ICF13

Beijing (China)

2013

Vol. B

New strategy for identification parameters of a micromechanical model coupled with ductile damage

Jean-Claude Rakotoarisoa[a,c], Donné Razafindramary[b,c], Akrum Abdul-Latif[b,c,*]

[a] Université d'Antsiranana Madagascar

[b] Université Paris 8

[c] Laboratoire d'Ingénierie des Systèmes Mécaniques et des Matériaux (LISMMA),
Supméca, 3, rue Fernand Hainaut - 93407 St Ouen Cedex – France
*e-mail: aabdul@iu2t.univ-paris8.fr

Abstract
A low-cyclic fatigue micromechanical model proposed recently [1] for emphasizing the concept of damage induced anisotropy is used. The solution of these nonlinear constitutive relations is an important topic since it requires an important computational time. With a high nonlinearity due to damage, the identification of model parameters represents consequently an important subject. In fact, a combination of the genetic algorithm (for the global optimization) with pattern search algorithm (for the local optimization) is proposed. A comparative study is conducted under complex cyclic loadings showing the ability of the proposed approach in calibrating model parameters.

Keywords Low-cyclic fatigue, parameters identification, global minimum and local minimum optimization

1. Introduction

Despite the existence of increasingly powerful computers, the progress in the constitutive equations development is continuous and can be conducted via computational optimization process. Several types of modes like micromechanical approaches are proposed for describing mechanical complex phenomena. Non-linear responses under cyclic loading, for example, make the related resolutions very expensive in computing time and in memory capacity. Numerically, it has been recently reported that the algorithm of Burlisch–Stöer gives the best compromise between computational time and precision compared to other well-known algorithms.
For a given model, the identification of parameters is an important issue and should be as accurate as possible to describe efficiently the material behavior. In fact, the use of reliable optimization algorithms is to minimize the difference between the model prediction and experimental behavior. Different methods have been developed to resolve this type of problem. They can, in general, be divided into two major groups: the first one which converges quickly is for local optimization. However, its major disadvantage is the possibility of converging towards local minimums. The Pattern Search algorithm is part of this group. It does not require the gradient calculation of the objective function and accepts parallel computing on different computer processors. The second group is formed by the evolutionary method based on the evolution of individuals. The genetic algorithm is a part of this group which is related to the global minimum convergence. However, it is slow because it requires several evaluations of the objective function.
Therefore, this study highlights the concept of damage induced anisotropy via the used model. Numerical solutions of these nonlinear constitutive equations require normally an important computational time. Therefore, a new strategy of model parameters calibration is considered. In fact, a hybrid approach is used, in this paper, to exploit the benefits of these groups of algorithms. Hence, a combination of the genetic algorithm (GA) with pattern search algorithm (PSA) is proposed. The basic idea of this approach is to look for the global minimum with the GA, then move to the local

minimum search via the PSA to improve the obtained result. Since the identification of the model parameters is of particular interest in this paper, therefore, several applications are presented. They deal with cyclic plasticity with damage induced anisotropy behavior of polycrystals and its related phenomena under complex history of loading path conditions. To conduct the identification process, the two methods (GA&PSA) are complementary and have different applications. The GA optimizes globally the model parameters leaving the field to the local method, PSA, to determine the final values of these parameters. Then, in order to evaluate the performances of the proposed method, a comparative study is performed under complex cyclic loadings showing the ability of such strategy to identify the model parameters.

2. Employed Micromechanical Model

The used micromechanical model utilizes three operating levels which are: microscale (slip system), mesoscale (granular) and macroscale (overall). The theoretical formulation of the developed model is presented in detail in [1]. However, a short description of the main features of the model equations at the overall level is illustrated below.

$$\underline{\underline{\Sigma}} = \sum_{i=1}^{3} \sum_{i}^{*} p_i \otimes \underline{p}_i \tag{1}$$

$$\underline{\underline{Q}} = \sum_{i=1}^{3} p_i \otimes p_i \tag{2}$$

$$\underline{\underline{Q}}^{+} = \sum_{i=1}^{3} H(\Sigma_i^{*})\, p_i \otimes p_i \tag{3}$$

$$p_{ijkl}^{+} = Q_{ia}^{+} Q_{jb}^{+} Q_{ka}^{+} Q_{lb}^{+} \tag{4}$$

$$\underline{\underline{\underline{\underline{D}}}} = D^{T}\, \underline{\underline{\underline{\underline{p}}}}^{+} \tag{5}$$

$$\underline{\underline{\underline{\underline{R}}}}^{d} = \left(\underline{\underline{\underline{\underline{I}}}} - \underline{\underline{\underline{\underline{D}}}}^{T} \right) : \underline{\underline{\underline{\underline{R}}}}^{o} \tag{6}$$

$$\dot{\underline{\underline{\underline{\underline{R}}}}}^{d} = \left(\dot{D}^{T}\, \underline{\underline{\underline{\underline{p}}}}^{+} + \dot{D}^{T}\, \underline{\underline{\underline{\underline{p}}}}^{+} \right) : \underline{\underline{\underline{\underline{R}}}}^{o} \tag{7}$$

$$\dot{\underline{\underline{\Sigma}}} = \dot{\underline{\underline{\underline{\underline{R}}}}}^{d} : \underline{\underline{E}}_{e} + \underline{\underline{\underline{\underline{R}}}}^{d} : \dot{\underline{\underline{E}}}_{e} + \dot{\underline{\underline{M}}} \tag{8}$$

$$\dot{\underline{\underline{M}}} = -\frac{1}{2} \dot{D}^{T} \frac{\partial\, \underline{\underline{\underline{\underline{p}}}}^{+}}{\partial\, \underline{\underline{E}}_{e}} : \underline{\underline{\underline{\underline{R}}}}^{o} : \underline{\underline{E}}_{e} : \underline{\underline{E}}_{e} - \frac{1}{2} D^{T} \frac{\partial\, \dot{\underline{\underline{\underline{\underline{p}}}}}^{+}}{\partial\, \underline{\underline{E}}_{e}} : \underline{\underline{\underline{\underline{R}}}}^{o} : \underline{\underline{E}}_{e} : \underline{\underline{E}}_{e} - D^{T} \frac{\partial\, \underline{\underline{\underline{\underline{p}}}}^{+}}{\partial\, \underline{\underline{E}}_{e}} : \underline{\underline{\underline{\underline{R}}}}^{o} : \dot{\underline{\underline{E}}}_{e} : \underline{\underline{E}}_{e} \tag{9}$$

To determine the overall damage tensor $\underline{\underline{D}}$ (Eq. 5), the spectral decomposition concept of stress tensor is adopted (Eqs. 1-4). Σ_i^* is the i^{th} principal strain and p_i the i^{th} corresponding to the unit principal direction of eigenvalue and eigenvector of Σ^*. The symbol $\otimes$ represents the tensor product. The 4^{th} order positive spectral projection tensor $\underline{\underline{P}}^+$ given in (Eq. 4) is determined by equations (Eq. 2) and (Eq. 3). According to (Eq. 5), the damage is considered to be entirely active when all the eigenvalues are positive in the three principal directions; whereas, it becomes fully passive once the eigenvalues are negative, i.e., depending on the $\underline{\underline{P}}^+$ configuration. Hence, $\underline{\underline{P}}^+$ allows verifying naturally the complexity of the damage activation/deactivation phenomenon whatever the applied loading path. The overall rigidity tensor for a damaged material $\underline{\underline{R}}^d$ and its evolution $\dot{\underline{\underline{R}}}^d$ are defined respectively by equations (Eq. 6) and (Eq. 7), where $\underline{\underline{R}}^o$ is the classical 4^{th} order rigidity tensor for an initially isotropic material. As recently proposed [1], the overall stress tensor evolution coupled with damage activation/deactivation phenomenon is mathematically described by (Eq. 8). In (Eq. 9), the second term in the right-hand side depends explicitly on the eigenvectors variation during cyclic loading. Thus, when the loading is applied according to laboratory reference axes, the principal vectors coincide with the latter. In this case, these vectors are constant, i.e., their characteristics vary neither with respect to time, nor according to the deformation. Hence, the second and third terms in the right-hand side of (Eq. 9) vanishes. As a result, (Eq. 8) has the advantage to successfully treat a great number of loading types especially the multiaxial ones.

3. Algorithms of optimization

The identification process is to find numerically a set of model coefficients, which correlates the best possible predictions and experimental results. It is based on minimizing the difference between the recorded model response and the given experimental result. Such a difference can never be zero. However, the rule states that when the difference is smaller, the set of coefficients is better. In this work, identification (calibration) of the model parameters is to find a search space where these values should minimize the gap between experimental results and predictions. Solving this problem is realized by minimizing the following function:

$$F(P) = \sum_{n=1}^{N} F_n(P), \tag{10}$$

$$F_n(P) = \frac{1}{t_1 - t_0} \int_{t_0}^{t_1} \left(V_{\exp} - V_{sim}\right)^T D \left(V_{\exp} - V_{sim}\right) dt. \tag{11}$$

where, P: Model parameters, N: number of tests, $[t_0, t_1]$: time interval of the test n, V_{exp}-V_{sim}: difference between observed experiments and their simulations for the test n, D: weighting matrix of the test n.

The complexities of search space are the minimum function using radically different methods of resolutions. As a first approximation, the deterministic method is suitable for search in small

state-space; whereas for complex and large search state-space, this requires rather a method of stochastic search (genetic algorithm, pattern search ...).
The difficulties of these problems via conventional optimization methods give rapidly this family of algorithms able to handle large combinatorial problems with mixed variable. It is more interested for solving practical problems by a general classification of optimization problems and solved methods [2,3]. Briefly, genetic algorithms are adaptive heuristic search algorithm based on the evolutionary idea of natural selection and genetic. Moreover, they are a part of evolutionary computing, a rapidly growing area of artificial intelligence.
The strategy proposed in this work is to utilize a combination of the GA with the PSA. We will briefly describe these two algorithms.

3.1 Genetic Algorithm

This algorithm starts with the creation of the initial population of individuals and terminates with the convergence towards the best individuals of population giving therefore the optimized solution. The transition from one generation to another is accomplished by applying the following process: (i) mechanism of evaluation, (ii) selection and (iii) modification, up to obtaining a stopping criterion. The structure of this algorithm is given by the flowchart [4] (figure 1).

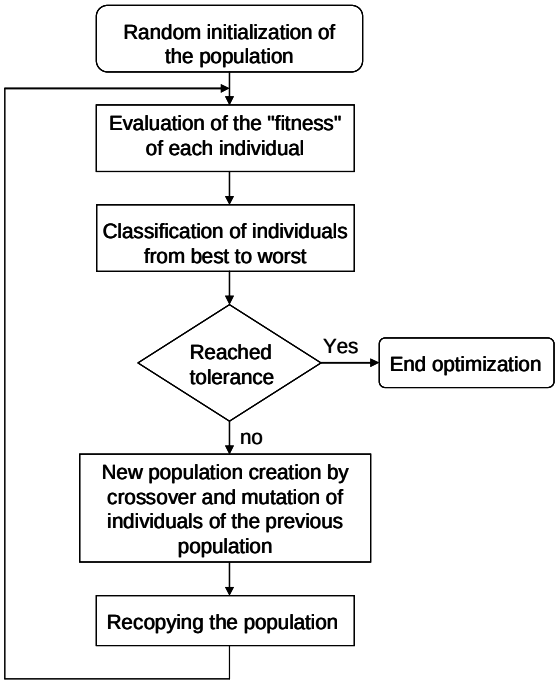

Figure 1 Structure of the genetic algorithm

Each individual of a given population is defined by a chain of genes that correspond to the different parameters to be identified. To avoid the difficulties that may arise in the binary coding and decoding of individual, a real coding GA is used [4]. The values of each parameter are bounded by

an interval [x_{min}, x_{max}] normally determined in this type of modeling according to mechanical bases. The main reason to establish these limits is to make the search process more efficient by reducing its space.

The initial population is produced by:

- Initial solutions (individuals) proposed based on the expert opinion and on experimental observations;
- Solutions chosen randomly in the search space.

This allows, in fact, to start the search from various solutions of the search space incorporating expert opinion.

Different numerical tests should be conducted and led to choice of stochastic operators as follows:

- Selection type elitism, which allows to highlight the best individuals in the population. These are the most developed individuals which will participate in the improvement. Such a technique has the advantage of faster convergence to the best individuals to the detriment of individuals which seem less appropriate and could provide elements for the creation of new individuals.
- Crossover scattered, which is cut individuals into several portions (2 or 3 portions) to obtain new individuals
- Adapt feasible mutation which randomly generates directions that are adaptive compared to the last generation successful or not. The feasible region is limited by the constraints. A pitch length is selected along each direction in such a manner that the bounds constraints are satisfied.

3.2. Pattern Search Algorithm

Pattern search is a direct search method. This method is employed for solving optimization problems that does not require any information about the gradient of the objective function. The pattern search begins at the initial point x_o. At the first iteration the mesh size is 1 and the GPS (Generalized Pattern Search) algorithm adds the pattern vectors to the initial point x_o to compute the following mesh points. The algorithm computes the objective function at the mesh points using the following approach:

$$xm_i = x_n + v_i \Delta_n \tag{12}$$

$$x_{n+1} = xm_j \,/\, f(xmj) = \min_i(f(xm_i)) \tag{13}$$

Where xm_i: the mesh points, x_n: the current point, v_i: the pattern vector and Δ_n: the current mesh size.

A pattern is a set of vectors $\{v_i\}$ that the PSA utilizes to define which points to search at each iteration. The set $\{v_i\}$ is determined by the number of independent variables in the objective function. For example, if there are three independent variables in the optimization problem, the default for a 2N positive basis consists of the following pattern vectors:

$$\begin{cases} v_1 = [1 \quad 0 \quad 0] \\ v_2 = [0 \quad 1 \quad 0] \\ v_3 = [0 \quad 0 \quad 1] \\ v_4 = [-1 \quad 0 \quad 0] \\ v_5 = [0 \quad -1 \quad 0] \\ v_6 = [0 \quad 0 \quad -1] \end{cases} \tag{14}$$

For a more description of this, see Kolda, Lewis, and Torczon [5].

To accelerate the convergence, we stop the iteration as soon as it finds a mesh point whose fitness value is smaller than that of the current point.
After a successful poll, the algorithm multiplies the current mesh size by 2. If none of the mesh points has a smaller objective function value at current point, so the poll is unsuccessful, the algorithm does not change the current point at the next iteration and multiplies the current mesh size by 0.5.
In our application the criteria for stopping the pattern search are the number of objective function evaluations.

4. Numerical applications

The evaluation of the proposed new strategy for identification is carried out through the description of the elastic-inelastic cyclic behavior of a polycrystal under uniaxial tension-compression (TC), biaxial tension-torsion with 90° out-of-phase angle (TT90). Our polycrystal is a random orientation distribution of 40 grains of a single-phase FCC. Initially, a database for both cyclic loading (TC and TT90) is numerically made up to final damaging of this grains distribution using the coefficients summed up in (Table 1)

Table 1 Coefficients used to create the database

Elastic-Inelastic parameters												
Model parameters	E (MPa)	ν	α	z	K	b^s	K_o (MPa)	Q^s (MPa)	$h_1=h_2=\ldots=h_5$	h_6	C^g (MPa)	a^g
coefficients	215000	0.32	1	20	50	13	240	256	1	2.29	95100	10

Damage parameters						
Model parameters	S^s	s_o	w^s	d_1	d_2	γ_0
coefficients	2	0.95	1	1	1.4	1.25

Such a database is considered as an experimental one. Thereafter, the identification process of model parameters is started by setting the damage parameters changing six key parameters related to the inelastic behavior (b^s, k_o, Q^s, h_6, C^g and a^g). Therefore, the identification process by the global minimum optimization concept is made through the genetic algorithm. After several tests on the population size, a population of 600 individuals is employed to optimize 6 coefficients of the model. Several iterations are made obtaining several families of model parameters followed by a local identification using the pattern search algorithm. The optimized model parameters are summed up

in (Table 2).

Table 2 Initial and optimized coefficients

Elastic-inelastic parameters												
Model parameters	E (MPa)	ν	α	z	K	b^s	k_o (MPa)	Q^s (MPa)	$h_1=h_2=\ldots=h_5$	h_6	C^g (MPa)	a^g
Initial	215000	0.32	1	20	50	24.5	340	100	1	1.7	75100	6
Optimized	215000	0.32	1	20	50	14.5	267.5	397.6	1	6.3	33830	8.71

Damage parameters						
Model parameters	S^s	s_o	w^s	d_1	d_2	γ_0
Initial	2	0.95	1	1	1.4	1.25
optimized	2	0.95	1	1	1.4	1.25

One of the main reasons which promotes this association is that both algorithms are parallelizable as shown in [2,3]. This allows gaining in computation time by exploiting computer multiprocessor. The experimental recorded fatigue lives are 38, and 14 cycles for TC and TT90, respectively. The model predicts these lives faithfully giving therefore 38, and 12 cycles in TC and TT90, respectively.

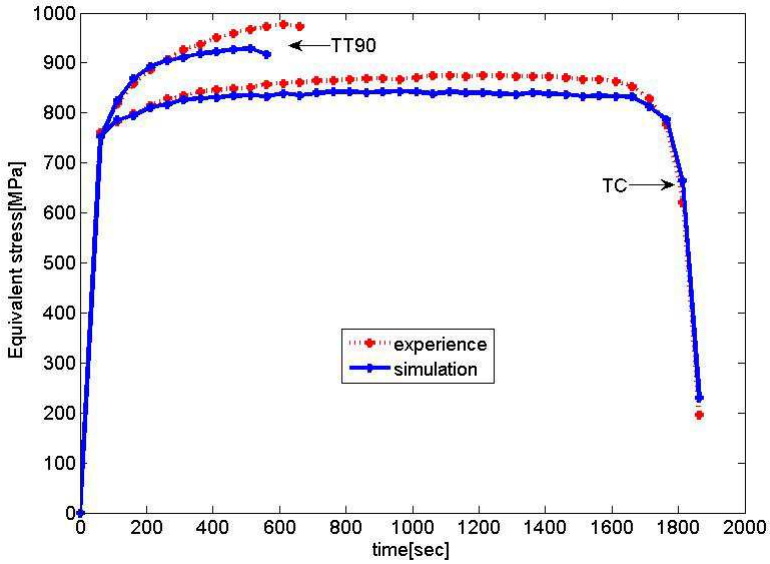

Figure 2 Evolution of the overall stress during TC and TT90 up to the final fracture

Figure 2 represents the typical evolutions of the maximum overall stress (pick stress value for each cycle) versus cyclic time using the same maximum von-Mises equivalent macro-strain for the two cyclic loading paths (TC and TT90). The predicted responses describe properly the experimental

results. Note that these predicted results are computed with the optimized model parameters summarized in table 2.

5. Conclusion

The objective of this work is to propose a new strategy to optimize the identification parameters of a micromechanical model coupled with damage [1]. Hence, a combination of genetic algorithm with pattern search algorithm is developed. The genetic algorithm optimizes globally the model parameters; whereas the pattern search algorithm, considered as a local method, has a role to determine the final values of these model coefficients. This model is tested under different cyclic loading complexities. It is recognized that this combination shows its ability to optimize the identification process. Consequently, the predicted responses describe faithfully the experimental results.

Acknowledgements

The authors are grateful to the AUF and SCAC of the Embassy France in Madagascar for supplying their financial support.

References

[1] Abdul-Latif, A., and Mounounga T., B. S., (2009), Damage Deactivation Modeling under Multiaxial Cyclic Loadings for Polycrystals, International Journal of Damage Mechanics, 18, 177-198.
[2] Dréo J., Pétrowski A., Siarry P,.and Taillard E. (2003), Métaheuristiques pour l'Optimisation Difficile, Eyrolles, ISBN : 2-212-11368-4.
[3] Smith R.E., Perelson A.S., and Forrest S., (1993), Searching for diverse, cooperative populations with genetic algorithms, Evolutionary Computation, 1(2), pp.127–149.
[4] Christophe Bontemps, Principes Mathématiques et Utilisations des Algorithmes Génétiques, Extrait de cours, Novembre 1995.
[5] Kolda, Tamara G., Robert Michael Lewis, and Virginia Torczon. "A generating set direct search augmented Lagrangian algorithm for optimization with a combination of general and linear constraints." Technical Report SAND2006-5315, Sandia National Laboratories, August 2006.

Advanced Assessment of Ductile Tearing in Nuclear Reactor Pressure Vessel Steel Using X-ray Tomography

Michael Daly[1*], Fabien Leonard[1], John K Sharples[2], Andrew H Sherry[1]

[1] Dalton Nuclear Institute, The University of Manchester, Pariser Building - G Floor, Sackville Street, Manchester, M13 9PL, UK
[2] AMEC Technical Services, Walton House, Birchwood Park, Warrington, Cheshire, WA3 6AT, UK
* Corresponding author: michael.daly@postgrad.manchester.ac.uk

Abstract Reactor pressure vessels (RPV) are manufactured from medium strength low allow ferritic steel specifically selected of its high toughness and weldability. The ability of the RPV to withstand crack propagation is crucial to maintaining the operational safety of the reactor plant. Current generations of RPV steels operate at sufficiently high temperatures to ensure that the material remains ductile during its service life. Furthermore, new materials are engineered to exhibit greater ductility and fracture toughness throughout their operating life. Therefore understanding and being able to predict the ductile fracture behaviour is critical for assuring the safety of RPV steels during operating conditions.

This paper presents the results of an experimental programme aimed at using 3D X-ray tomography to quantify the volume fraction of ductile voids in tested pre-cracked specimens manufactured from A508 Class 3 RPV steel.

The results indicate a high concentration of voids very close to the fracture surface and voids extending 3.6mm below the crack. The data and experimental methodology could be used to calibrate predictive mechanistically based models such as the Gurson-Tvergaard-Needlman (GTN).

Keywords Ductile, Tearing, Steel, X-ray, Tomography

1. Introduction

The mechanism of ductile fracture is characterised by the nucleation, growth and coalescence of voids at initiating particles. These particles are categorised as inclusions and second phase particles, and in ferritic steel are most often manganese sulphide (MnS) inclusions and metallic carbide particles (M_nC). The voids form at these particles within the volume of high plastic strain and triaxial stresses ahead of a crack-tip or stress concentrator.

Two nucleating processes have been observed [1]: voids formation by either decohesion of the interface between the matrix and the inclusion/particle, or by cracking of the inclusion/particle itself. Voids then grow under the influence of increasing plastic strain and high hydrostatic stress within the material. A crack will propagate once neighbouring voids coalesce and/or reach a critical size producing a macroscopic flaw. The coalescence of the voids can be considered as the final stage in the crack growth mechanism.

The larger particles nucleate voids at lower stresses and strains [2] . Smaller particles will start contributing to void nucleation when the material is subjected to greater plastic deformation. The nucleation of these smaller voids at proximity to smaller particles, often between larger voids or

microcracks where intense shear bands are present, may result in a void sheeting effect further contributing to void coalescence [3, 4].

The metallurgical characteristics of the microstructure, including the size and distribution of the initiating particles which can often concentrate close to or on the grain boundaries will contribute to the nucleation and coalescence process. The distribution of these particles may also be uneven within the material with banding regions of greater concentration of particles or varying grain sizes [5].

There exists a range of mechanistically based models that have been developed to describe the ductile fracture process. One of these is the Gurson-Tvergaard-Needleman (GTN) model [6] which characterises failure by defining a material yield function which depends greatly on the stress states and on material specific characteristics. These characteristics need to be calibrated to enable a simulation of ductile crack growth.

1.1 The Gurson Tvergaard Needleman

The GTN model assumes the material is homogeneous and behaves as a continuum with an idealised void volume fraction distribution. Crucially, the model takes into consideration both the strain softening effects of void nucleation, growth and coalescence as well as the competing effect of the matrix hardening behaviour to define a material yielding function Φ, defined as (Eq.1):

$$\Phi\left(\sigma_e,\sigma_m,\bar{\sigma},f^*\right)=\left(\frac{\sigma_e}{\bar{\sigma}}\right)^2+2q_1f^*\cosh\left(\frac{3q_2\sigma_m}{2\bar{\sigma}}\right)-\left(1+q_3f^{*2}\right)=0 \quad (1)$$

Where:
σ_e = macroscopic Von Mises Stress
σ_m = macroscopic mean stress
$\bar{\sigma}$ = flow stress for the matrix material
f^* = current void fraction

The values for q_1, q_2 and q_3 were introduced by Tvergaard and Needleman to better simulate the experimental observations. These are often taken as $q_1 = 1.5$, $q_2 = 1.0$ and $q_3 = q_1^2$. The rate of void growth is related to the plastic part of the strain rate tensor $\dot{\varepsilon}^p_{kk}$ and the void nucleation rate is related to the equivalent plastic strain rate, $\dot{\varepsilon}^p_{eq}$ in (Eq. 2):

$$f^*=f_{growth}+f_{nucleation}=(1-f)\dot{\varepsilon}^p_{kk}+\Lambda\dot{\varepsilon}^p_{eq} \quad (2)$$

The first term expresses the growth rate of existing voids assuming the matrix material is incompressible and the second term defines the quantity of new voids that have nucleated as a result of the increasing plastic strain.

The scaling coefficient, Λ is characterised by (Eq. 3):

$$\Lambda = \frac{f_N}{s_N\sqrt{2\pi}} \exp\left[-\frac{1}{2}\left(\frac{\varepsilon_{eq}^{p} - \varepsilon_N}{S_N}\right)^2\right] \quad (3)$$

Where:
f_N= volume fraction of void nucleating particles
s_N = standard deviation
ε_N = mean value
ε_{eq}^{P} = equivalent plastic strain.

An additional feature of the GTN model, introduced by Tvergaard and Needleman, was to take into consideration the initial void fraction f_0, a critical void volume fraction for coalescence f_c, and a critical void fraction that corresponds to the failure of the matrix, f_F.

$$f^* = \begin{cases} f & \text{for } f \le f_c \\ f_c - \dfrac{f_u^* - f_c}{f_F - f_c}(f - f_c) & \text{for } f > f_c \end{cases} \quad (4)$$

Where:
f_c = critical void volume fraction (typically $f_c = 0.15$ for carbon steel)
f_F = actual void volume fraction at final fracture
f_u^* = modified void volume fraction (typically $f_u^* = 1/q_1$)

The distribution of the initiating particles as well as their void volume fraction are key microstructural features that are needed to accurately calibrate the GTN model. These material specific parameters are usually calibrated using metallographic observations of the non-fractured material and the material volume around fractured test specimens from carefully controlled experiments. The fracture tests can be performed using a range of specimens introducing different levels of constraint and stress states. The highly constrained pre-cracked compact test (CT) specimen is frequently used to measure fracture toughness and will be used and discussed throughout this paper.

Previous experiments have shown that void volume fractions (VVF) may vary by material but also by specimen types. Work by Kerry et al [7] on a high strength and low toughness aluminium alloy AL2024-T351 have shown that there is a difference in the distribution of the void volume fraction below the fracture surface for notched tensile specimens when compared with CT specimens. Using 3D X-ray tomography Taylor et al demonstrated that the CT specimens exhibited a higher concentration of voids close to the fracture surface when compared with that measured close to the fracture surface in notched tensile specimens. On the other hand, the voids extended further below the fracture surface in notched tensile specimens than was observed in CT specimens.

Further work has recently been performed by Daly et al [8] with respect to an A508 Class 3 RPV ferritic steel to quantify the void volume fraction using 2D optical micrographs. Similar

observations showed a higher concentration of voids for pre-cracked specimens than for notched tensile specimens. Additionally, a greater analysis of the area below the fracture surface has shown that the void volume fraction can extend to a few millimetres below the fracture surface with large clusters of voids extending up to 3.5mm below the fracture surface.

The aim of this paper is to extend the observations made in this previous work by using 3D X-ray tomography to further quantify the void volume fraction below the fracture surface in pre-cracked CT specimens of A508 Class 3 RPV ferritic steel. The methodology and observations will be discussed as well as its implications for the calibration and application of the GTN model.

2. Experimental

2.1 Material

The material used throughout this experiment was an A508 Class 3 ferritic steel. The specimens were extracted from the outer ring of an upright wedge-shaped block originating from a larger ring forging. All the specimens were extracted from the same location and in the same orientation. The chemical composition (wt%) of the ferritic steel was evaluated using spectographic analysis and the results are indicated in Table 1.

Table 1: Chemical composition in wt% of A508 Class 3 steel.

C	Si	Mn	P	S	Cr	Mo	Ni	Al	Co	Cu	Sn	Ti	V
0.18	0.23	1.3	<0.005	<0.005	0.25	0.55	0.81	0.02	0.01	0.04	0.005	<0.01	0.01

2.2 Mechanical testing

The tensile properties of the material were determined using standard round-bar test specimens oriented in the hoop direction. Three tensile specimens were tested on a Zwick 1464 at room temperature using a strain rate of 0.025% s^{-1} according to BS EN ISO 6892 procedure [9].

Ten fracture toughness tests were performed according to the ESIS P2-92 [10] standard using CT specimens with standard dimensions of thickness, B = 25mm, width, W = 50mm and a crack length to specimen width ratio, a/W = 0.53. Specimens were 20% side-grooved following fatigue pre-cracking. Tests were performed using both the unloading compliance and the multi specimen methods. Out of the ten tested CT specimens, two were left intact in order to preserve the crack tip for analysis.

2.3 Metallographic analysis

The cracked and parent material was imaged using optical and scanning electron microscopes. The parent material was imaged to characterise the general microstructure of the ferritic steel with a specific interest on grain size and inclusion/particle type and distribution. The cracked specimens were analysed to characterise the ductile fracture mechanism and distribution of voids below the

fracture surface.

For the parent material, metallographic sections were taken to view the material in the axial-radial plane. The fractured sections were machined through the tested specimen halves in the region where plain strain fracture was expected to take place. The metallographic sections were progressively ground and polished to a mirror finish of 0.25 μm using diamond paste and etched using colloidal silica and 2% Nital.

2.4 X-ray Tomography Analysis

The test samples for X-ray tomography imaging were machined below the fracture surface of three CT specimens using electrical discharge machining (EDM). The samples were approximately 0.5mm in diameter and 12mm in length and were extracted at regular intervals starting at the pre-cracked region but before the initiation of ductile tearing. The remaining specimens were extracted from below the ductile crack path and beyond the crack arrest point. The sections were extracted as close as possible to the region where plane strain was expected to take place with the greatest amount of ductile tearing damage. The surfaces of these small cylinders were lightly polished to remove any rust or scaling resulting from the EDM.

The top 4mm very close to the fracture surface of these specimens were scanned at the Henry Moseley X-ray Imaging Facility at The University of Manchester using the Nikon Metrology 225/320 kV Custom Bay system equipped with a 225 kV static multi-metal anode source and a PerkinElmer 2000 × 2000 pixels 16-bit amorphous silicon flat panel detector.

The scanning was performed with a molybdenum target using a voltage of 80 kV and a current of 130 μA. The data acquisition was carried out with an exposure time of 1000 ms with no filtration. The number of projections was set to 3,142 and the number of frames per projection was 1. The entire volume was reconstructed at full resolution with a voxel size of 2.0 μm along the x, y, and z directions.

The data processing was performed with Avizo® Fire 7.0 software. An edge preserving smoothing filter was applied to the raw data to reduce image noise in each data set. Standard data processing was used to determine the void size distribution whereas a methodology similar to [11] was employed to determine the void to fracture surface distance and evolution of void volume fraction.

2.5 Quantification of ductile tearing damage

Using the Avizo Fire data, the void volume fraction was estimated by measuring the voxel counts of metallic voxels against the count of porous voxels below the fracture surface. The VVF was calculated for each Regions Of Interest (ROI). A ROI of 100μm in height was utilised to divide the specimens into smaller cylinder regions which were comparable to the units used in Daly et al [8]. The VVF was calculated for the specimens originating below the pre-cracked surface as well as the region below the ductile tearing surface and beyond the crack arrest.

3. Results

The results from the three tensile tests at room temperature are summarised in Table 2. The average yield stress was 446 MPa and the ultimate tensile stress was 594 MPa.

The fracture toughness properties of the A508 Class 3 steel are illustrated as a J R-curve in Figure 1 which includes data from both the unloading compliance tests and monotonically loaded tests presented together. The data from both test types are in agreement and the initiation toughness, measured by the intersection of the blunting line including 0.2 mm tearing and the power-law curve fit to the data is ~ 475 kJ/m^2. The specimens for tomography analysis were extracted from test samples B, G and C as these specimens were subjected to the most ductile tearing.

Table 2: Tensile Test results

Specimen No.	1	2	3	Average
Modulus (GPa):	211	210	208	210
0.2 % Stress (MPa):	445	457	436	446
UTS (MPa):	595	602	586	594
Elongation (%)	29	27	27	28
Reduction of Area (%)	75	75	74	75

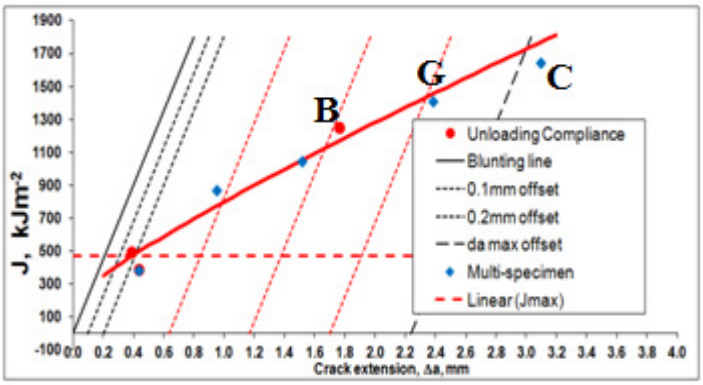

Figure 1: J R-curve for A508 Class 3 material tested in the hoop-radial direction at 23°C.

Figure 2 illustrates the general upper bainitic microstructure of the ferritic steel under the optical microscope and SEM respectively. The average grain size was estimated at 11µm. But the microstructure is interspersed with clusters of very small grains and regions where very large grains are present.

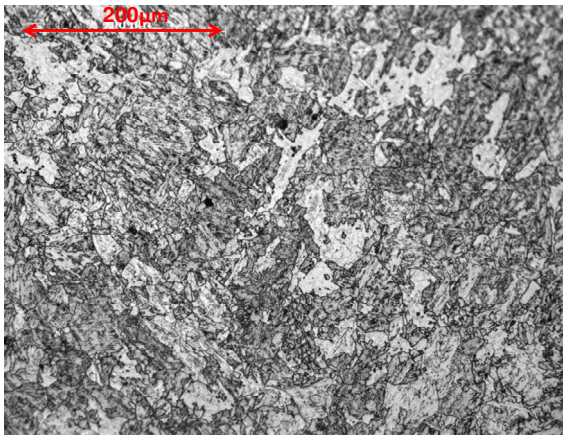

Figure 2: General microstructure of the bainitic steel under optical microscope.

Figure 3Figure 4 illustrate selected microstructural observations of voids in the material. Microvoids

were observed to initiate and grow by the decohesion of carbides from the matrix. Larger voids, in some cases, were shown to nucleate at large particles. These larger voids were observed to be present well below the fracture surface and ahead of the crack tip.

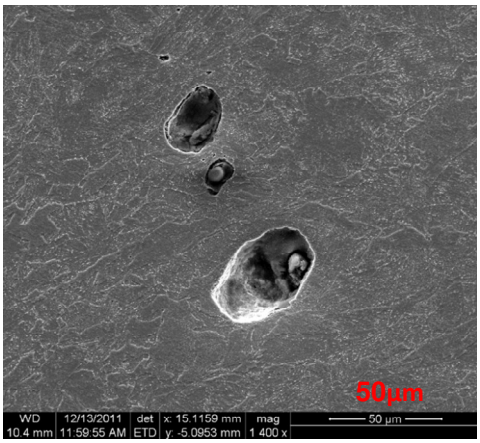

Figure 3: Large macroscopic voids with an inclusion

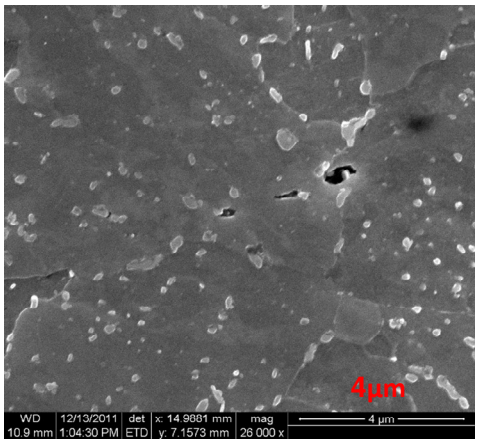

Figure 4: Microvoids nucleating at proximity of carbides

3.1 X-ray Tomography

The X-ray tomography images of Figure 5 shows the typical distribution of voids below the fracture surface for a specimen extracted from the fracture surface. Voids as small as 10µm in diameter could be resolved with a high degree of confidence. Figure 6 shows a render of the range of shapes and sizes of voids observed. Some voids have dumbbells morphologies possibly indicating coalescence. The ability to use the X-ray tomography technique enabled the imaging of voids in their entirety. Furthermore, this technique demonstrated the ability to visualise and quantify voids and in some cases, clusters of voids up to 3.6mm below the fracture surface.

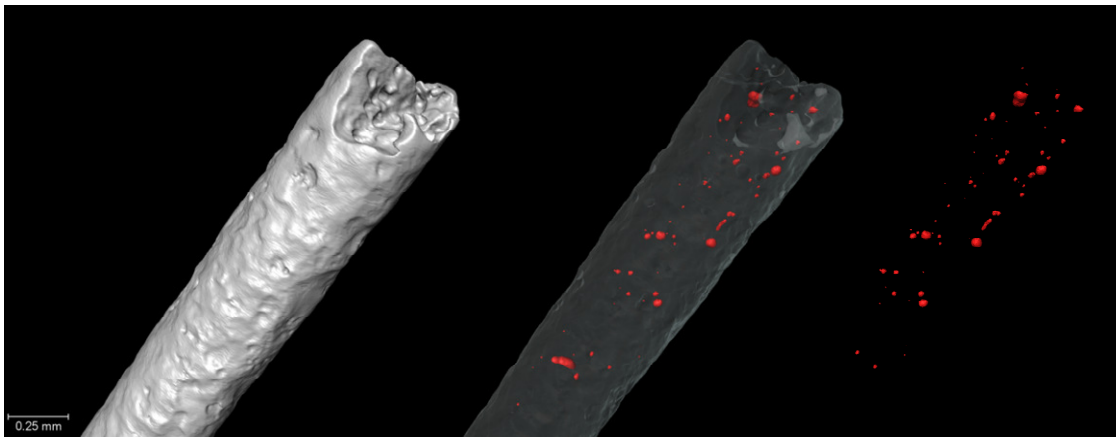

Figure 5: 3D tomographic image of the ferritic steel samples and the void distribution below the fracture surface.

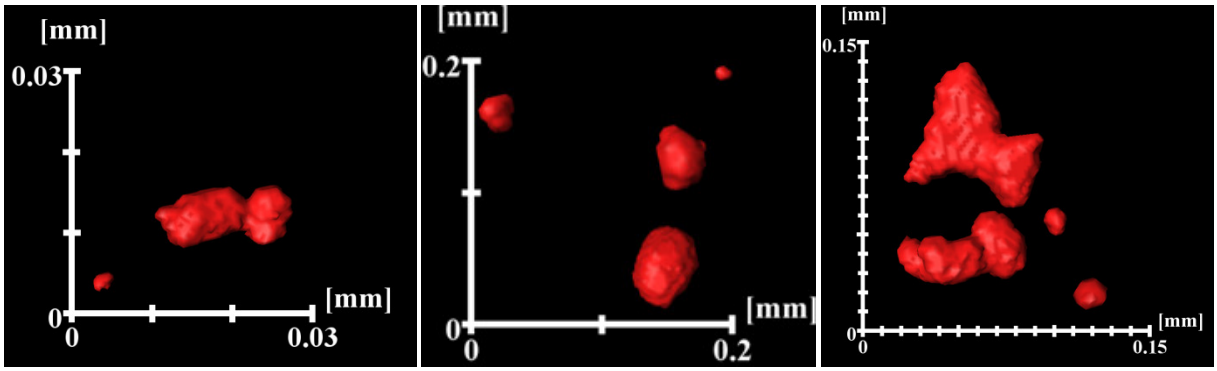

Figure 6: Magnified 3D tomographic images showing the range of sizes and shapes of voids quantified below the fracture surface.

3.2 Quantification results

The variation of the void volume fraction as a function of distance below the fracture surface in the CT specimens is illustrated in Figure **7**. The data were calculated by quantifying the average VVF for cylindrical cells of 100µm in height and starting from the fracture surface. The VVF for each specimen location (0mm, 0.5mm…) was averaged over all three specimens (B, C and G) to obtain an average VVF for the first 100µm below the fracture surface and every 100µm down to 3.6mm.

The presence of voids ahead of the final crack tip was also taking into consideration. Samples B and G had crack extensions of approximately 2mm, the extractions beyond the crack front were averaged separately and labeled as “beyond crack tip” on the plot.

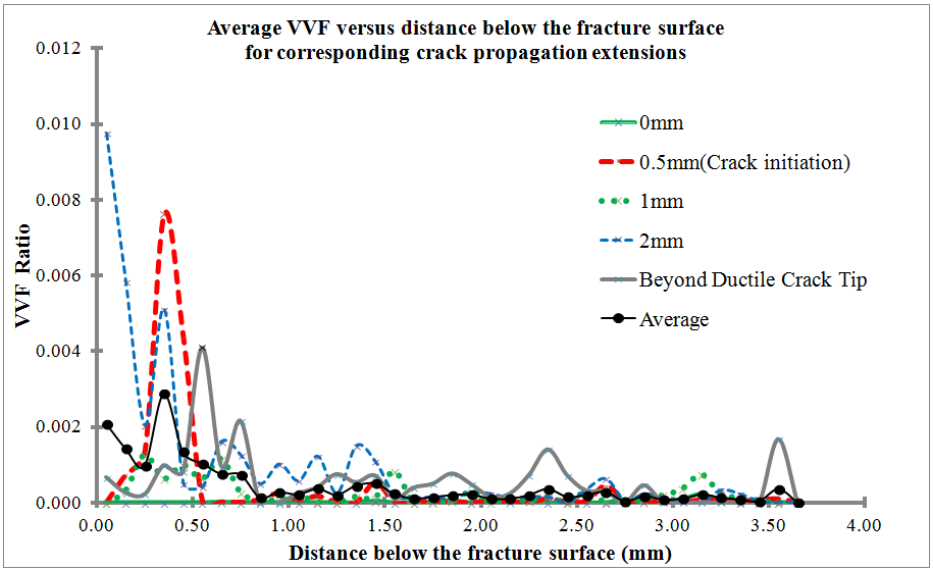

Figure 7: VVF as a function of distance below the fracture surface

The following observations can be made:

- The void volume fraction is highest close to the fracture surface and reduces to zero as a function of distance below the crack. A maximum VVF of 9.75×10^{-3} is measured

for the 2mm specimens. The VVF remains relatively high up to 800μm below the fracture surface.

- Secondary peaks are observed well below the fracture surface especially for the specimens extracted below extensive ductile tearing. The peaks are often representative of clusters of voids or very large voids at depths ranging from 1mm to 3.6mm.
- Pre-cracking of the fracture toughness specimens produces very little observable ductile tearing damage.
- At 2mm of ductile tearing, the ductile damage is immediately quantifiable very close to the fracture surface. For the other specimens, voids only become visible after 250μm below the fracture surface and peaks at a ratio of 7.60×10^{-3}.
- The data captured within the volume of material at proximity to the crack initiation and blunting (0.5mm) produce some of the highest VVF values with a maximum of 7.60×10^{-3} at 350μm below the crack surface.
- Voids have been imaged and quantified beyond the crack tips indicating ductile tearing damage ahead of the crack path.

4. Discussion

Taylor et al [7] quantified the void volume fraction below the fracture surface in failed CT specimens of AL2024-T351 aluminium alloy using optical and X-ray tomography. A critical void volume fraction f_f of approximately 1.0×10^{-2} was calculated for the aluminium alloy which compares favourably with the results obtained for the RPV ferritic steel of $f_f = 9.75\times10^{-3}$.

It is worth noting that the peaks within the void volume fraction data may disproportionately increase the average volume fraction well below the fracture surface for the three test specimens. But as the material should be considered as a continuum with an even distribution of initial voids and initiating particles, the average void volume fraction over a large number of tests should be representative of the material's bulk and fracture characteristics.

On the other hand, the ductile damage extends further beyond the crack surface in the ferritic steel than in the aluminium alloy. The aluminium alloy exhibits a sharp reduction in the VVF which reaches $f = 0$ at 300μm below the fracture surface. The ferritic steel exhibits ductile tearing damage up to 3.6 mm below the fracture surface identified by large voids and clusters of voids. The extent of the ductile damage was equally observed by previous work from Daly et al [8] using optical imaging analysis.

The substantial extent of the ductile damage was further observed in an equivalent HY100 ferritic steel. The work from Everett et al [2] identified voids below the fracture surface of fractured notched tensile specimens using a synchrotron source with equivalent resolutions. The distribution of voids deep below the fracture surface was attributed to microstructural banding and larger MnS inclusions. These larger MnS inclusions preferentially promoted the nucleation of voids at relatively low strains.

The effect of the plastic strain field produced from the propagating crack may provide sufficient strains at inclusions and particles to nucleate and grow relatively large voids deep below the fracture surface. A correlation of the experimental work with a finite element analysis is required to attain an estimate of the gradient of strains ahead and below the crack during propagation.

Finally, the tomographic images suffered from a blurring effect as a result of the X-ray beam hardening and X-ray spot being too large in comparison with the void sizes that were being imaged. Consequently, a substantial number of voids were only partially resolved and quantified since the pixel colours of these voids matched other metallic areas of the specimens and needed to be culled to obtain a reproducible and systematic quantifying tool. Further work will aim to use a synchrotron facility that will reduce such imaging artefacts and will ultimately increase the overall void volume fraction within the specimens.

5. Conclusions

This paper has described preliminary work undertaken to characterise the ductile fracture properties and fracture mechanism in A508 Class 3 steel using X-ray tomography analysis. The main conclusions from the work are as follows:

- The mechanical and fracture toughness properties have been quantified in the hoop direction. The average yield stress is 446 MPa and the initiation toughness defined by the 0.2 mm blunting line is ~ 475 kJ/m^2.
- The ductile fracture mechanism was identified to occur by the decohesion of the matrix from inclusions and second phase particles.
- The ductile damage was successfully imaged and quantified in 3D using X-ray laboratory sources to image voids of approximately 10µm in diameter and larger below the crack surface of compact test specimens.
- A relatively high VVF was quantified for specimens extracted at a 2mm crack extension but high concentrations of voids were also observed at 350µm and intermittently until 3600µm for specimens extracted along the length of the crack path. The results differ from experiments carried out with aluminium alloys where the VVF reached the background level at 300µm below the fracture surface.
- As a result of the limitations of the X-ray machine and software, a proportion of the voids were not quantified which has produced a VVF lower than is actually present in the material.
- The distribution of the voids deep below the fracture surface is attributed to microstructural banding and larger inclusions requiring lower strains.

6. Acknowledgements

The authors are grateful to AMEC in Risley for their support in the use of their material testing and

microscopy equipment. And, Fabien Leonard and Tristan Lowe from the University of Manchester Henry Moseley X-ray Imaging Facility for the use of the machines and their expertise.

7. References

[1] R. H. Van Stone, T. B. Cox, J. R. Low and J. A. Psioda, "Microstructural aspects of fracture by dimpled rupture," *International Metals Reviews ,* vol. 30, no. 4, pp. 157-179, 1985.

[2] R. K. Everett, K. E. Simmonds and A. B. Geltmacher, "Spatial distribution of voids in HY-100 Steel by X-ray Tomography," *Scripta Materialia,* vol. 44, pp. 165-169, 2001.

[3] T. Pardeon and J. W. Hutchinson, "An Extended Model for Void Growth and Coalescence," *Journal of the Mechanics and Physics of Solids,* vol. 48, pp. 2467-2512, 2000.

[4] V. Tvergaard, "Ductile Fracture by Cavity Nucleation Between Larger Voids," *Journal of the Mechanics and Physics of Solids,* vol. 30, pp. 265-286, 1982.

[5] C. I. A. Thomson, M. J. Worswick, A. K. Pilkey and D. J. Loyd, "Void Coalescence Within Periodic Clusters of Particles," *Journal of the Mechanics and Physics of Solids,* vol. 51, pp. 127-146, 2003.

[6] Z. L. Zhang, "A Complete Gurson Model," *Non Linear Fracture and Damage Mechanics,* pp. 223-248, 2001.

[7] K. L. Taylor and A. H. Sherry, "The characterization and interpretation of ductile fracture mechanisms in AL2024-T351 using X-ray and focused ion beam tomography," Vols. 60 (2012) 1300-1310, 2012.

[8] M. Daly, J. K. Sharples and A. H. Sherry, "Advanced Assessment of the Integrity of Ductile Components," in *ASME Pressure Vessels and Piping Division Conference*, Toronto, 2012.

[9] British Standards, ""Metallic materials. Tensile Testing. Method of test at ambient temperature" BS EN ISO 6892-1:2009".

[10] European Structural Integrity Society, "ESIS Standard No. P2-92: Procedure for determining the fracture behaviour of materials," ESIS, 1992.

[11] F. Leonard, J. Stein, A. Wilkinson and P. Withers, "3D Characterisation of Void Distribution in Resin Film Infused Composites," in *Conferene on Industrial Computed Tomography*, 2012.

3D synchrotron laminography assessment of damage evolution in blanked dual phase steels

Mouhcine Kahziz[1,2,*], Thilo Morgeneyer[2], Matthieu Mazière[2], Lukas Helfen[3], Eric Maire[4], Olivier Bouaziz[1,2]

[1] ArcelorMittal Research S.A., voie Romaine, F-57239 Maizières-lès-Metz, France
[2] Mines ParisTech, Centre des Matériaux, UMR CNRS 7633, BP 87, 91003 Evry Cedex, France
[3] Institute for Synchrotron Radiation – ANKA, Forschungszentum Karlsruhe, D-76021 Karlsruhe, Germany
[4] Université de Lyon, INSA-Lyon, MATEIS CNRS UMR 5510, 20 avenue Albert Einstein, 69621 Villeurbanne, France
* Corresponding author: mouhcine.kahziz@mines-paristech.fr

Abstract
The mechanical performance of automotive structures made of advanced high strength steels (AHSS) is often seen reduced by the presence of cut-edges. Here an attempt is made to gain insight into the initial damage state and the damage evolution during loading of a cut-edge. This is assessed in 3D and in-situ by synchrotron laminography observation during simultaneous tensile and bending loading of a cut-edge produced by stamping. Laminography is a technique that allows to observe regions of interest in thin sheet-like objects. It is found for the DP600 laboratory steel grade that the fracture zone is very rough and that needle voids from the surface and in the material bulk follow ferrite-martensite flow lines. During loading the needle voids grow from the fracture zone surface and coalesce with voids in the bulk. The needle cracks coalesce with the burnish zone though narrow zones, called void sheets. The formed cracks are inclined by 45° compared to the load direction.

Keywords: Dual phase steels, cutting edges, X-ray laminography, damage

1. Introduction

Advanced High Strength Steels (AHSS) grades remain the most widely used and developed materials in the automotive industry in order to reduce the "weight" of structural parts. Among these AHSS grades, dual phase (DP) steels with their ferrite-martensite composite microstructure present a good compromise between strength and formability. DP steels consist of a ferritic matrix containing a hard martensitic second phase in the form of islands. They are produced by controlled cooling from the austenite phase (in hot-rolled products) or from the two-phase ferrite plus austenite phase (for continuously annealed cold-rolled and hot-dip coated products) to transform some austenite to ferrite before a rapid cooling transforms the remaining austenite to martensite. However, the forming processes could affect the mechanical behavior of these grades. Some observations have shown that the cutting step tended to alter the good mechanical properties of this grade [1,2]. These studies have shown that the cutting process of DP sheets affects the adjacent material that extends into the bulk region of the sheet. This affected zone is characterized by a hardening and microstructural deformation which leads to local decohesion of ferritic and martensitic phases [1,11]. This drop in mechanical performance can significantly reduce the properties and then the use of AHSS.

While ductile fracture mechanisms of this steel and its base materials (i.e. ferrite and austenite separately) have been discussed in the past [5,6,7,8], the damage mechanisms of DP cut-edges are not well known. This study aims at offering knowledge of the microstructural initial state of a cut-edge and the evolution of damage from using three dimensions in-situ X-ray synchrotron laminography adapted to 3D observation of regions of interest sheet-like specimen and to identify the damage mechanisms leading to the crack formation initiating from the cut-edge.

X-ray synchrotron laminography has been used in the present study to visualize for the first time

damage evolution from a cut-edge during in-situ tensile bending test. The method, in contrast to computed tomography which is for axisymetric objects, allows to image in three dimensions a region of interest (for instance the crack tip) inside a sheet-like sample without cutting it. The laminography set-up used here is located at the ID19 beam line at the European Synchrotron Radiation Facility (ESRF) in Grenoble (France). The acquisition was performed with a voxel size of 0.778 μm^3. Applications in the study of damage of an aluminum grade can be found in the literature [12]. More details about the laminography technique are also given elsewhere [12,13].

2. Material and experiment

2.1. Studied material

The material used in this study is a laboratory dual phase steel with a ultimate tensile strength of approximately 600 MPa and a fracture strain of around 17 % at the as-received condition. The material was supplied as a 0.8mm thick cold rolled sheet. The chemical composition and microstructure are given in figure1.

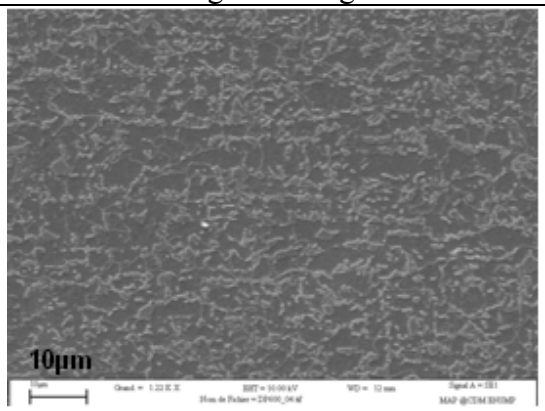

(a)

C	Mn	Si	Cr
0.08	0.8	0.23	0.68

(b)

Figure 1: (a) DP microstructure visualized by scanning electron microscopy (after nital 0.2% etching). (b) Chemical composition of DP600 steel (weight %)

The martensite islands appear to be aligned along the rolling direction. In the following the rolling direction will be referred to as L, the long transverse direction as T and the short transverse direction as S.

2.2. The cut-edge profile

The shearing, which is a cutting in a straight line over the entire width of the sheet by the action of a moving blade perpendicular to the plane of the sheet, is the most widely used and least expensive process for separating metal panels. In this study, we assume that the shearing and punching have the same effects on the cut edge as the 2D descriptions of these processes are identical. Figure 2 shows an optical micrograph of the polished surface of a sample after the cutting process. The sheared surface profile is characterized by the existence of 4 characteristic zones: rollover, fracture, burnish and burr (figure2). This observation is consistent with the results found in the literature [1,3].

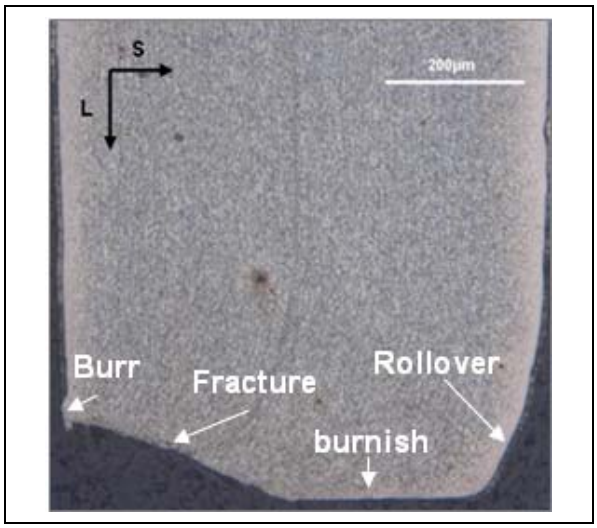

Figure 2: optical micrograph of a DP600 cut-edge profile (after 0.2% nital etching)

The proportion of these 4 characteristic zones are heavily dependent on cutting parameters such as the material nature, clearance, cutting edge radius and cutting speed [3,4,9]. The fracture zone displays the highest damage and presents a high roughness. Some zones of decohesion at the ferrite-martensite interfaces can be observed in the fracture zone and are aligned along the flow lines [1].

2.3. Experiment

The experimental technique used in this study was synchrotron radiation computed laminography (SRCL). It is a non-destructive technique similar to synchrotron radiation computed tomography (SRCT), for three dimensions imaging of objects that are extended in two dimensions. It provides a unique opportunity to observe internal damage mechanisms in three dimensions during extended crack propagation in sheet materials [12]. Unlike SRCT which is especially adapted to compact or one-dimensionally elongated objects which stay in the field of view of the detector system under rotation, SRCL is optimized to image regions of interest (ROIs) out of flat, sheet-like specimens. For this, the specimen rotation axis is inclined at an angle of $\theta < 90°$ with respect to the beam direction ($\theta = 90°$ corresponds to the case of CT). For sheet-like specimens, this enables a relatively constant average X-ray transmission over the entire scanning range of 360°, which allows reliable projection data to be acquired [12]. Although the 3D Fourier domain of the specimen is not sampled completely [13], which leads to imaging artefacts, these artefacts are often less disruptive than the ones produced by (limited-angle) CT [13].

The sample geometry shown in figure3 (a) was used. A hole with a radius of 5 mm was punched out from a sheet of DP steel and an elongated crack was machined up to one edge. The loading was achieved perpendicular to the crack, via a two-screw displacement-controlled wedging device that controls the specimen notch crack mouth opening displacement (CMOD) similar to the one used in Ref. [13,14].

To avoid the sample buckling and out-of-plane motion, an anti-buckling device was used. The entire rig was mounted in a dedicated plate that was removed from the SRCL rotation stage between loading steps. The loading was applied via stepwise increases in the CMOD, one turn of the screw corresponding to 1 mm of CMOD. 3 scans were performed before any loading in order to map and image the initial state of the cut-edge. After each loading step, a scan of the ROI containing the crack tip was carried out.

Observation was performed on the laminography instrument installed at ID19 at the European Synchrotron Radiation Facility (ESRF) in Grenoble (France). The axis inclination angle used was around 30° and a white beam was set up, centered around a 60 keV X-ray energy. The scanned region of interest (ROI) was about 1 mm^3.

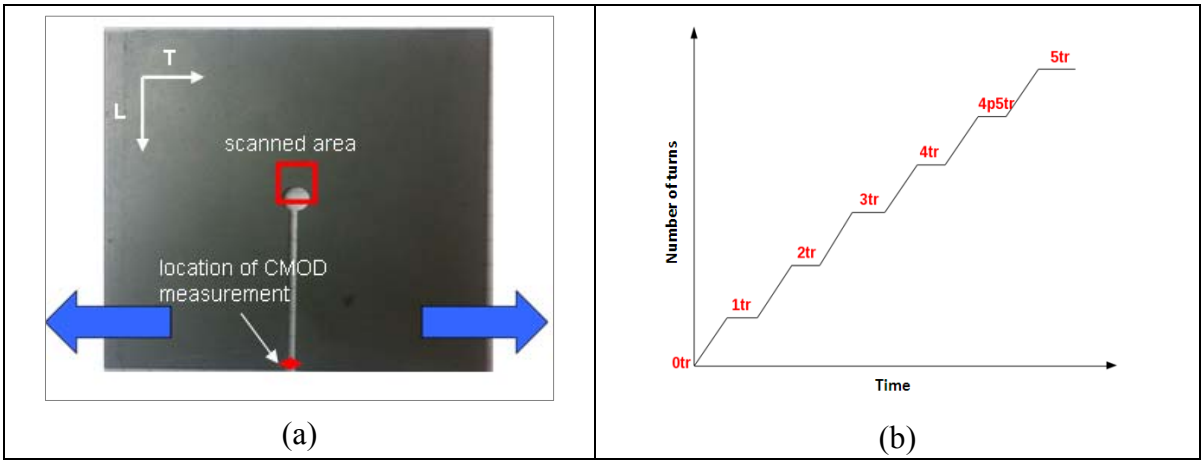

Figure 3: (a) the sample used in in-situ laminography observation and loading direction. (b) Schematic demonstration of stepwise loading applied during the in-situ observation.

3. 2D in-situ visualization of damage evolution from a cut-edge

The figure 4a-f shows the reconstructed 2D laminography sections at different loading stages. Ferrite and martensite phases have the same grayscale due to the fact that the phases have similar attenuation coefficients. They are shown in gray and the initial internal voids can be seen in black in the matrix (ferrite+martensite). Figure 4a shows the material at delivery state after punching in the L-T plane. The 2D sections (figures 4a-f) were taken from the burnish zone. The circular punched hole can be seen at the bottom of the sample. Some artifacts can be observed (cf [12]) that do not influence the segmentation of the voids (figure 5). The 2D sections (figure 4a-f) were taken from the burnish zone. A geometrical defect can be seen in the cut-edge.

Figure 4c, taken from at loading step corresponding to a CMOD equal to 2 mm, shows that a microcrack initiates on the cut-edge close to the geometrical defect. These observations of ductile crack propagation from a cut-edge and coalescence with internal porosities have never been seen before using SRCL with such a high level of details. The coalescence sheets are inclined by 45° compared to the L-direction. Other microcracks initiate from cut-edge but the crack located close to the geometrical defect grows faster. This is consistent with the increased level of stress triaxiality caused by the geometrical defect.

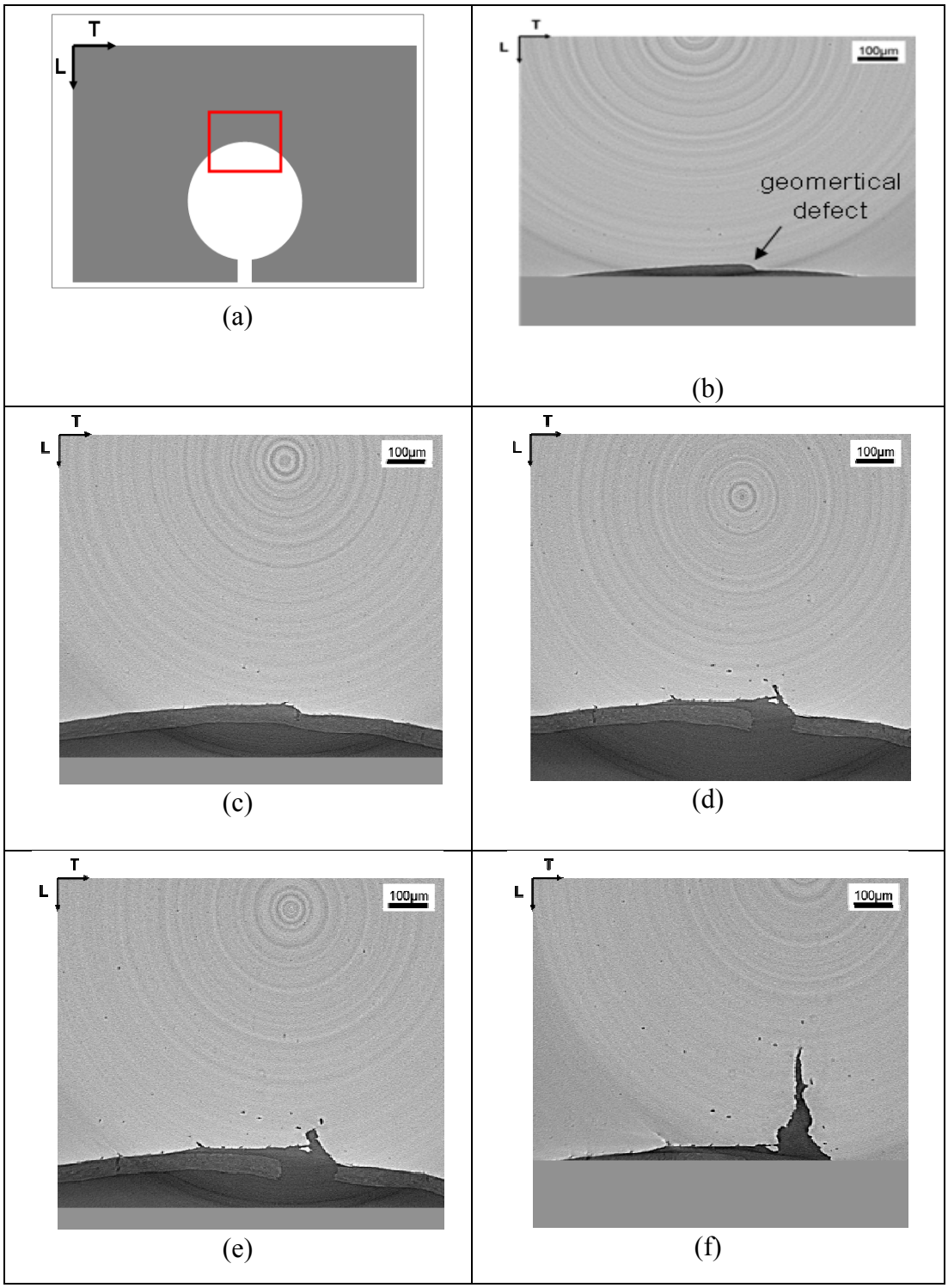

Figure 4: 2D sections at the burnish zone of the steel sheet plane of reconstructed laminography data of damage evolution from a cut-edge at CMODs. (a) The scanned zone (b) material at delivery state; (c) CMOD = 2 mm; (d) CMOD = 3 mm; (e) CMOD = 4 mm; (f) CMOD = 4.5 mm.

4. 3D in-situ observation of damage evolution from a cut-edge

Thanks to SRCL it is possible to visualize the voids in three dimensions, as shown in figure 5a-f, where voids are shown in volumes taken around the mid-thickness at different CMODs. Figure 4a shows the as-received material after punching. The fracture and burnish characteristic zones

surfaces and the geometrical defect located in the fracture-to-burnish transition zone can be seen. The initial porosities can be seen in the bulk of the specimen in black. These voids are aligned along the martensite alignments (interfaces ferrite-martensite) [1]. Coalescence sheets can be seen in figure 5e-f where needle voids growing from the cut-edge, i.e. fracture zone surface, coalesce with the internal needle voids corresponding to the decohesion of ferrite-martensite interfaces. These needle voids then coalesce with the burnish zone though narrow areas known as void sheets.

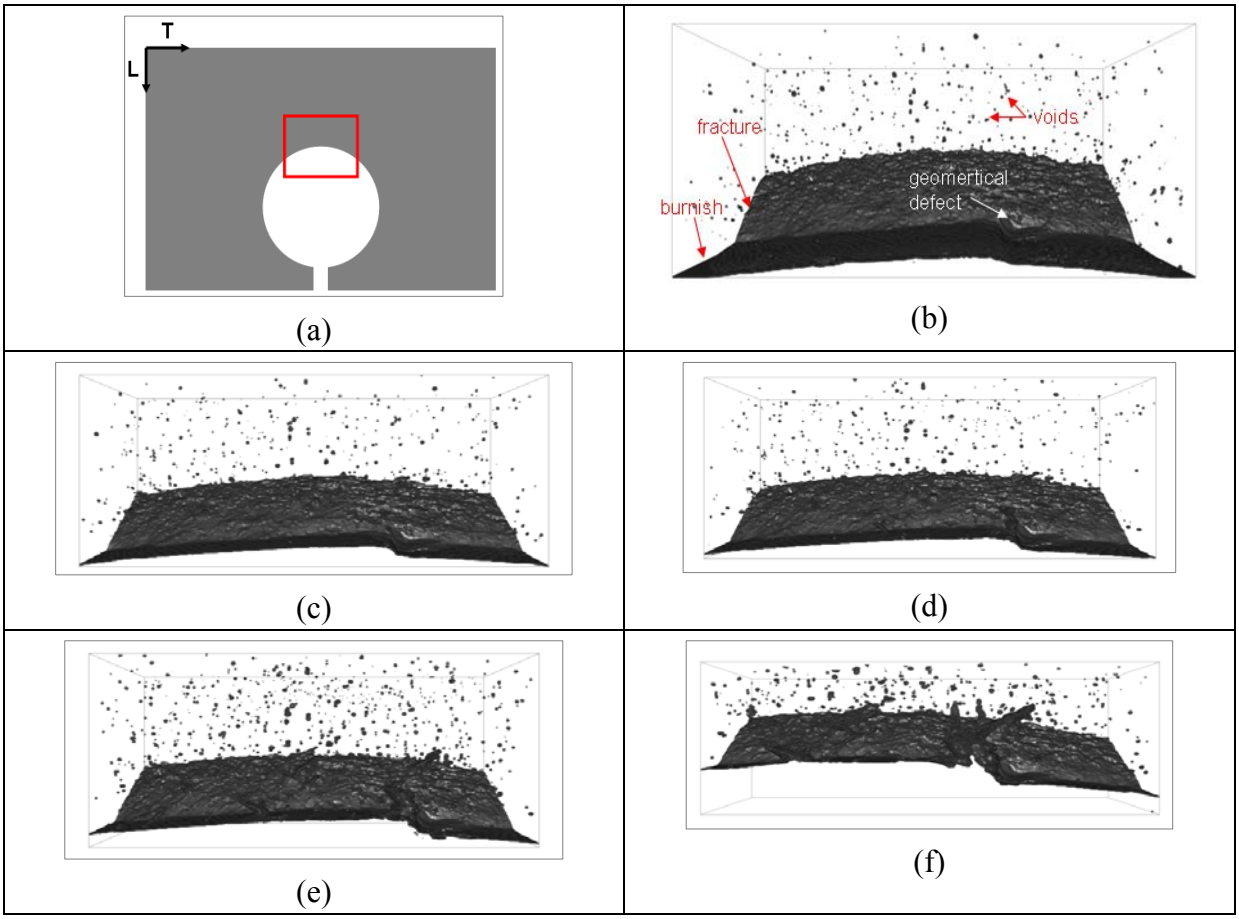

Figure 5: L-T views of 3D volumes of the steel sheet plane of reconstructed laminography data of damage evolution from a cut-edge at CMODs. (a) The scanned zone (b) material at delivery state (700x350x504 μm^3); (c) CMOD = 1 mm, (700x350x294 μm^3); (d) CMOD = 2 mm, (700x350x294 μm^3); (e) CMOD = 3 mm, (700x350x294 μm^3); (f) CMOD = 4 mm, (700x300x260 μm^3).

Figure 6 shows the shape of needle voids grown from the fracture zone surface and in the bulk. These needle voids consist with the decohesion of ferrite-martensite interfaces (i.e. the flow lines) characterized in Ref [1].

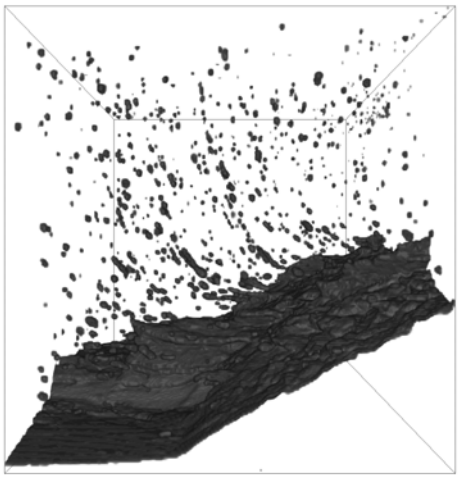

Figure 6: L-S 3D view of reconstructed laminography data of a DP600 cut-edge at CMOD = 3 mm (260x350x700 μm^3)

Figure 7 shows L-S views of reconstructed laminography data of DP600 cut-edge. Figure 7a illustrates the cut-edge profile with the 4 characteristic zones. Microcracks, needle voids from the fracture zone surface and needle voids in the bulk can be seen in figure 7a. Figure 7b shows the coalescence sheet of needle voids growing from the fracture zone and the burnish zone.

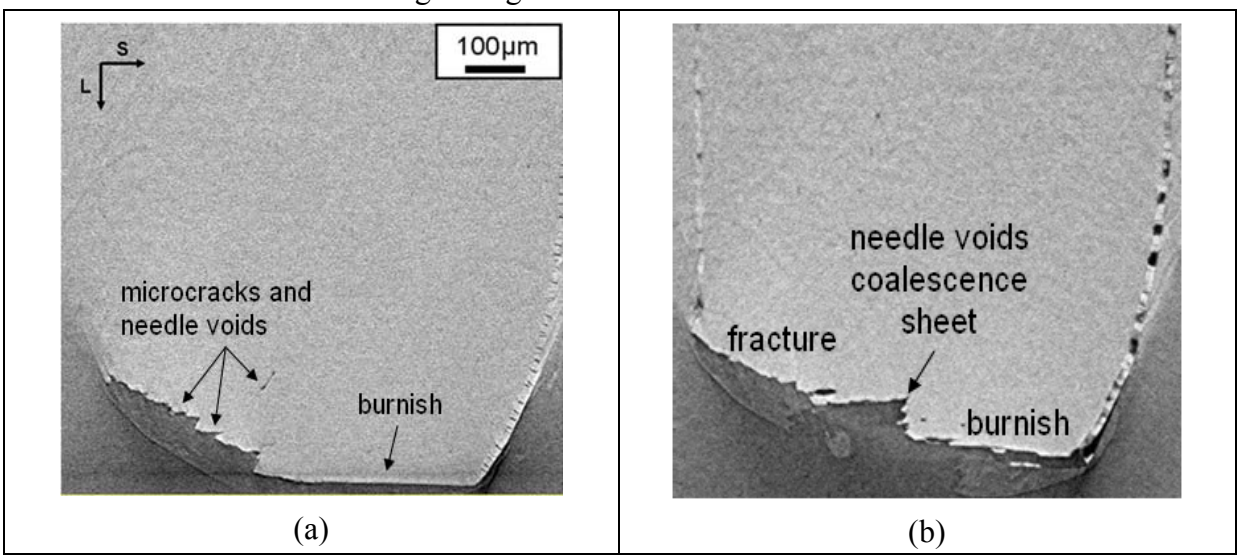

Figure 7: L-S 2D sections of reconstructed laminography data. (a) cut-edge profile at initial state. (b) Coalescence sheet at CMOD = 3 mm.

5. Conclusion

The experimental study presented in this paper aims at gaining insight into the initial damage state and subsequent damage evolution during mechanical loading from DP600 steel grade cut-edges. 3D imaging using synchrotron radiation computed laminography has allowed us to identify different defects that a cut-edge at initial state contains. These include roughness in the fracture zone, needle voids in the bulk from fracture zone and alignment of needle voids along the flow lines i.e. martensite alignments. These results are consistent with the ones found in Ref. [1,3].

The 3D in-situ laminography observation, particularly adapted to the observation of sheet-like objects, carried out on a sample with a circular punched hole has allowed us to characterize, for the first time, the damage evolution from a cut-edge in-situ and in 3D during mechanical tension and bending loading. The growth of needle voids was especially along flow lines from fracture zone surface but also in the bulk along the martensite alignments. The initial void growth direction is parallel to the burnish plan and normal to the loading direction. We observe that the coalescence of needle voids from the fracture zone with the burnish zone occurs via narrow coalescence zones. These cracks are inclined by 45° compared to the L-direction. Several cracks are formed, especially in the fracture zone, but the one located close to the geometrical defect grows faster. This is consistent with the increased level of stress triaxiality that is known to favor ductile damage growth.

References

[1]: A. Dalloz, J. Besson, A.-F. Gourgues-Lorenzon, T. Sturel, A. Pineau, Effect of shear cutting on ductility of a dual phase steel, Engineering Fracture Mechanics, 76 (2009) 1411 – 1424.
[2]: Daniel J. Thomas, Effect of Mechanical Cut-Edges on the Fatigue and Formability Performance of Advanced High-Strength Steels, Failure Analysis and Prevention, 12 (2012) 518-531.
[3]: X. Wu, H. Bahmanpour, K. Schmid, Characterization of mechanically sheared edges of dual phase steels, Materials Processing Technology, 212 (2012) 1209 – 1224.
[4]: H. So, D. Fasmann, H. Hoffmann, R. Golle, M. Schaper, An investigation of the blanking process of the quenchable boron alloyed steel 22MnB5 before and after hot stamping process, Materials Processing Technology, 212 (2012) 437-449.
[5]: C. Landron, O. Bouaziz, E. Maire, J. Adrien, Characterization and modeling of void nucleation by interface decohesion in dual phase steels, Scripta Materialia, 63 (2010) 973–976.
[6]: C. Landron, E. Maire, O. Bouaziz, J. Adrien, L. Lecarme, A. Bareggi, Validation of void growth models using X-ray microtomography characterization of damage in dual phase steels, Acta Materialia, 59 (2011) 7564–7573.
[7]: X. Sun and K.S. Choi and A. Soulami and W.N. Liu and M.A. Khaleel, On key factors influencing ductile fractures of dual phase (DP) steels, Materials Science and Engineering, 526 (2009) 140 – 149.
[8]: M. Ben Bettaieb, X. Lemoine, O. Bouaziz, A. M. Habraken and L. Duchane, Numerical modeling of damage evolution of DP steels on the basis of X-ray tomography measurements, Mechanics of Materials, 43 (2011) 139 – 156.
[9]: B.S. Levy and C.J. Van Tyne, Review of the Shearing Process for Sheet Steels and Its Effect on Sheared-Edge Stretching, Material and Engineering Performance, (2011) 1-9.
[10]: B.S. Levy and C.J. Van Tyne, Effect of a Strain-Hardening Rate at Uniform Elongation on Sheared Edge Stretching, Materials Engineering and Performance, (2012) 1-8.
[11]: M. Azuma, S. Goutianos, N. Hansen, G. Winther and X. Huang, Effect of hardness of martensite and ferrite on void formation in dual phase steel, Materials Science and Technology, 28 (2012) 1092-1100.
[12]: T.F. Morgeneyer, L. Helfen, I. Sinclair, H. Proudhon, F. Xu and T. Baumbach, Ductile crack initiation and propagation assessed via in situ synchrotron radiation-computed laminography, Scripta Materialia, 65 (2011),1010–1013.
[13]: L. Helfen, T. Baumbach, P. Mikulik, D. Kiel, P. Pernot, P. Cloetens, J. Baruchel,High-resolution three-dimensional imaging of flat objects by synchrotron-radiation computed laminography, Applied Physics Letters, 86 (2005) 071915.
[14]: L. Helfen, A. Myagotin, P. Mikulík, P. Pernot, A. Voropaev, M. Elyyan, M. Di Michiel, J. Baruchel, and T. Baumbach, On the implementation of computed laminography using synchrotron radiation,Review of Scientific Instruments, 82 (2011) 063702.

Numerical Simulation Method of radiation damage effects in plate-type dispersion nuclear fuel elements

Yunmei Zhao, Shurong Ding*, Xin Gong, Yongzhong Huo
Department of Mechanics and Engineering Science, Fudan University, Shanghai 200433, China
* Corresponding author: dsr1971@163.com

Abstract A metal-matrix dispersion nuclear fuel plate is composed of dispersion nuclear fuel meat and metal cladding. The fuel meat is similar to a kind of particle composite with the fuel particles embedded in the metal matrix. The extremely harsh irradiation environment results in the complex thermo-mechanical coupling behaviors occurring in the dispersion fuel plate. Especially, this complexity stems more from the irradiation damage effects, such as irradiation hardening and creep in the metal materials induced by the high-energy fission fragments and neutrons, and the thermal conductivity degradation of fuel particles as well. In this study, for heterogeneous irradiation conditions, the three-dimensional large deformation constitutive relations and stress update algorithms are built and validated for the homogenized fuel meat and cladding in the co-rotational coordinate system through forming subroutines in ABAQUS. The obtained results for the whole fuel plate indicate that when the non-homogeneous irradiation condition introduced: (1) both the mechanical and temperature fields show remarkable non-uniform characters along the length direction; (2) the deformation of the plate surface tends to be an arch, which could affect the normal flow of coolant with increasing burnup. The developed numerical simulation method provides a convenient way to simulate the heterogeneous irradiation damage. This study can lay a basis for establishing failure criteria for metal materials in the irradiation environment.

Keywords radiation damage, stress update algorithm, non-homogeneous irradiation condition, thermo-mechanical coupling

1. Introduction

Dispersion nuclear fuel elements are composed of metal cladding and fuel meat [1] with a certain volume fraction of fuel particles embedded in the matrix. Compared to the presently used nuclear fuel elements in nuclear plants, they have much better thermal conductivity and thus can reach higher burnup. They have a promising usage in the advanced nuclear reactors and disposal of nuclear wastes. The thermo-mechanical behaviors evolution of nuclear fuel elements and assembly is one of the mostly concerned issues for their in-pile safety, and it is a critical issue in their optimal design as well. Recent researches on thermo-mechanical behaviors in dispersion fuel elements with the finite element method (FEM) have been becoming a development trend, and the numerical simulation method is expected to be an important way for their optimal design. Some finite element method codes, such as FASTDART [2-3], PLATE [4-5], MAIA [6-7] and DART-TM [8], were developed with the attempt to study their thermal and thermal-mechanical behaviors. Van Duyn's study [9] treated the rod-like dispersion fuel pellet as a composite and established a three-dimensional model with the mutual interaction between the particles and matrix considered. Shurong Ding [10-11]studied the thermal and mechanical behaviors and Qiming Wang [12] studied the interfacial behaviors of the plate-type dispersion nuclear fuel elements based on the Representative Volume Element (RVE) method. In the demanding environment of nuclear reactors,

irradiation swelling occurs in nuclear fuels, and their thermal conductivity is degraded due to nuclear fissions; the metal materials within fuel elements experience irradiation damage effects, such as irradiation hardening and creep [13]. Besides, for the dispersion nuclear fuel plate, the research of nuclear reactor physics indicates that the irradiation damage along the length direction is heterogeneous owing to the non-homogeneous distribution of fast neutrons. All the above researches haven't well taken the irradiation damage effects into account, and a good simulation method for un-uniform irradiation conditions is waiting to be developed.

In order to study the thermo-mechanical behaviors of a whole fuel plate under non-homogeneous irradiation conditions, in this study, based on micromechanics, an equivalent fuel meat is obtained with the homogenized thermo-mechanical material properties related to the ones of fuel particles and metal matrix. With the thermo-elastic and irradiation swelling effects in the equivalent fuel meat, and with the thermo-elasto-plastic and irradiation hardening behaviors involved in the metal cladding, the respective three-dimensional thermo-mechanical constitutive relations and stress update methods are constructed. Assuming that the heat generation rates and neutron flux along the plate length direction are linear with the maximums appearing in the middle location, the numerical simulation methods are realized through several subroutines in ABAQUS. The material points have been given different constitutive relations according to time and their locations, thus the time and location-dependent constitutive relation can be carried out. The proposed numerical method is validated and the un-uniform thermo-mechanical fields are obtained and analyzed.

2. The constitutive relations and numerical simulation methods

The whole fuel plate is regarded as the research object in this study and its thermo-mechanical behaviors evolution is focused on under the heterogeneous irradiation conditions. In the fuel meat, there contain a large number of fuel particles. It is impossible to consider the mutual interactions between the fuel particles and the matrix in the finite element model and it is necessary to deal with it as an equivalent homogenous material. As follows, the equivalent thermo-mechanical parameters are obtained on the base of homogenization theory. Owing to the temperature-dependent and time-dependent performances of the component materials together with the resultant location-dependent ones due to the heterogeneous irradiation conditions, the equivalent meat also has the above special properties. For the fuel cladding, the irradiation hardening effect is included in the large-deformation thermo-elasto-plastic behaviors.

For the fuel meat and cladding, the thermal constitutive relations are comparably simple, which can be implemented with the subroutine UMATHT. According to the temperature, location and real time of the incremental step, the integration points can be applied with different thermal constitutive relations. In the following, the mechanical constitutive relations are mainly built and the relative numerical simulation methods are given.

2.1. Constitutive models of the equivalent fuel meat

2.1.1. Parameters of the equivalent meat

Homogenization theory [14-15] has been introduced to a dispersion nuclear fuel meat, and the

material properties including both the mechanical and thermal properties are obtained as follows.

According to the mean field model by MAXWELL [16], the conductivity of the equivalent meat $\mathrm{K(T,t,X)}$ can be described as:

$$\mathrm{K(T,t,X)} = \frac{K_m(2K_m+K_p-2V_f(K_m+K_p))}{2K_m+K_p+V_f(K_m-K_p)}, \tag{1}$$

Where K_m and K_p separately represent the conductivity of the matrix and the inclusion phase of fuel particles.

This analysis adopts Mori-Tanaka Method [17] to calculate the equivalent Young's modulus and Poisson's ratio. That's:

$$\mathrm{E(T,t,X)} = E_m(1+\frac{V_f(\frac{E_p}{E_m}-1)}{1+(1-V_f(E_p/E_m-1)}; \upsilon = \upsilon_m(1+\frac{V_f(\frac{\upsilon_p}{\upsilon_m}-1)}{1+(1-V_f(\upsilon_p/\upsilon_m-1)}, \tag{2}$$

where E is equivalent Young's modulus (MPa) and υ is the equivalent Poisson's ratio, they are related to the Young's Modula and Poisson's ratios of fuel particles and matrix.

Only the fuel particles in the dispersion fuel meat can generate heat, and the heat generation rate of the particles corresponds to their fission rate. The heat generation rate of the fuel particles $\dot{q_p}$ can be expressed as

$$\dot{q_p}(X) = c \cdot \dot{f}, \tag{3}$$

with the unit is W/mm^3. Where $\mathrm{c} = 3.204 \times 10^{-11}$J/fission is the generated heat energy every fission event and $\dot{f}$ is the fission rate of fuel particles, while in this analysis the value of $\dot{f}$ is linearly distributed along the length direction like the fast neutrons, which has the largest one $0.6408\ \mathrm{W}/mm^3$ in the middle location as twice as the lowest one at the margin of the fuel meat.

The corresponding heat generation rate of the equivalent meat can be obtained as:

$$\dot{q(X)} = V_f \cdot \dot{q_p} \tag{4}$$

The swelling rate of the equivalent meat is obtained similarly as

$$\mathrm{SW(T,t,X)} = \frac{\Delta \mathrm{V}}{\mathrm{V_0}} = V_f \cdot \mathrm{SW}_p, \tag{5}$$

where $\dot{q_p}$ and SW_p separately denote the heat generation rate and swelling rate of fuel particles, they are both location-dependent and SW_p increases with burnup [3].

The thermal expansion of the equivalent meat α_c can be expressed as

$$\alpha_c(T) = 5.84 \times 10^{-6} + 1.9 \times 10^{-7} \times \frac{V_f-0.1}{0.05} + 2 \times 10^{-7} \times \frac{T-350}{450}, \tag{6}$$

where T is temperature in Kelvin with the application range from 350K to 730K.

In the above equations, the subscript p represents the material parameters of the fuel particles and subscript m represents the ones of matrix, and V_f denotes the volume fraction of fuel particles in the fuel meat. In this study, the considered volume fraction is 10%. Under heterogeneous irradiation conditions, the above obtained equivalent parameters vary with location, temperature and time.

2.1.2. Constitutive relationship of the equivalent meat

The large-deformation elastic constitutive relationship for the equivalent meat in a co-rotational coordinate system can be expressed as the following relation between Cauchy stress and elastic logarithmic strain:

$$\sigma_{ij} = \lambda(T,t,X)\delta_{ij}{\varepsilon_{kk}}^{el} + 2\mu(T,t,X){\varepsilon_{ij}}^{el}, \tag{7}$$

where $\lambda(T,t,X)$ and $\mu(T,t,X)$ is the Lame constants, they are related to the Young's Modulus and Poisson's ratio in Eq. (2).

The incremental form for a time step from t to $t+\Delta t$ with the temperature change from T to T+ΔT in a corotational framework can be obtained as

$$\Delta\sigma_{ij} = \lambda(T+\Delta T, t+\Delta t, X)\Delta\varepsilon_{kk}^{el}\delta_{ij} + 2\mu(T+\Delta T, t+\Delta t, X)\Delta\varepsilon_{ij}^{el} + \Delta\lambda\varepsilon_{kk}^{el(t)}\delta_{ij} + 2\Delta\mu\varepsilon_{ij}^{el(t)} \quad (8)$$

$$\Delta\varepsilon_{ij}^{el} = \Delta\varepsilon_{ij} - \Delta\varepsilon_{ij}^{th} - \Delta\varepsilon_{ij}^{sw} \quad (9)$$

$$\Delta\lambda = \lambda(T+\Delta T, t+\Delta t, X) - \lambda(T, t, X),\ \Delta\mu = \mu(T+\Delta T, t+\Delta t, X) - \mu(T, t, X) \quad (10)$$

where $\Delta\varepsilon_{ij}$ represents the total strain increment and $\Delta\varepsilon_{ij}^{el}$ represents the elastic one, $\varepsilon_{ij}^{el(t)}$ depicts the elastic strain at time *t*; $\Delta\varepsilon_{ij}^{th}$ and $\Delta\varepsilon_{ij}^{sw}$ mean the thermal strain increment and swelling one as the following

$$\Delta\varepsilon_{ij}^{th} = (\ln(1+\alpha_{c(T+\Delta T)}(T+\Delta T-T_0) - \ln(1+\alpha_{c(T)}(T-T_0))\delta_{ij} \quad (11)$$

$$\Delta\varepsilon_{ij}^{sw} = \frac{1}{3}\delta_{ij}(\ln(1+\mathrm{SW}(\mathrm{T}+\Delta\mathrm{T}, \mathrm{t}+\Delta\mathrm{t}, \mathrm{X})) - \ln(1+\mathrm{SW}(\mathrm{T}, \mathrm{t}, \mathrm{X}))) \quad (12)$$

Where T_0 is the reference temperature which is set as 350K.

2.2. Constitutive relationship of the cladding

2.2.1. Irradiation hardening model for the cladding material

The strain-hardening curve of unirradiated Zircaloy is described as [18]

$$\sigma = \mathrm{K}\varepsilon^n \cdot (\frac{\dot{\varepsilon}}{10^{-3}})^m \quad (13)$$

where σ is the true stress(Pa), ε is the true strain, n is the strain-hardening exponent, *K* is the strength coefficient and *m* is the strain rate sensitivity exponent. $\dot{\varepsilon}$ is the true strain rate. If $\dot{\varepsilon} < 10^{-5}/s$, set $\dot{\varepsilon} = 10^{-5}/s$.

$$\mathrm{K} = 1.17628\times10^9 + T(4.54859\times10^5 + T(-3.28185\times10^3 + 1.72752T)) \quad (14)$$

$$\mathrm{n} = -9.49\times10^{-2} + T(1.165\times10^{-3} + T(-1.992\times10^{-6} + 9.588\times10^{-10}T)) \quad (15)$$

$$\mathrm{m} = 0.02 \quad (16)$$

where *T* is the temperature in Kelvin ranged from 300 K to 730K.

Due to the irradiation hardening effect, the strain hardening exponent [18] is described by further multiplying the coefficient given in Eq. (17)

$$k_2 = 1.369 + 0.032\times10^{-25}\cdot(\phi\cdot t) \quad (17)$$

The strength coefficient under irradiation [18] is given by adding the value given in Eq. (14) to Eq.(18)

$$k_3 = 5.54\times10^{-18}\cdot(\phi\cdot t) \quad (18)$$

The factors in Eqs. (17-18) are both dimensionless, and $\phi\cdot t$ denotes the fast neutron fluence (n/m^2); $\phi$is the fast neutron flux, which is location-dependent due to the heterogeneous irradiation conditions.

2.2.2. Three-dimensional constitutive relation for the cladding

The incremental constitutive relation for the cladding is similar to Eq. (8) as

$$\Delta\sigma_{ij} = \lambda(T+\Delta T, t+\Delta t, X)\Delta\varepsilon_{kk}^{el}\delta_{ij} + 2\mu(T+\Delta T, t+\Delta t, X)\Delta\varepsilon_{ij}^{el} + \Delta\lambda\varepsilon_{kk}^{el(t)}\delta_{ij} + 2\Delta\mu\varepsilon_{ij}^{el(t)}$$

Since the large-deformation thermo-elasto-plastic behaviors are considered, the elastic strain increment can be expressed as:

$$\Delta\varepsilon_{kk}^{el} = \Delta\varepsilon_{ij} - \Delta\varepsilon_{ij}^{th} - \Delta\varepsilon_{ij}^{p}, \quad (19)$$

Where $\Delta\varepsilon_{ij}^{p}$ can be obtained according to the backward Euler Integration and plastic constitutive

theory [19] as

$$\Delta\varepsilon_{ij}^{p} = \frac{3S_{ij}^{t+\Delta t}}{2\bar{\sigma}^{t+\Delta t}}\Delta\bar{\varepsilon}^{p}; \tag{20}$$

$$\sigma_{ij}^{t+\Delta t} = \sigma_{ij}^{t} + \Delta\sigma_{ij} \tag{21}$$

Where $S_{ij}^{t+\Delta t}$ are the components of the deviatoric tensor of the Cauchy stress at $t+\Delta t$; $\bar{\sigma}^{t+\Delta t}$ is the Mises stress at $t+\Delta t$, which is dependent on the equivalent plastic strain increment $\Delta\bar{\varepsilon_p}$. After some manipulations, a closed form expression for $\Delta\bar{\varepsilon}^{p}$ can be obtained:

$$\bar{\sigma}^{t+\Delta t} + 3G\Delta\bar{\varepsilon_p} - \bar{\sigma}^{pr(t+\Delta t)} = 0, \tag{22}$$

Where the Mises stress and equivalent plastic strain at $t+\Delta t$ should obey the irradiated strain-hardening curve in Section 2.2.1; $\bar{\sigma}^{pr(t+\Delta t)}$ is the trial Mises stress with the assumption of no plastic strain increments in Eq. (19). Eq. (22) is a nonlinear equation of $\Delta\bar{\varepsilon_p}$. Newton Iteration is applied to solve this nonlinear equation. When the converged equivalent plastic strain increment is obtained, the stress and strain can be updated.

Based on the developed constitutive relations and stress update methods for the fuel meat and cladding, the subroutines UMAT are written to simulate the non-homogeneous irradiation-induced mechanical behaviors.

3. Finite element model

3.1. Finite element geometric model

A dispersion nuclear fuel plate is taken as the research object, whose length and width is much larger than its thickness. The bonding between the fuel meat and the cladding is assumed perfect. As mentioned above, the thermo-mechanical behaviors evolution for un-uniform irradiation conditions is to be simulated. According to the symmetry in geometry and loading, a 1/8 part of the whole fuel plate is set as the finite element geometric model including the corresponding parts of fuel meat and cladding, as illustrated in Fig.1. Using the reduced Integration element C3D8RT, the FE model in Fig.1 is meshed with 49950 elements and 56848 nodes.

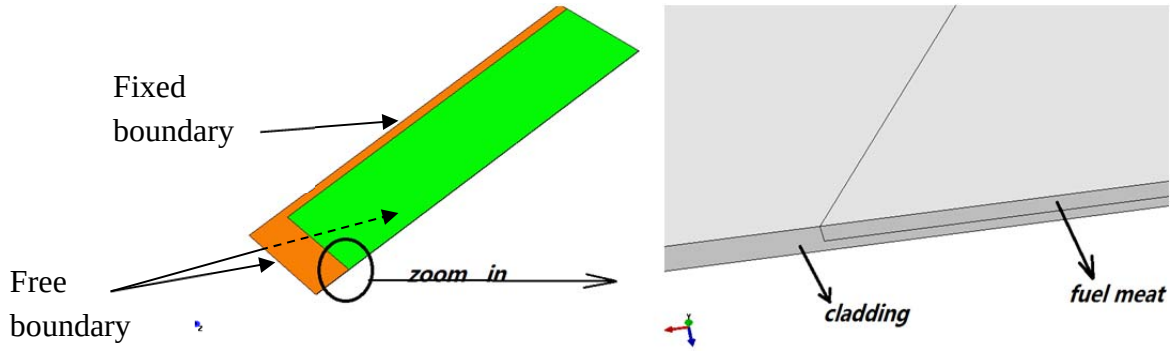

Figure.1 FEM Model

3.2 .boundary conditions

The boundary conditions to determine the temperature field are given as

(1) The surface to contact with the coolant water satisfies the convection boundary condition $-\mathrm{K}\frac{\partial T}{\partial n} = h(T - T_f)$, where the temperature of periphery fluid T_f is 573K. And the used heat transfer coefficient is $2\times10^{-2}\ W/mm^2K$.

(2) Other surfaces satisfy: $-\mathrm{K}\frac{\partial T}{\partial n} = 0$.

The used boundary conditions to determine the mechanical field are as follows
(1) Fixed boundary condition is applied to the side surface, shown as Fig.1
(2) The unseen lower surface and the front surface are set as free boundaries.
(3) Other surfaces are applied with symmetric boundary conditions.

4. Results and discussion

In this section, the effectiveness of the irradiation hardening simulation is validated, and the obtained temperature field and mechanical ones are to be shown and discussed.

4.1. Validation of irradiation hardening simulation

In order to make the correctness of irradiation hardening simulation confirmed, node M in the cladding is selected and the calculated Mises stresses and equivalent elasto-plastic strains at different time have been output. Taking them as the longitudinal and transverse ordinates respectively, three points can be produced in Fig.3. Meanwhile the irradiation hardening curves of the cladding material at the corresponding irradiation damage and temperature are plotted in Fig.3. It can be seen that the obtained computation results obey the irradiation hardening curves, which denotes that the irradiation hardening effect is correctly simulated.

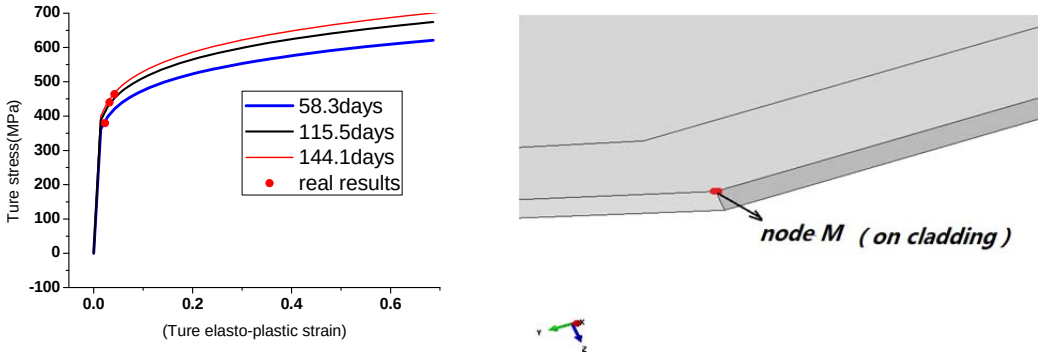

(a) (b)

Figure.2 (a) The stress-strain curves and the numerical results of (b) node M in the cladding

4.2. The temperature results

The calculated temperature field under heterogeneous irradiation condition is depicted in Fig.3 (a). It can be observed that the highest temperature with the red color locates in the fuel meat, precisely speaking, in the middle location along both the length and thickness directions. These phenomena result from the higher heat generation rate there. Thus, two paths in Fig.3 (b) are chosen to output the calculated temperatures at different time. The results under the uniform irradiation condition in Fig.4 are unchanged along the length direction of fuel plate. However, the temperature distribution under non-homogeneous conditions is approximately linear along the two paths, which is closely related to the heat generation rate of fuel meat. From 1.1 days to 144.1 days, the temperature

changes only 0.5 K, it is obvious that the temperature variation with burnup is very slight with a constant irradiation condition. Meanwhile, from comparison of the results along Path 1 and Path 2, it can be found that the maximum temperature in Path 1 is about 9K higher than the one in Path 2, which is for the reason that Path 2 is closer to the coolant water.

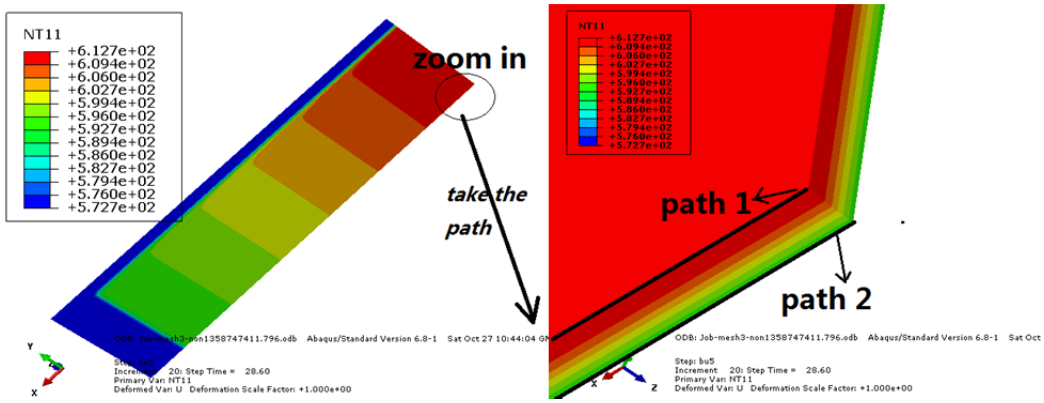

(a) (b)

Figure.3 (a) Temperature distribution at 144.1days and (b) the paths to output the results

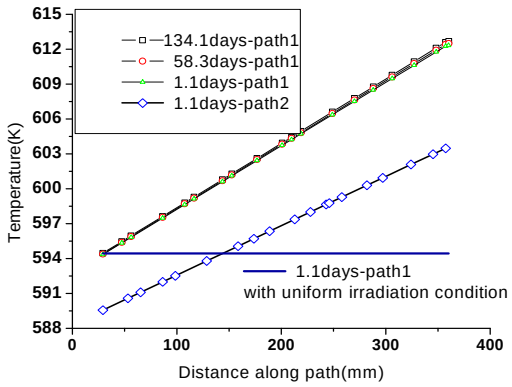

Figure. 4 Temperature distribution in the fuel meat

4.3. Mechanical behaviors in the cladding

The cladding is the first barrier to keep the radioactive substance from leakage. It's of huge importance to maintain its integrity. For the metal material, the Mises stress is firstly concerned. The contour plot at 144.1days is given in Fig.5. One can see that a stress concentration zone exists in the corner of cladding with the largest Mises stress reaching 468.4MPa, which is caused by the fixed boundary condition. To investigate the Mises stress distribution in the zone, two paths were taken in Fig.6. Through comparison of the results on path1 and path2, it can be discovered that path1 has slightly higher Mises stress than path2, as is shown in Fig. 6(a). Also, one can find that with increasing time the Mises stress demonstrate the same variation law on path1 as that the maximum numerical result always appears at the tip of the stress concentration zone. Meanwhile, from 29.7days to 144.1days, the maximum Mises stress on path1 increases from 341.52MPa to 465.4MPa. Observation of Mises stress distribution in the cladding part with the fuel meat

underneath shows that there exist the largest results in the middle location of fuel plate, that is, they locates at the right zone of the finite element model. It is induced by the fact that there exists the largest neutron flux which leads to the highest heat generation and irradiation swelling of fuel meat together with strengthened irradiation hardening in the cladding. This is the result of un-uniform irradiation conditions. In a word, it is necessary to optimize the constraint and irradiation conditions for fuel elements in order to assure their safety.

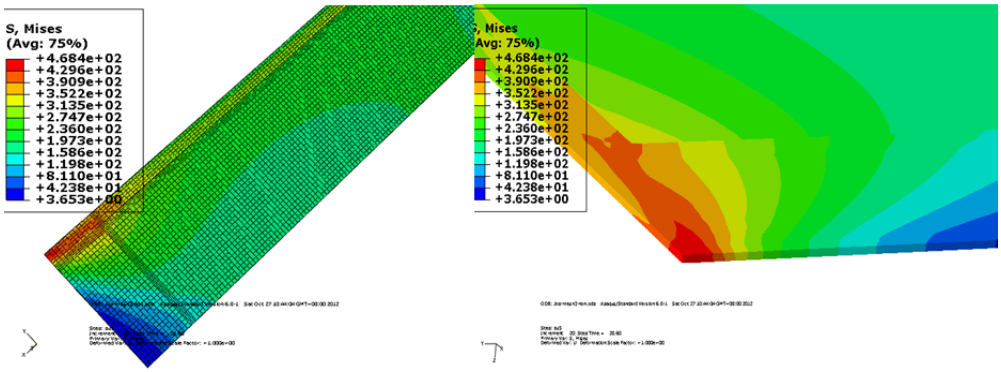

(a) (b)

Figure.5 (a) The Mises stress contours and (b) the stress concentration zone in cladding at 144.1days

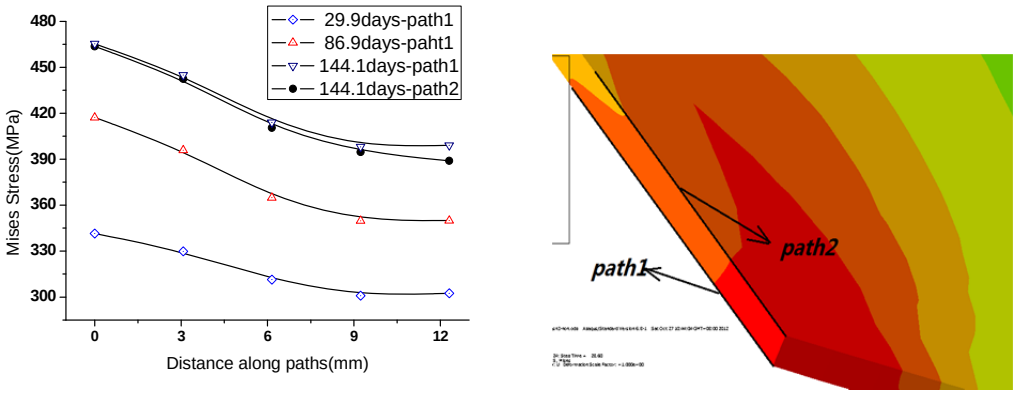

Figure.6 (a) The Mises Stress in different time along (b) the two paths in cladding

4.4. Deformation in the thickness direction

It is well known that the exceeding deformation along the plate thickness direction will narrow the coolant water channel, which will further lead to degradation of the heat transfer coefficient between the fuel plate and the coolant water. This could even result in accident with rapid temperature rise. Thus, the deformation in the thickness direction of fuel plate under nonhomogeneous neutron flux is mainly investigated. Fig.7 (a) reveals the displacements in the thickness direction of fuel plate along the surface path depicted in Fig. 7 (b). It can be observed that (1) the displacements is very small at the part with no fuel meat underneath and they change little with time; (2) the large displacements mainly exist in the part with the fuel meat underneath, and they increase with time distantly; (3) as expected, the maximum deformation arises in the middle part along the plate length direction, and its increasing rate with time is highest. The fuel plate tends to be an arch. As can be easily understood, the main contribution of the above deformation is from

the irradiation swelling of fuel meat, and the swelling is largest in the middle together with the highest temperature there. For the sake of in-pile safety, the initial gap between the fuel elements in the fuel assembly should be properly designed.

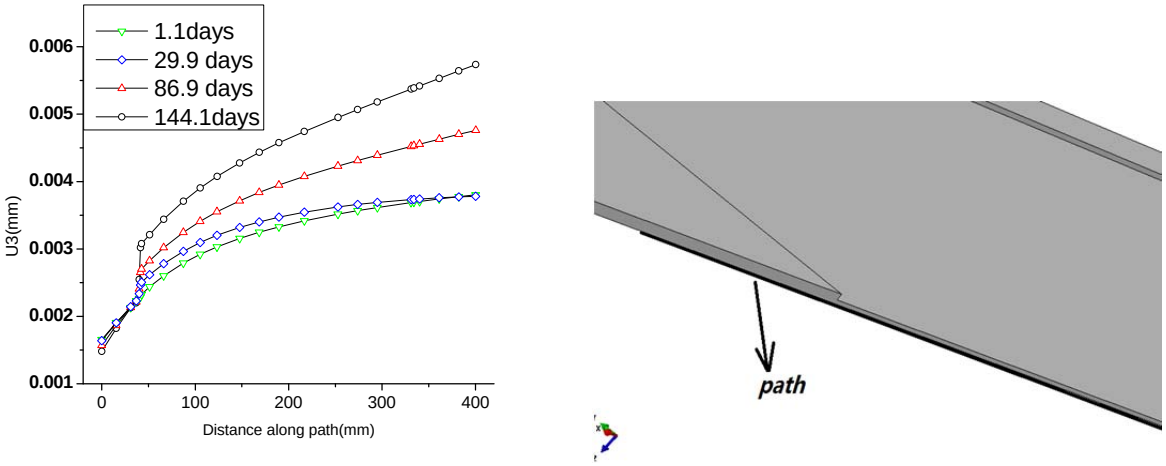

(a) (b)

Figure.7 (a) The displacements in the thickness direction along (b) the plate surface path

5. Conclusions

The stress update algorithms and UMAT subroutines for the dispersion nuclear elements are effective to simulate the thermal-mechanical behaviors under the assumed linearly distributed irradiation condition. Several conclusions can be obtained as the following

(1) The temperature distribution in the equivalent meat is corresponding to the heat generation setting and the middle position holds the highest temperature.

(2) The fixed long side of the cladding causes a stress concentration zone in the fuel plate corner, and the high neutron flux in the middle location leads to existence of the relatively large stress with the fuel meat underneath.

(3) Deformation of the thickness is un-uniformly distributed along the plate length direction and the largest one is at the middle position with the highest neutron flux.

In the future, other irradiation damage effects will be further included in our constitutive relation and numerical simulation, and different constraint conditions and more practical heterogeneous irradiation conditions for dispersion fuel plates will be studied.

Acknowledgement

The authors thank for the supports of the Natural Science Foundation of China (11172068, 91226101, 11272092,11072062, 91026005), the Research Fund for the Doctoral Program of Higher Education of China (20110071110013), Strategic Priority Research Program" of the Chinese Academy of Sciences (Grant No. XDA01020304).

References

[1] A.Leenaers, S. Van Den Berghe, S. Dubois, J. Noirot, M, Ripert, P. Lemoine, Microstructural

Analysis of Irradiated Atomized U(MO) Dispersion Fuel in an Al Matrix with Si Addition, RRFM2008 Transactions, Section2: Fuel Development and Fabrication,pp. 106-110.

[2] H.Taboada.J. Rest, MV. Moscarda, M, Markiewicz, E. Estevez, in: Proceedings of the 24th International Management on Reduced Enichement for Rearch and Test Reactors, San Carlos de Bariloche, Argentina, 3-8 November 2002.

[3] Rest, J., 1995. The DART Dispersion Analysis Research Tool: A Mechanistic Model for Predicting Fission-Product-Induced Swelling of Aluminum Dispersion Fuels, ANL-95/36.

[4] Hayes, S.L., Hofman, G.L., Meyer, M.K., Rest, J., Snelgrove, J.L., 2002. in: 2002 International Meeting on Reduced Enrichment for Research and Test Reactors, Bariloche, Argentina, 3–8 November.

[5] Hayes, S.L., Meyer, M.K., Hofman, G.L., Snelgrove, J.L., Brazener, R.A., 2003. in: Proceedings of the 2003 International Meeting on Reduced Enrichment for Research and Test Reactors, Chicago, IL, 5–10 October.

[6] Marelle, V., Dubois, S., Ripert, M., Noirot, J., Lemoine, P., 2007. in: The RERTR-2007 International Meeting on Reduced Enrichment for Research and Test Reactors, 23–27 September, Diplomat Hotel – Prague, Prague, Czech Republic.

[7] Marelle, V., Huet, F., Lemoine, P., 2004. in: Proceedings of the Eighth International Topical Meeting on Research Reactor Fuel Management, München, Germany, 21–24 March.

[8] Saliba, R., Taboada, H., Moscarda, M.V., 2003. in: 2003 International Meeting on Reduced Enrichment for Research and Test Reactors, Chicago, IL, 5–10 October.

[9] Lee Van Duyn, 2003. Evaluation of the Mechanical Behavior of a Metal-matrix Dispersion Fuel for Plutonium Burning, Georgia Institute of Technology: A Thesis for the Degree Master of Science in Mechanical Engineering.

[10] Shurong Ding, Xin Jing, Yongzhong Hou, Lin and Li, Journal of Nuclear Materials 374(2008)453-460.

[11] Shurong Ding, Yongzhong Huo, XiaoQing Yan, Journal of Nuclear Materials (2009), doi:10.1016/j.jnucmat. 2009.04.015.

[12] Qiming Wang, Xiaoqing Yan, Yongzhong Huo, Shurong Ding, Mechanical behaviors of the dispersion nuclear fuel plates induced by fuel particle swelling and thermal effect I: effects of variations of the fuel particle volume fractions, *Journal of Nuclear Materials*, Vol. 400, No. 2, May 2010, pp. 157-174..

[13] N.Okubo,Y. Miwa, K. Kondo,Y. Kaji, J. Nucl. Mater. 386-388(2009)290-293.

[14] Aboudi J., Mechanics of composite materials[M, Elsevier, Amsterdam, 1991.

[15] Aboudi J., Micromechanical analysis of composites by the method of cells-update[J]. Appl. Mech. Rev., 1996,49: S83-S91.

[16] J.C.Maxwell, A Treatise on Electricity and Magnetism[M]. Oxford: Clarendon Press, 1873.

[17] Mori T., Tanaka K., Average stress in matrix and average elastic energy of materials with misfitting inclusions[j]. Acta Matal, 1973, 21: 571-574.

[18] D.L.Hagman.G.A Reyman.MATPR-Verson11, A Handbook of Materials Properties for use in the Analysis of Light Water Reactor Fuel Rod Behavior, NUREG/CR-0497, TREE-1280,Rev, vol,3,1979..

[19] Belytschko, T., Liu, W.K., Moran, B.,2000. Nonlinear Finite Elements for Continua and Structures, John Wiley & Sons Ltd., U.K.

Effect of interfacial defect on surface crack behavior of an air plasma sprayed thermal barrier coating

Xu Rong, Zhang Weixu, Fan Xueling, Wang Tiejun*

State Key Laboratory for Strength and Vibration of Mechanical Structures, School of Aerospace Engineering, Xi'an Jiaotong University, Xi'an 710049, China
* Corresponding author: wangtj@mail.xjtu.edu.cn

Abstract Multiple surface cracking has significant effect on the failure of thermal barrier coating system (TBCs). The surface cracking is influenced by interface defects. It is of significance to study the relationship between the interface defect and the surface crack. In present work, the effect of interface defect on the surface crack behavior of TBCs has been investigated by using finite element method. The strain energy release rate (SERR) of the surface vertical crack is obtained as functions of the interfacial defect length and location. The results show that both the defect location and the defect length have a significant influence on the driving force of surface crack. It is concluded that the interface defect under the surface crack may induce a more intense facilitation on the surface cracking behavior than the remote defect. Moreover, a large scale interface defect may also induce a larger SERR of the surface crack which may promote its propagation.

Keywords Thermal barrier coating, Surface crack, Interfacial delamination, Strain energy release rate

1. Introduction

Thermal barrier coating systems (TBCs) are widely used in gas turbines or diesel engines due to their excellent heat-insulating property, which can efficiently prolong the life of the turbines blades[1, 2]. The major role contributing to the heat-insulating is the top layer of the TBCs, a ceramic coat with low thermal conductivity, which provides a temperature reduction of the metallic substrate[3, 4]. In order to protect the substrate from oxidation and make a better bond strength of the top coat to the substrate, a metallic bond coat is deposited between the top coat and the substrate. The top ceramic coat, metallic bond coat and substrate build up the typical TBCs.

Due to the mismatch of the geometric dimensions and the material properties, some fracture phenomena are inevitable in the TBCs[5, 6]. The common fracture behaviors observed during the service are the multiple surface cracks and the interface cracks[7, 8]. Considerable work was focused on the surface cracking behavior in the film/substrate system. Schulze and Erdogan[9] analyzed the periodic cracking of an elastic coating bonded to a homogeneous substrate. Vlassak[10] studied the channel cracking in thin films on substrates of finite thickness in order to simulate the segmentation of the ceramic layer of TBCs. Recently, by using finite element method, Fan *et al*.[11, 12] and Zhang *et al*.[13] built a three-layer model to investigate the effects of several important characteristic parameters, e.g. the interface roughness, thermally grown oxide (TGO), etc., on the periodic surface crack behavior. However, it is assumed in most of the aforementioned investigations that the ceramic/bond coat interface of TBCs is perfect, which ignores the fact that interface cracks may be initiated due to stress concentration.

The interface cracks have been frequently observed during the service, which lead to the spalling of ceramic coating and eventual failure of TBCs. The analyses and explanations for the appearances of interface cracks were presented by many researchers. Rice[14] developed the elastic fracture mechanics concepts for interfacial cracks between dissimilar solids, which made a great contribution to the interface cracks analysis in TBCs. Mumm and Evans[15] focused on the interface crack induced by the TGO growth. In their study, the morphological imperfections in the TGO played a great role in the failure of TBCs. Another significant reason for the initiation of interface cracks is the natural restrictions of depositing process especially the air plasma spraying. Currently, it is generally accepted that the ceramic coating of air plasma spraying TBCs exhibits laminar structural characteristic. Pores and micro-cracks are inevitable due to the internal thermal

stress in the process of thermal spraying[16-18]. The defects near the interface may coalesce during the service, leading to the interface cracks[19, 20].

The original motivate of present work is the author's experiment observations to TBCs that the surface cracks intensively appears in some areas of the ceramic coating of TBCs. Generally, one reason for the phenomenon is that, after air plasma spraying, as previous mentions, the ceramic/bond coat interface usually contains numbers of small scale delamination, which may promote the surface crack emerging above it. Another one is that the facilitation of the interfacial delamination induced by TGO growth or material property mismatch to the surface cracks. In general, the interaction between the interface defect and surface rupture make a great contribution to the experiment observations. In order to understand the fracture mechanisms of the TBCs clearly, the analyses of the mutual effects between the interface defect and surface rupture should be extremely necessary. More recently, investigations focus on the interaction of interfacial delamination and surface cracks[21, 22]. Among these studies, much attention has been paid on the effect of the surface cracks on the interfacial delamination, the basic assumption of which is that the interfacial delamination initiated from roots of surface channel cracks. However, for most cases, the interface cracks exist before the top ceramic coating starts to failure. Therefore, it is important to investigate the effect of the pre-existing interfacial defect on the ceramic failure especially on the initiation and propagation of the surface vertical crack. Zhou and Kokini[21] investigated the effect of pre-existing surface crack morphology on the interfacial thermal fracture and demonstrated that the large density of the period surface cracks can postpone the interfacial delamination, Fan *et al*. [22] used FEM to obtain the critical spacing of the periodic surface cracking below which the surface channel cracks have a dramatic effect on the interfacial delamination. However, much less attention has been paid directly to the effect of interface defect on the coating rupturing. In practice, actual spalling failure of TBC is followed by multiple surface cracks that propagate through the top coat and coalesce with interfacial crack between the top coat and the bond coat[22]. Therefore, to design excellent TBCs with high durability, it is necessary to study the effect of the interface cracks on the surface cracks which determines the coalescent of the surface cracks and interface cracks. In this paper, we build a multiple-layers TBCs model which contains pre-existing interfacial defect to investigate the effect of pre-existing interfacial defect on surface cracking. In Section 2, we firstly descript the numerical model for the problem of surface cracks and interfacial defect in TBCs. In Section 3, the crack driving forces for surface cracks are calculated, and moreover the effect of interfacial defect on surface cracks is discussed in detail. Section 4 summarizes the concluding remarks and emphasizes the effect of interfacial cracks on the durability of TBC system.

2. Statement of the problem

Due to the pre-existing interfacial defect after air plasma spraying or the interface cracks induced by thermal stress, the interfacial delamination probably emerges in some small areas, which effects the inevitable following surface cracks and the subsequent coalescent of the surface cracks and interface cracks. A steady state concept for cracks in multilayer structure is essential for many situations, where the crack driving force of surface crack is independent of the tunnel length if the length is enough long. Once the steady state is reached, the crack driving force can be calculated by using a two-dimensional (2D) plane strain model[23]. As a result, a three-dimensional TBCs model with surface cracks and interface defects is reduced to a 2D plane stain model. Fig. 1 shows the 2D plane strain model of steady state multiple surface cracks accompanied with interfacial cracks, in which h, a and W are the ceramic coating thickness, the surface crack length, and the cell model width, respectively. Based on our experimental observation[22], when the distance between adjacent surface cracks is large enough (about ten to twenty times the film thickness), the interaction between neighboring surface cracks can be ignored. Therefore, a unit cell model with single surface crack and interfacial defect can be constructed to simulate the actual TBCs with multiple cracks by setting the W equal twenty times the ceramic coating thickness.

The coordinate system (x, y) is set at the top surface of the film with surface crack, whose length a is along to y-axis. An interface defect with length l is presetting at the top/bond coating interface, the center of which offsets from the y-direction by c.

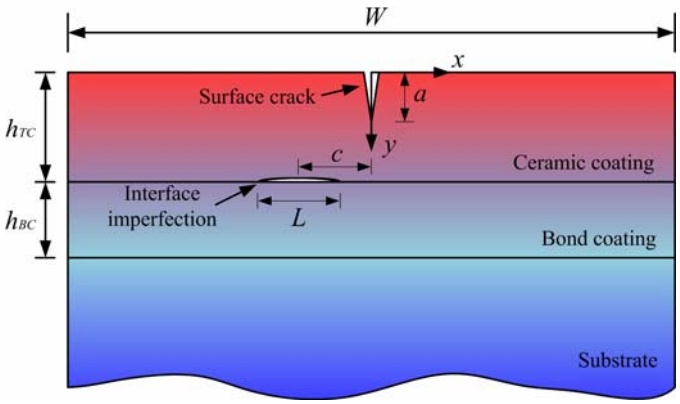

Figure 1. The TBCs model with surface crack in the TC and interfacial crack at TC/BC interface.

Assume a uniform strain is remotely applied to the TBCs system in the x-direction, the remote stress in the top coating is given by

$$\sigma_0 = \frac{\varepsilon_0 E_1}{1-\upsilon_1^2} \tag{1}$$

where E_1, υ_1 are the Young's modulus and Poisson's ratio of top coating. Therefore, the mixed boundary conditions on the surface crack faces can be expressed as

$$\begin{cases} \sigma_{ij}(0,y) = 0, & 0 < y < a \\ u_i(0+0,y) = u_i(0-0,y), & a < y < h \end{cases} \tag{2}$$

where σ_{ij} $(i,j=x,y)$ is the stress component and u_i $(i,j=x,y)$ is the displacement in x-direction or y-direction, respectively.

Moreover, the stress on the interface crack face at interfacial delamination area should be zero and in other area at the interface the displacement should be continuous. The mixed boundary conditions at the interface are shown as

$$\begin{cases} \sigma_{ij}(x,h) = 0, & -c-\dfrac{l}{2} < x < -c+\dfrac{l}{2} \\ u_i(x,h-0) = u_i(x,h+0), & x < -c-\dfrac{l}{2} \text{ and } x > -c+\dfrac{l}{2} \end{cases} \tag{3}$$

The problem can be solved by the superposition technique. The film/substrate system without any cracks is solved first and then added the stresses to the crack faces to represent the applied external loads σ_0. Then the numerical solution for mode I stress intensity factor (SIF) of the surface crack in a film/substrate system without any interfacial defect has been given by Beuth[24]

$$K/\sigma_0\sqrt{h} = 1.1215\sqrt{\pi}\left(a/h\right)^{1/2}\left(1-a/h\right)^{1/2-s}\left(1+\lambda a/h\right) \tag{4}$$

where the λ is a curve fitting parameter which is dependent of a/h, The value of λ also been given by Beuth[24]. The s is the singularity exponent which depends on elastic mismatch, and is the root to

$$\cos(s\pi) - 2\frac{\alpha-\beta}{1-\beta}(1-s)^2 + \frac{\alpha-\beta^2}{1-\beta^2} = 0 \tag{5}$$

where α, β are two non-dimensional Dundurs' parameters representing the material mismatch between adjacent layers[25]. For the plane strain problem, the Dundurs' parameters α, β can be

expressed as

$$\alpha = \frac{\bar{E}_1 - \bar{E}_2}{\bar{E}_1 + \bar{E}_2} \tag{6}$$

$$\beta = \frac{1}{2}\frac{\mu_1(1-2\upsilon_2) - \mu_2(1-2\upsilon_1)}{\mu_1(1-\upsilon_2) - \mu_2(1-\upsilon_1)} \tag{7}$$

where $\bar{E}_i = E_i / \left(1 - v_i^2\right)$, E_i, υ_1 and μ_1 are the plane strain modulus, Young's modulus, Poisson's ratio, and shear modulus of film/substrate systems' components, respectively. For homogeneous materials, the Dundurs' parameters are written as $\alpha = \beta = 0$.

Strain energy release rate (SERR) is another basic concept to study the driving force of an crack. A larger SERR value of the surface crack tip presents the more probability of surface rupturing. The SERR can be calculated by SIF and the Young's modulus of the top coating

$$G = \frac{K^2}{\bar{E}} \tag{8}$$

In present work, the multiple layers TBCs model with pre-existing interface crack has tiny differences with the typical film/substrate system. In detail, the interfacial defect existence may make it difficult to investigate the fracture mechanism in TBCs by using classical fracture mechanism. Fortunately, the finite element method can calculate the value of SIF and SERR accurately. Therefore, the commercial soft ABAQUS is adopted in present work to obtain the effect of the interfacial defect on the surface crack driving force (e.g. SERR). In the preliminary calculation, we found that a relatively small interfacial defect has little influence on the crack mode. In general, the mode II SIF is less than one-tenth of the mode I SIF, which means that the mode I crack dominates the fracture behavior and mode II crack can be ignored in the following analyses. Therefore, the SERR for the surface crack can be written in a similar form with Eq. (4)

$$K / \sigma\sqrt{h} = w(\alpha, \beta, \bar{a}, \bar{L}, \bar{c}) = \eta(\alpha, \beta, \bar{a}, \bar{L}, \bar{c})\bar{w}(\alpha, \beta, \bar{a}) \tag{9}$$

where the function w is the value of normalized SIF of surface crack obtained by FEM, and $\bar{w}$ represents the right expression of Eq. (4), which is determined by the Dundurs' parameters α, β and surface crack length $\bar{a} = a / h$. The revised function η is regarded as the function of the interface crack geometric characteristic, the crack length $\bar{L} = L / W$ and the crack location $\bar{c} = c / W$. Similarly, the SERR can also be written as follow by using the Eq. (8) and Eq. (9)

$$\frac{G\bar{E}}{\sigma^2 h} = Z(\alpha, \beta, \bar{a}, \bar{L}, \bar{c}) = \kappa(\alpha, \beta, \bar{a}, \bar{L}, \bar{c})\bar{Z}(\alpha, \beta, \bar{a}) \tag{10}$$

where the function Z, κ and $\bar{Z}$ represent the SERR value function, the revised function of the interfacial defect and the original SERR function without interfacial defect, respectively.

Since it is intractable to calculate SIF and SERR for an crack in TBCs, the more convenient calculation of SERR is applied in this paper. In the linear elastic fracture mechanics, the SIF and the SERR can be represented by the value of J-integral. Therefore, SERR associated with crack length can be calculated by J-integral method. For a virtual crack advance $\lambda(s)$, the value of J-integral can be calculated by [26]

$$\bar{J} = \int_A \lambda(s)\mathbf{n} \cdot \mathbf{H} \cdot \mathbf{q} dA \tag{11}$$

where dA is the total areas of a layer of elements enclosing the crack tip, $\mathbf{n}$ is the outward normal vector to the corresponding integral contour, and $\mathbf{q}$ is the direction of virtual crack extension, $\mathbf{H}$ is given by

$$\mathbf{H} = \left(W\mathbf{I} - \boldsymbol{\sigma} \cdot \frac{\partial \mathbf{u}}{\partial \mathbf{x}} \right) \tag{12}$$

where W is strain energy.

The finite element code ABAQUS is employed for numerical calculations. A fine mesh near

the crack tip is necessary for the regular finite element method in the typical TBCs model. Eight-node bilinear plane strain quadrilateral reduced integration elements are selected for all three layers except the crack tip region, where very fine mesh of singular elements are constructed. In addition, The J contour integral values are independent to the mesh configuration if the mesh configuration is fine enough around the crack tip. Herein, each layer in TBC is taken to be homogeneous, isotropic and linear elastic materials whose geometry and material properties are $h = h_{TC} = 0.2$ mm , $h_{BC} = 0.1$ mm , $h_S = 30$ mm , $E_{TC} = 60$ GPa , $E_{BC} = 200$ GPa , $E_S = 211$ GPa , $\nu_S = \nu_{BC} = \nu_{TC} = 0.3$ and $W / h = 20$, where the subscripts TC, BC and S represent top coat, bond coat and substrate, respectively.

3. Result and Discussion

In fracture mechanics, SERR at the crack tip can regarded as the driving force of the crack. Therefore, obtaining the SERR value of the surface crack for different lengths can detailedly describe the initiation and propagation of it. Fig.2 shows reduced revised function $\kappa(\bar{a},\bar{L},\bar{c})$ as a function of interfacial defect location for different surface crack length. Noted that the length of presetting interface crack is fixed as a uniform value $\bar{L} = 0.15$ in order to investigate the separate effect of interface crack location on the driving force of surface crack. As discussed earlier, the SERR for the surface crack in the TBCs with interface defect can be written as Eq. (10) which consist two functions, the revised function and the original SERR function without interface defect, respectively. In Fig.2, the value of $Z(\alpha,\beta,\bar{a},\bar{L},\bar{c}) / \bar{Z}(\alpha,\beta,\bar{a})$ in Eq. (10) for a constant $\bar{L} = 0.15$ equals to the normalized SERR $G / \bar{G}$. Therefore, the reduced revised function $\kappa(\bar{a},\bar{L},\bar{c})$ (α,β is constant since the material parameter is uniform) for $\bar{L} = 0.15$ can be obtained from the normalized SERR. The $\kappa(\bar{a},\bar{L},\bar{c})$ for $\bar{L} = 0.15$ is always larger than 1 for all surface crack length, a / h , which means the interface defect always promotes the initiation and propagation. This promotion is the result of the constrain reducing for the top coating caused by the interface defect. The close analyses have also been made by Tsui *et al.*[27] and Thouless *et al.*[28].

Noted that the $\kappa(\bar{a},\bar{L},\bar{c})$ curve for small a / h slightly deviates from the dash line standing for the SERR function without interface defect $\bar{Z}(\alpha,\beta,\bar{a})$ while the $\kappa(\bar{a},\bar{L},\bar{c})$ for relatively large a / h is much bigger ,which means that the interface defect effects the propagation of the surface crack more dramatically than the initiation. That's to say, the initiation of the surface crack appears to be impendent on the interface defect offset while the propagation intensively depend on the interface defect location. In addition, when the surface crack approach to the interface, the $\kappa(\bar{a},\bar{L},\bar{c})$ seems to decrease slightly (i.e. the curves for a / h =0.8 or 0.9 is in a low degree compared to that for a / h =0.6 or 0.7).

As shown in Fig.2, the interface defect offset $\bar{c}$ is a significant factor to affect the propagation of the surface crack. For the large offset $\bar{c}$, the $\kappa(\bar{a},\bar{L},\bar{c})$ is approach to 1, indicating the variation of SERR is exactly similar to the solution for perfect interface. Therefore, in this case, the remote interface defect appears to have relatively little influence on the surface cracking behavior. Conversely, when the offset is equal to zero, the $\kappa(\bar{a},\bar{L},\bar{c})$ seems to largely deviate from the dash line(i.e. the solution for perfect interface). In other words, the interface defect under the surface crack may promote the surface crack propagation more vigorously than the remote one. As a result, the surface cracks centralizing in some areas under of which there exists potential interface cracks may propagate much faster. Then they easily penetrate into the interface and coalesce with the interface cracks, which lead the eventual spalling of the ceramic coating. Therefore, we consider the interface defect as a significant reason for the premature failure of TBCs during service.

As the absolute value of $\bar{c}$ enlarges to a critical value, the $\kappa(\bar{a},\bar{L},\bar{c})$ for $\bar{L} = 0.15$ becomes

asymptotic to 1. Therefore, $Z(\alpha,\beta,\bar{a},\bar{L},\bar{c})$ seems to approach to $\bar{Z}(\alpha,\beta,\bar{a})$ which indicates the influence of interface can be ignored. In present model, the critical offset value is about 0.15 above which the interaction between surface crack and interface defect can be ignored. Moreover, a interesting finding in Fig.2 is that the $\kappa(\bar{a},\bar{L},\bar{c})$ for $a/h=$ 0.8 and 0.9 exhibits an irregular convex at $\bar{c}=\pm 0.05$. This irregular effect on surface cracking behavior is related to the extra deviating driving force induced by an asymmetric loading and restraint which are a result of the offsetting interface defect. Next part we will discuss this irregular behavior.

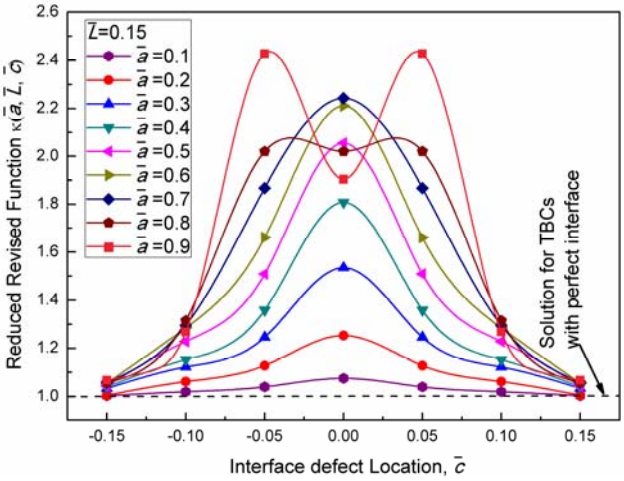

Figure 2. The reduced revised function $\kappa(\bar{a},\bar{L},\bar{c})$ as a function of interface defect location for different surface crack length.

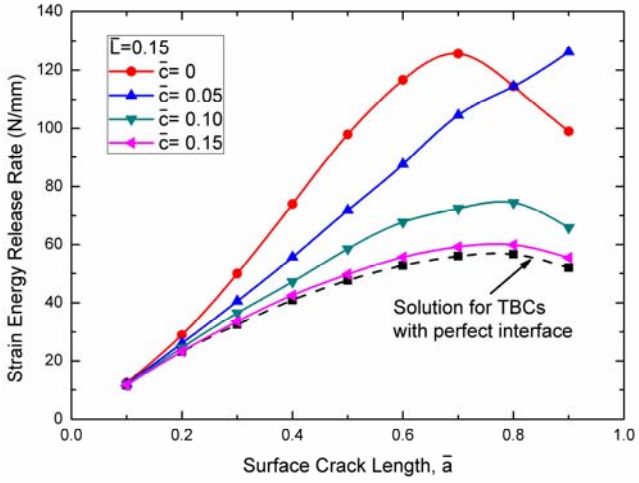

Figure 3. The SERR as a function of surface crack length for different interface defect offset.

Figure 3 shows the variations of SERR with normalized crack length a/h for the different offset of the interfacial defect. Moreover, SERR for the TBCs model with perfect interface is also plotted in Figure 3 for comparing. It is seen that the SERR for perfect interface rises to the maximum value as surface crack propagates and then drops as the crack approaches to interface, which coincides with the results obtained by Beuth[24]. Moreover, it is interesting to find that the overall trend of SERR curve in Figure 3 would change as the offset decrease. For the remote defect (e.g. $\bar{c}=0.15$), the curve of is much similar to the solution for perfect interface which, as previous described, rises to the maximum value as surface crack propagates and then drops as the crack approaches to interface. However, when the defect offset diminishes to 0.05, the SERR curve turns to monotonously ascend (e.g. $\bar{c}=0.05$). Then, Continue to decrease the offset of the defect, the

oscillation of SERR curve appears again (e.g. $\bar{c} = 0$) and the SERR reduces to a relatively low value. This behavior seems to be a result of the asymmetric loading and restraint causing by the offset of interface defect. An asymmetric loading and restraint may induce the extra deviating force for the surface crack. Therefore, the driving force would continue to increase instead of dropping as the crack approaches to interface, which may facilitate the deviation of the surface crack when it approaches to interface. Obviously, it can explain why the SERR curve for $a/h =$ 0.8 and 0.9 exhibit irregular convex at $\bar{c} = \pm 0.05$.Interestingly, this deviation has been observed by present researchers in their experiments[6]. If the defect is remote from the surface crack, its influence on surface crack is much small so that the deviating force is inconspicuous. Therefore, for the remote defect (e.g. $\bar{c} = 0.15$), the curve of SERR do not appear monotonous increasing.

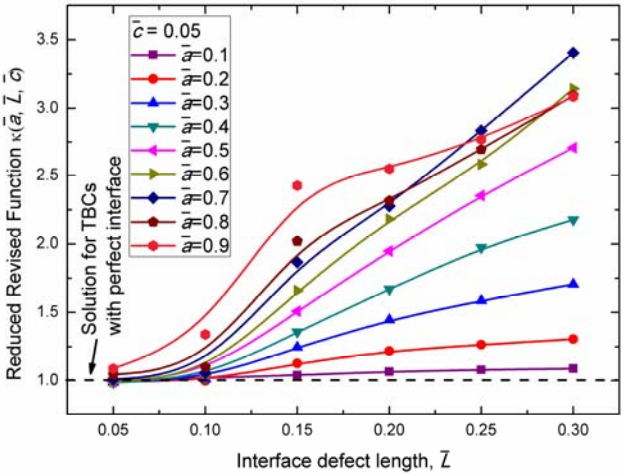

Figure 4. The reduced revised function $\kappa(\bar{a}, \bar{L}, \bar{c})$ as a function of interface defect length for different surface crack length.

The reduced revised function $\kappa(\bar{a}, \bar{L}, \bar{c})$ as a function of normalized surface crack length for different interfacial defect length is plotted in Fig. 4. In present figure, the interface defect offset $\bar{c}$ has been fixed as 0.05 and the surface crack length has been enlarged in order to simulate the spread of interface defect during the service of TBCs. Since the interface defect location has been fixed, the altering of $\kappa(\bar{a}, \bar{L}, \bar{c})$, which is obtained, as mentioned earlier, by the normalized SERR, can separately demonstrate the effect of defect length. In Fig. 4, it is seen that interfacial defect length is also a significant factor that affects the surface crack driving force.

For a small interface defect, the interface defect seems to have little influence to the surface crack. Noted that when the $\bar{L}$ is about 0.05, the value of SERR is close to the solution for perfect interface (the dash line in Fig. 4), which indicates that there may be an asymptotic curve for very low values of interface defect length. In other words, in present model, when the normalized length of interface defect with offset $\bar{c} = 0.05$ is smaller than 0.05, the interface can be regarded as a perfect one. For a relatively large interface defect, the value of $\kappa(\bar{a}, \bar{L}, \bar{c})$ rises to a high degree. For example, when the surface crack propagates about seventy percent of the ceramic coating, the $\kappa(\bar{a}, \bar{L}, \bar{c})$ for the $\bar{L} = 0.3$ is about 3.3, which indicate an interface defect with a length $\bar{L} = 0.3$ would make the driving force of surface crack more than three times larger since the substrate restrain is greatly reduced due to the interface defect. Obviously, the facilitation of the large scale interface defect may induce the premature coalescent of the surface crack and the interface crack, which contributes to the spalling of the ceramic coating. Therefore, a well bonded interface should be ensured in order to enhance the durability of the TBCs.

Compared to the Fig. 2, it seems that the effect of lengthening the interface defect length on the surface crack driving force is very similar to the effect of diminishing the offset of the interface

defect. They both promote the propagation of surface crack dramatically. Interestingly, as the interface defect length enlarges, the transformation of the SERR curves from oscillation (e.g. $\overline{L}=0.05$) to monotone (e.g. $\overline{L}=0.15$) and then back to oscillation (e.g. $\overline{L}=0.25$), which, as previous discussed, is induced by the extra deviating force, can also been found in Fig. 4.

As discussed above, it is concluded that the interface defect would promote the surface cracking behavior by increasing the SERR around the crack tip. Herein, it is generally accepted that the maximum increment of SERR induced by the interface defect is critical to estimate emanation of surface crack. Fig. 5 shows the maximum normalized SERR increment as a function of interfacial defect length and location. Two most important characteristics of interface defect, the length and the location, have been taken into consideration to investigate the their combined effect on surface crack. As shown in Fig. 5, the maximum normalized SERR increment for a remote interface defect ($\overline{c}=0.15$) is near to zero for a relatively small critical defect length (e.g. when $\overline{L}$ is less than 0.15), which means the remote and small defect has less potential to affect the surface cracking behavior. However, when interface defect is closer to the surface crack(e.g. $\overline{c}=0.05$), the critical defect length below which the defect can be ignored correspondingly decreases (e.g. $\overline{L}$ is less than 0.05). The most extreme situation is that the interface defect locates under the surface crack, in which the small defect cannot be ignored (as the black line in Fig. 5). In general, the maximum normalized SERR increment for a central interface defect is higher than the counterpart for the offsetting defect excepted the appearance of the extra deviating force for the surface crack, as discussed earlier, induced by asymmetric loading and restraint. The oscillation of the maximum normalized SERR increment curve stands for the extra deviating force.

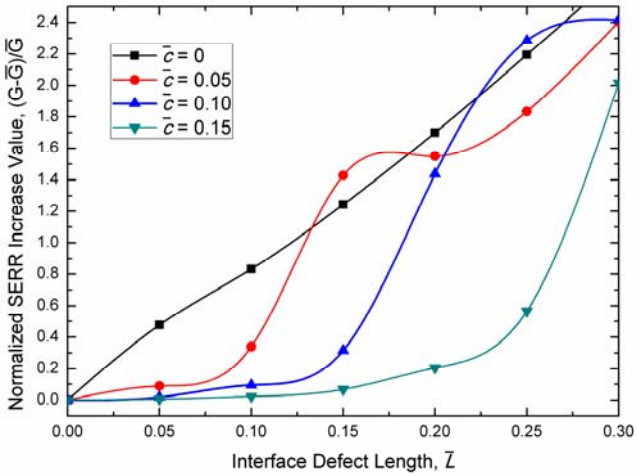

Figure 5. The maximum normalized SERR increment as a function of interfacial defect length and location.

4. Conclusions

The effects of interface defect on the surface fracture behavior of thermal barrier coating system (TBCs) are investigated in this work. The results show that the two important characteristic parameters, defect location and defect length, both have a significant influence on the driving force of surface crack. It is concluded a surface crack initiated above an interface defect propagates more easily since the enhancement of surface crack driving force is largest for the defect directly beneath the surface crack. Similarly, the surface crack propagates easier as the defect length increases. In present work, the critical value of the defect offset (below which the effect of an interface defect can be ignored) has been obtained and so does the critical value of defect length. By understanding the effect of the interface detect on the surface crack and using the critical value of the defect offset and defect length, the surface cracking behavior can be partially controlled. It is beneficial for

improving the durability of TBCs no matter by increasing the surface crack density to enlarge the strain tolerance of ceramic coating or reducing the surface crack to prolong the spalling of the ceramic coating.

Acknowledgements. This work is supported by the State 973 Program of China (2013CB035700), NSFC (11002104, 11021202, 11272259 and 11172227) and MOE fund.

References

[1] D. Clarke, C. Levi, Materials design for the next generation thermal barrier coatings. Annual review of materials research, 33 (2003) 383-417.
[2] R. Vaßen, M.O. Jarligo, T. Steinke, D.E. Mack, D. Stöver, Overview on advanced thermal barrier coatings. Surface and Coatings Technology, 205 (2010) 938-942.
[3] N.P. Padture, M. Gell, E.H. Jordan, Thermal barrier coatings for gas-turbine engine applications. Science, 296 (2002) 280.
[4] I. Zaplatynsky, Thermal expansion of some nickel and cobalt spinels and their solid solutions, National Aeronautics and Space Administration, 1971.
[5] T. Xu, S. Faulhaber, C. Mercer, M. Maloney, A. Evans, Observations and analyses of failure mechanisms in thermal barrier systems with two phase bond coats based on NiCoCrAlY. Acta materialia, 52 (2004) 1439-1450.
[6] Y.C. Zhou, T. Tonomori, A. Yoshida, L. Liu, G. Bignall, T. Hashida, Fracture characteristics of thermal barrier coatings after tensile and bending tests. Surface and Coatings Technology, 157 (2002) 118-127.
[7] A.G. Evans, D. Mumm, J. Hutchinson, G. Meier, F. Pettit, Mechanisms controlling the durability of thermal barrier coatings. Progress in Materials Science, 46 (2001) 505-553.
[8] W. Tie-Jun, Micro-and macroscopic damage and fracture behaviour of welding coarse grained heat affected zone of a low alloy steel: Mechanisms and modelling. Engineering Fracture Mechanics, 45 (1993) 799-812.
[9] G.W. Schulze, F. Erdogan, Periodic cracking of elastic coatings. International Journal of Solids and Structures, 35 (1998) 3615-3634.
[10] J.J. Vlassak, Channel cracking in thin films on substrates of finite thickness. International Journal of Fracture, 119 (2003) 299-323.
[11] X. Fan, W. Zhang, T. Wang, G. Liu, J. Zhang, Investigation on periodic cracking of elastic film/substrate system by the extended finite element method. Applied Surface Science, 257 (2011) 6718-6724.
[12] X.L. Fan, W.X. Zhang, T.J. Wang, Q. Sun, The effect of thermally grown oxide on multiple surface cracking in air plasma sprayed thermal barrier coating system. Surface and Coatings Technology, (2012).
[13] W. Zhang, X. Fan, T. Wang, The surface cracking behavior in air plasma sprayed thermal barrier coating system incorporating interface roughness effect. Applied Surface Science, (2011).
[14] J.R. Rice, Elastic fracture mechanics concepts for interfacial cracks. J. Appl. Mech.(Trans. ASME), 55 (1988) 98-103.
[15] D. Mumm, A. Evans, On the role of imperfections in the failure of a thermal barrier coating made by electron beam deposition. Acta materialia, 48 (2000) 1815-1827.
[16] D.L. Ruckle, Plasma-sprayed ceramic thermal barrier coatings for turbine vane platforms. Thin solid films, 73 (1980) 455-461.
[17] R.A. Miller, Current status of thermal barrier coatings--An overview* 1. Surface and Coatings Technology, 30 (1987) 1-11.
[18] Y. Bai, Z. Han, H. Li, C. Xu, Y. Xu, Z. Wang, C. Ding, J. Yang, High performance nanostructured ZrO2 based thermal barrier coatings deposited by high efficiency supersonic plasma

spraying. Applied Surface Science, (2011).
[19] O. Trunova, T. Beck, R. Herzog, R.W. Steinbrech, L. Singheiser, Damage mechanisms and lifetime behavior of plasma sprayed thermal barrier coating systems for gas turbines—Part I: Experiments. Surface and Coatings Technology, 202 (2008) 5027-5032.
[20] S.H. Song, P. Xiao, L.Q. Weng, Evaluation of microstructural evolution in thermal barrier coatings during thermal cycling using impedance spectroscopy. Journal of the European Ceramic Society, 25 (2005) 1167-1173.
[21] B. Zhou, K. Kokini, Effect of surface pre-crack morphology on the fracture of thermal barrier coatings under thermal shock. Acta materialia, 52 (2004) 4189-4197.
[22] X.L. Fan, R. Xu, W.X. Zhang, T.J. Wang, Effect of periodic surface cracks on the interfacial fracture of thermal barrier coating system. Applied Surface Science, 258 (2012) 9816-9823.
[23] J. Hutchinson, Z. Suo, Mixed mode cracking in layered materials. Advances in applied mechanics, 29 (1992) 191.
[24] J. Beuth, Cracking of thin bonded films in residual tension. International Journal of Solids and Structures, 29 (1992) 1657-1675.
[25] D. Dugdale, Yielding of steel sheets containing slits. Journal of the Mechanics and Physics of Solids, 8 (1960) 100-104.
[26] ABAQUS User's Manual, Dassault Systèmes Simulia Corporation, (2009).
[27] T.Y. Tsui, A.J. McKerrow, J.J. Vlassak, Constraint effects on thin film channel cracking behavior. Journal of materials research, 20 (2005) 2266-2273.
[28] M. Thouless, Z. Li, N. Douville, S. Takayama, Periodic cracking of films supported on compliant substrates. Journal of the Mechanics and Physics of Solids, (2011).

Experimental Observation and Constitutive Equations of Fracture Propagation

Alexander Chudnovsky[1], Zhenwen Zhou[1], Haiying Zhang[1,*]

[1] Department of Civil and Materials Engineering, University of Illinois at Chicago, 60607, USA
* Corresponding author: haiyin@uic.edu

Abstract There is a long list of empirical slow crack growth (SCG) equations that present the crack propagation rate as a function of stress intensity factor (SIF) or energy release rate (ERR). Experiments with crack growth through a heterogeneous stress field reveal the limitations of such type of equations resulting from existence of a process zone (PZ) surrounding the crack. PZ is a material "defense" against stress concentration caused by the crack and is commonly observed in most of engineering materials. It plays an important role in determination of the direction and rate of fracture propagation. Therefore, the PZ and crack are treated as two coupled elements of one Crack Layer (CL) system and CL propagation is represented by two coupled possesses: (i) the PZ evolution by transformation of the original material into a "damaged" and often anisotropic PZ material and (ii) crack growth into PZ. The CL driving forces are introduced as the negative derivative of Gibbs free energy with respect to CL geometrical parameters. The constitutive equations of CL propagation are formulated in form of simple relations between the crack and PZ growth rates and corresponding thermodynamic forces. Qualitative analysis of these equations suggests two distinctly different patterns of CL propagation: continuous and discontinuous, stepwise growth. A special experimental setup and test material have been selected to simplify and examine the proposed constitutive equations of CL growth. CL model provides a very good agreement with a large set of experimental data at various load levels, temperatures and specimen geometries.

Keywords Crack layer model, slow crack growth, process zone, constitutive equations

1. Introduction

Crack in engineering materials formed under fatigue and creep conditions usually appears as a narrow cut with small amplitude random deviations from a straight or slightly curved trajectory. A close observation of such crack reveals a presence of a process zone (PZ) (also called damage zone, plastic deformation zone, etc.) that precedes and surrounds the crack. Depending on material chemical composition and morphology, temperature, loading rate, specimen geometry, etc. various types of micro defects such as crazes, shear bands, microcracks, micro-voids constitute PZ. In general, micro-defects are strain localizations on micro scale and based on their orientation one can distinguish brittle, such as crazes and micro-cracks, and ductile like shear bands and micro-voids, types of damage. The micro-defects are commonly formed in response to stress concentration, and shield the vicinity of the crack front from high elastic stresses by increase of an effective (inelastic) material compliance. The crack growth is closely coupled with formation and evolution of the micro-defects population within PZ. A system of coupled crack and PZ is referred to as Crack Layer (CL).

There is a strong interaction between micro-defects in a vicinity of the crack front and the crack [1–4]. It results in significant modification of the crack tip fields. Apparently, it also affects the stress intensity factor (SIF) K. Figure 1 illustrates the effect of micro-cracking (displacement discontinuities) on SIF. An individual micro-crack is modeled as a displacement discontinuity across an elementary segment (area in 3D) with orientation $\underline{n}$ and displacement jump $\underline{b}$. In the specific example shown in Figure 1 all micro-cracks are considered to be parallel to the crack and have opening in the normal direction. The arrays of curves emanating from the crack tip forward and backward present contours of equal level of the mode I SIF Green's function $G_1^{SIF}(\underline{\xi})$ due to unit normal displacement dipole with $\underline{n}(0,1)$ and $\underline{b}(0,1)$ at the point $\underline{\xi}$ [3–5]. The continuous lines indicate SIF amplification effect due to the discontinuities located on the lines in front of the crack; whereas the two "butterfly wings" of dotted lines show the reduction of SIF, i.e., shielding effect of the discontinuities located on the lines

on both sides of the crack. The numbers above the lines indicate the magnitude of amplification and reduction of SIF. The external solid line indicates schematically the boundary of the process zone and therefore CL.

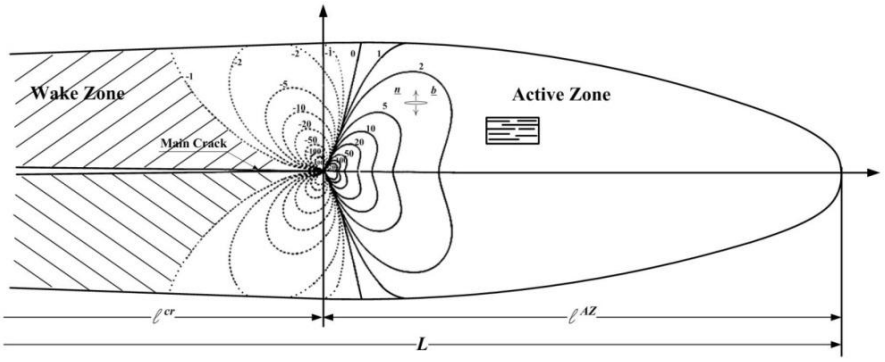

Figure 1. Dimensionless Mode-I SIF Green's Function due to a unit normal displacement dipole with orientation (θ = 0°) with respect to the x-axis.

By distributing the individual micro-cracks and passing to a continuum damage, we introduce damage density as a bivector $\rho(\underline{\xi})$ that represents the total micro-cracks area per unit volume (with dimensions $[\rho] = mm^2/mm^3$). There is a domain of PZ, where the defects constituting PZ strongly interact with crack by shielding and/or amplifying the crack tip fields. The crack in turn causes the new defects formation and growth, i.e., $\dot{\rho} \geq 0$ in that domain. Such domain is referred to as active zone (AZ) of CL. It leads to material degradation in the immediate vicinity of crack front and crack movement into PZ. As the crack advances through AZ, the latter "moves" away from the crack by forming new defects and leaves behind a wake zone (WZ) constituted by the defects that remain after unloading of AZ. Thus, CL propagation occurs as AZ "movement" in material frame of reference and crack advancement into AZ.

The total SIF is the sum of SIF K_I^0 due to remote load and the increment of SIF due to distributed micro-cracks with opening $\underline{b}$ dependent on the main crack – micro-cracks array interaction [3–5]:

$$K_I^{tot} = K_I^0 + \int_V G_I^{SIF}(\xi_i) \cdot b(\xi_i) \wedge \rho(\xi_i) dV \,. \tag{1}$$

The calculations suggest that the shielding effect (a negative SIF increment) is stronger than the amplification and the total SIF in some cases is vanishing [4]. In such cases the "beak" type crack tip opening displacement profile is observed [1].

2. Experimental and Results

To observe the details of CL evolution a set of creep tests was conducted at various loads and temperatures. The creep testing machine equipped with high temperature chamber with four creep stations and two observation windows, pneumatic system of graduate load application and continuous displacement monitoring device is used for tests (see Figure 3 (a)).

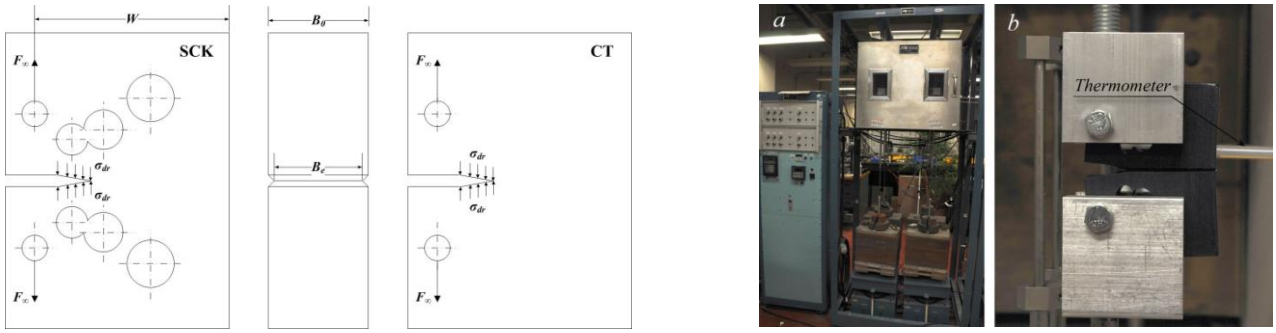

(b) (a)

Figure 3. (b) The geometry and loading of SCK and CT specimens; (a) Slow crack growth test setup.

Various specimen geometries have been used in the tests. One is the standard compact tension (CT) specimen. Another is a specially design stiff constant-*K* (SCK) specimen. SCK specimen poses the highest stiffness among comparable specimen geometries and provides a constant *K* within the crack size range $0.15 < a/W < 0.4$. The diameters and locations of holes are designed to maintain the constancy of SIF while crack is propagating. The side grooves are introduced to reduce the plane stress effect within the surface layers and guide the crack growth along the plane of symmetry. The CT specimen has the same shape and dimension as that in SCK, but does not have holes, as shown in Figure 3 (b). Both types CT and SCK specimens were machined from a commercial large diameter HDPE pipe with $3''$ wall thickness. The SIF is continuously increasing with crack growth in CT specimen. We selected HDPE material for this study since it displays the simplest, but not trivial PZ geometry observable in fracture experiments: a narrow wage shape domain of cold drawn fibers and membranes with sharp boundaries separating PZ and original bulk material.

Figure 4 shows the records of the load-point displacement vs. time monitored in the creep tests at various loads (SIFs) and temperatures. Curve *a* in Figure 4 (initial SIF: $K_0 = 10MPa \cdot \sqrt{mm}$ and $T = 80^{o}\mathrm{C}$) clearly shows a transition from continuous to stepwise growth. The same but subtler transition is also observed in Curve *b* (initial SIF $K_0 = 12MPa \cdot \sqrt{mm}$ and the same temperature compared to Curve *a*). At the same temperature, if the SIF is increased to $K_0 = 18MPa \cdot \sqrt{mm}$ (initial SIF), a pure stepwise growth is observed as displayed by Curve *c*. The length of individual step in CT specimen is continuously increasing due to the increasing SIF in contrast with that in SCK specimen (reported in [6]). However, there are no visible steps in load-point displacement record (Curve *d*), even for a significantly higher load ($K_0 = 48MPa \cdot \sqrt{mm}$ initial SIF), if the temperature is reduced to room temperature ($T = 23^{o}\mathrm{C}$),.

The continuous, discontinuous as well as transitional mechanisms of SCG are revealed even more explicitly by CL side view and fracture surfaces. For example, a homogeneous and continuous CL growth occurs at an elevated temperature with a much lower initial SIF ($K_0 = 10MPa \cdot \sqrt{mm}$) (see Figure 5 (a)). The upper picture in Figure 5 (a) presents a general view of CL developed during 290 hours of creep with initial SIF $K_0 = 10MPa \cdot \sqrt{mm}$ at 80°C. There are no steps as well, rather monotonically decreasing width of the triangular CL and crack opening toward a very weakly visible PZ tip. The bottom picture shows a homogeneous surface without any striations. At the very end, we can see a smooth strip that corresponds to the last process zone broken in liquid nitrogen.

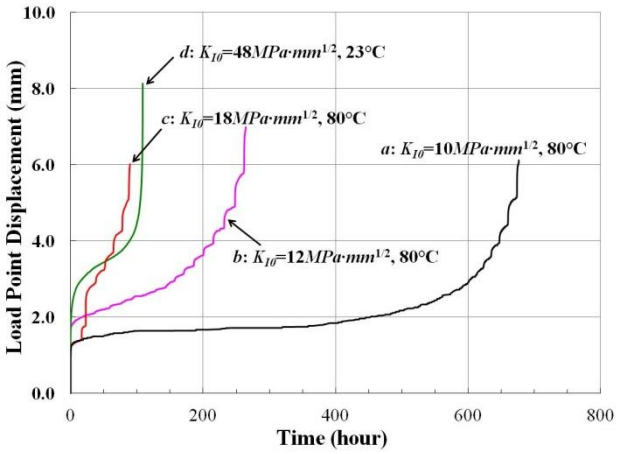

Figure 4. Load-point displacement vs. time recorded in creep test conducted at *a*) $K_0 = 10MPa \cdot \sqrt{mm}$, $T = 80^{\circ}\mathrm{C}$; *b*) $K_0 = 12MPa \cdot \sqrt{mm}$, $T = 80^{\circ}\mathrm{C}$; *c*) $K_0 = 18MPa \cdot \sqrt{mm}$, $T = 80^{\circ}\mathrm{C}$; *d*) $K_0 = 48MPa \cdot \sqrt{mm}$, $T = 23^{\circ}\mathrm{C}$.

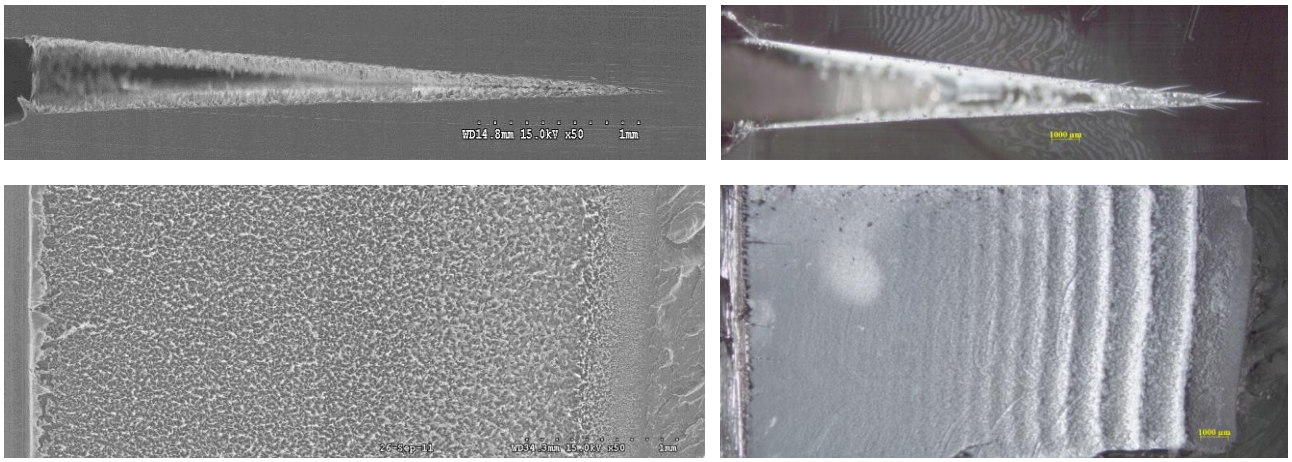

(a) (b)

Figure 5. CT specimens tested at 80°C with initial $K_0 = 10MPa \cdot \sqrt{mm}$: (a) tested for 290 hours, Upper: side view; Lower: fracture surface. (b) tested for 680 hours, Upper: side view; Lower: fracture surface.

The striking observation is that, given the same testing conditions ($K_0 = 10MPa \cdot \sqrt{mm}$, 80°C), if the test is conducted longer (680 hours), a transition from continuous to stepwise growth occurs. The upper picture in Figure 5 (b) depicts a monotonically decreasing opening of crack toward the tip, and pairs of symmetrical "flankers" emanating from two sides of the boundary in the region close to the crack tip. The positions of flankers correspond to white shining striations observed in the lower image, and are signs of discontinuous growth. This evolution from continuous to stepwise growth is manifested in the lower image in such a way that fracture surface first shows homogeneity then striations gradually appear with a wider and wider spacing due to increasing SIFs.

When the initial SIF is increased to certain level, the discontinuous fracture propagation takes place from the beginning. It is illustrated in Figure 6 that shows CL in a CT specimen tested at 80°C with initial SIF $K_0 = 18MPa \cdot \sqrt{mm}$ (Note: the sample was step loaded from $K = 12MPa \cdot \sqrt{mm}$ to $K = 18MPa \cdot \sqrt{mm}$ during a short period, and the latter is considered as the initial SIF.). A wedge-type pulsating domain indicates a discontinuously CL grown with six well defined steps in upper image

(the very first step is neglected for reason addressed above). Five steps are filled with drawn and broken fibers. The sixth one, a weakly visible and elongated wedge type domain, is the process zone with freshly drawn intact fibers. The fibrillated process zone is separated by a sharp boundary from a uniform grey domain of the original HDPE. It is also obvious that five completed steps exhibit an increasing size of PZ, in contrast with an equal size PZ in SCK specimen [6].

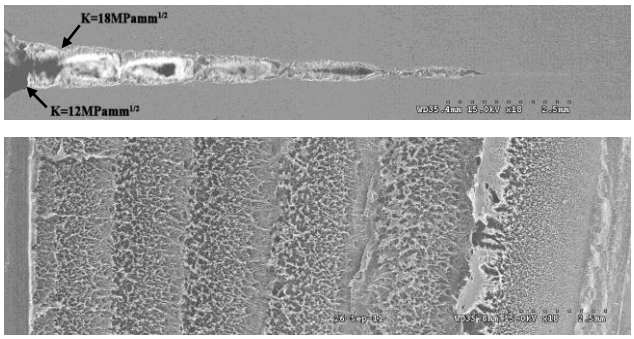

Figure 6. CL in CT specimen tested at 80°C with an initial SIF $K_0 = 18MPa \cdot \sqrt{mm}$ for 90 hours, Upper: side view; Lower: fracture surface (18×).

The data presented above clearly indicate that there are two different mechanisms of SCG: continuous and discontinuous ones. The transition from continuous to discontinuous SCG strongly depends on stress and temperature. A SCG mechanisms map has been proposed and discussed in [6, 7]. The equilibrium process-zone sizes are recorded using micrographs similar to that shown in Fig.6 and used for evaluation of CL parameters. Details of such work are presented in the accompanying paper [8].

3. Constitutive Equations of CL Model

As stated above, CL in PE poses the simplest PZ that displays the characteristic features of PZ evolution. Therefore, we use it as a showcase for formulation of CL constitutive equations.

3.1. Crack Layer Thermodynamic Forces

The active zone of CL in PE has narrow wedge shape geometry with a sharp boundary separating PZ from the surrounding original material (see upper Fig.5a). It consists of cold drawn fibers connected with original material. The crack propagation is the process of breaking fibers under creep condition and forming a fracture "surfaces" (see lower Fig 5a). The width of CL is very small in comparison to the CL length. Therefore we employ the conventional Fracture Mechanics formalism in modeling the external with respect to CL domain. However, addressing the fracture propagation through AZ we use an effective continuum with properties reflecting discrete fibrillated and oriented AZ material. In energy balance, we also consider the energy of transformation of the original material into cold drawn, highly oriented structure of PZ. For such analysis, it is convenient to decompose the specimen with CL into a specimen with CL cutoff and a thin wedge shape CL domain with variable width ω_0 of original material that undergoes cold drawing in process of PZ formation (see Figure 8). The stress analysis problem shown in Figure 8 (a) is presented as superposition of the same specimen geometry and external load with a cut of CL. The mechanical interaction between AZ of CL and the specimen is taken into consideration by application of the drawing stress σ_{dr} along the boundaryof AZ since there is a mechanical equilibrium between the drawn and original materials along that boundary (see Figure 8,b). The second part of the superposition is CL cutoff with stress σ_{dr} acting on the AZ from the specimen side (Figure 8,c). The width of AZ in the reference configuration ω_0 is a function of

location x, $0 \le x \le \ell^{AZ}$ within AZ and time t, since AZ evolves in time: $\omega_0 = \omega_0(x,t)$. Fig 8a should be AZ instead of PZ

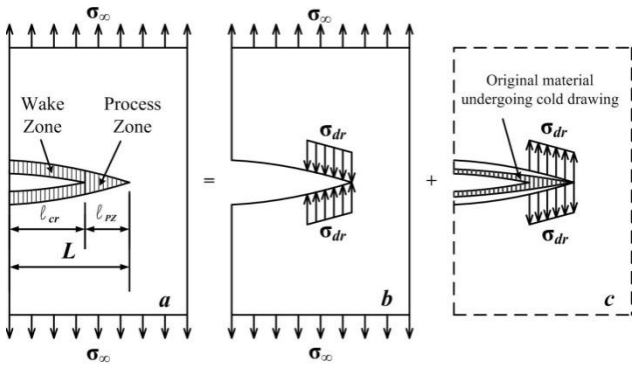

Figure 8. Decomposition of the stress analysis problem of CL

The width of AZ in actual configuration (after drawing) is $\omega = \lambda \cdot \omega_0$ (λ is the natural draw ratio). Thus, the displacement discontinuity in normal to the crack direction due to cold drawing is $(\lambda - 1)\omega_0$. To determine the amount of material that undergoes cold drawing and builds up AZ, i.e., the width ω_0, we consider crack opening displacement (COD) as an approximation of the opening of a slit in the specimen with CL cutoff. The approximation is quite accurate due to presence of a small parameter: the ratio of the width over the length of the slit. Then, we make use of conventional Fracture Mechanics formalism and compute COD for the boundary value problem depicted in the Figure 8b. Thus, ω_0 is found from the continuity conditions of the original problem: the COD $\delta(x, t)$ in the specimen with PZ cutoff and the traction σ_{dr} along AZ boundary should be equal to the displacement discontinuity in drawing process within AZ:

$$\omega_o(x,t) = (\lambda - 1)^{-1} \cdot \delta(x,t)\,. \tag{2}$$

The Eq. (2) establishes the functional relation between the width ω_0 and COD in the specimen and loading shown in the Figure 8b. The COD depends on applied load σ_∞, σ_{dr} and the specimen dimensions W, crack length ℓ^{cr}, AZ length ℓ^{AZ} and CL lengths L ($L = \ell^{cr} + \ell^{AZ}$). Thus, in this case, we have only two independent geometrical parameters of CL (ℓ^{cr} and ℓ^{AZ}), since ω_0 is not an independent one. That is the reason for simplification of CL in PE: it is reduced to two-parameter model. The stationary state of a solid with two-parameter CL is determined by the minimum of the total Gibbs potential G_{tot} for the problem of Fig 8a. Based on the decomposition of Fig. 8, the total Gibbs potential is the sum of the Gibbs potentials of the specimen with CL cutoff G_0 and the PZ potential G_{PZ} illustrated in Figure 8:

$$G_{tot} = G_0(\sigma_\infty, T, \sigma_{dr}; L, \ell^{AZ}, W) + G_{PZ}(\sigma_{dr}; \ell^{cr}, \ell^{AZ}, T)\,. \tag{3}$$

The Gibbs potential of PZ in turn consists of the wake zone G_{WZ} and active zone G_{AZ} potentials (see the definitions on WZ in Figure 1). AZ consists of homogeneous drawn material with properties different from that of the surrounding original material. It is also separated from the original by distinct boundary with drawing stress acting along it. As a result, the AZ Gibbs potential can be presented as:

$$G_{AZ} = \gamma^{tr} \cdot V_{AZ}\,. \tag{4}$$

The multiplier γ^{tr} in Eq. (4) stands for the specific energy of transformation of a unit mass of original material into the oriented drawn state under drawing stress σ_{dr}: $\gamma^{tr} = g^{tr}(T) - g^0(T)$, where the Gibb potential density is defined as $g(\sigma,T) = f(\varepsilon,T) - w$, where $f(\varepsilon,T)$ is the strain energy density and w stands for work density [9].

The potential of WZ is different in two ways: 1) it does not contain the strain energy of the stretched

fibers, since the crack is traction free; and 2) it contains the surface energy term of the crack faces:

$$G_{WZ} = \gamma_0^{tr} \cdot V_{PZ} + \gamma \cdot \ell^{cr} . \tag{5}$$

Finally, the total Gibbs potential can be expressed as follows:

$$G_{tot} = G_0(\sigma_\infty, \sigma_{dr}; L, \ell^{AZ}, W) + \gamma^{tr} \cdot V_{AZ}(\sigma_{dr}; \ell^{cr}, \ell^{AZ}) + \gamma_0^{tr} \cdot V_{WZ}(\ell^{cr}, L) + \gamma \cdot \ell^{cr} . \tag{6}$$

We compute the volume V^{AZ} of AZ material in the reference state by integrating the AZ width, which is expressed in terms of total COD in the specimen with PZ cutoff (Eq. (2)):

$$V^{AZ} = B_{eff} \int_{\ell^{cr}}^{L} \omega_o(x) dx = \frac{B_{eff}}{\lambda - 1} \int_{\ell^{cr}}^{L} \delta_{tot}\left(x; \ell^{cr}, \ell^{AZ}, W; \sigma_\infty, \sigma_{dr}\right) dx . \tag{7}$$

The total COD δ_{tot} in Eq. (7) is obtained as the superposition of COD $\delta_\infty = \delta_\infty(\sigma_\infty, L)$ due to remote load σ_∞ and crack "closure" $\delta_{dr} = \delta_{dr}(\sigma_{dr}; \ell^{cr}, \ell^{AZ})$ by the traction σ_{dr} acting along AZ boundary as shown in Figure 8.

The thermodynamic forces X^{AZ} and X^{CR} responsible for AZ (ℓ^{AZ}) and crack (ℓ^{cr}) growth are expressed as the partial derivative of total Gibbs potential G_{tot} with respect to corresponding parameters ℓ^{cr} and ℓ^{AZ}, since they are the only independent geometrical characteristics of CL:

$$X^{CR} = -\frac{\partial G_{tot}}{B_{eff} \partial \ell^{cr}}; \qquad X^{AZ} = -\frac{\partial G_{tot}}{B_{eff} \partial \ell^{AZ}} . \tag{8}$$

The derivative with respect to crack length ℓ^{cr} of the first term of G_{tot} decomposition Eq. (6) is zero, when CL length L is fixed. The derivative of the second and third terms of Eq. (6) is the energy release rate (ERR) J_1^{cr} due to crack extension into PZ, when PZ is stationary (L is constant); and the derivative of the fourth term is simply 2γ. Thus, the thermodynamic force reciprocal to crack length is:

$$X^{CR} = J_1^{cr} - 2\gamma . \tag{9}$$

We compute the thermodynamic force reciprocal to AZ in a similar manner considering the specimen with PZ cutoff as a linear elastic solid. The derivative of the first term of decomposition Eq. (6) gives the energy release rate in the specimen with crack of length L loaded by remote load σ_∞ and traction σ_{dr} applied on ℓ^{AZ} part of L:

$$-\frac{\partial G_0}{B_{eff} \partial \ell^{AZ}} = G_1 = \frac{K_{tot}^2}{E'} , \tag{10}$$

where E' is the plain strain Young's modulus and K_{tot} is the sum of SIFs due to remote load and traction along the AZ boundary:

$$K_{tot} = K_\infty(\sigma_\infty, L, W) - K_{dr}(\sigma_{dr}, W, L, \ell^{AZ}) , \tag{11}$$

The derivative of the V^{AZ} (Eq. (7)) with respect to ℓ^{AZ} is expressed as the following integral:

$$\frac{\partial V^{AZ}}{B_{eff} \partial \ell^{AZ}} = \frac{1}{\lambda - 1} \int_{\ell^{cr}}^{L} \frac{\partial \delta_{tot}}{\partial \ell^{AZ}}\left(x; \ell^{cr}, \ell^{AZ}, W; F_\infty, \sigma_{dr}\right) dx . \tag{12}$$

It is evaluated numerically and found to be approximately equal to COD at the root of PZ with a reasonable accuracy (any estimation of accuracy?):

$$\frac{\partial V^{AZ}}{B_{eff}\partial \ell^{AZ}} \cong \left.\frac{\delta_{tot}\left(x;\ell^{cr},\ell^{AZ},L,W;F_{\infty},\sigma_{dr}\right)}{\lambda-1}\right|_{x=\ell^{cr}}. \tag{13}$$

Since the WZ does not change if ℓ^{cr} is fixed, the derivative of the third term in Eq. (6) with respect to ℓ^{AZ} is zero. Finally, putting together Eq. (6), Eq. (8), Eq. (10) and Eq. (13) we obtain the expression for X^{AZ}:

$$X^{AZ} = \frac{K_{tot}^2}{E'} - \left.\frac{\gamma^{tr}}{\lambda-1}\cdot\delta_{tot}(x)\right|_{x=\ell^{cr}}. \tag{14}$$

The AZ reaches equilibrium when the thermodynamic force is vanishing. Therefore, the equilibrium AZ length ℓ_{eq}^{AZ} is determined by the following equation:

$$\frac{K_{tot}^2}{E'} - \left.\frac{\gamma^{tr}}{\lambda-1}\cdot\delta_{tot}(x)\right|_{x=\ell^{cr}} = 0. \tag{15}$$

For a given external load, and crack length, the equilibrium AZ size depends on γ^{tr} and drawing stress σ_{dr}. The cold drawing phenomenon in PE is long studied using macroscopical specimens. It is well established that the drawing stress σ_{dr} increases with the loading rate [7]. Unfortunately, it is difficult to evaluate σ_{dr} on microfibers. Therefore, we use the linear relations between σ_{dr} and log strain rate obtained in macroscopical tests. Since the loading rate of the AZ material changes with CL growth, the σ_{dr} acting along AZ boundary is also varies with CL growth and can be estimated on the basis of either a combination of COD rate and macroscopical $\sigma_{dr}\sim\ln\dot{\varepsilon}$ relations or indirectly on duration of AZ stationary state. Regarding γ^{tr}, the transformation of the original continuum media into highly oriented fibrillated structure within PZ is a complex process. It starts with cavitation ahead of the crack front as a precursor of drawing. The cavitation makes it possible to draw thin membranes between the cavities. Further drawing leads to splitting some of the membranes into thin fibers. For such micron scale of processes, a surface energy of microfibers and membrane becomes comparable to the bulk material energy. It complicates a theoretical evaluation of γ^{tr}. A comparison of the value of AZ size ℓ_{eq}^{AZ} resulting from solution of the Eq. (16) with actual ℓ_{eq}^{AZ} observed in the experiment allows evaluating of an effective (phenomenological) value of γ^{tr}. This estimation has been performed and reported in a separate paper accompanying this one.

3.2. Kinetic Equations of Crack Layer Growth in PE

A stationary CL configuration takes place, when the CL thermodynamic forces are not positive, i.e., $X^{AZ}\le 0$ and $X^{CR}\le 0$. The equilibrium is achieved, when the forces equal 0 (for example Eq. (15) for AZ equilibrium). At a small deviation from equilibrium, a thermodynamic system has a tendency to return to the equilibrium state. However, fracture is an essentially irreversible process: there is no return, when the crack is moving into AZ by breaking fibers, or AZ advances into the original material via cavitation followed by cold drawing of the material between the cavities and formation of membranes and fibers. Thus, when CL departs from equilibrium stationary state, it evolves to the next stationary configuration.

Close observation of the micromechanisms of CL growth reveals that there is always formation of AZ first in a vicinity of a a micro defect or specially made notch. After some time of growth, AZ reaches a stationary state, at which its length does not visibly change. It implies that the thermodynamic force reciprocal to AZ length has vanished. During that time, however, we observe an increasing load point displacement. It can be noticed from the load point displacement records of discontinuous (stepwise) SCG (Figure 4). The increase of load point displacement during a stationary AZ size stems from the macroscopical creep of the bulk material accompanied by an increasing width of AZ. The later may result from either drawing of an additional material across AZ boundary or creep of the drawn material of AZ or both.

The absence of a crack growth from a macroscopical view point means that the crack driving force $X^{CR} \leq 0$, i.e., $J_1^{CR} \leq 2\gamma$. This inequality may change the sign after a certain time of creep and degradation of fibers within AZ, since the specific fracture energy γ decays due to degradation of microfibers. Then, the crack moves into AZ for the distance controlled by an interplay between J_1^{CR} and $2\gamma(x,t)$. The advancement of the crack into AZ reduces AZ length and thus violates the AZ equilibrium condition, giving rise to an increase of AZ force that result in the AZ growth.

Thus, the role of AZ is in moderating high stress concentration caused by a crack. It is achieved by strain localization (displacement discontinuity) in form of cavitation and cold drawing. However, AZ can only delay the fracture propagation process: the creep and/or other types of degradation of the AZ material reduce its toughness with time and ultimately allow crack penetration into AZ. Such process of CL propagation continues by crack and AZ assisting mutual growth. The described scenarios of CL growth is formalized in the following system of coupled ordinary differential equations with respect to ℓ^{cr} and ℓ^{AZ}:

$$\begin{cases} \dot{\ell}^{cr} = k_1 X^{CR}, & if\ X^{CR} \geq 0,\ and\ \dot{\ell}^{cr} = 0,\ if\ X^{CR} < 0 \\ \dot{\ell}^{AZ} = k_2 X^{AZ}, & if\ X^{AZ} \geq 0,\ and\ \dot{\ell}^{AZ} = 0,\ if\ X^{AZ} < 0 \end{cases}. \tag{16}$$

The kinetic coefficients k_1 and k_2 in Eq. (16) as well as the parameters entering the CL driving forces X^{AZ} and X^{CR} are evaluated by matching the model predictions with observed CL evolution reflected by load point displacement vs. time plot like shown in Figure 4, side views and fracture surface micrographs similar to that shown in Figures 5, 6, and 7.

The crack and AZ thermodynamic forces are non-linear functions of crack and AZ lengths. Thus, the system of Eq. (17) despite of its simple appearance is a nonlinear system of ODE, solution of which calls for numerical methods. An illustration of numerical simulation of CL growth in a CT specimen is presented in the accompanying paper [8].

4. Conclusion

The focus of the paper is brittle fracture resulting from SCG. The limitation of the conventional approach of lifetime assessment in brittle fracture originates from complexity of SCG process. Specifically, relatively new data on continuous vs. discontinuous modes of SCG is presented in details. Only continuous CL growth takes place for low enough load. Above that value, both continuous and discontinuous modes of SCG are possible at different temperature.

The active zone of CL constituted by cold drawn microfibers and the energy dissipation associated with AZ formation play a major role in fracture process. A brittle fracture of microfibers in process

of drawing or soon after completion of drawing results in a continuous CL growth. In contrast with that, a ductile behavior (creep) of drawn microfibers within AZ is the underlying cause of the discontinuous CL growth.

A transition in the mechanism and kinetics of SCG takes place at certain combination of temperature and SIF. It suggests that commonly used extrapolation of data obtained at elevated temperature into service condition is limited by the requirement of similarity in the mechanisms and kinetics of fracture process. Therefore, the commonly used acceleration technique based on extrapolation of 1-1.5 years elevated temperature test data into 50 and 100-year life in service condition is a suspect. In addition, there is a hidden assumption that after decades of services the material retains the same properties as the one tested for a year or two. The material aging process (chemical degradation and/or physical aging) commonly takes place over time. It should be taken into consideration. An alternative approach to the lifetime assessment problem is a formulation of a sound physical model of initiation and SCG processes and numerical simulation of brittle fracture.

References

[1] A. Chudnovsky, Experimental and theoretical studies of slow crack growth in engineering polymers, Key Eng Mat, 345 (2007) 493–496.
[2] A. Chudnovsky, A. Dolgopolsky and M. Kachanov: Elastic interaction of a crack with a microcrack array—I. Formulation of the problem and general form of the solution, Int J Solids Struct, 23 (1987) 1–10.
[3] A. Chudnovsky, A. Dolgopolsky and M. Kachanov: Elastic interaction of a crack with a microcrack array—II. Elastic solution for two crack configurations (piecewise constant and linear approximations), Int J Solids Struct, 23 (1987) 11–21.
[4] M. Ben Ouezdou and A. Chudnovsky, Semi-empirical crack tip analysis, Int J Fracture, 37 (1988) 3–11.
[5] S. Wu and A. Chudnovsky, A., Elastic interaction of a crack with a random array of microcracks, Int J Fracture, 49 (1991) 123–140.
[6] Z. Zhou, H. Zhang and A. Chudnovsky, Temperature effects on slow crack growth in pipe grade PE, Proceedings of the 68th Annual Technical Conference & Exhibition, ANTEC 2010, Society of Plastics Engineers, Orlando, FL, 2010, pp. 679–684.
[7] A. Chudnovsky, Z. Zhou, and H. Zhang, Lifetime Assessment of Engineering Thermoplastics, Int J Eng Sci, 59 (2012) 108–139.
[8] H. Zhang, Z. Zhou and A. Chudnovsky, Computational Method for CL Model, …
[9] J. D. Eshelby, Energy relations and the energy-momentum tensor in continuum mechanics, in: M. F. Kannien, W. F. Adler, A. R. Rosenfeld, and R. I. Taffee (Eds.), Inelastic Behavior of Solids, McGraw-Hill, New York, 1970, pp. 77–115.

Investigation of Void Linkage in Magnesium Using SEM and Micro Computed X-ray Tomography

Michael J. Nemcko[1,*], David S. Wilkinson[1]

[1] Department of Materials Science and Engineering, McMaster University, Hamilton L8S 4L8, Canada
* Corresponding author: nemckomj@mcmaster.ca

Abstract Ductile fracture in metallic materials occurs by the nucleation, growth, and linkage of microvoids within the bulk of the material. As a result, two dimensional techniques must be complimented with three dimensional techniques in order to completely characterize the fracture process. In the present study, tensile testing coupled with: scanning electron microscope (SEM) imaging, electron backscattered diffraction (EBSD) patterning, and micro computed x-ray tomography (XCT), have been used to analyze void linkage in magnesium, which exhibits poor formability at room temperature. SEM imaging and EBSD patterning have been used to characterize the mechanisms responsible for void linkage and to determine the effects of void fraction and void orientation on the failure strain. Micro XCT has been used to examine the evolution of internal voids. It has been established that void fraction and void orientation have a weak influence on the failure strain due to the premature linkage of voids. EBSD analysis has shown that this premature void linkage is associated with the failure of twin and grain boundaries. The results suggest that (in contrast with more ductile fcc metals) the local microstructure has a significant impact on void linkage.

Keywords Magnesium, Void Linkage, Micro computed tomography

1. Introduction

Magnesium exhibits limited ductility when deformed at room temperature. The HCP crystal structure of the material does not provide an adequate amount of slip systems to satisfy the von Mises criterion. As a result, mechanical twins are activated to accommodate stress concentrations [1]. Void nucleation typically occurs within the bulk of the material. As a result, characterization techniques which can detect internal flaws are required to fully understand fracture. In the past, model materials were fabricated to better understand void growth and coalescence [2]. The 2D model materials consisted of thin sheets containing laser drilled holes through the thickness which simulated voids [3]. These model materials were pulled in tension within the SEM such that the growth and linkage of the holes could be analyzed in increments of deformation. FCC materials (aluminum and copper) were studied which are more isotropic than HCP materials. The results showed that void growth was uniform. Linkage of the voids occurred by the internal necking mechanism observed by Puttick [4]. Furthermore, experiments were carried out to determine the effects of the void fraction and void orientation on the failure strain. It was concluded that both parameters had a strong correlation with the failure strain.

The experiments were then extended to 3D to determine if the 2D experiments were representative of what occurs in the bulk [5]. 3D model materials were fabricated by diffusion bonding multiple sheets containing laser drilled holes between hole free sheets. These were used to simulate a 3D distribution of internal voids. The 3D model materials were tested in situ. The voids in the material are resolved using x-ray tomography from a synchrotron source based on the difference in the attenuation coefficient between the metal and the void. The use of tomography in materials science has significantly increased in the past few years [6]. In the present work, tomography is coupled with EBSD and SEM to understand the fracture of magnesium materials which display mechanical anisotropy.

2. Experiments

Commercially pure magnesium was hot rolled to a thickness of 125 µm. Tensile specimens were machined using electrical-discharge wire cutting. The tensile specimens had a reduced gage section with a length of 2 mm and a width of 1 mm. The samples were polished with 0.05 µm colloidal silica to ensure a smooth surface for laser machining. Holes with a diameter of approximately 13 µm, were laser drilled into the gage section of the tensile samples using a Ti:sapphire laser system. For one set of experiments, samples with a single row of holes perpendicular to the tensile axis were tested with different center to center hole distances to examine the effects of void fraction on the failure strain. The distances used were 40, 55 and 70 µm. In another set of experiments, samples with a single row of holes oriented at various angles with respect to the tensile direction were tested to analyze the effects of void orientation on failure strain. The angles were 45, 60 and 75˚. After laser drilling, the samples were annealed in a tube furnace purged with argon, at 450 ˚C for 1 hour, to remove the heat affected zone in the vicinity of the holes. The average grain size was approximately 50 µm with a standard deviation of 25 µm, after the final annealing process.

EBSD patterns were obtained to determine the initial texture in the vicinity of the holes. Tensile tests coupled with electron microscopy have been used to visualize void growth and linkage in-situ. Samples were pulled in uniaxial tension at room temperature under the SEM. The tensile stage utilizes a 220 N load cell and experiments were carried out at a constant test speed of 10 µm/s. Images were obtained in increments during deformation. Tests were stopped when microstructural features or damage was observed. EBSD was carried out on the deformed samples and micro computed tomography scans were employed to observe the bulk of the deformed samples. The Skyscan 1172 micro computed tomography unit was used in the analysis.

3. Results

The EBSD patterns obtained on the deformed samples allowed for characterization of the microstructural features which led to failure. Figure 1 shows the SEM image series of a row of holes perpendicular to the tensile axis with a center to center hole distance of 40 µm. The EBSD patterns have been overlaid on the SEM images where necessary.

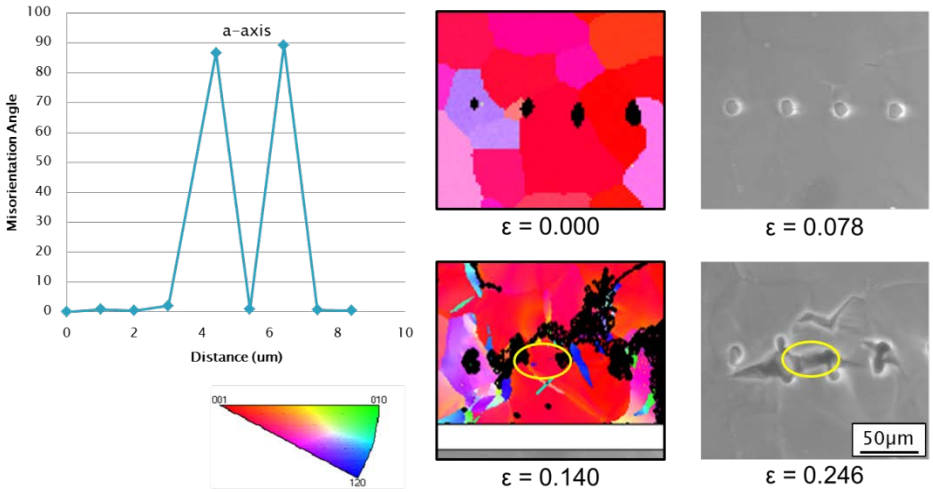

Figure 1: SEM image series at various far field strains and misorientation profile across the twin circled.

At a far field strain of 0.14, a twin was resolved which is circled in Figure 1. The twin was identified as an extension twin, which forms along the $\{10\bar{1}2\}$ plane in magnesium. The misorientation profile in Figure 1 displays a rotation of approximately 86˚ about the $<11\bar{2}0>$ direction (a-axis) with respect to the parent grain. This geometrical relationship is characteristic of the extension twin. The twin became a site for crack propagation at a far field strain of 0.246. It has been established that extension twins form at lower stresses to accommodate extension along the <0001> direction (c-axis). However, once nucleated the twins become stress concentrators and eventually become failure sites.

Figure 2 shows the SEM image series of a row of holes perpendicular to the tensile axis with a center to center hole distance of 70 μm. EBSD patterns were overlaid in the increments where they were obtained.

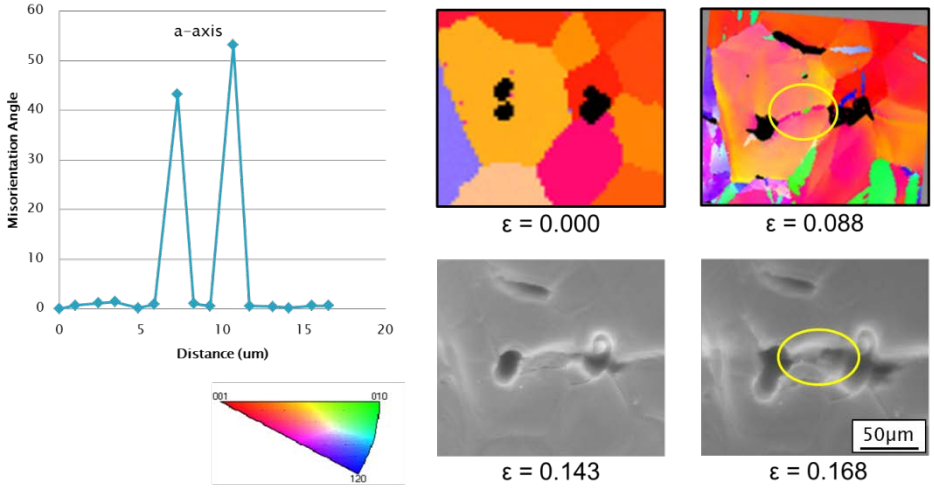

Figure 2: SEM image series at various far field strains and misorientation profile across the twin circled.

A twin was resolved by EBSD at a far field strain of 0.088 which is circled in Figure 2. The twin was characterized as a compression twin, which forms along the $\{10\bar{1}1\}$ plane in magnesium. The misorientation profile in Figure 2 reveals a rotation which is approximately 56˚ about the a-axis with respect to the parent grain. This is characteristic of the compression twin which accommodates compression along the c-axis. The twin boundary failed at a far field strain of 0.168. It has been established that this twin type requires high stresses to activate. The twin nucleated at a relatively low far field strain. This suggests that a complex stress state occurs within the material. Some grains experience much higher stresses than others due to the mechanical anisotropy of the material. Figures 1 and 2 both show failure at grain boundaries. Grain boundary failure is another dominant fracture mechanism.

The effects of void fraction on failure were observed by performing tests on void rows with different center to center holes distances. The center to center hole distance can be related to the void fraction f by

$$f = \frac{2r}{\lambda} \qquad (1)$$

where r is the radius of the hole and λ is the center to center spacing. The normalized length of the

voids which contributed to the first crack was plotted as a function of the void fraction. The normalized length in the tensile direction represents the local displacement field within the vicinity of a void. The results are shown in Figure 3.

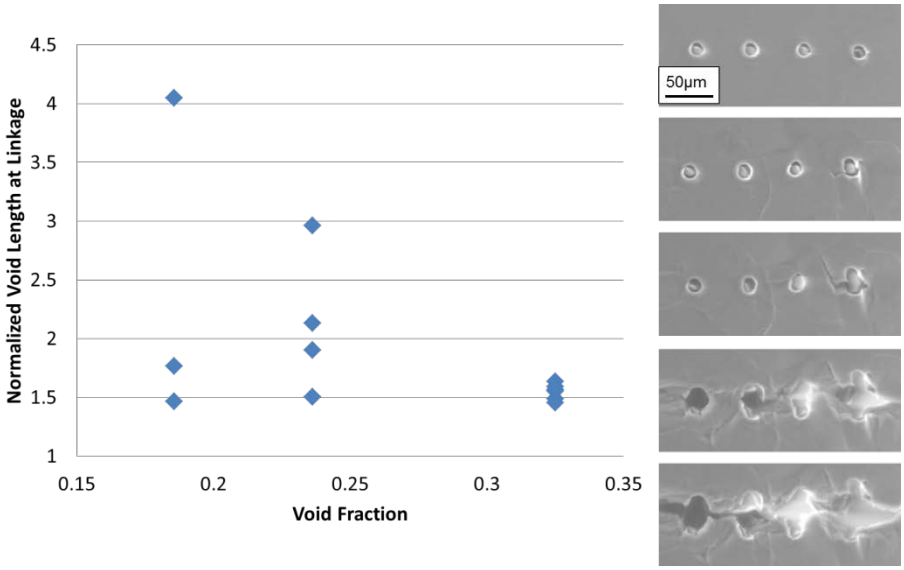

Figure 3: Normalized void length vs. void fraction.

The data does not show a strong correlation between the void lengths at failure and void fraction. This is different from what has been observed in isotropic materials. The variability of the data for a given void fraction suggests that the voids do not grow uniformly.

The effects of void orientation on failure were examined by testing samples with the holes oriented at various angles from the tensile axis. The center to center spacing of the holes was held constant in these experiments at 40 μm. The results are shown in Figure 4.

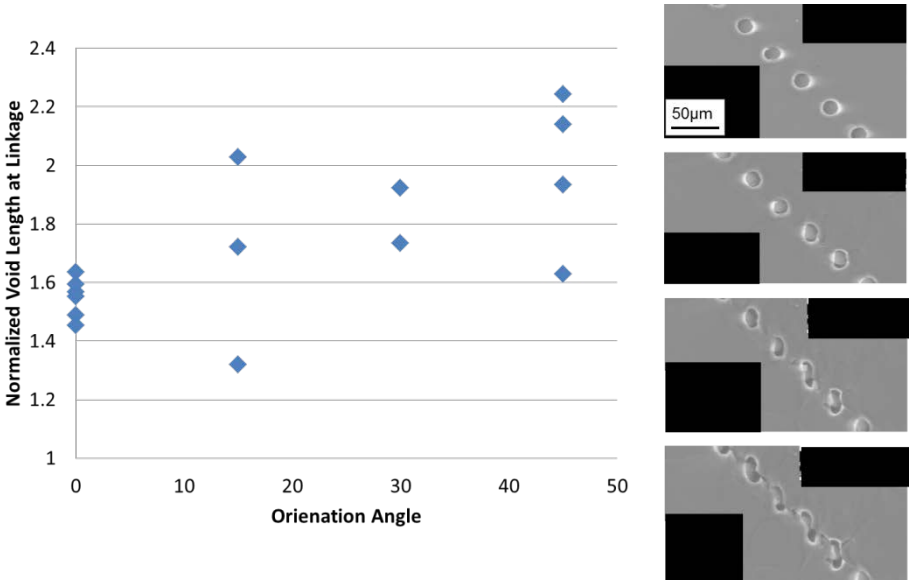

Figure 4: Normalized void length vs. void orientation.

The correlation between the void lengths at failure and void orientation is not strong. This is different from what was predicted in the work of Hosokawa et al [5]. However, in the previous work isotropic materials were tested where void growth was uniform and linkage occurred by internal necking of the voids. In the magnesium materials tested premature linkage occurs by grain and twin boundary failure. Therefore, the weak relationship between the void fraction and void orientation can be attributed to the fact that the linkage of the holes is not driven solely by plasticity in the magnesium materials tested.

Micro XCT has been used to investigate the bulk of the deformed samples. Figure 5 shows a deformed sample with a row of voids perpendicular to the tensile axis with a center to center hole distance of 70 µm. A grain boundary crack was detected by SEM shown in Figure 5a). The reconstructed 3D volume is shown in Figure 5b).

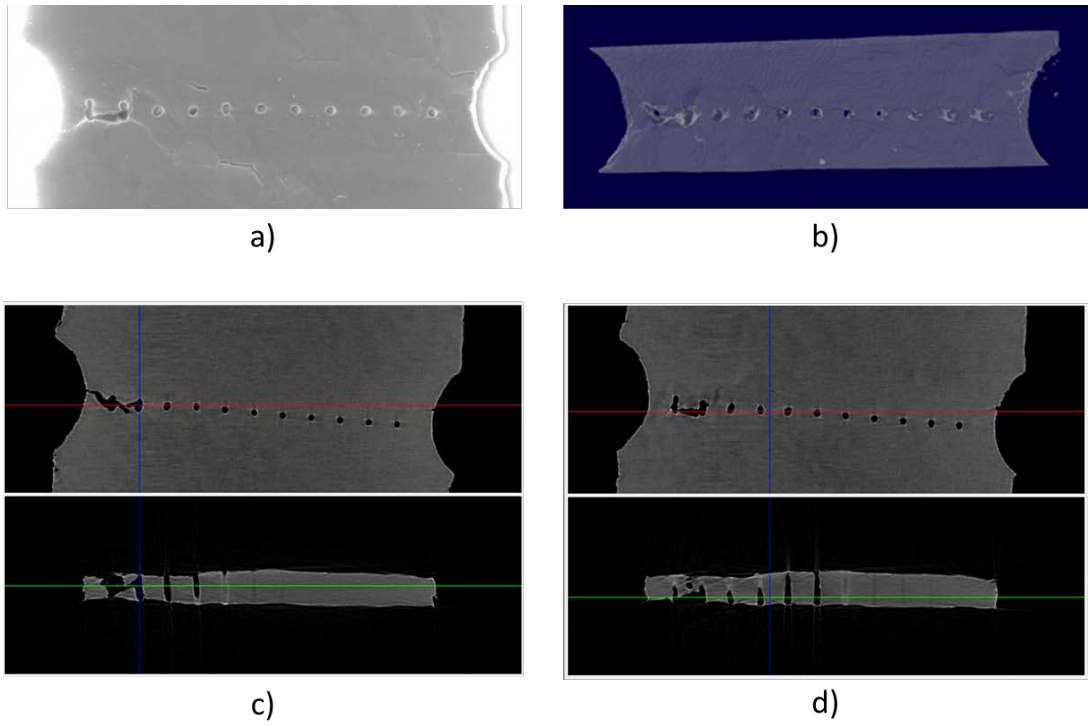

Figure 5: a) SEM image b) Reconstructed 3D volume c) Data slice at the back of the sample d) Data slice at the front of the sample.

The volume was examined using the Data Viewer software developed by SkyScan which allows the user to view the reconstruction slice by slice. Figure 5c) reveals that a crack has already developed on the side of the sample which cannot be detected by SEM. Figure 5d) shows the depth of the crack that is shown in the SEM image. The results suggest that the failure of the materials tested is very complex and the 3D structure must be accounted for to accurately predict the failure of these materials.

4. Discussion

Void linkage occurs prematurely in the magnesium materials tested. The premature linkage is associated with the failure of grain and twin boundaries. Both extension and compression twins have been characterized and contribute to the final failure. The weak correlation between the void fraction and void orientation on failure is a direct consequence of the fact that void linkage is not entirely driven by plasticity. Tomography tests have shown that the failure of the materials is quite complex and 3D techniques must be used to determine where the first failure site occurs.

5. References

[1] Barnett, M.R., Twinning and the ductility of magnesium alloys: Part I: “Tension” twins. Materials Science and Engineering: A, 2007. 464(1–2): p. 1-7.

[2] Weck, A. and D.S. Wilkinson, Experimental investigation of void coalescence in metallic sheets containing laser drilled holes. Acta Materialia, 2008. 56(8): p. 1774-1784.

[3] Weck, A., et al., Femtosecond laser-based fabrication of a new model material to study fracture. Applied Physics A, 2007. 86(1): p. 55-61.

[4] Puttick, K.E., Ductile fracture in metals. Philosophical Magazine, 1959. 4(44): p. 964-969.

[5] Hosokawa, A., et al., Effect of triaxiality on void growth and coalescence in model materials investigated by X-ray tomography. Acta Materialia, 2012. 60(6–7): p. 2829-2839.

[6] Salvo, L., et al., X-ray micro-tomography an attractive characterisation technique in materials science. Nuclear Instruments and Methods in Physics Research Section B: Beam Interactions with Materials and Atoms, 2003. 200(0): p. 273-286.

A new macroscopic model based on non-local interactions to predict damage and failure in quasibrittle materials

Laura B. Rojas-Solano[1], David Grégoire[1,*], Gilles Pijaudier-Cabot[1]

[1] Univ Pau & Pays Adour, LFC-R, UMR5150, 64600 Anglet, France
* Corresponding author: email@address.aa.b.cc

Abstract The purpose of this paper is to propose a new macroscopic approach to describe the evolving non-local interactions during damage and failure in quasi-brittle materials. A new integral-type non-local model is proposed where the weight function is directly built from these interactions. The structure is considered as an assembly of inclusions, which are successively elastically dilated in order to characterize the transfer of information inside the material. By this way, the new macroscale weight function takes into account intrinsically the interactions evolution during the material failure similarly as a mesoscale model does. This new model is first validated on simple 1D cases and its performances are compared with the performances of other models proposed in the literature. It is shown that the new model is able to describe the continuous/discrete transition during the dynamic failure of a rod. It is also shown that the new model is able to describe boundary effect during a spalling test. Finally, the model is used to predict damage and failure during 3 points bending fracture tests on notched and unnotched concrete beams.

Keywords Non-local model, interactions, damage, quasi-brittle materials

1. Introduction

Classical failure constitutive models involve strain softening due to progressive cracking and a regularization technique for avoiding spurious strain and damage localization. Different approaches have been promoted in the literature such as integral-type non-local models (e.g. [1]), gradient damage formulations (e.g. [2]), cohesive cracks models (e.g. [3] with classical finite elements and e.g. [4] with extended finite elements), or strong discontinuity approaches (e.g. [5]). Such macroscale failure models have been applied on a wide range of problems, including the description of damage and failure in strain softening quasi-brittle materials [1], softening plasticity [6–8], creep [9] or composite degradation [10]. They may exhibit, however, some inconsistencies such as (*i*) incorrect crack initiation, ahead of the crack tip; (*ii*) propagating damage fronts after failure due to non-local averaging, (*iii*) incorrect shielding effect with non-zero non-local interactions across a crack surface; (*iv*) deficiencies at capturing spalling properly in dynamics, with spalls of zero thickness when the expected spall size is below the internal length of the model (see e.g. [11–14]). Moreover changing geometry, e.g. from tensile to bending loads or from unnotched to notched specimens, results generally in the loss of predictive capabilities of the macro-scale non-local models [15, 16]. On the contrary, it has been shown recently [15, 17] that meso-scale models gave good prospect in the prediction of failure and size effect for notched and unnotched concrete beams. Indeed meso-scale results have been compared to a new experimental database [16] consisting in 3 point bending failure tests for similar notched and unnotched concrete specimens of four different sizes but made from the same formulation. Not only the different peak loads for all geometries are recovered but also the failure softening phase is well predicted which is a more challenging issue. It means that the meso-scale models intrinsically contain relevant information leading to a good description of the size effect, the boundary effect and the whole failure process.
At the macro-scale, the prediction of failure in quasi-brittle materials needs enhancement of existing non-local damage models and the way the non-locality is taken into account in the macro-scale models has to be redefined. Non-locality finds its origin in the interaction between material points

undergoing damage in the course of failure [18, 19]. There are several mechanisms, which should be considered when looking at the non-locality due to the interaction between damaged points: (*i*) an interaction exists if there is damage, which produces this interaction. Assuming that damage corresponds to the growth of micro-cracks, this interaction grows with the size of the defect; (*ii*) shielding effects are also expected: the interaction between two points located apart from a crack should not exist; (*iii*) on free existing or evolving boundaries, and along the normal to these boundaries, non-local interactions should vanish as demonstrated in [20]. The internal length in the non-local model is the parameter inside the weight function that encompasses the non-locality and there is a consensus that this quantity may not be constant, but should depend on the geometry of the specimen or on the state of damage. Therefore enhanced non-local models accounting for a variation of the internal length have been proposed recently [13, 20, 21]. Proposals discussed in [13, 20] are considered on academic one-dimensional problems. Their implementation and extension to 2D or 3D problems are really not trivial as they involve the computation of path integrals, which are tedious in a finite element setting. The stress-based model in [21] is more tractable in 2D/3D computations but the evolution of non-locality is rather empirical.
The purpose of this paper is to discuss a new approach to non-local interactions during failure in quasi-brittle materials and to upscale the relevant information present from the meso-scale to the macro-scale. Therefore, the paper focuses on the estimation of the non-local weight function directly from interactions. The material is modeled as an assembly of inclusions and the elastic interactions upon dilation of each inclusion are computed in a similar ways to a classical Eshelby's problem [22]. A new interaction-based weight function is then built from these interactions. This new interaction-based non-local model is validated on simple 1D problems and its performances are compared with the classical integral-type nonlocal model.

2. A new interaction-based non-local model

2.1. Non-locality in integral-type macro-scale models

In classical non-local models, such as the integral-type [1], the internal length is the parameter inside the weight function that encompasses the non-locality. Associated with a classical Gaussian weight function, it set how and how far the interactions produce inside the materials. However, the main drawback of the formulation is that this parameter is constant whatever the geometry and the failure process. For instance, close to a boundary, the part of the nonlocal averaging domain that protrudes outside the boundary is classically chopped off [1]. Improved models can be found in the literature, with a different averaging process close to the boundary of the solid [12,23] or with a varying internal length in the course of damage [13, 20, 21]. However, even if the internal length variations are based on micro-mechanical concepts, such as the crack growth interaction effect or the transfer of information through a damaged area, the final choice of the weigh function and thus the evolution of non-locality are rather empirical.

2.2. Non-locality in meso-scale models

In meso-scale models, the non-locality is intrinsically included by representing the meso-structure of the materials (e.g. granular, matrix and interfaces in concrete). Therefore, the non-locality does not behave the same close to a boundary, close to a damaged area, at initiation or during the failure process. It has been shown recently that such models are able to capture challenging issues of quasi-brittle materials failure such as predicting the peak loads and even the whole softening load-displacement responses of notched and unnotched beams in three-point bending [15, 17]. In the following, we aim at building a new interaction-based non-local weight function, which will evolve intrinsically when damage occurs inside the materials.

2.3. A new interaction-based non-local weight function

The purpose of the paper is to discuss a new approach to non-local interactions during failure in quasi-brittle materials and to upscale the relevant information present from the meso-scale to the macro-scale. Therefore, we aim at estimating the non-local weight function directly from interactions.

Before we get to the weight function to be inserted in a non-local integral model, let us first consider elastic interactions. In order to compute the effect of point ξ on point x, we look at the strain induced at point x due to the dilation of ε^* of a circular inclusion of radius a centered at point ξ (see Fig. 1).

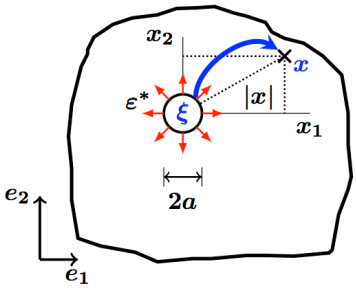

Figure 1. Non-local contribution seen by a point x when a perturbation is produced in ξ.

Assuming now that the induced strain at point x has been computed, numerically for instance. The growth of damage is often defined from energy considerations and we shall look at a norm of this strain, denoted as A, instead of the strain tensor itself:

$$A(x,\xi,\varepsilon^*,a)=\sqrt{\sum_{i=1}^{3}\left|\varepsilon_i(x)\right|^2} \tag{1}$$

where $\varepsilon_i(x)$ is the ith principal strain. Note that we could have chosen the true elastic energy instead of a norm of the strain tensor. It would not have changed much the following development. Then, the interaction is represented by this norm transmitted from the dilation in the inclusion centered at ξ to x. It depends on the geometry of the solid, on the inclusion size a, and on the material elastic properties inside and outside the inclusion. Formally, the norm A transmitted to x by the dilation ε^* writes also:

$$A(x,\xi,\varepsilon^*,a)=\left\|\varepsilon^*\right\|A^*(x,\xi,a) \tag{2}$$

where A^* represents the interaction produced at x due to ξ for a unit dilation.

2.4. Final formulation

2.4.1. Non-local averaging

We assume now that it is this interaction A^*, which governs the weight function involved in non-local averaging. This non-local averaging writes:

$$\bar{\varepsilon}_{eq}(x)=\frac{1}{\Omega_r}\int_\Omega \psi(x,\xi)\varepsilon_{eq}(\xi)\,d\xi \quad \text{with} \quad \Omega_r=\int_\Omega \psi(x,\xi)\,d\xi \tag{3}$$

where $\bar{\varepsilon}_{eq}$ is the non-local strain and ε_{eq} is the effective strain defined by Mazars [24] as:

$$\varepsilon_{eq}=\sqrt{\sum_{i=1}^{3}\left\langle\varepsilon_i\right\rangle_+^2} \tag{4}$$

where $\langle \bullet \rangle_+$ is the positive part function, Ω is the volume of the structure, Ω_r is a characteristic volume introduced in such a way that the non-local operator does not affect an uniform distribution of equivalent strain far away from the boundary when no damage occurs in the structure. The analogy between the interactions defined above and the weight function ψ suggests:

$$\psi(x,\xi) \equiv A^*(x,\xi,a) = \frac{A(x,\xi,\varepsilon^*,a)}{\|\varepsilon^*\|} \equiv \frac{\sqrt{\sum_{i=1}^{3} |\varepsilon_i(x)|^2}}{\|\varepsilon^*\|} \quad \text{with} \quad \Omega_r = \int_\Omega A_0^*(x,\xi,a)\,d\xi \tag{5}$$

where $A_0^*(x,\xi,a)$ is the interaction function reconstructed when no damage occurs in the structure (typically at the beginning of the computation).

Practically, the computation of the interactions (function A∗) is performed using a finite element setup, which is identical to that of the mechanical problem to be solved, with the same mesh. The finite elements which belong to each inclusion centered on a given integration point are subjected to a thermal expansion ($\varepsilon^* = \alpha \Delta T I$) where α is the thermal expansion coefficient, I is the identity tensor, and T is the temperature. If the structure has n inclusions (integration points), n elastic computations are performed to build the weight function at each loading step. Since the construction process of the interaction-based weight function is cinematically driven by the successive thermal expansions, all boundary conditions are clamped during the reconstruction process in order to avoid the perturbation of the kinematics on the boundary.

The single model parameter which remains to be determined is the inclusion size a. This inclusion size is the internal length involved in the formulation. It ought to be related to the average size of the heterogeneities in the underlying heterogeneous material to be modeled.

2.4.2. Constitutive model

Damage is considered to be isotropic. Temperature and time-dependent effects are neglected. Damage is a function of the amount of extension in the material, defined locally by the equivalent strain (see Eq. 4). The evolution of damage is a function of the non-local equivalent strain and it is governed by the Kuhn-Tucker loading-unloading condition (see [15] or [16] for details).

3. Validation and performances

3.1. Clamped bar in tension

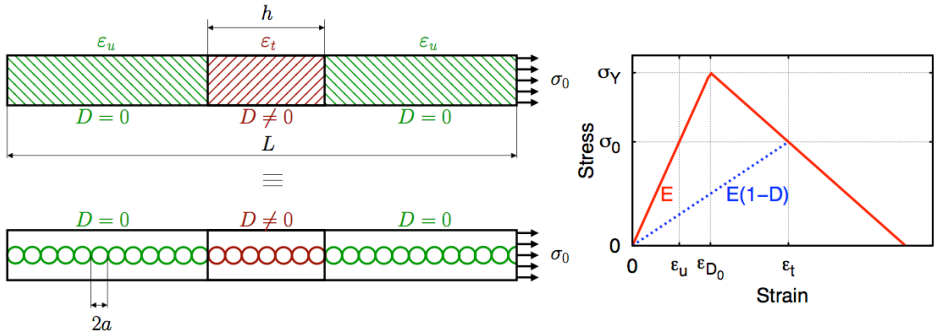

(L =10 cm, σ_Y =3 MPa, E =30 GPa, ε_{D0} =10^{-4}, σ_0 =1.8 MPa, D =70 %)

Figure 2. Simple problem of a clamped bar in tension.

We are going to illustrate the influence of the inclusion size a on the weight function and we shall look at the evolution of the non-local contributions nearby the boundary of a damaged zone. For this purpose, we look at a one-dimensional problem of a clamped bar subjected to tension. The bar has a damaged zone in the middle, the rest being undamaged. The distribution of damage is fixed a priori. The strain distribution inside the bar corresponds to the onset of evolution of damage from this initial state. The strains ε_u and ε_t are obtained from a bilinear softening constitutive law (see Fig. 2).

Although the bar is one-dimensional, the interactions are computed following a 2D, plane stress description. The weight functions are computed from a discrete set of circular inclusions located on the neutral axis of the bar (see Fig. 2). Their size is much smaller than the bar depth in order to avoid interactions with upper and lower boundaries. The finite element meshes consist in triangular elements with 1 integration point and the meshes are built in such a way that there are always 4 elements in the inclusion diameter. Each inclusion is dilated successively in order to reconstruct the weight functions. The weight functions are normalized afterwards so that their integral over the bar is equal to 1 (through the functional Ω_r in Eq. 5).

Fig. 3 presents the influence of the size of the inclusion on the weight function in the case where damage is equal to zero.

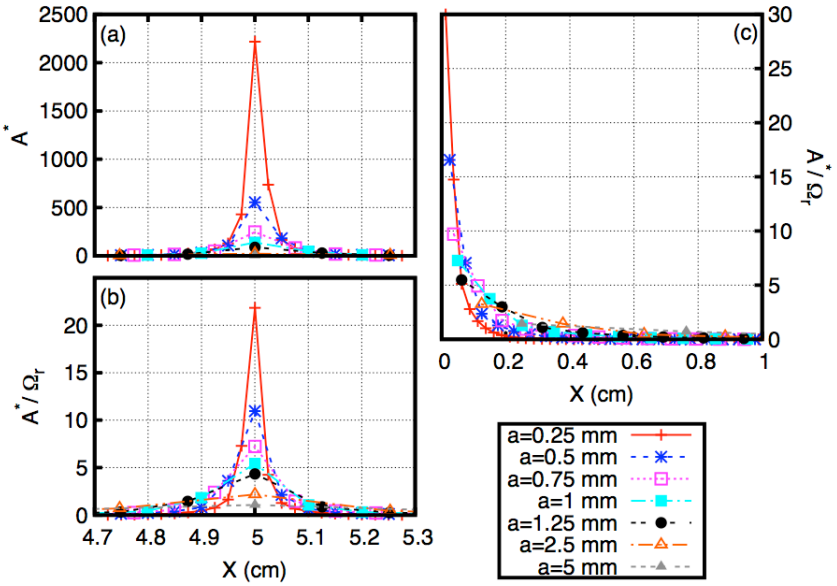

Figure 3. Influence of the inclusion size on the weight function (Reproduced from [25]):
(a) computed far from the boundaries; (b) normalized and computed far from the boundaries;
(c) normalized and computed near the boundary.

Far away from the center of the inclusion (Fig. 3.a), the weight function does not depend on the inclusion size and decreases as $1/X^2$ following the Eshelby's theory (see e.g. [22]). Fig. 3.b presents the same influence of the size of the inclusion but on the normalized weight function. If the inclusion size tends to zero, the computation of the interactions reduces to the construction of Green functions in which it is well known that no internal length is involved. One can demonstrate from the construction of the normalized weight function that it becomes a Dirac delta function and the constitutive model becomes local. Fig. 3.c shows the same calculation nearby the boundary of the solid. The weight function is centered in the inclusion, which sits right next to the boundary. Again, upon decreasing of the radius of the inclusions, the weight function converges toward a Dirac Delta function. According to the results due to [12], [20] and [23], it is expected that at the boundary of

the solid the response becomes local. In mesoscale models, there is a wall effect on the boundaries and large inclusions may not be fitted in a boundary layer smaller than their radius. Nearby a boundary, the inclusion size is constrained by the distance to the free surface, as it cannot protrude outside the solid. This feature can be easily introduced in the present model: at points located close to the boundary, the inclusion size is decreased so that it cannot protrude outside the solid. In a boundary layer of thickness l, inclusions of diameter l shall be considered only when $l < a$. Thus interactions tend to vanish as we consider points closer and closer to the boundary of the solid.

Fig. 4.b presents the normalized non-local contributions when the non local strain is computed at the center of the inclusion located close to the damage band in the region which unloads on the left side. The damage band contains 7 inclusions ($a = 1.25mm$, $h = 8.75mm$). A comparison with the gauss-type weight function used in the classical non-local damage model is also provided (Fig. 4.a). With the Gauss weight function and because the strain inside the damage band is larger than outside the damage band, the non-local contribution from points lying inside the band is much larger than those of points lying outside the band. This will trigger the propagation of the damage band, which should expand in the course of the calculation eventually. Fig. 4.b shows that a shielding effect is observed with the new formulation. The non-local weights outside the damage band are the most important. As a matter of fact, the weight at points lying inside the band is decreasing with increasing damage. There is a shielding effect due to damage, which derives directly from the method used for the calculation of interactions. In the extreme case of a fully damaged band, the dilation of an inclusion sitting inside the band will not be transmitted to the stiffer zone outside the band.

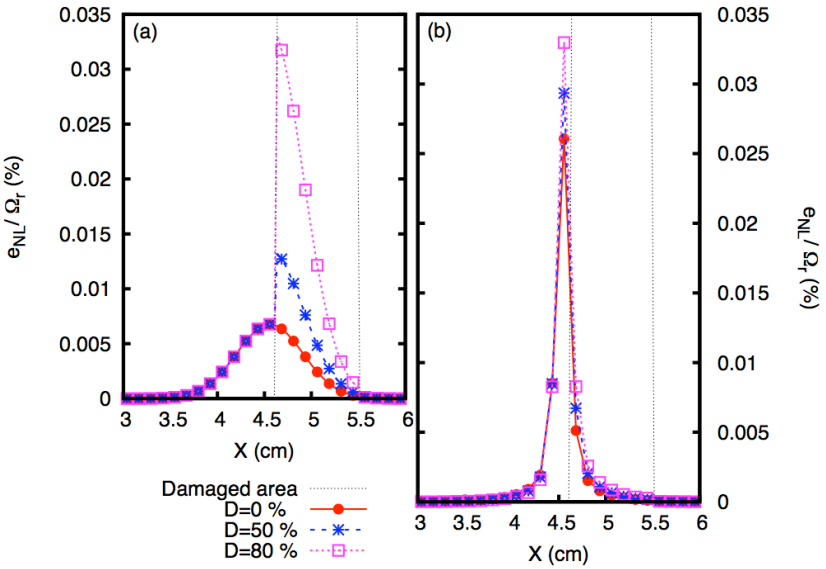

Figure 4. Response close to a damaged area (Reproduced from [25]):
(a) original formulation; (b) interaction-based formulation.

There is, however, a limitation to the shielding effect when the radius of the inclusions is larger than the width of the damage band. In this case, the interaction induced by the dilation of the inclusion will extend across the band. It is expected then that a point lying on one side of the band will feel the interaction from points lying on the other side. We recover here the case of an inclusion located near a boundary, a fully formed crack being two free boundaries facing each other. In order to avoid this problem, we impose that the radius of the circular inclusion reduces as damage grows and we adopt the following rule, which encompasses the situation where an inclusion is centered at a point nearby a damage zone or near a boundary of the solid:

$$a(x) = \min(a_0\sqrt{1-D(x)}, d(x)) \tag{6}$$

where *a(x)* represents the radius of the sphere containing the integration points where the thermal expansion is imposed to reconstruct the interaction-based weigh function, a_0 is a model parameter related to the maximum aggregate size, D is the local damage, d is the minimal distance from any boundary of the structure.

3.2. Dynamic failure of a rod

This example is used to test the relevance of the proposed model and its capabilities to describe progressive failure and complete failure. A bar is submitted at both extremities to constant strain waves, which propagate toward the center in the linear elastic regime (see Fig. 5 and Table 1). When the two waves meet at the center, the strain amplitude is doubled, the material enters the softening regime suddenly, and failure occurs. In all computations, the time step is chosen to be equal to the critical time step.

Table 1. Characteristics of the rod dynamic failure test

Parameter	L	v	E	ρ	l_c/a_0	ε_{D0}	α_t	A_t	B_t	α_c
Unit	cm	cms^{-1}	MPa	kgm^{-3}	cm					
Value	30	0.7	1	1	4	1	1	1	2	0

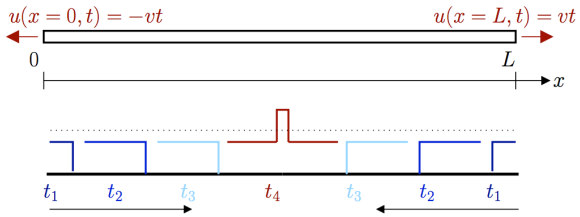

Figure 5. Dynamic failure of a rod: test description and time evolution of the strain amplitude repartition along the rod.

In the course of damage, the crack opening displacement (COD) can be estimated using the method proposed by [26] and compared to an ideal crack opening profile obtained from a strong discontinuity analysis (single crack). The comparison, e.g., the distance between the two profiles, indicates how close the strain and damage distributions are from those corresponding to a single crack surrounded by a fracture process zone. Details may be found in [13] based on [26].

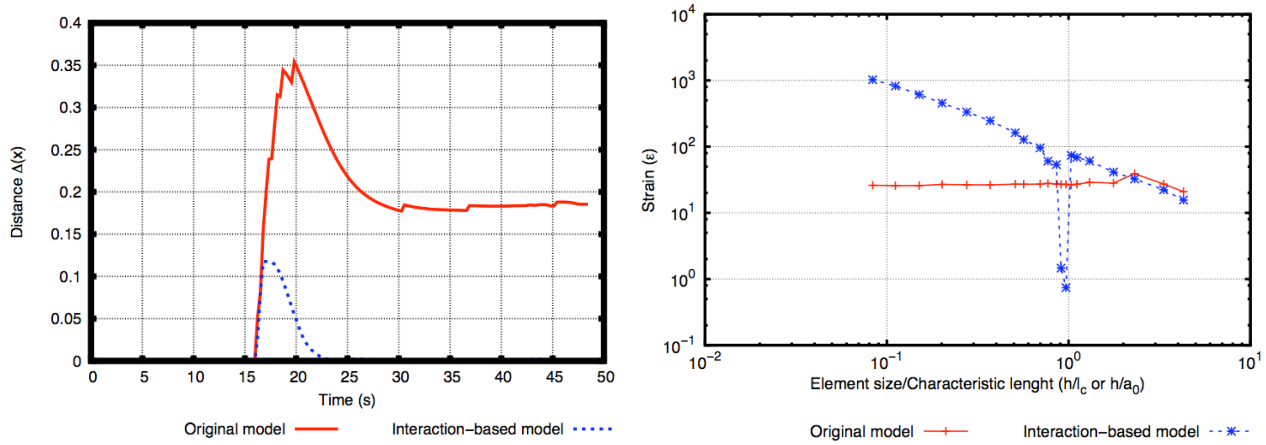

Figure 6. Dynamic failure of a rod (Reproduced from [25]): (left) distance between the computed COD and an ideal opening profile obtained for a strong discontinuity versus time; (right) strain in the cracked element versus adimensional element size at complete failure.

Figure 6 shows that the failure process is better described with the interaction-based model since the distance between its crack opening profile and the one corresponding to a strong discontinuity COD tends rapidly to zero. At complete failure, the crack opening computed according to the same technique should be independent of the element size. In a simple 1D setting, for instance, and assuming that the crack opening is smeared over the finite element that contains the discontinuous displacement at complete failure, the crack opening is equal to the strain distribution times the element size. Therefore, after complete failure, the strain in the cracked element should evolve in inverse proportion of the element size (for constant strain element). Figure 6 shows that the complete failure is better described with the interaction-based model since the strain versus adimensional element size curve follows a linear trend in a logarithmic plot. Moreover the slope is coherent with the CMOD estimated at complete failure. Note that in the original model, the element size is dimensioned by the internal length l_c whereas in the new model, it is dimensioned by the characteristic length a_0 . For the integration-based model, a peak discontinuity is observed when the element size is approximately equal to the characteristics length a_0. It means that several elements are needed inside the inclusion where the perturbation is produced to well reconstruct the interaction-based weight function.

3.3. Spalling test

A second 1D example is used to test the response of the new model close to a boundary. This 1D example consists of a spalling test presented by [12] based on a split Hopkinson pressure bar test primarily developed by [27] for material dynamic behavior characterization, but often adapted for dynamic fracture testing [28, 29]. A striker bar generates a square compressive wave that then propagates along the bar in the linear elastic regime. When this compressive wave reaches the free extremity of the bar, it is converted into a tensile wave and added to the incoming compressive wave (see Fig. 7 and Table 2). The resulting wave stays equal to zero until the tensile one reaches a distance from the boundary equal to half the initial signal length. Failure is initiated at this point if the amplitude is greater than the tensile strength, generating a spall at a controlled distance from the boundary that depends on the initial compressive signal duration. For all numerical studies, the time step is chosen to be equal to the critical time step of the corresponding element size.

Figure 7 shows that the spalling failure is better described with the interaction-based model since the spall location is predicted inside the bar whereas the damage is maximum on the boundary with the original model.

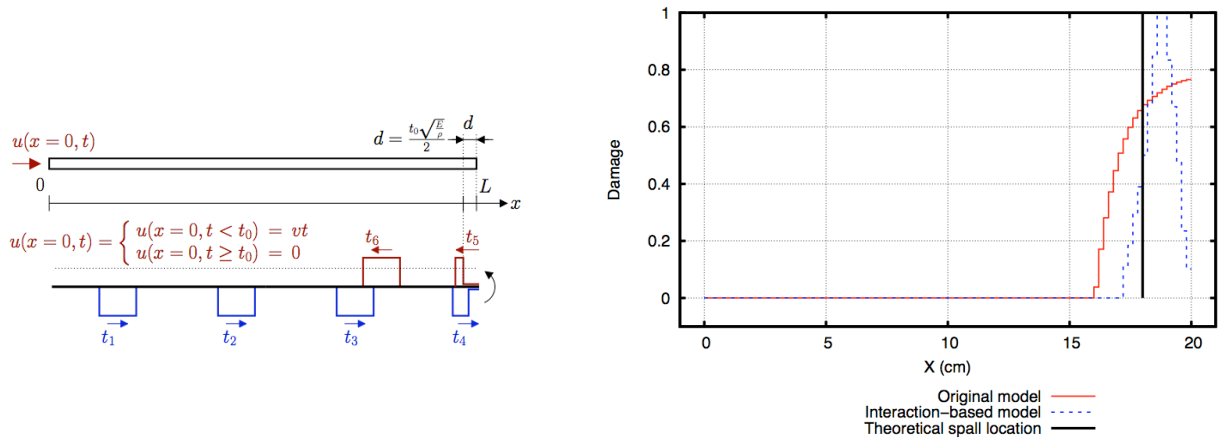

Figure 7. Spalling test: test description, time evolution of the strain amplitude repartition along the rod (left) and damage repartition along the bar after failure (right).

Table 2. Characteristics of the spalling test

Parameter	L	t_0	v	E	ρ	l_c/a_0	ε_{D0}	α_t	A_t	B_t	α_c
Unit	cm	s	cms^{-1}	MPa	kgm^{-3}	cm					
Value	20	4	1,5	1	1	4	1	1	1	2	0

4. Concluding remarks

A new interaction-based non-local formulation has been proposed. In this formulation, the material is modeled as an assembly of inclusions and the elastic interactions upon dilation of each inclusion are computed in a similar ways to a classical Eshelby's problem. A new interaction-based weight function is then built from these interactions. This new interaction-based non-local model has been first validated on simple 1D problems and its performances have been compared with the classical integral-type non-local model.

Different results have been presented in the paper:
(i) In the course of damage, the crack opening displacement has been estimated and the comparisons show that the failure process is better described with the new formulation. Indeed the crack opening profile is very close to an ideal opening profile obtained for a strong discontinuity.
(ii) At complete failure, the crack opening should be independent of the element size. Therefore, after complete failure, the strain in the cracked element should evolve in inverse proportion of the element size, assuming that the crack opening is smeared over the finite element that contains the discontinuous displacement. It has been shown that for the new formulation, the strain versus element size curve follows a linear trend in a logarithmic plot. Moreover the slope is coherent with the CMOD estimated at complete failure.
(iii) Close to a boundary, it has been shown that the spalling failure is better described with the interaction-based model since the spall location is predicted inside the bar whereas the damage is maximum on the boundary with the original model.

Finally, it has been shown that this new interaction-based formulation fulfill several deficiencies of the classical integral-type non-local model and the formulation has to be implemented in 2D in order to test its performance on more challenging issues of quasi-brittle materials failure such as reproducing the peak loads and even the whole softening load-displacement responses of notched and un-notched beams in three-point experimental bending tests [16].

Acknowledgements
Financial support from ERC advanced grant Failflow (27769) is gratefully acknowledged.

References

[1] G. Pijaudier-Cabot, Z.P. Bažant, Nonlocal Damage Theory. J Eng Mech, 113 (1987) 1512–1533.
[2] R. Peerlings, R. De Borst, W. Brekelmans, J. De Vree, I. Spee, Some observations on localisation in non-local and gradient damage models. Eur J Mech A-Solid, 15 (1996) 937–953.
[3] G. Wells, L. Sluys, A new method for modelling cohesive cracks using finite elements. Int J for Numer Meth Eng, 50 (2001) 2667–2682.
[4] N. Moës, T. Belytschko, Extended finite element method for cohesive crack growth. Eng Fract Mech, 69 (2002) 813–833.
[5] J. Oliver, A. Huespe, E. Samaniego, E. Chaves, Continuum approach to the numerical simulation of material failure in concrete. Int J Numer Anal Met, 28 (2004) 609–632.
[6] V. Tvergaard, A. Needleman, Effects of nonlocal damage in porous plastic solids. Int J Solids Struct, 32 (1995) 1063–1077.

[7] Z. Bažant, M. Jirásek, Nonlocal integral formulations of plasticity and damage: survey of progress. J Eng Mech, 128 (2002) 1119–1149.
[8] P. Grassl, M. Jirásek, Plastic model with non-local damage applied to concrete. Int J Numer Anal Met, 30(2006) 71–90.
[9] K. Saanouni, J. Chaboche, P. Lesne, On the creep crack-growth prediction by a non local damage formulation. Eur J Mech A-Solid, 8 (1989) 437–459.
[10] N. Germain, J. Besson, F. Feyel, Composite layered materials: Anisotropic nonlocal damage models. Comput Method App M, 196 (2007) 4272–4282.
[11] A. Simone, H. Askes, L. Sluys, Incorrect initiation and propagation of failure in non-local and gradient-enhanced media. Int J Solids Struct, 41 (2004) 351–363.
[12] A. Krayani, G. Pijaudier-Cabot, F. Dufour, Boundary effect on weight function in nonlocal damage model. Eng Fract Mech, 76 (2009) 2217– 2231.
[13] D. Grégoire, L. Rojas-Solano, G. Pijaudier-Cabot, Continuum to discontinuum transition during failure in non-local damage models. Int J Multiscale Com 10 (2012) 136.
[14] M. Jirásek, S. Rolshoven, P. Grassl, Size effect on fracture energy induced by non-locality. Int J Numer Anal Met, 28 (2004) 653–670.
[15] D. Grégoire, P. Grassl, L.B. Rojas-Solano, G. Pijaudier-Cabot, Macro and mesoscale models to predict concrete failure and size effects, in: G. Pijaudier-Cabot, F. Dufour (Eds.), Damage Mechanics of Cementitious Materials and Structures, ISTE Ltd and John Wiley & Sons, London, 2012.
[16] D. Grégoire, L.B. Rojas-Solano, G. Pijaudier-Cabot, Failure and size effect for notched and unnotched concrete beams. Int J Numer Anal Met, doi: 10.1002/nag.2180 (2013).
[17] P. Grassl, D. Grégoire, L.B. Rojas-Solano, G. Pijaudier-Cabot, Meso-scale modelling of the size effect on the fracture process zone of concrete. Int J Solids Struct, 49 (2012) 1818–1827.
[18] Z. Bažant, Nonlocal damage theory based on micromechanics of crack interactions. J Eng Mech, 120 (1994) 593–617.
[19] G. Pijaudier-Cabot, Y. Berthaud, Effets des interactions dans l'endommagement d'un milieu fragile. formulation non locale. Cr Acad Sci II, 310 (1990) 1577–1582.
[20] G. Pijaudier-Cabot, F. Dufour, Non local damage model. Eur J Environ Civ En, 14 (2010) 729–749.
[21] C. Giry, F. Dufour, J. Mazars, Stress-based nonlocal damage model. Int J Solids Struct, 48 (2011) 3431–3443.
[22] T. Mura, Micromechanics of defects in solids, vol. 3, Springer, 1987.
[23] Z. Bažant, J. Le, C. Hoover, Nonlocal boundary layer (nbl) model: overcoming boundary condition problems in strength statistics and fracture analysis of quasibrittle materials, in: Proc. FraMCoS-7, 2010, pp135–143.
[24] J. Mazars, A description of micro-and-macroscale damage of concrete structures. Eng Fract Mech, 25 (1986) 729–737.
[25] L.B. Rojas-Solano, D. Grégoire, G. Pijaudier-Cabot, Interaction-based non-local damage model for failure in quasi- brittle materials. Mech Res Commun, (2013) submitted.
[26] F. Dufour, G. Pijaudier-cabot, M. Choinska, A. Huerta, Extraction of a crack opening from a continuous approach using regularized damage models. Comput Concrete, 5 (2008) 375–388.
[27] H. Kolsky, An investigation of the mechanical properties of material at a very high rate of loading. Proc Phys Soc, London, Sec B, 62 (1949) 676–700.
[28] D. Grégoire, H. Maigre, J. Réthoré, A. Combescure, Dynamic crack propagation under mixed-mode loading – Comparison between experiments and X-FEM simulations. Int J Solids Struct, 44 (2007) 6517–6534.
[29] D. Grégoire, H. Maigre, A. Combescure, New experimental and numerical techniques to study the arrest and the restart of a crack under impact in transparent materials. Int J Solids Struct, 46 (2009) 3480– 3491.

Thermomechanical fatigue life of a TBC – comparison of computed and measured behaviour of delamination cracks

Sören Sjöström[1,*], Håkan Brodin[1,2], Magnus Jinnestrand[1]

[1] Department of Management and Engineering, Linköping University, SE-58183 Linköping, Sweden
[2] Siemens Industrial Turbomachinery AB, SE-61283 Finspång, Sweden
* Corresponding author: email@address.aa.b.cc

Abstract **Abstract** Thermal barrier coatings (TBCs) are used in hot parts of gas-turbine engines in order to increase gas temperatures and improve thermal efficiency. A TBC consists of a metallic bond coat (BC) and a ceramic top coat (TC).
During high-temperature service, thermally grown oxide will form in the BC/TC interface. This together with the general difference in mechanical and thermal expansion properties leads to a tendency of spalling damage, by which areas of the coating will flake off during thermomechanical cycling.
The modelling of this damage process is rather difficult, but the authors have managed to set up a fracture-mechanically based model, which takes thermal cycling, mechanical cycling and oxide growth into account. The model has been tested and verified under controlled laboratory conditions, using thermal cycling furnaces and continuous inspection of damage development. It has also been used in an FEM computation environment for prediction of TBC spalling in real gas-turbine components.
In this article, the model is described, computations are shown of the development of a typical delamination crack in the BC/TC interface, and the computed results are compared with actual delamination crack behaviour seen in the corresponding testing.

Keywords TBC, fracture-mechanical model, experimental, FEM, interface crack

1. Introduction

A thermal barrier coating (TBC) is a ceramic coating applied for thermal insulation purposes on a metallic substrate.

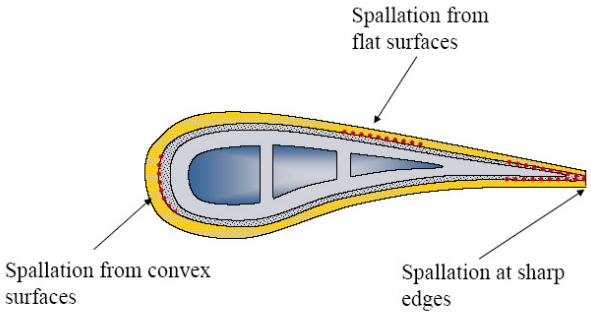

Figure 1. Schematic figure of a TBC-coated gas-turbine blade. Typical spalling mechanisms marked are explained below

Fig. 1 shows a schematic example of a TBC-coated gas-turbine blade. The TBC consists of a substrate (light grey in Fig. 1) on which a metallic bond coat (darker grey in Fig. 1) is applied. On top of the bond coat, finally, the top coat ceramic (yellow in Fig. 1) is applied. The substrate is usually a nickel-based superalloy, the bond coat is an alloy, rich in Al, and the top coat ceramic is usually

ZrO2 with an addition of 6 à 8% Y2O3. . The purpose of the bond coat is to improve the adhesion and to prevent the oxidation by itself forming a dense oxide with as good mechanical properties as possible..

In the typical gas-turbine application, such components will be loaded by the thermomechanical start/stop cycle, *i.e.*, a start, followed by a full-load high-temperature period of from a couple of hours up to several days, finally followed by a shut-down. The design life requirements between inspections for a land-based gas turbine can typically be 3 000 cycles and 30 000 full-load high-temperature hours, after which the TBC must still be functional.

This document deals with air-plasma-sprayed (APS) TBC, which is the type most commonly used in stationary gas turbines.

2. TBC fatigue life

Thermomechanical fatigue (TMF) aspects. Experience shows that with time (and, consequently, accumulated load cycles) TBCs are prone to failing by spalling (flaking). The most dangerous spalling mechanisms have been shown to appear at the end of the shutdown after a long high-temperature full-load period. At the end of the high-temperature full-load period, the stress state in the interface-near region will be low due to high-temperature creep, and as the top coat (ceramic) has a much lower thermal expansion than the metallic layers below, the top coat will be in strong compression at the end of the shut-down (at 'room temperature'). This leads to the three main spalling mechanisms illustrated in Fig. 1.

Of the spalling mechanisms shown in the figure, most research has been concentrated on the explanation and analysis of the spalling from flat surfaces.

TBC life models: history and present status. Early research (see, for instance, [1]) showed that the geometry of the interface (which has a pattern of repeated ridges and valleys caused by the plasma-spray process) leads to tensile stress normal to the interface during the stop cycle of the gas turbine, so that the initiation and growth of cracks in the interface is made possible. Similar analyses on an improved 3-D FE model in [2] confirmed this mechanism. This insight led us to the set-up of a fracture-mechanicallly based life model

3. Fracture-mechanical model of a TBC

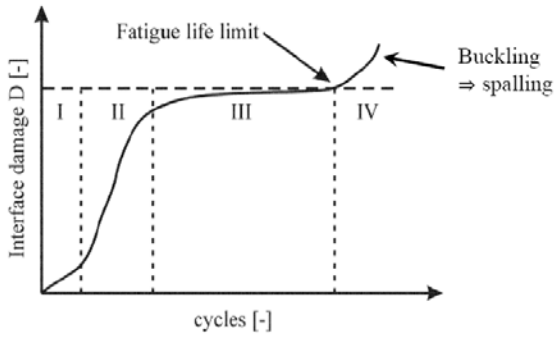

Figure 2. Measured damage evolution in APS TBC

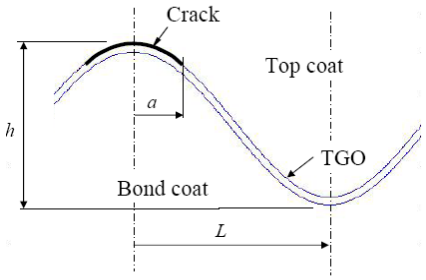

Figure 3. Idealised interface/crack geometry for the FM model

For the fracture-mechanical computations, a least representative cell has been defined, consisting of a substrate+bond coat+TGO+top coat cell, having the width L (= half the period of the idealised cosine wave of Fig. 3). This cell has been given boundary conditions corresponding to symmetry along the left-hand vertical boundary.

The model bases on an idealised (sinusoidal) bond coat (BC)/top coat (TC) interface profile, in which the thermally grown oxide (TGO) is assumed to grow. See Fig. 3. Equal cracks grow symmetrically from all profile tops, *i.e.*, when $D = a/L = 1.0$, cracks extend along the whole interface, leading to complete failure. Further essential model assumptions:

- Plane strain
- Stress-free TBC system at the end of the high-temperature part of the cycle
- The maximum damage-driving energy release rate G and stress intensity factors K_I and K_{II} appear after cooling down from the maximum temperature (low thermal expansion of the TC)
- The material behaviour of all components of the TBC aggregate during the cooling down from maximum temperature is assumed to be linearly elastic

G, K_I and K_{II} are computed by a virtual crack extension method and by interface crack theory (see [3] and appendix)

Fig 4 shows examples of the FE geometry and of the stress pattern in the interface region for 4 typical h/L cases

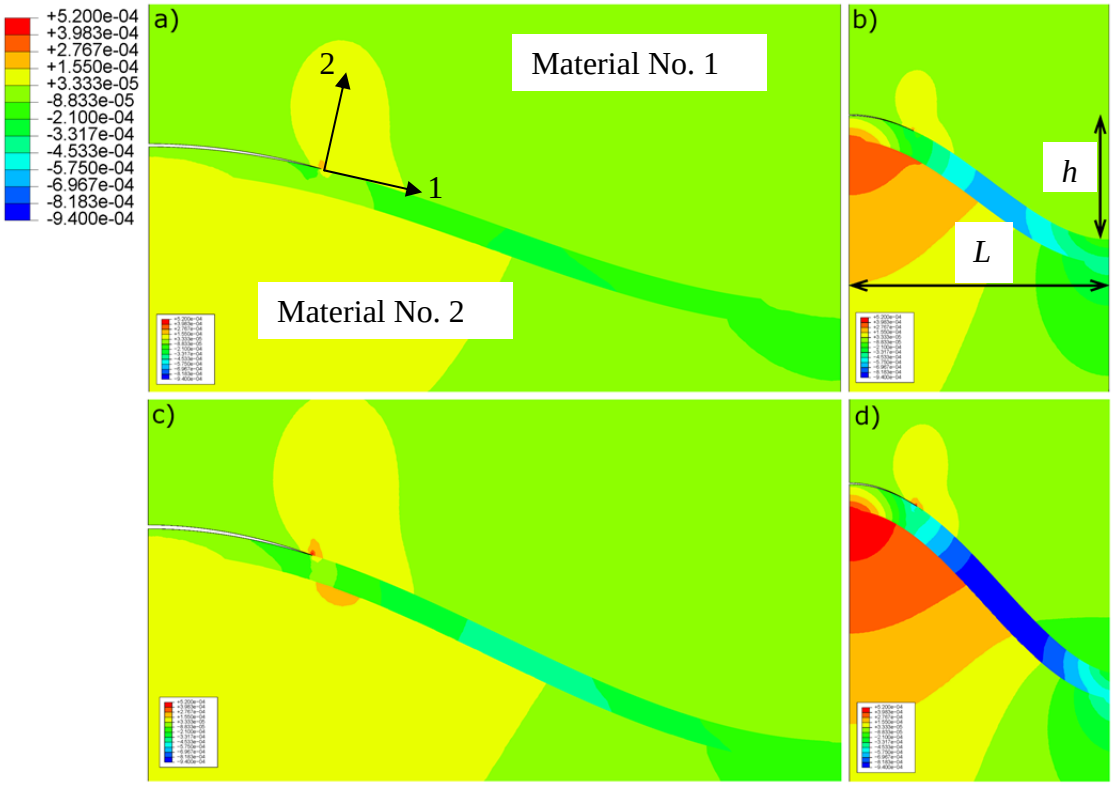

Figure 4. Examples of the FE geometry and of the stress pattern in the interface region for 4 typical *h/L* cases.

Most of the FE computations so far have been done in an in-house code. We have, however, moved over to the commercial code Abaqus for a planned continuation, which will, among other things, in-

volve creep modelling of the bond coat.

G, K_I and K_{II} have been computed for different h/L, different δ_{TGO} and continuously increasing crack lengths corresponding to damage $D_m = a/L$ in the interval $0.0 < D_m < 1.0$. See examples in Fig.5.

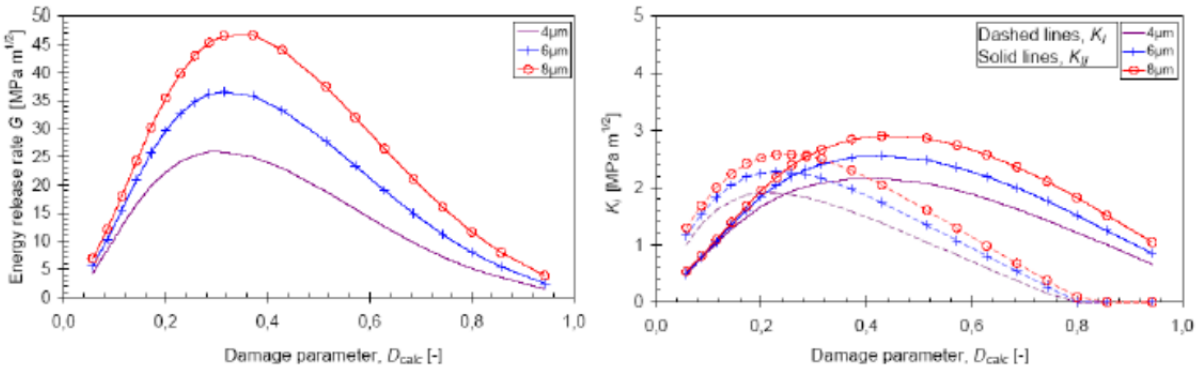

Figure 5. Energy release rate G and stress intensity factors K_I and K_{II} computed for the TCF test.

4. Experimental details

An experimental study has been conducted with the aim at giving quantitative data on crack propagation at a ceramic / metal interface. Evaluations are done on thermally cycled material and material exposed to engine conditions. The coatings evaluated are thin thermal barrier NiCoCrAlY coatings, with nominal thicknesses of top coat equal to 300µm and bond coat thickness of 150µm.

Thermal cycling is performed in air with furnace heating and cooling by forced air. The furnace cycling consists of a standard cycle type where small coupons 30x50x5 mm are exposed to a thermal cycle with 60 minutes dwell time in the furnace at constant temperature. Heating and cooling parts of the cycle are 10 minutes respectively. Data have been retrieved for interrupted tests where the cycling has been stopped after approximately 30% of the expected fatigue. Ex-serviced material has been included with corresponding conditions, i.e. 30-40% of the expected service life.

Coating infiltration by epoxy ensures that the exposed microstructure is retained and that the structure studied is not an artifact after sample preparation. After the epoxy infiltration, the material is cut and mounted for grinding and final polishing. All evaluations are done on as polished cross sections.

Cracks at the top coat / bond coat interface are identified and measured. Measurements are registered for the general microstructure geometry in regions where isolated defects are detected, see Figure 6. In Figure 6 the typical microstructure TBC is shown (a). The interface is undulating and a least representative cell is not easily detected. Instead the morphology of individual undulations needs to be considered (b). The structure is necessarily not similar to the structure observed in the modeling approach (c). In general, the microstructure is assumed to be described with the height over width ratio as defined for modeling purposes.

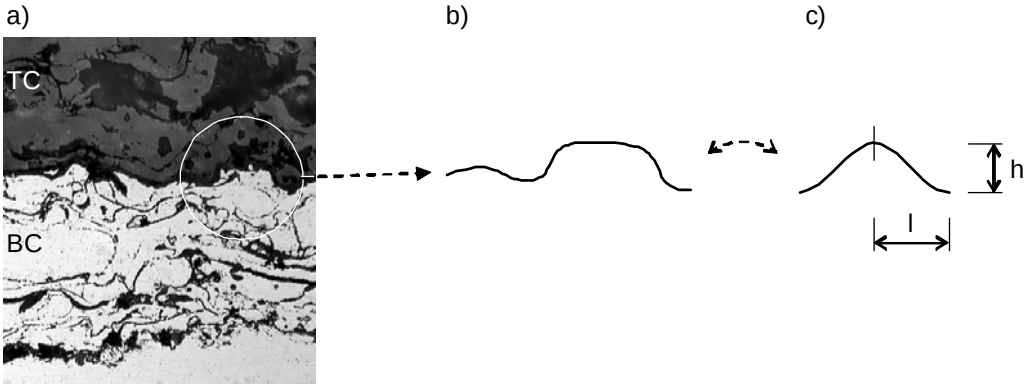

Figure 6. Comparison of interface microstructure / morphology in actual thermal barrier coatings.

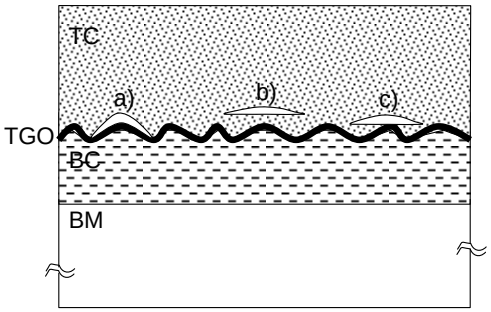

Figure 7. Crack patterns observed in thermal barrier coatings. (a) black interface crack, (b)ceramic white crack and (c) mixed black/white crack with the crack partly at the interface, partly in the top coat.

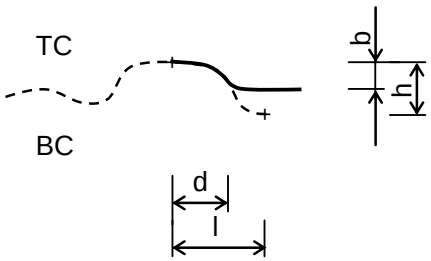

Figure 8. Definition of measurement on deflected kink crack.

Different crack types can theoretically be observed in the ceramic / metal material system. The three typical crack patterns are shown in **Error! Reference source not found.**. The different crack patterns (a), (b) and (c) are identified as black TC/BC interface cracks, white ceramic TC cracks and mixed kink cracks with portions of the crack both at the TC / BC interface as well as portions in the ceramic TC respectively. Cracks of type (c) are contained inside the TGO layer especially if the oxide is formed on an alloy with relatively low Al concentration. In such cases, the oxide is often observed to contain many defects and can be described as layered. During thermal fatigue exposure of the coatings, damages of type (a) are common. Also damage of type (c) is frequently observed after furnace testing and engine exposure. Damage of type (b) is not frequently occurring. This damage pattern is more related to high heat flux situations in burner test rigs and corresponding engine situations with high thermal loads

A schematic picture of the measurements taken is shown in **Error! Reference source not found.**. The measure *d* is defined as the distance from a ridge to the location where a crack deflects away from the interface into the top coat projected on a plane parallel to the interface (and the TBC outer surface). Also the distance vertically (perpendicular) from the ridge to the location of crack deflection is measured, in **Error! Reference source not found.** defined as *b*.

At the location of crack deflection from interface to TC crack the curve shape tangent *dy/dx*, or curve shape first derivative, is measured (a). On the corresponding model, the curvature has been described by a tangent as shown in (b) and (c). The tangent (b) is the slope at the inflexion point

with the highest value of *dy/dx*. This is to be compared to the average *dy/dx* value measured as the measure peak–to–valley over half wavelength, i.e. *h/l.*

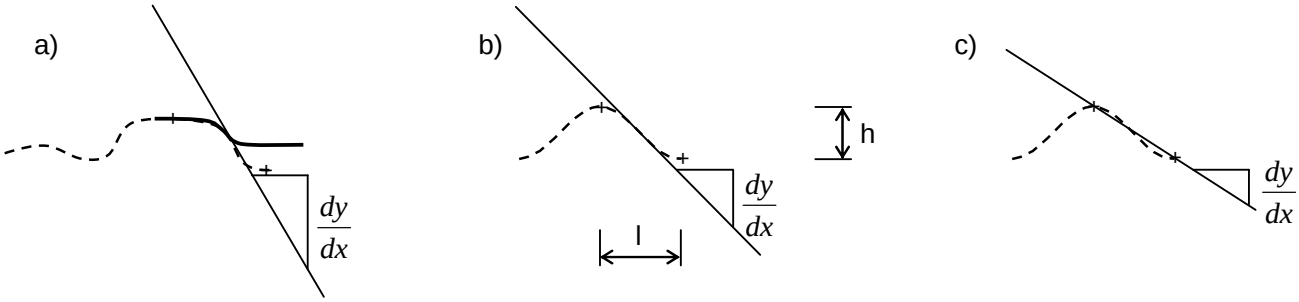

Figure 9. Definition of measurements for determination of angle for crack deflection. Figure (a) represents a real interface, (b) measurement of maximum slope for theoretical sinusoidal interface and (c) measurement of average slope for theoretical sinusoidal interface.

5. Comparison of fracture-mechanical model results and microstructural damage evolution

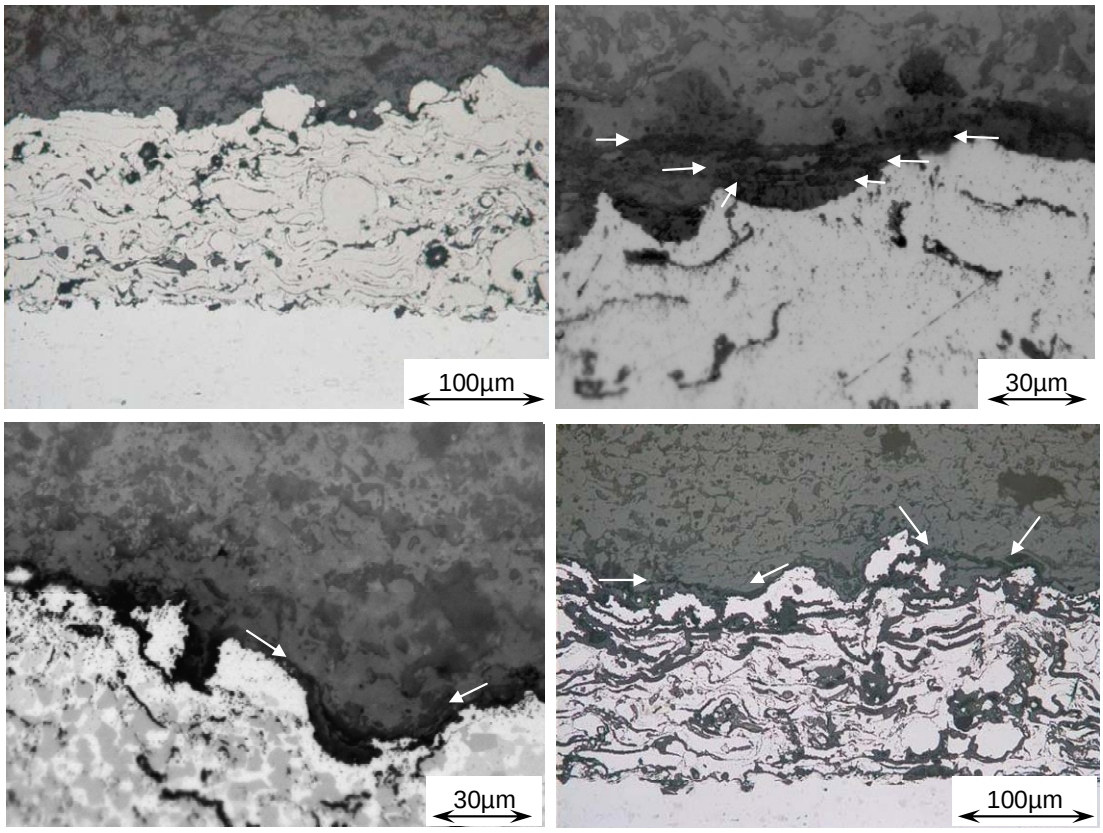

Figure 10. Typical microstructures of virgin (a) and ex-serviced materials (b) – (d). Multiple kink cracks (b) interface crack (c) and kink/white cracks after furnace testing (d).

Examinations of thermally cycled material (furnace and engine exposed) reveal that the material damage is similar. To a large extent the material damage is of interface type (black) but mixed cracking (black/white kink cracks) is frequently detected. Typical microstructures are shown in Figure 10. Image (a) is as manufactured, (b) and (d) indicate mixed (kink) deflected cracks from

furnace-cycled and engine-exposed, respectively. An interface crack formed during furnace cycling is shown in image (c).

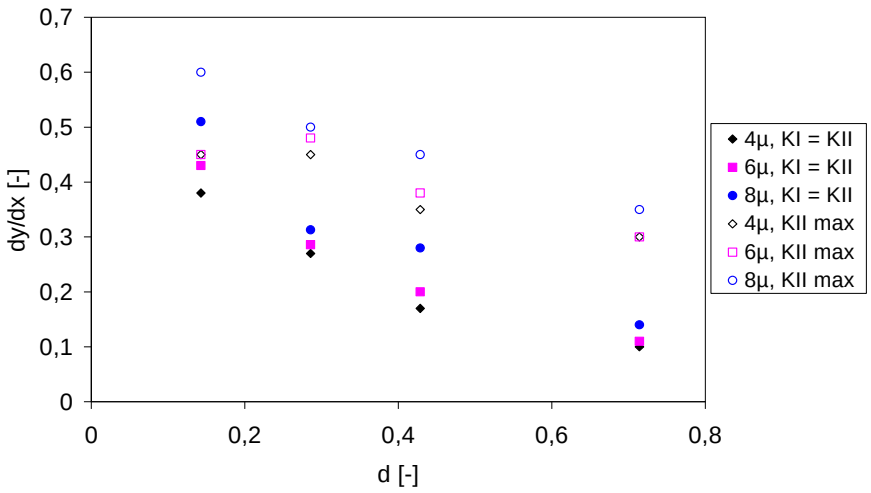

Figure 11. Correlation $dy/dx = f(\mathrm{D}, K_I = K_{II})$ and $D = f(K_{II\ max})$.

From the data in Figure 5 the damage level D for $K_I = K_{II}$ and maximum K_{II} are determined. These data are presented in Figure 11. Data in Figure 11 are for interface roughness 10/70, 20/70, 30/70 and 50/70 µm/µm. Series are included for a range of oxide thickness values.

For individual kink cracks data are collected for peak-to-valley h, half-wavelength l, distance b and d for crack deflection and interface slope dy/dx at location for crack deflection.

Data indicate that the actual location for crack deflection from an interface crack to a deflected kink crack best can be described by a correlation of peak to location for deflection b along the surface normal rather than the projection on a plane parallel to the interface. It is also obvious that the condition for crack deflection best is described by a correlation to the maximum slope of the generalised model interface.

Results according to Figure 13 should be interpreted with the stress state at the interface in mind. For short cracks, the stress state is K_I dominated. As the crack progresses, the stress state will be increased dominated by shear stresses. Considering crack growth in an isotropic material, the general assumption is that a crack growing in a mixed mode stress field will try to grow in the direction that enables growth under a K_I modus. In the case of crack growth at a biomaterial interface, this is not necessarily true. A crack can continue to grow at the interface, if, for instance, the interface acts a weak link. An example of this is the TBC system with a thick thermally grown oxide that acts as a prescribed crack path. In cases where the thermally grown oxide is dense and adherent to the underlying metallic material, the crack should, in principle, be able to deflect away from the interface and into the top coat where crack growth can take place under a K_I dominated stress field. Figure 14 visualises the criterion that can be used to determine when the crack should have possibility to deflect into the top coat. For short cracks and low stress intensities, the crack is confined to the interface. As the crack grows longer and the interface oxidizes, the shear stress increases and the conditions for crack deflection can be fulfilled at $D=D_m$. It is important to notice that not all cracks will deflect. One important factor can be local TGO growth. It is well-known that the oxide thickness is not constant throughout a thermally exposed TBC coating even if the temperature is known and constant over the coating at T_{max}.

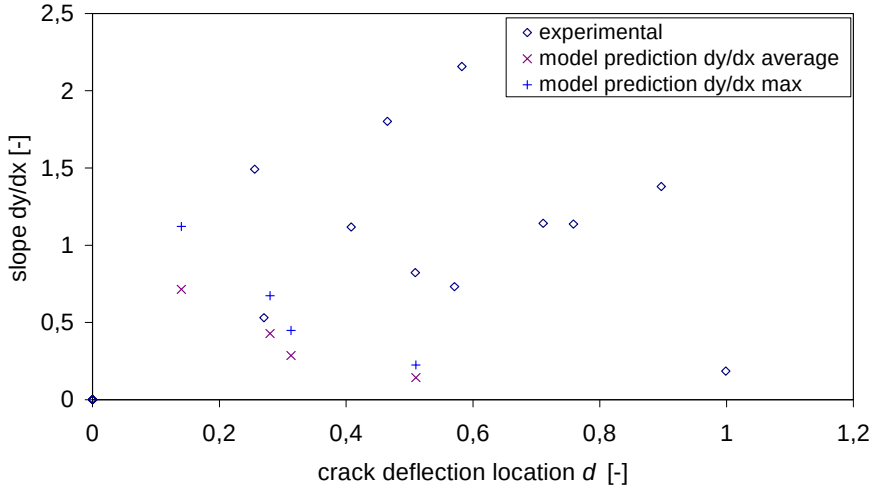

Figure 12. a) Correlation $dy/dx = f(d)$ and $dy/dx_{average} = d(K_I = K_{II})$ for experimental data and model results. b) Correlation $dy/dx = f(d)$ and $dy/dx_{max} = d(K_I = K_{II})$ for experimental data and model results.

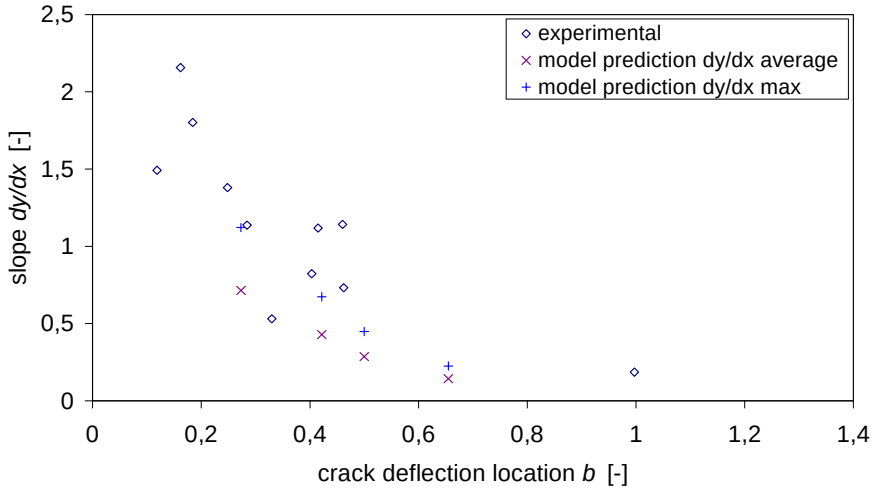

Figure 13. Correlation $dy/dx = f(b)$ and $dy/dx_{average} = b(K_I = K_{II})$ for experimental data and model results. b) Correlation $dy/dx = f(b)$ and $dy/dx_{max} = b(K_I = K_{II})$ for experimental data and model results.

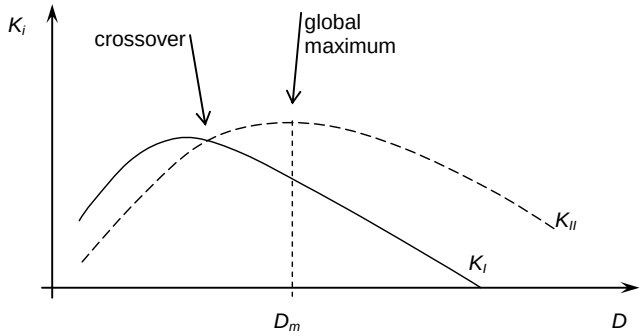

Figure 14. Possible criteria for change from interface crack to kink crack.

To some extent, the model tends to underestimate the slope required for transfer form mixed mode crack growth over to crack growth under a K_I dominated stress state. Hence, it can be argued that the stress state is overestimated at the interface. From these facts the conclusion could be that the

stress state determined by an FE-model is in the correct order of magnitude, and that the location for crack deflection can be described by $K_{II\,MAX}$ correlated to interface slope. However, it is likely that the stress level should be subject to further investigation. If $K_{II\,MAX}$ can be used as a criterion for crack deflection and the model prescribes this phenomenon to occur prematurely, the material response causes stresses to be exaggerated. Factors that can play a role in the mathematical modelling can be top coat stiffness, interface geometry, BC constitutive model, oxidation behaviour and thermal/mechanical load.

6. Conclusions

The current paper compares experimental findings and modelling results coupled to conditions for when a TBC delamination will change from an interface crack to a kink crack contained partly at the interface, partly in the ceramic top coat. It is shown that the condition for change from interface to kink crack can be fulfilled by comparison of interface slope and interface geometry in terms of asperity height. Comparisons indicate that the interface slope plays an important role ad that experimental and modelling results correlate if the distance from peak to deflection point is taken into consideration. In the comparison, modelling results give the best agreement if the location for KII max is chosen as a criterion for when deflection is to be expected.

References

[1] G.C. Chang, W. Phucharoen, Behavior of thermal barrier coatings for advanced gas turbine blades, Surf. and Coat. Techn. 30 (1987) 33-38
[2]M. Jinnestrand, S. Sjöström, Investigation by 3D FE simulations of delamination crack initiation in TBC caused by alumina growth, Surf. and Coat. Techn. 135 (2001) 188-195
[3] J.W. Hutchinson, Z. Suo, Mixed mode cracking in layered materials, Adv. Appl. Mech. 29 (1990). 63-187

Appendix: Mechanics of the interface crack

For a description of the theory of an interface crack see, for instance, [3].

From the FE solution, the energy release rate G and the crack flank displacements $u_1^{(u)}$, $u_1^{(l)}$, $u_2^{(u)}$ and $u_2^{(l)}$ at a number of nodes along the crack flank are used. (For definition of materials Nos. 1 and 2 and coordinate directions 1 and 2, see Fig. 4.)
The relation between G, K_I and K_{II} is given by

$$G = \left(\frac{1}{E_1^*} + \frac{1}{E_2^*}\right) \cdot \frac{1}{2\cosh^2(\pi\epsilon)} (K_I^2 + K_{II}^2) \tag{1}$$

in which

$$\epsilon = \frac{1}{2\pi} \ln \frac{\frac{1+\nu_2}{E_2} + \kappa_1 \frac{1+\nu_1}{E_1}}{\kappa_2 \frac{1+\nu_2}{E_2} + \frac{1+\nu_1}{E_1}} \tag{2}$$

$$\kappa_i = \begin{cases} 3 - 4\nu_i \text{ ; plane strain} \\ \dfrac{3-\nu_i}{1+\nu_i} \text{ ; plane stress} \end{cases} ; i = 1,2 \tag{3}$$

$$E_i^* = \begin{cases} \dfrac{E_i}{1-\nu_i^2} \text{ ; plane strain} \\ E_i \text{ ; plane stress} \end{cases} ; i = 1,2 \tag{4}$$

Using the general fracture-mechanical solution for an interface crack, $\delta_1 = u_1^{(u)} - u_1^{(l)}$ and $\delta_2 = u_2^{(u)} - u_2^{(l)}$ (where superscripts *(u)* and *(l)* stand for upper and lower crack flanks, respectively) are then given by

$$\begin{bmatrix}\delta_1 \\ \delta_2\end{bmatrix} = \Psi \cdot \begin{bmatrix}\sin(\epsilon \ln r) - 2\epsilon\cos(\epsilon \ln r) & 2\epsilon \sin(\epsilon \ln r) + \cos(\epsilon \ln r) \\ 2\epsilon \sin(\epsilon \ln r) + \cos(\epsilon \ln r) & -\sin(\epsilon \ln r) + 2\epsilon\cos(\epsilon \ln r)\end{bmatrix}\begin{bmatrix}K_I \\ K_{II}\end{bmatrix} \tag{5}$$

where

$$\Psi = \frac{1}{2}\left(\frac{1}{E_1^*} + \frac{1}{E_2^*}\right) \cdot \frac{8}{(1+4\epsilon^2)\cosh(\pi\epsilon)} \cdot \left(\frac{r}{2\pi}\right)^{\frac{1}{2}} \tag{6}$$

Eq. (6) is only used for establishing an expression for $\beta = K_I/K_{II}$:

$$\beta = \frac{K_I}{K_{II}} = \frac{-[\sin(\epsilon \ln r) - 2\epsilon\cos(\epsilon \ln r)] \cdot \delta_1 - [2\epsilon \sin(\epsilon \ln r) + \cos(\epsilon \ln r)] \cdot \delta_2}{-[2\epsilon \sin(\epsilon \ln r) + \cos(\epsilon \ln r)] \cdot \delta_1 + [\sin(\epsilon \ln r) - 2\epsilon\cos(\epsilon \ln r)] \cdot \delta_2} \tag{7}$$

In order to improve numerical performance, this computation of β is done for a number of positions along the crack, and the average of these is used together with Eq. (1) for the final computation of K_I and K_{II}:

$$\begin{cases} K_I = \sqrt{\dfrac{GH}{1+\dfrac{1}{\beta^2}}} \\ K_{II} = \sqrt{\dfrac{GH}{1+\beta^2}} \end{cases} \tag{8}$$

General laws of multiple fracture at static, cyclic and dynamic loading

Luidmila R. Botvina

Department of SSA, A.A.Baikov Institute of Metallurgy and Materials Science, Russian Academy of Sciences, 119991 Moscow, Russia, botvina@imet.ac.ru

Abstract Multiple fracture patterns of specimens from low - and medium carbon steel tested in conditions of static, dynamic and cyclic loading were studied. Cumulative distributions of microcracks by length under static and cyclic loading, distributions of the number of fragments by their mass under dynamic loading and amplitude distributions of acoustic emission signals were plotted. The parameters of these distributions at different stages of loading were estimated. It was studied the influence of specimen thickness, the distance to the fracture surface, the grain size and the failure mechanism on these parameters. The general laws characterizing multiple fractures at different loading conditions were found. They include, in particular, a change in function describing the distributions and a reduction of the exponents of these functions before fracture. The physical meaning of the estimated distribution parameters, the possibility of their use for the fracture prediction and material selection are discussed.

Keywords Multiple fracture, Damage evolution, General fracture laws

1. Introduction

The fundamental problem of materials science is associated with the need to relate macro characteristics of mechanical behavior of material with parameters of structure and its response to the loading conditions. This response is expressed in the formation of the localized plastic zone with a certain geometry and accumulation of internal damage, characterized by the size and density of microcracks. The evaluation of these parameters by the method of replicas removed from the surface of the polished specimens tested under different types of loading showed that there are some general regularities of the damage accumulation or the multiple fracture at the stage of macrocrack initiation, which will be discussed below.

2. Results of the study

2.1 Two stage of defect growth

Multiple fracture under conditions of irradiation and thermal fatigue [1], was studied using the histograms of the number - size distribution of voids in the aluminum irradiated using different neutron doses [2] and histograms of the distribution of thermal fatigue microcracks in the 06Cr18Ni11steel tested at different number of cycles [3].

Analysis of the cumulative number - size distributions of radiation defects with size of several angstroms in the aluminum [1] showed that these curves corresponding to different neutron doses can be reduced to a single distribution curve by normalization. This demonstrates the self-similarity of the process of accumulation defects at this early stage of their growth [4].

The thermal fatigue microcracks are longer than the radiation voids by several orders of magnitude. Figure 1 shows that the first self-similar stage of defect accumulation is described by an exponential law (the curves 1 – 3, Fig.1, a, b) and the second stage, by a power law (the curves 4 - 5). The exponents in the exponential laws decrease with the number of cycles and are 0.38, 0.17, 0.09 (R^2>0.92), respectively. The distribution curves 4 - 5 corresponding to stage of coalescence of voids are well described by a power law with the exponent 0.91 (R^2=0.98) (Fig.1, b, solid lines).

Thus, there are two stages of accumulation of defects: the first stage of growth of isolated voids

characterized by exponential distribution curves and the stage of accelerated growth due to void coalescence which is described by the power - law function.

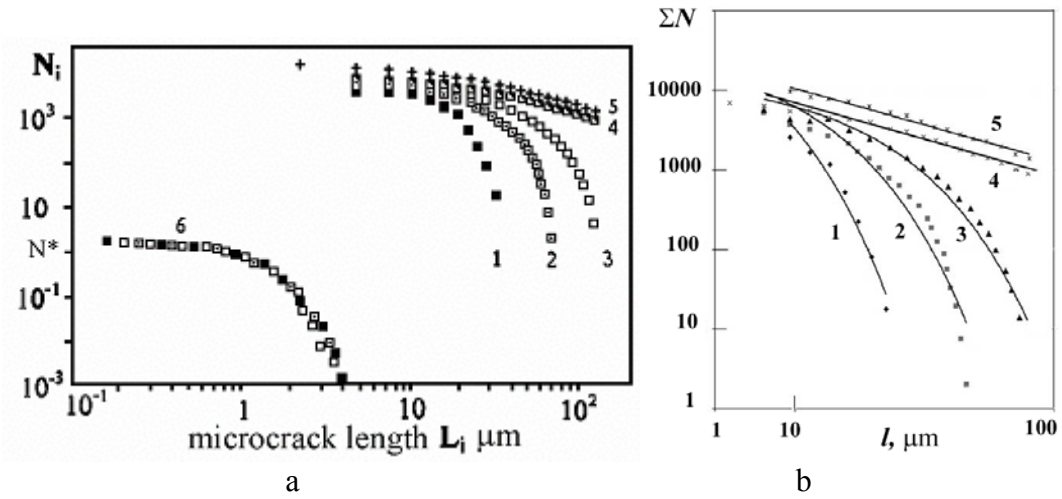

Figure 1. The cumulative number - size distributions of thermal fatigue microcracks in steel X6CrNi181 plotted using initial data [3] on microcrack growth at various numbers of cycles *N*: 2500 (curve 1), 4500 (2), 6500 (3), 11000 (4), 15000 (5). The curve 6 was obtained by normalizing the curves 1 - 3 with respect to the coordinates of their knee points. Solids lines in (b) correspond to the exponential (1-3) and power law (4, 5) relations

We assume that both the initial stages may obey the hypothesis of self-similarity, even though the characters of the laws describing these two stages of damage accumulation are different. It is important to note that the exponents in the exponential functions characterizing the first stage decrease with increasing a number of cycles.

2.2. Distributions of microcracks by their length at static loading

Similar results were obtained by means of analyzing the multiple fracture patterns in plastic zone of notched specimens from low carbon steel [5, 6]. The cumulative length - frequency distributions of microcracks in the plastic zones are shown in Fig. 2, which allows us to observe evolution of the distribution curves over different loading stages. It shows that as the tensile load increases, the change in these curves is similar to the change observed in thermal fatigue.

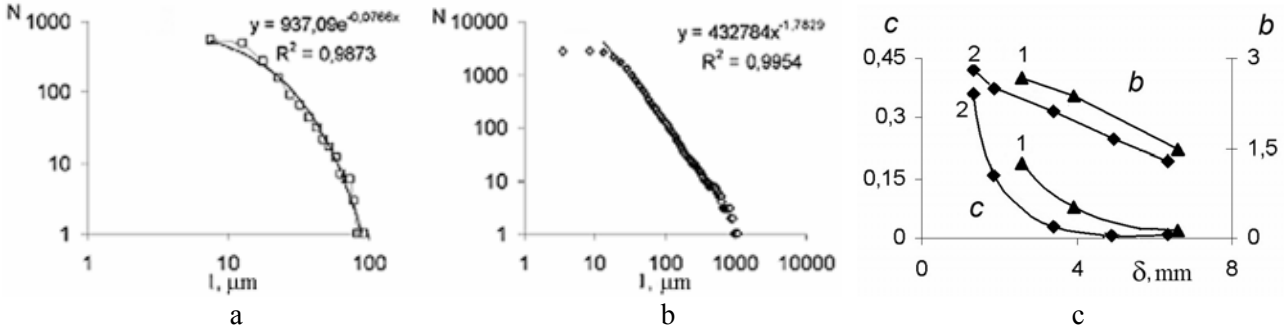

Figure 2. The cumulative distributions of microcracks in notched specimens from low carbon steel at different tension stages (a, b) (the specimen thickness is 6 mm): (a) – δ =2.8, P/P_{gy}=1,7; (b) –δ = 5.2, P/P_{gy} = 2.1, and dependencies (c) of the b - and c - values in the power-law and exponential cumulative number-length distributions of microcracks on the displacement of specimens (1) 16 and (2) 4 mm thick [4]

At the stage of the main crack formation, the exponential law

$$N \sim A \exp(-cl) \quad (1),$$

which describes multiple fracture patterns at the initial loading stage (Figure 2 a) is replaced by the power law

$$N \sim B\, l^{-b} \quad (2)$$

(Fig. 2 b). Both laws are characterized by the respective c and b exponents, whose absolute values decrease with load (Figure 2 c) and the specimen thickness.
An analysis of the amplitude distributions of the acoustic emission signals evaluated during tension has revealed the regularities similar to those, which were observed during tension; these are the change of the type of cumulative functions describing the number-amplitude distributions of signals and the reduction in the exponents of these functions before fracture.

2.3. Distributions of microcracks by their length at cyclic loading

The analysis of the distribution curves of fatigue microcracks in mild steel leads to the conclusion that the change of function describing these curves occurs with increasing a number of cycles (Fig. 3 a) and decreasing a distance from the specimen fracture surface (Fig. 3 b). As in the case of thermal fatigue, the change is accompanied by a reduction of the exponents of these functions.

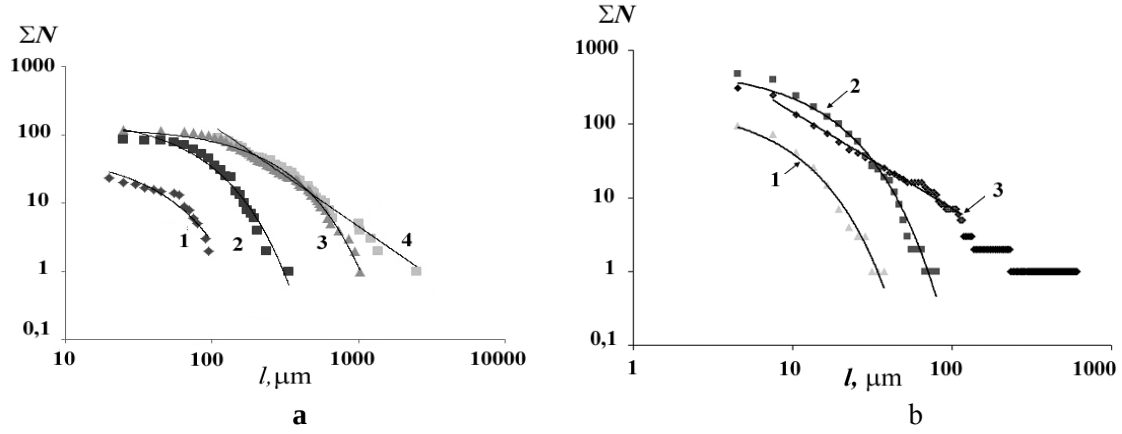

Figure 3. The cumulative distributions of fatigue microcracks in mild steel plotted on the data of Suh et al [7] at different relative number of cycles (a): n/n_f= 0,17 (1), 0,43 (2), 0,87 (3), 0,95 (4) and on data [5, 6] for microcracks located at a distance of 5.39 (1) 2.31 (2) and 0.79 mm from the fracture surface (b). Solid lines obey the exponential (a-curves 1-3, and b -1, 2) and power- law functions (a- curve 4, b- curve 3)

2.4. Distributions of fragments by their mass at dynamic loading

The similar conclusion was also made in studying the dynamic fracture [8, 9] (Fig. 4). The data presented in the Figure 4 show, firstly, that the number - mass distributions of fragments of shells made of brittle and ductile steels may be described by a simple exponential function:

$$\sum N \sim N_O \exp(-m/m_o) \quad (3),$$

and, as is seen from Fig. 4 b, the fragment distributions for the ductile material approach the power law N - m dependence. Secondly, the exponents of these distributions ($1/m_o$) are determined by the

mechanical properties of the fragment material and, in particular, by impact toughness of material in initial state (Fig. 4 c).

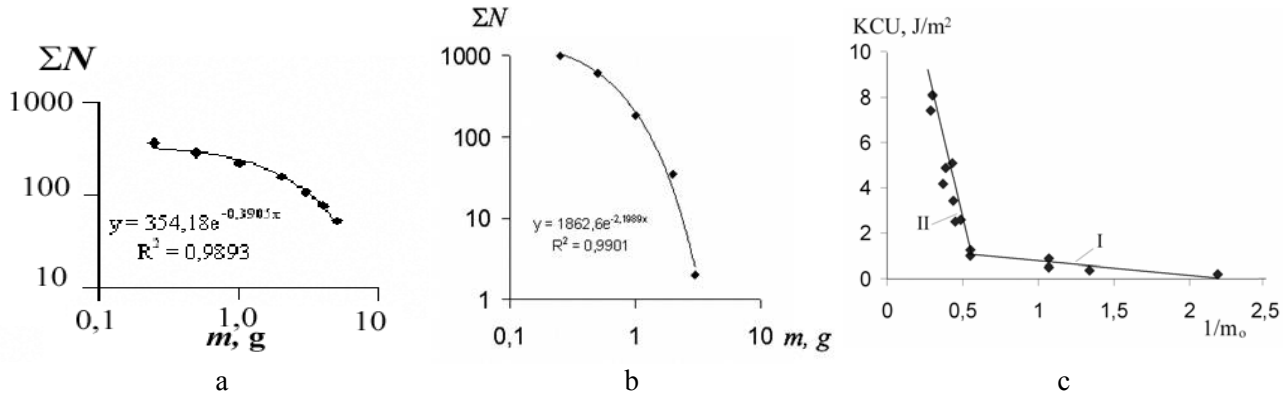

Figure 4. Cumulative number-mass distributions of shell fragments from brittle (a) and ductile (b) carbon steels, and dependence of impact toughness of the brittle (I) and ductile (II) steels on the exponents in the exponential relations describing distributions of fragments (c)

2.5. Concentration criterion of defects

At different stages of tension and fatigue, the average length of the microcracks L_{av}, their density n, fraction of the damages ω, and the values of concentration criterion k suggested in [10] and estimated by the relation

$$k = n^{-1/2} / L_{av} \tag{4}$$

were evaluated. It allowed to find that the transition from the exponential to the power - law relation with development of damage accumulation process is accompanied by reduction of the concentration criterion related to the coalescence of microcracks in the plastic deformation zone.

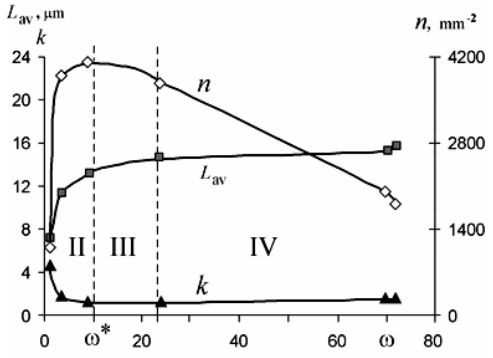

Fig. 5. Dependences of the average length (L_{av}), density of microcracks (n) and the concentration criterion (k) on the relative fraction of damages (ω) at the different loading stages of damage development (II, III, IV) (at the stage I plastic zone forms)

Four stages of the damage accumulation were found. At the first (I) stage, in the notch tip of specimen, slip bands appear and plastic zone is formed (before approaching the yield strength); at the second stage (II), the formation and the accumulation of the microcracks occur. Interaction of microcracks at the third stage (III) leads to their coalescence and initiation of macrocrack. At the fourth stage (IV), the main crack appears in a secondary plastic zone in its tip; the area of the

damaged surface grows as a result of the opening of microcracks. The development of the main crack leads to the complete fracture. Changes of the damage parameters at the observed stages of multiple fracture are shown in Fig. 5. It follows from the graphs that the critical situation appears at reaching the area of damages (ω*) close to 10%, when the microcrack opening increases, density of defects decreases as a result of their coalescence, and concentration criterion falls to the constant value (k~1.5). The value of ω*=10% is close to the threshold of percolation for many systems; therefore, changes at the third stage precede the critical event (specimen fracture). With reaching ω*, the exponential relation, which describes the cumulative distributions of microcracks and acoustic emission signals, becomes close to the power relation, and exponents in these relations reduce.

2.6. Activation energy of fracture process

An analysis of the established regularities of changes in exponents of the functions describing the statistical distributions allows us to connect them with a change in another important parameter of kinetic process, namely, in the activation energy of fracture.

According to Arrhenius – Zhurkov equation of [11], the lifetime (t) of solids is the function of the activation energy of fracture process $U(\sigma)$, the absolute temperature T, the energy of a thermal motion R and obeys the exponential relation:

$$t = t_0 \exp\left[\frac{U_0 - U(\sigma)}{RT}\right] \tag{5}$$

This relation may be obtained from a correlation $\lg t = \lg t_0 + b(\sigma)/T$, where $b(\sigma)$ is the slope of dependence $\lg t - 1/T$, $b(\sigma) = b = \Delta(\lg t)/\Delta(1/T)$,

or $t = t_0 \exp(\beta/T)$, where $\beta = 2.3b$.

Multiplying the numerator and denominator of the exponential function index by the Boltzmann constant and denoting $k\beta = U$ leads to (Eq. 5).

Thus, the activation energy is evaluated on the slope coefficient b of creep curves plotted in semi logarithmic coordinates [12]. The stress dependence of the activation energy of fracture of polymethylmethacrylate, which was plotted using these data [13], showed that the activation energy decreases with increasing the stress and the stress dependence of activation energy corresponds to the exponential relation with the exponent equal to 0.02 and R^2=0.98. Similar decrease of the slope coefficient with increasing the load or specimen displacement is presented in Fig. 2 c.

The activation energy of solids is traditionally related (by the analogy with that of chemical reactions) to the energy given for the overcoming of inter-atomic interaction by thermal fluctuations. Although the fracture process in the whole is determined by the strength of atomic bonds in the region of fracture localization, this approval calls for the special confirmation. Indeed, the slope coefficient of strength dependencies obtained for laboratory specimens is the macroscopic parameter revealing the kinetics of initiation and accumulation of microcracks and growth of a macrocrack. These processes are connected to changes in the fracture process zone size and damage accumulation in this zone. Therefore, the decrease in the activation energy with increasing stress may be a consequence of considered above regularities of damage accumulation in the fracture process zone that are due to the interaction of defects resulting in a decrease in the slope coefficients of statistical distributions. This assumption is confirmed by an analysis performed in [6, 13], which showed an interrelationship between the activation energy and exponents in power law equations characterizing the fracture development, namely, in both the Paris relation and the equation based on the phase transition theory.

3. Summary

The patterns of multiple fractures in carbon steel specimens at different stages of tension, cyclic and dynamic loading were studied; characteristics of damage accumulation were estimated and the cumulative distributions of microcracks and shell fragments were plotted. Analysis of damage accumulation process with the use of mechanical and physical methods allows us to establish some general laws characterizing this process on different stages. They include, in particular, the following.

- Distributions of microcracks under static and cyclic loading and amplitude distributions of acoustic emission signals measured during static loading are described by an exponential function at the initial stage of fracture and a power –law one at the final stage of fracture.
- Cumulative number-mass distributions of the shell fragments obey the exponential relations with the slope coefficients, which decrease for the brittle materials.
- There is a quantitative relationships of the exponents of functions approximating the distributions with material properties and loading parameters.
- Parameters of the cumulative distributions of microcracks and amplitude distributions of acoustic emission signals, as well as the concentration criterion are reduced at the stage of pre-fracture and can serve as diagnostic signs of the approaching fracture.

Acknowledgements

This study was partially supported by the Russian Foundation for Basic Research, project no. 12-08-13182 and 11-08-00983.

References

[1] L.R. Botvina, N.A. Zharkova, Self - similarity of the radiation defects accumulation process, Scripta metall. 38 (1998) 1829 – 1833.
[2] N.H. Paskan, Fluence and dependence of void formation in pure aluminum, J. of Nucl. Mater., 40 (1971) 11 – 17.
[3] K. Bethge, D. Munz, J. Neumann, Crack initiation and crack propagation under thermal cyclic loading, High Temp. Techn., 8 (1990) 98 – 104,
[4] L.R. Botvina, G.I.Barenblatt, Self-similarity of damage accumulation, Problems of Strength, 12 (1985)17 – 24,
[5] M.R. Tyutin, L.R. Botvina, N.A. Zharkova, T.B. Petersen, J.A. Hudson, Evolution of damage in low - carbon steel in tension condition, Strength, Fract. and Compl., 3 (2005) 73 – 80.
[6] L.R. Botvina, Fracture: kinetics, mechanisms, common regularities, Nauka, Moscow, 2008.
[7] C.M. Suh, R.Yuuki, H. Kitagawa, Fatigue microcracks in low carbon steel, Fatigue Fract. Eng. Mater. Struct., 8 (1985) 193 – 203.
[8] L.R. Botvina, V.N. Mochov, On parameters determining a character of dynamic fragmentation of steel shells, Deform. and Fract. of Mater., 12 (2006)19 – 25.
[9] L.R. Botvina. Dynamic fragmentation that reflects the effect of composition and mechanical properties of a material and loading conditions, Russian Metallurgy (Metally), 10(2011) 973 – 980.
[10] S.N. Zhurkov, V.S. Kuksenko, A.I. Sluzker, Formation of submicroscopic cracks in polymers under load, Physics of solid, 11 (1969) 296 – 302.
[11] S.N. Zhurkov, Kinetic concept of the strength of solids, Intern J. of Fracture Mechanics 1 (1965) 311–323.
[12] S. B. Ratner, Yu. I. Brochin, Temperature-time dependence of the limit stress of induced

elasticity for polymers, Reports of USSR Academy of Science 188 (1969) 807–810.
[13] L.R. Botvina, On correlation of various approaches for description of kinetic processes, Intern. J. of Fracture. 99 (1999) 131–141.

In-situ SEM/EBSD Study of Deformation and Fracture Behaviour of Flake Cast Iron

Mattias Lundberg[1,*], Mattias Calmunger[1], Ru Lin Peng[1]

[1] Department of Management and Engineering, Linköping University SE-581 83 Linköping
*Corresponding author: mattias.lundberg@liu.se

Abstract Cast irons' position as an important engineering material is un-disputed. They are widely used in many important industrial applications such as the automotives and workshop machinery. Nevertheless, fracture mechanisms in cast irons are not fully understood. In this study the fracture path and non-linear elastic behaviour of a fully pearlitic flake cast iron under uniaxial tensile loading have been investigated in a Scanning Electron Microscope (SEM) equipped with an Electron Backscattering Diffraction (EBSD) detector. The tensile load was applied via a specially made sample stage. Under uniaxial tensile loading the graphite flakes act as notches or cracks and therefore the fracture process starts at one or many graphite tips. The crack can propagate in many different ways, at the graphite and matrix interface, through the graphite, at the interface between cementite and ferrite or through the pearlitic grains. At the point where the stress strain curve deviates from its linear path plastic deformation at graphite tips can be noticed. Interface cracking between graphite and the matrix also starts at this point.

Keywords in-situ SEM, deformation, fracture, flake cast iron, EBSD

1. Introduction

Flake cast iron exhibits brittle failure under tension loading. Due to its many graphite tips acting as notches or small cracks they are considered to be initiation points for cracks in the material. The common knowledge on how cracks propagates in flake cast irons is that the crack initiation point is one or several of the many graphite tips, from the tips the crack propagates along the graphite flakes in the graphite-matrix interface. At strains just before break down, the crack propagates through the matrix and connecting graphite tips.

In a work done by Diószegi at al [1] the crack path was found to be through eutectic cells and along the graphite flakes. Depending on cooling condition the main crack path varied so to propagate along dendrites.

The mechanisms explaining the non-linear stress-strain curve founded for flake cast irons involves a small plastic zone at graphite tips [2]. A typical stress-strain curve for a flake cast iron with σ_{UTS} of 290 MPa can be seen in Figure 3. As can be seen there is a small portion when the curve is straight linear; according to literature the explanation for this linear part is the atomic bonds and the interface forces between the graphite and the matrix [3, 4]. Plastic deformation at graphite tips and separation between graphite and matrix seems to be an excepted description what happens in the material when the stress-strain curve starts to deviate from its linear path during tensile loading [4].

An electron backscatter detector (EBSD) uses kikuchi patterns and a database to identify crystal structure and crystallographic orientation. Especially grain lattice orientation and grain size is commonly determined with this technique [5-10]. Texture analysis of metallic material using EBSD is a commonly usages of this technique [8, 10-11]. Strain variations in each grain near the machined surface give vital information on damages from machining processes [12]. From distribution and amount of low angle grain boundaries (LAGB) in the material, strain variations from external forces as well as from the solidification process can gathered. In a work done by Bjerkaas at al. on an AlMgSi alloy the benefits of this technique (EBSD) shows that grain lattice orientation during

tensile testing depends much on originally un-tested grain orientation, so different slip systems becomes active depending on grain orientation [6].

Several different research groups have performed tensile in-situ scanning electron microscope (SEM) investigations, studying microstructural changes and deformation and/or fracture mechanisms on different materials [6, 10, 13-15]. From their experiments one can conclude that in-situ SEM investigations can give very accurate information about microstructural changes due to external forces. Some of the recent works in this field have also performed EBSD to analyse the microstructural changes, e.g. grain orientation and grain reorientation, due to loading.

In this study the crack initiation point(s) and crack propagation in a grey cast iron where studied during axial loading in a SEM. Thanks to a specially designed stage mounted to the SEM, in-situ analysis of the crack initiation and its propagation as well as crystallographic changes were detected with EBSD and analysed. The microstructural features associated with different proportions of the stress-strain curve were investigated and explained.

2. Experimental details

The flake cast iron had a fully pearlitic matrix and the composition of the material used is listed in Table 1 below.

Table 1. Nominal composition of flake cast iron used

Element	C	Si	Mn	P	S	Cu	Cr	Mo	Fe
Wt %	3.1	1.8	0.65	<0.08	0.12	0.90	0.14	0.25	Bal.

The samples were cut out to a thickness of 1.0 mm from an as-cast cylinder head, using an electronic discharge wire to minimize the effects of surface hardening and residual stresses. On one side of the sample a notch was cut out with a total depth of 1.0 mm and a notch root radius of 0.25 mm. Both sides of the samples were carefully grinded and one side future prepared for EBSD analysis. On the rougher side of the sample a strain gauge were attached to enhance the accuracy of the actual loading when inside the SEM. Due to the brittleness of flake cast iron and the small elongation before rapture, some points on the stress strain curve in vacuum could then be conducted. Strain gauge signals were transmitted through pins on the stage specially designed for signal transmission from the vacuum chamber.

The samples were investigated at loadings of approximately 0 MPa, 50 MPa, 90 MPa, 140 MPa, 200 MPa and 250 MPa. EBSD mapping with a step size of 0.3 µm and SE images on each loading were performed in a Hitachi SU-70 FEG-SEM equipped with an OXFORD Electron Backscatter Diffraction system with HKL software. Due to contamination of the surface (carbon diffusion from the material when the electron beam hits the sample) from the EBSD analysis two different locations were used.

In all the figures the loading axis is in the horizontal plane, excluding Figure 3 and Figure 7.

3. Results

The un-tested material shows a great amount of LAGB, Figure 1c display the frequency distribution of LAGB and grain boundaries (GB). Revealing that LAGB of 2-3° is most common and that GB most commonly have angels around 30° and 60°. Figure 1b also reveals where the LAGB and GB are located; the most common LAGB is represented as red line and is randomly distributed in the microstructure. This resulted in two different LAGB intervals in this analysis to increase the detectability of LAGB changes. They are denoted as type I (2-6 °, red lines) and type II (6-12 °, green lines) LAGB respectively.

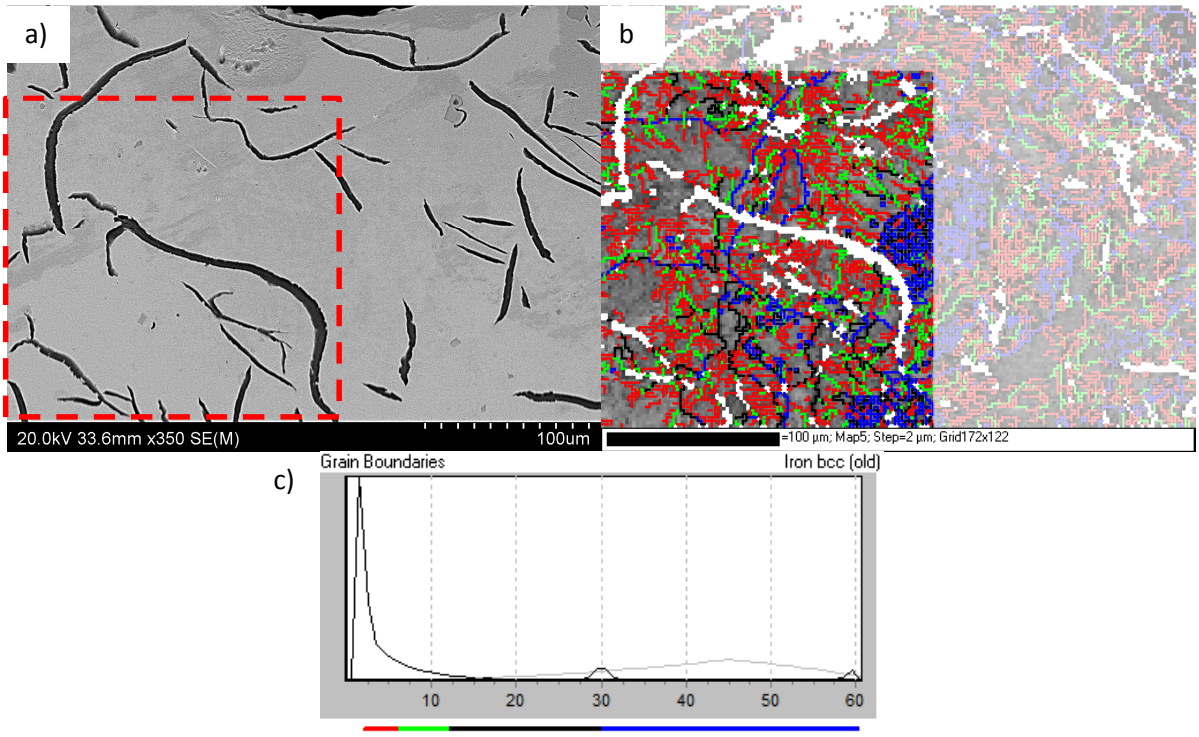

Figure 1. Display a) SE-picture with red marked EBSD-analysis area, b) EBSD-map showing band slope and the distribution of LAGB and grain boundaries (GB) and c) the grain boundary legend shows the colour of corresponding angle [°] and the frequency distribution of LAGB and GB. Zero solution is marked white.

In Figure 2 the LAGB distribution can be seen when a force corresponding to 200 MPa is applied. In Figure 2a graphite flakes have become larger due to internal cracking and matrix-graphite interface delamination, despite this the LAGB:s is unchanged.

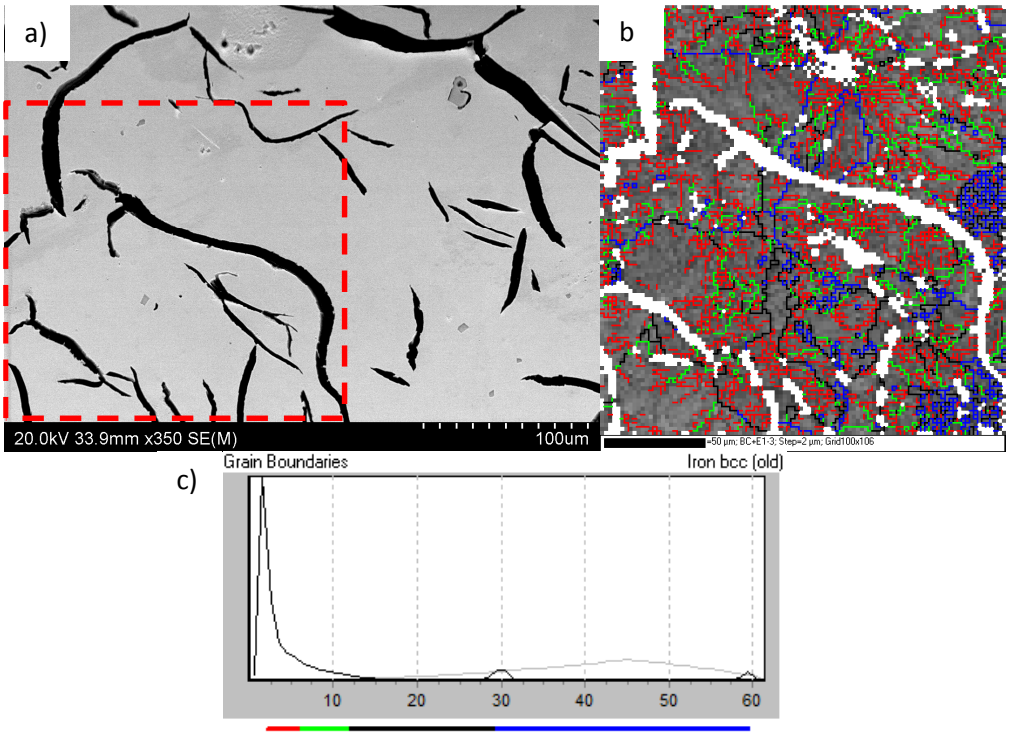

Figure 2. Display a) SE-picture with red dots marking the area of EBSD-analysis, b) EBSD-map showing band slope and the distribution of LAGB and grain boundaries (GB) and c) the grain boundary legend shows the colour of corresponding angle [°] and the frequency distribution of LAGB and GB. Zero solution is marked white.

The pure linear elastic part of a typical stress-strain curve for a flake graphite iron can related to the small tensile load that the graphite can withstand without microscopic yielding [16, 17] and the atomic forces. In this region the SE images did not revile any changes in the microstructure in neither the matrix nor the graphite. Also the EBSD mapping looks the same as in the un-stressed case, no statistical significant changes were found.

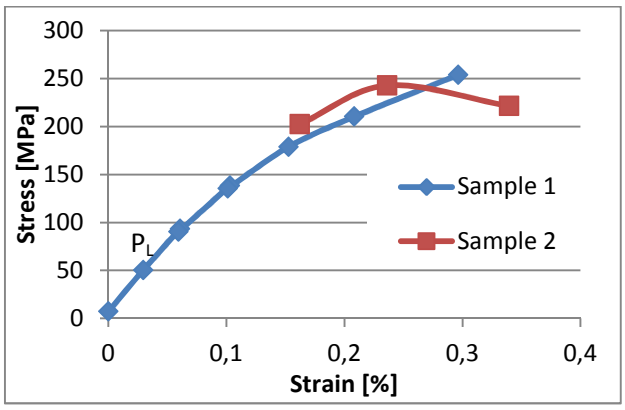

Figure 3. Obtained stress-strain curve from the experiment.

What then can be seen in SE-images, see Figure 2, when the applied load is slightly more than the critical value $P_{L;}$ (were the stress-strain curve starts to deviate from its linear path) the flaky graphite tends to open in the middle and a void appears inside. This phenomenon can be seen and detected in graphite orientated both perpendicular and parallel to the loading axis at loading levels above P_L ,

see Figure 3. At this stage the changes in the matrix is still too small to be detected with the set-up used.

When increasing the load, ($P>P_L$) the interface between the flaky graphite and the matrix starts to separate at several places in the material, mostly graphite flakes oriented perpendicular to the load shows this phenomenon. Still the cracks/voids earlier founded inside the flaky graphite opens more independent of the graphite's orientation, but the degree of opening is more evidence in graphite perpendicular to the load axis. The pearlitic matrix also starts to undergo microplasticity at several graphite tips, the matrix undergo local plastically deformation which can be seen in Figure 4 and Figure 5.

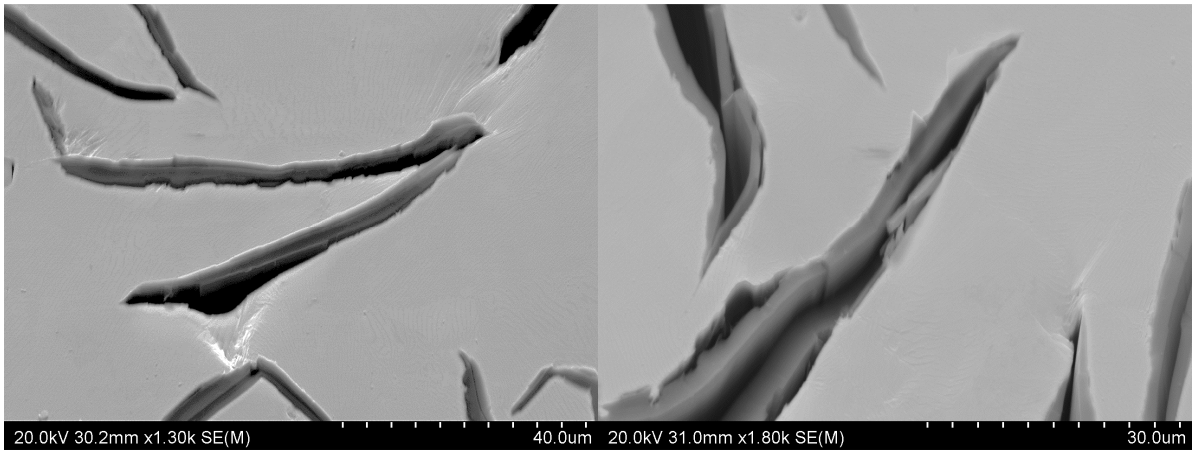

Figure 4. Plastic deformation at graphite tips and a bulge is evidence in the left picture. To the right multiple cracking with crack path both inside the graphite and at the graphite-matrix interface can be seen.

The delamination of the graphite-matrix interface is easy to identify and when increasing the load even more, above 200 MPa, small bulges in the separated graphite-matrix interface is evidence of the weakest pearlite, see Figure 4. Here at these bulges the matrix limited plasticity results in a crack path when the load is increased even more, local necking in the matrix.

At loads above $\sigma_{ys0.2\%}$ the crack also finds its way through the matrix in the ferrite-cementite interface as can be seen in Figure 5 below.

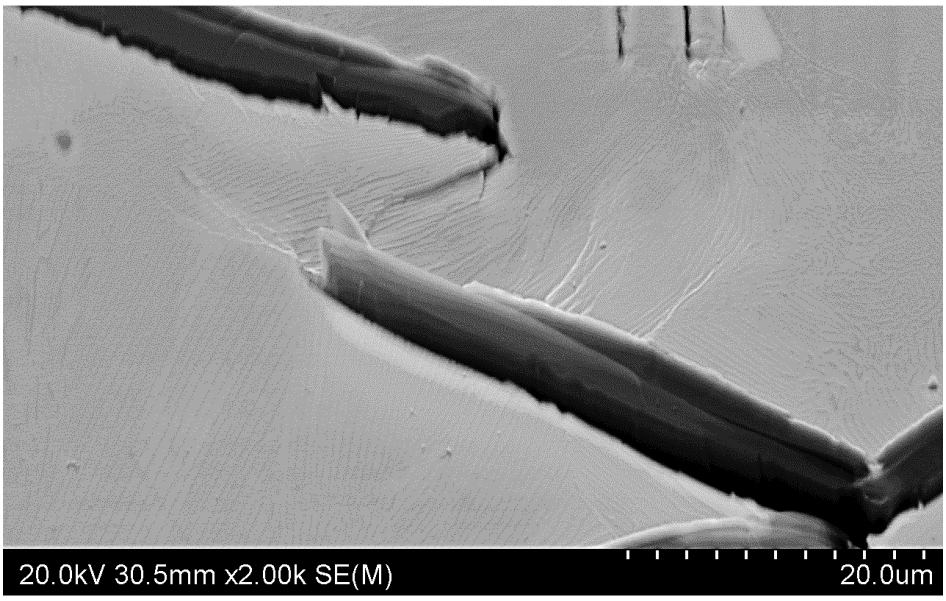

Figure 5. Cracking in the ferrite-cementite interface between two graphite tips.

At stresses above $\sigma_{ys0.2\%}$ the phenomenon of multiple cracking is also evident in the material, showing the complexity of the fracture behaviour of the material. In Figure 6 below this phenomenon can easily be seen in the left picture. The right picture is zoomed out from the left showing obviously multiple cracking.

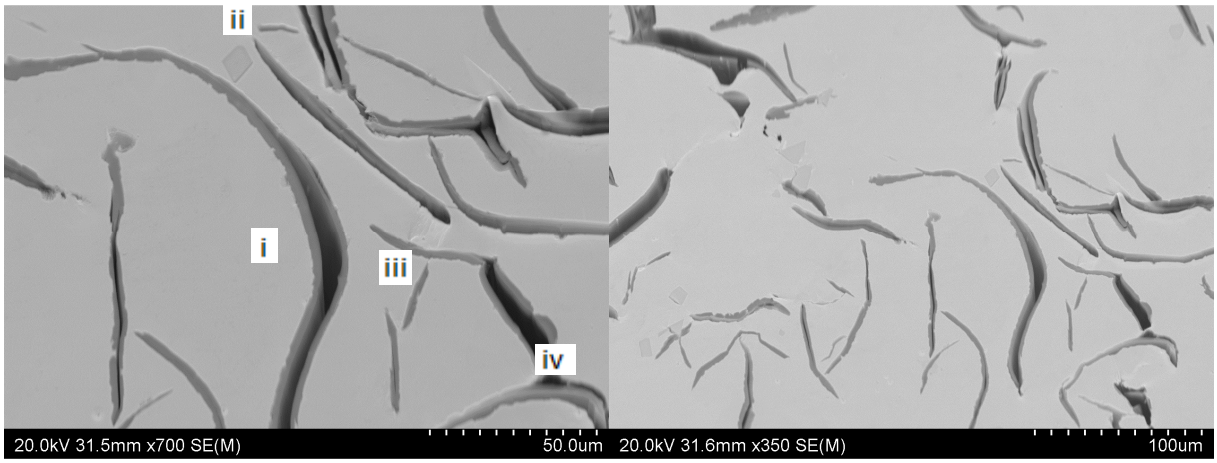

Figure 6. Showing voids inside graphite flakes (i), delamination of the graphite-matrix interface (ii), plastic deformation at graphite tips (iii) and a bulge (iv).

Fractorgraphy revealed that both ductile-like and cleavage-like fracture is present in flake cast iron. Near the notch almost all pearlite grains showed evidence of ductile crack surface, whereas the opposite side of the sample showed mainly river-pattern in the cracked pearlite associated with cleavage fracture. In Figure 7 below both these features can be seen along with a part of a graphite flake.

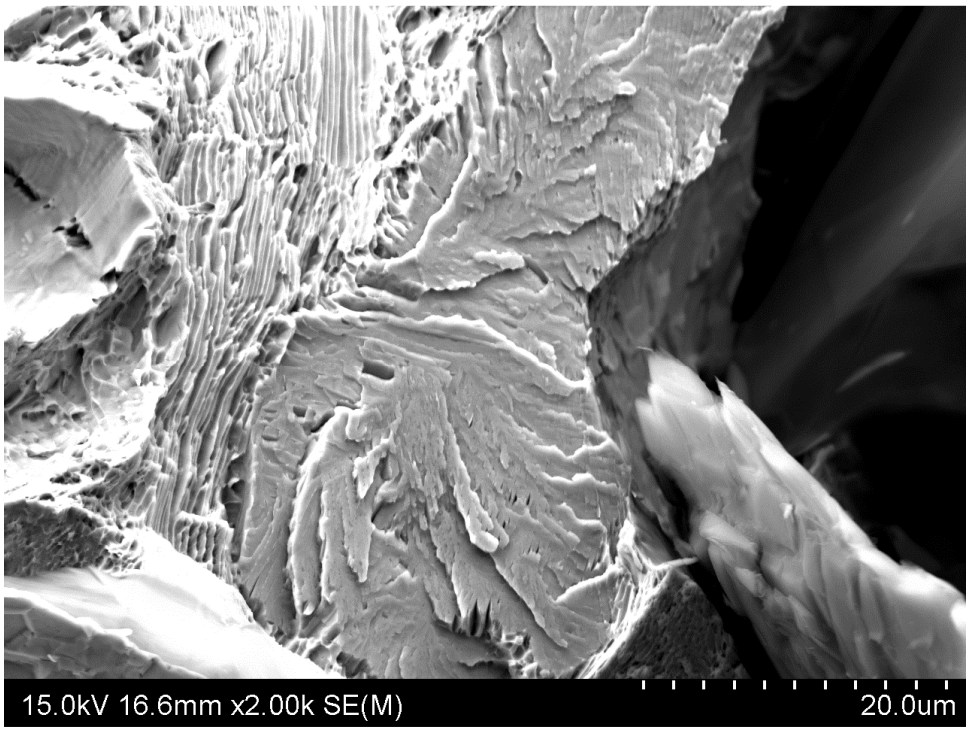

Figure 7. Fracture surface showing features associated with both ductile and brittle fracture in the pearlite matrix. On the right side a part of a graphite flake is seen.

4. Discussion

Even though pearlitic flake cast iron is widely used and is an important engineering material the knowledge on its fracture behaviour and the deformation due to axial loading is still very limited. One of the main goals with this research was to gain deeper knowledge on the deformation and fracture behaviour of a pearlitic flake cast iron. The use of the special designed stage in the SEM together with EBSD analysis can give a unique insight in the deformation and fracture behaviour of the material studied. In this study the amount of pre-existing LAGB's made the analysis of their changes due to loading very difficult and no clear effects where shown. The great amount of LAGB's detected is an effect of the solidification process and the material used had not been stress-relived. The heat treatment should decrease the amount of LAGB's once the internal thermal residual stresses from the solidification process minimizes. One aim with this study was to investigate the LAGB changes and the grain orientation due to axial loading and from these results no changes were detected.

The deformation of a flake cast iron under axial loading can be divided into several different main events. First deformation detected in the material was the development of voids inside graphite flakes. This material deformation was detected at loads as low as 50 MPa and the strength of the weakest slip plane in the graphite is approximately 40 Mpa which then makes the fact that it separates at 50 Mpa very understandable. With compressive residual stresses presence at the surface this deformation would not be seen at this load-level and thanks to careful polishing this effect could be discovered. Interesting to see is that when increasing the load these voids can be found in graphite flakes independent of its orientation to the load axis. Delamination of the graphite-matrix interface was the second kind of deformation detected in the material. This deformation requires slightly more applied load and a suggested explanation for this is that the interface forces between the two phases is just greater than the weakest slip plane in the graphite. By looking at the stress strain curve seen in Figure 3 one can see that curve deviates from its linear path at stresses between 50 and 90 Mpa and it is proposed by the authors that this is an effect of both the delamination of the graphite-matrix interface and the presence of voids inside the graphite flakes. These effects are also responsible in the change of Young´s modulus as seen in for flake cast iron subjected to cyclic loading, less elastic deformation is possible for this multi-phased material. Plastic deformation at graphite tips was the third permanent deformation detected in the material. Loads generating stresses in the magnitude of 140 Mpa and more results in plastic deformation at graphite tips. With increasing load the size of the plastic zone is increased and also amount of plastic deformation around graphite tips increases with increasing load. This is expected to be seen but not that the sizes of voids inside graphite flakes to decrease for those voids lying a bit away from the real crack path. Obviously some kind of stress relaxation occurs in the material when the pearlite starts to hardens due to the plastic deformation at the graphite tips. The last type of deformation detected was the development of bulges just before rapture, as a consequence of stress concentrations at the graphite. When study the final fracture it was then evident that the crack path had been via these bulges. The plastic deformation at these bulges is severe and a phenomenon of local necking is present.

Fracture behaviour becomes more and more complex as the applied load increases and several distinct features acting simultaneously resulting in final failure. The graphite tips acts as notches and clearly the plastic deformation at the tips indicates where the crack later will propagate. Due to multiple cracking not every graphite flake with local plastic deformation at the tip will be a part of the final cracking. Fractography reviled a ductile fracture where the bulges earlier had been detected leading to the conclusion that severe plastic deformation at the tips results in the ductile-like fracture found in the material.

Not every graphite flake that opens inside contributes to the final crack but once they have opened it affects the mechanical properties of the cast iron. It has been identified in this investigation that the first fracture observed in the material actually occurs inside the graphite flakes followed by delamination of the graphite-matrix interface. The non-linear elastic behaviour and the decrease in Young´s modulus observed in flake cast iron is proposed by the authors to a result of these two permanent deformation phenomenon´s in the material.

5. Conclusions

The fracture behaviour of flake cast iron can be summarized in a few steps of main events. The first noticeable microstructural feature due to the axial loading is the opening of graphite. Graphite flakes opens inside the flakes and this feature can be found in graphite flakes independent of its orientation to the applied load. As a second important and noticeable event is the delamination of the graphite-matrix interface. Parallel to this event one can see that the graphite that had opened inside opens even more. The third crack feature is the local plasticity at graphite tips laying perpendicular to the loading. Fourth and last important feature is the bulge of the matrix at the delaminated interface, where the crack later will propagate. Some of the graphite with an opening inside had also generated a delamination of the graphite-matrix interface. Development of bulges start once the plastic deformation at graphite tips is evidence but stresses close to and above $\sigma_{ys0.2\%}$ is needed to clarifying that a bulge is developed and not just local plastic deformation. At applied loadings just before rapture the fracture behaviour of flake cast iron results in multiple cracking, which makes it possible for the main crack to “jump” relatively large distances due to the network of flaky graphite. The weakest points in the sample will then link together which results in a rough topography of the fracture surface. As a final occurrence of fracture behaviour in flake cast iron subjected to axial loading the crack propagates in one of the following alternatives:

- Through the opening inside the graphite.
- Through the delaminated interface.
- Via the closest distance between graphite tips where the local plastic deformation results in a ductile-like fracture appearance.
- At the pearlitic grain boundaries leaving a ductile-like fracture.
- Straightforward through the matrix resulting in a cleavage fracture.
- Along the ferrite-cementite interface giving cleavage fracture.

Grain orientation and changes of LAGB’s in flake cast iron due to axial loading is very small, if existing, the relative fine step-size used could not show any differences. Fractography give instant insight why the crack propagated to the right in Figure 1 and not on the left side as large graphite flakes where located just below the surface to the right and not to the left. Analyse of the fractured surface revealed both ductile and cleavage fracture and an increase in fracture topology where multiple cracks was easily detected.

Acknowledgment

The authors would like to thank Maqsood Ahmad from Volvo Powertrain for providing the material. Agora Materiae graduated school at Linköping University.

References

[1] A. Diószegi, V. Fourlakidis, I.L. Svensson, Fracture Mechanics of Gray Cast Iron, Material Science Forum, 649 (2010) 517-522.
[2] L. Haenny, G. Zambelli, Strain Mechanisms in Grey Cast Iron, Engineering Fracture Mechanics, 18 (1983) 377-387.
[3] H.T. Angus, Cast Iron, Butterworth, London, 1976.

[4] T. Sjögren, Influence of the Graphite Phase on Elastic and Plastic Deformation Behaviour of Cast Irons, Linköping Studies in Science and Technology Dissertations No. 1080, Linköping.
[5] A.J. Schwartz, Electron Backscattering Diffraction in Material Science, Springer Science + Business Media, New York, 2009.
[6] H. Bjerkaas, S.K. Fjeldbo, H.J. Roven, J. Hjelen, R. Chiron, T. Furu, Study of Microstructure and Texture Evolution using In-situ EBSD Investigations and SE Imaging in SEM, Material Science Forum, 519-521 (2006) 809-814.
[7] S. Ifergane, Z. Barkay, O. Beeri, N. Eliaz, Study of Fracture Evolution in Copper Sheets by In-situ Tensile Test and EBSD Analysis, Journal of Material Science, 45 (2010) 6345-6352.
[8] M.F. de Campos, L.C. Rolim Lopes, P. Magina, F.C. Lee Tavares, C.T. Kunioshi, H. Goldenstein, Texture and Microtexture Studies in Different Types of Cast Irons, Material Science and Engineering A, 398 (2005) 164-170.
[9] M. Kamaya, Assessment of Local Deformation Using EBSD: Quantification of Local Damage at Grain Boundaries, Materials Characterization, 66 (2012) 56-67.
[10] M. Ferry, W. Xu, Microstructural and Crystallographic Features of Ausferrite in As-cast Gray Iron, Materials Characterization, 53 (2004) 43-49.
[11] G. Rivera, P.R. Calvillo, R. Boeri, Y. Houbaert, J. Sikora, Examination of the Solidification of Spheroidal and Flake Graphite Cast Irons using DAAS and EBSD, Materials Characterization, 59 (2008) 1342-1348.
[12] R. Lin Peng, Y.D. Wang, G. Chai, N. Jia, G. Wang, S. Johansson, On the Development of Grain-orientation-dependent and Inter-phase Stresses in a Super Duplex Stainless Steel Under Uniaxial Loading, Material Science Forum, 524-525 (2006) 917-922.
[13] V. Di Cocco, F. Iacoviello, M. Cavallini, Damaging Micromechanisms Characterization of a Ferritic Ductile Cast Iron, Engineering Fracture Mechanics, 77 (2010) 2016-2023.
[14] F. Iacoviello, O. Di Bartolomeo, V. Di Cocco, V. Piacente, Damaging Micromechanisms in Ferritic-Pearlitic Ductile Cast Irons, Materials Science and Engineering A, 478 (2008) 181-186.
[15] A. Ghahremaninezhad, K. Ravi-Chander, Deformation and Failure in Nodular Cast Iron, Acta Materialia, 60 (2012) 2359-2368.
[16] J.R. Dryden, G.R. Purdy, The Effect of Graphite on the Mechanical Properties of Cast Irons, Acta Metallurgica, 37 (1989) 1999-2006.
[17] D.D. Double, A. Hellawell, Defects in Eutectic Flake Graphite, Acta Metallurgica, 19 (1971) 1303-1306.

An Advanced Damage Percolation Model of Ductile Fracture

Cliff Butcher[1,*], Zengtao Chen[2], Michael Worswick[1]

[1] Department of Mechanical and Mechatronics Engineering, University of Waterloo, Canada
[2] Department of Mechanical Engineering, University of New Brunswick, Canada
* Corresponding author: cbutcher@uwaterloo.ca

Abstract

A multi-scale damage percolation model has been developed to predict fracture in advanced materials with heterogeneous particle distributions. The percolation model was implemented into a commercial finite-element code using so-called "percolation elements" to capture the complex stress- and strain-gradients that develop within the microstructure during deformation. In this approach, fracture is predicted as a direct consequence of the stress state, material properties and local conditions within the microstructure. Void nucleation, growth and coalescence models are applied for ellipsoidal voids subjected to general loading conditions. A novel void nucleation rule is employed for particle cracking based upon the particle morphology and stress state. A particle field generator has been implemented into the percolation software to generate representative particle fields based upon the field statistics obtained using x-ray micro-tomography. The percolation model was validated numerically and experimentally for an automotive-grade aluminum alloy in a notched tensile test used for material characterization.

Keywords: Void, Particle, Nucleation, Coalescence, Multi-scale

1. Introduction

The traditional approach to modeling ductile fracture involves homogenizing the microstructure of a material into a simple, equivalent geometry from which the relevant constitutive laws can be derived [1]. While attractive from a modeling perspective, critical details of the microstructure are lost in this homogenization process such as the particle size, shape, orientation, distribution and degree of clustering. Since void initiation and evolution is a highly localized phenomenon originating within heterogeneous particle clusters, these models fail to reliably predict fracture without requiring many calibration parameters. These limitations can be overcome using a damage percolation model that relies upon measured particle distributions obtained using digital imaging or x-ray micro-tomography. Micromechanical models can then be applied to each void and particle within the material to forge a direct link between local changes in the microstructure and the overall material behaviour. An advanced damage percolation model has been developed by Butcher [2] that was directly integrated into a commercial finite-element code as illustrated in Figure 1. The performance of this percolation model is evaluated by applying it to a notched tensile test specimen of AA5182 sheet. The predicted fracture strains, porosity and nucleation trends are compared and validated with the experiment data and the porosity data available in the literature.

1.1 Basics of the percolation model

The basics of the damage percolation model were established by Worswick et al. [3-4] and Chen [5] where particle fields are obtained via digital imaging techniques or micro-tomography. The particle field is then tessellated to extract the size, shape, location, and nearest neighbours of each particle and void within the field. This information is then used to re-create the particle field so that micromechanical models can be applied to each particle and void and thus predict fracture within heterogeneous particle distributions. The particles, voids and cracks are all assumed to be ellipsoidal where cracks are first formed by the coalescence of voids. The cracks are formed via a bounding box method and are subject to the same evolution laws as the voids. In the coupled

FE-percolation model of Butcher [2], the particle field is decomposed into "percolation elements" based upon the resolution of the finite-element mesh to better capture local stress and strain gradients within the microstructure. Void nucleation and coalescence occur within each percolation element with a global search for void coalescence occurring between elements at the end of each time step. The general percolation modeling strategy is outlined in Figure 2 and discussed in the subsequent sections. The interested reader is referred to [2] for additional details.

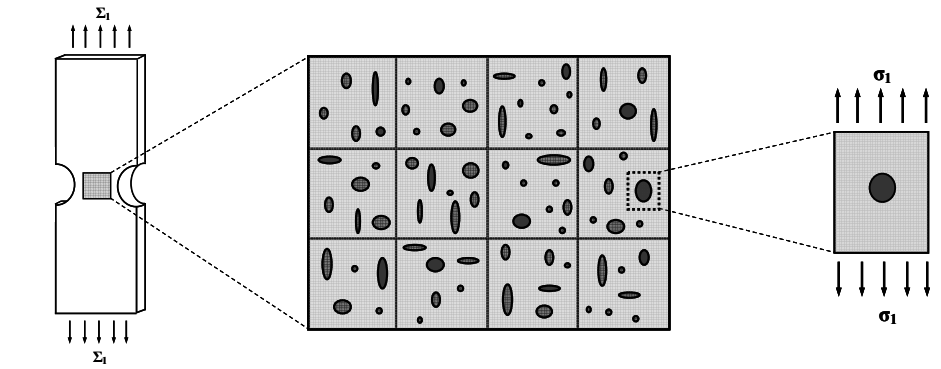

Finite-element model of a notched tensile test

Finite-elements are mapped onto a measured particle field

Micromechanical models are applied to each particle to characterize local void initiation and evolution leading to fracture

Figure 1: Multi-scale percolation model applied to a finite-element simulation of a tensile test.

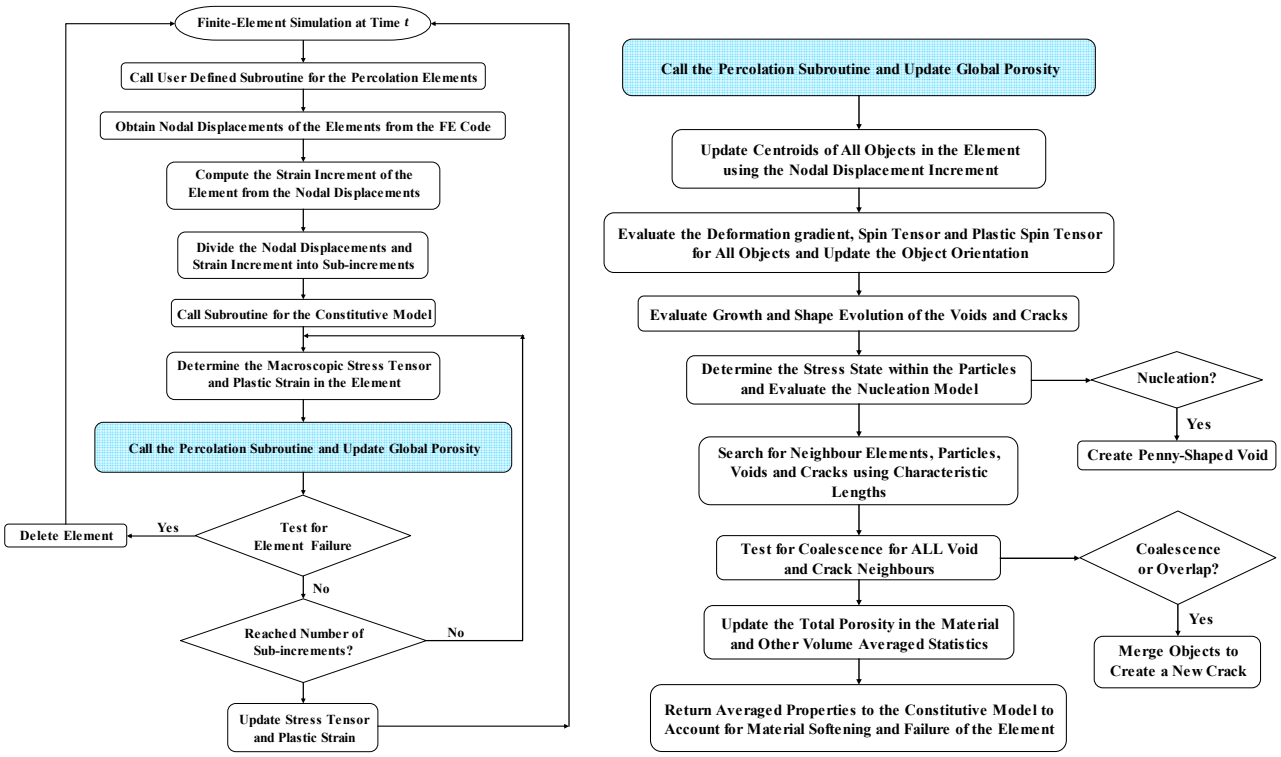

Figure 2: Flow-chart of the percolation modeling process

2. Constitutive model

The percolation material model was written as a user-defined subroutine for LS-DYNA [6] to integrate the stress state, analyze the microstructure for void evolution and return the stress tensor

and plastic strain to the finite-element program. The macroscopic stress and strain rate tensors are denoted as, Σ_{ij}, and D_{ij}, respectively. The porosity (void volume fraction), spheroidal aspect ratio and void spacing ratio are denoted as f, W, and χ, respectively. A Gurson-based yield criterion [1,7] using the modification of Ragab [8] for the q_i parameters is employed to account for material softening within the percolation element and is expressed as

$$\Phi = \left(\frac{\Sigma_{\text{eq}}}{\bar{\sigma}}\right)^2 + 2\bar{f}_d q_1(\Sigma_{\text{hyd}}, \Sigma_{\text{eq}}, n)\cosh\left(\bar{q}_2 \frac{3}{2}\frac{\Sigma_{\text{hyd}}}{\bar{\sigma}}\right) - q_1^2(\Sigma_{\text{hyd}}, \Sigma_{\text{eq}}, n)\bar{f}_d^2 - 1 = 0 \tag{1}$$

where the global porosity and average q_2 value of the voids and cracks are defined as

$$\bar{f}_d = \sum_{i=1}^{n_v} f_i^v + \sum_{i=1}^{n_c} f_i^c \qquad \bar{q}_2 = \frac{1}{\bar{f}_v}\sum_{i=1}^{n_v} f_i^v q_{2i}^v + \frac{1}{\bar{f}_c}\sum_{j=1}^{n_c} f_j^c q_{2j}^c \tag{2, 3}$$

with the subscripts v and c denote quantities for the voids and cracks, respectively, and an overbar symbol denotes a global quantity. The q_1 parameter does not require an averaging procedure since it is a function of the stress triaxiality and hardening exponent and these quantities are assumed to be homogeneous in the element. Alternatively, the q_2 parameter is a function of the void shape and stress state and will typically be different for each void and crack. The relations for the q_i parameters and the triaxiality, T, are

$$q_1 = A_0 + A_1 T + A_2 T^2 + A_3 T^3 \qquad q_2 = W^{\eta(T,n)} \qquad T = \Sigma_{\text{hyd}}/\Sigma_{\text{eq}} \tag{4-6}$$

where A_i, and η are coefficients found in Ragab [8]. The associated flow rule of the GT model yields the void growth relation that is applied for each void and crack as

$$\dot{f}_{\text{growth}} = \frac{3f(1-f)q_1 q_2 \sinh\left(q_2 \frac{3}{2}\frac{\Sigma_{\text{hyd}}}{\bar{\sigma}}\right)}{3\left(\frac{\Sigma_1 - \Sigma_{\text{hyd}}}{\bar{\sigma}}\right) + fq_1 q_2 \sinh\left(q_2 \frac{3}{2}\frac{\Sigma_{\text{hyd}}}{\bar{\sigma}}\right)} D_1^{\text{p}} \tag{7}$$

where Σ_1 and D_1^{p} are the stress and plastic strain rate in the principal loading direction.

Void coalescence is modeled using the criterion of Pardoen and Hutchinson [9] for internal necking coalescence. The onset of coalescence occurs when the following constraint is satisfied:

$$\frac{\Sigma_1}{\bar{\sigma}\left(1-\kappa_{uc}\chi^2\right)} \geq \left(\left(0.1 + 0.22n + 4.8n^2\right)\left(\frac{1-\chi}{W\chi}\right)^2 + \frac{1.24}{\sqrt{\chi}}\right) \tag{8}$$

where $\kappa_{uc} = \pi/4$ for a cubic cell. The void spacing ratio and the cell aspect ratio, λ, are defined as

$$\chi = \left(\frac{f}{\gamma}\frac{\lambda}{W}\right)^{\frac{1}{3}} \qquad \lambda = \frac{L_y}{\sqrt{L_x L_z}} \tag{9a,b}$$

where $\gamma = \pi/6$ for a cubic unit cell and L_i are its side-lengths that evolve with the applied strain. The criterion in Eq. (8) is also used to identify the onset of profuse void coalescence and failure of the percolation element. In this case, the global void aspect ratio and spacing ratios are:

$$\bar{W} = \frac{1}{\bar{f}_v}\sum_{i=1}^{n_v} f_i^v W_i^v + \frac{1}{\bar{f}_c}\sum_{j=1}^{n_c} f_j^c W_j^c \qquad \bar{\chi} = \left(\frac{\bar{f}_d \lambda_e}{\gamma \bar{W}}\right)^{\frac{1}{3}} \qquad (10,11)$$

where λ_e is the aspect ratio of the finite-element with respect to the principal loading direction.

2.1 Calibration of the void evolution and coalescence models

To ensure that the extended GT constitutive model described in the previous section is accurate for a single void, an extensive study of axisymmetric unit cells containing a dilute concentration of voids was performed with initial void aspect ratios ranging from 0.001 to 6. Each unit cell was subjected to constant triaxial loadings ranging from, T = 1/3 - 3, for a material with a hardening exponent of 0.1. Following the method of Ragab [8], the q_2 coefficient in Eq. (7) was calibrated for each void shape to ensure accurate predictions of the porosity. Second-order polynomials were used to describe the evolution of the void aspect ratios to high accuracy. See Butcher [2] for the complete results of this numerical study along with the calibrated coefficients for void evolution. When void growth and shape evolution are properly modeled, the coalescence strains predicted using Eq. (8) were in very good agreement with the numerical results. An example of the accuracy of the calibrated porosity trends for penny-shaped voids is shown in Figure 3a when the unit cell data is used to evaluate Eq. (7). Similarly, the predicted porosity and coalescence strains are shown in Figure 3b when the GT model in Eq. (1) is used to integrate the stress state. The good agreement of the calibrated GT model in Fig. 3b demonstrates that the predictions for void evolution and coalescence within the particle field are well represented for isolated voids.

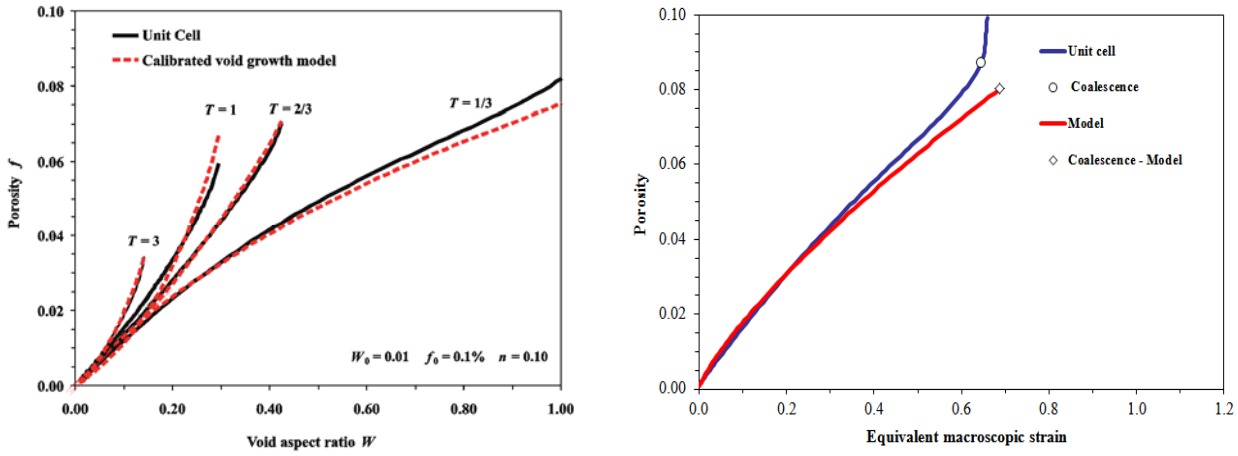

Figure 3: (a) Comparison of the porosity evolution in the unit cell and with Eq. (7) when it is evaluated using the stress state from the unit cell. (b) Comparison of the predicted void evolution and coalescence when using the GT yield criterion in Eq. (1) to integrate the stress state for a penny-shaped void in uniaxial tension.

2.2 Void nucleation

The secant-based particle homogenization scheme of Tandon and Weng [10] was implemented using the procedure of Butcher et al. [11]. Using this method, the stress state within the particles can be estimated based upon the global stress state, particle shape, volume fraction and its mechanical properties. For AA5182, the iron-rich intermetallic particles are assumed to remain elastic during deformation and nucleate voids via a penny-shaped crack in a brittle-type fracture.

Butcher et al. [11] adapted the volume-based criterion of Moulin et al. [12] for the break-up of irregularly shaped particles during rolling to ellipsoidal particles for void nucleation as:

$$\sigma_N = \frac{1}{\sqrt{\pi}} \frac{K_{1c}^*}{\sqrt[6]{V_p}} \qquad K_{1c}^* = K_{1c}\sqrt{\alpha} \qquad \alpha \approx 1 \tag{12}$$

where K_{1C}^* is the effective critical toughness of the particle material, V_p is the average particle volume and α is a geometry parameter in the Griffith mode I crack criterion to account for various effects such as crack blunting. This criterion contains only one physically-based parameter, K_{1c}, and captures the particle size-effect where small particles nucleate at high strains while large particles nucleate at low stresses [13]. The nucleation model also predicts that brittle phases are more likely to crack than more ductile phases.

3. Generation of representative particle fields

A particle field generator was developed and implemented into LS-DYNA [6] as a pre-processor for the percolation model. The measured probability distributions from micro-tomography studies were then re-created using rejection-sampling techniques. In this work, the distributions obtained by Orlov [14] were adopted for the semi-axes, orientations, volume fractions, and spacings of the voids and particles found in AA5182. The coupling of the percolation model with a particle field generator can enable stochastic predictions of fracture by performing multiple percolation model simulations. A typical particle field with a volume of 200 µm x 200 µm x 200 µm is shown in Figure 4 where the clustering of the voids and particles is evident along with their preferential orientation along the rolling direction. The respective number of voids, Mg_2Si and Fe-rich particles in this volume are 447, 616, 5273, corresponding to volume fractions of 0.053%, 0.049% and 0.483%.

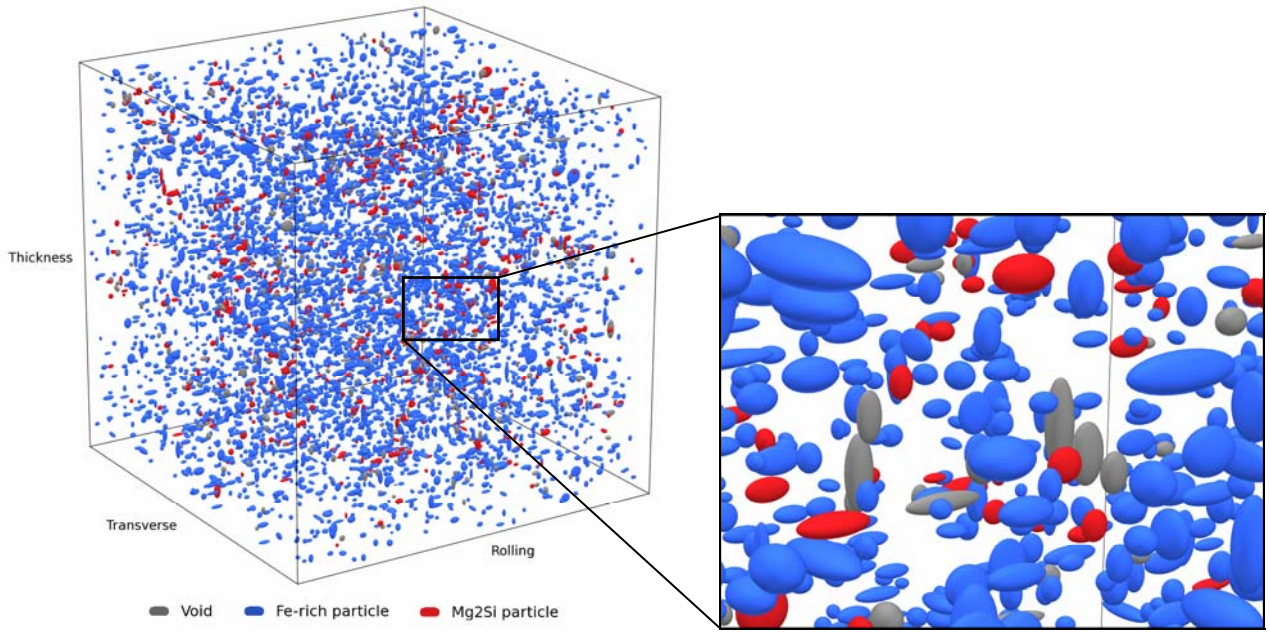

Figure 4: Generated particle field of AA5182 with a volume of 200 µm x 200 µm x 200 µm.

4. Application to a notched tensile test

Six notched tensile specimens of 1.5 mm thick AA5182 sheet with a notch radius, *R*, of 3 mm, gage length, *L*, of 12.5 mm, width, *w*, of 18 mm, and total sample length of 80 mm were tested to failure under quasi-static conditions. The notch ligament length is characterized using the notch ratio defined as $\rho = 2R/w = 0.25$ in this study. Fracture is characterized using both the ligament strain and axial or elongation strains. The ligament strain is representative of deformation in the region where fracture originates whereas the axial strain provides a metric for fracture based upon the bulk elongation of the material. The axial and ligament strains at fracture are defined as

$$\varepsilon_{a_f} = \ln\left(\frac{L_f}{L_o}\right) \qquad \varepsilon_{lig_f} = \ln\left(\frac{lig_f}{lig_o}\right) \tag{13,14}$$

where the initial ligament length is: $lig_o = w_o - 2R = 12$ mm. The axial strain at failure is recorded at the appearance of a macro-crack at the notch root and not final failure since the objective of the finite-element models is to predict the formation of a macro-crack and not the subsequent tearing process. Tensile specimens with notch ratios smaller than 1/3 exhibit visible cracking at the notch root prior to fracture and the appearance of a macro crack corresponds to a sharp drop in the experimental load displacement curve [15].

4.1 Material characterization

Three tensile specimens were evaluated to characterize a Voce hardening law for AA5182 as:

$$\bar{\sigma}(\text{MPa}) = 398.1 - 275.4\exp\left[-7.631\left(\bar{\varepsilon}^{p}\right)^{0.905}\right] \qquad n = \frac{\bar{\varepsilon}^{p}}{\bar{\sigma}}\frac{d\bar{\sigma}}{d\bar{\varepsilon}^{p}} \tag{15a, b}$$

with a yield stress of 122.7 MPa, and elastic moduli, $E = 65.33$ GPa and $\nu = 0.33$. Void nucleation in the AA5182 alloy is attributed to the iron-rich intermetallics and not the Mg_2Si particles based upon the micro-tomography study by Orlov [14]. The elastic constants of the Fe-rich particles are taken as those of steel with an elastic modulus of 200 GPa and a Poisson ratio of 0.28. It is assumed that the Fe-rich particles nucleate penny-shaped voids with an aspect ratio of 0.01 via particle cracking. The fracture toughness of the Fe-rich particles in Eq. (12) is taken as 2.15 MPa-$m^{1/2}$ based upon the measurements of Rathod and Katsuna [16].

4.2 Finite-element model

A one-eighth finite-element model of the notched specimen containing 24000 constant stress brick elements is shown in Figure 5a. For computational efficiency, only percolation elements are placed at the notch root (Figure 5b) to capture the initiation of the macro-crack while the remaining elements obey J_2 plasticity using the hardening rule in Eq. (15). The percolation model is computationally expensive and the size of the global particle field in this specific model is limited to a size of 4000 particles split into four elements. The placement of only several percolation elements at the notch root is acceptable for this specific notch geometry because deformation is

highly localized at the notch root. A previous study by Butcher and Chen [15] using a Gurson-based constitutive model has shown that the only appreciable damage occurs within this region (Figure 5c). The resulting ligament and axial strains are extracted from the FE model upon the onset of element deletion. The simulations are repeated five times for particle fields denoted P1-P5 that were generated from the tomography data of Orlov [14].

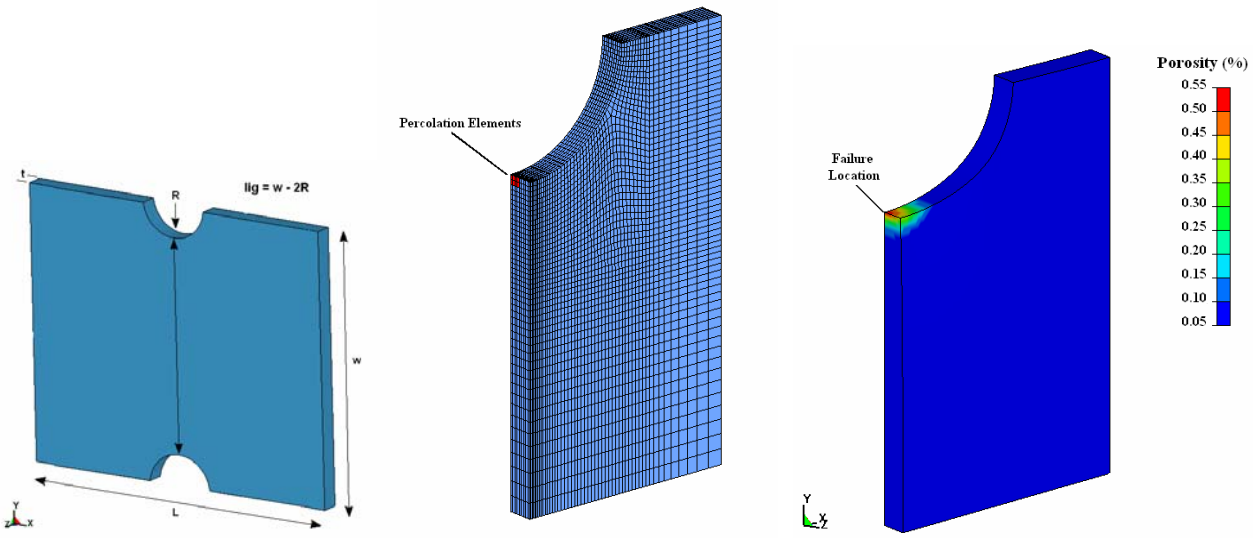

(a) (b) (c)

Figure 5: (a) Typical notch geometry. (b) 1/8th FE mesh showing percolation elements and (c) Porosity distribution obtained by Butcher and Chen (2011) using a traditional GT damage model.

5. Results and discussion

The predictions of the percolation model for the axial and ligament strain with the experimental values are shown in Figures 6a and 6b. The fracture strains are presented as 95% confidence intervals due to the stochastic nature of the percolation model. Although only five particle fields were considered, the variation in the axial strain predicted by the percolation model is comparable to the experimental variation.

The predicted porosity distributions of the five particle fields considered are shown in Figure 7a. All of the particle fields are in excellent agreement with the experimental porosity data of [14] at a plastic strain up to 0.10 and show generally good agreement at the higher strain levels. All of the particle fields considered, P1-P5, exhibit the same behaviour where deformation is relatively homogenous until the commencement of void nucleation at higher strains. The start of nucleation is followed by localized coalescence which promptly sweeps throughout the particle field causing failure. The fracture porosities are also in good agreement with the metallographic observations of Smerd et al. [17] who reported failure porosities on the order of 0.3%.

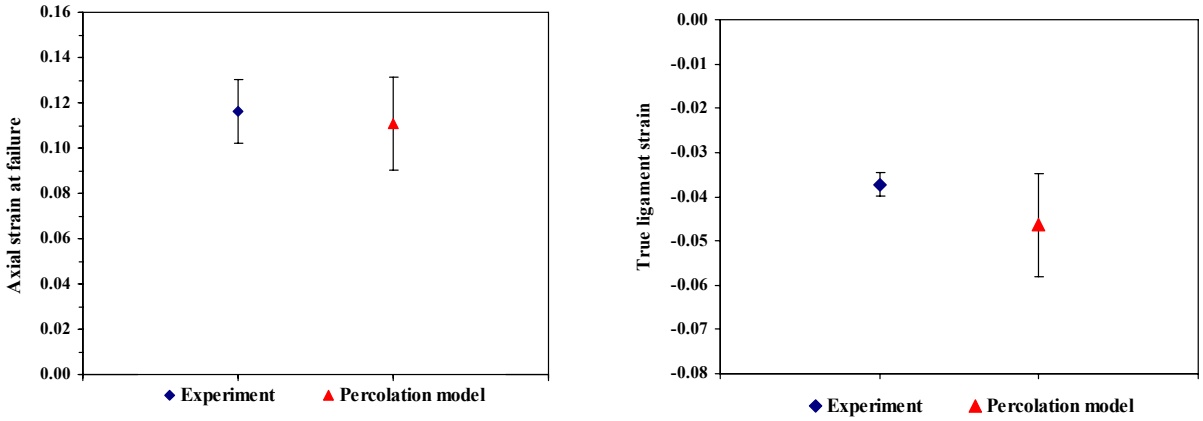

Figure 6: (a) Comparison of the experimental and predicted 95% confidence intervals for the true axial strain at failure and (b) true ligament strain.

The number of voids in the particle field is representative of void nucleation and the experimental and numerical predicted values are presented in Figure 7b. The predicted number of voids in each of the particle fields are in are in very good agreement with the experimental measurements of Orlov [17]. The convergence of the nucleation predictions demonstrates that only several particle fields are required to obtain the general trends. The porosity and fracture strains in the previous figures are expected to exhibit the most variation because they are related to coalescence which is strongly dependent upon the local microstructure. This agreement with the experimental nucleation trends is very encouraging for the physical foundation of both the percolation and the nucleation models.

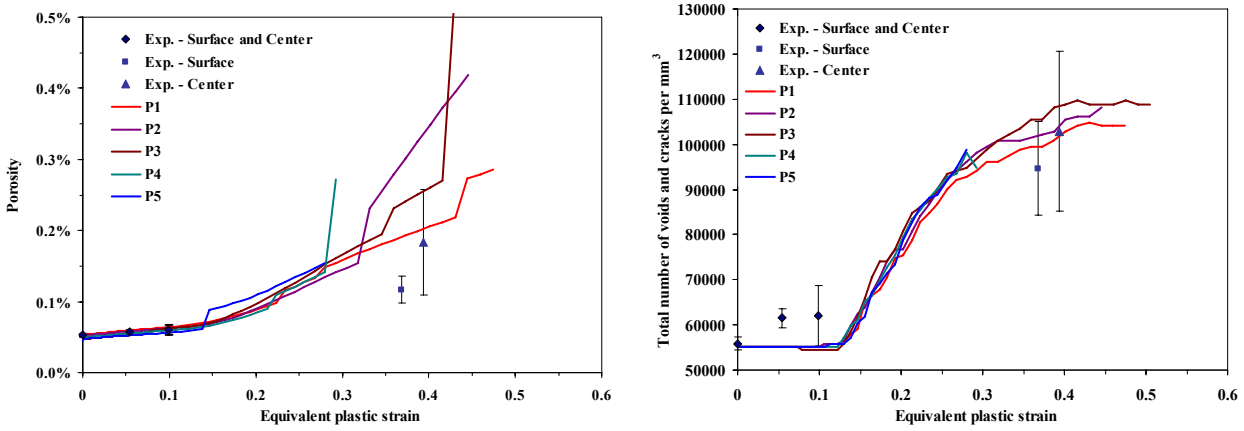

Figure 7: (a) Comparison of the predicted porosity and (b) total number of voids and cracks in the center of the notch root. The experimental tomography data is from [17] using a standard tensile specimen.

The average principal stress in the particles upon cracking (void nucleation) is shown in Figure 8a. Large particles crack at low stresses early in the deformation process while the smaller particles do not nucleate until the later in the deformation process. From this result, the stress required to fracture an Fe-rich particle is about 950 MPa. A strain-based nucleation criterion can also be developed by comparing the average volume of a broken particle to the global plastic strain

at which it nucleated as shown in Figure 8b. All of the particle fields display the well-known behaviour that small voids will nucleate only at high strains while larger particles display a negligible size effect and have a near constant nucleation stress or strain. Orlov [14] experimentally observed that no particles that had a volume smaller than 17.8 μm^3 nucleated a void and this is in accordance with the predictions of the model.

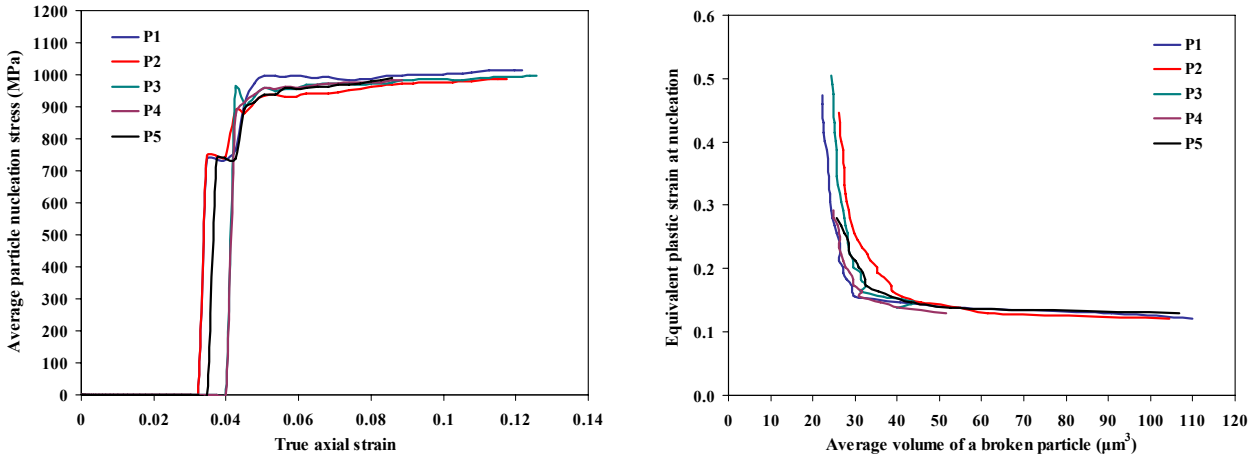

Figure 8: (a) Comparison of the average maximum principal stress in the particles at nucleation and (b) equivalent plastic strain in the matrix upon nucleation.

6. Summary

The complete damage percolation model was used to predict fracture and damage evolution in a notched tensile sheet specimen of AA5182 sheet. Representative particle distributions were created and mapped to the percolation elements located at the notch root where fracture initiates in the sample. The fracture strain, porosity, and nucleation predictions of the model are in very good agreement with the experiment data of Orlov [14]. No calibration or adjustable parameters were employed in the model and its good predictions of the experiment data attest to the strong physical foundation of the model. Fracture is a sole consequence of the stress state, material composition and the particle distribution. The main advantages of the present percolation model are that it is directly coupled into a finite-element code, contains a particle field generator as a preprocessor, and rests upon a minimum of assumptions regarding void evolution. At present, the main limitation of the model is its significant computational cost. The next phase of development of the percolation model will address this limitation and involve a large-scale application to a practical metal forming operation.

References

[1] Gurson, A.L. (1977). Continuum theory of ductile rupture by void nucleation and growth – Part I. Yield criteria and flow rules for porous ductile media. *J. Eng. Mech. Tech.* **99**, 2-15.

[2] Butcher, C. (2011). A multi-scale damage percolation model of ductile fracture. Ph.D. thesis, University of New Brunswick, Canada: http://dspace.hil.unb.ca:8080/handle/1882/35391

[3] Worswick, M.J., Pilkey A.K., Thomson C.I.A., Lloyd D.J. and Burger G. (1998), Percolation damage predictions based on measured second phase particle distributions, *Micro. Sci.*, 507-514

[4] Worswick, M.J., Chen Z.T., Pilkey A.K., Lloyd D., Court S. (2001). Damage characterization and damage percolation modeling in aluminum alloy sheet. *Acta Mater.* **49**, 2791-2803.

[5] Chen, Z.T. (2004). The role of heterogeneous particle distribution in the prediction of ductile fracture. Ph.D. Thesis, University of Waterloo, Canada.

[6] Hallquist, J.O. (2006). LS-DYNA Theory Manual. Livermore Software Technology Corp.

[7] Tvergaard, V. (1981). Influence of voids on shear band instabilities under plane strain conditions. *Int. J. Frac.* **17**, 389-407.

[8] Ragab, A.R. (2004). Application of an extended void growth model with strain hardening and void shape evolution to ductile fracture under axisymmetric tension. *Eng. Fract. Mech.* **71**, 1515-1534.

[9] Pardoen, T., Hutchinson, J. (2000). An extended model for void growth and coalescence. *J. Mech. Phys. Solids* **48**, 2567-2512.

[10] Tandon, G.P. and Weng, G.J.: Average stress in the matrix and effective moduli of randomly Oriented composites. *Compos. Sci. Tech.* **27**, 111-132 (1986)

[11] Butcher. C., Chen, Z.T. and Worswick, M.J. (2013). Integration of a particle-based homogenization theory into a general damage-based constitutive model to improve the modelling of void nucleation to coalescence. *Acta Mech.* **224**, 139-156.

[12] Moulin N., Jeulin D., Klöcker H., (2009). Stress concentrations in non-convex elastic particles embedded in a ductile matrix. *Int. J. Eng. Sci.* **47**, 170–191

[13] Thomason, P. (1990). *Ductile fracture of metals*. Pergamon Press Inc., Oxford.

[14] Orlov, O. (2006). A three-dimensional damage percolation model. Ph.D. Thesis, University of Waterloo, Waterloo, Ontario, Canada

[15] Butcher, C., Chen, Z.T. (2011). Characterizing void nucleation in a damage-based constitutive model using notched tensile sheet specimens. *Theor. Appl. Frac. Mech.*, **55**, 140-147.

[16] Rathod, M.J., Kutsuna, M. (2004). Joining of Aluminum Alloy 5052 and Low-Carbon Steel by Laser Roll Welding. *Welding Research*, January, 16-26.

[17] Smerd, R., Winkler, S., Salisbury, C., Worswick, M., Lloyd, D. and Finn, M. (2005). High strain rate tensile testing of automotive aluminum alloy sheet. *Int. J. Impact. Eng.* **32** 541-560.

Strength properties of a Drucker-Prager porous medium reinforced by rigid particles

Zheng He[1,*], Luc Dormieux[1], Kondo Djimedo[2]

[1] E.N.P.C, Institut Navier, 77455 Marne-la-Vallee, France

[2] U.M.P.C, Institut d'Alembert, 75252 PARIS CEDEX 05, France

* Corresponding author: hez@lmsgc.enpc.fr

Abstract In the present study, we investigate the strength properties of ductile porous materials reinforced by rigid particles. The microporous medium is constituted of a Drucker-Prager solid phase containing spherical voids; its behaviour is described by means of an elliptic criterion (issued from a modified secant moduli approach) whose corresponding support function is determined. The later is then implemented in a limit analysis approach in which a careful attention is paid for the contribution of the inclusion matrix-interface. This delivers parametric equations of the effective strength properties of the porous material reinforced by rigid particles. The predictions are compared to available results obtained by means of variationnal homogenization methods successively applied for micro-to-meso and then for meso-to-macro scales transitions. Moreover, we discuss in detail the predictions of the material strength under isotropic mechanical loadings. To this end, additional static solutions are derived and compared to the kinematics limit analysis ones. Finally, we derive an approximate closed-form expression of the macroscopic strength which proves to be very accurate.

Keywords Porous; Strength; Drucker-Prager; inclusion-matrix, interfaces.

1. Introduction

Being hard clayey rocks, COx Argillite is a porous clay matrix in which quartz or silica inclusions are embedded. In the present study, we mainly aim to derive new closed-form results for the strength of the COx argillite, under the assumption that the solid phase of the clay is a Drucker-Prager perfectly plastic material. Therefore, the behaviour of the microporous clay is described by means of an elliptic criterion [2] whose corresponding support function is determined in this paper. Then by using this support function, we explore an alternative approach which can be viewed as an extension of the original Gurson model. Instead of a spherical cavity surrounded by a matrix, the proposed 'rigid core sphere model' consists of a rigid spherical core surrounded by the homogeneous porous material. The failure criterion of this 'rigid core sphere model' is derived in the framework of the cinematic approach of limit analysis (LA). It is worth noting that from the LA point of view the failure mechanism can include a strain concentration at the core-matrix interface which can be described mathematically. ([1-3],[6],[9],[11],[12]). **Notations:** $\mathbf{1}$ and $\mathbb{I}$ are the second and fourth order identity tensors. $\mathbb{J}=(1/3)\mathbf{1}\otimes\mathbf{1}, \mathbb{K}=\mathbb{I}-\mathbb{J}$ are respectively the spherical and deviatoric projectors of isotropic fourth order symmetric tensor.

2. The micro-to-meso transition: support function of porous matrix

The first homogenization step approach starts at the microscopic scale. At this scale, the porous clay matrix is described as a heterogeneous material being made up of a Drucker-Prager perfectly plastic solid in which pores are embedded. Let $\tilde{\boldsymbol{\sigma}}_d=\tilde{\boldsymbol{\sigma}}-\tilde{\sigma}_m\mathbf{1}$ denote the deviatoric part of the stress tensor $\tilde{\boldsymbol{\sigma}}$ at the microscopic scale. The scalar deviatoric stresses $\tilde{\sigma}_m$ are defined as $\tilde{\sigma}_d=\sqrt{\tilde{\boldsymbol{\sigma}}:\mathbb{K}:\tilde{\boldsymbol{\sigma}}}$ and $\tilde{\sigma}_m=(\mathbf{1}:\mathbb{J}:\tilde{\boldsymbol{\sigma}})/3$ and the Drucker-Prager criterion reads:

$$\tilde{\sigma}_d + T(\tilde{\sigma}_m - h) \le 0\,. \tag{1}$$

The parameters T and h respectively characterize the friction coefficient and the tensile strength of the solid phase of the clay matrix.

The result of the first homogenization step is the derivation of the strength properties of the porous clay matrix at the mesoscopic scale where it is described as a homogeneous material. These properties were estimated successfully in [6] by means of the modified secant method. Now $\boldsymbol{\sigma}_d = \boldsymbol{\sigma} - \sigma_m \mathbf{1}$ denotes the deviatoric part of the stress tensor $\boldsymbol{\sigma}$ at the mesoscopic scale and we introduce $\sigma_d = \sqrt{\boldsymbol{\sigma} : \mathbb{K} : \boldsymbol{\sigma}}$ and $\sigma_m = (\mathbf{1} : \mathbb{J} : \boldsymbol{\sigma})/3$. In the situation of associated plasticity, the domain of admissible stress states is an ellipse in the (σ_m, σ_d)-plane:

$$F^{meso}(\boldsymbol{\sigma}, f, T) = \frac{1+2f/3}{T^2}\sigma_d^2 + (\frac{3f}{2T^2} - 1)\sigma_m^2 + 2(1-f)h\sigma_m - (1-f)^2 h^2 \le 0\,. \tag{2}$$

Note that $0 < T \le \sqrt{3f/2}$ (see [6]), f is the porosity. At the mesoscopic scale, the clay matrix is described by the elliptic criterion (2). In the framework of limit analysis theory (see e.g. [10]), a dual characterization of the strength criterion $F(\sigma) \le 0$ is the support function $\pi_{_F}(\mathbf{d}) = \sup(\sigma : \mathbf{d}, F(\sigma) \le 0\}$ of the convex set of admissible stress states. The support function $\pi(\mathbf{d})$ associated with (2) of the porous matrix finally takes the form

$$\pi_{_F}(\mathbf{d}) = \sigma_0 d_{_{EQ}} - \lambda d_v \qquad \text{with} \quad d_{_{EQ}} = \sqrt{\frac{2}{3}\mathbf{d} : H : \mathbf{d}}\,. \tag{3}$$

$$\sigma_0 = (1-f)h\sqrt{\frac{3}{2}}\sqrt{\frac{3f}{3f-2T^2}\frac{T^2}{1+2f/3}} \quad ; \quad \lambda = (1-f)h\frac{2T^2}{3f-2T^2}\,. \tag{4}$$

where $\mathbb{H} = \frac{1}{\alpha}\mathbb{J} + \mathbb{K}$ is a fourth order tensor, with

$$\alpha = \frac{3f/2 - T^2}{3+2f}\,. \tag{5}$$

3. Overall dissipation at the mesoscopic scale

We now focus on the transition from the mesoscopic scale to the macroscopic scale which constitutes the second homogenization step and is the main subject of the present paper. We seek the macroscopic criterion by means of a Gurson-type approach. As already stated, the microstructure at the mesoscopic scale is described by a composite sphere Ω with a rigid core surrounded by the homogenized clay resulting from the micro-to-meso transition. The external (resp. internal) radius is denoted by r_e (resp. r_i). The shell Ω_m ($r_i \le r \le r_e$) around the core represents the clay. The volume fraction $\rho = (r_i / r_e)^3$ of the core in the composite sphere is equal to the volume fraction of the rigid inclusions in a representative volume element of argillite.

3.1 Velocity field at the mesoscopic scale

For geomaterials, we define here a family of cinematically admissible (k.a.) velocity fields with $\mathbf{D}$, depending on one compressible parameter A:

$$r \ge r_i : \quad \underline{v}_A = A\underline{x} + (D_m - A)\frac{r_e^3}{r^2}\underline{e}_r + \mathbf{D}_d \cdot \underline{x}\,. \tag{6}$$

The strain rate in the clay ($r_i \le r \le r_e$) can be determined from (6):

$$\mathbf{d}_A = A\mathrm{l} + \mathbf{D}_d + (D_m - A)\frac{r_e^3}{r^3}\left(1 - 3\underline{e}_r \otimes \underline{e}_r\right). \tag{7}$$

From (7), with $D_d^2 = \mathbf{D_d} : \mathbf{D_d}$, the expression of d_{EQ} in (3) can be written as

$$d_{EQ}{}^2 = \frac{2A^2}{\alpha} + 4(D_m - A)^2 \frac{r_e^6}{r^6} + \frac{2D_d^2}{3} + \frac{4(D_m - A)}{3}\frac{r_e^3}{r^3}\mathbf{D}_d : \left(1 - 3\underline{e}_r \otimes \underline{e}_r\right). \tag{8}$$

The velocity is $\underline{v}_O = 0$ in the rigid core. Note that the condition $\underline{v}_A = 0$ on the boundary $r = r_i$ cannot be fulfilled by the velocity field defined in (6). This implies that the dissipation associated with a discontinuity of velocity must be considered at the boundary I ($r = r_i$) (section 3.4).

3.2 Macroscopic support function

Defining the macroscopic strength domain G^{hom} as the set of admissible macroscopic stress states Σ, the macroscopic support function reads $\Pi^{hom}(\mathbf{D}) = \sup(\Sigma : \mathbf{D}, \Sigma \in G^{hom})$. Considering the set K of k.a. velocity fields with $\mathbf{D}$, $\Pi^{hom}(\mathbf{D})$ is characterized as [5]:

$$\Pi^{hom}(\mathbf{D}) = \frac{1}{|\Omega|}\inf_{\mathrm{v}\in K}\left(\int_{\Omega_m} \pi_F(\mathbf{d}_A)\, dV + \int_I \pi(\underline{v}_A)\, dS\right). \tag{9}$$

where $|\Omega| = 4\pi r_e^3/3$. In the surface integral, $\underline{v}$ denotes the velocity discontinuity at the core boundary I and $\pi(\underline{v})$ represents the associated surface density of dissipation. In the line of reasoning of Gurson approach, $\Pi^{hom}(\mathbf{D})$ is approximated by the minimal dissipation obtained among the velocity fields $\underline{v}_A$ defined in (6):

$$\Pi^{hom}(\mathbf{D}) = \frac{1}{|\Omega|}\inf_{A\in R}\left(\int_{\Omega_m} \pi_F(\mathbf{d}_A)\, dV + \int_I \pi(\underline{v}_A)\, dS\right). \tag{10}$$

For further use, let us introduce the following notation:

$$\frac{1}{|\Omega|}\int_{\Omega_m} \pi_F(\mathbf{d}_A)\, dV = \tilde{\Pi}^m(\mathbf{D}, A) \quad ; \quad \frac{1}{|\Omega|}\int_I \pi(\underline{v}_A)\, dS = \tilde{\Pi}^I(\mathbf{D}, A). \tag{11}$$

Accordingly:

$$\Pi^{hom}(\mathbf{D}) = \inf_{A\in R} \tilde{\Pi}(\mathbf{D}, A). \tag{12}$$

$$\tilde{\Pi}(\mathbf{D}, A) = \tilde{\Pi}^m(\mathbf{D}, A) + \tilde{\Pi}^I(\mathbf{D}, A). \tag{13}$$

Once $\Pi^{hom}(\mathbf{D})$ is determined, the macroscopic admissible stress states on the boundary ∂G^{hom} are derived according to:

$$\Sigma = \frac{\partial \Pi^{hom}}{\partial \mathbf{D}}(\mathbf{D}). \tag{14}$$

The stress state of (14) lies on the boundary of G^{hom} at the location where the normal is parallel to $\mathbf{D}$. The overall dissipation of (12) proves to read in the following form:

$$\tilde{\Pi}(\mathbf{D},A)=\sigma_0\left[\,Narcsinh\left(\frac{uN}{M}\right)-\frac{\sqrt{M^2+u^2N^2}}{u}\right]_1^{\frac{1}{\rho}}+\sigma_0\sqrt{\frac{2}{3}}Y-3\lambda D_m\,. \tag{15}$$

with the notations introduced in (19), (27) and (28). For the sake of completeness, sections 3.3 and 3.4 respectively determine the contribution (18) of the shell Ω_m (volume integral in (10)) and the contribution (26) of the interface *I* (surface integral in (10)) which has led to (15). Section 4 will consider the minimization w.r.t. parameter *A*.

3.3 Contribution of the shell to dissipation

For a given value of parameter *A*, the contribution of the matrix to the macroscopic dissipation reads

$$\tilde{\Pi}^m(\mathbf{D},A)=\frac{1}{|\Omega|}\int_{\Omega_m}\left(\sigma_0 d_{EQ}-\lambda d_v\right)dV\,. \tag{16}$$

In order to obtain an analytical expression of $\tilde{\Pi}^m(\mathbf{D},A)$, the approximation introduced in [4] is applied. Let $S(r)$ denote the sphere of radius *r*. As a consequence of the Cauchy-Schwarz inequality, it is readily seen that

$$\int_{S(r)} d_{EQ}\,dS\le\sqrt{4\pi r^2}\sqrt{\int_{S(r)} d_{EQ}^2\,dS}\,. \tag{17}$$

We observe that the average $\left\langle \mathbf{1}-3\underline{e}_r\otimes\underline{e}_r\right\rangle_{S(r)}$ of $\mathbf{1}-3\underline{e}_r\otimes\underline{e}_r$ over the orientations of $\underline{e}_r$ on the sphere $S(r)$ is equal to 0. Then, using (8) and (17) in (16), $\tilde{\Pi}^m(\mathbf{D},A)$ reads

$$\begin{aligned}\tilde{\Pi}^m(\mathbf{D},A)&=\frac{4\pi\sigma_0}{\Omega}\int_{r_i}^{r_e} r^2\sqrt{\frac{2A^2}{\alpha}+4(D_m-A)^2\frac{r_e^6}{r^6}+\frac{2D_d^2}{3}}dr-\frac{\lambda}{\Omega}\int_{\Omega^m} d_v dV\\&=\sigma_0\left[\,Narcsinh\left(\frac{uN}{M}\right)-\frac{\sqrt{M^2+u^2N^2}}{u}\right]_1^{\frac{1}{\rho}}-3(1-\rho)\lambda A\end{aligned}\,. \tag{18}$$

with

$$M^2=\frac{2A^2}{\alpha}+\frac{2D_d^2}{3},\quad N^2=4(D_m-A)^2\,. \tag{19}$$

3.4. Inclusion-matrix interface

Unlike the classical Gurson's 'hollow sphere model', the model proposed in this paper substitutes a rigid core for the void in the center of the thick-walled sphere. Therefore, owing to null velocity ($\underline{v}_O=0$) in the rigid core, a velocity discontinuity tales place at the core boundary: $\underline{v}_A=\underline{v}_A(r_a\underline{e}_r)-\underline{v}_O=\underline{v}_A(r_a\underline{e}_r)$.

3.4.1. Surface density of dissipation

The velocity field $\underline{v}_A$ being discontinuous across the surface *I* (rigid core boundary), its gradient and the associated strain rate are to be defined in the sense of the distribution theory:

$$\mathbf{d} = \{\mathbf{d}\} + \frac{1}{2}\left(\underline{n} \otimes \underline{v}_A + \underline{v}_A \otimes \underline{n}\right)\delta_I \,. \tag{20}$$

where $\{\mathbf{d}\}$ is the standard expression of the strain rate corresponding to its smooth part, δ_I is the Dirac distribution which support is the surface of discontinuity I and $\underline{n} = \underline{e}_r$ is the unit normal to this surface. The surface density of dissipation $\pi(\underline{v}_A)$ contributed by the velocity jump $\underline{v}_A$ is therefore related to the support function $\pi_{_F}$ according to (see e.g. [10]):

$$\pi(\underline{v}_A) = \pi_{_F}(\mathbf{d}^I) \,. \tag{21}$$

where $\mathbf{d}^I$ is defined as

$$\mathbf{d}^I = \frac{1}{2}\left(\underline{n} \otimes \underline{v}_A + \underline{v}_A \otimes \underline{n}\right). \tag{22}$$

Recalling (6) and (22), the strain rate $\mathbf{d}^I$ associated with the velocity jump can be obtained and written as

$$\mathbf{d}^I = r_i\left(\left(\frac{1}{\rho}D_m + (1-\frac{1}{\rho})A\right)\underline{e}_r \otimes \underline{e}_r + \frac{1}{2}\left((\mathbf{D}_d \cdot \underline{e}_r) \otimes \underline{e}_r + \underline{e}_r \otimes (\mathbf{D}_d \cdot \underline{e}_r)\right)\right). \tag{23}$$

Eventually, the surface density of dissipation is derived from the combination of (21) and (3)

$$\pi(\underline{v}_A) = \sigma_0 d^I_{_{EQ}} - \lambda d^I_v \qquad \text{with} \quad d^I_{_{EQ}} = \sqrt{\frac{2}{3}\mathbf{d}^I : H : \mathbf{d}^I} \quad ; \quad d^I_v = \operatorname{tr}\mathbf{d}^I \,. \tag{24}$$

3.4.2. Contribution of the interface to dissipation

Recalling (16), the macroscopic dissipation related to the part of inclusion-matrix interface depending also on the scalar *A* can be written as

$$\tilde{\Pi}^I(\mathbf{D}, A) = \frac{1}{\Omega}\int_{r=r_i}\left(\sigma_0 d^I_{_{EQ}} - \lambda d^I_v\right)dS \,. \tag{25}$$

Again, the integration of d^I_{eq} is approximated by the upper bound (17) which yields

$$\tilde{\Pi}^I(\mathbf{D}, A) = \sigma_0\sqrt{\frac{2}{3}}Y - \lambda X \quad ; \quad Y = \frac{\sqrt{4\pi r_i^2}}{\Omega}\sqrt{\int_{r=r_i}\mathbf{d}^I : H : \mathbf{d}^I dS} \,. \tag{26}$$

Using (23), *Y* takes the form

$$Y = \sqrt{\frac{P^2 + Q^2}{15\alpha}} \,. \tag{27}$$

with

$$Q^2 = \left(\frac{51}{2}\alpha + 6\right)\rho^2 D_d^2, \quad P^2 = 45(1+2\alpha)\left[D_m - A(1-\rho)\right]^2 . \tag{28}$$

In turn, observing that the average $\left\langle \underline{e}_r \cdot \mathbf{D}_d \cdot \underline{e}_r \right\rangle_{r=r_i}$ of $\left\langle \underline{e}_r \cdot \mathbf{D}_d \cdot \underline{e}_r \right\rangle_{r=r_i}$ over the orientations of $\underline{e}_r$ on the sphere *I* is equal to 0, it is readily seen that

$$X = \frac{1}{\Omega}\int_{S(r_a)} d^I_v dS = 3\left(D_m - A(1-\rho)\right). \tag{29}$$

4. Macroscopic criterion

The macroscopic support function can be determined by minimizing the sum $\tilde{\Pi}(\mathbf{D},A)=\tilde{\Pi}^{m}(\mathbf{D},A)+\tilde{\Pi}^{I}(\mathbf{D},A)$ with respect to the parameter A. Accordingly, the boundary of G^{hom} is determined according to (14)[7]:

$$\Sigma=\frac{\partial\tilde{\Pi}(\mathbf{D},A)}{\partial\mathbf{D}},\qquad\text{with}\qquad\frac{\partial\tilde{\Pi}(\mathbf{D},A)}{\partial A}=0\,. \tag{30}$$

5. Comparison with the result obtained by a variational approach

Predictions according to (30) of the macroscopic criterion derived in the framework of the cinematic approach of limit analysis are now compared with the result obtained by the variational approach [11]. For the derivation of their criterion, these authors consider a variational approach in the two homogenization steps. Their criterion reads:

$$F^{\hom}(\Sigma,f,T)=\Theta\Sigma_d^2+\left(\frac{3f}{2T^2}-1\right)\Sigma_m^2+2(1-f)h\Sigma_m-\frac{3+2f+3f\rho}{3+2f}(1-f)^2h^2=0\,. \tag{31}$$

with

$$\Theta=\frac{\frac{1+2f/3}{T^2}+\frac{2}{3}\rho\left(\frac{3f}{2T^2}-1\right)}{\frac{4T^2-12f-9}{6T^2-13f-6}\rho+1}\,. \tag{32}$$

Applying the parameters f=0.25 and T=0.525, the comparison between the results predicted by the two different methods is shown in Fig.1 As it can be seen in Fig.1, the analytical estimate (31) obtained by the variational approach and the prediction from (30) based on the 'rigid core sphere model' show a very good agreement for purely isotropic stress states, both in traction and compression. It is noteworthy that the strength under purely isotropic stress seems surprisingly almost unaffected by the volume fraction ρ of the rigid core. Although the shapes of the yield surfaces predicted by the two methods are similar, the strength predicted by limit analysis always overestimates that predicted by the variational method. In particular, as far as the strength under pure shear loading is concerned, the difference becomes very important when the volume fraction of the rigid core ρ is larger. In order to gain a deeper understanding of the effect of the parameter ρ, the isotropic strength will now be compared with the exact solution predicted by the so-called static approach (sections 6). On the other hand, we note that the strength predicted by limit analysis (upper bounds) overestimates that predicted by the variational method under shear loading.(*We focus on the strength proprieties under isotropic loading. The strength under shear loading has not been discussed in the present paper.)*

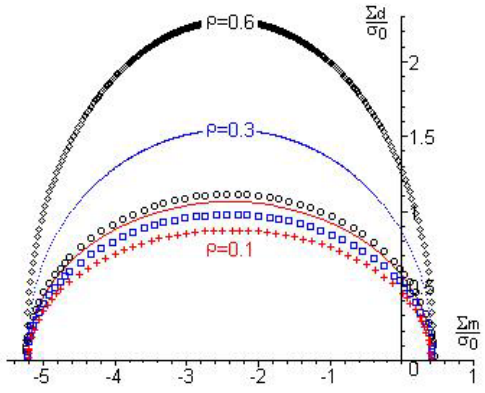

Figure 1. Comparison between the results predicted by limit analysis and the variational approach for different volume fractions of the rigid inclusion
-'line': limit analysis with ρ=0.1, -'cross': variational approach with ρ=0.1,
-'point': limit analysis with ρ=0.3, -'box': variational approach with ρ=0.3,
-'diamond': limit analysis with ρ=0.6, -'circle': variational approach with ρ=0.6

6. Strength under isotropic loading

6.1. Static approach of the limit analysis problem

The theory of limit analysis teaches that a cinematic approach like the Gurson one provides an upper bound of the true strength. In order to check the accuracy of a cinematic estimate, it is therefore highly desirable to derive a static approach which in turn will deliver a lower bound of the true strength. We therefore seek the stress field solution to an isotropic loading (traction or compression) in the framework of the 'rigid core sphere model'. The macroscopic stress state is of the form $\Sigma_m 1$. Accordingly the external boundary ($r = r_e$) is subjected to a radial surface force $\sigma \cdot \underline{n} = \Sigma_m \underline{n}$. We implement the so-called static approach of limit analysis. It consists in deriving a mesoscopic stress field σ which must be statically admissible with these boundary conditions and meet the criterion $F^{meso}(\sigma) = 0$ (see (2)). Owing to the spherical symmetry, this statically admissible stress field can be sought in the form (spherical coordinates):

$$\sigma = \sigma_{rr}(r)\underline{e}_r \otimes \underline{e}_r + \sigma_{\theta\theta}(r)\left(\underline{e}_\theta \otimes \underline{e}_\theta + \underline{e}_\varphi \otimes \underline{e}_\varphi\right). \tag{33}$$

The boundary condition on the surface $r = r_e$ reads

$$\sigma_{rr}(r_e) = \Sigma_m . \tag{34}$$

The momentum balance equation $div\sigma = 0$ reduces to

$$\frac{d\sigma_{rr}}{dr} = 2\frac{\sigma_{\theta\theta} - \sigma_{rr}}{r} . \tag{35}$$

With the notation $X = \sigma_{\theta\theta} - \sigma_{rr}$ (note that $X^2 = \frac{3}{2}\sigma_d^2$), it is found that $\sigma_m = \sigma_{rr} - \frac{2}{3}X$, so that the criterion (2) yields

$$\frac{2}{3}\frac{\left(1+\frac{2}{3}f\right)X^2}{T^2} + \frac{3f-2T^2}{2T^2}\left(\sigma_{rr} + \frac{2}{3}X\right)^2 + 2(1-f)h\left(\sigma_{rr} + \frac{2}{3}X\right) - (1-f)^2h^2 = 0 . \tag{36}$$

The values of *X* solutions of (36) read:

$$X = \frac{3}{2}\frac{(3f-2T^2)\sigma_{rr} - 2hT^2(f-1) \pm \sqrt{\Delta}}{2T^2 - 5f - 3}, \quad \text{with} . \tag{37}$$

$$\Delta = (2f+3)(2T^2-3f)\sigma_{rr}^2 + 4hT^2(2f+3)(f-1)\sigma_{rr} + 2h^2T^2(5f+3)(f-1)^2 . \tag{38}$$

Recalling (35), an ordinary differential equation with respect to σ_{rr} is obtained in the form:

$$X(\sigma_{rr}) = \frac{r}{2}\frac{d\sigma_{rr}}{dr} . \tag{39}$$

Introducing (37) into (39) and integrating over the interval $\left[r_i, r_e\right]$, one obtains

$$\frac{1}{3}\ln(\rho)=\int_{c}^{\Sigma_m}\frac{1}{3}\frac{2T^2-5f-3}{(2T^2-3f)\sigma_{rr}+2hT^2(f-1)+\varepsilon\sqrt{\Delta}}d\sigma_{rr}\,. \tag{40}$$

where the notation $c=\sigma_{rr}(r_a)$ and the boundary condition (34) at $r=r_e$ have been used. Note that no boundary condition is available at $r=r_i$. The physical meaning of (40) is the following: Whenever there exists a constant *c* such that (40) is fulfilled (with $\varepsilon=+1$ or -1), then Σ_m is an admissible loading for the value of ρ at stake. We seek the highest possible value $\Sigma_m^+>0$ of Σ_m (isotropic strength in traction) and the lowest one, denoted by $\Sigma_m^-<0$ (isotropic strength on compression). For the simplification of the following discussion, the denominator in the integral of (40) is denoted by D_ε:

$$D_\varepsilon=(2T^2-3f)\sigma_{rr}+2hT^2(f-1)+\varepsilon\sqrt{\Delta}\,. \tag{41}$$

In order for this integral to be defined, two mathematical conditions are to be met, namely $\Delta\geq 0$ and $D_\varepsilon\neq 0$. This remark leads to introduce the solutions to the equations of $\Delta=0$ and of $D_\varepsilon=0$.

First, let $\Sigma_{1m}^{\pm}$ denote the solutions to $\Delta=0$, which read:

$$\Sigma_{1m}^{+}=\frac{\left[2T(3+2f)-\sqrt{6f(3+2f)(5f-2T^2+3)}\right](1-f)hT}{(3+2f)(2T^2-3f)}$$
$$\Sigma_{1m}^{-}=\frac{\left[2T(3+2f)+\sqrt{6f(3+2f)(5f-2T^2+3)}\right](1-f)hT}{(3+2f)(2T^2-3f)} \tag{42}$$

Secondly, let Σ_{2m}^{+} (resp. Σ_{2m}^{-}) denote the solution to $D_+=0$ (resp. $D_-=0$):

$$\Sigma_{2m}^{-}=\frac{\left(2T+\sqrt{6}\sqrt{f}\right)(f-1)Th}{3f-2T^2}\,. \tag{43}$$

$$\Sigma_{2m}^{+}=\frac{\left(2T-\sqrt{6}\sqrt{f}\right)(f-1)Th}{3f-2T^2}\,. \tag{44}$$

After some reasoning, the static solution can be finally determined by numerical integration. Then the static solution is compared to the cinematic solution in the following subsection.

6.2. Comparison between static and cinematic solutions

The comparison between the static solution and the cinematic solution as functions of the rigid core volume fraction ρ (f=0.25 and T=0.525) has been performed. It is found that the two solutions can hardly be differentiated. it can be concluded that they can be regarded as the exact strength of the composite material, within the rigid core model. .

6.3. Analytical expressions of the strength under isotropic loading

Due to the complexity of the integrals in (40), these equations can hardly be solved analytically.

However, we observe that $\Sigma_m^{\pm}$ remain in the neighborhood of $\Sigma_{2m}^{\pm}$. We therefore propose to approximate the functions D_+ and D_- by series expansions in the neighborhood of Σ_{2m}^{+} and Σ_{2m}^{-}. In the case of of series expansion to the second order, The analytical solutions at order 2 read:

$$\Sigma_m^{\pm} = \eta + \rho \frac{c-\eta}{\kappa(c-\eta)(1-\rho)+1}. \tag{45}$$

with the following parameters for isotropic compression or traction:

$$\begin{cases} \eta = \Sigma_{2m}^{-} \\ \kappa = \dfrac{1}{2\sqrt{6}} \dfrac{3+2f}{(f-1)\sqrt{f}\,hT} \\ c = \Sigma_{1m}^{-} \end{cases} \quad \text{or} \quad \begin{cases} \eta = \Sigma_{2m}^{+} \\ \kappa = \dfrac{1}{2\sqrt{6}} \dfrac{3+2f}{(1-f)\sqrt{f}\,hT} \\ c = \Sigma_{1m}^{+} \end{cases}. \tag{46}$$

7. An approximate analytical macroscopic criterion

We seek an approximation of the criterion by an ellipse in the (Σ_m, Σ_d) plane. The ellipse intersects the Σ_m-axis at the points $(\Sigma_m^{-}, 0)$ and $(\Sigma_m^{+}, 0)$. The center of the ellipse is located at the middle of these points. We still have to determine the ordinate of the center of the ellipse which corresponds to the strength under pure shear ($D_m = 0$).

With the condition $D_m = 0$, it is readily seen that the value of the parameter A which minimizes $\tilde{\Pi}(\mathbf{D}, A)$ is A=0. With D_m=0 and A=0, closed-form expressions of the mean stress and the maximum shear stress can be obtained from (30):

$$\Sigma_{m,c} = -\lambda \quad ; \quad \Sigma_{d,c} = \sigma_0 \left[\sqrt{\frac{2}{3}}(1-\rho) + \sqrt{\frac{17\alpha+4}{15\alpha}}\rho \right]. \tag{47}$$

where $\lambda, \sigma_0, \alpha$ have been defined in (4) and (5). The subscript c recalls that this point is the center of the ellipse.

Now let us try to approximate the criterion given in parametric form (obtained by means of cinematic approach) found in section 4 by an analytical elliptic criterion. Analytical expressions of the strength have been established at particular stress states, namely under isotropic loading and under pure shear loading (with $\Sigma_m = -\lambda$). Recalling (45) (46) for the expressions of $\Sigma_m^{+}, \Sigma_m^{-}$ in the case of a second order expansion, together with (47) for the expression of $\Sigma_{d,c}$, the macroscopic criterion can be approached by the following analytical elliptic function:

$$\left(\frac{\Sigma_m - \lambda}{\Sigma_L / 2} \right)^2 + \left(\frac{\Sigma_d}{\Sigma_{d,c}} \right)^2 = 1. \tag{48}$$

with $\Sigma_L = \Sigma_m^{+} - \Sigma_m^{-}$ and $\lambda = (\Sigma_m^{+} + \Sigma_m^{-})/2$. Recall that $\Sigma_m^{+}, \Sigma_m^{-}, \Sigma_{d,c}$ are quantified in (45),(47) by (42),(43),(44); and $\lambda, \sigma_0, \alpha$ are given in (4),(5).

According to the comparison between the predictions of the analytical macroscopic criterion, (48), and the parametric criterion predicted by (30). We found that the comparison shows an excellent accuracy of (48).

8. Conclusion

On the basis of a limit analysis approach, we have proposed an extension of available models (devoted to the macroscopic strength of porous media). This extension concerns porous materials with a Drucker- Prager solid phase, reinforced by rigid particles. The proposed model concerns in particular, the Callovo Oxfordian clay as a composite material made up of rigid inclusions embedded in a porous clay matrix. The obtained results has been compared to the estimate of the strength recently derived by [4] on the basis of a variational non linear homogenization approach. A good accuracy of the estimate of the strength under isotropic loadings has been shown by a comparison with the results of a static (stress based) approach of the limit analysis problem. An interesting observation is that the estimates of the isotropic strength in traction or in compression do not depend on the homogenization method (limit analysis, variational method). Furthermore, the isotropic strength proves to be only slightly affected by the rigid core volume fraction. The practical implication is that the isotropic strength properties of the clay matrix and of the Callovo Oxfordian argillite are very close, irrespective of the quartz/calcite content. In contrast, a significant discrepancy between the failure envelopes is observed on the shear strength for large values of the rigid inclusions concentration.

Acknowledgements

The work presented in this paper was partly funded by ANDRA, the French national Agency for the management of radioactive wastes, which is gratefully acknowledged.

References

[1] A. Abou-Chakra Guery, F. Cormery, J.-F. Shao, D. Kondo, 2008. A micromechanical model of elasto-plastic and damage behavior of a cohesive geomaterial. Int. J. Solid. Struct., 45 (5), 1406–1429.

[2] Andra, 2005. Referentiel du site meuse-haute marne. Report.

[3] L. Dormieux, D. Kondo, 2010. An extension of gurson model incorporating interface stresses effects. International Journal of Engineering Science, 48(6), 575–581.

[4] A.L. Gurson, 1977. Continuum theory of ductile rupture by void nucleation and growth: Part I–Yield criterion and flow rules for porous ductile media, J. Engrg. Mat. Technol. 99, 2–15.

[5] J.-B. Leblond, G. Perrin, P. Suquet., 1994. Exact results and approximate models for porous viscoplastic solids. International Journal of Plasticity, 10(3):213–235.

[6] S. Maghous, L. Dormieux, J. Barthelemy, 2009. Micromechanical approach to the strength properties of frictional geomaterials. European Journal of Mechanics A/Solids., 28, 179–188.

[7] V. Monchiet, E. Charkaluk, D. Kondo, 2007. An improvement of Gurson-type models of porous materials by using Eshelby-like trial velocity fields. Comptes Rendus Mecanique., 335(1), Pages 32–41

[8] P.Ponte Castaneda, 1991. The effective mechanical properties of nonlinear isotropic composites. J. Mech. Phys. Solids, 39, 45–71.

[9] J-C. Robinet, P. Sardini, D. Coelho, J-C. Parneix, D. Pret, S. Sammartino, E. Boller and S. Altmann., 2012. Effects of mineral distribution at mesoscopic scale on solute diffusion in a clay-rich rock: Example of the Callovo-Oxfordian mudstone (Bure, France). Water Resources Research, 48, W05554, doi:10.1029/2011WR011352.

[10] J. Salencon, 1990. An introduction to the yield theory and its applications to soil mechanics. European Journal of Mechanics A/Solids, 9(5),477–500.

[11] W.Q. Shen, L. Dormieux, D. Kondo, J.F. Shao, 2013. A closed-form three scale model for ductile rocks with a plastically compressible porous matrix, Mechanics of Materials, 59 73--86

[12] W.Q. Shen, J.F. Shao, D. Kondo, B. Gatmiri., 2012. A micro-macro model for clayey rocks with a plastic compressible porous matrix, International Journal of Plasticity, 36, 64–85

Elasto-Dynamic Behaviour of Interacting Inhomogeneities and Cracks

Shaker A. Meguid[1,*], **Xiaodong Wang**[2]

[1]Department of Mechanical and Industrial Engineering, University of Toronto, Toronto, Canada M5S 3G8
[2]Department of Mechanical Engineering, University of Alberta, Edmonton, Canada T6G 2G8
* Corresponding author: meguid@mie.utoronto.ca

Abstract The paper presents a theoretical treatment of the dynamic behavior of fibre reinforced composites containing matrix cracks and reinforcing inhomogeneities. A pseudo-incident wave method is used to treat the dynamic interaction between cracks and inhomogeneities. Using this method, the original interaction problem is reduced to the solution of coupled single crack/inhomogeneity subproblems, for which analytical solutions could be derived. The interaction effects are introduced via the superposition of the different subproblems. The steady state solution of the interacting crack problem is obtained using integral transform method and the solution of the inhomogeneity problem is determined using Fourier expansion. The dynamic stress intensity factors (SIFs) at the matrix crack are obtained and numerical examples are provided to show the effect of the frequency, geometry of microdefects and material properties upon the dynamic SIFs.

Keywords Dynamic interaction, Crack, Inhomogeneity, Composite

1. Introduction

A major issue in modeling the micromechanical behaviour of advanced composites is how to deal with the interaction between cracks and inhomogeneities, which governs the overall failure mechanism of the materials [1-4]. The quasi-static interaction problem in composite materials has received considerable attention but the dynamic interaction between cracks and inhomogeneities is still limited [5-9]. Compared with quasistatic problems, the formulation of dynamic problems is much more complicated and difficult to deal with and the experimental data are difficult to obtain. It should be mentioned that most advanced composite materials are currently being used or considered for use in situations involving dynamic loading. Numerical methods, such as finite element analysis or boundary element method, can be used for this type of dynamic analyses under certain conditions but has their own limitations when multiple defects are involved. Analytical study of interacting cracks under dynamic loads is still attracting researchers [10-12] because of its high reliability and accuracy in simulating the dynamic response of multiple defects in composite materials.

It is the objective of the present paper to review and present the usage of the pseudo-incident wave method for the analysis of steady state dynamic interaction problems. Based on this method, the original interaction problem is reduced into single crack and single inhomogeneity subproblems, which are coupled through the scattered waves. The single crack and single inhomogeneity problems are solved analytically using integral transform method and Fourier expansion, respectively. Following this introduction, the paper is divided into three more sections: the formulations, results and discussions and conclusions.

2. Formulation of the Problem

Consider now the dynamic interaction between arbitrary defects, which could be in forms of cracks or inhomogeneities, in an infinite elastic isotropic solid under steady state dynamic antiplane loading, as shown in Fig.1. The displacement field corresponding to a steady state dynamic loading can be generally expressed in terms of the frequency ω as

$$w^*(x,y,t) = w(x,y)e^{i\omega t} \tag{1}$$

For the sake of convenience, the time factor $e^{i\omega t}$ will be suppressed and only the magnitude $w(x,y)$ will be considered. The harmonic displacement field must satisfy the Helmholtz equation [13],

$$\frac{\partial^2 w}{\partial x^2}+\frac{\partial^2 w}{\partial y^2}+\frac{\omega^2}{c_T^2}w=0 \tag{2}$$

where $c_T=(\mu/\rho)^{1/2}$ is the shear wave speed of the medium. The non-vanishing shear stress components are

$$\tau_{yz}=\mu\frac{\partial w}{\partial y} \quad , \quad \tau_{xz}=\mu\frac{\partial w}{\partial x} \tag{3}$$

where μ is the shear modulus of the material.

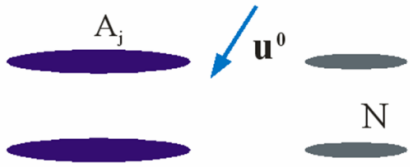

Figure 1. Interacting defects subjected to an incident wave

Instead of solving the original interaction problem, single defect problems will be considered. For any individual defect the interaction with other ones will be treated as an unknown wave, pseudo-incident wave. This wave represents the scattered waves from all other defects and will be determined by considering the consistency condition between defects.

2.1 Single crack problem

Consider the single defect problem first. For a single crack subjected to a dynamic antiplane loading, the boundary conditions along the crack surfaces are,

$$w(x,0)=0 \quad |x|\geq c \quad , \quad \tau_{yz}(x,0)=-\tau_1(x) \quad |x|<c \qquad sgn(y)=\begin{cases}1 & y>0\\ -1 & y<0\end{cases} \tag{4}$$

with τ_1 being the shear stress caused by the incident wave. x is the axis along the crack surface and c is the half length of the crack.

By making use of Fourier transform, the general solution of the displacement and stress fields in the transformation domain can be expressed as

$$w^*(s,y)=-\frac{sgn(y)}{2\pi i}\int_{-c}^{c} f(u)\frac{1}{s}e^{isu-\alpha|y|}du \tag{5}$$

where y is an axis starts from the centre of the crack and is perpendicular to the crack surfaces, s is the Fourier transform parameter of x, $f(x)$ represents the deformation of the crack surfaces, defined by

$$f(x)=\frac{\partial w(x,0)}{\partial x} \tag{6}$$

and

$$\alpha=\sqrt{s^2-\frac{\omega^2}{c_T^2}} \quad with \quad Re(\alpha)\geq 0$$

The solution of the problem can be obtained by using Chebyshev polynomial expansion of $f(x)$ as,

$$f(x)=\sum_{j=0}^{\infty}\frac{c_j}{\sqrt{1-\frac{x^2}{c^2}}}T_j(\frac{x}{c}) \tag{7}$$

where T_j are Chebyshev polynomials of the first kind and c_j are unknown constants. By satisfying the boundary condition at selected collocation points along the crack surfaces, the parameters c_j can be determined in terms of the boundary stress as,

$$[S]\{A\} = \{f\} \tag{8}$$

where $[S]$ is a known matrix, $\{A\}=\{c_1, c_2, \dots\}^T$ and $\{f\}$ is a matrix containing the boundary stresses at the collocation points along the crack surfaces. From this solution, the stress and displacement field caused by this crack can be calculated in terms of $\{A\}$.

2.2 Interaction problem

The solution of other single defect problems can also be determined and the solution can be expressed in the similar format as shown in Eq. (8). When multiple defects are involved, for defect A_j, as shown in Fig.2(a), all scattered waves from other defects will become an incident wave, i.e. the pseudo-incidenr wave (u_j^p). Therefore, defect A_j is subjected to both the original incident wave and the pseudo-incident wave and results in a scattered wave, as shown by Fig.2(b).

(a) (b)

Figure 2 Illustration of pseudo-incident waves
(a) scattering from other defects, (b) total incident wave for a defect

Based on the relation between defects discussed above, for defect A_j the solution can be expressed as

$$[S_j]\{A_j\} = \{f_j\} + \{f_j^p\} \tag{9}$$

where $[S_j]$ is the matrix given by (8) for A_j, and the two terms on the right hand side represent the original incident wave and the pseudo-incident wave.

If Eq. (9) is applied to all the defects and the pseudo-incident waves are represented in terms of the scattered waves, the governing equation for the interaction problem can be determined,

$$\left\{\begin{bmatrix}[S_1] & \cdots & 0\\ \vdots & \ddots & \vdots\\ 0 & \cdots & [S_n]\end{bmatrix} + \begin{bmatrix}[Q_1]\\ \cdots\\ [Q_n]\end{bmatrix}\right\}\begin{Bmatrix}\{A_1\}\\ \cdots\\ \{A_n\}\end{Bmatrix} = \begin{Bmatrix}\{f_1\}\\ \cdots\\ \{f_n\}\end{Bmatrix} \tag{10}$$

where $[Q_j]$ are determined by the scattered waves of the defects, $\{f_j\}$ are the original incident wave at different defects. It should be mentioned that both $[S]$ and $[Q]$ matrices are obtained from the analytical solution of single defects. By solving this linear equation, the solution of the interaction problem can be determined.

3. Results and Discussion

The solution presented in the previous section can provide reliable and accurate prediction of the stress field caused by the dynamic interaction. The method can be used to treat interaction between different defects [8,10,11]. Although only the single crack solution is presented in the previous section, solutions of other single defects can be similarly and easily assembled into Eq. (10). In this section, typical examples are presented to illustrate the dynamic interaction between different defects. The numerical simulation is conducted by solving Eq. (10) and the convergence of the solution has been carefully evaluated. Specifically, numerical results are presented to illustrate the dynamic interaction between a main crack and a second crack or an inhomogeneity. The incident antiplane wave is perpendicular to the crack surface.

To evaluate the accuracy of the current method, Fig. 3 shows the static interaction between a circular inhomogeneity and a collinear crack subjected to an initial stress intensity factor (K_0). Comparing with the closed form solution (lines) [14] excellent agreement is observed.

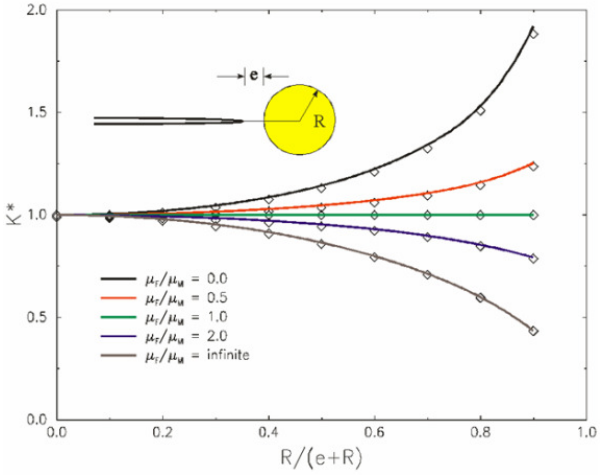

Figure 3. Static interaction

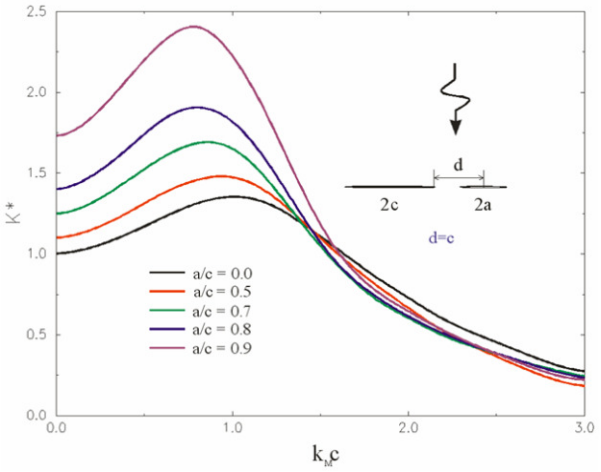

Figure 4. Interacting cracks

Fig.4 shows the effect of a collinear crack of length *2a* on the normalized stress intensity factor crack of a main crack of length *2c*. *a/c=0* corresponds to the case of a single crack. Comparing these curves indicates that significant interaction between cracks exists for low frequencies. But the interaction effect is significantly reduced at higher frequencies.

Fig.5 shows the result of interaction between a crack and an inhomogeneity. The variation of the normalized stress intensity factor for different crack-inhomogeneity configurations is presented. Unlike the collinear crack case where only amplification effects are observed, when the inhomogeneity, with a higher stiffness, is ahead of crack, the stress field is shielded. i.e. the dynamic stress intensity factor at the main crack attains a value lower than the dynamic single crack solution. Fig.6 presents the result of a similar inhomogeneity with a partially debonded interface near the crack tip, as shown. With the increase of the size of the debonded interface, the stress intensity factor at the crack tip increases and indicates an amplification effect. For high loading frequencies, the interaction effect becomes insignificant because the distance between the crack and the inhomogeneity is much larger than the wave length.

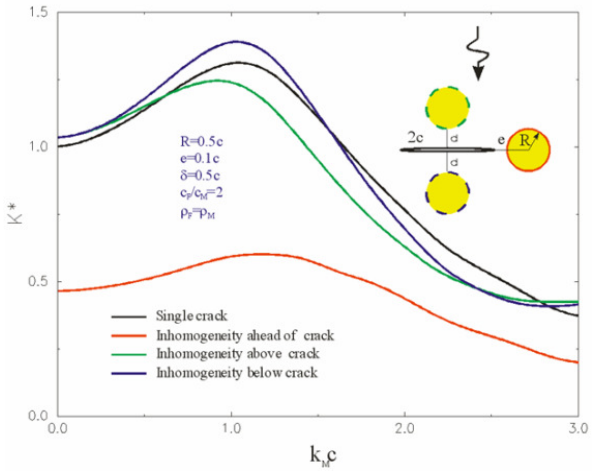

Figure 5. Crack and inhomogeneity

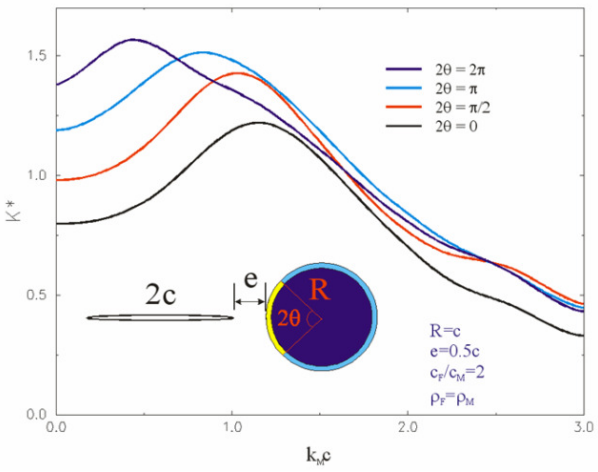

Figure 6. Crack and debonded inhomogenity

4. Conclusions

A pseudo-incident wave method is developed to predict the dynamic interaction effects between cracks and inhomogeneities. This approach enabled us to reduce the original interaction problem into the solution of coupled single crack/inhomogeneity subproblems, for which analytical solutions could be easily obtained which are coupled through the scattered waves. The steady state solution of the crack problem is obtained using integral transform method and the solution of the inhomogeneity problem is determined using Fourier expansion. The dynamic stress intensity factors (SIFs) at the matrix crack are obtained and numerical examples are provided to show the effect of the frequency, geometry of microdefects and material properties upon the dynamic SIFs. Both shielding and amplification effects are experienced and discussed.

Acknowledgements

This research is supported by the Natural Sciences and Engineering Research Council of Canada.

References

[1] R. G. Hoagland, G. T. Hahn and A. R. Rosenfield, Influence of microstructure on the fracture propagation in rock. Rock Mech. **5**, (1973), 77-106.

[2] N. Claussen, J. Steeb, R. F. Pabst, Effect of inducted micro-cracking on the fracture toughness of ceramics. Bull. Am. Ceram. Soc. **56**, (1977), 559-562.

[3] A. G. Evans, K. T. Faber, Crack-growth resistance of micro cracking brittle materials. J. Am. Ceram. Soc., **67**, (1984), 255-260.

[4] M. Ruhle, A. G. Evans, R. M. McMeeking, P. G. Charalambides, J. W. Hutchinson, Microcrack toughening in alumina/Zirconia. Acta Metall. **35**, (1987), 1701-1710.

[5] D.K.L. Tsang, S.O. Oyadiji, A.Y.T. Leung, Multiple penny-shaped cracks interaction in a finite body and their effect on stress intensity factor. Eng. Frac. Mech. **70**, (2003), 2199-2214.

[6] X. Yan, C. Miao, A numerical method for a void-crack interaction under cyclic loads, Acta Mech **223**, (2012), 1015-1029.

[7] D. Gross, Ch. Zhang, Diffraction of SH waves by a system of cracks: solution by an integral equation method. Int. J. Solids Structures. **24**, (1988), 41-49.

[8] S. A. Meguid, X. D. Wang, On the dynamic interaction between a microdefect and a main crack. Proc. R. Soc., Lond. **A409**, (1995), 449-464.

[9] Ch. Zhang, Elastodynamic analysis of a periodic array of mode III cracks in transversely isotropic solids. J. Appl. Mech. **59**, (1992), 366-371.
[10] S.A. Meguid, X.D. Wang, On the dynamic behaviour of interacting microdefects in advanced composite materials, Int. J. Impact Eng. **19**, (1997), 503-514.
[11] X. D. Wang, S. A. Meguid, Diffraction of SH-wave by interacting matrix crack and an inhomogeneity. *ASME J. App. Mech.* **64**, (1997), 568-575.
[12] W.T. Ang, L. Athanasius, Dynamic interaction of multiple arbitrarily oriented planar cracks in a piezoelectric space: a semi-analytic solution. Eur. J. Mech. A-Solid. **30**, (2011), 608-618.
[13] J.D. Achenbach, Wave propagation in elastic solids. North-Holland Publishing Company, Amsterdam (1973).
[14] E. Turska-Klebek, M. Sokolowski, On the influence of defects upon stress concentration at the crack. Arch. Mech. **36**, (1984), 121-126.

Fracture Behavior in Timber Element Under Climatic Variations

Frédéric Lamy [1], Frédéric Dubois [1,*], Octavian Pop [1], Mokhfi Takarli [1], Nicolas Angellier [1], Nicolas Larcher [1]

[1] Heterogeneous Material Research Group, Civil Engineering and Durability department, University of Limoges, Egletons, 19300, France
* Corresponding author: frédéric.dubois@unilim.fr

Abstract Timber elements placed in outdoor conditions are solicited by mechanical loadings and climatic variations. Joints or notched beams are subjected to stress concentrations which can cause a crack growth process due to drying phases. This paper deals with the experimental and analytical approaches about the fracture process in timber element subjected to different moisture content conditions. Two lots of SEN specimens are conditioned in different air conditions and tested in opening mode. A quasi-brittle fracture behavior is studied using a thermodynamic approach taking into account the dissipation based on the crack surface separation and the development of a process zone around the crack tip. The model includes the fracture and damage energy release rate concepts. Based on fracture and damage approaches, the dissipation separation is realized using the coupling of a finite element approach and image analysis tracking the visible crack tip during the experimental test. Experimental results and numerical treatments allow highlighting the moisture content effect on damage and crack growth with an increase of the ductility for high moisture content levels caused by the increase of the process zone size. This work allows envisaging the comprehension of the crack growth process under climatic variations introducing mechano-sorptive aspects.

Keywords Fracture mechanic, Viscoelastic behavior, Mechano-sorptive effects

1. Introduction

Timber elements placed in outdoor conditions are solicited by mechanical loadings and climatic variations. Around knots and joints, stress concentrations can induce crack growth initiation until fracture. Around these singularities, moisture content can be concentrated accentuated with climatic variations, .This coupling is usually treated by a mechano-sorptive approach coupling mechanical fields and moisture content gradients. In the past, a lot of works has been developed in order to understand this interaction at a material scale and for bending behavior. If we take the example of timber joints, the toughness can be accelerate by moisture content variations by provoking a crack initiation and the crack propagation until a partial collapse [1]. The one difficulty meet by the scientist community is the illustration of the mechano-sorptive effects in the fracture mechanic kinetic. Several scientific explorations have shown that coupling between moisture content variations and mechanical loading is subject to shrinkage-swelling effects and a modification of elastic or viscoelastic properties. In terms of thermodynamic visions, the last phenomenon is traduced, for constant mechanical loadings, by an increase of compliance properties during moistening phases and a blocking of strains during drying process corresponding to a partial storage of the free energy. These last observations request to put in evidence the local fracture behavior in moistening and drying phases. However, before to highlight the mechano-sorptive effects during wetting and drying phases, it is necessary to characterize the mechanical properties for dry and wet conditions.

The first section deals with the experimental setup based on a double cantilever beam specimen in Douglas fire using a electromechanical testing machine associated with a regulated environment chamber. These tests allow the determination of the specimen compliance and the critical energy release rate versus the crack tip position for dry and wet conditions.

Moisture content variations are stud in the second session. This part allows showing effects of a drying phase on the crack growth initiation under a creep loading.

2. Experimental setup

2.1. Material and methods

Experimental tests are based on the use of a double cantilever beam in Douglas fire submitted at a displacement control loading. Two sample groups are conditioned in dry and wet environments, respectively. In the other hand, for initial moistened specimens, a ramp of drying is imposed. All tests are filmed by CCD camera in order to record the crack tip advance. The Douglas fire specimen is a Double Cantilever Beam. Dimensions are fixed in Figure 1. The initial crack is oriented in the longitudinal axis with an initial length of 50mm. Its thickness is 20mm. The loading axes have a diameter of 10mm. The crack propagation is assumed to be in the Radial Longitudinal plane.

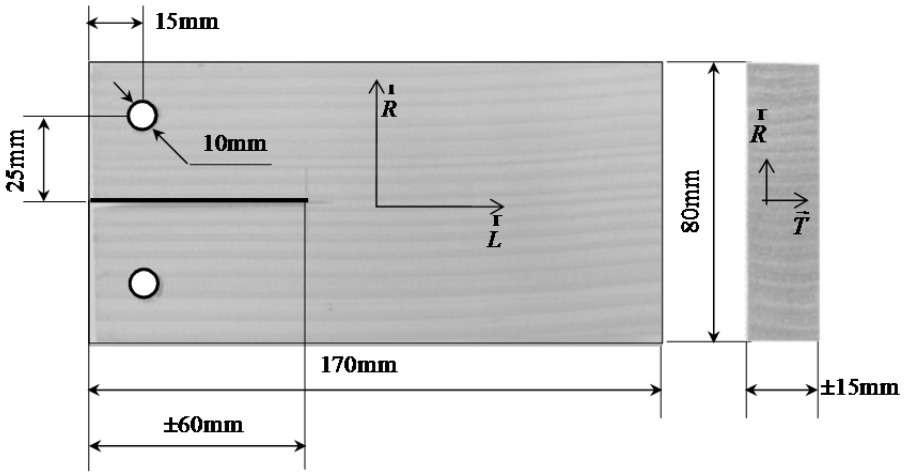

Figure 1. Double Cantilever Beam geometry

Two families of four specimens are placed in a dry (20°C, 40%HR) and wet (20°C, 85%HR) climate corresponding to moisture contents of approximately 9% and 19%, respectively. These specimens are acclimated during several weeks in order to obtain a moisture content homogeneity. The testing machine is a Zwick electromechanic incorporating an environmental chamber allowing the time synchronization between force-displacement and temperature/humidity histories, Figure 2.

Figure 2. Zwick electromechanic machine and CCD camera

The experimental device is completed by the crack tip advance monitoring using a CCD camera. The synchronization between images and mechanical data (force and displacement of the machine crossbar) is permitted by using a tracking marker technique of the point of force application, Figure 3.

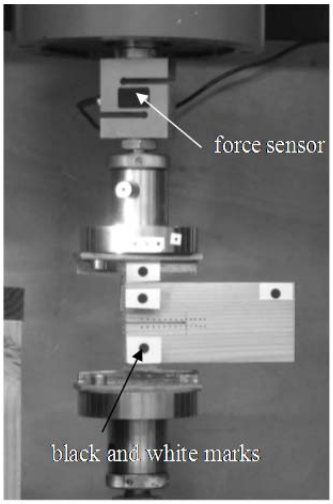

Figure 3. Synchronization with marker tracking method

During tests, the environment chamber is regulated in order to impose the equivalent moisture content conditioning. In order to limit creep effects, we impose a high constant displacement speed of 0,5mm/min until the total specimen collapse. In these conditions, the total test time does not exceed 4 minutes. Viscoelastic effects can be neglected in the following of this study.

2.2. Experimental results

Experimental results are composed of the force evolutions and the crack tip advance versus displacements. The force displacement curves are posted in Figure 4. First results highlight a decrease of the initial sample stiffness and the strength with eth moisture content increasing. In the other hand, wet samples seem to be characterized by a higher ductility.

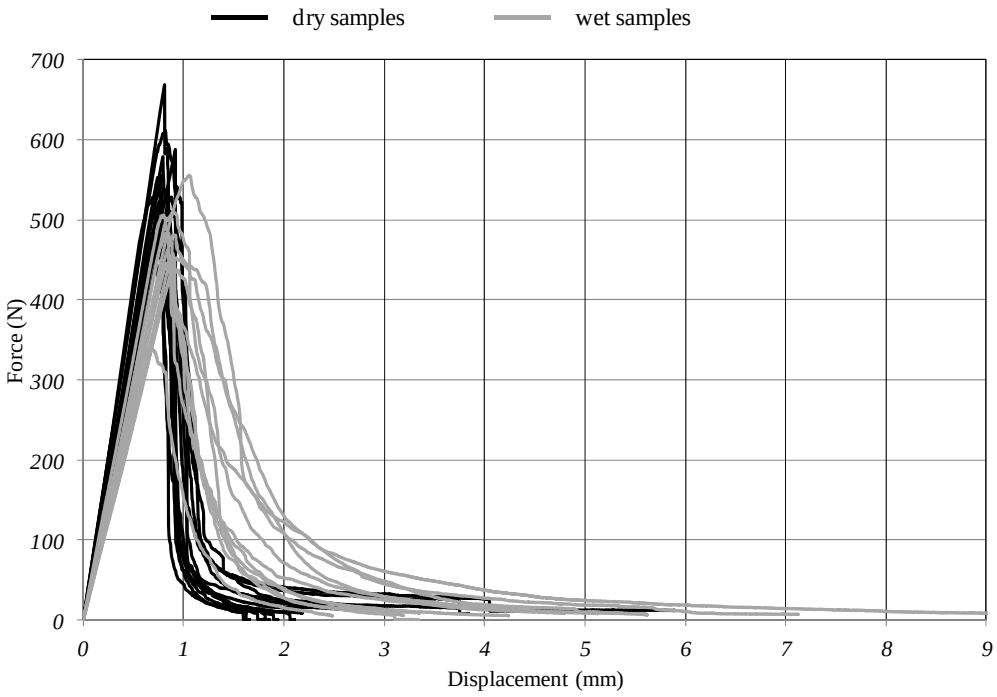

Figure 4. Force displacement curves under dry and wet conditions

All tests being filmed, the visible crack tip position can be noted versus displacements. In Figure 5, they are plotted crack length versus critical displacement corresponding to the crack tip advance. The graph highlights moisture content effect with an increase of sample compliance at a given crack length at high moisture content level (grey marks).

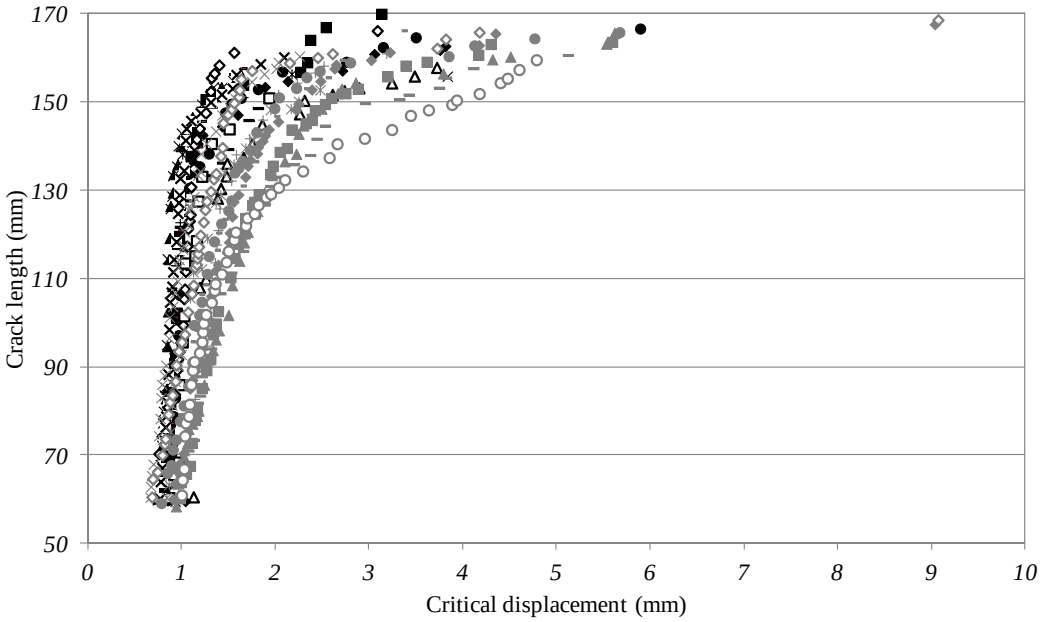

Figure 5. Visible crack length vs critical displacement

These observations prompt us to understand the cracking process by an energy approach. This one will clearly identify the effects of moisture content on the crack growth process by identifying energetic dissipation in terms of crack surface formations and process zone development.

3. Global thermodynamic approach

3.1. Thermodynamic formalism

Experimental results, shown in Figure 4 and 5, enables us to describe, at a global scale, energetic balance by introducing the global Helmholtz free energy $\psi[J]$ defined by observable variables represented by the total displacement d and an internal variable inducing softening of the sample stiffness [2]. By analogy with a damage theory, we introduce a virtual damage variable D and the effective stiffness $\tilde{k}(D)$. D represents the effects of the crack growth surface and the damage evolution in the process zone. Its form can be calculated from the non damage stiffness k such as :

$$D = 1 - \frac{\tilde{k}}{k} \quad \text{or} \quad \tilde{k} = (1 - D) \cdot k \tag{1}$$

Considering $F[N]$ as the reaction force, the global sample behavior can be defined as the relationship between this force and the global displacement u such as:

$$F = \tilde{k}(D) \cdot u \tag{2}$$

According to the thermodynamic approaches introduced by Lemaître, let us introduce the global thermodynamic potential in the form of the Helmholtz free energy variation is defined as:

$$\dot{\psi} = \frac{\partial \psi}{\partial u} \cdot \dot{u} + \frac{\partial \psi}{\partial D} \cdot \dot{D} \tag{3}$$

By assuming a total crack closure after unloading, the global elastic behavior (2) provides the first state equation:

$$F = \frac{\partial \psi}{\partial u} \tag{4}$$

Crossing expressions (2) and (4), the Helmholtz free energy can take the following form:

$$\psi = \frac{1}{2}\tilde{k}(D)\cdot u^2 \tag{5}$$

The energy release rate Y_D (associated to damage variable) can be defined as follow:

$$Y_D = \frac{\partial \psi}{\partial D} \tag{6}$$

Introducing equation (5) in (6), its definition becomes:

$$Y_D = \frac{u^2}{2}\cdot\frac{\partial \tilde{k}}{\partial D} \tag{7}$$

Considering the damage definition in expression (1), the energy release rate (7) can be rewritten by:

$$Y_D = -\frac{1}{2}\cdot k \cdot u^2 \tag{8}$$

By considering the Clausius-Duhem relationship, the dissipation, induced by the crack growth process φ can be defined by, Figure 6:

$$\dot{\varphi} = -Y_D \cdot \dot{D} \tag{9}$$

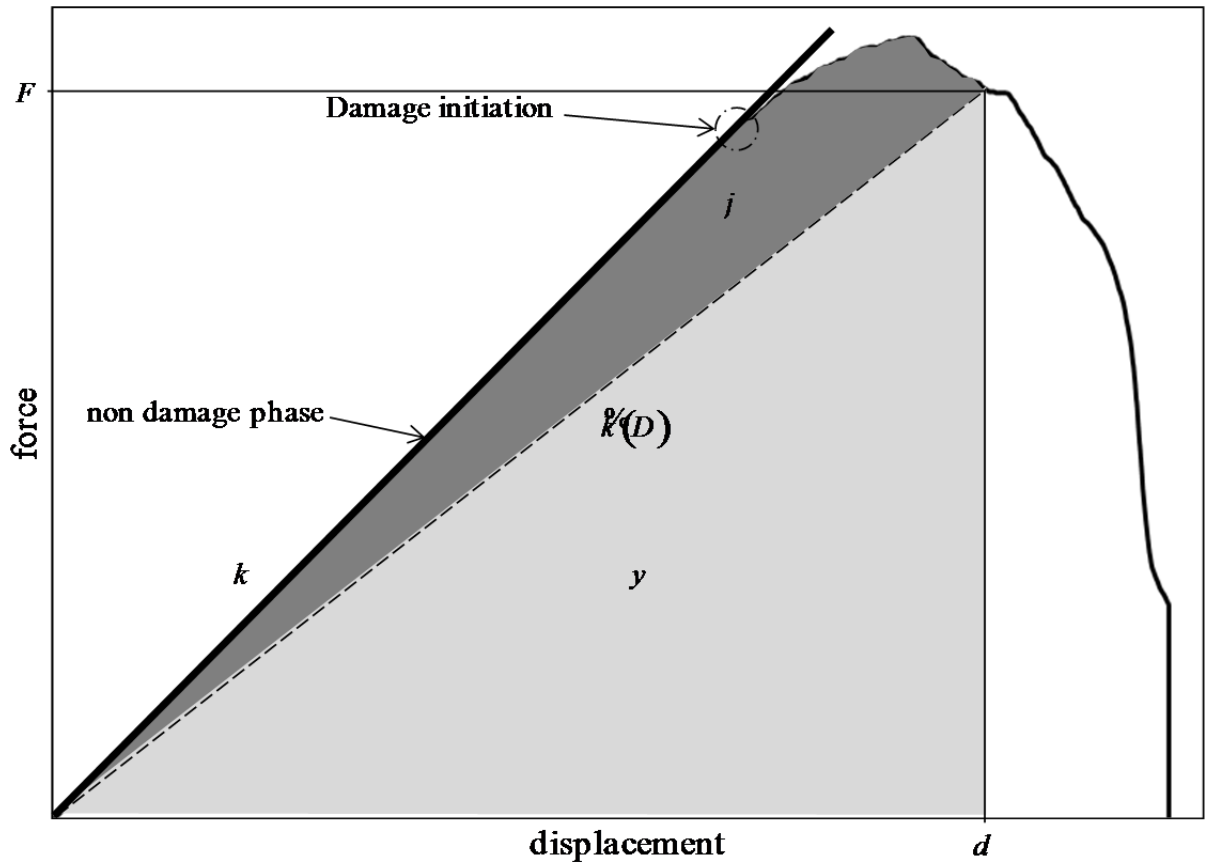

Figure 6. Experimental force-displacement he curve and thermodynamic description

3.2. Thermodynamic formalism

In the thermodynamic approach, an additional behavior law consists on the relationship between energy release rate and the global damage variable. Experimentally crossing expressions (1) and (8), we can easily plot the energy release rate – damage curve as shown in Figure 1. We can clearly note a behavior difference between dry and wet samples with a higher ductility at high moisture content levels. The behavior law can be separated into two regions. The first concerns the damage growth initiation which can be described by the following criterion:

$$D = 0 \quad \text{and} \quad \dot{D} = 0 \quad \text{if} \quad |Y_D| < Y_c \tag{10}$$

Where Y_c is a critical energy release rate value corresponding to a damage growth initiation. The second is the damage evolution function versus energy release rate. According to the global form, we propose an evolution under a Prony's serie form such as:

$$D = \chi_1 \cdot \left(1 - \exp\left(\frac{Y_D + Y_c}{Y_1}\right)\right) + \chi_2 \cdot \left(1 - \exp\left(\frac{Y_D + Y_c}{Y_2}\right)\right) \tag{11}$$

For dry and wet samples, **Error! Reference source not found.** and **Error! Reference source not found.** fixe thermodynamic parameters, respectively.

Table 1. Thermodynamic parameters for dry samples

	$Y_c\ (mJ)$	$Y_1\ (mJ)$	$Y_2\ (mJ)$	χ_1	χ_2	$k\ (N/mm)$
Average	207	88	794	0.94	0.06	709
Standard Variation	57	28	26	0.05	0.05	79

Table 2. Thermodynamic parameters for wet samples

	$Y_c\ (mJ)$	$Y_1\ (mJ)$	$Y_2\ (mJ)$	χ_1	χ_2	$k\ (N/mm)$
Average	169	183	787	0.81	0.19	571
Standard Variation	41	67	19	0.15	0.15	50

3.3. Average global behavior

The average behavior for dry and wet samples can be built by the following algorithm. Firstly, a global displacement history $u(t)$ is fixed. The energy release rate Y_D is calculated according to expression (8). The equation (11) allows defining the damage evolution. In a last time, the global sample behavior (2) after updating the effective stiffness (1). Results can be shown in Figures 7 and 8. The model can represent the differences in terms of ductility behavior between average dry and wet tests. The main criticism that we could do on this approach and the non decoupling process of crack propagation and the process zone. If our approach allows reproducing experimental test, it cannot be generalized for other geometry and doesn't take into account a scale effect induced by the

process zone existence.

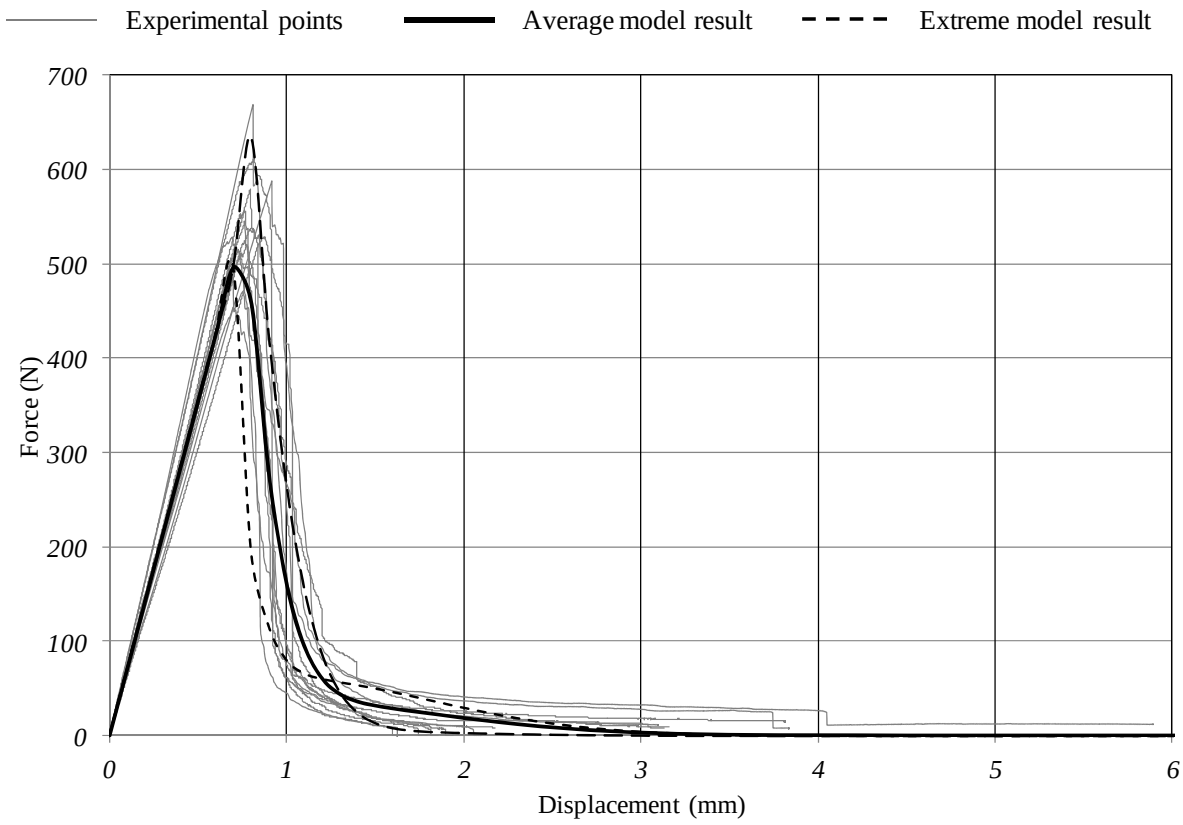

Figure 7. Modeling of fracture process for dry samples

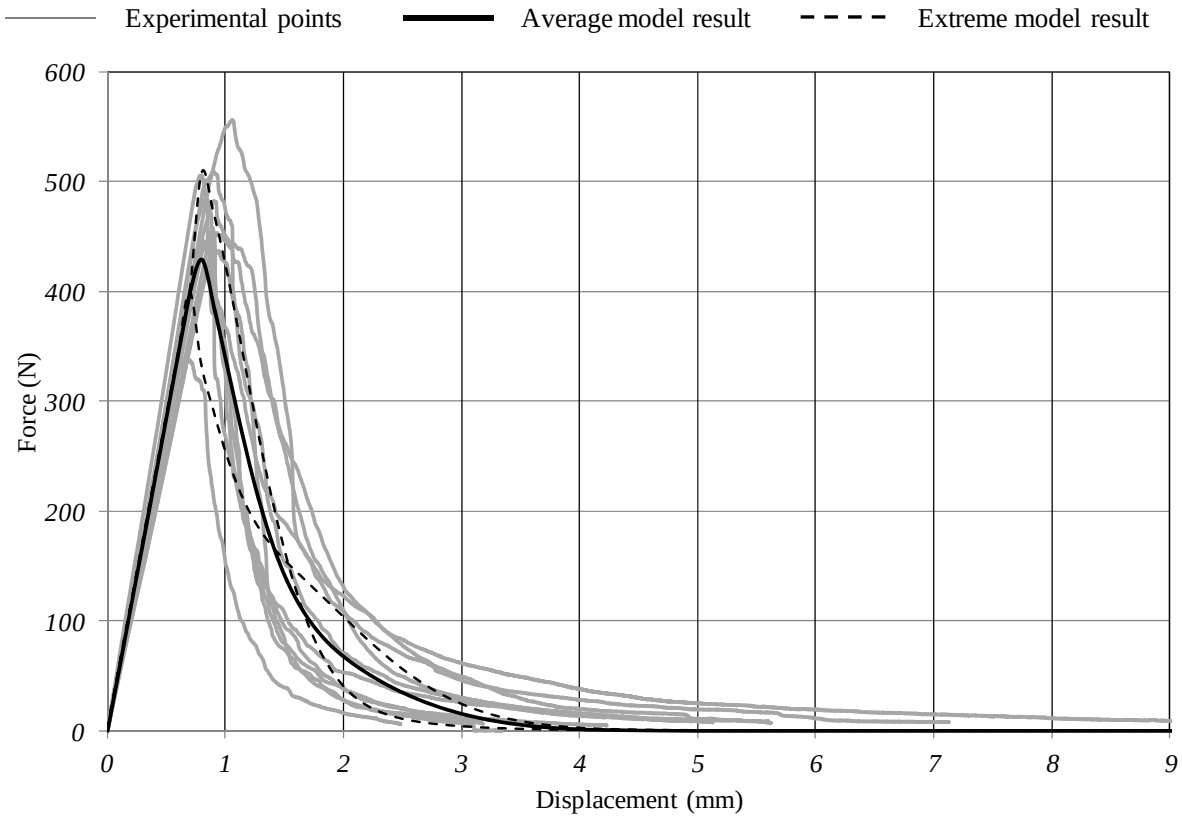

Figure 8. Modeling of fracture process for wet samples

4. Mechanical tests under variable climate

The mechanical test under variable climate conditions is based on a creep loading accompanied by relative humidity changes. This test allows the introduction, in the fracture behavior, effects of the viscoelasticity, the shrinkage or swelling and mechano-sorptive process. In this paper, we focus our investigation of drying process.

4.1. Loading history

The association of the mechanical loading with the decrease of the relative humidity requests to introduce the time as synchronization variable. In your case, we choose to load the specimen conditioned in a wet environment (20°C, 85%HR). The loading value is chosen according to a static displacement of 1mm with a displacement speed of 0,5mm/min. At this time, the force is fixed as constant during 10 minutes in order to observe creep response in constant wet climate. The next step is characterized by a drying phase by changing climate conditions at a dry state (20°C, 30%HR). The experimenters expect now the complete collapse of the sample. The Figure 8 summarizes the hygro-mechanical loading.

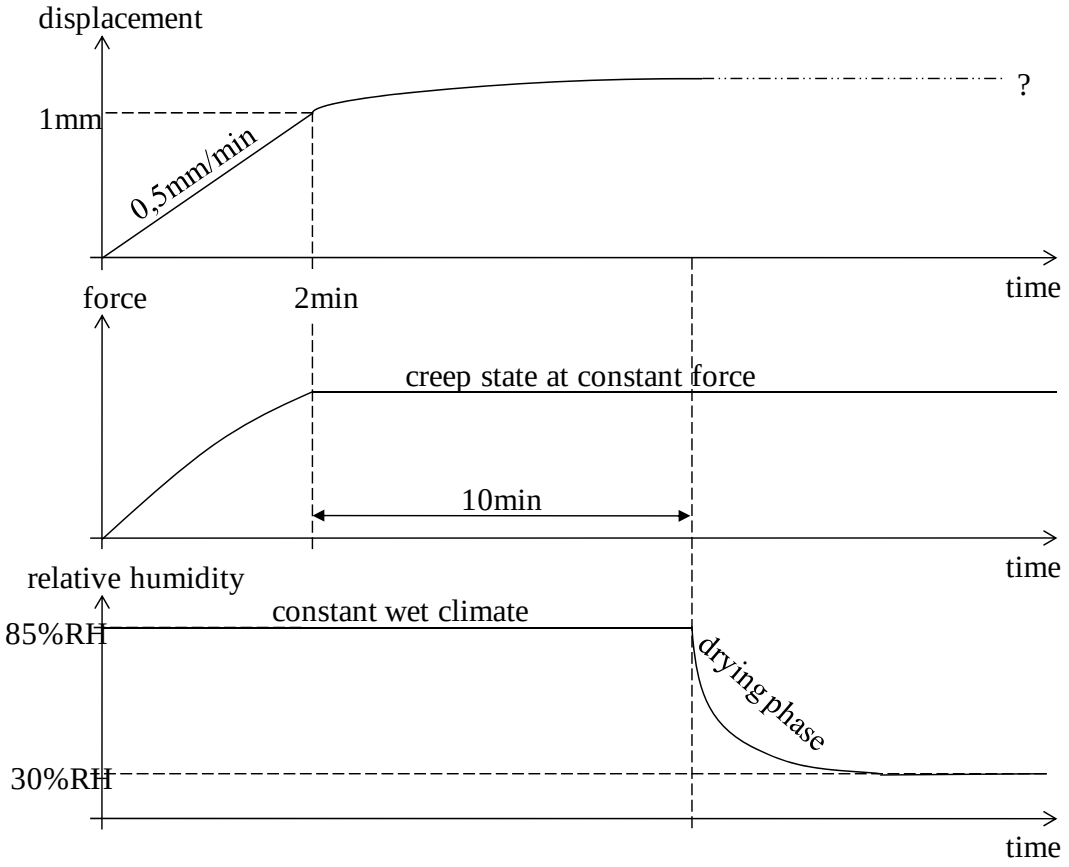

Figure 9. Hygro-mechanic loading history

4.2. Experimental results

The force-displacement curve vs time is posted in Figure 10. The graph can be separated in four

specific zones.

1- This zone corresponds to the loading of the wet sample with a displacement speed of 0,5mm/min. The overall stiffness is equal to 260N/mm. According to a finale displacement of 1mm, the corresponding force is 355N.

2- During ten minutes, the force is kept constant. The sample mechanical state is in a creep configuration. We can observe the displacement evolution versus time. At this state, the relative humidity is maintained at 85%.

3- At this time, the phase of drying starts. According to diffusion process, the specimen begins to dry from the outside surface. The creep response results on the combination of mechano-sorptive and shrinkage effects. We can observe a displacement blocking characterizing of mechano-sorptive effects and, more particularly, its hygro-lock properties [3], [4], [5].

4- The last phenomenon is characterized by a continuum increase of displacements. According to a non linear behavior, this phase can be assimilated at a secondary creep state accentuated by the 3D diffusion process. The total collapse can be observed after a total time of 2h40.

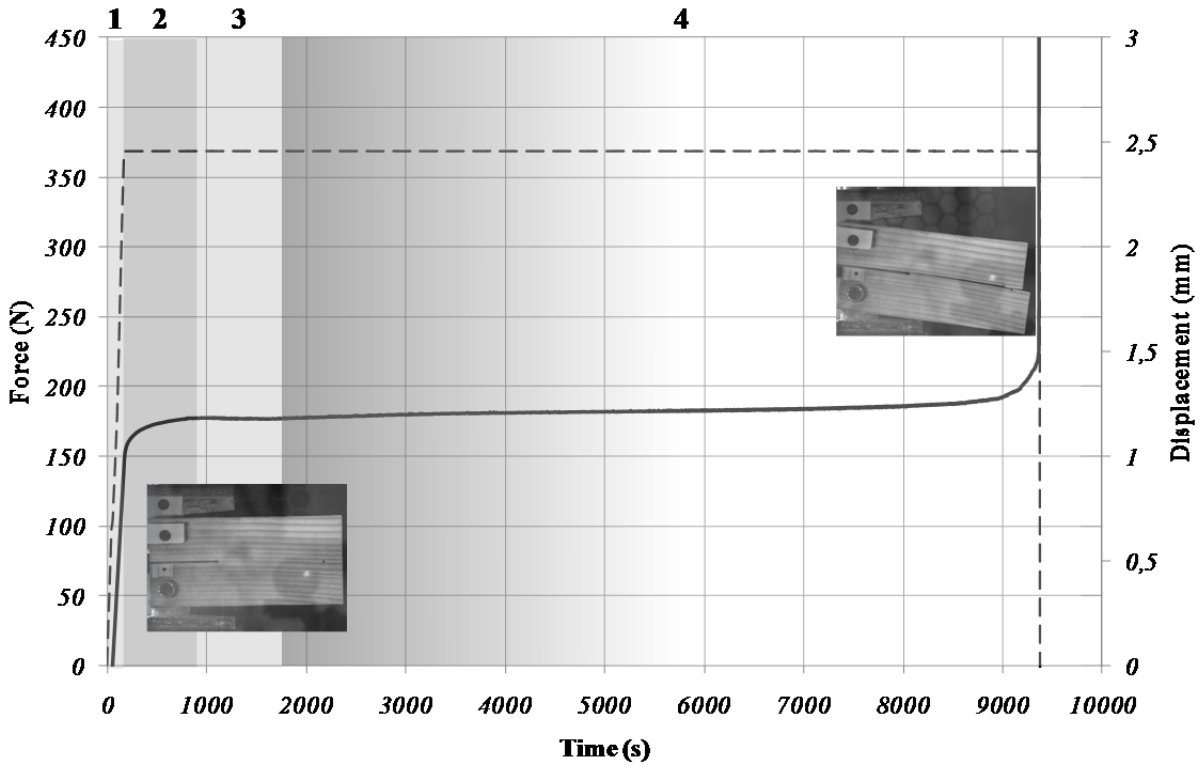

he th

Figure 10. Experimental results

5. Conclusion and outlook

This present thermodynamic approach allows studding the crack growth process by taking into account the global dissipation process induced by the new crack surfaces formations and a process zone development. The generalization of this approach for climatic variations request introducing mechano-sorptive behavior in the energetic balance. In the same time, the global behavior needs the uncoupling of shrinkage-swelling effect. In this last case, a finite element modeling allows the prediction of the free displacement induced by moisture content level taking into account orthotropic properties in the specimen thickness and diffusion process in the transverse section.

References

[1] M. Chaplain, T. Dethan, G. Valentin, Crack propagation in wood under relative humidity variations, 12th International Conference on Fracture, Ottawa, 2009.

[2] J. Lemaitre, J.L. Chaboche, Mécanique des matériaux solides, Dunod Press, Paris, 1988.

[3] J.M. Husson, F. Dubois, N. Sauvat, Elastic response in wood under moisture content variations: analytic development, Mechanics of Time Dependent Materials, doi: 10.1007/s11043-009-9104-y, MTDM149.2, 2009.

[4] F. Dubois, J. M. Husson, N. Sauvat, N., Manfoumbi Modeling of the viscoelastic, mechano-sorptive behavior in wood, Mechanics of Time Dependent Materials, doi: 10.1007/s11043-012-9171-3, 2012.

[5] J. Gril, International COST 508 Wood mechanics Conference, 1996.

Crack initiation and growth in an Zn-Cu-Al PE alloy

Vittorio Di Cocco[1,*], Francesco Iacoviello[1], Luigi Tomassi[1], Stefano Natali[2], Valerio Volpe[2]

[1] Department DICeM, University of Cassino and Southern Lazio, 03043, Italy
[2] Department DICMA, University of Rome "Sapienza", 00184, Italy
* Corresponding author: v.dicocco@unicas.it

Abstract Cu–Zn–Al shape memory alloys exhibit shape memory behavior within a certain range of composition. They are characterized by a stable high temperature disordered bcc structure named β-phase, followed by a transition to a B2 structure after appropriate cooling and from secondary B2 to DO3 ordering under other cooling procedures. It is also know that martensite stabilization can be reduced by a step-quenched treatment. Shape memory properties are often absolutely interesting and many grades of shape memory alloys are extensively used in the technological world, e. g. in surgery and dentistry. Copper-based shape memory alloys are preferred for their good memory properties and low cost of production.

In this work, the main crack initiation and its propagation in an tensile test is analyzed in order to evaluate crack path and its behavior corresponding to low and to high deformation values. Furthermore, results are associated to X-Ray diffraction in order to correlate structural transition involved in an Cu-Zn-Al alloy characterized by a PE behavior.

Keywords Shape Memory Alloy; Pseudo-Elastic Behaviour; Fracture; CuZnAl alloy.

1. Introduction

Shape memory alloys (SMA) and pseudo-elastic alloys (PEA) are able to recover their original shape after high mechanical deformations: the first ones by heating up to characteristic temperature (Shape Memory Effect, SME), and the second ones simply by removing the mechanical load (Pseudo-elastic Effect, PE). Different shape memory alloys have been optimized in the last decades, such as the copper-zinc-aluminum (ZnCuAl), copper-aluminum-nickel (CuAlNi), nickel-manganese-gallium (NiMnGa), nickel-titanium (NiTi), and other SMAs obtained alloying zinc, copper, gold, iron, etc.. However, the near equiatomic NiTi binary system shows the most interesting properties and it is currently used in an increasing number of applications in many fields of engineering, for the realization of smart sensors and actuators, joining devices, hydraulic and pneumatic valves, release/separation systems, consumer applications and commercial gadgets [1, 2]. Due to their good biocompatibility, another important field of SMA application is medicine, where the pseudo-elasticity is mainly exploited for the realization of several components such as cardiovascular stent, embolic protection filters, orthopedic components, orthodontic wires, micro surgical and endoscopic devices [3].

From the microstructural point of view, shape memory and pseudo-elastic effects are due to a reversible solid state microstructural transition from austenite to martensite, which can be activated by mechanical and/or thermal loads [4].

Copper-based shape-memory alloys are very sensitive to thermal effects, and it is possible that in

thermal cycles its properties change (e.g., shape-recovery ratio, transformation temperatures, crystal structures, hysteresis and mechanical behavior).
Cu–Zn–Al shape memory alloys exhibit shape memory behavior within a certain range of composition. It is characterized by a stable high temperature disordered bcc structure named β-phase. After a customized cooling process, a B2 structure is obtained followed a DO3 ordering. It is also know that martensite stabilization can be reduced by a step-quenched treatment.
Cu ZnAl alloys mechanical properties are influenced by [5]:

- martensite stabilization;
- grain size;
- processes procedure (e.g., temperature, heat treatment cycles number).

Other investigations carried out on CuZnAl alloys, showed a strain influence on the macroscopic behavior and on martensite morphology. Martensitic transformation occurs initially in deformed material and the manufact shape follows the transformation [6]. Larger grains dimensions allow an easier transformation process, allowing the growth of 18R martensite [7].
In this work, damaging micromechanism during a tensile test in a CuZnAl alloy has been investigated, focusing the crack inititiation and its stable growth. Deformation influence on alloy microstructure has been investigated during the tensile test by means of X-Ray diffraction .

2. Material and methods

In this work a CuZnAl pseudo-elastic alloy, made in laboratory by using controlled atmosphere furnace and characterized by chemical composition shown in Table 1, has been used to investigate mechanical behavior in tensile conditions.

Table 1. Chemical composition of CuZnAl investigated alloy

Cu	Zn	Al	Other
73.00	21.80	5.04	0.16

The evolution of the microstructure during uniaxial deformation was analyzed by a miniature testing machine (Fig. 1) which allows in-situ scanning electron microscopic (SEM) observations as well as X-Ray micro-diffraction analyses.
In particular, the testing machine is equipped with a simple and removable loading frame, which allows SEM and X-Ray analyses at fixed values of applied load and/or deformations. The machine is powered by a stepping motor, which applies the mechanical deformation to the specimen through a calibrated screw, with pitch of 0.8mm, and a control electronic allows simultaneous measurement and/or control of applied load and stroke of the specimen head. The stroke is measured by a Linear Variable Differential Transformer (LVDT) while the load is measured by two miniaturized load cells with maximum capacity of 10 kN. Miniature dog bone shaped specimens were machined from alloy samples obtained by cold cutting of mini sheets from as cast ingots, by wire electro discharge machining.
Step by step isothermal tensile tests were carried out, at room temperature, at increasing values of

the specimens elongation. For each loading step, the loading frame containing the specimen was removed from the testing machine, at fixed values of deformation. The specimens, under load condition, was analyzed by means of:

1) a light optical microscope, characterized by a wide observation field; all the investigated specimen length was observed in order to identify the crack initiation site. The investigated steps are ε_{eng} = 0%, 5%, 10%, and 14% (failure);
2) a diffractometer in order to evaluate XRD spectra. XRD measurements were made with a Philips X-PERT diffractometer equipped with a vertical Bragg–Brentano powder goniometer. A step–scan mode was used in the 2θ range from 40° to 90° with a step width of 0.02° and a counting time of 2 s per step. The employed radiation was monochromated CuKα (40 kV – 40 mA). The calculation of theoretical diffractograms and the generation of structure models were performed using the PowderCell software [8]. The investigated steps are at ε_{eng} = 0% and 5%.

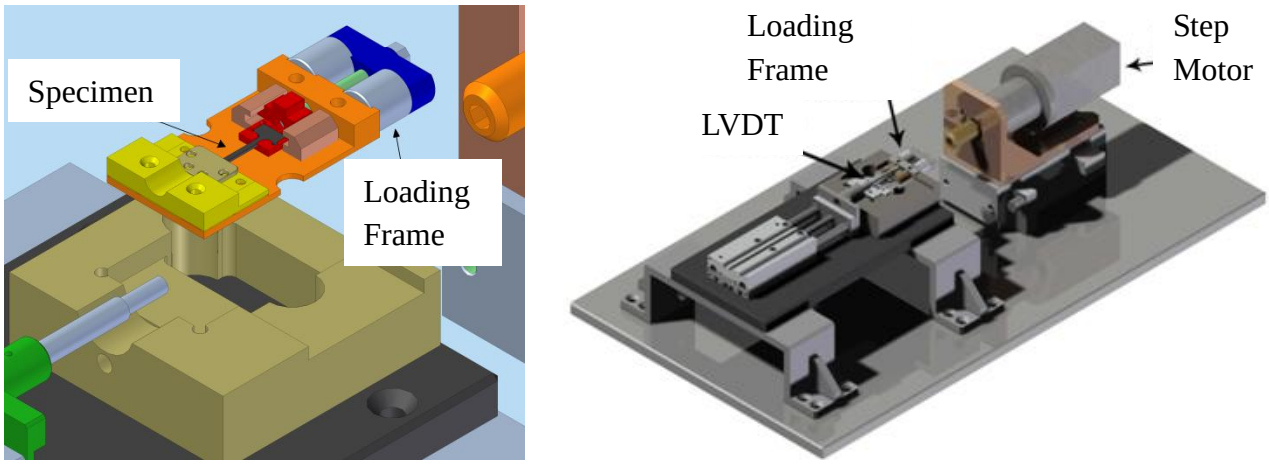

a) b)

Figure 1. Tensile equipment: a) loading frame, b) tensile machine.

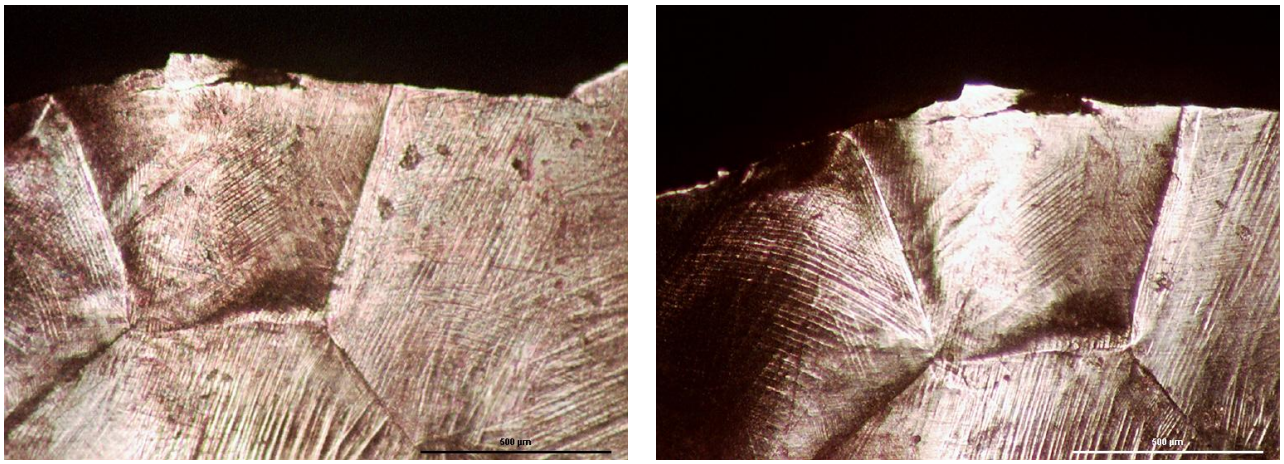

a) b)

Figure 2. Etched surface: a) etched-deformed and observed, b) deformed, cleaned and re-etched.

Finally, SEM observations on fracture surface have been performed in order to evaluate the main fracture micromechanisms.
In order to check the correctness of the LOM observation procedure, a preliminary test has been performed. An unloaded and metallographically prepared specimen has been deformed up to ε_{eng}=0% and then LOM observed (Fig. 2a). Subsequently the same specimen (loaded) has been metallographically prepared and LOM observed (Fig. 2b). It is evident the possibility to follow the grains modifications in the investigated SMA only performing the first metallographic preparation.

3. Results

Engineering stress strain curve of investigated alloy is shown in Fig. 3, where a plateau has not been observed. The investigated deformation conditions correspond to:

1. ε_{eng} = 0% - starting test conditions;
2. ε_{eng} = 5% - near yield point;
3. ε_{eng} = 10% - plastic zone;
4. ε_{eng} = 14% - specimen failure.

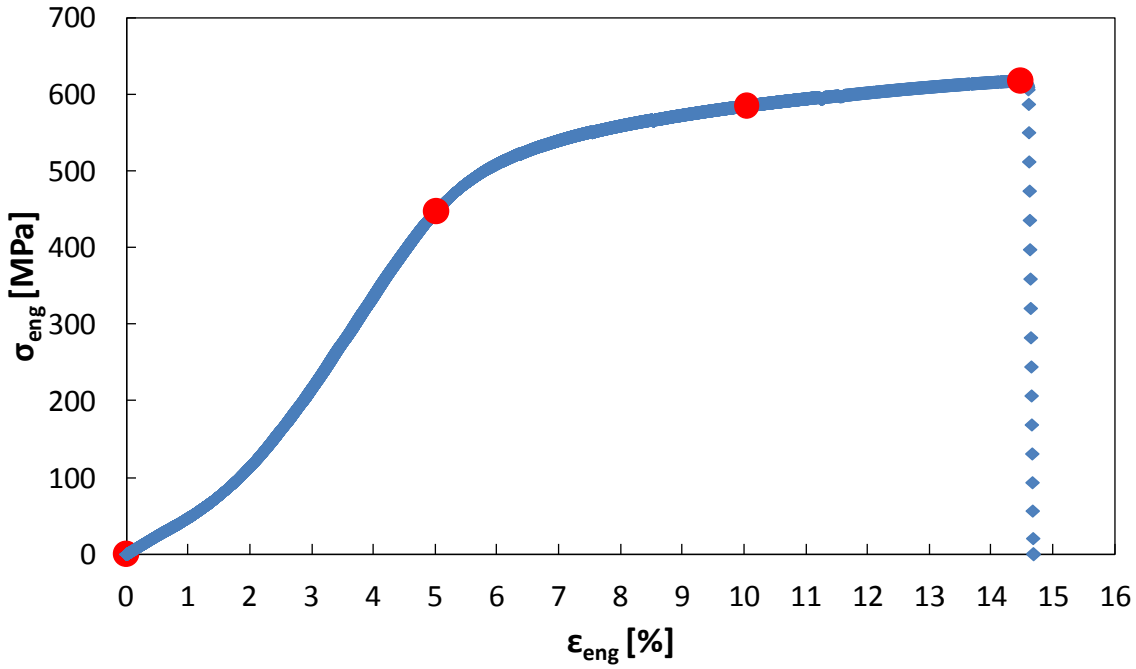

Figure 3. Engineering Stress-Strain curve (red points correspond to the investigated conditions).

The failure initiation site (Fig. 4), for ε_{eng} = 0%, is characterized by the presence of three grains (Fig. 4a). For ε_{eng} = 5% (Fig. 4b) the three grains show an unchanged orientation, no sub-grains nucleation and a grain boundary deformation from linear to curved shape, probably due to phase transition. This is more evident in the grain on the left, where a surface modification is observed (sort of zig-zag lines on the surface). For ε_{eng} = 10% (Fig. 4c), an intergranular crack initiate from the lateral specimen surface, with a secondary intergranular crack, that is more or less parallel to the applied load. This secondary crack is probably due to the phases transition in grains with different orientations, with a consequent τ stress increase at the grain boundary [7]. The increase of the macroscopical deformation implies an increase of the localized damage level, with the coalescence

of main and secondary cracks (Fig. 4d). Final failure is obtained by means of a crack propagation from one side to the opposite side of the specimen ("fracture ending zone").
In Fig. 5, the "fracture ending zone" is shown. For ε_{eng} = 0, 5 and 10%, corresponding respectively to Fig. 5a, b and c, no transformations are evident: surface modifications due to phase transformations are not observed in this zone. For ε_{eng} = 14% (Fig. 5d), it is possible to observe a localized ductile deformation.

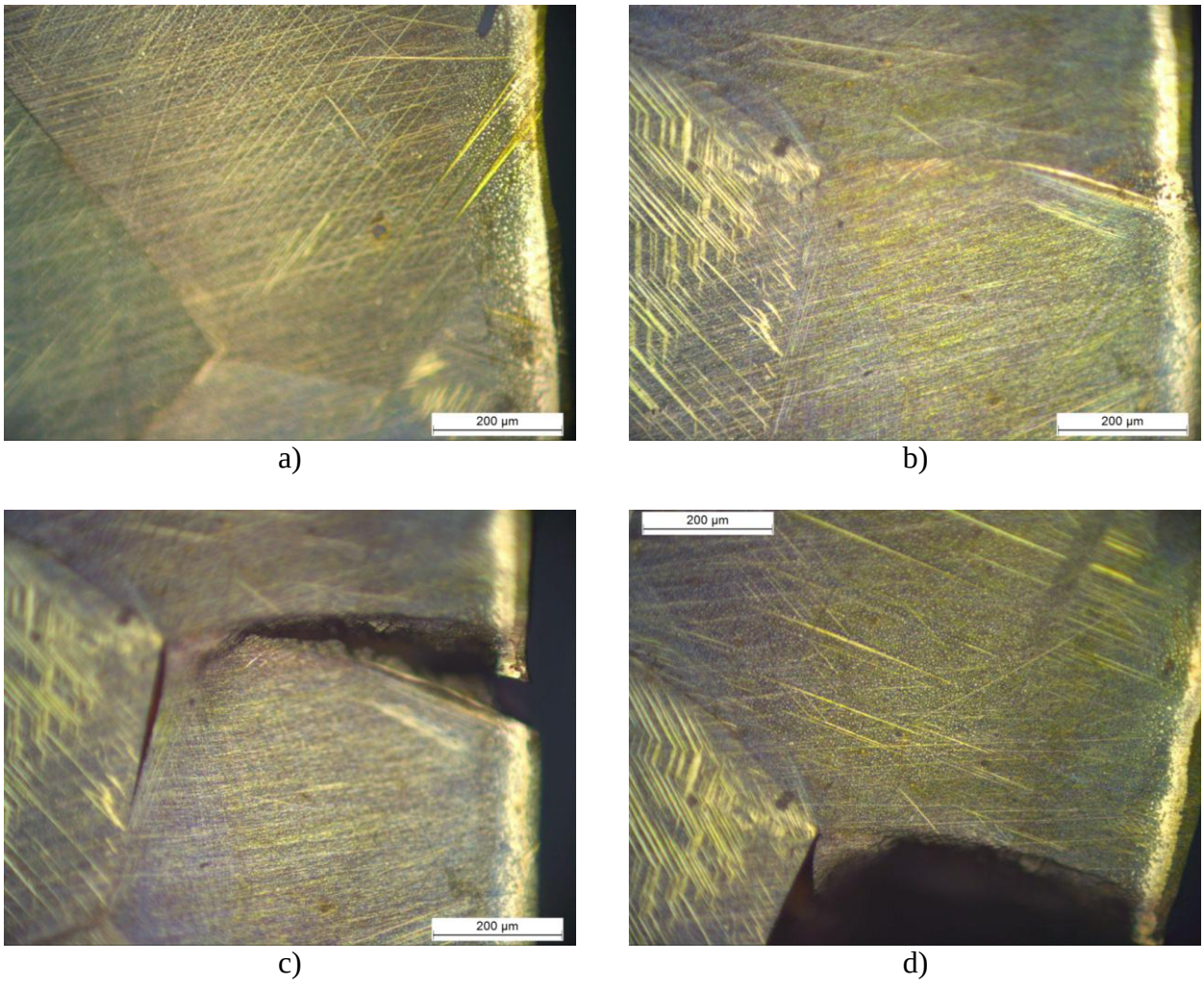

a) b)

c) d)

Figure 4. Fracture initiation zone: a) ε_{eng} = 0%, b) ε_{eng} = 5%, c) ε_{eng} = 10%, d) ε_{eng} = 14% (failure).

Evidence of structure transitions are in Fig. 6, where two diffractograms show respectively the undeformed and the deformed at ε_{eng} = 5% specimen. The undeformed specimen spectrum shows four peaks corresponding to 42.35°, 43.71°, 70.39°, 80.23°. The ε_{eng} = 5% deformed specimen shows also four peaks but corresponding to different diffraction angles (42.27°, 43.43°, 43.85° and 85.71°). Peaks modifications (considering both angles and intensity) show the mechanical deformation influence on the microstructure modifications.
Fracture surfaces are characterized by a brittle morphology, as the intergranular cleavage shown in Fig.7a, which confirms the path observed on the lateral surface (Fig. 4c, d). According to the LOM damaging micromechanisms analysis and to SEM fracture surface analysis, grains decohesion seems to be main damaging micromechamisms.
Inclusions presence implies the initiation of secondary microcracks (Fig. 7b), probably due to the same mechanism which characterizes the grains decohesion.

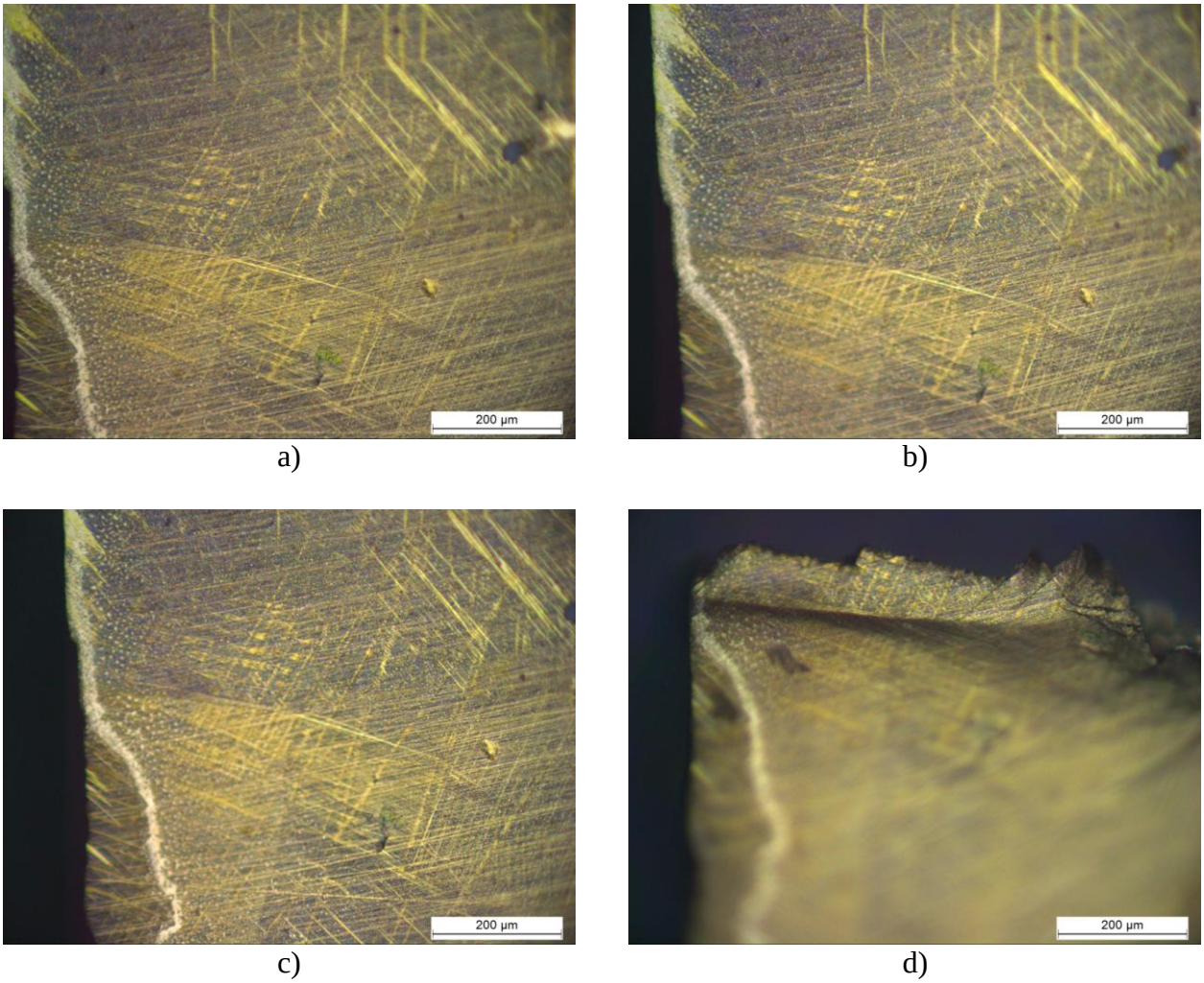

a) b)

c) d)

Figure 5. Fracture ending zone: a) ε_{eng} = 0%, b) ε_{eng} = 5%, c) ε_{eng} = 10%, d) ε_{eng} = 14% (failure).

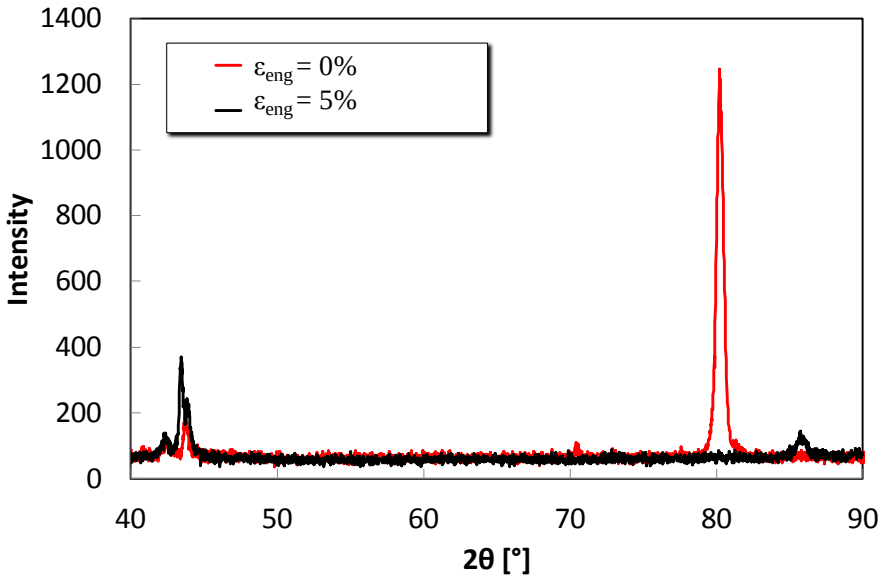

Figure 6. Diffraction spectra.

In the "ending fracture zone", corresponding to the highest deformation values (Fig. 5d), ductile fracture micromechanisms are shown (Fig 8). Two ductile morphologies are observed in Fig. 8 (respectively indicated by arrows with letters A and B). Morphology in A is characterized by an oriented plastic deformation, while morphology in B is characterized by an unoriented deformation.

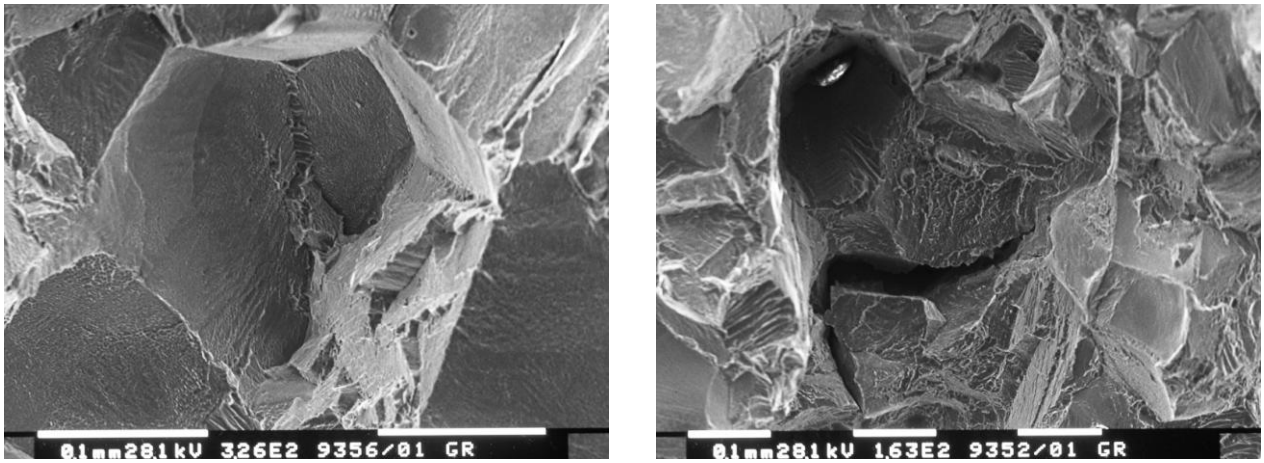

a) b)

Figure 7. Fracture surface: a) intergranular cleavage, b) secondary crack in presence of inclusion.

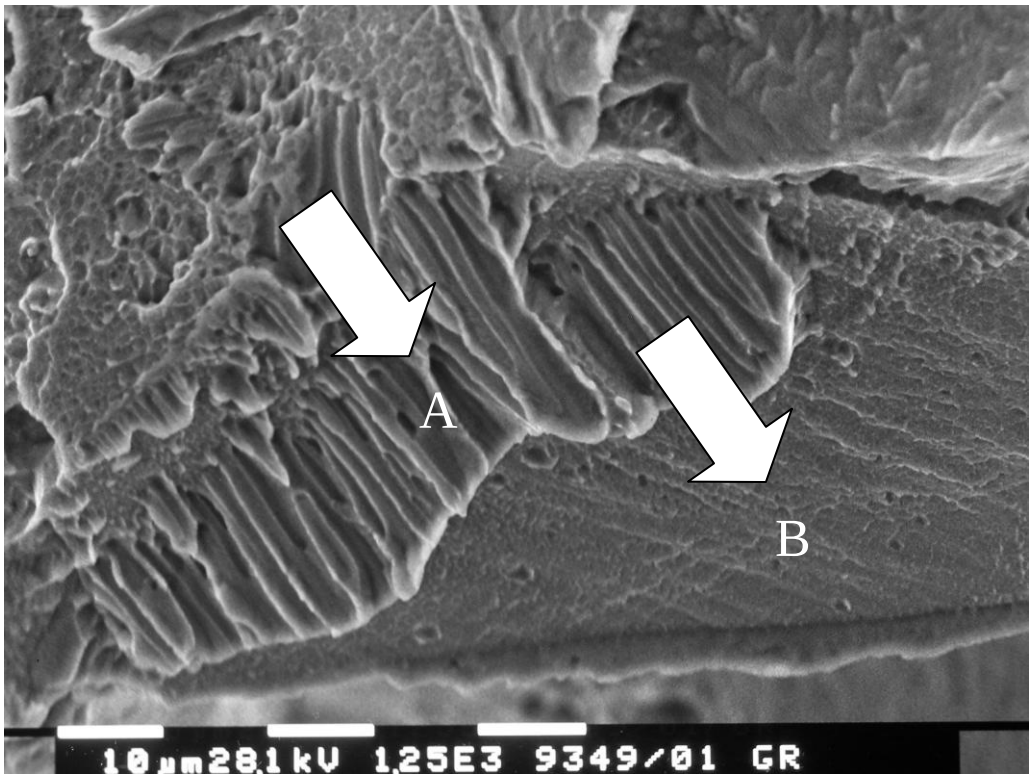

Figure 8. Fracture surface in the ending zone (as Fig. 5d)

Higher magnifications SEM observations (Fig. 9a and b) allow to confirm the ductile morphology of the fracture surface shown in Fig. 8.

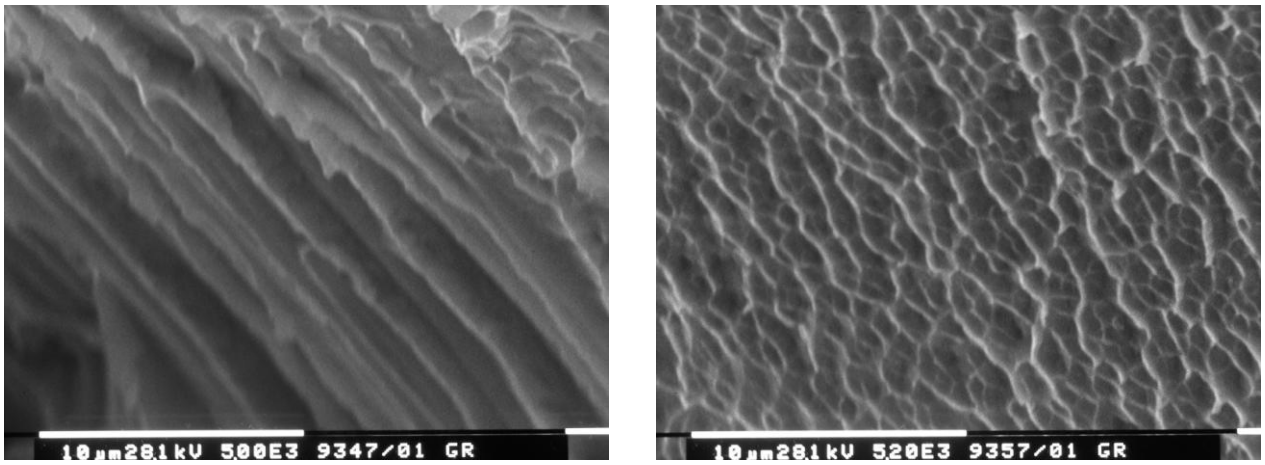

a) b)

Figure 9. Fracture surface with high deformation: a) morphology of zone A of Fig. 8, b) morphology of zone B of Fig. 8.

4. Conclusions

In this work, the main crack initiation and propagation micromechanisms during tensile tests performed on a CuZnAl SMA has been analyzed. According to the experimental results, the following conclusions can be summarized:

- Cracks initiate at grains boundaries due both to high deformation values and to phases transitions;
- Memory effect is not only due to phases transitions, but also to the unchanging of numbers of grins boundary;
- The main fracture surface morphology is brittle and is characterized by intergranular cleavage;
- Corresponding to the highest deformation values (“ending fracture zone”) the main damaging micromechanism is ductile.

5. References

[1] K. Otsuka, X. Ren, Physical metallurgy of Ti–Ni-based shape memory alloys, Progress in Materials Science (2005) 511.
[2] Y. Dong, Z. Boming, L. Jun, A Changeable Aerofoil Actuated by Shape Memory Alloy Springs, Materials Science and Engineering A, 485 (2008) 243–250.
[3] B. Chen, C. Liang, D. Fu, Pitting Corrosion of Cu-Zn-Al Shape Memory Alloy in Simulated Uterine Fluid, J. Mater. Sci. Technology, 21(2) (2005) 226-230.
[4] Y. Liu, G.S. Tan, Formation of interfacial voids in cast and micro-grained γ′-Ni3Al during high temperature oxidation, Intermetallics (2000) 8 1385-1391.
[5] P. Arneodo Larochette, M. Ahlers, Grain-size dependence of the two-way shape memory effect obtained by stabilisation in Cu–Zn–Al crystals, Materials Science and Engineering. A361 (2003) 249–257
[6] N. Kayali, S. Ozgen, O. Adiguzel, Strain effects on the macroscopic behaviour and martensite morphology in shape-memory CuZnAl alloys, Journal of Materials Processing Technology. 101 (2000) 245-249.
[7] J.X. Zhang, Y.F. Zheng, L.C. Zhao, The Structure and Mobility of Intervariant Boundaries in 18R Martensite in a Cu-Zn-Al Alloy, Acta mater. 47(7) (1999) 2125-2141.

[8] PowderCell 2.3—Pulverdiffraktogramme aus Einkristalldaten und Anpassung experimenteller Beugungsaufnahmen, in http://www.bam.de/de/service/publikationen/powder_cell.htm.

Evaluation of delamination mechanisms from Charpy impact test in API-X70 steel

Hudison Haskel[1], Ederson Pauletti[1], Juliana P. Martins[2], André L.M.Carvalho[1*]

[1] Department of Materials Engineering, States University of Ponta Grossa-UEPG
[2] Department of Chemical Engineering, Federal Technological University of Paraná-UTFPR
* Corresponding author: andrelmc@uepg.br

Abstract In this article was investigated the mechanisms of delamination phenomena occurs in the X70 steel during fracture process from the Charpy impact testing. Microtexture and Taylor factor map analysis were performed by electron backscatter diffraction (EBSD) technique in two fractured surface regions, namely, in the perpendicular and parallel regions to the propagation fracture direction where delamination occurred. As result, was observed two types of delaminations during fracture process, the crack arrester-type delamination and crack divider-type delamination. The main microtexture components obtained in the perpendicular and parallel regions to the direction of fracture propagation from orientation distribution function (ODF) were (221) [1-10] (223) [1-10] (112) [1-3 -2] (332) [023] and (223) [0-32] and (332) [1-10] orientations, respectively. It was also observed the presence of the (100) planes and Taylor factor value close to 2.7 in the respective regions investigated, consequently, a smaller stored energy was observed.

Keywords Delamination, Charpy impact test, crystallography orientation

1. Introduction

The transport of oil and gas through pipelines requires steels that are characterized by a combination of high strength and toughness, these steels are specified by the API 5L standard. However, during the fracture process by Charpy impact test, these steels exhibit the phenomenon known as delamination. This delamination can be attributed to crystallographic texture, intergranular fracture along grain boundaries of retained austenite, segregation of elements such as phosphorus and sulfur, microstructural anisotropy, banding, inclusions and aligned particles [1]. In this context many studies have been conducted to determine the relationship between microstructure and mechanical properties, where the technique by electron backscatter diffraction (EBSD) has been gained the ability to relate the spatial distribution of plastic deformation with the microstructural characteristics. Besides it allows a better understanding of the mechanisms responsible for the nucleation and propagation of cracks from delamination, which is a major problem in HSLA steels [2,3].The aim of present work is to investigate the mechanisms of delamination phenomena takes place in the API 5L X70 steel during fracture process from the Charpy impact testing in specimens with L-T and T-L orientations. Evaluation of microtexture and Taylor factor mapping were performed from the EBSD technique in two regions, namely, in the perpendicular and parallel regions to the propagation fracture direction where delamination occurred.

2. Experimental procedures

2.1 Material

The material used in this investigation was microalloyed steel specified by API 5L Grade X70 standards. The same was obtained by thermomechanical treatment by controlled rolling. The chemical composition obtained by optical spectrometry technique is shown in Table 1:

Table 1. Chemical composition of API X 70 steel

C	Si	Mn	P	Al	Cu	S
0.14	0.27	1.45	0.01	0.05	0.03	0.00076
Nb	V	Ti	Cr	Ni	Mo	
0.051	0.041	0.018	0.0005	0.001	0.0045	

2.2 Procedures

2.2.1 Charpy impact testing

Charpy impact testing specimens were removed from the orientation and dimensions according to ASTM E-23 [4], as can be seen in Fig. 1.

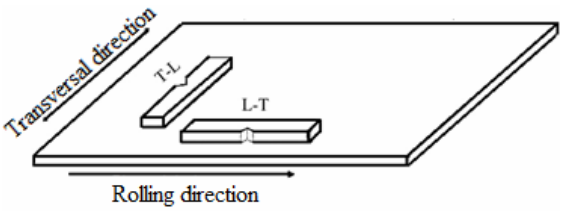

Figure 1. Schematic drawing of the orientation notch specimens

The tests were carried out in a range of temperature variation at 27°C up to -196°C, the specimens were immersed in a cryogenic bath of nitrogen and anhydrous alcohol liquids for 10 minutes, after that the same were withdrawn of the mixture and positioned on the machine. To increase the accuracy of this procedure the hammer would only be released whether all process occurred within 8 seconds.

2.2.2 Microtexture

Microtexture analyses were performed by EBSD technique. To carry out these measurements were used two samples from the fractured specimens in the L-T orientation by impact testing at -25 °C and 226J of absorbed energy in the ductile brittle transition temperature region. The surface specimens analyzed were carried out in the perpendicular region to the direction of fracture propagation and near the edges of the crack generated by crack divider-type delamination, as shown in Fig. 2a), another analysis was performed parallel to the direction of fracture propagation and near the edge separation caused by delamination, as shown in Fig. 2b). Samples were polished in the

solution of OP-S (colloidal silica), and then etched with Nital 2%. For EBSD data collection was used software TSL 5 IOM Data collection and for data processing was used software OIM Analysis 5. The scanning electron microscope used for performing of such measures was the EDAX TSL EVO MA 10.

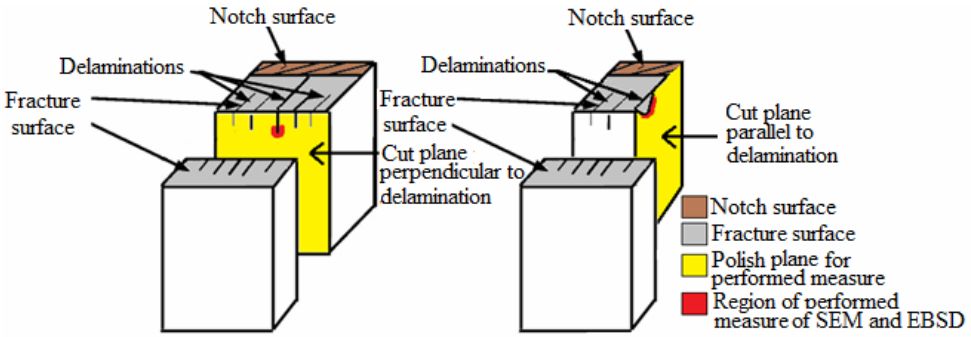

Figure 2. Schematic representation of removed samples for performing EBSD. a) Cut plane of the perpendicular direction of fracture propagation, b) Cut plane in the parallel region to the direction of fracture propagation.

3. Results and Discussion

3.2 Charpy impact testing

Fig. 3a) shows the curve of absorbed energy versus temperature for L-T and T-L orientations. It is possible to notice that there was a greater dispersion of energy values for the samples of L-T orientation when compared to the T-L orientation. At the lower upper shelf energy where the cleavage fracture occurs, both directions have obtained the same amount of energy, 5J. The L-T orientation has a higher upper shelf energy regarding T-L orientation, consequently this direction has higher absorbed energy for all temperatures. Concerning the ductile-brittle transition temperature, the L-T orientation has also obtained the highest absorbed energy values as a function of orientation, as can be seen in Fig. 3b).

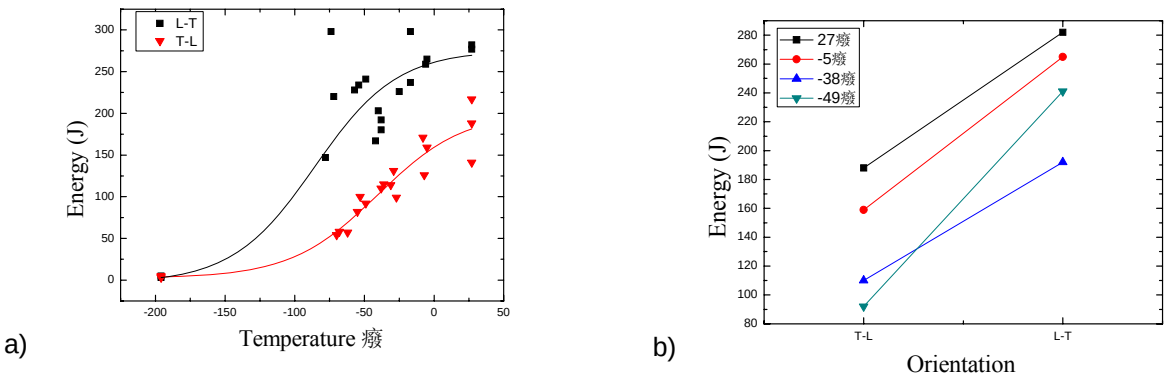

Figure 3. Charpy impact testing a) as a function of temperature, b) as a function of the orientation (for some temperatures)

The ductile-brittle transition temperature was estimated by comparing the percentage of ductile fracture area following the specifications of ASTM E-23[4]. Specimens with L-T orientation showed range lower values of transitions temperature between -38°C to -57°C, while the specimens with T-L orientation exhibited a greater range of the transition temperature values between -8 ° C up to -38 ° C.

3.3. Aspects of delamination phenomenon

Fig. 5) shows fractured surface samples with delaminations from the Charpy impact test. In Fig. 5a) is possible to observe crack arrester-type delamination from the specimen tested at -5°C and 265J of absorbed energy. Fig. 5b) also shows a set of crack divider- type delamination from the specimen tested at -36°C and 100J of absorbed energy.

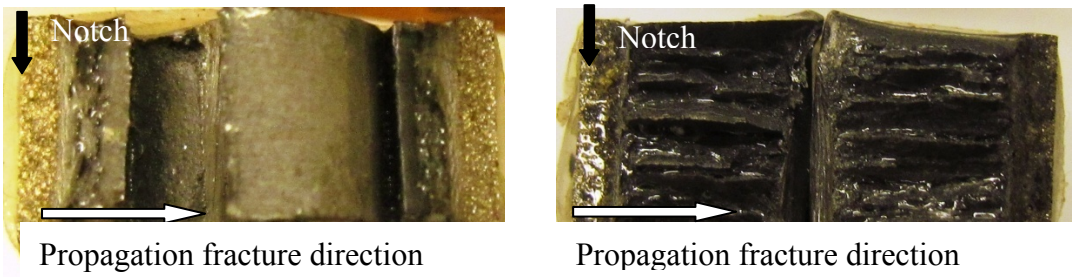

a) b)

Figure 4. Fractured surface by impact test showing the phenomenon of delamination. a) Crack arrester-type delamination, b) Crack divider-type delamination

It can be seen in Fig. 4a) the crack arrester-type delamination is formed perpendicular to the propagation fracture direction and parallel to the notch, while the crack divider-type delamination (Fig. 4b)) occurs parallel to the propagation fracture direction and perpendicular at notch. Cracks arrester-type delaminations are known by their beneficial effect to increase upper shelf energy [5], this suggests a higher tendency of the L-T orientation specimens present crack arrester-type delamination, which may contribute to increase of energy values for L-T orientation independent on the temperature used, as can be seen in Fig 3a).

3.4. Microtexture

Fig. 5 shows an image obtained by scanning electron microscopy in the regions in front of propagated crack by crack divider-type delamination, the distribution map of orientations, the inverse pole figure, the orientation distribution function (ODF) for Bunge angle $\Phi_2 = 45°$, and the pole figures of the (100) and (110) planes. Quantification of microtexture was made by EBSD technique, with the following parameters: Fig. 5b) was used step size of 1 micron and 1000 X magnification and Fig. 5c) was used step size of 3 microns and a magnification of 3000X.
From Fig. 5b) is possible to notice the presence of dark regions, where shows a crack produced by the formation of delamination. The remaining points may be regions of perlite, which have very

thin lamella (about 200nm). As the distance between layers is smaller than the step size used, the occurrence to indexation of crystallographic planes to these regions was not possible, resulting in dark regions. Another plausible explanation is associated to the material deformation, which can contribute to the accumulation of dislocations at grain boundaries, resulting in the non-indexed regions. In Fig. 5b) there is a grain size distributions quite heterogeneous and the absence of (100) plans. While in Fig.5c) shows the propagated crack region by delamination, the same propagates in the grain boundary, featuring an intergranular fracture mechanism. It is confirmed by separation of grains with [111]||ND and [101]||ND texture components indicated by 1 up to 5 grains, respectively.

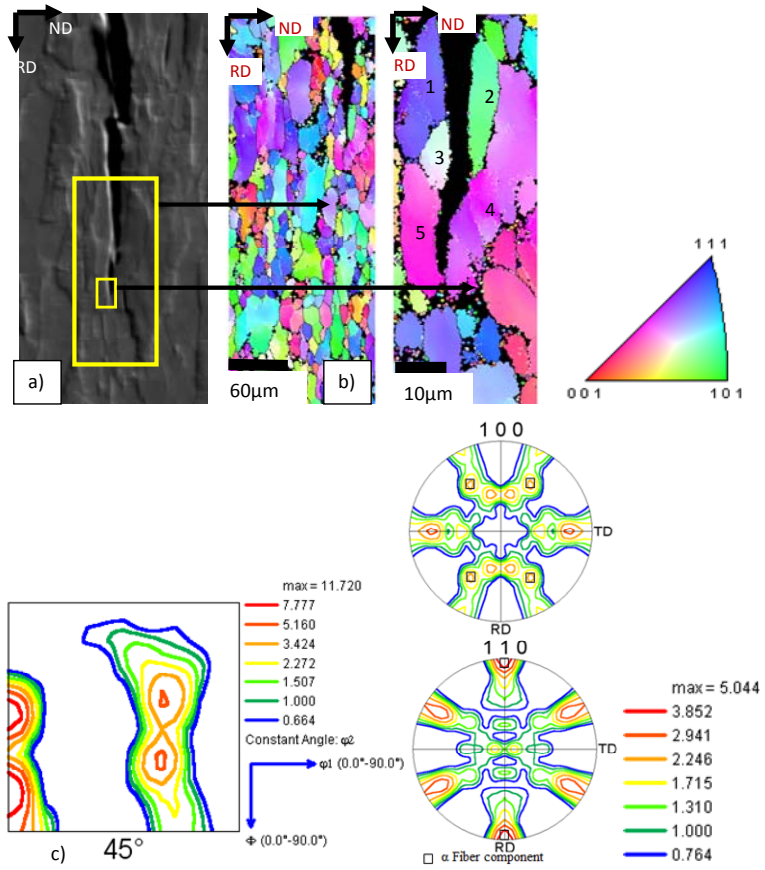

Figure 5. Microtexture in the region near the crack delaminated. a) SEM from the scanned region, b) distribution maps of orientation and inverse pole figure c) orientation distribution function (ODF) and pole figures.

It is well known that intergranular propagation occurs through high angle boundaries. In this context the Fig. 6 shows the misorientation obtained by EBSD technique from the scanned region (Fig 5b)). For generation of statistical data points only disorientation greater than 2° was considered. It is possible to see at Fig. 6 that approximately 42% of the misorientation angles between adjacent grains are smaller than 10° (low angle boundaries) while the other 58% are distributed randomly between 10° and 110°, indicating a high grain boundary angle.

For the generation of pole figures and ODF shown in Fig 5c) was used an orientation map from Fig. 5 b) which provides a better precision in the information due to its higher scanned area. The ODF shown in Fig. 5c) reveals that the orientations have α fiber components. The main components

obtained from ODF are (221) [1-10] (223) [1-10] (112) [1-3 -2] and (332) [023] orientations. Pole figures shown in Fig. 5c) confirm the presence of the α fiber components identified by the ODF.

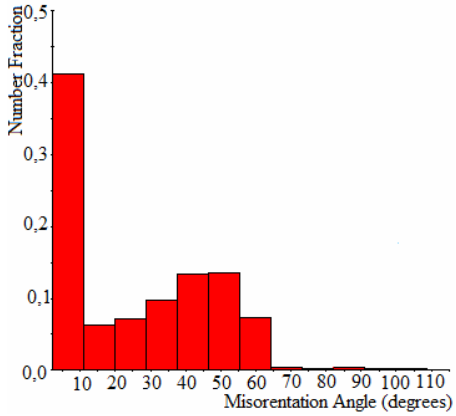

Figure 6. Misorientation angles between adjacent grains near to edges of delamination

Furthermore, materials with crystallographic plane with (100) orientation aligned in the rolling direction show a strong tendency to occur cleavage fracture during impact [1,2,6,7,8,9,10]. To identify whether in this case occurred the separation of the (100) planes were measured microtexture on the edge of the fractured surface where was generated the delamination. This sample was the same used in the analysis of Fig. 6b), but using step size of 1 micron and 1000X magnification, and the results obtained are displayed in Fig. 7. It can be observed in Fig. 7a) the difference of depth between the ferrite and pearlite. While in Fig. 7b) shows the distribution orientations map, there is a heterogeneous distribution of grain sizes and a few areas where there were not indexing of the plans, there is also the presence of (100) plans. The ODF to Bunge angle $\Phi_2 = 45°$ is shown in Fig 7c) and its indexing shows the main texture components was (223) [0-32] and (332) [1-10]. The pole figures are shown in Fig. 7d) where it is possible to notice that higher centering occurred in the (111) plane, however, it also notice that occurred to the (100) plane and indexing of some components reveals the presence of {100} planes families and the <011> families directions. As seen in Fig.5c) the crack nucleated by delamination separated grains with (111)||ND and (101)||ND texture components. It is evident that in this case should be noticed, the presence of the (111)||ND components close to the delamination, confirming the separation of ferrite plans. However the presence of the (100) planes was also confirmed. Whereas when if analyzes the microtexture, it cannot confirm whether this is a general rule for the nucleation of delamination in the material under study.

Experimentally, it is known that the stored energy during deformation changes with the crystallographic orientation of the grains. The Taylor factor is a parameter that correlates to macroscopic deformation behavior with microstructural characteristics of the material [11]. According to the theory of plasticity, the stored energy increases with the Taylor factor which in turn, depends on the crystallographic orientation of the grain in relation to the direction of applied stress [12]. The Taylor factor is defined as:

$$M = \sum \delta\gamma_i / \delta\varepsilon \tag{1}$$

Where $\delta\gamma_i$ represent shear portions in each of activated sliding systems in determinate grain while the sample receives a macroscopic deformation $\delta\varepsilon$ [13].

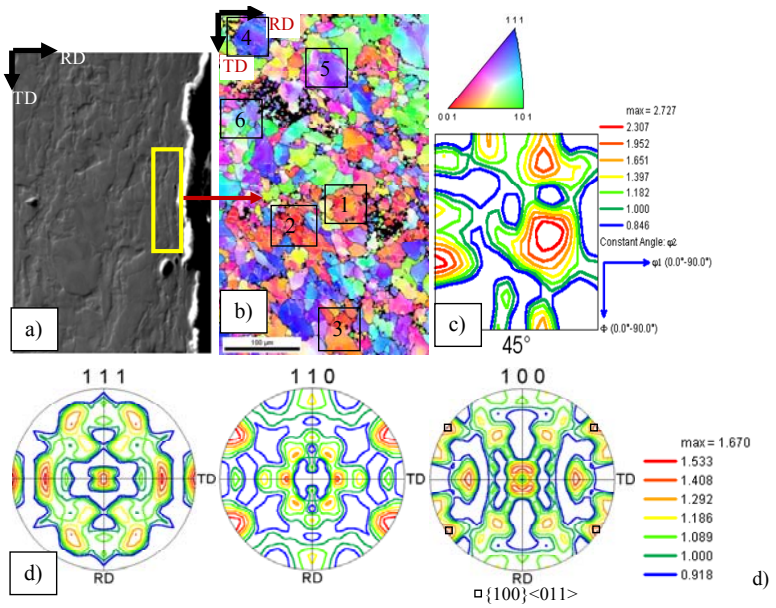

Figure 7. Microtexture analysis by EBSD. a) SEM scanning region, b) Distribution maps of orientation, magnification of 1000X, c) Inverse pole figure and ODF, d) pole figures

Fig. 8 shows the mapping of Taylor factor in front of the crack region for sample shown in Fig. 5b). It is possible to note in Fig. 8a) that mapping shows the separating generated by propagation crack occurs with grains with different Taylor factor values, indicating that the crack delamination intergranular propagate mode. The first and second grains were separated with factor Taylor value around 4.8 and 3.5, respectively. The same situation took place for 5 and 7 grains. Already the 3 and 4 grains also show Taylor factor values in the range of 3.0 and 3.6 respectively, the same has occurred with 5 and 6 grains. It notes that approximately 14% of the grains have Taylor factor values between 4.7 and 4.8 and close to 57% of the grains have Taylor factor values between 2.9 and 3.6.

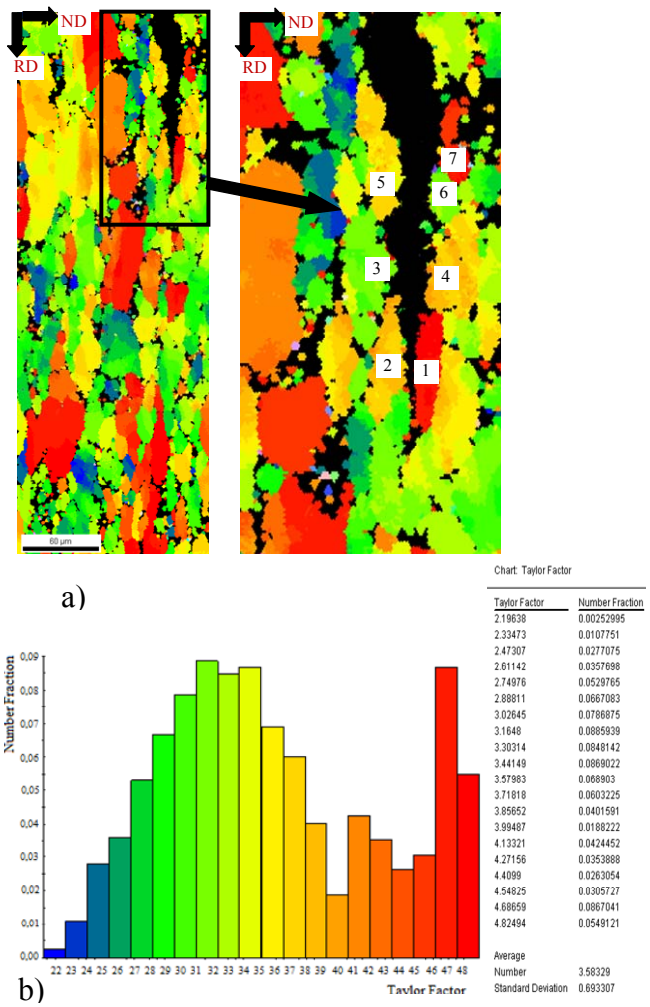

Taylor Factor	Number Fraction
2.19638	0.00252995
2.33473	0.0107751
2.47307	0.0277075
2.61142	0.0357698
2.74976	0.0529765
2.88811	0.0667083
3.02645	0.0786875
3.1648	0.0885939
3.30314	0.0848142
3.44149	0.0869022
3.57983	0.068903
3.71818	0.0603225
3.85652	0.0401591
3.99487	0.0188222
4.13321	0.0424452
4.27156	0.0353888
4.4099	0.0263054
4.54825	0.0305727
4.68659	0.0867041
4.82494	0.0549121
Average	
Number	3.58329
Standard Deviation	0.693307

Figure 8. Mapping of Taylor Factor. a) Scanned region, b) Histogram of number fractions

Besides, in the Fig. 9 shows the mapping of Taylor factor from the sample region shown in Fig. 7b). In the Fig. 9 is possible to observe that approximately 55.34% of the grains have Taylor factor between 2.7 and 3.4.

The stored energy in low carbon steels can be different conform to the sequence: $E_{(110)} > E_{(111)} > E_{(211)} > E_{(100)}$ where hkl plans are related to rolling plans in each grain (12). Thus a comparison can be made from the 1, 2 and 3 numbered regions of the following Figs. 7b) and 9a), where is observed the presence of the (100) planes and Taylor factor value close to 2.7 in the respective regions, consequently, a smaller stored energy was absorbed. Whereas, the 4, 5 and 6 numbered regions of the same figures show a predominance of the (111) planes and Taylor factor value close to 4.5, but the number fraction of grains with this Taylor factor value is low (about 1.53).

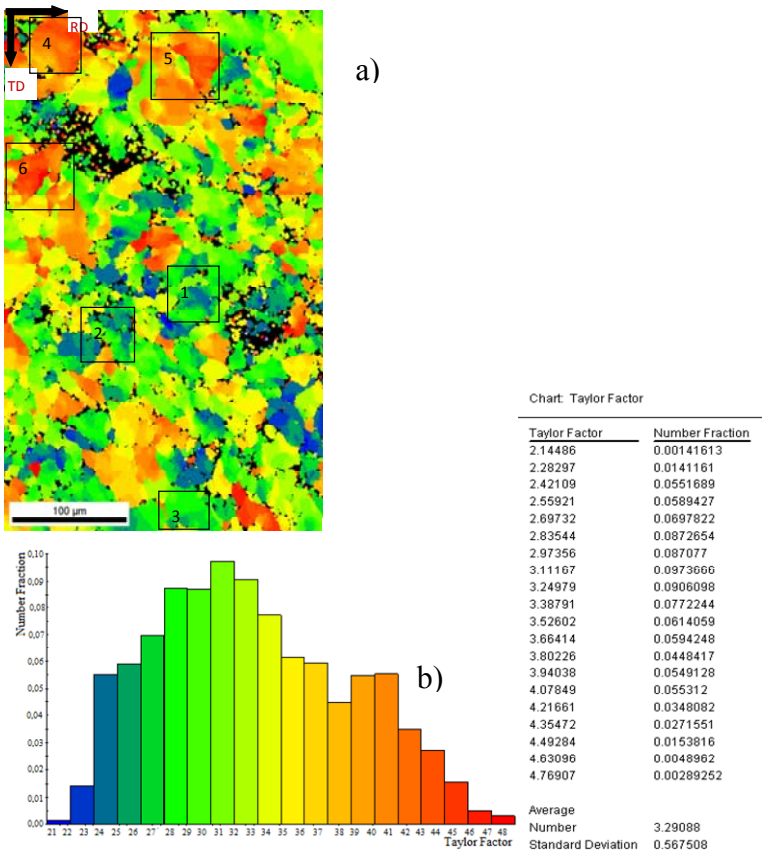

Chart: Taylor Factor

Taylor Factor	Number Fraction
2.14486	0.00141613
2.28297	0.0141161
2.42109	0.0551689
2.55921	0.0589427
2.69732	0.0697822
2.83544	0.0872654
2.97356	0.087077
3.11167	0.0973666
3.24979	0.0906098
3.38791	0.0772244
3.52602	0.0614059
3.66414	0.0594248
3.80226	0.0448417
3.94038	0.0549128
4.07849	0.055312
4.21661	0.0348082
4.35472	0.0271551
4.49284	0.0153816
4.63096	0.0048962
4.76907	0.00289252
Average Number	3.29088
Standard Deviation	0.567508

Figure 9. Mapping of Taylor Factor a) Scanned region, b) Histogram of number fractions

4. Conclusions

Charpy impact testing showed that specimens with L-T orientation absorbed more energy than specimens with T-L orientation. It was observed two types of delaminations during fracture process, the crack arrester-type delamination and crack divider-type delamination. The first type propagates parallel to the notch, while the second propagates perpendicular to notch. Crack arrester-type delamination tends to increase upper shelf energy during Charpy impact testing, and both types of delaminations tend to disappear with decreasing temperature.

The results obtained by EBSD technique shows the propagation mode of a crack generated by a divider-type delamination was intergranular. The main microtexture components obtained in the perpendicular region to the direction of fracture propagation from ODF were (221) [1-10] (223) [1-10] (112) [1-3 -2] and (332) [023] orientations. While in the parallel region to the direction of fracture propagation the (223) [0-32] and (332) [1-10] orientations were the main microtexture components.

The Taylor factor analysis display the difference in the Taylor factor values with crystallographic orientation, as expected. It was also observed the presence of the (100) planes and Taylor factor value close to 2.7 in the respective regions investigated, consequently, a smaller stored energy was observed. This confirms the fracture mechanisms from the delaminations are given by little plastic deformation, namely, brittle fracture.

Acknowledgements

The authors thank the USIMINAS by providing the material under study, the UFF-Federal Fluminense University by performing the EBSD measurements. The CAPES by providing scholarship and financial support from the project (PNPD- Case N°. 23038.008242/2010-08)

References

[1] M.S. Joo, D.W. Suh, J.H Bae, H.K.D.H. Bhadeshia, Role of delamination and crystallography on anisotropy of Charpy toughness in API-X80 steel. Materials Science and Engineering A, 546, (2012) 314-322**.**

[2] H. Yu, Influences of microstructure and texture on crack propagation path of X70 acicular ferrite pipeline steel. Journal of University of Science and Technology Beijing, 15, (2008) 683-687.

[3] P. Shanmugam, S.D Pathak, Some studies on the impact behavior of banded microalloyed steel. Engineering fracture mechanics, 53, (1996) 991-1005.

[4] AMERICAN SOCIETY FOR TESTING AND MATERIALS. Standard Test Methods for Notched Bar Impact Testing of Metallic Materials: ASTM E23. New York: ASTM International, 2002.

[5] M. Jafari, J. Kimura, K. Y. Tsuzakik. Enhancement of upper shelf energy through delamination fracture in 0,05 pct P doped High Strength steel. Metallurgical and materials transactions A, 43A (2012), 2453-2465.

[6] T. Inoue, F.Yin, J. Kimura, Y. Tsuzakik, S. Ochiai, Delamination effect on impact properties of ultrafine-grained low carbon steel processed by warm caliber rolling. Metallurgical and materials transactions A, 41, (2009) 341-355.

[7] C. J. Baczynski, J. J. Jonas, L. E. Collins, The influence of rolling practice on notch toughness and texture development in high-strength linepipe. Metallurgical and materials transactions A, 30, (1999) 3045-3054.

[8] J. I. Verdeja, J. Asensio, J. A. Pero-Sanz, Texture, formability, lamellar tearing and HIC susceptibility of ferritic and low carbon steels. Materials characterization, 50, (2003) 81-86.

[9] W. Yan, W. Sha, L. Zhu, W. Wang, Y. Shan, K. Yang, Delamination Fracture Related to Tempering in a High-Strength Low-Alloy Steel. Metallurgical and materials transactions A, 41 A, (2010) 149-161.

[10] H. Jian, F. Jiang, L. Wei, X. Zheng, K. Wen, Crystallographic mechanism for crack propagation in the T7451 Al-Zn-Mg-Cu alloy. Materials Science and Engineering A, 527, (2010) 5879-5882.

[11] F. Yin, T. Hanamura, T, Inque, K. Nagai, Fiber texture and substrutural features in the caliber-rolled low-carbon steels. Metallurgical and materials transactions A, 35 A, (2004) 665-677.

[12] S.F. Castro, J. Gallego, F. J. F. Landgraf, H. J. Kestenbach, Estudo da laminação de encruamento em aços elétricos semi-processados: correlação como os fatores de Taylor. 60° Congresso Anual da ABM, 60°, (2005) 9.

[13] C.S.C. Viana, A. S. Paula, Texturas de deformação. II workshop sobre Textura e Relações de Orientação: deformação plástica, recristalização e crescimento de grão, 2, (2003) 35-54.

Influence of delamination on microtexture and J-R curve in API X60 steel

Ederson Pauletti[1], Hudison L. Haskel[1], Juliana P. Martins[2], André L M Carvalho[1*]

[1] Department of Materials Engineering, States University of Ponta Grossa-UEPG
[2] Department of Chemical Engineering, Federal Technological University of Paraná-UTFPR
* Corresponding author: andrelmc@uepg.br

Abstract: Large–diameter, high-pressure gas transmission pipelines have been used more and more widely all over the world. With the development of the pipeline network, safety and maintenance become an important task. Controlled thermo-mechanical processing is considered as the primary route for the development of API grade linepipe steels because it provides desirable and fine grained microstructure. It is known that crystallographic orientation can generate anisotropy of mechanical properties. Furthermore, studies on pipeline steels, such as X60, X70 and X80, suggest that delamination phenomenon the fracture surface in fracture toughness test specimens affects the measured fracture toughness and therefore safety evaluation of pipeline steels. Microtexture analysis by electron backscattering diffractions (EBSD) was carried out to obtain crystallographic orientation from the fracture process in which occurs the delamination phenomenon. Experimental results obtained by EBSD technique have shown that delamination phenomenon occurs in the {100}<011>crystallographic orientation. The α fiber texture such as :{113}<110>, {112}<110> and {223}<110>, have produced anisotropic mechanical properties that during fracture process act to reduce the plastic constraint and contributing to increase the stress plane

Keywords Delamination, fracture toughness test , crystallographic orientation, API X70 steel

1. Introduction

One of the most widely used classes of steel pipes is based on the standard API (American Petroleum Institute), which are classified according to chemical composition and mechanical properties [1]. These steels generally undergo thermomechanical processing, associated with addition of alloying elements such as Nb and Ti to obtain a material with high toughness and ductility, as well as good weldability, well known as HSLA steels (high strength low alloy) [2]. The thermomechanical processing imposed on HSLA leads to generation of preferential orientation (texture), resulting in anisotropy mechanical properties [3-6]. The occurrence of texture is most evident during the controlled rolling process which can produce recrystallization, transformation and deformation texture [3].

Special attention should be given the {100} <110> texture component which is parallel to the rolling plate direction. During the monotonic and dynamic test this component contributes to the occurrence of cleavage planes [3, 7 ,8 ,9, 10]. This cleavage planes also contribute to appearance of the delamination (split), as can be seen in Fig. 1. Other factors leading to the occurrence of delaminations are the formation of precipitates at grain boundaries [11, 12], inclusions [13, 14], elongated grains [11, 15], decohesion of grain boundaries [13, 14].

The aim of present work was to investigate the microtexture from the delamination region takes

place in the API 5L X70 steel during fracture process from the fracture toughness testing. Evaluation of microtexture and Taylor factor mapping were performed from the EBSD technique in the perpendicular region to the propagation fracture direction where delamination occurred.

2. Experimental Procedure

The material used in the investigation was obtained from an API X60 steel plate grade of 5/8 inch thickness. Table 1 shows the chemical composition of API X60 steel and the requirement of the API standard.

Table 1. Chemical Composition obtained for API X60 steel and maximum specification through API standard (in wt. %) [1].

Element	C	Mn	P	S	Ni +V+T	Cr	Cu	Co	Si
Composition	0,15	1,45	0,014	0,005	0,011	0,032	0,037	0,02	0,3
API Specification	0,26	1,40	0,030	0,030	0,015				

To obtain the tensile properties, three specimens from the rolling direction (RD) and transverse direction (TD) were extracted in each direction. The specimens were tested in tensile testing SHIMADZU machine at room temperature according to ASTM E8M [16].

The single edge tension SE(T) specimens were used to obtain *J-R* curves. All specimens crack planes were oriented in the LT orientation according to ASTM E1820 [17]. The SE(T) specimen has following dimensions: length of reduction section of 156 mm, radius of fillet of 10 mm, overall length of 276 mm, width, W, of 32 mm and thickness of 12.5 mm. This specimen was loaded with a centered pin at center distance of 214 mm. Crack length to width ratios of 0.21 and 0.52 were investigated, corresponding shallow and deep cracks respectively. The specimens were loaded in three-point bending with a span of 128 mm, after precracking by fatigue according to the procedure in ASTM E1820. The specimens were side grooved using a Charpy cutter to a total thickness reduction of 20%, in an attempt to develop plane strains conditions along crack front. The fracture toughness tests were performed in MTS Flex Test GT servo hydraulic machine according to ASTM E1820 [17]. All specimens were tested at room temperature. The J-R curves were obtained from unloading compliance technique using clip gage to measure the crack mouth opening displacement (CMOD). Procedure to calculate the J-R resistance such as, k, η, γ factors were obtained from the results of Cravero [18].

Microstructure analysis were performed from the rolling direction (RD), transverse (TD) and normal direction (ND) which were grinding, polished and chemically etched with Nital 2%.

The microtexture was carried out by EBSD technique. The sample was obtained from perpendicular fracture surface in the delamination region, as can be seen in Figs. 1.a e 1.b. Samples were polished in the solution of OP-S (colloidal silica), and then etched with Nital 2%. For EBSD data collection was used software TSL 5 IOM Data collection and for data processing was used software OIM Analysis 5. The scanning electron microscope used for performing of such measures was the EDAX TSL EVO MA 10.

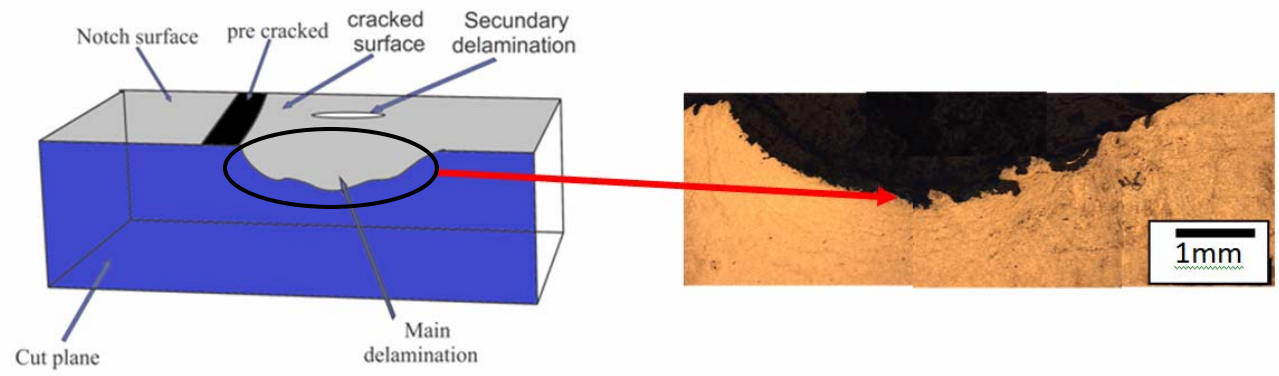

Figure 1 a) Schematic drawing shows the specimen section where was made cut perpendicular to the fracture surface b) fractured surface from the delamination region.

The scan was performed with step size of 1μm and magnification of 1000 times. Pole figures were obtained from the (100), (110) and (111) centered planes. While orientation distribution functions (ODF) was performed from the Euler space and the Bunge notation. Whereas, Taylor factor maps and misorientation angles distribution were generated in software for further analysis.

3. Results and Discussion

The chemical composition is according to the API standard [1], as shown the Table 1. The tensile properties obtained for the API X70 steel are shown in Table 2. The yield strength (YS), ultimate tensile strength (UTS) and elongation values are according to API standard [1].

Table 2. The tensile properties obtained from the tensile test for API X70 steel.

YS (MPa)	UTS (MPa)	Elongation (%)	Hardening exponent (%)	Modulus Elastic (GPa)
515	586	23	15	207

Fig. 2.a shows the three dimensional view of the API X70 microstructure steel. It can be observed a microstructure consisting of alternated layer of ferrite and pearlite in the RD and TD directions as also random distribution of ferrite and pearlite in the DN direction. Fig. 2.b shows the delamination region which can be noticed the banded microstructure caused by delamination.

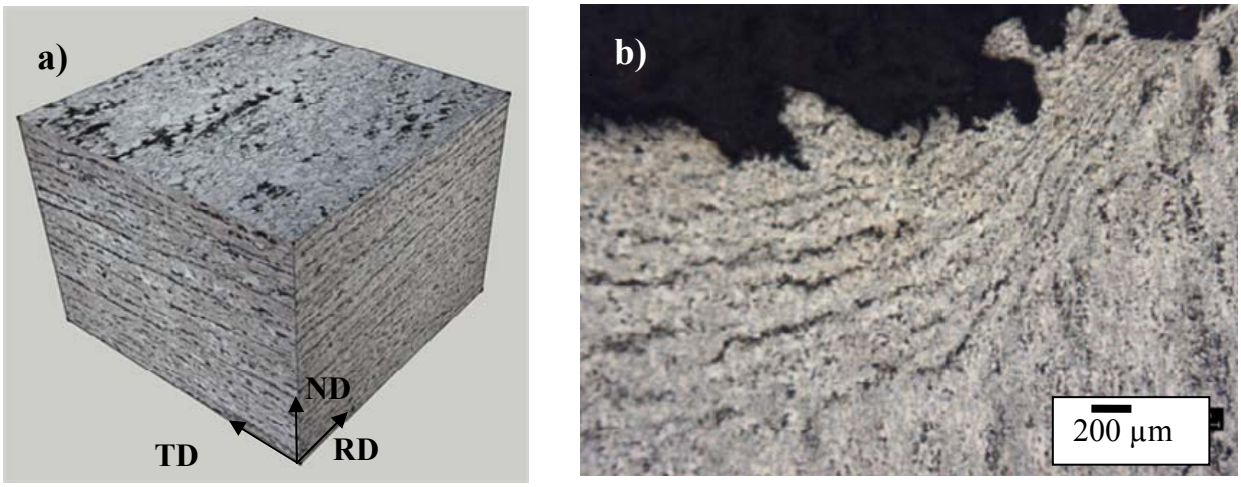

Figure 2. Microstructure of API X70 steel: a) three-dimensional view of the API X70 steel microstructure b) banded microstructure in the delamination region.

Fig. 3.a shows the fractured surface from tested specimen where it can be seen the notch, pre-fatigue crack, ductile crack extension. As the out-of-plane constraint is highest at the centre of the specimen, accordingly the delamination is most severe. Secondary delaminations are concentrated at the 1/4 thickness points from the free surfaces and similar to the main delamination [19, 20]. Fig. 3.b shows the P x CMOD curve from the unloading compliance method indicating the occurrence of delamination on the curve. It is possible to notice load-displacement curve a degree or register sequence failure. This feature is associated to the occurrence delamination phenomenon.

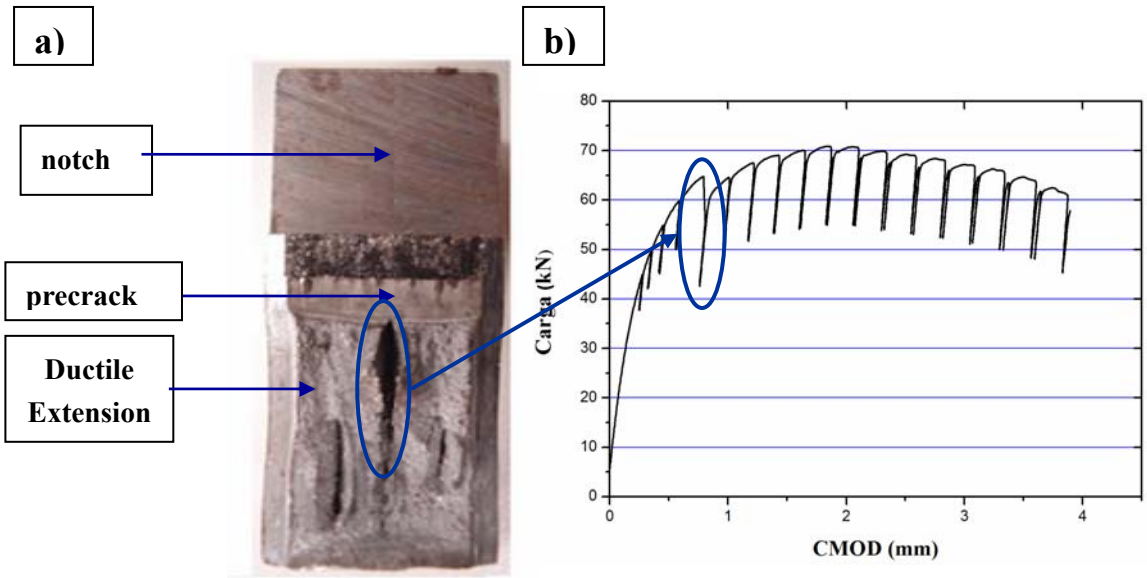

Figure 3. a) Fractured surface of sample from the fracture toughness test showing the notch, pre-fatigue and ductile extension, b) PxCMOD curve from the unloading compliance method indicating the occurrence of delamination on the curve.

Fig. 4.a shows the delamination region that was investigated by EBSD technique to obtaining of the microtexture. Fig. 4.b displays the orientation map, as well orientation triangle, where it can be observed a random grain sizes distribution from the rolling process occurred in the (α + γ) range, as also the higher predominance of <111> and <100> orientations. Also in Fig. 4.b displays the remaining points may be perlite regions, which have very fine lamella (about 200nm). As the distance between lamellas is smaller than the step size used, the occurrence to indexation of crystallographic planes to these regions was not possible, resulting in dark regions. Another plausible explanation is associated to the material deformation, which can contribute to the accumulation of dislocations at grain boundaries, resulting in non-indexed regions.

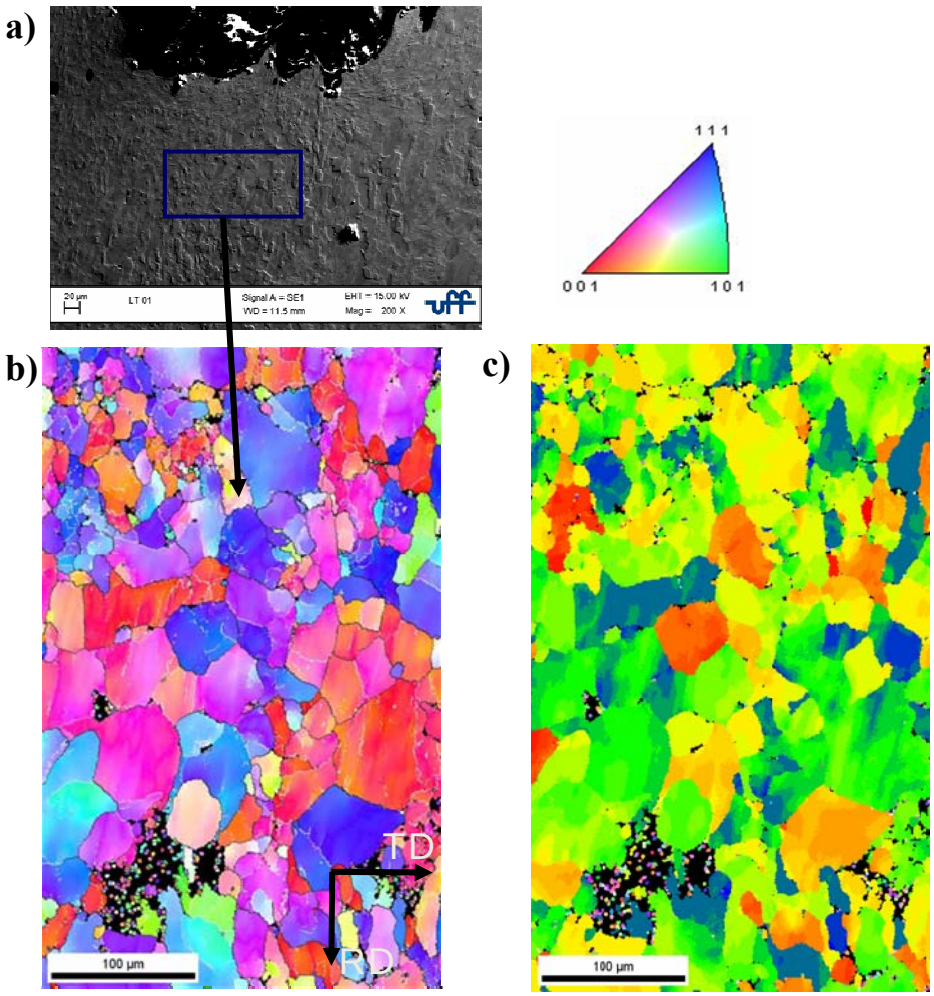

Figure 4. a) Delamination region used for microtexture analysis by EBSD technique b) orientation map of the selected region in the figure 3.a c) The Taylor factor Map of the same region.

Fig. 5 shows the Taylor factor distribution from the delamination region. It is possible to note the higher predominance of Taylor factor value between 2.5 to 3.5 corresponding 68% of grains. Moreover, 41% of grains have Taylor factor value lower 3 indicating lower absorbed energy. This indicates that the delamination phenomenon occur in the lower Taylor factor values. While the higher Taylor factor value (4) corresponded only 6% of grains.

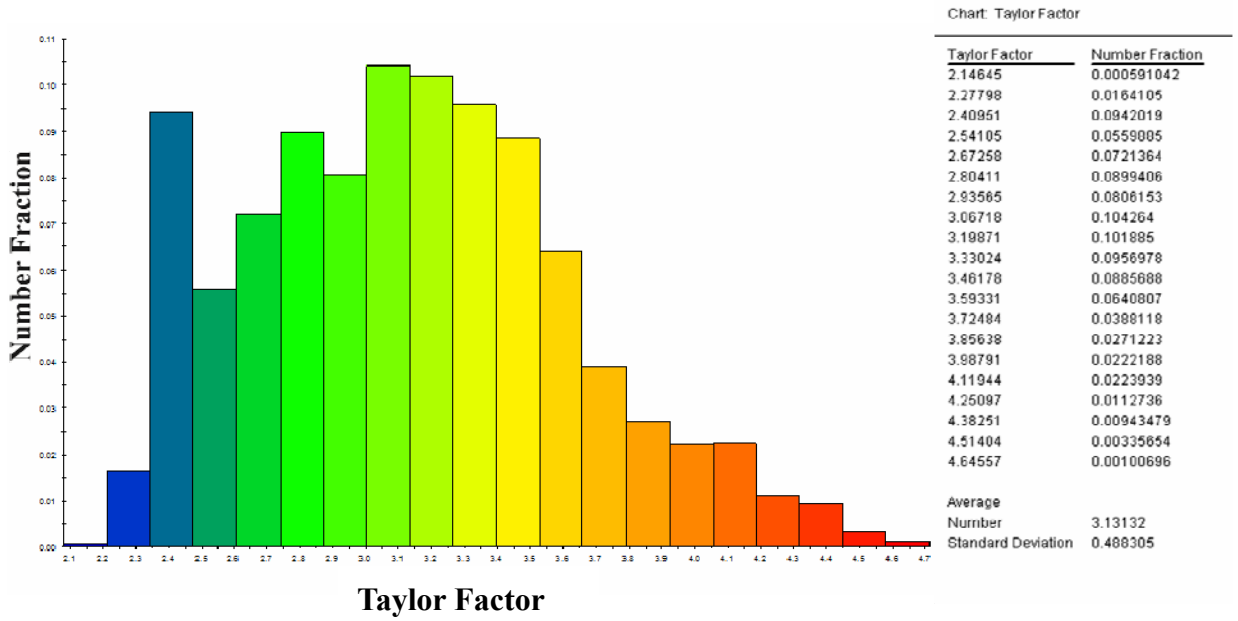

Figure 5. Histogram the Taylor factor distribution from Fig. 4.c.

Fig. 6.a shows the pole figures from the (111), (110) and (100) centered plans in the delamination region. Fig. 6.b shows the orientation distribution function (ODF) obtained for the section $\varphi_2 = 45$ °, which is the most important section on steels analysis, φ_1 is Euler angle aligned with RD while Φ is aligned to TD. The main components were obtained from ODF's because pole figures provide incomplete information [21]. It can be seen in Figs. 6.a and 6.b the formation of fiber texture: α fiber or fiber DL, γ fiber or fiber DN and cube textures. The presence these components are common in low carbon steel from the controlled rolling process. It can suffer change in the intensity value according to different processing and composition chemical of the steel [3].

The α fiber components more intense were: {113} <110>, {112} <110> and {223} <110>, which it can cause anisotropy mechanical properties [3, 5, 6]. This manner, the {113} <110> fiber component is generated from the deformed austenite recrystallization {112} <111> component. While the {112} <110> and {223} <110> fiber components both are produced by deformation from the {113}<110> rotation component. The same components can be contributing to ductile crack propagation during the test.

The cube fiber components were: {100} <120> and {100} <230>. These components usually are the lower intensity than γ and α fiber texture, this feature is attributed to recrystallization process [3]. The {100} <110> texture component was also found, the same is parallel to the rolling direction and contribute to both occurrence the cleavage plane and delamination phenomenon [3, 7, 8, 9, 10].

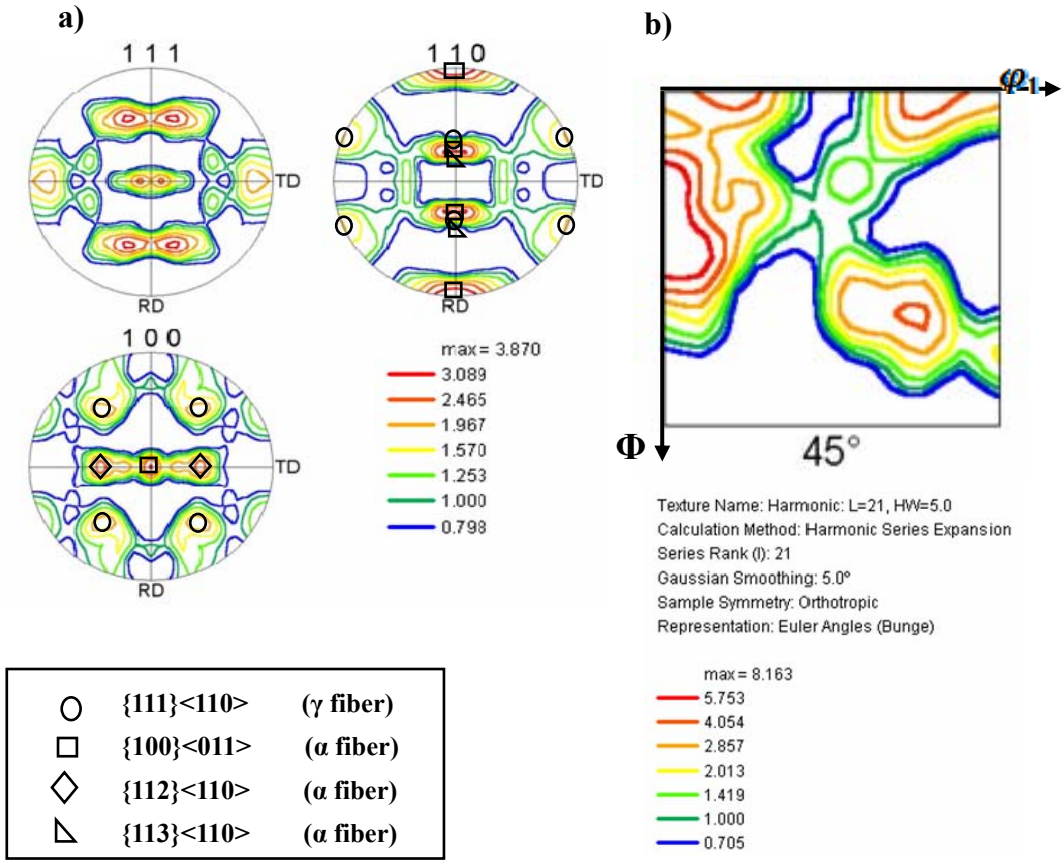

Figure 6. a) Pole figures from the (111), (110) and (100) centered planes obtained in the delamination region. b) orientation function o distribution for the section $\varphi_2 = 45°$.

5. Conclusions

The orientation maps close to the delamination region have displayed a heterogeneous grain size distribution. The Taylor factor values were the lower absorbed energy with <100> type orientation. While the <111> type orientation has shown higher absorbed energy, consequently, a higher Taylor factor value. The orientation distribution function and pole figure have shown the presence of the α fiber texture such as :{113}<110>, {112}<110> e {223}<110>, these components produce anisotropic mechanical properties that during fracture process act to reduce the plastic constraint and contributing to increase the stress plane. The {100}<110> cube fiber component has been found in the delamination region, it is main responsible to the occurrence of phenomenon in HSLA.

Acknowledgements

The authors thank the USIMINAS by providing the material under study, the UFF-Federal Fluminense University, for performing the EBSD measurements, and CAPES for providing scholarship and the project (Case No. PNPD-23038.008242/2010-08)

References

[1] Specification for line pipe steel API5L, API, 2007.
[2] D. Porter, A. Laukkanen, P. Nevasmaa, K. Rahka, K. Wallin, Performance of TMCP steel with respect to mechanical properties after cold forming and post-forming heat treatment. Int J Press Vessels Pip, 22 (2004) 867–877.
[3] R. K. Ray, J. J. Jonas, Transformation textures in steels. Int Mater Rev, 35 (1990) 1-36.
[4] F. J. Humphreys, M. Hatherly, Recrystallization and related annealing phenomena. Amsterdam, Elsevier, 2004.
[5] G.J. Baczynski, J.J. Jonas, L. E. Collins, The influence of rolling practice on notch toughness and texture development in high-strength linepipe. Metall Mater Trans A, 30 (1999) 3045 – 3054.
[6] P.K.C. Venkatsurya, Z. Jia, R.D.K. Misra, M.D.Mulholland, M. Manohar, J.E. Hartmann. Understanding mechanical property anisotropy in high strength niobium-microalloyed linepipe steels. Mater Sci Eng A, 556 (2012) 194-210.
[7] R.D.K. Misra, H. Nathani, F. Siciliano, Effect of texture and microstructure on resistance to cracking of high-strength hot-rolled nb-ti microalloyed steels. Metall Mater Trans A, 35 (2004) 3024-3029.
[8] D.L. Bourell, Cleavage delamination in impact tested warm-rolled**.** Metall Trans A, 14 (1983) 1983-2487.
[9] M.S. Joo, W. Suh, J.H. Bae, H.K.D.H. Bhadeshia, Role of delamination and crystallography on anisotropy of Charpy toughness in API-X80 steel. Mater Sci Eng A, 546 (2012) 314-322.
[10] T. Inoue, F. Yin, Y. Kimura, K. Tsuzaki, S. Ochiai, Delamination Effect on impact properties of ultrafine-grained low-carbon steel processed by warm caliber rolling. Metall Mater Trans A, 41 (2010) 341-355.
[11] W. Yan, W. Sha, L. Zhu, W. Wang, Y. Y. Shan, K. Yang, Delamination fracture related to tempering in a high-strength low-alloy steel. Metall Mater Trans A, 41 (2010) 159-171.
[12] T. Otárola, S. Hollner, B. Bonnefois, M. Anglada, L. Coudreuse, A. Embrittlement of a superduplex stainless steel in the range of 550–700 °C, Eng Fail Anal, 12 (2005) 930–941.
[13] T. Tanaka, Controlled rolling of steel plate and strip. Int Mater Rev, 4 (1981) 185-212.
[14] C. Grobler, G. T. Van Rooyen, The mechanisms by which splitting occurs along sheared edges and in charpy specimens of a 12% chromium steel, Can Metall Q, 27 (1988) 49- 58.
[15] B.L. Bramfitt, A.R. Marder, A study of the delamination behavior of a very low-carbon steel. Metall Mater Trans A, 8 (1977) 1263-1273.
[16] American Society for Test and Materials, Standard test method for tension test of metallic materials [metric], ASTM E8M, Philadelphia, 2004.
[17] American Society for Test and Materials. Standard test method for measurement of fracture toughness, ASTM E1820, Philadelphia, 2005.
[18] S. Cravero, C. Ruggieri, Estimation procedure of J-resistance curves for SE(T) specimens using unloading compliance. Eng Fract. Mech, 74 (2007) 2735-2757.
[19] E. Hippert Jr, Investigação experimental do comportamento dúctil de aços API-X70 e aplicação de curvas de resistência J-Δa para previsão de colapso em dutos. M. Sc. thesis, Polytechnic School of São Paulo, Univesity of São Paulo, 2007.
[20] W. Guo, H. Dong, M. Lu, X. Zhao, The coupled effects of thickness and delamination on

cracking resistance for X70 pipeline steel. Int J Press Vessels Pip, 79 (2002) 403 - 412.
[21] V. Randle, O. Engler, Introduction to Texture Analysis: macrotexture, microtexture, and orientation mapping, CRC Press, 2000.

Anti-plane problem of a lip-shape crack in one-dimensional hexagonal quasi-crystal materials

Jing Yu[1,2], JunHong Guo[1,*] , YongMing Xing[1]

[1] College of Science, Inner Mongolia University of Technology, Hohhot 010051, China
[2] College of general education, Inner Mongolia Normal University, Hohhot 011517, China
* Corresponding author: jhguo@imut.edu.cn

Abstract By introducing a conformal mapping and using the complex variable function method, the fracture behavior of a lip-shape crack in one-dimensional hexagonal quasi-crystals materials is investigated under anti-plane loading at infinity. The expressions for stress, strains, displacements and field intensity factors of the phonon and the phason fields in the vicinity of the crack tip are obtained. When the height of the lip-shape crack approaches to zero, the present results can be reduced to the solutions of the Griffith crack

Keywords one-dimensional hexagonal quasi-crystals; lip-shape crack; complex variable function method; stress intensity factor

1. Introduction

The discovery of quasi-crystals (QCs) in 1984 is a significant breakthrough for condensed matter physics, which won the Nobel's award in 2011 [1]. A theoretical description of the deformed state of QCs requires a combined consideration of interrelated phonon and phason fields. The phonon field describes the motion of lattices in physical space, while the phason field describes quasiperiodic arrangement of atoms in the complementary orthogonal space, which interact with one another. Since the discovery of QCs, they have attracted the extensive attention of researchers engaged in experimental and theoretical work. A quantity of significant achievements of QCs have been done [2-11] recent years. Experiments have shown that quasi-crystals are quite brittle and the defects of quasicrystalline materials have been observed [12,13]. When quasicrystalline materials are subjected to mechanical stresses in service, the propagation of flaws or defects produced during their manufacturing process may result in premature failure of these materials. Therefore, the study of crack problem of quasicrystalline materials is meaningful both in theoretical and practical applications.

At present, the study on the fracture problems of quasicrystalline materials is mainly confined to relatively simple defects. Thus, the elastic problem of one-dimensional (1D) hexagonal quasicrystal materials becomes the primary object and made many of significant achievements. A moving screw dislocation in 1D hexagonal QCs was investigated [14]. The exact solutions of a semi-infinite crack and two semi-infinite collinear cracks in a strip of 1D hexagonal QCs were obtained [15,16]. The interaction of between dislocations and cracks in 1D hexagonal QCs were considered by the complex variable function method. Very recently, the analytical solutions of several complicated defects such as cracks originating from holes in 1D hexagonal QCs were obtained [17-19].

In this paper, by using the Stroh-type formulism for anti-plane deformation in 1D hexagonal QCs, the fracture mechanic of a lip-shape crack in a 1D hexagonal QC is investigated under uniform remote anti-plane shear loadings of the phonon field and the phason field. By introducing a conformal mapping and using the complex variable function method, which is further solved analytically. The expressions for stress, strains, displacements and field intensity factors of the

phonon and the phason fields in the vicinity of the crack tip are obtained. The exact solutions of the stress intensity factors for the phonon field and the phason field are obtained respectively, which are very useful in practice.

2. Basic equations

When defects parallel to the quasi-periodic axis of 1D hexagonal QCs exist, the geometrical properties of the materials will be invariable along the quasi-periodic direction. In this case, the corresponding elasticity problem can be decomposed into two independent problems, i.e., a plane elasticity of conventional hexagonal crystal which can be solved by the route of the linear elastic theory [19] and an anti-plane phonon-phason field coupling elasticity problem [4]. Thus, we only need consider the latter one. The physical problem considered in this paper is shown in Fig. 1.

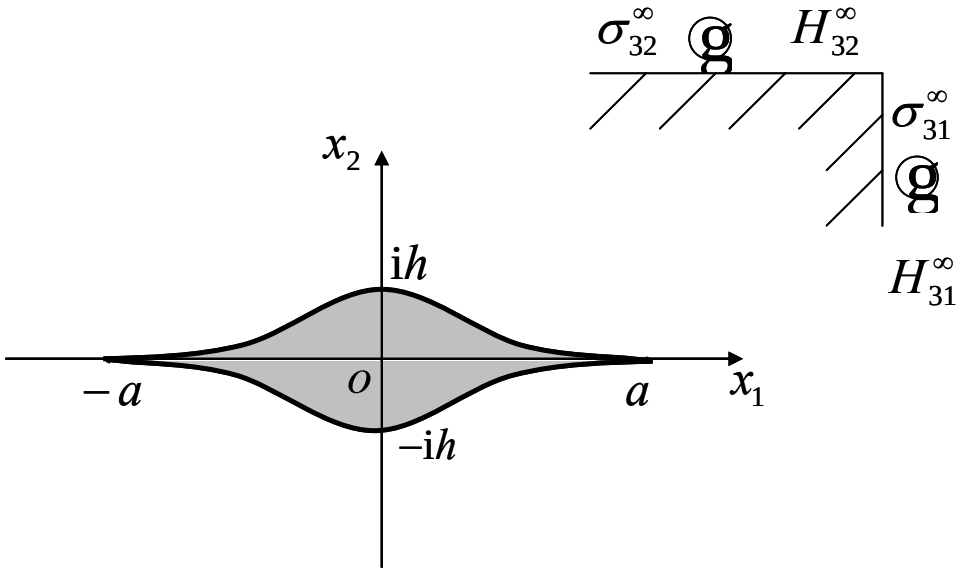

Figure 1. A lip-shape crack in 1D hexagonal QCs.

It is assumed that the quasi-periodic direction of 1D hexagonal QCs is along the positive direction of x_3 axis. In this case, all field variables are independent of x_3 and we have the following deformation geometrical equations [4]

$$\varepsilon_{3j} = \varepsilon_{j3} = u_{3,j}/2, \qquad w_{3j} = v_{3,j}, \tag{1}$$

the equilibrium equations

$$\sigma_{3j,j} = 0, \qquad H_{3j,j} = 0, \tag{2}$$

and the generalized Hooke's law

$$\sigma_{3j} = C_{44}u_{3,j} + R_3 v_{3,j}, \qquad H_{3j} = R_3 u_{3,j} + K_2 v_{3,j}, \tag{3}$$

where $j = 1, 2$; the repeated indices denote summation; a comma in the subscripts stands for a

partial differentiation; σ_{ij}, ε_{3j}, u_3 are the stress, strain and displacement of the phonon field, respectively; H_{ij}, w_{3j}, v_3 are the stress, strain and displacement of the phason field; C_{44} and K_2 are the elastic constants of the phonon field and the phason field, respectively; R_3 is the phonon-phason coupling elastic constant.

Substituting Eq. (3) into Eq. (2) ,then we can obtain the following result

$$\mathbf{B}_0 ? \nabla^2 \mathbf{u} \quad \mathbf{0}, \tag{4}$$

where ∇^2 indicates the two-dimensional Laplace operator, and

$$\mathbf{u} = [u_3, v_3]^T, \ \mathbf{B}_0 = \begin{matrix} 矩 \\ 阵 \end{matrix} \begin{matrix} C_{44} & R_3 \\ R_3 & K_2 \end{matrix}, \tag{5}$$

where the superscript T represents the transpose.

Because $C_{44}K_2 - R_3^2 \neq 0$, $\mathbf{B}_0^{-1}$ exists and thus Eq. (4) is equivalent to

$$? \nabla^2 \mathbf{u} \quad \mathbf{0}. \tag{6}$$

The general solution to Eq. (6) is

$$\mathbf{u} = \mathbf{f}(z) + \overline{\mathbf{f}(z)}, \qquad z = x_1 + \mathrm{i}x_2, \tag{7}$$

where $\mathbf{f}(z)$ is an unknown complex vector; and $\overline{\mathbf{f}(z)}$ stands for the conjugate of $\mathbf{f}(z)$.

To introduction Stroh-type formalism for anti-plane deformation, we take a generalized stress function vector $\sum$, such that [21,22]

$$[s_{31}, H_{31}]^T = - \boldsymbol{\sigma}_{,2} \ [s_{32}, H_{32}]^T = \boldsymbol{\sigma}_{,1} \tag{8}$$

Inserting Eq. (3) into Eq. (8) results in

$$- \boldsymbol{\sigma}_{,2} = \mathbf{B}_0 \frac{\partial \mathbf{f}}{\partial x_1} + \mathbf{B}_0 \frac{\bar{\mathbf{f}}}{x_1} \tag{9}$$

$$\boldsymbol{\sigma}_{,1} = \mathbf{B}_0 \frac{\partial \mathbf{f}}{\partial x_2} + \mathbf{B}_0 \frac{\bar{\mathbf{f}}}{x_2} \tag{10}$$

Eq. (9) or Eq. (10) gives

$$\boldsymbol{\sigma} = \mathrm{i}\mathbf{B}_0 \mathbf{f}(z) - \mathrm{i}\mathbf{B}_0 \overline{\mathrm{f}(z)} \tag{11}$$

Eqs. (7) and (11) can be rewritten as

$$\mathbf{u} = \mathbf{A}\mathbf{f}(z) + \overline{\mathbf{A}\mathbf{f}(z)}, \tag{12}$$

$$\boldsymbol{\sigma} = \mathbf{B}\mathbf{f}(z) + \overline{\mathbf{B}\mathbf{f}(z)}, \tag{13}$$

where

$$\mathbf{A} = \mathbf{I}, \qquad \mathbf{B} = \mathrm{i}\mathbf{B}_0 \tag{14}$$

where $\mathbf{I}$ is a 2×2 unit matrix.

Eqs. (12) and (13) are the general solutions of anti-plane deformations. It is seen that the stresses and stains of the phonon field and the phason field can be obtained from Eqs. (7) and (8) if the complex potential vector $\mathbf{f}(z)$ is available.

3. Stress fields and stress intensity factors

We consider a lip-shape crack in a 1D hexagonal quasicrystal solid infinitely large. It is assumed that the quasi-periodic direction of 1D hexagonal QCs is along the positive direction of x_3 axis. The solid is subjected to uniform remote anti-plane shear loadings of the phonon field and the phason field, as shown in Fig. 1 $2a$ is the crack length and $2h$ is the crack height. For the current case, we will study the complex potentials and the stress intensity factors under anti-plane shear loadings of the phonon field and the phason field at infinity. In this case, the complex function $\mathbf{f}(z)$ has the following form [21]

$$\mathbf{f}(z) = \mathbf{c}^{\text{¥}}\, z + \mathbf{f}_0(z), \tag{15}$$

c^{∞} is a complex constant related to the remote loading conditions, and $\mathbf{f}_0(z)$ is an unknown complex function vector, which vanishes at infinity, i.e., $\mathbf{f}_0(?\ )\quad 0$.

Differentiating Eqs. (12) and (13) with respect to x_1, we have

$$\mathbf{u}_{,1} = \mathbf{A}\mathbf{F}(z) + \overline{\mathbf{A}\mathbf{F}(z)}, \tag{16}$$

$$\sum_{,1} = \mathbf{B}\mathbf{F}(z) + \overline{\mathbf{B}\mathbf{F}(z)}, \tag{17}$$

where $\mathbf{F}(z) = d\mathbf{f}(z)/dz$. Substituting Eq. (15) into Eqs. (16) and (17), and then taking $z \to \infty$, results in

$$\mathbf{u}_{,1}^{\infty} = \mathbf{A}\mathbf{c}^{\infty} + \overline{\mathbf{A}}\,\overline{\mathbf{c}^{\infty}}, \tag{18}$$

$$\sum_{,1}^{\infty} = \mathbf{B}\mathbf{c}^{\infty} + \overline{\mathbf{B}}\,\overline{\mathbf{c}^{\infty}}, \tag{19}$$

$$\sum_{,1}^{\infty} = \left[\sigma_{32}^{\infty}, H_{32}^{\infty}\right]^T, \qquad \mathbf{u}_{,1}^{\infty} = \left[\varepsilon_{31}^{\infty}, w_{32}^{\infty}\right]^T. \tag{20}$$

The boundary along the surfaces of cracks is

$$\mathbf{B}\mathbf{f}(z) + \overline{\mathbf{B}\mathbf{f}(z)} = \int_s t_s\, ds, \qquad t_s = \left[t_3, h_3\right]^T, \tag{21}$$

where t_3 and h_3 represent the anti-plane shear traction of the phonon field and the phason field along the boundaries of cracks. In the current case, the surfaces of the cracks are free of external loadings, thus, Eq. (21) becomes

$$\mathbf{Bf}\left(z\right)+\overline{\mathbf{Bf}\left(z\right)}=0. \tag{22}$$

Inserting Eq. (15) into Eq. (22) gives

$$\mathbf{Bf}_0\left(z\right)+\overline{\mathbf{Bf}_0\left(z\right)}=-\left(\mathbf{Bc}^{\infty}z+\overline{\mathbf{Bc}}^{\infty}\bar{z}\right). \tag{23}$$

In order to obtain the complex function $\mathbf{f}_0\left(z\right)$ from Eq. (23), we introduce the following mapping function [23]

$$z=\omega\left(\zeta\right)=\frac{a}{2}\rho\mathrm{i}\left[m\zeta+\frac{1}{\zeta}-\frac{\zeta}{\rho^2\left(1+m\zeta^2\right)}\right], \tag{24}$$

in which

$$\rho=\frac{1}{1-m},\qquad \beta=\frac{h}{a}=\frac{1}{2}\frac{1+m}{1-m}\left[1-\frac{\left(1-m\right)^2}{\left(1+m\right)^2}\right]^2 \tag{25}$$

$\beta<1$,the approximate representations are

$$\rho\approx1+\frac{\beta}{2}+\frac{\beta^2}{4},\qquad m\approx\frac{\beta}{2}-\frac{\beta^2}{8} \tag{26}$$

It can be shown that Eq. (24) maps the exterior region of a lip-shape crack in the z plane into the interior of a unit circle in the ζ plane, and the boundary of the lip-shape crack is transformed the unit circle τ, where we take $\omega^{-1}\left(a\right)\to$ –i, $\omega^{-1}\left(-a\right)\to$ i, as shown in Fig. 2.

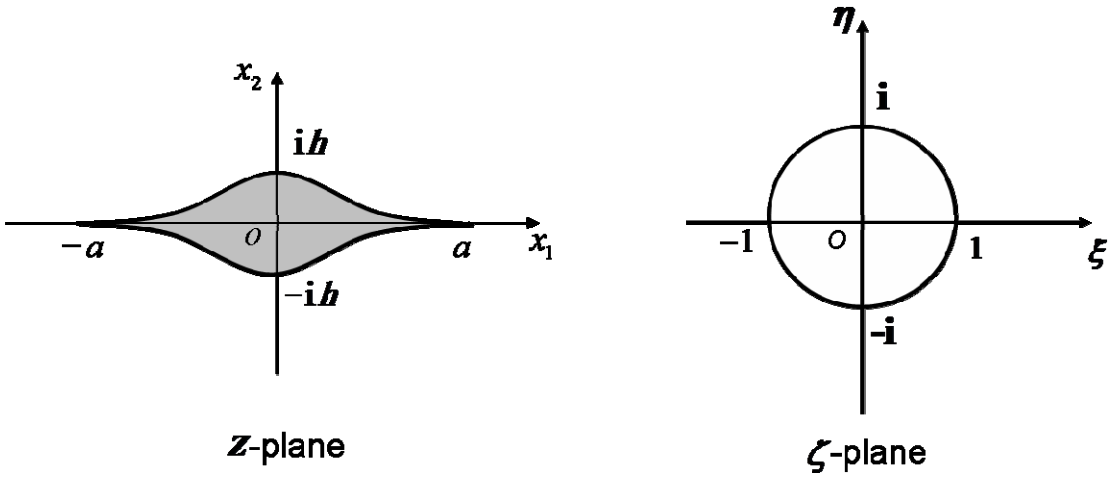

Figure 2. Mapping function of lip-shape crack into a unit circle.

Inserting Eq. (24) into Eq. (22),and then taking $\zeta = \sigma$, results in

$$\mathbf{B}\mathbf{f}_0(\sigma) + \overline{\mathbf{B}}\overline{\mathbf{f}_0(\sigma)} = -\left[\mathbf{B}\mathbf{c}^{\infty}\omega(\sigma) + \overline{\mathbf{B}}\overline{\mathbf{c}^{\infty}}\overline{\omega(\sigma)}\right], \tag{27}$$

where σ is the point on the unit circle, and $\mathbf{f}_0(\sigma) = \mathbf{f}_0(\omega(\sigma))$ is defined.

Multiplying Eq. (27) by $d\sigma/\left[2\pi\mathrm{i}(\sigma-\zeta)\right]$, where ζ is an arbitrary point inside the unit circle, and performing the Cauchy integral along the unit circle τ in the anticlockwise direction, we have

$$\mathbf{B}\mathbf{f}_0(\zeta) = -\mathbf{B}\mathbf{c}^{\infty}\frac{1}{2\pi\mathrm{i}}\int\frac{\omega(\sigma)}{\sigma-\zeta}d\sigma - \overline{\mathbf{B}}\overline{\mathbf{c}^{\infty}}\frac{1}{2\pi\mathrm{i}}\int_{\tau}\frac{\overline{\omega(\sigma)}}{\sigma-\zeta}d\sigma \tag{28}$$

$\omega(\zeta)$ is analytic inside the unit circle, except for a simple pole at $\zeta = 0$. Since $\overline{\omega(\zeta)}$ is analytic inside the unit circle, except for the simple poles at $\zeta = 0$, $\zeta = \sqrt{m}\mathrm{i}$, $\zeta = -\sqrt{m}\mathrm{i}$. By the residue theorem in complex variable function, one has

$$\frac{1}{2\pi\mathrm{i}}\int\frac{\omega(\sigma)}{\sigma-\zeta}d\sigma = \omega(\zeta) - \frac{a}{2}\rho\mathrm{i}\frac{1}{\zeta}, \tag{29}$$

$$\frac{1}{2\pi\mathrm{i}}\int_{\tau}\frac{\overline{\omega(\sigma)}}{\sigma-\zeta}d\sigma = \overline{\omega(\zeta)} + \frac{a}{2}m\rho\mathrm{i}\frac{1}{\zeta} - \frac{a}{2}\mathrm{i}\frac{\zeta}{\rho\left(m+\zeta^2\right)}. \tag{30}$$

The following result can be obtained by Eq.(18),Eq.(19),Eq.(20)

$$\mathbf{B}\mathbf{c}^{\infty} = \frac{1}{2}\left\{\left[\sigma_{32}^{\infty}, H_{32}^{\infty}\right]^T + \mathrm{i}\left[\sigma_{31}^{\infty}, H_{31}^{\infty}\right]^T\right\}, \tag{31}$$

$$\overline{\mathbf{B}}\overline{\mathbf{c}^{\infty}} = \frac{1}{2}\left\{\left[\sigma_{32}^{\infty}, H_{32}^{\infty}\right]^T - \mathrm{i}\left[\sigma_{31}^{\infty}, H_{31}^{\infty}\right]^T\right\}, \tag{32}$$

Substituting Eqs. (31) and (32) into Eq. (28), then differentiating the obtained results with respect to ζ leads to

$$\mathbf{B}\mathbf{F}_0(\zeta) = \frac{a\rho}{4}\left[m+1-\frac{1-m\zeta^2}{\rho^2\left(1+m\zeta^2\right)^2}\right]\begin{bmatrix}\sigma_{31}^{\infty}\\ H_{31}^{\infty}\end{bmatrix} - \frac{a\rho}{4}\left[m-1-\frac{1-m\zeta^2}{\rho^2\left(1+m\zeta^2\right)^2}\right]\begin{bmatrix}\sigma_{32}^{\infty}\\ H_{32}^{\infty}\end{bmatrix} \tag{33}$$

$\mathbf{F}_0(\zeta) = d\mathbf{f}_0(\zeta)/d\zeta$.

$\omega'(\zeta)$ and $\left[\overline{\omega(\zeta)}\right]'$ can be given by Eq. (24) as follows

$$\omega'(\zeta) = \frac{a}{2}\rho\mathrm{i}\left[m - \frac{1}{\zeta^2} - \frac{1-m\zeta^2}{\rho^2\left(1+m\zeta^2\right)^2}\right], \tag{34}$$

$$\left[\overline{\omega(\zeta)}\right]' = -\frac{a}{2}\rho\mathrm{i}\left[1-\frac{m}{\zeta^2}-\frac{m-\zeta^2}{\rho^2\left(m+\zeta^2\right)^2}\right], \tag{35}$$

It is found from Eq. (33) that the stress fields can be obtained from the relations between the stress and stress function.

The stress intensity factor at the crack tip is a very important physical quantity in fracture mechanics, which can reflect the stress intensity around the crack tip. The vector of the stress intensity factors can be defined as

$$\boldsymbol{k} = \left[K_{III}^{h}, K_{III}^{\perp}\right]^T = \lim_{z\to z_1}\sqrt{2\pi\left(z-z_1\right)}\sum\nolimits_{,1}, \tag{36}$$

where K_{III}^{h} and $K_{III}^{\perp}$ denote the stress intensity factors of the phonon field and the phason field, respectively.

Substituting Eq. (17) into Eq. (36) gives

$$\boldsymbol{k} = \left[K_{III}^{h}, K_{III}^{\perp}\right]^T = 2\lim_{z\to z_1}\sqrt{2\pi\left(z-z_1\right)}\mathbf{B}\mathbf{F}_0\left(z\right) \tag{37}$$

in which the condition that $\mathbf{B}\mathbf{F}_0\left(z\right)$ is imaginary along the x_2 axis is used.

In the ζ plane, Eq. (37) becomes

$$\boldsymbol{k} = 2\sqrt{2\pi}\lim_{\zeta\to-\mathrm{i}}\sqrt{\omega(\zeta)-\omega(-\mathrm{i})}\frac{\mathbf{B}\mathbf{F}_0\left(\zeta\right)}{\omega'\left(\zeta\right)}, \tag{38}$$

where $\zeta = -\mathrm{i}$ is the corresponding point of the crack tip $z = a$.

It is obvious from Eqs. (33) and (34) that one finds $\lim_{\zeta\to-\mathrm{i}}\omega'\left(\zeta\right)$ exists and $\lim_{\zeta\to-\mathrm{i}}\mathbf{B}\mathbf{F}_0\left(\zeta\right)\neq 0$. Thus, by the L'Hospital rule, Eq.(38) results in

$$\boldsymbol{k} = 2\sqrt{2\pi}\lim_{\zeta\to-\mathrm{i}}\frac{\mathbf{B}\mathbf{F}_0\left(\zeta\right)}{\sqrt{\omega''\left(\zeta\right)}}, \tag{39}$$

$\omega''(\zeta)$ can be obtained by Eq.(34)

$$\omega''(\zeta) = \frac{a}{2}\rho\mathrm{i}\left[\frac{2}{\zeta^3}-\frac{2m^2\zeta^3-6m\zeta}{\rho^2\left(1+m\zeta^2\right)^3}\right], \tag{40}$$

Inserting Eqs. (33) and (40) into Eq. (39), the analytic expressions of the stress intensity factors at the crack tip $\left(a,0,0\right)$ for the anti-plane shear problem are derived as follows

$$\boldsymbol{k} = \begin{bmatrix}\sigma_{32}^{\infty}\\ H_{32}^{\infty}\end{bmatrix}\sqrt{\pi a}K, \tag{41}$$

where

$$K=\sqrt{\frac{\rho}{1+3m\rho+m^2\rho}}. \tag{42}$$

If the crack height h tends to zero, one has $m=0,\ \rho=1$ and then Eq. (41) reduces to

$$K=\sqrt{\frac{\rho}{1+3m\rho+m^2\rho}}=1. \tag{43}$$

which is the solution of Griffith cracks in a 1D hexagonal QC [15].

4. Numerical examples

We consider the variation of K with $\beta=\frac{h}{a}$. It can be shown from Fig. 3 that if $\beta<1$, the dimensionless field intensity factor K decreases with the value of β becomes large. It indicates that an increase of the height of the tip-shape crack will retard the crack propagation. In particular, when the height of the lip-shape crack approaches to zero, the current case can be reduced to the Griffith crack, i.e., $K=1$, which is easier to propagate.

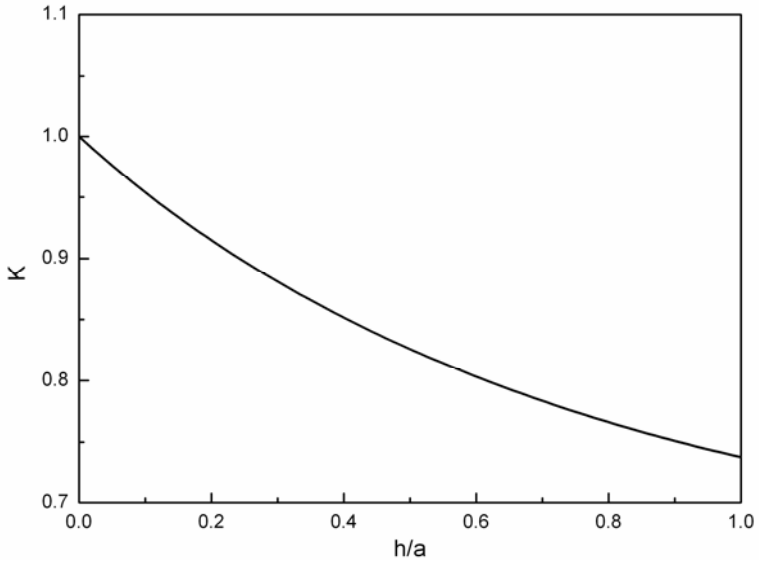

Figure 3. Variation of K with $\beta=\frac{h}{a}$

Acknowledgements

The authors thank the support from the National Natural Science Foundation of China (Nos.11262012 and 11262017), the Scientific Research Key Program of Inner Mongolia University of Technology (Grant No. ZD201219).

References

[1] D. Shechtman, I. Blech, D. Gratias, J.W. Cahn, Metallic phase with long-range orientational

order and no translational symmetry, Phys. Rev. Lett 53(1984) 1951 – 1953.

[2] S.B. Rochal, Second-order terms of the phonon – phason dynamic matrix of an icosahedral quasicrystal: Diffuse intensity and the profile shape around the Bragg peaks, Phys. Rev. B 64 (2001) 144204.

[3] S.B. Rochal, V.L. Lorman, Minimal method of the phonon – phason dynamics in icosahedral quasicrystals and its application to the problem of internal friction in the i-AlPdMn alloy, Phys. Rev. B 66 (2002) 144204.

[4] T.Y. Fan, The Mathematical Theory of Elasticity of Quasicrystals and its Applications, Science Press, Beijing/Springer-Verlag, Heidelberg, 2010.

[5] P De and R A Pelcovits, Phys. Rev. B35, 8609 (1987)

[6] W G Yang, R H Wang, D H Ding and C Z Hu, Phys. Rev. B48, 6999 (1993)

[7] Ding, D.H., Yang, W.G., Hu, C.Z., Wang, R.H., 1993. Generalized elasticity theory of quasicrystals. Phys. Rev. B 48, 7003 – 7010.

[8] R H Wang, W G Yang, C Z Hu and D H Ding, J. Phys. Condens. Matter 9, 2411(1997)

[9] Liu, G.T., Fan, T.Y., Guo, R.P., 2004. Governing equations and general solutions of plane elasticity of one-dimensional quasicrystals. Int. J. Solids Struct. 41,3949 – 3959.

[10] X.F. Li, T.Y. Fan New method for solving elasticity problems of some planar quasicrystals and Chin. Phys. Lett., 15 (1998), pp. 278–280

[11] Y.Z. Peng, T.Y. Fan Perturbation method solving elastic problems of icosahedral quasicrystals containing circular crack Chin. Phys., 9 (10) (2000), pp. 764–766

[12] X.M. Meng, B.Y. Tong, Y.K. Wu, Mechanical properties of Al65 Cu20 Co15, Acta Mech. Sin. 30 (1994) 60 – 64 (in Chinese).

[13] Z. Zhang, K. Urban, Transmission electron microscope observation of dislocation and stackling faults in a decagonal Al-Cu-Co alloy, Phil. Mag. Lett. 60 (1989) 97 – 102.

[14] T.Y. Fan, X.F. Li, Y.F. Sun, A moving screw dislocation in a one-dimensional hexagonal quasicrystals, Phys. Sin. Overseas Edition 8 (1999) 288 – 295.

[15] T.Y. Fan, 1999 The Mathematical Theory of Elasticity of Quasi-crystals and Applications, Beijing:Beijing Institute of Technology Press. (in chinese)

[16] L.H. Li, T.Y. Fan, Exact solutions of two semi-infinite collinear cracks in a strip of one dimensional hexagonal quasicrystal, Appl. Math. Comput. 196(2008) 1 – 5.

[17] J.H. Guo, G.T. Liu, Analytic solutions of the one-dimensional hexagonal quasicrystals about problem of a circular hole with asymmetry cracks, J. Appl. Math. 30 (2007) 1066 – 1075 (in Chinese).

[18] J.H. Guo, G.T. Liu, Analytic solutions to problem of elliptic hole with two straight cracks in one-dimensional hexagonal quasicrystals, Appl. Math. Mech. 29 (2008) 485 – 493.

[19] J.H. Guo, G.T. Liu, Exact analytic solutions for an elliptic hole with asymmetric collinear cracks in a one-dimensional hexagonal quasi-crystal, Chin. Phys. B 17 (2008) 2610 – 2620.

[20] N.I. Muskhelishvili, Some Basic Problems of Mathematical Theory of Elasticity, Noordhoff, Groningen, 1963.

[21] T.Y. Zhang, C.F. Gao, Fracture behaviors of permeable multi-cracks in a piezoelectric material, Theor. Appl. Frac. Mech. 41 (2004) 339 – 379.

[22] J.H. Guo, Z.X. Liu, Exact solution of four cracks originating from an elliptical hole in one-dimensional hexagonal quasicrystals. Appl. Math. Comput. 217 (2011) 9397-9403

[23] Z.B. Kuang, Stress analysis for plane curved polygonal defects containing cusps only, Chin. J. Theo. Appl. Mech., 14 (1979)218-228. (in chinese)

Introduction of a reverse simulation approach to identify the fatigue SIF crack arrest threshold from fretting cracking experiments

Alix de Pannemaecker[1&2,*], Siegfried Fouvry[1], Jean-Yves Buffière[2]

[1] LTDS, Ecole Centrale Lyon, 69134 Ecully, France
[2] MATEIS, INSA Lyon, 69100 Villeurbanne, France
* Corresponding author: alix.de-pannemaecker@ec-lyon.fr

Abstract

Fretting is a small amplitude oscillatory movement appearing between two contacting surfaces subjected to vibrations. This phenomenon may generate crack growth propagation. The aim of the present work is to estimate the ΔK_{Ith} (Crack arrest stress intensity factor) related to the crack arrest condition of a material subjected to partial slip fretting loadings by coupling experimental results and numerical simulations. The study is limited to cylinder/plane models TA6V/Al-alloys. In this approach, fretting tests are first performed for each configuration to obtain the crack length as a function of fretting cycles in order to establish the length of the arrested crack. Then an automatic program based on FEM simulations of the experimental test is developed to estimate the stress intensity factor corresponding to the crack arrest. Using a reverse analysis, the ΔK_{th} corresponding to the crack arrest condition is identified and different materials are compared.

Keywords Fretting tests, Fatigue crack arrest, Crack closing, Stress intensity factor

1. Introduction

Araujo et al. [1] demonstrated that the fretting fatigue endurance can be formalized using a short crack arrest methodology. This approach has been adopted in [2] to estimate the crack arrest boundary in the fretting fatigue map approach. Such analysis consists in computing the evolution of the stress intensity factor as a function of the crack length and to evaluate if this K-factor loading path intercepts or not the short crack arrest boundary. If the ΔK loading path overpasses this boundary, then a fretting fatigue failure is expected. Note that the short crack arrest boundary is approximated using either KT or El Haddad formalism.

Such a methodology usually considers a crack localized at the contact border and perpendicular to the contact surface. However, experimental results show that the crack path below the interface is more complex and usually displays an oblique angle oriented toward the inner part of the contact. A major question is to know if the normal crack approximation is relevant to describe the real crack path evolution.

A second aspect concerns the short crack methodology which is usually applied to approximate the crack arrest condition. In this research work, we consider an original reverse approach which consists in estimating the ΔK_{Ith} related to the studied material by applying a reverse identification method of our experimental results.

2. Materials and experimental procedure

2.1. Materials

A 2000 series al alloy (2196) aluminum alloy was investigated with the chemical composition detailed in Table 1.

Table 1. Chemical composition of the 2196 aluminum

% Cu	% Li	% Mg	% Mn	% Ag	% Zr	% Zn	% Si	% Fe
2.5-3.3	1.4-2.1	0.25-0.8	< 0.35	0.25-0.6	0.04-0.18	< 0.35	< 1.2	< 0.15

Two different heat treatments were applied: the industrial peak aged on one side called T8, and the experimental treatment at low temperature (120°C during 96 hours) on the other, called UA (Under-Aged). These two ageing treatments involve equivalent elastic properties with an elastic modulus E about 79000 MPa and the Poisson's coefficient about 0.305, but different monotonic and fatigue properties like the ultimate stress R_m, the yield stress $R_{0.2}$ and the elongation's rate A% (Table 2), which imply different ΔK_{th} values. Note that for confidential reasons, all data regarding fatigue properties are not available.

Table 2. Mechanical properties of the 2196 aluminum, depending on the heat treatment

State	$R_{0.2}$ (MPa)	R_m (MPa)	A%
T8	559	594	5.9
UA	428	520	11.1

For each alloy, small cubic specimen were machined and polished to achieve a 0.2 µm R_a roughness. Samples were adjusted so that the fretting loading was applied along the rolling direction of the alloy (Fig. 1).

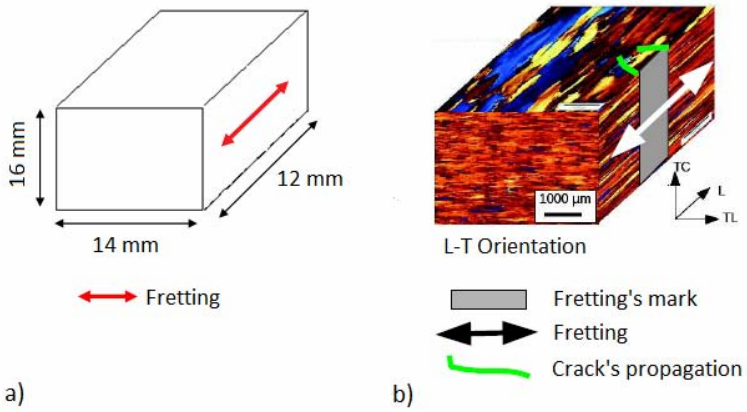

Figure 1. a) Sample's geometry - b) Microstructure [3]

2.2. Plain Fretting Experiment

Plain partial slip fretting tests were performed on a hydraulic set up at the LTDS previously described by Heredia [2]. The normal force (P) is kept constant, while the tangential force (Q) and displacement (δ) amplitudes are recorded. The fretting loop can be plotted and the corresponding amplitude values (respectively Q* and δ*) defined (Fig. 2).

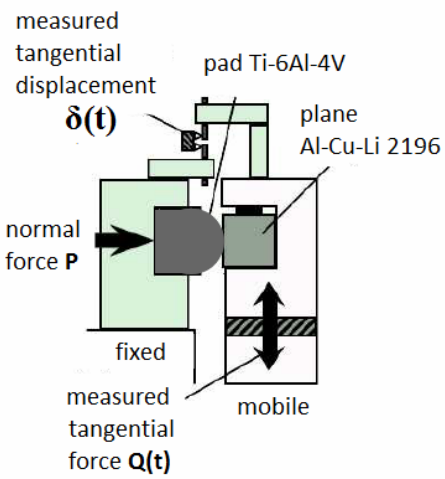

Figure 2. Experimental set up [2&3]

In the present fretting cracking investigation the displacement amplitude was monitored in order to maintain partial slip conditions, keeping constant the tangential force amplitude during the whole test duration. A cylinder/plane configuration was applied. The fretting pad consists of a Ti-6Al-4V alloy which displays the following elastic properties: 119500 MPa for the elastic modulus and 0.287 for the Poisson's coefficient. The cylinder's radius was fixed at 80 mm and the applied normal force at P=436.5 N/mm which induces a maximum hertzian constant pressure p_0=300 MPa and a hertzian constant radius a_H=0.92 mm. The lateral width of the cylinder pad was about 8 mm which corresponds to plain strain conditions along the median axis of the fretting scar. Previous tests were done to determine the friction coefficient at the sliding transition μ_t=0.85. [4]

3. Experimental results

Our objective was to identify the evolution of the crack length as a function of the fretting cycle to establish the "plateau" value related to the crack arrest condition. The tangential force was kept constant for all the experiment with Q*=200 N/mm. This tangential loading was previously adjusted to guarantee significant fretting cracking for elastic configurations (i.e. the stress is inferior to the yield stress $R_{0.2}$).

Figure 3 shows a typical crack path observed for the studied configuration after 2.10^6 cycles. As usually observed the incipient crack propagation a near 45° orientation compared to the normal of the surface until about 30 µm in depth. Below 200 µm, the crack propagation direction is normal to the plan. Between 30 and 200 µm, the crack path is considered to be linear with a 10° angle with respect to the normal of the surface. A schematic description of the crack path is given in Figure 3. The major part of the crack expertise leads to similar evolutions, so that the overall crack path description can be provided by linear segments (Fig. 3), and by making the average, we kept the first angle at 47.5°, the second at 15.5 and the last at 0° for the numerical model exposed hereafter.

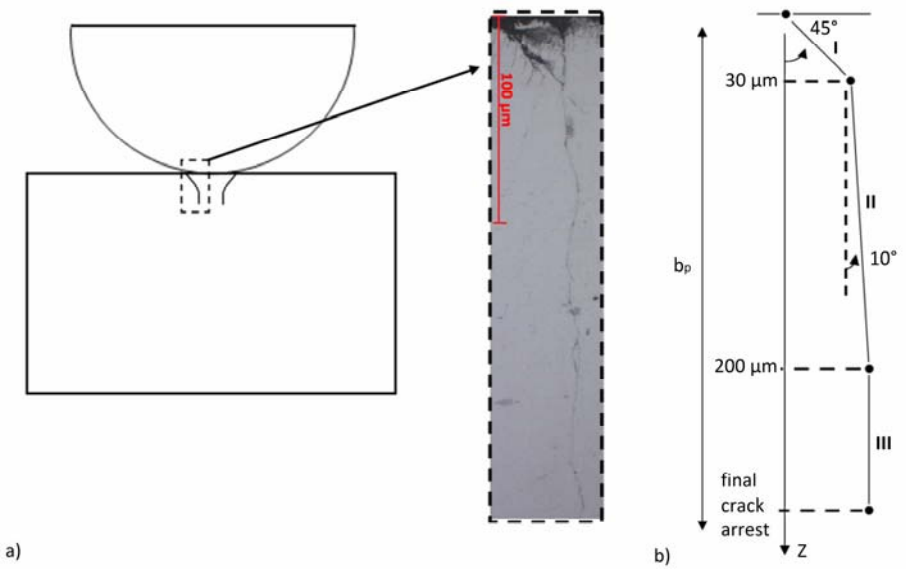

Figure 3. Crack path description a) Schematic and photo of the 2196-UA at N=2.10^6 - b) Discretization of the real crack path

This typical crack path evolution will be considered later for the crack modelling. To simplify the crack length analysis only the projected crack length (b_p parameter on Fig. 3) was considered. Figure 4 compares the evolution of the maximum projected crack length which was represented as a function of the fretting cycle.

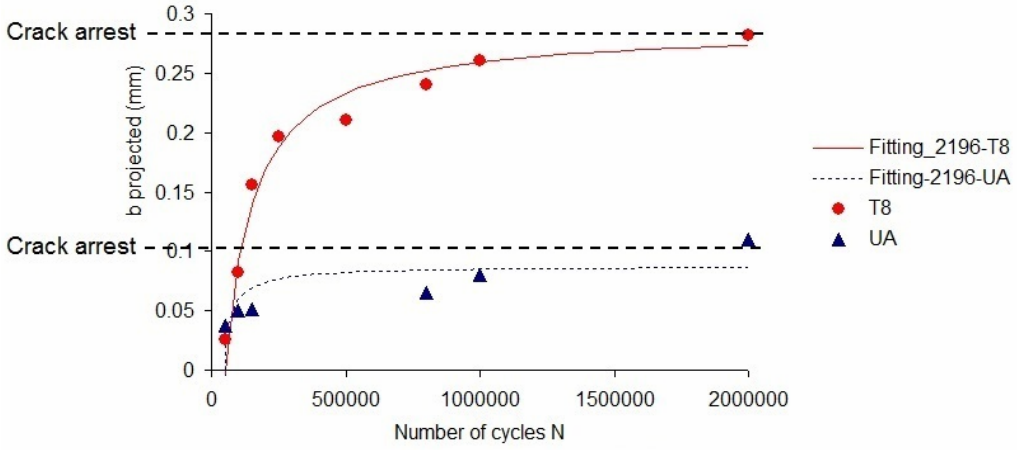

Figure 4. Propagation's curves

For the two materials, asymptotic evolutions can be observed. This analysis shows that the maximum crack length stabilized after 10^6 cycles. This allows us to estimate the crack length related to the crack arrest condition for the studied (P=436.5 N/mm; Q*=200 N/mm) plain fretting condition. We found respectively for the T8 and UA ageing treatments the following b_{pth}(T8)=280 µm and b_{pth}(UA)=100 µm crack length values. Because the maximum crack length achieved for the T8-ageing is longer than the one observed for the UA-ageing, it can be intuited that the threshold Stress Intensity Factor (SIF) related to the T8-treatment is significantly smaller than the one expected for the UA-ageing. The following analysis will consist in quantifying this aspect.

4. FEM computation of the Stress Intensity Factor's (SIF) evolution below the fretting contact

4.1. Contact modeling

A 2D-plain strain FEM modeling of the studied plain fretting test was developed. All the elastic and friction properties previously defined during experiment tests were implemented in the FEM-model. The fretting model is composed of a fixed plane and a moving cylindrical pad (Fig. 5). The mesh is composed of triangular (CPE3) and quadratic (CPE4R) linear elements. Quadratic elements were used to define the crack tip zone in a round domain of a radius of 5µm. Outside the crack tip zone, triangular elements were considered in order to reduce time costs. The mesh size in the contact zone was refined down to 20 µm in order to provide a more accurate estimation of the contact stress fields. The contact and the crack were described by a master-slave algorithm, and the tangential loading was determined by Lagrange multipliers through a constant friction coefficient (μ_t=0.85). During a computation, a fretting cycle were reproduced through the introduction of a normal load P=436.5 N/mm and through the application of a cyclic tangential cycle with a Q*=200 N/mm.

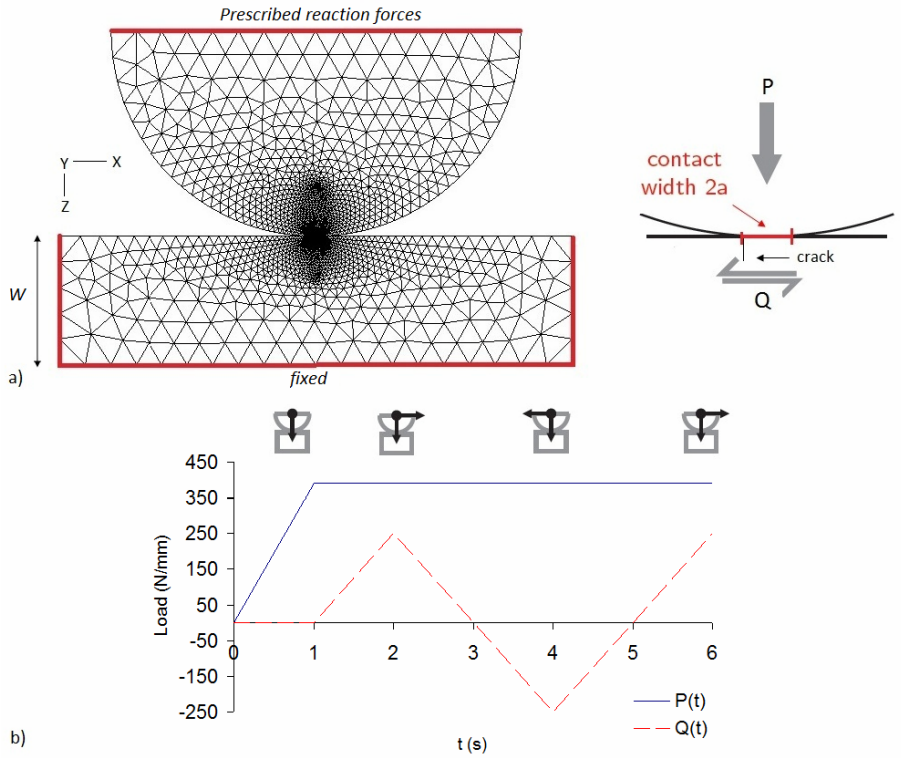

Figure 5. FEM description of the plain fretting cracking experiments a) FEM model - b) Loads applied

As elastic loads were imposed, the cracking computation was restricted to a single loading cycle. Results and interpretations were made for a single crack located at the trailing contact border ($x=-a_H$) at the loading stage (Q=Q*) which infers an open crack condition (Fig. 5).

4.2. Computation of the SIF parameter, crack meshing

An automatic Matlab code was developed to generate Abaqus input scripts, which remesh the cracks in a fretting cylinder/plane interface during the propagation's stage. This model with its mesh was inspired by the work of H. Proudhon [5]. The crack patch can be located anywhere in the plane's interface and can be described using sequential segments to reproduce as close as possible the real crack path. In the present investigation, crack nucleation is located at the contact border which is confirmed by experimental observations and multiaxial fatigue Modelling [1, 2, 6]. Two different crack path descriptions will be considered in the present analysis:

a) **The crack is normal to the surface**. Indeed, as indicated in the introduction, in numerous works published in the literature [1, 2] the crack is assumed to propagate in the normal direction of the surface in a fretting configuration. For such conditions only, one segment is required for the FEM simulation.

b) **The crack is kinked**. The path is described thanks to three segments provided in Figure 6.b. to approximate the real evolution of the crack propagation. This involves an angle of nearly 47.5° on the surface down to 0° deeper below the interface. This description is more complex to implement but it is also more relevant considering the real crack path evolution.

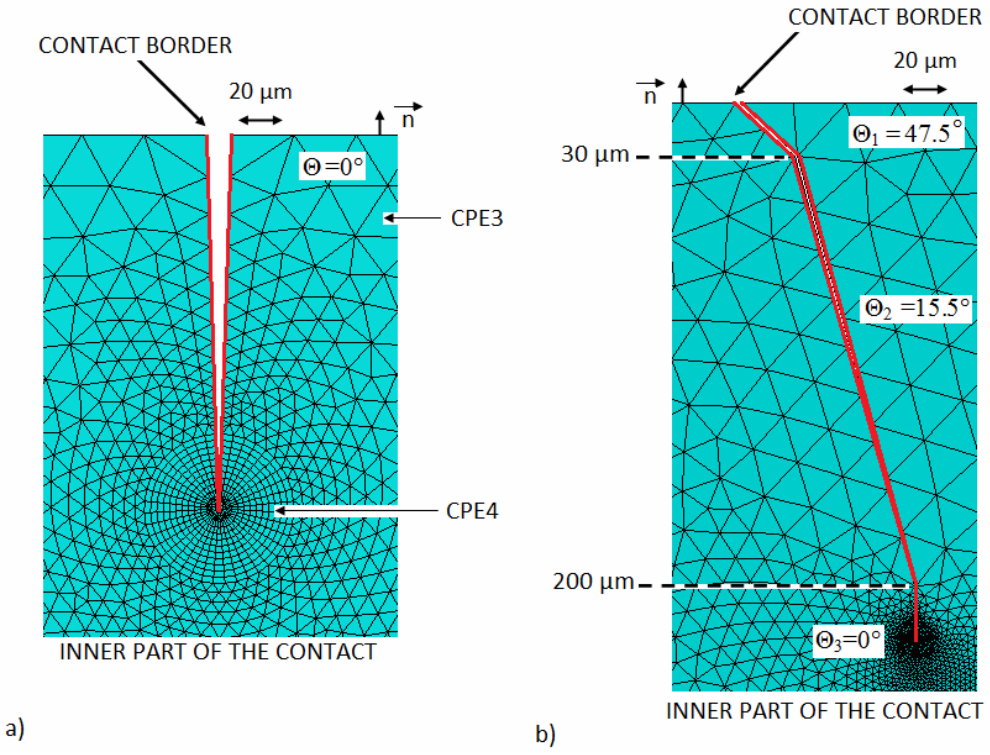

Figure 6. Illustration of the two crack mesh developed in the present investigation a) Plain normal crack hypothesis - b) Kinked crack's description

The Contour Integral's method (CI) is used by Abaqus 6.9 to estimate Stress Intensity Factors (SIF) at the crack tip. First, the Rice's integral (J-integral) is calculated, to then be related to K_I and K_{II} [7]. CPE3 triangular elements are used everywhere in the model except for the crack tip, where CPE4 quadrilateral elements are used for the CI. In the present analysis, only the mode I component (K_I) will be considered as it is applied in many fretting fatigue modelling description [1]. Although the

model allows us to consider the friction coefficient within the crack lips, in this first analysis, this friction's value (which highly influences the value of the SIF in second mode) is presently assumed to be equal to zero. The stress state below the interface is very complex, to quantify the crack propagation. An effective SIF value based on the ELBER formalism is addressed:

$$\Delta K_{Ieff} = K_{Imax} - 4 \quad \text{for } R>0$$

$$\Delta K_{Ieff} = K_{Imax} - (4.R + 4) \quad \text{for } -1<R<0 \qquad \text{with} \quad R = \frac{K_{Imin}}{K_{Imax}}$$

$$\Delta K_{Ieff} = K_{Imax} \quad \text{for } R<-1 \qquad (1)$$

An important aspect of this coupled FEM simulation is the fact that the fretting contact description includes the crack's presence in the contact stress analysis. Indeed, the crack can induce a local pressure's and shear's discontinuity at the contact border which will successively modify the contact loading and finally the crack's propagation process (Fig. 7). Note that such coupled interaction between crack and contact stressing is not considered in usual decoupled approaches involving dislocation methods or weight functions [8].

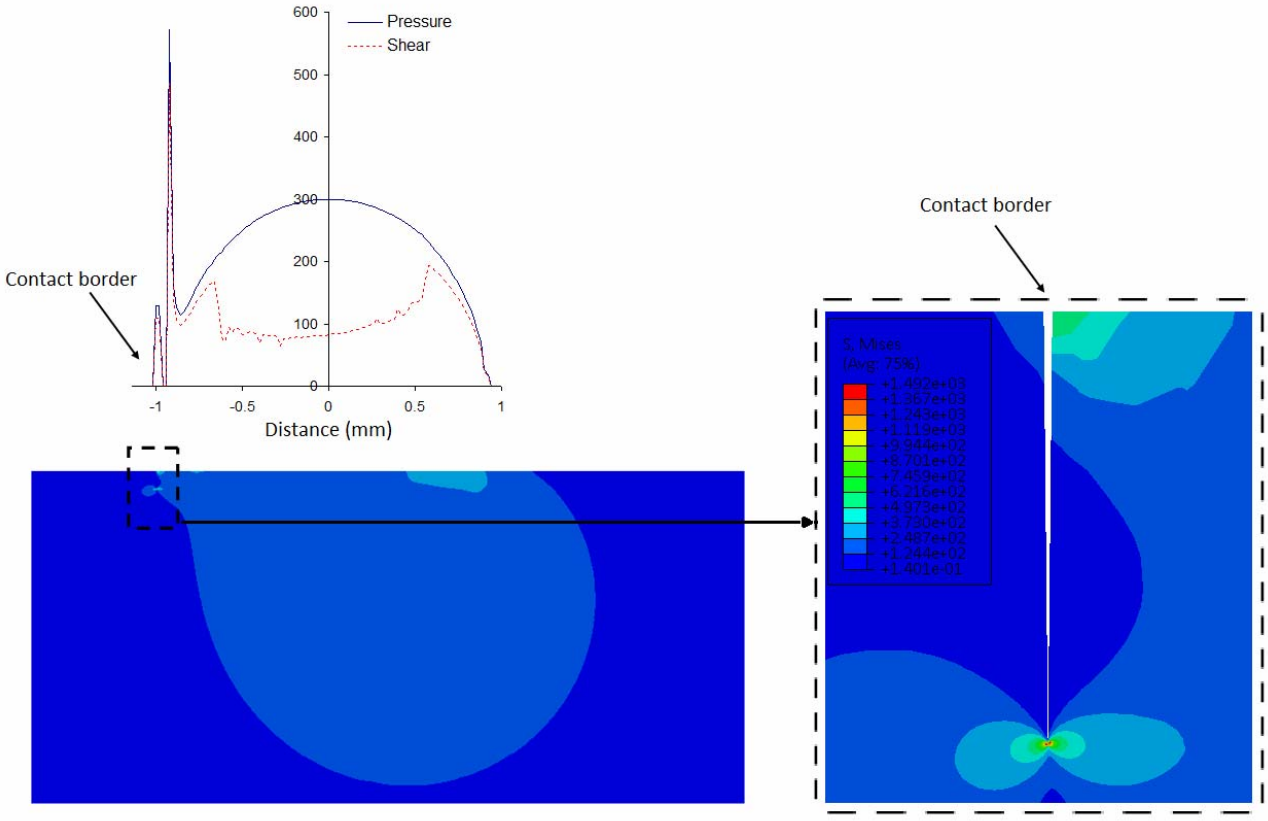

Figure 7. Illustration of the interaction between the contact stress and the crack's presence in the interface (Q=Q*, case of a normal crack with b_p=100 µm)

4.3. Results: comparisons between normal and kinked cracks

Figure 8 compares the evolution of the K_{Imax} as a function of the projected crack length obtained for the two crack descriptions.

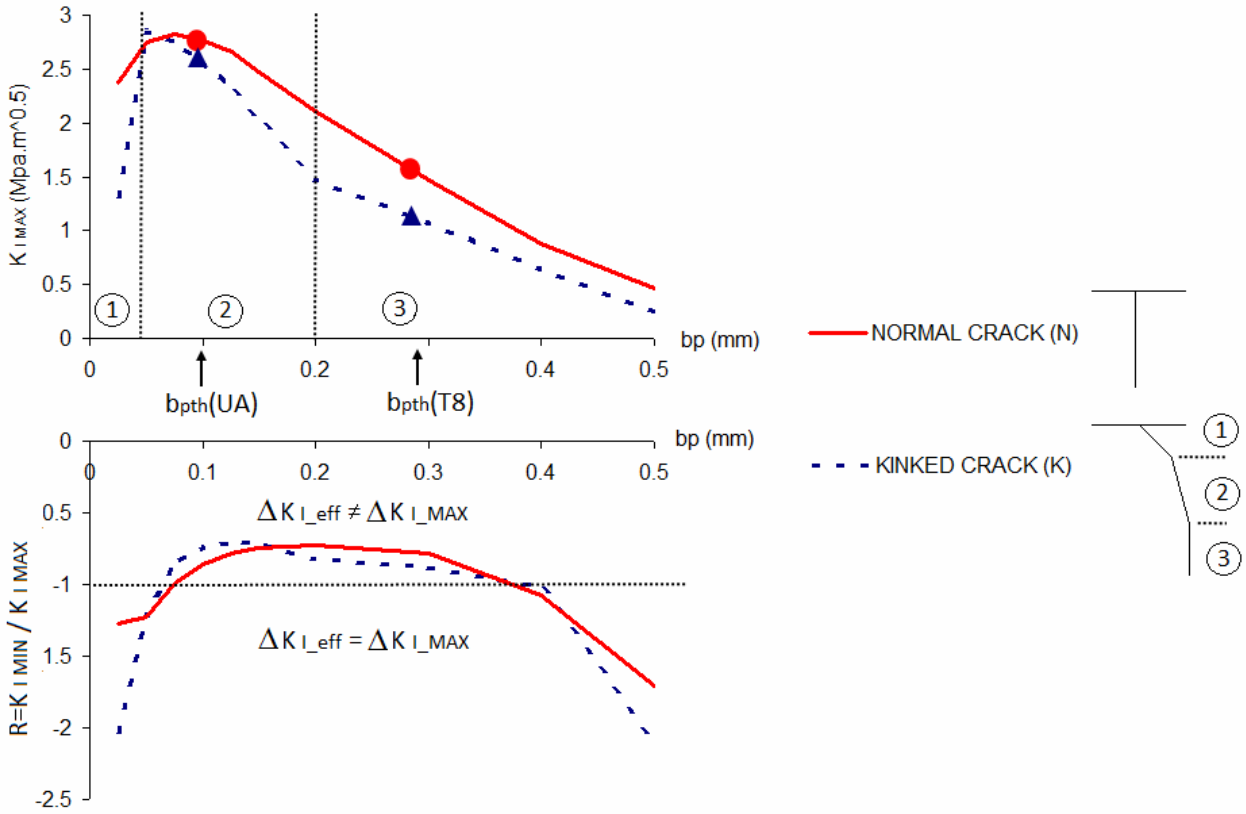

Figure 8. Evolution of the K_{Imax} and R ratio as a function of the projected crack length (P=436.5 N/mm; Q=200 N/mm) computed for the two normal and kinked crack descriptions

Both normal and kinked descriptions lead to similar non monotonic evolutions of the K_{Imax} values. As previously depicted in [9], the K_{Imax} value first increases with the crack length but then decreases when the tip of the crack is more and more remote from the surface due to the very sharp stress decrease induced by the severe contact stress gradients. Focusing on the comparison between kinked and the normal crack path descriptions, it can be said that in the zone 1, next to the surface, the crack angle ($\Theta_1 = 47°$) which is considered in the kinked description tends to reduce the mode I SIF value compared the normal crack description (Fig. 8. zone 1). Then, in the deeper zone 2, the angle decreases ($\Theta_2 = 15.5°$) so that the K_{Imax} value extrapolated from the kinked description is becoming closer to one defined from the normal crack approximation. Finally, in the very deep region 3, the crack orientation turns to the normal direction ($\Theta_3 = 0°$), however the K_{Imax} value provided by the kinked description is still smaller than the value extrapolated using the normal crack description. This difference can be explained by the fact that the lateral position of the crack tip is not the same. Indeed, if the crack tip is still at the vertical of the contact border for the normal crack description, it is now located in the inner compressive part of the contact for the kinked description. A major conclusion of this comparison is the fact that the two approximations of the crack path are in fact rather close. Note that the gap between the K_{Imax} values tends to decrease in

depth. Beside the normal approximation leads systematically higher K_{Imax} values providing conservative descriptions of the crack propagation's risk. Confirming former analytical analyses [9], it can be concluded that the usual "normal" crack path description provides relevant and conservative estimations of the fretting K_{Imax} evolutions. This result is important because it supports numerous plain fretting and fretting fatigue crack propagation's descriptions given in the literature.

4.4. Identification of the ΔK_{th} crack arrest value

By reporting the maximum projected crack length b_{pth}(T8) and b_{pth}(UA) on the previous graph, it is possible to extrapolate the related ΔK_{Ith} crack arrest value. Hence assuming the "Normal" crack's description we found:

$\Delta K_{Ith\_N}(T8) = 1.6MPa.\sqrt{m}$ (R=-0.9) and $\Delta K_{Ith\_N}(UA) = 2.7MPa.\sqrt{m}$ (R=-0.9)

Whereas using the "kinked" crack description we obtain:

$\Delta K_{Ith\_K}(T8) = 1.2MPa.\sqrt{m}$ (R=-0.9) and $\Delta K_{Ith\_K}(UA) = 2.6MPa.\sqrt{m}$ (R=-0.75)

The extrapolated values are rather small but quite representative of values for such aluminium alloys. Note that such values come from very low stress ratios (R) conditions, which is quite uncommon in conventional fatigue investigations. Considering the "Normal" crack description, which is usually the case in the literature for fretting fatigue cracking's characterizations, we can compare the obtained values with the ultimate stress values (Fig. 9.).

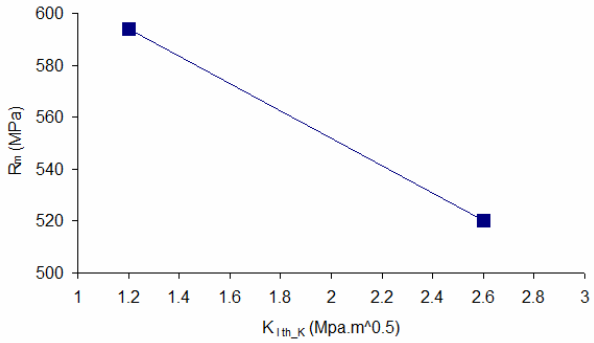

Figure 9. The ultimate stress as a function of ΔK_{th}

We confirm that for a given alloy, a heat treatment inducing an increase of the ultimate stress, leads to a decrease of the ΔK_{Ith}. Further developments will consist in comparing the ΔK_{Ith} identified from this inverse fretting identification's approach with conventional crack propagation fatigue analysis, thus to evaluate the pertinence of this approach and to estimate how very low stress R ratios can be considered regarding the crack arrest process. Besides, mixed mode descriptions including the mode II contribution and the friction coefficient in the crack lips will be addressed.

5. Conclusion

Using this reverse analysis, the ΔK_{Ith} values related to two different microstructures of a similar

Al-alloy were extrapolated. We confirmed that a heat-treatment inducing higher ultimate stresses leads to lower crack arrest stress intensity factors. This investigation underlines that despite its simplicity, a normal description of the fretting crack propagation path provides relevant and above all conservative estimations of the maximum Stress Intensity Factor (K_{Imax}). In the present work, plain fretting conditions involving very low R ratios (close to -1 or inferior) and a basic mode I description were considered. Besides the effect of the microstructure relate to the multi-crack process is not considered [10]. Future developments will consist in investigating fretting fatigue and fretting on pre-stressed specimen to consider higher R ratio and by implementing a mixed-mode [11] description of the SIF taking into account the coefficient of friction which is operating between the crack edges during the unloading compressive stage.

Acknowledgements

The authors want to thank the Carnot institute (I@L) for the partial financial support of this research and Constellium CRV company for the furnishing of material specimens.

References

[1] J.A. Araújo, D. Nowell, Analysis of pad size effects in fretting fatigue using short crack arrest methodology, International Journal of Fatigue, 21 (1999) 947–956.

[2] S. Fouvry, K. Kubiak, Development of a fretting–fatigue mapping concept: The effect of material properties and surface treatments, Wear, 267(2009) 2186–2199

[3] S. Heredia, S. Fouvry, Introduction of a new sliding regime criterion to quantify partial, mixed and gross slip fretting regimes: Correlation with wear and cracking processes, Wear, 269, Issues 7-8, (2010) 515-524.

[4] J. Delacroix, Etude des Mécanismes de Fissuration en Fatigue et/ou Fretting d'Alliages Al-Cu-Li, PhD, thesis, Institut National des Sciences Appliquées de Lyon, 2011.

[5] H. Proudhon, S. Basseville, Finite element analysis of fretting crack propagation, Engineering Fracture Mechanics, 78 (2011) 685-694.

[6] H. Proudhon , S. Fouvry, J-Y Buffiere, “Characterisation of fretting fatigue damage using synchrotron X-ray micro-tomography ”, Tribology International 39 (2006) 1106–1113.

[7] J.R. Rice, A path independent integral and the approximate analysis of strain concentration by notches and cracks, Journal of Applied Mechanics, 35, (1968) 379-386.

[8] H.F. Bueckner, A novel principle for the computation of stress intensity factors, Zeitschrift für Angewandte Mathematik und Mechanik, 50 (1970) 529-546.

[9] S. Fouvry, D. Nowell, K. Kubiak and D.A. Hills, Prediction of fretting crack propagation based on a short crack methodology, Engineering Fracture Mechanics, 75, Issue 6, (2008) 1605-1622.

[10] J. Delacroix, S. Cazottes, A. Daniélou, S. Fouvry, J.Y. Buffière, Influence of microstructure on the fretting resistance of Al-Cu-Li alloys, ICAA13 13th International Conference on Aluminium Alloys, 2012.

[11] M.C. Dubourg, A. Chateauminois Experimental and theoretical investigation of the contact fatigue behaviour of an epoxy polymer under small amplitude sliding micro-motions, European Structural Integrity Society, 32 (2003) 51-62.

The Model and Application of Fatigue Life Based on Fracture Mechanics and Fuzzy Theory

Xing-liang MA[1,*] , Hui-li WANG[2] , Si-feng QIN[3]

1. Bridge Science Research Institute Dalian University of Technology, Dalian, Liaoning province, 116023,China
2. Bridge Science Research Institute Dalian University of Technology, Dalian, Liaoning province, 116023,China
3. The corresponding author: Research Center for Numerical Tests on Material Dalian University, Dalian, Liaoning province, 116022,China

* Corresponding author: 512792881@qq.com

Abstract: Based on fracture mechanics and fuzzy theory, a model of fatigue life is developed to predict the fatigue life of structure. The dangerous point and stress amplitude can be gotten by finite element analysis method. According to fracture mechanics theory, considering fuzziness of fatigue life factors, the Paris' formula is combined with fuzzy theory and the model of fatigue life based on fuzzy theory is developed. The fuzziness of fatigue life factors is considered in the model so the results are more close to real situation. The model offers reference for fatigue life analysis.

Keywords : fracture mechanics, fuzzy, fatigue

1. Introduction

In vessels, pipelines, bridges, ships, offshore structures and many other engineering structures, there were a lot of disastrous accidents because of fatigue cracks. A report from American National Standards Institute indicates that cracks cause America a loss of 119 billion dollars every year. It is about 4 percents of American cross national products in 1982. According to a survey result of Committee of the Fatigue and Fracture, a sub-committee of ASCE, about 80-90% destruction of steel structures relates to fatigue cracks. From 1978 to 1981, America did a research against 20 states and Ontario Province in Canada. They collected the data of 142 bridges which had cracks. Among them, they found that the cracks on 115 bridges resulted from fatigue fracture[1]. How to analyze and estimate the fatigue life of member in construction correctly has become an important issue. This paper proposes a analysis modal which is based on fuzzy theory and combined with fracture mechanics.

2. Fuzzy phenomenon in analysis of fatigue life

The fuzziness of objects means the boundary is not clear, we cannot distinguish the difference between the right and wrong in its implication correctly, and we cannot divide its boundaries in our discussion range. The fuzziness is a natural characteristic of objects, it is a transient process between difference of objects.[2,3]

Broadly speaking, strength includes fatigue life, fracture toughness, residual strength and so on. In order to judge a structure is invalid or reliable, we must know the strength of material and structure. But because we get the data of strength from experiment, so it's inevitable to bring fuzziness.[4,5] It's feasible to apply the method of S-N curve and fracture mechanics. This paper is based on fuzzy theory, applys the method of fracture mrchanics to predict the fatigue life of structure.

Paris formula[9] is a always used to calculate the fatigue life in fracture mechanics, namely

$$\frac{da}{dN} = C\left(\Delta K\right)^m \quad , \tag{1}$$

Among it, a-crack size; N-number of load cycles; C, m-material constants; ΔK - stress strength

amplitude
Based on theory of fracture mechanics,

$$\Delta K = Y\Delta\sigma\sqrt{a\pi} \quad , \tag{2}$$

Y-coefficient of crack shape (generally it is 1),
$\Delta\sigma$ -alternative stress amplitude
We make (2) type substitute (1) type, we can get

$$N = \frac{1}{C}\int_{a_0}^{a_c}\frac{da}{(\Delta K)^m} = \frac{1}{C}\int_{a_0}^{a_c}\frac{da}{\left(\Delta\sigma\sqrt{a\pi}\right)^m} \quad , \tag{2-1}$$

Integrating, we can get

$$N = \begin{cases} \dfrac{a_c^{1-m/2} - a_0^{1-m/2}}{C\pi^{m/2}(1-m/2)(\Delta\sigma)^m} & m \neq 2 \\ \dfrac{\ln a_c - \ln a_0}{C\pi(\Delta\sigma)^2} & m = 2 \end{cases} , \tag{1}$$

Implied by some statistical data, initial crack length a_0 of welded structure is about 0.1~1.0mm. On average, we can think that a_0 is equal to 0.5mm[6]. Critical crack size a_c depends on the fracture toughness and stress level of material. According to the theory of fracture, we can get:

$$a_c = \frac{1}{\pi}\left(\frac{K_c}{\sigma}\right)^2 \quad , \tag{2}$$

Among it, K_c -the fracture toughness of material, we can get it from material data;
σ -structure stress
Because of some uncertain factors, such as fabrication technology, material properties and environment for use, we cannot get a most realistic number of C, so there are different numbers of C in different documents. For this reason that C is a variable quantity with fuzzifrfication, we can select some point among C's feasible region and on its edge. Then we put them into formula (3) and get their fatigue life respectively. Finally, based on the method of fuzzy comprehensive evaluation, we can make a forecast of its fatigue life.

3. Model of fuzzy comprehensive evaluation

3.1 Degree of membership

Assuming $C = (c_1, c_2, \mathrm{L}\ , c_m)$ which is the factor set that affect structure's fatigue life, $V = (v_1, v_2, \mathrm{L}\ , v_n)$ which is the set of evolution level. Among them, $c_i (i = 1, 2, \mathrm{L}\ , m)$ means number i influencing factors, $v_j (j = 1, 2, \mathrm{L}\ , n)$ means evolution level. So the array of degree of membership of set V is:

$$R=\begin{bmatrix} r_{11} & r_{12} & \mathrm{L} & r_{1n} \\ r_{21} & r_{22} & \mathrm{L} & r_{2n} \\ \mathrm{L} & \mathrm{L} & \mathrm{L} & \mathrm{L} \\ r_{m1} & r_{m2} & \mathrm{L} & r_{mn} \end{bmatrix}=\left(r_{ij}\right)_{m\times n} \quad , \tag{5}$$

among it, $i=1,2,\mathrm{L}\ m$, $j=1,2,\mathrm{L}\ n$ 。

In the factor set, for reflecting the different importance of each factor, we give each factor c_i a corresponding weight. The degree of membership of proposal j[7]:

$$u_j=\frac{1}{1+\left(\dfrac{\sum_{i=1}^{m}\left[w_i\left(r_{ij}-1\right)\right]}{\sum_{i=1}^{m}\left(w_i r_{ij}\right)}\right)^2} \tag{6}$$

We can get the fatigue life through the weighting factor method:

$$\bar{N}=\sum_{j=1}^{n}u_j N_j \tag{3}$$

Among it, N_j is the fatigue life of structure when evolution level is j.

2.2 Weight vector

For decreasing the affection of human factors, the method of getting the weight w_i is based on its relative degree of fuzziness membership. Generally speaking, the higher degree of membership of target, the bigger attention will be pay. In other words, the bigger weight will be given. According to the fuzzy set, we can regard the degree of membership as the weight. So we transpose the array R, and get the array of relative degree of membership which is target to the “importance”, namely

$$W=\begin{bmatrix} w_{11} & w_{12} & \mathrm{L} & w_{1m} \\ w_{21} & w_{22} & \mathrm{L} & w_{2m} \\ \mathrm{L} & \mathrm{L} & \mathrm{L} & \mathrm{L} \\ w_{n1} & w_{n2} & \mathrm{L} & w_{nm} \end{bmatrix}=(w_{ji})_{n\times m}=R^T \tag{7-1}$$

From array W, we can know the vector $\mathrm{r}_{w_{(i)}}=(w_{1i},w_{2i},\mathrm{L}\ ,w_{ni})^T$ of relative degree of membership. It is a vector of n proposals that are about factors c_i to the “importance”. Because each proposal in set V completes fairly, so n proposals have the same weight to the importance of factor c_i. So weight vector is[7]:

$$w_{(i)}=(1+d_{yi}^2\cdot d_{zi}^{-2})^{-1} \tag{4}$$

Among it： $d_{yi}=\left\{\sum_{j=1}^{n}(1-w_{ji})^p\right\}^{1/p}$, $d_{zi}=\left\{\sum_{j=1}^{n}w_{ji}^p\right\}^{1/p}$

p is the index of distance, when p is one， it is Hamming distance; when p is two, it is Euclidean distance

4. Calculation example

The stiffening girder of steel truss on one over-sea bridge is composed by main truss, main beam and upper and lower bracing. Main truss is connected by integral joint plate, and all the members' sections are closed box. Main truss is composed by top chord members, lower chord members, vertical web members and inclined web members. Main truss is 10m tall, and each standard segment is 10m long. The structure of integral joint on top chord member is shown in figure1. It is made of Q345steel. This joint is under multi-direction stress, it has a complicated stress field. It is connected by large numbers of variable welding lines, so vehicle load could cause fatigue problem easily.

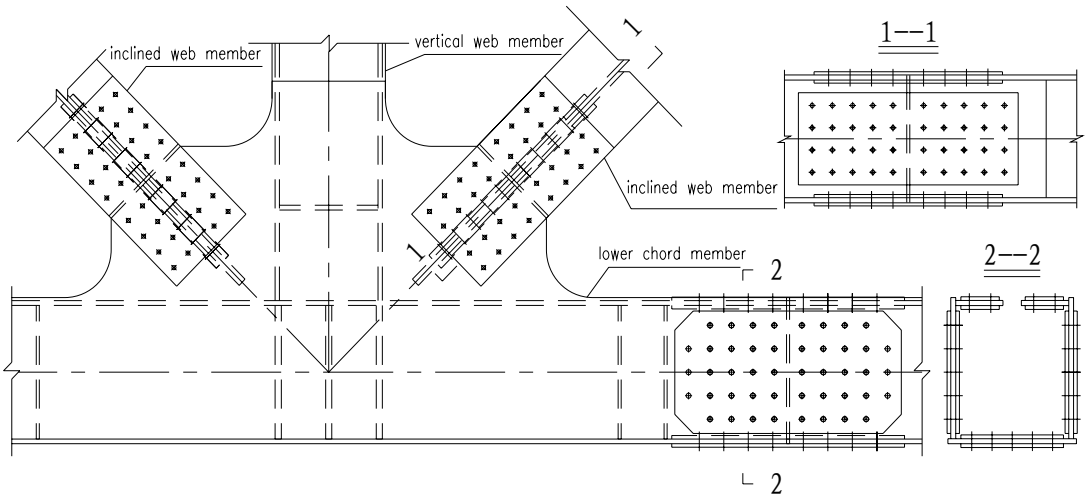

Fig.1 Schematic diagram of integral joint

4.1 Analysis based on crack mechanics

Through finite element analysis, we know that there is obvious stress concentration at the intersection of integral joint plant and inclined web member. As shown in figure2, the biggest stress amplitude $\Delta\sigma = 84.4Mpa$.

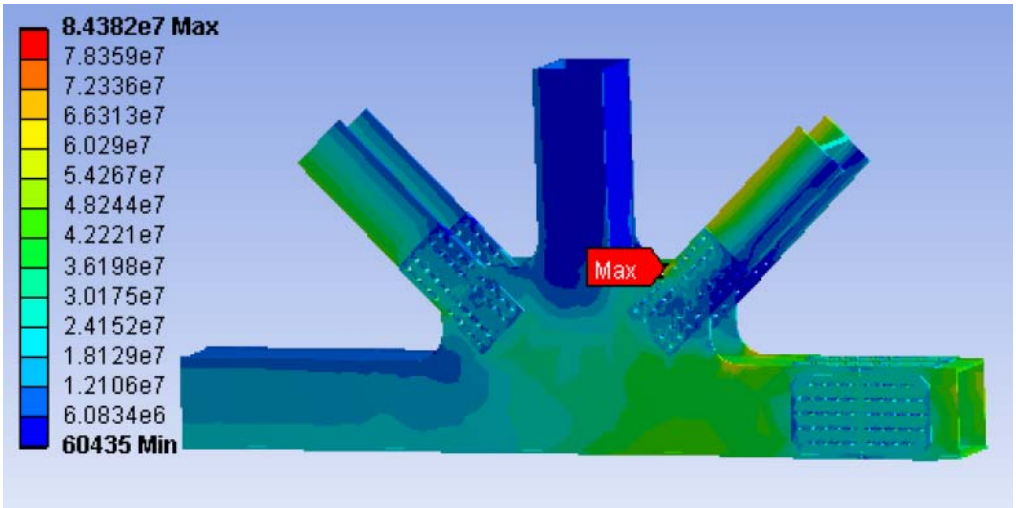

Fig.2 Equivalent stress nephogram of integral joint

The crack toughness of Q345steel is: $K_c = 207.91 Mpa \bullet mm^{\frac{1}{2}}$. According to formula (4), we can get the critical crack size:

$$a_c = \frac{1}{\pi}\left(\frac{K_c}{\sigma}\right)^2 = \frac{1}{\pi}\left(\frac{207.91}{84.4}\right)^2 = 1.93mm$$

Initial crack size: $a_0 = 0.5mm$, material constant $m = 3.0$, material constant C, average $\mu_c = 2.12 \times 10^{-13}$, coefficient of variation $C_v = 0.15$ [8].
According to formula (3), we can get the fatigue life is 2310340 times, 2123015 times, 1963789 times, 1826781 times and 1707643 times under different levels.

4.2 Create the factor set

Considering the specific condition of truss structure, the influencing factors of fatigue life of integral joint plate are as follows:
$C = (c_1, c_2, c_3)$

Among it, c_1 means fabrication technology, c_2 means material properties, c_3 means environment for use.

4.3 Create the evolution set

According to the trends consistency principle, five evolution indexes should be created which are shown in table1.

Tab.1 Grade of each evaluation factors

	v_1	v_2	v_3	v_4	v_5
c_1	excellent	good	average	bad	worse
c_2	excellent	good	average	bad	worse
c_3	excellent	good	average	bad	worse

4.4 Create the array of degree of membership

By the evolution of experts and technical staffs, array of degree of membership should be created as follows:

$$R=\begin{pmatrix} 0.10 & 0.45 & 0.30 & 0.10 & 0.05 \\ 0.05 & 0.50 & 0.35 & 0.05 & 0.05 \\ 0.05 & 0.10 & 0.25 & 0.45 & 0.15 \end{pmatrix}$$

According to (6) and (8) formula, we can get:

$u=(0.010,0.511,0.322,0.139,0.018)$.

So the fatigue life is:

$$\bar{N}=\sum_{j=1}^{5}u_j N_j = 2024965 \text{ times.}$$

5. Conclusion

In this paper, we propose an analysis model of fatigue life which is based on fuzzy theory. If we can combine it with actual construction situation, combine the fuzzy theory with crack mechanics, and we consider the fuzziness of factors which affect fatigue life, we can get a more accurate calculation result, and offer reference for fatigue life analysis.

6. Reference

Journal article:

[1] ASCE. Committee on fatigue and fracture reliability of the committee on structural safety and reliability of the structural division, fatigue reliability. J Struct Eng ASCE. 1982, 108.

[2] Degrauwe D, Roeck GD, Lombaert G. Uncertainty quantification in the damage assessment of a cable-stayed bridge by means of fuzzy numbers. Computers & Structures, 2009, 87(17):1077-1084.

[3] Wang Xuliang, N ieHong. A Study of the Fuzziness in Fatigue Life Estimation. Mechanical Science and Technology for Aerospace Engineering. 2008, 27(9).

[4] Muc A. A fuzzy set approach to interlaminar cracks simulation problems. International Journal of Fatigue. 2002, 24.

[5] CHI Sho-yan,HONG Ming,ZHAO De-you.Fuzzy Assessment of Fatigue Life for Plate Joints.China Offshore Platform. 2002, 17(6).

[6] Liu Chang-hong, Liu Wei-qi. Reliability Analysis Method Taking Account Of Fuzziness In Fatigue Failure Probability of The Main Beam of Bridge Crane. Journal of Mechanical Strength. 1994, 16(1).
[7] ZHANG Zhe, WANG Hui-li, SHi Le, HUANG Cai-liang. Application of multi-levels and multi-objectives fuzzy optimization model of bridge type selection. Journal of Harbin Institute of Technology.2006, 38(9).

Book:
[8] Li Hong-sheng, Zhou Cheng-fang. Engineering Fracture Mechanics. Dalian: Dalian University of Technology Press,1990.
[9] Fisher. JW. Fatigue and fracture in steel bridges : case studies. New York Wiley, 1984.

Fatigue and dwell-fatigue behavior of nano-silver sintered lap-shear joint at elevated temperature

Yansong Tan[1], Xin Li[2], Chengjun Li[1], Xu Chen[1,*]

[1] School of Chemical Engineering & Technology, Tianjin University, Tianjin 300072, China
[2] School of Material Science and Engineering, Tianjin University, Tianjin 300072, China
* Corresponding author: xchen@tju.edu.cn

Abstract Load-controlled fatigue and dwell-fatigue tests were conducted at elevated temperature to describe the high temperature behavior of nano-silver sintered lap-shear joints. The results show that the shear strength of nano-silver sintered lap-shear joints are strongly temperature dependent, and almost halved at the temperature of 325℃. To describe the temperature effect on fatigue life under fully-reversed loading, Basquin's equation is developed by introducing temperature factor, and shows a good agreement with experiment results. In dwell-fatigue tests, creep is found the main factor resulted in failure acceleration and cyclic life reduction.

Keywords lap-shear, fatigue, dwell-fatigue, Basquin' equation, temperature dependent

1. Introduction

Nowadays, the use of tin-lead solder in certain application has been banned for its damage on healthy. However, there still are some fields such as power electronics packaging using high lead solder as interconnected material [1], which can be mainly attributed to the absence of appropriate substitution. Therefore, the introducing of environmental friendly die-attaching material becomes more and more important due to increasing stringent requirements of weight reduction, size miniaturization, high thermal dissipation, etc. [2].

In the 1970s, the view of diffusion welding silver film had been introduced by O'brien et al.[3], and thus a new die-attaching technology named low-temperature joining technology was remarkably promoted. With the assistance of mechanical pressure of about 40MPa, micro-sized silver powder could be sintered at temperature below 300℃ [4]. From then on, silver is used widely in microelectronic packages as a promising interconnection material between substrates and chips because of its superior electrical/thermal conductivity, high melting temperature (1,233 K), and good reliability. Though, for brittle silicon chips and ceramic substrates, the aided pressure might be destructive even slightest irregularities [5]. To raise the sintering driving force of this interconnection material, the paste formed by nano-sized silver powder, which gained the close attention of both scientists and power electronics engineers, was introduced by Lu et al [6].

Before the sintering technology coming into practical application, the processing profile and the property of nano-silver paste had been studied. In recent years, A low-temperature sintering profile with sintering temperature of 285℃, heating rate of 10℃/min, and holding time of 60 min was introduced by Wang et al [7]. Yu et al. studied the tensile behaviors of low-temperature sintered nano-silver films and proved that accumulation of plastic strain took place in silver-bonding layer during thermal cycling, which might lead to the final failure of the chip-attachment [8]. Chen et al. stated that the process of damage evolution of the nano-silver films was temperature independent by

mass of creep test data at elevated temperatures [9]. However, these studies only revealed the properties of sintered silver film, which in turn imposed a limitation to consider the thermally induced strain due to thermal expansion coefficient mismatch between substrate and chip in actual applications. Li et al. [10, 11] constructed a lap-shear structure to study the mechanical property of sintered nano-silver as a joint. Following this lap-shear structure, further research on fatigue and dwell-fatigue property of sintered nano-silver joint was conducted in this study.

Not only tensile and fatigue tests but also creep-fatigue tests were conducted in this article in order to understand the failure mechanism of nano-silver sintered lap shear joint at elevated temperature, study any possible relation between creep and fatigue in the low-cycle regime and learn the probabilistic observed mechanisms The creep-fatigue tests were conducted at the temperature of 325℃, at which both dwell time and fatigue process interacted and failure occurred in the low-cycle regime.

2. Sample preparation and experiment procedure

Details about lap-shear joint preparing have been presented elsewhere [11]. The well prepared sintered nano-silver structure with 2mm×1mm×50μm joint used in this study is showed in Fig. 1. All the tests were conducted on Micro Uniaxial Fatigue Testing System (MUT-1020) provided by CARE Measure & Control Co., Ltd. as shown in Fig. 2.

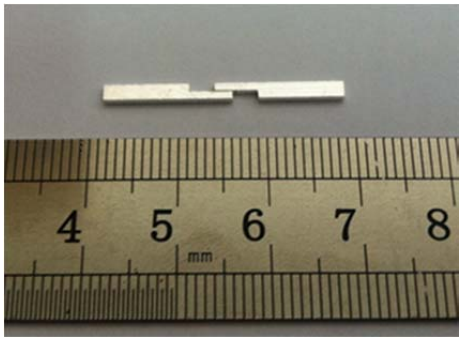

Fig. 1 Prepared sintered nano-silver lap-shear structure

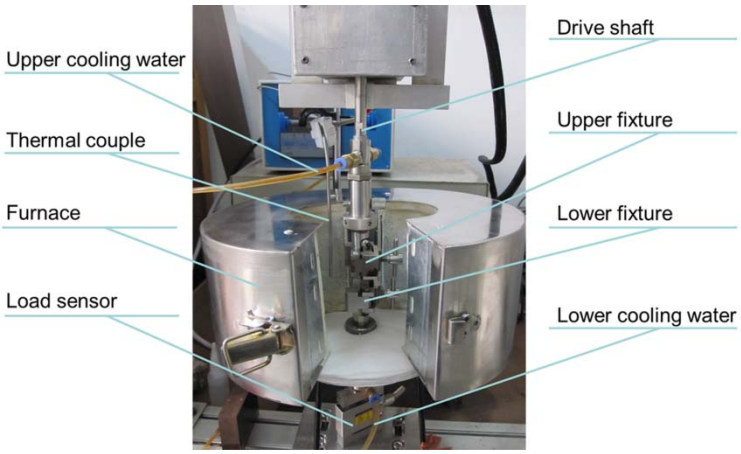

Fig.2 The testing apparatus

In order to obtain the shear stress-strain relations of sintered lap shear joints as the base for cyclic tests, a series of shear tests were conducted at four different ambient temperatures of 25℃, 225℃, 275℃ and 325℃. For fatigue and dwell-fatigue tests, the loading conditions are listed in Table 1. 3 samples were conducted for each loading condition. All the shear and cyclic tests were conducted under stress-controlled mode with loading rate of 2MPa/s.

Table 1. Loading conditions for low-temperature sintered nano-silver lap-shear joints

Name	Temperature /℃	Stress amplitude /MPa	Mean stress /MPa	Dwelling time /s
A1	325	10	0	0
A2	325	9	0	0
A3	325	8	0	0
A4	325	7	0	0
A5	325	6	0	0
A6	325	5	0	0
A7	325	6	0	1
A8	325	6	0	3
A9	325	6	0	5
A10	325	6	0	7
A11	325	6	0	9
A12	325	0	6	0
B1	225	10	0	0
B2	225	9	0	0
B3	225	8	0	0
B4	225	7	0	0
B5	225	7	0	1
B6	225	7	0	7
B7	225	7	0	9

3. Results and discussion

3.1 Shear behavior at elevated temperatures

As shown in Fig.3, the effect of temperature on strain level of nano-silver joints can be concluded. At room temperature of 25℃, the failure strain is less than 1.5%, which contains a small part of plastic strain and thus a brittle failure. With the temperature increasing, the shear modulus is decreased and the plastic flow of the joint was more obvious. The average shear strength under 4 ambient temperatures is given in Fig. 4. When the temperature is higher than 225 ℃, the shear strength drops dramatically, and almost halve at the temperature of 325℃ (14MPa).

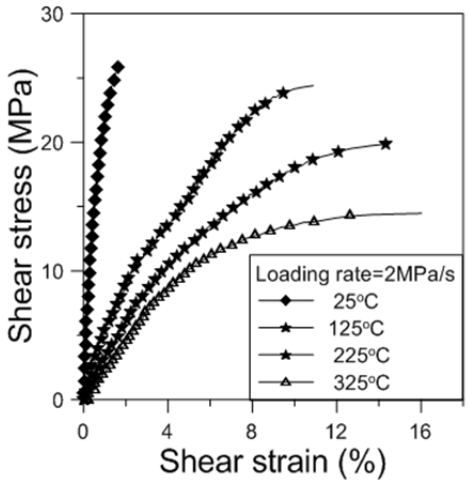

Fig.3 Shear stress-strain relationship of sintered nano-silver joint

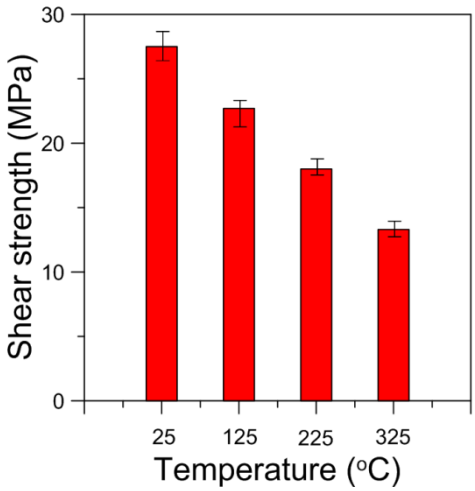

Fig.4 Shear strength of sintered nano-silver joint

3.2 Fatigue tests of fully reversed at elevated temperature

3.2.1 Fatigue behavior

Figure 5 shows shear stress-strain hysteresis loop under different loading amplitudes. From Fig. 5 we can find that the shear strain amplitude increases with the loading amplitude increasing under fully reversed loading situation. The increasing of hysteresis loops with loading amplitudes demonstrates the larger energy dissipating per unit volume during a cycle, which results in fewer cycles.

The plot of shear strain range versus number of cycles as shown in Fig.6 illustrates that the initial shear strain range increases as the increasing of the loading amplitudes. The evolution of shear strain range can be divided into three stages. The first stage has the longest duration of about 60-80 percent of the fatigue life and takes almost constant shear strain amplitude. When the fatigue test steps into the second stage of 80-90 percent of fatigue life, the shear strain slowly increases, which can be considered as the crack initiation. The final 10 percent of fatigue life is involving the third stage, during which the fatigue damage accumulation accelerates and results in ultimate failure.

The true strain-stress hysteresis loops of the nano-silver joint at load amplitude of 6MPa and 8MPa are displayed at Fig. 7. The enclosed area of the hysteresis loop represents the cyclic plastic energy consumed in each cycle. At certain loading amplitude, with the increasing of the cycles, the enclosing area increases gradually. The enclosed area of hysteresis loop experiences a rapid increase before the nano-silver joint comes to the final failure.

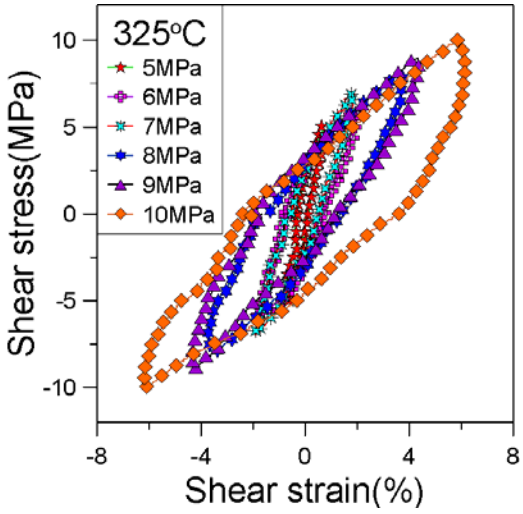

Fig. 5 Comparison of hysteresis loop under different loading amplitudes

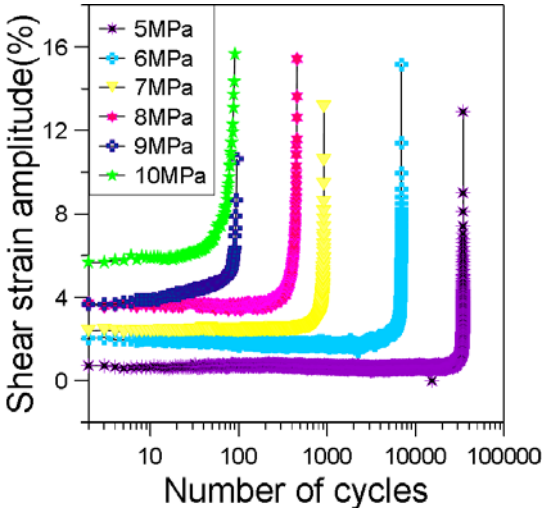

Fig. 6 Comparison of strain amplitude under different loading amplitudes at the temperature of 325℃

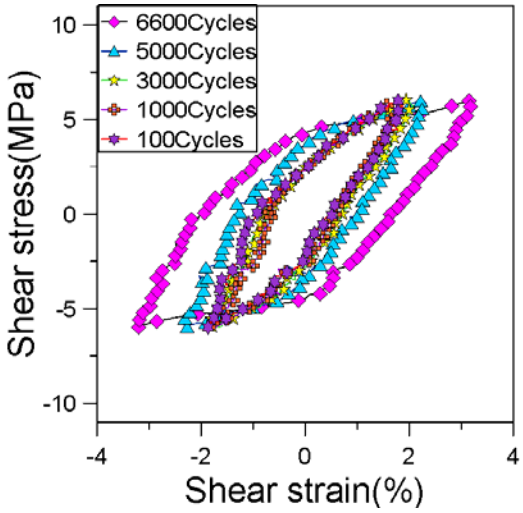

(a) At the loading amplitude of 6 MPa

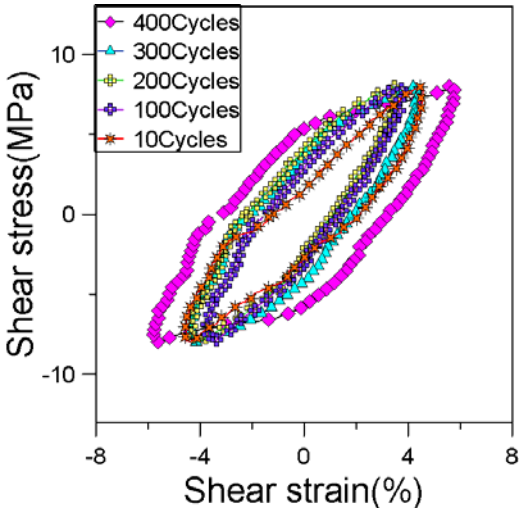

(b) At the loading amplitude of 8MPa

Fig. 7 Comparisons of hysteresis loops under different cycles

The temperature effects on hysteresis loops under 7MPa and 9MPa loading amplitude are shown in Fig. 8. It can be found that at higher temperature of 325℃, more plastic strain is present and the loops are wider, which causes the cyclic plastic deformation in the joint to be more severe. As a result, the fatigue life at the temperature of 325℃ is shorter than that at the temperature of 225 ℃. It should not be ignored that higher temperature could mobilize the dislocation of the nano-silver joints, which leads to a significant reduction of fatigue life.

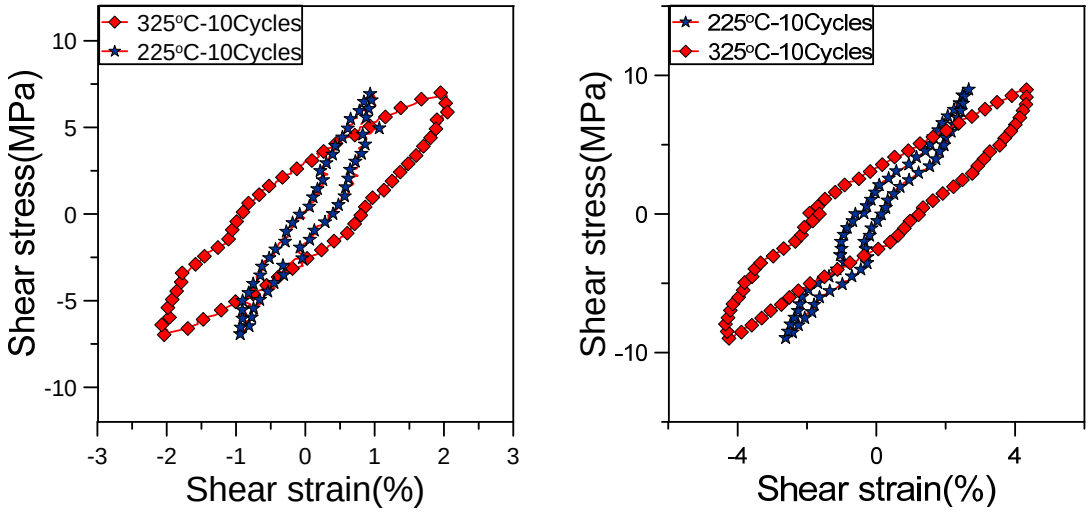

(a) At the loading amplitude of 7MPa (b) At the loading amplitude of 9MPa

Fig. 8 Comparison of the hysteresis loops at the temperature of 325℃ and 225℃

3.2.2 Fatigue life prediction

The stress-life (S-N) data can be plotted linearly in a log-log scale which is firstly observed by Basquin [12]. Here the formula can be expressed as

$$\Delta\tau/2 = \sigma'_{ft}(2N_f)^b \quad \text{(Eq. 1)}$$

The relationship between the shear stress amplitude and the fatigue life for sintered nano-silver lap shear joint at 325℃ and 225℃ are linearly fitted as Basquin's equation in the logarithm coordinate system as shown in Fig. 9. The fatigue strength exponent b and fatigue strength coefficient σ'_{ft} for sintered lap shear joint are given in Table 2. It can be obviously observed that the fatigue strength coefficient increased with decreasing temperature. The fatigue strength exponent has little change at different temperature as is shown in Fig. 9. The fatigue life of the nano-silver sintered lap-shear joints at the temperature of 325℃ and 225 ℃ are fitted well.

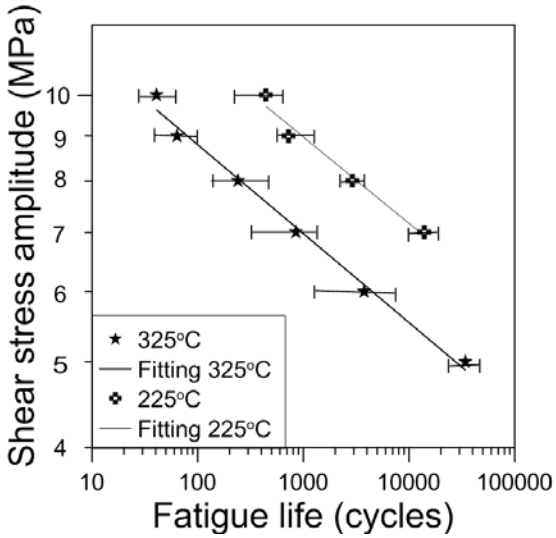

Fig. 9 S-N curve for nano-silver sintered lap-shear joints

Table 2. Comparison of fatigue properties between experimental value and empirical value

Temperature (℃)	σ'_{ft}	B
225	19.2	-0.1056
325	15.3	-0.1061

3.3 The dwell-fatigue behavior of nano-silver sintered lap-shear joints

As listed in Table 2, a series of dwell-fatigue tests (A7-A11) are conducted at the loading amplitude of 6MPa and the temperature of 325℃. From the results show in Table 3 we can find that with the increasing of dwell time, the fatigue life in cycle decreases at a rapid rate. But the total creep time (dwell time summation) holds between 2000-4000s, which indicates that the creep take a more important part in the failure process and might lead to the final failure. A point should be put forward that dwell sensitivity accelerates the fatigue failure while the cyclic loading prolong the creep life, since the creep life of the joints under the same loading amplitude is only 415s.

Table 3. The dwell-fatigue tests data under different dwell time.

Spec. ID	Temperature /℃	Dwell time (s)	Fatigue Life (cycles)	Total creep Time (s)
A6	325	0	6925	0
A7	325	1	2538	2538
A8	325	3	1226	3678
A9	325	5	438	2180
A10	325	7	536	3752
A11	325	9	239	2151
B4	225	0	9800	0
B5	225	1	4590	4590
B6	225	7	919	6433
B7	225	9	409	3681

Fig.10 indicates that the number of cycles verses dwell time is a straight line on the semi-log plot. The life in cycles reduces with the increasing of dwell time. It should be pointed out that the effect of dwell time at the temperature of 325℃ is more significant than that of 225℃. In other words, as the creep behavior of nano-silver sintered lap-shear joints is significantly influenced by temperature, so creep plays a more important part to the final failure of specimens at the temperature of 325℃ than 225℃. However, a series of creep-fatigue tests need to be conducted for further study of the effect of creep on creep-fatigue tests.

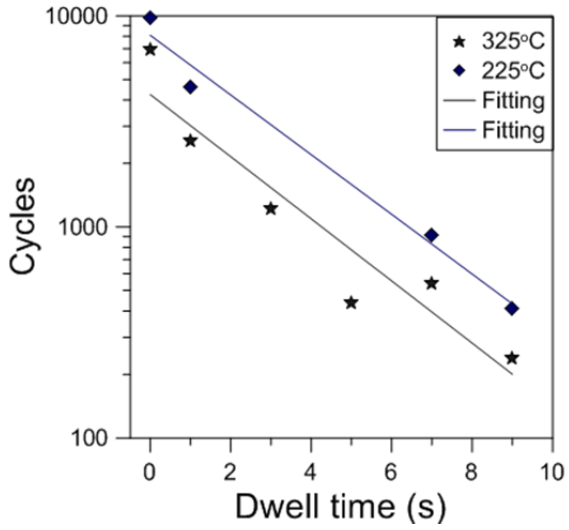

Fig.10 The fatigue data with different dwelling time

4. Conclusions

Firstly, the shear tests of nano-silver sintered lap-shear joints at elevated temperatures were conducted to study the effect of temperature on shear behavior. Secondly, a series of fatigue tests under fully reversed loading indicated how temperature affected the Basquin equation. Finally, the effect of creep on fatigue was studied at high temperature of 325 ℃. The following conclusions are obtained.

(1) Shear behaviors are temperature dependent. The shear strength decreases with the increased of temperature. The shear strength at room temperature is as high as 28MPa, which halve at the temperature of 325℃.

(2) Basquin's equation is presented to predict the fatigue life of the nano-sintered lap-shear joints at different temperatures, where the fatigue strength exponent b is a constant and the fatigue strength coefficient σ_{ft}' is a value dependent on temperature, which decreases with the elevated temperature

(3) With the increasing of the dwell time, the effect of creep becomes more and more significant. It can be concluded from the dwell-fatigue tests at the temperature of 325℃ that creep is the main factor that lead to the final failure of the specimen.

Acknowledgements

The project was supported by NSFC (No. 10802056 and No.11072171).

References

[1] L. Nie, M. Osterman, FB. Song, J. Lo, SWR. Lee, M. Pecht, Solder ball attachment assessment of reballed plastic ball grid array packages. IEEE translations on components and packaging, 32 (2009) 901–908.

[2] T. Wang, X. Chen, G.Q. Lu, G. Lei., Low-temperature sintering with Nano-silver paste in Die-Attached interconnection. Journal of electronic materials, 36 (2007) 1333–1340

[3] O'brien M, Rice C. R., Olson D. L., High strength diffusion welding of silver coated base metals. Welding Journal, 55 (1976) 25–27.

[4] Z. Zhang, G. Q. Lu, Pressure-assisted low-temperature sintering of silver paste as an alternative die-attach solution to solder reflow. IEEE translations on Electronics Packaging manufacturing, 25 (2002) 279–283.

[5] M. Knoerr, S. Kraft, A. Schlitz, Reliability assessment of sintered nano-silver die-attachment for power semiconductors, In: Proceedings of the Electronics Packaging Electronics Packaging Technology Conference (EPTC), 2010, pp. 56– 61.

[6] J.G. Bai, G. Q. Lu, Thermo mechanical Thermo mechanical reliability of low-temperature sintered tired silver die-attached SiC power device assembly. IEEE translations on Device Mater. Reliability, 6(2006) 436–441.

[7] T. Wang; X. Chen, G. Q. Lu.; Lei, G.; Low-Temperature sintering with Nano-silver paste in Die- Attached interconnection. Journal of electronic materials, 36(2007) 1333–1340

[8] D. J. Yu, X. Chen, G. Chen, G. Q. Lu; Applying Anand model to low-temperature sintered nano-scale silver paste chip attachment. Materials and design, 30(2009) 4574–4579

[9] G. Chen, X. H. Sun, P. Nie, X. Chen, G. Q. Lu, High-Temperature Creep Behavior of Low-Temperature-Sintered Nano-Silver Paste Films. Journal of electronic materials, 41(2012) 782–790

[10] X. Li, G. Chen, X. Chen, Mechanical property evaluation of nano-silver paste sintered joint using lap-shear test, Soldering & surface mount technology, 24(2012) 120-126

[11] X. Li, G. Chen, X. Chen, High temperature ratcheting behavior of nano-silver paste sintered lap shear joint under cyclic shear force, Microelectronics Reliability, 2012 in press

[12] Julie A. Bannantine, Jess J. Corner, James L. Handrock, Foundamentals of metal fatigue analysis, Prentice Hall press, New Jersey, 1990.

Fretting fatigue properties under the effect of hydrogen and the mechanisms that cause the reduction in fretting fatigue strength

Jader Furtado[1,*], Ryosuke Komoda[2], Masanobu Kubota[3]

[1] Air Liquide R&D, Centre de Recherche Claude Delorme Paris-Saclay,
1 Chemin de la Porte de Logas, Les Loges-en-Josas, 78354, France
[2] Graduate School of Kyushu University, 744 Motooka, Nishi-ku, Fukuoka 819-0395, Japan
[3] Kyushu University, Air Liquide Industrial Chair on Hydrogen Structural Materials and Fracture,
WPI-I2CNER and AIST, 744 Motooka, Nishi-ku, Fukuoka 819-0395, Japan
* kubota.masanobu.304@m.kyushu-u.ac.jp

Abstract Fretting fatigue, which is a composite phenomenon of metal fatigue and friction, is one of the major factors in the design of mechanical components as it significantly reduces fatigue strength. Since hydrogen can influence both fatigue and friction, fretting fatigue is one of the important concerns in designing hydrogen equipment. The authors carried out the fretting fatigue tests on austenitic stainless steels in order to characterize the effect of hydrogen and to explain the mechanism responsible for hydrogen embrittlement. In this study, the significant reduction in fretting fatigue strength due to hydrogen is shown including other factors influencing the fretting fatigue strength such as surface roughness, hydrogen content and the addition of oxygen. The cause of the reduction in the fretting fatigue strength in hydrogen is local adhesion between the contacting surfaces and subsequent formation of many small cracks. Furthermore, hydrogen enhances crack initiation under fretting fatigue conditions. Transformation of the microstructure from austenite to martensite is another possible reason. A hydrogen charge also reduces the fretting fatigue strength. The cause is the reduction in the crack growth threshold, ΔK_{th}, due to hydrogen.

Keywords Hydrogen, Fretting, Fatigue, Austenitic stainless steels, Adhesion

1. Introduction

Hydrogen embrittlement is a classic problem, but recent studies on hydrogen embrittlement have clarified that there are many technical challenges to achieving a balance between reducing the cost of hydrogen equipment and ensuring their safety. In this study, fretting fatigue in hydrogen is the focus, since fretting fatigue is one of the major factors in the design of mechanical components due to the significant reduction in fatigue strength. It has been reported that fretting can cause a reduction in fatigue strength by half to one-thirtieth of that of a smooth specimen [1]. Fretting fatigue occurs at the position where metal fatigue and fretting occur simultaneously. Fretting is the cyclic relative slip motion involving wear between the contacting surfaces of components mechanically fastened. In hydrogen equipment, fretting fatigue is definitely an important issue, since hydrogen can have an influence on both fatigue and friction phenomena. A significant reduction in the fretting fatigue strength due to hydrogen and the mechanisms causing the reduction are described. Several factors influencing the fretting fatigue properties in hydrogen are also investigated.

2. Procedures

2.1 Fretting fatigue test method

Figure 1 shows the fretting fatigue test method under tension and compression loading. In addition, a bending fretting fatigue test was also carried out. Detailed configurations of the specimen and contact pad are shown in refs. [2, 3]. In either case, two contact pads were pressed onto the front and back side surfaces of the fatigue test specimen. When a fatigue load is applied to the specimen, fretting is induced between the contacting surfaces due to the difference in the

deformation between the specimen and contact pad. The shape of the contact pad is the so-called bridge type in which there are two contact parts. As shown in Fig. 1, a strain gage was cemented at the midpoint of the contact parts to measure the friction force.

The nominal contact pressure was 100MPa. The tangential force coefficient, ϕ, was defined as the ratio of the friction force and the contact force. The fretting fatigue test was carried out with a stress ratio, *R*, of -1 at a loading frequency, *f*, of 20Hz. The test environment was hydrogen and laboratory air. The hydrogen pressure was 0.2MPa. The test temperature was room temperature. The fretting fatigue test in this study was terminated at 10^7 cycles if no specimen failure occurred.

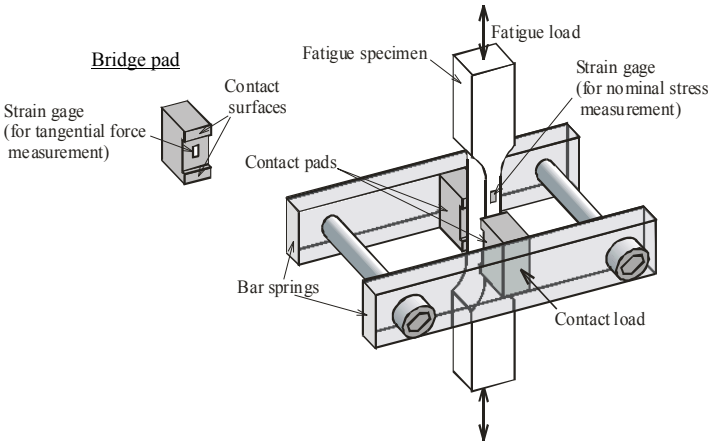

Figure 1. Fretting fatigue test method

2.2. Material

The test materials were three kinds of austenitic stainless steels, JIS SUS304, SUS316 and SUS316L. The chemical compositions of the materials are listed in Table 1. A solution heat treatment was done to the materials by quenching following heating at 1303K for 3.9ks.

Since fretting is a surface phenomenon, hydrogen diffusion into the material is one of the important issues. Therefore, hydrogen pre-charged materials were used in a part of the fretting fatigue test. The method of hydrogen pre-charging was thermal hydrogen charging.

Table 1. Chemical composition

Material	C	Si	Mn	P	S	Ni	Cr	Mo	Fe
SUS 304	0.06	0.51	0.92	0.033	0.004	8.08	18.8	-	Bal.
SUS 316	0.05	0.49	1.31	0.030	0.027	10.22	17.0	2.04	Bal.
SUS 316L	0.012	0.19	1.64	0.031	0.012	12.19	16.6	2.22	Bal.

3. Effect of hydrogen on fretting fatigue strength

3.1. *S-N* curves

Figure 2 shows the fretting fatigue *S-N* diagrams. For the SUS304, the fretting fatigue strength of the uncharged material was significantly lower in the hydrogen than in air (□ and ○). The effect of hydrogen pre-charging is also shown in Fig. 2. The details of the hydrogen pre-charging are found in ref. [1]. In air, the fretting fatigue strength was significantly reduced by the hydrogen pre-charging (● and ○). The fretting fatigue strength of SUS304 is reduced by not only gaseous hydrogen, but also internal hydrogen. When the fretting fatigue test of the hydrogen-charged material was done in hydrogen, the reduction in the fretting fatigue strength was very significant (■). The gaseous hydrogen and internal hydrogen synergistically works in decreasing the fretting fatigue strength. The mechanisms will be discussed in the latter part of this paper.

Figure 2 also shows the fretting fatigue strength of SUS316L. A failure of the hydrogen-charged specimen occurred at the fretting fatigue limit of the uncharged material. There was a trend that the finite life of the hydrogen-charged material was shorter than that of the uncharged material. Although the amount of the reduction in the fretting fatigue was small compared to SUS304, hydrogen reduced the fretting fatigue strength of the SUS316L. Since this material is recognized as a hydrogen compatible material [4, 5], the result which shows the reduction in fatigue strength is important for the design of hydrogen equipment. The hydrogen embrittlement during the fatigue of SUS316L was also reported by Murakami et al [6].

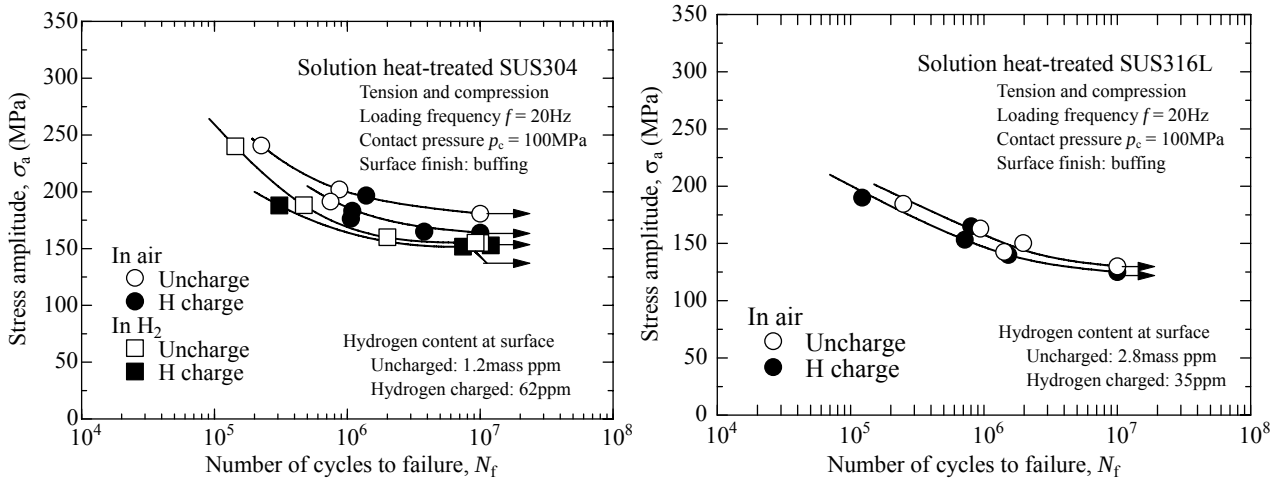

(a) Solution heat-treated SUS304 (b) Solution heat-treated SUS316L

Figure 2. Effect of hydrogen on fretting fatigue strength

3.2. Mechanism that causes the reduction in fretting fatigue strength due to hydrogen

3.2.1. Local adhesion between contacting surfaces

Figure 3 shows the characteristic phenomenon that occurs during fretting fatigue in hydrogen. The specimen and contact pad adhered to each other during the fretting fatigue in hydrogen. During the fretting in air, oxidized fretting wear particles separate the specimen and pad. In air, the fretting damage is produced by an oxidation dominant process. On the other hand, during the fretting in non-oxidative environments, such as a vacuum [7] or nitrogen [8], the fretting damage mechanism changes to an adhesion dominant process. In hydrogen, a similar mechanism may occur.

Figure 3 also shows the tangential force coefficient in each environment. An increase in the tangential force in hydrogen is clearly shown. The adhesion between the contacting surfaces is the cause of the increased tangential force in hydrogen. The stress conditions on the fretted surface are determined by the fatigue stress, contact stress and tangential stress due to friction [9]. The tangential force is a dominant factor of the fretting fatigue strength [10]. The increase in the tangential force in hydrogen causes an increase in the mechanical stresses on the contact surface. Consequently, the increase in the tangential force due to adhesion is one of the possible reasons for the reduced fretting fatigue strength in hydrogen.

Figure 4 shows the section along the specimen axis of the adhered specimen and contact pad during the fretting fatigue test in hydrogen. There were many small cracks at the interface between the specimen and pad. The small cracks propagated in two directions at which the small cracks made angles of approximately 45 or 135 degrees to the contact surface. During the fretting fatigue in air, small oblique cracks and multiple small cracks are the typical characteristics [11]. However, the angle of the oblique small cracks is constant [12]. Furthermore, the small cracks observed in this experiment propagated into both the specimen and the contact pad. Fretting fatigue cracks are

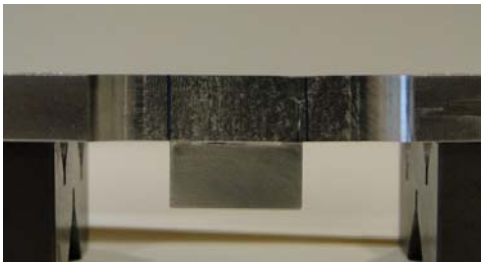

(a) Adhered specimen and contact pad (SUS316L, uncharged, σ_a = 200MPa, $N_f = 5.4\times10^5$)

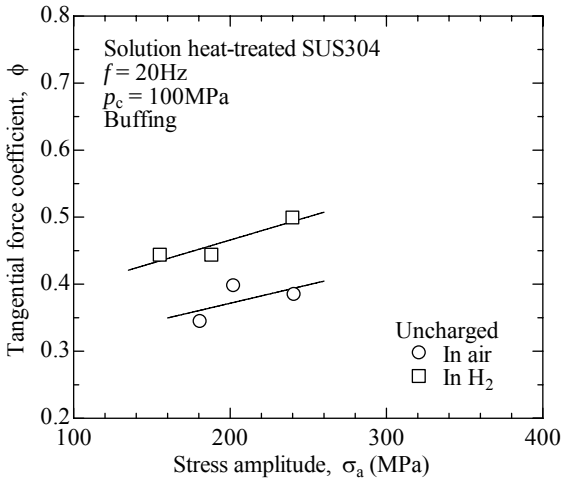

(b) Increase in tangential force coefficient

Figure 3. Adhesion between contacting surfaces during fretting fatigue test in hydrogen

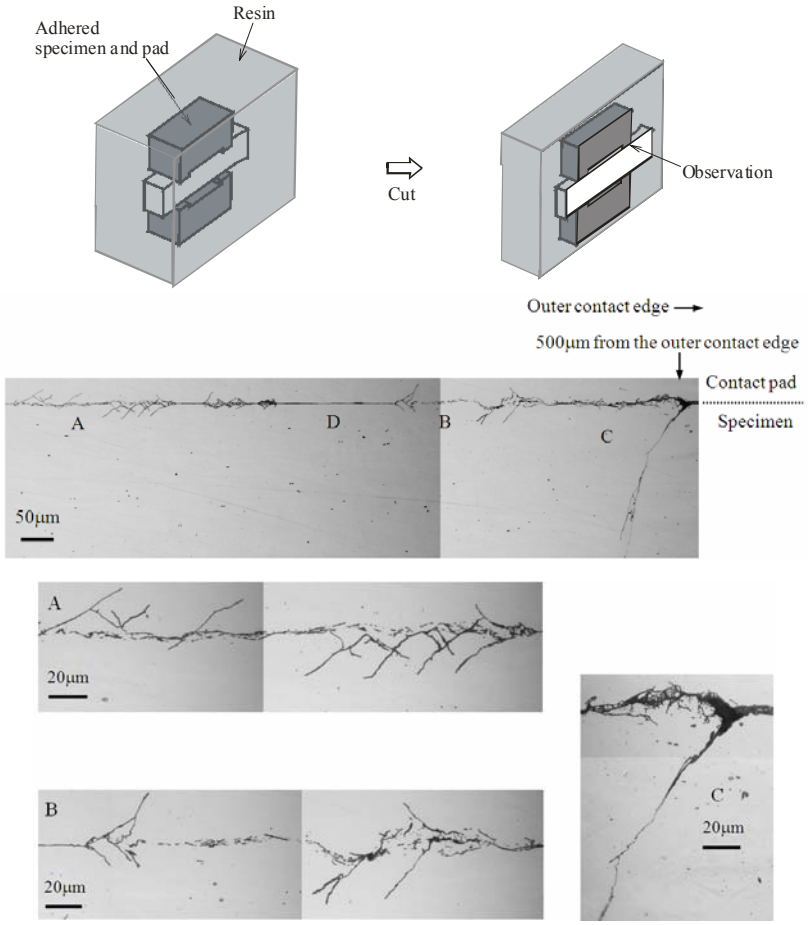

Figure 4. Observation of adhered part at the longitudinal section of the adhered specimen and pad (SUS304, σ_a = 180MPa, $N = 1.0\times10^6$).

typically found in a specimen because no fatigue stress is applied to the contact pad. The morphology of the small fretting fatigue cracks in hydrogen was unique compared to that observed in air.

If a contact pad is simply placed on the specimen without fretting, the boundary of the specimen and pad should be a straight line. However, at positions A, B and C, the interface was not

continuous and winding. These are microscopic evidence of adhesion. At position D where a straight line was observed, there was no fretting fatigue cracks. Therefore, the formation of the small cracks is related to the local adhesion.

There was a major crack leading to specimen failure at position C. The major crack started to grow from one of the small cracks that emanated from the adhered spot. Therefore, the adhesion and the subsequent formation of many small cracks are one of the root causes of the reduced fretting fatigue strength in hydrogen. Based on this observation, a model to describe the fretting fatigue failure in hydrogen is shown in Fig. 5.

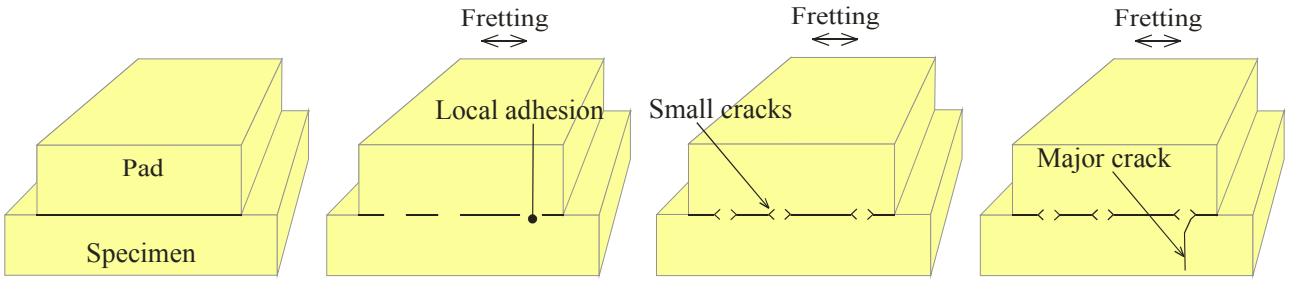

(a) Before test (b) Local adhesion (c) Crack initiation (d) Specimen failure

Figure 5. Model to cause fretting fatigue failure in hydrogen

3.2.2. Effect of hydrogen on fretting fatigue crack initiation

Figure 6 shows the test method used to investigate the effect of hydrogen on the initiation of a fretting fatigue crack. The specimen and contact pads were welded using a spot welding machine to mimic adhesion during fretting fatigue in hydrogen. A compressive load, which corresponds to the contact load in the fretting fatigue test, was applied. The fatigue test was interrupted at 10^5 cycles and identification of a small crack was then carried out. The details of the experiment are described in ref. [13].

Figure 7 shows an example of the fatigue crack in the adhesion mimic test. About 100 μm-deep cracks were found. The morphology of the cracks is similar to that observed in the fretting fatigue test in hydrogen as shown in the figure.

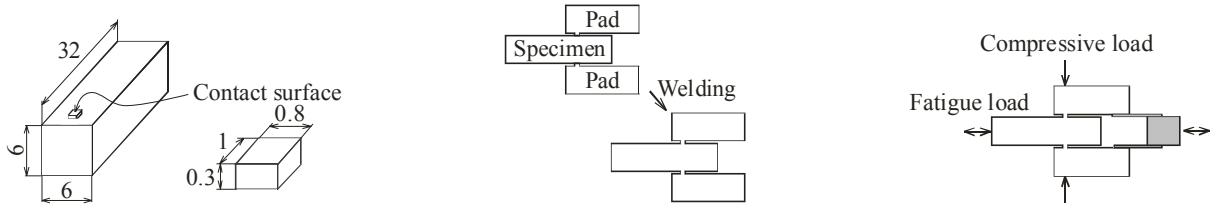

(a) Contact pad (b) Welding of specimen and pad (c) fatigue test method

Figure 6. Adhesion mimic fatigue test (dimensions are in mm)

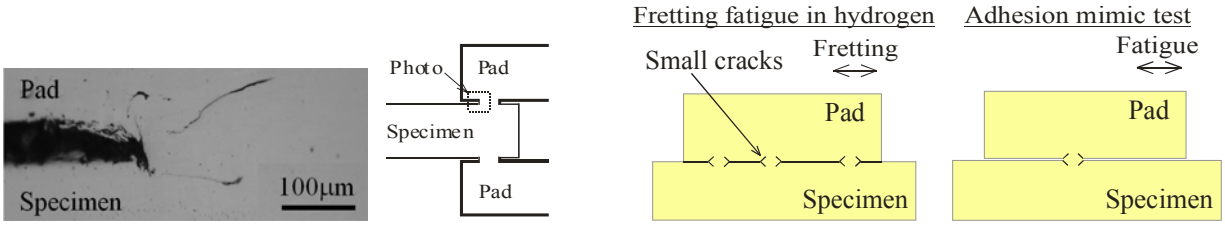

(a) Small crack in adhesion mimic test (b) Morphology of small crack

Figure 7. Observation of small cracks

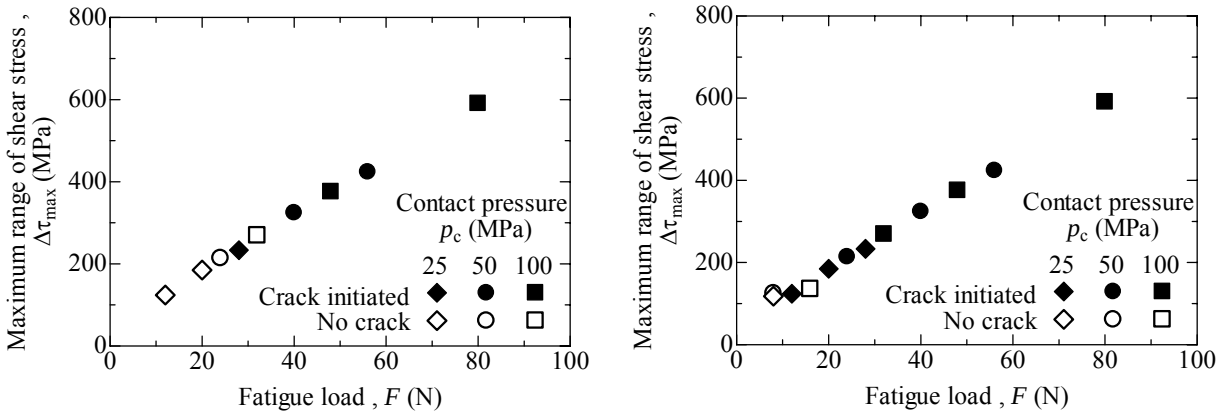

(a) In air (b) In hydrogen

Figure 8. Effect of hydrogen on crack initiation under adhesion condition

The result of the local adhesion mimic fatigue test is shown in Fig. 8. The maximum range of shear stress was obtained by an elastic-plastic finite element (FE) analysis [13]. The crack initiation occurred in a significantly lower maximum shear stress range in hydrogen than in air. It was confirmed that hydrogen assisted the crack initiation in this experiment. This is one of the mechanisms other than stress concentration due to local adhesion that causes a reduction in the fretting fatigue strength in hydrogen.

The maximum shear stress range was greater than the proof strength of the material. Since the regions with a higher strain attract more hydrogen [14] and mobile dislocations transport hydrogen [15], it is presumed that the local adhesion activates the hydrogen embrittlement. As further evidence, the authors confirmed the facilitating of crack initiation due to hydrogen in a low-cycle fatigue of austenitic stainless steel [16]. Furthermore, fretting wear removes the oxidized surface which may prevent the diffusion of hydrogen into the material. There is a possibility that such a higher stress causes a microstructure change from austenite to martensite. The microstructure change during the fretting fatigue will be described in the next section.

3.2.3. Microstructure change

Figure 9 shows the result of the electron backscatter diffraction (EBSD) observations of the adhered part. Alpha-prime, which is considered to be strain-induced martensite, was detected at the adhered part. Martensite is vulnerable to hydrogen. Besides this, the diffusivity of hydrogen is significantly greater in the martensitic phase than in the austenitic phase [17]. As a result, the transformed martensite in the austenitic stainless steel can act as a low resistance diffusion pathway for hydrogen diffusion [18]. The transformation of the microstructure is one of the important mechanisms that cause a reduction in the fretting fatigue strength in hydrogen.

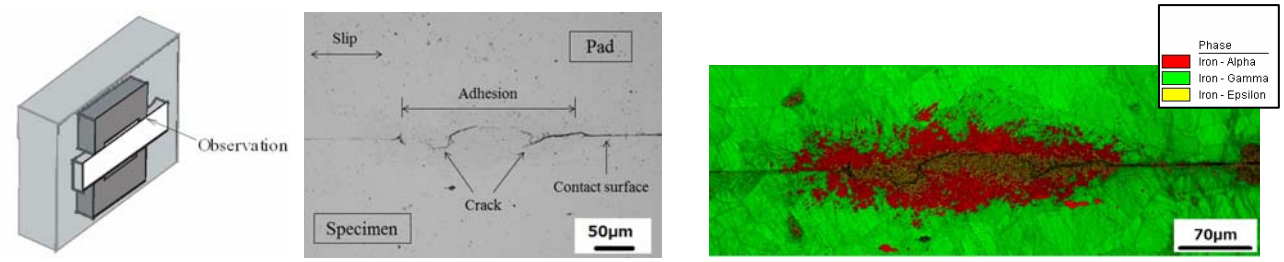

(a) SEM image (b) Phase map obtained by EBSD

Figure 9. Microstructure change due to local adhesion between fretting surfaces
(SUS316, σ_a = 182MPa, $N_f = 10^6$)

3.2.4. Reduction in fatigue threshold by absorbed hydrogen

Figure 10 shows the result of the crack growth test. The details of the test method are found in ref. [19]. In the hydrogen-charged specimen, the reduction in the threshold stress intensity factor, ΔK_{th}, is clearly shown. The reduction in ΔK_{th} is one of the causes of the reduced fretting fatigue strength by a hydrogen charge. The fretting fatigue limit of both the hydrogen-charged and uncharged materials can be quantitatively evaluated by the model based on the ΔK_{th} [19].

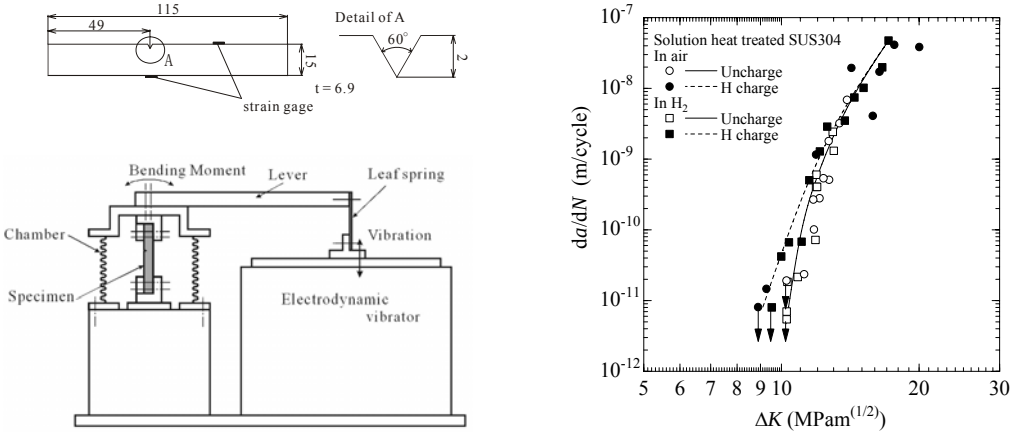

(a) Specimen and test method (b) Crack growth curves

Figure 10. Effect of hydrogen on crack growth threshold of SUS304

4. Effect of work-hardening

Work-hardening is a fundamental method of increasing the strength of austenitic stainless steels. Strengthened austenitic stainless steels are frequently used for high-pressure components. A 40% plastic strain was applied to the solution heat-treated materials by the tensile test at room temperature. The mechanical properties of the work-hardened austenitic stainless steels are shown in Table 2.

Figure 11 shows the result of the fretting fatigue test of the work-hardened SUS304. When the fretting fatigue strength of the uncharged material in air was compared between the solution heat-treated material (Fig. 2) and work-hardened material, it was found that the work-hardening improved the fretting fatigue strength (○ in each graph). However, the reduced fretting fatigue strength due to hydrogen was almost equivalent between the solution heat-treated material and the work-hardened material. The effect of the work-hardening was suppressed by the hydrogen. This indicates that special consideration is required in the design of hydrogen equipment made of work-hardened austenitic stainless steels.

5. Effect of surface roughness

For mechanical components requiring a gas tightness, surface roughness is one of the design factors. Figure 12 shows the fretting fatigue *S-N* curves of SUS316 in which the specimens have two

Table 2. Mechanical properties and Vickers hardness

Material	Conditions	Proof strength $\sigma_{0.2}$ (MPa)	UTS σ_B (MPa)	Elongation δ (%)	Vickers hardness HV
SUS304	Solution heat-treated	294	667	60	242
	40% pre-strained	955	1027	26	358

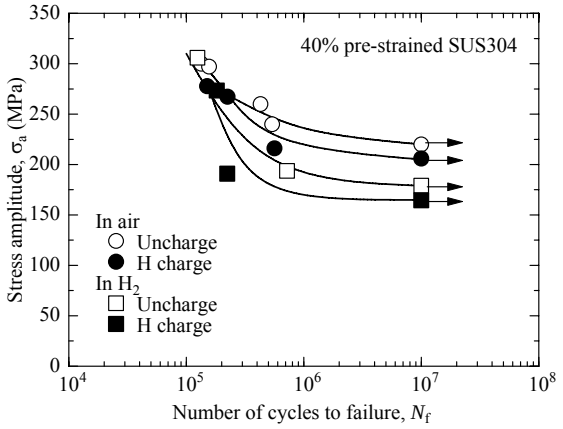

Figure 11. Effects of work-hardening and hydrogen on fretting fatigue strength of SUS304.

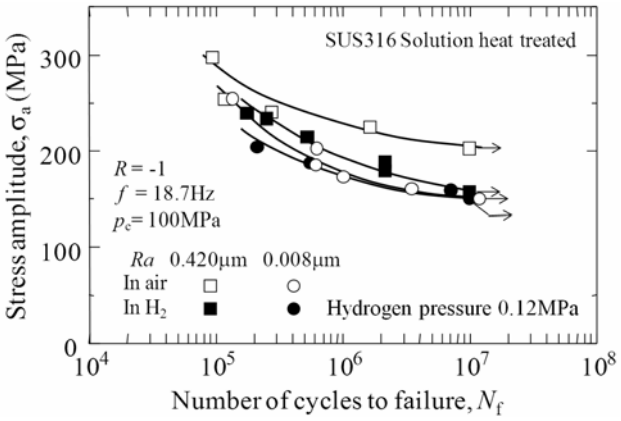

Figure 12. Effects of surface roughness and hydrogen on fretting fatigue strength of SUS316.

different contact surface roughnesses. The smoother surface specimen showed a considerably lower fretting fatigue strength than the rougher surface one (○ and □). The effect of hydrogen was significant in the rougher surface specimen (□ and ■), but not so in the smoother surface specimen (○ and ●).

These results can be interpreted by the crack nucleation mechanism. Figure 13 shows the major crack in the smoother surface specimen used for the fretting fatigue test in air. The major crack started to grow from the locally adhered spot similar to that observed in hydrogen. That is, when the contact surface has an extremely low surface roughness, adhesion occurred even in air and the adhesion played a dominant role in causing the fretting fatigue failure.

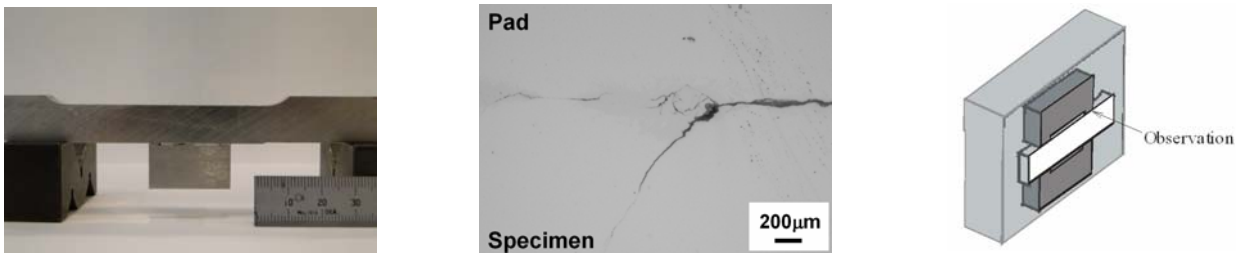

(a) Adhered specimen and pad (b) Major crack emanated from adhered spot

Figure 13. Fretting fatigue test of smooth contact surface specimen in air

6. Effect of hydrogen content

Figure 14 shows the fretting fatigue strength of the SUS316 for specimens having different hydrogen contents. The hydrogen content in the material was increased by the thermal hydrogen charging at 573K for 200h. The fretting fatigue strength of the SUS316 decreased with an increase in the hydrogen content.

7. Effect of hydrogen-containing oxygen as minor impurity

The purity of hydrogen used in hydrogen equipment is one of the most important concerns in terms of the performance of hydrogen equipment and the cost of hydrogen. Figure 15 shows the effect of oxygen addition on the fretting fatigue strength of the SUS304 in hydrogen. The oxygen content was 100vol ppm. The fretting fatigue strength in the oxygen-hydrogen mixture was between that in the pure hydrogen and in air.

One of the causes of the increase in the fretting fatigue strength in the oxygen-hydrogen mixture is the reduction of the tangential force between the contacting surfaces due to generation of oxidized fretting wear particles. Another cause is the increase in the crack initiation limit. Based on the adhesion mimic test (section 3.2.2), the critical maximum shear stress range to crack initiation in the hydrogen-oxygen mixture was between that in hydrogen and air [20].

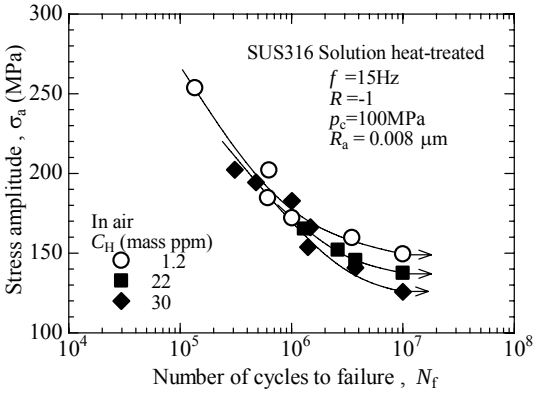

Figure 14. Effect of hydrogen content on fretting fatigue strength of SUS316

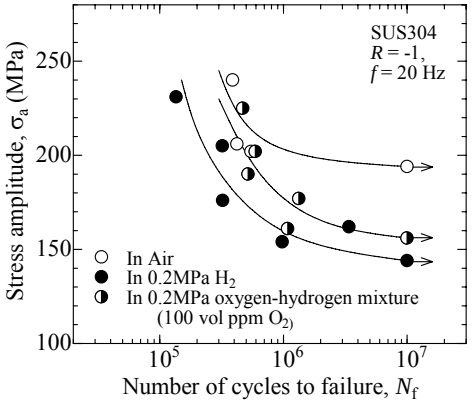

Figure 15. Effect of addition of oxygen on fretting fatigue strength of SUS304 in hydrogen

8. Conclusions

Fretting fatigue is one of the major concerns in various engineering fields such as railway, energy, aviation, automobile, etc., because fretting fatigue strength is significantly lower than the fatigue strength of a smooth specimen. This study showed the additional reduction in fretting fatigue strength due to hydrogen. The major results can be summarized as:

- ***S-N* curves:** the fretting fatigue strength of SUS304 and SUS316L is reduced by gaseous hydrogen. When the fretting fatigue test of the hydrogen-charged material, such as SUS304 was done in hydrogen, the reduction in the fretting fatigue strength was more affected due to the synergistic effect of gaseous hydrogen and internal hydrogen;
- **Mechanisms that cause the reduction in fretting fatigue strength in gaseous hydrogen:** The first mechanism is explained by the action of hydrogen as the cause for local adhesion between contacting surfaces in fretting-fatigue samples of both SUS304 and SUS316L. The second one is the microstructure change to martensite in the local adhesion part. Both mechanisms will act together in lowering the fretting fatigue strength of these stainless steels in contact with gaseous hydrogen;
- **Reduction in fatigue threshold by absorbed hydrogen:** The reduction in ΔK_{th} is one of the causes of the reduced fretting fatigue strength by a hydrogen;
- **Effect of surface roughness:** The effect of hydrogen was significant in the rougher surface specimen, but not so in the smoother surface specimen. Rough surfaces present more stress concentrators to attract hydrogen;
- **Effect of hydrogen content:** The fretting fatigue strength of the SUS316 decreased with an increase in the hydrogen content;
- **Effect of hydrogen-containing oxygen as minor impurity:** The oxygen content of 100vol ppm in gaseous hydrogen had a beneficial effect by improving fretting fatigue strength of SUS304. Even at this low impurity level, oxygen causes the reduction of the tangential force between the contacting surfaces due to generation of oxidized fretting wear particles, and the increase in the crack initiation limit.

Despite all these findings, additional work is needed to better explore the mitigating effects of oxidizing impurities in hydrogen environments.

Acknowledgements

This work has been carried out in the donated laboratory by the AIR LIQUIDE, France and AIR LIQUIDE JAPAN. A part of this work has been supported by the NEDO project "Fundamental Research Project on Advanced Hydrogen Science" (2006-2012). This work was also supported by the World Premier International Research Center Initiative (WPI), MEXT, Japan. The International Institute for Carbon-Neutral Energy Research (WPI-I2CNER) is supported by the World Premier International Research Center Initiative (WPI), MEXT, Japan.

References

[1] Y. Kondo, M. Bodai, Study on fretting fatigue crack initiation mechanism based on local stress at contact edge. Trans. JSME, A63-635 (1997) 1567-1572.
[2] M. Kubota, T. Nishimura, Y. Kondo, Effect of hydrogen concentration on fretting fatigue strength. Journal of solid mechanics and materials science, 4-6 (2010) 1-14.
[3] M. Kubota. et al., Mechanism of reduction of fretting fatigue limit caused by hydrogen gas in SUS304 austenitic stainless steel, Tribology international, 44 (2011) 1495-1502.
[4] NASA, Safety standard for hydrogen and hydrogen systems, NSS 1740.16 (1997).
[5] Japan Automobile Research Institute, JARI S 001 (2004).
[6] Y. Murakami, T. Kanezaki, Y. Mine, S. Matsuoka, Hydrogen embrittlement mechanism in fatigue of austenitic stainless steels, Metallurgical and materials transactions, 39A (2008) 1327-1339.
[7] A. Iwabuchi, T. Kayaba, K. Kato, Effect of atmospheric pressure of friction and wear of 0.45%C steel in fretting wear. Wear, 91(1983) 289-305.
[8] B. Bethune, R. B. Waterhouse, Adhesion of metal surfaces under fretting conditions. I. Like metals in contact. Wear, 12 (1968) 289-296.
[9] S. Faanes, U. S. Fernando, Life prediction in fretting fatigue, in: R. B. Waterhouse, T. C. Lindley (Eds.), Fretting fatigue, ESIS publication 18, Mechanical Engineering Publications Limited, London, 1994, pp. 149-159.
[10] K. Nishioka, K. Hirakawa, Fundametal investigations of fretting fatigue (Part 5, The effect of relative slip amplitude), Bulletin JSME, 12-52 (1969) 692-697.
[11] Endo K, Goto H, Initiation and propagation of fretting fatigue cracks. Wear 1976; 38: 311-24.
[12] K. Nishioka, K. Hirakawa, "Fundamental investigation of fretting fatigue – Part 3. Some phenomena and mechanisms of surface cracks", Bulletin JSME, 12-51 (1969) 397-407.
[13] R. Komoda, M. Kubota, Y. Kondo, J. Furtado, Fundamental mechanisms causing reduction in fretting fatigue strength by hydrogen, Trans. JSME, Reviewing.
[14] K. A. Nibur, B. P. Somerday, D. K. Balch, C. San Marchi, The role of localized deformation in hydrogen-assisted crack propagation in 21Cr-6Ni-9Mn stainless steel. Acta Materialia, 57 (2009) 3795-3809.
[15] K. Horikawa, N. Ando, H. Kobayashi, W. Urushihara, Visualization of hydrogen gas evolution during deformation and fracture in SCM440 steel with different tempering conditions. Materials Science and Engineering, 534A (2012) 495-503.
[16] M. Kubota, et al., Effects of multiple overloads and hydrogen on high-cycle fatigue strength of notched specimen of austenitic stainless steels. Trans. JSME, 77A-782 (2011) 1747-1759.
[17] H. G. Nelson, J. E. Stein, Gas-phase hydrogen permeation through alpha iron, 4130 steel and 304stainless steel from less than 100C to near 600C. NASA TN D-7265 (1973).
[18] T. Kanezaki, C. Narazaki, Y. Mine, S. Matsuoka, Y. Murakami, Effects of hydrogen on fatigue crack growth behavior of austenitic stainless steels. Hydrogen energy, 33 (2008) 2604-2619.
[19] K. Mizobe, Y. Shiraishi, M. Kubota, Y. Kondo, Effect of hydrogen on fretting fatigue strength of SUS304 and SUS316l austenitic stainless steels. Proc. the JSME/ASME 2011 International Conference on Materials and Processing ICM&P2011, 2011, Corvallis, OR, USA.
[20] M. Kubota, Y. Adachi, Y. Shiraishi, R. Komoda, J. Furtado, Y. Kondo, Effect of hydrogen and addition of oxygen on fretting fatigue properties, Proceedings of 2012 Hydrogen conference, 2012, Moran, WY, USA.

Hydrogen Effect on Fatigue Crack Initiation Behavior of Structural Materials

Ryuichiro Ebara*
Institute of Materials Science and Technology, Fukuoka University, Fukuoka-city, 814-0180,Japan
* ebara@gold.megaegg.ne.jp

Abstract Hydrogen effect on fatigue crack initiation behavior of structural materials related to the internal hydrogen embrittlement and hydrogen environment embrittlement is reviewed. Mechanisms of hydrogen effect on fatigue crack initiation behavior of structural materials are briefly summarized. The emphasis is focused upon the hydrogen related corrosion fatigue crack initiation behavior of structural materials in aggressive gas and sour crude oil environments. Finally recommended researches in hydrogen effect on fatigue crack initiation of structural materials are touched on briefly.

Keywords Hydrogen, Fatigue, Corrosion fatigue, Corrosion pit, Crack initiation

1. Introduction

Hydrogen effect has been investigated on structural materials used for important machinery components in oil and energy related industries so far. It is well recognized that hydrogen drastically accelerate crack propagation rate of structural materials [1]. However hydrogen effect on crack initiation behavior of structural materials is not well understood. Prevention of hydrogen related fatigue crack initiation of structural materials is indispensable for safety use of fuel cell vehicle and hydrogen fueled internal combustion engine yet to come[2,3]. In this paper hydrogen related fatigue crack initiation behavior of structural materials is reviewed mainly on the basis of the author's experimental results. First the proposed mechanisms of hydrogen effect on fatigue crack initiation and propagation behavior of structural materials are briefly summarized. Then the corrosion related fatigue crack initiation behavior of structural materials in steam, humid air and aqueous solution including industrial gas such as H_2S, SO_2 and CO_2 are summarized. Hydrogen related corrosion fatigue crack initiation behavior of ship hull structural steels in sour crude oil environment is also emphasized. Finally recommended studies in hydrogen effect on fatigue crack initiation behavior of structural materials are touched on briefly.

2. Mechanism of hydrogen effect on fatigue crack initiation behavior of structural materials

It has been well recognized that fatigue strength of structural materials is affected by oxygen and humidity in air. Therefore oxygen effect on fatigue crack initiation of structural materials has been well investigated. The mechanisms for oxygen effect on fatigue crack initiation such as the oxygen intake mechanism with dislocation motion [4] were proposed so far. However the decisive mechanism for hydrogen effect on fatigue crack initiation has not yet proposed so far. Hydrogen effect on fatigue strength of mild steel with round notched plate specimen was not significant as compared with effect of oxygen and humidity [5]. Suzuki et al. conducted low cycle fatigue tests for normalized S45C round bar specimens with different purity with P,S,N,O and Al in order to investigate the pre-charged hydrogen effect [6]. The pre-charged hydrogen effect on low cycle fatigue life was not significant for high purity S45C steel. On the contrary low cycle fatigue life of low purity S45C steel was 50 to 90 % lower than that of conventional normalized S45C steel. They concluded that cyclic softening reduce the dislocation density in S45C steel with high purity and make the steel insensitive to hydrogen. Low cycle fatigue tests were also conducted for 21/4 Cr-1Mo steel in high temperature and

high pressure hydrogen environment (P_{H_2}:24.5MPa,733K) [7].The low cycle fatigue life was50% lower than that in nitrogen environment. The low cycle fatigue life in hydrogen environment was dependent on loading frequency and the hydrogen effect on crack initiation was observed. In order to ensure the safety of pipe and vessel used in high pressure hydrogen gaseous environment Nakamura et al. conducted cyclic pressurization fatigue tests for plane and pre-cracked austenitic stainless steels such as SUS304 steel, SUS316 steel, 32% cold worked SUS316 steel, precipitation hardening A286 steel and SCM435 low alloy steel with different tensile strength in hydrogen environment (P_{H_2}:35MPa) [8]. The stable austenitic stainless steel SUS316 showed no reduction of fatigue life in high pressure hydrogen gaseous environment. In contrast significant reduction of fatigue life was observed on metastable SUS304 steel, precipitation hardening A-286 steel and SCM 435 steels. They concluded that hydrogen condensation at austenitic phase for metastable 304 steel and hydrogen trapping at cementite for A286 steel is the cause of fatigue life reduction in high pressure hydrogen embrittlement.

Fatigue crack propagation process in structural materials is significantly affected by hydrogen. It has been reported that fatigue crack propagation rate was significantly accelerated by hydrogen for various kinds of structural materials such as Nickel base alloy, Inconel 718 and Waspaloy for space shuttle engine[9], 21/4Cr-1Mo steel[10],mild steel,HT790 steel[11],low alloy steel, super dual phase stainless steel,super ferritic stainless steel[12,13] and BS4360 steel[14]. R.P.Wei proposed hydrogen embrittlement mechanism at local stressed area ahead of crack tip [15]. Hydrogen by transportation process diffused into the local processed area (fracture zone) where embrittlement reaction occurs. Quantitative relation of plastic zone size during fatigue crack propagation and hydrogen embrittlement fracture zone size is recommended to evaluate. The potential hydrogen trap site might be martensite laths, carbides, sulfides or oxy sulfides[16].Certain gaseous activities to a hydrogen atmosphere can stop a running crack in 4340 steel[17].The hydrogen-metal interactions was prevented by the addition of gaseous specie such as O_2,CO_2 and N_2O[18]. In the results of accelerated fatigue crack propagation rate by hydrogen fracture surfaces such as intergranular, cleavage and quasi cleavage are predominantly observed [18,19 and 20].

Hydrogen effect on fatigue crack initiation in structural materials seems not to be prominent as compared with that on fatigue crack propagation. Nagumo explained that hydrogen embrittlement fracture surface is characterized by hydrogen assisted nano scale failure such as vacancy defect and dislocation interaction in ductile fracture process [21]. Hydrogen embrittlement is deeply related to plastic slip [22, 23]. The microscopic mechanism related to dislocation motion is recommended to investigate in order to understand hydrogen effect on fatigue crack initiation of structural materials more in detail.

3. Hydrogen related corrosion fatigue crack initiation behavior of structural materials

In order to determine the design stress of machinery components in oil and energy related industries it is indispensable to consider the effect of gaseous environment such as H_2, H_2S, SO_2 and CO_2, and sour crude oil on fatigue strength of structural materials. However, these environments are aggressive and injurious to human health. Therefor corrosion fatigue data under such aggressive environments are very few to find because of difficulty to conduct corrosion fatigue testing.

3.1 Effect of aggressive gas in steam and humid air

Fig. 1 shows S-N diagrams of plain bar specimens for 12Cr stainless steel and Ti-6Al-4V alloy in steam containing industrial gases such as H_2S and CO_2[24]. Reduction of corrosion fatigue strength in 12 Cr stainless steel is 87.5% in steam containing 20ppm H_2S gas, while the reduction of corrosion fatigue strength in Ti-6Al-4V alloy is only 4%. The SO_2 gas effect in humid air was as same as that of H_2S gas in humid air. The CO_2 gas effect in steam was not remarkable as compared with that of H_2S gas in steam. In the results of fatigue crack propagation tests with frequency of 30 Hz for 12 Cr plate specimen the effect of 20ppm H_2S gas containing in humid air on corrosion fatigue crack propagation rate of 12 Cr stainless steel was scarcely noticeable. Therefore it can be concluded that the major cause of the reduction in corrosion fatigue strength of 12Cr stainless steel is acceleration of corrosion fatigue crack initiation by H_2S gas in steam and humid air. In fact fracture surface observations revealed that crack initiated at a corrosion pit with about 10 μm depth and propagated in association with intergranular fracture as shown in Fig.2.

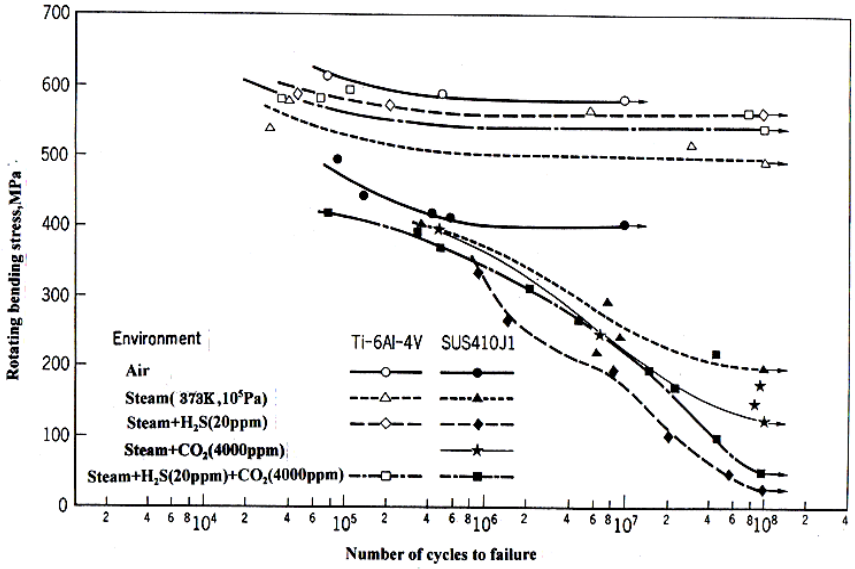

Figure1. Influence of industrial gas in steam on fatigue strength of SUS410J1and Ti-6Al-4V[Ebara[24]].
Rotating bending, 60Hz, R=－1

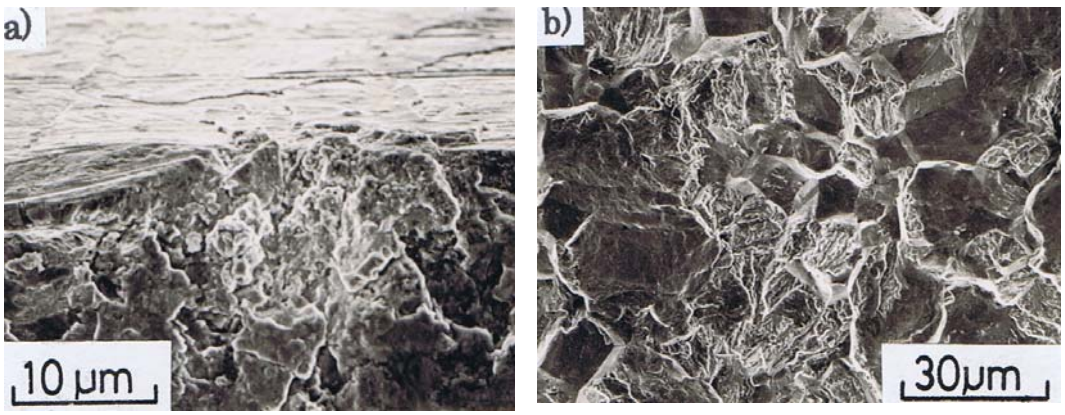

Figure 2. Corrosion fatigue fracture surface of 12 Cr stainless steel in 20ppm H_2S and 4000ppm CO_2 in steam［Ebara[24]］.
171.6MPa, 2.36X10^7cycles
a) Corrosion pit at initiation area
b) 2mm from initiation

The corrosion pit initiated in the result of reaction between 12Cr stainless steel and H_2S gas in humid air. Intergranular fracture surface was induced by hydrogen occurred in the corrosion reaction.Fig.3 also shows plane bending corrosion fatigue testing results for T type welded joints of high 17-4PH stainless steel 5000ppm H_2S and 99.9% CO_2 gas in a humid air[25]. The remarkable reduction of corrosion fatigue strength of T type welded joints can be observed. The similar results were obtained on AISI410 and AISI4330 steel [26]. The higher the ultimate tensile strength of the steel, the larger the influence of H_2S gas environment was. In 5000ppm H_2S and 99.9% CO_2 environment corrosion fatigue crack initiated from corrosion pit at welded toe. Striation was predominant at crack propagation area. Typical fracture surface of 17-4 PH steel in humid H_2S gas environment is shown in Fig. 4. The following reaction can be considered.

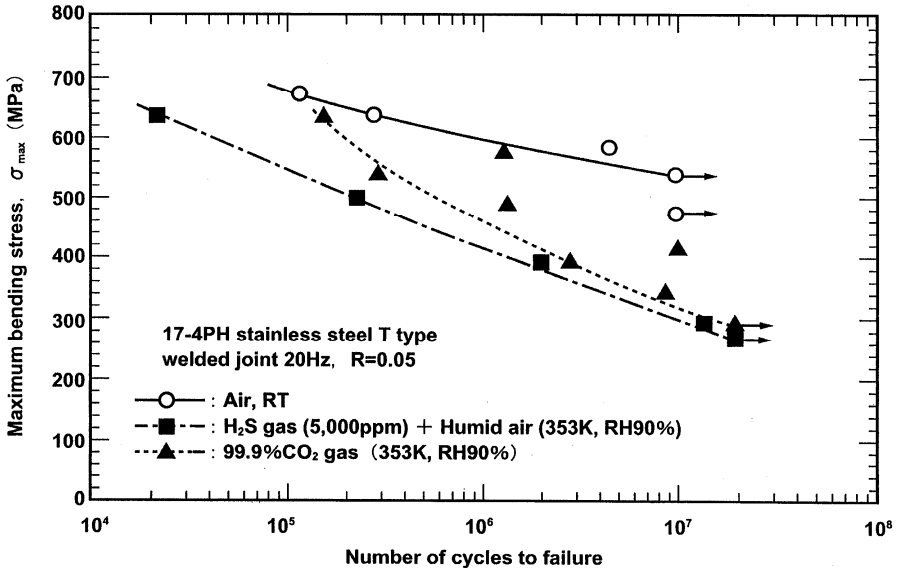

Figure 3. S-N curves of T type welded joints of 17-4pH T type welded joints in H_2S and CO_2 gas environment［Ebara et al. [26]］.
Plane bending, 20Hz, R=0.05

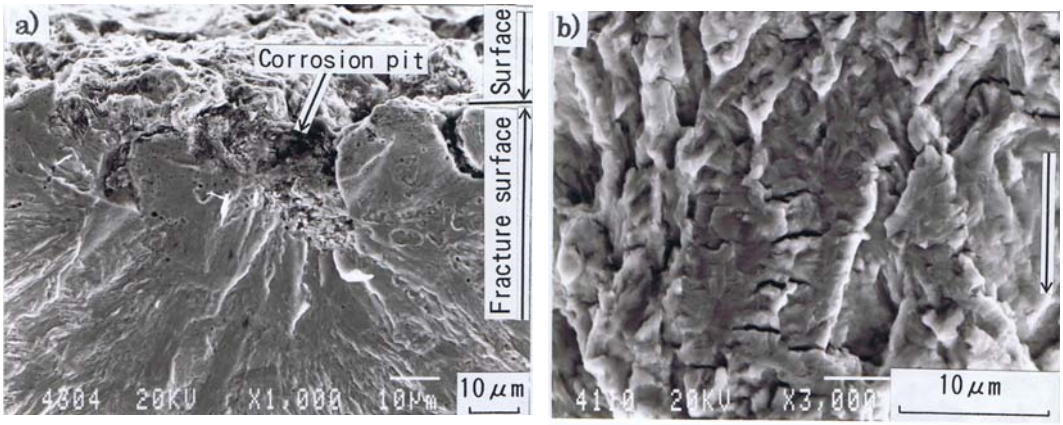

Figure 4. Corrosion fatigue fracture surface of 17-4pH T type welded joint in humid air(353K, 90% relative humidity) containing 5000ppm H_2S gas［Ebara et al.[26]］.
294.3MPa,1.4x10 ^{7}cycles
a) corrosion pit at crack initiation area
b)3mm from initiation area,
Arrow shows crack propagation direction

In humid H_2S gas environment

$$Fe + H_2S \rightarrow FeS + H_2 \quad (1)$$

$$Fe + H_2S + H_2O + 3/2O_2 \rightarrow FeSO_4 + 2H_2 \quad (2)$$

In humid CO_2 gas environment

$$CO_2 + H_2O \rightarrow H_2CO_3 \quad (3)$$

$$Fe + H_2CO_3 \rightarrow FeCO_3 + H_2 \quad (4)$$

In the results of reaction between these steels' welded joints and aggressive gas such as H_2S and CO_2 corrosion products such as $FeSO_4$ and $FeCO_3$ were formed and corrosion pit initiated at corrosion fatigue crack initiation area. H_2 also evolved in the result of reaction. However the role of hydrogen in fatigue crack initiation is not understood well. Corrosion fatigue behavior of structural steels in geothermal steam environment at Onikobe and Katayama have been reported on power plant steels such as 13CrMo,12CrMoV,3.7NiCrMo and CrMoV. Reduction rate of corrosion fatigue strength of these steels was dependent on Cr content in steel. It was concluded that the major cause of corrosion fatigue strength reduction was stress concentration at corrosion pit formed at corrosion fatigue crack initiation area [27]. Corrosion fatigue strength reduction was also reported on AISI 403, AISI422 steel at Geysers geothermal steam [28] and 13Cr, 2.5NiCrMoV steel at Otake geothermal steam [28]. Fatigue life decrease of a medium carbon steel for compressor valve springs and sucker rods was observed in hydrogen sulfide environment[29].Quasi cleavage fracture and FeS reaction product was observed on fracture surface[30]. Thus it is apparent that major cause of reduction of corrosion fatigue strength of structural steels and welded joints in humid aggressive gas such as H_2S and CO_2 can be attributed to corrosion pit formed at corrosion fatigue crack initiation area. Mechanism of hydrogen effect on corrosion fatigue crack initiation in structural materials is still veiled in aggressive gas in steam and humid air.

3.2 Effect of aggressive gas in aqueous solution

Corrosion fatigue strength decrease of plain carbon steel used for machinery of oil and gas production in brine with H_2S was due to hydrogen effect [31]. The similar findings were obtained by plane bending and axial corrosion fatigue testing on oil well sucker rods [32,33]. Tsukada et al. conducted corrosion fatigue life tests for a SAE4135 steel and a modified SAE 4135 steel in a 0.5% percent acetic acid solution in saturated with H_2S gas [34]. The modification of SAE4135 steel consists of an increase in molybdenum content of 0.20 to 0.75 percent and addition of 0.036 percent columbium. Corrosion pits and sub cracks were severely observed at the corrosion fatigue crack initiation area of these steels in H_2S gas environment. High cycle corrosion fatigue strength for the modified steel was 66 percent higher than that of the standard steel. They concluded that the improvement was attributed to an increase in resistance of hydrogen embrittlement brought about by a higher tempering temperature which reduces the amount of phosphorus on grain boundaries, as well as the beneficial scavenging effects associated with the increase in molybdenum content and the presence of columbium. They also conducted crack propagation tests for both steels. However crack propagation behavior of these steels were similar and hydrogen effect was significant at lower ΔK region. Fatigue life decrease of weathering steel in artificial sea water saturated with H_2S [35] and work hardened nickel in hydrogen sulfide saturated water [36] were also observed.

3.3 Effect of aggressive gas in crude oil

Fig.5 shows S-N diagrams of high strength steel (HT50,TMCP) notched round bar specimen with stress concentration factor of 4.02 in air and in sour crude oil with 400ppm H_2S[37]. The

effect of sour crude oil on the fatigue life of round notched specimen is pronounced in high stress region and tends to decrease as decreasing the stress. At nominal stress of about 470MPa the fatigue life in the sour crude oil decreased to about 10 % of the fatigue life in air. Decreasing the stress the effect of sour crude oil on fatigue life decreased. At nominal stress of about 200MPa specimen did not fail after $2x10^6$ cycles. Fatigue life testing results on boxing fillet welded specimens in air and in sour crude oil are also shown in Fig 5. At axial stress of 150MPa specimen in sour crude oil did not fail even after 10 times of the number of cycles to fail in air. Macroscopic fracture surface observation for round notched bar specimen revealed that fatigue crack initiated at notched root as shown in Fig.6 a). It is apparent from SEM observation that corrosion pit was not observed at crack initiation area[Fig. 6 b)]. Brittle striation was predominant at crack propagation area [Fig.6 c)]. It is well understood that crack propagation rate of ship structural steels and line pipe steels is accelerated in sour crude oil environment[37,38 and 39]. Hydrogen effect on crack propagation rate of these steels and welded joints was drastically observed at high ΔK region. Cleavage fracture surface and brittle striation were predominant at crack propagation area. At axial stress of 196MPa a couple of small fatigue cracks initiated at notched root as shown in Fig.7 a).Figure 7.b) is one of the forced fracture surface from these cracks. The depth of the corrosion fatigue crack was 0.2mm and notched area was brown in color. But corrosion pit was not observed at fatigue crack initiation area [Fig.7 b)]. Ductile striation was predominant at crack propagation area [Fig.7c)]. This means that crack propagation rate was not affected by hydrogen in low stress region. After corrosion fatigue life test for 2393hrs crude oil exhibited less H_2O content (340 to 210ppm), lower pH value(7.3 to 4.3) and more total S content than those before test. All these facts suggest that hydrogen (H_2) was produced through the reaction of H_2O and H_2S in sour crude oil with steel. Thus, in high stress region it can be considered that atomic hydrogen (H) accumulated in the plastic zone at fatigue crack tip accelerate crack propagation rate and reduce the fatigue life of the specimen. In the low stress region, plastic zone size is small and hydrogen does not accelerate fatigue crack propagation rate. It is assumed that wedge effect [40] of crude oil retarded corrosion fatigue crack propagation rate of notched bar specimen and boxing fillet welded specimen. Corrosion fatigue mechanism in sour crude oil is schematically illustrated in Fig, 8. Corrosion fatigue behavior is a time dependent phenomenon. If corrosion pit formed at initiation area in

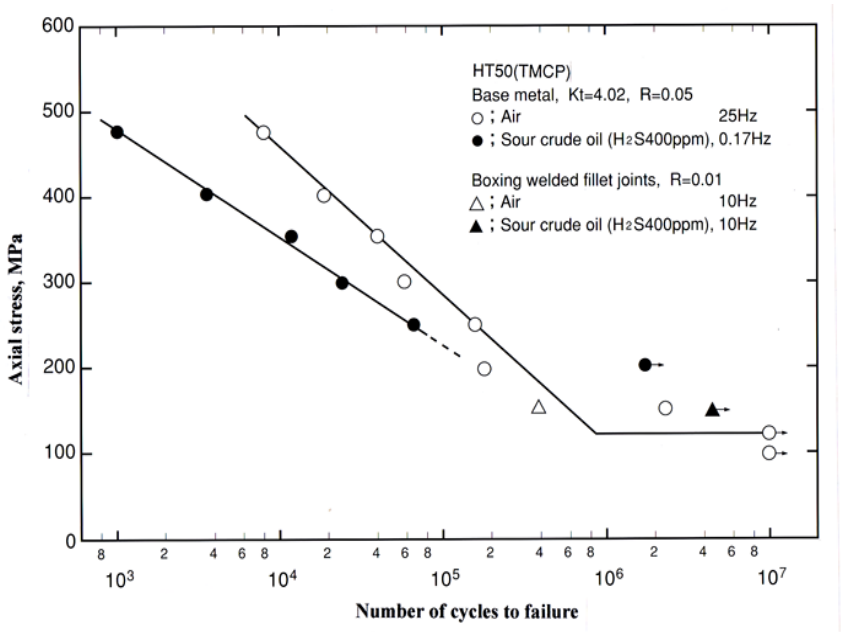

Figure 5. S-N curves of round notched HT50(TMCP) specimen in air and sour crude oil environment［Ebara et al.[37]］

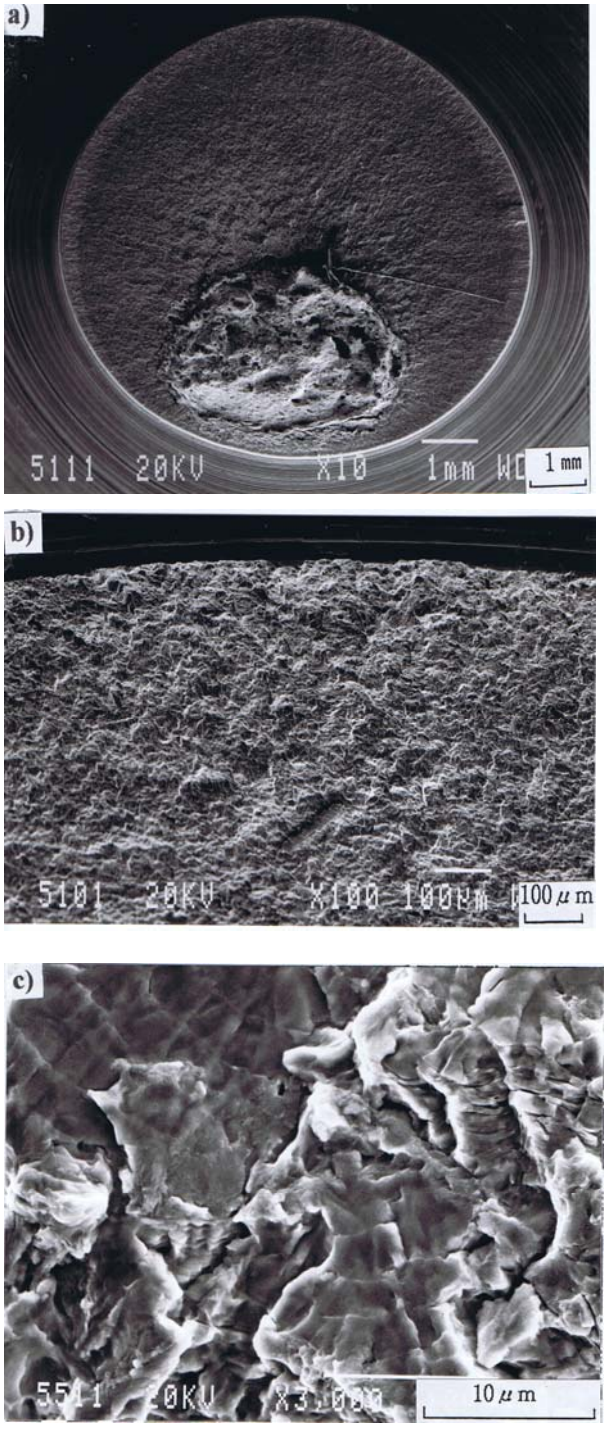

Figure 6. Corrosion fatigue fracture surface of HT50(TMCP) steel in sour crude oil (H_2S400ppm) [Ebara et al.[37]].
round notched bar specimen
294,2MPa,2x104 cycles
a) macroscopic fracture surface
b) crack initiation area
c) 1.8mm from initiation

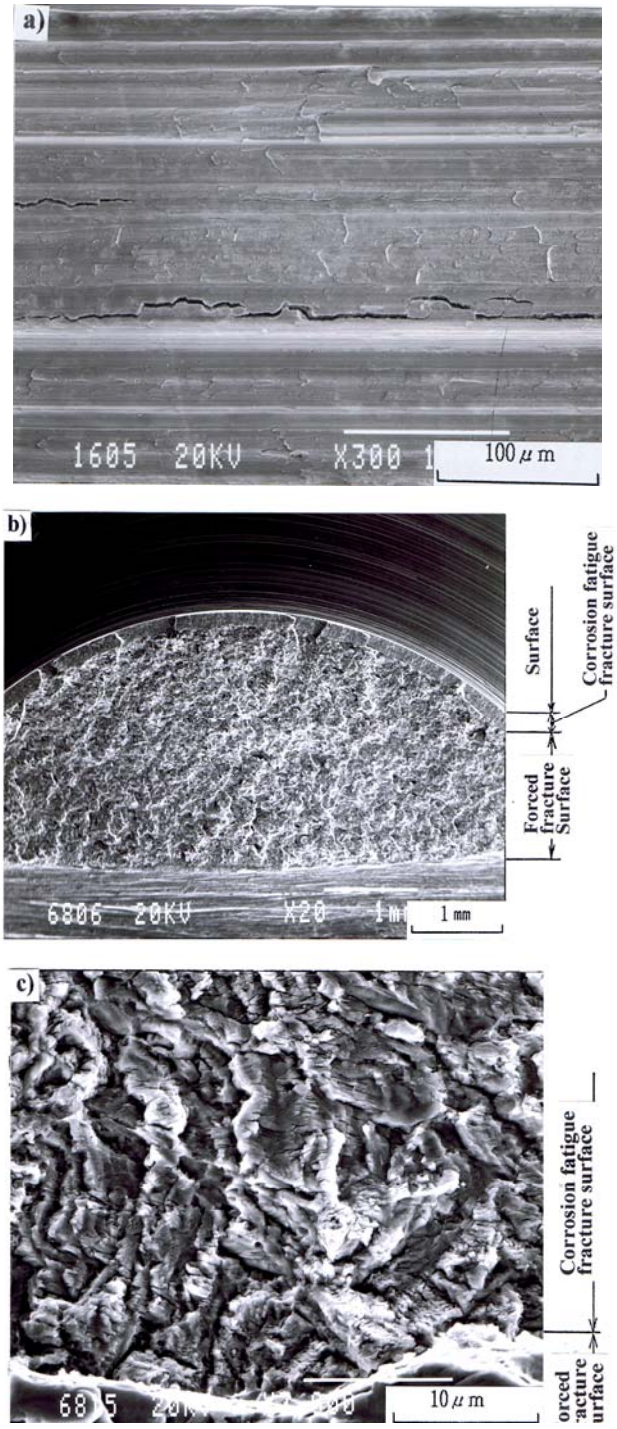

Figure 7.Surface crack and fracture surface of HT50(TMCP) steel in sour crude oil (H_2S400ppm) [Ebara et al.[37]].
round notched bar specimen
196.1MPa, unfailed after $1.66x10^6$ cycles
a) surface crack
b)macroscopic fracture surface
c) 0.12 mm from surface

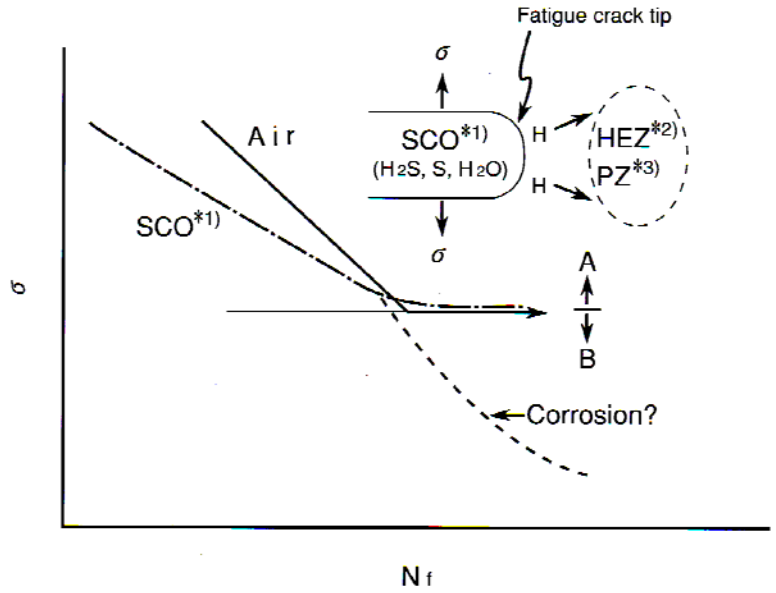

Figure 8. Schematic illustration of corrosion fatigue mechanism in sour crude oil environment[Ebara et al.[37]]. Note: *1) SCO:Sour Crude Oil *2) HEZ; Hydrogen Embrittlement Zone *3) PZ; Plastic Zone

lower stress level drastic reduction of corrosion fatigue strength may be anticipated. The long term corrosion fatigue test is expected to conduct in lower stress level.

4. Concluding remark

This paper has briefly summarized hydrogen effect on fatigue crack initiation behavior of structural materials. In aggressive gas such as H_2S, CO_2 and SO_2 in steam, humid air and aqueous solution corrosion fatigue crack initiation from corrosion pit reduce corrosion fatigue strength of structural materials. Under these environments it is stressed that corrosion pit initiated at fatigue crack initiation area drastically reduced fatigue strength of structural steels. On the contrary, in sour crude oil environment hydrogen from reaction of steel with H_2S accelerated corrosion fatigue crack propagation rate of steels. It can be concluded that hydrogen effect on corrosion fatigue crack initiation in sour crude oil is still veiled. For safety use of structural materials in hydrogen environment prevention of fatigue crack initiation is indispensable. Definite fatigue crack initiation mechanism in hydrogen environment is expected to propose. In order to evaluate the hydrogen related fatigue life of the structural components more precisely the following studies are recommended to investigate.

1) Microscopic crack initiation mechanism with dislocation motion
2) Quantitative evaluation of the relation between the plastic zone and hydrogen embrittlement zone size at the fatigue crack tip
3) Hydrogen effect on ΔK_{th} and near ΔK_{th} region in da/dN
4) Hydrogen resistant materials to prevent fatigue crack initiation

References

[1] R.Ebara,Hydrogen effect on fatigue strength of structural steels, Key Engineering Materials,261-263(2004)1251-1256.

[2] Y.Murakami, J.Nagata,Effect of hydrogen on high cycle fatigue failure of high strength steel,SCM435,J. of The Soc. of Materials Science,Japan,54(2005)420-427.
[3] K.Yokogawa, Hydrogen embrittlement and high pressure hydrogen storage in fuel-cell car, Invited Lecture, Zairyo-to Kankyo Annual Meeting at Chugoku-Shikoku Branch ,2007.
[4] F.E.Fujita,Oxidation and dislocation mechanisms in fatigue crack formation,Fracture of Solids,John wiley & Sons,1963,657-670.
[5] I.Masumoto,K.Ueda,R.Ebara,Effect of atmosphere on the fatigue strength of mild steel,J.of the Japan Welding Soc., 39(1970)771-778.
[6] G.Suzuki,K.Oishi,A.Kato,K.Tokuno,Y.Tsuchida ,Effect of hydrogen pre-charging on fatigue life on medium carbon steels of different purity,Tetsu-to-Hgane,98(2012)39-44.
[7] R.Ebara,Y.Kobayashi,H.Nakashima,H.Makimoto, Y.Kaji, Influence of stress on hydrogen embrittlement of pressure vessel steels,Paper presented for the 96th Annual Meeting of the Japn Inst.of Metals,1985.
[8] J.Nakamura,M.Miyahara,T.Omura,H.Senb ,M.Wakita,Fatigue properties and degradation mechanism for stainless steel in high pressure gaseous environment, J. of the Soc. of Materials Science,Japan,60(2012)1123-1129.
[9] P.Jewett, R.J.Walter ,W.T.Chandler,Influence of high pressure hydrogen on cyclic load crack growth in metals,Corrosion Fatigue Technology, ASTM STP642, H.L.Craig Jr.,T.W.Crooker and D.W.Hoeppner Eds.,1978,243-263.
[10] R.Brazill,G.W.Simons, R.P.Wei, Fatigue crack growth in 21/4Cr-1Mo steel exposed to hydrogen containing gases, J. of Engineeruing Materials and Technology,101(1979) 199-204.
[11] M.Tanaka,The influence of hydrogen gas on fatigue crack growth in low carbon structural steels, paper presented for Pacific Corrosion’87 ,1987.
[12] J.T.Marrow,C.A.Hippsley,J.E.King,Effect of hydrogen assisted fatigue crack propagation in duplex stainless steel,Acta metall. mater.,39(1991)1367-1376.
[13] J.T.Marrow,P.J.Cotterill ,J.E.King,Temperature effects on the mechanism of time independent hydrogen assisted fatigue crack propagation insteels, Acta metall.mater., 40(1992)2059-2068.
[14] P.J.Cotterill ,J.E.King,The Influence of a coal gasfier atmopsphere on fatigue crack growth rates in BS 4360 steel,Int.J. Fatigue,15(1993)27-30.
[15] R.P.Wei,On Understanding environment enhanced fatigue crack growth-A fundamental approach,Fatigue Mechanisms,ASTM STP675, J.T.Fong Edit.,1979,816-840.
[16] W.W.Gerberich,T.Livne,X.-F.Chen ,M.Kaczorowski,Crack growth from internal hydrogen-Temperature and microstructural effects 4340steel.Metallurgical Transactions, 19A(1988) 1319-1334.
[17] V.Skirishnan, P.J.Ficalora.Selective adsorption and hydrogen embrittlement, Metallurgical Transactions,7A(1976)1669-1675.
[18] J.D.Frandsen ,H.L.Marcus,Environmentally assisted fatigue crack propagation in steel, Metallurgical Transactions,8A(1977)265-272.
[19] I.M.Austen,P.McIntyre,Corrosion fatigue of high-strength steel in low-pressure hydrogen gas,Metal Science,13(1979)420-428.
[20] S.Fukuyama,K.Yokogawa,M.Araki,Fatigue crack growth of SNCM439 steel in high pressure hydrogen at room temperature,J.of the Soc. of Material Science,Japan, 34(1984) 709-714.

[21] M.Nagumo,Characteristics features of hydrogen-related failure, Zairyo-to- Kankyo,56 (2007)132-147.
[22] M.Iino,Hydrogen-defect interactions and hydrogen-Induced embrittlement in iron and steel,Iron and Steel,74(1988)601-608.
[23] Y.Fukai,K.Tanaka ,H.Uchida,Hydrogen and Metals,Uchidarokakuho,1998.
[24] R.Ebara, Corrosion fatigue behaviour of structural materials in an industrial gaseous environment, Fatigue Life Analysis and Prediction, Proc.of the International Conference and Exposition on Fatigue, Corrosion Cracking, Fracture Mechanic sand Failure Analysis, ASM,1986,325-331.
[25] R.Ebara,Y.Yamada,H.Shinohara,Corrosion fatigue strength of high strength steel welded joints in H_2S and CO_2 gas environments,J. of the Soc. of Materials Science,Japan,46 (1997)613-617.
[26] R.Ebara,Y.Yamada ,Y.Fukaya,Corrosion fatigue strength of steel welded joints in H_2S and CO_2 gas environments,Boshoku Gijutsu,39 (1990)538-543.
[27] S.Okazaki,H.Nakamura,On corrosion fatigue of steels in geothermal steam, J.of the Soc.Mat.Sci., Japan,24(1975)15-21.
[28] S.T Ivy,Corrosion fatigue of Type 402 and 422 stainless steel in geothermal steam,paper presented for NACE Corrosion 79,Paper No.58,1978,58/1-58/9.
[29] P.E.Ellis,D.M.Anliker,Geothermal power plant corrosion experience-A Global survey, Materials Performance,21(1982)9-16.
[30] R.L.Prowse,M.L.Wayman,Effect of environment on the fatigue behavior of a medium carbon steel,Corrosion ,30(1974)280-284.
[31] P.Mehdizadeh,R.L.McGlasson,J.E.Landers,Corrosion fatigue performance of a carbon steel in brine containing air,H_2S and CO_2,Corrosion, 22(1966)325-335.
[32] L.M.Dvoracek,Corrosion fatigue testing of oil well sucker rods, Materials Protection and Performance, 12(1973)16-19.
[33] P.Mehdizadeh, Effect of metallurgical variables on corrosion of sucker rods in brine containing CO_2 and H_2S,Materials Protection and Performance, 13(1974)13-16.
[34] K.Tsukada,K.Minakawa ,A.J.McEvily,On the corrosion fatigue behavior of a modified SAE4135 type steel in a H_2S environment,Metallurgical Transactions,14A(1983)1737-1742.
[35] Y.Minami,T.Ogawa,K.Hashimoto, J. of the Soc. Mat.Sci.Japan, 17(1968)718-722.
[36] C.Laird,G.C.Smith,Initial stage damage in high stress fatigue in some pure metals, PhilosophicalMagazine,(1963)1945-1963.
[37] R.Ebara,Y.Yamada,A.Fushimi,D.Sakai,E.Watanabe,H.Yajima, Corrosion fatigue strengt strength of ship structural steel plates in sour crude oil, J.of the Soc. of Naval Architects of Japan,No.173(1993)337-347.
[38]Y.Nakano,S.Matsumoto,E.Sugie,H.Yajima,R.Ebara E.Watanabe,Corrosion fatigue strength of ship structural steel plate in sour crude oil (2)-Corrosion fatigue strength of welded joints-, J. of the Naval Architects of Japan,No.174,(1993)571-578.
[39] O.Vosikovsky, Fatigue crack growth in an X65 line-pipe steel in sour crude oil,Corrosion,32(1976)472-475.
[40] K.Endo,K.Komai, Metal Corrosion Fatigue and Strength Design(in Japanese),62,1982.

SENSITIVITY TO HYDROGEN EMBRITTLEMENT OF 2 PIPE STEELS

G Pluvinage*[1]and J. Capelle[2]

*Fiabilité Mécanique. Conseils Silly sur Nied France
ENIM Metz France

* Corresponding author : pluvinage@cegetel.net

Fracture toughness and fatigue résistance of two pipe steels (X52and X70) has been determined using curved specimens (roman tiles) directly extracted from pipes. In both case, hydrogen embrittlement is done by electrolytic method.
The comparative assessment of local fracture initiation at notches have been done for conditions of electrochemical hydrogenating. The factor of hydrogen concentration in metal was taken into account. The relationship between hydrogen concentration in metal and work for initiation of the local fracture emanating from the notch has been derived. The existence of some critical hydrogen concentration, which causes the significant loss of local fracture resistance of material, was also shown and discussed.
The concept of ΔK_ρ has been extended to fatigue initiation emanating from notch and under hydrogen embrittlement. Here, fatigue initiation is detected by acoustic emission. It has been found that the fatigue initiation decreases after hydrogen absorption. This can be explained by interaction of hydrogen and plasticity as can be seen for tensile and fracture behaviour steel after introduction of hydrogen.

Keywords : pipe steel, hydrogen embrittlement, local fracture energy, fatigue initiation

1.INTRODUCTION

General reason, which increases of attention to the problem hydrogen degradation of pipeline steels, is fact that hydrogen will play a decisive role in a future energy system, when fossil fuels have become scarce and thus expensive and/or unsuitable from ecological reasons. The number of aspects related to the technical feasibility and economics of developing a hydrogen energy infrastructure are presented and discussed in literature during last decades [1, 2]. The possible use of existing pipeline networks for mixtures of natural gas and hydrogen offers a unique and cost-effective opportunity to initiate the progressive introduction of hydrogen as part of the development of a full hydrogen energy system [3].
From this reason, the safety, durability and integrity issues related to hydrogen/natural gas mixtures in the existing natural gas system become actual and important. First of all, there is a potential problem of so-called “hydrogen embrittlement” of pipeline material - the effects of transported hydrogen on material mechanical properties [4].
Moreover, the specific long-term exploitation of pipelines promotes the hydrogenating of steel. The external environmental conditions cause free corroding processes, where hydrogen can evaluate on metal surface as result of cathodic counterpart of the anodic dissolution reaction. This fact has been proved by several studies [5-7].
External interference incidents are characterised by potentially severe consequences: leaks and ruptures. In majority, these types of incidents are caused by initial damaging of the pipe external surface as result of third party interference e.g. by scratches and gouges and also pitting corrosion.

Such defects can be considered as typical stress concentrators and consequently the privileged sites where the further damaging and failure processes occur.

In this paper, evidence on a critical hydrogen concentration for the ductile brittle transition of two pipe steels X52and X70 is presented. The strong influence of hydrogen embrittlement on fatigue crack initiationis the second point which focuses our attention.

2. OBJECT OF STUDY AND EXPERIMENTAL PROCEDURE

The objects of study were two API grade pipeline steels, namely: X52 and X70. Nowadays, the steel X52 is the most usable in existed gas pipelines.

The specimens for tests were machined from real pipes (Table 1). The chemical composition of steels and their mechanical properties in air are given in Table 2 and 3 respectively.

Table 1 Size of pipes

Steel grade	Outer diameter D, mm	Wall thickness t, mm
X52	610	11.0
X70	710	12.7

Table 2 Chemical compositions of steels (wt %)

Steel grade	*C*	*Mn*	*Si*	*Cr*	*Ni*	*Mo*	*S*	*Cu*	*Ti*	*Nb*	*Al*
X52	0.206	1.257	0.293	0.014	0.017	0.006	0.009	0.011	0.001	<0.03	0.034
X70	0.125	1.68	0.27	0.051	0.04	0.021	0.005	0.045	0.003	0.033	0.038

Table 3 Mechanical properties of steels in air at ambient conditions

Steel grade	σ_U, *MPa*	σ_Y, *MPa*	*Elongation. %*
X52	528	410	30.2
X70	712	590	18.3

For tests (fatigue and fracture), the special “Roman tile” [8] specimens were used. The specimens were notched for modelling of the longitudinal external defects under operating internal pressure. The specimen view and notch geometry are given in Fig. 1. The study was conducted in special soil solution NS4 with *pH=6.7* [9]

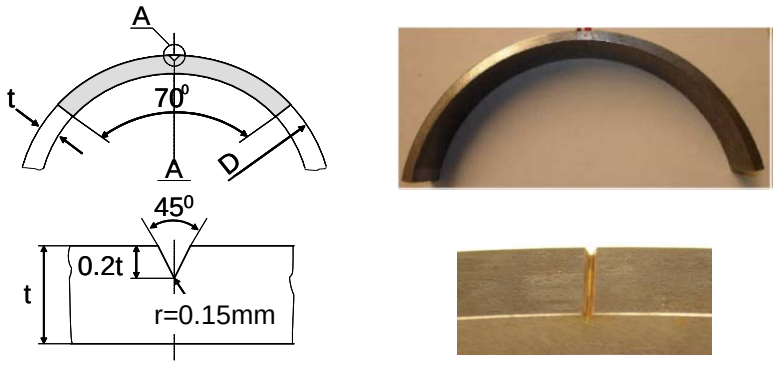

Fig. 1 “Roman tile” specimen and geometry of notch

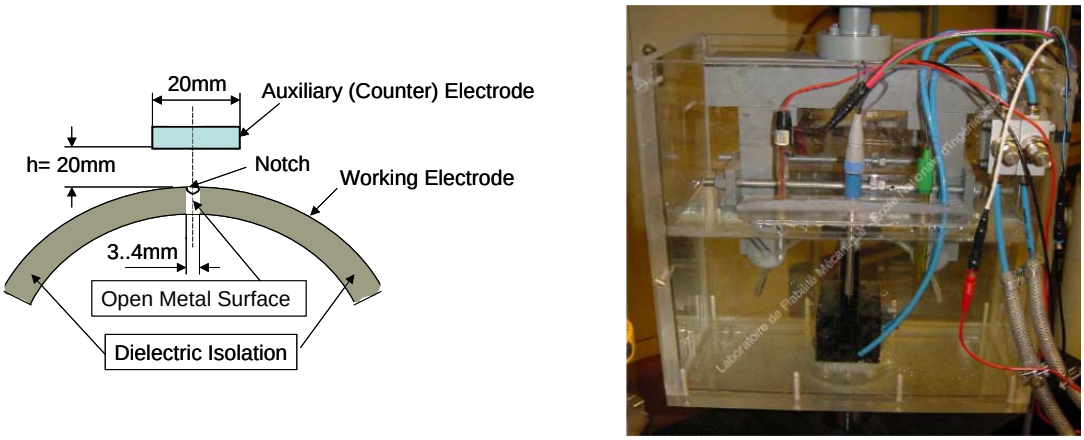

a) b)

Fig. 2 Mutual location of working electrode (specimen) and auxiliary (counter) electrode (a) and general view of corrosion cell (b)

The specimens were coated by special dielectric isolation, excepting the small area at the notch (Fig. 3). The size of auxiliary (counter) electrode was 20x40 mm. In this case its square is significantly larger than the working electrode area, which to be polarised. During testing the specimens were immersed into the cell with NS4 solution (Fig. 2) and exposed under constant potential of cathodic polarisation $E_{cath} = const$. For this experimental procedure the Potentiostat VMP has been used. During all test the level of pH was controlled and regulated between 6.6 and 6.7 by bubbling of CO_2 gas.

In given tests, the specimens were hydrogen charged at some constant potential of polarisation, which is slightly negative than free corrosion potential for the given steels. Taking into account that for studying steels the free corrosion potential is about $E_{corr} = -800mV(SCE)$, it has been chosen. Moreover, for simulating of the service conditions, the specimens were loaded during the hydrogen-charging process. The level of load was defined as the gross hoop stress σ_{gross} =194 and 195.7 MPa respectively which corresponds of the internal pressure in pipe under exploitation $p_{\exp} = 70\,bar$

The hydrogen-charging process was controlled by registration of the cathodic polarisation current $I_{cath}(\tau)$. The total quantity of evaluated hydrogen on metal surface during time of exposition τ_{exp} can be found as:

$$Q_H^{ev} = \int_0^{\tau_{\exp}} I_{cath}(\tau)d\tau \quad under\ E_{cath} = const. \tag{1}$$

Hydrogen concentration in metal has been determined on the base of hydrogen discharging process under anodic polarisation with using of hydrogen electrochemical oxidation method proposed in work [10]. For this aim, the standard three-electrode electrochemical cell has been used. The hydrogen discharging of specimen was carried out in *0.2 M NaOH* (*pH=12.4*) solution under anodic polarisation $E_{anodic} = +168\,mV(SCE)$ during some defined time τ_{dis} The total quantity of absorbed hydrogen by metal can be defined as:

$$Q_H^{abs} = \int_0^{\tau_{dis}} \left[I_H(\tau) - I_{ref}(\tau)\right]d\tau \quad under\ E_{anodic} = const. \tag{2}$$

Here $I_H(\tau)$ is anodic polarisation current for hydrogen charged specimen and $I_{ref}(\tau)$ is anodic polarisation current for specimen without hydrogen (reference curve). Calculation of hydrogen concentration was done according to formula:

$$C_H = \frac{Q_H^{abs}}{zFv}. \tag{3}$$

Where z is the number of electrons take in reaction; F is the Faraday constant; v is the effective volume of specimen: $C_H \left[mol/cm^3\right]; Q_H^{abs} \left[A \cdot s\right]; \; z = 1; \; F = 9{,}65 \cdot 10^4 \; C/mol$.

After assigned exposition under hydrogenating conditions, all specimens were tested to failure under increasing static loading or fatigue according to 3-point bending scheme. The "load – displacement" diagram and acoustic emission (AE) signals were simultaneously registered by PC during the tests. The start of fracture process has been defined by acoustic emission method.

3. RESULTS AND DISCUSSION

Process of hydrogen charging of pipeline steels at the given conditions of cathodic polarisation was characterised by following parameters: averaged meaning of cathodic current density i_c; total quantity of evaluated Q_{ev} and absorbed Q_{abs} hydrogen; coefficient of efficiency of hydrogen permeation in metal $k = Q_{abs}/Q_{ev}$ and hydrogen concentration in metal C_H. It can be seen that for assigned testing conditions, i.e. in deoxygenated, near-neutral pH NS4 solution and under loading by tensile stress, which simulates of operating conditions, the resistance to hydrogen absorption decreases with decreasing of steel strength.

Based on received experimental results, the hydrogen concentration in given steels versus time of exposition of specimens in the hydrogenating conditions can be described by power relation:

$$C_H = A \cdot 10^{-6} \cdot \tau^m. \quad \left[mol/cm^3\right]. \tag{4}$$

Where A and m are constants (see Table 4).

Table 4 Meanings of constants in formula (4)

Steel	A	m
API X52	0.30	0.57
API X70	0.40	0.42

3.1Local strength

The study of local strength of notched specimens in presence of hydrogen was resulted in the dependencies of total work U_i for initiation of the local fracture emanating from the notch. The scheme of determination of parameter U_i is presented in Fig. 3

$$U_i = \int_0^{\Delta_i} P(\Delta) \cdot d\Delta. \tag{5}$$

Here the hydrogen concentration C_H in metal was calculated by using of the analytical relation (4). The main observation based on these results is the existence of some critical time of exposition and as a consequence – some critical hydrogen concentration C_H^*, when the essential

decreasing of fracture toughness value is occurred (Fig. 3). The values of C_H^* for studied steels are given in Table 5.

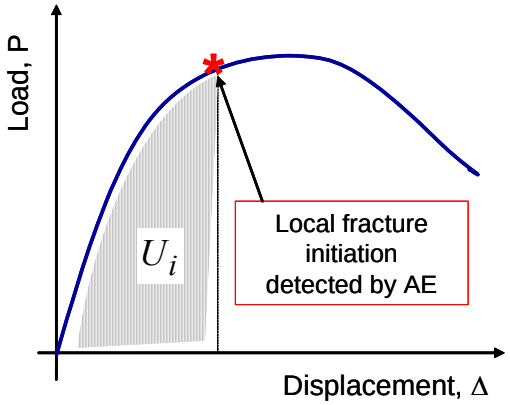

Fig 3. Scheme of determining of work for local fracture initiation

Table 5 Critical hydrogen concentrations C_H^* for API grade pipeline steels

Steel	$C_H^*, 10^6\ mol/cm^3$
X52	4.3
X70	2.3

The steel X70 demonstrates very high sensitivity to notch effect even in air and the presence of hydrogen strengthens this tendency. The hydrogen concentration about $C_H^* \approx 2.3 \cdot 10^{-6}\ mol/cm^3$ can be considered as critical, because at this conditions the given steel losses in 2.5 times its local strength with comparison of test in air. Therefore, for assigned testing conditions, steel X52 is preferable than steel X70 from the point of view of local strength at notches under hydrogen embrittlement.

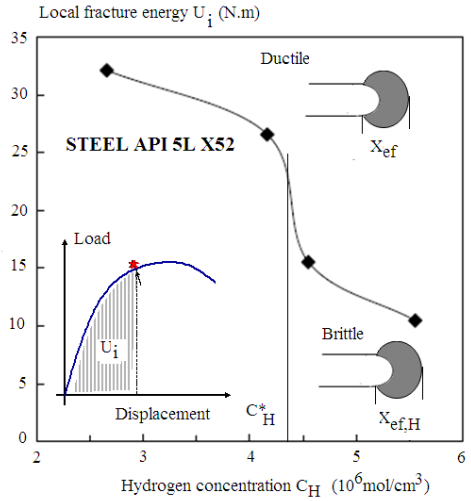

Fig .4 Ductile-brittle transition with hydrogen concentration in API5L X52 steel.

This critical hydrogen concentration at ductile brittle transition can be explained by a competition to the fracture process volume and the hydrogen affected fracture process volume. In an area approach, the effective distance X_{ef} represents the diameter of the fatigue process zone assumed as

cylindrical. Its determination is based on a procedure involving the relative stress gradient to determine an inflexion point on the notch tip opening stress distribution [8]. If X_{ef} is smaller than $X_{ef,\,H}$, the corresponding value after hydrogen embrittlement, the effective stress in the fracture process volume is greater and then the work done for fracture is higher.

There is the tendency of monotonic decreasing of C_H^* values with increasing of yield stress σ_Y or ultimate stress σ_U steel (Fig. 10). This dependency can be described by power function, like to:

$$C_H^* = B_1 \cdot (\sigma_Y)^{n_1} \text{ or } C_H^* = B_2 \cdot (\sigma_U)^{n_2}, \tag{6}$$

where B_1, B_2, n_1, n_2 are the some constants of material's properties and testing conditions. Here, the standard deviation R^2 = 0.98-0.99 that is fully acceptable. As first approximation, it can be concluded that

$$C_H^* \sim \frac{1}{\sigma_U^2}. \tag{7}$$

3.2 fatigue initiation

The fatigue resistance to initiation of the API 5L X52 and X70 steels has been measured in radial direction at room temperature using non-standard curved notched specimens, namely, "Roman tile" specimens because the pipe dimensions do not permit to measure through thickness mechanical characteristics.

The applied load, frequency and the fatigue cycle (sinusoidal) were monitored on the control panel. Hydrogen charging was made using the same cell filled with NS4 solution. Tests conditions are given in Table 6.

Table 6 : Fatigue test conditions

Shape of the cycle used	Sinus:
Frequency :	0.05 Hz
Load ratio	0.5
Working potential	- 1 V_{sce}
Electrolytic solution	New Solution 4 (NS4)
Solution pH	between 6.66 and 6.74

Wöhler curves were drawn at both initiation and failure. Results are presented in a bi logarithmic graph of stress amplitude versus number of cycles to failure. The classical power fit of the stress range versus the number of cycles to failure is in accordance with Basquin's law:

$$\Delta\sigma = \sigma'_f (N_R)^b \tag{8}$$

where σ'_f is the fatigue resistance and b the Basquin's exponent. Results are presented in Table 7.

Table 7: Fatigue resistance parameters with and without hydrogen charging for X 52and X70 steels

Steel, environment	σ'_f fatigue resistance (MPa)	exponentβ	R^2
X70 air	436	-0.023	0.94
X70 Hydrogen	395	-0.015	0.94
X52 air	343	-0.022	0.89
X52 Hydrogen	301	-0.012	0.95

Fatigue phenomenon consists of two parts, fatigue initiation and crack propagation until failure. When using optical devices, definition of initiation depends on optical resolution of the equipment. In our tests, we detect fatigue initiation by acoustic emission which is more sensitive than optical method. Acoustic emission is registered during test by two sensors. Fatigue initiation is easily detected by an energy burst. This method is also reliable and gives supplementary information on fatigue mechanism. Stress range versus number of cycles to initiation is fitted by a power law similar to Basquin's one.

$$\Delta\sigma = \sigma_i^{'}\left(N_i\right)^{\beta} \tag{9}$$

where σ'_i is fatigue initiation resistance and β an exponent. $\Delta\sigma$ is the gross stress range.

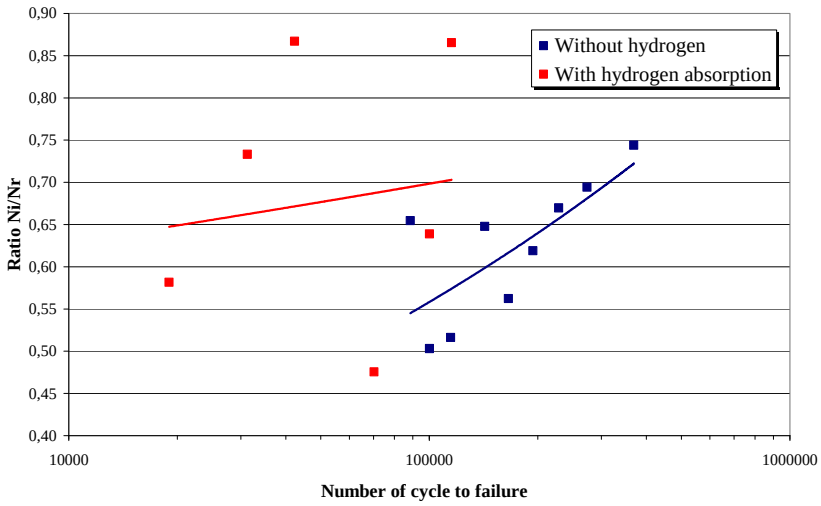

Figure 5: Evolution of ratio N_i/N_r versus number of cycles to failure for X52 steel.

Table 8: Fatigue initiation resistance parameters with and without hydrogen charging for X 52and X70 steels

Steel, environment	σ'_i fatigue initiation resistance (MPa)	Exponent β	R^2
X70 air	395	-0.016	0.96
X70 Hydrogen	368	-0.010	0.97
X52 air	325	-0.018	0.90
X52 Hydrogen	296	-0.011	0.95

Evolution of ratio N_i/N_r versus number of cycles to failure is plotted in Figure 6. We note that fatigue crack propagation is faster in presence of hydrogen because the difference N_r-N_i is strongly reduced.

Barsom and McNicol [11], Jack and Price [12], Clark [13] and Truchon [14] have used the parameter $\Delta K/\sqrt{\rho}$ to express fatigue resistance on notched specimens. Boukharouba et Al [15] have compare fatigue initiation criteria with a criterion based on the elasto plastic notch stress intensity factor K_ρ on welded specimen made in low strength steel. The same parameter has been used to plot a fatigue initiation curve K_ρ (= $f(N_i)$. One notes that this curve are not sensitive to pipe steels but sensitive to environment.

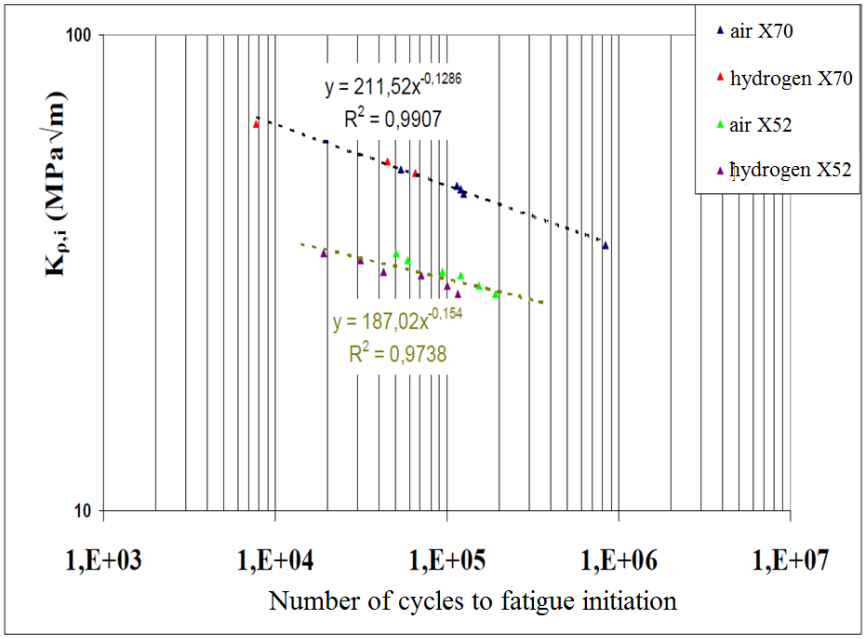

Figure 6 : Fatigue initiation curves for both steels with and without hydrogen embrittlement.

The hydrogen concentration increases as a power function of time (see equation 4) and then depends on number of cycles to initiation N_i and test frequency f. The local hydrogen concentration depends on hydrostatic stress σ_h. The average hydrogen concentration is the local one computed over the effective distance V_{ef} :

$$\overline{C}_H = \frac{1}{X_{ef}} \int_0^{X_{ef}} A\left(N_i \times \frac{1}{f}\right)^m \cdot \exp\left[-\frac{V_H \cdot \sigma_h(r)}{R \cdot (T - T_0)}\right] dr \qquad (10)$$

Where A and m are constants of equation 4, R Perfect gas constant, V_H molar hydrogen volume.

Notch Stress Intensity Factor is given according to [8] :

$$K_{\rho,air} = \sigma_{\text{ef}} \cdot \sqrt{2\pi \cdot X_{ef}} \qquad (11)$$

In hydrogen, NSIF takes the following form because maximum hydrogen concentration is localised at peak stress

$$K_{\rho,H} = \sigma_{\text{max,H}} \cdot \sqrt{2\pi \cdot X_{ef,H}} \qquad (12)$$

Effective stress σ_{ef}, peak stress $\sigma_{max,\,H}$, effective distance X_{ef} and effective distance under hydrogen concentration $X_{ef\,,H}$ are obtained by computing notch tip stress distribution by finite element and using stress strain behavior with and without hydrogen embrittlement respectively.

A plot of the following ratios $\left(\frac{\sigma_{\text{max,H}}}{\sigma_{\text{ef}}}\right)$ and $\left(\frac{X_{ef,H}}{X_{ef}}\right)$ indicates an exponential dependence with average hydrogen concentration.

$$\sigma_{\max,H} = \sigma_{ef} \cdot \exp\left(A_1 \cdot \overline{C}_H + B_1\right) ;\ X_{ef,H} = X_{ef} \cdot \exp\left(A_2 \cdot \overline{C}_H + B_2\right) \quad (13)$$

$$\begin{cases} A_1 = -9 \cdot 10^{-5} & B_1 = 0{,}1182 \\ A_2 = -5 \cdot 10^{-4} & B_2 = -0{,}0442 \end{cases}$$

So the Notch Stress Intensity factor under hydrogen can be expressed as a function of Kρ, air

$$K_{\rho,H} = K_{\rho,air} \cdot f\left(\overline{C}_H, \alpha\right) \quad (14)$$

With $f\left(\overline{C}_H\right) = \exp\left[\left(A_1 + \frac{1}{2}A_2\right) \cdot \overline{C}_H + \alpha \cdot \left(B_1 + \frac{1}{2} \cdot B_2\right)\right]$

The prameter a is introduced in order to get $K_{\rho,H} \rightarrow K_{\rho,air}$ when $\overline{C}_H \rightarrow 0$

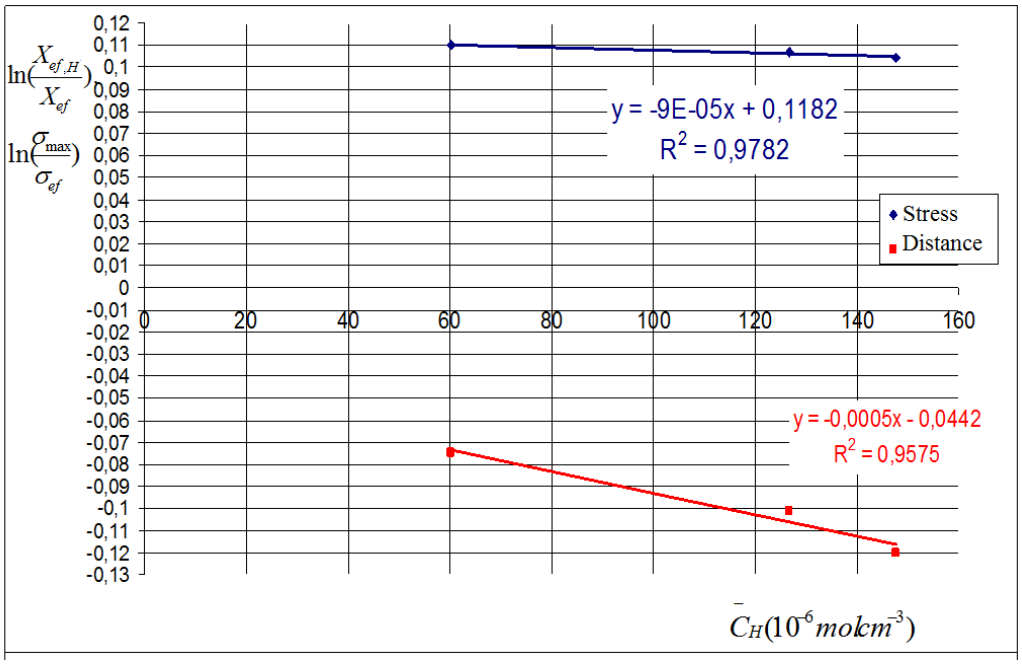

Figure 7 : Evolution of ratios $\left(\frac{\sigma_{\max,H}}{\sigma_{ef}}\right)$ and $\left(\frac{X_{ef,H}}{X_{ef}}\right)$ with average hydrogen concentration.

4. CONCLUSION

It is important to note that hydrogen concentration provides a fracture resistance transition .similarly to temperature, loading rate and notch acuity in pipe steels X52 and X. This phenomenon is describes for the first time (according to our knowledge) in this paper.

Some critical hydrogen concentration C_H^* exists for tested steels, which causes the significant loss of local fracture resistance of material at notches. The tendency of monotonic decreasing of C_H^* values with increasing of yield stress σ_Y or ultimate stress σ_U of steels has been derived.

Critical hydrogen concentration C_H^* may be considered as an important engineering parameter for forecasting of strength and reliability of exploited pipelines and under designing of new pipelines for hydrogen transportation as well.

Hydrogen embrittlement reduces fatigue life by increasing fatigue crack propagation and reducing number of cycles to initiation. Fatigue initiation can be described by the Notch Stress Intensity Factor which is sensitive to average hydrogen concentration.

References

[1]. Mulder G., Hetland J. and Lenaers G. Towards a sustainable hydrogen economy: Hydrogen pathways and infrastructure. International Journal of Hydrogen Energy, 32, Issues 10-11 (2007) 1324-1331

[2]. Wietschel M., Hasenauer U. and de Groot A. Development of European hydrogen infrastructure scenarios - CO_2 reduction potential and infrastructure investment. Energy Policy, 34, Issue 11 (2006) 1284-1298

[3]. NaturalHy Project, *http://www.naturalhy.net*

[4]. Hanneken J. W. Hydrogen in metals and other materials: a comprehensive reference to books. bibliographies. workshops and conferences. International Journal of Hydrogen Energy. 24. No 10. (1999) 1005-1026.

[5]. Cheng Y.F. Fundamentals of hydrogen evolution reaction and its implications on near-neutral pH stress corrosion cracking of pipelines. Electrochimica Acta 52 (2007) 2661–2667

[6]. Dey S., Mandhyan A.K., Sondhi S.K., Chattoraj I. Hydrogen entry into pipeline steel under freely corroding conditions in two corroding media. Corrosion Science 48 (2006) 2676–2688

[7]. Shipilov S.A., May I.L. Structural integrity of aging buried pipelines having cathodic protection. Engineering Failure Analysis 13 (2006) 1159–1176

[8]. Adib-Ramezani H.. Jeong J.. Pluvinage G. Structural integrity evaluation of X52 gas pipes subjected to external corrosion defects using the SINTAP procedure. International Journal of Pressure Vessels and Piping 83 (2006) 420–432

[9]. Capelle J., Gilgert J., Dmytrakh I., Pluvinage G. Sensitivity of pipelines with steel API X52 to hydrogen embrittlement. International Journal of Hydrogen Energy 33 (2008) 7630-7641

[10]. Yan M., Weng Y. Study on hydrogen absorption of pipeline steel under cathodic charging. Corrosion Science 48 (2006) 432–444

[11]. M. Barsom and R. C. McNicol, Effect of stress concentration on fatigue-crack initiation in HY-130 steel. *ASTM STP* **559,** 183-204 (1974).

[12]. A. R. Jack and A. T. Price, The initiation of fatigue cracks from notches in mild steel plates. *Int. J. Fracture Mech.* **6 (4) (1970).**

[13]. W. G. Clark, Jr, Evolution of the crack initiation properties of type 403 stainless steel in air and steam environment. ASTM STP 559, 205-224 (1974).

[14]. M. Truchon, Amorçage de fissures en fatigue à partir d'entaille, application aux joints soudés. Bulletin Technique duBureau Veritas 67 (5) (1985).

[15]. Boukharouba,T. Tamine,L. Niu, C. Chehimi and G. Pluvinage The use of notch stress intensity factor as a fatigue crack initiation parameter**.** Engineering Fracture Mechanics Vol. 52, No. 3, pp. 503-512, (1995).

The tensile properties of NiCrMo1 steel under conditions of hydrogen charging studied using the linearly increasing stress test

Qian Liu[1], Bartolomeus Irwanto[2], Andrej Atrens[1*]

[1] The University of Queensland, Materials Engineering, St Lucia, Qld 4072, Australia
[2] Alstom (Switzerland) Ltd, CH-5242 Birr, Switzerland
* Corresponding author: Andrejs.Atrens@uq.edu.au

Abstract The tensile properties of NiCrMo1 steel were investigated using the linearly increasing stress test (LIST) in air and with hydrogen charging. Hydrogen charging was carried out by applying an increasingly negative applied potential to -1550 $mV_{Ag/AgCl}$ in acidified 0.1 M Na_2SO_4, pH 2 solution. The LIST results showed that the yield stress of the steel was similar in air or with hydrogen charging. SEM examination showed that the specimens tested in air had no surface cracks, and the fracture surfaces comprised dimples. The failure in air was due to ductile overload. The specimens tested with hydrogen charging had obvious surface cracks in the necked region, and their length increased to about 550 μm with a more negative potential. However, the fracture surfaces were nevertheless dominated by ductile feature. These results imply that the influence of hydrogen was only associated with the final ductile fracture after the onset of necking.

Keywords: Steel 1, LIST 2, hydrogen embrittlement 3, SEM 4.

1. Introduction

Operation of metallic components is required in hydrogen (H) in the H economy being developed in response for the need for clean energy. The H economy requires pressure vessels resistant to hydrogen embrittlement (HE) for the production, distribution, storage and use of gaseous H_2. Though laboratory scale vessels can be made from expensive exotic materials, there are significant cost imperatives to use less expensive materials like steels in a commercial H economy. Some steels are susceptible to hydrogen, particularly high strength steels [1-11]. Some medium strength steels are resistant to hydrogen even under severe hydrogen charging conditions [12-15]. Using the linearly increasing stress test (LIST) [16], our previous investigation of 3.5NiCrMoV steel [15] showed that there was negligible influence of hydrogen on the yield stress and fracture stress, though the ductility was decreased for some tests. Detailed examination of the surface appearance and the fracture surfaces indicated that (i) there was no influence of hydrogen up to the yield stress of the steel; and (ii) hydrogen caused some small brittle fracture events in small localised areas associated with the final ductile fracture after the onset of necking. The LIST [16] is a stress-controlled version of the constant extension rate test (CERT) [17]. A LIST is identical to a CERT up to the onset of yielding, or the onset on subcritical crack growth. It is expect that the same apparent threshold stress would be measured using CERT as measured using LIST, an apparent threshold that related to the onset of plastic deformation.

The aim of this research was to evaluate using LIST the behavior of medium strength NiCrMo1 steel under hydrogen conditions. The results could be considered as a reference to the suitability of this steel for the H economy.

2. Experimental procedure

The material was the nickel chromium molybdenum steel, NiCrMo1. It is a quenched and tempered martensitic steel; the microstructure is tempered martensite as shown in Fig. 1. Table 1 presents the chemical composition. The steel was machined into specimens with 10 mm gauge length, 3 mm diameter and an overall length of 110 mm. The specimen was evaluated by LIST. The threshold stresses were measured with the potential drop (PD) measurement. LISTs were carried out in air, and in solution, (i) at the free corrosion potential (E_{corr}) and (ii) under hydrogen charging conditions.

The solution was acidified 0.1 M Na_2SO_4 pH 2 solution. Details about hydrogen charging, LIST and SEM sample preparation are as in [15]. After each LIST, the fracture surface was examined by SEM.

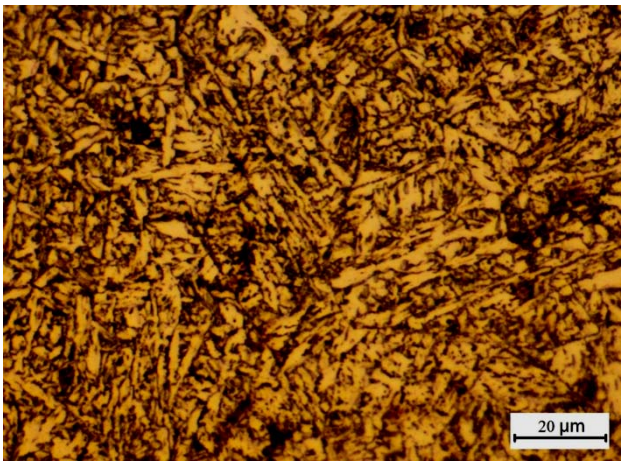

Figure 1. The microstructure of the NiCrMo1 steel.

Table 1. Chemical composition of NiCrMo1 (wt%) as determines by two independent measurements.

Steel	Composition, wt%									
	C	Ni	Cr	Mo	V	Mn	Si	S	P	Cu
NiCrMo1	0.09	1.04	0.52	0.60	0.01	0.88	0.31	0.01	0.01	0.06
	0.08	0.98	0.48	0.60	0.01	0.91	0.31	0.01	0.01	0.06

The stress rate was mostly the moderate stress rate: 0.02 MPa s^{-1}. The yield stress in air, σ_y, or the threshold stress, σ_{th}, was determined by the PD measurement. The precision for σ_y or σ_{th} was ± 5 MPa. The precision of the fracture stress was ± 2 MPa. The reduction of area, R_A, of each specimen was evaluated from the original specimen gauge diameter and the measured minimum diameter after each test. For the evaluation of σ_{th} or σ_f, in most cases the area used was the original specimen cross-section area. For tests in solution at E_{corr}, corrosion reduced the cross section area of the specimen during the LIST. In those cases, the area used was the cross section area that had undergone uniform plastic deformation.

The specimen designation can be explained by the following example: S1200.02a, where the letter ‘‘S’’ identified a specimen tested in solution (alternatively ‘‘A’’ identified a specimen tested in air), ‘‘1200’’ identified the applied potential (alternatively “ocp” identified a specimen tested in solution at the free corrosion potential), ‘‘.02’’ identified the applied stress rate, and the subsequent letter identified specimens tested under the same conditions.

3. Experimental procedure

3.1. Tensile properties

Fig. 2 shows a typical PD record for NiCrMo1 tested at 0.02 MPa s^{-1} in acidified 0.1 M Na_2SO_4 pH 2 solution at three negative potentials. Similar plots were obtained from the other experiments. Table 2 presents the measured data for σ_y, σ_{th} at which subcritical cracking appeared to initiate in solution, σ_f and R_A. The E_{corr} was about -500 $mV_{Ag/AgCl}$.

The σ_y or σ_{th} in air or at negative applied potentials were in the range of 600 to 660 MPa, while the σ_f was varied from 690 to 760 MPa. The values of R_A were about 70 ~76 %.

LIST for specimens in solution at E_{corr} produced values of the σ_{th} varying from 625 to 690 MPa, values of the σ_f varying from 710 to 800 MPa, and values of the R_A varying from 69% to 79%.

These values were comparable, or somewhat higher than, the values in air.

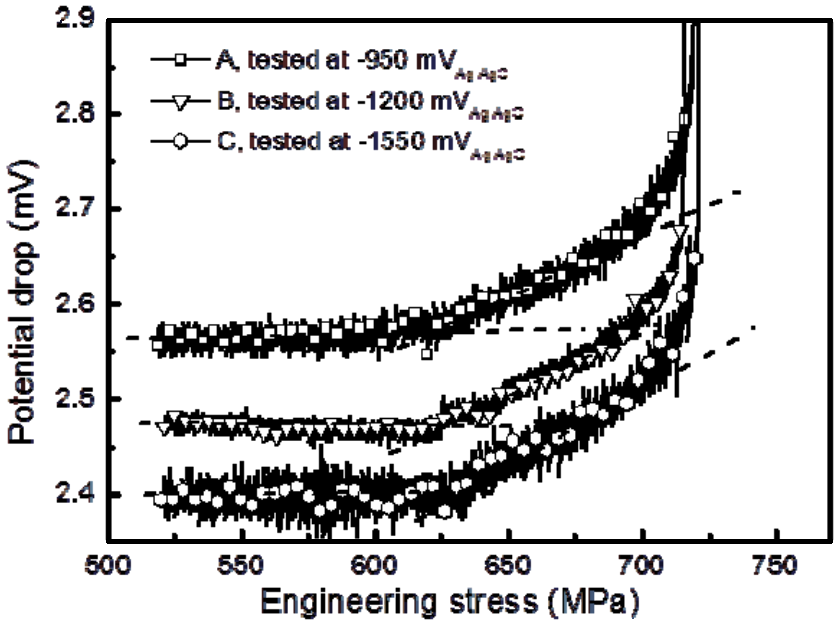

Figure 2. A typical plot of potential drop (mV) vs. engineering stress (MPa) for NiCrMo1 tested at 0.02 MPa s^{-1} in acidified 0.1 M Na_2SO_4, pH 2 solution at three potentials.

Table 2 Yield stress in air (as an engineering stress), σ_y, the apparent threshold stress at which subcritical cracking appeared to initiate in solution (as an engineering stress), σ_{th}, the fracture stress (as an engineering stress), σ_f, the reduction of area, R_A. Solution: ①0.1 M Na_2SO_4, pH=2.

Applied stress rate (MPa/s)	Sample	Solution	Applied potential ($mV_{Ag/AgCl}$)	σ_{th}±5	σ_f±2	R_A
0.02	A.02a	air	0	664	763	74%
0.02	A.02b	air	0	603	693	76%
0.02	A.02c	air	0	631	726	75%
0.02	A.02d	air	0	620	717	72%
0.002	A.002	air	0	646	740	75%
0.02	Socp.02a	①	E_{corr}	683	798	77%
0.02	Socp.02b	①	E_{corr}	625	714	79%
0.02	Socp.02c	①	E_{corr}	693	796	69%
0.02	S950.02	①	-950	619	719	73%
0.02	S1200.02	①	-1200	624	715	73%
0.02	S1400.02	①	-1400	664	759	73%
0.02	S1550.02	①	-1550	633	720	70%

3.2. Surface appearance in the necked region

Visual examination of the surface appearance of each specimen showed that there was obvious necking for all the specimens. Black corrosion products, which were easily removed by EDTA, were produced on the specimens during tests at E_{corr}. For specimens tested at negative potentials, there were cracks on the specimen surface concentrated at the fracture site.

For specimens tested in air at a rate of 0.02 MPa s^{-1}, SEM observation showed necking and shallow cracks at about 45 ° to the stress direction, and linear features parallel to the stress direction in the necked region. Specimens tested at E_{corr} showed similar surface appearance except that the surface was more rough due to corrosion.

Fig. 3 presents the surface appearances of specimens tested under hydrogen charging at 0.02 MPa

s^{-1}. Specimens tested at negative potentials showed necking, and surface cracks perpendicular to the stress direction, and cracks oriented at 45 ° to the stress direction (Fig. 3(c)). The surface cracks were concentrated at the fracture site, and the number density of cracks decreased as a function of distance from the fracture surface. The surfaces of specimens tested at negative potentials were essentially similar. Fig. 3 shows that the surface cracks increased in size with increasingly negative potential.

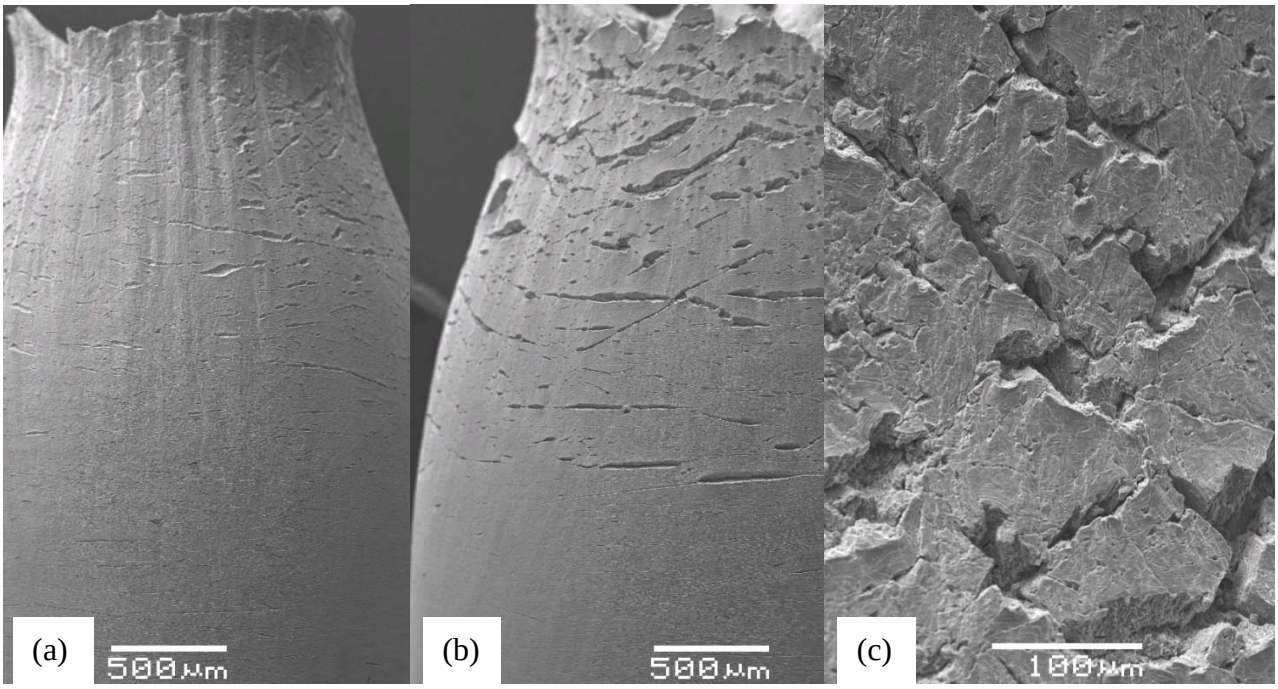

Figure 3. The surface appearances of specimens tested at negative potentials at 0.02 MPa s^{-1}. (a) -950 $mV_{Ag/AgCl}$; (b) -1550 $mV_{Ag/AgCl}$; (c) magnified view of (b) in the necked region. Tensile direction is vertical

3.3. Cross sections through fracture surface (specimen S1550.02)

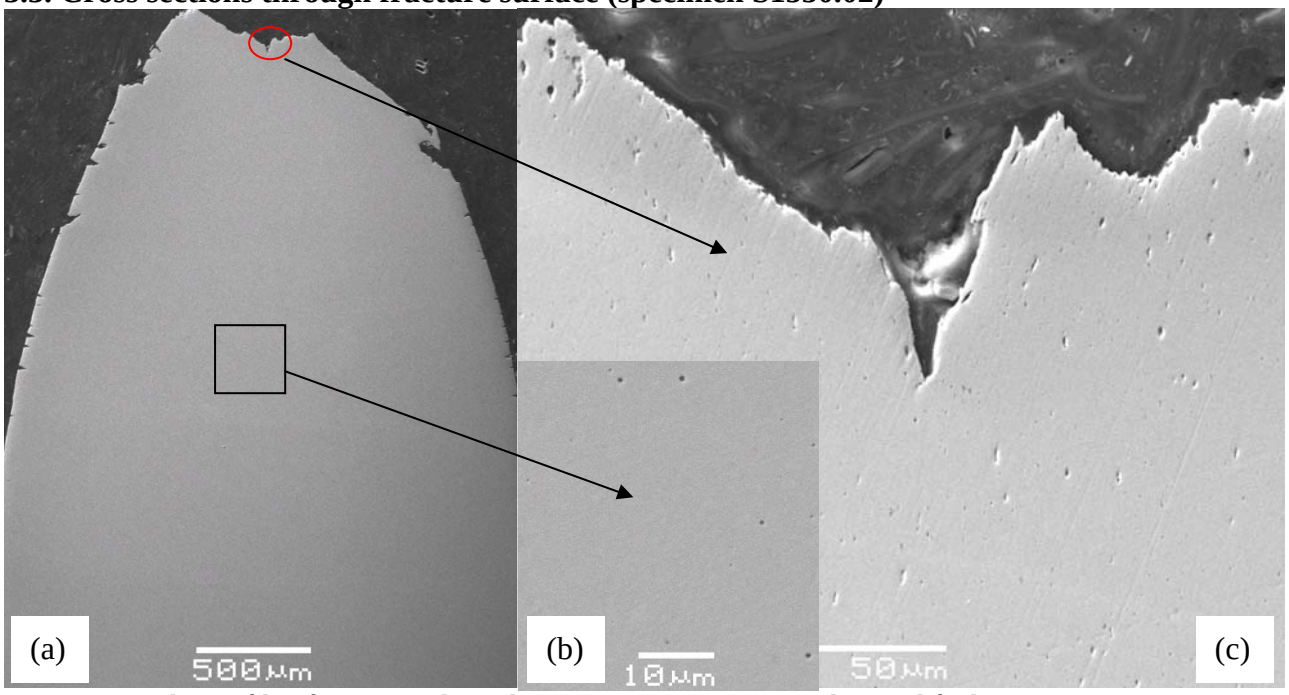

Figure 4. The profile of a section through specimen S1550.02 tested in acidified 0.1 M Na_2SO_4, pH 2 at -1550 $mV_{Ag/AgCl}$ at an applied stress rate of 0.02 MPa s^{-1}. (a) overview; (b) detailed view in the center; (c) detailed view near fracture surface. The tensile loading was in the vertical direction.

The longitudinal cross-section of specimen S1550.02 is shown in Fig. 4. Cracks initiated from the surface and extended into the specimen interior. The density of the surface cracks decreased as a function of distance from the fracture surface. Fig. 4(b) shows the detailed view in the interior of the specimen. There were small round voids, but no cracks. A magnified view of the region near the fracture surface (Fig. 4(c)) indicates that there were small holes near the fracture surface. As these sections were taken at random, it is concluded that there were no cracks in the interior of the specimens, apart from the small round voids.

3.4. SEM fractography

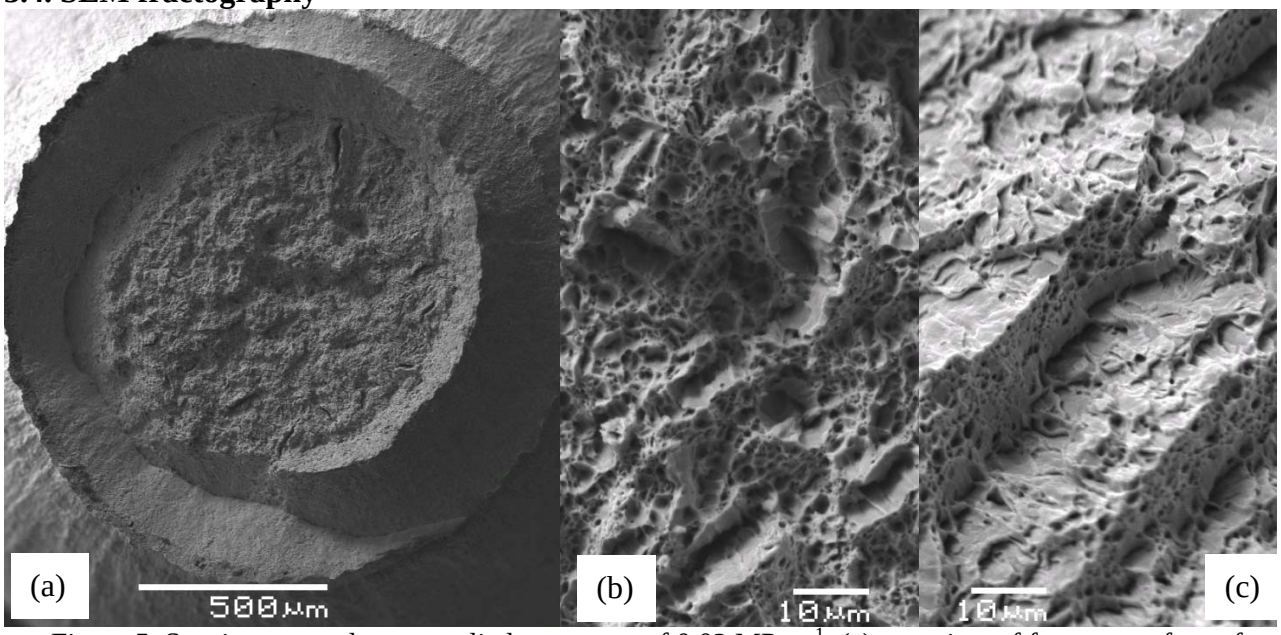

Figure 5. Specimen tested at an applied stress rate of 0.02 MPa s^{-1}: (a) overview of fracture surface of specimen A.02c, (b) a magnified view of cone part of specimen A.02c; and (c) brittle facets steps on the fracture surface of Socp.02c.

The fracture surface of specimen A.02c tested in air (Fig. 5) presented a cup and cone fracture with secondary cracks up to 140 μm in size, and showed significant ductility. These secondary cracks were surrounded by dimples, and had a small number of orientations. A magnified view of the fracture surface shown in Fig. 5 (b) indicates that the fracture surface comprised dimples, due to ductile microvoid coalescence (MVC) and secondary ductile cracks. All the secondary cracks were ductile and were surrounded by dimples. The fracture surfaces of other specimens tested in air were similar to specimen A.02c.

Similar to that obtained in air, the fracture surface of specimens Socp.02a and Socp.02b tested at E_{corr} showed a cup and cone fracture with a big secondary crack about 270 μm in size, and small secondary cracks less than 100 μm in size. However, one specimen Socp.02c tested at E_{corr} showed dimples and secondary cracks as well as some brittle facets, as shown in Fig. 5(c). Those brittle facets built up horizontal steps; dimples were like a linker between those steps. These brittle facets covered a substantial area in the middle of the fracture surface. Nevertheless, they were entirely surrounded by microvoid coalescence.

The fracture surface of specimen S950.02 tested at -950 $mV_{Ag/AgCl}$ at a rate of 0.02 MPa s^{-1} showed a cup and cone fracture as illustrated in Fig. 6. Fig. 6(b) presents a magnified view of region A, which comprised dimples and some secondary cracks. Region B at the edge, shown in Fig. 6(c), comprised brittle facets at the edge and shear dimples, i.e. dimples which had formed in the shear lips of the

cup and cone fracture at ~45° to the tensile axis, and were heavily sheared.

The fracture surfaces of specimens tested at -1200 $mV_{Ag/AgCl}$ and -1400 $mV_{Ag/AgCl}$ also showed obvious ductility, presenting a cup and cone fracture with a large secondary crack about 170 µm in size and small secondary cracks less than 150 µm in size completely surrounded by dimples.

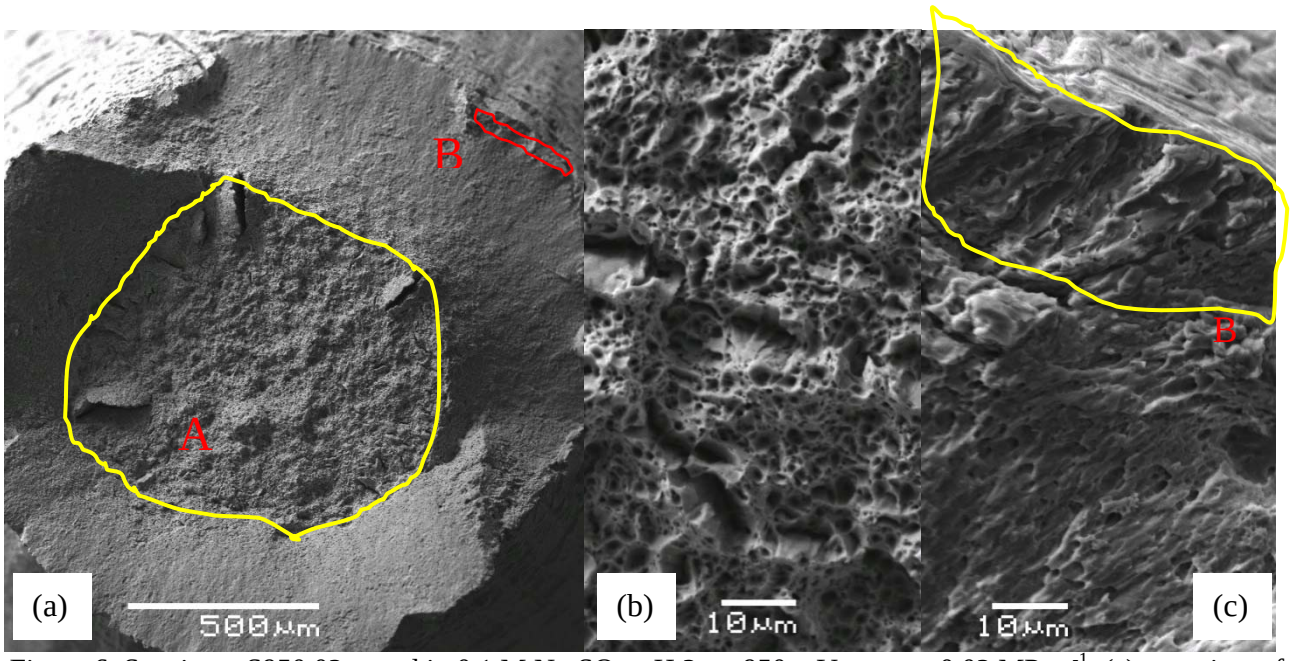

Figure 6. Specimen S950.02 tested in 0.1 M Na_2SO_4, pH 2 at -950 $mV_{Ag/AgCl}$ at 0.02 MPa s^{-1}: (a) overview of the fracture surface, (b) a magnified view of region A, and (c) a magnification of region B.

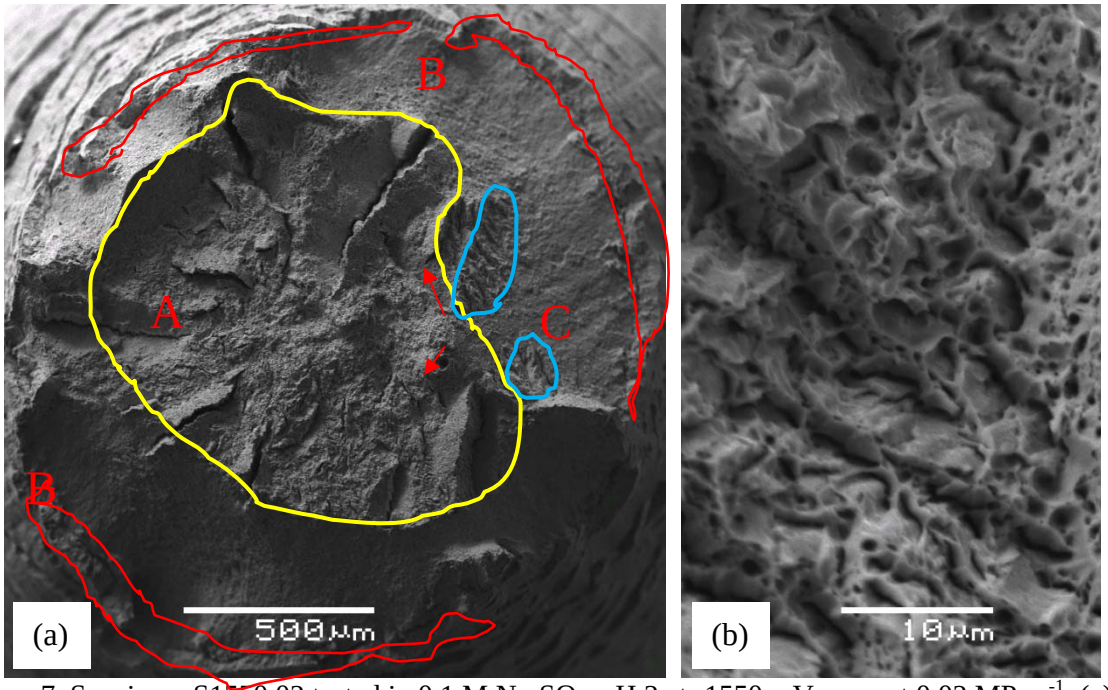

Figure 7. Specimen S1550.02 tested in 0.1 M Na_2SO_4, pH 2 at -1550 $mV_{Ag/AgCl}$ at 0.02 MPa s^{-1}: (a) an overview of the fracture surface, and (b) a detailed view in region C.

Fig. 7(a) presents the fracture surface of specimen S1550.02 tested at -1550 $mV_{Ag/AgCl}$ at a rate of 0.02 MPa s^{-1}. Region A of the fracture surface, similar to that shown in Fig. 6(b), was mainly MVC with some secondary cracks up to 550 µm. These secondary cracks surrounded by dimples were

oriented radially to the centre of the specimen. Region B was similar to that shown in Fig. 6(c). Fig. 7(b) presents a detailed view in regions C, showing small brittle facets.

4. Discussion

4.1. Tensile properties

All the specimens showed significant ductility, as demonstrated by obvious necking and high values of R_A. At the applied potentials, hydrogen was produced during each experiment at the specimen surface. The increasingly negative potentials increased the amount of H (and the H fugacity) at the specimen surface [18], and concomitantly the hydrogen concentration in the specimen. However, Table 2 indicates that decreasing applied potential did not cause any significant changes in the values of σ_{th}, σ_f and R_A. The influence of hydrogen on the tensile parameters of the NiCrMo1 steel was negligible.

4.2. Surface appearance

There were cracks at about 45° to the tensile direction on the necked surface of specimens tested in air and in solution at E_{corr}. These shallow surface cracks are attributed to the surface intersection of localised bands and stress, as the shear stress is maximum at 45 ° to the tensile direction.

For each of the specimens tested at negative potentials from -950 $mV_{Ag/AgCl}$ to -1550 $mV_{Ag/AgCl}$, there were no cracks on the surface that had undergone uniform plastic deformation, while the surface of the necked region contained cracks perpendicular to the tensile direction, and cracks about 45° to the tensile direction. The number of these cracks decreased as a function of the distance from the fracture surface. These cracks became longer with increasingly negative potential, which was attributed to high H fugacity at the specimen surface [18]. These cracks were due to the influence of hydrogen on the localized plastic deformation at the surface in the necked region of the specimen.

It can be concluded that (i) there was no hydrogen influence for stresses up to the yield stress of the material; and (ii) the influence of hydrogen was associated with localised plastic deformation and fracture. These conclusions were similar to those for the 3.5NiCrMoV steel in our previous research [15].

4.3. Cross Section

The examination of cross section of specimen S1550.02 indicated that hydrogen only had an effect (i) on the edge and places near the edge of the necked region and (ii) locations close to the fracture surface in the heavily deformed region. These facts indicate the occurrence of cracks was associated with high levels of localised plastic deformation during the process of necking during final ductile fracture. This is consistent with the results obtained from the surface appearance.

However, it is possible that the duration was not long enough for hydrogen to reach a stable concentration though the specimen, therefore, the influence of hydrogen in the centre of specimen was weaker than that of on the surface. This might provide an alternative explanation for hydrogen influence only obvious on the surface of the necked region. Nevertheless, the fact that the secondary cracks extended to the centre of the specimen tested at -1550 $mV_{Ag/AgCl}$ in Fig. 7 implies that there was sufficient hydrogen throughout the specimen under this test condition to cause hydrogen related fracture events throughout the cross section. The absence of hydrogen damage inside the specimen was not due to insufficient hydrogen inside the specimen.

4.4 Fracture surfaces

The fracture surfaces obtained in air and at E_{corr} were dominated by dimples, due to ductile

microvoid coalescence, interspersed with some secondary cracks. The difference between various specimens seems to be a slightly different amount and size of secondary cracks. These results indicated that the specimen tested in air and at E_{corr} failed due to ductile overload.

The specimens tested under negative potentials showed a significant amount of ductile features on the fracture surface, similar to those in air. Most of the substantial cracks on the fracture surfaces were oriented radially. With increasingly applied negative potential, cracks on the fracture surfaces grew longer, up to about 550 μm at -1550 $mV_{Ag/AgCl}$. However, it is hard to say that these cracks were due to hydrogen, since there were similar cracks on the fracture surfaces for specimens tested in air. The initiation of these cracks may be due to inclusions [19]. Yet the presence of hydrogen did accelerate the growth rate of these cracks.

Brittle features at the edge associated with surface cracks in the neck region were deeper at a more negative potential indicating that hydrogen had a greater influence.

There were brittle features in small localised areas in the presence of hydrogen, associated with final ductile fracture. However, these brittle features were all surrounded by regions of ductile fracture. Even at the most negative potential, the fracture surface was predominately ductile, indicating that the specimens tested under hydrogen charging also failed due to ductile overload. The influence of hydrogen was not significant.

4.5 Mechanistic interpretation

Due to (i) no measureable influence of hydrogen on the yield stress; (ii) no surface cracks in the uniformly deformed part of the specimen gauge section for any specimen, the PD technique measured the onset of plastic deformation rather than the onset of subcritical crack growth.

The influence of hydrogen was on the final fracture process after the onset of necking via two ways: (i) causing localized brittle fracture events, and (ii) accelerating crack growth rate on the fracture surface. The brittle hydrogen associated fracture events in the present study occurred simultaneously with a ductile fracture process throughout the necked region of a fracturing specimen. However, the hydrogen fracture mechanism was not comparable to the other ductile fracture mechanism attributable to the stress reaching the fracture stress, and to mechanically unstable of the specimen. The dominant fracture mechanism was ductile microvoid rupture.

There were secondary cracks on the fracture surfaces not only for the specimens tested in solution, but also from the specimens tested in air. This implies that even though these secondary cracks were accelerated by hydrogen, inclusions [19] instead of hydrogen might be responsible for the initiation of these cracks.

4.6 Implications for service

Considering the results discussed above, (i) the properties of the NiCrMo1 might be improved by reducing the inclusion density; and (ii) if the material will be used at a stress under the yield stress, the influence of hydrogen can be negligible, indicating that it is safe to use this material under the yield stress in an environment containing hydrogen for the H economy.

5. Conclusions

The tensile and fracture properties of NiCrMo1 steel under conditions of hydrogen charging were investigated by LIST and SEM. The results showed that:

1. The influence of hydrogen on the tensile parameters (σ_y, σ_{th} and R_A) was negligible;
2. There were no surface cracks in the region that had undergone uniform plastic deformation,

implying that there was no influence of hydrogen up to the yield stress of the steel;
3. There were surface cracks in the necked region on the specimens tested under hydrogen charging, implying that the influence of hydrogen was associated with the final ductile fracture process after the onset of necking.

Acknowledgements

This work is supported by an ARC linkage grant & Alstom (Switzerland) Ltd.

References

[1] S. Ramamurthy, W.M.L. Lau, A. Atrens, Influence of the applied stress rate on the stress corrosion cracking of 4340 and 3.5NiCrMoV steels under conditions of cathodic hydrogen charging, Corrosion Science, 53 (2011) 2419-2429.
[2] S. Ramamurthy, A. Atrens, The influence of applied stress rate on the stress corrosion cracking of 4340 and 3.5NiCrMoV steels in distilled water at 30 °C, Corrosion Science, 52 (2010) 1042-1051.
[3] E. Villalba, A. Atrens, Hydrogen embrittlement and rock bolt stress corrosion cracking, Engineering Failure Analysis, 16 (2009) 164-175.
[4] E. Gamboa, A. Atrens, Stress corrosion cracking fracture mechanisms in rock bolts, Journal of materials science, 38 (2003) 3813-3829.
[5] E. Gamboa, A. Atrens, Environmental influence on the stress corrosion cracking of rock bolts, Engineering Failure Analysis, 10 (2003) 521-558.
[6] R. Rieck, A. Atrens, I. Smith, The role of crack tip strain rate in the stress corrosion cracking of high strength steels in water, Metallurgical and Materials Transactions A, 20 (1989) 889-895.
[7] A. Oehlert, A. Atrens, Stress corrosion crack propagation in AerMet 100, Journal of materials science, 33 (1998) 775-781.
[8] A. Atrens, A. Oehlert, Linearly-increasing-stress testing of carbon steel in 4 N NaNO3 and in Bayer liquor, Journal of materials science, 33 (1998) 783-788.
[9] A. Atrens, Z. Wang, ESEM observations of SCC initiation for 4340 high strength steel in distilled water, Journal of materials science, 33 (1998) 405-415.
[10] M. Wang, E. Akiyama, K. Tsuzaki, Effect of hydrogen and stress concentration on the notch tensile strength of AISI 4135 steel, Materials Science and Engineering A, 398 (2005) 37-46.
[11] M. Wang, E. Akiyama, K. Tsuzaki, Effect of hydrogen on the fracture behavior of high strength steel during slow strain rate test, Corrosion Science, 49 (2007) 4081-4097.
[12] L. Marchetti, E. Herms, P. Laghoutaris, J. ChAne, Hydrogen embrittlement susceptibility of tempered 9%Cr-1%Mo steel, International Journal of Hydrogen Energy, 36 (2011) 15880.
[13] E. Villalba, A. Atrens, An evaluation of steels subjected to rock bolt SCC conditions, Engineering Failure Analysis, 14 (2007) 1351-1393.
[14] E. Villalba, A. Atrens, SCC of commercial steels exposed to high hydrogen fugacity, Engineering Failure Analysis, 15 (2008) 617-641.
[15] Q. Liu, B. Irwanto, A. Atrens, The influence of hydrogen on 3.5NiCrMoV steel studied using the linearly increasing stress test, Corrosion Science, (2012) DOI: 10.1016/j.corsci.2012.10.019.
[16] A. Atrens, C. Brosnan, S. Ramamurthy, A. Oehlert, I. Smith, Linearly increasing stress test (LIST) for SCC research, Measurement Science and Technology, 4 (1993) 1281.
[17] N. Winzer, A. Atrens, W. Dietzel, G. Song, K. Kainer, Comparison of the linearly increasing stress test and the constant extension rate test in the evaluation of transgranular stress corrosion

cracking of magnesium, Materials Science and Engineering: A, 472 (2008) 97-106.
[18] A. Atrens, D. Mezzanotte, N.F. Fiore, M.A. Genshaw, Electrochemical studies of hydrogen diffusion and permeability in Ni, Corrosion Science, 20 (1980) 673-684.
[19] K. Yoshino, C. McMahon, The cooperative relation between temper embrittlement and hydrogen embrittlement in a high strength steel, Metallurgical and Materials Transactions B, 5 (1974) 363-370.
[20] A.M. Brass, J. Chêne, Influence of tensile straining on the permeation of hydrogen in low alloy Cr–Mo steels, Corrosion Science, 48 (2006) 481-497.
[21] M. Hashimoto, R. Latanision, Theoretical study of hydrogen transport during plastic deformation in iron, Acta Metallurgica, 36 (1988) 1837-1854.

Recovery of ductility observed in liquid gallium induced embrittlement of polycrystalline silver

Kodai Yamamoto, Kohei Arakawa, Hirokazu Koizumi*

Department of Physics, School of Science and Technology, Meiji University, Kawasaki 214-8571, Japan
* Corresponding author: koizumi@isc.meiji.ac.jp

Abstract Polycrystalline silver is embrittled by liquid gallium immediately after intimate contact between the solid and the liquid metals is made. When the tensile test is performed at room temperature, recovery of ductility has been observed if the contact time is long enough. This recovery is induced by formation of an intermetallic compound between silver and gallium. When the specimen is stressed above 420 K, embrittlement is not observed even if the contact time between the solid and liquid metals is short. This is the ductility trough reported in various solid and liquid metal couples that cause the liquid metal embrittlement. Although loss of embrittlement occurs as a function of contact time and as a function of test temperature, it may be difficult to connect the ductility trough with contact time dependent recovery from embrittlement, and there seems two independent recovery processes.

Keywords liquid metal embrittlement, ductility trough, sliver, gallium

1. Introduction

Liquid metal embrittlement (LME) is a phenomenon that normally ductile metals become brittle when they are stressed in close contact with certain kinds of liquid metals. Embrittlement appears as a decrease in maximum stress and fracture strain in a tensile test. Characteristic features of LME are [1]:
(1) LME occurs only in some solid and liquid metal couples. This is called "selectivity" and solid and liquid metal couples that cause LME are listed in ref. [2]. Solid and liquid metal couples such as polycrystalline aluminum and liquid gallium show a significant reduction of the maximum stress and fracture strain, while in case of a steel and liquid lead the maximum stress decreases to only a half of the original maximum stress [3]. The factors that determine the selectivity are not known.
(2) The embrittlement takes place immediately after intimate contact between solid and liquid metal is made. For polycrystalline aluminum-liquid gallium and polycrystalline silver-liquid mercury couples, embrittlement occurs even after the surface liquid metal is removed before stressing, if the contact time of the solid and liquid metals is long enough. In these cases, the degree of embrittlement increases with the contact time after a certain incubation time [4].
(3) The degree of embrittlement is severe near the melting temperature of the liquid metal, and the embrittlement disappears at a higher temperature. This temperature range is called "ductility trough", and is often explained as a result of temperature dependence of the yield stress [3] or stress relaxation at potential crack initiation site [5].

We have reported that liquid gallium induced embrittlement of polycrystalline silver is transitory [6, 7]. The silver tensile specimens with a small amount of gallium on the surface were kept in a furnace at the temperature T_h for a period of time t_h. The tensile test was performed to the specimens at 308 K. When t_h is small, the specimens undergo severe reduction of maximum stress and fracture strain, while for large t_h, the specimens show ductile behavior. The duration of brittleness is short when the quantity of gallium is small and the temperature of the furnace is high. For silver-gallium couple ductility trough exists as a function of the contact time.

The objective of the present investigation is to show that the ductility trough exits as a function of temperature as many other embrittlement couples, and to discuss differences between the ductility

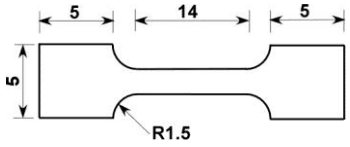

Fig. 1 Tensile specimen. The thickness is 2 mm.

trough as a function of temperature and that as a function of time.

2. Experimental

The tensile specimens used in this investigation is shown in Fig. 1. They were cut out from a silver plate of 99.98 % purity by electrodischarge machining. After mechanical polishing, the specimens were annealed at 1073 K for 2 hours. The average grain size of the specimens was 0.3 mm. A small amount of liquid gallium, 10 mg in weight and saturated with silver at 308 K, was deposited on the specimen, so that one of the four faces of the gauge section was completely covered with the gallium. To ensure the contact between the solid specimen and the liquid, the surface covered with liquid gallium was scratched with a needle. After immersing the specimen in liquid nitrogen to freeze the gallium, the specimen was placed in the tensile machine. The tensile test was performed on the specimen in a hot silicone oil bath in the temperature between 300 K and 465 K and in water between 274 K and 300 K. The strain rate was 1.2×10^{-2} s^{-1}.

The fracture surface was observed by the scanning electron micrograph (SEM).

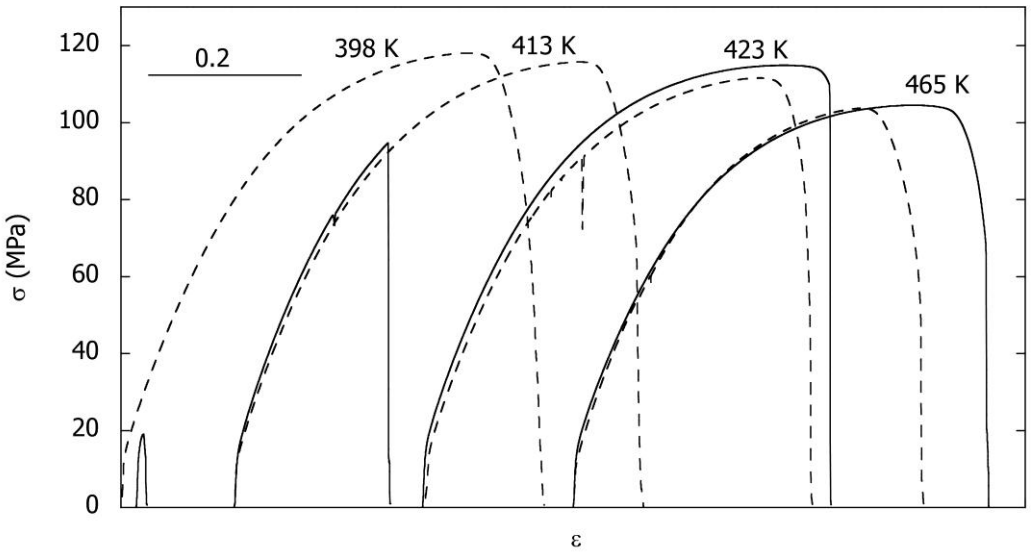

Figure 2. Stress-strain curves of silver specimen with gallium (solid lines) and without gallium (dashed lines). The test temperature is shown in the figure.

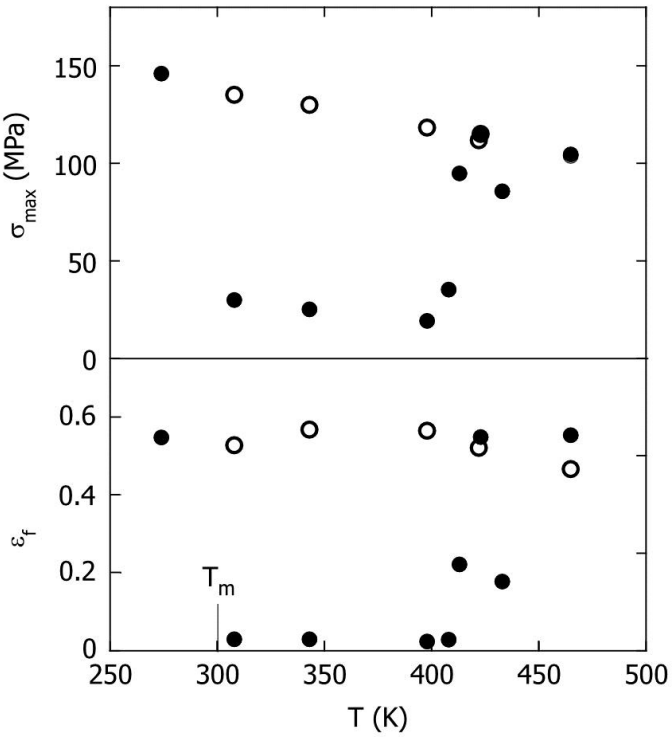

Figure 3. Temperature dependence of maximum stress σ_{max} and frcture strain ε_f of silver specimens tested with liquid gallium (solid circles) and without gallium (open circles). T_m indicates the melting point of gallium.

3. Results

Figure 2 shows some typical stress-strain curves of the specimens without and with liquid gallium on the surface. The test temperature is shown in the figure. Below 400 K, liquid gallium induces a significant reduction of the maximum stress σ_{max} and the fracture strain ε_f, while at 465 K liquid gallium has no effect on σ_{max} and no reduction of ε_f is observed. Around the transition temperature (413 K and 423 K in the figure), in the specimens with gallium the stress drops abruptly after the stress-strain curve reaches the maximum, while the decrease of the stress is gradual in the specimens without gallium at all temperatures measured and in the specimen with gallium at 465 K.

In Fig. 3 the maximum stress σ_{max} and the fracture strain ε_f are shown as a function of test temperature T. When the specimen is pulled without gallium, the maximum stress decreases with temperature, while the fracture strain is almost constant. Since the specimen was immersed in liquid nitrogen before the test to prevent supercooling of gallium, embrittlement is not observed below the melting temperature T_m of gallium (303 K). Above T_m the maximum stress and the fracture strain are reduced significantly by liquid gallium. The brittleness disappears above 420 K. This means that ductility trough starts at the melting temperature of gallium and ends around 420 K.

Figure 4 shows the SEM images of the fracture surfaces and the optical micrographs of the tensile specimens. When the test temperature is below 413 K, the fracture surface is apparently intergranular, although the surface is partially covered with liquid gallium, and the optical micrograph shows that the fracture surface is nearly perpendicular to the tensile axis. At 465 K, necking is observed in the specimen. The fracture surface is covered with liquid gallium. This

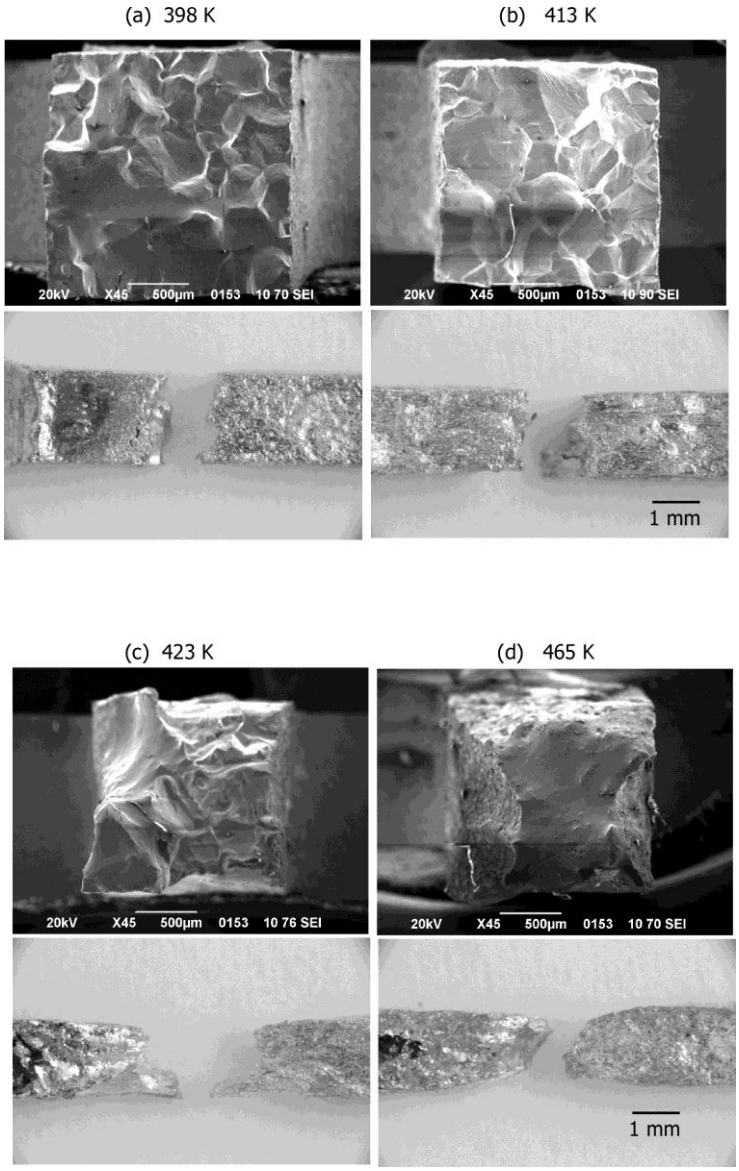

Figure 4. Scanning micrograph of the fracture surface (upper) and optical micrograph of the specimen (lower) tested at (a) 398 K, (b) 413 K, (c) 423K and (d) 465 K.

indicates that gallium is in liquid phase when the specimen fails. At 423 K, in spite of large maximum stress and fracture strain, the optical micrograph shows that reduction of cross-sectional area does not localize and the fracture surface is rough, which is different from the typical ductile fracture surface.

4. Discussion

In Fig. 3 we showed that the ductility trough exists as a function of temperature in polycrystalline silver-liquid gallium couple.

We have reported in [7] that for this couple the recovery from LME is observed if the contact time between the solid and liquid metals is long. In [7] the tensile test was performed at 308 K on the specimens with 10 mg of gallium after they were kept in a furnace at the temperature T_h for certain holding times t_h. Stress-strain curves are shown in Fig. 5(a) for the specimens of T_h =373 K. In Fig.

5(b) the maximum stress is shown as a function of the holding time t_h. Ductility recovers around 80 ks. Figure 5(c) shows the recovery time t_R as a function of the furnace temperature T_h. The recovery observed in the time dependence is considered due to formation of ζ'-phase or Ag_7Ga_3 by the X-ray diffraction analysis.

From Fig. 5(c), the recovery time of the specimen held at 465 K is estimated more than 10 ks, when it is stressed at 308 K. In the present experiment, however, the specimens stressed at 465 K is not embrittled, although the test was performed immediately after the specimen temperature became the test temperature, and the test ended in less than a few minutes. The specimen that is ductile at 465 K becomes brittle at 308 K. As shown in Fig. 4(d), the fracture surface of the specimen pulled at 465 K is covered with gallium flowing from the specimen surface. At this temperature the specimen

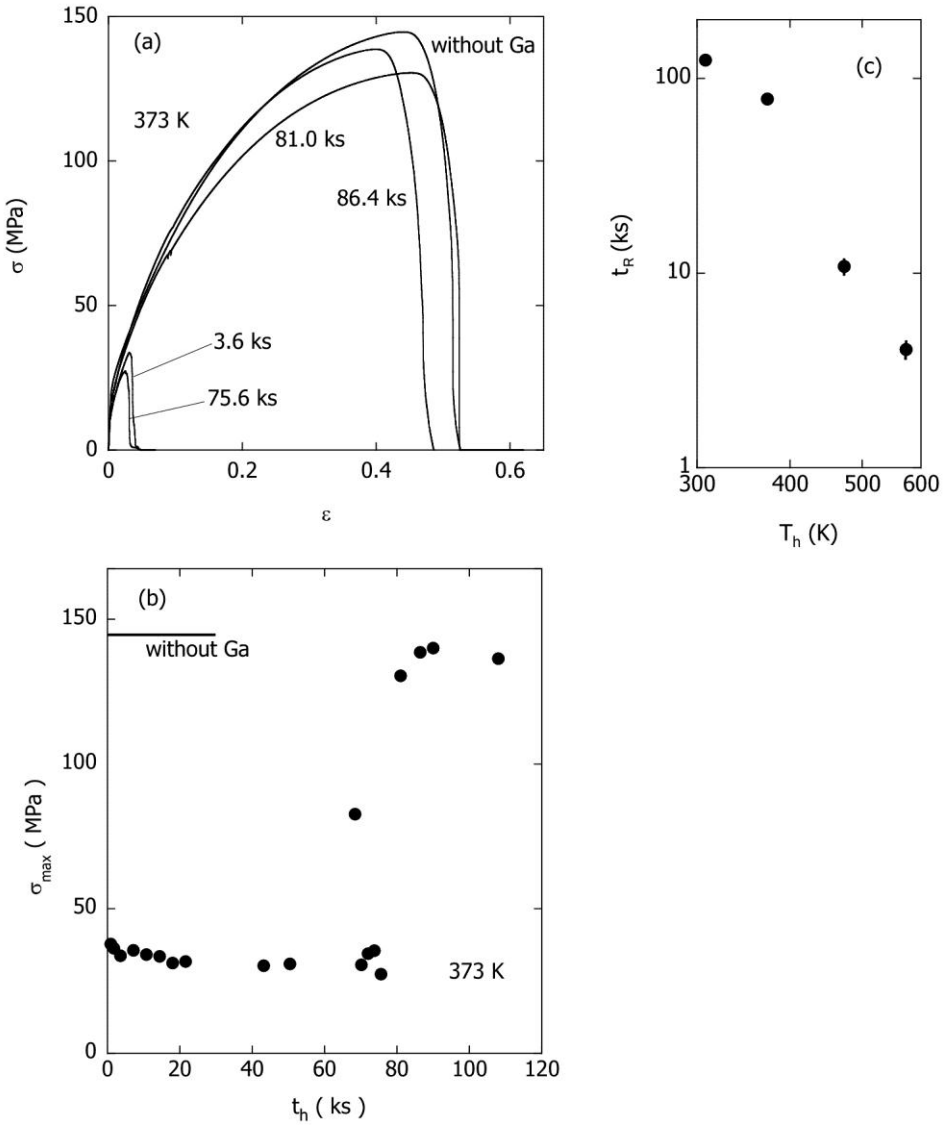

Figure 5. (a) The stress-strain curves. After the specimens were kept in contact with a small amount of gallium at 373 K for the time indicated in the figure, the tensile testing was performed at 308 K with a strain rate of 1.2×10^{-2} s^{-1}. (b) The maximum stress σ_{max} as a function of holding time t_h. (c) The time to recover ductility t_R as a function of the temperature of the furnace T_h [7].

is ductile despite gallium in liquid phase on the surface, and, therefore, the recovery of ductility at 465 K is not considered to be induced by formation of the intermetallic compound.

Various mechanisms of LME have been proposed, and it is still controversial whether crack initiation or crack propagation is a controlling process [1]. The specimen pulled at 423 K did not indicate clear necking (Fig. 4(c)), and the stress-strain curve shows abrupt drop after it reaches the maximum (Fig. 2). These indicate that a crack propagates very fast once a crack starts to move, and, therefore, a micro crack nucleation or start of crack motion seems to be especially blocked at this temperature.

5. Conclusion

Polycrystalline silver is embrittled by liquid gallium. Recovery from the embrittlement occurs if the contact time with liquid metal is long. This is considered induced by the formation of an intermetallic compound. Ductility trough is also observed as a function of test temperature in this solid and liquid metal couple. However, this ductility trough is not connected to forming the intermetallic compound.

References

[1] for a review: B. Joseph, M. Picat, F. Barbier, Liquid metal embrittlement: A state-of-the-art appraisal. Eur Phys J AP, 5 (1999) 19-31.
[2] F. A. Shunk, W. R. Warke, Specificity as an aspect of liquid metal embrittlement. Scripta metall, 8 (1974) 519-526.
[3] G. Nicaise, A. Legris, J. B. Vogt, J. Fost, Embrittlement of the martensitic steel 91 tested in liquid lead. J Nucl Mater 296 (2001) 256-264.
[4] K. Ina, H. Koizumi, Penetration of liquid metals into solid metals and liquid metal embrittlement. Mater Sci Engng A 387-389 (2004) 390-394.
[5] S. P. Lynch, Metal-induced embrittlement of materials. Mater Characterization 28 (1992) 279-289.
[6] K. Sakai, H. Koizumi, Time dependent embrittlement of polycrystalline Ag by liquid Ga, Procedia Engng 10 (2011) 643-648.
[7] K. Arakawa, K. Yamamoto, K. Sakai, H. Koizumi, to be submitted.

The Effects of Hydrogen on Mechanical Properties of Ni-base Alloys under the Static and Cyclic Loading.

Alexander Balitskii*, Lyubomir Ivaskevich, Volodimir Mochulskyi.

Department of Hydrogen Resistance of Materials Karpenko Physico-Mechanical Institute,
5 Naukova str., Lviv, 79601, Ukraine
* balitski@ipm.lviv.ua

Abstract The effect hydrogen on short-term strength, low-cycle durability and plane-stress fracture toughness of 04Cr16Ni56 and 05Cr19Ni55 alloys at pressure up to 35 MPa and temperature 293…1073 K was investigated. The modes of hydrogen action for which the mechanical properties of alloys are minimum were established: hydrogen pressure above 10 MPa (non-hydrogenated specimens of 04Cr16Ni56 alloy) and above 35 MPa (hydrogenated specimens of 05Cr19Ni55 alloy, hydrogen concentration C_H = 19 wppm). The plane-strain state conditions and, correspondingly, the conditions of the evaluation of plane-strain fracture toughness (K_{Ic}) were fulfilled on compact tension specimens of 04Cr16Ni56 with a thickness of 20 mm at hydrogen pressure above 10 MPa in the temperature range 293…473 K. Plane-stress fracture toughness K_c of 05Cr19Ni55 alloys was decreased at 293 K from 116 MPa·m$^{1/2}$ in helium to 78 MPa·m$^{1/2}$ in hydrogen under the pressure 30 MPa and to 68 MPa·m$^{1/2}$ in hydrogen under the pressure 30 MPa after preliminary high-temperature hydrogenation (with hydrogen concentration C_H = 19 wppm).

Keywords Hydrogen embrittlement, Fracture toughness, Alloy

1. Introduction

The production of turbine equipment requires a wide usage of dispersive hardened heat-resistant Fe-Ni alloys. In these products heat-resistant alloys are exploited at high temperatures in the contact with high-pressure hydrogen containing gas mixtures. Therefore one of the most important requirements for such alloys is their resistance to hydrogen degradation. In other words their ability to keep high level of mechanical properties under the action of hydrogen in wide range of exploitation parameters. At the same time, age-hardening alloys are known to be rather sensitive to hydrogen embrittlement [1-3].

The serviceability of structures in hydrogen is, as a rule, estimated according to the results of testing at room temperature [4-7]. This is explained by maximum sensitivity of steels and alloys to hydrogen degradation and complexity of experiments at elevated temperatures. However, the operating conditions of the equipment for hydrogen power engineering include static and cyclic loading of the products in hydrogen in fairly broad temperature ranges [7, 8], whereas the available literature data on the temperature dependences of mechanical properties in hydrogen are quite poor and ambiguous. In most cases, the influence of gaseous hydrogen on mechanical properties weakens as temperature increases and, according to the data presented in [6], the upper temperature of embrittlement under the analyzed conditions was equal to 573 K. At the same time, we reveal a significant decrease in the plasticity of heat-resistant nickel alloys in hydrogen under a pressure of 35 MPa at temperature1073 K [3, 7, 9].

In what follows, we study the influence of high-pressure gaseous hydrogen on short-term strength, low-cycle durability, and static crack resistance of nickel based alloys in the temperature range 293-1073 K.

2. Materials and Experimental Procedure

Two types of dispersion-hardened alloys were investigated: 04Cr16Ni56 and 05Cr19Ni55. Alloying

with niobium, vanadium, titanium, aluminum and boron leads to the formation of carbide TiC, borides Me_3B_2, and intermetallics $Ni_3(Al,Ti,Nb)$ in the amounts of to 8 % for 05Cr19Ni55 alloy and up to 15…17 % for 04Cr16Ni56 alloy, which substantially increases their high-temperature strength [8] and significantly influences the sensitivity to the action of hydrogen [3, 9]. Heat treatment regimes and the mechanical properties of alloys (Table 1) in helium and in hydrogen under a pressure of 35 MPa after preliminary hydrogenation to hydrogen content of 19 wppm (05Cr19Ni55 alloy) and 20 wppm (04Cr16Ni56 alloy). After heat treatment, the grain size was 40…60 μ, and the particle size of the intermetallic γ′-phase was 320…500 Å.

Table 1. Chemical Composition, Modes of Thermal Treatment and Mechanical Properties of Alloys in Helium/Hydrogen (35 MPa) at Room Temperature

Alloy	Thermal Treatment		Mechanical Properties					
	Solution treat-ment	Mode of aging	σ_u, MPa	σ_y MPa	δ %	ψ %	Number of cycles to frac-ture, ben-ding strain 1.6 %	K_c MPa·$m^{1/2}$
04Cr16Ni56 (C-0.04; Si-0.12; Cr-16.4; Mo-5.24; V-0.35; Nb-5.19; Ti-0.58; Al-1.0; Fe-15.14; Cu-0.49; Ni-bal)	1373K, 1 h	1023 K, 16 h + 923 K, 10 h	1320 880	840 750	34 4	48 12	3205 54	134 52
05Cr19Ni55 (C-0.05; Si-0.23; Cr-19.0; Mo-8.87; Nb-1.73; l-1.49; Fe-12.0; Cu-0.02; Ni-bal)	1323K, 1 h	1000 K, 15 h + 923 K, 10 h	1080 970	650 660	35 7	38 21	2560 199	116 68

Static tensile tests with recorded “stress-strain” curves were carried out on standard five-fold cylindrical specimens using displacement rate V = 0.1 mm/min. During the test the specimens were positioned into the chamber specially designed for high-temperature tests at 293...1093 K temperature range under 0.1...30 MPa hydrogen pressure. Specimens were tested in temperature range 293...1073 K under 30 MPa of hydrogen pressure and, as a comparison, in helium. The low-cycle durability for pure strain-controlled sign-preserving bending was investigated under pressures of 30 MPa for the strain amplitudes ε = 1.6% and loading frequency of 0.5 Hz on polished plane specimens with a working part size 3 x 6 x 20 mm. Stress intensity factor under static loading K_c was computed either for the maximum force F_c in the "F-V" linear diagram or for the force F_Q determined by using the 5% secant for nonlinear diagrams. Rectangular compact specimens 50 × 60 × 20 mm in size were tested for eccentric tension in a high-pressure chamber under pressures of 0.4-30 MPa at strain rate of 0.1 mm/min. The values of K_c can be calculated from the Srawley-Gross formula [10].

To determine the indicated mechanical characteristics in hydrogen, the working chambers were preliminarily evacuated, blown-out with hydrogen, again evacuated, and filled up with hydrogen to a given pressure. At high temperatures, the specimens were held under the testing conditions for 30 min until the attainment of thermal equilibrium.

Earlier we established that, at some region of hydrogen pressure and strain rate exists a maximum

influence of hydrogen on the plasticity, low-cycle fatigue life, and static and cyclic crack resistance of martensitic steels and high nickel alloys [3, 7, 9]. In short-term tension, austenitic dispersion-hardened steels are substantially embrittled by hydrogen only after preliminary hydrogenation at elevated temperatures when its content becomes greater than 12 wppm [3, 7]. This is why we held a part of the specimens for 10 h in a hydrogen atmosphere under 623 K and 35 MPa. These regimes provide the hydrogenation of specimens to hydrogen contents of 19 wppm (05Cr19Ni55 alloy) and 20 wppm (04Cr16Ni56 alloy). Hydrogenated and non-hydrogenated specimens were tested in helium and hydrogen under different pressures.
Hydrogen concentration (C_H) was determined with a LECO TCH 600 instrument [11] with precise 0.1 ppm (3 samples for point).

2. Hydrogen Pressure Influence on the Mechanical Properties.

It is known from the literature for almost materials and testing methods the influence of hydrogen increases proportionally to the square root of pressure [1, 4, 6, 12]. The pressure range for which this dependence is valid is studied insufficiently. In the process of short-term static tension, the properties of carbon steels deteriorate only in the range 0-10 MPa. Embrittlement of specimens made of Inconel-718 alloy begins only when the pressure reaches 10 MPa and increases up to 70 MPa [12]. Hydrogen influence on plasticity of steels and many other materials increases in the entire pressure range (0-70 MPa) [1, 3, 6, 12].
In the case of 04Cr16Ni56 alloy the dependence of low-cycle durability (N), the plasticity parameters (δ and ψ) (Fig.1a) and plane-stress fracture toughness (K_c) (Fig.2, curves 3, 4) on the hydrogen pressure consists of two regions. In the first region (low pressures), parameters N, δ, ψ and K_c drops abruptly, and in the second, the negative influence of hydrogen is practically independent of pressure (figs. 1, 2). This means that there exists a pressure which cause the limiting degradation of materials properties. An additional effect of preliminary dissolved hydrogen (C_H = 20 wppm) on the properties of 04Cr16Ni56 alloy was manifested at hydrogen environment pressure less than 10 MPa. The parameters of loading and the modes of hydrogen action for which the mechanical characteristics of the investigated alloys are minimum at 293 K can be formulated as follows: –the strain rate V_{def} = 0,1 mm/min ($6.7 \cdot 10^{-5}$ s^{-1}) at short-term static tension and static crack propagation; – the frequency and amplitude of bending under the conditions of low-cycle fatigue are ν = 0, 5 Hz and ε = 1.6% respectively, and the pressure of hydrogen must be higher than 10 MPa.

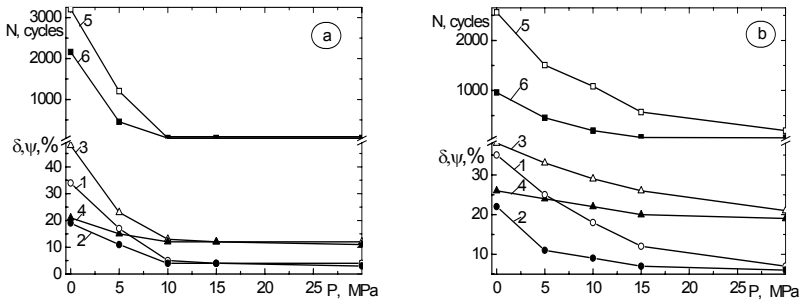

Figure 1. The relative elongation δ (1, 2), reduction of area ψ (3, 4) (V = 0,1 mm/min.) and number cycles to failure N (5, 6) (ε = 1,6%) specimens of 04Cr16Ni56 (a) and 05Cr19Ni55 (b) alloys versus hydrogen pressure P at 293 K: 1, 3, 5 – non-hydrogenated specimens; 2, 4, 6 – hydrogenated specimens.

In the case of 05Cr19Ni55 alloy the low-cycle durability N, plasticity parameters δ and ψ (Fig.2b, curves 1, 3, 5) and plane-stress fracture toughness K_c (Fig.3, curve 1) decrease in whole hydrogen pressure range. Preliminary dissolved hydrogen (C_H = 19 wppm) leads to a considerable additional decrease in the properties of this alloy (Fig.2b, curves 2, 4, 6; Fig.3, curve 2). Maximum hydrogen effect achieved on hydrogenated specimens at hydrogen pressure above 10 MPa.

Thus, to estimate the serviceability of alloy 04Cr16Ni56 it is suffices to test the specimens in gaseous hydrogen, while for alloy 05Cr19Ni55 there is a need for preliminarily hydrogenation.

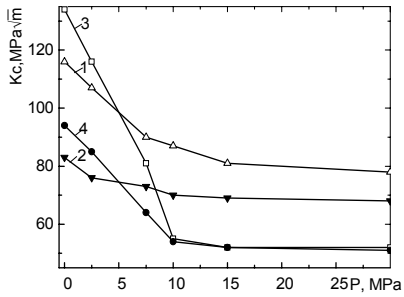

Figure 2. Fracture toughness K_c of 05Cr19Ni55 (1, 2) and 04Cr16Ni56 (3, 4) alloys versus hydrogen pressure P at 293 K: 1, 3 – non-hydrogenated specimens; 2, 4 – hydrogenated specimens.

Hydrogen decreases the stress intensity factor K_c and affects the fracture morphology. Under the conditions of maximum hydrogen embrittlement, the load-displacement diagrams become linear with sharp maxima (as functions of the load) (Fig.3a) and correspond to type I [10]. The fracture surfaces of the specimens are intergranular with cleavage facets typical of brittle fracture (Fig.4b), when in helium the honeycomb relief with ductile intergranular fracture portions is prevailed (Fig.4a). The values of K_c can be regarded as equal to K_{1c}, i.e., they satisfy the condition $l,b > 2.5(K_c^H/\sigma_{0,2}^H)^2$, where l is the crack length and b is the thickness of the specimen [10]. The indicated condition is satisfied at room temperature for alloy 04Cr16Ni56 under pressures of hydrogen higher than 10 MPa for which K_{1c} is equal to 52 MPa·m$^{1/2}$. The plane-strain state conditions were not fulfilled for the specimens made of alloy 05Cr19Ni55.

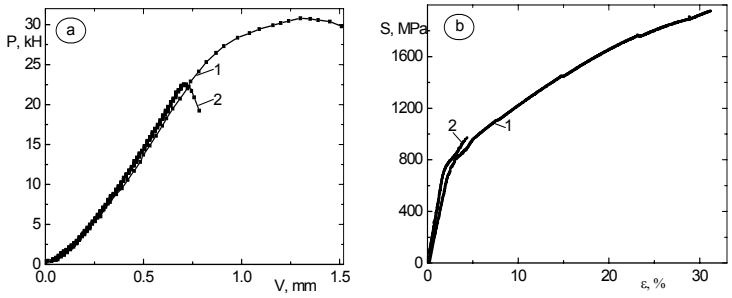

Figure 3. Diagrams "loading – crack opening displacement" (a) and true "stress-strain" diagram (b) of 04Cr16Ni56 alloys in helium (1) and hydrogen (2) under pressure 30 MPa at 293 K.

Hydrogen produced changes in true stress diagrams of both alloys in wide pressure and temperature range: essentially decrease failure stress and deformation of specimens (Fig.3b).

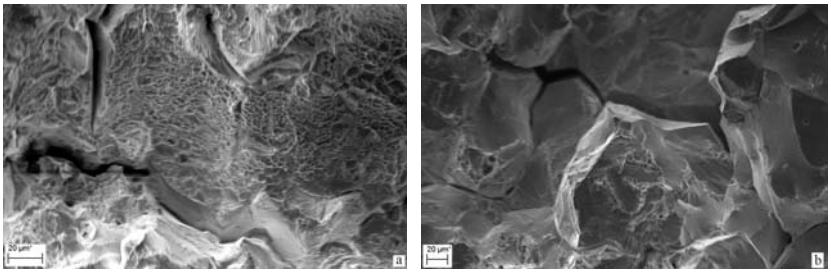

Figure 4. Fracture surface of 04Cr16Ni56 alloys under static loading of compact specimens in helium (a) and hydrogen (b) under pressure 30 MPa at 293 K.

3. Influence of Temperature on Hydrogen Embrittlement of the Alloys.

The strength of the alloy 05Cr19Ni55 significantly decreases in helium at temperatures higher than 873 K. This process is accompanied by a decrease in plasticity parameters for the alloy 05Cr19Ni55 at temperature 873 K and a significant increase in the relative elongation and reduction of area for specimens made of this alloy at temperatures 973…1073 K (Fig.5, curves 5, 6). At temperatures range 973…1073 K we observed a decrease in plasticity parameters for the alloy 04Cr16Ni56 (Fig.5, curves 7, 8).

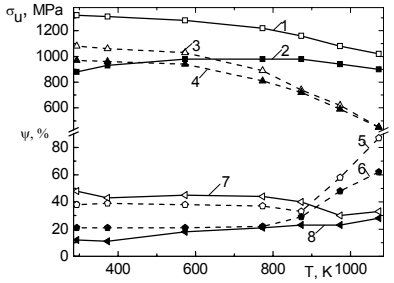

Figure 5. Temperature dependences of ultimate strength σ_u (1-4) and reduction of area ψ (5-8) of 04Cr16Ni56 (1, 2, 7, 8) and 05Cr19Ni55 (3, 4, 5, 6) alloys at helium (1, 3, 5, 7) and hydrogen (2, 4, 6, 8) under the pressure 30 MPa.

The drop of plasticity of the dispersion-hardening materials within the temperature range of intense phase transformations is caused by the localization of strains on the grain boundaries due to the intense redistribution of Ni, Ti, and Al in the boundary regions. Moreover, the increase in plasticity observed at higher temperatures is caused both by partial coagulation of hardening phases and possible dissolution of small amounts of finely divided precipitations [8]. In alloy 04Cr16Ni56 that contain higher amount of refractory elements (Table 1), the diffusion processes are decelerated and, therefore, the drop of strength is small and the temperature of plasticization is probably higher than 1073 K (Fig. 5, curves 1, 7).

The ultimate strength of alloy 04Cr16Ni56 is sensitive to hydrogen action (Fig. 5, curves 1, 2). At the same time σ_u of specimens made of alloy 05Cr19Ni55 decreases in hydrogen insignifically (Fig. 5, curves 3, 4). The hydrogen effect on plasticity parameters δ and ψ (Fig. 6), low-cycle durability N (Fig. 6) and plane-stress fracture toughness K_c (Fig. 7) of both alloys is essential in the temperature range 293…773 K and appreciable at all other temperatures. As temperature increases from 773 to 873 K the hydrogen effect on reduction of area of the alloy 05Cr19Ni55 specimens initially decrease and again increase at 973 and 1073 K (Fig. 5, curves 5, 6). That suggests that at 1073 K the hydrogen-induced processes of localization of strains and fracture (mainly intergranular) occur in this alloy so intensely that the coagulation of hardening phases is insufficient for the high-temperature plasticization observed in helium. This phenomenon we established earlier on dispersion-hardening austenitic steels [13].

The additional effect of preliminary hydrogenation on parameter of static growth resistance K_c for the alloy 05Cr19Ni55 is appreciable only at room temperature (Fig. 6, curves 3, 4, 6, 7). At 373 K the value of K_c for hydrogenated and non-hydrogenated specimens are almost equal, i.e., this temperature is sufficient for hydrogenation of dispersion-hardening nickel base alloys from the hydrogen atmosphere. For all loading modes, the degree and temperature interval of hydrogen degradation for alloy 04Cr16Ni56 is much larger than for alloy 05Cr19Ni55 (figs. 5-7).

The plane-strain condition required for the evaluation of K_{Ic} were fulfilled on compact tension specimens made of alloy 04Cr16Ni56 with a thickness of 20 mm at hydrogen pressure above 10 MPa in the temperature range 293…473 K. Fracture toughness K_c for alloy 05Cr19Ni55 was decreased at 293 K from 116 MPa·$m^{1/2}$ in helium to 78 MPa·$m^{1/2}$ in hydrogen under the pressure

30 MPa and to 68 MPa·m$^{1/2}$ in hydrogen under the pressure 30 MPa after preliminary high-temperature hydrogenation (with hydrogen concentration 19 ppm). The plane-strain conditions were not fulfilled at these two cases.

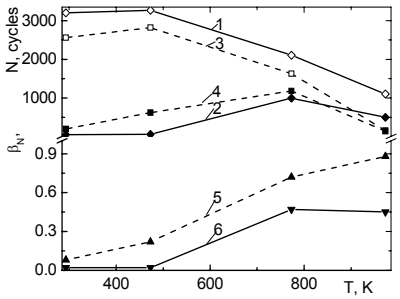

Figure 6. Temperature dependences of number cycles to failure N (1-4) (ε = 1,6%) and coefficients of hydrogen influence $\beta_N = N_H/N_{He}$ (5, 6) on 04Cr16Ni56 (1, 2, 6) and 05Cr19Ni55 (3, 4, 5) alloys: 1, 3 – helium, 2, 4 – hydrogen under the pressure 30 MPa.

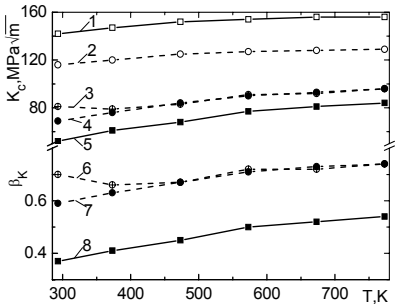

Figure 7. Temperature dependences of plane-stress fracture toughness K_c (1-5) and coefficients of hydrogen influence $\beta_K = K_c^H/K_c^{He}$ (6-8) on 04Cr16Ni56Nb5Mo5TiAl (1, 5, 8) and 05Cr19Ni55Nb2Mo9Al (2-4, 6, 7) alloys: 1, 2 – helium, 2, 3, 6 – hydrogen under the pressure 30 MPa, 4, 7 – hydrogen under the pressure 30 MPa after preliminary hydrogenation (623 K, 35 MPa H_2, 10 h).

Conclusions.

The parameters of loading and the modes of hydrogen action for which the mechanical characteristics of the investigated alloys are minimum at room temperature can be formulated as follows:

– strain rate $V_{def} \leq 6.7 \cdot 10^{-5}$ s^{-1} for tensile test and the strain amplitude ε = 1.6 % under the conditions of low-cycle fatigue at hydrogen pressures above 10 MPa for the alloy 04Cr16Ni56 and hydrogen pressures above 15 MPa at concentration of preabsorbed hydrogen 19 wppm for the alloy 05Cr19Ni55;

– for static crack propagation at hydrogen pressure above 10 MPa for the alloy 04Cr16Ni56 and hydrogen pressure above 15 MPa at concentration of absorbed hydrogen 19 wppm for the alloy 05Cr19Ni55.

The plane-strain conditions required for the evaluation of K_{Ic} were fulfilled on compact tension specimens made of alloy 04Cr16Ni56 with thickness of 20 mm at hydrogen pressure above 10 MPa in the temperature range 293…473 K.

For all loading modes, the degree and temperature interval of hydrogen degradation for 04Cr16Ni56 alloy is much larger than for 05Cr19Ni55 alloy.

References

[1] Chandler W.I. and Walter R.I. Testing to determine the effect of high pressure hydrogen environment on the mechanical properties of metals, in: Hydrogen Emrittlement Testing,

ASTM STP 543, Philadelphia, 1974, pp. 170–197.
[2] N.R. Moody, F.A Greulish, Hydrogen indused slip band fracture in Fe-Ni-Co superalloy. Scr. Metallurgica, 19 (1985) 1107-1116.
[3] A. I. Balitkii, L.M. Ivaskevich, V.M. Mochulskyi. Temperature Dependences of Age-Hardening Austenitic Steels Mechanical Properties in Gaseous Hydrogen, in: Proceedings on CD ROM of the 12th International Conference on Fracture, Ottawa, Canada, July 12-17, 2009, edited by M. Elboujdaini, Ottawa: NRC, 2009, Paper No T19.001. 7 p.
[4] Physicomechanical Institute: Development and Achievements [in Ukrainian], Lviv, 2001, 430 p.
[5] A. I. Belogurov, V. S. Radchuk, M. A. Rudis, A. M. Sushkov, and V. 1. Kholodnyi, Strength analysis of structural elements of hydrogen power-generating equipment, Materials Science, 40, (2004), No. 6, pp. 814—821.
[6] B. A. Kolachev, Hydrogen Brittleness of Metals [in Russian]. Metallurgiya, Moscow, 1985.
[7] V. I. Tkachev, L. M. Ivaskevich, V. I. Vitvitskii, Specific features of determination of the susceptibility of steels to hydrogen degradation. Altern. Energ., 32 (2005). No. 12, 46-51.
[8] C. T. Sims and W. C. Hagel (eds.). The Superalloys. Wiley, New York, 1972.
[9] V. I. Tkachev, I. M. Levina, L. M. Ivaskevich, Distinctive features of hydrogen degradation of heat-resistant alloys based on nickel, Materials Science, 33 (1997), No. 4, 524-531.
[10] W. F. Brown, J. E. Srawley. Plane Strain Crack Toughness Testing of High Strength Metallic Materials, ASTM Publ., No. 410, 1966.
[11] LECO TCH 600 – Series (Nitrogen, Oxygen, Hydrogen Determination), LECO Corporation : MI, USA, 2003. 6 p.
[12] H. R. Gray. Testing for hydrogen environment embrittlement: Experimental variables. In: Hydrogen Embrittlement Testing, ASTM STP 543, ASTM Baltimore, 1974, pp. 133-151.
[13] V. I. Tkachev, L. M. Ivaskevich, V.M. Mochulskyi, Temperature dependences of mechanical properties of austenitic and martensitic steels in hydrogen, Materials Science, 45, (2007), No 5, 654-666

Review of Hydrogen Diffusion Models for the Analysis of Hydrogen Embrittlement of Materials

Jesús Toribio[1,*], **Viktor Kharin**[1]

[1] University of Salamanca, Campus Viriato, 49022 Zamora, Spain
* Corresponding author: toribio@usal.es

Abstract Hydrogen-assisted fracture (HAF) of metals is the problem of major concern in structural integrity. HAF is rate limited by hydrogen accumulation in fracture sites in metals. Diffusion is a relevant stage of transport that supplies hydrogen to fracture process zones. Addressing the purposes of HAF analysis, modelling of hydrogen diffusion with account for physical-mechanical fields and factors of material microstructure (hydrogen trapping) is revisited. Generalised system of equations of trapping-affected hydrogen diffusion is derived from the kinetics principles. For circumstances, which are relevant to plenty of engineering HAF cases, specialised models of "microstructure informed" stress-strain-assisted hydrogen diffusion in metals are retrieved and collated under the prism of their suitability for HAF analyses.

Keywords Hydrogen assisted fracture, Hydrogen diffusion, Modelling

1. Introduction

Hydrogen is often the key factor in environmentally assisted fracture of metals, as far as it may be present *per se* in the environment or discharge in cracks due to favourable local electrochemistry [1]. Harmful effects of hydrogen on metals ("hydrogen embrittlement") form the long-standing problem of the mechanics of materials. Hydrogen transport to damage sites is ubiquitous component of every hydrogen assisted fracture (HAF) process, which is rate-limited by hydrogen delivery to meet requirements of operating fracture mechanism. A series of kinetic processes involved in HAF have been identified, among which hydrogen diffusion has been substantiated as the governing mode of hydrogen supply to fracture nuclei [1-3]. Continuum modelling of hydrogen diffusion has been focused as the key issue of HAF studies and their engineering applications [1,3-6].

Concerning hydrogen behaviour in metals, important disconformities [2,7,8] were witnessed between experience and the Fick's diffusion laws. Various issues have been pointed out as potential causes of these inconsistencies, and several analyses have been performed culminating in continuum equations of diffusion built up from microscopic or phenomenological considerations [1,4-11]. However, comprehensive accounting for a variety of potentially influencing factors is complicated undertaking, and numerous specialised diffusion models, which attended to different microstrictural features, have been raised [8]. An outlook of hydrogen diffusion modelling for the purposes of HAF analysis is here presented.

2. Background Theory of HAF [1,5]

HAF is considered a result of synergic action of stress, strain and hydrogen amount in material. Fracture event takes place in a locus identified by position vector **x,** when hydrogen concentration C accumulated there over time t reaches the critical level C_{cr} dependent on stress-strain state:

$$C(\mathbf{x},t) = C_{cr}\left(\boldsymbol{\sigma}(\mathbf{x},t), \boldsymbol{\varepsilon}_p(\mathbf{x},t)\right), \tag{1}$$

where $\boldsymbol{\sigma}$ y $\boldsymbol{\varepsilon}_p$ are, respectively, the tensors of stress and plastic strain. Condition of contact between the concentration and the criterial surfaces, $C(\mathbf{x},t)$ and $C_{cr}(\mathbf{x},t)$, respectively, which reads

$$\partial C(\mathbf{x},t)/\partial \mathbf{x} = C_{cr}\left(\boldsymbol{\sigma}(\mathbf{x},t),\boldsymbol{\varepsilon}_p(\mathbf{x},t)\right)/\partial \mathbf{x}, \tag{2}$$

accompanies the fracture criterion (1) to form the system of equations to define the location $\mathbf{x}_{cr}$ and time t_{cr} of HAF event [12]. Hydrogen transport towards fracture sites is dominated by diffusion, which defines the left-hand parts of Eqs. (1) and (2).

It is known that material damage is associated with crystal imperfections, and that they act as hydrogen traps (T-sites) for H atoms where their free energies G_T are less than that for ordinary lattice (L-)sites G_L (Fig. 1a). The ratio at.H/at.Me can there substantially exceed that in L-sites [2,3,4,6], as follows from the equilibrium partition of hydrogen between T- and L-sites [2,4,6,13]

$$\frac{\theta_T}{1-\theta_T} = \frac{\theta_L}{1-\theta_L} K \quad \left(K = e^{\beta E_b}\right), \tag{3}$$

where $\theta_X = C_X/N_X$ is hydrogen saturation of X-type sites (X = L or T) defined by volume concentrations of these sites in metal, N_X, and of hydrogen allocated to them, C_X, so that the total concentration $C = \Sigma C_X$, $E_b = G_L - G_T$ is the binding energy of hydrogen to trap, and $\beta = (RT)^{-1}$ is the Boltzmann's factor in terms of the gas constant R and temperature T. Then, e.g., for steels at usual HAF occurrence conditions $T \approx 300$ K and $\theta_L \sim 10^{-6}$ at utmost [3,6], reported values of E_b, being approximately in the range from 0.25 to 1.5 eV [2,14,15] yield $K \geq \sim 10^4$ and $\theta_T/\theta_L \geq \sim 10^4$.

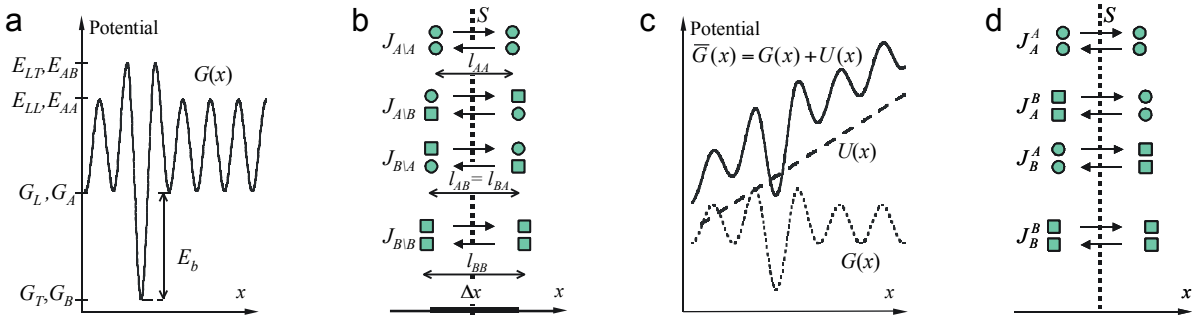

Figure 1. Schematics of (a) potential-position trace $G(x)$ for H in a lattice with different type sites L and T (or A and B); (b) combination of diffusion jumps between sites of different kinds (A – circles, B – quads) to evaluate partial fluxes; (c) distortion of lattice potential $G(x)$ by superposed field U; (d) combination of hops to establish partial balances.

To this end, whenever L/T-partition of hydrogen in volume element $d^3\mathbf{x}$ around a point $\mathbf{x}$ is in equilibrium, all partial concentrations $C_i(\mathbf{x},t)$ (i = 1,2,…) are related one to another via Eq. (3), so that all them, including the one corresponding to crystal imperfections responsible for HAF micro-mechanism, are biunivocally related to the total one $C(\mathbf{x},t)$. In this case, continuum description of local HAF event by Eqs. (1)-(2) holds, as well as it may be rewritten explicitly in terms of the responsible partial concentration C_X merely by changing there the variable according to Eq. (3). Otherwise, HAF should be described taking in Eqs. (1)-(2) responsible concentration C_X instead of C, and accounting for L/T-exchange kinetics in analysis of hydrogen transportation.

At any rate, hydrogen delivery to fracture sites proceeds by thermally activated hopping of H atoms between available sites in metal, i.e., by diffusion that turns out to be affected by trapping [2,4,6,7,10,13]. In this context, diffusion modelling is crucial for HAF analysis, prediction and control, as far as, combining with HAF experiments able to reveal fracture initiation time t_{cr} and location $\mathbf{x}_{cr}$, this allows to specify the critical concentration $C_{cr}(\boldsymbol{\sigma},\boldsymbol{\varepsilon}_p)$, i.e., the fracture criterion (1), and to employ this criterion for assessment of fracture time of structures [12,16].

3. Modelling of Hydrogen Diffusion with Trapping: Backgrounds Revisited

Both atomistic and thermodynamic arguments have been used to derive diffusion equations [1,4-11,13,15]. These approaches are not contradictory, but complementary [11] and capable to converge into the same field equations with certain insights about specific factors. Concerning traps, they were incorporated into resulting field equations in some cases via plausible postulating [4,6,7,17], but not from background principles (excepting few attempts with limited offspring [10,18,19] for HAF). In this section, diffusion equations grounding upon diffuser jumps probabilities is revisited.

3.1. Flux Equations

Isothermal diffusion by particles hopping among sites of kinds A and B is considered adopting the techniques used elsewhere [11,13,15,18-20]. Concerning the flux of the species through unit surface S normal to x-axis and situated there at position x, eight possible elementary steps can be grouped in pairs as shown in Fig. 1b, where l_{IJ} (I,J = A or B) are jump distances between specified sites, so that each couple renders the net flux $J_{A\backslash B}$ by forth and back hops between transboundary A and B sites, which are here diffuser releasers and receptors, respectively. The transition frequency Γ_{AB} from A-sites located at x' to B-ones at x'' per unit time depends on attempt frequency Ω_{AB} controlled by particle vibration frequency at given site ω_{0A} and by potential barrier $\Delta E_{AB} = E_{AB} - G_A$, where E_{AB} is the free energy at saddle point of lattice potential $G(x)$ between A and B (Fig. 1a). The frequency of successful hops depends on combined probability Y_B, which merges the probabilities γ_B that encountered receptor sites are the B-type ones and Θ_B that they are empty, that is

$$\Gamma_{AB} = \left[\Omega_{AB}\right]_{x'}\left[Y_B\right]_{x''} \text{ at } \Omega_{AB} = \omega_{0A}^{x}\exp\left(-\beta\Delta E_{AB}\right),\ Y_B = \gamma_B\Theta_B,\ \gamma_B = N_B/N\ ,\ \Theta_B = 1 - \theta_B, \qquad (4)$$

where $\omega_{0A}^{x} = \omega_{0A}f_A^{x}$ to reckon up the fraction f_A^{x} of hops that contribute to the flux through S having directions towards it, and $N = \Sigma N_i$ is the volume concentration of all available sites. (Note, that process parameters f_A, l_{AB} and ΔE_{AB}, according to the crystal symmetry, can depend on the x-axis orientation with respect to the lattice, causing this way diffusion anisotropy. They are isotropic, e.g., for interstitial sites in cubic lattice, and can be for "spherical" point-wise defects there, yielding $f_A = f = 1/6$ irrespectively of orientation.) Jump probability to any site is assumed to be not conditioned by that to another.

When some imposed potential field $U(x)$ distorts the lattice relief $G(x)$, Fig. 1c, ΔE_{AB} depends on jump sense, which biases the hopping probabilities. This implies modification of hopping frequency (4) with the factor $\exp(\pm\frac{1}{2}\beta\Delta x\nabla_x U)$, where the lower/upper sign corresponds to jumps pro-/counter-wise the x-direction, $\Delta x = x' - x''$, and ∇_x is the x-component of a gradient.

Reckoning up the hops of particles from A to B sites through control surface S at position x, using Taylor series expansions of involved variables about x with respect to Δx and truncating them at the second term, the net partial transfer by forth and back A→B jumps can be obtained

$$\mathbf{J}_{A\backslash B} = -d_{AB}\left\{Y_B \nabla C_A - C_A\left(\nabla Y_B - \beta Y_B \nabla U\right)\right\}, \tag{5}$$

where the diffusivity $d_{AB} = \Omega_{AB} l_{AB}^2$ when $\Delta x = l_{AB}$ is taken. The total diffuser flux vector $\mathbf{J}$ is the sum of the net partial ones $\mathbf{J}_{A\backslash B}$ over all pairs of site kinds A and B, which reads:

$$\mathbf{J} = \sum_{A,B} \mathbf{J}_{A\backslash B} = -\sum_{A,B} d_{AB} Y_B C_A \nabla \ln\left(e^{\beta U} C_A / Y_B\right). \tag{6}$$

This holds for arbitrary number m of site types, e.g., the L-sites and (m – 1) kinds of traps T_i (i=1,…,m – 1). Presented flux equations advance those derived elsewhere [18] in that arbitrary occupation degrees θ_i (i = 1,…,m) towards saturation are here admitted for all kinds of sites, and that alteration of lattice potential relief by some superposed field $U(x)$ is taken into account.

Description of diffusion in terms of specified partial fluxes can be supplemented with mass-balance relation being now the usual continuity equation:

$$\frac{C(\mathbf{x},t)}{\partial t} = -\nabla \cdot \mathbf{J}\left(= \nabla \cdot \sum_{A,B} d_{AB} Y_B \left[\nabla C_A - C_A \nabla \ln\left(e^{-\beta U} Y_B\right)\right]\right). \tag{7}$$

3.2. Mass Balance

In contrast to the one-level system (single kind of sites), Eq. (7) does not accomplish description of diffusion in terms of concentrations C_i (i = 1,…,m) for the m-level case (m > 1) where a system of m balance equations must be built up. This requires to combine the same diffusion steps as shown in Fig. 2d to gather all forth and back jumps across S that fill/vacate the sites of the sort A in a region Δx around a point x by surmounting saddle points at $x \pm \Delta x/2$. Desired equations are derived here following the random walk theory and its continuum implementation [19,20].

Considering two-level system and addressing the net species supply into A-sites in a domain $\Delta x \ni x$ by overcoming saddle point at $x - \Delta x/2$ from all outer A- and B-sites, involved diffusion steps include the net income flux $J_{A\backslash A}$, and the resulting B⇆A-exchange flux, which is as follows:

$$J_A^B = \left\{e^{-\frac{1}{2}\beta \Delta x \nabla_x U}\left[C_B l_{AB} \Omega_{BA}\right]_{x-\Delta x}\left[Y_A\right]_x - e^{\frac{1}{2}\beta \Delta x \nabla_x U}\left[C_A l_{AB} \Omega_{AB}\right]_x \left[Y_B\right]_{x-\Delta x}\right\}. \tag{8}$$

The net exit from A-sites in a domain Δx towards all sites beyond $x + \Delta x/2$ is defined similarly. Then, balancing transitions at both extremes of Δx, using power series expansions and disregarding higher order terms with Δx, mass balance for the species dwelling in A-sites can be derived. However, calculations in general terms are overly long and tedious, so that now we content ourselves with particular case when the sites characteristics are isotropic and uniform, i.e., jump frequencies $\Omega_{...}$ and lengths $l_{...}$ are constant, for which the following is deduced:

$$\frac{\partial C_A}{\partial t} = d_{AA}\nabla\cdot\left[Y_A C_A \nabla \ln\left(e^{\beta U} C_A / Y_A\right)\right] + d_{BA} Y_A \nabla\cdot\left[C_B \nabla \ln\left(e^{\beta U} C_B\right)\right] - d_{AB} C_A \left(\nabla^2 Y_B - \beta \nabla Y_B \cdot \nabla U\right) + \\ + \left[k_{BA} C_B \left(N_A - C_A\right) - k_{AB} C_A \left(N_B - C_B\right)\right], \quad (9)$$

where $k_{AB} = f^{-1}\Omega_{AB} / N = d_{AB} / (fNl_{AB}^2)$. Similarly, balance for a diffuser dwelling in B-sites can be derived rendering the result that differs from Eq. (9) by permutation of the site labels A and B. This description is extensible for arbitrary number m of site types by taking in the right-hand part of Eq. (9) the sum over all site kinds from a set {B;B≠A}. The last term in brackets in Eq. (9) represents transitions between the nearest neighbour sites of different types in a volume $d^3\mathbf{x}$ around a point $\mathbf{x}$.

This way, the system of nonlinear differential equations (9) is derived for partial concentrations C_i (i=A,B,… or 1,…,m). Balance in terms of total concentration $C = \Sigma C_i$ can be obtained summing up the equations of the system (9) over site kinds totality {A}. After all, the result coincides with Eq. (7). One may notice here the similarity with equations built up by Leblond-Dubois [10] following distinct approach based on construction of Boltzmann type transport equations. Present derivation advances the previous one [19] with respect to the sites saturability, their concentrations non-uniformity, and the contribution of a field U.

3.3. Equilibrium

The chemical potential μ_A of hydrogen residing in metal in sites of whichever type A is [13,15]

$$\mu_A(\theta_A) = \overline{G}_A + RT \ln\left(\theta_A / (1-\theta_A)\right), \quad (10)$$

where $\overline{G}_A$ is the free energy at the site with account for imposed potential U, $\overline{G}_A = G_A + U$ (Fig, 1c). At equilibrium, μ_A must be the same throughout a solid and in equilibrium with the input fugacity of hydrogen imposed by an environment, e.g., H_2 gas at pressure p that has chemical potential of hydrogen μ_p = const. Then, for all sites at equilibrium $\mu_A = \mu_p$, which yields

$$\left[\frac{\theta_A}{1-\theta_A}\right]_{eq} = e^{\beta\left(\mu_p - \overline{G}_A\right)} = e^{\beta\left[\mu_p - (G_A + U)\right]} \text{ or } \left[\frac{C_A}{\left(N_A - C_A\right)S_A}\right]_{eq} = \frac{1}{NS_A}\left[\frac{C_A}{Y_A}\right]_{eq} = e^{\beta\mu_p}, \quad (11)$$

where $S_A = \exp\left(-\beta \overline{G}_A\right)$ is the solubility factor. From the kinetics point of view, the numbers of forward and backward jumps between the nearest neighbour sites of distinct types in equilibrium are equal to each other in a volume $d^3\mathbf{x}$ around a point $\mathbf{x}$. This is expressed by detailed balance relation [20] being nothing else than equilibrium partition Eq. (3), which gets now more forms:

$$C_A \Omega_{AB} Y_B = C_B \Omega_{BA} Y_A \text{ or } C_A d_{AB} Y_B = C_B d_{BA} Y_A \text{ or } \theta_B\left(1-\theta_A\right) = \theta_A\left(1-\theta_B\right)\exp\left[\beta\left(G_A - G_B\right)\right]. \quad (12)$$

One can verify that fluxes $J_{I\backslash I}$ (I = A,B,…) are nil at equilibrium by virtue of Eq. (11), and that the sum $J_{A\backslash B} + J_{B\backslash A}$, A ≠ B, does the same with the aid of detailed balance (12). So, the total flux (6) is nil at equilibrium. As well, Eq. (9) at equilibrium yields $\partial C_A/\partial t = 0$ for all A-s by virtue of Eqs. (11) and (12), being the last term in brackets in Eq. (9) a paraphrase of the detailed balance (12).

4. Special Field Equations and Retrieval of the Known Models

4.1. One-level System

In the case of diffusion over identical sites, say L-sites, Eqs. (5), (6), and (9) in the absence of any potential field $U(\mathbf{x})$ render Fick's laws for isothermal diffusion with lattice diffusivity $D_L = d_{LL} = \Omega_{LL} l_{LL}^2$ [11,13,15]. As well, they lead to the equations of uphill diffusion under imposed potential U, e.g., due to lattice dilatation under hydrostatic stress σ, when $U = -V_H \beta\sigma$, V_H is the partial molar volume of H in metal, as they are known both for dilute solutions at $\theta << 1$ [1,2,11,21] (hereafter the site type labelling is skipped wherever convenient) and for arbitrary degree of saturation $\theta = C/N$ [22]. For the latter more general case, corresponding reduction of Eq. (5) reads:

$$\mathbf{J} = -D_L\left[\nabla C + \beta C(1-\theta)\nabla U\right]. \tag{13}$$

The balance equation is established then by common continuity relation, cf. Eq. (7).

4.2. Multi-level System, Implicit Description of Trapping: The Variable Solubility Model

Since the origin of potential $U(\mathbf{x})$ was not relevant in derivations, it can incorporate the intrinsic own lattice potential relief with variable depths of wells at interstitial sites, which yields variable solubility S($\mathbf{x}$) according to the well bottom $\overline{G}(\mathbf{x})$at location $\mathbf{x}$. This can be complemented with variable saddle point energy $E(\mathbf{x})$. Then, skipping site labels that become irrelevant, both Eqs. (5) and (6) can be rewritten in terms of the non-uniform both solubility and diffusivity as follows:

$$\mathbf{J} = -D(1-\theta)C\nabla \ln\left(\frac{C}{(1-\theta)S}\right) = -D(1-\theta)^2 S\nabla\left(\frac{C}{(1-\theta)S}\right), \tag{14}$$

where (cf. expressions (4), (5) and (11))

$$D(\mathbf{x}) = \omega_0(\mathbf{x})\exp\left[-\beta\left(E(\mathbf{x}) - \overline{G}(\mathbf{x})\right)\right]/2 \quad \text{and} \quad S(\mathbf{x}) = \exp\left(-\beta\overline{G}(\mathbf{x})\right). \tag{15}$$

With these flux equations, the mass balance is established by usual continuity relation, cf. Eq. (7).

This mode to describe diffusion, named [10] the non-uniform solubility model, deals with a system where neither interstitial positions nor saddle points are all identical, and so, it treats in effect a multilevel system. Though, specific sites are here indiscernible within each elementary volume $d^3\mathbf{x}$ around a point $\mathbf{x}$, where the values $\overline{G}(\mathbf{x})$ and $E(\mathbf{x})$ can be interpreted as effective averages over different sites with account for their amounts in regions, which are small in macroscopic sense, but large enough in microscopic one. Such averaging counts implicitly on equilibrium partition of a diffuser between sites of different kinds in $d^3\mathbf{x}$ disregarding traps filling/emptying kinetics.

Anyhow, excepting the term $(1 - \theta)$ that accounts for sites saturability, these equations render fairly the same as established for dilute solutions ($\theta << 1$) elsewhere booth within the frameworks of microscopic kinetics [10] and macroscopic thermodynamics [1,5,9]. To this end, built up upon

phenomenological account of measurable variables, but not relying on specification of atomic mechanisms, the latter approach extends the suitability of hydrogen diffusion description by means of Eq. (14) over much wider range of circumstances, such as non-uniformity of alloy composition, transient external fields (e.g., mechanical stresses), simultaneous (e.g., strain induced) phase transformations, cold working, non-isothermal diffusion (Soret effect), etc. [1,5,9,11]. Till now, these factors could not be incorporated satisfactorily in diffusion models via kinetics considerations. From another side, diffusion modelling accounting for the kinetics of H transitions between different microstructural entities ("sites") is not feasible on the way of thermodynamics.

4.3. Multi-level System, Explicit Description of Trapping

When conditions of system equilibrium are not fulfilled, it evolves to equilibrium. Various transitions can be discerned there. One of them is rather long-distance transfer that drives to global equilibrium via fluxes represented by respective equations of the previous section. Besides, localised processes of H exchange between the nearest sites of different kinds are there involved, too, which tend to local equilibrium expressed by the detailed balance (12). Corresponding process rates, which may depend on both intrinsic (e.g., vibration frequency and jump length) and extrinsic (such as diffusion distance) factors, may be so distinct, that in the time scale of interest (e.g., for membrane permeation or for hydrogen delivery to fracture locations) some processes may have attained equilibrium while others have not yet.

4.3.1. Diffusion under Traps-Lattice Equilibrium

One possibility of the mentioned partial equilibrium is when detailed balance is quickly reached and maintained during diffusion, e.g., when relatively long diffusion distances x_{cr} with corresponding times $t \sim x_{cr}^2/(4D)$ [23] are of interest. Suggested by Oriani [17] to be kept during diffusion, the hypothesis of local equilibrium assumes that detailed balance (12) holds for all nearest neighbour A and B sites, so that partial balance (9) in the case of multiple B-sites yields the following:

$$\frac{\partial C_A}{\partial t} = d_{AA}\nabla\cdot\left[Y_A C_A \nabla \ln\left(\left(e^{\beta U} C_A / Y_A\right)\right)\right] + \sum_B d_{AB}\frac{C_A}{C_B}\nabla\cdot\left[Y_B C_B \nabla \ln\left(\left(e^{\beta U} C_B / Y_B\right)\right)\right]. \qquad (16)$$

The global balance (7) for two-level system (for multi-level one the sum is to be taken over all site types) under local equilibrium is reduced to the next:

$$\frac{\partial C}{\partial t} \equiv \frac{\partial\left(C_A + C_B\right)}{\partial t} = \nabla\cdot\left[\left(d_{AA}Y_A C_A + 2d_{AB}Y_B C_A + d_{BB}Y_B C_B\right)\nabla \ln\left(\frac{C_A}{S_A Y_A}\right)\right]. \qquad (17)$$

Accompanying Eq. (17) with the detailed balance (12), which may be solved with respect to C_B,

$$C_B = \frac{N_B C_A K / N_A}{1 + C_A\left(K-1\right)/N_A} \quad \left(K = e^{\beta E_b},\ E_b = G_A - G_B\right), \qquad (18)$$

the system of partial-differential equations of diffusion with trapping converts into the system of

one partial-differential and a series of algebraic equations (17) and (18) with respect to partial concentrations C_I (I = A,B,…). This system transforms into the sole differential equation (17) with respect to C_A by substitution there C_B according to Eq. (18).

It can be verified that, labelling A ≡ L to be lattice sites and B ≡ T traps, at $\theta_L << 1$ and $\gamma_T << \gamma_L \approx 1$, and so, $Y_T << 1$, which are usually met in HAF of engineering alloys [6], and $d_{BX}/d_{AX} \sim \exp(-\beta E_b) < \sim 10^{-4}$ at $E_b > 0.2$ eV [2,14,15] for X = L or T, Eqs. (17)-(18) convert into the equation of trap-assisted diffusion [4] as implementation of Oriani's [17] equilibrium hypothesis:

$$\left(1+\frac{\partial C_T}{\partial C_L}\right)\frac{\partial C_L}{\partial t} = \nabla\cdot\left[D_L\left(\nabla C_L - C_L\nabla\ln S_L\right)\right] \text{ at } C_T = C_L K N_T/\left(N_L + K C_L\right). \tag{19}$$

4.3.2. Diffusion with Account for Lattice/Trap Exchange Kinetics

The system of equations (9), which describes hydrogen diffusion affected by traps in rather general terms, is tough to solve. Taking advantage of circumstances usually met in HAF, it can be reduced to more suitable forms. Namely, $\theta_L << 1$, $\gamma_T << \gamma_L \approx 1$, and thus $Y_T << Y_L \approx 1$, as well as $d_{TX}/d_{LX} << 1$ (X = T and L) usually hold in HAF, but the matter of local L/T-equilibrium is not ensured *a priori*. Then, taken for granted that T→T jumps are fairly improbable, the total flux **J**, Eq. (6), and the partial balance for C_T, Eq. (9), can be assessed as follows:

$$\mathbf{J} = \mathbf{J}_{L\backslash L}\left\{1+\frac{d_{TT}}{d_{LL}}\left[Y_T O\left(\frac{|\nabla C_T|}{|\nabla C_L|}\right)+O\left(\frac{C_T}{C_L}\right)\right]+\frac{d_{LT}}{d_{LL}}\left[Y_T O(1)+o(C_L)\right]+\frac{d_{TL}}{d_{LL}}O\left(\frac{|\nabla C_T|}{|\nabla C_L|}\right)\right\}, \tag{20}$$

$$\frac{\partial C_T}{\partial t} = \frac{d_{LT}}{d_{LL}}Y_T\nabla\cdot\mathbf{J}_{L\backslash L}+\frac{1}{fl^2}\left(d_{LT}Y_T C_L - d_{TL}C_T\right). \tag{21}$$

Accordingly, if neither ratios of partial concentrations C_T to C_L and their gradients nor the divergence of lattice-hopping flux $\mathbf{J}_{L\backslash L}$ are too large to forbid the disregard of terms with $d_{TX}/d_{LX} << 1$ and $Y_T << 1$ in Eqs. (20) and (21), then Eqs. (17)-(18) convert into the system of partial- and ordinary-differential equations postulated by McNabb-Foster [7], which is now extended for variable solubility S_L:

$$\frac{\partial}{\partial t}\left(C_L + C_T\right) = \nabla\cdot\left[D_L\left(\nabla C_L - C_L\nabla\ln S_L\right)\right];\ \frac{dC_T}{dt} = \left(k_{LT}/N\right)\left(N_T - C_T\right)C_L - k_{TL}C_T. \tag{22}$$

Obviously, these specialised equations of trap-affected diffusion are additively extensible for the case of multiple trap kinds T_i (i = 1,…) as the antecedent general Eqs. (7) and (9) do.

The system of equations (22) with respect to a number of concentrations C_i (i = 1,…,m) may complicate numerical simulations of diffusion making corresponding discrete approximations of the boundary-value problems oversized. However, the second of Eqs. (22) has the closed-form solution

$$C_T = \exp\left(-\int_0^t P_T(\xi)d\xi\right)\left[\int_0^t\left(\exp\left(\int_0^\xi P_T(\xi)d\xi\right)Q(\xi)\right)d\xi + C_T^0\right], \tag{23}$$

where $P_T(t) = k_{TL} + k_{LT}C_L(t)/N$, $Q(t) = k_{LT}N_TC_L(t)/N$, and $C_T^0 = C_T\big|_{t=0}$ is the initial condition. Substitution of the expression (23) into the first of Eqs. (22) reduces the problem to the sole integro-differential-equation with respect to C_L. Its computational implementation, e.g., via available finite element routines [4-6], requires modification only of calculation of concentration capacity matrices.

5. Summation: Suitability of Models for HAF Analysis

The system of equations of diffusion with trapping, which is derived here from kinetics principles, provides generalisation of pertinent previously suggested models, as well as it retrieves special ones typically either raised on the thermodynamics bases or postulated partially from microscopic arguments. This way, simpler equations of specialised models gain clarification of involved approximations and, respectively, of the requisites of their applicability. This allows reasoned pondering of their advantages and limitations to select optimal models for HAF-case analyses.

Demonstrated relation of general kinetics-based equations of trapping-affected diffusion with thermodynamics-grounded variable-solubility model visualises the incorporation of traps in this latter. However, its solid thermodynamics foundation makes it capable of accounting of wider variety of factors that influence hydrogen diffusion in metals, but are not amenable to incorporation in kinetics analysis. These are phase transformations under loading (e.g., $\gamma\rightarrow\alpha$ transition in steels), variable alloy composition, thermodiffusion, and all microstructural features, such as inclusions, grain boundaries or dislocations, which, strictly speaking, can hardly be treated as point-wise lattice irregularities that the majority of kinetics-based models deal with. With variable solubility model, numerous factors of H behaviour in metals can be incorporated in HAF analyses and simulations through macro-level determined, i.e., apparent or measurable, diffusivities and solubilities dependent on microstructure, cold working, etc. It is the advantage of this model in addition to its linearity, which substantially streamlines computations. However, the prominent deficiency of this model is inability to describe dissymmetry between hydrogenation and dehydrogenation kinetics. Meanwhile, the significance of this fault for HAF analysis seems to be case-dependent, e.g., it may be irrelevant whenever only monotonic hydrogenation occurs, but can be substantial under load or hydrogenation cycling. As well, this model discounts the lattice/trap exchange kinetics, which may be desired in particular HAF analyses. The importance of these deficiencies is also case-dependent, as far as HAF involves definite diffusion distances towards fracture sites x_{cr}, and corresponding diffusion times $t_{dif} \sim x_{cr}^2/(4D)$, which may be short or long compared with the characteristic time of approaching trap-lattice equilibrium $t_{T\text{-}L}^{-1} \sim k_{TL} + k_{LT}C_L/N$ according to the solution (23). E.g., the role of trap-filling kinetics may be noticeable for hydrogen assisted crack growth in high-strength or brittle materials, where sub-micrometer diffusion distances of the order of crack-tip opening displacement are involved [1,5], and it can be irrelevant otherwise.

Concerning diffusion models that account for trapping explicitly, they lack of the majority of attractions of the preceding one, as far as they cannot account for a series of cited diffusion-influencing factors. In return, they describe hydrogenation-degassing dissymmetry and a series of other trap-related abnormalities of diffusion. However, this improvement raises computational expenses of managing non-linear partial-differential or integro-differential equations. These models

count on micro-level determined mobility, binding and kinetics rates characteristics, which complicates their implementation in engineering. Regarding suitability for HAF description of explicit models of trapping-affected diffusion with or without lattice-trap equilibrium, this is basically the matter of transportation distances and corresponding times relevant to HAF process, so that whenever they are short, account for lattice-trap exchange kinetics may be advisable. However, one ought to be aware that large concentration gradients that can be met, e.g., in the proximity of hydrogen entry surface at short diffusion times can invalidate the requisites of smallness of the ratios of partial concentrations and their gradients, which justify the reduction of general system of diffusion equations (9) to the special case (22) of McNabb-Foster.

At any rate, recognising that trap populations may be affected by plastic deformation ε_p, $N_T = N_T(\varepsilon_p)$, and that the most relevant field for HAF is the stress field, $U \propto \sigma$, all considered equations describe the process of stress-strain assisted diffusion [1,4-6,16]. This way, present study gives an outlook of "microstructure informed" models of stress-strain affected hydrogen diffusion able to account for various physical variables relevant to HAF.

Acknowledgements

This undertaking was inspired by challenges of the EU's 7FP Project "MultiHy" (http://multihy.eu).

References

[1] J. Toribio, V. Kharin, Corr. Rev., 19 (2001) 207–252.
[2] J.P. Hirth, Met. Trans., A11 (1980) 861-890.
[3] R.P. Gangloff, in: Comprehensive Structural Integrity. Vol. 6, Elsevier, 2003, pp. 31–101.
[4] P. Sofronis, R. McMeeking, J. Mech. Phys. Solids 37 (1989) 317-350.
[5] J. Toribio, V. Kharin, ASTM STP 1343 (1999) 440-458.
[6] A. Krom, A. Bakker, Met. Trans., B31 (2000) 1475-1482.
[7] A. McNabb, P. Foster, Trans. AIME 227 (1963) 618-627.
[8] I. Bekman, in: Interaction of Hydrogen with Metals, Moscow, 1987, pp. 143-177.
[9] J. Waisman, G. Sines, L. Robinson, Met. Trans. 4 (1983) 291-302.
[10] J. Leblond, D. Dubois, Acta Met. 31 (1983) 1459-1469.
[11] S. Bokshtein, et al, Thermodynamics and Kinetics of Diffusion in Solids, Oxonian Press, 1985.
[12] V. Kharin, Sov. Materials Sci. 23 (1987) 348-357.
[13] R. Kirchheim, Acta Met. 30 (1982) 1069-1078.
[14] A. Pisarev, B. Chernikov, in: Interaction of Hydrogen with Metals, Moscow, 1987, pp. 233-264.
[15] Y. Fukai, The Metal-Hydrogen System, Springer, 2005.
[16] J. Toribio, V. Kharin, Materials Sci. 42 (2006) 263-271.
[17] R. Oriani, Acta Met. 18 (1970) 147-157.
[18] R. Barrer, J. Membrane Sci. 18 (1984) 25-35.
[19] J.M. Hill, Scr. Met. 13 (1979) 1027-1031.
[20] A. Allnatt, A. Lidiard, Atomic Transport in Solids, Cambridge Univ. Press, 2003.
[21] H. Wipf, Phys. Scripta T94 (2001) 43-51.
[22] R. Fuentes-Samaniego, J. Hirth, Phys. Stat. Solidi 106 (1981) 359-371.
[23] R. Barrer, Diffusion in and Through Solids, Cambridge Univ. Press, 1951.

Hydrogen Embrittlement in Metals: Analysis of Directionality of Hydrogen Diffusion Assisted by Stress and Strain

Jesús Toribio[1,*], Viktor Kharin[1], Diego Vergara[1], Miguel Lorenzo[2]

[1] Department of Materials Engineering, University of Salamanca, Avda. Requejo 33, 49022 Zamora, Spain
[2] Department of Mechanical Engineering, University of Salamanca, Avda. Fernando Ballesteros 2, 37700 Béjar, Spain
* Corresponding author: toribio@usal.es

Abstract Hydrogen diffusion within a metal or alloy is conditioned by the stress-strain state therein. For that reason it is feasible to consider that hydrogen diffuses in the material obeying a Fick type diffusion law including an additional term to account for the effect of the stress state represented by the hydrostatic stress. According to this law hydrogen diffuses not only to the points of minimum concentration (driven by its gradient), but also to those of maximum hydrostatic stress (driven by its gradient), the diffusion itself being also conditioned by the gradient of plastic strain. In this paper the hydrogen transport by diffusion in metals is modelled in notched specimens where loading generates a triaxiality stress state. To this end, two different approaches of stress-assisted hydrogen diffusion, one-dimensional (1D) and two-dimensional (2D), were compared in the vicinity of the notch tip in four notched specimens with very distinct triaxiality level at two different loading rates. The 2D approach predicts lower values of hydrogen concentration than the 1D approach, so that a *loss of directionality* of hydrogen diffusion towards the location of highest hydrostatic stress appears in the 2D case. This loss of directionality of hydrogen diffusion depends on both notch geometry parameters (radius and depth) and loading rate (or straining rate).

Keywords Hydrogen diffusion, Numerical models, Notched samples, Directionality of diffusion.

1. Introduction

Catastrophic fracture of structural materials in harsh environments for lower loading level than in air is caused many times by hydrogen diffusion towards material lattice and accumulation in certain places where damage at microstructural level is produced [1-4]. This phenomenon, known as *hydrogen embrittlement* (HE) or *hydrogen-assisted fracture* (HAF), has a key role in prestressed concrete structures due to the high susceptibility of the prestressing steel to this type of fracture [5-7]. At the critical fracture instant, the hydrogen concentration C reaches a critical value C_{cr} in a certain material locus $\vec{x}_{cr}$. The critical value of hydrogen concentration depends on the stress-strain state at the critical instant in the critical place or prospective location for fracture initiation [8]. Thus, the fracture criterion can be expressed as follows:

$$C_{cr} = C_{cr}(\sigma_i, \varepsilon_i) \quad \text{in} \quad \vec{x} = \vec{x}_{cr}, \tag{1}$$

where $\vec{x}$ is the spatial vector coordinates. In this equation the influence of the stress-strain state on the critical value of hydrogen concentration is included by means of both tensor invariants represented by the principal stresses, σ_i, and principal plastic strains ε_i (i = 1, 2, 3).

To study this phenomenon, constant-extension-rate tensile (CERT) tests in a hydrogenating environment are commonly used. The mechanical load applied during the test generates a certain stress-strain state in the material according to the geometry of the tested specimen. Although specimens for this type of test could exhibit different shapes, diverse studies [9,10] consider round notched bars as the best suited to the evaluation of these fracture phenomena. Obviously, under CERT test load conditions the stress and strain state varies with time and, consequently, a transient analysis of the hydrogen diffusion must be carried out.

The analysis of the HAF process presents a serious difficulty: the experimental determination of the value of hydrogen concentration $C(\vec{x},t)$ at certain point, $\vec{x}$, for a given time t. This difficulty becomes particularly important in the analysis of HAF process for critical conditions, $C_{cr} = C(\vec{x}_{cr},t_{cr})$. To solve this objection is essential (i) to find the HAF focus by means of metallographic techniques of the fractured specimens analysis [9,11,12], and (ii) to determine the local values of the variables governing the diffusion process, i.e., hydrogen concentration C, the hydrostatic stresses σ_i and equivalent plastic strains ε_i^P (i = 1,2,3).

The mechanical variables representing the stress-strain state in the hydrogen diffusion model can be obtained by numerical simulation revealing the evolution of stress-strain state in the notched specimen during CERT test. Unfortunately, nowadays an advanced numerical simulation code of general use that solves the problem stated in this paper is not available: the analysis of transient hydrogen diffusion assisted by stresses considering a 2D approach. To overcome this difficulty, the hydrogen concentration at any place and time of the transient diffusion assisted by stress state can be obtained by means of an *ad hoc* numerical code based on the finite element method (FEM) developed by the authors [13]. With the help of this tool the analysis of the time evolution of hydrogen concentration can be developed in the notched samples considered in this study during the CERT tests performed under different extension rates. The numerical simulations were carried out taking into account both approaches of the hydrogen diffusion assisted by stress state: *one-dimensional* (1D) and *two-dimensional* (2D). The differences between both simulations reveal a loss of directionality of hydrogen diffusion into metal.

2. Problem Statement

The numerical modelling of this problem raises a huge complexity due to the following fact: the hydrogen diffusion equation must consider the stress field generated by the remote load applied during CERT test. In general terms hydrogen diffusion in metals obeys a Fick type diffusion law including an additional term to account the effect of the stress state, which is time dependent, i.e. transient for the analyzed cases. Thereby, the stress-assisted diffusion flux of hydrogen is:

$$\boldsymbol{J} = D\nabla C + D\frac{V_H}{RT}C\nabla\sigma, \tag{2}$$

where D is the diffusion coefficient, V_H the molar partial volume of hydrogen in metal, R the ideal gases constant and T the absolute temperature.

The role of stress in hydrogen diffusion is commonly associated with one of the stress tensor invariants: the hydrostatic stress (or mean normal stress) σ. The relevance of stress in hydrogen transport by diffusion and HAF is well known from previous references [14-16], and, according to Eq. (2) is established that hydrogen diffuses not only to the points of minimum hydrogen concentration C (driven by the gradient of concentration), but also to the sites of maximum hydrostatic stress σ (driven by the gradient of stresses) [17]. So, the hydrogen diffusion process assisted by stress in non-homogeneous stress fields can be expressed as follows [8]:

$$\frac{\partial C}{\partial t} = D\left(\nabla^2 C - \frac{V_H}{RT}\nabla C\nabla\sigma - \frac{V_H}{RT}C\nabla^2\sigma\right). \tag{3}$$

i.e., a parabolic-type partial differential equation given in terms of hydrogen concentration C and hydrostatic stress s as the relevant variables of the process od hydrogen transport.

Free of hydrogen specimens before the test were considered and, consequently, the initial condition of null hydrogen concentration at the initial time ($C(\vec{x},t)|_{t=0} = 0$) was applied in simulations. The material considered in this study is a hot rolled bar of eutectoid pearlitic steel (C 0.75%, Mn 0.67%, Si 0.200%, P 0.009%, S 0.009%, Cr 0.187%, V 0.053%), whose mechanical properties are: Young´s modulus 195 GPa, Yield Strength 720 MPa and ultimate tensile strength (UTS) 1270 MPa.

Finally the values of relevant parameters of metal-hydrogen interaction were obtained from previous works [18,19] as $D = 6.6\ 10^{-11}$ m^2/s y $V_H = 2\ 10^{-6}$ m^3/mol. The geometry of a round notched specimen can be defined by two parameters (Table 1): the notch tip radius ρ and notch depth a. To have results independent of sample dimensions these parameters were normalized with the specimen diameter d (where $d = 12$ mm for all the notched geometries analyzed in this study).

Table 1. Notch parameters of the analyzed notched specimens

Parameter	A	B	C	D
ρ/d	0.03	0.05	0.40	0.40
a/d	0.10	0.30	0.10	0.30

Fig. 1 shows a scheme of the four analyzed notched specimens, including the corresponding notation used to identify each one. To analyze the effect on hydrogen diffusion of the extension rate during the CERT tests, two different values were considered: fast extension rate, 0.1 mm/min, and slow extension rate, 0.001 mm/min.

Two numerical approaches of hydrogen diffusion model, based in previous research [13,20], are used in present work: the *one-dimensional approach* (1D) and the quite more realistic (although time-consuming) *two-dimensional approach* (2D). Transient stress state generated in the specimen by remote loading during CERT test is included as input data in the FEM code developed *ad hoc* for both simulations of diffusion process. The specimen stress state is obtained from a previous mechanical simulation of the CERT test with a commercial FEM code considering small-strain. The same stress field was considered in the two approaches (1D and 2D) used in this paper.

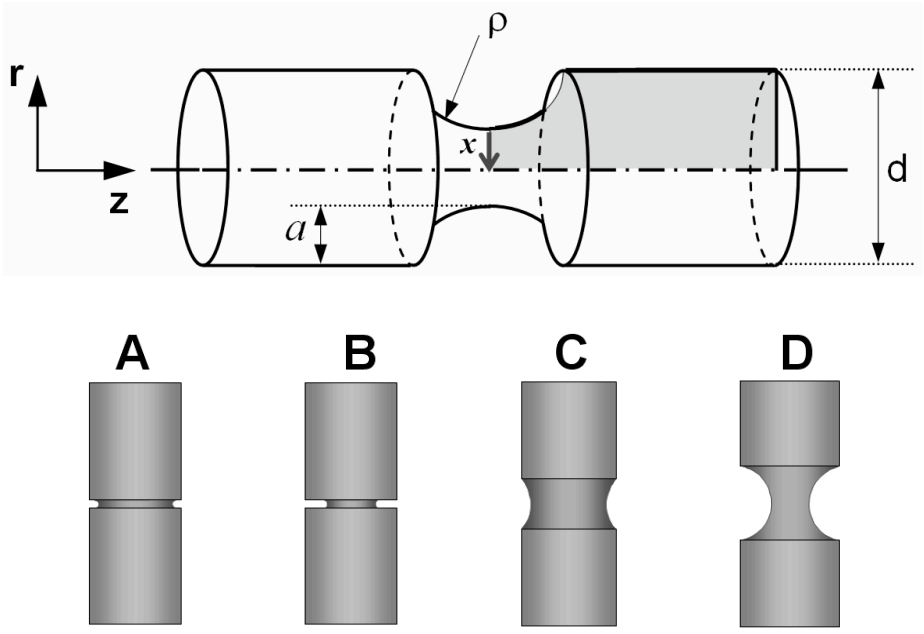

Fig. 1. Scheme of the notched specimens and parameters used for describing the notch

The 1D approach considers hydrogen diffusion is exclusively developed in radial direction (r), i.e., through the wire radius placed at notch symmetry plane. However, in 2D approach the hydrogen diffusion proceeds in both radial (r) and axial direction (z). Therefore, differences in the hydrogen concentration given by the two considered approaches can be associated to a *geometric factor*. The FEM simulation of the hydrogen diffusion assisted by stresses was performed with linear elements for both approaches (1D and 2D).

In these simulations the exposure time to harsh environment was chosen equal to the fracture time (t_f) obtained in the study [21], where similar specimens –material and notched geometries– were tested in an inert environment (air). This way, data related to fracture time due to HAF (t_{HAF}) are included in the results of the simulation performed since $t_{HAF} < t_f$ [12].

The results of the displacement at fracture instant, u_f(A) = 0.4 mm, u_f(B) = 0.13 mm, u_f(C) = 1.2 mm and u_f(D) = 0.42 mm, obtained in [21] with an extensometer of 25 mm gage length, were used to determine the time of fracture in air (t_f) according to the following relation $t_f = u_f / \dot{u}$ for each one of the two considered extension rates $\dot{u}$ (0.1 and 0.001 mm/min).

3. Numerical Results

The hydrogen accumulation in the material is represented by the relative hydrogen concentration C_r ($C_r = C/C_0$), which can be defined as the hydrogen concentration normalized with the equilibrium hydrogen concentration in a virgin material C_0, i.e., free of stress and strains. Fig. 2 shows the distribution of the relative hydrogen concentration (C/C_0) through the considered notch symmetry plane for a diffusion time lower than the fracture time in air (t_f) obtained for each one of the two extension rates considered, 0.1 mm/min and 0.001 mm/min.

As can be shown in Fig. 2 two different trends were obtained according to the extension rate: on one hand, for the highest extension rate of 0.1 mm/min (Fig. 2 left) slightly differences appear in hydrogen concentration obtained by 1D and 2D approaches of diffusion model. On the other hand, when the lowest extension rate of 0.001 mm/min is applied (Fig. 2 right) a clear influence of the geometric factor on hydrogen diffusion is revealed, especially, in the notched geometry type A where high differences in relative hydrogen concentration are obtained considering 1D and 2D approaches. Therefore the use of 1D approach (less realistic than 2D approach) leads to a loss of accuracy in the determination of relative hydrogen concentration, it being more accused for low extension rate tests and sharp notches.

According to these results hydrogen diffuses not only through the notch symmetry plane but also towards other directions. However, most of hydrogen is preferentially accumulated in the radial notch symmetry plane direction, as could be expected since H diffuses towards the location where the highest hydrostatic stress appears (situated in the notch symmetry plane [13]). So, according to Fig. 2, the lower the extension rate the more accused the effect of the *geometric factor* on hydrogen diffusion, it becoming inappreciable for high extension rate test where the hydrogen diffusion is performed practically through the notch symmetry plane with a negligible *loss of directionality*.

The influence of geometric factor on hydrogen diffusion is dependent of notch geometry parameters (radius and depth). So, the influence of this factor is lower for blunt notched samples with a high notch radius (notches C and D) than for sharply notched geometries (notches A and B) with a low notch radius (Fig. 2). According to that, a stronger influence of the geometric factor on hydrogen diffusion appears for high values of the depth (distance) from the notch tip (x).

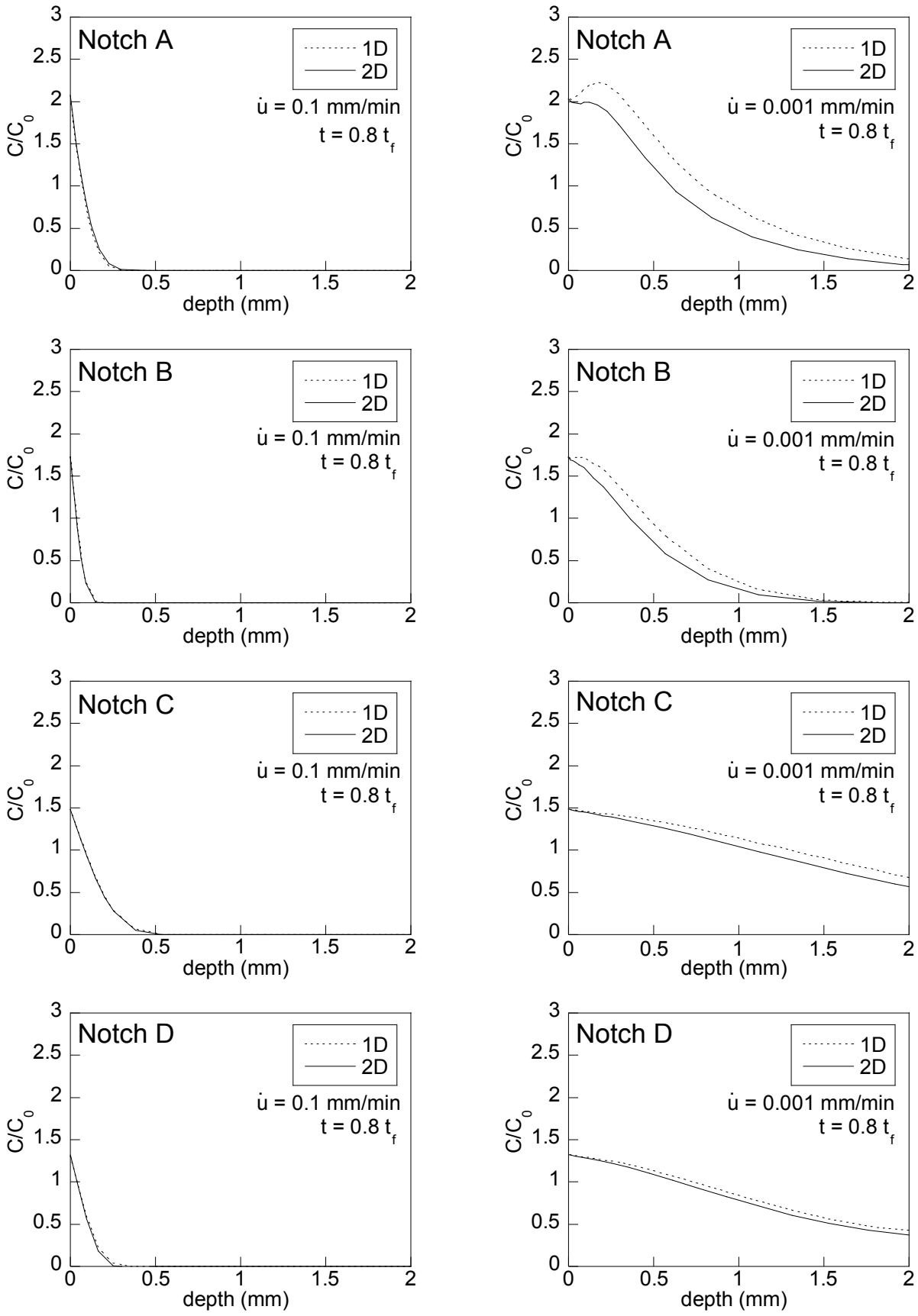

Figure 2. Distribution of hydrogen concentration through the notch symmetry plane for the geometries analyzed and an extension rate of 0.1 mm/min (left) and 0.001 mm/min (right) at exposure time $t = 0.8t_f$

The loss of accuracy of 1D approach with regard to the more realistic 2D approach can be quantitatively estimated by a new parameter λ defined as the amount of diffused hydrogen out of the notch geometry plane, thus, λ represents the *loss of hydrogen diffusion directionality:*

$$\lambda = \frac{C_r(1D) - C_r(2D)}{C_r(1D)}. \quad (4)$$

As a sketch, the 1D approach could be considered as a hollow cylindrical tube through hydrogen diffuses and the 2D approach could be considered as a hollow cylindrical tube with small holes placed in the cylinder walls. So, in first case (1D approach) a fluid that flows inside the cylinder is trapped inside it and is not able to pass through the cylinder walls whilst in second case (2D approach) the fluid can escape out of the cylinder through the holes causing a loss of fluid flux in relation to the first case.

To get a clear view of the influence of the parameters defining the different notched geometries on the loss of directionality, in Fig. 3 the distribution of the parameter through the notch symmetry plane is represented for each one of the four notched geometries simulated under the lowest loading rate, 0.001 mm/min, for a exposure time to harsh environment of 80% of the time to fracture in air, $t = 0.8\ t_f$. Fig. 3 shows a common trend for notched wires with the same notch tip radius, ρ. For blunt geometries with a higher notch radius (notches C and D) a low loss of directionality is obtained, i.e., the loss of accuracy of the 1D approach is low, cf. Fig. 2, whereas for sharp notches with a low notch radius (notches A and B) the 2D approach is required to obtain an adequate simulation.

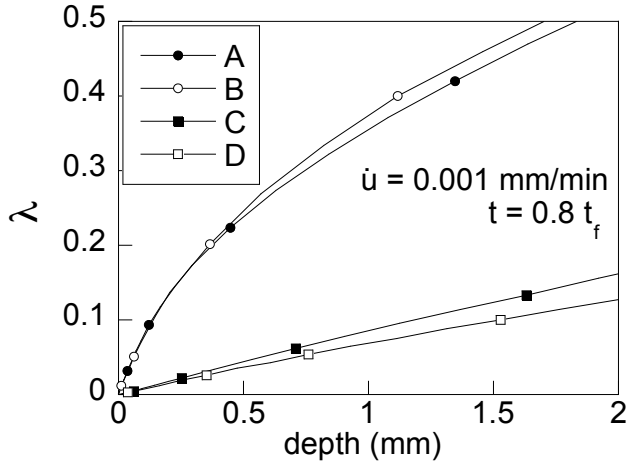

Figure 3. Distribution of loss of hydrogen diffusion directionality, through notch symmetry plane for the four notched geometries simulated under an extension rate of 0.001 mm/min at diffusion time $t = 0.8t_f$

According to these results, the notch tip radius (ρ) is the parameter governing the amount of hydrogen available for diffusing toward points out of notch symmetry plane in axial direction, with a second order effect of the notch depth (a). Fig. 4 shows a scheme of the diffusion path followed by hydrogen inside the material as a function of the dimensional approach (1D or 2D) to the process of hydrogen diffusion in the solid.

The reason why hydrogen diffuses toward the axial direction out of the notch symmetry plane can be attributed to the key role that stress state plays in the hydrogen diffusion assisted by stress model (Eq. 3). According to this model, hydrogen diffuses to the places where the maximum hydrostatic stress appears [17]. In the case of 1D approach these points are placed inside the notch symmetry

plane, which means that hydrogen diffuses exclusively inside that plane. However, in the case of 2D approach, the maximum hydrostatic stress σ appears over a *zone* [13] allowing hydrogen to move towards diverse places. Fig. 3 shows a null loss of hydrogen diffusion directionality in points near the notch tip. The same figure indicates that the deeper is the considered point the higher is the loss of directionality, which is represented in the scheme shown in Fig. 4.

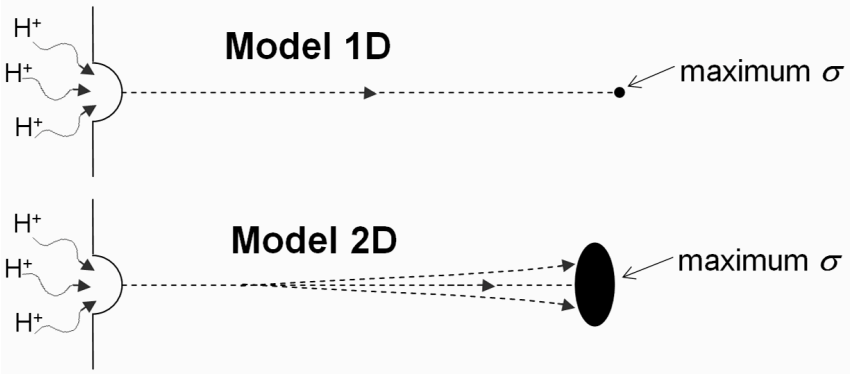

Figure 4. Scheme of hydrogen diffusion path inside a material taking into account the diffusion model approaches considered in numerical simulations.

4. Conclusions

- For high loading rates the hydrogen concentration predicted by the 1D approach to hydrogen diffusion in the material is practically equal to that predicted by the 2D approach, and therefore the influence of the *geometric factor* is not significant.
- For low loading rates during the constant extension rate tensile (CERT) tests the loss of accuracy of results obtained with the 1D approach to hydrogen diffusion in the material becomes more significant due to the loss of directionality in diffusion path.
- During the CERT tests, certain amount of hydrogen diffuses towards points placed out of the notch symmetry plane. This supposes a *loss of hydrogen diffusion directionality* in relation to the radial path obtained in 1D approach.
- The loss of directionality of hydrogen diffusion is more accused for low extension rates during the CERT tests and points placed far away from the notch tip, it becoming more significant in sharp notches with low notch radius.
- Obtained results reveal that the notch tip radius (sharp or blunt notched geometries) is the most relevant geometric parameter governing the loss of directionality of hydrogen diffusion, the notch depth exhibiting minor importance.
- Hydrogen diffusion toward points placed out of the notch symmetry plane is strongly dependent on the distribution of hydrostatic stress inside the material. In the 1D approach the maximum hydrostatic stress location is a single point, whereas in the 2D approach it is a zone.

Acknowledgements

The authors wish to acknowledge the financial support provided by the following Spanish Institutions: Ministry for Science and Technology (MCYT; Grant MAT2002-01831), Ministry for Education and Science (MEC; Grant BIA2005-08965), Ministry for Science and Innovation (MICINN; Grants BIA2008-06810 and BIA2011-27870), Junta de Castilla y León (JCyL; Grants SA067A05, SA111A07 and SA039A08).

References

[1] L. Vehovar, V. Kuhar, A. Vehovar, Hydrogen-assisted stress-corrosion of prestressing wires in a motorway viaduct. Eng Fail Anal, 5 (1998) 21–27.
[2] M. Perrin, L. Gaillet, C. Tessier, H. Idrissi, Hydrogen embrittlement of prestressing cables. Corros Sci, 52 (2010) 915–926.
[3] J. Ahmad, J. Purbolaksono, Hydrogen embrittlement due to mild condensate contamination by sea water ingress through condenser tube leakages: a case study. Desalination, 274 (2011) 302–307.
[4] J. Capelle, J. Gilgert, I. Dmytrakh, G. Pluvinage, The effect of hydrogen concentration on fracture of pipeline steels in presence of a notch. Eng Fract Mech, 78 (2011) 364–373.
[5] B.G. Pound, Hydrogen trapping in high-strength steels. Acta Mater, 46 (1998) 5733–5743.
[6] G. Wayne, Ph. D. Thesis, Corrosion and embrittlement of high-strength steel bridge wires. Columbia University (2001).
[7] S. Ramadan, L. Gaillet, C. Tessier, H. Idrissi, Detection of stress corrosion cracking of high-strength steel used in prestressed concrete structures by acoustic emission technique. Appl Surf Sci, 254 (2008) 2255–2261.
[8] J. Toribio, V. Kharin, Evaluation of hydrogen assisted cracking: the meaning and significance of the fracture mechanics approach. Nucl Eng Des, 182 (1998) 149–163.
[9] D.G. Enos, J.R. Scully, A critical-strain criterion for hydrogen embrittlement of cold-drawn ultrafine pearlitic steel. Metal Mater Trans, A33 (2002) 1151–1166.
[10] J. Toribio, F.J. Ayaso, Optimization of the round-notched specimen for hydrogen embrittlement testing of materials. J Mater Sci Lett, 39 (2004) 4675–4678.
[11] D.G. Enos, A.J. Williams, J.R. Scully, Long-term effects of cathodic protection of prestressed concrete structures: hydrogen embrittlement of prestressing steel. Corrosion, 53 (1997) 891–908.
[12] J. Toribio, A.M. Lancha, M. Elices, Macroscopic variables governing the microscopic fracture of pearlitic steels. Mater Sci Eng, A145 (1991) 167–177.
[13] J. Toribio, V. Kharin, D. Vergara, M. Lorenzo, Two-dimensional numerical modelling of hydrogen diffusion in metals assisted by both stress and strain. Adv Mat Res, 138 (2010) 117–126.
[14] M. Wang, E. Akiyama, K. Tsuzaki, Crosshead speed dependence of the notch tensile strength of a high strength steel in the presence of hydrogen. Scripta Mater, 53 (2005) 713–718.
[15] S. Takagi, S. Terasaki, K. Tsuzaki, T. Inoue, F. Minami, A new evaluation method of hydrogen embrittlement fracture for high strength steel by local approach. ISIJ Inter, 45 (2005) 263–271.
[16] M. Wang, E. Akiyama, K. Tsuzaki, Effect of hydrogen on the fracture behavior of high strength steel during slow strain rate test. Corros Sci, 49 (2007) 4081–4097.
[17] J. Toribio, V. Kharin, A hydrogen diffusion model for applications in fusion nuclear technology. Fusion Eng Des, 51-52 (2000) 213–218.
[18] R.S. Lillard, D.G. Enos, J.R. Scully, Calcium hydroxide as a promoter of hydrogen absorption in 99.5% Fe and a fully pearlitic 0.8% C steel during electrochemical reduction of water. Corrosion, 56 (2000) 1119–1132.
[19] J.P. Hirth, Effects of hydrogen on the properties of iron and steel. Metal Trans, 11A (1980) 861–890.
[20] J. Toribio, V. Kharin, D. Vergara, M. Lorenzo, Optimization of the simulation of stress-assisted hydrogen diffusion for studies of hydrogen embrittlement of notched bars. Mater Sci, 46 (2011) 819–833.
[21] F.J. Ayaso, Ph. D. Thesis, Fractura de alambres entallados de acero eutectoide progresivamente trefilado (in Spanish). University of La Coruña, Spain (2001).

Effect of Second-Stage-Aging on the Fatigue Properties of Maraging Steel

Norio Kawagoishi[1], Kohji Kariya [1], Takanori Nagano [2], Yuzo Nakamura [3]

[1] Department of Mechanical System Engineering, Daiichi Institute of Technology
Kirishima 899-4395, Japan
[2] Department of Mechanical Engineering, Miyakonojo National College of Technology
Miyakonojo 885-8567, Japan
[3] Department of Mechanical Engineering, Graduate School of Science and Engineering
Kagoshima University, Kagoshima 890-0065, Japan

* Corresponding author: nakamura@mech.kagoshima-u.ac.jp

Abstract Maraging steels are known to have not only ultrahigh strength but also large toughness so that they are promised to be as used as components or parts with structural integrity. It is also known that maraging steels are conventionally aged in two steps to obtain such good mechanical properties. Some of the present authors showed that one-step-aged maraging steels exhibited the increase in fatigue strength at intermediately high temperatures of 473 K and 673 K, compared with the strength obtained at room temperature. In addition, when low-temperature aging at 473 K and 673 K was given to one-step-aged maraging steels by varying the aging time, this second-step-aging increased the hardness of the steel. It also increased fatigue strength in an environmental situation where high humidity markedly reduced the fatigue life of one-step-aged steels. These results strongly suggest that the second-step-aging at low temperatures produces some additional microstructures which impede plastic deformation and increases resistance to fatigue cracking, even in the environmental conditions which accelerate the deformation and fracture. In the present report, a microstructural model will be proposed to interpret the effect of second-step-aging on the mechanical properties of maraging steel, which will explain the improvement of fatigue strength at intermediately high temperature and in high humidity condition.

Keywords Maraging steel, Fatigue, Two-step-aging, Microstructure, Environmental effect

1. Introduction

The high strength of maraging steels is principally based on the strengthening due to the martensitic transformation of Fe-18mass%Ni alloy, which also accompanies the introduction of dislocations with high density [1, 2]. According to a recent study of Nakashima *et al*. [3], the dislocation density introduced by martensitic transformation becomes 7×10^{15} /m^2 in ultra-low carbon Fe-18mass%Ni (0.002mass%C), leading to the yield strength of 0.66 GPa. The addition of alloying element such as Mo, Ti and Co increases the strength of maraging steels substantially by the precipitation hardening obtained by aging [1, 2]. As a result, the maraging steels exhibit the ultrahigh strength up to more than 2 GPa, without losing ductility and fracture toughness significantly. These mechanical properties are beneficial from the viewpoints of the structural integrity and the reduction in weight in practical applications.

The high strength and large ductility generally improve the fatigue strength. However it is well known that the fatigue properties of steels are very sensitive to environment [4]. Exposure to humid air or to aqueous solutions leads to the prominent deterioration of fatigue strength in high strength steels like maraging steel. Our previous studies [5−7] showed that the fatigue strength of 18Ni maraging steels aged at 753 K was lowered markedly by exposing the steel to humid air with a relative humidity (RH) of 85%. The susceptibility of fatigue strength to humidity increases with aging time in one-step-aged maraging steel, which leads to the lowest fatigue strength at peak-aging [6, 7]. The application of the second-step-aging at 673 K to the one-step-aged steel, however,

recovered the susceptibility comparable to the under-aged states. In another previous study [8], the fatigue strength of a 300G maraging steel under-aged at 753 K was shown to increase at test temperatures of 473 K and 673 K. It was also demonstrated that the hardness increases with the number of cycles at these temperatures. The second-stage-aging of this type is, hence, very effective to improve the fatigue properties at moderately elevated temperatures.
The results in the previous studies mentioned above suggest that microstructural change is induced by the static second-step-aging to improve the fatigue strength in humid air, and that dynamical aging is also caused during deformation at moderately elevated temperatures. In addition, these effects appear prominently in fatigue properties. In the present study, we try to understand the effects of the second-step-aging on the fatigue properties of maraging steels from the microstructural aspect. For this purpose, we reassess the results of previous studies. In particular, we investigate the dependence of hardness change on aging time and temperature in detail, taking into account the microstructural analyses by means of transmission electron microscopy (TEM). Based on these reassessment and analyses, the strengthening mechanism due to the second-step-aging and its role in suppressing the deterioration of fatigue properties will be discussed.

2. Experimental procedures

Chemical compositions of 300G and 350G maraging steels used are shown in Table 1. Both steels were supplied as rods of 13 mm diameter, and experienced the solution treatment conducted at 1123 K for 5.4 ks. The 300G steel was aged at 753 K for 48 ks, which led to an under-aging state. For the 350G steel, two under-aging conditions were obtained at 753 K by using the aging times of 11 ks and 100 ks, while the peak-aging was attained by heating the specimen at 753 K for 150 ks. The 300G steel specimens were subjected to rotating bend test with a frequency of 50 Hz at room temperature, 473 K and 673 K, to examine the effect of test temperature on the fatigue properties. For the 350G steel, the peak-aged specimens were subjected to second-step-aging at 473 K and 673 K by changing the keeping time, prior to tensile and rotating bend tests at room temperature. The fatigue tests of the 350G steel specimens were carried out in air with the RH of 25% and 85% to examine the influence of humidity on the fatigue properties. The details of experimental procedures used for the above fatigue tests had been reported in the previous papers [5–8]. Hereafter we assign S and D to the one-step-aging and two-step-aging, and U, P and O to the under-, peak- and over-aging, respectively, as will be shown in Table 2.
The second-stage-aging at 473 K and 673 for various time up to 800 ks was applied to the under-aged 300G steel and the peak-aged 350G steel. The Vickers hardness of the polished surfaces of these specimens was measured by using a load of 9.8 N to examine the change in hardness during the second-step-aging. The microstructures of one-step-aged and two-step-aged 350G specimens were also observed by TEM. In addition, an electrolyte extraction technique was used to identify the precipitates and evaluate their contents.

Table 1. Chemical compositions of maraging steels (mass%).

Grade	Ni	Mo	Co	Ti	Al	Mn	Si	S	C	Fe
300G	18.4	5.14	9.09	0.89	0.11	0.01	0.05	0.002	0.005	bal.
350G	17.89	4.27	12.36	1.3	0.08	0.01	0.01		0.001	bal.

3. Results

3.1 Relation between the tensile properties and hardness

Table 2 shows the yield strength (σ_y) given by 0.2% proof stress, the tensile strength (σ_{max}), the

reduction of area and the Vickers hardness (H_V) obtained for age-hardened 300G and 350G maraging steels. The aging conditions are also listed in this table. One can see from this table that under-aged 300G steel (SA-U0) has the lowest strength and hardness. It also exhibits the smallest reduction of area which represents the ductility. The increase of keeping time in one-step-aging heightens the static strength of 350G steel to the peak strength obtained at 150 ks. However, when the aging-time is longer than this, softening appears. This result suggests that over-aging is induced by the coarsening of precipitates. Fig. 2 shows the relation of the yield strength and tensile strength with the Vickers hardness. It is well known that the strength measured by tensile tests has a linear relationship with the Vickers hardness, *i.e.*, $\sigma = CH_V$, where C is a numerical constant and generally about 1/3 [9, 10]. As can be seen from solid lines depicted in Fig. 2, this relation is satisfied in the one-step-aged specimens and the value of C becomes 0.334 for yield strength and 0.346 for tensile strength. However the two-step-aged specimens do not exhibit such linear relations in both of the yield and tensile strengths. It has not been clarified why this phenomenon occurs, but the change in hardness seems to be more sensitive to microstructural change than the macroscopic properties obtained by tensile tests.

Table 2 shows the tensile properties and Vickers hardness of 300- and 350G steels

Grade	Aging condition (specification)	Yield strength, σ_y (GPa)	Tensile strength, σ_{max} (GPa)	Reduction of area (%)	Vickers hardness, H_V (GPa)
300	753 K, 48 ks (SA-U0)	2.07	2.16	47	6.21
350	753 K, 11 ks (SA-U1)	2.19	2.23	54	6.52
	753 K, 100 ks (SA-U2)	2.27	2.31	54	6.76
	753 K, 150 ks (SA-P)	2.30	2.44	54	6.91
	SA-P + 673 K, 72 ks (DA-U)	2.33	2.42	52	7.35
	SA-P + 673 K, 400 ks (DA-P)	2.42	2.55	51	7.69
	SA-P + 673 K, 673 ks (DA-O)	2.34	2.44	55	7.35

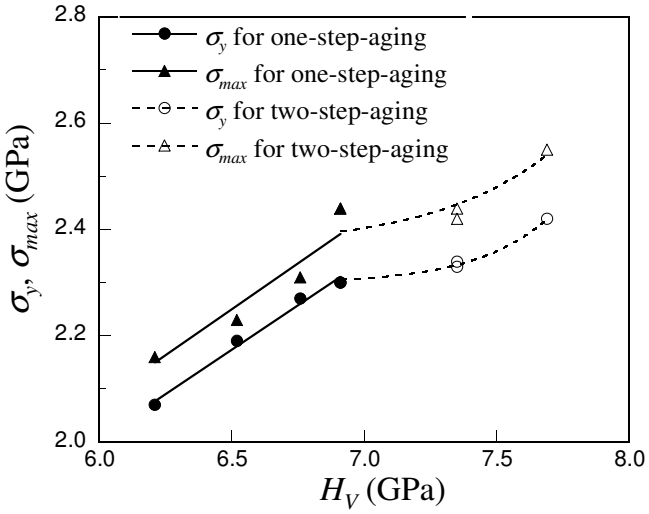

Fig. 2. The relation of yield and tensile strengths with hardness.

3.2 Change in hardness during second-step-aging

Fig. 3 shows the change in hardness with the time of second-step-aging at 473 K and 673 K, which is obtained for SA-P and SA-U0 specimens. The hardness increases very slowly at short time and then rapidly at longer time. SA-P specimen aged at 673 K, however, shows the saturation of hardness increase at 400 ks and the softening due to over-aging at longer time. Instead, the increase

in hardness due to the second-step-aging is retarded in SA-P specimen aged at 473 K, and the saturation of hardness does not appear during the time investigated. The same trend can be seen in SA-U0 specimens aged at 473 K and 673 K, while the increase in hardness occurs earlier than SA-P specimens.

The increase in hardness, ΔH_V, during the second-step-aging is considered to arise from the formation of atmosphere of solute atoms or precipitates due to this aging, as will be mentioned later. It is well known that the evolution of precipitates frequently obeys the Johnson-Mehl-Avrami equation in which the volume fraction of precipitates can be written as [11]

$$f = f_o \{1 - \exp(-kt^n)\}, \quad (1)$$

where f_o is the saturation value of volume fraction, t is time, and k and n are constants. It is believed that the hardening during the second-step-aging till the peak-hardening is caused by the shear-cutting of the newly formed precipitates by mobile dislocations. Thus the increase in hardness may be given by $\Delta H_V = Ar^{1/2}f^{1/2}$, where A is a constant and r is the radius of particles, according to the theory of precipitation hardening [12]. As will be discussed later, the coefficients of lattice diffusion of substitutional solute atoms are too small to contribute to the precipitation at 473 K. Instead their diffusion along dislocations (pipe diffusion) is considered to play a major role in the precipitation at such low temperatures. In this case the particle size is given by [13]

$$r = B\{D_d/(RT)\}^{1/5}t^{1/5}, \quad (2)$$

where B is a constant, D_d is the coefficient of pipe diffusion, R is the gas constant and T is the absolute temperature. Taking into account the incubation time t_i, which appears as the retardation of the hardness increase at 473K, we can obtain the following formula for the increase in hardness.

$$\Delta H_V = \beta(t - t_i)^{1/10}\{1 - \exp[-k(t - t_i)^n]\}^{1/2}, \quad (3)$$

where $\beta = ABf_o\{D_d/(RT)\}^{1/10}$. This equation reproduces the measured values of ΔH_V fairly well in each specimen and for each second-step-aging condition, as is shown by solid curves in Fig. 3.

Table 3 shows the values of parameters in Eq. (3). The values of β and n at 473 K are nearly equal in SA-U0 and SA-P specimens, which suggests that the precipitation proceeds with the same

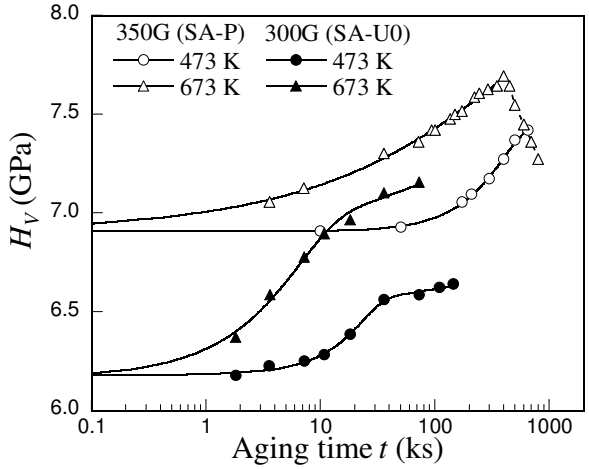

Fig. 3. Change of hardness with time during second-step-aging.

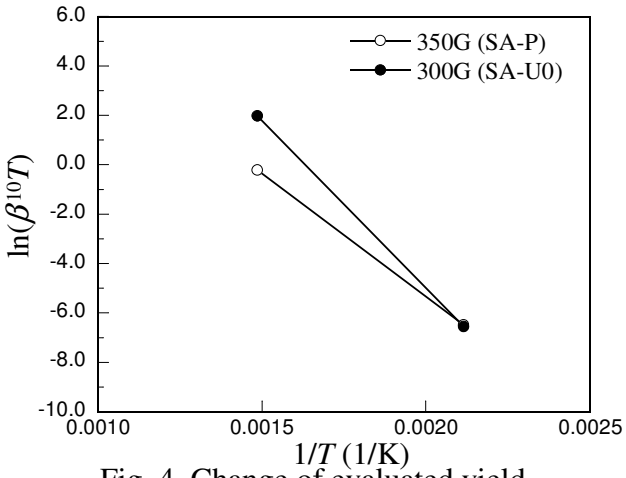

Fig. 4. Change of evaluated yield strength with aging time.

Table 3. The values of parameters in equation (4) and the activation energy of diffusion.

Specimen	T (K)	β (GPa/ks$^{1/10}$)	n	k (/ks^n)	t_i (ks)	Q_d (kJ/mol)
300G (SA-U0)	473	0.281	2.35	4.63 x 10^{-4}	~0	113
	673	0.636	1.44	0.0531	0.02	
350G (SA-P)	473	0.283	2.34	4.37 x 10^{-7}	6.47	82.9
	673	0.511	0.54	0.0377	0.01	

mechanism in both specimens. This trend can be seen at 673 K. However, since the value of n indicates the morphology of precipitates or the precipitation process [11], the smaller values of n at 673 K suggest that the nature of precipitates at this temperature may differ from that of 473 K. It should be also noted that the evaluated incubation time is very small except SA-P specimen aged at 673 K, suggesting that the precipitation starts very quickly. The assumed activation energy of pipe diffusion, Q_d, can be evaluated from the values of $\beta^{10}T$. Fig. 4 shows the Arrhenius plots of $\beta^{10}T$ evaluated for SA-P and SA-U0 specimens. The slopes of straight lines in this figure yield 82.9 kJ/mol and 113 kJ/mol for the value of Q_d in SA-P and SP-U specimens, respectively (Table 3).
These values of Q_d are nearly one third or half of the activation energy of lattice diffusion, Q_l (for instance, Q_l = 244 kJ/mol for Ni in pure Fe), and close to the activation energy of dynamic strain aging in Fe-Ni alloys (~110 kJ/mol) and Fe-Si alloy (125 kJ/mol) measured by Cuddy and Leslie [14]. Cuddy and Leslie suggest that the pipe diffusion of substitutional solute atoms which have large solution-hardening effects contributes to the occurrence of dynamic strain aging, since C atoms in the alloys they used are believed to be removed by the addition of Ti. The contribution of C atoms is also believed to be negligibly small in the maraging steels investigated here, because the content of C atoms is too small to yield the observed increase of hardness and the diffusion coefficients of C atoms at 473 K and 673 K are too large to explain the very slow increase of hardness at these temperatures.

3.3 Dynamic aging during fatigue tests

Fig. 5 shows the *SN* curves of SA-U0 specimen tested at room temperature, 473 K and 673 K. The increase in test temperature markedly increases the fatigue strength in high cycle fatigue region, and the increase of fatigue strength at the number of cycles larger than about 5 x 10^5 seems to be larger at 673 K than at 473 K. These results are in contrary with the fact that the yield strength decreases as the test temperature is increased [5]. In order to reassess the previous data, we use the following formula for the relation of stress amplitude (σ_a) with the number of cycles (N_f).

$$\sigma_a = \sigma_{ao} + k\{(N_f/N_{fo})^{-a} - 1\}^b. \quad (4)$$

Here N_{fo} is a reference number of cycles to failure, σ_a is the fatigue strength at the reference number, k is the strength factor, and a and b are numerical constants. Since the fatigue fracture does not take place at cycles larger than 10^7, as is shown by arrows in Fig. 5, the value of N_{fo} is set to be 10^7. The fatigue limit defined by σ_{ao} is evaluated to be 597 MPa, 745 MPa and 796 MPa at roomtemperature, 473 K and 673 K, respectively. In Fig. 6, the abscissa of Fig. 5 is converted into the time to failure t_f and the extrapolation to low cycle fatigue region is conducted by using Eq. (4). The σ_a-t_f curves of

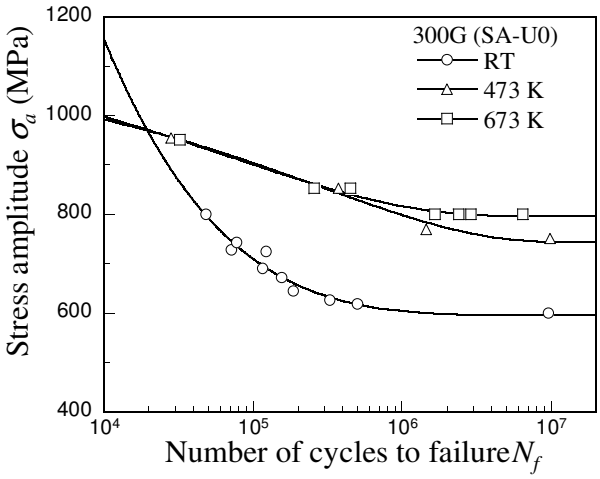

Fig. 5. SN curves of 300G steel tested at room temperature, 473 K and 673 K.

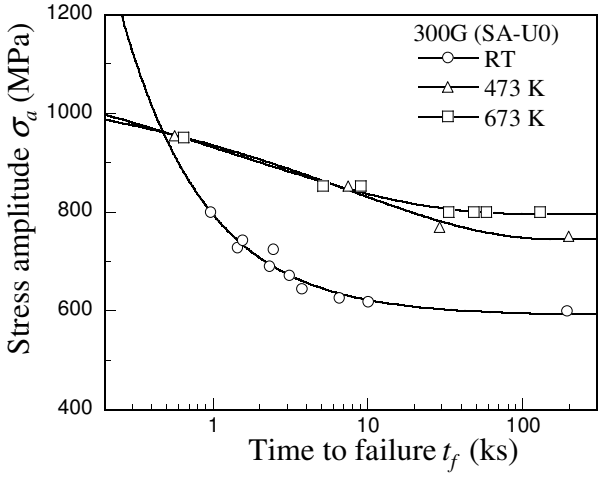

Fig. 6. Relation of stress amplitude with time to failure in 300G steel.

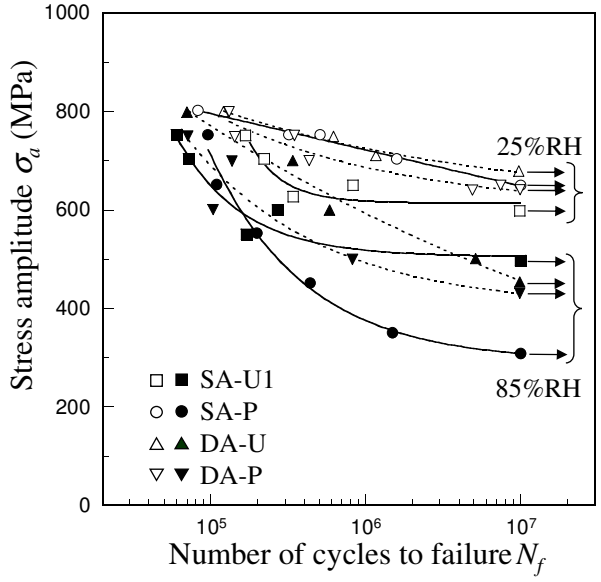

Fig. 7. SN curves of 350G maraging steels in dry and humid airs.

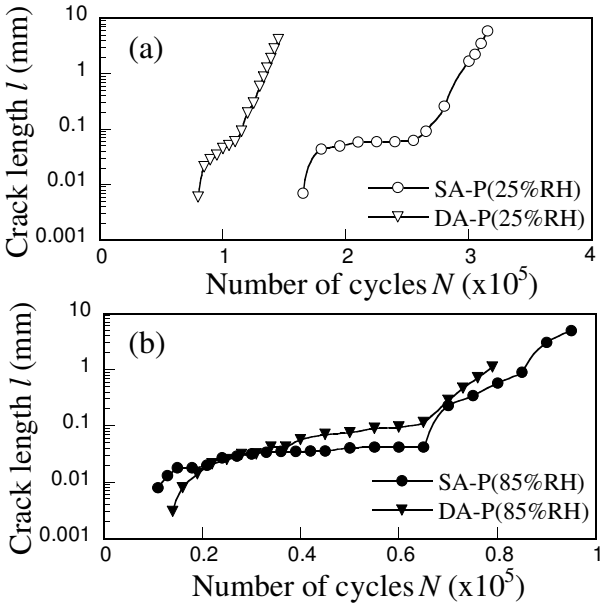

Fig. 8. Crack growth (a) in dry air and (b) in humid air.

473 K and 673 K intersect with that of room temperature at 0.4 ks ($N_f \approx 2$ x 10^4), and the dynamic aging becomes prominent at longer time than this. It also predicts that low cycle fatigue region at shorter time than 0.4 ks shows normal temperature-dependence in which the fatigue strength is lowered by increasing temperature. One can see from Fig. 3 that static aging at 673 K already appears at shorter time than 0.4 ks. However there is no increase in hardness within 2 ks when the second-step-aging is conducted at 473 K, while dynamic aging resulting in the same increase of fatigue strength as that of 673 K starts in much shorter time. These results suggest that the microstructural change at 473 K and 673 K is enhanced with the motion of dislocations during fatigue tests. From the analysis of static aging described in the previous section, it is believed that solute atoms segregate at dislocations and impede their motion. Almost the same increase of stress amplitude at 473 K and 673 K suggests that the atmosphere of solute atoms around dislocations is saturated so quickly as to have the same suppression effect on the motion of dislocations. However, the enrichment of solute atoms may lead to the formation of dense or large precipitates at 673 K for longer duration, which results in larger fatigue limit than that of 473 K as the stress level is lowered.

3.4 Effect of two-step-aging on environmentally assisted fatigue cracking

Fig. 7 shows the *SN* curves of one-step-aged and two-step-aged 350G maraging steel specimens which were tested in the air of 25% RH (dry) and 85% RH (humid) at room temperature [7]. In the dry air, the one-step-aged specimens show larger fracture strength in peak-aging than in under-aging, while fatigue strength is not affected by two-step-aging. Fatigue tests in the humid air, however, result in a marked decrease in fatigue strength, especially at high cycle fatigue region. The one-step-aged specimens exhibit the increase in the susceptibility to the humid air as the aging time increases from under-aging (SA-U1) to peak-aging (SA-P). As a result, the peak-aged specimens showed the lowest fatigue strength. The addition of second-step-aging at 673 K to the SA-P specimens increases the fatigue strength significantly compared to the original value of SA-P specimens.

Cracks are initiated at very small number of cycles in the humid air compared to in the dry air, as demonstrated by Fig. 8. After the initiation stage, cracks grow steadily in both conditions, but the crack growth is accelerated in the humid air. In particular, abrupt crack propagation seems to occur

in SA-P specimen tested in the humid air (Fig. 8(b)), while such abrupt growth does not appear in DA-P specimen. This result suggests that the second-step-aging suppresses the occurrence of abrupt crack growth in the humid air, which may lead to the larger resistance to fatigue cracking than is observed in SA-P specimen (Fig. 7).

3.5 Microstructures

Fig. 9 shows the TEM images of microstructures in DA-U specimen. It is obvious from the bright field image that there are two types of precipitates having rod and spherical shapes, which are homogeneously distributed in grains. The analysis of diffraction patterns show that the rod-shaped particles are Ni_3Ti, as is shown by the dark field image (Fig. 9(b)). The fine particles of spherical shape have much larger density than that of rod-shaped Ni_3(Ti, Mo) particles. These features are common to the specimen one-step-aged to peak-hardening stage (SA-P) and the specimens two-step-aged at 673 K (DA series). The size and number of Ni_3Ti particles do not seem to differ significantly between these specimens.
The electrolyte extraction technique revealed that all of the specimens except SA-U1 specimen contained the particles of Ni_3Ti, Ni_3Mo, Ni_3Al, FeMo and Fe_2Mo [15]. In particular, the fractions of Ni_3Ti, Ni_3Mo and FeMo are much larger than that of Fe_2Mo. However, the contents of these phases were much less in SA-U1 specimen. This suggests that the under-aging state of SA-U1 specimen contains much more solute atoms or finer precipitates of which content cannot be measured by the electrolyte extraction technique. Over-aging at 753 K in one-step-aging led to a drastic decrease in FeMo content and a marked increase in Fe_2Mo instead, though the fractions of Ni_3(Ti, Mo) particles increase very slightly. Thus it is suspected that FeMo particles dissolve and more stable Fe_2Mo particles are formed at longer duration. On the other hand, no significant change was observed in the nature and contents of precipitates between SA-P and DA-P specimens. The similarity in the nature and contents of precipitates was also observed in DA-O specimen and the two-step-aged specimen in which the second-step-aging was conducted at 473 K. These results suggest that the static and dynamic hardening due to the second -step-aging at 473 K and 673 K are caused by very fine microstructures which are not identified by TEM observation and electrolyte extraction technique.

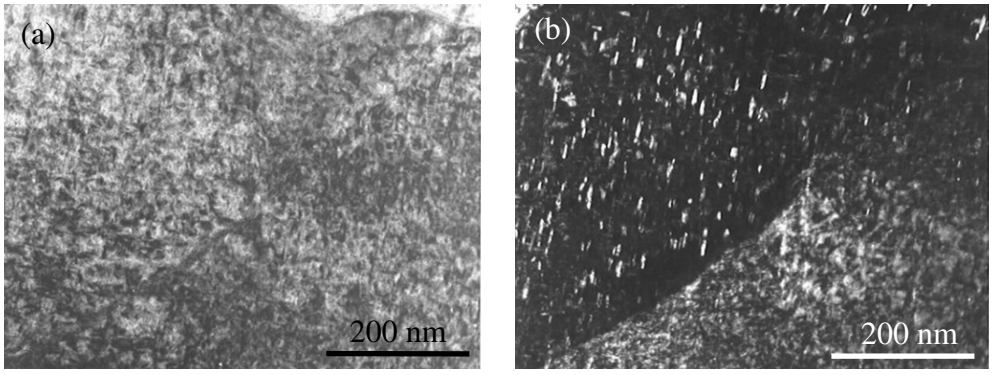

Fig. 9. Microstructures in 350G steel two-step-aged to under-aging state (DA-U) .
(a) Bright field image and (b) dark field image.

4. Discussion

The present results clearly indicate that the hardness of one-step-aged maraging steels is increased by the addition of static aging at 473 K and 673 K. The rapid increase in fatigue strength within the duration of 0.4 ks at these temperatures also suggests that the microstructural change is promoted by the motion of dislocations. As mentioned in section 3.2, both of the static and dynamic agings are

considered to be related with the precipitation which occurs via the pipe diffusion of substitutional solute atoms. In this case it is considered that the segregation of the solute atoms at dislocations precedes the precipitation at the initial stage of aging. It is well known that the misfit parameters of solute atoms in atomic size and modulus determine the magnitude of the elastic interaction of the solute atoms with dislocations. The analysis of the hardness data of ferrous alloys measured by Stephans and Witzke [16] indicate that Mo atoms have the second largest interaction with dislocations, which is comparable to that of Ti atoms [15]. From the thermodynamical viewpoint, the degree of supersaturation of solute atoms is another significant factor which enhances the segregation at dislocations. According to the phase diagrams of Fe-Mo alloy [17] and Fe-Ti alloy [18], the solubility of Ti and Mo decreases rapidly as the temperature is lowered below 773 K. It is expected that more excess Mo atoms are present during the second-step-aging or the fatigue tests at 473 K and 673 K than Ti atoms, since the content of Mo is much larger than that of Ti in the maraging steels used here. Thus such excess Mo atoms play a predominant role in interacting with dislocations at these temperatures. One can see from Fig. 3 that under-aging state accelerates the increase in hardness due to the following second-step-aging. Since the degree of supersaturation of solute atoms is expected to be larger in the under-aging state, the driving force for the segregation increases.

According to Nitta *et al*. [19] the coefficient of lattice diffusion of Mo in Fe is given by D_{Mo} = 0.0148exp(−282.6 kJ/mol/RT) m^2/s. The diffusion coefficient at 473 K is too small to explain the static and dynamic agings observed at this temperature. The present results rather indicate that the pipe diffusion of solute atoms is attributable to the static aging, as mentioned in section 3.2. It is considered that Mo atoms very close to dislocations migrate to the dislocations with the assistance of their elastic interaction and then diffuse along the dislocations. The stress-induced migration followed by pipe diffusion may serve effectively at 473 K. Thus the evaluated values of Q_d are considered to involve the contribution of stress-induced diffusion of solute atoms close to dislocations. Recently Christien *et al*. [20] have shown by using neutron diffraction that the dislocation density of 4 x 10^{15} /m^2 are generated during martensitic transformation of 17-4PH steel and it is kept nearly constant with increasing aging temperature up to 773 K. The dislocation density measured by them agrees well with 7 x 10^{15} /m^2 in Fe-18mass%Ni evaluated by Nakashima *et al* [3]. Nakashima *et al*. also reported that the dislocation density was lowered to 4 x 10^{15} /m^2 by plastic deformation. Assuming that these results are applicable to the maraging steels investigated here, the mean spacing of dislocations becomes about 16 nm and the stress level between dislocations is 1 GPa. It is therefore considered that such high dislocation density enables the stress-induced and pipe diffusions of solute atoms to operate effectively at low temperatures.

The present results clearly show that hardness is a good measure to get insight into the microstructural change with aging time or testing temperature. Viswanathan *et al*. [21] measured the Rockwell hardness (H_{RC}) of 350G maraging steel aged at temperatures from 673 K to 823 K for various time. In order to compare their result with the present Vickers hardness data, the Rockwell hardness measured by Viswanathan *et al*. is converted into the Vickers hardness in GPa by using the hardness conversion table for steels given in ASTM E140-7. Fig. 10 shows the aging time-temperature-hardness (TTH) diagram deduced from the converted Vickers hardness data. The TTH curves have a nose-shape which is oriented toward higher temperature at shorter time. This indicates the general tendency of aging in which the nucleation and growth of precipitates proceed from the supersaturation of solute atoms to the peak aging and then decomposition and coarsening take place. It should be noted that the hardness increases to its maximum value at 673 K and 1000 ks, as the temperature is lowered. Tewari *et al*. [22] proposed a time-temperature-transformation (TTT) diagram for 350G maraging steel which is shown by broken curves in Fig. 11. The TTT curves proposed by them are conceptual ones and do not present exact profiles. The overlapping of the TTT curves on the TTH contours, however, provides a general trend pertinent to the dependence of hardness on microstructure at temperatures of 673 K ~ 823 K over a wide range of aging time.

The TTT diagram suggests that, at 753 K used as one-step-aging temperature in the present study, Ni_3(Ti, Mo) particles precipitates first and these particles grow accompanying the formation of fine Fe_2Mo particles which leads to the peak hardening. Our microstructural investigation, rather, indicates that Ni_3(Ti, Mo) and FeMo particles with much larger contents than that of Fe_2Mo are attributable to the peak hardening at 753 K. Tewari *et al*. reported that S phase was initially formed at 673 K, which was followed by the precipitation of ω phase in 10 ks. Sha *et al*. [23] found ω phase ($Ni_{47}Fe_{12}Co_1Mo_{40}$) in Fe-Ni-Mo-Co model alloy aged at 687 K for 57 ks by using APFIM. They also showed that Fe_7Mo_6 particles were formed at this aging condition. According to these results, very fine particles of S phase, ω phase and Fe_7Mo_6 are considered to play a major role in the slow hardening at 673 K.

The low-temperature boundaries of TTH curves suggests the possibility that age-hardening continues as the temperature is lowered below 673 K, and it requires longer time with the decrease in temperature. The extrapolation of the boundaries to 473 K, however, does not predict the hardness observed at this temperature. It is rather considered that the solute atoms absorbed at dislocations migrate along them to agglomerate as very fine clusters as the aging time is increased, as shown schematically in Fig. 11. Dissimilar to the aging at 673 K where lattice diffusion may also contribute to the growth of precipitates for prolonged duration, the transition from such clusters to precipitates is considerably retarded at 473 K. In fatigue tests at 473 K, however, dislocations encounter excess solutes atoms during their motion. This leads to the quick formation of solute atmosphere around the dislocation, which in turn impedes the dislocation motion and increases the resistance to fatigue cracking.

It has not been made clear why the second-step-aging improves the fatigue strength in humid air. The specimens tested in 85%RH air showed that cleavage-like facets in several grains were formed at the initiation of cracks and the cracks propagated along lath boundaries, irrespectively of the aging conditions. On the other hand, the crack initiation in 25%RH air was associated with slip in grains, followed by the crack propagation along lath boundaries. These fractographic features obtained in the previous study [24] do not provide the information on the effects of second-step-aging on fatigue cracking. The present results, however, suggest that the increase in fatigue strength in humid air is also closely related with the microstructures formed by the second-step-aging.

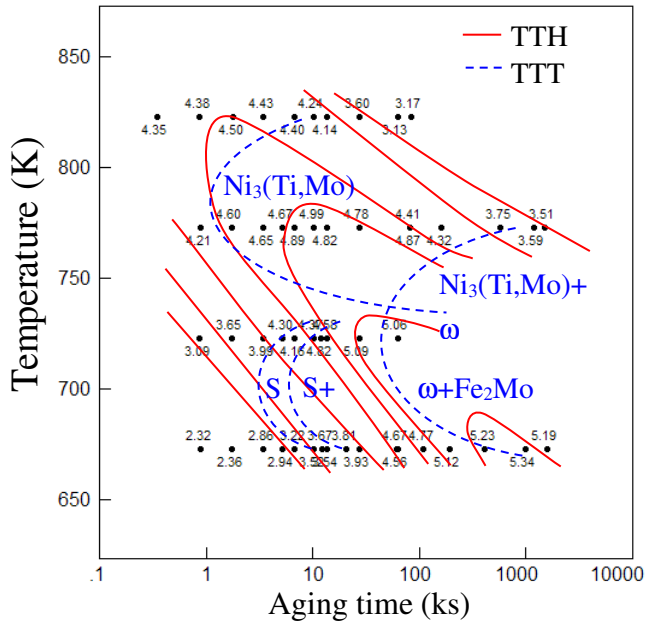

Fig. 10. TTH and TTT diagrams deduced from [21] and [22].

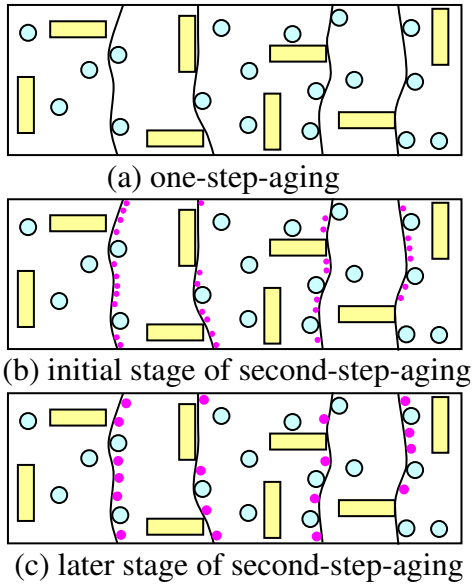

Fig. 11. Segregation and precipitation process during second-step-aging.

5. Summary

In the present study, the effects of the artificial second-step-aging prior to deformation as well as the effects of dynamical aging during deformation in Fe-18Ni maraging steels (300 and 350 grades) were investigated. The analysis of the increase in hardness with aging time in the second-step-aging at 473 K and 673 K showed that the activation energy of second-step-aging is 113 kJ/mol for initially under-aged 300G steel and 82.9 kJ/mol for initially peak-aged 350G steel. This activation energy corresponds to that of the pipe diffusion of solute atoms along dislocations. The solute atmosphere is considered to form around dislocations via the pipe diffusion and impede the motion of dislocations. Particularly the dynamic aging process takes place in the fatigue tests at 473 K and 673 K, of which effect is nearly the same. This also indicates that the fast diffusion of solute atoms to mobile dislocations causes the dynamic aging which improves the fatigue strength markedly. The microstructural observations do not provide clear evidence that new precipitates are formed during the second-step-aging. This fact also is indirect evidence that the evolution of solute atmosphere, very fine clusters or precipitates invisible in TEM are responsible for the hardening during the static and dynamic aging. The improvement in fatigue strength in humid air by the second-step-aging may be correlated closely with the microstructural change and hardening mechanism mentioned above.

References

[1] W. Sha, Z. Guo, Maraging Steel, Modelling of Microstructure, Properties and Applications, Woodhead Publishing Limited, Oxford, 2009.
[2] W.C. Leslie, The Physical Metallurgy of Steels, McGraw-Hill, New York, 1981.
[3] K. Nakashima, Y. Fujimura, H. Matsubayashi, T. Tsuchiyama, S. Takaki, Tetsu-to-Hagane, 93 (2007) 459–465.
[4] N.E. Frost, K.J. Marsh, L.P. Pook, Metal Fatigue, Dover, New York, 1999.
[5] N. Kawagoishi, T. Nagano, M. Moriyama, Y. Ohzono, T. Ura, Trans JSME A, 71 (2005) 14–20.
[6] N. Kawagoishi, M. Miyazono, T. Nagano, M. Moriyama, J-JSMS, 58, (2009) 787–792.
[7] N. Kawagoishi, K. Hayashi, T. Nagano, Y. Nakamura, M. Moriyama, Y. Maeda, J-JSMS, 61 (2012) 787–794.
[8] N. Kawagoishi, T. Iwamoto, T. Nagano, K. Morino, J-JSMS, 58 (2009) 781–786.
[9] D. Tabor, The Hardness of Metals, Oxford Press, Oxford, 1951.
[10] K.L. Johnson, Contact Mechanics, Cambridge University Press, Cambridge, 1985.
[11] J.W. Christian, The Theory of Transformations in Metals and Alloys, Part I, 2nd Edition, Pergamon Press, Oxford, 1975.
[12] V. Gerold, Precipitation Hardening, in F.R.N. Nabarro (Ed.), Dislocations in Solids, Vol. 4, North-Holland, Amsterdam, 1979, pp.219–260.
[13] F.C. Larché, Nucleation and Precipitation on Dislocations, in: *ibid.*, pp. 135–153.
[14] L.J. Cuddy, W.G. Leslie, Acta Met, 20 (1972) 1157–1167.
[15] Y. Nakamura, N. Kawagoishi, unpublished.
[16] J.R. Stephens, W.R. Witzke, J Less Common Metals, 48 (1976) 285–308.
[17] A.F. Guillermet, Calphad, 6 (1982) 127–140.
[18] K.C. Hari Kumar, P. Wollants, L. Delaey, Calphad, 18 (1994) 223–234.
[19] H. Nitta, T. Yamamoto, R. Kanno, K. Takasawa, T. Iida, Y. Yamazaki, S. Ogu, Y. Iijima, Acta Mater, 50 (2002) 4117–4125.
[20] F. Christien, M.T.F. Telling, K.S. Knight, Scripta Mater, to be published.
[21] U.K. Vsiwanathan, G.K. Dey, M.K. Asundi, Met Trans A, 24 (1993) 2429–2442.
[22] R. Tewari, S. Mazumder, I.S. Batrai, G.K. Dey, S. Banerjee, Acta Mater, 48 (2000) 1187–1200.
[23] W. Sha, G.D.W. Smith, A. Cerezo, Surface Science, 266 (1992) 378–384.
[24] N. Kawagoishi, K. Kariya, T. Nagano, M. Moriyama, Y. Nakamura, Y. Maeda, Proc 31st Symp on Fatigue, JSMS, 2012, pp.119–123.

Ductility loss in Hydrogen-charged Ductile Cast Iron

Hisao Matsunaga[1, 2, 3, 4, *], **Teruki Usuda**[5], **Keiji Yanase**[4, 6], **Masahiro Endo**[4, 6]

[1] Department of Mechanical Engineering, Kyushu University, Fukuoka 819-0395, Japan
[2] International Institute for Carbon-Neutral Energy Research (I2CNER), Kyushu University, Fukuoka 819-0395, Japan
[3] Research Center for Hydrogen Industrial Use and Storage (HYDROGENIUS), Kyushu University
[4] Institute of Materials Science and Technology, Fukuoka University, Fukuoka 814-0180, Japan
[5] Graduate School of Fukuoka University, Fukuoka 814-0180, Japan
[6] Department of Mechanical Engineering, Fukuoka University, Fukuoka 814-0180, Japan
* Corresponding author: matsunaga@mech.kyushu-u.ac.jp

Abstract Hydrogen-induced ductility loss in ductile cast iron (DCI) was studied by conducting a series of tensile tests with three different crosshead speeds. By utilizing the thermal desorption spectroscopy and the hydrogen microprint technique, it was found that most of the solute hydrogen was diffusive and mainly segregated at the graphite, graphite/matrix interface zone and the cementite of pearlite in the matrix. The fracture process of the non-charged specimen was dominated by the ductile dimple fracture, whereas that of the hydrogen-charged specimen became less ductile by accompanying the interconnecting cracks between the adjacent graphite nodules. Inside of the hydrogen-charged specimen, the interspaces generated by the interfacial debonding between graphite and matrix are filled with hydrogen gas in the early stage of the fracture process. In the subsequent fracture process, such a local hydrogen gas atmosphere coupled with a stress-induced diffusion attracts hydrogen to the crack tip, which results in a time-dependent ductility loss.

Keywords Hydrogen, Hydrogen embrittlement, Ductile cast iron, Ductility loss

1. Introduction

Ductile cast iron (DCI) is widely used for pipes in city gas pipelines and is a prospective candidate material for hydrogen gas pipes. However, to the authors' knowledge, there exist few studies about the effect of hydrogen on the strength properties of cast irons. On the other hand, with respect to the hydrogen-induced ductility loss in the ferritic or ferritic-pearlitic steels (*e.g.* carbon steels), a number of studies have examined the degradation process in the tensile properties [1-8]. These studies clarified that the ductility loss was mainly attributed to the hydrogen-induced acceleration of the fracture process (*e.g.* nucleation of voids or cracks and their subsequent growth). In addition to the ferritic-pearlitic matrix, DCI contains numerous spheroidal graphites, which can serve not only as stress-concentration sites but also as hydrogen-trap sites. Therefore, the process of hydrogen-induced degradation in cast iron, if any, could be more complex than carbon steels due to the presence of graphites. In this study, as a first attempt to understand the hydrogen effect on the various strength properties of DCI, our focus is primarily on the ductility loss due to internal hydrogen. A unique degradation process associated with solute hydrogen behavior is demonstrated and discussed based on the observations of the fracture process and the microscopic hydrogen segregation behavior.

2. Material and experimental methods

2.1. Material and specimen

The test specimens were cut out from a ductile cast iron pipe that was produced by centrifugal casting. The chemical composition in mass% was 3.70 C, 1.78 Si, 0.34 Mn, 0.058 P, 0.007 S and bal.

Fe. The microstructure was composed of a ferrite/pearlite matrix in conjunction with spheroidal graphites. The volume fraction of each phase, which was measured at a mirror-finished section, was 21 % for pearlite, 15 % for graphite and bal. ferrite. The average value of the Vickers hardness, *HV*, measured with a load of 9.8 N, was 169 in the ferrite section and 217 in the pearlite section. The round bar specimens, having a diameter of 5 mm and a gage length of 30 mm, were used for the tensile tests. The surface of the specimen was finished by polishing with emery papers and then by buffing with an alumina paste.

2.2. Hydrogen-charging, TDS analysis and microscopic visualization of solute hydrogen

The specimens were charged with hydrogen by soaking them in an aqueous solution of 20 mass% ammonium thiocyanate at 313 K for 48 hours. The hydrogen-charged specimens were re-polished before tensile tests to remove the corrosion layer produced by the charging. A number of studies (*cf.* [9-12]) have reported that cast irons as well as steels are vulnerable to surface cracking due to hydrogen-charging. To confirm the presence or absence of a crack in the specimen after the charging, the surface was mirror-polished with buff and then etched with nital. In this study, no crack was detected on the specimen surface.

The hydrogen content in the specimens was measured by the thermal desorption spectroscopy (TDS). Circular disks of 0.8 mm-thick were sliced from the specimen cross section and used for the TDS analysis. The measurements were carried out up to a temperature of 873 K (600 °C) at a heating rate of 0.5 K/s.

The hydrogen emission from the cast iron was visualized by using the hydrogen microprint technique (HMT) [13-15].

2.3. Tensile test

Displacement controlled tests were carried out with three different crosshead speeds (CHSs) of 50, 1 and 0.02 mm/min by using a hydraulically-controlled testing machine in ambient air. By assuming that crosshead displacement is equal to the elongation of the test section, the strain rate $\dot{\varepsilon}$ for each CHS is rendered as 2.8×10^{-2}, 5.6×10^{-4} and 1.1×10^{-5} s^{-1}, respectively. During the experiment, strain was measured with a clip gauge extensometer.

3. Results and discussion

3.1. Hydrogen content in specimen and the desorption behavior

Figure 1 displays the residual hydrogen content, $C_{H,R}$, as a function of the total hold time after hydrogen-charging, Δt. The content decreased gradually while the charged specimen was exposed to ambient air. After 200 hours, the content reduced to the same level of hydrogen content as in the non-charged specimen. From the reduction of hydrogen content, an apparent hydrogen diffusion coefficient at room temperature, D', was estimated by means of Demarez *et al.'s* solution for the hydrogen diffusion from a finite cylinder [16]. The least-square fitting rendered the coefficient to be $D' = 9.1 \times 10^{-13}$ m^2/s, which is relatively smaller than the diffusion coefficient in steels. In the hydrogen-charged specimens, all the tensile tests were initiated within 2 hours after hydrogen-charging, and they were finished within 3 hours after the initiation of the test; *i.e.* around 3-5 mass ppm of hydrogen seemed to be present in the specimen during the tensile test.

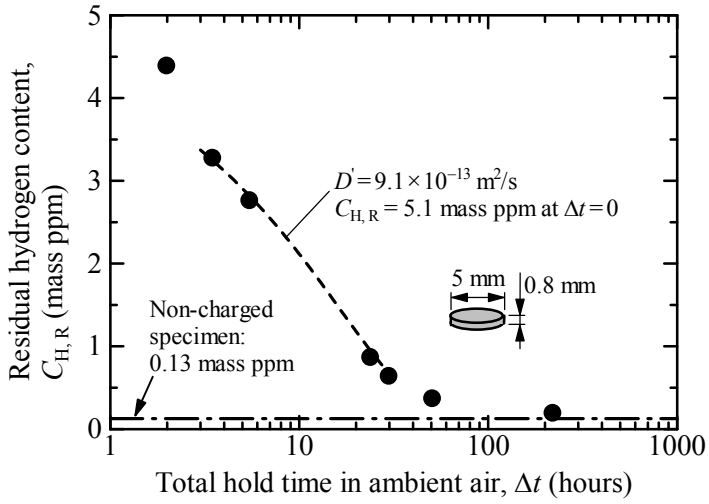

Figure 1. Residual hydrogen content as a function of total hold time in ambient air (Broken line shows the least-square fitting with Demarez et al.'s solution for the hydrogen diffusion from a finite cylinder [16])

3.2. Hydrogen segregation in microstructure

Figure 2 shows the result of HMT observation on a longitudinal section of a hydrogen-charged specimen. Numerous white spots in the photographs represent the silver particles to which the silver bromide particles were reduced by emitted hydrogen. The silver particles were mainly observed at the cross section of graphite nodules as exhibited in Figure 2(a). The particles were also observed along the cementite lamellae in pearlite colonies as shown in Figure 2(b), but were barely observed at ferrite. It is noted that in the non-charged specimens, no hydrogen emission was detected by the HMT.

Figure 3 shows the HMT images on the fracture surface of the hydrogen-charged specimen. The HMT was applied right after the tensile test. As shown, hydrogen emission was observed not only at the graphite nodules, but also at the concaves apart from the graphite nodules. This result implies that a great amount of hydrogen exists at or near the graphite/matrix interface as well as in the graphite itself.

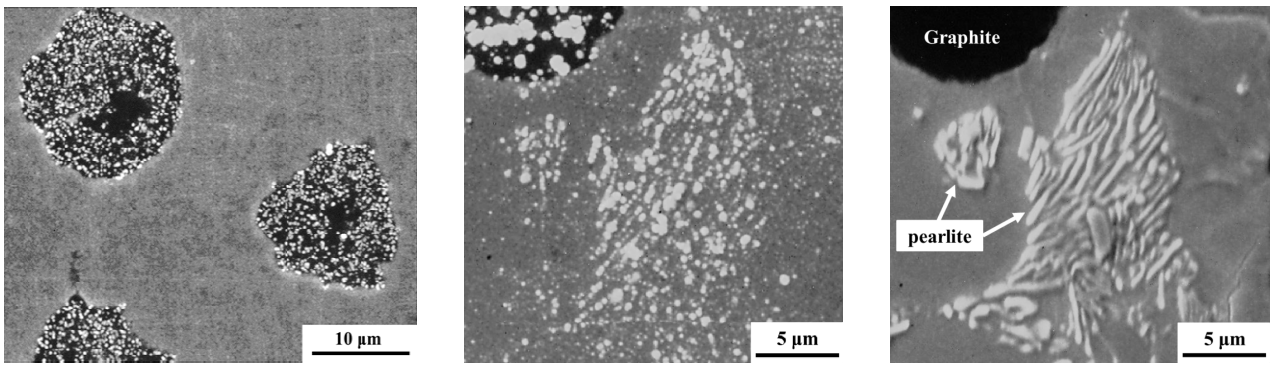

(a) Hydrogen emission from graphite (b) Hydrogen emission from pearlite, HMT image (*left*); Etched microstructure at the same area (*right*)

Figure 2. HMT images on a longitudinal section of the hydrogen-charged specimen

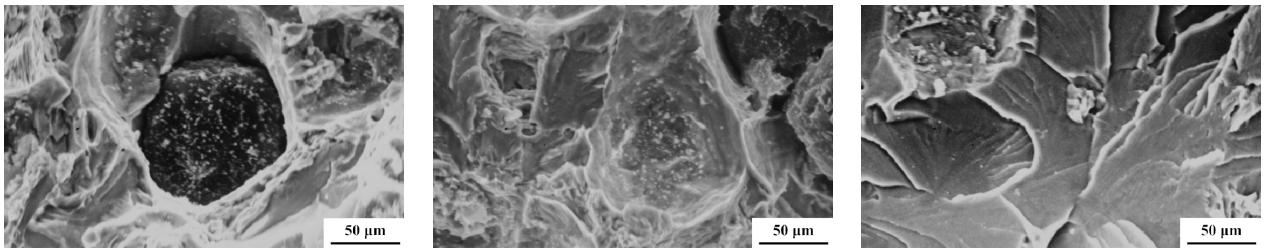

(a) Spheroidal graphite (b) Concave apart from graphite (c) Less ductile surface

Figure 3. HMT images on the fracture surface of the hydrogen-charged specimen (Crosshead speed: 1.0 mm/min)

3.3. Results of tensile testing under different CHSs

Figure 4 displays the engineering stress-strain curves. As demonstrated, hydrogen-charging markedly reduced the percentage elongation after fracture. In addition, Figure 5 illustrates the relationship between the percentage reduction of area (%RA) and CHS. For the sake of more general illustration of the experimental data, the approximated scale of strain rate, $\dot{\varepsilon}$, is additionally indicated on the top of the figure. It is noted that the strain rate was calculated by the CHS divided by the gage length of the specimen. In the non-charged specimen, %RA was nearly constant irrespective of CHS. On the other hand, in the hydrogen-charged specimen, %RA was gradually reduced with a decrease in CHS, *i.e.* a strain-rate-dependent ductility loss was manifested.

3.4. Fracture process

Figure 6 shows the SEM micrographs at the central part of fracture surfaces, and the non-charged (left-hand side) and the hydrogen-charged (right-hand side) specimens are compared. In the non-charged specimens, the ductile fracture with dimples was dominantly observed regardless of CHS. In the hydrogen-charged specimen tested at a CHS of 50 mm/min, the ductile dimple fracture was still dominant, but a small fraction of less ductile fracture surface appeared. In contrast, in the hydrogen-charged specimen tested at a CHS of 0.02 mm/min, the fracture morphology apparently became much less ductile.

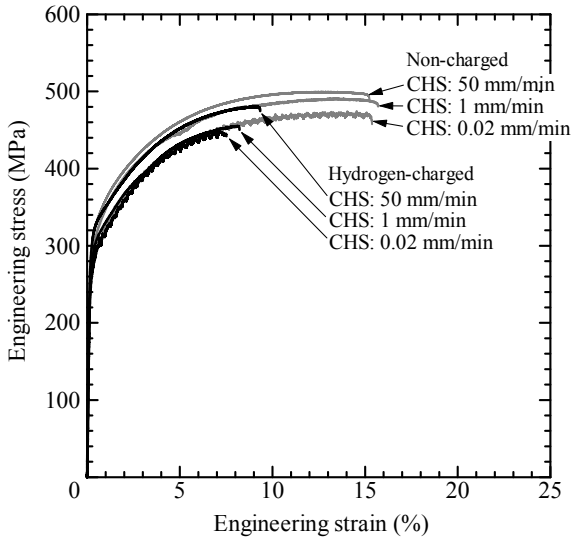

Figure 4. Engineering stress-strain curves

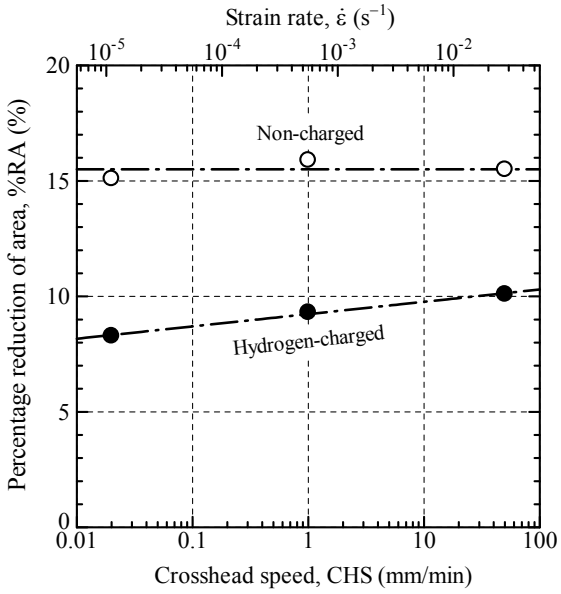

Figure 5. Relationship between the percentage reduction of area and the crosshead speed

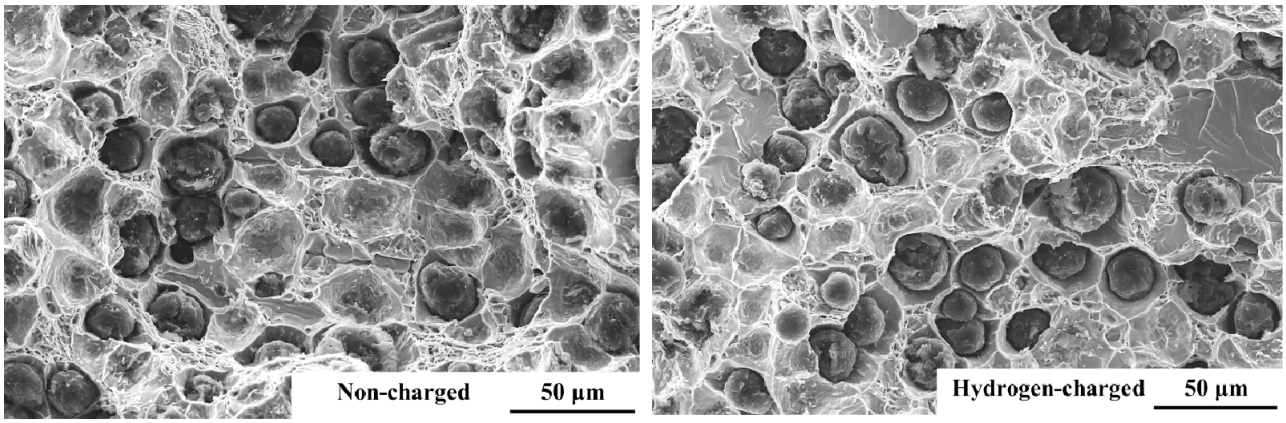

(a) CHS: 50 mm/min ($\dot{\varepsilon} \approx 2.8\times10^{-2}$ s^{-1})

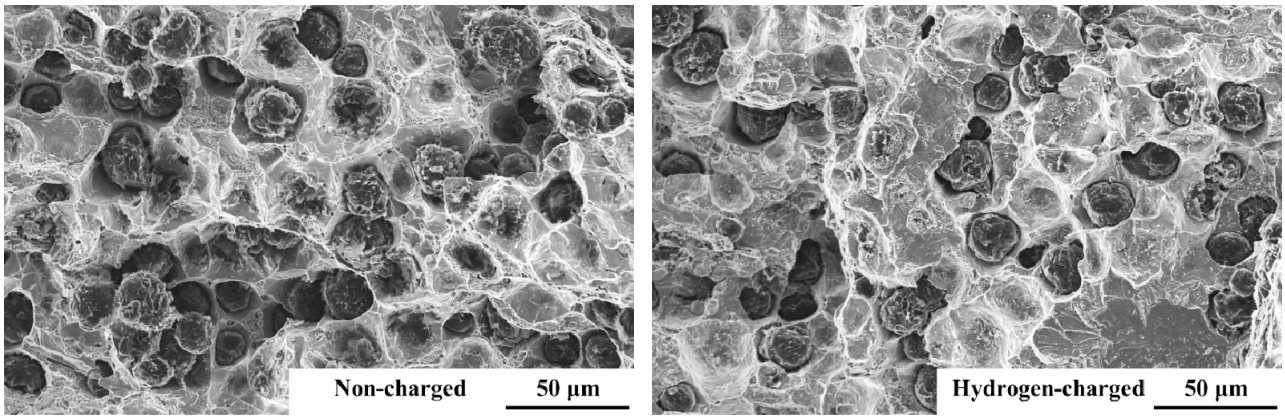

(b) CHS: 1 mm/min ($\dot{\varepsilon} \approx 5.6\times10^{-4}$ s^{-1})

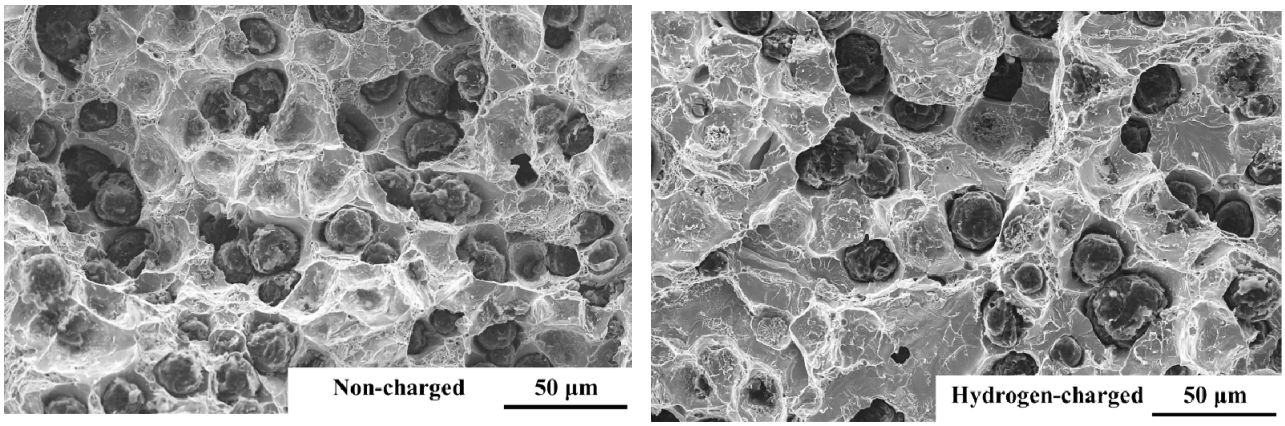

(c) CHS: 0.02 mm/min ($\dot{\varepsilon} \approx 1.1\times10^{-5}$ s^{-1})

Figure 6. SEM micrographs at the central part of the fracture surfaces (CHS: Crosshead speed)

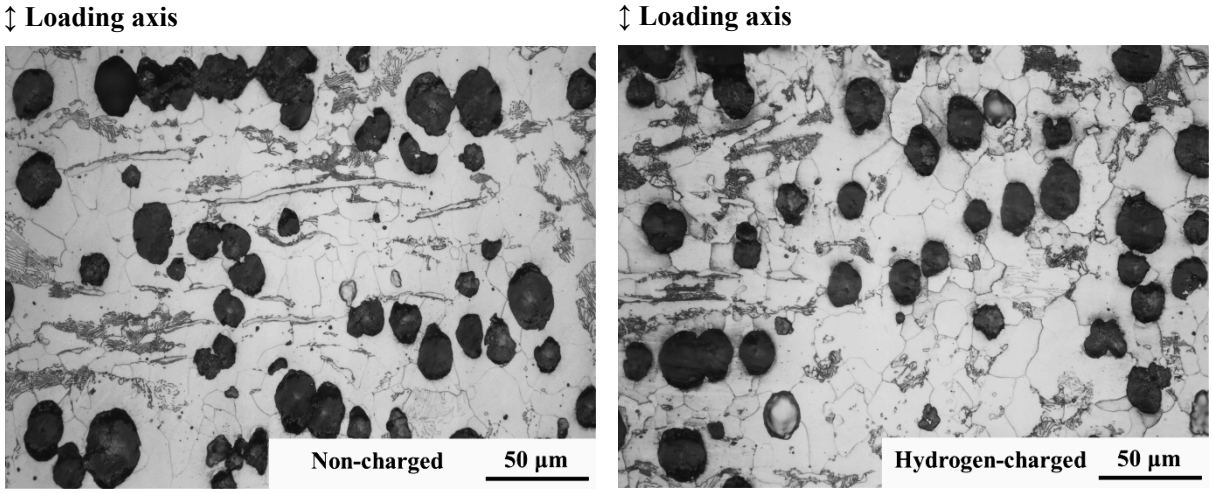

(a) CHS: 50 mm/min ($\dot{\varepsilon} \approx 2.8\times10^{-2}$ s^{-1})

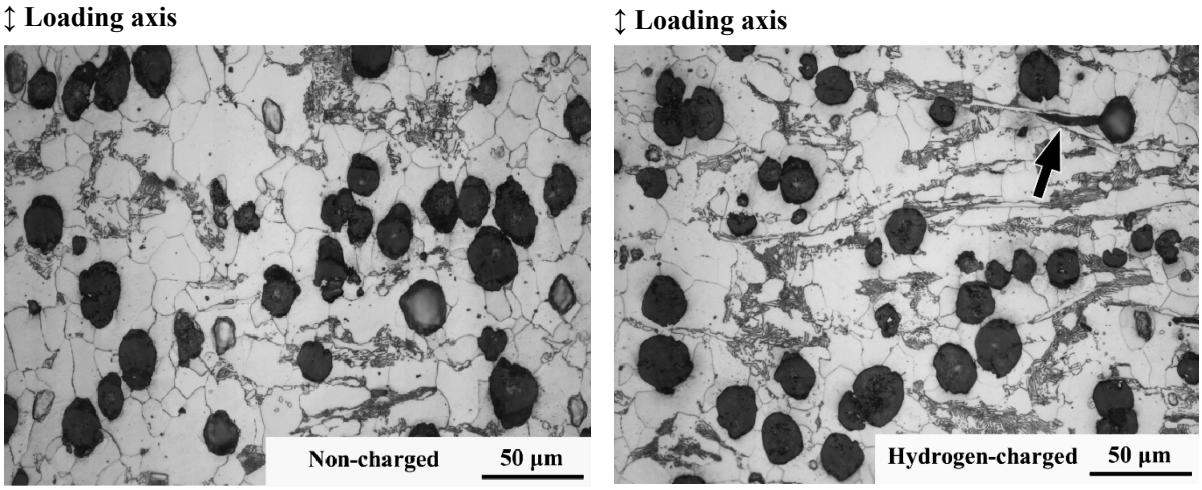

(b) CHS: 1 mm/min ($\dot{\varepsilon} \approx 5.6\times10^{-4}$ s^{-1})

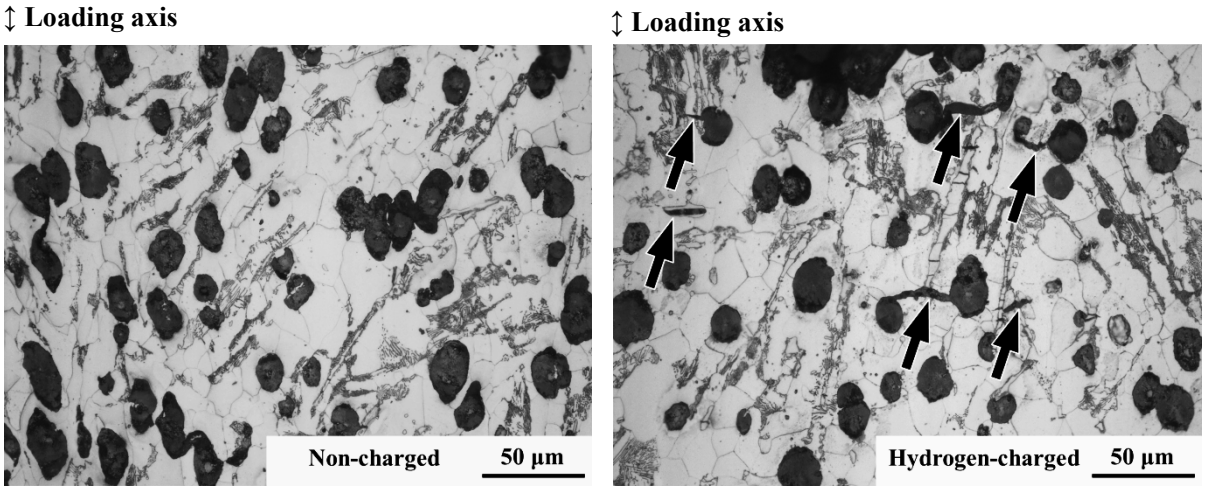

(c) CHS: 0.02 mm/min ($\dot{\varepsilon} \approx 1.1\times10^{-5}$ s^{-1})

Figure 7. Fracture morphology on the etched cross sections just beneath the fracture surfaces (Arrows indicate interconnecting cracks. CHS: Crosshead speed)

Figure 7 exhibits the fracture morphology on the etched cross sections just beneath the fracture surfaces. In the non-charged specimens (left-hand side), most of the graphites coalesced with each other leading to a typical ductile behavior, regardless of CHS. On the other hand, in the hydrogen-charged specimens (right-hand side), the fracture process was accompanied with the interconnecting cracks between adjacent graphites. This tendency appeared prominently at lower CHS (*cf*. Figure 7(c)).

Figure 8 illustrates two distinct fracture modes in the non-charged and the hydrogen-charged specimens, which were based on the observation of fracture processes. As illustrated for the hydrogen-charged specimen, in the presence of the interconnecting cracks between graphites, less graphite nodules tend to appear on the fracture surface.

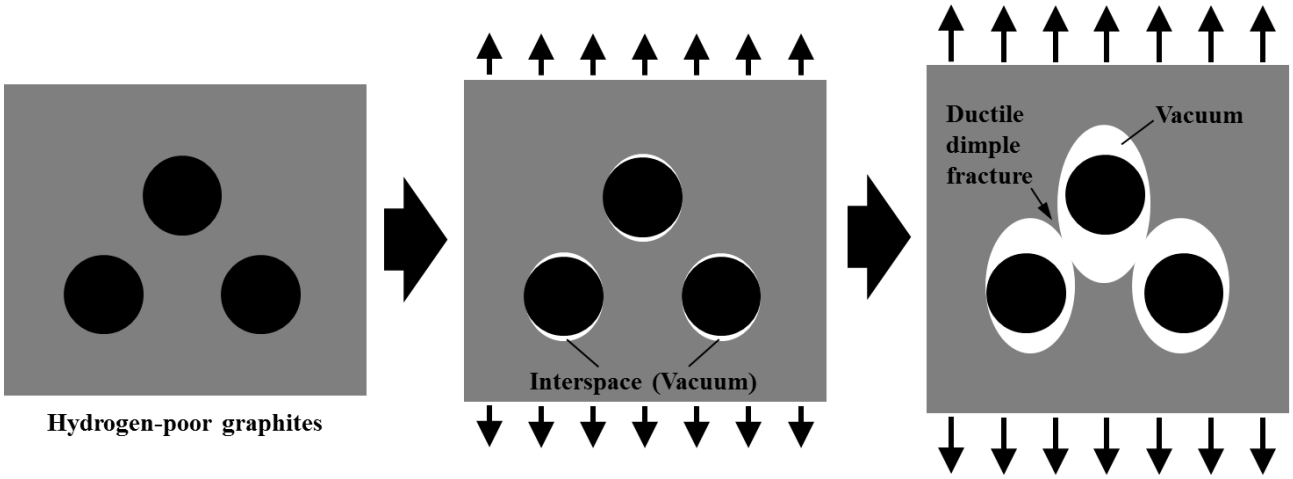

(a) Ductile dimple fracture (Non-charged specimen)

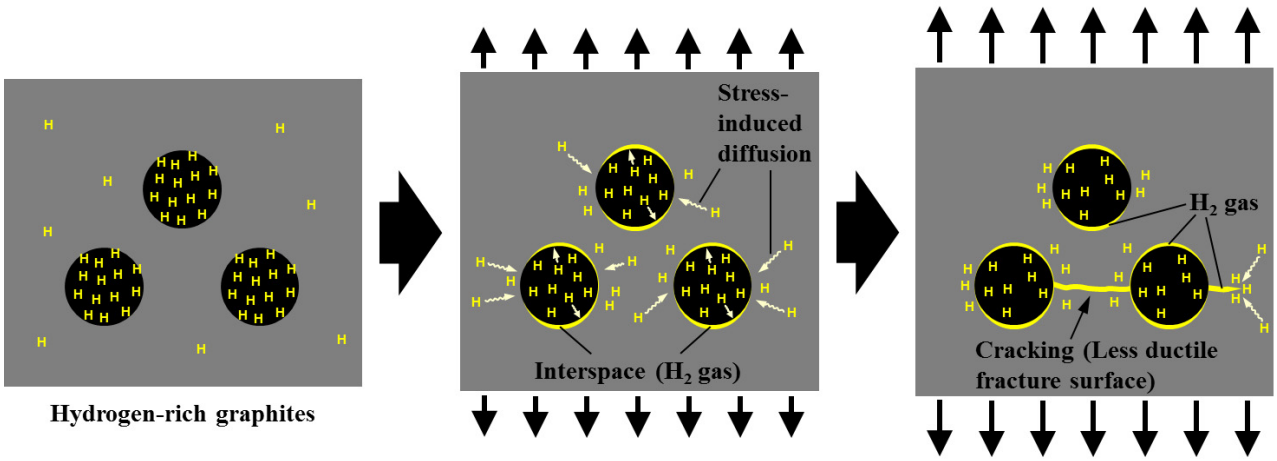

(b) Cracking in local hydrogen gas environment (Hydrogen-charged specimen)

Figure 8. Two typical fracture processes in the non-charged and the hydrogen-charged specimens

3.5. Influencing factors for degradation

Considering the hydrogen segregation and fracture process together with the strain-rate-dependent degradation in the hydrogen-charged specimen, it is possible to postulate the role of graphite in the degradation process as follows. In the deformation process of the non-charged specimen, an interspace generated by interfacial debonding between graphite and matrix maintains a vacuum environment. In this case, the surrounding matrix material can be relatively ductile; thereby, the fracture surface exhibits the dimple fracture accompanied with the interconnection of graphites (*cf*. Figure 8(a)). On the other hand, in the hydrogen-charged specimen, a great amount of hydrogen exists at or near the graphite/matrix interface zone, as illustrated by Figures 2 and 3. Therefore, in the early stage of the fracture process, the interspace between graphite and matrix is immediately filled with hydrogen gas (*cf*. Figure 8(b)). It is noted that the hydrogen in the interspace is of molecular in nature. Then, a certain amount of hydrogen as atom can spread into the surrounding matrix near the graphite nodule. Simultaneously, the stress-induced hydrogen diffusion inside the matrix can also contribute to increase the hydrogen concentration near the graphite. It has been shown that solute hydrogen enhances a localization of plasticity [17, 18], which hinders the formation of ductile dimple by facilitating the cracking [5-7, 17]. After the crack initiation from a graphite nodule, hydrogen is incessantly outgassed from the inside of the graphite nodule and supplied to the crack tip via the local hydrogen gas environment. The stress-induced hydrogen diffusion can also attract a certain amount of hydrogen to the crack tip. Such a process results in the localization of plasticity at the crack tip and thereby facilitates the crack growth [17]. As a consequence, smaller CHS enables more hydrogen to be concentrated to the crack tip. This time-dependent process causes the ductility loss associated with a decrease in CHS only for the hydrogen-charged specimen.

As was discussed, the DCI possesses the unique characteristics regarding the influence of hydrogen. Therefore, for proper evaluation of the hydrogen-induced degradation in DCI, the pivotal role of graphites as a *local hydrogen supplier* should be taken into consideration.

4. Conclusions

The effect of hydrogen-charging on ductility loss in the ductile cast iron (DCI) was investigated by conducting a series of tensile tests with three different crosshead speeds (CHSs). According to the present study, the following conclusions were obtained:

(1) Hydrogen-charging led to a marked decrease in the percentage reduction of area (%RA). In the non-charged specimens, %RA was nearly constant irrespective of CHS, whereas in the hydrogen-charged specimens, %RA was reduced with a decrease in CHS.

(2) Thermal desorption spectroscopy (TDS) and the hydrogen microprint technique (HMT) revealed that most of solute hydrogen in the hydrogen-charged specimen was diffusive, and they were mainly segregated at the graphite, graphite/matrix interface zone and the cementite of pearlite.

(3) Hydrogen-charging accelerated the coalescence of graphites during the fracture process. In the non-charged specimen, the fracture process involved the ductile dimple fracture associated with the coalescence of neighboring graphites. On the other hand, in the hydrogen-charged specimen, the fracture process involved interconnecting cracks between neighboring graphites, which appeared prominently at lower CHS.

(4) The variation in fracture morphology is attributed to a great amount of hydrogen stored in the

graphite and graphite/matrix interface zone. In the early stage of the fracture process in the hydrogen-charged specimen, the interspace generated by interfacial debonding between graphite and matrix is filled with hydrogen gas, which hinders the formation of ductile dimple by facilitating the cracking. Even in the subsequent fracture process, hydrogen is incessantly emitted from graphites. Such a local hydrogen gas atmosphere coupled with a stress-induced hydrogen diffusion inside the material attracts hydrogen to the crack tip. Accordingly, the delayed hydrogen supply causes the time-dependent degradation. To evaluate the hydrogen-induced degradation in DCI, the pivotal role of graphite as a *local hydrogen supplier* should be taken into consideration.

Acknowledgements

The authors gratefully acknowledge Mr. Kenshin Matsuno of ShinMaywa Industries, Ltd. and Mr. Kazuhisa Hatakeyama of National Institute of Advanced Industrial Science and Technology (AIST) for their support in the experimental work. This research has been supported in part by:

(1) The International Institute for Carbon-Neutral Energy Research (WPI-I2CNER), sponsored by the Japanese Ministry of Education, Culture, Sport, Science and Technology.

(2) The NEDO, Fundamental Research Project on Advanced Hydrogen Science (2006 to 2012).

References

[1] R. Garber, I.M. Bernsteln, A.W. Thompson, Effect of hydrogen on ductile fracture of spheroidized steel. Scripta Metallurgica, 10 (1976) 341-345.

[2] H. Cialone, R.J. Asaro, The role of hydrogen in the ductile fracture of plain carbon steels. Metallurgical and Materials Transactions A, 10 (1979) 367-375.

[3] H. Cialone, R.J. Asaro, Hydrogen assisted fracture of spheroidized plain carbon steels. Metallurgical and Materials Transactions A, 12 (1981) 1373-1387.

[4] S.P. Lynch, Environmentally assisted cracking: Overview of evidence for an adsorption-induced localised-slip process. Acta Metallurgica, 36 (1988) 2639-2661.

[5] H. Nishiguchi, Y. Fukushima, S. Matsuoka S, Y. Murakami, Effects of hydrogen and pre-strain on tensile properties of carbon steel STPG 370 (0.19C-0.21Si-0.56Mn, mass%) for 1 MPa hydrogen gas pipelines. Transactions of the Japan Society of Mechanical Engineers A, 74 (2008) 1016-1025.

[6] H. Nishiguchi, Y. Fukushima, S. Matsuoka, Y. Murakami, Effects of hydrogen on tensile properties of ferritic-pearlitic carbon steels. Transactions of the Japan Society of Mechanical Engineers A, 76 (2010) 1459-1468.

[7] T. Matsuo, N. Homma, S. Matsuoka, Y. Murakami, Effect of hydrogen and prestrain on tensile properties of carbon steel SGP (0.078C-0.012Si-0.35Mn, mass%) for 0.1MPa hydrogen pipelines. Transactions of the Japan Society of Mechanical Engineers A, 74 (2008) 1164-1173.

[8] K. Yokogawa, S. Fukuyama, K. Kudo, Tensile fracture surfaces of carbon steels in high pressure hydrogen in room temperature. Journal of the Japan Institute of Metals, 44 (1980) 870-875.

[9] K. Ogi, H. Hagi, A. Tahara, A. Sawamoto, H. Ikeda, Y. Hayashi, Behavior of hydrogen in ferritic spheroidal graphite cast iron with heavy section. Journal of Japan Foundry Engineering Society, 64 (1992) 186-191.

[10] A. Sawamoto, Y. Hayashi, N. Ohtani, Journal of the Japan Institute of Metals, 43 (1979) 513-519.

[11] T. Sakai, H. Kaji, Nucleation and growth of bubbles formed by hydrogen attack in carbon and low alloy steels. Tetsu-to-Hagané, 64 (1978) 430-438.
[12] S. Nomura, M. Hasegawa, Effect of cementite distribution in low carbon steel on hydrogen attack. Tetsu-to-Hagané, 61 (1975) 2579-2588.
[13] J. Ovejero-García, Hydrogen microprint technique in the study of hydrogen in steels. Journal of Materials Science, 20 (1985) 2623-2629.
[14] K. Ichitani, M. Kanno, Visualization of hydrogen diffusion in steels by high sensitivity hydrogen microprint technique. Science and Technology of Advanced Materials, 4 (2003) 545-551.
[15] H. Matsunaga, H. Noda, Visualization of hydrogen diffusion in a hydrogen-enhanced fatigue crack growth in type 304 stainless steel. Metallurgical and Materials Transactions A, 42 (2011) 2696-2705.
[16] A. Demarez, A.G. Hocks, Meuniers FA. Diffusion of hydrogen in mild steel. Acta Metallurgica, 2 (1954) 214-223.
[17] C.D. Beachem, A new model for hydrogen-assisted cracking (hydrogen "embrittlement"). Metallurgical and Materials Transactions B, 3 (1972) 441-455.
[18] H.K. Birnbaum, P. Sofronis, Hydrogen-enhanced Localized Plasticity — A Mechanism for Hydrogen-related Fracture. Materials Science and Engineering: A, 176 (1994) 191-202.

Small Crack Effect on Threshold Stress Intensity K_{TH} for High Strength Steel with Internal Hydrogen

Yukitaka Murakami[1*], Hisao Matsunaga[1, 2, 3], Arezou Abyazi[4], Yoshihiro Fukushima[1, 3]

[1] International Institute for Carbon-Neutral Energy Research (I2CNER), Kyushu University, Fukuoka 819-0395, Japan
[2] Institute of Materials Science and Technology, Fukuoka University, Fukuoka 814-0180, Japan
[3] Department of Mechanical Engineering, Kyushu University, Fukuoka 819-0395, Japan
[4] Department of Materials Engineering, Sahand University of Technology, Tabriz, Iran
* Corresponding author: murakami.yukitaka.600@m.kyushu-u.ac.jp

Abstract The size effect of the threshold stress intensity K_{TH} for hydrogen-precharged specimens of SAE52100 were investigated. Four types of tensile specimens were used: (i) smooth specimens and (ii) specimens having various shapes of artificial defects with sizes of about 35 ~ 500 μm. In the smooth specimens, fracture origins were nonmetallic inclusions with the size of 10 ~ 30 μm (*e.g.* $Al_2O_3{\cdot}(CaO)_x$, TiN and TiC). The fracture toughness determined for the small defects at fracture origin, *i.e.* the K_{TH} calculated from the defect size $\sqrt{area}$ and the fracture tensile stress σ_f, showed a defect size dependence, where, *area* denotes the area of the domain defined by projecting the defect on a plane normal to the cylindrical axis of the specimen. The values of K_{TH} for both the nonmetallic inclusions and artificial defects were much smaller than those for large cracks measured by the standard WOL and CT specimens.

Keywords Threshold stress intensity, Defect size, Nonmetallic inclusion, Hydrogen embrittlement, High strength steel

1. Introduction

Hydrogen causes degradation of various strength properties, such as tensile strength, ductility, fatigue strength, fracture toughness and *etc*. [1-3] Among them, the fracture toughness such as K_{IC} and J_{IC} is recognized as one of the most important property for the structural integrity of high-pressure hydrogen storage vessels and hydrogen supply systems. Moody *et al.* [4] showed how the fracture toughness K_{TH} of low alloy steels varies with yield strength and hydrogen pressure. Figure 1 schematically shows the relationship between K_{TH} of a steel in hydrogen gas as a function of the yield strength σ_{YS} [1]. Once σ_{YS} exceeds about 1500 MPa, K_{TH} reachs a lower limit between 10 and 20 MPa$\sqrt{\text{m}}$. Similar results on the hydrogen effect on the fracture toughness have been reported also by the other researchers [5 and others].

In most cases, K_{TH} for various materials has been measured for *large cracks* by using standard specimens, *e.g.* WOL and CT. On the other hand, in order to evaluate the effect of small defects on the fracture toughness of high strength steels, Murakami *et al.* [6] carried out a series of tensile tests using hydrogen-precharged (H-precharged) specimens. They determined the K_{TH} values from the fracture stresses and sizes of the nonmetallic inclusions at fracture origins. They reported the followings:

(i) K_{TH} was decreased with an increase in the residual hydrogen content in the material.
(ii) K_{TH} was decreased with a decrease in the defect size. This crack size dependence was similar to that of ΔK_{th} for the small fatigue crack or defect [7, 8].

Above experimental facts caution that the use of the threshold values measured for the *large cracks* leads to an unconservative estimation in the fracture toughness design against *small cracks* or *small defects*. However, the significance of the size effect has not been well recognized despite the presence

of detrimental flows, *e.g.* nonmetallic inclusions and small fatigue cracks, in the real components [9].

In this study, for a more extended understanding of the defect size dependence on the fracture toughness of H-precharged high strength steels, tensile tests of SAE52100 were carried out using specimens having various shapes of artificial surface defect with sizes of about 35 ~ 500 μm. The smooth specimens were also tested to investigate the fracture toughness for subsurface nonmetallic inclusions with sizes of about 10 ~ 30 μm.

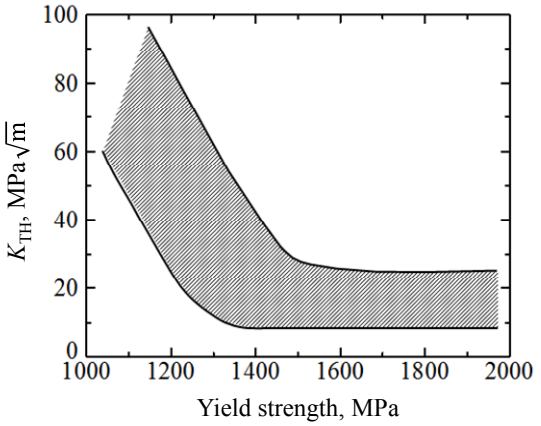

Figure 1. Schematic relationship between the threshold stress intensity factor K_{TH} of a steel in hydrogen gas as a function of the yield strength σ_{YS} [4]

2. Experimental

2.1. Material and specimen

A commercial grade SAE52100 bearing steel was used. The chemical composition in mass% is 1.00 C, 0.26 Si, 0.38 Mn, 0.013 P, 0.001 S, 0.10 Cu, 0.08 Ni, 1.40 Cr, 0.03 Mo, 0.0016 Ti, 0.0005 O and bal. Fe. The steel was heat-treated so that he average Vickers hardness, *HV*, measured with a load of 9.8 N had 712.

Figure 2 shows the shape and dimensions of specimen. In some specimens, the following four types of artificial defects with various sizes were introduced onto the specimen surface; (i) a rectangular slit made by the focused ion beam (FIB) technique, (ii) a semi-circular slit made by the electrical discharging, (iii) a drilled hole which has crack-like thin slits made by the FIB technique and (iv) a hole made by the electrical discharging having the FIB slits. Figure 3 shows the shapes and dimensions of the defects, which are designated as Type A ~ D, respectively.

2.2. Hydrogen precharging (H-precharging) and Tensile testing

The specimens were charged with hydrogen by soaking them in an aqueous solution of 20mass % ammonium thiocyanate at 313 K for 48 hours.

Displacement controlled tests were carried out under a crosshead speed V of 1 mm/min corresponding to the strain rate $\dot{\varepsilon}$ of about 6.5×10^{-5} s^{-1} by using a hydraulically-controlled testing machine in ambient air. All the tensile tests were initiated within 2 hours after the charging. The *time after the H-precharging* means the total hold time in ambient air.

2.3. Measurement of hydrogen content

After each tensile test, the residual hydrogen content $C_{H,R}$ in the specimen was measured by the thermal desorption spectroscopy (TDS). Right after the final fracture of the specimen, circular disks of 2.0 mm-thick were sliced from the broken specimen and used for the TDS analysis.

2.4. Characterization of fracture origins and nonmetallic inclusion rating

The size of the defect was represented by the $\sqrt{area}$, where *area* denotes the area of the domain defined by projecting the crack or defect on a plane normal to the cylindrical axis of the specimen [7, 8, 10].

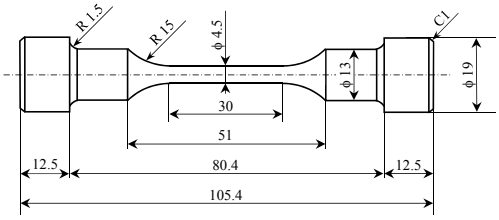

Figure 2. Shape and dimensions of test specimen in mm (Control volume: V_s = 477 mm^3)

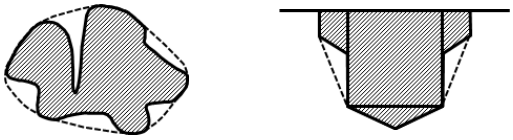

(a) Non-metallic inclusion (b) Artificial defect

Figure 4. Irregularly shaped defects and estimation method for effective area [8]

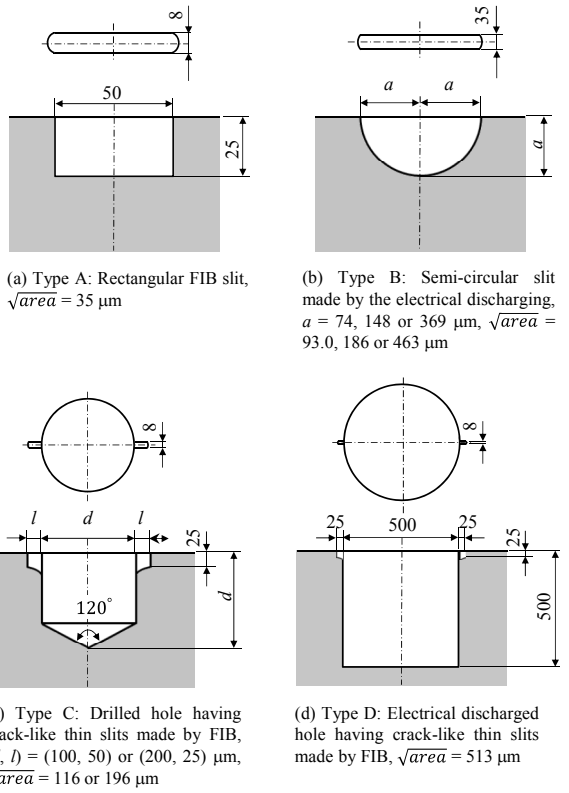

(a) Type A: Rectangular FIB slit, $\sqrt{area}$ = 35 μm

(b) Type B: Semi-circular slit made by the electrical discharging, a = 74, 148 or 369 μm, $\sqrt{area}$ = 93.0, 186 or 463 μm

(c) Type C: Drilled hole having crack-like thin slits made by FIB, (d, l) = (100, 50) or (200, 25) μm, $\sqrt{area}$ = 116 or 196 μm

(d) Type D: Electrical discharged hole having crack-like thin slits made by FIB, $\sqrt{area}$ = 513 μm

Figure 3. Shapes and dimensions of artificial defects

The effective area for the defect size $\sqrt{area}$ was estimated by considering a contour which envelopes the original irregular shape of the defect, as shown in Fig. 4 [8].

A newly proposed inclusion rating method [11] based on the statistics of extremes was used.

3. Results and discussion

3.1. Hydrogen content in specimen and the desorption behavior

Figure 5 shows the hydrogen thermal desorption spectra for the H-precharged specimen [12]. Figure 6 displays the residual hydrogen content, $C_{H,R}$, as a function of the total hold time after the charging, Δt, in laboratory air. The content decreased gradually with the hold time. After 100 hours, the content reduced to almost the same level of hydrogen content as in the non-charged specimen. From the reduction of hydrogen content shown in Fig. 6 [12], an apparent hydrogen diffusion coefficient at room temperature, D', was estimated by means of Demarez *et al.'s* solution [13]. The least-square fitting rendered the coefficient to be $D' = 8.6 \times 10^{-13}$ m^2/s. In the H-precharged specimens, all the tensile tests were initiated within 2 hours after the charging, and they were finished within 2 minutes after the initiation of the test; *i.e.* around 4 mass ppm of hydrogen seemed to be present in the specimen during the tensile test.

3.2. Fracture data and fracture origins

Figure 7 shows examples of the uniaxial tension stress-strain curves [12]. All the H-precharged specimens failed at a much lower stress as compared to the non-charged specimens irrespective of the presence or absence of the artificial defect, as shown in Fig. 7, *i.e.* the so-called *hydrogen embrittlement* was demonstrated in the H-precharged specimens. Moreover, the presence of an artificial

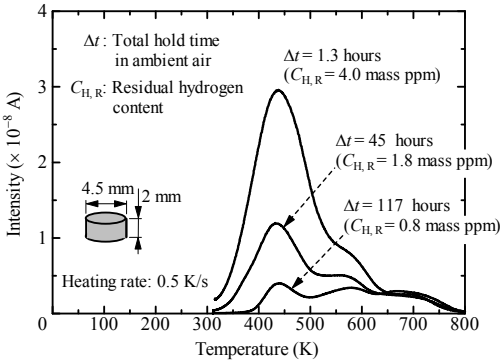

Figure 5. Hydrogen thermal desorption spectra for the hydrogen-charged specimen [12]

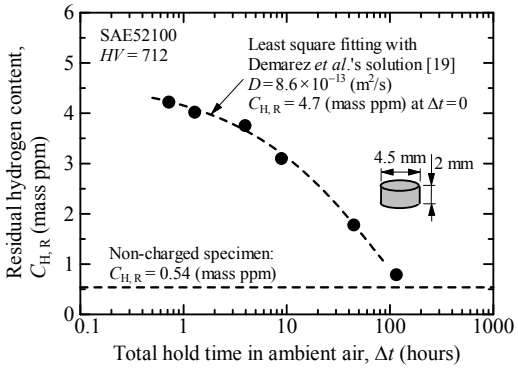

Figure 6. Residual hydrogen content as a function of total hold time in ambient air [12]

defect significantly decreased the nominal stress at the final fracture of specimen, σ_f, which was decreased with an increase in the defect size.

Table 1 lists the chemical compositions of all the inclusions at fracture origin together with a series of experimental data. The inclusion size $\sqrt{area}$ ranged from about 10 to 30 μm. The fracture processes of specimens originated from two types of inclusions, *i.e.* $Al_2O_3 \cdot (CaO)_x$ and TiN, has been reported in a separate paper [6]. Figure 8 illustrates crack initiation processes from the two kinds of nonmetallic inclusions in the non-charged and H-precharged specimens [6]. In an early stage of the fracture process from the $Al_2O_3 \cdot (CaO)_x$ type inclusion, an interfacial cracking occurs at the pole of the inclusion/matrix interface where the tensile stress becomes maximum owing to a large modulus of the inclusion. Subsequently, the complete separation of the interface between the inclusion and matrix creates a spherical-like cavity, which shifts the location of the highest tensile stress from the pole to the equator of the cavity. On the other hand, the fracture process from the TiN type inclusion is initiated by the cracking of inclusion itself. These processes for two types of inclusions take place while the overall deformation of the specimen is elastic as shown in [6].

Figure 9 [12] shows the statistics of extremes distribution of nonmetallic inclusions at the fracture origin of the H-precharged tensile specimens, where y' is the reduced variant, F is the cumulative distribution fraction and T' is the return period. The distribution of the extreme value $\sqrt{area}_{max}$ shows a good linearity and provides a justification for the use of the distribution of extremes.

In the H-precharged specimens having artificial defect, the fracture was originated from the defect. It is worth noting that there was an exception, *i.e.* the fracture of the specimen having the smallest artificial defect (*cf.* Fig. 3(a)) was not originated from the artificial defect but from a nonmetallic inclusion, though the size of the inclusion was definitely smaller than that of the artificial defect,

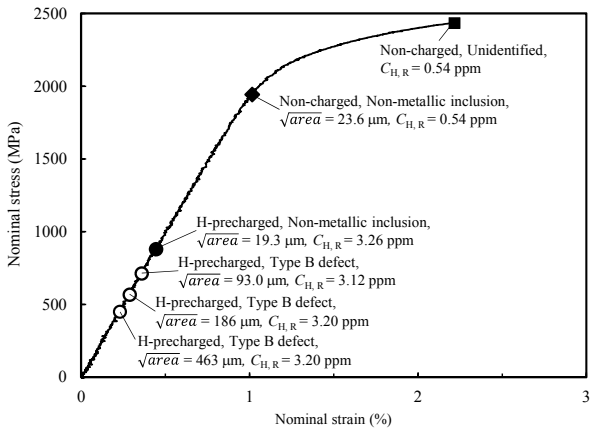

Figure 7. Example of the stress-strain curve and fracture points

as compared in Table 1 [12]. This is due to the non-uniform distribution of hydrogen concentration in the specimen from the surface to the center.

3.3 Dependence on the threshold stress intensity on defect size and hydrogen concentration

In order to quantitatively characterize the hydrogen effect together with the defect size dependence on the fracture toughness, the fracture data will be analyzed in terms of the macroscopic fracture stress σ_f, the defect size $\sqrt{area}$ and the residual hydrogen content $C_{H,R}$.

3.3.1. Smooth specimens

Firstly, we associate the fracture stress σ_f with K_{TH} for the onset of a crack from a spherical inclusion. After the interfacial debonding between inclusion and matrix, the spherical inclusion can be regarded as a traction free cavity (*cf.* Fig. 8). Figure 10 shows the normalized stress intensity factor $K_I/\sigma_0\sqrt{a'+\lambda}$ for a crack emanating from an ellipsoidal cavity as a function of the parameter λ/a',

Table 1. Experimental data of SAE52100 [12]

	t_1 (min)	t_2 (min)	Fracture origin	$C_{H,R}$ (mass ppm)	σ_f (MPa)	$\sqrt{area}$ (μm)	K_{TH} (MPa $\sqrt{m}$)
H-precharged specimens	27	76	Al, Ca, Mg, Si, S	3.29	795	15.0	2.73
	49	111	Al, Ca, Si	3.17	785	19.3	3.06
	27	89	Ti, C	2.46	1027	11.6	3.10
	21	90	Al, Ca, Mg, Si, S	3.64	769	22.4	3.23
	45	108	Al, Ca, Mg, Si, S	3.00	897	18.8	3.45
	32	90	Al, Ca	3.79	779	25.0	3.45
	21	89	Al, Ca, Mg, Si	3.06	943	16.3	3.37
	31	94	Al, Mg	3.26	883	19.3	3.44
	47	108	Al, Ca, Mg, Si	3.08	802	23.9	3.47
	32	89	Al, Ca, P, Si	3.89	845	22.3	3.54
	25	75	Al, Ca, Mg, Si	2.95	773	27.6	3.60
	29	97	Al, Ca, Si	3.05	1001	19.8	3.95
	34	94	Al, Ca, Mg, Si	2.69	1031	19.0	3.98
	20	85	Ti, N, Mn, S	2.32	1041	19.3	4.05
	24	105	Semi-circular slit	3.12	714	93.0	7.93
	24	94	Semi-circular slit	3.20	567	186	8.90
	27	94	Semi-circular slit	3.20	450	463	11.15
	21	102	Drilled hole + FIB slits	3.39	657	116	7.28
	28	117	Drilled hole + FIB slits	3.95	668	196	10.47
	30	112	Electro discharged + FIB slits	3.77	471	513	11.67
	20	102	Al, Ca, Mg, Si, S	3.03	960	12.4*	3.00
			Rectangular FIB slit			35.0	
Non-charged specimen	—	—	Al, Ca, Mg, S	0.54	1943	23.6	8.37
	—	—	Unidentified	0.54	2436	—	—

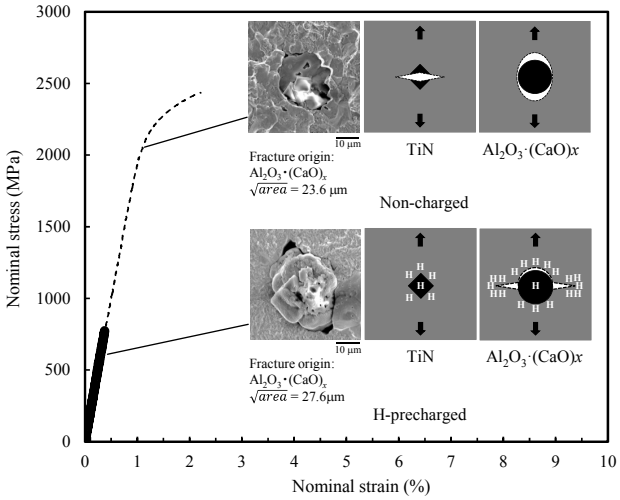

Figure 8. Illustration of crack initiation processes from two kinds of non-metallic inclusions [6]

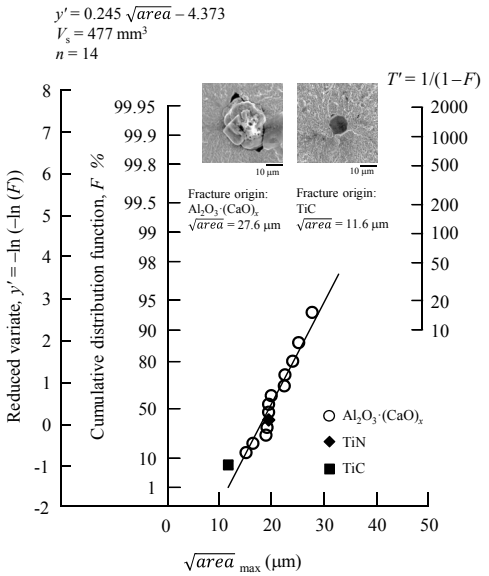

Figure 9. Statistics of extremes distribution of inclusions at the fracture origin [12]

where σ_0 is the remote tensile stress, a' is the large semi-axis of the ellipsoid and λ is the crack length measured from the equator of the ellipsoid [15]. As shown in Fig. 10, K_I for a crack with λ/a' of 0.2 is approximately equal to the stress intensity factor for a penny shaped crack with the radius of $a'+\lambda$. By considering such a steep growth in K_I value together with the presence of the interfacial cracking or cracked inclusion in the early stage of the fracture process (*cf.* Fig. 8), it can be deemed that the ellipsoidal nonmetallic inclusions are mechanically equivalent to a penny-shaped crack. Such an equivalence has experimentally been confirmed for the small fatigue cracks and defects [7, 8, 10]. Accordingly, we approximate K_{TH} in terms of σ_f and the inclusion size as follows:

$$K_{TH} = (2/\pi)\ \sigma_f \sqrt{\pi a'} \tag{1}$$

As illustrated in Fig. 8, most of the $Al_2O_3\cdot(CaO)_x$ type inclusions yield a spherical-like cavity [6]. The shape of the cavity is determined by the inclusion shape, which is not perfectly spherical but is irregular in nature. Also in the case of the TiN type inclusion, the shape of the original crack generated

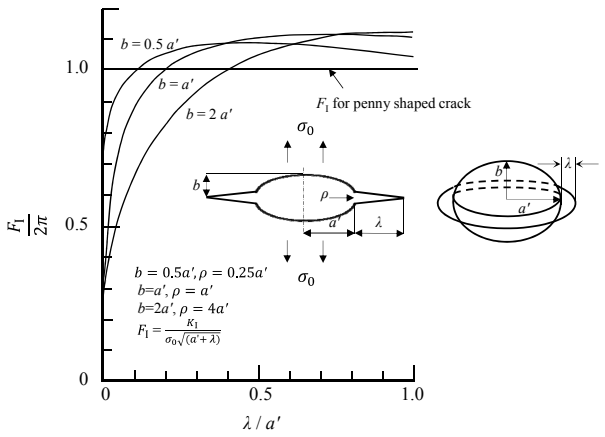

Figure 10. Normalized stress intensity factor for an annular crack emanating from an ellipsoidal cavity [15]

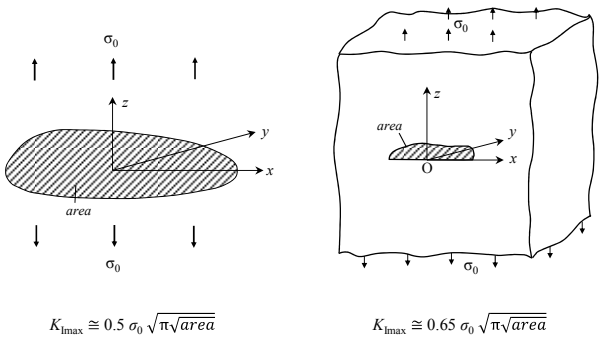

(a) Internal crack (b) Surface crack

Figure 11. Stress intensity factor for planer cracks with arbitrary shapes [7, 8, 10]

by the cracking of inclusion itself is not circular but somewhat angular in accordance with the inclusion shape. Hence, we approximate the cracks forming at nonmetallic inclusions as planar cracks by projecting the 3-D shape of the inclusion onto the plane perpendicular to the tensile axis of the specimen [7, 8, 10]. For a planar internal crack with arbitrary shape under tension shown in Fig. 11(a), K_{Imax} along the crack front is approximately given by [7, 8, 10].

$$K_{\mathrm{Imax}} = 0.5\sigma_0\sqrt{\pi\sqrt{area}} \tag{2}$$

Thus, K_{TH} for H-precharged smooth specimens associated with K_{Imax} is expressed by

$$K_{\mathrm{TH}} = 0.5\sigma_{\mathrm{f}}\sqrt{\pi\sqrt{area}} \tag{3}$$

K_{TH} obtained through this equation yields a magnitude which differs from that of Eq. (1) for the perfectly penny-shaped crack by only about 4%. All the fracture data are listed in Table 1.

The primary objective in this study is to determine the initiation threshold K_{TH} for the onset of crack propagation from small cracks in components exposed to high pressure hydrogen gas. It is well known in metal fatigue that ΔK_{th} for small cracks is not a material constant; ΔK_{th} for small cracks is smaller than that for long crack [7, 8, 10, 16]. In this study, we will explore whether such a size dependence exists or not in the case of small cracks in H-precharged specimens under static loading. Figure 12 shows K_{TH} plotted respectively against the inclusion size $\sqrt{area}$ and the residual hydrogen content measured right after the final fracture of each specimen $C_{\mathrm{H,\,R}}$ [12]. Regardless of some visible scatter in the experimental data in Fig. 12, one can note the following trends:

- K_{TH}, decreases with an decrease in the inclusion size $\sqrt{area}$.
- K_{TH}, decreases with an increase in the residual hydrogen content $C_{\mathrm{H,\,R}}$.

By means of these two dominant factors, the experimental data shown in Fig. 12 can be linearly interpolated by

$$K_{\mathrm{TH}} = 3.89 + 0.0555\sqrt{area} - 0.494C_{\mathrm{H,\,R}} \tag{4}$$

Where, $\sqrt{area}$ is in μm and $C_{\mathrm{H,\,R}}$ is in mass ppm. Figure 13 replots the data in Fig. 12 modified based on Eq. (4) [12]. Equation (4) is expressed as a linear function of $\sqrt{area}$ and $C_{\mathrm{H,\,R}}$, because the variation range of these variables are small such as 10-30μm of inclusion size. However, the equation applicable to wider variation range of these variables must be reconstructed as described later.

The reason for the dependence of K_{TH} on the inclusion size is explained as follows. Recall that the distribution of tensile stress along the axis of symmetry (x direction) ahead of the crack of length $2a$ in an infinite plate under remote tensile stress σ_0 in the y direction is described by

$$\sigma_{\mathrm{yy}} = \frac{\sigma_0 x}{\sqrt{x^2 - a^2}} \tag{5}$$

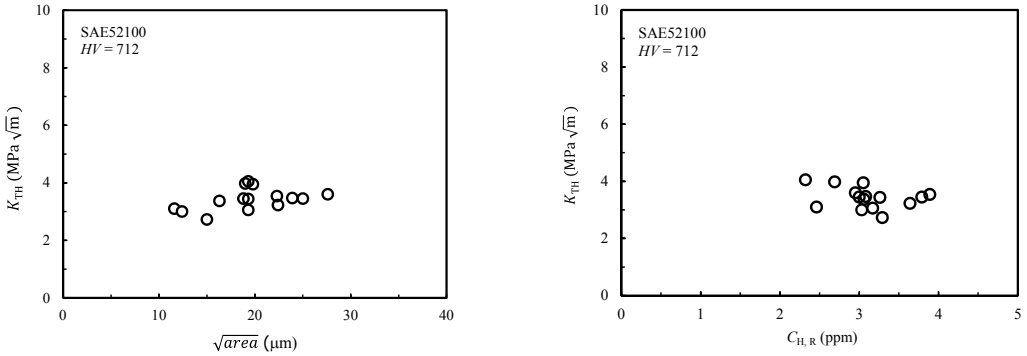

(a) K_{TH} as a function of $\sqrt{area}$ (b) K_{TH} as a function of $C_{H,R}$

Figure 12. K_{TH} data plotted respectively against $\sqrt{area}$ and $C_{H,R}$ [12]

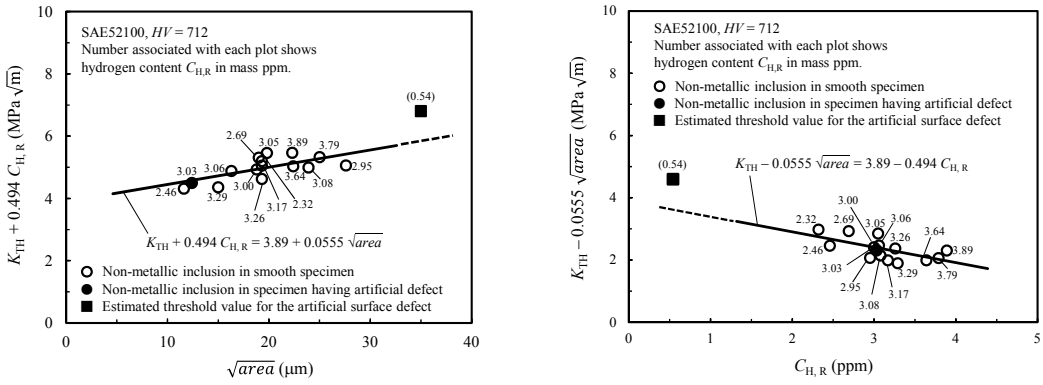

Figure 13. Threshold K_{TH} for SAE52100 expressed in terms of $\sqrt{area}$ and $C_{H,R}$ [12]

Particularly for very small distances, r, from the crack tip along the axis of symmetry, Eq. (5) yields

$$\sigma_{yy} = \frac{K_I}{\sqrt{2\pi r}} \tag{6}$$

Where, $K_I = \sigma_0 \sqrt{\pi a}$ is the stress intensity factor. Figure 14 shows an example of the comparison of stress field ahead of the tip of two different sizes of cracks under a stress intensity factor K_I of 10 MPa$\sqrt{m}$ which were obtained by Eq. (5). In both cases, σ_0 was determined so that K_I is equal to 10 MPa$\sqrt{m}$. In the *large crack* (*e.g.* $2a$ = 20 mm), the singular stress field decays very fast from the crack tip. In this case, Eq. (5) can be well represented by Eq. (6) to characterize the stress field near the crack tip. On the other hand, in the *small crack* (*e.g.* $2a$ = 0.02 mm), a large discrepancy arises between the stress fields in these two cracks. Such a discrepancy in the stress field near crack tip between small crack and large crack also arises even if the material is not the perfectly elastic but the elastic-plastic. For this reason, the tensile stress field ahead of the tip of small crack cannot be determined uniquely through the stress intensity factor alone, and therefore the calculated threshold values for small cracks show a crack size dependence.

3.3.2. Specimens having artificial surface defects

For a planar cracks with arbitrary shape at specimen surface (*cf.* Fig. 11(b)), K_{Imax} along the crack front can be approximated by [7, 8, 10].

$$K_{\mathrm{Imax}} = 0.65\sigma_0\sqrt{\pi\sqrt{area}} \tag{7}$$

Thus, considering the mechanical equivalence between small crack and defect as discussed in the previous section, K_{TH} for surface defects associated with K_{Imax} is expressed by

$$K_{\mathrm{TH}} = 0.65\sigma_{\mathrm{f}}\sqrt{\pi\sqrt{area}} \tag{8}$$

Figure 15 shows the K_{TH} values both for the artificial surface defects and nonmetallic inclusions as a function of the defect size $\sqrt{area}$ [12]. The data are shown in a double logarithmic diagram, as has widely been used for the arrangement of ΔK_{th} data of the small fatigue cracks [7, 8, 10, 16]. It is well known that in fatigue crack the threshold stress intensity factor range ΔK_{th} has the following relation with the defect size in the small crack regime, *e.g.* $\sqrt{area} < 1$ mm.

$$\Delta K_{\mathrm{th}} \propto (\sqrt{area})^{1/3} \tag{9}$$

Also in the present results for K_{TH}, we can see a definite size dependence in the range between about 10 and 500 μm in Fig. 15, *i.e.* K_{TH} was reduced with a decrease in $\sqrt{area}$. However, the exact dependence of the threshold value on the defect size is not clear at present since the threshold value can be varied also with the hydrogen concentration at the location of fracture origin, as will be discussed in the next section. As a reference data, in Fig. 15, the shaded area shows the Moody *et al.*'s K_{TH} data for a large crack in the standard CT and WOL specimens of AISI4340 steel with the yield strength σ_{YS} of 1500 ~ 1900 MPa, which was determined from tests in hydrogen gas, NaCl solutions and H-precharged specimens [4]. The values of K_{TH} for both the nonmetallic inclusions and artificial defects were definitely smaller than those for the large cracks, though the effect of some influencing factors, *e.g.* material type, strength level, hydrogen content, strain rate *etc*., should further be clarified in the future.

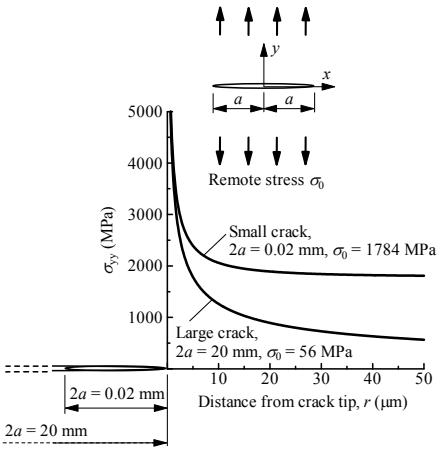

Figure 14. Comparison of stress field ahead of tip of *large* and *small* cracks under a stress intensity factor $K_{\mathrm{I}} = 10$ MPa$\sqrt{\mathrm{m}}$

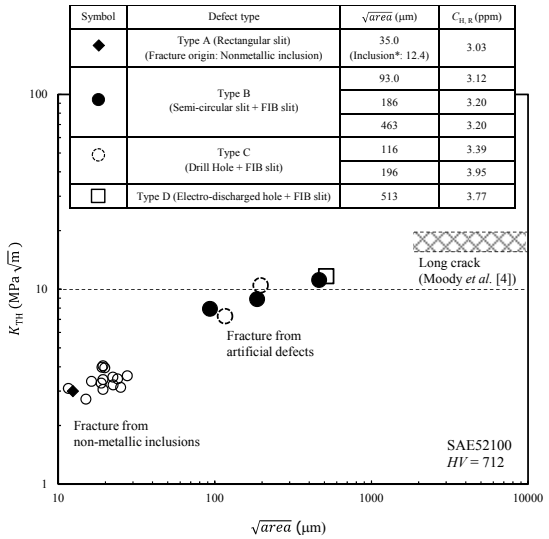

Figure 15. Relationship between K_{TH} and $\sqrt{area}$ for both short and long cracks in SAE52100. ◆: The specimen had the artificial defect, but was fractured from a non-metallic inclusion [12]

4. Conclusions

A series of uniaxial tensile tests of a H-precharged SAE52100 steel were carried out to determine the fracture toughness for the failure originated from nonmetallic inclusions and small artificial defects. The results are summarized as follows:

(1) All the H-precharged specimens failed in the elastic regime irrespective of the presence or absence of the artificial defect.
(2) In the smooth specimens, fracture origins were nonmetallic inclusions with the size of 10 ~ 30 μm (*e.g.* $Al_2O_3{\cdot}(CaO)_x$, TiN and TiC).
(3) Fracture of specimens having the artificial defect with sizes of about 100 ~ 500μm were originated from the defects.
(4) The threshold intensity factor K_{TH} was decreased with a decrease in defect size in the small crack regime. The values of K_{TH} for small defects were much smaller than those for large cracks in the standard specimens such as CT and WOL. For the safer design against the fracture toughness for small cracks, the crack size dependence should be taken into consideration.

Acknowledgements

This research has been supported in part by:

(1) The International Institute for Carbon-Neutral Energy Research (WPI-I2CNER), sponsored by the Japanese Ministry of Education, Culture, Sport, Science and Technology.
(2) The NEDO, Fundamental Research Project on Advanced Hydrogen Science (2006 to 2012).

References

[1] Y. Murakami, S. Matsuoka, Y. Kondo, S. Nishimura, Mechanism of Hydrogen Embrittlement and Guide for Fatigue Design. Yokendo, Tokyo, Japan (2012).
[2] R.P. Gangloff, B.P. Somerday, Ed., Gaseous hydrogen embrittlement of materials in energy technologies, Volume 1, Woodhead publishing, Oxford, UK (2012).
[3] Y. Murakami, H. Matsunaga, International Journal of Fatigue, 28 (2006) 1509-1520.
[4] R.N. Moody, S.L. Robinson, W.M. Garrison Jr., Res Mechanica, 30 (1990) 143-206.
[5] R.O. Ritchie, M.H. Castro Cedeno, *et al.*, Metall. Trans. A, 7 (1978) 35-40.
[6] Y. Murakami, T. Kanezaki, P. Sofronis, Engng. Frac. Mech., 97 (2013) 227-243.
[7] Y. Murakami, M. Endo, Int. J. Fatigue, 7 (1994) 163-182.
[8] Y. Murakami, Metal Fatigue: Effects of Small Defects and Nonmetallic Inclusions. Elsevier Ltd., Oxford, UK (2002).
[9] T. Miyamoto *et al.*, J. Soc. Mater. Sci., Japan, 59 (2010) 916-923.
[10] Y. Murakami, M. Endo, J. Soc. Mater. Sci., Japan, 35 (1986) 911-917.
[11] S. Fujita, Y. Murakami, Metall. Mater. Trans. A, 44 (2012) 2013-2033.
[12] Y. Murakami, H. Matsunaga, A. Abyazi, Y. Fukushima, Defect size dependence on threshold stress intensity for high strength steel with internal hydrogen, submitted (2013).
[13] A. Demarez, A.G. Hocks, F.A. Meuniers, Acta Metallurgica, 2 (1954) 214-223.
[14] K.A. Nibur, *et al.* SAND2010-4633, Sandia National Lab. (2010).
[15] Y. Murakami, Ed. in chief, Stress Intensity Factors Handbook, Vol. 2. 871-873, Pergamon Press, UK (1987).
[16] H. Kitagawa, S. Takahashi, Trans. Japan Soc. Mech. Engineers, Ser. A, 45 (1979) 1289-1303.

Study on damage tolerance properties of fiber metal laminates

Yu E Ma[1,*] Zhongchun Xia[1] Shuang Yun[1] XiaoFeng Xiong[2] QingMao Zhang[2]

[1] BOX 118, School of Aeronautics, Northwestern Polytechnical University, 710072, P.R. China,

[2] AVIC ChengDu Aircraft Design & Research Institute, ChengDu, P.R. China, 610041

* Corresponding author: ma.yu.e@nwpu.edu.cn

Abstract Fatigue crack growth rates in different notched fiber metal laminates under constant amplitude fatigue loading were studied experimentally and numerically. An modified numerically approach was used for predicting the crack growth rate with delamination growth, where the effective stress intensity factor in the metal layer is modulated by a bridging stress intensity factor. Then, fatigue lives of different notched fiber metal laminates were calculated. Good agreement was achieved between the predictions and experimental results.

Keywords Fiber metal laminates, crack growth , delamination growth, bridge stress, fatigue lives

1.Introduction

In modern aircraft fuselage design, advanced composite materials are increasingly utilized. A special family of such materials are the hybrid composites, also known as fiber metal laminates (FMLs), consisting of alternating layers of Al alloy and glass fiber reinforced epoxy. This material provides improved fatigue characteristics, considerable fire resistance and provides improved damage behaviour[1].

This paper deals with a numerical approach of this material, focusing on the fatigue crack growth rates in different notched FMLs. The numerical approach developed by Alderliesten[2] for predicting the fatigue crack propagation of FMLs is modified, and good agreement is achieved between the predictions and experimental results.

2.Experiments

The FMLs studied in this paper were consists of three layers of Al alloy 2024-T3 with the thickness of 0.254mm per layer and two layers of [0/90/0] glass/epoxy prepreg with the thickness of 0.15 mm per glass fiber layer. The dimensions of the specimens are 700 mm in length (L) and 140 mm in width (W). FMLs specimens were designed with 3 different notch sizes($2a_s$): 5mm, 10mm and 20mm. Constant amplitude fatigue testing was conducted using an MTS testing machine, as is shown in Fig 1. Fatigue tests were performed according to ASTM E 468-2004 at room temperature with a frequency of 10 Hz and a stress ratio of R = 0.1. The maximum applied stress was 160 MPa. Crack lengths and the cycles correspondingly were recorded. Crack growth rates were plotted in Fig 2.

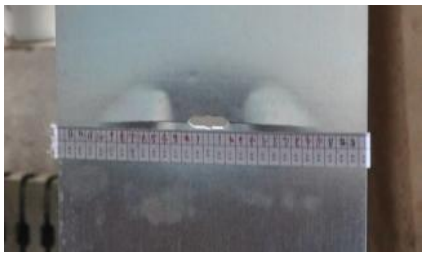

Fig 1 Delamination shape in FML during testing

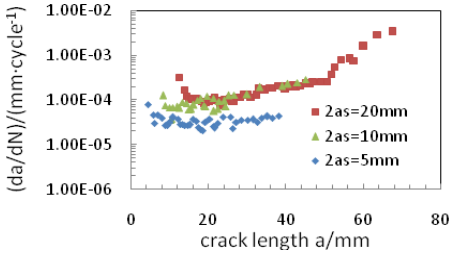

Fig 2 Crack growth rates

3.Model development

In this study, some details of the numerical approach developed by Alderliesten[2] were modified so that the predictions will have a better agreement with the experimental results. The numerical approach is based on a crack opening displacement relationship, as shown in Fig 3.

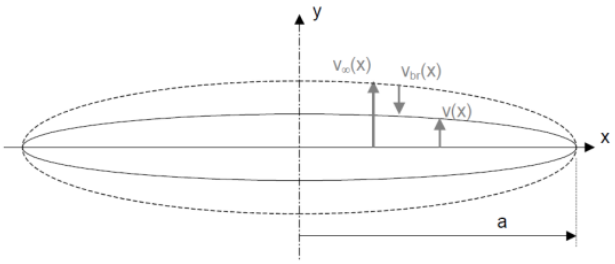

Fig 3 Definition of the crack opening displacement

$$v_\infty(x) - v_{br}(x) = \delta_f(x) + \delta_{pp}(x) \tag{1}$$

where $v_\infty(x)$ and $v_{br}(x)$ denote the crack opening displacement due to the remote applied stress and bridging stress in Al layer, respectively. $\delta_f(x)$ and $\delta_{pp}(x)$ are the deformation in the glass/epoxy prepreg and adhesive layers, respectively. The crack opening displacement away from the notch caused by the remote stress can be expressed as below

$$v_\infty(x) = 2\frac{S_{al}}{E_{al}}\sqrt{a^2 - x^2} \tag{2}$$

where E_{al} and S_{al} are the elastic modulus and the remote stress of the Al layer, respectively. The crack opening displacement $v_{br}(x)$ caused by bridging stress in Al layer can be calculated

$$v_{br}(x) = \int_0^a v(x, x_p)dx_p \tag{3}$$

The crack opening displacement $v(x, x_p)$ caused by point load is expressed as equation (4) and (5).

If $|x| < x_p$

$$v(x, x_p) = \frac{4S_{br,al}dx_p}{\pi E_{al}}\left(\tanh^{-1}\sqrt{\frac{a^2 - x_p^2}{a^2 - x^2 + b^2(x)}} + \frac{\frac{1}{2}(1+\upsilon)b^2(x)}{x_p^2 - x^2 + b^2(x)}\sqrt{\frac{a^2 - x_p^2}{a^2 - x^2 + b^2(x)}}\right) \tag{4}$$

and if $|x| > x_p$

$$v(x, x_p) = \frac{4S_{br,al}dx_p}{\pi E_{al}}\left(\tanh^{-1}\sqrt{\frac{a^2 - x^2}{a^2 - x_p^2 + b^2(x)}} + \frac{\frac{1}{2}(1+\upsilon)b^2(x)}{x_p^2 - x^2 + b^2(x)}\sqrt{\frac{a^2 - x^2}{a^2 - x_p^2 + b^2(x)}}\right) \tag{5}$$

where υ is Poisson ratio of the Al layer. $b(x)$ is the delamination shape function. $S_{br,al}$ is the bridging stress in Al layer.

The deformation caused by the elastic fiber extension is expressed as (6)

$$\delta_f(x) = \frac{S_f + S_{br,f}(x)}{E_f}b(x) \tag{6}$$

where E_f is the elastic modulus of glass/epoxy prepreg, and $S_{br,f}$ is the bridging stress in glass/epoxy prepreg. S_f is the stress in glass/epoxy prepreg at the notched zone. The bridging

stress in Al layer and glass/epoxy prepreg has a relationship given as(7)

$$\frac{S_{br,al}}{S_{br,f}} = \frac{n_{f1}t_{f1} + n_{f2}t_{f2}}{n_{al}t_{al}} \tag{7}$$

For the numerical solution, the crack geometry is divided into N elements with equal width $w = \frac{a - a_s}{N}$.

The stress intensity factor as a result of the far field stress present in the Al layers follows from the linear elastic theory for monolithic metals

$$K_{farfield} = S_{al}\sqrt{\pi a} \tag{8}$$

Since the bridging stress in Al layer for a given delamination shape is calculated, the stress intensity factor caused by the bridging stress is expressed as followed

$$K_{bridging} = 2\sum_{i=1}^{N} \frac{S_{br,al}(x_i)w}{\sqrt{\pi a}} \frac{a}{\sqrt{a^2 - x_i^2 + b^2(x_i)}} \left(1 + \frac{1}{2}(1+\upsilon)\frac{b^2(x_i)}{a^2 - x_i^2 + b^2(x_i)}\right) \tag{9}$$

The bridging stress in Al layer impedes the crack growth, so the stress intensity factor at the crack tip is expressed as(10)

$$K_{tip} = K_{farfield} - K_{bridging} \tag{10}$$

In order to calculate the crack growth rate with Paris equation, an effective stress intensity factor range must be determined. Take the effect of stress ratio and the geometry into consideration, the effective stress intensity factor is expressed as(11)

$$\Delta K_{eff} = \left(1 - R^{1.35}\right) K_{tip} \sqrt{\sec\left(\frac{a\pi}{W}\right)} \tag{11}$$

where W is the width of the specimen.

Now, the crack growth rate can be obtained as (12)

$$\frac{da}{dN} = C_{cg}\Delta K_{eff}^{n} \tag{12}$$

4.Results and conclusions

All the equations above are solved by MATLAB. Triangle is chosen as the delamination shape, that is $b(x) = b(a_s) \times \left(1 - \frac{x - a_s}{a - a_s}\right)$. $b(a_s)$ is a ratio of maximum delamination length to crack length, which is based on experimental observations. $b(a_s)$ for the FMLs with notch length of 20mm is 0.35 . $b(a_s)$ for the FMLs with notch length of 10mm is 0.35. $b(a_s)$ for the FMLs with notch length of 5mm is 0.175. Bridging stresses distributions in the FMLs with 3 differernt notch sizes along the crack length was plotted in Fig 4 when crack lengths comes to 65mm.The comparisons between experimental and predicted crack growth rates are plotted in Fig 5, Fig 6, Fig 7 when notch length is 20mm,10mm,5mm ,respectively.

The fatigue lives of FMLs can be obtained by the equation (13)

$$N = \int_0^a \frac{1}{C_{cg}\Delta K_{eff}^{n}} da \tag{13}$$

Using above equations, the fatigue lives for the notched fiber metal laminates can be calculated, as is plotted in Table 1.

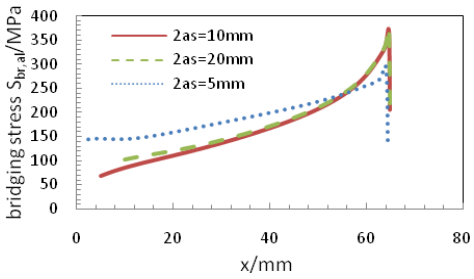

Fig 4 Bridging stresses distributions in t

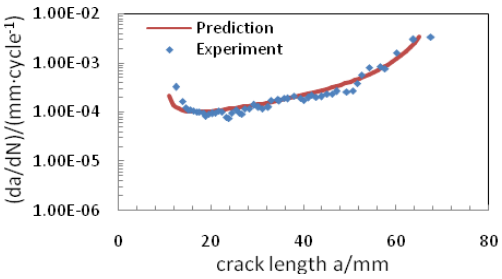

Fig 5 Comparison for as is 20mm

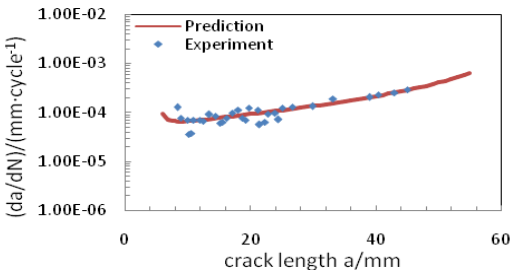

Fig 6 Comparison for as is 10 mm

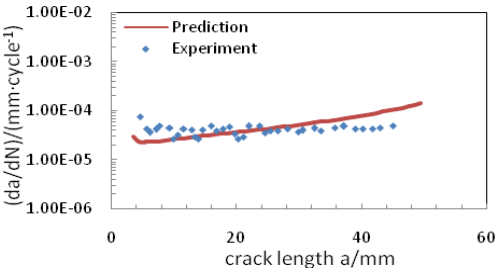

Fig 7 Comparison for as is 5mm

Table 1 The comparisons between experimental and predicted fatigue lives of FMLs

$2a_s$ (mm)	Experiments （N）	Predictions （N）	Errors（%）
5	1024000	1067019	4.2
10	355600	363672	2.3
20	296000	277720	6.2

Actually, the accuracy of this numerical approach depends on the delamination shape and the ratio . The delamination shape can be ellipse, parabola, triangle and cosine. Through the calculation, triangle seems to be the best delamination shape, cosine to be the second, parabola and triangle don'tfit well with the experimental results. The predictions are also sensitive to the radio .But a range of the radio can be determined by experimental observations so that the errors can be controlled.

This paper proposes a modified numerical approach for predicting the fatigue crack growth rates in different notched FMLs. By using MATLAB, the fatigue crack growth rates and the fatigue lives of different notched FMLs are calculated, and good agreement is achieved between the predictions and experimental results.

References

[1] Roebroeks G.H.J. Towards GLARE - The development of a fatigue insensitive and damage tolerant aircraft material [D]. PhD Thesis, Delft University of Technology, Delft, 1991.

[2] Alderliesten R.C. Fatigue crack propagation and delamination growth in GLARE[D]. PhD Thesis, Delft University of Technology, Delft, 2005.

Simulating the bluntness of TBM Disc Cutters in Rocks using Displacement Discontinuity Method

Hadi Haeri[1, *], Kourosh Shahriar[2], Mohammad Fatehi Marji[3], Parviz Moarefvand[4]

[1]PhD candidate of rock mechanics, Mining Engineering Department, Science and Research Branch, Islamic Azad University, Poonak, Hesarak, Tehran, Iran

[2]Prof., Department of Mining and Metallurgical Engineering, Amirkabir University of Technology, Tehran, Iran

[3]Associate Prof., Head of Mine exploitation Engineering Department, Faculty of Mining and Metallurgy, Institution of Engineering, Yazd University, Yazd, Iran

[4]Assistant Prof., Department of Mining and Metallurgical Engineering, Amirkabir University of Technology, Tehran, Iran

* Corresponding author: hadihaeri@ymail.com

Abstract

Underground accessibility includes several steps which the cutting step is the one of most basic and most important of them. Indentation of TBM disc cutters into the rock and producing of the chips in different scales are well known as an indentation process. This phenomena passé from producing the micro cracks to the coalescing into macro cracks. The present research focuses on the linear elastic fracture mechanics of rock and maximum shear stress criterion to investigate the micro crack propagation and its direction under disc cutters. A higher order indirect boundary element method (using quadratic displacement discontinuity elements) is used to estimate the stress intensity factors in rocks under single disc cutter. Also to eliminate errors caused by stress and displacement singularity near the crack tip, three special crack tip elements are used. As the TBM disc cutters will be eroded after a period of working, the effects of eroded and not eroded discs are numerically modeled, analyzed and compared with each other. To create the eroded disc model, we considered 4 small elements to generate the curvature of the cutter tip, which reducing the computing efficiency and increasing the required specific energy for chips formation.

Keywords: eroded disc, micro crack propagation, specific energy, SDDM, TBM

1. Introduction

One of the most complex engineering problems is cutting and indentation of mechanical tools into the rock which has been considered by human primitively. The investigation on rock fracture mechanics with mechanical tools in mining and civil operations is significant duo to its widespread applications. These investigations can be used to predict and estimate rock fracture mechanism for optimization and risk-reducing of planning, temporal and economic schematization [1]. The key parameters in TBM head design are head diameter, number of cutters, thrust force, rolling force, RPM, penetration depth, and cutter spacing [2, 3 and 4]. Many experimental studies and numerical simulations have been reported for the breakage mechanism of rock under disc cutters of tunnel boring machines (TBMs) [5-16]). Recently, Cho et al [4] investigated the optimum spacing of TBM

disc cutters using numerical simulations. Their results are in good agreement with those obtained from experimental studies (LCM). Propagation and coalescence mechanism of micro cracks due to indentation of TBM disc cutters into the rock and production of chips in indent process is highly complex and important. The mechanism of micro crack propagation and coalescence has not been widely studied and its real reasons (micro crack propagation and coalescence) have not been fully found. Because of the complexity of the micro crack propagation and coalescence problem under TBM disc cutters, nowadays, numerical or analytical-numerical approaches are mostly used for simulating the rock breakage mechanism [17]. A numerical model, the higher order semi-infinite displacement discontinuity ($HOSDD_{2D}$) code, a two-dimensional code based on the linear elastic fracture mechanics (LEFM) which uses quadratic displacement discontinuity formulation with three special crack tip elements at each micro crack initial and end is used to simulate the rock breakage mechanism. Based on this numerical method, stresses near the crack tip and distribution of displacements can be clearly defined to determine the accurate strain energy release rate and stress intensity factors. There are three important fracture initiation criteria, which are applicable in action: the maximum tangential stress (σ_θ-criterion), the minimum energy density criterion (S-criterion) and the maximum energy release rate (G-criterion) or any modified form of those mentioned issues, (e.g. F-criterion which is A modified energy release rate criterion) has mostly been used to study the breakage mechanism of rock [18-24,14]. Although this criteria act prosperously for predicting the crack initiation under TBM disc cutters, the maximum tangential stress criterion is used here to predict the direction of micro crack initiations resulted from artifact cracks of TBM disc cutters. In the present research, the rock breakage mechanism under eroded disc cutters of tunnel boring machines (TBMs) is modeled and studied by the proposed method. A comparison of results between eroded and non-eroded disc models is presented.

2. Higher Order Displacement Discontinuity In a Half-plane

The semi-infinite displacement discontinuity method (SDDM) is an indirect boundary element method that is solved problems on the basis of fracture mechanics principles given the boundary conditions and calculates stresses and displacements at discontinuities in all boundary elements. cruch and starfield [25] used the analytical solution of a constant element displacement discontinuity, over the line segment $|x| \le a$, $y = 0$ in the semi-infinite area $y \le 0$ as shown in Fig. 1. For complete computaion of displacements and stresses in semi-infinite body, due to the real displacement discontinuity, its portrait and its resulting from the supplementary solution are denoted by u_i^R and σ_{ij}^R, u_i^P *and* σ_{ij}^P, u_i^S and σ_{ij}^S, respectively.
The complete solution for the semi-infinite plane $y \le 0$ can be expressed as:

$$u_i = u_i^R + u_i^P + u_i^S \qquad \text{and} \qquad \sigma_{ij} = \sigma_{ij}^R + \sigma_{ij}^P + \sigma_{ij}^S \tag{1}$$

$\bar{x}, \bar{y}$ and x, y are local coordinates and global coordinates, respectively, that can be transformed by the following two formulas:

$$\begin{aligned} \bar{x} &= (x - c_x)\cos\varphi + (y - c_y)\sin\varphi \\ \bar{y} &= -(x - c_x)\sin\varphi + (y - c_y)\cos\varphi \end{aligned} \tag{2}$$

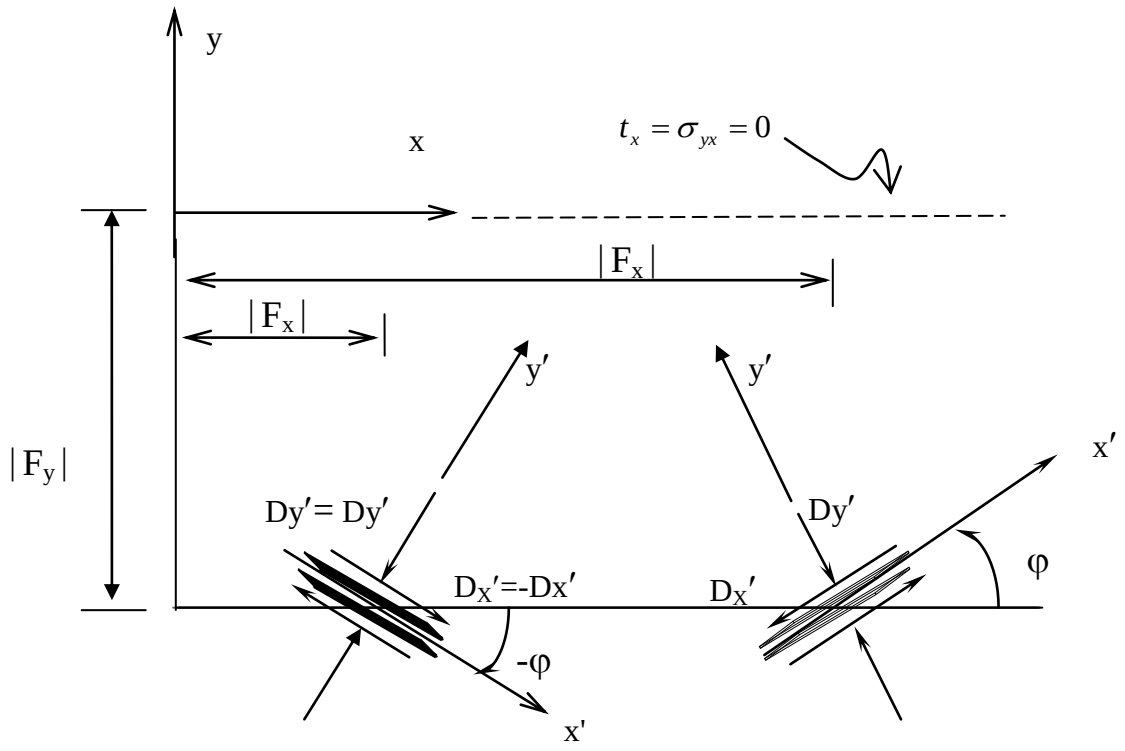

Figure 1. Real and portrait displacement discontinuities in half-plane $y \leq 0$, with a traction-free surface (after Crouch and Starfield [25]).

In the present study, in order to obtain high precision, quadratic collocation displacement discontinuity modified for half plane crack problems with a traction free surface are used. $D_k(\xi)$ is equation that can be used to calculate two fundamental variables of each element (the opening displacement D_y and sliding displacement D_x).

$$D_j(\xi) = \sum_{i=1}^{n} \Pi_i(\xi) D_i^k, k = x, y \tag{3}$$

Where $D_1^k (i, e. D_1^x$ and $D_1^y)$, $D_2^k (i.e. D_2^x$ and $D_2^y)$, $D_3^k (i.e. D_3^x$ and $D_3^y)$ are the quadratic displacement discontinuities, and using the equal length of each sub element $a_1 = a_2 = a_3$

$$\begin{aligned}
\Pi_1(\xi) &= -(3a_1^3 - a_1^2\xi - 3a_1\xi^2 + \xi^3)/(48a_1^3), \\
\Pi_2(\xi) &= (9a_1^3 - 9a_1^2\xi - a_1\xi^2 + \xi^3)/(16a_1^3), \\
\Pi_3(\xi) &= (9b_1^3 + 9a_1^2\xi - a_1\xi^2 - \xi^3)/(16a_1^3)
\end{aligned} \tag{4}$$

are their quadratic element shape functions.

In Fig. 2, A quadratic displacement discontinuity (DD) element is divided into three equal sub-elements (each sub-element contains a central node for which the nodal displacement discontinuities are evaluated numerically) [26].

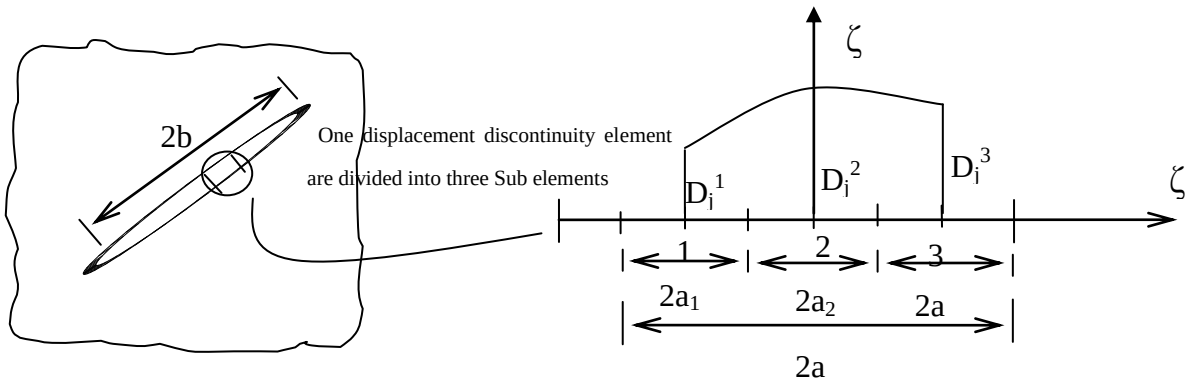

Figure 2. Higher order displacement discontinuity (HODD) elements by quadratic elements

To increase the accuracy in computing of the displacement discontinuities and stresses near original crack tips, the special crack tip elements are used. In previous works, usually, one or two special elements for crack tip were used, but in the present research, three special elements are used. Following equation can be used three elements, particularly for crack tip:

$$D_i(\xi) = [\Pi_{T1}(\xi)]D_i^1(b) + [\Pi_{T2}(\xi)]D_i^2(b) + [\Pi_{T3}(\xi)]D_i^3(b) \tag{5}$$

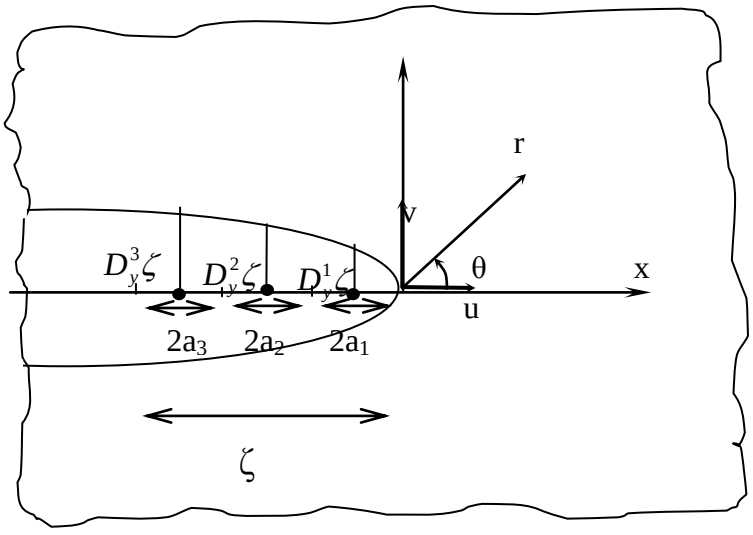

Figure 3. Quadratic element for the higher order displacement discontinuity variation

3. Verification of the semi-infinite displacement discontinuity method (using quadratic elements)

Verification of this method is made through the solution of a simple example problem i.e. a center inclined micro crack in a semi-infinite body which is shown in Fig. 4. The tensile stress is acting parallel to the x axis at infinity. Considering a 30 degrees center inclined micro crack under uniform normal tension σ= *10 MPa*, a half micro crack length b= 1 meter, fracture toughness K_{IC}= *2 MPa*

√m, modulus of elasticity *E=10 GPa*, Poisson's ratio *v= 0.2* are assumed. The analytical solution of mode I and mode II stress intensity factors, K_I and K_{II}, for the infinite body problem are given as [27]:

$$K_I = \sigma(\pi b)^{\frac{1}{2}} \sin^2 \beta \; and \; K_{II} = \sigma(\pi b)^{\frac{1}{2}} \sin \beta \cos \beta \tag{6}$$

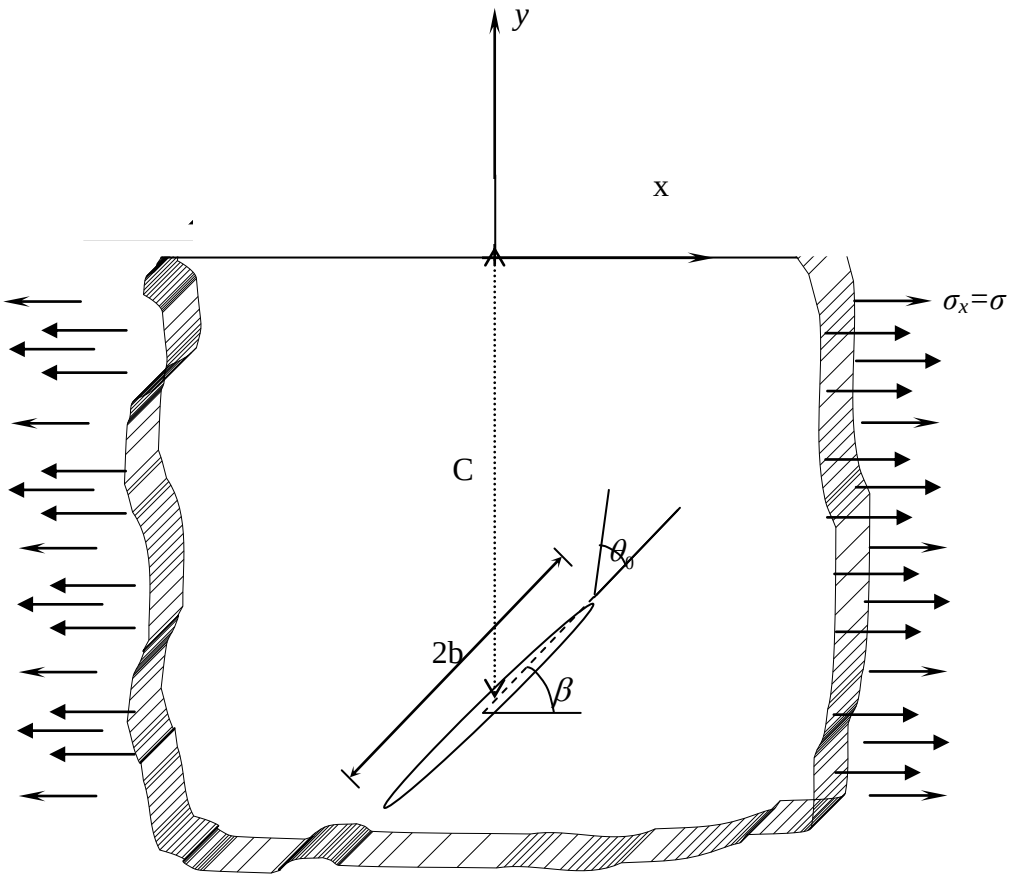

Figure 4. A center inclined micro crack in a semi- infinite body.

The semi-infinite center inclined micro crack problem is selected to verify the proposed code (see Fig. 4).

Fig.5 is based on the normalized stress intensity factors which compare the different results obtained for the upper cracks (the cracks near to the free surface of the half plane), and the lower cracks, with the available analytical results of the center inclined micro crack in an half plane.

The numerical results show that as the depth of the micro crack (*C/R* ratio) increases the mixed mode stress intensity factors K_I and K_{II}, and the crack initiation angle θ_0 tend to their corresponding analytical values of the center inclined micro crack in an infinite plane.

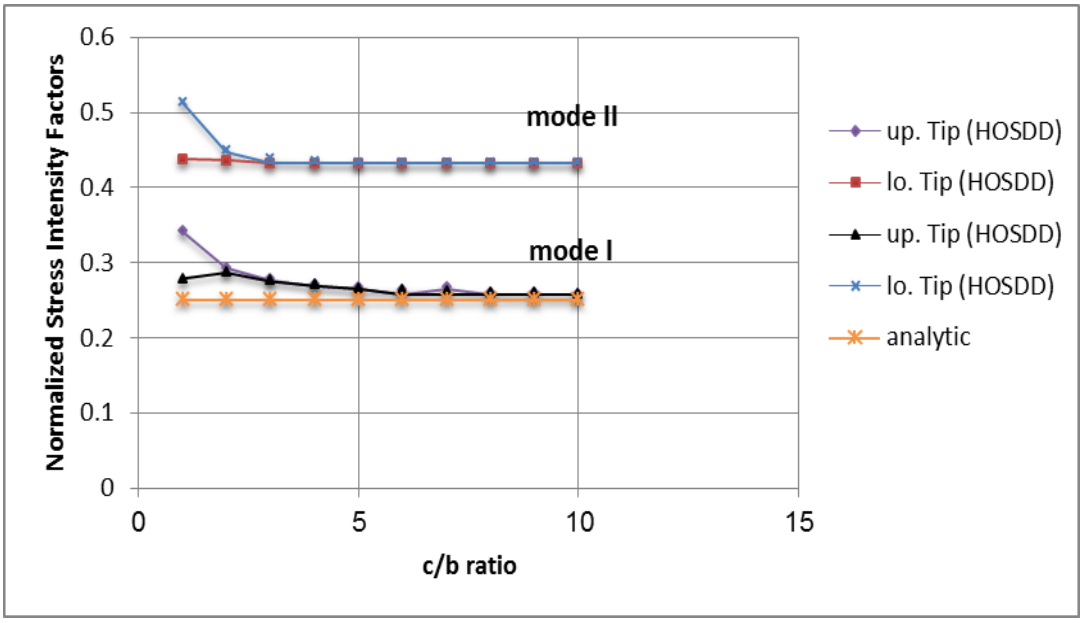

Figure 5. The normalized stress intensity factors $K_I/(p\sqrt{\pi\rho R})$ and $K_{II}/(p\sqrt{\pi\rho R})$, for different *C/R* ratios, for a center inclined micro crack , in a semi-infinite plane

4. Modeling of eroded disc cutter

Since, after a while, TBM disc cutters erosion caused by contact with the rock, therefore, the effect of erosion is modeled numerically. For this purpose, four special elements are used to simulate the disc cutter tips. This model estimates the required curvature near the disc cutter tips, reducing the computing efficiency and increases the required specific energy for chips formation under disc cutters during a rock indentation process. In the Figure 6, the micro crack propagation path for artifact cracks of AC1, AC2, AC3 and AC4 which represents the coalescing of propagated micro cracks from artifact cracks, and also this path for $S/P_d=10$, disc edge angle $\psi=60$, $P_d=6mm$ and extended length of $\delta=4mm$ (8 iteration) are estimated. Micro cracks propagate with respect to direction of the artifact cracks, then after several (8) iteration propagated micro cracks from artifact cracks coalesce to each other at the region between cutters. Considering a typical TBM with a thrust of *250 kN* per cutter, with disc cutters of 15 mm width and 432 mm diameter. The typical rock is the Aspo diorite with the Mode I and Mode II fracture toughnesses $K_{IC}=3.83\ MPa\ m^{1/2}$, and $K_{IIC}=5.09\ MPa\ m^{1/2}$ respectively. The other parameters of this rock as quoted by Backers (2004) are: $\sigma_t = 15$ *MPa*, $\sigma_C = 220$ *MPa*, and $E= 68\ GPa$ and $\nu = 0.24$ [20].

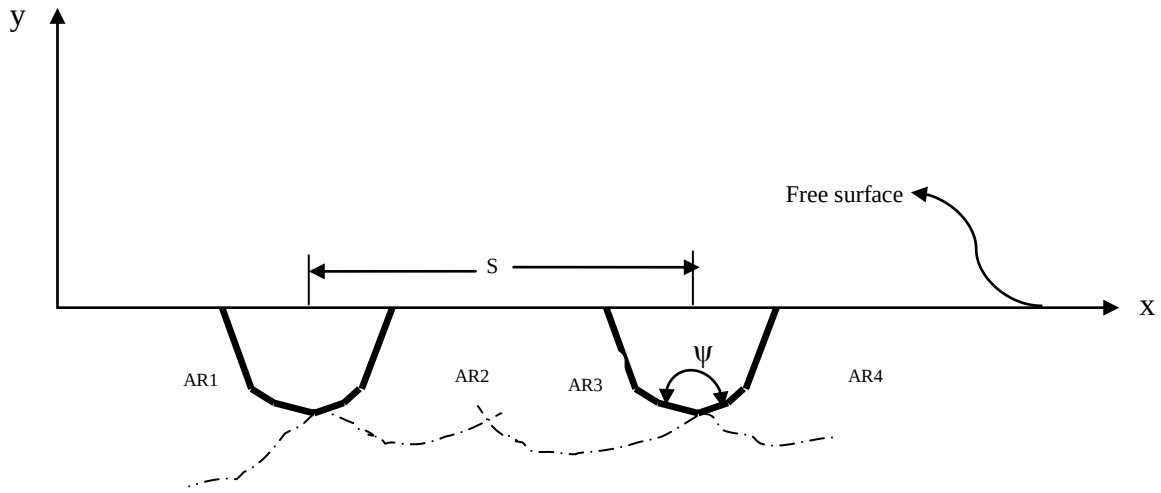

Figure 6. The micro crack propagation path for *S/Pd=10* edge angle *ψ =60, Pd=6*, mm and extended length of *δ=4mm* (8 iteration).

In order to investigate the effect of erosion on the TBM, the results of modeling as illustrate in Figs. 7- 9. According to the Fig. 7, because the cutters are blunted under erosion, as a result, more specific energy for eroded cutters than non-eroded cutters is required. The figure shows that in both cases, the optimum ratio *S/Pd* is in range of 7.5–15, which is in well agreement with the experimental results. Figs. 8 shows comparison between eroded and non-eroded disc cutters for the Mode I and Mode II stress intensity factors, K_I, K_{II} *(MPa* $m^{1/2}$*)* versus different *S/Pd* ratios. Figs. 9 shows comparison between eroded and non-eroded disc cutters for the Mode I and Mode II stress intensity factors, K_I, K_{II} *(MPa* $m^{1/2}$*)* versus different *Pd* ratios.

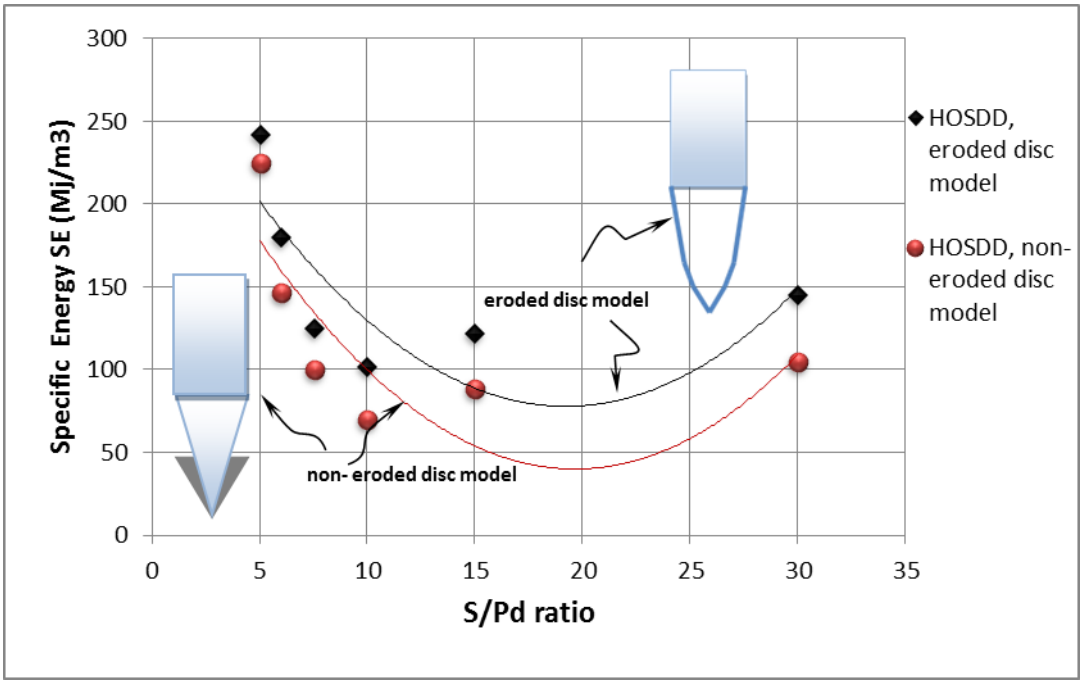

Figure 7. Comparison between eroded and non-eroded disc cutters for specific energy *SE (Mj/*m^3*)* versus different *S/Pd* ratios

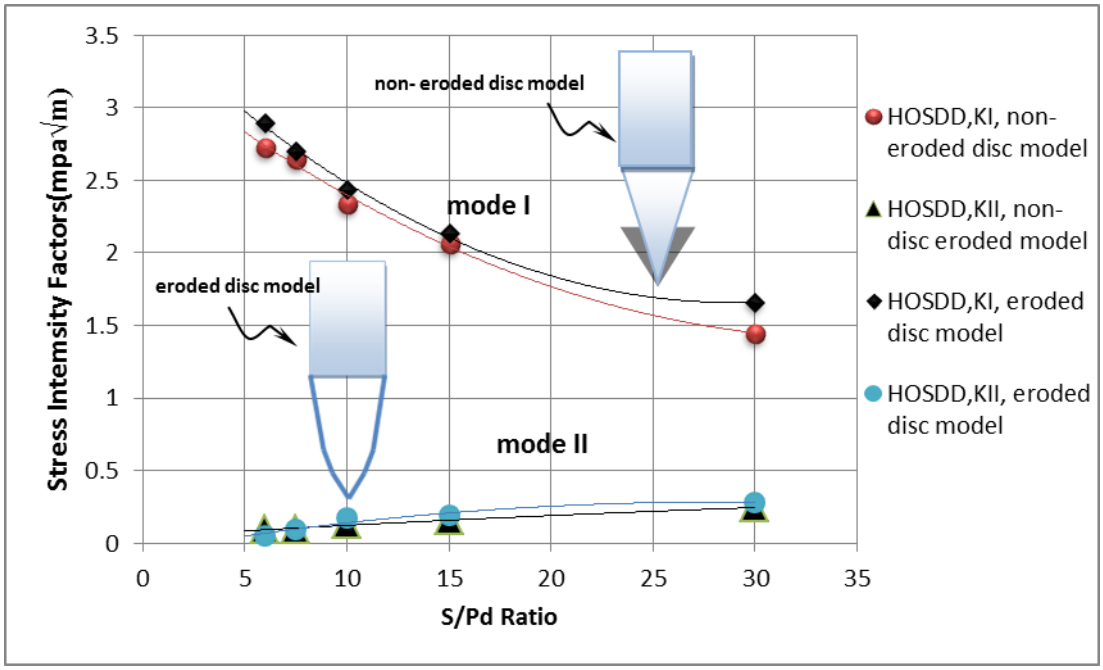

Figure 8. Comparison between eroded and non-eroded disc cutters for the Mode I and Mode II stress intensity factors, K_I, K_{II} ($MPa\ m^{1/2}$) versus different *S/Pd* ratios

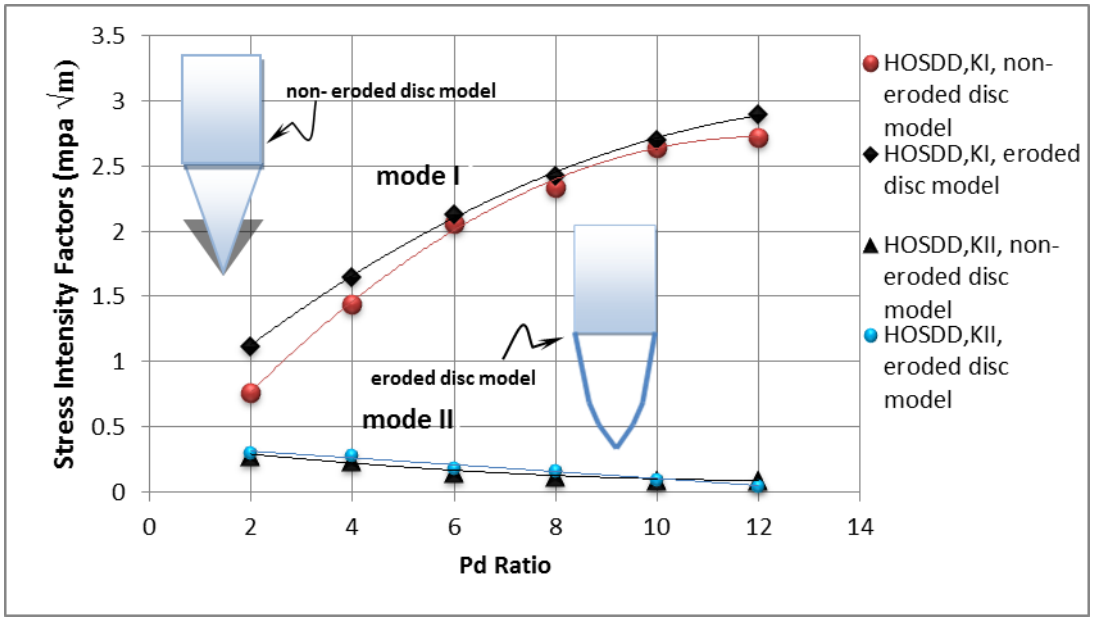

Figure 9. Comparison between eroded disc cutter and non-eroded disc cutters for the Mode I and Mode II stress intensity factors, K_I, K_{II} ($MPa\ m^{1/2}$) for various penetration depths *Pd*

5. Conclusions

A two-dimensional code based on a semi-infinite displacement discontinuity method (Known as $HOSDD_{2D}$) is used to simulate rock-cutting behavior under TBM disc cutter during rock indentation. The produced micro cracks under the disc cutters are coalesced during their propagation into the

underneath rock mass. The disc edges are assumed to behave as artifact cracks. The propagation and coalescence mechanism of the micro cracks emanating from each artifact crack tips are investigated by discretizing it into three ordinary and three special crack tip elements at the tip. The maximum tangential tensile stress criterion (σ_θ-criterion) is implemented into $HOSDD_{2D}$ code. In the present research, the effects of erosion on the Mode I and Mode II stress intensity factors and specific energy (SE) for TBM disc cutters are investigated by simulating the penetrating artifact cracks (disc cutters) into a rock mass. The main purpose of the present modeling was to compare the results obtained for the eroded disc cutters with those of non-eroded disc cutters. As a result, for the eroded disc cutters, higher forces (more specific energy) are required to propagate the micro cracks emanating from the artifact cracks compared to those for non-eroded disc cutters

6.References

[1] X. C. Tan, S. Q. Kou, P. A. Lindqvist, Simulation of Rock Fragmentation by Indenters Using DDM and Fracture Mechanics, Rock Mechanics, Tools and Techniques; Aubertin M., Hassani F., and Mitri H. (Eds.); Balkema, Roterdam, 1996

[2] J.Rostami, , L. Ozdemir, A new model for performance prediction of hard rock TBMs. In: Proceedings, Rapid Excavation and Tunneling Conference (RETC), 1993, pp. 793–809.

[3] O. Acaroglu, L. Ozdemir, B. Asbury,. A fuzzy logic model to predict specific energy requirement for TBM performance prediction. Tunn. Undergr. Space Technol, 23 (2008) 600–608.

[4] J.W. Cho, S. Jeon, S.H. Yu, S.H. Chang, Optimum spacing of TBM disc cutters: A numerical simulation using the three-dimensional dynamic fracturing method, Tunnelling and Underground Space Technology 25 (2010) 230–244.

[5] N.G.W. Cook, M. Hood, F. Tsai, Observations of crack growth in hard rock loaded by an indenter. Int. J. Rock Mech. Min. Sci. Geomech. Abstr, 21 (1984) 97– 107.

[6] Y. Uga, K. Sakoi, S. Sugiyama, Y. Kondo, K. Nishimura, H. Ono,. Development of new tunnel boring machine with slurry transport system – penetration efficiency of disc cutters, Kawasaki Heavy Industry Report 91, 1–8 (in Japanese), 1986.

[7] B. Nilsen, L. Ozdemir, Hard rock tunnel boring prediction and field performance. In: Proceedings, Rapid Excavation and Tunneling Conference (RETC), 1993, pp. 833–852.

[8] N. Bilgin, H. Tuncdemir, C. Balci, H. Copur, S. Eskikaya, A model to predict the performance of tunneling machines under stressed conditions, In: Proceedings, AITES-ITA 2000 World Tunnel Congress, 2000, pp. 47–53.

[9] H.Y. Liu, S.Q. Kou, P.A. Lindqvist, C.A. Tang, Numerical simulation of the rock fragmentation process induced by indenters. Int. J. Rock Mech. Min. Sci. 39 (2002) 491–505.

[10] S.H. Baek, H.K. Moon, A numerical study on the rock fragmentation by TBM cutter penetration. Tunn. Undergr. Space (J. Korean Soc. Rock Mech.) 13 (2003) 444–454 (in Korean).

[11] N. Bilgin, C. Feridunoglu, D. Tumac, M. Cinar, Y. Palakci, O. Gunduz, L. Ozyol, The performance of a full face tunnel boring machine (TBM) in Tarabya (Istanbul). In: Proceedings, 31st ITA-AITES World Tunnel Congress, 2005, pp. 821–826.

[12] S. Eskikaya, N. Bilgin, C. Balci, H. Tuncdemir,. From research to practice – development of rapid excavation technologies. In: Proceedings, 31st ITA-AITES World Tunnel Congress, 2005, pp. 435–441.

[13] N. Bilgin, M.A. Demircin, H. Copur, C. Balci, H. Tuncdemir, N. Akcin, Dominant rock properties affecting the performance of conical picks and the comparison of some experimental and theoretical results. Int. J. Rock Mech. Min. Sci. 43 (2006) 139–156.
[14] S.H. Chang, S.W. Choi, G.J. Bae, S. Jeon,. Performance prediction of TBM disc cutting on granitic rock by the linear cutting test. Tunn. Undergr. Space Technol, 21 (2006), 271.
[15] K.I. Park, S.H Chang, S.W Choi, S. Jeon, Prediction of the optimum cutting condition of TBM disc cutter in Korean granite by the linear cutting test. In: Proceedings, Korean Society for Rock Mechanics Conference, 2006, pp. 217–236 (in Korean).
[16] R.Gertsch, L. Gertsch, J. Rostami, Disc cutting tests in Colorado red granite: implications for TBM performance prediction. Int. J. Rock Mech. Min. Sci. 44 (2007) 238–246.
[17] H. Haeri,. Numerical Modeling of the Interaction between Micro and Macro Cracks in The Rock Fracture Mechanism Using Displacement Discontinuity Method. PhD Thesis, department of mining engineering, Science and Research branch, Islamic Azad University, Tehran, Iran, during work, 2011.
[18] A. R. Ingraffea, Numerical Modeling of Fracture Propagation, Rock Fracture Mechanics; Rossmanith H. P. (Editor); Springer Verlagwien; New York, 1983, pp. 151-208.
[19] S. Melin,. When does a crack grow under mode II condition? International Journal of Fracture, 30(1986) 103-114.
[20] D. Broek,. The Practical Use of Fracture Mechanics, 4th Edition, Kluwer Academic Publishers, Netherland.70. Whittaker BN, Singh RN, Sun G. Rock fracture mechanics: Principles, design and applications. Amsterdam: Elsevier, 1989.
[21] B. N. Whittaker, R. N Singh, G. Sun, Rock Fracture Mechanics, Principles, Design and Applications, Elsevier, Netherlands, 1992 .
[22] B.Shen, O. Stephansson 'Modification of the G-criterion for Crack Propagation Subjected to Compression', Engng. Fract. Mech., 47(1994)177-189.
[23] J.F. Shao, J.W. Rudnicki,. A micro crack-based continuous damage model for brittle geomaterials. Mechanics of Materials, 32(2000)607-619
[24] D.J.C Bremaecker, MC. Ferris, D. Ralph, Compressional fractures considered as contact problems and mixed complementarity problems, Eng. Fract. Mech., 66(2000) 287-303.
[25] S. L Crouch, A. M. Starfield, Boundary Element Methods in Solid Mechanics; Allen and Unwin, London, 1983.
[26] M.F. Marji, H. Hosseini-Nasab, A. H Kohsary, On the uses of special crack tip elements in numerical fracture mechanics, Int. Journal of solids and structures 43(2006) 1669-1692.
[27] C. Scavia, Fracture Mechanics Approach to Stability Analysis of Crack Slopes, Engng. Fract. Mech., 35(1990)889-910

Modeling the propagation mechanism of two random micro cracks in rock Samples under uniform tensile loading

Hadi Haeri[1, *], Kourosh Shahriar[2], Mohammad Fatehi Marji[3], Parviz Moarefvand[4]

[1]PhD candidate of rock mechanics, Mining Engineering Department, Science and Research Branch, Islamic Azad University, Poonak, Hesarak, Tehran, Iran

[2]Professor, Department of Mining and Metallurgical Engineering, Amirkabir University of Technology, Tehran, Iran

[3]Associate Professor, Head of Mine exploitation Engineering Department, Faculty of Mining and Metallurgy, Institution of Engineering, Yazd University, Yazd, Iran

[4]Assistant Professor, Department of Mining and Metallurgical Engineering, Amirkabir University of Technology, Tehran, Iran

* Corresponding author: hadihaeri@ymail.com

Abstract

The breakage mechanism of brittle substances such as rocks under uniform tensile loading is considered. The random micro cracks are mostly produced in all of Polycrystalline substances resulting from stress concentration. This paper focuses on the interaction of two pre-existing micro cracks. The quality of the growing and coalescing of micro cracks in rock-like specimen are studied by using a Fortran Code $HDDMCR_{2D}$ which is based on a two dimensional displacement discontinuity method for the crack analysis (a boundary element computer code based on the linear elastic fracture mechanics (LEFM) theory). In order to improve the accuracy of the results and reduce the errors in calculating displacement discontinuity in the proposed model, the higher-order elements (quadratic elements) are used to discretize a sufficient number of boundary elements. Also to eliminate errors caused by stress and displacement singularity near the crack tip, three special elements has been used to discretize each crack end. In this research, the problems of wing cracks propagated at different angles from the original micro crack tips in an infinite specimen under uniform tension are considered.

Keywords micro crack interaction, crack initiation, LEFM, BEM, crack coalescence

1. Introduction

The presence of micro cracks in brittle substances may have higher effect on their macro mechanical behavior. It has been observed that the macro mechanical behavior of rocks is due to their micro mechanical structure [1]. The micro cracks initiate from their tips and extend at an angle with respect to the original micro crack plane [2]. In the path of development of micro cracks, the kinked and curved cracks may be produced and these types of cracks usually occur under shear or mixed mode loading [3]. The breakage mechanism of brittle substances with random micro cracks depends on the degree of their interaction and coalescence path that may leads to the formation of a macro crack [4].

In studying the breakage mechanism of brittle substances under uniaxial tensile stress, crack initiation and specimen breakage may happen very soon and the crack initiation is normally expected to occur in a direction perpendicular to the maximum tensile stress. In rocks, crack initiation in tension is preferred due to the lower toughness of rock substances in tension than in shear [5]. The mechanism of propagation and coalescence of micro cracks in forming of macro cracks or rupture of rock is still not a well understood subject and the problem of interaction between the micro cracks and macro cracks is always noted by the researchers [6]. A number of

experimental investigations on the propagation and coalescence of micro cracks in rock-like specimens under uniaxial and biaxial compression have been published [7-14]. Some useful and modern numerical models such as FROCK code, damage model, Rock Failure Process Analysis ($RFPA^{2D}$) are used in this field [5, 15-19]. There has never been a random investigation on the effect of fracturing in brittle substances altering positions of random micro cracks which is under tension. In this research, a numerical model is proposed using a higher order displacement discontinuity code for micro crack analysis ($HDDMCR^{2D}$ code). This model is designed on the basis of the linear elastic fracture mechanics (LEFM) principles so that it is able to simulate the micro crack interaction of specimens containing random micro cracks. In this paper, the numerical analysis of the growth of wing cracks from pre-existing micro cracks in rock-like specimens under uniform normal tensile stress is studied. In order to verify the validity of proposed numerical model, the experimental and numerical results of the wing crack initiation directions (given by Guo et.al. [20]) for different micro crack inclination angles of a center slant micro crack under uniform tension have been used. The crack propagation mechanism of two pre-existing micro cracks are investigated (for a specimen under uniform tension) in which the propagation direction of micro cracks is estimated by using the maximum tangential stress fracture criterion (σ-criterion) proposed by Erdogan & Sih [21].

2. The higher order displacement discontinuity method

In the higher order displacement discontinuity method, the boundaries are discretized into multiple segment elements. The formulations of three types of displacement discontinuity variations with: a constant variation of the displacement along the elements, a linear variation, and a quadratic variation were previously mentioned and used in the literature [22-24]. The quadratic element displacement discontinuity is fundamentally based on integrating the quadratic element shape functions over collinear, straight-line displacement discontinuity elements.

Fig. 1 shows the displacements distribution at quadratic collocation point ‘m’, which can be calculated as:

$$D_j(\zeta) = \sum \Omega_m(\zeta) D_j^m \ for\ m = 1, to 3,\ j = x, y \tag{2}$$

where D_j is the fundamental variable. It should be noted that two fundamental variables are calculated in each collocation point. Using $c_1 = c_2 = c_3$, it can be written:

$$\Omega_1(\varepsilon) = \zeta(\zeta - 2c_1)/8c_1^2,\ \Omega_2(\zeta) = -(\zeta^2 - 4c_1^2)/4c_1^2,\ \ \Omega_3(\zeta) = \zeta(\zeta + 2c_1)/8c_1^2 \tag{3}$$

which are the shape functions of the quadratic collocation point ‘m’. In the quadratic collocations, there are three collocation points for each element, for which the displacements are typically calculated. These collocations are located in the center of the elements (Fig. 1).

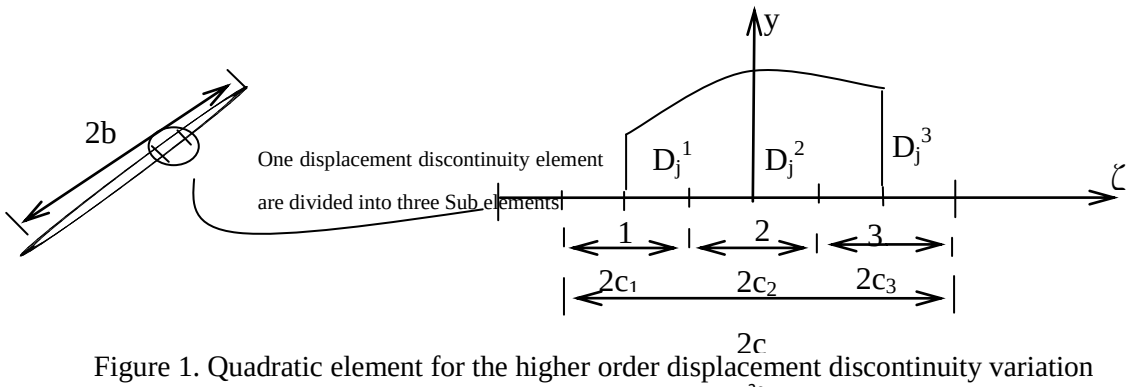

Figure 1. Quadratic element for the higher order displacement discontinuity variation

To eliminate the singularity of the displacements and stress calculation near the micro crack ends and increase the accuracy of order higher displacement discontinuity method around the original micro crack tip, a special treatment of the micro crack at the tip is necessary [24-27]. In this research three special crack tip elements at the end and initiation of each micro crack are used in the general higher order displacement discontinuity method. As shown in Fig. 2, using a special crack tip element with the length of 2c.The displacement discontinuity variations along this element can be written in the following form [24]: given as:

$$D_j(\zeta) = [\Omega_{T1}(\zeta)]D_j^1(c) + [\Omega_{T2}(\zeta)]D_j^2(c) + [\Omega_{T3}(\zeta)]D_j^3(c) \tag{4}$$

The crack tip element has a length $c = c_3 + c_2 + c_1$. Considering $c_1 = c_2 = c_3$, the shape functions $\Omega_{T1}(\zeta)$, $\Omega_{T2}(\zeta)$ and $\Omega_{T3}(\zeta)$ can be written as:

$$\Omega_{T1}(\zeta) = \frac{15\zeta^{\frac{1}{2}}}{8c_1^{\frac{1}{2}}} - \frac{\zeta^{\frac{3}{2}}}{c_1^{\frac{3}{2}}} + \frac{\zeta^{\frac{5}{2}}}{8c_1^{\frac{5}{2}}}, \qquad \Omega_{T2}(\zeta) = \frac{-5\zeta^{\frac{1}{2}}}{4\sqrt{3}c_1^{\frac{1}{2}}} + \frac{3\zeta^{\frac{3}{2}}}{2\sqrt{3}c_1^{\frac{3}{2}}} - \frac{\zeta^{\frac{5}{2}}}{4\sqrt{3}c_1^{\frac{5}{2}}} \quad \text{and}$$

$$\Omega_{T3}(\zeta) = \frac{3\zeta^{\frac{1}{2}}}{8\sqrt{5}c_1^{\frac{1}{2}}} - \frac{\zeta^{\frac{3}{2}}}{2\sqrt{5}c_1^{\frac{3}{2}}} + \frac{\zeta^{\frac{5}{2}}}{8\sqrt{5}c_1^{\frac{5}{2}}} \tag{5}$$

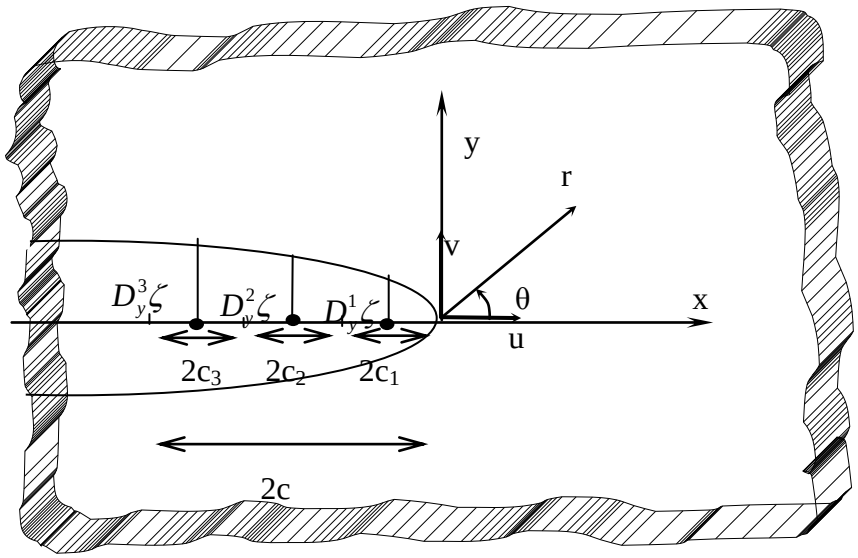

Figure 2. Quadratic element for the higher order displacement discontinuity variation

The mode I and Mode II stress intensity factors k_I and k_{II} can be estimated based on LEFM theory as the opening and sliding displacements [23]:

$$K_I = \frac{\rho}{4(1-\nu)}\left(\frac{2\pi}{c}\right)^{\frac{1}{2}} D_y(c), \quad \text{and} \quad K_{II} = \frac{\rho}{4(1-\nu)}\left(\frac{2\pi}{c}\right)^{\frac{1}{2}} D_x(c) \tag{6}$$

3. Verification of DDM with quadratic elements

A simple problem for verifying the numerical results and the proposed code is presented in this paper. This problem is the center slant micro crack in an infinite specimen shown in Fig. 3. The slant angle ψ, changes counter clock wise from the x (horizontal) axis, and the tensile stress σ^{∞} = 10 MPa is acting. Half of the micro crack length, b= 1 meter, modulus of elasticity E=10 GPa, Poisson's ratio $\nu = 0.2$, fracture toughness K_{IC}= 1.8MPa $m^{1/2}$ are assumed.

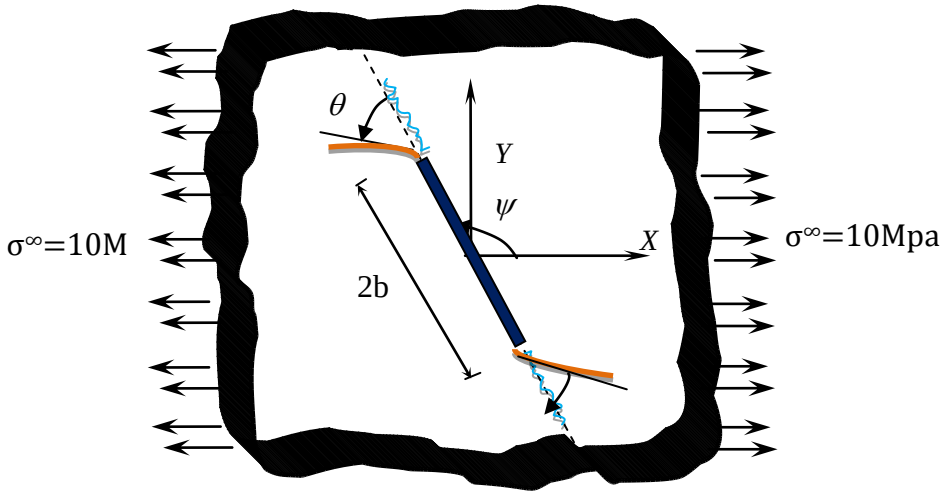

Figure 3. A center slant micro crack in an infinite body under uniform tension (parallel to the x axis)

The center slant micro crack problem has been solved by different researchers e.g. Guo et.al [20] to get a simple analysis, also these researchers used the constant element displacement discontinuity with a special crack tip element for angles 30, 40, 50,60,70,80 degrees. To evaluate the micro crack initiation angle θ_0, they used two initiation criteria: Maximum tangential tensile stress criterion (σ_θ-criterion), and Minimum strain energy density criterion (S-criterion), and compared their results with the results from other models. Fig. 4 compares the numerical results for the wing crack initiation directions θ_0 (obtained by $HDDMCR_{2D}$ code) and the results given by Guo et. al [20].

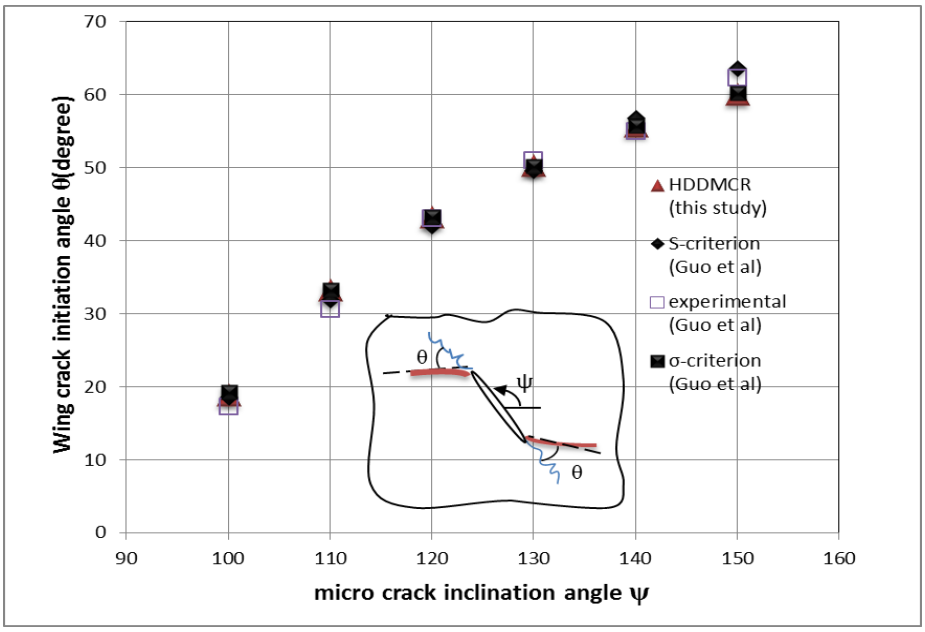

Figure 4. The micro crack initiation angle θ_0 as a function of micro crack inclination Angle ψ

4. The initiation and propagation of two non-parallel pre-existing micro cracks

In addition to the formation and growth of micro cracks in a rock mass, the reciprocal effects among the micro cracks may also be considered in the breakage process of the rock. The micro crack interactions can be modeled by the present numerical method which may allow micro cracks to interact reciprocally. It can be concluded that by increasing the number of micro cracks, the induced stresses among the original micro crack tips may have a significant effect on their initiation and some new micro cracks may also be produced. In fact, in rock specimens a series of micro cracks may remain closed during loading and propagation. In order to find out how the micro cracks connect under uniform tension (parallel to y axis), two micro cracks (of the same size as shown in Fig. 5), are considered. The body containing the micro cracks is an infinite plane, and the plane strain condition is assumed. It is under a uniform far field tensile stress, $\sigma^{\infty} = 10mpa$ with modulus of elasticity, $E=10\ GPa$, Poisson's ratio, $\nu=0.2$, fracture toughness, $K_{IC}=1.8MPa\ m^{1/2}$. In the present research, the effects of micro cracks randomness and spacing are considered.

The mode I and mode II stress intensity factors, K_I and K_{II}, near the original tips of two random micro cracks are estimated numerically. The non-dimensional mode I and mode II stress intensity factors, $\frac{k_I}{\sigma^{\infty}\sqrt{(\pi b)}}$ and $\frac{k_{II}}{\sigma^{\infty}\sqrt{(\pi b)}}$ are mainly used in the micro crack analyses. The negative sign of K_I value shows the micro crack closure, while the positive and negative signs in K_{II} only show the direction of relative shear between the two surfaces of micro crack.

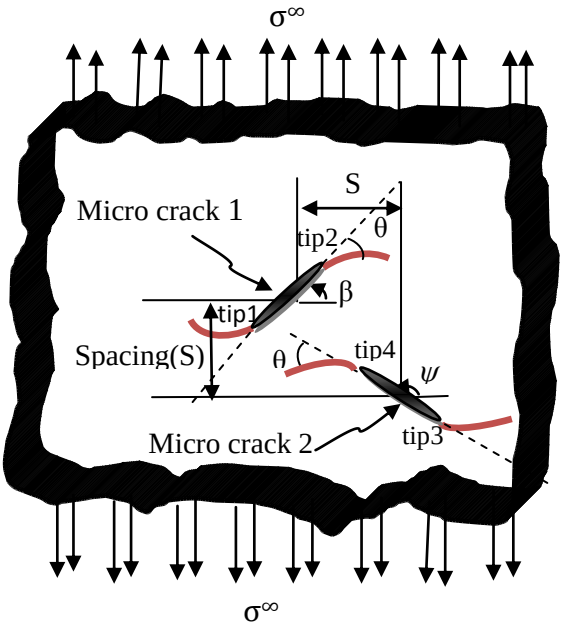

Figure 5. Two randomly slant micro cracks in an infinite specimen under uniform tension with the spacing, S=2b

4.1. Effects of inclination and randomness of micro cracks on SIF

Two random and completely non-parallel micro cracks are shown in Fig. 5. These micro cracks are known as micro crack 1 and micro crack 2. Their vertical and horizontal distances (center to center) are defined by S, and their inclination angles are denoted by β and ψ. The micro cracks are located in an infinite specimen under uniform tension (parallel to y axis). The normalized stress intensity factors $\frac{k_I}{\sigma^\infty\sqrt{(\pi b)}}$ and $\frac{k_{II}}{\sigma^\infty\sqrt{(\pi b)}}$ are shown graphically in Figs. 6 and 7. These normalized intensity stress factors are evaluated for four original tips of the two micro cracks (keeping a constant inclination angle, β=60°, for micro crack 1 but different angles, ψ= 150°, 140°,120°, 100°,80° and 60° for micro crack 2). For the original micro crack tips 3, 4, which have the most effect compared to other original tips, k_I value has decreased with an increase in the inclination angle of micro crack 2 (angle ψ) from 50° to 90°. In fact, k_I gets negative values when ψ is close to 90°. In tension field, the closing of micro crack is due to shear stress because shearing mode occurs sooner than opening mode in this field. The stress intensity factor k_I increases considerably as the inclination angle ψ increases from 90° to 150°. For the original micro crack tips 1 and 2, the effects of randomness are lower than those of other tips. The maximum value of k_I (~0.772) occurs at ψ=150° due to the complete non-orientation of both the micro cracks. The behavior of mode II SIFs of four original tips of micro cracks is notably different from that of mode I SIFs. For original tips 3, 4, $|k_{II}|$ value

has increased in the inclination angle ψ from 50° to 130° and decreased from 130° to 150°, when the micro crack 1 and micro crack 2 are completely non-oriented. For original micro crack tips 1 and 2, there aren't any noticeable effects with a change in the micro crack inclination angle ψ. As it was shown in Figs. 6 and 7, the most changes were in original micro crack tips 3 and 4, when the original tips 3 and 4 are close to the other of original micro crack tips, both of modes I and mode II stress intensity factors, k_I and k_{II} are increased. In nearly vertical micro cracks, k_{11} plays a more important role than k_I. Fig. 8 shows the wing crack initiation angle of four tips versus the changes of inclination angle ψ. This figure shows that in tips 3, 4, wing crack initiation angle θ has increased in the inclination angle ψ from 60° to 90° and decreased from 90° to 150°. The maximum of wing crack initiation angle θ occurs at ψ= 90°. And also for tips 1 and 2, the changes of ψ are not noticeable due to non-orientation of micro cracks and it is assumed that there is zero interaction.

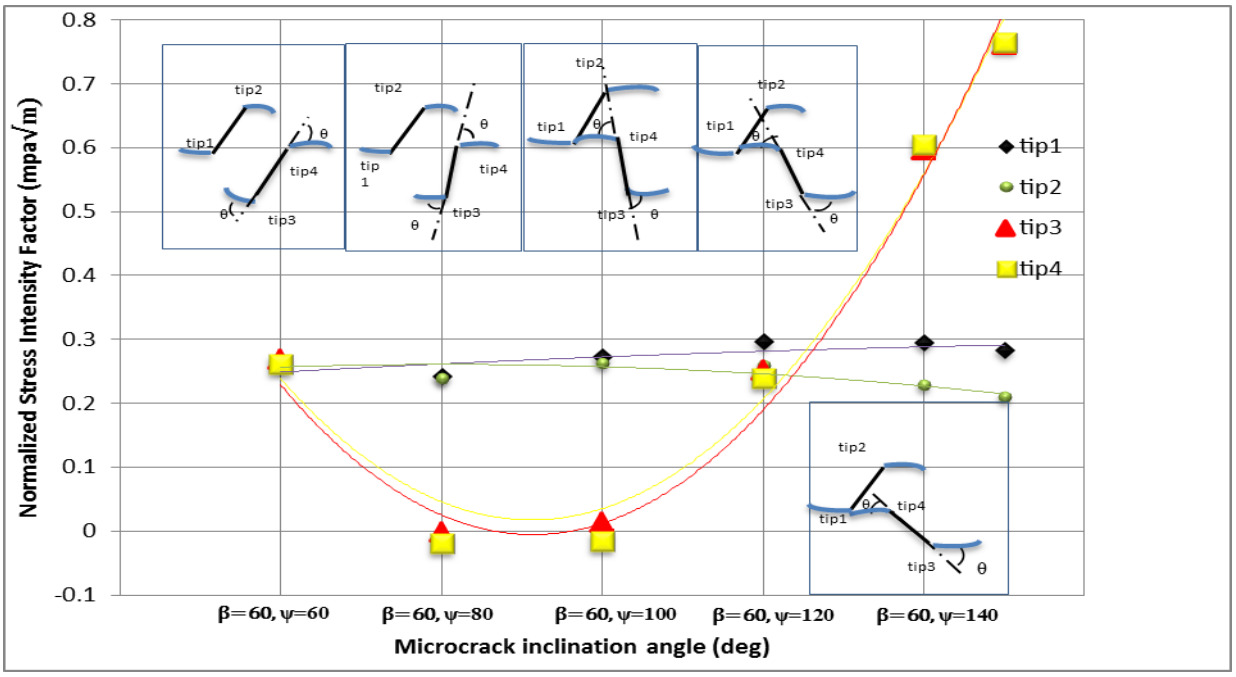

Figure 6. Treatment of mode I SIFs versus the locations of two micro cracks, under uniform tension (parallel to the y axis), for L/b=0.1 and 360+6 nodes for each micro crack

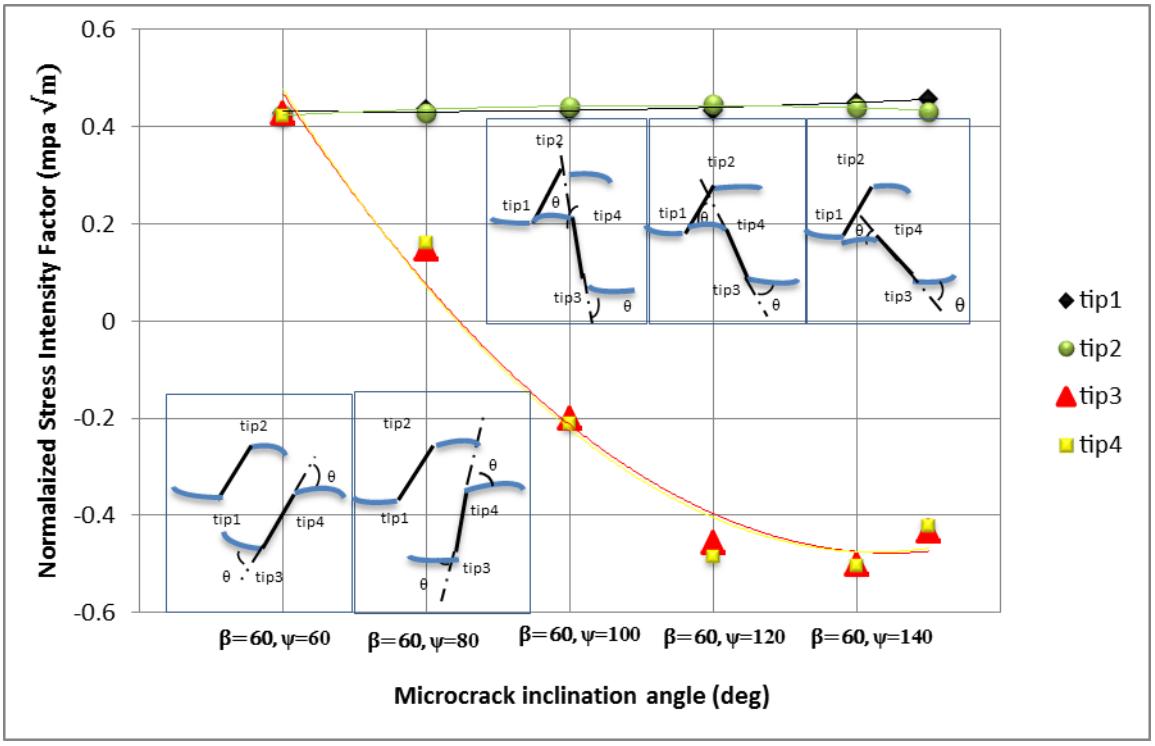

Figure 7. Treatment of mode II SIFs versus the locations of two micro cracks, under uniform tension (parallel to the y axis), for L/b=0.1 and 360+6 nodes for each micro crack

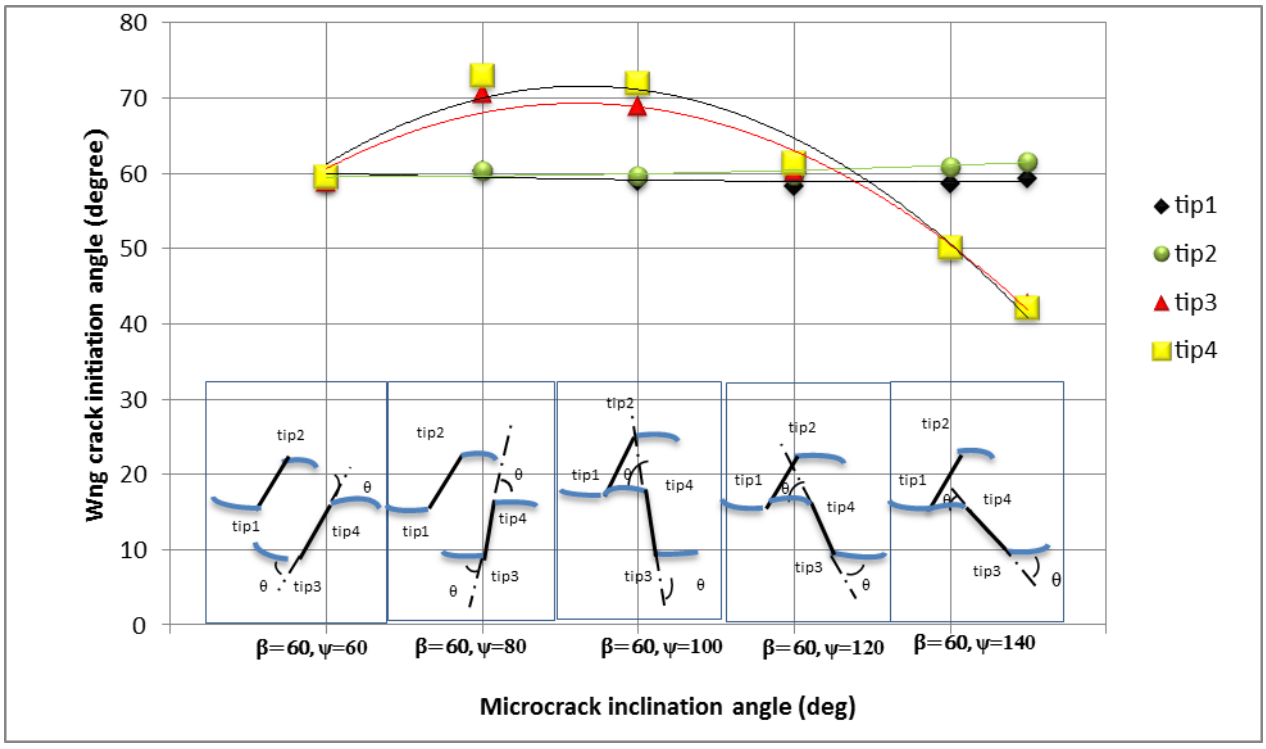

Figure 8. Wing crack initiation angle versus the locations of two micro cracks, under uniform tension parallel to the y axis, for L/b=0.1 and 360+3 nodes for each micro crack

5. Conclusions

A numerical model on the basis of computing the stress intensity factors and wing crack initiation angles for cracked substances under normal uniform tension is presented. In the present work, based on the Linear Elastic Fracture Mechanics (LEFM), the maximum tangential stress criterion or σ-criterion is implemented into code HDDMCR to investigate the interaction of micro cracks. In order to verify the validity of the proposed model, analytical solution of a typical sample problem e.g. a center slant micro crack under uniform tension is used, and its propagation mechanism is compared with numerical solution. In the present model, quadratic collocations with three special crack tip elements for each micro crack tip at the same time are implemented into code $HDDMCR_{2D}$. The numerical simulation is carried out considering infinite planes with two micro cracks under uniform tension. Comparing the parallel and non-parallel micro cracks, the effects of inclinations of two micro cracks show that these factors have a strong influence on the breaking path.

6. References

[1] A. Golshani, Y. Okui, M. Oda, T. Takemura, Micromechanical model for brittle failure of rock and its relation to crack growth observed in triaxial compression tests of granite, int. j. Mechanics of Materials, 38 (2005) 287-303.
[2] J. Niu, S.W.U. MAO, Analysis of asymmetric kinked cracks of arbitrary size, location & orientation – Part I. Remote compression, Int. J. Frac., 89(1998) 19–57.
[3] M. F. Marji, I. Dehghani, Kinked crack analysis by a hybridized boundary element/boundary collocation method, Int. j Solids and Structures, 47(2010)922–933.
[4] T. Li, W. Yang, Expected coalescing length of displacement loading collinear micro cracks. Theoret. Appl. fracture mechanics, 36(2001) 17-21.
[5] C. H. Park, Coalescence of Frictional Fractures in Rock Materials, PhD Thesis, Purdue University West Lafayette, Indiana, 2008.
[6] H. Haeri, Numerical Modeling of the Interaction between Micro and Macro Cracks in The Rock Fracture Mechanism Using Displacement Discontinuity Method. PhD Thesis, department of mining engineering, Science and Research branch, Islamic Azad University, Tehran, Iran, during work, 2011.
[7] E. Hoek, Z.T Bieniawski, Brittle Rock Fracture Propagation in Rock under Compression, South African Council for Scientific and Industrial Research Pretoria, Int. J. Frac. Mech., 3(1965) pp. 137-15.5.
[8] H. Horii, S. Nemat-Nasser, Compression-Induced Micro crack Growth in Brittle Solids: Axial Splitting and Shear Failure, Journal of Geophysical Research, 90(1985) 3105-3125.
[9] M. Sagong, A. Bobet, Coalescence of multiple flaws in a rock-model material in uniaxial compression, Rock Mechanics and Mining Sciences, 39(2002) 229-241.
[10] Y.P. Li, L.Z. Chen, Y.H. Wang, Experimental research on pre-cracked marble under compression, Int.J. Solids and Structures, 42(2005) 2505-2516.
[11] T. Y. Ko, H.H. Einstein, J. Kemeny,. Crack Coalescence in Brittle Material under Cyclic Loading, Golden Rocks , 41st U.S. Symposium on Rock Mechanics (USRMS), ARMA/USRMS 2006, pp.06-930.

[12]L.N.Y. Wong, H.H. Einstein, Fracturing Behavior of Prismatic Specimens Containing Single Flaws, Golden Rocks, 41st U.S. Symposium on Rock Mechanics (USRMS), 50 Years of Rock Mechanics - Landmarks and Future Challenges, Golden, Colorado, ARMA/USRMS, 2006, pp.06-899

[13] M. F. Marji, J. Gholamnejad , M. Eghbal,. On the crack propagation mechanism of brittle rocks under various loading conditions. Proceedings of International Multidisciplinary Scientific Geo. Conference, Bulgaria, 2011, pp.561-568

[14] M. F. Marji, A. Manouchehrian, Numerical Prediction of Crack Path in Pre-Cracked Rocks under Uniaxial Compression Using a Bonded Particle Model, 19th European Conference on Fracture, Kazan, Russia, 2012.

[15] H.C.M. Chan, Automatic Two-dimensional Multi-fracture Propagation Modelling of Brittle Solids with Particular Application to Rock, Sc. D. Thesis, Massachusetts Institute of Technology, Cambridge, U.S.A,1986.

[16] H.C.M. Chan, V. Li, H.H. Einstein, A hybridized displacement discontinuity and indirect boundary element method to model fracture propagation, Int. J. Fract., 45(1990) 263-82.

[17] O. Reyes, H.H. Einstein, Failure Mechanism of Fractured Rock- A Fracture Coalescence Model, Proceedings 7th International Congress of Rock Mechanics, 1(1991)333-340.

[18] A. Bobet, H.H. Einstein, Fracture Coalescence in Rock-type Materials under Uniaxial and Biaxial Compression, Int. J. Rock Mech and Min. Sci., 35(1998a) 863-888.

[19] H.Y. Liu, S.Q. Kou, P.A. Lindqvist, C.A. Tang,. Numerical Simulation of Shear Fracture (ModeII) in Heterogeneous Brittle rock, Int. J.Rock mech. Min.sci., 41(2004).

[20] H. Guo, N. I. Aziz, L. C. Schmidt, Linear Elastic Crack Tip Modeling by Displacement Discontinuity Method, Eng. Fract. Mech. 36(1990) 933-943.

[21] F. Erdogam, G. C. Sih, On the Crack Extension in Plates Under Plane Loading and transverse Shear, J. Bas. Engng., 85(1963)519-527.

[22] S. L. Crouch, A. M. Starfield, Boundary Element Methods in Solid Mechanics, Allen and Unwin, London,1983.

[23] K. J. Shou, S. L. Crouch, A Higher Order Displacement Discontinuity Method for Analysis of Crack Problems, Int. J. Rock Mech. Min. Sci. and Geomech. Abstr., 32(1995) 49-55.

[24] M. F. Marji, H. Hosseinin_Nasab, A. H. Kohsary, On the Uses of Special Crack Tip Elements in Numerical Rock Fracture Mechanics, Int. j Solids and Structures, 43(2006)1669-1692.

[25] D. Broek, The Practical Use of Fracture Mechanics, 4th Edition, Kluwer Academic Publishers, Netherland.70. Whittaker BN, Singh RN, Sun G. Rock fracture mechanics: Principles, design and applications. Amsterdam: Elsevier,1989.

[26] B.N. Whittaker, R.N. Singh, G. Sun,. Rock fracture mechanics: Principles, design and applications, Amsterdam: Elsevier,1992.

[27] M. H. Aliabadi, Fracture of Rocks, Computational Mechanics Publications, Southampton, U.K, 1999.

Evaluation Using Digital Image Correlation and Finite Element method of Stress Intensity Factors and T-stress

M.L.Hattali*, H. Auradou, M. François, V. Lazarus

Laboratoire FAST, Université Paris-Sud, Université Pierre et Marie Curie–Paris 6, CNRS, Bat. 502, Campus Univ., Orsay, F-91405, France
* Corresponding author: hattali.lamine@gmail.com

Abstract A controlled crack growth in PMMA was achieved in Wedge-Splitting Test (WST) by regulating the cross-head speed of loading by a computer-driving testing device. The fracture behavior of a crack propagating was investigated quantitatively by both numerical modeling and experiment using Finite Element Method (FEM) and Digital Image Correlation (DIC). A two-parameter fracture mechanics approach, describing the near-crack-tip stress field, was applied to determine the stress intensity factor (SIF) and the coefficient of higher order term (T-stress). In both methods, it was shown that the stress intensity factor versus crack length remains constant whereas the T-stress varies from negative to positive. This later variation is similar to the three point bend beam, but different from the compact tension specimen, for which the T-term is always positive. Using Digital Image Correlation (DIC), the stress intensity factor and T stress were estimated with 10% and 15% uncertainty in a complex loading set-up without having to do a numerical modeling of the experiment.
Keywords Crack path propagation, Digital Image Correlation, Finite Element Method, Stress intensity factor, T-stress

1. Introduction

Fracture propagation in brittle or quasi brittle material is dominated mainly by the near-tip stress field. The stress intensity factors "K" gives the magnitude of the stress field ahead of a crack tip and fracture propagates when a critical stress intensity factor is reached. There are experimental evidences that the stress contributions acting at largest distance from the crack tip may affect fracture mechanics properties [1]. The constant stress contribution (first "higher-order" term of the Williams stress expansion, denoted as the T-stress term) is the next important parameter. It is well known that for crack growth under mode I loading (i.e., $K_{II} = 0$) the straight crack path is stable when $T < 0$ and unstable for $T > 0$ [2]. In the brittle or quasi-brittle materials, the determination of a two-parameter fracture mechanics "K" and T-stress as function of crack length or crack velocity is often difficult. To measure the stress field during the fracture propagation, we need to perform stable fracture tests beyond the maximum load. This is not an easy task! Sophistical and expensive test stability control apparatus (i.e. closed loop control unit with e.g. crack tip opening displacement as a feedback signal) may be used to perform such tests. . However, these systems are often not available inlaboratories.
The wedge-splitting test (WST), first used by Linsbauer and Tscheg [3] and later developed by Brühwiler and Wittmann [3], is a test that permits to propagate stable cracks. . The WST has been extensively used for experimental (e.g. [5-6]), numerical (e.g. [7-8]) and inverse analysis studies (e.g. [9]). In spite of its advantages, the fracture parameters for the WST are not widely reported. The purpose of this paper is to study, using both numerical and experimental approaches, the variation of stress intensity factor or T-stress as function of crack path position. Digital Image Correlation (DIC) is used to follow the crack propagation. Based on displacements evaluation, crack tip position, Stress intensity factor "K" and T-stress are determined. Secondly, we performed by means of a constraint-based two-parameter fracture mechanics approach, a numerical analysis of near-crack-tip stress field using the Finite Element Method (Abaqus 6.6 software) [10]. In the numerical approach, the wedge

displacement load versus crack tip position data was used as boundary load conditions to calculate both stress intensity factor "K" and T-stress. Their values are compared with the result obtained by the Digital Image Correlation (Q4-DIC software) [11]. Finally, the performances of the two global approaches are compared.

2. Experimental configuration

The experimental setup is shown in Figure 1a and b. A vertical load is applied by means of a metallic wedge at the mouth of the notched sample. The sample is supported along its basis. To minimize friction between wedge and lateral supports, two lines of rollers are used. During testing, the wedge pierces the sample and the crack generated at the tip of the notch propagates in stable way. The crack grows until it reaches the bottom of the sample, splitting it into halves.

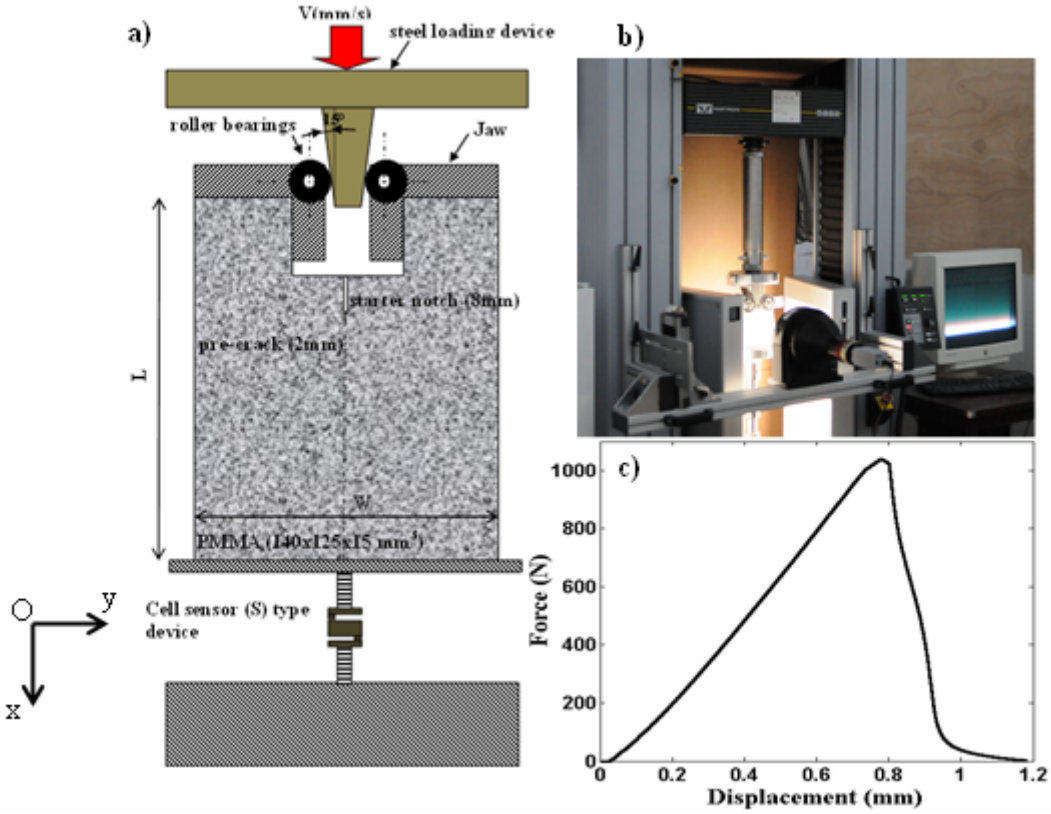

Figure 1. a) Experimental set-up of the Wedge Splitting loading. b) A telecentric lens is used to minimize artifacts induced by out-of-plane motions. c) Typical load- wedge displacement curve from PMMA fracture test.

Due to the compressive stresses in front of the crack tip and due to the small amount of elastic energy stored in the specimen, the crack propagates with a velocity proportional to V_{wedge}. The elastic energy stored in the testing device is much lower compared to other common test methods because the wedge angle (here choose to 15°) enhances the effect of the vertical force applied by the machine. The material used is Polymethyl methacrylate (PMMA) from Altuglas International (Perspex sheets). This material is brittle with a Young's modulus E= 2800 MPa and Poisson's ratio ν=0.33. The specimen is prepared from rectangular plates of length L=140mm, width W=125mm, and thickness H=15mm. A notch is machined i) by cutting out a 25x25x15mm^3 parallelepipeds from the middle of one of the WxH edges; ii) by subsequently adding a 8 mm long 800 µm thick groove with a diamond saw; and

iii) by finally introducing a seed crack (~2mm-long) with a razor blade. The test is conducted at room temperature (20 °C), under displacement control at 1 µm/s using a testing machine of 1 kN capacity (Instron 5882). The specimens exhibited a linear load–displacement diagram prior to fracture, confirming the predominantly linear elastic behavior of the material (Figure 1c). During the test, the surface of the sample is observed, with a CCD camera, (pixeLINK®, definition: 2500 x 1600 pixels, digitization: 8 bits) operating at 0.1 Hz and equipped with a telecentric objectif (GO Edmund, Techspec® gold series, Max distorsion: 0.35%, telecentricity: < 0.2°). The telecentric is used to minimize artifacts related to out-of-plane motions. The physical pixel size corresponds to 44.2 µm. Prior to the experiment, surface of the sample is painted in white and speckled with black paint. Two halogen lights are used for illuminating. For a realistic simulation, we need to obtain the typical wedge displacement-crack length curve from mechanical test and the crack path trajectory. These informations are directly measured from the location of crack tip via the camera using Digital Image Correlation (Figure 2a and b).

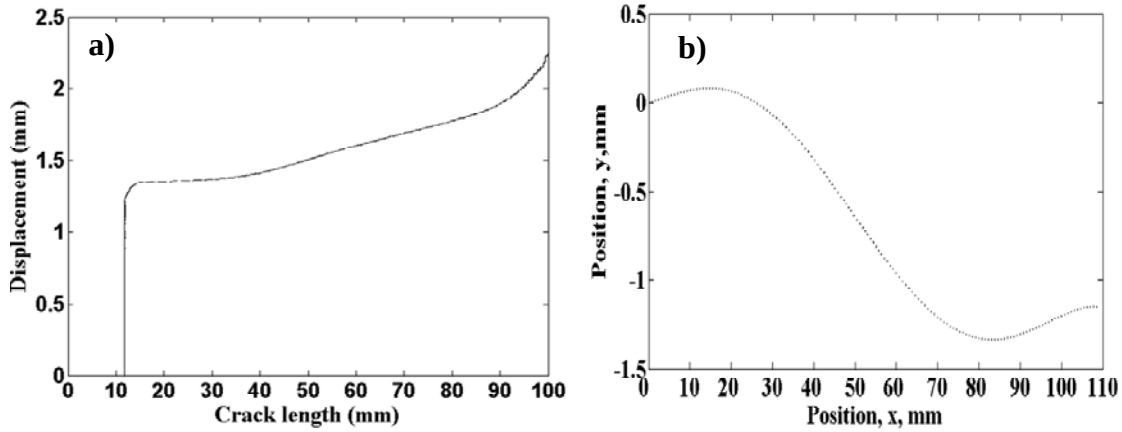

Figure 2. a) Displacement-crack length curve from PMMA fracture test, b) Crack path trajectory determined by DIC.

3. Finite element analysis (Abaqus)

Two-dimensional linear elastic fracture mechanics is retained to model the Wedge Splitting Test (WST) using a finite element method (Abaqus 6.6 software). To be in agreement with the experimental conditions, the choice of plane-stress state conditions was assumed. The computation of the stress intensity factor (K) and T-stress based on the domain integral "J" is carried out using six contours [10,12]. Apart from the first contour, the J-integral is path independent for the remaining 5 contours surrounding the crack tip. The material model was linear elastic, with the same properties for the experimental tests. The loading wedge is modeled as rigid bodies. The specimen is loaded by applying a displacement to the wedge in the vertical direction using an experimental displacement versus crack length data in the loading boundary conditions and taking under consideration the crack path trajectory (see Figure 2a and b. All other motions of the wedge are restrained. Surface-to-surface contact with a finite-sliding formulation is defined between the wedge and the rolling specimens, on the one side, and the specimen and the support, on the other. We assume that the contact is frictionless. Two analysis steps are used. In the first step, contact is established between the wedge and the rolling specimen by applying a small displacement (1×10^{-3} mm) in the vertical direction. In the second step controlled displacement loading of the wedge is applied. The virtual crack extension direction is specified with the q-vector. In the present model, it is defined with the starting point at the crack tip and the end point at the red dot, as shown in Figure 3.

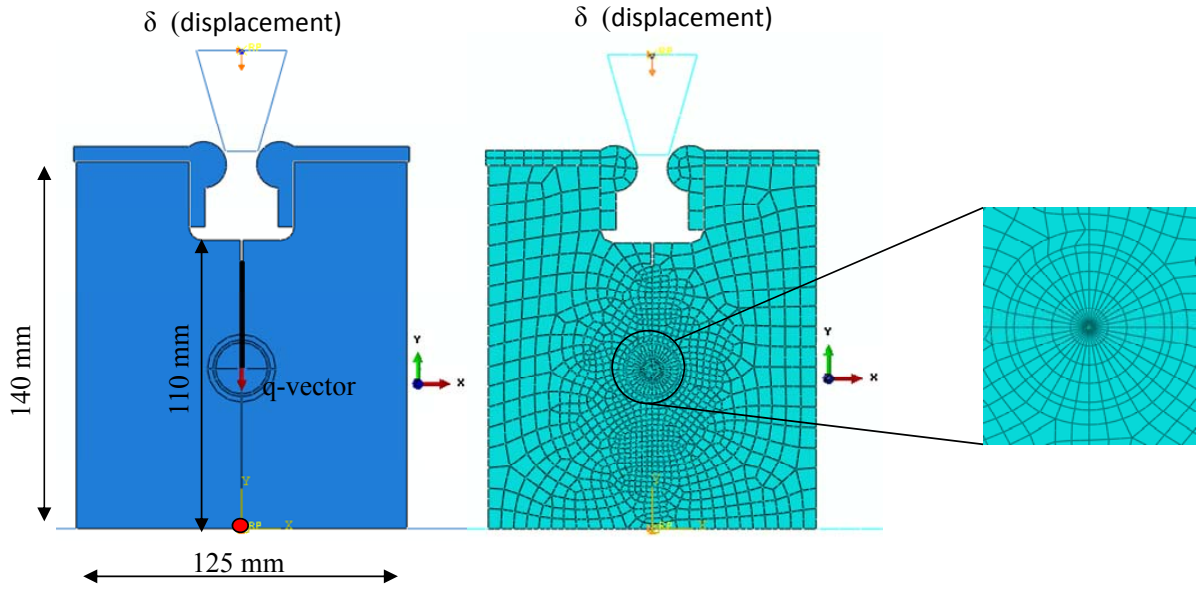

Figure 3. Partitioned two-dimensional Wedge Splitting Test and mesh strategy adopted around crack-tip.

For a sharp crack, the strain field becomes singular at the crack tip. Including the singularity at the crack tip for a small-strain analysis improves the accuracy of strain calculations, the J-integral and stress intensity factors. The partitioning of the geometry is defined by the circular lines centered on the crack tip (Figure 3); this partitioning strategy facilitates the generation of a focused mesh. The remaining portion of the model is free meshed using the "medial axis" meshing algorithm. The crack tip is meshed using a ring of collapsed 8-node bilinear, reduced integration (CPS8R) elements. To obtain a $1/\sqrt{r}$ singularity term, the following conditions must be met:

1. The elements around the crack tip must be focused on the crack tip. One edge of each element must be collapsed to zero length so that the nodes of this zero length edge are located at the crack tip.
2. The "midside" nodes of the edges radiating out from the crack tip of each of the elements attached to the crack tip must be placed at one-quarter of the distance from the crack tip to the other node of the edge.

4. Digital Image Correlation Analysis (Q4-DIC)

Digital image correlation is a technique that allows one to retrieve displacement fields separating two digital images of the same sample at different stages of loading.
We summarize the main points here, for more information the reader shall refer for instance to [11, 15]. Generally, it is not possible to find the correspondence of a single pixel in an image in the deformed state to the image in the reference state. This is because there is not a unique correspondence. The subsets which are comprised of finite number of pixels are utilized to locate the same material point between deformed and reference states. To correlate the deformed image $\boldsymbol{g}$ to the undeformed reference image $\boldsymbol{f}$, each image is divided into small subsets and the correlation algorithm is executed from subset to subset. A digital image of a body is simply a discrete intensity record of the light levels present at various positions of the body in the smallest unit of digitization, the pixel. In an eight-bit system, light intensity at each pixel ranges in value from 0 to 255 (represented as $0 < p(x,y) < 255$). The point P(x,y) in

the reference image becomes P'(x^*,y^*) in the deformed image and Q(x,y) becomes Q'(x^*,y^*). DIC is run by comparing group of similar light intensity numbers between the two digital images to track points P and Q. Depending on the use of a first or second order approximation, 6 or 12 unknowns are available and can be found by correlation between the two images. This can be done by minimizing the global residual between the reference image f and the deformed image corrected by the displacement field g(x+u(x)) over the whole region of interest:

$$\eta^2 = \iint_\Omega \left[g(x+u(x)) - f(x)\right]^2 dx \tag{1}$$

In the following, 4-noded elements are considered (*i.e.* a Q4-DIC approach [11]). The DIC procedure applied herein consists in measuring displacement field discretized with quadratic Q4 elements. The elements size was chosen to be equal to 8 pixels. This value is a good compromise between measurement uncertainly and spatial resolution. Extracting some mechanically meaningful information using the detailed map of displacement can be performed by identifying the amplitudes of relevant reference displacement fields namely, William's series [13]. These field $\mathbf{u}=u_x+iu_y$ take the following expression in the crack frame (crack tip at the origin, and crack path along the negative x axis) resorting to the complex plane, $z=re^{i\theta}$

$$u(z) = \sum_n \left[\omega_n \Omega_n(z) + \upsilon_n \psi_n(z)\right] \tag{2}$$

With, for a mode I regime:

$$\Omega_n(z) = \frac{(-1)^{(1-n)/2}}{2\mu\sqrt{2\pi}} r^{n/2}\left[\kappa \exp\left(\frac{in\theta}{2}\right) - \frac{n}{2}\exp\left(\frac{i(4-n)\theta}{2}\right) + \left((-1)^n + \frac{n}{2}\right)\exp\left(-\frac{in\theta}{2}\right)\right] \tag{3}$$

And a mode II regime:

$$\Psi_n(z) = \frac{i(-1)^{(1-n)/2}}{2\mu\sqrt{2\pi}} r^{n/2}\left[\kappa \exp\left(\frac{in\theta}{2}\right) + \frac{n}{2}\exp\left(\frac{i(4-n)\theta}{2}\right) + \left((-1)^n - \frac{n}{2}\right)\exp\left(-\frac{in\theta}{2}\right)\right] \tag{4}$$

Where μ is Lamé's modulus, and κ is a dimensionless parameter dependent on Poisson ratio ν (*i.e.* $\kappa = \frac{3-\upsilon}{1+\upsilon}$ in plane stress, or 3-4ν in plane strain condition).

Amplitudes ω_1 and ν_1, associated with field Ω_1 and Ψ_1, are the mode I and II SIFs, K_I and K_{II}, respectively. Amplitudes ω_0 and ν_0 correspond to rigid body translations. Amplitudes ω_2 and ν_2 give access to the T-stress component, and the rigid body rotation. The crack-tip is located by canceling out amplitude ω_{-1} of the first supersingular field.

5. Results and discussion

Experimental results were obtained from the displacement fields obtained with a mesh size of 8 pixels (1 pixel→44.2 μm), over a region of interest of 2500 x 350 pixels (Figure 4).

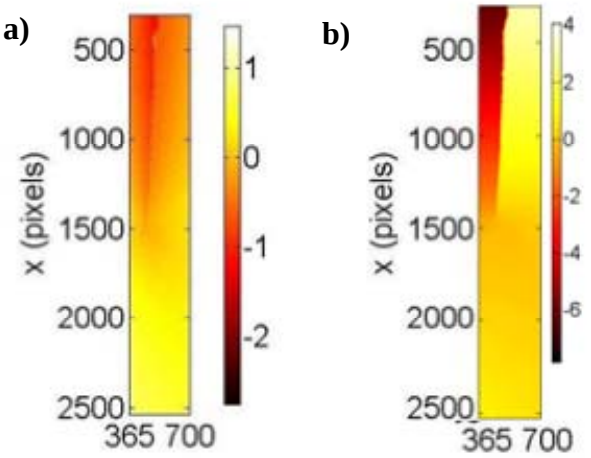

Figure 4. Horizontal (a) and vertical (b) component of the displacement field expressed in pixels as projected onto the basis of suited functions in post-processing of the measured displacement (1 pixel → 44.2 μm).

From the amplitudes ω_n and ν_n, it is possible to plot the SIF and T-stress as function of crack length. In figure 5a and 5b, the SIF obtained by DIC are shown together with the SIF obtained by Abaqus. In average the differences is 9%. For the DIC method, an error bars was estimated by extracting extreme positions of crack tip and measuring the corresponding change in K (average error bars were 11 %). For both methods, we found that K_I is constant from 40 mm to the end of sample, demonstrating that the crack propagation is stable (ie. The cracks propagates with a constant velocity), whereas K_{II} fluctuates around zero (Fig 5b). Despite an average difference of 22 %, a good agreement is found in the case of the T-stress component when compared to the FE results. This difference is compensated by error bars (an average error bar were 15%) (Fig 5c). In both case, the T-stress varies from negative value for short cracks to positive value for crack lengths above 5 mm, contrary to the compact tension geometry, where T values are always positive [14]. Compared to the stress intensity factor, the error bar in the case of T-stress is higher because the T-stress is the coefficient of higher order terms of the displacement field expansions.

Without surprise, those measures confirms Irwin's criterion $K_I=K_c$ during stable propagation and the Principle of Local Symmetry $K_{II}=0$. It confirms also Cotterell and Rice crack path stability criterion. As soon the T-stress becomes positive, the crack path doesn't remain straight (fig. 2b) and find another, not straight, path which satisfies nevertheless Irwin's criterion and the Principle of Local Symmetry. This is one more [16] experimental demonstration that this double criterion doesn't lead to a unique solution: the observed crack path is not the trivial straight one but another more stable bifurcated one.

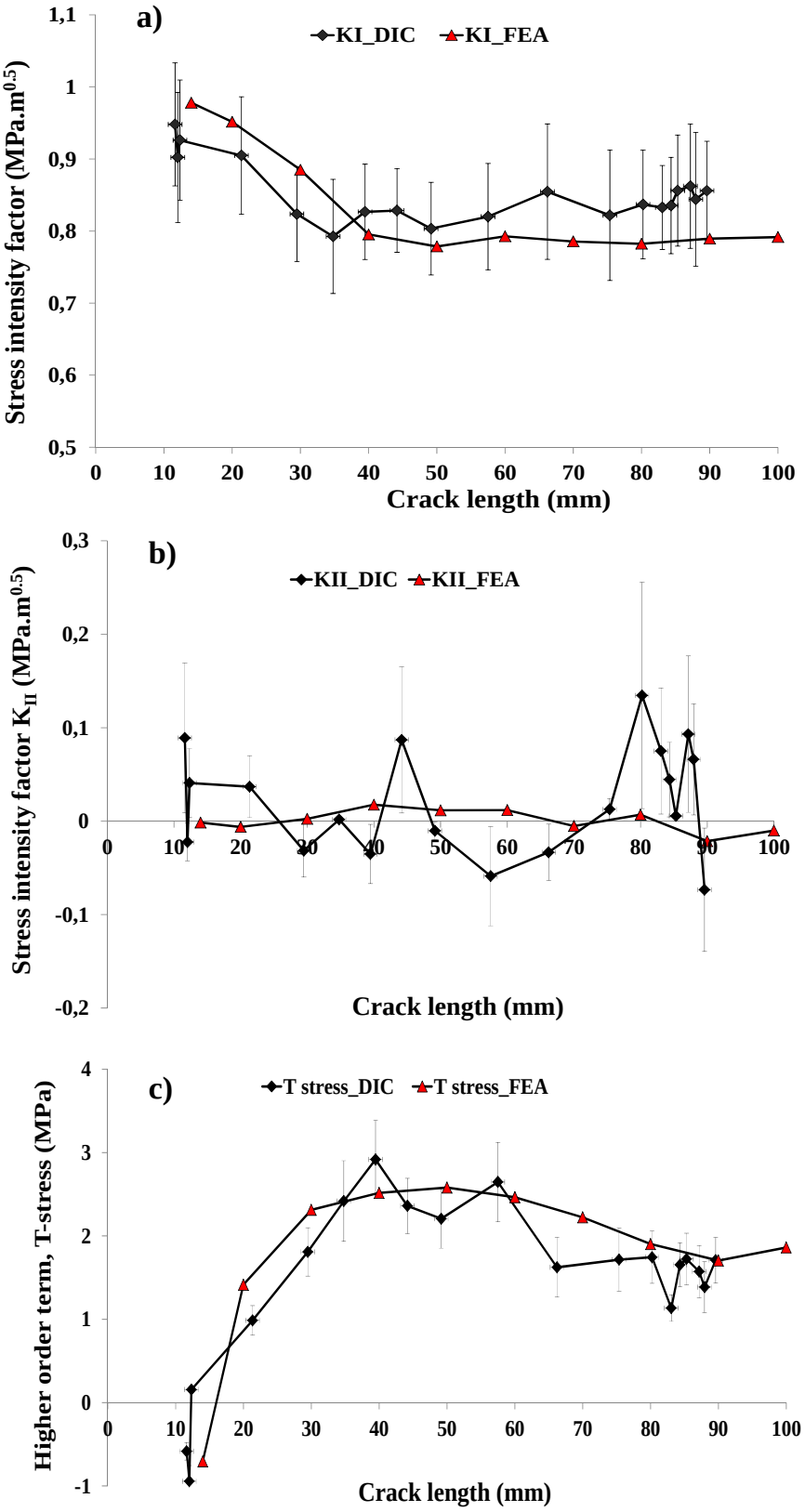

Figure 5. Comparison of (a)-(b) stress intensity factor, (c) T-stress determining using Finite Element Analysis and Digital Image correlation.

6. Conclusions

The Finite element Analysis and Direct measurement of the crack tip displacement field is performed using Abaqus software and Digital Image Correlation (Q4-DIC). In Finite Element Analysis, the two parameter fracture mechanics approach, describing the near–crack-tip stress field (SIF and T-stress) were calculated using the domain integral "J". In Digital Image Correlation, these parameters were obtained by adjusting the first supersingular term of William's series. One the crack tip was determined, the crack growth increment is estimated in addition to other global parameters such as the stress intensity factor range and T-stress. In both method, good agreement is shown and finite element analysis can be validated. The stress intensity factor versus crack length remains constant whereas the T-stress varies from negative to positive. This later variation is similar to the three point bend beam, but different from the compact tension specimen, for which the T-term is always positive. Using Digital Image Correlation (DIC), the stress intensity factor and T stress were estimated with 10% and 15% uncertainty in a complex loading set-up without the need for a numerical modeling of the experiment. The displacement and crack extension at the onset of crack propagation is important. It is expected that any model that can match all the experimentally observed features of the test will provide a significant enhancement to our present capability to predict any fracture parameter. Our wedge splitting test is particularly attractive for fundamental research and model validation because of the enhanced length of stable crack propagation. This advantage allows us the identification of crack propagation parameters during all propagation from one single test.

Acknowledgement

The authors acknowledge support of the ANR Program SYSCOMM grants ANR-09-SYSC-006 (France).

References

[1] T.Fett, A Green's function for T-stresses in an edge-cracked rectangular plate. Eng Frac Mech, 57(4) (1997) 365-373.
[2] B. Cotterell, J.R. Rice, Slightly curved or kinked cracks. Int J Fracture, 16(2) (1980) 155-169.
[3] H.N. Linsbauer and E.K. Tschegg, Fracture energy determination of concrete with cube-shaped specimens. Zement und Beton, 31 (1986) 38-40.
[4] E. Bmhwiler and E H. Wittmann, The wedge splitting test: A method of performing stable fracture mechanics tests. Engineering Fracture Mechanics, 35 (1990) 117-125.
[5] M. Elser, E. K. Tschegg, N. Finger, S. E. Stanzl-Tschegg, Fracture behaviour of polypropylene-fibre reinforced concrete: an experimental investigation. Compos Sci Technol, 56 (1996) 933–45.
[6] J. Scheibert, C. Guerra, F. Célarié, D. Dalmas and D. Bonamy, Brittle-Quasibrittle Transition in Dynamic Fracture: An Energetic Signature. Physical Review Letters, 104 (2010) 045501.
[7] L. Ostergaard, Early-age fracture mechanics and cracking of concrete-experiments and modelling. Ph.D. Thesis. Department of Civil Engineering, Technical University of Denmark; 2003.
[8] G.V. Guinea, M. Elices, J. Planas, Stress intensity factors for wedge-splitting geometry. Int J Fracture, 81 (1996) 113–24.

[9] N.S. Que, F. Tin-Loi, An optimization approach for indirect identification of cohesive crack properties. Comput Struct, 80(16-17) (2002) 1383-92.
[10] ABAQUS Software (2006) User's manual, version 6.6. Karlsson and Sorensen Inc, Hibbitt.
[11] S.Roux, F. Hild, Stress intensity factor measurement from digital image correlation:post-processing and integrated approaches. Int J Fract, 140 (2006) 141–157.
[12] F. Erdogan, G. C. Sih, On the crack extension in plates under plane loading and transverse shear. J of Basic Eng, 85 (1963) 519-527.
[13] M.L. Williams, On the stress distribution at the base of a stationary crack. ASME J. Appl. Mech, 24(1957) 109-114.
[14] Q.Z. Xiao, B.L. Karihaloo, Coefficients of the crack tip asymptotic field for a standard compact tension specimen. Int J Fract, 118(1) (2002) 1-15.
[15] M. Grédiac, F. Hild Mesures de champs et identification en mécanique des solides. Collection Mécanique et Ingénierie des matériaux. Ed. Lavoisier, 2011.
[16] VB Pham, H-A Bahr, U. Bahr and H. Balke and H-J Weiss. Global bifurcation criterion for oscillatory crack path instability. Physical Review E (Statistical, Nonlinear, and Soft Matter Physics). 77 (2008), 66-114.

A strain based criterion for creep crack initiation

A. Hobt[1,*], A. Klenk[1], K. Maile[1]

[1] MPA University of Stuttgart, Pfaffenwaldring 32, 7569 Stuttgart Germany
* Corresponding author: alexander.hobt@mpa.uni-stuttgart.de

Abstract
Commonly, for components under creep loading, the maximum tolerable inelastic strain is limited to 1 %. The strains are calculated for components which are free from defects, using appropriate material models. Within the fabrication process internal defects such as crack or cavities cannot be avoided, especially for large thick-walled components. For these internal defects fracture mechanic concepts must be applied for safety assessment.
Existing fracture mechanics concepts such as the Two-Criteria-Diagram or the Time-Dependent-Failure-Assessment-Diagram do not include the effect of the material's ductility which has a clear effect on crack initiation process. Under creep load, the strains within the crack tip region dominate local material separation. Therefore a concept is introduced, which formulates a deformation exhaustion rule. With this procedure a better material utilisation is achieved.
In a next step, crack initiation is calculated using an internal damage variable, which can be used as a life time parameter. Within this approach, the influence of a multiaxial state of stress on the damage evolution must be implemented. This procedure simplifies crack initiation assessment, replacing fracture mechanic methods by the evaluation of the damage variable.

Keywords Creep, crack initiation, failure criterion, creep strain

1. Introduction

For components under creep loading, the maximum tolerable accumulated inelastic strain must be limited, [1]. This limitation in strain is well-founded on evaluations of the remaining life-span with reference on microstructural damage, [2]. If an inelastic strain of 1 % is accumulated, monitoring arrangements must be established. This does not account for internal defects or cracks. For a safe operation of the component, the assessment must include the description of crack initiation and crack growth. If now the period to crack initiation is longer, than the period to accumulate the limit strain, the assessment procedure could be simplified. This can be described by the relation of the time to crack initiation t_A to the time, say for 1 % inelastic strain, $t_{1\%}$:

$$t_A \geq t_{1\%}. \tag{1}$$

The aim of this work was to identify crack sizes for which **Eq. (1)** is met. Therefore the time to crack initiation t_A must be identified, which requires an appropriate assessment concept. Commonly used concepts, such as the Two-Criteria-Diagram, [3], (TKD, see **Figure 1**) or the Time-Dependent-Failure-Assessment-Diagram, [4], [5], are based on stress relations. The TKD differs between three damage modes. Within the crack-tip-damage region the specimens or components have large cracks with a low mean stress. Within the ligament-damage region there are small cracks with a high mean stress and a high accumulated strain within the far-field region of the specimen. In between there is the mixed-mode damage region. Ligament damage is defined by accumulation of 1 % strain in the farfield of the specimen, [3], [4]. The analysed specimens within this work are aimed to have an $R_\sigma = 0.75 \div 1$ and $R_K \approx 0{,}5$ and lie on the edge of the ligament-damage field.
Over the past decade, there have been analysed various steels used in power plant operation generating a wide database for describing the material's behaviour and crack initiation, [5], [6], [7], [8], [9]. Modern high chromium steels however, exhibit a high creep ductility influencing strongly the

crack initiation behaviour. The ductility in this case is represented comfortably by the material's creep rupture strain. The more deformation within the region of the crack tip is attainable, the later the crack initiation will start. Therefore it is sensible to set up a strain based criterion to describe crack initiation. With this, the influence of ductility is directly implemented. To gain a concept which is valid for either high or low ductility, materials differing in their ductility must be analysed to validate the concept. Describing crack initiation applying a stress formulated concept - such as the commonly used assessment procedures- will be too conservative. The influence of ductility on crack initiation have been analysed theoretically or have been approximated, [10], [11], [12], [13]. Concerning the TKD, a modification based on the creep rupture strain has been proposed in [13]. This was done mainly for the crack-tip-damage region. For the ligament-damage mode a dependency of ductility could not yet be established.

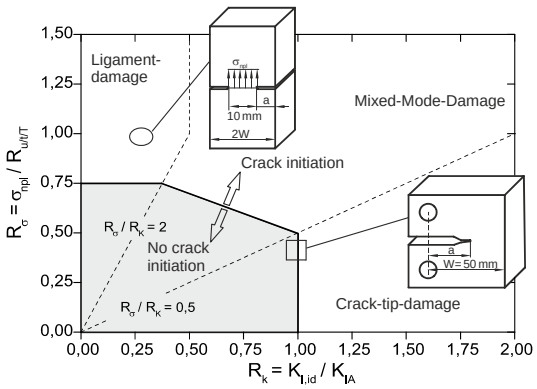

Figure 1. Creep rupture strains of a 10Cr-steel at T = 600 °C, different heats

The specimens investigated will have Double-Egde-Notched-Tension (DENT) in different sizes or compact-tension (CT) geometry. The loading times for the numerically treated specimens are up to operational relevant times of 200.000 h. The aim is the determination of initial crack sizes as a function of the creep rupture strain for different specimen sizes which account for Eq. 1. Below this limit of initial crack size a_{limit}, a fracture mechanics assessment is not necessary. The creep data used to set up the material law is available up to 140.000 h for uniaxial creep tests. The fracture mechanics experiments are available up to 20.000 h.

2. Investigated materials

To account for the influence of the material's ductility, one 10Cr-steel and two 1Cr-steels have been considered. The creep rupture strain of the 10Cr-steel is shown in **Figure 2**.

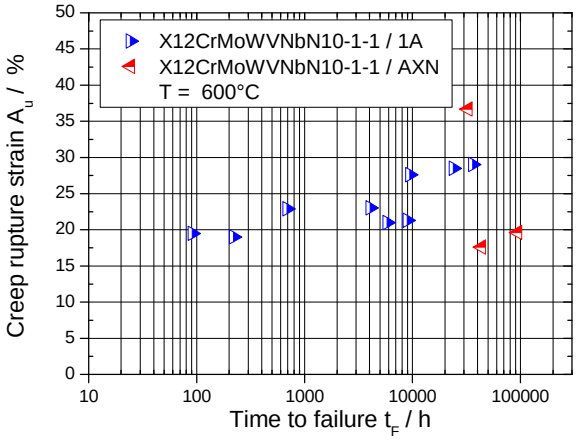

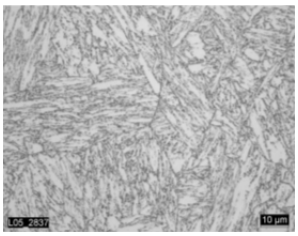

X12CrMoWVNbN10-1-1

Figure 2. Creep rupture strains of a 10Cr-steel at T = 600 °C, different heats

There are two heats shown, which differ only with respect to the initial heat treatment. Due to the loading times up to 100.000 h the material properties are not supposed to differ. As shown, the creep rupture strain is about 20%-25% and can be approximated by a constant.
The creep rupture strain of the two 1Cr-steels is shown in **Figure 3**. It can clearly be seen, that the rupture strain is decreasing with increasing loading time. Both steels differ in the initial heat treatment.
The creep rupture strain itself, however, is not an appropriate measured variable, due to the influence of the reduction of area gained in creep tests on materials with high ductility. Concerning thick-walled components, no transverse strain is observed. To meet this problem a reference strain was introduced, which does not include the influence of the reduction of area on the creep rupture strain value, see **Figure 4**. Two different formulations have been analysed. One is based on the volume of the creep test specimen. This method was preferred for the implementation of the failure criterion. The second method is based on the strains at the onset of the tertiary creep stage.

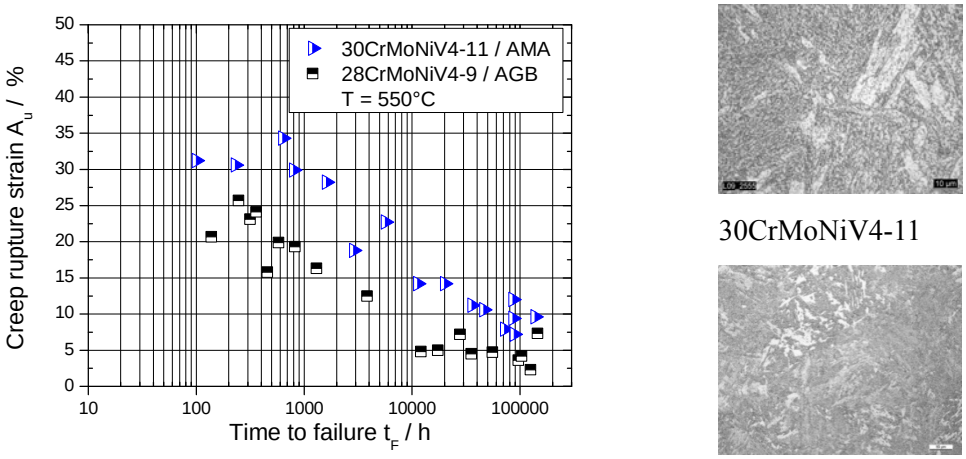

Figure 3. Creep rupture strains of 1Cr-steels at T = 550 °C

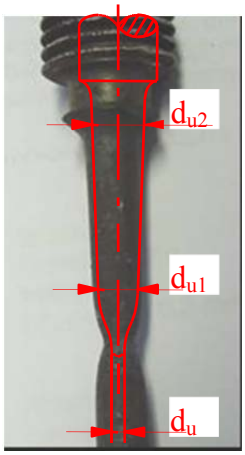

$$\varepsilon_{r,1} = \left(\frac{2 \cdot d_0}{(d_{u1} + d_{u2})} \right)^2 - 1 \qquad (2)$$

$$\varepsilon_{r,2} = \varepsilon_{2/3} + \dot{\varepsilon}_{min} (t_u - t_{2/3}) \qquad (3)$$

with: t_u – time to failure,

$\varepsilon_{2/3}$ – Strain at onset of tertiary creep

$t_{2/3}$ – Timepoint at onset of tertiary creep

Figure 4. Definition of a reference strain

The reference strain according to **Eq. (2)** is used as material parameter within the failure criterion, which relates a characteristic strain within the specimens to the reference strain. The reference strain is referred as ε_r. The reference strain can be plotted over the creep rupture strain, see **Figure 5**. This yields the correlation of the creep rupture strain and the calculated initial limit crack length a_{limit}.

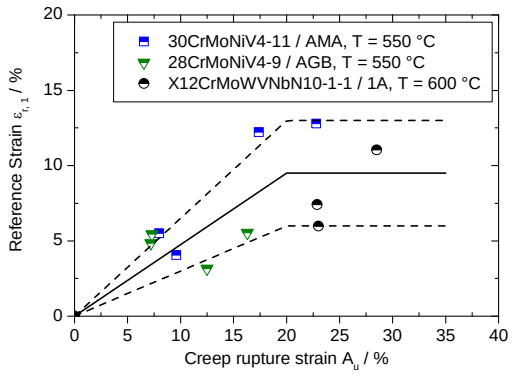

Figure 5. Correlation between reference strain and creep rupture strain

3. Investigation of small cracks

To analyse the dependence of the pre-loading crack size a_{limit} on the material's ductility, 3D models of specimens with DENT geometry have been used. The crack was modelled with a crack tip radius of 0.1 mm, which is valid for the experiments. The crack tip was meshed with a fine mesh to represent the stress and strain gradients correctly. For the description of the material's behaviour a modified Graham-Walles formulation have been implemented, [14]. The calculations were conducted with the Finite-Element-Code ABAQUS ©.

The numerical analysis of specimens with loading times up to 200.000 h requires a failure criterion to correlate with crack initiation. Within the creep regime and with respect to the dependence on ductility, a strain based formulation of the failure criterion is appropriate. Since the creep deformation and the creep damage is dependent on the multiaxiality of the stress state, this must also be considered, [15], [16], [17], [18]. With higher multiaxiality, the deformability is reduced. To account for that effect, the concept of Cocks&Ashby is applied, [19].

To correlate the calculated strains with the material dependent reference strain, a characteristic point within the crack tip region to evaluate the strains and the multiaxiality must be chosen. The calculated strains were evaluated at the point of maximum triaxiality near the modelled crack tip. Due to the high constraints, crack initiation begins at this point by formation, growth and coalescence of creep cavities. In addition a definition of crack initiation in the experiment must be set up. Crack initiation is defined for a crack growth of $\Delta a = 0.1$ mm.

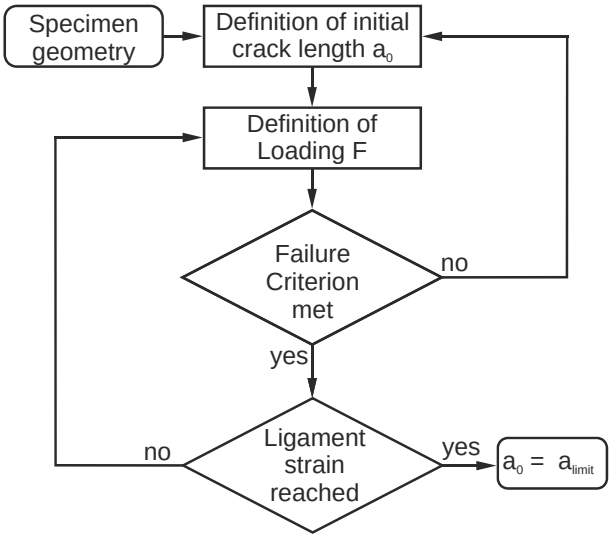

Figure 6. Schematic overview of calculation of a_{limit}

This value was chosen on the one hand to avoid the need of modelling crack propagation in the FE-calculations and on the other to be able to detect crack initiation within the experiments. In **Figure 6** the calculation procedure is schematically shown. The optimisation of the results with respect to the initial crack length and the accumulated strain within the ligament are done iteratively.

The concept for describing crack initiation was first validated by applying on already run experiments. In **Figure 7** are the results shown for the analysed 10Cr and 1Cr-steels. The results of the FE-calculations are in good agreement with the defined reference strain for all materials and different ductility. The failure criterion now can be applied to find out, if there is a limit crack size below a fracture mechanics assessment is not necessary. The limit of initial crack size a_{limit} will be determined in correlation to the creep rupture strain corresponding to loading times of 100.000 h and more, which cannot be done experimentally. The creep rupture strain for the 10Cr-steel is assumed to be constant between 100.000 h and 200.000 h. For the 1Cr-steels the low creep rupture strain at 100.000 h is extrapolated as constant up to 200.000 h.

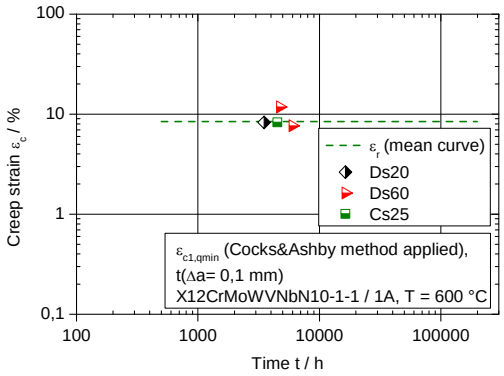

a) X12CrMoWVNbN10-1-1

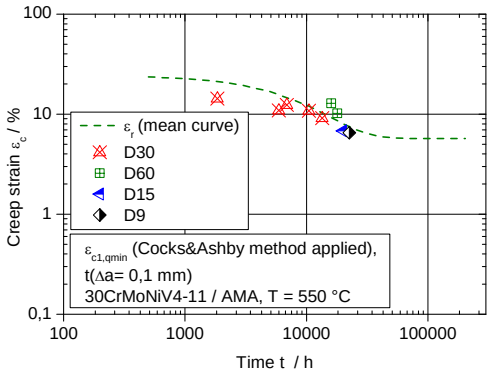

b) 30CrMoNiV4-11

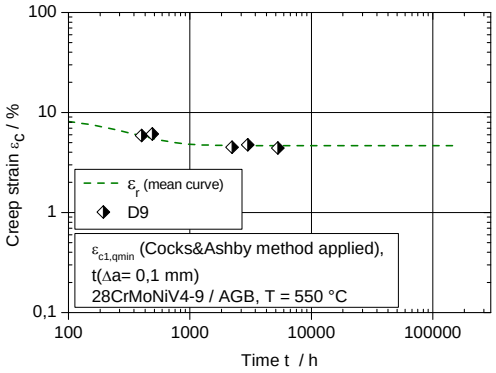

c) 28CrMoNiV4-9

Figure 7. Validation of the strain based failure criterion for 10Cr and 1Cr-steels

The limit of initial crack size a_{limit} sought, is defined dependent on the accumulated inelastic strain within the ligament of the specimen. It is that size of surface type crack for the DENT specimen, when simultaneously the failure criterion in the crack-tip region is met and the selected creep strain is reached. To quantify the influence of specimen geometry and size, these have been varied. The results of the calculations are shown in **Figure 8**. It can be seen, that there is small scatter of the data with respect to geometry and size of the specimens at a constant creep rupture strain. In general it can be stated, that with increasing size (especially breadth) the limit of initial crack size increases, too. An increasing ductility also leads to a higher limit of initial crack size. Also different levels of ligament strain have been analysed. This is derived for the operation of different components. A strain level of 1 % within the net section stress area is valid for thick-walled components and is

founded on [1]. For turbine runners, this strain would lead to component failure due to the component tolerances. In this case a strain level in the ligament of the components of 0.2 % is discussed.

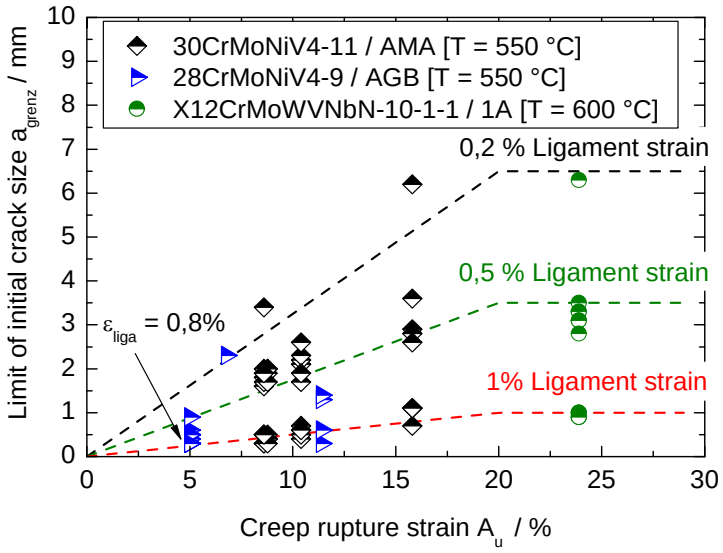

Figure 8.

With a decreasing ligament strain, the net section stress is reduced, which results in a reduced crack tip loading for constant crack length. As it is shown in Figure 8, the limit in initial crack size therefor increases. It is clear, that with growing of a_{limit}, the wall thickness must have a minimum larger than a_{limit}.

For the creep-brittle 1Cr-steel 28CrMoNiV4-9 a ligament strain of 1 % could not be attained even for crack sizes of 0.3 mm. Instead of modelling initial crack sizes below 0.3 mm a ligament strain of 0.8 % was accepted, too.

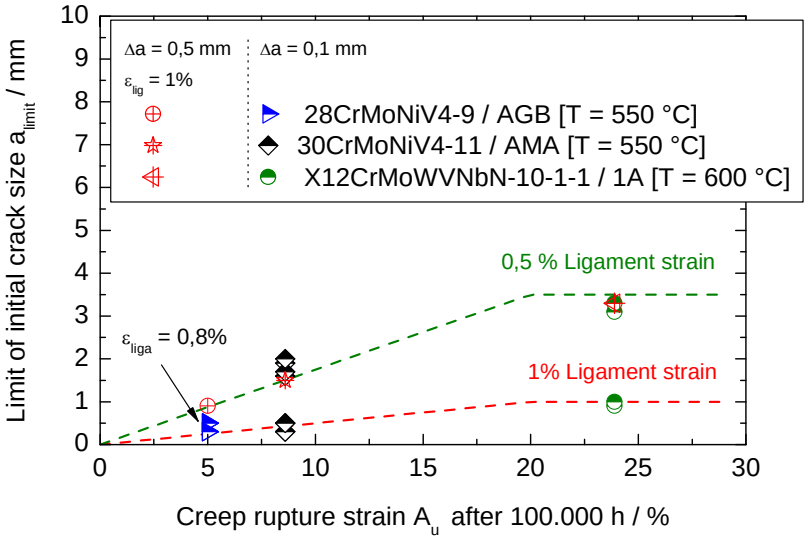

Figure 9.

Considering the relation between the reference strain and the creep rupture strain (see Figure 5) it correlates well with the observed dependence of the initial crack size and the creep rupture strain, i.e. above 20 % of creep rupture strain a_{limit} and ε_r remain constant.

This analysis was conducted defining crack initiation at a crack growth of 0.1 mm. In general a crack propagation of 0.5 mm is assumed. So the above applied strain based failure criterion is met

at earlier loading times, i.e. it is more conservative, if a crack growth of 0.5 mm is tolerable. Otherwise, for a fixed loading time and net section stress, a larger initial crack size is tolerable if at crack initiation a defined ligament strain is reached. This was investigated for a fixed loading time of 100.000 h, shown in **Figure 9**. It can clearly be seen, that the initial crack sizes increase if crack initiation occurs for a crack growth of 0.5 mm at the same ligament strain.
Since no crack propagation was modelled in the numerical analysis, the crack growth was approximated using:

$$\frac{da}{dt} = m \cdot (C^*)^k \tag{4}$$

With the C*-parameter, see [14], [22]. The parameters C and m are dependent on the material and are listed in Table **1**.

Table 1. Crack propagation parameters

	X12CrMoWVNbN10-1-1	30CrMoNiV4-11
	T = 600 °C	T = 550 °C
m	0,25	0,25
k	0,18	1,05

Within the small crack propagation of 0.4 mm a constant crack growth rate can be assumed. The total time span of 100.000 h is then the sum of the time to reach the strain based failure criterion with a crack propagation of 0.1 mm and the crack growth to $\Delta a = 0.5$ mm.

4. Summary

Modern steels for high temperature operation, e.g. in power plants, are showing high deformability. Classical methods, determining failure formulated on the stress field, are highly conservative. Improving the assessment aiming at a better material usage requires a concept which includes the actual deformability. Additionally, for high ductile materials, crack initiation does not readily start before a certain strain within the net section stress region is accumulated, defining monitoring measures or the replacement of the component. To be able to determine this crack size dependent on the material´s ductility a more accurate failure criterion is needed.
A strain based concept has been introduced and applied on three 10Cr- and 1Cr-steels with different ductility. It correlates a characteristic strain within the crack tip region of the specimen and a material dependent reference strain. Determining the stress and strain field within the crack tip at a certain loading time requires Finite-Element modelling and calculations to crack initiation. With a crack initiation criterion with a crack growth of 0.5 mm modelling of the crack propagation is essential. To avoid this effort, crack initiation was attained for a smaller crack growth of 0.1 mm. The concept was validated on fracture mechanics specimens with loading times up to 20.000 h.
It could be shown that the initial crack sizes of interest, i.e. such sizes which does not show crack initiation before a certain strain is reached within the ligament section, is dependent on the materials ductility. For a ligament strain of 1 % the limit of initial crack size is up to 1 mm for creep rupture strains of 20 % and more. Reducing the ligament strain is leading to an increase of the limit of initial crack size.

5. Discussion and conclusions

Within the creep regime, local failure can be described through the available deformability of the material. With regard to crack initiation it would lead to a less conservative concept, than using stress based formulations, since the deformability does markedly have impact. The formulation of failure set up could be validated on fracture mechanics experiments, providing a limit of initial crack size for practical operation times. This limit characterises crack sizes for which crack initia-

tion does not occur before a certain strain within the ligament (in the net section stress region) is reached. If now the operation period of the component is defined by these creep strains within the net section stress area, pre-loaded cracks would not tend to initiate. For this cracks and internal defects, a fracture mechanics assessment is not necessary. So, the results of this work can be used to simplify the assessment of components, depending on the ductility, i.e. the creep rupture strain at a given loading period. In addition for materials with a high ductility a more precise failure assessment could be provided.

Acknowledgements

This work is the result of a research project provided by the Research Union for Combustion Engines, (FVV). The work was conducted at the Materials Testing Facility (MPA) Stuttgart and the Institute of Materials Science of the Technical University of Darmstadt.
The work was funded by the Research Union of the iron and metal-working Industrie (AVIF), No A252. It was coordinated by the working group W14, of the Community of Heat Resistant Steels of the VdeH and the FVV.

Literature

1. TRD508, Technische Regeln für Dampfkessel, Zusätzliche Prüfung an Bauteilen, berechnet mit zeitabhängigen Festigkeitskennwerten. Carl Heymanns Verlag (Taschenbuchausgabe 2007, Stand 2002)
2. VGB-Richtlinie-TW 507: Richtreihen zur Bewertung der Gefügeausbildung und Zeitstandschädigung warmfester Stähe für Hochdruckleitungen und Kesselbauteile. 2. Auflage (2005)
3. Ewald, J.: A Two Criteria Diagram for Creep Crack Initiation. In : Int. Conf. on Creep Tokyo, Japan, p.p. 173/8 (1986)
4. R5 Issue 3, An Assessment Procedure for the High Temperature Response of Structures. British Energy Generation Ltd. Procedure (2003)
5. R6 Revision 4, Assessment of the Integrity of Structures Containing Defects. Britisch Energy Generation Ltd. Procedure (2011)
6. Ewald, J., Maile, K., Tscheuschner, R.: Creep Crack Growth Assessment by Means of a Crack Tip/ Far Field Concept. Nuclear Engineering and Design 117, 185/95 (1989)
7. Berger, C., Granacher, J., Roos, E., Maile, K.: Kriechrissverhalten ausgewählter Kraftwerksstähle in erweitertem praxisnahem Parameterbereich. Schlussbericht zum AVIF-Forschungsvorhaben Nr. A78, Institut für Werkstoffkunde der TU Darmstadt und Staatliche Materialprüfungsanstalt, Universität Stuttgart (1999)
8. Berger, C., Granacher, J., Roos, E., Maile, K.: Rissverahlten typischer warmfester Kraftwerksbaustähle im Kriechermüdungsbereich. Schlussbericht zum AiF-Forschubsvorhaben Nr. 10395 I/II, Institut für Werkstoffkunde der TU Darmstadt und Staatliche Materialprüfungsanstalt, Universität Stuttgart (1999)
9. Berger, C., Scholz, A., Roos, E., Maile, K., Müller, F., Schellenberg, G.: Einfluss inerter Atmosphäre auf das Rissverhalten warmfester Stähle im Kriech- und Kriechermüdungsbereich. Abschlussbericht zum AiF-Forschungsvorhaben Nr. 11722 N, Institut für Werkstoffkunde der TU Darmstadt und Staatliche Materialpfürungsanstalt (2002)

10. Kloos, K. H., Kußmaul, K., Granacher, J., Maile, K., Tscheuschner, R., Eckert, W.: Kriechrisseinleitung und Kriechrisswachstum warmfester Kraftwerksbaustähle unter Berücksichtigung des Größeneinflusses. Abschlussbericht des AiF-Vorhabens Nr. 6038, Institut für Werkstoffkund der TH Darmstadt und Staatliche Materialprüfungsanstalt, Universität Stuttgart (1988)
11. Berger, C., Scholz, A., Roos, E., Maile, K., Müller, F., Stadtmüller, W.: Hochtemperaturverhalten der neuen 600 °C-Stähle für Wellen und Gehäuse von Dampfturbinen. Abschlussbericht zum AVIF-Forschungsvorhaben A127, Institut für Werkstoffkunde der TU Darmstadt und Staatliche Materialprüfungsanstalt, Universität Stuttgart (2002)
12. Ewald, J., Wellinger, K.: Stützwirkung bei höherer Temperatur, Zeitstandversuche an Biegeproben. Technisch wissenschaftlicher Bericht, Staatliche Materialprüfungsanstalt, Universität Stuttgart (1972)
13. Gooch, D. J., Haigh, J. R., King, B. L.: Relationship between Engineering and Metallurgical Factors in Creep Crack Growth. In : Metal Science. (1977) pp. 545-550
14. Riedel, H.: Fracture at High Temperatures. Springer-Verlag Berlin, Heidelberg, New York, London, Paris, Tokyo (1986)
15. Ewald, J.: Zwei-Kriterien-Daigramm für Kriechrisseinleitung: Berücksichtigung des Kriech-Verformungsvermögens (für ferritische Werkstoffe). In : Vortrag auf der 26. Vortragsveranstaltung der Arbeitsgemeinschaft für warmfeste Stähle und der Arbeitsgemeinschaft für Hochtemperaturwerkstoffe, Düsseldorf (2003)
16. Roos, E., et.al.: Bewertung von Bauteilen in Abhängigkeit vom Kriechverformungsvermögen. Abschlussbericht zum AVIF-Forschungsvorhaben A252, Materialprüfungsanstalt, Universität Stuttgart und Institut für Werkstoffkunde der TU Darmstadt (2011)
17. Maile, K., Meyer, L. W.: Einfluss der Mehrachsigkeit der Belastung auf die Kriechporenbildung und die zeitliche Schädigungsentwicklung bei typischen Kraftwerksbaustählen. Abschlussbericht des Forschungsvorhabens AVIF A105, MPA Stuttgart, TU Chemnitz (2000)
18. Maile, K., Klenk, A.: Influence of the multiaxial stress state on component failure in the creep range. In : International Conference on Advanced Technology in Experimental Mechanics 2003, JSME-MMD, Nagoya (2003)
19. Hobt, A., Klenk, A., Roos, E., Mao, T., Scholz, A., Berger, C.: Bewertung von Bauteilen mit Fehlstellen in Abhängigkeit vom Kriechverformungsvermögen. In : Abschlussbericht FVV Frühjahrstagung, Bad Neuenahr (2011)
20. Maile, K., et.al.: Kriterien zur Schädigungsbeurteilung von Hochtemperaturbauteilen aus martensitischen 9-11 %-Cr-Stählen. Abschlussbericht des Forschungsvorhabens AVIF A229, MPA Stuttgart, Siempelkamp Prüf und Gutachter Gesellschaft (2008)
21. Cocks, A., Ashby, F.: Intergranular fracture during power-law creep under multiaxial stresses. Metal Sciennce, 395-402 (1980)
22. Vishwanathan, R.: Damage Mechanisms and Life Assessment of High-Temperature Components. ASM INTERNATIONAL, Metals Park Ohio (1989)

CMOD-Based J Integral Measurement for Surface Cracked Specimens

Xudong Qian[1,*], **Ya Li**[1]

[1] Department of Civil and Environmental Engineering, National University of Singapore, Singapore 117576, Singapore
* Corresponding author: qianxudong@nus.edu.sg

Abstract This paper proposes an experimental approach based on the measured crack-mouth opening displacement (CMOD) to determine the mode I energy release rate for surface cracks in plate specimens subjected to four-point bending. The proposed experimental scheme measures the load versus CMOD relationships in a surface cracked specimen under four-point bending, and computes the relative rotation, θ, between the two crack planes based on the measured CMOD, and the bending moment (M) applied on the cracked cross section based on the measured load. The energy release rate, measured by the J-integral value, computes from the area under the M-θ curve, similar to the eta-approach originally proposed by Rice and co-workers for single-edge-notched bend, SE(B), specimens. This study examines the above approach for four plate specimens with fatigue pre-cracked, machined surface notches. The measured J value shows close agreement with the energy release rate computed using the domain integral approach.

Keywords surface crack, crack-mouth opening displacement, energy release rate, domain integral, compliance.

1. Introduction

The standard procedure to derive the fracture resistance curve, namely the J-R curve restricts to small-scale planar specimens with a straight, through-thickness crack front [1-2] under high-constraint, small-scale yielding conditions. The fracture resistance thus measured characterizes the capabilities of the material in resisting fracture failure in an idealized, plane-strain condition. In contrast, realistic cracks in structural details often entail a complex topology with a curved crack-front, sometimes resembling a semi-elliptical shape. The varying crack-extensions along the curved crack fronts impinge inevitably on the resistance against crack growth at individual crack-front locations, due to the stress redistribution caused by the non-uniform crack extensions along the curved crack front. The plane-strain fracture resistance obtained using the conventional through-thickness fracture specimens may not, therefore, represent the fracture resistance reserved at different crack-front locations in curved surface cracks. The fracture resistance measured from the through-thickness specimens may thus not provide an accurate description of the evolving fracture resistance as the surface crack grows in the integrity assessment for engineering structures, *e.g.*, the level 3C ductile tearing assessment. An experimental method to measure the J-integral values for surface crack specimens becomes much-needed to overcome the transferability of the J-R curve from the material level to the specimen/structural level.

This study proposes such an experimental approach to determine the energy release rate for surface cracked plate specimens. The calculation of the energy release rate utilizes the CMOD-based approach, frequently used in the conventional through-thickness fracture specimens in evaluating the energy release rate. The experimental procedure determines the gross energy release rate along the entire crack front using the area under the moment-rotation curve of the crack plane, similar to the η-approach originally proposed by Rice *et al*. [3]. The rotation of the crack plane derives from a numerically determined center of rotation. The dimensionless η-value is, on the other hand, determined by coupling the numerical strain energy (the area under the M-θ curve computed from finite element [FE] models with a stationary crack) and the domain-integral values. The energy release rate determined from the compliance method agrees closely with the energy release computed using the domain-integral approach implemented in WARP3D [4].

2. Proposed *J*-Measurement for Surface Cracks

The proposed approach to measure the energy release rate, quantified by the *J*-integrals, predicates the fundamental principle prescribing the variation of the strain energy with respect to the crack extension,

$$J = -\frac{1}{B}\frac{dU}{da}, \tag{1}$$

where B refers to thickness of the conventional planar fracture specimen with a through-thickness straight crack. The definition of the J value in Eq. (1) requires that the parameter B characterizes the length of the crack front, as the physical interpretation of the J refers to the energy released per extended crack area. Replacing B by the crack-front length for a curved surface crack, Eq. (1) becomes,

$$J_{avg} = -\frac{\partial U}{\partial A_{crack}}, \tag{2}$$

where A_{crack} denotes the crack area. The J-value determined from Eq. (2) thus represents the energy release rate averaged over the entire curved crack front in the surface crack specimens.

To facilitate the experimental measurement of the energy release rate, previous researchers [3, 5] have developed an η-approach for different fracture specimens with a through-thickness crack,

$$J = \frac{\eta U}{Bb}, \tag{3}$$

where η remains as a dimensionless parameter dependent on the specimen geometry, and equals 2.0 for SE(B) specimens [3]. The parameter b in Eq. (3) denotes the length of the remaining ligament in a fracture specimen with a through-thickness crack. The η parameter needs to be re-calculated for surface cracked specimens. Equation (3) provides a convenient calculation of the energy release rate based on some simple geometric parameters and the strain energy U, which often derives from the area under the load versus the load-line displacement. The denominator in Eq. (3) quantifies the remaining net area of the cracked cross section in the fracture specimen. When applied to specimens with a surface crack, Eq. (3) becomes,

$$J_{avg} = \frac{\eta U}{A_{net}}, \tag{4}$$

where A_{net} refers to the net intact area of the cracked cross section, or,

$$A_{net} = A_{total} - A_{crack}, \tag{5}$$

where A_{total} denotes the gross cross-sectional area of the specimen.

Equation (4) allows the determination of a single characteristic energy release rate for a surface crack in the experimental procedure. In contrast, the numerical domain integral approach often computes the varying energy release rates along the curved front for a surface crack. The energy release rate, averaged over the entire crack front, thus derives from the individual J-values along the crack front,

$$J_{avg} = \frac{\sum_{i}^{n} B_i J_i}{B_{total}}. \tag{6}$$

In calculating the average energy release rate along the crack front, Eq. (6) divides the curved crack front into multiple segments, each with a length B_i and a corresponding energy release rate J_i. B_{total}

in Eq. (6) denotes the total crack-front length. Equating Eqs. (4) and (6) allows the determination of the value of the dimensionless parameter η.

3. Experimental Validation

3.1. Specimen Configuration and Set-up

The experimental program includes four specimens made of high-strength steels extracted from a large-scale circular hollow section joint [6]. Figure 1 illustrates the geometric configuration of the steel plate specimens with a machined surface notch. The shape of the surface notch follows a semi-elliptical configuration with the crack aspect ratio (a/c) equal to 0.5, *i.e.*, the machined crack depth equals 10 mm.

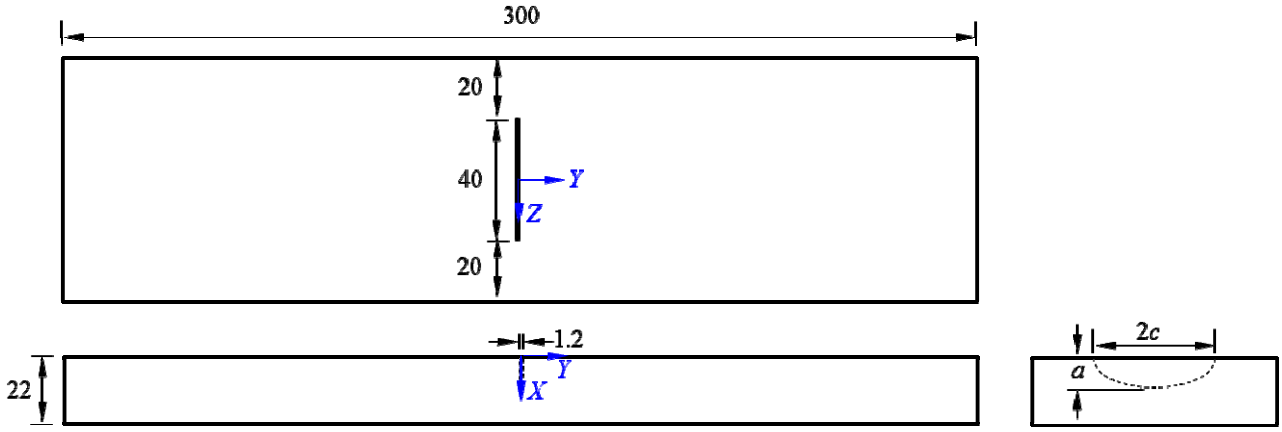

Figure 1. Configuration of the surface cracked plate specimens.

Figure 2 shows the uniaxial true stress-true strain curve obtained from the axial tension test following the ASTM E-8M [7]. The steel material has a specified grade of S690, with a measured yield strength equal to 810 MPa, and a tensile strength of 866 MPa. The Young's modulus of the material equals 206 GPa, with a Poisson's ratio of 0.3.

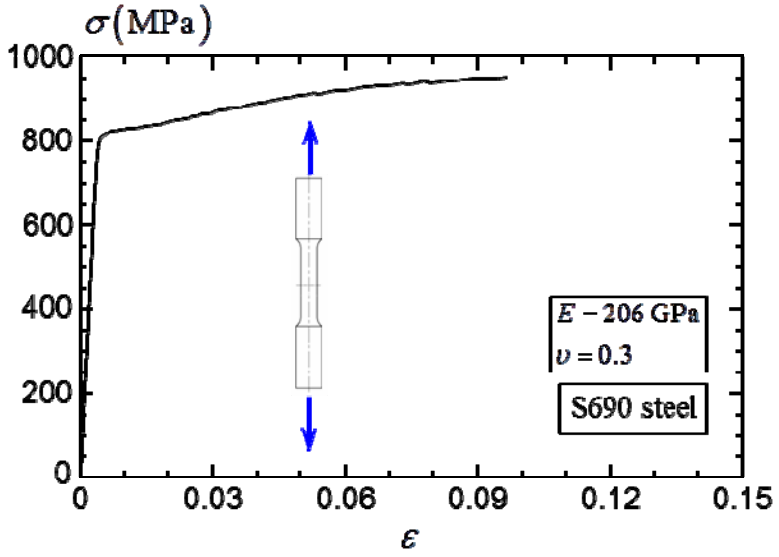

Figure 2. True stress-true strain curve of the S690 steel.

Figure 3 illustrates the four-point bend test set-up for the plate specimens. This four-point bend set-up, in contrast to the three-point bend set-up, prevents the plastic deformation caused by the indentation of the loading point to impinge on the plastically deformed crack tip under large deformations, which has frequently occurred in SE(B) specimens made of highly ductile materials.

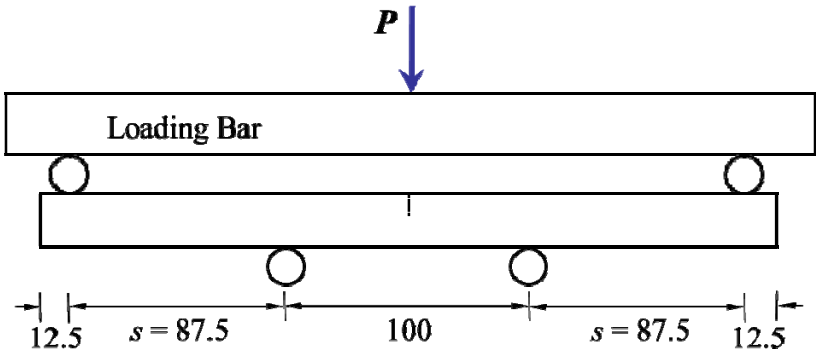

Figure 3. The four-point bend test set-up for the plate specimens.

3.2. Experimental Procedures

The experimental procedure separates into two stages: 1) a load-controlled fatigue pre-cracking cyclic load to generate a sharp crack-front along the machined notch; 2) a displacement-controlled monotonic loading coupled with multiple unloading-reloading cycles to monitor the compliance of the specimen, measured by the ratio of the measured CMOD range over the corresponding range of the applied load, throughout the procedure. The increasing compliance measured during the test indicates a growing crack during the test.

The experimental procedure monitors the specimen compliance during the fatigue pre-cracking stage, which terminates as the compliance increases by 20% to 30% of the initial compliance of the specimen. Table 1 lists the fatigue pre-cracked sizes for all four specimens.

Table 1. Fatigue pre-cracked sizes for the plate specimens

Specimen	Machined Crack Size		Fatigue Pre-crack	
	a (mm)	a/c	a (mm)	a/c
SP1	10	0.5	12.0	0.497
SP2			12.0	0.496
SP3			12.4	0.484
SP4			12.3	0.483

Figure 4 shows the load-CMOD measured during the experiment for the specimen SP1 shown in Table 1. The CMOD in Figure 4 refers to the crack mouth opening displacement measured at the center of the surface crack (Z = 0 in Figure 1).

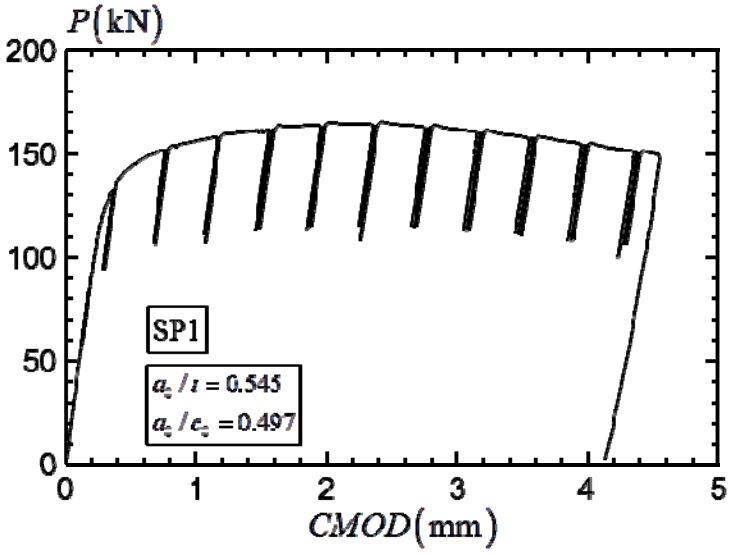

Figure 4. Definition of the crack-plane rotation angle θ.

3.3. Evaluation of Energy Release Rate

The calculation of the energy release rate in the plate specimens shown in Figures 1 and 3 depends on the evaluation of the strain energy U for the surface cracked specimens. The strain energy U, for the four-point bend specimens, follows,

$$U = 2\int_0^{\theta} M d\theta \,, \tag{7}$$

in which the angle θ defines the rotation of one of the two crack planes and M refers to the bending moment applied on the cracked section. Assuming a center of rotation at a distance of r ($W - a$) away from the crack tip, the rotation of the crack plane thus derives from the measured crack-mouth opening displacement (CMOD),

$$\theta = \frac{CMOD}{2\left[a + r(W-a) + h\right]}, \tag{8}$$

where h denotes the thickness of the knife-edge aluminum plate glued to the surface of the plate specimens in order to mount the crack-opening displacement (COD) gauge, as shown in Figure 5.

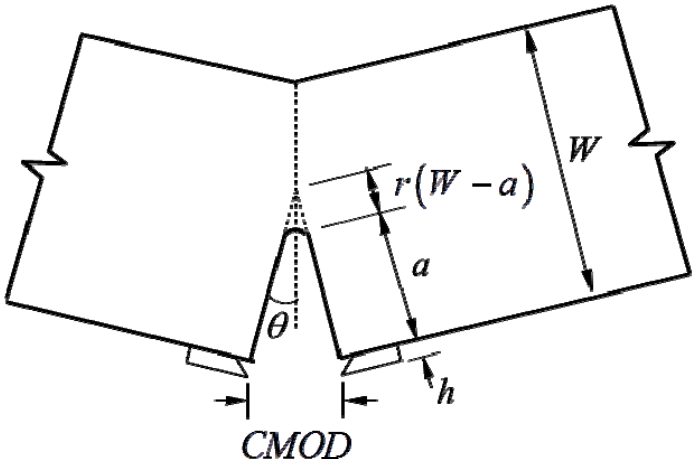

Figure 5. Definition of the crack-plane rotation angle θ.

The value of r in Eq. (8) equals 0.44 for SE(B) specimens, as outlined in standard material testing procedures [1]. This value of r, however, requires re-evaluation for the plate specimens subjected to the four-point bending shown in Figure 3. This study determines the r value through a detailed, large-deformation finite element analyses for plate specimens with a stationary crack. Figure 6 compares the deformed crack plane computed from the finite element analyses (represented by the discrete symbols) with the deformed shape calculated from a regressed rotation center with $r = 0.18$. The displacement u_Y in Figure 6 refers to the displacement in a direction perpendicular to the crack plane (see Figure 1 for the coordinate system X-Y-Z), while the Z value defines the crack-front position corresponding to which the displacements on the crack plane are measured. The results in Figure 6 indicates that the deformed crack plane aligns along a rotated plane with the rotation center calculated using $r = 0.18$.

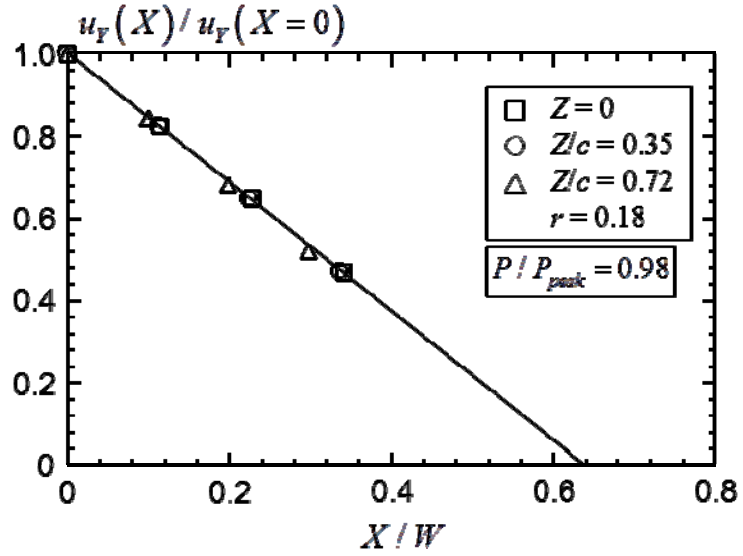

Figure 6. The r value for the plate specimens subjected to four-point bending.

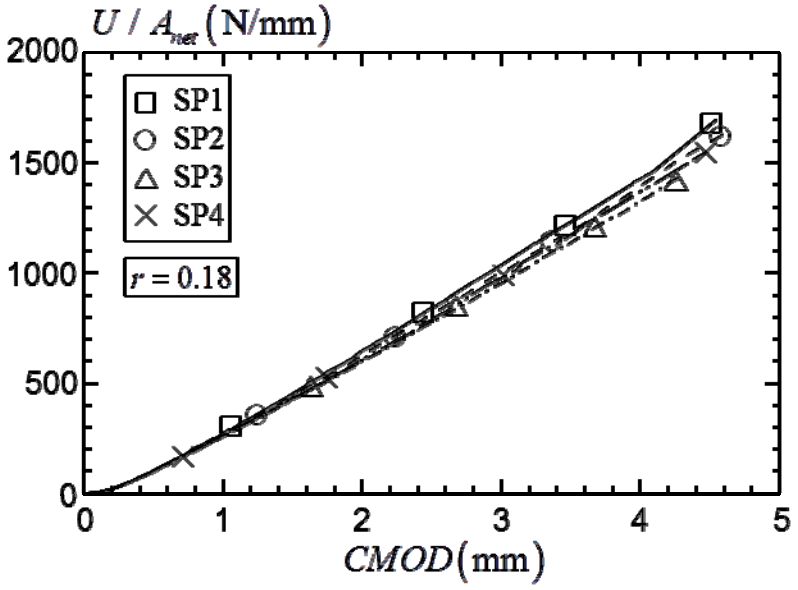

Figure 7. Evolution of the strain energy U for the four plate specimens.

Using an r value of 0.18, the strain energy U for the plate specimen can now derive from Eqs. (7)

and (8). Figure 7 presents the evolution of the strain energy U with respect to the crack mouth opening displacement measured at the center of the crack ($Z = 0$) for all four plate specimens.

The evaluation of the energy release rate requires the determination of the dimensionless η-value. This study determines the η-value using FE models with stationary cracks via equating Eqs. (4) and (6). The strain energy value U in Eq. (4) is computed using the strain energy derived from the area under the moment-rotation curve of the crack plane computed from the large-deformation finite element analyses, as shown in Eq. (7). Figure 8 illustrates the variation of the η-value as the applied load increases for the four plate specimens. The η-value remains approximately at the same magnitude at different load levels in all four specimens. The current study utilizes, therefore, a constant η-value of 1.1 for all plate specimens.

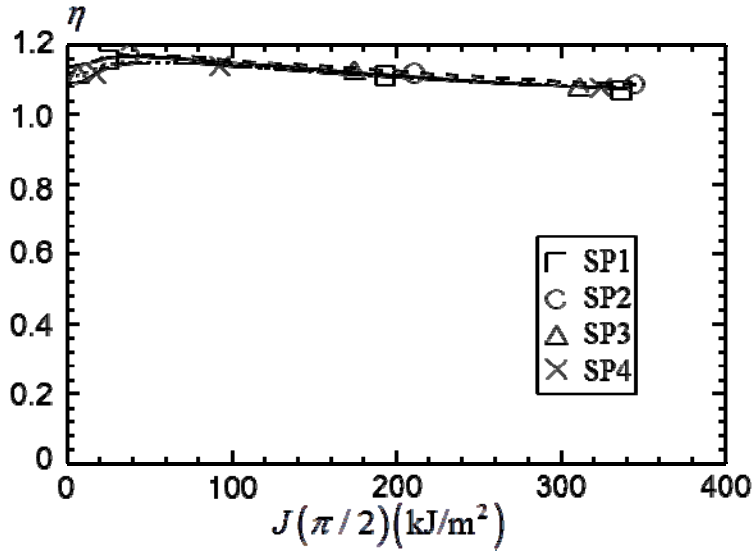

Figure 8. The dimensionless η-values for the plate specimens.

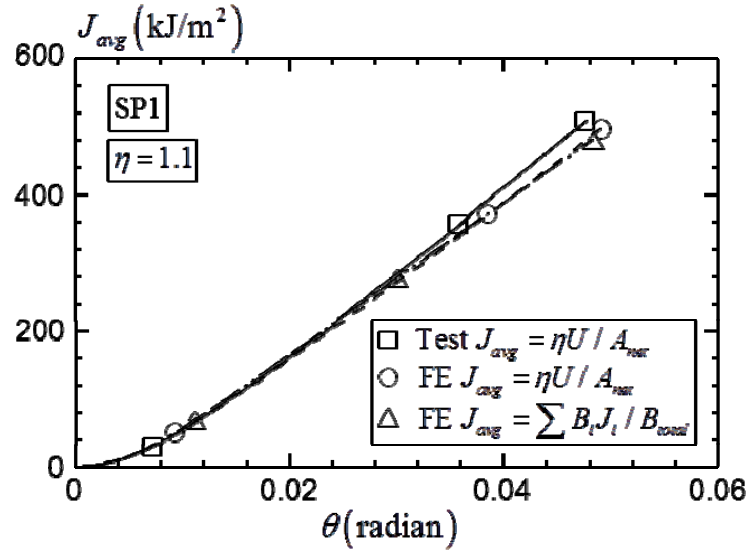

Figure 9. Comparison of the energy release rate for the surface cracked plate specimen SP1.

Figures 9 and 10 compare the energy release rate computed from the finite element model and those measured from the experiments for two selected specimens SP1 and SP4. The average J-values computed from the finite element analysis in Figures 9 and 10 correspond to the plate models with a stationary crack. The comparison in Figures 9 and 10 therefore limits the comparison for the

experimental energy release rate to a small deformation level, at which the amount of ductile crack extension remains small. For both specimens, the numerically computed energy release rate agrees closely with those measured from the experiments.

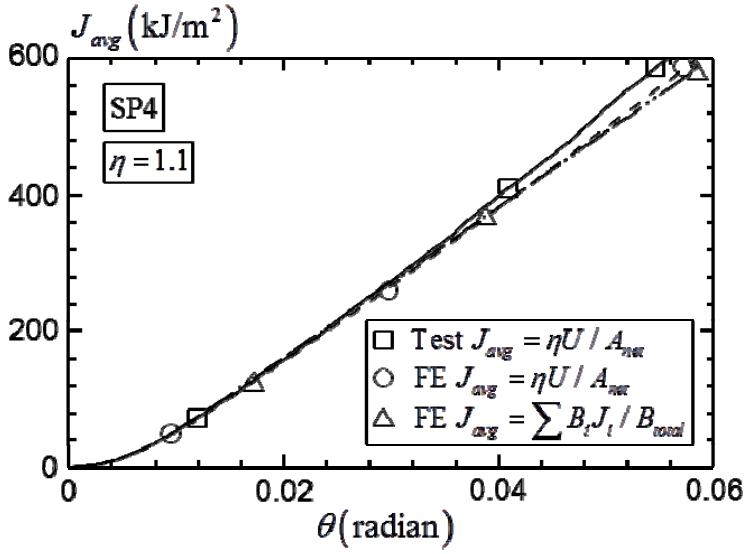

Figure 10. Comparison of the energy release rate for the surface cracked plate specimen SP4.

4. Summary and Conclusions

This study describes a compliance-based procedure to measure the energy release rate for surface cracks in plate specimens subjected to four-point bending. The average energy release rate along the crack front derives from the η-approach using the area under the M-θ curve for the cracked section. The center of rotation for the crack plane remains at about 18% of the remaining ligament measured from the crack tip at the deepest crack-front location, for the four surface cracked specimens considered in this study. This value, however, requires further validation when the η-approach is extended to other types of surface cracked specimens under different loading conditions. The energy release rate calculated using the η-approach based on the area under the numerical moment-rotation curves of the cracked section matches closely with the average energy release rate based on the domain-integral values computed in the large-deformation, elastic-plastic analyses. The energy release rate estimated using the η-approach from the experimental M-θ curves agrees well with that estimated using the numerical M-θ curve, before substantial crack extensions occur in the experimental specimen. Together with a compliance based method to determine the crack size in the surface cracked plate specimen, the approach proposed here provides a basis to determine the J-R curve for surface cracked specimens [8].

References

[1] American Society for Testing and Materials, Standard test method for measurement of fracture toughness. ASTM E1820-11. West Conshohocken, PA, United States, 2011.

[2] X. K. Zhu, J. A. Joyce, Review of fracture toughness (G, K, J, CTOD, CTOA) testing and standardization. Eng Fract Mech 85 (2012) 1-46.

[3] J. R. Rice, P. C. Paris, J. G. Merkle, Some further results of J-integral analysis and estimates. ASTM STP 536, American Society for Testing and Materials, Philidelphia, PA, (1973) 23-245.

[4] A. Gullerud, K. Koppenhoefer, A. Roy, S. RoyChowdhury, M. Walters, B. Bichon, K. Cochran, A. Carlyle, R. H. Jr. Dodds. WARP3D: 3-D dynamic nonlinear fracture analysis of solids using parallel computers and workstations. Structural Research Series (SRS) 607 UILU-ENG-95-2012 University of Illinois at Urbana Champaign.

[5] Y. Zhang, X. Qian, An eta-approach to evaluate the elastic-plastic energy release rate for weld-toe cracks in tubular K-joints. Eng Struct, under review (2012).
[6] X. Qian, Y. Li, Z. Ou, Ductile tearing assessment of high-strength steel X-joints under in-plane bending. Eng Fail Ana, 28 (2013) 176-191.
[7] American Society for Testing and Materials, Standard test methods for tension testing of metallic materials, ASTM E8/E8M, West Conshohocken, PA, United States, 2011.
[8] X. Qian, Y. Li. A compliance-based approach to measure fracture resistance curve for surface cracked steel plates. Int J Fract, under review (2012).

Determination of crack surface displacements for a radial crack emanating from a semi-circular notch using weight function method

D H Tong, X R Wu*

AVIC Beijing Institute of Aeronautical Materials , Beijing 10095 , China
* Corresponding author: xueren.wu@gmail.com)

Abstract A radial crack emanating from a semi-circular notch is of significant engineering importance. Accurate determination of key fracture mechanics parameters is essential for damage tolerance design and fatigue crack growth life predictions. The purpose of this paper is to provide an efficient and accurate closed-form weight function approach to the calculation of crack surface displacements for a radial crack emanating from a semi-circular notch in a semi-infinite plate. Results are presented for two load conditions: remote applied stress and uniform stress segment applied to crack surfaces. Based on a correction of stress intensity factor ratio, highly accurate analytical equations of crack surface displacements under the two load conditions are developed by fitting the data obtained by using the weight function method. It is demonstrated that the Wu-Carlsson closed-form weight functions are very efficient, accurate and easy-to-use for calculating crack surface displacements for arbitrary load conditions. The method will facilitate fatigue crack closure and other fracture mechanics analyses where accurate crack surface displacements are required.

Keywords: Radial crack, Semi-circular notch, Dugdale strip-yield model, Crack surface displacement, Weight function method.

1. Introduction

In fracture mechanics analysis and fatigue crack growth life predictions for structural components, the strip-yield model (modified Dugdale models) [1] have been employed for crack configurations like middle-crack tension [1-5] and compact specimens [6-8]. Reference [9] discussed the application of the model to analyze double radial cracks emanating from a circular hole. This crack configuration and a radial crack emanating from a semi-circular notch are among the most important crack types for aircraft structures. Stress intensity factors for such cracks under various loading conditions can be found in the literature [10-11]. However, crack surface displacements for various load conditions, preferably in analytical form, which are needed in crack-closure-based fatigue crack growth life prediction models and other fracture mechanics analyses, are rarely available.

A modified Dugdale model is proposed by Newman [1]. The modification is to leave plastically deformed materials in the wake of the crack. The primary advantage in using this model is that the plastic-zone size and crack surface displacements are obtained by superposition of two elastic problems: a crack in a plate subjected to a remote uniform stress and a uniform stress applied over a segment of the crack surfaces. In the Newman model, crack surface displacements under remote applied stresses and a segment uniform pressure (partial loading) in the immediate wake of the crack tip are both required for calculating the crack opening stress, S_{op}. The accuracy of these displacements will significantly influence S_{op}, and further, fatigue crack growth rates.

The motivation of the present paper is to explore an analytical approach, based on the closed-form weight functions, to the calculation of crack surface displacements for a radial crack emanating from a semi-circular notch in a semi-infinite plate. Results are presented for the two loading conditions: remote applied stress and uniform segment stress (partial load) applied to a segment of the crack surfaces. Based on a correction of stress intensity factor ratio, highly accurate analytical equations of the crack surface displacements are developed to fit the data from weight function

method. It is envisaged that the closed-form weight function approach will provide an efficient and reliable method for calculating crack-surface displacements under arbitrary loadings. The analytical equations of the crack surface displacement can contribute to a more rapid and reliable fatigue crack growth life predictions for a radial crack emanating from a semi-circular notch in a semi-infinite plate.

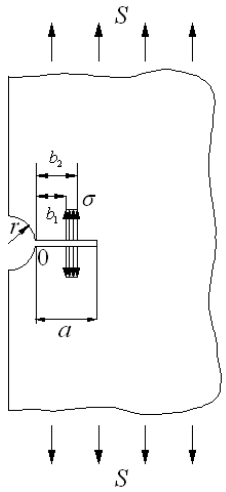

(a)

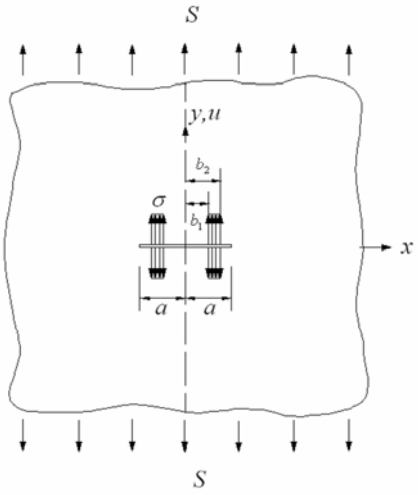

(b)

Figure.1 Crack geometry. (a) A radial crack emanating from a semi-circular notch in a semi-infinite plate. (b) Middle crack in an infinite plate

2. Theoretical procedures

The weight function method [10] is a very powerful method for the determination of key fracture mechanics parameters for cracks under arbitrary load conditions, e.g. stress intensity factors and crack surface displacements. The high efficiency of this method lies in that the weight function is a property of crack geometry only, and is independent of loading. For given crack configuration, once the weight function is obtained, fracture mechanics parameters for the same crack configuration under arbitrary loadings can be easily determined through a simple quadrature.

For stress intensity factors [10]:

$$K = f\sigma\sqrt{\pi a} \tag{1}$$

$$f = \int_0^a \frac{\sigma(x/a)}{\sigma} \cdot \frac{m(a,x)}{\sqrt{\pi a r}}\,\mathrm{d}x \tag{2}$$

where $m(a, x)$ is the weight function for the given crack geometry, which can be derived from the crack opening displacements $u(a, x)$ for a reference load case.

$$m(a,x) = \frac{E'}{K(a)}\frac{\partial u(a,x)}{\partial a} \tag{3}$$

where $E' = E$ for plane stress and $E' = E/(1-\eta^2)$ for plane strain.

For the corresponding crack surface displacements [10]:

$$u(a,x) = \frac{\sigma}{E'}\int_{a_0}^{a}[f(s)\sqrt{\pi s}]\cdot m(s,x)\mathrm{d}s \tag{4}$$

From the above equations, it is seen that the central issue in the weight function method is the determination of weight function $m(a, x)$ for the crack geometry in consideration. Various approaches have been used for determining $m(a, x)$. One effective way is to derive $m(a, x)$ through a reference load case. With this procedure, systematic derivations for the weight functions $m(a, x)$ for a large number of two-dimensional crack configurations have been given by Wu and Carlsson [10], which can be readily utilized for the present analysis.

For the edge crack configuration, which is applicable to the present case, i.e. a radial crack emanating from a semi-circular notch in a semi-infinite plate, the stress intensity factor and the corresponding crack face loading for the reference load case are expressed in polynomials of the type:

$$f_r(\frac{a}{r}) = \sum_{i=0}^{I}\alpha_i(\frac{a}{r})^i \tag{5}$$

$$\frac{\sigma_r(\frac{x}{r})}{\sigma} = \sum_{m=0}^{M} S_m(\frac{x}{r})^m \tag{6}$$

where r is the notch radius, and the coefficients α_i and S_m for the present crack configuration are given in Section 3.

The weight function was expressed in closed-form by Wu and Carlsson [10], as

$$m(a,x) = \sqrt{\frac{r}{2\pi a}}\sum_{i=1}^{4}\beta_i(\frac{a}{r})\cdot(1-\frac{x}{a})^{i-\frac{3}{2}} \tag{7}$$

where

$$\left.\begin{aligned}
\beta_1(\frac{a}{r}) &= 2.0 \\
\beta_2(\frac{a}{r}) &= \frac{[4\frac{a}{r}f_r^{'}(\frac{a}{r}) + 2f_r(\frac{a}{r}) + \frac{3}{2}F_2(\frac{a}{r})]}{f_r(\frac{a}{r})} \\
\beta_3(\frac{a}{r}) &= \frac{\left\{\frac{a}{r}F_2^{'}(\frac{a}{r}) + \frac{1}{2}[5F_3(\frac{a}{r}) - F_2(\frac{a}{r})]\right\}}{f_r(\frac{a}{r})} \\
\beta_4(\frac{a}{r}) &= \frac{[\frac{a}{r}F_3^{'}(\frac{a}{r}) - \frac{3}{2}F_3(\frac{a}{r})]}{f_r(\frac{a}{r})}
\end{aligned}\right\} \tag{8}$$

where

$$\left.\begin{aligned}
F_1(\frac{a}{r}) &= 4f_r(\frac{a}{r}) \\
F_2(\frac{a}{r}) &= \frac{15\left[\sqrt{2}\pi\phi(\frac{a}{r}) - E_1(\frac{a}{r})\cdot F_1(\frac{a}{r})\right] - E_3(\frac{a}{r})\cdot F_1(\frac{a}{r})}{15E_2(\frac{a}{r}) - 3E_3(\frac{a}{r})} \\
F_3(\frac{a}{r}) &= \frac{E_2(\frac{a}{r})\cdot F_1(\frac{a}{r}) - 3\left[\sqrt{2}\pi\phi(\frac{a}{r}) - E_1(\frac{a}{r})\cdot F_1(\frac{a}{r})\right]}{15E_2(\frac{a}{r}) - 3E_3(\frac{a}{r})}
\end{aligned}\right\} \tag{9}$$

with

$$\phi(\frac{a}{r}) = \frac{1}{a^2}\int_0^a (s\cdot\left[f_r(\frac{s}{r})\right]^2)\mathrm{d}s \tag{10}$$

$$E_j(\frac{a}{r}) = \sum_{m=0}^{7}\frac{2^{m+1}m!S_m(\frac{a}{r})^m}{\prod_{k=0}^{m}(1+2j+2k)}, \quad j=1,2,3 \tag{11}$$

where r is the radius of the semi-circular notch; f_r and S_m are defined in Eq. (5) and Eq. (6).

3. Crack surface displacements for a radial crack emanating from a semi-circular notch in a semi-infinite plate

For a radial crack emanating from a semi-circular notch in a semi-infinite plate, uniform remote tension is chosen as the reference load case, and the corresponding non-dimensional stress intensity

factor and the reference crack face loadings are expressed in Eq. (5) and Eq. (6) with the following coefficients, respectively:

a_i : 3.4345, -6.9715, 14.5781, -19.9230, 16.9424, -8.5301, 2.3134, -0.2595. ($a/r \leqslant 2.0$)

S_m : 3.0643, -6.6864, 13.1677, -16.9513, 13.7335, -6.6293, 1.7273, -0.1861. ($x/r \leqslant 2.0$)

3.1. Uniform remote tension

The normalized stress intensity factor of a radial crack emanating from a semi-circular notch in a semi-infinite plate under uniform remote tension, $f_{B,S}$, is given in Eq. (5), as:

$$f_{B,S} = \sum_{i=0}^{7} \alpha_i \left(\frac{a}{r}\right)^i \tag{12}$$

With the information of $f_{B,S}$ and $m(a, x)$, the crack surface displacements can be easily calculated from Eq. (4). Figure 2 shows the normalized crack surface displacements of a radial crack emanating from a semi-circular notch in a semi-infinite plate under uniform remote tension for non-dimensional crack length a/r = 0.05 to 1. The circular symbols in Fig. 2~3 are obtained by the crack surface displacement analytical equations, which will be explained later.

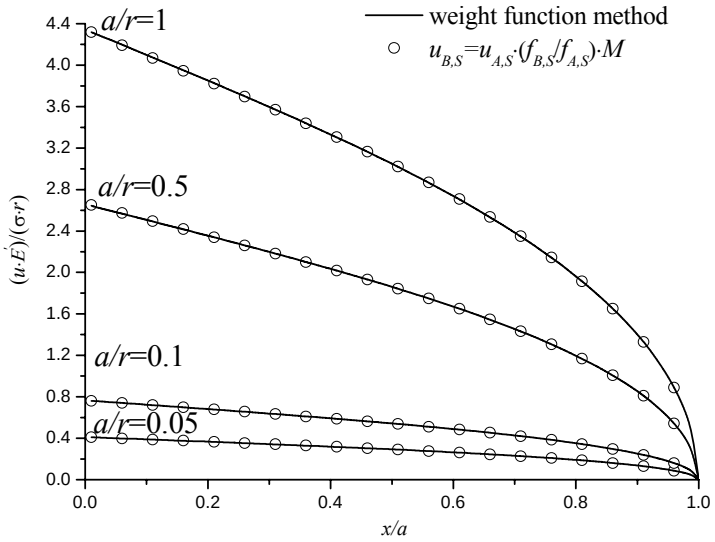

Figure.2 Non-dimensional crack surface displacements for a radial crack emanating from a semi-circular notch in a semi-infinite plate subjected to uniform remote tension.

3.2. Partial crack surfaces subject to Dugdale loading

For partial crack surfaces subject to Dugdale loading (see Fig. 1(a), $b_2=a$), the stress distribution is expressed in a simple form:

$$\sigma(x) = \sigma \qquad (b_1 \leq x \leq a) \tag{13}$$

For partial crack surfaces subject to Dugdale loading, the normalized stress intensity factor of a radial crack emanating from a semi-circular notch in a semi-infinite plate is easily calculated by inserting Eq.(13) and Eq. (7) into Eq. (2), with

$$f_{B,\sigma}=\frac{\sqrt{2}}{\pi}\left[\sum_{1}^{4}\frac{1}{(2i-1)}\beta_i(\frac{a}{r})\cdot(1-\frac{b_1}{a})^{i-\frac{1}{2}}\right] \tag{14}$$

With the above $f_{B,\sigma}$-expression and $m(a, x)$, the crack surface displacements (Eq. (4)) for partial crack surfaces subject to Dugdale loading can be readily calculated from the following equation:

$$u_{B,\sigma}=\frac{\sigma}{E'\pi}\int_{a_0}^{a}\left(\left[\frac{1-\frac{b_1}{s}}{1-\frac{x}{s}}\right]^{\frac{1}{2}}\cdot\sum_{i=1}^{4}\frac{\beta_i(s/r)}{2i-1}\cdot(1-\frac{b_1}{s})^{i-1}\cdot\sum_{i=1}^{4}\beta_i(s/r)\cdot(1-\frac{x}{s})^{i-1}\right)\mathrm{d}s \tag{15}$$

Figure 3 present the results, the normalized crack surface displacements of a radial crack emanating from a semi-circular notch in a semi-infinite plate with crack surfaces subject to Dugdale loading (b_2=a，b_1=d). The non-dimensional crack lengths in Fig. 3 are: a/r=0.05, 0.1, 0.5 and 1.0.

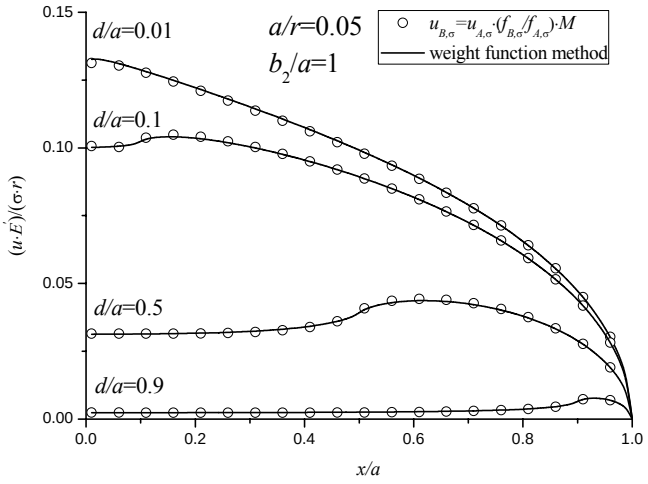

(a)

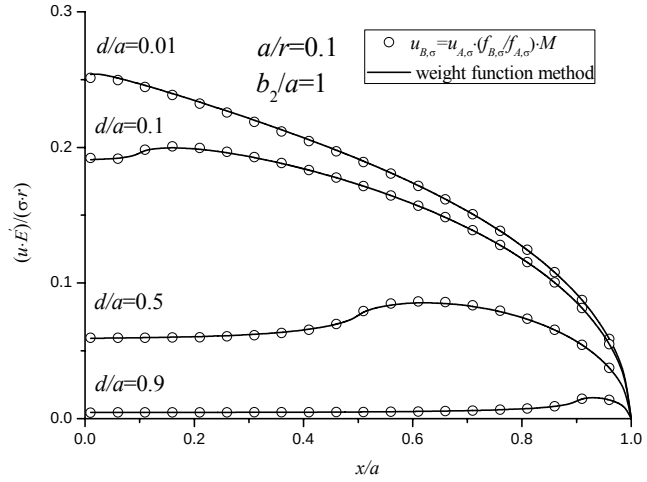

(b)

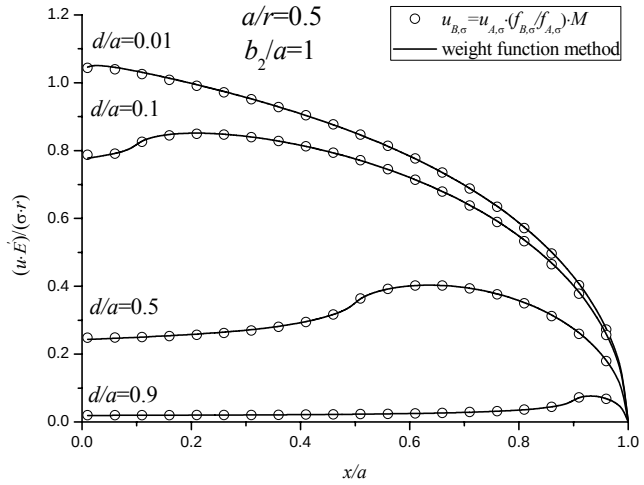

(c)

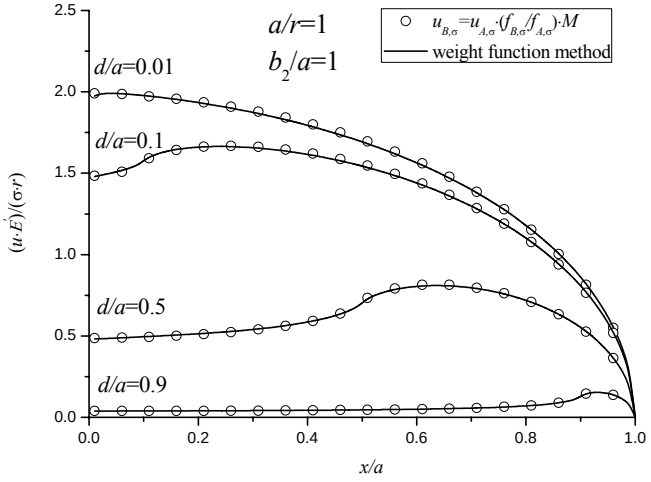

(d)

Figure.3 Non-dimensional crack surface displacements for a radial crack emanating from a semi-circular notch in a semi-infinite plate subjected to Dugdale loading in the immediate wake of crack tip, with (a) a/r=0.05. (b) a/r=0.1. (c) a/r=0.5. (d) a/r=1.0.

4. Analytical crack surface displacement equations for a radial crack emanating from a semi-circular notch in a semi-infinite plate

It has been a common practice in the literature that the crack surface displacements for one case (B) can be estimated from available crack surface displacements for a similar known case (A), by multiplying a correction factor. Recently, Tong and Wu proposed a general expression for an edge crack in a semi-infinite plate and double radial cracks at a circular hole with good success [12,13]. The correction is composed of two parts: the ratio of stress intensity factors for the two cases, f_B /f_A and a fitted correction factor M, as the following:

$$u_B = u_A \cdot \frac{f_B}{f_A} \cdot M \tag{16}$$

where the subscripts A and B represent the two load cases.

Because the crack surface displacements of a center crack in an infinite plate (see Fig. 1(b)) have exact solutions, this case (see Fig. 1(b)) is selected as load case A, a radial crack emanating from a semi-circular notch in a semi-infinite plate is selected as load case B.

For a center crack in an infinite plate under uniform remote tension, the exact crack surface displacement equation is [11]

$$u_{A.S} = \frac{2(1-\eta^2)S}{E}\sqrt{a^2 - x^2} \quad |x| \le a \tag{17}$$

The normalized stress intensity factor is

$$f_{A,S} = 1 \tag{18}$$

For a center crack in an infinite with crack surfaces subject to Dugdale loading, the exact crack surface displacement equation is [11]

$$u_{A,\sigma} = h(x) + h(-x) \quad |x| \le a \tag{19a}$$

$$h(x) = \frac{2(1-\eta^2)\sigma}{\pi E}\left[\begin{array}{l}(d-x)\operatorname{arccosh}\left(\dfrac{a^2 - dx}{a|d-x|}\right) + \\ \sqrt{a^2 - x^2}\,\arcsin\left(\dfrac{d}{a}\right)\end{array}\right]_{d=b_1}^{d=a} \tag{19b}$$

The normalized stress intensity factor is [11]

$$f_{A,\sigma} = \left[\frac{2}{\pi}\sin^{-1}\left(\frac{d}{a}\right)\right]_{d=b_1}^{d=a} \tag{20}$$

4.1. Analytical crack surface displacement equation for uniform remote tension

For a radial crack emanating from a semi-circular notch in a semi-infinite plate under uniform remote tension, the crack-surface displacement analytic equation can be expressed as

$$u_{B,S} = u_{A,S} \cdot \frac{f_{B,S}}{f_{A,S}} \cdot M_{B,S} \tag{21a}$$

where $f_{B,S}$, $f_{A,S}$ and $u_{A,S}$ are given in Eq. (12), Eq. (18) and Eq. (17), respectively. The factor $M_{B,S}$ is determined by fitting the crack opening displacement results obtained from the weight function method. The fitted expression is

$$M_{B,S}=\frac{1+3.52\cdot\frac{a}{r}+0.12\cdot\frac{x}{a}+0.38\cdot(\frac{a}{r})^2+0.645\cdot(\frac{x}{a})^2+2.15\cdot\frac{x}{a}\cdot\frac{a}{r}}{0.774+2.364\cdot\frac{a}{r}+0.45\cdot\frac{x}{a}+0.44\cdot(\frac{a}{r})^2+0.545\cdot(\frac{x}{a})^2+3.28\cdot\frac{x}{a}\cdot\frac{a}{r}}\quad (a/r\le 1.0) \tag{21b}$$

Figure 2 shows that this analytical expression fits the weight function results very well. The maximum error is 0.36% (for $a/r = 0.5$).

4.2. Analytic crack surface displacement equation for Dugdale loading

For a radial crack emanating from a semi-circular notch in a semi-infinite plate with crack surfaces subject to Dugdale loading, the analytical crack-surface displacement equation is

$$u_{B,\sigma}=u_{A,\sigma}\cdot\frac{f_{B,\sigma}}{f_{A,\sigma}}\cdot M_{B,\sigma} \tag{22a}$$

where $u_{A,\sigma}$, $f_{A,\sigma}$ and $f_{B,\sigma}$ are given by Eq. (19), Eq. (20) and Eq. (14), respectively. The factor $M_{B,\sigma}$ is determined by fitting the crack opening displacement results obtained from the weight function method, Eq.(15):

$$M_{B,\sigma}=\frac{0.921-0.713\cdot\frac{a}{r}-0.728\cdot\frac{d}{a}+0.63\cdot\frac{x}{a}+2.98\cdot\frac{a}{r}\cdot\frac{d}{a}+1.65\cdot\frac{a}{r}\cdot\frac{x}{a}-2.26\cdot\frac{d}{a}\cdot\frac{x}{a}-0.14\cdot(\frac{a}{r})^2+0.454\cdot(\frac{d}{a})^2+3.1\cdot(\frac{x}{a})^2}{0.718-0.287\cdot\frac{a}{r}-0.594\cdot\frac{d}{a}+0.723\cdot\frac{x}{a}+2.91\cdot\frac{a}{r}\cdot\frac{d}{a}+1.544\cdot\frac{a}{r}\cdot\frac{x}{a}-2.33\cdot\frac{d}{a}\cdot\frac{x}{a}-0.37\cdot(\frac{a}{r})^2+0.392\cdot(\frac{d}{a})^2+3.2\cdot(\frac{x}{a})^2} \tag{22b}$$

Figure 3 shows some typical comparisons between the fitted expression, Eq. (22), and the weight function results. For a radial crack emanating from a semi-circular notch in a semi-infinite plate, Eq. (22) represented by the circular symbol, is in very good agreement with the results from weight function method (the solid curves) for all points along crack surface. The maximum difference occurs in the loading segment (a/r=0.05, b_1/a=0.9), and is about 2.4%.

With this analytical equation of crack surface displacements for the Dugdale loading, crack surface displacements for a segment (width Δb) pressure acting at an arbitrary location along the crack faces can readily be obtained by using the same procedure as Ref [12,13], i.e. taking the difference between two Dugdale loadings with $b_2=a$, b_1 and $b_1+\Delta b$ in Fig.1.

$$u_{\mathrm{B},\sigma,\Delta b}=(u_{\mathrm{A},\sigma}\cdot\frac{f_{\mathrm{B},\sigma}}{f_{\mathrm{A},\sigma}}\cdot M_{\mathrm{B},\sigma})\Big|_{d=b_1}-(u_{\mathrm{A},\sigma}\cdot\frac{f_{\mathrm{B},\sigma}}{f_{\mathrm{A},\sigma}}\cdot M_{\mathrm{B},\sigma})\Big|_{d=b_1+\Delta b} \tag{24}$$

Equation (23) will not only significantly improve the accuracy of fatigue crack closure analysis for the specific crack geometry in consideration, but also will improve the computational efficiency for the modified strip-yield-model-based fatigue crack growth predictions by eliminating the time -consuming numerical integrations for crack surface displacements under partial loading.

5. Summary and conclusions

Crack surface displacements for a radial crack emanating from a semi-circular notch in a semi-infinite plate are determined, and analytical equations have been developed. Two load cases have been treated, i.e. uniform remote tension and crack face Dugdale loading. The weight function method was used for the analysis. The following conclusions can be drawn.

(1) The closed-form weight function method provides a powerful means for accurate determination of crack surface displacements under arbitrary load conditions.

(2) Based on a correction of stress intensity factor ratio, highly accurate analytical equations of the crack surface displacements for a radial crack emanating from a semi-circular notch in a semi-infinite plate are developed, which fit the results from the weight function method very well.

References

[1] J.C. Newman, Jr., A crack-closure model for predicting fatigue crack growth under aircraft spectrum loading, ASTM STP 748 (1981) 53-84.
[2] B. Budiansky, J.W. Hutchinson, Analysis of closure in fatigue crack growth, J Appl Mech 45 (1978) 267-276.
[3] J.H. Kim, S.B. Lee, Fatigue crack opening stress based on the strip-yield model, Theor Appl Fract Mech 34 (2000) 73-84.
[4] J.Z. liu, X.R. Wu, Study on fatigue crack closure behavior for various cracked geometries, Eng Fract Mech 57 (1997) 475-491.
[5] B. Ziegler, Y. Yamada, J.C. Newman, Jr., Application of a strip-yield model to predict crack growth under variable-amplitude and spectrum loading – Part 2: Middle-crack-tension specimens, Eng Fract Mech 78 (2011) 2609-2619.
[6] G.S. Wang, A.F. Blom, A strip model for fatigue crack growth predictions under general load conditions, Eng Fract Mech 40 (1991) 507-533.
[7] Y. Yamada, B. Ziegler, J.C. Newman, Jr., Application of a strip-yield model to predict crack growth under variable-amplitude and spectrum loading – Part 1: Compact specimens, Eng Fract Mech 78 (2011) 2597-2608.
[8] S. Mall, J.C. Newman, Jr., The Dugdale model for compact specimen, ASTM STP 868 (1985) 113-128.
[9] J.C. Newman, Jr., A nonlinear fracture mechanics approach to the growth of small cracks, In: Zocher H, editor, Behaviour of short cracks in airframe materials, vol. 328, AGARD CP (1983) P: 6.1-6.26.
[10] X.R. Wu and A.J. Carlsson, Weight Functions and Stress Intensity Factor Solutions, Oxford, Pergamon Press, 1991.
[11] H. Tada, P.C. Paris, G.R. Irwin, The stress analysis of cracks handbook, 3rd ed, New York, ASME Press, 2000.
[12] D.H. Tong and X.R. Wu, Determination of crack surface displacements for cracks emanating from a circular hole using weight function method, Fatigue Fract Eng Mater Struct 2013, in press.
[13] D.H. Tong and X.R. Wu, Weight function solutions of crack surface displacements for double cracks emanating from a circular hole in an infinite plate, Acta Aeronautica et Astronautica Sinica 2013, in press, in Chinese.

Acoustic Emission Technique (AET) for Failure Analysis in wood materials

Frédéric LAMY [1], Mokhfi TAKARLI [1,*], Frédéric DUBOIS [1], Nicolas ANGELLIER [1], Ion-Octavian POP [1]

[1] Groupe d'Etude des Matériaux Hétérogènes, Université de Limoges, Egletons 19300, Country, France
* Corresponding author: Mokhfi.takarli@unilim.fr

Abstract Understanding failure mechanisms of construction materials as well as their damage evolution are two key factors to improve design tools of structures. Depending on failure modes to be highlighted, and studied, several tests methods, and analysis tools have been developed, in particular AET. This latter is an experimental tool well suited for characterizing material behavior by monitoring fracture process. Despite the wide use of AET to characterize and monitor damage evolution of composite materials, few research studies focused on using AET to characterize the mechanical behavior of wood materials.
In this work, the failure process in wood material under monotonic loading is studied by confronting three experimental methods; by analyzing stress-strain curves, AE measurements, and digital image acquisition. First, results show good correlation and complementarity between the used methods. Second, simple approach in analysis of AE signals (cumulative event and energy) gives important information about crack initiation and growth without the material. Moreover, advanced analysis of AE data (determination of source locations and the study of mechanism of individual events; study of amplitude distributions; investigation of frequency characteristics of emission events) will allows us to understand some key damage mechanisms such as the fracture process zone.

Keywords Acoustic Emission, Cracking, Wood, Fracture Energy

1. Introduction

Knowledge of the failure mechanisms of construction material as well as their damage evolution are two key factors to improve design tools of structures. In this context, Seismic **N**on-**D**estructive **T**echniques **(NDT)** which are based on stress wave propagation are interesting techniques for monitor structural integrity and characterize the behavior of materials when they undergo deformation, fracture, or both. These techniques can be divided into two methods: passive and active. This paper focuses on the **A**coustic **E**mission **T**echnique (**AET**) which is a passive method. Acoustic emission may be defined as transient elastic waves generated by the rapid release of strain energy in a material. A number of micro and macro processes contribute to both the deformation and the deterioration of a material under strain, resulting to a series of acoustic events. Thus, the events released by the material contain information regarding the general deformation process.
Kawamoto and Williams [1] reported literature review on the feasibility of AET for monitoring defects in wood. The advantages and the disadvantages of this technique were also described. It was noted that the AE investigations for wood products can be classified into five fields: (i) monitoring and control during drying; (ii) prediction of deformation; (iii) estimation of strength properties; (iv) fracture analysis, and (v) machine control.

This introduction focuses on fracture analysis by AET. Ansell [2] related the AE-strain characteristic from three softwoods tested in tension to mechanisms of deformations observed by scanning electron microscopy. The authors also reported correlation of EA total count with fracture toughness. Similar relationship was obtained by Suzuki and Schniewind [3] during cleavage failure in adhesive joints. Landis and Whittaker [4] compared the energy released by a mode I crack propagation in wood with the resulting acoustic emission energy. Results of the energy comparison indicated a good correlation. Reiterer et al., [5] investigated the mode I fracture behavior of softwoods and hardwoods under the splitting test associated to acoustic emission measurements. The measured AE parameters included cumulative counts, amplitude and frequency spectra. The results showed that

the AE counts until the maximum force was reached are much higher for the softwoods supporting the interpretation that the softwoods behave more ductile and therefore build a process zone containing much more microcracks. It was also shown that the differences in macrocrack formation and propagation can be visible in the shape of the cumulated AE counts and the AE amplitudes. More recently, Ando et al., [6] used AET to examine the microscopic process of shearing fracture of old wood.

In conclusion, the potential of laboratory AET to examine the fracture process in wood has been clearly demonstrated in the literature review. Simple AE approaches were used, for example: recording the events by expressing them in the form of event rate or cumulative events; study of amplitude distributions; investigation of frequency characteristics of emission events. All these approaches were performed by considering AE events without determination of source locations. The purpose of this study is to investigate mode I fracture of wood using determination of the position of developing cracks with AE measurements. The AE source is determined from the time differential of AE signals among two piezoelectric transducers (linear location). The determination of source locations associated to the attenuation curve in the tested sample allows correction of the output signal amplitude of the AE transducer. In this study, AE measurements were associated to digital image acquisition during the tensile test.

2. Experimental Procedure

For the present study specimens were cut from softwood (Douglas) and conditioned, in climate-controlled room, to constant moisture content for about 10%. The temperature and relative humidity were regulated at 20 °C and 40% RH, respectively. The specimens had the following dimensions: W = 80 mm; L = 170 mm; T = 15 mm (Fig. 1). Next, a 50 mm notch was cut along the grain to create a mode I double cantilever configuration. The starter notch was introduced with a band saw (3mm) and the notch orientation was chosen such that crack propagation took place in longitudinal direction.

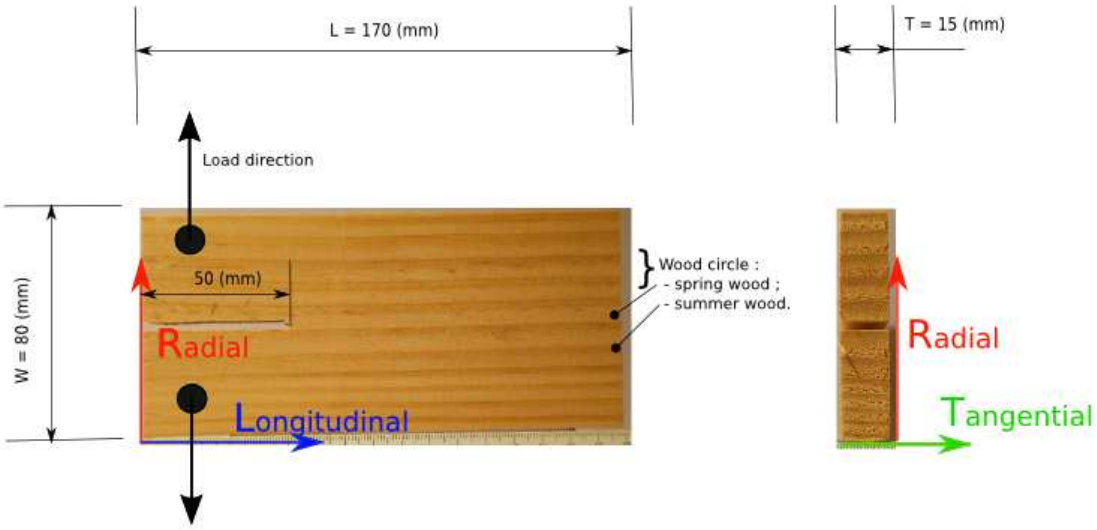

Figure 1. Photography of mode I fracture specimen.

The specimens were loaded under displacement control in an universal testing machine with a 50 kN load capacity. Load was applied to the specimen through the use of shafts that are pushed into holes drilled through the top and bottom cantilevers. A total of 4 specimens were tested at constant displacement-rate of 0.5 mm/min. Synchronized with the testing machine, an 8-bit Charge-Coupled Device camera measured the displacement fields. Thanks to this full-field optical method, the displacement evolution on the specimen surface could be recorded throughout the test. Also note that the image rate of the camera was set at 2 frames/s.

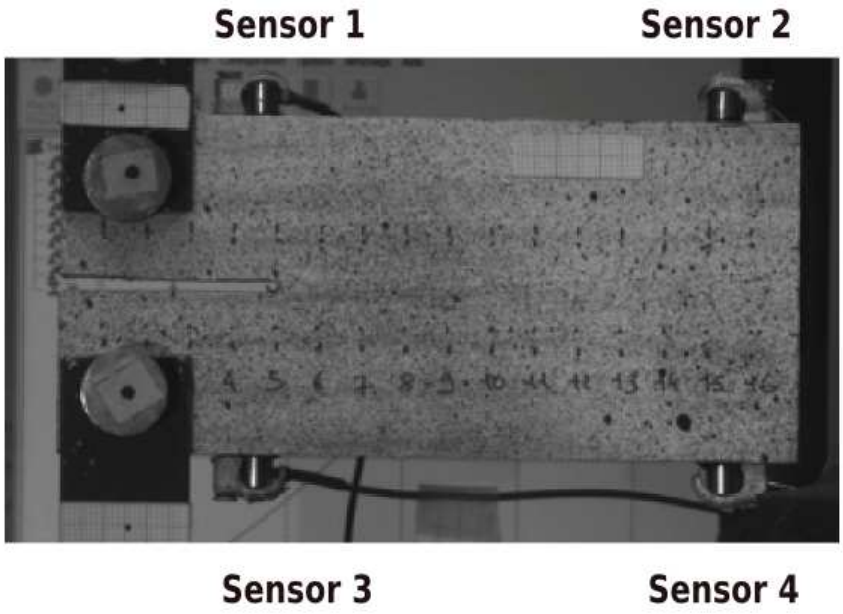

Figure 2. Photography of a specimen instrumented with AE sensors

During the test, AE event signals were monitored and recorded using a Euro Physical Acoustics (EPA) system:

- Four piezoelectric transducers (Nano30), with a band characteristic from 125 to 750 kHz, and 140 (and 300) kHz resonant frequency, were mounted on the specimen (Fig. 2). The transducers were coupled to the specimen with a silicon grease to avoid loss of acoustic signal at the transducer-sample interface;
- Pre-amplification of the AE signals was provided by four preamplifiers (IL40S model) with a gain set for 40 dB;
- AE signals were sampled at 20 MHz and filtered with amplitude threshold about 40 dB. It is clear that the detected events depend on the value of this threshold. Before the loading test, the effective propagation velocity of the longitudinal waves was determined by generating an elastic wave using the conventional pencil lead breaking.
- A signal conditioner and software that allow recording the AE features in a computer for further analysis.

3. Data Analysis and Discussion

3.1. Calibration of Acoustic Emission Measurements

For wood, the wave velocities are very dependent on propagation direction. Consequently, conventional AE source location techniques such as 2D planer location mode, which assume isotropic velocity, cannot easily be used for wood. Thus, AE source location, the most identifiable and beneficial factor of the AE technique for homogenous materials, is difficult to use on wood. In order to overcome these difficulties, we adopted in this study a liner location mode combined with a specific calibration procedure. The value of effective AE wave velocity (5350 m/s) was evaluated by the conventional pencil lead breaking.

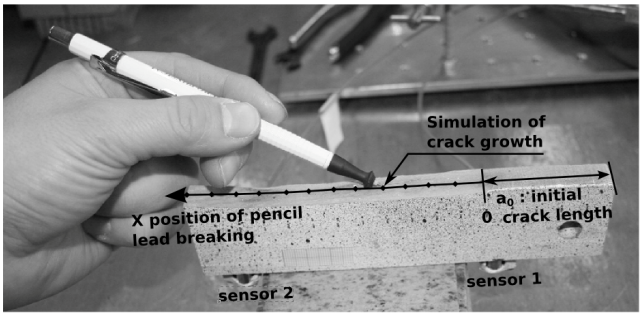

(a)

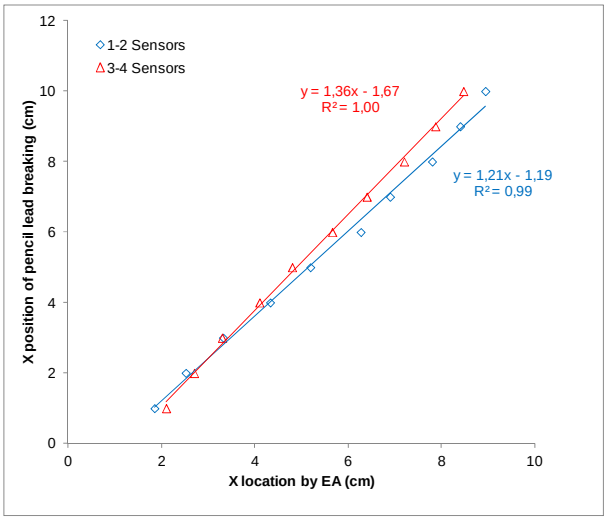

(b)

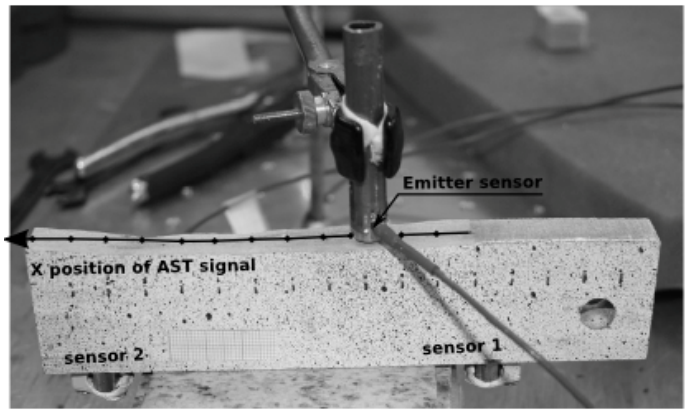

(c)

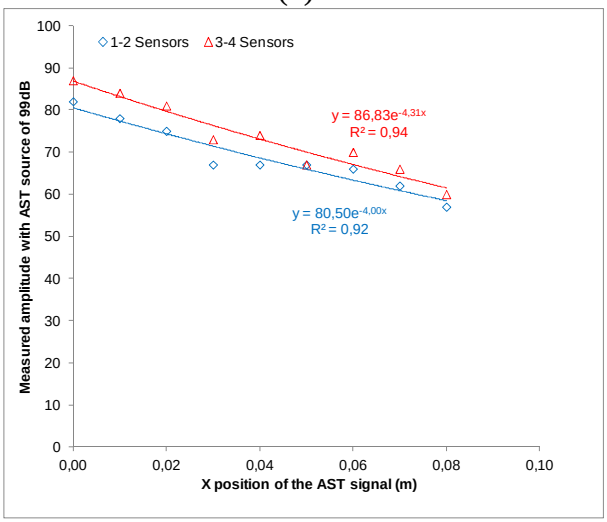

(d)

Figure 3. Calibration of Acoustic Emission Measurements. a) Photography of the pencil lead break method. b) calibration curve of the acoustic emission location. c) Photography of the AST method for attenuation measurements. d) Attenuation profile of the AE response on the wood sample.

All specimens were tested, after the fracture loading, using pencil lead break to simulate the burst signal propagation. The device (pencil lead break) is an aid to simulate an acoustic emission event using the fracture of a brittle graphite lead in a suitable fitting. This generates an intense acoustic signal, quit similar to a natural AE source, which the sensors detect as a strong burst. Figure 3 presents the principle of the pencil lead break method preformed on the fractured sample (Fig. 3.a) and the calibration curve of the acoustic emission location (Fig. 3.b).

The amount of AE wave attenuation depends on the proprieties on the material. For the tested samples, attenuation curve (Fig. 3.d) is performed by using the AST procedure (Auto Sensor Test, Fig. 3.c). AST provides an automated means of pulsing and receiving of simulated AE burst that is coupled to the structure. Similar results of attenuation curve can be also obtained by using the pencil lead break method. The attenuation curve plotted in figure 3.b is the consequence of several phenomena taking place as AE waves propagate along the sample: dispersion, scattering and eventually dissipation. The results presented in these figures highlight the importance of the AE calibration procedure in the analysis of AE data.

3.2. Analysis of Energy Balance

The energy approach states that crack extension occurs when the energy available for crack growth is sufficient to overcome the resistance of the material. The material resistance may include the surface energy, plastic work, or other type of energy dissipation associated with a crack propagation. Figure 4.a illustrates the load-displacement behavior of tested wood specimens with a growing crack. Consider point A on the presented curve. The crack has grown with Δa length from initial length a_0. The crosshatched area represents energy that would be stored in the material where considering linear elastic behavior; the remainder is the energy dissipation associated with a propagation crack.

Examination of the plot of figures 4.c&d illustrates a number of things. First, crack growth initiation detected by image analysis occurs closely after the end of the linear elastic behavior. The progression of the crack front propagation according to the displacement loading is quasi-linear showing stable crack growth in the tested specimens. A second point to observe is the over shape similarity when we compare the fracture energy curve and the crack front propagation curve. Thus we can assume validity of the initial hypothesis, linear release of stored elastic energy, used in the energy balance analysis.

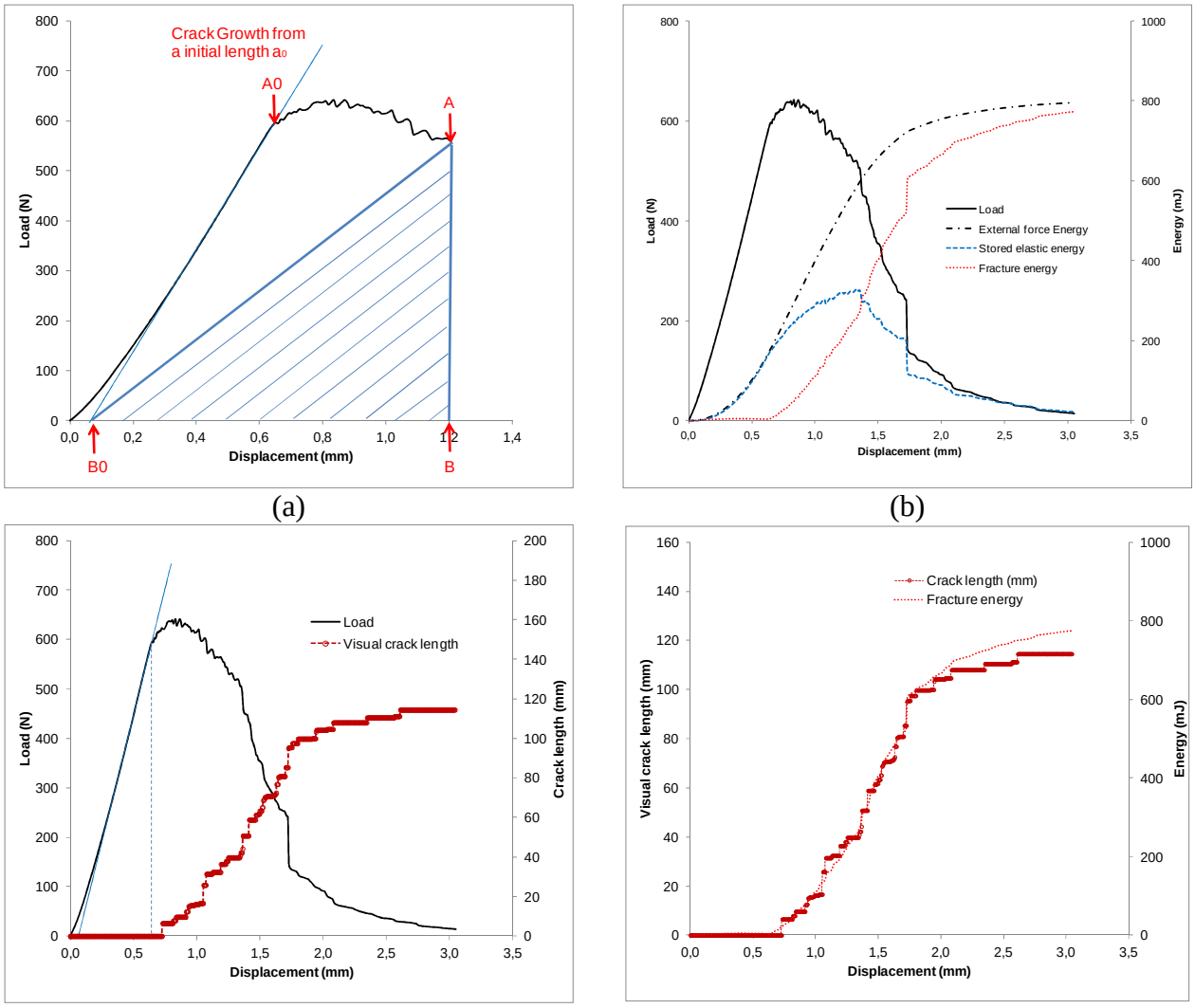

Figure 4. a) load-displacement curve for a specimen with a crack that grows with Δa length from initial length a_0: A_0ABB_0 (External force energy); ABB_0 (Stored Elastic Energy) and B_0A_0A (Fracture energy). b) Energy balance according to the displacement loading. c) Plot of load-displacement curve and crack front propagation measured by image analysis. d) Plot of fracture energy curve and crack front propagation.

3.3. Acoustic Emission Analysis

The recorded AE data are presented with respect to both AE-event (located material change giving rise to acoustic emission) and AE-hit (detected and measured signal for each cannel). To perform comparison with the mechanical results (energy balance) we consider one of the most important characteristic parameter of the AE in the amplitude-time domain, namely AE energy. With conventional AE energy analysis, the AE waveforms are squared and integrated over time. Although that analysis produces an energy measure, the resulting units do not lend themselves to direct comparisons with other energy analyses.

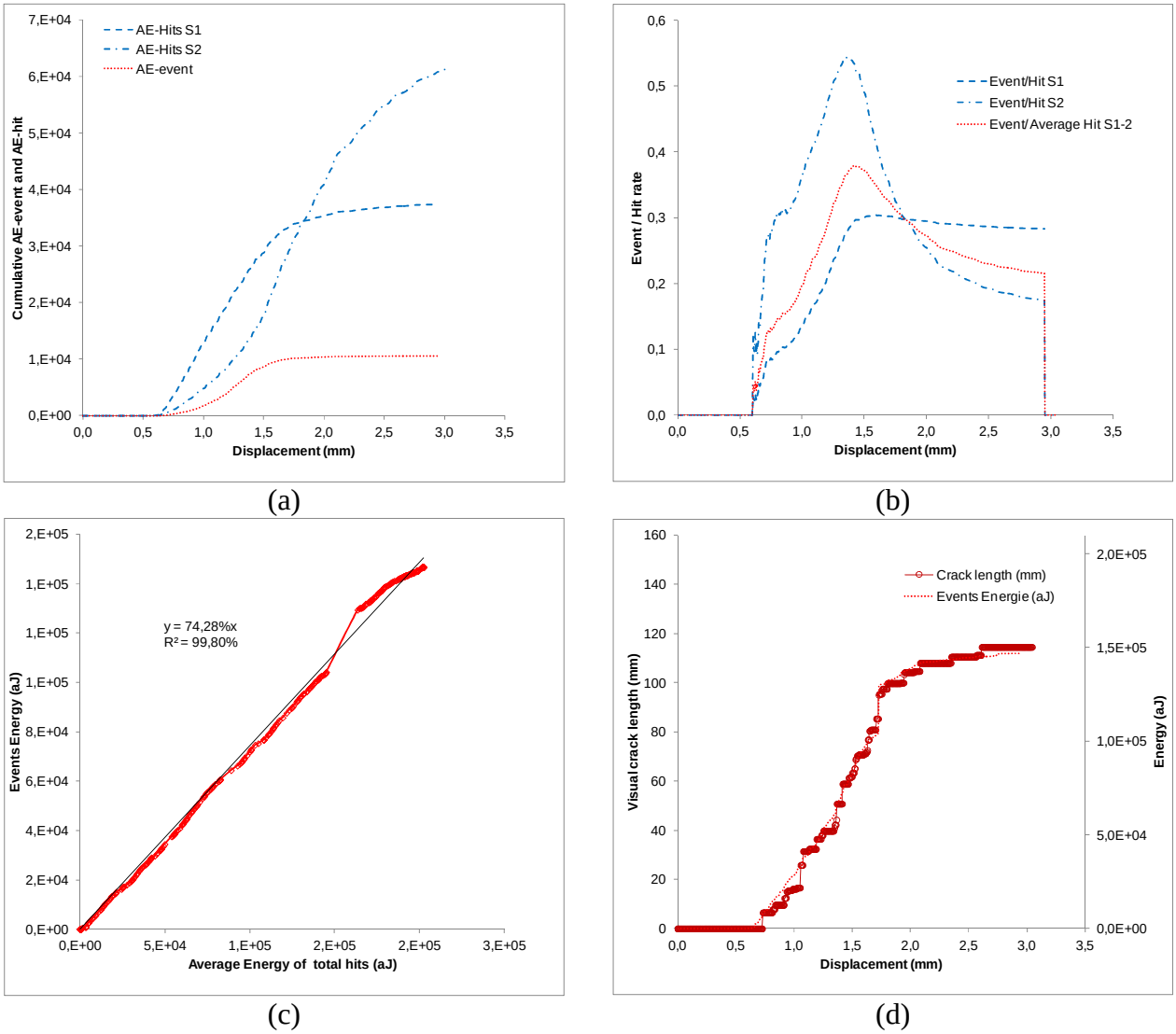

Figure 5. AE data. a) Cumulative AE-event and AE-hit for 1-2 sensor's group location. b) ratio between cumulative AE-event and cumulative AE-hit. d) Comparison of AE-event energy and AE-hit energy. d) Plot of AE-event energy curve and crack front propagation.

Plotted in figure 5 is, for each AE sensor, the cumulative AE-event along with the cumulative AE-hit. Similar results was observed between 1-2 sensor's group location and 3-4 sensor's group location, and only data from the first group are plotted. For linear location mode of AE source, calculation of x-position of each event is based on the measurement of the differences in first wave arrival times between two recorded AE-waveforms (Hits). The first wave arrival time is detected as the first threshold crossing by AE signal. Another parameter necessary for time difference location method is effective velocity. It can be established experimentally with or without considering different wave propagation modes (longitudinal, shear and Rayleigh waves). In this study, the value of effective AE wave velocity was evaluated by the conventional pencil lead breaking, and the obtained value is 5350m/s. The propagation modes were not separated inducing AE-hits which cannot be located. Indeed, figures 5.a&b show that approximately 30% of the average recorded hits from the 1-2 sensor's group location are located. However, figure 5.c shows a good correlation between AE-event energy and AE-hit energy. It should be noted that AE-hit energy is not corrected according to the attenuation curve. Some part of the no-located events can be caused by external noise such that caused by the loading system. Finally, if we compare figures 4.d and 5.d it can be shown that greater correlation between the energy release and the crack front propagation is obtained

from the AE measurements.

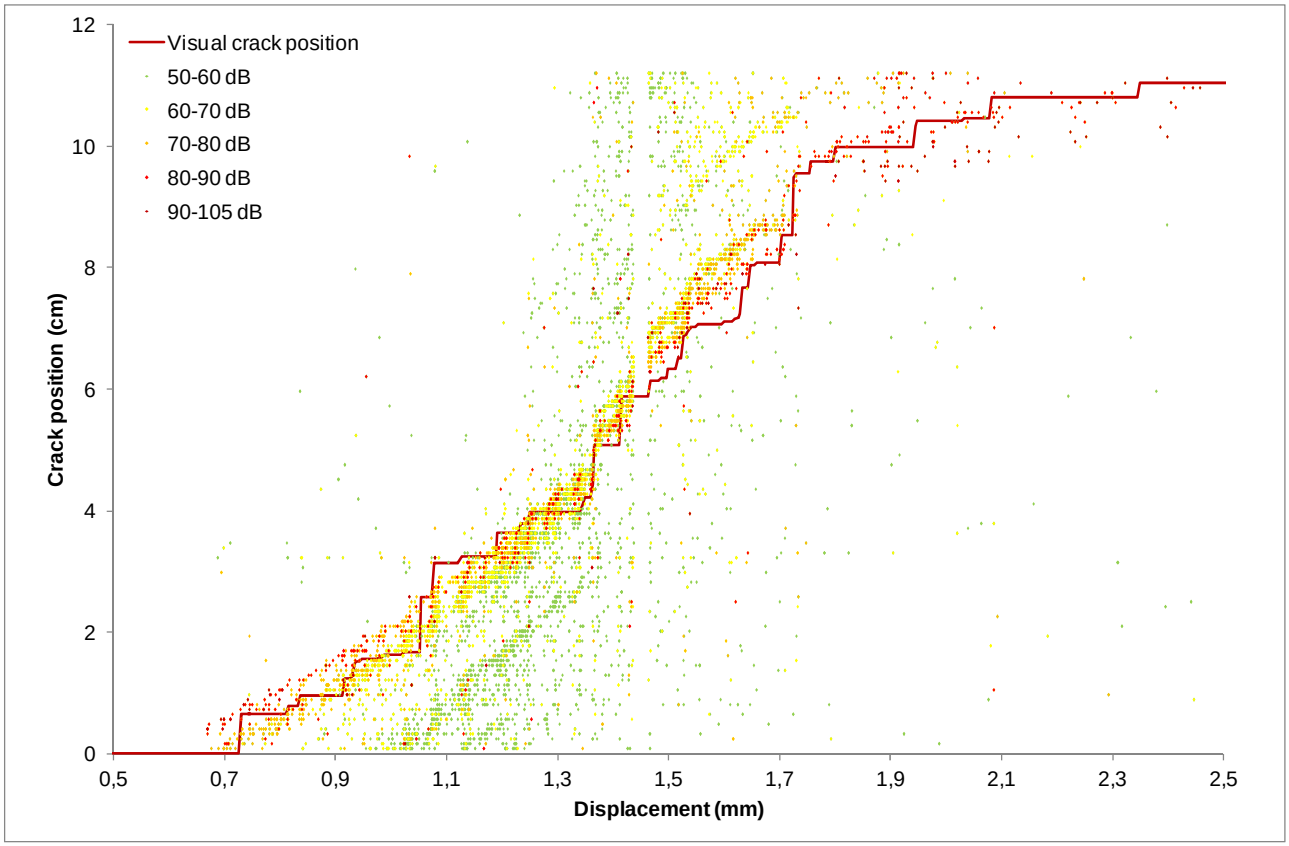

Figure 6. AE-events location and visual crack position vs. displacement loading.

In figure 6 is presented the crack front propagation curve obtained from the AE location process. The dynamic of the crack propagation is in good agreement with the results obtained with the image analysis. In addition, it was observed that the crack front appears to be associated with a Fracture Process Zone. Future works, based on AE waveform analysis using moment tensor components, will allow the crack classification and understand the mechanisms of this localized area.

4. Conclusion

In this study, we observed that the AE technique is an efficient tool for characterizing the failure process in wood materials. First, the experiment showed that crack initiation and crack growth detected by the AE activities is in a good agreement with the image analysis results. A second point to observe is that progress in AE-energy, during the test, is very similar to changes in fracture energy calculated from the load-displacement curve. These results were obtained for the both approaches used in the analysis of acoustic data: global approach with considering AE-hit signals and localization approach by using AE-event signals. For future works, this experimental investigation shows that the use of the localization approach seems to be a very promising method to investigate the cracks mechanisms such as the process zone.

References

[1] S. Kawamoto, R. Sam Williams, Acoustic Emission and Acousto-Ultasonic Techniques for Wood and Wood-Based Composites, A review. Gen. Tech. Rep. FPL-GTR-134. Madison, WI: U.S. Department of Agriculture, Forest Service, Forest Products Laboratory., 2002

[2] Ansell, M.P. 1982. Acoustic emission from softwoods in tension. Wood Science and Technology. 16: 35–58.

[3] M. Suzuki, A.P. Schniewind, Relationship between fracture toughness and acoustic emission during cleavage failure in adhesive joints, Springer, Wood science and technology, 1987

[4] Eric N. Landis, Douglas B. Whittaker, Acoustic Emissions and the Fracture Energy of Wood, in Condition Monitoring of Materials and Structures, Farhad Ansari, ed. ASCE, 2000 pp 21-29

[5] A. Reiterer, S. E. Stanzl-Tschegg, E. K. Tschegg, Mode I fracture and acoustic emission of softwood and hardwood, in Wood Science and Technology 34 (2000) 417-430 © Springer-Verlag 2000

[6] K. Abdo, Y. Hirashima, M. Sugihara, S. Hirao, Y. Sasaki, Microscopic processes of shearing fracture of old wood, examined using the acoustic emission technique in The Japan Wood Research Society 2006

Analysis of Metallic Ductile Fracture by extended Gurson models

Wei Jiang[1,*], Yazhi Li[1], Yixiu Shu[1], Zhenxing Fan[1]

[1] Department of Aeronautics, Northwestern Polythchnical University, 710000, China
* Corresponding author: jiangwei0525@mail.nwpu.edu.cn

Abstract Ductile fracture of metallic materials is usually the result of void nucleation, growth and coalescence. The original Gurson-Tvergaard (GT) model deals with the homogenous deformation related to void nucleation and growth. However, it takes no consideration on the localized deformation due to the void coalescence. In this paper extended GT damage models incorporating two different void coalescence criteria are developed, respectively. One of the void coalescence criteria is based on the plastic limit load model by Thomason; the other decides the onset of void coalescence by a critical equivalent plastic strain as a power law of stress triaxiality (defined by the ratio of the hydrostatic stress over the equivalent stress). Hence, void coalescence is controlled by physical mechanisms, rather than by a critical void volume fraction which cannot be taken as a constant. The extended constitutive models are implemented into an implicit finite element code via a user defined material subroutine (UMAT) in ABAQUS. Detail analyses are performed for a series of notched round tensile bars. The predictions of the fracture behavior based on the proposed approach, from void nucleation to final material failure, are compared with experiment data. Both results agree pretty well. In the end, the effects of stress triaxiality are discussed.

Keywords ductile failure, mechanism-based approach, Gurson model, void coalescence

1. Introduction

Mechanism-based fracture mechanics attempts to link micro-structural variables and continuum properties of material to macroscopic fracture behavior. The macroscopic ductile fracture process due to the presence of voids can be separated into two phases, the homogenous deformation with void nucleation and growth, and the localized deformation due to void coalescence (Zhang et al., 2000) [1].The famous porous material model for analyzing the ductile failure, in which the material yielding is coupled with damage (void volume fraction, f) and hydrostatic stress, was proposed by Gurson (1977) [2]. Tvergaard (1981, 1982) [3], [4] modified Gurson model by introducing two adjustment factors to account for void interaction effects and material strain hardening. Needleman and Tvergaard (1984) [5] extended Gurson model to simulate the rapid loss of load carrying capacity during void coalescence. Chu and Needleman (1980) [6] supplemented it by various kinds of void nucleation criteria.

In the early research, the criterion for the onset of void coalescence states that void coalescence starts at a critical void volume fraction f_c which has tend to be regarded as a material constant. However, further studies show that f_c depends strongly on parameters such as initial void volume fraction, void shape, void spacing, stress triaxiality, as well as strain hardening, etc.(Zhang et al., 2000; Pardoen and Hutchinson, 2000) [1], [7]. Thomason (1985, 1998) [8], [9] proposed a plastic limit load model for void coalescence. In this model, the start of void coalescence is controlled by the mechanism of the plastic localization in the void ligament, which is able to unify the material and stress states dependencies. Bao (2005) [10] conducted a series of experiments and finite element analyses on an aluminum alloy 2024-T351 and obtained a coalescence criterion in terms of the critical equivalent strain E_c as a function of the stress triaxiality ratio T. When the macroscopic equivalent strain reaches the critical value E_c, void coalescence occurs and the material quickly loses its load carrying capacity. However, Gao and Kim (2006) [11] argued that the extra parameter lode angle θ should be introduced and the critical equivalent strain should have the

form $E_c(T,\theta)$.

In this paper, two different void coalescence criteria are combined with the original GT model to simulate the whole process of voids nucleation, growth and coalescence. Axisymmetric round tensile bars with different notch root radii are simulated using the extended damage models to investigate the variation of critical damage at coalescence as a function of stress triaxiality.

2. Extended Damage Models

2.1. Modeling the void growth process

The growth of a void and the associated macroscopic softening is adequately captured by GT constitutive relationship. The most widely used form, which applies to strain hardening materials under the assumption of isotropic hardening, has the shape

$$\Phi=\left(\frac{q}{\bar{\sigma}}\right)^2+2q_1 f\cosh\left(-\frac{3q_2}{2}\frac{p}{\bar{\sigma}}\right)-1-q_3 f^2=0, \tag{1}$$

where p represents the macroscopic hydrostatic pressure

$$p=-\frac{1}{3}\sigma:I, \tag{2}$$

q denotes the macroscopic Mises equivalent stress

$$q=\sqrt{\frac{3}{2}s:s}, \tag{3}$$

σ is stress tensor; s is stress deviator; I is the second order identity tensor; $\bar{\sigma}\left(\bar{\varepsilon}_m^p\right)$ is the current flow stress of the fully dense matrix material as a function of $\bar{\varepsilon}_m^p$, the equivalent plastic strain in the matrix; and f is the current void volume fraction in the material. Tvergaard (1980, 1981) [3] introduced the constants q_1, q_2 and $q_3=q_1^2$ to account for void interaction effects due to multiple-void arrays and to give a better agreement with experimental data.

The hardening of the matrix material is described through $\bar{\sigma}=\bar{\sigma}\left(\bar{\varepsilon}_m^p\right)$. The evolution of $\bar{\varepsilon}_m^p$ is assumed to be governed by the equivalent plastic work expression:

$$(1-f)\bar{\sigma}d\bar{\varepsilon}_m^p=\sigma:d\varepsilon^p, \tag{4}$$

where $d\varepsilon^p$ is the macroscopic plastic strain rate tensor; $d\bar{\varepsilon}_m^p$ is equivalent plastic strain rate of the matrix material.

The change in volume fraction of the voids is due partly to the growth of existing voids and partly to the nucleation of voids. It can be expressed as [12]:

$$df=df_{growth}+df_{nucleation}, \tag{5}$$

with

$$df_{growth}=(1-f)d\varepsilon^p:I, \tag{6}$$

Nucleation of voids can occur as a result of micro-cracking and/or decohesion of the particle-matrix interface. It can be assumed to be strain controlled, so that the rate of increase of void volume fraction due to nucleation of new voids is given by

$$df_{nucleation}=Ad\bar{\varepsilon}_m^p, \tag{7}$$

The void nucleation intensity, A is a function of $\bar{\varepsilon}_m^p$ the equivalent plastic strain in the matrix material, and is assumed to follow a normal distribution as suggested by Chu and Needleman (1980) [6]:

$$A = \frac{f_N}{s_N\sqrt{2\pi}} \exp\left[-\frac{1}{2}\left(\frac{\bar{\varepsilon}_m^p - \varepsilon_N}{s_N}\right)^2\right], \tag{8}$$

where f_N is determined so that the total void volume nucleated is consistent with the volume fraction of particles; ε_N is the mean equivalent plastic strain for void nucleation; and s_N is the standard deviation of the distribution.

2.2. Void coalescence criterion

2.2.1 Plastic limit load criterion

Thomason (1985, 1998) [8] found that the localized deformation mode by intervoid matrix necking can be characterized by a plastic limit load which is not fixed but is strongly dependent on the void geometry and stress states. The condition for void coalescence can be written as:

$$\sigma_1 = \sigma_1^L, \tag{9}$$

where σ_1^L represents the capacity of the material to resist void coalescence; and σ_1 is the maximum principal stress at current yield surface of a material point.

Using a 3D unit cell containing an axisymmetric ellipsoidal void, Thomason acquired the plastic limit load to void coalescence with the following form

$$\frac{\sigma_1^L}{\bar{\sigma}} = \left(\alpha\left(\frac{R_z}{X - R_x}\right)^{-2} + \beta\left(\frac{R_x}{X}\right)^{-1/2}\right)\left(1 - \frac{\pi R_x^{\,2}}{X^2}\right), \tag{10}$$

where R_x, R_z and X are the current radii of the ellipsoidal void in the x- and z- axes and the current length of the cell in the x-axis, respectively; the local coordinates system is constructed so that x-, y- and z- axes represent the minor, medium and maximum principal stress directions. α and β are constants which are suggested as 0.1 and 1.2 by Thomason. Pardeon and Hutchinson (2000) [7] conducted a large number of cells calculations and found the dependence of α and β on hardening exponent n. Their simulation results showed that β is almost a constant and can be taken as 1.24 while

$$\alpha(n) = 0.1 + 0.217n + 4.83n^2 \quad (0 \le n \le 0.3), \tag{11}$$

If the void is assumed to be always spherical, the void/matrix geometry in Eq. 10 can be directly determined from the current void volume fraction f and current principal strain $\varepsilon_1, \varepsilon_2, \varepsilon_3$ by following equations (Zhang, 2001)[13]:

$$R_x = R_y = R_z = \sqrt[3]{\frac{3}{4}\frac{f}{\pi}e^{\varepsilon_1+\varepsilon_2+\varepsilon_3}}, \tag{12}$$

$$X = Y = \sqrt{e^{\varepsilon_1+\varepsilon_2}}/2, \tag{13}$$

2.2.2 Equivalent plastic strain criterion

By assuming the existence of a periodic distribution of voids, the material can be considered as an array of cubic blocks with each block being a unit cell having a void at its center. Failure of the unit cell occurs when localization of plastic flow takes place in the ligament (Koplik and Needleman,

1988) [14]. In macroscopic, a critical value of equivalent plastic strain is always used as a measurement of material ductility. Therefore, critical equivalent plastic strain can be used to denote material failure by void coalescence. To implement this concept, a possible approach is to establish a failure criterion based on equivalent plastic strain at the location where failure is most likely to initiate.

In practical, for axisymmetric round tensile bars, failure always initiates in the center of the minimum section in specimens, where corresponds to the site with the highest stress triaxiality. In addition, stress triaxiality is often used as the sole parameter to characterize the effect of the triaxial stress states on ductile fracture. So the critical equivalent plastic strain can be established as a function of the stress trixiality ratio T .

The power law form of the equivalent plastic strain criterion for API X65 steel proposed by Oh et al. (2007) [15] can be written as:

$$E_{ef} = 3.29e^{-1.54T} + 0.10, \tag{14}$$

with

$$T = -\frac{p}{q}, \tag{15}$$

where E_{ef} represents the critical equivalent plastic strain. This criterion is also used to develop extended damage model in this paper.

2.3. Post coalescence response

The f^* function, introduced by Tvergaard and Needleman (1984) [5], is adopted, to account for the effects of rapid void coalescence at failure. After void volume fraction reaches critical value determined by voids coalescence criteria, f is replaced by f^* in the extended damage models.

$$f^* = \begin{cases} f & for \quad f < f_c \\ f_c + \dfrac{f_u^* - f_c}{f_F - f_c}(f - f_c) & for \quad f \geq f_c \end{cases}, \tag{16}$$

where f_c is the critical void volume fraction at which voids begin coalesce; $f_u^* = 1/q_1$ is the f^* value at zero stress; and f_F denotes the void volume fraction at final complete failure.

3. Finite element applications

API X65 steel which is main pipe material largely utilized in gas transportation networks is discussed in this paper. To investigate the effect of triaxial stress states on tensile ductility of the material, three tensile round bar specimens with different notch root radii are analyzed, see Fig. 1. These specimens are also analyzed by Oh et al. (2007) [15] and the present simulation results are compared to their experimental data.

The extended damage models described in the previous section are implemented in ABAQUS via a user defined material subroutine (UMAT). Two critical numerical procedures are involved in the finite element implementations. The integration of the rate form constitutive equations is following the backward Euler method by Aravas (1987) [16]. In an implicit code, the linearization modulus is needed to construct the stiffness matrix (Jacobin) for Newton scheme which is used to solve the global equilibrium equations. The explicit consistent tangent modulus based on a return mapping

algorithm provided by Zhang (1995) [17] is adopted in this paper. The coalescence criterion 1, the plastic limit load criterion, and the coalescence criterion 2, the equivalent plastic strain criterion, are totally incorporated into the extended damage model, respectively.

As the specimens are axisymmetric, eight-node axisymmetric element with reduce integration (CAX8R) are used in the finite analyses. The finite element meshes of specimens are presented in Fig. 2. The element length of the minimum section where failure will first initiate in the specimen is 0.15mm.

API X65 steel is high strength and low alloy and the tensile properties of the present material are Yong's modulus, $E = 210.7\,\text{GPa}$; Poisson ratio, $\nu = 0.3$; initial yield strength, $\sigma_0 = 464.5\,\text{MPa}$. The uniaxial true stress-strain relationship of the present API X65 steel is approximated using the Ramberg-Osgood form fitted to the test data by Oh et.al (2007) [15].

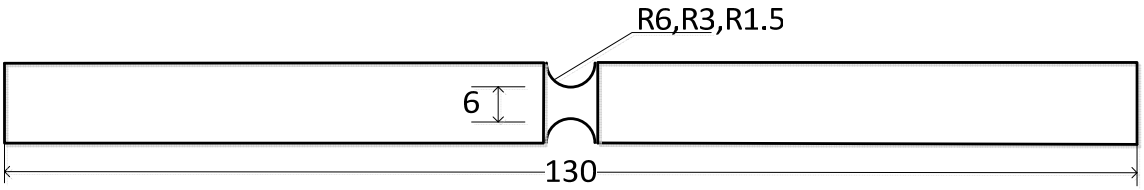

Figure 1. Geometries of notched tensile specimens

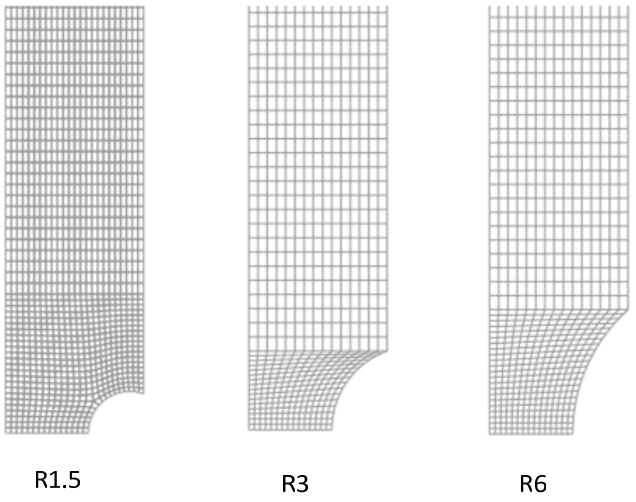

Figure 2. Axisymmetric finite element meshes for notched tensile bars

3.1. Determination of damage model parameters

In order to apply the present extended damage models to simulate ductile fracture, eight parameters should be first determined, including two adjustment factors for Gurson yield function (q_1, q_2); six parameters related to void volume fraction (f_0, f_c, f_F, ε_N, s_N and f_N).

The classic values ($q_1 = 1.5$ and $q_2 = 1.0$) given by Tvergaard (1982) [4] have been applied by many researchers as the constants for the GT model. Koplik and Needleman (1988) [18] carried out micromechanics studies about void growth and coalescence and found that the values of $q_1 = 1.25$ and $q_2 = 1.0$ provide best agreement between the GT model and the finite element results of voided cells calculations. Faleskog et al. (1998) [19] found that the q-values exhibit dependence

on both the hardening exponent (n) and the ratio of initial yield strength over Young's modulus (σ_0 / E). The studies of Kim et al. (2004) [20] have shown that, for a given material, the q-parameters should vary with stress triaxialities.

The nucleation parameters, ε_N and $s_N = 0.1$, determined by Chu and Needleman (1980) [6], are considered reasonable values for the current application. $f_N = 0.04$ is also suggested and is widely used by many researchers. However, the API x65 steel is a high-grade pipeline steel which is very clean steel and thus void nucleation is not significant and also delayed until very late in the deformation process. For this reason a much smaller value of f_N, 0.0008 is adopted in this study.

Some authors suggests that, as a first approximation, initial void volume fraction f_0 could be taken as the volume fraction of MnS inclusions, which is estimated from Franklin's formula [21]

$$f_v = 0.054\left(S\% - \frac{0.001}{Mn\%} \right), \tag{18}$$

where, $S\%$ and $Mn\%$ are the weight-% of sulfur and manganese, respectively. While voids coalescence is automatically determined by two type's criteria in the extended damage models, f_0 is the only unknown parameter and is to be fitted.

The void volume fraction at final fracture f_F is strongly dependent on f_0. Since f_F has been considered as an unimportant parameter, it can be extrapolated from the empirical equation by Zhang (2001) [13]:

$$f_F = 0.15 + 2 f_0, \tag{19}$$

In the present study, two sets of damage model parameters are involved. For these two groups, ε_N, s_N and f_N are to be take the same values as discussed previously; f_0 is determined by fitting to the experiment results for one notched tensile bar and then with this f_0, the void volume fraction at final fracture, f_F is obtained by Eq. 19. The critical coalescence porosity f_c is decided by the two coalescence criteria: plastic limit load criterion and equivalent plastic strain criterion. The q-values are also disparate for the two groups. The classic values ($q_1 = 1.5$ and $q_2 = 1.0$) are adopted in the first group. For the second, $q_1 = 1.704$ and $q_2 = 0.846$ are interpolated from the Faleskog's tabulated results based on the measured values of hardening exponent (n) and the ratio of initial yield strength over Young's modulus (σ_0 / E). Both sets of damage model parameters are illustrated in Table 1.

Table 1. Damage models parameters

	ε_N	s_N	f_N	f_0	f_c	f_F	q_1	q_2
Set1	0.3	0.1	0.0008	0.000125	Criteria1	0.15025	1.5	1.0
Set2	0.3	0.1	0.0008	0.0005	Criteria2	0.151	1.704	0.846

3.2. Comparison with experimental results

The finite element analyses are applied to predict mechanical behavior for the notched tensile bars that had notch root radii of 6mm, 3mm and 1.5 mm. These specimens have different levels of stress triaxiality. Porous metal material based on Gurson plasticity theory is also provided by ABAQUS in both implicit and explicit code; however, the failure definition is only available in

ABAQUS/Explicit. Therefore, it is essential to develop a complete damage model with the ability of simulating the whole process from void nucleation to the final damage. Finite element predictions both using the developed damage models and porous metal material provided by ABAQUS, and experimental results given by Oh et al. (2007) [15] are presented in Fig. 3. Since the axial displacement is monitored with the length of 25mm in experiments, the nominal strain and nominal stress of FEM results are derived from the mean nodal displacements and total nodal force at the section which is 12.5mm from the middle section, respectively.

It can be seen from Fig. 3 that the extended damage models with two different coalescence criteria can give almost identical predictions that are very close to the experimental results for all the specimens, irrespective of geometry. Simulations without the coalescence model can still predict the experimental curve very well before void coalescence. The FEM predictions without the coalescence response definition, however, cannot predict the sharp reduction in the slope of the nominal stress versus nominal strain curve after instability.

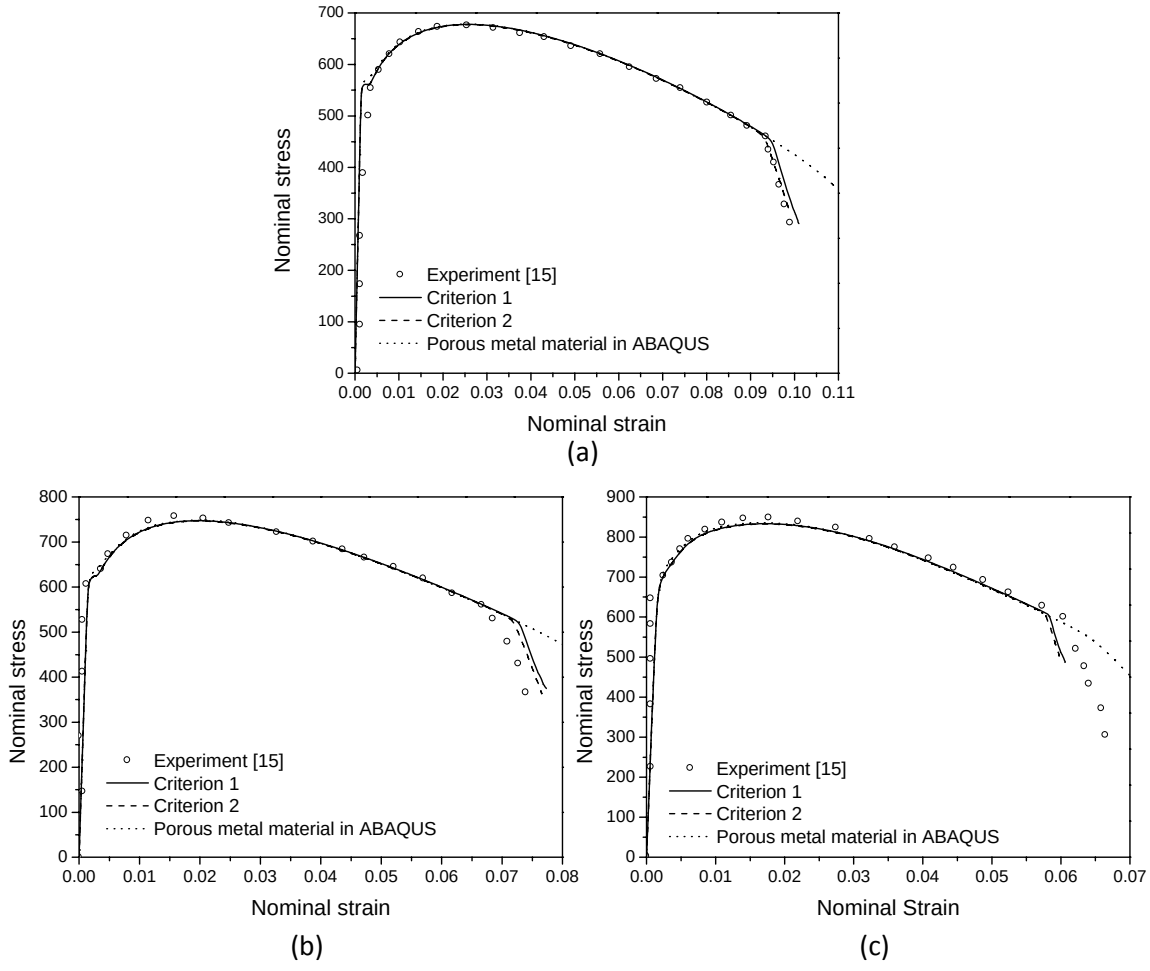

Figure 3. Comparison of FEM results with notched tensile tests: (a) R6; (b) R3; (c) R1.5

3.3. Crack formation in the notched bars

One of advantages of the developed model is that both the crack initiation site and propagation path can be simulated. Fig. 4 (a) shows the crack initiation location of the R6 notched tensile bar, the center site in the minimum section, which is in accordance with results observed from experiments.

Fig. 4 (b) illustrates the crack growth path, from the center to the free surface through the minimum section of the specimen. The void volume fraction at crack initiation is presented in Fig. 4 (c) and the highest void volume fraction site appears in the center of notched bars with no surprise.

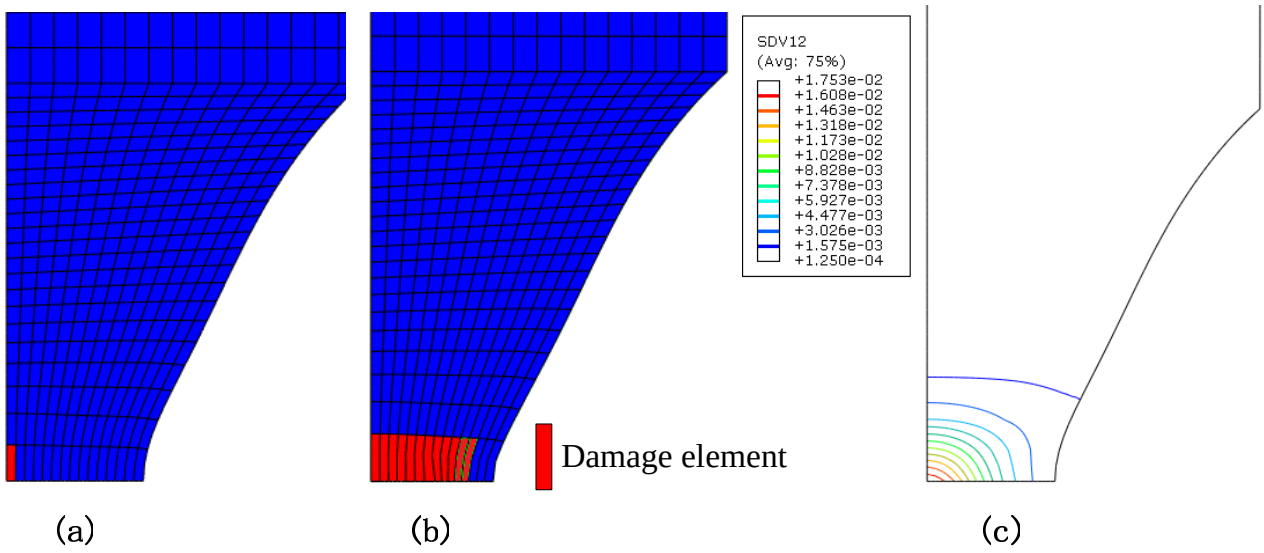

Figure 4. The FEM results of R6 notched tensile bar: (a) (b) Damage elements at and after crack initiation; (c) The void volume fraction at crack initiation

3.4. The effect of stress triaxiality

For each specimen, stress triaxiality is highest at the center and lowest at the free edge. Fig. 5(a) demonstrates the stress triaxiality value along the minimum section at the loading level corresponding to the onset of crack. Higher values of stress triaxiality together with increased plastic deformation in the center region of notched specimens accelerate crack initiation and growth according to the GT constitutive relationship. Thus, it is not surprising to find that crack initiates at the center of specimens.

For specimens with different notch root radii, various stress triaxialities are determined by geometry. Larger notch root radii results in smaller stress trixiality ratio. The curve of stress triaxiality ratio T versus equivalent plastic strain $\bar{\varepsilon}_{ef}$ at the center of specimen with load proceeding is presented in Fig. 5(b). Various stress triaxialities lead to void coalescence at different plastic deformation measured by equivalent plastic strain, illustrated in Fig. 6.

4. Concluding remarks

By incorporating two coalescence criteria, the extended damage models succeed in simulating the ductile failure in round tensile bars and also provide a practical approach to simulate the crack formation and propagation in small-scale tensile specimens. The present predictions show that:

(1) The extended damage models with two different coalescence criteria can give almost identical predictions that are very close to the experimental results for all the specimens.
(2) For each round tensile bar, crack initiates in the center of specimen where the highest stress triaxiatity and largest void volume fraction appear. In addition, crack propagation along the minimum section in specimens.
(3) Distinct geometries represent different stress triaxiatities and different stress triaxiatities lead

to void coalescence starting at diverse equivalent plastic strain.

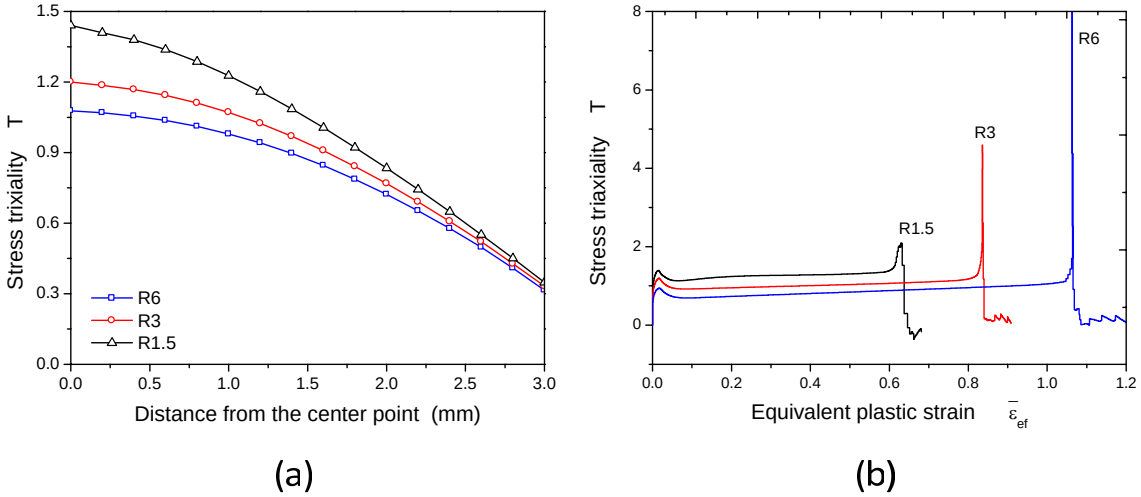

Figure 5. (a)Variation in stress triaxiality along minimum section at crack intiation; (b) Different stress triaxialities at the center of specimens

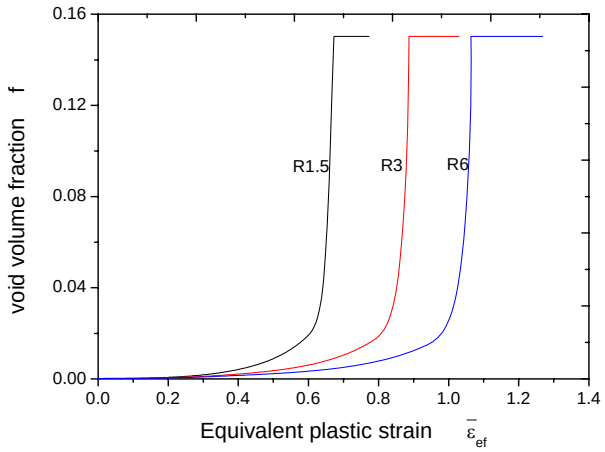

Figure 6. Void volume fraction versus equivalent plastic strain

References

[1] Z.L. Zhang, C. Thaulow, J. Odegard, A complete Gurson model approach for ductile fracture. Eng Fract Mech, 67(2000)155–168.

[2] A.L. Gurson, Continuum theory of ductile rupture by void nucleation and growth: part I yield criteria and flow rules for porous ductile media. J Eng Mater Technol, 99(1977)2–15.

[3] V. Tvergaard, Influence of voids on shear band instabilities under plane strain conditions. Int J Fract, 17(1981)389–407.

[4] V. Tvergaard, On localization in ductile materials containing spherical voids. Int J Fract, 18(1982)237–252.

[5] V. Tvergaard, A. Needleman, Analysis of the cup-cone fracture in a round tensile bar. Acta Metall, 32(1984)157–169.

[6] C.C. Chu, A. Needleman, Void nucleation effects in biaxial stretched sheets. J Eng Mater Technol, 102(1980) 249–256.
[7] T. Pardoen, J.W. Hutchinson, An extended model for void growth and coalescence. J Mech Phys Solid, 48(2000)2467–2512.
[8] P.F. Thomason, A three-dimensional model for ductile fracture by the growth and coalescence of micro-voids. Acta Metall, 33(1985)1087–1095.
[9] P.F. Thomason, A view on ductile-fracture modelling. Fatigue Fract Eng M, 21(1998)1105–1022.
[10] Y. Bao, Dependence of ductile crack formation in tensile tests on stress trixiality, stress and strain ratios. Eng Frcat Mech, 72(2005)505–522.
[11] X.S. Gao, J. Kim, Modeling of ductile fracture: Significance of void coalescence. Int J Solids Struct, 43(2006) 6277–6293.
[12] ABAQUS, Standard User's Manual, Version 6.11, 2012.
[13] Z.L. Zhang, A complete Gurson model, in: M.H. Alibadi, Nonlinear Fracture and Damage Mechanics, WIT Press, Southampton, UK, 2001, pp. 223–248.
[14] J. Koplik, A. Needleman, Void growth and coalescence in porous plastic solids. Int J Solids Struct, 24(1988)835–853.
[15] C.K. Oh, Y.J. Kim, J.H. Baek, W.S Kim, Development of stress-modified fracture strain for ductile failure of API X65 steel. Int J Fract, 143(2007)119–133.
[16] N. Aravas, On the numerical integration of a class of pressure-dependent plasticity models. Int J Numer Meth Eng, 24(1987)1395–1416.
[17] Z.L. Zhang, Explicit consistent tangent moduli with a return mapping algorithm for pressure-dependent elastoplasticity models. Comput Method Appl M, 121(1995)29–44.
[18] J. Koplik, A. Needleman, Void growth and coalescence in porous plastic solids. Int J Solids Struct, 24(1988)835–853.
[19] J. Faleskog, C.F. Shih, Micromechanics of coalescence I: Synergistic effects of elasticity, plastic yielding and multi-size-scale voids. J Mech Phys Solids, 45(1997)21–45.
[20] J. Kim, X.S. Gao, T.S. Srivatsan, Modeling of void growth in ductile solids: effects of stress triaxiality and initial porosity. Eng Fract Mech, 71(2004) 379–400.
[21] B.A. Bilby, I.C. Howard, Z.H. Li, Prediction of the first spinning cylinder test using ductile damage theory. Fatigue Fract Eng M, 16(1992) 1–20.

Strain Rate Effect on the Failure Behavior of Kevlar 49 Fabric and Single Yarn

Deju Zhu[1,*], Barzin Mobasher[2], Subramaniam D. Rajan[2]

[1] College of Civil Engineering, Hunan University, Changsha, 410082, China
[2] School of Sustainable Engineering & the Built Environment, Arizona State University, Tempe, 85287, USA
* Corresponding author: dzhu@hnu.edu.cn

Abstract: High strength woven fabrics are ideal materials for use in structural and aerospace systems where large deformations and high-energy absorption are required. Their high strength to weight ratio and ability to resist high-speed impacts enables them to be more efficient than metals in many applications, including ballistic armors, propulsion engine containment systems and fabric-reinforced composites. In order to facilitate the design and improvement of such applications, this study investigates the mechanical behavior of Kevlar 49 fabric and single yarn under quasi-static and dynamic tensile loadings. The experimental results show that the fabric exhibits non-linear in tension, and can deform up to 20% before complete failure under quasi-static loading. The fabric has identical Young's modulus in warp and fill directions, but has different crimp strain, tensile strength and ultimate strain. The sample size has little effect on the mechanical properties of the fabric. The dynamic tensile behaviors of the fabric and single yarn were investigated at strain rates from 25 to 170 s^{-1} by using a high rate servo-hydraulic testing machine. Results show that their dynamic material properties in terms of Young's modulus, tensile strength, maximum strain and toughness increase with increasing strain rate.

Keywords: Fabrics, Dynamic, Strain rate, Kevlar 49

1. Introduction

High strength woven fabrics are ideal materials for use in structural and aerospace systems where large deformations and high energy absorption are required. Their high strength to weight ratio and ability to resist high speed impacts enables them to be more efficient than metals. Materials loaded at high strain rates can exhibit mechanical characteristics that are different from those obtained under quasi-static loading. High strain rate applications are quite varied and include structural, military, aerospace, and sports disciplines. Aramid and other high strength fibers and fabrics have been studied extensively in a wide range of applications, creating a demand for numerical modeling of fibers, yarns, and fabrics. While quasi-static tensile strength data for the single fibers is available, results cannot be extrapolated and scaled up for yarns consisting of many fibers, woven, knitted, or bonded fabrics with a 2-D or 3-D microstructure. Furthermore, the strain rates observed in static experiments is not in the same order of magnitude as those observed in ballistic applications [1]. Five types of testing systems are commonly used in generating the rate dependent material data: the conventional screw drive load frame, servo-hydraulic system, high rate servo-hydraulic system, impact tester and Hopkinson bar system. However, the experimental techniques to generate stress-strain data at the medium strain rates in the range of 1~100 s^{-1} are not well established [2]. Two types of equipment have been used to generate data in this strain rate range: high rate servo-hydraulic testing machines [3-5] and drop-weight impact machines [6, 7].

The primary objective of our research is to investigate the effects of gage length and strain rate on the mechanical properties of Kevlar 49 fabric and single yarn, as a part of the project on explicit finite element modeling of multi-layer composite fabric for gas turbine engine containment systems [8-12]. In the next section we present the experimental procedure and results of fabric and single

yarn specimens under quasi-static and dynamic tensile loadings and the results of Weibull statistical analysis. Images captured during loading process are used to study the deformation and failure mechanisms of the fabric and yarn.

2. Experimental Program

2.1. Specimen preparation

The plain-woven Kevlar® 49, a high performance fabric for ballistic protection application, made by EI du Pont de Nemours & Co., is used in this study. The fabric is manufactured using a plain-weave of 17×17 yarns (per linear inch) each consisting of hundreds of filaments. The bulk density (mass per unit of volume) and linear density (mass per unit of length) are 1.44 g/cm^3 and 1.656 × 10^{-3} g/cm, respectively. The cross-sectional area of each yarn was calculated as 1.15 × 10^{-3} cm^2 by dividing the linear density of the material by its bulk density [13]. This value is then taken as the total c/s area of individual fibers within the yarn.

To make a strip specimen for quasi-static tests, the fabric was first cut into an oversized rectangular strip, and then a number of yarns along the fabric length were removed from both sides, thereby producing a sample without yarn crossovers along the edges. This step is necessary to ensure that the edge defects are minimized and that the loaded yarns will not slip out of the cross yarns during the test. The final sample dimension had a length of 250 mm with two alternate widths of 30 mm and 60 mm. In each set, yarns are removed from both sides of the strip such that the samples are left with 17 and 34 longitudinal yarns, respectively. The initial gage length was 200 mm. The total cross-sectional area of a specimen was defined as the cross-sectional area per yarn multiplied by the number of yarns within the width. In order to investigate the effect of gage length on the mechanical properties of the fabric, additional specimen sizes of 25 × 280 mm and 25 × 355 mm were also tested in warp direction under the same loading rate.

Smaller specimens were used for dynamic tensile tests. The fabric was cut to the width using an electric scissor allowing eight yarns in the section of gage length. Thin aluminum sheets were glued using high-strength epoxy to the ends of the test specimen to reduce the stress concentration and improve load transfer in grips so as to prevent any slippage, as shown in Fig. 1. The single yarn specimen was constructed to contain one yarn in the central position by removing the rest of the yarns as shown in Fig. 2. Two different gage lengths of 25 mm and 50 mm were tested for both fabric and single yarn specimens.

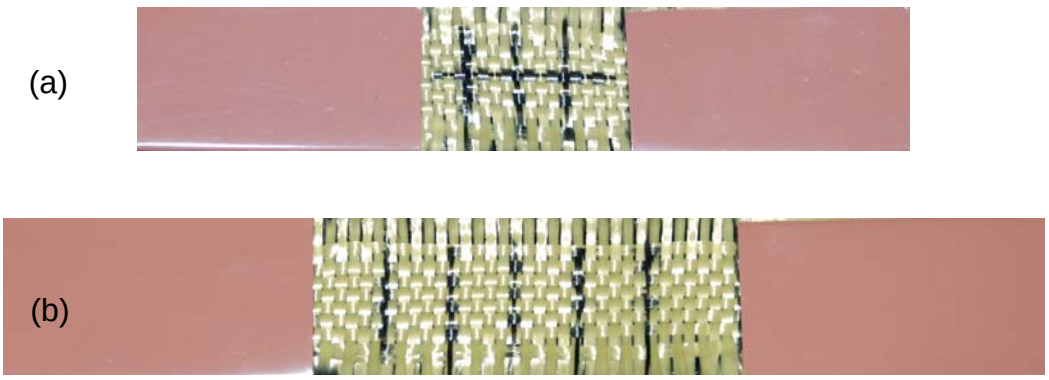

Figure 1. Fabric specimens with (a) 25mm and (b) 50mm gage length for dynamic tensile tests

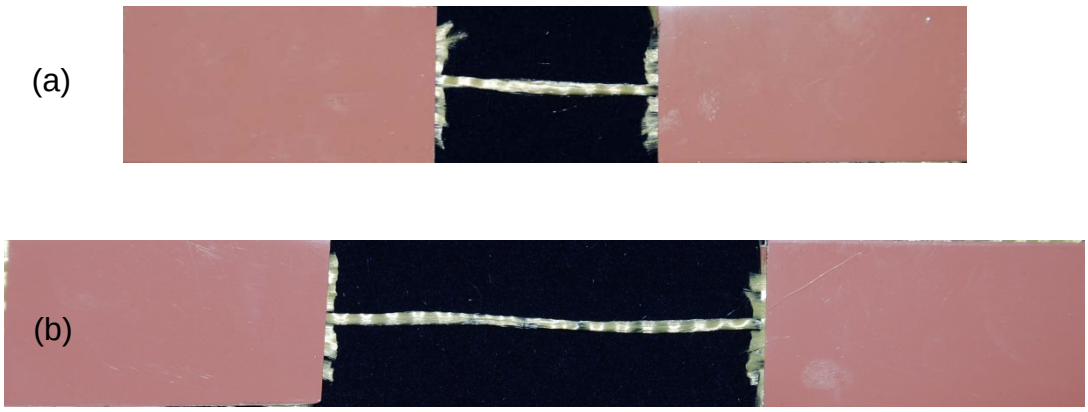

Figure 2. Single yarn specimens with (a) 25mm and (b) 50mm gage length for dynamic tensile tests

2.2. Quasi-static tensile testing

Quasi-static tensile tests of Kevlar fabric were performed on a 90 kN INSTRON machine operated under closed-loop displacement control with a displacement rate of 2.5 mm/min. Digital data acquisition was used to collect data at a sampling rate of 2 Hz. The test was continued until complete failure of the specimen. The overall specimen deformation was measured by stroke movement. The two plates were held together within the hydraulic grips to ensure uniform pressure application and prevent any fabric slippage (more details in Naik et al. [9]). Five replicates were tested for each specimen size in both warp and fill directions, and the deformation and failure behaviors of the specimens were recorded by a CCD monochrome camera.

In order to measure the mechanical properties of the yarn, single yarns were extracted from fabrics and only the warp yarns were tested. A low capacity load cell (275N) was used to record the force. A universal joint was connected to the testing frame to allow rotation of the grip and remove any potential bending moment. The universal joint also helped in the alignment of yarn during test. To avoid any slipping of test sample during testing, the yarn was wrapped around the upper and lower mandrels and aligned using a laser beam alignment level [14]. Ten replicate samples of six different gage lengths (50, 125, 200, 275, 350, 425 mm) were tested on an MTS test frame under displacement control at a strain rate of 4.2×10^{-4} s^{-1} (quasi-static).

2.3. Dynamic tensile testing

Dynamic tensile tests were conducted on an MTS high rate servo-hydraulic testing machine operated in open-loop control [3]. The speed of the stroke is controlled by the opening and closing of the servo-valve of hydraulic supply. By manually turning the servo-valve, the rate of flow of hydraulic fluid can be controlled, resulting in different stroke speeds. However there are some differences in the actual stroke speeds between individual tests although the opening of servo-valve is not changed, especially at higher stroke speeds. The actual stroke speeds of individual tests are determined by the slopes of real-time displacement-time curves obtained from the tests. A description of the high strain rate testing system, test setup and data processing procedure are

provided in the references [3, 13]. The fabric samples of two different gage lengths (25mm and 50 mm) were tested at strain rates ranging from 25 to 170 s^{-1}. The Young's modulus, tensile strength, maximum strain, and toughness were investigated at these strain rates. Single yarn samples were tested at strain rates of 30, 50 and 100 s^{-1} for the 25 mm gage length, and at strain rates of 20 and 60 s^{-1} for the 50 mm gage length. It should be noted that the strain rates listed above are the average values and the actual strain rate of an individual test may be slightly different.

3. Results and Discussion

3.1. Quasi-static response

The typical stress versus strain relationship and the fabric deformation under uniaxial tension are shown in Fig. 3. There are four distinct regions in the stress-strain behavior of both warp and fill directions: crimp region, linear pre-peak region, linear post-peak region and non-linear post-peak region. In the undeformed, but undulated state (strain ε=0), the warp and fill yarns are orthogonal to each other and free of any stretch. In the crimp region, the stress increase is relative low due to the straightening of the undulated yarns in loading direction with limited yarn stretching. The maximum strain in crimp region in warp and fill directions is only 0.0065 mm/mm and 0.0025 mm/mm, respectively. These strain values are negligible when compared with the strain at failure. As the strain increases, the yarns in the loading direction are extended, and when fully straightened (ε=0.01 to 0.02), the fabric exhibits a linear response with no visible failure signs. The Young's modulus (elastic stiffness) is defined by the slope of the stress-strain curve in this region. Both the crimp and pre-peak regions are fitted by linear curves to obtain corresponding stiffnesses [9]. As the stress level reaches the strength of the constituent yarns, the yarns in the loading direction start to fail, resulting in a dramatic decrease in the fabric load-carrying capacity until reaching a transition point at about 200 MPa (the end of linear post-peak region) where the yarns/fibers are broken. After that the stress decreases gradually to zero when the strain increases up to about 0.2 mm/mm, representing the nonlinear post-peak region where the failed yarns/fibers slip out of the fabric and the load is carried by the friction between sliding fibers (ε=0.02 to 0.04). The toughness of the fabric is defined by the area under the entire stress-strain curve.

Analysis of the stress versus strain curves in both warp and fill directions for both specimen sizes (50 mm × 200 mm and 25 mm × 200 mm), indicates that the pre-peak elastic stiffness (Young's modulus) of warp direction is almost identical to that of fill direction, and the stiffness in the crimp region for warp and fill directions is as much as 6% and 20% of the elastic stiffness (Young's modulus) in pre-peak region, respectively. The absolute value of the stiffness in linear post-peak region of warp and fill directions is 2.2 and 5.6 times of the elastic stiffness in pre-peak region. Comparing the stress-strain behavior between warp and fill directions, the major difference is the crimp strain, tensile strength (peak stress) and the ultimate strain (strain at peak stress) in both directions. The crimp strain in warp direction is about 2.6 times larger than that of fill direction. The tensile strength in warp direction is approximately 10~15% lower than that in fill direction, while the ultimate strain in warp direction is approximately 7~12% higher than that in fill direction. This

is due to the fact that the warp yarns have sustained more damage from weaving process and have higher initial crimps. The stress-strain curves of specimens tested are highly repeatable for both sizes and directions.

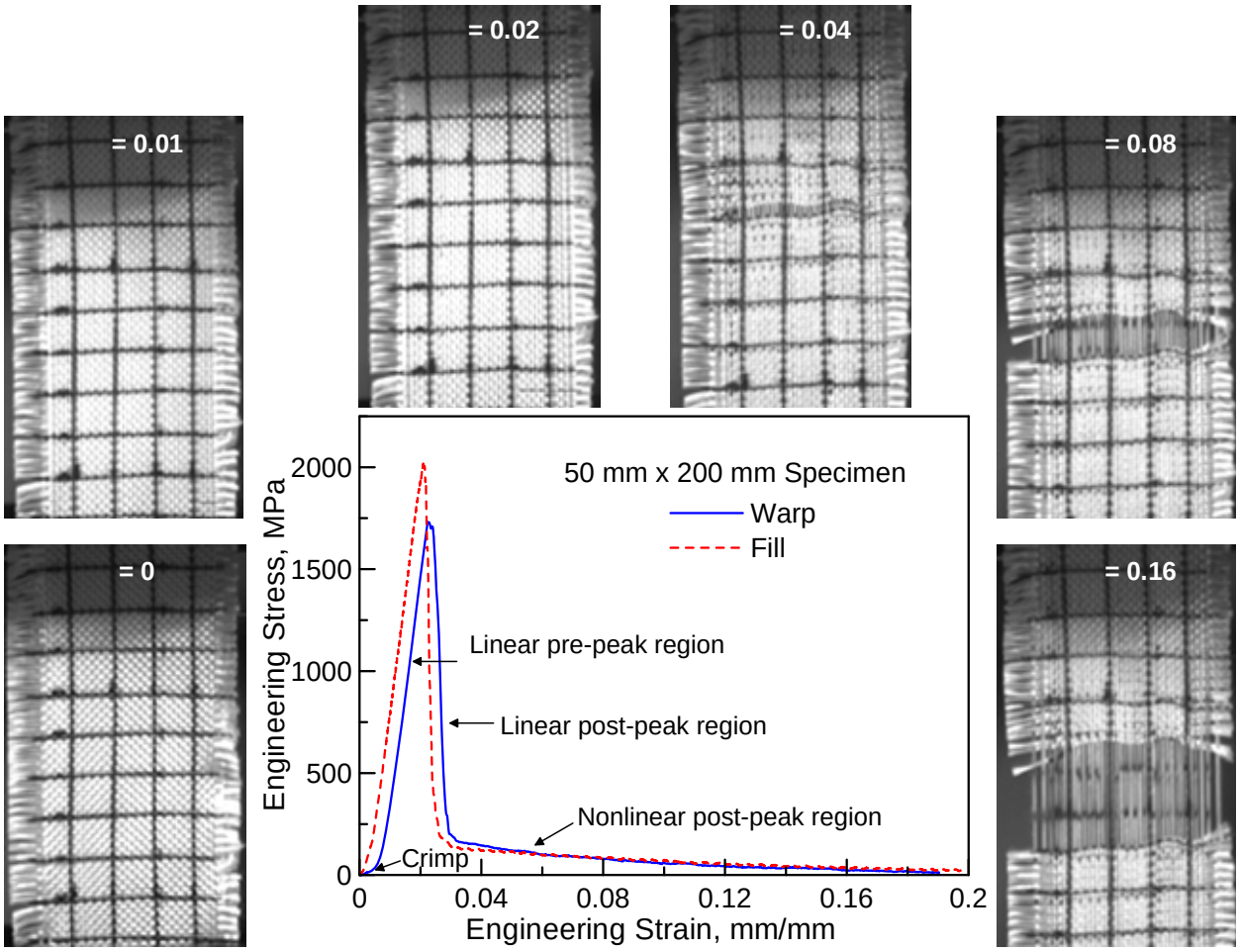

Figure 3. Typical stress-strain relationship and fabric deformation under quasi-static uniaxial tension

Table 1 Summary of Tensile Properties of Kevlar 49 Fabric

Specimen Size (mm × mm)	Material Direction	Tensile Strength (MPa)	Young's Modulus (GPa)	Toughness (MPa)	Ultimate Strain (mm/mm)
50×200	Warp	1748 ± 56	117.2 ± 3.3	32.4 ± 3.0	0.0223 ± 0.0012
	Fill	2013 ± 44	117.1 ± 3.0	33.9 ± 1.3	0.0201 ± 0.0010
25×200	Warp	1859 ± 109	117.9 ± 2.5	32.9 ± 1.4	0.0215 ± 0.0015
	Fill	2055 ± 72	119.7 ± 4.0	33.2 ± 1.2	0.0200 ± 0.0009
25×280	Warp*	1776 ± 100	126.5 ± 4.6	26.9 ± 1.7	0.0197 ± 0.0014
25×355	Warp*	1811 ± 61	132.1 ± 5.8	27.1 ± 1.8	0.0181 ± 0.0008

*These tests were stopped once the load acting on the specimen fell below 222N.

Tables 1 summarizes the tensile properties of both specimen sizes in both warp and fill directions. There is no apparent size effect in terms of Young's modulus, toughness and ultimate strain, but the average tensile strength of 50 mm wide specimens is slightly lower (2~6%) than those of 25 mm wide specimens in both directions. For longer specimens (25 × 280 mm and 25 × 355 mm), the tests were stopped once the load on the specimen fell below 222N (corresponding to approximately 10% maximum strain). Toughness in these samples is underestimated as much as 16~20% lower than those of 200 mm long specimens. However, the toughness remains almost same when the gage length increases from 280 mm to 355 mm, so does the tensile strength, Young's modulus, and ultimate strain, indicating that gage length effect on the fabric's mechanical properties is negligible.

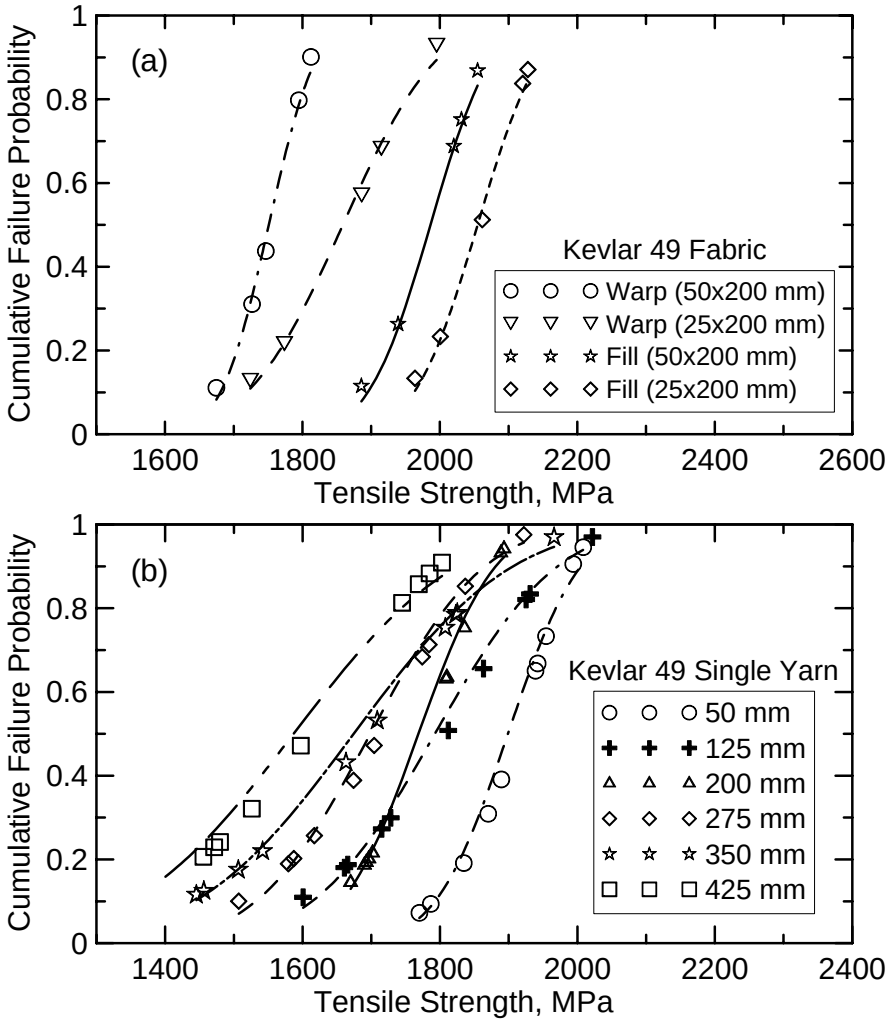

Figure 4. Comparison of cumulative failure probability versus tensile strength: (a) fabric and (b) single yarn under quasi-static loading

Weibull parameters were obtained using a 2-parameter Weibull equation:

$$P_f(\sigma) = 1 - \exp\left[-\left(\frac{\sigma}{\sigma_0}\right)^m\right] \tag{1}$$

where σ_0 is the characteristic yarn strength and m is the shape parameter, characterizing the spread

in the distribution of strengths. P_f was estimated using the following equation:

$$P_f = \frac{i}{N+1} \tag{2}$$

where N is the total number of tests and i is the current test number [15].

Figure 4a and b shows the Weibull curve fitting to experimental data of both fabric and single yarn samples, respectively. The fabric data clearly indicate that the fabric breaks at lower stress in warp direction than in fill direction, and wider samples (50 mm) have lower tensile strength. For the single yarn data, as the gage length increases, the cumulative probability plot shifts towards lower stress values, which is a clear indicator of dependence of tensile strength on the gage length. The Weibull parameters identified from both fabric and single yarn tests are presented in Table 2.

Table 2. Weibull Parameters of Kevlar 49 Fabric and Single Yarn under Quasi-Static Loading

	Fabric				Single Yarn					
Size (mm)	25 × 200		50 × 200		50	125	200	275	350	425
Material Direction	Warp	Fill	Warp	Fill	Warp					
σ_0 (MPa)	1857	2064	1759	2001	1933	1829	1795	1724	1726	1652
m	13.3	27.0	27.5	27.4	21.7	11.5	14.3	11.9	7.9	8.8

3.2. Dynamic response

Figure 5(a-d) shows the dependence of the dynamic material properties of Kevlar 49 fabric, defined in terms of Young's modulus, tensile strength, maximum strain and toughness on strain rates, respectively. There is an apparent dependence of the dynamic material properties on the strain rates discussed as follows: For 25 mm gage length specimen, the Young's modulus increases from 120 ± 14 GPa at initial strain rate of 30 s^{-1} to 131 ± 23 and 147 ± 10 GPa at strain rates of 100 s^{-1}, and 170 s^{-1} respectively. The tensile strength increases from 1489 ± 54 MPa at a strain rate of 30 s^{-1} to 1968 ± 109 and 2340 ± 134 MPa at strain rates of 100 s^{-1}, and 170 s^{-1} respectively. Maximum strain increases from 2.92 ± 0.17% to 3.27 ± 0.32% and then to 3.66 ± 0.27%, and toughness increases from 24.6 ± 2.6 MPa to 30.6 ± 1.5 MPa and to 41.4 ± 4.8 MPa when the strain rate increases from 30 to 100 and then to 170 s^{-1}. For 50 mm gage length specimen, the Young's modulus increases from 127 ± 16 GPa to 144 ± 12 GPa and then to 162 ± 11 GPa, the tensile strength increases from 1677 ± 136 MPa to 1954 ± 104 MPa and then to 2108 ± 83 MPa, the maximum strain increases from 2.58 ± 0.34% to 2.82 ± 0.18% and then to 2.83 ± 0.28%, and toughness increases from 21.6 ± 3.8 MPa to 22.2 ± 3.3 MPa and then to 25.8 ± 1.8 MPa when the strain rate increases from 25 to 60 and then to 100 s^{-1}.

Figure 6(a-d) shows the dependence of the dynamic material properties of Kevlar 49 single yarn on the strain rate. There is an apparent dependence of the dynamic material properties on the strain rate; however there is no clear dependence between the properties and gage lengths investigated. For the

25 mm gage length specimen, the Young's modulus increases from 109 ± 11 GPa at a strain rate of 30 s^{-1} to 111 ± 10 and 128 ± 11 GPa at strain rates of 50 s^{-1}, and 100 s^{-1} respectively. The tensile strength increases from 1622 ± 104 MPa at a strain rate of 30 s^{-1} to 1675 ± 51 and 1707 ± 82 MPa at strain rates of 50 s^{-1}, and 100 s^{-1}, respectively. Maximum strain increases from 0.0245 ± 0.003 mm/mm to 0.0253 ± 0.0017 mm/mm and then to 0.0282 ± 0.0022 mm/mm, and toughness increases from 20.1 ± 2.6 to 20.5 ± 1.4 MPa and to 26.0 ± 4.3 MPa when the strain rate increases from 30 to 50 and then to 100 s^{-1}. For the 50 mm gage length specimen, the Young's modulus increases marginally from 118 ± 28 to 121 ± 22 GPa when the strain rate increases from 20 to 60 s^{-1}. While the tensile strength increases by as much as 23.5% from 1579 ± 100 to 1874 ± 110 MPa, the maximum strain increases about 15% from 0.0217 ± 0.003 mm/mm to 0.025 ± 0.0026 mm/mm, and toughness increases about 29 % from 18.8 ± 2.5 MPa to 24.3 ± 4.0 MPa.

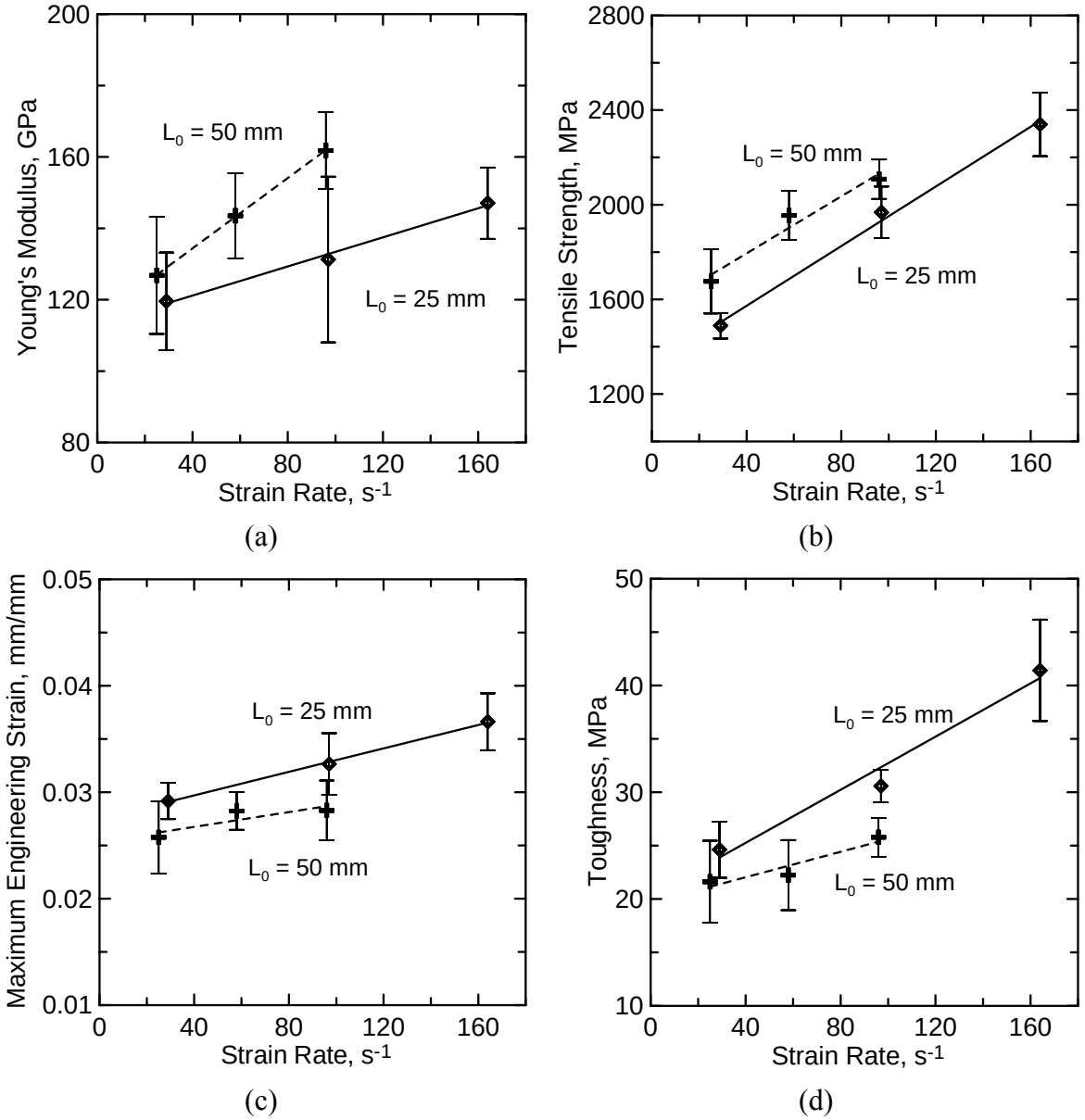

Figure 5. Strain rate effect on the dynamic material properties of Kevlar 49 fabric: (a) Young's modulus, (b) tensile strength, (c) maximum strain, and (d) toughness. L_0 is the gage length.

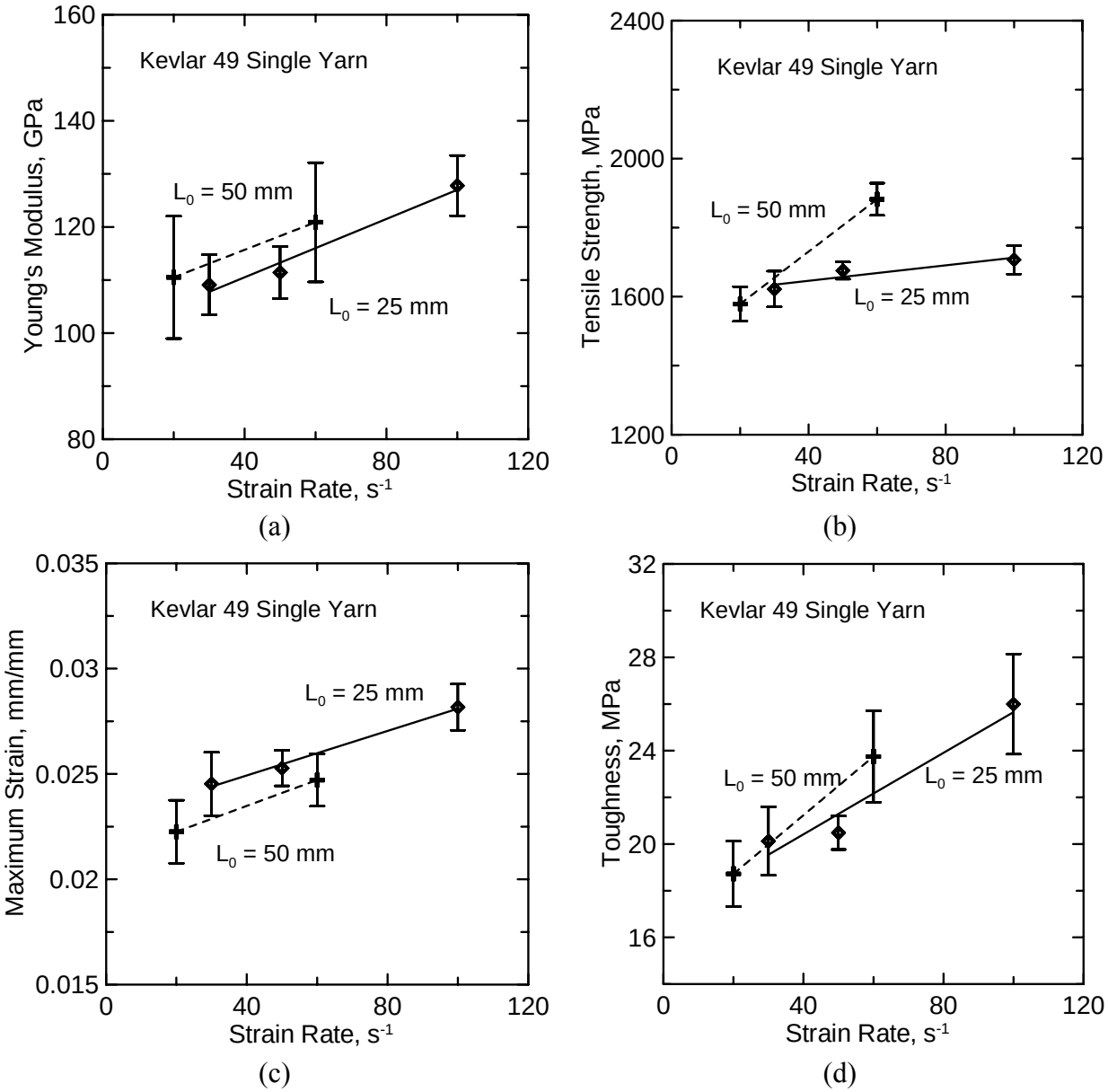

Figure 6. Strain rate effect on the dynamic material properties of single yarn: (a) Young's modulus, (b) tensile strength, (c) maximum strain, and (d) toughness

4. Conclusions

This work investigated the mechanical behaviors of Kevlar 49 fabric and single yarn under quasi-static and dynamic tensile loadings. Weibull parameters have been obtained to characterize the considerable scatter in the mechanical properties due to different amount and distribution of imperfections in the fabric and yarn specimens. The following conclusions can be reached:

(1) Under quasi-static loading, the stress-strain response of Kevlar 49 fabric exhibits non-linear and orthogonal behavior in both warp and fill directions, and the fabric can deform up to 20% before the stress decreases to zero. The Young's modulus is almost identical to one another in both directions. The major difference between warp and fill directions is the crimp strain, the tensile

strength and the ultimate strain. The tensile strength of single yarn decreases with increasing gage length.

(2) Under dynamic loading, Young's modulus, tensile strength, maximum strain and toughness of the fabric and yarn increase with increasing strain rate over the strain rate range from 20 to 170 s^{-1}. However, based on the current results, it is not clear what the effect of the gage length is on the dynamic properties.

References

[1] B. Farsi Dooraki, J. A.Nemes, M. Bolduc, Study of parameters affecting the strength of yarns. Journal of Physics IV, 134 (2006) 1183–1188.

[2] X.R. Xiao, Dynamic tensile testing of plastic materials. Polymer Testing, 27(2008) 164–178.

[3] D. Zhu, S.D. Rajan, B. Mobasher, A. Peled, M. Mignolet, Modal analysis of a servo-hydraulic high speed testing machine and its application to dynamic tensile testing at an intermediate strain rate. Experimental Mechanics, 51(2011) 1347–1363.

[4] D. Zhu, B. Mobasher, S.D. Rajan, Characterization of dynamic tensile testing using aluminum alloy 6061-T6 at intermediate strain rates. ASCE Journal of Engineering Mechanics, 137(2011) 669–679.

[5] D. Zhu, A. Peled, B. Mobasher, Dynamic tensile testing of fabric-cement composites. Construction and Building Materials, 25(2011) 385–395.

[6] S. Sahraoui, J.L. Lataillade, Analysis of load oscillations in instrumented impact testing. Engineering Fracture Mechanics, 60(1998) 437–446.

[7] D. Zhu, M. Gencoglu, B. Mobasher, Low velocity impact behavior of AR glass fabric reinforced cement composites in flexure. Cement and Concrete Composites, 31(2009) 379–387.

[8] S. Bansal, B. Mobasher, S.D. Rajan, I. Vintilescu, Development of fabric constitutive behavior for use in modeling engine fan blade-out events. ASCE Journal of Aerospace Engineering, 22(2009) 249–259.

[9] D. Naik, S. Sankaran, B. Mobasher, S.D. Rajan, J.M. Pereira, Development of reliable modeling methodologies for fan blade-out containment analysis, Part I: experimental studies. International Journal of Impact Engineering, 36(2009) 1–11.

[10] Z. Stahlecker, B. Mobasher, S.D. Rajan, J.M. Pereira, Development of reliable modeling methodologies for fan blade-out containment analysis, Part II: finite element analysis. International Journal of Impact Engineering, 36(2009) 447–459.

[11] D. Zhu, C. Soranakom, B. Mobasher, S.D. Rajan, Experimental study and modeling of single yarn pull-out behavior of Kevlar 49 fabric. Composites Part A, 42(2011) 868–879.

[12] D. Zhu, B. Mobasher, A. Vaidya, S.D. Rajan, Mechanical behaviors of Kevlar 49 fabric subjected to uniaxial, biaxial tension and in-plane large shear deformation. Composites Science and Technology, 74(2013)121–130.

[13] D. Zhu, B. Mobasher, S.D. Rajan, Dynamic tensile testing of Kevlar 49 fabrics. ASCE Journal of Materials in Civil Engineering, 23(2011)230–239.

[14] S. Bansal, Development of micro-mechanical model for dry fabrics. M.S. Thesis, Arizona State University, 2007.

[15] D. Zhu, B. Mobasher, J. Ermi, S.Bansal, S.D. Rajan, Strain rate and gage length effects on tensile behavior of Kevlar 49 single yarn. Composites Part A, 43(2012) 2021–2029.

Three-dimension dynamic simulation of thin epoxy-resin plate and comparison with experiment

Hao Chen[1,*] **, Tomoo Okinaka**[2]

[1] Key Laboratory of Earthquake Engineering and Engineering Vibration,
Institute of Engineering Mechanics, CEA, Sanhe, 065201, China
[2] Kinki University, Higashi-Osaka, 577-8502, Japan
* Corresponding author: chenhao@iem.ac.cn

Abstract This paper presents a 3D dynamic failure analysis of linear elastic body by using particle discretization scheme finite element method (PDS-FEM). PDS-FEM uses two sets of non-overlap characteristic function to discretize function and function derivative. Unlike ordinary FEM, PDS-FEM can easily calculate crack, which is the discontinuity in displacement function. The target is a thin epoxy plate with two anti-symmetric notches under uni-axial tensile boundary condition. A time depend failure criterion, called Tuler - Butcher criterion is applied. The simulation results are compared with the experimental results, which are captured by an image sensor at the rate of one million frames per second. In real world, no ideal isotropic homogeneous body exists. Disturbances exist everywhere. Crack is sensitive to local heterogeneity. Since the mesh configuration determines the candidate crack distribution in PDS-FEM, the uncertainty can be modeled by adding disturbance to the mesh configuration. By using Monte-Carlo simulation, the crack patterns observed in experiment, including bending, kinking and bifurcation are successfully simulated by using PDS-FEM.

Keywords Three dimensional dynamic simulation of fracture, stochastic model, brittle failure, photo-elastic experiment

1. Introduction

The simulation of fracture has been a challenging problem in solid continuum mechanics [1-2]. There are two difficulties in reproducing experiment results numerically: 1, accuracy and efficient numerical method is needed; 2, due to the limitation of observing technology, a stochastic model, which can represent the uncertainties, needs to be carefully designed.

For simulation of crack growth, varieties of numerical methods have been developed, such as E-FEM, X-FEM [3], discontinuous Galerkin method and meshfree methods. However, the original version of these methods has two common drawbacks: (1), the bifurcation or branching could not be calculated, which is essential for brittle materials, such as epoxy resin, rock and concrete; (2), the crack configuration is simple, normally in one dimension, so complex and detail configuration cannot be expressed. Recently, the improved version of above methods has been proposed by many researchers. The static, quasi-static and dynamic analysis can be successfully carried out [4-7].

Besides aforementioned methods, the newly developed method, called particle discretization scheme finite element method (PDS-FEM) is another candidate [8], for its numerical efficiency and capability of calculating bifurcation. In order to verify the accuracy and numerically efficiency of this method, a thin epoxy resin plate with two notches located anti-symmetrically in the middle under uni-axial tensile has been carried out numerically and experimentally. The quasi-static state of PDS-FEM has been developed by Oguni et al [9]. The comparison results show similarity between the simulation and experiment results.

In order to study the dynamic crack growth, we extend PDS-FEM to dynamic state [10]. PDS-FEM is originally formulated for Lagrangean at quasi-static state, and hence the extension to dynamic state is straightforward. Special attentions, however, have to be paid to time integration since

cracking releases strain energy and changes stiffness matrix drastically. High robustness is required for the time integration, and we adopt Hamiltonian formulation so that most robust algorithm which is proposed in the field of computational quantum mechanics can be employed for the time integration.

In real world, there is no ideal isotropic homogeneous body. Various kinds of disturbances exist everywhere. Due to limitation of the observation technology, the material property and boundary condition can hardly measure accurately. The difference between numerical setting and reality is called disturbance. Since crack is sensitive to local heterogeneity, even with the same setting, the crack paths of experimental samples are still somehow different from each other. In this paper, the authors try to reproduce a fracture experiment of a thin epoxy resin plate. In order to model the heterogeneity, a stochastic model is proposed, which introduces certain perturbation to the homogeneous body. Then, a Monte-Carlo simulation is carried out, from which, the crack patterns observed from corresponding experiments are successfully simulated.

The content of the present paper is as follows: section 2 briefly explains the extension of PDS-FEM to dynamic state. We formulate the dynamic extension of PDS-FEM by using discretized Hamiltonian, so that a robust algorithm can be applied to the time integration. Section 3 is devoted to discuss modeling of weak heterogeneity. The modeling is made by using different candidates of possible crack extensions, which is realized by using different meshes. Section 4 contains a Monte-Carlo simulation for a thin epoxy resin plate with a pair of anti-symmetric notches located in the middle. Also, the simulation results are compared with corresponding experiments, which are captured by a high frequency image sensor at the rate of 1 million frames per second. Concluding remarks are pointed out in section 5.

2. Extension of PDS-FEM to dynamic state

On the viewpoint of the numerical computation, it is not easy to analyze the crack growth, since cracking not only releases strain energy, but also changes the stiffness matrix. A robust algorithm that can handle such a change is required. The algorithm is also required to guarantee symplecticity, i.e., the total energy and momentum should be conserved during the crack growth.

A robust algorithm of time integration has been studied in the field of computational quantum mechanics [11]. To implement such an algorithm, we formulate the dynamic extension of PDS-FEM using Hamiltonian. We start from the following Lagrangean of a linearly and isotropically elastic solid, denoted by B, with elasticity $\mathbf{c}$, density ρ, displacement $\mathbf{u}$, stress $\boldsymbol{\sigma}$ and strain $\boldsymbol{\varepsilon}$:

$$L[\mathbf{u},\dot{\mathbf{u}};\boldsymbol{\varepsilon},\boldsymbol{\sigma}]=\int_B \frac{1}{2}\boldsymbol{\varepsilon}:\mathbf{c}:\boldsymbol{\varepsilon}-\frac{1}{2}\rho\dot{\mathbf{u}}\cdot\dot{\mathbf{u}}+\boldsymbol{\sigma}:(\nabla\otimes\mathbf{u}-\boldsymbol{\varepsilon})\,dv\,. \tag{1}$$

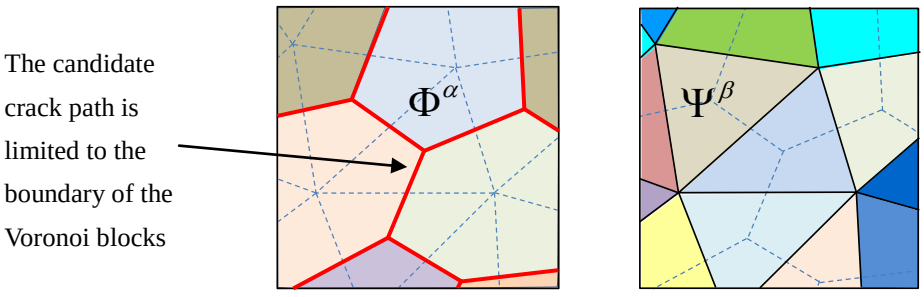

Figure 1. Two dimension decomposition by using particle discretization scheme

The discretization is made by using dual Voronoi $\{\Phi^{\alpha}\}$ and Delaunay tessellations $\{\Psi^{\beta}\}$, and their characteristic functions $\{\phi^{\alpha}\}$ and $\{\psi^{\beta}\}$ are used as basis functions. Note that, the displacement is discretized by Voronoi tessellations, while strain and stress are discretized by Delaunay tessellations:

$$\begin{aligned} u(x,t) &= \sum_{\alpha} u^{\alpha}(t)\phi^{\alpha}(x), \\ (\varepsilon,\sigma)(x,t) &= \sum_{\beta} \left(\varepsilon^{\beta},\sigma^{\beta}\right)(t)\psi^{\beta}(x). \end{aligned} \tag{2}$$

The following discretized wave equation is derived from L and the discretized functions:

$$M^{\alpha}\ddot{\mathbf{u}}^{\alpha}(t) + \sum_{\alpha'} \mathbf{K}^{\alpha\alpha'} \cdot u^{\alpha'}(t) = 0, \tag{3}$$

where M^{α} is the mass of the α^{th} Voronoi tessellation, the superscript α' stands for the α'^{th} adjacent Voronoi tessellation. Note that $\mathbf{K}^{\alpha\alpha'}$ is the stiffness matrix of PDS-FEM. This $\mathbf{K}^{\alpha\alpha'}$ coincides with an element stiffness matrix of FEM with linear tetrahedron elements [8]. Also, it should be noted that Eqn. 3 automatically leads to a lumped mass matrix. No approximation is needed to derive the lumped mass matrix, unlike ordinary FEM. This is the advantage of PDS-FEM, since, as shown in Eqn. 3, displacement is discretized as a set of rigid body displacement, or a continuum is regarded as an assembly of rigid body particles.

From this discretized wave equation, a discretized Hamiltonian of the following form is defined:

$$H = \sum \frac{1}{2}\mathbf{q}^{\alpha} \cdot \mathbf{K}^{\alpha\alpha'} \cdot \mathbf{q}^{\alpha} + \frac{1}{2\mathbf{M}^{\alpha}}\mathbf{p}^{\alpha} \cdot \mathbf{p}^{\alpha}, \tag{4}$$

where $\mathbf{p}^{\alpha} = \dfrac{\partial L}{\partial \dot{\mathbf{u}}^{\alpha}}$ and $\mathbf{q}^{\alpha} = \mathbf{u}^{\alpha}$ are the momentum and displacement of the α^{th} Voronoi tessellation.

We take advantage of the bilateral symplectic algorithm [12] as a robust algorithm of the time integration of Eqn. 4. The main advantage of this algorithm is that in order to achieve the accuracy of the order of Δt^N with Δt and N being time increment and an integer, it needs $2N$ times iteration for the interval of $2\Delta t$. Until now the highest order derived for this algorithm are four. In this paper, the fourth order is used.

3. Modeling of weakly heterogeneity for cracking

For brittle materials, it is usually observed that a crack propagates in an unpredictable manner, when subjected to dynamic loading. For instance, kinking and brunching are induced during the process of crack growth, or shattering due to multiple cracking is observed at high loading rate.

The key task of this paper is a numerical experiment that uses a set of weakly heterogeneous bodies. In the numerical model, several parameters, such as failure criteria, material properties, flaws' positions, can hardly be obtained accurately. However, it is not necessary at all to make all these parameters to be the stochastic variables, we can assign only a few to be stochastic variables, and others can be assigned as constants according to experience for simplicity. In this way, all the variability of unknown parameters can be represented by the designed stochastic variables.

Generally speaking, two methods can be used to model heterogeneity, adding perturbation to material properties of either deformation or fracture. PDS-FEM takes a simple treatment of weak heterogeneity, as: material properties are uniform except for a parameter for fracture, and cracking are allowed only on some of predetermined weak plane segments.

PDS-FEM uses a boundary facet as a set of pre-determined weak plane segments for possible crack extensions. The location of the weak plane is pre-determined by mesh configuration. In order to model the weak heterogeneity, we add disturbance to the location of mesh mother points, from which, a lot of samples with slightly different fracture property can be generated. However, there are two difficulties in this method: generating unbiased distribution may result in ill-shaped Delaunay elements, i.e., some elements with large aspect ratio; a simple solution of forcing the aspect ratio of the Delaunay elements in a certain range leads to biased distribution of some clusters of Voronoi mother points. The unbiased distribution of the Voronoi mother points and the aspect ratio control of the Delaunay elements are in a trade-off relation. As a compromise, we start from one distribution of the Voronoi mother points with majority of the Delaunay elements being well shaped, and modify this distribution randomly to generate other distributions without changing the geometry of the target model.

The mesh size is regarded as a parameter which represents the degree of material heterogeneity; the size becomes smaller as the distribution of material parameters is closer to being uniform. For designing the stochastic model of a real experiment, we need to identify the degree of material heterogeneity or the mesh size. However, with limited observation equipment, the degree of heterogeneity of real samples cannot be measured easily. Therefore, the authors try to start from a standard mesh configuration, which takes a balance between the accuracy and computation overload. If the crack path solutions of the numerical experiments show that the variability is not large enough to include the experimental results, then we have to find ways to increase the degree of heterogeneity in the stochastic model: (1), apply larger mesh size, while ensuring the required accuracy; (2), add additional perturbation to material properties of deformation. Thus, in the numerical experiment presented in section 4, we start from a standard mesh configuration as this: finer meshing is used near the crack tip, to allow a wider choice of crack extension, while meshing becomes coarser farther from the crack tip to save computation overload.

4. Monte-Carlo simulation of crack propagation

This section carries out a numerical experiment of executing Monte-Carlo simulation of heterogeneous samples, in order to reproduce the real experiments' phenomena.

4.1. Problem setting

We study a thin plate of 5×24.5×140 mm, which includes two anti-symmetric parallel notches of height 0.6 mm; see Fig. 2. It is assumed that the material is linearly elastic; see Table 1. For dynamic analysis of brittle material we need to consider the time effect, since dynamic fracture is a time-dependent phenomenon [13-14] which depends on the stress pulse duration, also from experiment study, it is observed that, the material strength is higher than static strength for high loading rate [15-16]. Concerning about this, a time dependent material strength failure criterion called Tuler Butcher criterion [17] is adopted in this paper:

$$\int_0^{\tau_f} \left(\sigma_1 - \sigma_0\right)^{\beta} dt \geq K_f , \tag{5}$$

for $\sigma_1 \geqq \sigma_0 \geqq 0$, where σ_0 and σ_1 are a threshold stress and the maximum stress, τ_f is fracture duration and K_f is the stress impulse for failure. This criterion means that a crack grows if accumulated stress in fracture duration reaches a critical value. It is assumed that $\beta = 2$ and $K_f = 10^{-8}$, σ_0 is equal to the static tensile strength, and τ_f is assigned to be the time step used in time integration; these parameters should be calibrated according to experimental data, which are not

available at this moment. However, as mentioned above, the variability of the parameters can be presented by the disturbance in mesh configuration.

Table 1. Material properties of epoxy resin

Young's modulus (Mpa)	3300
Poisson's ratio	0.38
Tensile strength (Mpa)	35.0
Epoxy density (kg/m^3)	1180

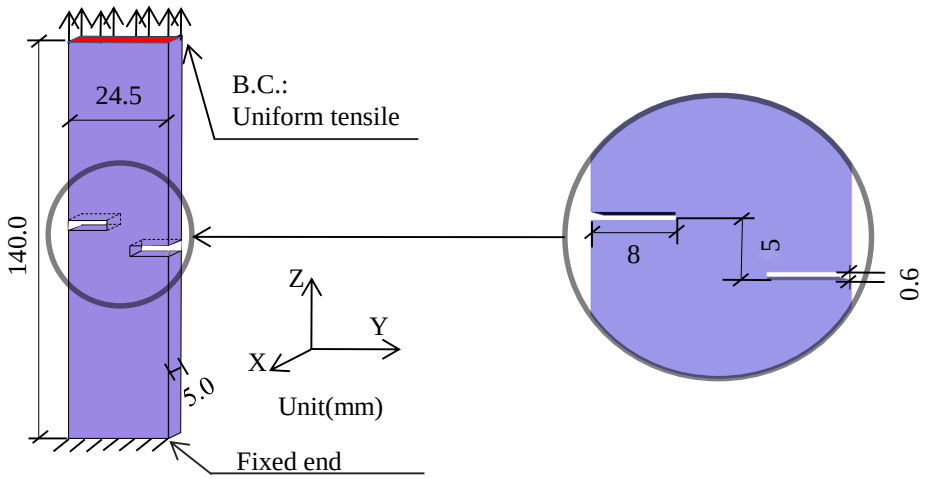

Figure 2. Analysis model

The force boundary condition is posed. The bottom end of the model is fixed, and the top end is pulled up in longitudinal direction. The loading rate is set to be 5N/s. Since the loading rate is small, the initial load of simulation is set to be 135N to save computation time. No element failure exists under this initial load. Following the PDS-FEM discretization, the crack tip is modeled as a notch with 0.6 mm height; the vertical surface of the notch is discretized by using 2 elements. The average mesh size is 1.0 mm at the top and bottom surfaces of the model to save computational overload. The time increment is set to be $\Delta t = 5.0 \times 10^{-9}$s.

200 samples with slightly different mesh configurations or distributions of candidate crack path for PDS-FEM are prepared for Monte-Carlo simulation. The number of samples is decided by checking the convergence of average crack path position through the specified cross-sections.

4.2. Simulation results and experimental comparison

For numerical simulation, the crack patterns can be classified into two groups: (1), the crack paths are symmetrically distributed; (2), one crack is fully developed horizontally from either of the notches. Fig. 3 shows eight typical crack path solutions of the model with small heterogeneity. Bifurcation is also observed in the simulation results; see Fig. 3.5~Fig.3.8.

In order to record the development of crack growth and stress changes of the epoxy resin thin plate, an ultra high speed video camera, which can capture images at the rate of 1 million frames per second, is used herein [18]. The photo-elastic technology [19] is used to show the stress distribution of experimental samples. Fig. 4 shows the final stages of four typical photo-elastic fringe patterns.

Within 16 samples, no sample with perfect anti-symmetric distribution of the two crack paths has been found. This is because the number of experimental samples is too few to include a sample with sufficiently homogenous material property and symmetrical boundary condition at the same time. The typical crack patterns can be classified into two groups: (1), one main crack path develops from either one of the two notches; (2), the two crack paths are more or less anti-symmetrically distributed. From experiments, some cracks bifurcate at the end of experiments.

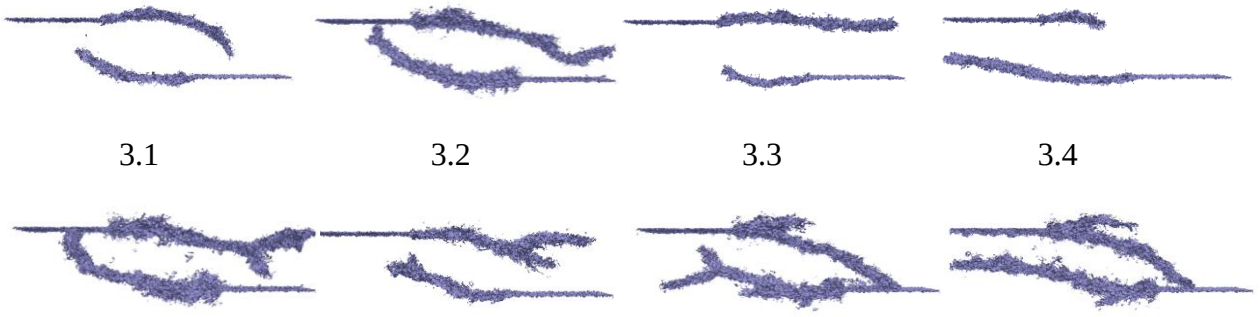

3.1 3.2 3.3 3.4

3.5 3.6 3.7 3.8

Figure 3. The typical crack paths projection into YZ plane
under force boundary condition of loading rate 5N/s

Among 200 numerical samples, we find the samples, whose crack paths coincide with experimental results. In order to make further comparison between the simulation results and experimental results, the stress distribution of simulation has been converted into photo elastic fringe patterns. Fig. 5 and 6 shows the experimental photo-elastic fringe patterns and the numerically synthesized fringe patterns. From these comparisons, the crack growth processes of these two samples are successfully simulated by the method proposed in this paper.

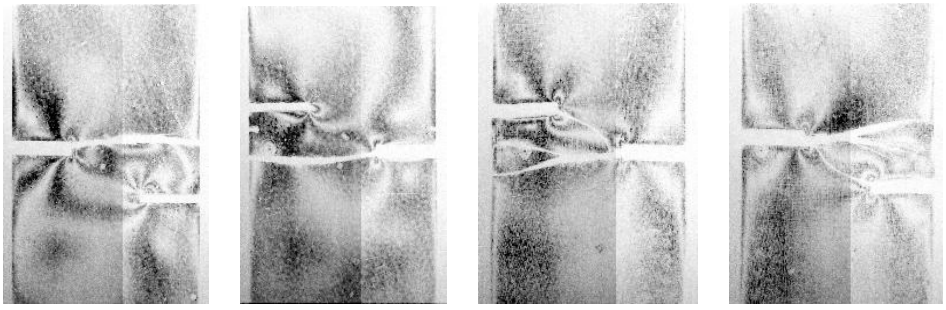

4.1 4.2 4.3 4.4

Figure 4. Photo elastic frames of experiments' final stages, $t = 100\mu s$ (with colors reversed)

Experiments

$t = 40\mu s$ $t = 70\mu s$ $t = 100\mu s$

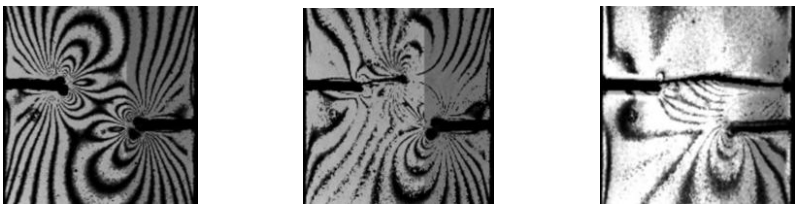

(a), fringe patterns of experimental sample 4.1

Simulations

$t_0 = 76,179,191\mu s$ $t = t_0 + 40\mu s$ $t = t_0 + 70\mu s$ $t = t_0 + 100\mu s$

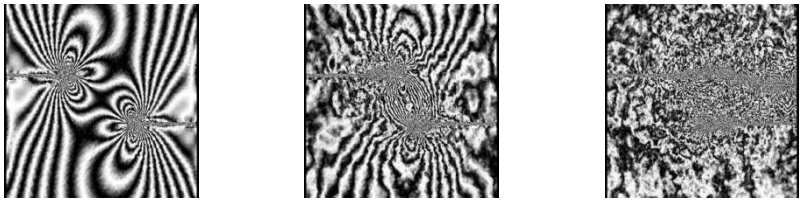

(b), synthesized fringe patterns of numerical sample 3.3

(c), crack growth process of numerical sample 3.3

Figure 5. One main crack path

Experiments

$t = 30\mu s$ $t = 50\mu s$ $t = 70\mu s$

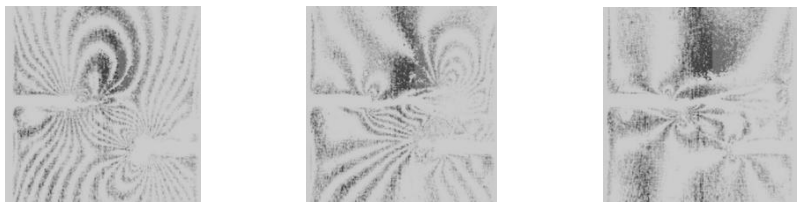

(a), fringe patterns of experimental sample 4.4

Simulations

$t_0 = 76,179,191\mu s$ $t = t_0 + 30\mu s$ $t = t_0 + 50\mu s$ $t = t_0 + 70\mu s$

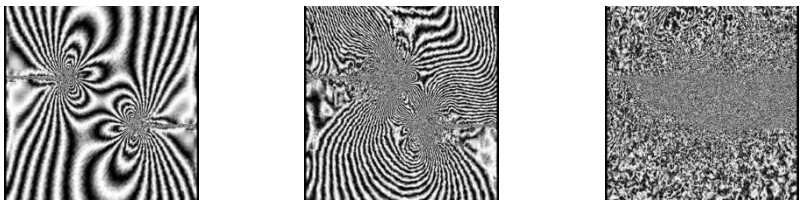

(b), synthesized fringe patterns of numerical sample 3.6

(c), crack growth process of numerical sample 3.6

Figure 6. Bifurcation

(The colour of all images in Fig. 6.a and b has been reversed, since the records are too dark to see.)

Before crack starts, the experimental fringe patterns and simulation results show significant similarity. However, when crack develops, the stress distribution of the simulation becomes blurred. There are three possible reasons for this:

(1) The mesh density is not large enough near the crack tips. In the simulation, the element size is still large, so the energy of the stress wave released from broken elements is significant. On the contrary, the granularity of the epoxy resin is small, and the energy released from the broken of crystalline grain is small and continuous in real experiments.

(2) Friction, thermal as well as acoustic energy consumption mechanics due to cracking have not been considered in this simulation. The released strain energy blurs the simulated photo-elastic fringe patterns.
(3) Ductile fracture may happen in the experiments under indoor temperature.

5. Conclusion

There is no ideal homogeneous body in the world. In order to model the heterogeneity, PDS-FEM offers a nature way by adding disturbance in the mesh configuration. This paper conducts a tensile fracture experiment of a thin epoxy resin, and builds a stochastic model with the distribution of candidate crack path set as stochastic variables. Monte-Carlo simulation is carried out. With specified basic mesh configuration, the simulation results reproduce the crack growth of corresponding experiments, including bending, kinking and bifurcation. The heterogeneity is successfully modeled.

Before crack develops, the stress distribution of simulation shows great similarity with experimental photo-elastic fringe patterns captured by a high speed camera. When crack begins, the fringe patterns of simulation become blurred. Three possible reasons have been proposed and more realistic problem setting is needed to increase the similarity between the results of simulation and experiment in future study.

Acknowledgements

This research is partially supported by the Central Public-interest Scientific Institution Basal Research Fund of China (Grant No. 2011B-05), China postdoctoral Science Foundation, and Natural Science Foundation of Hei Longjiang Province of China (Grant No. LC2012C32). These supports are greatly appreciated.

References

[1] J. Oliver, Modelling strong discontinuities in solid mechanics via strain softening constitutive equations. Part 2: Numerical simulation. *Int. J. Num. Meth. Eng*., 39(21), (1996) 3601-3623.
[2] N. Moes, J. Dolbow, T. Belytschko, A finite element method for crack growth without remeshing. Int. J. Num. Meth. Eng., Vol. 46:1, (1999) 131–150.
[3] J. Oliver, A. Huespe, and P. Sanchez, A comparative study on finite elements for capturing strong discontinuities: E-FEM vs X-FEM. Computer methods in applied mechanics and engineering, 195(37), (2006) 4732-4752.
[4] T. Rabczuk, S. Bordas, and G. Zi, A three-dimensional meshfree method for continuous multiple-crack initiation, propagation and junction in statics and dynamics. Comput. Mech., 40(3), (2007) 473-495.
[5] S. Bordas, T. Rabczuk, and G. Zi, Three-dimensional crack initiation, propagation, branching and junction in non-linear materials by an extended meshfree method without asymptotic enrichment. Eng. Fract. Mech., 75(5), (2008) 943-960.
[6] F. Stan, Discontinuous Galerkin method for interface crack propagation. Int. J. Mater. Forming 1, (2008) 1127-1130.
[7] N. Sukumar, B. Moran, T. Black, and T. Belytschko, An element-free Galerkin method for three-dimensional fracture mechanics. Comput. Mech., 20(1), (1997) 170-175.
[8] M. Hori, K. Oguni, and H. Sakaguchi, Proposal of FEM implemented with particle discretization for analysis of failure phenomena. J. Mech. Phys. Solids: 53(3), (2005) 681-703.

[9] K. Oguni, L. Wijerathne, T. Okinaka and M. Hori, Crack propagation analysis using PDS-FEM and comparison with fracture experiment. Mech. Mater. Phys. Solid, 41(11), (2009) 1242-1252.
[10] H. Chen, L. Wijrathne, M. Hori, and T. Ichimura, Stability analysis of dynamic crack growth using PDS-FEM. Struct. Eng. Earthq. Eng., 29(1), (2012) 1s-8s.
[11] M. West, Variational integrators, California Institute of Technology, 2004.
[12] L. Casett, Efficient symplectic algorithms for numerical simulations of Hamiltonian flows. Phys. Scripta, 51, (1995) 29-34.
[13] T. Nojima, T. Crack stability in rate sensitive ceramics and their rate dependence. J. Phys. IV:4, (1994) C8-689-C8-694
[14] A. Nyoungue, Z. Azari, M. Abbadi, S. Dominiak, and S. Hanim, Glass damage by impact spallation. Mater. Sci. Eng.: A, 407(1), (2005) 256-264.
[15] J. Jeong, H. Adib, and G. Pluvinage, Proposal of new damage model for thermal shock based on dynamic fracture on the brittle materials. J. Non-cryst. Solids, 351(24), (2005) 2065-2075.
[16] Y. Xia, X. Wang and B. Yang, Brittle-ductile-brittle transition of glass fibre-reinforced epoxy under tensile impact. J. Mater. Sci. Lett., 12(18), (1993) 1481-1484
[17] B.M. Butcher, L.M. Barker, D.E. Munson and C.D. Lundergan. Influence of Stress History on Time-dependant Spall in Metals. AIAA, Vol. 2:6, (1964) 977-990.
[18] T.G. Etoh, D. Poggemann, G. Kreider, et al. An image sensor which captures 100 consecutive frames at 1000000 frames/s. Electron Devices, IEEE Transactions on, 50(1), (2003) 144-151.
[19] M. Wijerathne, K. Oguni, and M. Hori, Inverse analysis method for photoelastic measurement of 3D stress state. Key Engng. Mater., Vol. 261, (2004) 753–758.

Calculation of bearing loads for fractured specimens by FRASTA simulation

Yuguang Cao[1,*], Shihua Zhang[1], Xiaoyu Sun[2], Kiyoshi Tanaka[3]

[1] Department of Engineering Mechanics, China University of Petroleum, 266580, China
[2] Drilling Technology Institute of Shengli Petroleum Bureau, 257017, China
[3] Department of Mechanical Systems Engineering, Toyama Prefectural University, 939-0398, Japan

Abstract Based on the previously proposed simple bar hypothesis, the fracture surfaces can be assumed to be composed of independent rectangular bars. In this paper, by dividing the plastic deformation into single bars, the original lengths of these bars were deduced and then the global strains of these bars during the course of failure were calculated. According to the relationship between true stress and true strain of the material, the normal stress on the cross section of each bar was determined. Multiply the stress with the cross section area, the load acted on each single bar was obtained. Adding all loads on all bars together led to the total applied load of the specimen.

Keywords Fracture surface; FRASTA; Fatigue load

1. Introduction

To investigate the fractured surfaces always reveals a lot of useful information. For example, details of the processes that lead to failure can be determined from these surfaces, making it useful to investigate their morphology.

In order to investigate the reasons for a material's failure, it is necessary to know the temperature, environment and load imposed on it. Since these records are often unavailable, the reasons for failure must be deduced by analyzing fracture surfaces.

Dr. Kobayashi firstly proposed fracture-surface topography analysis (FRASTA) in 1987 [1]. FRASTA considers that as the crack extends, the material immediately beneath the newly formed fracture surfaces undergoes no further inelastic deformation. Based on this understanding, the process of fracture can be rebuilt from the conjugate fractured surfaces. Using the FRASTA technique, the details of the void nucleation and growth, the coalescence of the voids and cracks, and the crack propagation process can be clarified visually [2]. However, the FRASTA application has previously focused on smaller size scales and localized behaviors [3].

A novel method [4] of measuring the CTOA and determining the J integral using FRASTA was proposed in 2006. It extended the application of FRASTA to global fracture surfaces. Software [5] was developed for researching the global fracture surfaces based on this principle. The relationship between J integral and fracture surface average profile [6] and the relationship between J integral and COD [7] were proposed respectively based on FRASTA reconstruction.

The main goal of this paper is to propose a new method to calculate the specimen applied load during failure from the fracture surfaces. Based on the above researches especially the proposed simple bar hypothesis, the fracture surfaces will be divided into independent rectangular bars. The calculation of elongation, global strain, cross-section normal stress and so on of these bars will be deduced. By adding the applied force of each bar together, the total applied force of the specimen during the course of failure will be derived.

2. Method for calculating the applied loads of fractured specimens

The simple bar hypothesis was firstly proposed for determining the J integral [4]. Then it was used in the research of relationship between J integral and fracture surface average profile [6]; and relationship between J integral and COD [7] respectively. Results in these researches verified the validity of the proposed simple bar hypothesis. Based on the hypothesis, a new method for determining the applied loads of fractured specimens during the course of failure will be proposed and experiments will be performed to verify it.

It is well known that, by means of Mises yield criterion, for the Mode Ⅰ stress field, the boundary of plastic zone around crack tip for plain strain [8] can be expressed as Eq. (1)

$$r(\theta)=\frac{K_{\mathrm{I}}{}^{2}}{2\pi\sigma_{y}{}^{2}}\cos^{2}\frac{\theta}{2}\left[(1-2\nu)^{2}+3\sin^{2}\frac{\theta}{2}\right]. \tag{1}$$

where K_{I} is the stress intensity factor and ν is the Poisson's ratio. In plastic zone, the distribution of strain component that perpendicular to fracture surface is

$$\varepsilon(y)=\frac{K_{\mathrm{I}}}{2G(1+\nu')\sqrt{2\pi r}}\cos\frac{\theta}{2}\left[(1-\nu')+(1+\nu')\sin\frac{\theta}{2}\sin\frac{3\theta}{2}\right]. \tag{2}$$

where $\nu'=\nu$ and $\nu'=\nu/(1-\nu)$ for plain stress and plain strain respectively, G is shear modulus.

Introduction of Eq. (1) into Eq. (2) leads to Eq. (3)

$$\varepsilon(y)=\frac{\sigma_{y}}{2G(1+\nu')\sqrt{(1-2\nu)^{2}+3\sin^{2}\dfrac{\theta}{2}}}\left[(1-\nu')+(1+\nu')\sin\frac{\theta}{2}\sin\frac{3\theta}{2}\right], \tag{3}$$

where σ_{y} is the yielding stress. It is clear that, on the boundary of plastic zone, for certain material, $\varepsilon(y)$ is only relative to θ. And for $\theta=\pi/2$, $\varepsilon(y)$ can be represented as Eq. (4),

$$\varepsilon(y)_{\frac{\pi}{2}}=\frac{\sigma_{y}}{2G(1+\nu')\sqrt{(1-2\nu)^{2}+\dfrac{3}{2}}}\left(\frac{3}{2}-\frac{\nu'}{2}\right). \tag{4}$$

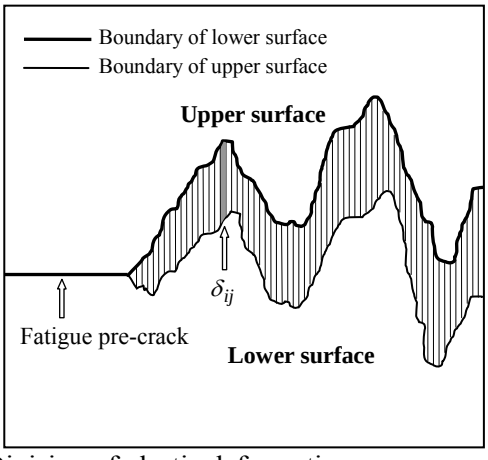

Figure 1. Division of plastic deformation on cross-sectional plot

This paper defines

$$\varepsilon_y = \varepsilon(y)_{\frac{\pi}{2}}. \tag{5}$$

It is obvious that ε_y is a constant. According to elastic-plastic fracture mechanics, at the crack tip, when the strain component along y axis direction reaches some certain value, crack extends. This certain value is defined as ε_f in this paper.

Fig. 1 displays a cross-sectional plot of a compact tension specimen. The hatched area is the overlap of the upper and lower fracture surfaces when driven to the initial position (state before test started) after being broken. It refers to the plastic deformation left on the specimen. In order to simplify the calculation, this paper supposes the plastic deformation is symmetry about the fracture surface as shown in Fig. 2. It means that the specimen fractures along x axis. Furthermore, this paper defines the area which is plastically deformed during the course of testing as plastic field. It is worth noting that plastic field is different from plastic deformation as shown in Fig. 2.

In this paper, according to the simple bar hypothesis, the fracture surfaces are assumed to be composed of independent rectangular bars. The sizes of these bars in the X and Y directions (the directions of crack extension and specimen thickness, respectively) are determined by the resolution of the laser microscope for the X and Y axes (represented by p and q, respectively). In this paper, they are both 50 μm. Thus, along the direction of crack extension, the amount of plastic deformation which is gray-scaled in Fig. 2 can be considered as the elongation of the bar. This paper supposes the original half length of the bar is l and the half elongation is Δl.

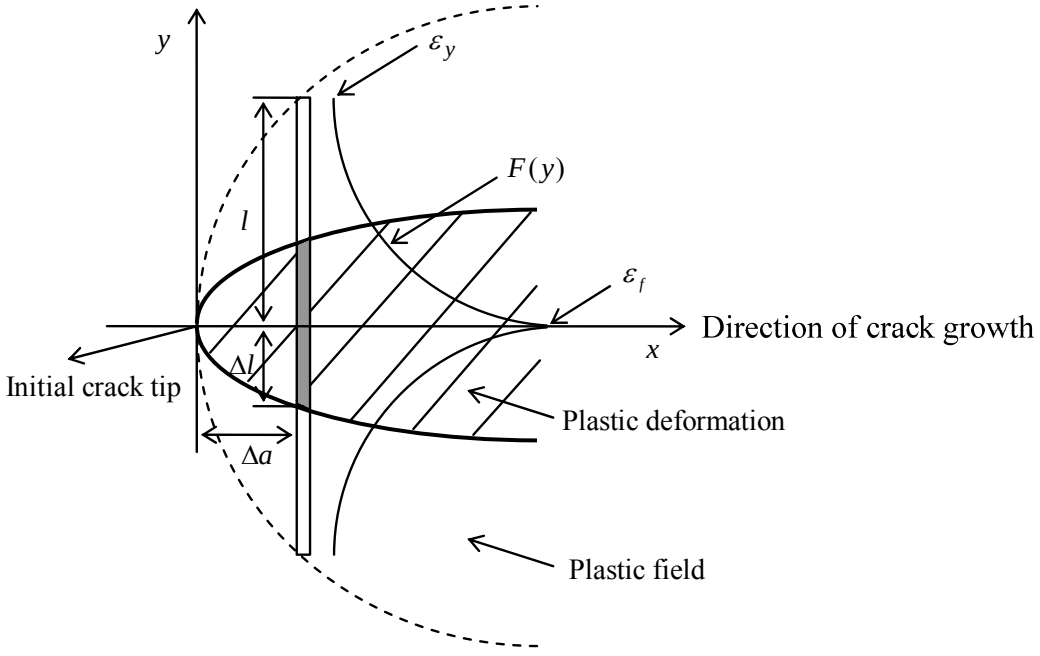

Figure 2. Principle of determining plastic field left on specimen

As introduced in [4], the strain distribution of a simple rectangular bar along the axis can be expressed as the curve shown in Fig. 2. The function of curve was supposed to can be written as Eq. (6),

$$F(y) = a\exp(by). \tag{6}$$

According to what discussed above,

$$F(0) = \varepsilon_f ,$$

$$F(l) = \varepsilon_y . \tag{7}$$

The substitution of Eq. (7) into Eq. (6) provides Eq. (8),

$$a = \varepsilon_f ,$$

$$b = \frac{1}{l} \ln \frac{\varepsilon_y}{\varepsilon_f} . \tag{8}$$

So, the elongation of the bar can be expressed as Eq. (9),

$$\Delta l = \int_0^l F(y)\, dy = \frac{\varepsilon_f - \varepsilon_y}{\ln \varepsilon_f - \ln \varepsilon_y} l . \tag{9}$$

Thus, the ratio of elongation of the bar can be expressed as Eq. (10),

$$P = \frac{\Delta l}{l} = \frac{\varepsilon_f - \varepsilon_y}{\ln \varepsilon_f - \ln \varepsilon_y} . \tag{10}$$

Because ε_f and ε_y are material constants, P is a constant, too. That is to say, the dimension of plastic field left on specimen is in proportion to the plastic deformation. At the same time, because Δl can be acquired from FRASTA, the plastic field left on specimen can be determined.

Return to the state as shown in Fig. 1, δ_{ij} represents the elongation of the bar at (x_i, y_j), where i and j represent the number of position along x and y axis respectively. The sizes of these bars along x and y direction (the direction of crack extension and specimen thickness respectively) are determined by the step lengths of laser microscope, which are represented by p and q respectively in this paper. Then, the original length l_{ij} of each bar should be

$$l_{ij} = \frac{\delta_{ij}}{P} , \tag{11}$$

the length of each bar after being broken is

$$l_{ij}' = \frac{\delta_{ij}}{P}(1 + P) . \tag{12}$$

In order to calculate the load applied to the specimen during the course of fatigue, based on the above simple bar hypothesis, the fracture surfaces are assumed to be composed of independent rectangular bars. Once the normal stress on the cross section of each bar was obtained, the force applied on the bar can be determined by multiplying the normal stress with the cross section area. By this means, adding the force applied on each bar together, the load applied on the specimen can be obtained.

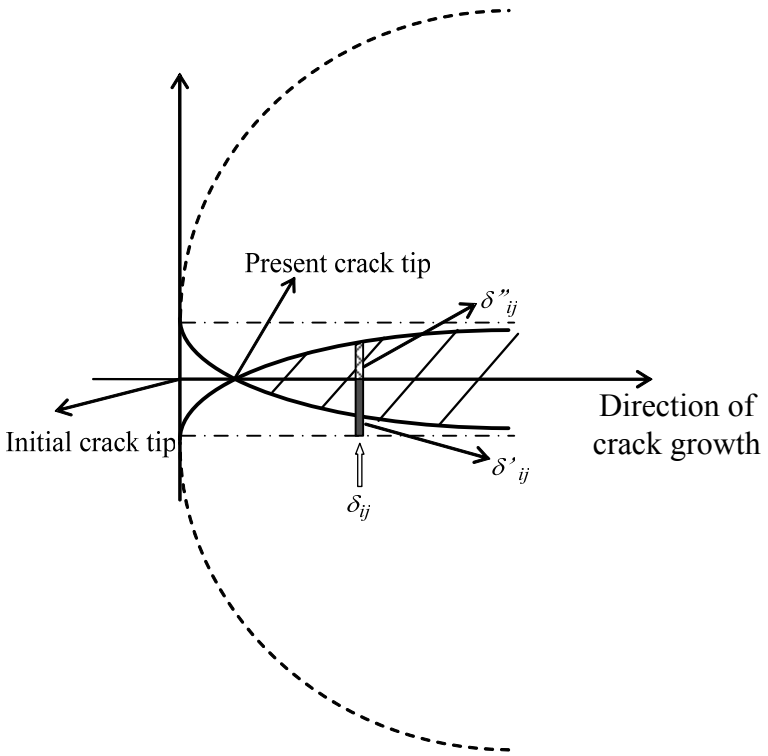

Figure 3. Two parts of the elongation of a single bar

According to this idea, we should firstly determine the global strain of each single bar during the course of failure. As shown in Fig. 3, using FRASTA to reconstruct the process of fracture, considering that the crack has extended to the "present crack tip", that is material behind the present crack tip (between the "initial crack tip" and the "present crack tip" in Fig. 3) has been fractured, thus forces acting on the bars composing this part had been released. While for material in front of the "present crack tip", it still bears load before failure. Add the loads acting on these bars together, the applied load of the specimen can then be determined. As shown in Fig. 3 and introduced above, suppose the final elongation of the bar is δ_{ij} and divide the elongation into two parts, δ'_{ij} and δ''_{ij}, where δ'_{ij} represents the elongation of the bar when the crack extends to the "present crack tip" and δ''_{ij} represents the residual elongation of the bar with the crack extending further from the "present crack tip" until final failure.

As introduced above, it is easy to get δ_{ij}, δ'_{ij} and δ''_{ij} by reconstructing the process of crack extension using FRASTA. According to Eq. (11), the initial length of the bar can then be calculated and the global strain of the bar when the crack reaches to the "present crack tip" can be calculated as Eq. (13),

$$\varepsilon_{ij} = \frac{\delta'_{ij}}{l_{ij}}. \tag{13}$$

Furthermore, the relationship between true stress σ and true strain ε can be expressed as Eq. (14),

$$\sigma = K\varepsilon^n, \tag{14}$$

where K is a constant and n is work hardening exponent.

Introduction of Eq. (13) into Eq. (14) leads to Eq. (15),

$$\sigma_{ij} = K\varepsilon_{ij}^{\ n}, \tag{15}$$

where σ_{ij} is the normal stress on the cross section of the single bar l_{ij}. Thus the applied load of the specimen can be calculated as Eq. (16),

$$F = \sum p \times q \times \sigma_{ij} = p \times q \times K \times \sum \varepsilon_{ij}^{\ n} \tag{16}$$

In order to simplify the calculation, use the average deformation of the fracture surfaces for instead, that is to add all deformations of the single bars with the same x coordinate together and divide it by the number of bars. By this means, Eq. (16) can be converted into Eq. (17),

$$F = p \times q \times K \times k \times \sum \varepsilon_{i}^{\ n} \tag{17}$$

where ε_i is the average strain at x_i and the k is the number of bars with the same x coordinate .

3. Conclusions

From the results presented in this paper, it is clear that by using FRASTA reconstruction, that is recording the elevation data of fracture surfaces and reconstructing the process of crack extension, it is possible to obtain the plastic deformation with crack extension. Based on the simple bar hypothesis and by dividing the plastic deformation into single bars, the original lengths of these bars can be determined thus the global strains of these bars during the course of failure can also be calculated. According to the relationship between true stress and true strain of the material, the normal stress on the cross section can thus be determined. Multiply the stress with the cross section area, the load acted on each single bar can be got. Adding all loads on all bars together leads to the total applied load of the specimen.

Acknowledgements

The work was supported by “the National Nature Science Foundation of China” (Contract No. 11242004) and “the Fundamental Research Funds for the Central Universities” (Contract No. 12CX04068A).

References

[1] T. Kobayashi, D.A. Shockey, Metall. Trans. A 18 (1987) 1941-1949.
[2] H. Miyamoto, M. Kikuchi, T. Kawazoe, Int. J. Fracture 42 (1990) 389-404.
[3] W.R. Lloyd, Eng. Fract. Mech. 70 (2003) 387-401.
[4] Y.G. Cao, K. Tanaka, Int. J. Fracture 139 (2006) 253-266.
[5] Y.G. Cao, K. Tanaka, Acta Metall. Sin. (English Letters) 19 (2006) 165-170.
[6] Y.G. Cao, S.F. Xue, K. Tanaka, Acta Metall. Sin. (English Letters) 20 (2007) 40-48.
[7] Y.G. Cao, X.Y. Sun, K. Tanaka, Acta Metall. Sin. (English Letters) 20 (2007) 417-424.
[8] M.F. Kanninen, C.H. Popelar, Advanced Fracture Mechanics, Oxford University Press, New York, 1985.

The Master Failure Curve of Pipe Steels and Crack Paths in Connection with Hydrogen Embrittlement

M. Hadj Meliani[1,2,*],A. Elhussein[2], A. Elhoud[3], Z. Azari[2], Y.G. Matvienko[4], G. Pluvinage[2] T. Boukharouba[5]

[1] LPTPM, FS, Hassiba BenBouali University of Chlef, 02000, Chlef, Algeria.
[2] LaBPS-ENIM, Ile de saulcy 57045, Paul Verlaine university of Metz, France.
[3] Sinal, Materials and metallurgical services division, Rue de Madrid, Annaba, Algeria.
[4] Mechanical Engineering Research,4.M. Kharitonievsky Per., 101990 Moscow, Russia.
[5] Laboratoire de Mécanique Avancée, LMA, USTHB, Algeries, Algeria.
* Corresponding author: hadjmeliani@univ-metz.fr

Abstract This paper provides some critical review of the history and state of two elastic fracture mechanics (K and T) and relationship to crack paths. A particular attention is given in the case of hydrogen embrittlement. A fracture toughness transferability curve ($K_{\rho c}$-T_{ef}) has been established for the X52 pipe steels described by a linear relationship where T_{ef} is the average value of T stress over the characteristic length of the fracture process. A mechanism involving influence of the $T_{ef,c}$-stress on void growth for ductile failure is proposed; the effects of hydrogen on crack paths from the viewpoint of microstructural aspects are disputed.

Keywords crack paths, hydrogen embrittlement, transferability curve, fracture toughness, T-stress

1. Introduction

Fracture toughness is now considered as not intrinsic to material but depends on geometry, thickness, loading mode and more generally to constraint. Recent numerical and experimental studies have attempted to describe fracture in terms of two or three fracture parameters [1-3].The elastic stress fields in a region surrounding the crack tip can be characterized by the following solution [1]:

$$\sigma_{ij} = \frac{K_I}{\sqrt{2\pi r}} f_{ij}(\theta) + T\delta_{xi}\delta_{xj} + A_3\sqrt{2\pi r} + 0(r) \qquad (1)$$

where K_I is the stress intensity factor, $f_{ij}(\theta)$ is the angular function, δ_{ij} is the symbol of Kronecker's determinant. A polar coordinate system (r,θ) with origin at crack tip is used. Several methods have been proposed in literature to determine the T-stress for cracked specimen. The stress difference method has been proposed by Yang et al. [4]. It was noted [5-8] that T-stress characterizes the local crack tip stress field for elastic linear material, and the elastic plastic material with the restriction of small-scale yielding conditions. Various studies have shown that T-stress has significant influence on fracture toughness, crack growth direction, A_3 has some influence crack stability [9-15].

The K-T and K-A_3 approaches lead to a two-parameter fracture criterion. With K as the driving force and T or A_3 a constraint parameters, a master failure curve can be successfully used to take into account the constraints of stress fields for various proposed geometry and loading structure configurations. Recently, the master curve has been evolved into a mature technology for characterizing the notch fracture toughness to quantify constraint effects for different testing specimen and structures [16].

The effect of T-stress on crack paths has been investigated for various specimen configurations and materials [17-19]. But some results of the crack path estimation give ambiguous data; for example, it was shown [20] that if the T-stress in front of a flat crack is negative then the crack grows along the crack plane. In the case of a positive T-stress, the crack deviates from its initial plane. It was also observed that the crack did not turn immediately when the T-stress became positive but at a considerably higher value. The method employed in Ref. [21,22] was developed for a kink which is formed at a given angle to the main crack [23]. Actual attention has been paid to problem of hydrogen pipeline systems due to strong world asking in energy and environmental problems. One future way is to use hydrogen as energy vector. In one European project [24], hydrogen transport will be provided way by adding hydrogen to natural gas in existing networks. Experience shows that the majority of pipeline failure initiates from defects or cracks [25-27]. Effects of transported hydrogen affect material mechanical properties, namely, hydrogen embrittlement [28,29]. The external environmental conditions cause free corroding processes, where hydrogen is product on metal surface as result of cathodic counterpart of the anodic dissolution reaction [30,31]. The gas pipeline industry recognizes this well as a major problem.

The aim of present work is to study the influence of hydrogen coupled with constraint (T stress is used as constraint parameter) on master failure curve and crack path direction and stability. In the first part the influence of hydrogen on master failure curve determined from fracture tests performed on different specimens geometries (CT, SENT, RT and DCB) has been studied. In a second part, fracture path under low constraint (negative T-stress) has been studied. Fracture has been obtained by burst tests under hydrogen pressure of pipes. In the third part, fracture path under high constraint (positive T-stress) has been studied from fracture of DCB specimens. Finally, a proposed mechanism of crack extension with constraint and hydrogen embrittlement has been proposed.

2. Material

The material used in this study is an X52 steel meeting requirements of API 5L standard. API X52 steel was the most common gas pipeline material for transmission of oil and gas during 1950-1960. Chemical composition of the studied steels is given in Table 1. In table 2, the mechanical properties of API X52 steel have been presented. E, σ_Y, σ_u, A%, n, k and K_{Ic} are the Young's modulus, yield stress, ultimate stress, elongation at fracture, strain hardening exponent and hardening coefficient of Ramberg-Osgood law, and fracture toughness, respectively. Stress strain curves of X52 steel have been determined with and without hydrogen absorption and reported in Figure 1. Classical tensile properties such as yield stress and ultimate strength increases also when hydrogen is absorbed in steel as indicated in Table 2. A small increase of yield stress has been noted (2.5%) as an important reduction of elongation at failure (38%). Static stress-strain is obtained by fitted tensile test results using hardening power law $\sigma = K.\varepsilon^n$. Microstructure of API 5L X52 steel in the longitudinal and transverse orientation is shown in Figure 2 (a) and Figure 2 (b), respectively. These pictures show the distribution of the ferrite and pearlite with respect to orientation. The distribution of pearlite in

upper surface (Figure 2.a) appears to be relatively isotropic when compared to the pearlite bands in inner the surface (Figure 2.b). However, Figure 2 shows pearlite bands in different sections of the API 5L X52 specimen.

Table 1. Chemical composition of API X52 steel (weight %).

C	Mn	P	Si	Cr	Ni	Mo	S	Cu	Ti	Nb	Al
0.22	1.220	-	0.240	0.16	0.14	0.06	0.036	0.19	0.04	<0.05	.032

Table 2. Mechanical properties of API X52.

E, GPA	σ_Y, MPa	σ_u, MPa	A, %	n	K	$K_{Ic}\ MPa\sqrt{m}$
210	410	528	32	0.164	876	116.6

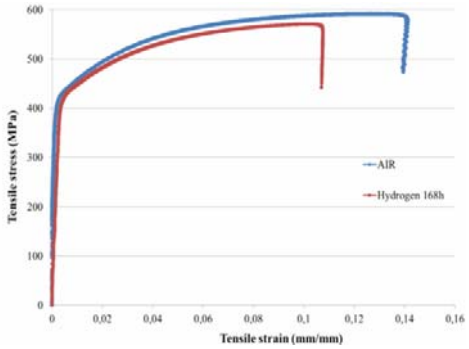

Figure 1. stress strain curves of X52 pipe steel with and without hydrogen absorption.

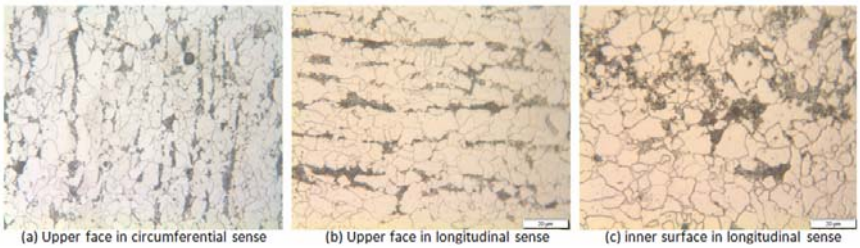

Figure 2. X52 metallographic sections showing ferrite-pearlite microstructure with bands (nital etching- originally taken at (a) 100x and (b) 500x)

3. Influence of Hydrogen on Master Failure Curve

Due to the assumptions, that pipes failure emanates mainly from external interferences i.e. that defect promoting failure are considered as notch, the notch fracture toughness (critical notch stress intensity factor) $K_{\rho,c}$ and the critical effective T-stress ($T_{ef,c}$) were employed to describe the material failure curve $K_{\rho,c} = f\left(T_{ef,c}\right)$. The critical notch stress intensity factor $K_{\rho,c}$ is determined by the Volumetric Method (VM) [32]. Averaging the T-stress distribution inside the effective distance (determined by Volumetric Method), the effective T-stress (T_{ef}) can be defined in the following

form:

$$T_{ef} = \frac{1}{X_{ef}} \int_0^{X_{ef}} T_{xx}(r).\Phi(r).dr \tag{3}$$

$K_{\rho c}$–$T_{ef,c}$ has been determined with [6] and without[2] the presence of hydrogen. Different specimens geometries (CT, SENT, RT and DCB) are used, all with a notch and a depth ratio of 0.5 (a/t = 0.5). Specimens have been submitted to hydrogen environment during 30 days. Fracture initiation is detected by acoustic emission and provides load for crack initiation P_i, more details are given in [12]. Results are compared with results of [2] and summarized in Figure 3. The material master curve is approximated by the following equation

$$K_{\rho,c} = a\, T_{ef,c} + b \tag{4}$$

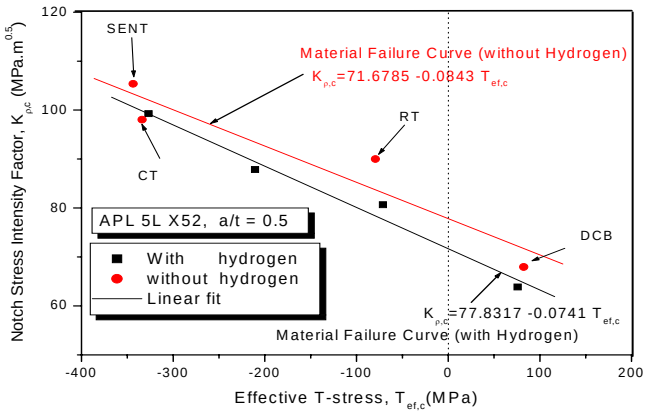

Figure 3. The experimental assessment points ($K_{\rho,c}, T_{ef,c}$) and the material failure curve $K_{\rho,c} = f\left(T_{ef,c}\right)$ for X52 pipe steel with and without hydrogen effect [6].

where a = -0.0843 and b =71.6785 for the X52 pipe steel without hydrogen embritlement and a =-0.0741 and b = 77.83 for the X52 pipe steel with hydrogen embrittlement. One notes a small decreases of fracture toughness decreases in the range [5.8 %– 9.8 %] when T_{ef} increases in the range [- 400 MPa- +100 MPa] with a small difference for SENT specimen and larger for DCB specimen (about 10 %). One note a parallel with the decrease of fracture resistance in term of master failure curve and increase of the yield stress after hydrogen introduction. A small increase of yield stress has been noted (2.5%), as an important reduction of elongation at failure (38%). Also one notes that increasing the yield stress increases the constraint parameter.

4. Hydrogen and Constraint Effect on Kinking Direction

4.1 Fracture under low constraint

Fracture of pipe under internal pressure is performed under low constraint. Notched tubes were used for burst tests under pressure of hydrogen gas. Tubes were manufactured with steel X52, which

chemical composition, mechanical properties at elongation and environmental conditions of tests are given in [33].

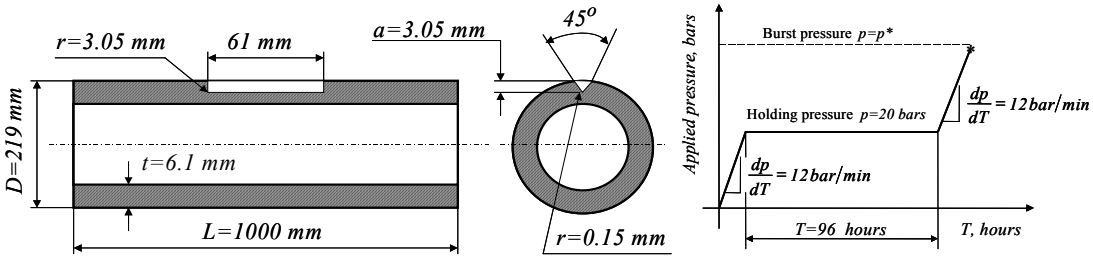

Figure 4. Tubes- Specimen for test

a) b)

Figure 5. Burst tests of the model specimens made from Ukrainian tube:
a - elastoplastic failure; b – catastrophic brittle fracture.

Tubes-specimens have a longitudinal notch on the outer surface and their geometry is given in Figure 4. Pipes were tested until burst according to the test sequence described in Figure 5. T-stress distribution indicates that T stress is negative and increases with internal pressure (see Fig.6). Test results showed that burst pressure for test in methane is equal $p_{max} = 118\ bar$ and burst pressure for test in hydrogen is equal $p_{max} = 122bar$. Therefore, there is no gaseous hydrogen effect on the strength of notched pipes for considered testing conditions. At this critical pressure effective T-stress T_{ef} is equal to – 22.268 MPa. This negative value indicates a relatively low constraint.

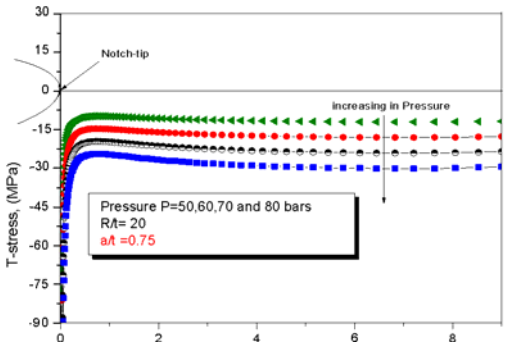

Figure 6. Evolution of T- stress versus distance over ligament. Pipe submitted to internal pressure. Diameter 400 mm thickness 10 mm (pressure 50-80 bars)

After burst tests, fracture surfaces were examined with a Scanning Electron Microscopy (SEM) for determination of fracture initiation points and also for checking of eventual fracture surface modification under influence of hydrogen. It has been found for hydrogen tests, inner fracture surface is characterized by an array of surface cracks (see Fig. 7-a). Careful examination shows that, surface cracks density is higher and average crack length is smaller. View of surface cracks under hydrogen conditions is given in Fig. 7.b at magnification X250.

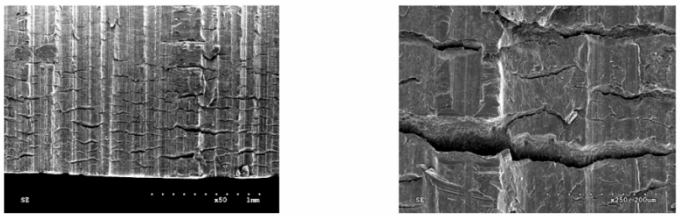

(a) (b)

Figure 7. (a) surface cracks mesh at the edge of fractured notch for test in hydrogen. (b) magnification X250.

Examination of the notch bottom shows that fracture is originated at centre of notch (± 1 at 2 *mm*).The mechanism of fracture initiation is developing of micro cracks from notch bottom (Fig. 7.a). Generally fracture surface consist of two parts. First part is a flat surface created by micro cracks growth from notch bottom and second part is final failure surface, which is made by shear mechanisms. This second part prevails at the inner surface of tube along notch and it may be considered as final ductile failure (Fig. 8.a). For test in hydrogen, the following aspect was observed. There is alternation of brittle and ductile sites of fracture character (Fig.8.b). The depth of particular surface aspect doesn't exceeds a distance of about 50 μm from notch bottom. No crack bifurcation was observed with or without hydrogen and this fact is considered as the result of fracture occurring under low constraint.

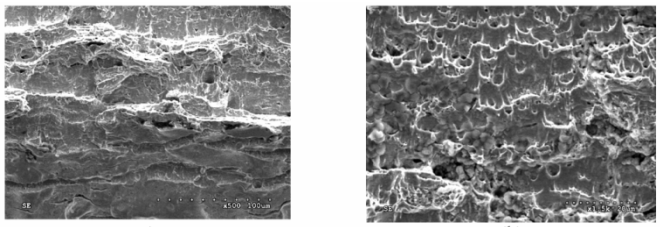

a) (b)

Figure 8. (a) Micro cracks at the notch bottom as source of fracture initiation for test in hydrogen. (b) fracture character at the inner surface.

4.2 Fracture under high constraint

Fracture tests have been made on DCB specimen made in X52 steel. Geometry and dimensions of specimen ~~is~~ aregiven in figure (9).

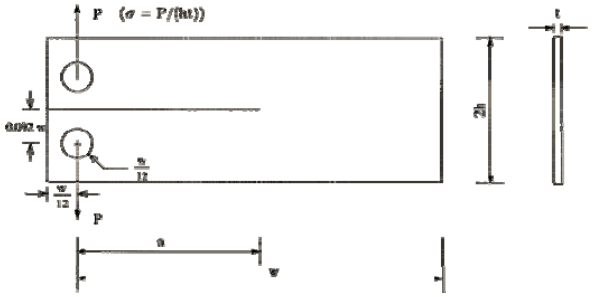

Figure 9**.** Geometry and dimensions of DCB specimens made in X52 steel.

Effective T stress has been determined by computed T stress distribution by Finite Element method along ligament and applying the Stress Difference Method, SDM [4]. Effective T stress distribution is presented in Figure 10. T is positive and indicates a low of constraint. $T_{ef,c}$ at failure is equal to (+151.657 MPa). Observation of hydrogen effects by SEM on crack paths is shown in Figure 11 on CT and DCB specimens. Presences of hydrogen also induce another feature on crack growth that will contribute to the acceleration effect. A comparison is made with CT specimen which develops higher constraint. For CT in air and hydrogen crack grows perpendicular to the principal opening stress in mode I. For DCB under hydrogen, there is facility to extend crack in perpendicular direction and this could cause microscopic deviations in the crack path (Figure 11). These deviations can lead into crack branching or kinked crack paths [12].

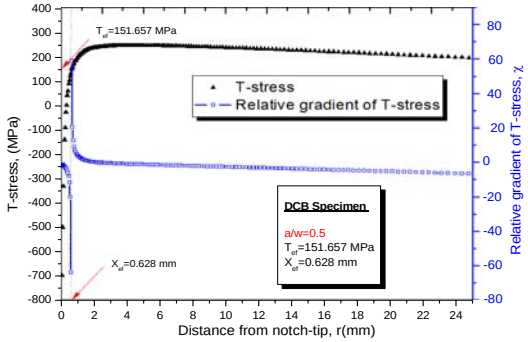

Figure 10. Evolution of the T-stress along of ligament for DCB specimen.

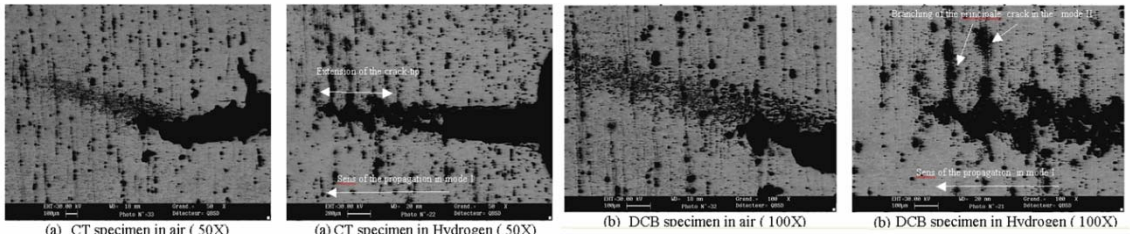

Figure 11. Observation by SEM of the cracks formation in pipeline during its service in different environments: air and hydrogen for CT and DCB specimens.

Crack propagation in air shows perlite debonding and ferrite matrix cracking as in Figure 12. In air, crack propagates by mode I in ferrite phase. Somes cracks are arrested in the perlitic phase, and continue as second crack in ferrite. Extension of second crack, is probably prolongation of the first crack in third dimension. The perlite phase play the role of crack arrestator.

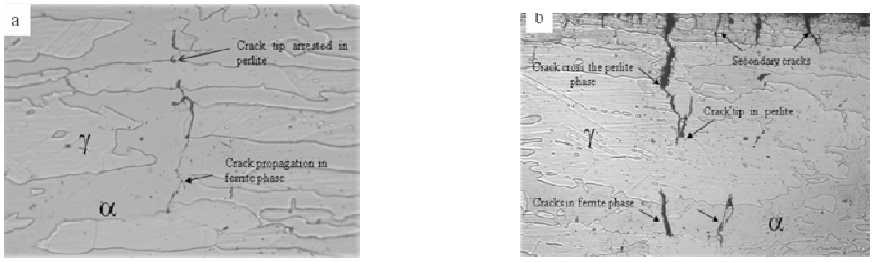

(a) 40µm (50X) (b) 100µm (20X)

Figure 12. Optical photographs for cross section through the cracks and secondary cracks (a) –without hydrogen & (b) –hydrogen environment

With hydrogen environment, fracture is sometimes initiated from secondary cracks and very close to the surface due to pitting under hydrogen attack as shown in Figure 12.b. The crack stress field will produce a strain magnification in adjacent micro-cracks and penetration of hydrogen atoms will result in further cracking of ferrite phase at the crack tip. The crack cross the perlitic phase and will propagate in the straight direction, facilitating hydrogen propagation and weeping.

5. Discussion

It can be seen that critical effective $T_{ef,c}$-stresses have ~~the~~ influence on crack paths. Pipe submitted to internal pressure has higher negative critical value of the T-stress, $T_{ef,c}$, range and consequently lower constraint in comparison with bending specimens. SENT and CT specimens have also a high negative value of the $T_{ef,c}$-stress for cracks emanating from notch tip but lower than a notched pipe. For these specimens and pipe submitted to internal pressure, crack extension is observed along x direction, i.e. perpendicular to the principal tensile stress (Fig. 13.a). DCB specimens exhibits a particular positive $T_{ef,c}$-stress values (Fig. 13.b). In this case, crack bifurcation appears after fracture initiation.

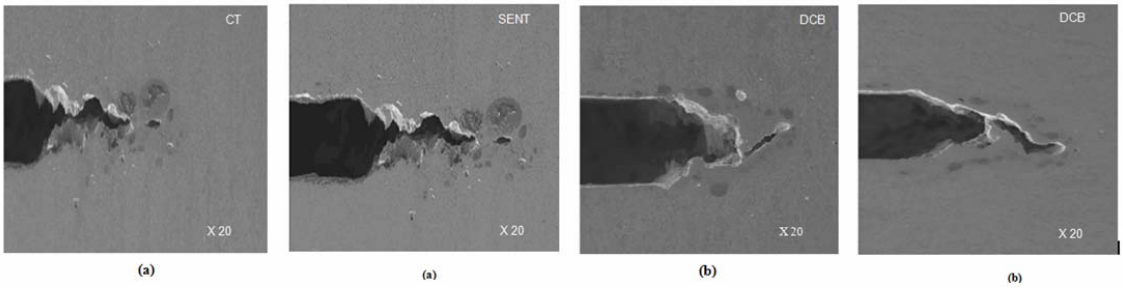

Figure 13. Kinking direction for (a) SENT and CT specimen, (b) DCB specimen.

Crack extension in API 5L X52 steel is governed by ductile failure mechanism, namely, nucleation of microvoids, growth and coalescence of these microvoids. However, pipe under internal pressure, CT, and SENT specimens, voids close to the notch are not elongated along the direction of loading but are elongated along shearing stress direction component which induced failure by mode II superimposed with mode I. Therefore, crack extension has a zigzag path characteristic of mixed mode (I + II failure mode). This zigzag mechanism can be seen on Figure 14.a with and without the hydrogen effect.

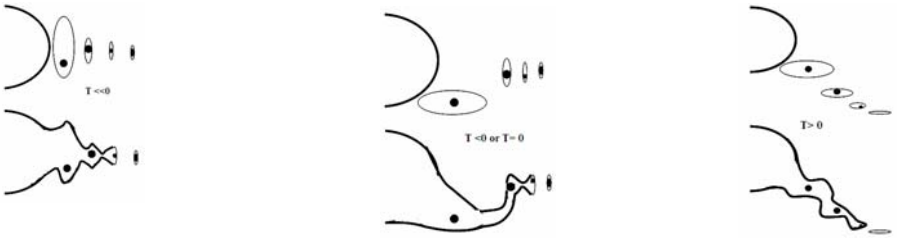

(a) strong negative T stress (b) low negative T-stress (c) positive T-stress

Figure 14. Proposed mechanisms for ductile crack extension under negative or positive $T_{ef,c}$ -stresses.

For DCB specimen, the T-stress component is positive and voids are elongated closed to shearing direction. Crack path is linear along a direction which is close to pure mode II bifurcation angle (70°) (see Fig. 14.b). Therefore, ductile crack extension is governed by the intensity of shearing mode induced by the T-stress. Thus, the following model of crack extension can be assumed to describe crack paths as a function of the critical effective T-stress. Due to hard particles inside voids (these particles promote voids nucleation by stress concentration), voids cannot be closed by compressive (negative) T-stress and crack extension is then stable in notch direction according to scheme in [12]. If the T-stress is positive and higher than opening stress at some distance ahead of the notch tip, void extension then occurs in x direction which is corresponding to the maximum $T_{ef,c}$-stress direction. In this case, crack extension is made by bifurcation.

6. Conclusion

Fracture toughness is not really intrinsic to material but depend on constraint. The critical notch stress intensity factor versus the effective T stress build up a master curve which coupled the fracture driving force gives the critical conditions for any kind of geometry and loading mode. For the pipe steel API X52,the master curve exhibits a linear decreasing behavior. Slope and value at origin are few affected by hydrogen embrittlement. Crack path after fracture initiation is affected by constraint evaluated by T stress. A loss of constraint corresponds to high negative T effective value. This situation occurs in notched pipe submitted to internal pressureand crack path remains normal to maximum principal stress. This is unchanged after hydrogen embrittlement but fracture appearance is then modified. Over a short distance ahead of notch tip , there is a mixture of dimples and brittle facets. Fracture of DCB specimens occurs under high constraint characterized by a positive value of T stress. Crack kinking occurs due to mixed mode I +II induced by superposition of T stress. It has been seen on CT specimen with a lower constraint than DCB specimen that hydrogen embrittlement promotes this crack kinking. Further works are required to understand the shift of critical T effective value to promote crack kinking to lower value. The assumption of decreasing shearing mode cohesion energy with hydrogen will be investigated. Following the same idea, evolution of ratio of shearing and opening mode cohesion energy will be determined by appropriate experiments.

References

1. Chao, Y.J., Liu, S., and Broviak, B.J. (1999). Variation of fracture toughness with constraint of PMMA specimens. Proceedings of ASME-PVP 393, 113–120.
2. Hadj Meliani M., Pluvinage G., Matvienko Y.G. (2011). Two Parameter Fracture Criterion (K_ρ-T_{ef}) Derived From Notch Fracture Mechanics. Internal Journal of Fracture. 167:173–182.
3. M. Hadj Meliani, Z. Azari, G. Pluvinage, Y.G.Matvienko (2011).Variation of Material Failure Curve with Constraint. Procedia Engineering. **10**. 710-715.
4. Yang, B. Ravi-Chandar, K. (1999). Evaluation of elastic T-stress by the stress difference method. Engng Fract Mech. 64:589-605.
5. Chao Y.J., Liu S. and Broviak B.J. Brittle fracture (2011). variation of fracture toughness with constraint and crack curving under mode I conditions .Experimental Mechanics, 41, 3, pp 232-241.
6. Hadj Meliani M., Azari Z., Matvienko Y.G., Pluvinage G. (2011).The Effect of Hydrogen on the Material Failure Curve of APL 5L Gas Pipe Steels. Procedia Engineering. **10**. 942-947
7. Hadj Meliani M, Azari Z, Pluvinage G, Capelle J (2010). Gouge assessment for pipes and associated transferability problem. Engng Failure Analysis; **17**: 1117-1126.
8. Ayatollahi, M.R., Pavier, M.J., and Smith, D.J. (2002). Mode I cracks subjected to large T-stresses. International Journal of Fracture 117(2), 159–174.
9. Chao YJ, Reuter WG (1997). Fracture of surface cracks under bending loads. In: Underwood JH, MacDonald B, Mitchell M(eds) Fatigue and fracture mechanics, vol 28,ASTMSTP 1321. American Society for Testing and Materials, Philadelphia, pp 214–242.
10. Sumpter, J.D.S (1993). An experimental investigation of the T stresses approach. Constraint effects in Fracture, ASTM STP 1171 (Edited by E. M. Hackett, K.-H. Schwalbe and R.H. Dodds), American Society for Testing and Materials, Philadelphia, 492-502.
11. Hancock, J.W, Reuter, W.G and Parks, D.M. (1993). Constraint and toughness parameterized by T. constraint effects in Fracture, ASTM STP 1171 (Edited by E.M. Hackett, K.-H. Schwalbe and R.H. Dodds), American Society for Testing and Materials, Philadelphia, 21-40.
12. Hadj Meliani M., Azari Z., Pluvinage G., Matvienko Y.G. (2011). The effective T-stress estimation and crack paths emanating from U-notches. Engineering Fracture Mechanics. 77(2010):1682–1692.
13. Hadj Meliani M., Azari Z., Pluvinage G. (2009).Constraint Parameter for a Longitudinal Surface Notch in a Pipe Submitted to Internal Pressure. Key Engineering Materials. Advances in Strength of Materials. Vol. 399 (2009) pp 3-11.
14. Hadj Meliani M., Benarous M., Moustabchir H., Harriri S., Azari Z. (2009).Three-dimensional T-stress to Predict the Directional Stability of Crack Propagation in a Pipeline with External Surface Crack. Springer Edition, Mars 2009**.**
15. Ayatollahi, M.R, Pavier, M.J, and Smith, D.J. (1998). Determination of T-stress from finite element analysis for mode I and mixed mode I/II loading. Int. J. of Fracture 91, 283-298.
16. Hadj Meliani M, Matvienko Yu.G, Pluvinage G (2011). Corrosion defect assessment on pipes using limit analysis and notch fracture mechanics. Engng Failure Analysis; **18**: 271-283.
17. Meshii T., Tanaka T(2010). Experimental T_{33}-stress formulation of test specimen thickness effect on fracture toughness in the transition temperature region. Engineering Fracture Mechanics **77** 867–877.

18. Matvienko Yu.G. (2011). A damage evolution approach in fracture mechanics of pipelines**.** In: Integrity of Pipelines Transporting Hydrocarbons, NATO Science for Peace and Security Series C: Environmental Security / eds.: G. Bolzon, T. Boukharouba, G. Gabetta, M. Elboujdaini and M. Mellas, Springer Netherlands: 227-244.
19. Maleski M.J., Kirigulige M.S. and Tippur H.V. (2004). A method for measuring Mode I crack tip constraint under dynamic and static loading conditions. Society for ExperimentalMechanics, vol 44, N° 5.
20. Cotterell B, Rice JR(1980). Slightly curved or kinked cracks. Int J Fract; 16: 155-69.
21. Selvarathinam AS, Goree JG (1998). T-stress based fracture model for cracks in isotropic materials. EngFractMech; 60: 543-61.
22. Sumi Y, Nemat-Nasser S, Keer LM (1985). On crack path stability in a finite body. EngFractMech; 22: 759-71.
23. Cotterell B (1980). Notes on fracture paths and stability of cracks. EngFractMech; 13: 526-33.
24. European project. NaturalHy Project, http://www.naturalhy.net
25. Hadj Meliani M., Moustabchir H., Azari Z. (2007). T-stress by stress difference method (SDM): Numerical analysis on mode (I) loading. Particle and continuum aspect of mesomechanics. Mesomechanics 2007, Lille, France. p 253-260, edited by ISTE publishing Knowlge.
26. SofronisP.and Lufrano J.(1999). Interaction of local elastoplasticity with hydrogen: embrittlement effects. Materials Science and Engineering, A260, pp. 41-47.
27. Eliezer D., Eliuaz N., Senkov O. N., Froes F. H (2000). Positive effects of hydrogen in metals. Materials Science and Engineering, A280, pp. 220-224.
28. Wilkowski G. (2000). Leak-before-break: what does it really mean? Journal of Pressure Vessel Technology, Transaction of ASME. Vol. 122, No 3, pp. 267-272.
29. Liu Y. H. Cen Z. Z., Chen H. F., Xu B. Y. (2000). Plastic collapse analysis of defective pipelines under multi-loading systems. International Journal of Mechanical Science. Vol. 42, pp. 1607-1622.
30. Hanneken J. W. (1999). Hydrogen in metals and other materials: a comprehensive reference to books, bibliographies, workshops and conferences, International Journal of Hydrogen Energy, Vol. 24, No 10, pp. 1005-1026.
31. Capelle J, Gilgert J, Dmytrakh I, Pluvinage G.(2008). Sensetivity of pipelines with steel API X52 to hydrogen embrittlement. Int J Hydrogen Energy; **33**: 7630-7641.
32. Capelle J., Gilgert J., Dmytrakh I., Pluvinage G. (2011) . The effect of hydrogen concentration on fracture of pipeline steels in presence of a notch. Engineering Fracture Mechanics **78**;364–373.
33. Naturalhy-Project(2005). Burst tests on pipes under pressure of mixture of hydrogen and natural gaz. Contract N^{o} SES6/2004/502661.Durability and Integrity Work-packages. Subcontract N^{o} 1401-2005.

Research on the mechanical properties of the CNT composites

Luodan Su, Qingsheng Yang*

Department of Engineering Mechanics, Beijing University of Technology, Beijing 100124, China
*Corresponding author: qsyang@bjut.edu.cn

Abstract Carbon nanotube (CNT) can be used as a good reinforcement embedded into polymer matrix. However, properties of composites reinforced by CNT can't be improved efficiently, because of the damage of interface between CNT and polymer in CNT composites. In this paper, the cohesive zone model (CZM) was employed to express the damage and fracture of interface between CNT and the epoxy matrix. The key parameters of the bilinear CZM were deduced based on the existing theory work. The whole deformation and fracture process of the interface has been revealed through the FE simulation results. The performance of the interface decides the mechanical property of the CNT composites and the stress-strain curve of composites has been plotted. It is with great importance to study the mechanical property of the interface to improve the performance of CNT composites.

Keywords Carbon nanotude, Composite, Interface, Damage, Crack Growth

1. Introduction

Since the discovery of carbon nanotube (CNT) by Iijima [1], CNT has wide application potential because of their wonderful physical and mechanical property, it has been thought as a promising candidate as the ideal reinforcing fibers for advanced composite with high strength and low density. However, mechanical property of composites reinforced by CNT can't be improved efficiently, owing to the deep affect of interface between CNT and polymer in CNT composites. The damage and fracture of the interface leads to stress redistribution in CNT composite, and decides the effective mechanical property of the composite. The mechanical property of the interface is the key factor of the CNT reinforced composite [2].

The Cohesive zone Model (CZM) describes material separation with a traction-separation law (T-S law) and links the micro-structural failure mechanism to the effective properties of the composite [3,4]. Because of the nano-scale interface in CNT composite, the van der Waals force plays an important role in the property of the interface [5,6]. The Cohesive zone Model(CZM) can reflect the characteristic and working principles of the van der Waals force phenomenologically, by two important parameters, the cohesive strength Tc and the energy release rate Gc, as shown in Fig.1[7]. The effective separation and damage parameter from view point of stiffness reduction are employed. The different T-S law has been developed with continuous study of the cohesive model, and the CZM has been widely used in interface decohesion and crack growth.

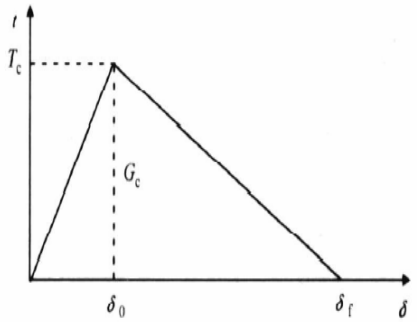

Figure 1. Bilinear cohesive law

Nowadays, many researchers have realized the significance of the van der Waals force in the

interface between the CNT and the matrix, and study mechanical property of the interface of CNT composite with various method, such as the experimental method and the Melecular Dynamics (MD) method [8]. There are still many technical limitations in experimental method, and the calculation cost of the MD method is too huge. The Finite Element Method (FEM) combined with the CZM is the effective and economy method to study mechanical property of the interface of CNT composite, and the CZM was utilitied in this paper to predict local damage initiation and fracture propagation.

2. CZM Model of Interface

The key problem of the CZM is the definition of the two important parameters, the cohesive strength *Tc* and the energy release rate *Gc* . There is few experimental data providing the interface parameters accurately and directly for the CZM. Gou[9] has calculated the shear strength by the MD simulation of the CNT's pull out from the matrix. The result 75MPa was adopted to be the shear strength .Tan[6] has deduced the normal strength 470MPa and the energy release rate 0.107Jm^{-2}, from the Lennard-Jones potential from the van der Waals interactions, the results was adopted as the normal cohesive strength and the energy release rate *Gc* . The interface between the CNT and the matrix was modeled by the 2 dimension, 4 node cohesive element COH2D4 to reproduce the damage of interface between the CNT and polymer. The Young's modules of the CNT and the epoxy matrix are respectively 1 TPa and 4GPa.
The FEM model of the CNT composite was established by the generally used software ABAQUS. It is with three phases: the CNT fiber phase, the cohesive interface phase employing the CZM and the epoxy matrix phase. The unit cell was extracted to represent the effective properties of CNT composite based on the homogenization theory, as is shown in Fig. 2.

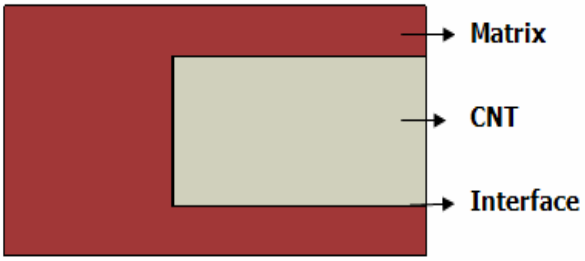

Figure 2. Unit cell of CNT composite

Since composite structures are usually designed for the loading in the reinforcement orientation, the displacement load was exerted at one side of the unit cell, and the other side was fixed, the boundary conditions of the unit cell was demonstrated in Fig. 3.

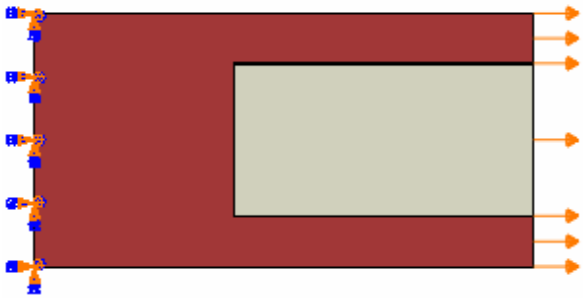

Figure 3. Boundary conditions of unit cell

3. Results and discussion

One of the advantages of the FE simulation is that the whole deformation and damage process can be observed clearly in the simulation. From the FE results, three obvious stages of mechanical properties of the interface were found: the linear elastic stage, the damage initiation stage and the crack propagation stage, as is shown in Figs. 4-6. The unit of the labels of the stress distribution nephogram is GPa.

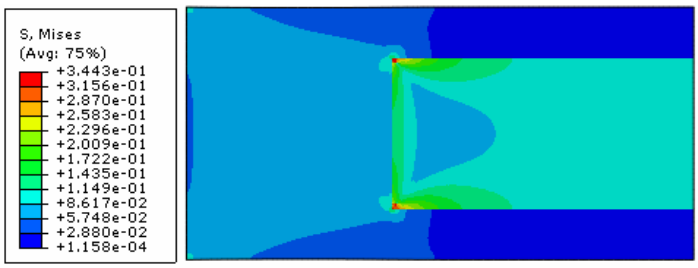

Figure 4. Stress distribution at linear elastic stage

In the linear elastic stage, the epoxy matrix and the CNT were bonded by the interface. The high cohesive strength ensures the effective transfer of the stress between CNT and the matrix. CNT takes more load than the matrix, the properties of CNT composites have been improved by the strong interface. The stress in the matrix where near by the CNT end is larger than the other positions in the matrix, and the stress in the CNT where near by the interface is larger than the other positions in CNT. In addition, the stress concentration appears at the corner of the CNT end.

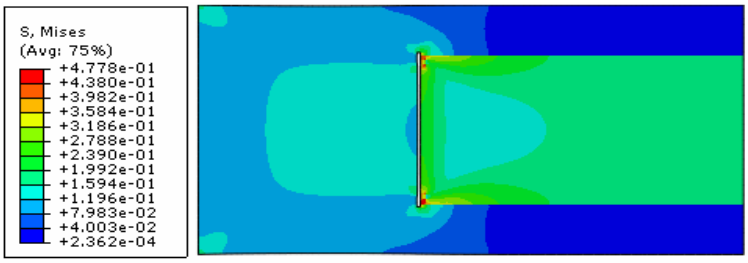

Figure 5. Stress distribution at damage initiation stage

As the displacement increasing, the damage initiation stage comes up, the damage initiated at the corner of the interface due to stress concentration. The damage of the interface leads to the stiffness reduction and stress redistribution in the composite, although the composite still has the capacity to bear the load. Then the microcracks at the corner grows, the crack extends to the end side of the interface.

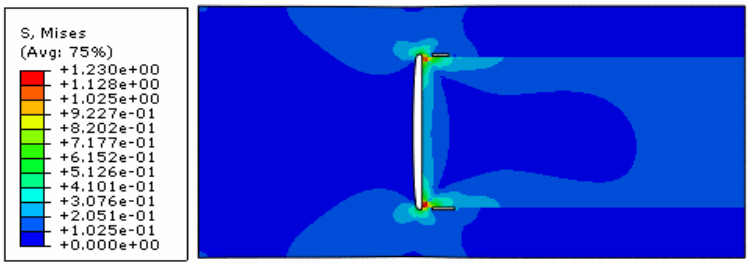

Figure 6. Stress distribution at crack propagation stage

At the crack propagation stage, the shear sliding comes up after the normal debond in the corner of

the interface, as can be seen from the Fig.6, the normal crack hasn't connected to the shear crack, the shear crack initials at a position near the interface end . For the damage and the debond of the interface, the CNT composite has been failed to take the load. The interface plays an important role to the mechanical property of the composites. The maximum stress appears in the corner of the interface, the stress concentration effect should be considered to predict the damage initiation and the crack propagation.

4. The discussion of mechanical property of CNT composites

The crack progress and the fracture mechanism of the interface has been studied by the CZM model. The influence of the interface to the CNT composites can be reflected in the stress--strain curve of the whole unit cell, as is shown in Fig.7. Because of the effect of the interface, the relationship between stress and strain is nonlinear. At first, the composite displays linear characters, on account of the valid function of the interface before the stress gets to its strength value. The effective modules of the composites in the linear stage is 9.44GPa, CNT has the obvious reinforcing performance. Then accompanies with the crack propagation in the interface, the stress has an abrupt drop. The performance of the interface decides the mechanical property of the CNT composites.

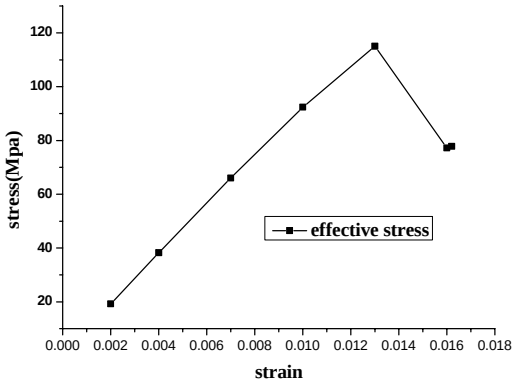

Figure 7. Stress-strain curve of CNT composites

5. Conclusion

1. The CZM of the interface between the matrix and CNT has been established to predict the mechanical property of interface, and it is proved that CZM is effective in the nanocomposites.
2. The whole deformation and damage process of the interface has been studied through the FE simulation results.
3. The stress--strain curve of composites has been plotted to research the mechanical properties of the composites. It is with great importance to study the mechanical property of the interface to improve the performance of CNT composites.

Acknowledge
This work is supported by the National Natural Science Foundation of China under the Project Number 11172012, and the Ph. D programs foundation of the Ministry of Education under the Project Number 20101103110005, which are gratefully acknowledged.

Reference

[1] Iijima S. Helical microtubules of graphite carbon . Nature, Vol 354(1991)56-61.
[2] Tserpes,K.I. , Papanikos, P. , Labeas,G. Multi-scale modeling of tensile behavior of carbon nanotube-reinforced composites. Theoretical and Applied Fracture Mechanics, 49(2008)51-60.
[3] N.Chandraa，H.Lia. Some issues in the application of cohesive zone mode For metal-ceramic interfaces. International Journal of Solids and Structures, 39(2002)2827-2855.
[4] D.Stevanovic. FEA of crack-particle interactions during delamination in inter layer toughened polymer composites. Engineering Fracture Mechanics,72(11)(2005)1738-1769.
[5] Jiang LY, HuangY, Jiang H, et al. A cohesive law for carbon nanotube/polymer interfaces based on the van der Waals force. J of Mech and Phys of Solids, 54(11) (2006)2436-52.
[6] H.Tan, L.Y.Jiang, Y.Huang, et al. The effct of van der Waals-based interface cohesive law on carbon nanotube-reinforced composite materials. Composites Science and Technology, 67(2007)2941-2946
[7] X. Guo, aA.Y.T. Leung ,A.Y. Chen. Investigation of non-local cracking in layered stainless steel with nanostructured interface. Scripta Materialia, Vol 63(2010)403-407.
[8] Li C Y, Chou T W. Modeling of elastic buckling of carbon nano-tubes by molecular Structural mechanics approach. Mechanics of Materials,36(2004)1047-1055
[9] Gou J H, Minaie B, Wang B, et al. Computational and experimental Study of interfacial Banding of single-walled nano-tube reinforced composites. Computational Materials Science, 31(2004)225-236

A experimental study of I-II-III mixed mode crack fracture of rock under different temperature

LI Li-yun[1,*], XU Zhi-qiang[1], LI Ming-xiu[1], LIU Yi[1], FAN Chen[1], TANG Tie-Wu[1], LIU Da-an[2]

[1]China University of Mining and Technology, Beijing 100083, China;
[2]Institute of Geology and Geophysics, Chinese Academy of Science, Beijing 100029, China
[*] Corresponding author: lly@cumtb.edu.cn

Abstract A series of critical fracture toughness of two kinds of rock materials under different temperature which varied from -50°C to 240 °C are measured by I-II-III mixed mode fracture experiments adopting atypical three point bending specimens. Relative stress intensity factors of crack initiation are calculated by finite element method. Combining with calculated values, the experiment result shows that, the mixed mode fracture toughness of the rocks decreases with the increase of temperature. The experimental and calculated results can be used in the design of deep underground engineering and disaster prevention and mitigation engineering。

Key words rock crack fracture, I-II-III mixed mode , temperature, experiments, finite element method.

1. Introduction

The rock mass whole structure failure in underground engineering is the process of damage, crack fracture and propagation. Deep mining engineering and geological disposal engineering such as nuclear waste, carbon dioxide and garbage deeply buried belong to the underground geotechnical engineering combining with temperature variation. Therefore, the investigation of the propagation behavior of rock crack under different temperature will be very important. Preliminary studies on temperature effect are mainly concentrated in mode I rock crack[1-3], a small amount of studies are concentrated in mixed-mode I-II rock crack[4-7]. About three-dimensional propagation behavior of rock crack which containing mode III stress intensity factor, the authors have done some researches under the room temperature in the recent time [8-9]. But the research about mixed mode I-II-III rock crack fracture coupling with temperature effect, there is almost no published paper, but it has important significance in deep underground engineering, for this mixed mode crack coupling with temperature is the basic existence in deep underground engineering. Consider of this, three point bending I-II-III mixed mode fracture experiments of two kinds of granite were carried out under 6 temperature levels in this paper. The variation law of critical fracture load v.s. temperature was measured. Combined with finite element method (FEM) calculation, the stress intensity factors in crack tip line under the critical load were got. The results of the paper both in experiments and in numerical calculation can provide a valuable reference for the deep underground engineering design and disaster prevention engineering design.

2. Experimental investigation

2.1. Preparation of specimen

The rocks used in this experiment investigation are two kinds of granite: white linen granite and red linen granite. They have different grain sizes. The grain size of the former is smaller than later. Specimen contours are both 140mm×40mm×24mm (Figure 1). From specimen central section, in the position L=15mm and L=30mm, an edge crack which width is not more than 1mm were cut by diamond wheel blade. Crack length a=20mm.

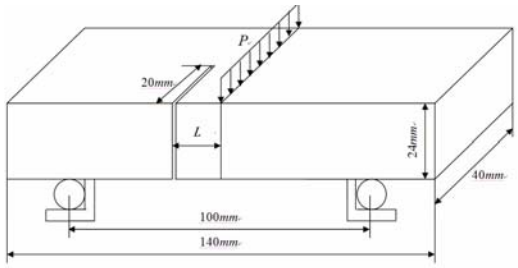

Figure 1 Specimen diagram and loading mode

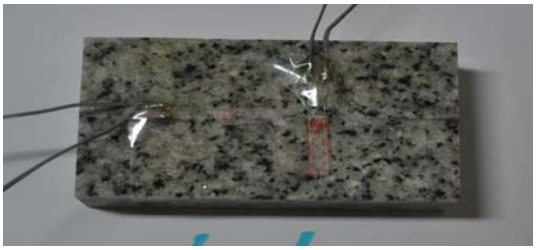

Figure 2 Uniaxial compression experiment specimen

2.2. The process of experiment

For the finite element method (FEM) calculation subsequently in this paper, the elastic modulus of two rocks under different temperature was measured by uniaxal compression experiments. The contour of uniaxal compression specimen and test situation is shown in Figure 2 and Figure 3. The elastic modulus E measured under different temperature are listed in Table 1. Due to the difficulty of test technique，the Poisson's ratio of the two rocks under different temperatures were not measured except under ambient temperature. And then, about the variation law of Poisson's ratio in different temperature was not mentioned in published documents. So in this paper Poisson's ratio are assumed that it has no change when temperature changes; and it is measured under ambient temperature that: for white linen granite μ = 0.26 and for red linen granite μ = 0.3.

The loading way of abnormal three point bending test is shown in Figure 1. The experimental situation is shown in Figure 4. For the two kinds of granite, under different temperature and different crack position L, the critical fracture loads F measured by experiments are listed in Table 2.

Table 1 ： Elastic modulus E of two kinds of granite under different temperatures

Type of specimen	Elastic modulus E/GPa					
	-50^0C	-25^0C	Room temperature	80^0C	160^0C	240^0C
White linen granite	18.8685	17.643	15.3455	17.1	18.3985	17.087
Red linen granite	17.033	15.992	17.713	17.56	17.9665	19.196

Whether in high temperature test or in low temperature test, before a test, the specimen must be placed in the oven in which temperature has arrived demand level half an hour in order to get a well-distributed temperature within specimen. In the experimental process, the loading way of test machine was controlled by displacement. Loading rate is 0.015mm/min. In experiment it can be observed that the crack tip point at the bottom of the specimen starts fracture, it leads the specimen failure. The fracture section of specimen is not a plane, and presents a three-dimensional

morphology. The failure pattern of the specimen is shown in Figure 5. The critical fracture loads under different temperature are shown in Table 2. The relative variation rate η which was compared with the critical fracture load under ambient temperature, the values of η v.s. temperature are listed in Tab. 3. η is defined as:

$$\eta=(F-F_0)/F_0 \quad (1)$$

F_0 and F are the critical fracture load under ambient temperature level and other temperature levels. η can reflect the deviation extent between F and F_0 under different temperature.

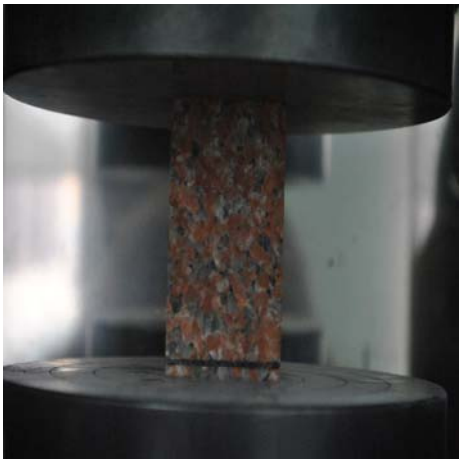

Figure 3 Uniaxial compression test

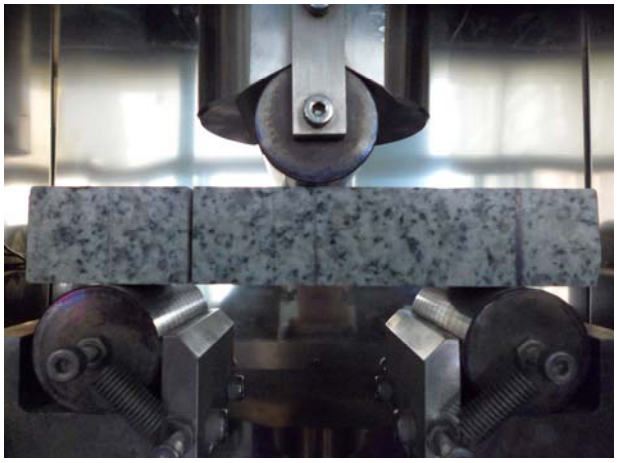

Figure 4 Abnormal three point bending experiment

Table 2 The critical fracture load F v.s. temperature

Type of specimen	Distance from the central position/mm	The critical fracture load F/（kN）					
		-50^{0}C	-25^{0}C	Room temperature	80^{0}C	160^{0}C	240^{0}C
White linen granite	L=30	2.67	-	2.07	2.01	1.71	1.62
	L=15	1.47	1.51	1.25	1.17	1.06	0.84
Red linen granite	L=30	2.35	1.90	1.72	1.27	0.95	0.97
	L=15	1.55	1.21	1.21	1.42	0.99	0.75

Table 3 The deviation rate η between F and F_0 under different temperature.

Temperature /^{0}C	White linen granite		Red linen granite	
	L=30mm	L=15mm	L=30mm	L=15mm
-50^{0}C	28.95%	17.86%	37.02%	27.95%
-25^{0}C	-	21.10%	10.61%	-0.47%
Room temperature	0	0	0	0
80^{0}C	-2.86%	-6.20%	-26.02%	17.28%
160^{0}C	-17.32%	-15.12%	-44.53%	-18.25%
240^{0}C	-21.71%	-33.07%	-43.39%	-37.82%

2.3. The relationship between parameters and temperature

It can be seen from Table 1 that in the range of -50^{0}C to 240^{0}C, with the temperature increases, the variation of elastic modulus E is not obvious. It has only a little volatility.

From Table 2, for the same type of specimen, It can be seen that the critical fracture load reduce with the temperature increase. It is unconcerned with the crack location and the type of rock. Under the same temperature, the value of the critical load is related with the crack position. The shorter the distance between crack and central position of the specimen is, the lower the critical load is.

In the rang of -50^{0}C to 240^{0}C, for different specimens, with the temperature increase, the deviation rate η between F and F_0 gradually reduce. For white linen granite, when L = 30 mm, η gradually reduce from 28.95% down to -21.71%. when L = 15 mm, η gradually reduce from 17.86% down to -33.07%. For red linen granite, when L = 30 mm, η gradually reduce from 37.02% down to -43.39%. When L = 15 mm, η gradually reduce from 27.95% down to -37.82%.

Figure 5 Specimen after fracture

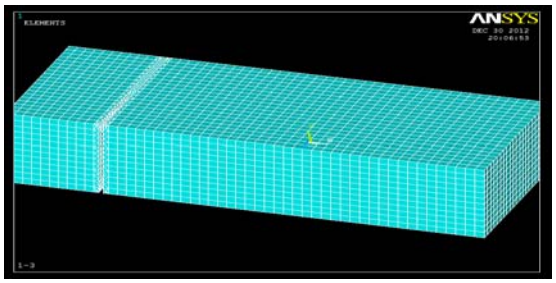

Figure 6 Divide grid

3. Finite element analysis

For abnormal three point bending I-II-III mixed mode fracture specimens in this paper, numerical solution of stress intensity factors for every point in crack tip line were not got in other documents, no more than analytic solutions. In this paper the distribution laws of stress intensity factors K_{I}、K_{II}、K_{III} and their critical values in crack fracture initiation point were obtained by FEM calculation under different temperatures.

3.1.Finite element modeling

By try of FEM calculations many times, it had been known that if the short sections outside the two lower supports of the specimen were ignore, it did not affect the simulation results obviously, so in this paper, the sections between the two lower supports of specimen were choose into FEM calculation. By this modeling way, unnecessary elements can be reduced. It can improve the calculation speed. Cartesian coordinate system was defined as follows: X axis is along the length of the specimen, Y axis is up along the specimen thickness direction, Z axis is forward along the width direction (Figure 6). The width of edge crack is not more than 1mm. The crack surface is a free surface, and the crack front is a rectangular shape. It is consistent with the crack front in the specimens of experiments. Scanning grid division is used. In order to get accurate stress values near crack tip, refined grids around crack tip are also used. Divided elements situation are shown in Figure 6. Substitute the material parameters E, μ and critical load F into the FEM program, critical values (mixed mode critical fracture toughness) of K_{I}, K_{II}, K_{III} in failure crack tip can be calculated.

3.2. The relation between stress intensity factors of initiation points and temperatures

After the stress field calculated within the specimens by the finite element method, the three formulas following can be directly applied to calculate the stress intensity factors of the crack tip[10-11]:

$$K_{\mathrm{I}} = \lim_{r\to 0}\sqrt{2\pi r}\sigma_x \tag{2}$$

$$K_{\mathrm{II}} = \lim_{r\to 0}\sqrt{2\pi r}\tau_{xz} \tag{3}$$

$$K_{\mathrm{III}} = \lim_{r\to 0}\sqrt{2\pi r}\tau_{xy} \tag{4}$$

r is the short distance from stress point to the crack tip

Put r values and stress values of every point on crack extension cord into the formulas, and drew a straight line of K_{I}、K_{II}、K_{III} v.s. r, through the straight line, the real values of K_{I}、K_{II}、K_{III} can be got at the point $r = 0$[10-11].

In abnormal three point bending experiments (Figure 4), the crack fracture just initiated from the tension point which was on the crack tip point located on the bottom of specimen (Figure 4), so the relations between critical stress intensity factors and temperatures are listed in Table 4 and Table 5, and shown in Figure 7 to Figure 10.

Table 4 Critical stress intensity factors v.s. temperature (white linen granite)

Temperatures	L=30mm			L=15mm		
	K_{I}/MPam$^{1/2}$	-K_{II}/MPam$^{1/2}$	-K_{III}/MPam$^{1/2}$	K_{I}/MPam$^{1/2}$	-K_{II}/MPam$^{1/2}$	-K_{III}/MPam$^{1/2}$
-50^{0}C	2.285	0.453	0.248	2.114	0.258	0.148
-25^{0}C	-	-	-	2.172	0.265	0.152
Normal temperature	1.772	0.351	0.180	1.794	0.219	0.126
80^{0}C	1.721	0.341	0.186	1.682	0.205	0.118
16^{0}0C	1.465	0.290	0.159	1.522	0.186	0.107
24^{0}0C	1.387	0.275	0.150	1.200	0.147	0.084

Table 5 Critical stress intensity factors v.s. temperature (red linen granite)

Temperatures	L=30mm			L=15mm		
	K_{I}/MPam$^{1/2}$	-K_{II}/MPam$^{1/2}$	-K_{III}/MPam$^{1/2}$	K_{I}/MPam$^{1/2}$	-K_{II}/MPam$^{1/2}$	-K_{III}/MPam$^{1/2}$
-50^{0}C	2.014	0.399	0.218	2.229	0.272	0.156
-25^{0}C	1.626	0.322	0.176	1.734	0.212	0.121
Normal temperature	1.470	0.291	0.159	1.676	0.205	0.117
80^{0}C	1.318	0.261	0.143	2.043	0.249	0.143
160^{0}C	0.816	0.162	0.088	1.218	0.149	0.085
240^{0}C	0.794	0.157	0.086	1.083	0.132	0.076

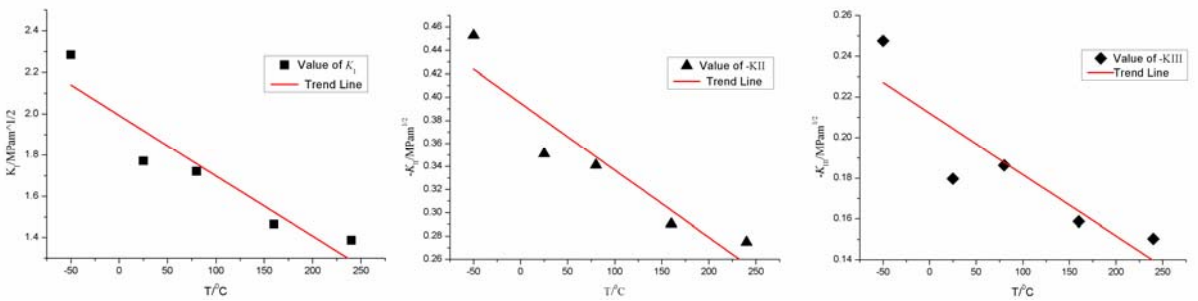

(a) Curves of K_I (b) Curves of -K_{II} (c) Curves of -K_{III}

Figure 7 The critical stress intensity factors v.s. temperature (white linen granite, L =30mm)

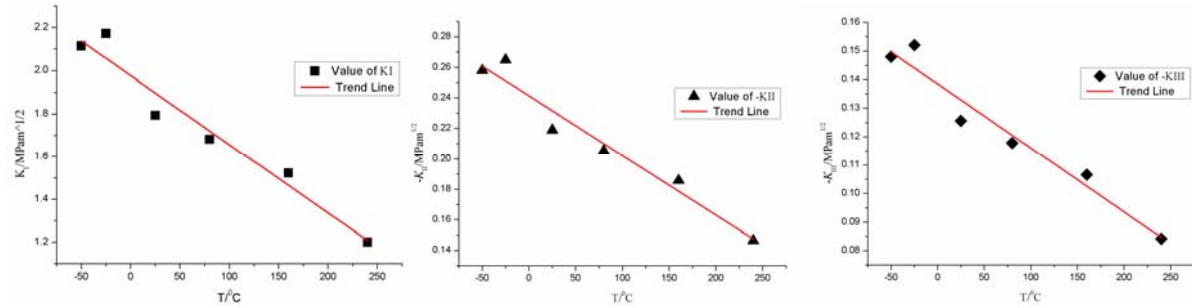

(a) Curves of K_I (b) Curves of -K_{II} (c) Curves of -K_{III}

Figure 8 The critical stress intensity factors v.s. temperature (white linen granite, L =15mm)

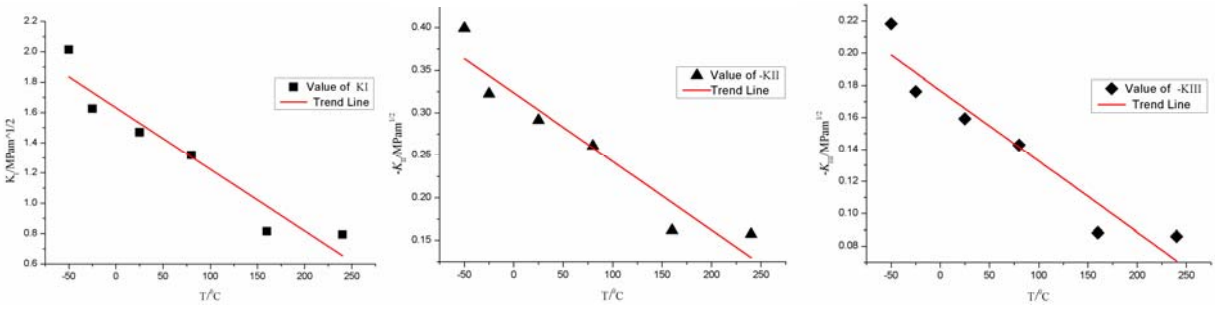

(a) Curves of K_I (b) Curves of -K_{II} (c) Curves of -K_{III}

Figure 9 The critical stress intensity factors v.s. temperature (red linen granite, L =30mm)

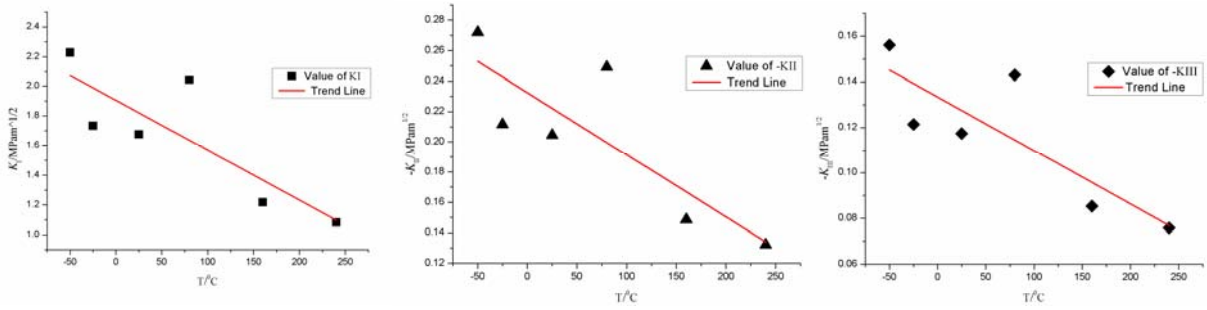

(a) Curves of K_I (b) Curves of -K_{II} (c) Curves of -K_{III}

Figure 10 The critical stress intensity factors v.s. temperature (red linen granite, L =15mm)

3.3.Result analysis

From the Figures above，it can be seen that the absolute values of critical stress intensity factors decrease with the temperature increase. It is unconcerned with rock type and crack positions L. The reason is the critical fracture loads decrease with the temperatures increase, so the critical stress intensity factors K_{I}、K_{II}、K_{III} decrease relevantly.

From the Tab. 4 and Tab. 5, it can be seen that the K_{I} (>0) values at the initiation points for L=30mm specimen are generally smaller than the K_{I} (>0) values for L=15mm specimen. And the critical loads of the former are generally bigger than the latter. From this it can be known that, let the L=30mm specimen failure is more difficult than let the L=15mm specimen failure. But the relevant absolute values K_{II} and K_{III} of former are bigger than latter. It shows that, if K_{I} value who dominates the crack fracture initiation is not big enough, a I-II-III mixed mode rock crack tip can begin to expand, it has to have bigger K_{II} and K_{III} values. This result reflects a comprehensive effect of mixed mode rock crack fracture sufficiently.

4. Conclusion

(1) In the range of -50^{0}C to 240^{0}C, with the increase of temperature, the variation of elastic modulus E of two kinds of granite is not obvious; i.e. E values had no obvious differences between ambient temperature and some other temperature levels.

(2) For the same kind of rock crack specimen, with the increase of temperature, the critical fracture load is gradually reduced. The deviation rate η decrease gradually from (20% to 40%) under -50^{0}C to (-20% to -40%) under 240^{0}C, i.e. at the lower temperature -50^{0}C, the crack initiation load will be higher (20% to 40%) than at ambient temperature; at the higher temperature +240^{0}C, the critical fracture load will be lower (20% to 40%) than at ambient temperature .

(3) For the same specimen, the critical stress intensity factor K_{I}, K_{II}, K_{III}, at the crack fracture point, decrease with the temperature increase.

(4) At the same temperature, the longer the distance between crack and center of the specimen, the value of K_{I} (caused by tensile stress) in crack fracture point will be lower; and the critical load will be higher. It reflects the rock crack fracture initiation is mainly caused by tensile stress. If the K_{I} value is smaller, is the higher absolute value of K_{II}, K_{III} at crack fracture initiation point required. It reflects the comprehensive effects in I-II-III mixed mode rock crack fracture.

Acknowledgements

This study is financially supported by Natural Science Foundation of China (No: 41072242) and National Basic Research Program under Grant No. 2010CB226802, 2011CB201201.

References

[1] Xu Xiaoli , Gao Feng , Ji Ming. Damage Mechanical Analysis of Fracture Behavior of Granite Under Temperature[J]. Journal of Wuhan University of Technology, 2010, 32(1):143-147.

[2] T Funat su, M Seto, H Shimada, et al. Combined effects of increasing temperature and confining pressure on the fracture toughness of clay bearing rocks[J]. International Journal of Rock Mechanics and Mining Sciences, 2004, 41(6): 927-938.

[3] Zuo Jianping, Zhou Hongwei, Liu Yujie. Research on characteristic parameters of sandstone three-point bending failure under different temperatures[J].Chinese Journal of Rock Mechanics

and Engineering,2010,29(4):705-712.

[4] N.A. Al-Shayea, K. Khan, S.N.Abduljauwad. Effects of confining pressure and temperature on mixed-mode (I–II) fracture toughness of a limestone rock[J]. International Journal of Rock Mechanics and Mining Sciences. 2000, 37(4): 629-643.

[5] Naser A. Al-Shayea. Crack propagation trajectories for rocks under mixed mode I－II fracture[J]. Engineering Geology, 2005, 81(1): 84-97.

[6] Xie Hai feng, Rao Qiu hua, Xie Qiang,et al. Plane shear (Mode Ⅱ) fracture experiment analysis of brittle rock at high temperature[J].The Chinese Journal of Nonferrous Metals,2008,18(8):1534-1540.

[7] Kang Jian, The rock thermal fracture research and application[M]. Dalian: Dalian University of Technology Press,2008.

[8] Li Liyun, Wong R H C, Han Zhichao, et al. Experimental and theoretical analysis of three-dimensional surface crack propagation[J]. Chinese Journal of Rock Mechanics and Engineering, 2012,31(2):311-318.

[9] Li Liyun, Xu Fengguang, Xie Heping,et al. Fracture Study on Mode I-III Crack of Rock[J]. Key Engineering Materials, 2006, 325(2): 1217-1220.

[10] He Qingzhi，Li Zhengneng. Engineering fracture mechanics[M]. Beijing：Beijing University of Aeronautics and Astronautics Press, 1993.

[11] Li Shiyu, Yin Xiangchu. Rock fracture mechanics[M].China University of Science and Technology Hefei: Press,2010.

Numerical study of the deformations of two coplanar circular cracks during their coalescence

L. Legrand[a], V. Lazarus[b]

[a] *UPMC Univ Paris 6, CNRS, UMR 7190, Institut Jean Le Rond d'Alembert, France, legrand@lmm.jussieu.fr*
[b] *Univ Paris-Sud, UPMC Univ Paris 6, CNRS, UMR 7608, FAST, France*

Abstract

Consider two planar circular cracks embedded in an infinite linear elastic media and submitted to mode I tensile loading. Bueckner-Rice weight functions theory allows us to update the stress intensity factor when the crack fronts are slightly deformed in their plane. Using an incremental numerical method based on this theory, we study the propagation of these two cracks when they interact each other taking into account the non-linearities induced by their deformations. The advantage of this method in comparison to more standard finite element methods is that only the crack fronts have to be meshed. Using a Griffith threshold law, we notice important deformations of the crack fronts are observed and a drastically decreasing threshold loading when the fronts approach each other.

Keywords: Brittle fracture, Toughening, Finite element method, Elastic line model

The present study focuses on the coalescence phenomenon of two circular cracks. What is the critical loading to reach the coalescence? Is the crack advance facilitated due to the presence of the secondary crack? What is the shape of the cracks during their propagation? Those questions are considered in the present article. To do it accurately, the main difficulty is to calculate the three-dimensional stress intensity factors along all the fronts by taking into account the crack shape changes induced by the interaction between the cracks.

In the literature, we can find papers treating of interacting cracks but they never take into account the cracks fronts deformation during propagation (see [2 − 5] and [8]).

Here, the effects of the crack front shape changes are analized independently of the edge effects. For this purpose, two small cracks are considered, so we can make the assumption that the medium is infinite and subjected to remote loading. For this reason, methods based on integral equations are adapted here: the sole cracked area is needed. Moreover, in the present case of in-plane propagation, it is just necessary to mesh the 1D outline of the cracks. Using Bueckner-Rice formalism [7], the work of Bower and Ortiz [1] provides some examples of this approach in mode I. More recently, Lazarus [6] developped a simplified variant of their method without significant loss of accuracy. All these works only deal with a sole crack. In the present paper, we extend to two cracks in order to study their final coalescence.

1. Objectives

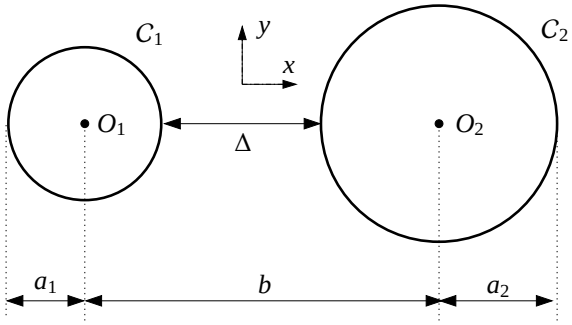

Figure 1: Two circular cracks.

Let us consider two circular coplanar cracks embedded in an isotropic elastic body (such as depicted in figure 1). The aim of this paper is to predict the in-plane propagation of these cracks subjected to remote tensile stress σ_∞ at infinity in brittle fracture. The method consists in coupling the Bueckner-Rice formalism with a propagation law starting from a configuration for which the needed quantities, namely the stress intensity factor (SIF) along the front and a certain kernel, are known. The procedure consists of different steps:

- Determination of the SIF for a given geometry:
  Knowing the geometry and the loading, how to calculate the SIF along the fronts?
- Propagation problem with a threshold:
  In brittle fracture, it is assumed that the propagation law is given by Irwin's criterion:

$$\left\{ \begin{array}{lcl} K < K_c & : & \text{no propagation} \\ K = K_c & : & \text{possible propagation} \end{array} \right. \tag{1}$$

  For a given crack geometry, there is a critical loading σ_∞^c such as: if $\sigma_\infty < \sigma_\infty^c$ then $K(M) < K_c$, $\forall\, M$ and if $\sigma_\infty = \sigma_\infty^c$, there is at least one point M of the front that verifies $K(M) = K_c$. We want to determine this stability threshold σ_∞^c all along the propagation.

2. Numerical approach

2.1. Adimensionalization

Let us define the dimensionless problem for which the distance between cracks centers b is taken at 1. The quantities of interest become: a_1/b and a_2/b, with a loading unit $\sigma_\infty = 1$, letting $K(M) = \sqrt{b}\,\sigma_\infty\,\widehat{K}(M)$, where $\widehat{K}$ is a dimensionless quantity.

2.2. Rice incremental formulae

Suppose that the crack geometry is slighty perturbed in its plane and consider a point $M_i \in C = C_1 \bigcup C_2$.

Let us set $\alpha = (1\,,\,2)$ and $\beta = (1\,,\,2)\,,\,\beta \neq \alpha$.

Then Rice's first formula reads ([7]):

$$\begin{aligned} \delta\widehat{K}_\alpha(M_i) &= \frac{1}{2\pi}\ VP \int_C \frac{W(M_k, M_i)}{D^2(M_k, M_i)} \widehat{K}(M_k)[\delta a(M_k) - \delta_* a(M_k)] ds(M_k) \\ &= \frac{1}{2\pi}\ VP \int_{C_\alpha} \frac{W_{\alpha\alpha}(M_i, M_k)}{D^2_{\alpha\alpha}(M_i, M_k)} \widehat{K}_\alpha(M_k) \delta a_\alpha^{(\alpha)}(M_k) ds(M_k) \\ &+ \frac{1}{2\pi} \int_{C_\beta} \frac{W_{\alpha\beta}(M_i, M_k)}{D^2_{\alpha\beta}(M_i, M_k)} \widehat{K}_\beta(M_k) \delta a_\alpha^{(\beta)}(M_k) ds(M_k) \end{aligned} \tag{2}$$

with:

$$\delta a_{\alpha}^{(\gamma)}(M_k) = \delta a_{\gamma}(M_k) - (\delta a_{\alpha}(M_i)\overrightarrow{n_{\alpha}}(M_i)).\overrightarrow{n_{\gamma}}(M_k) \quad , \quad \gamma = 1,2$$

and where $W_{\alpha\gamma}(M_i, M_k)$ is a kernel expressing the effect of the advance of $M_i \in C_\alpha$ over the SIF at point $M_k \in C_\gamma$. Rice's second formula can be written of the form:

- if $M_i \in C_\alpha$ and $M_k \in C_\alpha$ (points belong to the same crack front):

$$\begin{aligned}\delta W_{\alpha\alpha}(M_i, M_k) &= \frac{D^2(M_i, M_k)}{2\pi}\ VP \int_C \frac{W(M_i, M)W(M; M_k)}{D^2(M_i; M)D^2(M; M_k)}\,[\delta a(M) - \delta_{**}a(M)]ds(M) \\ &= \frac{D^2_{\alpha\alpha}(M_i, M_k)}{2\pi}\ VP \int_{C_\alpha} \frac{W_{\alpha\alpha}(M_i, M)W_{\alpha\alpha}(M_k, M)}{D^2_{\alpha\alpha}(M_i, M)D^2_{\alpha\alpha}(M_k, M)}\delta a^{(\alpha)}_{\alpha\alpha}(M)ds(M) \\ &+ \frac{D^2_{\alpha\alpha}(M_i, M_k)}{2\pi} \int_{C_\beta} \frac{W_{\alpha\beta}(M_i, M)W_{\alpha\beta}(M_k, M)}{D^2_{\alpha\beta}(M_i, M)D^2_{\alpha\beta}(M_k, M)}\delta a^{(\beta)}_{\alpha\alpha}(M)ds(M)\end{aligned} \tag{3}$$

- if $M_i \in C_\alpha$ and $M_k \in C_\beta$ (points belong to different crack fronts):

$$\begin{aligned}\delta W_{\alpha\beta}(M_i, M_k) &= \frac{D^2_{\alpha\beta}(M_i, M_k)}{2\pi}\ VP \int_{C_\alpha} \frac{W_{\alpha\alpha}(M_i, M)W_{\alpha\beta}(M, M_k)}{D^2_{\alpha\alpha}(M_i, M)D^2_{\alpha\beta}(M, M_k)}\delta a^{(\alpha)}_{\alpha\beta}(M)ds(M) \\ &+ \frac{D^2_{\alpha\beta}(M_i, M_k)}{2\pi}\ VP \int_{C_\beta} \frac{W_{\alpha\beta}(M_i, M)W_{\beta\beta}(M_k, M)}{D^2_{\alpha\beta}(M_i, M)D^2_{\beta\beta}(M_k, M)}\delta a^{(\beta)}_{\alpha\beta}(M)ds(M)\end{aligned} \tag{4}$$

with: $\delta a^{(\gamma)}_{\alpha\beta}(M) = \delta a_{\gamma}(M) - \overrightarrow{V_{i,k}}(M).\overrightarrow{n_{\gamma}}(M)$, where $\overrightarrow{V_{i,k}}$ is a geometric transformation such as:
$\delta a^{(\gamma)}_{\alpha\beta}(M_i) = \delta a^{(\gamma)}_{\alpha\beta}(M_k) = 0$.

These formulae give us the first order perturbation of the SIF and kernels, knowing the perturbation δa and the initial SIF and W. Here comes the natural idea of an iterative procedure to predict the propagation. For this purpose, it's necessary to start from a configuration for which the quantities $\widehat{K}_\alpha$ and $W_{\alpha\gamma}$ are known. We assume that for two circular cracks which are distant enough, the SIF and functions $W_{\alpha\gamma}$ are those for single crack that is :

$$\begin{cases} \widehat{K}_\alpha(M) = 2\ \sqrt{a/\pi} \\ W_{\alpha\alpha} = 1 \\ W_{\alpha\beta} = 0 \end{cases} \tag{5}$$

This situation will serve as starting point of our method, corresponding to two circular cracks of size $a_0/b << 1$.

2.3. Propagation

Assumption is made that propagation is governed by the SIF so that we have:

$$\delta a\,(M) = \delta a_{max}\left[\frac{K(M)}{K_{max}}\right]^{\beta} \tag{6}$$

where δa_{max} is a small given quantity.

It is presumed here that this law simulates brutal fracture if $\beta \gg 1$ and fatigue propagation otherwise.
Subjected to Irwin's criteria, cracks are supposed to propagate in a quasistatic way under a remote loading σ_∞, varying

at each numeric step such as: $\max_{M \in C} K(M)/K_c = 1$. This condition ensures that $K(M) < K_c, \forall M \in C$ and that there is always an "active" part of the front. The loading is thus recalculated at each numerical step:

$$\sigma_\infty \sqrt{b} = \frac{K_c}{\max_{M \in C} \widehat{K}} \tag{7}$$

We can define here the real nondimensionalized loading as follows:

$$\sqrt{b} \frac{\sigma_\infty}{K_c} = \frac{1}{\max_{M \in C} \widehat{K}(M)} \tag{8}$$

3. Determination of the SIF along two coplanar circular cracks of same radius $a_1 = a_2 = a$

In this section, the SIF values obtained for two coplanar penny-shaped cracks in interaction are presented. Unfortunately, to our knowledge, no 3D analytical solution exists for this problem that should serve as benchmarks. For weakly interacting cracks (that is the SIF remains close to their value for one single crack), Isida et al. [4], Fabrikant [3], Kachanov and Laures [5], Chen and Lee [2] and Zhan and Wang [8] provide numerical results that are in agreement with each other. We thus believe that those values must be correct and shall serve to validate our code and test the influence of our numerical parameters a_0/b, N and $\delta a/a$ (section 3.1). For closely spaced cracks, the numerical approximations are more questionable and few studies exist. Among them those of Fabrikant [3], Kachanov and Laures [5] and Zhan and Wang [8] will serve to compare with our simulations (section 3.2).

3.1. Weak interaction

Figures 2 reflect the influence of different parameters: the number of nodes N on each front, the initial adimensionless radius a_0/b and the crack advance $\delta a/a$. In this section, cracks are subjected to a uniform advance defined as follows: $\frac{\delta a}{a} = \gamma \; min\left(a \,, \frac{\Delta}{2}\right)$.
All the figures 2 represent K_{max}/K_0 as a function of $\Delta/2a$ in the same y-range to make easier comparisons. Moreover it shall be noticed that the SIF of all points within the frame are less diffent than 10 % from the ones for a single isolated crack.

The initial cracks should not be too small because of the incremental nature of the method, numerical errors would accumulate. Typically, one shall choose a_0/b between 0.05 and 0.1.

There is a few dependence on the number of points, provided that $N > 100$. Moreover we notice that $K(s)$ presents some irregularities for $N < 160$. Thus values of $N \geq 160$ shall be used. Since the CPU depends on N, we shall be reasonable. Typically $N = 160$ seems a good compromise.

Once again due to the incremental nature of the method, we notice on figure (2c) that $\delta a/a$ shall be not too small but enough to use the first order perturbation formulae. Typically, $\delta a/a \in (0.025 - 0.1)$ is acceptable.

We shall use $a_0/b = 0.1$, $N = 160$, $\delta a/a = 0.025$ in the sequel.

3.2. Strong interaction

In the sequel, let's define: $l = \min(a, \Delta)$.
It shall be noticed that the method is unstable for some set of parameters. It is linked to the incremental nature of the method and to the amplification of K as soon as some angular points appear along the crack front. For instance, one can notice on figure (3c) that for $N = 160$, ($a_0/b = 0.1$, $\delta a/l = 0.01$ the value of K_{max} diverges. In the sequel, we consider those calculations as ill and arrange to find well suited set of parameters. A systematic study of numerical stability is under consideration and will be published in the future.

From those results, we can conclude that the method is able to give qualitatively correct values of K but quantitatively, is quiet sensitive to the numerical parameters. In particular for cracks as close as $\Delta/2a < 10^{-4}$, a relative dispersion (standard deviation/mean value) can be observed of approximately 100 % by choosing reasonable parameters ($N = 100 - 200$, $a_0/b = 0.1 - 0.2$, $\delta a/l = 0.01 - 0.05$). For higher values of $\Delta/2a$, the dispersion decreases. It is of 50 % for $\Delta/2a \sim 10^{-2}$, 10 % for $\Delta/2a \sim 10^{-1}$, 1 % for $\Delta/2a \sim 0.5$, 0.1 % for $\Delta/2a \sim 1$.

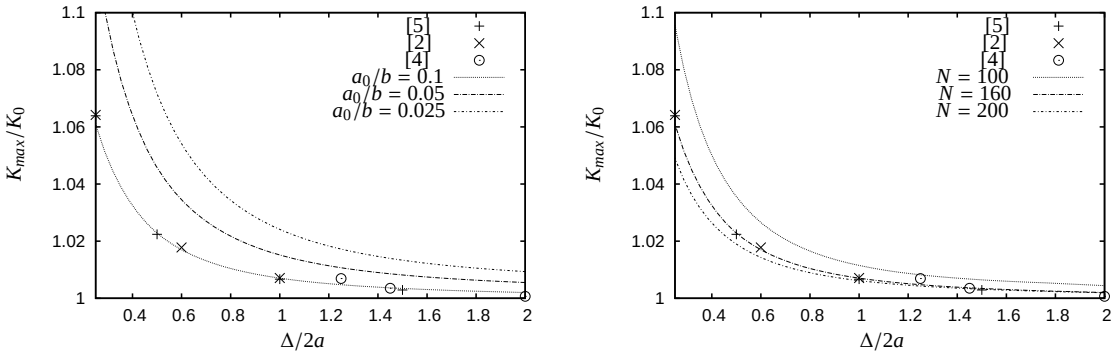

(a) $N = 160$, $\delta a/a = 0.025$

(b) $\delta a/a = 0.025$, $a_0/b = 0.1$

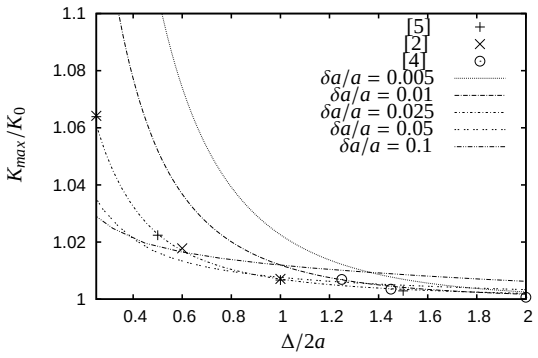

(c) $\delta a/a$ ($N = 160$, $a_0/b = 0.1$

Figure 2: Dependance on the initial size a_0/b (a), on the number N of points in the mesh (b), on the crack advance (c)

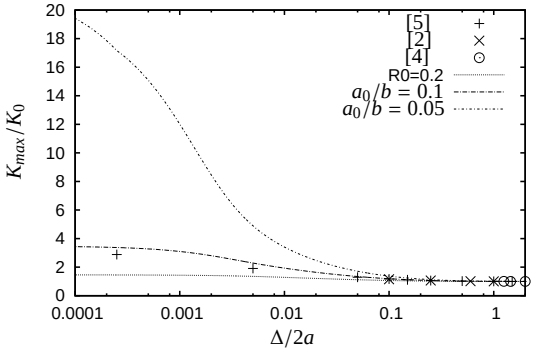

(a) $N = 160$, $\delta a/a = 0.025$

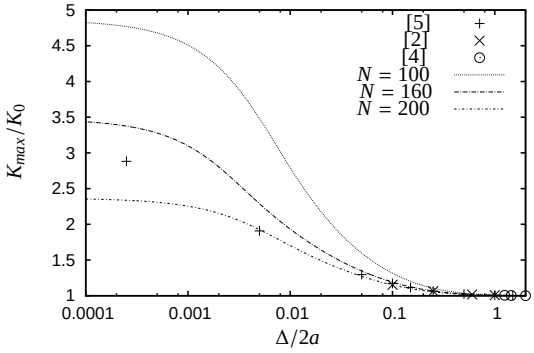

(b) $\delta a/l = 0.025$, $a_0/b = 0.1$

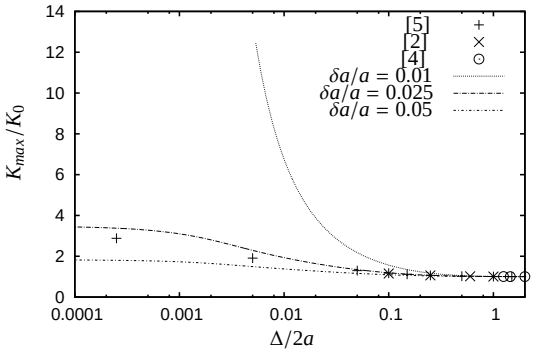

(c) $\delta a/l = 0.025$, $a_0/b = 0.1$

Figure 3: Dependance on the initial size a_0/b (a), on the number N of points in the mesh (b), on the crack advance (c)

Nevertheless we achieve to obtain very similar results than previous authors Fabrikant [3], Kachanov and Laures [5] and Zhan and Wang [8] by choosing $a_0/b = 0.1$, $N = 160$, $\delta a/a = 0.025$ (see figure 4 where *phi* is the polar angle). We shall use those parameters as reference in the sequel.

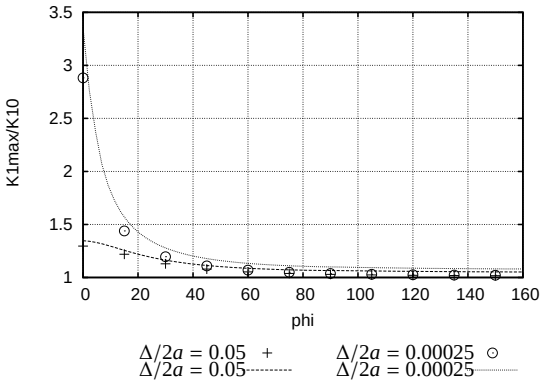

Figure 4: Points corresponds to the values of Kachanov and Laures [5] given in table 1. Lines correspond to our simulations for $a_0/b = 0.1$, $N = 160$, $\delta a/l = 0.025$.

4. Propagation of two circular cracks in brittle fracture

We present here our results for simulations in brittle fracture. For numerical purposes, Irwin's law can be remedied by a Paris type law provided to choose an exponent β large enough. In practice, above $\beta = 30$, results are very close and become independent of β. That is why the sole case $\beta = 30$ is presented here. Crack deformation is consequent so that we had to set up a remesh procedure to redistribute nodes.

Figure (5a) shows the successive positions of the fronts for different values of the dimensionless loading $\sigma_\infty \dfrac{\sqrt{b}}{K_c}$. When the cracks are distant, threshold is reached for the entire set of points because the SIF values are almost uniform along the fronts.

When a/b reaches about $1/4$, interaction between cracks leads to an increase in SIF of points near the opssite crack. In consequence, the threshold is only achieved at these nodes whence a pronounced front deformation. It should be noted that coalescence couldn't be reached because of the values larger and larger of the SIF. Indeed, SIF values are asymptotically infinite at the vinicity of the "interaction area".

Figure (5b) represents the real loading in terms of cracks advance, characterized by the dimensionless quantity a_{int}/b for the case of coalescence and for the isolated crack. It can be noticed that the loading strongly decreases during propagation and tends to almost disappear when cracks are close to one another.

5. Conclusion and perspectives

The purpose of this work was to apply Lazarus's numerical code to study the coalecence of circular cracks.
To validate the code, we compared the SIF values, obtained for different configurations, with those found in the literature. Good agreements with Fabrikant [3], Kachanov and Laures [5] and Zhan and Wang [8] were achieved. After validation with literature, brittle propagation was experimented. It shoud be emphasized that each front was highly perturbed by the presence of the other crack. Our simulations showed cracks with a strongly elongated profile within the "interaction area". It can also be observed a significant decrease of the fracture loading as soon as the interaction between cracks was felt.
The possibility of extending the code to more complex geometries is considered.

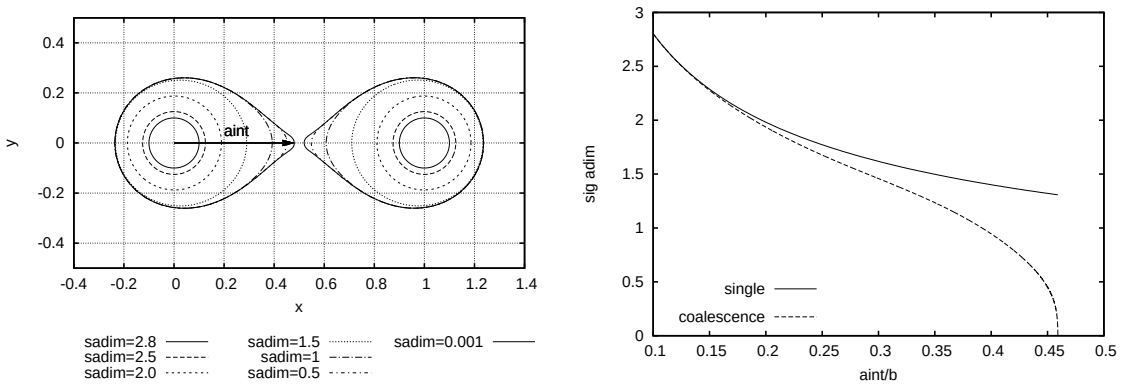

(a) Successive positions of the crack

(b) Critical loading during propagation

Figure 5: $\beta = 30$, $N = 160$, $\delta a_{max}/l = 0.001$, $a_0/b = 0.1$, remesh each 1000 numerical cycles

Acknowledgements

[1] A. F. Bower, M. Ortiz, 1990, Solution of three-dimensional crack problems by a finite perturbation method, J. of the Mechanics and Physics of Solids 38(4), 443 480.
[2] Y. Chen, K. Y. Lee, 2002, Solution of flat crack problem by using variational principle and differential-integral equation, Int. J. of Solids and Structures 39 (23), 578797.
[3] V. Fabrikant, 1987, Close interaction of coplanar circular cracks in an elastic medium, Acta Mechanica 67, 3959.
[4] M. Isida, K. Hirota, H. Noguchi, T. Yoshida, 1985, Two parallel elliptical cracks in an infinite solid subjected to tension, Int. J. of Fracture 27, 3148.
[5] M. Kachanov, J.-P Laures, 1989, Three-dimensional problems of strongly interacting arbitrarily located penny-shaped cracks, Int. J. of Fracture 41, 289313.
[6] V. Lazarus, 2003, Brittle fracture and fatigue propagation paths of 3D plane cracks under uniform remote tensile loading, Int. J. of Fracture 122 (1-2), 2346.
[7] J. R. Rice, 1989, Weight function theory for three-dimensional elastic crack analysis, in R. P. Wei and R. P. Gangloff, eds, Fracture Mechanics: Perspectives and Directions (Twentieth Symposium), American Society for Testing and Materials STP 1020, Philadelphia, USA, pp. 2957.
[8] S. Zhan, T. Wang, 2006, Interactions of penny-shaped cracks in three-dimensional solids, Acta Mechanica Sinica 22, 341353.

Failure Analysis Procedure of Steel Wire Drawing Fracture

LIU Lihua, SUN Jie*, WANG Huan

Jiangsu Fasten Hopesun Group Co., Ltd., 214434, China
* Corresponding author: jason8246@163.com

Abstract Failure analysis procedure of steel wire drawing fracture process was introduced, which includes background information collection, visual inspection and low magnification test, microscopic analysis, metallographic examination, etc. The importance of each step on fracture failure analysis results was also explained. In accordance with the stress condition in drawing process of steel wire, the typical characteristics of the mainly drawing fracture failure modes including pencil-point shaped, plane shaped and inclined shaped were investigated. The process of microscopic analysis and metallographic examination were optimized with macro morphology characteristics, and a faster and more precise analytical approach of metallic wire drawing fracture failure was proposed which was of important engineering significance and practical value to improve product competitiveness.

Keywords failure analysis, fracture, drawing, SEM, metallographic examination

1. Introduction

This is a template to prepare the full paper manuscript for the 13th International Conference on Fracture, which will be held at Beijing, China, June 16–21, 2013.
Fracture failure was inevitable during steel wire drawing which was affected by equipment, weather, operation, etc [1]. Many researchers had made great efforts to investigate the causes of fracture failure, the major fracture morphology included pencil-point shaped, plane shaped, and inclined shaped fracture [2]. And microstructure of wire rod, drawing die, lubrication and other factors which lead to fracture were analyzed.

An optimized procedure of circle section steel wire fracture failure analysis which was depended on macroscopic fracture morphology was proposed. The importance of every step of failure analysis was emphasized, and failure analysis of the pencil-point shaped, plane shaped, and inclined shaped fracture were introduced respectively.

2. Failure Analysis Procedure

The main procedure failure analysis procedure of steel wire drawing fracture was: background information, visual inspection and low magnification test, microscopic analysis, metallographic examination, chemical analysis and mechanical tests if necessary [3].

2.1. Background Information

The object of failure analysis was not only the fracture wire but an integration of wire, equipment, environment and person. Failure analysis should consider the relationships include: fracture wire and normal wire of the same batch, fracture wire and drawing equipment, fracture wire and production environment, fracture and operating person.

First of all, make sure the location of fracture wire, number of drawing pass, reduction of fracture pass and other relevant information as much as possible. Generally, fracture wire located in drawing die hole, around the reel, post-straightener, or take-up device. That information was used to judge the stress condition of fracture. Secondly, find out the fracture frequency of the same batch and

other similar fracture samples. Then, make sure whether the drawing equipment was well, such as broken of drawing die, hole eccentric of die, water shortage of die case would lead to wire fracture. Because the influence of temperature and humidity on wire drawing performance, production environment and operating person would not be ignored.

2.2. Visual Inspection and Low Magnification Test

The purpose of visual inspection and low magnification test were to determine the fracture mode by the macro morphology and surface defects, and photo with relevant information should be recorded. For circle section steel wire fracture, visual inspection and low magnification test included: (1) Original surface defects, such as fold and pitting. (2) Surface defects caused by drawing, such as broken of drawing die, hole eccentric of die, water shortage of die case, etc. (3) Color of wire surface, such as corrosion and welding joints.

2.3. Microscopic Analysis and Metallographic Examination

The purpose of microscopic analysis and metallographic examination was to find microstructural characteristic which caused wire fracture.

Scanning electron microscope (SEM) was used to observe fracture and surface morphology. The feature of wire fracture could be divided into two categories: (1) Dimple character, which was composed of round or oval holes with different sizes, sometimes inclusions or second-phase particles could be found in dimple. (2) Cleavage character, which included river pattern, scallop pattern, grainy pattern and intergranular fracture character.

Metallographic examination was used to analysis internal cracks, grain size, decarburized layer, defect microstructure, etc. And typical defect microstructure included: martensite, net carbide, widmanstatten, etc.

3. Drawing Fracture Analyses

Steel wire was under drawing force, pressure and friction during the drawing that was a plastic deformation. If the drawing equipment had poor lubrication, shortage of cooling water, or die eccentric, wire drawing would be caused to fracture. Fracture and surface morphology were very important to failure analysis of wire drawing fracture. Generally, fracture modes were corresponded to macro fracture morphology and surface state of wire.

Failure analysis procedure of typical macro fracture morphology was optimized, such as, pencil-point shaped, plane shaped and inclined shaped fracture.

3.1. Pencil-point Shaped Fracture

One end of the pencil-point shaped facture was conical tip, and the other conical hole which was matched with each other. The conical surface was angel of 45° to drawing direction and its morphology was shown in Fig. 1. Many investigations showed that the cause of pencil-point shaped fracture was central brittle phase. During wire drawing, brittleness microstructure in center could not be well deformed with outer steel wire, cracks firstly initialized surround the brittle phase, then the cracks which extended along 45° direction to wire axis leas to fracture [4,5]. Central brittle microstructure of wire that was shown in Fig.2 consists of inclusion, net carbide, martensite, etc.

The above research showed that defects of pencil-point shaped fracture usually in center of wire, therefore the procedure of microscopic analysis and metallographic examination should be: (1) SEM was used to search inclusion or pin of it in conical tip. (2) Longitudinal metallographic examination was used to seek central brittle phase. Transversal metallographic examination was also used by some researchers to judge brittle microstructure. Longitudinal metallographic examination was suggested that could found brittle phase and its discontinuous deformation (shown in Fig. 3) more easily.

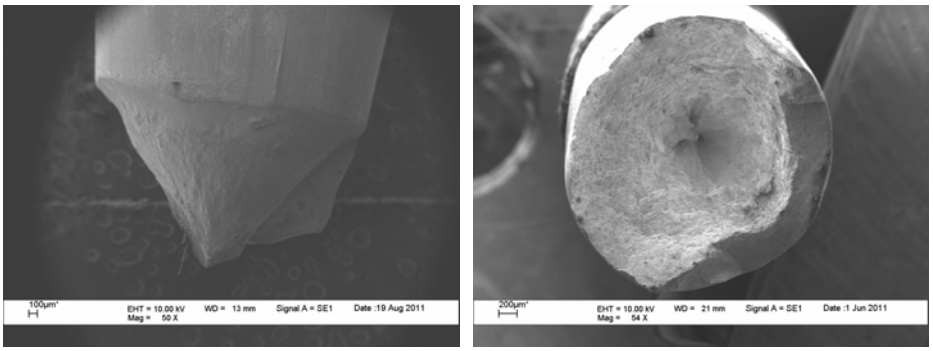

(a)conical tip (b) conical hole

Figure. 1 Morphology of pencil-point shaped fracture

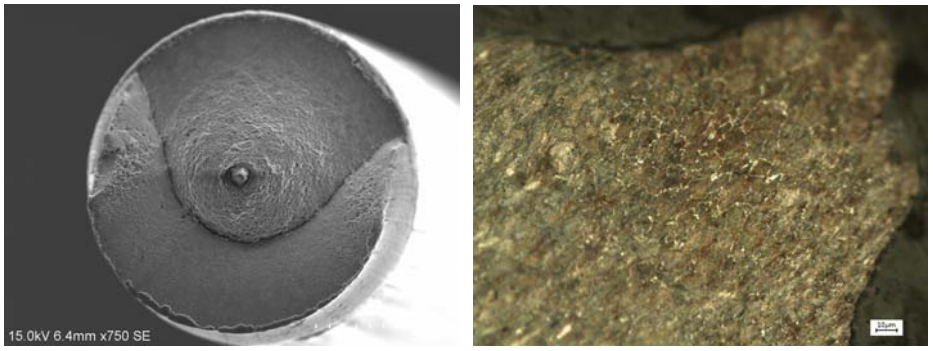

(a) Inclusion (b) net carbide

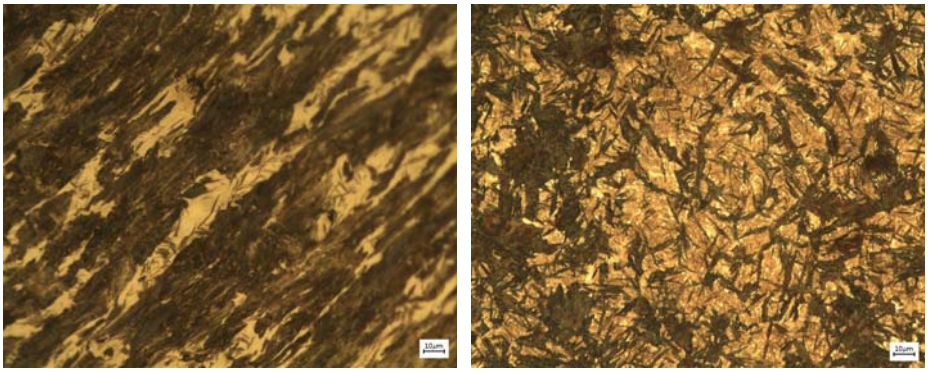

(c) martensite (longitudinal) (d) martensite(transversal)

Figure. 2 Central brittle microstructure of pencil-point shaped fracture

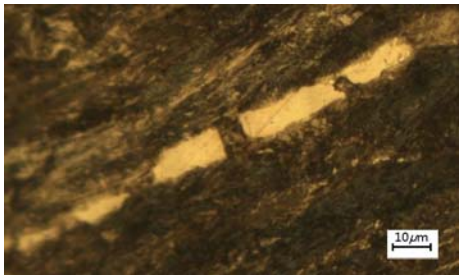

Figure. 3 Discontinuous martensite in center of steel wire

3.2. Plane shaped fracture

There was almost no necking or significant surface defects of plane shaped fracture, whose fracture surface was likely a plane shown in Fig. 4, so called as plane shaped fracture. Generally, the cause of plane shaped fracture was abnormal microstructure or larger grain which increased brittleness of wire [6]. Cleavage character and its microstructure of a plane shaped fracture were shown in Fig. 5.

Bad welding zone could lead to plane shaped fracture as well [7], and the unusual color of blue or white could be the proof of joint. There were cleavage character, inclusion and dimples of different region of fracture, and longitudinal metallographic examination could show variation tendency of grain size which were shown in Fig. 6.

Therefore microscopic analysis and metallographic examination procedure of plane shaped fracture should be: (1) wire surface should be inspected whether had defects or unusual color. (2) SEM was used to observe cleavage character, dimple, inclusion or other microstructural feature. (3) Transversal metallurgical examination should be adopted if cleavage character was found. Longitudinal metallurgical examination should be adopted if there were more than one microstructural character or unusual color of wire surface.

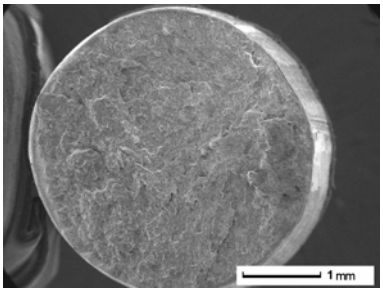

Figure. 4 Morphology of plane shaped fracture

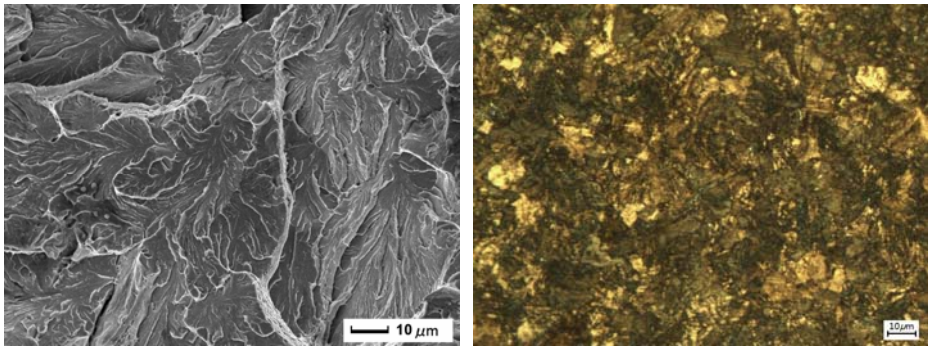

(a) Cleavage Character (b) Metallurgical analysis

Figure. 5 Cleavage character and Metallurgical analysis of plane shaped fracture

(a) Unusual color

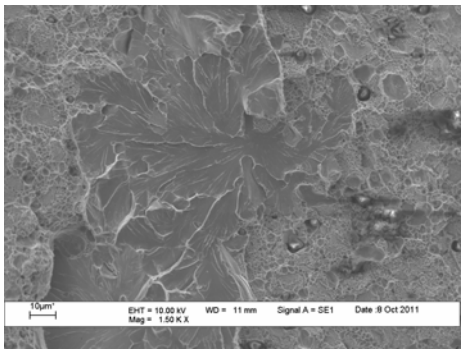

(b) Microscopic character

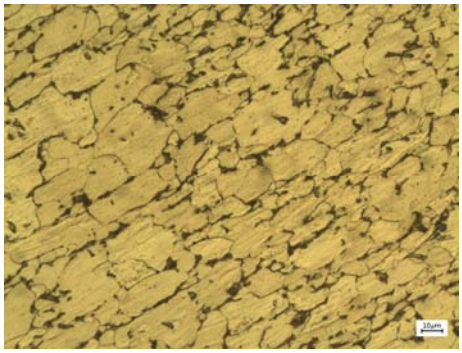

(c) Variation trend of grain size

Figure. 6 Plane shaped fracture of bad welding

3.3. Inclined shaped fracture

The fracture surface of inclined shaped was an angle to wire drawing direction, and crack, little hole or other defects would be found nearby fracture. Different wire surface defects corresponded to fracture cause which included scratching, abrasions, die broken, poor lubrication, etc [8]. Morphology of inclined shaped facture and a typical surface defect was showed in Fig. 7 and Fig. 8, respectively.

Microscopic analysis of inclined shaped fracture was brittle fracture feature, shown in Fig. 9. Trend of surface crack and poor deformability microstructure would be observed by longitudinal metallographic examination, shown in Fig. 10.

Microscopic analysis and metallographic examination procedure of inclined shaped fracture should be: (1) Wire surface of fracture should be examined to find defect of crack, scratches and so on. (2) SEM would be used to identify microstructural character and defect mode. (3) Longitudinal metallurgical examination would be used to observe trend of crack and poor deformability.

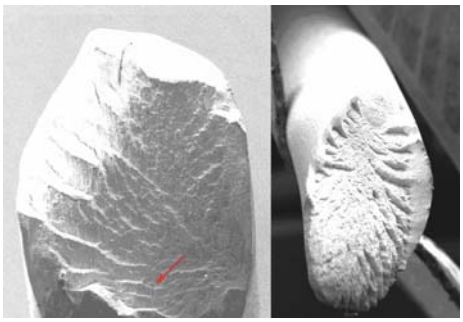

Figure. 7 Morphology of inclined shaped facture

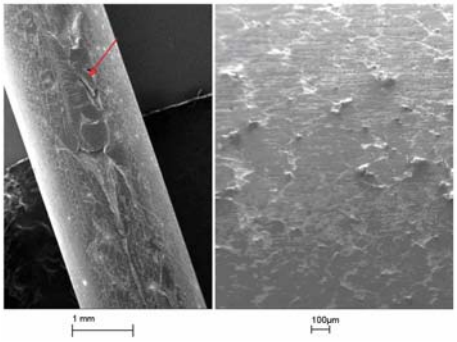

Figure. 8 Surface defect of inclined shaped facture

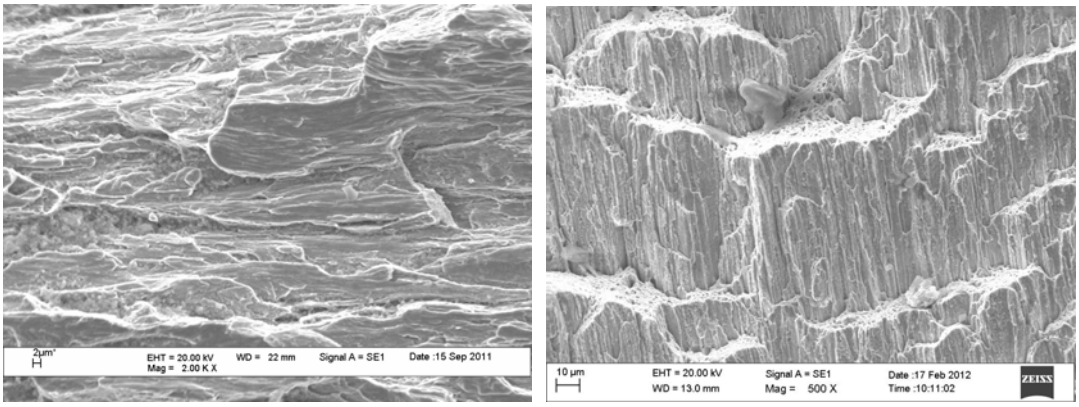

Figure. 9 Micro-morphology of inclined shaped facture

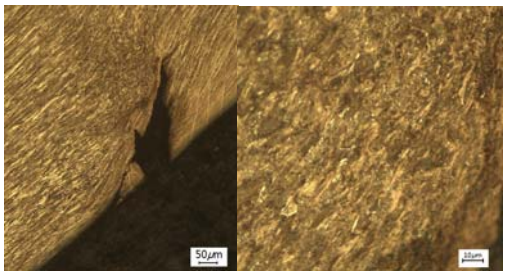

Figure. 10 Poor deformability microstructure of inclined shaped facture

4. Conclusion

Failure analysis procedure of steel wire drawing fracture was proposed and the significance of every step was explained. Microscopic analysis and metallographic examination of pencil-point shaped, plane shaped and inclined shaped fracture were optimized by fracture modes and investigation of fracture failure.

References

[1] H. Uchikawa, S. Hanehara, T. Shirasaka, D. Sawaki, Effect of water curing. Cem Concr Res, 22 (1992) 115–120.
[1] ZHONG Qunpeng, ZHAO Zihua, Fractography, Higher Education Press, Beijing, 2006.
[2] SUN Jie, LIU Lihua, CHENG Xiaonong, etc, Fracture mode and cause analysis of 82B wire rod, Metal Products, 38(2011) 61-64.
[3] ZHANG Zheng, Failure analysis procedure, PTCA(PART: A Physics Test), 41(2005) 105-107.
[4] LI Qingyan, ZHAO Cheng, Analysis of fracture reasons of 62A cold-drawing steel wire, Journal of Qingdao University of Science and Technology(Natural Science Edition), 30(2009) 57-60.

[5] MENG Xiancheng, WANG Yong, LIU Yazhengm, Analysis of pencil-tip shaped fracture of cord steel 72A during cold drawing and improvement of process, Special steel, 30(2009) 55-57.
[6] YAO Ganying, PAN Yingjun, Causes of brittle fracture of 82B wire rod, Journal of Wuhan University of Science and Technology(Natural Science Edition), 29(2006) 457-459.
[7] CAO Wenkui, XU Zhongliang, FANG Feng, etc, Fracture analysis of high carbon steel strand welding zone, Jiangsu Merallury, 34(2006) 6-9.
[8] MA Peng, OU Yangqi, FU Junhong, etc, Cause analysis of SWRH82B wire rod drawing fracture, Metal Products, 36(2010) 57-59

The Effect of the Changing State of Stress Around the Crack Tip on the Determination of Stress Intensity Factors by the Method of Caustics

Emmanuel Gdoutos*

Civil Engineering, Democritus University of Thrace, GR-671 00 Xanthi, Greece
* egdoutos@civil.duth.gr

Abstract The state of stress in the vicinity of the crack tip changes from plane strain at the tip to plane stress at a critical distance (about half the specimen thickness) from the tip through an intermediate region where the state of stress is three-dimensional. In the optical method of caustics, the caustic is the image of a circle on the specimen centered at the crack tip, and, therefore, yields information on the stress state along this circle. In the method conditions of plane stress are assumed along this circle. This condition imposes restrictions on the geometrical dimensions of the optical arrangement, specimen thickness, crack length and applied loads for the correct determination of stress intensity factors. In the present work the limits of applicability of the method of caustics are studied. The use of optically anisotropic materials is introduced to obtain a double caustic which provides the correct state of stress (plane strain, plane stress or three-dimensional) along the initial curve. When the state of stress is known the proper values of stress-optical constants can be used for the correct determination of stress intensity factors.

Keywords Cracks, Stress intensity factors, The method of caustics, Triaxial state of stress

1. Introduction

The optical method of caustics is sensitive to stress gradients, and it has extensively been used for the determination of stress intensity factors in crack problems [1-6]. According to the method the stress singularity at the crack tip is transformed to an optical singularity. A highly illuminated curve, so-called caustic, is obtained on a viewing screen at a distance from the crack tip. The dimensions of the caustic are related to the state of stress near the crack tip. Thus the stress intensity factor which governs the stress field can be determined by measuring characteristic dimensions of the caustic, usually, its diameter perpendicular to the crack. The method is based on the assumption that the state of stress near the crack tip is plane stress. However, experimental and analytical solutions have shown that the state of stress changes from plane strain near the crack tip to plane stress away from the tip through an intermediate region where the stress state is three-dimensional. The changing state of stress results to changing values of stress-optical constants which enter in the equations for the determination of stress intensity factors. In the present work the method of caustics is critically reviewed, and its limits of applicability are studied. Furthermore, the use of optically anisotropic material is introduced for the determination of stress intensity factors.

2. The Optical Method of Caustics

In the optical method of caustics a specimen is illuminated by a light beam and the reflected or transmitted rays undergo a change of their optical path dictated by the stress field (Fig. 1). The change of the optical path is caused by the variation of the thickness and refractive index as the specimen is loaded. At stress gradients resulting at crack tips, the reflected or transmitted rays generate a highly illuminated three-dimensional surface in space. When this surface is intersected by a reference screen, a bright curve, the so-called caustic curve, is formed. For transparent

materials three caustics are formed by the light rays reflected from the front and rear surfaces and those transmitted through the specimen. For opaque materials, only one caustic is formed by the reflected light rays from the front surface of the specimen. The dimensions of the caustic are related to the state of stress near the crack tip. For the case of a mode-I through-the-thickness crack the stress intensity factor K_{exp} is given by [1]

$$K_{exp} = 0.0934 \frac{D^{5/2}}{z_0 c t m^{3/2}} \tag{1}$$

where z_0 is the distance between the specimen and the viewing screen where the caustic is formed, c is the stress optical constant of the specimen under conditions of plane stress, t is the specimen thickness, m is the magnification factor of the optical arrangement defined as the ratio of a length on the reference screen where the caustic is formed divided by the corresponding length on the specimen and D is the transverse diameter of the caustic at the crack tip. The above equation is valid when the state of stress in the vicinity of the crack tip is plane stress, so that the value of stress-optical constant under conditions of plane stress is used.

For optically isotropic materials, the caustic is created by the light rays reflected from the circumference of a circle, the so-called initial curve, which surrounds the crack tip. The radius of the initial curve is given by

$$r = 0.316\ m\ D \tag{2}$$

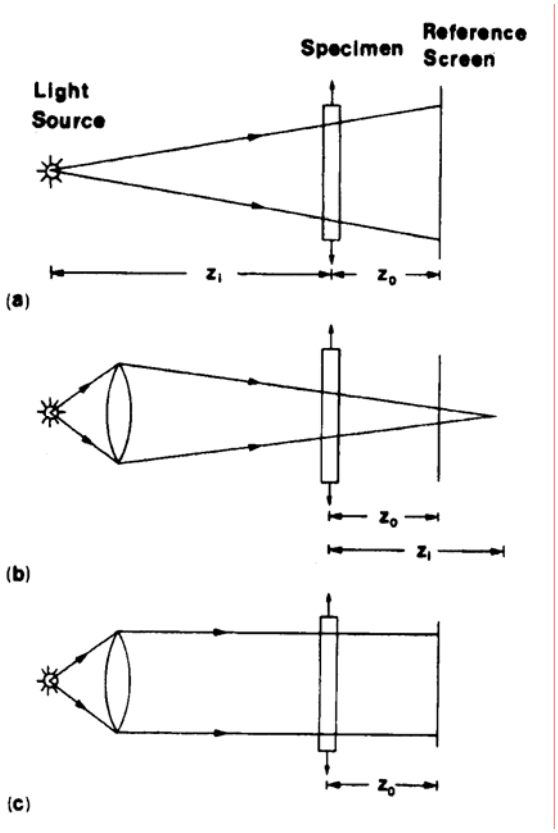

Figure 1. Optical arrangement for divergent (a), convergent (b) and parallel (c) light

3. Experimental

Specimens made of Plexiglas, of thickness d = 3.0, 4.5, 9.5 and 12.5 mm and width w = 42.4, 47.5, 51.5 and 63.5 mm, with an edge notch of length a = 15.5 mm were subjected to a progressively increasing tensile loading in an Instron testing machine. The specimens were illuminated by a convergent, divergent or parallel monochromatic light beam produced by a Ne-He laser. The caustic curves obtained from the light rays reflected from the front or rear faces of the specimen, or those transmitted through the specimen, were recorded on a viewing screen placed at a distance z_0 from the specimen. Caustics were obtained at different load levels for various values of the magnification factor of the optical arrangement, m, and the distance z_0. In this way, a host of caustics were obtained from different values, r, of the initial curve from the crack tip.

Experimental values of stress intensity factor, K_{exp}, were obtained. These values were compared with theoretical values of stress intensity factor K_{th} given by [7]

$$K_{th} = \sigma\sqrt{\pi a}\left[1.12 - 0.23\left(\frac{a}{w}\right) + 10.55\left(\frac{a}{w}\right)^2 - 21.72\left(\frac{a}{w}\right)^3 + 30.95\left(\frac{a}{w}\right)^4\right] \quad (3)$$

Note that the experimental values of stress intensity factor are obtained under the assumption that the initial curve of the caustic lies in the region near the crack tip where plane stress conditions dominate. Thus, if the values of K_{exp} and K_{th} coincide, this means that the initial curve of the caustic lies in the region where the state of stress is plane stress. In case the values of K_{exp} and K_{th} do not coincide, this implies that the initial curve lies in the region where the state of stress is three-dimensional

Fig 2 present the variation of K_{exp}/K_{th} versus r/d for a value of the specimen thickness d = 4.5, and different values of specimen width. Points in figure correspond to different values of the applied load, P, the magnification factor of the optical arrangement, m, the distance between the specimen and the viewing screen where the caustic is formed, z_0, and the specimen thickness, d. Note form figure that the ratio K_{exp}/K_{th} increases with r/d and reaches a plateau value equal to one as the radius of the initial curve takes a limiting value r_c. At that value of $r = r_c$ the state of stress in the neighborhood of the crack tip becomes plane stress. For distances r smaller than r_c the state of stress is three-dimensional, while for values of r larger than r_c plane stress conditions dominate. It was obtained that the critical value of r for which the state of stress becomes plane stress depends not only on d, but also on the geometrical characteristics of the cracked plate, especially the ratio of the crack length to specimen thickness.

4. Limit of Applicability of the Method of Caustics

The condition that the initial curve of the caustic should lie at distances from the tip approximately greater than half the specimen thickness introduces limitations in the parameters (distance between the specimen and the viewing screen where the caustics is formed, the magnification factor of the optical arrangement, the specimen dimensions and thickness, and applied loads) entering in the determination of stress intensity factors. These factors should be properly selected so that the initial

curve lies in the region where plane stress conditions dominate. In that case the value of stress-optical constant corresponding to plane stress should to be used.

In order to obtain caustics generated from the region of plane stress the radius of the initial curve of the caustic should be larger than a fraction of the specimen thickness. By taking this distance equal to half the specimen thickness we obtain

$$\left(\frac{3.385 z_0 cK}{m}\right)^{2/3} > d \tag{4}$$

Inequality (4) establishes a condition the quantities, z_0, c, K, m, d should satisfy in order to obtain caustics generated by an initial curve that lies in the plane stress region Fig. 3 presents the variation of the critical (minimum) value of specimen thickness, z_0, versus K_I for a parallel light beam illuminating a notched Observe that the critical thickness z_0 increases as the thickness of the specimen increases and K_I decreases. Fig. 4 presents the variation of r_0 versus stress intensity factor K_I for a Plexiglas specimen of thickness d = 1 mm illuminated by a parallel light beam. The caustic is created by transmitted light rays (c_t = 1.08x10^{-10}m^{2}N^{-1}) and the reference screen is placed at distances z_0 = 0.1,1 and 10 m from the specimen. K_I varies up to 1 MPa√m corresponding to the value of fracture toughness of Plexiglas. In the same figure the line r_0 = d/2 is drawn. Observe that r_0 increases as K_I and z_0 are also increased. Only for the part of curves above the line r_0 = d/2, does the radius of the initial curve lie in the region of plane stress. It is observed that the realm of validity of the method of caustics under conditions of plane stress increases with K_I and z_0.

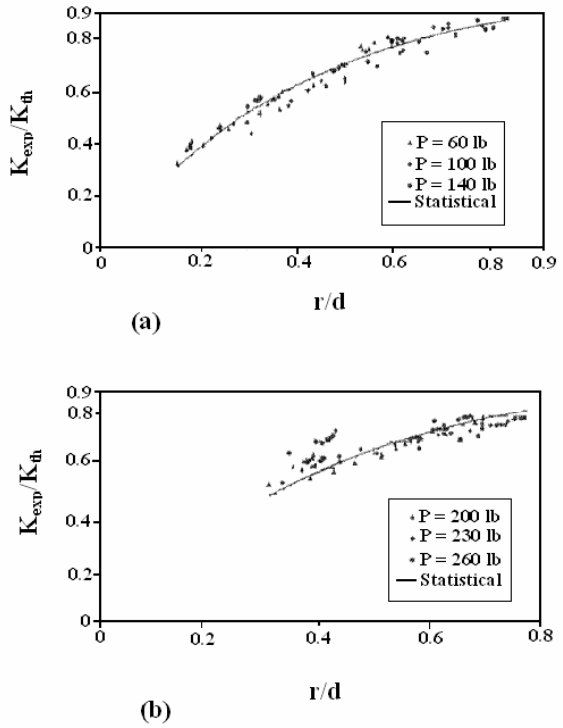

Figure 2. Variation of K_{exp}/K_{th} versus r/d for a = 15.5 mm, d = 4.5 mm and w = 47.5 mm (a) and w = 63.5 mm (b)

5. Determination of Stress Intensity Factors

When the initial curve of the caustic lies at distances where three-dimensional effects dominate the proper value of the stress-optical constant, c, should be used. The value of the stress-optical constant changes from its plane strain value near the tip to its plane stress value at distances away from the tip approximately equal to half the specimen thickness. In order to characterize the three-dimensionality of the stress field near the crack tip an empirical triaxiality factor k is introduced, such that

$$\sigma_z = k\,\nu\,(\sigma_x + \sigma_y) \tag{5}$$

where σ_z is the normal stress perpendicular to the plane of the specimen, and σ_x and σ_y are the in-plane stresses. k takes the values of 0 and 1 for plane stress ($\sigma_z = 0$) and plane strain [$\sigma_z = \nu\,(\sigma_x + \sigma_y)$], respectively.

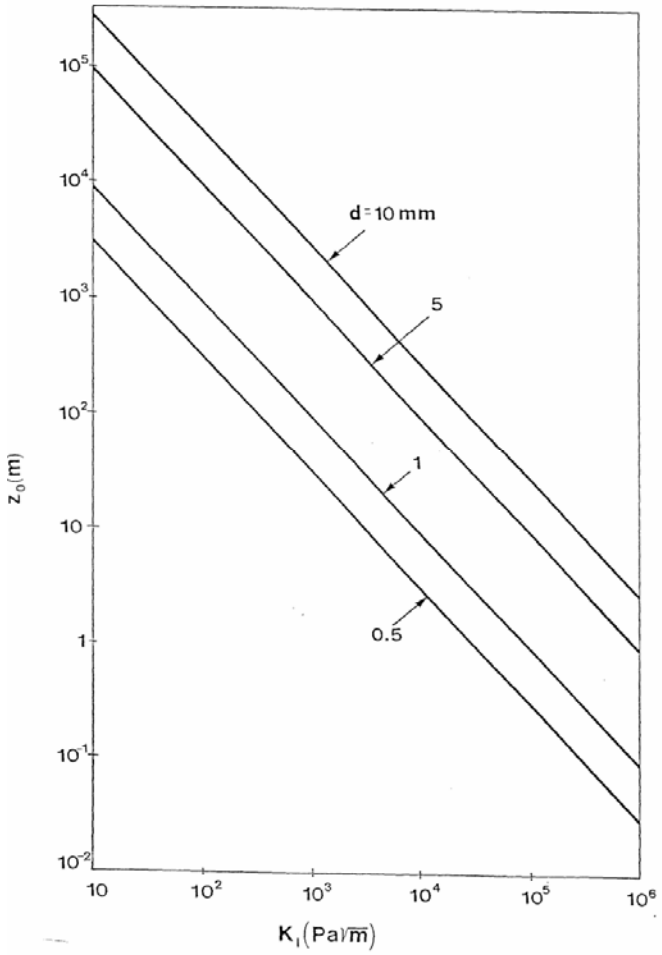

Figure 3. Variation of minimum value of z_0 versus K_I for parallel light. d= 0.5, 15 and 10 mm.

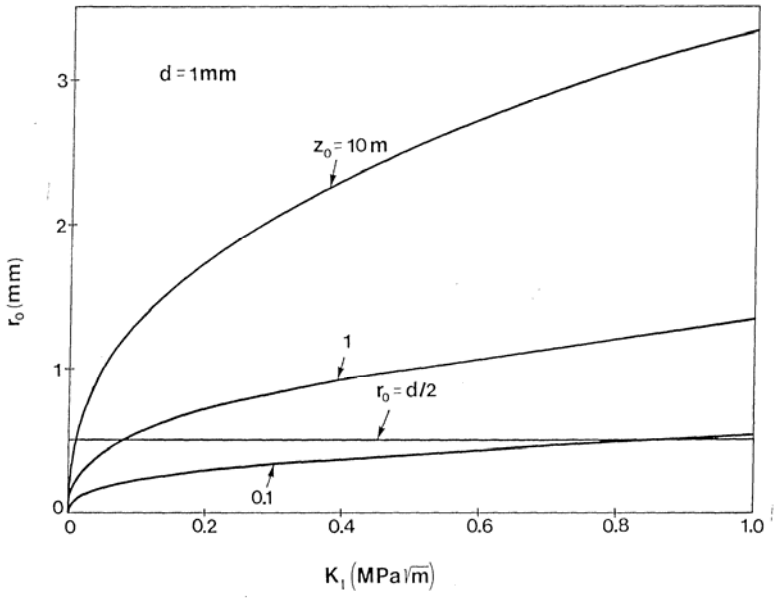

Figure 4. Variation of r_0 versus K_I for parallel light. d = 1 mm, z_0 = 0.1, 1 and 10 m

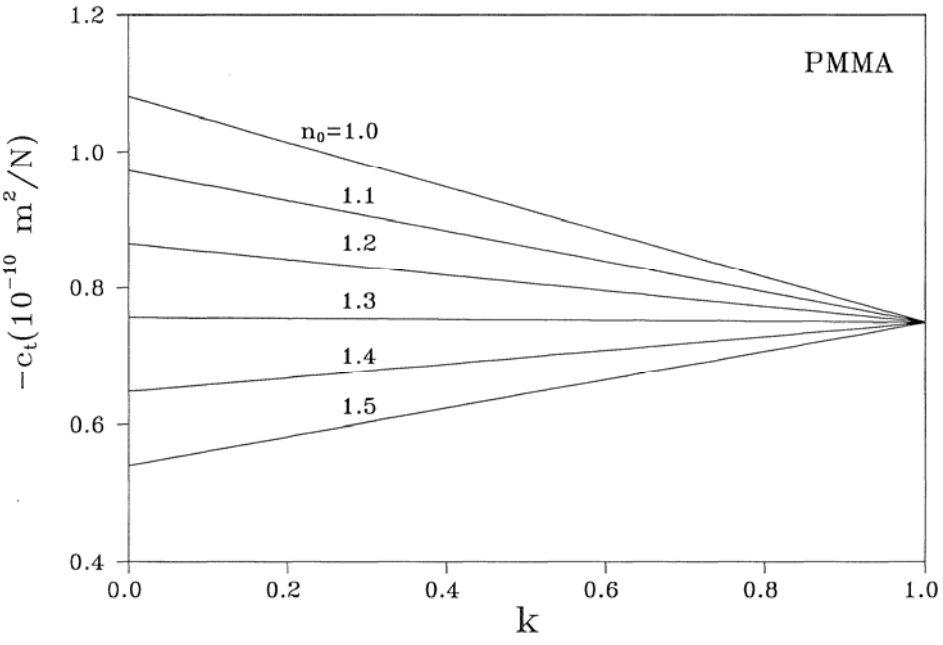

Figure 5. Variation of stress-optical constant c_t versus triaxiality coefficient k for PMMA for various values of the index of refraction n_0 of the surrounding medium. k = 0 and 1 correspond to conditions of plane stress and plane strain, respectively.

When the triaxiality factor is determined the corresponding value of the stress-optical constant, c, is calculated which subsequently is used for the determination of stress intensity factor. Fig. 5 presents the variation of the stress-optical constant c_t for transmitted light for Plexiglas (PMMA) versus the triaxiality coefficient k from its plane stress (k = 0) to its plane strain value (k = 1) for various

values of the index of refraction n_0 of the surrounding medium. Note that c_t varies linearly with k. From Fig. 5 it is observed that c_t remains almost constant for $n_0 = 1.35$. This means that when the index of refraction of the medium surrounding the specimen is equal to $n_0 = 1.35$ the stress-optical constant c_t is independent of the state of stress near the crack tip. Under such circumstances Eq. (1) can be used for the correct determination of stress intensity factor K_I for any values of the parameters entering in Eq. (1). Analogous results for the stress-optical constant c_r are shown in Fig. 6. Note that in this case c_r does not become constant for any value of n_0.

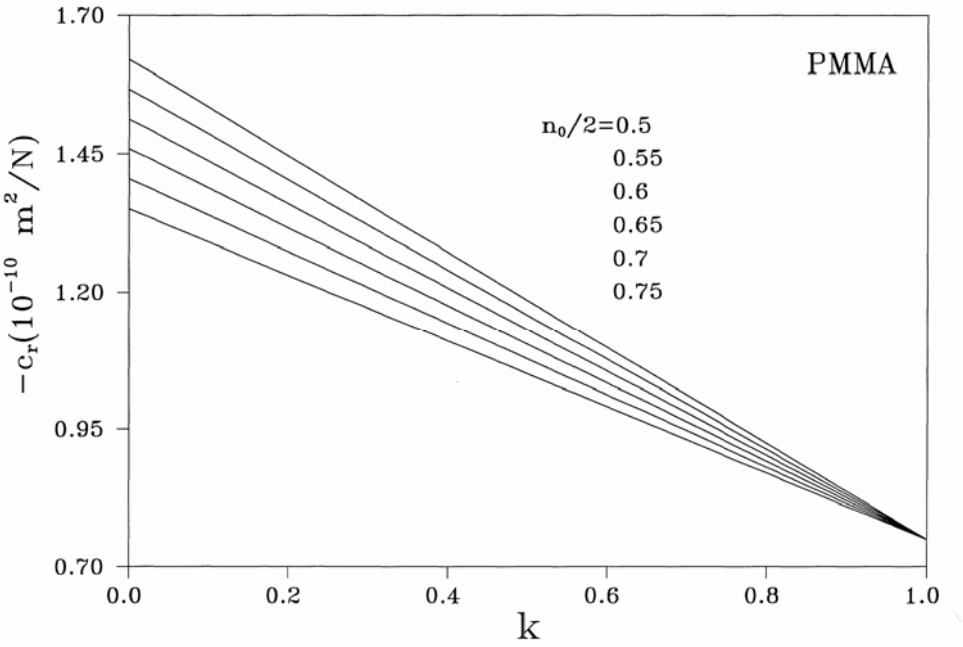

Figure 6. Variation of stress-optical constant c_r versus triaxiality coefficient k for PMMA for various values of the index of refraction n_0 of the surrounding medium. k = 0 and 1 correspond to conditions of plane stress and plane strain, respectively.

6. Use of Optically Anisotropic Materials

In optically anisotropic materials the variation of the optical path of a light ray traversing the specimen along the two principal stress directions is given by:

$$\Delta s_{t1,2} = c_t \left[(\sigma_1 + \sigma_2) \pm \xi_{r,t} (\sigma_1 - \sigma_2) \right] d \tag{6}$$

where the coefficient $\xi_{r,t}$ characterizes the optical anisotropy of the material for light rays reflected from the rear face (r) or traversing (t) the specimen. The plus and minus signs in equation correspond to the values σ_1 and σ_2 of the principal stresses. Under such conditions the parametric equations of the caustic are given by [8]:

$$X_{r,t} = \left(\frac{3}{2}C_{r,t}\right)^{2/5}\left[A^{2/5}\cos\theta + \frac{2}{3}A^{-3/5} + \left\{\left(\cos 3\theta/2\right) \pm \frac{3}{4}\xi_{r,t}\sin 2\theta\right\}\right] \tag{7a}$$

$$Y_{r,t} = \left(\frac{3}{2}C_{r,t}\right)^{2/5}\left[A^{2/5}\sin\theta + \frac{2}{3}A^{-3/5} + \left\{\left(\sin 3\theta/2\right) \pm \frac{1}{4}\xi_{r,t}\left(1+3\cos 2\theta\right)\right\}\right] \tag{7b}$$

where:

$$A = \pm\frac{1}{4}\xi_{r,t}\sin\theta + \left[1 \pm \frac{1}{4}\xi_{r,t}\left\{\left(7\sin\theta/2 + \left(\sin 3\theta/2\right)\right\} + \frac{1}{32}\xi_{r,t}^2\left(25+9\cos 2\theta\right)\right]^{1/2} \tag{8}$$

$$C_{r,t} = \frac{\varepsilon z_0 dc_{r,t}K_I}{\left(2\pi\right)^{1/2}} \tag{9}$$

The equation of the initial curve is given by:

$$r = r_0 = \left\{\frac{3}{2}C_{r,t}A\right\}^{2/5} \tag{10}$$

Equations (7) express the equations of the caustic curve for optically anisotropic materials. Two caustics are obtained corresponding to the plus and minus signs in equations. These caustics are referred to the two principal stress directions. Note that for $\xi_{r,t}$ = 0 equations (7) and (9) reduce to the equations of the caustic for optically isotropic materials. Fig. 7 shows the initial curves and respective caustics in a plate with crack subjected to tension made of birefringent materials with ξ = 0, 0.2, 0.4, 0.6, 0.8 and 1.0 [8]. Observe that as ξ increases the shapes of the initial curves and caustics are progressively distorted. The distance between the two caustics increases as ξ also increases. The value of ξ depends on the state of stress, being plane strain, plane stress or three-dimensional. Thus the experimental caustics obtained can be used for the determination of the triaxiality factor k and the subsequent calculation of the stress-optical constant for the correct determination of stress intensity factors.

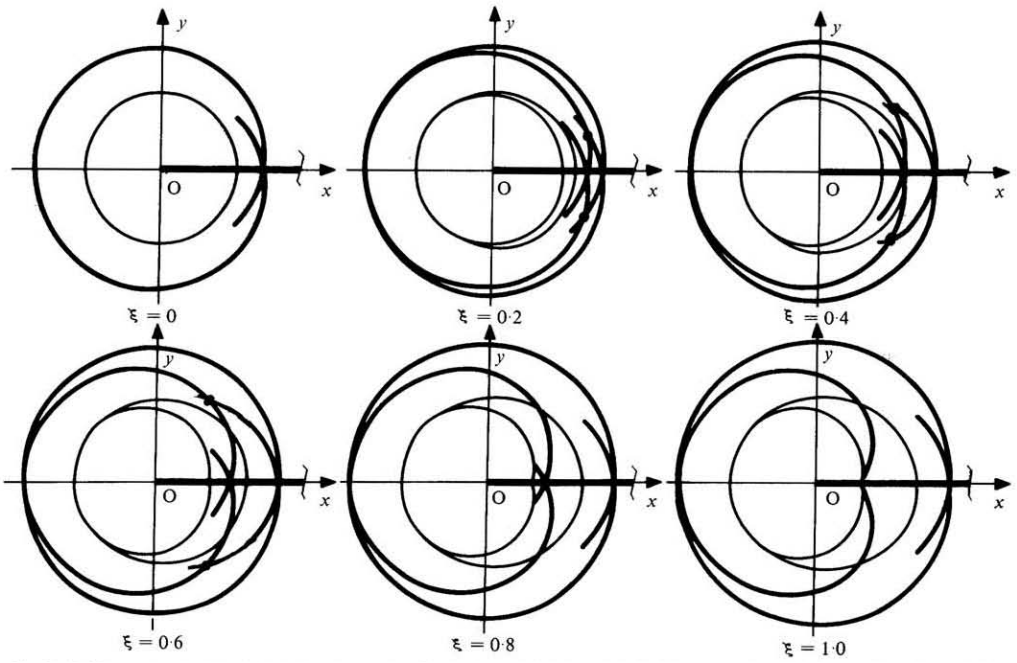

Figure 7. Initial curves and respective caustics in a plate with crack subjected to tension made of birefringent materials with ξ = 0, 0.2, 0.4, 0.6, 0.8 and 1.0

7. Conclusions

From the results of the present work the following conclusions may be drawn:

a. Direct application of the method of caustics without taking special precautions for the determination of stress intensity factors may lead to erroneous results.
b. The material, dimensions of the specimen, applied loads and geometrical dimensions of the optical arrangement should be properly selected to ensure that the initial curve lies in the plane stress region.
c. For specimens made of Plexiglas the stress-optical constant for transmitted light rays is independent of the state of stress around the crack tip for a value of the index of refraction of the medium surrounding the specimen approximately equal to 1.35. Under such condition the plane stress stress-optical constant of the material can be used for any location of the initial curve of the caustic. On the contrary, for light rays reflected from the rear face of the specimen the stress-optical constant does not become independent of the state of stress around the crack tip for any value of the index of refraction of the medium surrounding the specimen.
d. Optically anisotropic materials can effectively be used for the determination of the state of stress around the initial curve of the caustic and the correct determination of stress intensity factors. For such materials the two caustics formed can be used for the determination of the triaxiality coefficient and the subsequent calculation of the corresponding stress-optical constant.

Acknowledgements

The work contained in this paper was supported by the TSMEDE research project of the Democritus University of Thrace.

References

[1] P.S. Theocaris, Elastic stress intensity factors evaluated by caustics, in Mechanics of Fracture, Vol. 7, G.C. Sih (Ed), Martinus Nijhoff, The Netherlands, 1981, pp. 189-252.

[2] P.S. Theocaris, E.E. Gdoutos, An optical method for determining opening-mode and edge sliding-mode stress intensity factors. J Appl Mech, 39 (1972) 91-97.

[3] J.F. Kalthoff, Shadow optical method of caustics, in Handbook on Experimental Mechanics, Second Ed., A.S. Kobayashi (Ed), Prentice-Hall, Eaglewood Cliffs, NJ, USA, 1994, pp.407-476.

[4] A.J. Rosakis, K. Ravi-Chandar, On crack tip stress state: An experimental evaluation of three-dimensional effects. Int J Sol Struct, 22 (1986) 121-134.

[5] M. Konsta-Gdoutos, E.E. Gdoutos, Some remarks on caustics in mode-I stress intensity factor evaluation. Theor. Appl Fract Mech, 17 (1992) 47-60.

[6] M. Konsta-Gdoutos, E.E. Gdoutos, Guidelines for applying the method of caustics in crack problems. Exp Tech, 16 (1992) 25-28.

[7] E.E. Gdoutos, Fracture Mechanics – An Introduction, Second Edition, Springer, 2005.

[8] P.S. Theocaris, G.A. Papadopoulos, Stress intensity factors from reflected caustics in birefringent plates with cracks. J Strain Anal, 16 (1981) 29-36.

Transition of ductile and brittle fracture during DWTT by FEM

YouYou WU[1], Hailiang YU[1,2*], Cheng LU[1], Kiet TIEU[1], Ajit GODBOLE[1], Guillaume MICHAL[1]

[1] School of Mechanical, Materials & Mechatronic Engineering, University of Wollongong, NSW 2500, Australia
[2] School of Mechanical Engineering, Shenyang University, Shenyang, 110044, China
* Corresponding author: hailiang@uow.edu.au or yuhailiang1980@tom.com

Abstract Globally, steel pipelines are widely used to transport energy in the form of liquid petroleum and natural gas. The steel used in the manufacture of these pipelines must have high strength and toughness, and high resistance to fracture. The Drop Weight Tear Test (DWTT) is the most widely used test to assess brittle fracture characteristics in steel. The zones of ductile and brittle fracture during DWTT characterize the quality of pipeline steels. In this paper, the Gurson-Tvergaard-Needleman (GTN) fracture models are coupled in a Finite Element model. The ductile and brittle fracture zones in the samples are analyzed under different conditions. The results show that the change in fracture mode during the DWTT is from the brittle to the ductile, then again to the brittle. The calculated absorbed energies during DWTT compare well with experimental findings. Finally, we present an analysis of the transition from ductile to brittle fracture under different conditions.

Keywords Energy pipeline; ductile fracture; brittle fracture; DWTT

1. Introduction

Oil and gas provide 60% of the world's primary fuel and a large proportion is transported in pipelines. There is more than 33,000 km of high-pressure steel pipelines in Australia. The pipelines are designed, built and operated to well-established standards and rules, because the products they carry can pose a significant hazard to the surrounding population and environment. A combination of good design, adequate material properties and sound operating practices are therefore necessary, to ensure that transmission pipelines operate safely and efficiently.

Line pipe specifications specify minimum requirements for the shear area in a Drop Weight Tear Test (DWTT) to ensure the arrest of a long running brittle fracture. The DWTT, as specified in API RP 5L3 [1] or ASTM E436 [2], was developed by Battelle Memorial Institute in 1962 during the course of the American Gas Association NG-18 Research Program [3] to overcome some limitations of the Pellini drop-weight test which was developed by the US Naval Research Laboratory. In a DWTT, the test specimen is a rectangular bar with a length of 305 mm, a width of 76 mm and of the full material thickness (up to at least19mm). The specimen has a shallow pressed notch and is subjected to three-point bending, as shown in Fig. 1. The standards specify a 5 mm deep notch made by a sharp indenter with a 45° included angle resulting in a tip radius that is normally between 0.0127 to 0.0254 mm [1]. A series of specimens are broken under impact loading at various temperatures and the proportions of ductile fracture (shear) and brittle fracture (cleavage) on the fracture surfaces are measured. From correlations with full-scale pipe burst tests, a transition temperature corresponding to about 85 percent shear is normally defined in application standards as the fracture propagation transition temperature (FPTT) [4-5].

In this paper, a numerical method has been used to simulate the fracture behavior of pipelines. The most commonly used fracture model in computational fracture mechanics to characterize the toughness of line pipe steels is the modified Gurson model [6]. The Gurson model includes the influence of micro-voids on the plastic flow in a constitutive framework. The Gurson model was later modified extended by Tvergaard [7] and Needleman [8]. The modified Gurson- Tvergaard-Needleman(GTN) model is used to describe the acceleration of void growth. In this model, the

material is regarded as a continuum, composed of a ductile matrix with microvoids. There have been a limited number of studies applying this model to ductile materials [9-11].

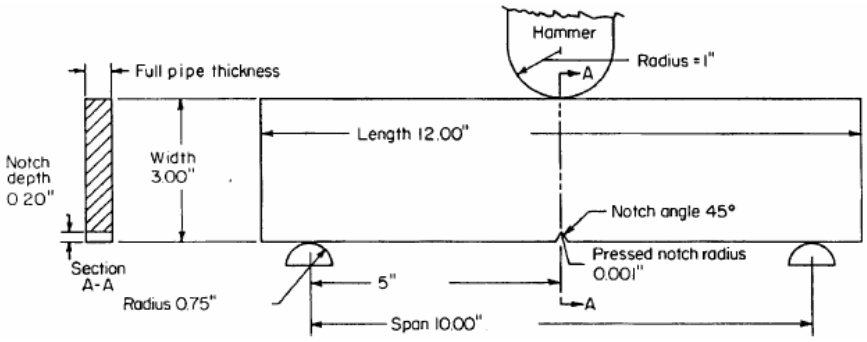

Fig. 1 Drop weight tear test (DWTT) specimen [2]

As opposed to simulations of the DWTT, simulations of Charpy tests are widely carried out to characterize the toughness of line pipe steels. Koppenhoefer and Dodds [12] investigated specimen size and loading rate effects on cleavage fracture of ferritic steels tested in the ductile-to-brittle transition region in pre-cracked Charpy specimens. The probability distribution for fracture of a cracked solid is defined by a two-parameter Weibull distribution [12]. Eberle et al. [13] developed 2D as well as 3D explicit dynamic finite element analyses, in combination with the rate-dependent Gurson model, to simulate Charpy tests. The simulated load-displacement curve and crack front are in close agreement with experimental observations. Tanguy et al. [14] conducted a numerical simulation of the Charpy V-notch test in the ductile-brittle transition regime using a modified Gurson-type model for ductile damage and Beremin model for cleavage fracture. Folch et al [15] also developed a local coupled brittle/ductile fracture approach model to predict either Charpy energy or fracture toughness and to investigate conditions for correlations between them using the Beremin and Gurson models. The modified Beremin model is based on the principles of Weibull statistics for the distribution of the defects and their size as is the standard Beremin model. The modified Gurson model, which incorporates a yield function for porous metal plasticity, was utilized in this work in conjunction with the Lemaitre and Beremin models. Thibaux and van den Abeele [16] reported on the fracture mechanics of instrumented Charpy tests performed on an X70 material. The tests were then simulated using a finite element method and the GTN constitutive model. Damage is represented by an internal variable, f, representing the void volume fraction which is assumed to be isotropic.

There have been very few reports on studies of the ductile-to-brittle transition region during a DWTT. Nonn et al [17] performed numerical simulations of a DWTT by applying the GTN model and compared the simulation results with experimental results from an instrumented DWTT. The results show that GTN model gives a reliable prediction of the load level variation with time when considering strain rate dependence. By applying GTN parameters validated on quasi-static fracture mechanics tests, the maximum load level including the beginning of the load drop for a DWTT can be well described quantitatively. The model equations were not provided in the publication.

In this paper, we used the GTN model to simulate the fracture behavior during DWTT. The stress at the notch was included as an initial condition in this model for the first time. The equivalent stress, nucleation of voids, void size distribution, etc, were analyzed. We found that the fracture propagates in a triangular shape at the crack tip, and the inverse fracture occurs when the fracture propagated about 3/4 of sample width in current study case. Some of the cases show that the transition during DWTT test is from the brittle to the ductile and then again to the brittle zone.

2. Models and simulation

The GTN damage model could be used to analyze the ductile fracture behavior under tension loads. In this paper, we also used the model to predict the damage behavior, as shown in Eq. (1),

$$\Phi = \frac{\sigma_{eq}^2}{\sigma_0^2} + 2q_1 f^* \cosh\left(-q_2 \frac{3p}{2\sigma_0}\right) - \left(1 + q_1^2 f^{*2}\right) \quad (1)$$

where p the hydrostatic pressure, σ_{eq} the effective Von Mises stress, σ_0 the yield stress of the matrix (function of the plastic deformation), q_1, q_2 are material parameters and f^* is the effective porosity. Material grade API 5L X80 was adopted in the models and the parameters are listed in Table 1.

Table 1 Main material parameters

Parameters	Value
Density, kg/m^3	7850
Young's Modulus, GPa	206
Yield stress, MPa	610
f^*	0.06
q_1,q_2	1.5,1.0

As specified in the ASTM E436 [2], the DWTT specimen is loaded in three-point bending by a drop hammer with 400kg weight and loading span of 254 mm. The simulated fracture test comprises two steps employed, as shown in Fig. 2: (1) pressing the notch and, (2) fracturing the sample under the action of the hammer. A three-dimensional geometrical model of the DWTT process was created with a pressed crack was set up with the above parameters and computational meshes with 8-node elements. The elements around the expected fracture zone are much finer than elsewhere in order to accommodate steeper gradients in parameters. In the models, there are 124864 elements and 127002 nodes. In the DWTT process, the hammer descends with an initial impact speed of 7 m/s.

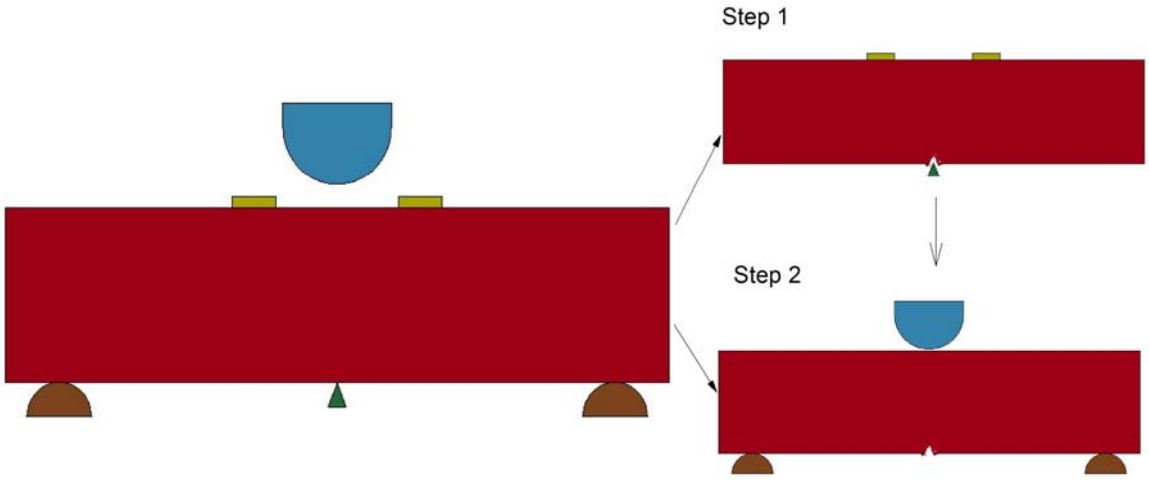

Fig. 2 Geometry of the full simulation process

3. Results and discussion

Fig.3 shows the equivalent stress distribution around the pressed notch position. After the pressed notch was introduced (step 1) at the centre of the specimen, stress concentration in the notch tip

area is observed prior to commencement of fracture. In the figure, we observe the maximum initial stress appeared in the notch tip zone, and this will affect the fracture behavior during the DWTT process.

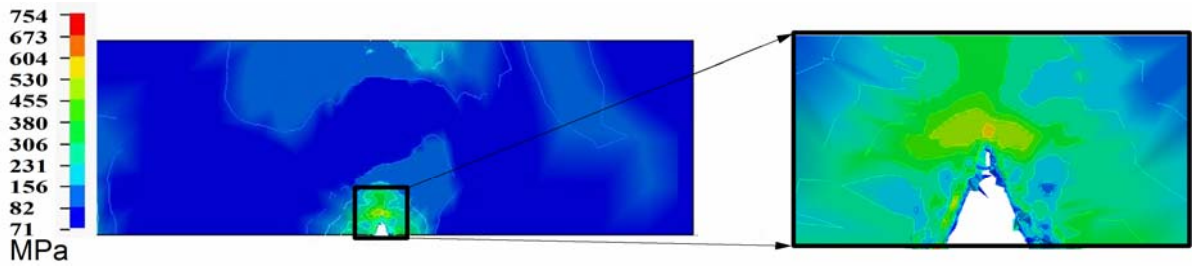

Fig. 3 Equivalent stress distribution and detail around the notch (MPa)

Fig.4 shows the equivalent stress distribution sequence during crack propagation (step 2). The equivalent stress is a three-dimensional stress calculated by Eq.(2). A maximum stress of 813 MPa is found at the notch tip and at the loading point, due to high stress concentration at these places. The stress value in the central area between the notch tip and the loading point is relatively small. A 'butterfly-wing' stress distribution is observed at the crack tip and at the loading point. The stress distribution is almost symmetrical about the loading line. As the crack propagates, the maximum stress distribution extends along the loading line till the specimen fractures.

$$\sigma_v = \sqrt{\frac{3}{2} s_{ij} s_{ij}} \qquad (2)$$

Where S_{ij} are the components of the stress deviator tensor.

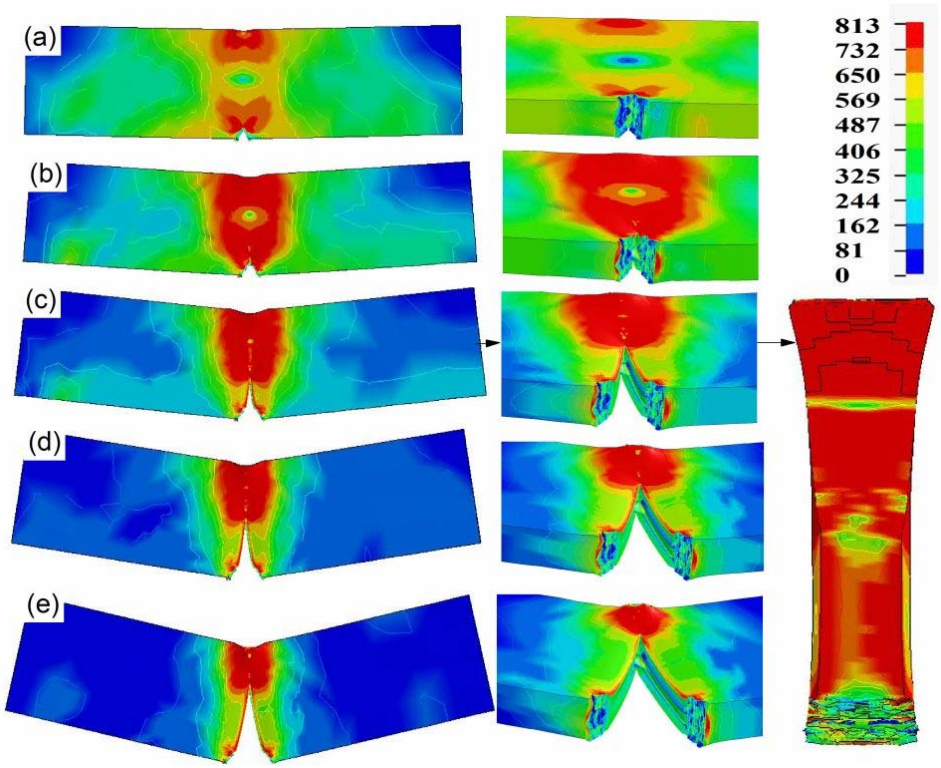

Fig.4 Equivalent stress distribution in DWTT sample (MPa)

Figure 5 shows the development of void nucleation during crack propagation from the notch tip to the impact side. The maximum void density always occurs at the two sides of the fracture surface where fully ductile fracture is seen. The voids appear to peak faster near the plane of symmetry. Which implies that the plasticity at the two sides of the sample is larger than that near the plane of symmetry.

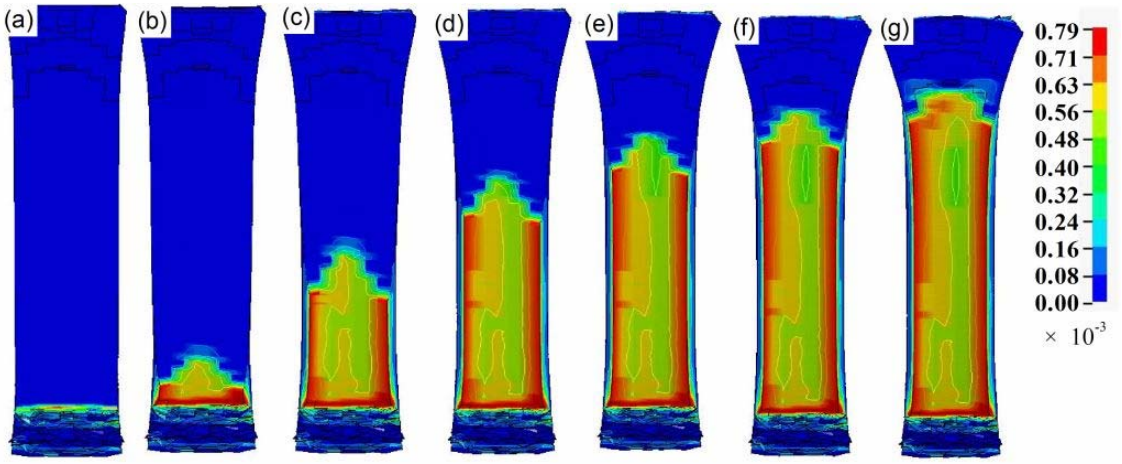

Fig.5 Nucleation of voids in DWTT samples

Fig.6 shows the void volume fraction distribution in the DWTT sample at different stages. It is seen that the void volume fraction in the pressed notch zone is slightly larger than in the other zone, suggesting that the process of notch pressing affects the initiation of fracture in the test sample. Hong et al. [18] concluded that the stress was less concentrated at the notch tip in the pressed-notch specimens compared to a Chevron notch, and this makes the initiation of fracture of pressed-notch specimens more difficult, and accordingly the deformation preceding the fracture initiation resulted in strain hardening in the hammer-impacted region increased.

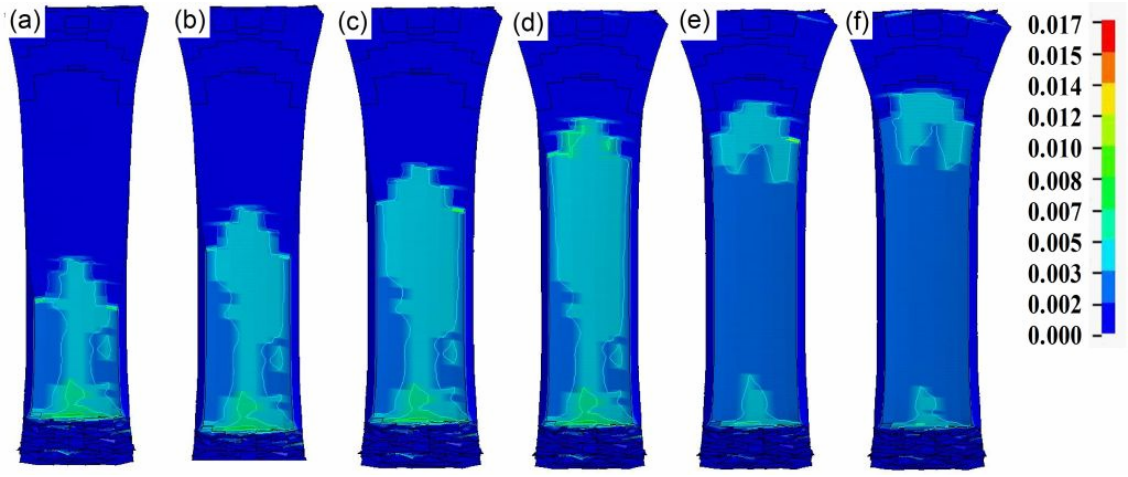

Fig. 6 Void volume fraction distribution in DWTT samples

As seen in Fig.7, the effective strain rate shows a peak near the plane of symmetry until the specimen fractures. This is consistent with the higher crack growth rate due to stress concentration near the surface of symmetry. As expected, the shape of effective strain rate distribution is found to be similar to the shape of the voids distribution. In Fig. 7 (g), it was observed that the inverse

fracture occurred when the fracture propagation reached 3/4 of sample width. The fracture also occurred at impact zones at same time.

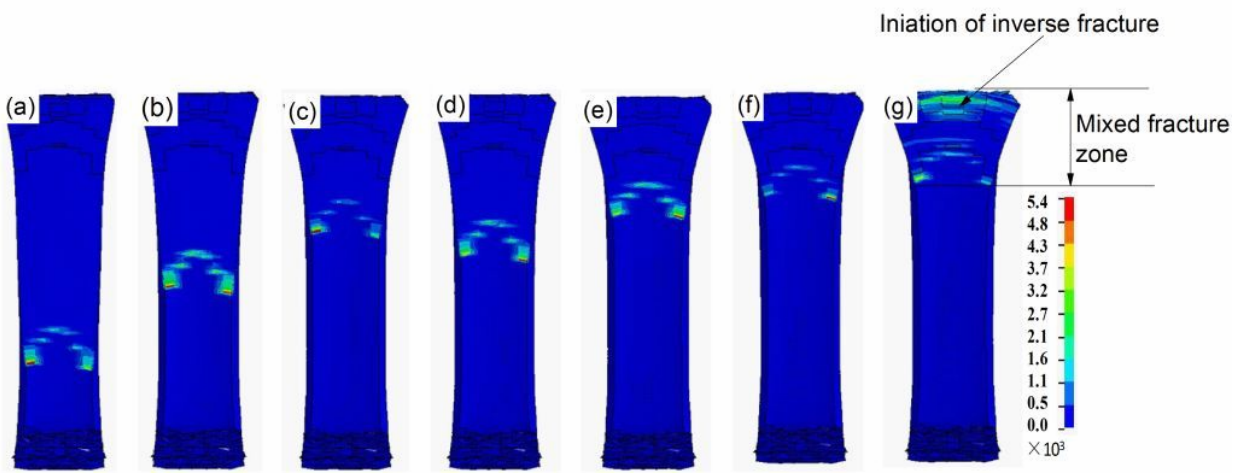

Fig. 7 Effective strain rate distribution in DWTT samples (s^{-1})

The appearance of the simulated fracture surface is in close agreement with the experimental results [18] in terms of stress distribution and fracture morphology as shown in Fig.8. Fracture was initiated as cleavage fracture followed by shear fracture, and then an inverse fracture occurred at the impact zone of the sample. Further analyses on ductile-brittle transition will be carried out by developing a coupled brittle/ductile fracture model in the near future. The relationship between the initiation of inverse fracture and the length of mixed fracture zone need to be further investigated.

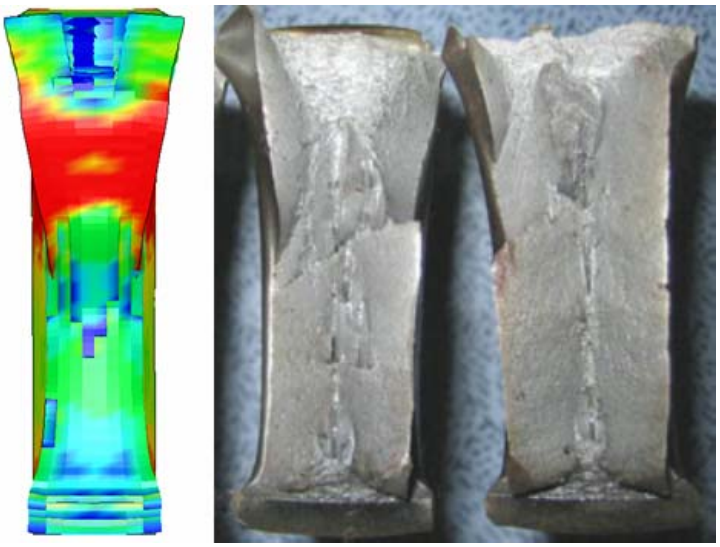

Fig. 8 Simulated results versus the experimental results obtained in ref 18.

4. Conclusions

(1) A finite element model using the Gurson-Tvergaard-Needleman damage model was employed to simulate the fracture process of pipeline steel during DWTT, in particular, considering the state of initial stress around the pressed notch.

(2) During DWTT, the fracture follows a triangular shape in the sample due to higher constraint at

the mid-thickness. This is compatible with the simulation results for void nucleation distribution and effective strain rate distribution.

(3) The simulated results are in good agreement compared with the experimental results in terms of stress distribution and fracture morphology. The relationship between the initiation of inverse fracture and the length of mixed fracture zone need to be further investigated.

Acknowledgements

The authors appreciate Prof. Valerie Linton (Energy Pipeline CRC), Dr. John Piper (John Piper & Associates) and Leigh Fletcher (Welding and Pipeline integrity) for the suggestions in revision of the manuscript.

This work was funded by the Energy Pipeline CRC, supported through the Australian Government's Cooperative Research Centre Program. The funding and in-kind support from the APIA RSC is gratefully acknowledged.

The corresponding author gratefully acknowledges the financial support from the Vice-Chancellor's Fellowship Grant at the University of Wollongong, the National Natural Science Foundation of China through Grant 51105071 and the Doctorate Foundation of the Ministry of Education of China through the Grant 20090042120005.

References

[1] ANSI/API, Recommended Practice for Conducting Drop-Weight Tear Tests on Line Pipe, Third Edition, 1996.
[2] ASTM, Standard Test Method for Drop-Weight Tear Tests of Ferritic Steels, 2008.
[3] A. Cosham, D. G. Jones, R. Eiber, P. Hopkins, Don't drop the drop weight tear test. Journal of Pipeline Engineering, 9(2010).69-84.
[4] R. J. Eiber, B. N. Leis, Fracture control technology for natural gas pipelines circa 2001, Report No. PR-003-00108 to PRCI, 2001.
[5] R. J. Eiber, Correlation of full scale tests with laboratory tests. 3rd Symposium on Line Pipe Research, American Gas Association, November 1965, 83-118.
[6] A. L. Gurson, Continuum theory of ductile rupture by void nucleation and growth: part i---yield criteria and flow rules for porous ductile media. Journal of Engineering Materials and Technology, 99(1977) 2-15.
[7] V. Tvergaard, Influence of voids on shear band instabilities under plane strain conditions. International Journal of Fracture, 17 (1981) 389-407.
[8] V. Tvergaard, A. Needleman, Analysis of the cup-cone fracture in a round tensile bar, Acta Metallurgica, 32(1984) 157-169.
[9] G. Bernauer, W. Brocks, Micro-mechanical modelling of ductile damage and tearing – results of a European numerical round robin. Fatigue & Fracture of Engineering Materials & Structures, 25 (2002) 363-384.
[10] C. Ruggieri, T.L. Panontin, R.H. Dodds, Numerical modeling of ductile crack growth in 3-D using computational cell elements, International Journal of Fracture, 82 (1990) 67-95.
[11] X. Gao, J. Faleskog, C.F. Shih, Cell model for nonlinear fracture analysis – II. Fracture- process calibration and verification. International Journal of Fracture, 89(1998)375-398,
[12] K. C. Koppenhoefer, R. H. Dodds Jr, Loading rate effects on cleavage fracture of pre-cracked CVN specimens: 3-D studies. Engineering Fracture Mechanics, 58 (1997) 249-270.
[13] A. Eberle, D. Klingbeil, W. Baer, P. Wossidlo, R. Liicker, The Calculation Of Dynamic

Jr-Curves From 2d And 3d Finite Element Analyses Of A Charpy Test Using A Rate-Dependent Damage Model, Elsevier Science Ltd, 2002.

[14] B. Tanguy, J. Besson, R. Piques, A. Pineau, Ductile to brittle transition of an A508 steel characterized by Charpy impact test. Part II: Modeling of the Charpy transition curve. Engineering Fracture Mechanics, 72(2005) 413-434.

[15] L. C. A. Folch, F. M. Burdekin, Application of coupled brittle-ductile model to study correlation between Charpy energy and fracture toughness values. Engineering Fracture Mechanics, 63(1999) 57-80.

[16] P. Thibaux, F. Van Den Abeele, Determination of crack initiation and propagation energy in instrumented Charpy V-notch impact tests by finite element simulations. Pipeline Technology Conference, Ostend, 2009, Ostend 209-093.

[17] C. K. A. Nonn, Modelling of Damage Behaviour of High Strength Pipeline Steel, Europipe, 2010. http://www.europipe.com/73-0-2000-2012.html

[18] S. Hong, S. Shin, S. Lee, N.J. Kim, Effects of specimen thickness and notch shape on fracture modes in the drop weight tear test of API X70 and X80 linepipe steels. Metallurgical and Materials Transactions A, 2011, Doi: 10.1007/s11661-011-0697-9.

Structure responses in the riveted and the friction stir welded stringer panel under the tensile loading

MA Yu E [1,*], ZHAO ZhenQiang [1]

[1] School of Aeronautics, Northwestern Polytechnical University, 710072, P.R. China,

* Corresponding author: ma.yu.e@nwpu.edu.cn

Abstract In this paper, applications of friction stir welding in the integral fuselage structure are studied. In order to compare with the traditional riveted stringer panel, the integral panels are joined by two ways: one is by single-row rivets and the other one is by friction stir welding. Two kind finite element models are built by Abaqus 6.10. Stress distributions are analyzed and compared. For welded panel, a FORTRAN program of the SIGINI subroutine is made to input the residual stress profile to the finite element model of friction stir welded panel. Compared with the rivet joint, friction stir welded joint can reduce the weight of fuselage. In the same applied stress, the sample joint with rivets has the higher stress areas around the rivet hole, the sample joint with friction stir welding avoids the stress concentration in junctions.

Keywords Friction stir weld; riveted stringer panel; welded panel; stress distribution.

1. Introduction

Friction stir welding (FSW) is a solid state welding process that has received the world wide attention, particularly for joining aluminum alloys. Because FSW has a lower heat input than the traditional fusion welding, the plastic shrinkage of joint induced by heat in FSW is also lower, which will help to reduce the welding residual stress and distortion of structure. Consequently, FSW has been widely used in modern aero structures.

A significant amount of work has been conducted in the past few years to understand the properties of friction stir welding joints. Aidy studied the crack coalescence in 2024-T351 Al alloy friction stir welded joints and discussed the fatigue endurance of FSW joint [1]. Zhang established the two-dimensional numerical models of friction stir welding and gave the numerical simulation of FSW process [2]. Dinaharan studied the effect of friction stir welding on microstructure, mechanical and wear properties of AA6061/ZrB_2 [3]. Xu studied the residual stress in thick aluminum friction stir welded butt joints [4].

2. Numerical Simulation

2.1 Parameters settings

Finite element analysis is run by Abaqus 6.10. The riveted stringer panel and the welded panel are of the same size (shown in Fig.1). The length of the panel is 1113mm, the width in the middle is 200mm and in both ends is 288mm, and the thickness is 2mm. There are three rows of rivet hole along the direction of the riveted stringer panel width, one of which is located in the middle and the other two rows are located on both sides, 150 mm from the middle rivet holes. Three stringers (shown in Fig.2) will be fixed on the panel by 30 rivets. The width of the surface of the stringer which contacts with the panel is 28mm, the height of the stringer is 28mm, and the thickness is always 2mm in every part of the stringer. The material of panel and stringers is aluminum-lithium alloy, the Young's modulus is 77000 and the Poisson's ratio is 0.33. The material of rivet is 45 steel; two parameters are 210000 and 0.269. Welded panel is joined by welding instead riveting to joint panel and stringers, and the size of the welded panel are the same with the riveted stringer panel except using 10 mm width weld zone to replace the three rows of rivet hole. The material parameters in the weld zone are 55000 and 0.33. After assembly, contact surface between different

parts of the panel has been set up. In the riveted stringer panel, each group of mutually contacting surface are defined as an contact pair, then four contact pairs in the riveted stringer panel were built. In the welded panel, the constraint tie were set up to characterize the welded areas in panel and stringers, other contact areas were defined as contact pairs in same parameters with riveted stringer panel.

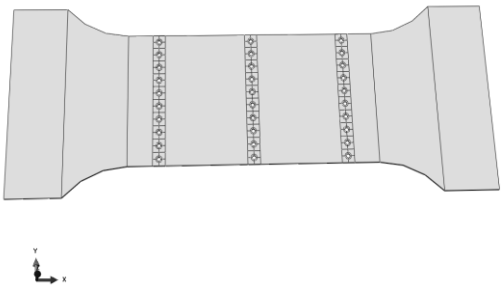

Fig.1 Riveted stringer panel

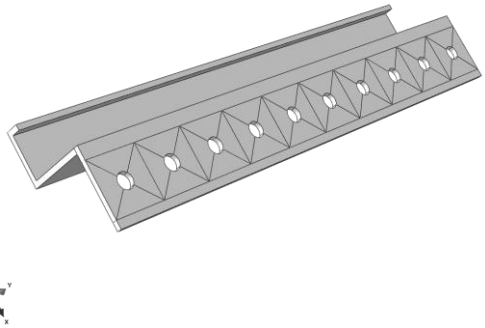

Fig.2 Stringer

2.2 Mesh

Reasonable mesh of complex structure need appropriate partition (Fig.1 illustrates the partition of each part of this panel). In order to get a more accurate calculation result, the rivet must be meshed carefully. The areas around the rivet holes are critical areas where stress concentrate will emerge in tensile load, so these areas also need meticulous grid. Based on this principle, the panel were meshed carefully (shown in Fig.3). Mesh of the welded panel is easier because there is no rivet in welded model.

2.3 Loads

The same load is applied to the two models. 200MPa tensile pressure is loaded along the x direction, in addition, a FORTRAN program of the SIGINI subroutine is made to input the residual stress profile to the finite element model of friction stir welded panel before tensile pressure is loaded.

2.4 Results

Fig.4 shows the numerical simulation result of riveted stringer panel, the high stress areas appears around the rivet holes (especially the middle row) and the curved areas on both sides, the stress in stringers is lower compare with the panel. The maximum stress around the rivet holes reaches more than 600MPa (exceed the ultimate strength of the material) and the stress in the curved areas reaches from 400MPa to 500MPa (shown in Table.1), stress in other areas is much lower than these areas. So the rivets connection areas on the panel may be the first to be destroyed in proper tensile load.

Fig.5 shows the numerical simulation result of welded panel, the high stress areas appears in the top of the welded areas and the curved areas on both sides, stringers are also the low stress areas. The maximum stress in the curved areas is nearly 400MPa, a little higher than 350MPa in the top of the welded areas, however, the tensile strength of the welded area is much lower than the base material (about 70% of the base material), and so the welded areas will be weak zone.

After comparison of the results of two different models show in Table 1, under the same tensile load，stress profile in welded panel is uniform and much lower than it in riveted stringer panel, so we can predict that the welded panel could withstand the larger tensile load than riveted stringer panel.

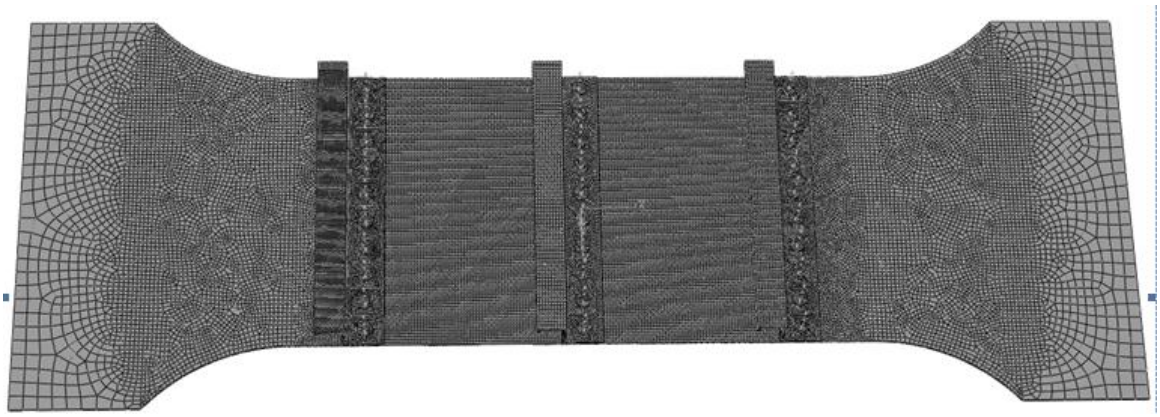

Fig.3 Mesh of riveted stringer panel

Table.1 Comparison of stress

Stress in Riveted panel (MPa)			Stress in Welded Panel (MPa)		
Panel	Around Holes	Stringers	Panel	Welded Areas	Stringers
<300	>600	<100	<300	200~400	<200

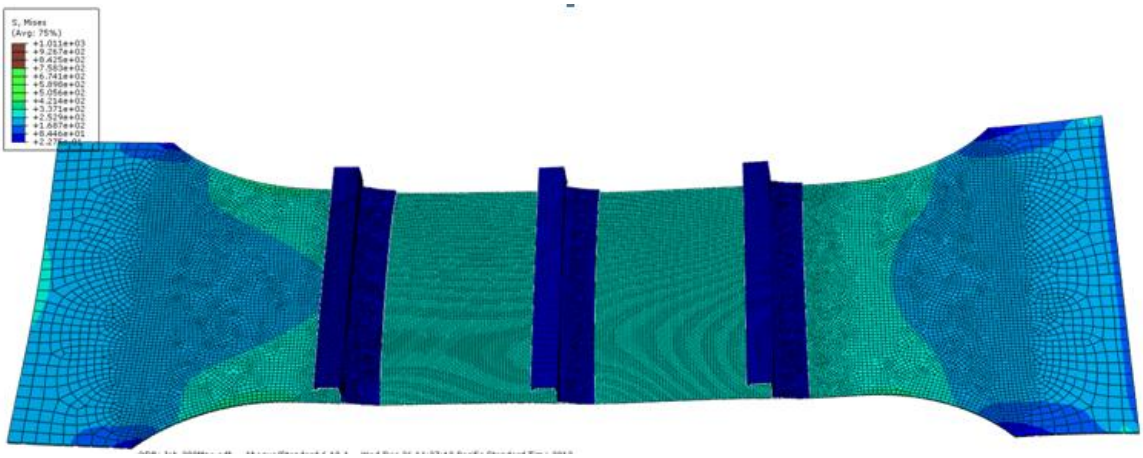

Fig.4 Riveted stringer panel

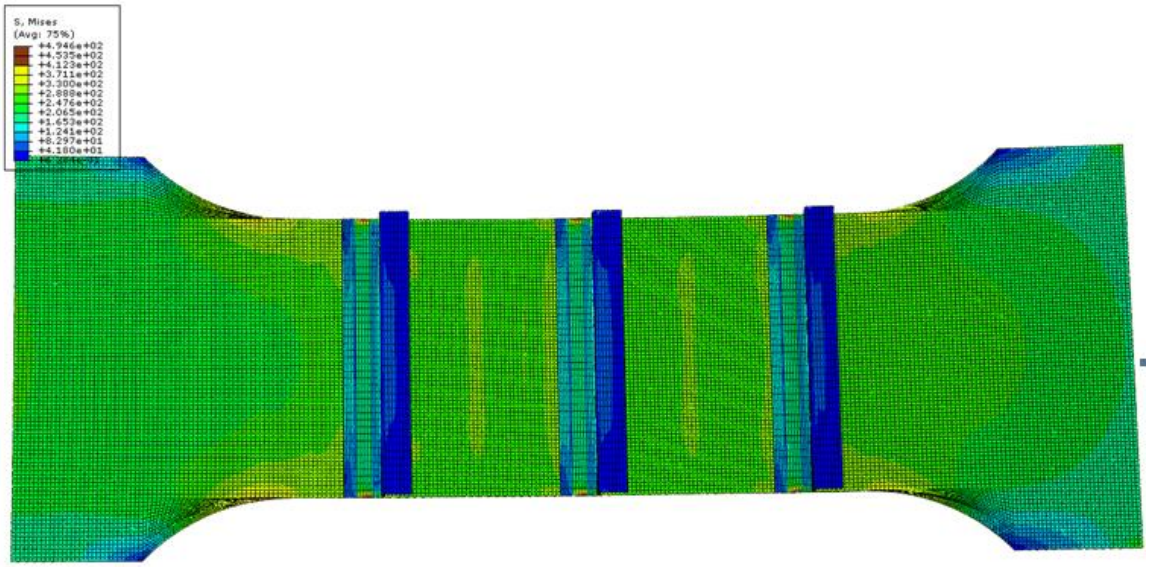

Fig.5 Welded panel

3. Comparison with the Test Results.

Tests were performed to compare this two kinds of structures in tensile load. Six panels consist of three riveted stringer panels and three welded panels were tested by MTS, and the results are shown in Table.2. Two of riveted stringer panels were destroyed in rivet holes on one side and the other one is destroyed in the middle row of rivet holes, the welded panels are all destroyed in welded areas. These results can be used as validation of the numerical simulation.

Table.2 Testing and simulation results

			Simulation Result
	Number	Failure Position	High Stress Area
Riveted panel	1	Left holes	Around holes
	2	Left holes	
	3	Middle holes	
Welded panel	1	Left weld	Welded areas
	2	Middle weld	
	3	Middle weld	

4. Summary

In this study, the main conclusions are

(1) A more uniform stress distribution in welded panel than riveted stringer panel under the same applied stress, the sample joint with friction stir welding avoids the stress concentration in junctions.

(2) The tensile strength of welded structure is higher than riveted stringer structure in certain situation.

References

[1] Aidy Ali, M.W.Brown, C.A.Rodopoulos, Modelling of crack coalescence in 2024-T351 Al alloy friction stir welded joints, International Journal Fatigue 30(2008)2030-2043.

[2] Zhang Hong Wu, Zhang Zhao, Chen Jin Tao, Finite element simulation of friction stir welding process, Transactions of the china welding institution, Vol.26, No.9, September 2005.

[3] Dinaharan, N.Murugan, Effect of friction stir welding on microstructure, mechanical and wear properties of AA6061/ ZrB_2 in situ cast composites, Materials Science and Engineering A, 543(2012)257-266.

[4] Weifeng Xu, Jinhe Liu, Hongqiang Zhu, Analysis of residual stresses in thick aluminum friction stir welded butt joints, Materials and Design 32(2011)2000-2005.

Modeling of deformation and failure behavior of dissimilar resistance spot welded joints under shear, axial and combined loading conditions

Sebastian Burget[1,*], **Silke Sommer**[1]

[1] Crash-Safety, Damage Mechanics, Fraunhofer-Institute for Mechanics of Materials IWM, 79108 Freiburg, Germany
* Corresponding author: Sebastian.Burget@iwm.fraunhofer.de

Abstract This paper presents the modeling of deformation and failure behavior of dissimilar resistance spot welded joints (RSW) between hot-stamped ultra-high strength (22MnB5) and microalloyed (HC340LAD) steels. To determine the deformation and failure behavior of the different material zones of the weld, tensile and shear specimens, which were cut from the base metals, the weld nugget and heat treated sheets were tested and modeled using the Gologanu-Leblond model coupled with the fracture criteria of Thomason and Embury. The joints were modeled using detailed 3-dimensional finite element models taking into account the different weld zones, i.e. base metal (BM), heat affected zones (HAZ) and weld metal (WM), their dimensions and their mechanical properties. Simulations of the spot welded joints' behavior under shear, axial and combined axial and shear loading were carried out and compared to experimental results such as force vs. displacement curves, load bearing capacities, fracture mode and fracture locations. Maximum loads and force vs. displacement curves from experiments and simulations showed good agreements for all loading situations examined. Despite of its superior strength compared to the microalloyed steel, pull-out fracture of the joints took place in the coarse grain HAZ of the hot-stamped ultra-high strength steel in experiments and simulations.

Keywords Resistance spot welding, Mechanical properties, Combined loading, Failure criterion, Ultra-high strength steel

1. Introduction

With several thousands of spot welds in a body-in-white, spot welding still represents the most widely used thermal joining process in steel-based automotive production. With the development of hot-stamped ultra-high strength steels, new light-weight potentials have been created, that combine thin steel sheets and thereby reduce weight, with a simultaneous optimization of passive safety requirements. To implement these potentials joining technologies have been adapted to ensure a combination of optimized material and joint strength. At present hot-stamped manganese-boron steels (22MnB5) are widely used, especially for load-bearing structural components in parts of the passenger cabin, where deformation and intrusion should be kept at a minimum.
To increase the reliability and accuracy of crash-simulations failure of the joints has to be taken into account using simplified models like solid or beam elements [1][2][3] in combination with simplified mostly force based failure criteria depending on the occurring axial and shear loads acting on the joints. To identify the model parameters of such criteria, failure of the joints can be characterized experimentally under different loading situations, as e.g. shown in [4][5]. For different welding parameters, which lead to a change in the joints' geometry in terms of different diameters of the weld nugget and the heat-affected zone [6], the procedure has to be repeated to determine the load bearing capacities of each particular joint.
In this work the deformation, fracture and load bearing capacity of dissimilar spot welds between hot-stamped and microalloyed steels is investigated in detailed finite-element simulations in several loading situations such as pure shear and pure axial loading as well as combined axial and shear loading. Material data for the modeling of the different material zones of the weld were obtained in tensile, notched tensile and double notched shear tests. The material models calibrated based on these tests are used for the simulation of experiments on spot-welded tensile-shear, KS2- and coach-peel specimens.

2. Experimental results

2.1. Dissimilar spot welded joints between ultra-high strength and low-alloyed steels

The joints investigated in this work are dissimilar resistance spot welded joints between a hot-stamped ultra-high strength steel (22MnB5) with a nominal ultimate tensile strength (UTS) of 1500 MPa and a microalloyed high strength low-alloy steel (HC340LAD) with an UTS of 415 MPa. Spot welding and testing of spot welded KS2-specimens was carried out at the Laboratory for Materials and Joining Technology (LWF) at the University of Paderborn [7].
On the left Fig. (1) shows the etched cross section of the dissimilar joint. The upper sheet shows the microalloyed HC340LAD with a sheet thickness of 1.5 mm. The hot-stamped 22MnB5 steel sheet with a thickness of 1.0 mm can be seen as the lower sheet in Fig. (1) (left). The averaged weld nugget diameter measured from cross-sections of three different spot welds was 5.2 mm.

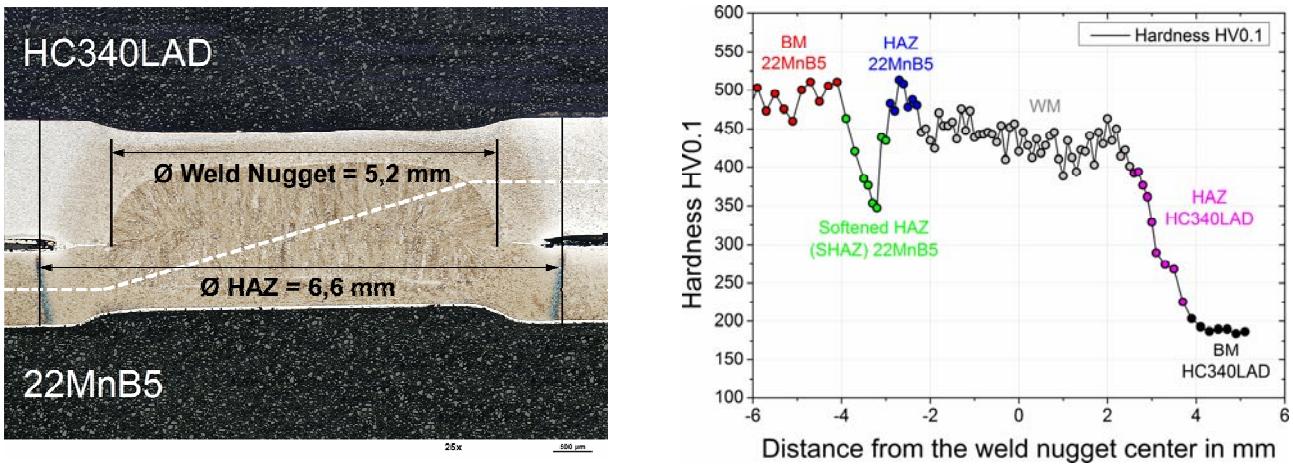

Figure 1. Etched cross section (left) and hardness measurements along the dashed white line shown in the cross section of the investigated spot welded joint between hot-stamped 22MnB5 and HC340LAD (right)

The base metal (BM) of the microalloyed steel shows a ferritic-perlitic microstructure with a hardness of 190HV0.1. Inside its HAZ the microstructure is ferritic-bainitic and a continuous increase in hardness up to 380HV0.1 adjacent to the weld nugget can be observed. The microstructures of the BM and the HAZ of the hot-stamped 22MnB5 are fully martensitic with averaged hardness values of 475HV0.1. Inside the subcritical HAZ a significant decrease in hardness can be seen. Due to the heat input during spot welding tempering of the martensitic microstructure occurs in this region (SHAZ) and leads to softening of the material. This phenomenon has also been observed during spot or laser welding of dual-phase steels as e.g. shown in [8]. The microstructure of the weld metal (WM) of the dissimilar weld is martensitic and has slightly lower hardness values than the BM and the HAZ of the hot-stamped manganese-boron steel.

2.2. Testing of dissimilar spot welded joints

The mechanical behavior of the dissimilar spot welded joints was characterized under shear, axial and combined axial and shear loading conditions using different tests and specimens such as tensile-shear- (TS), LWF-KS2- and coach-peel (CP) specimens. The LWF-KS2 concept [9] is based on double-U formed specimens, which are spot welded in their center and tested under different loading angles and/or velocities using different clamping conditions. The CP- and the KS2-specimen as well as the fixtures of the KS2-specimen for tests with different loading angles

are shown in Fig. (2). By using a pin-joint connecting the grips with the specimens fixtures no additional constraining forces arise during loading and only the applied vertical force acts on the joint.

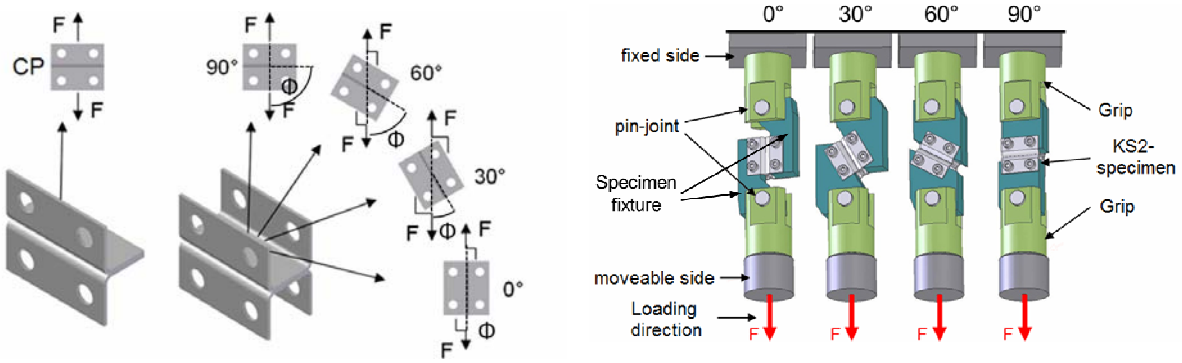

Figure 2. Coach-peel and KS2-specimens with loading angles 0°, 30°, 60° and 90° (left). Clamping conditions for the KS2-specimens tested under different loading angles (right) [9]

Assuming constant loading angles Φ, defined as the angle between the joining plane and the loading direction during deformation of the specimens, the measured forces F in KS2-experiments can be decomposed into their axial F_N and shear F_S parts as

$$F_N = F \cdot \sin\phi\,, \qquad F_S = F \cdot \cos\phi\,. \tag{1}$$

Based on this decomposition simplified force-based failure criteria for spot welded joints as proposed by several authors [4][10][11] can be constructed. Fig. (3) (left) shows the force vs. displacement curves of all the KS2-experiments carried out on the investigated dissimilar spot welded joint. The decomposition of their load bearing capacities assuming constant loading angles is shown on the right. The gray dashed circular lines in Fig. (3) (right) indicate lines of constant resulting forces. The highest maximum load of the joint was measured under shear loading conditions in experiments on KS2-0° specimens. With increasing loading angles the load bearing capacity of the joint decreases to a minimum of 4.2 kN under pure axial loading in KS2-90° tests. Fracture of all tested specimens occurred as pull-out fracture from the hot-stamped 22MnB5 sheets. Cross-sections of failed specimens, loading capacities and results of TS- and CP-specimens will be shown in section 3.3.

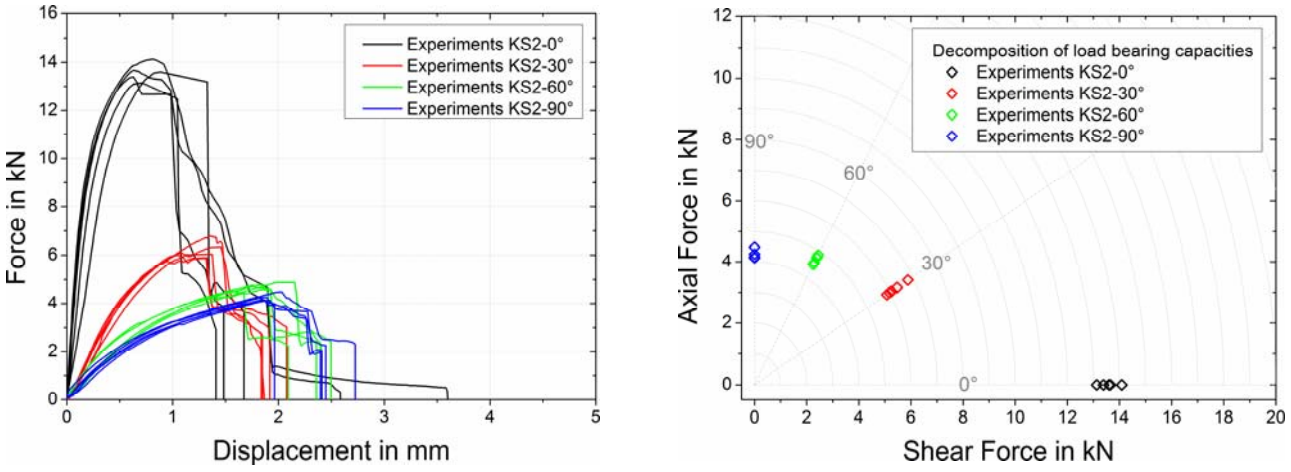

Figure 3. Force vs. displacement curves of KS2-specimens with loading angles 0°, 30°, 60° and 90° (left). Decomposition of load bearing capacities of the KS2 experiments into axial and shear forces (right)

3. Modeling of deformation and failure behavior of dissimilar spot welded joints

3.1. Material model

The constitutive model developed by Gologanu and Leblond [12] for porous media is an extension of the Gurson model [13] which takes into account the effect of void shape. In addition to the porosity *f*, the void shape *S* or *w* is considered in the flow potential of the model. Considering an oblate or prolate axisymmetric spheroidal void, shown in Fig. (4), with the semi-axes a along the x_2-(axial direction) and b along the x_1- and x_3-direction (radial direction), *w* and the *S* are defined as $w=a/b$ and $S=ln(a/b)=ln(w)$. Spherical voids are characterized by $S = 0$ and $w = 1$ respectively. The shape parameters for prolate voids are $S > 0$ and $w > 1$, while $S < 0$ and $w < 1$ is true for oblate voids.

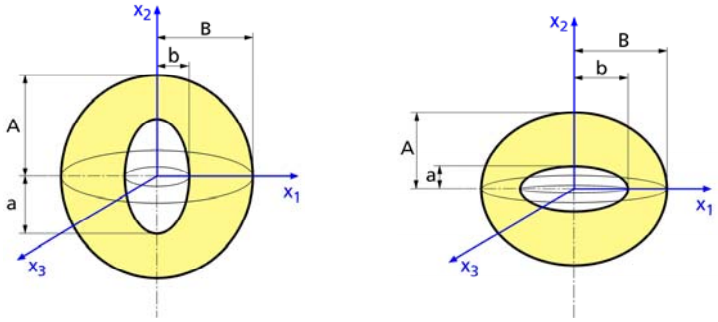

Figure 4. Spheroidal axisymmetric prolate (left) and oblate (right) void in a representative volume element with the shape of a confocal spheroid with the semi-axis A along x_2 and B along x_1 and x_3

The porosity of the representative volume element is given by

$$f = \frac{ab^2}{AB^2}. \tag{2}$$

The functional form of the flow potential, which was derived by Gologanu using an approximate load limit-analysis, is given in Eq. (3).

$$\Phi = C\frac{\|T_{ij}\|^2}{\sigma_M^2} + 2q_1(g+1)(g+f)\cosh\left(\frac{\kappa\Sigma_h}{\sigma_M}\right) - (g+1)^2 - q_1^2(g+f)^2 = 0 \tag{3}$$

with

$$\|T_{ij}\| = \sqrt{\frac{3}{2}T_{ij}T_{ij}} \tag{4}$$

T_{ij} and Σ_h are anisotropic generalizations of the deviatoric and the hydrostatic stresses. σ_M is the equivalent yield stress of the matrix material. The parameters *C*, q_1, *g* and κ are functions of the void volume fraction *f* and the void shape *S*. The evolution of the void shape $\dot{S}$ and the porosity in terms of the rate of void growth $\dot{f}_{growth}$ and nucleation $\dot{f}_{nuc}$ are given in Eq. (5) and Eq. (6) – (8).

$$\dot{S} = S_a\dot{\varepsilon}_a^{p'} + S_b\dot{\varepsilon}_{kk}^{p} \tag{5}$$

The parameters S_a and S_b are functions of the void shape and the stress triaxility. $\dot{\varepsilon}_a^{p'}$ and $\dot{\varepsilon}_{kk}^{p}$ are the deviatoric part of the plastic strain rate in the direction of the semi-axis a and the rate of

volumetric strain. Compared to the Gurson model, no modifications are needed to describe the evolution of porosity. The rate of f consists of two terms describing growth and nucleation of voids.

$$\dot{f} = \dot{f}_{growth} + \dot{f}_{nuc} \tag{6}$$

Void growth is governed by the rate of volumetric plastic strain, whereas void nucleation is assumed to be controlled by the equivalent plastic strain $\varepsilon_{pl,M}$ of the matrix material. Under the assumption that void nucleation follows a normal distribution, its rate is given by Eq. (8).

$$\dot{f}_{growth} = (1-f)\dot{\varepsilon}_{kk}^{pl} \tag{7}$$

$$\dot{f}_{nuc} = \frac{f_n}{S_N\sqrt{2\pi}} \exp\left(-\frac{1}{2}\left(\frac{\varepsilon_{pl,M}-\varepsilon_N}{S_N}\right)^2\right)\dot{\varepsilon}_{pl,M} \tag{8}$$

f_n denotes the overall volume fraction of void nucleating inclusions, ε_N is the mean value of the equivalent plastic strain, at which inclusions nucleate voids and S_N is the standard deviation of the normal distribution.

Together with the Gologanu model the fracture criteria of Thomason [14], in a modified version of Pardoen and Hutchinson [15], and Brown and Embury [16] are used. The Thomason model assumes that void coalescence begins once the plastic limit load on the ligament between the voids is reached. The limit load is derived using an axisymmetric unit-cell containing one ellipsoidal void of a regular array shown in Fig. (5).

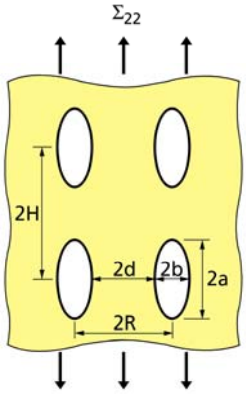

Figure 5. Geometrical quantities of the void distribution used for the Thomason model

The coalescence criterion is then expressed by Eq. (9), where α and β are material parameters. Unit cell analyses suggest to choose α = 0.1 and β = 1.2 [15]. Based on the geometry the ligament size ratio can be written as Eq. (10).

$$C_{\text{Thomason}} = \frac{\Sigma_{22}}{\sigma_M} - \left(1-\left(\frac{b}{R}\right)^2\right)\left(\alpha\left(\frac{R/b-1}{w}\right)^2 + \beta\left(\frac{R}{b}\right)^{1/2}\right) = 0 \tag{9}$$

$$\frac{\mathrm{b}}{\mathrm{R}} = \left[\frac{3}{2}\frac{\mathrm{f}}{\mathrm{w}}\frac{\mathrm{H}_0}{\mathrm{R}_0}\exp\left(\tfrac{3}{2}\varepsilon'_{22}\right)\right]^{1/3} \tag{10}$$

The Gologanu model calculates f, w, Σ_{22} and σ_M in Eq. (9) and (10). The initial aspect ratio H_0/R_0 can be considered, besides α and β, as a third material parameter of the failure criterion.

To model material failure at low stress triaxilities, the criterion of Brown and Embury [16] is used here. This model is based on the assumption that the formation of shear bands takes place in the ligament between two voids and leads to ductile fracture, if the mean radius of a void equals half the distance between the centers of the two voids. Using the void aspect ratio w, calculated by the

Gologanu model, this criterion can by written as

$$C_{Embury} = \sqrt{1+w^2} - \frac{R}{b} = 0\,. \tag{11}$$

The model has been implemented by Andrieux [17] into the finite element code ABAQUS/Explicit.

3.2. Identification of model parameters of the different weld zones

The parameters of the Gologanu model and the fracture criteria were identified by inverse simulations of smooth and notched tensile specimens as well as double notched shear specimen, which were cut from the base materials, the weld nugget itself and heat treated sheets with microstructures corresponding to the heat affected zones. In case of the specimens cut from the weld nugget reduced dimensions have had to be used, due to the geometry of the weld nuggets. All specimens have been modeled using detailed finite element models meshed with 3-dimensional brick elements with edge lengths of 0.1 mm in the regions of interest. Using the symmetry of the specimens only one eighth of the smooth and notched tensile specimen and half of the double notched shear specimen has been modeled. The finite element models are shown in Fig. (6).

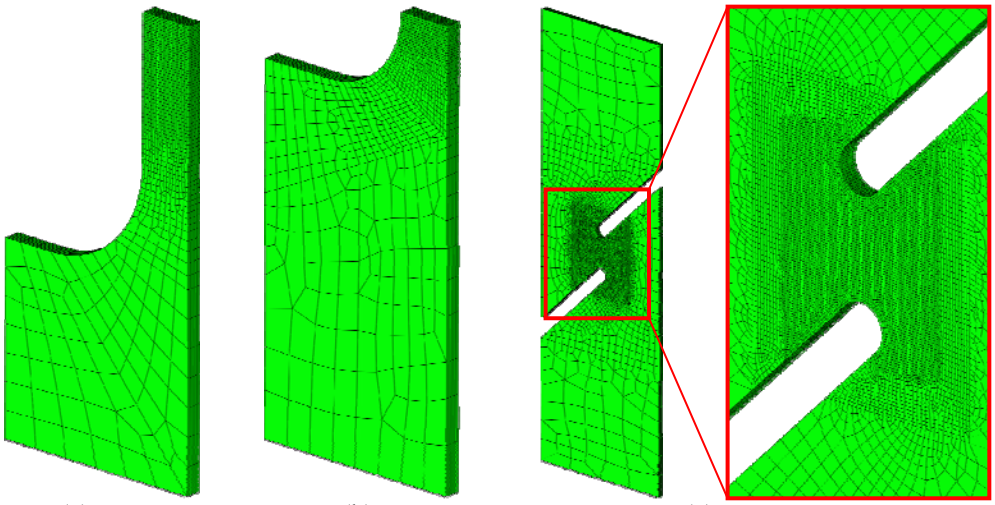

(a) (b) (c)

Figure 6.Finite element models of smooth (a) and notched tensile (b) and double notched shear (c) specimens

Up to uniform elongation the true stress-strain curves of the base material, heat affected zones and the weld metal were measured in smooth tensile tests. Subsequently the true stress vs. true strain curves are determined in simulations of the smooth tensile tests. The damage and failure parameters for the different material zones of the weld were identified by simulating the smooth and notched tensile tests and the shear tests on double notched shear specimens and adjusting the parameters to match the numerical results with the experimental ones. The parameters identified are given in Table (1).

Table 1. Parameters of the material model and the failure criteria

	f_0	ε_N	f_N	S_N	q	S_0	H_0/R_0	α	β
22MnB5 BM	0.002	0.20	0.02	0.1	1.5	0.0001	1.2	0.1	1.2
22MnB5 SHAZ	0.002	0.30	0.008	0.1	1.5	0.0001	1.2	0.1	1.2
HC340LAD BM	0.002	0.85	0.003	0.1	1.5	0.0001	0.5	0.1	1.2
HC340LAD HAZ	0.002	0.15	0.005	0.1	1.5	0.0001	0.5	0.1	1.2
WM	0.002	0.15	0.02	0.1	1.5	0.0001	1.8	0.1	1.2

The comparison of experimental and numerical results for the 5 different material zones is shown in Fig (7) – Fig. (9). The simulation results show good agreements with the experimental measurements for all loading conditions and stress triaxilities. It should be noted that the specimens for the characterization of the weld metal and the smooth tensile specimens from the HAZ of HC340LAD have been manufactured and tested with reduced dimensions and gauge lengths to obtain valid experimental data. The materials' ductility in terms of technical fracture strains in tensile tests cannot be compared in these cases.

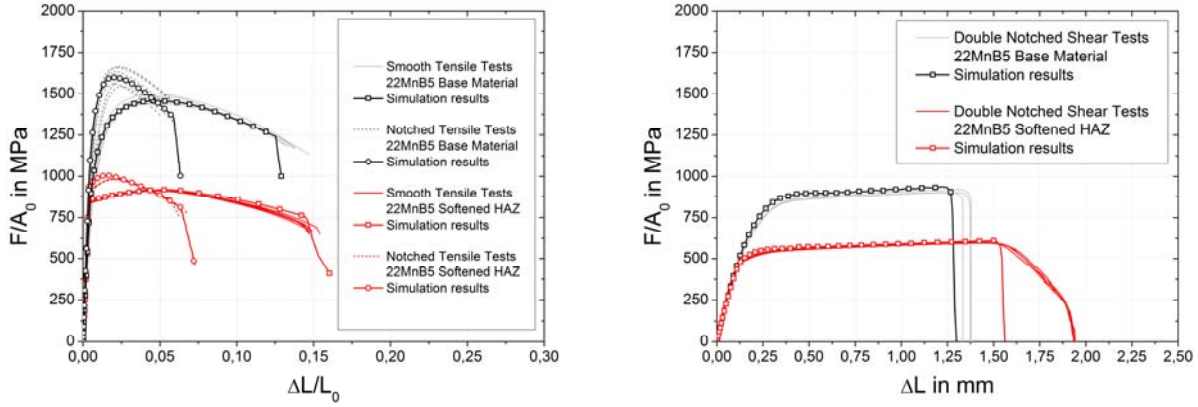

Figure 7. Comparison of measured and calculated F/A_0 vs. $\Delta L/L_0$ curves of smooth and notched tensile tests (left) and F/A_0 vs. ΔL curves of double notched shear tests (right) for 22MnB5 (BM and softened HAZ)

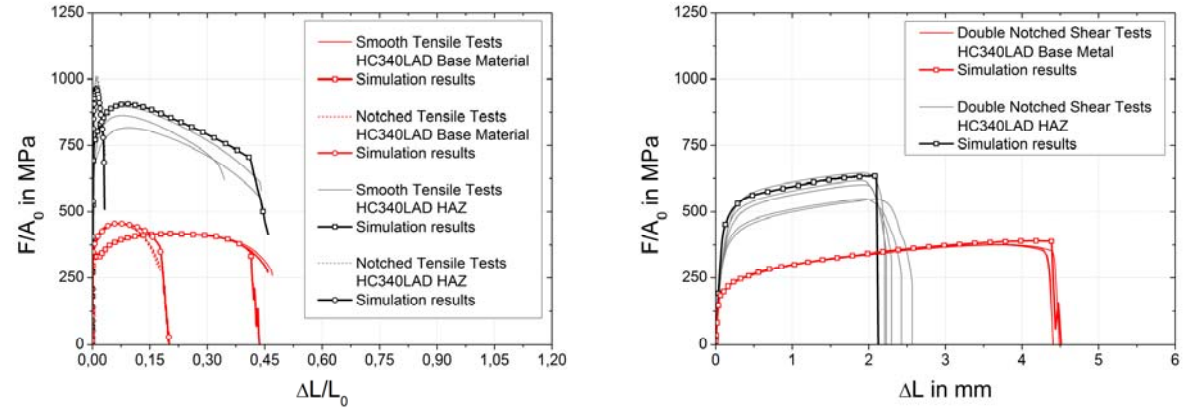

Figure 8. Comparison of measured and calculated F/A_0 vs. $\Delta L/L_0$ curves of smooth and notched tensile tests (left) and F/A_0 vs. ΔL curves of double notched shear tests (right) for HC340LAD (BM and HAZ)

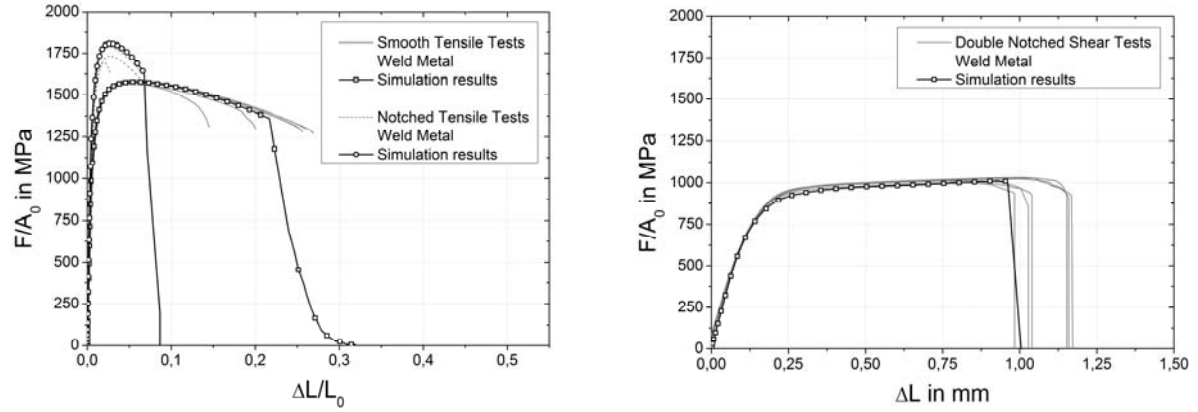

Figure 9. Comparison of measured and calculated F/A_0 vs. $\Delta L/L_0$ curves of smooth and notched tensile tests (left) and F/A_0 vs. ΔL curves of double notched shear tests (right) for the WM

3.3. Simulation of tensile-shear-, KS2- and coach-peel tests

For the simulation of deformation and failure behavior of dissimilar spot welded joints in tensile-shear- (TS), KS2- and coach-peel (CP) tests, the calibrated material and failure models were used for the different material zones of the weld. Due to the negligible differences in the mechanical behavior between the base material of 22MnB5 and the weld metal as well as the similar hardness values of the base metal, the weld metal and the non-softened HAZ in 22MnB5, the mechanical properties of the non-softened HAZ were assumed to be identical to those of the weld metal. A detailed finite-element model of the spot weld, shown in Fig. (10), was built up taking into account the geometry of the weld and its material zones measured in etched cross-sections and hardness measurements of spot welded specimens (see Fig.(1)). The nugget diameter and the diameter of the HAZ of the spot weld were modeled as 5.2 mm and 6.6 mm respectively. The softened HAZ in the hot-stamped 22MnB5 sheet was modeled with a width of 0.6 mm. The edge length of the elements in the spot welded region is approximately 0.1 mm.

Figure 10. Detailed finite element model of the spot weld between 22MnB5 and HC340LAD

The finite-element models of TS-, KS2- and CP-specimens are shown in Fig. (11). Due to the symmetry only one half of each specimen was modeled. The parts of the specimens that are clamped in the experiments, shown in dark gray, are taken as rigid bodies. The grips and the specimen fixtures of the KS2-tests were not explicitly taken into account. Instead of that the clamping conditions of the specimens have been modeled by connecting all nodes of the clamped rigid bodies via kinematic constraints to one node representing the pin-joint between the specimen fixtures and the grips (see Fig. (2)). This is shown schematically in Fig. (11).

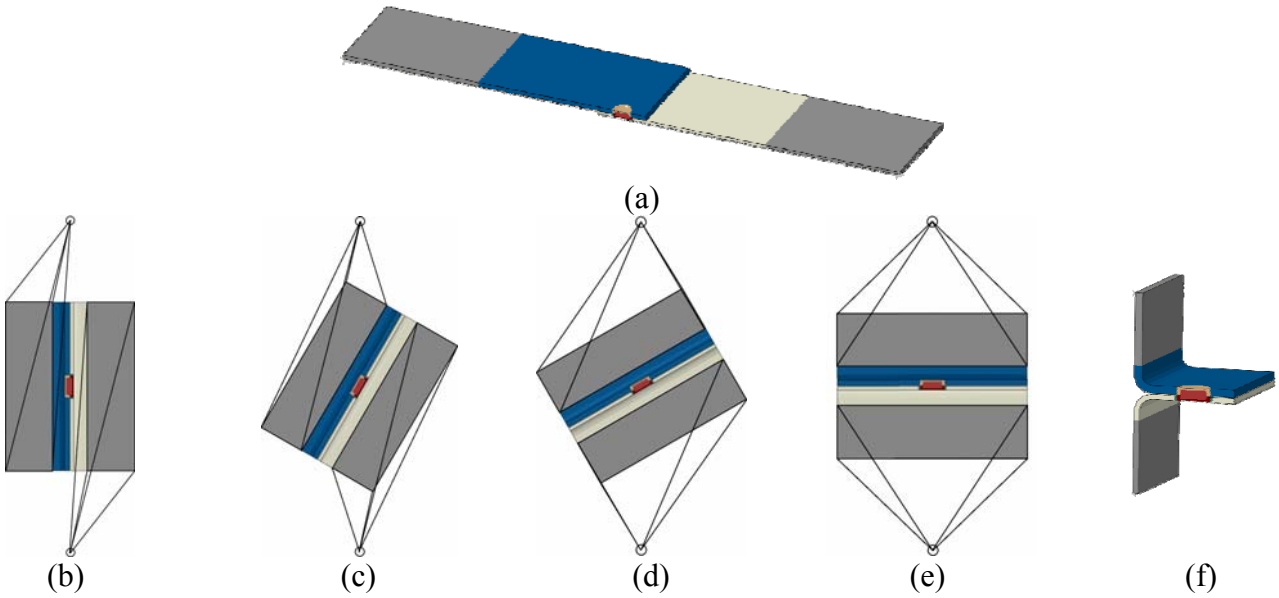

Figure 11. Detailed finite element models of the spot welded tensile-shear specimen (a), KS2-0° (b), -30° (c), -60° (d), -90° (e) specimens and the coach-peel specimen (f)

All simulations were performed using the finite element code ABAQUS/Explicit version 6.9. The calculated force vs. displacement curves for the six different loading situations of the spot welded joints are shown together with the corresponding experimental data in Fig. (12). The measured force vs. displacement curves of all specimens are reproduced well by the numerical results. Also the calculated and experimental load bearing capacities (see Table (2)) agree well.

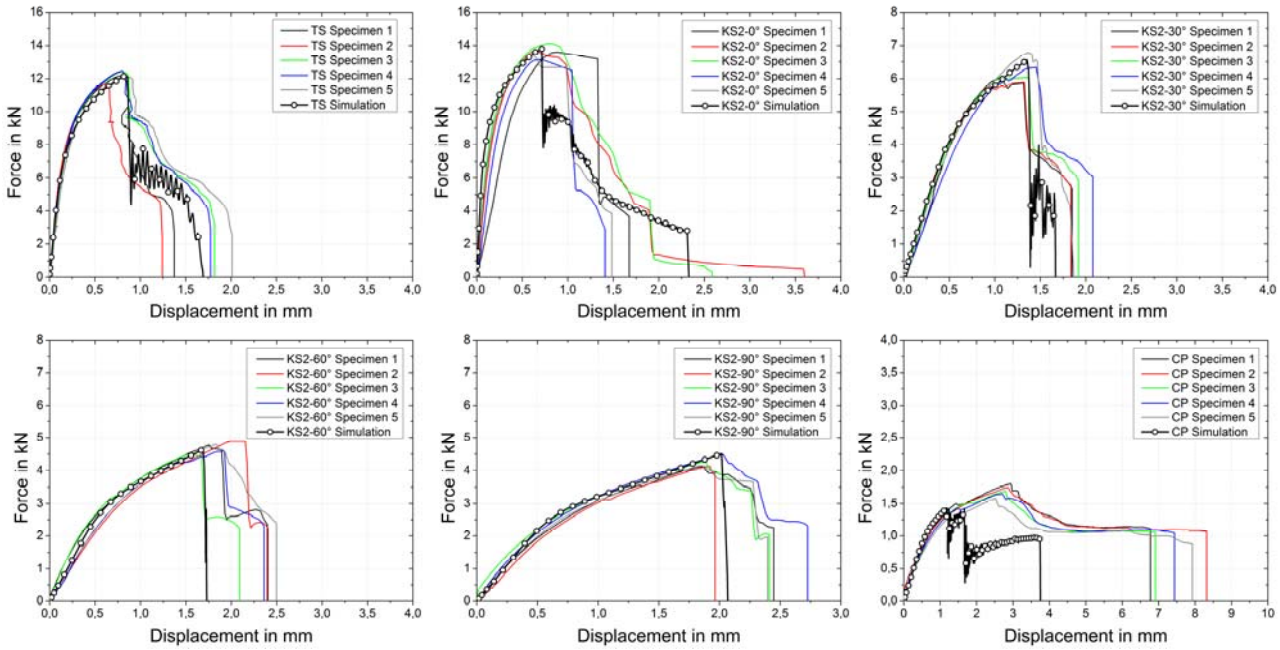

Figure 12. Comparison of measured and calculated force vs. displacement curves for tensile-shear- , KS2-0°, -30°, -60° and -90° and coach-peel specimens

Failure of the joints in shear tests, i.e. TS- and KS2-0° tests, is calculated as pull-out fracture inside the softened HAZ of the hot-stamped 22MnB5. During loading of both of the shear-specimens deformation localizes inside the SHAZ of 22MnB5 leading to pull-out fracture of the joint. Failure of the SHAZ occurs due to the Thomason criterion. The calculated fracture location was confirmed in observations of polished and etched cross-sections of the tested TS-specimens (see Fig. (13)).

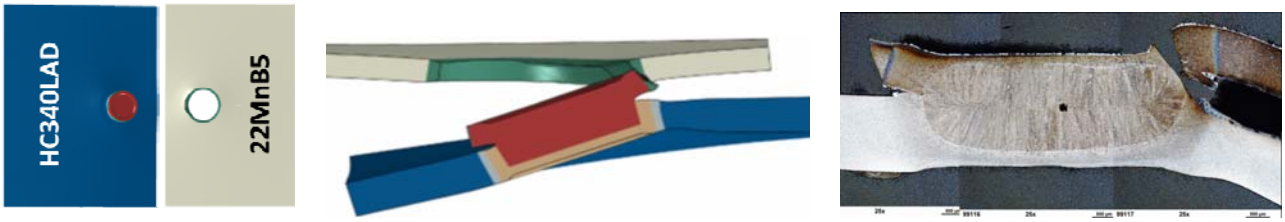

Figure 13. Calculated pull-out fracture of TS-specimen inside the softened HAZ of 22MnB5 (left and middle) Polished and etched cross-section of a tested TS-specimen showing pull-out fracture inside the SHAZ (right)

In pure axial loading situations in KS2-90° tests, pull-out fracture of the joints does not initiate inside the softened HAZ, but occurs inside the coarse grain HAZ of 22MnB5 directly adjacent to the weld nugget. The same fracture behavior is observed under combined loading conditions in KS2-30° and KS2-60° tests as well as in CP-tests. Fracture occurs in the ultra-high strength steel due to the lower sheet thickness and the lower ductility of its HAZ compared to that of the microalloyed steel. In all cases the critical criterion for failure initiation of the joints in simulations was found to be the Thomason criterion. As an example Fig. (14) shows the comparison between calculated and experimentally observed fracture appearance and locations for KS2-90° specimens.

Table 2. Comparison of measured and calculated load bearing capacities of the dissimilar joints

	TS	KS2-0°	KS2-30°	KS2-60°	KS2-90°	CP
$F_{max,av}$ Exp.	12.16 kN	13.57 kN	6.20 kN	4.67 kN	4.20 kN	1.66 kN
F_{max} Sim.	12.19 kN	13.78 kN	6.56 kN	4.64 kN	4.51 kN	1.43 kN
Deviation in %	+ 0,25	+ 1,55	+ 5,81	- 0,64	+ 7,38	-13,86

Figure 14. Calculated pull-out fracture of KS2-90° specimen (left and middle). Polished and etched cross-section of a tested KS2-90° specimen showing fracture inside the coarse grain HAZ of 22MnB5 (right)

Based on the simulations of TS- and KS2-specimens the applied loads were decomposed into axial and shear forces according to the current loading angles during deformation of the specimens as shown in Fig. (15). It can be seen that the loading angles of all specimens, except the KS2-90° specimen, which is loaded under pure axial forces, deviate from their original values due to rotation of the weld nuggets during deformation. In KS2-60° and KS2-30° tests only minor rotations of the weld occur. Therefore the deviation from their original loading angle is negligible. In this case the measured load bearing capacities from experiments could be directly decomposed into their components to be used as values for the adjustment or construction of force-based failure criteria. In shear loading conditions larger weld rotations were observed. Up to the maximum forces rotations of 12.2° and 9.6° were calculated for TS- and KS2-0° specimens respectively. Caused by the rotation the axial forces acting on the joints increase to 2.6 kN for TS- and 2.3 kN for KS2-0° specimens. The assumption of constant loading angles for the adjustment or the construction of simplified force based failure criteria should not be made in this case, but can be taken from numerical simulations.

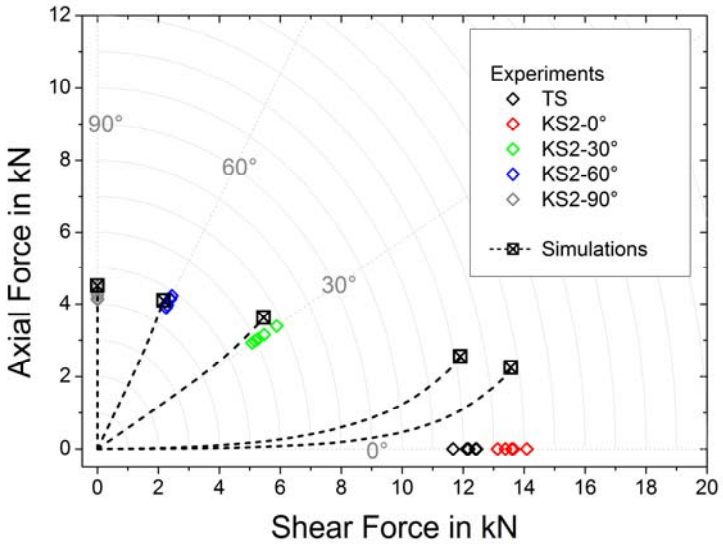

Figure 15. Decomposition of measured and calculated load bearing capacities into axial and shear forces acting on the joint. The evolution of axial and shear forces during deformation of the specimens in simulations are shown by the dashed black lines

4. Conclusion

Based on the calibrated Gologanu material models and failure criteria of Thomason and Brown and Embury for the different material zones of resistance spot welded joints between the hot-stamped ultra-high strength steel and the microalloyed HSLA steel, the joints' behavior in terms of force vs. displacement curves, load bearing capacities, fracture mode and fracture locations can be calculated using detailed finite-element models according to the joints geometry. In the cases investigated pull-out fracture of the joints under shear loading took place inside the softened HAZ of 22MnB5 due to localization of plastic deformation. Under combined axial and shear loading as well as under pure axial loading situations a change in fracture location can be observed. In these cases fracture occurred as pull-out fracture in the coarse grain HAZ of 22MnB5 directly adjacent to the weld nugget. Fracture initiation of all joints is calculated due to the Thomason criterion.
The evolution of axial and shear forces acting on the weld during different loading situations could be obtained by decomposing the applied loads into their axial and shear components according to their true loading angles. Such results can be used for the adjustment or the identification and construction of simplified force based failure criteria used for simplified spot weld models in crash simulations. Furthermore, factors influencing the load bearing capacity of the joints, as e.g. sheet thickness, weld nugget diameter or other geometrical quantities can be investigated by means of detailed finite-element modeling of spot welded joints between the investigated materials without further experimental effort.

Acknowledgements

The results presented are part of the research project P806/A262. The research project was conducted with professional supervision and financial support of the Research Association for Steel Application (FOSTA), Düsseldorf, Germany and the Research Association of the Working Group of the Iron- and Metal-processing Industry e.V. (AVIF), Ratingen, Germany by the Stiftung Stahlanwendungsforschung. Sincere thanks are given for the sponsorship.

References

[1] LS-DYNA Keyword User´s Manual, Version 971, Livermore Software Technology Corporation (LSTC), 2010.
[2] PAM-CRASH/SAFE Solver Notes Manual, ESI Software GmbH, 2004.
[3] ABAQUS Analysis user's manual, Version 6.9. Hibbit, Karlsson & Sorensen Inc., 2004.
[4] J.H. Song, H. Huh, Failure characterization of spot welds under combined axial-shear loading conditions, International Journal of Mechanical Sciences, 53 (2011) 513 – 525.
[5] S.-H. Lin, J. Pan, S.-R. Wu, T. Tyan, P. Wung, Failure loads of spot welds under combined opening and shear static loading conditions, International Journal of Solids and Structures, 39 (2002) 19 – 39.
[6] S. Aslanlar, The effect of nucleus size on mechanical properties in electrical resistance spot welding of sheets used in automotive industry, Materials & Design, Vol. 27 (2006), 125 – 131.
[7] S. Sommer, S. Burget, F. Klokkers, D. Hein, D. Krätschmer, H.-J. Wink, Charakterisierung und Ersatzmodellierung des Bruchverhaltens von Punktschweißverbindungen aus ultrahochfesten Stählen für die Crashsimulation unter Berücksichtigung der Auswirkungen der Verbindung auf das Bauteilverhalten, Final report FOSTA/AVIF P806/A262, to be published
[8] V.H. Baltazar Hernandez, S.K. Panda, M.L. Kuntz, Y. Zhou, Nanoindentation and microstructure analysis of resistance spot welded dual phase steel, Material Letters, 64 (2010), 207 – 210.
[9] O. Hahn, D. Gieske, A. Rhode, Probe und Probenspannvorrichtung zum Einsatz in

Zugmaschinen, Patent specification DE 195 22 247 A1, 1996
[10] S.-H Lin, J. Pan, T. Tyan, P.Prasad, A general failure criterion for spot welds under combined loading conditions, International Journal of Solids and Structures, 40 (2003), 5539 – 5564.
[11] P. Wung, A force-based failure criterion for spot weld design, Experimental Mechanics, 41 (2001), 107 – 113.
[12] G. Gologanu, J.B. Leblond, G. Perrin, J. Devaux, Recent Extensions of Gurson's Model for Porous Ductile Metals, Continuum Micromechanics, CISM Courses and Lectures No. 377, ed. by P. Suquet, pp. 61-130, 1997.
[13] A.L. Gurson, Continuum Theory of ductile rupture by void nucleation and growth Part I. Yield criteria and flow rules for porous ductile media, J. of Eng. Materials and Technology, 99 (1977), 2 – 15.
[14] P.F. Thomason, Ductile Fracture of Metals, Pergamon Press, Oxford, 1990
[15] T. Pardoen, J.W. Hutchinson, An extended model for void growth and coalescence, J. Mech. Phys. Solids, Vol.48 (2000) , 2467 – 2512.
[16] L.M. Brown, J.D. Embury, Proc. 3rd Int. Conf. on Strength of Metals and Alloys, London Institute of Metals, 1973
[17] F. Andrieux, D.-Z. Sun, H. Riedel, Troyes France, Proc. Int. Forum on Advanced Material Science and Technology IFAMST04 on CD, 2004

Comparative Study on Fatigue Properties of Friction Stir Welding Joint and Lap Joint

Teng Zhang[1], Yuting He[1,*], Qing Shao[1], Haiwei Zhang[1], Liming Wu[1]

[1] Aeronautics and Astronautics Engineering College, Air Force Engineering University, Xi'an 710038, China
* Corresponding author: hyt666@tom.com

Abstract Friction Stir Welding (FSW) is a new type of solid-state connection which can reduce structural weight significantly. In this paper, fatigue tests and finite element analysis were employed to study fatigue properties of aerial aluminum alloy 2524-T3 FSW joint and lap joint. The S-N curves of specimens show that the fatigue strength of FSW joint is better than that of lap joint. Finite element models of two joints were established by ANSYS software. The residual stress of FSW joint were obtained by a nonlinear direct coupled-field analysis, and the detailed stress distribution of lap joint which under pulling force were simulated. On the basis of finite element analysis results, the fatigue lives of two types of joints were estimated. It is verified that the analytic and estimated results agree with that of experiment. The residual stress is the main factor affecting the fatigue life of FSW joint and the failure of lap joint is mainly caused by stress concentration of hole edge.

Keywords Friction stir welding, Fatigue test, S-N curve, Finite element analysis, Lap joint

1. Introduction

Friction stir welding (FSW) [1] is a new solid-state joining technology invented at the welding institute (TWI) of Britain in 1991. It is a technique well suit for joining many hard-to-weld metals without filler materials. Compared with traditional bolt or rivet jointing techniques, FSW can reduce connective weight significantly and has higher link efficiency. In order to reduce design, manufacture, and maintenance costs, FSW is applied to the fabrication of aircraft primary structures. In North America, Eclipse Aviation has developed the Eclipse 500 business jet, utilizing FSW in both wing and fuselage skin-stiffener-frame fabrication [2].

Extensive research has been carried out on FSW with the wide application of this technology. In order to improve the mechanical properties of FSW joint, many studies have been performed on welding procedure and microstructure of joint, and many researchers have explored the thermomechanical numerical simulation technology of FSW.

Thermal and mechanical behaviors are mutually dependent during the FSW process. Many researchers [3-7] have simulated this process by finite element method and have obtained the distribution of residual stress, but they didn't discuss the relationship between residual stress and fatigue life of FSW joint. Furthermore, reference [8] pointed out that the influence of residual stress on fatigue life of FSW joint is a problem need to be solved.

Reference [9] has studied the fatigue properties of aerial aluminum alloy 2524-T3 base metal specimens and three different sizes of FSW joints, fatigue tests have been carried out and the S-N curves have been obtained. Although the fatigue properties of base metal specimens and FSW joints have been compared, the fracture mechanism of FSW joints has not been identified.

Nowadays, structures such as skins and stringers are jointed together by bolts or rivets in most aircrafts, however, the comparative study on fatigue properties of FSW joint and bolt or rivet

connected joint is rare. In this paper, fatigue tests and finite element analysis (FEA) were employed to study the fatigue properties of 2524-T3 FSW joint and riveted lap joint. Test results show that the fatigue strength of FSW joint is better than that of lap joint. The residual stress of FSW joint and the detailed stress distribution of lap joint were obtained by FEA. Furthermore, the fatigue life of FSW joint was estimated according to the result of residual stress distribution and base metal S-N curve; the fatigue life of lap joint was estimated according to the results of stress-strain distribution and local stress-strain method.

2. Experiments

Fatigue tests of FSW joint specimens and lap joint specimens were made by machine MTS-810-500 at room temperature, just as shown in Fig.1 and Fig.2.

Figure 1. Fatigue test of FSW joint specimen

Figure 2. Fatigue test of lap joint specimen

2.1. Specimens and Fixture Design

Two types of specimens, which simulate different connective types of skins in airframe, are shown in Fig.3 and Fig.4. Pieces of specimens are made of aluminum alloy 2524-T3 and rivets are made of titanium alloy TC4. FSW joint specimens were produced by machine FSW2-4CX-006. The tool shoulder diameter is 8mm. The pin is cylindrical with a hemispherical tip, its dimensions are 2.6mm in diameter and in 1.7 mm length. The tool rotation speed is set at 1000 rpm, and the translation speed is fixed at 100mm/min. While the rotating tool moves along the welding line, a forging pressure of 1.5kN is applied. Lap joint specimens are connected by staggered rivets.

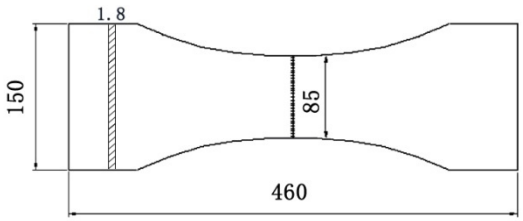

Figure 3. FSW joint specimen (mm)

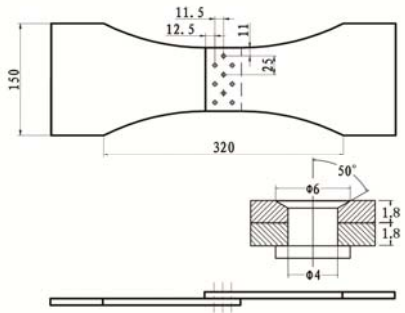

Figure 4. Staggered riveted lap joint specimen (mm)

The weight of lap joint specimen and FSW joint specimen are 297g and 271g separately. This means the FSW technique could reduce structural weight significantly than traditional jointing techniques.

For the purpose of simulating the actual force condition, anti-bend fixtures were designed for lap joint specimens, just as shown in Fig.5. The anti-bend fixture I and II are designed to prevent out-of-plane bending and the function of shims is to ensure specimens loaded in the same plane. In order to reduce the friction between specimens and fixtures during test, some effective measures were applied such as injecting lubricant oil or inserting plastic films between contact surfaces.

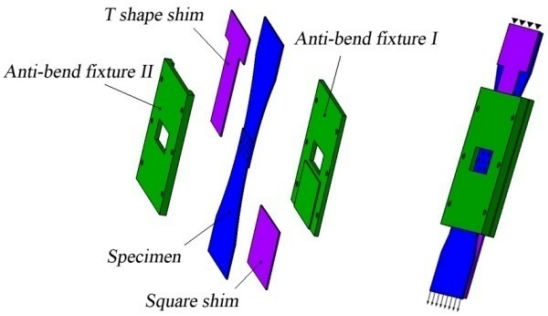

Figure 5. Configuration of anti-bend fixtures

2.2 Fatigue test

All specimens were subjected to constant amplitude loads; the stress ratio R=0.06 and the load frequency f=10. In order to obtain S-N curves, each type of specimens were divided into three groups, which loaded under different stress levels (illustrated in Table 1).

Table 1. The maximum stress endured by different types of specimens during fatigue test (MPa)

	FSW specimen	Lap joint specimen
1	240	150
2	210	120
3	180	100

2.3 Test results

Fig.6 shows the fracture forms of specimens. The fracture position of FSW specimens locates on the thermomechanical affected zone and the lap joint specimens break on the line of the first row of rivets.

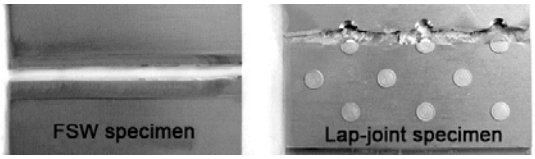

Figure 6. Fracture forms of two type specimens

Chauvenet criterion was used for all test results to abandon dubious data. And S-N curves of two

type specimens were obtained by group test method, the formulas of S-N curves are,

$$\text{FSW specimen:} \quad N=1.89\times10^{11}(S-122)^{-3.36}, \tag{1}$$

$$\text{Lap joint specimen:} \quad N=1.18\times10^{8}(S-72.9)^{-1.84}. \tag{2}$$

S-N curves are illustrated in Fig.7.

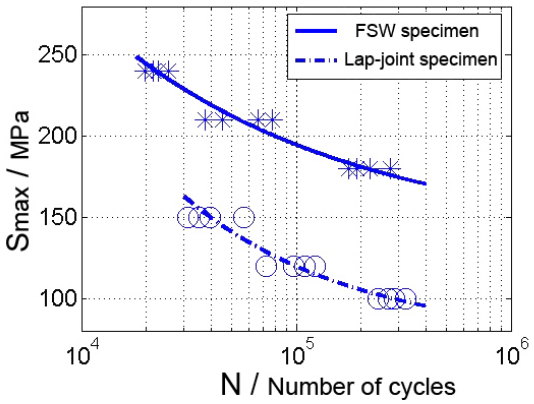

Figure 7. S-N curves of two type specimens

The S-N curves show that the fatigue strength of FSW joint is better than that of lap joint. At the fatigue life of 1×10^5 cycles, the fatigue strength of FSW joint (195MPa) is about 61% higher than that of lap joint(120MPa).

3. Finite element analysis

In order to reveal the fracture mechanism of two jointing techniques, three-dimensional elasticplastic FEA for two types of specimens was conducted by ANSYS 14.0 software.

Through FEA, the residual stress of FSW joint and detailed stress distribution of lap joint were obtained, and both of them provide necessary conditions for life prediction.

3.1 FEA of FSW joint

FSW is a coupled-field (structural-thermal) process. The temperature field affects the stress distribution during the entire process. Also, heat generated in structural deformation affects the temperature field. In this paper, a direct FEA of coupling is developed using a coupled-field element SOLID226. The simulation occurs over three load steps, representing the dwell, traverse and cool phases. The schematic diagram of FEA model is shown in Fig.8.

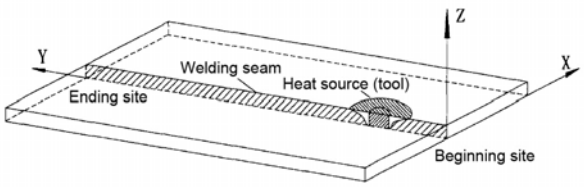

Figure 8. Schematic diagram of FEA model

The material properties of aluminum alloy 2524-T3 are shown in Table 2.

Table 2. Material properties of aluminum alloy 2524-T3

Temperature(℃)	25	150	300	500
Young's modulus(GPa)	68	60	51	38
Poisson's ratio	0.31	0.32	0.33	0.35
Density(kg/m^3)	2810	2785	2750	2708
Coefficient of thermal expansion(um/m℃)	23	25.5	29	33
Yield stress(MPa)	370	330	115	50
Tangent modulus(GPa)	23.5	22	19.8	17
Thermal conductivity(W/m℃)	120	134	146	159
Specific Heat(J/kg℃)	860	920	980	1050

The temperature rises at the contact interface due to frictional contact between the tool and workpieces. FSW generally occurs when the temperature at the weld line region reaches 70 to 90 percent of the melting temperature of the workpiece material [10].

A moving heat source was used to simulate the heat generated by friction. Meanwhile, a moving pressure of 1.5kN is applied synchronously to simulate the forging pressure of tool.

According to reference [11] and [12], the heat flux density of shoulder is expressed as,

$$q_s = \frac{\pi\omega\mu P(R_1^2 + R_1R_2 + R_2^2)}{45(R_1 + R_2)}, \tag{3}$$

and the heat flux density of stirring pin is,

$$q_p = \frac{\pi\omega\mu PR_2(1.5h+1)}{45}. \tag{4}$$

where,

ω: Rotating speed of tool, μ: Friction coefficient, P: Forging pressure of tool,

R_1: Radius of shoulder, R_2: Radius of stirring pin, h : Height of stirring pin.

The boundary conditions include thermal boundary conditions and mechanical boundary conditions. On the top and side surfaces of the workpiece, convection and radiation account for heat loss to the ambient [4], the value of the convection coefficient is set as 30 W/m^2℃. Conduction losses also occur from the bottom surface of the workpiece to the backing plate, and a high heat-transfer coefficient of 300 W/m^2℃ is set. The workpiece is fixed by clamping plate [4], and the clamped portions are constrained in all directions. To simulate support at the bottom of the backing plate, all bottom nodes of the workpiece are constrained in the Z direction.

The simulated FSW process consists of three primary phases: dwell, traverse and cool. Three load

steps are applied corresponding with the three phases. Dwell phase means the heat source dwells at the initial position until the temperature reaches to the value required for the welding. Traverse phase means the rotating tool moves along the welding line, this is the most important phase during FSW. During the cool phase, the temperature of workpiece drops to initial value (25 ℃) and then the fixture will be removed; accurate residual stress of FSW joint will be obtained after this phase.

The temperature distribution during the second load step is shown in Fig.9. The melting temperature of aluminum alloy 2524 is about 550℃, and the maximum temperature at the welding line is well below it.

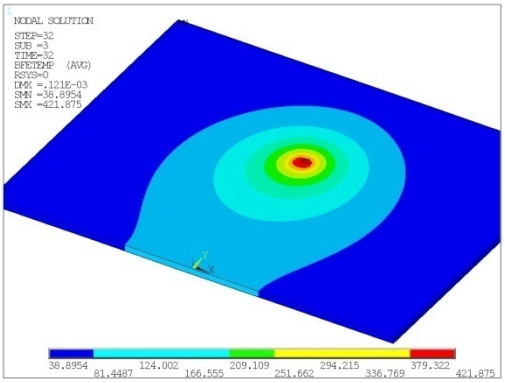

Figure 9. Temperature distribution during load step 2

The distribution of residual stress (X direction) after the third load step is shown in Fig.10. The residual stress distribution of middle site is different from that of the beginning and ending site. Because the FSW joint specimens are cut out from a big workpiece, the residual stress distribution of specimens can be considered as that of middle site.

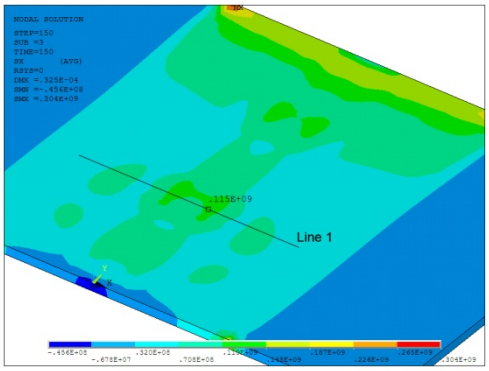

Figure 10. Distribution of residual stress (X direction)

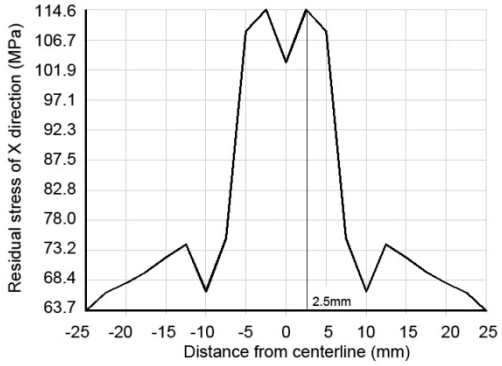

Figure 11. The residual stress distribution of line 1

Fig.11 shows the distribution of residual stress of line 1 (Fig.10). The maximum stress is 115MPa at the point of 2.5mm from the weld center, which shows a good agreement to the fracture position of FSW specimen.

3.2 FEA of lap joint

Three-dimensional lap joint specimen model is created as shown in Fig.12. The full scale joint is modeled considering the features of material nonlinearity, out-of-plane bending, pin-load and friction contact.

Both the pieces and rivets are meshed by 10 nodes tetrahedron solid element SOLID92. All the possible contact areas are modeled, and the rivets are modeled as 'neat fit' to holes and plates. The surface of model has the same displacement restriction as the specimen for the best boundary condition approximation.

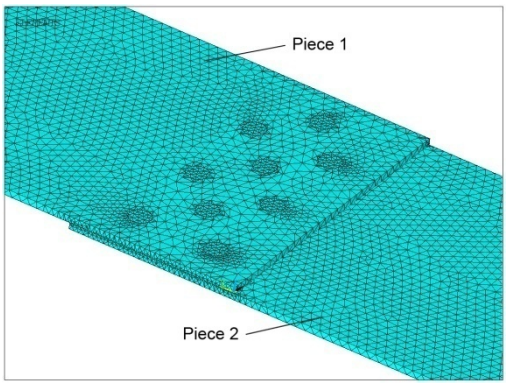

Figure 12. Finite element model of lap joint specimen

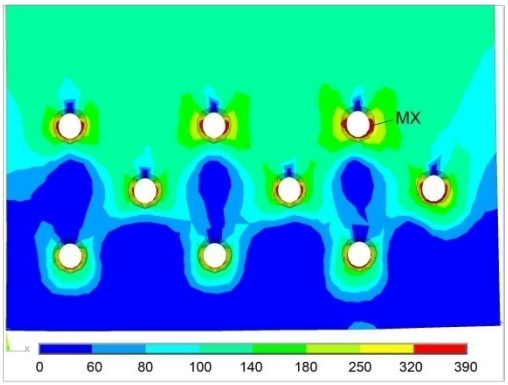

Figure 13. Von Mises stress of piece1

Three-DOF constrain was applied on one side of the model, and pulling stress (120MPa) was evenly applied on the other side. Fig.13 shows the stress distribution of piece 1.

The maximum stress concentration of lap joint locates on the right hole's edge of the first rivets row, it shows an excellent accordance with the crack initiation locations observed in tests. The maximum stress is 385MPa and the maximum strain is 0.0068 when the pulling stress is 120MPa; the maximum stress is 59.8MPa and the maximum strain is 0.00088 when the pulling stress is 7.2MPa.

4. Fatigue life estimate

In order to verify the validity of simulation method and establish links between FEA and test, fatigue lives of two different joints were estimated.

4.1 Fatigue life estimate of FSW joint

The fatigue life of FSW joint is estimated according to residual stress result and base metal S-N curve [9] on the bridge of *Goodman formula*.

We have known that the maximum residual stress of FSW joint is 115MPa. When the FSW joint under the constant amplitude load spectrum which maximum stress is 180MPa and stress ratio is 0.06 (accord to Fig.7, the fatigue life is 224566), the maximum local stress of joint is 295MPa ($\sigma'_{max}=180+115$) and the stress ratio is 0.42 ($R'=\frac{180\times 0.06+115}{180+115}$).

Assume the decline of fatigue performance of FSW joint is only affected by residual stress. We can estimate the fatigue life of FSW joint by base metal S-N curve according to the maximum local stress of FSW joint.

Goodman formula is used to establish the relationship between the maximum local stress and the base metal S-N curve. *Goodman formula* is a constant life formula, which is expressed as,

$$S_a = S_{-1}[1-\frac{S_m}{\sigma_b}]. \tag{5}$$

where,

S_a : The stress amplitude of load spectrum, S_m : The mean stress of load spectrum,

S_{-1} : Stress amplitude when the stress ratio is -1, σ_b : The ultimate strength of material.

Through calculation, the fatigue life of FSW joint is equal to that of base material specimen under the constant amplitude load spectrum which maximum stress is 247.6MPa and stress ratio is 0.06.

According to Fig.4 in reference [9], the fatigue life of base material specimen which considering the influence of residual stress is 252674 cycles, with an error of 12.5%. This result is basically identical with the experimental one, means that the residual stress is the main factor affecting the fatigue life of FSW joint.

4.2 Fatigue life estimate of lap joint

The fatigue life of lap joint is estimated according to stress-strain results and *local stress-strain method*. Calculation formulas of local *stress-strain method* are shown as,

$$\varepsilon_a = (\varepsilon_{\max} - \varepsilon_{\min})/2, \tag{6}$$

$$\sigma_m = (\sigma_{\max} + \sigma_{\min})/2, \tag{7}$$

$$\varepsilon_a = \frac{\sigma_f^{'} - \sigma_m}{E}(2N)^b + \varepsilon_f^{'}(2N)^c. \tag{8}$$

where,

$\varepsilon_{\max}$, $\varepsilon_{\min}$: The maximum and minimum strain, $\sigma_f^{'}$, $\varepsilon_f^{'}$, E, b, c : Material parameter,

$\sigma_{\max}$, $\sigma_{\min}$: The maximum and minimum stress, N : Fatigue life.

According to the simulation results of FEA, the fatigue life of lap joint is 90400 cycles under the constant amplitude load spectrum which maximum stress is 120MPa and stress ratio is 0.06. The

estimate error is 8.2%, which satisfies engineering demands. The coincidence of estimate result and test result prove that the failure of lap joint is mainly caused by stress concentration of hole edge.

5. Conclusions

This paper has studied the fatigue properties of aerial aluminum alloy 2524-T3 FSW joint and lap joint by fatigue tests and FEA.

The S-N curves of different specimens have been obtained by fatigue tests to compare the fatigue strength of them. It has been shown that the fatigue strength of FSW joint is better than that of lap joint. At the fatigue life of 1×10^5 cycles, the fatigue strength of FSW joints is about 61% higher than that of lap joint.

The three-dimensional elasticplastic FEA for two types of specimens have been developed to explore the fracture mechanism of two jointing techniques. The residual stress of FSW joint were obtained by a nonlinear direct coupled-field analysis, and the detailed stress distribution of lap joint which under pulling force were simulated. The maximum residual stress of FSW joint is 115MPa at the point of 2.5mm from the weld center, and the maximum stress concentration of lap joint locates on the right hole's edge of the first rivets row.

Finally, fatigue lives of specimens have been estimated, and both estimated results agree with that of experiment. Results show that the residual stress is the main factor affecting the fatigue life of FSW joint and the failure of lap joint is mainly caused by stress concentration of hole edge.

References

[1] W.M. Thomas, E.D. Nicholas, J.C. Need ham, M.G. Murch, P. Templesmith, C.J. Dawes, Friction Stir Welding, International Patent Application No. PCT/GB92102203 and Great Britain Patent Application No. 9125978.8, 1991
[2] Alves de Sousa RJ, Yoon JW, Cardoso RPR, Fontes Valente RA, On the used of a reduced enhanced solid-shell finite element for sheet metal forming applications. Int J Plasticity, 23(2007) 490-515.
[3] H.W. Zhang, Z. Zhang, J.T. Chen, The finite element simulation of the friction stir welding process. Materials Science and Engineering A, 403 (2005) 340-348.
[4] Zhu X.K.,and Y.J.Chao, Numerical Simulation of Transient Temperature and Residual Stresses in Friction Stir Welding of 304L Stainless Steel. Journal of Materials Processing Technology, 146.2(2004)263-272.
[5] Z. Feng, X.L. Wang, S.A. David, et al, Modelling of residual stresses and property distributions in friction stir welds of aluminium alloy 6061-T6. Science and Technology of Welding and Jointing, 4(2007)348-356.
[6] G.J. Bendzsak, C.B. Smith, An experimentally validated 3D model for friction stir welding, Proceedings of the Second International Symposium on Friction Stir Welding. Gothenburg, Sweden: TWI, 2000.
[7] T. li, Q.Y. Shi, H.K. Li, Residual stresses simulation for friction stir welded joint. Science and Technology of Welding and Joining, 8(2007)634-640.
[8] Zhou Caizhi, Yang Xinqi, Luan Guohong, Research Progress on the Fatigue Behavior of

Friction Stir Welded Joints. Rare Metal Materials And Engineering, 7(2006) 1172-1176.
[9] Zhang Teng, He Yuting, Wu Liming, Wang Xinbo, Fatigue Performance of Friction Stir Welded Butt Joints for 2524-T3 Aluminum Alloy. Materials for Mechanical Engineering, 5(2012) 47-49.
[10] Prasanna P., B.S. Rao, G.K. Rao, Finite Element Modeling for Maximum Temperature in Friction Stir Welding and its Validation. Journal of Advanced Manufacturing Technology, 51(2010)925-933.
[11] H.Schmidt, J.Hattel, J.Wert, An analytical model for the heat generation in friction stir welding Model. Simul.Mater.Sci.Eng, 12(2004)143-157.
[12] Wang Jianhua, Yao Shun, Wei Liangwu, Thermal and thermo-mechanical modeling of friction stir welding. Transactions Of The Chian Welding Institution, 4(2002)61-64.
[13] Chen Chuanrao, Fatigue and Fracture , Huazhong University of Sicence and Technology Press, Wu Han, 2001.

Effects of loading rate and temperature on crack arrest behavior of hull steel in stiffened plate construction

Chunhuan Guo, Yanmei Song, Fengchun Jiang* and Ruitang Liu

Key Laboratory of Superlight Materials & Surface Technology of Ministry of Education

Harbin Engineering University, Harbin 150001, P.R. China

* Corresponding author: fengchunjiang@hrbeu.edu.cn

Abstract Based on the residual strength diagram of non-stiffened plate construction, a residual strength diagram of hull steel in stiffened plate construction was proposed using the linear-elastic fracture mechanic theory in this work, the effects of loading rate and temperature on the crack arrest behavior of the stiffened plate construction were discussed, the lower limit of the residual strength and the dimension of a valid arrested crack were obtained via the theoretical analysis. The results demonstrated that, whether loading rate or temperature significantly influence the lower limit of the residual strength of the hull steel in a stiffened plate construction; under the conditions of 273K and 293K, the stiffened plate construction is a stiffener critical construction when the applied loading rate $\dot{K}$ is in the order of $\sim 10^5 MPa\sqrt{m}/s$, while under the loading rate of $\sim 10^6 MPa\sqrt{m}/s$, it becomes a skin critical construction due to the decrease of the fracture toughness of the full steel, the lower limit of residual strength is reduced to one fourth of the steel yield strength under this loading condition. In this case, the stiffened shipping construction is no longer adaptable to such a high loading rate, the crack arrest design is therefore highly desirable for protecting the full plate construction.

Keywords stiffened plate, residual strength, crack arrest, loading rate and temperature effect

1. Introduction

In order to enhance strength and stiffness, the stiffened plate construction is always often used in the structure design of the hull. Therefore, it must be considered the effect of stiffener when analyzing the deformation and fracture behavior of hull structure. Vliege and Brock studied the crack propagation behavior and crack arrest characteristic in stiffened plate structure of the plane, and proposed the residual strength diagram of non-stiffened plate structure to analyze and predict the crack propagation characteristic of the stiffened plate structure [1, 2]. The design of crack arrest is an important aspect of ship design, while the study associated with of the crack arrest behavior of hull steel under dynamic loading is quite limited at present. The ships especially naval vessels are often subjected to impact load in their service processing. The fracture toughness of hull steel may be reduced due to the effect of high loading rate, for example, the fracture toughness (K_{IC}) of hull steel used in this paper is $\sim 180 MPa\sqrt{m}$ (loading rate $\sim 10^0 MPa\sqrt{m}/s$) under the temperature ~273K, while the fracture toughness decreases to $\sim 64 MPa\sqrt{m}$ under the loading rate $\sim 10^6 MPa\sqrt{m}/s$, which is one third of static fracture toughness. Thus, it is essential to design ships in terms of crack arrest principle. Based on the linear-elastic fracture mechanic theory and residual strength diagram (when temperature is 273K, $\sim 10^5 MPa\sqrt{m}/s$ and 293K, $\sim 10^6 MPa\sqrt{m}/s$) of the hull, the present paper discusses the crack arrest behavior of the stiffened plate structure of the hull, the conclusions drawn from this work can be used as the reference for the design of crack arrest of the hull steel.

2 Mechanical properties of materials and stiffened plate construction

The hull steel used for skin plate and stiffener of stiffened plate structure is a low alloy steel in this paper, and its mechanical properties of the hull steel are listed in Table 1,

Table 1 The mechanical properties of hull steel

material	σ_s (MPa)	σ_b (MPa)	δ(%)	φ(%)
hull steel	480	580	21.4	74
weld metal	400	505	28	74

The Charpy impact specimens were used in experiments, which firstly were cut notch ~3mm by EDM (electrical charge machine), and then pre-fatigue for achieving a relative crack length a/W≈0.5. The dynamic fracture toughness of hull steel under different loading rate conditions were tested by pendulum impact test ($\sim 10^5 MPa\sqrt{m}/s$) and Hopkinson bar apparatus ($\sim 10^6 MPa\sqrt{m}/s$), respectively. The experimental results are shown in Table 2. The impact energy tested by pendulum impact experiment can be used to calculate the dynamic fracture toughness by the following Equation [3]:

$$K_{\mathrm{Id}}^2 = 1290.17 + 108.03\mathrm{CVN} \tag{1}$$

It can be seen from Equation (1) that the dynamic fracture toughness under loading rate $\sim 10^5 MPa\sqrt{m}/s$ can be obtained using the value of CVN. The dynamic fracture toughness of tested material under higher loading rate $\sim 10^6 MPa\sqrt{m}/s$ can be gained using Hopkinson bar loading apparatus, details for testing procedures can be found elsewhere [4].

Table 2 The dynamic fracture toughness and dynamic strength of hull steel

loading rate	$\sim 10^5 MPa\sqrt{m}/s$		$\sim 10^6 MPa\sqrt{m}/s$	
Temperature (K)	273	293	273	293
$K_{Id}(MPa\sqrt{m})$	119	128	64	74
$K_d(MPa\sqrt{m})$	282	343	71	89
$\sigma_{Yd}(MPa)$	567	565	640	638
$\sigma_b(MPa)$	691	678	774	768

As the dynamic yield strength of tested material is a necessary parameter in next analysis, the dynamic yield strengths under different strain rate and temperature were carried out using dynamic compression test in Hopkisnon bar apparatus in order to investigate the rate sensitivity of this material. Thus the dynamic compression test was carried out on the Hopkinson pressure bar test for determining the dynamic yield strength of hull steel. The relationship between dynamic yield strength and strain rate and temperature can be established as following according to our experimental data:

$$\sigma_{yd} = \sigma_s\left[1+\left(\dot{\varepsilon}/59213\right)^{0.281}\right]\left[1.13\exp\left(-0.0004T\right)\right] \tag{2}$$

Where T is the experimental temperature, σ_s is the yield strength under quasi-static, $\dot{\varepsilon}$ is the strain

rate. Using the Equation (2), the dynamic yield strengths of hull steel under different strain rate and temperature were evaluated and listed in Table 2.

The data listed in Table 2 and the thickness of skin were confirmed to be meet the plane strain condition in terms of ASTM E-399 standard. Therefore, it needed to use the Irwin Equation to transform the data listed in table 2 to plane stress fracture toughness K_d [5, 6]:

$$\beta_{Id}=\frac{1}{B}(\frac{K_{Id}}{\sigma_{yd}})^2 \quad , \quad K_d^{\,2}=K_{Id}^{\,2}(1+1.4\beta_{Id}^{\,2}) \tag{3}$$

The value of plane stress fracture toughness K_d transformed were also listed in Table 2.

The simple stiffened plate construction with two stiffeners was analyzed, as shown in Figure 1. The stiffeners are symmetrically distributed at both sides of central crack 2a, and the crack plane passes through the rivet hole. The stiffener and skin plate are connected by rigid rivet. The corresponding construction parameters are as following: thickness of the skin plate B=24*mm*, sectional area of stiffener A_s=20*mm*×80*mm*, interval of stiffeners b=600*mm*, interval of rigid rivet p=b/12=50*mm*, modulus of elasticity E_s=E=2.1×10^5*MPa*, Reinforcement ratio [7]:

$$\mu=A_sE_s/(A_sE_s+EbB) \tag{4}$$

where E_s is elastic modulus of stiffeners, E is elastic modulus of skin plate. The value of μ is calculated using Equation (4) to be 0.1.

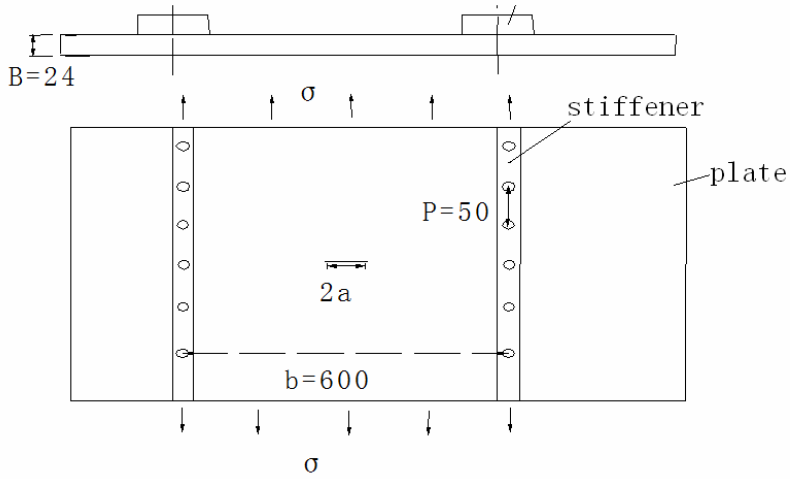

Figure1. Construction diagram of stiffened plate construction

3 The residual strength of stiffened plate construction

According to linear-elastic fracture mechanical theory, the relationship between stress and plane strain fracture toughness is following for the infinite wide plate with a penetrated central crack that bears the average tensile stress in both surface [8].

$$\sigma_c=K_{Ic}/\beta\sqrt{\pi a_c} \text{ (for infinite width plate, a<<w, } \beta=1) \tag{5}$$

Here, σ_c is fracture stress, a_c is the half length of critical crack and K_{Ic} is quasi-static plane strain fracture toughness. If the dynamic fracture toughness does not meet the plane strain condition, the equivalent value must be calculated by Equation (3). According to the Equation (5), the curve of

residual strength of non-stiffened plate can be calculated, that is to say the curve of $\sigma_c - a$ can be computed. However, it must be modified by Fedderson revision [9] when the crack length is quite small.

When stiffened plate construction is subjected to load, partial load would transfer to stiffeners by way of rivet, which lower the stress intensity factor in the crack tip of stiffened plate. Simultaneously, the stress concentration occurs around the stiffeners. The decreasing coefficient of stress intensity factor of crack tip of stiffened plate C is calculated as [10,11] ,

$$C = K_{stiffened} / K_{nonstiffened} \quad (6)$$

where, $K_{stiffened}$ is the stress intensity factor of stiffened plate construction with crack, $K_{nonstiffened}$ is the stress intensity factor of non-stiffened plate construction with crack. It can be seen from Equation (6) that the value of C is less than 1, i.e. C≤1. The coefficient of stress concentration L is written as,

$$L = \sigma_{max} / \sigma \quad (7)$$

where, σ is nominal stress of stiffened plate construction, σ_{max} is concentrated stress of stiffener, the parameters of C and L can be found in the stress intensity factor manual [8].

If the stiffened plate and non-stiffened plate construction with the same crack length fracture under the same stress intensity factor, the following Equation will be exist:

$$\sigma_{cstiffened} = \sigma_{cnonstiffened} / C \quad (8)$$

where， $\sigma_{cstiffened}$ is fracture stress of stiffened plate construction, $\sigma_{cnonstiffened}$ is fracture stress of non-stiffened plate construction. It can be seen from Equation (8) that the fracture stress of stiffened plate increases by 1 / C times. Using the Equation (8), the residual strength curve of stiffened plate construction can be calculated by that of non-stiffened plate construction.

Under the non crack condition, when the stress of stiffeners reaches to tensile strength σ_b, the stiffeners will fracture. Contrary, if the concentrated stress σ_{max} reaches to tensile strength σ_b, stiffeners would fracture. The following Equation can be derived from Equation (7):

$$\sigma = \sigma_b / L \quad (9)$$

Where, σ is nominal stress of stiffeners. According to the Equation (9), failure curve of stiffeners can be attained.

The residual strength curve of stiffened plate construction can be achieved by putting the residual strength curve of non-stiffened plate and stiffened plate construction and the failure curve of stiffener together into a common coordinate system， as shown in Figures 2 and 3.

4 Analysis of the crack arrest behavior of the stiffened plate construction

The residual strength diagram of stiffened plate construction of the hull under the loading rates $\sim 10^5 MPa\sqrt{m}/s$ and $\sim 10^6 MPa\sqrt{m}/s$ at the temperature of 273K and 293K can be determined using

the related data listed in table 2 and Equations (3)-(8), as shown in Figures 2 and 3.

Whether Figure 2(a) and (b) or Figure 3(a) and (b), all of them indicate that for stiffened plate construction with penetrable crack in center, the residual strength curve nearly coincides with that of non-stiffened plate construction when the crack length is small, which shows that reinforcement effect of stiffener is not obvious. When the crack propagated near the stiffener, the amplitude decrease of stress intensity factor become larger due to the load beard by stiffeners increasing, and the stress intensity factor reaches to maximum value while the crack propagates to the central line of stiffeners. At the same time, the residual strength curve of stiffened plate construction is much higher than that of non-stiffened plate construction. The reinforcement effect of stiffener decreases again and the residual strength curve of stiffened plate construction falls with increasing crack

According to the relative position between the failure curve of stiffeners and the residual strength diagram of stiffened plate construction, the crack arrest behavior of the stiffened plate construction includes a stiffener critical construction (Figure 2) and a skin critical construction (Figure 3). In skin critical construction (Figure 3), the unstable expansion of crack is arrested when the lengths reaches a_1' under stress state of σ_1 and the initial length of crack satisfying $a_0<a_1<a_s$. Under this condition, the crack is in stable state. That is to say, any expansion of crack would lead to further increase of the fracture resistance. It can be concluded that crack is in controlled state or crack arrest state. As the stress increased to σ_0, crack would steadily spread to a_s and then unsteadily propagate. Following, the stiffener would fracture because of the high stress applied, which results in structural failure. However, in the skin critical construction, as shown in Figure 2, when crack spread to a_s, since the stress of stiffener reaches its fracture stress, fracture would occur and the reinforced influence of stiffener released. As a result, crack of skins spread instability and led to structural failure.

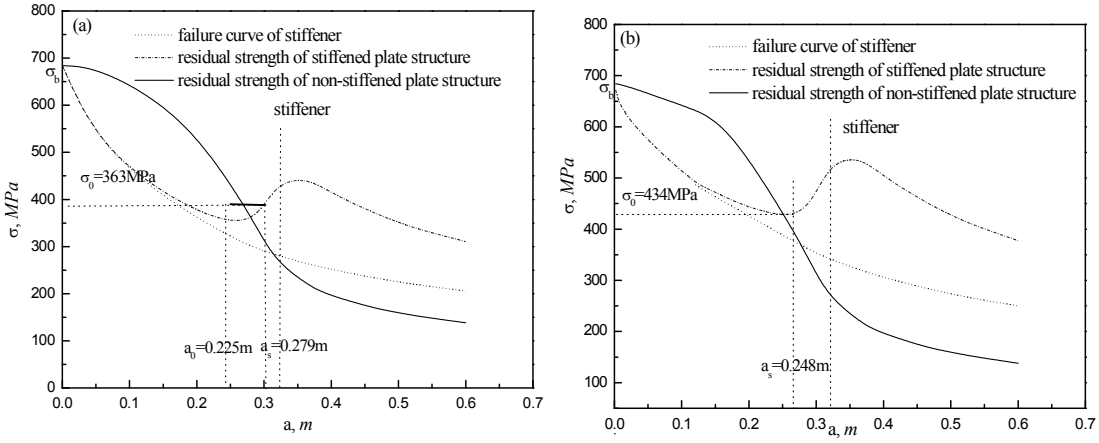

Figure2. Residual strength diagram of stiffened plate construction of the hull under loading rate $\sim 10^5 MPa\sqrt{m}/s$ and temperature 273K (a) and 293K (b)

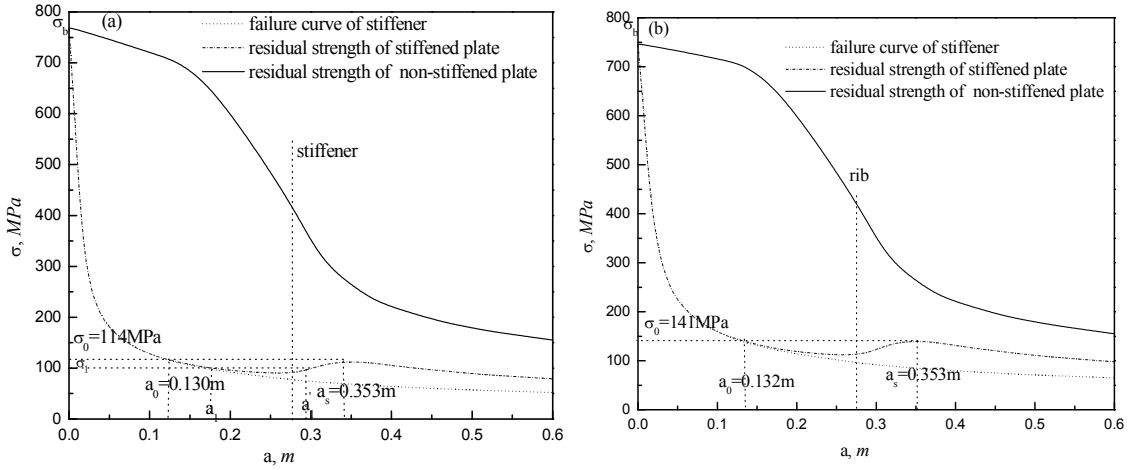

Figure3. Residual strength diagram of stiffened plate construction of the hull under loading rate $\sim 10^6 MPa\sqrt{m}/s$ and temperature 273K (a) and 293K(b)

The above analysis with respect to the crack behavior shows that the residual strength of stiffened plate construction has a "platform" stress σ_0 to which corresponding the range of cracks length $a_0 \sim a_s$. At this scope, the stiffened plate construction can play a part in crack arrest. Therefore, it can be obtained that the lower limiting value of residual strength of stiffened plate construction is σ_0, and the effective range of crack length for crack arrest is $a_0 \sim a_s$.

The stiffened plate construction of the hull analyzed in this paper shows elastic-plastic fracture with large plastic deformation under the loading rate $\sim 10^5 MPa\sqrt{m}/s$ and temperature 273K and 293K. At this condition, the stiffened plate construction belongs to a stiffener critical construction (details seen in Figure 2). For example, when the loading rate is $\sim 10^5 MPa\sqrt{m}/s$, the fracture toughness of hull steel are $282 MPa\sqrt{m}$ and $343 MPa\sqrt{m}$ under temperature 273K and 293K, respectively. While, under the loading rate $\sim 10^6 MPa\sqrt{m}/s$, the fracture toughness obviously decrease to $71 MPa\sqrt{m}$ and $89 MPa\sqrt{m}$, which is only quarter of the fracture toughness under quasi-static loading rate (seen Table 2). Thus, the residual strength curve of stiffened plate construction decreases largely. As a result, under the loading rate $\sim 10^6 MPa\sqrt{m}/s$, the stiffened plate construction belongs to a skin critical construction (Figure 3). The lower limiting value σ_0 and the range of crack length for crack arrest $a_0 \sim a_s$ for stiffened plate construction of the hull are listed in Table 3.

Table 3 $\sigma_0 (MPa)$ and $a_0 \sim a_s (m)$ of stiffened plate construction of the hull

loading rate	$\sim 10^5 MPa\sqrt{m}/s$		$\sim 10^6 MPa\sqrt{m}/s$	
temperature (K)	273	293	273	293
$\sigma_0 (MPa)$	363	434	114	141
$a_0 \sim a_s (m)$	0.225-0.279	0.248	0.130-0.353	0.132-0.353

It can be seen from Table 3 that the lower limiting value of residual strength is strongly dependent

upon the loading rate and temperature, which is the same as the fracture toughness of steel. That is to say, at the same loading rate, the lower limiting value of residual strength under temperature 293K is higher than that under temperature 273K; on the other hand, at the same temperature, the lower limiting value of residual strength decreases drastically with increasing loading rate, especially under loading rate $\sim 10^6 MPa\sqrt{m}/s$, the lower limiting value of residual strength reduces to the level of a quarter of σ_s. Suggesting the hull construction is no long suitable for use under impact condition with a loading rate $\sim 10^6 MPa\sqrt{m}/s$. Thus, it is necessary to use stiffened plate construction according to the strength level. However, it is worth noting that the stiffened plate construction is the skin critical construction that has a limit crack arrest capacity. Therefore the stiffened plate construction is needed to modify to enhance the crack arrest performance of the construction.

The data listed in Table 3 indicates that the crack length range of effective crack arrest in the skin critical construction is more than that in the stiffener critical construction. Under the loading rate $\sim 10^5 MPa\sqrt{m}/s$, the crack length range at temperature 273K is 0.225 *m* ~0.279 *m*, while at temperature 293K there is no crack arrest after the crack instable state. Under the loading rate $\sim 10^6 MPa\sqrt{m}/s$, the crack length range of effective crack arrest is 0.130 *m* ~ 0.353 *m* whether temperature 273K or 293K because the stiffened plate construction belongs to the skin critical construction.

5 Conclusions

Based on the linear-elastic fracture mechanic theory and the residual strength diagram of non-stiffened plate construction, the residual strength diagram of stiffened plate construction of the hull was proposed, and the crack arrest behavior, temperature and loading rate effects in the stiffened plate construction were discussed. The following conclusions can be drawn:

(1) The lower limiting value of residual strength of stiffened plate construction is significantly influenced by temperature and loading rate.

(2) The stiffened plate construction belongs to the stiffener critical construction at temperature 273K and 293K under loading rate $\sim 10^5 MPa\sqrt{m}/s$. While stiffened plate construction belongs to the skin critical construction because the fracture toughness of hull steel decreases sharply under loading rate $\sim 10^6 MPa\sqrt{m}/s$.

(3) The lower limiting value of residual strength of stiffened plate construction discussed in this paper and the crack length range of effective crack arrest are found to be 0.225 *m* ~ 0.279 *m* for the loading rate $\sim 10^5 MPa\sqrt{m}/s$ and temperature 273K and 0.130 *m* ~ 0.353 *m* for the loading rate $\sim 10^6 MPa\sqrt{m}/s$ and temperature 273K or 293K.

References

[1] H. Vlieger. The residual strength characteristics of stiffened panels containing fatigue cracks. Eng. Frac. Mech.,5(1973) 447-477

[2] D. Brock. Engineering fracture mechanics foundation. K.Y. Wang (translator). Science press, Bingjing, 1981.

[3] R.T. Liu, J.Wang. A discussion on the relationship between dynamic fracture toughness and impact toughness. Mater. Eng.. suppl (2003) 271-275.(In Chinese)

[4] Fengchun Jiang and Kenneth S. Vecchio. Hopkinson bar experimental technique: a critical review on

dynamic fracture toughness measurement. Appl. Mech. Rev.. 2009, 62(4):060802 1-39

[5] J.C.Newman Jr., D.S.Dawicke,B.R.Seshadri. Residual strength analysis of stiffened and unstiffened panels—Part Ⅰ:laboratory specimens. Eng. Frac. Mech..70(2003):493-507

[6] B.R.Seshadri,J.C.Newman,Jr.D.S.Dawicke,B.R.Seshadri:Residual strenghth analysis of stiffened and unstiffened panels—Part Ⅱ:wide panels. Eng. Frac. Mech.. 70(2003) :509-524

[7] C.C Jr.Poe., Stress intensity factor for a cracked sheet with riveted and uniformly spaced stiffeners.NASA TR R-358

[8] D.P.Rooke, D. J.Cartwright. Compendium of stress intensity factors. London :Her Majesty's Stationery Office,1976:293

[9] C. E. Fedderson. Evaluation and Prediction of the residual strength of center cracked tension panels. ASTM STP,1971,50-78

[10] R.J Dexter, P.J. Pilarski, N. H. Mahmoud. Analysis of crack propogation in welded stiffened panels. Inter. J. of Fati..25(2003):1169-1174

[11] C.C Jr. Poe. Fatigue cracked propagation in stiffened panels. Damage Tolerance in aircraft structures.ASTM STP 486.Ametican Society for testing and Materials.1971:79-97

13th International Conference on Fracture
June 16-21, 2013, Beijing, China

Fatigue Failure of Outlet Pipe Work of Flare System at Natural Gas Processing Plant

Abdel-Monem El-Batahgy [1,*], Martin Wheeler[2]

[1] Manufacturing Technology Department, Central Metallurgical R&D Institute, Cairo, Egypt
[2] Process and Operational Safety Department, Rashid Petroleum Company, Cairo, Egypt
[*] Corresponding author: elbatahgy@yahoo.com

Abstract

The natural gas produced from subsea wells is processed through different stages before being supplied through pipelines for local market or export. Processing of the produced natural gas is started with separation of gas and liquid using a slug catcher that is connected to a flare system. The flare system consists of piping made of 16" diameter branches connected to 20" diameter header using circumferential weld with a total of seven joints. The pipe work of the flare system is made of 316L stainless steel and it is operated in an interrupted mode. Design and operation pressures are 142 bar g and 88 bar g while design and operation temperatures are -40^{o}C and 20^{o}C, respectively. After five years of normal service, one of the seven joints of 16" branch/20" header has experienced failure. Based on different non-destructive and destructive tests, it is concluded that this premature failure is attributed mainly to fatigue damage. It is believed that acute or sharp angle of 16" branch/20" header connection that acts as a local stress raiser played a remarkable role in initiation of fatigue damage on outer surface, just beside circumferential weld. In addition, low stress high frequency vibration of the subject pipe work, due to mainly several emergency shut down operations, has accelerated initiation of fatigue damage. In order to minimize the possibility of such failure in future, design of 16" branch to 20" header connection was modified where a compensation plate fitted was used to minimize stress concentration at this connection zone.

Keywords: Natural gas processing, Flare system, 316L stainless steel, Stress concentration, Vibration, Fatigue

1. Background

A natural gas production plant has been set into operation about twelve years ago. The natural gas produced from subsea wells is processed through different stages before being supplied through pipelines for local market or export. Processing of produced natural gas is started with separation of gas and liquid using a slug catcher that is connected to flare system to be used in case of emergency plant shutdown. The flare system consists of piping is made of 16inch diameter pipes connected to 20inch diameter header using circumferential weld with a total of seven joints. Nominal thickness of 16" pipes is 4mm while that of 20" header is 6mm. The pipe work of the flare system is made of 316L stainless steel and it is operated in an interrupted or irregular mode. Design and operation pressures are 142 bar g and 88 bar g, respectively. Design and operation temperatures are -40^{o}C and 20^{o}C, respectively.

After five years of normal service, one of the seven joints of 16" pipe/20" header has experienced failure where

fracture has occurred at its conjunction zone. A spool including fracture zone was subjected to different non-destructive and destructive investigations for failure analysis.

2. Investigations

The failed spool was subjected to different non-destructive and destructive tests including visual investigation, liquid penetrant test, radiographic test, chemical analysis, thickness measurement, macro-, optical and scanning electron microscopic examinations, hardness measurements, tensile and impact tests. General and enlarged views of the fracture zone of the spool are shown in Fig. 1. The important notice is that fracture had occurred at the acute or sharp angle zone of 16" pipe/20" header assembly, just beside its circumferential weld. Based on visual investigation, it can be deduced that fracture was started at its mid-length then, propagated in tow opposite directions along circumference. The fracture extended less than half way around the circumference of 16" pipe/20" header. Visual and dye penetrant inspections indicated surface cracks on both sides of the fracture termination zones (Fig. 1-b). Generally, the outer surface of the failed spool is clean and free from deposits or indications for corrosion. Visual investigation of the weld face and root sides of the circumferential weld of 16" pipe/20" header as well as that of 16" pipe showed less weld quality. However, dye penetrant test of both root and face sides of circumferential weld of 16" pipe showed no surface cracking.

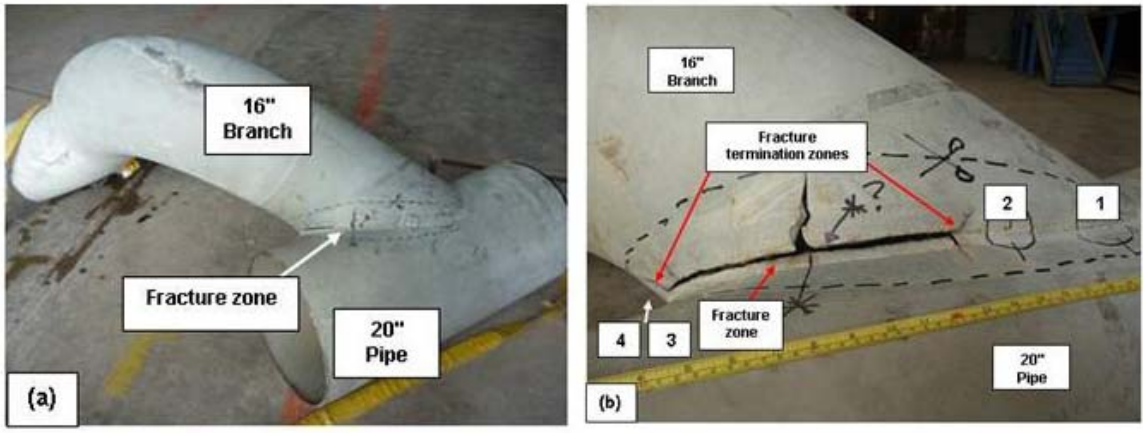

Figure 1. General (a) and enlarged (b) views of fracture zone of the spool. Note that fracture had occurred at sharp angle zone of 16" pipe/20" header assembly, just beside its circumferential weld.

Visual investigation of the internal surface of the failed spool showed damage at the inner surface of 16" pipe, which could be related to mechanical action. Except that, the internal surface of the spool showed smooth surface with no indications for internal corrosion. In other words, no thinning or variation in the wall thickness was observed, where almost uniform wall thickness (~6.0mm for 20" pipe and ~4mm for 16" branch) was obtained at both fractured and non-fractured zones. Macro- and microscopic investigations of a cross section taken from mechanically damaged zone showed internal localized reduction of about 0.6mm depth in the wall thickness of mechanically damaged zone. Optical microscopic investigation showed no indication for cracking at mechanically damaged zone.

Surface cracks zones observed around the fracture termination zones (zones 1, 2, 3 & 4, in Fig. 1-b) were subjected to detailed investigation. Close-up views of zones 4 and 1 at front of the fracture termination zones are shown in Fig. 2-(a) and (b). It can be noticed that surface cracks are existed just beside

circumferential weld of 16" pipe/20" header. Visual and dye penetrant examinations of zones 3 and 4 showed similar results.

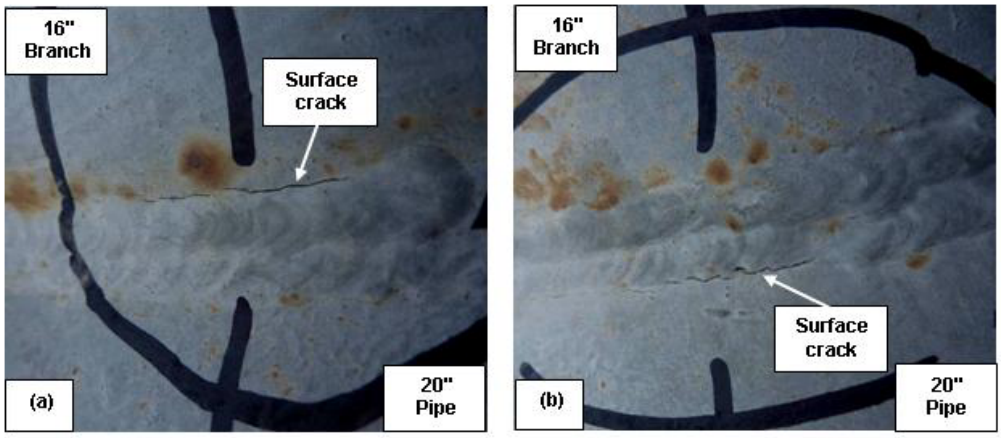

Figure 2. Close-up views of zones 4 and 1 at front of fracture termination zones of Fig. 1-b. Note surface cracks on both sides of circumferential weld of 16" pipe/20" header.

After detailed visual and dye penetrant investigations, specimens from both fractured and non-fractured zones of the spool were cut out and prepared for chemical analysis, macro- and microscopic examinations, scanning electron microscopic examination, hardness measurements, tensile and impact tests. Results of chemical analysis of the failed spool together with the specified chemical composition range for type 316L stainless steel are shown in Table 1. It is obvious that the chemical composition of the used spool is a typical for the austenitic stainless steel type 316L.

Table 1. Results of chemical analysis (wt%) of the failed spool together with the specified chemical composition range for ASME-SA213, 316L stainless steel.

Material	C	Si	Mn	S	P	Cr	Ni	Mo
Failed spool (BM)	0.017	0.41	1.45	0.018	0.031	17.73	11.26	2.16
Failed spool (WM)	0.017	0.37	1.23	0.006	0.029	16.91	10.18	2.01
316L St. St.	<= 0.03	<= 1.0	<= 2.0	<= 0.03	<= 0.04	16.0~ 19.0	9.0~ 12.0	2.0 ~ 3.0

Cracked zones 1, 2, 3 and 4 in Fig. 1-(b) were cross sectioned where its cracking features were clarified. Macrographs of a cross section taken from cracked zone 2 are shown in Fig. 3. It is clear that the observed cracks are weld toe cracking type. Similar results were obtained for samples taken from zones 1, 3 and 4 in Fig. 1-b. Weld toe cracks of zones 2 and 3 (~18cm away from fracture termination zones) were propagated through thickness of 16" pipe. Weld toe cracks of zones 1 and 4 in Fig. 1-b (~35cm away from fracture termination zones) were propagated through thickness of 20" header. It is obvious that cracks were initiated at weld toe on outer surface then, propagated through thickness. Optical micrographs with high magnification of cross sections taken from zones 1 and 4 in Fig. 1-b are shown in Fig. 4. It can be noticed that normal austenitic microstructures for both base metal, HAZ and weld metal were obtained and cracks were propagated through grain boundaries. Survey of the hardness measurements indicated

reasonable hardness values for the base metal, HAZ and weld metal, where average hardness values of 181HV, 183HV and 179HV were obtained for base metal, HAZ and weld metal respectively (Table 2). The given hardness values are the average of five readings. Results of the tensile test for both base metal and welded joint of the failed spool are shown in Table 3. The given tensile values are the average of three specimens. Results of the impact test, at different temperatures, of the base and weld metals of the failed spool are shown in Table 4. The given impact values are the average of three specimens. Results of both tensile and impact tests showed normal values based on specified properties for the used material.

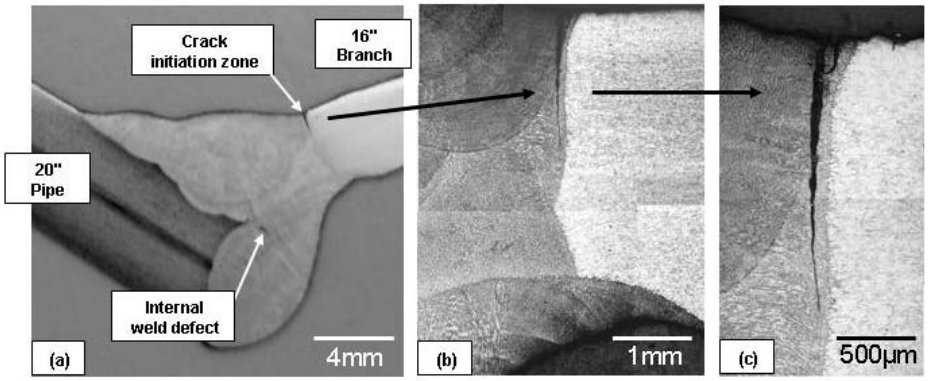

Figure 3 Macrographs of a cross section taken from zone 2 in Figure 1-b showing toe cracks propagated through thickness of 16" pipe.

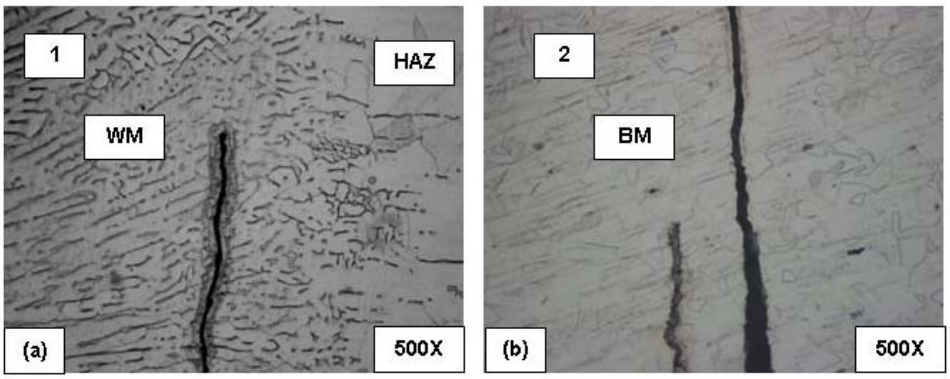

Figure 4 Optical micrographs with high magnification of cross sections taken from zones 1 and 4 in Figure 1-b. Note normal austenitic microstructures for base metal, HAZ and weld metal. Cracks were propagated through grain boundaries.

Table 2. Results of hardness measurements (HV) of fractured spool together with the specified value for ASME-SA213, 316L stainless steel.

Hardness \ Zone	Base Metal	HAZ	Weld Metal	ASME-SA 213, 316L St. St.
HV	182	185	180	217 max.

The given hardness values are the average of five readings.

Table 3. Results of tensile test of circumferential welded joints together with the specified values for ASME-SA213, 316L stainless steel.

	0.2% Proof Strength (MPa)	Tensile Strength (MPa)	Elongation (%)
Base Metal	359	597	52
Welded Joint	---	593	---
ASME-SA 213, 316L St. St.	170 min.	485 min.	40 min.

The given values are the average of three tested samples.

Table 4. Results of impact test of circumferential welded joint together with the specified values for ASME-SA213, 316L stainless steel.

	Absorbed Energy, J		
	-5°C	-10°C	-15°C
Base Metal	107	101	98
Weld Metal	107	97	95
ASME-SA 213, 316L St. St.	88-134 J (65-100 Ft.lb) at 23°C		

The given values are the average of three tested samples.

In order to help in identification of failure mechanism, fracture surface was carefully examined using stereoscope and scanning electron microscope. Low magnification photographs of fracture surface of 16" pipe side of the spool are shown in Fig. 5. Crack initiation zones and fracture propagation directions are highlighted with arrows. It is obvious that multi-cracks were initiated at the outer surface, where smooth fracture surface can be seen, then propagated toward inner surface. In other words, crack suspected initiation zones at the outer surface appeared relatively smooth and associated with beach marks and a propagating ductile crack. Crack termination zones at the inner surface had a rough texture associated with the final fracture.

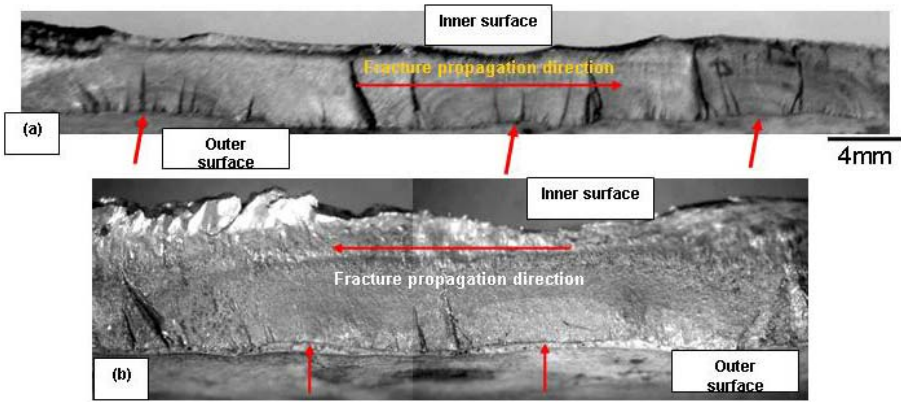

Figure 5. Low magnification photographs of fracture surface of 16" pipe side of spool. Crack initiation zones and fracture propagation directions are highlighted with arrows. Note beach marks at crack suspected initiation zones.

Scanning electron microscopic photographs with different magnifications of fracture surface including suspected initiation zones are shown in Fig. 6. Crack initiation sites can be seen on the outer surface, where a single macroscopic direction of crack propagation is impossible to be defined. This is because crack size is still in the microcrack zone, where multiple cracks form at the surface, initiating at different locations and with different orientations. The important notice is the unclear fatigue striations at the fracture initiation zones.

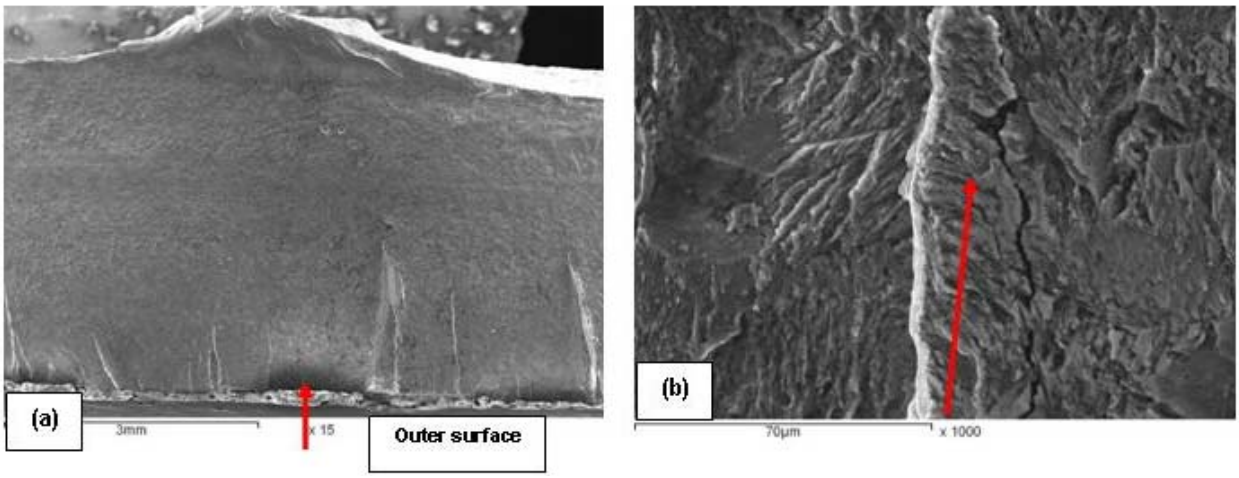

Figure 6. Scanning electron microscopic photographs of fracture suspected initiation zones at outer surface showing unclear fatigue striations.

3. Discussion

Visual and dye penetrant examinations of the failed spool showed that the fracture zone was confined to the acute or sharp angle of 16" pipe/20" header assembly, just beside circumferential weld line. Such sharp angle is considered as stress concentration zone. The fracture was initiated at the outer surface and propagated through thickness in two opposite directions where it was extended less than half way around the circumference. No indications for corrosion attack were observed on spool outer or inner surface. Only, mechanically damaged zone was observed at the inner surface of 16" pipe and this could be occurred long time ago during construction or repair works. However, such mechanical damage played no role in the current failure. In general, non-destructive investigations showed less weld quality. Meanwhile, fracture was not directly related to welding defects since fracture had occurred in the base metal just beside weld line.

Based on the results of chemical analysis, hardness measurements, tensile and impact tests and microscopic examination of the failed spool, materials of both base and weld metals were found to be within the specification of type 316L austenitic stainless steel. Macro- and microscopic examinations of cross sections around the fracture zone showed multi-cracks initiated at the weld toe that is considered as another stress concentration zone. Stereoscopic examination of the fracture surface showed that multi-cracks were initiated at the outer surface where smooth surface with beach marks was observed. Scanning electron microscopic investigation of the fracture surface showed unclear fatigue striations at the fracture suspected initiation zones. These findings support fatigue damage as a failure mechanism [1-5].

Fatigue failure is the phenomenon leading to fracture under repeated or fluctuating stresses that are less than the tensile strength of the material. Fatigue fractures are progressive, beginning as minute cracks that grow under the action of fluctuating stress. There are three stages of fatigue failure: initiation, propagation, and final fracture. The location of the initiation is at a stress concentration [6-9]. It is believed that stress concentration in the subject case is attributed mainly to the acute or sharp angle zone of 16" pipe/20" header assembly. In other words, such acute or sharp angle worked as site for initiation of fatigue damage at weld toe on outer surface of 16" pipe/20" header assembly, just beside its circumferential weld line.

The current piping system is subjected to more than just static forces. They can have severe vibrations induced mainly due to several start up operations. Vibration can be also induced due to temperature change. Since the piping system is operated in an interrupted or irregular mode, it is subjected to low stress high cycles fatigue. Under such repeated conditions, fatigue crack could be initiated at the highest stress concentration zone (acute angle zone). After the original fatigue crack is formed, it becomes an extremely sharp stress concentration that tends to drive the crack ever deeper into the metal with each repeating of the stress. The local stress at the tip of the crack is extremely high because of the sharp “notch,” and with each crack opening, the depth of the crack advances by one “striation”. Fatigue striation is not clear at the fracture initiation zone due to low stress cycles. As the propagation of the fatigue crack continues, gradually reducing the cross-sectional area, it eventually weakens the material so greatly that final, complete fracture occurs.

Conclusions and Recommendations

Based on the results obtained in this investigation, it can be concluded that the subject premature failure is attributed mainly to fatigue damage. High stress concentration at the acute or sharp angle of 16" pipe/20" header assembly and low stress high frequency vibration due to mainly several start up-shut down operations, both have shortens the lifetime of the spool. Fatigue failure is the phenomenon leading to fracture under repeated or fluctuating stresses that are less than the tensile strength of the material. The initiation site of fatigue failure is minute, never extending for more than two to five grains around the origin. The location of the initiation is at a stress concentration. It is believed that the acute or sharp angle of 16" pipe/20" header assembly that acts as local stress raiser played a remarkable role in initiation of the fatigue damage on the outer surface, just beside circumferential weld. It is obvious that the fracture initiated at the outer surface and propagated across the thickness in two opposite directions. As the propagation of the fatigue crack continues, gradually reducing the cross-sectional area, it eventually weakens the material so greatly that final, complete fracture occurs.

As a preventive measure, the other six connections of 16" pipe/20" header were subjected to visual and dye penetrant tests where absence of external surface cracks was confirmed. In order to minimize the possibility of such failure in future, the design of 16" pipe to 20" header connection was modified, where a compensation plate fitted was used to minimize stress concentration at this connection zone. Besides, circumferential welds were made with a better quality even it had no direct relation with the failure.

References

[1] R. D. Barer and B. F. Peters, Why Metals Fail, 6th ed., Gordon and Breach Science Publishers, New York, 1991.

[2] ASM Handbook, Failure Analysis and Prevention, Vol. 11, Materials Park, OH: ASM International, 1996.

[3] V. J. Colangelo, F.A. Heiser, Analysis of Metallurgical Failures, 2nd. ed., New York, NY: Wiley, 1987.

[4] C. R. Brooks, A. Choudhury, Metallurgical Failure Analysis, McGraw-Hill, New York, 1993.

[5] M. G. Fontana, Corrosion Engineering, 3rd ed. (New York, NY: McGraw-Hill, 1987.

[6] Abdel-Monem El-Batahgy: "Influence of HAZ and Stress Concentration on Fatigue Strength of Welded Structural Steel", Materials Letters, 21 (1994).

[7] Abdel-Monem El-Batahgy and Wafaa Metwally. “Weld Defect and Design Induced Failure of Draught Fan of Boiler Flow Gases”, Al-Azhar Engineering Fifth International Conference, 19-22 February 1997, Cairo, Egypt

[8] A. El-Batahgy. and B. Zaghloul: " Fatigue Failure of Off Shore Condensate Recycle Line of Production Separator at Natural Gas Production Field”, International Conference on Fracture ICF 11, 20-25 March 2005, Turin, Italy.

[9] A. El-Batahgy and M. Abdalla: “Catastrophic Failure of HP Steam Transferring Pipeline of a Newly Erected Boiler”, Doc. X1601-06, Annual Assembly of IIW, Aug. 27-Sept.2, 2006, Quebec, Canada.

Ductile to brittle transition concept on fracture behavior of poly(vinylidene fluoride) / poly(methyl methacrylate) blends

Lucien Laiarinandrasana[1,*], Yannick Nziakou[2], Jean-Louis Halary[2]

[1] Centre des Matériaux CNRS UMR 7633, Mines ParisTech, Evry Cedex 91003, France
[2] SIMM-Lab. UPMC/CNRS/ESPCI UMR 7615, ESPCI ParsTech, Paris Cedex 05 75231, France
* Corresponding author: Lucien.Laiarinandrasana@mines-paristech.fr

Abstract The fracture behavior of blends of poly(ninylidene fluoride) (PVDF) and poly(methyl methacrylate) (PMMA) was investigated by gradually increasing the PVDF content. The study focuses on semi-crystalline blends. The trends of net stress versus crack opening displacement curves were analyzed. From these plots, two fracture energies were defined: the fracture energy to crack initiation corresponding to the area under the curve up to the maximum net stress and the fracture energy to crack propagation considering the last part of the curve where the load continuously decreases. Fracture surface inspections confirmed typical semi-crystalline polymer features. Critical values of the degree of crystallinity corresponding to brittle to ductile transition were determined, depending on the selected fracture energy.

Keywords Blends, Poly(methyl methacrylate), Poly(vinylidene fluoride), Fracture toughness, Brittle to Ductile transition

1. Introduction

Mechanical parameters at failure are key factors to assess the durability of engineering components. For structural polymeric materials, fracture toughness is often characterized by the impact strength (Charpy or Izod tests). These are dynamic tests, accurate for brittle failure characterization. They might be inappropriate when the material exhibits significant ductility. Theoretically, fracture mechanics approaches suggest a methodology to define fracture toughness, whatever the mechanical response of the material. Whereas comprehensive research has been carried out for years on metallic materials concerning the equivalence between impact strength and fracture toughness, there is no such amount of work on polymers. Some attempts were made in this way but failed because, for instance, of the difficulty to fulfill requested plane strain conditions. Nevertheless, impact strength or toughness of polymeric materials was currently plotted as a function of the test temperature, in order to find a ductile to brittle transition temperature. The essential motivation of such a plot is to check whether the modification of the material process actually leads to an improvement of the toughness or the impact strength, by shifting the brittle to ductile transition temperature away from in-service temperature.

The present contribution focuses on blends of poly(vinylidene fluoride) (PVDF) and poly(methyl methacrylate) (PMMA). Indeed, in recent years, PMMA/PVDF blends got a renewal of interest with studies aiming at assessing their mechanical response. In terms of processing, they exhibited a transition from miscible amorphous to semi-crystalline structures. At room temperature and for approximately the same given crosshead speed, PMMA is basically brittle and neat PVDF exhibits ductile failure. By gradually increasing the PVDF content, toughening effects were evidenced according to a given fracture mechanics parameter based on fracture energy. The motivation here is then to determine a critical degree of crystallinity able to characterize the transition between brittle (low fracture energy) and ductile (high fracture energy) failures, for the same test conditions (room temperature/ crosshead speed). It was demonstrated that depending on the fracture energy definition,

corresponding to either fracture toughness or impact strength, the value of this critical degree of crystallinity was changed.

2. Experimental procedure

2.1. Materials - Specimen

The PVDF/PMMA blends were prepared from the homopolymers PVDF Kynar® 721 and PMMA Oroglas® V825, both provided by the company Arkema France. Blending was achieved by co-precipitation from a homogeneous solution [1]. Depending on the fraction of PVDF, either amorphous or semi-crystalline blends were produced. Typically, the blends remain amorphous when their PVDF content is less than about 50 wt%. In the following, blend identification was based on weight composition. For instance, %F = 20 or F/M 20:80 deals with a blend containing 20 wt. per cent of PVDF and 80 wt. per cent of PMMA. Of course, blend composition influenced the values of the glass transition temperature. Moreover, the presence of amorphous PVDF segments constrained by the crystallites was evidenced in the crystalline blends [1].

Table 1. Blends characteristics

Sample	%F	T_g (°C)	χ (%)
M	0	110	0
F/M 20:80	20	85	0
F/M 30:70	30	77	0
F/M 40:60	40	58	0
F/M 50:50	50	66	14
F/M 60:40	60	54	19
F/M 70:30	70	45	27
F/M 80:20	80	54	36
F/M 90:10	90	53	45
F	100	-40	55

Table 1 recalls the main characteristics of the blends under study, namely overall wt percentage of PVDF, %F, glass transition temperature, T_g and the degree of crystallinity, χ.

The blends were compression-molded in the form of 5 mm-thick sheets. Then, single edge notch bending (SENB) specimens were machined out of the sheets. Their characteristic dimensions were kept constant: thickness T = 5 mm, width W = 12 mm, crack depth a = 5 mm (thus a/W = 0.42), length L = 70 mm, span S = 50 mm. The pre-crack was machined with a notch root radius of approximately 250 µm.

2.2. Fracture energy measurements

Fracture tests on SENB specimen were carried out at room temperature on an Inströn testing machine with a constant crosshead speed of 0.5 $mm.s^{-1}$ for all tests. For the sake of reproducibility, all tests were repeated twice. The load F, the notch opening displacement δ and the crosshead displacement were recorded as a function of the running time. The net stress (σ_{net}) is defined as the

load F divided by the area of the initial net section: T (W –a).

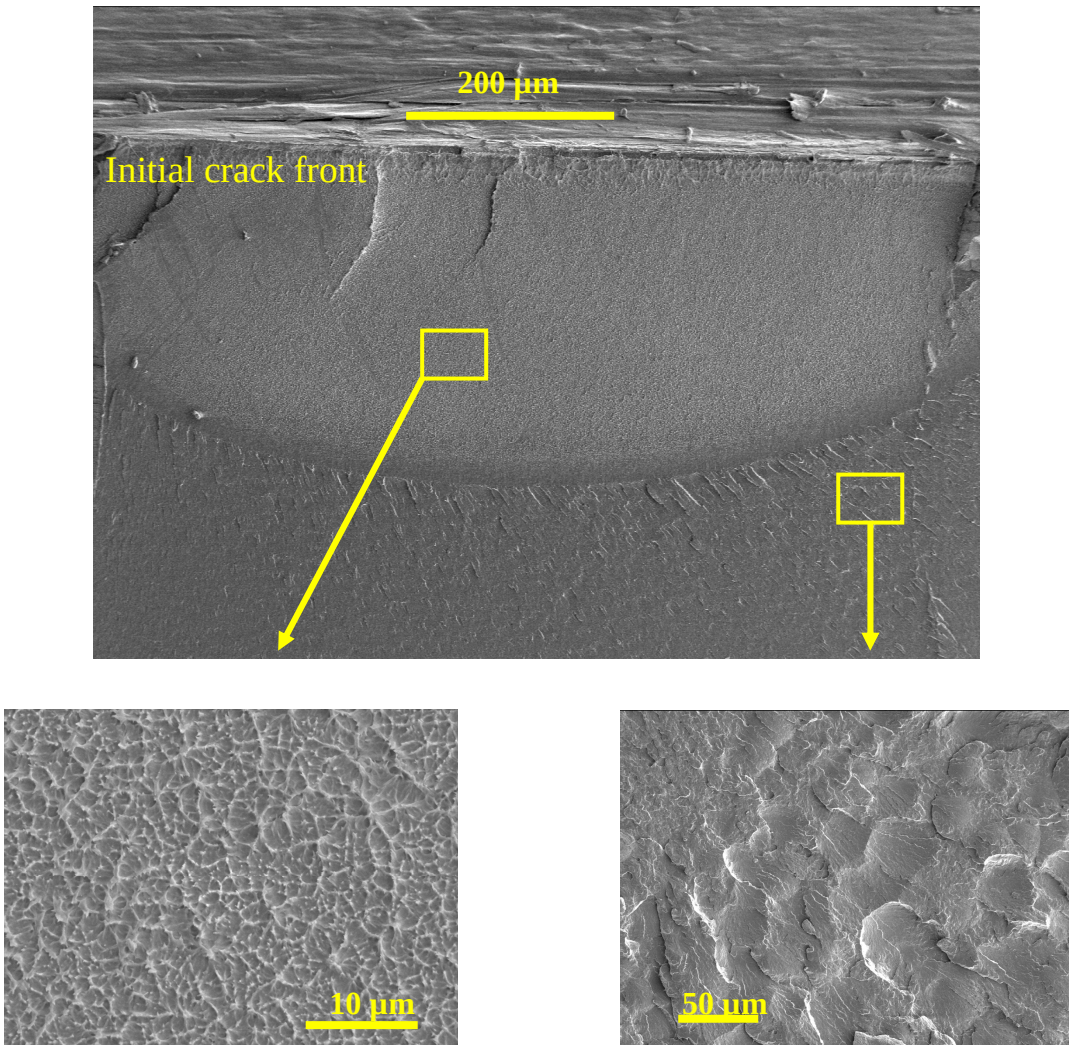

Figure 1. Typical features of semi-crystalline fracture surfaces for 50 ≤ %F ≤ 80

Following fracture mechanics theory [2], the energy release rate G can be expressed as:

$$G = f(a/W)\, U \qquad (1)$$

where $f(a/W)$ is a function of the crack depth ratio and the specimen geometry; U the area under the load versus δ plot. Here both a/W and specimen geometry were kept constant so G was assumed to be proportional to the area under σ_{net} versus δ. Note that this area is homogeneous to an energy density and can be directly calculated from experimental data. In the following, it will be integrated and split into two fracture energies: E_i during the loading path up to the maximum σ_{net} and E_p corresponding to the consecutive decrease in σ_{net}. For brittle fracture $E_p = 0$, E_i is therefore related to the critical energy release rate. It is representative of the toughness of the material. For the general case where $E_p \neq 0$, the total fracture energy $E_t = E_i + E_p$ can be linked to the Charpy impact fracture strength [3-5] but adapted here to quasi-static loading of the specimen. Both E_i and E_t will then be considered here to follow the toughness improvement according to the PVDF content.

3. Results

3.1. Fractography

In Table 1, the degree of crystallinity χ is zero for %F ranging from 0 to 50. Additionally, T_g values were "stabilized" for %F ≥ 50. As already mentioned, the blends were considered as semi-crystalline when their PVDF content was more than 50 wt%. By examining fracture surfaces of broken SENB specimens (fig.1), it was demonstrated that typical semi-crystalline features were identified on blends corresponding to 50 ≤ %F ≤ 80. Accordingly, investigations focused on blends for which %F ≥ 50, *that is* 14% ≤ χ ≤ 55%. Indeed, to better assess the transition between brittle (low fracture energy) and ductile (high fracture energy) fractures, the failure mechanisms should be ensured to be the same. Moreover, since T_g does not vary so much for semi-crystalline blends and since all tests were carried out the room temperature, the degree of crystallinity χ was selected as the relevant parameter allowing for the characterization of this transition.

3.2. Mechanical parameters

3.2.1. Net stress versus δ curves

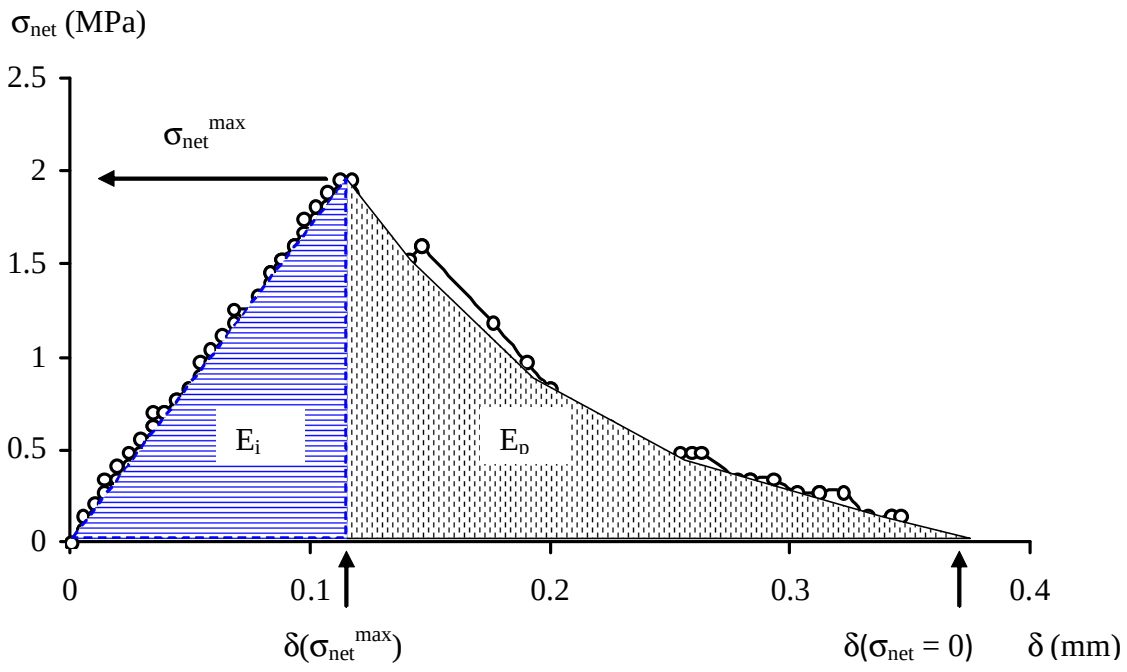

Figure 2. Typical net stress versus opening displacement curve for %F = 50.

The main mechanical parameters were derived from the curve of net stress versus the opening displacement δ as illustrated in fig.2. The definitions of σ_{net}^{max}, $\delta(\sigma_{net}^{max})$ and $\delta(\sigma_{net} = 0)$ were clearly indicated. Moreover, two specific steps could be distinguished in this plot: i) the loading stage (up to maximum net stress), where the crack is supposed to be stationary at the initial value of a/W = 0.42. This part is concerned with "crack initiation" process and therefore to E_i; ii) the crack

growth stage, characterized by the decrease of net stress, related then to E_p.

3.2.2. Maximum net stress

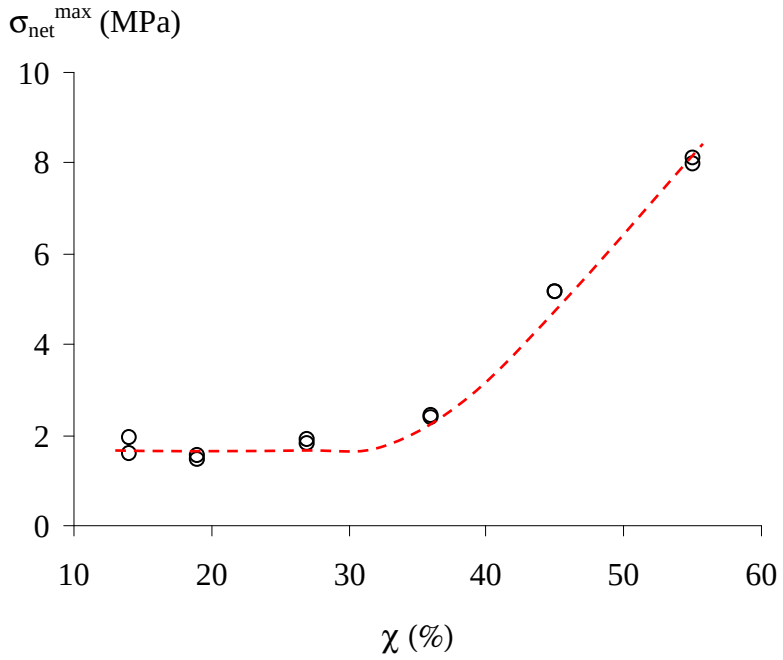

Figure 3. σ_{net}^{max} as a function of the degree of crystallinity χ (%)

The maximum values of the net stress (σ_{net}^{max}) were plotted as a function of χ (%) in fig.3. A continuous increase in σ_{net}^{max} is observed, slightly between 14% and 35% then significantly for the last values of the degree of crystallinity. Moreover, excellent reproducibility of (σ_{net}^{max}) values could be noticed.

3.2.3. Opening displacements: $\delta(\sigma_{net}^{max})$ and $\delta(\sigma_{net} = 0)$

Fig.4 displays the crack opening displacements δ corresponding to respectively, $\sigma_{net} = 0$ at the complete failure of the specimens (first Y-axis) and σ_{net}^{max} (second Y-axis). The same trend as in fig.3 is observed for $\delta(\sigma_{net}^{max})$. This similarity indicates that during the loading step, the net stress versus δ curve was quasi-linear.

Instead, the evolution of $\delta(\sigma_{net} = 0)$ versus χ (first Y-axis) exhibited a jump between 20% and 30%. Actually, this jump was essentially due to the propagation stage where additional deformation of the crack tip (blunting) was observed. For $\chi \geq 35\%$ a saturation of $\delta(\sigma_{net} = 0)$ value was observed.

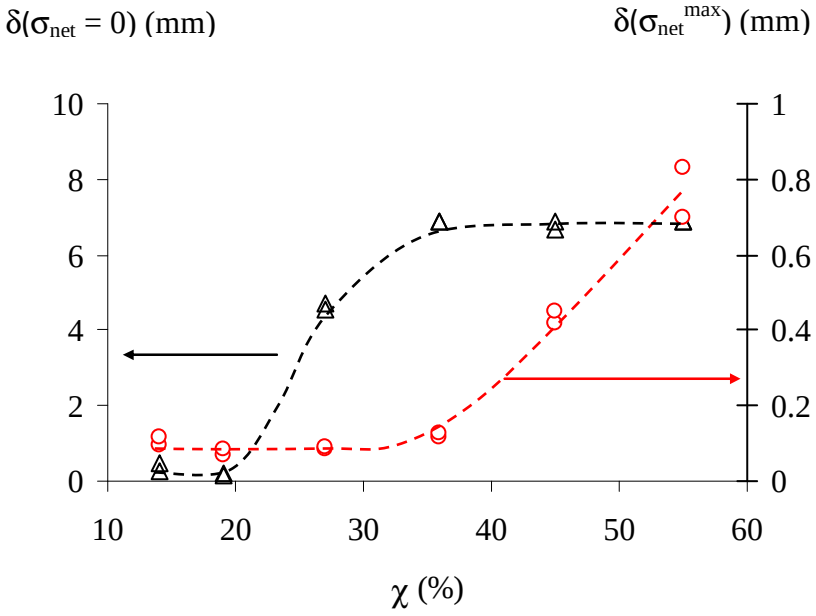

Figure 4. $\delta(\sigma_{net}^{max})$ and $\delta(\sigma_{net} = 0)$ as a function of the degree of crystallinity χ (%)

3.2.3. Fracture energies E_i and E_t

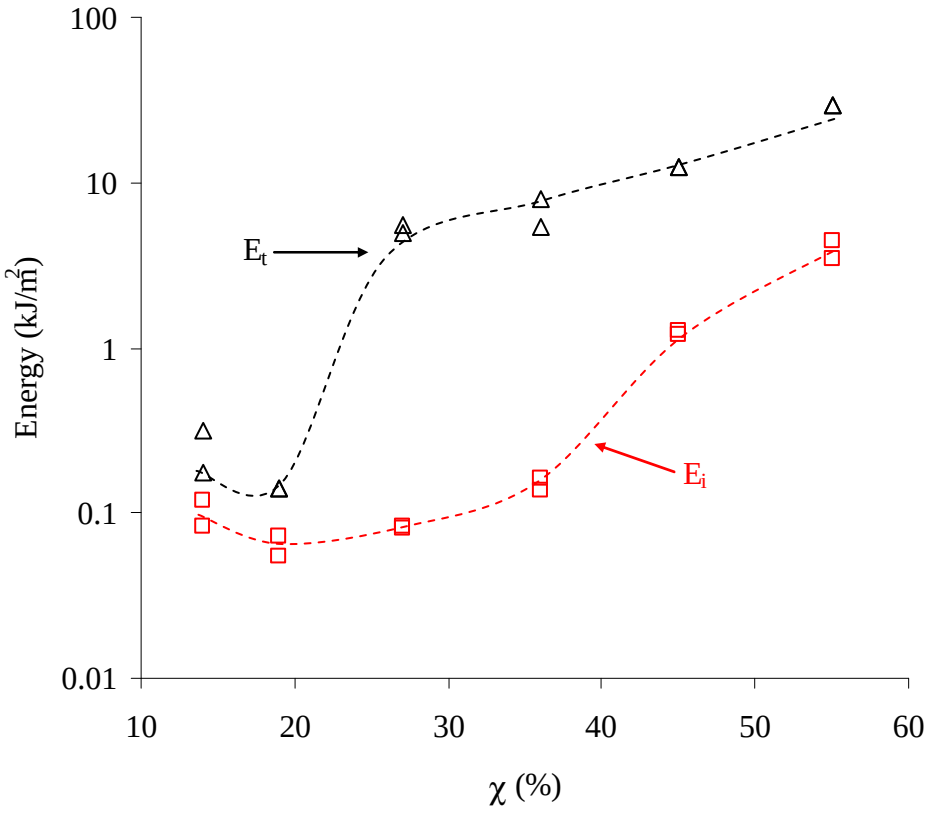

Figure 5. Fracture energies plotted as a function of the degree of crystallinity χ (%)

Fig.5 displays the fracture energies E_i and E_t in a semi-logarithmic scale versus χ. For E_i, the trend was the same as that of σ_{net}^{max} and $\delta(\sigma_{net}^{max})$, whereas the jump of E_t between 20% and 30%

coincided to that of $\delta(\sigma_{net} = 0)$. Furthermore, fig.5 showed that at low values of fracture energy ($\chi \leq$ 20%), $E_t \approx 2E_i$. This was due to that E_i and E_p had approximately the same value. In the upper shelf of the fracture energy ($\chi > 40$) E_p was of higher order of magnitude than E_i.

4. Discussion

The effects of the PVDF content on the fracture energies were analyzed for %F ≥ 50 corresponding to $\chi \geq 14\%$. Depending on the selected fracture parameter, the observed gain in fracture energy may significantly differ in their absolute value (factor 10). Indeed, a jump in the total fracture energy E_t was clearly established whereas a smoother increase in E_i was evidenced at the same time. It should be recalled that E_t is representative of the Charpy impact strength. The "gain in toughness" observed for both parameters was shown to be of the same order of magnitude. In practice, the shape of E_t suggests that the degree of crystallinity corresponding to the brittle to ductile transition was estimated at about $\chi = 23\%$. Around this transition, E_t value drastically increased from 0.13 kJ/m^2 to 5.3kJ/m^2 (factor 40). It is to be noted that for higher values of χ, E_t was still growing from 5.3 kJ/m^2 to 29 kJ/m^2.

For the fracture toughness parameter E_i, a slight and progressive transition was observed at χ values ranging from 30% to 45%. In this χ range, E_i increased from 0.08 kJ/m^2 to 1.2 kJ/m^2 (factor 10).

5. Conclusion

Consideration of the blends of PVDF and PMMA all over the composition range proved to be a powerful tool to assess the characteristics that govern the fracture behavior of polymers. The amorphous blends (PMMA-rich materials) corresponding to PVDF content lower than 50% exhibited zero degree of crystallinity, low values of fracture energy and no particular pattern on their fracture surfaces. They were not taken under consideration in this work.

The PVDF-richer blends exhibited higher degrees of crystallinity $\chi \geq 14\%$. The fracture surfaces issued from tested SENB samples showed dimples characteristics of semi-crystalline polymers. Transitions from brittle to ductile fracture behavior of these semi-crystalline blends were identified, in terms of critical degree of crystallinity χ. The value of such a transition was found to depend on the fracture mechanics parameter: either the fracture toughness (fracture energy to crack initiation E_i) or the equivalent of the Charpy impact strength in quasi-static case (total fracture energy E_t).

The transition for E_i and E_t was estimated at $\chi \sim 38\%$ and $\chi = 23\%$, respectively. At these χ-transitions, E_i was found to increase from 0.08 kJ/m^2 to 1.2 kJ/m^2 (factor 10) whereas E_t jumped from 0.13 kJ/m^2 to 5.3kJ/m^2 (factor 40).

Acknowledgements

The authors would like to acknowledge Julie Heurtel (Mines ParisTech) for technical support.

References

[1] L. Laiarinandrasana, Y. Nziakou, J.L. Halary, Fracture behavior of amorphous and semi-crystalline blends of poly(vinylidene fluoride) and poly(methyl methacrylate). Journal of Polymer Science Part B: Polymer Physics, 50 (2012) 1740-1747.

[2] J.D. Landes, J.A. Begley, Fracture Analysis, STP 560. American Society for Testing Analysis. Philadelphia 1974, pp. 170-186.

[3] L.C.A. Folch, F.M. Burdekin, Application of coupled brittle–ductile model to study correlation between Charpy energy and fracture toughness values. Engineering Fracture Mechanics 63 (1999), 57-80.

[4] A. Rossol, C. Berdin, C. Prioul, Determination of the fracture toughness of a low alloy steel by the instrumented Charpy impact test. International Journal of Fracture, 115 (2002) 205-226

[5] B. Tanguy, C. Bouchet, S. Bugat, J. Besson, Local approach to fracture based prediction of the ΔT_{56J} and ΔT_{KIc100} shifts due to irradiation for an A508 pressure vessel steel. Engineering Fracture Mechanics 73 (2006) 191-206

Fracture of Metallic Ring Samples under static and dynamic loading

Viktor A. Morozov[1*], Yuriy V. Petrov[1], Anton A. Lukin[1], Viktor M. Kats[1], Svetlana A. Atroshenko[1], Georgii D. Fedorovskii[1], Dmitriy A. Gribanov[1], Olga K. Zaichenko[1]**

[1] Saint-Petersburg state university, 7-9, Universitetskaya nab., St. Petersburg, 199034, Russia

[*] viktor.morozov@math.spbu.ru, [**] yp@yp1004.spb.edu

Abstract

A study on the destruction of thin aluminum and copper samples in a wide range of loading times was made. Static loading of samples in the form of strips on a tensile testing machine was carried out. For dynamic loading magnetic-pulse method with a period of 1 μs loading and 7,5 μs applied. The samples were made in the form of rings. The mechanism of fracture in each time range, and the peculiarities of the behavior of materials was studied. A mathematical model for fracture process was proposed. Comparison of the mechanical properties of materials under static and dynamic range tests was realized.

Keywords: static loading, dynamic loading, fracture, magnetic pulse technique, metallic ring samples.

1. Introduction

A large number of experiments on loading of continuum shows fundamental differences between destruction process under the influence of slow quasistatic loadings and "fast" dynamic destruction. In case of quasistatic deformation critical value of strength parameters is much less dependent on experimental conditions, than at dynamic influence. As observed critical characteristics of destruction at dynamic deformation it is essential volatile and behave it is rather unpredictable, one of the main objectives at definition of dynamic strength characteristics is research of interrelation of the limit power parameters conducting to destruction of a material with duration, amplitude and growth rate of enclosed loading. Results of microstructural research of the destroyed samples. The mathematical model, allowing to describe destruction of materials both at static, and under dynamic conditions of loading is considered.

Results of a experimental study on a rupture of thin aluminum and copper samples in the form of narrow strips as in the conditions of static loading by breaking machine, and at dynamic harmonic stretching impact with the period 1μs are given in this work. In the second case the magnetic-pulse method of loading was applied, and samples were carried out in the form of rings. The destroying static tension of materials is determined and the assessment of their dynamic breaking points with use of the offered method of measurement of time from the beginning of loading until destruction is made. Comparison of breaking points in static and dynamic conditions is carried out. Results of microstructural research of the destroyed samples are given. The mathematical model, allowing to describe destruction of materials both at static, and under dynamic conditions of loading is considered.

2. Deformation and destruction of thin aluminum and copper samples at quasistatic loading

2.1. The methodology of the experiments

The experimental study on mechanical deformation and strength properties of aluminum (Al) and copper (Cu) condenser foils by h=0,015 mm thickness in solid (cold-worked [1]) condition is conducted at stretching of strips in the breaking machine Tinius Olsen H10KN (fig. 1) at a speed of movement of mobile grab of the breaking machine of 10 mm/min.

Fig. 1. General view of the test machine: 1 - frame, 2 - PC 3 - moving cross-arm, 4 – machine`s grabs, 5 - sample clips, 6 – sample.

Control of operation of the machine and data acquisition was carried out by the computer. Charts of stretching of samples were received: "effort - lengthening" and "stress – deformation". The test machine`s computer automatically chose scales of charts in the set size of speed of deformation, thickness and sample width, its working length. Start of movement of mobile grab (cross-arm) was carried out at not completely straightened condition of samples - foils, because of complexity of exact definition of the effort beginning in them. Therefore at charts there was an initial area (fig. 2, 3), having, generally small nonzero ordinates (efforts and stress), the achievements caused by process by samples of the straightened condition, and also operation (friction) of additional tiny hinged devices (clips) for samples mount. Further, when processing charts, this area excluded.

2.2. About a type of samples and their production

In [2] requirements to aluminum foils for condensers, a view and sizes of samples (length of 150 mm, width of 15 mm) and conditions of mechanical (quasistatic) tests are provided. However, for an exception of influence of a large-scale factor by comparison of these quasistatic tests in comparison with dynamic experiments on the ring samples received by gluing together or the soldering of strips foils, in our case the sizes of samples – strips for quasistatic tests were accepted considerably the less size, namely: rather close with sizes of strips applied to rings. Preparations – strips for quasistatic tests of an aluminum foil were cut out 60 mm long and width b about 6 mm,

and copper - respectively, 50 and b=1,7 mm, with width deviation no more, than $\pm 0{,}05$ mm. The choice of bigger width (and lengths) aluminum preparations was connected with considerably smaller durability of this material, in comparison with copper, - for providing a sufficient correctness of tests. Length of working part of aluminum samples equaled l_0=28 mm, copper 20 mm. Thus, the speed of relative deformation of samples equaled $\dot{\varepsilon}(t) = \frac{\Delta l}{l_0}$ aluminum samples it was equal 0,357 min^{-1}, copper – 0,5 min^{-1}. Conditional stretching tension stress in samples was determined by a formula $\sigma = \frac{P}{h \cdot b}$ with initial values h and b. Other parts of samples (ends) were used for fastening of samples in grabs of the test machine so that the rupture of a sample was carried out not in capture zone, and in its working zone. For this purpose the ends were bent before acceptance of double thickness, with placement of cardboard laying in a bend, and, then, the ends were pasted over with a paper adhesive tape. Before the placing of samples in the test machine on these ends tiny aluminum clips with the hinges, necessary for more exact axial loading of samples that it is difficult to provide at direct use of large rigid grabs of the test machine Were attached. At test samples fastened in test machine grabs through tiny clips.

2.3 . Results of quasistatic experiments

In fig. 2 are provided received by means of the computer of the test machine the chart of "loading - lengthening" and "stress - deformation" for one sample from an aluminum foil, and on fig. 3 – for one of a copper foil.

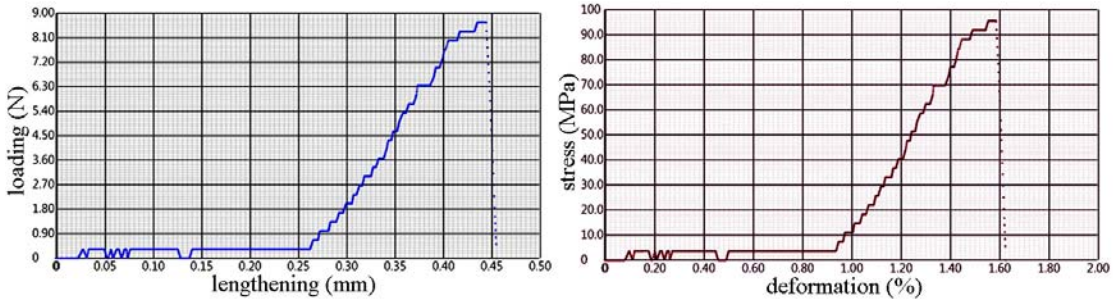

Fig. 2. Charts of stretching of an aluminum foil

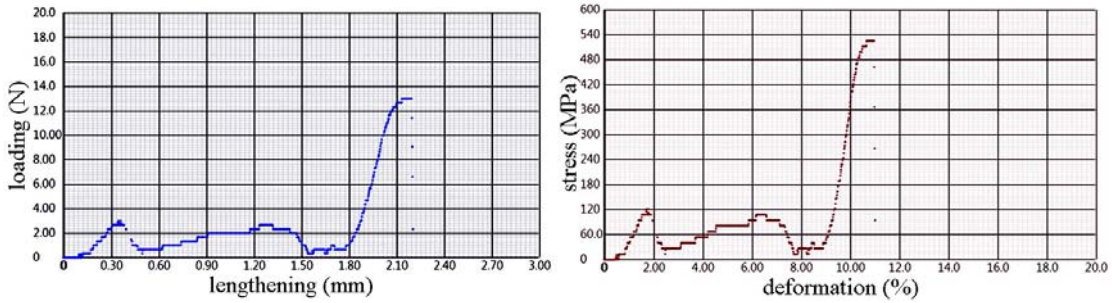

Fig. 3. Charts of stretching of a copper foil

When processing initial areas of the charts "stress - deformation" (0 – 0,9) for aluminum and (0 – 9) for copper were excluded. The same was carried out when processing charts of all other samples.
Stretching charts σ - ε aluminum and copper foils have an appearance typical for plastic materials: with an initial site of elasticity, viscoplasticity and destruction. On the chart for a copper foil before destruction small falling of conditional stress ((increase of true stress) before a direct prompt macrorupture of a sample – germination of the main crack, the events for an aluminum foil in time ~ 0,12 sec., and for copper 0,05 sec. is observed.

In table 1 are provided average on three measurements (to charts σ - ε) data on mechanical characteristics aluminum and copper foils at stretching with speeds of $\dot{\varepsilon}(t) = 0{,}357$ min^{-1} and 0.5 min^{-1} respectively, in parentheses – discrepancy in %. Designations are accepted: E - Young's modulus; σ_e - elasticity limit; $\sigma_{\max}$ - the maximum conditional stress on the chart "stress - deformation"; σ_c - conditional stress of destruction (temporary resistance) corresponding to the moment of the beginning of a macrorupture of a sample; ε_c - destruction deformation; t_c - destruction time.
Essential distinction of all mechanical characteristics foils is established to Al and Cu.

Table 1. Mechanical characteristics of an aluminum and copper foils

Material	E, GPa	σ_e, MPa	$\sigma_{\max}$, MPa	σ_c, MPa	ε_c, %	t_c, s
Al	13 (±12%)	60 (±15%)	99 (±1%)	99 (±1%)	0,76 (±14%)	1,275 (±14%)
Cu	38 (±28%)	400 (±18%)	527 (±3%)	508 (±3%)	2,27 (±18%)	2,730 (±18%)

Very insignificant dispersion of characteristics attracts attention $\sigma_{\max}$ and σ_c. It is possible to claim about experimental stability of these characteristics.

2.4. The microstructural analysis of destruction at quasistatic loading

The type of two samples of an aluminum foil and two samples of a copper foil after destruction is presented on figs. 4. In fig. 4 destruction of samples on a working site is noticeable l_0.
Research of destruction surfaces of aluminum and copper samples after tests was carried out on an optical microscope of Axio-Observer-Z1-M in a dark field, and research of structure cross microsection – in a light field or polarized light. The structure was studied on cross microsection after the corresponding etching. The size of grain and quantity of a pores defined on a surface microsection.
Microstructural studying is carried out on three aluminum and three copper destroyed samples. The analysis of samples structure of copper and aluminum showed that samples mainly collapse viscously – have a “cup” break. Comparison of samples of copper and aluminum revealed that the

Fig. 4. The destroyed samples aluminum (at the left) and copper (on the right) foils

fiber percent in a break of statically loaded copper is less, than in aluminum, i.e. copper collapses is more fragile in these conditions.

On fig. 5 structures of aluminum samples after static tests are presented. Porosity in a sample 4, cracks in a sample 5 and the main crack in a sample 6 is visible.

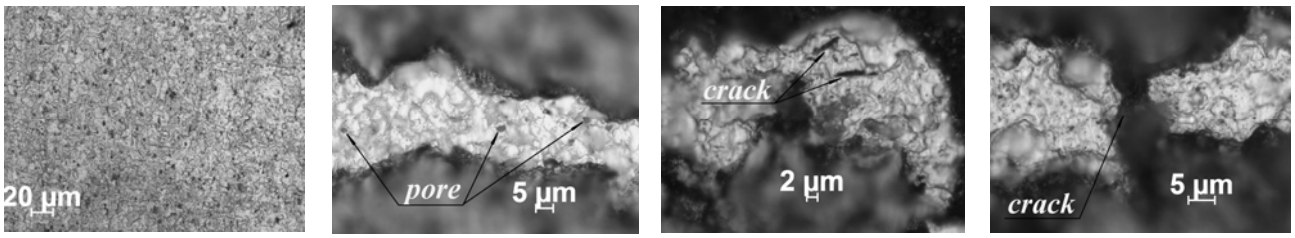

a b c d

Fig. 5. Structure of aluminum samples after static tests: a – in an initial condition; b – pores in a sample 4; c – crack in a sample 5; d – the main crack in a sample 6.

In figure 6 structures of samples of copper after static tests are presented.

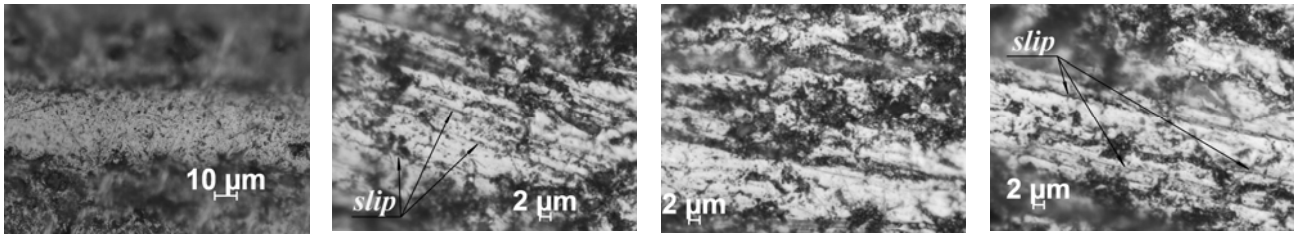

a b c d

Fig. 6. Structure of copper samples after static tests: a – in an initial condition; b – sliding strips in a sample 4; c– homogeneous structure in a sample 5; d – sliding strips in a sample 6.

In samples 4 and 6 sliding strips are observed, and in a sample 5 the homogeneous structure prevails, as is noticeable by appearance of samples in fig. 4. The sample 5 is destroyed at an angle about 45^0, i.e. in the direction of the maximum tangent stress on the planes of more dense packing.

3. Deformation and destruction of aluminum and copper samples at dynamic loading

Experiments on deformation and destruction of samples were carried out with use of the modified magnetic-pulse method on the basis of the generator of short high-voltage impulses of GKVI-300 providing formation of electric voltage with amplitudes of 30 - 300 kV. As samples rings from thin aluminum and copper foils with a diameter of 28,6 mm and 1 - 2 mm wide were used.

On fig.7 the loading scheme is shown. The current passing on the coil on which the ring sample coaxially settles down, directs in it induction current, and interaction of these currents generates pushing away force between the solenoid and a ring.The coil is made of a copper wire by diameter 1mm, has 5 rounds, diameter of the coil - 25 mm. The current passing through the coil, was measured by a Rogovsky coil (RC) and displayed on a digital oscillograph (OSC) information with which registered on the electronic carrier. At a rupture of the ring (Sample) which has been coaxially fixed on the middle of the coil (L), there was a spark which allowed to fix the moment of destruction of a sample by means of the photo diode (PD). At test of samples installation when via the coil current with the period of fading fluctuations T=1μs was passed was applied. Its flowchart is provided on fig. 8.

Appearance of installation is given on fig. 9.

On fig. 10 current oscillograms via the coil and a signal from the photo diode fixing the moment of a rupture of a sample are represented.

Experiments on rings from aluminum and copper foils 0.015 mm thick and 1.0 - 2.0 mm wide were made. Samples tested with a cut and without a cut.

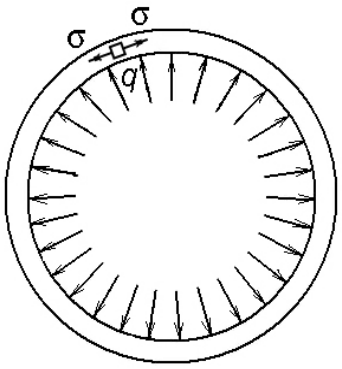

Fig. 7. Scheme of sample loading
(q – loading, σ– the stretching stress)

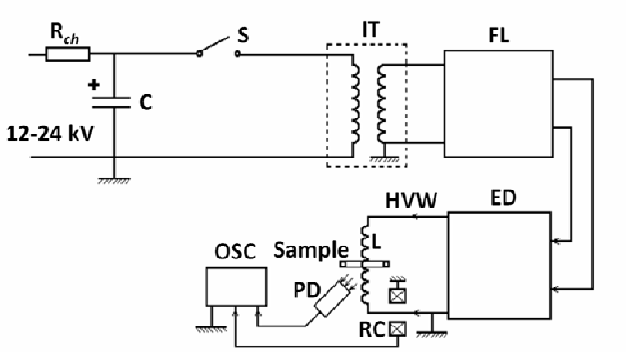

Fig. 8. The block-scheme of the setup for sinusoidal electromagnetic load of period 1 μs: Sample – a sample; IT – the pulse transformer; FL – the forming line; ED – the output device; HVW – a high-voltage electrode; PD – the photo diode; RC – a Rogovsky coil; OSC - an oscillograph

The assessment of the radial force operating on a ring from rounds of the coil, was carried out by a technique stated in work [3], submitted on ICF 13. Tangential stretching stress was calculated on Laplace's formula for thin-walled covers

$$\sigma(t) = \frac{q(t)R}{h},$$

where $q(t) = F(t)/c -$ the distributed radial loading acting on an internal surface of a ring, F (t) – force acting on a ring, c, R, h – width, internal radius and ring thickness, respectively.

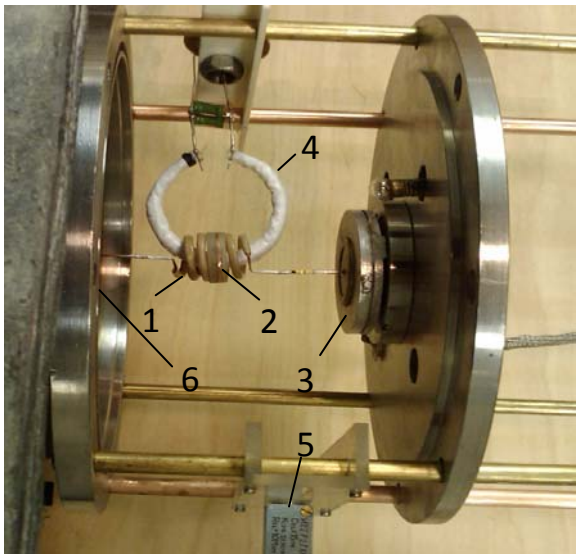

Fig. 9. General view of installation,
1 – solenoid; 2 – sample; 3 - Rogovsky coil, measuring current in the coil; 4 – Rogovsky coil, measuring current in a ring;
5 – photo diode; 6 – output device.

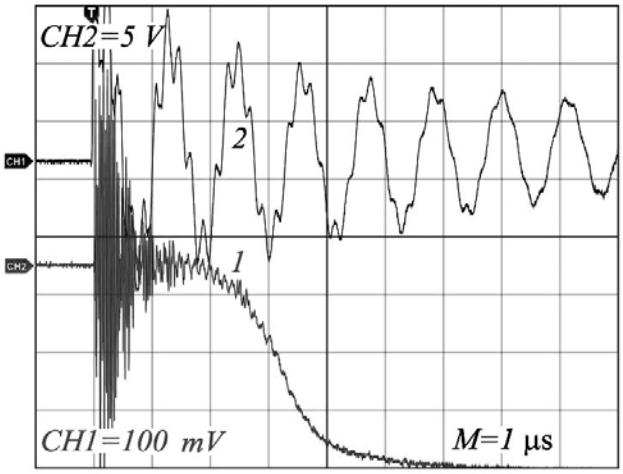

Fig. 10. Oscillograms from the photo diode 1 and current from a Rogovsky coil 2.

At determination of the stretching tangential stress its pulsing value $\sigma(t)$ it was replaced average in the form of a rectangular impulse with an amplitude σ_0 and duration equal to time from beginning of giving of current in coil until rupture of a ring t_c:

$$\int_0^{t_c} \sigma(t)dt = \sigma_0 t_c, \quad \sigma_0 = \frac{\int_0^{t_c} \sigma(t)dt}{t_c}$$

Time t_c was measured in experiences.

Characteristics of samples, conditions of experiments and results are provided in table 2, where: T - the period of fluctuations of current in the coil; h - ring thickness; c - ring width; ∅ - diameter of a ring; U - tension of a charge of the condenser; σ_0 - the stretching stress of a ring rupture; τ - time before destruction; W - energy of the charged condenser; I - current amplitude via the coil.

Table 2. Characteristics of samples, conditions of experiments and results

Material	T, μs	h, mm	c , mm	∅, mm	U, kv	σ_0, MPa	τ, μs	W, J	I, A
Al	1	0,015	1,50	28,6	20	162	4,17	100	4200
Cu	1	0,015	1,00	28,6	20	577	4,68	100	5800
Cu notch	1	0,015	1,55	28,6	20	376	6,60	100	8400

3.1. Results of microstructural research

Microstructural studying is carried out by the same technique that is presented in item 2.4. Microhardness measured on the PMT-3 device at loading 20g. Results of microstructural researches are given in photos (фиг.11) and in table 3, where: T - the period of fluctuations of current in the coil; S=hxb - sample section; D - grain size; n - quantity of a time on the area 400 μm2; HV – microhardness.

Table 3. Results of microstructural researches

Material	T, μs	hxb, μm^2	D, μm	n, 1/400 μm^2	HV, MPa
Al	1	$68,4\times10^3$	3,0	70	639,1
Al initial		120 x10^3	4,6	53	720,4
Cu	1	$29,9\times10^3$	2,5	96	340,2
Cu notch	1	75,8 x10^3	0,8	380	103,3
Cu initial		15 x10^3	-	282	644,6

The copper sample before loading represented a monocrystal, and after loading as a result of dynamic recrystallization there are fine grains – the size – 0,8-2,5 μm. And dynamic recrystallization in a sample with a cut – here grains smaller is more developed. Quantity of a time in a sample with a cut too much more, than in a sample without a cut. Besides, in a sample with a cut a large number of strips of shift (fig.11d).

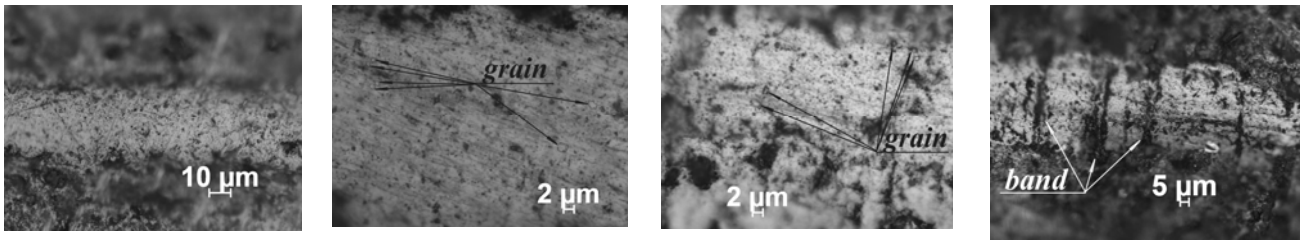

a b c d

Fig. 11. Copper structure: (a) - in an initial condition; (b) - after loading with the period of T=1μs (S=0,03mm2); (c) – sample with a cut after loading with the period of T=1μs (S = 0,08 mm2); (d) - sample with a cut after loading with the period of T=1μs (S = 0,08 mm2). Designations: grain – the recrystallized grains, band – shift strips.

4. Results comparison of static and dynamic materials destruction

It should be noted essential distinction of dynamic and static strength characteristics.
Comparison of structural changes at static and dynamic loading shows that at short-term influence there is a dynamic recrystallization – formation of new fine grains. Extent of dynamic recrystallization the greatest in samples with the bigger duration of loading and the maximum cross section (a large-scale factor). Aluminum samples after loading show big tendency to cavitation at increase in the period of loading in comparison with the initial. Besides, at increase in duration of influence in samples there is an origin of a multiple splitting off.

5. Conclusion

1. Techniques of experimental studying of quasistatic and dynamic properties metal foils are developed and applied.
2. Deformation and strength characteristics aluminum and copper foils are defined.
3. Analytical expressions for mechanical characteristics of materials are received.
4. The microstructural analysis of destruction zones is made at quasistatic and dynamic loading.
5. Comparison of properties of materials in the conditions of the static and dynamic loading, shown their essential distinction is carried out.

References

[1] Physical quantities: The directory / Under the editorship of I.S.Grigoriev, E.Z.Meylikhova. – M: Energoatom, 1991. – 1332 pages.
[2] Foil aluminum for condensers. Specifications. GOST 25905-82. – 27 pages.
[3] V.A Morozov, Yu. V. Petrov, A. A. Lukin, V. M. Kats, S. A. Atroshenko, G. D. Fedorovskii, Fracture of Metallic Ring Samples under Magnetic Pulse Shock Action (2013) in ICF 13.

Evaluation of ductile fracture models in high velocity impact problems

Ying Li[1,*], Xiaobin Li[1], Xiangshao Kong[1], Xing-xing Wu[1]

1. School of Transportation, Wuhan University of Technology, Wuhan, 430063
* Corresponding author: liying198842@126.com

Abstract: As resourceful stress states, high strain rates, and large plastic deformation were involved, the Taylor test can be used to identify the most suitable fracture criterions for high velocity impact problems. A systematic evaluation is carried out for the maximum principal stress, the maximum principal strain, equivalent plastic strain and Johnson–Cook fracture models by numerical simulations. The applicability of the ductile fracture models are discussed, finally.

Keywords: Taylor impact, Ductile fracture, Johnson–Cook fracture model

1. Introduction

Considering high temperature and high strain rates, strength models and fracture criterions are needed in impact response calculation of metal material. There are J-C, ZA, MTS strength models and the maximum principal stress, the maximum principal strain, equivalent plastic strain and Johnson–Cook fracture models to chose from. It is necessary to evaluate these fracture models.

The Taylor test can get high strain rate (10^4~10^6), in which a deformable flat-nosed cylinder is fired against a fixed, rigid wall and was originally proposed to determine dynamic yield stresses of materials [1]. Taylor test results are used to validate or to estimate coefficients for phenomenological strength models needed for simulating dynamic loading processes using inverse identification procedures[2-4].

When Taylor bar runs fast, cracks and fragmentation phenomenon are very common. Couque (1998)[5] observed several spiral cracks which formed on the lateral surface of the cylinder in symmetric Taylor tests on swaged tungsten alloys.

Material mechanics performance test of Q235 was taken to calculate parameters of fracture criterions. The display dynamic analysis software AUTODYN was used to forecast failure modes of Taylor tests. The differences and limitations of the ductile fracture models are discussed, finally.

2. Mechanical property testing of Q235

To get parameters of the fracture criterions, cold quasi static single axis tensile test was done on MTS. Specimens were processed according to <GB/T228-2002>, whose diameter was 10mm, length of test part was 100mm (see Fig.1). Loading rate of this test was 0.6mm/min (strain rate was 2×10^{-4}/s).

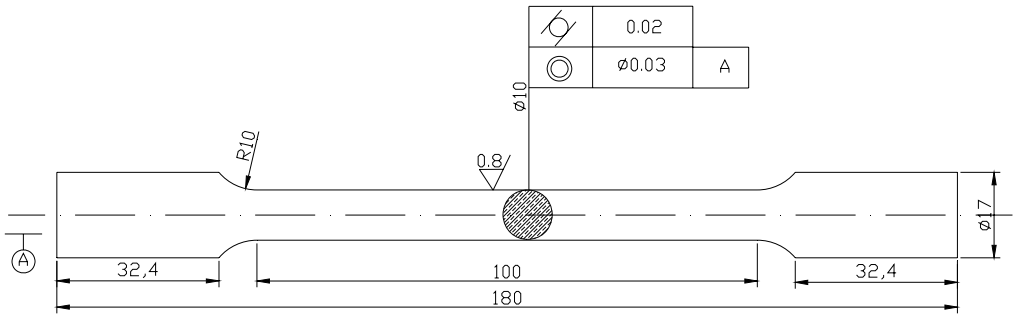

Fig.1 Schematic of specimen for quasi static single axis tensile tests

Engineering stress strain curve was got by the load-displacement curve. Parameters of the maximum principal stress, the maximum principal strain, equivalent plastic strain and Johnson–Cook fracture models were got by Stress triaxial degree test and tensile test at high temperature.

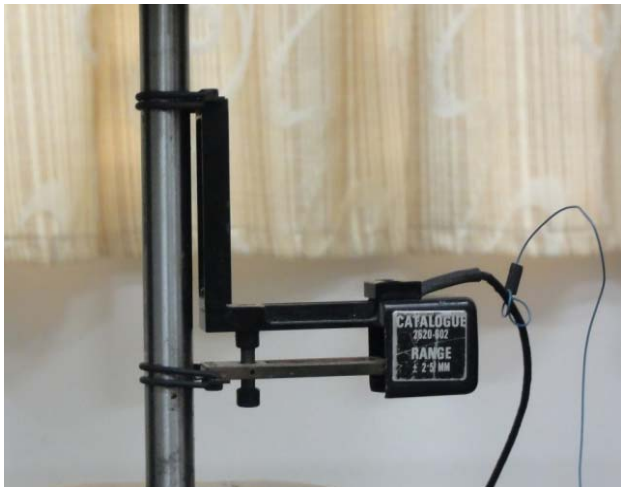

Fig.1 quasi static single axis tensile test

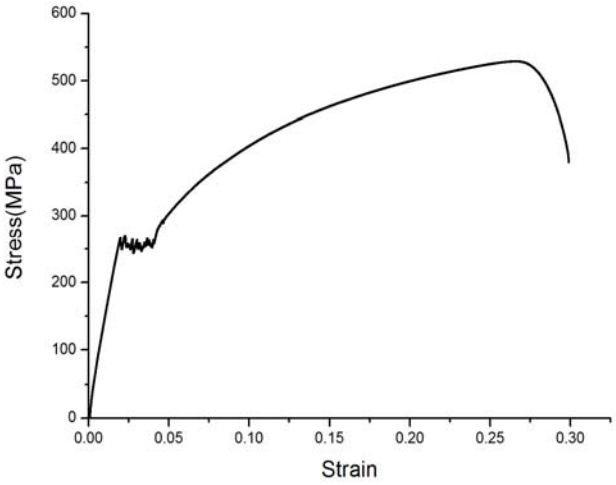

Fig.2 stress-strain curve of Q235

3. The numerical simulation model and the strength model

3.1 The numerical simulation model

Generally, in the Taylor test a deformable flat-nosed cylinder is fired against a fixed rigid wall (see Fig. 3). The cylindrical projectile is of the diameter d= 6mm and the length l= 30mm. The friction coefficient between the front surface of the projectile and the rigid wall is assumed to be $\mu = 0.1$.

Smoothed Particle Hydrodynamics method (SPH) was used to simulate the failure phenomena of cylinder. A 3-D solid finite element model was built rather than an axisymmetric model (see Fig. 4).

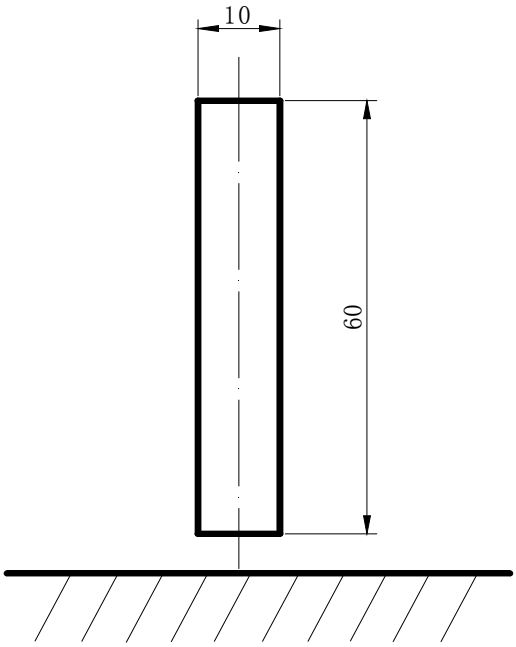

Fig. 3 Schematic of a cylindrical projectile impacting a rigid wall

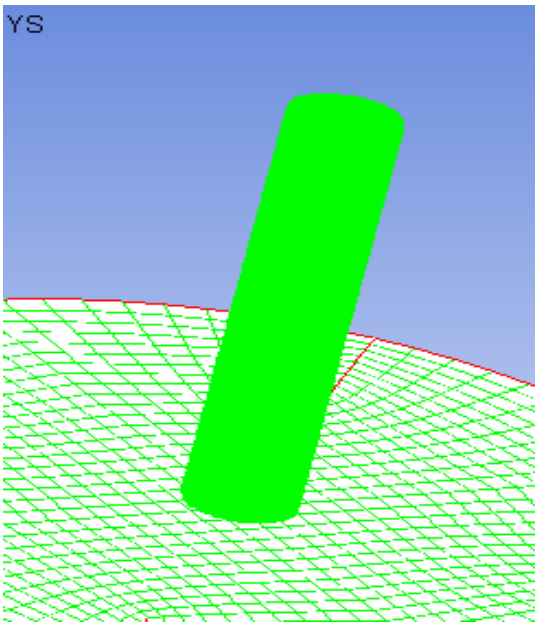

Fig.4 Finite element model of the projectile-target system

3.2 The strength model

Due to simplicity and availability of material coefficients, the Johnson–Cook (JC) material model implemented in AUTODYN was used in the present calculation. The material model should not be confused with the fracture model which will be discussed later. In the JC model the equivalent stress σ is an explicit function of the equivalent plastic strain ε_{eff}, the temperature T, and the plastic strain rate $\dot{\varepsilon}$.

$$\sigma = (A + B\varepsilon^{n})(1 + C\ln\dot{\varepsilon}^{*})(1 - T^{*m}) \tag{1}$$

Where the reference plastic strain rate $\dot{\varepsilon}^{*} = \dot{\varepsilon}/\dot{\varepsilon}_{0}$, $T^{*} = (T - T_{r})/(T_{m} - T_{r})$, T_{r} and T_{m} are the room temperature and the material melting temperature respectively, and A, B, n, C, and m are five material constants. The JC model accounts for isotropic strain hardening, strain rate sensitivity, and thermal softening in the uncoupled form. The first term of the right hand side of Eq. (1) represents the quasi-static stress–strain relation at room temperature; the second term signifies the strain-rate hardening; the third term means the temperature dependence of the stress–strain relation. It should be pointed out that in the computation, the material behaves elastically up to the point of initial yield and then follows Eq.(1).

The material parameters in the JC model for Q235 were listed in Table 1.

Table 1 Material parameters for Q235

Material	A（MPa）	B（MPa）	n	C	m
Q235	249.2	45.6	0.875	0.32	0.76

4. Results and analysis

4.1 The maximum principal stress failure criterion

Refering to quasi static tensile tests, the maximum principal stress of Q235 was 560MPa , The maximum shear stress of Q235 was 448MPa. With the simulation computation, failure mode of the maximum principal stress for different velocity is showing in Fig.5 and 6.

After impacting on the rigid wall, the Taylor bar was smashed. The fragments were very small and almost in the same volume (v=400m/s).

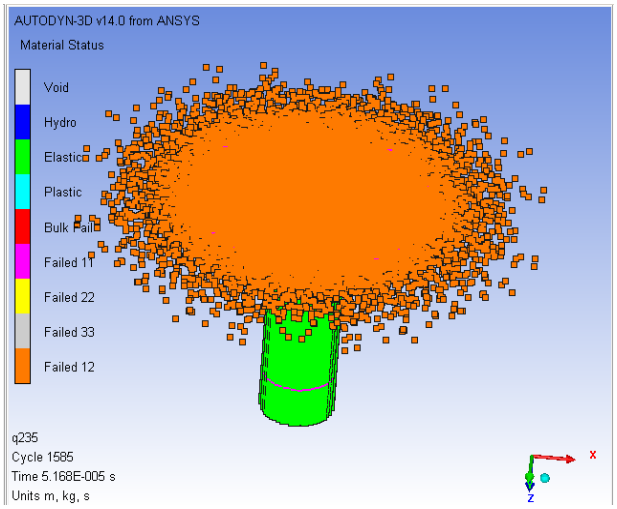

Fig.5 Failure mode of the maximum principal stress (v=300m/s)

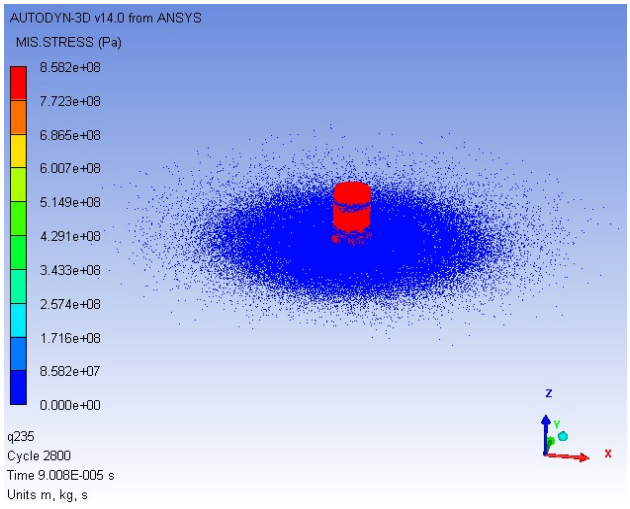

Fig.6 Failure mode of the maximum principal stress (v=400m/s)

4.2 The equivalent plastic strain failure criterion

Refering to quasi static tensile tests, the equivalent plastic strain, $\varepsilon_f = 2\ln\left(\frac{d}{d_0}\right)$, for Q235 $\varepsilon_f = 1$.

Through the simulation, failure mode of equivalent plastic strain for different velocities (v=300m/s, 400m/s) are showing in Fig.7and 8.

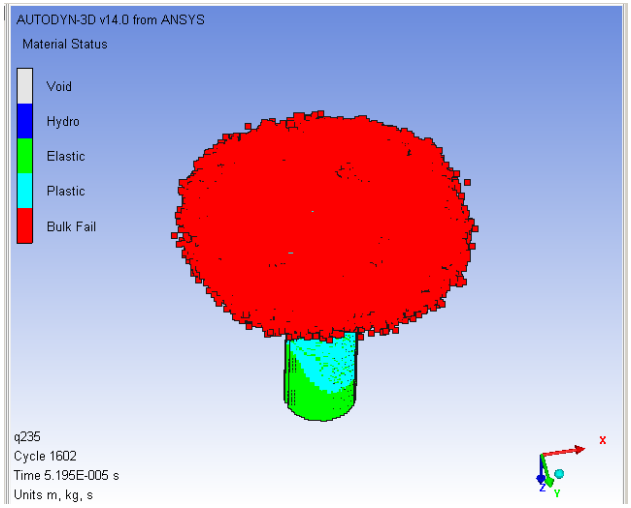

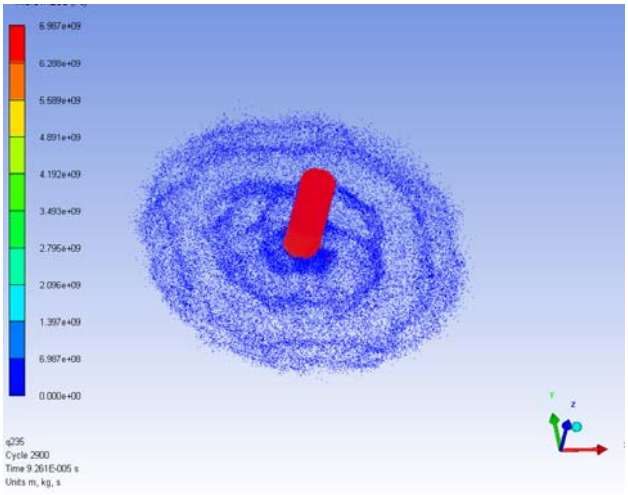

Fig.7 Failure mode of equivalent plastic strain (v=300m/s)

Fig.8 Failure mode of equivalent plastic strain (v=400m/s)

4.3 The maximum principal strain fracture criterion

Refering to quasi static tensile tests, The maximum principal strain was 0.33. Through the simulation, failure mode of the maximum principal strain in different velocities (v=300m/s, 400m/s) are showing in Fig.9 and 10.

About thirty fragments produced in this process, and the fragment volume was larger than that of above two fracture criterions.

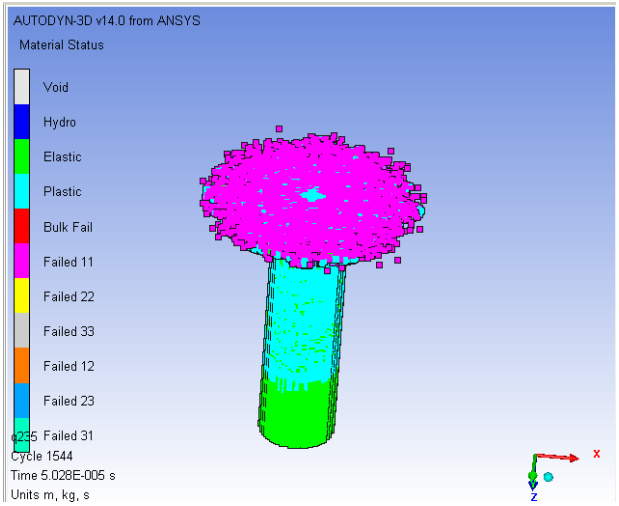

Fig.9 Failure mode of the maximum principal strain (v=300m/s)

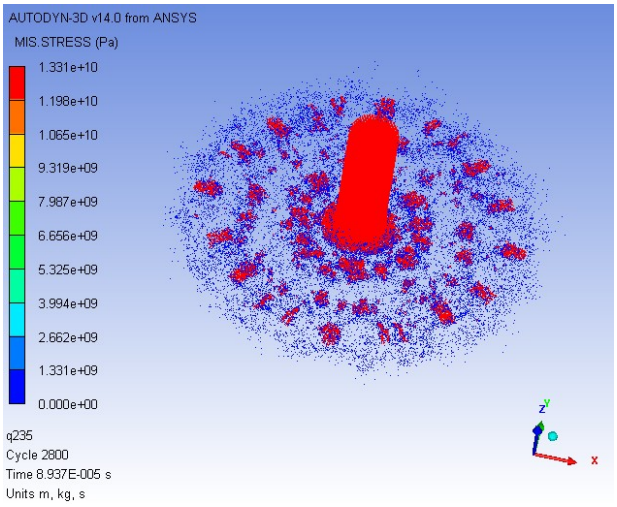

Fig.10 Failure mode of the maximum principal strain (v=400m/s)

4.4 J-C fracture criterion

The influence of the stress triaxiality in these models is based on the void growth equation proposed[6, 7].The expression of J-C fracture strain ε_f is[3]

$$\varepsilon_f = \left(D_1 + D_2 e^{\left(D_3 \sigma^*\right)} \right)\left(1 + D_4 \ln \dot{\varepsilon}^*\right)\left(1 + D_5 T^*\right) \tag{2}$$

D_1, D_2, D_3, D_4 and D_5 are material parameters; $\sigma^* = p/\sigma_{eff} = -\sigma_{kk}/\sigma_{eff} = -R_\sigma$, p is pressure, σ_{eff} is equivalent stress, R_σ is stress triaxiality; $\dot{\varepsilon}^* = \dot{\varepsilon}/\dot{\varepsilon}_0$ is dimensionless plastic strain rate, $\dot{\varepsilon}_0$ is Referenced plastic strain rate; $T^* = (T - T_r)/(T_m - T_r)$, T_r and T_m are the room temperature and the material melting temperature. For Q235, D_1=0.38, D_2=1.47, D_3=2.58, D_4=-0.0015, D5=8.07.

Through the simulation, failure modes of J-C in different velocities (v=300m/s, 400m/s) are showing in Fig.11 and 12.

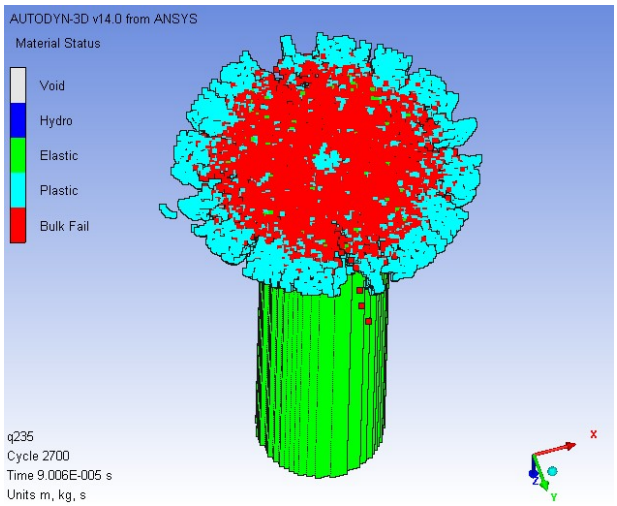

Fig.11 Failure mode of J-C(v=300m/s)

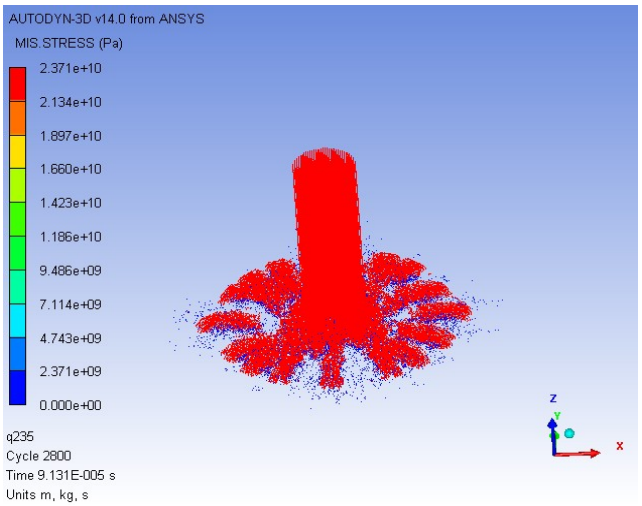

Fig.12 Failure mode of J-C(v=400m/s)

4. Conclusion

Through the above analysis and Taylor test, in which the Taylor bar was broken like petals, Finally, conclusions are summarized:
(1) Failure modes in high velocity impact problems are quite different because of choosing different fracture criterions.

(2) J-C fracture criterion is the most accurate fracture criterion in four fracture criterions for ductile metal in high velocity impact problems.

(3) The maximum principal stress and the equivalent plastic strain failure criterions lead to many fragments for ductile metal in high velocity impact problems.

References

[1] Taylor, G. The Use of Flat-Ended Projectiles for Determining Dynamic Yield Stress. I. Theoretical Considerations[J]. Mathematical and Physical Sciences, 1948, 194(1038): 289-299.

[2] GR Johnson, W. C. A Constitutive Model and Data for Metals Subjected to Large strains,High Strain Rates and High Temperature[C]. Proceedings of the seventh international symposium on ballistics, Netherland. 1983.

[3] GR Johnson, W. C. Fracture Characteristics of Three Metals Subjected to Various Strains, Strain Rates, Temperatures and Pressures[J]. Engineering Fracture Mechanics, 1985, 21: 31-48.

[4] Holmquist, G. R. J. T. J. Evaluation of cylinder - impact test data for constitutive model constants [J]. J Appl Phys, 1988, 64(8): 3901-3910.

[5] Couque, H. On the use of the symmetric Taylor test to evaluate dynamic ductile compression fracture properties of metals.[C]. Proceedings of the 5th International Conference on Structures Under Shock and Impact, Billerica,MA, USA. 1998.

[6] Yingbin Bao, T. W. On fracture locus in the equivalent strain and stress triaxiality space[J]. International Journal of Mechanical Sciences, 2004, 46 81–98.

[7] Rice, J. R., Tracey, D.M. On the ductile enlargement of voids in triaxial stress fields[J]. Mech Phys Solids, 1969, 17: 210-217.

Several kinds of Calculation Methods on the Crack growth Rates for Elastic-Plastic Steels

Yangui Yu*

Zhejiang GuangXin New Technology Application Academy of Electromechanical and Chemical Engineering
Hangzhou, 310007, China
* gx_yyg @126.com

Abstract Research interdependent correlations among various calculations models, relationship between their calculations parameters, and relationship between their materials constants in equations on strengths and life predictions, which are elastic-plastic steels with cracks. Thereby obtain and suggest to adopt several new calculations models and their calculations methods on crack propagation rates, which are respectively suitable for calculations of crack propagation rates under different stress ratio loading, or are suitable for calculations under symmetrical and unsymmetrical cyclic loadings, the work stresses less than or greater than the yield limit. Also the material constants B_2 in new models are defined as comprehensive material constants and give also out their physical meaning and geometric significances that are having a function relation with other parameters. Moreover provide yet a calculation example of crack propagation rate. Anticipate that the works will be having practical significances for fatigue - damage - fracture tests to save experimental times, fund inputs and to expand engineering applications.

Keywords Elastic-Plastic-materials, Comprehensive material constants, Crack growth rate, Calculation methods

1. Introduction

In the engineering fields, loading conditions are very complicated. In the engineering designs and calculations, there are a lot of calculating models are applied. In traditional design methods, for their calculating parameters, for their material constants adopted in the models, in addition to some key calculating parameters, in addition to some limited materials constants which are showing the material properties, they must be by means of the experiments to take data. However there are also some of the traditional calculating models, their calculating parameters and material constants had been already extensively applied, which had been derived usually from the relationships between various calculation parameters or from the relationships between all kinds of material constants, afterwards again applied to engineering design calculation and analysis.

The same, for including cracks structures and materials undergone to very complicated loadings, the calculations on their strengths, crack propagation rates and service life, in all kinds of calculation models also must refer to many calculation parameters and material constants, but these required parameters of designs and calculations got from experiments are always limited. In fact, between these calculations parameters or between these materials constants each other, there are also usually some functional relations. So that to research and analyze these calculations models, their calculations parameters and materials constants, of course, some new models and their parameters and constants can also be derived from them and would be applied to designs and calculations in engineering.

The author researches various strengths, crack propagation rates and life calculations models, to analyze and find interdependent relationships between the various calculation parameters and all kinds of material constants, proposes respectively several new calculation models and calculation methods for the elastic-plastic steels with cracks. But also puts forward specially the new concepts of comprehensive material constants and their calculation methods, its purpose is in combination

with limited experimental data and conventional material constants, thereby to realize the calculations for the crack growth rates and to do the life predictions which are in different stress ratio under complicated loading conditions. Moreover, provides yet homologous calculation examples. Anticipate that the works will be having practical significances for fatigue - damage - fracture tests to save experimental times, fund inputs and to expand engineering applications.

2. The calculations of crack growth rate for elastic-plastic steels

In references [1，2] provide the relation between the fracture life N_{2fc} and half-cycle of amplitude value $\Delta\delta_t/2$ of crack tip open displacement at crack growth stage,

$$\frac{\Delta\delta_t}{2} = \delta_{fc} \times 2N_{2fc}^{c'_2} \tag{1}$$

But if it is expressed to adopt one-cycle of crack tip open displacement range $\Delta\delta_t$, it become as following form

$$\Delta\delta_t \times N_{2fc}^{-c_2} = B_2^{c_2} \tag{2}$$

And relation between the crack growth rate da_2/dN_2 and one-cycle of crack tip open displacement range $\Delta\delta_t$ is as discussed [3~4],

$$da_2/dN_2 = B_2\Delta\delta_t^{\lambda_2} \tag{3}$$

Where the equations (1) and (2) can be described as the reversed beeline C_2C_1 in bidirectional combined coordinate system and bidirectional curves in the whole process(Fig.1) ［5~7］, that is predigested by logarithm transacting just is showed the relation between the life and the crack tip open displacement. And the equations (3) can be described as the positive direction beeline C_1C_2, it just is showed for the relation between the crack growth rate and the crack tip open displacement.

Research and discover that in fact the relations among equations (1), (2) and (3) are consistent. Here the parameters λ_2, c_2 and B_2 are all material constants. λ_2 and c_2 are exponents of equations, $\lambda_2 = -1/c_2$, its geometrical meaning is the slope of force triangle bevel edge. Of course some key material constant in the engineering calculations must be obtained from experimentations. But actually in a number of calculation models, there are functional relationps between some parameters or between some material constants each other, so that we can use the kinds of having

important significances of correlations, can derive a number of beneficial formulas, obtain some calculation methods on the strengths, crack propagation rates and life predictions. For example between the material constant B_2 and other constants are having functional relations as formulas below,

$$B_2 = 2(2\delta_{2\,fc})^{-\lambda_2}(a_{2c} - a_{02})/(N_{2c} - N_{02})\ (\sigma_m = 0) \tag{4}$$

$$B_2 = 2\left(2\delta_{2\,fc}(1 - \frac{\delta_m}{\delta_{2\,fc}})\right)^{-\lambda_2} \times (a_{2c} - a_{02})/(N_{2c} - N_{02}),(\sigma_m \neq 0) \tag{5}$$

Where $\delta_{2\,fc}$ in (4~5) are critical value of the crack tip open displacement, $\delta_{2\,fc} = \delta_c$, the B_2 is defined as comprehensive material constants. Its physical meaning is a concept of power, is a maximal increment value, and also is given out energy in one cycle made specimens to failure. Its geometrical meaning is a maximal micro-trapezia area to approximate to beeline, and is also an intercept between $O_3 - O_4$ (Fig.1). And slope of micro-trapezium bevel edge just is corresponding to the exponent λ_2 of formula (4, 5). a_{2c} is a critical crack size, a_{02} is initial (or precrack) crack size. N_{02} is initial life, $N_{02} = 0$; N_{2c} is a critical life. δ_m is a mean value of the crack tip open displacement, $\delta_m = (\delta_{\max} + \delta_{\min})/2$, here $\delta_{\max}$ and $\delta_{\min}$ are the maximal and minimal values of the crack tip open displacement. Moreover if its unit of the parameter B_2 is calculated by 'mm', then the value of B_2 must be again multiplied by 1000.

For the sake of safety, the comprehensive constant B_2 should be calculated as following form,

$$B_{2eff} = 2\left(2\delta_{2eff}(1 - \frac{\delta_m}{\delta_{2\,fc}})\right)^{-\lambda_2} \times (a_{2eff} - a_{02})/(N_{pv} - N_{02}) \tag{6}$$

Where B_{2eff} is also an effective comprehensive material constant, its physical meaning is a given out effective energy in one cycle made specimens before failure. Here $(a_{2eff} - a_{02})/(N_{pv} - N_{02}) = v_{pv}$, v_{pv} is defined to be the virtual rate, $v_{pv} = v^*(m/cycle)$ [6,8]. $v_{pv} \approx 3\times10^{-8} \sim 3\times10^{-7} = v^*,(m/cycle)$. a_{eff} is an effective size during steady growth course. N_{pv} is a virtual life. δ_{2eff} is an effective value of crack tip open displacement, that is the parameters during steady growth course, they must be all obtained from experiment. Here suppose that

$\delta_{2eff} = (0.3 \sim 0.4)\delta_c$.

It should point that for elastic-plastic materials, the calculating validity of the crack tip open displacement is restricted by different work stresses σ, their calculation expressing forms would be different for work stress under $\sigma < \sigma_s$ or $\sigma > \sigma_s$ condition. Such, calculations of the crack growth rate in equation (3), in addition to directly calculate from the experiment achieved data, and can also use the following varied calculation methods to calculate it.

2.1 Calculations for crack growth rate under work stress $\sigma < \sigma_s$ condition

According to the D-M' as discussed by [9] mathematical model to calculate the crack tip open disparagement δ_t, it can be adopted as following equation.

$$\delta_t = \left(\frac{8\sigma_s a_2}{\pi \cdot E} \ln \sec \frac{\pi \times \sigma}{2\sigma_s} \right) \tag{7}$$

Under $\delta_t -> \delta_c$, $K_1 -> K_{1c}$ condition, and the work stress $\sigma / \sigma_s << 1$ ($\sigma \le 0.5\sigma_s$), for the D-M' model is made by simplify treatment, it is

$$\delta_t = \beta \frac{y_2 K_2^2}{E \cdot \sigma_s} \tag{8}$$

Here y_2 is correction coefficient related to crack size and shape. The coefficient β is $\beta = 1$ under plane stress condition, and $\beta = (1 - \nu^2)/2$ under plane strain condition. ν is Poisson's ratio. If $\beta = 1$ and under cyclic loading, the crack tip open displacement can adopt three of kinds calculations methods as following forms.

(1) The calculations methods used by the stress intensity factor $K_2 (= K_I)$

For this method, the comprehensive material constant B_{2eff} and the crack tip open displacement $\Delta\delta_t$ range in the crack propagation rate equation da_2 / dN_2 are all to adopt the stress intensity factor to express. Here the crack tip open displacement range $\Delta\delta_t$ can be [9],

$$\Delta\delta_t = \frac{y_2 \Delta K_2^2}{2E \cdot \sigma_s} \tag{9}$$

$$\frac{da_2}{dN_2} = B_{2eff} \times v_{pv} \times \left(\frac{y_2 \Delta K_2^2}{2E \cdot \sigma_s} \right)^{\lambda_2}, (m/cycle), (\sigma_m = 0) \tag{10}$$

Here for $\sigma < \sigma_s$, and under the symmetrical cyclic loading ($R_\delta = \delta_{\min} / \delta_{\max} = -1$),

$$B_{2eff} = 2 \left(\frac{K^2{}_{eff}}{2E \cdot \sigma_s} \right)^{-\lambda_2} \times v_{pv} \tag{11}$$

But for $R_\sigma = \sigma_{\min} / \sigma_{\max} \neq -1$ (or $R_\delta = \delta_{\min} / \delta_{\max} \neq -1$), for $\beta = 1$, the parameters δ_m in equations (6) should be also changed as follow forms,

$$B_{2eff} = 2 \left\{ \frac{K^2{}_{eff}}{2E \cdot \sigma_s} \times \left(1 - \frac{K_{1\max}^2 + K_{1\min}^2}{2K_{1c}^2} \right) \right\}^{-\lambda_2} \times v_{pv} \tag{12}$$

$$K_{eff} \approx \sqrt{K_{th} K_{1c}} \quad \text{or} \quad K_{eff} \approx (0.25 \sim 0.55) K_{1c} \tag{13}$$

Where K_{eff} is an effective stress intensity factor, K_{th} is threshold stress intensity factor. $K_{1\max}$ and $K_{1\min}$ are respectively the Maximums and minimums value of stress intensity factor. E is a modulus of elasticity. In fact the (12) is consistent with (6).

(2) The calculation methods used by the stress σ

For this method, the comprehensive material constant B_{2eff} and the crack tip open displacement $\Delta\delta_t$ range in the crack propagation rate equation are all to use the stress to express. Here the crack tip open displacement δ_t and $\Delta\delta_t$ are as below [10]

$$\delta_t = \pi \sigma_s y_2 (\sigma / \sigma_s)^2 a_2 / E, (m) \tag{14}$$

Under cyclic loading, and for stress ratio $R_\delta = \delta_{\min} / \delta_{\max} = -1$, the crack tip open displacement

range is,

$$\Delta\delta_t = \frac{y_2 \Delta\sigma^2 \pi a_2}{4\sigma_s E}, (m) \tag{15}$$

Then equation of crack growth rate is

$$\frac{da_2}{dN_2} = B_{2eff} \times \left(\frac{y_2 \Delta\sigma^2 \pi a_2}{4\sigma_s E} \right)^{\lambda_2}, (m/cycle) \tag{16}$$

And for different stress ratio, the B_{2eff} are respectively,

$$B_{2eff} = 2\left[4(\pi\sigma_s(\sigma_{meff}/2\sigma_s)^2 a_{meff}/E)\right]^{\lambda_2} \times v_{pv}, (\sigma_m = 0) \tag{17}$$

$$B_{2eff} = 2\left\{4(\pi\sigma_s(\sigma_{meff}/2\sigma_s)^2 a_{meff}/E)\left(1 - \frac{a(\sigma_{\max}^2 + \sigma_{\min}^2)}{2a_{meff}\sigma_s^2}\right)\right\}^{-\lambda_2} \times v_{pv}, (\sigma_m \neq 0) \tag{18}$$

Where σ_{meff} is maximal effective stress, $\sigma_{meff} = (0.5 \sim 0.55)\sigma_s$. a_{meff} is a maximal effective crack size,

$$a_{meff} = \frac{K_{eff}^2}{\sigma_s^2 \pi} = \frac{(0.5 \sim 0.55)K_{1c}^2}{\sigma_s^2 \pi}, (m) \tag{19}$$

(3) Calculation method of combination of the stress and the stress intensity factor

For this method, the comprehensive material constant B_{2eff} in the crack propagation rate equation adopts the stress intensity factor to express, and the crack tip open displacement $\Delta\delta_t$ range adopts the stress to express. So their forms are as bellows

$$\frac{da_2}{dN_2} = 2\left(\frac{K^2{}_{eff}}{2E \cdot \sigma_s} \right)^{-\lambda_2} \times v_{pv} \times \left(\frac{y_2 \Delta\sigma^2 \pi a_2}{4\sigma_s E} \right)^{\lambda_2} (\sigma_m = 0) \tag{20}$$

$$\frac{da_2}{dN_2} = 2\left(2(K_{eff}/\sigma_s)^2 \times \frac{\sigma_s}{E}\left[1 - \frac{K_{2\max}^2 + K_{2\min}^2}{2 \cdot K^2{}_{1c}}\right] \right)_{eff}^{-\lambda_2} v_{pv} \times \left(\frac{y_2 \Delta\sigma^2 \pi a_2}{2\sigma_s E} \right)^{\lambda_2} (\sigma_m \neq 0) \tag{21}$$

It must point that the equations (10), (16), (20) and (21) can also only apply to work stress $\sigma/\sigma_s << 1$($\sigma \le 0.5\sigma_s$).

2.2 Calculations for crack growth rate under work stress $\sigma => \sigma_s$ condition

On the other hand, for work stress $\sigma => \sigma_s$ condition, it must be changed to use as following calculating equations. Here there are also two kinds of methods

(1) The calculation methods used by the stress σ

It also can directly use the stress σ to calculate the δ_t and $\Delta\delta_t$ [10]. Here the crack tip open displacement δ_t and $\Delta\delta_t$ are as bellows [10]

$$\delta_t = \frac{0.5\pi\sigma_s y_2(\sigma/\sigma_s + 1)a_2}{E} \quad (m) \tag{22}$$

$$\Delta\delta_t = \frac{\pi\sigma_s y_2(\Delta\sigma/2\sigma_s + 1)a_{02}}{E}, (m) \tag{23}$$

$$\frac{da_2}{dN_2} = B_{2eff} = \left(\frac{\pi\sigma_s y_2(\Delta\sigma/2\sigma_s + 1)a_2}{E}\right)^{\lambda_2}, (m/cycle) \tag{24}$$

$$B_{2eff} = 2\left\{2\left[(\pi\sigma_s(\sigma/\sigma_s + 1)a_{meff}/E\right]\right\}^{-\lambda_2} \times v_{pv} \ (\sigma_m = 0) \tag{25}$$

$$B_{2eff} = 2\left\{\left[2(\pi\sigma_s(\sigma/\sigma_s + 1)a_{meff}/E\right] \times \left(1 - \frac{a(\sigma_{\max}^2 + \sigma_{\min}^2)}{2a_{meff}\sigma_s^2}\right)\right\}^{-\lambda_2} \times v_{pv} \ (\sigma_m \neq 0) \tag{26}$$

$$a_{meff} = \frac{E\delta_{eff}}{\pi\sigma_s(\sigma/\sigma_s + 1)}, (m) \tag{27}$$

Where $\delta_{eff} = (0.3 \sim 0.35)\delta_c$.

(2) The calculation methods combined by stress and strain

Its method is that the comprehensive material constant B_{2eff} to adopt the δ_{eff} to express, and the crack tip open displacement to adopt the stress σ to express, its form as follow

$$\frac{da_2}{dN_2}=2\left(2\delta_{eff}(1-\frac{\delta_m}{\delta_c})\right)^{-\lambda_2}\times v_{pv}\left(\frac{y_2\pi\sigma_s(\Delta\sigma/2\sigma_s+1)a_2}{E}\right)^{\lambda_2},(\sigma_m\neq 0) \tag{28}$$

Here can take $\delta_m\approx 0$.

3. Calculation example

A pressure vessel is made with steel 16MnR, its strength limit of material $\sigma_b=573MPa$, yield limit $\sigma_s=361MPa$, modulus of elasticity $E=200000MPa$. Critical stress intensity factor $K_{2c}=K_{1c}=92.7\text{MPa}\sqrt{\text{m}}$. Suppose shape correcting coefficient of long crack $y_2=1.01$. Its local stress $\sigma_{\max}=450\,MPa$ at stress concentration point, $\sigma_{\min}=0$. Other computing data is all in table 1. Try to calculate the growth rate da_2/dN_2 at crack size $a_2=0.001m$ under $\sigma=450MP>\sigma_s=391\ \ MPa$ conditions.

Table 1. Calculation data

$K_{1c},MPa\sqrt{m}$	$K_{eff},MPa\sqrt{m}$	$K_{th},MPa\sqrt{m}$	v_{pv}	m_2	$\delta_{2\,fc},m$	λ_2	y_2	β
92.7	28.23	8.6	2×10^{-7}	3.91	0.00018	2.9	1.01	1

(1) Calculations for relevant parameters

1) According to table 1, take the virtual rate, $v_{pv}=2\times10^{-7}\,(\text{m/Cycle})$.

2) Take effective crack tip open displacement,

$\delta_{eff}=0.35\times\delta_c=0.35\times0.00018m=6.3\times10^{-5}(m)$; Take $\delta_m\approx 0$.

3) Calculation for effective crack size

$$a_{eff}=\frac{\delta_{eff}E}{\pi\sigma_s(\sigma/\sigma_s+1)}=4.94537\times10^{-3}(m)$$

4) According to (26), calculation for comprehensive material constant B_{2eff}

$$B_{2eff}=2\left[2\times(\pi\sigma_s(\sigma/\sigma_s+1)a_{eff}/E)\right]^{\lambda_2}\times v_{pv}$$
$$=2\left[2\times3.1416\times361(450/361+1)\times0.00494537/200000\right]^{2.9}\times2\times10^{-7}=84151(m^{\lambda_2}\cdot m/cycle)$$

The experiment value of Steel 16MnR, $B_2=84570$, and here its calculation value 84151, so that it is close to experimental data.

5) According to equation (23), computing for crack tip open displacement range $\Delta\delta_t$

$$\Delta\delta_t = \frac{y_2\pi\sigma_s(\Delta\sigma/2\sigma_s+1)a_2}{E} = \frac{1\times3.1416\times361(450/2\times361+1)0.001}{200000} = 9.204\times10^{-6},(m)$$

(2) Calculation for crack growth rate under $\sigma = 450MPa > \sigma_s$ condition.

According to equation (24), at $a_2 = 0.001m$, its crack growth rate is

$$\frac{da_2}{dN_2} = 2\left[2\times(\pi\sigma_s(\sigma/\sigma_s+1)a_{eff}/E)\right]^{\lambda_2}\times v_{pv}\left[\frac{\pi\sigma_s y_2(\Delta\sigma/2\sigma_s+1)a_2}{E}\right]^{\lambda_2}$$
$$= 2\left[2\times3.1416\times361(450/361+1)\times0.00494537/200000\right]^{2.9}\times2\times10^{-7}$$
$$\times\left[\frac{3.1416\times361(450/2\times361+1)0.001}{200000}\right]^{2.9} = 84151\times2.4869\times10^{-15} = 2.062\times10^{-10},(m/cycle)$$

4. Conclusions

(1) The correlating equation $\Delta\delta_t/2 = \delta_{fc}\times2N_{2fc}^{c'_2}$ between half-cycle of crack tip open displacement amplitude $\Delta\delta_t/2$ and life N_{2fc}, the correlating equation $\Delta\delta_t\times N_{2fc}^{-c_2} = B_2^{c_2}$ between one-cycle of crack tip open displacement range $\Delta\delta_t$ and life N_{2fc} and the correlating equation $da_2/dN_2 = B_2\Delta\delta_t^{\lambda_2}$ between one-cycle of crack tip open displacement range $\Delta\delta_t$ and crack growth rate da_2/dN_2, which the interrelations among three of kinds relation- expressions actually are consistent.

(2) The crack growth rate equations (10), (16), (20), (21), (24) and (28) of suitable for elastic-plastic steels are also consistent with the rate equation (3) in [3, 4]. But the material constant B_2 in latter (3) is obtained from experiment under constant stress ratio condition, so that only applying to corresponding loading. And the former, they can respectively do calculations for cracks growth rates of suitable for different stress ratio and loading conditions which they are only in combination with a small number of experiment data, Therefore they can expand the application ranges, and increase the calculating reliabilities and safeties.

(3) The comprehensive materials constants B_2 and B_{2eff} in crack growth rate equations are to have interdependent functional relationships with parameters δ_{eff}, λ_2, δ_m and v_{pv}. Its physical

meaning of the B_{2eff} is to give out effective value of energy in one cycle made specimens before to failure. Its geometrical meaning is a maximal micro-trapezia area to approximate to beeline.

(4) The crack growth rate equations (24) and (28) are generally suitable for under $\sigma => \sigma_s$; and the (10), (16), (20) and (21) can only applied to under $\sigma <= 0.5\sigma_s$. If the (10), (16), (20), (21) are applied to under $\sigma > 0.5\sigma_s$ and $\sigma < \sigma_s$, their calculation error are larger.

Acknowledgments

Author thanks sincerity the Zhejiang Province Natural Science fund Committee to support and provide subsidization of research funds. Numbers of supporting project is Y1111267.

References

[1] Yu Yangui, Tan Jianrong. The calculations in whole process of fatigue-damage-fracture for components. Advances in fracture research. ICF9, PERGAMON, Sydney, 1997, pp.1401–1409.

[2] Yu Yangui. The Correlation among Each Parameter in Some Equation on Crack Growth Stage, Advances in Fracture Research, ICF9, Sydney, Volume 3. PERGAMON. pp.1395-2002. 1997.

[3] W. D. Dover, Engineering Fracture Mechanics, Vol. 5, Nol. 5, (1973)11.

[4] B. B. Pokrovsky, B. Kaplunenko G. Influence of asymmetry cycle on the characteristics of the cyclic crack resistance for thermostable steels. Problems of strength. (1987), 11, 8–13.
(В. В. Покровский, В. Г. Каплуненко, Влияние асимметрии цикла на характеристики циклической трещиностойкости Теплоустойчивых сталей. Проблемы Прочности. (1987) 11. 8~13.)

[5] Yu Yangui, Sun Yiming, MaYanghui and XuFeng. The Computing of intersectant relations for its Strength Problem on Damage and Fracture to Materials with short and long crack. International Scholarly Research Network ISRN Mechanical EngineeringVolume 2011, Article ID 876396.

[6] Yangui Yu，The Calculations of Evolving Rates Realized with Two of Type Variables in Whole Process for Elastic-Plastic Materials Behaviors under Unsymmetrical Cycle. Mechanical Engineering Research; Vol. 2, No. 2; ISSN 1927-0607(print) E-ISSN 1927-0615(Online). Canadian Center of Science and Education (2012) 77-87.

[7] Yu Yangui, Bi Baoxiang, MaYanghau, Xu Feng. Damage Calculations in Whole Evolving Process Actualized for the Materials Behaviors of Structure with Cracks to Use Software Technique. 12^{th} International Conference on Fracture Proceeding. 2009, July 12-19, Ottawa, (CD, Author Index Y, Yangui).

[8] S. Ya. Yaliema. Correction about Paris's equation and cyclic intensity character of crack. J. Strength Problem. Vol, 147，(1981) 9:20–28. (In Russian).

[9] Dugdale, D. s. J. Mech Physiss Solids 8 (1960),100–104.

[10] GB/T 19624-2004, Safety assessment for in-service pressure vessels containing defects (2005), China. 2005; 24–26 (in Chinese).

Effect of corrosion pits on fatigue life and crack initiation

Xin-Yan Zhang [1], Shu-Xin Li [1,*], Rui Liang [1], R. Akid [2]

[1] School of PetroChemical Engineering Lanzhou University of Technology, Lanzhou 730050, China
[2] Corrosion & Protection Centre, School of Materials, University of Manchester, Manchester M13 9PL
* Corresponding author: li_shuxin@163.com

Abstract Corrosion fatigue is identified as one of the main failure mechanism for structures working in corrosive environment. The existing study on pit corrosion showed that cracks do not necessarily initiate from the bottom of the pit. Where the crack initiate from pit depends on the pit shape (aspect ratio), loading and the corrosive environment. In this study, firstly, the corrosion pit development in size and shape and its effect on fatigue life were reviewed. Fatigue tests were conducted on pre-pitted and smooth samples to further investigate the pit effect. Then various aspect ratios of pits were modeled to calculate the SCF in a round bar under tension and bending loadings.In addition, the SCF of a wide range of aspect ratios of pits were calculated, by which it is expected to offer the engineering practice and researchers convenience to find SCF value.

Keywords Corrosion pits 1; Aspect ratio 2; Stress concentration factor 3; Fatigue life 4

1. Introduction

Pitting corrosion is considered to be one of the principal degradation mechanisms for many metallic materials subjected to corrosive environment. The fatigue life was shortened due to formation of corrosion pits on surface of the material causing the initial damage and then cracks initiated from these pits. Pit development and its effect on corrosion fatigue crack growth have been extensively studied, but there is little consensus with regard to the exact relationship between the pit size and the time due to the interaction of environment and loading and the dependence on microstructural state and stress level.

The main purpose of the present paper is to provide a review of the pit formation and its effect on fatigue lives, attempting to develop a generalized understanding of how the pits develop. Then fatigue tests were conducted on pre-pitted and smooth samples to further investigate the pit effect. Finally, various aspect ratios of pits were modeled to calculate the SCF in a round bar under tension and bending loadings.

2. Corrosion pit development

2.1 Pit size development

Corrosion pit size varies as exposure time in solution increases and depends on electrochemical and mechanical conditions. Many researchers have conducted extensive studies on pit development and various relationships between and pit size and time were proposed. Sriraman et al [1] developed a model that considers the coexistence of corrosive environment and fatigue loading conditions and took into account the influence of cyclic stresses in the pitting corrosion process. Boag et al [2] observed stable pit formation on AA2024-T3 in a NaCl environment, and indicated that local clustering played an important role in pit initiation. Ryuichiro Ebara [3] emphasizes initiation and growth of corrosion pits in the corrosion fatigue crack initiation process. The pit size distribution

data in [4] suggests that the depth of the pits in alloys such as 7075-T6 increases by the interconnection of the pits that have nucleated at constituent particles at various depths through the thickness of the exposed alloy. Rybalka's study [5, 6] on pitting development on Stainless Steel 403 Steel and 20Kh13 showed that the size of pit is affected by the PH and temperature of the solution and the electrode rotation. Additionally, the depth of growing pits as a function of time can be described by the equation $h = 2.25+3.39t^{1/2}$. While the depth h of growing pits on 20Kh13 steel in 0.01 M NaCl solution at ΔE= 30 mV increases with the time as $h \sim t^{1/2}$, and an average pit diameter d obeys the relationship $d = d_0(1-e^{-0.07t})$. P. Ernst [7, 8] proposed that the pit width increases almost linearly with time, and the pit growth in depth follows a parabolic law with time ($\propto \sqrt{t}$) and is independent of the potential, whereas lateral pit growth is linear with time and dependent upon potential. Harlow and Wei [9] assumed that the pit maintained hemispherical geometry and grew at a volumetric rate determined by Faraday's law, and the aspect ratio is a continuous function of time. The relationship between the depth (a) and the diameter ($2c$) of pits was studied by Kondo [10] and showed that the pit growth occurred at the same aspect ratio $a/c \approx 0.7$. The corrosion pit growth law can be formulated as $2c \propto t^{1/3}$. Cavanaugh [11] used optical profilometry and Weibull functions to characterize pit depth and diameter distributions and found pit growth kinetics varied by environment, but most followed approximately $t^{1/3}$ kinetics. Sriraman [12] proposed the depth a_p is considered proportional to the cube root of t through the relationship of $a_p = Bt^{1/3}$. Buxton [13] described the pit growth law following a typical power law curve ($x = Bt^{\beta}$) with a relatively large exponent value of 0.596. Turnbull [14] also assumed that the depth can be described by $x = \alpha t^{\beta}$, and examples of the results [15] for three environmental exposure conditions in terms of the variation of aspect ratio with pit depth are illustrated.

As illustrated above that various relationship was developed for pit depth and width. But the literature mostly suggests that the pit width follows a linear relationship with time shown in Fig. 1 (left) and the pit depth is linearly proportional to the square root of time in Fig. 1 (right).

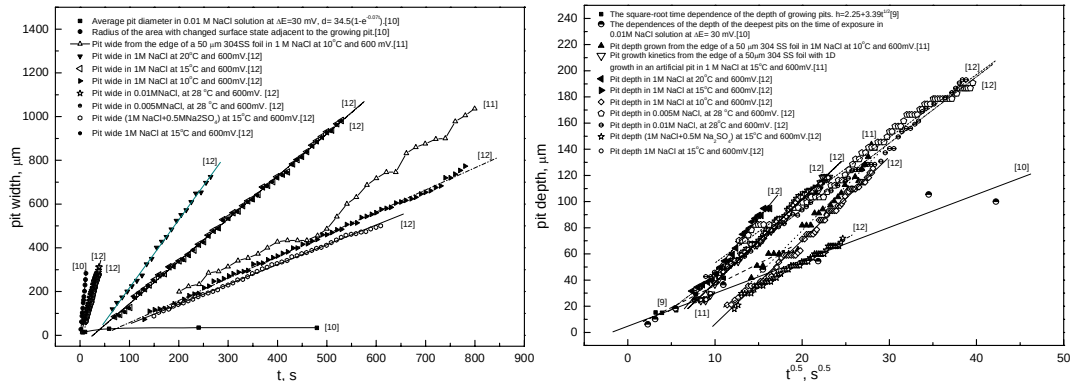

Fig. 1. Corrosion pit width vs t and depth vs $t^{0.5}$.

2.2 Pit shape development

Pidaparti et al [16] noted that the pit/defect profile changing its shape (both depth and width) from slightly conical to more hemispherical shape with increasing corrosion time and stress distribution and levels vary non-linearly around a single pit/defect. Melchers [17] proposed that the sequence consists of the development of anodic areas, development of small pits and shallow broad pits, the apparent coalescence of small pits into larger localized corrosion and eventually the appearance of

stepped or benched, perhaps irregular shaped broad or macro-pits. Ernst [7, 8] carried out a semi-quantitative model to explain lacy pit cover formation and pit growth, representing the shape of a pit and pits within pits grown from the edge of a 50 μm 304 SS foil in 1 M NaCl at 15℃ and 600 mV. An SEM microfractograph of a typical nucleating corrosion pit on the fracture surface of a specimen that had been precorroded for 384 h was given by Dolley [18]. And elliptical pits developed from the artificial pit were given in [19].

3. Effect of the corrosion pit on fatigue lives (crack initiation)

3.1 Effect of the corrosion pit on crack initiation and propagation.

Corrosion pits acted as pre-existing flaws in the material to nucleate fatigue cracks. Burstein [20] and Li Lei [21] indicated that the evolution of corrosion pit followed three stages: nucleation, metastable growth and stable growth. The pit size observed on the fracture surface is considered to give the critical pit size that depends on the cyclic stress amplitude at which the transition occurred [10]. A comprehensive seven-stage model is developed in [22, 23] for pitting corrosion fatigue damage process, including pitting nucleation, pit growth, transition from pit growth to short crack, short crack growth, transition from short crack to long crack, long crack growth, and fracture. Bastidas-Arteaga [24] assessed the total corrosion-fatigue life as the sum of three critical stages: corrosion initiation and pit nucleation; pit-to-crack transition, and crack growth. Turnbull [14, 15] noted that fundamental steps in the overall process of crack development include pit initiation, pit growth, the transition from a pit to a crack, short crack growth and long crack growth, and suggested that cracks do not necessarily initiate from the bottom of the pits, for the reason that there were many cracks with a depth smaller than that of the corresponding pit. While Ebara [25] found that the crack initiated at the bottom of corrosion pit where stress concentration is large and is presumably electrochemically active, and indicated that corrosion fatigue cracks essentially nucleated and grew from one or two large pits at the circular hole surface near the area of maximal stresses [26]. It is indicated that the largest pits did not nucleate cracks, which is due to the result of a combination of the ‘bluntness’ of the larger pits, and they were not located at the root of the notch, where the stress concentration is highest [27]. As regards to the SUS 630 specimen, the fracture surface showed that the fatigue crack propagation displayed high non-linear in route [28].

The initiation and growth of corrosion pit, crack initiation from corrosion pit and the crack propagation appearance can be vividly identified in [25]. Based on the modeling results of Bastidas-Arteaga [24], G. S. Chen [26] and Medved [27], two criteria are proposed to describe the transition from pit growth to fatigue crack growth: (1) the stress intensity factor of the equivalent surface crack has to reach the threshold stress intensity factor, ΔK_{th}, for fatigue crack growth, assuming that a corrosion pit may be modeled by an equivalent semi-elliptical surface crack; (2) the time-based corrosion fatigue crack growth rate also exceeds the pit growth rate.

The results of Sriraman and Pidaparti [1, 12] indicated crack initiation from pit sites can be extremely fast at high stress levels and can occur even from relatively small pits. And Kondo [10] pointed that at higher stress levels, transition occurred at fairly small pit sizes. On the other hand, at lower stress levels, transition occurred at larger pits. Medved [27] arrived at the conclusion that pits were deeper than wide with aspect ratios up to 4, many of which nucleated fatigue cracks were not

singular pits, but rather comprised of multiple needlelike pits. The observed synergistic effects of environmental, material and loading parameters on the environmental acceleration of fatigue crack growth in low-alloy RPV steels are discussed in [29]. Sivaprasad [30] noted the mechanism of corrosion fatigue crack growth for the two HSLA steels changes with attendant change in the Paris slope, and temperature, water flow speed, ionic concentration, material quality, and load condition play a crucial role in the behavior of fatigue crack propagation of SUS 630 [28]. Bjerkén [31] examined the manners in which the cracks grow and coalesce on the surface and showed that the cracks avoid each other initially and coalesce crack tip to crack side.

3.2 Stress intensity factor/ stress concentration factor around corrosion pits

Ramsamooj [32] suggested the parameters needed to predict corrosion fatigue might be the crack velocity caused by stress-corrosion, the applied mechanical stress, frequency, and the threshold stress intensity factor. Cerit and Genel [33] investigated the stress distribution at the semi-elliptical corrosion pits and pointed out that the aspect ratio is the main parameter affecting the stress concentration factor (SCF). The initiation and propagation of the non-propagating crack at the bottom of the artificial corrosion pit, were explained with the stress concentration factor of the pits and the stress intensity factor (SIF) range of the crack tip in [34]. Sankaran et al [4] concluded that the effects of pitting corrosion on fatigue lives can be related to the effects of equivalent stress concentration factors that are routinely used in structural design. Eduardo R. de los Rios [35] proposed an equation to evaluate the stress concentration as a function of distance from the pit center. Carpinteri et al [36-38] calculated the SIF of elliptical-arc surface cracks and the maximum stress-intensity factor is obtained at the deepest point on the crack front. W. Guo [39] showed that the SIF is strongly dependent on SCF, and the influence of notch geometry is negligibly weak for a given stress concentration coefficients. Toribio's [40] review on SIF for surface cracks in round bars under tension loading indicated that SIF increases with the crack depth and decreases with the crack aspect ratio and changes continuously from the crack center to the crack surface.

3.3 Effect of the corrosion pit on fatigue life

The influence of the pitting was on initiation and very early growth stages of fatigue. Further reductions in fatigue lives were associated with increases in pit size. And corrosion fatigue lives were reduced by 40-50% from those of pristine samples [27]. Y. Kondo [10] proposed a residual life prediction method for fatigue crack initiation for the case where crack initiation is controlled by pitting. P. Shi [22] studied on the damage tolerance approach for probabilistic pitting corrosion fatigue life prediction and found that pit nucleation time and the material constant for short crack growth are the two most important random variables affecting corrosion fatigue life. Emilio Bastidas-Arteaga [24] developed a model to predict the corrosion fatigue lifetime. The results showed that the coupled effect of corrosion-fatigue on structures strongly affects its performance, leading to large reduction in the expected lifetime.

Together with the rotating bending fatigue tests with various loads on shaft specimens in various extent of pitting corrosion conditions and the fatigue fracture surface analyses, the fatigue lifetime of SUS 630 shaft under various extent of pitting corrosion condition is found to be in a range of

only 2.5-27% of that of the uncorroded condition [28]. Sriraman [12] presents a simple integrated deterministic model for life prediction in a high-strength aluminum alloy subject to pitting corrosion under cyclic stresses. The overall corrosion-fatigue life is the sum of crack initiation and propagation. At higher stress levels, there is not enough time for pits to develop and hence failure is not associated with stress concentration at the base of a pit, whereas life prediction at low stress amplitude is possible using only pit growth times [13]. Dolley [18] interpreted the reduction in fatigue life depending upon the pre-corrosion time and in turn the initial pit size. Rokhlin [19] established an empirical relation to predict fatigue life $N = N_{th}(d/h)^{-3/4}$. Yongming Liu [41] predicted the probabilistic fatigue life by using an equivalent initial flaw size (EIFS) distribution, which is independent of applied load level and only uses fatigue limit and fatigue crack threshold stress intensity factor. A method for estimation of the cumulative distribution function (CDF) for the lifetime is demonstrated to predict the lifetime, reliability, and durability beyond the range of typical data by integrating the CDFs of the individual RVs into a mechanistically based model [42].

4. Corrosion fatigue testing

To further illustrate the effect of corrosion pit on fatigue life, the test on pre-pitted in air and in corrosion solution of 3.5% NaCl were conducted. Fig.2 shows the *S-N* data for air and corrosion fatigue tests. It can be seen that the air fatigue P1200 samples have the longest fatigue lifetimes. The stress concentration factor of the pre-pitted samples, with a pit aspect ratio of 0.11, is around 1.5 [33]. This geometry of defect significantly reduces the fatigue life by over 60%. At 298 MPa, the air fatigue life of the pre-pitted sample is only 16% of that of the P1200 samples, while the corrosion fatigue lives are further reduced. The corrosion fatigue strength reduced from 279 MPa (in air) to 126 MPa (in 3.5 % NaCl) at 10^7 cycles. A previous study by Masaki et al [34] showed that the fatigue strength of pitted specimens for 316NG at 10^8 cycles is approximately half that of unpitted specimens, where the SCF of the pre-pit was assumed to be approximately 2, almost equivalent to the fatigue strength reduction factor. However, the present study shows that the fatigue strength reduction factor is much greater than the stress concentration factor.

The corrosion pits have smaller stress concentration factor than the pre-pit due to their smaller depth [33], implying that pre-pitted samples having longer fatigue lives than initially-smooth samples that develop pits within a corrosive solution. Furthermore, the smooth samples in 3.5%NaCl have shorter fatigue lives than the pre-pitted samples in air, indicating that electrochemical effects, i.e., localized corrosion, has a greater effect on fatigue life than mechanical effects, especially as stress levels fall below the in-air fatigue limit.

5. Modeling of corrosion pit development

As literatures stated above that the corrosion pits can be simplified as semi-elliptical pits. Cracks originates from pits where the SCF is the biggest. To calculate the SCF around pits, a 3-D model is developed on a round bar under uniaxial tension and bending loading by using FEM. The 3-D model has various pit diameter ($2c$) and depth (a) ranging from 80 to 1000 μm. A total of 82878 finite elements and 118406 nodes are employed.

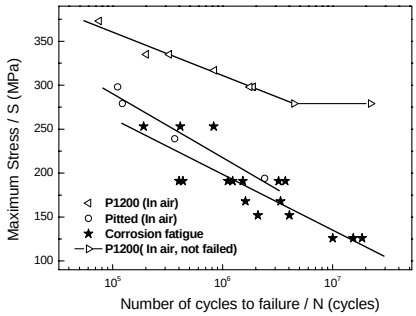

Fig. 2. S-N data for air and artificial seawater environments.

Figs. 3 show the maximum stress within the pit. The maximum stress is not always at the bottom of corrosion pit and it moves to the mouth with the aspect ratio *a/2c* increasing. The maximum stress occurs at the bottom when *a/2c* is less than 1/7 under tension loading and *a/2c* less than 1/10 under bending loading.

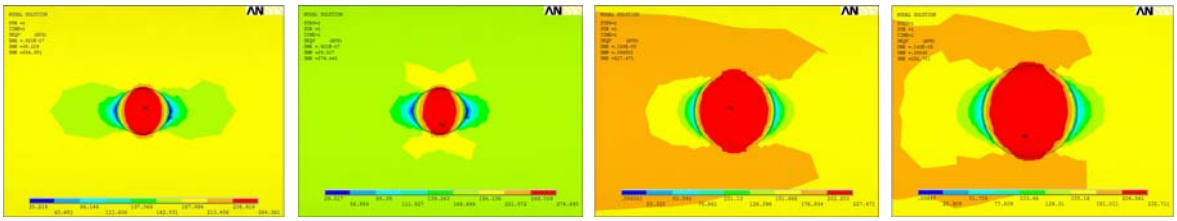

(a) *a/2c* =1/7 (b) *a/2c* =1/6 (c) *a/2c* =1/10 (d) *a/2c* =1/9

Fig. 3.The maximum stress distribution at various aspect ratios under tension (a), (b) and bending (c), (d).

Cracks initiate from the point where the stress concentration is highest. Then the corrosion pit transfers to crack when the stress intensity factor for the equivalent surface crack growth for the pit reaches the threshold stress intensity factor for the fatigue crack growth, and the corrosion fatigue crack growth rate exceeds the pit growth rate.

The SCF is largely influenced by the aspect ratio (*a/2c*) and the type of loading mode, as shown in Fig.4. The SCF increases greatly with increasing aspect ratio when *a/2c* is less than 1, and slow down when *a/2c* is between 1-2. It remains unchanged as *a/2c* is greater than 2. The tension loading produces bigger SCF than the bending. Also compared is the depth effect and width effect, illustrated in Fig. 5. The pit depth has much bigger effect than the pit width.

6. Conclusion

The corrosion pit size and shape development and its effect on crack initiation and fatigue life were reviewed. It suggested the following:

1) Various relationships were developed for corrosion pit depth and pit width. But the literatures mostly suggest that the pit width follows a linear relationship with time and the pit depth is linearly proportional to the square root of time.

2) The higher the stress amplitude the more corrosion pits formed. Compared to artificially-induced pits, real corrosion pits have a smaller stress concentration factor, but lead to shorter fatigue lifetimes.

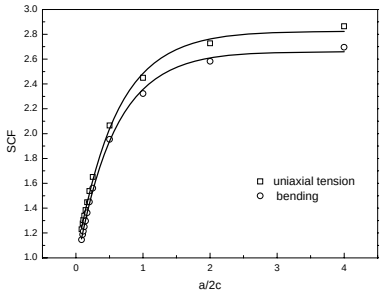

Fig. 4 SCF variation with *a/2c* Figure.

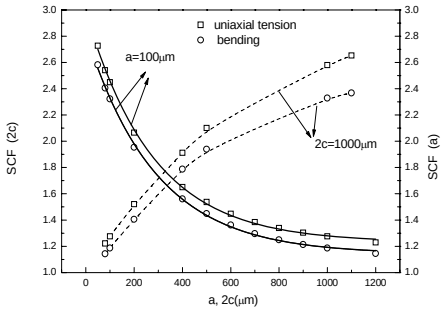

Fig.5 SCF variation with *2c* and *a*

3) Cracks do not necessarily originate from the bottom of the pit. Rather, it starts from the point which has the biggest SCF. The aspect ratio affects the SCF greatly when *a/2c* is less than 1 but almost has no effect when *a/2c* is greater than 2. The pit depth has much bigger effect on SCF than the pit width does.

Acknowledgements

The authors would like to thank National Science Foundation of China (No. 51275225) for financial support and PHD foundation of Lanzhou University of Technology (SB05200801) for which due acknowledgement is given.

References

[1] Sriraman M R, Pidaparti R M, Crack initiation life of materials under combined pitting corrosion and cyclic loading. J. Mater. Eng. Performance, 19 (2010) 7-12.

[2] Boag A, Taylor R J, Muster T H, Goodman N, McCulloch D, Ryan C, Rout B, Jamieson D, Hughes A E, Stable pit formation on AA2024-T3 in a NaCl environment. Corro. Sci., 52 (2010) 90-103.

[3] Ebara R, Corrosion fatigue crack initiation in 12% chromium stainless steel. Mater. Sci. Eng. A, 468 – 470 (2007) 109-113.

[4] Sankaran K K, Perez R, Jata K V, Effects of pitting corrosion on the fatigue behavior of aluminum alloy 7075-T6: modeling and experimental studies. Mater. Sci. Eng.: A, 297 (2001) 223-229.

[5] Rybalka K V, Shaldaev V S, Beketaeva L A, Malofeeva A N, Development of pitting corrosion of stainless steel 403 in sodium chloride solutions. Russian J. Electrochem., 46 (2010) 196-204.

[6] Rybalka K V, Beketaeva L A, Shaldaev V S, Kasparova L V, Davydov A D, Development of pitting corrosion on 20Kh13 steel. Russian J. Electrochem., 45 (2009) 1217-1225.

[7] Ernst P, Newman R C, Pit growth studies in stainless steel foils. I. Introduction and pit growth kinetics. Corro. Sci., 44 (2002) 927-941.

[8] Ernst P, Newman R C, Pit growth studies in stainless steel foils. II. Effect of temperature, chloride concentration and sulphate addition. Corro. Sci., 44 (2002) 943-954.

[9] Harlow D G, Wei R P, A probability model for the growth of corrosion pits in aluminum alloys induced by constituent particles. Eng. Fract. Mechan., 59 (1998) 305-325.

[10] Kondo Y, Prediction of fatigue crack initiation life based on pit growth. Int. J. Fat., 11 (1989) 280.

[11] Cavanaugh M K, Buchheit R G, Birbilis N, Modeling the environmental dependence of pit growth using neural network approaches. Corro. Sci., 52 (2010) 3070-3077.
[12] Sriraman M R, Pidaparti R M, Life Prediction of Aircraft Aluminum Alloys Subjected to Pitting Corrosion Damage Under Cyclic Stresses. J. AIRCRAFT, 46 (2009) 1253-1259.
[13] Buxton D C, Cottis R A, Scarf P A, McIntyre P, Life prediction in corrosion fatigue, in: Proc. Int. Conf. Corrosion-Deformation Interaction, Fontainebleau, France, 1992, pp. 901-913.
[14] Turnbull A, McCartney L N, Zhou S, A model to predict the evolution of pitting corrosion and the pit-to-crack transition incorporating statistically distributed input parameters. Corro. Sci., 48 (2006) 2084-2105.
[15] Turnbull A, Zhou S, Pit to crack transition in stress corrosion cracking of a steam turbine disc steel. Corro. Sci., 46 (2004) 1239-1264.
[16] Pidaparti R M, Patel R K, Investigation of a single pit/defect evolution during the corrosion process. Corro. Sci., 52 (2010) 3150-3153.
[17] Jeffrey R, Melchers R E, The changing topography of corroding mild steel surfaces in seawater. Corro. Sci., 49 (2007) 2270-2288.
[18] Dolley E J, Lee B, Wei R P, The effect of pitting corrosion on fatigue life. Fat. Fract. Eng. Mater. Struct., 23 (2000) 555-560.
[19] Rokhlin S I, Kim J Y, Nagy H, Zoofan B, Effect of pitting corrosion on fatigue crack initiation and fatigue life. Eng. Fract. Mechan., 62 (1999) 425-444.
[20] Burstein G T, Pistorius P C, Mattin S P, The nucleation and growth of corrosion pits on stainless steel. Corro. Sci., 35 (1993) 57-62.
[21] Li L, Li X, Dong C, Huang Y, Computational simulation of metastable pitting of stainless steel. Electrochimica Acta, 54 (2009) 6389-6395.
[22] Shi P, Mahadevan S, Damage tolerance approach for probabilistic pitting corrosion fatigue life prediction. Eng. Fract. Mechan., 68 (2001) 1493-1507.
[23] Shi P, Mahadevan S, Corrosion fatigue and multiple site damage reliability analysis. Int. J. Fat., 25 (2003) 457-469.
[24] Bastidas-Arteaga E, Bressolette P, Chateauneuf A, Sánchez-Silva M, Probabilistic lifetime assessment of RC structures under coupled corrosion – fatigue deterioration processes. Struct. Safety, 31 (2009) 84-96.
[25] Ebara R, Corrosion fatigue crack initiation behavior of stainless steels. Procedia Eng., 2 (2010) 1297-1306.
[26] Chen G S, Wan K C, Gao M, Wei R P, Flournoy T H, Transition from pitting to fatigue crack growth-modeling of corrosion fatigue crack nucleation in a 2024-T3 aluminum alloy. Mater. Sci. Eng.: A, 219 (1996) 126-132.
[27] Medved J J, Breton M, Irving P E, Corrosion pit size distributions and fatigue lives—a study of the EIFS technique for fatigue design in the presence of corrosion. Int. J. Fat., 26 (2004) 71-80.
[28] Ma F Y, Wang W H, Fatigue crack propagation estimation of SUS 630 shaft based on fracture surface analysis under pitting corrosion condition. Mater. Sci. Eng.: A, 430 (2006) 1-8.
[29] Seifert H P, Ritter S, Corrosion fatigue crack growth behaviour of low-alloy reactor pressure vessel steels under boiling water reactor conditions. Corro. Sci., 50 (2008) 1884-1899.
[30] Sivaprasad S, Tarafder S, Ranganath V R, Tarafder M, Ray K K, Corrosion fatigue crack growth behaviour of naval steels. Corro. Sci., 48 (2006) 1996-2013.

[31] Hejman U, Bjerk E N C, Environmentally assisted initiation and growth of multiple surface cracks. Int. J. Solids and Structures, 47 (2010) 1838-1846.
[32] Ramsamooj D V, Shugar T A, Modeling of corrosion fatigue in metals in an aggressive environment. Int. J. Fat., 23, Supplement 1 (2001) 301-309.
[33] Cerit M, Genel K, Eksi S, Numerical investigation on stress concentration of corrosion pit. Eng. Failure Analysis, 16 (2009) 2467-2472.
[34] Masaki K, Ochi Y, Matsumura T, Small crack property of austenitic stainless steel with artificial corrosion pit in long life regime of fatigue. Int. J. Fat., 28 (2006) 1603-1610.
[35] de Los Rios E R, Mechanisms and Modelling of Cracking under Corrosion and Fretting Fatigue Conditions. Shot Peening, 241-254.
[36] Carpinteri A, Elliptical-arc surface cracks in round bars. Fat. Fract. Eng. Mater. Structu., 15 (1992) 1141-1153.
[37] Carpinteri A, Vantadori S, Surface cracks in round bars under cyclic tension or bending. Key Eng. Mater., 378-379 (2008) 341-354.
[38] Carpinteri A, Brighenti R, Vantadori S, Surface cracks in notched round bars under cyclic tension and bending. Int. J. Fat., 28 (2006) 251-260.
[39] Guo W, Shen H, Li H, Stress intensity factors for elliptical surface cracks in round bars with different stress concentration coefficient. Int. J. Fat., 25 (2003) 733-741.
[40] Toribio J, Alvarez N, Gonzalez B, Matos J C, A critical review of stress intensity factor solutions for surface cracks in round bars subjected to tension loading. Eng. Failure Analysis, 16 (2009) 794-809.
[41] Liu Y, Mahadevan S, Probabilistic fatigue life prediction using an equivalent initial flaw size distribution. Int. J. Fat., 31 (2009) 476-487.
[42] Harlow D G, Wei R P, Probability approach for prediction of corrosion and corrosion fatigue life. AIAA j., 32 (1994).

Using Triaxiality Dependent Cohesive Zone Model in Low Cycle Fatigue

Xuan Cao[1,*], Michael Vormwald[1]

[1] Material Mechanics Group, Technische Universität Darmstadt, 64287 Darmstadt, Germany
* Corresponding author: cao@wm.tu-darmstadt.de

Abstract: Cohesive zone models (CZM) are widely used for material fracture analysis. In monotonic loading process, the cohesive parameters are remarkably dependent on the specimens' triaxiality conditions. A cyclic CZM is now introduced for crack initiation life and fatigue crack growth analysis. These two types of fatigue phenomena - crack initiation and fatigue crack growth - are to be described by the cyclic CZM with a unique set of parameters. Fatigue crack initiation is usually investigated using smooth specimen and fatigue crack growth is measured using compact tension specimen. The triaxiality condition in the CZM of these two standard specimens is strongly different. Realistic modelling of the phenomena therefore requires taking the triaxiality into account in the damage evolution law of the cyclic CZM. As a consequence in this paper a cyclic CZM combined with triaxiality dependent characteristic is proposed. This new model can be applied for specimens with different triaxiality conditions. The computation results including crack initiation life and fatigue crack growth simulation are compared with experimental data. In the very low cycle fatigue regime, a reasonable accordance of experimental and calculated results is achieved.

Keywords: Cohesive zone model, Triaxiality dependence, Low cycle fatigue, Damage evolution

1. Introduction

In actual engineering, fracture of the materials and structures is a very dangerous failure form and usually causes serious consequence. Thus, research on mechanisms of material fracture, controlling and reducing occurrence of fracture accidents are always important issues. Fracture mechanics provides the theoretical basis and application approaches for material fracture research. But sometimes the modelling expenses are very high for fracture mechanics concepts and other ideas should be introduced. Among all these methods, the cohesive zone model is very attractive for researchers.

Cohesive zone model (CZM) is an interface damage model, it simplifies the fracture process zone into a narrow cohesive strip. Originally, the concept of CZM has been proposed by Dugdale [1] and Barenblatt [2]. In 1976, the CZM was firstly used by Hillerborg [3] in finite element calculation for concrete material. From then on, the CZM was applied widely as a numerical simulation model for material fracture. In the last 30 years, the CZM was developed by many investigators and scientific groups [4-10]. Now, it becomes a universal tool for material fracture analysis. Especially for material fracture under monotonic loading, the applications of the CZM are successful.

However, using the CZM in material fatigue fracture is still at a starting stage. In the late 1990's, the CZM was firstly extended by De-Andrés et al. [11] for fatigue crack growth simulation. A damage parameter was introduced to indicate the irreversible damage process. But in this model no description about the damage evolution is supplied. Soon afterwards, Yang et al. [12] developed a damage locus in the CZM to simulate fatigue crack growth. However, in this model the unloading and reloading stiffness have different definitions and the damage evolution is just dependent on the damage locus, these treatments are not convenient and accurate for application. Then the cyclic CZM proposed by Roe and Siegmund [13] explicitly introduced a damage variable and a damage evolution equation. The stiffness and traction of the cohesive zone degraded with the damage variable. The numerical calculation results of this model can reproduce many basic characteristics which are similar to the experimental phenomena in fatigue fracture. Nevertheless, there is no experimental verification for the damage evolution process and the other important factors for CZM

are not considered, such as surrounding continuum element influence, element friction influence and constraint condition influence. Base on Roe and Siegmund's method, some authors did further research work [14-16].

2. Cohesive zone model

2.1. Fundamentals

The CZM intends to describe the real physical fracture process by phenomenological equations. It treats the material separation in the fracture process zone as material damage. Separation is the displacement jump occurring in the cohesive element. In the CZM, the material separation behaviour is described within a constitutive equation relating the cohesive traction T to the material separation δ, called traction separation law (TSL). The TSL represents the material deterioration occurring in the damage zone under the monotonic loading condition. For the shape of the TSL many proposals have been given, but no one can easily decide which is right or wrong. For all TSLs, two parameters are contained: maximum traction T_0 and critical separation δ_0. The area under the TSL represents the cohesive energy Γ_0. If the shape of the TSL is selected, the cohesive parameters should be determined from the correlative experiment. In this paper, the TSL from Scheider et al. is taken as a basis (Equation (1) and Figure 1). More details on application of this CZM can be taken from references [8-9].

$$T(\delta)=T_0 f(\delta)=T_0\begin{cases}2\left(\dfrac{\delta}{\delta_1}\right)-\left(\dfrac{\delta}{\delta_1}\right)^2 & \delta<\delta_1\\ 1 & \delta_1\le\delta\le\delta_2\\ 2\left(\dfrac{\delta-\delta_2}{\delta_0-\delta_2}\right)^3-3\left(\dfrac{\delta-\delta_2}{\delta_0-\delta_2}\right)^2+1 & \delta_2<\delta\le\delta_0\end{cases} \tag{1}$$

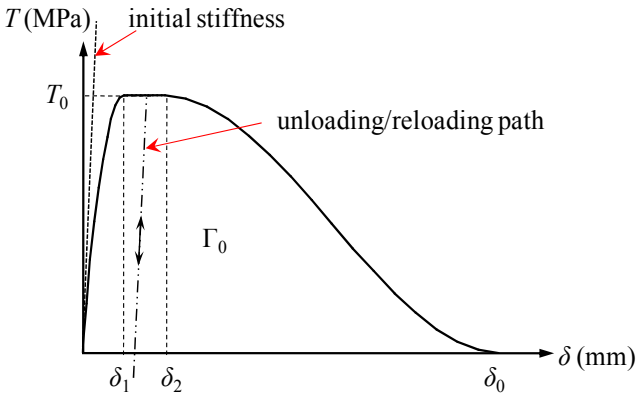

Figure 1. Traction separation law according to Scheider et al. [8], given by Equation (1)

2.2. Triaxiality dependent behaviour

When the phenomenological TSL is applied for ductile fracture analysis, it is possible to find a fundamental relationship between this TSL and micromechanics. A micromechanical model - GTN model [17] is used to simulate a biaxial tension test for one volume element, a cohesion-decohesion curve can be obtained. Such cohesion-decohesion curve is considered as the micromechanical TSL and can be used to fit the phenomenological TSL. For this micromechanical traction separation curve, some investigators found that it was strongly dependent on the triaxiality condition of the

element. Here, the triaxiality value means the ratio between the hydrostatic stress and the von Mises equivalent stress, see Equation (2).

$$H = \frac{\sigma_h}{\sigma_{Mises}} \tag{2}$$

H is the triaxiality value for unit volume element. σ_h is the hydrostatic stress in the element. σ_{Mises} is the von Mises equivalent stress in the element.

The conclusions for triaxiality dependent behavior can be summarized as: the cohesive parameters are not pure material constants but dependent on the triaxiality conditions. With increasing the triaxiality value, the material maximum traction T_0 becomes bigger but the material critical separation δ_0 and cohesive energy Γ_0 become smaller. Details about this investigation can be consulted in references [18-20]. When the triaxiality dependent behaviour is implemented into the CZM, the triaxiality value can only be obtained from the surrounding continuum element and has to be transferred to the cohesive element.

3. Extended CZM for fatigue fracture

3.1. Overview

The ordinary TSLs just describe the material fracture failure under monotonic loading condition. For material fatigue fracture properties, other approaches need to be introduced. By reviewing some ideas from pioneers, a tentative method of Roe and Siegmund [13] is chosen as starting point. Considering the theory of continuum damage mechanics, a damage variable and a corresponding damage evolution law are introduced in the CZM following ideas of Scheider [8]. This cyclic CZM is used for fatigue fracture analysis.

In respect to the fatigue fracture process, the important research topics focus on fatigue crack initiation life and fatigue crack growth rates analysis. In experimental investigation, fatigue crack initiation is usually tested using uncracked smooth specimen and fatigue crack growth is measured using pre-cracked specimen. The triaxiality conditions for these two standard specimens are totally different. When the CZM is applied for simulation of these two fatigue phenomena, it is necessary to take the triaxiality influence into account in the damage process.

So, a triaxiality dependent cyclic CZM is now proposed. The model should be implemented to reproduce fatigue experimental phenomena which contain fatigue crack initiation and fatigue crack growth, just using a unique set of parameters. For simplicity, in this paper just mode-I fracture is considered. This means in the CZM just normal separation contributes to the damage.

3.2. Fatigue damage process

With the damage variable D, the cohesive strength and normal stiffness of the cohesive element will degrade (Equation (3) and Equation (4)).

$$T_0^N = \left[T_{0\,(H)}^N \right] (1 - D) \tag{3}$$

$$k_N = k_N (1 - D) = \frac{2T_0^N}{\delta_1} \tag{4}$$

T_0^N and $\overline{T}_0^N$ are the initial and current normal cohesive strength, the subscript (*H*) represents that the initial cohesive strength is dependent on the triaxiality condition. k_N and $\overline{k}_N^0$ are the initial and current normal stiffness of the cohesive element. δ_1 is a parameter relating to the critical separation δ_0, the meaning is the same as in Equation (1).

For the triaxiality dependent cyclic CZM, it is difficult to judge the loading and unloading conditions because the separation δ and the critical separation δ_0 of the cohesive element alter simultaneously. So, a relative normal separation and its increment are defined by Equation (5) and Equation (6):

$$\delta_{re}^N = \frac{\delta^N}{\delta_{0\,(H)}^N} \tag{5}$$

$$\Delta\delta_{re}^N = \frac{\delta_t^N}{\delta_{0\,(H_t)}^N} - \frac{\delta_{t-\Delta t}^N}{\delta_{0\,(H_{t-\Delta t})}^N} = \delta_{re\,(t)}^N - \delta_{re\,(t-\Delta t)}^N \tag{6}$$

δ_{re}^N and δ^N are the relative and absolute normal separation, respectively. δ_0^N is the critical normal separation, the subscript (*H*) represents that it is dependent on the triaxiality condition. $\Delta\delta_{re}^N$ is the relative normal separation increment. The subscripts *t-Δt* and *t* stand for the previous and current calculation time increment. $\delta_{t-\Delta t}^N$ and δ_t^N, $\delta_{0\,(H_{t-\Delta t})}^N$ and $\delta_{0\,(H_t)}^N$, $\delta_{re\,(t-\Delta t)}^N$ and $\delta_{re\,(t)}^N$ correspond to the absolute normal separation, the critical normal separation and the relative normal separation in the time increment *t-Δt* and *t*, respectively. If in the different time increment the triaxiality condition does not change, the two critical separations $\delta_{0\,(H_{t-\Delta t})}^N$ and $\delta_{0\,(H_t)}^N$ should be the same.

A loading step is indicated by $\Delta\delta_{re}^N > 0$, an unloading step is indicated by $\Delta\delta_{re}^N < 0$. At the first loading step, the traction separation response goes along the monotonic TSL's path (Equation (1)). Afterwards the unloading and reloading process is defined by Equation (7).

$$T_t^N = T_{t-\Delta t}^N + \overline{k}_N^0 \left[\Delta\delta_{re}^N * \delta_{0\,(H_t)}^N \right] \tag{7}$$

$T_{t-\Delta t}^N$ and T_t^N are the normal traction in the time increment *t-Δt* and *t*. The meanings for the other symbols can be checked in the previous paragraphs.

In every loading process a maximum relative normal separation $\delta_{re\,\max}^N$ may be reached. During the reloading process, when the current relative normal separation exceeds this maximum value, Equation (8) is used for the new path.

$$T^N = \begin{cases} \overline{T}_0^N \left[2\left(\dfrac{\delta^N}{\delta_1}\right) - \left(\dfrac{\delta^N}{\delta_1}\right)^2 \right] & \delta_{re}^N \le \dfrac{\delta_1}{\delta_{0\,(H)}^N} \\ \overline{T}_0^N & \delta_{re}^N > \dfrac{\delta_1}{\delta_{0\,(H)}^N} \end{cases} \tag{8}$$

In the unloading process, it is still an open topic how the triaxiality influences the cohesive parameters. In this paper, a simple assumption is made. The triaxiality value keeps constant in the unloading process and a part of the reloading process. The definition about this part of the reloading

process is like Equation (8). When the current relative normal separation is less than δ_{re}^{N}, the triaxiality value keeps constant. Once δ_{re}^{N} is exceeded, the triaxiality value updates again.

After the cohesive element is broken, in the unloading or compression period in order to avoid the adjacent continuum element penetrating each other, a contact condition should be considered. Here, when δ^{N} <0, Equation (9) is used.

$$T^{N} = k_{N}\delta^{N} \tag{9}$$

A new damage evolution equation is proposed here, as Equation (10)

$$\dot{D} = \left(\frac{A^{\frac{1}{H}} e^{(\lambda - H)}}{H} \right) \Delta\delta_{re}^{N} \left[\frac{T^{N}}{\left[T_{0}^{N}{}_{(H)} \right](1-D)} - \frac{\sigma_{e}}{T_{0}^{N}{}_{(H)}} \right]^{m} \qquad \dot{D} \geq 0 \tag{10}$$

D is the damage variable. $\dot{D}$ is the damage evolution. It is always a positive value. $T_{0}^{N}{}_{(H)}$ is the triaxiality dependent normal cohesive strength. T^{N} is the cohesive traction. $\Delta\delta_{re}^{N}$ is the relative normal separation increment. σ_{e} is the material endurance limit. H is the triaxiality value. A and m are the material dependent damage controlling parameters. λ is the material dependent triaxiality influence coefficient.

A schematic illustration for the cyclic process of the CZM is shown in Figure 2. The new cyclic CZM is contained in a user defined subroutine, and it is connected with the commercial finite element program ABAQUS. The fatigue damage is calculated for every time increment.

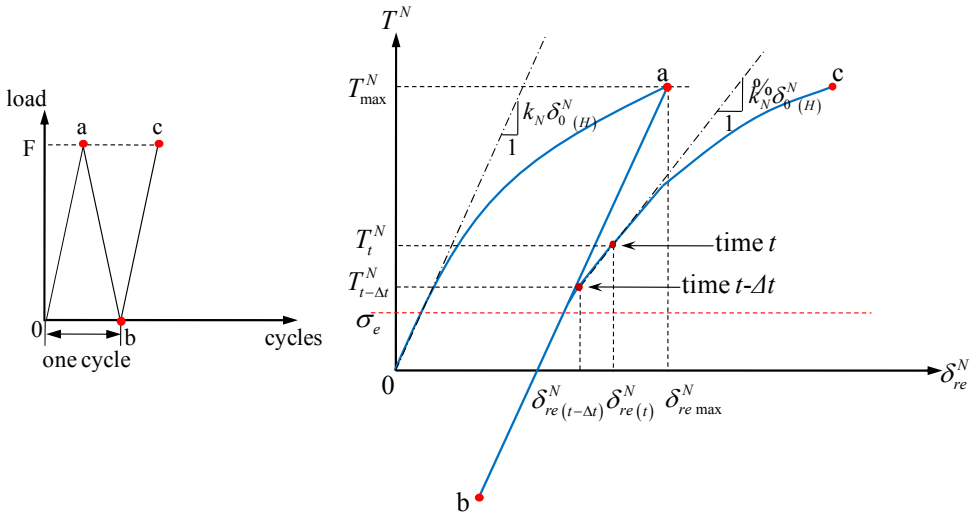

Figure 2. Schematic illustration for cyclic process of the CZM

4. Numerical application

The triaxiality dependent cyclic CZM is applied for fatigue simulation. For triaxiality dependent behavior, some results from literature [20] are used. In reference [20], the examined material is S460N. For convenience, material S460N is chosen for the whole investigations in this paper, too. Some basic mechanical properties for material S460N are shown in Table 1.

Table 1. Mechanical properties for material S460N

Material	E(MPa)	σ_Y(MPa)	R_m(MPa)	K'	n'	σ_e(MPa)
S460N	208000	470	682	1181	0.161	312

E is the material Young's modulus. σ_Y is the material yield stress. R_m is the material ultimate tensile strength. K' is the material cyclic hardening coefficient. n' is the material cyclic hardening exponent. σ_e is the material endurance limit.

4.1. Damage parameters analysis

For the chosen material, the unknown damage parameters in the damage evolution law are just A, m and λ. The material dependent triaxiality influence coefficient λ is fixed first for λ=1.2. The decision for this parameter is based on many trial calculations and a little supposition. The recommendation λ value for material S460N ranges between 0.8 and 1.2, a change of the parameter λ will influence the other two parameters A and m. After λ is chosen, a simple simulation is applied to analyze the material dependent damage controlling parameters A and m. The finite element model consists of two plane strain elements (CPE4) connected by one cohesive element. The model is loaded by cyclic displacement, the loading ratio is R=-1.

In order to reflect the real material response under cyclic loading, the material behavior for continuum element uses a nonlinear kinematic hardening model in ABAQUS. Three different ways are offered by ABAQUS to define the nonlinear kinematic hardening component, specifying the material parameters directly, specifying half-cycle test data or specifying test data from a stabilized cycle. In this paper, nonlinear kinematic hardening model is identified from the stabilized cyclic test. Series of the parameters A and m are investigated and the calculation results are plotted in the material strain-life curve, shown in Figure 3.

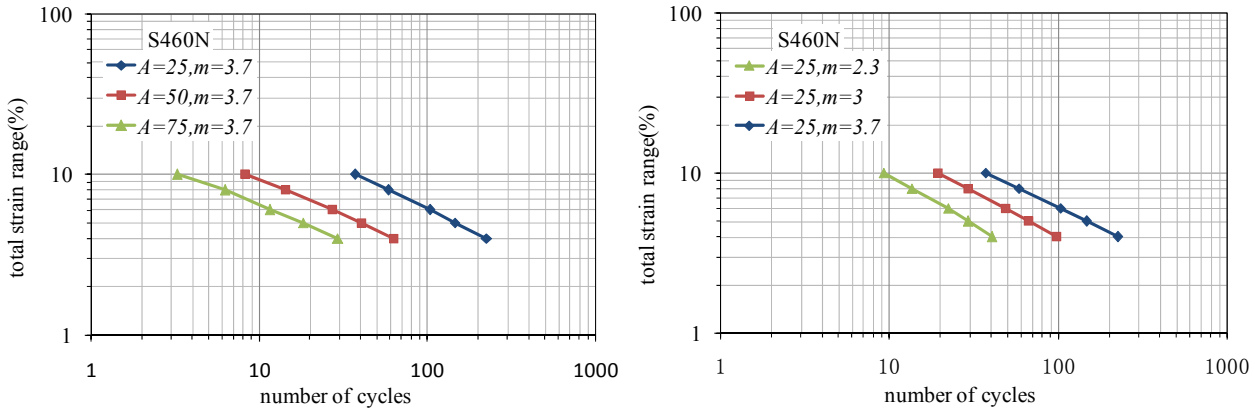

Figure 3. Effect of damage controlling parameters A and m

It is obvious that the parameter m influences the slope of the strain life curve. With increasing the value of m, the slope of the strain-life curve becomes flatter. The parameter A does not influence the slope of the strain-life curve. However, it makes the curve moving parallelly. According to these rules, the parameters A and m can be identified by fitting the numerical results to the experimental strain-life curve.

4.2. Fatigue crack initiation simulation

The strain-life curve of the material S460N is expressed by Equation (11)

$$\varepsilon_a = \varepsilon_{a,el} + \varepsilon_{a,pl} = \frac{\sigma_f'}{E}(2N)^b + \varepsilon_f'(2N)^c \tag{11}$$

ε_a is the strain amplitude. $\varepsilon_{a,el}$ and $\varepsilon_{a,pl}$ are the elastic and plastic part for the strain amplitude. E is the Young's modulus. N is the fatigue life, it stands for fatigue crack initiation life or fatigue fracture life. Here it means the fatigue crack initiation life. σ_f' is the fatigue strength coefficient. b is the fatigue strength exponent. ε_f' is the fatigue ductility coefficient. c is the fatigue ductility exponent. Values are taken from reference [21] and shown in Table 2.

Table 2. Experimental strain-life curve parameters

Material	E(MPa)	σ_f'(MPa)	ε_f'	b	c
S460N	208000	1218	0.452	-0.104	-0.536

In the previous section, the influence rules of the damage controlling parameters A and m are discussed. By fitting the simulation results to the experimental strain-life curve, the parameters A and m can be determined. Here the simulation model is also two plane strain elements connected by one cohesive element. The loading condition and the material behaviour are like in the previous section. The investigations just focus on the very low cycle fatigue regime, so the calculated number of cycles is within 600. For material S460N, the parameters A and m are fitted as: A=25, m=3.7. The experiment and simulation results are plotted in Figure 4.

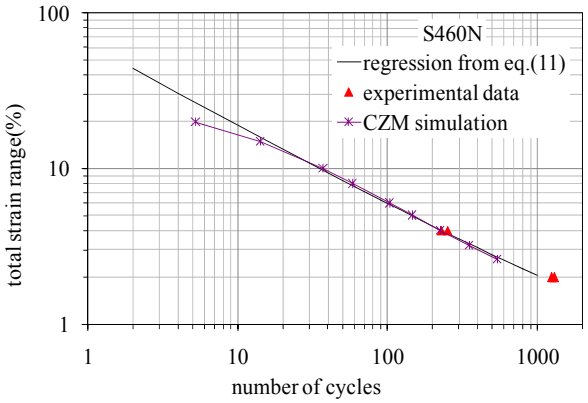

Figure 4. Comparison of strain-life curve for material S460N

4.3. Fatigue crack propagation simulation

For the material S460N, the damage parameters are determined: λ=1.2, A=25 and m=3.7. These parameters need further validation. As an important part of fatigue fracture, the fatigue crack growth simulation is applied here to validate the damage parameters.

The experimental data of fatigue crack growth for the material S460N are taken from reference [22]. The experimental fatigue crack growth rate curve includes four different strain range levels, i.e. $\Delta\varepsilon$=0.4%, $\Delta\varepsilon$=0.6%, $\Delta\varepsilon$=1.0% and $\Delta\varepsilon$=2.0%. Because the investigations focus on very low cycle fatigue regime, just the experimental data at fast crack growth rate are used for comparison.

The numerical model is a two dimensional compact tension specimen. The dimension of the model is width 50mm and height 60mm. The initial crack length a_0 is 25mm and the ligament length is 25mm, too. The type of the continuum element is plane strain. The material behaviour of the continuum elements is the same as in the previous section. The cohesive elements locate along the

ligament and the size of the element is 0.125mm. The details for the finite element model are depicted in Figure 5.

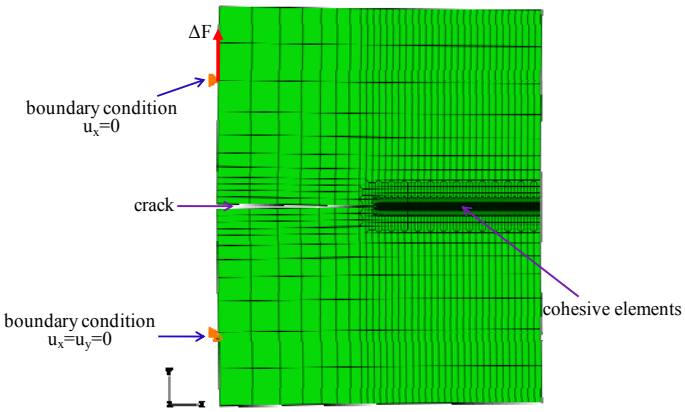

Figure 5. Finite element model for simulated compact tension specimen

In the calculation, three different cyclic loading ranges are used: ΔF=1200N, ΔF=950N and ΔF=800N. All loading ratios are R=0. The fatigue crack growth rate $\Delta a/\Delta N$ can be calculated directly from the numerical model, but the cyclic ΔJ integral will be computed by another approach. A finite element model of the CT specimen without cohesive zone is built. The crack length inserted in this model is $(a_0+\Delta a)$. One cycle is calculated and the cyclic ΔJ integral is computed by Equation (12) [23].

$$\Delta J = \int_{\Gamma}\left(\Delta W dy - \Delta t_i \frac{\partial \Delta u_i}{\partial x} ds\right) \qquad \Delta W = \int_0^{\Delta\varepsilon} \Delta\sigma_{ij} d\Delta\varepsilon_{ij} \tag{12}$$

$\Delta\sigma_{ij}$ and $\Delta\varepsilon_{ij}$ are the cyclic stress and strain range. W is the cyclic deformation energy. x and y are the Cartesian coordinates with the x-axis parallel to the crack surface. Γ is the integration path. ds is the line element lying on the integration path. Δt_i is the cyclic stress vector on the integration path. Δu_i is the cyclic displacement variation.

The simulation results under three loading ranges are plotted together with the scatter band of experimental data in Figure 6.

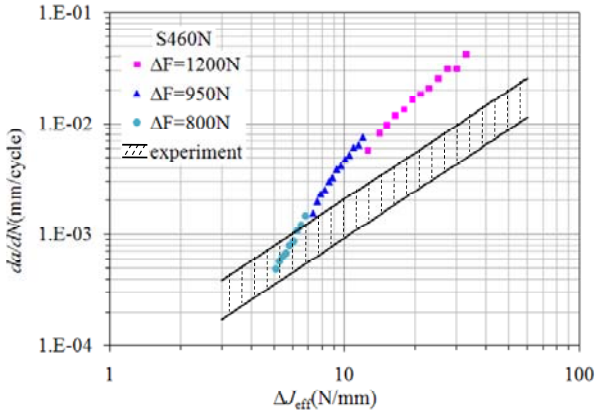

Figure 6. Comparison of fatigue crack growth rates curve for material S460N

A reasonable accordance of experimental and simulated results is achieved. The simulated fatigue crack growth rates are a little bit faster than the experimental data, but the total trend for fatigue

crack growth is very similar. One possible reason for this diversity is from the influence of the model dimension. In experiment, the specimen is a three dimensional model, but in simulation a two dimensional model is used. The calculation about the energy integral ΔJ is bigger for two dimensional problems than for three dimensional problems. The other possible reason is from the new CZM. This numerical model may express the real cyclic process inaccurately.

5. Conclusions

CZM is a very robust numerical tool for material fracture analysis. It is simple enough for theoretical understanding and practical application. For the material monotonic fracture, the implementation of the CZM is particularly mature. But for fatigue fracture analysis, the application is just in developing. In this paper, according to the pioneers' idea [13], a triaxiality dependent cyclic CZM is proposed. This model can be applied for various triaxiality conditions, and only one set of unique material damage parameters is used. In the very low cycle fatigue regime, using the triaxiality dependent cyclic CZM in fatigue crack initiation and fatigue crack growth simulation, the reasonable comparison results between experiment and simulation can be obtained.

However, this new CZM is still in a testing process. Many improvements and developments need to be done in the future. More materials should be chosen in the simulation to validate the new CZM. The cyclic process for the CZM needs more discussions, especially in unloading and compression period. The format of the damage evolution law maybe modified. The triaxiality dependent behavior in the whole cyclic process needs much more investigations.

Acknowledgements

Author would like to thank Dr. Ingo Scheider from Helmholtz-Zentrum Geesthacht, Institut für Werkstoffforschung, for providing many helpful suggestions in cohesive zone model application.

References

[1] D.S. Dugdale, Yielding of steel sheets containing slits. Journal of the Mechanics and Physics of Solids, 8 (1960) 100-104.
[2] G.I. Barenblatt, The mathematical theory of equilibrium cracks in brittle fracture. Advances in Applied Mechanics, 7 (1962) 55-129.
[3] A. Hillerborg, M. Modéer, P.E. Petersson, Analysis of crack formation and crack growth in concrete by means of fracture mechanics and finite elements. Cement and Concrete Research, 6 (1976) 773-782.
[4] A. Needleman, A continuum model for void nucleation by inclusion debonding. Journal of Applied Mechanics, 54 (1987) 525-531.
[5] A. Needleman, An analysis of decohesion along an imperfect interface. International Journal of Fracture, 42 (1990) 21-40.
[6] V. Tvergaard, J.W. Hutchinson, The relation between crack growth resistance and fracture process parameters in elastic-plastic solids. Journal of the Mechanics and Physics of Solids, 40 (1992) 1377-1397.
[7] H. Yuan, G.Y. Lin, A. Cornec, Verification of a cohesive zone model for ductile fracture. Journal of Engineering Materials and Technology, 118 (1996) 192-200.
[8] A. Cornec, I. Scheider, K.H. Schwalbe, On the practical application of the cohesive model. Engineering Fracture Mechanics, 70 (2003) 1963-1987.
[9] I. Scheider, W. Brocks, Simulation of cup-cone fracture using the cohesive zone model. Engineering Fracture Mechanics, 70 (2003) 1943-1961.

[10] N. Chandra, H. Li, C. Shet, H. Ghonem, Some issues in the application of cohesive zone models for metal-ceramic interfaces. International Journal of Solids and Structures, 39 (2002) 2827-2855.
[11] A. De-Andrés, J.L. Pérez, M. Ortiz, Elastoplastic finite element analysis of three-dimensional fatigue crack growth in aluminium shafts subjected to axial loading. International Journal of Solids and Structures, 36 (1999) 2231-2258.
[12] B. Yang, S. Mall, K. Ravi-Chandar, A cohesive zone model for fatigue crack growth in quasibrittle materials. International Journal of Solids and Structures, 38 (2001) 3927-3944.
[13] K.L. Roe, T. Siegmund, An irreversible cohesive zone model for interface fatigue crack growth simulation. Engineering Fracture Mechanics, 70 (2003) 209-232.
[14] A. Abdul-Baqi, P.J.G. Schreurs, M.G.D. Geers, Fatigue damage modeling in solder interconnects using a cohesive zone approach. International Journal of Solids and Structures, 42 (2005) 927-942.
[15] J.L. Bouvard, J.L. Chaboche, F. Feyel, F. Gallerneau, A cohesive zone model for fatigue and creep-fatigue crack growth in single crystal superalloys. International Journal of Fatigue, 31 (2009) 868-879.
[16] Y.J. Xu, H. Yuan, On damage accumulations in the cyclic cohesive zone model for XFEM analysis of mixed-mode fatigue crack growth. Computational Materials Science, 46 (2009) 579-585.
[17] P. Nègre, D. Steglich, W. Brocks, Crack extension in aluminium welds: a numerical approach using the Gurson-Tvergaard-Needleman model. Engineering Fracture Mechanics, 71 (2004) 2365-2383.
[18] T. Siegmund, W. Brocks, The role of cohesive strength and separation energy for modeling of ductile fracture. Fatigue and Fracture Mechanics, 30 (2000) 139-151.
[19] M. Anvari, I. Scheider, C. Thaulow, Simulation of dynamic ductile crack growth using strain-rate and triaxiality-dependent cohesive elements. Engineering Fracture Mechanics, 73 (2006) 2210-2228.
[20] I. Scheider, Derivation of separation laws for cohesive models in the course of ductile fracture. Engineering Fracture Mechanics, 76 (2009) 1450-1459.
[21] CHR. Boller, T. Seeger, Materials data for cyclic loading-part B: low-alloy steels, Elsevier Science Publishers B.V., Amsterdam, 1987.
[22] M. Vormwald, Ermüdungslebensdauer von Baustahl unter komplexen Beanspruchungsabläufen am Beispiel des Stahles S460. Materials Testing, 53 (2011) 98-108.
[23] C. Wüthrich, The extension of the J-integral concept to fatigue cracks. International Journal of Fracture, 20 (1982) 35-37.

Healing of Fatigue Crack Treated with Surface-Activated Pre-Coating Method by Controlling High-Density Electric Current

Atsushi Hosoi, Tomoya Kishi, Yang Ju*

Department of Mechanical Science and Engineering, Nagoya University, Nagoya 464-8603, Japan
* Corresponding author: ju@mech.nagoya-u.ac.jp

Abstract A technique to heal a fatigue crack for a stainless steel by controlling a high-density electric current field was studied. The high-density electric current was applied at the crack tip using electrodes. A surface-activated pre-coating technique was used in order to improve adhesion of the crack surface. The crack on the specimen surface was observed by scanning electron microscope (SEM) before and after the application of the high-density electric current to examine the effect of the fatigue crack healing. The experimental results showed that the fatigue crack was closed and the crack growth rate of a healed specimen was decreased by the electrical stimulation.

Keywords Crack Healing, Fatigue, Crack Closure, Electric Current, Stainless Steel

1. Introduction

Fatigue is the main reason of failure accidents in metallic structures. To improve long term durability and reliability of structures, various methods are studied. The techniques to improve the fatigue strength, such as high-frequency quenching, carburizing, nitriding and shot peening, had been developed. They can prolong the fatigue life of materials by suppressing the crack initiation on the material surface. However, the advantages of these methods are limited for the materials where a crack had been existed. If damage of materials can be healed, it is possible to improve the reliability and durability of the industrial materials remarkably. Recently, some researchers have studied crack healing techniques in polymer materials and ceramic materials [1-3]. However, a technique to heal essentially a fatigue crack detected in metallic materials has not been established.

The studies to improve the mechanical properties of metallic materials have been conducted by the application of the electric current for a few decades. Karpenko et al. [4] showed that the fatigue life of a steel was prolonged by the application of the electric current during fatigue loadings. Golovin et al. [5] studied the effect of the high-density pulse current on the crack propagation of a silicon iron during the dynamic tensile loading. They showed that the crack propagation halted when the high-density pulse current was applied just before the crack initiation. Conrad and coauthors [6-10] investigated the influence of high-density pulse current on materials in detail. They showed that the action of drift electrons influenced the dislocation mobility. As other effects, the following phenomena are known, such as the generation of Joule heating [11], the cause of the compressive stress due to Joule heating [12-14], the induction of Lorentz force [15], the cause of the electron wind force due to the flow of the electric current [16].

Although some studies to improve the mechanical and material properties by applying the electric current in metallic materials have been conducted, a method for the essential healing of a fatigue crack has not been established yet. Therefore, the authors developed the technique to heal a fatigue crack in a stainless steel by controlling the high-density electric current field [17, 18]. In these researches, it is revealed that the crack was closed and the bridging by partial melting was formed between the crack surfaces. However, the adhesion between the crack surfaces is prevented due to the oxide layer on the crack surfaces. In this study we proposed to improve the adhesion of the crack surfaces by treating surface-activated pre-coating technique, which eliminates oxide layer and coats Ni on the crack surfaces. In addition, we evaluated quantitatively the healing effect of the

fatigue crack treated with the surface-activated pre-coating method by controlling high-density electric current.

2. Experiments

2.1. Specimens

Austenite stainless steel SUS316 was used as the experimental material. The chemical compositions and the mechanical properties of SUS316 are shown in Tables 1 and 2, respectively. The dumbbell-shaped specimens were used, and the schematic is represented in Fig. 1. A notch was introduced at the center of the one-side edge in the specimens. The specimens were treated with stress relief annealing to remove the residual stress caused in machining process. The heat treatment process is as follows. The specimens are heated to 1173 K for 4 hours, and the temperature is kept at 1173 K for 10 minutes. After that, the specimens are cooled slowly to a room temperature in a furnace. The surfaces of the specimens were polished to a mirror plane by using a buffing machine to observe the surface condition.

2.2. Experimental conditions

2.2.1. Fatigue test conditions

The tensile fatigue tests were conducted to introduce a fatigue crack with the annealed specimen, and were carried out at the room temperature in the atmosphere under load control conditions with a hydraulic driven testing machine. All of the tests were conducted at a stress ratio of R=0.05 and a frequency of f=10 Hz. The details of the fatigue test conditions are shown in Table 3. The crack length under cyclic loading was measured by in-situ observation using a digital microscope. In this paper, the test conditions and results of two major examples were indicated. Each specimen is named Specimen A and B. For comparison, the specimen which is not applied electric current is named Standard specimen.

2.2.2. Surface-activated pre-coatings

The surface-activated pre-coating technique, which eliminates the oxide layer and coats Ni film for preventing reoxidation, was treated on the crack surfaces. The surface-activated pre-coating technique was composed of three stages as follows. The first stage is electrolytic cleaning, the second stage is HCl activating and the third stage is Ni striking. The schematic of surface-activated pre-coating technique is represented in Fig. 2. The specimen is washed by using pure water between every stage. In the stage of the electrolytic cleaning, the specimen is washed in alkali solution. The composition of the alkali solution is 30 g/L NaOH, Na_2Co_3 and Na_4SiO_3. The anode was connected to Al plate and the cathode was to the specimen. The electrolytic cleaning current density is 10 A/dm^2, a time of current duration is 60 seconds and the alkali solution is maintained at a temperature of 60 °C. In the stage of the HCl activating, the oxide layer on the specimen was eliminated in 37 % HCl solutions for 10 seconds. At the stage of Ni striking, the oxide layer on the specimen was eliminated and the Ni film was coated for preventing reoxidation. The composition of the Ni coating solution is 240 g/L $NiCl_2$ and 80 g/L 37%HCl. The anode was connected to Ni plate and the cathode was to the specimen in the coating solution. The current density is 10 A/dm^2 and a time of current duration are 60 seconds.

2.2.3 Conditions of electric current application

The electric current was applied to heal the fatigue crack. The application of electric current was carried out using a transistor type power source. The pulse current was applied through the electrodes striding across the notch as shown in Fig. 3. The chromium cupper electrodes of 5 mm in diameter were used. Two electrodes were connected straddling the notch of the specimen. The distance between two electrodes was 1.3 mm. The conditions of the application of the electric current are shown in Table 4. The pulse electric current was applied to the specimen once and more, and the crack state on the specimen surface was observed with a scanning electron microscope (SEM) before and after every application of the electric current.

Table 1. Chemical compositions of the stainless steel SUS316 (wt. %)

C	Si	Mn	P	S	Ni	Cr	Mo	Fe
0.05	0.26	1.3	0.028	0.03	10.1	17.09	2.01	Balance

Table 2. Mechanical properties of SUS316

Yield stress [MPa]	Tensile strength [MPa]	Young's modulus [GPa]	Poisson's ratio	Hardness HBW
300	573	193	0.3	161

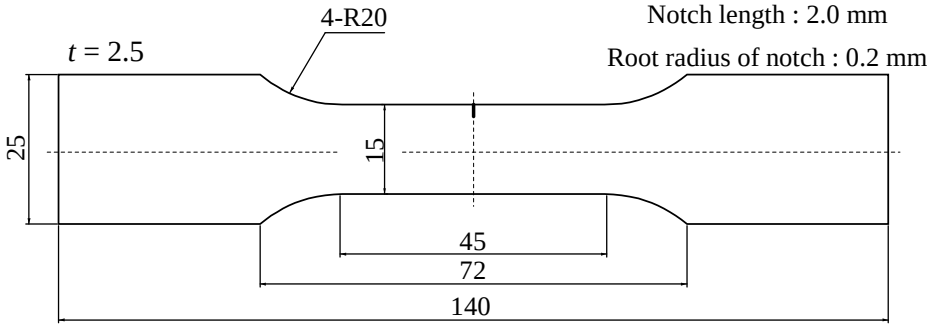

Figure 1. Schematic of specimen

Table 3. Fatigue test and crack conditions before current application

	Specimen A	Specimen B	Standard
The maximum gross stress σ_{max} [MPa]	180	150	150
Stress ratio R	0.05	0.05	0.05
Frequency f [Hz]	10	10	10
Pre-crack length a [mm]	1.55	1.08	-

Table 4. Conditions of the electric current

	Specimen A	Specimen B
Applied current [A]	4000	8000
Pulse duration [msec]	2.0	1.0
The Number of current application	12	1

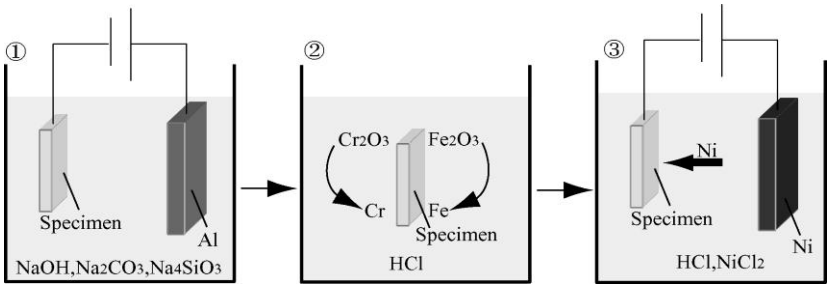

(a) (b) (c)

Figure 2. Schematic diagram of surface-activated pre-coating technique:
(a) Electrolytic cleaning, (b) HCl activating, (c) Ni striking

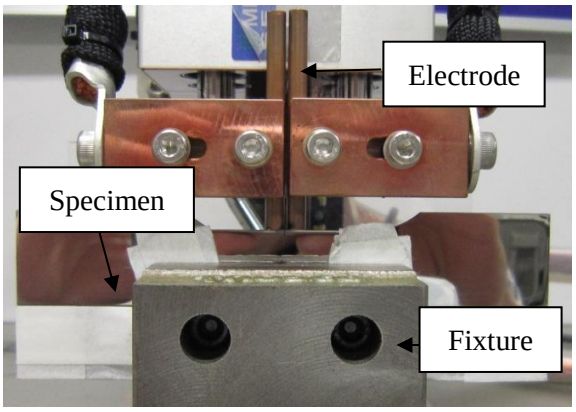

Figure 3. Applying electric current

3. Experimental results

3.1. Observation of fatigue crack

The elemental components were observed with an auger microprobe to confirm the effect of the surface-activated pre-coating technique. Figure 4 shows the relationship between atomic concentration of O, Cr, Fe and Ni and depth from the specimen surface after Ni striking. The Fe and Cr are the main element of the specimens, SUS316, and Ni is the element coated by the surface-activated pre-coating technique. It is observed that the oxide layer, O is almost eliminated at the surface of the specimen and Ni coating film is approximately 630 nm thick.

The crack state on the specimen surface was observed with SEM. Figure 5 shows the fatigue crack shape before the application of the electric current in Specimen A. The points to measure the change of the crack width were indicated. Figure 6 shows the change of the fatigue crack shape at each application of the electric current in Specimen A. It is observed that the crack was closed for almost every application of the electrical current. Figure 7 is an enlarged picture at the area near the point 3 which is approximately 900 μm away from the crack tip before the application and after the 12th application of the electric current in Specimen A. The adhesion between the crack surfaces was observed and it is observed that the application of electric current also has an effect on the area far from the crack tip. Figure 8 shows the change of crack width for every application of the electric current. Compared to before the application and after the twelfth application of the electric current, the crack width near the notch decreased from approximately 39 μm to 8.5 μm. After the twelfth application of the electric current, the whole crack was closed 75-97 % from original crack, and the whole crack width was less than 10 μm. The bonding of the crack surfaces was confirmed by

cutting the specimen vertically to the direction of the crack propagation.

The elemental components at the inside of the crack were observed with the auger microprobe. Figure 9 shows the auger spectrum at the bridge formation inside of the crack after the application of the electric current. It is observed that the intensity of the spectral line is strong at the electron energy of Fe and Ni, and Fe and Ni are alloyed on the crack surface.

3.2. Evaluation of crack growth behavior

The behavior of the crack growth was evaluated quantitatively in order to research the effect of the crack healing. The crack closure was confirmed at the Specimen B in the same way like Specimen A. Figure 10 shows the crack growth rate as a function of the stress intensity factor range, Paris law, with Standard specimens without the application of the electric current. The fatigue test was conducted at σ_{max} = 150 MPa in the Specimen B after the application of the electric current. Figure 11 shows that before and after the application of the electric current in the Specimen B. The solid line indicates the approximate line of the results of Standard specimens without applying the electric current. The open and solid symbols B show the behavior of the crack growth in specimen B before and after the application of the electric current, respectively. It was observed that the crack growth rate decreased from 3.69×10^{-8} to 2.52×10^{-8} m/cycle just after the application of current compared to that of Standard specimens.

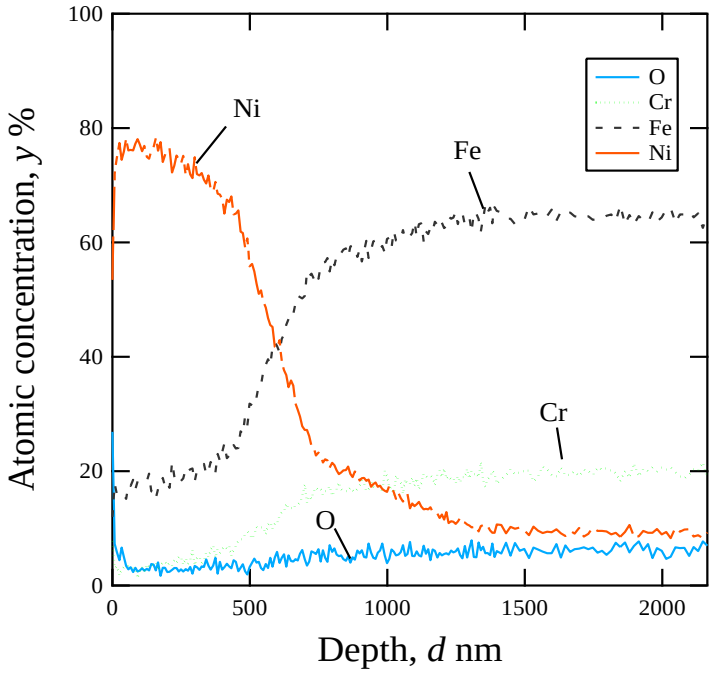

Figure 4. The relationship between atomic concentration of O, Cr, Fe and Ni and depth from the specimen surface after Ni striking

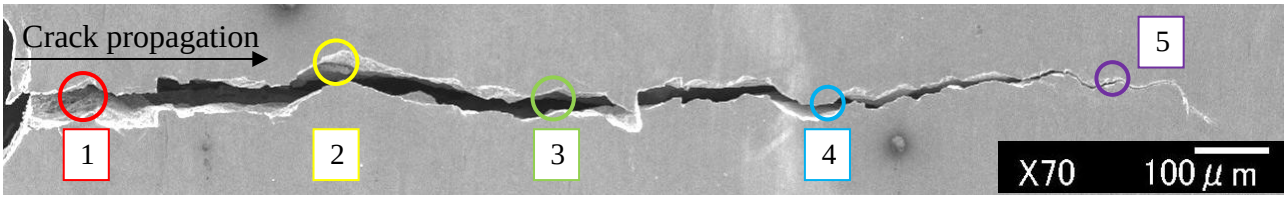

Figure 5. Image of fatigue crack before the application of the electric current and the measurement points of the crack width in Specimen A

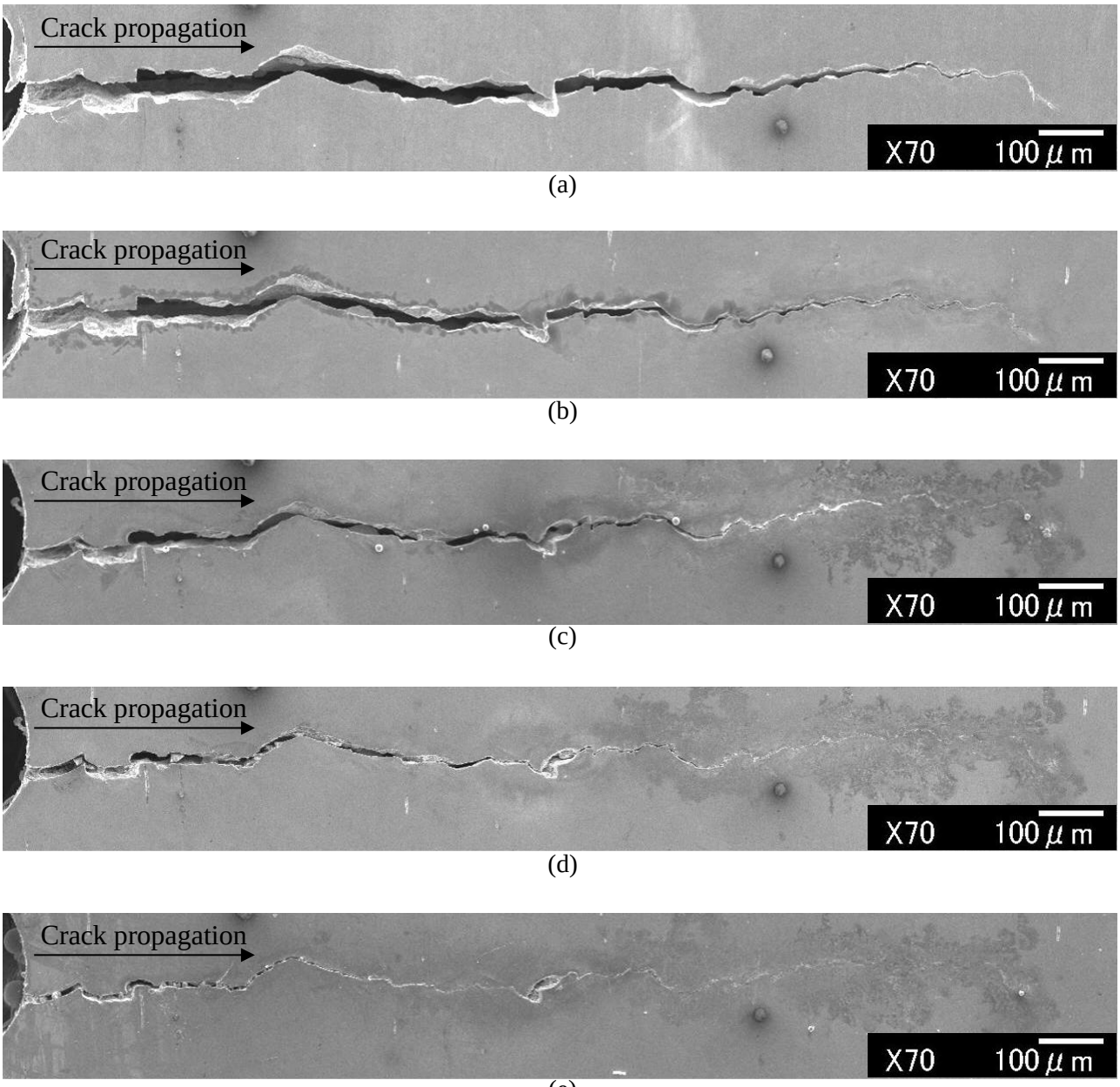

Figure 6. Images of fatigue crack in Specimen A: (a) before, (b) after first, (c) after forth, (d) after sixth and (e) after twelfth application of electric current

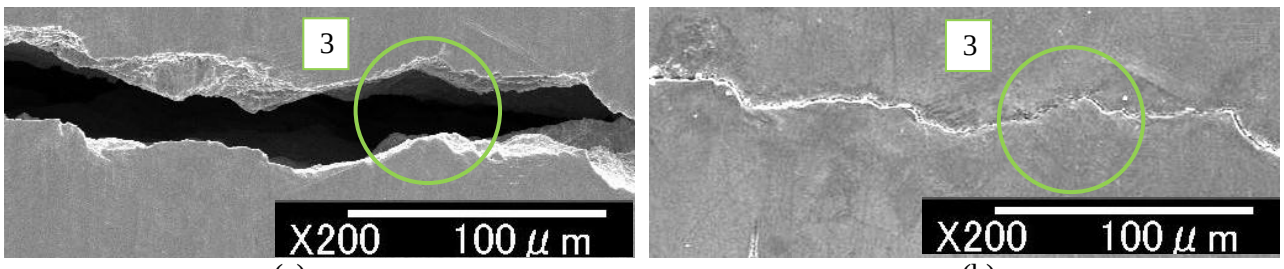

Figure 7. Magnified images of fatigue cracks in Fig. 5: (a) before and (b) after the twelfth application of electric current

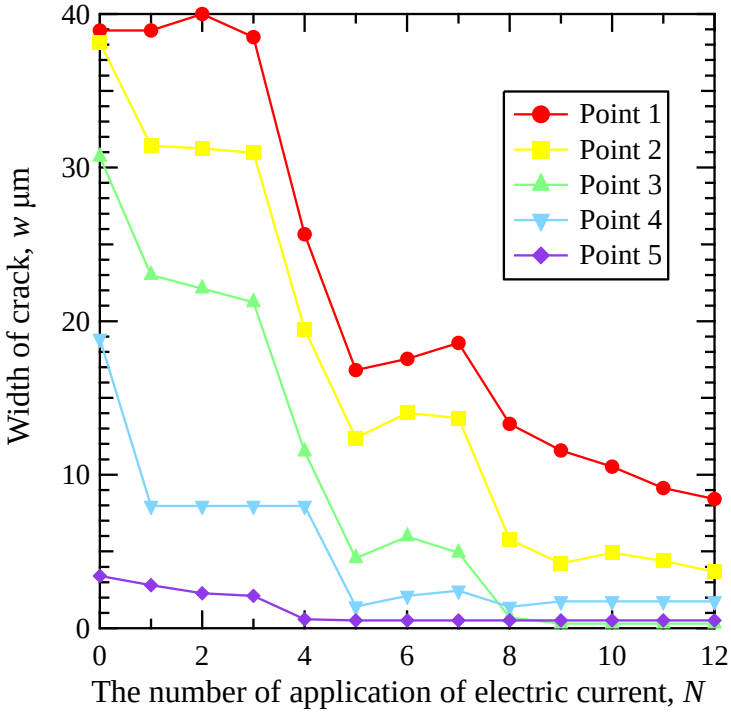

Figure 8. Change of crack width at the measure point in Fig. 5 for every application of the electric current in Specimen A

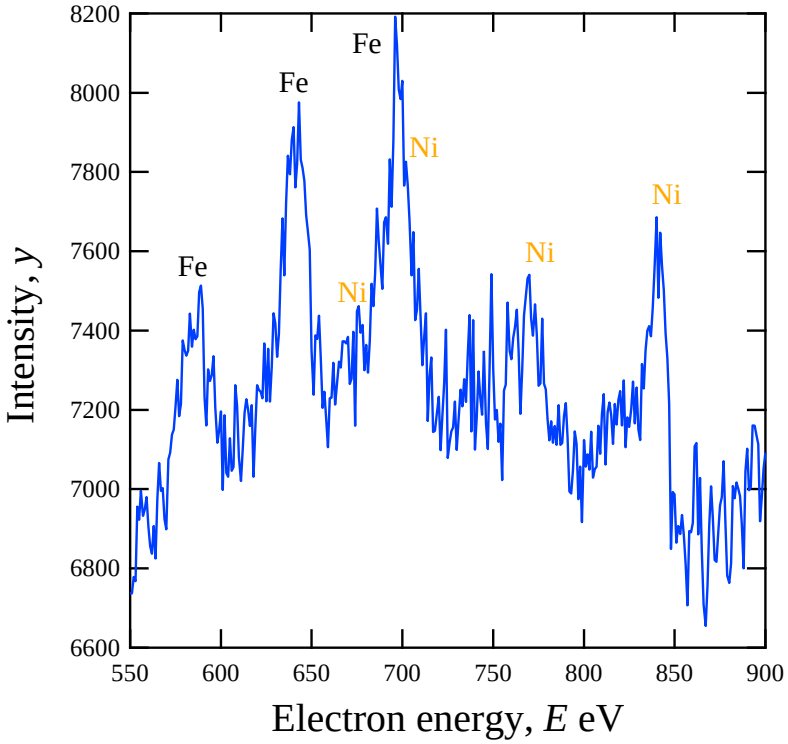

Figure 9. Auger spectrum at the inside of the crack after the application of the electric current

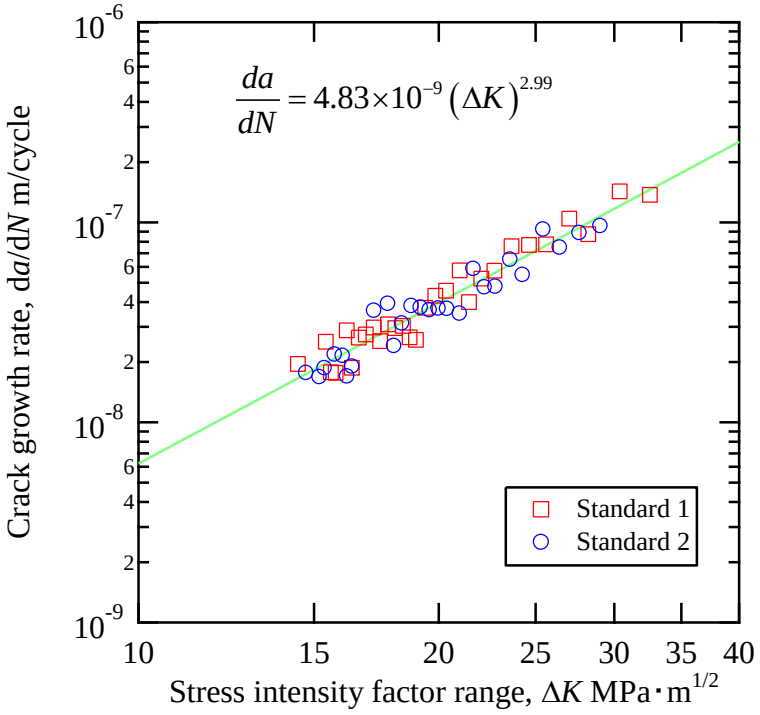

Figure 10. Fatigue crack growth rate as a function of stress intensity range with Standard specimens without the application of the electric current

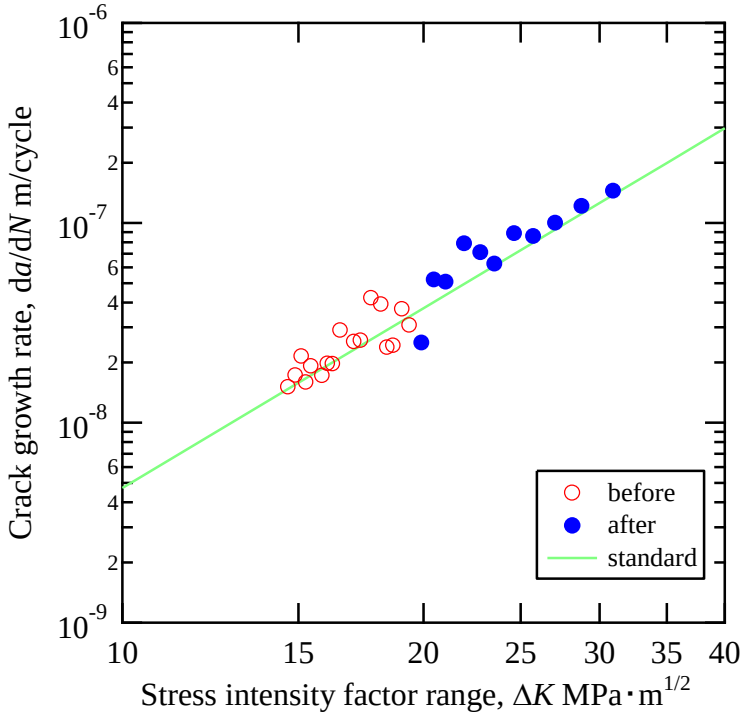

Figure 11. Fatigue crack growth rate as a function of the crack length before the application and after the application of the electric current in Specimen B

4. Discussions

One of the reasons that the crack was closed and healed as shown in Figs. 6 and 7 is thought to be thermal compressive stress due to Joule heating caused by the high-density electric current field formed at the clack tip. When the electric current is applied as crossing a crack, it flows along the crack because of the electric resistance on the crack surface. Therefore, the high-density electric current field is formed at the crack tip. The area at the tip and the vicinity of the crack is heated rapidly and expands due to Joule heating. On the other hand, the outside area of the crack tip where the high-density electric field is not caused remains intact. Therefore, the direction of expansion is restricted and the thermal compressive stress toward crack closure is caused due to the thermal expansion and it is thought that the crack is closed. Moreover, it is thought that the crack surfaces are easily bonded because the oxide layer preventing the bonding between each crack surfaces is eliminated by the surface-activated pre-coating technique, and the Ni film works as the well-adhesion inner layer. In addition, for every application of the electric current, the crack is closed, and the crack tip transfers to the direction to the notch. Therefore, the area of the current concentration continuously transfers to the direction of the notch and the whole crack was closed by the application of electric current.

On the other hand, the crack growth rate decreased temporarily as shown Fig. 11. The reason the crack growth was decreased is thought that the crack closure and bonding between the crack surfaces influenced on fatigue crack growth by applying electric current. The crack closure reduces the driving force for the crack propagation because of the decrease of the crack opening displacement. The bonding between the crack surfaces also makes the crack opening suppressive.

5. Conclusion

The technique to heal fatigue crack treated with surface-activated pre-coating method by controlling high-density electric current field was researched. The closure of the crack and the bonding between crack surfaces were realized by applying high density electric current. The crack was closed 75-97 % from original crack by improving adhesion between crack surfaces and applying the multiple electric current. Moreover, it was observed that the crack growth rate was decrease temporarily after the application of the electric current. As a result, it was indicated that the technique with the electrical stimulation has the potential to heal a fatigue crack.

Acknowledgements

This work was supported by the Japan Society for the Promotion of Science under Grant-in-Aid for Young Scientists (A) 23686021.

References

[1] X. Chen, M.A. Dam, K. Ono, A. Mal, H. Shen, S.R. Nutt, K. Sheran and F. Wudl, A thermally re-mendable cross-linked polymeric material, Science, 295 (2002) pp. 1698-1702.
[2] S.R. White, N.R. Sottos, P.H. Geubelle, J.S. Moore, M.R. Kessler, S.R. Sriram, E.N. Brown and S. Viswanathan, Autonomic healing of polymer composites, Nature, 409 (2001) pp. 794-797.
[3] K. Ando, Y. Shirai, M. Nakatani, Y. Kobayashi and S. Sato, (Crack-healing + proof test): a new methodology to guarantee the structural integrity of a ceramics component, J Eur Ceram Soc, 22 (2002) pp. 121-128.
[4] G.V. Karpenko, O.A. Kuzin, V.I. Tkachev and V.P. Rudenko, Influence of an electric current upon the low-cycle fatigue of steel, Sov Phys Dokl, 21 (1976) pp. 159-160.
[5] Y.I. Golovin, V.M. Finkel and A.A. Sletkov, Effects of current pulses on crack propagation

kinetic in silicon iron, Strength Mater+, 9 (1977), pp.204-210.
[6] K. Okazaki, M. Kagawa and H. Conrad, A study of the electroplastic effect in metal, Scripta Metall Mater, 12 (1978) pp. 1063-1068.
[7] A.F. Sprecher, S.L. Mannan and H. Conrad, On the mechanisms for the electroplastic effect in metals, Acta Metall Mater, 34 (1986) pp. 1145-1162.
[8] H. Conrad, J. White, W.D. Cao, X.P. Lu and A.F. Sprecher, Effect of electric current pulses on fatigue characteristics of polycrystalline copper, Mater Sci Eng, A 145 (1991) pp. 1-12.
[9] W.D. Cao and H. Conrad, On the effect of persistent slip band (PSB) parameters on fatigue life, Fatig Fract Eng Mater Struct, 15 (1992) pp. 573-583.
[10] H. Conrad, Electroplasticity in metal and ceramics, Mater Sci Eng, A 287 (2000) pp. 276-287.
[11] M. Saka and H. Abé, A path-independent integral for 2-dimensional cracks in homogeneous isotropic conductive plate, Int J Eng Sci, 21 (1983) pp. 1451-1457.
[12] M. Saka and H. Abé, Path-independent integrals for heat conduction analysis in electrothermal crack problems, J Therm Stresses, 15 (1992) pp. 71-83.
[13] G.X. Cai and F.G. Yuan, Electric current-induced stresses at the crack tip in conductors, Int J Fracture, 96 (1999) pp. 279-301.
[14] T.J.C. Liu, Thermo-electro-structural coupled analyses of crack arrest by Joule heating, Theor Appl Fract Mec, 49 (2008) pp. 171-184.
[15] G.X. Cai and F.G. Yuan, Stresses around the crack tip due to electric current and self-induced magnetic field, Adv Eng Softw, 29 (1998) pp. 297-306.
[16] R.P. Gupta, The electron wind force in electromigration, J Chem Solids, 47 (1986) pp. 1057-1066.
[17] Hosoi, T. Nagahama and Y. Ju, Fatigue Crack Healing by Controlling High-Density Electric Current Field, Mater Sci Eng, A 533 (2012) pp. 38-42.
[18] Hosoi, T. Nagahama and Y. Ju, Effect of High-Density Electric Current Field on Fatigue Cracks in Stainless Steel, ASME 2010 International Mechanical Engineering Congress and Exposition (2010), IMECE2010-37819 pp. 123-128.

Fatigue Life Prediction of Polycrystals under Multiaxial Straining

Gustavo M. Castelluccio[1,*], David L. McDowell[1,2]

[1] Woodruff School of Mechanical Engineering

[2] School of Materials Science and Engineering

Georgia Institute of Technology, 771 Ferst Drive, N.W, Atlanta, Georgia 30332, USA

* Corresponding author: castellg@gatech.edu

Abstract: In the high cycle fatigue, the initiation of fatigue cracks is significantly affected by microstructure, loading conditions, and specimen geometry. However, fatigue life estimation traditionally considers microstructure and geometric effects via semi-empirical methods without explicit consideration of the early stages of crack formation, which tends to dominate the total lives in high cycle fatigue. Such a strategy has been useful for existing materials that have been characterized with extensive fatigue experiments, but is less applicable to the design of fatigue-resistant alloys or modification of existing alloy microstructures to enhance fatigue resistance. This paper employs a framework developed to assess the early stages of crack formation and growth through the microstructure in smooth and notched specimens. The methodology employs finite element simulations that render an unimodal grain-size microstructure and a crystal plasticity-based fatigue model that estimates 3D transgranular fatigue growth on a grain-by-grain basis. The crystal plasticity model parameters were calibrated for Ni-base superalloy RR1000. In these simulations, cracks form in near surface grains with highest slip-based driving force and then propagate through the field of adjacent grains.

Keywords Fatigue Indicator Parameter, Microstructurally Small Cracks, Fatigue Life

1 Introduction

In spite of its significance in industrial applications, the influence of microstructure on the early stages of fatigue cracks in engineering alloys is still poorly understood. The formation and early growth of fatigue cracks can consume a significant portion of the high cycle fatigue life and is strongly influenced by the size and shape of grains, and the crystallographic orientation. Fatigue models have been able to predict the fatigue life as a function of the microstructure by employing parameters aimed at reflecting the role of microstructure without strong physical connections. These methodologies can assess and perhaps compare materials, but they are not fully appropriate to design of fatigue-resistant engineering alloys.

During the past decade computational simulations have been increasingly used for designing materials. These models simulate microstructure-sensitive mechanical responses with the aim of reducing experimental effort. Castelluccio [1][2] developed a computational methodology for predicting the number of fatigue cycles required to crack an individual grain with highest driving force. The algorithm employs finite element simulations and a crystal plasticity framework to compute nonlocal fatigue indicator parameters (FIPs) which are correlated with the cycles required to crack a grain. This methodology has been successfully employed to assess the effect of bimodal

grain size distributions on fatigue resistance [2].

This work employs similar fatigue and crystal plasticity models to assess the effect of multiaxial straining and stress concentration on early fatigue life. The finite element simulations are calibrated to represent RR1000 Ni-base superalloy and render the microstructure explicitly. The fatigue lives are correlated to a variant of the Fatemi-Socie FIP that is averaged over nonlocal volumes that are oriented as bands aligned with the crystallographic slip planes. The model considers the influence of grain size effects for fatigue cracks that nucleate and extend into neighboring grains.

2 Modeling and simulation

2.1 Constitutive model

At the scale of individual grains we employ a physically-based crystal plasticity constitutive model for RR1000 superalloy adapted from the work of Lin et al. [3]. The crystallographic shearing rate is given by

$$\dot{\gamma}^{(\alpha)} = \dot{\gamma}_0 \exp\left[-\left(\frac{F_0}{k_b T}\right)\left\langle 1-\left\langle \frac{\left|\tau^{(\alpha)}-B^{(\alpha)}\right|-S^{(\alpha)}\mu/\mu_0}{\tau_0\mu/\mu_0}\right\rangle^{p}\right\rangle^{q}\right] sgn\left(\tau^{(\alpha)}-B^{(\alpha)}\right), \quad (1)$$

in which $\dot{\gamma}^{(\alpha)}$ is the shearing rate of slip system α, $\tau^{(\alpha)}$ is the resolved shear stress, T is the absolute temperature, F_o, p, q, $\dot{\gamma}_0$, τ_0, μ, and μ_0 are material parameters that may differ for octahedral and cube slip systems, as listed in Table 1 for 650°C, and k_b is Boltzmann's constant. The evolution laws for slip resistance ($S^{(\alpha)}$) and back stress ($B^{(\alpha)}$) are written as

$$\dot{S}^{(\alpha)} = \left[h_S - d_D\left(S^{(\alpha)}-S_0^{(\alpha)}\right)\right]\left|\dot{\gamma}^{(\alpha)}\right|, \quad (2)$$

$$\dot{B}^{(\alpha)} = h_B\dot{\gamma}^{(\alpha)} - r_D^{(\alpha)}B^{(\alpha)}\left|\dot{\gamma}^{(\alpha)}\right|, \quad (3)$$

in which $r_D^{(\alpha)} = \frac{h_B\mu_0}{S^{(\alpha)}}\left\{\frac{\mu_0'}{f_c\lambda}-\mu\right\}^{-1}$ and S_0, h_B, h_S, d_D, μ_0', f_c, λ, are constants that differ for octahedral and cube slip planes (see Table 1). The initial values are specified as S_0 for the slip resistance and zero for the back stress. This formulation considers 12 octahedral and 6 cube slip systems and was implemented as a user-material subroutine (UMAT) in ABAQUS 6.9 [4] using an implicit integration scheme. Discussion of model parameters and their estimation can be found in Ref. [1].

2.2 Fatigue driving force

During crack nucleation and early growth, the local fatigue driving force is affected by the microstructure, which has particular implications for microstructurally small cracks (MSCs). Hence,

Table 1. Parameters of the constitutive model at 650°C for octahedral and cube slip systems.

	F_0 kJ/mol	p	Q	$\dot{\gamma}_0\ s^{-1}$	τ_0 *GPa*	S_0 *MPa*	f_c	h_B *GPa*	h_S *GPa*	d_D *MPa*	μ_0' *GPa*
Oct.	295	0.31	1.8	120	810	350	0.42	400	10	6024	72.3
Cube	295	0.99	1.6	4	630	48	0.18	100	4.5	24	28.6

Other: λ=0.85, μ_0' = 192GPa. Elastic constants: C_{11} = 166.2GPa, C_{12} = 66.3GPa, C_{44} = 138.2GPa.

the driving force for early stage fatigue needs to be characterized with fatigue indicator parameters (FIPs) describing the local fields (rather than far field basis of the stress intensity factor in LEFM). The present approach quantifies the driving force with a crystallographic version of the Fatemi-Socie parameter adapted to evaluate the FIP on each octahedral slip system, i.e.,

$$\mathrm{FIP}^{\alpha} = \frac{\Delta\gamma_p^{\alpha}}{2}\left(1 + k\frac{\sigma_n^{\alpha}}{\sigma_y}\right) \tag{4}$$

where $\Delta\gamma_p^{\alpha}$ is the cyclic plastic shear strain range on slip system α, σ_n^{α} is the peak stress normal to this slip system, σ_y is the cyclic uniaxial yield strength of the polycrystal, and *k=0.5*, as proposed by Fatemi and Socie [5]. Several investigators have successfully employed approaches akin to the Fatemi-Socie parameter along with crystal plasticity formulations for studying the effects of microstructure on fatigue life [6][7]. The value of such a parameter was further explored by Reddy and Fatemi [8], who postulated that the Fatemi-Socie parameter represents the fatigue driving force and plays a role similar to that of the ΔK or the ΔJ in predicting fatigue crack formation and early growth. Recently, Castelluccio and McDowell [9] correlated the Fatemi-Socie parameter with the cyclic crack tip displacement using crystal plasticity simulations. To numerically regularize the FEM discretization and also to represent the finite physical scale of the fatigue damage process zone, the FIP^{α} values are calculated at each integration point and then averaged along bands (i.e., nonlocal FIPs), parallel to slip planes across entire grains, as depicted in Figure 1.

2.2.1 Life estimation

This approach focuses on the interaction between small fatigue cracks and the microstructure at a mesoscale level; therefore, crack growth on a grain-by-grain basis. In other words, the number of cycles to crack the first grain (nucleation) is first computed, and then the cycles required to extend the microstructurally small crack within each of the neighboring grains is computed. Each nonlocal FIP is employed in fatigue life correlations using a hierarchical approach to estimate the life to completely crack a grain along a band. The nucleation relation is assumed to follow the semi-empirical empirical law [6]

$$N_{nuc} = \frac{\alpha_g}{d_{gr}}(FIP^{\alpha})^{-2}, \tag{5}$$

where α_g is an irreversibility coefficient and d_{gr} is a length scale of the current grain calculated as:

$$d_{gr} = D_{st} + \sum_{i}^{n} \omega^i D_{nd}{}^i, \tag{6}$$

in which ω^i is the disorientation factor for grain i, D_{st} is related to the length of the band considered and D^i_{nd} relates to the length of all n intersecting bands in adjacent grains. The values of D_{st} and D^i_{nd} are calculated for each averaging band as the square root of the area of the band. The disorientation factor is computed as

$$\omega = \left\langle 1 - \frac{\theta_{dis}}{20^o} \right\rangle \tag{7}$$

Here, θ_{dis} is the disorientation angle between two grains, and the Macaulay brackets satisfy that $<a>=a$ if $a > 0$, $<a>=0$ if $a \le 0$. Thus, ω = 1 when there is no disorientation (i.e., the grain and the neighbor have exactly the same orientation and should be a single grain) and ω = 0 if the disorientation is 20° or larger. The disorientation factor for randomly oriented grains results in non-zero values for fewer than 10% of the grain boundaries.

The MSC crack growth rate is assumed to be controlled by the mechanical irreversibility of dislocations emitted from the crack tip and proportional to the crack tip displacement range, i.e.,

$$\left.\frac{da}{dN}\right|_{msc}^{\alpha} = \phi \left\langle A \quad \mathrm{FIP}^{\alpha} - \Delta \mathrm{CTD}_{\mathrm{th}} \right\rangle, \tag{8}$$

where $(A \sim 2)$ is a scaling constant that depends on microstructure attributes, $\Delta \mathrm{CTD}_{\mathrm{th}}$ is a threshold that has a value close to the magnitude of the Burgers vector. The factor $\phi=0.077$ measures the mechanical irreversibility at the crack tip process zone and depends on environment. The number of cycles to extend the crack front through the i^{th} grain along slip system α in the MSC regime, $N_{G_i}|_{MSC}^{\alpha}$, is determined by integrating Equation (8) with respect to the crack length. The crack growth rate

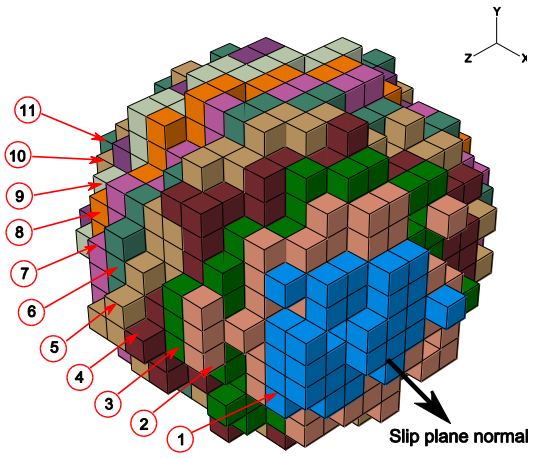

Figure 1: Schematic representation of elements, bands and grains in which FIPs are averaged to estimate transgranular fatigue crack growth. The implementation in a FEM model with unstructured, voxellated meshing is shown, with bands color coded and numbered for a single spherical grain.

depends on the crack length/size within the i^{th} grain, which varies from an uncracked to a fully cracked grain. To integrate analytically Equation (8), we consider that the mean evolution of FIP^{α} inside the grain follows a decreasing law, i.e.,

$$\mathrm{FIP}^{\alpha} = \mathrm{FIP}_o^{\alpha}\left(1-\frac{1}{2}a_i^2\right) \tag{9}$$

Here, a_i is defined here as the *fraction* of the area of the i^{th} grain to have cracked (nondimensional measure of cracked area of slip plane within the grain), and FIP_o^{α} represents the FIP value for the i^{th} grain on the α^{th} slip system along which a_i is measured, *before the grain is cracked*. Interestingly, Equation (9) resembles the empirical laws proposed by Hobson et al. [10] [11] and Miller [12] and has been validated using FEM simulations [1].

After integrating, the total life consumed in the MSC regime (N_{MSC}) is the sum of the lives for each grain involved in the growth process for a given 3D crack, i.e.,

$$N_{MSC} = \sum_i N_i\,|_{MSC}^{\alpha} \,. \tag{10}$$

where
$$N_i\,|_{MSC}^{\alpha} = N_{G_i}\,|_{MSC}^{\alpha} - N_{History} = \frac{1}{\sqrt{c_1 c_2}}\tanh^{-1}\left(D_{st}\sqrt{\frac{c_2}{c_1}}\right) - N_{History} \tag{11}$$

$$c_1 = \phi\,\frac{D_{st}+\sum_i^n \omega^i D_{nd}{}^i}{d_{gr}^{ref}}\,2\mathrm{FIP}_0^{\alpha} - \phi\,\Delta\mathrm{CTD}_{th} \quad \text{and} \quad c_2 = \phi\,\frac{\mathrm{FIP}_0^{\alpha}}{\left(D_{st}+\sum_i^n \omega^i D_{nd}{}^i\right) d_{gr}^{ref}} \tag{12}$$

Here, $N_{History}$ corresponds to the number of cycles undergone since the band considered has intersected the crack perimeter, and is necessary to include since cracks grow in multiple grains along a 3D crack front. Further details can be found in Refs. [1][2].

2.3 Crack growth model

To compute stress redistribution due to an increment in crack length, we employ an isotropic damage model along the bands having FIP values that lead to minimum fatigue lives. For the elements within these bands, the elastic stiffness tensor $\bar{\mathbf{C}}$ is degraded according to damage parameter d_1, i.e.,

$$\bar{\mathbf{C}} = (1-d_1)\mathbf{C} \tag{13}$$

Here, d_1 varies from 0 (uncracked) to 0.99, at which point full damage is assumed. The elastic stiffness is degraded for those elements in bands along which the crack is assumed to grow. The degradation of the elastic stiffness requires a gradual increase of parameter d_1 to achieve convergence of the FEM solution. Accordingly, the degradation is imposed over several time steps, i.e., for the current time step Δt^i we write

$$d_1^{(i+1)} = d_1^{(i)} \pm \nu \, \Delta t^i \tag{14}$$

For example, a value of $\nu = 2$ was enough to increase d_1 up to 0.99 by the end of the 1-second half loading cycle; of course, ν can be varied to accelerate crack stiffness reduction and to allow for convergence while computing stress redistribution effects in the polycrystal over a few computational cycles. Of course, this represents evolution over a much larger number of applied fatigue loading cycles. The plus sign corresponds to the case in which the stress normal to the band is positive and the crack plane is in tension. On the contrary, if the stress normal to the band is in compression, the crack is assumed to be closed and d_1 is decreased to zero at a rate proportional to the time step, as described by the minus sign in Equation (14).

When roughness- or plasticity-induced closure conditions are detected by virtue of compressive traction normal to the crack face on individual elements, the value of d_1 is decreased to 0 such that the initial elastic stiffness is restored. Hence, the degradation of the stiffness tensor is performed on a grain-by-grain basis by increasing the parameter d_1 in all the elements after predicting the path of the crack in the following grain. Such a prediction is performed every two computational loading cycles to allow for stiffness degradation and the update of the stress and strain fields.

In summary, the fatigue algorithm starts by calculating the nonlocal FIP values on every band in every grain over the third computational cycle, and proceeds by calculating the number of expected cycles to nucleate crack on all bands for all grains using Equation (5). The elements within the band with the lowest nucleate life are marked as "cracked," and the model applies again a couple of computational loading cycles to update the FIP values and to degraded (d_1 increased) the stiffness tensor as necessary to represent crack growth. Thereafter, the algorithm computes the MSC life of all FIP averaging bands that intersect the crack perimeter and renders the elements in the band with minimum life as cracked. The simulation proceeds by applying further loading cycles, in which the stiffness tensor is degraded on the cracked elements to redistribute stress and plastic strain, while checking for grain level closure effects of cracked grains, and the MSC life is evaluated again on the remaining grains. Since we seek to describe the dominant crack, only one crack nucleates per realization.

3 Simulation results

3.1 Specimens and loading conditions

Figure 2 depicts the C3D8R-element meshes employed for modeling smooth and notched specimens, each color representing a different crystallographic orientation. The grain size follows a lognormal distribution based on the algorithm by Musinski [13] with a mean value of 18μm. The straining sequence consisted of triangular relative displacement of the upper and lower boundary planes at a 0.05%/s strain rate under shear or tensile mode loading to achieve an overall nominal strain range of 0.8%; lateral faces are free of traction. Simulations with different strain ratios employed a similar strain range to assess only the effect of applied strain ratios (strain/displacement conditions).

To achieve equivalence with tensile straining, the magnitude of the displacement vector in shear straining was computed by assuming an elastic model with cubic symmetry. The value of Poisson's

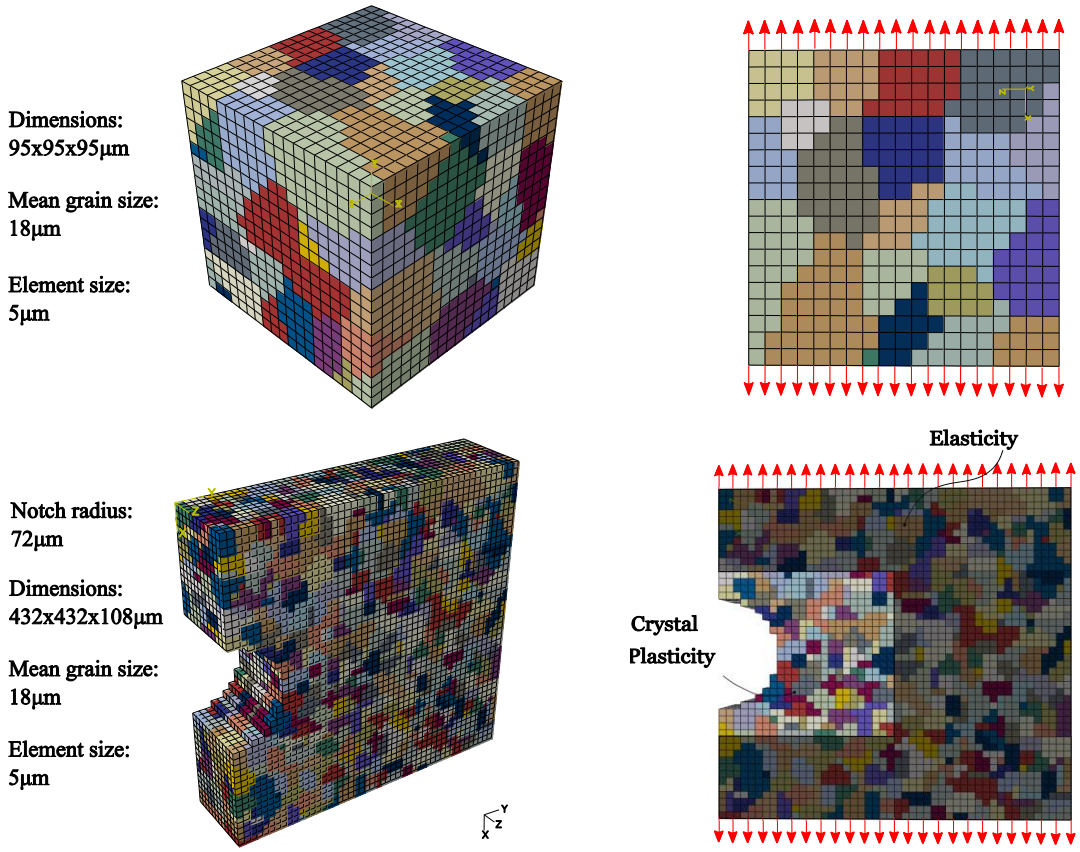

Figure 2. Example of voxellated meshes representing the explicit polycrystalline microstructure for axial straining of smooth (top) and notched (bottom) specimens. Triangular straining sequence is applied by displacing the upper and bottom faces of the meshes at 0.05%/s strain rate.

ratio was deduced to compute the equivalent pure shear strain for $R_\varepsilon = 0$. The 0.8% uniaxial strain range is equivalent in shear to

$$\Delta\gamma_{eq} = (1+\nu)\Delta\varepsilon_1 = (1+\nu)0.8\% = (1+0.3989)0.8\% = 1.119\% \tag{15}$$

Thus, the upper and lower faces were displaced in shear up to a nominal shear strain of 1.119% for equivalence in this particular case. The Poisson's ratio was deduced using an elastic model with cubic symmetry, i.e.,

$$\nu = \frac{C_{12}}{C_{11}} = \frac{66.3}{166.2} = 0.399 \tag{16}$$

3.2 Crack growth vs cycles for smooth specimens

Smooth specimens were employed to simulate shear and tension-compression straining at 650°C for under three strain ratios $R_\varepsilon = \varepsilon_{min} / \varepsilon_{max}$ = -1, R_ε = 0 and R_ε = 0.5, all undergoing an equivalent nominal strain range of 0.8% at 0.05%/s strain rate. For each loading condition, a total of 10 equivalent microstructure realizations were simulated. The simulations considered unidirectional periodic boundary conditions, with lateral faces free of traction. Figure 3 presents crack length vs. life on a semi-log scale. Each data point corresponds to extending the crack by one grain and only lives below 10^9 are considered (otherwise considered as crack arrest, giving rise to run-out

behavior). These results support that uniaxial tension-compression straining is more detrimental than cyclic shear, by a factor of nominally two or greater on life.

Fatigue crack nucleation rather than fatigue crack growth seems particularly influenced for $R_\varepsilon = 0$ and $R_\varepsilon = 0.5$, which suggests that crack nucleation assisted by stress concentration (e.g., notch, pore, or inclusion) might exhibit a reduced dependence on the strain ratio. Furthermore, tension-compression fatigue life results seem to show slightly less variability, and for both displacement conditions, the variability seems to increase with decreasing strain ratio.

Figure 4 presents an example of the stress-strain evolution for one realization in tension after 20 straining cycles for three different strain ratios. As expected, higher strain ratios lead to higher tensile mean stresses. The mean stress evolves slowly and after 20 cycles the change is less 10%; therefore we may consider that the fatigue life estimations are performed at a relatively stable mean stress level for each strain ratio. Even when mean stress assessed may differ from a fully relaxed state, the fatigue model was calibrated under similar conditions [1], which reduces the inaccuracies.

3.3 Crack growth vs cycles for notched specimens

Figure 5 presents the simulation results for three strain ratios using models with a notch root radius of 144 μm and a similar microstructure. Compared to the smooth specimens, the results from models with a notch show a reduction in fatigue life of about an order of magnitude. As expected, the lower the strain ratio, the larger the fatigue life, while tension-compression simulations resulted in lower lives than shear loading. However, the separation in life between tension-compression and shear cases increases with decreasing strain ratio, which was not clearly observed in simulations with smooth specimens. Note that the cracks for the shear case did not nucleate at the notch, but grew in the bulk of the specimen. The computed results for tension-compression, which nucleated the crack at the notch, lie within two orders of magnitude on life. In the case of shear loading, the life is longer and exhibits greater scatter as the cracks formed in the bulk of the specimen.

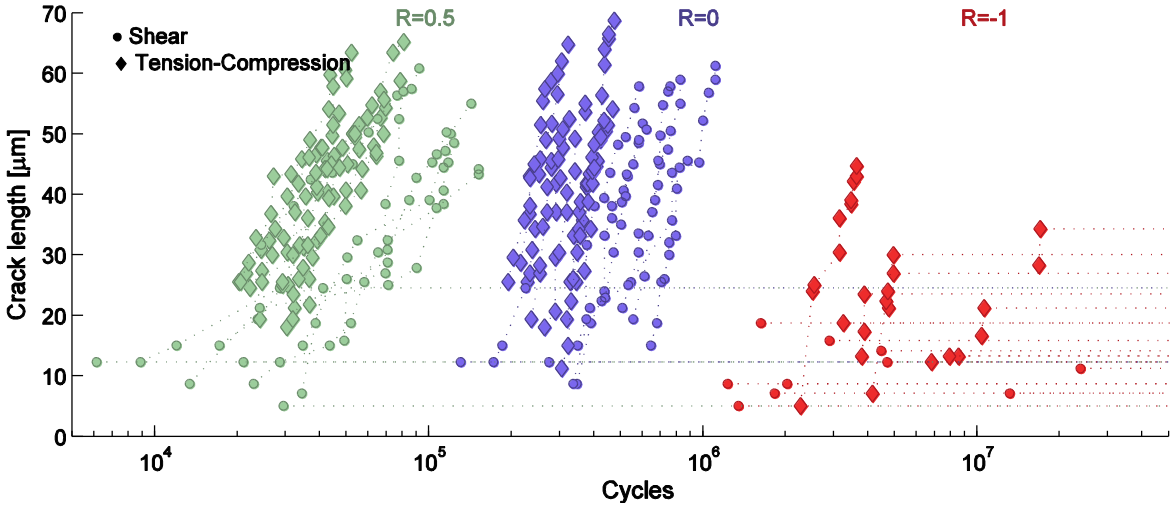

Figure 3. Comparison of the results for strain ratios $R_\varepsilon = 0$, $R_\varepsilon = 0.5$ and $R_\varepsilon = -1$ using simulations with unidirectional periodic conditions undergoing an equivalent nominal strain range of 0.8%.

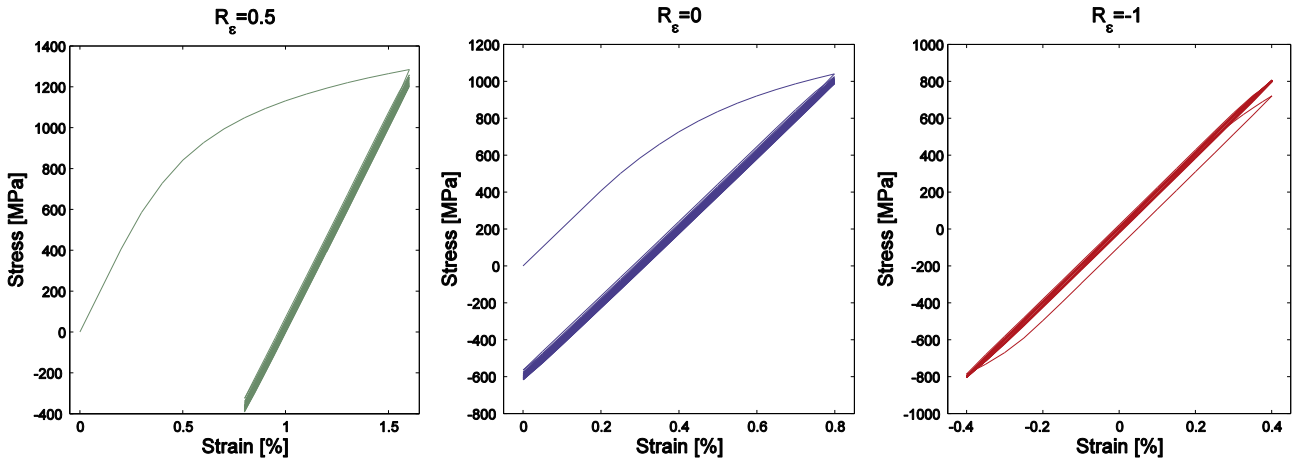

Figure 4. Stress-strain responses of a smooth specimen microstructure realization and three strain ratios over 20 uniaxial straining cycles.

4 Discussion and conclusions

The simulations showed quantitatively the detrimental effects of higher strain ratios, which change orders of magnitude the cycles required to grow a crack of similar lengths. Furthermore, in all cases tension-compression straining was more damaging than shear straining, which has been reported in the literature for other materials [14][15]. The results for smooth specimens exhibited a spread of fatigue life over three orders of magnitude for strain ratios between $R_\varepsilon = 0.5$ and $R_\varepsilon = -1$, for shear and tension-compression loading. Notched specimens under tension-compression loading showed a smaller spread, which is explained by a reduction of the variability in nucleating a crack. This effect dominates over the reduction of the highly strained volume around the notch. In the case of notches under shear, the cracks nucleated within the bulk of the specimen (not at the notch), and the results are comparable to those found for smooth specimens.

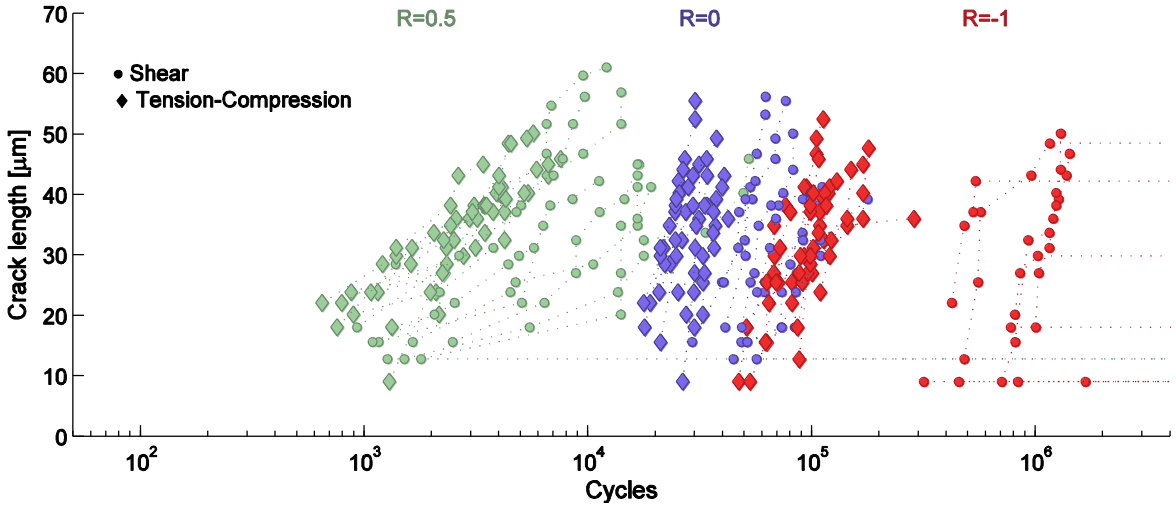

Figure 5. Comparison of the results for strain ratios $R_\varepsilon = 0$, $R_\varepsilon = 0.5$ and $R_\varepsilon = -1$ on a logarithmic scale for notched specimens undergoing an equivalent nominal strain range of 0.8%.

Acknowledgements

G. M. Castelluccio and D.L. McDowell are deeply grateful for the support provided by Integrated Systems Solutions, Inc. (Technical Monitor: Dr. Nam Phan, NAVAIR).

References

[1] G. M. Castelluccio, 'A study on the influence of microstructure on small fatigue cracks', PhD Thesis, Georgia Institute of Technology, Atlanta, GA, USA, 2012.

[2] G. Castelluccio, D. L. McDowell, 'Fatigue Life Prediction of Microstructures'. In *Proceedings of the ASME International Mechanical Engineering Congress and Exposition*. Houston, Texas, USA: ASME, 2012.

[3] B. Lin, L. G. Zhao, J. Tong, and H.-J. Christ, 'Crystal plasticity modeling of cyclic deformation for a polycrystalline nickel-based superalloy at high temperature', *Mater. Sci. Eng., A,* 527(15), 3581–3587, 2010.

[4] ABAQUS, *FEM software V6.9, Simulia Corp., Providence, RI, USA*. Providence, RI, USA: Simulia, Inc., 2009.

[5] A. Fatemi, D. F. Socie. A critical plane approach to multiaxial fatigue damage including out-of-phase loading. *Fatigue Fract. Eng. Mater. Struct.*, 11(3), 149--165, 1988.

[6] M. Shenoy, J. Zhang, and D. L. McDowell, "Estimating fatigue sensitivity to polycrystalline Ni-base superalloy microstructures using a computational approach," *Fatigue Fract. Eng. Mater. Struct.*, (10) , 889-904, 2007.

[7] C. Przybyla, R. Prasannavenkatesan, N. Salajegheh, and D. L. McDowell, 'Microstructure-sensitive modeling of high cycle fatigue', *Int. J. Fatigue*, 32 (3), 512–525, 2010.

[8] S. C. Reddy and A. Fatemi, 'Small Crack Growth in Multiaxial Fatigue', in *Advances in Fatigue Lifetime Predictive Techniques*, ASTM, 1992, 276–298.

[9] G. M. Castelluccio and D. L. McDowell, "Assessment of Small Fatigue Crack Growth Driving Forces in Single Crystals with and without Slip Bands, *Int. J. Fracture*, 176(1), 49-64 2012.

[10] P. D. Hobson, "The formulation of a crack-growth Equation for short cracks," *Fat. Eng. Mater. Struct.*, 5 (4) , 323-327, 1982.

[11] P. D. Hobson, M. W. Brown, and E. R. de los Rios, "Two Phases of Short Crack Growth in a Medium Carbon Steel," in *The behaviour of short fatigue cracks* (London: Mechanical Engineering Publications, 1986), 441-459.

[12] K. Miller, "The three thresholds for fatigue crack propagation," in *Fatigue and Fracture Mechanics: 27th volume*, ASTM STP 1296 (1997), 267-286.

[13] W. D. Musinski, D. L. McDowell, Microstructure-sensitive probabilistic modeling of HCF crack initiation and early crack growth in Ni-base superalloy IN100 notched components. *Int. J. Fatigue*, 37, 41–53, 2012.

[14] F. A. Kandil, M. W. Brown, and K. J. Miller. "Biaxial Low Cycle Fatigue Failure of 316 Stainless Steel at Elevated Temperatures," In *Metal Society Book 280*, 203–210. Varese, Italy: Metal Society of London, 1982.

[15] H. A. Suhartono , K. Pötter, A. Schram, and H. Zenner. "Modeling of Short Crack Growth Under Biaxial Fatigue: Comparison Between Simulation and Experiment," 323–339. ASTM STP 1387, 2000.

Variability of the Fatigue Driving Force within Grains of Polycrystals

Gustavo M. Castelluccio[1,*], David L. McDowell[1,2]

[1] Woodruff School of Mechanical Engineering
2 School of Materials Science and Engineering
Georgia Institute of Technology, 771 Ferst Drive, N.W, Atlanta, Georgia 30332, USA
* Corresponding author: castellg@gatech.edu

Abstract Experimental studies in the last few decades have exhibited higher fatigue crack growth rates for cracks with size on the order of grains than would be predicted using growth laws based on LEFM. Small crystallographic fatigue cracks are affected by microstructure features that are not captured by traditional homogenous fracture mechanics theories (i.e., LEFM, EPFM). Since far-field driving force parameters cannot capture the intrinsic variability of the local fatigue driving force of small cracks induced by microstructure, alternative measures of the fatigue driving force are sought. This work employs finite element simulations that explicitly render the polycrystalline microstructure to compare nonlocal fatigue indicator parameters (FIPs) averaged over multiple volumes. The model employs a crystal plasticity algorithm in ABAQUS calibrated to study the effect of microstructure on early fatigue life of Ni-base RR1000 superalloy at elevated temperature under constant amplitude loading. The results indicate slight differences in the extreme values of distributions of FIPs for each element, slip plane cross-section (bands) and grain volumes. Furthermore, the grain average FIP better reflects the driving force for cracks on the cross section at the center of the grain while the extremes values of the FIPs averaged along bands tend to be located away from the grain centers.

Keywords Fatigue Indicator Parameter, Microstructurally Small Cracks, Fatigue Driving Force

1 Introduction

Extensive literature shows that fatigue experiments on metals in the high cycle fatigue (HCF) regime present variability in fatigue life of over a factor of 10. Multiple investigators have demonstrated that the underlying microstructural attributes [1][2] (i.e., grain size effects, elastic and plastic anisotropy, pre-existing defects) are usually responsible for the large variation in fatigue life. Indeed, in the HCF regime, the heterogeneous plastic deformation within favorably oriented and/or highly stressed grains controls the nucleation and early growth of fatigue cracks.

Recent finite element approaches that render the microstructure of metallic alloys have estimated the fatigue damage by assessing nonlocal fatigue indicator parameters (FIPs). These parameters typically refer to the value of the FIP averaged over certain mesoscale volumes (e.g., grain volumes). In contrast to local magnitudes within each finite element, these nonlocal FIPS mitigate effects of the mesh sensitivity and represent the physical length scale over which the fatigue damage occurs. Recent work [3][4] pursued definition of the averaging volume in terms of bands

that lie parallel to the crystallographic slip planes and have a width of one element. These bands seek to reflect domains in which cyclic plastic deformation localizes via dislocation dipole structures and in experimentally observed persistent slip bands.

By averaging the local FIPs over bands [3], a methodology was developed that predicts the path of a fatigue crack along bands through multiple grains, considering grain size effects [4]. The fact that FIPs can be averaged over multiple volumes (sizes and shapes) raises questions about the role of volume domains for averaging on the variability of nonlocal FIPs and the influence of grain size effects on the variance of the distribution of fatigue life.

This work employs a crystal plasticity finite element model for RR1000 Ni-base superalloy to compare the variability of the Fatemi-Socie FIPs averaged over grains or bands, and its local magnitudes for a number of realizations of ostensibly the same microstructure. The influence of grain size effects on normalized FIP distributions is also considered.

2 Modeling and simulation

2.1 Constitutive model

At the scale of individual grains we employ a physically-based crystal plasticity constitutive model for RR1000 superalloy adapted from the work of Lin et al. [5]. The crystallographic shearing rate is given by

$$\dot{\gamma}^{(\alpha)} = \dot{\gamma}_0 \exp\left[-\left(\frac{F_0}{k_b T} \right) \left\langle 1 - \left\langle \frac{\left| \tau^{(\alpha)} - B^{(\alpha)} \right| - S^{(\alpha)} \mu/\mu_0}{\tau_0 \mu/\mu_0} \right\rangle^p \right\rangle^q \right] sgn\left(\tau^{(\alpha)} - B^{(\alpha)} \right), \quad (1)$$

in which $\dot{\gamma}^{(\alpha)}$ is the shearing rate of slip system α, $\tau^{(\alpha)}$ is the resolved shear stress, T is the absolute temperature, F_o, p, q, $\dot{\gamma}_0$, τ_0, μ, and μ_0 are material parameters that may differ for octahedral and cube slip systems, as listed in Table 1 for 650°C, and k_b is Boltzmann's constant. This formulation considers 12 octahedral and 6 cube slip systems, the latter representing a zigzag deformation mechanism [6] along octahedral planes, but producing net slip along cube planes. The model was implemented as a user-material subroutine (UMAT) in ABAQUS 6.9 [7] using an implicit integration scheme based on the Newton-Raphson and the backward-Euler methods. Discussion of model parameters and their estimation can be found in Ref. [8].

The slip system shearing rate relation includes a directional slip resistance $S^{(\alpha)}$ that functions as a theshold stress below which no plastic flow occurs and a back stress $B^{(\alpha)}$ that accounts for directional hardening (Bauschinger effects) on the slip system. The evolution laws for slip resistance and back stress are written as

$$\dot{S}^{(\alpha)} = \left[h_S - d_D \left(S^{(\alpha)} - S_0^{(\alpha)} \right) \right] \left| \dot{\gamma}^{(\alpha)} \right| \quad (2)$$

$$\dot{B}^{(\alpha)} = h_B \dot{\gamma}^{(\alpha)} - r_D^{(\alpha)} B^{(\alpha)} \left| \dot{\gamma}^{(\alpha)} \right|, \tag{3}$$

in which $r_D^{(\alpha)} = \frac{h_B \mu_0}{S^{(\alpha)}} \left\{ \frac{\mu_0'}{f_c \lambda} - \mu \right\}^{-1}$ and S_0, h_B, h_S, d_D, μ_0', f_c, λ, are constants that differ for octahedral and cube slip planes (see Table 1). Both evolution equations follow a hardening-dynamic recovery format and the initial values are specified as S_0 for the slip resistance and zero for the back stress.

Table 1. Parameters of the constitutive model at 650°C for octahedral and cube slip systems.

	F_0 kJ/mol	p	Q	$\dot{\gamma}_0 s^{-1}$	τ_0 *GPa*	S_0 *MPa*	f_c	h_B *GPa*	h_S *GPa*	d_D *MPa*	μ'_0 *GPa*
Oct.	295	0.31	1.8	120	810	350	0.42	400	10	6024	72.3
Cube	295	0.99	1.6	4	630	48	0.18	100	4.5	24	28.6

Other parameters: λ=0.85, μ_0= 192GPa.
Elastic constants: C_{11} = 166.2GPa, C_{12} = 66.3GPa, C_{44} = 138.2GPa.

2.2 Simulations

Figure 1 depicts a mesh composed of "brick" elements (C3D8R) employed for modeling smooth specimens, containing 6859 elements and 118 grains, with colors representing different crystallographic orientations. The loading sequence consisted of relative displacement of the upper and lower boundary planes at a 0.05%/s strain rate under tensile mode loading to achieve overall nominal peak strains of 0.8% and strain ratio (R_ε) equal to zero, typical of the HCF regime. The lateral faces are free of traction and the model has unidirectional periodic boundary conditions along the loading direction (Y-axis) such that the sum of the displacement perturbations of the nodes on top and bottom faces relative to the mean is null, leaving only the imposed net relative displacement. The grain size follows a lognormal distribution based on the algorithm by Musinski [9] and has a mean grain size about 18 μm.

2.3 Fatigue driving force measures

Since the local driving force to nucleate and grow fatigue cracks is affected by the microstructure, several FIPs have been proposed to consider these effects. Fatemi and Socie [10] proposed a FIP based on the critical plane approach that plays a role similar to that of the mixed mode ΔCTD or ΔJ-integral in correlating with growth of small fatigue cracks [11][12][13]. Subsequently, several investigators have successfully employed approaches akin to such FIP along with crystal plasticity formulations for studying the effects of microstructure on fatigue crack formation and early growth within the first few grains [14][15][16].

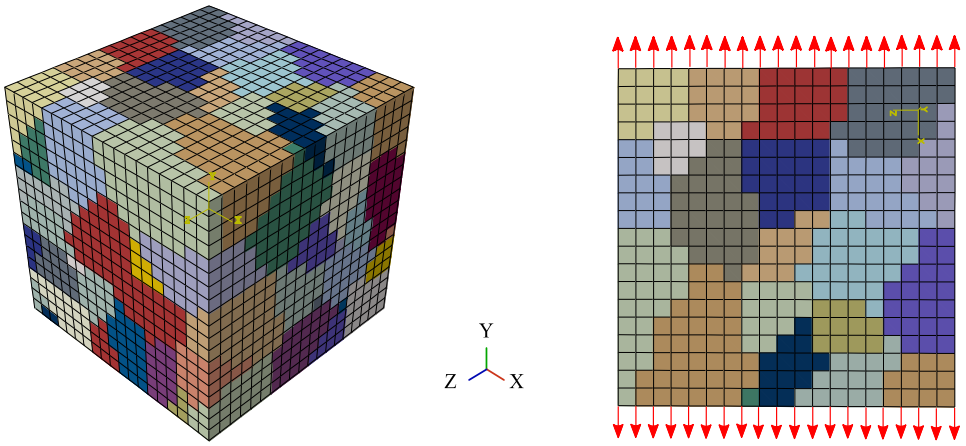

Figure 1. Example of a mesh with the explicit microstructure for axial loading of smooth specimens. Quasistatic mean relative displacement of the upper and lower boundary planes is depicted by the red arrows.

Castelluccio and McDowell [3] proposed to quantify the driving force for transgranular failure with a crystallographic version of the Fatemi-Socie FIP defined for each octahedral slip system, i.e.,

$$\mathrm{FIP}^{\alpha} = \frac{\Delta\gamma_p^{\alpha}}{2}\left(1 + k\frac{\sigma_n^{\alpha}}{\sigma_y}\right) \tag{4}$$

where $\Delta\gamma_p^{\alpha}$ is the cyclic plastic shear strain range on slip system α, σ_n^{α} is the peak stress normal to this slip system, σ_y is the cyclic uniaxial yield strength of the polycrystal, and $k = 1$, as proposed by Fatemi and Socie [10]. The algorithm computes the FIP on each slip system and for each element using the range of plastic strain over the third loading cycle [3]. This methodology allows for an approximate stress redistribution to almost represent "steady state" cyclic conditions in terms of stress and plastic strain redistribution within the polycrystal in the HCF regime, since the microstructure exerts a dominant influence on the transient cyclic plastic deformation fields.

2.3.1 Mesoscale averaging volumes for FIPs

To numerically regularize the FEM discretization and also to represent the finite physical scale of the fatigue damage process zone, the FIPs calculated at each integration point in the mesh are averaged over a selected mesoscale volume. In the present approach we consider three volumes (Figure 2): (i) individual elements, (ii) bands parallel to slip planes, and (iii) entire grain volume. Figure 2 presents a cluster of finite elements that form one grain. Each grain is subdivided in bands of one element of width that are parallel to slip planes as described in Refs. [3][4][8]. The nonlocal FIP is averaged separately over each of these volumes—elements, bands and grains.

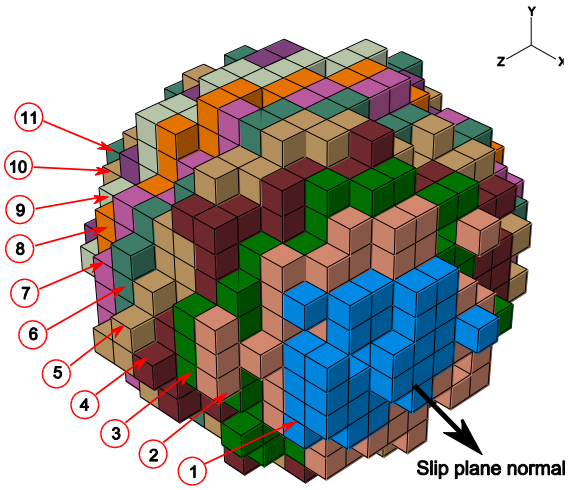

Figure 2: Schematic representation of elements, bands and grains in which FIPs are averaged to estimate transgranular fatigue crack growth. The implementation in a FEM model with unstructured, voxellated meshing is shown, with bands color coded and numbered for a single spherical grain.

3 Assessment of non-local FIP averaging volumes

A total of 50 equivalent realizations with random grain distributions for nominally the same microstructure with mean grain size of about 18 μm were utilized to compare the FIP averaged over grains (FIP_{grains}), bands (FIP_{band}), or the local FIP on every element ($FIP_{element}$). In each case, the average is computed for each octahedral slip system over the corresponding domain.

Figure 3 presents the distributions of the FIP for each element ($FIP_{element}$) and the averages over bands (FIP_{band}) and grains (FIP_{grains}) compiled from 50 equivalent realizations considering all the octahedral slip systems. Since fatigue life is dominated by the extreme distributions, these results consider only values larger than FIP_{thresh} =MAX(FIP_{grains})/1000. The three cases present similar distributions and the extreme value of the three distributions lie between $2x10^{-3}$ and $3x10^{-3}$. Since elements are smaller than the grain scale, the FIPs averaged over elements have somewhat higher extreme values than either grain- or band-averaged FIPs.

Figure 4 presents the distributions of band-averaged FIPs that result from dividing the grain into seven regions, each aligned along slip planes which are oriented perpendicular to the slip plane normal. Note that the number of bands per grain is not constant, so each region may include more than one band from a single grain and slip system. The FIP_{band} presents similar distributions from all sections of the grains, which suggests that there is no dependence of the FIPs on the section from which it belongs (e.g., closer to the center of the grain).

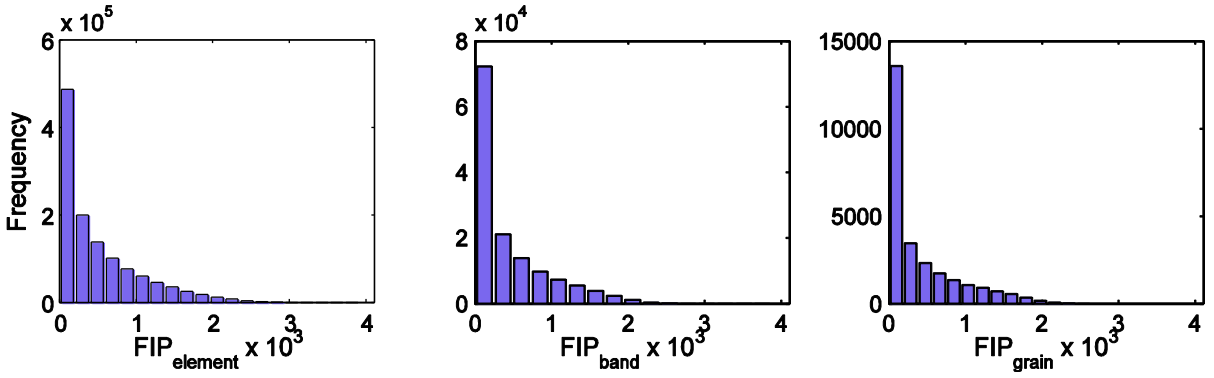

Figure 3. Distributions of the FIP from each element, band and grain for values larger than FIP_{thresh} from 50 equivalent realizations.

To assess the difference between averaging over bands or grains, Figure 5 presents a series of histograms with ratio FIP_{band}/FIP_{grain}; such ratios are presented in a semi-log scale between 0.1 and 10 only considering FIP values larger than FIP_{thresh} for bands or grains. Furthermore, we classified the histograms with the sections from which they belong (rows 1 to 7) or the range of the FIP_{grain} (columns, the FIP increases to the right).

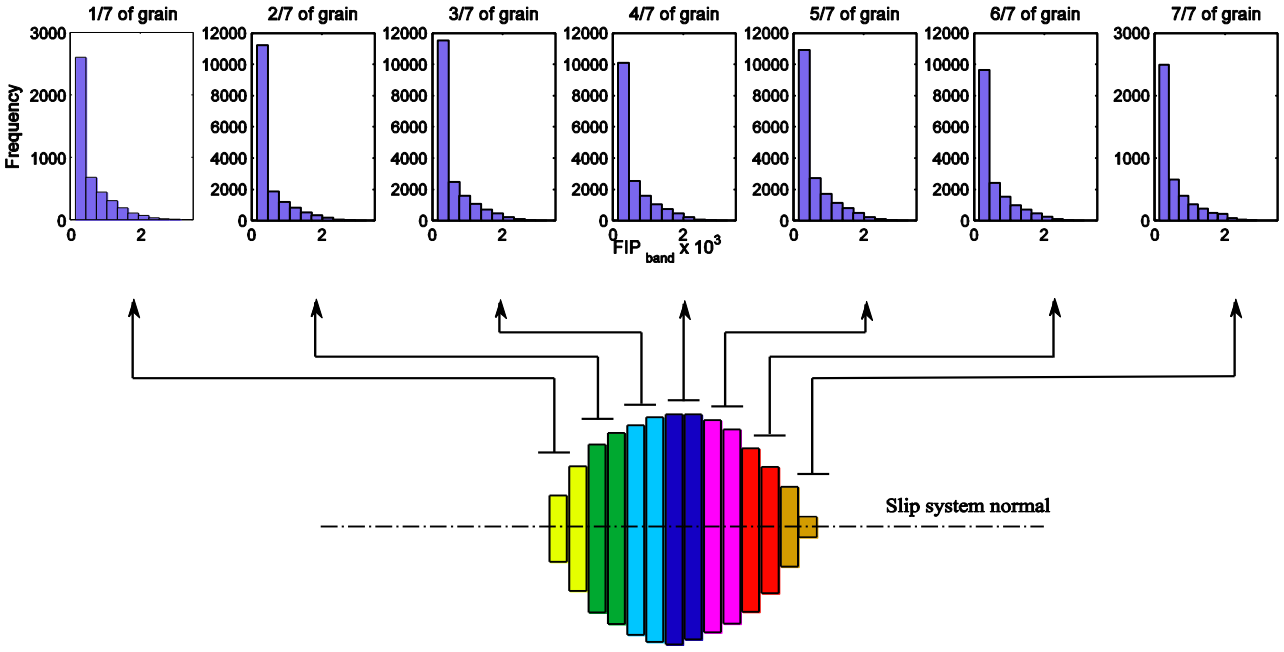

Figure 4. FIP_{band} distributions classified by the region they occupy within a grain, computed from 50 realizations. Only values larger than FIP_{thresh} are considered.

The results show that the variability of the ratio FIP_{band}/FIP_{grain} decreases both towards larger FIPs and the center of the grain. Therefore, the average of the FIP over the entire grain closely mimics the FIP computed at the center cross section of the grain for large values of FIPs.

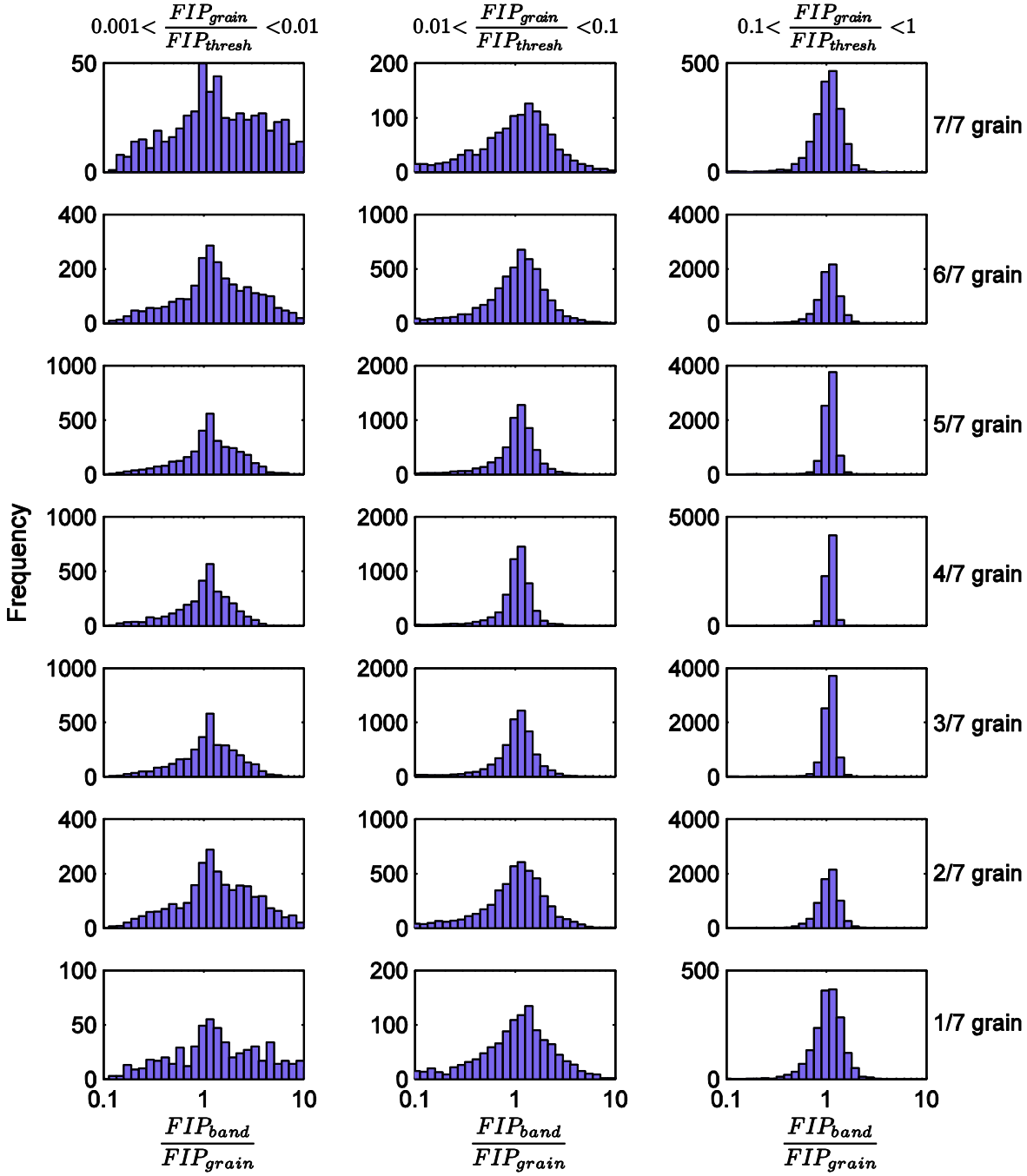

Figure 5. Distributions of the ratio between FIP_{band} and FIP_{grain}, classified by region they occupy in the grain (rows) and the intensity of the FIP_{band} and FIP_{grain} (columns).

3.1 Grain size effects

Grain size effects on fatigue crack formation and early transgranular growth have been modeled by

introducing a dependence of plastic deformation (or the FIP) on the grain size. Such a definition can be ambiguous since the "cross sectional area of the grain" differs for each slip plane that cuts through it. For example, the grain size can be computed for each band as the square root of the cross sectional area or as the diameter of a spherical grain with equivalent volume. Figure 6 presents the distributions of the size of the bands (scales as the square root of the number of elements within) and grains (scales as the cubic root of the number of elements within) normalized by the reference grain size (d_{gr}^{ref} =18μm.); the distributions are clearly different, with the same extreme values but a lower mean value for the band size distribution. In previous work [3][8] we have estimated the fatigue life to nucleate a crack by assuming a proportional dependence of the FIP on the normalized grain size, d_{gr}, (either the size of the band or the diameter of the grains) described by

$$A = d_{gr} \Big/ d_{gr}^{ref} \tag{5}$$

By multiplying A by the FIP we obtain the normalized driving force

$$A \cdot FIP = d_{gr} \Big/ d_{gr}^{ref} \; FIP \tag{6}$$

Distributions in Figure 7 present normalized values of $A \cdot FIP$. It is noted that, because the extreme values associated with FIP_{band} do not tend to be associated with the center of grains, the cross sectional dimension of their associated planes is usually smaller than the grain diameter based the cube root of the grain volume. Accordingly, the distributions of $A \cdot FIP_{band}$ and $A \cdot FIP_{grain}$ are very similar. However, the maximum extreme values of the grain-averaged FIPs are somewhat higher.

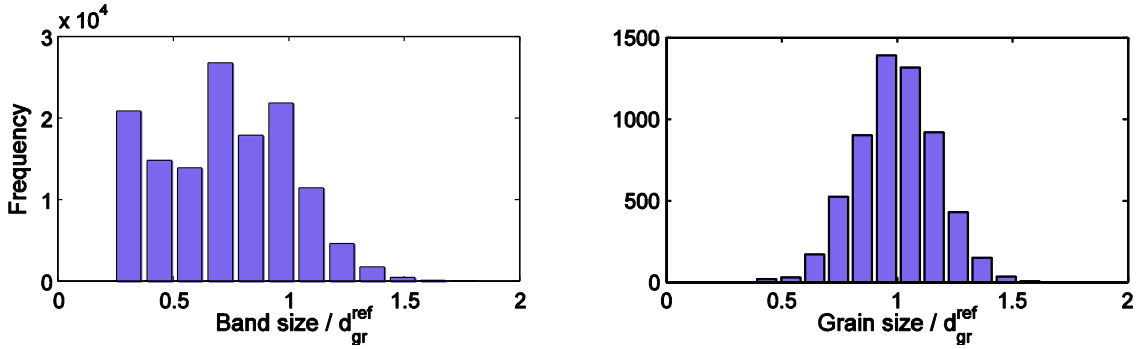

Figure 6. Distributions of the normalized size of bands (left) and grains (right).

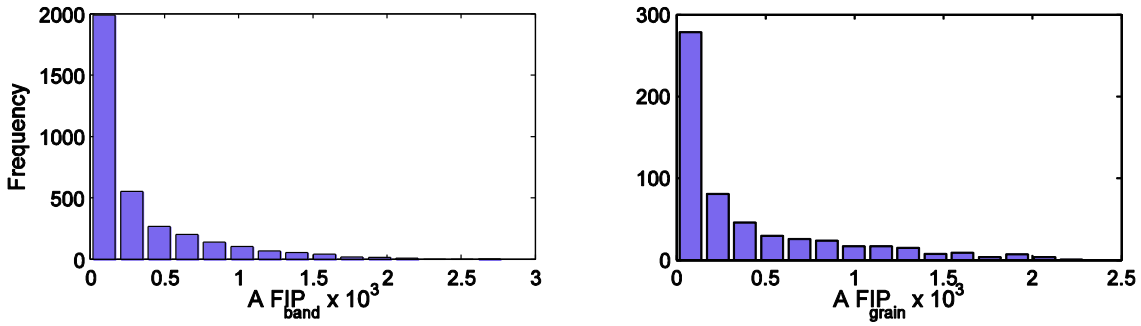

Figure 7. Distributions of the FIPs regularized with the grain size effects for bands, FIP_{band}, (left) and grains, FIP_{grain}, (right).

4 Conclusions

Results of this work support the following conclusions:

- The distributions of FIPs for each element, slip plane cross-section (bands) and the grain volume are very similar with only slight differences in the extreme values.
- Grain averages of FIP represents better the largest cross section representative of the center of the grain.
- The extremes values of the FIPs averaged along the slip plane cross-sectional area tend to be located away from the center of the grains.
- The methodology employed to define grain size effects can affect the variability of the fatigue driving force and modify the distribution of extreme FIP values.

Acknowledgements

G. M. Castelluccio and D.L. McDowell are deeply grateful for the support provided by Integrated Systems Solutions, Inc. (Technical Monitor: Dr. Nam Phan, NAVAIR).

References

[1] K. Gall, H. Sehitoglu, and Y. Kadioglu, 'A Methodology for Predicting Variability in Microstructurally Short Fatigue Crack Growth Rates', *J. Eng. Mater. Technol.*, vol. 119, no. 2, pp. 171–179, 1997.

[2] V. P. Bennett and D. L. McDowell, 'Polycrystal orientation distribution effects on microslip in high cycle fatigue', *Int J. Fatigue*, vol. 25, no. 1, pp. 27–39, Jan. 2003.

[3] G. Castelluccio, D. L. McDowell, 2013 Effect of annealing twins on crack initiation under high cycle fatigue conditions. *J.Mater. Sci.*, 48, 2376-2387, 2013.

[4] G. Castelluccio, D. L. McDowell, 'Fatigue Life Prediction of Microstructures'. In *Proceedings of the ASME International Mechanical Engineering Congress and Exposition*. Houston, Texas, USA: ASME, 2012.

[5] B. Lin, L. G. Zhao, J. Tong, and H.-J. Christ, 'Crystal plasticity modeling of cyclic deformation for a polycrystalline nickel-based superalloy at high temperature,' *Mater. Sci. Eng., A*, 527(15), 3581–3587, 2010.

[6] W. Österle, D. Bettge, B. Fedelich, and H. Klingelhöffer, 'Modelling the orientation and

direction dependence of the critical resolved shear stress of nickel-base superalloy single crystals', *Acta Mater.*, vol. 48, no. 3, pp. 689–700, Feb. 2000.

[7] ABAQUS, *FEM software V6.9, Simulia Corp., Providence, RI, USA*. Providence, RI, USA: Simulia, Inc., 2009.

[8] G. M. Castelluccio, 'A study on the influence of microstructure on small fatigue cracks', PhD Thesis, Georgia Institute of Technology, Atlanta, GA, USA, 2012.

[9] W. D. Musinski, D. L. McDowell, Microstructure-sensitive probabilistic modeling of HCF crack initiation and early crack growth in Ni-base superalloy IN100 notched components. *Int. J. Fatigue*, 37, 41–53, 2012.

[10] A. Fatemi, D. F. Socie, D. F., 1988. A critical plane approach to multiaxial fatigue damage including out-of-phase loading. *Fatigue Fract. Eng. Mater. Struct.*, 11(3), 149—165.

[11] S. C. Reddy and A. Fatemi, 'Small Crack Growth in Multiaxial Fatigue', in *Advances in Fatigue Lifetime Predictive Techniques*, ASTM, 1992, pp. 276–298.

[12] D. L. McDowell and J. Y. Berard, 'A ΔJ-based approach to Biaxial Fatigue', *Fatigue Fract. Eng. Mater. Struct.*, vol. 15, no. 8, pp. 719–741, 1992.

[13] G. M. Castelluccio and McDowell D. L., "Assessment of Small Fatigue Crack Growth Driving Forces in Single Crystals with and without Slip Bands, *Int. J. Fatigue*, 176(1) (2012): 49-64.

[14] K. Kirane, S. Ghosh, M. Groeber, and A. Bhattacharjee, 'Grain Level Dwell Fatigue Crack Nucleation Model for Ti Alloys Using Crystal Plasticity Finite Element Analysis', *J. Eng. Mater. Technol.*, vol. 131, no. 2, pp. 021003 1–14, 2009.

[15] C. Przybyla, R. Prasannavenkatesan, N. Salajegheh, and D. L. McDowell, 'Microstructure-sensitive modeling of high cycle fatigue', *Int. J. Fatigue*, vol. 32, no. 3, pp. 512–525, 2010.

[16] M. M. Shenoy, J. Zhang, and D. L. McDowell, 'Estimating fatigue sensitivity to polycrystalline Ni-base superalloy microstructures using a computational approach', *Fatigue Fract. Eng. Mater. Struct.*, vol. 30, no. 10, pp. 889–904, 2007.

Fatigue Crack Growth Rate Tests of High Performance Steel HPS 485W

Lan Duan[1], Chun-sheng Wang[1,*], Shi-chao Wang[1]

[1] Engineering Research Center for Large Highway Structure Safety of Ministry of Education, College of Highways, Chang'an University, 710064, China
* Corresponding author: wcs2000wcs@163.com

Abstract Research in this paper is about fatigue and fracture behavior of high performance steel HPS485W produced in Wuyang Steel Factory in China. Fatigue crack growth rate (da/dN) test was conducted for HPS 485W compact specimens with thickness of 7.5mm, 12.5mm and 19.5mm under different fatigue load ratio ($R=F_{min}/F_{max}$=0.1, 0.5 and 0.8), respectively. The seven-point incremental polynomial method was adopted for local fitting to obtain fatigue crack growth rate. The test results show that HPS485W has better crack growth resistance compared with traditional steel 14MnNb. What's more, specimen thickness is an influencing factor for crack growth rate, and fatigue crack growth rate increases with the increase of fatigue load ratio R. For 19.5mm specimen under fatigue load with R=0.1, the engineering threshold was tested and numerical calculation was conducted to obtain theoretical threshold. The calculated theoretical threshold is 7.22MPa.$m^{0.5}$. Fatigue life of high performance steel bridge can be predicated based on tested fatigue crack growth rate curve. Study in this paper serve as test basic for the fatigue control and fracture control of high performance steel bridge.

Keywords high performance steel, fatigue crack growth rate, stress intensity factor, threshold value, fracture

1. Introduction

High performance steel (HPS) for highway bridges was developed, which has superior characters in strength, weldability, toughness and corrosion resistance. Compared with steel bridge fabricated by traditional steel, these material characters bring several advantages to HPS bridges such as longer span length, easier fabrication, greater crack tolerance, elimination of painting in operation stage and so forth [1, 2]. Nowadays, about 250 HPS bridges have been constructed in the U.S., and all of these HPS bridges have demonstrated to be structural efficient and economical in whole life cycle [1]. So, the construction of HPS bridge is an attractive choice for modern society. However, with assumption that HPS detail has the same fatigue performance as conventional structural steel, effectively use of HPS may not be possible when fatigue limit state controlling the design [3].

Fatigue and fracture are typical failure mode for steel bridge. With purpose of ensuring high performance steel bridge operation safety, fracture failure control and remaining fatigue life calculation should be studied clearly. Thus, it's necessary in this paper to carry out study for fracture toughness and fatigue characters study for high performance steel Q&T HPS 485W, which is produced by Chinese Wuyang Iron and Steel Co., Ltd. [4]. In this paper, with purpose of remaining life calculation and safety assessment, fatigue crack growth rate test was conducted under different load ratio to acquire fatigue crack growth parameters by Paris equation under cyclic loading, and threshold value was also tested and calculated. The test study in this paper provide important parameters in high performance steel bridge fracture control design and its remaining fatigue life calculation.

2. Fatigue crack growth rate test

Fatigue crack growth rate (da/dN) tests were conducted to determine the fatigue crack growth rate according to ASTM E647-08 and referencing to Chinese GB/T 6398-2000 [5, 6].

2.1. Test specimens

d*a*/d*N* tests were conducted for compact specimen [C(T)] with different HPS 485W thickness under load ratio of *R*=0.1, 0.5 and 0.8. The prefabricated crack for all the specimen is oriented perpendicular to the rolling direction of the steel plate (L-T). The dimension and specimen are shown in Figure 1 and Table 1.

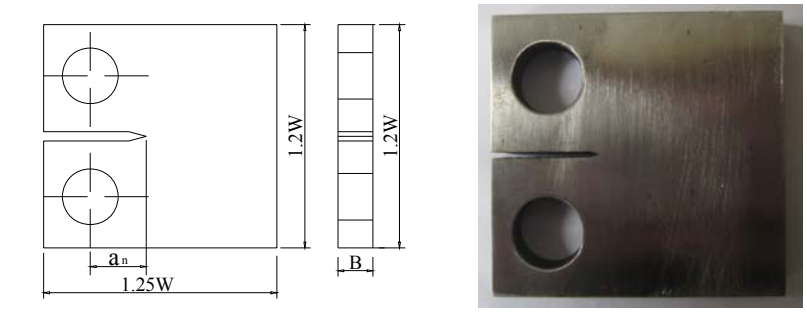

(a) Dimension of C(T) specimen (b) Fabricated C(T) specimens

Figure 1. Dimension of C(T) specimen

Table 1. Specimens dimensions (mm)

B	$1.25W$	$1.2W$	a_n
7.5	50	48	9
12.5	75	72	15
19.5	125	120	23

The loading frequency during test is 15 Hz, considering low frequency of the alternating cycle load in practical traffic transportation. Fatigue crack precracking is conducted before test to provide a sharpened fatigue crack. During the test, the electro-hydraulic servo-controlled fatigue testing machine was used and the crack growth length is read by the microscope with min scale of 0.01mm. The load cycle number and corresponding crack length are recorded at certain intervals from near-threshold to fatigue crack propagate unstably.

2.2. Test result

After the test, the stress-intensity factor range ΔK_i under each crack length is calculated, according to Eq.1. In Eq. 1, $\alpha=a/W$ 错误！未找到引用源。, and $a/W\geq 0.2$.

$$\Delta K = \frac{\Delta P}{B/W}\frac{(2+\alpha)}{(1-\alpha)^{3/2}}\cdot (0.886+4.64\alpha-13.32\alpha^2+14.72\alpha^3-5.6\alpha^4) \quad (1)$$

Using Paris equation to fit tested ΔK_i and $(da/dN)_i$ data. The parameters are obtained including material constant m and C, the standard deviation S, and correlation coefficient. The d*a*/d*N* test result for HPS 485W is shown in Table 2 and Figure 2.

The fracture surface of d*a*/d*N* specimen presents fibrous, and grey or dark grey. Figure 3 shows fracture surface for one of test specimens. The fatigue fracture is composed with crack propagation phase and ultimately quickly failure phase, corresponding to smoothing region and intense coarse region. The fracture surfaces of specimens, shown in Figure 3, are characterized with secondary

cracks. The fracture surface has strong stereoscopic impression.

Table 2. Fatigue crack growth rate of Q&T HPS 485W steel

Thickness	R	Regression Parameters				
		m	C（m/cycle）	log$C$	Correlation coefficient	S
7.5mm	0.1	2.84	1.05×10^{-11}	-10.98	0.96	0.06
	0.5	4.13	2.37×10^{-13}	-12.62	0.97	0.05
	0.8	3.26	3.64×10^{-12}	-11.44	0.96	0.05
12.5mm	0.1	2.53	2.19×10^{-11}	-10.66	0.87	0.12
	0.5	2.72	1.48×10^{-11}	-10.83	0.84	0.11
	0.8	3.16	6.11×10^{-12}	-11.21	0.73	0.1
19.5mm	0.1	3.28	2.29×10^{-12}	-11.64	0.99	0.05
	0.5	3.29	2.82×10^{-12}	-11.55	0.98	0.05
	0.8	3.29	3.24×10^{-12}	11.49	0.99	0.05

错误！未找到引用源。错误！未找到引用源。

(a) Test result for 7.5mm specimen (b) Test result for 12.5mm specimen

错误！未找到引用源。

(c) Test result for 19.5mm specimen

Figure 2. log(da/dN) and log(△K) curves for HPS485W specimens

2.3. Threshold value test

Threshold value (ΔK_{th}) is a significant factor in fracture control design of steel structures and load decreasing procedure is used for ΔK_{th} test. ΔK_{th} for 19.5mm HPS 485W specimen under R=0.1 is tested and the test result is shown in Figure 4 [7]. The calculated theoretical threshold value is 7.22MPa•m$^{0.5}$.

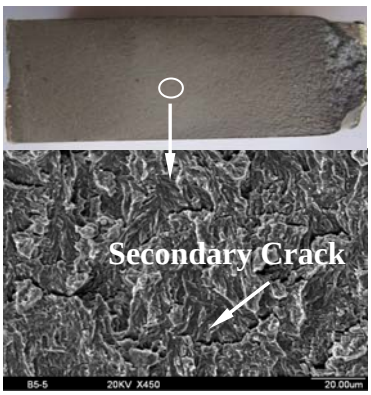

Figure 3. Fracture surface of specimen

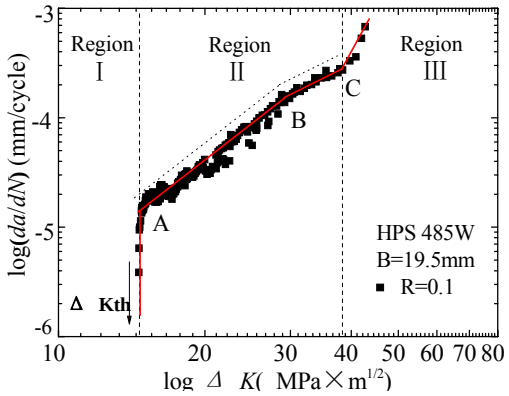

Figure 4. log(da/dN) and log(△K) curve for 19.5mm specimens

3. Test result analysis

Ren et al. conducted da/dN test for 24mm, 32mm and 50mm 14MnNb steel under load ratio of R=0.1, 0.2 and 0.5 [8]. The test result of Ren Weixin is shown in Table 3. Neglecting thickness effect, compare da/dN test result of HPS 485W and 14MnNb was conducted. For R=0.1, the tested m is ranging from 2.53 to 3.28 and C is ranging from 2.29×10^{-12}m/cycle to 2.19×10^{-11}m/cycle for HPS 485W, while the tested m is ranging from 2.67 to 3.74 and C is ranging from 5.83×10^{-10}m/cycle to 1.98×10^{-8}m/cycle for 14MnNb. For R=0.5, the tested m is ranging from 2.72 to 4.13 and C is ranging from 2.37×10^{-13}m/cycle to 1.48×10^{-11}m/cycle for HPS 485W, while the tested m is ranging from 3.39 to 4.08 and C is ranging from 3.08×10^{-10}m/cycle to 1.76×10^{-9}m/cycle for 14MnNb. Learn from comparative result, the tested value of m is similar for traditional bridge steel 14MnNb and HPS 485W, which is about 3. However, the tested value of C for HPS 485W is much smaller than 14MnNb. Fatigue crack growth rate is increasing with the increase of C and m, so compared with traditional 14MnNb, HPS 485W has superior fatigue crack resistance.

The average value of m in Table 3 is 3.17. Using this average value of m=3.17, the log(da/dN) and log(△K) curves are re-fitted by Paris equation for HPS485W specimens. The re-fitting test result is shown in Table 4. The correlated coefficient in Table 4 means the derivation from average value for all the HPS 485W specimens. Learn from Table 4, firstly, for the same load ratio R, thickness of specimen has obvious affection for fatigue crack propagate rate. Secondly, for specimen with same thickness, with the increase of R, value of C is increasing, which means fatigue crack growth rate is increasing.

Table 3. da/dN test result for 14MnNb

Thickness	R	Regression Parameters		
		m	C（m/cycle）	Correlation coefficient
23.5mm	0.1	3.59~3.74	$5.83\sim8.38\times10^{-10}$	0.97～0.99
	0.2	3.31~3.72	$6.55\times10^{-10}\sim 1.31\times10^{-9}$	0.97～0.99
	0.5	3.81~3.97	$3.83\sim5.39\times10^{-10}$	0.97～0.99
31.5mm	0.1	2.67~2.91	$1.02\sim1.98\times10^{-8}$	0.99
	0.2	3.45~3.52	$1.01\sim1.62\times10^{-9}$	0.99
	0.5	3.39~3.75	$4.81\times10^{-10}\sim1.76\times10^{-9}$	0.95~0.99
49.5mm	0.1	2.97~3.24	$2.87\sim6.43\times10^{-9}$	0.99

	0.2	3.16~3.33	$2.25\sim4.29\times10^{-9}$	0.99
	0.5	3.58~4.08	$3.08\sim9.28\times10^{-10}$	0.99

Table 4. Re-fitting result after HPS 485W da/dN test

Thickness	R	Regression Parameters			
		m	C（m/cycle）	log$C$	Correlation coefficient
7.5mm	0.1	3.17	3.71×10^{-12}	-11.43	0.91
	0.5	3.17	4.58×10^{-12}	-11.34	0.87
	0.8	3.17	4.65×10^{-12}	-11.33	0.93
12.5mm	0.1	3.17	2.85×10^{-12}	-11.54	0.82
	0.5	3.17	3.95×10^{-12}	-11.4	0.61
	0.8	3.17	5.24×10^{-12}	-11.28	0.61
19.5mm	0.1	3.17	2.95×10^{-12}	-11.53	0.83
	0.5	3.17	3.85×10^{-12}	-11.41	0.96
	0.8	3.17	4.20×10^{-12}	-11.38	0.95

Zhang et al. conducted da/dN test for 24mm 14MnNbq at room temperature by three-point loading specimen, which is applied in steel and concrete composite railway bridge in Qinghai-Tibet railway system [9]. For 14MnNbq base steel, the tested parameters in Paris equation is C=1.4763×10^{-10}m/cycle and m=2.1413, which shows HPS 485W has greater fatigue crack growth resistance than 14MnNbq. The comparative results demonstrate better fatigue resistance of HPS 485W.

4. Conclusions

This paper conducted fatigue crack growth rate (da/dN) test to study fatigue resistance of high performance steel HPS 485W. The da/dN test result shows HPS 485W has better fatigue crack growth resistance than traditional steel. The fatigue crack growth rate of HPS 485W is determined by Paris equation, which provides significant parameters in remaining fatigue life calculation of HPS bridge. Research in this paper demonstrates HPS 485W has superior fatigue resistance, and HPS 485W is suggested to be prior used in stress complex part of steel bridge.

Acknowledgements

The writers would like to acknowledge the financial support provided by Fok Ying Tung Education Foundation (Grant No. 101078), Program for New Century Excellent Talents in University of the Ministry of Education of the P.R. China (Grant No. NCET-07-0121) and the HPS 485W steel plate provided by Wuyang Iron and Steel Co., Ltd.. The writes would also gratefully acknowledge the technical support provided by State Key Laboratory for Mechanical Behavior of Material in Xi'an Jiaotong University.

References

[1] G. Hamby, G. Clinton, R. Nimins, et al., High Performance Steel Designer' Guide, Second Edition, U.S. Department of Transportation, San Francisco, 2002.

[2] International Association for Bridge and Structural Engineering (IABSE), Use and Application of High Performance Steels for Steel Structures, Structural Engineering Documents 8, 2005.

[3] R. Sause, Barriers to the use of high performance steel in I-girder highway bridges, In: Proceedings of ASCE structures congress XIV, (1996) 108-115.
[4] T. Guo, M. Wei, L. Liu, Development of new type atmospheric corrosion resisting steel A709M-HPS 485W for bridge, Steel Construction, (2009) 17-20.
[5] ASTM, E647-08. Standard test method for measurement of fatigue crack growth rates, 2008.
[6] GB/T 6398-2000，Standard test method for fatigue crack growth rates of metallic materials. Beijing: China Plan Publications, 2000.
[7] R. Xu, X. Duan, Z. Zhan, Investigation on theoretical threshold, Structure & Environment Engineering, (1995) 12-16.
[8] W. Ren, Experiment on fatigue crack growth rate of 14MnNb new type bridge steel, Journal of Changsha Railway University, (1994) 57-65.
[9] Y. Zhang, Study on performance and safety design of fatigue and fracture in large-scale railway steel welded bridge, Tsinghua University, 2004.

Dissipated Energy Measurements of Metal Material during High-cycle Fatigue Test Process

Yuan LI[*,a,b], Francois MAQUIN[c], Zhicheng LIU[a], Chao JIANG[a], Xu HAN[a]

[a] *State Key Laboratory of Advanced Design and Manufacturing for Vehicle Body, College of Mechanical and Vehicle Engineering, Hunan University, Changsha, 410082, China*
[b] *Department of Traffic and Transportation Engineering, College of Basic Education for Commanding Officers, National University of Defense and Technology, Changsha, 410003, China*
[c] *Laboratoire de Mecanique et Procedes de Fabrication(LMPF), Arts et Metiers ParisTech, BP 508 Rue St Dominique, Chalons-en-Champagne, 51006, France*

Abstract

In this paper, the high-cycle fatigue characterization of 316L stainless steel was studied based on dissipated energy measurement. At first, the dissipated energy per cycle was deduced from temperature field of specimen surface using an experimental mechanical method. Then, variations of dissipation energy per cycle were in-situ monitored during each high-cycle fatigue test under different stress levels. The results show that dissipated energy is mainly constant after the initial 5% cycles of total fatigue lifetime. Dissipated energy versus fatigue lifetime fitting curve shows the same pattern as the traditional stress versus fatigue lifetime curve.

Key words: Dissipated energy, metal material, high-cycle fatigue, fatigue lifetime

1. Introduction

High-cycle fatigue characterization of metal material is a time consuming and expensive statistical process. Thus, various theories and alternative accelerated methods to estimate fatigue characteristics have been of great interest at home and abroad [1] over a number of years. From an energy point of view, under the repeated mechanical energy input provided by the loading, dislocation are created and rearranged into the specific micro-structures. These micro-structural modifications accompanied with heat dissipation energy, lead to progressive energy storage.

By observing the local temperature rise, many authors developed many accelerated methods to estimate fatigue limit or S-N curve, such as one curve method [2]and two curve method [3], Amiri method [4], quantitative thermographic method [5], self-heating method [6] et.al. Unfortunately, fatigue characteristics resulting from these approaches are questionable: the local temperature rise is correlated with heat-conduction, heat-convection and heat-exchange, and especially affected by the environment temperature fluctuation, and the physical reasons leading to these estimations are not yet well understood. A better understanding of the physical origin of dissipated energy is required to better interpret the local temperature rise. The relative dissipated energy was firstly deduced from local temperature

[*]Corresponding author: yuanli@nudt.edu.cn

rise using a two-dimensional convolution local heat conduction equation under fatigue loadings [7, 8]. Considering the environment temperature and the thermo-elastic effect, the accurate dissipated energy per cycle was achieved [9]. In this paper, a precise temperature measurement experiment program was developed to compute dissipated energy. The variation of dissipated energy per cycle was in-situ monitored during each high-cycle fatigue test process under different stress levels.

2. Theory and Experiment Set-up

To achieve the goal of this work, it is necessary to perform precise energy dissipation measurements in high cycle fatigue processing.

2.1. Materials

Stainless steel 316L is a low-carbon stainless austenitic steel. It's composed of 0.03 C, 2 Mn, 0.045 P, 0.03 S, 0.75 Si, 16-18 Cr, 0.01 N, 2-3 Mo, 10-14 Ni (in wt.%). The thermo-mechanical properties of 316L stainless steel are reported in Tab.1. The specimens were machined from a 3mm thick cold rolled sheet and machined in the rolling direction. Before the high cycle fatigue test, three tensile tests was performed to determine the 0.2% yield stress ($\sigma_{0.2\%} = 295MPa$) and ultimate tensile stress ($\sigma_b = 587MPa$).

Table 1: Thermo-mechanical and Mechanical properties(at 20 ^{o}C)

	ρ (kg.m^{-3})	C (J.kg^{-1}K^{-1})	k (m^{-1}.K^{-1})	α (10^{-6}.K^{-1})	E (GPa)	$\sigma_{0.2\%}$ (MPa)	σ_b (MPa)	Ref.
316L	7960	500	14	14.8	195	295	585	[10]

2.2. Dissipated energy measurements

The dissipative source d_1 of the material were computed from the surface temperature fields of the loaded specimen with a rectangular active gauge section (width l=20mm and length lu=30mm). As the surface temperature variations with plastic strain are very small, precise temperature field measurements are required. A step-by-step mathematical description and details about the method performance are available in [9, 11].

A loaded sheet specimen and a dummy specimen were used to dissipated energy measurement. The dummy specimen localized next to the loaded specimen was made from the same material as the loaded one (Fig.1, left picture). It's used to monitor the environment temperature variation during the temperature filed acquisition. Both loaded and dummy specimens were coated with a thin layer of black paint to enhance their emissivity. To lower the environment noise, an insulation equipment was designed and placed around the specimen. Besides, a black curtain was surrounded to avoid external radiative reflections onto the specimens (Fig.1,right picture).

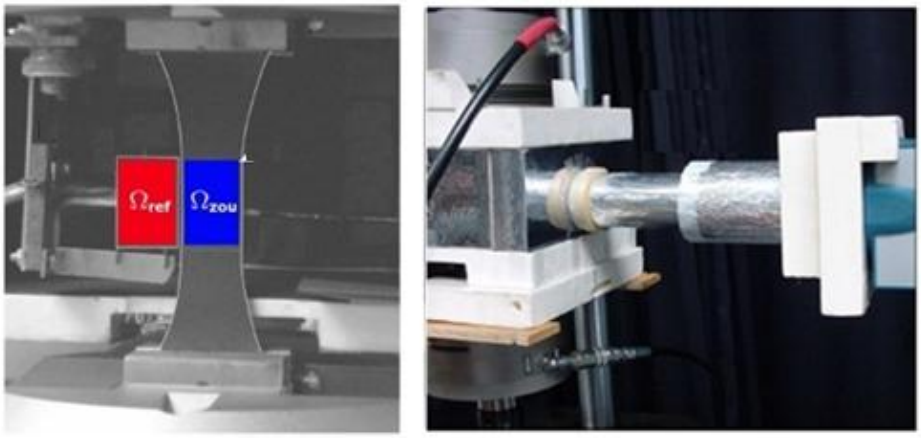

Figure 1: Specimens position (left) under fatigue machine and thermal insulation box (right).

Experiments under cyclic loading were conducted with a INSTRON 8801 axial servo-hydraulic load frame at room temperature. Each high cycle fatigue test was load-controlled. The temperature field of the observed Ω_{sp} and Ω_{dum} were measured using a 350Hz sampling and an integration time of 1200 μs infrared camera (CEDIP Jade MW) with a resolution of 160×120 pixels. The camera, which sensor is cooled down by a Rotary Stirling engine, was started about 4h before the tests in order to ensure its thermal stability. Moreover, the origin manufacturer calibration was used to ensure the precise dissipated energy measurement in this study. Fig.2 shows the dissipated energy $E^i_{d_1}$ obtained with and without the insulation calibration.

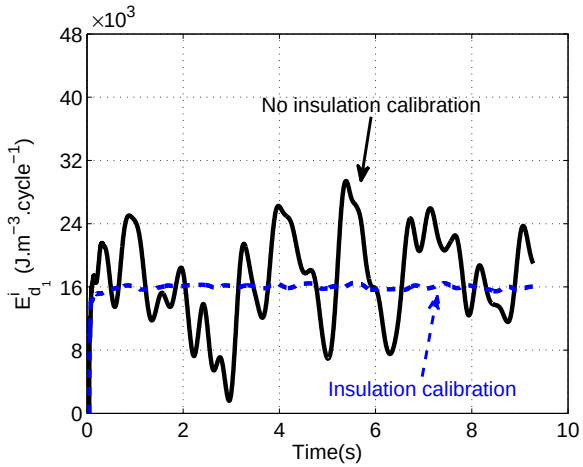

Figure 2: Evolution of dissipated energy difference with and without the insulation calibration.

During each test, the thermal fields of the observed areas Ω_{sp} and Ω_{dum} were stored for 20s (7000 images), which divided in two sequences (Fig.3):

-At the first 5s, the applied stress on the specimen was constant and equal to the mean stress σ_m. The mean stress being small compared to the material yield stress, creep and associated dissipated energy is negligible. Thus, during these 5s, the intrinsic dissipative sources d_1 of both specimen and dummy were assimilated to zero. The measured thermal drifts are due to the convection (loaded specimen and dummy) or conduction (loaded specimen) and represent the initial conditions.

-At the second 15s, the specimen was loaded with a stress such as σ=σ_m+$\sigma_a \cos(2\pi f t)$, where σ_a is the alternate stress amplitude and f is the loading frequency (f=14Hz). The temperature fields acquisition was from t=5s and lasted 15s (210 cycles). The temperature field variations acquired due to the intrinsic thermo-mechanical sources. The alternative temperature variation are due to the thermo-elastic sources S_{th} (thermoelastic coupling effect) while the mean temperature increase is due to the dissipative sources d_1.

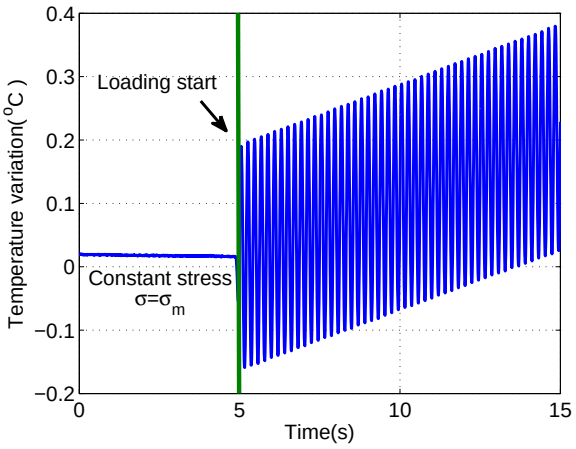

Figure 3: Temperature variation during a temperature field measurement under R_σ=0.2, σ_{max}=380MPa, 316L specimen.

The measured temperature fields were assumed to be representative of the material temperature through the specimen thickness, and the thermo-mechanical sources d_1 and S_{th} were estimated using the local energy balances equations. By combining the balance energy equations before and after the start of the the loading on both loaded specimen and dummy, the following energy balance equation was obtained:

$$\rho C(\frac{\partial \theta}{\partial t} - [\frac{\partial \theta}{\partial t}]_{t=0^-}) - k\Delta_2\theta + \rho C(\frac{\theta}{\tau_{th}^{2D}}) = d_1 + S_{th} \quad (1)$$

where ρ is the material density, C is the calorific capacity, k is the thermal conductivity and Δ_2 is the Laplacian operator, θ is the local temperature variation of the specimen due to the thermo-mechanical sources. Eq.(1) underlines that these thermo-mechanical sources produce three major effects: a change in heat rate ($\rho C(\frac{\partial \theta}{\partial t} - [\frac{\partial \theta}{\partial t}]_{t=0^-})$), energy exchanges by conduction ($k\Delta_2\theta$) and energy exchanges by convection and radiation ($\rho C(\frac{\theta}{\tau_{th}^{2D}})$). τ_{th}^{2D} is here a time constant characterizing the convection and radiation losses.

The dissipative and thermo-mechanical sources are coupled in Eq.(1)(thermo-mechanical coupling effects), although only the dissipative sources d_1 are of interest in this work. The loading signal was used to compute and remove the thermo-mechanical sources S_{th} and associated temperature variations from Eq.(1). As a result, dissipative sources d_1 were obtained. Eq.(1) was also integrated over the observed area Ω_{sp} and Ω_{dum} to lower the measurement noise level.

In this work, the mean dissipative sources were defined as $\bar{\bar{d}}_1$ to underline the spatial averaging. The spatial average $\bar{\bar{d}}_1$ is supposed to be representative of the dissipative sources field over the area Ω_{sp}. This hypothesis has been validated by computing the fields of dissipative sources d_1 using the method described in [9]. Eventually, the dissipated energy per cycle $E^i_{d_1}$ was computed by integrating $\bar{\bar{d}}_1$ over each cycle:

$$E^i_{d_1} = \int_{t_i}^{t_i+1/f} \bar{\bar{d}}_1 dt \tag{2}$$

Where t_i is the starting time of cycle i.

As the dissipated energy measurement is achieved in the elastic hysteretic domain, the dissipated energy should be constant during the test (15s). This characteristic was used a posteriori to check whether the test was performed in the elastic domain. The mean of the dissipated energy per cycle $E^m_{d_1}$ was thus computed over a time t_m=12s to lower the noise level (Fig.4):

$$E^m_{d_1} = \frac{1}{t_m} \int_{t_0}^{t_0+t_m/f} E^i_{d_1} dt \tag{3}$$

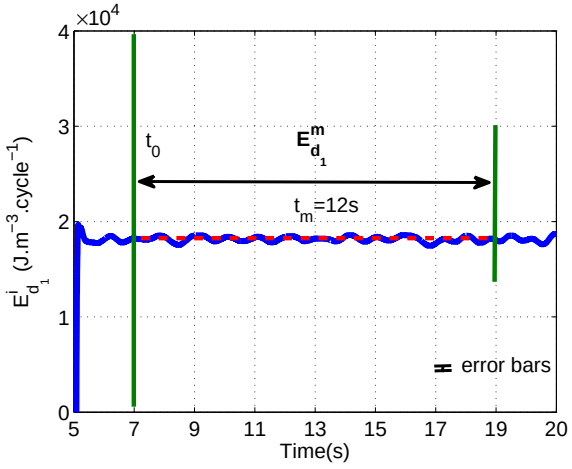

Figure 4: Definition of the mean dissipated energy per cycle $E^m_{d_1}$ (316L specimen).

The dissipated energy measurements have proved to be a reliable method[12]. With this method, the detection threshold of $E^m_{d_1}$ is as small as $\pm 222 J{\cdot}m^{-3}{\cdot}cycle^{-1}$ ($2\sigma_{E^m_{d_1}}$) for a 316L stainless steel specimen.

3. Results and discussion

It's known that in high fatigue test, damage is created slowly by dislocation pile-ups due to the small and gradual changes in the material microstructure. A test sequence was proposed to observe dissipated energy variation during the high cycle fatigue process, to better underline the in-situ thermo-mechanical modifications of materials. Serval specimens were loaded from σ_{max}=280MPa to 440MPa in steps of 20MPa with R_σ=0.2 and f=14Hz.

Different constant amplitude fatigue tests (13 levels,30 specimens) were run until the specimen complete separation under traction-traction loadings (Tab.2). In each fatigue test, serval dissipated energy measurements were performed every 5,000, 10,000 or 30,000 cycles for different stress levels fatigue tests.

Table 2: Fatigue test results of 316L stainless steel (R_σ=0.2, f=14Hz)

Specimen number	σ_{max} (MPa)	σ_m (MPa)	σ_a (MPa)	N_f to failure	$E_{d_1}^m$ at 30,000 cycles $(J{\cdot}m^{-3}{\cdot}cycle^{-1})$	Results
1	440	264	176	64,300	40,633	Failure
2	420	252	168	72,897	36,842	Failure
3	420	252	168	76,087	38,425	Failure
4	400	240	160	91,580	34,568	Failure
5	400	240	160	105,348	34,183	Failure
6	390	236	156	127,456	–	Failure
7	380	228	152	145,770	–	Failure
8	380	228	152	146,425	28,712	Failure
9	380	228	152	149,296	25,245	Failure
10	375	225	150	172,776	20,792	Failure
11	375	225	150	184,285	19,982	Failure
12	370	222	148	178,784	19,875	Failure
13	350	210	140	164,713	19,178	Failure
14	350	210	140	245,817	18,303	Failure
15	320	192	128	291,264	9,532	Failure
16	320	192	128	277,642	10,475	Failure
17	310	186	124	305,381	8,502	Failure
18	310	186	124	663,809	6,006	Failure
19	310	186	124	719,016	6,882	Failure
20	310	186	124	345,773	–	Failure
21	310	186	124	581,912	6,917	Failure
22	310	186	124	503,891	7,582	Failure
23	310	186	124	513,625	7,690	Failure
24	310	186	124	465,469	6,560	Failure
25	310	186	124	551,751	6,940	Failure
26	310	186	124	482,605	7,429	Failure
27	300	180	120	696,100	6,559	Failure
28	300	180	120	1,200,000	4,773	No Failure
29	290	174	116	2,000,000	4,317	No Failure
30	280	168	112	2,000,000	3,499	No Failure

Fig.5 and Fig.6 are dissipated energy variations in term of fatigue cycles ratio at different stress levels from

420MPa to 280MPa during fatigue test process, where N is the loading cycle, N_f is the cycles to failure (i.e. fatigue lifetime) and N/N_f represents fatigue loading cycles ratio. Dissipated energy per cycle $E_{d_1}^m$ was almost constant after 10% of total fatigue lifetime (N/N_f=0.10) beyond σ_{max}=370MPa) and 5% of total fatigue lifetime (N/N_f=0.05 in below σ_{max}=350MPa).

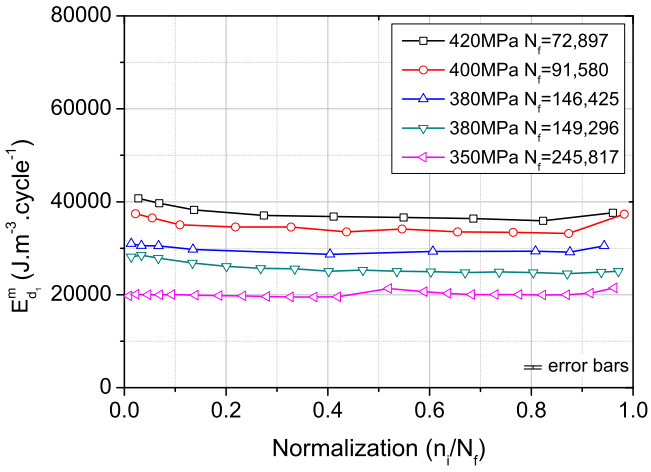

Figure 5: Dissipated energy variation during high cycle fatigue tests from 420MPa to 350MPa (R_σ=0.2, f=14Hz).

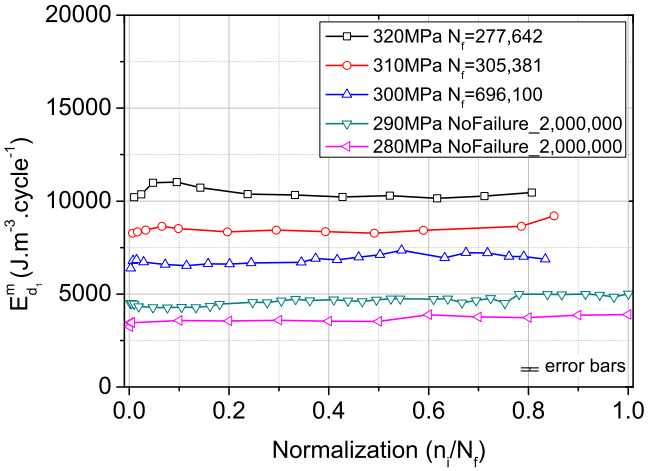

Figure 6: Dissipated energy variation during high cycle fatigue tests from 330MPa to 280MPa (R_σ=0.2, f=14Hz).

The same phenomenon about dissipated energy variation were observed by $Meneghetti, G$ [8, 13]. In his method, the fatigue test must suddenly stop many time to measure the cooling curves to calculate the specific heat loss Q. The

measured values of Q for each specimen were whin 15% with respect to the mean value. Thanks to the precise experiment set-up, the dissipated energy per cycle $E_{d_1}^m$ are with 5% of the mean value in these fatigue tests.

The constant stress amplitude fatigue tests (12 stress levels, 30 specimens in Tab.2) were performed to obtain the S-N curve by the traditional procedure (Fig.7). Meanwhile, Fig.8 shows that the relationship between the dissipated energy $E_{d_1}^m$ and fatigue lifetime N_f is very similar to the S-N curve. This curve was defined as $E_{d_1}^m$-N curve in this work. The scatter bands of the two curves are given for 10% and 90% survival probability.

The linear fitting equation of $E_{d_1}^m$-N curve is written as,

$$log(E_{d_1}^m) = -0.77log(N_f) + 8.33 \tag{4}$$

where the related coefficient $R^2_{E_{d_1}^m - N}$ between $E_{d_1}^m$ and N_f equals to 0.94.

The linear fitting equation of S-N curve is written as,

$$log(\sigma_a) = -0.13log(N_f) + 2.85 \tag{5}$$

where the related coefficient R^2_{S-N} between σ_a and N_f equals to 0.89.

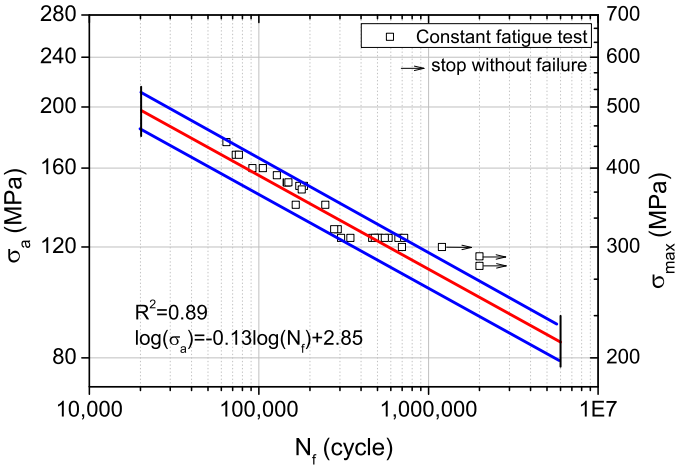

Figure 7: S-N curve by traditional staircase procedure of 316L material (R_σ=0.2, f=14Hz).

As $R^2_{E_{d_1}^m - N} > R^2_{S-N}$, $E_{d_1}^m$-N curve by dissipated energy measurements shows more accurately than S-N curve by traditional fatigue test method. In such a case, it's possible to extrapolate the $E_{d_1}^m$-N curve by dissipated energy measurements to predict the residual fatigue lifetime during various stress amplitude fatigue test under traction-traction cyclic loadings (i.e. R_σ=0.2).

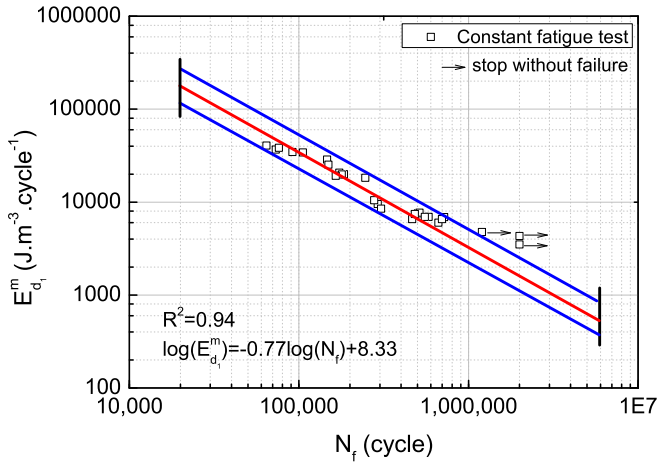

Figure 8: $E_{d_1}^m$-N curve by dissipated energy $E_{d_1}^m$ method of 316L material (R_σ=0.2, f=14Hz).

4. Conclusion

In conclusion, dissipated energy per cycle $E_{d_1}^m$ is constant under traction-traction cyclic loadings during constant and various stress amplitude high cycle fatigue tests of 316L stainless steel while the material reached a stabilized thermo-mechanical state (5% of total fatigue lifetime). Dissipated energy versus fatigue lifetime fitting curve shows the same pattern as the traditional stress versus fatigue lifetime curve. Further studies and specific microstructural analysis are still required to better understand the correlation between the dissipated energy and the microstructural material state.

Acknowledgements

The work is partially supported by CSC(visiting scholarship) and NSFC(51175160). And I also especially acknowledge the supervision of Prof. Fabrice PIERRON and Dr. Francois MAQUIN in LMPF, ENSAM in France.

References

[1] C. Mareau, V. Favier, B. Weber, A. Galtier, and M. Berveiller. Micromechanical modeling of the interactions between the microstructure and the dissipative deformation mechanisms in steels under cyclic loading. *International Journal of Plasticity*, 2012.

[2] G. Fargione, A. L. Geraci, G. La Rosa, and A. Risitano. Rapid determination of the fatigue curve by the thermographic method. *International Journal of Fatigue*, 24(1):11–19, 2002.

[3] M. P. Luong. Fatigue limit evaluation of metals using an infrared thermographic technique. *Mechanics of Materials*, 28(1-4):155–163, 1998.

[4] M. Amiri and M. M. Khonsari. Life prediction of metals undergoing fatigue load based on temperature evolution. *Materials Science and Engineering A*, 527(6):1555–1559, 2010.

[5] X. G. Wang, V. Crupi, X. L. Guo, and Y. G. Zhao. Quantitative thermographic methodology for fatigue assessment and stress measurement. *International Journal of Fatigue*, 32(12):1970–1976, 2010.

[6] C. Doudard, S. Calloch, P. Cugy, A. Galtier, and F. Hild. A probabilistic two-scale model for high-cycle fatigue life predictions. *Fatigue and Fracture of Engineering Materials and Structures*, 28(3):279–288, 2005.

[7] T. Boulanger, A. Chrysochoos, C. Mabru, and A. Galtier. Calorimetric analysis of dissipative and thermoelastic effects associated with the fatigue behavior of steels. *International Journal of Fatigue*, 26(3):221–229, 2004.

[8] G. Meneghetti and M. Ricotta. The use of the specific heat loss to analyse the low- and high-cycle fatigue behaviour of plain and notched specimens made of a stainless steel. *Engineering Fracture Mechanics*, 2011.

[9] N. Connesson, F. Maquin, and F. Pierron. Experimental energy balance during the first cycles of cyclically loaded specimens under the conventional yield stress. *Experimental Mechanics*, 51(1):23–44, 2011.

[10] J. P. Strizak and L. K. Mansur. The effect of mean stress on the fatigue behavior of 316 ln stainless steel in air and mercury. *Journal of Nuclear Materials*, 318(SUPPL):151–156, 2003.

[11] F. Maquin and F. Pierron. Heat dissipation measurements in low stress cyclic loading of metallic materials: From internal friction to micro-plasticity. *Mechanics of Materials*, 41(8):928–942, 2009.

[12] N. Connesson, F. Maquin, and F. Pierron. Dissipated energy measurements as a marker of microstructural evolution: 316l and dp600. *Acta Materialia*, 59(10):4100–4115, 2011.

[13] G. Meneghetti. Analysis of the fatigue strength of a stainless steel based on the energy dissipation. *International Journal of Fatigue*, 29(1):81–94, 2007.

Measurement of Effective Stress Intensity Factor Range of Mode II Fatigue Crack Growth using Hysteresis Loop

Shigeru Hamada[1,*], **Minjian Liu** [2]

[1] Department of Mechanical Engineering, Faculty of Engineering, Kyushu University,
744 Moto-oka, Nishi-Ku, Fukuoka 819-0395, Japan
[2] Department of Mechanical Engineering, Graduate School of Engineering, Kyushu University,
744 Moto-oka, Nishi-Ku, Fukuoka 819-0395, Japan
* Corresponding author: hamada@mech.kyushu-u.ac.jp

Abstract A method was proposed for measuring the effective stress intensity factor ranges of Mode II fatigue crack growth by using the hysteresis loop for a specimen's surface strain. Many cases of rolling contact fatigue failure, such as those that occur in railway rails, bearings and gears are due to repeated high shear loads. In order to prevent such fatigue failures, the resistance of a material to repeated high shear loads must be determined. The fatigue crack growth characteristics are dependent on the Mode II stress intensity factor range. However, conventionally measured Mode II fatigue crack growth characteristics vary according to the measurement methods. Therefore, the authors improved the experimental measurement method proposed by Murakami, and proposed a way to measure the Mode II effective stress intensity factor range. Improvements to the jigs and specimen were made based on the ideal mechanical model of the experimental method. Furthermore, to measure the Mode II fatigue crack growth behavior, strain gauges were applied to the specimen and the hysteresis loop of the strain was measured with high accuracy by using a newly developed subtraction circuit.

Keywords Rolling contact fatigue, Friction, Mode II fatigue crack, Effective stress intensity factor, Fracture mechanics

1. Introduction

Mechanical failures such as spalling and pitting can occur in rails, bearings, and other components when they are subjected to heavy repeated rolling contact loading. In order to prevent these types of failures, it is necessary to determine the resistance of certain materials to them. A fatigue crack under repeated rolling contact loading, which is what leads to the failure, propagates in Mode II. Therefore, the resistance to fatigue crack propagation which is caused by stress concentration sources such as flaws or inclusions can be evaluated by using the Mode II fatigue threshold stress intensity factor range, ΔK_{IIth}.

Methods for measuring Mode I fatigue crack propagation have already been established and standardized [1]. However, for Mode II fatigue crack propagation, systematic research is limited because this type of fatigue crack propagation is difficult to produce in a laboratory and there are no standard tests. Early systematic research was conducted by Otsuka et al. [2]. However, the method they developed could only be applied to soft metals such as aluminum alloys, even though hard metals are used for the components for which Mode II fatigue crack become a problem. After this study, Murakami et al. [3, 4] developed an experimental method that could also be applied to hard metals such as bearing steel. Later, Otsuka et al. [5] improved their method so that it could also be applied to hard metals. However, different values were obtained for the threshold stress intensity factor range ΔK_{IIth} when these two methods [4, 5] were used for the same material. It seems that interference by the crack faces affected the result. The study conducted by Matsunaga et al. [6] on the shear mode threshold proved that friction on the crack face increases the value of ΔK_{IIth}. Therefore, it is thought to be necessary to take the friction on the crack faces into account when determining the Mode II effective stress intensity factor range, $\Delta K_{\mathrm{IIeff}}$.

In the previous work by the authors, a new method was proposed [7, 8] to measure the friction at the crack faces and $\Delta K_{\mathrm{IIeff}}$. Moreover, a more appropriate assumption for the friction distribution on

the crack faces was made and a new method was proposed. This paper discusses, Mode II fatigue crack growth experiments that were conducted using the proposed method, along with the obtained results.

2. Experimental procedures

2.1. Mechanical model

Figure 1(a) shows the mechanical model of the Mode II fatigue crack growth experiment that was proposed by Murakami et al. [3]. In this paper, this model is referred to as the "former mechanical model." Load P was applied to the upper cantilever. By inserting a ceramic cylinder in the slit, load P was assumed to be divided into two equal halves and applied to both cantilevers. In a real machine, a Mode II crack propagates under the condition of compressive stress. Therefore compressive load S was applied using the pre-tightening force of bolts. Mode II fatigue crack growth experiments were performed by applying the former mechanical model. However, because of the plastic deformation of the specimen where the ceramic cylinder made contact with it, load P could not be divided as expected. In fact, dents were found on the specimen where the ceramic cylinder inserted into the slit made contact, and a considerable reduction in the slit width was observed during the fatigue experiment. This reduction in the slit width was thought to be caused by a gap formed as a result of plastic deformation when the load was applied and, as a result, the load applied to the lower cantilever was thought to be considerably reduced.
In order to equally divide the load P between the cantilevers, a new mechanical model has been proposed [7, 8]. Figure 1(b) shows this new mechanical model, which was based on the experimental setup shown in Fig. 1(c). The new model was discussed with springs and rigid blocks in the previous study [7, 8]. This discussion showed that if the pre-tightening force S was larger than $P/2$, then the load was divided into two equal halves and applied to the two cantilevers, and the width of the slit did not change during the experiment even if a cylinder was not in place. In addition to the compressive load S by the pre-tightening force of the bolts, compressive load Q was applied on the fatigue crack face in order to avoid crack branching in Mode I during the fatigue crack propagation.

2.2. Material

The experiments were carried out using commercial grade Japanese Industrial Standards (JIS) SS400 steel (400 MPa minimum tensile strength) which is rolled steel designed for general structures. Table 1 presents its chemical composition.

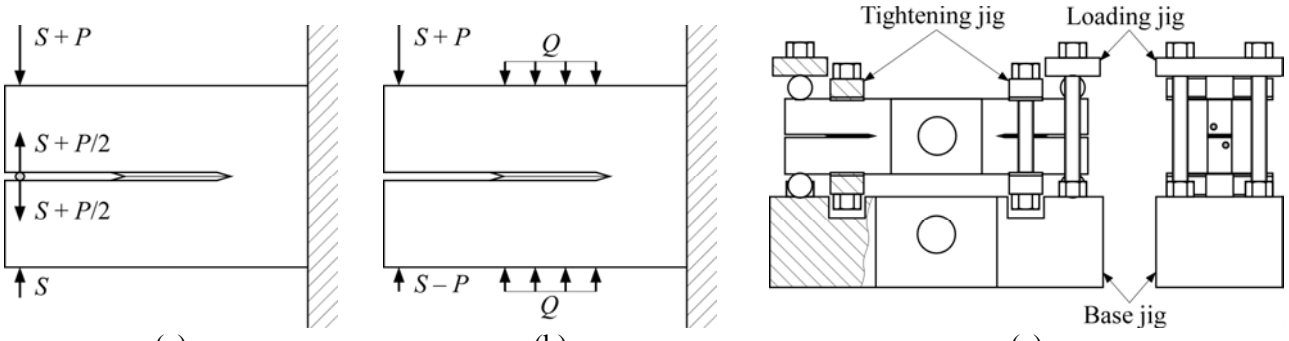

Figure 1. Mechanical models for Mode II experimental method: (a) former mechanical model [3], (b) new mechanical model [7, 8], and (c) new experimental setup

2.3. Specimen

Figure 2 shows the shape and dimensions of the specimen that was used in this study. The specimen had a chevron notch and side grooves. The fatigue crack initiated at the tip of the chevron notch, where the stress intensity factor was high. The groove on the side of the chevron notch caused Mode II fatigue crack growth in the section with the maximum shear stress and prevented crack branching in the direction of the maximum tensile stress, which was a Mode I crack. Two crack propagations were simultaneously carried out on a single specimen. Compressive force Q was applied on the crack face with the middle jigs to avoid crack branching in Mode I. In order to reduce the unexpected horizontal force applied to the specimen, three of the four grooves on the end of the cantilever were made flat and one was made larger with a radius of 1 mm to 4 mm. The three flat grooves allowed for the relative displacement caused by the elastic deformation between the specimen and the jigs. The large circular groove prevented the specimen from moving.

2.4. Experimental setup

Figure 3 shows the setup of the experiment. Four ceramic cylinders were placed between the cantilevers and the loading jigs. As a result, the load applied to the specimen was divided into two equal halves on the cantilevers. A cyclic tensile load P in the form of a sine wave, ranging from 0.5 kN to 10 kN (stress ratio: $R = 0.05$) was applied to the center holes in the jig and specimen through two pins using a servo-hydraulic fatigue testing machine operating at a frequency of 6 Hz. In order

Table 1. Chemical composition of specimen (mass %)

C	Si	Mn	P	S	Fe
0.11	0.27	0.55	0.021	0.023	Bal.

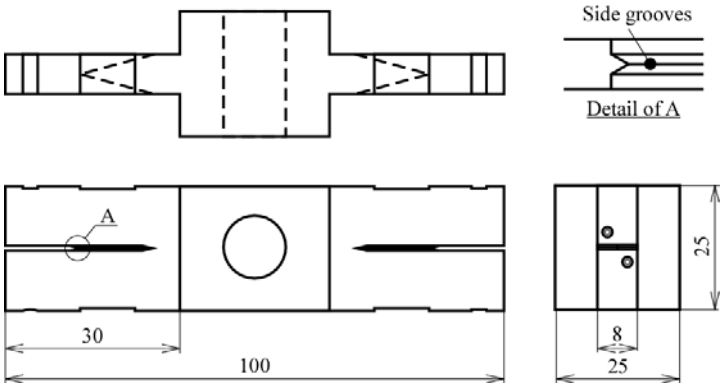

Figure 2. Shape and dimensions of specimen (unit: mm)

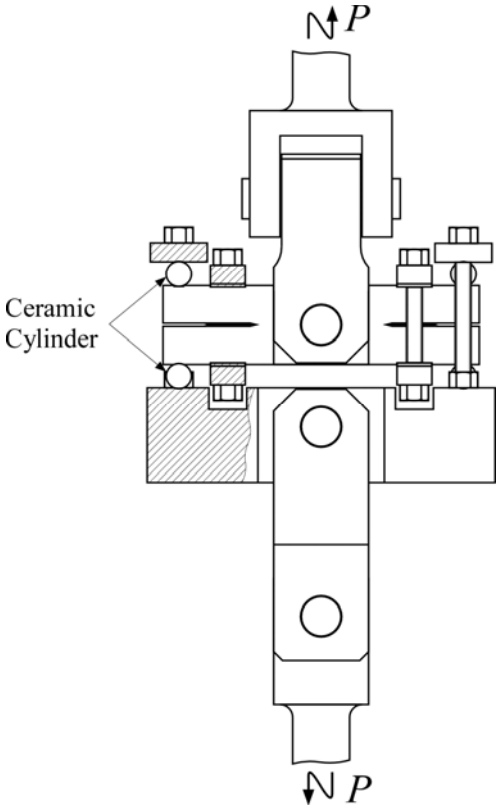

Figure 3. Experimental setup

to suppress the tendency for Mode I crack branching, the pre-tightening load S of a bolt was applied to the ends of the cantilevers and vertical compressive load Q was applied to the crack faces using the loading jigs and tightening jigs. The ceramic cylinder diameter (8 mm) was larger than that used in the former setup (1 mm) in order to reduce the plastic deformation of the specimen on the contact face. Moreover, a set of universal joints was used to cancel out the unexpected moment applied to the specimen.
The specimen and jigs were designed considering their compatibility with the fatigue crack growth experiment equipment using a "CT (Compact Tension) specimen." Therefore, the experimental setup shown in Fig. 3 could be used with environmental experiments equipment that is designed for a "CT specimen."

2.5. Crack length measuring method

The crack length during the fatigue crack growth experiment was measured by using the AC potential method [3]. Two electrodes were connected to the ends of the cantilevers. As the crack between the two cantilevers grew, the electrical resistance between these two electrode points increased. Then, the resistance was measured and converted into the crack length. The ratio of the increase in the electric potential (ΔE) caused by the crack growth to the electric potential at the beginning of the experiment (E_0) correlated with the crack length. Therefore, the crack length could be measured without interrupting the experiment. The specimen was insulated from the jig using the ceramic cylinders.

3. Derivation of friction between crack faces

In order to measure the friction between the fatigue crack faces, two strain gauges (Kyowa Electronic Instruments Co., Ltd., KFG-2N-120-C1) were placed on the specimen surface. Figure 4 shows the strain measurement positions on the specimen. The friction force on the crack face was derived from the load-strain curve over one cycle using the outputs of the strain gauges.
Figure 5 shows the basic model for the derivation of the friction, which represents a mass spring model with a rough ground and a mass subjected to a cyclic load P. The load-displacement curve over a cycle is shown in Fig. 5(b). Because the direction of the friction changes over a cycle, the friction can be derived from the hysteresis in the load-displacement curve.
However, for the real experiment, the curve became more complicated. When the loading began, the portion of the crack faces at the notch began to slide, and all of the other parts of the crack faces soon followed. As a result, the linear part of the curve marked (i) became nonlinear. Thus, because of the plastic deformation that occurred around the crack tip, the portion of the linear part of the curve marked (ii) also became nonlinear. The same phenomena also occurred at the portions marked (iii) and (iv). Therefore, the load-strain curve over one cycle was estimated to be that is shown in Fig. 6. The friction could still be derived from the load-strain curve. The vertical dashed line shown in Fig. 6 starts from point A and intersects at point B with the extended line of the elastic portion of the curve at the unloading. The length of dashed line AB is related to the friction, where the relation is determined using a finite element method (FEM).

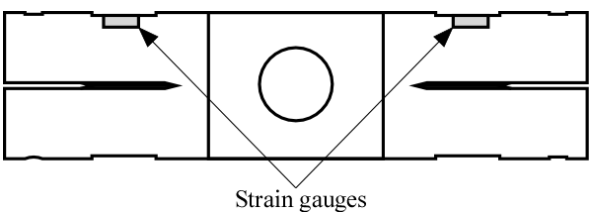

Figure 4. Strain gauges placed on specimen

4. Results and discussion

The fatigue crack growth experiment was ended by the action of the displacement limiter at $N = 2.08 \times 10^6$ cycles. A fatigue crack that nucleated and grew at the root of the cantilever caused the limiter action. Figure 7 shows the displacement range ($\Delta\delta$) of the load piston during the fatigue experiment. Until $N = 1.0 \times 10^6$ cycles, the displacement range maintained a constant value. However, at $N = 2.0 \times 10^6$ cycles, the value rose slightly and then suddenly began to increase. This sudden increase was thought to indicate the fatigue crack growth at the root of the cantilever. Therefore, in this case, the intended fatigue crack growth experiment was performed until around $N = 1.0 \times 10^6$ cycles.

4.1. Mode II fatigue crack growth behavior

Figure 8 shows the relationship between the potential difference and the number of cycles measured using the AC potential method. In this experiment, because the effect of electric noise was not removed, averaged data were considered. From Fig. 8, it can be seen that the crack began to grow from $N = 5 \times 10^3$ cycles, after which the crack growth depended on the number of cycles.

4.2. Fracture surface of Mode II fatigue crack

After the fatigue crack growth experiment, the fracture surface was observed using a scanning electron microscope (SEM). Figure 9 shows the result of this observation. In this figure, lines that were parallel to the crack growth direction and cracks branching in the Mode I direction were found, which are characteristic of a Mode II fatigue fracture surface [3, 4]. Therefore, the success of the Mode II fatigue crack growth experiment was verified.

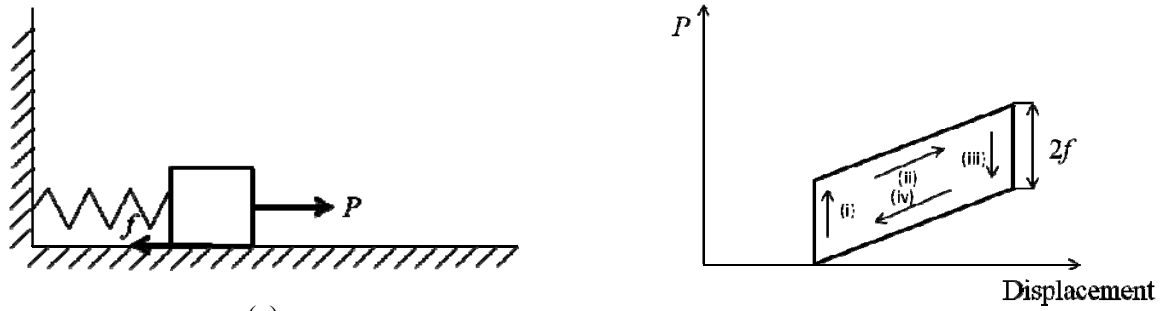

Figure 5. Models for derivation of friction: (a) mass-spring model and (b) load-displacement curve

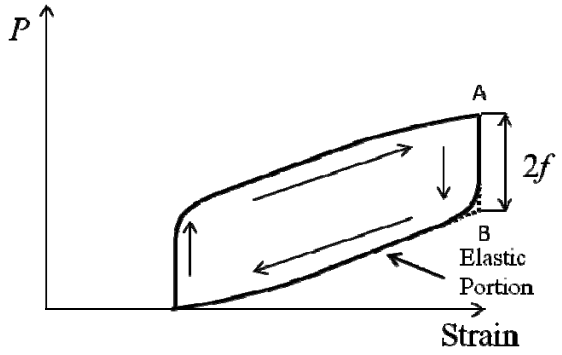

Figure 6. Estimated load-strain curve

4.3. Friction force measurement

Figure 10(a) shows an example of the relationship between the load and the strain at $N = 4.0 \times 10^4$ cycles. In order to measure the hysteresis loop of the strain with high accuracy, a subtraction circuit was developed. The input data were the strain at a jig and the strain at a specimen, as measured by strain gauges. These strains were converted to electric potentials and subtracted in the circuit. Figure 10(b) shows that the relationship between the load and the subtracted strain. From Fig. 10(b), the hysteresis loop was observed during a load cycle. As seen from a comparison of Fig. 10(b) with Fig. 6, the hysteresis loop was the same at a low load, whereas a difference existed at a high load. At present, the exact reason for this result is not known. However, through an analysis of the obtained load-strain hysteresis loop, the friction force and values of $\Delta K_{\mathrm{IIeff}}$ and ΔK_{IIth} could be determined in a future study.

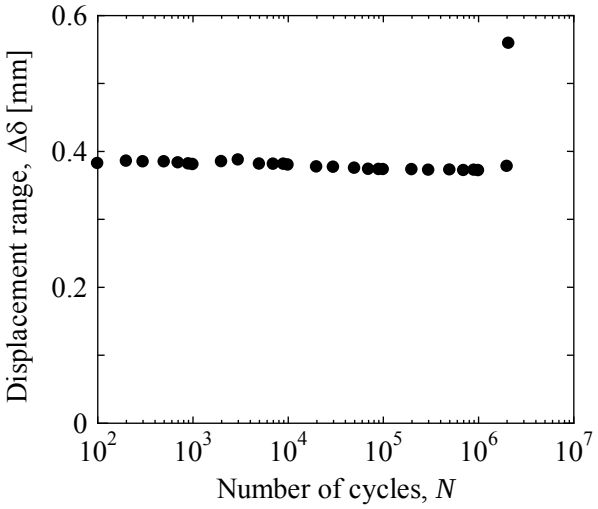

Figure 7. Relationship between displacement range of pull-rod and number of cycles

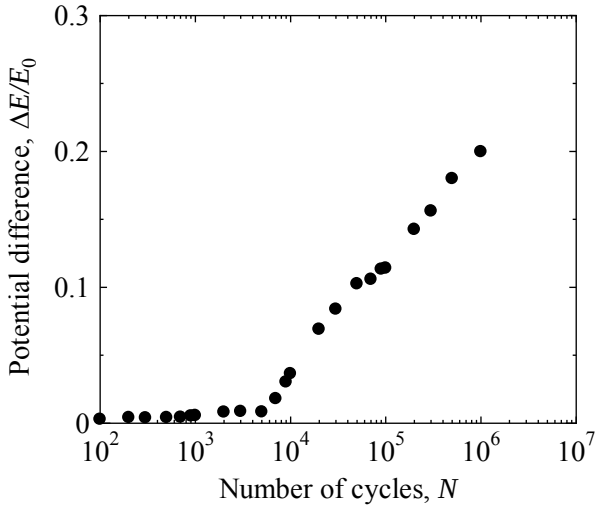

Figure 8. Relationship between potential difference and number of cycles

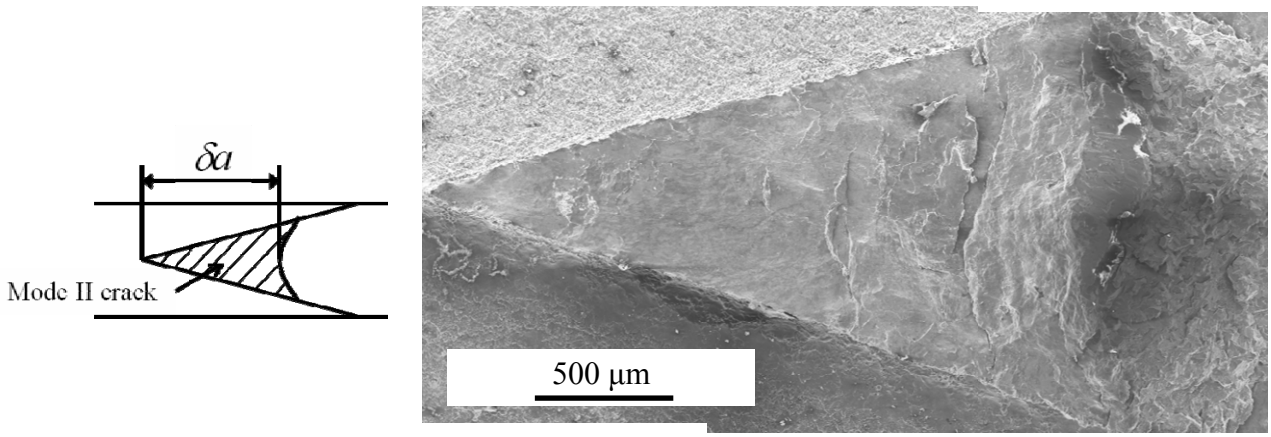

Figure 9. Fracture surface of Mode II fatigue crack

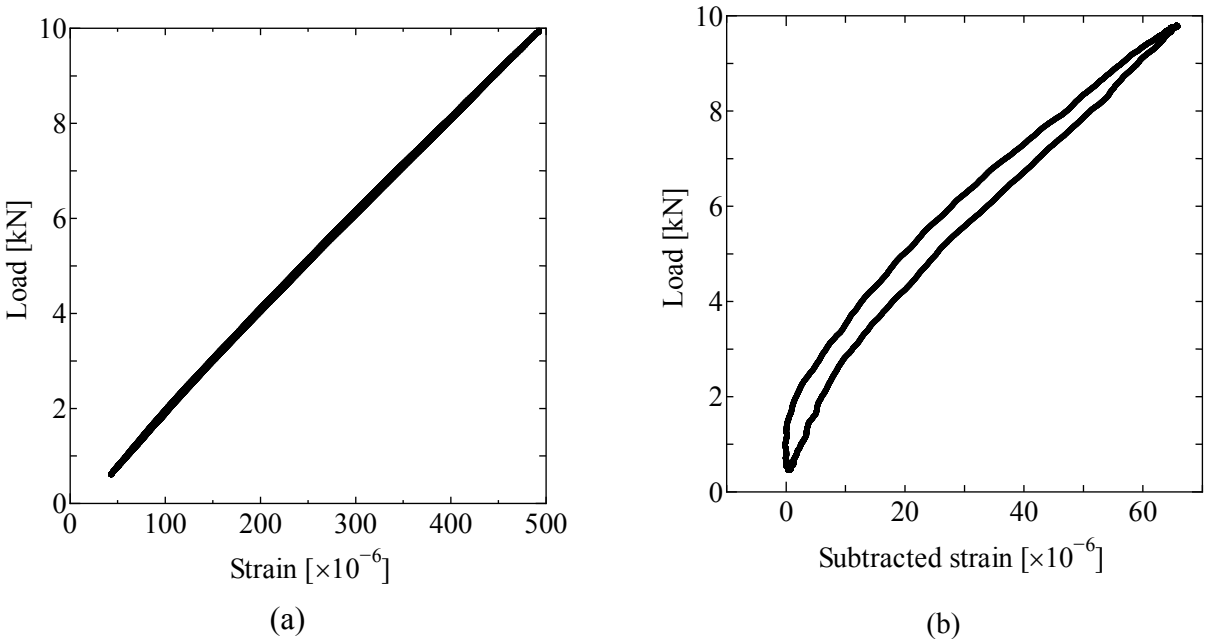

Figure 10. Example of relationship between load and strain (at $N = 4.0 \times 10^4$ cycles): (a) strain is measured strain and (b) strain is subtracted strain

5. Conclusions

The mechanical model for the Mode II experimental method proposed in the previous paper was modified. Thus, the load was considered to be equally divided into two halves and applied to each cantilever of the specimen. Furthermore, a new method for determining the friction between the crack faces was proposed. The crack length and friction between the crack faces were measured using an AC potential method and deduced from the load-strain curve, respectively. From this measurement and deduction, $\Delta K_{\mathrm{IIeff}}$ could be determined. However, the value of ΔK_{IIth} has not yet been determined. It will be determined using this method in a future study.

Acknowledgements

This work was supported by JSPS KAKENHI Grant Number 24560103.

References

[1] American Society for Testing and Materials, ASTM E647-11$^{\varepsilon 1}$: Standard test method for measurement of fatigue crack growth rates, 2011.
[2] A. Otsuka, K. Mori and K. Tohgo, Current research on fatigue cracks, material research series, The society of materials science, Japan, 1 (1985) 127-55.
[3] Y. Murakami, S. Hamada, Fatigue Fract. Engng. Mater. Struct., 20 (1997) 863-70.
[4] Y. Murakami, C. Sakae and S. Hamada, Engineering Against Fatigue, edited by J. H. Beynon, M.W. Brown, T. C. Lindley, R. A. Smith & B. Tomkins, Taylor & Francis, UK.
[5] A. Otuska, Y. Fujii and K. Maeda, Fatigue Fract. Engng. Mater. Struct., 27 (2004) 203-212.
[6] H. Matsunaga, N. Shomura, S. Muramoto and M. Endo, Fatigue Fract. Engng. Mater. Struct., 34 (2011) 72-82.
[7] M. Liu, S. Hamada, Procedia Engineering, 10 (2011) 1949-1954.
[8] M. Liu, S. Hamada, Proceedings of 19th European Conference on Fracture (ECF19), (2012) ID 455.

On the tolerance to short cracks departing from notch roots

Hao Wu[1,*], Jaime Tupiassú Pinho de Castro[2], Zheng Zhong[1]

[1] Tongji University, Siping Road 1239, 200092 Shanghai, P.R. China
[2] Pontifical Catholic University of Rio de Janeiro, PUC-Rio, Brazil
* Corresponding author: wuhao@tongji.edu.cn

Abstract
It is well known that it is impossible to guarantee that structural components are really free of cracks smaller than the detection threshold of the non-destructive method. Nevertheless, most components are still designed against fatigue crack initiation using procedures that do not recognize such cracks. Consequently, their "infinite life" predictions may become unreliable when cracks are introduced by any means and not quickly detected or properly removed. Therefore, structural components that must last for very long fatigue lives should be designed to be tolerant to undetectable short cracks. Indeed, continuous work under fatigue loads cannot be guaranteed if any crack can propagate during their service lives. Since most structural components designed for long lives work in spite of not recognizing such cracks, and they certainly are somehow tolerant to short cracks. However, the question "how much tolerant" cannot be answered by traditional fatigue design procedures alone, but such a problem can be avoided by adding proper short crack concepts to their "infinite" life design criteria. This work proposes such a damage-tolerance requirement to quantify the behavior of short cracks. This methodology can also be used to quantify the difference between the fatigue K_f and the static stress concentration factor K_t.
Keywords: Fatigue; Short crack; stress gradient; non-propagating crack; tolerance

1. Introduction

During the manufacture or service of structural components, small defects ranging in length from tens microns to several millimeters are unavoidable. Industrial experiments have shown that the rupture of components is often produced by these "short cracks", which develop in most cases from the instinct faults of these structures and propagate when they are subjected to cyclic loading. As the initiation fatigue life is largely influenced by the behavior of short cracks, not taking into account of the propagation of short cracks can lead to potentially dangerous overestimation of fatigue life [1, 2]. It is therefore essential to thoroughly understand their growth rules and effectively predict the structure life by considering the initiation and propagation of short cracks.

As we know, growing short cracks from sharp notches can stop completely even when the remote applied stress amplitude remains constant. This phenomenon was discovered as early as 1949 by Frost [3] as shown in Fig.2. In the succeeding research of short cracks, inspired by Frost's report about the non-propagating cracks, people normally tend to focus on the behavior of short cracks departing from the sharp notch root which corresponds to the evident notch sensitivity coefficient and significant stress gradient. It has a non-propagating cracks zone where the cracks initiated from a sharp notch ($K_t > 3$); and the driving force ΔK, which should increase along with the short cracks growth, is not high enough to propagate the cracks under the constant remote applied stress and K_t. These analyses contribute to the quantification of fatigue crack initiation life and non-propagating crack length. Hence, it is certainly reasonable to expect that such phenomenon can be used to quantitatively explain why the fatigue stress concentration factor K_f differs from the conventional stress concentration factor K_t of sharp notches. The stop of short cracks has been attributed to the decrease of ΔK as short cracks lengthen, which relates to significant stress gradient at the edge of notch.

Recently, Castro et al. have indicated in [4] that the high stress gradient at the narrow notch root

was drastically reduced due to the short crack growth, which may lead to the non-propagating crack phenomena. In the present paper, based on their analytical methodology, a modified method has been provided to quantify the short crack behavior. And the variation of the stress gradient and the resulting ΔK along with the short cracks growth has been presented.

2. Stress gradient at the sharp notch root along with the short cracks growth

It is well known that the stress concentration is usually caused by geometrical discontinuity or heterogeneity of microstructure which involves an appearance of the maximum stress compared to the calculated median values based on the smooth section. In mechanical design, one attaches rather importance to the high stress fields which arise in the majority of the industrial components (shoulder, holes, fillets etc.). The stress concentrations can be regarded as the origin of the fatigue cracks or the unstable ruptures.

In this paper, the authors are devoted to the investigation of the stress concentrations due to the geometry imposed by the industrial design. The notch effect is modeled by an increase of the local stress in a restricted volume, compared to the distribution of nominal stress. However, the concept of stress gradient can be generalized with any cross-section of a specimen or with any volume element of a mechanical component. Therefore, for a plate containing cracks at the bottom of an elliptic notch as illustrated in Fig. 1, the stress σ_y, which acts in the remaining ligament of an infinite plate with an elliptic hole, is given by Eq. (1) at points ($x \geq b$, 0) (see [5]).

$$\frac{\sigma_y}{\sigma_n} - 1 = \frac{\left(b^2 - 2bc\right)\left(x - \sqrt{x^2 - b^2 + c^2}\right)\left(x^2 - b^2 + c^2\right) + bc^2\left(b - c\right)x}{\left(b - c\right)^2\left(x^2 - b^2 + c^2\right)\sqrt{x^2 - b^2 + c^2}} \tag{1}$$

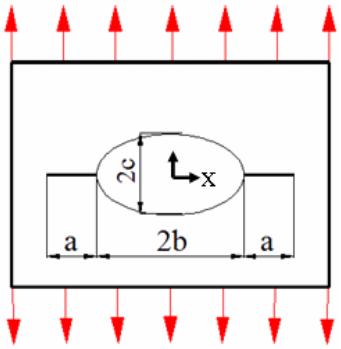

Fig. 1. Centre elliptic notch with a fatigue cracks formed at the notch roots

The σ_y/σ_n can be defined as the stress concentration factor in the presence of short crack K_{tf}. Thus, the gradient of σ_y at the bottom of notch (at the edge of the elliptic hole) is given by the following equation:

$$d\sigma_y / dx\big|_{x=b} = -\left(2K_t + 1\right)\sigma_n / \rho = -\left(3 + 4b/c\right)b\sigma_n / c^2 \tag{2}$$

The stress gradient increases with the increase of K_t and/or the reduction of ρ, where $K_t = 1 + 2\sqrt{b/\rho}$ according to [6]. In this paper, five different configurations with the same dimension of elliptic notch b = 27.5 mm (see Table 1) have been analyzed, and five radii values of which have been

tested on a purely comparative basis (ρ = 0.5, 1, 2.5, 3 and 27.5mm), which correspond to the critical value of the elliptic notch.

ρ (mm)	b (mm)	c (mm)
0,5	27,5	0,5
1	27,5	1
2,5	27,5	2,5
3	27,5	3
27,5	27,5	27,5

Table 1. Notches dimensions

The high value $K_{tf} = \sigma_y/\sigma_n$ in the presence of a short crack is always localized close to the edges of the hole according to the curves of Fig. 2. In fact, in the case of an elliptic notch ($b > c$), the ratio of the stress $\sigma_y(x)$ along the remaining ligament and the nominal stress σ_n, i.e. K_{tf}, is roughly equal to 3 for the distance $x = 1.1b$. This ratio falls to a value of 2 independently of the radius ρ when x reaches approximately $1.2b$. The Eq. (3) enables us to quantify the influence of the stress gradient on the variation of the K_{tf} according to x/b.

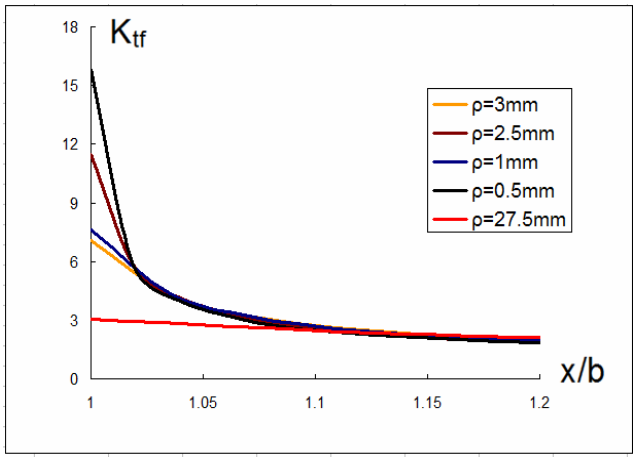

Fig. 2. Evolution of the stress concentration in the presence of a short crack

Fig. 3 illustrates explicitly the relationship between the stress concentration K_t (without crack) and the stress concentration ($K_{tf} = \sigma_y/\sigma_n$) (in the presence of a crack) with respect to the distance away from the edge of the notch. The reduction of K_{tf}/K_t is practically linear and not very sensitive to the value of K_t. The ratio decreases steeply from 1 for a point located at the end of the notch to 0.9 for a point which is very close to the crack length $a = b/20$. This rather high stress gradient can cause an initiation of the fatigue short crack, even in the case of a nominal stress lower than the yield stress.

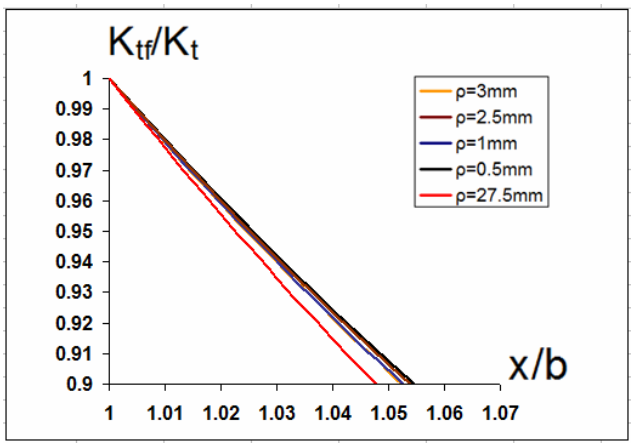

Fig. 3. Evolution of the ratio K_{tf}/K_t with respect to the relative length of the short crack

After the above discussion of the stress gradient with the propagation of short cracks at the sharp notch root, the variation of ΔK which associates with the fatigue stress concentrations K_f can be better understood. The K_f is defined as the ratio of the fatigue limit of a smooth specimen, S_0, to that of a notched specimen, S_0', under the same experimental conditions. Obviously, it is related to the size and geometry of the specimen and dimension of the notch. However, to determine experimentally the K_f with the grand variation of the notch shape (from the blunt notch to the critical condition "crack") is too laborious. Thus the analytical method based on some experimental results to predict the K_f is rather necessary. Indeed, if the crack is regarded as the critical condition of "notch", the nominal stress which can initiate the existing crack will be equal to the value of S_0'. That implies that the K_f is not only the key point for the crack initiation life analysis but also for the short crack growth estimations.

In 1979, El Haddad et al. associated the fatigue limit with the crack threshold through the Eq. (3) – Eq.(4) [7].

$$\Delta K = \eta \cdot \Delta\sigma \sqrt{\pi (a + a_0)} \geq \Delta K_0 (a) = \Delta K_0 \cdot \sqrt{a/(a + a_0)} \tag{3}$$

$$a_0 = (1/\pi) \cdot \left(\Delta K_0 / (\eta \cdot \Delta S_0) \right)^2 \tag{4}$$

Following Bazant's reasoning in [8], a more general threshold expression as Eq. (5) was presented by introducing an adjustable parameter γ to fit experimental data as described by Eq.(5)

$$\Delta K_0(a) = \Delta K_0 \cdot \left[1 + (a_0/a)^{\gamma/2} \right]^{-1/\gamma} \tag{5}$$

For the case where the crack is much smaller or much larger than the notch dimensions, the stress intensity range of a semi-elliptical notch has been mentioned in [9] with the expression in Eq.(6) and Eq.(7).

$$\Delta K = \eta \cdot K_t \cdot \Delta\sigma \cdot \sqrt{\pi (a + a_0)} \qquad \text{for} \quad a << b \tag{6}$$

$$\Delta K = \eta \cdot \Delta\sigma \cdot \sqrt{\pi (a + b)} \qquad \text{for} \quad a >> b \tag{7}$$

For the case of very small crack with $a << a_0$, $\Delta\sigma$ is the notch root stress range; for the long crack with $a >> b$, $\Delta\sigma$ tends to the nominal stress $\Delta\sigma_n$. In most cases, the K_t is used to indicate the stress concentration factor of the notch root without the crack growth. Hence, the function $\varphi(a)$ in Eq. (8)

can be used to reflect the effects of the notch root stress concentration instead of K_t. It is remarkable that the $\varphi(a)$ tends to the notch root stress concentration factor as the crack length a tends to zero.

$$\Delta K = \alpha \cdot \varphi(a) \cdot \Delta\sigma \cdot \sqrt{\pi(a + a_0)} \tag{8}$$

According to these theories, Meggiolaro et al. have proposed an effective method which could analytically estimate the K_f (see [9]). They associated ΔK and $\Delta K_{th}(a)$ so that the short crack will propagate when:

$$\Delta K = \eta \cdot \varphi(a/\rho) \cdot \Delta\sigma\sqrt{\pi a} > \Delta K_{th}(a) = \Delta K_0 \cdot \left[1 + (a_0/a)^{\gamma/2}\right]^{-1/\gamma} \tag{9}$$

Accordingly, a crack propagation criterion was stated using two dimensionless functions φ and g with the following expression:

$$\varphi\left(\frac{a}{\rho}\right) > \frac{\left(\Delta K_0/\Delta S_0\sqrt{\rho}\right)\cdot(\Delta S_0/\Delta\sigma)}{\left[\left(\eta\sqrt{\pi a/\rho}\right)^{\gamma} + \left(\Delta K_0/\Delta S_0\sqrt{\rho}\right)^{\gamma}\right]^{1/\gamma}} \equiv g\left(\frac{a}{\rho}, \frac{\Delta S_0}{\Delta\sigma}, \frac{\Delta K_0}{\Delta S_0\sqrt{\rho}}, \gamma\right) \tag{10}$$

The second term $\Delta S_0/\Delta\sigma$ in the function g will be equal to the K_f when the $\Delta\sigma$ corresponds to the minimum stress range that can cause crack initiation and propagation from the notch border by fatigue, without arrest.

In general, K_f and a_{max} can always be found by solving the system

$$\begin{cases} \varphi/g = 1 \\ \partial(\varphi/g)/\partial x = 0 \end{cases} \Rightarrow \begin{cases} \varphi\left(\dfrac{a_{max}}{\rho}\right) = g\left(\dfrac{a_{max}}{\rho}, K_f, \kappa, \gamma\right) \\ \partial\varphi\left(\dfrac{a_{max}}{\rho}\right)\Big/\partial x = \partial g\left(\dfrac{a_{max}}{\rho}, K_f, \kappa, \gamma\right)\Big/\partial x \end{cases} \tag{11}$$

To verify the accuracy of the models to evaluate the tolerance to short cracks, a methodology is proposed to design notched fatigue test specimens specially conceived to induce non-propagating short cracks. The geometric configuration is that of a modified compact tension specimen C(T), having a machined notch with a circular hole with radio ρ at the tip, as is shown in 错误!未找到引用源。a. The line of size a represents the crack length. The external dimensions and the notch length $b = 15(mm)$ is chosen according to ASTM E647 recommendations to assure that the loading condition at the crack tip is not influenced by the loading-pin holes.

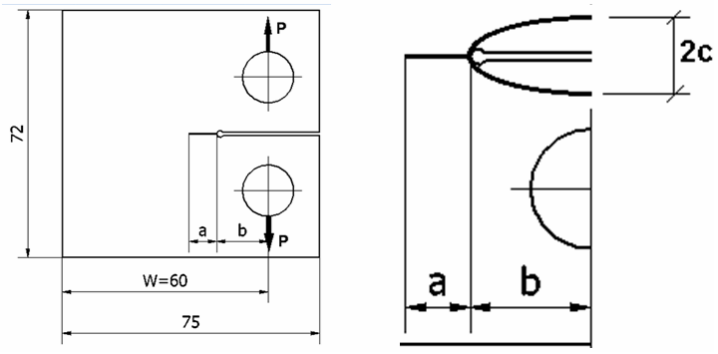

(a) (b)

Fig. 4 a) Modified C(T) specimens, dimensions in mm.

b) Approximation to a semi-elliptical notch.

The specimen notch is approximated by a semi-elliptical notch with semi-axes b and c (see **Fig.** b). The value of c can be expressed as a function of the notch root tip ρ, $\rho = c^2 / b$.

From an elastic stress analysis, considering the C(T) as a cantilever beam, the nominal stress range applied at the notch can be calculated as

$$\Delta\sigma_n = \frac{\Delta P}{t \cdot (W - b)} \cdot \left(1 + 3 \cdot \frac{W + b}{W - b}\right) \tag{1}$$

Therefore, after the value of $\Delta\sigma_n$ is determined by solving the system of equations in Eq. (11), the load ΔP to be applied to the specimen will be found by applying Eq. (12), in the next section are presented the numerical results for that combination.

3. Numerical results

Assuming the fatigue limit of smooth specimen as $S_L' = 0.5 \cdot S_u$, for a load ratio $R = -1$ (fully reversed loading), by Goodman it can be interpolated for $R = 0$ (pulsating tension), resulting in $\Delta\sigma_0 = 2 \cdot S_u / 3$.

Following the Frost's statement, it is the difference between K_t and K_f that define the generation of non-propagating cracks. The figure also shows the stress concentration factor K_t and how its value tends to K_f as the notch root ρ increases. Therefore, for this material and specimen configuration, notch with root radii $\rho <\sim 1.5$ will be able to generate non-propagating cracks (see **Fig. 5**).

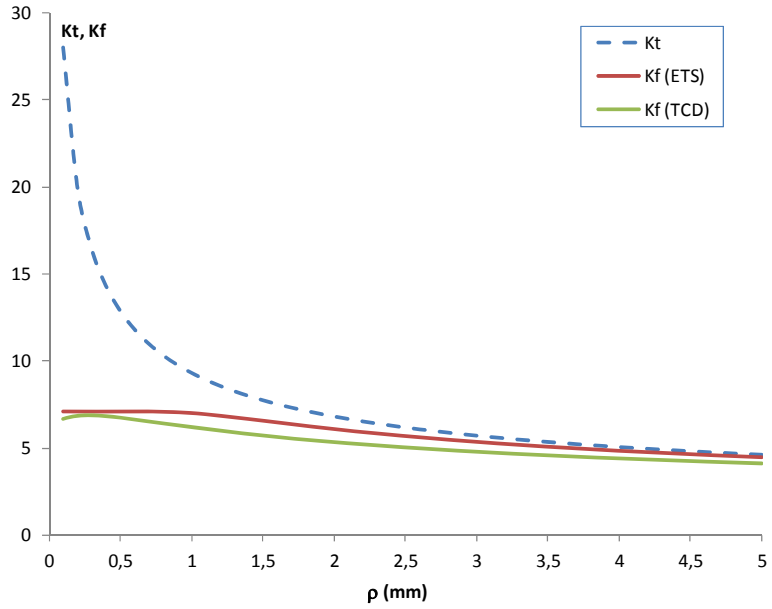

Fig. 5 Comparison of predictions of the notch fatigue factor K_f with the stress concentration K_t as a function of the notch root ρ.

In addition to K_f, the model also allows calculating the largest non-propagating crack $a_{\max}$ that can arise from fatigue alone. **Fig.** shows the value of $a_{\max}$ as a function of the notch root ρ.

Ideally, it would be better to deal with high values of ρ because they are easier to machine at the notch tip. In the other hand, the smaller the notch root radius ρ, the greater the maximum non-propagating crack $a_{\max}$ is, and, consequently, the more reliably the method can be applied to predict non-propagating cracks that can be robustly measured. According to the numerical results shown in **Fig.** , for $\rho <\sim 1.5$ it can be expected that the maximum non-propagating crack size should be $0.309mm < a_{\max} < 0.83mm$. Those values can be easily measured by an optical microscope.

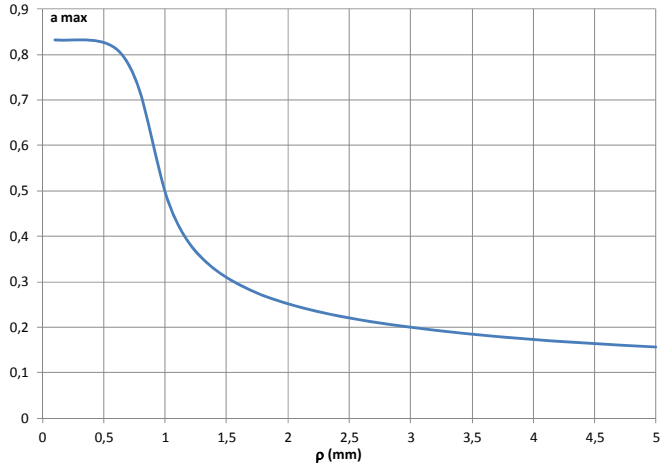

Fig. 6 Comparison of predictions of the maximum non-propagating crack a_{max} as a function of the notch root ρ.

4. Conclusions

A method was used to predict the notch factor K_f and, therefore, the fatigue limit for a notched specimen can be designed to induce non-propagating short cracks at the notch root. The configuration of the notch was approximated as a semi-elliptical notch and its fatigue limit was determined as a function of the radius of the notch root ρ. The largest non-propagating crack length can be calculated.

References

[1] B. Bhattacharya, B. Ellingwood, Continuum damage mechanics analysis of fatigue crack initiation. Int. J. Fatigue. 20 (1998) 631-639.
[2] C. Kaynak, A. Ankara, T.J. Baker, A comparison of short and long fatigue crack growth in steel. Int. J. Fatigue. 18 (2006) 17-23.
[3] Frost NE, Marsh KJ,Pook LP. Metal Fatigue, Dover, 1999.
[4] J.T.P. Castro, M.A. Meggiolaro, M.A.C. Oliveira, H. Wu, A. Imad, N. Benseddiq, Prediction of fatigue crack initiation lives at elongated notch roots using short crack concepts. Int. J. Fatigue. 42 (2012) 172-182.

[5] J. Schijve, Fatigue of Structures and Materials, Kluwer, Dordrecht, 2001.

[6] C.E. Inglis, Stresses in a plate due to the presence of cracks and sharp corners. Trans. Inst. Naval Architects., 55(1913) 219-241.
[7] M.H. El Haddad, T.H. Topper, K.N. Smith, Prediction of non-propagating cracks. Eng. Fract. Mech. 11(1979) 573-584.
[8] Z.P. Bazant, Scaling of quasibrittle fracture: asymptotic analysis. Int. J. Fracture. 83(1997)

19-40.
[9] M.A. Meggiolaro, A.C.O. Miranda, J.T.P. Castro, Short crack threshold estimates to predict notch sensitivity factors in fatigue. Int. J. Fatigue. 29 (2007) 2022–2031.

Some Microstructural Aspects on Humidity-Enhanced Deterioration in the Fatigue Strength of Age-Hardened 7075 Al Alloy

Yuzo Nakamura[1,*], Kohji Kariya [2], Norio Kawagoishi [2]

[1] Department of Mechanical Engineering, Graduate School of Science and Engineering, Kagoshima University
Kagoshima 890-0065, Japan
[2] Department of Mechanical System Engineering, Daiichi Institute of Technology
Kirishima 899-4395, Japan
* Corresponding author: nakamura@mech.kagoshima-u.ac.jp

Abstract Age-hardened 7075 Al alloys are one of the materials which possess large strength and large toughness. Their weight and large resistance to corrosion are also attractive in practical use. We have recently shown that the fatigue behavior of extruded 7075-T6 Al alloy is strongly influenced by the humidity in atmospheric air, and the fatigue strength decreases markedly at the humidity higher than about 60%. In addition, shear-type fracture with high crack growth rate occurs at high humidity, while tensile-type fracture dominates at low humidity. The occurrence of the change in fracture mode, however, depends on the conditions used in fatigue tests. In the present study, microstructures of the 7075 T6 Al alloy subjected to fatigue tests in various conditions and humidity are examined by using electron backscattering diffraction (EBSD) and X-ray diffraction (XRD). The results of EBSD and XRD analyses indicate that the microstructures depend on the history of metalworking and heat treatment and that the fatigue properties in high humidity environment are influenced by the difference of the microstructures in addition to the effect of humidity. A crytallographic geometry model is also shown to interpret the preferential occurrence of the shear-type fracture based upon the EBSD analyses.

Keywords Fatigue, Humidity, Fracture mode, 7075-T6 Al alloy, Microstructure

1. Introduction

Age-hardened Al alloys are very attractive from the viewpoints of those large strength, large fracture toughness and light weight. In particular, Al-Mg-Zn(-Cu) alloys (7000 series) are commonly strengthened by the precipitation of spheric GP zone, hexagonal η' phase ($MgZn_2$) and hexagonal η phase ($MgZn_2$), and the degree of strengthening depends on the heat treatment conditions used for aging [1]. It is well established that 7000 series Al alloys are very susceptible to stress corrosion cracking in aggressive corrosion environment [1]. The fatigue properties of age-hardened Al alloys are very sensitive to environment, and a drastic decrease in fatigue strength occurs in the air of relative humidity (RH) higher than 85% [2]. Our previous studies [3-7] have also shown that the fatigue strength of 7075 T6 alloy decreases markedly as RH is increased to more than about 60 %. Anodic dissolution of particles or stress concentration arising from large particles may become the causes of initiating cracks. However, the previous studies strongly suggest that hydrogen-enhanced local plasticity mechanism plays a major role in the deterioration of fatigue properties.

The difference in microstructure especially due to under-, peak- and over-aging has been considered to be another key issue to understand the susceptibility of age-hardened Al alloys and improve their resistance to environmental attacks. Commercial Al alloys, however, commonly experienced metalwork processes such as rolling and extrusion in order to obtain products with desired strength, shape and size. Thus, we have to consider the effect of these microstructures produced by manufacturing processes. The previous studies have shown that the extruded rods of 7075 T6 alloy exhibit unique deformation and fracture behaviors in cyclic loading. The initiation of crack and its propagation takes place at angles of about 35^o inclined from the loading axis in certain atmospheres and for certain test conditions. In the rotating bend tests with the frequency of 50 Hz, this shear-type cracking is observed in high humidity more than 60% RH at high stress levels, while the decrease in

stress level or the decrease in frequency to 6 Hz alters the shear mode to the tensile mode.
In the present study, microstructural analyses of the extruded 7075 T6 Al specimens subjected to fatigue tests were carried out by EBSD and XRD, in order to obtain an insight into the influence of extrusion texture on the fatigue properties in high humidity environment. Since EBSD analyses are restricted in local regions and insensitive to internal stresses, XRD analyses were also conducted to obtain the information on the macroscopic texture structure as well as the internal stresses remaining due to extrusion. The microstructural analyses were carried out on another specimen into which different microstructures were introduced by using different heat treatment. In order to deepen the understanding of the relation of fatigue properties influenced by humid environment with microstructures, some of the previous results on fatigue tests were reassessed and compared with the results of microstructural analyses.

2. Experimental procedure

Commercial rods of 7075 T6 Al alloy with the diameters of 18 mm were used as a starting material. The alloy has the chemical composition listed in Table 1, but the degree of extrusion was not known. Some of the as-received rods were solution treated at 733 K for 10.8 ks, and some rods were solution treated at 773 K for 118.8 ks. These solution treatments were carried out to increase grain sizes. The solution treated specimens were aged at 393 K for 86.4 ks, *i.e.*, under ordinary T6 temper condition. In order to distinguish the heat conditions, the as-received specimens and the specimens solution treated at 733 K and 773 K will be hereafter called A, B and C specimens, respectively. Table 2 shows the tensile properties and grain size of these rods. It is clear from this table that the solution treatment increased grain size considerably, and lowered the yield strength markedly compared to that of as-received ones.
The fatigue tests were conducted for A and B specimens, while C specimens were used only for the comparison of microstructure with these specimens. A specimens were subjected to rotating bend (RB) tests at 50 Hz and ultrasonic loading (US) tests at 20 kHz. On the other hand, B specimens were RB-tested at 50 Hz and 6 Hz. The shape and size of the fatigue test specimens are shown in Fig. 1. The humidity was varied from 0% RH in N_2 gas to 100% RH in distilled water. The details of the fatigue tests and conditions had been mentioned in the previous studies [3-7]. EBSD and XRD analyses were conducted by using disk specimens with a height of 10 mm cut from A, B and C rods (Fig. 2). The surfaces of these specimens to be used for EBSD analyses were mechanically polished to the final polishing with 20 nm silica particles, followed by low-energy Ar ion etching. XRD profiles were obtained by using Cu Kα beam from the same transverse cross-section as was subjected to EBSD analyses. Subsequently the disc specimens were cut longitudinally at the

Table 1. Chemical composition of 7075 T6 Al.

Element	Zn	Mg	Cu	Cr	Si	Fe	Mn	Ti + Zr	Al
Mass fraction (%)	5.46	2.56	1.47	0.19	0.09	0.25	0.03	0.03	bal.
Atomic fraction (%)	2.35	2.96	0.65	0.10	0.09	0.13	0.02	0.01	bal.

Table 2. Tensile properties and grain size of 7075 T6 Al.

Specimen	Heat treatment	Yield strength (MPa)	Tensile strength (MPa)	Reduction in area (%)	Nominal grain size (μm)
A	as-received ordinary T6	630	691	9.5	8
B	733 K, 10.8 ks 393 K, 86.4 ks	527	673	11.3	13
C	773 K, 118.8 ks 393 K, 86.4 ks	553	685	11.6	40

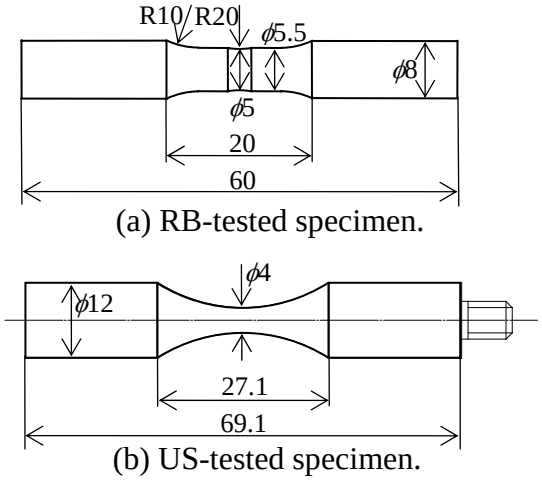

Fig. 1. Shape and size (mm) of specimens.

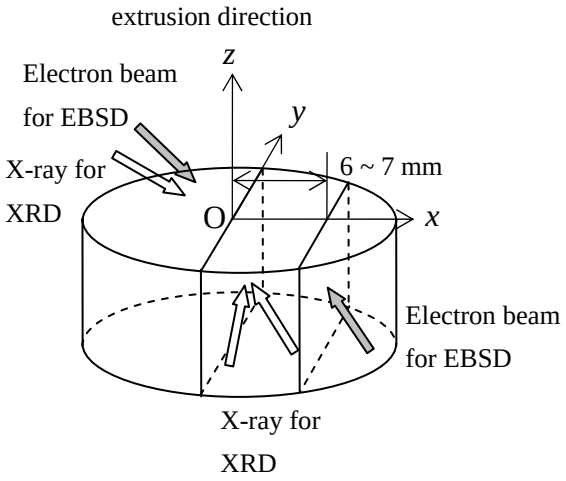

Fig. 2. Locations for EBSD and XRD analyses.

distance of 6 ~ 7 mm from the center, and the cut surfaces were polished in the same way and then subjected to EBSD and XRD analyses. In the XRD analyses of the longitudinal cross-sections, the projection of X-ray beam on the cross-section was aligned in directions along *x* and *y* axes to examine the difference in microstructure in these directions. The same procedure was applied to the microstructural analysis of longitudinal cross-sections at the center of disc.

3. Results

3.1 Effect of humidity on fatigue strength

Fig. 3 shows a comparison of *SN* curves obtained for A and B specimens which are subjected to RB tests with 50 Hz in humid atmospheres ranging 0% RH (N_2 gas) to 100% RH (distilled water). Symbols in the figure are experimental data of the stress amplitude (σ_a) and the number of cycles to failure (N_f), and the curves can be expressed by

$$\sigma_a = \sigma_{ao} + k\{(N_f/N_{fo})^{-m} - 1\} \quad (1)$$

where σ_{ao} and k are the strength coefficients, m is a numerical constant and N_{fo} is a reference number of cycles to failure and set to be 10^7 cycles in the present analysis. The as-received A specimens in N_2 gas show the largest fatigue strength among all of the testing conditions, which exhibits larger strength by 30 ~ 60 MPa than that of B specimens fatigue-tested in N_2 gas. This is consistent with the fact that the yield and tensile strengths of A specimens are larger than B specimens. Humidity does not change the fracture strength of B specimens significantly until RH is increased to 50 %, and a marked reduction of fatigue strength occurs at the humidity larger than 50 %. Previous studies showed that this transition appeared distinctly at the humidity of about 60 %. In contrast to B specimens, the humidity-induced deterioration in A specimens is prominent from the RH of 25 %, and the fatigue strength of A specimens at the humidity from 25% RH to 85% RH is lower than that of B specimens for identical RH. These results indicate that A specimens with larger yield strength is more susceptible to the environmentally assisted fatigue cracking.

Fig. 4 shows the change of the fatigue strength (σ_{ao}) for $N_f = 10^7$ as a function of RH. The fatigue strength of A specimens RB-tested at 50 Hz decreases monotonically with increasing RH. The fatigue strength of B specimens tested in the same condition, however, is insensitive to the humidity up to 50 % and shows a rapid decrease at higher humidity. Nevertheless, the fatigue strength of B specimens RB-tested at 6 Hz is kept to be constant up to 85% RH. The application of US loading with 20 kHz to A specimens results in a slight degradation from N_2 gas to 25% RH, a high-stress-level plateau from 25% to 50% RH, a drastic degradation from 50% to 75% RH, and

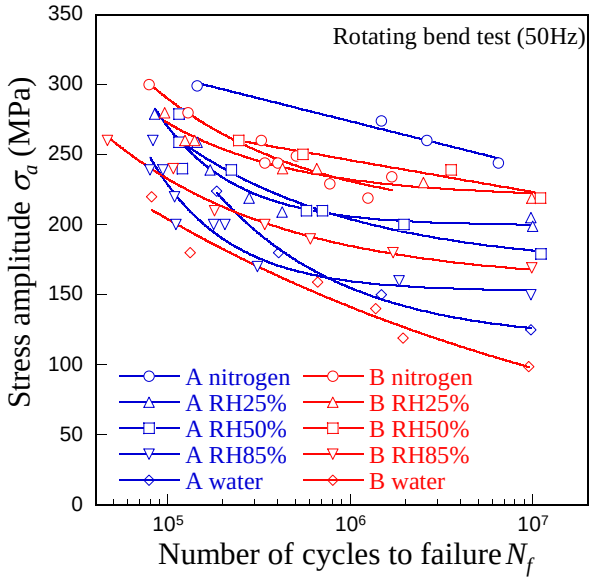

Fig. 3. SN curves of A and B specimens.

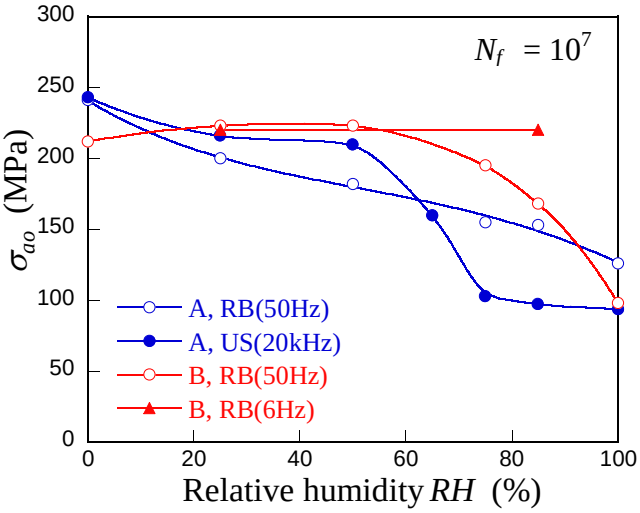

Fig. 4. Dependence of fatigue strength on RH.

then a low-stress-level plateau above 75% RH. It is obvious that these different fatigue behaviors cannot be explained only by the effect of humidity.

3.2 Crack initiation and growth

SEM observations conducted in previous studies [3-7] showed different morphologies of fatigue cracks in extruded 7075 T6 Al alloy, which are depicted schematically in Fig. 5 (a)~(d). These morphologies are macroscopically classified into (a) tensile-mode-initiation followed by tensile-mode-propagation (TT-type), (b) tensile-mode-initiation and shear-mode-propagation (TS-type), (c) shear-mode-initiation and shear-mode-propagation (SS-type), and (d) multiple-shear-mode-initiation followed by coalescence of cracks leading to apparent tensile fracture (MST-type). Typical examples of fracture surfaces are also shown in Fig. 5. In A specimens RB-tested at 50 Hz, crack initiation takes place in tensile manner and their macroscopic fracture mode becomes TT-type in all of the humid conditions and TS-type in N_2 gas. On the other hand, the application of US loading to A specimens changes the crack initiation from tensile mode to shear mode, except at low humidity. Hence US-tested A specimens show TS-type fracture at low humidity and SS-type or MST-type fracture for other conditions. This tendency appears in B specimens RB-tested at 50 Hz, too. The common feature to US-tested A specimens and RB-tested B specimen is that MST-type fracture is induced at 85% RH and in water at low stress level. This fact suggests that many cracks are initiated at the surface exposed to such high humidity for longer time. Both of the initiation and propagation of S-type cracks take place at an angle of about 35^o inclined from the loading axis in both of the RB and US tests. In particular, the morphologies of initial cracks are important, since they may be indicative of the slip prior to the initiation as well as the slip associated with the initiation.

Fig. 6 shows typical examples of T-type and S-Type short cracks observed on the surfaces of B specimens RB-tested at 25% RH and 85 % RH, respectively. The T-type crack exhibits some irregularities in propagation path, some of which are inclined by $\pm 35^o$ from the loading axis, but it develops in a direction perpendicular to the loading axis. On the other hand, the S-type crack develops in a shape of "V" of which edges are symmetrically inclined by $\pm 35^o$ from the loading axis. The symmetry of crack initiation with a definite geometry, which can be microscopically observed in the zigzag path of T-type crack, indicates that slip leading to the crack initiation may take place

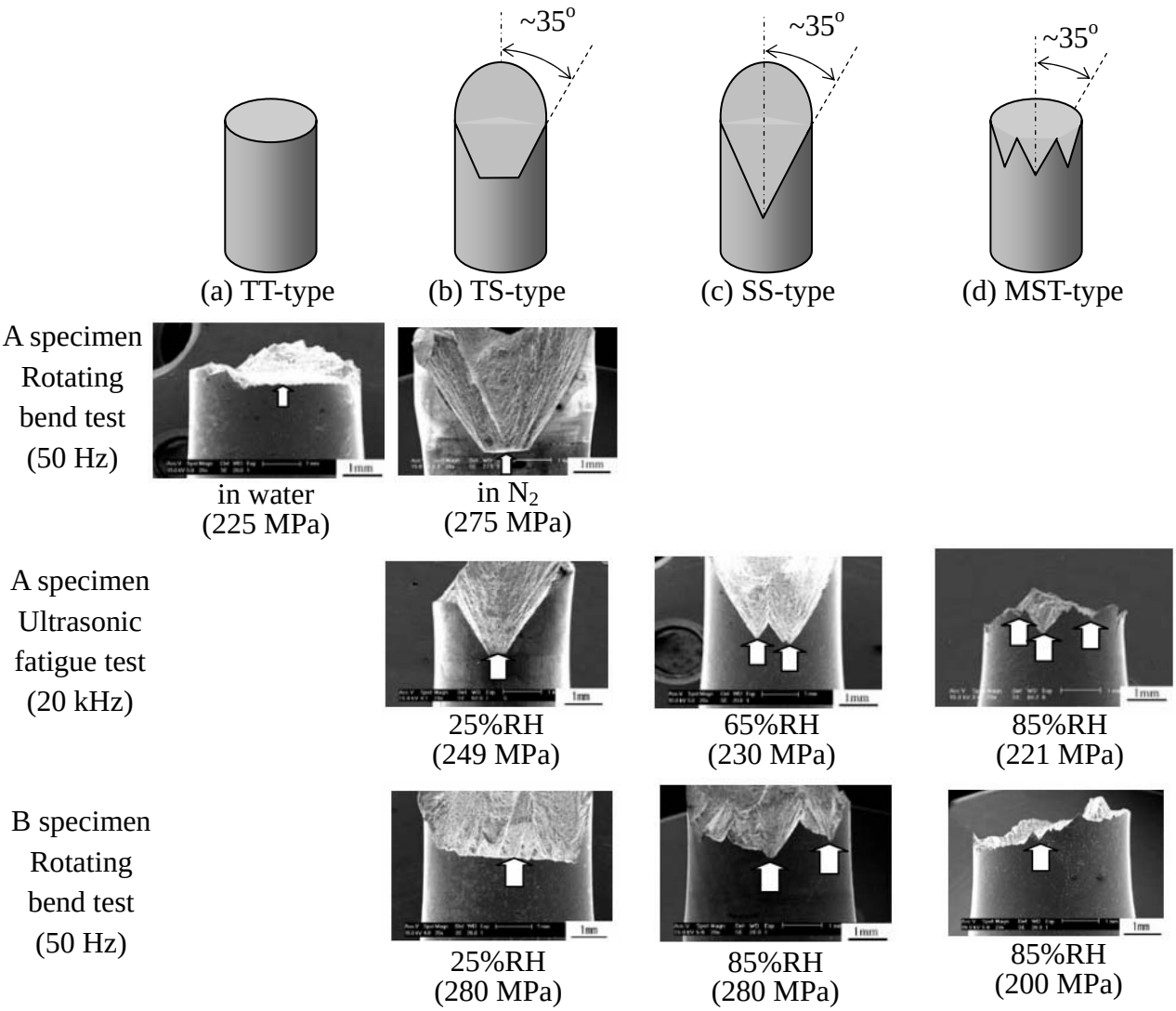

Fig. 5. Macroscopic features of fatigue fracture.

preferentially in this direction. One can see that the crack propagation in macroscopic scale shows the same tendency in certain circumstances. Thus, the evolution of plastic zone in front of crack tip may also have orientation-dependence intrinsic to the microstructure.

Fig. 7 shows typical relations of crack length (l) and number of cycles (N) in B specimens RB-tested at 50 Hz. The values of crack length were measured in transverse direction. Thus the length of a pure S-type crack developing with an angle of 35°, for example, becomes $l/\sin 35^{o} = 1.74l$. As shown in Fig. 5, there are some mixtures of T- and S-type crack propagations so that the real length of crack along its path is always larger than the measured value of l in such mixtures. Reminding this effect, one can see from Fig. 6 that the growth of S-type cracks formed at 85% RH occurs much faster than that of T-type cracks at 25% RH. It is also recognized that the initiation of S-type cracks at such high humidity is induced at very small cycles compared with the initiation of T-type cracks at low humidity. On the other hand, A specimens tested in the same test condition show T-type crack initiation irrespectively of environment, while its sensitivity to humid environment appears from low humidity. US tests with 20 kHz enables A specimens to exhibit the S-type cracking so that the crack growth as a function of N becomes much larger than RB-tested A specimens. This result suggests that the formation and propagation of cracks may be rate-controlled. This was also demonstrated in B specimen; the reduction of frequency from 50 Hz to 6 Hz in RB tests transformed the fracture mode from S-type to T-type [7].

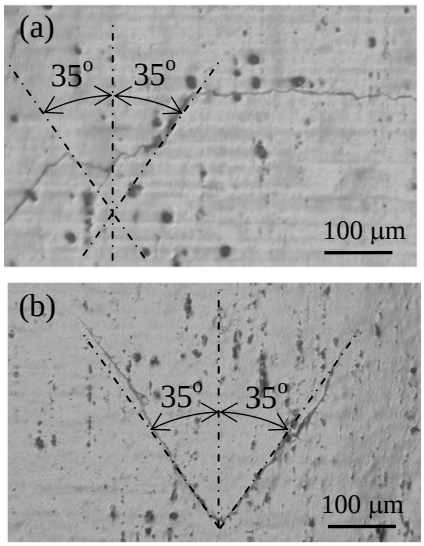

Fig. 6. Crack initiations in (a) T-type and (b) S-type modes.

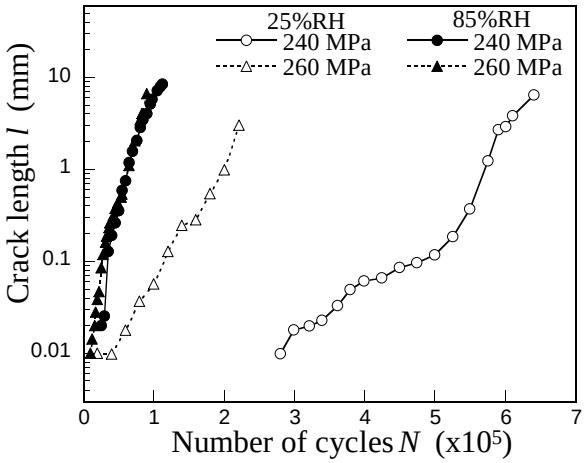

Fig.7. Relation of crack growth with the number of cycles in B specimens.

3.3 Microstructure

Fig. 8(a) shows the SEM image of the transverse cross-section at the center of B specimen, which is inclined by 70° for EBSD analyses. Fig. 8 (b), (c) and (d) are the maps (IPF maps) of crystallographic orientations of grains in *z*, *x* and *y* directions, respectively, which are obtained from the square region depicted in Fig. 8(a). Grains are distinguishable by those relief and contrast in SEM image. The grain size estimated by using the SE image is 12 μm, which is nearly the same as the grain size evaluated by using large misorientation angle. The IPF image along *z* axis shows that the transverse surface are dominated by large grains close to <111> direction (hereafter called <111> grains) and the remaining large grains have orientations close to <001> (hereafter called <001> grains). The areal fraction of <111> grains is estimated to be about 80 %. However, the IPF images along *x* and *y* axes clearly indicate that these large grains involve subgrains, and the average grain size including the subgrains is estimated to be 3.9 μm by using a misorientation angle of 0.5° for grain boundary detection. The IPF (Fig. 7(e)) along *z* axis also shows the largest fraction of <111> grains and the second one of <001> grains. The crytallographic orientations are uniformly distributed along <101>-<112> circle in *x* and *y* directions, as is shown by Figs. 7(f) and 7(g).
Figs. 9 and 10 are the IPF images of A and C specimens, respectively. It is obvious that the grains in C specimens have round corners compared to A specimens, which indicates the grain growth takes place in C specimen by the solution treatment. The grain growth appearing as round grains can be seen in B specimen by comparing Fig. 8(b) with Fig. 9(a). The grain sizes listed in Table 4 show that the as-received A specimen has the smallest grain sizes in both large misorientation and small misorientation including subgrains. In addition the fraction of <111> grains in A specimen is 61 %, while the fraction in the other specimens are nearly 80%. This result indicates that the solution treatments done for B and C specimens induce the preferential growth of <111> grains.
Fig. 11(a), (b) and (c) are the pairs of IPF image and IP figure taken from the longitudinal cross-section at the center of B specimen along *z*, *x* and *y* axes, respectively. The longitudinal cross-section is mainly covered with <111> grains which involve the elongated islands of <001> grains (Fig. 11(a)). The extrusion ratio is estimated to be more than 800 % from the shape of island <001> grains. In contrast to the transverse cross-section, subgrains involved in large <111> grains do not have large misorientation between neighboring ones. It is also noted that some of the <001> grains observed in *z* axis analysis disappear in *x* and *y* axes, which indicate that these disappeared grains have continuous relation with surrounding <111> grains. Thus the texture structure is

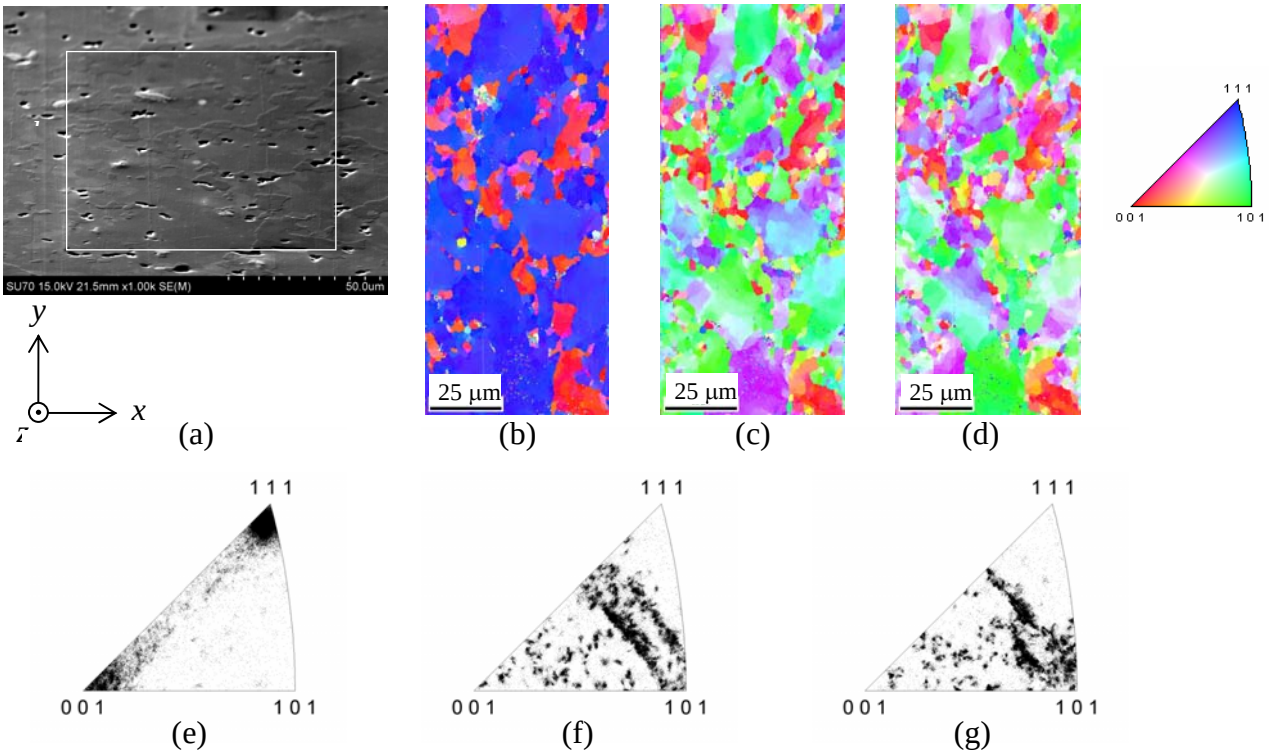

Fig. 8. Results of EBSD analyses obtained for the transverse cross-section at ceneter of B specimen. (a) SE image, (b) IPF map along z axis, (c) IPF map along x axis, (d) IPF map along y axis, (e) IP figure along *z* axis, (e) IP figure along *x* axis, and (f) IP figure along *y* axis.

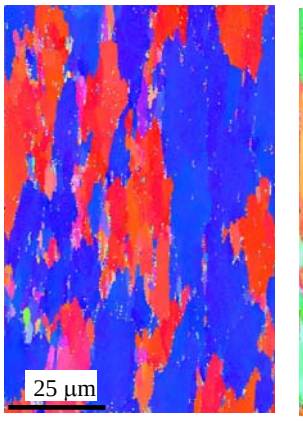

(a) z axis

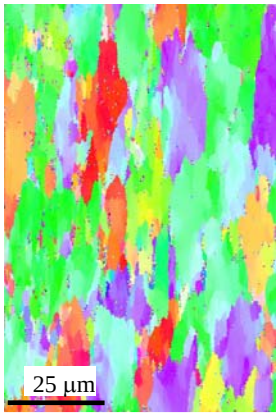

(b) x axis

Fig. 9. IPF maps of transverse cross-section at center of A specimen.

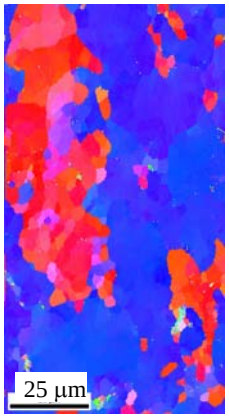

(a) z axis

(b) x axis

Fig. 10. IPF maps of transverse cross-section at center of C specimen.

consisted of fibrous grains of 3.9 μm diameter elongated in the extrusion direction, but is regarded as having the single-crystal-like nature within several 10 μm in the transverse directions. These trends are common in all specimens investigated. However A specimen exhibits a larger fraction of <001> grains, as is shown in Fig. 9 (a).

3.4 XRD profiles

Fig. 12 shows the XRD peaks taken from the transverse cross-section in B specimen. The height of (111) reflection peak was considerably large in all of the specimens due to the texture of <111>

Table 4. Estimated grain sizes and fraction of <111> grains.

Specimen	Grain size with large misorientation (μm)	Grain size involving subgrains (μm)	Fraction of <111> grains (%)
A	10	1.8	61
B	12	3.9	80
C	50	5.5	85

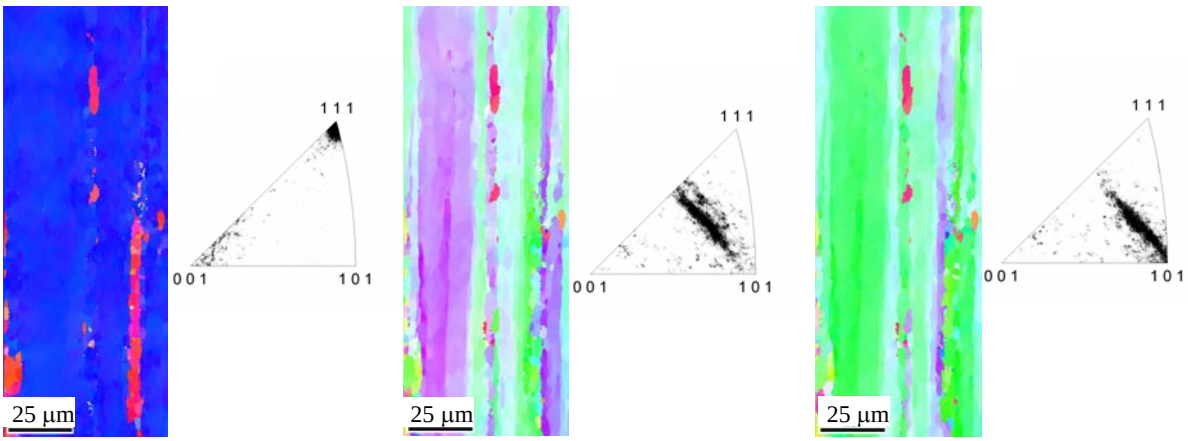

(a) *z* axis (b) *x* axis (c) *y* axis

Fig. 11. IPF images and IP figures of longitudinal cross-section at center of B specimen.

grains, as is typically demonstrated by Fig. 12. This result is consistent with the results of EBSD analyses mentioned above. However, A specimen has the broadest peaks, while C specimen has the most narrow peaks, as shown in Fig. 13. Since the grain sizes of the present specimens are too large to contribute to the broadening of XRD peaks, the internal stress is attributed to the broadening in A and B specimens [6]. The internal stress due to precipitates is considered to be nearly the same in all specimens, because the same aging condition is applied. Therefore the broadening of XRD peaks is considered to be brought by the difference in the dislocation density; A specimen has the largest dislocation density, the density in B specimen is the second largest and the density in C specimen is comparable to that of the annealed one which shows distinct peaks of $K_{\alpha 1}$ and $K_{\alpha 2}$ X-rays.

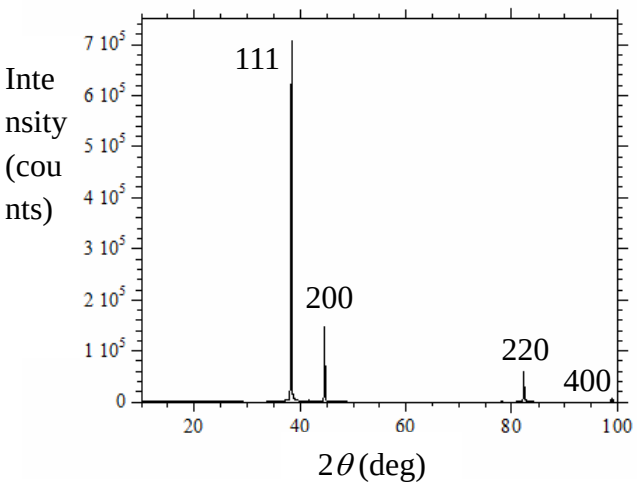

Fig. 12. X ray peaks in B specimen.

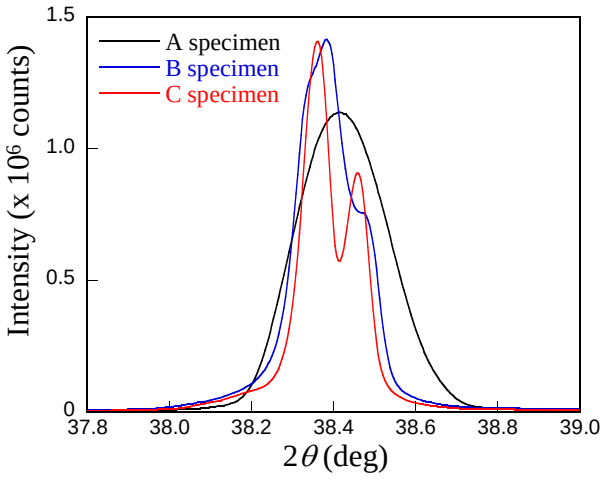

Fig. 13. Peaks of (111) reflection.

4. Discussion

Birnbaum and Solfronis [8] calculated the interaction of H interstitials with dislocations and indicated that the motion of dislocations trapping H interstitials becomes easier and planar. Ferreira *et al*. [9] showed that the cross slip of screw dislocations in pure Al becomes difficult in hydrogen atmosphere. Further, Bond *et al*. [10] showed that the velocity of dislocations is enhanced and therefore the resistance to cracking is reduced in 7050 and 7075 alloys exposed to hydrogen atmosphere. These theoretical and experimental results strongly support that hydrogen-enhanced local plasticity (HELP) accompanying the reduction of flow stress and the planar slip is induced in Al and its alloys, when they are exposed to environments which enable H atoms to enter the materials. It is also considered that H atoms formed by the reaction of H_2O with freshly created surfaces close to crack tips enter the material during the fatigue cracking of 7075 T6 alloy in high humidity. The HELP mechanism works at the crack tips and lowers the flow stress in the plastic zone in front of the crack tips. This deterioration mechanism explains the present results well. However, the difference in the sensitivity to humidity as well as the fracture mode between A and B specimens, which is shown by Figs. 3-7, has not been made clear [13].

As mentioned in sections 3.3 and 3.4, as-received A specimens have finer grains containing dislocations with a high density. In contrast, B specimens solution-treated at 733 K for 10.8 ks exhibit the preferential growth of <111> grains and their dislocation density is lowered. Such grain growth as well as the reduction in dislocation density is manifested in C specimens. These results suggest that the grain size, the structure of texture and the dislocation density influence the HELP mechanism in environmentally assisted fatigue cracking. In A specimens, both of the <111> and <100> grains are relatively hard as is shown by the yield strength in Table 2. In addition, the faction of <100> grains in A specimens is larger compared with that of B specimens. It is hence considered that the propagation of slip between neighboring grains is more difficult in A specimens. On the other hand, the grains in B specimens are softer and mostly governed by <111> grains, and the misorientations between the subgrains are very small (Fig. 11). Therefore it is considered that the texture structure of B specimens enables selected slips to propagate smoothly from grain to grain. This consideration explains well why the shear mode fracture takes place more preferentially in B specimens than in A specimens under the same RB test condition using 50 Hz (Fig. 5).

Kariya [11] found by using etch pit technique that the humidity-induced shear mode cracks propagate in <110> direction and the cracks lie on {001} plane in B specimens RB-tested at 50 Hz. This result seems to be consistent with the morphology of observed S-type cracks, since the angle between <111> and <001> is 35.3^o. On the other hand, the present EBSD analyses yield such angle of S-type cracks in other geometries as shown in Fig. 14. In a <100> grain, the intersections of two slip planes with the specimen surface make the angle of $\pm 35.3^o$, when <110> direction of the grain is normal to the surface (Fig. 14(a)). The "V"-shaped crack can be formed only in this geometry. In a <111> grain, a slip direction makes an angle of 35.3^o with the specimen surface, when this slip direction is parallel to the surface (Fig. 14(b)). It is suspected from these geometries that the cracks of "V" shape are initiated in such <100> grains emerging at the specimen surface. It should be also noted that the "V"-shaped cracks in <100> grains can induce the slip in neighboring <111> grains with the same angle, when <011> directions of both grains are aligned like Fig. 14(a) and (b). Further the slip in <100> grains can be continuously connected with the slips in <111> grains, when the slips on two slip planes involving the selected direction operate simultaneously in <111> grains. This situation leads to the macroscopic {001} slip plane in <111> grains which is microscopically composed of two slip planes (Fig. 14(c)). As a result, {111} and {001} planes become preferential planes for crack propagation in <100> and <111> grains, respectively. It is also considered that edge dislocations glide on these planes so that the interaction of H atoms with the edge dislocations induces the acceleration of inclined crack propagation. It is suspected that the continuous slip propagation between <100> and <111> grains in A specimens is more difficult than in B specimens

for the reasons mentioned above. In the present study, we have not yet obtained the full understanding on the mechanisms by which the fatigue properties are influenced by the test conditions such as RB, US and frequencies. It is believed that such effects involve some rate-controlled processes like the diffusion and trapping of H atoms in different microstructures.

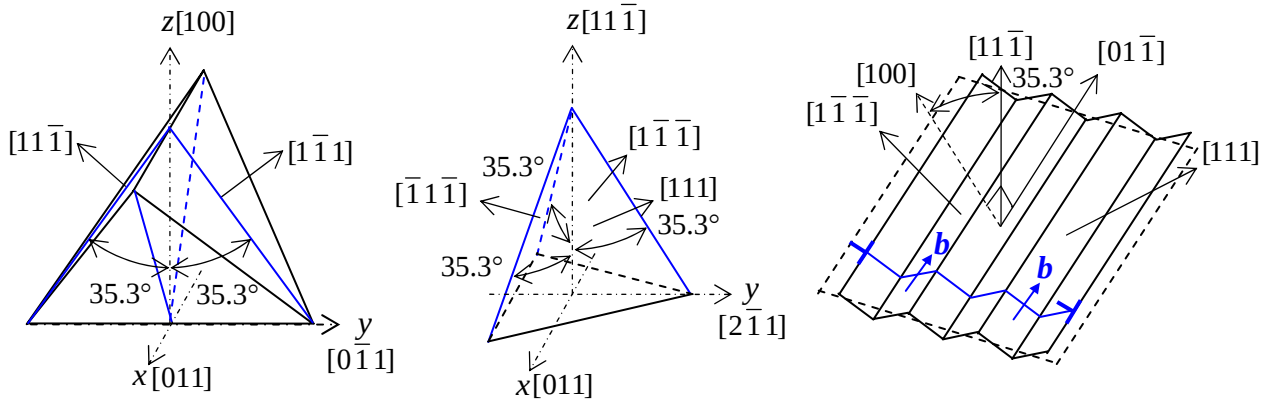

(a) <100> grain. (b) <111> grain. (c) {100} fracture in <111> grain.

Fig. 14 Crytallographic geometries. Thompson tetrahedron is used in (a) and (b).

5. Summary

The present study shows that extruded 7075 T6 Al alloy exhibits the deterioration of fatigue strength in high humidity environment. However the fracture mode strongly depends not only on the history of the metalworking and heat treatment, but also on the test conditions. The results of EBSD and XRD analyses indicate that these differences may arise from the grain size, texture structure and dislocation density. In particular, the shear mode cracking with the angle of 35^{o} from loading axis can be correlated with the crytallographic geometry of slips which are selected in the texture strongly aligned in <111> direction. In order to interpret the whole phenomena including the test conditions, more analyses taking into the characteristics of microstructures will be needed.

References

[1] I.J. Polmear, Light Alloys, Second Edition, Edwald Arnold, London, 1989.
[2] N.E. Frost, K.J. Marsh, L.P. Pook, Metal Fatigue, Dover, New York, 1999.
[3] N. Kawagoshi, T. Fukudome, Y. Nakamura, Y. Ozono, M. Goto, J JSME A, 76 (2010) 938-946.
[4] K. Kariya, N. Kawagoishi, T. Fukudome, Y. Nakamura, E. Kondo, J-JSMS, 60 (2011) 339-344.
[5] N. Kawagoishi, K. Kariya, Q. Chen, M. Goto, Y. Nakamura, J-JSMS, 60 (2011) 890-897.
[6] K. Kariya, N. Kawagoishi, S. Furumoto, Y. Nakamura, E. Kondo, J-JSMS, 60 (2011) 1015-1022.
[7] K. Kariya, H. Maeda, N. Kawagoishi, Q. Chen, Y. Nakamura, K. Morino, J-JSMS, 61 (2012) 712-718.
[8] A. Guinier, X ray Diffraction in Crystals, Imperfect Crystals, and Amorphous Bodies, Dover, New York, 1994.
[9] C.D. Beacham, Met Trans, 3 (1972) 437-451.
[10] H.K. Birnbaum, P. Sofronis, Mater Sci Eng, A176 (1994) 191-202.
[11] P.J. Ferreira, I.M. Robertson, H.K. Birnbaum, Acta Mater, 47 (1999) 2991-2998.
[12] G.M. Bond, I. M. Robertson and H. K. Birnbaum, Acta Metall, 35 (1987) 2289-2296.
[13] K. Kariya, Doctoral Thesis, Kagoshima University, Japan (2012).

Influence of Surface Rolling Time on Short Fatigue Crack Behavior of LZ50 Axle Steel

Bing Yang*, YongXiang Zhao

State Key Laboratory of Traction Power, Southwest Jiaotong University, 610031, China
* Corresponding author: yb@home.swjtu.edu.cn

Abstract Based on the mean fatigue life of LZ50 axle steel specimens which were unrolled before testing, five surface rolling times were determined according to the fatigue life fraction, i.e., f=0.0, 0.3, 0.5, 0.6, and 0.7. Five groups of smooth hourglass shaped specimens which were turned and rolled at above surface rolling times were tested by a replication technique. Results show that with a given dominant short crack size, crack growth rate after surface rolling occurs much slower than that before rolling. However, the more prolonged the surface treatment is performed, the greater the growth rate occurs at the transition point between the micro-structural short crack (MSC) stage and the physical short crack (PSC) stage. Furthermore, influenced by the change of surface hardness and residual compressive stress, the effective short crack density in all the specimens, which is the average number of short cracks per unit area, decreases significantly after rolling than before. Focusing on the density after surface rolling, it is evident that the highest effective short crack density for the five studied groups of specimens increases from 662 mm^{-2} to 941 mm^{-2} with postponed rolling time. On the other hand, the average fatigue life for each group of specimens decreases with postponed surface treatment time. The average life of the initial rolled specimens was 882,562 cycles, while that of specimens turned and rolled at a 0.7 fatigue life fraction is 618,640 cycles. Therefore, the surface rolling procedure can improve the fatigue performance characteristics of the material. The choice of rolling time may affect the short fatigue crack behavior greatly. The earlier the surface treatment is performed, the better the collective effect of short cracks can be restrained as well as the longer the fatigue life of the material will be.

Keywords Fatigue, short crack, surface rolling time, LZ50 axle steel

1. Introduction

With the development of the high speed and heavy haul railway in China, the service load conditions for structures and components of railway vehicles are much poorer than before[1]. As one of the important parts for vehicle running gear, axle bears complicated alternate loadings in service, and is the component with the highest loading frequency and the most complex failure modes[2]. If the axle failure caused by fatigue damage is uncontrollable, vehicles are likely to derail, and railway operation safety will be gravely affected. For components with smooth surface under alternate loadings, short fatigue crack (SFC) initiation, coalescence and propagation normally occupy more than 70% the fatigue life[3]. For example, with a overhaul cycle of 100,000 km and a reliability of 0.999, the critical size of semi-elliptical crack on the load relieving groove of RD_2 axle is 1.23 mm, and the size of circumferential crack is only 0.94 mm[4, 5]. Thus it can be seen that the fatigue damage process of axle belongs primarily to SFC stage.

The maintenance strategy for load relieving groove of RD_2 axle, for which the final processing method is turning, is finish turning and surface rolling. However, the impact of surface treatment time choice on maintenance effect, i.e., how the surface rolling time affects the short fatigue crack behavior, is still an on-going research issue.

LZ50 axle steel is one of the widely applied axle materials in Chinese railway manufacturing

industry, its production technology adopted the axle standard of AAR M-101[6]. Present research is based on the fatigue tests by a replication technique of this material. Different surface treatment times are chosen for five groups of specimens. The influence of surface rolling time on short crack propagation, crack density, and fatigue life is revealed.

2. Materials, Rolling Simulation, and Replication Tests

2.1. Test Materials and Specimens

Test material of present work is LZ50 axle steel. Its chemical composition and mechanical properties are shown in Tables 1 and 2, respectively. The heat treatment is double normalizing and then tempering in accordance with the Chinese railway standard, TB 2945-1999. After heat treatment, the microstructure of material is coarse ferrite particles and layered pearlite particles. The banded structure is quite obvious (Figure 1a), the mean value of intervals between two rich pearlite bands, d_2, is about 109 μm with high dispersion. Gathering effects exist in both ferrite structure and pearlite structure (Figure 1b). Average equivalent diameters for ferrite grains, d_1, is 14.6 μm[7]. Totally 33 smooth axial hourglass shaped specimens with 10 mm diameter were machined (Figure 2).

Table 1. Chemical composition of LZ50 axle steel (wt. %)

C	Si	Mn	Al	Cr	Ni	Cu	P	S
0.47	0.26	0.78	0.021	0.02	0.028	0.15	<0.014	<0.01

Table 2. Mechanical properties of LZ50 axle steel

σ_b / MPa	σ_s / MPa	δ / %	Ψ / %	E / MPa
656.43	383.57	54.71	26.57	209750

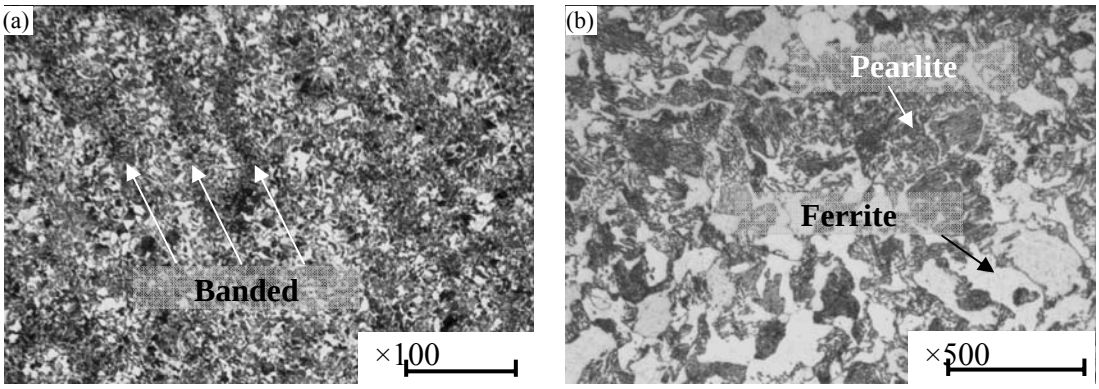

Figure1. Low (a) and high (b) magnified OM images of LZ50 axle steel after heat treatment

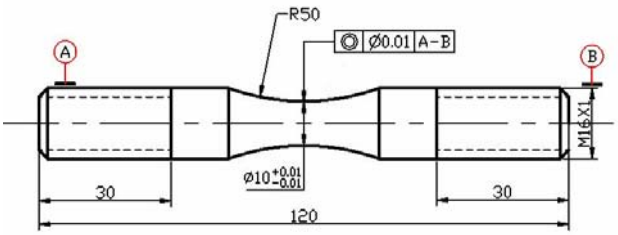

Figure 2. Schematic of shape and dimension of the specimen for fatigue test (Unit: mm)

2.2. Surface Rolling Simulation

The machining technology for load relieving groove of RD_2 axle is listed in Table 3 in detail. The purpose of finish turning is to remove possible surface cracks, while surface rolling is to strengthen the surface of load relieving groove. Surface treatment parameters of present research are also listed in Table 3. It can be seen that the simulation technology meets the maintenance requirements of real RD_2 axle. After rolling, surface Vickers hardness of specimens increases from 201.68 $HV_{0.1}$ to 222.90 $HV_{0.1}$. Meanwhile, absolute value of axial and circumferential compressive stress for specimens after surface rolling is about 170 MPa and 101 MPa higher than that before rolling[8].

Table 3. Practical repair procedure for RD2 axle and simulated surface treatment procedure for specimen

Procedure	Indicator	In practice	In simulation
Finish turning	Equipment	Numerical control machine	Numerical control machine
	Rotate speed of axle	≥350 r/min	=350r/min
	Cutting thickness	≤0.2 mm	≤0.15 mm
	Feeding speed	40~70 mm/min	=50 mm/min
Surface rolling	Equipment	Numerical control machine	Numerical control machine
	Rotate speed of axle	330~400 r/min	=350 r/min
	Rolling time	1	1
	Diameter deformation	≤0.02 mm	≤0.02 mm

2.3. Replication Tests

Replication technique is a widely applied fatigue test method in short crack research field. Test is interrupted at given time intervals (depending on the number of cycles), then replicate specimen surface with softened acetyl cellulose films, and finally these films can be dried and preserved for subsequent observation[9]. Present tests were performed under a stress-controlled sine wave mode on Rumul 250 kN high frequency fatigue test machine. The symmetrical cyclic stress amplitude was 230 MPa. To study the relationship between cracks and micro structures, specimen surfaces were etched by 4% nitric acid alcohol and the metallographic structure was exposed.

Firstly, all specimens without surface rolling were tested according to replication technique. Secondly, when cyclic loading number met predetermined cyclic number for surface treatment, test was suspended and specimens were dismounted. Thirdly, above specimens were turned and surface rolled complying with Table 3. Finally, processed specimens were mounted on test machine again and still tested at 230 MPa by replication method to final failure. Two things are important to note:

(1) Number of loading cycles according to surface rolling time.

Previous test result has shown that the average fatigue life of LZ50 axle steel specimens without surface rolling is 137705 cycles[7]. To investigate the influence of rolling time, surface treatment time for five groups of specimens was determined according to this life. That is, surface rolling was applied when life fraction, f, was 0.0, 0.3, 0.5, 0.6 and 0.7, respectively. To facilitate the presentation, specimens were indexed according to their surface rolling time, i.e., S0.0, S0.3, S0.5, S0.6, and S0.7 specimens.

(2) Test stress amplitude after surface rolling.

After turning and surface rolling, axle diameter will be slightly smaller than before, which will lead to higher local stress level even at same service loading condition. However, the purpose of present research is to investigate the influence of surface treatment time and maintenance technology on short fatigue crack behavior for LZ50 axle steel. Increase of stress amplitude caused by size decrease at changeless test load can make subsequent analysis more complex. Therefore in present study, test load was recalculated based on actual specimen diameter after surface rolling, so that replication test could be finished still at 230 MPa.

Number of effective specimens for S0.0 to S0.7 is 6, 6, 7, 7, and 7, respectively. After tests, dried replication films, which had been flattened with two glass slides, were observed using an

Auto-Montage micro-observation system by an inverted sequence method[10]. Thus, the information of short crack initiation and propagation, such as crack size, number, and angle, was obtained.

3. Results and Discussions

3.1. Comparison of Dominant Short Crack Growth Rate

Inheriting the idea of effective short fatigue crack criterion[10-12], the relation curves between dominant short crack (DSC) growth rate, d*a*/d*N*, and its size, *a*, with five different surface rolling times are shown in Figure 3. Following conclusions can be drawn:

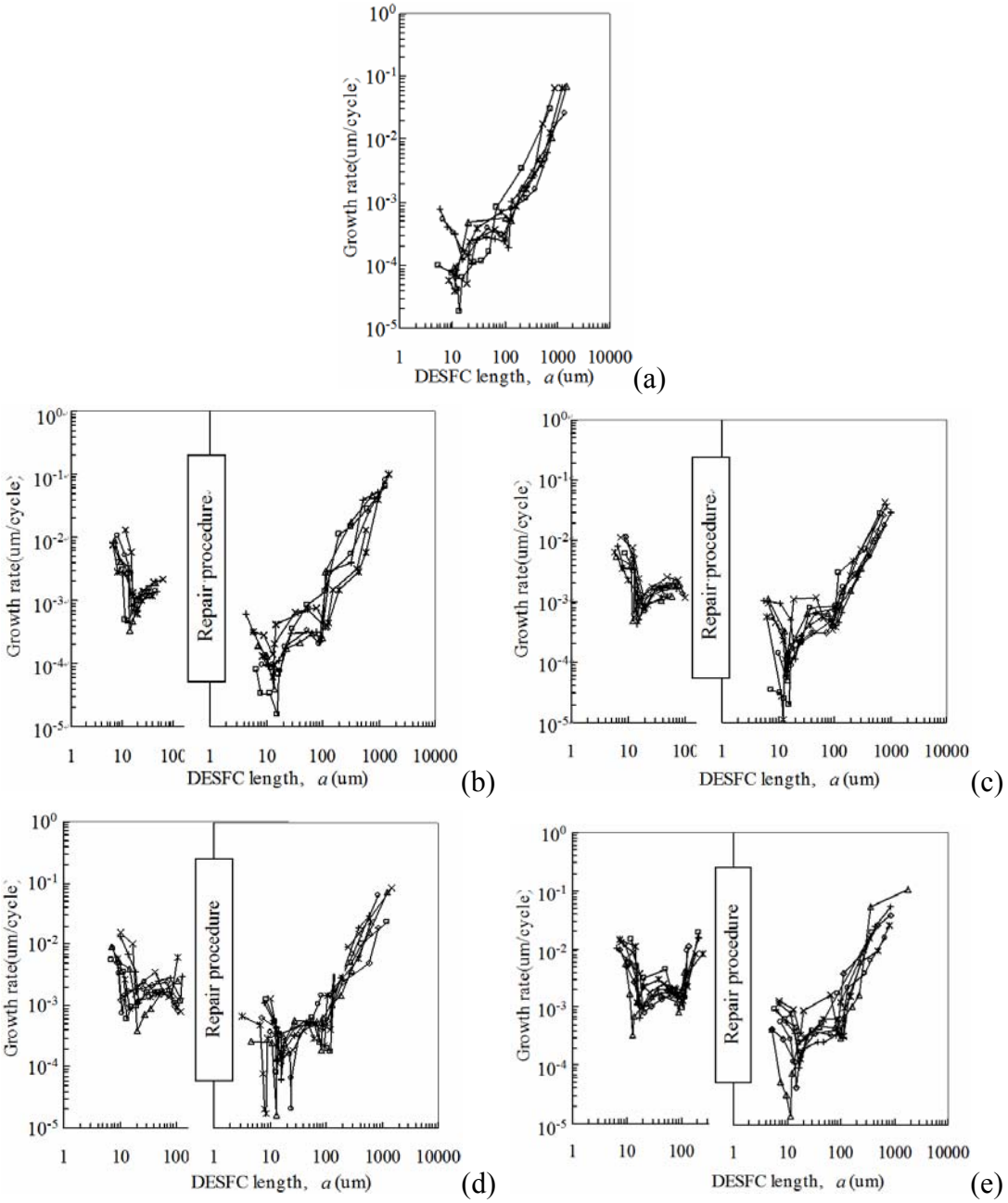

Figure 3. Dominant short crack growth rate for each group of LZ50 axle steel specimens repair times for specimens are (a) *f*=0.0, (b) *f*=0.3, (c) *f*=0.5, (d) *f*=0.6, and (e) *f*=0.7

(1) During crack growth process, the growth rate decelerates once or twice clearly for all these five groups of specimens. If only the crack propagation after surface rolling is taken into

consideration, it is clearly that no matter when surface treatment is performed, the crack growth rate exhibits decelerations twice in MSC stage, and corresponding DSC sizes can be seen in Table 4. At the same time, DSC sizes corresponding to growth rate decelerating time for specimens before rolling are also listed in Table 4. For S0.3 and S0.5 specimens, there are no DSC size data, because the second obvious deceleration has not appeared yet. Combined with previous study results[7], it is evident that whether or not the specimens are rolled, DSC growth rate decelerates when its size approaches ferrite grain boundary firstly and then to the pearlite banded structure. These micro-structural barriers restrain the growth of short cracks. They are inherent resistances of material, and do not change with surface rolling time.

(2) Comparing the crack growth rate curves for specimens before and after surface rolling, it is easy to judge that DSC of unrolled specimens grows much faster than specimens after rolling at the same DSC size. This may due to the difference in specimens surface condition. While surface is not rolled, its hardness and absolute value of residual compressive stress are both smaller than specimens after rolling. Fatigue performance characteristics of the material is not strengthened, thus its constraint force for crack initiation and growth is relatively weak.

Table 4. Mean value of dominant short crack size while crack growth decreases for each group of specimens

Repair time	Before repair		After repair	
	a_1, μm	a_2, μm	a_1, μm	a_2, μm
f=0.0	---	---	15.90	101.43
f=0.3	15.51	---	14.19	91.51
f=0.5	16.08	---	15.34	100.92
f=0.6	15.55	106.90	16.29	97.56
f=0.7	17.62	104.53	15.02	105.16

Note: f---fatigue life fraction according to previous test results[7], a_1, a_2---mean value of dominant short crack size while crack grow decreases for the first and the second time

3.2. Comparison of Effective Short Crack Density

LZ50 axle steel owns the character of two-stages, i.e. MSC stage and PSC stage, for the crack initiation and growth[7, 13]. Effective short crack density is the average number of short cracks per unit area in the initial zone of DSC in MSC stage. While in PSC stage, the observation regions transfer to the two zones ahead of DSC tips. The density can reflect the inherent difference of local micro-structure, and is one of the proper parameters to describe the evolutionary collective effect and statistical scatter of SFC behavior[14]. Higher density indicates the formation of micro-structural conditions for short crack growth, and also reflects the strengthen of SFC collective effect.

The changes in effective short crack density with respective fatigue life fraction for S0.0 to S0.7 specimens are shown in Figure 4. It is clear that crack density of specimens after surface rolling is much less than that of unrolled specimens. Surface treatment effectively limits the collective initiation of short cracks, and consequently weakens the promotive impact of SFC collective effect on crack propagation. However, crack density of all groups of specimens shows the same overall trend, i.e., increases in MSC stage and decreases in PSC stage. It attains the peak value at the transition point from MSC stage to PSC stage. DSC size according to density peak value is about the mean value of intervals for rich pearlite bands. It can be concluded from above discussions that the rich pearlite banded structure instead of the ferrite grain boundary is the strongest micro-structural barrier. When DSC grows to this size, SFC collective effect is further embodied. DSC is about to coalesce with other short cracks through further propagation, and enters PSC stage.

Moreover, the maximum density value for each group of specimens increases with the delay of surface rolling time. For S0.0 specimens, the mean value of maximum density is 662 mm^{-2}, while for S0.7 specimens, surface rolling time, *f*, is postponed to 0.7, and the density increases to 941 mm^{-2}. So postponed rolling time will lead to strengthened SFC collective effect, so that local micro-structure conditions get more and more advantageous to DSC growth.

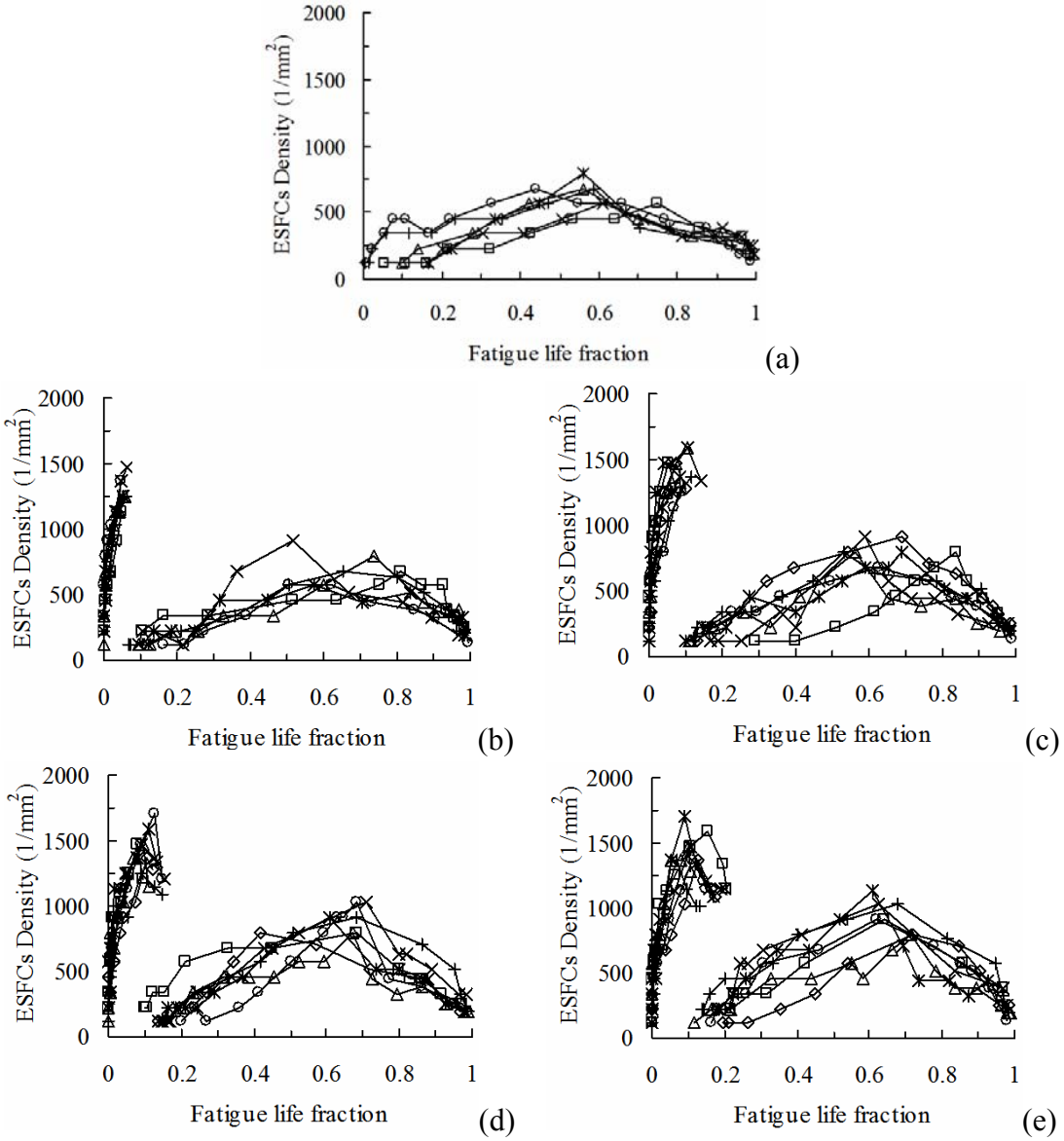

Figure 4. Effective short crack density for each group of LZ50 axle steel specimens repair times for specimens are (a) *f*=0.0, (b) *f*=0.3, (c) *f*=0.5, (d) *f*=0.6, and (e) *f*=0.7

3.3. Comparison of Fatigue Life

Fatigue life is the most direct indicator to reflect surface rolling effect. Table 5 gives the cyclic numbers before rolling, after rolling, and in total. To calculate the prolonged-life rate (defined as the ratio of total cyclic number to standard life), an average fatigue life of 137705 cycles, which was obtained from previous unrolled specimens fatigue tests[7], is cited as the standard life. It can be seen from the table that surface turning and rolling extends the fatigue life greatly than that of

unrolled specimens. The prolonged-life rate increases from 4.49 to 6.41 with the advance of surface rolling time.

Theoretically, average fatigue life for S0.0 specimens to S0.7 specimens should be close to each other due to the same test stress amplitude. However, the choice of surface rolling time makes great difference in life extension effect. For example, the average life of initial rolled specimens (S0.0) is about 1.69 times the cyclic number after rolling of S0.7 specimens. The later surface treatment is performed, the slighter the life extension effect may be. Possible reasons are: Fatigue damage cumulated in material before surface turning and rolling can not be eliminated entirely. This residual damage gets more and more serious with delayed rolling time. Secondly, to remove existed surface cracks as thoroughly as possible, cutting thickness has to be increased with the postponement of rolling time. Thus, diameter and effective section of specimen are also reduced more seriously. Assume the same short cracks initiate in two specimens, local stress level for specimen with smaller diameter is relatively higher.

Table 5. Mean value of fatigue life and corresponding prolonged-life rate for each group of specimens

Repair time	Cyclic number before repair, cyc	Cyclic number after repair, cyc	Total cyclic number, cyc	Prolonged-life rate
f=0.0	--	882562	882562	6.41
f=0.3	41311	720580	761891	5.53
f=0.5	68852	627380	696232	5.06
f=0.6	82623	567379	650002	4.88
f=0.7	96393	522247	618640	4.49

4. Conclusions

(1) Ferrite grain boundary and rich pearlite banded structure are two primary micro-structural barriers to short fatigue crack growth for LZ50 axle steel. No matter surface rolling or not, dominant short crack growth data of all specimens exhibits deceleration twice in MSC stage due to above micro-structural obstacles. Growth rate of specimens after surface rolling is significantly slower than that of specimens before rolling.

(2) Effective short crack density for all five groups of specimens indicates the same overall trend, i.e., first rises then falls. Density after specimen rolling is much less. Surface rolling effect restrains the initiation of collective short cracks. However, this effect is weakened with the delay of rolling time.

(3) Surface turning and rolling to specimens prolongs the fatigue life greatly compared to the life of unrolled specimens. It is because turning cuts off possible existed short cracks in material surface and rolling improve the fatigue performance of new surface. But postponed implementation of surface rolling make the accumulated fatigue damage can not be eliminated thoroughly. In addition, increase of cutting thickness also increase the actual local stress.

In conclusion, for unrolled specimens, the earlier the surface treatment is performed, the better the collective effect of short cracks can be restrained as well as the longer the fatigue life of the material will be.

Acknowledgements

Present research is supported by Natural Nature Science Foundation of China (No. 51205326), Fundamental Research Funds for the Central Universities (No. SWJTU11CX075), and Opening

Project of State Key Laboratory of Traction Power, Southwest Jiaotong University (No. 2011TPL _T02).

References

[1] Z.Y. Shen, Y.X. Zhao, B. Yang, J.C. Peng. Progresses on the fatigue reliability research of China railway. Adv Mater Res, 44-46 (2008) 1-14.
[2] Y.X. Zhao, Q. Gao, B. Zhang, K.J. Diao. Chin J Solid Mech, 31 (2010) 716-730.
[3] S. Pearson. Initiation of fatigue cracks in commercial aluminum alloys and the subsequent propagation of very short cracks. Eng Fract Mech, 7 (1975) 235-247.
[4] Y.X. Zhao, B. Yang, M.F. Feng. Critical safety fatigue crack sizes for the RD2 type axle of Chinese railway freight car, in: S.J. Wu, P.E.J. Flewitt, Z. Zhang (Eds.), Proc 9th Int Conf on Engineering Structural Integrity Assessment, China Machine Press, Beijing, 2007, pp. 1194-1199.
[5] Y.X. Zhao, B. Yang, M.F. Feng, Y. Li, M.J. Liu, G.X. Song. Probabilistic critical fatigue safety state of the RD2 type axle of China railway freight car. Adv Mater Res, 44-46 (2008) 751-758.
[6] Z. He, W.W. Yao. Rotating bending fatigue property of LZ50 steel axle. Mater Mech Eng, 36 (2012) 94-96.
[7] B. Yang, Y.X. Zhao. Experimental research on dominant effective short fatigue crack behavior for railway LZ50 axle steel. Int J Fatigue, 35 (2012) 71-78.
[8] B. Yang, Y.X. Zhao. Influences of final processing methods on surface physical properties and fatigue life for railway LZ50 steel. Adv Mater Res, 463-464 (2012) 85-89.
[9] Swain M H. Monitoring small-crack growth by the replication method, in: J.M. Larsen, J.E. Allison (Eds.), Small-Crack Test Methods. American Society of Testing and Materials, Philadelphia, 1992, pp. 34-56.
[10] Y.X. Zhao, Q. Gao, J.N. Wang. Interaction and evolution of short fatigue cracks. Fatigue Fract Eng Mater Struct, 22 (1999) 459-468.
[11] Y.X. Zhao, Q. Gao, J.N. Wang. Microstructural effects on the short crack behaviour of a stainless steel-weld metal during low-cycle fatigue. Fatigue Fract Eng Mater Struct, 22 (1999) 469-480.
[12] Y.X. Zhao. Size evolution of the surface short fatigue cracks of 1Cr18Ni9Ti pipe-weld metal. J Mater Sci Technol, 19 (2003) 129-132.
[13] B. Yang, Y.X. Zhao. Influence of surface rolling on short fatigue crack behavior for LZ50 axle steel. Acta Metall Sin, 48 (2012) 922-928.
[14] B. Yang, Y.X. Zhao. Surface rolling effect on effective short fatigue cracks density for railway LZ50 axle steel . Adv Mater Res, 118-120 (2010) 75-79.

Effect of Humidity on Fracture Mechanism of Age-hardened Al Alloys under Ultrasonic Loading

**Norio Kawagoishi[1,*], Kohji Kariya[1], Hironori Matsusako[2]
Yuzo Nakamura[3], Xishu Wang[4], Qingyuan Wang[5]**

[1] Department of Mechanical System Engineering, Daiichi Institute of Technology, Kirishima 899-4395, Japan
[2] All Nippon Airways Co., Tokyo 105-7133, Japan
[3] Department of Mechanical Engineering, Kagoshima University, Kagoshima 890-0065, Japan
[4] Department of Engineering Mechanics, Tsinghua University, Beijing 100084, China
[5] Department of Civil Engineering & Mechanics, Sichuan University, Chengdu 610065, China
* Corresponding author: n-kawagoishi@daiichi-koudai.ac.jp

Abstract Effect of humidity on the propagation mechanism of a fatigue crack in age-hardened Al alloy 2017-T4 was investigated under ultrasonic loading in relative humidity of 25% and 85%, respectively. Plain specimen of both extruded and drawn Al alloys were tested. In the extruded alloy, fatigue cracks that propagated macroscopically in tensile mode in low humidity changed to extend in shear mode to failure, comparing to that fatigue cracks always grew in shear mode in high humidity. On the other hand, in the drawn alloy, fatigue cracks propagated in tensile mode to final fracture in low humidity, and in a combined mode of tensile and shear in high humidity. In the both alloys, the growth of cracks shorter than a specific length, e.g. ~1 mm, which is stress level dependent, was accelerated in high humidity, but it was not or little influenced by humidity beyond that specific length. The difference in fatigue crack propagation behavior between the two alloys and the effect of humidity on the fracture mechanism were discussed based on fractographic and crystallographic analyses.

Keywords Fatigue, Ultrasonic loading, Age-hardened Al alloy, Humidity, Texture

1. Introduction

High strength Al alloys have excellent properties such as high specific strength, corrosion resistance and easiness to recycle, from viewpoint of reduction of environment load. However, Al alloys have no definite fatigue limit, meaning that once a crack initiates it will continue to grow and lead to failure. Therefore, the fatigue property of Al alloys in long life region is important, though the examination of fatigue behavior in long life region is a time consuming task. Recently, ultrasonic fatigue test has attracted much attention because it is a time-saving technology for the evaluation of fatigue properties in long life region in comparison with the conventional low frequency fatigue method [1]. However, the effect of high frequency on fatigue properties has not been fully understood. Especially, the effect of environment such as corrosion is one of important factors to be clarified, because corrosion is a time-dependent damage and high strength metals are highly sensitive to corrosive environment [2-4].

In the present study, fatigue tests at ultrasonic frequency (20kHz) were carried out in relative humidity of 25% and 85% respectively, for two kinds of age-hardened Al alloys 2017-T4 (Al-Cu-Mg alloy), i.e. the extruded and the drawn alloys, which have nearly the same static strengths but different microstructure to investigate the effects of microstructure and atmospheric moisture on fatigue crack propagation behavior under ultrasonic loading.

2. Material and Experimental Procedure

Materials used were an extruded and a drawn bar of age-hardened Al alloy 2017-T4. The chemical

composition (mass %) of each alloy is shown in Table 1. The mean grain sizes of the extruded and the drawn alloys were about 13 μm and 18 μm, respectively. Their mechanical properties are shown in Table 2.

Figure 1 shows inverse pole figure on the cross section of the bars. The extruded alloy has marked texture on (111) plane, but a specified orientation is not observed in the drawn one. This difference in texture may be related to the difference in severity during fabrication processes. From the material properties of both alloys mentioned above, the important difference in both alloys is the degree of texture.

Table 1. Chemical composition (mass %)

	Si	Fe	Cu	Mn	Mg	Cr	Zn	Ti
Extruded	0.42	0.3	4.06	0.73	0.58	0.05	0.02	0.05
Drawn	0.41	0.32	3.87	0.7	0.62	0.04	0.03	0.04

Table 2. Mechanical properties

	$\sigma_{0.2}$ (MPa)	σ_B (MPa)	σ_T (MPa)	ϕ(%)
Extruded	350	471	638	32.4
Drawn	303	464	718	43.7

$\sigma_{0.2}$: 0.2% proof stress σ_B: Tensile strength
σ_T : True breaking stress ϕ: Reduction of area

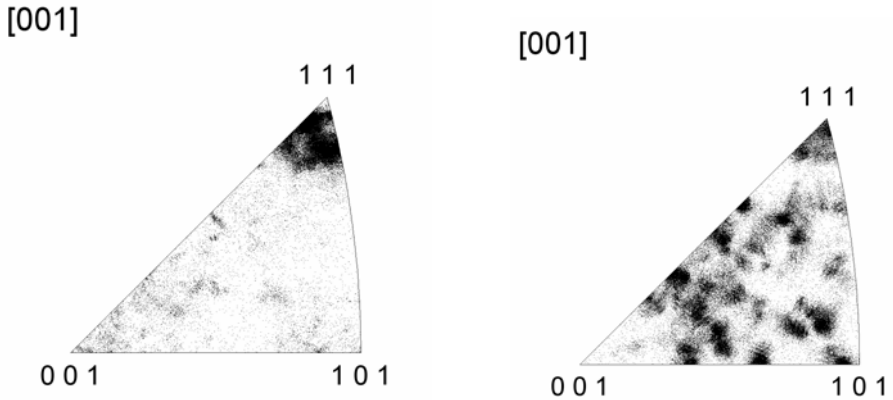

(a) Extruded (b) Drawn

Figure 1. Inverse pole figure

Figure 2 shows shape and dimensions of specimens. Prior to fatigue testing, all of the specimens were slightly electro-polished by 40 μm in diameter to remove the work affected layer and secure direct surface observation. The observation of fatigue damage and the measurement of crack length were conducted under a scanning electron microscope (SEM) or under an optical microscope by using the plastic-replica technique. Surface crack length, ℓ, was measured in the circumferential direction of the specimen in both tensile and shear mode propagations. The crystallographic analysis was performed by using Electron Back Scatter Diffraction Pattern (EBSD) method. The fatigue tests were carried out using a 20 kHz piezoelectricity actuated ultrasonic machine in relative

humidity (RH) of 25% and 85%. In addition, rotating bending fatigue tests (50Hz) were carried out in nitrogen gas (N_2>99.995%, O_2<5ppm, H_2O<10ppm) and RH25% to investigate the effects of oxygen and humidity. In the ultrasonic fatigue, pulse-pause tests were employed with a pulse length of 1s and a pause length of 5s to reduce temperature rise under high frequency cycling. By this method, temperature rise during ultrasonic fatigue was controlled below 3K. The humidity conditions were selected by considering the daily humidity and the significant influence of humidity on fatigue strength [4]. The deviation of humidity was controlled in the range of RH±5% with the temperature at 298±3K in each humidity condition.

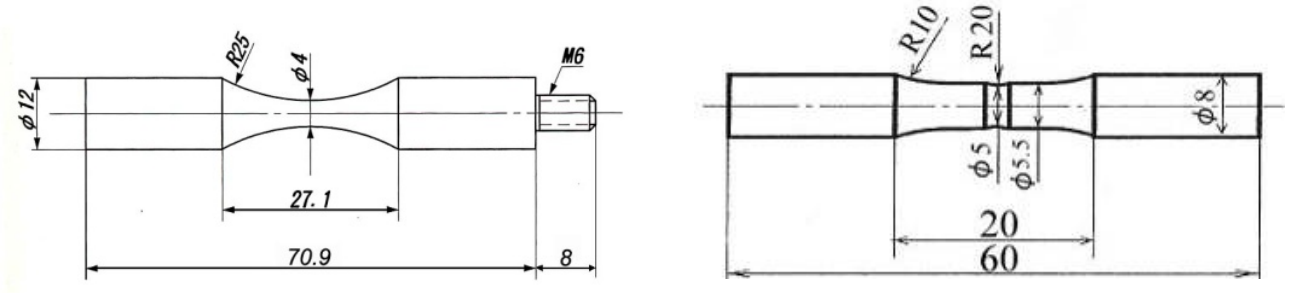

(a) Ultrasonic fatigue (b) Rotating bending fatigue

Figure 2. Shape and dimensions of specimens (mm)

3 Experimental Results and Discussion

Figure 3 shows *S-N* curves of both alloys in RH25% and RH85%. In Fig. 3, results under rotating bending fatigue tests were also displayed by lines only [5]. Fatigue strength is larger in ultrasonic loading than in rotating bending in both alloys. Moreover, fatigue strengths of both alloys in both fatigue tests were largely decreased in high humidity with the drop in fatigue strength is larger under ultrasonic loading than under rotating bending, though the time consumed at given fatigue life was much shorter in ultrasonic fatigue. The effect of humidity on fatigue strength was larger in the extruded alloy than in the drawn one. For example, fatigue strength at 10^7 cycles of the extruded alloy in RH85% was decreased to about 30% of that in RH25%.

Figure 4 shows crack propagation curves of both alloys. In both alloys, a crack initiated at the early stage of stress repetitions, so most of fatigue life was occupied by the growth life of a crack in both humidity. Moreover, the propagation of cracks shorter than a specified length ℓ_0, e.g. about 1 mm, was accelerated in high humidity, and there was no or little influence of humidity on the propagation of a fatigue crack over ℓ_0. The existence of crack length ℓ_0 is clearly confirmed in RH25%, though the value of ℓ_0 changed with stress level.

Optical feature of surface cracks and SEM morphology of fracture at different stage of crack growth are shown in Fig. 5, in which the results of Fig. 4 are rearranged into two groups so as to better understand whether or not and how the humidity affects crack growth behavior in the two alloys. It is found that the crack growth in each alloy can be classified into two regions, i.e. region I and II. In the region I ($\ell<\ell_0$), crack growth is accelerated by high humidity, while in the region II ($\ell>\ell_0$), no distinct effect of humidity is recognized. In the extruded Al alloy, cracks propagated in tensile mode

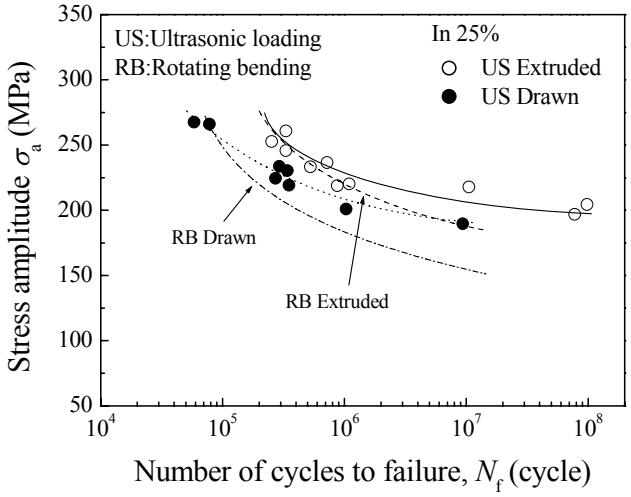

(a) In RH25%

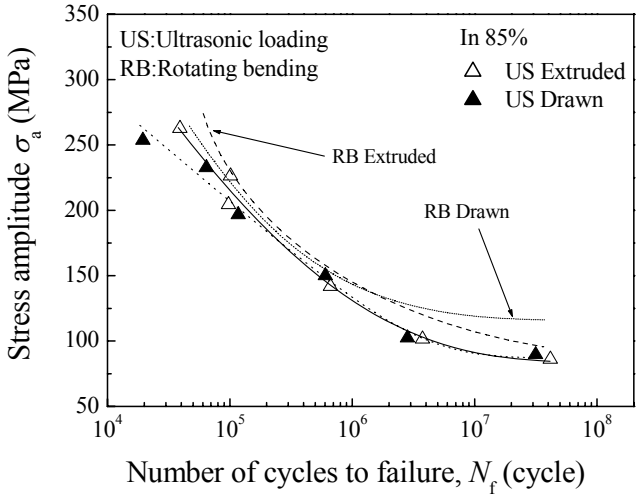

(b) In RH85%

Figure 3. *S-N* curves of extruded and drawn Al alloys

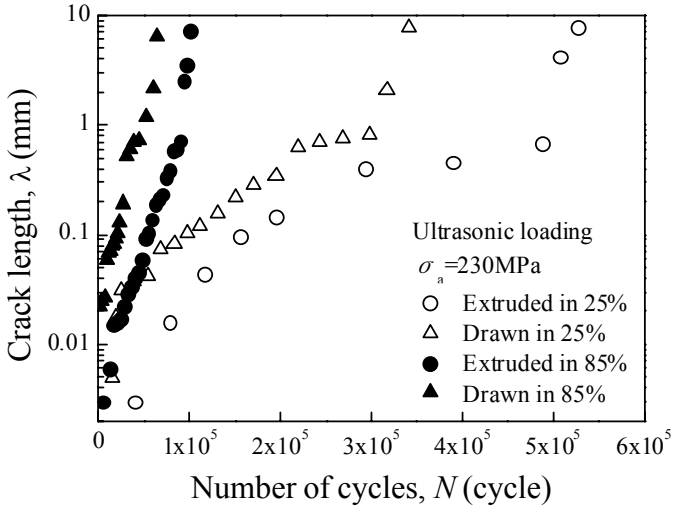

Figure 4. Crack growth curves of extruded and drawn Al alloys

macroscopically, then changed growth mode to shear one in low humidity (D), in comparison with that the whole fatigue crack propagation process was occupied by shear mode cracks in high humidity (C). The crack length corresponding to the above mentioned crack growth mode change coincides with the specific length, ℓ_0, as described before. The angle between the propagation direction of the shear mode crack and the load axis, θ, is about 35°. In the drawn Al alloy, however, fatigue cracks propagated in tensile mode entirely in low humidity (J) and in a combined mode of tensile and shear in high humidity (I). On the other hand, fracture morphology also depends on the microstructure of the alloy and humidity. In the extruded alloy, fracture surfaces are different even in the same propagation of a macroscopic shear mode crack. For example, fracture surfaces in the region II in RH25% (E) and RH85% (A) are mostly occupied by slip planes, while those in the region I in RH85% (B) feature with ripple-like pattern in addition to slip planes. On the other hand, in case of the drawn alloy which is characteristic of a macroscopic tensile mode crack in both humidity, many facets of a grain size and tearing of matrix between facets are observed in the regions I and II in RH25% (K, L), and in the region II in RH85% (G), though ripple-like pattern is also observed in the region I in RH85% (H). These facets are confirmed as slip planes by etch pit method (Fig. 6) and by EBSD analysis. Moreover, there was no brittle facet observed as in the corrosion fatigue of Al alloys [6] and high strength steels [7].

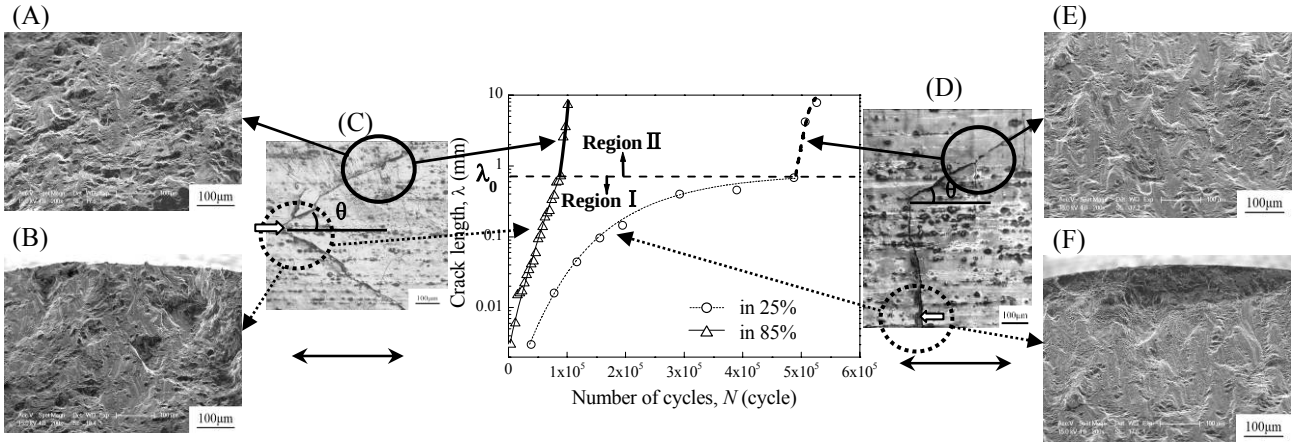

(a-1) RH85% (a-2) RH25%

(a) Extruded Al alloy

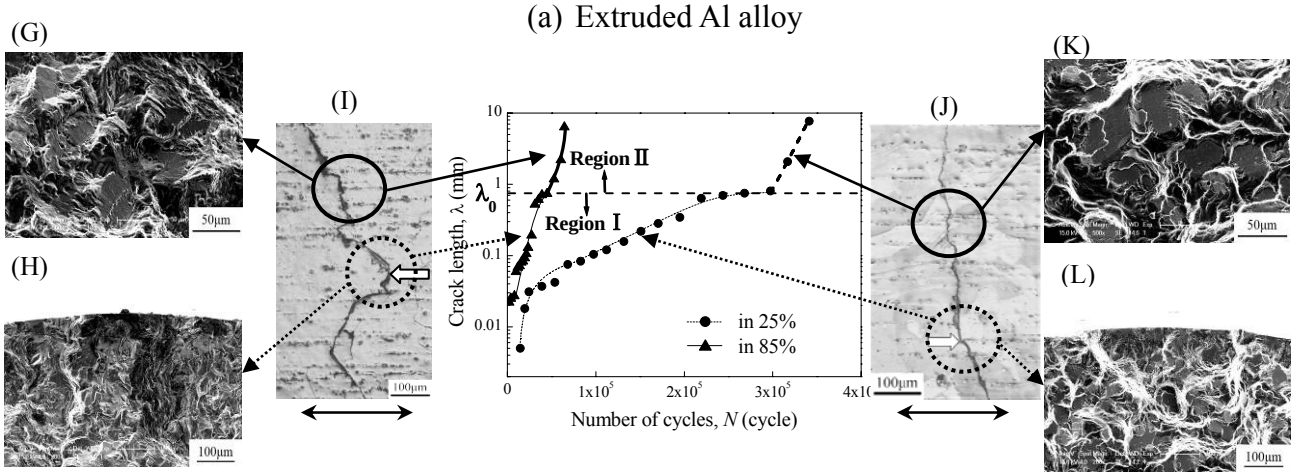

(b-1) RH85% (b-2) RH25%

(b) Drawn Al alloy

Figure 5. Optical photos featuring surface cracks and SEM micrographs characterizing fracture morphology at different stage of crack growth (⟷ :axial direction, ⇒ : crack initiation site)

The observation of fracture surfaces caused by the propagation of a macroscopic tensile mode crack in low humidity, e.g. (F) and (L), was difficult because of the sever contacting at crack tips. However, striations were recognized on the fracture surface of extruded Al alloy 7075-T6 under ultrasonic loading [8], which means that cracks propagated in a ductile manner regardless of humidity. As stated above, fracture mechanism is different depending on humidity when the crack length is smaller than ℓ_0, but there is no difference in fracture mechanism when the crack length is larger than ℓ_0 in both alloys. These findings on the effect of humidity on fracture mechanism agree well with those on crack propagation rate as shown in Fig. 4.
From the results mentioned above, it is concluded that the shear mode crack propagated along slip planes, therefore, cracks in the extruded alloy propagated in shear mode macroscopically because of

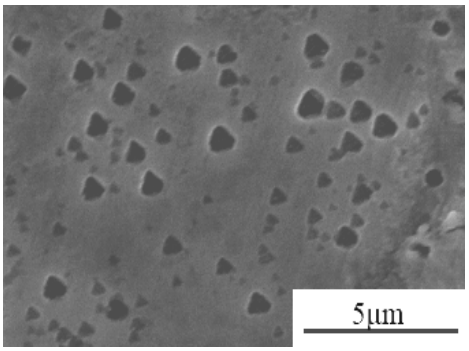

Figure 6. Etch pit figure observed at fracture surface in drawn Al alloy

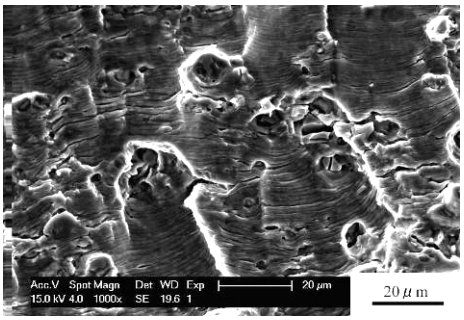

(a-1) RH25%

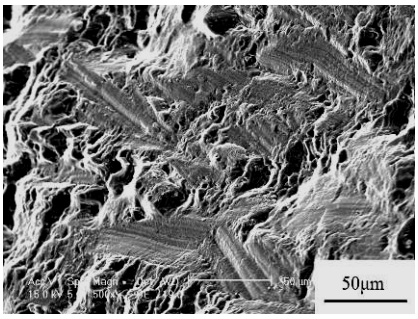

(a-2) N_2 gas

(a) Extruded alloy

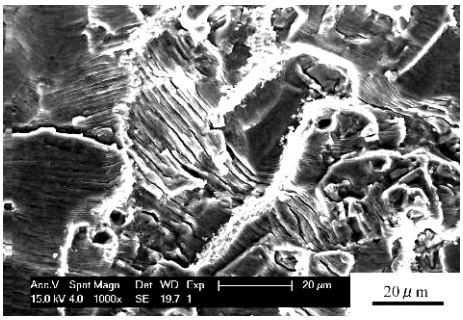

(b-1) RH25%

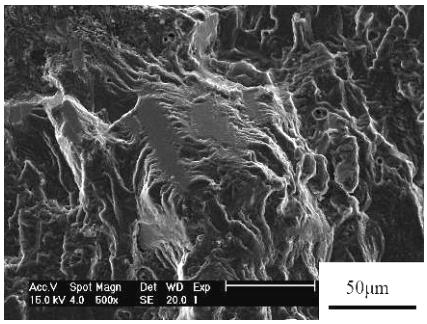

(b-2) N_2 gas

(b) Drawn alloy

Figure 7. Fracture surfaces under rotating bending

its marked texture. This can be explained by considering that the angle between the propagation direction of the shear mode crack and the load axis, 35°, is related to the angle between the composed plane (100) of fracture surface with the plane (111) of texture. On the other hand, the effect of humidity on crack propagation behavior may be explained as follows. A crack whose growth was accelerated in high humidity propagated in a ductile manner, which means that fatigue deformation was assisted by hydrogen because the hydrogen enhanced localized plasticity (HELP) [9] is assumed as the propagation mechanism of a fatigue crack in high humidity. Moreover, the reason for the indistinct effect of humidity on crack propagation behavior in the region II may be related to the high crack growth rate under ultrasonic loading or in other words, atmosphere is difficult to reach at crack tips so that the environment at the crack tips is similar to vacuum. As a result, crack propagation mode changed and the effect of humidity disappeared.

In order to confirm this assumption, fatigue tests under conventional loading frequency (50Hz) were carried out in RH25% and in nitrogen gas as well to simulate vacuum condition. Figure 7 shows fracture surfaces in the region II in both RH25% and N_2 gas after rotating bending fatigue. In both alloys, fracture surfaces of specimens subjected to rotating bending in N_2 gas are similar to those under ultrasonic loading, though definite striations characteristic of general propagation mechanism are observed in RH25%.

4. Conclusions

Fatigue tests under ultrasonic loading frequency (20kHz) were carried out for two kinds of age-hardened Al alloys, extruded and drawn alloys of 2017-T4 (Al-Cu-Mg alloy) with nearly the same static strengths in relative humidity of 25% and 85%, to investigate the effects of microstructure and humidity on propagation behavior of a fatigue crack under ultrasonic loading. The extruded Al alloy has a marked texture with plane (111) in the cross section, but the drawn alloy has not any specified orientation. In the both alloys, the propagation of small cracks shorter than a specific length, e.g. about 1 mm, which is stress level dependent, was accelerated in high humidity, causing large decrease in fatigue strength, though there was no or little influence of humidity on the propagation of a fatigue crack beyond that length. In the extruded Al alloy, fatigue cracks propagated in tensile mode macroscopically, and then changed to grow in shear mode in low humidity, in comparison with that all of fatigue crack propagation process was occupied by the shear mode crack growth in high humidity. On the other hand, in the drawn alloy, a fatigue crack propagated in tensile mode to final fracture in low humidity and in a combined mode of tensile and shear in high humidity. Fracture surfaces caused by the propagation of a shear mode crack were covered with many slip planes. The difference in fatigue crack propagation behavior between the two alloys was mainly caused by the texture. The effect of humidity on crack propagation was yielded through the acceleration to the propagation of a ductile crack.

References

[1] QY. Wang, C. Bathias, N. Kawagoishi, Q. Chen , Effect of inclusion on subsurface crack initiation and gigacycle fatigue strength, International Journal of Fatigue, 24 (2002) 1269–1274.

[2] K. Komai, K. Yamaji, K. Endo, Effect of atmosphere on fatigue crack propagation of aluminum alloy,

Journal of the Society of Materials Science, Japan, 29 (1980) 162–167.

[3] K. Endo, K. Komai, Fatigue crack growth of aluminum alloy in ultra-high vacuum, Journal of the Society of Materials Science, Japan, 26 (1977) 143–148.

[4] N. Kawagoishi, T. Fukudome, K. Kariya, Q. Chen, M. Goto, Fatigue strength of age-hardened & extruded Al alloy under high humidity (Rotating bending and ultrasonic loading), Transactions of the Japan Society of Mechanical Engineers, Series A, 76 (2010) 1651–1658.

[5] N. Kawagoishi, A. Higashi, Q. Chen, Y. Nakamura, K. Morino, Effect of microstructure on fatigue properties of Al alloys 2017 in high humidity, Journal of the Society of Materials Science, Japan 61 (2012) 556–563.

[6] Haftirman, S. Hattori, T. Okada, Fatigue strength of aluminum alloys in high-humidity environment, Transactions of the Japan Society of Mechanical Engineers, Series A, 62 (1996) 1140–1145.

[7] K. Asami, H. Emura, The influence of moisture on fatigue crack propagation characteristics of high-strength steels, Journal of the Society of Materials Science, Japan, 49 (1990) 425–431

[8] N. Kawagoishi, M. Oki, M. Goto, Q. Chen, QY. Wang, Crack propagation behavior of Al Alloy 7075-T6 under ultrasonic fatigue, Transactions of the Japan Society of Mechanical Engineers, A, 72 (2006) 1356–1363.

[9] P.J. Ferreira, I.M. Robertson, H.K. Birnbaum, Hydrogen effects on the interaction between dislocations, Acta Materialia, 46 (1997) 1749–1757.

Experimental Investigation of Mode I Fatigue Crack Growth Behavior of Titanium Foils

Lee Chang-Woo[1], Liu Liu[2,*], Holmes W John[3]

[1]Department of Advanced Analysis and Characterization, Korea Institute of Materials Science, Chang won, Korea
[2] School of Aerospace Engineering, Beijing Institute of Technology, Beijing, 100081, China
International Research Center for Clean Energy Materials and Systems, Beihang University, Beijing, 100191,China
* Corresponding author: liuliu@bit.edu.cn

Abstract A low-cost experimental apparatus has been developed to investigate the Mode I fatigue crack growth behavior of thin metallic foils and sheets. The apparatus utilizes magnetic coupling between a ceramic magnet and a rotating steel disk to induce cyclic tensile loads in notched rectangular test specimens.To illustrate the testing apparatus, Mode I fatigue crack growth in 30 μm thick high purity titanium foils was studied. Experiments were performed at ambient temperature using a loading frequency of 2 Hz and a nominal stress ratio of 0.1. The cyclic crack growth data could be fit to a Paris relationship between crack growth rate and stress-intensity range. The stress intensity factor exponent, *m*, in the Paris relationship was between 4 and 5, which is comparable to the relatively high values found in the literature for the tension-tension fatigue of other metallic bulk materials. Self-similarity analysis was used to explain the observed higher m values for thin metallic foils.

Keywords Fatigue testing, Mode I crack growth, foil

1. Introduction

Foil thickness materials, with a thickness in the range of 10 μm to 250 μm are used in a variety of applications, including micro-electro-mechanical systems (MEMS), integrated circuits, fuel cells and printers. The progressive trend of miniaturization of structural components leads requires knowledge regarding the mechanical behavior and properties of thin metallic materials. As discussed below, the tensile, fracture and fatigue behavior of foil-thickness materials can be very different from that observed in bulk materials. In addition to influencing the tensile properties (ductility and strength) of thin foils, grain size and grain orientation can have a major effect on crack initiation, crack growth and fracture toughness. Compared to bulk materials, microstructural inclusions or precipitates in thin foils will also have a larger impact on fracture toughness and crack growth. Surface damage, in the form of roughness, oxidation or corrosion will also have a much larger effect on the mechanical behavior of thin metallic foils.

Several experimental and theoretical investigations of the mechanical properties of foils have been carried out during last two decades. Klein *et al* [1] studied the stress-strain behavior of Cu and Al with thicknesses ranging from 10 and to 250 μm and observed a thickness effect on fracture strain, which decreased with decreasing specimen thickness. In experiments with thin Cu films, Zhang *et al* [2] observed an increase in yield strength and a decrease in fatigue life as thickness was decreased. In another study, Zhang *et al* [3] found that although the mode of fatigue damage in 25 μm thick 304 stainless steel followed that of the bulk material, the fatigue strength was higher for the 25 μm foils; the increase in fatigue strength was attributed in part to the smaller grain size of the foils

Fracture-mechanics-based test results. In a review of fatigue test techniques and experimental results for materials used in MEMS, Sharp and Turner found that the majority of available fatigue data for foils was in the form of S-N curves obtained from bending fatigue. Limited fatigue data was found for uniaxial loading with a positive mean stress [4]. The cyclic crack growth behavior from a pre-existing notch in free-standing thin foils is still a relatively unexplored area of research.

Holmes *et al* [5, 6] studied the mode I fatigue crack growth behavior of 250 μm thick center-notched Ni-base specimens, which were subjected to tension-tension fatigue at a loading frequency of 2 Hz. Using the Paris relationship, it has been found that the stress intensity factor exponent, *m* was significantly higher than commonly reported for bulk Ni-base specimens [7, 8]. A similar trend was also observed in Ti-6Al-4V foils. The high cyclic crack growth rate in thin foils was attributed to the lower Mode I lower fracture toughness commonly observed for thin metallic foils [5, 6, 9]. In a very informative study, Meirom *et al* [9] observed that ~500 nm thin films exhibit low fracture toughness and inferior resistance to fatigue crack growth when compared to conventional micro-scale-grained bulk forms of the materials. Their studies showed that thickness had a substantial effect on the Paris power law exponent and the estimation of fracture toughness. At first glance, the high crack growth rates found during Mode I testing of thin metallic foil [5, 6] is at odds with observations of higher fatigue strength found from standard (S-N) tests with un-notched thin metallic foils [2,3]. Standard fatigue life (S-N) tests include cycles to crack initiation, which may be strongly influenced by yield strength and residual stresses as well as surface finish and microstructural features such as grain size. However, fracture toughness can play an important role in the cyclic crack growth behavior of materials. For certain metals, fracture toughness exhibits a “bell-shaped” dependence on thickness, with fracture toughness reaching a maximum at intermediate thickness. In experiments with Cu, Wang *et al* [10] observed that J_c initially increased with increasing thickness, reached a maximum at a thickness of about 0.3 mm, and decreased at larger thicknesses.

Because of the very low applied loads, the cyclic crack growth behavior of metallic foils requires specialized testing approaches. For lower frequency testing (up to 1000 Hz with specially designed load frames) servo hydraulic and electro-mechanical load frames can be used for tension-tension fatigue loading histories [11, 12]. However, because of the low load levels required, the use of servo hydraulic load frames for fatigue testing is generally limited to foil thicknesses above 50 μm. Moreover, because of high cost, servo hydraulic and electro-mechanical load frames are generally not used for long duration testing of materials. The cost to perform long duration fatigue and fatigue crack growth experiments is of particular concern for low loading frequencies in the range of 0.01 to 5 Hz, which is a frequency range of general interest for many practical devices which utilize foil-thickness materials, including MEMS, fuel cells with metallic interconnects, and printer drives.

The objective of the present investigation was to develop a reliable low-cost experimental apparatus to study the low frequency high cycle Mode I cyclic crack propagation behavior of thin foils under tension-tension loading. The approach, which involves use of magnetic coupling between a clamped rectangular specimen and a rotating steel disk, is well suited for studies of Mode I fatigue crack growth. In order to illustrate the test apparatus, the cyclic crack growth rate of 30 μm thick edge-notched high-purity (99.6%) annealed titanium (Ti) foils was investigated at RT.

2. **Development of Testing Apparatus**

The overall design goal was to develop fatigue test apparatus using commercially available components and conventional machining. As shown in Figures 1, this was accomplished by magnetic coupling between a magnet attached to a sliding grip and a rotating eccentric steel disk mounted to a DC motor. As shown in Fig. 1, the specimen is clamped in face-loaded (friction) grips. One of the specimen grips is attached to a linear bearing slide, which is free to translate parallel to the specimen centerline; motion perpendicular to the centerline is constrained by the linear rail. The grip at the other end of the specimen was fixed to a load cell (Honeywell Model 41) which was rigidly fixed to the test frame. A ceramic magnet attached to the end of the translating specimen grip provides magnetic coupling with a rotating eccentric steel rotor. The strength of the couple, and

hence tensile force in the specimen, is controlled by the magnet strength and the air gap between the rotor and magnet. The air gap varies with the rotation of the eccentric rotor; therefore, the force varies in a cyclic manner. A mean tensile stress is achieved by use of a weight applied through a cable and pulley attached to the sliding grip/magnet assembly. To control the cyclic loading frequency, the eccentric steel rotor is driven by variable speed DC motor. For the test apparatus shown, the DC motor had a power rating of ½ HP, and a maximum rotational speed of 34 RPM.

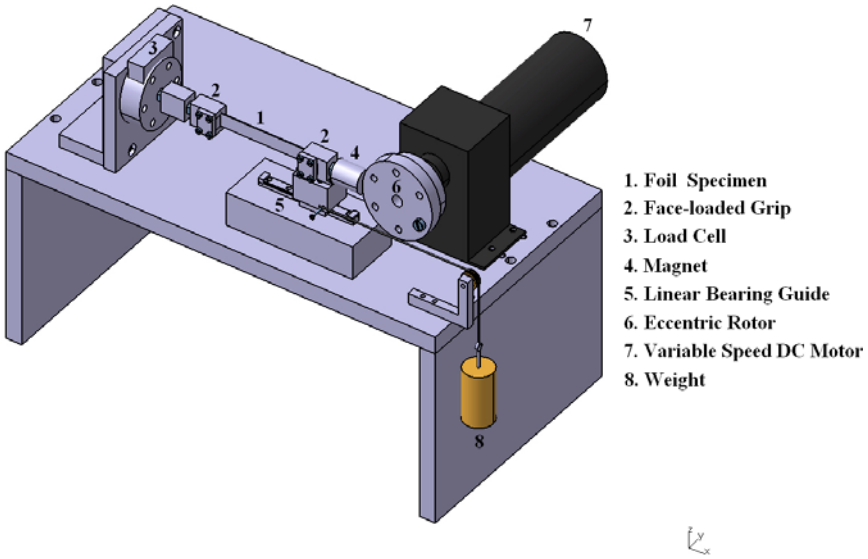

Figure 1. Schematic illustration of the fatigue testing apparatus.

For a given magnet strength and rotor speed, the waveform of the applied axial load is determined by the geometry of the rotor (shape and number of lobes). For the current test configuration, the motor speed was adjusted to provide a loading frequency of 2 Hz. Although a simple eccentric rotor was used in the present investigation, a multi-lobed rotor can also be used to increase the fatigue loading frequency or provide different peak and mean load levels within a given cycle. The shape of the rotor lobe (s) can also be changed to produce other load *versus* time waveforms. Alternatively, the shape or number of magnets that interact with the rotor can be altered to achieve a desired waveform.

Signal monitoring. An impulse counter was used to record the number of fatigue cycles. The load cell and impulse counter signals were monitored by a data acquisition board and DASYLAB software.[1] By monitoring the load cell signal, the DA board also enabled stopping the motor when the specimen failed. Figure 2 shows a close-up view of the actual fatigue testing apparatus with a 30 μm thick specimen installed.

3. Experimental Procedure

3.1. Material and Specimen Preparation

The material used for this study, commercially available annealed Ti foil (99.6% purity), was obtained as 30 μm thick sheets.[2] General information regarding the composition and mechanical

[1]Measurement Computing Corporation, Norton, MA USA.
[2]Goodfellow Corp., 125 Hookstown Grade Road, Coraopolis, PA 15108-9302 USA.

behavior of 99.6% purity Ti foil can be found in Refs [13, 14]. Single-edge-notched specimens were cut from the foil sheets using a single-blade paper cutter. To determine if differences in specimen geometry with the same notch to width ratio would affect test results, specimens with widths of 12 mm and 10 mm were tested. The first type of specimen (Group A) had a nominal thickness of 30 μm, a width of 12 mm and an overall length of 120 mm. Group A specimens had a notch length of 1.6 mm along one edge of the specimen. A second group of specimens (Group B), with the same thickness and length, but a smaller 10 mm width and shorter 1.35 mm long edge-notch were also tested. Note that both specimen groups had the same notch-to-width ratio of 0.13.

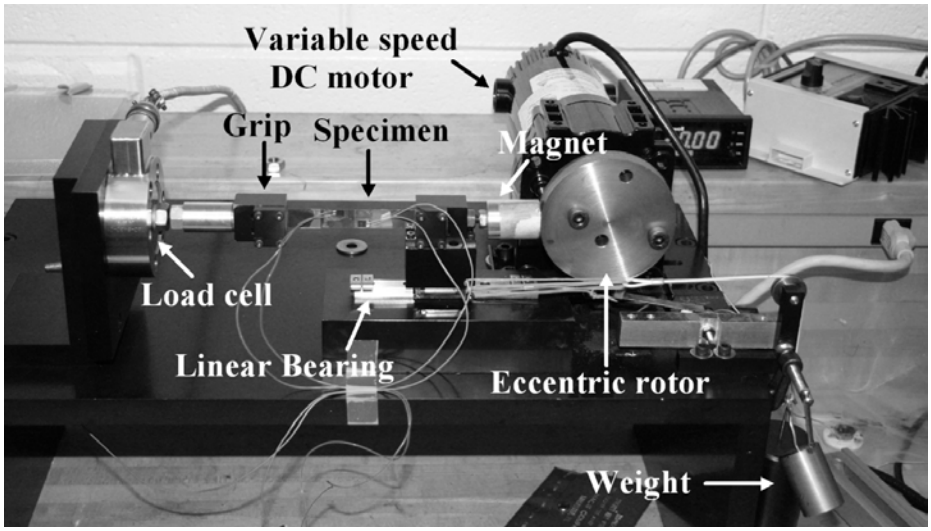

Figure 2. Close-up of the experimental setup

3.2 Experimental Procedure

All fatigue experiments were performed at room temperature at a nominal stress ratio of 0.1 and loading frequency of 2 Hz. At the start of each experiment, and with a specimen installed, the distance between the rotor and magnet was adjusted to achieve the desired maximum stress level in the specimen; in parallel, the tensile mean stress (and therefore the minimum load level) was adjusted by use of a weight applied through the cable attached to the moving grip/magnet assembly.

Table 1. Overview of the test conditions used to investigate the Mode I fatigue crack growth rate of thin titanium foils

	Type A	Type B
Loading mode	Tension-Tension	Tension-Tension
Stress ratio, R	0.1	0.1
Frequency, f	2 Hz	2Hz
Max stress, σ_{max}, MPa	111~124	122~ 124

Table 1 summarizes the specimens and test conditions that were used in the investigation. Two types of specimens having different width. For specimen in fatigue tests, crack length was measured with a 20X optical microscope attached to a video camera and digital micrometer. During the fatigue tests, crack length was measured at the end of each fatigue loading block. The optical microscope had a resolution of 0.002 mm and a repeatability of 0.005 mm. At the completion of testing, fracture surface characteristics were examined by optical and scanning electron microscopy.

4. Data analysis

As discussed in the results section, the cyclic crack growth behavior of the Ti foils could be described by the Paris relation between cyclic fatigue crack growth rate (*da/dN*) and applied stress intensity, ΔK :

$$\frac{da}{dN} = C\Delta K^m \tag{1}$$

C and m are obtained from a linear curve fit to the experimental data. For a single-edge-notched specimen, the applied stress intensity range, ΔK, is related to the far field stress amplitude, $\Delta\sigma$ and the crack length, a, by

$$\Delta K = Y\Delta\sigma\sqrt{\pi a} \tag{2}$$

Y is a geometry correction factor defined in terms of the ratio of the crack length a to the specimen width w. The determination of the geometry correction factor depends on the specimen's geometry and the applied loading type. For a single-edge-notched specimen, *Y* is given by

$$Y = 1.12 - 0.231\left(\frac{a}{w}\right) + 10.55\left(\frac{a}{w}\right)^2 - 21.72\left(\frac{a}{w}\right)^3 + 30.39\left(\frac{a}{w}\right)^4 \tag{3}$$

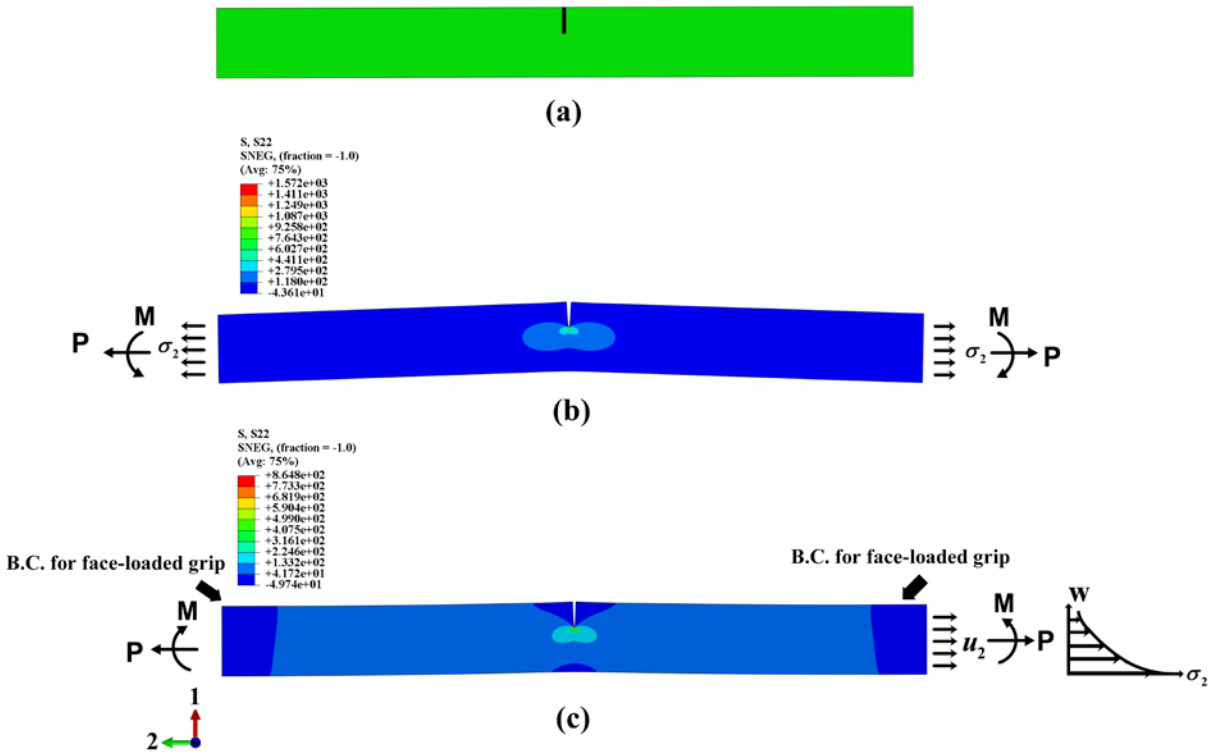

Figure 3. FEM models of the foil specimen. (a) FEM model of unloaded foil specimen. (b) Foil specimen under a uniform stress, which represents the condition used for the intensity factor given by Eq. 3. (c) Foil specimen loaded through the face-loaded grips with a uniform displacement u_2 boundary condition is applied along the right grip.

Correction of the effective stress intensity factor

Eq.3 is limited to loading configurations which can provide a uniform stress throughout the specimen cross section. In the present investigation, the foil specimen is constrained to move parallel to the applied tensile load by the linear bearing; this most closely represents a fixed-displacement end condition. The application of Eq. 3 to a fixed-end displacement loading configuration can overestimate the applied stress intensity factor [15]. The center line of the specimen shift can cause a bending moment which increases the applied Mode I stress intensity factor. This overestimation is of particular importance as a crack grows and the

crack-depth-to-width ratio increases.

To estimate a corrected K_I, a finite element analysis of the end conditions for the magnetic-driven fatigue apparatus was performed. The foil, which is rigidly clamped by the face-loaded grips along its ends, is under a uniform fixed-end displacement boundary condition (Figure 3c). Due to the non-uniform tensile stress σ_2 distribution along the specimen width, a closing moment is imposed on the specimen, which reduces the effective stress intensity at the crack tip. A summary of the results of the analysis for the loading cases examined is provided in Figure 4. The corrected stress intensity factors obtained from the FEM analysis were used in the subsequent analysis of ΔK versus crack growth rate presented below.

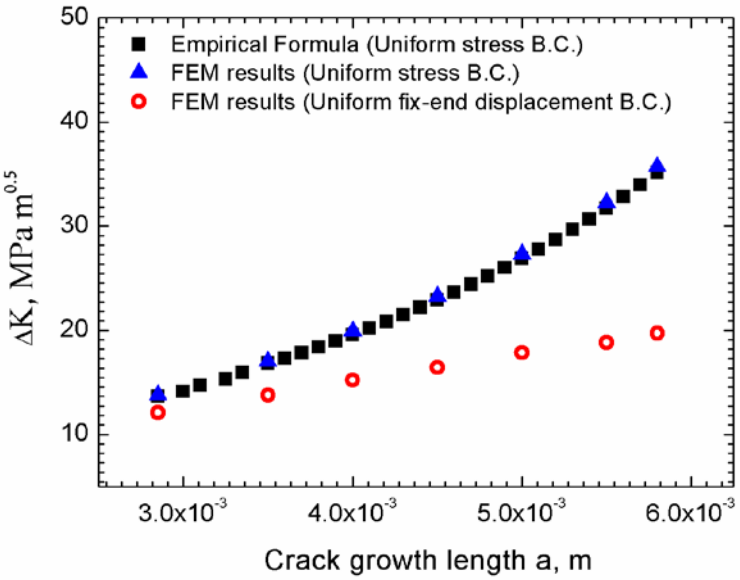

Figure 4. Variation of stress intensity factor K_I with the crack length. The data defined by solid squares represents K_I calculated from the empirical Eq. 2; the triangular data point represents K_I is determined by FEM analysis. A comparison of the data shows that the overestimation of K_I by Eq. 2 increases as crack length increases.

5. Results and discussion

5.1 Results

All fatigue cracks started from the root of the machined notch; cyclic crack propagation behavior, which remained perpendicular to the applied load, was similar for all specimens, indicating adequate alignment of the specimen was achieved during the experiments. Figure 5 shows typical results for crack length versus number of cycles. All specimens behaved in a similar manner, and the amount of scatter was limited for similar test parameters.

Figure 6 shows crack growth rate *vs.* corrected stress intensity for all specimens. The double-logarithmic plot shows that the data can be fit reasonably well using a simple Paris-equation relationship between crack growth rate and applied stress intensity range (corrected with FEM analysis). The measured stress intensity factor exponent m ranged from 3.94~5.08 for the eight specimens tested (Table 2). The small change in specimen width from 12 mm to 10 mm (Group A and Group B), did not have a measurable influence on the test results. The crack growth rate data for thin foils is quite limited and the Paris “m” value for similar pure Ti foils is not available. However, the m values found in the current investigation are similar to elevated m values of around

4~5 reported for other metals [5,6].

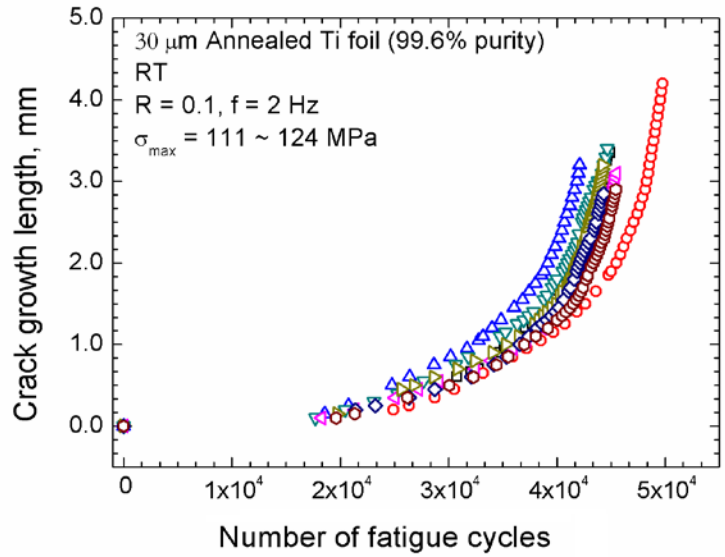

Figure 5. Crack growth length versus fatigue cycles for 30 μm thick single-edge notch Ti foil specimen foil specimens subjected to tension-tension fatigue at RT. The data scatter is very limited for similar experimental conditions.

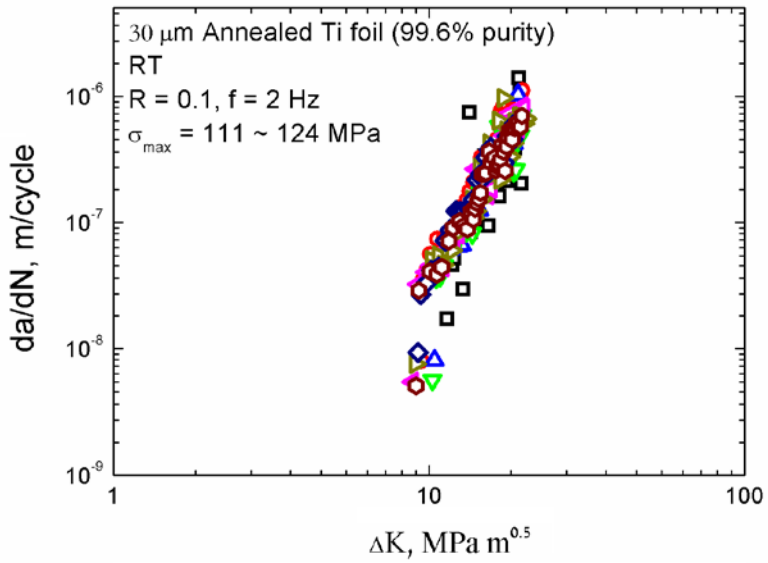

Figure 6. Cyclic crack growth rate data for 30 μm thick Ti foil specimens subjected to tension-tension fatigue loading at room temperature.

The typical crack growth path is observed after specimen failure; these images show the side view of the flat fracture surface in crack growth region II, and the corrugated facture surface in the high crack growth rate region prior to failure. The crack growth was generally perpendicular to the tensile loading direction until a final shear slip forms during failure. According to experimental measurements, the stable crack growth length was around 7~8 mm, which covers two crack growth regimes. For instance, in crack growth region II, the applied ΔK is lower than 30 MPa $m^{1/2}$ and the crack growth rate is less than 10^{-6} m/cycle. In this crack growth regime, the crack growth rate *vs.* applied ΔK can be described by the Paris relationship with the exponent value m between 4~5. With the crack growth length increasing, the applied ΔK increases and the crack propagation fit in very high crack growth regime (crack growth region III). The angle of the "knife edge" fracture surface ranges between 44° and 48°. To evaluate the morphological characteristics of Ti foil fracture

surface, fractography for foil specimens was investigated by scanning electron microscopy (SEM). All SEM images exhibited similar fracture surface appearances. Representative SEM images taken of specimens that failed during cyclic loading are shown in Fig. 7. These images show the complicated fracture surface appearance for crack growth within the Paris region with occasional striations visible. Fractography features also indicate a ductile, void rupture along with indications of transverse (through thickness) necking.

Table 4. Overview of the experimental conditions and test results for the cyclic fatigue crack growth behavior 30 μm thick Ti.

ID	Δσ, MPa	Corrected ΔK$_{max}$, MPa m$^{1/2}$	Corrected ΔK$_{min}$, MPa m$^{1/2}$	a$_i$ mm	N$_{tot}$	C	m
						correlated with FEM results	
A-1	111	19.5	11.4	1.6	44,941	2.55E-13	4.96
A-2	100	19.7	9.46	1.6	49,751	8.62E-13	4.72
A-3	112	19.1	10.4	1.6	42,104	3.34E-13	4.9
A-4	110	19.7	10.2	1.6	44,667	9.25E-13	4.58
B-1	109	19.9	8.9	1.35	45,476	4.48E-13	4.80
B-2	109	20.3	9.04	1.35	44,234	2.31E-13	5.01
B-3	110	19.0	9.22	1.35	44,330	3.61E-13	5.02
B-4	112	19.6	9.07	1.35	45,449	4.84E-14	5.45

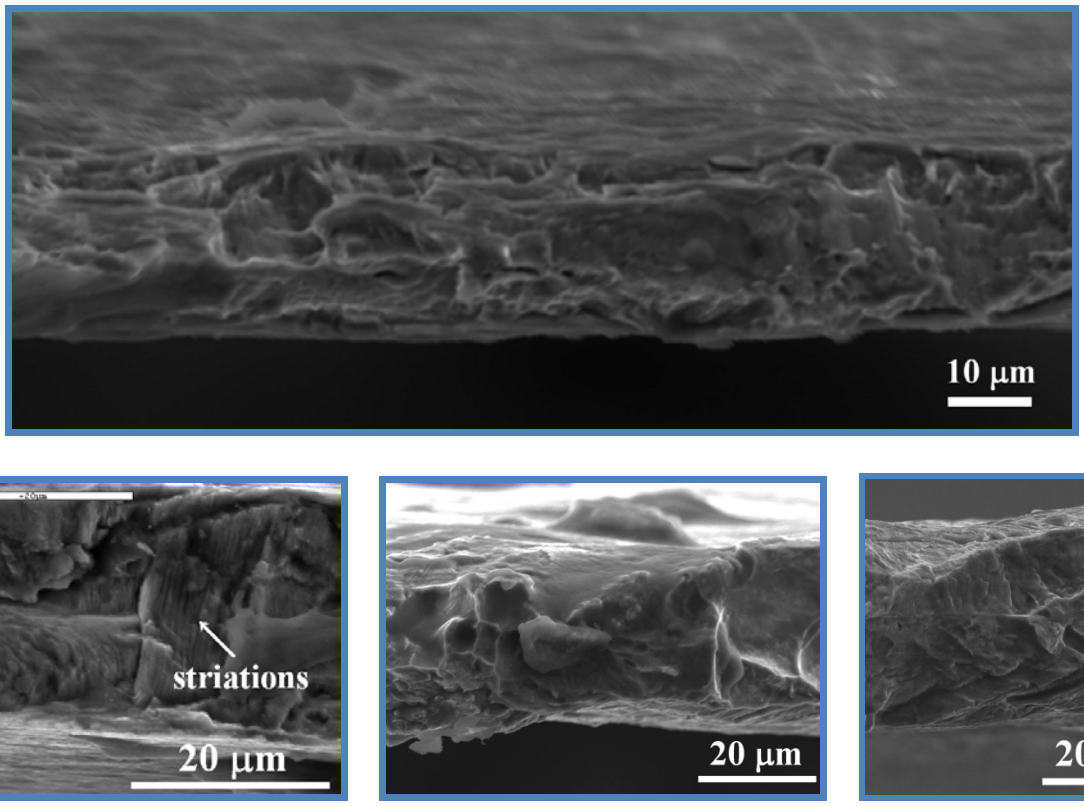

Figure 7. SEM fractography images fracture surfaces of a typical specimen subjected to tension-tension fatigue until failure. The fracture surface exhibited complicated fracture features including striations and transverse necking.

5.2 Similarity Analysis

Incomplete self-similarity of higher crack growth rate for foils

The crack growth rate can be correlated with the corrected stress intensify factor ΔK_I by a power-law relationship (Paris relationship), which is a notable scaling law [16], between the fatigue-crack growth rate per cycle, *da/dN*, and the stress intensity factor range, ΔK. This relationship has been shown to apply over a wide range of cyclic crack growth rates for metallic, polymeric and ceramic materials. For the limited number of foil-thickness materials that have been studied, the m value of is higher than that commonly found for bulk (thicker) samples [5,6].

The Paris relationship (Eq. 1) is an empirical equation that provides little information of the effect that other parameters might influence cyclic crack growth behavior. Obviously, the average crack growth depends on (i) fatigue loading parameters, *i.e.* loading ratio *R* and frequency *f*, (ii) material properties, such as yield strength, σ_y and fracture toughness, K_c and (iii) specimen size. To examine the effect of various parameters on fatigue crack growth behavior, following the mathematical similarity approach from the work of Barenblatt *et al* [17] and Ritchie [18] crack growth rate can be expressed as:

$$\frac{da}{dN} = \left(\frac{\Delta K}{\sigma_y}\right)^2 \Phi\left(\frac{\Delta K}{K_c}, R, z, f t\right) \tag{4}$$

z is the basic similarity parameter, given in terms of material constants and a characteristic specimen length scale *h*:

$$z = \frac{\sigma_y \sqrt{h}}{K_c} \tag{5}$$

If incomplete similarity is assumed in the parameter $\Delta K << K_c$, then

$$\Phi = \left(\frac{\Delta K}{K_c}\right)^{\alpha} \Phi_1(R, z), \quad \frac{da}{dN} = \frac{(\Delta K)^{2+\alpha}}{\sigma_y^2 K_c^{\alpha}} \Phi_1(R, z) \tag{6}$$

Comparison with the Paris relation (Eq. 1) gives,

$$C = \frac{\Phi_1(R, z)}{\sigma_y^2 K_C^{\alpha}}, \quad m = 2 + \alpha(R, z) \tag{7}$$

where α is a function of loading ratio R and similarity parameter *z*. From Eqs. 6 and 7, the incomplete self-similarity infers that the constants C and m in the Paris power law relationship depend not only experimental parameters, such as ΔK, and material parameters, but also (through the similarity parameter *z*) on a specimen length scale h. For a set of loading parameters, the exponent α (and therefore m in Eq. 7) depends only on the parameter *z*.

It has been first reported by proposed *et al* [17] and interpreted by Ritchie [18] that there is a trend of increasing Paris exponents *m* with increasing *z* corresponding to the transition from ductile (low *m* value) to brittle fracture (high *m* value). For the fatigue crack growth behavior of the Ti foils investigated, the experimentally measured Paris constant *m* varied between 4 to 5, which is slightly higher than the *m* value typically associated with bulk metal materials. The result implies accelerated fatigue crack growth rate due to foil thickness effect. According to incomplete self-similarity method, higher *m* value occurs with increasing *z* value and it corresponds to a transition from ductile fatigue fracture (m = 2~4) to more brittle fatigue fracture (m > 4). The higher *m* value induced by higher *z* value results from the competing mechanism between decreasing sample characteristic dimension *h*, fracture toughness K_c and increasing yield strength σ_y in the similarity parameter of *z*. Taking specimen thickness as the characteristic length scale *h*, would lead

to the conclusion that foil thickness materials should have smaller *z* values, however compared to the dependence on yield strength and fracture toughness, *z* has a weaker, square-root, dependence on *h*. Although the mode I fracture toughness K_{Ic} and yield strength σ_y of 30 μm pure Ti foil were not determined in the present investigation, it can be expected, in line with results for foil-thickness metals, that the mode I fracture toughness K_{Ic} *decreases* with decreasing sample thickness [10]. Therefore it is indicated from the slightly higher value of m that although the sample thickness *h* decreases for foils, the effect of σ_y/K_{Ic} on the similarity parameter of *z* is more significant. The foil samples investigated also demonstrated complicate ductile combined brittle fatigue fractures features (Fig. 7). The fatigue behavior of the Ti foils, which was characterized by slightly elevated *m* values and both ductile and brittle fracture surface characteristics, is consistent with the speculation that the higher *m* value induced by higher *z* value with decreasing sample characteristic dimension *h*, fracture toughness K_c and increasing yield strength σ_y.

To summarize, a preliminary incomplete self-similarity analysis, indicates that that the slightly higher *m* values observed for the Ti foil specimens, and in other metal foils [5, 6] is related to a the reduction in the fracture toughness and the rising in the yield strength with decreasing metal thickness. It can also be inferred from the incomplete similarity that with a further decrease in fracture toughness with decreasing thickness even higher values of m indicative brittle crack growth could occur.

6. Conclusions

A new experimental approach to study the tensile fatigue behavior of ultra-thin metal foils was developed. The technique, which involves magnetic coupling between an eccentric steel rotor and a ceramic magnet attached to a specimen grip mounted to a linear bearing slide. Cyclic tensile loads are induced in the specimen during rotation of the eccentric disk which is attached to a variable speed DC motor. The apparatus can be readily fit with a small furnace for testing at elevated temperatures. For the proof-of-concept experiments, fatigue crack growth tests were performed with commercially pure 0.03 mm thick Ti foils. Based on the observations, test results and a preliminary similarity analysis, the following conclusions can be made:

1. The test apparatus shows considerable promise as a low-cost method to study tensile fatigue and mode I cyclic crack growth of thin foils and wires at ambient and elevated temperatures.

2. Analysis showed that a shift in the centerline of loading can occur when testing edge-notched specimens, which induces an opening moment at the crack tip. If not accounted for, this effect can lead to overestimation of the mode I stress intensity factor.

3. Crack growth data for specimens with the same notch-to-width ratios, exhibits similar trends and fatigue crack growth parameter values. For all test cases, stable crack growth was observed.

4. The effective stress intensity factor ΔK_I corrected by FEM analysis for face-loaded specimens were used to correlate the crack growth rate *da/dN*. The crack growth rate can be described by a Paris relationship with a *m* value between 4~5. The results are consistent with other studies of thin metal foils where high m values are commonly observed.

An incomplete self-similarity theory was used to gain additional insight to the higher *m* value in Paris law and possible trends with decreasing specimen thickness. It is proposed that due to a significant reduction in fracture toughness K_{Ic} for foil thickness metals, the basic similarity parameter *z* increases, which leads to an increasing *m* value. This also infers that there is a transition

from ductile fracture to brittle facture behavior with decreasing thickness. It is suggested that with continuing decreasing specimen thickness, *m* could increase until a constant maximum value is achieved and brittle fatigue fracture behavior dominates the crack growth process.

Acknowledgements

Dr. L. Liu was supported by the National Natural Science Foundation of China under Grant No. 11002020 and the Program for New Century Excellent Talents at Chinese Universities. Professor John W. Holmes was supported by the National Thousand Talent Plan of China and by the International Center for Clean Energy Systems and Materials at Beihang University.

References

[1] M. Klein, A. Hadrboletz, B. Weiss, and G. Khatibi, The ‘size effect’ on the stress–strain, fatigue and fracture properties of thin metallic foils. *Material Science and Engineering A*, 319–321, (2001) 924-928.

[2**]** G.P. Zhang, K.H. Sun, B. Zhang, J. Gong, C. Sun C and Z.G. Wang, Tensile and fatigue strength of ultrathin copper films. *Material Science and Engineering A*, 483–484, (2008) 387–390.

[3**]**G.P. Zhang, K. Takashima, and Y. Higo, Fatigue strength of small-scale type 304 stainless steel thin films. *Material Science and Engineering A*, 426, (2006) 95-100.

[4] W.N. Sharpe and K.T. Turner, Fatigue testing of materials used in microelectro mechanical systems. in: X.R. Wu, Z.G. Wang (Eds.), Fatigue 99, EMAS, UK, (1999)1837–1844.

[5] E. Vanswijgenhoven and J.W. Holmes JW, Fatigue Crack Growth in Inconel 718 Superalloy Foil at Elevated Temperature. Fifth International Special Emphasis Symposium on Superalloys 718, 25, 706, and Derivatives, (2001) Pittsburgh, June, USA.

[6]L. Liu and J.W. Holmes, Experimental technique for elevated temperature Mode I fatigue crack growth testing of Ni-base metal foils. *Journal of Engineering Materials and Technology-TRANSACTIONS OF THE ASME*, 129, (2007) 594-602.

[7] J.Z. Xie, Low Cycle Fatigue and Fatigue Crack Growth Behavior of Alloy in 718 *Superalloy 718, 625 and various Derivatives*, The Minerals, Metals & Materials Society, (1991) 491–500.

[8] L. A. James and W.J. Mills Effect of Heat-Treatment and Heat-to-Heat Variations in the Fatigue Crack Growth Response of Alloy 718. *Eng. Fract. Mech.*, 22, (1985)797–817.

[9] R.A. Meirom, T.E. Clark and C.L. Muhlstein, The role of specimen thickness in the fracture toughness and fatigue crack growth resistance of nanocrystalline platinum films. Acta Materialia, 60, (2012)1408–1417.

[10] H.W. Wang, Y.L. Kang, Z. F. Zhang and Q.H. Qin, Size effect on the fracture toughness of metallic foil. *Int J Fract.*, 123(3/4), (2003) 177–85.

[11] Jong-Sung Bae, Chung-Seog Oh, Kyoung-Seok Park, Sang-Kyo Kim and Hak-Joo Lee, Development of a high cycle fatigue testing system and its application to thin aluminum film. *Eng. Fract. Mech.*, 75, (2008) 4958-4964.

[12] Chung-Youb Kim, Ji-Ho Song and Do-Young Lee, Development of a fatigue testing system for thin films. *Int. J. Fatigue*, **31**, (2009)736-742.

[13] Q.Y. Sun and H.C. Gu. Tensile and low-cycle fatigue behavior of commercially pure titanium and Ti–5Al–2.5Sn alloy at 293 and 77 K. *Materials Science and Engineering A*, 316, (2001)80-86.

[14] Kenichi Takao and Kazuhiro Kusukawa, Low-cycle fatigue behavior of commercially pure titanium. *Materials Science and Engineering A*, 213, (1996)81-85.

[15] T. Hanlon, E.D. Tabachnikov and S. Suresh, Fatigue behavior of nanocrystalline metals and alloys. *International Journal of Fatigue*, 27, (2005)1147–1158.

[16] G.I. Barenblatt, *Scaling*, Cambridge University Press, Cambridge, U.K. 2003.

[17] G.I. Barenblatt and L.R. Botvina, Incomplete self-similarity of fatigue in the linear range of crack growth. *Fatigue Eng Mater Struct*, 3(3), (1980)193–202.

[18] R.O. Ritchie RO. Incomplete self-similarity and fatigue-crack growth. *Int. J. Fract.*, **132(3)**, (2005) 197–203.

Determination of statistical secured residual lifetime based on sensitivity analysis and stochastic crack propagation simulation

Jens Lebahn*, Manuela Sander

Institute of Structural Mechanics, University of Rostock, Rostock 18059, Germany
* Corresponding author: jens.lebahn@uni-rostock.de

Abstract To consider uncertainties due to the scattering of input parameters common residual lifetime calculations are deduced from conservative deterministic crack propagation simulations. Conclusions about the reliability of the residual lifetime are not possible in general. Those can be obtained from stochastic crack propagation simulations. Therefore the significant input parameters have to be identified and statistically modelled. In the present investigations quantil curves of the crack propagation data of 42CrMo4 are derived. From those the fracture mechanical material parameters were statistically modelled. After identifying the significant material parameters by performing a sensitivity analysis stochastic input vectors of the relevant input parameters are generated. Using the Monte Carlo simulation and the analytical crack propagation software NASGRO stochastic residual lifetime calculations are performed and statistically analyzed. Afterwards residual lifetimes can be related to survival probabilities.

Keywords residual lifetime calculation, sensitivity analysis, Monte Carlo method, *Forman*/*Mettu*-equation

1. Introduction

The residual lifetime of components and structures can be calculated by crack propagation simulations [1]. Those are mostly performed analytically due to the low computational effort. Therefore, deterministic simulations are commonly used. Uncertainties through the scattering of input parameters e.g. the crack propagation curves are considered by conservative appreciated material parameters and safety factors [2]. As a result of this approach, it is not possible to derive conclusions about the failure probability of the calculated residual lifetimes. Alternatively stochastic crack propagation simulations e.g. the Monte Carlo simulation [3–5] can be performed instead of deterministic ones. Therefore, the significant stochastic input parameters must be statistically characterized. From those, independent input vectors are calculated and a multiplicity of crack propagation simulations are performed. Afterwards the residual lifetimes are statistically analyzed.

To identify the significant stochastic input parameters a sensitivity analysis [6–8] was used in the present study. Therefore, only scattering of the crack propagation curve was considered. From crack propagation curves of 42CrMo4 for different stress ratios quantile curves were deduced. By fitting those curves with the *Forman/Mettu*-equation [9] its parameters and the related distribution functions of the parameters could be obtained. Hereby, stochastic input vectors were calculated and crack propagation simulations performed by use of the analytical crack propagation software NASGRO 6 [9]. The sensitivity analysis respectively the robustness analysis provided the significant input parameters of the resistance against cyclic crack propagation. Those were used to perform stochastic crack propagation simulations.

2. Theoretical background

In this chapter some basics of analytical crack propagation simulation, sensitivity analysis and Monte Carlo simulation are provided.

2.1. Analytical crack propagation simulation

The basic requirements for an analytical crack propagation simulation are the solution of the stress

intensity factor (SIF) and a relationship between the cyclic SIF ΔK and the crack propagation *da/dN* [1]. An equation to describe the crack propagation curve is the *Forman*/*Mettu*-equation

$$\frac{da}{dN} = C \cdot \left(\frac{1-\gamma}{1-R} \cdot \Delta K\right)^n \cdot \left(1 - \frac{\Delta K_{\mathrm{th}}}{\Delta K}\right)^p \cdot \left(1 - \frac{K_{\max}}{K_{\mathrm{C}}}\right)^{-q}. \tag{1}$$

This function, which is implemented in NASGRO [9], characterizes the whole crack propagation curve. The empirical coefficients C, n, p and q have to be fitted to test data. K_{C} is the fracture toughness. The R-dependence in eq. (1) is explained by the crack closure effect and considered by *Newman*'s crack closure function

$$\gamma = \frac{K_{\mathrm{op}}}{K_{\max}} = \begin{cases} \max(R, A_0 + A_1 \cdot R + A_2 \cdot R^2 + A_3 \cdot R^3) & R \geq 0 \\ A_0 + A_1 \cdot R & -2 \leq R < 0 \end{cases} \tag{2}$$

with the coefficients

$$\begin{aligned} A_0 &= (0{,}825 - 0{,}34\alpha_{\mathrm{CF}} + 0{,}05\alpha_{\mathrm{CF}}^2) \cdot \left[cos\left(\frac{\pi}{2} \cdot \frac{\sigma_{\max}}{\sigma_{\mathrm{F}}}\right)\right]^{\frac{1}{\alpha_{\mathrm{CF}}}} \\ A_1 &= (0{,}415 - 0{,}071\alpha_{\mathrm{CF}}) \cdot \frac{\sigma_{\max}}{\sigma_{\mathrm{F}}} \\ A_2 &= 1 - A_0 - A_1 - A_3 \\ A_3 &= 2A_0 + A_1 - 1. \end{aligned} \tag{3}$$

The constraint factor α_{CF} varies between 1 for the plane-stress condition and 3 for the plane-strain condition. The constraint factor and the ratio of maximum stress $\sigma_{\max}$ and yield stress σ_{F} are also considered as fitting coefficients [9]. To describe the R-dependence of the cyclic threshold value

$$\Delta K_{th} = \Delta K_1 \cdot \sqrt{\frac{a}{a + a_0}} \cdot \left(\frac{1-R}{1-\gamma}\right)^{\left(1 + C_{th}^{+} \cdot R\right)} / (1 - A_0)^{(1-R) \cdot C_{th}^{+}} \tag{4}$$

for $R \geq 0$ and

$$\Delta K_{th} = \Delta K_1 \cdot \sqrt{\frac{a}{a + a_0}} \cdot \left(\frac{1-R}{1-\gamma}\right)^{\left(1 + C_{th}^{-} \cdot R\right)} / (1 - A_0)^{\left(C_{th}^{+} - C_{th}^{-} \cdot R\right)} \tag{5}$$

for $R < 0$ again *Newman*'s crack closure function is used. The cyclic threshold value ΔK_1 for $R \to 1$ as well as C_{th}^{+} and C_{th}^{-} are fitting coefficients. All in all ten parameters are needed to describe the resistance against cyclic crack propagation by the *Forman*/*Mettu*-equation.

2.2. Sensitivity analysis

With a sensitivity analysis the significance of input parameters X_{i} or rather factors and their effects on an output value Y is investigated [6]. The importance of a factor is denoted as sensitivity S_{i}. The effect is distinguished in main effect (first order effect) and interaction effect, which describes the effect of a factor according to the properties of another factor. Sensitivity analysis can be divided in factor screening, local and global sensitivity analysis [8]. While with factor screening only qualitative influences of factors are investigated with local and global sensitivity analysis also quantitative influences are analyzed. If the effect of a factor on an output value is investigated in a small domain of the factor with consideration of its distribution function a local sensitivity analysis or rather a robustness analysis is performed [8]. To determine sensitivities different methods e.g. the contrast method, the regression analysis or the analysis of variance (ANOVA) exists [7, 8].

The regression analysis is based on a regression model in which the dependencies between input and output factors are described analytically [8]. Therefore, linear or quadratic models are used commonly. For n_f input factors without error term a linear regression model

$$\hat{y} = b_0 + \sum_{i=1}^{n_f} b_i \cdot x_i + \sum_{i=1}^{n_f-1} \sum_{j=i+1}^{n_f} b_{ij} \cdot x_i \cdot x_j \tag{6}$$

contains one constant b_0, n_f regression coefficients b_i and $n_f \cdot (n_f - 1)/2$ independent regression coefficients b_{ij}. If the domain of the input factors is normalized on [-1 , 1], the coefficients b_i are a measure of the main effects and the coefficients b_{ij} are a measure of the interaction effects [8]. Here the scattering of the input and output factors is not considered *Saltelli* et al. [7] recommend

$$S_i = b_i \cdot \frac{s_i}{s_y} \tag{7}$$

as a measure of the sensitivity. Herein, s_i and s_y are the standard deviations of the input factor X_i and the output value Y.

To check the predictive of the regression model and thus the accuracy of the calculated sensitivities the coefficient of determination

$$R^2 = \frac{\sum_j (\hat{y}_j - \bar{y})^2}{\sum_j (y_j - \bar{y})^2} \tag{8}$$

is calculated. For a linear regression model a small coefficient of determination can be caused by non-linear effects. In such a case a transformation of the output value can lead to a better accordance. To find a valid transformation the Box-Cox-transformation [8]

$$z = \begin{cases} \dfrac{y^\lambda - 1}{\lambda \cdot g^{(\lambda-1)}} & ,\lambda \neq 0 \\ g \cdot ln(y) & ,\lambda = 0 \end{cases} \tag{9}$$

with the geometric mean value

$$g = (y_1 \cdot y_2 \cdot \ldots \cdot y_{n_r})^{\frac{1}{n_r}}. \tag{10}$$

can be performed. For different values of λ a multiplicity of transformations is realized. For each of them the coefficients of determination can be calculated to find the optimum transformation.

2.3. Monte Carlo simulation

The Monte Carlo simulation is a numerical method for the approximate solution of mathematic tasks by use of random input vectors [3]. It is e.g. used to solve multi-dimensional integrals. The generation of linear independent random vectors x_{ij} based on the input factor's distribution functions $g_i(x)$ is the main object of the Monte Carlo simulation. If $f(x)$ is a function of the factor X and $g(x)$ its' distribution function the expected value

$$E[f(x)] = \int_{-\infty}^{+\infty} f(x) \cdot g(x) dx \approx \frac{1}{N} \cdot \sum_{j=1}^{N} f(x_j) \pm \sqrt{\frac{\sigma^2}{N}} = \frac{1}{N} \cdot \sum_{j=1}^{N} f(x_j) \pm s_{\bar{F}} \tag{11}$$

of $f(x)$ can approximately calculated by the mean of the function values of the N random input values x_j [3]. The sum converges against the integral, if the standard error $s_{\bar{F}}$ of the expected value of $f(x)$ gets small. Therefore, a high number N of samples is required, depending on the variance σ^2

of the function $f(x)$. However, the accuracy of the Monte Carlo simulation is independent of the number n_f of input factors [3, 5] so it becomes attractive for systems with a multiplicity of factors.

For the basic Monte Carlo simulation the input vectors are generated by a random number generator based on the factor's distribution functions. Therefore, taking into account a statistical error of 10 %

$$N = \frac{100}{P_A} \tag{12}$$

samples are required [5]. It is obvious that the computational effort is high for small probability of failure P_A. Against this background different variants of the Monte Carlo simulation were developed to minimize the variance and therefore to increase the computational efficiency. Some of them are the Latin Hypercube sampling and the Importance sampling [5].

3. Analysis of crack propagation data

For the crack propagation simulation an analytical relationship $da/dN = f(\Delta K, R)$ is required. To obtain its coefficients this function is fitted through experimental crack propagation data. Therefore, visual criteria and a conservative approximation are commonly used [2]. An automated adaption of the *Forman*/*Mettu*-equation is not documented. This is also the case for a complete statistical analysis of its coefficients and building on a sensitivity analysis or rather a robustness analysis referred to the residual life. To consider the scattering of crack propagation data of metallic materials usually the coefficients C [2,10 – 14], ΔK_0 [2, 10, 11, 13] and K_C [2, 11] are statistically analyzed. ΔK_0 is the cyclic threshold value for $R \rightarrow 0$ which is related to ΔK_1 [9].

3.1. Automated adaption of fitting parameters

To perform an automated analysis of crack propagation data by the *Forman/Mettu*-equation a MATLAB program was developed. The adaption of the fitting coefficients on the experimental data is divided in two steps. First the threshold values against cyclic crack propagation are calculated for different stress ratios and therewith the coefficients ΔK_1, C_{th}^{+} and C_{th}^{-} of equations (4) and (5) are determined. Next the coefficients C, n, p and q of the *Forman/Mettu*-equation (1) are calculated. The remaining coefficients a, a_0, α_{CF}, σ_{max}/σ_F and K_C have to be supported for the adaption.

After loading the crack propagation data the threshold values for the different stress ratios are calculated by use of the DLR-method [15]. Therefore the user has to set an upper bound da/dN_{max} of the crack propagation data used for the analysis of the threshold value. This limit should be below the transition from the threshold to the *Paris*-domain [15]. The threshold data are analyzed in a linear scaled coordinate system, Figure 1. Every data set with R = constant is fitted by a linear function. Therewith, the threshold value is obtained for $da/dN = 0$. The crack propagation data of 42CrMo4 contains of the stress ratios $R = 0{,}1$, $R = 0{,}3$ and $R = 0{,}5$. The analyzed threshold values for each stress ratio are plotted in Figure 2.

Referring to the determination of the experimental threshold values the coefficients ΔK_1, C_{th}^{+} and C_{th}^{-} for the analytical threshold value calculation are adapted. Therefore two algorithms are available in the program. The first one is a simple search algorithm, in which the search domain is divided into intervals. The second one is a gradient based algorithm. For both methods start values of the fitting coefficients must be set. Furthermore, the coefficients $a = 45$ mm, $a_0 = 0{,}0381$ mm, $\alpha_{CF} = 1{,}9$ and $\sigma_{max}/\sigma_F = 0{,}3$ are pretended. At the beginning the number of stress ratios is checked. If only positive stress ratios are available at least two otherwise three discrete threshold values are required. Since the crack propagation data only contains positive stress ratios C_{th}^{-} could not be analyzed, see equation (4) and (5). The adaption of the threshold value is visualized in Figure 2.

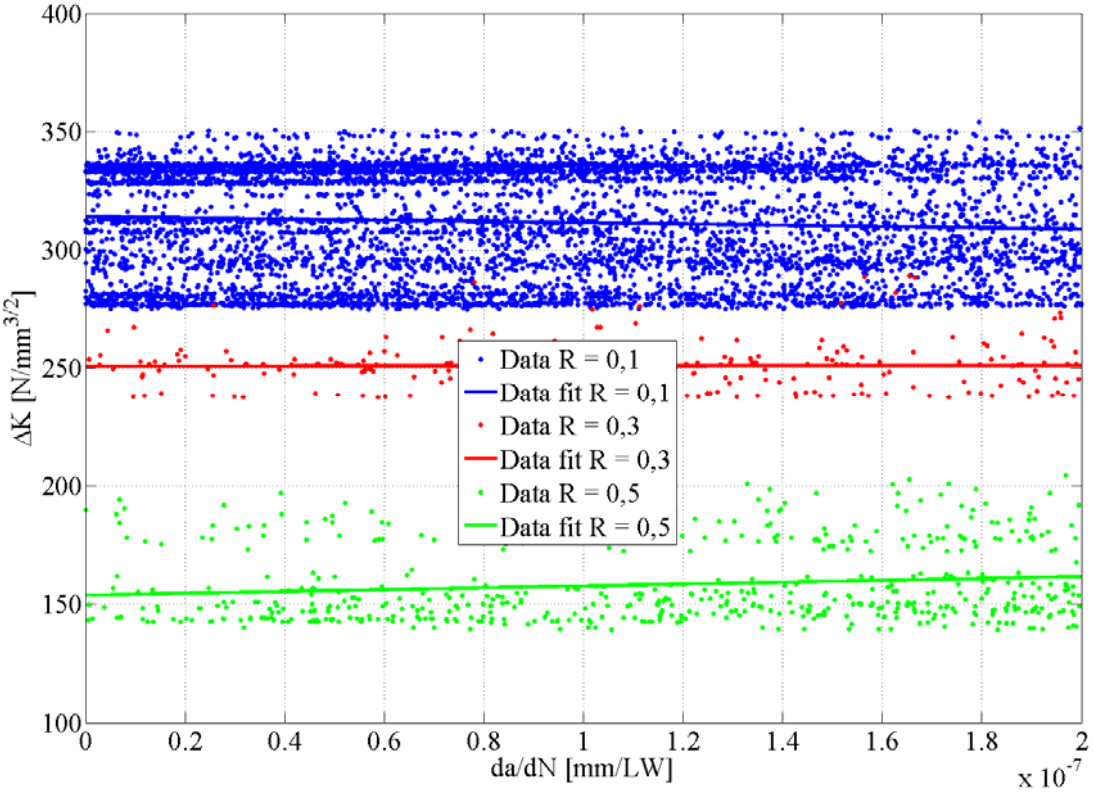

Figure 1: Determination of threshold values from crack propagation data by DLR-method

In the second step of the adaption the coefficients C, n, p and q are calculated by use of a search algorithm with nested intervals. Therefore, the four-dimensional search domain is divided into intervals. In every iteration loop a weighted effective error is calculated for every parameter combination. The parameter combination leading to a minimum error is used as center for the search domain of the next iteration loop. Additionally, the search domain is reduced, so that the intervals become smaller. Due to the nested intervals a convergence behavior of the algorithm is realized. Since error values of the threshold domain are much smaller compared to those of e.g. the K_C-domain the error values are weighted with the inverse of the crack propagation. For the adaption a fracture toughness $K_C = 4.200$ N/mm$^{3/2}$ is used. The results of the adaption together with the crack propagation data of 42CrMo4 are shown in Figure 3. The appropriated mean fitting coefficients are listed in Table 1 and consists with a probability of survival $P = 50$ %.

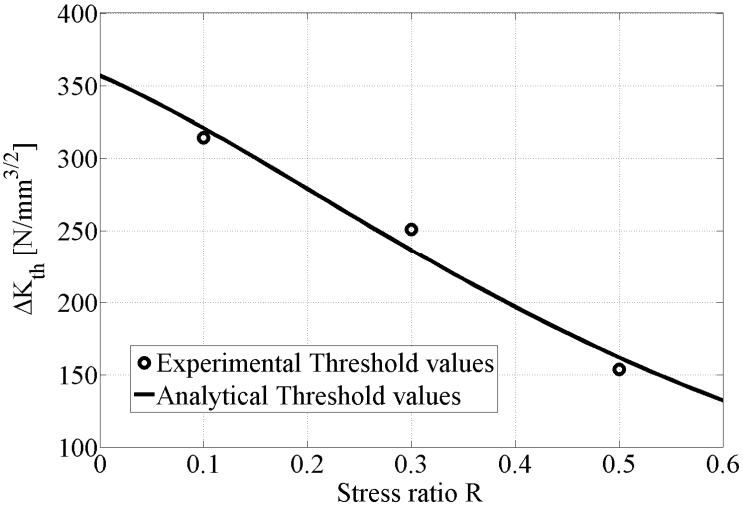

Figure 2: Experimental and analytical threshold values

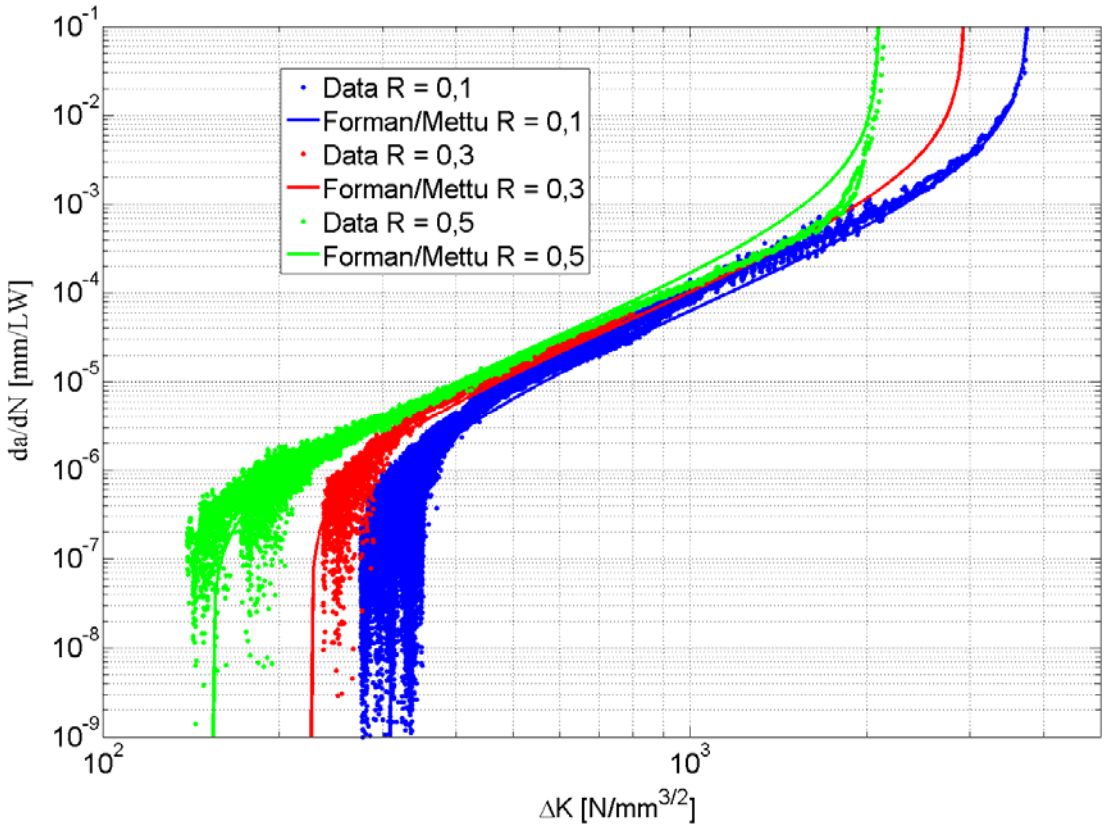

Figure 3: Crack propagation data of 42CrMo4 and the adaption by the *Forman/Mettu*-equation

3.2. Statistical analysis

The statistical analysis of the crack propagation data is divided in three steps. First for each stress ratio quantile curves are calculated for different probabilities of survival. Next, for each probability of survival the quantile curves are fitted by the *Forman/Mettu*-equation to obtain the fitting coefficients. Those are statistically analyzed in the last step to obtain their distribution functions.

To determine quantile curves the logarithm is taken from the crack propagation data. Afterwards the co-domain of the crack propagation data is divided into intervals. For each interval a polynomial regression function and a confidence interval for a pretended confidence probability are calculated. Therewith and for each domain discrete values are calculated for the mean and the upper and lower bound of the confidence interval. By use of interpolation functions the transition between the domains is smoothed and equidistant spaced values are calculated. Taking the antilogarithm the three quantile curves are obtained e.g. for a stress ratio $R = 0{,}1$, Figure 4. This procedure is also applied to the crack propagation data of the other stress ratios.

Every quantile curve corresponds to a probability of survival P. Taking the quantile curves for one probability of survival the fitting coefficients of the threshold value and the *Forman/Mettu*-equation are determined by use of the adaption program. For the statistical analysis of the crack propagation data of 42CrMo4 the probabilities of survival $P = 5\,\%$, $P = 50\,\%$ and $P = 95\,\%$ are used. The corresponding fitting coefficients are listed in Table 1. As can be seen the analytical crack propagation curve is shifted to top left with increasing probability of survival.

In the last step every fitting coefficient is statistically analyzed. This contains the choice of a distribution function and the calculation of the mean value and the standard deviation. For all fitting coefficients a normal distribution is used to describe the scattering, except of the coefficient C, Table 1. Here, a logarithmic normal distribution leads to the best results.

Table 1: Fitting coefficients of the *Forman/Mettu*-equation and their distribution functions

Parameter	ΔK_1 [N/mm$^{3/2}$]	C_{th}^{+}	C [mm/LW]	n	p	q	K_C [N/mm$^{3/2}$]
P = 5 %	71,0	3,1	$8{,}6 \cdot 10^{-12}$	2,5	0,65	1,1	4350
P = 50 %	55,75	3,4	$1{,}2 \cdot 10^{-11}$	2,4	0,8	0,9	4200
P = 95 %	42,0	3,83	$1{,}8 \cdot 10^{-11}$	2,3	1,0	0,7	4050
Distribution	normal	normal	log-normal	normal	normal	normal	normal
μ	56,3	3,44	-10,91	2,4	0,82	0,9	4200
s	8,81	0,22	0,0975	0,06	0,11	0,12	91,2

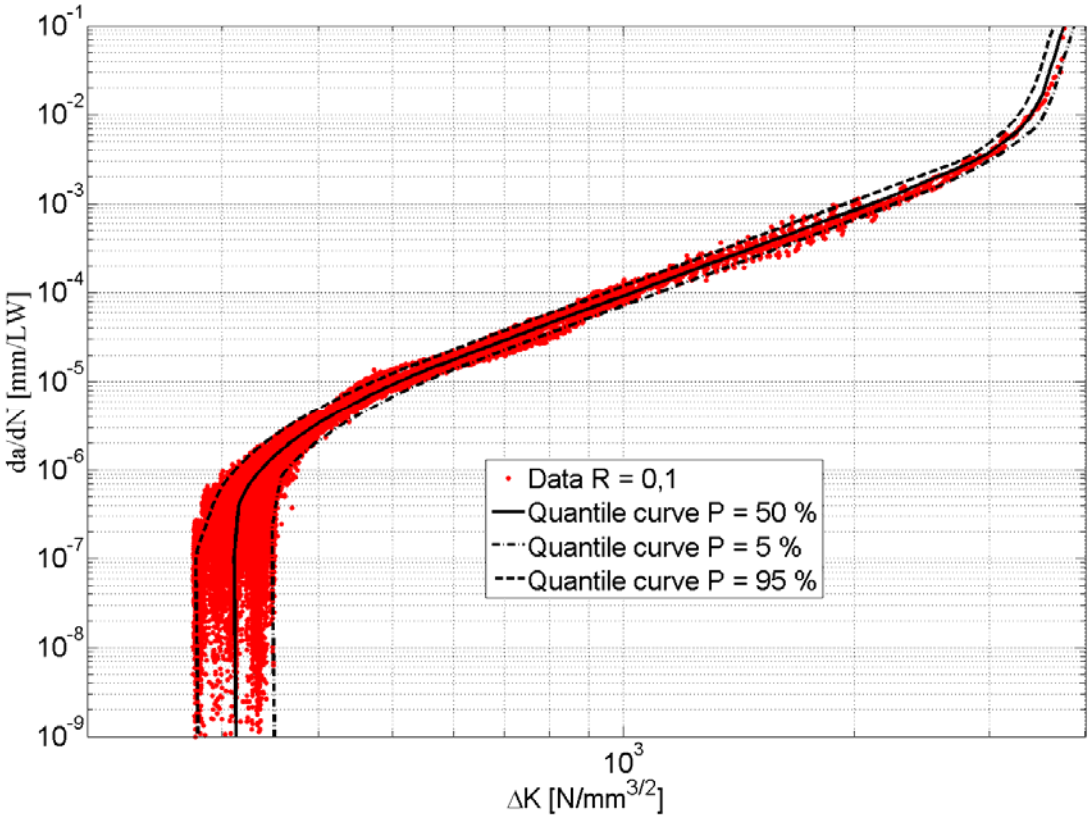

Figure 4: Crack propagation data of R = 0,1 and the adaption by quantile curves

4. Stochastic crack propagation simulation

To perform a sensitivity analysis of the fitting coefficients and to deduce statistical secured residual lifetimes stochastic crack propagation simulations were carried out by use of the analytical crack propagation software NASGRO 6.0 [9]. In a MATLAB script random input vectors of the fitting coefficients were generated using the determined distribution functions and a random number generator. To assure a probability of failure P_A = 1 % the input vectors contain of 10.000 elements, according to equation (12). For every element the MATLAB script generates an input file, starts the crack propagation simulation and reads in the residual lifetime.

The crack problem is a semi-elliptical surface crack in a hollow cylinder. The cylinder is loaded by a positive constant mean stress and a reverse bending stress. The amplitude of the bending stress is defined by a load frequency distribution. The initial crack size and the load were adapted, that the

frequency distribution is at least repeated 30 times to prevent load sequence effects [16]. The non-interaction material model was used.

4.1. Sensitivity analysis of the fitting coefficients on the residual lifetime

To identify the dependencies of the residual lifetime a sensitivity analysis was performed by use of the software Visual-XSel 12.0 [17]. The input factors are the seven fitting coefficients C, n, p, q, ΔK_1, C_{th}^+ and K_C. The output factor is the residual lifetime. To derive the sensitivities a regression analysis was performed by use of a quadratic model with interaction effects [17]. To increase the accuracy of the regression model the output factor was transformed by the natural logarithm, which followed from the Box-Cox-transformation. The reduced model, containing only the significant factors, explains 99,8 % of the data. The relative effects of the input factors are plotted in Figure 5. As can be seen the coefficients C, n and q are inversely proportional to the residual lifetime.

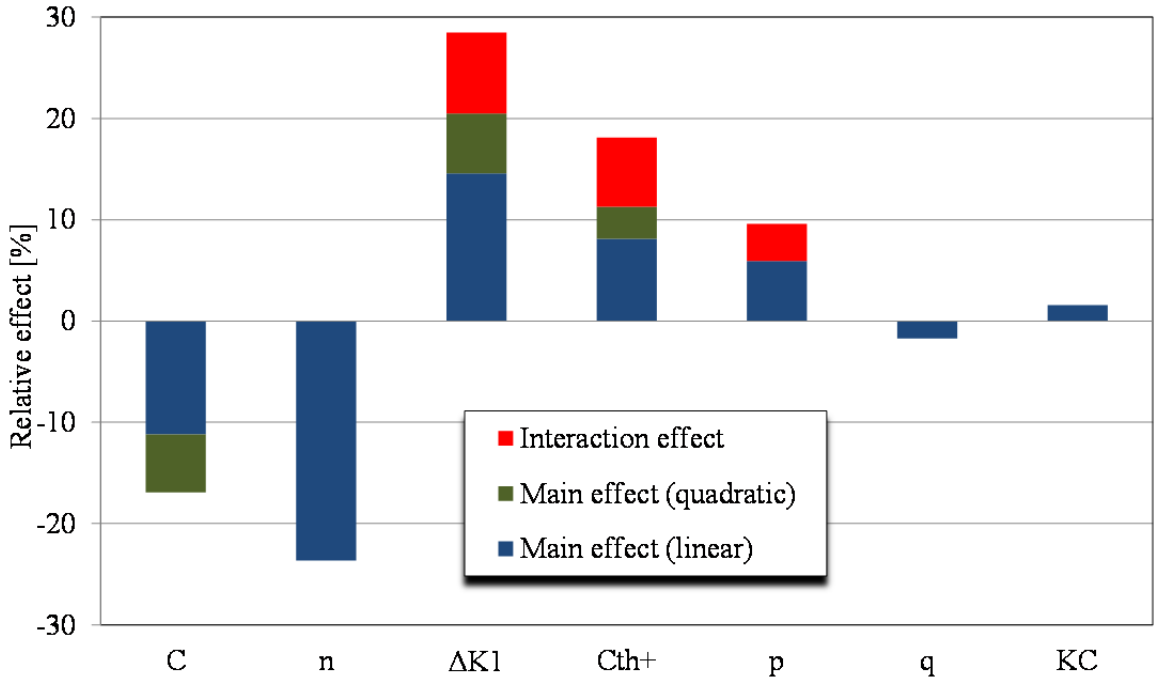

Figure 5: Relative effects of the fitting coefficients on the residual lifetime

Furthermore, it is obvious that the coefficients q and K_C are less significant and thus are not required as stochastic parameters in the stochastic crack propagation simulation. The coefficients C, n, ΔK_1, C_{th}^+ and p are significant. That means they have to be statistically analyzed and are required for the stochastic crack propagation simulation. Although, p has a small effect it cannot be neglected, due to the interaction effects between ΔK_1 and C_{th}^+.

The results of the sensitivity analysis are inconsistent to the statistical analysis of crack propagation data in literature [2, 10 – 14]. On the one hand it is not necessary to statistically analyze K_C in terms of a residual lifetime calculation. On the other hand a statistical analysis should include the coefficients n, p and C_{th}^+.

4.2. Determination of statistical secured residual lifetime

The stochastic crack propagation simulations with stochastic input vectors, created by a random number generator correspond to a basic Monte Carlo simulation. Additionally and based on the results of the sensitivity analysis a second stochastic crack propagation simulation was performed in

which only the five significant parameters were stochastically modeled. Afterwards, the residual lifetimes were statistically analyzed by use of the distribution fitting toolbox in MATLAB. The scattering of the residual lifetimes corresponds to a logarithmic normal distribution, Figure 6. By knowledge of the distribution function residual lifetimes can be calculated for arbitrary probabilities of failure. Furthermore it is able to determine the range of scattering

$$T_N = 1{:}\frac{N_{P=90\%}}{N_{P=10\%}} = 1{:}\frac{3{,}0 \cdot 10^6}{0{,}83 \cdot 10^5} = 1{:}3{,}6 \tag{13}$$

which is equal for both stochastic simulations. So the results of the sensitivity analysis are confirmed and the coefficients q and K_C are insignificant.

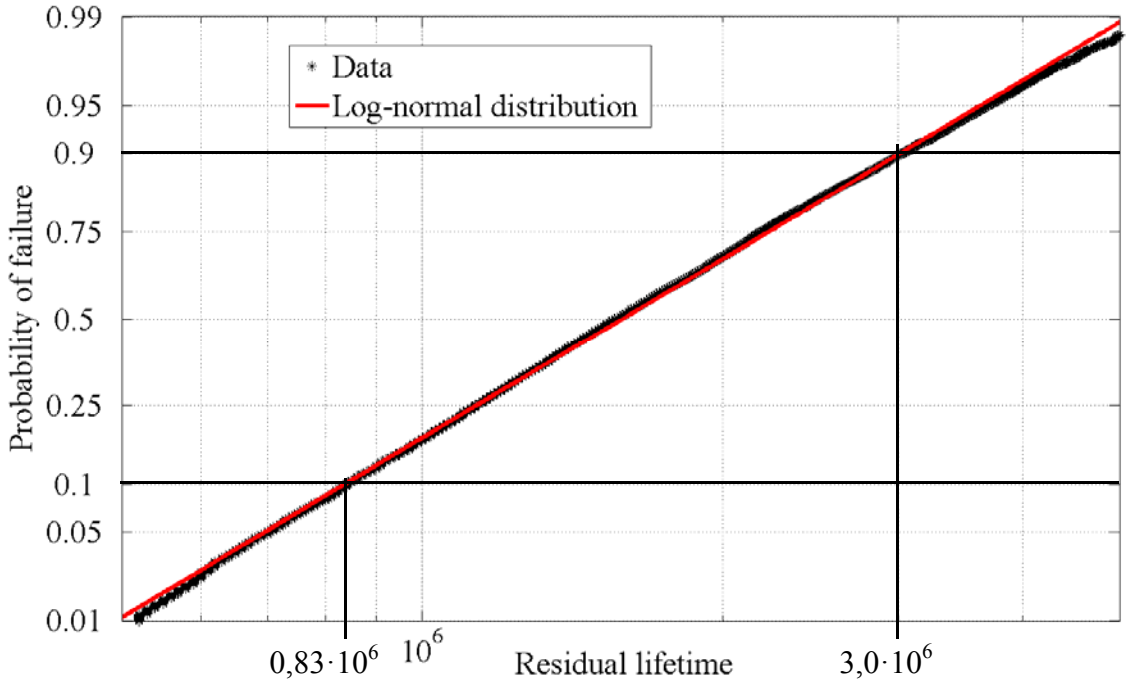

Figure 6: Residual lifetimes of stochastic crack propagation simulation with 7 stochastic parameters

5. Conclusion

In the current investigations crack propagation data of 42CrMo4 are analyzed. This includes the determination of fitting coefficients of the *Forman/Mettu*-equation which describes the crack propagation curve analytically. For the automated adaption of the crack propagation curve a MATLAB program was developed. Herewith, first the experimental threshold values are calculated and analytically described by use of a one criteria concept. Next the whole crack propagation curve is adapted by the *Forman/Mettu*-equation. Therefore, the limits of cyclic crack propagation (threshold value and fracture toughness) are required. For the determination of the optimum fitting coefficients a search algorithm with nested intervals is used. Problematically in this context is the calculation of an error value by reason that the co-domain reaches about eight decades.

Furthermore, the crack propagation data is statistically analyzed. By dividing the co-domain in several intervals regression functions and confidence intervals are calculated for each domain. Therewith, discrete quantile curves for pretended probabilities of survival are calculated using interpolation functions. From the adaption of quantile curves with constant probability of survival by the *Forman/Mettu*-equation the corresponding fitting coefficients are determined. The statistical analysis of these fitting coefficients leads to its distribution functions.

To obtain statistically secured residual lifetimes stochastic crack propagation simulations are

performed by use of MATLAB and the analytical crack propagation software NASGRO. Therefore, the significant parameters are stochastically modeled. To identify the significant parameters of the *Forman/Mettu*-equation a sensitivity analysis was performed. The results are inconsistence to the statistical analysis of crack propagation data used in literature. For instance the fracture toughness is insignificant to the scattering of the residual lifetime and can be neglected in the stochastic crack propagation simulation. As simulation method the basic Monte Carlo simulation was used. The stochastic input vectors are determined by a random number generator. After the simulation the residual lifetimes are statistically analyzed. Thus, it is possible to obtain residual lifetimes for pretended probabilities of survival.

References

[1] M. Sander, H. A. Richard, J. Lebahn, M. Wirxel, Fracture mechanical investigations on wheelset axles. Proceedings of 16th International Wheelset Congress, Cape Town, 2010.
[2] P. Hübner, G. Pusch, U. Zerbst, Ableitung von Quantilrisswachstumskurven für Restlebensdauerberechnungen. DVM-Bericht 236, Berlin, 2004, pp. 121–130
[3] C. Theis, W. Kernbichler, Grundlagen der Monte Carlo Methoden. Institut für Theoretische Physik, TU Graz, 2002
[4] J. D. Sørensen, Notes in structural reliability theory and risk analysis. Institute of Building Technology and Structural Engineering, Aalborg University, 2004
[5] OptiSLang – Sensitivity Analysis, Multidisciplinary Optimization, Robustness Evaluation, Reliability Analysis and Robust Optimization. version 3.1, DYNARDO GmbH, Weimar, 2010
[6] J. P. C. Kleijnen, Sensitivity Analysis and Related Analysis. Schriftenreihe 706, Faculty of Economics and Business Administration, Tilburg University, 1995
[7] A. Saltelli, M. Ratto, T. Andres, F. Campolongo, J. Cariboni, D. Gatelli, M. Saisana, S. Tarantola, Global Sensitivity Analysis: The Primer. Wiley, Chichester, 2008
[8] K. Siebertz, D. van Bebber, T. Hochkirchen, Statistische Versuchsplanung: Design of Experiments (DoE). Springer-Verlag, Berlin Heidelberg, 2010
[9] NASGRO – Fracture Mechanics and Fatigue Crack Growth Analysis Software. Reference manual, version 6.0, 2009
[10] S. Beretta,M. Carboni, Experiments and Stochastic Model for Propagation Lifetime of Railway Axles. Engineering Fracture Mechanics 73, 2006, pp. 2627–2641
[11] S. Henkel, P. Hübner, G. Pusch, Zyklisches Risswachstumsverhalten von Guss-Eisenwerkstoffen – Analytische und statistische Aufbereitung für die Nutzung mit dem Berechnungsprogramm ESACRACK. DVM-Bericht 240, Berlin, 2008, pp. 251–259
[12] P. Hübner, U. Zerbst, M. Berger, T. Brecht, The Fracture of a Wobbler in a Heavy Plate Mill. Engineering Failure Analysis 16, 2009, pp. 1097–1108
[13] Wheelset Integrated Design an Effective Maintenance (WIDEM). 6th Framework Program, Sustainable Development, project number TST-CT-2005-516196, 2005
[14] W. F. Wu, C. C. Ni, A Study of Stochastic Fatigue Crack Growth Modeling Through Experimental Data. Probabilistic Engineering Mechanics 18, 2003, pp. 107–118
[15] H. Döker, Fatigue crack growth threshold: implications, determination and data evaluation, Int. J. Fatigue 19, 1997, pp. 145–149
[16] J. Lebahn, M. Sander, Untersuchungen zur Restlebensdauerberechnung mit NASGRO an eigenspannungsbehafteten, abgesetzten Hohlwellen. DVM-Bericht 242, 2010, pp. 103–112
[17] C. Ronniger, Design of Experiments & Statistics. Visual-XSel 12.0, CRGRAPH, Munich, 2012

Fatigue crack growth in a metastable austenitic stainless steel

D.F. Martelo and M.D. Chapetti*

Laboratory of Experimental Mechanics (LABMEX) Research Institute for Material Science (INTEMA)
CONICET - Faculty of Engineering, National University of Mar del Plata
J.B. Justo 4302, 7600 Mar del Plata, Argentina
* Corresponding author: mchapetti@fi.mdp.edu.ar

Abstract Fatigue crack growth in a metastable austenitic stainless steel was investigated in thin specimen under positive stress ratio. Annealed conditions were used to test the influence of the microstructure. The influence of load ratio on propagation threshold and propagation behavior was analyzed using the Elber`s closure approach, the Donald and Paris partial crack closure and the empirical Kujawski $(\Delta K \bullet Kmax)^{\alpha}$ parameter. Results show that load ratio effects are not completely explained by these approaches. It was found that the threshold of the material in the annealed condition depends on the load history, especially when the load ratio is low. It seems that the amount of martensite transformation is responsible for the observed differences in fatigue crack growth resistance.

Keywords: Fatigue, crack propagation, thresholdMetastable austenitic stainless steel

1. Introduction

In the last years, the competitiveness in the automotive sector and the compliance with higher environmental standards has forced the development of new light-weight materials. One of the materials that fulfill with the exigencies of automotive sector are the metastable stainless steels because of they combine good corrosion resistance with versatile mechanical properties [1,2]. Due to his high ultimate strength, metastable stainless steel allows the use of components of less thickness. One of the more important aspects in the automotive sector is the design again fatigue damage.Traditionally, the approach to fatigue design based on the cyclic stress range ΔShas been used [3]. However, thin walled light components must be designed using more conservative approach, basedmainly in linear elastic fracture mechanics.

AISI 301LN steels belong to the metastable austenitic steels and have an austenitic structure in annealed conditions which confers them an excellent ductility. Besides, they have an extraordinary strain hardening because of the transformation of austenite to martensite during deformation. This particular class of steels are called TRIP steels [4]. Significant researches have been conducted on the fatigue behavior of TRIP steels [4-12], and depending of the testing condition, different behaviors have been reported. In the high cycle (HCF) regime, i.e. test under load control or test under K control, the conclusion of the studies show that exists a relationship between the martensitic transformation around the crack tip and the decrease in the fatigue crack growth rate (FCGR) [4-8,10,12], with the exception of reference [9], where it attributed the decrease in the FCGR to the slip characteristic rather than the martensitic transformation. Until now various mechanisms have been proposed trying to explain how the martensitic transformation can affect the FCGR. However, there is no mechanism that can explain satisfactorily the effect of the martensitic transformation over the FCGR having accounted the entire picture of the stress state.

The most recurrent mechanism to explain the crack growth retardations in fatigue is the crack closure, which was introduced by Elber in 1971 [13], after observing that fatigue crack surfaces contact under cyclic tensile loading. Even direct measurements have not been achieved, is felt that the martensitic transformation cause crack closure because of the involved volume expansion of 1-4 % [14]. The first mechanism used to explain the premature contact between the faces of the crack is the plasticity induced crack closure. However, others mechanisms induced crack closure

have been identified, as oxide induced crack closure or roughness induce crack closure. The vast majority of mechanisms to explain crack closure are explained, for instance, in the book "Fatigue of Material" written by S.Suresh [3]. Traditionally, in some expression obtained from experimental investigations have been indicated that the crack opening stress intensity factor K_{op} is only function of the stress ratio R [13,15]. However, some authors recognized that K_{op} is also influenced by the specimen geometry, the stress state, the stress intensity factor range and the environment. Some models have been theoretically developed in order to explain how the crack opening stress is influenced by the stress ratio R, the maximum applied stress or load level P_{max}, and the crack front constraint (plane stress or plane strain behavior).

In this work the fatigue crack growth behavior of an annealed metastable austenitic stainless steel was investigated in thin specimen under positive stress ratio. The influence of load ratio on propagation threshold and propagation behavior was analyzed using the Elber`s closure approach, the Donald and Paris partial crack closure approach and the empirical Kujawski $(\Delta K \bullet Kmax)^{\alpha}$ parameter. Results are analyzed in order to look for answers about the influence of the martensitic transformation on the fatigue behavior of this kind of steel and for a unique relationship between fatigue crack propagation rate and the applied driving force.

2. Experiments

The material utilized in the current study was an annealed austenitic stainless steel AISI 301LN provided by OCAS NV, Arcelor-Mittal R&D Industry Gent (Belgium) The chemical composition of this material is shown in Table 1. The microstructure of the material is shown in figure 1. The α'martensite content was calculated by mean of X-ray diffraction and results showed that the martensite content was less than 2%.

Table 1.Chemical Composition

AISI 301LN	FE	Cr	Ni	Mo	C	Si	P	S	Mn	Cu
Annealed	bal	17.94	6.30	0.18	0.016	0.513	0.032	0.005	1.481	0.135

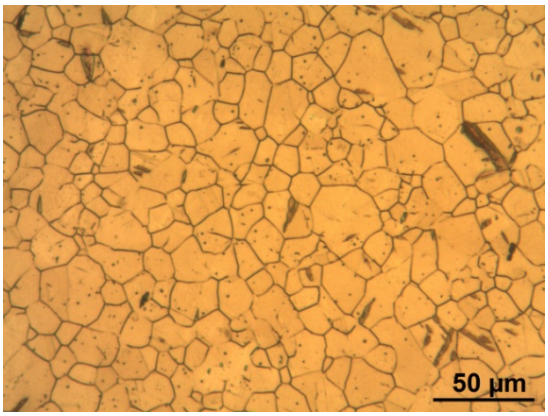

Figure 1.Microstructure of annealed AISI 301LN stainless steel

Table 2.Mechanical and thermo-mechanical properties

σ_{ys}	σ_{UTS}	Elongation (Pct)	Ms (^{o}C)	M_{d30} (^{o}C)	M_d (^{o}C)
343 MPa	973 MPa	39,39	-66.015	49.042	100*

*For AISI 301 stainless steel.

Single edge notch test specimen (SENT) of 1 mm thickness and a width of 35 mm and 40 mm, were

machined with the rolling direction parallel (T-L) and perpendicular (L-T) to the notch. The specimens were fatigued in air and at room temperature.

The FCGR test were conducted in an Instron‘s servo-hydraulic machine with closed loop to computers for automatic test control and data acquisition. The crack extension was measured with a krak-gages® technique, which is principally an indirect DC potential measurement procedure. The krag-gages® theory is explained in reference [16]. For instance, the crack gauge KG-B20, whose full scale is 20 mm, has a sensitivity of measurement to crack extension that is better than 0.02mm [17]. The crack extension was also measured using the compliance technique by means of a clip gage in the crack mouth and a strain gauge fixed in the back surface.

The crack closure measurementwere made by using a sampling rate of 400 data pairs (load and displacement) per cycle according to some of the recommendations made by Song et al. [18]. The signal noise was reduced by using low-pass digital filters [19]. The determination of the opening force was done by comparing slope segments of 10 percent of the load- displacement data with the linear region of the load-displacement curve.

The fatigue tests were performed at a frequency of 20 Hz. Three different values of load ratio R ($=\sigma_{min}/\sigma_{max}$) 0.1, 0.3, 0.5, 2 different stress level at the same load ratio, and 3 decreasing ΔK at different load ratio were employed. For ΔK decreasing test the rate of force shedding with increasing crack size was according to the ASTM standard (20). The details of the experiments are listed in table 3.

The martensite transformation around the crack tip was observed by optical microscopy. The material was ground in the surface where the fatigue crack was going to appear with SiC emery paper up to a roughness of 1200 grit and then polished. Because of the mechanical grinding can induce martensitic transformation,the material was electro-polished with a solution consisting of 5vol% perchloric acid and 95% ethanol at 45V for 15 s. The martensitic phase was revealed by chemical etching in a solution of 100 ml ethanol, 20 ml HCl, 1.5 g K_2S2O_5 and 2 g $NH_4F{\cdot}HF$. The electro-polished was used until no peak (100) (200) (211) (α`martensite peak according to M. Karimi et al [21]) was found by X-ray diffraction.

Table 3.Details of test configuration

	Specimen	R ($\sigma_{min}/\sigma_{max}$)	Load level [N] (P_{max}- P_{min})	Notch [mm]	Test Type	w [mm]	C [mm^{-1}]
1	NL2	0.5	2625	8.729	Constant amp. load	35	-
2	NL3	0.1	2625	8.600	Constant amp. load	35	-
3	NL4	0.1	1815	13.817	Constant amp. load	35	
4	NL6	0.3	1890	14.020	Constant amp. load	35	-
5	NL7	0.7	2625	8.927	Constant amp. load	35	-
6	NL9	0.1	variable	9.777	ΔK decreasing	40	-0.08
7	L3G	0.5	variable	11.55	ΔK decreasing	40	-0.065
8	NNL4	0.7	variable	9.088	ΔK decreasing	35	-0.055
9	NNL7	0.7	variable	8.897	ΔK decreasing	35	-0.09
10	NNL1	0.5	variable	8.912	ΔK decreasing	35	-0.08

3. ΔK expressions

In situations where the linear elastic fracture mechanics theory (LEFM) is valid the crack driving force is traditionally represented by using the stress intensity factor ΔK. For the specimen type used in this investigation and for the grid constraint of our test‘s machine, the stress intensity factor for the specimen of this investigation is not tabulated in books, therefore the finite element method (FEM) was employed to obtain the value of the stress intensity factor. Figure 2 shows the ΔK solutions used for the two configurations that have been used for test. The typical solution available in literature for SENT specimens is also shown and the difference in the given *K* values for a given crack length can be clearly observed. The curve was normalized by dividing the stress intensity factor by the applied stress and the crack length by the specimen length.

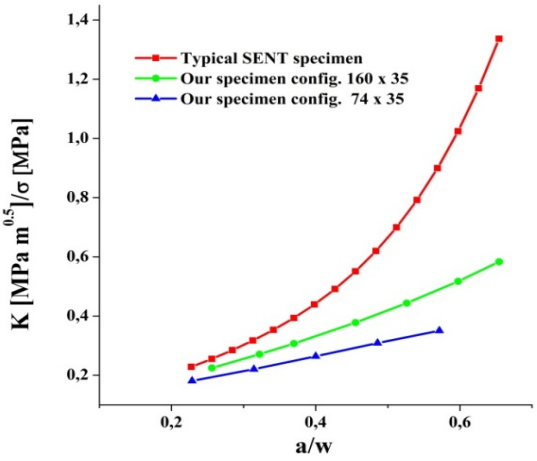

Figure 2. Stress intensity factor obtained by finite element models for the used configurations.

4. Experimental Results

4.1. Results using the range of the stress intensity factor

The fatigue crack growth rates of austenitic stainless steel 301LN at room temperature, at 3 different load ratios and different load levels are shown in Fig. 3(a). For all test conditions the crack growth rate increases with increase in ΔK. The curves show a trend that can be considered linear with positive and constant slope. The influence of load level is negligible, in spite of we found some papers that mention that some austenitic stainless materials in specimen with thin section [7,22] suffer the influence of stress level on fatigue crack growth rate.

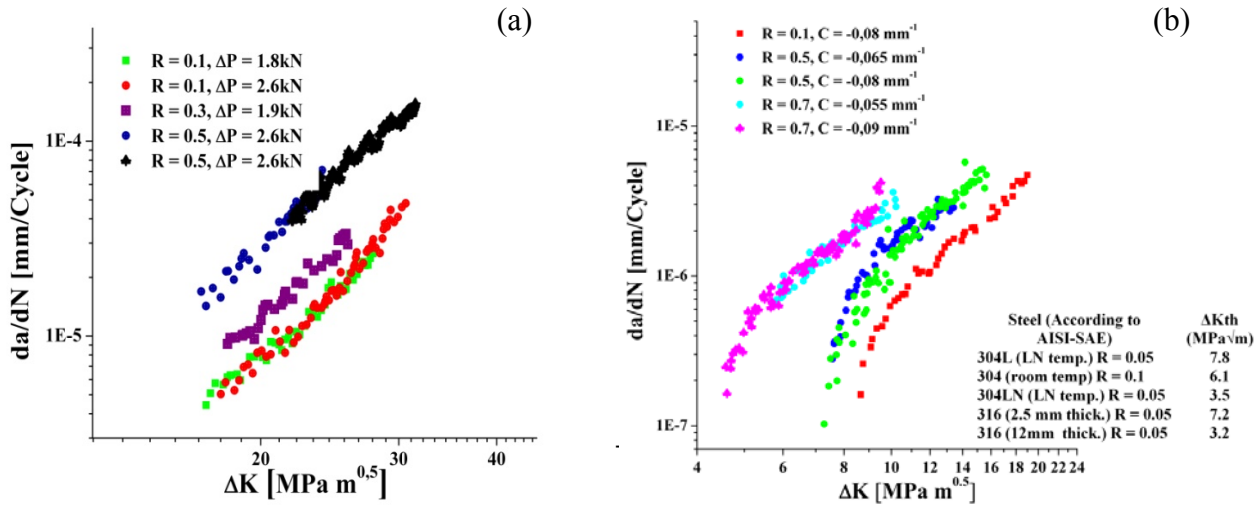

Figure 3. Fatigue crack growth rate vs stress intensity factor range at different load ratios (a) in the stable crack propagation region and (b) in the near threshold region.

The influence of R values on near threshold crack growth rates is shown in Fig. 3(b). It can be seen how the ΔK_{th} decreases with the increment in load ratio. The values of ΔK_{th} are relatively high, especially at R = 0.1 and R = 0.5, in comparison with other austenitic stainless steel alloys or even other steel alloys. However the results are not surprising, according to the results found for other austenitic stainless steel that are shown in the table of Fig.3(b), where it can be observed that materials with martensitic transformation and/or in conditions of plane stress, produce high thresholds.

4.2. Results using the effective stress intensity factor

The fatigue crack growth rate was plotted also by using the conventional Elber's approach and defining the effective stress intensity range as:

$$\Delta K_{eff} = K_{max} - K_{op} \tag{1}$$

Fig. 4 shows the obtained results. They show that in the stable region (far from thresholds) the crack closure is practically constant in the total range of crack propagation for the same test. It is only observes the same average value of $S_o/S_{max} \approx 0.35$ for both cases at low load ratio (R = 0.1 and 0.3). The analysis was based in the work of J. Song et al [18], from which the offset criterion that better estimate load ratio effects in the Paris region is 4% (this analysis will be detailed in a paper that will be soon submitted for publication).

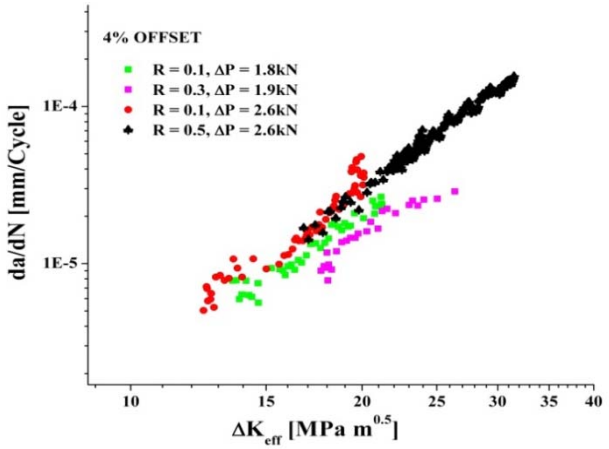

Figure 4. Fatigue crack growth rate as a function of the effective stress intensity factor

Fig. 5 shows the correlation obtained using Eq. (1) for the near threshold behavior. It shows that with the use of crack closure concepts the curves move closer each other but it is still not possible to join them in a unique curve. In this region of slow growth rate the relation of K_{op}/K_{max} increase with decreasing the range of the stress intensity factor (approaching the threshold).

4.3. Results using the Donald`s effect

The original concept of crack closure indicates that the crack cannot grow if the crack is not fully open. However Donald and coauthors have shown that the interference of crack faces does not

shield completely the crack tip from fatigue damage [23]. Based on this concept, Donald proposed to calculate an effective stress intensity factor range as:

$$\Delta K_{2/PI} = \Delta K_{app} - \frac{2}{\pi}\left(K_{op} - K_{min}\right) \quad (2)$$

This is one of several methods that have been used to estimate ΔK_{eff}, although this method distinguishes over other because of his simplicity and because has provided successful correlation of the crack growth rate data for aluminum alloys. Fig. 6 shows the fatigue crack growth rate as a function of the effective stress intensity factor proposed by Donald. It can be observed that for our analyzed material the Donald`s effect does not provide a better correlation of the R-ratio effects than the traditional ΔK_{eff} calculated by using the Eq. (1).

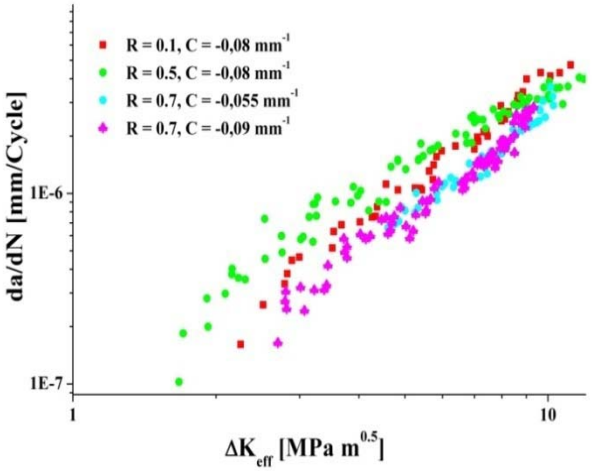

Figure 5. Fatigue crack growth rate as a function of the effective stress intensity factor

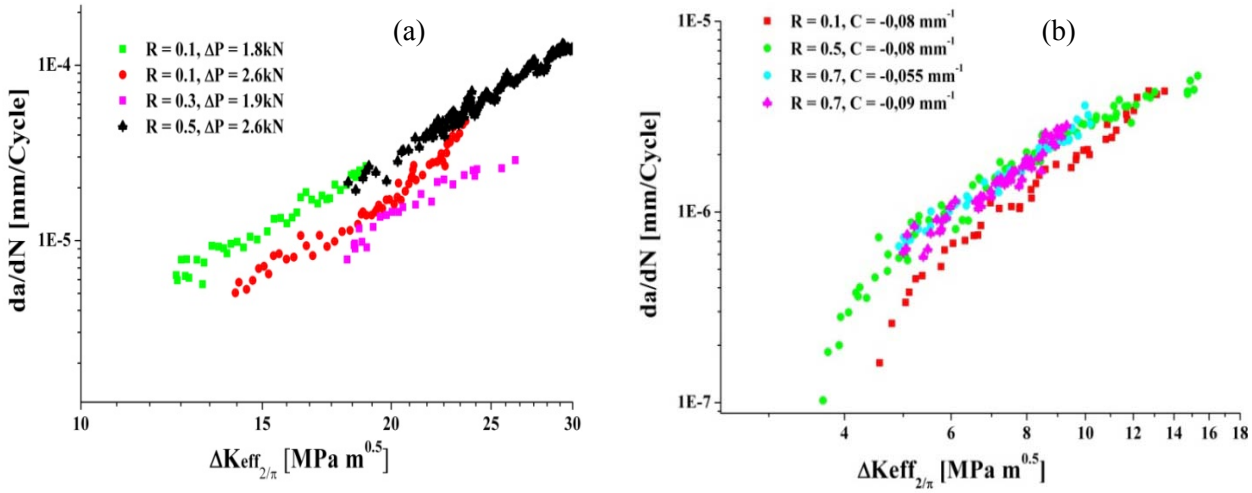

Figure 6. Fatigue crack growth rate as a function of the effective stress intensity factor proposed by Donald et al. (a) in the stable crack propagation region and (b) in the near threshold region.

4.3. Results using the Kujawski`s Parameter

To explain the load ratio effects in fatigue crack growth, and because of the inconsistency in the measurement of crack closure and the difficulties to determine the fatigue damage associated to a crack partially open, Kujawski proposed a crack driving force parameter that is calculated by using

K_{max} and ΔK [24] as follow:

$$K^* = (K_{max})^{\alpha}(\Delta K)^{1-\alpha} \tag{3}$$

Where ΔK is the positive part of the range of the applied stress intensity factor. This parameter is characterized, among other things, by the use of two separate variables that could describe unambiguously the load cycle at least if the load ratio is positive and K_{max} is greater than 0, like in the present case. The α value is a factor that determines the importance of K_{max} or ΔK and it is calculated by means of the following expression:

$$\alpha = \frac{log(\Delta K_1/\Delta K_2)}{log((1-R_1)/(1-R_2))} \tag{4}$$

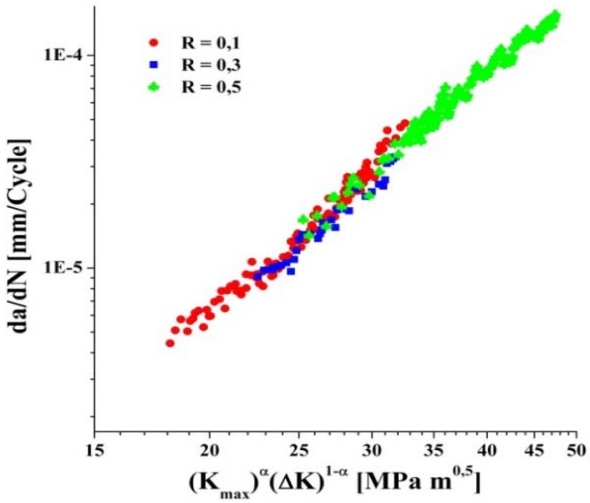

Figure 7. Fatigue crack growth rate as a function of the Kujawski`s parameter with α equal to 0.6.

Using Eq. (4) the average α value, for the AISI 301 LN in the paris region, was equal to 0.6. This was the same α value found for the metastable austenitic stainless steel AISI 304L tested at 77K [8], although in that case the scatter was higher. Fig. 7 shows the correlation obtained by plotting the fatigue crack growth rate vs the Kujawski`s parameter far from the threshold region. It is seen that kujawski`s parameter can unify the curves of the test performed to constant load ratio into a master curve that can be described by using Eq (5) with C = 1.33×10^{-11} [mm/cycle MPa $m^{0.5m}$] and m = 3.619.

$$\frac{da}{dN} = C(\Delta K^{1-\alpha}K_{max}^{\alpha})^m \tag{5}$$

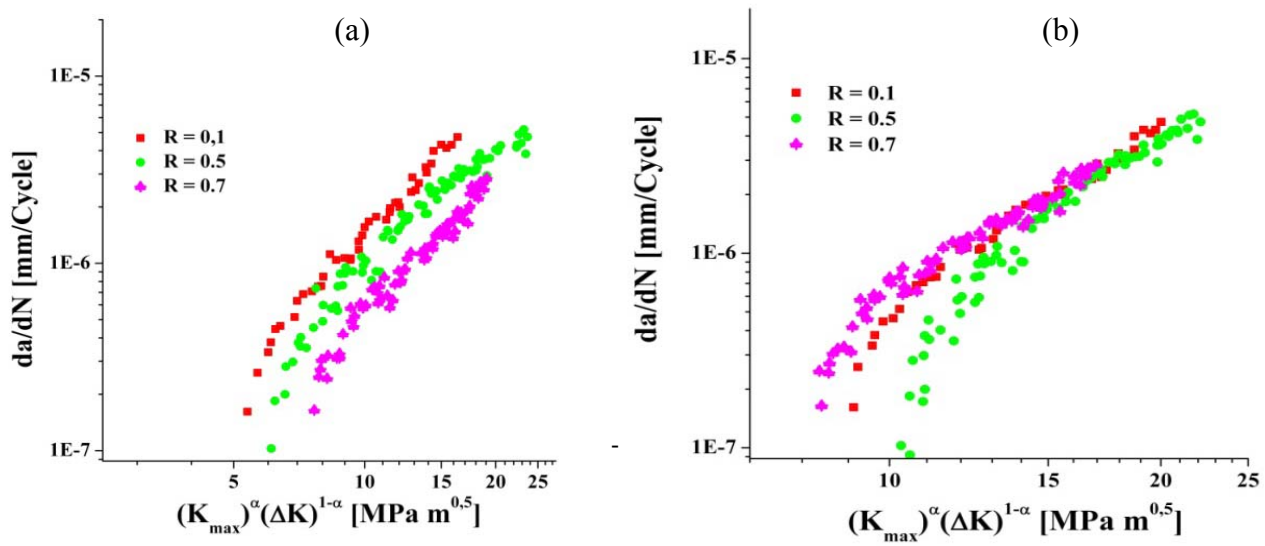

Figure 8.Fatigue crack growth rate as a function of the Kujawski`s parameter with (a) α equal to 0.6 and (b) α equal to 0.5

The same parameter α that was found to correlate the fatigue crack growth rate curves in Fig. 7 has been used to analyze the near threshold region, and results are shown in Fig 8(a). It can be observed that in this case the approach cannot success as in Fig. 7. Fig.8(b) shows results obtained by using an α value equal to 0.5. Even though results seem to be somehow better, the approach does not success.

It is interesting to note that the value of α parameter calculated for the AISI 301LN decrease with the decrease of the stress intensity factor range and/or with the decrease of the martensite content. This result agree with those of the work of S.Kalnaus et al [11], were they estimated an α parameter equals to 0.36 for an austenitic steel without transformation. According to our measurements, the martensite content decreases in the near threshold region of crack propagation with respect to measurement made in the relative high ΔK fatigue crack propagation region. It is clear that further and more detailed analyses are needed in order to explain the influence of the load ratio R in this region.

5. Concluding remarks

Fatigue crack growth of aannealed metastable austenitic stainless steel was investigated in thin specimen under positive stress ratio. The influence of load ratio on propagation threshold and propagation behavior was analyzed using the Elber`s closure approach, the Donald and Paris partial crack closure and the empirical Kujawski $(\Delta K \bullet Kmax)^{\alpha}$ parameter.

Results show that load ratio effects are not completely explained by these approaches. The crack closure effect approaches (both, the traditional Elber approach and its modification by Donald and Paris) cannot explain the influence of the stress ratio R on the fatigue crack propagation rate on the analyzed thin specimens of a TRIP material.

The two parameter crack driving force $(\Delta K \bullet Kmax)^{\alpha}$, with $\alpha = 0.6$, seem to be a proper parameter to uniquely explain the fatigue behavior of the analyzed TRIP steel for positive R ratios far from the threshold region. However, it seems to fail in the threshold region, where the crack closure levels are important, and a unique α value cannot be found. So, further investigation should be carried out in order to explain these results.

Acknowledgements

Authors wish to express their gratitude to the funding provided by CONICET (National Research Council), and by Agencia Nacional de Promoción Científica y Tecnológica (ANPCyT), Argentina (PICT2010 Nro.0379).

References

[1] S. Lamb, Handbook of Stainless Steels and Nickels Alloy, CASTI Publishing Inc, Edmonton, 2001.

[2] H. Hallberg, L. Banks-Sills, M. Ristinmaa, Crack tip transformation zones in austenitic stainless steel. ENG FRACT MECH, 79 (2012) 266-280.
[3] S. Suresh, Fatigue of Materials, Cambridge University Press, Cambridge, 1998.
[4] G.R. Chanani, S.D. Antolovich, W.W. Gerberich, fatigue Crack Propagation in Trip Steels. METALL MATER TRANS B, 3 (1972) 2661 - 2672.
[5] A.G. Pineau, R.M. Pelloux, Influence of Strain-induced Martensitic Transformation on fatigue Crack Growth rates in Stainless Steels. METALL MATER TRANS B, 5 (1974) 1103-1112.
[6] E. Hornbogen, Martensitic Transformation at a Propagating Crack. ACTA METALL MATER, 26 (1978) 147-152.
[7] G. Schuster, C. Altstetter, Fatigue of Annealed and Cold Worked Stable and Unstable Stainless Steels. METALL TRANS A, 14 (1983) 2077-2084.
[8] Z. Mei, J.W. Morris, Influence of deformation-induced martensite on fatigue crack propagation in 304-type steels. METALL TRANS A, 21 (1990) 3137-3152.
[9] W.Y. Maeng, M.H. Kim, Comparative study on the fatigue crack growth behavior of 316L y 316LN stainless steel: Effect of microstructure of cyclic plastic strain zone at crack tip. J NUCL MATER, 282 (2000) 32-39.
[10] S. Biswas, S. Sivaprasad, N. Narasaiah, S. Tarafder, P.C. Chakraborti, Load history effect on FCGR behaviour of 304LN stainless steel. INT J FATIGUE, 29 (2007) 786-791.
[11] S. Kalnaus, Y. Jiang, A.K. Vasudevan, An experimental investigation of Fatigue crack Growth of stainless steel 304L. INT J FATIGUE, 31 (2009) 840-849.
[12] X. Cheng, R. Petrov, L. Zhao, M. Janssen, Fatigue Crack growth in TRIP steel under positive R - ratios. ENG FRACT MECH, 75 (2008) 739-749.
[13] W. Elber, The significance of fatigue crack closure, in: M.S. Rosenfeld (eds.), Damage tolerance in aircraft structures ASTM STP 486, Philadelphia, 1971, pp. 230-242.
[14] P. Hedstrom, Deformation induced martensitic transformation of metastable stainless steel AISI 301, Lulea, Lulea University of Technology, 2005.
[15] J. Schijve, Some formulas for the crack opening stress level. ENG FRACT MECH, 14 (1981) 461-465.
[16] H.R. Hartmann, R.W. Churchill. KRAK-GAGE: A new Transducer for Crack Growth Measurement. Presented at the Society for Experimental Stress Analysis Fall Meeting, sponsored by the Society for experimental Stress Analysis, 1981.
[17] TTI Division, Hartrun Corporation. Krak-gage Accuracy and Resolution. Chaska Minnesota : s.n., 1981. KRAK-TIP No. 8109-1.
[18] J.H. Song, Y.I. Chung, Improvement of ASTM compliance offset method for precise determination of crack opening load. INT J FATIGUE, 31 (2009) 809-819.
[19] C.Y. Kim, J.H. Song, An automated procedure for determining crack opening level from differential displacement signal data, INT J FATIGUE, 15 (1993) 477-489.
[20] E647-08E01, standard Test Method for Measurement of fatigue Crcak Growth Rates. Annual Book of ASTM Standards ASTM. Philadelphia : s.n., 2010.
[21] M. Karimi, A. Najafizadeh, A. Kermanpur, M. Eskandari. Effect of martensite to austenite reversion on the formation of nano/submicron grained AISI 301 stainless Steel. MATER CHARACT, 60 (2009) 1220-1223.
[22] D.G. Rickerby, P. Fenici, Fatigue Crack Growth in thin section Type 316 Stainless Steel. ENG FRACT MECH, 19 (1984) 585-599.
[23] P. Paris, H. Tada, J.K. Donald, Service load fatigue damage — a historical perspective. INT J FATIGUE,21 (1999) S35-S46.

[24] D. Kujawski, A fatigue crack driving force parameter with load ratio effects. INT J FATIGUE, 23 (2001) S239-S246.

Creep-fatigue interaction model for crack growth of nickel-based superalloys with high temperature dwell time

Hongqin Yang [1,*], Rui Bao[2], Jiazhen Zhang[1]

[1] Beijing Aeronautical Science & Technology Research Institute of COMAC, Beijing 100083, PR China
[2] Institute of Solid Mechanics, Beihang University (BUAA), Beijing 100191, PR China
* Corresponding author: yanghongqin@comac.cc

Abstract A three-term crack growth model was developed by adding a creep-fatigue interaction term to the traditional linear superposition law. It is based on the hypothesis that the maximal creep-fatigue interaction occurs when creep and fatigue crack growth rates are comparable. Thereby a novel exponential form of interaction intensity factor was proposed. In order to verify the model, the creep-fatigue crack growth behaviour of a nickel-based powder metallurgy superalloy (FGH97) was experimentally investigated. Creep-fatigue crack growth rates were obtained at 750 °C with various dwell times. Comparison of the crack growth rates between fitted and measured values at 0s, 90s, 450s and 1500s dwell times show great agreement. Encouragingly, excellent predictive ability of the model was verified by the experiment at 25s dwell time. Furthermore, to test the applicability of the interaction law on other materials, experimental data of two additional superalloys from references, namely Alloy 718 and Hastelloy® X, were used to fit the model. The results are also satisfactory.

Keywords Crack growth rate modelling, high temperature, dwell time, nickel-based superalloys

1. Introduction

As for the quantitative description of creep-fatigue crack growth rate, several models have been developed. Tong et al. [1] proposed single term models, in which creep damage is taken into account by modifying the coefficient of the basic fatigue model. Other researchers [2] have used an alternative approach. They assumed that creep-fatigue behaviour is governed by competing mechanisms of creep and fatigue crack growth, and whichever gives a higher growth rate dominates the entire crack growth process. A more universal model is based on simple linear superposition of creep crack growth and fatigue crack growth [3]. However, such methods tend to overlook the effect of creep-fatigue interaction, which cannot be ignored by many materials.

For this reason, a three term model considering the interaction effect separately was referred in [4], expressed in the form of linear superposition of fatigue crack growth rate, creep crack growth rate and their interactions. However, the quantitative relationship between the creep-fatigue interaction and the loading condition for certain materials is still an open question. The work of Grover and Saxena [5] indicated that the intensity of the creep-fatigue interaction is directly related to the relative sizes of the creep zone and cyclic plastic zone.

Recently, the authors [6] presented an exponential formed interaction intensity factor to help describing the interaction effect. The accuracy of the model proposed was experimentally confirmed by a nickel-based superalloy FGH97. The study presented here is a continuation of that work and applicability of the model on other materials was verified.

2. Creep-fatigue interaction model

The simple linear superposition equation, as shown in Eq. (1), is preferentially considered to model the creep-fatigue crack growth rate[3].

$$\frac{\mathrm{d}a}{\mathrm{d}N} = \left(\frac{\mathrm{d}a}{\mathrm{d}N}\right)_{\text{fatigue}} + \left(\frac{\mathrm{d}a}{\mathrm{d}N}\right)_{\text{creep}} \tag{1}$$

where $(\mathrm{d}a/\mathrm{d}N)_{\text{fatigue}}$ denotes the fatigue crack growth rate, including the effect of environment (oxidation for example). It can be achieved by Eq. (2) according to the Paris law. $(\mathrm{d}a/\mathrm{d}N)_{\text{creep}}$ represents the creep crack growth rate. Selecting K as the creep crack growth dominant parameter due to its practicability, $(\mathrm{d}a/\mathrm{d}N)_{\text{creep}}$ is thereby expressed by Eq. (3).

$$\left(\frac{\mathrm{d}a}{\mathrm{d}N}\right)_{\text{fatigue}} = C(\Delta K)^n \tag{2}$$

$$\left(\frac{\mathrm{d}a}{\mathrm{d}N}\right)_{\text{creep}} = A(K_{\max})^m t_{\mathrm{h}} \tag{3}$$

where $K_{\max} = \Delta K / (1 - R)$, C, n, A and m are material related parameters.

In order to take the creep-fatigue interaction into account, a three-term crack growth model was developed by adding a third-term to the traditional linear superposition equation, see Eq. (4).

$$\frac{\mathrm{d}a}{\mathrm{d}N} = \left(\frac{\mathrm{d}a}{\mathrm{d}N}\right)_{\text{fatigue}} + \left(\frac{\mathrm{d}a}{\mathrm{d}N}\right)_{\text{creep}} + \left(\frac{\mathrm{d}a}{\mathrm{d}N}\right)_{\text{interaction}} \tag{4}$$

where $(\mathrm{d}a/\mathrm{d}N)_{\text{interaction}}$ denotes the influence of creep and fatigue interaction on the crack growth rate, and the expression should be discussed.

As Grover and Saxena [5] indicated, at short t_{h}, the creep zone size is small relative to the cyclic plastic zone size during all the crack growth period since the creep zone grows very slowly, resulting in fatigue dominating cracking. At long t_{h}, the creep zone grows larger than cyclic plastic zone size, and the crack growth rate becomes time dependent. In between, the cracking will rely on both creep and cyclic plastic damage. The most significant interaction occurs when creep and cyclic plastic damage size are comparable. Also provided in their study is that the ratio of the creep and cyclic plastic zone sizes is dependent on the dwell time t_{h}, load ratio R and the material related parameters. This implies that the creep fatigue interaction should also depend on these parameters. Based on these, a factor, η, was proposed to characterize the intensity of the creep and fatigue interaction, as shown in Eq.(5).

$$h = \exp(- p_1(\ln f + p_2 \mathrm{D}K + p_3)^2) \tag{5}$$

where, p_1, p_2 and p_3 are material related parameters, $f = (T+t_h)^{-1}$ is the frequency of the load waveform and T is the load period of the baseline triangular waveform. It can be seen that there are two extreme cases. On one extreme, η approaches zero, indicating that there is almost no interaction between creep and fatigue. For the other extreme case in which η approaches 1, it implies that the interaction reaches the most significant.

Accordingly, taking $D(\Delta K)^q$ as the basic term, $(da/dN)_{interaction}$ can thereby be expressed as following:

$$(\frac{da}{dN})_{interaction} = D(\Delta K)^q \cdot h \tag{6}$$

where $K_{max} = \Delta K / (1 - R)$, D and q are material related parameters.

3. Crack growth experiment on FGH97

The material in this study is a nickel based PM superalloy, named FGH97, taken from a turbine disk. It was strengthened by the formation of γ′ precipitates based on Ni_3Al and received both the solid-solution-strengthening and age-hardening treatment. The nominal chemical composition is as follows (wt%): C 0.02-0.06, Cr 8.0-10, Mo 3.5-4.2, W 5.2-5.9, Al 4.8-5.3, Ti 1.6-2.0, Co 15.0-16.5, Nb 2.4-2.8, Hf 0.1-0.4, Mg ≤ 0.02, Zr ≤ 0.015, B ≤ 0.015, Ce ≤ 0.010 and the balance nickel[7]. Compact tension (CT) specimens were employed, where width W = 50 mm and initial crack length a_0 = 22.5 mm. More details can be found in Ref.[6].

The baseline loading cycle is a triangular wave of load ratio R = 0.05. Different dwell time t_h = 90s, 450s and 1500s at the maximum load are superimposed to the baseline loading cycle to obtain a trapezoidal creep-fatigue loading condition, see Fig. 1. The baseline triangular fatigue loading cycle can be reasonably regarded as t_h = 0s reasonably. A typical service temperature of 750°C was conducted.

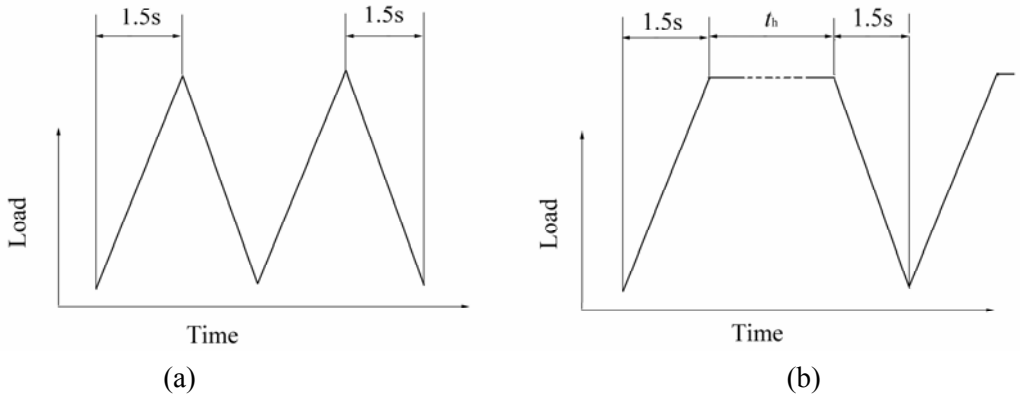

Figure 1. Schematic of loading waveforms (a) Triangular; (b) Trapezoidal

In order to clarify the creep-fatigue interaction, the da/dN vs. f data of the present alloy at four specified ΔK in log-log scale is plotted in Figure 2(a). For pure fatigue loading, according to Eq. (2), the crack growth rate showing no influence by f, therefore, ln(da/dN) vs. ln(f) curves should be parallel to the abscissa f at specified ΔK. And for pure creep crack growth, according to Eq. (3), the da/dN is proportional to t_h at certain stress level, hence, the gradients for ln(da/dN) vs. ln(f) curves should be -1. Thereby, the solid lines in Figure 2(a), calculated by Eq. (1), denote the simple linear superposition of the fatigue and creep components. The experimental data at four specified ΔK are also provided in the figure by various symbols.

It can clearly be seen from that, first, the t_h effect on da/dN is nonlinear in the log-log scale. With the t_h increases, the effect is initially increased and then decreased, especially at low ΔK stage. Second, the experimental data in the medium ΔK and t_h are much greater than the solid lines. Comparisons between the fitted and experimental crack growth rates are presented in Figure 2(b). The results show good agreements at all four dwell times, ignoring slight deviation in the quite low ΔK and ln(f) stage. Thereby, interaction intensity factor η, as expressed in Eq.(5), can depict this interaction satisfactory.

Comparisons between the fitted and experimental crack growth rates are presented in Figure 2(b). The results show good agreements at 0s, 90s, 450s and 1500s. Furthermore, to verify the predictive capability of the model, additional crack growth rate for t_h = 25s is computed by Eq. (4) and are compared with the experimental data, also shown in Figure 2(b). Excellent correlation between the predicted and observed growth rates was obtained. It appears that the model can provide accurate descriptions of the influence of t_h and ΔK on the crack growth behaviour at 750°C.

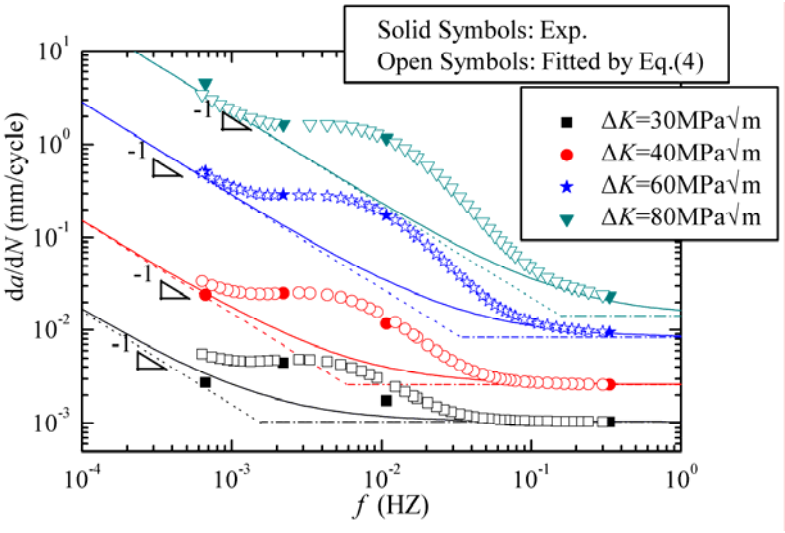

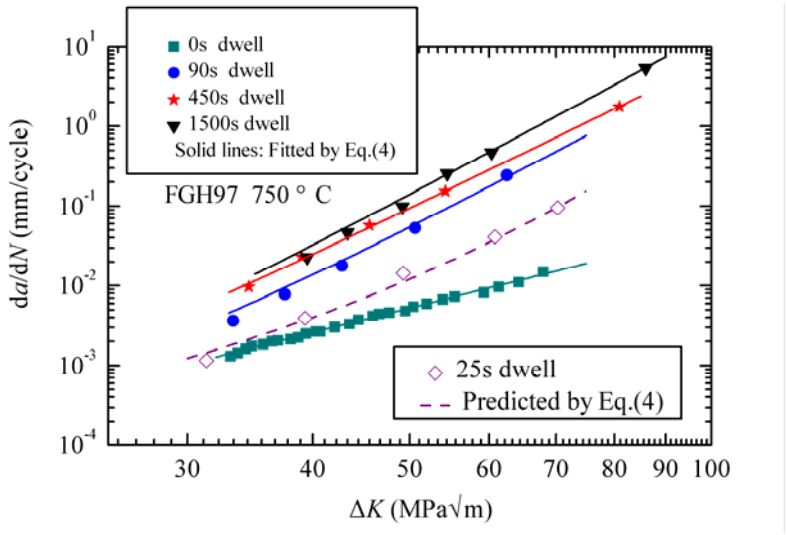

(a) d*a*/d*N* versus *f* (b) d*a*/d*N* versus Δ*K*

Figure 2. Comparisons between the fitted and experimental d*a*/d*N* of FGH97 at 750 °C

4. Applicability on Alloy 718 and Hastelloy® X

In order to verify the applicability of the model on other materials, two additional nickel-based superalloys from the references, namely Alloy 718 and Hastelloy® X, were analysed. Alloy 718 is a wrought polycrystalline nickel based superalloy with a large amount of Fe and Cr. The crack growth experiments [8] were conducted on Kb-type specimens with rectangular cross sections of 4.3×10.2 mm. Hastelloy® X alloy is a solid-solution strengthened nickel-based superalloy that combines exceptional oxidation resistance, good fabricability, and excellent high-temperature strength. And the experiments [9] were conducted on CT specimen with thickness of 3.2 mm, height of 61.0 mm and width of 63.5 mm. Here, two temperatures with three or four dwell times were involved for each material. Details of the experiments can be found in references [8] and [9], respectively.

Figure 3 and Figure 4 present the comparisons between the fitted and experimental d*a*/d*N* of Alloy 718 and Hastelloy® X, respectively. Where, the solid lines in the figures were fitted by Eq. (4). Encouragingly, the results show excellent correspondences for these two alloys.

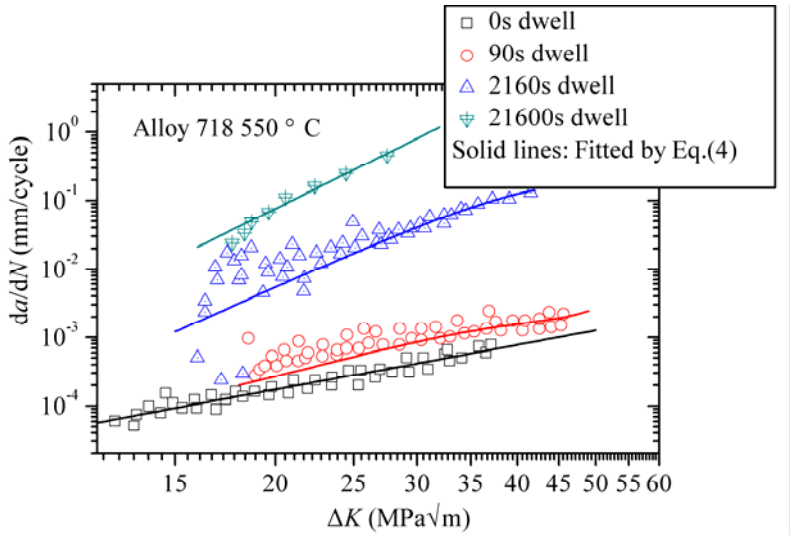

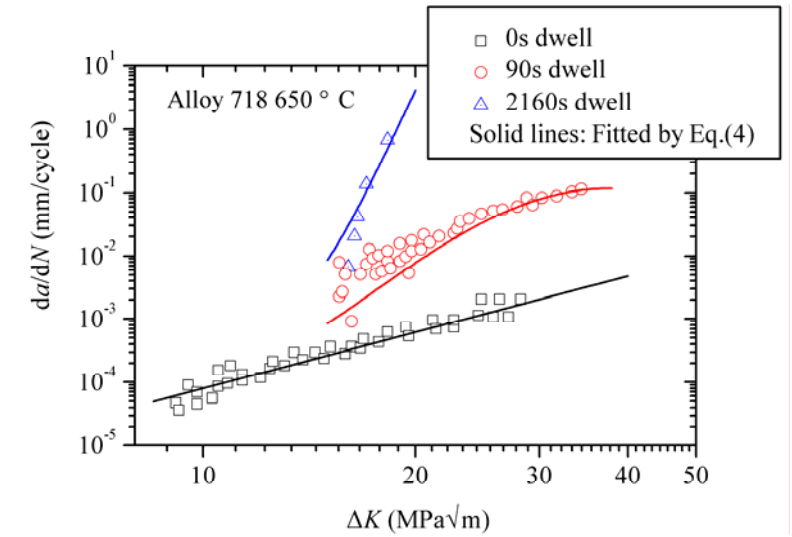

(a) 550 °C (b) 650 °C

Figure 3. Comparisons between the fitted and experimental d*a*/d*N* of Alloy 718

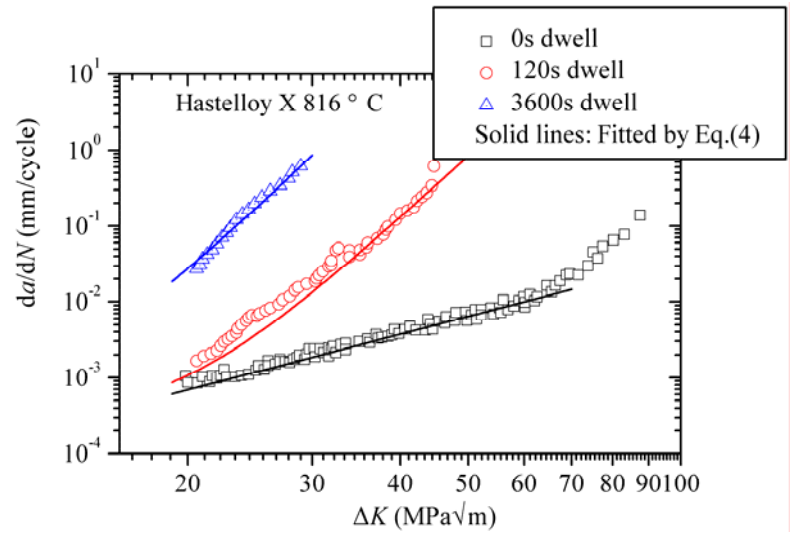

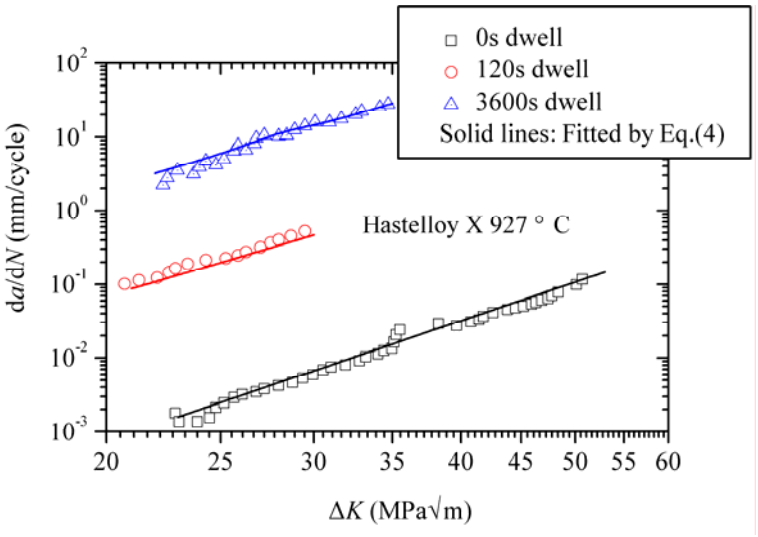

(a) 816 °C (b) 927 °C

Figure 4. Comparisons between the fitted and experimental da/dN of Hastelloy® X

5. Summary

Key results and conclusions drawn from this investigation are summarized below: (1) The exponential form of interaction factor, η, could successfully characterize the intensity of the creep and fatigue interaction. (2) The established three-term crack growth model is capable of accurately representing and predicting the creep-fatigue crack growth behavior of FGH97. (3) The applicability of the three-term model on the nickel-based superalloys Alloy 718 and Hastelloy® X is satisfactory.

References

[1] J. Tong, S. Dalby, et al, Creep, fatigue and oxidation in crack growth in advanced nickel base superalloys. Int J Fatigue, 23(2001), 897-902.

[2] R. Ohtani, T. Kitamura, et al, High-temperature low cycle fatigue crack propagation and life laws of smooth specimens derived from the crack propagation laws, in: H.D. Solomon, G.R. Halford, et al (Eds.), Low Cycle Fatigue, ASTM STP 942, Philadelphia, 1988, pp. 1163-1180.

[3] F. Djavanroodi, Creep-fatigue crack growth interaction in nickel base supper alloy. American Journal of Applied Science, 5(2008), 454-460.

[4] F. Z. Xuan, S. D. Tu, et al., Time-dependent fatigue fracture theory and residual life assessment techniques for defective structures. Chinese Journal of Advances in Mechanics, 35(2005), 391-403.

[5] P. S. Grover, A. Saxena, Modelling the effect of creep-fatigue interaction on crack growth. Fatigue Frac Eng M, 22(1999), 111-122.

[6] H.Q. Yang, R. Bao, et al., Creep-fatigue crack growth behaviour of a nickel-based powder metallurgy superalloy under high temperature. Eng Fail Anal, 18(2011), 1058-1066.

[7] Y. Zhang, Y. W. Zhang, et al, Heat treatment processes and microstructure and properties research on P/M superalloy FGH97. Journal of Aeronautical materials, 28(2008), 5-9.

[8] M. HÖrnqvist, T. Månsson, et al., High temperature fatigue crack growth in Alloy 718-Effect of tensile hold times. Procedia Engineering, 10(2011), 147-152.

[9] Y. L. Lu, P. K. Liaw, et al., Tensile-hold effects on high-temperature fatigue-crack growth in nickel-based Hastelloy X alloy. Mat Sci Eng A, 433(2006), 114-120.

Residual stress effects on the propagation of fatigue cracks in the weld of a CA6NM stainless steel

Alexandre Trudel[1,*], Myriam Brochu[1], Martin Lévesque[1]

[1] Department of Mechanical Engineering, École Polytechnique de Montréal, Montreal, Canada
* Corresponding author: alexandre.trudel@polymtl.ca

Abstract The fatigue crack growth behavior in an automatic flux core arc weld was investigated for stainless steel alloy CA6NM. As-welded and heat treated compact tension specimens were prepared with the crack propagation plane perpendicular to the weld. Constant stress intensity factor range tests were performed at a load ratio R = 0.1 to reveal intra-specimen fatigue crack growth rate variations and differences between the fatigue crack growth behavior of as-welded and heat treated specimens. Comparing the fatigue crack growth rate of as-welded and heat treated specimens revealed that the crack propagates at a faster rate in the as-welded specimens where indications point to the existence of tensile residual stresses acting on the crack tip by inhibiting crack closure. As for the heat treated specimens, when the crack is in the base metal, the fatigue crack growth rate decreases accompanied by an increase in crack closure levels. Tensile residual stresses that may have remained after the post-weld heat treatment and their subsequent relaxation with crack growth could explain this behavior.

Keywords Welding, Stainless Steel, Fatigue Crack Growth, Residual Stresses, Crack Closure

1. Introduction

Cast martensitic stainless steel alloy CA6NM has been used to manufacture hydraulic turbine runners for many decades. Its high strength, weldability and resistance to corrosion and cavitation damage make it a prime candidate for this application. Turbine runners are manufactured by welding cast blades to a cast core using a matching filler metal such as 410NiMo. During service, the cyclic loads acting on the runners can lead to fatigue failures [1]. A damage tolerance approach for the stress analysis of turbine runners can be an efficient strategy to account for the discontinuities, such as casting and welding defects as well as partial penetration weld joint designs, found in these components. A good knowledge of material resistance to fatigue crack growth is therefore needed.

During welding, residual stresses develop and are believed to have a significant influence on the fatigue crack growth behavior of CA6NM welds. Weld-induced residual stresses arise from the elastic interactions between the constraining base metal and the weld metal shrinkage upon solidification and cooling. In stainless steel CA6NM, the volumetric expansion resulting from the austenite to martensite transformation, in conjunction with the low transformation temperature, contributes to the buildup of residual stresses during the welding process [2]. Previous studies have shown that significant tensile and compressive residual stresses can be found in as-welded CA6NM welds [2, 3]. These studies have also shown that post-weld heat treatment (tempering) can reduce the residual stress level. Thibault and al. obtained a 75 percent reduction of the maximum tensile residual stress measured in a five beads V-preparation weld (534 MPa to 136 MPa) [2]. Moisan and al. also showed that the maximum average tensile residual stress in a multi-pass T-joint was reduced after post-weld heat treatment by an amount of 73 percent (204 MPa to 56 MPa) [3].

A fatigue crack growing in a weld can be under the influence of tensile or compressive residual stresses, depending on the geometry of the joint and the position of the crack tip. Under tensile residual stresses, the crack tip is submitted to higher maximum and minimum loads resulting in a higher effective load ratio. This can also affect the effective stress intensity factor range as it can prevent closure, often resulting in higher fatigue crack growth rates (FCGR) [4-6]. On the other hand, compressive residual stresses can accentuate crack closure and be beneficial if they reduce the effective stress intensity factor range and thus the fatigue crack growth rate [5].

The main objective of this study was to characterize the effect of residual stresses on the fatigue crack growth behavior of a flux-cored arc weld consisting of alloy CA6NM and filler metal 410NiMo. Intra-specimen fatigue crack growth rate variations between the filler metal (FM), heat affected zone (HAZ) and base metal (BM), as well as the effect of post-weld heat treatment on fatigue crack growth behavior were studied. Microhardness profiles and metallographic observations were realized on as-welded (AW) and heat treated (HT) specimens encompassing the three zones (FM, HAZ and BM) in order to position the fusion line and determine the width of the heat affected zone. Fatigue crack growth tests were carried out at constant stress intensity factor ranges in order to highlight the effect of residual stresses on the fatigue crack growth behavior. The results are discussed based on the effect of the residual stresses as well as crack closure.

2. Experimental procedure

2.1. Materials

The materials used in this study are base metal martensitic stainless steel alloy CA6NM, and the matching filler metal 410NiMo. The chemical composition and mechanical properties of the CA6NM alloy used are given in Table 1 and Table 2, respectively. Using a fully automated flux-cored arc welding (FCAW) process, 40 mm of weld was built up at the surface of a 50 mm thick CA6NM plate. The welding parameters are given in Table 3. The welded plate was cut in two parts, one of which underwent a post-weld heat treatment at 600°C for two hours. Specimens were prepared from both plates for microhardness measurements and fatigue testing.

Table 1. Chemical composition of base metal CA6NM (weight %) [7]

Material	C	Mn	Si	S	P	Cr	Ni	Mo
CA6NM	0.02	0.66	0.59	0.008	0.031	13.04	4.07	0.53

Table 2. Mechanical properties of base metal CA6NM [7]

Yield strength	Tensile strength	Young's Modulus	Elongation	Reduction Area
763 MPa	837 MPa	206 GPa	27.0 %	58.8 %

Table 3. Welding parameters

Process	Shielding gas	Wire diameter	Voltage	Current	Speed	Heat input
FCAW	75% Ar, 25% CO_2	1.6 mm	27.5 V	260 A	5 mm/s	1.4 kJ/mm

2.2 Microhardness measurements and metallographic observations

As-welded (AW) and heat treated (HT) specimens encompassing the three zones (FM, HAZ and BM) were sampled for microhardness measurements and metallographic observations. A rough polish was performed with abrasive paper of grit sizes ranging from 240 to 600, followed by a final polish using polycrystalline diamond suspension of sizes 6 μm, 3 μm and 1 μm. Vickers microhardness profiles were taken across the as-welded and heat treated specimens using a force of 100 gf and a dwell time of 15 seconds. The indentation spacing was 100 μm and measurements were taken on a length of 12 mm starting in the filler metal up to the unaffected base metal. A modified Fry's reagent was used to chemically etch the specimens and metallographic observations were realized to position the fusion line.

2.3. Fatigue testing

Compact tension (CT) specimens having a width of 50.8 mm and a thickness of 12.7 mm were machined from heat treated and as-welded plates in accordance with ASTM E647 [8]. The notches were aligned perpendicularly to the welding direction to allow for the crack to grow through each zone of the joint (FM, HAZ and BM). As seen in Fig. 1, the crack tip was positioned in the filler metal at 7 mm from the fusion line (FL). Constant stress intensity factor range tests in river water environment were performed at a constant load ratio R = 0.1 and at a frequency of 20 Hz using a 100 kN MTS servo-hydraulic machine. As-welded and heat treated specimens were tested at stress intensity factor ranges of 8 MPa·m^{½} and 20 MPa·m^{½}. The crack length was continuously monitored using the compliance method with a crack mouth clip gauge. The load and crack opening displacement (COD) were recorded for every cycle and used to determine the closure loads. The closure stress intensity factor (K_{cl}) was defined for a compliance offset of 2 percent [8]. The effective stress intensity factor range (ΔK_{eff}) was calculated by the difference between the maximum applied stress intensity factor (K_{max}) and the closure stress intensity factor (K_{cl}).

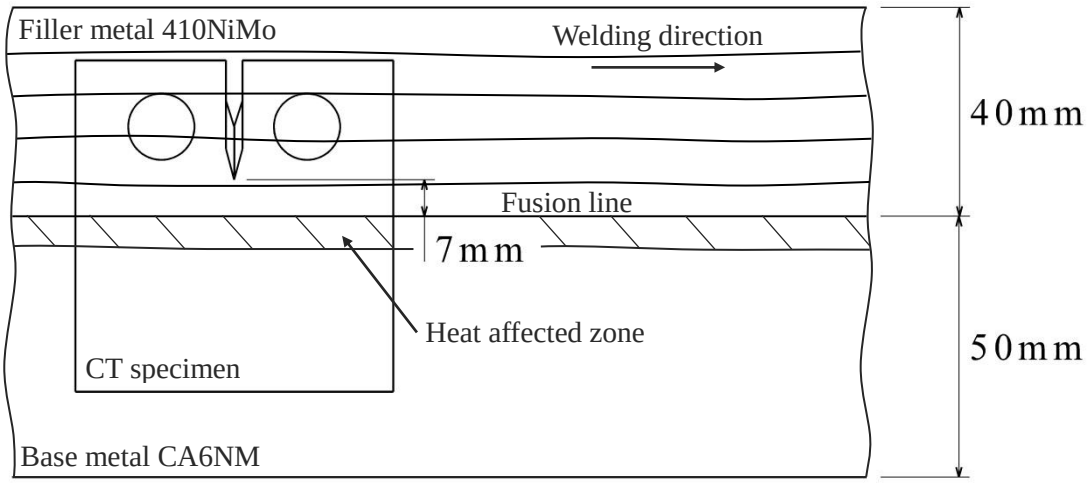

Figure 1. Compact tension specimen sampling layout. Starter notch aligned perpendicularly to the welding direction. Crack tip positioned at 7 mm from the fusion line in the FM.

3. Results

3.1. Microhardness measurements and metallographic observations

The microhardness profiles of the as-welded and heat treated specimens are shown in Fig. 2a and b, respectively. Metallographic observations were realized to identify the position of the fusion line as shown in Fig. 3 for an as-welded joint. The microstructure of the heat treated joint is visually similar and has been omitted. The heat affected zone extends from the fusion line to the microhardness plateau characterizing the base metal, as indicated in Fig. 2. The shape of the microhardness profile is similar for both specimens. The microhardness has its highest value in the filler metal and decreases from the fusion line down to characteristic values of the base metal. The heat affected zone extends up to about 5 mm from the fusion line. The main difference between the two profiles is the microhardness of the filler metal, which is 360 HV on average in the as-welded condition and 325 HV following the tempering heat treatment. These results are in good agreement with what was measured by Thibault and al. from a FCAW CA6NM joint using filler metal 410NiMo [9].

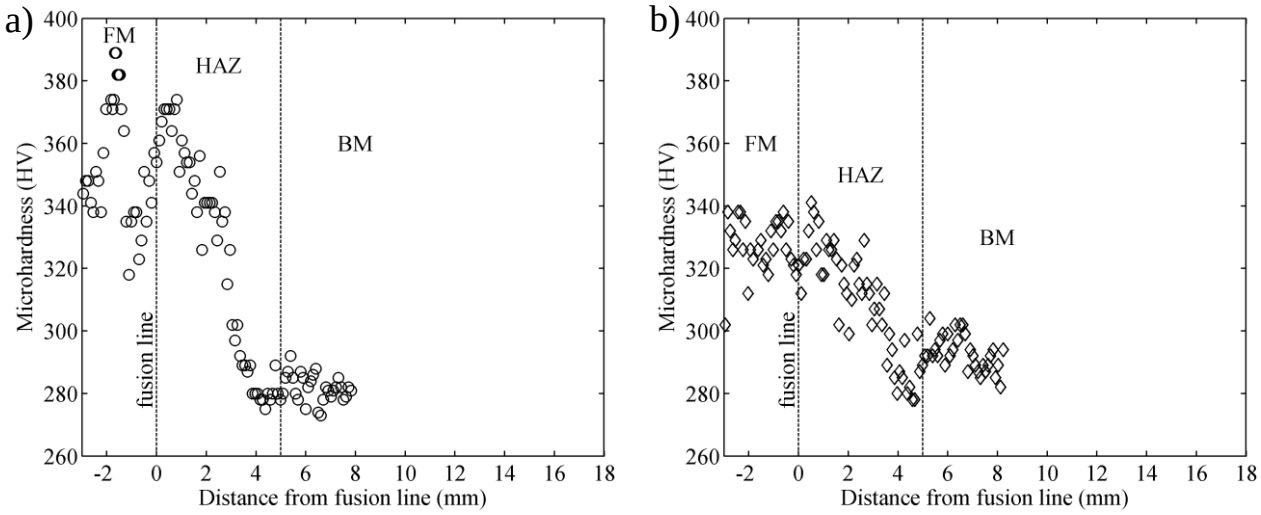

Figure 2. Microhardness profiles a) As-welded specimen b) Heat treated specimen, 2 hours at 600°C

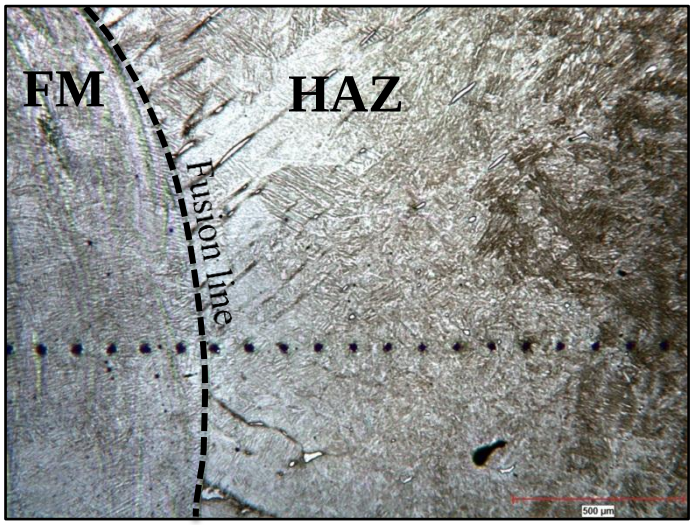

Figure 3. As-welded joint microstructure near the fusion line revealed by etching (50X).

3.2 Fatigue tests

Fig. 4 shows the results of the fatigue tests for as-welded and heat treated specimens at $\Delta K = 8$ MPa·m^{½} and $\Delta K = 20$ MPa·m^{½}. Table 4 shows the mean fatigue crack growth rate in the three zones (FM, HAZ and BM) of as-welded and heat treated specimens. When comparing a given zone at a given stress intensity factor range, the fatigue crack growth rate is always lower in the heat treated specimens than in the as-welded specimens, suggesting that the post-weld heat treatment improves the fatigue crack growth resistance. Pukasiewicz et al. found a similar behavior where the fatigue crack growth rate in the fusion zone of an as-welded CA6NM welded joint was considerably lowered after post-weld heat treatment [10]. In as-welded specimens, the fatigue crack growth rate decreases regularly from the filler metal and into the heat affected zone, before stabilizing in the base metal for both stress intensity factor ranges. These intra-specimen variations are believed to be attributed to microstructural effects and are the subject of an ongoing research. The gradual decrease of the fatigue crack growth rate is not observed in the heat treated specimen. At $\Delta K = 8$ MPa·m^{½}, the fatigue crack growth rate remains fairly constant up to 9 mm from the fusion line (4 mm into the base metal), then decreases by approximately 50 percent and stabilizes at 13 mm from the fusion line. The same behavior, though less pronounced, is also observed at $\Delta K = 20$ MPa·m^{½}, where the fatigue crack growth rate decreases by approximately 20 percent.

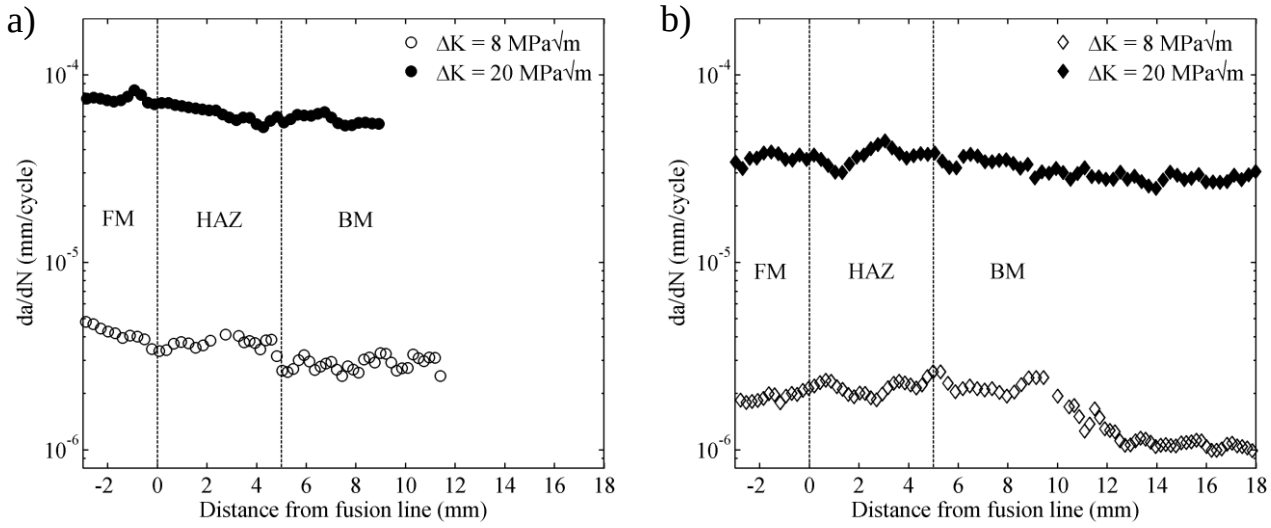

Figure 4. Constant ΔK test results a) As-welded specimens b) Heat treated specimens

Table 4. Mean FCGR in the FM, HAZ and BM of as-welded and heat treated specimens

ΔK (MPa·m^{½})	Fatigue crack growth rate (mm/cycle)						
	As-welded specimens			Heat treated specimens			
	FM	HAZ	BM	FM	HAZ	BM	
						Up to 9 mm from FL	After 13 mm from FL
8	$4.2\cdot10^{-6}$	$3.7\cdot10^{-6}$	$2.9\cdot10^{-6}$	$1.9\cdot10^{-6}$	$2.1\cdot10^{-6}$	$2.2\cdot10^{-6}$	$1.1\cdot10^{-6}$
20	$7.5\cdot10^{-5}$	$6.3\cdot10^{-5}$	$5.8\cdot10^{-5}$	$3.6\cdot10^{-5}$	$3.7\cdot10^{-5}$	$3.5\cdot10^{-5}$	$2.8\cdot10^{-5}$

4. Discussion

This section presents an analysis of the constant stress intensity factor range tests results. The higher fatigue crack growth rates found in the as-welded specimens are discussed in terms of tensile residual stresses causing the opening of the crack. The fatigue crack growth rate variations observed in the heat treated specimens are discussed in terms of residual stress relaxation and crack closure.
Fig. 5 shows the base metal fatigue crack growth curves obtained at load ratios R = 0.1 and R = 0.7 [1], along with the mean fatigue crack growth rate obtained in the base metal from the constant stress intensity factor range test results (Table 4). The mean fatigue crack growth rate in the base metal of the heat treated specimens was calculated from the stabilized data starting at 13 mm from the fusion line. For the heat treated specimens, a good agreement is found between the R = 0.1 base metal fatigue crack growth curve and the fatigue test results, for both stress intensity factor ranges. These results, along with the intra-specimen fatigue crack growth rate variations noted in the last section (Fig. 4b), are discussed further in terms of residual stress relaxation and crack closure. Furthermore, the fatigue crack growth rates in the as-welded specimens at $\Delta K = 8$ MPa·m^{½} (empty circles) and $\Delta K = 20$ MPa·m^{½} (filled circles) correlate well with the R = 0.7 base metal baseline. Several indications suggesting the presence of tensile residual stresses responsible for the higher effective load ratio seen by the as-welded specimens are discussed next.

4.1. Fatigue crack growth behavior of as-welded specimens

The typical load-compliance offset curve for as-welded specimens is shown in Fig. 6a. For both stress intensity factor ranges and at all crack lengths, the specimen's response does not deviate from the fully-open crack compliance. This indicates that the crack remains fully-open and that the effective stress intensity factor range is equal to the applied stress intensity factor range. This corresponds to an effective stress intensity factor range ratio ($U = \Delta K_{eff}/\Delta K$) equal to unity in Fig. 6b (circles). It is well known that, for ductile materials free of residual stresses, plasticity-induced crack closure plays a significant role in reducing the effective stress intensity factor range [11].

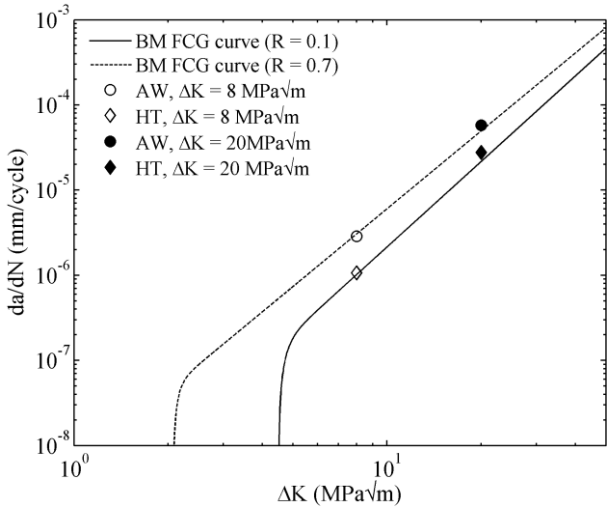

Figure 5. Comparison between the mean FCGR in the BM obtained from the constant ΔK tests and the BM fatigue crack growth curve in the Paris regime at load ratios R = 0.1 and R = 0.7 [1]

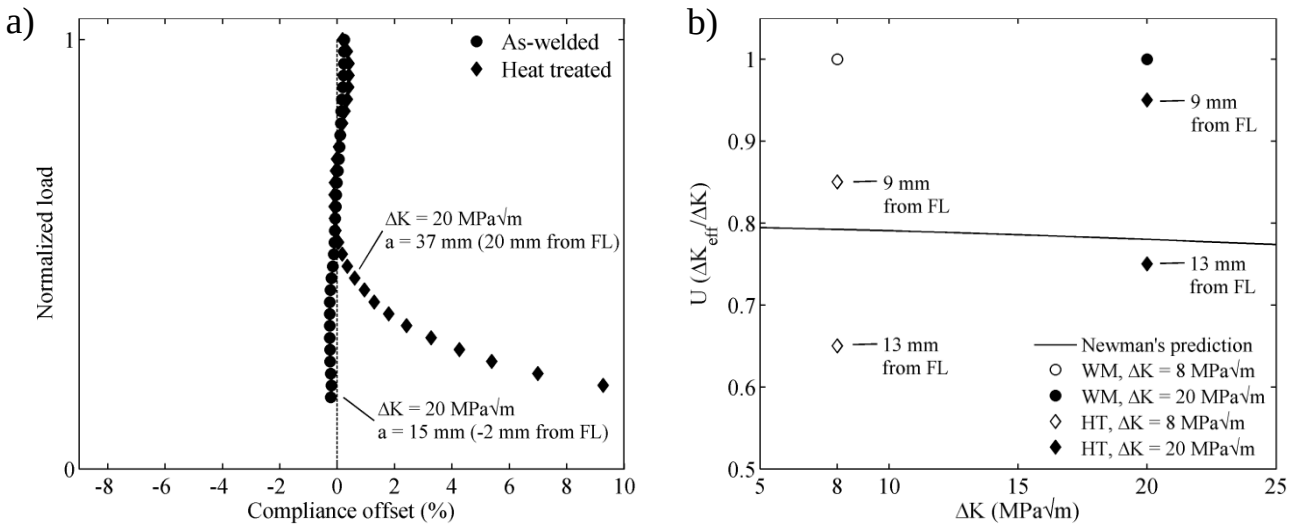

Figure 6. a) Typical load-compliance offset curves for as-welded and heat treated specimens. b) Comparison between experimental values of U and Newman's prediction

The solid line in Fig. 6b was calculated using Newman's plasticity-induced closure stress equation [12, 13] and represents an upper bound of the effective stress intensity factor range ratio. Experimental data above this upper bound indicate the existence of a crack opening mechanism. Tensile residual stresses are believed to act as such a mechanism in the as-welded specimens, since tensile residual stresses are typically found in CA6NM welds.

To further assess the presence of tensile residual stresses, an as-welded compact tension specimen with a crack length of 20 mm was incrementally loaded from 500 N to -12000 N and the crack opening displacement was recorded (Fig. 7). A closure load of -1000 N was found with a 2 percent compliance offset criterion. The existence of a negative closure load is another strong indication that tensile residual stresses are acting on the crack by preventing it to close at positive loads. A similar behavior has been observed in the welds of three different kinds of steels where tensile residual stresses caused the crack to remain fully open at a load ratio R = 0, resulting in higher fatigue crack growth rates than that of the base metal [5].

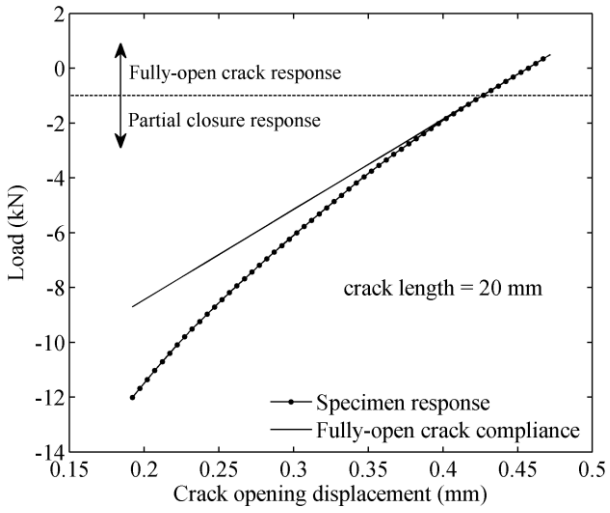

Figure 7. As-welded specimen load-COD curve from a single compression excursion (a = 20 mm)

4.2. Fatigue crack growth behavior of heat treated specimens

The crack closure behavior of the heat treated specimens is different. Crack closure was observed at both stress intensity factor ranges and for all crack lengths and the typical load-compliance offset curve is shown in Fig. 6a. Fig. 6b shows the effective stress intensity factor range ratio for the heat treated specimens when the crack is at 9 mm from the fusion line and at 13 mm from the fusion line. As a first observation, crack closure is more important at $\Delta K = 8$ MPa·m^{½} for equal crack lengths. This is expected since crack closure is more pronounced for low stress intensity factor ranges [14]. Furthermore, up to 9 mm from the fusion line, the effective stress intensity factor range ratio remains above Newman's theoretical upper bound for both stress intensity factor ranges. This is an indication that tensile residual stresses may have remained after post-weld heat treatment, partially inhibiting crack closure. These results are consistent with previous studies that showed that the post-weld heat treatment may not completely eliminate the residual stresses in CA6NM welds [2, 3]. On the other hand, the effective stress intensity factor range ratio of the crack at 13 mm from the fusion line is below the upper bound predicted by Newman for plasticity-induced crack closure for both stress intensity factor ranges. This is an indication that tensile residual stresses at the crack tip may have relaxed with crack growth and that crack closure is not inhibited. Tensile residual stresses are known to redistribute and eventually relax following the growth of a fatigue crack [15]. After complete relaxation of the tensile residual stresses, common closure mechanisms such as plasticity-induced, roughness-induced and oxide-induced crack closure become fully active and the global closure level is increased.

The evolution of the measured effective stress intensity factor range ratio against the crack length is shown in Fig. 8 (triangles). Crack closure is rather constant up to 9 mm from the fusion line, than it increases as the crack grows and eventually stabilizes. A good correlation is observed between the profiles of the fatigue crack growth rate (circles) and the effective stress intensity factor range ratio (triangles). This shows that the fatigue crack growth behavior of the heat treated specimens is directly affected by the variation of crack closure.

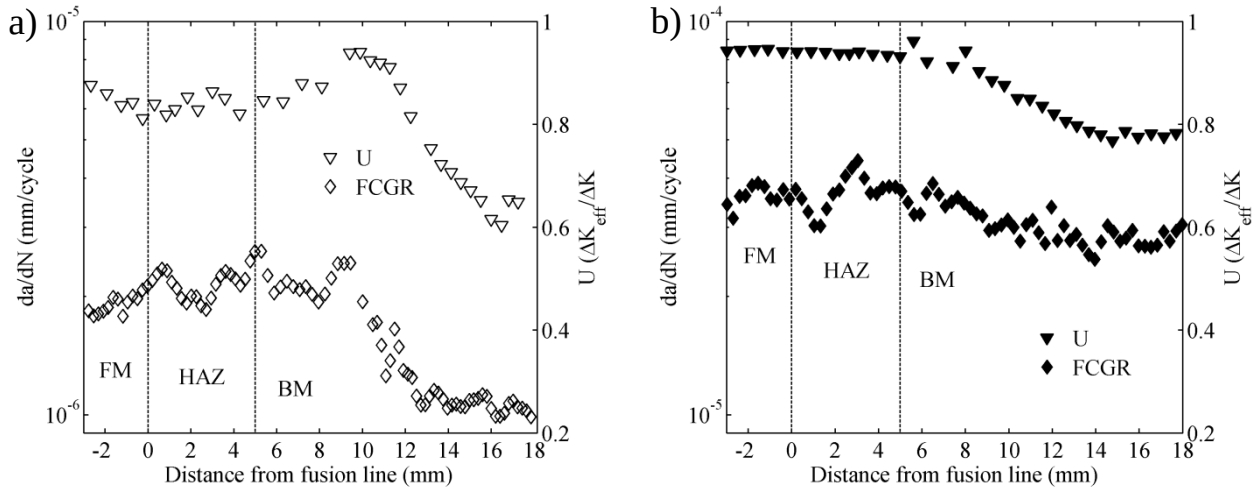

Figure 8. Relationship between U and the FCGR against the crack length for heat treated specimens a) $\Delta K = 8$ MPa·m^{½} b) $\Delta K = 20$ MPa·m^{½}

5. Conclusion

The main objective of this study was to investigate the effect of residual stresses on the fatigue crack growth behavior of a stainless steel alloy CA6NM welded joint. From the results, the following conclusions can be drawn.

In as-welded specimens, many clues point to the fact that tensile residual stresses are present at the crack tip and are having an effect on the fatigue crack growth behavior. This hypothesis is supported by: (1) A higher effective load ratio indicated by the agreement between the mean R = 0.1 experimental base metal fatigue crack growth rate and the R = 0.7 base metal fatigue crack growth curve. (2) An effective stress intensity factor range ratio equal to unity for all crack lengths meaning that a crack opening mechanism is present. (3) A negative closure load on an as-welded specimen at a crack length of 20 mm.

It is also believed that some tensile residual stresses remain after post-weld heat treatment, as evidenced by the effective stress intensity factor range ratio being superior to Newman's prediction for plasticity-induced crack closure. In addition, an increase in crack closure when the crack is in the base metal points to the fact that the tensile residual stresses were relaxed with crack growth and that closure mechanisms become fully active.

This study showed that tensile residual stresses, which are strongly believed to be present in the as-welded specimens, caused the crack to remain fully open, this having a detrimental effect on the fatigue crack growth resistance of CA6NM welds. Moreover, the fatigue crack growth resistance was found to be improved in the heat treated specimens compared to the as-welded specimens. This is attributed to the residual stresses relaxation after tempering and with crack growth, allowing closure mechanisms to become active and reducing the fatigue crack growth rates. This shows the importance of a good residual stress level control through post-weld heat treatment.

Acknowledgements

This study was made possible by the support of Alstom Hydro, Hydro-Québec and the National Science and Engineering Research Council of Canada (NSERC). The authors wish to thank Prof. Yves Verreman for his invaluable technical insights as well as technologists Carlo Baillargeon and Benedict Besner for their help with the fatigue testing procedure.

References

[1] M. Sabourin, D. Thibault, D. A. Bouffard, and M. Levesque, "New parameters influencing hydraulic runner lifetime," presented at the 25th IAHR Symposium on Hydraulic Machinery and Systems, Timisoara, Romania, 2010.

[2] D. Thibault, P. Bocher, M. Thomas, M. Gharghouri, and M. Côté, "Residual stress characterization in low transformation temperature 13%Cr–4%Ni stainless steel weld by neutron diffraction and the contour method," *Mat Sci Eng A-Struct*, vol. 527, pp. 6205-6210, 2010.

[3] É. Moisan, M. Sabourin, M. Bernard, and T. Bui-Quoc, "Residual stress measurements in hydraulic turbine welded joints," presented at the IAHR 23rd Symposium on Hydraulic Machinery and Systems, Yokohama, Japan, 2006.

[4] Y. B. Lee, C. S. Chung, Y. K. Park, and H. K. Kim, "Effects of redistributing residual stress on the fatigue behavior of SS330 weldment," *Int J Fatigue*, vol. 20, pp. 565-573, 1998.

[5] A. Ohta, N. Suzuki, and Y. Maeda, "Unique fatigue threshold and growth properties of welded joints in a tensile residual stress field," *Int J Fatigue,* vol. 19, pp. 303-310, 1997.

[6] C. Jang, P.-Y. Cho, M. Kim, S.-J. Oh, and J.-S. Yang, "Effects of microstructure and residual stress on fatigue crack growth of stainless steel narrow gap welds," *Mater Design,* vol. 31, pp. 1862-1870, 2010.

[7] J. Lanteigne, M. Sabourin, T. Bui-Quoc, and D. Julien, "The characteristics of the steels used in hydraulic turbine runners," presented at the IAHR 24th Symposium on Hydraulic Machinery and Systems, Foz Do Iguassu, Brazil, 2008.

[8] ASTM, "E647-11e1 Standard Test Method for Measurement of Fatigue Crack Growth Rates," ed: ASTM International, 2011.

[9] D. Thibault, P. Bocher, and M. Thomas, "Residual stress and microstructure in welds of 13%Cr–4%Ni martensitic stainless steel," *J Mater Process Tech,* vol. 209, pp. 2195-2202, 2009.

[10] A. G. M. Pukasiewicz, S. L. Henke, and W. J. P. Casas, "Effect of post-weld heat treatment on fatigue crack propagation in welded joints in CA6NM martensite stainless steel," *Welding International,* vol. 20, pp. 947-952, 2006.

[11] W. Elber, "The significance of fatigue crack closure," *Damage Tolerance in Aircraft Structures, ASTM STP 486,* pp. 230-242, 1971.

[12] J. C. Newman, "A crack opening stress equation for fatigue crack growth," *Int J Fracture,* vol. 24, pp. 131-135, 1984.

[13] J. C. Newman Jr, J. H. Crews Jr, C. A. Bigelow, and D. S. Dawicke, "Variations of a global constraint factor in cracked bodies under tension and bending loads," *Constraint Effects in Fracture Theory and Applications: Second Volume, ASTM STP 1244,* pp. 21-42, 1995.

[14] S. Suresh and R. O. Ritchie, "Near-threshold fatigue crack propagation: a perspective on the role of crack closure," presented at the Symp. on Concepts of Fatigue Crack Growth Threshold, Philadelphia, USA, 1983.

[15] R. C. McClung, "A literature survey on the stability and significance of residual stresses during fatigue," *Fatigue Fract Eng M,* vol. 30, pp. 173-205, 2007.

Analysis of the transition from flat to slanted fatigue crack growth in thin metallic sheets

Jean-Baptiste Esnault [1,2], Véronique Doquet [1,*], Patrick Massin[2]

[1] : Laboratoire de Mécanique des Solides, CNRS, Ecole Polytechnique, Palaiseau France

[2] LaMSid, EDF – CNRS - CEA, Clamart, France

*corresponding author: doquet@lms.polytechnique.fr

Abstract Fatigue crack growth in thin sheets of 7075 T651 aluminium alloy and S355 steel were characterized in 3D, using crack front markings and topographic reconstructions of fracture surfaces. Tests performed in air or in salt water produced different crack paths for similar mechanical conditions, shear lips being reduced by the corrosive environment, in the aluminium alloy as well as in steel. Before the onset of shear lips development, tunnelling crack fronts were observed, due to the difference in closure effects at mid-thickness and near the free surfaces. Tunnelling was progressively reduced and cancelled as slanted crack growth developed, even though ΔK_I was reduced locally by crack twisting. This indicates a significant contribution of shear modes to the crack driving force, even though mode I striations are present in the slanted zones. Elastic three-dimensional X-FEM computations were performed to analyse the observed crack growth kinetics, based on ΔK_I, ΔK_{II} and ΔK_{III}. The crack growth rates correlated much better to $\Delta K_{eq} = \sqrt{\Delta K_I^2 + \Delta K_{II}^2 + \frac{\Delta K_{III}^2}{(1-\nu)}}$ than to ΔK_I. Elastic-plastic finite element simulations and the local application of a fatigue criterion with an amplitude-dependent critical plane were found to capture qualitatively the transition in fracture mode.

Keywords fatigue crack, shear lips, thin sheet, mixed-mode, X-FEM, slanted crack

1. Introduction

Fatigue crack growth normal to the tensile axis becomes unstable in thin metallic sheets, above a material, environment and frequency-dependent amplitude, even though, in many cases, small scale yielding conditions still prevail. Shear lips development has been investigated mainly in aluminium alloys by Schijve and coworkers [1-2] Zuidema et al. [3-4] or Shanyavsky and Koronov [5], while a few studies were devoted to steel [6] or titanium alloys [7]. Walker et al [7] first reported an influence of environment on shear lips development in titanium alloys. The corrosive environment appeared to postpone crack twisting in Ti-8Al-1Mo-1V, while no systematic effect was found in Ti-6Al-AV. Vogelesang and Schijve [2] observed complete crack twisting in 7075 T651 aluminium alloy for a lower apparent ΔK_I in vacuum than in air and for a higher apparent ΔK_I in 3,5%NaCl solution. Horibe et al [6] reported a similar effect of salt water in low strength steel, but a less pronounced effect of environment for high strength steel. Shanyavsky and Koronov [5] measured the shear lips width in thin aluminium alloy cruciform specimens cyclically loaded in two orthogonal directions and reported that a positive biaxiality ratio reduced the shear lips, while a negative ratio increased it. They also observed a reduction in shear lips width when the R ratio increased. This observation conflicts with the conclusion of Zuidema et al. [3-4] that the

"steady-state" shear lips is a linearly increasing function of the effective ΔK, which usually increases with R.

The analyses of experimental data in the literature are essentially two-dimensional. Slanted crack growth kinetic data is analysed as if it was mode I and as if the growth rate and driving force were uniform along the front. Based on "constant ΔK_I tests", empirical relations between the steady-state shear lips width, the loading frequency and the "effective ΔK_I" were derived for aluminium alloys [3-4]. This parameter will be denoted below by "apparent ΔK_I", since it is computed in 2D for a normal crack of same length as that observed on the free surface, with an empirical correction for closure effects deduced from the R ratio. The meaning of "constant ΔK_I tests" is also questionable in view of the large gradient in K_I, K_{II} and K_{III} along the front of a partially or completely slanted crack and of the reduction in ΔK_I associated with crack twisting.

In an effort toward 3D analysis, Pook [8] performed finite element computations of the stress intensity factors along the front of a fully slanted crack in specimens of different thickness. He found that K_I was 0.51 to 0.71 smaller than its apparent value (computed in 2D for a normal crack of same length). He also found that K_{III} had the same order of magnitude as K_I, while K_{II} raised near the free surfaces with a skew-symmetric profile. Bakker [9] performed 3D computations of stress intensity factors for fully or partially slanted crack. However, as in the case studied by Pook, a straight crack front was considered, while tunnelling probably plays a role in crack twisting in fatigue.

The present work re-examines the problem from a 3D perspective, in order to determine what mechanical parameters control the onset of crack deviation and the kinetics of slanted crack growth. Since environment seemed to influence shear lips development, a 3D experimental characterization of the crack paths and kinetics was performed, both in air and in salt water and the crack paths were compared. A 3D numerical analysis of the crack growth rates was done, based on linear elastic fracture mechanics, taking mode-mixity into account. Elastic-plastic computations of stress and strain fields ahead of the crack front were used to rationalize the observed crack paths. A method to predict the onset of crack twisting and the twist angles was proposed.

2. Experimental procedures

Fatigue crack growth tests were performed with a frequency of 5Hz and R=0.1 on 6mm-thick, 100mm-wide, 300mm-high Center-Cracked Panels (CCP) specimens. Two material were investigated: 7075-T651 aluminium alloy ($\sigma_{0,2}$= 376MPa, σ_u= 537MPa, E= 75 GPa) and S355 low-alloy steel ($\sigma_{0,2}$= 349MPa, σ_u= 510MPa, E= 205 GPa). Both sides of the specimens were polished to allow crack propagation monitoring with an optical microscope, at a magnification of one hundred. The tests were performed in air or in a transparent reservoir filled with 3,5g/l NaCl solution, under different loading amplitudes indicated in Table 1. Marker block loading sequences with and increased K_{min} but the same K_{max} were periodically applied, so that the R ratio became temporary 0.7, until approximately 100 μm propagation was achieved, in order to mark the position of the crack front and be able to derive the mean crack growth rate between consecutive markings, for any point along the front. Ten to twelve marker blocks were applied at 20Hz. To characterize crack front tunnelling, the difference in crack length between the mid-thickness and the average length on free surfaces was measured and denoted by Δa.

Table 1: Test conditions

Material	7075 T651			S355 steel	
Test n°	CCP7a	CCP7Na	CCP5a	CCP2a	CCP2Na
Environment	air	NaCl	air	air	NaCl
Range of apparent ΔK_I (Mpa$\sqrt{m}$)	7-18	7-18	9-20	18-35	18-35
Stress range (MPa)	34	34	40	100	100
Cycles for crack initiation	30000	10000	15000	35000	27000
Cycles of crack growth until fracture	202440	110260	59000	157730	138730

Fracture surface topographies were reconstructed using a digital optical microscope. The results were obtained as (x, y, z) triplets, where x denotes the distance from the notch root, y, the position in depth, and z the height from the notch plane. Transverse height profiles, z(y) were derived. Polynomial expressions were fitted to these profiles and used to compute the local twist angle as arctang (dz/dy). The shear lips width, denoted by t_s, was deduced from these height profiles.

3. Experimental results

Salt water reduced the number of cycles for crack initiation by a factor of 3 in the aluminium alloy and 1.3 in steel. Crack growth was significantly accelerated in the aluminium alloy, but not in steel. Figure 1 shows examples of crack transverse profiles, z(y), and twist angle profiles at different stages of crack growth.

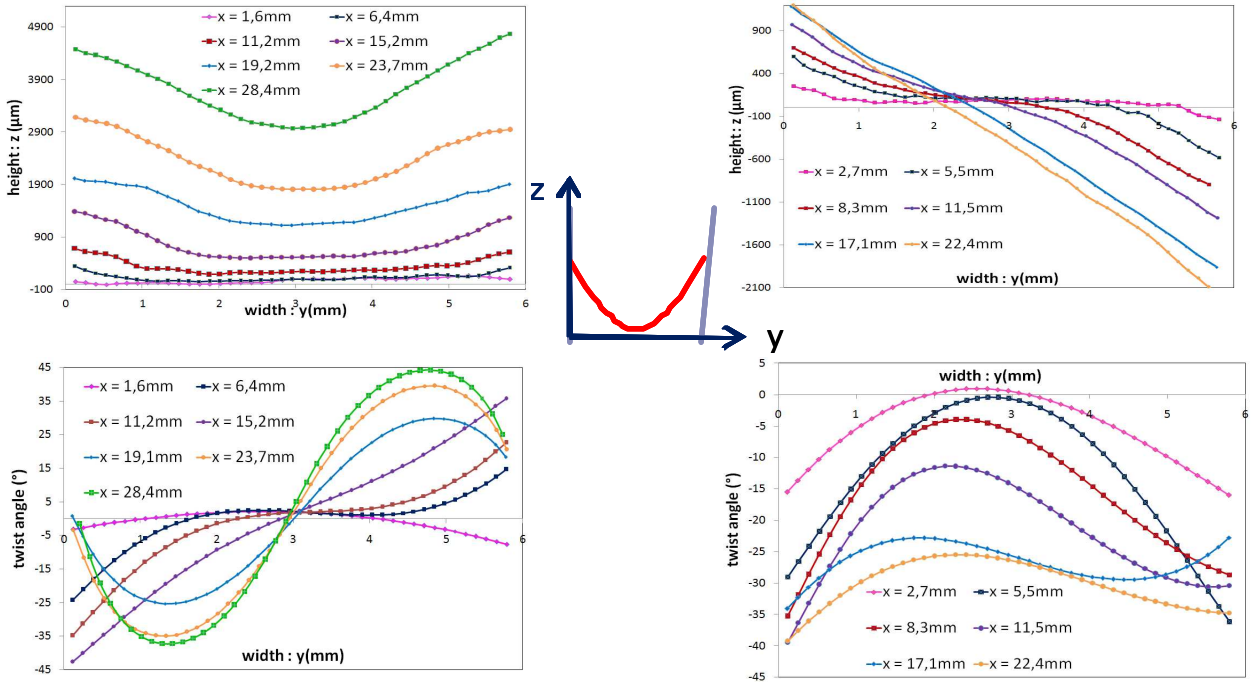

Fig 1: Topographic reconstructions of fracture surfaces. a) transverse profiles and b) twist angles for specimen CCP5a. c) transverse profiles and d) twist angles for specimen CCP2a.

The twist angle is neither uniform along the shear lip, nor constant as the crack grows. It is substantially less than 45°. In some cases, the peak value is not observed at the free surface but up to 1mm in depth. The evolutions of the shear lips width in air and NaCl solution under the same mechanical conditions are compared on Fig 2.

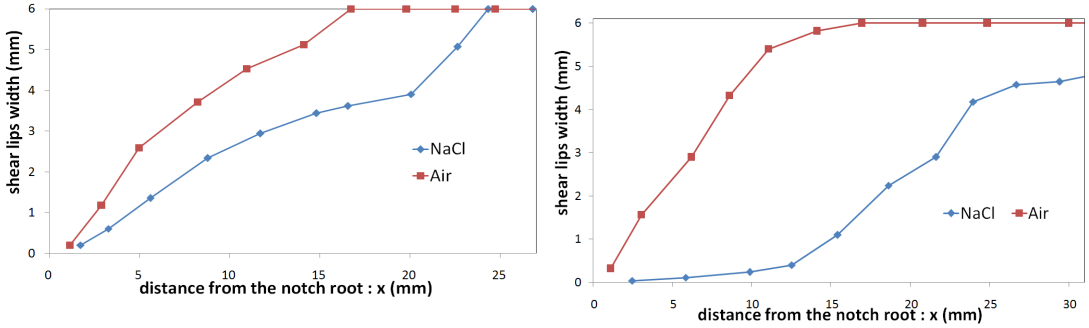

Fig 2: Evolution of shear lips width in air and NaCl solution under similar loading conditions
a) specimens CCP7a and CCP7Na and b) steel specimens CC2a and CCP2Na

Shear lips development was delayed and less complete in the NaCl solution, in agreement with some observations from the literature [2, 6]. The evolution of crack front tunnelling, Δa, is plotted on Fig 3.

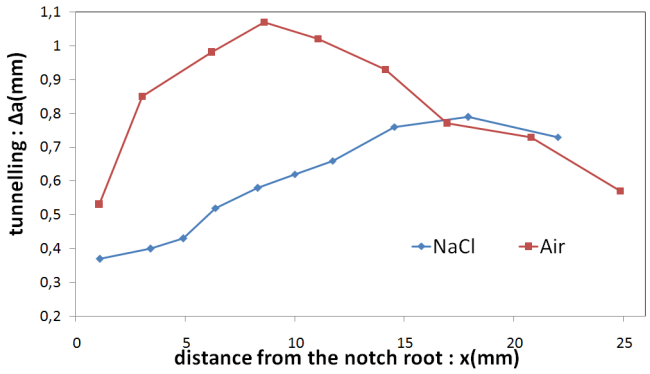

Fig 3: Evolution of crack front tunnelling, in steel specimens, in air or NaCl solution

In air, tunnelling was progressively reduced and cancelled by the development of shear lips, in spite of a drop in nominal ΔK_I in the slanted zones and of a probable local increase in closure effects, generally more important at low ΔK_I. Both factors should reduce the crack growth rate near the free surfaces and thus increase the convexity of the front. A reverse effect is observed. The reduction of tunnelling provides evidence for an effective contribution of shear modes to the crack driving force. However, fractographic observations revealed fatigue striations in normal zones as well as in slanted areas, where a few isolated rubbing marks were also observed near the side surfaces. Hence mode I still contributed to crack growth in the slanted zones and it would be incorrect to describe crack twisting as a transition from tension to shear-mode, as sometimes done in the literature.

4. Numerical study

The numerical study is constituted of two parts: 1) an elastic analysis in an extended finite element code (X-FEM, implemented in *Code_Aster* at EDF R&D, *www.**code-aster**.org/*) well fitted to

estimate the stress-intensity factors (SIFs) taking into account the real geometry of slanted cracks, but not suitable for the simulation of cyclic plasticity and 2) an elastic-plastic analysis carried out in the framework of the classical finite element method with Cast3M software (*www-**cast3m**.cea.fr/)*, therefore limited to flat tunnelling cracks. The stress-intensity factors issued from the X-FEM computations will be used to analyse the measured crack growth rates and to determine the parameter which best correlates the data. But the SIFs are considered useless for the prediction of crack paths, since none of the bifurcation criteria based on those parameters can predict that a fatigue crack loaded in mode I changes its path to grow in mixed-mode along a shear lip. In the present case, the crack paths are believed to be determined by the stress and strain fields just ahead of the crack front, which must be computed by elastic-plastic cyclic computations.

4.1 ***The X-FEM computation***

4.1. a General framework

The extended finite element method, introduced by Moes et al. [10], allows the simulation of complex crack shapes where the structural finite element mesh does not have to conform to the crack surface. The crack surface and its front are defined geometrically by two signed distance functions named “level sets”. In order to take into account the displacement jump due to the presence of the crack and the crack tip singularity the discretized displacement field is “enriched” with discontinuous shape functions. The displacement field is approximated as follows:

$$u(x) = \sum_{i \in I_0} N_i(x) u_i + \sum_{i \in I_H} N_i(x) H(x).a_i + \sum_{i \in I\gamma} N_i(x) \left(\sum_{k=1,4} \gamma_k(x).b_{i,k} \right) \quad (1)$$

In which H denotes the Heavyside function: $H(x) = \begin{cases} -1 \, if & x < 0 \\ +1 \, if & x > 0 \end{cases}$ (2)

I_0 is the set of the standard finite element nodes, I_H the set of nodes whose support is completely cut by the crack and I_γ the set of nodes whose support contains the crack front, a_i and $b_{i,k}$, the corresponding additional degrees of freedom. N_i are the standard finite element shape functions, u_i the nodal displacements and γ_k is the base of Westergaard’s solution representing the asymptotic displacement field at the crack tip of a semi-infinite crack in an infinite medium:

$$\gamma_k(x) = \left\{ \sqrt{r} \sin(\frac{\theta}{2}), \sqrt{r} \cos(\frac{\theta}{2}), \sqrt{r} \sin(\frac{\theta}{2}) \sin(\theta), \sqrt{r} \sin(\theta) \cos(\frac{\theta}{2}) \right\} \quad (3)$$

4.1. b Representation of the crack.

One of the ways to generate the level–sets used to represent the crack is to mesh both the crack surface and the crack front. This mesh is used only for the geometrical description of the crack and not for the resolution of the problem. An algorithm was thus developed to turn the measured topographic data, that is: a set of (x, y, z) triplets plus polynomial fits of crack front markings, into a mesh representative of the crack. The first step is to fit a polynomial interpolation to the cloud of points extracted from the topography, using the least square method, in 3D. Then a regular, flat grid of points is deformed, using both the equation of the crack surface z(x, y), and the polynomial fit of its front, x(y) (Fig. 4). This grid is then meshed with quadrangles and the linear elements of the

crack front are extracted.

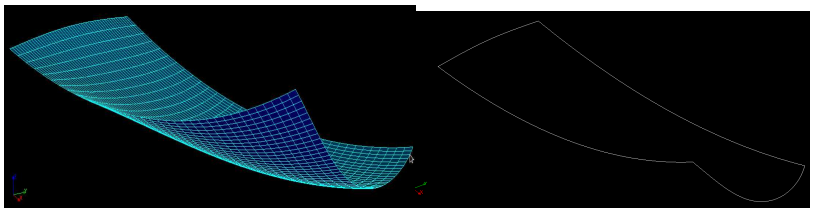

Fig 4: example of mesh of a crack surface used for level-sets computation

The G-θ method proposed by Destuynder et al. [11] was used to compute the SIFs. Due to corner point singularities, the values computed at surface points were not included in the analysis.

4.1. c The structural mesh.

Half of the CCP specimen was modelled with linear hexahedral (50µm*50µm*50µm) elements in a parallalepidal zone centered at the crack tip, linked to tetrahedral elements, via pyramidal elements, out of the process zone. The boundary conditions are indicated on Fig. 5.

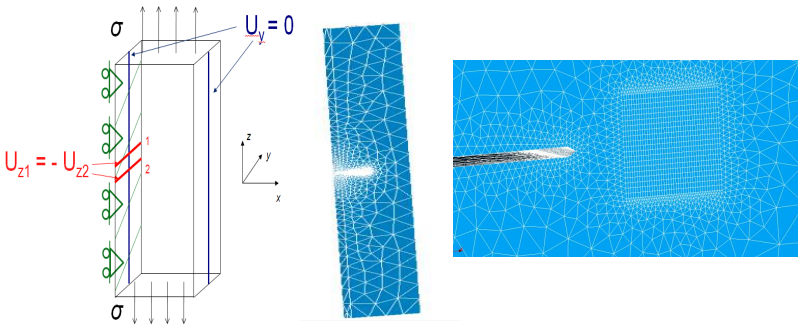

Fig 5: Boundary conditions and mesh of the CCP specimen in the X-FEM model

4.2. Elastic-plastic finite element analysis

This part focuses on the onset of crack twisting and thus considers flat, normal cracks, but takes tunnelling into account. Only a quarter of the CCP specimen was modelled, taking advantage of the symmetries. A 3D mesh with a straight crack front was first prepared, using linear elements, 30*30*150µm-wide near the crack front, which was then deformed, using the polynomial equation describing best the observed tunnelling front (Fig 7).

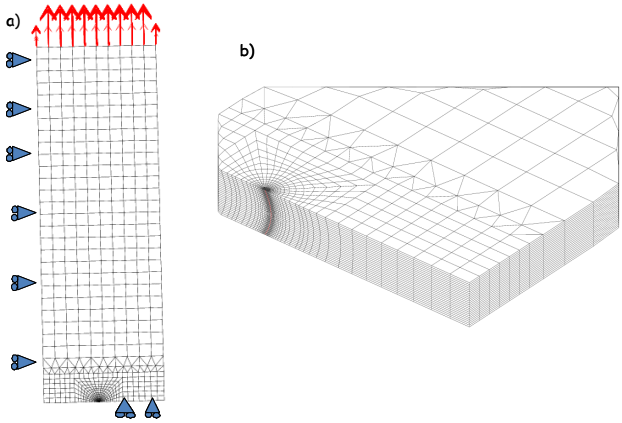

Figure 7: a) F.E. mesh of a quarter CCP specimen and boundary conditions, b) tunnelling crack front

Elastic-plastic constitutive equations with isotropic and non-linear kinematic hardening, identified from the stress-strain loops obtained from push-pull tests were used. Cyclic loading with R=0.1 was simulated. The stress and strain fields computed at maximum and minimum load were used for a local application, ahead of each node of the front, of a fatigue criterion derived from that identified by Zhao and Jiang from an extensive multiaxial fatigue database on 7075 T6 [12]. Their criterion successfully captured the transition in fracture mode observed in torsion as well as in push-pull or combined loading: when the loading range increases, fatigue damage changed from normal-stress-driven to shear-driven, yet with an assistance of an opening stress. Their damage function (DF) was thus:

$$DF = 2b\Delta\varepsilon_n \left\langle \sigma_{n\max} \right\rangle + \frac{1-b}{2}\Delta\tau\Delta\gamma \tag{4a}$$

$$b = \left\langle a_1 - a_2 \Delta\sigma_{eq} \right\rangle \tag{4b}$$

in which <x> denotes the positive part of x, a_1 and a_2 two fitted constants (0.862 and 0.00125), $\Delta\varepsilon_n$, $\Delta\gamma$, $\Delta\tau$, σ_{nmax}, respectively the normal strain, shear strain and stress range and peak opening stress, all computed along the critical plane. The latter is that for which the damage function, DF is maximum. As a consequence of Eq. 4b, the normal stress and strain play a major role at low stress range, but their influence decreases as the stress range increases, down to a transition stress range above which damage is merely driven by shear (b=0). In the present study, this criterion was slightly modified. The transition in fracture mode occurs in the low-cycle fatigue regime, where fatigue tests are usually strain-controlled, while the equivalent stress range evolves due to cyclic hardening. The value of $\Delta\sigma_{eq}$ which enters equation 4b was thus not clearly defined. The parameter b was thus considered to be more clearly related to the applied equivalent strain range, rather than to the stress range. Equation 4b was therefore turned into:

$$b = \left\langle 1 - \frac{2.\Delta\varepsilon_{eq}}{\Delta\varepsilon_{eq\,trans}} + \left(\frac{\Delta\varepsilon_{eq}}{\Delta\varepsilon_{eq\,trans}}\right)^2 \right\rangle \tag{5}$$

in which $\Delta\varepsilon_{eq,trans}$ corresponds to the equivalent strain range for which the transition from one fracture mode to the other is observed. A smoother evolution of b is predicted, compared to Eq. 4b. In addition, b tends toward 1 when the strain range vanishes, so that fracture is controlled merely by the normal stress and strain, which was not the case in the original criterion, for which the maximum value of b was 0.862. To apply the criterion ahead of each node of the crack front, $\Delta\varepsilon_{eq}$ was first averaged over a 90μm-long segment parallel to the x axis, comprising three elements. The local value of b was then computed using Eq. 5 with $\Delta\varepsilon_{eq,trans}$=0.92% for the aluminium alloy and 0.45% for steel. For each node, the damage function was computed, using the local value of b, along all potential twisted planes, for a twist angle θ ranging from 0 to 45°. The value of θ corresponding to the maximum of DF was considered as the local direction of crack extension. Here again stresses and strains were averaged over a distance of 90μm. This arbitrary distance, which influences the predicted crack paths should be considered as an adjustable parameter.

5. Numerical analysis of the experimental results

5.1. Computed SIFs and analysis of crack growth rates

Figure 8 shows the computed K_I, K_{II} and K_{III} computed at peak load along the 7th crack fronts in specimens CCP5a and CCP2a.

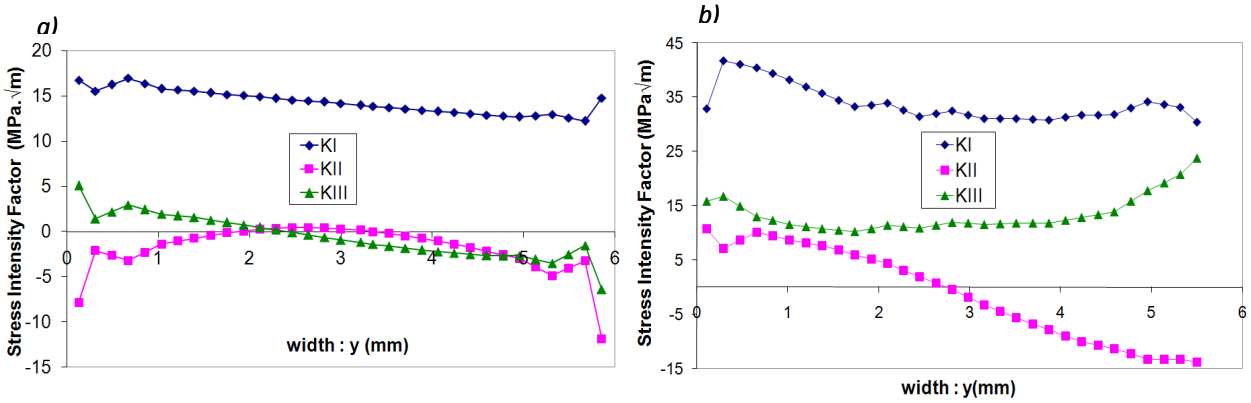

Figure 8: SIFs at peak load along the 7th crack fronts in a) Al specimen CCP5a b) steel specimen CCP2a.

The crack growth rates measured at various depths in these specimens are plotted versus ΔK_I on Fig. 9a and versus $\Delta K_{eq} = \sqrt{\Delta K_I^2 + \Delta K_{II}^2 + \frac{\Delta K_{III}^2}{(1-\nu)}}$ on Fig. 9b. While ΔK_I fails to correlate all the data, ΔK_{eq} provides a much better correlation, which gives additional evidence that opening and shear modes cooperate for slanted crack growth.

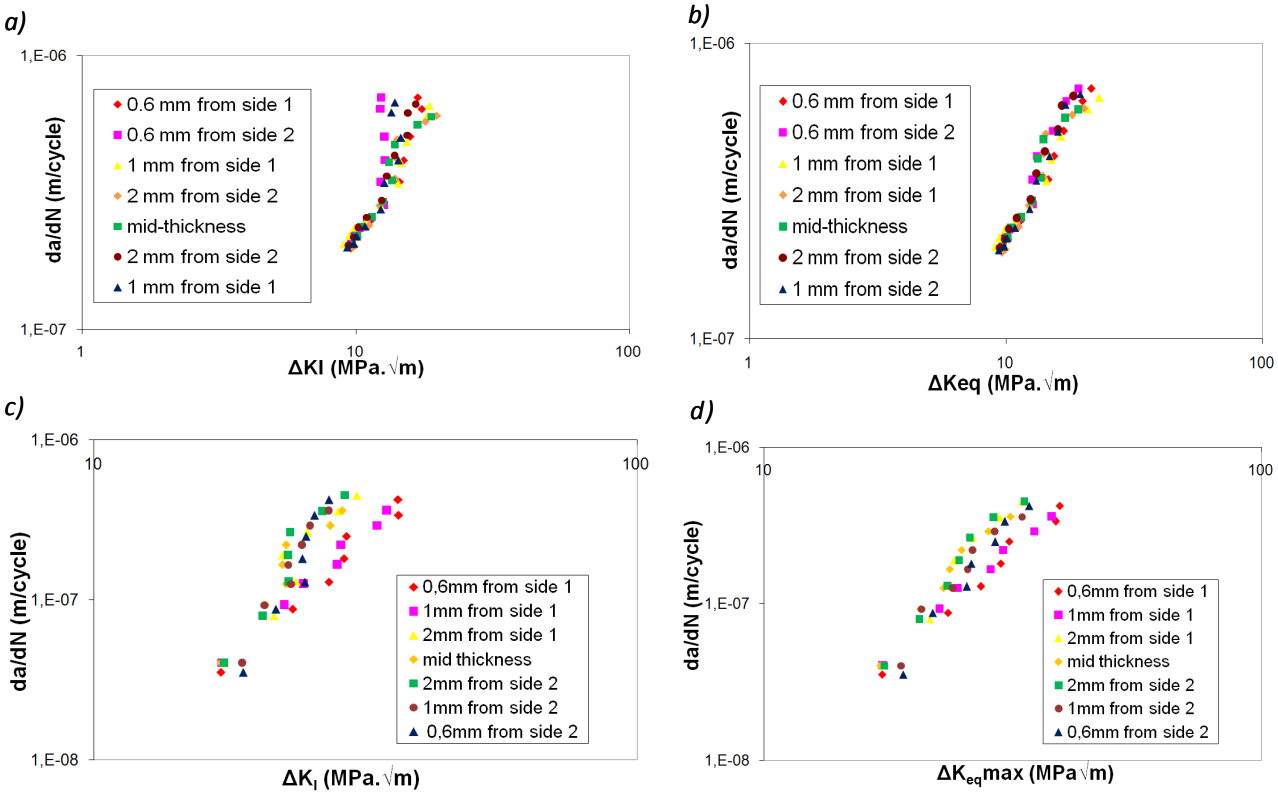

Figure 9: Correlation of measured crack growth rates in 7075-T6 with a) ΔK_I or b) ΔK_{eq} and in S355 steel with c) ΔK_I and d) ΔK_{eq}

5.2. Analysis of crack paths based on the local approach

Figure 10 shows the computed profiles of von Mises equivalent strain range ahead of the successive crack fronts for specimens CCP5a and CCP2a. Since ΔK increases as the crack grows, so does the equivalent strain range. $\Delta\varepsilon_{eq}$ rises near side surfaces. According to the fatigue criterion presented above, this should trigger a change in fracture mode (normal to slanted crack growth) there.

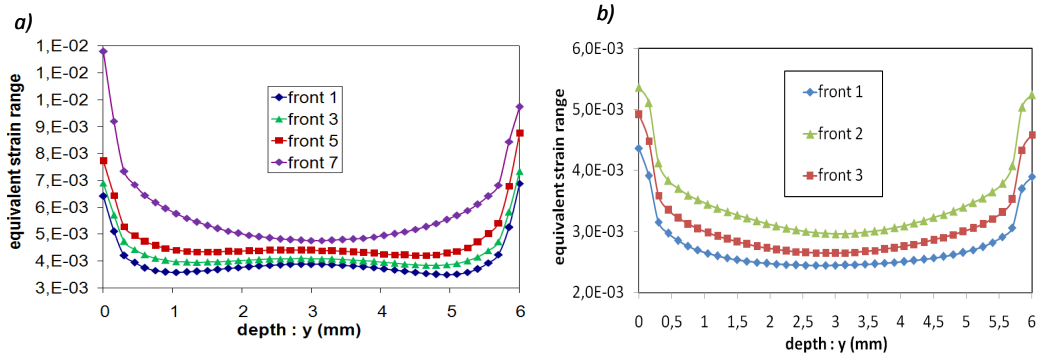

Figure 10: Profiles of Δ∈eq ahead of various crack fronts for a) specimen CCP5a and b) specimen CCP2a

Figure 11 shows the profiles of predicted twist angles. A progressive increase in twist angle as the crack grows is predicted near side surfaces. In some cases, as for the measured twist angles shown on Fig. 1b and 1d, the peak value of θ was not found at the free surface but somewhat inside.

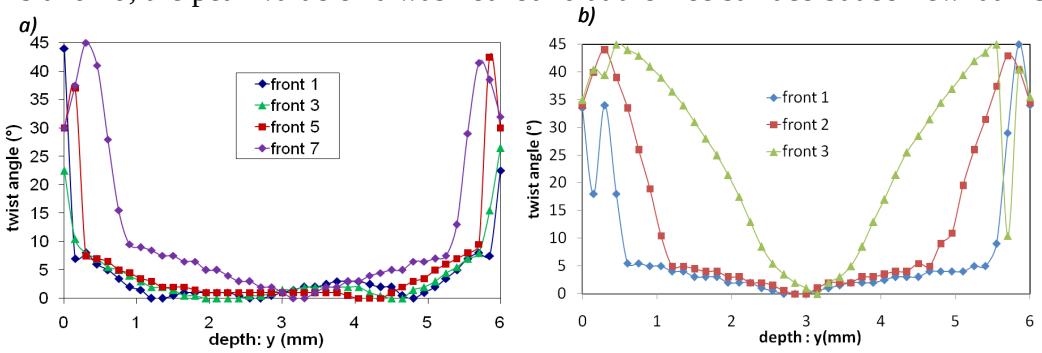

Figure 11: Profile of predicted twist angles for a) specimen CCP5a and b) specimen CCP2a

The shear lips width, t_s, was computed from such profiles, as the width of the part where $\theta \geq 4°$ in average. Figure 12 compares the predicted and measured evolutions of t_s. The model qualitatively captures the progressive increase in t_s.

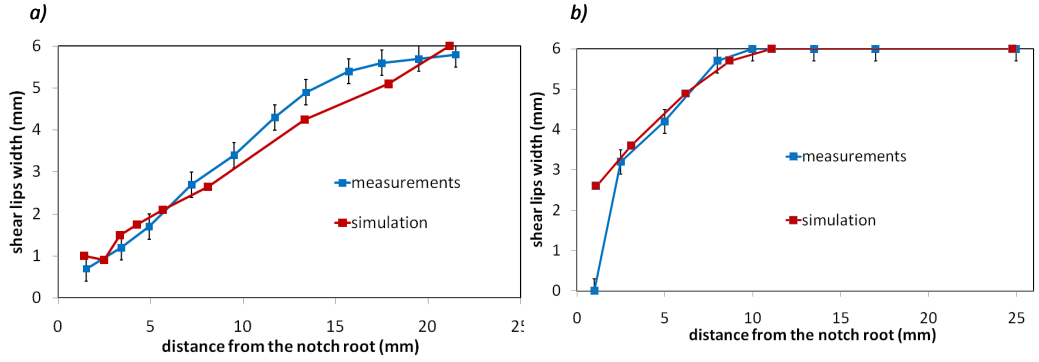

Figure 12: Predicted and measured evolution of shear lips width. a) ccp5a and b) ccp7a.

6. Conclusions and further work

Fatigue crack paths in thin sheets of aluminium alloy and mild steel were characterized in 3D in air and salt water. Crack twisting was delayed by a corrosive environment, which makes normal mode I crack growth more stable. Real 3D crack geometries were taken into account in an X-FEM model allowing the computation of K_I, K_{II}, K_{III} at any point along the front. Both the opening and shear modes contribute to slanted crack growth, whose rate correlates much better with $\Delta K_{eq} = \sqrt{\Delta K_I^2 + \Delta K_{II}^2 + \frac{\Delta K_{III}^2}{(1-\nu)}}$ than with ΔK_I. 3D elastic-plastic F.E. simulations and a local application of a fatigue criterion with a strain range-dependent critical plane qualitatively predicted the transition in crack growth mode and the twist angles. The challenge is now to develop incremental 3D simulations of mixed-mode slanted crack growth in a unified framework. The X-FEM method has to be modified to incorporate cyclic plasticity. This should allow predictions of both the crack growth kinetics and crack paths, based on the local approach mentioned above.

References

[1] J. Schijve, Shear lips on fatigue fractures in aluminium alloy sheet metal, *Eng. Fract. Mech*. 14 (1981), 789-800

[2] L.B. Vogelesang, J. Schijve, Environmental effects on fatigue fracture mode transitions observed in aluminium alloys, *Fat. Fract. Eng. Mat. & Struct*. 3 (1980) 85-98

[3] J. Zuidema, H.S. Blauw, Slant fatigue crack growth in Al 2024 sheet material, *Eng. Fract. Mech*. 29 (1988) 401-413

[4] J. Zuidema, M. Mannesse, Interaction of fatigue crack growth properties and crack surface geometry in Al 2024 , *Engng. Fract. Mechanics* 40 (1991) 105-117

[5] A.A. Shanyavsky, M.Z. Koronov, Shear lips on fatigue fractures of aluminium alloy sheets subjected to biaxial cyclic loads at various R-ratios, *Fat. Fract. Engng. Mat. Struct.* 17 (1994) 1003-1013

[6] S. Horibe, M. Nakamura, M. Sumita, The effect of seawater on fracture mode transition in fatigue, *Int. J. Fatigue* 7 (1985) 224-227

[7] K. Walker, S. Pendleberry, R. McElwee , Tensile and shear-mode cracking of titanium sheet in air and in salt water, in: *Effects of environment and complex load history on fatigue life*, p234-240, ASTM STP 462, ASTM Philadelphia (1970)

[8] L.P. Pook (1993), A finite element analysis of the angle crack specimen in*"Mixed-mode fracture and fatigue"* p 285-302, H.P. Rossmanith and K.J. Miller eds, ESIS 14, MEP, London

[9] A.Bakker, Three dimensional constraint effects on stress intensity distributions in plate geometries with through-thickness cracks, *Fat. Fract. Engng. Mat. Struct.*, 15 (1992) 1051-1069

[10] N. Moes, J. Dolbow and T. Belytschko, A finite element method for crack growth without remeshing *Int. Journ. Numerical Methods in Engineering* 46 (1999) 131-150

[11] Ph. Destuynder, M. Djaoua, S. Lescure, Quelques remarques sur la mécanique de la rupture elastique, *Journ. Mécanique Théorique & Appliquée* 2 (1983) 113-135

[12] T. Zhao, Y. Jiang Fatigue of 7075-T651 aluminum alloy *Int. J. Fatigue* 30 (2008) 834–849

PaperTemplatefor 13th International ConferenceonFracture

Yina F. M.Moscoso[1], Anderson S. Barbosa[2],João B. Uchôa[3],Luciano M. Bezerra[4], Marcus Sa[5]

[1,2,3,4,5] Departamento de Tecnologia,Universidade de Brasilia, Cep:70910-900, Brasil
Eletronic account:yifemunoz@gmail.com

Abstract

Ceramic coatings are generally used on the facades of buildings. These materials provide acoustic and thermal insulation, achieving a reasonable comfort in buildings. The coatings are run in layers: plaster, adhesive mortar, grout and ceramic. They are subject to different weather and thus prompted the actions coming from sudden temperature variation or thermal shock. When you combine these actions with different physical and mechanical characteristics of the materials used, states of stress and strain on the facades are produced, creating different pathologies, such as peeling parts, which can cause accidents on pedestrians. This paper presents a methodology for evaluating the fatigue resistance, using experimental, analytical and numerical analysis via Finite Elements and considering the system under the action of heat loss shock temperature characteristic in the city of Brasilia. Studies are in particular the influence of thermo mechanical stresses in fatigue failure of the adhesive mortar. Experimentally a Whöler curve (or "SN" curve) is obtained for the adhesive mortar. With the appropriate models for fragile materials, the fatigue strength of the mortar under compressive and tensile-compression is deduced. With the values of temperatures and correspondent stresses obtained via analytical and numerical analysis it is possible, with this methodology, to assess the fatigue resistance of the adhesive mortar on the coating system.

Keywords: Fatigue coating, Coatingsystem, Stress facades

1. Introduction

Coatings on facades of buildings are used, among other purposes, for protection against the weather which have aggressive agents that reduce its lifespan. They also, have the property to give thermal and acoustic comfort to the user inside the building. Thus, the facades are exposed to various situations of thermal loads, arising from changes in temperature and isolation, which results in thermal stresses requested by the materials that make up the coating.

A ceramic coating system is an element for presenting different materials in different applications that must always maintain a balance between the stresses acting on the system and tension resistance of the materials so as not to compromise the integrity of the facade. In this paper we present the stresses inside the structure produced by outside thermal shock, when using clearceramic (low energetic absorption of heat) and dark ceramic (high-energetic absorption of heat), evaluating the structure performance against thermal shock cycles, which cause fatigue. The fatigue is evaluated by tracing the experimental curve or Wöhler SN, based on the principle that the thermal stresses acting on the system tend to cause their rupture by fatigue and using a coating structure composed of ceramic pieces and groutconstituting the outermost layer, connected with a thin layer of adhesive mortar in turn connected to a base composed of plaster. These structures are superposed on a masonry wall, which is coated with a layer of plaster facing the inside of the building. We tried to represent such a constructive disposition commonly used in Brazil.

2. Fatigue

The degradation process by fatigue is linked to deterioration under cyclic loading which leads to the emergence and development of microcracks or microfissures on the pre-existing material, and may cause rupture of the structure. The higher the stress level used, the lower the number of cycles achieved, and thus more rapidly deteriorate the mortar by fatigue, for the same frequency of loading. Coating systems are subject to an increase of stress due to temperature differences between the top and bottom of the wall and the coating system, causing large thermal differential that origin the warpage of the coating.

For the static fatigue analysis breakthrough curves are usually used that can be adapted to cyclic loading. In the analysis of fatigue strength material such as mortar which is a brittle material a classical curve that may be used is the Mohr-Coulomb curve. This curve defines the fatigue resistance of the material and the expected life of the material can be used with the stresses generated by the thermal shock on the system, and indicate whether there is a risk of collapse due to fatigue mortar.

3. Characterization of mortar

In this work the mortar ACII Votomassa was used, prepared according to the manufacturer's recommendations.

3.1. Definition of the body-of-evidence

Fatigue tests in compression, body-of-proof cylindrical 10x20cm were chosen according to the study by SUELEN, 2009.

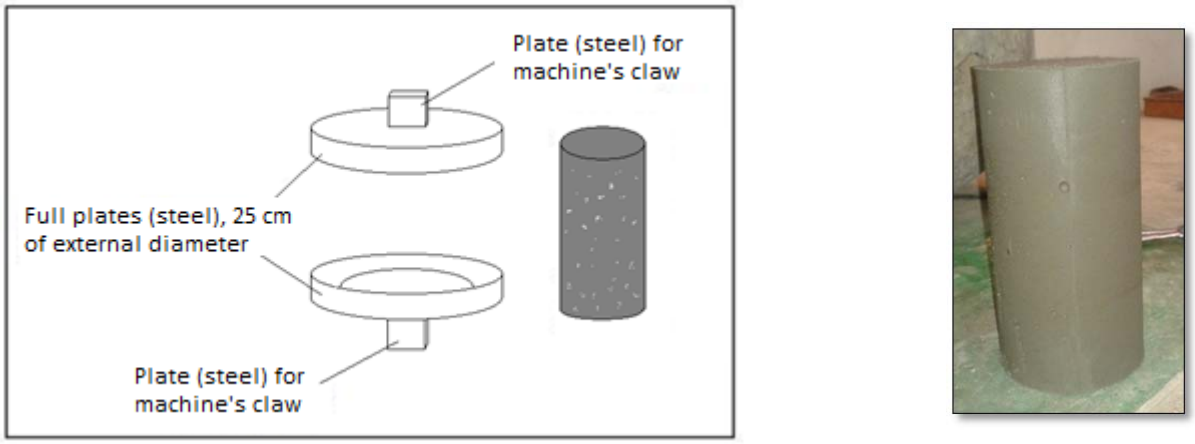

Figure 1 - Mechanism to support the fatigue test and compression test specimen.

3.2 Fatigue Testing

The fatigue test consists in applying a cyclic compression load on a body-of-evidence in order to measure how many cycles the body-of-evidence resists before rupturing. Thus, we obtain the Wöhler curve or SN curve. This assay is also capable of supplying a characteristic alternated stress for each material, below which the body of the test piece no longer breaks. The main results of this assay are: Narrow fatigue resistance (σ_{Rf}), ie the alternating stress value below which the body of

the test piece not further ruptures by fatigue; Life fatigue (N_f), or the number of cycles that rupture occurs in the body of the test piece for a particular alternated stress level (S) above (σ_{Rf}).
After sizing the body-of-evidence, the realization of the mortar compression fatigue test is next. The tests were performed on a universal testing machine MTS 810, being made via control force which results in constant amplitude alternating stress across the tests.
The body of the test piece was cast in a mold iron, running in three layers of 4 cm each, and applying 25 blows on each layer. The procedure for determining the body-of-evidence to the MTS 810 was given as follows: initially, for the specimen used in the compression test, we used two circular steel plates holding the specimen fixed. As can be seen in Figure 2a and Figure 2b.


(a)


(b)

Figure 2– (a) - (b)Endurance test compression.

4. Thermal Analysis

The purpose of the thermal analysis was to determine how the temperature distribution behaves inside the wall, and therefore inside coating structure, after the incidence of atmospheric thermal shock abroad. The first mathematical simplification was made to adopt an equivalent wall composed of only one material, which replaces the conventional wall, composed of five layers of materials. Thus it was possible to work with only one equivalentthermal diffusivity parameter(α_{eq}).
The temperature distribution analyticalequation$U(y,t)$varies in function of the wall thickness (direction$y$) and time (t).It was obtained from the problem depicted in partial differential equation of heat diffusion:

$$\alpha_{eq}\frac{\partial^2 U}{\partial y^2}=\frac{\partial U}{\partial t} \tag{3}$$

The boundary conditions of the problem, then, represent the heat exchanges by conduction and convectionat the faces facing the interior and exterior of the building:

$$-K_{eq}\frac{\partial U(d,t)}{\partial y}=h_e\big(U(d,t)-U_\infty(t)\big)-\gamma I_g(t) \tag{4}$$

$$-K_{eq}\frac{\partial U(0,t)}{\partial y}=h_i\big(U_i-U(0,t)\big) \tag{5}$$

Where$U_\infty(t)$is the air temperature outside the building, and$I_g(t)$represents the supply of thermal energy from the sun to the facade over time, modeling it as a source of heat within the system. Having in mind that τ is the time instant at which occurs the heat shock, these features were modeled as it follows:

$$U_{\infty}(t) = U_a + (U_c - U_a)H(t-\tau) \tag{6}$$

$$I_g(t) = \gamma I_g\big(1 - H(t-\tau)\big) \tag{7}$$

Where,$H(t-\tau)$is the Heaviside mathematical function (step function) definedby

$$H(t-\tau) = \begin{cases} 0, & t < \tau \\ 1, & t \geq \tau \end{cases} \tag{8}$$

Other variables of the problem are:

- $K_{eq} = 1{,}19$ W/m°C: Thermal Conductivity of the equivalent wall;
- $\alpha_{eq} = 6{,}33 \times 10^{-7}$m²/seg: Equivalent Thermal diffusivity. Single value of thermal diffusivity for the entire coating structure;
- $d = 25{,}15$cm: Total thickness of the wall where the structure of ceramic coating, outward looking;
- $l_1 = 2$cm: Thickness of plaster layer facing the interior of the building. Not part of the structure of the ceramic coating;
- $l_2 = 20$cm: Thickness ofthe masonry wall layer. Substrate where theceramic coating structure is applied;
- $h_i = 9$W/m² °C: Coefficient of air heat transfer from inside the building into the wall structure where the internal plaster layer lays;
- $h_e = 18$W/m² °C: Coefficient of atmospheric air heat transfer from outside the building into the wall structure where the ceramic coating lays;
- $U_i = 21$°C: air temperature inside the building where is the wall subjected to thermal shock;
- $U_a = 34{,}60$°C: Temperature of the atmospheric air outside the building moments immediately prior to the occurrence of thermal shock;
- $U_c = 22{,}14$°C: Temperature of the atmospheric air outside the building moments immediately following the occurrence of thermal shock;
- λ_n:∶ Eigenvalues obtained numerically by the following equation:

$$\lambda \cos \lambda d - \frac{\lambda^2 K_{eq}}{h_i} \sin \lambda d + \frac{h_e}{K_{eq}} \sin \lambda d + \frac{\lambda h_e}{h_i} \cos \lambda d = 0 \tag{9}$$

- CF_n: Coefficients of Fourier Series describing the temperature distribution;
- γ: Coefficient of Solar Radiation Absorption of ceramic coating. Worth 0.45 to 0.95 for clear anddark ceramic pottery.
- $I_g = 692$ W/m²: Solar Thermal Energy Incident on the ceramic surface, moments immediately prior to heat shock.

The values of the parameters described were obtained in Saraiva (1998), Moaveni (2008), Uchôa (2007) and Rosa (2001). Thus the modeled thermal shock itself contains a mathematical simplification, which consists in the instant change of atmospheric conditions in contact with the

outer face of the wall. A further simplification is the admission that before the heat shock event, the wall is in a steady state temperature distribution, simplification considered conservative.
Thus, solving the problem has been that the coating structure in equation ($t \geq 0$) is given by:

$$U(y,t) = \frac{h_e U_c K_{eq} + h_i U_i K_{eq} + h_i h_e U_i d + [h_e h_i (U_c - U_i)](y + l_1 + l_2)}{K_{eq}(h_e + h_i) + d h_e h_i} - \sum_{n=1}^{\infty} CF_n e^{-\alpha_{eq} \lambda_n{}^2 t} \left(\sin \lambda_n (y + l_1 + l_2) + \frac{\lambda_n K_{eq}}{h_i} \cos \lambda_n (y + l_1 + l_2) \right) \quad (10)$$

$$CF_n = \frac{2\lambda_n{}^{-1} h_i \left[h_i{}^2 (\sin \lambda_n d - \lambda_n d \cos \lambda_n d) + \lambda_n{}^2 K_{eq} \sin \lambda_n d \, (h_i d + K_{eq}) \right] \left[h_e (U_c - U_a) - \gamma I_g \right]}{\left(2\lambda_n K_{eq} h_i (\sin^2 \lambda_n d) + \left(\lambda_n{}^2 K_{eq}{}^2 - h_i{}^2 \right) \sin \lambda_n d \cos \lambda_n d + \lambda_n d \left(\lambda_n{}^2 K_{eq}{}^2 + h_i{}^2 \right) \right) \left(K_{eq}(h_e + h_i) + d h_e h_i \right)} \quad (11)$$

Therefore, we obtain values of temperature in each wall layer in the form of one-dimensional distribution.

5. Adopted numerical model

To evaluate the stresses that arise in the three outer layers of the wall(which characterize the structure of the coating)regarding the temperature distribution described by the analytical equation obtained, we choose to model the coating structure with a finite element mesh. Modeling in a coating system of 4.90 m length in each direction, having in mind that Fiorito (1994) suggests that, on a wall, positioning the drive joints should be at least every 4.90 m distance. However, as been done in previous studies of Uchôa (2007) and Saraiva (1998), it is appropriate to focus the analysis in only a small region of that piece of facade. Therefore, a region containing only three ceramic riding up a region equivalent shell around the three ceramics is choosen, as shown in Figure 3 below:

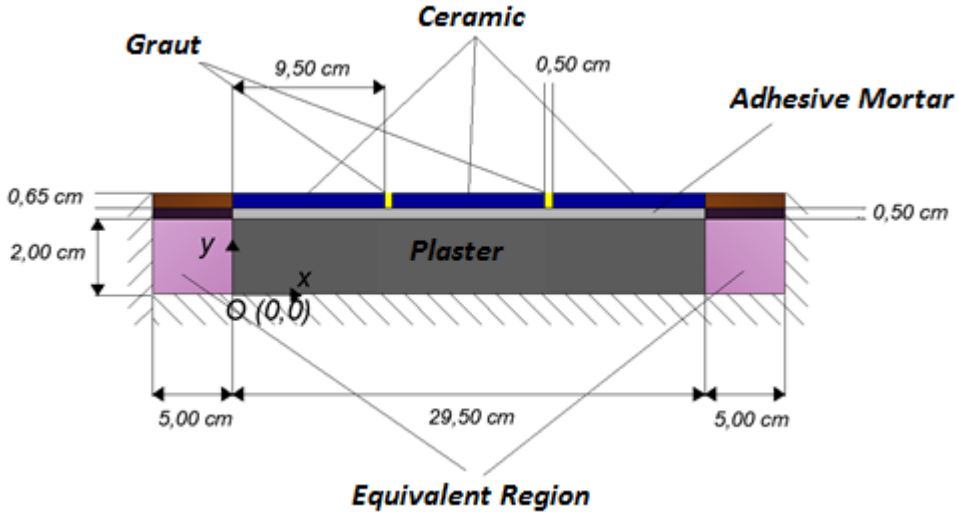

Figure 3-Structure model to be analyzed and dimensions.

The boundary condition used to simulate the structure is based in the assumption that the substrate is rigid.Thus, in the boundary between the coating and the substrate the displacements in the y-axis must be equal to zero. The equivalent regions and their very neighborhoodare not considered objects of study, being focus the central regions of the system. The idea would be to avoid disturbances generated at the boundary, which does not produce consistent results, as argued by Saraiva (1998).

Table1- Material properties of the coating structure and facade equivalent.

Material	**ElasticityModulus - E (GPa)**	**Thermal Expansion Coefficient - α ($°C^{-1}$)**	**Poisson'sRatio - ν**
Plaster	5,499	$11,5 \times 10^{-6}$	0,2
Mortar	3,562	$8,7 \times 10^{-6}$	0,2
Graut	7,879	$4,2 \times 10^{-6}$	0,2
Ceramic	41,600	$6,8 \times 10^{-6}$	0,2
Eq.Plaster	0,11941	530×10^{-6}	0,2
Eq.Mortar	0,07735	400×10^{-6}	0,2
Eq.CeramicandGraut	0,78891	310×10^{-6}	0,2

Once modeled of the facade, the application ANSYS (1994) is ran to convert it into finite elements. Among the factors contained in the library of ANSYS (1994) the element named PLANE42 was used, which has four nodes having two degrees of freedom per node: the displacements in the directions *"x"* and *"y"*.The PLANE42 element accepts temperature as charging, and allows inputting parameters such as elasticity modulus, thermal expansioncoefficient of, Poisson's ratio in the materials and structures modeled with the element.

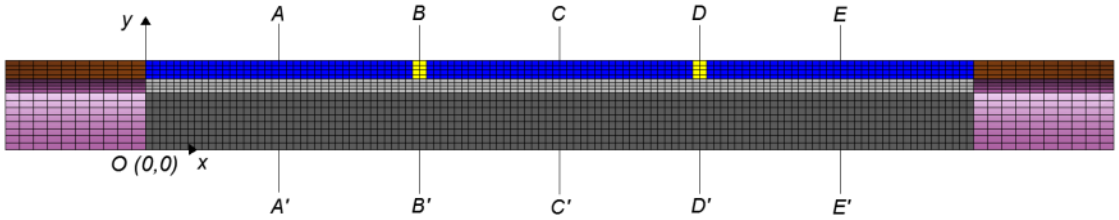

Figure 4 - Finite element mesh structure characterizing the coating studied.

6. Results Presentation

After insertingnodal temperatures in each nodal layer the model, obtained through the temperature distribution equation, the application ANSYS (1994) is ran again, outputtingthestresses that affect the coating structure. The stresses obtained were: SX to the normal stresses in the x direction; SY to the normal stress in the y direction; SXY for the shear stresses; and S1 and S2 to the principal stresses.

According to the above, two constructive situations were studied: using clear ceramic, and using dark ceramic. In each case were evaluated three sections shown in Figure 4: AA ', passing through

the center of the first ceramic; BB' passing through the layer of grout, and CC 'passing through the ceramic core. Therefore, the influence of ceramic and cross-sectional analysiswere evaluated.

6.1 Temperature Distribution

As explained in the item 4, we adopted the simplifying assumption that, before the heat shock, the coating structure presented steady state temperature distribution. Therefore the most critical condition in which the structure has higher temperatures is the initial. When the thermal shock atmospheric occurred, the coating structure begins to gradually lose heat to the air, seeking new situation of steady state, with higher speed of temperature decrease in the first few minutes. The clear ceramic shows lower temperatures than the dark because it has a lower coefficient of thermal absorption.

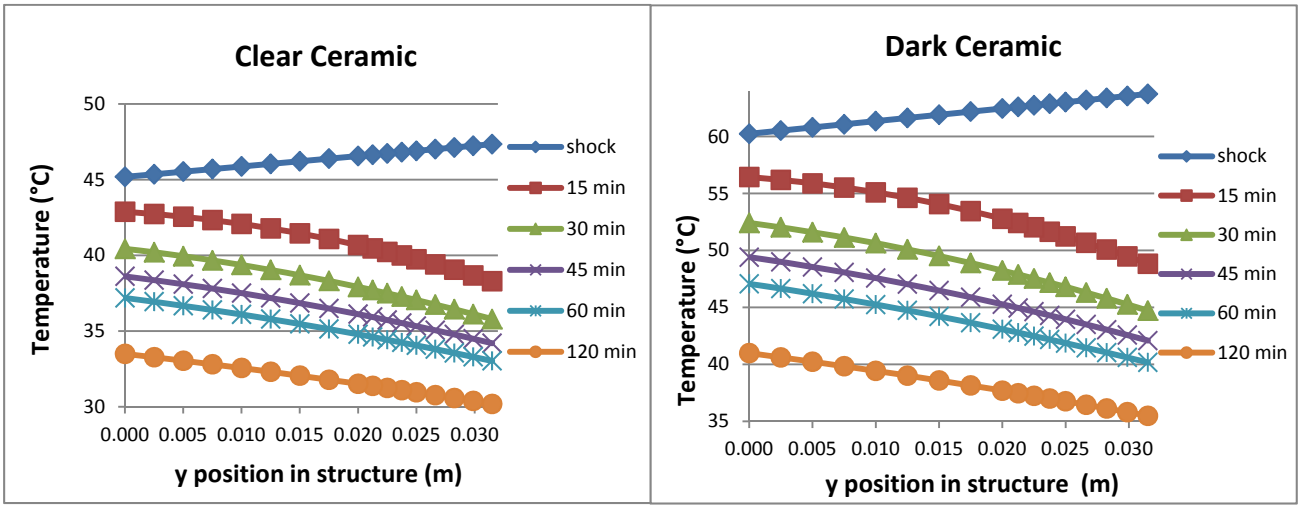

Figure 5 – Temperaturesobtained for ceramics dark and clear

6.2Analysis of stresses

Considering that the highest temperatures are shown at the beginning, also the highest stressesare present at that moment. Because the model with clear ceramic works with lower temperatures, stresses values in this model were lower when compared with the dark ceramic. During the cooling of the layers of the structure, due to thermal shock, there is also the relief of the stresses that request it. Negative values indicate compressive stresses, and the positive tensile stresses.

With regard to stresses SX, it was found that the models worked with compressive stresses in all three layers. This is due to the fact that when the structure is heated before heat shock, it tends to swell; however, their deformation is prevented by the boundary conditions of zero displacement at the ends. From here the compressive stress analysis are originated. The ceramic pieces in sections AA 'and CC' have the highest stress values because they have the higher modulus of elasticity (41.6 GPa). Because of high modulus of elasticity, the ceramic ultimately absorb much of the compressive stress that would be passed on to lower layers. Moreover, the grout atBB' top is significantly less rigid than the ceramic (modulus of 7.879 MPa) and therefore ends up being compressed by the ceramic part, deforming and allowing major deformations, thus,allowing the passage of more stresses for the subsequent layers of adhesive mortar and plaster, which is why

tensions SXin plaster and adhesive mortarof BB’ section are higher than observed in sections AA’ and BB’.

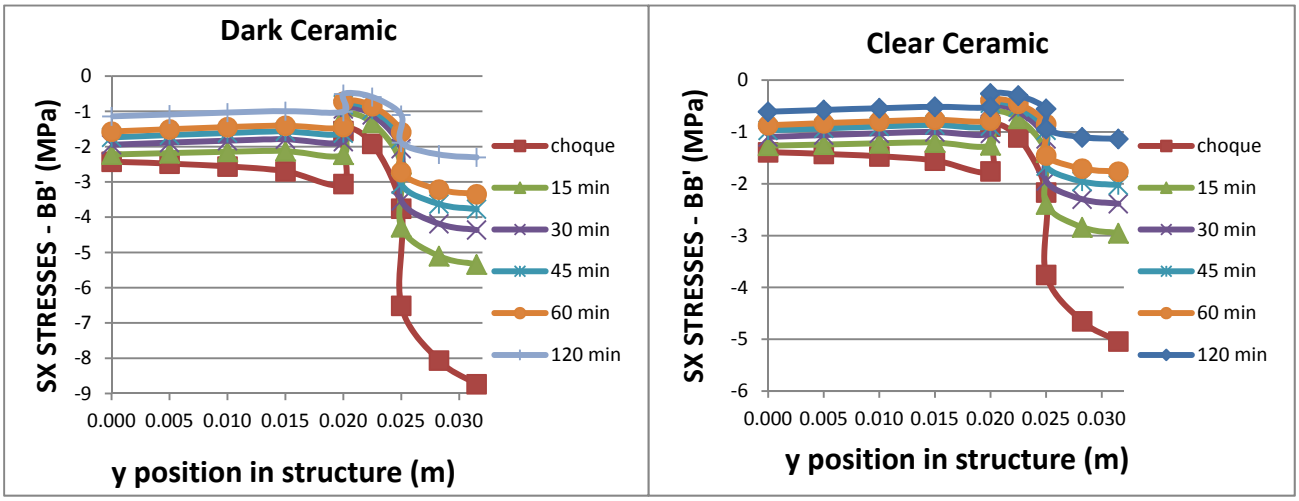

Figure 6 –SX stresses in section BB’ after thermal shock, ceramicsclear and dark

Regarding the SY stresses, due to the compressive stress in the x direction, the sections AA’ and CC’ there were tensile stresses in the sense tendency to detachment between layers of the structure. The highest stress values were observed in these layers beneath the layer of plaster, where was restrictionof no movement. Moreover, layers of plaster and adhesive mortar section BB’ worked with SY compression stresses, and the main reason is because the ceramic parts are compressing the grout in the x direction. In response, crushed grout spreads up and down in the vertical direction, compressing both the adhesive mortar as the plaster situated below it.

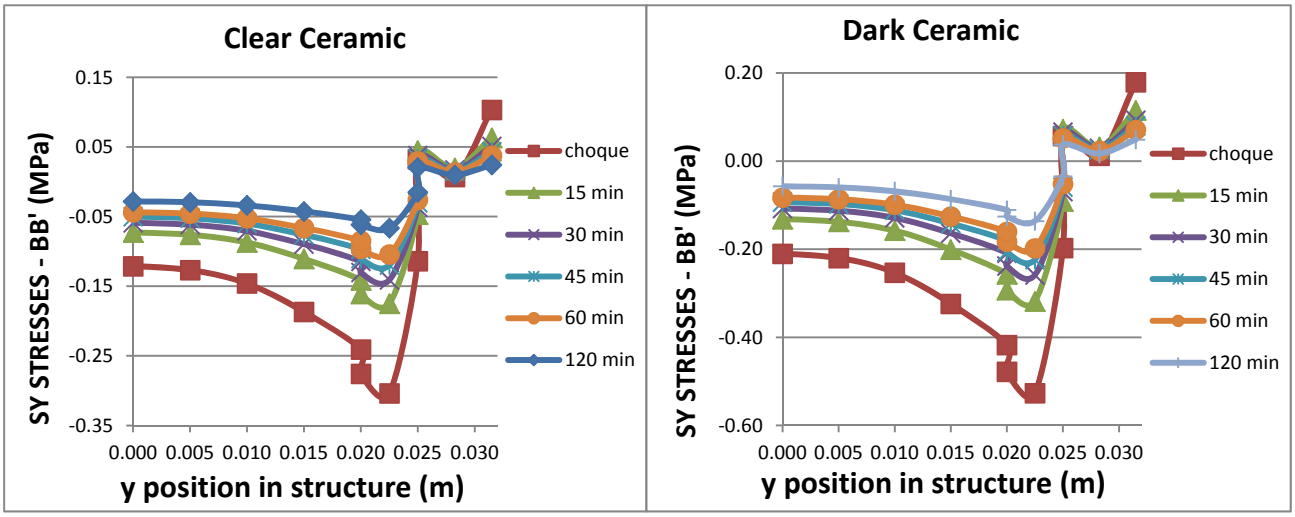

Figure 7 – SY stresses in section BB’ after thermal shock, ceramicsclear and dark.

TheSXY shear stresses encountered to the coating structure in both models were very low compared to the stresses SX and SY. In section CC’ the values were effectively zero, due to the central position of this section. The reason for the low values of SXY is because of the deformations within the structure are of thermal nature, which normally do not produce shear stresses. As a result, the values should be more restrictions on movement imposed on the structure than the thermal loading

properly. So, it follows that the principal stresses S1 and S2 have almost the same values SY and SX, respectively.

6.3Performance of the mortar layer on the fatigue

Given that the thermal shock is a transient phenomenon, which produces variation in the stress state along time, one can understand the difference between the final state and the initial state of stresses as the alternated loads that affect the structure. Then it is appropriate to evaluate the performance of the structure (specifically the adhesive mortar) as fatigue, determining how many cycles of alternating stresses (S) are necessary to the rupture.
In this paper, only the performance of the layer of adhesive mortar is evaluated. For this, Equations 12 and 13 are used, which displays the linearized equation of SN curve (or Wöhler curve) for the adhesive mortar, obtained under test. The critical situations, where the highest stresses occurred, in the mortar, were on top of layer (grout interface) to the stresses S2, and at the base of the layer (plaster interface) to stress S1, both in section BB' section.

$$S = 9{,}5771 - 0{,}7523\log(N), \quad N < 1{,}1 \times 10^6 \tag{12}$$

$$S = \sigma_{Rf} = 5{,}06\,MPa, \quad N > 1{,}1 \times 10^6 \tag{13}$$

Table 3 – Calculation of alternatedstress

CASE1 (CLEAR CERAMIC)			
	PRINCIPAL STRESSES (MPa)		ALTERNATED STRESSES(MPa)
	during shock	120 min	ΔS = S (120 min) - S (Shock)
S1	-0,27579	-0,06181	-0,06181 – (-0,27579) = 0,21398
S2	-2,16630	-0,55252	-0,55252 – (-2,16630) = 1,61378
CASE2 (DARKCERAMIC)			
	PRINCIPAL STRESSES (MPa)		ALTERNATED STRESSES(MPa)
	during shock	120 min	ΔS = S (120 min) - S (Shock)
S1	-0,47798	-0,12571	-0,12571 – (-0,47798) = 0,35227
S2	-3,75780	-1,10190	-1,10190 – (-3,75780) = 2,65590

So for both cases, there is no risk of fatigue failure in any of the directions of principal stress, because the variation of both principal stresses ΔS1 and ΔS2 is smaller than the threshold fatigue resistance (σ_{Rf}=5,06 MPa).

7. Final Thoughts

The methodology consisted of three phases: characterization tests of the behavior of the adhesive mortar when subjected to cyclic loading; the conception of an analytical equation to explain the temperature distribution inside the coating structure, in responseto the incidence of heat loss shock;

and using numerical model in finite elements to determine the stresses arising within the coating due to the temperature distribution over time.

In step test was determined the 5,06Mpavalue as the limit of fatigue resistance of the adhesive mortar. In consequence, as the alternated stresses levels in the mortar layer does not reach this value, according to this methodology there is no risk of breakage of this layer to either case. This is due to the fact that among the materials that compose the structure, the mortar is the one with the lowest value of elasticity modulus.

However, it is recommended to apply the methodology also for the other layers, especially layers of grout (subjected to large compression caused by the movement of ceramics) and ceramic (because they are subject to the higher stress levels, including bending stresses). Consequently, it is necessary to perform characterization tests for types of grout, besides testing flexural behavior for ceramic pieces.

References

ANSYS.Analysis System. Houston, PA: ANSYS, 1994. 5.4v.

FIORITO, A J. S. I.Manual de Argamassas e Revestimentos – Estudos e Procedimentos de Execução", Editora Pini. São Paulo, SP, 1994

MOAVENI, Finite Element Analysis, Theory and Application with ANSYS.Prentice Hall Inc..New Jersey, United States, 2008

ROSA, J. A. Determinação dos Campos de Velocidade e Temperatura em Ambientes Ventilados, Dissertação de Mestrado apresentada à Universidade Federal do Rio Grande do Sul, Porto Alegre, RS, 2001

SARAIVA, A G. Contribuição ao Estudo de Tensões de Natureza Térmica em Sistemas de Revestimento Cerâmico de Fachada. Dissertação de Mestrado apresentada à Faculdade de Tecnologia da Universidade de Brasília, Brasília, DF. 1998.

UCHÔA, J. C. B. Procedimento numérico e experimental para a avaliação da resistência à fadiga de sistemas de revestimento, Dissertação de Mestrado apresentada à Faculdade de Tecnologia da Universidade de Brasília, Brasília, DF, 2007.

Statistical Model of Submicrocrack Evolution under Cyclic Loading

Oleg Plekhov*, **Oleg Naimark**

Institute of continuous media mechanics Ural Branch Russian academy of science, 614013, Perm, Russia
*poa@icmm.ru

Abstract To describe the damage evolution under high- and gigacyclic fatigue we develop a generalization of statistical model of microcrack evolution. The statistical model combined with a stochastic description of damage accumulation process allows us to describe the interaction of microplastisity and damage (submicrocracks) under cyclic deformation and propose a model of fatigue crack initiation. Considering a fatigue crack initiation as a blow-up regime of damage accumulation we propose a method for prediction of SN-curves of materials. The SN-curve has dual form caused by shift the location of crack initiation from surface to the bulk of specimen.

Keywords statistical model of defects, gigacyclic fatigue, dual Woller curve

1. Introduction

It is now well known that real metals have complex structure, which is a hierarchy of different levels. Under deformation process the structural evolution observed at all scale levels and leads to irreversible deformation and destruction. The most interesting situation observed under gigacyclic fatigue when the stress amplitude is less than the yield stress of materials and fracture emergence under macroscopic “pure” elastic conditions. One of most critical issue of the gigacyclic fatigue is the location of fatigue crack initiation. The decreasing of stress amplitude leads to the shift of crack initiation from specimen surface to the bulk.

To develop a model of defect evolution under small stress amplitude we have to choice of the basic physical level of description of the material microstructure and describe the geometry of the elementary defects. Analysis of the experimental results of the study of structural levels of plastic deformation and fracture [1,2] and resent experimental investigation of damage evolution of fine grain metals can hypothesize that scale level with the size of submicrocracks 0.1-0.3 mm plays a key role in this process [3]. The failure process includes both the nucleation of new microcracks and their development. The contribution of these processes in the failure varies depending on the structure of the material conditions of its loading.

The defect kinetics is different near specimen surface and in the bulk. The rate of microcracks nucleus initiation in the surface layers of one to three orders of magnitude higher than in the bulk material. It is also well known that for high concentration the defect ensemble exhibits both collective and nonlocal effects.

One of the possible descriptions of defect kinetics is the statistical model of defect ensample. This model has to take into account the stochastically properties of defect initiation, their nonlinear integration and link between micropalsticity and damage accumulation.

This work is devoted to the development of such model in the application to cyclic loading of metals. The paper is organized as follow. The first part is devoted to the statistical description of submicrocrack ensemble. The statistical description was developed based on the mean field approximation of defect interaction and allows us to investigate the effect of initial nucleus concentration of defect evolution process and determine the equilibrium state of materials with

defects.

The second part of the paper devoted to the thermodynamic description of deformation process. Based on the results of solution of the statistical problem we introduce a new thermodynamic variable and derive the constitutive equation for metals with submicrocracks.

In the last part the proposed constitutive equation applied for the description of defect kinetics near specimen surface and in the bulk. The model allows us to describe the shift of crack initiation location from the specimen surface to the bulk and numerically obtain dual S-N curve for 2023 T3 aluminum alloys.

The discuses about physics of the investigated process and proposition for father experimental verification of the model presented in conclusion.

2. Statistical description of damage accumulation in metals

The data obtained from systematic studies of defects evolution, carried out at Physical technical institute named after A.F. Ioffe RAS shows that the volume defects (submicrocracks with characteristic size about 0.1 mkm) play the important role in deformation process [3]. These defects emerge at the early stage of deformation and effect on the microplasticity and failure processes. The same situation could be observed under cyclic loading. The best materials for the experimental proofing of this hypothesis are the fine grain metals which contained the high concentration of volumes defects (micropores) after manufacturing procedures (equals channel pressing).

The value, geometrically representing the real microcracks with allowance made for a variety of their shapes, sizes and arbitrary orientations as well as or the crack initiated material loosening, can be introduced in terms of the dislocation theory [4].

The dislocation loop D, bounding the surface S, where the displacement vector undergoes a finite increment equal the Burgers vector b, is characterized by the tensor of the dislocation moment $S\nu_i b_k$. The sum of N dislocation loops, which is equivalent to a microcrack, introduces the tensor of dislocation moment of a microcrack:

$$s_{ik} = \sum_{l=1}^{N} S^l \nu_i^l b_k^l, \tag{1}$$

where $\vec{\nu}^l$ is the vector of a normal to the surface S of the 1-th loop. Small sizes and multiple character of microcrack nucleation as well as size and orientation distributions of microcracks permit averaging of their parameters over elementary volume to obtain the macroscopic tensor

$$p_{ik} = n\langle s_{ik} \rangle, \tag{2}$$

where n is a concentration of microcracks.

A solution of equation (2) was presented in [4]. The solution depends on structural parameter δ and defect concentration n. Figure 1 presents two solutions of the equation (2) for $\delta = 1.1$ and different values of initial defect concentration (curves 1,2).

To describe a real deformation process which characterized by the growth of defect concentration we propose that the representative material volume V_r contains $n_0 V_r$ defects

nucleuses. Following [5] we propose that the applied stress activates the defects and this process can be described as a stochastic Poisson point process with intensity function $n(\Sigma)$.

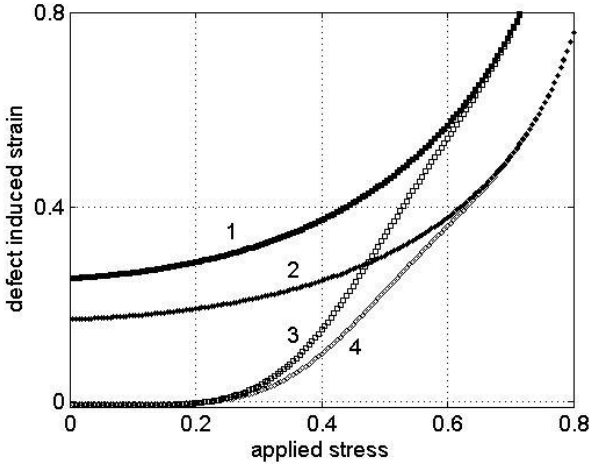

Figure 1. Equilibrium defect induced strain versus applied stress for different values of initial defect concentration (curves 1,2) and the mean values of defect induced strain during deformation process (curves 3,4).

Intensity function describes both the growth of active defects (which contribute to the defect induced strain) and growth defect nucleuses. Following the experimental data [5] about evolution of microcrack concentration we can assume the following approximation for intensity function

$$n(\Sigma)=\frac{\alpha_0}{2}\left(1+Erf\left(\frac{\Sigma-\Sigma_0}{\Sigma_1}\right)\right)(n_0+\alpha_1\Sigma), \tag{3}$$

where $\alpha_0,\alpha_1,\Sigma_0,\Sigma_1$ - material constants.

The probability of find N active defects in representative material volume is $P(N)=\frac{n(\Sigma)^N Exp(-n(\Sigma))}{N!}$.

The stochastic consideration of defect evolution process change the self-consistency equation for defect induced deformation. The solution of equation (2,3) is presented in figure 1 (curves 3,4). For small stress values we observe a pure elasticity which passes to the plastic deformation with different intensity. The intensity of plastic deformation and damage accumulation depends on the initial concentration of defect nucleuses.

3. Thermodynamics of metals with defects

A thermomechanical process of plastic deformation obeys the momentum balance equation and the first and second laws of thermodynamics. In the case of small deformation, these equations involve the following thermodynamic quantities: volumetric mass ρ, specific internal energy e, strain and stress tensors ε_{ik} and σ_{ik}, heat supply r, heat flux vector $\vec{q}$, specific Helmholtz free

energy F, and specific entropy η. The energy balance and the entropy can be written as

$$\dot{e} \equiv \left(\dot{F} + \eta\dot{T} + \dot{\eta}T\right) = \frac{1}{\rho}\sigma_{ik} : \dot{\varepsilon}_{ik} + r - \overline{\nabla} \cdot \overline{q}\,, \tag{4}$$

$$\dot{\eta} - \overline{\nabla} \cdot \left(\frac{\overline{q}}{T}\right) - r' \geq 0\,,$$

where $\overline{\nabla} = \left(\frac{\partial}{x_1}, \frac{\partial}{x_2}, \frac{\partial}{x_3}\right)$, the superposed dot stands for the material time derivative.

We assume the following kinematical relationship for the material under study

$$\tilde{\varepsilon} = \tilde{\varepsilon}^{e} + \tilde{\varepsilon}^{p} + \tilde{p} + \tilde{\beta}\left(T - T'\right), \tag{5}$$

where ε_{ik}^{e} is the elastic strain tensor, $\tilde{\varepsilon}^{p}$ is the plastic strain tensor (related to the defect motion), $\tilde{\beta}$ is the thermal expansion coefficient tensor, and T' is the reference temperature.

To introduce the list of independent variables for the free energy $F\left(\tilde{\varepsilon}^{e}, T, \tilde{p}\right)$ the equations (4) give

$$-\vec{q} \cdot \frac{\overline{\nabla} T}{T} - F_{\tilde{p}} : \dot{\tilde{p}} + \frac{1}{\rho}\tilde{\sigma} : \left(\dot{\tilde{\varepsilon}}^{p} + \dot{\tilde{p}}\right) \geq 0\,, \tag{6}$$

$$c\dot{T} = \overline{\nabla}\overline{q} + r + Q^{e} + Q^{p}\,, \tag{7}$$

where $Q^{e} = TF_{T\varepsilon^{e}} : \dot{\tilde{\varepsilon}}^{e}$ - heat production due to thermoelastic effect; $Q^{p} = TF_{Tp} : \dot{\tilde{p}} + \frac{1}{\rho}\tilde{\sigma} : \dot{\tilde{\varepsilon}}^{p} + \left(\frac{1}{\rho}\tilde{\sigma} - F_{p}\right) : \dot{\tilde{p}}$ - represents the inelastic part to the heat production; $c = -TF_{TT}$ - the specific heat capacity.

To assume the linear links between thermodynamic forces and the thermodynamics fluxes, we obtain the constitutive equations

$$\dot{\tilde{\varepsilon}}^{p} = l_{\varepsilon^{p}} F_{\tilde{\varepsilon}^{e}} + l_{\varepsilon^{p}p}\left(F_{\tilde{\varepsilon}^{e}} - F_{\tilde{p}}\right), \tag{8}$$

$$\dot{\tilde{p}} = l_{p}\left(F_{\tilde{\varepsilon}^{e}} - F_{\tilde{p}}\right) + l_{\varepsilon^{p}p} F_{\tilde{\varepsilon}^{e}}\,, \tag{9}$$

where the function F_{p} follows from the presentation of free energy given by the statistical model of solid with mesodefects.

The specific free energy of the system can be calculated as $F = -n_0 Q \cdot \ln Z$ or

$$F(p) = \frac{1}{2}\lambda p_{ik}^2 - n(\sigma_{ik})Q \cdot ln \int exp\left\{\left[(\gamma\sigma_{ik} + \lambda p_{ik})s\nu_i\nu_k - \alpha s^2\right]/Q\right\} ds d^3\vec{\nu}. \quad (10)$$

The equation (10) request a determination materials constants at micro level and complex calculation. At macroscopic level the equation (10) can be approximated by corresponding function [4].

To consider the influence of diffusion processes on defect nucleation and evolution and to study the localization effects of the damage accumulation, we have introduced in the expression of the total free energy F the term describing spatially-nonuniform distribution of microcrack density tensor p_{ik}

$$\mathrm{F} = \frac{1}{2}K\varepsilon_{ll}^{e\,2} + \mu\left(\varepsilon_{ik}^e - \frac{1}{3}\varepsilon_{ll}^e\delta_{ik}\right)^2 + F(p_{ik}) + \frac{1}{2}\kappa\left(\frac{\partial p_{ik}}{\partial r}\right)^2. \quad (11)$$

In order to evaluate tensor F_p, we have to consider the equation (11) as a functional determined for a representative material volume. For one dimension problem we can write

$$F_p = \frac{\delta \mathrm{F}}{\delta p_{ik}} = \frac{\partial \mathrm{F}}{\partial p_{ik}} - \frac{\partial}{\partial x_l}\left[\frac{\partial \mathrm{F}}{\partial(\partial p_{ik}/\partial x_l)}\right]. \quad (12)$$

The system (8)–(9) in the case of uniaxial cyclic loading ($\sigma_{zz} = \sigma$, $e_{zz} = e$, $p_{zz} = p$) takes the form

$$\dot{\varepsilon}^p = l_{\varepsilon^p}\sigma + l_{\varepsilon^p p}\left(\sigma - \frac{\partial F}{\partial p} - \frac{\partial}{\partial x}D\frac{\partial p}{\partial x}\right), \quad (13)$$

$$\dot{p} = l_p\left(\sigma - \frac{\partial F}{\partial p} - \frac{\partial}{\partial x}D\frac{\partial p}{\partial x}\right) + l_{\varepsilon^p p}\sigma, \quad (14)$$

where D is the coefficient of self-diffusion which is known to obey the Arrenius law, $D = D_0\, exp(-E_{sd}/T)$ (E_{sd} is the activation energy of self-diffusion) and largely depends on the defect concentration.

4. **Defect evolution under cyclic loading**

To describe the defect evolution in bulk and near specimen surface let us to reduce the equations (13,14). Under high cyclic and gigacyclic fatigue we can propose a weak interaction of defect accumulation and microplastisity processes ($l_{\varepsilon^p p} -> 0$) and write the equation (14) in the form

$$\dot{p} = l_p\left(\sigma - \frac{\partial F}{\partial p} - \frac{\partial}{\partial x} D \frac{\partial p}{\partial x}\right). \tag{15}$$

Let us to consider two representative material volumes V_{sur}, V_{bulk} located near specimen surface (part of the surface volume coincides with specimen surface) and into specimen volume, respectively. If we introduce a mean defect induced strain in the considering volume as $p_m = \frac{1}{v_i}\int_{v_i} p dv$ we can rewrite the equation (15) as

$$\dot{p}_m + \frac{h\, l_p}{V} p_m = l_p\left(\sigma - \frac{\partial F}{\partial p}\right)_m, \tag{16}$$

where we used the following boundary conditions

$$D \frac{\partial p}{\partial x}\bigg|_{p\in S} = -\frac{h}{V}\int_{v_i} p dv\,. \tag{17}$$

The equation (16) requests an approximation of function $\sigma - \frac{\partial F}{\partial p}$ which determined the equilibrium states of materials with defects. Taking into account the solution of equations (2) we can propose the following approximation for defect evolution law

$$\dot{p}_m + \frac{h\, l_p}{V} p_m = l_p\left(\frac{n\sigma^2}{n_0 E^2}\left(p_m + p_0\right)^2 - a\, p_m\right), \tag{18}$$

where n is initial defect concentration, σ is mean stress for the considered volume, p_0, l_p, a are materials constants, h the constant which determine the boundary conditions for considered volumes.

To explain the different mechanisms of crack initiation on specimen surface and in the bulk we have to consider a surface as a physical object with high concentration of incomplete atomic planes and other defect of different nature. As a result we can consider the surface as negative source with infinite capacity which has a great influence on the defect evolution. This influence can be described by the value of constant h in the boundary condition (18).

There are two limiting cases for equation (18). The first case is $h \to \infty \Rightarrow p\big|_{p\in S} = 0$. It means the surface is the sink of infinite capacity and this condition can be used for the description of defect evolution close to specimen surface (V_{sur}). The second case is $h \to 0 \Rightarrow D\frac{\partial p}{\partial x}\Big|_{p\in S} = 0$. The surface is closed for the defect diffusion. This condition can be used for the description of defect evolution in the bulk of specimen (V_{bulk}).

Let us to introduce the following dimensionless variables $\tau = t\, l_p a$, $n' = n / n_0$, $\Psi = \sigma /(E a)$, $h' = h /(V a)$, taking into account the fact that the initial defect (submicrocrack) concentration near specimen surface is in one or two order high then in the bulk of specimen [6] ($n'_{sur} >> n'_{bulk}$) and the difference in boundary conditions we can write the equation (18) for V_{sur}, V_{bulk} as

$$\dot{p}_m = n'_{sur}\Psi^2\left(p_m + p_0\right)^2 - \left(1 + h'\right)p_m, \tag{19}$$

$$\dot{p}_m = n'_{bulk}\Psi^2\left(p_m + p_0\right)^2 - p_m. \tag{20}$$

Under one dimension loading the stress is equal for both representative volumes and can be written as $\Psi = \Psi_0 \cos(\omega\tau)$. The numerical solutions of equations (19,20) are presented in figure 2.

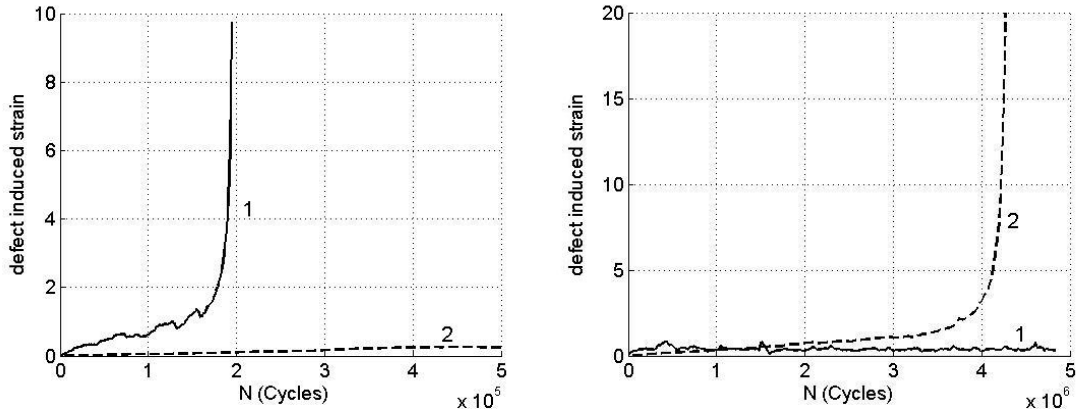

a) b)

Figure 2. Defect induced strain evolution near specimen surface (1) and in the bulk of specimen (2) for high (a) and small stress amplitudes (b).

At high stress amplitude the initial defect concentration plays the main role and leads to the sharp increasing of defect density near specimen surface (Fig.2a). The blow-up regime of defect accumulation can be considered as damage to fracture transition and can manifest the emergence of macroscopic crack.

At small stress amplitude the defect diffusion and defect annihilation on specimen surface lead to the low defect growth near specimen surface and blow-up regime of defect accumulation can be observed in the bulk of specimen (Fig. 2b).

The calculation of critical times corresponding the blow-up of defect accumulation allows us to determine the S-N of the material which describes the two possibilities of fatigue crack initiation. The materials constants l_p, a, p_0, n_0, h, V were selected to describe the two stage S-N curve experimentally obtained by C. Bathias and P. Paris for 2023-T3 aluminum alloy [6]. The numerical result presented in figure 3.

The S-N curve has dual form. First branch describes the ordinary surface fatigue crack

initiation. The second part has high fracture times and describe the volume fatigue crack initiation.

The equation (19,20) allows as to propose the analytical representation for S-N curve of material. To obtain the upper bound for life time we can take into account the stress amplitude, only.

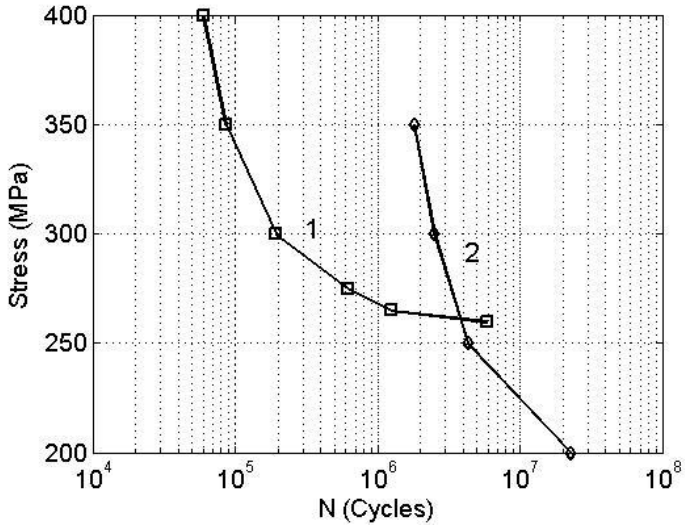

Figure 3. S-N curve for aluminum alloy 2024-T3. Failure caused by surface crack initiation (1), failure caused by under surface crack initiation (2).

In the case of proposed approximation of equilibrium solution of (2) the critical time in the equation (19) can be estimated as follows

$$t_f = \int_0^{\infty} \frac{(1+h')p_m}{n'_{sur}\Psi^b(p_m + p_0)^b}\,dp\,. \tag{21}$$

To describe the full S-N curve we have to use several equation (19) with different values h', n' which could be connected with initial heterogeneity of materials. The equation (21) gives the traditional representation of S-N curve in Basquin form

$$ln(N_f) = a - b\,ln(\Psi), \tag{22}$$

where $a = \nu \int_0^{\infty} \frac{(1+h')p_m}{n'_{sur}(p_m + p_0)^b}\,dp$, ν is loading frequency.

5. Conclusion

Analysis of experimental data devoted to the study of microcracks kinetics in the bulk and surface layer of the metals allowed us to choice of scale level for description of fracture of metallic materials - the level of submicrocracks with the size of 0.1-0.3 microns. To describe the geometry of these defects, as well as their effect on the mechanical material properties were used dislocation theory.

The high initial concentration of these defects in metals and their initiation during initial stage of deformation process allows us to propose the importance of the consideration of their evolution

under cyclic loading. The high concentration of these defect experimentally observed in fine grain metals after equals channel pressing allows us to propose the fine grain metals as model materials for verification of the theoretical predictions obtained in this work.

The small size and high concentration of submicrocracks in metals, the existing of their size and orientation distributions allows us to develop a statistical description of microcrak evolution in metals under cyclic loading and introduce a new thermodynamical variable – defect induced strain. The new variable gives a natural description of thermodynamics of metals with microcracks and allows one to describe the interaction of plasticity and failure processes.

The combination of statistical description of microcrack ensemble with stochastic consideration of defect initiation process allows us to describe the effect of initial nucleus concentration of the deformation process. This model coupled with a description of nonlocal effect in the defect ensemble gives us a key parameter for the description of defect kinetics in the bulk and near specimen surface under cyclic loading.

Based on the developed model the new equation for defect kinetics in the bulk and near specimen surface have been proposed. The surface was considered as a physical object with high concentration of incomplete atomic planes and other defect of different nature. It allows us to explain the difference in the defect kinetics far and close to specimen surface and describe the damage to fracture transition both in the bulk and near specimen surface.

It was show that the stress amplitude can influence on the location of macro fatigue crack initiation. At small stress amplitude the defect induced strain reaches an equilibrium value near specimen surface due to the defect diffusion and annihilation processes. It can be considered as an infinite fatigue life but in this case there is possibility of blow-up regime of defect kinetics in the bulk of specimen. It leads to the shift of location of crack initiation from the surface to the bulk of specimen.

These two modes of crack initiation leads to dual form of S-N curve of materials. The calculated S-N curve has a good quantitative agreement with experimental data obtained by C. Bathias and P. Paris for 2023-T3 aluminum alloy [6]. Each part of the dual S-N curve has the traditional Basquin representation. The micromechanical model allows as to propose the link of macroscopic parameters a, b with defect accumulation kinetics and used the experimentally determined S-N curve for the estimation of microscale model variables.

The developed theoretical model describes the important role of specimen surface and its physical state in the process of defect accumulation under cyclic loading. This model proposes a physical mechanism of the shift of crack initiation location from specimen surface to the bulk that experimentally observed under gigacyclic fatigue (cyclic loading with small stress amplitude). It is interesting to note that the best experimental verification of the model could be carried out based on the structural investigation of microcrack accumulation in fine grain metals (materials with high concentration of initial submicrocracks) under gigacyclic fatigue.

Acknowledgements

This work was carried out during the stay of first author at the department DuMAS I2M (Bordeaux, France). The authors sincerely thank prof. T. Palen-Luc and prof. N. Saintier for his hospitality and fruitful discussions.

The work is partly supported by grant of President of the Russian Federation for support of young Russian scientists and leading scientific schools (MD-2684.2012.1) and RFBR (grant N 11-01-00153).

References

[1] Panin V.E., Grinyaev Yu.V., Danilov V.V., at al, Structural levels of plastic deformation and fracture. Novosibirsk:Nauka, 1990, 255 p. (in Russian).

[2] Rybin V.V., Severe plastic deformation and failure of metals. M.:Metalurgiya. 1986. 224 p. (in Russian).

[3] Betekhtin V. I., Kadomtsev A. G. Evolution of microscopic cracks and pores in solids under loading. Physics of the solid state, Vol. 47, No. 5, (2005) 825–831.

[4] Naimark O., Defect Induced Transitions as Mechanisms of Plasticity and Failure in Multifield Continua In "Advances in Multifield Theories of Continua with Substructure", Birkhauser Boston, Inc., 2003, pp.75.

[5] Doudard C. Calloch S., Cugy P., Galtier A., Hild F. A probabilistic two-scale model for high-cycle fatigue life predictions. Fatigue and Fracture of Engineering Materials and Structures 28, (2005), 279–288.

[6] Bathias C., Paris P. Gigacycle Fatigue in Mechanical Practice Taylor & Francis, 2004, 328 p.

Formulation and Characterization of Fatigue Strength Diagrams of Notched Specimens Based on Equivalent Cyclic Stress Ratio, Attending Especially to Material Dependence and Notch Size Effects

Hiroshi Matsuno[1,*]

[1] Department of MECHANICAL ENGINEERING, SOJO University, Kumamoto 860-0082, Japan
* Corresponding author: hi-matsuno@par.odn.ne.jp

Abstract In the present paper, a fatigue strength diagram is formulated and characterized as a function of an equivalent cyclic stress ratio (named as R_{EQ}-ratio). The R_{EQ}-ratio is derived from a hypothesis of plastic adaptation that reflects micro-mechanical behavior of a fatigue slip band, and it was proposed as a corresponding parameter between cyclic stress-conditions of notched and un-notched specimens in the previous paper. The R_{EQ}-ratio is given as a function of a theoretical stress concentration factor K_t and a nominal cyclic stress ratio R_N, and it is noteworthy that the R_{EQ}-ratio materializes a similitude relation between the fatigue strength diagrams of notched and un-notched specimens in the case where the notch depth is greater than about 1*mm* (where the notch size effect is negligible). Therefore, the R_{EQ}-ratio can be applied as a main variable to the formulation of the fatigue strength diagram. The formulation is extended to the case of the extremely shallow notch where the size effect is dominant, and finally the generalized equations expressing the fatigue strength diagrams are proposed. These equations are applied to regression analyses on fatigue data of practically used metallic materials. Consequently, the material- and size-dependence in notch effects are considered and characterized.

Keywords Fatigue strength diagram, Cyclic plastic-adaptation, Equivalent cyclic stress ratio (R_{EQ}-ratio), Notch behavior map, Notch size effect

1. Introduction

A fatigue strength diagram is formulated and characterized as a function of an equivalent cyclic stress ratio (named as R_{EQ}-ratio). The R_{EQ}-ratio is derived from a hypothesis of cyclic plastic adaptation that reflects micro-mechanical behavior of a fatigue slip band, and it was proposed as a corresponding parameter between cyclic stress condition of notched and un-notched specimens in the previous paper [1]. A graphic method estimating the R_{EQ}-ratio on the basis of the hypothesis is developed in the present paper. It is described that the R_{EQ}-ratio materializes a similitude relation between the fatigue strength diagrams of the notched and un-notched specimen in the case where the notch depth is comparatively large size of *mm*-order (where the notch size effect is negligible). It means that the R_{EQ}-ratio can be applied as a main variable to the formulation of the fatigue strength diagram. Next, the notch behavior is characterized and mapped by making the notch root radius and depth into variables. The notch size effect is discussed on the basis of the notch behavior map and the size effect factors are introduced. As a result, the formulation of the fatigue strength diagram can be extended to the case of the extremely small size notch, such as the depth of 10 and 100 μm-order, where the size effect is dominant, and finally the generalized equations expressing the fatigue strength diagrams are proposed. These equations are applied to regression analyses on fatigue data of practically used metallic materials.

2. Graphic method estimating an equivalent cyclic stress ratio (R_{EQ}-ratio)

2.1. A hypothesis of cyclic plastic-adaptation

Irreversible microscopic expansion developing in the slip direction of a crystal of a persistent slip

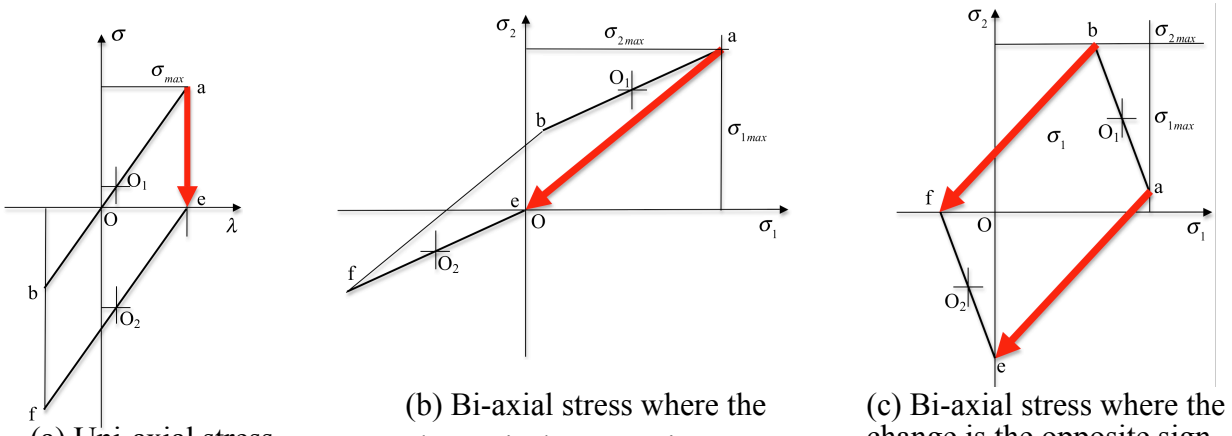

(a) Uni-axial stress (b) Bi-axial stress where the change is the same sign (c) Bi-axial stress where the change is the opposite sign

Fig. 1 Change of the stress path under cyclic plastic-adaptation

band is released on the surface and forms surface relief [2-4]. On the other hand, it is inside restrained and produces inherent compressive stress. A hypothesis that reflects such microscopic mechanical behavior in the persistent slip band is introduced from a viewpoint of macro-mechanics as follows. At the weakest spot of a surface layer, a notch root and a fatigue crack tip, the elastic expansion arising at the maximum stress is transformed into the irreversible expansion inherent in fatigue. As a result, the maximum stress at the weakest spot is substantially decreased and the elastic energy is relieved. Therefore, it is termed as the hypothesis of cyclic plastic-adaptation by author. Such stress relief is materialized for each maximum principal stress in a multi-axial stress condition, too. The expansion arising by the plastic adaptation behaves as a mechanical misfit and lowers the mean stress of substantial cyclic stress. Accordingly, the cyclic behavior of stress can be imaged as shown in Figs. 1(a)-(c). They show the cases of uni-axial stress (a), bi-axial stress where the change is the same (b) and opposite sign (c). At the weakest spot of the surface layer, the stress path moves from a site *ab* to a site *ef*, in common in each figure, though the outward path remains at a site *ab*. The cyclic plastic-adaptation is accomplished completely at the site *ef*. As mentioned later, it should be noted that the movement of the stress path caused by growth of irreversible expansion means not a change of itself but the movement of the potential field that it has.

2.2. Derivation of the equivalent cyclic stress ratio (R_{EQ}-ratio)

How to reproduce the cyclic stress potential field at a notch root as that in the surface layer of the un-notch condition is illustrated based on the hypothesis of cyclic plastic-adaptation. Concretely speaking, the cyclic stress that activates microscopic slip behavior in the un-notch condition as much as the cyclic stress does at the notch root is pictured on the diagram of the stress path. From this diagram, the equivalent cyclic stress ratio R_{EQ} and the equivalent mean stress $\sigma_{mean\,EQ}$ are graphically estimated. R_{EQ} and $\sigma_{mean\,EQ}$ behave just like a hydrostatic stress ratio and hydrostatic mean stress in the process of the cyclic plastic-adaptation, respectively. This is due to the following reasons; (1) the irreversibility of expansion caused by cyclic plastic-adaptation and (2) the addibility of volume expansion which is produced under each principal cyclic stress. These two matters give the important hint to quantitative interpretation of cyclic plastic-adaptation; it is the potential described by Mises' equivalent stress that generates a driving force advancing cyclic plastic adaptaion and it is the algebraic sum of the maxmum value of principal stresses that provides the capability producing the cyclic plastic-adaptation. So, in the present study, in order to estimate the

potential at the notch root, Mises' equivalent stress concentration factor K_{teq} is defined by Eq. (1) where $\sigma_{xN},\cdots,\tau_{zxN}$ are the stress components of the nominal condition and $\sigma_{xNR},\cdots,\tau_{zxNR}$ are those of the notch root. Moreover, Eq. (2) that has been rewritten by principal stresses is obtained by dividing Eq. (1) with K_{teq}. Then, the principal stresses σ_{iNR} (i=1-3) are already not those arising actually at the notch root but those of which nominal values σ_{iN} (i=1-3) are expanded to the same potential level as the notch root has. After all, the principal stress of the un-notch condition where the potential is equal to that of the notch root is given by σ_{iNR} (i=1-3) in Eq. (3). The difference in the stress path of the nominal condition (magnified by K_{teq}) and the notch root condition is disregarded in the present method. As it is mentioned in the following section 2.3, such disregard does not affect the correspondence between fatigue strength of the notch and un-notch condition.

$$
\begin{aligned}
K_{teq} &= \frac{\sigma_{eq\,NR}}{\sigma_{eq\,N}} \\
&= \frac{\left(1/\sqrt{2}\right)\sqrt{\left(\sigma_{x\,NR}-\sigma_{y\,NR}\right)^2+\left(\sigma_{y\,NR}-\sigma_{z\,NR}\right)^2+\left(\sigma_{z\,NR}-\sigma_{x\,NR}\right)^2+6\left(\tau_{xy\,NR}^2+\tau_{yz\,NR}^2+\tau_{zx\,NR}^2\right)}}{\left(1/\sqrt{2}\right)\sqrt{\left(\sigma_{x\,N}-\sigma_{y\,N}\right)^2+\left(\sigma_{y\,N}-\sigma_{z\,N}\right)^2+\left(\sigma_{z\,N}-\sigma_{x\,N}\right)^2+6\left(\tau_{xy\,N}^2+\tau_{yz\,N}^2+\tau_{zx\,N}^2\right)}} \\
&= \frac{\left(1/\sqrt{2}\right)\sqrt{\left(K_{tx}\sigma_{x\,N}-K_{ty}\sigma_{y\,N}\right)^2+\left(K_{ty}\sigma_{y\,N}-K_{tz}\sigma_{z\,N}\right)^2+\left(K_{tz}\sigma_{z\,N}-K_{tx}\sigma_{x\,N}\right)^2+6\left(K_{ts\,xy}^2\tau_{xy\,N}^2+K_{ts\,yz}^2\tau_{yz\,N}^2+K_{ts\,zx}^2\tau_{zx\,N}^2\right)}}{\left(1/\sqrt{2}\right)\sqrt{\left(\sigma_{x\,N}-\sigma_{y\,N}\right)^2+\left(\sigma_{y\,N}-\sigma_{z\,N}\right)^2+\left(\sigma_{z\,N}-\sigma_{x\,N}\right)^2+6\left(\tau_{xy\,N}^2+\tau_{yz\,N}^2+\tau_{zx\,N}^2\right)}}
\end{aligned}
\tag{1}
$$

$$
1=\frac{\sigma_{eq\,NR}}{K_{teq}\sigma_{eq\,N}}=\frac{\left(1/\sqrt{2}\right)\sqrt{\left(\sigma_{1\,NR}-\sigma_{2\,NR}\right)^2+\left(\sigma_{2\,NR}-\sigma_{3\,NR}\right)^2+\left(\sigma_{3\,NR}-\sigma_{1\,NR}\right)^2}}{\left(1/\sqrt{2}\right)\sqrt{\left(K_{teq}\sigma_{1N}-K_{teq}\sigma_{2N}\right)^2+\left(K_{teq}\sigma_{2N}-K_{teq}\sigma_{3N}\right)^2+\left(K_{teq}\sigma_{3N}-K_{teq}\sigma_{1N}\right)^2}} \tag{2}
$$

$$
\therefore\quad \sigma_{1\,NR}=K_{teq}\sigma_{1N},\quad \sigma_{2\,NR}=K_{teq}\sigma_{2N},\quad \sigma_{3\,NR}=K_{teq}\sigma_{3N} \tag{3}
$$

One example of the process of the cyclic plastic-adaptation at the notch root of material subject to cyclic torsion is shown in Fig.2, where plane stress is assumed. The segments *ab* and *cd* show the stress path of the nominal condition and the expanded one of the un-notch condition of which the potential is equal to the notch root, respectively. The segment *ef* shows the stress path where the

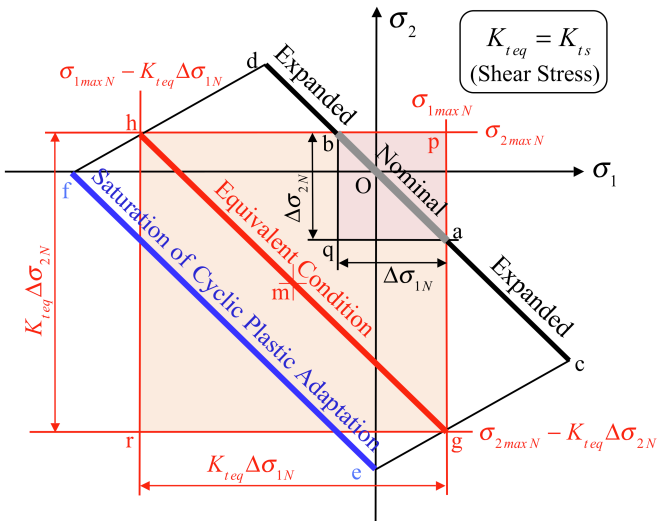

Fig. 2 Illustration of the graphic method of how to estimate R_{EQ} and $\sigma_{mean\,EQ}$ (cyclic torsion)

cyclic plastic-adaptation is accomplished completely. On the way of the cyclic plastic-adaptation process, as it is shown by the segment *gh*, each maximum values of the principal stress become equal to that of the nominal stress path, respectively. This is an important matter which should be mentioned specially; for, it means that, if the cyclic stress shown by the segment *gh* is applied to the un-notched material, the cyclic plastic-adaptation process at the notch root can be reproduced at the surface layer of the un-notched material. Therefore, it can be said that the segment *gh* corresponds to the equivalent cyclic stress condition between the notched and un-notched specimens. In the present study, the stress ratio R_N^* is newly defined for multi-axial stress condition other than the usual nominal stress ratio R_N. The R_N^* is formulated as a ratio of the algebraic sum of the x/y-coordinate value for each of the peak point *p* and *q* of the rectangle *paqb* with the line segment *ab* as a diagonal line (henceforth, the basic equations are shown with the three-dimensional form);

$$R_N^* = \frac{\left(\sigma_{1\,max\,N} - \Delta\sigma_{1N}\right) + \left(\sigma_{2\,max\,N} - \Delta\sigma_{2N}\right) + \left(\sigma_{3\,max\,N} - \Delta\sigma_{3N}\right)}{\sigma_{1\,max\,N} + \sigma_{2\,max\,N} + \sigma_{3\,max\,N}} \tag{4}$$

Next, the equivalent cyclic stress ratio R_{EQ} is formulated as the ratio of the algebraic sum of the x/y-coordinate values for each of the peak points *p* and *r* of the rectangle *pgrh* with the line segment *gh* as the diagonal line, and the expression is moreover simplified by using Eq. (4);

$$\begin{aligned} R_{EQ} &= \frac{\left(\sigma_{1\,max\,N} - K_{t\,eq}\Delta\sigma_{1N}\right) + \left(\sigma_{2\,max\,N} - K_{t\,eq}\Delta\sigma_{2N}\right) + \left(\sigma_{3\,max\,N} - K_{t\,eq}\Delta\sigma_{3N}\right)}{\sigma_{1\,max\,N} + \sigma_{2\,max\,N} + \sigma_{3\,max\,N}} \\ &= R_N^* - \left(K_{t\,eq} - 1\right)\left(1 - R_N^*\right) \end{aligned} \tag{5}$$

Last, the equivalent mean stress $\sigma_{mean\,EQ}$ is formulated as the algebraic sum of the x/y-coordinate values of the middle points *m* of the rectangle *pgrh* with the line segment *gh* as a diagonal line;

$$\begin{aligned} \sigma_{mean\,EQ} &= \left(\sigma_{1\,max\,N} + \sigma_{2\,max\,N} + \sigma_{3\,max\,N}\right) - K_{t\,eq}\left(\Delta\sigma_{1N} + \Delta\sigma_{2N} + \Delta\sigma_{3N}\right)\Big/2 \\ &= \left(\sigma_{1\,max\,N} + \sigma_{2\,max\,N} + \sigma_{3\,max\,N}\right) - K_{t\,eq}\left(\sigma_{1a\,N} + \sigma_{2a\,N} + \sigma_{3a\,N}\right) \end{aligned} \tag{6}$$

where, $\sigma_{i\,a\,N}$ (i=1-3) are the principal stress amplitude of the nominal condition. Saying again, R_{EQ} and $\sigma_{mean\,EQ}$ behave just like a hydrostatic stress ratio and hydrostatic mean stress in the process of the cyclic plastic-adaptation, regardless whether the stress components constituting them synchronizes or not, respectively. For the un-notch condition of $K_{t\,eq} = 1$, $\sigma_{mean\,EQ}$ of Eq. (6) is coincident with the mean hydrostatic stress that Sines introduced into his criterion [5].

2.3. Applicability of the R_{EQ}-ratio to fatigue strength diagramming

In order to prove the applicability of the equivalent cyclic stress ratio R_{EQ} and the equivalent mean stress $\sigma_{mean\,EQ}$, the fatigue strength of the specimen containing a comparatively large size notch (from the reason why influence of the notch size effect is little) is plotted on the diagram where the abscissa shows R_{EQ} and $\sigma_{mean\,EQ}$ and the ordinate does the notch root stress range $\Delta\sigma_{NR}$. Fig. 3 shows the fatigue test result concerning the notched and un-notched round-bar specimen of SM400 (low carbon structural steel) subject to cyclic axial loading under mean stress of tension side [1] and suject to rotating bending. Fig. 3(a) and (b) represent the R_{EQ}-based and $\sigma_{mean\,EQ}$-based fatigue strength diagram, respectively. The depth of the circumferential notch t is 3 *mm* for axial cyclic loading test and 1.5 *mm* for rotating bending test. The notch root radius ρ is changed in the range

from 0.1 to 3 *mm*. The R_{EQ} for axial cyclic load is estimated by FEM based on Mises' equivalent

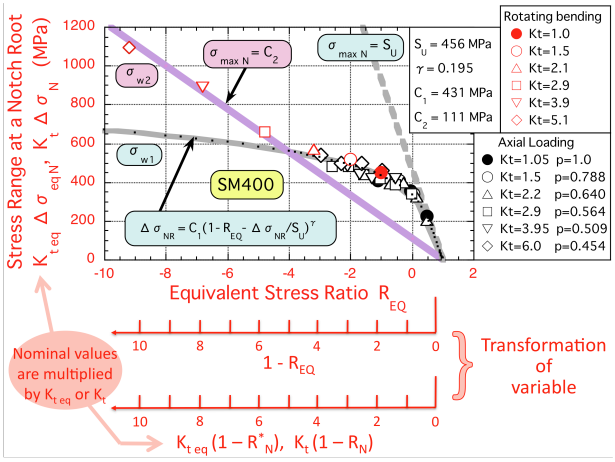

(a) R_{EQ} *vs.* $K_t\Delta\sigma_N$ diagram and similarity

(b) $\sigma_{mean\,EQ}$ *vs.* $K_t\sigma_{amp\,N}$ diagram and identity with that of the un-notch condition

Fig. 3 Fatigue strength diagram of SM400 steel round-bar specimen with the large-size notch (The fatigue tests were performed by cyclic axial load under mean stress [1] and rotating bending)

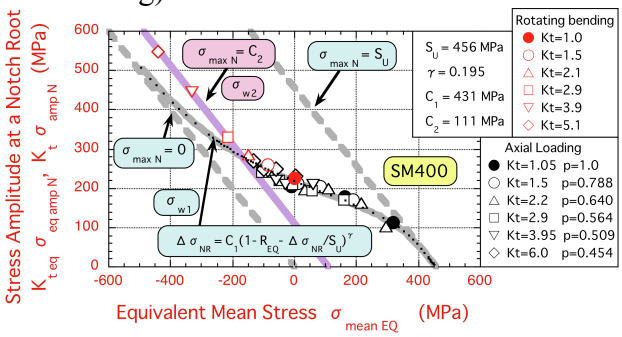

stress and the factor p done as the ratio of the average equivalent stress in the notch section $\bar{\sigma}_{eq}$ to the nominal stress σ_N [1]. In Fig. 3, the colored plot represents the experimental result. From the dispersion state of a plot, it is found, the fatigue strength is systematically arranged in spite of differences of stress concentration factors and mean stress, and it is clearly separable into the two groups of σ_{w1} and σ_{w2}. The curved and straight lines represent the fatigue strength diagrams of σ_{w1} and σ_{w2}, respectively, and they are drawn on the basis of the regression equations derived in the following chapter. The horizontal axis of the graph in Fig. 3(a) can be converted from the scale of R_{EQ} to the scale of $K_{t\,eq}\left(1-R_N^*\right)$ and $K_t\left(1-R_N\right)$ as shown in the lower berth of the graph;

$$1-R_{EQ}=K_{t\,eq}\left(1-R_N^*\right)=K_{t\,eq}\left(\Delta\sigma_{eq\,N}/\sigma_{eq\,max\,N}\right)=\Delta\sigma_{eq\,NR}/\sigma_{eq\,max\,N} \quad \text{(for axial load)} \quad (7)$$

$$1-R_{EQ}=K_t\left(1-R_N\right)=K_t\left(\Delta\sigma_N/\sigma_{max\,N}\right)=\Delta\sigma_{NR}/\sigma_{max\,N} \quad \text{(for rotating bending)} \quad (8)$$

Both the axes of the graph take the scale proportional to K_t. Therefore, it can be said that a similitude relation between the diagrams is materialized. This means that R_{EQ} is very useful as the correspondence parameter between the fatigue strength of the notched and un-notched specimen. The coincidence of a diagram in Fig. 3(b) means that the $\sigma_{mean\,EQ}$-based fatigue strength diagram obtained from the fatigue data of the notched specimen turns into the $\sigma_{mean\,N}$-based fatigue strength diagram of the un-notched specimen as it is.

3. Formulation of the fatigue strength diagram based on the R_{EQ}-ratio

3.1. Characterizing and mapping of the notch behavior

The notch is characterized by two parameters of ρ/t and $\sqrt{\rho t}/L_0$ as shown in Fig. 4(a) and (b), where the notch depth t and the notch root radius ρ are expressed as the co-ordinates after normalized by the size L_0. L_0 is introduced as an index for judging large size or small size notch. In the present study, $L_0=1mm$ is set emprically. The parameter ρ/t shows the sharpness of the notch which K_t depends on and the parameter ρt does the scale of the notch which the size effect depends on. Taylor classified the character of the notch behavior into three and drew the

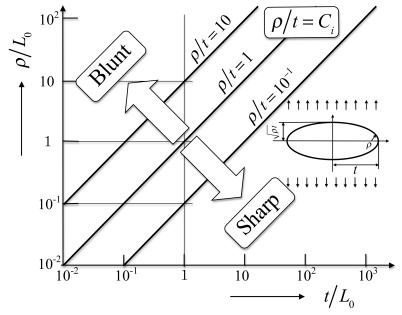

(a) Notch sharpness: ρ/t

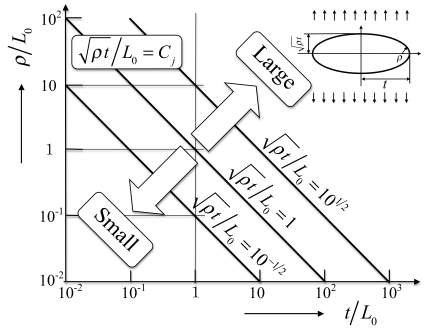

(b) Notch size scale: $\sqrt{\rho t}/L_0$

Fig. 4 Index parameter of notch sharpness and notch size scale: ρ/t and $\sqrt{\rho t}/L_0$

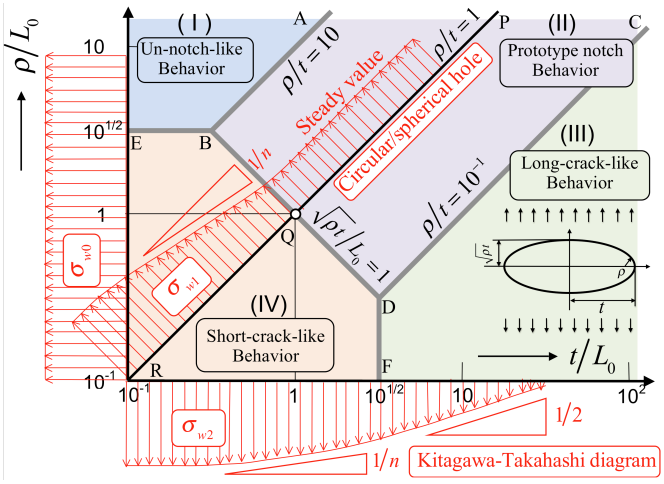

Fig. 5 Notch behavior map and a few typical distributions of fatigue strength threshold stress

distribution map on the key map [6]. His map seems to be rather suitable for expressing the characteristic of the fatigue strength σ_{w2}. So, a new map is created so that it can express the characteristic of the fatigue strength inclusive of the fatigue strength σ_{w1}. The new map is shown in Fig. 5, where the character of the notch behavior is classified into four domains; (I) Un-notch-like behavior, (II) Prototype notch behavior, (III) Long-crack-like behavior and (IV) Short-crack-like behavior. The four domains are partitioned with three characteristic lines AB, CD and BD and with the outgoing lines BE and DF drawn in the horizontal and perpendicular directions from the two intersections. The characteristic lines AB, CD and BD are expressed by the following simple formulas, $\rho/t=10$, $\rho/t=10^{-1}$ and $\sqrt{\rho t}/L_0=1$, respectively. A straight line PR formulated as $\rho/t=1$ expresses the size change of the circular or spherical hole that represents typical notch behavior. The distribution of the fatigue strength can be diagramed in a logarithmic scale by taking the z-axis in the direction perpendicular to space of the map. Three examples are schematically shown in Fig. 5. One is the diagram of the fatigue strength σ_{w1} for the circular or spherical hole. The diagram makes $\sqrt{\rho t}/L_0$ a variable and it is shown as a $\sigma_{w1}-\sqrt{\rho t}/L_0$ diagram on the line where $\rho/t=1$. As mentioned later, a $\sigma_{th}-\sqrt{area}$ diagram that makes Murakami's parameter of $\sqrt{area}$ a variable is a particular case of the $\sigma_{w1}-\sqrt{\rho t}/L_0$ diagram where $\rho/t=1$ and $\sqrt{\rho t}/L_0<1$. Another is Kitagawa-Takahashi diagram that makes a crack length a/a_2 a variable and the diagram is known as a $\sigma_{th}-a/a_2$ diagram [7]. The $\sigma_{th}-a/a_2$ diagram is depicted as a $\sigma_{w2}-t/L_0$ diagram on the horizontal axis (x-axis) in Fig. (5) where the crack length a/a_2 is replaced by the notch depth t/L_0. Moreover, Kitagawa and Takahashi prepared another critical size a_1 that represents the substantial transition from large size crack to small size one. This type of transition size on the fatigue strength σ_{w2} is expressed by replacing a_1/L_0 by t_0/L_0; the transition notch size is shown as $t_0/L_0=10^{1/2}$ in Fig. (5). The third is the fatigue strength of the un-notch condition σ_{w0} that is distributed on the vertical axis (y-axis) as a uniform value. This value is thought to be materialized in common where both ρ/L_0 and t/L_0 are extremely small.

3.2. Primary equations at the onset of formulation and their modification (Domain II)

The fatigue strength diagram is formulated first for the prototype notch of the domain II ($\sqrt{\rho t} \geq L_0$), where the notch size effect is not taken into consideration. In the following section 3.3, the equation is developed into a general form including the short-crack-like notch of the domain IV ($\sqrt{\rho t} < L_0$), where the notch size effect is taken into consideration. Primary equations that become a starting point of formulation are as follows, where Eq. (9) is quoted from Ref. [8];

$$\left(\Delta\sigma_{NR}\right)_{w1} = C_1\left(1 - R_{EQ}\right)^{\gamma}, \qquad \text{(Fatigue strength } \sigma_{w1}\text{)} \tag{9}$$

$$\left(\Delta\sigma_{NR}\right)_{w2} = C_2\left(1 - R_{EQ}\right). \qquad \text{(Fatigue strength } \sigma_{w2}\text{)} \tag{10}$$

Eq. (10) is rewritten by using the conversion expression of Eq. (8), as follows;

$$\left(\sigma_{max\,N}\right)_{w2} = C_2. \qquad \text{(Fatigue strength } \sigma_{w2}\text{)} \tag{11}$$

Eq. (12) is adopted as an asymptotic equation of Eq. (9) on σ_{w1}, so that the ultimate strength of material S_U may be gradually approached with an increase of the value R_{EQ};

$$\left(\sigma_{max\,N}\right)_{w1} = S_U \quad \text{i.e.} \quad \left(\Delta\sigma_{NR}\right)_{w1} = S_U\left(1 - R_{EQ}\right). \tag{12}$$

Solving Eqs. (9) and (12) about $\left(1 - R_{EQ}\right)$ and susequently transposing those algebraic sum to new $\left(1 - R_{EQ}\right)$, Eq. (13) can be expressed;

$$\left(\Delta\sigma_{NR}\right)_{w1} = C_1\left\{1 - R_{EQ} - \frac{\left(\Delta\sigma_{NR}\right)_{w1}}{S_U}\right\}^{\gamma}. \qquad \text{(Fatigue strength } \sigma_{w1}\text{)} \tag{13}$$

Eq. (13) is a very important as the expression which not only improves the precision for calculating the fatigue strength σ_{w1} but also explains how the tensile strength of material S_U relates quantatively with σ_{w1}. The equation expresses that the SCF-criterion (K_t-criterion) is materialized for σ_{w1} by using the equivalent cyclic stres ratio R_{EQ}. On the otherhand, for the fatigue strength σ_{w2}, Eq. (10) and (11) is used in a form as it is. It should be noted that, at this stage, γ, C_1 and C_2 are not material constants but variables. Strictly speaking, C_1 includes free boundary correction and C_2 includes a function of the notch depth t.

3.3. The equations generalized by incorporation of notch-size effects (Domain IV)

The factor of a notch size effect is incorporated into the euations derived in the foregoing paragraph. The judgement whether it is necessary to take the notch size effect into consideration or not is performed according to the value of a notch size $\sqrt{\rho t}$. In the present study, the value of $\sqrt{\rho t} = L_0$ is selected as the critical value as shown in Fig. 5. As it is mentioned in the foregoing section 3.1, the fatigue strength σ_{w1} depends on the notch size $\sqrt{\rho t}$ and the fatigue strength σ_{w2} does on the notch depth t. Therefore, the size factors F_{S1} and F_{S2} are introduced in the forms of the functions of $\sqrt{\rho t}$ and t, respectively;

$$F_{S1} = f_1\left(\sqrt{\rho t}\right), \tag{14}$$

$$F_{S2} = f_2\left(t\right). \tag{15}$$

Generally, the nominal stress of the plate and round-bar specimen containing a hole, a defect and a pre-crack is shown by gross-sectional stress. On the other hand, that of the plate and round-bar specimen containing an edge and circumferential notch is shown by net-sectional stress. These specimens are often furnished with the net-sectional area unified for different K_t and accordingly their gross-sectional area is different every specimen. Such difference has serious influence for the asymptotic process ofthe fatigue strength σ_{w1} to the ultimate strength of material S_U. So, a factor of F_G is introduced for the fatigue strength σ_{w1} expressed by the net-sectional stress, as follows;

$$F_G = A_{G0} / A_G\ , \tag{16}$$

where, A_{G0} and A_G are the gross-sectional area for $\sqrt{\rho t} = L_0$ and $\sqrt{\rho t} < L_0$, respectively. Also, it should be noted that the fatigue strength σ_{w2} in torsion is not subjected to the influence of the notch depth t. A concrete form of the function of F_{S1}, F_{S2} and F_G is summarized in Table 1. By using these factors, Eq. (9) and (12) are rewritten for the σ_{w1} as Eq. (17) and (18), respectively;

$$F_{S1}\left(\Delta\sigma_{NR}\right)_{w1} = C_1\left(1-R_{EQ}\right)^{\gamma}, \tag{17}$$

$$F_G\left(\sigma_{max\,N}\right)_{w1} = S_U \quad \text{i.e.} \quad F_G\left(\Delta\sigma_{NR}\right)_{w1} = S_U\left(1-R_{EQ}\right). \tag{18}$$

Eq. (18) is adopted as an asymptotic equation of Eq. (17) so that the ultimate strength of material S_U may be gradually approached with an increase of the value R_{EQ}. The final equation on the fatigue strength σ_{w1} is obtained as follows;

$$F_{S1}\left(\Delta\sigma_{NR}\right)_{w1} = C_1\left\{1-R_{EQ}-\frac{F_G\left(\Delta\sigma_{NR}\right)_{w1}}{S_U}\right\}^{\gamma}. \tag{19}$$

Eq. (19) is obtained by solving Eqs. (17) and (18) about $\left(1-R_{EQ}\right)$ and subsequently transposing those sum to new $\left(1-R_{EQ}\right)$. The final equation for the fatigue strength σ_{w2} is shown as follows;

$$F_{S2}\left(\Delta\sigma_{NR}\right)_{w2} = C_2\left(1-R_{EQ}\right) \quad \text{i.e.} \quad F_{S2}\left(\sigma_{max\,N}\right)_{w2} = C_2\,, \tag{20}$$

Table 1 Summary of the notch size correction factors

σ_w	F	Center hole (Gross-sectional stress)		Edge/circumferential notch (Net-sectional stress)		Small-size defect
σ_{w1}	$\sqrt{\rho t}$	$\sqrt{\rho t} \ge L_0$	$\sqrt{\rho t} < L_0$	$\sqrt{\rho t} \ge L_0$	$\sqrt{\rho t} < L_0$	$\sqrt{area} < L_0$
	F_{S1}	$F_{S1}=1$	$F_{S1}=\left(\sqrt{\rho t}\right)^{1/8}$	$F_{S1}=1.12$	$F_{S1}=1.12\left(\sqrt{\rho t}\right)^{1/8}$	$F_{S1}=\left(\sqrt{area}\right)^{1/6}$
	F_G	$F_G=1$		$F_G=1$	$F_G=\frac{A_{G0}}{A_G}=\left(\frac{d+2L_0}{d+2\sqrt{\rho t}}\right)^2$	$F_G=1$
σ_{w2}	t	$t \ge t_0$	$t < t_0$	$t \ge t_0$	$t < t_0$	$\sqrt{area} < L_0$
	F_{S2}	$F_{S2}=t^{1/2}$	$F_{S2}=t^{1/7}$	$F_{S2}=1.12t^{1/2}$	$F_{S2}=1.12t^{1/7}$	$F_{S2}=\left(\sqrt{area}\right)^{1/7}$

Note 1) $L_0 = 1mm$.
2) $t_0 = \sqrt{10}\,L_0 = \sqrt{10}\,mm$.
3) A value of 1.12 means a free boundary correction (F_0).

where, γ, C_1, C_2: Material constants.

4. Regression analysis on the fatigue data currently introduced in literature

Eq. (19) and (20) are applied to the regression analyses of fatigue data picked up from literatures. It is confirmed whether the function form of the equation derived in the preceding chapter 3 is appropriate as a regression equation. A part of the result is described below. Fig. 6 shows the result of a rotating bending test of S45C annealed steel with a round-bar specimen containing a small drill-hole. In the experiment [9], the diameter of a hole d was changed in the range from 0.04 to 0.5 *mm* and the depth t changed from 0.04 to 1 *mm*. The fatigue strength σ_{w1} is shown as a function of $\sqrt{area}$ -parameter in Fig. 6. The plot represents the experimental result and the curve shows the calculated result from the regression equation. The horizontal line represents the strength level of an un-notched specimen σ_{w0} is calculated backward from the regression equation. It turns out that the regression equation fits the experimental result very well. Fig. 7 shows the result of a rotating bending test of S45C annealed steel with a round-bar specimen containing an extremely shallow circumferential-notch. In the experiment [10], the notch root radius ρ was changed in the range from 0.01 to 0.6 *mm* and the depth t changed from 0.005 to 1.5 *mm*. The fatigue strength σ_{w1} and σ_{w2} were measured and they were shown as a function of a stress concentration factor K_t in Fig. 7(a) and (b), respectively. The colored plot represents the experimental result and the colored thin curve/line shows the calculated result. The horizontal thick gray line represents the strength level of an un-notched specimen σ_{w0} calculated backward from the regression equation. The thick gray curve obtained by dividing σ_{w0} by K_t is drawn for reference. In both Fig. 7(a) and (b), it turns out that the regression equation fits the experimental result very well. The regression analysis using the proposed equation has applied to the fatigue testing result of the total

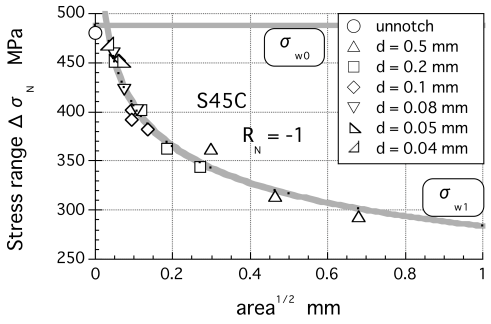

Fig. 6 Result of a regression analysis on rotating bending fatigue strength of S45C round-bar specimens containing small drill-holes (data from Ref. [9])

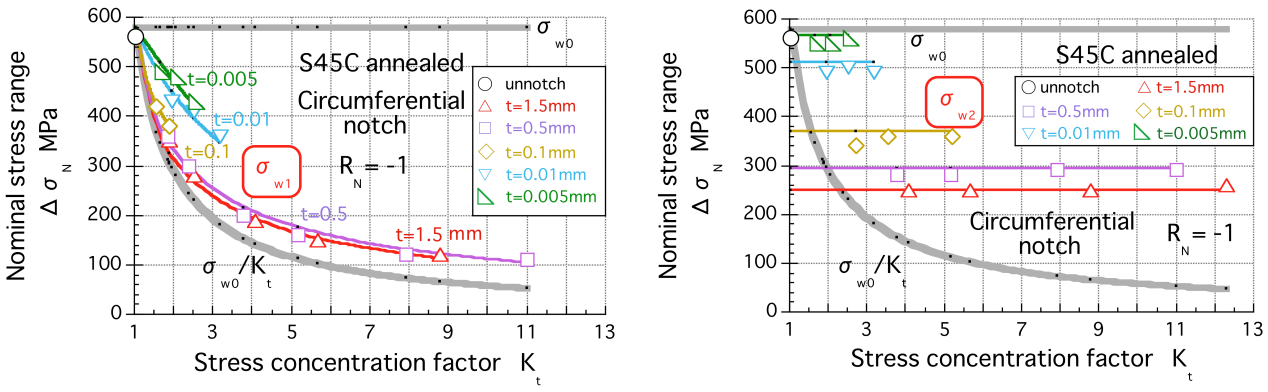

(a) Fatigue strength σ_{w1} (b) Fatigue strength σ_{w2}

Fig. 7 Result of a regression analysis on rotating bending fatigue strength of S45C round-bar specimens containing small size circumferential notches (data from Ref. [10])

number of about 25 sorts of ferrous materials and their heat-treatment conditions in the present stage. As a result, it is found that the equation is materialized with less than 10% of error.

5. Conclusions

(1) A fatigue strength diagram is formulated and characterized as a function of the equivalent cyclic stress ratio (R_{EQ}-ratio). The R_{EQ}-ratio is derived from a hypothesis of cyclic plastic adaptation that reflects micro-mechanical behavior of a fatigue slip band.

(2) The graphic method estimating R_{EQ}-ratio based on the hypothesis of the plastic adaptation is developed in the present paper. R_{EQ}-ratio materializes a similitude relation between the fatigue strength diagrams of the notched and un-notched specimen in the case where the notch depth is comparatively large size of *mm*-order (where the notch size effect is negligible). It means that R_{EQ}-ratio can be applied as a main variable to the formulation of the fatigue strength diagram.

(3) The notch behavior is characterized and mapped by making the notch root radius and depth into variables. The notch size effect is systematically considered on the basis of the notch behavior map and the size effect factor is proposed for each of the fatigue strength σ_{w1} and σ_{w2}.

(4) The formulation of the fatigue strength diagram can be extended to the case of the extremely small size notch, such as the depth of 10 and 100 μm-order, where the size effect is dominant, and finally the generalized equations expressing the fatigue strength diagrams are proposed. These equations are applied to regression analyses on fatigue data of practically used metallic materials. As a result, it is found that the equations are materialized with less than 10% of error.

References

[1] H. Matsuno, Y. Mukai, A stress parameter for correspondence between notched and un-notched specimen fatigue data: strength of fatigue macro-crack initiation at a notch root in plates and round-bars, Proc. APSCFS & ATEM'01, JSME-MMD, Oct. 20-22, 2001, JSME No. 01-203, 394–399.

[2] U. Essmann, U. Gösele, H. Mughrabi, A model of extrusions and intrusions in fatigued metals, I. Point-defect production and the growth of extrusions, Phil. Mag. A, 44-2 (1981) 405–426.

[3] E.A. Repetto, M.A. Ortiz, A micromechanical model of cyclic deformation and fatigue-crack nucleation in f. c. c. single crystals, Acta Materialia, 45 (1997) 2577–2595.

[4] J. Polák, J. Man, K. Obrtlik, AFM evidence of surface relief formation and models of fatigue crack nucleation, International J. Fatigue, 25 (2003) 1027–1036.

[5] G. Sines, Failure of materials under combined repeated stresses with superimposed static stresses, Tech. Note 3495, National Advisory Committee for Aeronautics, Washington, DC, (1955).

[6] D. Taylor, A Mechanistic Approach to critical-distance methods in notch fatigue, Fatigue Fract. Engng Mater. Struct., 24 (2001) 215–224.

[7] H. Kitagawa, S. Takahashi, Fracture mechanics approach to very small fatigue crack growth and to the threshold condition, Trans. JSME. A, 45, 399 (1979) 1289–1303.

[8] H. Matsuno, A new interpretation of notch-sensitivity in fatigue of metals, Proc. 9-th International Fatigue Congress, May 14-19, 2006, Atlanta, Georgia, USA.

[9] Y. Murakami, M. Endo, A geometrical parameter for the quantitative estimation of the effects of small defects on fatigue strength of metals, Trans. JSME, A, 49, 438 (1983) 127–136.

[10] H. Nisitani, M. Endo, Unifying treatment of notch effects in fatigue, Trans. JSME, A, 51, 463 (1985) 784–789.

Crack growth rate in friction stir welded nugget under different R ratio fatigue load

Yu E Ma[1,*], BaoQi Liu[1], ZhenQiang Zhao[1]

[1]School of Aeronautics, Northwestern Polytechnical University, 710072, P.R. China

[*]Email: ma.yu.e@nwpu.edu.cn

Abstract 2.0 mm thick 2198-T8 Al-Li alloy sheets with the parallel friction stir welds in the middle were used in this work. The center cracked tension (CC(T)) specimens with transverse welds were designed and welded by different welding parameters. Fatigue tests were performed and fatigue crack growths in the nuggets were measured and compared. Effects of rotation speed and welding speed on fatigue crack growth rates parallel to the friction stir welds were studied. It was shown crack growth rate in the nuggets can relate to the welding parameter. Residual K (K_{res}) approaches was used to predict fatigue crack growth rates in residual stress fields. Finite element models of the samples were built and the measured residual stress data put into the model. The virtual crack closure technique was used to calculate K_{res} and then K_{res} was used to calculate effective R values. Predicted crack growth rates were compared with experimental results.

Keywords Friction stir weld, Welded nugget, Fatigue crack growth rate, different R ratio.

1. Introduction

Friction stir welding (FSW), invented at The Welding Institute (TWI) in 1991, was widely used in modern aerospace industry. This new welding technique have successfully taken the pilot study stage and developed into a useful alternative in the manufacture of industrialized aluminum structures solid phase connection technology. Compared to traditional welding techniques, FSW strongly reduces the presence of distortions and residual stresses [1-4]. Also, the FSW performed well in the strength, fatigue and fracture resistant of aerospace aluminum welds, which has long inhibited the widely use of those alloys such as 2XXX and 7XXX series [5, 6]. These aluminum alloys are generally classified as non-weldable because of the poor solidification microstructure and porosity in the fusion zone [7]. Previous studies show that the grain size of the weld nugget has a strong effect on the mechanical properties [8]. In 2007, the air bus published a report which claimed that the FSW application in fuselage longitudinal seam connection of A340-500s and A340-600s has reduced 0.9 kg weight per meter relative to traditional riveting technology. A similar instance occurred in Boeing that the production efficiency in the manufacture of C-17 Global/MasterⅢ has improved tenfold with the FSW application.

2. Experimental procedure

2.1. Fatigue test procedure

2198-T8 Al-Li alloy plates were friction stir welded. The welding directions are perpendicular to the rolling direction. Cracks are the weld centre and grow in the weld. Center cracked tension (CC(T)) specimens ware chosen for the fatigue experiment. All samples have been cut into 220mmX70mm. The specimens have different rotation speed and welding speed: 800(rpm)/400(mm/min), 600(rpm)/200(mm/min) and 400(rpm)/100(mm/min). Fig.1 shows the sample geometries.

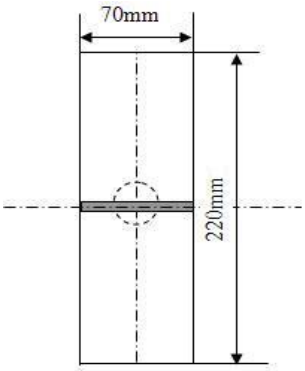

Fig.1 Sample size

Instron8872 hydraulic servo fatigue testing machine was used. Samples with different rotation speed and welding speed were tested in three different R ratio: R=0.1, R=0.3 and R=0.6. Δ P was set a constant value 6.3 KN.

2.2 Results

In Fig.2, crack growth rates under three different R ratio fatigue loads were shown. For three different welding parameters, crack growth rates at R=0.1, 0.3 were shown in Fig. 3.
The experimental data from all specimens was compared in Fig.2 and Fig.3, for samples with crack, da/dN versus $\Delta K_{applied}$. Even though had different rotation speed, welding speed and R ratio, the crack growth rate of these samples tended to be the same tendency. Previous studies [9] indicated that the fatigue life was based on the R ratio, which shown the stress level played an important role in crack growing. However, the fatigue life of the three kinds of samples certificated that even in different rotation speed and welding speed, the microstructure was the primary factor controlling the crack propagation for cracks grow in the welded nugget.

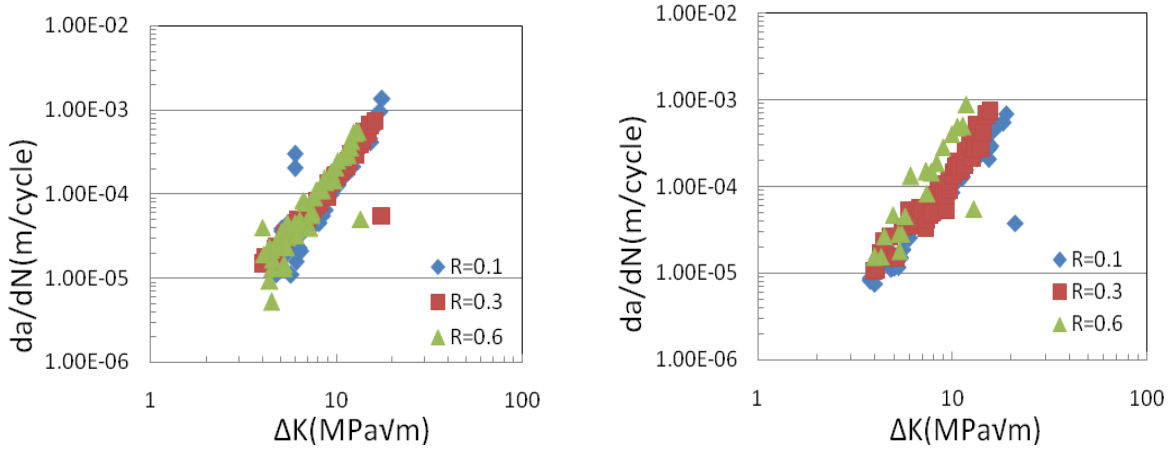

(a) 400/100 (b) 800/400

Fig.2 Crack growth rates at R=0.1, 0.3, 0.6

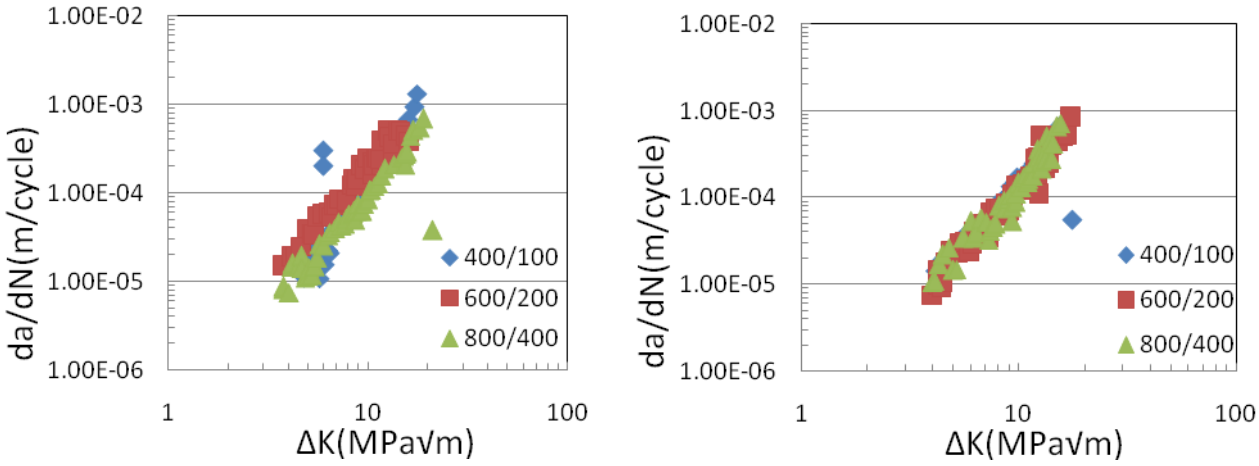

(a) R=0.1 (b) R=0.3

Fig. 3 Crack growth rate under different ratios for three different welding conditions

3. Numerical simulation

3.1 Numerical solution of K_{res}

The evaluation of residual K (K_{res}) was considered as a mature method of predicting fatigue crack growth rates in residual stress fields. Finite element analysis was used to calculate the stress intensity factor K_{res} from residual stress by using ABAQUS 6.10. The models were built using C3D8R (an 8-node linear brick, reduced integration, hourglass control.) entity elements around the notch tip and along the crack lines. The unit size gradual transition from 2.5mm to 0.5mm length. The virtual crack closure technique (VCCT) [10] was used for calculating strain energy release rate for unit sample thickness.

For plane stress, the relation between the strain energy release rate and stress intensity factor (SIF) was as follows:

$$K_{res} = \sqrt{GE} \tag{1}$$

$$\Delta K = \frac{\Delta P}{B}\sqrt{\frac{\pi\alpha}{2w}\sec\frac{\pi\alpha}{2}} \tag{2}$$

$$R_{eff} = \frac{K_{res}+K_{min}}{K_{res}+K_{max}} \tag{3}$$

If residual stresses were input to this model, K_{res} can be derived from Eqs. (1), R_{eff} can be derived from Eqs. (2) and (3). The crack growth rate can be calculated with the Paris formula.

3.2 Fatigue life in simulation

The fatigue life in weld nugget were compared to the experimental data, as shown in Fig.4 For ΔK less than 10MPa $\sqrt{m}$, the experimental data was consistent with the parent material. When ΔK grew breakthrough 10MPa $\sqrt{m}$, the experimental data was more in line with simulations.

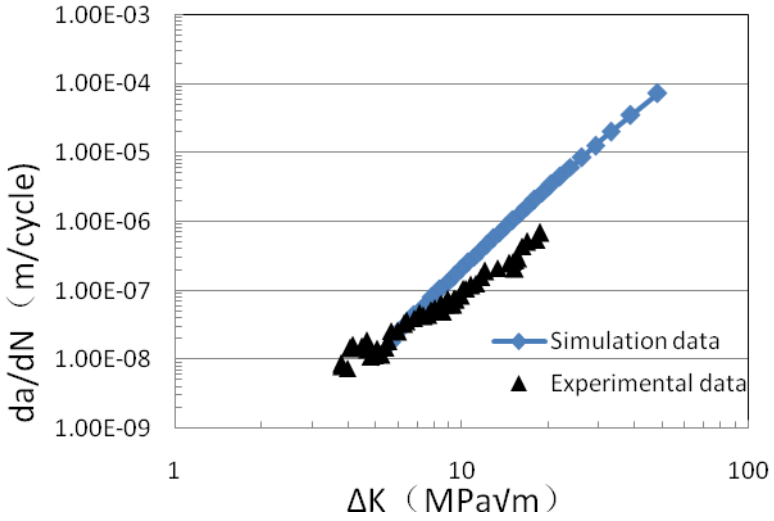

Fig.4 The crack growth rate in parent material and weld nugget

4. Conclusion

The crack growth rate in weld nugget of Al-Li alloy 2198-T8 friction stir welded was mainly decided by the microstructure, not the R ratio as common understanding.

Acknowledgement

This paper is sponsored by "National Natural Science Foundation of China (11002111)

References

[1] P. Cavaliere, M. Cabibbo, F. Panella, A. Squillace, 2198 Al–Li plates joined by Friction Stir Welding: Mechanical and microstructural behavior, Materials & Design, Volume 30, Issue 9, 2009, pp. 3622–3631.

[2] G Bussu, P.E Irving. The role of residual stress and heat affected zone properties on fatigue crack propagation in friction stir welded 2024-T351 aluminium joints, International Journal of Fatigue, Volume 25, Issue 1, 2003, pp.77-88.

[3] R John, K.V Jata, K Sadananda, Residual stress effects on near-threshold fatigue crack growth in friction stir welds in aerospace alloys, International Journal of Fatigue, Volume 25, Issues 9–11, 2003,pp.939-948.

[4] P. Cavaliere, A. De Santis, F. Panella, A. Squillace, Effect of anisotropy on fatigue properties of 2198 Al–Li plates joined by friction stir welding, Engineering Failure Analysis, Volume 16, Issue 6, 2009, pp.1856–1865

[5] P.M.G.P. Moreira, M.A.V. de Figueiredo, P.M.S.T. de Castro, Fatigue behaviour of FSW and MIG weldments for two aluminium alloys, Theoretical and Applied Fracture Mechanics, Volume 48, Issue 2, 2007, pp.169–177

[6] M. Pedemonte, C. Gambaro, E. Lertora, C. Mandolfino, Fatigue assessment of AA 8090 friction stir butt welds after surface finishing treatment, Aerospace Science and Technology, 2012, in press.

[7] R.S.Mishra, Z.Y.Ma, Friction stir welding and processing, Materials Science and Engineering: R: Reports, Volume 50, Issues 1–2, 2005, pp. 1–78.

[8] Z.L. Hu, X.S. Wang, S.J. Yuan, Quantitative investigation of the tensile plastic deformation characteristic and microstructure for friction stir welded 2024 aluminum alloy, Materials Characterization, Volume 73, 2012, pp. 114–123.

[9] B. Holper, H. Mayer, A.K. Vasudevan, S.E. Stanzl-Tschegg, Near threshold fatigue crack growth at positive load ratio in aluminium alloys at low and ultrasonic frequency: influences of strain rate, slip behaviour and air humidity, International Journal of Fatigue, Volume 26, Issue 1, 2004, pp.27-38.

[10]Krueger Ronald. The virtual crack closure technique: history, approach and applications. NASA/CR-2002-211628.

Effect of Loading Frequency in Fatigue Properties and Micro-Plasticity Behavior of JIS S15C Low Carbon Steel

Benjamin Guennec[1,*], Akira Ueno[2], Tatsuo Sakai[2], Masahiro Takanashi[3], Yu Itabashi[3]

[1] Student Member: Graduate School of Science and Engineering, Ritsumeikan University, Kusatsu, Shiga 525-8577, Japan
[2] College of Science and Engineering, Ritsumeikan University, Kusatsu, Shiga 525-8577, Japan
[3] Research Laboratory, Structural Strength Department, IHI Corporation, Yokohama, Kanagawa 235-8501, Japan
* Corresponding author: gr0081rh@ed.ritsumei.ac.jp

Abstract Ultrasonic testing method has allowed some impressive improvements in order to better grasp fatigue properties of various metallic materials the latest 20 years. It is particularly the case in the very high cycle regime since ultrasonic fatigue tests are conducted at very high stressing frequencies. However, the question of a potential difference of fatigue strengths due to huge frequency gap between ultrasonic method (usually carried out at 20 kHz) and servo-hydraulic one (usually in the range of 1~100 Hz) is still unclear and needs to be studied for a various kind of metallic materials. The case of low carbon steels presents a singularity, as fatigue properties are significantly different between these two fatigue tests methods. It seems particularly interesting to study this kind of materials in order to get a better overview of frequency effect in metallic materials fatigue. Aim of the present work, which consists of a general survey of JIS S15C steel (0.15% C) fatigue properties, is firstly to reconfirm such a frequency effect. Secondly, based on several experiments related to micro-plasticity behavior, some discussions will be held in order to explain this frequency effect in the case of low carbon steels.

Keywords Frequency effect, Low carbon Steel, Ultrasonic test, Cyclic hardening, EBSD observations

1. Introduction

The past 20 years in the field of fatigue test marks increase of ultrasonic testing method for various industrial uses. Since study of the very high cycle regime has become a topical issue, ultrasonic stressing frequency allowed by this fatigue testing method is essential to conduct fatigue test in a definite time. It is indeed almost impossible to reach 10^9~10^{10} cycles with a conventional fatigue testing machine.

However, question of a potential influence of stressing frequency on fatigue test result, usually known as “frequency effect”, have been studied by numerous literatures and is still unclear, except for some particular materials. Low carbon steels reveal usually a clear difference of fatigue strength between usual fatigue testing (servo-hydraulic as instance) and ultrasonic testing method.

As a consequence, it was decided to make a focus on the effect of loading frequency on low carbon steels. The present work discusses some phenomenon possibilities involved in frequency effect of low carbon steels.

2. Experimental Procedure

In the present study, material tested is JIS S15C steel, extracted from as rolled material. Chemical composition and mechanical properties are indicated in Tables 1 and 2, respectively. Figure 1 shows the microstructure of this steel, with typical ferritic and pearlitic composition. One can see that grains are elongated in the rolling direction.

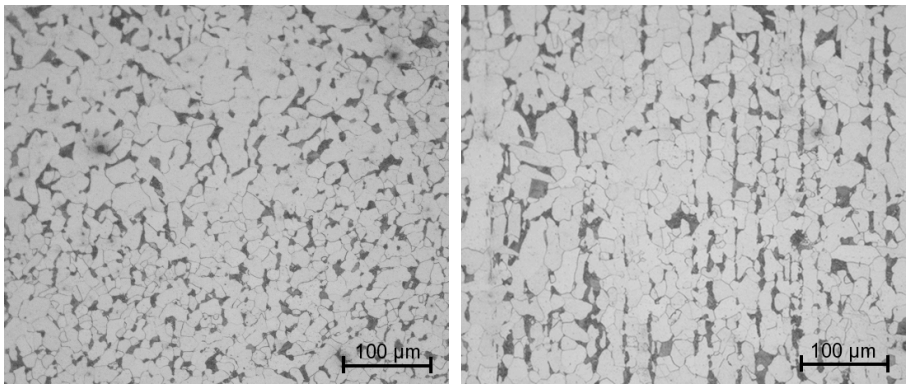

(a) Along transversal axis (b) Along longitudinal axis

Fig.1. Microstructure of S15C steel

Table 1. S15C chemical compositions (mass %)

C	Si	Mn	Cu	Ni	Cr	Fe
0.15	0.21	0.40	0.02	0.02	0.15	*Re*

Table 2. Mechanical properties of S15C steel

Mechanical properties	Value
Lower yield stress (MPa)	273
Tensile strength (MPa)	441
Young modulus (GPa)	207
Elongation (%)	40.2
Reduction of area (%)	65.8
Vickers hardness (HV)	161

Fatigue tests have been conducted at several frequencies: 20 kHz using an ultrasonic type machine, under displacement control; 140 Hz using an electro-magnetic type machine under stress control; 20 Hz, 2 Hz and 0.2 Hz using servo-hydraulic type machine under stress control. An air-cooling system and intermittent loading conditions were admitted to avoid temperature rising of specimen in the case of ultrasonic fatigue tests. For fatigue tests performed at 140 Hz, an air-cooling system has been also added for the same reason.

All fatigue tests were performed in air, at room temperature, with a stress ratio R = -1. Configurations of fatigue specimens are presented in Fig. 2. Diameter of tested portion was fixed at 5 mm, whatever the testing method used. After machining, center portion of specimens are electro-polished to remove residual stresses. As a consequence, we avoid any size effect and residual stress effect on the *S-N* properties of S15C steel.

One can see that servo-hydraulic and electro-magnetic specimens present a cylindrical shape at center rather than usual hour glass shape. It allows us to carefully attach a 4-strain gauge system in order to follow micro-plasticity behavior during fatigue test. Choice of this type of full-bridge system has been done in order to obtain accurate measures and to avoid heating influence on strain measures.

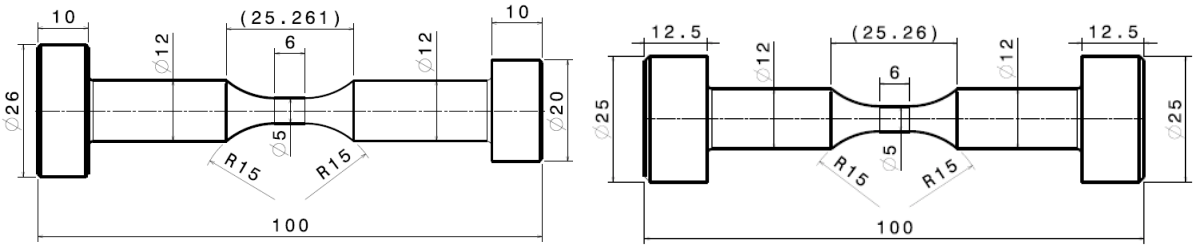

(a) Specimen for servo-hydraulic type machine (b) Specimen for electro-magnetic type machine

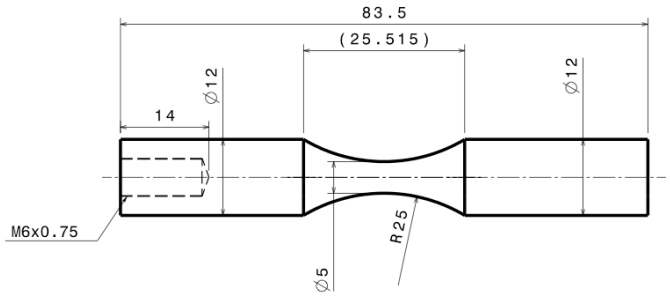

(c) Specimen for ultrasonic type machine
Fig.2. Shape and dimensions of fatigue specimen

3. Experimental Results

3.1. *S-N* data

S-N diagram of JIS S15C steel used here is depicted in Fig. 3. One can see a clear difference of fatigue strength between ultrasonic 20 kHz fatigue test results and other results from servo-hydraulic and electro-magnetic machines. Fatigue limits found under these four fatigue tests conditions are 248 MPa, 200 MPa for 20 kHz and 140 Hz respectively, and a similar fatigue limit of 185 MPa has been found in the case of servo-hydraulic fatigue tests at a testing frequency of 2 and 20 Hz. This kind of large discrepancy between fatigue tests performed in usual testing frequency range and ultrasonic frequency has been also found in several other literatures as Kikukawa *et al.*[1], Yokobori *et al.*[2] or Setowaki *et al.*[3] for different other kinds of low carbon steels.

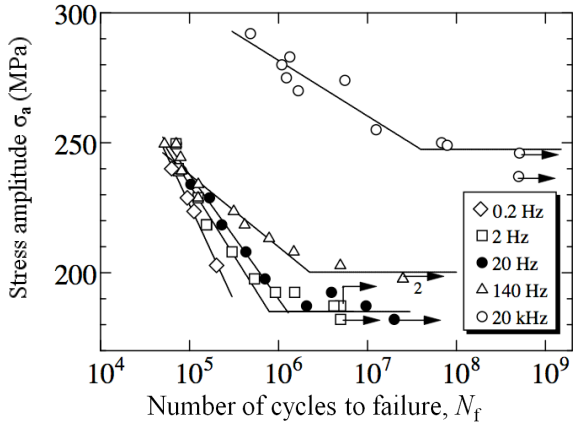

Fig.3. General *S-N* property of S15C steel

In addition, one can see that there are some fatigue strength differences between tests performed in the range from 0.2 Hz to 140 Hz. The fatigue properties are equivalent for high stress tests in this frequency range. However, as the stress level decreases, some fatigue life differences can be seen. In a general way, the higher is frequency, the higher becomes the fatigue strength. Particularly, even though tests performed at 2 and 20 Hz reveals the same fatigue limit, a relatively higher fatigue limit is found for 140 Hz tests. Nevertheless, those fatigue strength differences are far smaller than compared with ultrasonic fatigue test results.

3.2. Fracture surface observation

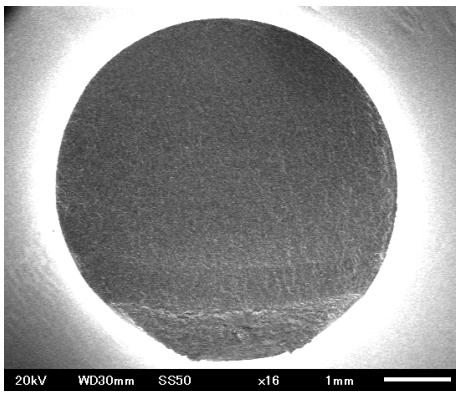

(a) f=20 kHz, σ_a=255 MPa, N_f=1.25×10^7

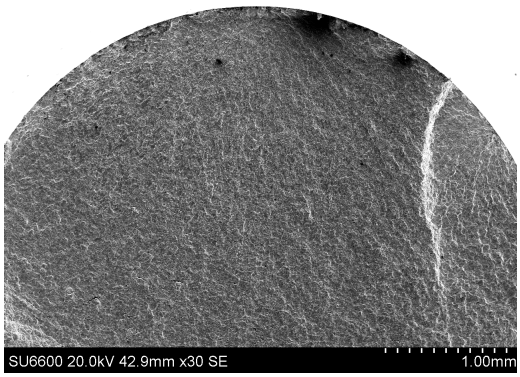

(b) f=2 Hz, σ_a=228.8 MPa, N_f=1.25×10^5

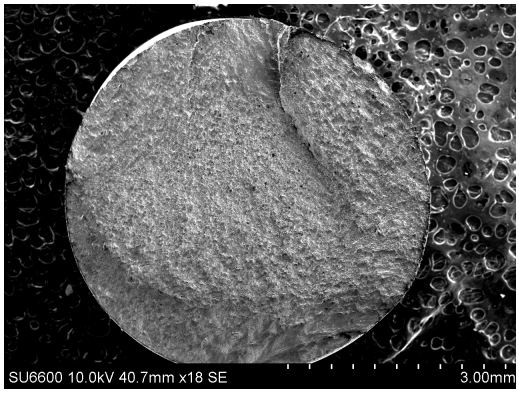

(c) f=140 Hz, σ_a=244.4 MPa, N_f=7.29×10^4

Fig. 4 Typical examples of fracture surface

Fracture surface observation reveals that, for all the fatigue tests conducted up to failure, fracture has been initiated from the specimen surface, even under ultrasonic fatigue loading. This fact is usual for this kind of low strength steels, where number of inclusions, and so main factor of fish-eye fracture occurrence, is low. Figure 4 shows some typical examples encountered in the present study. Two kinds of fracture conditions have occurred. On the one hand, Fig. 4(a) presents a fracture behavior initiated by only one crack. On the other hand, Figs. 4(b) and (c) depict a clear multiple cracks conditions before specimen's failure. In order to gather such these data, Fig. 5 is an *S-N* diagram, which makes clearly distinction between simple and multiple cracks behavior found.

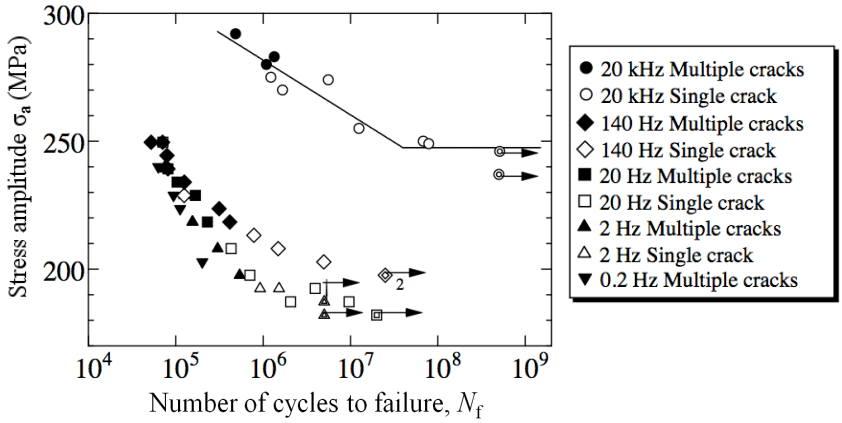

Fig.5. General fracture crack behavior

It is not surprising at all to see that multiple crack behavior is able to occur only for relatively high stress level tests, whereas simple crack condition is more likely to happen for low stress levels. One important finding related to this fracture behavior is that the transition between multiple to single crack appears around fatigue strength of 10^6 cycles, regardless testing frequency. In other words, this fracture behavior is not directly related to the stress level, but is mainly governed by the fatigue strength at a specific fatigue test condition. As fatigue strength of S15C steel is dependent of the testing frequency, the stress level where takes place this fracture behavior transition tends also to increase when testing frequency is increasing.

3.3. Stress-strain hysteresis

Stress-strain behavior in the present study has been studied for 0.2, 2, 20 and 140 Hz loading frequencies; as such a study is not possible in the case of ultrasonic method. Stress signal was directly recorded from testing machine load cell, whereas strain was measured from strain gauge system introduced before. As failure of fatigue specimen occurs almost all the time at the extremity of central cylindrical shape due to a slight stress concentration factor K_t=1.04, crack propagation does not influence measures on strain gauge at the center.

General evolution of stress-strain hysteresis loop of S15C studied here is presented in Fig. 6. In this diagram, hysteresis loop's area A_h from some fatigue tests is plotted against the number of cycles. One can clearly see on Fig. 6(a) that an increasing general trend occurs. In other words, as those tests are stress controlled, S15C is generally softening when fatigue goes. This result can be explained by the fact that this material is as rolled, and so has a hardened initial condition.

In addition, it is obvious that increasing trend becomes dramatic as the stress level increases. This result is natural, since cyclic softening phenomenon becomes usually more remarkable when material is subjected to higher stress amplitude. One can note that softening get to saturation at a certain number of cycles and then a slight cyclic hardening behavior is observed, as hysteresis loop's area tends to decrease. This phenomenon is particularly obvious for high stress tests.

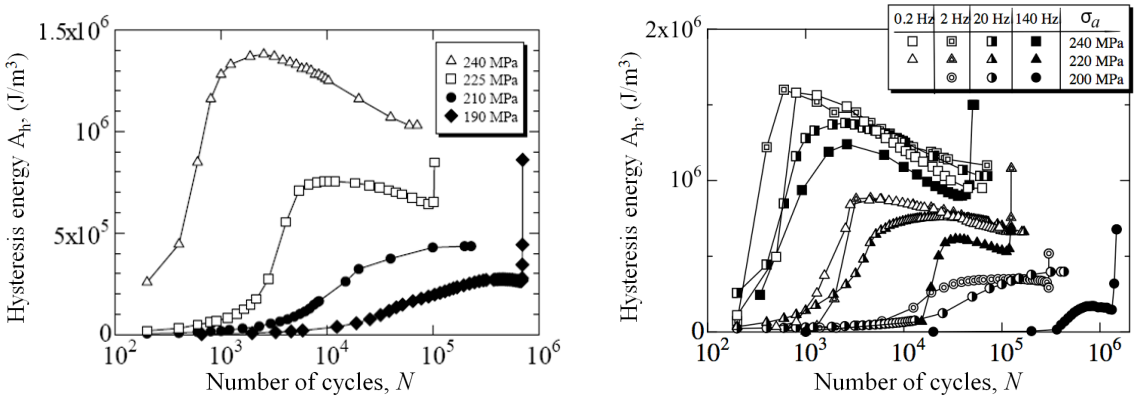

(a) Hysteresis area under 20 Hz tests (b) Hysteresis area for several tests conditions

Fig.6. Evolution of stress-strain hysteresis loop's area

Figure 6(b) allows a comparison of hysteresis loop's area value between 0.2 Hz, 2 Hz, 20 Hz and 140 Hz fatigue tests at three different stress amplitudes. One can see clearly that hysteresis loop's area is dependent of the fatigue test as the smaller is the frequency, the higher becomes hysteresis energy. In addition, primary cyclic softening behavior is also more severe when frequency decreases.

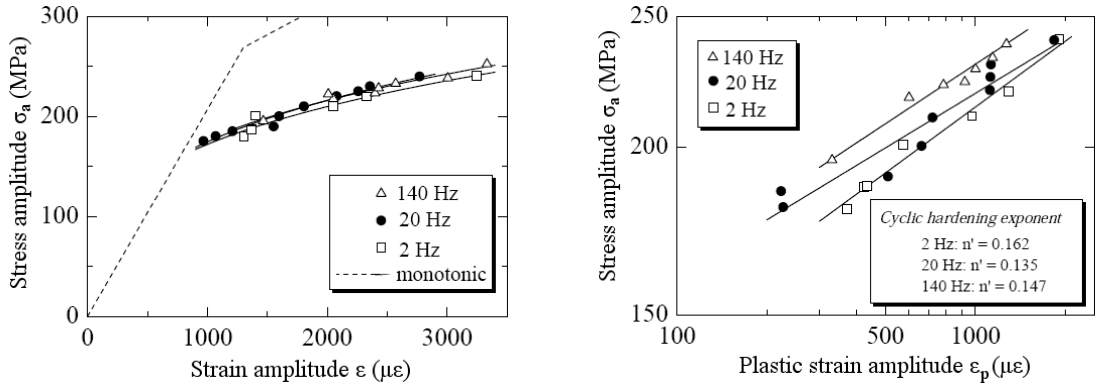

(a) Comparison Monotonic and CSSC (b) Determination of cyclic hardening exponent

Fig.7. Comparison of CSSC under 2 and 20 Hz

Let us pay now a particular attention on the cyclic stress-strain curve (CSSC). Figure 7(a) allows a comparison of monotonic and cyclic stress-strain curves from fatigue tests at 2, 20 and 140 Hz. One can find that cyclic stress-strain data are lower than monotonic ones. This behavior is in accordance with general cyclic softening already mentioned[4].

In addition, if we consider only plastic strain of hysteresis loops as in Fig. 7(b), the cyclic hardening exponent is equal to 0.162, 0.135 and 0.147 for 2, 20 and 140 Hz fatigue tests respectively. One can note that theses values are close to the usual estimation 0.15 for most of metallic materials[5], regardless its initial conditions. Even though CSSC from 20 and 140 Hz fatigue tests are really close one to each other, one can see that for a similar stress amplitude, total strain amplitude and particularly plastic strain amplitude decreases when the testing frequency is increasing. This fact is of course correlated with the decrease of hysteresis energy already highlighted.

4. Discussion

A clear effect of the testing frequency on the fatigue properties of JIS S15C steel has been reconfirmed in the previous section. Now let us make a discussion on some phenomena, which can be involved in fatigue behavior for the present material.

4.1. Yield stress influence

Effect of strain rate on the yield stress value for this kind of low carbon steels has been reported in some publications[3,6]. This phenomenon is most of the time considered as one of the main phenomena that can explain frequency effect observed.
Figure 8 shows results of tensile tests conducted at different speeds in order to assess the strain rate effect on the present S15C steel. These tensile tests have been conducted according to JIS Z2201 standard, with a 14 mm diameter tested section. Results are compared with data from Tsuchida[7].

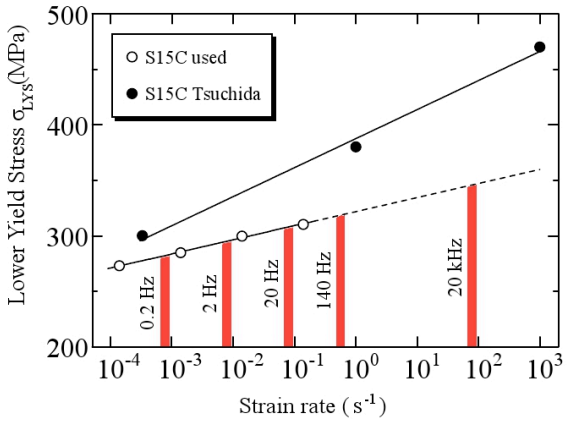

Fig.8. Strain rate effect on yield stress

One can easily find that S15C lower yield stress tends to increase when strain rate is increasing. This trend may be certainly linked with resistance of deformation, which decreases under high-speed tests.
Accordingly to literature from Tsuchida, a logarithmic law has been chosen. Difference of slope between the present work and Tsuchida's results may comes from that tensile test specimens in the case of very high stain rate are significantly smaller than those in usual strain rate range.
The present S15C used shows a regression with a correlation coefficient of 0.998, in the strain rate range from 10^{-4} to 10^{0} s^{-1}. This regression was extrapolated up to a strain rate of 10^{2} s^{-1} in order to assess yield stress value under equivalent ultrasonic fatigue strain rate. For instance, by this means, we obtain a difference of lower yield stress value between 20 Hz and 20 kHz fatigue test conditions of nearly 40 MPa.
This difference has been compared with the fatigue properties of S15C steel already introduced in Fig. 3. The following diagram, in Fig. 9, takes into consideration variation of yield stress by using normalized stress amplitude σ_a by the lower yield stress σ_{LYS} previously assessed.

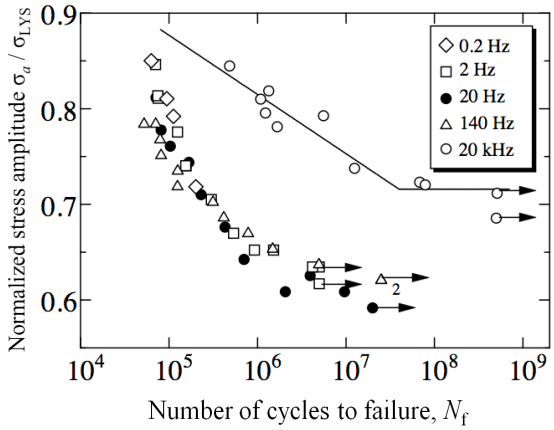

Fig.9. Evaluation of yield stress variation on *S-N* properties

Such a diagram gives us two very interesting points, which have to be discussed. First, if we consider only results from tests performed at 0.2, 2, 20 and 140 Hz, one can see that fatigue strength of S15C steel gathers in a thin area. Besides, fatigue limits from 2 and 140 Hz fatigue tests become really close each other. As a consequence, such a diagram is significant in order to evaluate the yield stress influence on the *S-N* property of S15C steel.

The second main point is of course the case of fatigue results from ultrasonic tests. Due to relatively high difference of yield stress introduced before between ultrasonic tests conditions and usual test frequency conditions, the huge gap of fatigue strength seen in Fig. 3 is significantly lower by taking into consideration the effect of strain rate. Nevertheless, it is not enough to claim that *S-N* properties are similar with other results from usual range frequency. So, the strain rate effect on yield stress is not sufficient to give an entire explanation of fatigue strength gap found in Fig. 3.

4.2. Cyclic hardening / softening behavior

In Figs. 6 and 7, a difference of stress-strain hysteresis phenomenon can be highlighted between 0.2, 2, 20 and 140 Hz fatigue tests. In other words, cyclic softening and hardening behavior seems to be slightly influenced by fatigue test frequency in this range. Of course, it is impossible to undertake similar stress-strain hysteresis study in the case of ultrasonic testing method, as real stress applied on specimen in unknown under ultrasonic technique. So, we cannot assess in the same way a potential discrepancy between ultrasonic and fatigue tests conducted in usual frequency range.

In order to highlight anyway a possible frequency effect on the cyclic hardening and softening, misorientation observation by EBSD method has been performed. This comparison involves 20 kHz and 20 Hz fatigue tests.

The samples used in this study have been prepared following hereafter instructions. For each frequency, two particular stress levels have been chosen, which are the fatigue limit plus 10 and 30 MPa. These stress levels are called S_w+10 and S_w+30 in the rest of the present paper.

For each stress level, corresponding fatigue strength is given by *S-N* model shown in Fig. 3. Three different specimens were stopped at 5%, 10% and 25% of the calculated fatigue strength. So, 12 different specimens have been fatigued in this process considering both 20 kHz and 20 Hz fatigue tests. After fatigue test has been stopped, center section of the specimen has been extracted, and then polished. Sample final condition has been prepared by OP-AA polishing method in order to

prepare samples for EBSD observations.

Aim of these observations is to determine how lattice misorientation in ferrite phase evolves when fatigue goes. As well-known, cyclic hardening / softening behavior has an impact on dislocation structure[8-9]. This type of experiments can be considered as a first step to evaluate dislocation changes, before conducting direct observation of dislocations.

For each sample, two distinctive map scans of a 200x180 μm^2 area have been conducted. Misorientation curves presented in Figs. 10 and 11 are the average of these two scans. Figure 10(a) reveals that misorientation distribution does not significantly change between stages 5 and 25% of N_f for 20 Hz tests. This is less the case of ultrasonic tests, according to Fig. 10(b), even though dramatic change cannot be seen between these three fatigue stages. However, main result that has to be pointed out here is the drift of distribution into lower misorientation values for fatigued specimens, compared to the condition before fatigue test.

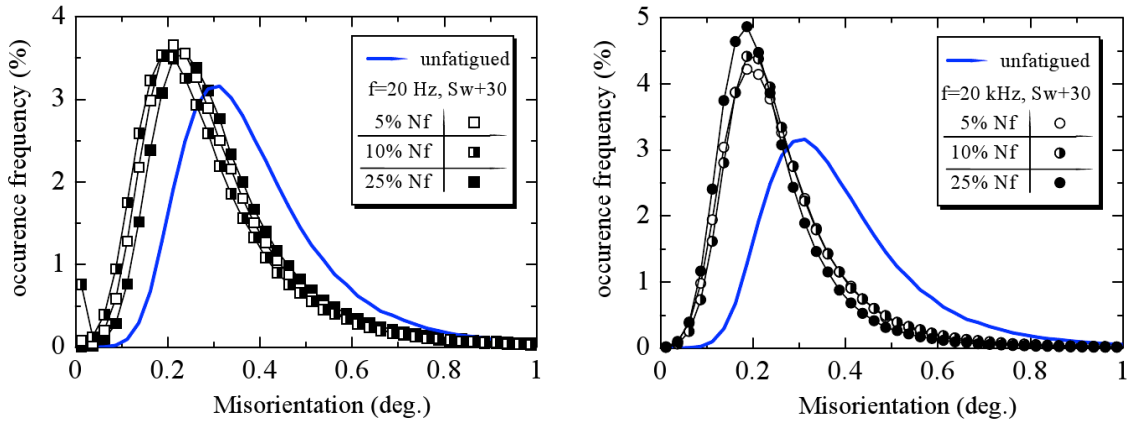

(a) Case of 20 Hz loading frequency (b) Case of 20 kHz loading frequency

Fig.10. Change of misorientation distribution for S_w+*30* stress level

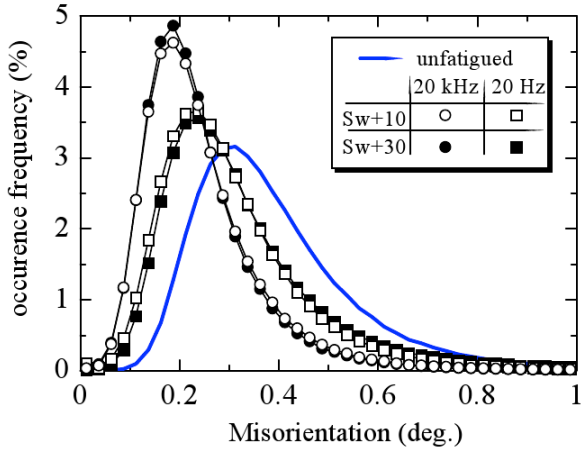

Fig.11. Comparison of misorientation distributions for 20 Hz and 20 kHz conditions at N=25% N_f

Such a result is confirmed in Fig. 11, where results at N=25% N_f for both stress levels studied are presented. It is found at a same frequency, distribution from S_w+*10* and S_w+*30* are similar. However, mode of distributions from 20 kHz tests is obviously lower than 20 Hz. This significant change of mode is certainly linked with dislocation structure changes. More precisely, such a result is an

indication that dislocation structure changes due to fatigue loading at 20 Hz and 20 kHz is not equivalent. A possible explanation of this fact is the time allowed to dislocations to move is necessarily different for a same material fatigued under 20 Hz and 20 kHz conditions.
As a consequence, we can assess that fatigue frequency has an effect on cyclic behavior of S15C steel. Nevertheless, other results are needed to conclude in this way. It is particularly expected to undertake direct dislocations observation in order to be able to detect such a discrepancy in dislocations substructures.

5. Conclusions

(1) Frequency effect on fatigue properties of S15C low carbon steel has been reconfirmed. Fatigue strength tends to increase when testing frequency is increasing.
(2) Strain rate has a clear effect on yield stress value of S15C steel. This phenomenon is involved in the trend described before and explains the slight change of fatigue strength between 0.2 and 140 Hz. However, it is not sufficient to explain the *S-N* properties gap found from ultrasonic method.
(3) Comparison of stress-strain hysteresis loops and EBSD observations indicate a frequency dependence in cyclic behavior. This fact urges us to consider the cyclic hardening / softening properties as one other main phenomenon involved in frequency effect of S15C steel.
(4) Some other works have to be conducted to finalize the study of frequency effect on S15C steel. Particularly, further experiments on cyclic hardening / softening behavior will be undertaken, like dislocation observations.

References

[1] M. Kikukawa, K. Ohji, K. Ogura, Push-Pull Fatigue Strength of Mild Steel at Very High Frequencies of Stress Up to 100 kc/s. J. Basic Eng. T. ASME D, 87 (1965) 857–864.
[2] T. Yokobori and T. Kawashima, Acoustical Fatigue with Special Emphasis on Ferrite Grain Size Dependence of Fatigue Strength. J. of the Japanese Society for Strength and Fracture of Materials, 4 (1969) 19–16. (In Japanese)
[3] S. Setowaki, Y. Ichikawa, I. Nonaka, Effect of Frequency on High Cycle Fatigue Strength of Railway Axle Steel. Proceedings VHCF-5 (2011) 153–158.
[4] C.E. Feltner, C. Laird, Cyclic Stress-Strain Response of F.C.C. Metals and Alloys-I. Acta Metall., 15 (1967) 1621–1632.
[5] L. Landgraft, J. Morrow, T. Endo, Determination of the Cyclic Stress-Strain Curve. Journal of Materials, 4 (1969) 176–188.
[6] N. Tsutsumi, A. Shiromoto, V. Doquet, Y. Murakami, Effect of Test frequency on Fatigue Strength of Low Carbon Steel, J. Jpn Soc. Mechanical Eng. A, 72, 715 (2006) 317–325. (In Japanese)
[7] N. Tsuchida, H. Masuda, Y. Harada, K. Fukaura, Y. Tomota, K. Nagai, Effect of Ferrite Grain Size on Tensile Deformation of a Ferrite-cementite Low Carbon Steel. Material Science and Engineering A, 488 (2008) 446–452.
[8] J.R. Hancock and J.C. Grosskreutz, Mechanisms of Fatigue Hardening in Copper Single Crystals, Acta Metall., 17 (1969) 77–97.
[9] H. L. Huang, A Study of Dislocation Evolution in Polycrystalline Copper during Low Cycle Fatigue at Low Strain Amplitude, Materials Science and Engineering A, 342 (2003) 38–43.

On the effect of fatigue crack plastic dissipation on the stress intensity factor

Nicolas Ranc[1,*], Thierry Palin-Luc[2], Paul C. Paris[3]

[1] Arts et Métiers ParisTech, PIMM, CNRS, 151 Boulevard de l'Hôpital, F-75013 Paris, France
[2] Arts et Métiers ParisTech, I2M, CNRS, Esplanade des Arts et Métiers, F-33405 Talence Cedex, France
[3] Parks College of Engineering, Aviation, and Technology, St. Louis University St. Louis, MO, 63103 USA
and visiting professor at Arts et Metiers ParisTech, France
* Corresponding author: Nicolas.ranc@ensam

Abstract In metals, during plastic strain, a significant part of the plastic energy is converted into heat. This generates a heterogeneous temperature field around the crack tip which depends on the intensity of the heat source associated with the plasticity and the thermal boundary conditions of the cracked structure under cyclic loading. Due to the thermal expansion of the material, the temperature gradient near the crack tip creates thermal stresses which contribute to stress field around the crack tip. This paper shows how this thermal effect modifies the mode one stress intensity factor for two cases: (i) the theoretical problem of an infinite plate with a semi-infinite through crack and (ii) a finite plate specimen with a central through crack. The comparison of the two cases allows the authors to discuss the effect of convection. The comparison of the simulated and experimental temperature field variation at the specimen surface (infra-red measurement on a mild steel) leads to identify the heat flux in the reverse cyclic plastic zone. This is the key parameter of the problem. Finally, the consequences of the calculation on the range, the ratio and the maximum and the minimum values of the stress intensity factor are discussed.

Keywords: stress intensity factor, plastic dissipation, reverse cyclic plastic zone, thermal stress

1. Introduction

During experimental study of fatigue crack propagation (for example the characterization of the propagation velocity versus the range of the stress intensity factor) the heating effects associated with the crack propagation are often neglected and the tests are considered as isothermal. This assumption is all the more legitimate when the loading frequency is small. However currently it is increasingly necessary to study the fatigue behavior of materials for long and very long life. Experimental techniques of accelerated tests thus are often carry out in order to reduce test durations : electromagnetic resonance fatigue testing machine with a loading frequency of about hundred Hertz and even ultrasonic fatigue machine with a loading frequency of about several tens of kHz. It is then necessary to know if the assumption of an isothermal process is always valid under these test conditions.

In metals, during plastic strain, a significant part of the plastic energy (around 90% [1,2]) is converted in heat. During a cyclic loading of a cracked structure, the plasticity is located in the reverse cyclic plastic zone near the crack tip [3,4]. This heat source generates a heterogeneous temperature field which depends on the intensity of the heat source associated with the plasticity and the thermal boundary conditions of the cracked structure. Due to the thermal expansion of the material, the temperature gradient near the crack tip creates thermal stresses which contribute to the stress field in this region and on the global stress intensity factor.
The objective of this communication is to propose a method in order to quantify the thermal contribution on the stress intensity factor. In a first part the identification of the heat source associated with the crack propagation will be detailed. In a second part the estimation of the thermal effect on the stress field near the crack tip and on the stress intensity factor will be made for the two geometries: an infinite plate with a semi-infinite through crack and a finite plate specimen with a central through crack and with convection boundary conditions on all the specimen faces. Finally, in the last part, all these results will be compared and discussed.

2. Heat source identification associated with the fatigue crack propagation

In order to identify the heat source associated with the crack propagation a cracked specimen which geometry is given in fig. 1, is subjected to a cyclic loading with a stress intensity factor range of about $20\,MPa\sqrt{m}$ and a stress ratio of 0.1. The loading frequency is about 100Hz and the material is a C40 mild steel with an ultimate tensile strength UTS=600 MPa. The mechanical and thermal properties of this steel are summarized in table 1.
The temperature field at the specimen surface was measured with an infrared camera (CEDIP Jade III MWR) whose spectral range is in the near infrared domain. The acquisition frequency and the aperture time of the camera were respectively 5Hz and 1100µs. In order to reduce the effect of the emissivity of the surface on the temperature determination, the specimen was covered with a fine coat of mat black paint.

Table 1. Mechanical and thermal properties of C40 steel

Material properties	density	Yield stress	Young Modulus	Poisson ratio	Thermal expansion	Heat capacity	Heat conduction	Heat diffusivity
Notation	ρ	σ_y	E	ν	α	C	k	a
Unit	kgm^{-3}	MPa	GPa		K^{-1}	$JK^{-1}kg^{-1}$	$WK^{-1}m^{-1}$	m^2s^{-1}
Value	7800	350	210	0.29	$1.2x10^{-5}$	460	52	$1.4x10^{-5}$

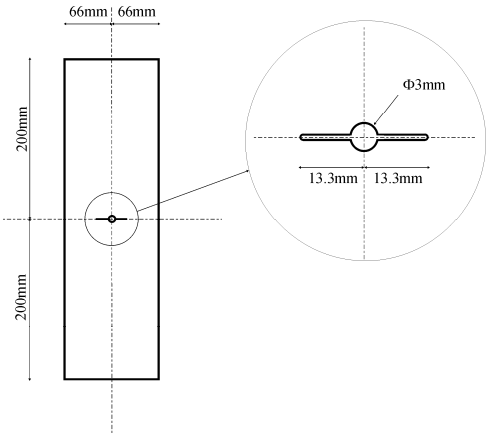

Figure 1. Cracked specimen geometry

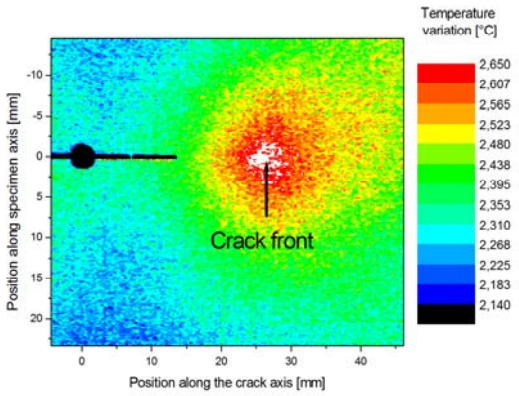

Figure 2. Temperature field near the crack front after 680s

Fig. 2 and fig. 3 show respectively the temperature variation field near the crack tip at time 680s and the temperature evolution according to time at a distance of 5mm from crack front. The temperature evolution on fig. 3 exhibits a superposition of a high frequency evolution of the temperature due to the thermoelasticity and a low frequency signal evolution corresponding to the dissipated power in the reverse cyclic plastic zone. Fig. 2 shows that the temperature distribution remains heterogeneous due to the highly localized form of the heat source in the reverse cyclic plastic zone. The total increase of the temperature in the specimen between the beginning and the end of the test corresponds to the heat source related to the plastic dissipation in the reverse cyclic plastic zone. This total increase in the temperature at a distance of 5mm from the crack front is about 2.5°C.

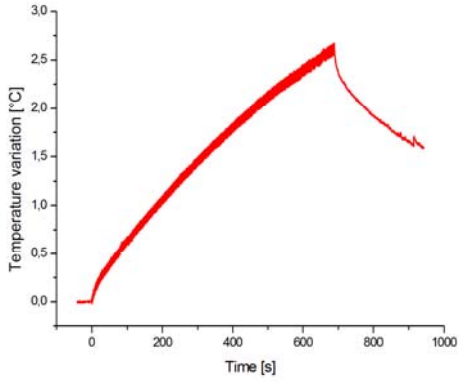

Figure 3. Temperature evolution versus time at a distance of 5mm from the crack front

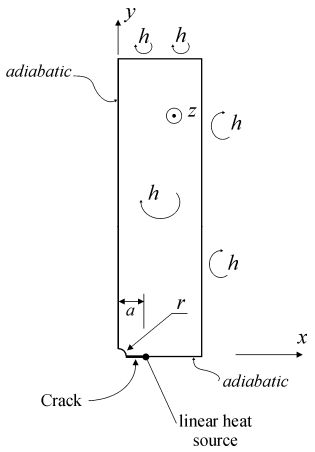

Figure 4. Thermal model, geometry and boundary conditions

In order to determine the heat source associated with the crack propagation. Under plane stress condition the radius of the reverse cyclic plastic zone can be quantified with the relation:

$$r_R = \frac{\Delta K^2}{8\pi\sigma_y^2} \tag{1}$$

For a stress intensity factor of $20\,MPa\sqrt{m}$ the radius of the reverse cyclic plastic zone is about 130µm. This value remains small compared to the size of the specimen. The heat source distribution will be thus considered as linear and centered in the reverse cyclic plastic zone.

For a slow moving crack, the heat source associated with the fatigue crack propagation can be considered to be motionless. This assumption can be justified by the calculation of the Péclet number, noted *Pe*, which compares the characteristic time of thermal diffusion with the characteristic time associated to the heat source velocity (i.e. the velocity of the reverse cyclic plastic zone at the crack tip). In our case the Péclet number is expressed by $Pe = Lv/a$ where L is the characteristic length of crack propagation, v the crack velocity and a the thermal diffusivity. For a crack length of around 1mm, a crack velocity of $0.1 mms^{-1}$ and a thermal diffusivity of 1.4×10^{-5} m^2s^{-1} the Péclet number is 6×10^{-3}. This value remains small compared to unit and therefore the heat source can also be considered as motionless.

In order to identify the heat source a thermal model of the plate was made and solved with the finit element method. The geometry and the thermal boundary conditions are detailed in fig. 4. The heat convection coefficient on the specimen faces and the room temperature are respectively taken equal to $10Wm^{-2}K^{-1}$ and 20°C. For C40 mild steel, the thermal and mechanical properties are given in table 1. A unit line heat source (q=$1Wm^{-1}$) is imposed on the crack front line. For a steady state regime the temperature variation at a distance of 5mm of the crack front is about 0.0163°C. Thanks to the linearity of the heat equation with the heat source, it is possible to deduce a heat source of $153Wm^{-1}$ associated with the fatigue crack loaded with a stress intensity factor range of $20\,MPa\sqrt{m}$.

3. The stress field and stress intensity factor due to the heterogeneous temperature field near the crack tip

2.2. An infinite plate with a semi-infinite through crack

This section is focused on the theoretical problem of an infinite plate with a semi-infinite through

crack loaded in fatigue in mode I. The main advantage of this problem is that it can be solved analytically. In the associated thermal problem, the thermal losses due to convection and radiation are neglected and the steady state regime is only considered. This problem is axi-symetric and the temperature variation distribution $\vartheta(r,t)$ is given by the heat equation:

$$\rho C \frac{\partial \vartheta}{\partial t} = q\delta(r) + k \frac{\partial^2 \vartheta}{\partial r^2}, \tag{2}$$

with δ the Dirac function. A solution of this equation is given in [5]:

$$\vartheta(r,t) = \frac{-q}{4\pi k} \mathrm{Ei}\left(-\frac{r^2}{4at}\right), \tag{3}$$

with $-\mathrm{Ei}(-x) = \int_x^\infty \frac{\mathrm{e}^{-u}}{u} \mathrm{d}u$ the integral exponential function and a the heat diffusivity.

In order to estimate the thermal stresses the thermo-mechanical problem with the temperature variation field previously calculated needs to be solved. The behavior of the material is considered elastic and perfect plastic. It is supposed that the plastic strain occurs only in the reverse cyclic plastic zone. With alternating plasticity, the boundary condition on the reverse cyclic plastic zone radius is radial stress equal to zero.

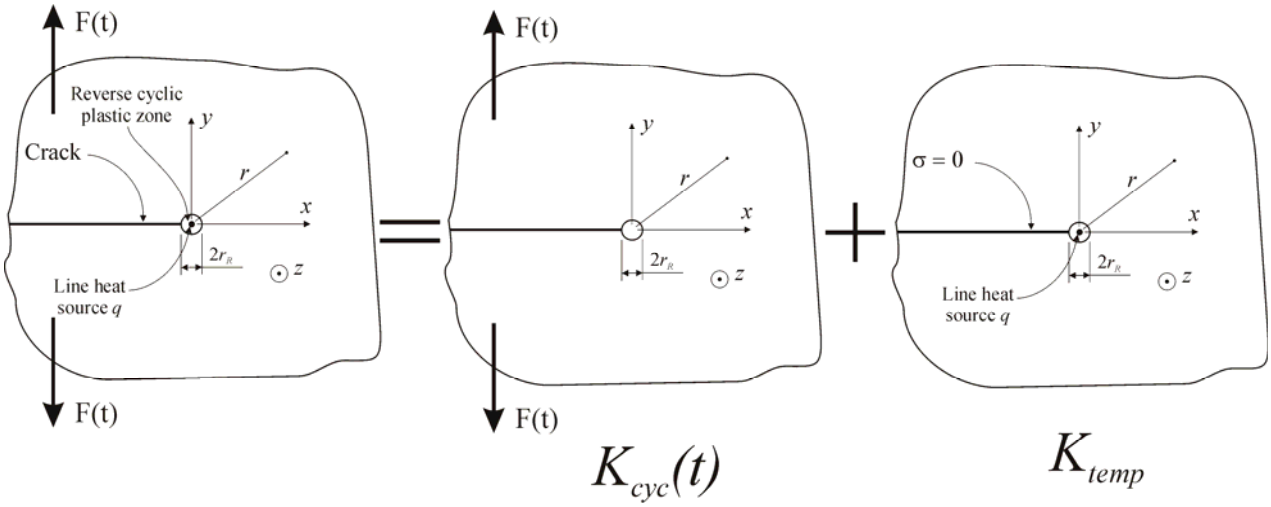

Figure 5. Decomposition of the thermomechanical problem

First the thermomechanical problem can be decomposed into two problems: the first problem (purely mechanical problem) is the cracked specimen subjected only to the cyclic loading $F(t)=F_m+F_a \sin(2\pi f\, t)$ without heat source due to the crack. The stress field associated with this problem is related to a mode one stress intensity factor $K_{cyc}(t)$. The second problem (purely thermal problem) is the cracked specimen subject to the line heat source q. The thermal stresses associated with this thermal loading create to a stress intensity factor named K_{temp}. The thermal effect generates a compressive stress field near the crack front and thus creates a negative contribution on the stress intensity factor ($K_{temp} < 0$) [6]. This decomposition is correct if crack closure due to the thermal effect is neglected and if the thermal effect does not affect significantly the reverse cyclic plastic zone radius. This assumption is realistic if the thermal correction remains small compared to the mechanical loading. The first pure mechanical problem is solved in a classical way and enable us to estimate the mode I stress intensity factor $K_{cyc}(t)$ according to the applied force $F(t)$. In order to solve the second problem, another decomposition is necessary. This second decomposition is illustrated in fig. 6.

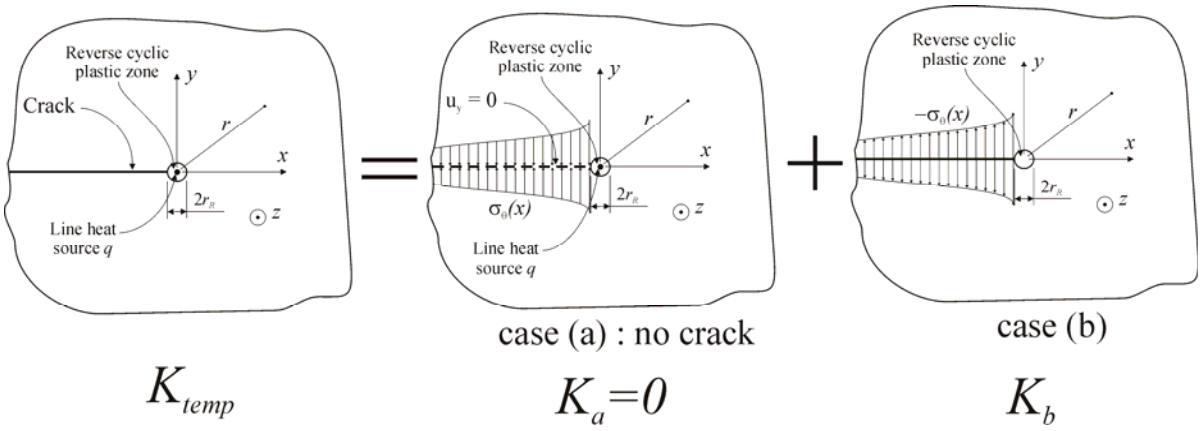

Figure 6. Decomposition of the thermal problem

In the first case (a) a normal stress $\sigma_\theta(r)$ is applied on the crack lips in order to imposed a crack opening equal to zero ($u_y = 0$). This stress $\sigma_\theta(r)$ is calculated from a thermoelastic problem without crack and with the heat source q. The stress intensity factor of case (a) is equal to zero and the stress intensity factor of case (b) is calculated with the Green function:

$$K_{temp} = \sqrt{\frac{2}{\pi}} \int_{r_R}^{\infty} \frac{\sigma_\theta(r,t)}{\sqrt{r - r_R}} \mathrm{d}r \,. \tag{4}$$

The case (a) thermo-mechanical problem is symmetric because both the geometry and the temperature field are symmetric. Only the case of plane stress is considered hereafter but plane strain solution is given in [6]. Further, outside of the reverse cyclic plastic zone since the constitutive behavior of the material is supposed to be elastic, it is expected in first approximation that the basic equations of thermo-elasticity will govern. The equilibrium equation is:

$$r\frac{\partial \sigma_r}{\partial r} + \sigma_r - \sigma_\theta = 0 \tag{5}$$

For which σ_r is the radial normal stress and σ_θ is the circumferential normal stress.
The isotropic elastic stress strain law gives with plane stress hypothesis:

$$\varepsilon_r = \frac{\partial u_r}{\partial r} = \frac{\sigma_r}{E} - \nu\frac{\sigma_\theta}{E} + \alpha\vartheta(r,t) \tag{6}$$

$$\varepsilon_\theta = \frac{u_r}{r} = \frac{\sigma_\theta}{E} - \nu\frac{\sigma_r}{E} + \alpha\vartheta(r,t) \tag{7}$$

A solution of this equation is given in [6] and the circumferential stress can be expressed with the following relation:

$$\sigma_\theta(r,t) = \frac{-\alpha E q}{8\pi k r^2}\left\{4at\left[\exp\left(\frac{-\mathrm{r}_\mathrm{R}^2}{4\mathrm{at}}\right) - \exp\left(\frac{-\mathrm{r}^2}{4\mathrm{at}}\right)\right] - \left[r_R^2 \mathrm{Ei}\left(\frac{\mathrm{r}_\mathrm{R}^2}{4\mathrm{at}}\right) + r^2 \mathrm{Ei}\left(\frac{r^2}{4at}\right)\right]\right\} \tag{8}$$

This circumferential normal stress is then calculated for a line heat source of 153 Wm^{-1} and at time $t = 680$s and this is represented in fig. 7. Near the reverse cyclic plastic zone ($r = r_R = 130\mu$m) the circumferential stress is negative (about -8.24 *MPa*) because the temperature is high and through the circumferential direction, the material is under compression due to the thermal expansion and the constraint effect.

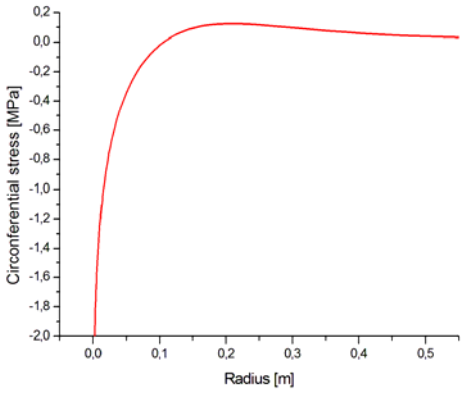

Figure 7. Circumferential stress distribution along radial axis

From equation (1) and (8) it is possible to expressed the associated stress intensity factor K_{temp}. We obtain after integration:

$$K_{temp} = \frac{-\alpha E q}{80k}\sqrt{\frac{2}{\pi}}\left\{40\sqrt{r_R} + \frac{20at\left(\exp\left(\frac{-r_R^2}{4at}\right)-1\right)}{r_R^{3/2}} + \sqrt{r_R}\,\mathrm{Ei}\left(\frac{-r_R^2}{4at}\right)\right.$$

$$+\frac{10(at)^{1/4}}{\Gamma\left(\frac{7}{4}\right)}\left(3{}_2F_2\left[\left(\frac{-1}{4},\frac{1}{4}\right),\left(\frac{1}{2},\frac{3}{4}\right),\frac{-r_R^2}{4at}\right]\right)+\frac{10(at)^{1/4}}{\Gamma\left(\frac{7}{4}\right)}\left({}_2F_2\left[\left(\frac{1}{4},\frac{3}{4}\right),\left(\frac{1}{2},\frac{7}{4}\right),\frac{-r_R^2}{4at}\right]\right)$$

$$\left.-\frac{8r_R}{(at)^{1/4}\Gamma\left(\frac{1}{4}\right)}\left(5{}_2F_2\left[\left(\frac{1}{4},\frac{3}{4}\right),\left(\frac{5}{4},\frac{3}{2}\right),\frac{-r_R^2}{4at}\right]\right)-\frac{8r_R}{(at)^{1/4}\Gamma\left(\frac{1}{4}\right)}\left({}_2F_2\left[\left(\frac{3}{4},\frac{5}{4}\right),\left(\frac{3}{2},\frac{9}{4}\right),\frac{-r_R^2}{4at}\right]\right)\right\}, \quad (9)$$

With the hypergeometric function

$${}_pF_q = \left(\{a_1,\ldots,a_p\},\{b_1,\ldots,b_q\},z\right) = \sum_{i=1}^{+\infty}\frac{(a_1)_i\ldots(a_p)_i}{(b_1)_i\ldots(b_q)_i}\frac{z^i}{i!},$$

where $(a)_i = \dfrac{\Gamma(a+i)}{\Gamma(a)} = a(a+1)(a+2)\ldots(a+i-1)$ is the Pochhammer symbol and $\Gamma(x) = \int_0^{+\infty} u^{x-1}\mathrm{e}^{-x}\mathrm{d}u$ the Euler Gamma function.

The value of K_{temp}, the thermal correction on the stress intensity factor, is estimated for a line heat source of 153Wm^{-1} and the typical material characteristics detailed in table 1. Eq. (9) gives a thermal correction on the stress intensity factor of -0.521 $MPa\sqrt{m}$.

2.2. A finite plate with a central through crack

For being representative of a real crack propagating problem let us now consider a finite plate with a central through crack. In such case thermal losses due to convection on the specimen faces, the effect of the temperature gradient near the crack front and thus the thermal correction of the stress

intensity factor cannot be neglected. For this type of thermomechanical problem it is not possible to find an analytical solution. That is the reason why computations of both the temperature field and the associated stresses and strains have been carried out by a finite element analysis.
First, the temperature field is calculated with the same model presented in section 2 for the thermal source identification. The steady state temperature field is thus calculated and represented on figure 8 for a line heat source of 153Wm^{-1}.

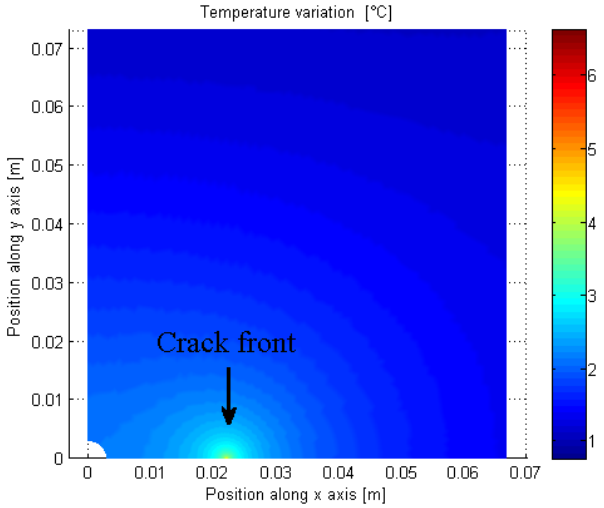

Figure 8. Temperature field near the crack front

The same type of decomposition and assumptions as presented for the previous geometry are used to calculate the stress field in the specimen. These two decompositions are detailed in figure 9 and 10.

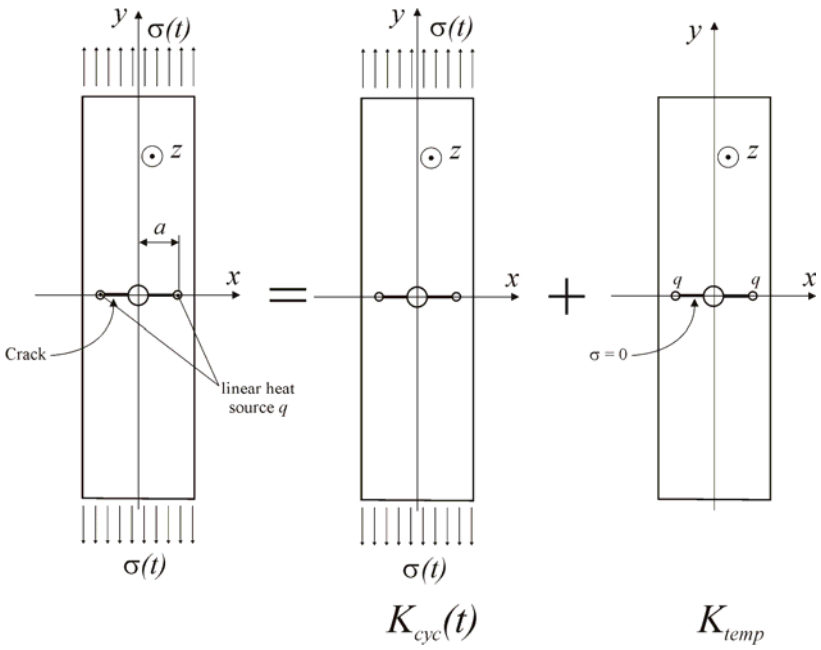

Figure 9. Decomposition of the general problem

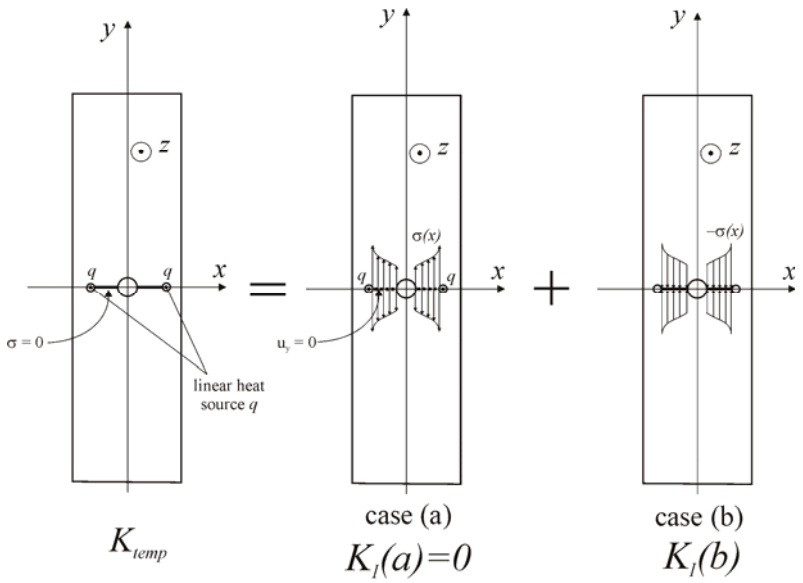

Figure 10. Decomposition of the thermal problem

Figures 11 and 12 show the normal stress in the direction of the y axis. The thermal effect on the stress intensity factor, K_{temp}, is calculated from the case (a) with the Green function and the stress field along the x axis calculated with the case (b) :

$$K_{temp} = \frac{2}{\sqrt{\pi}} \int_0^a \sigma(x) \frac{\sqrt{a}}{\sqrt{a^2 - x^2}} \mathrm{d}x \tag{10}$$

with a the crack length. The value of the thermal correction of the stress intensity factor K_{temp} for the plane problem with an centered through crack for a line heat source of 153Wm^{-1} is about -0.316 $MPa\sqrt{m}$.

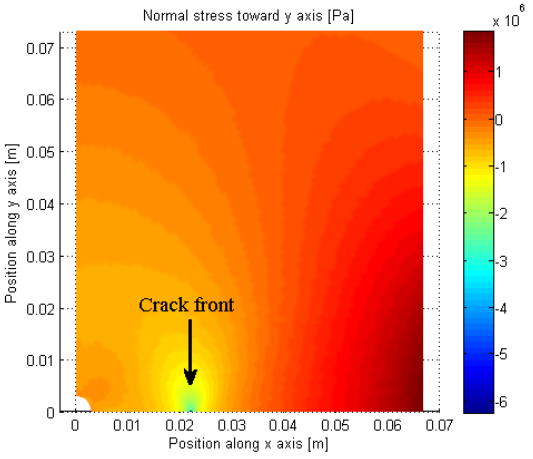

Figure 11. Normal stress field in the direction of the y axis

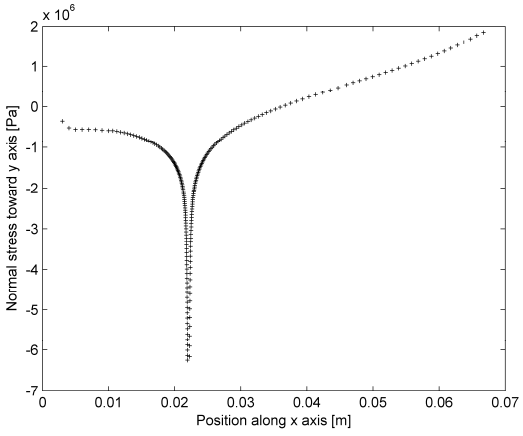

Figure 12. Normal stress in the direction of the y axis distributed along the x axis

2. Conclusion

The correction on the mode one stress intensity factor, K_{temp}, determined in the two previous sections is a value superimposed on the usual stress intensity factor due to the fatigue cyclic loading, noted K_{cyc}(t), which varies at each cycle between a maximum, $K_{cyc,max}$, and a minimum, $K_{cyc,min}$, of the stress intensity factor. As written before, due to the compressive thermal stresses around the

crack tip it has been shown that the stress intensity factor during a fatigue loading has to be corrected by the factor K_{temp}. This thermal effect on the stress intensity factor varies slowly with time and can be considered as constant during one cycle. Consequently the temperature has no effect on the stress intensity factor range ΔK but it has an effect on both the maximum, K_{max}, and minimum, K_{min}, values of the stress intensity factor:

$$K_{max}=K_{temp}+K_{cyc,max} \tag{11}$$

$$K_{min}=K_{temp}+K_{cyc,min} \tag{12}$$

However, K_{temp} can affect crack closure by changing the load ratio (equation 13) and because of the compressive nature of the thermal stresses around the crack tip:

$$R_K = \frac{K_{min}}{K_{\max}} = \frac{K_{temp} + K_{cyc,\max}}{K_{temp} + K_{cyc,\min}} \neq \frac{K_{cyc,\max}}{K_{cyc\min}} \tag{13}$$

In the two problem geometries presented in this paper, the results on the thermal correction of the stress intensity factor are very closed. For a stress intensity factor range of $20\,MPa\sqrt{m}$ and a stress ratio of 0.1 the thermal correction is about $-0.521\,MPa\sqrt{m}$ for an infinite plate with a semi-infinite through crack and $-0.316\,MPa\sqrt{m}$ for a finite plate with a central through crack with considering thermal losses due to convection. In conclusion the geometry of the specimen and the thermal boundary conditions have a very small effect on the results. For test on mild steel at a loading frequency of 100Hz, the values of K_{temp} remain very small and a new stress ratio of 0.087 (compared to 0.1, the initial stress ratio) can be calculated.

However, since the dissipated energy rate per unit length of the crack front is proportional to both the loading frequency and to $\Delta K^4/\sigma_y^4$ this effect should be more important for ductile metals (low yield stress) loaded under high stress intensity range. Revisiting the frequency effect on the fatigue crack growth could be also interesting by taking this thermal correction consideration.

References

[1] W.S. Farren, G.I. Taylor, The heat developed during plastic extension of metals. Proc Roy Soc A (1925)107 422–51.

[2] G.I. Taylor, H. Quinney, The latent energy remaining in a metal after cold working. Proc Roy Soc A, (1934) 143 307–26.

[3] P.C. Paris, Fatigue - the fracture mechanics approach, Fatigue an interdisciplinary approach, Syracuse University Press, 1964.

[4] J.R. Rice, The mechanics of crack tip deformation and extension by fatigue, Fatigue crack propagation, ASTM, Special Technical Publication 415, Philadelphia, 1967. pp. 247–311.

[5] H.S. Carslaw, J.C. Jaeger, Conduction of heat in solids, Oxford, Clarendon Press, 1947.

[6] N. Ranc, T. Palin-Luc, P.C. Paris, Thermal effect of plastic dissipation at the crack tip on the stress intensity factor under cyclic loading, Engineering Fracture Mechanics 78 (2011) 961–972

Rotating Bending Fatigue Tests of PH-42 steel Plasma Nitrided

José Divo Bressan[1,*], **Daniel Kohls**[2]

[1] Department of Mechanical Engineering, Center for Technological Sciences, University of Santa Catarina State, Campus Universitário, 89.223-100 Joinville, Santa Catarina, Brazil.
[2] Faculty of EEFF, Institute of GGHH, City Post Code, Country
* Corresponding author: dem2jdb@joinville.udesc.br

Abstract: The aim of this study was to evaluate the influence of plasma nitriding process on the fatigue limit of PH-42 Supra steel provided by Schmolz + Bickenbach of Brazil. The paper presents the experimental results of rotating bending fatigue tests for specimens as received and treated by plasma nitriding process with a nitrided layer of 0.3mm. This material is employed in manufacturing polymer injection molds and inserts, and offers high hardness and good machinability. The fatigue tests were carried out by a rotating bending fatigue machine which allowed to plot and compare the Wöhler's curve for both types of steel specimens. Moreover, the hardness of the nitrided layer and substrate, the hardness of the non-nitrided specimens, the ultimate strength from simple tensile tests were determined experimentally. The fatigue testing results were used to obtain the material empirical Basquin's fatigue life equations. Photographs by SEM of the fractured surface were obtained and provided a visual aspect analysis of nitrided and non-nitrided specimens in tensile and fatigue testing. The fatigue limit stress increased from 440 MPa to 710 MPa for non nitrided and plasma nitrided PH-42 steel respectively. In addition, the fatigue limit behavior and fracture mechanisms, depending on the application of advanced plasma nitrided layer, are also discussed.

Keywords: PH-42 steel, rotating bending test, plasma nitriding, fatigue limit.

1. Introduction

Rupture in a structural or mechanical component frequently initiate at metal surface under two loading conditions, owing to metal fatigue process. Firstly, it is related to high loading cycles of component, leading to resultant stresses greater than the material fatigue limit. Under this type of high loading, rupture occur at shorter number of cycles due to the inception of surface micro-cracks which are originated from shear bands in preferential sliding atomic planes and directions in the material.

Secondly, there are situations of fracture occurring in components due to surface crack nucleation which are originated from surface defects such as grooves, scratches, pores, holes or metallic inclusions, even for low stresses. However, fatigue cracks can also be originated from non-metallic inclusions and defects situated in sub-layers just below the component surface [1]. This kind of rupture has been referred in literature to explain the behavior of high strength steels. In surface treated steels, fatigue limit is expected to increase proportionally to hardness increase. However, it is worth to recall that for steels with hardness above 400 Vickers there is a reduction of fatigue limit which is related to non-metallic inclusions. This can be observed in Fig. 1, showing the fatigue limit of various steel grades versus hardness [2]: fatigue limit increases up to a maximum and then falls with increasing hardness.

Moreover, there are other issues related to fatigue resistance of steels such as the presence of profile of residual stresses near the surface site of crack nucleation due to machining and shot peening processes [3].

In metal fatigue, tensile stresses act to open crack tip and promotes crack growth. However, compressible stresses can increase the fatigue limit or have little or no contribution to crack generation and propagation. In this context, it is important to study the fatigue limit of machined steel components of high hardness and steel components with plasma nitriding surface treatment which increase even more the surface hardness.

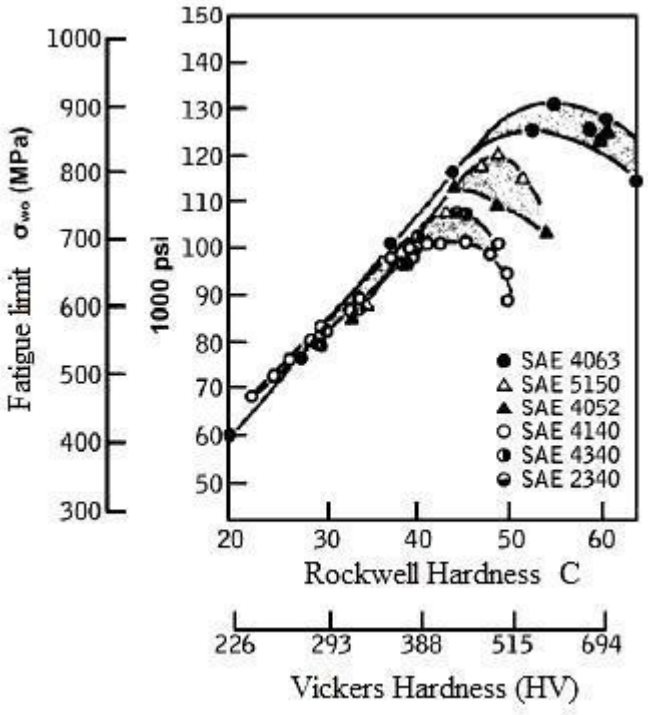

Figure 1. Fatigue limit of various steel grades versus hardness [2].

Hence, the main goal of this work is to present and compare the experimental results of rotating bending fatigue tests of PH-42 Supra steel plasma nitrided and non-nitrided which is low carbon steel and are employed to fabricate plastic injection molds and inserts.

2. Material and Experimental Procedure

Fatigue tests were performed using specimens of PH-42 Supra steel delivered by Schmolz + Bickenbach of Brazil. According to the steel supplier, the material had limit strength of 1250 MPa, elasticity modulus of 206 GPa and Rockwell hardness of 40HRC [4]. For the plasma nitrided steel specimens the attained surface hardness was 60HRC. The material chemical composition is shown in Table 1.

Table 1. Chemical composition of PH-42 Supra steel, according to supplier [5].

C %	Mg %	Ni %	Cu %	Al %
0.15	1.5	3.0	1.0	1.0

25 fatigue test specimens as received (non-nitrided) and 25 plasma nitrided specimens with a nitriding layer of 0.3mm, were tested in a rotating bending fatigue machine and the results were plotted and compared by Wöhler's curve for both types of steel specimens. Besides, the surface hardness of non-nitrided and plasma nitrided specimens and the limit strength were obtained by hardness and tensile tests respectively. Photographs by SEM of the fractured surface specimens were obtained and provided a visual analysis of fracture of nitrided and non-nitrided specimens in tensile and fatigue tests.

The fatigue test specimens were machined from one bar, according to the dimensions seen in Fig.2. Each specimen were polished to surface average roughness of Ra = 0.11μm in the useful region which had lower specimen diameter of 7.0mm.

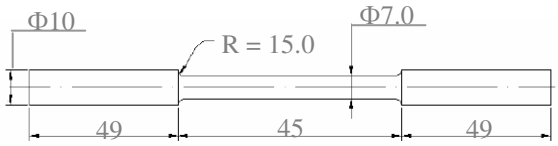

Figure 2. Geometry dimensions of rotating bending fatigue test specimens.

Figure 3 shows a photo of a non-nitrided specimen employed in the rotating bending fatigue test which attained a fatigue life over 10^6 cycles.

Figure 3. Photo of a rotating bending fatigue test specimen which attained fatigue life over 10^6 cycles.

2.1. Fatigue Tests

Fatigue tests were carried out in the rotating bending fatigue machine, type TYP RM 506, Budapeste/Hungary, seen in Fig. 4. The specimen bending load was applied by a load arm existing in the machine. The true bending load applied on the fatigue specimen corresponds to 10 times the load applied on the plate situated at the opposite arm end.

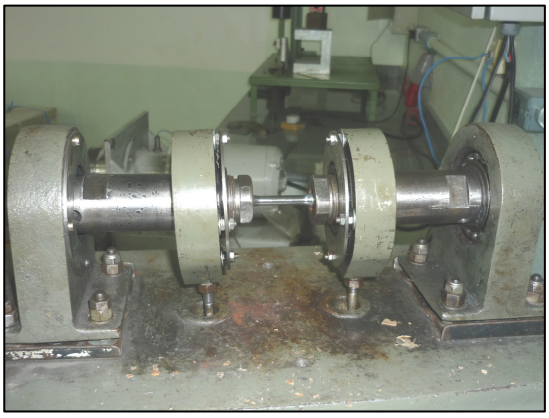

Figure 4. Photo of the rotating bending fatigue machine, type TYP RM 506, utilized in the fatigue tests.

Hence, the tensile and compression stresses on the specimen surface were calculated by the equation,

$$\sigma = 160\frac{P\,a}{\pi D^3} \quad (kgf/mm^2) \tag{1}$$

where D (= 7mm) is the diameter of the useful region in the specimen, P (kgf) is the applied load on the plate at the load arm end and "a" is the distance from the point of bending support (ball bearing) to the point of load application. For the nitrided specimens, the load varied from 4.8 to 8.0kgf and for non-nitrided specimens the load varied from 2.72 to 5.2kgf. The electric motor rotating velocity was fixed and equal to 3000 rpm.

The fatigue tests were initiated for high applied load until the specimen rupture. This high load was gradually reduced for the following specimens till obtaining the fatigue limit for the material. The fatigue limit was defined as the maximum stress for fatigue life of 10^6 cycles.

3. Results and Discussions

3.1. Vickers Micro-Hardness

Tables 2 and 3 shows the average Vickers micro-hardness (mHV), using indenter load of 500g, for the PH-42 Supra steel fatigue specimen plasma nitrided at two distinct regions: measured on the plasma nitrided surface layer of 0.3mm, Table 2, and at the substrate or bulk of material, Table 3. In addition, the correspondent Rockwell C hardness conversion is also presented. In Table 4, the average Vickers micro-hardness measured at surface, indenter load of 500g, for the non-nitrided specimen of PH-42 Supra steel fatigue specimen is presented. The nitriding process has increased the substrate material hardness from 454 to 885 mHV as can be observed from Table 3 and 4.

Table 2. Vickers micro-hardness of nitrided surface layer of PH-42 Supra steel nitrided specimen.

Load 500g	Vickers micro-hardness (mHV0.5)	Conversion to Rockwell C hardness (HRC)
	861.22	65.9
	900.56	67.0
	893.77	66.8
Average	885.2	66.6

Table 3. Vickers micro-hardness of substrate of PH-42 Supra steel nitrided specimen.

Load 500g	Vickers micro-hardness (mHV0.5)	Conversion to Rockwell C hardness (HRC)
	680.41	59.2
	588.70	54.6
	599.54	55.2
	727.31	61.2
Average	648.99	57.7

Table 4. Vickers micro-hardness of PH-42 Supra steel non-nitrided specimen.

Load 500g	Vickers micro-hardness (mHV0.5)	Conversion to Rockwell C hardness (HRC)
	446.0	45.0
	434.0	44.0
	484.0	48.0
	506.0	45.6
Average	454.2	45.6

3.2. Surface Roughness

Before fatigue tests, the arithmetic average surface roughness Ra of plasma nitrided and non-nitrided specimens were measured, utilizing a profilometer Supertronic 25 Taylor Robson, with total sliding distance of 4.0mm and Gausian filter of 0.8mm [5]. The experimental results for three specimens and total average Ra are presented in Table 6 for 10 measurements on each specimen. The plasma nitrided specimens have increased the surface roughness Ra in relation to the non-nitrided specimens, but they both can be considered polished for their very low values. This is due to the formation of precipitates and nitrides on the nitriding layer [6].

Table 7. Arithmetic average surface roughness Ra of plasma nitrided and non-nitrided specimens.

Specimen	Ra (μm) Plasma nitrided	Ra (μm) non-nitrided
1	0.31	0.14
2	0.44	0.11
3	0.29	0.08
Total average	0.35	0.11

3.2. Rotating Bending Fatigue Test Results

The fatigue limits for as received (non-nitrided) and plasma nitrided specimens were obtained directly from the plotted Wöhler's curve, seen in Fig. 5, which is the curve of fatigue life for the alternate bending stress tests versus total number of cycles to specimen fracture [7]. According to ASTM E466 standard recommendation, fatigue limit correspond to the maximum rupture stress for the number of cycles equal or superior to 10^6 cycles. The average values are presented in Table 5.

Table 5. Fatigue Limit Stress for PH-42 Supra steel specimens plasma nitrided and non-nitrided. Average values obtained from the plotted Wöhler's curve for fatigue life (1kgf/mm^2 ≅ 10 MPa).

Specimen	Fatigue Limit Stress σ_{fad} (MPa)
Ph-42 Supra steel plasma nitrided	710.0
Ph-42 Supra steel non-nitrided	440.0

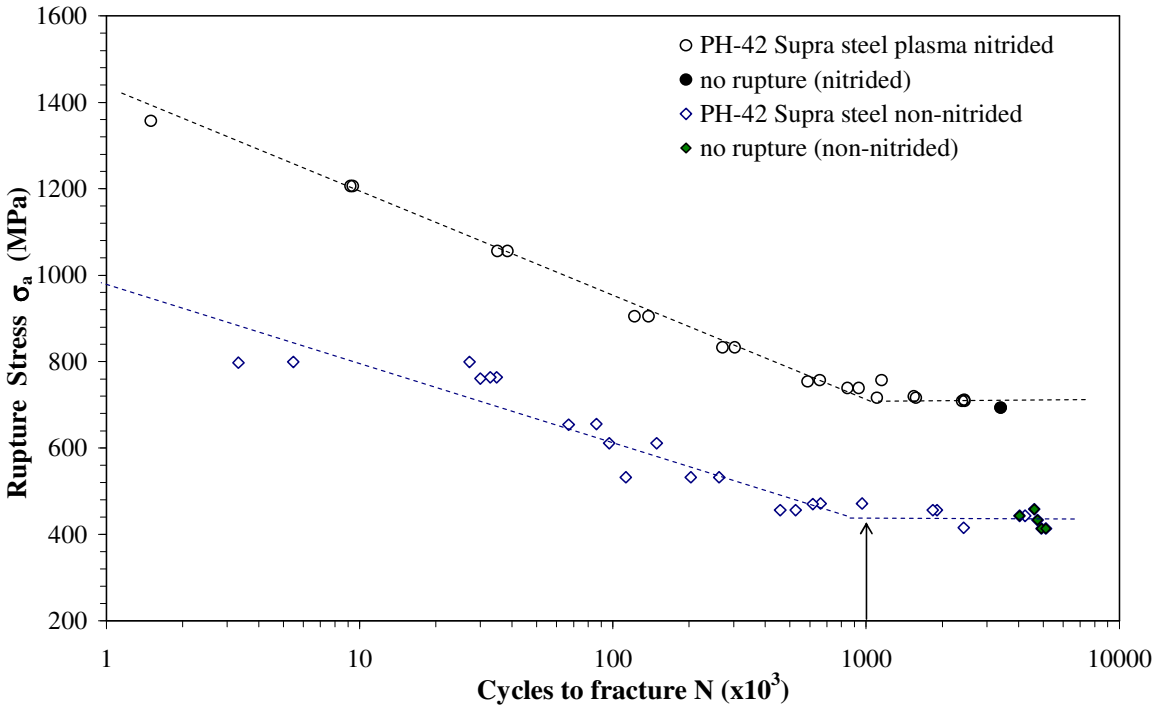

Figure 5. Stress versus number of cylces N to fracture curves for rotating bending fatigue test for PH-42 Supra steel non-nitrided and plasma nitrided with layer of 0.3mm. Fatigue limit is for $N=10^6$ cycles.

In Fig. 6, some fractured non-nitrided specimens after the rotating bending fatigue tests can be observed which fracture site is similar to the plasma nitrided specimens.

Figure 6. Photo of three non-nitrided specimens after the fatigue test.

3.3. Tensile Tests

Tensile tests were also performed, using the same fatigue test specimens of PH-42 Supra steel plasma nitrided with nitriding layer of 0.3mm and non-nitrided as seen in Fig. 2. The ultimate tensile strength values are shown in Table 6.

Table 6. Ultimate tensile strength obtained experimentaly from tensile tests.

Sperimen	Ultimate tensile strength σ_t (MPa)
Ph-42 Supra steel plasma nitrided	1174.3
Ph-42 Supra steel non-nitrided	1150.0

3.4. Basquin's Equation

The empiric law of Basquin for fatigue life [8] of PH-42 Supra steel plasma nitrided specimens obtained from the plotted mean curve in Fig. 5 is given by,

$$\sigma_a = 2921\ N_f^{-0.1024}\ (\text{MPa}) \tag{2}$$

and for PH-42 Supra steel non-nitrided specimens, the Basquin's equation is given by,

$$\sigma_a = 2182.7\ N_f^{-0.1159}\ (\text{MPa}) \tag{3}$$

where σ_a is the bending cyclic stress amplitude and N_f is the number of cycles to rupture.

3.5. Fractograph by SEM

Fracture surface by SEM of PH-42 Supra steel plasma nitrided tensile test specimens are shown in Fig. 7a and 7b. Surface cracks initiated in the nitrided layer and at 90 degree to the load line are seen. Hence, the fracture mechanism of the nitrided layer was brittle fracture due to principal maximum tensile stress. The measured plasma nitrided layer thickness was 337.87μm.

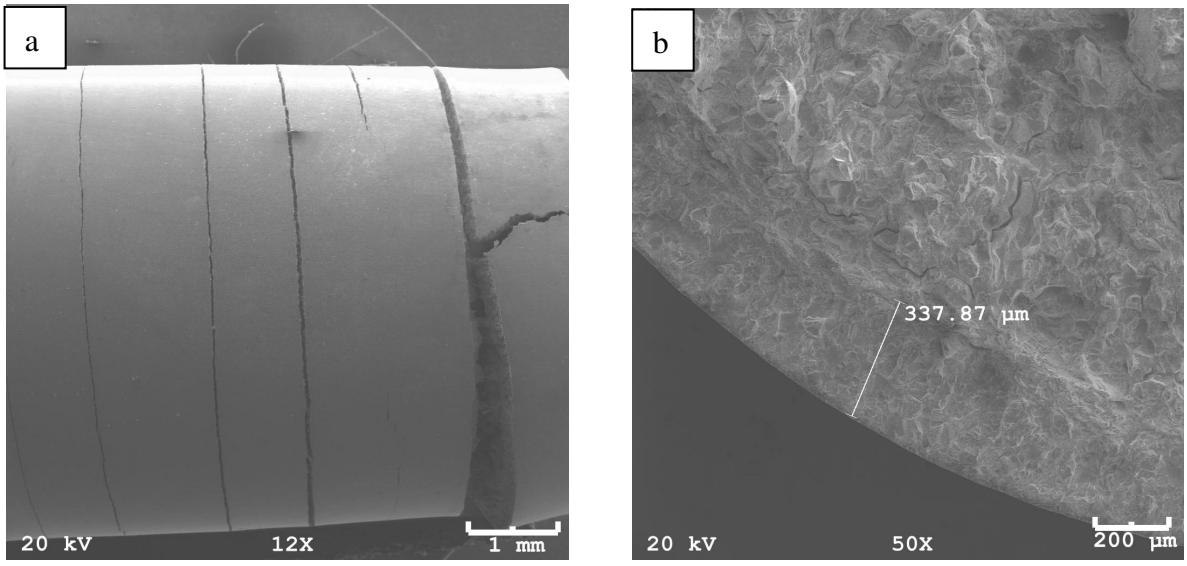

Figure 7. SEM photos of fractured PH-42 Supra steel plasma nitrided tensile test specimen: a) surface cracks and b) fracture surface showing the plasma nitrided layer thickness of 337.87μm.

In Fig. 8, fracture surface of fatigue test specimen of PH-42 Supra steel non-nitrided are presented. Brittle fracture mechanism in Fig. 8a and 8b and the fatigue crack length near the specimen surface can be observed. In Fig. 9a and 9b, fracture surface of fatigue test specimen of PH-42 Supra steel plasma nitrided are shown. Instantaneous rupture by brittle fracture and a very small fatigue region

near specimen surface are seen. The fatigue crack length near the specimen surface can be evaluated in Fig. 9b, approximately 20μm owing to plastic compressive deformations.

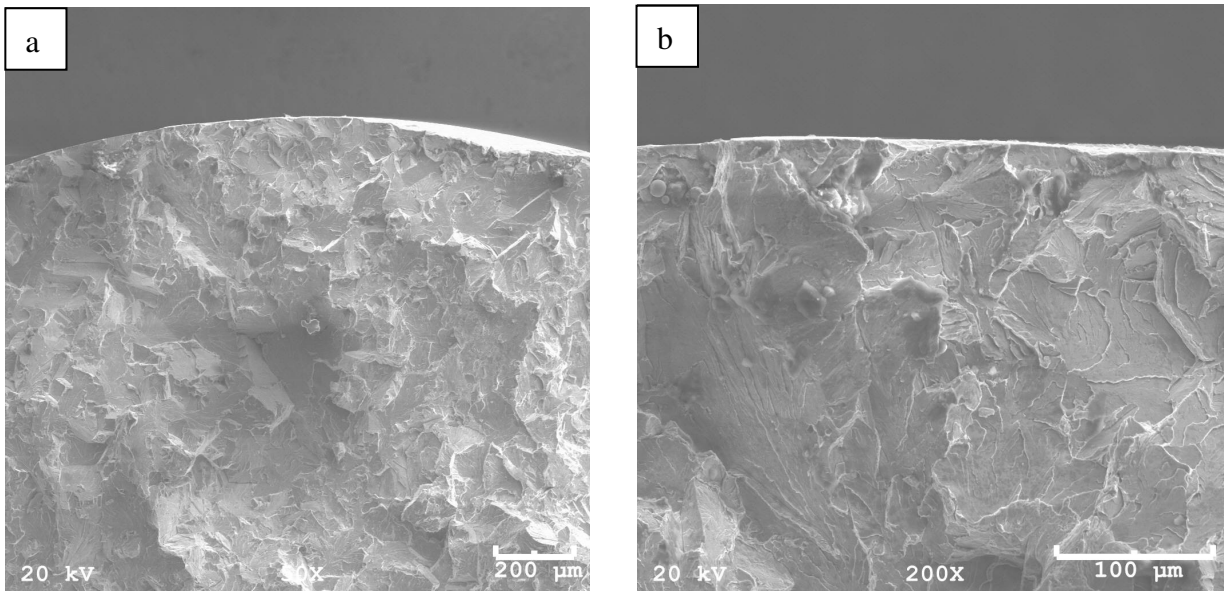

Figure 8. SEM photos of fracture surface of PH-42 Supra steel non-nitrided fatigue test specimen in rotating bending test: a) rupture by brittle fracture and b) detail of beginning of fatigue crack at specimen surface.

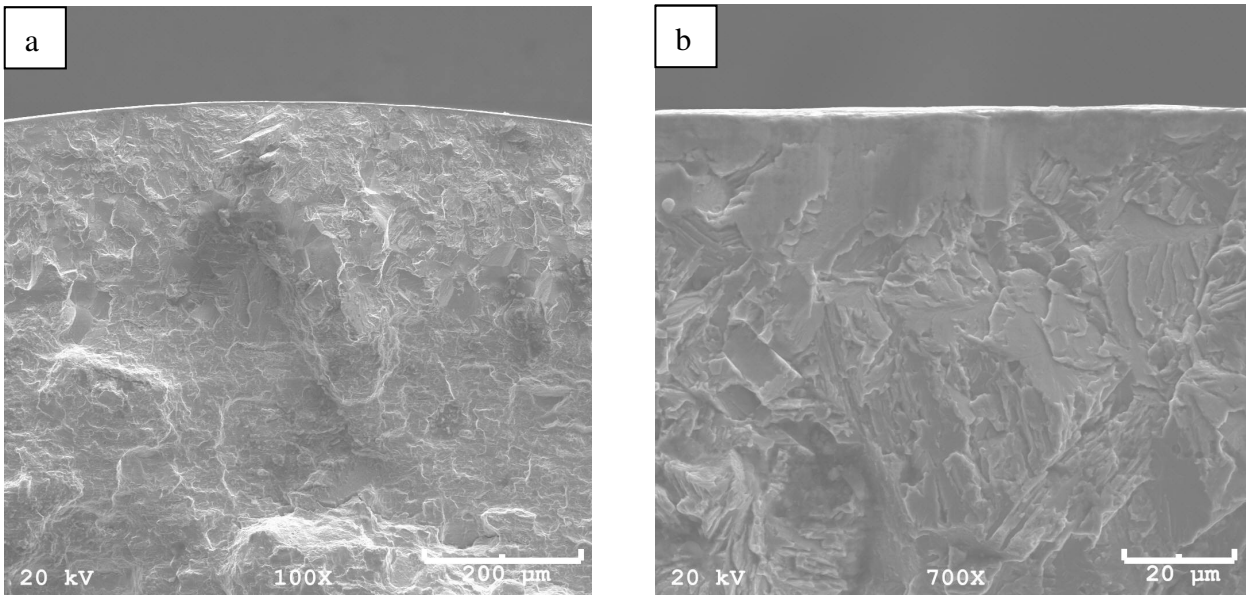

Figure 9. SEM photos of fracture surface of PH-42 Supra steel plasma nitrided fatigue test specimen in rotating bending test: a) rupture by brittle fracture and b) detail of fatigue crack growth at specimen surface.

4. Conclusions

From the experimental results of PH-42 Supra steel (Schmolz + Bickenbach do Brasil) plasma nitrided, nitriding layer of 0.3mm, and as received (non-nitrided) specimens tested in tensile test, Vickers micro-hardness and rotating bending fatigue testing and analysis of fracture surface by SEM, the following conclusion can be drawn,

a) Fatigue limit stress of PH-42 Supra steel plasma nitrided was 710 MPa which is much higher

than the bulk material or non-nitrided specimen of 440 MPa. Hence, the plasma nitriding process has increased the fatigue limit stress by 61%.

b) The plasma nitriding process has increased the material hardness from 454 to 885 mHV.

c) Basquin's empiric law for fatigue life of PH-42 Supra steel plasma nitrided specimens was $\sigma_a = 2921\ N_f^{-0.1024}$ (MPa) and for non-nitrided specimens, $\sigma_a = 2182.7\ N_f^{-0.1159}$ (MPa).

d) SEM analysis of fracture surface of fatigue test specimen of PH-42 Supra steel non-nitrided presented brittle fracture mechanism: the fatigue crack length near the surface was very small.

e) SEM analysis of fracture surface of fatigue test specimen of PH-42 Supra steel plasma nitrided had shown rupture by brittle fracture and a very small fatigue region near specimen surface. The fatigue crack length near the specimen surface was evaluated approximately 20μm owing to plastic compressive deformations.

f) The plasma nitrided specimens have increased the surface roughness Ra in relation to the non-nitrided specimens from Ra = 0.11μm to 0.35μm for non-nitrided and plasma nitrided respectively, but they both can be considered polished for their very low values.

g) In tensile tests, surface cracks initiated in the nitrided layer and at 90 degree to the load line are seen. Hence, the fracture mechanism of the nitrided layer in tensile test was brittle fracture due to principal maximum tensile stress.

Acknowledgements

The authors would like to thank the company TOX Pressotechnik of Joinville/Brazil for providing the specimens, University of Santa Catarina State and CNPq of Brazil for financial support.

References

[1] C.E.S. Amorim, Análise dos recobrimentos anticorrosivos aplicados sobre um aço aeronáutico de alta resistência no comportamento em fadiga. Thesis (Doutoramento in Mechanical Engineering), Faculdade de Engenharia de Guaratinguetá, Guaratinguetá/Brazil, 2003.

[2] Y. Murakami; S. Kodama; S. Konuma, Quantitative evaluation of effects of non-metallic inclusions on fatigue strength steels I: Basic fatigue mechanism and evaluation of correlation between fracture stress and the size and location of nonmetallic inclusions. Int. J. Fatigue, Sept. (1989) 291-298.

[3] H.J.C. Voorvald; M.P. Silva; M.Y.P. Costa; M.O.H. Cioffi, Improvement in the fatigue strength of chromium electroplated AISI 4340 steel by shot peening. Fatigue &Structures, 32 (2009) 97-104.

[4] Formadur PH-42 Superclean. Available in http://www.schmolz-bickenbach.com.br/fileadmin/files/schmolz-bickenbach.com.br/documents/Fichas_Tecnicas_novo_formato_dez2011/Moldes/Formadur_Ph42superclean.pdf> acessed on 4 december 2011.

[5] Rebrac Instrumentos de Medição, Rugosidade. Available in <http://www.rebrac.com.br/downloads/RUGOSIDADE%20-par%C3%A2metros-.pdf>. acessed on april 2011.

[6] Análise da rugosidade e Microestrutura de Camadas Nitretadas Obtidas pelos Processos Líquido, Gasoso e Iônico em Aço AISI H13. Available in <http://www.bodycote.com.br/artigos/artigoNitretacao.pdf> acessed on 23 april 2011.

[7] S.A. Meguid, Engineering Fracture Mechanics. Department of Mechanical Engineering, University of Toronto, Canada, Elsevier Applied Science, 1989, p. 75-79.

[8] Norman E. Dowling, Mechanical Behavior of Materials. 3rd edition, Prentice-Hall, USA, 2006.

Study of Stored Energy Evolution at Fatigue Crack Tip Based on Infrared Data

Anastasia Fedorova[*1], **Michael Bannikov**[1], **Oleg Plekhov**[1]

[1]Institute of continuous media mechanics Russian academy of science, 614013, Perm, Russia
*anastfed@mail.ru

Abstract The presented work is devoted to the experimental study of heat dissipation process caused by fatigue crack propagation. To investigate a spatial and time temperature evolution at the crack tip, set of experiments has been carried out using plate titanium specimens with pre-grown centered fatigue crack. An original mathematical algorithm for experimental data treatment has been developed to obtain a power of heat dissipation caused by plastic deformation at the crack tip. The algorithm includes spatial-time filtration and relative motion compensation procedures. The time dependence of the stored energy was calculated as difference between work caused by plastic deformation near the crack tip and heat dissipation energy obtained from experimental data. As a result, it has been shown that the stored energy has to accumulated during the fatigue test and has to be equal to zero when the crack reaches the critical length corresponding to the sample failure.

Keywords stored energy, plastic work, fatigue test, heat dissipation, infrared thermography

1. Introduction

Infrared thermography is the simple way to measure the temperature of surface and to monitor of crack propagation during cycling test. It is well know that the changing of the temperature correlates to the physical processes of damage and failures in metals [1]. The application of infrared thermography as a non-destructive method to detect the damage accumulation and to investigate the fatigue process of materials has become popular and has been wildly investigated in literature in last 25 years.

In materials under cyclic deformation, fatigue cracks are initiated in the area of plastic deformation localization and lead to an intensive heat dissipation [2]. Investigation of the heat dissipative and absorption laws can take information about dissipative ability of material and current state of structural evolution.

This work is devoted to investigation the time evolution of the stored energy during fatigue test using infrared technique and specially developed methods of data processing. Proposed approach allows us to measure parts of plastic work that dissipated as heat and stored in metals at fatigue crack tip. Study of these tasks enables to obtain information about the evolution laws describing the irreversibility of the fatigue process.

2. Materials and conditions of experiments

Experimental study of temperature evolution at the fatigue crack tip was carried out on the plane specimens of titanium Ti-4.2Al-1.6Mn. The specimens were manufactured from a commercial titanium sheet 3 mm thick.

Mechanical properties of material are modulus of elasticity - 64 GPa, yield stress - 800 MPa, ultimate stress 900 MPa, fatigue limit (R=-0.051) – 460 MPa, fracture toughness – 75.6 MPa$\sqrt{m}$.

The geometry of specimen is shown in Fig. 1. The specimens were weakened by holes to initiate fatigue crack at the specimen center. The fatigue crack (about 10 mm) was initiated at the initial stage of the experiment by high amplitude cyclic loading of the specimens at the average stress of 215MPa, stress amplitude of 238 MPa and loading frequency of 20 Hz. Then the load was decreased to slow down the rate of crack propagation, which allows a detailed analysis of the heat generation processes at the crack tip. The surface of the specimens was polished in several stages by

the abrasive paper (at the final stage of polishing the grit size does not exceed 3 μm). Before starting the experiment, the polished surface was covered by a thin layer of amorphous carbon.
The temperature evolution was recorded by infrared camera CEDIP Silver 450M. The spectral range of the camera is 3-5 mm. The maximum frame size is 320×256 pixels; the spatial resolution is 10^{-4} meters. The temperature sensitivity is 25 mK at 300 K. Calibration of the camera was made based on the standard calibration table.
Mechanical tests were carried out at 100 kN servo-hydraulic machine Bi-00-100. The test conditions comply with the conditions of the experiment was described in [3]. The process of crack propagation was studied at 5 Hz loading frequency.
The selected frequency of loading provides a close to adiabatically condition at crack tip. At low frequency (less that 5 Hz) the heat transfer process plays a great role and doesn't allow one to calculate the right value of heat source. The investigation of high loading frequency requests the high frame rate and treatment of large amount of infrared data.

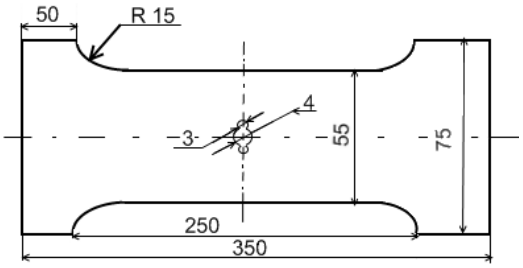

Figure 1. Geometry of sample (all sizes are in millimeters).

3. Experimental data processing and determination of the stored energy

At the beginning of data processing procedure, the first frame was subtracted from the film to eliminate the influence of infrared radiation from the camera lens on the determined temperature field. Due to the relative motion of the specimen and infrared camera lens under cyclic tests, there is the problem of motion compensation in order to obtain the correct temperature data at a given point on specimen surface. Compensation of relative motion was made based on the algorithm described in details in [4]. The main idea of this algorithm is the selection of marker-zone on the studied surface and searching this area on the surface in each next time step. Farther, displacement of each point on the surface is calculated for each time step. As a result of data processing, we obtained the temperature increment field (Fig. 2) based on which the heat sources field was determined.

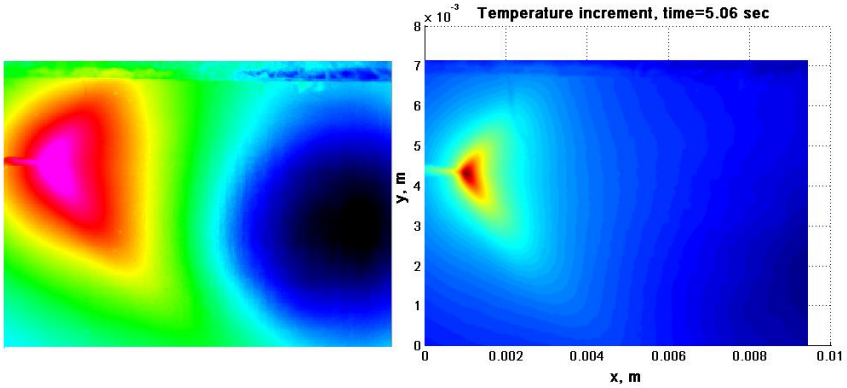

A **B**
Figure 2. Infrared image of sample before data processing (A) and obtained temperature increment field (B).

To calculate the specific power of the heat source, we have used a finite difference scheme of the equation for heat sources evolution (Eq. 1).

$$s = \rho c\left(\dot{T} + \frac{T}{\tau}\right) - k\Delta T, \tag{1}$$

where T – temperature, ρ – density (4550 kg/m^3), c – heat capacity (600 J/(kg·K)), k – heat conductivity (6.5 W/(m·K)), s – unknown specific power of the heat source (W/m^3), τ – a constant related to the losses of heat by heat exchange with the surroundings (10^3 J/(m^3·K)).
The heat power of sources close to fracture moment (at 5.06 sec after beginning of the last stage of test) is shown in Fig. 3. At the last moments before fracture, we can observe pronounced plastic deformation at crack tip and plastic zone has a "butterfly form" near the crack tip as it is presented in Fig. 3.

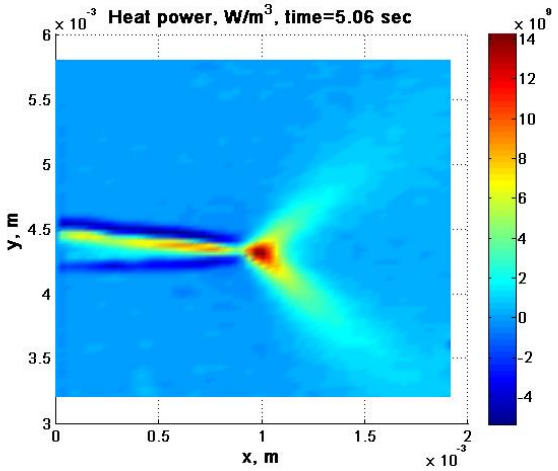

Figure 3. Experimental data of heat power field near the crack tip at the beginning of unstable crack propagation.

Taking into account assumption from [5, 6], we also suppose that some of the irreversible plastic work contributes to heat generation while the rest is stored as energy of crystal defects accompanying plastic deformation, traditionally known as the stored energy of cold work.
To define the plastic work near the crack tip we used the solution for stress distribution at crack tip obtained by Hutchinson, Rice and Rosengren (HRR-solution). Specific plastic work in the direction of crack propagation can be written as [7]:

$$w_p(x,t) = \int_0^{\varepsilon_p} \sigma d\varepsilon = \frac{n}{n+1}\frac{J(t)\sigma_e^{n+1}}{I_n x}, \tag{2}$$

where n – hardening coefficient (in our case n=4), I_n – function of hardening coefficient, x – distance from the crack tip, σ_e – tabulation function, $J(t)$ – energy J-integral that is the function of applied cycling loading and crack length. Time dependence of J-integral is presented in Fig. 4.

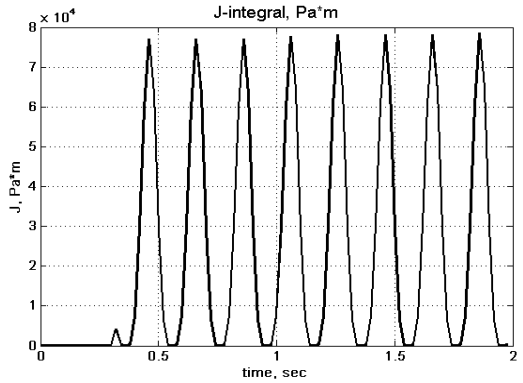

Figure 4. Time dependence of energy J-integral during cycling loading.

The stored energy was obtained as difference between accumulated plastic work (Eq. 3) and accumulated heat dissipation energy (Eq. 4) calculated at the point of the crack tip x_0 during all time moments of experiment as follows:

$$W_p(t) = \int_0^{t_i} w_p(x_0, t)dt \tag{3}$$

$$Q(t) = \int_0^{t_i} s(x_0, t)dt \tag{4}$$

The time dependence of accumulated plastic work, dissipative energy and stored energy that was calculated at the moving fatigue crack tip is shown in Fig. 5. Comparing time evolution of the plastic work and dissipative energy, the deformation process during cycling loading can be divided into three parts. The first one is about 1.3 seconds when two curves have a good correlation that can be connected with thermoelastic effect and existence the elastic part of the mechanical work.

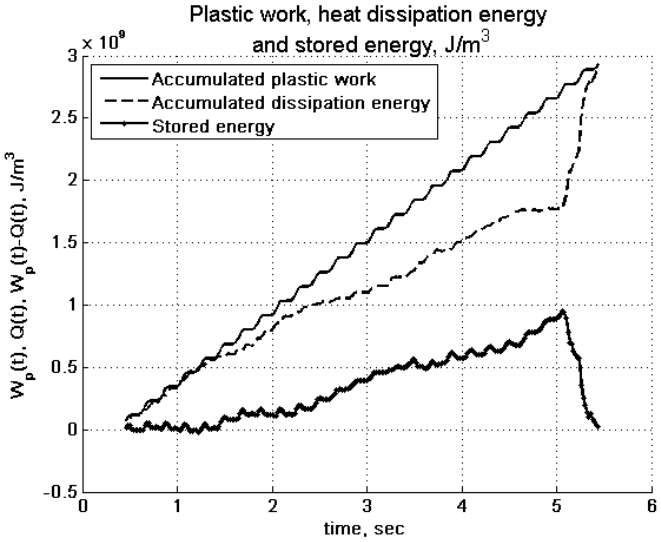

Figure 5. Time dependence of plastic work, heat dissipation energy and stored energy.

From 1.3 second to 5 second, dissipation energy increases slower than plastic work. In this period stored energy is monotonically accumulated in deformed material and spent on the potential energy of lattice distortion. At the last moments before fracture the heat dissipation energy increases explosively and reaches the value of the plastic work. The stored energy aims to the zero and material goes to the fracture stage when macroscopic displacements play important role and it is accompanied significant energy dissipation.

Data obtained for studied material displays that value of the stored energy increases to a critical point after that all mechanical energy goes to the heat and stored energy decreases explosively to zero, which ultimately leads to the destruction.

4. Conclusion

The effect of heat dissipation at the crack tip under cyclic loading has been studied based on the infrared thermography. To calculate the values of heat dissipation at crack tip an original data processing algorithms were applied. The algorithms include the relative motion compensation and spatial-time filtration procedures. As a result of infrared data treatment we determine the characteristics associated with the heat dissipation processes at the crack tip, which allowed us to propose method for determining the current values of the heat dissipation energy and stored energy

during cycling loading.
As a result, it has been shown that the value of the stored energy has to accumulate during the fatigue test and has to be equal to zero when the crack reaches the critical length corresponding to the sample failure. So, it can be used as a criterion for prediction of damage.
The set of developed mathematical algorithms and methods of the experiment allows us to develop in a future engineering methods for analyzing the current crack state inside of real constructions in a wide range of applied loads.

Acknowledgements

This work was supported by grant of President of the Russian Federation for support of young Russian scientists and leading scientific schools (MD-2684.2012.1) and RFBR (grant № 11-01-96005).

References

[1] X.D. Li, H. Zhang, D.L. Wu, X. Liu, J.Y. Liu, Adopting lock-in infrared thermography technique for rapid determination of fatigue limit of aluminum alloy riveted component and affection to determined result caused by initial stress. Int J Fatigue, 36 (2012) 18-23.
[2] A.A. Shanyavskiy, Bezopasnoe ustalostnoe razrushenie elementov aviakonstrukcii. Sinergetika v ingenernih prilogeniyah [Safe fatigue damage of aircraft construction elements. Synergetics in engineering applications]. Ufa, (2003) 803.
[3] M. Bannikov, A. Terekhina, O. Plekhov, Vestnik Permskogo gosudarstvennogo tehnicheskogo universiteta. Mehanika, 2 (2011) 14.
[4] A.Yu. Fedorova, M.V. Bannikov, O.A. Plekhov, Infrared thermography study of the fatigue crack propagation. Fracture and Structural Integrity, 21 (2012) 46-53.
[5] J.Hodowany, G. Ravichandran, A.J. Rosakis and P.Rosakis, Partition of plastic work into heat and stored energy in metals. Exp Mech, 40(2) (2000) 113-123.
[6] O. Plekhov, S. Uvarov, O. Naimark, Theoretical and experimental investigation of dissipated and stored energy ratio in iron under quasi-static and cyclic loading. Strength of materials, 1(391) (2008) 101-105.
[7] Yu.G. Matvienko, V.G. Avramenko, Dynamics of temperature field in the plastically deformed metal. II. Specimen with a crack. Deformation and fracture of materials, 10 (2009) 2-10.

Fatigue life prediction based on a mechanism-based simulation of crack initiation and short crack growth in forged Ti-6Al-4V

Hans-Jürgen Christ[1,*], Helge Knobbe[1], Philipp Köster[1,2], Claus-Peter Fritzen[2], Martin Riedler[3]

[1] Institut für Werkstofftechnik, Universität Siegen, D-57068 Siegen, Germany
[2] Institut für Mechanik und Regelungstechnik - Mechatronik, Universität Siegen, D-57068 Siegen, Germany
[3] Böhler Schmiedetechnik GmbH & Co KG, A-8605 Kapfenberg, Austria
* Corresponding author: Hans-Juergen.Christ@uni-siegen.de

Abstract Ti-6Al-4V was experimentally investigated in two different forged conditions with respect to fatigue crack initiation mechanisms and growth characteristics of microstructurally short fatigue cracks. The experimental findings show that the stage of short fatigue crack propagation is strongly affected by the microstructure and widely controls fatigue life under the testing conditions applied. The observations obtained were implemented into a mechanism-based short-crack model, which describes crack propagation as a partially irreversible dislocation glide on a crystallographic slip plane. The numerical model is based on dislocation dipole boundary elements. The non-uniform, oscillating propagation behaviour of short cracks is dealt with by defining grain boundaries and phase boundaries as obstacles to plastic slip and crack propagation. The model prediction in terms of short crack propagation behaviour allows for a quantitatively representation of the crack growth characteristics. Moreover, the simulation of short crack propagation was successfully used for the purpose of life assessment. Finally, by means of virtual microstructures, microstructural parameters such as grain size and volume fractions were systematically varied. Crack growth simulation calculations in these virtual microstructures are helpful to define those microstructural modifications which are desirable for improving the fatigue resistance.

Keywords Ti alloy Ti-6Al-4V, fatigue crack initiation, short fatigue crack propagation, microstructural barriers, fatigue life assessment, boundary element method

1. Introduction

The Ti6Al4V alloy is still by far the most common titanium material in use. It is used in many different fields, however the most important applications are probably found within the aerospace industry, where airframes and aero engine components are made of titanium alloys [1]. These employments are mainly driven by the superior structural efficiency of this alloy caused by an excellent combination of high strength and low density. Hence, a selection of high strength titanium forgings will always be found in the internal structure of planes.

A proper fatigue assessment is of course a crucial requirement for all structural components in flight service, since fatigue loading conditions always occur in these assemblies. Many approaches only consider the propagation of long cracks (damage tolerant approach) and thus make use of phenomenological equations such as Paris Law in classical linear elastic fracture mechanics [2]. As an alternative, total life approaches are used with S-N curves as basis for a fatigue life prediction according to Basquin/Coffin/Manson [3-5]. These methods do generally not distinguish between

crack initiation, short crack propagation and long crack propagation, which might be important in some cases. Another option, which is linked to physical properties of the material, is a microstructural-based short fatigue crack propagation model for lifetime prediction [6]. Since the loads arising in components associated with the internal structure are usually in the area of high cycle fatigue, up to 99% of the total lifetime can be spent with crack initiation and the propagation of short fatigue cracks. Thus, modeling short crack propagation in virtual microstructures promises a flexible and reliable approach for lifetime calculations. This paper presents firstly some selected experimental results from a study of the crack initiation and microstructurally short fatigue crack propagation mechanisms in two forged Ti6Al4V alloys. Then a mechanism-based model will briefly be introduced which tries to describe quantitatively the phenomena observed. This model will be verified by comparing experimental and predicted results. Finally it will be shown that by means of the generation of virtual microstructures the model is capable to identify microstructural parameters which are significant for a purposeful microstructure optimization with respect to fatigue resistance.

2. Material and experimental details

The Ti6Al4V alloy under investigation was delivered by Böhler Schmiedetechnik, where round bar stocks were forged into “V-shaped” pieces from which all specimens were machined. Two different heat treatments were applied after the forging process, (i) mill-annealing (ma) and (ii) solution heat treatment (sht). The most important chemical elements of the composition are given in Tab. 1. The analysis was done using spark emission spectroscopy. The figures represent mean values from three measurements and are within normal scatter. Some Fe content was found probably resulting from impurities of the alloying elements or from the process routine.

Table 1. Chemical composition in wt.%

Element	Al	V	Fe	Ti
Concentration	6.5	3.52	0.133	bal.

Micrographs using a scanning electron microscope with backscattered electron detector giving a channeling grain contrast of the resulting microstructures are shown in Fig. 1. A typical bi-modal microstructure was obtained in both conditions, thus no distinctive differences are present. The microstructures consist of primary alpha grains (α_p-grains) and colonies of secondary alpha lamellae (α_s-lamellae). A little content of remaining β-phase (app. 5-8%) can be found between the lamellae or at triple points.

The primary alpha grains of the sht microstructure are fully recrystallized due to the applied dwell time at a high temperature near the forging temperature, while the ma condition was cooled directly after forging, so some grains are only partially recrystallized. This can be deduced from orientation measurement data exhibiting large misorientation variations in single primary alpha grains along with subgrain boundaries.

The final heat treatment step was the same for both microstructures consisting of a plain stress relieve annealing above the Ti_3Al solvus temperature. The phase fractions are slightly different (α_p: 71% ma, 61% sht), and the mean grain sizes are larger for the sht condition (α_p: 3.1µm ma, 7.3µm sht; α_s: 3.3µm ma, 11.3µm sht). It should be mentioned that no subgrains were accounted for in the ma condition and that the α_s size refers to the colonies, meaning lamellae of the same orientation. Of course the mean lamella thickness is much smaller in case of the ma condition.

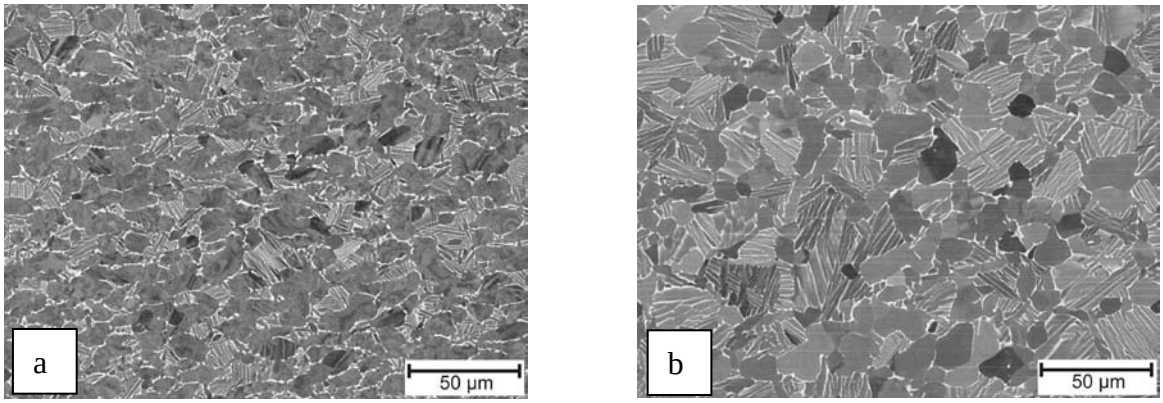

Figure 1. Microstructure of (a) ma condition and (b) sht condition.

All specimens except of the micro-sections were electro-chemically polished in a solution of perchloric acid and methanol prior to testing to meet the requirements for electron backscattered diffraction (EBSD) experiments. The surface should be as smooth as possible without any residual stresses from machining. This requirement can be perfectly met by grinding and vibration polishing (which was done in case of flat specimens for micro-sections), but is impossible for cylindrical specimens, where electrolytic polishing is the only possibility available. It should be pointed out that a slight surface roughness results from different metal removal rates of the different phases. The topography, measured by atomic force microscopy (AFM), was about 400nm from peak to valley.

Fatigue experiments were carried out in symmetrical push-pull with a servohydraulic MTS 810 test system under load control at a frequency of 20Hz. All experiments were stopped by specimen failure or at $6x10^6$ cycles. The samples which survived this number of cycles are referred to as run-out specimens. Cylindrical specimens with a milled shallow notch in the gauge length were used for the crack initiation and short crack growth investigations in order to limit the area to be observed. Some tests were interrupted after certain numbers of cycles to enable studying several cracks in the scanning electron microscope (SEM) together with EBSD. A Philips XL30 microscope equipped with automated orientation imaging microscopy (OIM^{TM}) was employed for all analytical research work. A FEI Helios DualBeam Microscope was used for sectioning cracks into the depth.

3. Experimental results

Two types of crack initiation sites were observed. Firstly, crack initiation is observed at the interface between two lamellae. Because of the Burgers relationship between alpha and beta phase

during phase transformation, this interface plane is parallel to one prismatic plane in the hcp crystal of the alpha phase, which is a possible slip system [7]. Secondly, cracks are found to initiate on slip bands inside of primary alpha grains.

Once initiated, different growth mechanisms were found for the short crack propagation in stage I. Inside of primary alpha grains or single lamellae, the crack grows on slip bands. By means of EBSD-measurements the cracks are identified to be either on the basal plane or the prismatic plane. The active slip bands are favorably orientated slip systems characterized by a high Schmid factor *S*. An example of such a crack is shown in Fig. 2a; the crack starts to grow on the basal plane with a Schmid factor of $S = 0.43$. After crossing a grain boundary the crack is slightly deflected and propagates on a prismatic plane, once again characterized by a high Schmid factor $S = 0.46$. Thus, the crack propagation rate is controlled by crack tip slide displacement range $\Delta CTSD$. The grain boundaries act as obstacles to crack propagation, as they prevent a transmission of slip into the neighboring grain. This yields a dislocation pile up in front of the barrier resulting in a decreased crack growth rate. If the boundary is overcome, the stress intensity will be relieved by slip in the next grain and the crack propagation rate will increase again, resulting in an oscillating crack growth rate. In addition to that, crack growth is also found on grain boundaries, as can be seen at the right crack tip in Fig. 2a. Here, the crack path is in a plane perpendicular to the applied load so that the normal stress, which causes a crack opening, seems to be responsible for crack propagation.

The crack in Fig. 2b grows on the interface between two lamellae. As this plane is equal to a prismatic plane with a Schmid factor of $S = 0.49$ the crack growth mechanism can be explained by slip as well. However, cracks were also found between two lamellae oriented normal to the applied load, where the Schmid factor on the respective prismatic plane is small.

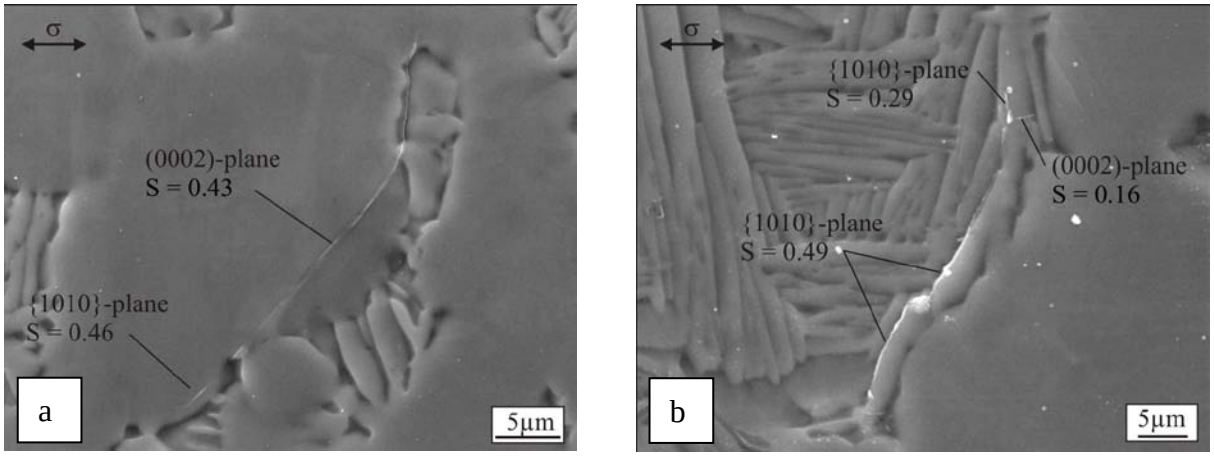

Figure 2. (a) Stage I-crack in primary alpha on slip plane and (b) crack growth on lamellae interface .

Since orientation data from the surface was used to calculate the possible slip plane, FIB sectioning was applied to determine the crack path direction into the interior (Fig. 3). A comparison between the calculated tilt angle of the slip plane with the surface and the crack path in the depth shows a good agreement. This strongly supports the assumption of crack growth occurring on a single slip system. However, as soon as a grain boundary is crossed (indicated by the white line) the crack is slightly deflected as can be observed on the surface as well.

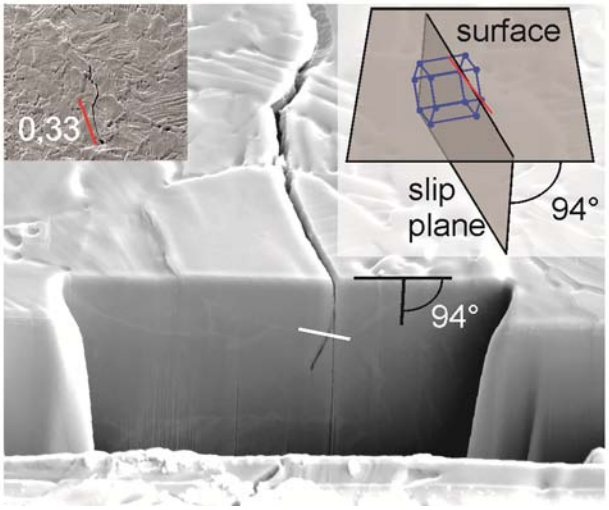

Figure 3. Cross section of a crack in primary alpha.

4. Short crack model

Several models for stage I-cracks have been presented, which consider the abnormal propagation behaviour of short cracks described above. Very promising one-dimensional analytical models for stage I-crack growth have been developed by Taira [8] and Navarro and de los Rios [9]. These models account for the barrier effect of grain and phase boundaries by blocking the extension of the plastic zone at the next grain boundary. Only if the stress on a dislocation source behind the grain boundary reaches a critical value, slip is transferred over the barrier resulting in an increased crack propagation rate. In order to take real microstructures with arbitrary grain shapes and orientations into account the analytical approaches have been extended to a two-dimensional model, which has been applied successfully to simulate crack growth in a duplex stainless steel [6,10]. This model is taken as the basis for the simulation of short crack growth in forged Ti6Al4V.

The crack problem is solved numerically by means of a discretisation with dislocation dipole boundary elements (see Fig. 4). Such a dipole element consists of a negative and a positive dislocation and represents a constant relative displacement over the element. Within a crack element two dipoles with a Burgers vector normal and tangential to the crack are combined to allow for an opening and a tangential displacement. On a slip band only a slide deformation is possible, so the respective boundary elements only consist of a dipole representing a tangential displacement. To monitor the stress state behind the grain boundary sensor elements with a constant length are positioned at the intersection point between active slip band and grain boundary. The sensor orientations match those of possible slip planes so that it is possible to calculate, in which direction a slip band is activated.

As grain boundaries act as obstacles to plastic deformation, the extension of the plastic zone is blocked by the next grain boundary. Thus, the crack propagation rate, which is controlled by the plastic deformation at the crack tip, decreases. Only if a critical stress intensity is reached on a dislocation source beyond the barrier in the neighbouring grain, the respective slip band is activated and the plastic zone extends into the new grain. The dislocation pile up in front of the grain

boundary is released resulting in a significant increase of the crack tip slide displacement and the crack propagation rate. This mechanism yields an oscillating crack growth rate that is characteristic of microstructurally short fatigue cracks.

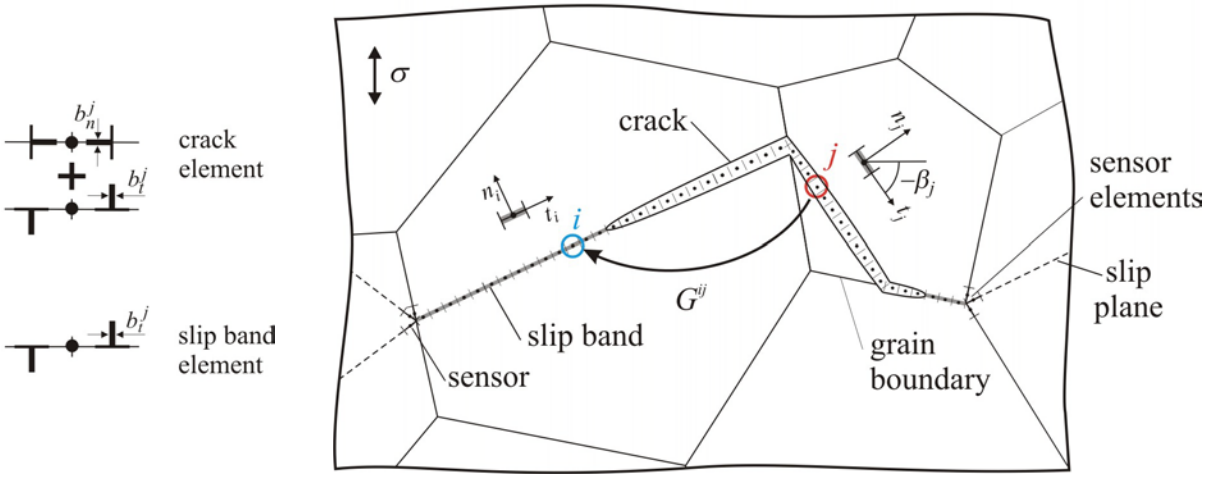

Figure 4. Stage I-crack model with boundary element discretisation.

In the plastic zone in front of the crack tip a differentiation between two cases is made, which results in different crack growth mechanisms. In the first case the crack propagates on a slip band and plastic slip occurs on this slip plane, if the resolved shear stress τ reaches the critical value for dislocation motion τ^b. In the second case the crack grows on a grain boundary, which does not represent a slip system of the crystal. Therefore, the only way to reduce the stress intensity in front of the crack tip is a plastic deformation inside the neighboring grains leading to a crack tip opening displacement. As the grains at each side of the grain boundary have different orientations, in general it is likely that more than one slip system is activated in each grain in order to ensure a compatible plastic deformation (Fig. 5a). In the model this plastic deformation is projected onto the yield strip on the grain boundary where both a tangential and a normal relative displacement is possible. As the plastic deformation occurs on multiple slip systems in the neighboring grains, the von Mises stress σ^m is used as the criterion for plastic deformation (Fig. 5b).

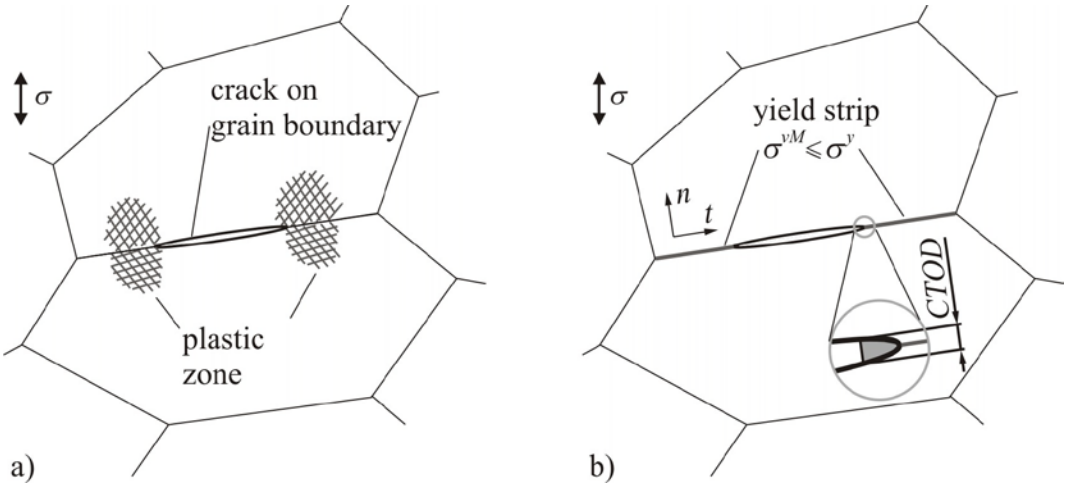

Figure. 5. Crack on grain boundary: a) plastic zone around the crack tip and b) yield strip model of the plastic zone.

The crack propagation on a slip band is calculated from the range of the crack tip slide displacement *ΔCTSD* by a power law function, which is analog to the model of [9]. A physical explanation for the mechanism of crack propagation is given in [11]. During the loading and the unloading cycle dislocations of opposite sign are created in a dislocation source in front of the crack tip and move towards the crack. Thus, vacancies are generated, which lead to a crack advance. For crack propagation on a grain boundary the crack growth is related to the range of the crack tip opening displacement *ΔCTOD*.

5. Virtual microstructure

The simulation model can be used for a virtual optimization of the microstructure for maximum high-cycle-fatigue strength. The aim is to carry out crack growth simulations in virtual microstructures with different properties to find out, how the stage I-crack growth resistance can be improved. Therefore, an algorithm for the generation of virtual microstructures has been developed, which is based on the Voronoi technique. Initially, such a Voronoi diagram has a normal distribution of the grain diameter and is single-phased. By assigning different phases to individual grains, a microstructure consisting of primary alpha grains and colonies of alpha lamellae is created. Furthermore, the average grain size and grain size distribution is modified by dividing selected grains.

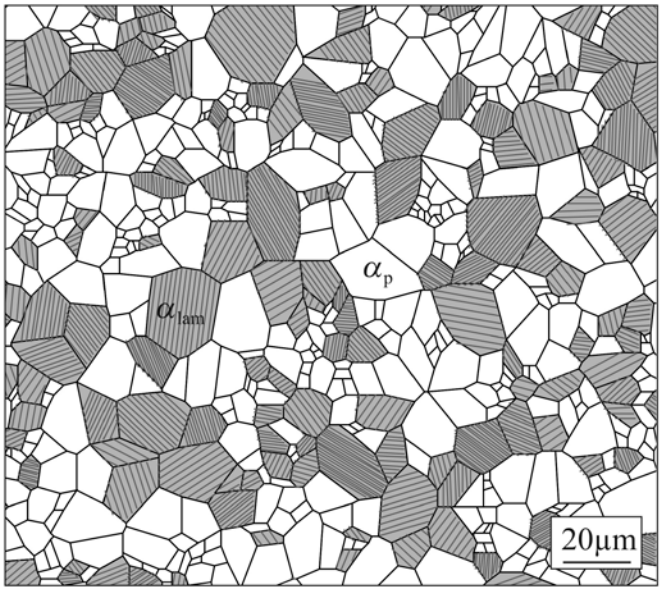

Figure 6. Virtual microstructure of forged Ti6Al4V in the sht condition.

In a first step a virtual microstructure has been generated, which represents the real microstructure of the ma condition shown in Fig. 1a. The virtual microstructure is shown in Fig. 6 and has a primary alpha volume fraction of 70.5%, compared to 70.9% of the real one. A good agreement is found in the mean diameter of the α_p-grains and lamellar grains, which are 10.0µm and 6.8µm for the virtual and 9.9µm and 6.8µm for the real microstructure. Also the grain size distribution shows a reasonably good agreement.

The slip systems in the model are chosen based on the experimental observations during the fatigue

tests. As cracks were found both on the basal plane and on prismatic planes in α_p-grains, the respective systems are considered in the model. In reality a lamellar colony consists of parallel alpha plates in a beta matrix and the orientation relation between both phases is defined by the Burgers relationship. This means that there are two parallel slip systems in both phases, and therefore slip can be easily transferred over the interface between alpha plate and beta matrix so that the effective slip length is equal to the colony diameter. As the effective slip length is the crucial parameter for crack initiation and crack growth, a lamellar colony is modeled as one grain in the virtual microstructure without resolving each single lamella.

6. Model capability

First, the model is verified by comparing simulation results to real fatigue crack propagation behavior. For this purpose the geometry of the crack shown in Fig. 7b is given as an input into the simulation model. Then, the simulation is started from the initial crack length until the crack tip reaches the end of the slip band. In Fig. 7a the projected crack length of the left and the right half is plotted over the number of cycles. It can be seen that the crack propagates fast on the left hand side on a slip band favorably oriented for slip. However, when the crack tip approaches the grain boundary the propagation rate decreases. On the right hand side the crack grows significantly slower on a grain boundary. The comparison of simulation and experimental data shows satisfying agreement.

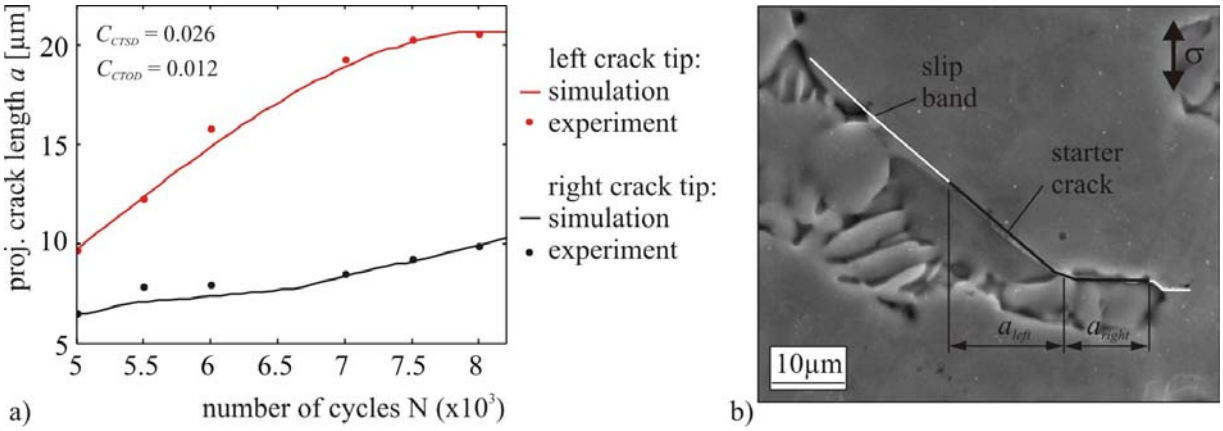

Figure 7. (a) Comparison between simulation and experimentally observed fatigue crack and (b) crack geometry.

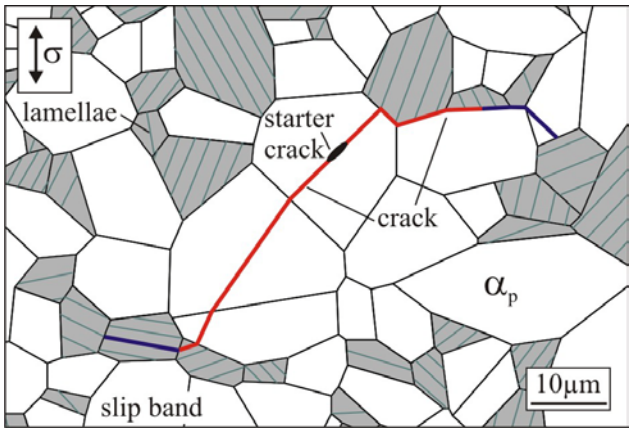

Figure 8. Crack growth simulation through several grains in virtual microstructure.

Crack growth simulations were carried out in virtual microstructures (Fig. 8). The simulation is started with an initial crack on a slip band in an α_p-grain. Then the crack grows autonomously through the microstructure. On the left hand side the crack propagates on a slip band, whereas intercrystalline crack growth on grain boundaries occurs on the right hand side.

On the basis of these calculations a fatigue life assessment is possible. For this purpose 100 calculations were carried out for each stress amplitude considered. A starter crack of 0.2µm in length is assumed to lie in the middle of an α_p grain, which is randomly selected from all α_p grains exhibiting a Schmid factor of higher than 0.4. In Fig. 9 the growth of the projected crack length with the number of cycles is shown for stress amplitudes of 500MPa and 600MPa. At the lower stress amplitude most of the cracks stop at microstructural obstacles.

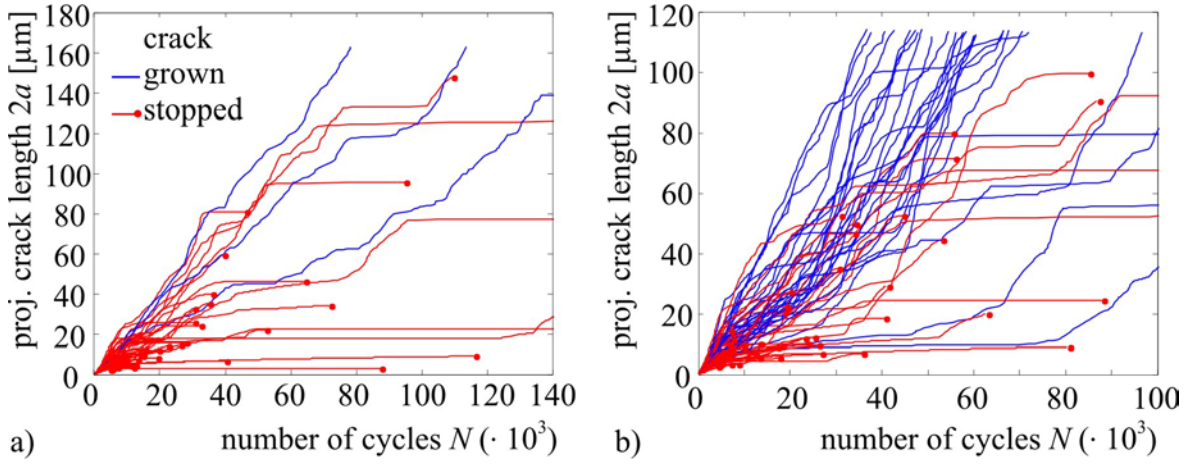

Figure 9. Crack growth simulation results for stress amplitudes of (a) 500MPa and (b) 600MPa (ma condition).

In these calculations, failure is defined to occur, when a critical value of the stress intensity factor at the crack tip is reached. This value is assumed to be 8 MPa $m^{½}$. In order to take into account that a real fatigue sample forms numerous fatigue cracks and that the fastest growing crack determines fatigue life, 20 cracks were randomly selected from the 100 cracks simulated and the one that fulfils the failure criterion first defines cyclic life. Hence 5 data points result for stress amplitude. This data is depicted in Fig. 10 together with the experimentally observed number of cycles until failure for both heat treatment conditions. The agreement appears very promising.

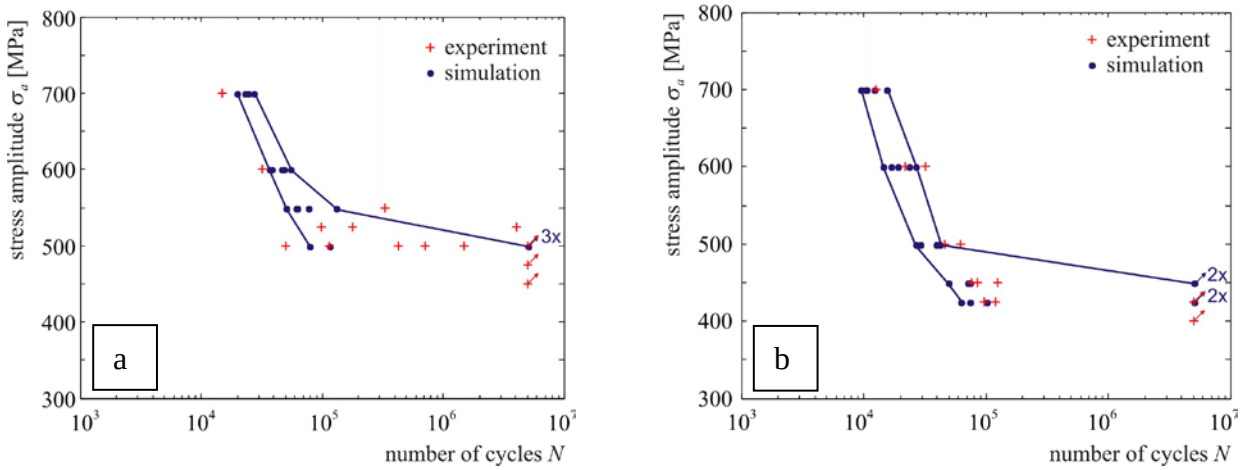

Figure 10. Comparison of observed and predicted fatigue lives for (a) ma condition and (b) sht condition.

7. Conclusions

This paper presents experimental investigations on crack initiation and short crack propagation in Ti6Al4V and shows, how the results are used in a numerical model. Crack growth mainly occurs on single slip systems (basal or prismatic) although in some cases cracks are found on boundaries where no slip system could be assigned. The numerical approach considers these crack growth mechanisms and uses either the range of the crack tip slide displacement or the crack tip opening displacement to describe the crack propagation rate. The modeling results show excellent agreement with propagation data of observed cracks. By means of calculations of the microstructurally controlled short fatigue crack growth in artificially generated “virtual” microstructures the significance and effect of microstructure parameters can be identified and analyzed, providing a mechanism-based foundation for a purposeful material development towards higher fatigue resistance. Moreover, a statistical treatment of the calculation results in terms of the evaluation of the distribution of the number of loading cycles necessary to reach a critical stress intensity factor under given loading conditions forms a sound methodology for fatigue life assessment.

Acknowledgement

The authors would like to express their gratitude to Böhler Schmiedetechnik GmbH & Co KG for financially supporting the project and supplying the material.

References:

[1] R.R. Boyer, An overview on the use of titanium in aerospace industry. Mat Sci Eng A, A213 (1996) 103-114.
[2] P.C. Paris, M.P. Gomez, W.E. Anderson, A rational analytic theory of fatigue. Trend Eng, 13 (1961) 9-14.
[3] O.H. Basquin, The exponential law of endurance tests. Proc Annual Meeting ASTM, 10 (1919) 625-634
[4] L.F. Coffin, Fatigue at high temperatures. ASTM STP, 520 (1973) 744-782.
[5] S.S. Manson, Fatigue: A complex subject-some simple approximations. J Exp Mech, 5 (1965) 193-226.
[6] B. Künkler, O. Düber, P. Köster, U. Krupp, C.P. Fritzen, H.-J. Christ, Modelling of short crack propagation – transition from stage I to stage II. Eng Frac Mech, 75 (2008) 715-725.
[7] G. Lütjering, J.C. Williams, Titanium (2nd Edition), Springe, Berlin-Heidelberg-New York, 2007.
[8] S. Taira, K. Tanaka, Y. Nakai, A model of crack-tip slip band blocked by grain boundary. Mechanics Research Communications, 5 (1978) 375-381.
[9] A. Navarro, E.R. de los Rios, Short and long fatigue crack growth: A unified model. Phil. Mag. A, 57 (1988) 15-36.
[10] O. Düber, B. Künkler, U. Krupp, H.-J. Christ, C.P. Fritzen, Experimental characterization and two-dimensional simulation of short-crack propagation in an austenitic–ferritic duplex steel. Int. J. of Fatigue, 28 (2006) 983-992.
[11] A.J. Wilkinson, S.G. Roberts, P.B. Hirsch, Modelling the threshold conditions for propagation of stage I fatigue cracks. Acta Mater, 46 (1998) 379-390.

Draft: SI8-043

Fatigue Behavior Investigation and Micro-Analysis of X80 High-Strain Line-pipe

Yang Li[1,2 *], Weiwei Zhang[2], He Li[2], Likang Ji[2], Chunyong Huo[2], Helin Li[2,3]

[1] School of material science and engineering, University of Science and Technology of Beijing, Beijing 100008, China
[2]Tubular Goods Research Institute of CNPC, Xi'an 710065, China
[3]School of material science and engineering, Xi'an Jiaotong University, Xi'an 710049, China
* Corresponding author: liyang011@cnpc.com.cn

Abstract Symmetrical push-pull low circle fatigue tests were carried out with conventional and high-strain X80 linepipe material respectively. Micro-analysis was performed for deformation mechanism as well. Results showed that high-strain X80 linepipe material exhibited a lower cyclic softening rate and a longer low-circle fatigue life than those of conventional X80 linepipe material. Cyclic response curves showed that the cyclic softening occurred at all strains amplitude (0.4%~1.4%) on two X80 line pipe materials. For conventional X80 linepipe material, cyclic softening was found after slight cyclic stress saturation at high strain amplitude of 1.0% ~1.4%. however, for high-strain X80 linepipe material, cyclic softening was observed after slight cyclic hardening at high strain amplitude of 1.0% ~1.4%. Fractography analysis suggested that transgranular fracture with well-developed fatigue striations and obvious second crack is the predominant failure mode. The amount of second crack was fewer detected in high-strain X80 linepipe material than that in conventional X80 linepipe material. TEM examination reveals that the primary deformation mode of two kinds of material was dislocation slipping. Abundant dislocation glide bands and dislocation cells were formed at grain boundary as strain amplitude increased. The number of dislocation blocked and wall thickness of dislocation cells in conventional X80 linepipe material are much greater than that in high-strain X80 linepipe material. The better cyclic deformation resistance of high-strain X80 linepipe material was ascribed to relative more M/A islands distributed inside the grains or grain boundaries.

Keywords High-strain line pipe; Low-circle fatigue; Strain amplitude; Dislocation; M/A

1. Introduction

Fatigue is a common failure mode of oil & gas pipeline. Fatigue fracture of pipeline is mainly caused by various alternating stress, which derives from pressure oscillation, layering of gas medium and all sorts of external variable load, such as vibration led by vehicle on the buried pipeline, fluvial abrasion of river, quicksand migration in desert and waves wash in offshore pipeline [1, 2]. Alternating stress can lead to local and alternative plastic deformation where stress concentration occurs, then fatigue failure of pipeline. In addition, since a lot of long distance, high pressure and large throughput pipeline set up in the harsh geological area, such as landslide, permafrost and seismic, buckling always caused by serious local plastic deformation of pipeline by bending, axial compression and axial tension stress. However, fracture can not be accomplished only once, low circle fatigue always becomes the final reason for the fracture of pipeline [3, 4]. Therefore, investigation on fatigue behavior of pipeline, especially low circle fatigue behavior is very significant for providing the theoretical suggestion for design, material selection and lifetime prediction of pipeline operating in the harsh condition. In this paper, the difference of low-circle fatigue performance between two X80 linepipe materials has been discovered by sub-structure evolution observation as well.

2. Experimental

The material of X80 conventional and high-strain line pipe used in this paper is obtained by TMCP and UOE forming technology. The microstructure of both X80 linepipe material mainly consists of granular bainite, polygonal ferrite and M/A as show in figure 1. While comparing the detailed

feature of conventional and high-strain X80 linepipe material, some differences can be detected that the grain size of first one is much finer and the content of polygonal ferrite and M/A of second one is much higher. The tensile properties of both X80 pipe are listed in table 1. It can be found that the tensile strength, ductility and strain hardening property of X80 high-strain pipe are much better than conventional pipe.

Since cyclic load that leads to fatigue failure always derives from axial stress, such as bending, compression and tension stress, round bar specimen with uniform section is cut from the pipe body along the longitudinal direction where is adjacent to the weld seam with 90° and machined with a gauge length of 12.5mm as shown in figure 2. Low circle fatigue test has been conducted on electro hydraulic servo fatigue testing machine Instron 1341 in terms of GB/T 15248-2008, in which tension-compression symmetric cycle and total axial strain control has been used. Triangle wave loading is adopted in tests to ensure a stable strain rate during the process of cyclic tension and compression and an obvious inflection point of sluggish loop. Strain amplitude of tests are 0.4%, 0.6%, 0.8%, 1.0%, 1.2% and 1.4%, strain rate used in tests is 4×10^{-3}mm/s, and strain ratio is -1.

Fatigue fracture has been investigated on SEM JSE-6700F. Specimen for TEM investigation was cut from the specimen in the range of gauge length along section direction after fatigue tests with EDM and machined by mechanical thinning and electrode polishing. Deformation microstructure observation has been carried out on the TEM JEM-200CX using an accelerating voltage as 200Kv.

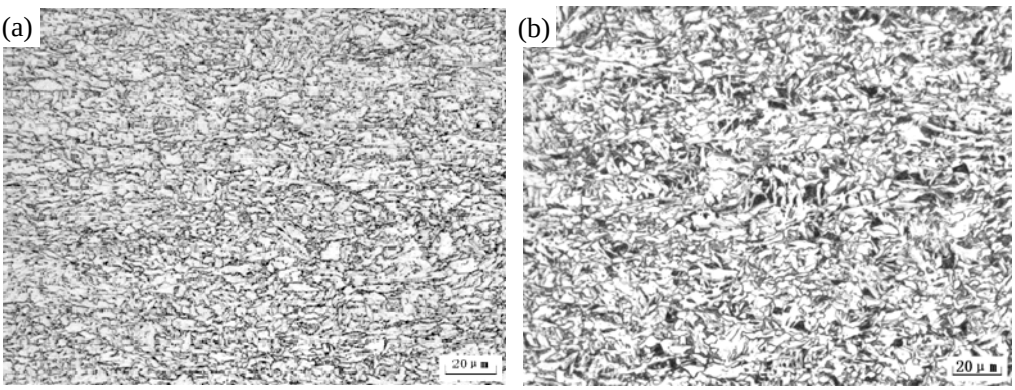

Figure 1. Micro-structure of X80 linepipe: a) conventional, b) high-strain

Table 1. longitudinal tensle property of X80 linepipe (round bar, gaugh length 50mm, diameter 12.7mm)

No.	σ_s/MPa	σ_b/MPa	δ/%	σ_s/σ_b	*UEL*/%	*n*
Conventional	580	653	24.1	0.89	7.25	0.0688
High-strain	569	729	24.3	0.78	7.87	0.1126

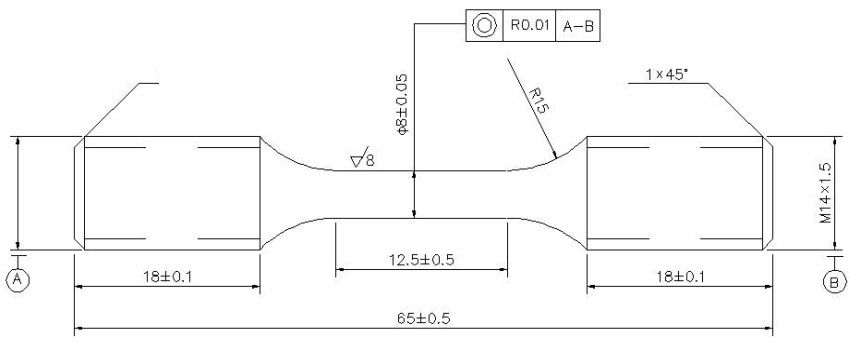

Figure 2. Specimen of low circle fatigue test

3. RESULTS

3.1. Cyclic stress response behavior

The relationship between stress amplitude and lifetime of two X80 linepipe steel material has been investigated with different strain amplitude 0.4%~1.4% as shown in figure 3. Comparing figure 3 (a) and (b), some common cyclic fatigue characteristics of X80 linepipe material suffered with different strain amplitude can be concluded: i. the stress amplitude of two X80 linepipe materials declines with the increment of cyclic time Nf, which means that material shows a general cyclic softening during the process of cyclic deformation with different strain amplitude. ii. softening rate is relative lower when material suffers with low strain amplitude 0.4%~0.8%, softening rate greatly increases as strain amplitude exceeds 0.8%, total softening rate of material shows an incremental tendency as strain amplitude increased. iii. cyclic fatigue lifetime is gradually shortened as strain amplitude increases. According to figure3, some different cyclic deformation feature also can be found: i. in the earlier phase of cyclic deformation, e.g. Nf lower than 4, two X80 linepipe material shows an obvious cyclic softening feature when materials suffer with lower strain amplitude 0.4%~0.8. However, as strain amplitude exceeds 0.8%, X80 conventional linepipe material shows a cyclic saturation feature, while X80 high-strain linepipe material presents a cyclic hardening behavior in which hardening level is prompted as stress amplitude increased. ii. the softening rate of X80 high-strain linepipe material is much higher than X80 conventional linepipe during the whole process of cyclic deformation with different strain amplitude. iii. under the same strain amplitude, cyclic stress amplitude of X80 high-strain linepipe material is always higher than X80 conventional linepipe material, which maybe ascribes to the much higher strength of X80 high-strain linepipe material.

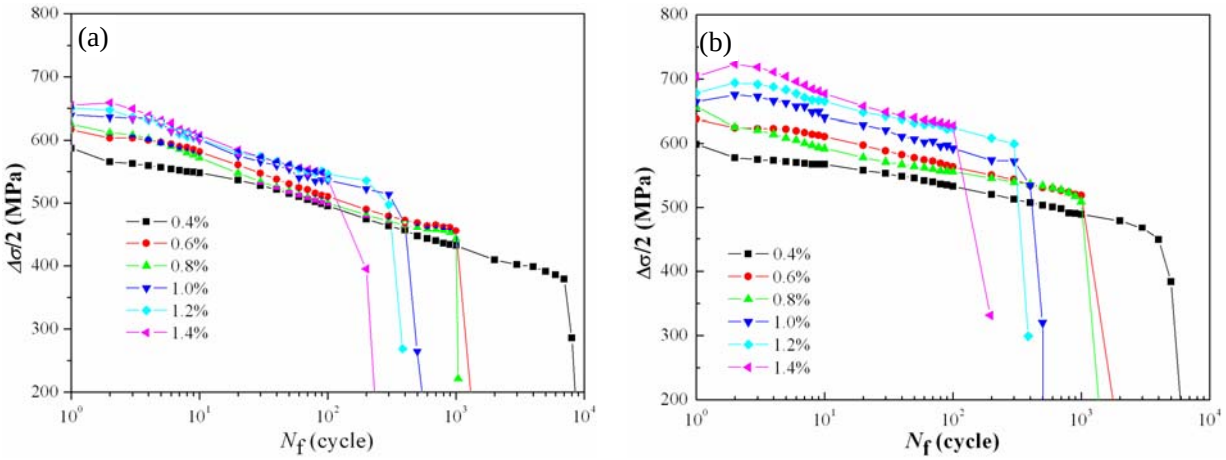

Figure 3. Relationship between stress amplitude and lifetime of X80 linepipe: (a) conventional, (b) high-strain

3.2. Cyclic stress strain behavior

Cyclic strain resistance in steady state of metallic material always can be indicated by cyclic stress strain curve. When comparing it with static tension curve, the feature of cyclic strain behavior can be found. In terms of relationship between $\Delta\sigma/2$ and $\Delta\varepsilon_p/2$, cyclic stress strain curve can be obtained after test data linear fitted in the logarithmic coordinates by least square method. Static tension curve and cyclic stress strain curve of two X80 linepipe material is shown in figure 4. It is found that two materials present cyclic softening characteristic in the range of strain amplitude. Softening level is much stronger under lower strain amplitude, while, softening level decreases with

the increment of strain amplitude. It can be observed that cyclic hardening rate of two X80 linepipe material is higher than that of static tension. It means that although the material apparently presents cyclic softening, since uniform distribution ability of deformation elevated by hardening, cyclic level is declined with the increment of strain amplitude [5].
Cyclic stress strain curve of two X80 linepipe material has been compared as figure 5 shown, it displays that cyclic softening level of X80 high-strain linepipe material is much lower than X80 conventional linepipe material under the same strain amplitude and the difference of stress amplitude between them gradually enhances as strain amplitude increases, which implies that X80 high-strain linepipe material has a much better cyclic strain resistance.

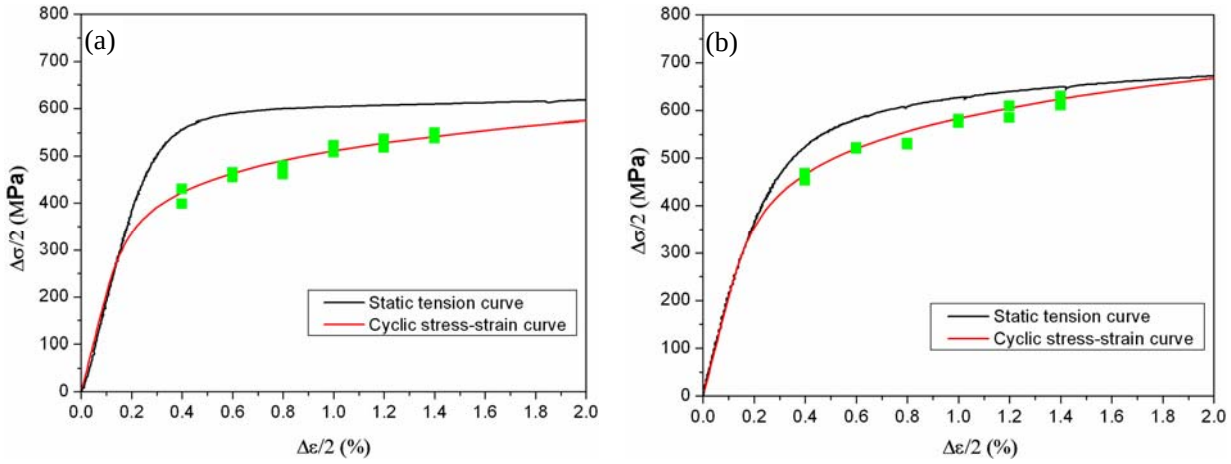

Figure 4. Cyclic strain stress curve and static tension curve of X80 linepipe material: (a) conventional, (b) high-stain

3.3. Fatigue lifetime

According to Manson-coffion equation, the relationship between strain and lifetime of X80 conventional and high strain linepipe material can be extrapolated as equation (1) and (2) after test data linear fitted in the logarithmic coordinates by least square method.

$$\frac{\Delta\varepsilon_t}{2}=\frac{\Delta\varepsilon_e}{2}+\frac{\Delta\varepsilon_p}{2}=0.0044(2N_f)^{-0.0677}+0.3171(2N_f)^{-0.5572} \quad \text{(conventional)} \quad (1)$$

$$\frac{\Delta\varepsilon_t}{2}=\frac{\Delta\varepsilon_e}{2}+\frac{\Delta\varepsilon_p}{2}=0.0073(2N_f)^{-0.1158}+0.2159(2N_f)^{-0.5032} \quad \text{(High-stain)} \quad (2)$$

Figure 6 shows the strain-lifetime curve of two X80 linepipe materials. It indicates that lifetime of X80 high-strain linepipe material is much higher than X80 conventional linepipe material when stain amplitude is much lower as 0.4%~1.0%. When strain amplitude exceeds 1.0%, the lifetime of two X80 linepipe materials almost has no difference. Generally, the lifetime of X80 high-strain linepipe material is much higher than X80 conventional linepipe material.

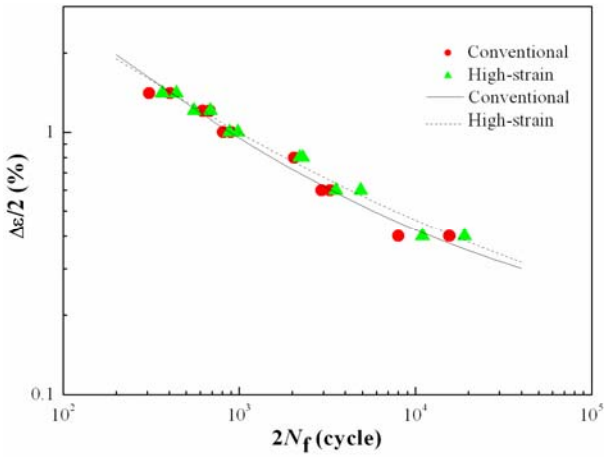

Figure 6. Strain-lifetime curve of X80 linepipe material

3.4. Fractography analysis

Fracture of low-circle fatigue specimens of two X80 linepipe material has been investigated by SEM. Figure 7 shows the facture appearance of specimen suffered with 1.2% strain amplitude. It is observed that fatigue fracture consists of 3 zones, including fatigue crack initiation, propagation and final fracture. Fatigue crack always initiates at surface and propagates along the direction perpendicular to the normal tensile stress (axial of specimen). The excircle edge of fracture fully distributes with fatigue steps presented with a radial pattern, and the amount of fatigue step increases with the increment of strain amplitude, which implies that the quantity of fatigue source increases accordingly. Comparing figure 7 (a) and (b), it can be found that the amount of fatigue step and radial stripe of X80 conventional linepipe material is much more than X80 high-strain linepipe material. Since fatigue specimen suffered tension-compression load, the zone adjacent to crack initiation presents obvious trail of extruding and grinding which resulted by the mutual extruding and rubbing between upper and lower surface of crack when fatigue crack stretched and closed repeatedly. Extruding and grinding become much heavier with the increment of strain amplitude and load applied on material, which makes the zone near the crack initiation much smoother as shown in figure 8. It also indicates that in initiation zone of X80 high strain linepipe material has a much smoother feature than X80 conventional linepipe material and its step is also much lower, which implies that high-strain linepipe material has a relative lower crack initiation rate.

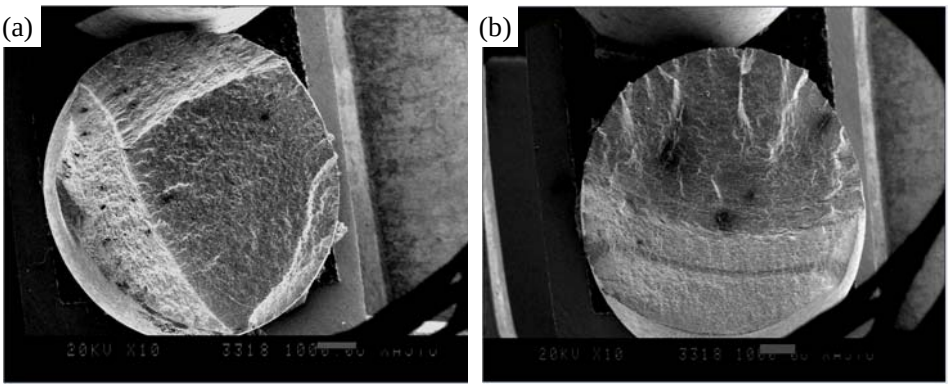

Figure 7. Macro-appearance of low-circle fatigue fracture of X80 linepipe material ($\Delta\varepsilon / 2$ =1.2%): (a) conventional, (b) high-strain

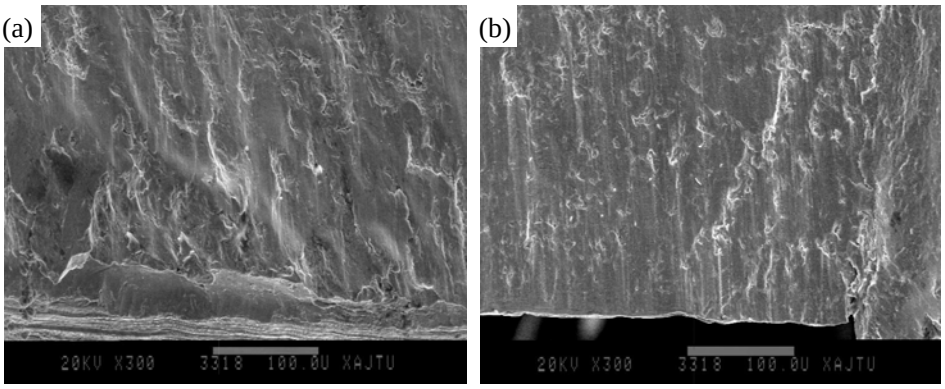

Figure 8. Micro mophology of fitigue crack intiation zone of X80 high-strain linepipe material ($\Delta\varepsilon/2$ =1.2%)

Micro-morphology of fatigue crack propagation zone of X80 linepipe material under the condition of different strain amplitude is shown in figure 9 and figure 10. It is found that the typical characteristic of propagation zone of specimen is fatigue striations and second crack which induced by cyclic load with the strain amplitude of 0.4%, as shown in figure 9. Comparing with figure 9 (a) and figure 9 (b), it can be found that the amount of second crack and the spacing of fatigue striation of X80 conventional linepipe material is much higher than X80 high-strain linepipe material, which means that fatigue crack propagation rate of X80 conventional linepipe material is much higher.

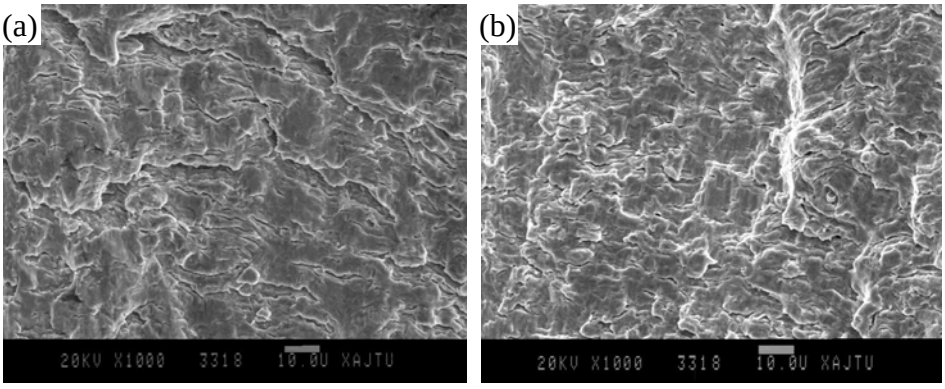

Figure 9. Micro mophology of fitigue crack propagation zone of X80 high-strain linepipe material ($\Delta\sigma/2$ =0.4%): (a) conventional，(b) high-stain

When strain amplitude increases to 1.2%, much more second cracks appear since load enhanced. Since the heavy extruding and grinding of fracture surface, propagation zone turns to be much smoother, tire-shaped pattern presents and fatigue striations almost disappears as shown in figure 10. The emergence of tire-shaped pattern means that fatigue crack speed dramatically increases under the condition of high strain amplitude which can enormously shorten the fatigue lifetime of material [6]. According to figure 10, X80 high-strain linepipe material presents a much obvious tire-shaped patter in crack propagation zone which presents a typical brittle fatigue feature.

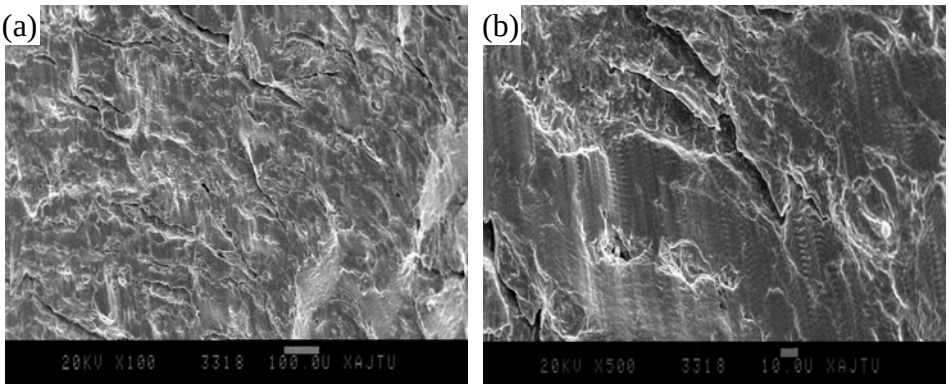

Figure 10. Micro mophology of fitigue crack propagation zone of X80 linepipe material ($\Delta\sigma/2$ =0.4%): (a) conventional，(b) high-stain

4. Sub-structure observation and Discussion

Low-circle fatigue tests results of two X80 linepipe materials as presented above show that cyclic deformation behavior of both X80 linepipe materials is cyclic softening. In addition, the softening rate of X80 high-strain linepipe material is much lower than that of X80 conventional linepipe material, the fatigue lifetime of X80 high-strain line pipe material is much longer as well. Generally, cyclic softening behavior always decides by the evolution of micro sub-structure of material suffered for cyclic loads. Usually, possible reasons for cyclic softening are reduction of dislocation density resulted by opposite screw dislocation meetion and counteraction, dislocation realignment and formation of sub-grain or dislocation cell, decline of friction stress induced by dislocation off-pining which original pinned by solute atoms. Therefore, some investigations on both X80 linepipe materials after cyclic deformed have to be performed to discover the different cyclic strain behavior of both X80 linepipe materials.

Since ferrite is relatively soft and has much fewer precipitated carbide, plastic deformation always preferentially happens inside it. Therefore, dislocation motion in ferrite can reflect the substructure evolution of material. Figure 11 presents substructure morphology of two ruptured X80 linepipe materials which suffered with lower cyclic strain amplitude 0.4%. X80 conventional linepipe material has a much heavier density of dislocation inside ferrite, and an incomplete dislocation cell is has formed by tangled dislocation as shown in figure 11 (a). However, it can be observed from figure 11 (b) that dislocation in ferrite and bainite is fairly higher and abundantly tangled on the grain boundary, while dislocation cell has not formed yet. The presence of dislocation of X80 high-strain linepipe material mainly is outcrop and dislocation line in ferrite due to much higher density of M/A constituent that can improve the deformation coordinate capability of material and postpone the occurrence of dislocation cell in ferrite. The difference of dislocation configuration between two materials results in the lower cyclic softening rate of X80 high-strain linepipe.

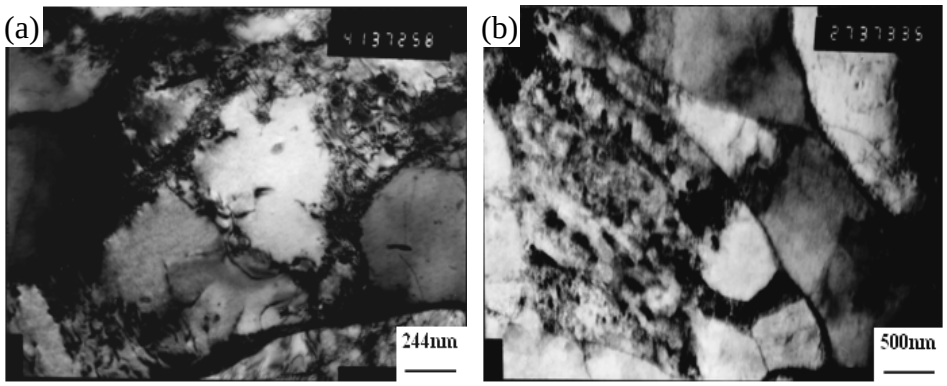

Figure 11 Substructure morphology of X80 linepipe material by 0.4% strain amplitude: (a) conventional (*Nf* =7800), (b) high-strain (*Nf* =9500)

Figure 12 (a) ~ (b) shows the dislocation configuration of X80 conventional linepipe material. With the increment of strain amplitude up to 0.8%, dislocation density in ferrite of X80 conventional linepipe material further decreases, single dislocation line almost disappears and complete dislocation has been formed as figure 12 (a) shown. Dislocation in M/A island begins to be polygonzaition and dislocation cell is going to be formed, in the same time, the amount of dislocation which bypasses second particles and accumulates around increases as shown in figure 12 (b) which results the realignment of dislocation. The formation of dislocation cell and declines of dislocation density causes the cyclic softening rate increase of material under 0.8% strain amplitude. Figure 12 (c) ~ (d) shows the dislocation configuration of X80 high-strain linepipe material. An obvious variation of dislocation configuration happens in X80 high-strain line pipe material with the increment of strain amplitude. Dislocation cell with relative thinner wall has started to be formed in ferrite in some area, which implies that with the occurrence of cellular structure, cyclic softening rate of X80 high-strain line pipe material suffered 0.8% strain amplitude is significantly improved comparing with 0.4% strain amplitude. Furthermore, it also can be observed that the tendency of dislocation cellular structure formation is much more obvious in ferrite surrounded by M/A as shown in figure 12 (c). While, the dislocation configuration in ferrite not surrounded by M/A is dislocation line or tangled dislocation as show in 12 (d). The reason for this phenomenon is that deformation inside material focuses primarily on coordinating deformation among structures. That is to say, deformation firstly happens on ferrite with a lower strength which can induce dislocation annihilation or formation of dislocation cell after dislocation movement and occurrence of ferrite softening [7]. Meanwhile, since deformation of ferrite is restrained by plenty of M/A constituent, once ferrite has been deformed to a certain level, deformation on M/A island begins. Furthermore, since much more ferrite exits in X80 high-strain linepipe material, the resource for dislocation movement is much more than X80 conventional linepipe material. Therefore, deformation in ferrite is further suppressed and the formation of dislocation cell in ferrite is accordingly delayed, which results in the reduction of softening rate of ferrite. Perhaps, that is certain reasons for inducing of much lower softening rate of X80 high-strain line pipe material [8].

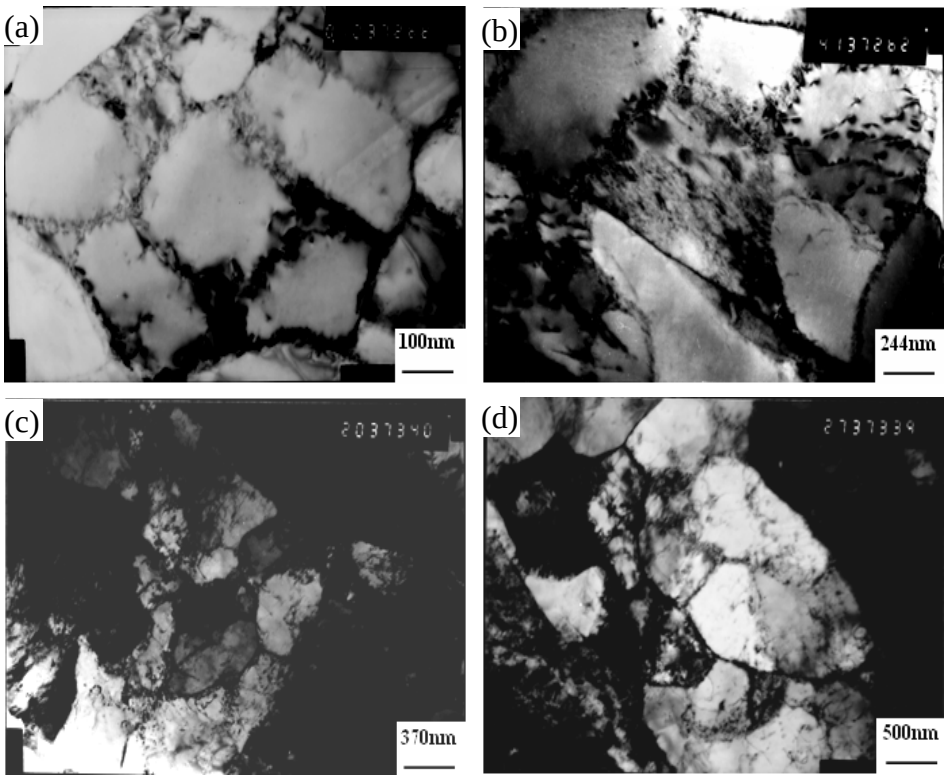

Figure 12. Substructure morphology of X80 linepipe material by 0.8% strain amplitude: (a)~(b) conventional (*Nf* =1027), (c)~(d) high-strain (*Nf* =1145)

Figure 13 presents the substructure morphology of two X80 linepipe material suffered 1.2% strain amplitude. For X80 conventional linepipe material, dislocation cell has been rapidly formed and cell wall-thickness obviously increases due to the dislocation pilling up nearby as indicted by figure 13(a). It is observed in figure 13 (b) that dislocation cell has been formed in ferrite surrounded by M/A, which further demonstrated the decrease of softening rate resulted by M/A that can obstruct deformation and postpone the development of dislocation cell in ferrite of X80 high-strain linepipe material.

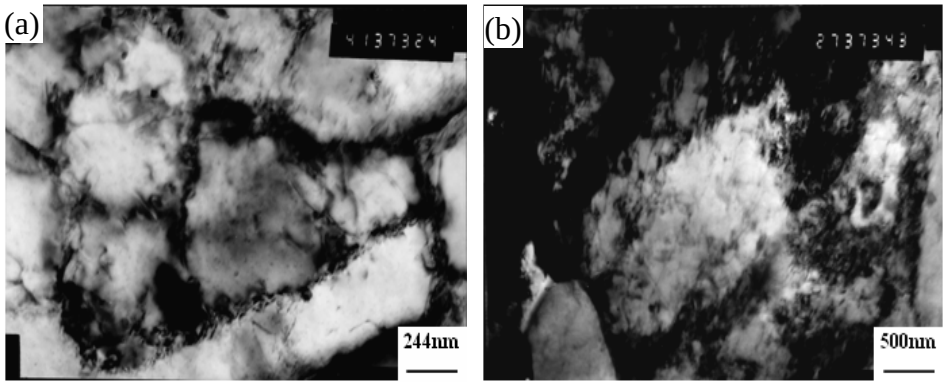

Figure 13. Substructure morphology of X80 linepipe material by 1.2% strain amplitude: (a) conventional (*Nf* =340), (b) high-strain (*Nf* =343)

5. Conclusion

Generally, two X80 linepipe materials exhibit a cyclic softening behavior under the cyclic load. Softening rate of two X80 linepipe materials show an incremental tendency as strain amplitude

increased. Cyclic fatigue lifetime of two X80 linepipe materials is gradually shortened as strain amplitude increases. In the earlier phase of cyclic deformation with strain amplitude exceeding 0.8%, X80 conventional linepipe material shows a cyclic saturation feature, while X80 high-strain linepipe material presents a cyclic hardening behavior. The softening rate of X80 high-strain linepipe material is much higher than X80 conventional linepipe during the whole process of cyclic deformation. Under the same strain amplitude, cyclic stress amplitude of X80 high-strain linepipe material is always higher than X80 conventional linepipe material, which maybe ascribes to the much higher strength of X80 high-strain linepipe material.

Cyclic softening level of X80 high-strain linepipe material is much lower than X80 conventional linepipe material under the same strain amplitude and the difference of stress amplitude between them gradually enhances as strain amplitude increases, which implies that X80 high-strain linepipe material has a much better cyclic strain resistance. The fatigue lifetime of X80 high-strain linepipe material is much higher than X80 conventional linepipe material.

In initiation zone of X80 high strain linepipe material has a much smoother feature than X80 conventional linepipe material and its step is also much lower, which implies that high-strain linepipe material has a relative lower crack initiation rate. the amount of second crack and the spacing of fatigue striation of X80 conventional linepipe material is much higher than X80 high-strain linepipe material, which means that fatigue crack propagation rate of X80 conventional linepipe material is much higher. X80 high-strain linepipe material presents a much obvious tire-shaped patter in crack propagation zone which presents a typical brittle fatigue feature.

Substructure evolution investigation reveals that the primary deformation mode of two X80 linepipe material is islocation slipping. As strain amplitude increased, dislocation cell developed gradually from dislocation line and tangled dislocation in two X80 linepipe materials. Dislocation density in X80 high strain linepipe material is much higher than X80 conventional linepipe material under various strain amplitude. The formation of dislocation cell or dislocation realignment of X80 high-strain linepipe material is always later than X80 conventional linepipe material. Ferrite deformation has been restrained in X80 high-strain linepipe material due to the higher amount of M/A and ferrite which postponed the formation and development of dislocation cell and caused a much lower softening rate.

Acknowledgements

Thanks for the financial support of Major Science and Technology Project of the 2nd WEGP of China National Petroleum Corporation.

References

[1] Levin SI. Causes and requency of failures on gas mains in the USSR [J]. Pipes and pipelines international, 91 (30): 149-176.

[2] Hagiwara N, Meziere Y, Oguchi N, et al. Fatigue Behavior of Steel Pipes Containing Idealized Flaws under Fluctuating Pressure [J]. JSME International Journal, 42(4): 610-617.

[3] Hagiwara N, Oguchi N. Fatigue Behavior of Line Pipes Subjected to Severe Mechanical Damage [J]. Journal of Pressure Vessel Technology, 121(4): 369-374.

[4] Fowler JR, Alexander CR, Kovach PJ, et al. Fatigue Life of Pipelines with Dents and Gouges Subjected to Cyclic Internal Pressure[C]. Proceeding of the Energy-Sources Technology Conference and Exhibition. Houston: ASME, 69: 17-35.

[5] Kiefner JF, Alexander CR, Fowler JR. Repair of Dents Containing Minor Scratches[C]. The 9th Symposium on Line Pipe Research. Houston: American Gas Association, 5:1-3.

[6] Chen M B, Wang R. Fatigue Crack Propagation of X60 Pipeline Steel after Pre-tension Deformation [J]. Material for mechanical engineering, 8 (7): 18-20.

[7] Diao S, Feng Y R, Zhuang C J, et al. Study on the Fatigue Properties of Oil Gas Pipeline and Its Prediction of Service Life [J].China safty science jurnal, 18 (1): 123-130.

[8] Liu W J, Chen Y F, Lu M X. Effect of overload on fatigue crack growth rate for X52 pipeline steel [J]. Transaction of material and heattreatment, 2008, 29 (4): 123-126.

Fracture mechanisms during intergranular hold time fatigue crack growth in Inconel 718 superalloy.

Sten Johansson[1,*], Leif Viskari[2], Krystina Stiller[3] Magnus Hörnqvist[4], Johan Moverare[1]

[1] Department of Engineering Materials, Linköping University, Linköping 581 83, Sweden
[2]Chalmers University of Technology and SKF Sweden
[3]Chalmers University of Technology Sweden
[4]Chalmers University of Technology and GKN Aerospace Engine Systems Sweden
* Corresponding author: Sten.Johansson@liu.se

Abstract Ni-base superalloy IN718 is known to display time-dependent intergranular crack growth under dwell time mechanical loading at high temperature under atmospheric conditions. Oxygen has been pointed out as a cause of the intergranular damage causing embrittled crack growth during both cyclic and hold time loading. Investigation of the mechanisms responsible for the embrittlement should not only focus on the effect of environment but also on the combined action of fatigue, creep, temperature and time. In this work material from experiments with fatigue crack growth in combination with hold times of different length at different temperatures has been investigated. Fractographic studies and metallographic cross sections of fatigued specimens has been subjected to careful analysis using ECCI- imaging in order to shed light on the fracture mechanisms. The results show that the damage is caused by the influence of a combination of environment and severe local damage manifested as a transformation of the microstructure into sub cells, micro twins and recrystallised areas close to the crack tip. The damage mechanism is thus influenced by a combination of oxidation and severe local plastic deformation.

Keywords Intergranular damage, Dwell time, ECCI, Fatigue, Fractography

1. Introduction

Ni-base superalloys are widely used in high temperature and for applications like rotating discs in gas turbines where IN718 is a popular alloy due to relatively low price/performance ratio, good corrosion resistance and mechanical properties with excellent weldability. The high temperature performance is limited to 650°C and an increase in temperature needed to increase efficiency has created demands of increasing temperature in steps of 50°C. Since IN718 has a strengthening phase of DO_{22} based on Ni and Nb called γ'' the max temperature is 650°C while a similar precipitate based on Ni and Al (γ') dissolves at a higher temperature. A newly developed γ'-former called Allvac718plus [1] is a replacement candidate for IN718.

The Ni-base superalloys are during service subjected to a combination of static loading and fatigue loading controlled by stress as well as strain. In addition to that high temperature and environment will act to reduce service life. The growth of fatigue cracks will be affected by temperature and environment so that the mode of crack growth is shifted from transgranular to intergranular. This embrittlement effect that most superalloys have in common [2] has been analysed in a great number of publications [3-8]and reviews [9-11] [12]. The fact that not only fatigue fracture crack growth is influenced by, frequency, temperature and environment but also growth of a static crack in conjunction with fatigue has been subject to analysis [13, 14]. The conclusions have so far been that the significance of the effect is minor under present service conditions but with increasing service temperature and load the effect might be a serious matter for the future.

The aim of this work is to study the effect of growth of fatigue cracks at high temperature in IN718 and Allvac718Plus in order to better understand the mechanisms behind the growth of fatigue

cracks especially dwell time cracking at hold times with varying length.

2. Experiments

Two alloys IN718 and Allvac718Plus have been subjected to fatigue testing with dwell time. The testing was performed in servohydraulic testing machines at constant stress amplitude using SEN specimens [8] with DCPD crack monitoring at high temperature using a radial furnace or induction heating [8, 15, 16]. Specimens with a crack were studied either as cross sections or as fracture surfaces using an Hitachi S70 analytical SEM with an annular Back scatter detector making it possible to produce images by Electron Channeling Contrast Image (ECCI). This method has been used with great success to study damage mechanisms in super alloy single crystals [17, 18]. The studied specimens have been chosen from crack growth experiments performed with Kb-type of specimens with cross sections of 4.3 X 10.2 mm with a 0.2 mm sparc cut starter notch. A baseline series of specimens were run at 0.5 Hz, R=0.005and the hold time testing (90s, 2160s and 21600s) was performed at 450, 550, 650 and 700°C in lab air environment except for Allvac718Plus that was also tested in pure oxygen atmosphere and the results presented as crack growth curves in ref. [5, 16, 19-21].

3. Results

In order to be able to distinguish between crack growth at different temperatures with and without dwell the results from crack growth without dwell will be presented first. In figure 1 the crack zone for baseline cracking at 450°C and 650°C is shown.

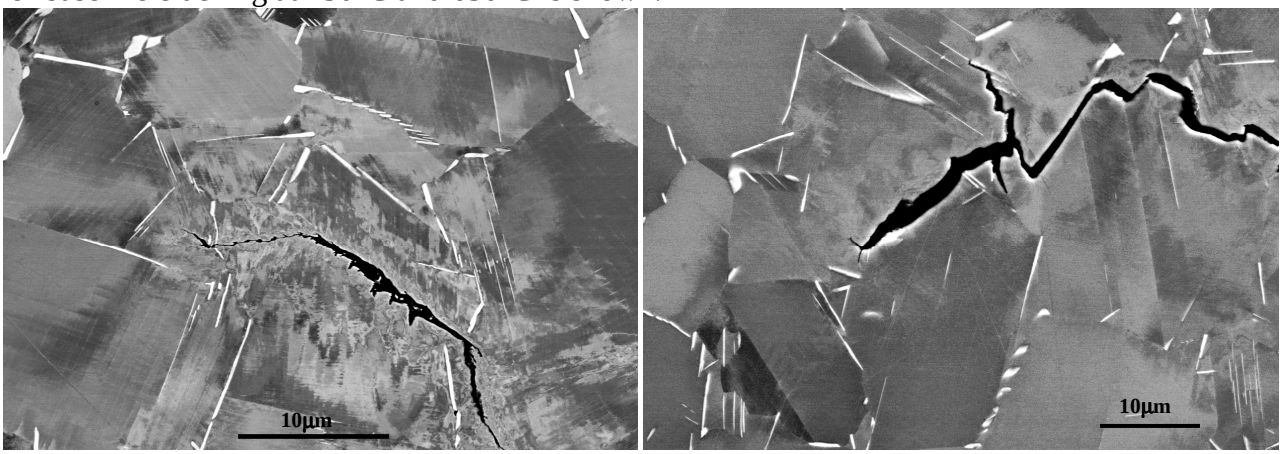

a b

Figure 1. SEM-ECCI micrograph showing cross section of the crack tip region of IN718 subjected to base line fatigue at a) 450°C showing high slip activity and 650°C with lower slip activity.

The lower temperature shows clear channeling contrast from plastic deformation caused by homogeneous slip on primary slip systems and in a narrow zone close to the crack localized more concentrated multiple slip. The crack path is transcrystalline with slight crack branching. The crack growth mechanism seems to be based on a weakening of interface at the crack tip by plastic deformation. For the higher temperature the crack path is more intergranular with more crack branching and the slip intensity is less pronounced.
The specimens subjected to dwell show more intergranular fracture and branching Figure 2 and the plastic deformation is more pronounced at 550°C but the fracture mode is varying along the crack

path and the crack growth seems to be assisted by both slip, plasticity induced dynamic recrystallisation sometimes with twins or formation of voids and cracking oxide at the crack tip. Although the crack growth is considered intercrystalline it can be divided into three different growth modes.

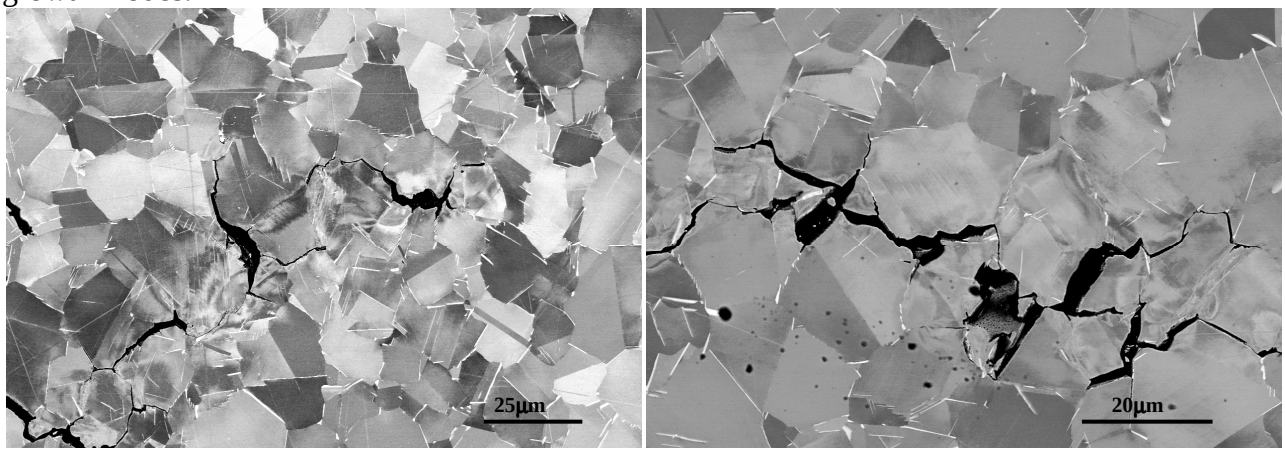

a b

Figure 2. SEM-ECCI micrographs showing cross sections of specimens with hold time at a) 550°C with intergranular branched cracks and clear signs of slip and b) 650°C with intergranular cracking and less pronounced plasticity.

The first one is the growth along grain boundaries where the mating grains are subjected to planar slip on one or two slip systems Figure 1a. The second growth mode is along grains with heavier homogeneous slip and a narrow zone close to the fracture surface with heavy non planar dislocation structure and sometimes twins and recrystallisation structure nicely shown in ECCI mode in the SEM Figure 3.

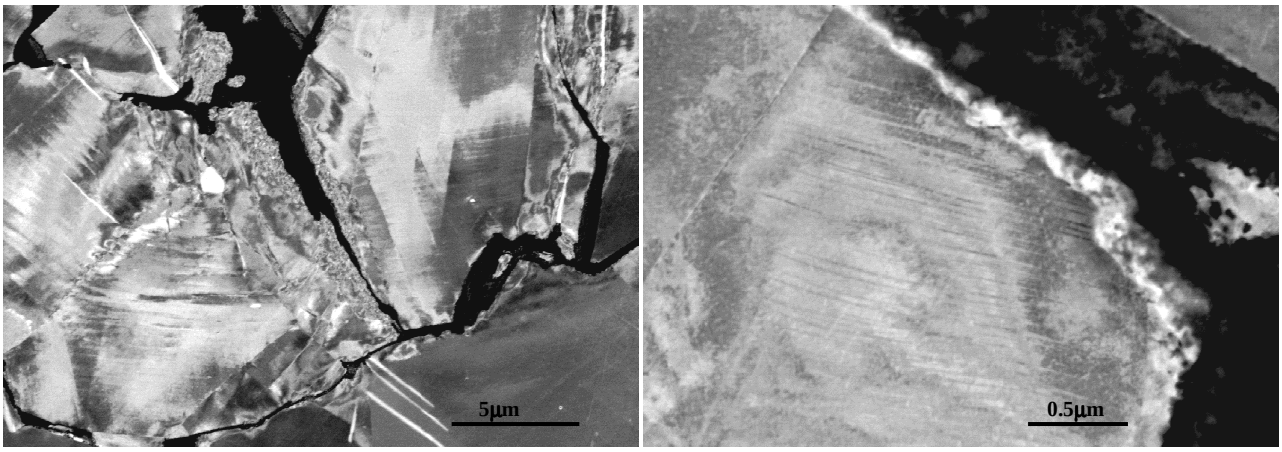

a) b)

Figure 3. SEM-ECCI micrographs showing a) the plastically damaged zone with sub grains and beginning recrystallisation close to the crack surface and b) deformation twins.

The third growth mode is cracking along δ-phase often oxidized into a sponge like structure in the interface between a δ-plate and the crack. It is thus difficult to say anything about the time-sequence of these events but the nanometric oxidized pores present at crack tips with a smallest size in the order of the hardening precipitates could trigger the onset of intercrystalline failure and the stress state and dislocation structure contributing factors Figure 4, 5, 6. The separate dwell time cracking

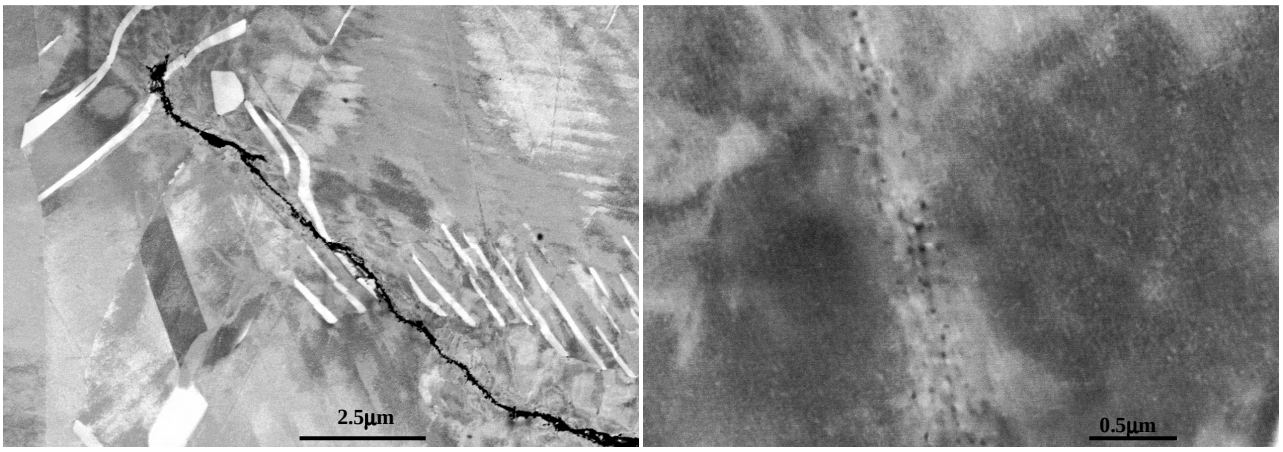

a b

Figure 4. SEM-ECCI micrograph showing a) the crack tip region and b the damage zone in front of the crack tip at higher magnification with stringers of pores.

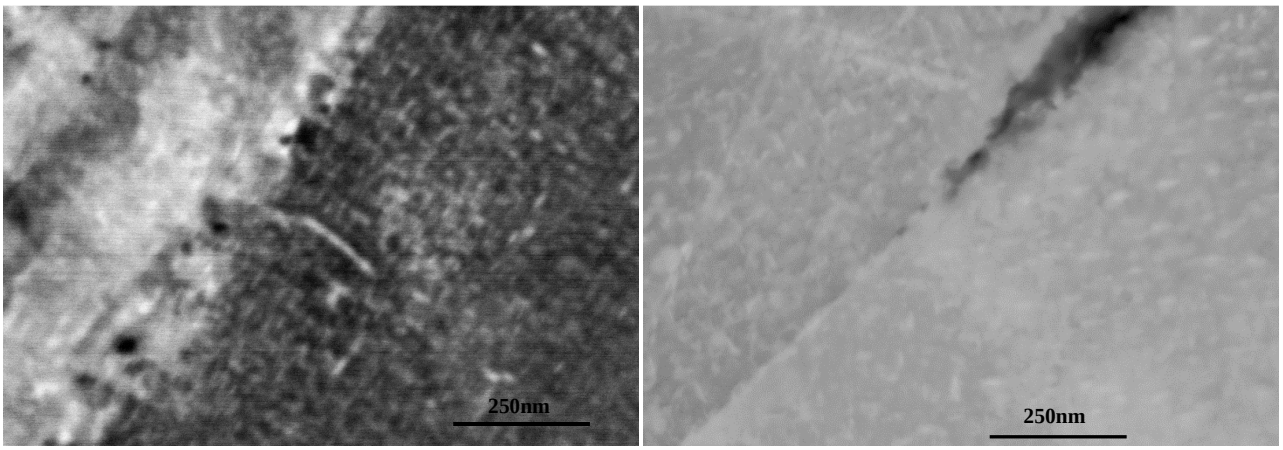

a b

Figure 5. SEM-ECCI picture of the damaged zone in IN718 at 550°C temperature close to the crack showing a) the hardening precipitates along with nano sized pores in an area with high plastic deformation and b) pores in a grain boundary with no plastic deformation.

events caused by unloading between each hold time are difficult to distinguish along the crack front. The crack front seems to have the character of a spherical discontinuous process zone (fig.2) with branched intergranular cracks rather than a single crack moving through the microstructure. Crack growth could then consist of environmental oxygen induced intercrystalline growth of cracks along sensitized paths in different directions and an interlinking between embrittled areas showing ligaments with more severe slip. The ligaments are severely plastically deformed to a level that is very close to dynamic recrystallization with characteristic pores shown as black dots in Fig. 4b, Fig. 5 indicating a future crack path. The growth of the main crack is also influenced by interaction with δ-plates acting either as a crack path or as a crack stopper (fig 4a) depending on orientation. The fact that the δ-phase is ductile makes it less probable as a crack path but the interface between δ and matrix is often acting as a crack [10] path through severely oxidized pores in the interface as observed in this work. Non propagating branched cracks are stopped due to blunting and/or geometrical reasons like going into mode II. Residual stress built up during growth manifested by a closure of the crack along the front also plays a role for the path taken by the crack.

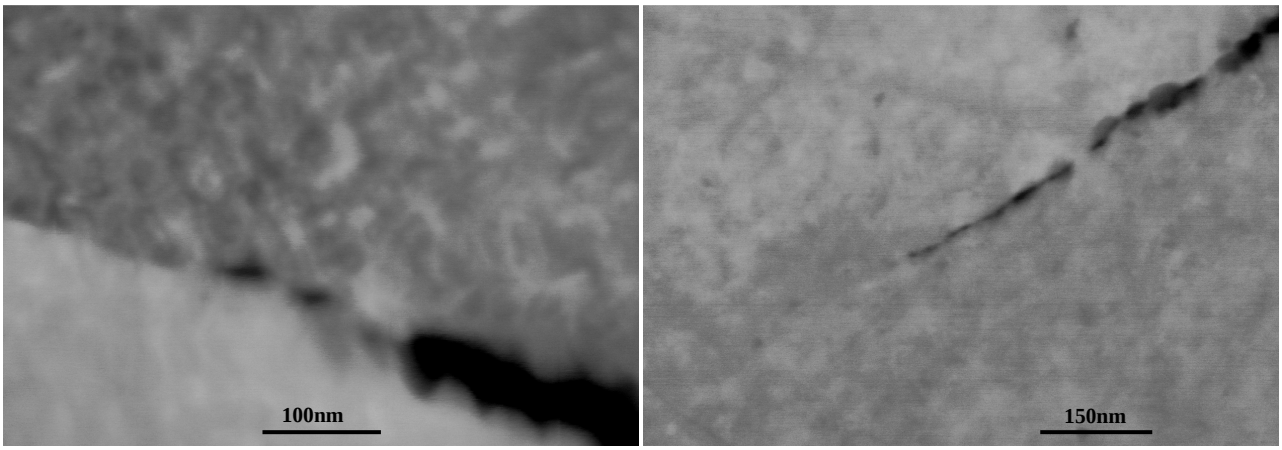

a b

Figure 6. SEM-ECCI micrographs of a) IN718 650°C during hold and b) ALVAC718plus 700°C during hold. Both alloys show voids in front of the crack tip. The smallest voids are in the same range of size as the hardening precipitates that are clearly visible in a).

The macroscopic crack path often shows a mismatch orthogonally indicating shear or grainboundary sliding along the crack growth direction. SEM ECCI pictures taken at a very high magnification of non propagating secondary cracks is shown in Fig. 6 where nanometric voids in the same size range as the clearly visible hardening precipitates Fig 6a are seen along the grain boundary. This type of voids is often seen along the crack front for longer cracks being coarser and more oxidized.

The dwell time cracking of Alvac718Plus in pure oxygen atmosphere shows (Fig. 7b) more clearly the intercrystalline character of the crack growth due to the absence of δ-plates (black in Fig. 7a) in this condition. The observable environmental action manifested by growth of oxidized pores in the grain boundaries seems to be the same as for IN718. The completely flat grain boundary surface has still slip bands and microscopic pores. The fatigue cycling in oxygen atmosphere at 700°C before the start of the dwell time cycle show clear striation like arrest markings indicating a continuous crack growth mode. Studying the fracture surfaces in higher magnification show signs of nano sized voids at the tip of branched cracks. The intergranular facets giving a smooth appearance at lower mag. (Fig 7b) show signs of voids at higher magnification (Figure 8, 9).

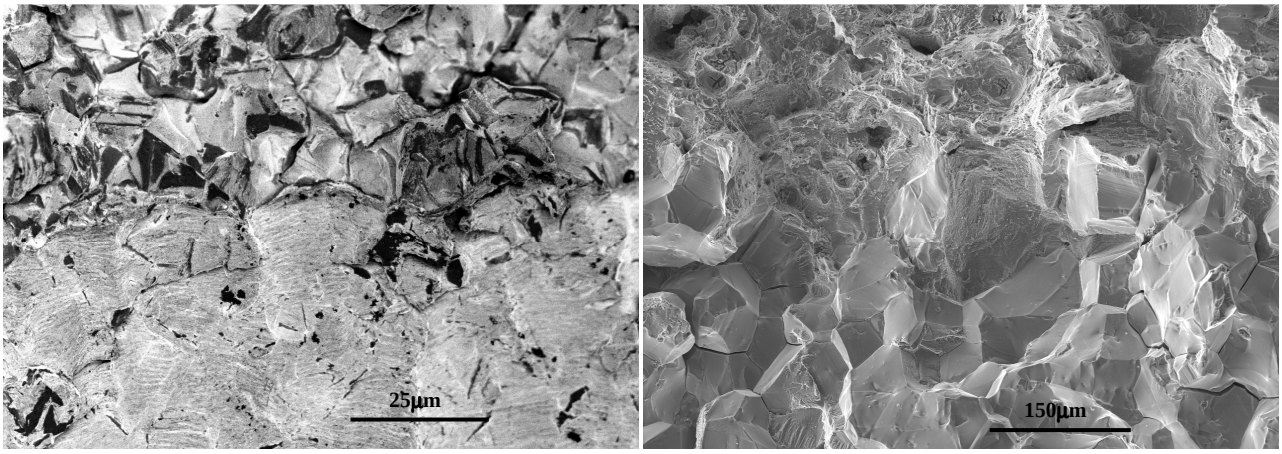

a b

Figure 7. SEM fractographs showing a) boundary between pre cracking at room temperature (lower) and dwell time growth at 550°C (upper), black contrast is δ-phase b) boundary between dwell cracking (lower) and final fracture (upper)in Allvac718plus at 700°C in pure oxygen atmosphere.

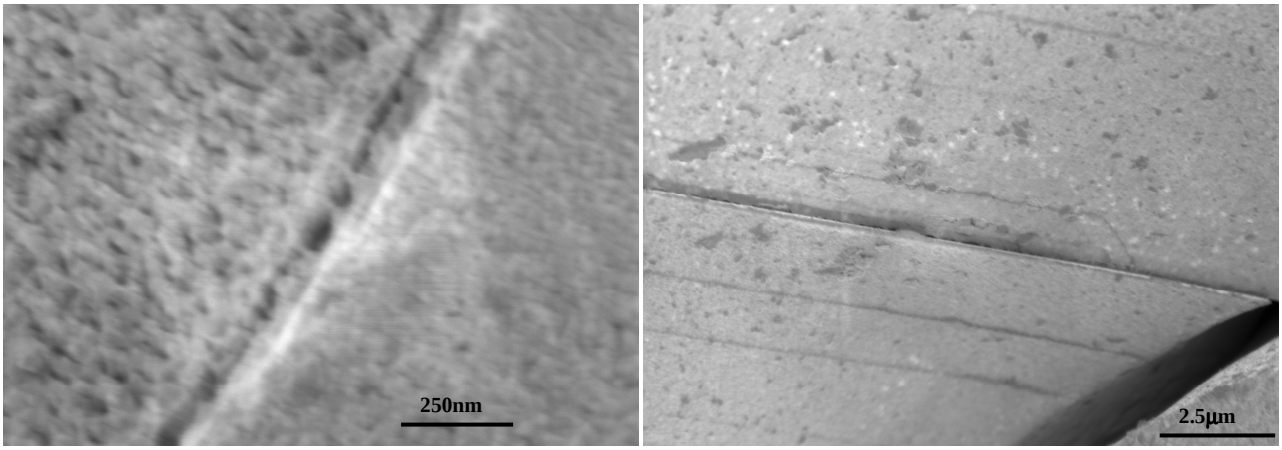

a b

Figure 8. SEM fractographs of grain facets in Allvac718plus (700°C dwell) a) oxidized surface with voids b) surface at lower magnification with one open and one closed secondary crack with voids.

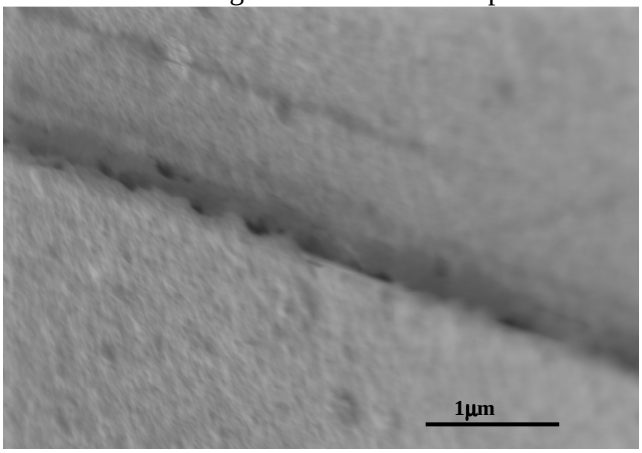

Figure 9. SEM fractograph showing the voids in the grain boundary shown in fig. 8b at higher magnification.

4. Discussion

The results from studies of the crack growth process of IN718 and Allvac718Plus under fatigue and dwell time loading conditions at high temperature will be discussed. The focus will be put on the effects of events taking place during the hold time periods.

The crack growth under the influence of temperature and cyclic loading is transgranular at 450°C with clear evidence of planar slip in the grains surrounding the crack going over to intense slip close to the fracture surface with phenomena like nano twins and local recrystallisation appearing. The crack path is sometimes branched and not as transgranular as during room temperature cycling indicating that the grain boundaries play a role even during base line cracking. With increasing temperature the crack path becomes more branched and the plastic deformation is less pronounced. This indicates that the environmental effect is gradually increasing with temperature.

The hold time experiments consist of applied constant load cycles between 90 to 21660 s where each cycle is separated by unloading to zero load level. The observed macroscopic change in growth rate caused by those events can unfortunately not by traced on a micro level. The reason for that is probably that the crack advance is a non continuous process. Gas phase embrittlement, GPE by oxygen is by far the most proposed damage mechanism in this case [12]. Still very little is

known about the damage on a micro scale. The conditions at the crack tip are probably controlled by the environment and the diffusion of oxygen towards and into the grain boundaries. This process is in turn controlled by the conditions at the grain boundary where slip bands, local stress, voids, oxide formation and local chemistry will affect the diffusion of embrittleing elements like oxygen. Depending on the local condition at the grain boundaries micro cracks will form and propagate till they are interfering and sometimes arrested by microstructure like δ phase or blunted at different locations in different directions creating a damaged volume where the final crack path will be formed when the ligaments between the micro cracks will break after plastic deformation or embrittlement. This crack model can explain the apparent non continuous crack growth and all the other phenomena like oxidized voids and plastic deformation together with embrittlement. Crack closure caused by local plasticity and observed mixed mode character along the crack path may also play a role both due to the unloading cycle between the cycle but also due to plasticity and oxide formation[10]. The environmental crack propagation during dwell at 700°C in Allvac718plus is observed as close to purely intergranular with limited fractographic information of microscopic direction of growth while the fatigue crack growth during the same conditions show clear crack arrest markings during intergranular growth. The fact that the there are virtually no crack arrest markings present during dwell does unfortunately not answer the question if the crack growth is continuous or not. Analysis of the crack tip with [15] advanced methods (SIMS) has shown that the penetration of oxygen is very limited in the crack tip region in front of the crack tip so the triggering of the crack growth event is probably caused by oxidation and growth of nano sized voids in the crack tip region. The voids can either be pure creep nano voids or γ'' or γ´particles from the matrix identified in this study. The origin of the voids found in this study could be from γ'' and/or γ´ growing under the influence of local stress and dislocation activity [10] and subsequently close to the crack tip being opened up and oxidized to form the observed pores. The oxidation of γ'' is probable in this environment since the δ-plates exposed to oxygen, with the similar composition as γ'' or even sometimes could be transformed to δ by dislocation particle [11] shearing, have been observed to be severely oxidized. Since the analysis with SIMS has shown that diffusion of oxygen in front of the crack tip is nonexistent a growth mechanism based on oxygen diffusion must be extremely local in character. This supports a mechanism where nanometric voids are created by a combined action of creep, transformation/oxidation of γ'' or γ´ into pores where the pore walls are thin enough to allow transportation of oxygen before they break and gradually open up the crack. In a review by Woodford [12] the cavities are supposed to be created by oxidation of carbon into gas phase where the voids are created from gas bubbles. The bubbles are not only acting as creep cavities but also to reduce the grain boundary sliding that normally takes place to relive stress concentrations in the grain boundary at higher temperatures. This is not contradicted by the observations in this work and could also explain the lack of expected oxide in front of the crack tip and also the fact that no oxygen at all was found by SIMS in ref. [16]. This also supports the observations in this work that there is a large amount of plastic deformation involved together with intergranular fracture in IN718 and no signs of embrittlement since the oxygen is not primarily causing embrittlement according to this model. Unfortunately evidence of a possible carbon source for the creation of gas bubbles to support the model proposed in Woodford has not been observed in this study but on the other hand not specifically been a subject of study.

Generally the growth of a crack during hold time constant loading is for IN718 a result of a number of growth mechanisms where microstructure together with plastic deformation and environment preferably oxygen are acting. For Allvac718Plus the dwell time effect at high temperature is more clear with pure intergranular growth mode but the growth mechanism during intergranular growth is very similar to IN718 with signs of oxidized pores in the [11]crack tip region.

5. Conclusions

A study of the growth of hold time cracks in IN718 and Allvac718Plus at high temperatures has led to the following conclusions.

- Growth of cracks in IN718 during dwell time show a mix between different growth modes with a marked shift in crack growth mode towards intergranularity with branching compared to fatigue crack growth under the same conditions.
- The growth mode during dwell time cracking is shifting towards more intergranular with increased branched cracking with increasing temperature for IN718 but local plasticity is still present.
- The dwell time cracking mode for Allvac718Plus is pure intergranular at high temperature with less pronounced local plasticity.
- Intergranular nanosized voids observed close to the crack tip region could be the responsible for intergranular cracking in both alloys.
- The origin of the nanosized voids is either pure mechanical or a result of oxidation of grain boundary precipitates

Acknowledgements

The authors wish to great fully acknowledge Turbo Power consortium, Siemens Industrial Turbines, Volvo Aero Corporation. Agora Materiae and Strategic Faculty Grant AFM at Linköping University are also acknowledged.

2.4. References

1. Melih Cemal Kushan, S.C.U., Yagiz Uzunonat, and Fehmi Diltemiz, *Recent Advances in Aircraft Technology*, in *ALLVAC 718 Plus™ Superalloy for Aircraft Engine Applications*, R. Agarwal, Editor. 2012, InTech.
2. Lei Zheng, G.S., Ye Meng, Reda Chellali & Ralf Schlesiger, *Mechanism of Intermediate Temperature Embrittlement of Ni and Ni-based Superalloys.* Critical Reviews in Solid State and Materials Sciences, 2012. **37:3**(181-214).
3. Gustafsson, D., Moverare, Johan, Johansson, Sten, Simonsson, Kjell, Hornqvist, M. Mansson, T, Sjöström, Sören, *Influence of high temperature hold times on the fatigue crack propagation in Inconel 718.* International Journal of Fatigue, 2011. **33**(11): p. 1461-1469.
4. Gustafsson, D., Moverare, Johan, Simonsson, Kjell, Johansson, Sten, Hörnqvist, Magnus, Månsson, Tomas, Sjöström, Sören, *Fatigue Crack Growth behaviour of Inconel 718 - the Concept of a Damaged Zone Caused by High Temperature Hold Times.* Procedia Engineering, 2011. **10**: p. 2821-2826.
5. David Gustafsson, Johan Moverare, Kjell Simonsson, Sten Johansson, Magnus, Hörnqvist, Tomas Månsson, and Sören Sjöström, *Fatigue crack growth behaviour of Inconel 718 – the concept of a damaged zone caused by high temperature hold times*, in *ICM11, P. Engineering*, Editor. 2011, Accepted: Como Lake Italy. p. 2821-2826.

6. Atsushi Sato, Johan Moverare,, Magnus Hasselqvist,,Roger Reed, *On The Oxidation Resistance of Nickel-Based Superalloys.* Advanced Materials Research, 2011. **278**: p. 174-179.
7. Sten Johansson, Johan Moverare,, Daniel Leidermark,, Kjell Simonsson,, Jan Kanesund, *Investigation of localized damage in single crystals subjected to thermalmechanical fatigue (TMF).* Procedia Engineering, Fatigue 2010, 2010. **2**(1): p. Pages 657-666
8. David Gustafsson, J., Moverare, Sten Johansson, Magnus Hörnqvist, Kjell Simonsson, Sören Sjöström, Babak Sharifimajd, *Fatigue crack growth behaviour of Inconel 718 with high temperature hold times. Procedia Engineering, Volume 2, Issue 1, April 2010, Pages 1095-1104,* 2010. **2**(1): p. *Pages 1095-1104*.
9. Andre Pineau, S.D.A., *High temperature fatigue of nickel-base superalloys – A review with special emphasis on deformation modes and oxidation.* Engineering Failure Analysis (2009) **16**: p. 2668-2697.
10. D.G. Leo Prakash, M.J.W., D. Maclachlan, A.M. Korsunsky *Crack growth micro-mechanisms in the IN718 alloy under the combined influence of fatigue, creep and oxidation.* International Journal of Fatigue 2009. **31**: p. 1966-1977.
11. Andre Pineau, Stephen D. Antolovich, *High temperature fatigue of nickel-base superalloys – A review with special emphasis on deformation modes and oxidation.* Engineering Failure Analysis 2009. **16**: p. 2668-2697.
12. Woodford, D., A.,, *Gas phase embrittlement and time dependent cracking of nickel based superalloys.* Energy Materials, 2006. **1**(1): p. 59-79.
13. A. Karabela, L.G.Z., J. Tong, N.J. Simms, J.R. Nicholls, M.C. Hardy, *Effects of cyclic stress and temperature on oxidation damage of a nickel-based superalloy.* Materials Science and Engineering A 2011. **528**: p. 6194-6202.
14. Wanhill, R.J.H., *Significance of dwell cracking for IN718 turbine discs*
International Journal of Fatigue) 2002. **24** p. 545-555.
15. L.Viskari, S. Johansson and K. Stiller, *Oxygen influenced intergranular crack propagation: analyzing microstructure and chemistry in the crack tip region*, in *Materials at high temperatures*. 2011: UK. p. 336-341.
16. Viskari, L., *Oxygen Induced High Temperature Crack Growth in NI-base Superalloys*, in *Department of Applied Physics*. 2011, Chalmers University of Technology: Gothenburg, Sweden.
17. Moverare, J.J., S. Johansson, and R.C. Reed, *Deformation and damage mechanisms during thermal-mechanical fatigue of a single-crystal superalloy.* Acta Materialia, 2009. **57**(7): p. 2266-2276.
18. Moverare, J.J. and S. Johansson, *Damage mechanisms of a high-Cr single crystal superalloy during thermomechanical fatigue.* Materials Science and Engineering a-Structural Materials Properties Microstructure and Processing, 2009. **527**(3): p. 553-558.
19. David Gustafsson, Kjell Simonsson,, Sören Sjöström,, Sten Johansson, *Influence of high temperature hold times on the fatigue crack propagation in Inconel 718* International Journal of Fatigue, 2011.
20. Viskari, L., Johansson, Sten, Stiller, Krystina, *Oxygen influenced intergranular crack propagation : analysing microstructure and chemistry in the crack tip region.* Materials at High Temperature. **28 (2011)**(4): p. 336-341.
21. Gustafsson, D., *Constitutive and fatigue crack propagation behaviour of Inconell 718*, in *Department of management and engineering*. 2011, Linköping University: Linköping, Sweden.

Fatigue life and initiation mechanisms in wrought Inconel 718 DA for different microstructures

Meriem Abikchi[1,2,*], Thomas Billot[3], Jerome Crepin[1], Arnaud Longuet[2], Caroline Mary[2], Thilo F. Morgeneyer[1], André Pineau[1]

[1] Mines ParisTech, Centre des Matériaux UMR CNRS 7633, BP 87, 91003 Evry cedex, France
[2] Snecma-SAFRAN group ; site de Villaroche, 77550 Moissy-Cramayel, France
[3] Snecma-SAFRAN group ; site de Gennevilliers, 92702 Colombes Cedex, France

* Corresponding author: meriem.abikchi@mines-paristech.fr

Abstract Wrought Inconel 718 DA superalloy disk zones present a wide range of behavior in fatigue life due to the variability of the microstructure. In order to link the effect of the forging conditions and achieved microstructure to the fatigue life, two microstructures have been tested in fatigue. Fatigue tests under strain control were performed at 450°C. Grain size distributions and phase distributions were characterized in the specimens and related to fatigue failure initiation modes. Fatigue crack initiation was seen to occur on large grains in stage I for the larger grain material whereas for the material with slightly smaller grains initiation from internal nitrides caused failure via so-called fish-eye cracks. The different steps of these failure modes are discussed using data from the literature to gather the ingredients for a quantitative assessment of the fatigue lifetime using fracture mechanics.

Keywords Inconel 718, Microstructure, Fatigue, Crack initiation, Propagation mechanism

1. Introduction

Inconel 718 is widely used in aircraft industry. Because of a good combination of formability fatigue and weldability properties and low price/performance ratio, this superalloy is widely used for aerospace applications like turbine disks [1, 2]. This wrought material is produced by forging followed by different heat treatments in order to obtain the desired microstructure. The fatigue behavior at high temperature of this superalloy was widely studied [3-6], the main objective is to predict the lifetime of aircraft engine disk by calculation according to microstructures parameters [7, 8].

To improve the fatigue durability, it is important to obtain the finest possible microstructure. A specific heat treatment called Direct Aging (DA) was developed to obtain this kind of microstructure [9]. Contrary to a classical heat treatment, here the material is directly quenched after forging then aged without adding an annealing step. Fatigue tests were carried out on 718DA and even if the fatigue life was improved thanks to a finer grain size, a strong scatter in test results was observed [10]. Fractography revealed that this scatter is linked to different microstructures and crack initiation mechanisms [11]. Two mechanisms were identified, one for the fine grain size material (5-10µm) and another one for the large grain size material (150µm). For the fine microstructure, initiation sites were systematically related to the presence of second phase particles (carbides and nitrides) on the specimen surface with a size of 10-20µm, then Stage II crack propagation occurs until the breaking point. On the other hand, in the larger grain size material, conventional Stage I crack initiation was observed along the slip bands. In conclusion of this work [11], crack initiation always occurs in the larger microstructural phase. For the fine grain size material, it corresponds to the particles. When the grain size is larger than the particles, crack initiation occurs within the grains themselves. Also, in the previous study, the fatigue properties

were compared at 600°C, and strong oxidation effects are observed in particular on the NbC particles. This oxidation mechanism increases the volume of the particles and allows the initiation and propagation of local cracks because of stress concentration [9].
In the present study, the two materials which were investigated have a mean grain size smaller than the particles size because of the forging parameters used and the DA heat treatment. Two grain sizes were selected. In the case of small grain size the scatter of fatigue life is always present [10]. So it is necessary to understand which one of these parameters really affects the fatigue life.
In the present study the microstructural features are assessed via experimental observation methods. Mechanical fatigue tests are carried out and fatigue crack initiation mechanisms assessed via fractography observations. The various modes of crack initiation encountered and subsequent propagation are discussed using data from the literature to gather the ingredients for a quantitative assessment of the contributions of each crack progression step on the fatigue lifetime.

2. Materials and experimental methods

The experimental pancakes used in this study were forged by Snecma. The pancakes, which were water quenched after forging, have been directly aged with the standard aging treatment, and will be designated as DA718 in the following. The standard aging treatment is: 720°C /8h/ Furnace cooling (50°C/h) down to 620°C/8h and subsequent air cooling. In the present study, two kinds of forging parameters have been investigated (such as temperature, strain amplitude or cooling speed). Indeed material 1 presents a cooling speed slower, as well as a hold time at temperature higher than the delta phase solvus temperature longer than the material 2.

Inconel 718 is a nickel based superalloy hardened by γ'' (Ni_3Nb) and γ' ($Ni_3[Ti,Al]$) precipitates. This alloy also contains δ (Ni_3Nb) phase. The δ phase particles are located both along the grain boundaries and within the grains, depending on the heat treatment applied to the alloy. Another category of coarse second phase particles present in the alloy are nitrides (TiN) and carbides (NbC) with a typical size ranging from 5 to 20 μm. These particles are preferentially located at grain boundaries [14].

Table 1 : Chemical composition of Inconel 718 in weigth %

Al	B	C	Cr	Co	Cu	Fe	Mn	Mo	Ni	Nb+Ta	Ti	O	N
0.56	0.0041	0.023	17.97	0.14	0.03	17.31	0.08	2.97	54.18	5.40	1.00	0.001	0.0062

Microstructures were assessed in term of grain size, particle (carbides and nitrides) and δ phase sizes and their distributions. Samples were polished up to 1μm diamond paste. Micrographs of these samples were taken using a Scanning Electron Microscope (SEM), LEO VP 1450 SEM. To measure precipitates and particles size and their distributions, image analysis software, ImageJ®, was used.
Electron back scatter diffraction (EBSD) scans were also carried out on polished samples. EBSD patterns were collected using a Hikari digital camera, installed on a LEO SEM system. LEO VP 1450 SEM is equipped with an EDAX TSL OIM EBSD data acquisition and processing software and a Hikari digital camera. Operating conditions: high voltage 30 kV, probe current 2000 pA, working distance 22.5 mm, tilt angle 70 deg, step size 0.5 micrometers (hexagonal grid). Four areas of 500μm² were scanned on each material. Data cleanup by "Grain dilation" with threshold values of grain size and misorientation angle of 2 pixels and 5 degrees, respectively.
All the mechanical tests were performed on specimens taken from the two forged material which were submitted to DA heat treatment. The specimens were oriented along the tangential direction of the pancakes.
Fatigue tests were performed using a servo-hydraulic MTS testing machine with a maximum loading of 250kN. This machine was equipped with a resistance heating furnace allowing a

maximum temperature of 1200°C. The fatigue tests were carried out in air at 450 °C ± 2 °C. The temperature control was realized with thermocouple welded on each head of the sample surface (outside the gauge length). These specimens had a diameter of 5 mm and a gauge length of 13 mm. The specimens were tested under 1Hz triangular cycles under strain control. SEM observations of the fracture surfaces allowed us to identify the nature of the fatigue crack initiation sites using a Zeiss Gemini SEM.

3. Results and discussion

3.1. Microstructure

Figure 1 shows EBSD data for the two materials. Differences in grain size are observed. In material 1, the average size of grains is about 10µm whereas it is only about 7µm in material 2. The distribution of the grain size is also different (Figure 2); the scatter of the distribution of grain size is larger in material 1. EBSD data also show that both materials do not have a preferred crystal orientation (i.e. texture in Figure 3).

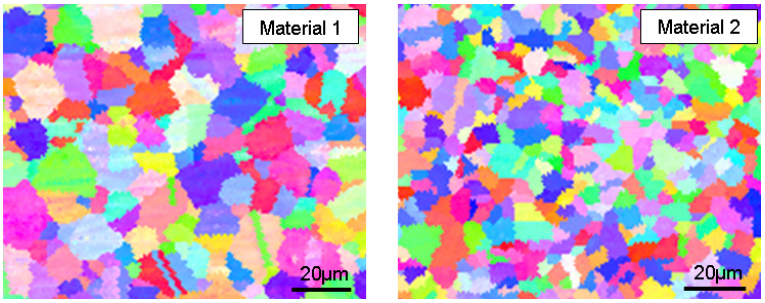

Figure 1 : Grain microstructures observed by EBSD scans with a step of 0.5 µm for a) material 1 and b) material 2

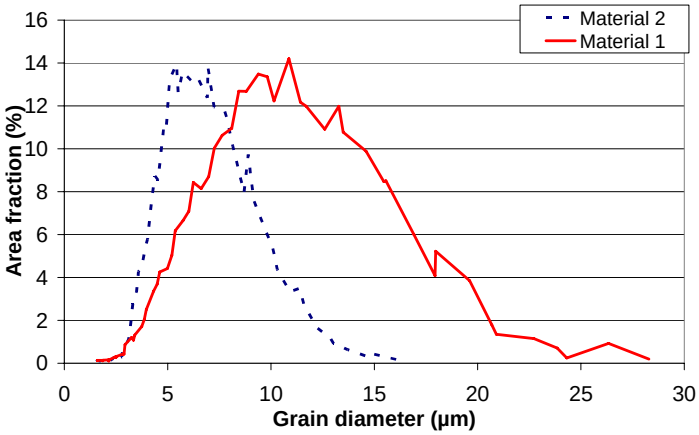

Figure 2 : Grain size distributions of the 2 materials calculated from the EBSD data on 1mm² zones

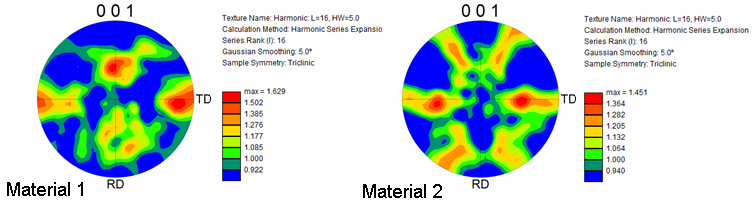

Figure 3 : Pole figure of the texture of the two materials

The size and the distribution of the particles (carbides and nitrides) were also determined by SEM observations on cut-sections first (Figure 4). Carbides are bigger in the initial, non-wrought material

than in the wrought materials, which is consistent with the fact that the carbides were “cut” during the forging process (Table 2). During forging, clusters of smaller carbides are formed that are oriented according to the fibre direction. These results were obtained from a 1mm² surface.

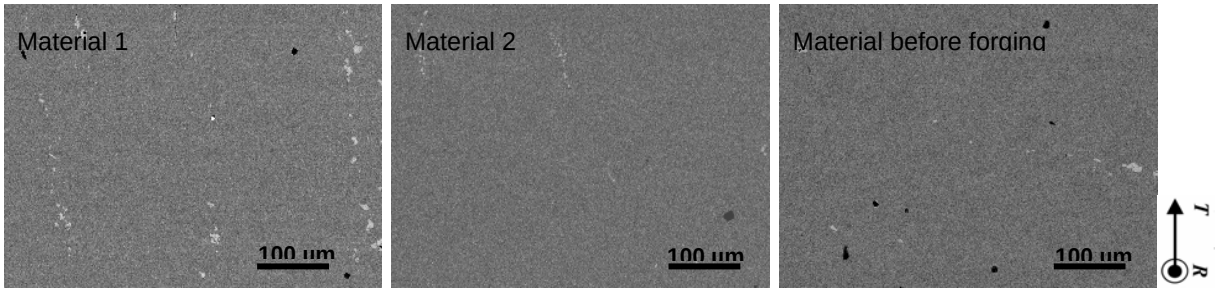

Figure 4 : Microstructures of the different materials, comparison of the distribution of carbides and nitrides, in the radial direction.

Table 2 : Comparison of the distribution and the size of the carbides in the three materials, analysis zones of 1mm².

	Numbers of carbides	Average size	Average diameter	Maximal size	Maximal diameter
	(±5)	µm² (±0,5)	µm	µm² (±0,5)	µm
Material 1	185	13.3	6.5	139.0	20.9
Material 2	115	16.9	7.3	121.5	19.5
Material before forging	95	25.6	9.0	220.5	26.3

The same analysis was carried out for the nitrides which are particles with sharper angles than the carbides (Figure 4). Their density seems similar in both materials, only their size differs weakly. To carry this study further, and compare the distribution of the nitrides in the two materials, a larger area of analyses should be used to assess enough particles for a statistical study.

Table 3 : Comparison of the distribution and the size of the nitrides in the three materials, analyse zones of 1mm².

	Numbers of nitrides	Average size	Average diameter	Maximal size	Maximal diameter
	(±5)	µm² (±0,5)	µm	µm² (±0,5)	µm
Material 1	23	33.3	10.2	204.1	25.3
Material 2	24	27.2	9.2	154.9	22.1
Material before forging	22	17.9	7.5	101.0	17.8

The last microstructural comparison concerns the proportion of δ phase in the two materials of the study (Figure 5). The fraction of δ phase is three times higher in material 2 compared to material 1; they are respectively of 3.0% and 1.1%. This δ phase precipitates preferentially on grain boundaries.

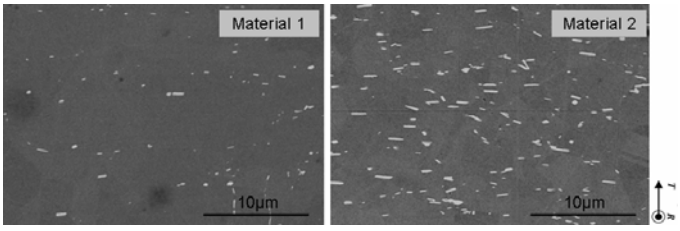

Figure 5 : Comparison of the delta phase distribution between the two materials.

3.2. Mechanical test results

The difference of yield stress between the material 1 and 2 is observed; they are respectively 1170 MPa and 1250MPa. Fatigue properties of these two materials are compared in relation with the grain sizes. The results are presented in Figure 6, the pseudo-stress values are normalised by the Young modulus divided by the mean yield stress of the material, and for proprietary reason this

value cannot be indicated. As shown in Figure 6, for tests conducted at 450°C, the small grain size material achieves significantly higher fatigue lives than the larger grain size material. The fatigue life of material 2 is at least twice superior to that of the material 1.

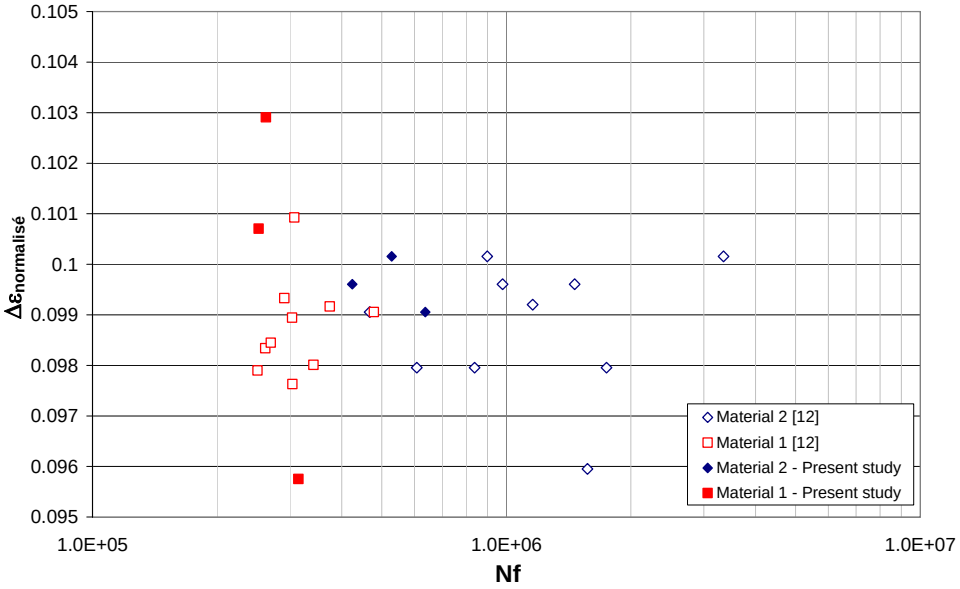

Figure 6 : Repartition of the fatigue life at 450°C, Comparison of the two microstructures**.**

3.3. Discussion of the fatigue crack initiation scenarios and crack propagation steps

In this section the different crack initiation and propagation scenarios are discussed in detail and compared with the literature to gather the elements necessary for a quantitative study of the contribution of each crack progression mechanism to the total fatigue lifetime.

Inconel 718 DA presents at least two known modes of crack initiation [9, 11] modes depending of the microstructure for smooth round bars:
1. Crack initiation on the surface particles for the lowest fatigue life
2. Stage I crack initiation for the longest fatigue life.
In this study, a supplementary crack initiation mode is observed:
3. Internal crack initiation on nitrides leading to fish-eye cracks.
This third crack initiation mode appears for long fatigue lifes and will be discussed in detail.

3.3.1. Crack initiation on surface particle

This type of fatigue crack initiation phenomenon is not shown here but it was clearly observed in the F. Alexandre's work [9, 11] for larger strain amplitude and temperature. These brittle particles may fracture during loading. In addition, the niobium carbides particles on the surface are strongly oxidized and transformed into Nb_2O_5 type oxide [9, 15], as shown in Figure 7. The increased volume of carbides and the stress concentration associated with the oxidation of carbides may lead to early crack initiation. The surface crack initiation probability is dependent of the probability to encounter a large oxidized particle on the specimen surface. This probability increases for large specimens. The fatigue life is then mainly spent in Stage II propagation from an initial crack size equal to the size of the larger grain.

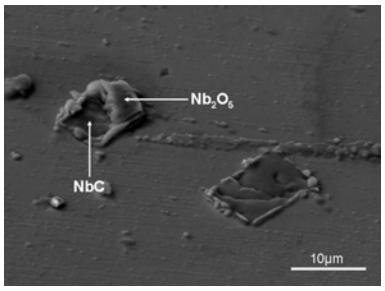

Figure 7 : SEM micrograph of the outer specimen surface away from the fracture surface after specimen failure; oxidized carbides surrounding nitrides are seen

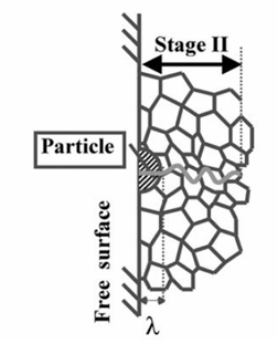

Figure 8 : Schematic representation of the fracture mechanisms for crack initiation from a surface particle [11]

3.3.2. Stage I crack initiation on large grains via persistent slip bands (PSB)

For the larger grain size material 1, the fatigue crack initiation corresponded to typical Stage I crack initiation along persistent slip bands as shown in Figure 9 for two specimens. The stage I crack initiation takes place over several grains, it occurs from the larger grains of material 1. This type of crack initiation was already observed in a previous study [9, 11] for larger mean grain size material, about 50µm.

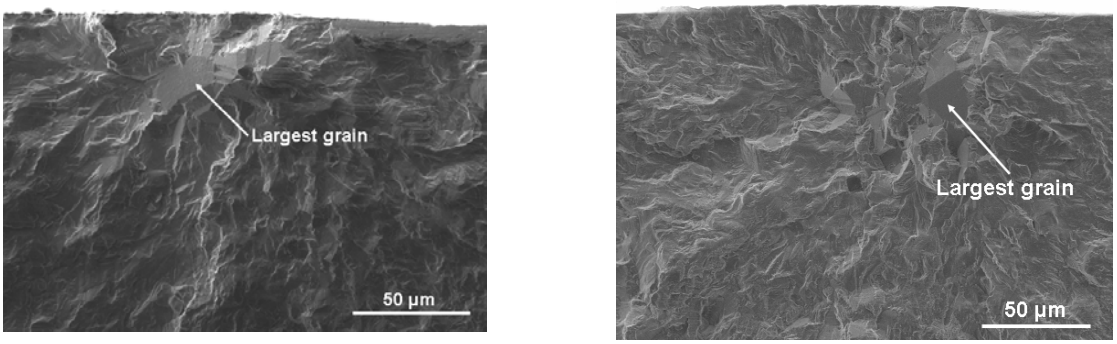

Figure 9 : Fatigue crack initiation sites on microstructure 1 with the biggest mean grains size (11 µm) : Stage I crack initiation across an area of several grains of (a) 70µm of diameter and (b) 150µm of diameter

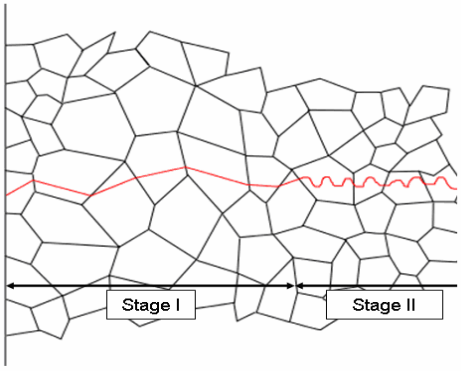

Figure 10 : Schematic representation of the fatigue crack initiation and propagation mechanisms for stage I initiation (for the material with larger grains in the present study)

A probabilistic life model was described by F. Alexandre [11] for this mechanism. The number of crack initiation cycles has been assessed using a Tanaka-Mura [16] type formulation with a modification to account for grain size effect.

$$N_i = \frac{1}{d}\frac{A_{StageI}}{(\Delta\varepsilon_p)^2} \quad (1)$$

where N_i is the number of cycles to initiation, d is the grain size (here, 7µm), $\Delta\varepsilon_p$ is the strain plastic amplitude (in our study, the macroscopic plastic strain is almost equal to zero), and A_{stageI} a constant depending on temperature. This model accounting for grain size effect is consistent with the findings of our study because crack initiation occurs on the largest grains for the material with the larger grains.

This stage I crack initiation is known to be sensitive to the size of the γ'' precipitates [17]. Indeed the γ'' precipitates influence the homogenization on the slip bands. Reducing the risk of crack initiation via PSBs [18].When the grain size is small, the size of the γ'' precipitates increases and the slip bands are more homogeneously distributed in the grains. So this theory may explain why stage I crack initiation occurs on the biggest grain of the material. The dislocation structure and the precipitate size have an effect on the fatigue life [19].

3.3.3. Internal crack initiation on particles leading to a fish-eye crack

This last mechanism is observed in material 2 with smaller grains; crack initiation occurs on an internal particle (nitrides) leading to a fish-eye crack. The mechanism was widely observed for other materials, like in steels for very cycle fatigue [20, 21]. Only a semi-quantitative discussion of crack initiation and propagation steps is presented here.

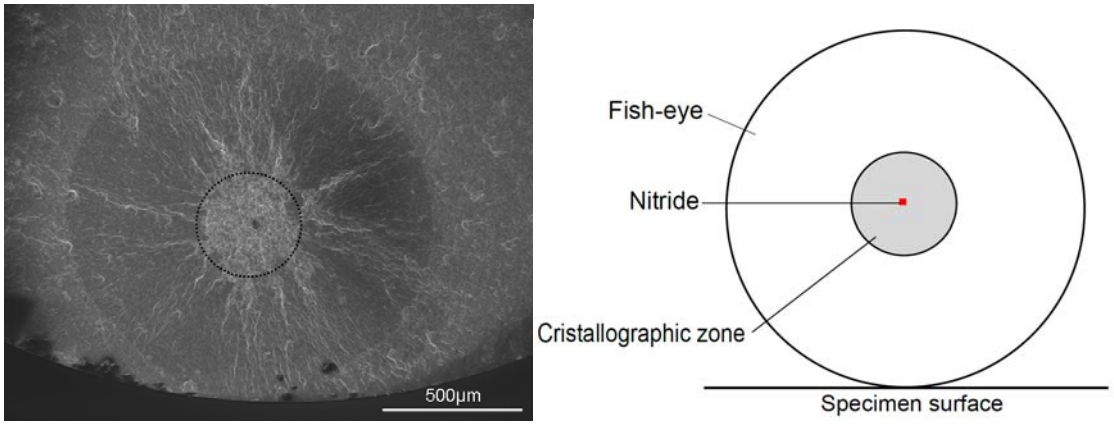

Figure 11 : SEM micrography of a fish-eye crack with a dark nitride particle in its centre for the small grain material 2 and the schematic representation

SEM observations (Figure 11) show an example of a fish-eye pattern formed on the fracture surface and the nitride at the centre of the fish eye. The difference of contrast between the three zones observed on the fracture surface suggests different crack growth mechanisms. At the centre of the fish-eye mark, a bright-facet area was found around the inclusion at the fracture origin as shown in Figure 12. The bright-facet area reveals a very rough topology compared to the area inside the fish-eye.

The propagation mechanism can be classified in five steps:

I. fracture of the large nitride during loading (or during forging)
II. Near threshold micropropagation with crystallographic character, under vacuum
III. vacuum stage II propagation (few striations),
IV. Air propagation with marked striations when the crack reaches specimen surface,
V. final ductile fracture

All these steps will be studied to gather elements to better understand the contribution of the

fracture phenomena on fatigue life.

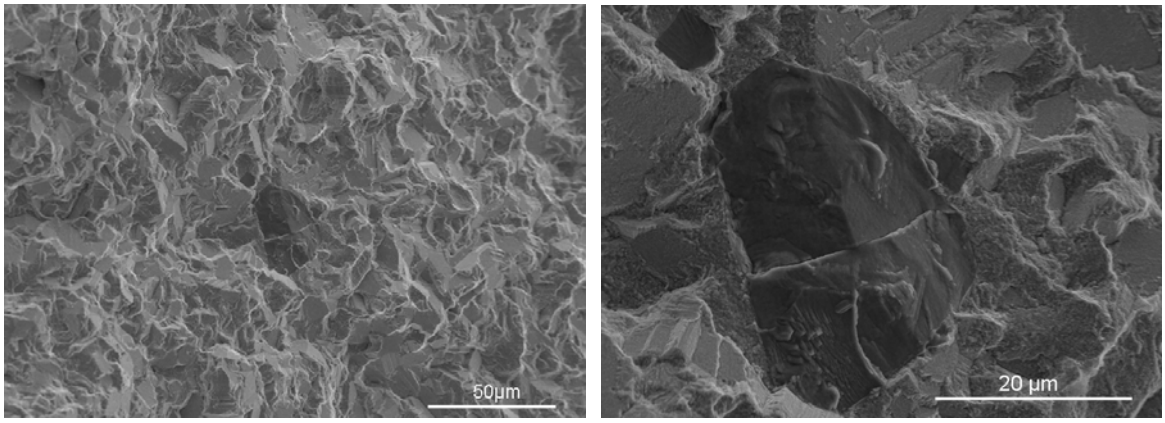

Figure 12 : SEM micrograph showing a zoom in the centre of the fish-eye crack displaying the fractured nitride particle and the rough micro-propagation with crystallographic character

I. Large nitride broken during loading (or during forging)

The nitride cracking is dependent on the particle size and applied stress [9, 11]. As a consequence the distribution of the nitrides through the material plays a role on the fatigue life of a structure. The crack initiation always occurred on the largest nitrides for the present study when comparing according to surface characterization of the nitrides distribution realised (Table 3).

II. Vacuum near threshold micropropagation with crystallographic character

The question is if a cracked nitride leads to crack propagation from the first load cycle onwards. If the value of stress intensity factor generated by the cracked nitride is superior to the threshold value this will be the case. Based on the size of the particles found in the crack initiation site, the initial stress intensity factor range, $\Delta K_{ini,}$ can calculated for a penny shaped crack in a cylinder using the following formula [22]:

$$\Delta K_{ini,inclusion} = 0{,}5\,\sigma_a\,\sqrt{\pi\sqrt{area_{inclusion}}} \qquad (2)$$

Where, σ_a is the stress amplitude. The initial stress intensity factor calculated from a nitride size is between 4MPa√m and 6MPa√m for different specimens displaying internal crack initiation. According to Lawless and King's studies [23, 24], the stress intensity threshold in air for 718 DA, at 538°C and 550°C respectively, is about 8MPa√m. At 427°C in air [19] the threshold for a fine microstructure varies between 5MPa√m and 9MPa√m depending of the heat treatment and the stress ratio. This threshold decreases when the grain size decreases [19, 23]. These values have been found for crack propagation in air; the initiation of the internal fish eye crack occurs, however, in vacuum. Few studies about propagation threshold were performed in vacuum. In [25] the threshold seems to be closed from the one in air when extrapolating the given curve. Material 2 of this study has a small mean grain size (about 7µm) which can reduce the propagation threshold. In addition the residual stress around the particle may be in tension and lead to an effective stress intensity factor which is higher than the one calculated here which would facilitate the propagation.

Furthermore most the threshold values given in the literature have been obtained for long cracks. However, for the fish eye crack initiation, the initial crack is the cracked nitride which is a short crack. It may be assumed that due to the short crack behavior crack progression may occur below threshold values obtained for long cracks [26].

The last parameter which can influence the initial stress intensity factor is the shape of the particle. The corners of the cubic nitrides may generate a stress intensity factor that is superior to the one obtained by the equation (2) for a penny shaped crack

The propagation speed and consequently the fatigue life of this step is certainly low because of the

roughness of the crystallographic surface [1, 13]

III. Vacuum stage II propagation (little striations)

The second area inside the fish-eye presents a classic stage II fracture surface, but the striations are not marked. This can be explained by the fact that this propagation step still occurs in vacuum [13]. Utilisation of Pedron's data [25] is certainly suitable in this step of the propagation. This step propagation stops when the crack reaches the specimen surface.

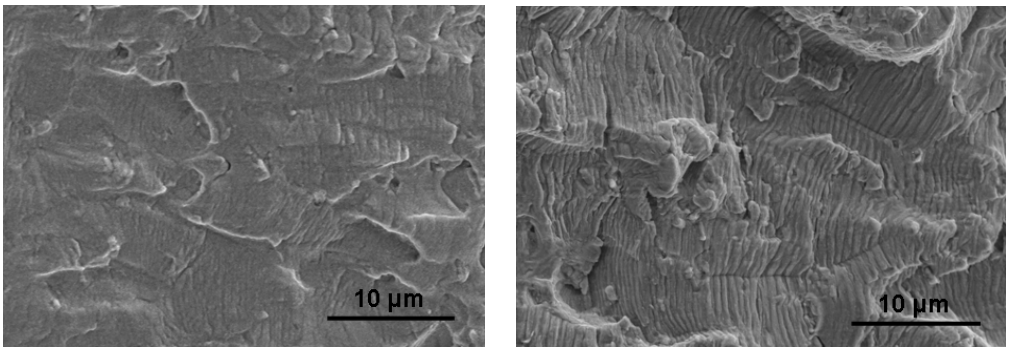

Figure 13 : SEM fractography of the stage II fatigue a) vacuum crack propagation in the fish eye b) air crack propagation beyond the fish-eye.

IV. Crack reaches specimen surface air propagation with marked striations

When the fish-eye crack reaches the specimen surface, the ligament between the penny-shaped fish-eye crack and the specimen surface will break very quickly due to the high local stress intensity factor.

In this step the surface crack can approximately be considered as semi-elliptical. The propagation occurs in air:

$$K = \sigma\sqrt{\pi d}\ F_I \quad (3)$$

Where σ is applied stress, *d* the crack depth from the surface and F_I the correction factor depending on the geometry of the specimen and crack. Values of this factor F_I can be found in handbooks [22]. The last step on the fracture mode corresponds to final ductile fracture.

In conclusion, 3 different crack initiation scenarios have been identified for Inconel 718. The likelihood of the occurrence of each of these scenarios depends on the microstructural heterogeneities, such as e.g. grain size distributions, particle size distributions and their spatial distributions. The link between the probability to encounter each crack initiation scenario and the total fatigue life of the specimens is schematically sketched in **Figure 14**. Further analysis of the resulting distributions in fatigue life is under progress.

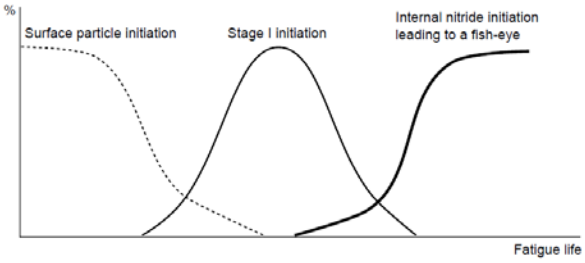

Figure 14 : Schematic representation of the relationship between probability to encounter each crack initiation scenario function with the total fatigue life of the specimen for a specific loading value (the relative position of the stage I initiation curve and the internal nitride initiation curve is dependent of a scale effect. These curves can be translated.)

Conclusions

The differences in fatigue life behavior in Inconel 718DA are studied here for two different microstructures. In both microstructures of the present study, the average grain size is smaller than the particle (nitrides) size and nevertheless crack initiation sites are different. In the larger (10μm) grain size material, stage I crystallographic cracking at or near the surface is initiated on the large grains of the material located at the free surface and having a diameter about 30 μm. In small (7μm) grain size material, crack initiation occurs preferentially on internal TiN particles followed by crack propagation with crystallographic character and subsequent Stage II crack propagation. A fish-eye crack is formed. The particles initiating the internal fatigue cracks are substantively larger than the largest particles observed on cut section from microstructural analyses. The internal crack occurs on nitrides of a mean diameter of 30μm. The different stages of the fish eye cracks are identified with: I. fracture of the large nitride during loading (or during forging), II. vacuum near threshold micropropagation with crystallographic character, III.vacuum stage II propagation (few striations), IV.crack reaches the specimen free surface, and propagation in air with marked striations and V.final ductile fracture. These crack progression stages are discussed using data from the literature to gather elements for quantitative assessment of the contribution of each crack progression step to the total specimen lifetime.

Acknowledgements

Snecma, Safran group, is gratefully acknowledged for financial support and material provision.

References

[1] C. Bathias, A. Pineau, Fatigue des Matériaux et des Structures 3, Hermes science publication, (2009).

[2] D. F. Paulinis, J.J. Schirra, Alloy 718 at Pratt & Whitney – Historical perspective and future challenges, Superalloys 718, 625, 706 and derivatives, ed. by E. E. Loria, TMS, (2001).

[3] R. L. Saha, K. Gopinath, K. K. Sharma and M. Srinivas, Low cycle fatigue behaviour of alloy 718 disc forging at elevated temperatures, Superalloys 718, 625, 706 and derivatives, ed. by E. E. Loria, TMS, (2001).

[4] W. L. Mills and C. M. Brown, Fatigue fracture surface morphology for alloy 718, Superalloys 718, 625, 706 and derivatives, ed. by E. E. Loria, TMS, (2001).

[5] J. Warren, D.Y. Wei, The cyclic fatigue behaviour of direct aged 718 at 149, 315, 454 and 538 °C, Materials Science and Engineering A 428, 106-115, (2006).

[6] S. P. Lynch, T. C. Radtke, B. J. Wicks and R. T. Byrnes, Fatigue crack growth in nickel-based superalloys at 500-700°C. II: Direct aged alloy 718, Fatigue Fract. Engng Mater. Struct. Vol. 17, No. 3, pp. 313-325, (1994).

[7] S. Deyber, F. Alexandre, J. Vaissaud and A. Pineau, Probabilistic life of DA718 for aircraft engine disks, Superalloys 718, 625, 706 and derivatives, ed. by E. E. Loria, TMS, (2005).

[8] M. Stoschka, M. Stockinger, H.Maderbacher and M. Riedler, A closed concept to associate the hot-forging process controlled microstructure with fatigue life, Proceedings Superalloys 2012, TMS, (2012).

[9] F. Alexandre, Probabilistic and microstructural aspect of fatigue crack initiation in IN718, PhD thesis, Ecole des mines de Paris, (2004).

[10] V. Zerrouki, Inconel 718 et tenue en fatigue oligocyclique. Influence de la microstructure et prédiction de la durée de vie, Mémoire de DRT Génie des Matériaux, université EVRY, (2000)

[11] F. Alexandre, S. Deyber, A. Pineau, Modelling the optimum grain size on the low cycle fatigue of a Ni based seperalloy in the presence of two possible crack initiation sites, Scripta Materialia, 50, pp. 25-30, (2004),.

[12] Y. Desvallèes, M. Bouzidi, F. Bois, N. Beaude, Delta phase in Inconel 718 : Mechanical

properties and forging process requirements, Superalloys 718, 625, 706 and various derivatives, (1994).
[13] S. Suresh, Fatigue of Materials Second Edition, Cambridge University Press, (1998).
[14] X. Huang et Al. Experimental investigations on microcrack initiation process in nickel-based superalloy DAGH4169. Int J Fatigue (2011).
[15] T. Connolley, P. A. S. Reed, J. M. Starink, Short crack initiation and growth at 600°C in notched specimens of Inconel 718, Materials Science and Engineering, A340 1-2, pp. 139-154, (2003).
[16] K. Tanaka and T. Mura, A dislocation model for fatigue crack initiation, journal of Applied Machanics, Vol.48, pp. 97-103, (1981),
[17] Effect of Direct Aging on the microstructure and the mechanical properties of Alloy 718 A.Devaux, L.Nazé, A.Organista, J.Y.Guédou, P. Héritier, In preparation.
[18] L. L. Li, P. Zhang, Z. J. Zhang, Z. F. Zhang, Effect of crystallographic orientation and grain boundary character on fatigue cracking behaviors of coaxial copper bicrystals, Acta Materialia 61, pp. 425-438, (2013).
[19] D. D. Krueger, Stephen D. Antolovich, and R. H. Van Stone, Effects of grain size and precipitate size on the fatigue crack growth behaviour of alloy 718 at 427°C, Metallurgical transactions A, Vol.18A, (1987)
[20] K. Shiozawa and L. Lu, Very high-cycle fatigue behaviour of shot-penned high-carbon-chromium bearing steel, Fatigue Fract Engng Mater Struct 25, pp. 813-822, (2002)
[21] T. Sakai, Y. Sato and N. Oguma, Characteristic S-N properties of high-carbon-chromium-bearing steel under axial loading in long-life fatigue, Fatigue Fract Engng Mater Struct 25, pp. 765-773, (2002).
[22] Y. Murakami, S. Kodoma and S. Konuma, Quantitative evaluation of effects of non-metallic inclusions on fatigue strength of high strength steel. Trans. JSME 54A, pp. 688-695, (1988)
[23] Bernard H. Lawless and A. W. Dix, Effect of processing/microstructure on threshold fatigue crack growth behaviour of alloy 718 forging, Superalloys 718, 625, 706 and various derivatives, (2001).
[24] J. E. King, Fatigue crack propagation in nikel-base superalloys – effects of the microstructure, load ratio and temperature, Materials science and technology, Vol.3, (1987).
[25] J. P. Pédron, A. Pineau, the effect of the microstructure and environment on the crack growth behaviour of inconel 718 alloy at 650°C under fatigue, creep and combined loading, Materials science and engineering, 56, pp. 143-156, (1982).
[26] A. Pineau, Short crack behavior in relation to three-dimensional aspects and crack closure effect, Small Fatigue Cracks. A publication of the Metallurgical Society, Inc. Warrendale, PA, (1986).

Effect of Ultrasonic Nanocrystal Surface Modification to the Fatigue Properties of S45C with Different Surface Hardness

Bo Wu[1,2], Jianxun Zhang[1], Young-Shik Pyoun[3], Ri-ichi Murakami[2*]

[1] State key laboratory for mechanical behavior of materials, Xian Jiaotong University, Xian 710049, People's Republic of China
[2] Department of Mechanical Engineering, The University of Tokushima, 2-1 Minami-josanjima-cho, Tokushima, Japan
[3] Institute for Manufacturing Systems Technology, Sun Moon University, Asan, Choongnam, Republic of Korea
* Corresponding author: murakami@me.tokushima-u.ac.jp

Abstract The Ultrasonic nanocrystal surface modification (UNSM) was employed to enhance the fatigue strength of S45C steel with different pre-plasma nitriding (un-nitrided, nitriding 8 h and 48 h) by improving the surface roughness and producing nanocrystalline on the sample surface. The parameters of UNSM were two different strike numbers, 34000 mm^{-2} and 68000 mm^{-2}. Different experimental processes including microstructure observation, microhardness, roughness and X-ray diffraction measurements have been performed to characterize the treated surface of specimens. The results shown that after UNSM treatment an improvement can be obtained for surface microhardness, surface roughness, and compressive residual stress. Under the same UNSM conditions more surface defects can be produced with the increasing strike number and with increase of surface hardness the effect to surface roughness decreased. For the higher hardness surface sample, smaller nanocrystalline can be obtained compared with other sample through XRD results. Higher compressive residual stress was found for un-nitrided S45C steel with increasing strike number, but a decrease was found for the nitriding sample. Rotating bending fatigue test was carried out to evaluate the effect UNSM to the fatigue strength. An improvement of fatigue strength for un-nitrided and nitriding 8 h sample was found and the surface defects were the main reason inducing the fatigue failure. However, for N48 samples, no improvement of fatigue strength as little effect of UNSM on the sub-surface crack induced by inclusion.

Keywords UNSM, Plasma nitriding, Surface Hardening, Fatigue

1. Introduction

Ultrasonic nanocrystal surface modification (UNSM), as one of severe surface plastic deformation (S^2PD) methods to improve material surface properties, has been used on many materials treatments [1-5]. The properties of wear [4, 5], fatigue [1-3] of materials can be improved as the reason of high surface hardness and compressive residual stress produced by the UNSM treatment. In the study of Cao [2], with the increase of strike number higher fatigue strength can be obtain and small fatigue crack can be restrained as the compressive residual stress produced by UNSM treatment. Suh's study [3] shows that the grain in the top surface zone can be refined into nano-size and the depth of gradual grain refined layer about 100 μm can be produced by UNSM treatment with the applied static force of 100 N. Amanov [5] has found that high impact load can get a lower friction and well wear characteristics and smaller nano-grain size can be obtained at the same time. So we can see that the processing parameters (the applied static force, the strike number per mm^{-2}, the size of tip ball) can be controlled accurately and all of these parameters have a close connection with the characters of specimen's surface zone after the UNSM treatment. Also the structure of the material receiving surface treatment plays an important role for the formation of microstructure in the surface processing layer. Zhou [6] showed that the SMAT steel sample has a thicker refined layer (with grain size < 100 nm) compared with pure Fe. Cho [7] and Lee [8] found that with more hard

phase smaller sized grain can be induced due to the easier formation of dislocation around the hard phase.

Although a few studies have been conducted on the UNSM treatment with many kinds of materials, few studies about the UNSMed sample with different surface hardness were found. In this paper, the specimens of S45C steel with different surface hardness introduced by pre-surface treatments were processed by the UNSM treatment under the same conditions. The surface morphology, microstructure, residual stress, microhardness and fatigue properties were investigated and the effect of different pre-hardening surface to the UNSM treatment on the surface properties was discussed.

2. Experiment

2.1. Materials preparation

The material used was a medium-carbon steel S45C shaft with a chemical composition (in wt.%) of 0.45%C, 0.15%~0.35%Si, 0.6~0.9%Mn, ≤0.03%P, ≤0.035%S, ≤0.3%Cu, ≤0.2%Ni, and ≤0.2%Cr, balanced with Fe. To test the fatigue properties, the specimens were machined to the dimensions shown in Fig. 1, resulting in a stress concentration factor, K_t, of approximately 1.08. The specimens were first quenched (austenitized, 1113 K, 150 min; oil quenched, room temperature, 60 HRC) and tempered (tempered, 773 K, 270 min, 31 HRC). The specimens were then polished by using sandpaper from grade 400 to grade 2000. Subsequently, the specimens were nitrided in a mixture gas (40%N_2-60%H_2) and at 400 Pa. Two nitriding time durations, 8 h (N8) and 48 h (N48), were used to obtain different nitriding properties.

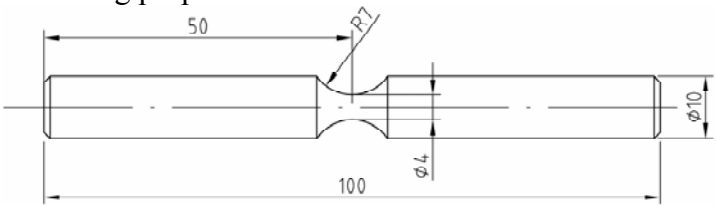

Figure 1. Dimension of the test specimen for S45C steel.

2.2. Surface treatment

After plasma nitriding, the surface layer (approximately 12 μm) was removed to avoid the effect of the nitriding layer on the subsequent UNSM treatment. The UNSM technique details have been previously published. An ultrasonic generator (a 30 μm amplitude and 20 kHz) and air compressor devices were used to produce a static force with a dynamic load to strike the material surface with a tungsten carbide (WC) ball (the diameter: 2.4 mm). Accurate surface strike numbers can be obtained by calculating the speed of the surface being treated when the specimen is rotated by a turning lathe. Thus, it is easy to process the material surface and control the static loads and strike numbers. Throughout the process, cold liquid was used to avoid high specimen surface temperatures.

Table 1. Specimen treatment conditions

Specimens	Untreated	U1	U2	N8	N8U1	N8U2	N48	N48U1	N48U2
34000 mm^{-2}	–	Y	–	–	Y	–	–	Y	–
68000 mm^{-2}	–	–	Y	–	–	Y	–	–	Y

To study the effect of strike number on the fatigue properties of the nitrided sample, two treating

parameters were selected: (U1) strike number of 34000 mm^{-2}; static load of 50 N; revolution rate of 37 rpm, feed rate of 0.07 mm/rev; and (U2) strike number of 68000 mm^{-2}; static load of 50 N; revolution rate of 18.5 rpm, feed rate of 0.07 mm/rev. The specimen processing conditions are listed in Table 1.

2.3. Materials characterization

To examine the grain-refined layer and the nitriding layer, the cross-section of the all specimens were observed by an optical microscope (Olympus BN2). Before test, the samples were mechanically polished with the sandpapers (from grade 150 to grade 2000) and then a polish cloth with a liquid suspension of alumina. The saturated picric acid solution was used to etch the specimens in this test.

X-ray diffraction (XRD) was employed to measure residual stress of all sample varieties, utilizing Cr-Kα radiation for a longer wavelength and deeper penetrating power. The test was carried out on a Rigaku XG-4026A1 using the classical sin2ψ method. Cu-Kα (on a Rigaku Rint-2000) was used to analyze the state of the surface layer nanostructure and the compound layer of nitrided samples to a depth of approximately 5 μm.

The microhardness of the plastic deformation zone and nitriding layer was measured on a micro-Vickers hardness tester (MVK-E3, Akashi). The parameters used in the microhardness test were 50 gf and a duration 15 s.

The surface roughness of the S45C specimens before and after the UNSM treatment was tested on a contact surface profiler (ULVAC DEKTAK3).

To compare the fatigue properties of S45C with the two process methods, a rotating bending fatigue test was carried out on a dual-spindle rotating bending fatigue test machine under atmospheric conditions. The rotating frequency used was 52.5 Hz, and the stress ratio was -1.

The failure fracturing of the samples was observed using scanning electron microscopy (SEM) (S-4700, Hitachi). Energy-dispersive X-ray spectroscopy (EDX), with the same machine, was used to detect the composition of any inclusions that induced the sub-surface fish-eye crack initiation.

3. Results and discussion

The surface morphology of before and after UNSMed specimens was shown in Figure 2. It is obvious that UNSMed processing marks were produced on the specimen surface. As the processing principle, these marks show parallel and as the increase of processing number these marks become more obvious. For the parallel marks, the distance between each other was approximately 70 μm. This value equals to the processing parameter of the feed rate which is 0.07 mm/rev. During surface treatment, only the surface under the center of the tip can receive most severe plastic deformation as the reason of ball shape of the process tip. Comparing the surface morphology results of UNSM samples with different pre-surface hardness, it can be seen that for the softest surface sample (un-treated) the UNSM process marks show the most obvious after the process of 68000 mm^{-2}. The surface roughness was test and shown in Figure 3. It can be found that the surface roughness (Ra) for the all UNSMed sample has an improvement and even there are a few of obvious UNSMed process marks on the UNSMed sample surface. As the increase of strike number, a little growth can be observed with the surface roughness. Combined with results of surface morphology it is easy to find that the UNSMed process marks produced during surface process were the main reason.

Though from magnified surface morphology results the region between two UNSMed marks was smoother the process of more strike number, the UNSMed marks mainly lead to the worse of the surface roughness. For the nitriding samples, the UNSMed marks show unobvious as the reason of nitrides within top surface region reducing the plastic deformation of sample surface. Compared with the soft un-nitriding sample, better surface roughness can be obtained for the sample surface with higher hardness. It also means fewer surface defects produced on the nitriding sample surface.

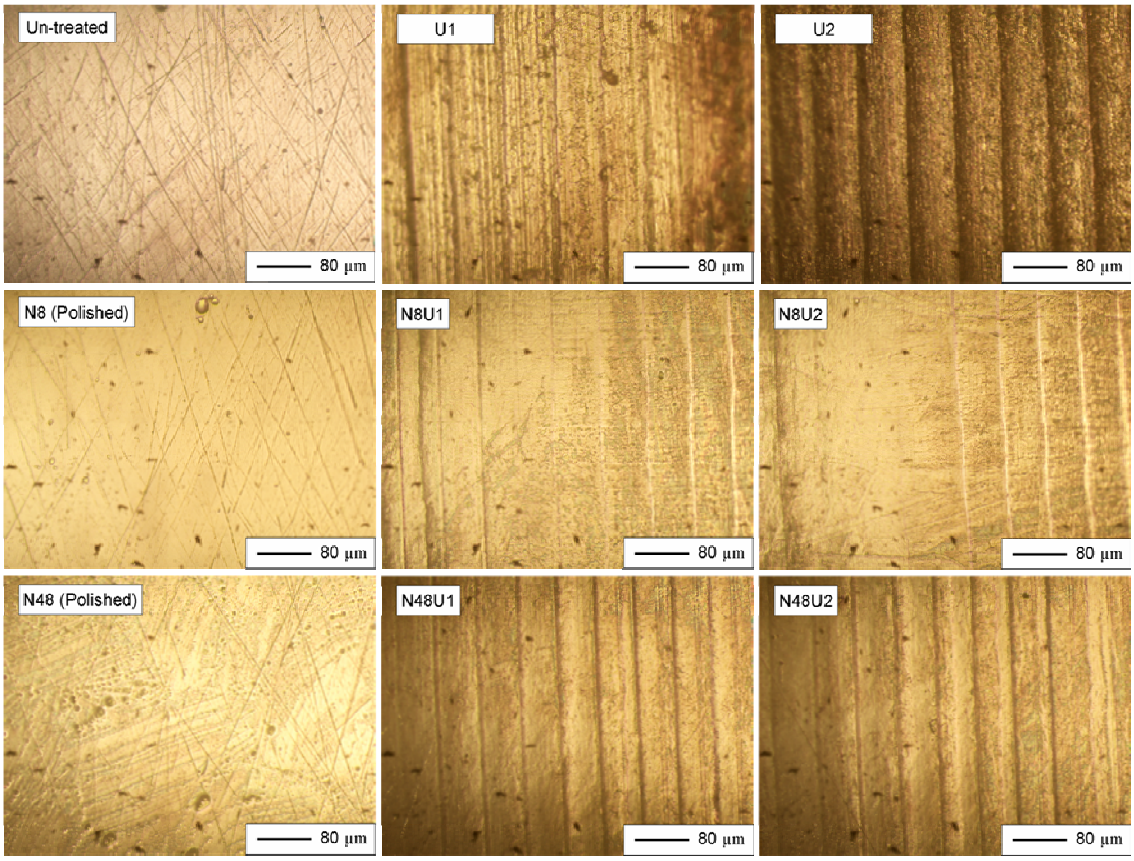

Figure 2. The surface morphology of specimens before and after UNSM.

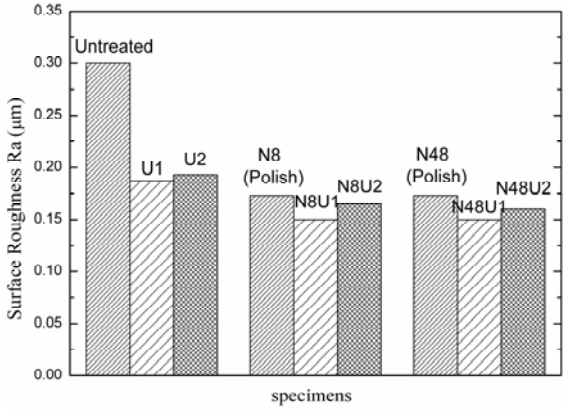

Figure 3. The surface roughness of specimens before and after UNSM.

The microstructures of the samples before and after UNSM treatment were shown in Figure 4. Through the other studies [3, 6] it can be seen that a gradual change microstructure from nano-sized grain in the sample top surface to the grain size of base material can be produced by the S^2PD treatment. With picric acid solution the grain boundaries can be etched easily. For the un-UNSMed samples the grain can be distinguished from top surface to interior and no difference between each

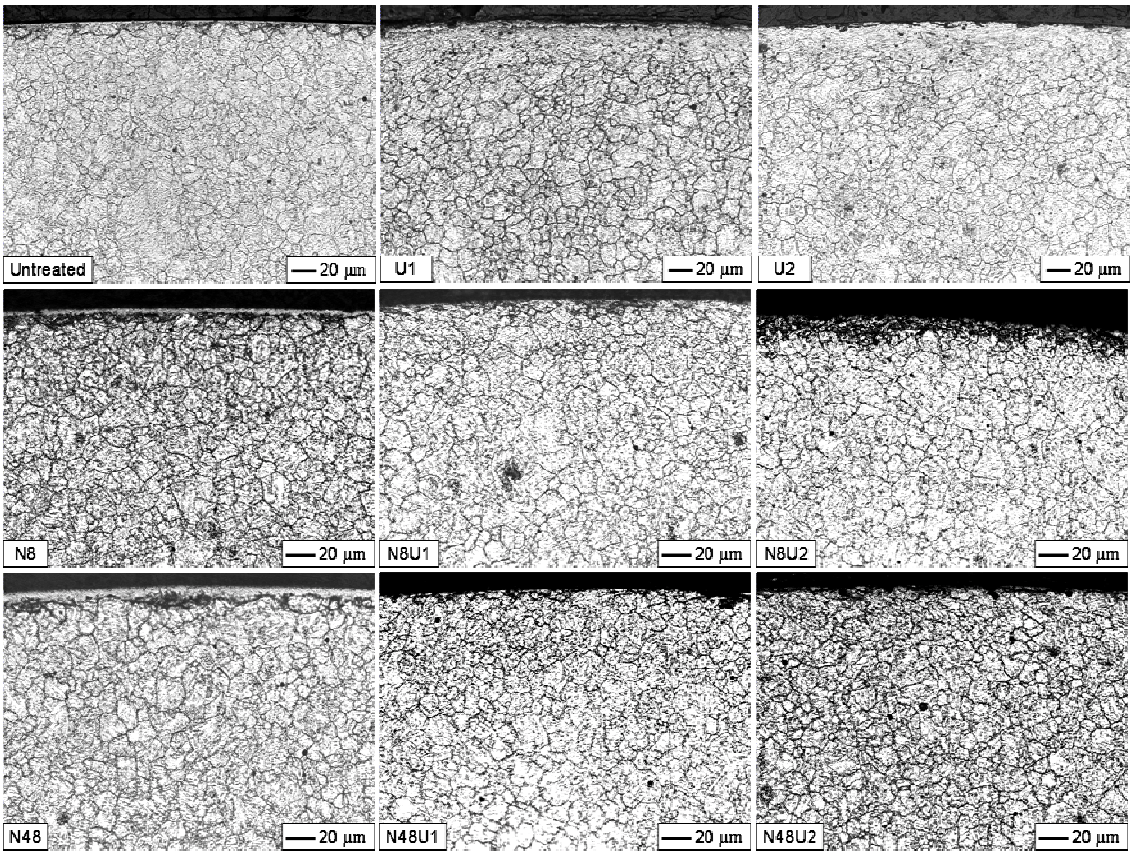

Figure 4. The microstructure of cross-section of specimens before and after UNSM.

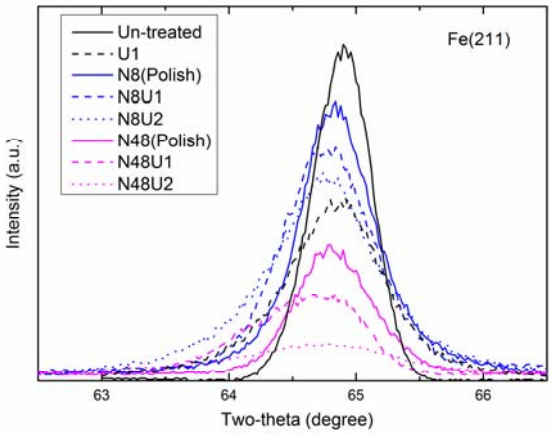

Figure 5. The XRD pattern of Fe (211) diffraction angles for the specimens before and after UNSM.

other can be observed. For the nitriding sample, a compound layer can be found on the nitriding sample surface (approximately 3 μm for N8 and approximately 8 μm for N48 sample). All the UNSMed samples can be found a grain refined layer at the edges of the cross-section. The refined layers are obvious for U1 and U2 samples approximately 40 μm for U1 specimens and approximately 70 μm for U2 specimens. However for the pre-nitriding samples, this layer is difficult to be distinguished and only some deformed grains can be found and the results show that the deformed layer induced by UNSM decreases with the increase of pre-sample surface hardness. The XRD was employed to scan the sample surface and the Fe (211) diffraction angles were scanned slowly and shown in Figure 5. Analyzing the XRD results and we can find that the Bragg diffraction peaks for all samples can be broadened by the UNSM. That means a grain refinement was induced on the sample surface according relation between grain size and the full width at half

maximum (FWHM). With FWHM results of all samples it can be found that though the nitrides within the sample surface zone and the XRD intensity of all un-UNSMed samples is different, the values of FWHM are close. And the degrees of the change are different. It is easy to find that the N48 samples were broadened easily compared with the un-treated and N8 samples. In many references [6-8], the hard phase can enhance the ability of the refinement of ferrite as different mechanism. So we can see that with the growth of nitrides concentration, harder sample surface can be obtained. More easy grain refinement can be found the harder sample, but thinner grain refined layer would be obtained as the reason of the surface with high hardness hindering the transfer of the plastic deformation energy produced by UNSM.

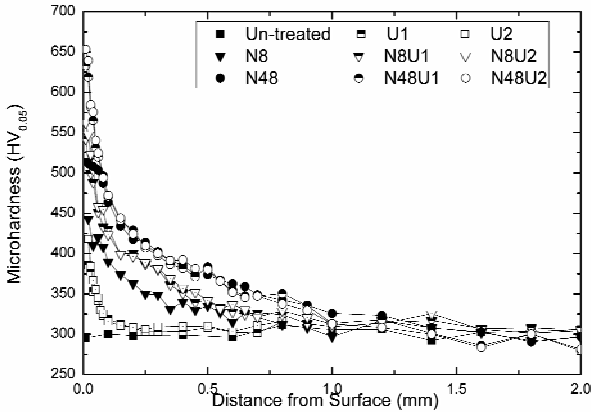

Figure 6. The microhardness of cross-section of specimens before and after UNSM.

The microhardness results of the all samples along the cross-section were shown in Figure 6. After UNSM treatment not only was surface hardness improved but also a gradual enhancement in the sub-surface region also can be observed. For the UNSM samples, the microhardness in the top nanostructured layer is 372 Hv for U1 sample and 418 Hv for U2 sample. For the N8 specimens, the surface hardness increased from 443 HV to approximately 540 HV after U1 treatment and to 560 HV after U2 treatment. These values were even higher than that of the N48 samples without UNSM treatment. For the N48 specimens, the surface hardness increased from 510 HV to 630 HV after U1 treatment and to 650 HV after U2 treatment. For all UNSMed samples the top surface hardness and the depths of effect increase with more strike number. It also can be found that the depths of effect regions are different with the change of samples. After the UNSM treatment, the materials surface was subjected to a severe plastic deformation induce a grain refinement. With the UNSM treatment, increased number of grain boundaries as the refined grains and generation of high density dislocation with strain hardening restrict the dislocation motion and render the material harder and stronger. According the microstructure results, we can also infer that the concentration of nitrides has a close connection with the hardening depth. Zhou [6] has found that compared with the strain-induced grain refinement in the pure Fe under the same SMAT processing, not only was refinement of ferrite much facilitated by the presence of dispersed cementite particles but also a thicker nanostructured layer can be obtained. The hard phase has the ability of transfer energy during S^2PD treatment. For soft surface materials, as the amplitude of 30 μm during UNSM processing energy of UNSM can not transfer too far as the absorption of energy by the top surface to have a plastic deformation. With the increase of nitrides concentration the hard phase of nitrides can transfer the energy to the deeper region. However when the surface hardness is too high, it is difficult to have a plastic deformation in the top surface and only induce a refinement of grains. So with just enough nitrides concentration, a deeper hardening layer can be produced.

The top surface residual stress was measured and shown in Figure 7. Before UNSM treatment un-treated and plasma nitriding samples all have a compressive residual stress on the surface

induced by QT (quenching and tempering) and nitriding process. After UNSM treatment the surface stress for all UNSMed samples was improved. However different trends with the increase of strike number can be observed for the UNSMed samples. For the un-treated sample, the surface residual stress increase from -217.4 MPa to -318 MPa with U1 and -395.1 MPa with U2 and it can be found that higher compressive residual stress can be obtained as the increase of UNSMed striking number. For the nitriding samples, the residual stress has a growth from -171.9 ~ -161.2 MPa (N8 and N48) to -925 MPa for N8 samples and -1089 MPa for N48 samples with U1 treatment. However a decrease (to -750 MPa for N8 samples and -778 MPa for N48 samples) was found with U2 treatment. This means that though with the growth of surface hardness higher compressive residual stress can be produced, a decrease was found as the increase striking number. This phenomenon is different from the U1, U2 results and other studies [2]. This may be the reason of the grain refinement of the nitrides in the surface zone inducing a relaxation of the surface stress.

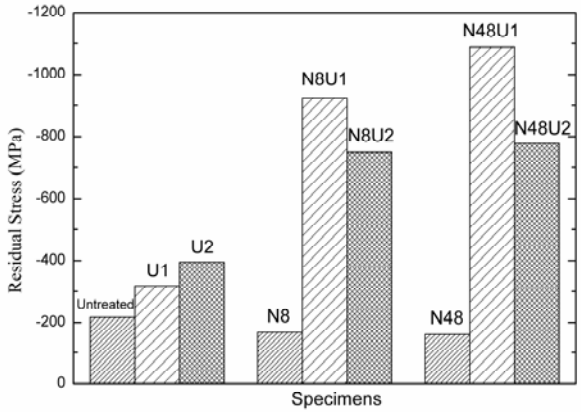

Figure 7. The residual stress on the surface of specimens before and after UNSM.

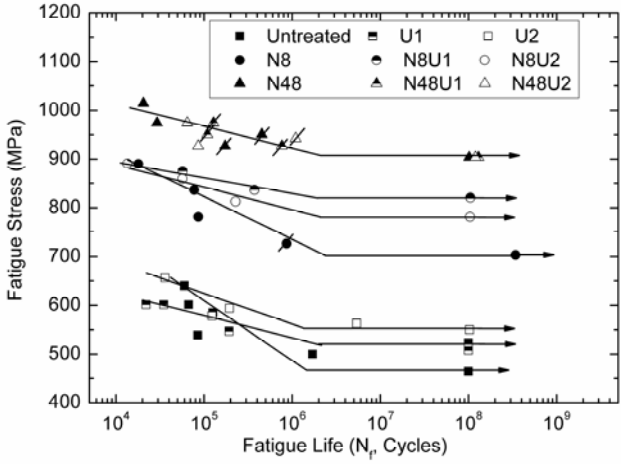

Figure 8. S-N curves of rotating-bending fatigue test

The fatigue test was employed on a rotating bending test machine and the S-N results are shown in Figure 8. The results show that after UNSM treatment the fatigue strength was enhanced for un-treated and N8 samples, but no improvement for the N48 samples. Compared with un-treated sample, more enhancements were obtained for N8 samples. At the same time the improvements of UNSMed samples have a close connection with the value of surface residual stress. Foe ever un-treated or N8 samples, the fatigue strength has a linear relation with the surface residual stress and with the higher residual stress, higher fatigue strength can be obtained. So we can find that a higher fatigue limit of N8 sample can be obtained after U1 treatment than after U2 treatment. It shows opposite compared with un-treated sample after UNSM treatment. This means that though

harder surface can be obtained by U2 treatment, the fatigue strength mainly depends on the level of surface stress. For the N48 samples, U1 process also introduced a higher compressive residual stress but the sub-surface fatigue crack initiation induced by inclusions hinders the improvement of fatigue strength.

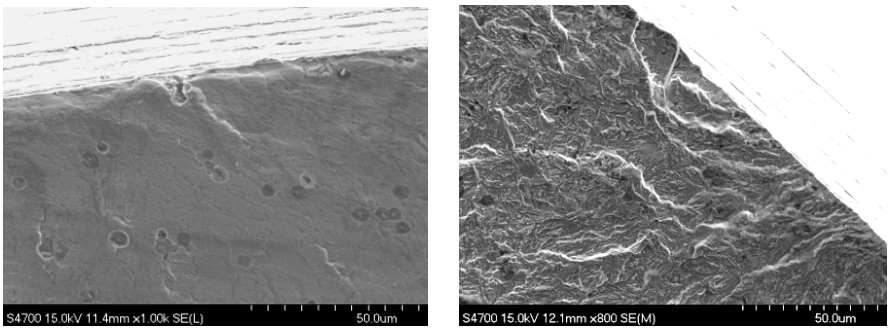

Figure 9. The fatigue crack initiating from surface defects (U2, 562MPa, $5.4x10^6$, left; N48U2, 974MPa, $6.46x10^4$, right)

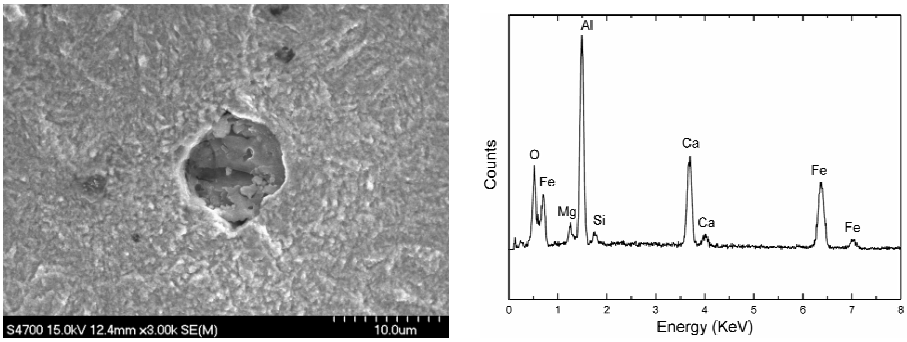

Figure 10. The sub-surface fatigue crack induced by inclusions (N48U1, 974.2MPa, $1.3x10^5$) (Left); EDX data on the inclusion.

The observations of the fatigue fractures were shown in Figure 9 and Figure 10. It obviously can be seen that the fatigue crack inducing the material's failure can be divided into two modes: one is the surface crack initiation induced by the persistent slip bands (PSBs) or surface defects; another is the sub-surface crack induced by the inclusions within materials. After plasma nitride, the surface of S45C steel can be enhanced effectively and the fatigue crack initiating from sample's surface becomes difficult. With the high cycle loading the inclusion within the sub-surface can induce a stress concentration and a fine granular area (FGA) (Figure 10, left), which was composed by the aluminum oxide, calcium oxide and magnesium oxide or other hard phases (Figure 10, right), was produced and expand to fracture. The mechanism of the formation of FGA is not clear and there are many theories explaining this phenomenon, for example, the theory of hydrogen diffusion, the dispersive decohesion of carbide and the grain refinement induced by stress concentration [9-11]. From the observations of fractures results, the UNSM treatment not only can improve the fatigue strength but also has an influence on the fatigue crack initiation. For the un-treated samples, the surface cracks transfer form surface crack induced by PSBs to the crack induced by the UNSM process marks (Figure 9, left) which we also can found in the surface morphology results. So we can also find that with increase of the test loading the fatigue life decreases as the reason of relaxation of residual stress and the stress concentration induced by the surface defects. For the nitriding samples, also were surface cracks induced by surface defects (Figure 9, right) found and the fatigue strength decreases with the increase of striking number (U2) as the reason of decrease of surface residual stress and more surface defects induced by the UNSM treatment after U2 process. We can also find more surface fatigue crack initiations for N48 samples with U1 treatment than U2

treatment. Combined with the results of surface roughness, it can be found that more surface defects can be introduced to the N48 samples' surface. So the fatigue strength is difficult to be enhanced as these defects inducing stress concentration easily. For the N48U1 samples, though high compressive residual stress and little defects were introduced, the inclusions within the sub-surface of samples still can form a fish-eye crack and hinder the improvement of fatigue strength. Also we found that as the high compressive residual stress induced by UNSM treatment the position of inclusions trend a deeper depth beneath the samples' surface [1]. With above results we can conclude that with the high loading during fatigue test the fatigue strength is more sensitive to the surface state of samples. At the same time, though high compress residual stress can be introduced by UNSM treatment, the sub-surface cracks induced by inclusions with materials are difficult to be hindered as the reason of limited depth of enhanced zone improved by UNSM treatment.

4. Conclusions

(1) With the increase of strike number, deeper UNSM processing marks can be introduced on the specimen surface; for the specimen with the higher surface hardness, little effect of UNSM to the surface roughness can be found.
(2) A gradual refined grain layer can be produced by the UNSM as multiple strikes to specimen surface; the thickness of the refined layer increases with the strike number and decreases as the growth of surface hardness; the top surface grains can be refined in to nano-size and for the sample with higher surface hardness grain refinement become easier.
(3) The surface hardness can be effectively improved by UNSM treatment and increases as the increasing strike number; N8 sample has a larger zone for the hardness increase as the effect of nitrides within sample.
(4) Higher compressive residual stress can be found for the nitriding specimens; increase of the residual stress can be obtained for un-nitriding samples as the increase of strike number; however opposite phenomenon was found for nitriding samples and residual stress decreases with the increasing strike number.
(5) The enhancement of fatigue strength mainly depends on the residual compressive stress in the surface zone produced by UNSM treatment; as the increase of fatigue strength the surface defects and sub-surface inclusions hinder the increase of fatigue strength definitely.

Acknowledgements

The authors thank Atsushi Onizawa of Neturen Company for assistance with plasma nitriding and DesignMecha Co., Ltd for assistance with UNSM. This study was supported by the Double Degree Program (DDP) of The University of Tokushima.

References

[1] B. Wu, P. Wang, Y.-S. Pyoun, J. Zhang, R.-i. Murakami, Effect of ultrasonic nanocrystal surface modification on the fatigue behaviors of plasma-nitrided S45C steel, Surface & Coatings Technology, 213 (2012) 271–277.
[2] X.J. Cao, Y.S. Pyoun, R. Murakami, Fatigue properties of a S45C steel subjected to ultrasonic nanocrystal surface modification, Applied Surface Science, 256 (2010) 6297-6303.
[3] C. Suh, G. Song, M. Suh, Y. Pyoun, Fatigue and mechanical characteristics of nano-structured tool steel by ultrasonic cold forging technology, Materials Science and Engineering: A, 443 (2007) 101-106.
[4] A. Amanov, I.S. Cho, Y.S. Pyoun, C.S. Lee, I.G. Park, Micro-dimpled surface by ultrasonic nanocrystal surface modification and its tribological effects, Wear, 286–287 (2012)

136–144.

[5] A. Amanov, O.V. Penkov, Y.-S. Pyun, D.-E. Kim, Effects of ultrasonic nanocrystalline surface modification on the tribological properties of AZ91D magnesium alloy, Tribology International, 54 (2012) 106-113.

[6] L. Zhou, G. Liu, X.L. Ma, K. Lu, Strain-induced refinement in a steel with spheroidal cementite subjected to surface mechanical attrition treatment, Acta Materialia, 56 (2008) 78–87.

[7] K.T. Cho, S. Yoo, K.M. Lim, H.S. Kim, W.B. Lee, Effect of Si content on surface hardening of Al–Si alloy by shot peening treatment, Journal of Alloys and Compounds, 509 (2011) S265-S270.

[8] W.B. Lee, K.T. Cho, K.H. Kim, K.I. Moon, Y. Lee, The effect of the cementite phase on the surface hardening of carbon steels by shot peening, Materials Science and Engineering: A, 527 (2010) 5852-5857.

[9] P. Grad, B. Reuscher, A. Brodyanski, M. Kopnarski, E. Kerscher, Mechanism of fatigue crack initiation and propagation in the very high cycle fatigue regime of high-strength steels, Scripta Materialia, 67 (2012) 838–841.

[10] K. Shiozawa, Y. Morii, S. Nishino, L.Lu, Subsurface crack initiation and propagation mechanism in high-strength steel in a very high cycle fatigue regime, International Journal of Fatigue, 28 (2006) 1521–1532.

[11] Y. Murakami, N.N. Yokoyama, J. Nagata, Mehhanism of fatigue failure in ultralong life regime, Fatigue and Fracture of Engineering Materials and Structures, 25 (2002) 735-746.

Research on Fatigue Damage and Crack Propagation of GH4133B Superalloy Used in Turbine Disk of Aero-engine

Rongguo Zhao[1,*], Dunhou Tan[1], Xiyan Luo[2], Hongchao Li[1], Junfei Li[1], Wei Li[1], Xuehui Liu[3]

[1] College of Civil Engineering and Mechanics, Xiangtan University, Xiangtan 411105, China
[2] College of Resources and Environmental Science, Chongqing University, Chongqing 401331, China
[3] Liyang Aero-Engine Corporation, Aviation Industry Corporation of China, Anshun 561102, China
* Corresponding author: zhaorongguo@163.com

Abstract The fatigue damage and fracture of GH4133B superalloy used in turbine disk of aero-engine are studied. Firstly, the fatigue limit is measured, and the relation between electric resistance change ratio and number of fatigue loading cycles is investigated for smooth samples. Then, the fatigue crack propagation tests are carried out at various stress ratios, and the fatigue crack propagation threshold values are measured for standard compact tension samples. The research results indicate that the theoretical fatigue limit agrees well with experimental one, the modified Chaboche model can predict the fatigue damage preciously, and the Paris formula considering fatigue threshold can describe the crack propagation behavior accurately. Finally, the crack propagation equations and loads are derived using the inverse deducing method based on the fractography of smaples. It is suggested that the inverse deduced equations can predict the crack propagation behavior, and the predict results can effectively prevent the occurrence of fatigue fracture.

Keywords Fatigue, Damage, Crack propagation, Fractrography, GH4133B superalloy

1. Introduction

In the fracture accidents of engineering components and structures, the fracture caused by fatigue accounted for about 70% to 80% of all the fracture accidents [1]. In the field of aviation industry, the damage tolerance design criterion has been introduced into the structural design of the aircraft and aero-engine, instead of the traditional minimum safe life design criterion [2, 3]. As far as the fatigue damage mechanism is concerned, from the point of view of damage mechanics, the process of crack growth in material from initiation to propagation to ultimate failure is a one of continuous damage evolution. The damage evolution equation is stated by the relationship between the change of damage variable and the number of loading cycles. Therefore, constructing a suitable damage evolution equation becomes a key issue of the damage tolerance design. Many damage theories for various metals and their alloys under different conditions had been devoloped, and these models were reviewed, and they were grouped into six categories: linear damage rules; nonlinear damage curve and two-stage linearization approaches; life curve modification methods; approaches based on crack growth concepts; continuum damage mechanics models; and energy-based theories [4]. In general, the elastic modulus, fatigue cycles, microhardness, interface shrinkage, as well as electric resistance, etc., can be used to describe the fatigue damage of material. For most of the metals and their alloys, the electric resistance change method can be adopted to charaterize the fatigue damage evolution, which has better accuracy and sensitivity [5–7].

Fatigue crack growth in metals and alloys is a process controlled by many variables, which includes both external factors such as temperature, frequency, loading rate, stress ratio, mean stress, and internal factors such as content, microstructure, and inclusion. GH4133B is a nickel-based superalloy. Such alloy is selected to manufacture components operated at high temperature, such as turbine disk of aero-engine, for its resistance to sensitization, adaquate high temperature tensile strength and creep resistance. Hu [8] investigated the creep-fatigue interaction and the effect of loading history on the creep-fatigue damage of GH4133B superalloy at 600ºC in three cases of loading as continuous cyclic loading (CF), prior fatigue followed by creep loading (F+C), and prior

creep followed by fatigue loading (C+F), and found that the creep-fatigue damage in the cases of CF and F+C was larger than unity, while that was smaller than unity at C+F. Luo [9] carried out a statistical analysis on the mechanical parameters of GH4133B superalloy at room temperature, and found that the three-parameter Weibull distribution was fit for the reliability assessment of this superalloy. Padula II [10] investigated the effect of grain size on high frequency fatigue crack propagation of nickel-based superalloys at various stress ratios. The results indicated that there is no effect of frequency on the fatigue behavior at ambient temperature. The threshold stress intensity for fatigue crack propagation decreases with decreasing grain size and with increasing stress ratio.
In this paper, the fatigue damage and fracture tests of GH4133B superalloy used in turbine disk of earo-engine are carried out at room temperature. The fatigue limit is measured for smooth samples at various stress amplitudes, and the fatigue crack growth rates are detected for standard compact tension samples under different stress ratios. A modified Chaboche model is applied to predict the accumulated damage of smooth samples of GH4133B superalloy at symmetrical cycle loading, and a Paris formula considering threshold stress intensity factor range is deduced to describe the fatigue crack growth behavior. The fracture surface morphologies of standard compact tension samples of GH4133B superalloy are investigated using scanning electron microscope, and the crack growth equations and loads are derived using the inverse deducing method.

2. Material and samples

The material used in this research is a nickel-based GH4133B superalloy with following chemical composition in % weight: C 0.06, Cr 19~22, Al 0.75~1.15, Ti 2.5~3.0, Fe 1.5, Nb 1.3~1.7, Mg 0.001~0.01, Zr 0.01~0.1, B 0.01, Ce 0.01, Mn 0.35, Si 0.65, P 0.015, S 0.007, Cu 0.07, Bi 0.0001, Sn 0.0012, Sb 0.0025, Pb 0.001, As 0.0025, and the balance nickel. The superalloy samples are machined from a turbine disk. The heat treatment process is as follows: 1080±10ºC, 8 hours, air cooling with 750ºC±10ºC, 16 hours air cooling. The samples for fatigue damage tests are machined in rod shape, as shown in Fig. 1. The samples for fatigue crack growth tests are machined in the shape of standard compact tension sample, as shown in Fig. 2.

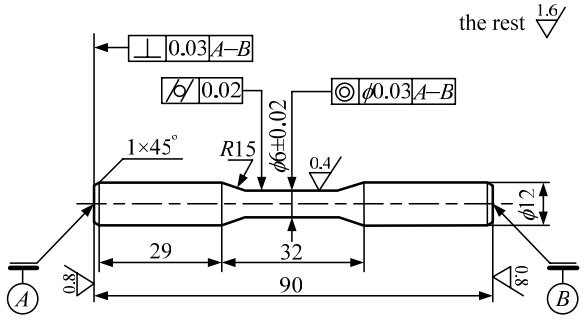

Figure 1. Dimensions of smooth sample (unit: mm)

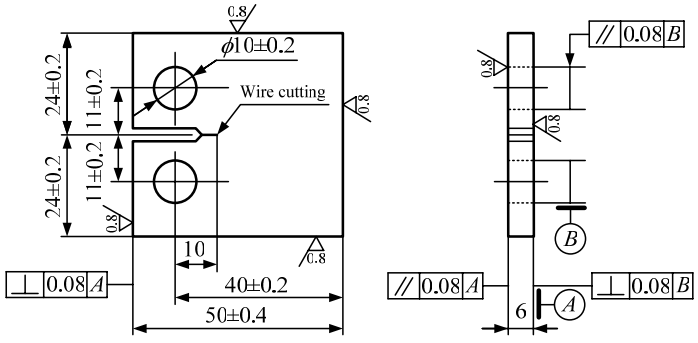

Figure 2. Dimensions of standard compact tension sample (unit: mm)

3. Fatigue life and fatigue damage analysis

3.1. Fatigue life test

At room temperature and atmospheric pressure, the fatigue tests for smooth samples of GH4133B superalloy are performed on a servo hydraulic test machine (CSS-280S-20) of ±20kN loading capacity. Under symmetrical cyclic loading condition (30 Hz sine wave, stress ratio R=–1), the fatigue life tests are carried out at various stress amplitudes. The fatigue limit is defined as 10^7 cycles. The stress amplitudes are assigned as 256MPa, 320MPa, 400MPa, 432MPa, 462MPa and 538MPa, respectively. In the case of stress amplitude as 256MPa or 538MPa, only one fatigue test for a smooth sample is carried out, while for the other stress amplitudes, four fatigue tests are performed for eight smooth samples of GH4133B superalloy. During the process of fatigue tests, a multi-parameter measurement mode is adopted, that is, except for recording the number of fatigue loading cycles, the values of electric resistance of smooth sample are measured every certain number of loading cycles by a QJ-57 type DC resistance bridge whose scale overs the range from 0.01μΩ to 1.1111kΩ, which is producted by Shanghai Sute Electrical Appliance Limited Company. Therefore, the accumulated fatigue damage for the sample of GH4133B superalloy during the fatigue process is monitored by measuring electric resistance change.

3.2. Fatigue life analysis

Using the up-down stress amplitude method, the fatigue life measured in the tests is determined as 288MPa, which is the mean value of stress amplitude 256MPa and 320MPa. The three-parameter power function expression is adopted to describe the fatigue *S-N* curve, that is

$$N_{\mathrm{f}} = \sigma_{\mathrm{f}}(\sigma_{\mathrm{a}} - \sigma_{\mathrm{ac}})^{-m}, \tag{1}$$

where, N_{f} is fatigue life, σ_{f}, σ_{a} and m are undetermined coefficients, and σ_{ac} is theoretical fatigue limit. Usually, the value m is obtained as 2 to 4. In this work, the value m is set as 2. Taking logarithm on both sides of above equation, and the equation can be rewritten as

$$\lg N_{\mathrm{f}} = \lg \sigma_{\mathrm{f}} - 2\lg(\sigma_{\mathrm{a}} - \sigma_{\mathrm{ac}}), \tag{2}$$

Eq. (2) shows a linear relationship between logarithmic fatigue life $\lg N_{\mathrm{f}}$ and $\lg(\sigma_{\mathrm{a}}-\sigma_{\mathrm{ac}})$, and the slope is 2. According to the experimental data obtained from the fatigue life tests, using a standard normal distribution function to calculate the values of fatigue life at survival probabilities as 50%, 90%, 95% at various stress amplitudes, the *P-S-N* equations at survival probabilities as 50%, 90% and 95% are individually achieved by using nonlinear regression method as

$$N_{\mathrm{f}} = 2.987\times10^{10}(\sigma_{\mathrm{a}} - 233.43389)^{-2}, \tag{3}$$

$$N_{\mathrm{f}} = 2.008\times10^{10}(\sigma_{\mathrm{a}} - 229.50659)^{-2}, \tag{4}$$

$$N_{\mathrm{f}} = 1.795\times10^{10}(\sigma_{\mathrm{a}} - 228.36174)^{-2}, \tag{5}$$

It can be seen that the theoretical fatigue limit σ_{ac} in Eq. (1) is calculated as 233.43389MPa, and the experimental one is measured as 288MPa, the relative error is about 18.95%. According to Eq. (3), Eq. (4) and Eq. (5), the *P-S-N* curves at survival probabilities as 50%, 90% and 95% are individually plotted, and are compared with the estimated values of fatigue life, as shown in Fig. 3. It can be found from Fig. 3 that the theoretical *P-S-N* curve is well fitted with the estimated values of fatigue life at survival probability as 50%, while at survival probabilities as 90% and 95%, there are some difference between the theoretical curves and the estimated values.

3.3. Fatigue damage analysis

As aforementioned above, during the process of fatigue life tests, the multi-parameter measurement

mode is applied to measure the electric resistance of GH4133B superalloy samples every certain numerber of loading cycles at various stress amplitudes. According to the definition of damage variable, the damage variable D charaterized by electric resistance can be written as

$$D = 1 - \frac{R_0}{R}, \text{ or } D = \frac{\Delta R}{R_0 + \Delta R}, \tag{6}$$

where, R_0 is the electric resistance before damage, R is the electric resistance after damage, and ΔR is the difference between R and R_0, which is called as electric resistance change. In this work, a modified Chaboche damage model is derived to describe the damage evolution, that is

$$D = 1 - \left(1 - \frac{N}{N_f}\right)^{1/(1+\beta_1(\sigma_a)+\beta)}, \tag{7}$$

Substituting Eq. (6) into Eq. (7), the fatigue damage evolution equation characterized by electric resistance change can be written as

$$\frac{\Delta R}{R_0} = \left(1 - \frac{N}{N_f}\right)^{-1/(1+\beta_1(\sigma_a)+\beta} - 1, \tag{8}$$

where, N is the number of fatigue loading cycles, N_f is the fatigue life, β and β_1 are the fatigue parameters, and the parameter β_1 is the function of the stress amplitude σ_a.

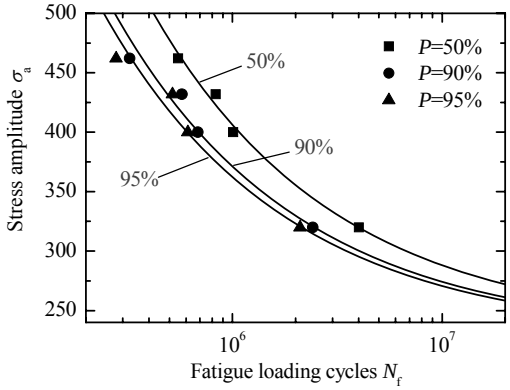

Figure 3. *P-S-N* curves at different survival probabilities

According to Eq. (8), the theoretical damage evolution equations at various stress amplitudes are derived using the nonlinear regression analysis of experiment data obtained in the electric resistance tests. Corresponding to stress amplitudes applied as 320MPa, 400MPa, 432MPa and 462MPa, the values of damage parameter $1+\beta+\beta_1(\sigma_a)$ are determined as 26.543, 31.571, 40.177 and 46.822, respectively. The comparisons between theoretical fatigue damage evolution curves and test data are shown in Fig. 4. Corresponding to the various stress amplitudes, the accumulated fatigue damages of two samples in each group are collected. In Fig. 4, the square symbols denote the test date obtained from the first sample, while the circle symbols denote the test data obtained from the second sample of each group, and the solid lines represent the theoretical results. It can be found from Fig. 4 that the theoretical predicted values are in good agreement with the experimental data, which indicates that the electric resistance change ratio under cyclic loading can be used to describe the process of fatigue damage evolution of GH4133B superalloy.

In the fatigue nucleation and small crack propagation stage (stage I), the fatigue damage is mainly dominated by a process of microdamge nucleation. Furthermore, due to the tension-pressure mode of cyclic loading, the action of compressive stress results in some small crack interfaces colsed, leading to the corresponding electric resistance change smaller, which can be reflected from Fig. 4(a) to (d), that is, the damage increases slowly with number of cycle in the early part of damage evolution curve. With the propagation and coalescence of small cracks, the damage degree becomes

larger, following with increasing electric resistance, and the electric resistance change ratio transits from a relatively flat stage to an acceleration stage, which is called stable fatigue crack propagation stage (stage II). With increasing number of loading cycles, the fatigue propagation moves from a stable stage to an acceleration stage (stage III), and finally leads to fracture failure. In this stage, the damage change rates very large, and the corresponding electric resistance change ratios are also large, as shown in the last parts of fatigue damage evolution curves.

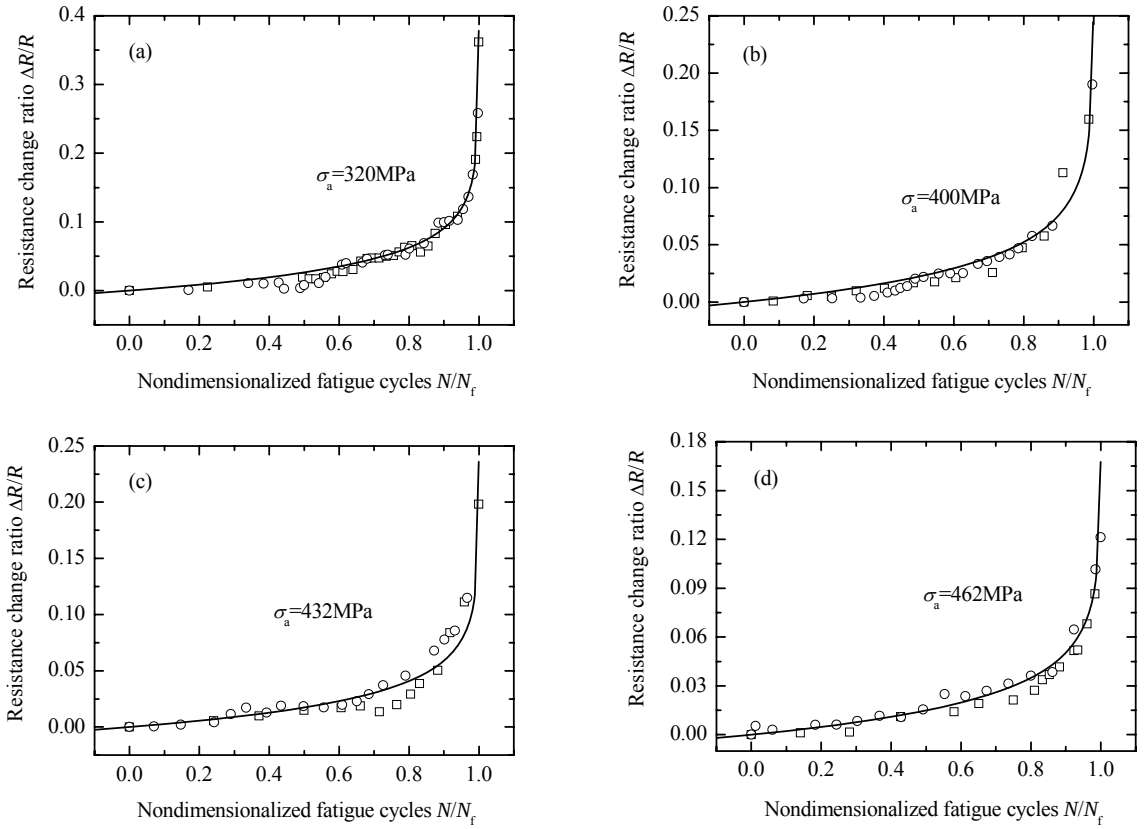

Figure 4. Fatigue damage evolution curves at various stress amplitudes

As aforementioned above, when the stress amplitude σ_a increases from 320MPa to 462MPa, the value of parameter $1+\beta+\beta_1(\sigma_a)$ increases from 26.543 to 46.882. However, the chang rate of electric resistance change ratio is reversed with increasing stress amplitude, which indicates that when the stress amplitude becomes higher, to achieve the same degree of damage as that at lower one, the proportion of consumed fatigue life over the total fatigue life will increase. That is, in the fatigue tests, as the stress amplitude increases, the proportion of fatigue life in the stage II and stage III of crack propagation will decrease, and the total fatigue life is mainly consumed in the stage I of fatigue crack initiation and small crack propagation. Therefore, the change rate of electric resistance change ratio is also relatively slow.

4. Fatigue crack propagation behavior and fractography reverse model

4.1. Fatigue crack propagation tests

The fatigue crack propagation tests for standard compact tension samples of GH4133B superalloy are performed on the CSS-280S-20 test machine. Under cyclic loading conditions (6Hz sine wave, stress ratio R=0.02, 0.1, 0.2, 0.4), the fatigue crack propagation tests are carried out. According to the different values of stress ratio, the tests are categorized as four groups, and two samples prepare

for each group. The approach of specified number of fatigue loading cycles is applied to determine the threshold stress intensity factor range ΔK_{th}, and an EVO scanning electron microscope is applied to investigate the fracture surface morphologies of samples of GH4133B superalloy.

4.2. Fatigue crack propagation behavior

As the stress ratio R=0.02, 0.1, 0.2 and 0.4, the threshold stress intensity factor ranges ΔK_{th} measured in the tests are 11.842MPa·m$^{1/2}$, 11.313MPa·m$^{1/2}$, 9.773MPa·m$^{1/2}$ and 7.440MPa·m$^{1/2}$, respectively. The relationship between the crack propagation rate da/dN and stress intensity factor range ΔK is shown in Fig. 5(a). It can be found from Fig. 5(a) that the crack propagation rate da/dN increases with increasing stress intensity factor range ΔK, and with increasing stress ratio. However, under the condition of low stress intensity factor ranges, the differences among the experimental data of crack propagation rate at different stress ratios are very small, which indicates that the effect of stress ratio on fatigue crack propagation rate are weak at low stress intensity factor ranges.

The Paris formula is applied to carry out a regression analysis for experimental data of fatigue crack propagation at various stress ratios. The Paris formula is written as

$$\frac{\mathrm{d}a}{\mathrm{d}N} = C(\Delta K)^m, \tag{9}$$

where, a is crack length, N is number of fatigue loading cycles, C and m are parameters determined by the crack propagation tests. Taking logarithm both sides of Eq. (9), Eq. (9) can be rewritten as

$$\lg\left(\frac{\mathrm{d}a}{\mathrm{d}N}\right) = \lg C + m\lg(\Delta K), \tag{10}$$

It can be seen from Eq. (10) that the relationship between crack propagation rate da/dN and stress intensity factor range ΔK shows a linear one in double-logrithmic coordinates, and the slope and intercept are individually m and lg$C$. At stress ratio R=0.02, 0.1, 0.2 and 0.4, the experimental data of fatigue crack propagation are analyzed by Eq. (10) using the least square regression method, and the crack propagation rate equations are individually derived as

$$\lg\left(\frac{\mathrm{d}a}{\mathrm{d}N}\right) = -8.229 + 2.700\times\lg(\Delta K), \tag{11}$$

$$\lg\left(\frac{\mathrm{d}a}{\mathrm{d}N}\right) = -8.403 + 2.858\times\lg(\Delta K), \tag{12}$$

$$\lg\left(\frac{\mathrm{d}a}{\mathrm{d}N}\right) = -8.807 + 3.171\times\lg(\Delta K), \tag{13}$$

$$\lg\left(\frac{\mathrm{d}a}{\mathrm{d}N}\right) = -8.587 + 3.176\times\lg(\Delta K), \tag{14}$$

According to Eq. (11), Eq. (12), Eq. (13) and Eq. (14), the theoretical curves of crack propagation rate versus stress intensity factor range are plotted, as shown the solid lines in Fig. 5(a). It can be found from Fig. 5(a) that the theoretical results are in good agreement with the experimental data, and the value of slope m increases monotonously from 2.700 to 3.176 with increasing stress ratio from 0.02 to 0.4, indicating that the crack propagation rate increases with increasing stress ratio, which is consistent with the aforementioned experiment results. Therefore, the Paris formula can be used to describe the fatigue crack propagation behavior of GH4133B superalloy.

Intending to describe the crack propagation behavior in the fatigue tests of GH4133B superalloy at any stress ratio more precisely, a threshold stress intensity factor range ΔK_{th} is introduced into Eq. (9), and the Paris formula is modified as

$$\frac{\mathrm{d}a}{\mathrm{d}N} = B(\Delta K - \Delta K_{th})^n, \tag{15}$$

where, B and n are material parameters determined by the fatigue crack propagation tests. Taking logarithm both sides of Eq. (15), Eq. (15) can be rewritten as

$$\lg\left(\frac{\mathrm{d}a}{\mathrm{d}N}\right) = \lg B + n\lg(\Delta K - \Delta K_{\mathrm{th}}), \tag{16}$$

It can be found from Eq. (16) that the relation between logrithmic crack propagation rate lg(da/dN) and lg(ΔK–ΔK_{th}) shows a linear one, and the slope and intercept are individually m and lg$B$. As aforementioned above, in the cases of stress ratio R=0.02, 0.1, 0.2 and 0.4, the threshold stress intensity factor ranges (ΔK_{th}) measured in the tests are 11.842, 11.313, 9.773 and 7.440MPa·m$^{1/2}$, respectively. The linear regression analysis on the experiment data is performed by using Eq. (16), and the crack propagation rate equations considering ΔK_{th} are individually derived as

$$\lg\left(\frac{\mathrm{d}a}{\mathrm{d}N}\right) = -6.858 + 2.055\times\lg(\Delta K - 11.842), \tag{17}$$

$$\lg\left(\frac{\mathrm{d}a}{\mathrm{d}N}\right) = -6.994 + 2.192\times\lg(\Delta K - 11.313), \tag{18}$$

$$\lg\left(\frac{\mathrm{d}a}{\mathrm{d}N}\right) = -7.326 + 2.457\times\lg(\Delta K - 9.773), \tag{19}$$

$$\lg\left(\frac{\mathrm{d}a}{\mathrm{d}N}\right) = -7.376 + 2.571\times\lg(\Delta K - 7.440), \tag{20}$$

Considering the threshold stress intensity factor range ΔK_{th}, and in double-logrithmic coordinates, the theoretical curves of crack propagation rate da/dN versus stress intensity factor rang ΔK are plotted by using Eq. (17), Eq. (18), Eq. (19) and Eq. (20), as shown the solid lines in Fig. 5(b).

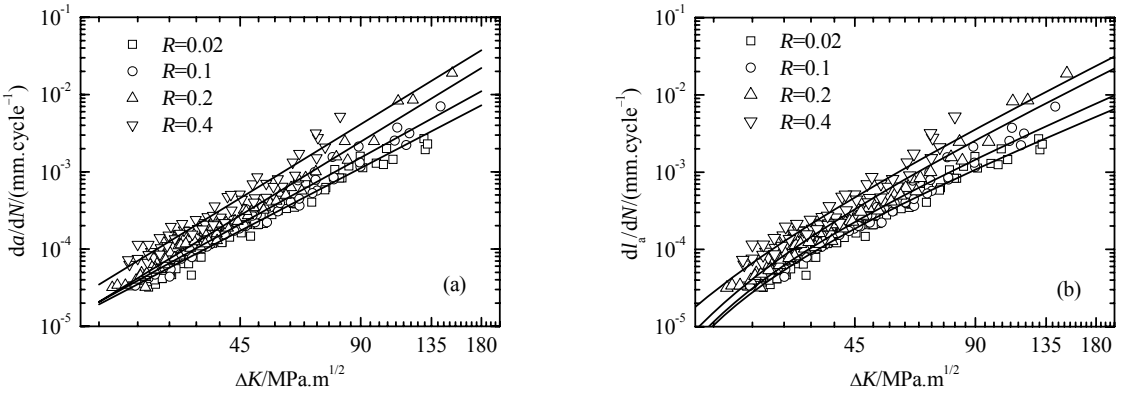

Figure 5. Curves of crack propagation rate: (a) by Paris formula; (b) by modified Paris formula

It can be found from Fig. 5(b) that the theoretical results are well fitted with test data, especially in the case of small values of stress intensity factor range ΔK, comparing with Eq. (11) to Eq. (14), the precise theoretical results are obtained by using Eq. (17) to (20), which can be seen from the comparison between theoretical curve and experimental data in Fig. 5 and Fig. 6. Therefore, the modified Paris formula can not only be used to predict the value of threshold stress intensity factor at different stress ratio, but also can describe the fatigue crack propagation behavior accurately.

4.3. Fractography reverse model

As aforementioned above, the fracture surface morphologies of standard compact tension samples of GH4133B superalloy are investigated using an EVO scanning electron microscope, and a series of fatigue striations are found in the crack steady propagation region. According to these fatigue striations on the fracture surface, the crack propagation rate equations and loads are derived using

the inverse educing method. For mode I crack, the expression of stress intensity factor range ΔK is

$$\Delta K = Y\Delta\sigma\sqrt{\pi a}\,, \tag{21}$$

where, $\Delta\sigma$ is external stress range, a is crack dimension parameter, Y is shape factor which relates to structure shape, crack location and dimension as well as load condition. Substituting Eq. (9) into Eq. (21), the expression of external stress range $\Delta\sigma$ is derived as

$$\Delta\sigma = \frac{1}{Y\sqrt{\pi a}}\left(\frac{1}{C}\cdot\frac{\mathrm{d}a}{\mathrm{d}N}\right)^{1/m}, \tag{22}$$

It can be found from Eq. (22) that if the values of crack propagation rate are measured, then the external stress range acted on the sample can be calculated using the inverse educing method. For standard compact tension sample (Fig. 2), the expression of stress intensity factor range ΔK is

$$\Delta K = \frac{\Delta P}{B\sqrt{W}}F(\alpha),\quad F(\alpha) = \frac{2+\alpha}{(1-\alpha)^{3/2}}\times(0.886+4.46\alpha-13.32\alpha^2+14.72\alpha^3-5.6\alpha^4), \tag{23}$$

where, ΔP is external load range, B is thickness, W is width, and α is the ratio of crack length a to width W. Substituting Eq. (9) into Eq. (22), the expression of external load range ΔP is derived as

$$\Delta P = B\sqrt{W}\left(\frac{1}{C}\cdot\frac{\mathrm{d}a}{\mathrm{d}N}\right)^{1/m}\Big/F(\alpha), \tag{24}$$

For example, in the case of R=0.4, the fracture surface morpologies in the steady propagation region at various stress intensity factors are shown in Fig. 6. Measuring the widths of damage striations on the fracture surface, and recording the corresponding number of loading cycles, thus the crack propagation rates are calculated. Using Eq. (23) and Eq. (24), the stress intensity factor ranges and external loads relating with crack propagation rates are derived.

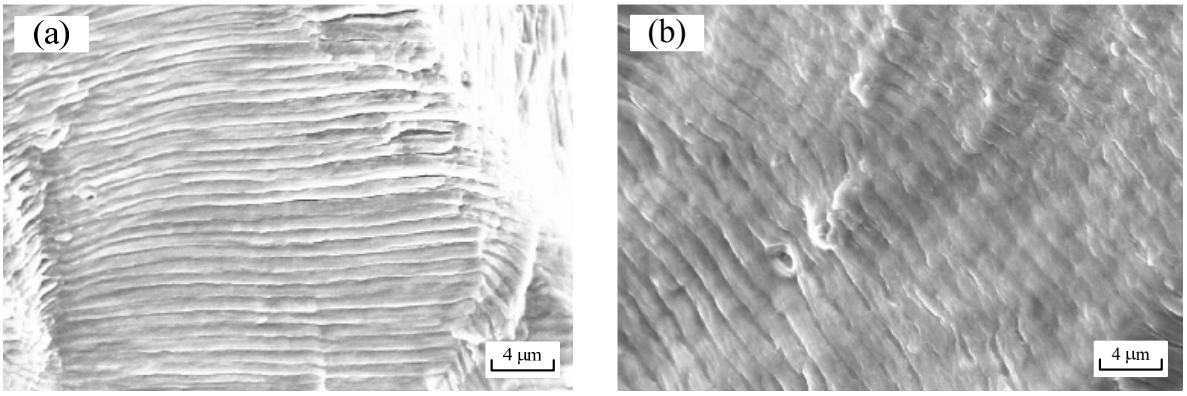

Figure 6. Fracture surface morpology: (a) ΔK=60.69MPa·m$^{1/2}$; (b) ΔK=80.53MPa·m$^{1/2}$

According to Eq. (16), the regression analysis on the calculated data obtained from the fractography is performed, and the inverse deduced equations on fatigue crack propagation are derived. In the cases of stress ratio R=0.02, 0.1, 0.2, 0.4, the inverse deduced equations are individually as

$$\lg\left(\frac{\mathrm{d}a}{\mathrm{d}N}\right) = -7.633+2.619\times\lg(\Delta K-11.842), \tag{25}$$

$$\lg\left(\frac{\mathrm{d}a}{\mathrm{d}N}\right) = -7.544+2.498\times\lg(\Delta K-11.313), \tag{26}$$

$$\lg\left(\frac{\mathrm{d}a}{\mathrm{d}N}\right) = -7.595+2.500\times\lg(\Delta K-9.773), \tag{27}$$

$$\lg\left(\frac{\mathrm{d}a}{\mathrm{d}N}\right) = -8.003+2.647\times\lg(\Delta K-7.440), \tag{28}$$

The comparison between the theoretical curves predicted by inverse deduced equations and analysis data obtain from the fractography is shown in Fig. 7. It can be seen from Fig. 7 that the theoretical curves are well fitted with analysis data, which indicates that the inverse deduced equations can be used to accuratelly describe the crack propagation behavior in the steady propagation region.

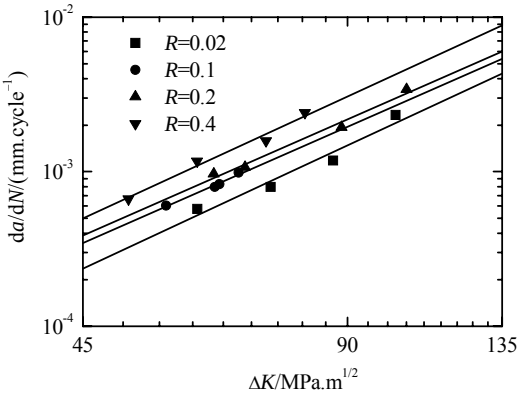

Figure 7. Inverse deduced curves of crack propagation rate

Following, these inverse deduced equations (from Eq. (25) to Eq. (28)) are generalized to describe the whole process of fatigue crack propagation. At various stress ratios, the comparisons between theoretical curves of fatigue crack propagation rate and experimental data are shown in Fig. 8.

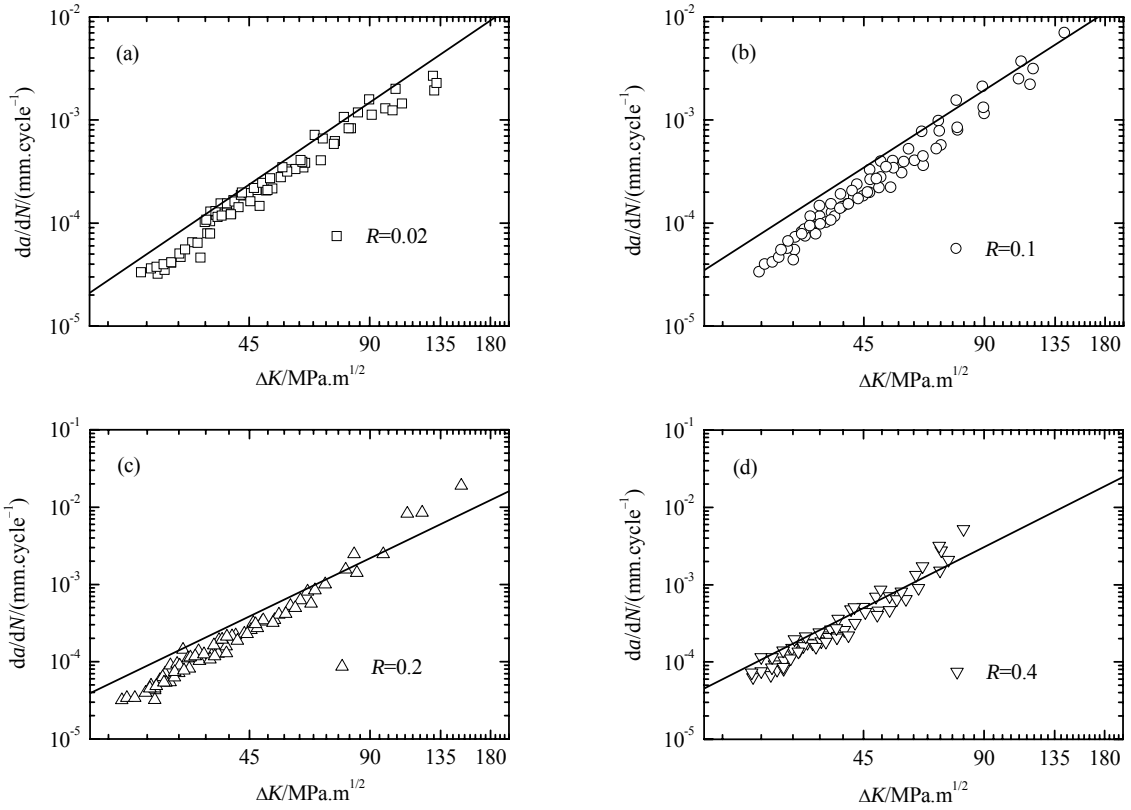

Figure 8. Crack propagation rate curves obtained by inverse deduced equations

It can be seen from Fig. 8 that the theoretical curves are basically consistent with experimental data, indicating that the inverse deduced equations derived from the analysis data obtained by measuring damage striations in steady propagation region of fracture surface, can still be used to predict the whole process of fatigue crack propagation. Furthermore, it can be found that if only the stress

intensity factor range ΔK is not too large, in other words, if only the fatigue crack is not at the later stage of accelerated growth region, the theoretical values are totally larger than that of experimental data, so the predicted results obtained by the inverse deduced equations tend to security.

5. Conclusions

(1) The fatigue life of GH4133B superalloy is measured, and the theoretical fatigue life is calculated, and the *P-S-N* curves at various survival probabilities are obtained. It is found that the theoretical fatigue limit agrees well with experimental one, and the fatigue life of GH4133B superalloy can accurately be estimated by the *P-S-N* curves.
(2) The modified Chaboche model can predict the accumulated damage of GH4133B superalloy preciously. Higher stress amplitude will result in a higher proportion of the fatigue life in stage I of fatigue crack initiation and small crack propagation to the total fatigue life, which is unfavorable to monitor the accumulative fatigue damage and to prevent fatigue fracture in the components.
(3) A modified Paris formula is achieved by introducing a threshold stress intensity factor range. The comparison between theoretical curves and experiment data shows that the modified Paris formula can not only be used to predict the value of threshold stress intensity factor range at different stress ratio, but also can describe the fatigue crack propagation behavior accurately.
(4) Based on the measurement data of fatigue striations and the modified Paris formula, the crack propagation rate equations and external loads are inversely deduced and calculated. It is found that the inverse deduced equations based on the fractography inverse model can predict the fatigue crack propagation behavior, and the predicted results tend to security.

Acknowledgements

The authors gratefully acknowledge the finanicial support of the Research Foundation of Education Burean of Hunan Province, China (No. 11B125).

References

[1] Q.P. Zhang, Z. Zhang, H.S. Wu, S.Z. Zuo. Physical and mathematical models of fatigue propagation and final rupture regions for metallic materials. Acta Aeronautica and Astronautica Sinica, 21(s), (2000) s11–s14. (in Chinese)
[2] E.J. Xu.The Effect of defects, damage and micro crack on total life and reliability of aeroengine components in service. Aeroengine, 29(2), (2003) 11–15. (in Chinese)
[3] J. Schijves. Fatigue damage in aircraft structures, not wanted, but tolerated? Int. J. Fatigue, 31(6), (2009) 998–1011.
[4] A. Fatemi, L. Yang. Cumulative fatigue damage and life prediction theories: A survey of the state of the art for homogeneous materials. Int. J. Fatigue, 20(1), (1998) 9–34.
[5] P. Starke, F. Walther, D. Eifler. New fatigue life calculation method for quenched and tempered steel SAE 4140. Materials Science and Engineering A, 523(1–2), (2009) 246–252.
[6] B. Sun, Y. Guo. High-cycle fatigue damage measurement based on electrical resistance change considering variable electrical resistivity. Int. J. Fatigue, 26(5), (2004) 457–462.
[7] D. Huang, P. C. Xu, Y.M. GUO. A research on the estimation of remaining service life for metals in fatigue. Journal of Experimental Mechanics, 18(1), (2003) 113–117. (in Chinese)
[8] D.Y. Hu, R.Q. Wang. Experimental study on creep-fatigue interaction behavior of GH4133B superalloy. Materials Science and Engineering: A, 515(1–2), (2009) 183–189.
[9] X.Y. Luo, R.G. Zhao, Y.Z. Jiang, H.C. Li, X.J. Li, X.H. Liu. Statistical analysis on mechanical properties of GH4133B superalloy used in turbine disk of aero-engine at ambient temperature. Chinese Journal of Mechanical Engineering, 46(22), (2010) 75–83. (in Chinese)
[10] S.A. Padula II, A. Shyam, R.O. Ritchie, W.W. Milligun. High frequency fatigue crack propagation behavior of a nickel-base turbine disk alloy. Int. J. Fatigue, 21(7), (1999) 725–731.

FATIGUE CRACK GROWTH SIMULATION OF SURFACE CRACKS UNDER ARBITRARY CRACK FACE LOADING

Xiaobin Lin

HBM (nCode) United Kingdom Limited, UK
Xiaobin.Lin@hbmncode.com

Abstract Fatigue crack growth was simulated for a surface crack subjected to arbitrary crack face loads. The simulation was based on the step-by-step integration of a proper fatigue crack growth law along the crack front, enabling complex crack shape changes to be directly predicted. The three-dimensional finite element method with the inverse square singularity near the crack tip considered was employed to calculate the stress intensity factors along the crack front, and the contact elements were also introduced into the cracked surface to avoid the possible overlapping between the crack faces. Several typical crack face loads were analysed, and the results including crack shape development, aspect ratio changes and stress intensity factor variations were given to validate the simulation technique. The results showed that the crack shape is dependent on the applied load and non-semielliptical surface crack profiles may be adopted by fatigue cracks. The simulation is particularly useful and necessary for the fatigue crack growth analysis in a residual stress field.

Keywords fatigue crack growth, stress intensity factor, surface crack, crack shape change

1. Introduction

Fatigue crack growth for surface cracks in plates has been extensively investigated both theoretically and experimentally. Surface cracks are very common in many engineering components and structures, such as pressure vessels, pipeline systems, off-shore and aircraft components *et al*. It has been widely observed from experimental investigations [1, 2] that a surface crack under fatigue loading always changes its crack front as it grows, and the shape by the fatigue crack subjected to both tension and bending loads is close to a semi-ellipse if neglecting the possible retardation of crack growth along the free surface.

Some efforts have been made to establish reasonable models to predict the fatigue crack growth of a two-dimensional surface crack, in which an experimental fatigue crack growth relation obtained from small specimen tests is employed. A typical model is that a surface crack is treated to have a semi-elliptical shape, and the change in crack aspect ratio is predicted. Newman and Raju [3] presented a two degree-of-freedom model, in which the change of crack aspect ratio is calculated by coupled integration of a Paris type of fatigue crack growth law along both crack depth and surface directions. In their model, the stress intensity factor (SIF) range at the free surface point was modified by the reducing 10% its value to consider the effect of the surface layer when the retardation of crack growth is often observed, and their own closed-form SIF equations were used.

For cracks subjected to a complex stress gradient, a method similar to those mentioned above is probably suitable if SIF solutions corresponding to such a stress distribution are available. Generally, these solutions are likely to be obtained by using a weight function method, or by superposing the SIF results for a series of polynomial stress distributions. However, this method is obviously incomplete. First, it includes a semi-elliptical shape assumption which is not adequate in some situations to define the actual shape adopted by the crack. Second, crack contact is not taken into account almost in all SIF solutions reported. This may happen if there are compressive stresses acting on the crack face. Using the SIF results obtained without considering crack contact might cause a big error in fatigue crack growth calculations. In this paper, a numerical method developed

by the author [4, 5] has been employed to simulate the fatigue crack growth of surface cracks under several typical and complex crack face loads. The method can directly predict, in a step-by-step way, the crack shape change without having to make a semi-elliptical crack shape assumption, and also take possible crack face contact into account. Various results are given to validate the numerical method for simulating fatigue crack growth with complex crack shape change.

2. Numerical simulation technique

It is usually considered reasonable to apply a fatigue crack growth law from small specimens that have a straight front to a curved crack front along which the stress intensity factor varies. The fatigue crack growth rate can then be expressed as a function of crack front position as follows

$$\frac{\mathrm{d}a(\xi)}{\mathrm{d}N} = f(\Delta K(\xi)) \tag{1}$$

where $a(\xi)$ and $\Delta K(\xi)$ are the local normal crack growth increment and the SIF range at an arbitrary crack front position, ξ, as shown in Fig.1. The crack growth increment can be written as

$$\Delta a(\xi) = \frac{f(\Delta K(\xi))}{f(\Delta K_{\max})} \Delta a_{\max} \tag{2}$$

where $\Delta a_{\max}$ is the maximum increment along the crack front, occurring at the point where the SIF is the largest. Fatigue cycles can then be calculated as follows

$$N_{\mathrm{i+1}} = N_{\mathrm{i}} + \frac{\Delta a_{\max}}{f(\Delta K_{\max})} \quad (\mathrm{i} = 0,1,...) \tag{3}$$

By choosing an appropriate small value of $\Delta a_{\max}$, both the crack shape change and the corresponding number of fatigue cycles can be predicted if the SIF solutions along the crack front are available. For a Paris type fatigue crack growth law, we have

$$\Delta a(\xi) = \left(\frac{\Delta K(\xi)}{\Delta K_{\max}}\right)^m \Delta a_{\max}, \quad N_{\mathrm{i+1}} = N_{\mathrm{i}} + \frac{\Delta a_{\max}}{C(\Delta K_{\max})^m} \quad (\mathrm{i} = 0,1,...) \tag{4}$$

The above equations have been used in the present simulation. However, it is worth indicating that a general fatigue crack growth rate equation including crack threshold and fracture toughness can be readily incorporated.

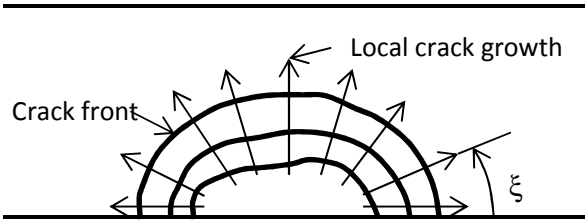

Figure 1. Illustration of fatigue crack growth of a surface crack

Stress intensity factors along the crack front were estimated by using the finite element (FE) method. The 1/4-point displacement method was used to achieve the inverse square-root stress singularity at the corner of a wedge element, and particularly possible contact between crack faces in a compressive stress field was taken into account in FE analyses. The method of estimating the SIF was detailed in [5]. Figure 2 illustrates a typical mesh created in the simulation. The mesh comprises both cracked and un-cracked blocks. Between them the “multiple point constraint” equations are applied to maintain the displacement compatibility. Both cracked and un-cracked blocks are filled with 20-node iso-parametric elements. In particular, three rings of elements are arranged surrounding the crack tip. In the simulation, the cracked block is recreated as the crack

grows whilst the un-cracked block remains unchanged.

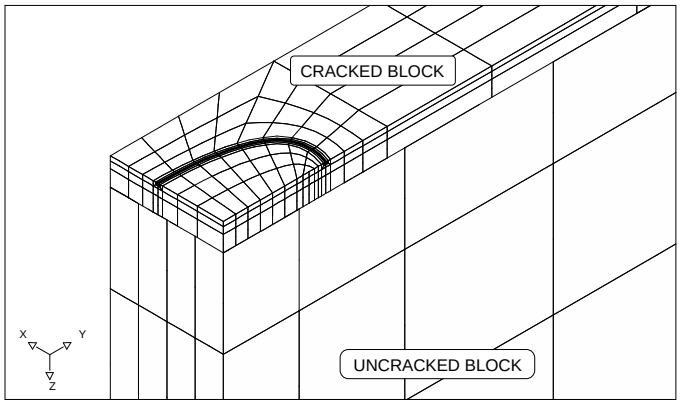

Figure 2. Type mesh configuration for stress intensity factor estimation

Local fatigue crack growth increments were calculated using the equation mentioned above, and a new crack front was established by fitting a cubic spline curve to the positions of the advanced corner nodes. Along the spline curve new corner and midside nodes were then relocated with them distanced properly. This method has been verified to be effective [6]. Automatic re-meshing of the FE model is part of the simulation technique, which makes the step-by-step simulation possible. More details can be found in [4, 6].

3. Analysis examples

Six different stress distributions varying along the plate thickness direction, as shown in Fig. 3, are considered in the present investigation. They are applied to the surface crack face in the plate as the maximum fatigue load. The minimum fatigue load is assumed to be zero.

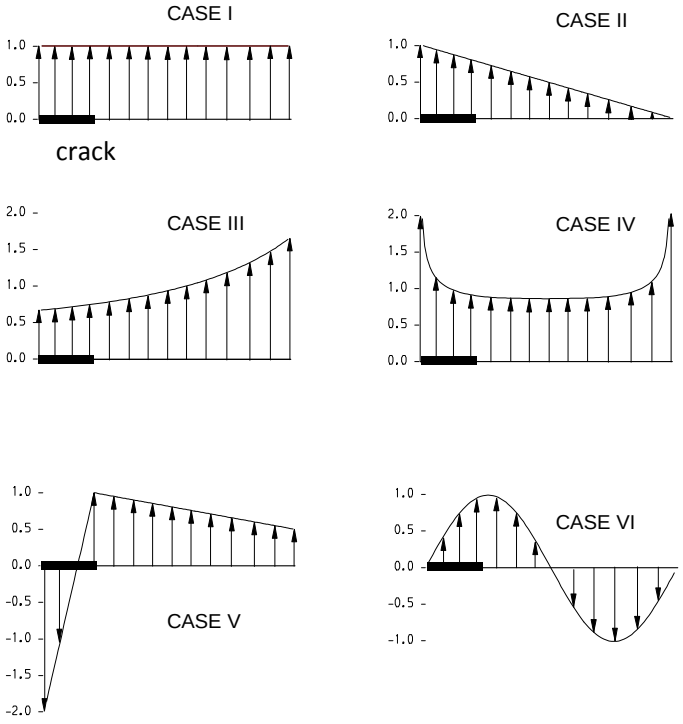

Figure 3. Crack face stresses considered in the investigation

Case I is the extensively studied loading configuration—uniform tension, i.e.

$$s(x)=1 \tag{5}$$

Case II is a combined tension and bending load that decreases linearly from unity to zero,

$$s(x)=-x/t+1 \tag{6}$$

This was selected as a representative of the linear stress variation.

Case III represents a stress variation existing on the wall of a cylindrical vessel subjected to a uniform internal pressure, which can be expressed as

$$s(x)=\frac{pR_{\mathrm{i}}^2}{R_{\mathrm{o}}^2-R_{\mathrm{i}}^2}\left(1+\frac{R_{\mathrm{o}}^2}{(R_{\mathrm{o}}-x)^2}\right) \tag{7}$$

where R_{i} and R_{o} are the inner and outer radii of the vessel, respectively; p is the internal pressure. In the simulation, the ratio of $R_{\mathrm{o}}/R_{\mathrm{i}}$ is chosen to be 2 and p to be 1 MPa. The location where x=0 corresponds to the external wall of the vessel, thus the modelled crack is similar to an external surface crack in a cylinder.

Case IV is a typical stress distribution existing in cruciform fillet welded joints [7], as shown in Fig. 5. Verreman *et al.* [7] proposed the following equations to describe the stress variation occurring at the weld toe

$$s(x)=\left(\frac{x}{t}\right)^{-\alpha}\sum_{i=0}^{4}\lambda_i\left(\frac{x}{t}\right)^i \quad 0\le x/t\le 0.5 \tag{8}$$

$$s(x)=\left(\frac{t-x}{t}\right)^{-\alpha}\sum_{i=0}^{4}\lambda_i\left(\frac{t-x}{t}\right)^i \quad 0.5\le x/t\le 1 \tag{9}$$

The above equations were obtained by fitting them to the two dimensional elastic element results. For the particular cruciform fillet joint shown in Fig. 4, the following parameters have been used: α=0, λ_0=0.414, λ_1=0.815, λ_2=-1.71, λ_3=4.16, λ_4=-3.7. High stress concentration can be found at the weld toe, which is the reason why the crack initiation is often induced there. This crack problem has been received a great deal of attention due to its importance in engineering practice.

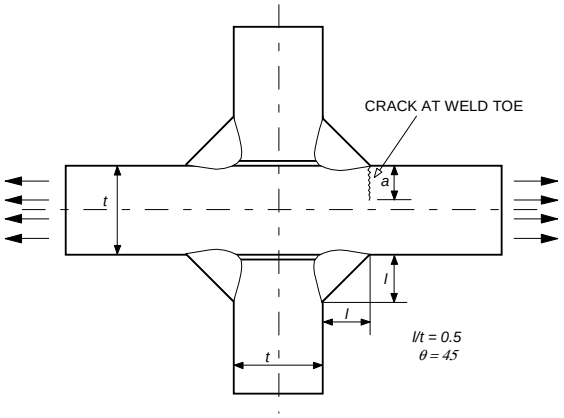

Figure 4. Cruciform fillet welded joint

Case V is used by the author to demonstrate the ability of the numerical technique to simulate the fatigue crack growth in a complex stress field containing compression. It is well known that compressive stresses are often generated on purpose to resist fatigue cracking as well as its subsequent growth. The shot peening is usually considered beneficial to delaying or even avoiding

the crack initiation from the free surface. The stress form devised here, to a certain extent, is similar to the residual stress generated by such a shot peening process. This hypothetical stress is expressed by the following equations

$$s(x)=\frac{15}{t}x-2 \qquad 0\le x\le t/5 \tag{10}$$

$$s(x)=\frac{5}{8t}x+\frac{9}{8} \qquad t/5\le x\le t \tag{11}$$

Case VI is also a hypothetical load case intended to demonstrate the capability of the numerical technique. The following is its stress distribution

$$s(x)=\sin\left(\frac{2\pi}{t}\right)x \tag{12}$$

The initial crack configuration was assumed to be a semi-circle (a/c=1) with depth ratio a/t=0.2. a, c and t are crack depth, crack surface half length, and plate thickness, respectively. The material properties employed in this investigation are: Poisson's ratio ν=0.3, Paris' fatigue crack growth relation $\mathrm{d}a/\mathrm{d}N=1.83\times10^{-13}(\Delta K)^3$

4. Results and discussion

4.1. Crack Shape Development

Figure 5 shows the fatigue crack shape development of the initially semi-circular surface crack in a plate subjected to different crack face loads. It is clear that the shape change is dependent on the load applied. The crack under uniform tension (Case I) grows with a similar growth increment along the crack front. The free surface has a slight effect on crack growth, which makes the crack advance relatively rapidly along the surface. It can be seen that the semi-elliptical shape is adequate to define the front of the propagating cracks in Fig. 5 (Case I). Crack shape change of different initial cracks for this load case has been investigated by the author [8]. It has been numerically confirmed that the widely used semi-ellipse is an adequate crack shape approximation.

The crack in Case II that has a decreasing stress value along the plate thickness propagates more rapidly in the direction of the free surface than in the direction of the plate thickness, gradually leading to a flatter crack profile. The semi-ellipse is also quite acceptable for the shape in this case, as indicated by the author [8] according to a numerical study of crack shape.

Contrary to Case II, the Case III crack extends faster at the depth than the free surface. This is due to the larger stress in the direction of crack depth. It seems that these crack profiles predicted can still be approximated with high accuracy by the semi-elliptical shape.

The stress concentration at the free surface in the Case IV load permits the crack to grow more easily along the surface compared to the crack under uniform tension fatigue (Case I). It is particularly obvious at the early stage of crack growth. The numerical crack profiles in Fig. 5 (Case IV) are basically in agreement with the experimental results obtained by Pang *et al.* [9, 10] using the beach-mark method. The growing cracks were also treated by them as those of semi-elliptical form during the crack growth calculation.

The crack face load of Case V produces an interesting result of crack shape development. The

initially semi-circular crack gradually evolves into a mushroom-shaped crack. The crack mouth is kept close and the crack, initially, is only given an opportunity of extending in a small region near the crack depth. As the cracked area becomes large, the portion of the crack front in a state of closure gradually shrinks. This is because of the increasing positive resultant stress. The maximum crack dimension can be seen to occur nearly at the *t*/4 position from the front surface, which is in accordance with the loading configuration that has the maximum tensile stress at the *t*/4 position. This phenomenon should be considered to be reasonable although no direct experimental result can be compared. The predicted crack fronts are obviously far from the semi-elliptical shape, and thus the widely used semi-elliptical crack shape assumption is not adequate for such load case. The crack shape evolution in Fig. 5 (Case V) also demonstrates that surface cracks can be effectively delayed by creating a compressive stress field near the plate surface, such as using the shot peening method.

The crack shape change illustrated in Fig. 5 for Case VI also shows that the semi-elliptical shape is not proper to be approximated to the crack fronts in this case. The lagging of crack growth along the surface can be observed, which is due to the zero stress value at the surface. The crack develops mainly in the depth direction at the early stage but the crack growth in this direction is slowed down and even stopped finally by the descending stress level as the crack extends further, see Fig. 3. The maximum crack growth is subsequently transferred to the crack front position, where the highest stress happens, i.e. at the *t*/4 position from the front surface.

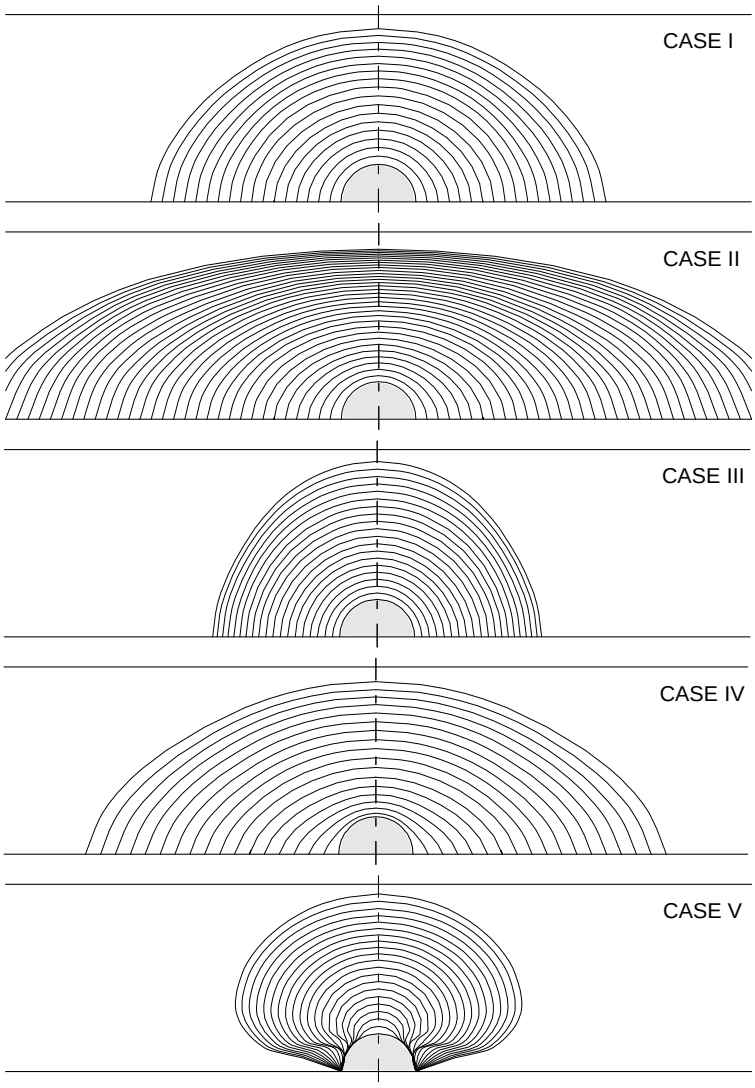

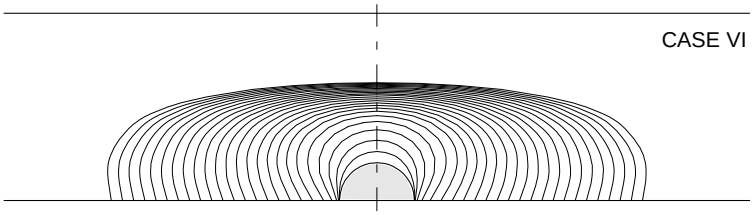

Figure 5. Fatigue shape development starting from an initially semi-circular surface crack under different crack face loads.

4.2. Aspect Ratio Change

The crack shape change is usually described quantitatively by the aspect ratio (*a*/*c*) variation with the crack depth ratio (*a*/*t*), but it should be aware that it is incomplete. The aspect ratio changes are shown in Fig. 6 for all six load cases. Clearly, the aspect ratio relation is strongly dependent on the load, as mentioned previously. The load with decreasing stress along the plate thickness makes the crack advance more difficult in this direction and eventually leads to a smaller *a*/*c* value, as seen for Cases II and IV; whilst the increasing stress along the plate thickness causes more rapid crack growth in this direction than along the surface. This can be seen in Case III. The *a*/*c* value of the Case V crack increases linearly with the *a*/*t* ratio, quickly exceeding the maximum value set in the figure. This is because no crack extension occurs along the plate surface due to the large compressive stress acting in the surface layer of the plate. However, for Case VI, the *a*/*c* value re-drops rapidly after its initial rise similar to the Case V crack, which is caused by the stress distribution with a decreasing value when the crack depth is in the region of *t*/4 and 3*t*/4. Obviously, the aspect ratio cannot give a proper description for the cracks that are not of semi-elliptical shape, like the Cases V and VI cracks.

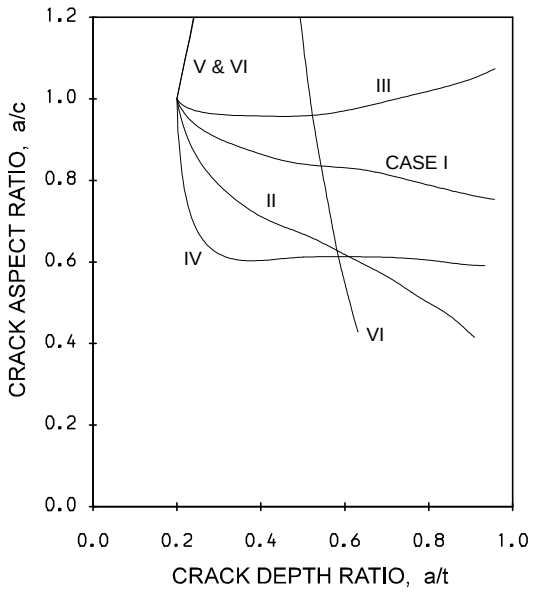

Figure 6. Aspect ratio change for surface crack under different crack face loading

Lin and Smith [8] compared the numerical results of aspect ratio predicted by the simulation technique with the experimental results for the pure tension case, i.e. Case I, and found that both the numerical and experimental results are in good agreement. This indicated that the simulation technique is effective. The numerical aspect ratio result of Case VI can be found to agree well with the experimental results of [9, 10], who carried out the fatigue test of welded joint containing a

surface crack similar to that analysed in this work for both the initial crack and joint geometries, if their result is included in Fig. 6. This further validates the present numerical technique.

4.3. Stress Intensity Factor Variation

Figure 7 shows the SIF distributions along the front of the initially circular crack (a/t=0.2) estimated by the 3D finite element method for all six load cases, where the SIF is normalised by $K_0 = \sqrt{\pi a}$. Obviously, the results vary with the applied load. The distributions along the crack front are basically uniform for Cases I, II and III, but not for Cases IV, V and VI. The SIF for Case IV shows a rapid rise at the plate surface, but that for Case VI drops when the crack front approaches the plate surface. The Case V crack gives a result that the SIF value is zero along the half crack front close to the surface, which means that the crack is in a state of partial closure under the load (Case V). It needs to be indicated that contact elements have been employed for this case. By looking at the crack face load in Fig. 3 for this case, these results are obviously reasonable.

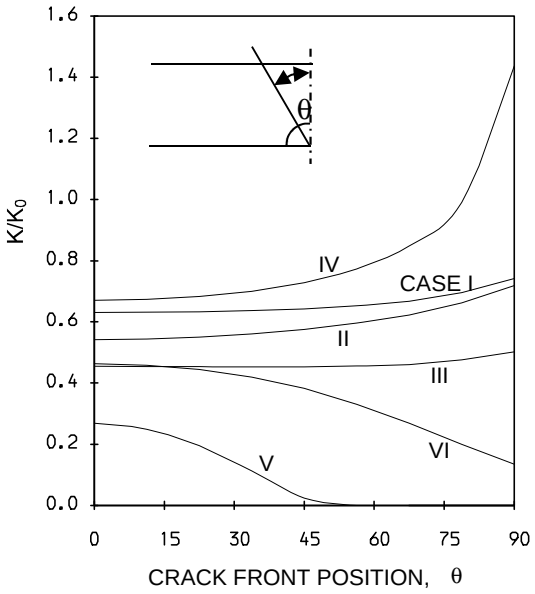

Figure 7. Stress intensity factor distributions along the initially circular crack front

The degree of the SIF non-uniformity along a crack front with crack growth is more clearly represented for all six loads in Fig. 8, where the ratio of $K_{\min}/K_{\max}$ is plotted against the crack depth ratio, a/t. It can be found that the equal K profile (the SIF value is identical around the crack front), generally, cannot be reached for non-uniform loads. Dependent on the load acting on the crack faces, complex variations exist. For Case V, rapid rise and subsequent drop in the $K_{\min}/K_{\max}$ ratio are due to the sine load, whilst for Case VI the zero variation is caused by the existence of partial closure along the crack front.

Figure 9 shows the SIF variations for all load cases at both the depth (θ=0°) and surface (θ=90°) points, where SIF has been normalized by $K_0 = \sqrt{\pi a}$. The SIF value at the depth generally increases with the crack advance except Case VI. The SIF decrease for Case VI is due to the rapid drop in stress after the crack propagates to the region of a/t<1/4. The SIF along the surface also tends to increase during crack growth, but that for Case V retains to be zero.

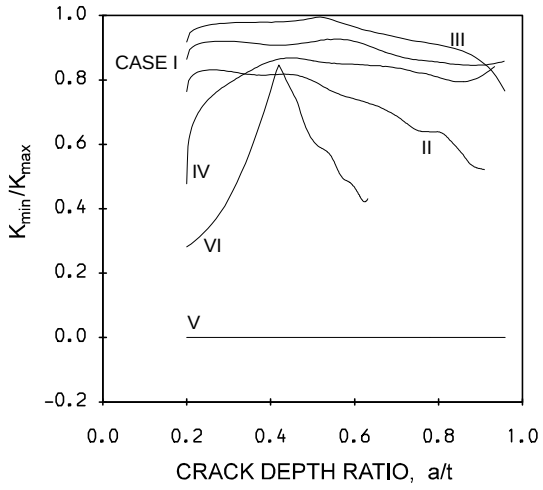

Figure 8. Change of $K_{\min}/K_{\max}$ along the crack front during crack development

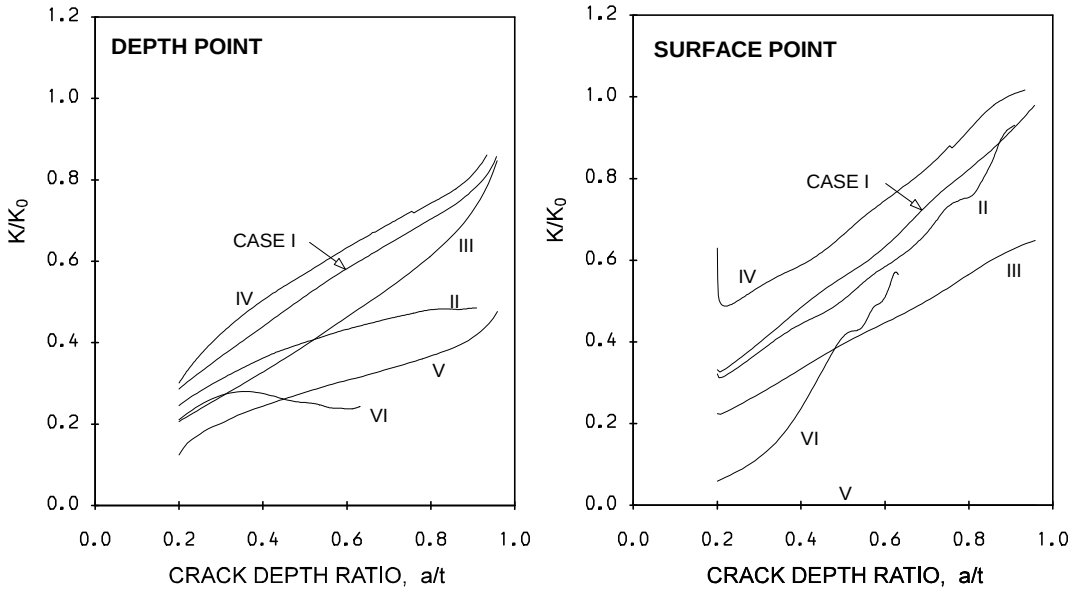

Figure 9. Stress intensity factor variations along both depth and surface points during crack growth

5. Concluding remarks

The effect of different crack face loads on fatigue crack growth of a surface crack in a plate has been investigated by using a multiple degree-of-freedom numerical method, which is based on a series of 3D FE analyses with including contact elements in cracked area and is able to directly obtain the crack shape development in a complex crack face stress field. It has been concluded that complex crack shape evolution in fatigue crack growth can be successfully predicted by the multiple degree-of-freedom numerical method. The crack profiles adopted by cracks are strongly dependent on the applied load. They might significantly deviate from the widely assumed semi-elliptical shape, although in many cases they can be approximated to such a shape. It has been also found that crack surface contact can be simulated by the contact elements introduced in the SIF calculations, so that negative SIF results can be correctly avoided.

References

[1] M.A. Mahmoud, Quantitative prediction of growth patterns of surface fatigue cracks in tension analysis. Engng Fracture Mech., 30 (1988), 735–746.
[2] M.A. Mahmoud, Growth patterns of surface fatigue cracks under cyclic bending - a quantitative analysis. Engng Fracture Mech., 31 (1989), 357–369.
[3] J.C. Jr. Newman, I.S. Raju, Analyses of surface cracks in finite plates under tension or bending loads. NASA Technical Paper 1578, 1979.
[4] X.B. Lin, R.A. Smith, Finite element modelling of fatigue growth of surface cracked plates-Part I: the numerical technique. Engng Fracture Mech., 63(5) (1999) 503–522.
[5] X.B. Lin, Estimation of stress intensity factors with considering crack surface contact. In The Thirteen European Conference on Fracture (ECF 13), San Sebastian, Spain, 6-9 September, Edited by M.R. Bache et al. 2000, pp. 1855–196.
[6] X.B. Lin, Numerical Simulation of Fatigue Crack Growth. Ph.D. thesis, The University of Sheffield, 1994.
[7] Y. Verreman, J.P. Baïlon, J. Masounav, Fatigue life prediction of welded joins—a re-assessment. Fatigue Fract. Engng Mater. Struct., 10(1), (1987) 17–36.
[8] X.B. Lin, R.A. Smith, Finite element modelling of fatigue growth of surface cracked plates-Part II: crack shape changes. Engng Fracture Mech., 63(5) (1999) 523–540.
[9] H.L.J. Pang, Analysis of weld toe profiles and weld toe cracks. Int. J. Fatigue, 15(1) (1993) 31–36.
[10] H.L.J. Pang, T.G.F. Gray, Fatigue analysis of surface cracks at fillet welded toes. Fatigue Fract. Engng Mater. Struct., 16(2) (1993) 151–164.

Characterization of the fatigue behavior of brazed steel joints by digital image correlation (DIC)

Michael Koster[1,*], **Christoph Kenel**[1], **Christian Leinenbach**[1]

[1] Empa - Swiss Federal Laboratories for Materials Science and Technology; Laboratory for Joining Technologies and Corrosion; Überlandstrasse 129; 8600 Dübendorf; Switzerland
* Corresponding author: Michael.Koster@empa.ch

Abstract
In the actual work, the fatigue induced damage evolution in brazed steel joints - in particular under the influence of artificial brazing defects - was investigated using digital image correlation (DIC). The brazed joints consist of the soft martensitic stainless steel AISI CA 6-NM as substrate material and Au 18wt.-% Ni as a filler metal. Brazing was performed in a shielding gas furnace with an H_2 atmosphere. Besides the lifetime-oriented investigations, the cyclic deformation behavior was investigated using DIC. The measurements show that it is possible to monitor localized accumulating fatigue damage in an early state of the experiment. Besides the determination of the local strains, the deformation zones in the vicinity of strain concentrations could be characterized in detail. A high frequency camera allowed characterizing the damage evolution in the brazing zone during cyclic loading and investigating crack initiation and crack propagation during cyclic loading. The results are in correlation with SEM investigations and allow a more profound understanding of the failure mechanisms of brazed steel joints.

Keywords brazing, fatigue, defect, fracture, DIC

Nomenclature

Roman Symbols

a	[mm]	Defect size
A	[%]	Elongation at fracture
BSE	[--]	Back scattered electrons
d	[mm]	Thickness of the braze layer
DIC	[--]	Digital image correlation
E	[MPa]	Young's Modulus
N_f	[--]	Number of cycles to fracture
Nmax	[--]	Maximum number of cycles
R	[--]	Load ratio
SEM	[--]	Scanning electron microscopy

Greek Symbols

σ_{UTS}	[MPa]	Ultimate tensile strength
σ_{max}	[MPa]	Maximum applied load for cyclic testing on the defect-free assumed cross section
σ_y	[MPa]	Yield strength

1. Introduction

Brazing has gained increasing importance as a favorable joining technology for many seminal applications in industry in the last years. Generally, brazing plays an essential role because the thermal stress of the joining partners and the processing times can be reduced, compared to e.g. welding. Furthermore, brazing allows joining of dissimilar materials as e.g. metals and ceramics at narrow tolerances. With the use of advanced brazing technologies, as e.g. high temperature (HT) vacuum furnace brazing, brazed joints can also be used for thermally and mechanically heavily loaded components in chemical engineering, power generation and for the production of power electronic components [1-3].

By definition, brazing is performed by heating an assembly over the melting point of the filler metal placed between two substrates without reaching the melting point of the substrate material. The liquid filler metal wets the surfaces of the substrate material and fills the joint gap. Subsequent adhesion and diffusion processes during the cooling of the assembly are essential for the final joint strength. The general differentiation between soldering and brazing is made according to the process temperatures used for the joining process. The above described process at $T < 450$ °C is referred to as soldering, whereas it is named brazing at $T > 450$ °C.

Generally, brazed joints form heterogeneous systems, consisting of base material, filler metal and diffusion zone. Under mechanical loading, the properties of brazed joints vary significantly from those of the individual joining partners. The complex deformation behavior of the brazed joint is characterized by geometrical and microstructural interactions as e.g. by different elastic-plastic properties of substrate material and thin braze layer. Uniaxial loading and the constrained deformation of the thin filler alloy layer can lead to a triaxial stress state which strongly influences the joint performance [4]. To estimate the influence of defects on bulk materials and on welded structures under quasi-static loadings, defect assessment procedures, such as R6, BS7910 or SINTAP have been developed [5 - 8]. In the scope of previous investigations [9], it has been shown that the R6-procedure can also be used to estimate the influence of defects on brazed joints. In previous studies, a rather unusual fatigue crack growth behavior of brazed steel joints, i.e. extremely steep da/dN-ΔK curves in comparison with the ones of bulk materials, was observed [4]. It could be shown that under defined boundary conditions, the influence of defects on the fatigue lifetime can be estimated based on the stress intensity factor caused by the defect [10], but up to date information on the general influence of brazing defects on the fatigue behavior of brazed joints is lacking. Therefore, a better understanding of fatigue crack initiation and propagation is very important for reliable life-time predictions of brazed joints.

Generally, during stress-controlled fatigue tests with metallic materials, fatigue is closely related to the evolution of (local) irreversible strains. In homogenous materials, the strains are relatively equally distributed over a macroscopic length scale and can therefore be averaged using integrating measurement techniques, e.g. with extensometers. However, plastic strains in brazed joints are usually localized in a small volume in or next to the brazing zone. The thickness of braze layers is usually in the range of 50-100 µm, so conventional strain measuring techniques cannot be applied reasonably. To measure local strains during cyclic loading with a sufficiently high resolution, digital image correlations (DIC) were performed. The technique was applied to monitor the fatigue induced damage evolution in brazed steel joints during cyclic loading, in particular under the influence of brazing defects. Furthermore, the fracture surfaces were analyzed by SEM to correlate the experimental results with characteristic deformation features and to obtain information on the underlying failure mechanisms.

2. Testing materials and experimental setup

The brazed joints used for the actual investigations consisted of the steel AISI CA 6-NM (X 3 CrNiMo 13-4) as substrate material and of the gold-nickel alloy Au-18wt.-% Ni as filler metal. The substrate material contains 0.05 wt.-% carbon, 13wt.-% chromium, 4 wt.-% nickel and small amounts of molybdenum. Brazing was performed using foils of the filler metal with a thickness of d = 100 µm. Besides its comparably low melting point of 955°C, the filler metal is characterized by good corrosion resistance and excellent wetting behavior. The brazing process was performed at T ≈ 1000°C in reducing atmosphere with H_2 as a shielding gas. After brazing, a two-step heat treatment procedure was performed at $T_1 \approx 700$°C and $T_2 \approx 650$°C with N_2 was as a shielding gas to optimize the mechanical properties of the brazed joints and to improve the materials resistance against stress corrosion cracking. The mechanical properties of the substrate material, filler metal and brazed joints taken from round specimens are shown in Table 1. The mechanical properties of the filler metal were measured in the scope of in situ SEM investigations [9].

Table 1: Mechanical properties of base material, filler metal and brazed joint

	E [GPa]	σ_y [MPa]	σ_{UTS} [MPa]	A [%]	HV0.05
AISI CA 6-NM	203	726	844	20.0	327
Au-18wt.-%Ni	110	555	940	6.5	271
Brazed, round	200	721	841	10.3	--

Further tensile tests were performed with T-joint specimens. Due to their specimen geometry, conventional strain measurements with an extensometer were not applicable. The experiments show that the σ_{UTS} of brazed T-joints without defects averages 835 MPa.

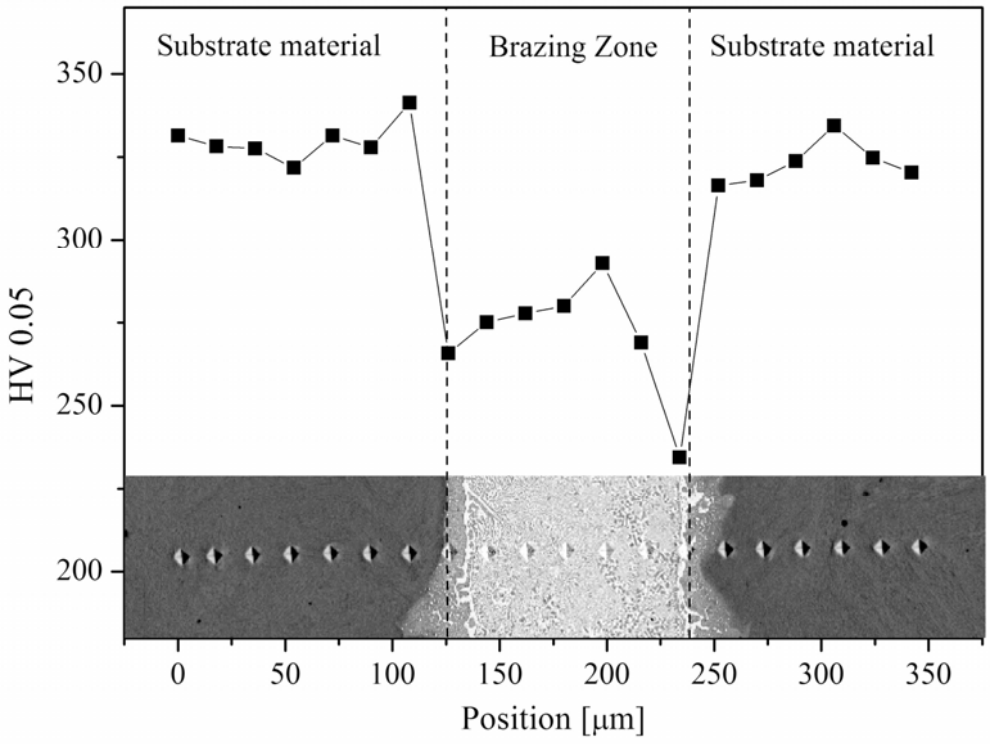

Figure 1: Microstructure and hardness measurements of a brazed joint

As shown in the BSE-micrograph in Figure 1, the joint consists of base material, filler metal and diffusion zone.

In the brazing zone, the filler metal consists of a gold-rich phase and an iron-nickel-rich phase whereas in the region between substrate material and braze layer, the penetration of gold into the substrate material was observed, as is also reported in the literature [11]. Adjacent to the diffusion zone, a layer of the precipitate-free gold-rich phase is formed, that provides the lowest hardness values of 235 HV 0.05.
For the actual experiments T-joints with and without artificial brazing defects were investigated. T-joints are characterized by a sudden change of the cross section area at the brazing zone, as shown in Figure 2. They were designed with respect to the original geometry of a turbo compressor impeller.

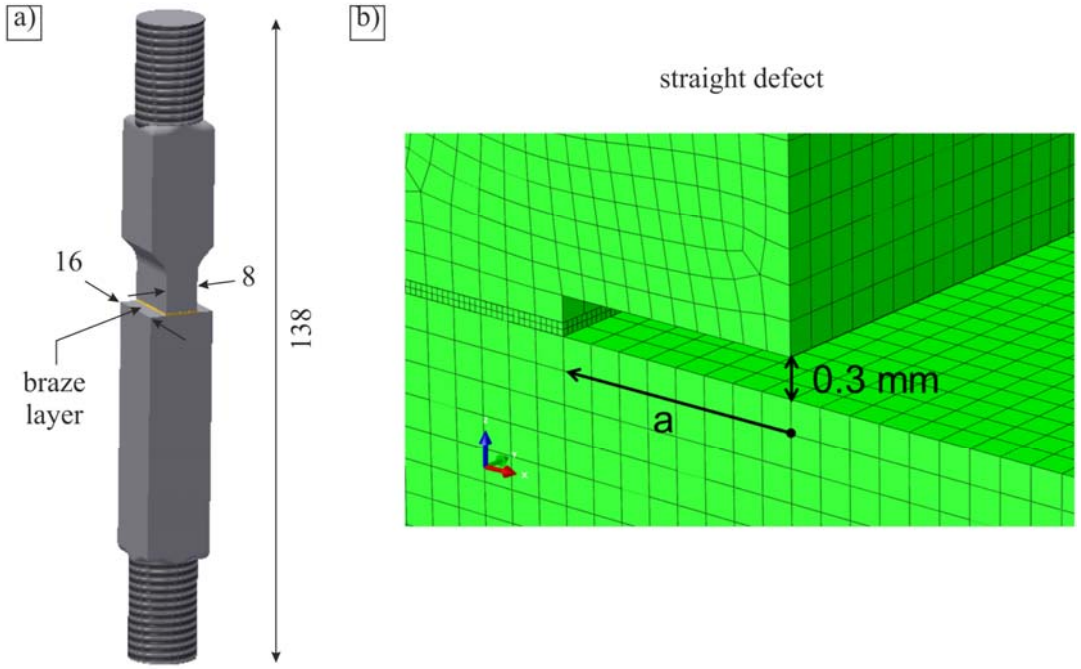

Figure 2: a) Geometry of the T-joint specimen and b) defects introduced into the braze layer

To simulate typical brazing defects like partly unfilled brazing gaps or large pores, straight defects with sizes of a = 0.5 mm, a = 1 mm and a = 2 mm (cf. Fig. 2b) were introduced into the braze layer by electrical discharge machining.
The stress-controlled cyclic loading experiments were performed on a servo-hydraulic testing machine at a frequency of 5 Hz. To simulate the influence of start/stop cycles, the experiments were performed at a load ratio of R = 0.1 until $N_{max}=2\cdot10^4$ cycles. Besides the lifetime oriented investigation of the fatigue behavior, event-oriented experiments were performed with DIC.
The DIC analysis was performed with a black speckle pattern on a white coating on the side surfaces of the T-specimens. To guarantee a sufficient resolution of the object displacements, the pattern was prepared with an average speckle size of 35 µm. The spray painting system used was an airbrush device with a nozzle diameter of 0.2 mm and gravity feed. The image acquisition was performed with a high speed camera (Redlake MotionExtra HG100K) that was focused on the brazing zone. Series of pictures were taken at a recording speed of 500 fps and an aperture time of 500 µs. The DIC was performed with the software Moiree Analysis V0.950© by correlating images of the maximum and the minimum force at defined loading cycles. The use of a high frequency camera allows investigating the development of strains during cyclic loading. Especially for brazed specimen, as a typical representative for heterogeneous systems, this technique allows to study the crack initiation, the crack propagation and the influence of stress concentrations as e.g. defects

locally with an adequate lateral and temporal resolution.
After the experiments, SEM investigations were performed to analyze the fracture surface and to correlate the results with DIC. To distinguish between volumes with different chemical compositions, a BSE detector was chosen for the investigations. Therefore, volumes containing heavy elements as gold are shown in bright contrast whereas comparably light elements are shown in dark contrast.

3. Results

Figure 1 shows the maximum applied loading amplitude of the defect-free assumed cross section as a function of the numbers of cycles to failure.

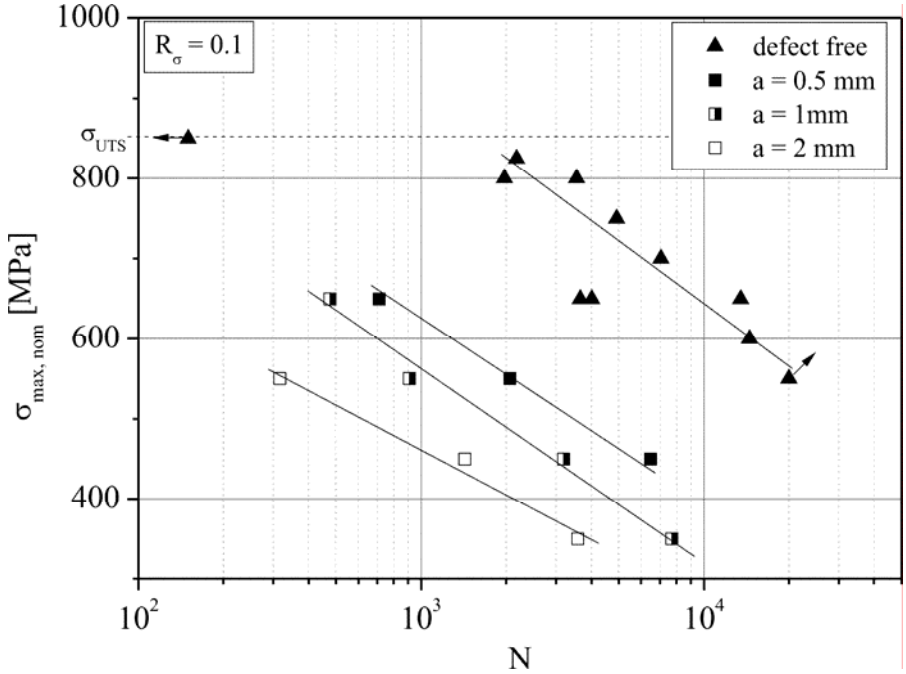

Figure 3: S,N curve of defect-free and defect containing T-joint specimens

The results of the experiments show that defects significantly influence the joint strength. As could be expected, defects lead to a decrease of the joint strength. The larger the defect, the more pronounced the decrease of the fatigue strength. Defect-free specimens can be loaded even up to the ultimate tensile strength of the substrate material for 50 loading cycles, as shown in Figure 3. This can be explained by the ductile deformation and hardening behavior of the substrate material. Loadings around the yield strength of the material lead to failure of the defect-free specimens at approx. 10^4 loading cycles. S,N-curves can be used to describe the influence of one defined defect, but they are not suitable to describe the influence of defects varying in form, shape and position reasonably. In a previous study, a fracture mechanical approach to estimate the influence of brazing defects on a universal scale is based on the stress intensity caused by a defect was successfully applied to make life-time predictions for joints of a less ductile steel [10]. However, this approach did not lead to reasonable results for the material used in this work.

The local strain evolution was characterized experimentally by DIC. Figure 6 shows a defect-free specimen at several stages during cyclic loading at $\sigma_{max} = 650$ MPa until $N_f = 13518$ cycles. The strain distribution in the first and in the loading cycle before failure occurred is shown in Figure 4 together with the speckle in the background.

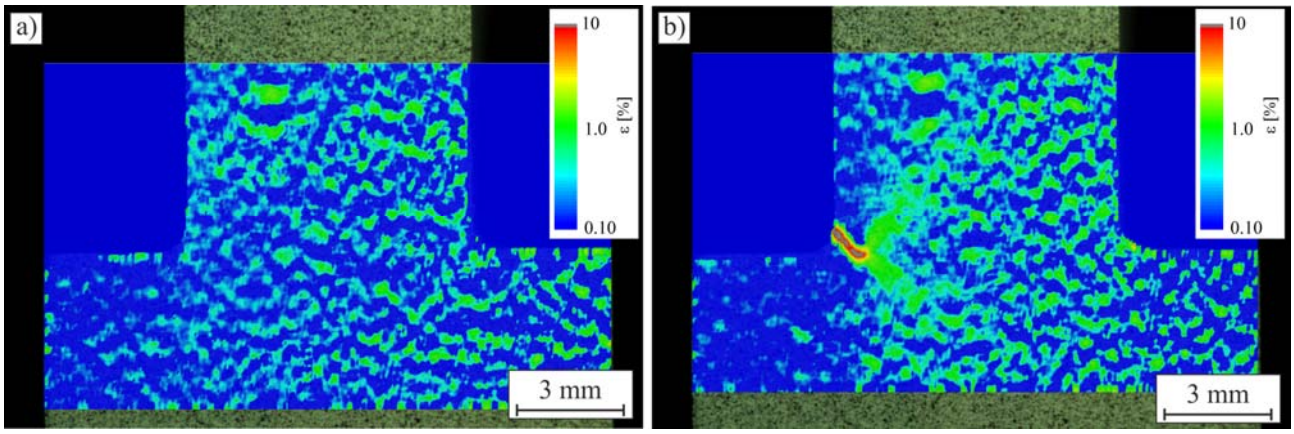

Figure 4: DIC with a defect free specimen

During the first loading cycles, the strains are equally distributed over the whole cross section (Figure 4 a). During further cycling, the fatigue damage accumulation leads to increased local strains and subsequent crack initiation and propagation. Figure 4b shows the deformations in the last cycle before fracture. Furthermore, Figure 4b shows that the crack initiates in the fillet, not directly in the braze layer, as could be expected. Then, it grows at an angle of approximately 45° to the loading direction until it changes its direction and propagates in the vicinity of the brazing zone, perpendicular to the loading direction.

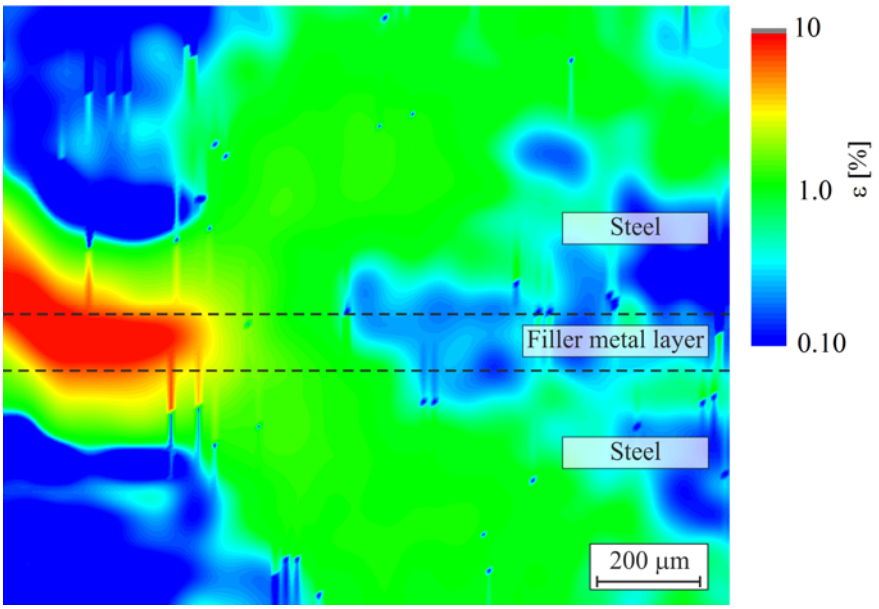

Figure 5: DIC – Strain field in the vicinity of the fatigue crack

Figure 5 shows a close-up image correlation of the crack tip region, the approximate position of the filler metal layer is indicated by dashed lines. Whereas the highest strains are found at the position of the crack due to the crack opening, the volume ahead of the crack tip exhibits also increased strains. With increasing distance these high strains are located in wing-shaped strain fields in the parent material. The filler metal is only subjected to a strain level comparable to the wing-shaped strain fields in a region of 300 µm ahead of the crack tip, whereas in further distance the enhanced stress levels are only observed in the parent material. Some of the data points shown in blue represent regions where no correspondence was found. The strain interpolation with the neighboring values leads to the vertical stripes in Figure 5.

A further experiment was performed with a defect containing specimen with a = 1 mm that was subjected to σ_{max} = 350 MPa. Failure occurred after N_f = 7711 loading cycles.

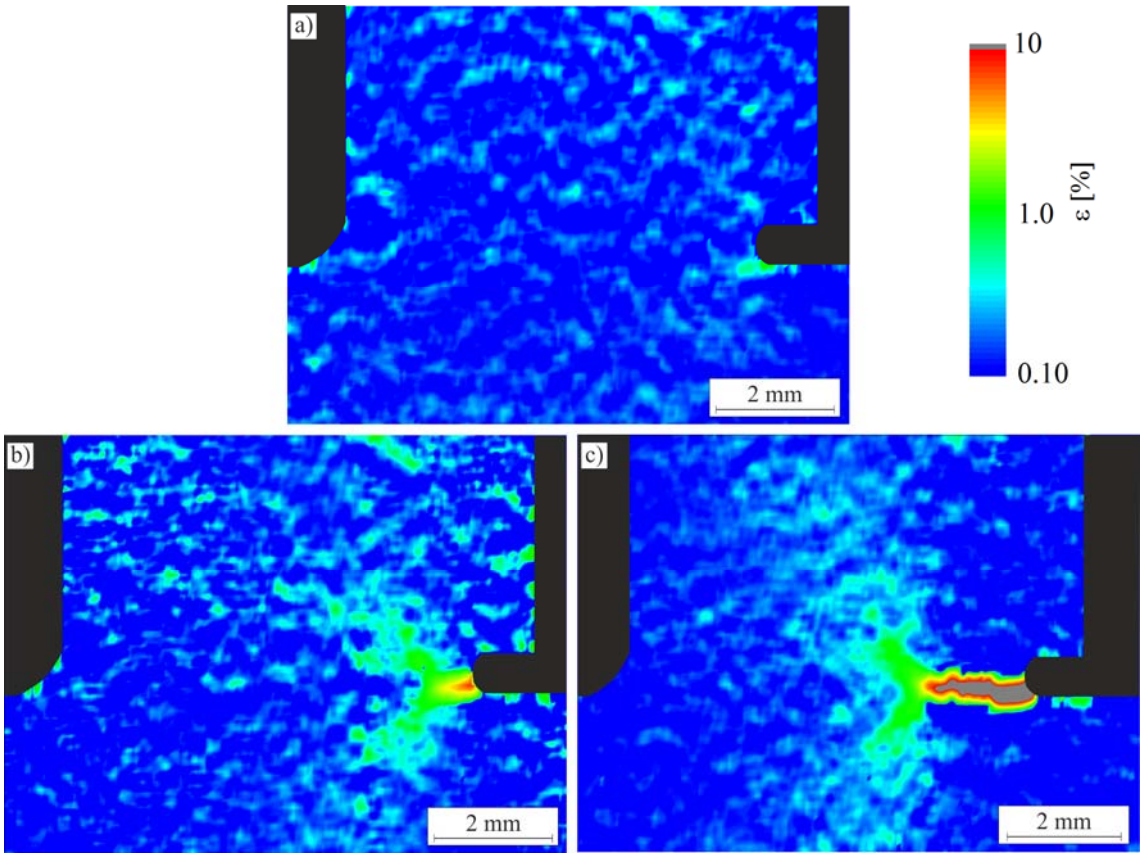

Figure 6: DIC of a defect containing specimen at a) N = 100 b) N = 0.8·N_f and b) N = N_f – 20

The results of the DIC show the inhomogeneous distribution of local strains due to increased stresses at the tip of the defect already in an early state of the experiment. After 100 loading cycles, a slight increase of the strains can be measured at the tip of the defect (Figure 6a) At N ≈ 6200 loading cycles (≈ 0.8·N_f), severe deformations indicate increasing strains as a result of accumulated fatigue damage at the approximate position of the braze layer at the tip of the defect (Figure 6b). Further cycling leads to crack initiation and crack growth. Figure 6c shows the local deformations 20 loading cycles before failure occurred. Due to the lacking possibility of differentiating between crack opening and a black speckle, the results in the direct proximity of the crack should be considered only qualitatively. Especially the volume ahead of the crack exhibits high strains that are distributed over a relatively large volume compared to the layer thickness of d = 100 µm. The wing shaped strain field that expands over 1 mm in front of the crack tip corresponds also to the strain field that has been determined for the defect free specimen (Figure 4b).

To investigate the mechanisms of crack growth, SEM investigations were performed on the fracture surfaces of the specimens shown in Figure 4 and Figure 6.

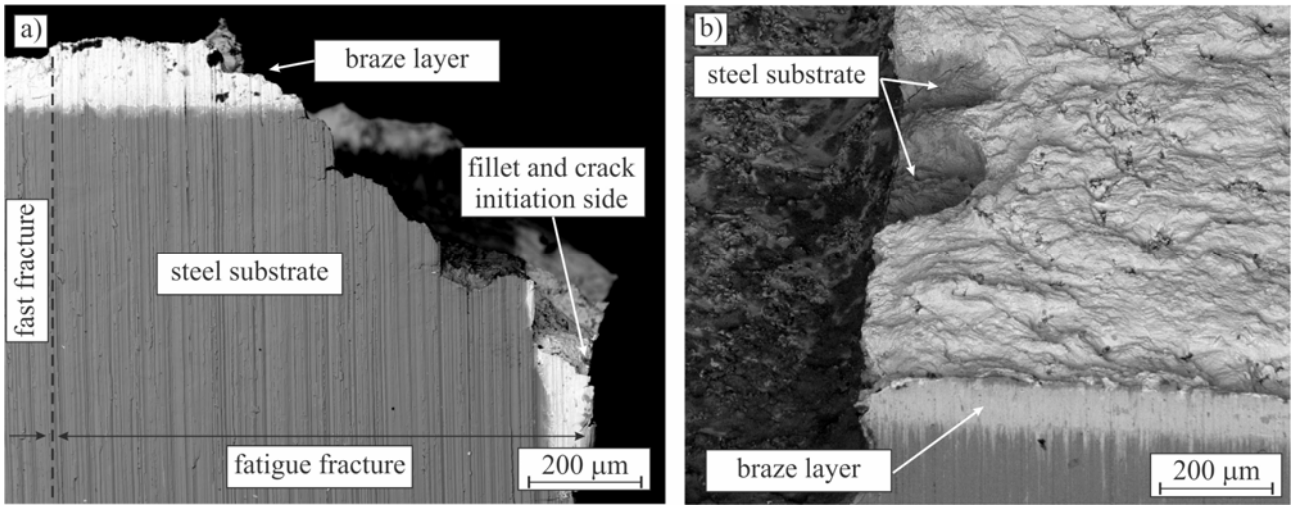

Figure 7: SEM investigations of the fracture surface for a) defect-free and b) defect containing T-joint

The SEM analysis correlates with the DIC calculations considering crack initiation and crack growth. Figure 7a shows the crack initiation side in the fillet and its growth at an angle of 45°, as was also shown in Figure 4b. The crack path through the substrate material is characterized by a discontinuous course. This could be an indicator for inter-crystalline crack growth that could result from the diffusion of liquid gold into the steel substrate between the grain boundaries, as described in [11]. Next to the main crack, multiple secondary cracks were found in the substrate material and in the braze layer. The crack growth follows the same direction until it has passed the braze layer and reached the opposite interface. There, it changes direction and follows the interfacial zone until it has reached a critical length and fast fracture occurs. The fracture surface of the defect containing specimen is shown in Figure 7b. Also for this specimen, the crack passes through the substrate material.

Conclusions

The results show that defects in the brazing zone strongly influence the fatigue lifetime of brazed components. It could be shown that DIC allows measuring local displacements during cyclic loading with a sufficiently high resolution. Continuing fatigue damage is indicated before final failure occurs by increasing strains around structural hot spots. Wing shaped strain fields in front of the crack tip extend over a comparable large volume of the substrate material. Furthermore, the results allow to draw conclusions on the mechanisms of crack initiation and to monitor crack growth during cyclic loading, which is important for braze joints. The results of the DIC show that for defect-free and for the defect containing T-joint specimen, the crack does not necessarily follow the softer filler metal but propagates through both the substrate material and the braze layer. Only when the crack reaches the opposite interface of the braze layer it changes its direction and follows the interfacial regions on its path. Further experiments will be performed to characterize the fatigue behavior of brazed joints with special interest on the influence of defects. In the future, DIC will be performed to investigate the fatigue crack growth behavior more precisely. In correlation with SEM investigations, the presented methods can be used to achieve a better understanding of the mechanisms that lead to failure of brazed steel joints.

Acknowledgement
The authors gratefully thank MAN Diesel & Turbo AG Zürich for financing this project

References

[1] T. Ma, M. Zeng, Y. Ji, H. Zhu, Q. Wang, Investigation of a novel bayonet tube high temperature heat exchanger with inner and outer fins. Int. J. Hydrogen Energy, 36 (2011) 3757-3768.

[2] J. Novacki, P. Swider, Producibility of brazed High-dimension Centrifugal Compressor Impellers. J. Mater. Process. Technol., 133 (2003) 174-180.

[3] L. Sáncheza, D. Carrillo, E. Rodrígueza, F. Aragóna, J. Sotelob, F. Torala, Development of high precision joints in particle accelerator components performed by vacuum brazing. J. Mater. Process. Technol., 211 (2011) 1379-1385.

[4] C. Leinenbach, H.-J. Schindler, Mechanics of fatigue crack growth in a bonding interface. Eng. Fract. Mech., 89 (2012) 52-64.

[5] Y.J. Kim, M. Koçak, R.A. Ainsworth, U. Zerbst, SINTAP defect assessment procedure for strength mismatched structures. Eng. Fract. Mech., 67 (2000) 529-546.

[6] British Energy Generation Ltd., Assessment of the integrity of structures containing defects. R6-Rev. 4 (2002).

[7] British Standard, Guide on methods for assessing the acceptability of flaws in metallic strcutures. BS 7910 (1999).

[8] S. Webster, A. Bannister, Structural integrity assessment procedure for Europe – of the SINTAP programme overview. Eng. Fract. Mech., 67 (2000) 481-514.

[9] C. Leinenbach, H.-J. Schindler, T.A. Başer, N. Rüttimann, K. Wegener, Quasistatic fracture behaviour and defect assessment of brazed soft martensitic stainless steel joints. Eng. Failure Anal., 17 (2010) 672-682.

[10] C. Leinenbach, M. Koster, H.-J. Schindler, Fatigue assessment of defect-free and defect containing brazed steel joints. J. Mater. Eng. Perform., 5 (2012) 739-747.

[11] D. Favez, L. Deillon, J.-D. Wagnière, M. Rappaz, Intergranular penetration of liquid gold into stainless steel. Acta Mater., 59 (2011) 6530-6537.

Study on Delamination Behavior and Crack Opening Contour of Advanced Hybrid Laminates during Fatigue Crack Propagation Process

Xiao Huang[1], Jianzhong Liu[1,*]

[1] Beijing Institute of Aeronautical Materials, Beijing 100095, China
* Corresponding author: jianzhongliu09@sina.com

Abstract To study crack opening contour and delamination behavior of one kind of advanced hybrid laminates during fatigue crack propagation process, this research accomplished fatigue crack propagation test under R=0.1 for two kinds of saw-cut length and two kinds of stress level, acquired the basic appearance of crack opening contour and delamination, obtained the effect of saw-cut length and stress level on crack opening contour and delamination size. The results indicate that crack opening contour becomes larger as the stress level or saw-cut length rises. Delamination size increases when the stress level becomes larger. The saw-cut length is almost not able to affect delamination size.

Keywords Fiber metal laminates; Advanced hybrid laminates; Delamination; Fatigue crack propagation; Saw-cut

1. Introduction

Fiber metal laminates (FML) have been developed in recent years[1]. Advanced hybrid laminates (AHL) applied to wing load-carrying structures have been developed from ARALL, GLARE and the concept of Selective Reinforcement[2]. One of the AHL, named CentrAl, developed by GTM-advanced structures and Alcoa Technical Center, will be applied in the wing box structure for airliner and cargo plane[3].

Significant research on fatigue crack propagation behavior has been adequately conducted for ARALL and GLARE. And various prediction models have been developed by researchers[4-15]. As Alderliesten said[13], bridging stress, crack opening contour and delamination shape are in balance. As a result of it, in order to calculate bridging stress and then predict fatigue crack propagation behavior effectively, there is significance for studying crack opening contour and delamination behavior deeply.

Existing a few papers[2, 16] present that it is very different from the fatigue crack propagation behavior of AHL and traditional FML. ARALL and GLARE is thin enough to show a nearly same fatigue crack propagation rate in each aluminum alloy sheet layers and a similar delamination shape and size between each layer. But there is a remarkable difference for crack length and delamination size between each layer because of a thickness effect. As the same time, research on the crack opening contour of AHL has not yet been published.

To understand the fatigue crack propagation behavior of AHL, this research accomplished fatigue crack propagation test under different saw-cut lengths and stress levels, recorded crack opening contour, obtained delamination shape and size by etching, got the initial results from the influence of saw-cut length and stress level on crack opening contour and delamination behavior, laid the foundation of validating theoretical analysis results.

2. Experiment

2.1. Materials and Specimen

The lay-up of AHL in this research is shown in Fig. 1. There is a 3/2 lay-up laminate bonded between two 2mm-thick 2A12-T4 aluminium alloy sheets by adhesive film. Central 3/2 lay-up was laid by three 0.5mm-thick LY12-M aluminium sheets and two prepregs. Prepregs are prepared by

HS2 glass fiber and TDE-85 epoxy resin.

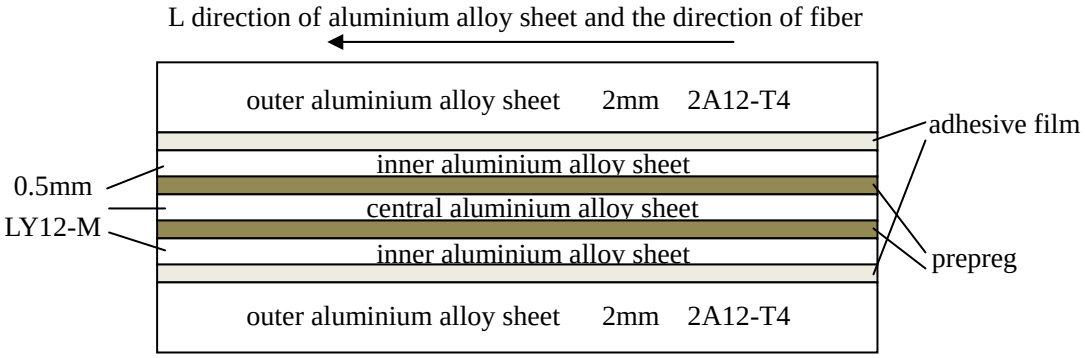

Figure 1. Lay-up of advanced hybrid laminates

Centre crack tension (CCT) specimen was selected for this research, as shown in Fig. 2. Two kinds of saw-cut size, $2a_s$=10mm and 15mm, were processed in order to explore influence of saw-cut length on crack opening contour and delamination behavior.

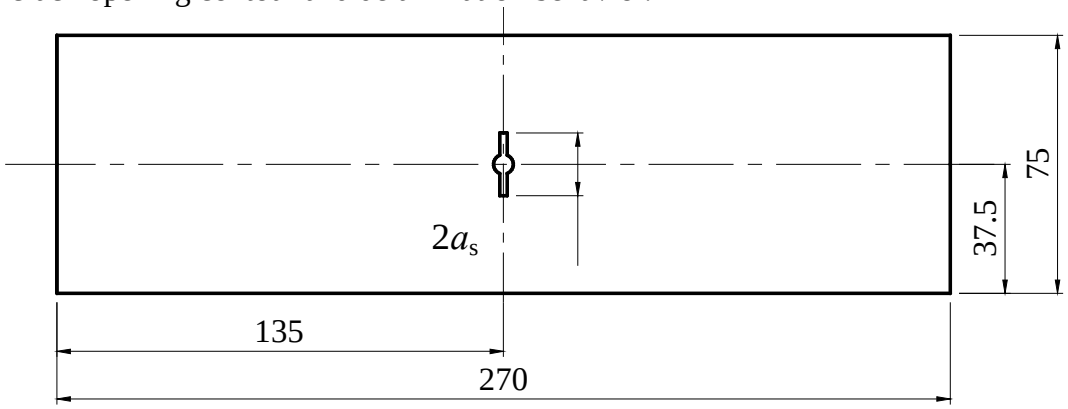

Figure 2. Centre crack tension (CCT) specimen

1.2 Fatigue Crack Propagation Test

Fatigue crack propagation test was finished with constant-amplitude sine wave fatigue loadings, the frequency of 10 Hz and the stress ratio R of 0.1 on 2.5T MTS-858 electohydraulic servocontrolled fatigue testing machine. Crack length was observed by two JDX-B magnification microscopes with scale of 30X. Average crack length a_m is obtained by averaging the front-left side crack length a_1 and back-right side crack length a_2. The matrix of the test is shown in Table 1.

Table 1. Matrix of fatigue crack propagation test

Saw-cut length $2a_s$/mm	Stress level σ_{max}/MPa	Target average crack length a_m/mm
10	60	12，17，22
10	85	12，17，22
15	60	12，17，22

Crack opening contours are captured when a_m reaches nearly 12mm, 17mm and 22mm. Specific measurement method is: take pictures of crack area with a ruler after applying a tension loading which equal to the maximum fatigue loading, then measure the crack opening contour by using image measurement software, and finally obtained the crack opening contour, as shown in Fig. 3.

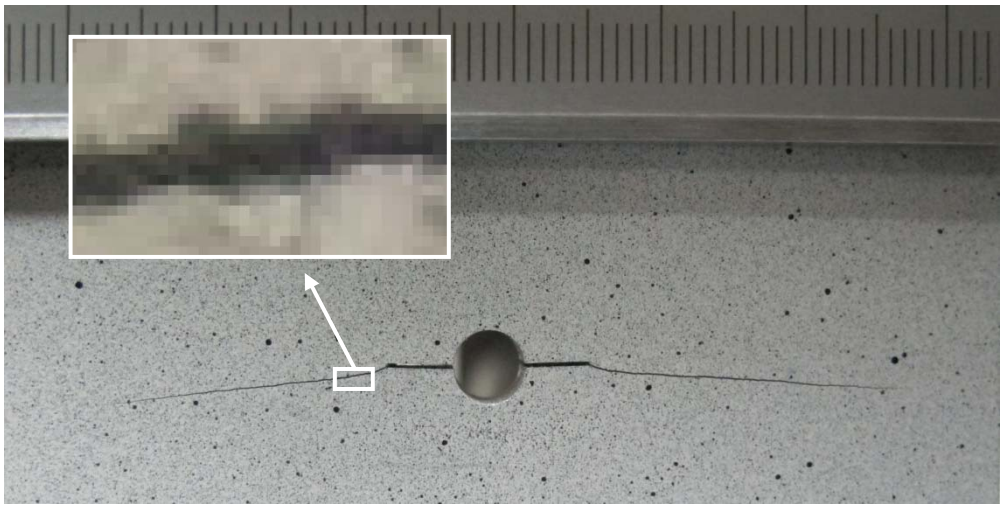

Figure 3. Image analysis measurement method for crack opening contour

To investigate delamination behavior, etch the specimen when a_m reaches nearly 12mm, 17mm and 22mm. Through image analysis measurement method, acquired delamination shape and size finally, as shown in Fig. 4.

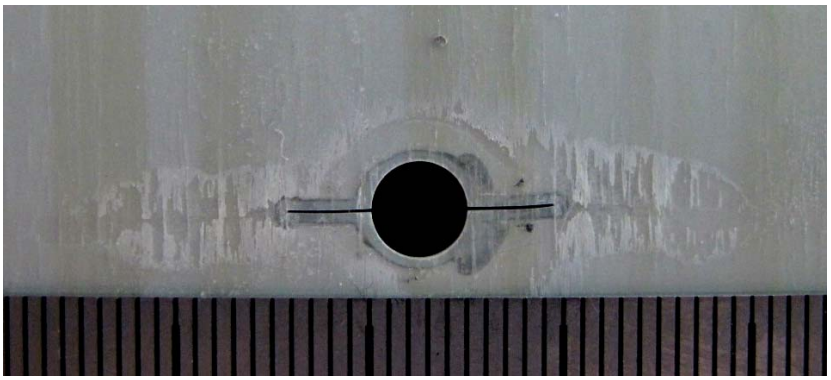

Figure 4. Image analysis measurement method for delamination shape and size after etching

2. Results and Analysis

2.1. Crack opening contour

Experimental data and fit curves are shown in Fig. 5. The direction of axis *x* represents the direction of crack propagation and the zero point in axis *x* is the location of the saw-cut tip.

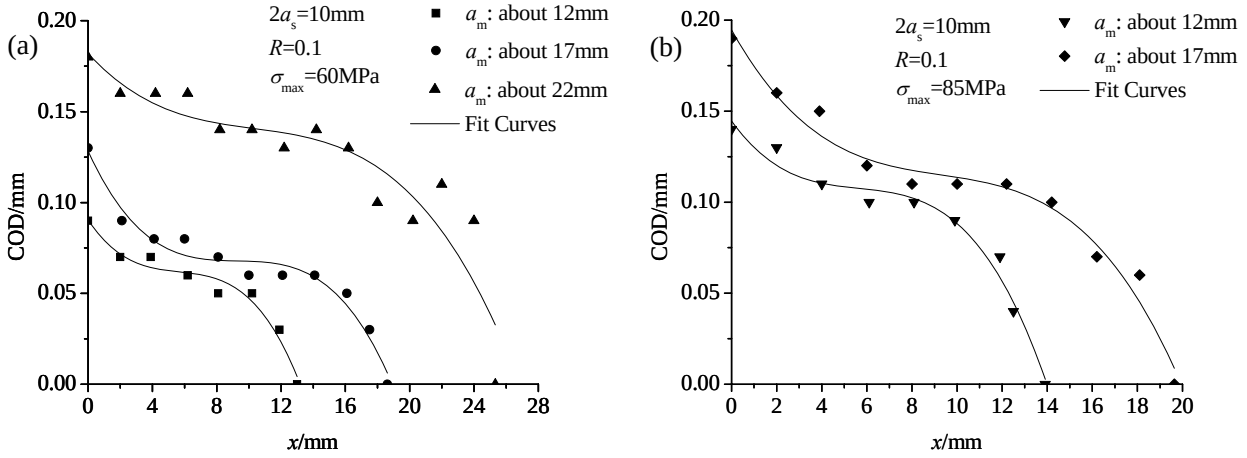

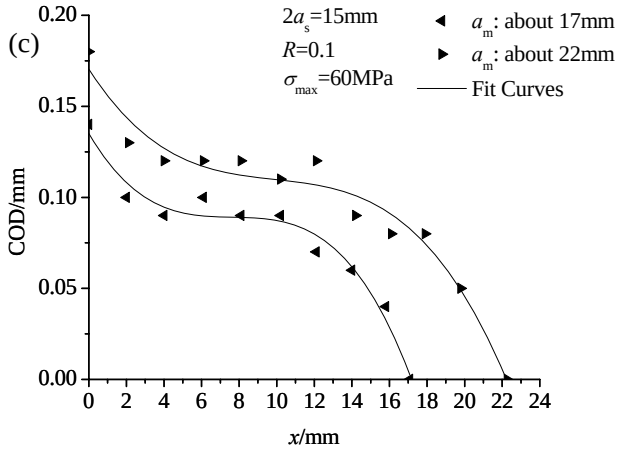

Figure 5. Variation of crack opening contour

As shown in Fig. 5, the crack opening contour can be described as: be maximum value near the tip of saw-cut, decline rapidly along the crack propagation direction, remain almost a constant value in the middle, and decrease to zero at the tip of the crack. Based on the distribution of data, it can be fitted to time by cubic polynomial equation perfectly.

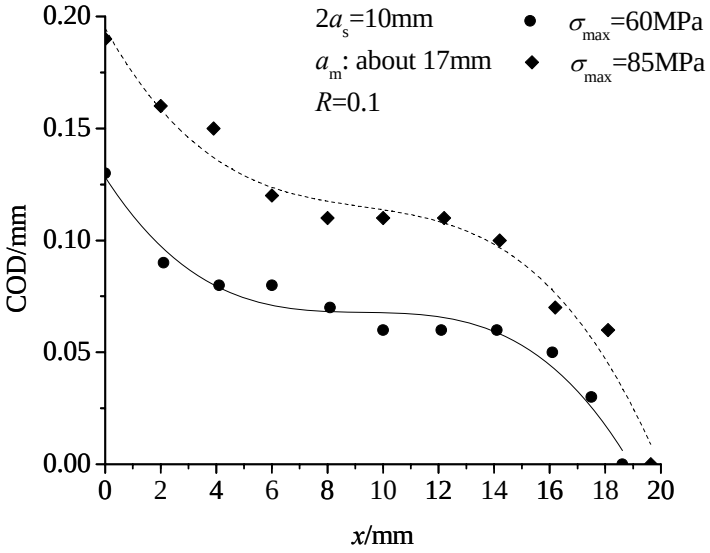

Figure 6. Influence of stress level on crack opening contour

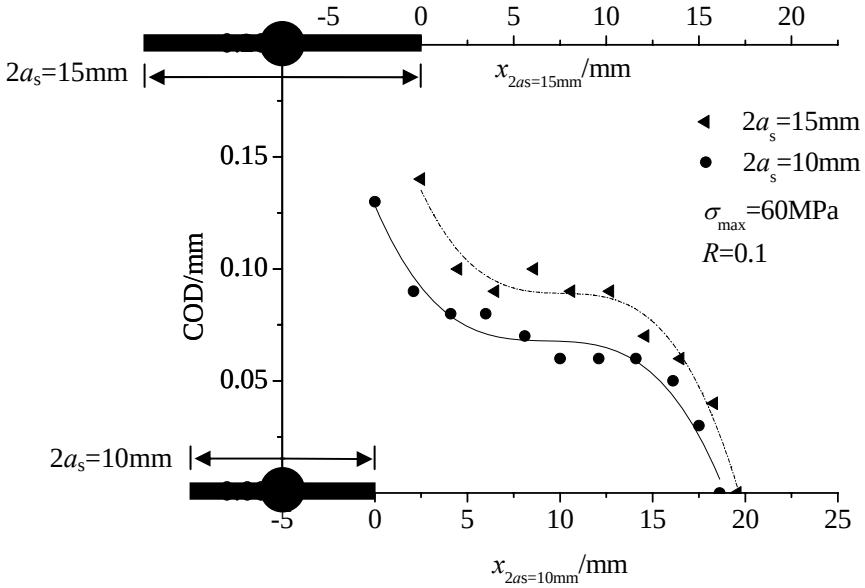

Figure 7. Influence of saw-cut length on crack opening contour

The crack opening contour for a nearly 17mm average crack length under two different stress level is shown in Fig. 6. It can be seen that crack opening contour increase significantly with a higher stress level.
On the other hand, Fig. 7 display the relationship between saw-cut length and crack opening contour. The crack opening contour in a larger 15mm saw-cut length is slightly larger.

2.2. Delamination shape and size

Past studies[2, 16] have described the crack length and delamination in each layer for AHL in detail, as shown in Fig. 8. The outer aluminium alloy sheet, adhesive film and inner aluminium alloy sheet own the same longer length crack without delamination inside. There is a large delamination size between inner aluminium alloy sheet and prepreg, and the sharp point of the delamination locate in the same place with the crack tip of inner aluminium alloy sheet. Crack in central aluminium alloy sheet is obviously shorter than other layers, meanwhile there is a smaller size delamination between prepreg and central aluminium alloy sheet.

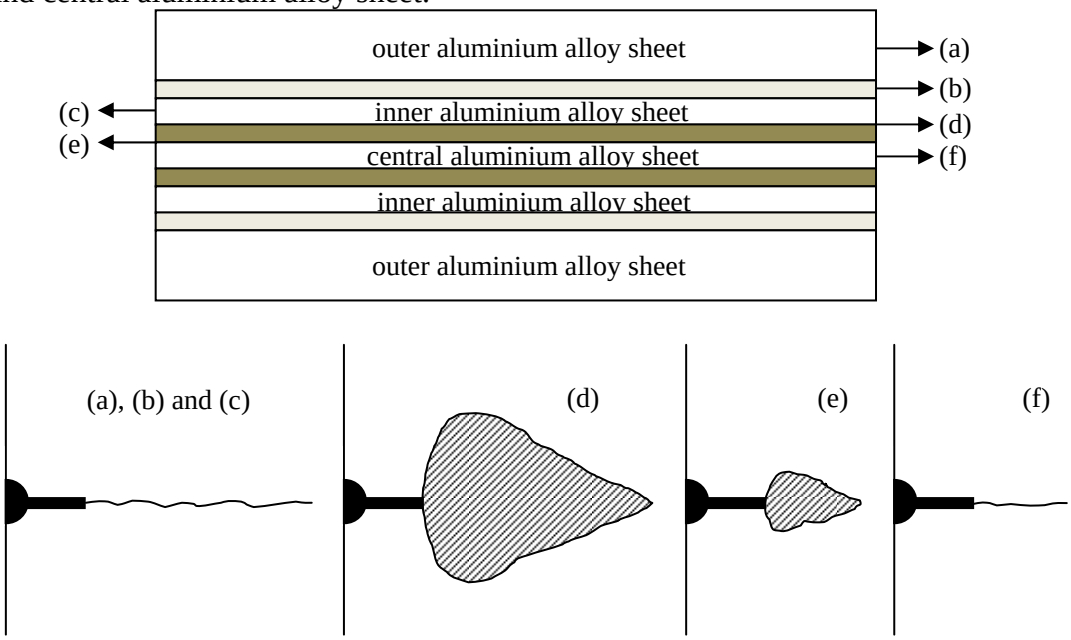

Figure 8. Crack and delamination in each layers

The delamination between inner aluminium alloy sheet and prepreg affect the fiber bridging effect markedly for its large scale, determine the fatigue crack propagation property of AHL, and thus is selected as the study object for delamination behavior.
The results are shown in Fig. 9(a-c). Similar with above, the direction of axis x represents the direction of crack propagation and the point in axis x=0 and axis y=0 is the location of the saw-cut tip.
Fig. 9(a-c) indicates the variation of delamination between inner aluminium alloy sheet and prepreg. With the increase of crack length, delamination grows larger while remaining a similar shape: the size close to zero in the crack tip, increase from crack tip to saw-cut tip, and decrease slightly near the saw-cut tip. Considering the symmetry of the delamination shape, delamination data were grouped and compared after adding together the data from two sides of crack. As shown in Fig. 10, data in axis d represent the width of the delamination shape in Fig. 9, that is $d=|y_1-y_2|$, in which y_1 and y_2 separately indicate the data of upper and lower delamination boundary.

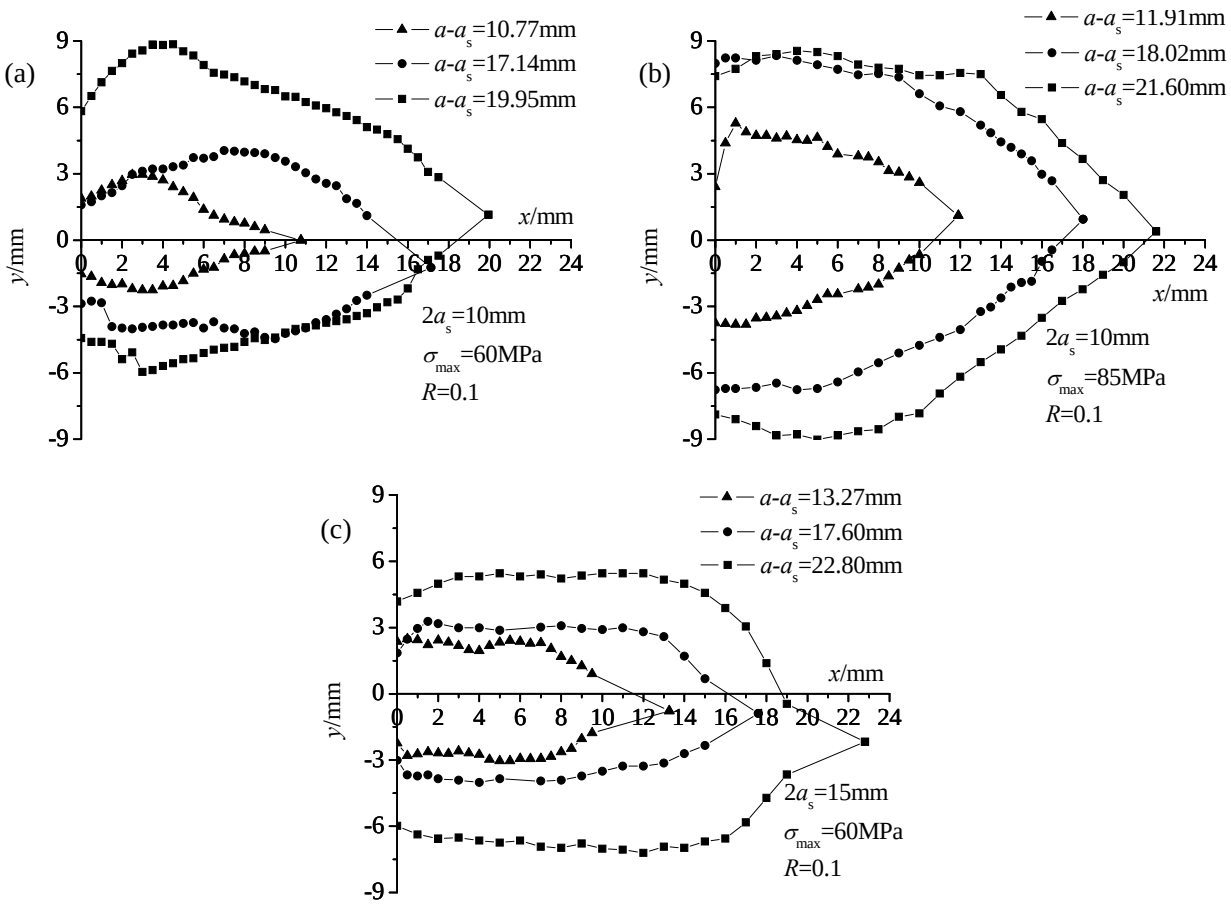

Figure 9. Variation of delamination between inner aluminium alloy sheet and prepreg

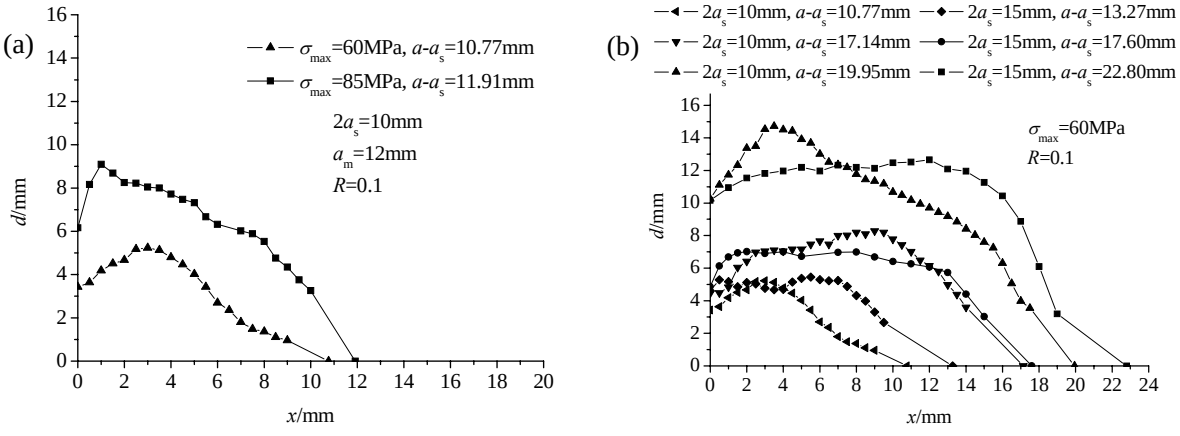

Figure 10. Influence of saw-cut length and stress level on delamination size

Delamination size in the higher stress level is clearly larger than it in lower stress level, as shown in Fig. 10(a). Stress level has a significant impact on delamination behavior. Previous work had shown that the bridging stress becomes too low in case the delamination growth is high, resulting in inefficient fiber bridging[15]. As a result, for AHL, in the condition of high stress level, the bridging effect drops so that the fatigue crack propagation property reduces.

However delamination size seems to be same with different saw-cut length, as shown in Fig. 10(b). Thus it can be seen that the influence of saw-cut length on delamination behavior for AHL is not distinct.

3. Conclusions and prospect

Based on the test data and analysis, it can be concluded as follows:
(1) The crack opening contour of AHL is typically regular, that is be the maximum value at the saw-cut tip, be zero at the crack tip, nearly remaining a constant value in the middle. And the data of crack opening contour is suitable for cubic polynomial fitting.
(2) The crack opening contour becomes larger as the stress level or saw-cut length rises when the other condition is the same.
(3) Delamination shape between inner aluminium alloy sheet and prepreg stays the same basically, that is be nearly zero at the crack tip, increase from crack tip to saw-cut tip, and decrease slightly near the saw-cut tip.
(4) The delamination size increases as the stress level rises when the other condition is the same. The influence of saw-cut length on delamination behavior is not distinct.
Because of the balance of bridging stress, crack opening contour and delamination, there is significance for the data of crack opening contour, delamination shape and size displayed in this research, which can support the creation and verification of fatigue crack propagation predict model for AHL.

Acknowledgements

Advanced hybrid laminates were prepared by Post Doctor Shigang Bai and Master Shiyu Wang in Harbin Institute of Technology. Specimen processing and fatigue crack propagation test were finished with great help of Engineer Shufen Li in Beijing Institute of Aeronautical Materials and Professor Liyang Xie, Professor Ruijin Zhang, Doctor Anshi Tong in Northeastern University (China). I would like to express my heartfelt gratitude to all the people mentioned above.

References

[1] A. Vlot, J.W. Gunnink, Fibre Metal Laminates, an introduction, Kluwer Academic Publishers, Dordrecht, The Netherlands, 2001.
[2] Geert H.J.J. Roebroeks, Peter A. Hooijmeijer, Erik J. Kroon. The development of CentrAl. First International Conference on Damage Tolerance of Aircraft Structures. 2007.
[3] Robert S. Fredell, J.W. Gunnink, R.J. Bucci, Jens Hinrichsen, "Carefree" hybrid wing structures for aging USAF transports, First International Conference on Damage Tolerance of Aircraft Structures. 2007.
[4] R. Marissen, Fatigue Crack Growth in ARALL, A hybrid Aluminium-Aramid Composite Material, crack growth mechanisms and quantitative predictions of the crack growth rate, PhD Thesis, Delft University of Technology, 1988.
[5] Y.J. Guo, X.R. Wu, A theoretical model for predicting fatigue crack growth rates in fibre-reinforced metal laminates, Fatigue Fract Eng Mater Struct, 21 (1998) 1133–1145.
[6] Y.J. Guo, X.R. Wu, Bridging stress distribution in center-cracked fiber reinforced metal laminates: modelling and experiment, Eng Fract Mech, 63 (1999) 147–163.
[7] Y.J. Guo, X.R. Wu, A phenomenological model for predicting crack growth in fiber-reinforced metal laminates under constant-amplitude loading, Compos Sci Technol, 59 (1999) 1825–1831.
[8] T. Takamatsu, T. Matsumura, N. Ogura, T. Shimokawa, Y. Kakuta, Fatigue crack growth of a GLARE3-5/4 fiber/metal laminate and validity of methods for analysing results, 20th symposium international committee on aeronautical fatigue, Bellevue Washington, USA, 1999.
[9] D.A. Burianek, Mechanics of fatigue damage in titanium-graphite hybrid laminates, PhD thesis, Massachusetts Institute of Technology, 2001.
[10] Y.J. Guo, X.R. Wu, Fatigue behaviour and life prediction of FRML under CA and VA loading, Fatigue Fract Eng Mater Struct, 25 (2002) 417–432.
[11] Wu XJ. A higher-order theory for fiber–metal laminates. In: Proceedings of the 23rd

International Congress on Aeronautical Sciences, Toronto, Canada, 2002.
[12] T. Takamatsu, T. Shimokawa, T. Matsumura, Y. Miyoshi, Y. Tanabe. Evaluation of fatigue crack growth behaviour of GLARE3 fiber/metal laminates using compliance method, Eng Fract Mech, 70 (2003) 2603–2616.
[13] R.C. Alderliesten, Fatigue Crack Propagation and Delamination Growth in Glare, PhD Thesis, Delft University of Technology, 2005.
[14] H.M. Plokker, Crack closure in GLARE, Master's Thesis, Delft University of Technology, 2005.
[15] R.C. Alderliesten, Analytical prediction model for fatigue crack propagation and delamination growth in Glare, Int J Fatigue, 29 (2007) 628–646.
[16] X. Huang, J.Z. Liu, Fatigue crack propagation and delamination behavior of advanced fiber metal hybrid laminate, Journal of Aeronautical Materials, 32 (2012) 97-102.

Subcycle Fatigue Crack Growth Mechanism Investigation for Aluminum Alloys and Steels

Jian Yang[1], Wei Zhang[1], Yongming Liu[1,*]

[1] Mechanical Engineering, Arizona State University, Tempe 85281, US
* Corresponding author: yongming.liu@asu.edu

Abstract In this paper, the existence of crack closure and its sufficiency for crack growth prediction is investigated by multi-resolution in-situ optical microscopy experiment and SEM experiment. In in-situ optical microscopy testing, the digital image correlation analysis is used to measure the plastic zone size in front of the crack tip. In in-situ SEM testing, the crack tip opening displacement and the crack growth kinetics are investigated. Besides, crack closure behavior under constant loading with a single overload is studied in in-situ SEM test. This experimental methodology is applied to two different metallic materials (aluminum alloys and steels). Detailed imaging analysis and experimental results are presented and compared. It is found that first, there exists crack closure phenomena for aluminum alloys, but not for steels in our current researches; second, the crack closure will significantly change the crack tip plasticity behavior; third, the crack closure concept is able to account for crack growth kinetics uniquely for constant loading, but it is insufficient for constant loading with a single overload. Finally, the necessarily and the insufficiency of crack closure for crack growth prediction is discussed.

Keywords fatigue, crack closure, crack growth, plastic zone, overload

1. Introduction

In the past half century, many existing studies have been done on fatigue crack growth mechanism and prediction models. The most famous and successful model should be Paris' Law, which based on the applied stress intensity range [1]. However, Paris' model cannot be applied to loadings with different load ratio and modification is required. In 1970, Elber introduced a crack closure mechanism and modified the applied stress intensity factor range in order to characterize the effect of load ratio [2]. Since Elber's discovery provides a physical meaning to the modification, many researches have been done to get crack-opening load in theoretical method or experimental way. In 1978, Budiansky and Hutchinson provided an analytical estimation of crack opening load with the assumptions of long crack and small scale yielding according to the ideally plastic Dugdale-Barenblatt model [3]. In 1984, Newman analyzed the crack closure problems by developing a strip yield model, which employs a strip yield type plastic zone for leaving residually stretched material in the wake of the crack, causing plasticity-induced closure [4]. However, it is found that the measurement is difficult and the result depends on the measuring location and technique employed such as by traditional gauge and acoustic method [5]. Others methods like electrical potential method [6], ultrasonic method [7][8], and numerical method [9] are also used to measure crack opening load. These methods mentioned are indirectly way to observe crack closure and measure the crack opening loading, and it might be affected by many other factors, for example, it is found that commonly employed notch-mouth clip-gauge method is not sensitive enough to detect the closure of short cracks in regions of notch plasticity [10].

In this paper, in-situ testing and imaging analysis is used to directly observe the crack closure level and its relationship with crack tip behavior. Compare to the other indirect method, it is non-contact and can provide direct evidence about the crack closure at very different resolutions. Next, the proposed methodology is applied to two different metallic material systems and the existence of crack closure is investigated in detail. Following the testing under constant loading, a variable loading situation is tested to investigate crack closure effects on crack growth rate. In mechanics,

the crack closure behavior under overloading load is investigated in detail. Meanwhile, a statistical crack growth rate under constant loading and overloading load is compared. Finally, a discussion for the existence and insufficiency of crack closure for the fatigue crack growth analysis is given based on the current investigation.

2. In-situ optical microscopy study for crack closure

In in-situ optical microscopy test, a unit load cycle is divided into several steps and images are taken at each step. By digital image correlation analysis, then the strain distribution can be calculated. When the load is decreasing, the plastic zone is increasing due to the reversed plastic flow. However, if the crack is closed, the crack surfaces will contact and begin to undertake the reversed stress, thus the reversed plastic zone size will stop increasing. The reversed plastic zone size is a better indicator for crack closure than many other methods due to the advantages of non-contact and a stable precision inherited from digital image correlation method.

2.1. Experiment set-up and procedure

The experimental set-up for in-situ optical microscopy experiment is shown in Figure 1. It contains two parts: a palm-sized tensile stage and an optical microscope system. The tensile stage is fixed on the microscope and the cyclic loading is applied to the specimen. A Nikon metallurgical microscope is used to monitor the specimen surface and a high resolution imaging acquisition system is used to record images during the testing.

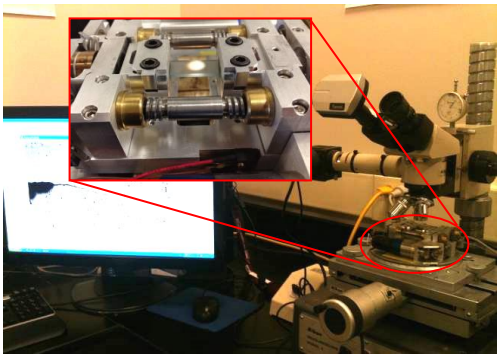

Figure 1. Experiment setup

The specimen is a ingle edge notched plate with width W = 8 mm, length L = 52 mm and thickness T = 0.86 mm. Due to the small thickness of specimens, it is assumed to be under the plane stress conditions for a relatively long crack. An edge notch of length 1mm is machined on the specimen. After machining, the specimens are pre-cracked until the initial crack reaches about 1 mm. The pre-cracking procedure follows the ASTM standard E647-08. Following this, both surfaces of the specimen are polished with the sandpaper whose average particle diameter is smaller than 10 um.

The experiment procedure contains four major steps.

Step 1: specimen manufacturing and pre-cracking. Single edge notched plate specimen is used for testing. After notching, the specimens are pre-cracked under a hydraulic tension machine INSTRON 1331 until the initial crack reaches about 1 mm. The pre-cracking procedure follows the ASTM standard E647-99;

Step 2: polish the specimen to form randomly distributed small dark regions on the smooth surface,

which is a requirement for digital image correlation (DIC) analysis. Both surfaces of the specimen should be polished with the sandpaper whose average particle diameter is smaller than 10 um. The final polishing is done using a vibration polishing machine with 1~3um polishing suspension;

Step 3: apply load on the specimen under the monitoring of a microscope, while image of the crack tip region is taken during the loading and unloading process. A unit load cycle is divided into several steps in the load profile. At each step, the image around the crack region is taken for strain calculation. The step load is set according to the precision requirement and computation resource limitation. An example profile is shown in Figure 2, which has about forty segments during the loading and unloading path.

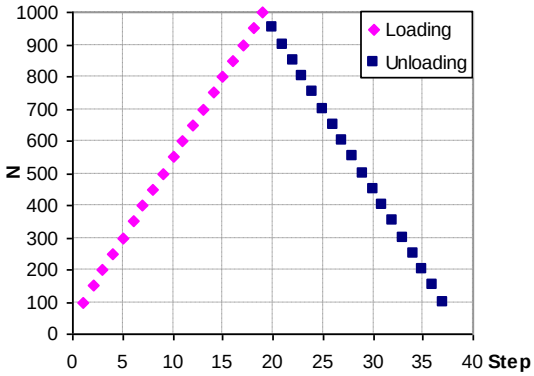

Figure 2. Load profile

Step 4, process the images by DIC software to get the strain field of the crack tip region and calculate the plastic zone using mechanical analysis. The plastic zone size is defined along the crack propagation direction and it can be measured directly from the processed image.

The theoretical reversed plastic zone under cyclic loading can be estimated by Eq. (1) without the consideration of crack closure [11]

$$\rho = \frac{1}{\pi}\left(\frac{\Delta K}{2\sigma_y}\right)^2, \tag{1}$$

where σ_y is the yielding strength and

$$\Delta K = F \cdot \Delta\sigma\sqrt{\pi a} = F \cdot (\sigma_{\max} - \sigma_{\min})\sqrt{\pi a} \tag{2}$$

where F is the geometry factor and

$$\mathrm{F} = 1.12 - 0.231\left(\frac{a}{W}\right) + 10.55\left(\frac{a}{W}\right)^2 - 21.72\left(\frac{a}{W}\right)^2 + 30.39\left(\frac{a}{W}\right)^3 \tag{3}$$

where a is the crack length.

2.2. Title and author information

With the above described experiment procedure, two sets of experiment are carried out to investigate the crack closure behavior under constant loading in Al 7075-T6 and Steel 4340 separately.

The chemical composition aluminum 7075-T6 is listed in Table 1. The aluminum is the balance in the total weight. The basic physical properties are listed in Table 2.

Following the above discussed general experiment methodology, the plastic zone size at each

loading step can be measured using the digital image correlation analysis. Three specimens have been tested and the reversed plastic zone size is shown in Figure 3. It can be found that there is a plat form when stress intensity factor (SIF) is less than about 3.5 MPa·m$^{0.5}$, which indicates the crack closes and the reversed stress is released by the surface contact.

Table 1. Chemical composition of Al 7075-T6 (weight, %)

Element	Zn	Mg	Cu	Fe	Si	Mn	Cr
Min	5.1	2.1	1.2	0	0	0	0.18
Max	6.1	2.9	2.0	0.5	0.4	0.3	0.28

Table 2. Basic mechanical properties of Al 7075-T6

Elastic Modulus /GPa	Yield Strength /MPa	Tensile Strength /MPa
71.7	502~516	573~582

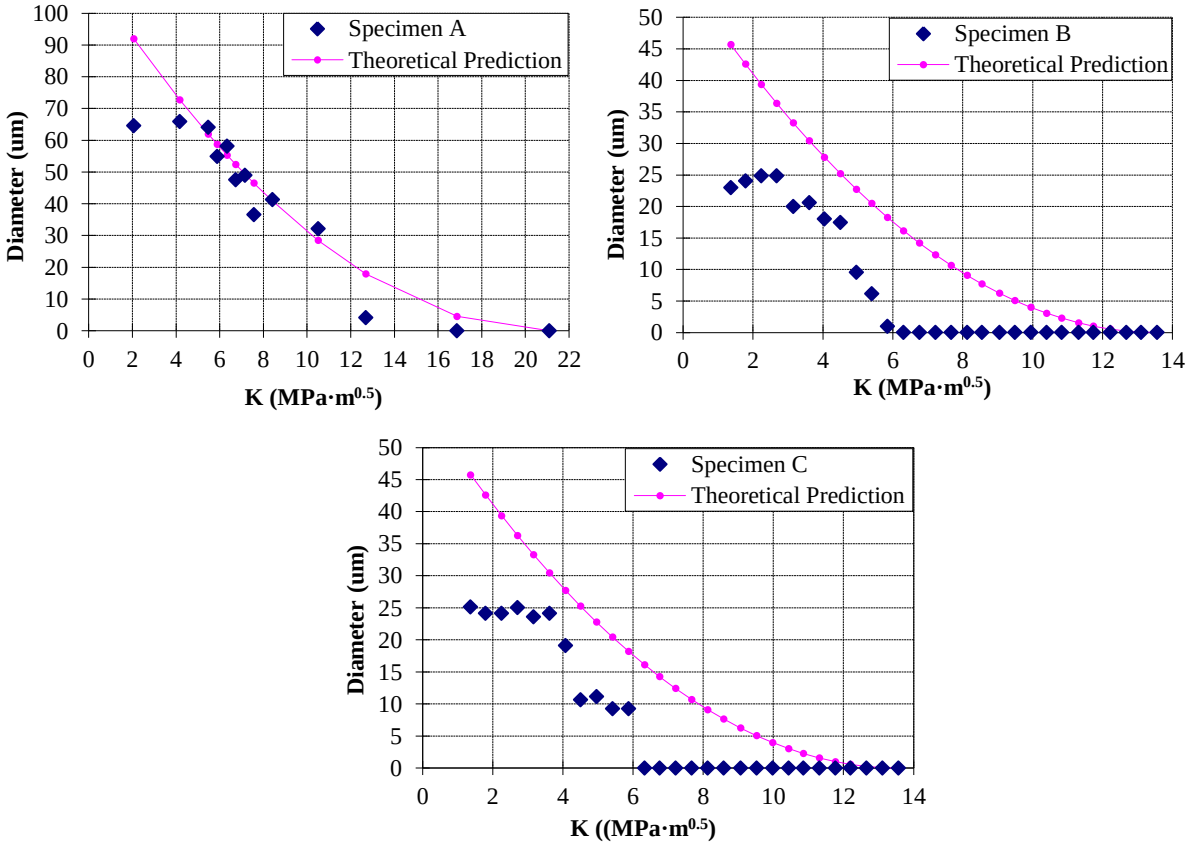

Figure 3. Plastic zone size of aluminum [12]

The same experiment is carried on steel 4340. AISI 4340 steel is a heat treatable, low alloy steel containing nickel, chromium and molybdenum. The chemical composition of this material and its basic physical properties are listed in Table 3 and 4.

Table 3. Chemical composition of AISI 4340 steel

Element	C	Cr	Mn	Mo	Ni	P	Si	S
Min	0.38	0.7	0.6	0.2	1.65	0	0.15	0
Max	0.43	0.9	0.8	0.3	2	0.035	0.3	0.04

Table 4. Basic physical properties of AISI 4340 steel

Elastic Modulus /GPa	Yield Strength /MPa	Tensile Strength /MPa
190~210	472.3	744.6

In the test, the load starts from 100 N to 1000 N at a step of 50 N. Result of the plastic zone size during the unloading process is obtained as shown in Figure 4. It is found that the reversed plastic zone size keeps increasing throughout the unloading process and these experiment data shows similar trends to the theory data without plastic closure phenomena. This is very different compared with the results of aluminum alloys and it indicates no crack closure for steel in these tests.

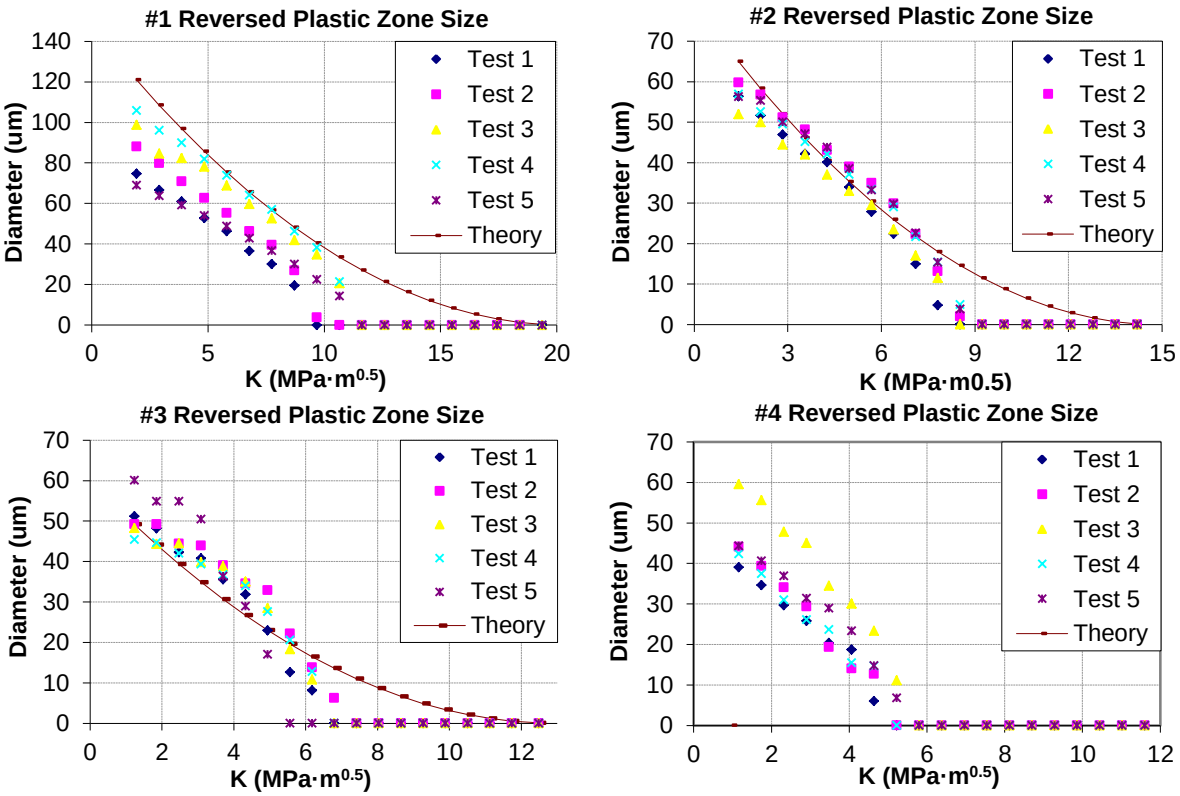

Figure 4. Plastic zone size of steel specimens

3. In-situ SEM study for crack closure

In order to verify the crack closure indications from optical microscope observation and get further information of the crack tip deformation behavior, in-situ SEM experiment is carried out on the two materials. Further, the behavior of crack closure under variable load is studied for the sufficiency of K_{eff} for crack growth prediction. In mechanics, crack closure behavior under a single overload is studied for the sufficiency of K_{eff} for crack propagation mechanics. In statistics, the crack growth rate under constant loading and overloading load is compared to show the sufficiency of K_{eff} for crack growth prediction. Detailed experimental procedure has been discussed in [13][14] and only a brief description of the experimental methodology is given below.

3.1. In-situ SEM study under constant amplitude loading

An in-situ SEM fatigue testing is performed to achieve the high resolution investigation for the hypothesis verification of crack growth kinetics and crack deformation in the vicinity of the crack tip. Compared with experiment under optical microscope, crack tip opening displacement (CTOD) is measured directly to find the crack is closed or not. Some details of the experimental set-up for the in-situ SEM experiment are shown in Figure 5. It consists of the tensile sub-stage and a field emission SEM (JEOL-7400F). The sub-stage is fixed in the SEM and the cyclic loading is applied during the experiment. Multiple resolution images are recorded during the testing for the

measurements of crack length and the crack tip deformation behavior.

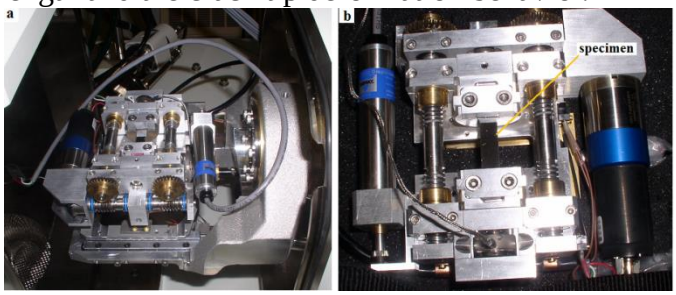

a) loading stage installed in SEM; b) specimen installed in loading stage.
Figure 5. In-situ SEM fatigue testing setup

The specimen configuration and preparation are almost the same as that in optical microscope experiment. In this experiment, the final polishing is done by a vibration polishing machine with 1~3 um polishing suspension.

The specimen is undergoing cyclic loading and observed in-situ under SEM. In the following comparison for aluminum and steel, the stress ratio is 0.1. The measurements are usually taken after 50 to 100 cycles to ensure the crack growth is stable. During the testing, one loading cycle is divided into many steps, similar with the testing under optical microscopy. The applied loading increases/decreases at a very slow rate. CTOD is measured directly from the processed images. The CTOD is defined as the distance of crack surface at the place of crack tip in last cycle. With the same reference, the crack growth rate at each cycle could be measured, as shown in Figure 6.

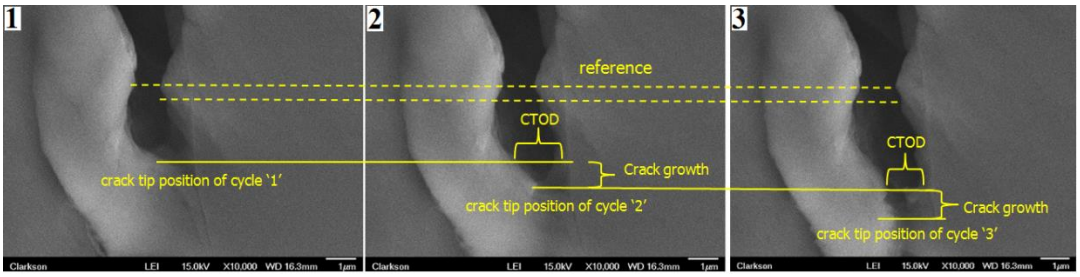

Figure 6. Images of crack tip position and CTOD under maximum loadings

Using the measuring method, two sets of experiments on steel 4043 and aluminum 7075-T6 have been performed. The results are shown in Figure 7. It shows that CTOD reduces to zero when SIF is less than 5 MPa·m$^{0.5}$ for Al 7075-T6, while for steel 4340, CTOD is not zero under the minimum loading. The crack tip details are shown in Figure 8. It shows the crack closure in Al 7075-T6 clearly but the crack remains open for steel 4340.

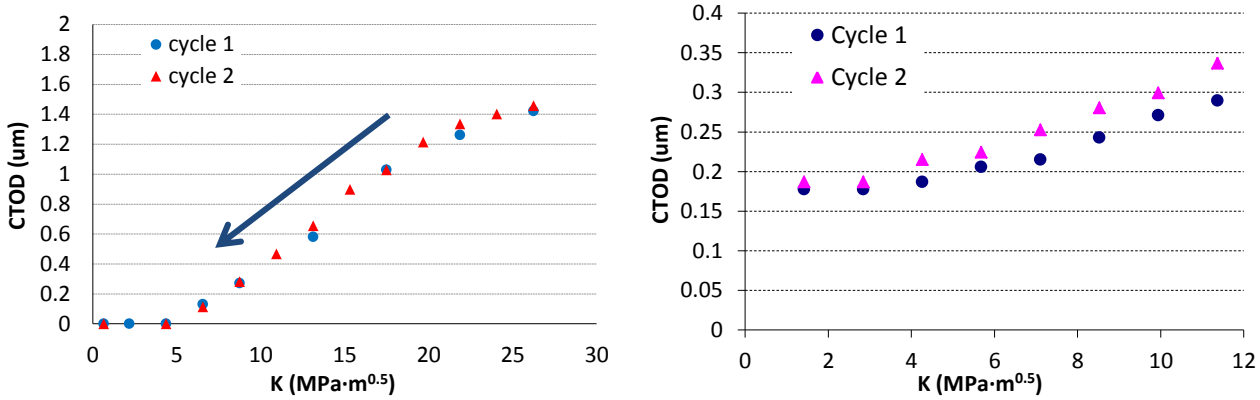

(a) Al 7075-T6 (b) Steel 4340

Figure 7. CTOD during unloading process on Al 7075-T6 and steel 4340

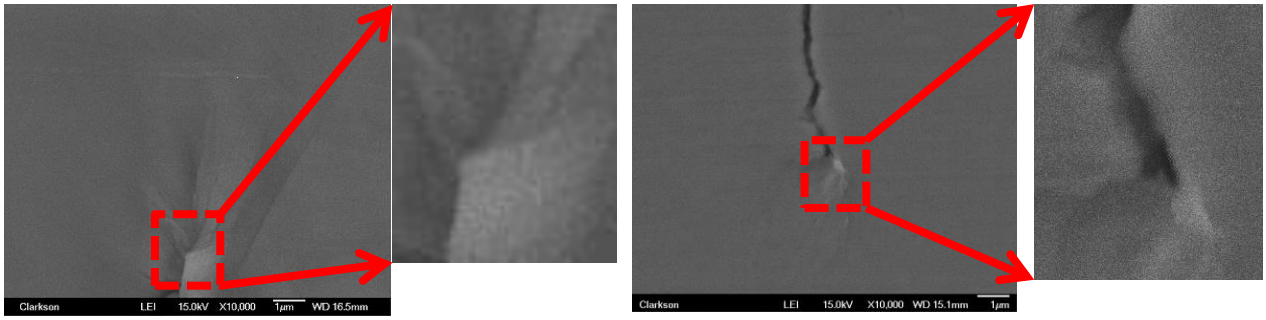

(a) Al 7075-T6 (b) Steel 4340

Figure 8. Crack tip under minimum loading of Al 7075-T6 and steel 4340

This result is consistent to the experiment under optical microscope and they show that the existence of crack closure in Al 7075-T6, but it is not observed in steel 4340 at this stage.

3.2. In-situ SEM study under variable loading with single overload

As crack closure is observed both under optical microscope and SEM, its effects on crack growth rate is not negligible for fatigue crack growth prediction for some metallic materials, if it happens. However, it is not clear that the crack closure is the only/dominant mechanisms for aluminum materials, especially under different loading conditions. Thus, the crack closure effect on crack growth rate under variable loading is investigated and is shown below.

The procedure of SEM experiment under variable loading is the same with that under constant loading. The only difference is the loading profile. In this experiment, a cycle of over-load is inserted in a constant loading spectrum. The constant loading ranges from 10 to 30 MPa·$m^{0.5}$ and the overload ranges from 10 to 36 MPa·$m^{0.5}$. Thus the over load ratio is 1.2 as the ratio of two maximum load. A schematic plot is shown in Figure 9.

In order to observe and compare the effects of overload loading, four types of loading cycle are chosen for observations. The first type is the constant loading cycles before the over load (cycle **A** in Figure 9), which provides the baseline information of the crack propagation kinematics. The second and the third type are the overload cycle (B) and the cycle right after it (C). The last type is the cycle 5~20 cycles after the overload (D). In this study, two experiments data are obtained. In the first experiment, the background stress ratio is 0.33 and the overload ratio is 1.2. In the second experiment, the background stress ratio is 0.025 and the overload ratio is 1.1. In the following discussion, the result of the first experiment will be discussed in detail and the second one will be given as a comparison.

Following the experiment procedure and the loading profile, the details of crack growing before, during, and after overload under SEM is obtained and compared.

For all testing measurements, the crack opening stress intensity factor at each observing cycle are plotted in Figure 10. The X axis is cycle number and Y axis is the ratio of crack opening SIF over the maximum SIF (K_{open}/K_{max}). It is shown that during the constant loading in stage 1 (cycle A), K_{open}/K_{max} is 0.57. In the overload cycle (B) and right after the overload cycle (C), the crack opening slightly decreases and increases to about 75% after more than 10 cycles (D). Another experiment has been performed with stress ratio R=0.025, the maximum SIF of the constant loading is 26.26 MPa·$m^{0.5}$ and the overload ratio 1.1. Very similar result is observed as shown in Figure 11.

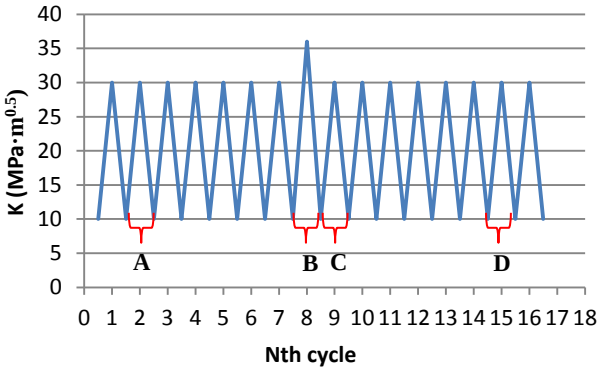

Figure 9. Schematic representation of single overload spectrum

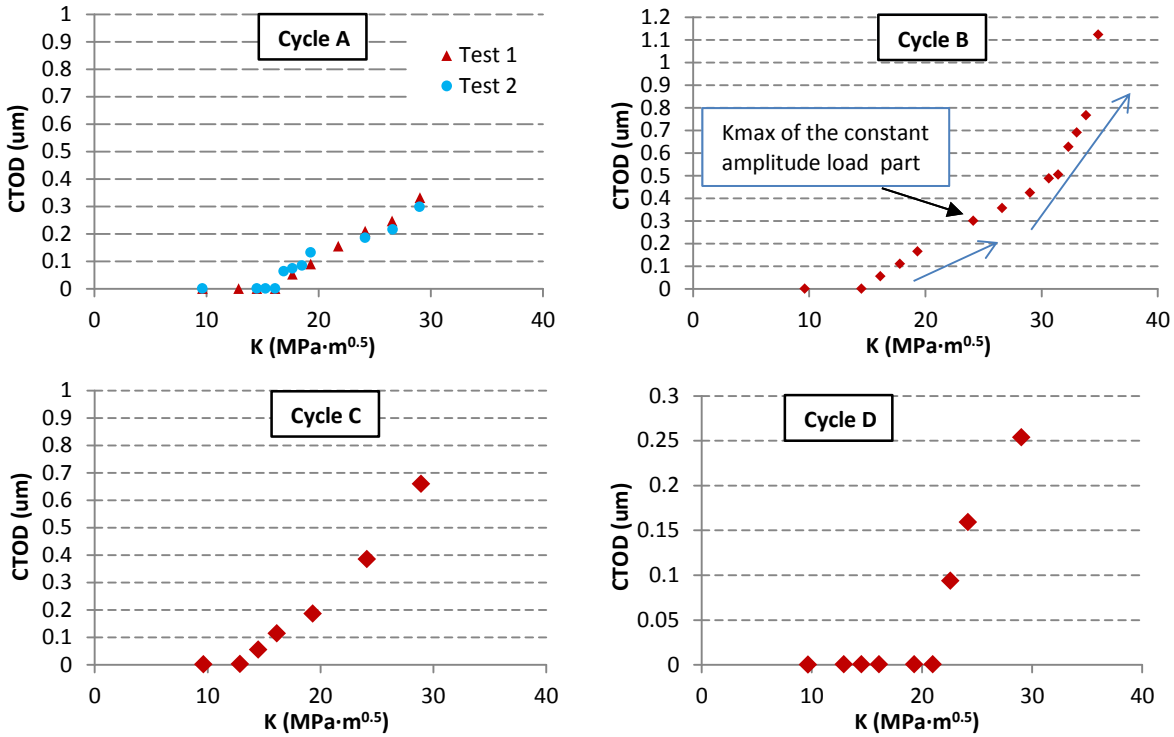

Figure 10. CTOD variation at each loading cycle in Figure 9

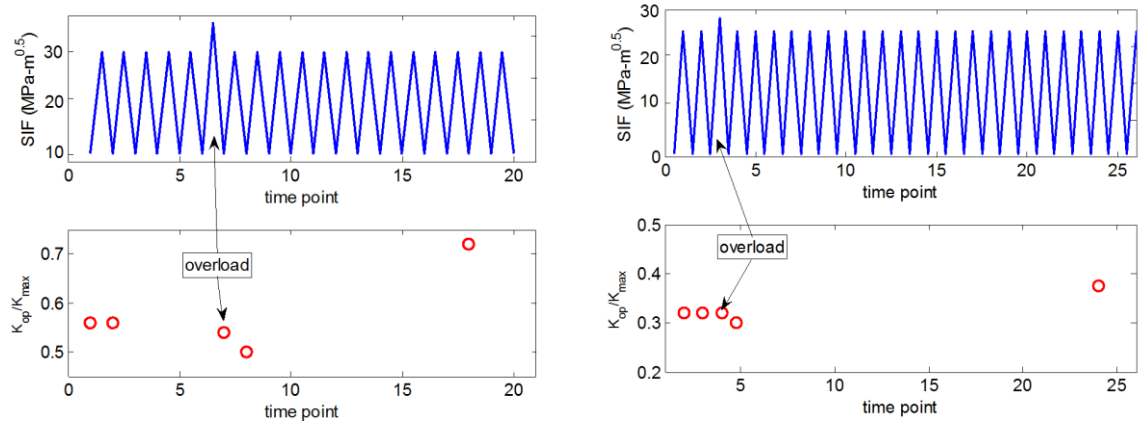

(a) R=0.33 (b) R=0.025

Figure 11. Illustration of the crack opening stress level variation

One important hypothesis in the classical crack closure theory is that the effective stress intensity

factor range (defined as the maximum SIF minus the opening SIF) can be used to uniquely correlate with crack growth rate under different loadings. However, this experiment shows that under single overload loading, crack opening SIF becomes variable and crack starts to kink and bifurcate. These mechanics cannot be explained only by the phenomena of crack closure.

Further, a statistical study of crack growth rate under constant load and overload lading is conducted to verify this hypothesis. Several experiments have been completed at stress ratio R=0.5, 0.33, 0.1 and 0.025, and the result of crack growth rate with the effective SIF is plotted in Figure 12. Figure 12 (a) shows the result under constant loading. It can be found that all the data shows a good linear relationship in log-log scale, except one data in red dashed circle. Figure 12(b) shows the data together with the single overload testing. It is observed that the two data points are not consistent with the linear trend from the constant amplitude loading data. This observation further indicates that other mechanism also contributes to the crack growth under single overload loading, such as crack branching and blunting as observed in the experiment.

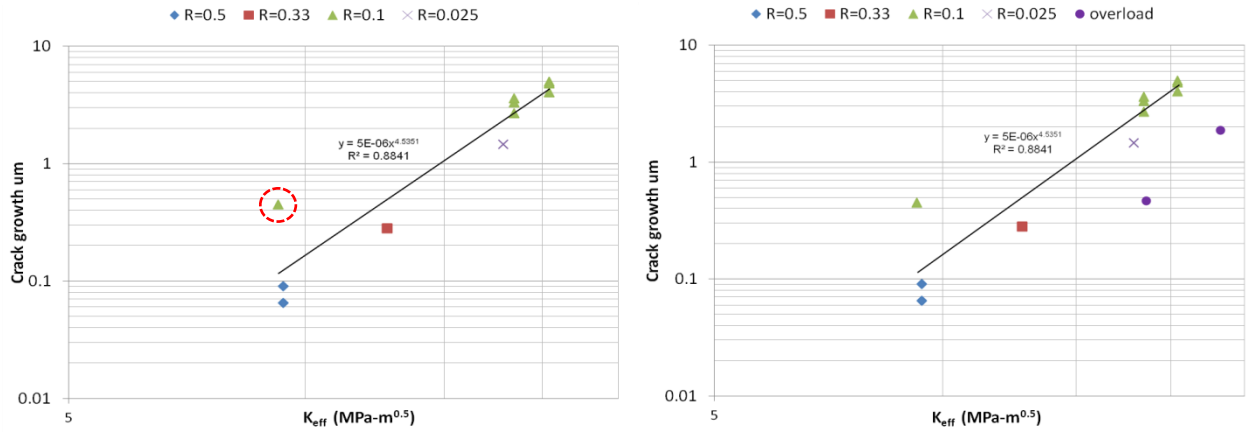

(a) Constant load (b) Constant loading and overloading load

Figure 12. Crack growth rate with SIF under constant load and overloading load

3. Conclusions

In this paper, in-situ experiment at micrometer scale and nanometer scale has been introduced and the observation of crack closure behavior of steel 4340 and aluminum 7075-T6 under constant loading has been obtained. Besides, preliminary crack closure behavior under single overload on aluminum 7075-T6 is studied. Several conclusions can be made from the experiments as follows.

1. Crack closure is directly observed in Al 7075-T6 under both constant and variable loads, but it is not observed in steel 4340 under constant loading at stress ratio 0.1.

2. The crack closure can significantly change the plasticity distribution in front of the crack tip;

3. K_{eff} defined as the difference of K_{max} and K_{open} in the classical fracture theory correlates with the unique crack growth rate under constant loading, but it not enough for crack growth prediction under variable loading. Additional parameter for the mechanism is need for the prediction;

The proposed study focus on simple variable loadings and more complex loading conditions require additional study. The current imaging analysis is for surface measurements and 3D imaging technique will be very helpful for the investigation of subsurface behavior near a crack tip.

Acknowledgements

The research was supported by funds from Air Force Office of Scientific Research: Young Investigator Program (Contract No. FA9550-11-1-0025, Project Manager: Dr. David Stargel). The support is gratefully acknowledged.

References

[1] P.C. Paris, M.P. Gomez, W.E. Anderson, A Rational Analytic Theory of Fatigue, Trend in Engineering. 13 (1961) 9–14.

[2] E. Wolf, Fatigue crack closure under cyclic tension, Engineering Fracture Mechanics. 2 (1970) 37–45.

[3] B. Budiansky, J. Hutchinson, Analysis of closure in fatigue crack growth, Journal of Applied Mechanics. 45 (1978) 267–276.

[4] J. J.C. Newman, A crack opening stress equation for fatigue crack growth, International Journal of Fracture. 24 (1984) R131–R135.

[5] D.E. Macha, D.M. Corbly, J.W. Jones, On the variation of fatigue-crack-opening load with measurement location, Experimental Mechanics. 19 (1979) 207–213.

[6] T.T. Shih, R.P. Wei, A study of crack closure in fatigue, Engineering Fracture Mechanics. 6 (1974) 19–32.

[7] D. Bouami, D. De Vadder, Detection and measurement of crack closure and opening by an ultrasonic method, Engineering Fracture Mechanics. 23 (1986) 913–920.

[8] D.S. Singh, A. Srivastav, S. Gupta, E. Keller, A. Ray, Ultrasonic measurement of crack opening load for life-extending control of mechanical structures, in: 2009 American Control Conference, IEEE, Piscataway, NJ, USA, 2009: pp. 210–215.

[9] W. Riddell, R. Piascik, M. Sutton, W. Zhao, S. McNeill, J. Helm, Determining Fatigue Crack Opening Loads from Near-Crack Tip Displacement Measurements, ASTM SPECIAL TECHNICAL PUBLICATION. 1343 (1999) 157–174.

[10] N. Fleck, C. Shin, Fatigue crack growth under compressive loading, Engineering Fracture Mechanics. 21 (1985) 173–185.

[11] J. Rice, A path independent integral and the approximate analysis of strain concentration by notches and cracks, Journal of Applied Mechanics. 35 (1968) 379–386.

[12] W. Zhang, Y. Liu, Plastic zone size estimation under cyclic loadings using in situ optical microscopy fatigue testing, Fatigue & Fracture of Engineering Materials & Structures. 34 (2011) 717–727.

[13] W. Zhang, Y. Liu, Investigation of incremental fatigue crack growth mechanisms using in situ SEM testing, International Journal of Fatigue. 42 (2012) 14–23.

[14] W. Zhang, Y. Liu, In situ SEM testing for crack closure investigation and virtual crack annealing model development, International Journal of Fatigue. 43 (2012) 188–196.

Application of Weakest Link Probabilistic Framework for Fatigue Notch Factor to Turbine Engine Materials

Oluwamayowa A. Okeyoyin[1,*], Gbadebo M. Owolabi[1]

[1] Department of Mechanical Engineering, Howard University, Washington DC 20059, USA
* Corresponding author: oluwamayowa.okeyoy@bison.howard.edu

Abstract

This paper is concerned with the extension of a recently developed probabilistic framework based on Weibull's weakest link and extreme-value statistics to aero-engine materials like titanium alloy and nickel-base super alloys using simulation strategies that capture both the essence of notch root stress gradient and the complexity of realistic microstructures. In this paper, notch size effects and notch root inelastic behavior are combined with probability distributions of microscale stress-strain gradient and small crack initiation to inform minimum life design methods. A new approach which can be applied using crystal plasticity finite element or closed-form solution is also proposed as a more robust approach for determining fatigue notch factor than the existing classical methods. The fatigue notch factors predicted using the new framework are in good agreements with experimental results obtained from literature for notched titanium alloy specimens subjected to uniaxial cyclic loads with various stress ratio.

Keywords: probabilistic mesomechanics, weakest link, microstructure-sensitive, fatigue notch factor, fatigue indicator parameters.

1. Introduction

Titanium alloy is widely used in aero engine components. The fatigue resistance of aero-engine components made from this material can be drastically reduced by the presence of small notches on the components formed from the ingestion of foreign objects causing foreign object damage (FOD) [1 - 2]. To account for the effects of FOD on the fatigue strength of these materials, the damage are usually modeled as notches with a certain depth and notch root radius [1- 2]. The severity of these notches in materials is characterized by the elastic stress concentration factor, k_t which is the ratio of peak (maximum) local stress at the notch root to the remotely applied stress, *S* as shown in Figure 1.

$$k_t = \frac{\sigma_{peak}}{S} \tag{1}$$

k_t is dimensionless and a compilation of its values for different notch geometries and loading modes can be found in Peterson's book [3]. However, k_t under-estimate fatigue life and several arguments have been attributed to this observation. The fatigue life of notched component is not only dependent on the peak stress as predicted by k_t, but also on the average stress that acts over a finite damage process zone. Consequently, fatigue life prediction methods based on k_t typically do not consider stress gradients which have been shown to influence the fatigue life of complex notched components [4 - 5]. Thus, the actual reduction factor on long fatigue lives is typically represented by the concept of fatigue notch factor, otherwise known as the fatigue strength reduction factor, k_f.

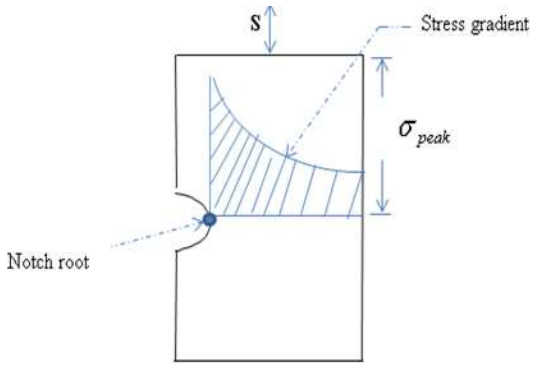

Figure 1. Stress distributions in a notched specimen

The fatigue notch factor, k_f, is determined at a given number of completely reversed cycles (typically 10^6 or 10^7) to crack initiation and is given as:

$$k_f = \frac{\sigma_f^{unnotched}}{\sigma_f^{notched}} \tag{2}$$

Where $\sigma_f^{unnotched}$ is the fatigue strength of the unnotched specimen and $\sigma_f^{notched}$ is the fatigue strength of the notched specimen. The difference between k_t and k_f for a given microstructure is typically represented by the notch sensitivity factor, q given as:

$$q = \frac{k_f - 1}{k_t - 1} \tag{3}$$

At $q = 0$, there is no notch sensitivity and at $q=1$ we have full notch sensitivity. i.e. full theoretical elastic concentration effect. Several empirical relations have been developed to estimate the fatigue notch factor of a material and its associated notch sensitivity index. These techniques include: the classical methods (Neubers [6 - 7], Peterson [3, 8] and Heywood [9]), stress field intensity method [10], and probabilistic method based on linear elastic fracture mechanics [11]. Detail review of these methods can be found in [12], each attempt to simplify the complex behavior of fatigue in notched components to a few geometric and characteristic material constants. However, these approaches suffer from some fundamental drawbacks. Among these drawbacks is that the fatigue notch factors are obtained through time consuming and costly experiments. Moreover, the relationship of microstructure to K_f, using these constants has proven difficult to establish. Recently, Owolabi et al. [14] have established a probabilistic framework based on weakest link theory and extreme-value statistics which incorporates information regarding the peak stress and stress gradient relative to microstructure length scales within a well defined fatigue damage process zone around the notch root. This paper combines the developed probabilistic framework with other existing probabilistic formulations that consider the size distribution and different competing damage mechanisms for aero-engine materials.

2. Material Systems

The alloy used for this study is a dual-phase titanium alloy, Ti-6Al-4V. Ti-Al alloys offer a range of properties such as high strength and fracture toughness at low temperatures to high strength and creep resistance at elevated temperatures. These wide ranges of properties have led to extensive use of Ti-Al

alloys in engineering applications from airframe components to compressor blades applications. The experimental data used in this work were obtained from Haritos et al [1], Lanning et al [13] and Naik et al. [15] on Ti-6Al-4V for various notch root geometries and stress ratios. The Ti-6Al-4V specimens used in these papers were obtained from forged bar, which were initially heat treated to 705^{o}C for 2 h, and then followed by static argon cooling to below 149^{0}C. The material was subsequently annealed in vacuum at 549^{0}C for 2 h. This is then followed by static argon cooling to below 149^{0}C. The microstructure of the resulting bar is as shown Figure 2.

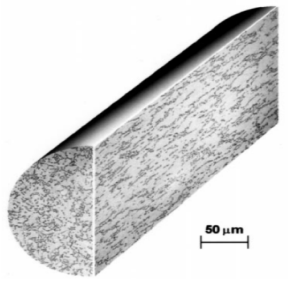

Figure 2. Ti-6Al-4V forged plate microstructure [1]

3.0. Crystal Plasticity model of Ti-6Al-4V

Crystal plasticity models are more suited for studying heterogeneity and interaction across grains in the notch root field as they relate grain scale stress to crystallographic slip response [16 - 18]. The use of crystal plasticity is thus relevant for the accurate prediction of the stress-strain field response at the notch root. The crystal plasticity model used in this work is based on 3D crystal plasticity models developed by Mayeur and McDowell (2007)[19]. Thus, only the summary of the crystal plasticity constitutive models is presented in this section.

The deformation in the material is based on a standard two term multiplicative decomposition of the deformation gradient into elastic and plastic parts, i.e.,

$$F=F^{e}F^{p} \tag{4}$$

Here, F is the total deformation gradient, F^{p} captures the dislocation glide through the lattice while F^{e} captures the rigid body rotation and elastic stretching of the lattice. The plastic velocity gradient $\hat{}L^{p}$ defined as the sum of the crystalline shear displacement rates over all slip systems k is given in the isoclinic, lattice invariant intermediate configuration as [20]:

$$\hat{L}^{p}=\dot{F}^{p}\cdot(F^{p})^{-1}=\sum_{k=1}^{N_{sys}}\dot{\gamma}^{k}(s_{0}^{k}\otimes n_{0}^{k}) \tag{5}$$

Here, γ^{k} is the slip system shearing rate, and S_0^{k} and n_0^{k} are fixed unit vectors in the slip direction and slip plane normal direction, respectively. The slip vectors S_0^{k} and n_0^{k} remain unchanged through deformation F^{p} from the reference to the intermediate configuration and maintain orthogonality through F^{e}. The relationship between the slip system shearing rate and the resolved shear stress of the k_{th} slip system is described by the power law flow rule given by McGinty [21] as:

$$\dot{\gamma}^{k}=\dot{\gamma}_{0}\left\langle\frac{\left|\tau^{k}-\chi^{k}\right|-\kappa^{k}}{D^{k}}\right\rangle^{M}\operatorname{sgn}(\tau^{k}-\chi^{k}) \tag{6}$$

Here, γ_0 is the reference shearing rate, M is the inverse strain-rate sensitivity exponent which controls the rate sensitivity of flow, τ^k is the resolved shear stress, χ^k is the back stress, κ^k is the length scale-dependent threshold stress and D^k is the drag stress. As developed by Zhang et al. [22], the drag stress is taken as a non-evolving constant, while the back stress evolves according to an Armstrong-Frederick direct hardening/dynamic recovery type of equation, i.e.,

$$\dot{\chi}^k = h\dot{\gamma}^k - h_D \chi^k \left|\dot{\gamma}^k\right| \tag{7}$$

With $\chi^k(0)=0$. The threshold stress is expressed as

$$\kappa^k = \frac{\kappa_y}{\sqrt{d^k}} + \kappa_s^k \tag{8}$$

3.1 Simulation of Notched Components

The crystal plasticity constitutive model was coded into ABAQUS 2006 UMAT, based on previous work by Zhang et al [22]; Mayeur and McDowell, 2007[19]. For textured Ti-6Al-4V alloy, some of the material parameters in the crystal plasticity are obtained from Bridier et al [23]. Finite element simulation was performed on three different geometries, meshed using 3D stress four-node linear tetrahedron element type (C3D4) and consisting of approximately 218940 elements to estimate the stress distribution and possible plastic straining that occur in the notched specimens. The dimensions of the specimens used and the different test cases are as given in Table 1. A diagram of the gage section of the specimen is provided in Figure 3.

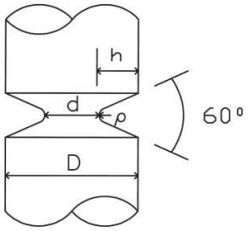

Figure 3. Gage section of the cylindrical specimen with a circumferential V-notch.[1]

To reduce computational time, the notched specimen geometries are decomposed into three different regions: an outermost region, far from the notch root, where isotropic linear elasticity is used; an intermediate transition region where macroscopic J_2 cyclic plasticity theory is used; and finally the notch root region where crystal plasticity theory is used. The element size at the crystal plasticity region was chosen to coincide with the average grain size of Ti-6Al-4V which is 45 μm. The domain decomposition is as shown in Figure 4. Also, One quarter of the cylindrical notched specimen was modeled because of the symmetry in loading and geometry of the specimen as shown in Figure 5.
The bottom of the notched specimen is encastre while symmetry boundary conditions are applied to the two planes of symmetry. The notched specimens were tested at four different load ratios; R=0.1, R=0.5 and R=-1. Average alternating HCF strength at 10^6 cycles, as determined by Naik et al [15] and as contained in Table 1 for different load ratios, are applied to the top of the specimen.

Table 1. The 7 different test cases

Test Case	K_t	Notch radius, **ρ** (mm)	Notch depth, h (mm)	R-ratio	Average alternating HCF strength at 10^6 cycles (MPa)
1	2.78	0.330	0.729	-1	173.6
2	2.78	0.330	0.729	0.1	158.9
3	2.78	0.330	0.729	0.5	104.6
4	2.78	0.203	0.254	0.10	167.2
5	2.78	0.203	0.254	0.50	105.2
6	2.78	0.127	0.127	0.10	144.7
7	2.78	0.127	0.127	0.50	111.0

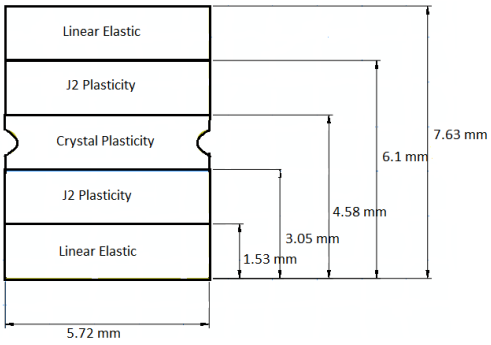

Figure 4. Domain decomposition of the cylindrical notched specimen geometry.

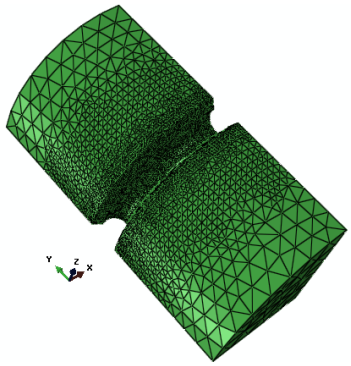

Figure 5 Finite element mesh for 0.33 mm notch root radius and K_t = 2.78 consisting of four-node linear tetrahedron element type (C3D4)

For a smooth specimen with defects having a fatigue damage process zone of volume V, the whole volume is divided into small volume elements, dV with probability of failure of a sufficiently small volume element given as:

$$dP = \lambda dV \tag{9}$$

Where here, λ is the critical defect density defined as the expected number of defects per unit volume of the smooth specimen. Using weakest link theory, the probability of survival of the entire volume is obtained from the probability of survival of all "m" number of sub-volumes i.e.

$$P_s = \prod_{i=1}^{m} (1 - dP_i) = \prod_{i=1}^{m} (1 - \lambda dV) \tag{10}$$

This equations assumes that the defects are randomly distributed within the volume and thus do not interact, which is only reasonable when considering the formation of a fatigue crack(s) in high cycle (HCF) and very high cycle fatigue (VHCF) regimes. Following the framework presented in [14], as the volume of each small element tends to zero, equation (10) can be transformed into

$$P_s = \exp\left(-\int_{V_d} \lambda dV \right) \tag{11}$$

Using the generalized extreme value distribution function, the distribution of defects, *a*, that are above the threshold, a_{th}, is modeled by a power law of the form

$$\lambda = \frac{1}{V_0}\left(1 + \xi\left(\frac{a - a_{th}}{a_0}\right)\right)^{-1/\varepsilon} \tag{12}$$

Where a_0 and ξ are the scale and shape parameters respectively. Substituting (12) into (11) yields

$$P_s = \exp\left\{-\frac{1}{V_0}\int_{V_d}\left(1+\xi\left(\frac{a-a_{th}}{a_0}\right)\right)^{-1/\varepsilon} dV\right\} \tag{13}$$

If $a_{th} = a_0^*\xi$, re-arranging equation (13) yields,

$$P_s = \exp\left\{-\frac{1}{V_0}\int\left(\frac{a}{a_0^*}\right)^{-1/\varepsilon} dV\right\} \tag{14}$$

Where a_0^* is regarded here as the mean defect size. Equation (14) is valid only if $\xi \neq 0$. The critical defect size is related to the microscopic stress (taking here as a random variable) through a power law relationship of the form

$$\sigma = \frac{A}{\sqrt[z]{a}} \tag{15}$$

where A and z are materials constants. Similarly, the stress amplitude, σ_0 corresponding to the mean defect size a_0^* can be taken as the fatigue limit of the reference volume V_o for 50% failure probability. The two parameters can also be related by a power law of the form:

$$\sigma_0 = \frac{A}{\sqrt[z]{a_0^*}} \tag{16}$$

Combining equations (15) and (16) we have

$$\frac{a}{a_0^*} = \left(\frac{\sigma_0}{\sigma_a}\right)^z \tag{17}$$

Substituting Equation (17) into Eq. (14) yields

$$P_s = \exp\left\{-\frac{1}{V_0}\int\left(\frac{\sigma}{\sigma_0}\right)^b dV\right\} \tag{18}$$

Where $b=z/\xi$. For $\xi>0$, b and σ_0 represents a 2-parameter Weibull shape and scale parameters. The cumulative probability of HCF failure of the component, specifically defined can be obtained from Eq. (18) as

$$P_f = 1-\exp\left\{-\frac{1}{V_0}\int\left(\frac{\sigma}{\sigma_0}\right)^b dV\right\} \tag{19}$$

To facilitate development of the expression for fatigue notch factor from Eq. (18), the concept of stress homogeneity factor that have been used is introduced here. Thus equation (18) can be re-written as,

$$P_f = 1-\exp\left\{-\frac{kV}{V_o}\left(\frac{\sigma_{\max}}{\sigma_0}\right)^b\right\} \tag{20}$$

where

$$k = \frac{1}{V}\int\left(\frac{\sigma}{\sigma_{\max}}\right)^b dV \tag{21}$$

is regarded as the stress homogeneity factor. Conventionally, the fatigue notch factor is the ratio of

unmatched to notched fatigue strength at the same probability of failure (usually 50%). Using equation 20, the probability of failure of unmatched specimen and a notched specimen will be the same when

$$\exp\left\{-\frac{k_s V_s}{V_o}\left(\frac{\sigma_{\max,s}}{\sigma_0}\right)^b\right\} = \exp\left\{-\frac{k_n V_n}{V_o}\left(\frac{\sigma_{\max,n}}{\sigma_0}\right)^b\right\} \tag{22}$$

where the subscripts *n* and *s* represent the respective value of the variable for notched and smooth (unmatched) specimens. The ratio of the smooth to notch fatigue driving force parameters (i.e., the stress amplitude) is used to define a new fatigue notch factor given as

$$k_f = \frac{\sigma_{\max,s}}{\sigma_{\max,n}} = \left(\frac{k_n}{k_s}\right)^{1/b}\left(\frac{V_n}{V_s}\right)^{1/b} \tag{23}$$

For smooth specimen that is loaded at a very low stress or strain amplitude in the HCF regime, the number of critically stressed grains (or elements) is very small. Thus for the life limiting case in which only one grain or element is critically stressed above the threshold, $V_s = V_e$ (i.e. volume of element or grain) and $K_s = 1$; thus Equation (23) becomes

$$k_f = \frac{\sigma_{\max,s}}{\sigma_{\max,n}} = (k_n)^{1/b}\left(\frac{V_n}{V_e}\right)^{1/b} = \left(\frac{1}{V}\int\left(\frac{\sigma}{\sigma_{\max,n}}\right)^b dV\right)^{1/b}\left(\frac{V_n}{V_e}\right)^{1/b} \tag{24}$$

However, if the materials contain some pores or inclusions, equation (23) must be used. It is important to state that Eqs. (23) and (24) can be used only if subsurface crack initiation is the failure process, if crack originates from the surface, then the volume parameter in this equation should be replace with the surface area.

5. Closed Form Solution for Fatigue Notch Factor

To resolve inelastic deformation at the scale of microstructure to facilitate next generation microstructure-sensitive notch root analyses inherently requires mesh refinement to the scale of microstructure, which is often several orders of magnitude finer than the scale of the component. Moreover, the kind of constitutive equations that must be used are often of advanced form and requiring rather sophisticated and time-consuming computational strategies to perform concurrent analyses at the component and notch root microstructure scales. Accordingly, direct application of multiscale finite element analysis is simply too computationally time consuming for practical microstructure-sensitive fatigue damage assessment of notched components under multiaxial loads. Thus, for practical engineering application, a more simplified and approximate model for fatigue notch factor is presented here based on closed form solution for stress distribution at the notch developed by Glinka using the Creager-Paris solutions of the stress field ahead of a crack. For a notch component with notch root radius ρ and stress concentration factor, k_t, the axial stress distribution along the notch root centre line is given as:

$$\sigma = \frac{1}{2}\left(\left(\frac{\rho}{x+\rho/2}\right)^{1/2} + \frac{1}{2}\left(\frac{\rho}{x+\rho/2}\right)^{3/2}\right)k_t S = \frac{1}{2}\left(\left(\frac{\rho}{x+\rho/2}\right)^{1/2} + \frac{1}{2}\left(\frac{\rho}{x+\rho/2}\right)^{3/2}\right)\sigma_{\max,n} \tag{25}$$

Finding the ratio of the stress amplitude to the maximum stress and substituting into equation (24) at x

= a_c (i.e., the critical distance) will allow the determination of an expression for the fatigue notch factor of the form

$$k_f = \left(\frac{1}{V} \int \left(\frac{1}{2} \left(\left(\frac{\rho}{a_c + \rho/2} \right)^{1/2} + \frac{1}{2} \left(\frac{\rho}{a_c + \rho/2} \right)^{3/2} \right) \right)^b dV \right)^{1/b} \left(\frac{V_n}{V_e} \right)^{1/b} \tag{26}$$

Assuming that the critical distance is constant for the notched component with a notch root radius ρ, Eq. (26) reduces to

$$k_f = \left(\frac{1}{2} \left(\left(\frac{\rho}{a_c + \rho/2} \right)^{1/2} + \frac{1}{2} \left(\frac{\rho}{a_c + \rho/2} \right)^{3/2} \right) \right) \left(\frac{V_n}{V_e} \right)^{1/b} \tag{27}$$

The above equation for k_f was derived using the fatigue damage process zone based on critical distance, probabilistic framework based on the weakest link, and the Glinka's closed form solution based on the notch root stress distribution. The expression in Eq. (25) has been shown to give a good prediction of the stress field for relatively blunt U-notches and be used over a distance of 3ρ from the notch root with an accuracy of approximately 7% [15].

6. Results and Discussion

The stress distribution obtained from the finite element analysis was used in determining the average k_f for the geometry using the proposed probabilistic framework based on Weibull's weakest link and extreme-value statistics. Also as a further validation of the proposed approach, the value of k_f was calculated using the closed form solution for fatigue notch factor in Eq. (27) and the result is compared to experimental results determined by R.A. Naik et al [15] as shown in Table 2. Both results are in agreement with the experimental results with minimal difference. The k_f determined using the Weibull's weakest link approach, when the loading ratio R =-1, is more accurate than for every other loading ratios tested.

Table 2. Comparison of measured and predicted K_f using FEM and closed form analysis

Test Case	K_t	Notch radius, **ρ** (mm)	Notch depth, h (mm)	R-ratio	Experimental average K_f	K_f using Weibull's weakest link	K_f using closed-form analysis
1	2.78	0.330	0.729	-1	2.79	2.73	2.66
2	2.78	0.330	0.729	0.1	1.80	1.89	1.88
3	2.78	0.330	0.729	0.5	1.75	1.82	1.84
4	2.78	0.203	0.254	0.1	1.71	1.86	1.80
5	2.78	0.203	0.254	0.5	1.74	1.83	1.83
6	2.78	0.127	0.127	0.1	1.98	2.05	2.01
7	2.78	0.127	0.127	0.5	1.65	1.72	1.77

Also, the radius of curvature at the notch root plays a vital role on the stress gradient at the notch. This effect is captured by the fatigue notch sensitivity factor q given in Equation 3. Figure 6 gives a plot of the notch sensitivity factor as a function of the notch root radius for the different load ratio. The

straight line plot represents the notch sensitivity factor calculated using the Neuber's formulation [7] given in Equation 28 where a_0 is a material constant taken to be 0.2 for Ti-6Al-4V [1]. The plot shows that the new approach and the closed-form solutions give more accurate result compared to the existing Neuber's formulation.

$$q = \frac{1}{1 + \sqrt{\frac{a_0}{\rho}}} \tag{28}$$

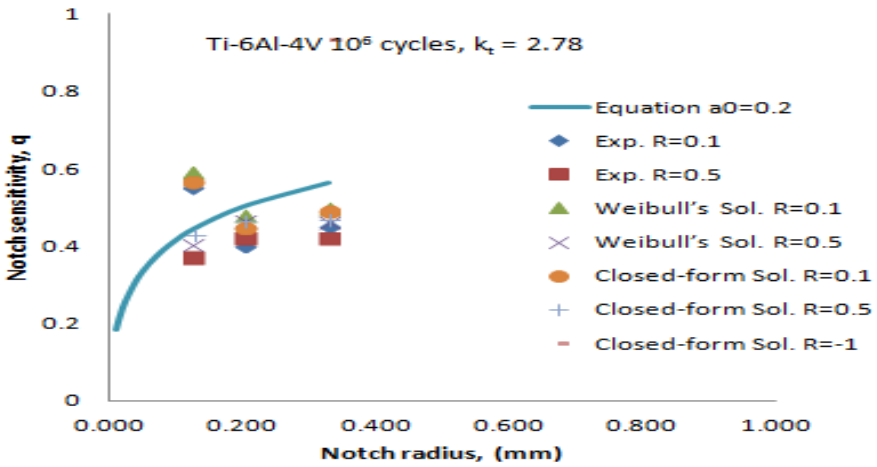

Figure 6. Notch sensitivity versus notch root radius for three notch sizes.

6. Conclusions

A probabilistic framework based on Weibull's weakest link extreme-value statistic that accounts for stress gradient at the notch root and the realistic microstructure of the material is presented. The fatigue notch factors, $k_{f,}$ estimated by this approach are compared with experimental k_f. The comparison shows that the proposed method accurately predicts the fatigue notch factor of Ti-6Al-4V for the different Load ratios applied to the specimen geometry analyzed. Also, k_f determined from a closed form solution of the proposed probabilistic approach validates the effectiveness of the proposed method. A plot of the notch sensitivity index against the notch root radius analyzed for the different load ratios as shown in Figure 6 shows that the proposed approach gives more accurate result compared to the existing Neuber's formulation.

Acknowledgements

The authors of this paper express their profound gratitude to the Department of Defense for the financial support provided through research and educational program for HBCU/MSI (contract # W911NF-11-1-014, L. Russel and D. Stargel, Program Managers.)

References

[1] Haritos, G.K., Nicholas, T., and Lanning, D.B., Notch Size Effects in HCF Behavior of Ti-6Al-4V. Int. J. Fatigue, 21 (1999) 643–652.

[2] Yoichi Yamashita, Yusuke Ueda, Hiroshi Kuroki, Masaharu Shinozaki, Fatigue life prediction of small notched Ti-6Al-4V specimens using critical distance. Engineering Fracture Mechanics, 77 (2010) 1439-1453.
[3] Peterson RE. Stress concentration factors. New York: Wiley; 1974.
[4] Philip CE, Heywood RB. The size effect in fatigue of plain and notched steel specimens under reversed direct stress. Proc Inst Mech Eng 1951; 165: 113-24.
[5] Bellett D, Taylor D, Marco S, Mazzeo E, Guillois J, Pircher T, The fatigue behaviour of three-dimensional stress concentrations. Int. J. Fatigue 27 (2005) 207–21.
[6] Neuber H. Theory of stress concentration in shear strained prismatic bodies with arbitrary non-linear stress law. J Appl Mech 1961;28:544–50.
[7] Neuber H. Theory of notch stresses: principle for exact stress calculations. Ann Arbor (MI): Edwards, 1946
[8] Peterson RE. Notch sensitivity. In: Sines G, Waisman JL, editors. Metal fatigue. New York: McGraw-Hill, 1959: 293-306.
[9] Heywood RB. Stress concentration factors, relating theoretical and practical factors in fatigue loading. Engineering London 179 (1955) 146- 8.
[10] Weixing, Y., Stress field intensity approach for predicting fatigue life. International Journal of Fatigue, vol. 15, no. 3, pp. 243-246, 1993.
[11] Anderson, T., Fracture Mechanics: Fundametals and Applications. Taylor &
Francis, Boca Raton, FL, third ed., 2005.
[12] William D. Musinski (2010) Novel methods for microstructure-sensitive probabilistic fatigue factor. Ph.D. thesis, Georgia Institute of Technology, Atlanta, USA.
[13] Lanning DB, Nicholas T, Haritos GK, On the use of critical distance theories for the prediction of the high cycle fatigue limit stress in notched Ti-6Al-4V. Int J Fatigue 27 (2005) 45–57.
[14] Owolabi GM, Prasannavenkatesan R, McDowell DL, Probabilistic framework for a microstructure-sensitive fatigue notch factor. Int J. Fatigue 32 (2010) 1378–1388.
[15] Rajiv A. Naik, David B. Lanning, Theodore Nicholas, Alan R. Kallmeyer. A critical plane gradient approach for the prediction of notched HCF life. Int. J. Fatigue 2005; 27: 481-492.
[16] Morrissey R, Goh CH, McDowell DL. Microstructure-scale modeling of HCF deformation. Mech Mater 2005;35:295-311
[17] Shenoy MM. Constitutive modeling and life prediction in Ni-base superalloys. Ph.D. Thesis, Georgia Institute of Technology; 2006
[18] Kumar RS, Wang AJ, McDowell DL. Effects of microstructure variability on intrinsic fatigue resistance of nickel-base superalloys – a computational micromechanics approach. Int J Fract 2006;137:173-210
[19] Mayeur, J.R., McDowell, D.L., 2007. A three-dimensional crystal plasticity model of duplex Ti-6Al-4V. Int. J. Plasticity 23, 1457-1485
[20] Asaro, R.J., 1983. Micromechanics of crystals and polycrystals. Adv. Appl. Mech. 23, 1-115.
[21] McGinty RD (2001) Multiscale representation of polycrystalline inelasticity. Ph.D. thesis, Georgia Institute of Technology, Atlanta, USA
[22] Zhang, M., Zhang, J., McDowell, D.L., 2007. Microstructure – based crystal plasticity modeling of cyclic deformation of Ti-6Al-4V. Int. J. Plasticity 23, 1328-1348
[23] Bridier F., McDowell D.L., Villechaise P., Mendez Jose., 2009. Crystal plasticity modeling of slip activity in Ti-6Al-4V under high cycle fatigue loading. Int. J. Plasticity 25, 1066-1082

A Prediction Model for Low Cycle Fatigue Crack Initiation under Axial Loading

Yajun Zhang, Lingqing Gao, Chunfen Wang

Luoyang Ship Material Research Institute, Luoyang 471023, China

* Corresponding author: zhangyj309@163.com

Abstract: A prediction model for low cycle fatigue crack initiation was proposed, based on damage mechanics theory, which indicated the relation of equivalent value *d* of low cycle fatigue crack initiation to stress attenuation percentage $\triangle S/S$. Then, parameter *d* will be calculated if $\triangle S/S$ is given, and the corresponding cyclic life is initiation life of fatigue crack. To validate the model, a group of 10CrNiMo structural steel specimens with a round-section were tested through low cycle fatigue test controlled by constant strain under axial loading, and the results manifested that the model is dependable and applicable; and the error of *d* to really measured value is not more than 5.0%; when the total strain amplitude is 0.6%, *d* is close to 2.0mm and the initiation life is approximately 900 cycles, which is nearly 80% of the entire life.

Keywords: Low cycle fatigue, Crack initiation， Prediction model, Initiation life

1. Introduction

In engineering, a crack which can be observed through a microscope with a low magnification (10×～20×), usually was defined as crack initiation and its length is 0.13mm to 0.25mm [1,2]. In design, crack initiation was deemed as a range from 0.25mm to 2.5mm [3]. When a crack increases to a certain length such as 0.1mm, 0.5mm, or 1.0mm, relevant fatigue cycle is called initiation life of fatigue crack. In general, there are three methods to measure crack initiationi, replication technique, potential drop method and observation through a microscope with a long focal length. Basically, the three methods have a high precision, and can meet engineering requirements. But all of them are inconvenient in real application [4]. In the fields of crack initiation and life prediction, many scholars proposed several models based on different parameters, for examples, Manson-Coffin Model [5] beginning with macro-mechanics, Mesomechanics Model [6] to describe microcosmic dispersivity using macroscopic parameters, Probability Model [7] calculating crack initiation life taking microcrack bulk density as index and so on. Many problems appeared when above models applied in reality [8]. In this paper, a new prediction model for low cycle fatigue crack initiation was proposed, based on damage mechanics theory, by which equivalent value of crack initiation could be calculated in case of an assuming condition, and crack initiation life could be measured combining with some simple tests, which would provide some reference for engineering design.

2. A prediction model for low cycle fatigue crack initiation based on damage mechanics

Damage mechanics is a subject studying evolution law of damage field of the deformable solid, including damage and its effect on mechanical properties of materials under action of outside factors such as load, changing temperature and corrosion and so on. Based on damage mechanics theory, a relation was deduced in literature [8] as follows:

$$\frac{\Delta A}{A}=\frac{\Delta S}{S} \tag{1}$$

where △A and △S were after damaged area, stress amplitude , accordingly.

Constant strain is admitted as control parameter generally, so low cycle fatigue is also called strain fatigue. Under cyclic action of constant strain, grains in material may come into microcracks because of repeated slips, which will damage the material. Simultaneously, effective area of the material will decrease gradually and capacity enduring the load may drop and nominal stress acted on the material will attenuate step by step. Supposing a crack or several cracks initiated, and damage effect produced by several cracks initiated in the same section or different sections is equivalent to one crack, then attenuation of the stress and the length of the crack should meet a certain mathematical relation. When cracks don't initiate, stress will keep constant; and cracks initiated and propagated to fracture the material, stress would drop to zero. That's to say, ratio of reduction of the specimen area perpendicular to the direction of the crack propagation to original specimen area should be equal to ratio of attenuation of the current stress to steady stress, that is Eq. (1). Reduction of the specimen area and length of the crack propagation should satisfy some mathematic relation, which would provide a basis of damage mechanics theory for setting up the expression of a equivalent value of crack initiation to stress attenuation. Attenuation of stress can be measured by a test, and the equivalent value of crack initiation be also obtained through the built expression, and corresponding cycle is called crack initiation life.

Literatures [9,10] indicated that several cracks initiated in the course of low cycle fatigue. It could be seen that several cracks sometimes initiated in the same section perpendicular to loading orientation, sometimes not from many tests. No matter one crack or several cracks initiated in the same section or not, damage effect should be deemed as that of one crack in one section. Figure 1 reveals above analysis. Parameters a, b and c are crack lengths located in one section or different sections, and parameters A, B and C are corresponding areas swept by above three cracks, see figure 1(1) for details. Damage effect produced by above three cracks or more equals to that by one crack *d,* with a corresponding swept area $\triangle A_{D,}$ see figure1(2). Figure1(3) shows the geometry relations of equivalent crack length *d,* its swept area $\triangle A_D$ and specimen radius *r,* and also is calculation model to predict crack initiation.

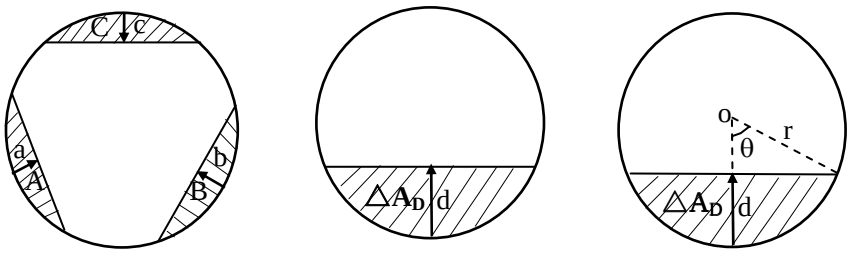

(1) (2) (3)

(1) Several cracks and corresponding swept areas (2) Equivalent to one crack and an area (3) Sketch of calculation model

Fig.1 Calculation model predicting crack initiation based on damage mechanics theory

From figure 1(3), some equations may be obtained:

$$\theta = \arccos\frac{r-d}{r} \tag{2}$$

$$\Delta A_D = r^2\theta - r(r-d)\sin\theta \tag{3}$$

$$d = r - \frac{r\theta - \pi\Delta A_D\theta}{\sin\theta} \tag{4}$$

From above analysis, ratio of reduction of the specimen area to original area $\Delta A_D/A_D$ should equal to ratio of attenuation of nominal stress to steady stress $\Delta S/S$, namely:

$$\frac{\Delta A_D}{A_D} = \frac{\Delta S}{S} \tag{5}$$

Based on above equations, when specimen radius r is determined (e.g. 5mm), the relation of equivalent length d of crack initiation and $\Delta S/S$ will be built. Through test data processed (see figure2), the following equation would be set up:

$$\frac{\Delta S}{S} = -0.1186d^3 + 1.7765d^2 + 4.1698d - 0.5006 \quad (R = 1) \tag{6}$$

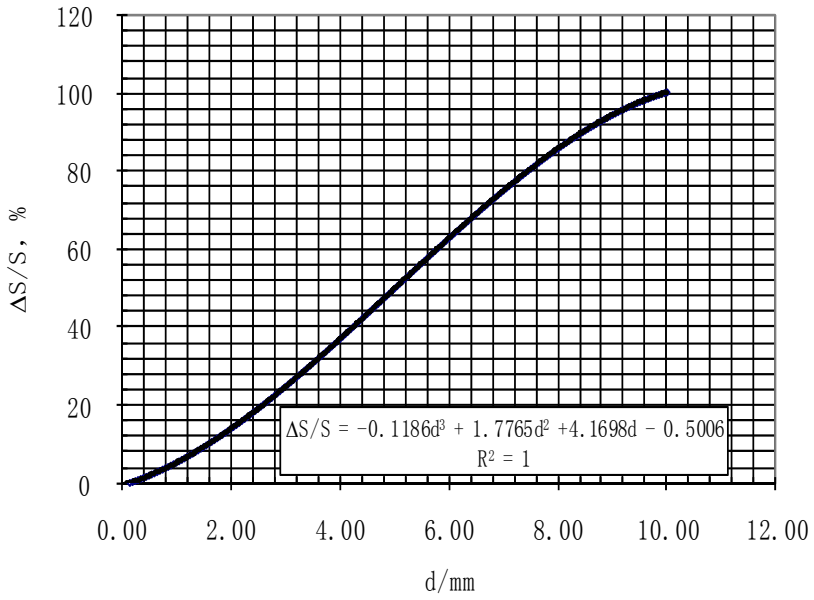

Fig.2 Relation curve and corresponding equation of △S/S-d

3. Correction for prediction model for low cycle fatigue crack initiation

Considering deviation of damage effect of one crack equivalent to several cracks in one section or several sections, damage coefficient λ (0～1) was introduced. Simultaneously, many factors including some measurement errors of attenuation of stress, areas swept by cracks and section distortion when specimen fractured and so on, which would directly influence calculation precision of equivalent crack length. Supposing calculating error is d_0 (a constant relevant to material), then expression (6) can be further amended:

$$\frac{\Delta S}{\lambda S} = -0.1186(d + d_0)^3 + 1.7765(d + d_0)^2 + 4.1698(d + d_0) - 0.5006 \quad (R = 1) \qquad (7)$$

From equation (7), we know, firstly, through a simple test, for each specimen, solve damage coefficient λ and material constant d_0, then, whatever equivalent length *d* of crack initiation is defined,

△S/S will be calculated .Vice versa, we can get *d* from the known ΔS/S and corresponding cycle is crack initiation life.

It could be seen from many tests, when ΔS/S reached 50% (corresponding equivalent crack length was 5mm), specimen fractured immediately. So, for formulas (6) and (7), the following boundary conditions will be satisfied: 0≤△S/S≤0.5, 0≤d≤r.

4. Verification of prediction model for low cycle fatigue crack initiation

In order to ensure correctness of the built prediction model, related test were carried out, with the following test conditions: four pieces used with series of number 1 to 4, constant strain amplitude 0.6%, test frequency 0.2Hz; when percentage of stress attenuation increased to 5.33%, 9.35%, 14.0%, 19.17% respectively (corresponding equivalent crack length was 1.00mm, 1.50mm, 2.00mm and 2.50mm accordingly), test ended. Afterwards, the tested specimens were heated about 30 minutes at a temperature from 300℃ to 400℃ and then fatigued again, and finally all specimens were fractured into two parts. Adopting PHOTOSHOP tool software, daubing fatigue crack propagation district black and re-fatigue and fractured distracts white, see figure 3(a) and (b).

Figure 3 showed that the specimen fracture appearance had different degree distortion, and measured area swept due to crack propagation was not uniform with the real area by reason of measurement error. So, it is necessary to correct the prediction model.

Percentage of black distract to the entire fractured area was measured by OLYCIAm3 Image Analysis System, and equivalent crack length was calculated per equation (7). Relative errors of real crack length to calculated crack length from prediction model, λ value of each specimen, and corrected value d_0 (difference between average of real equivalent crack length and that from prediction model) were listed in table1.

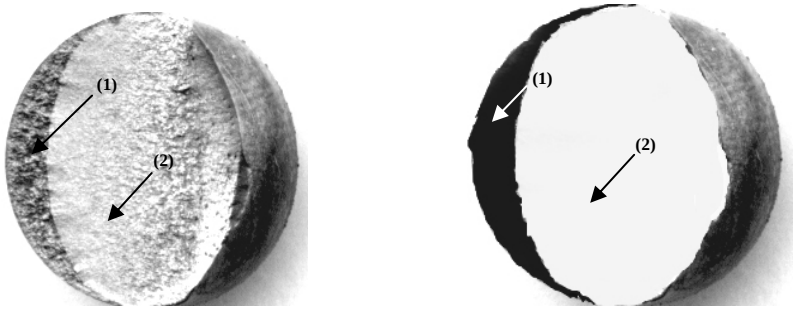

(a) before (magnification 5×) (b) after (magnification 5×)

(1) District of fatigue crack propagation (2) Districts of re-fatigue and fracture

Fig.3 Fracture appearance of the specimen processed before and after

Tab.1 Comparison of real value and calculated value from prediction model of equivalent length of crack initiation

Spec. No.	Specimen diameter /mm	ΔS/S /%	Damage coefficient λ	Measured $\Delta A_D/A_D$ /%	$\triangle A_D$ /mm^2	Calculated crack length /mm	Constant d_0/mm	Real crack length /mm	Corrected crack length /mm	Relative error /%
1	10.07	5.33	0.33	16.32	12.82	1.0	1.10	2.20	2.10	4.39
2	10.08	9.35	0.47	19.85	15.59	1.5		2.54	2.60	-2.46
3	10.07	14.00	0.53	26.56	20.86	2.0		3.15	3.10	1.61
4	10.10	19.17	0.57	33.545	26.35	2.5		3.74	3.60	3.72

Table 1 shows that parameter d_0 really is a constant. Although there is some difference between average of real equivalent crack length and that from prediction model, relative error is not more than 5.0%, which manifests that the prediction model is reliable and applicable.

5. Predetermination crack initiation life by means of the prediction model

Generally, for low cycle fatigue test using smooth specimen, specimen will fail quickly once crack initiates, due to larger stress and strain acted on the specimen. For most of metallic materials, crack initiation life will dominantly take up 80% or so of the entire life. It is very difficult to directly measure crack initiation life through normal low cycle fatigue tests using smooth specimen. In order to investigate applicability of the prediction model, relation of crack initiation life to entire life was studied below.

Simple-specimen-method was employed in order to avoid data distribution. Amount of cycle, corresponding to percentage of stress attenuation which relates to some equivalent crack length, is crack initiation life of the equivalent crack length. Different literatures defined different crack initiation, and it is difficult to determine one proper equivalent value for steel such as 10CrNiMo structural steel, which will rely on concrete test. In this paper, three of specimens were performed, with series of number 5 to 7, and percentage of stress attenuation was supposed to 0.65%, 2.0%, 5.33%, 9.35%, 14.0%, 19.17%, 20%, 30% and 50% from a low-level to a high-level, recording relevant repeated cycles. See figure 4 for final test results.

Curve of $\triangle$S/S-N in figure 4 indicates that with cycle increasing, percentage of stress attenuation is improved, and when the cycle is close to 800 to 1000 cycles, specimens fail quickly with a high speed. Based on above analysis, when repeated cycle attains to 800 to 1000 cycles, it is suitable taking corresponding equivalent crack length as crack initiation for 10CrNiMo steel. In the range from 800 to 1000 cycles, $\triangle$S/S of the three specimens are all 5.33% and corresponding equivalent length of crack initiation is 1.0mm. Considering of correctness of the prediction model, real crack initiation should be as 2.1mm. See table 2 for data analysis of three specimens.

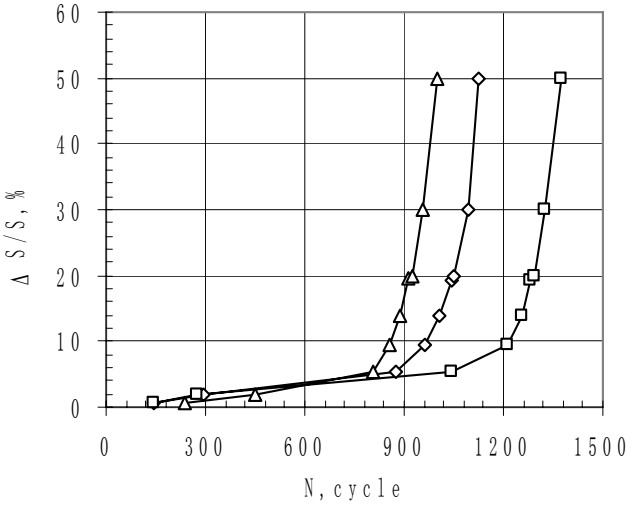

Fig.4 Relations of percentage of stress attenuation to cycle N

Table.2 Data of crack initiation and initiation life

Specimen No.	Percentage of stress attenuation ΔS/S， %	Crack initiation length a_0/mm	Crack initiation Life N_i	Entire life N	N_i/N /%
5	5.33	2.10	808	1003	80.6
6	5.33	2.10	876	1228	77.7
7	5.33	2.10	1044	1372	76.1
average	5.33	2.10	909	1168	78.1

Table 2 indicate that equivalent value of crack initiation of the structural steel 10CrNiMo is close to 2.0mm and initiation life is approximately 900 cycles, which is nearly 80% of the entire life.

6. Conclusions

(1)Any equivalent value of crack initiation, corresponding percentage of stress attenuation, can be calculated and crack initiation life be predetermined, according to prediction model for low cycle fatigue crack initiation proposed by damage mechanics theory, combining with some simple tests.

(2)Relative error between average of real equivalent crack length and that from prediction model is not more than 5.0%, which manifests that the prediction model is reliable and applicable.

(3) When the total strain amplitude is 0.6%, equivalent value of crack initiation of the structural steel 10CrNiMo is close to 2.0mm and initiation life is approximately 900 cycles, which is nearly 80% of the entire life, on the basis of prediction model and related tests, which will be referred to in engineering application and design.

References

[1] Fuchs H O and Stephens R I. Metal Fatigue in Engineering. New York: John Wiley and Sons,1980, 67.

[2] Pearson S. Roy. Air. Estab. Tech. Report 71109,1971.

[3] Socie D F. Fatigue life prediction using local stress-strain concepts. Exp. Mech.1977, 17:50.

[4] Zhang F, Luo X M. Determination for fatigue crack initiation life by using compliance method. Physical Testing and Chemical Analysis Part A: Physical Testing 2003, 39(7): 651-654.

[5] A. Tricoteaux, F. Fardoun, S. Degallaix, F. Sauvage. Fatigue crack initiation life prediction in high strength structural steel welded joints. Fatigue Fract. Engng. Mater. Struct. 1995,18: 189-200.

[6] R. G. Tryon, T. A. Cruse. A reliability- based model to predict scatter in fatigue crack nucleation life. Fatigue Fract. Engng. Mater. Struct. 1998, 21: 257-267.

[7] Lei W. S., Winfried Dahl. Weakest-link statistics of cleavage fracture. Int. J. Pres. & Piping. 1997, 74: 259-261

[8] Zhang Y J. Study on low cycle fatigue behavior of high-strength 10CrNiMo steel. A thesis for master's degree in Xi'an Jiaotong University, Xi'an 2009：3-6.

[9] Wang J G, Yang S L, Wang H Y, et al. Low-cycle fatigue properties of 800 MPa-grade ultrafine-grained steel. *J Univ Sci Technol Beijing*, 2005, 27(1):75-78.

[10] Yao J, Guo J T, Yuan C, et al. Low cycle fatigue behavior of cast nickel base superalloy K52. *Acta Metall Sin*, 2005, 41(4): 357-362.

Surface layer modification of 12Cr1MoVand 30CrMnSiNi2 steels by Zr^+ ion beam to improve the fatigue durability

Ilya Vlasov[1,2,*], Sergey Panin[1,2], Viktor Sergeev[2], Alfred Sungatulin[2], Mark Kalashnikov[2], Boris Ovechkin[1], Viktor Panin[1,2]

[1]Department of Material Science in Mechanical Engineering, Institute of High Technology Physics Tomsk Polytechnic University, 634050, Tomsk, Russia

[2] Laboratory of Polymer Composite Materials, Institute of Strength Physics and Materials Sciences SB RAS, 634021, Tomsk, Russia

* Corresponding author: good0@yandex.ru

Abstract A cyclic tension and alternating bending tests of 12Cr1MoV and 30CrMnSiNi2 steels specimens in as–supplied state and after surface nanostructuring by Zr^+ ion beam have been carried out. Distinctions in formation of strain induced relief, as well as the cracking pattern of modified surface layer are illustrated by methods of optical microscopy and interferential profilometry. Changes to occur in subsurface layer are characterized by means of nanoindentation and fractography (scanning electron microscopy) of fracture surfaces. The description of differences of deformation behavior is carried out with use of the multiple cracking concepts.

Keywords strength, nanostructuring, multiple cracking, deformation, fracture.

1. Introduction

The majority of products and machine parts during their exploitation experience the impact of variable loads, which can give rise to their fatigue fracture. In doing so regardless the long history of study the problem of fatigue fracture and approaches to increase fatigue durability are of substantial importance [1]. Surface modification is an effective way both to protect and to improve the mechanical properties of structural materials. On the other hand, under mechanical loading the distinction of elastic modules of a modified surface layer and adjacent bulk material causes the stress concentrators to occur, whose relaxation may give rise to localized development of plastic deformation or fracture [2]. Under cyclic loading such distinction of the properties brings to microcracking within strengthened surface layer, to act as structural micronotches. Therefore, the choice of modes and options for modifying the surface layer should be a compromise between strength/ductility of this layer and its thickness (this as well depends on several other factors, including adhesion etc.).

Ion implantation technique for a long time is widely used for industrial applications and is an extensively studied process. Recently, with the use of vacuum arc ion sources the modes of surface layer nanostructuring which allowed modifying surface layers with a thickness of some microns that is several times higher in contrast with ion implantation at conventionally used regimes were realized. Such nanostructured surface layers are not coatings yet, but no longer can be called ion-implanted ones [3]. Study of influence of such layers on fatigue life-time of structural steel specimens is of particular interest due to the possibility of simultaneously improvethe fatigue durability and wear resistance. To study the influence of surface layer nanostructuring of 12Cr1MoV and 30CrMnSiNi2 steels by Zr^+ ions on the fatigue durability increase is the purpose of this work.

2. Materials and research methods

Two types of steel were used in the current research for Zr+ ion beam surface modification: heat resistant ductile 12Cr1MoV steel intended for operation at high temperatures as well as 30CrMnSiNi2 high strength steel used for manufacturing of heavy-loaded machine parts [4]. The choice of 12Cr1MoVsteel for research was caused by the fact that the steel experiences no structural changes at the temperature at which the process of surface layer nanostructuring by ion beam is performed. Besides, the steel is quite ductile, so the study of processes of localized deformation and fracture under cyclic load provides much more evidence at lower rate of deformation processes.

High strength 30CrMnSiNi2 steel is used for manufacturing responsible and highly loaded parts that experience action of alternate loadings. Increasing of fatigue durability of this steel is a complex process since its low heat resistance and high level of alloying. Using the experience of 12Cr1MoV steel treatment new regimes for the surface nanostructuring were determined that make possible to slightly decrease mechanical properties while to enhance substantially fatigue durability.

Flat specimens of size 70×10×1 mm for 12Cr1MoVsteel and 70×8×1 mm for 30CrMnSiNi2 steel were made from a peace of a pipe by electro-spark cutting. For running fatigue tests the holes of 2 mm were drilled as a stress concentrator in the specimens at a distance of 50 mm from one of its edges. For static tension tests specimens in the shape of dog-bone with gauge length of 20×5×1 mm were also used, as well as ones with the stress concentrator (similar to the specimens for fatigue tests). The specimens were mechanically polished and divided into 2 groups: a) in initial state (without treatment) and b) specimens with a nanostructured surface layer by zirconium Zr^+ ion beam (after ion beam treatment). In the initial state steel 12Cr1MoV has the ferrite-pearlite structure with a characteristic grain size of 30 ÷ 50 μm.

Ion nanostructuring of surface layer of the steel specimens was carried out with a help of high current vacuum arc source of metal ions UVN-0.2 "Quant". Images of specimen's surface were obtained by means of optical microscopes Carl Zeiss Axiovert 25 CA and EPIQUANT, as well as scanning electron microscope Carl Zeiss EVO 50.Surface profilometry were performed with the help of Optical Interferometer of white light NewView 6200. X-ray phase analysis was conducted by X-ray difractometer DRON-7.

Tests on static tension were performed using electromechanical testing machine Instron 5582 while for the cyclic tension using servo hydraulic testing machine Biss UTM 150 were employed. Surface micrographs of specimen's were captured by Canon D550 digital photo camera during the process of fatigue tests. Nanohardness of specimens was measured by Nanotest (Micromaterials Ltd., UK).

2. The results of the experiments

2.1. Study of the modified surface layer of 12Cr1MoV steel

2.1.1. Electron-microscopy study

The structure of the surface layer of the steel in the initial state is represented by large ferrite grains >1 μm with inclusions of cementite (Fe_3C), whose average size makes 120 nm (fig. 1, a). Surface

layer structure after nanostructuring by the beam of Zr^+ ions is represented by phases of $FeZr_3$, $FeZr_2$, as well as ferrite grains. The average size of the grains in the surface layer is 100-150 nm (fig. 1, b-d).

2.1.2. Specimensnanoindentation

Strength properties of the specimens under study before and after the treatment were evaluated by nanoindentation to penetrate at the depth of 200 nm. It is revealed that due to nanostructuring the hardness of the surface layer increases approximately by 1.5 times. At the same time elastic modulus is reduced almost by 2 times.

2.1.3. X-raydiffraction

For specimens in the initial state structure is primarily represented by the α-Fe iron, whereas after nanostructuring the formation of intermetallic phases of the system Fe-Zr: $FeZr_2$ and $FeZr_3$, as well as the carbides ZrC into the subsurface layer takes place. Structural-phase micro-analysis of the specimen surface with nanostructured surface layer was performed. The data indicate that the overall content of zirconium in the subsurface layer of the specimen makes about 14.2 %.

2.2. Study of the modified surface layer of 30CrMnSiNi2 steel

Investigations of surface layer of 30CrMnSiNi2 steel specimens performed with the use of SEM have allowed to reveal nanosized particles in the modified layer (fig. 1,a). Average size of the particles made 80-10 nm. The particles are non-uniformly distributed over the specimen surface. The thickness of the modified surface layer was also estimated to show the depth of 2 μm (fig. 1,b). X-ray microanalysis has shown that iron in the layer has α-structure, while Zr-containing phases are as well revealed there.

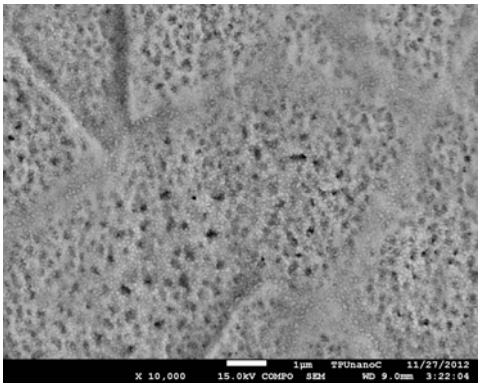

a)

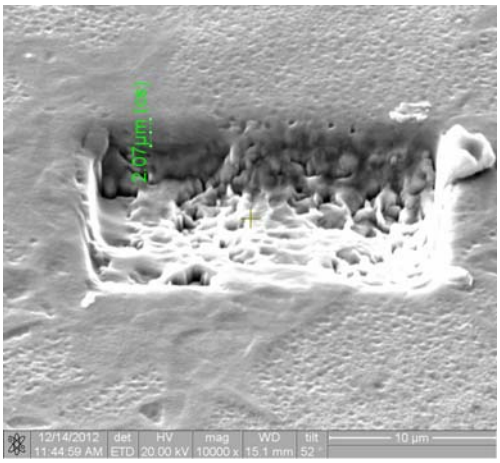

b)

Figure 1. SEM-micrographs of surface nanostructured specimen

2.3. Static tension tests

2.3.1. Mechanical properties

During tensile tests the loading diagram of 12Cr1MoV steel for dog-bone shape specimens was registered. It was found that for untreated specimens the presence of sharp yield point (yield tooth) is evident like it takes place for low carbon steels. Yield point of such specimens makes $\sigma_{0.2}$= 270 ± 25 MPa, ultimate strength –σ_u= 494 ± 36 MPa and elongation – ε = 20 ± 3 % which is close by values to the reference book data for this steel [4]. After the surface nanostructuring the value of ultimate strength is increased up to σ_u = 570 ± 17 MPa while elongation becomes lower ε = 16 ± 0.7 %. In doing so, there is no formation of the yield plateau at the diagram of the processed specimens.

2.3.2. Optical microscopy

Microscopic investigations of specimens surface near the area of the main crack at a certain distance from the fracture edge were performed (fig. 2). It is found that the specimen without surface treatment has the pronounced grain strain induced relief (fig. 2, a). At the same time undermore detailed observationit is seen that the surface of the nanostructured layer has small microcracks characterized by variation in their orientation in the modified layer (fig. 2, b). Whether, presence of the nanostructured layer on the surface of 12Cr1MoV steel hinders the formation of the grain relief that results in lower surface roughness of such specimens. The fracture surface of specimens after treatment shows signs of ductile fracture except for surface layer where the fracture was brittle. It is obvious that the thickness of the layer is not strictly constant which is manifested in the form of varying width of subsurface layer characterized by brittle fracture.

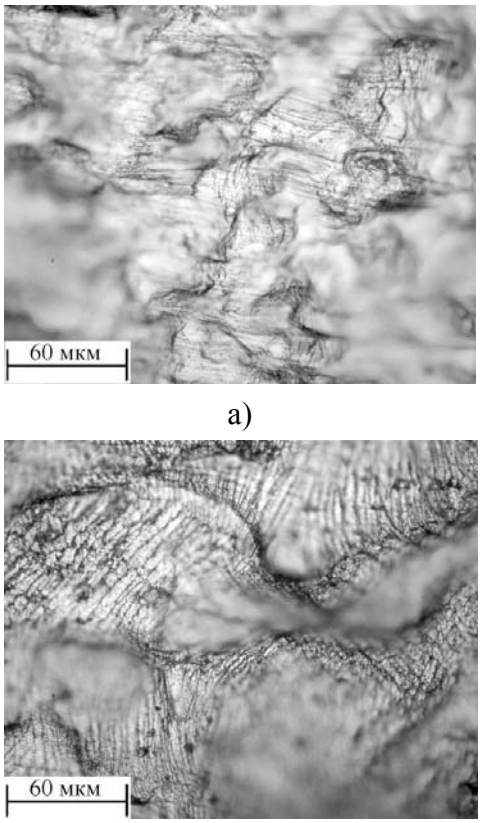

a)

b)

Figure 2. Surface images of failured specimens at static tensile tests: a) specimen without treatment; b) after nanostructuring surface; a), b) optical images, axis of loading is oriented horizontally

2.4. Cycling tension tests

2.4.1. Low-cycle fatigue (LCF) 12Cr1MoV

Results of cyclic tension tests have shown that under LCF the number of cycles prior to the fracture of the specimens with nanostructured surface layer is increased by 3 times. In doing so, the time before main crack initiation is increased approximately by3 times. The graphs of dependence of the main crack length versusthe number of cycles were plotted. It is clear that for the treated specimen later origination and more slow development of the main crack in the specimen is characteristic feature as compared with oneswithout the treatment. For the latter the rate of crack growth makes 0.085 μm/cycle while for one with nanostructured surface layer it makes 0.023 μm/cycle which is lower by more than 3.5 times. Thus, a modified surface layer effectively hinders the fatigue crack origination. In doing so the number of cycles before the main crack appearance is enlarged by 3 times and reduces the rate of its growth.

2.4.2. High-cycle fatigue (HCF) 12Cr1MoV

The results of tensile tests under HCF showed that the number of cycles prior to the fracture of specimens with nanostructured surface layer is increased by 2 times.The number of cycles before the crack nucleation is increased approximately by 2 times. Based on analysis of optical images the

dependence the crack length on the normalized and the absolute number of tension cycles were calculated and plotted. Much like to the case of LCFat comparisonthe graphs of specimens without treatment and after the surface nanostructuring differences in time of the main crack origination, as well as the rate of its development becomes visible. Crack growth rate of the specimens without treatment made0.03 μm/cycle, while for one with the nanostructurized surface layer its rate is reduced by 2 times that can be estimated as 0.015 μm /cycle.

2.4.3. Fractography study of cyclically fractured specimens 12Cr1MoV

Micrographs of specimens fractured under cyclic tensile were obtained using scanning electron microscope at high magnification (fig. 3). Micrographs gained in fatigue crack growth region (fig. 3, b) also point to the brittle pattern of the nanostructured surface layer fracture being compared with untreated specimens (fig. 3, a). It is seen that the surface layer of the nanostructured specimen is damaged by multiple cracks that does not bring to noticeable deformation localization. According to the author's opinion, multiple cracking allows to redistribute efficiently the loading and minimize the effect of the powerful stress macroconcentrator operating in the vicinity of the main fatigue crack tip.

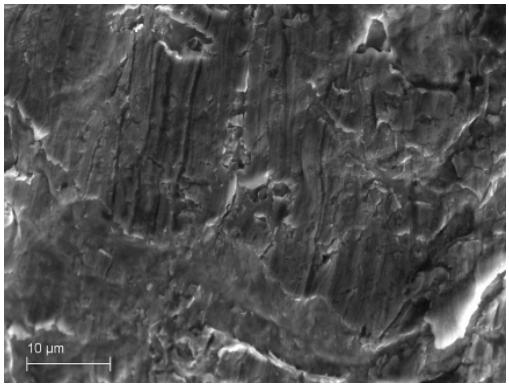

a)

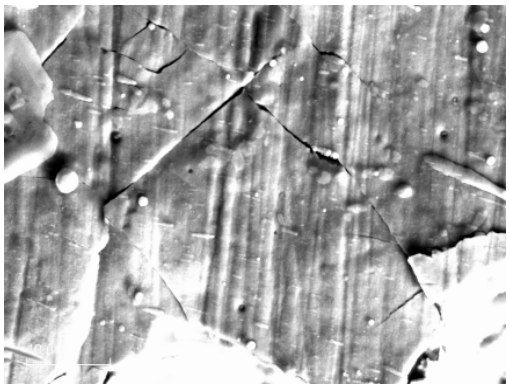

b)

Figure 3. SEM micrographs for the area of fatigue crack growth found at the flat face failured at cyclic tension tests; (a) specimens without treatment; b) with nanostructured surface layer; axis of loading oriented vertically

2.4.4. High-cycle fatigue (HCF) 30CrMnSiNi2

The tests on cyclic tension of 30CrMnSiNi2 steel specimens have shown that surface nanostructuring by Zr^+ ions gives rise to double-or-triple time increase of fatigue durability. In doing so nucleation of fatigue crack in specimens with the surface modification happens later, while rate of its growth is noticeably slower in contrast with non-treated specimens.

2.5. Test on cyclic alternating bending

According to the testingdata the fatigue life-time of specimens under cyclic alternating bending is increased due to nanostructuring of a surface layer by~ 2 times. The series of optical images were used for plotting the graphs to characterize dependence the crack length versus the number of loading cycles. At cyclic bending the main crack originates nearly at the same time for both types of specimens but has significant differences in thepropagation rate. Crack growth rate forthe untreated specimen was 0.05 μm/cycle while for the specimen with modified surface layer it made 0.024 μm/cycle. Thus, it is shown that nanostructuring of surface layer by ion beam to slow the rate of fatiguecrack growth by about 2 times.

2.5.1. Optical observation of strain induced relief

Images of surfaces of both type specimens after the different number of cycles before fracture to cause distinction in the formation of strain induced relief are given in fig. 4. One can see formation of manifested thin folds (fig. 4,a) located close to the fracture area (region of maximum curvature) in the specimen without treatment which shows an intensive deformation development in this area. Most likely their presence contributes to a rapid propagation of fatigue crack in this specimen. Reason of formation of these folds is apparently related to the testing scheme that governs periodical application of tensile and compressive stresses. Mechanism of material deformation for this case is similar to the corrugation formation which is formed as a result of greater deformation in the subsurface layer. In the nanostructured layer the number of such folds is slightly visible and deformation relief is smoother and changeable more lightly (fig. 4, b).

The analysis of surface roughness of failured specimens in the fracture area was carried out with a help of optical interferential profilometer. According to obtained values of roughness parameter R_a the surface roughness of the specimen without treatment is more than 1.5 times higher in comparison with one for the specimen with nanostructured surface layer.

During the test, in the specimen without the treatment clearly pronounced microcracks are formed along the grain boundaries and the main crackis more clearly manifested and propagates just along the microcracks. The specimen after the treatment has the number and size of the microcracks noticeably smaller and the main crack develops to a less extent. More detailed view of the main crack for specimen without treatment testifies for the fact that it is developed intensively not only on the surface, but into the bulk of the specimen as well. The main crack in the nanostructured specimen is less pronounced that could indicate that it develops mainly in the modified surface layer which hinders its spreading into the bulk of the material. This may cause a reduction in growth rate atmain fatigue crack propagation.

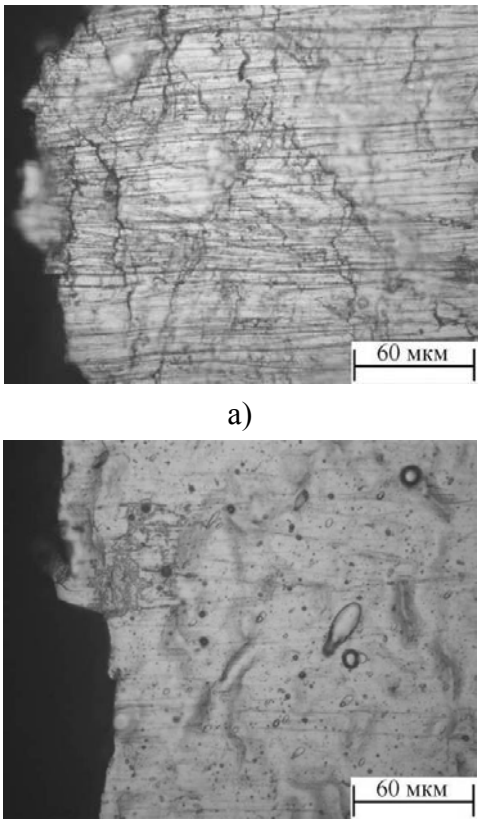

a)

b)

Figure 4. Optical micrographs to illustrate strain induced reliefonthe surfaceofspecimens: a) without treatment; b) withnanostructured surface layer

3. Discussion of results

The first effect of the surface layer nanostructuring which is to be stressed is the noticeable increase of flowstress with a ratherlow decrease of ductility. Traditionally, ion beam treatment is accompanied by the formation of a layer with thickness up to 0.1 micron, whereas under the treatment used the thickness of modified layer is estimated as 2 μm (according to the data of optical profilometry of the cracked layer) up to 10 μm (according to data of the scanning electron microscopy at observation of the fracturesurface after fatigue fracture).In doing so, presence of multiple cracksin the modified layerin the vicinity of neck exerts no significant impact on the reduction of plasticity due to the small thickness of the modified layer,as well as realization of multiple cracking. As a result, none of the cracks becomes the main oneand plastic deformation of the composition is determined mostlyby the development of plastic flow in the ductile material of the substrate.

The following key result is associated with notable changein the character of the localized plastic deformation development in the subsurface.It is shown that the layer to have the 1.5 times increased hardness and thickness of several microns can significantly change the pattern of the deformation relief formed. At low strain of the substrate (for example, at static tension out the neck area) deformation relief on the surface almost is not formed while in the region of intensive development of plastic deformation the size of strain induced relief elements is noticeably bigger than that in specimens without the treatment. This result is consistent with data on the cyclic bending tests

where during the process of cyclic loading the modified layer behaves much like a thin polymeric film placed on the water surface which is manifested both in dumping the deformation development and remarkable smoothing reliefto form at the specimen's surface. The hindering formation of strain induced relief under tests by another scheme (cyclic tension) when the surface relief to a large extent determines the origin of the main crack brings to increasing by more than twice the time period prior to origin of fatigue crack in the case of the ion beam modification.

Of particular interest in the light of the results obtained is observed difference in the character of the fatigue fractureunder cyclic tension and bending. It should be reminded that in the first case the crack originwas fixed at cyclic deformation not less than 0.75 N_F (the total number of loading cycles). At the same time, under alternating bending tests the main crack is already initiated at cyclic load of 0.15-0.2 N_F which in absolute terms corresponds to the same number of bending cycles of the non-treated specimens and ones with modified surfacelayer. Thus, for the case of cyclic bending the main crack in the specimen without the treatment originated very early but the rate of its growth was rather low in contrast with one under cyclic tension tests. This result, in principle, can be quite simply interpreted, because under the cyclic bending a surface layer is subjected to the periodic effects of maximum tensile and compressive stresses. Therefore, presence of the nanostructured layer on the surface hinders noticeable delay the origination (but not propagation!) of the crack.

However, its subsequent growth is realized significantly slower that was interpreted a result of fewer microcracks arising along the grain boundaryin the specimen without treatment, while the nanostructured layer hinders the formation of microcracks and, consequently, the rate of the crack growth. Another factor that may have a significant impact on the character and the rate of the origination and propagation of the crack is its depth. Despite the fact that in the work direct measurements of the depth of a forming fatigue crack was not carried out but judging by the size of its opening the depth of a crack in a specimen of the initial state should be noticeably higher, which in it turn should bring to its more rapid growth.

In contrast, under cyclic tension test a crack is originated sufficiently later that could be associated with roughly equal distribution of stresses through the cross section. As a result, it is the deformation relief of surface that can be a key factor in terms of origin of the main crack. A visible hindering in its formation has led not only to a multiple increasing of fatigue life-time of nanostructured specimens but also significantly slower rate of the main crack propagation.

It is proved by the notable difference in the rate of its propagation which under LCF (when influence of processes of localized plastic deformation is dominant) amounted up to 3.5 times (nanostructured layer hinders the development of plastic deformation), while under HCF when crack growth is governed by dominant mechanisms of the brittle fracture, the difference in the rate of the crack growth made two times.

In conclusion, one should point the role of multiple cracking processes, especially under conditions of high ductility of the substrate. In our view, the greater contribution to improving fatigue durability is associated with suppression of plastic deformation processes by nanostructured layer of higher strength causing substantial delay of the moment of the fatigue crack initiation. Noticeably smaller contribution to increasing the fatigue life-time is associated with the processes of multiple cracking. At the same time, usingmaterials of higher strength in contrast with substrate, as well as greater thickness of a coating will result in its cracking with their fast coalescence into the main one

resulting in a substantial reduction of fatigue durability of "coating-substrate" compositions.The combination oflow thickness of themodified surface layer and the ratio of the elastic characteristics compared with more ductile substrate material with high plastic deformations (for instance, in the area of a neck, or plastic tension under cyclic bending) has led to a formation of the system of multiple crackswhose orientation is not always in line with the normal to the direction of the external load.This is a fact that allows us to discuss the thesis of multiple cracking as one of the ways to improve the fatigue durability of "coating-substrate" compositions.

4. Conclusion

A study of structure and deformation behavior under static and cyclic tension and alternating bending the specimens of heat resistant 12Cr1MoVsteel subjected to surface layer nanostructuring by zirconium ion beam was performed. It is shown that ultra-dispersed particles of zirconates with the size about 100-150 nm were formed as a result of such treatment in a subsurface layer with a thickness up to several microns. Increase of strength properties by 15 % and decrease elongation before fractureby ~ 19 % is fixed due to thistreatmentat the static tensile.

It is found that the formation of the nanostructured surface layer increases the fatigue durability by 2-3 times at cyclic tension tests. The authors associate this with the delay of time the main crack initiationdue tohindering in deformation relief formation which play the key role in propagation of a crack.

At cyclic alternating bending the main crack origination in specimens of both types happens at almost equal numbers of cycles that is associated with the periodic occurrence in the surface layer of tensile and compressive stresses. However, at a subsequent stage the growth rate of the main crack is differing approximatelyin 2 times because of the nanostructured surface layer hinders microcracks origin on the grain boundaries of the substrate. This result is consistent with data of distinction comparison for both fatigue crack growth rate at the cyclic tensile and bending. For the second case, the growth rate is several times less.

The influence of multiple cracking on improving fatigue durability of specimens under study is discussed. It is shown that in the area of the main crack (predominantly under cyclic tensile) the finite length microcracks whose orientation does not always coincide with the direction of normal to the axis of the applied load are formed. This fact may be the manifestation of the effect of channeling plastic shears in the substrate material.

References

[1] Shaniavskii A.A. Safe fatiguefracture of elements aviastructures: Synergetics in engineering applications /–Ufa: Izdatel’stvoUGNTU, 2003. – 802 p.

[2] Didenko A.N., Sharkeev Yu.P., Kozlov E.V., Ryabchikov A.I. Effects of long-range interaction in ion-implanted metal materials / – Tomsk: Izdatel’stvoNTL, 2004. – 328 p.

[3] PaninV.E., Sergeev V.P., PaninA.V.Nanostructuringofsurface layers of structural materials and deposition of nanostructured coatings / – Tomsk: Polytechnic University, 2008. – 286 p.

[4] PaninV.E., EgorushkinV.E., PaninA.V.The effect of channeling plastic shears and nonlinear waves of localized plastic deformation and fracture// Phys. Mesomech. –2010. –T. 13. – N5. – P. 7-26.

Effects of Short-Time Duplex Heat Treatment on Microstructure and Fatigue Strength of Ti-6Al-4V Alloy

Satoshi Tanaka[1,*], Tatsuro Morita[1], Kosuke Shinoda[1]

[1] Department of Mechanical and System Engineering, Graduate School, Kyoto Institute of Technology, Kyoto 606-8585, Japan
* Corresponding author: satoshi.tanaka.10011@gmail.com

Abstract This study was conducted to investigate the effects of short-time duplex heat treatment on the microstructure, mechanical properties and fatigue strength of α+β titanium alloy Ti-6Al-4V. The duplex heat treatment was composed of short-time solution treatment (1203 K, 60 s) and short-time aging (753-903 K, 40 s). The first heat treatment transformed a part of prior β phase to acicular α' martensite phase. The second heat treatment precipitated fine α phase in metastable β phase. These change in microstructure increased the hardness of prior β phase. At the same time, the tensile strength and fatigue strength greatly improved without reduction in ductility and their maximum improvement rates reached 29 % and 22 %, respectively.

Keywords Ti-6Al-4V Alloy, Short-Time Duplex Heat Treatment, Microstructure, Mechanical Properties, Fatigue Strength

1. Introduction

Ti-6Al-4V alloy is a typical α+β titanium alloy possessing high specific strength (tensile strength/density) and excellent corrosion resistance, and has been widely used in the aerospace industry. For example, this titanium alloy is used to fix CFRP components in the airplanes recently developed because of its high electric corrosion resistance as well as high specific strength [1]. Ti-6Al-4V alloy occupies more than 50 % of the titanium market in the USA [2]. Accordingly, further improvement in the strength of this titanium alloy will have a great impact.

The strength of Ti-6Al-4V alloy is improved by controlling microstructure through heat treatment. Conventional heat treatment for titanium alloys is solution treatment and aging [3, 4]; however, it needs relatively long hours. In the previous study, one of the authors showed short-time solution treatment (1173-1263 K, 60 s) improves the tensile and fatigue strengths of Ti-6Al-4V alloy. Moreover, the above heat treatment was combined with short-time aging (753-953 K, 40 s). This duplex heat treatment further improved the tensile strength without reduction in ductility [5-8].

Although fatigue strength of metals is usually related to tensile strength, the fatigue strength of Ti-6Al-4V alloy markedly depends on the microstructure [9]. For the newly developed heat treatment, therefore, a detailed study was needed to investigate its effect on the fatigue strength.

From the above back ground, this study comprehensively investigated the effects of the short-time duplex heat treatment on the microstructure, mechanical properties and fatigue strength of Ti-6Al-4V alloy. To accumulate data, we conducted the metallographic examinations such as the optical observation of microstructure, TEM (transmission electron microscopy) observation and electron diffraction. Furthermore, the hardness measurement, tensile test and fatigue test were performed.

2. Materials and Experimental Procedures

Table 1 shows the chemical composition of Ti-6Al-4V used in this study. The material was supplied as round bars (diameter: 14 mm) and machined to the three specimen shapes shown in Fig. 1. For the short-time solution treatment, the specimens were kept at 1203 K for 60 s and quenched.

Hereafter, this heat-treated material is called "STQ material". In the short-time aging, STQ material was kept at 753, 803, 853 and 903 K for 40 s and air-cooled. They are called "STA materials". For comparison, the untreated material was also prepared.

The test sections of the button specimens (Fig.1 (a)) were polished to mirror surfaces with emery papers and alumina powder. The button specimens were used in the observation of the microstructure and hardness measurement. The test sections of the tensile and fatigue specimens (Fig. 1 (b), (c)) were polished with emery papers and electro-polished to mirror surfaces.

For TEM observation, thin small disks (diameter: 3 mm, thickness: 50 μm) were prepared from STQ and STA materials. The observation regions were polished with alumina powder and finally thinned by ion milling. Electron diffraction patterns of STQ material were obtained at the same positions where the microstructure was observed.

In the hardness measurement, a super micro-Vickers hardness tester with a CCD camera was used. The average hardness was measured under the test force of 2.94 N, and the hardness of α phase and prior β phase was measured under the test force of 19.6 mN. The tensile test was conducted in air at room temperature. The plane-bending fatigue test was performed under the conditions of frequency of 33 Hz and stress ratio R=-1 in air at room temperature. After the fatigue test, crack initiation sites were observed on the fracture surfaces by SEM (scanning electron microscopy).

Table 1 Chemical composition of Ti-6Al-4V alloy used in this study (mass %)

Al	V	C	N	O	Fe	H	Ti
6.18	4.20	0.001	0.01	0.17	0.17	0.0004	Bal.

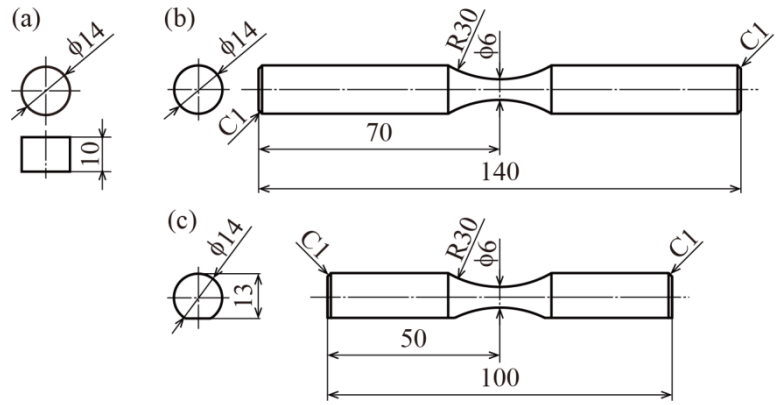

Figure 1 Specimen shapes (mm): (a) button specimen; (b) tensile specimen; (c) fatigue specimen.

3. Results and Discussion

3.1. Microstructure

Figure 2 shows the microstructures of the untreated, STQ and STA materials, and Fig. 3 shows the microstructures of prior β phase observed by TEM. Figure 3 includes the electron diffraction profiles of STQ material. Figure 4 shows a schematic illustration to explain the change in microstructure with the duplex heat treatment.

In the untreated material (Fig. 2(a)), a lot of small dark points correspond to β phase, and the

other bright regions are equiaxed α phase. In STQ material (Fig. 2 (b)), isolated regions are α phase and the regions surrounding α phase are prior β phase. As seen in Fig. 2 (b), the volume fraction of prior β phase increased with STQ treatment [5]. At the same time, a part of prior β phase was transformed to acicular α' martensite (Fig. 3(a)); however, the result of the electron diffraction showed the existence of metastable β phase. This point is important to think about the ductility of STQ material because strain-induced transformation can arise in metastable β phase.

Although the volume fraction of prior β phase was unchanged with the subsequent short-time aging, the inside of prior β phase became dark with increasing the treatment temperature (Fig. 2 (c)). This change in etching degree meant that metastable β phase was decomposed into fine α phase and stable β phase.

The change in microstructure with the duplex treatment was summarized as follows (Fig. 4): the untreated material was composed of α phase and stable β phase. Since the volume fraction of prior β phase increased with the short-time solution treatment, concentration of vanadium which is a β stabilizer decreased in prior β phase. As a result, acicular α' phase was generated in prior β phase through quenching. The short-time aging decomposed a part of remained metastable β phase into fine α phase and stable β phase during. The decomposition was accelerated by increasing the aging temperature.

3.2. Hardness and mechanical properties

Figure 5 shows the changes in the average hardness, hardness of α phase and prior β phase with the duplex heat treatment. Figure 6 shows the changes in the mechanical properties.

As shown in Fig. 5, the hardness of prior β phase was significantly increased by STQ treatment due to the formation of α' phase, although the hardness of α phase was almost unchanged. As a result, the average hardness also increased. The subsequent short-time aging generated fine α phase, so that the hardness of prior β phase further increased and it reached the maximum value at 803 K.

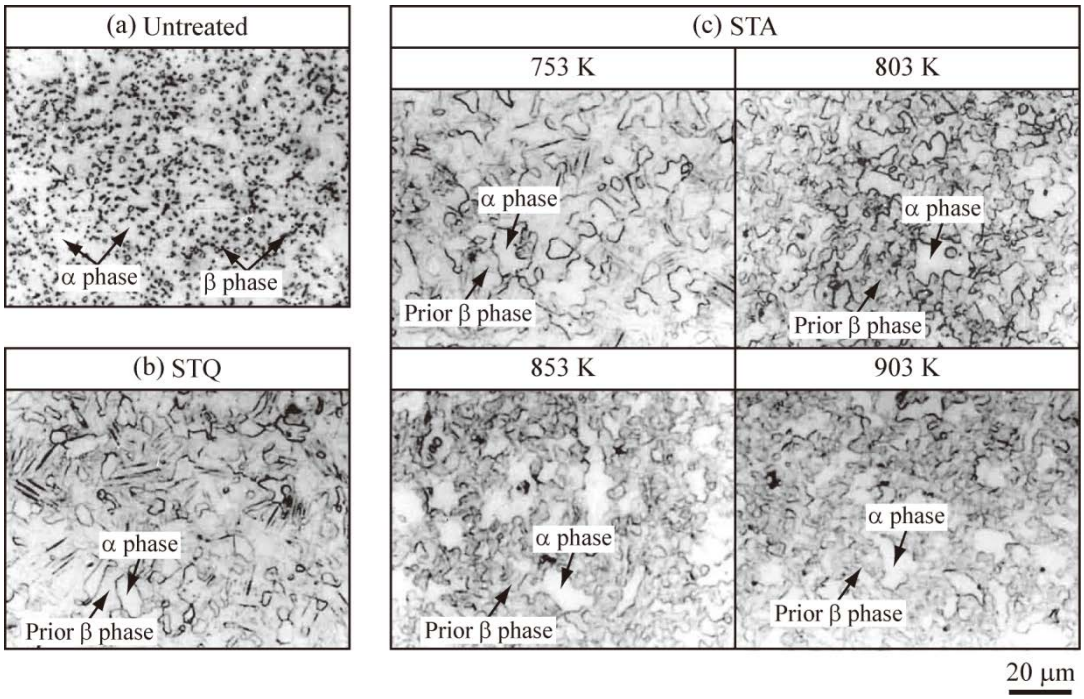

Figure 2 Microstructures optically observed after etching.

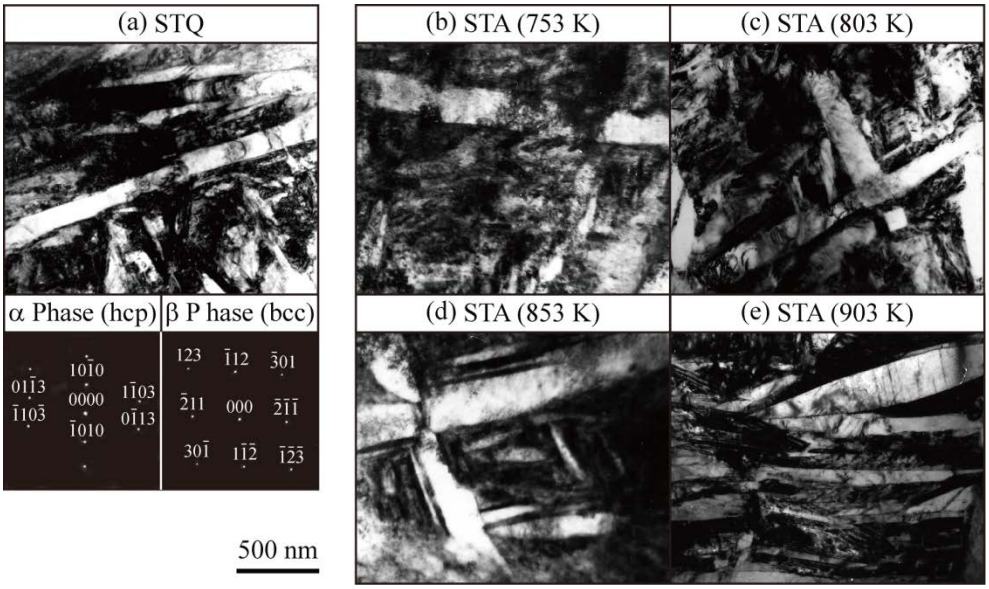

Figure 3 Microstructures of prior β phase observed by TEM and the electron diffraction patterns.

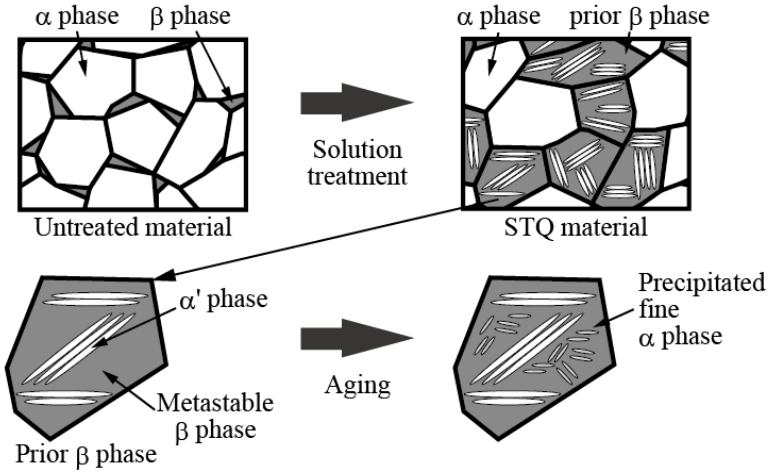

Figure 4 Schematic illustration to explain the change in microstructure with the duplex treatment.

If the aging temperature was increased beyond 803 K, the decomposition of prior β phase proceeded and the hardness showed a decline tendency.

The yield and tensile strengths obeyed the hardness of prior β phase (Fig. 6). Namely, the static strengths were improved by STQ treatment, and they were further increased by the subsequent short-time aging. The highest static strengths were achieved by STA treatment (aging temperature: 803 K), and their improvement rates were 46 % and 28 %, respectively.

The interesting point was found on the change in ductility. The reduction in area was increased by STQ treatment in spite of the great increase in the static strengths. This improvement will result from the strain-induced transformation of metastable β phase under tensile loading [3, 10]. Through the subsequent short-time aging, the ductility slightly decreased because a part of metastable β phase was decomposed. Nevertheless, the reduction in area was higher than that of the untreated material. As mentioned above, STA treatment greatly improved the static strengths without reduction in ductility.

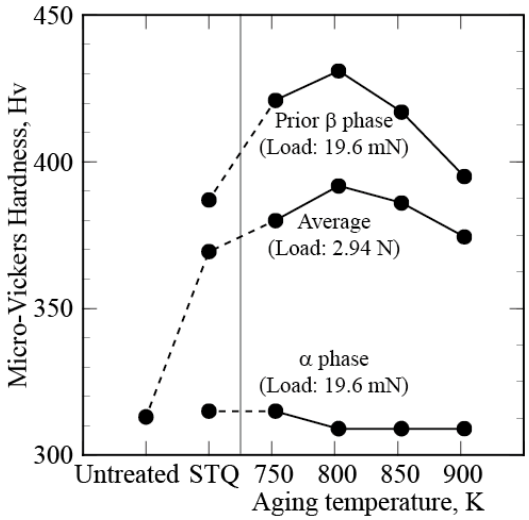

Figure 5 Changes in the average hardness, hardness of α phase and prior β phase with the duplex heat treatment.

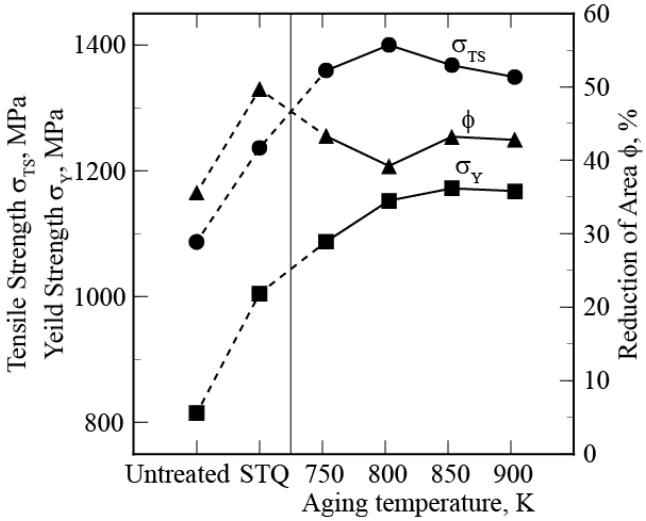

Figure 6 Changes in the mechanical properties with the duplex heat treatment.

3.3. Fatigue strength

Figure 7 shows the S-N curves of all materials, and Fig. 8 shows the change in the fatigue strength by STQ and STA treatments. Figure 8 includes the change in the ratio of the fatigue strength and the tensile strength, σ_W/σ_{TS}. Figure 9 shows the fatigue fracture surfaces of STQ material and STA material (aging temperature: 803 K).

The fatigue strength of Ti-6Al-4V alloy greatly increased with STQ treatment (Fig. 8). The maximum improvement in the fatigue strength was achieved by STA treatment (aging temperature: 803 K). As shown in Fig. 9, facets were observed at crack initiations sites of both materials, and their sizes were almost the same to α grain size. Moreover, no non-propagating crack was found on the test sections of the specimens which did not fracture until fatigue cycles of 10^7.

The above results meant that the fatigue strength was the maximum stress amplitude at which fatigue cracks did not initiate from α grain. The difference in the fatigue strength between STQ and STA materials resulted from the difference in the characteristics of prior β phase surrounding α phase. In the case of STA material, since the hardness of prior β phase was markedly higher than α phase, this region suppressed extension of slippages induced in α grain. In consequence, initiation of fatigue cracks was strongly restricted and the fatigue strength was improved.

On the other hand, STQ material also showed high fatigue strength although the hardness of prior β phase was lower than that in STA material. This will result from high ductility of prior β phase. That is, prior β phase in STQ material included much metastable β phase. Even if slippages in α phase generated a strain field in prior β phase, such strain field can be effectively cancelled through its strain-induced transformation. Consequently, the fatigue strength was improved by STQ treatment. As mentioned above, the improvement of the fatigue strength by the short-time treatments will be closely related to the two factors: the hardness of prior β phase and its ability for strain-induced transformation.

Finally, Fig. 10 summarized the tensile and fatigue strengths of the materials examined in this study. In addition, the figure includes the reference data [9]. As understood in this figure, STQ treatment effectively increased the fatigue strength although the improvement rate of the tensile

strength was relatively low; however, the subsequent short-time aging conducted at 803 K showed the great improvement of both strengths, and the reached level was markedly higher than the reference data.

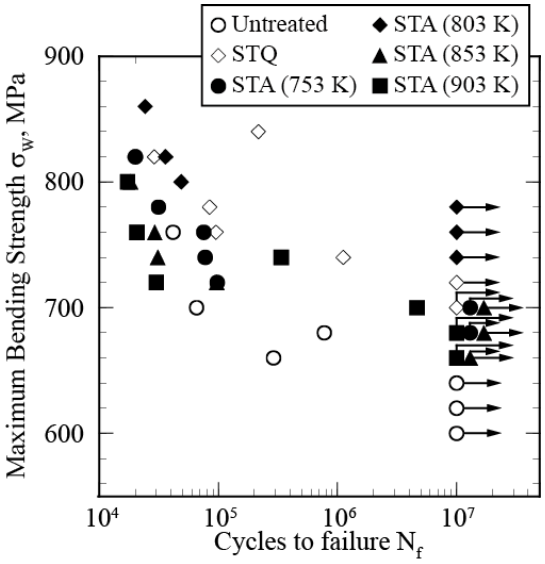

Figure 7 S-N curves.

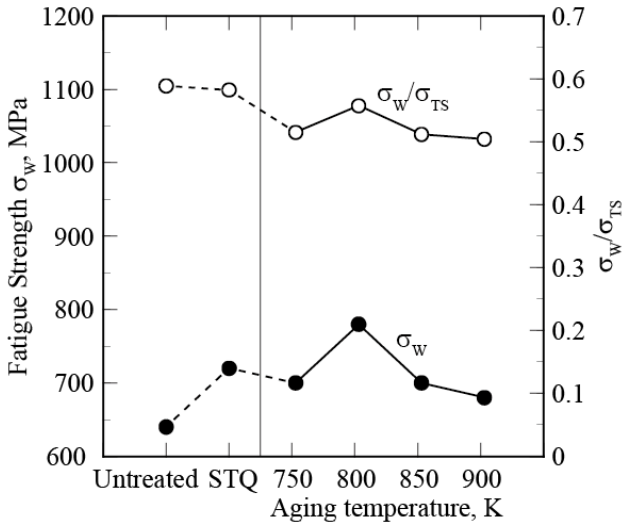

Figure 8 Change in the fatigue strength and the change in the ratio of the fatigue strength and tensile strength, σ_W/σ_{TS}.

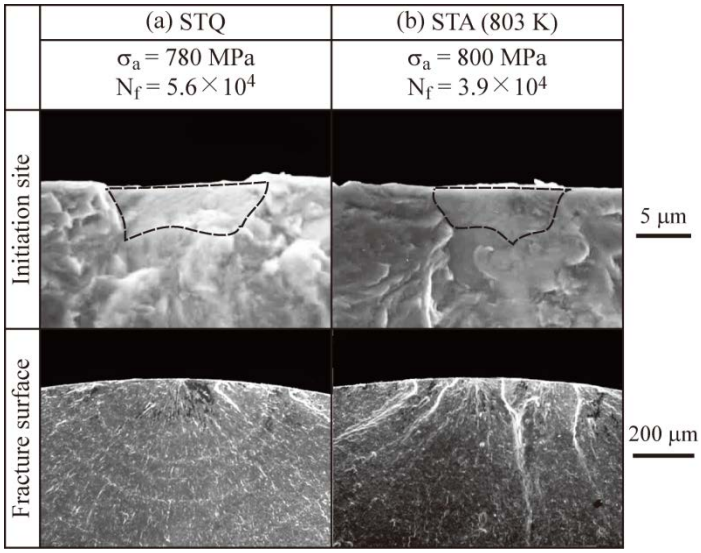

Figure 9 Fatigue fracture surfaces of STQ material and STA material (aging temperature: 803 K).

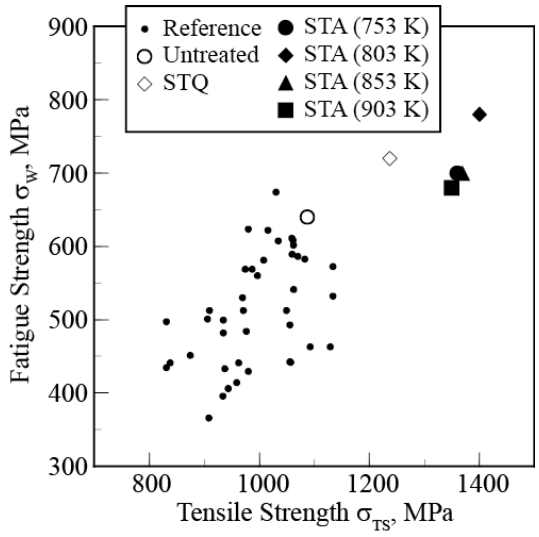

Figure 10 Changes in the tensile strength and the fatigue strength of Ti-6Al-4V alloy, including reference data [9].

4. Conclusions

(1) The short-time solution treatment transformed a part of prior β phase to acicular α' martensite phase. The subsequent short-time aging precipitated fine α phase in metastable β phase. These changes in microstructure increased the hardness of prior β phase.

(2) The short-time duplex heat treatment greatly increased the tensile strength and fatigue strength

of Ti-6Al 4V alloy without reduction in ductility. The most appropriate heat treatment was composed of STQ treatment at 1203 K for 60 s and short-time aging at 803 K for 40 s. Through this duplex heat treatment, the improvement rates of the tensile strength and fatigue strength reached 29 % and 22 %, respectively.

Acknowledgements

This work was supported by a Grant-in-Aid for Scientific Research (KAKENHI), No. 16560069 and No. 18560080. The authors gratefully acknowledge the generous support.

References

[1] T. Nishimoto, N. Nakanishi, J. Umeda, Mechanical Properties and Strengthening mechanism of pure Ti powder composite material reinforced with carbon nano particles, Transactions of JWRI, Vol. 40 (2011), No. 2, 66-68.

[2] G. Lutjering and J. C. Williams, Titanium, Springer-Verlag, Berlin, 2003, p.7.

[3] M. A. Imam and C. M. Gilmore, Fatigue and microstructural properties of quenched Ti-6Al-4V, Metallurgical Transaction A, Vol. 14A, pp. 233-240 (1983).

[4] J. R. Kennedy, Fatigue behavior of solution-treated and quenched Ti-6Al-4V alloy, Materials Science and Engineering, Vol. 57, pp. 197-204 (1983).

[5] T. Morita, W. Niwayama, K. Kawasaki and Y. Misaka, Strengthening of Ti-6Al-4V alloy by induction heat treatment, Transactions of the Japan Society of Mechanical Engineers (A), Vol. 64, No. 624, pp. 2115-2120 (1998).

[6] T. Morita, K. Kawasaki and Y. Misaka, Short-time heat-treatment of Ti-6Al-4V $\alpha+\beta$ type titanium alloy, JP. 3762528 (2006).

[7] T. Morita, K. Kawasaki and Y. Misaka, Short-time duplex heat-treatment of $\alpha+\beta$ type titanium alloy, JP. 3789852 (2006).

[8] T. Morita, K. Hatsuoka, T. Iizuka and K. Kawakami, Strengthening of Ti-6Al-4V alloy by short-time duplex heat treatment, Materials Transaction, Vol. 46, No. 7, pp. 1681-1686 (2005).

[9] K. Minakawa, Fatigue of titanium alloy, Tetu-to-hagane, Vol. 75, No. 7, pp. 1104-1111 (1989).

[10] G. Sridhar, R. Gopalan and D. S. Sarma, A microstructural characterization of solution-treated titanium alloy Ti-6Al-4V, Metallography, Vol. 20, pp. 291-310 (1987).

Effect of different micro-arc oxidation coating layer types on fatigue life of 2024-T4 alloy

Xi-Shu Wang[1,*], Xing-Wu Guo[2], Xu-Dong Li[3], Norio Kawagoishi[4]

[1] Department of Engineering Mechanics, Tsinghua University, Beijing 100084, P.R. China
[2] National Engineering Research Center for Light Alloy Net Forming School of Material Science & Engineering, Shanghai Jiao Tong University, Shanghai, 200030, P.R. China
[3] Department of Mechanical Engineering, Qingdao Campus of Naval Aeronautical Academy, Qingdao, 266041, P.R. China
[4] Department of Mechanical System Engineering, Daiichi Institute of Technology, Kirishima, 899-4395, Japan
* Corresponding author: xshwang@tsinghua.edu.cn

Abstract Due the fatigue life of aluminum alloys is strongly sensitive to the environmental effect in the most engineering applications, one of effectively improved methods on the strength and fatigue life of aluminum alloys is generally to take a coating process on the surface of these aluminum alloys. And the micro-arc oxidation ceramics coating method is not only to enhance the fatigue strength but also to avoid the environment corrosion. In this work, a dual-spindle rotating bending environment fatigue tests for two types aluminum alloys were carried out. The effects of differently relative humidity and oxidation ceramics coating types on fatigue life of aluminum alloys were discussed. These results indicated that the fatigue life (N_f>10^6) of 7074-T6 alloy began obviously to degrade when the relative humidity is over than 75% and there is a threshold. At the same time, the fatigue lives of 2024-T4 alloy by using the different oxidation ceramics coating treatments present the different changed tendencies. For example, the effect of micro-arc oxidation ceramics coating with sealing hole technology on fatigue life is positive and the effect of other two oxidation ceramics coating technologies on fatigue life is negative, such as micro-arc oxidation coating and hard oxidation coating.

Keywords Fatigue life, Aluminum alloy, Micro-arc oxidation technology, Coating layer, Relative humidity

1. Introduction

Aluminum alloys have been widely used for making structural parts in transport vehicles such as ships and aircraft for the purpose of reducing their weight. However, these structures are usually exposed to the natural environment throughout their lifetime. In these fields, very often the main requirements for the components include high-cycle fatigue (HCF) and corrosion resistance [1], especially the corrosion fatigue (CF) is defined as the sequential stages of aluminum alloys damage that develops during accumulated load cycling in an aggressive environment [2-4]. In addition, the effect of the relative humidity of over 60% on the HCF life of aluminum alloys can not be ignored. This is because the decrease in fatigue life was mainly the acceleration of crack growth caused by brittle fracture under rotating bending and the transition to shear mode crack accompanied with glide plane decohesion and void formation under ultrasonic loading respectively [5,6]. The first requirement is achieved usually by a proper material selection to enhance the fatigue resistance of aluminum alloy but not to avoid the higher cost. The second requirement for aluminum alloys is achieved by using corrosion resistance coatings [7,8]. Micro-arc oxidation ceramics process is a classical approach to enhance the fatigue properties [9] and to provide one of countermeasures against the fatigue corrosion damage of aluminum alloys. However, the enhanced behavior and effective mechanism to fatigue property of aluminum alloys exists still some arguments and/or there are not enough experimental evidences. In this work, we sum up the effect of the relative humidity on the fatigue life of aluminum alloys then investigate the effects of different micro-arc oxidation ceramics methods on the fatigue life of Al 2024-T4 alloy. The results indicated that the fatigue life (N_f>10^6) decreased obviously when the relative humidity scopes from 50% to 75% and the effect of micro-arc oxidation ceramics coating with sealing hole on the fatigue life of Al 2024-T4 alloy is

positive and the effect of other micro-arc oxidation ceramics coating technologies, such as micro-arc oxidation process and hard oxidation process, on the fatigue life of Al 2024-T4 alloy is negative.

2. Material and Experimental Procedure

Materials used were Al 2024-T4 alloy and Al 7074-T6 alloy. And the size and shape of the experimental specimens is shown in Figure. 1 including the morphology of specimen with the different micro-arc oxidation ceramics coating processes consisting of the different micro-arc oxidation ceramics coating technologies with sealing hole, micro-arc oxidation ceramics coating and hard oxidation ceramics coating surface technologies as shown in Fig. 1b. The oxidation ceramics coating layer of all experimental specimens by the different oxidation ceramics coating surface technologies has the approximate same ceramics coating layer thickness of about 0.15 mm. The center notch in these specimens was fabricated to control the stress concentration factor as about 1.08. The mechanical properties of aluminum alloys are presented in Table 1. All fatigue tests were performed by using the rotating bending machine including the addition relative humidity controlled device and 4-spindle loading device (by Yamamoto Metal Tech Co. LYD, Japan) as shown in Figure 2. The machine provides the cyclic loads at the frequency of 50 Hz and at the stress ratio of R=-1.

Table 1. Mechanical properties

	$\sigma_{0.2}$ (MPa)	σ_B (MPa)	E (GPa)	δ (%)
Al 2024-T4	325	470	70.0	20
Al 7075-T6	527	673	72.2	11

$\sigma_{0.2}$: 0.2% proof stress. σ_B: Tensile strength. E: Young's modulus. δ: Percentage elongation.

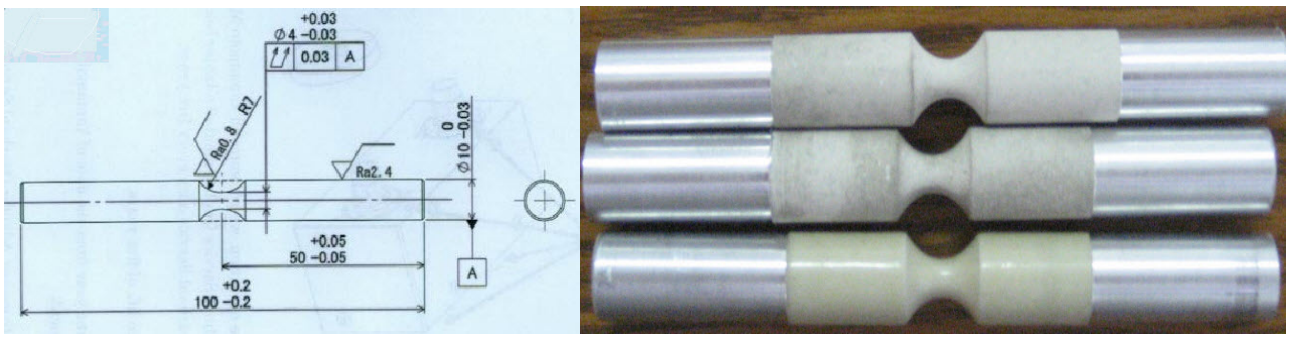

(a) (b)

Figure 1 Shape and dimensions of specimens (mm)

Figure 2 Experimental machine

3. Results and discussion

3.1 Effect of the relative humidity on fatigue life of Al 7075-T6 alloy

Figure 3 illustrates the S-N curves under the different relative humidity scopes of Al 7075-T6 alloy. The high-cycle fatigue (HCF) behavior of Al 7075-T6 alloy indicated that the effect of the relative humidity on the fatigue life can not be ignored. Especially when the relative humidity is over than 75% and the fatigue cycles is over than 2×10^6, the effect of the relative humidity on fatigue life of aluminum alloy is very obvious. At the same time, there is a difference about the fatigue behavior in the two relative humidity states of both 75% and 100% (in water), in which with the increasing of relative humidity, the fatigue life of Al 7075-T6 alloy observably decreases no matter what is the relative humidity of over than 75% and the low- or high- cycle fatigue life of aluminum alloy. Of course, the difference of fatigue life is much obvious when the cycles are over than 10^6. However, the decreasing trend of fatigue life was restrained at lower relative humidity scopes from 75% to 50% and low-cycle or $N<10^6$. The effect of the relative humidity on the fatigue life of aluminum alloy can be even ignored. It has previously been reported that the influence mechanism was expressed by the different fatigue fracture models [5,10]. One of main reasons is because the shear stress action occupies more than part in fatigue fracture process although the applied stress is only a compressive and tensile stress at the surface damage point of specimen. The shear stress at the fatigue fracture surface might be caused by the coupling action both stress state and hydrogen or oxygen on the fatigue crack initiation and growth mechanism of aluminum alloys. Therefore, the fatigue crack growth driven force of Al 7075-T6 alloy comes from the interaction both shear and normal stresses. With the corrosion effect of hydrogen or oxygen increasing, the shear stress occupied the proportion to increase. However, the composite damage behavior of humidity effect needs to be carefully discussed in further.

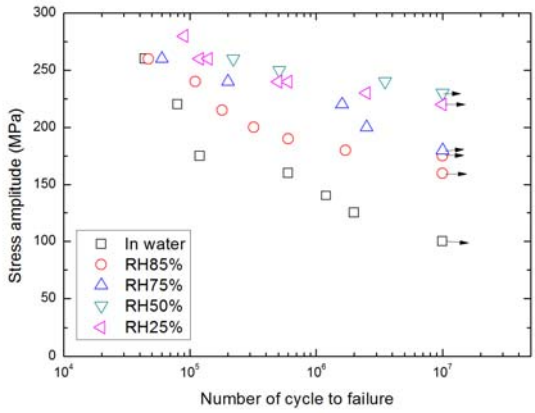

Figure 3 S-N curves under the different relative humidity scopes of Al 7075-T6 alloy

3.2 Effect of different micro-arc oxidation processes on fatigue life of Al 2024-T4 alloy

Considering the countermeasures against the effect of relative humidity on the fatigue life of aluminum alloy, the oxidation ceramics coating layer were carried out on the surface of Al 2024-T4 alloy specimens by using the micro-arc oxidation, micro-arc oxidation plus the sealing hole and hard oxidation technologies, respectively. All coating layers have an approximate same thickness of about 0.15 mm. in addition, to compare with the differently typical coating layer how to influence on the fatigue life of Al 2024-T4 alloy, the fatigue data without coating layer has been also plotted

in the S-N curves as shown in Figure 4. These experimental results indicated that the fatigue life (mark Δ) of Al 2024-T4 alloy is seriously injured with the hard oxidation ceramics coating layer, but the effect of micro-arc oxidation plus sealing hole method on the fatigue life of Al 2024-T4 alloy is positive. And the fatigue life (mark ○) of Al 2024-T4 alloy with the micro-arc oxidation ceramics coating layer is approximate same fatigue life (mark ■) of Al 2024-T4 alloy. By means of the fatigue data with and without oxidation ceramics coating layer of Al 2024-T4 alloy compared as shown in Figure 4, we clearly know that the coating layer is able to avoid the effect of humidity or corrosion on the fatigue strength of aluminum alloy but the different coating layer technologies cause the fatigue damage mechanism change of aluminum alloy. Therefore, we should pay close attention to the issue in future to optimize and improve the coating layer technology.

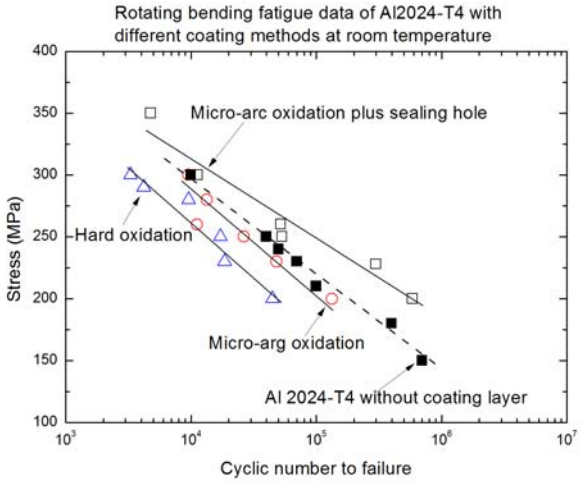

Figure 4 S-N curves under the different micro-arc oxidation processes of Al 2024-T4 alloy

(a) (b) (c)

Figure 5 Fatigue fracture surfaces for differently typical micro-arc oxidation processes of Al 2024-T4 alloy (a) micro-arc oxidation ceramics coating with sealing hole, (b) micro-arc oxidation ceramics coating, (c) hard oxidation ceramics coating.

Figure 5 illustrates the fracture appearances for the different oxidation ceramics coating layer technologies including (a) the micro-arc oxidation ceramics coating layer with sealing hole, (b) the micro-arc oxidation ceramics coating layer and (c) hard oxidation ceramics coating layer. All the applied stress amplitudes are 230 MPa, respectively. These fracture surfaces have much more different flat fracture surface such as the smooth area in the center or concave-convex surface in the marginal zone as shown in Figure 5a and 5b as well as 5c. This is a fact that the different flat fracture surface reflects the different fatigue crack propagation life. That is the fatigue crack propagation life for micro-arc oxidation ceramics coating layer with sealing hole is slower than that for micro-arc oxidation ceramics coating layer. This is because the center area and the fatigue crack propagation area in the marginal zone for the micro-arc oxidation coating ceramics layer with sealing hole are larger and relative smoother than that other two oxidation technologies. It means

that the surface quality in the oxidation ceramics coating layer processes plays an important part in fatigue damage of aluminum alloy. In additional, the fracture-resistant of the different fracture appearances is different under the different oxidation ceramics coating layer methods. The different oxidation ceramics coating layer methods cause unavoidably the different surface quality. The oxidation ceramics coating layer with sealing hole can much easily avoid the surface defects such as shrinkage cavity. And the shrinkage cavity causes unavoidably the stress concentration and fatigue life degradation of materials. At the same time, the residual stress affects on the fatigue life of Al 2024-T4 alloy to exist the different results in three oxidation ceramics coating processes.

4. Summary

Fatigue life of aluminum alloys may be either affected by relative higher humidity when the cycle is over than 2×10^6 or improved by the appropriate oxidation ceramics coating layer technology. For example, the effect of micro-arc oxidation with sealing hole process on the fatigue life of Al 2024-T4 alloy is positive and the effect of other micro-arc oxidation processes, such as micro-arc oxidation process and hard oxidation process, on the fatigue life of Al 2024-T4 alloy is negative. Therefore, the micro-arc oxidation ceramics coating layer with sealing hole technology is not only to enhance the fatigue strength but also to avoid the harmful or negative effect of the relative humidity on the fatigue life of Al 2024-T4 alloy.

Acknowledgements

The authors would like to thank the projects (Grants No: 11072124,11272173) supported by NSFC.

References

[1] Q.Y. Wang, C. Bathias, N. Kawagoishi, Effect of inclusion on subsurface crack initiation and giga-cycle fatigue strength. Int J Fatigue, 24 (2002) 1269–1274.

[2] X.D. Li, X.S. Wang, H.H. Ren, Y.L. Chen, Z.T. Mu, Effect of prior corrosion state on the fatigue small cracking behavior of 6165-T6 aluminum alloy. Corros Sci, 55 (2012) 26-33.

[3] K. Jones, D.W. Hoeppner, Prior corrosion and fatigue of 2024-T3 aluminum alloy. Corros Sci, 48 (2006) 3109-3122.

[4] W.F. Xu, J.H. Liu, Microstructure and pitting corrosion of friction stir welded joints in 2219-O aluminum alloy thick plate. Corros Sci, 51 (2009) 2743-2751.

[5] N. Kawagoishi, K. Kariya, Y. Nu, S. Furumoto, E. Kondo, Effect of humidity on fatigue strength of age-hardened Al alloy under rotating bending. Key Eng Mater, 452-453 (2011) 745-748.

[6] N. Kawagoishi, T. Fukudome, K. Kariya, Q. Chen, M. Goto, Fatigue strength of age-hardened and extruded Al alloy under high humidity (Rotating bending and ultrasonic loading). Trans Japan Soc Mech Eng A, 76 (2010) 1651-1658.

[7] H.M. Nykyforchyn, V.I. Pokhmurskii, M.D. Klapkiv, M.M. Student, J. Ippolito, Electrochemical characteristics of PEO treated electric arc coatings on lightweight alloys. Adv Mater Research, 138 (2010) 55-62.

[8] B. Lonyuk, I. Apachitei, J. Duszczyk, The effect of oxide coatings on fatigue properties of 7475-T6 aluminium alloy. Surf & Coat Tech 201 (2007) 8688-8694.

[9] N.P. Wasekar, A. Jyothirmayi, L.R. Krishna, G. Sundararajan, Effect of micro arc oxidation coatings on corrosion resistance of 6061-Al alloy. J Mater Eng & Perform, 17 (2008) 708-713.

[10] N. Kawagoishi, K. Hayashi, N. Yan, S. Furumoto, E. Kondo, Effect of humidity on fatigue strength of age-hardened Al alloy under rotating bending. Key Eng Mater, 452-453 (2011) 745-748.

Three-dimensional Fatigue Crack Growth Path Simulation under Non-proportional Mixed-mode Loading

Ying Yang[1,*], Michael Vormwald[1]

[1] Material Mechanics group, Technische Universität Darmstadt, Petersenstaße 12, 64287 Darmstadt (Germany)
* Corresponding author: yang@wm.tu-darmstadt.de

Abstract An algorithm based on linear elastic fracture mechanics (LEFM) for three-dimensional fatigue crack growth simulation under non-proportional mixed-mode loading is proposed in the present paper. Combined non-proportional cyclic tension and torsion loading with different phase angle and loading ratio M_T/F are considered. The maximum tangential stress (MTS) criterion is performed as the main theory to predict crack propagation direction. Under some specific loading cases, especially for high stress intensity factors, the crack growth direction needed to be modified in order to be in accordance with the experimental results. By analyzing the simulated crack growth paths, three distinct features are observed that are tension mode dominated crack paths, shear mode dominated crack paths and transitional crack paths. When crack growth changes from tension to shear mode, the latter is described by the maximum shear stress (MSS) criterion. A preliminary proposal is made to predict the transitional mode.

Keywords Linear elastic fracture mechanics, Non-proportional loading, Mixed mode, Transitional fracture

1. Introduction

Considering that a great amount of structures or components are subjected to mixed mode loading during the service time, research on material fracture under this kind of loading type has attracted more attention in recent years. Crack propagation direction is one of the major problems in this field. Since the maximum tangential stress criterion was first proposed by Erdogan and Sih [1], the minimum strain energy density criterion (S-Criterion), the maximum energy release rate criterion and maximum tangential strain criterion [2–4] and so on were suggested subsequently. All the mentioned criteria present similar crack propagation direction for proportional mixed mode loading, showing small deviation with the experiment results. The crack growth directions display a tension mode feature following the direction which minimizes the K_{II} values. However, large distinction between experimental crack propagation direction and the predicted crack kink angle were also observed for some materials. In these cases, the crack growth occurred in the plane that K_{II} values were maximum. As a result the maximum shear stress (MSS) criterion was proposed. Crack growth in shear mode was summarized in a literature review by H. W. Liu [5].

The criteria represented by MTS and MSS are deduced according to the stress field solution in the vicinity of crack tip on the basis of linear elastic fracture mechanics. Strictly speaking, these criteria are appropriate only in monotonic loading condition. Nevertheless, Highsmith et al. [6] pointed out that the criteria can be performed straightforward to fatigue crack growth under proportional mixed mode loading. Fatigue crack growth under non-proportional mixed mode loading is a more complex situation and there are insufficient experiments and hypotheses for application. Vormwald et al. [7] reviewed some research consequences in recent years. Six relevant factors which influence the crack growth behavior under non-proportional loading were denoted and an algorithm based on LEFM for three-dimensional fatigue crack growth simulation under non-proportional mixed-mode loading is proposed [8]. The emphasis in the present paper is focusing on the crack growth path behavior. A description of the algorithm is presented.

2. Application of the algorithm

The algorithm is applied to simulate the fatigue crack growth including path and propagation rate in a thin-walled, hollow cylindrical specimen (see Figure 1) with a notch. The corresponding experimental data were obtained by Brüning [9]. In the experiment two common used materials were tested, the aluminium alloy AlMg4.5Mn and steel S460N. The combined non-proportional cyclic tension and torsion loading with phase angles of 45° and 90° were applied to the specimens with an R ratio of -1. The results of 4 specimens marked as A7, A8, S7 and S13 could be used here for comparison purpose because the loading was relatively low to meet small scale yielding requirements.

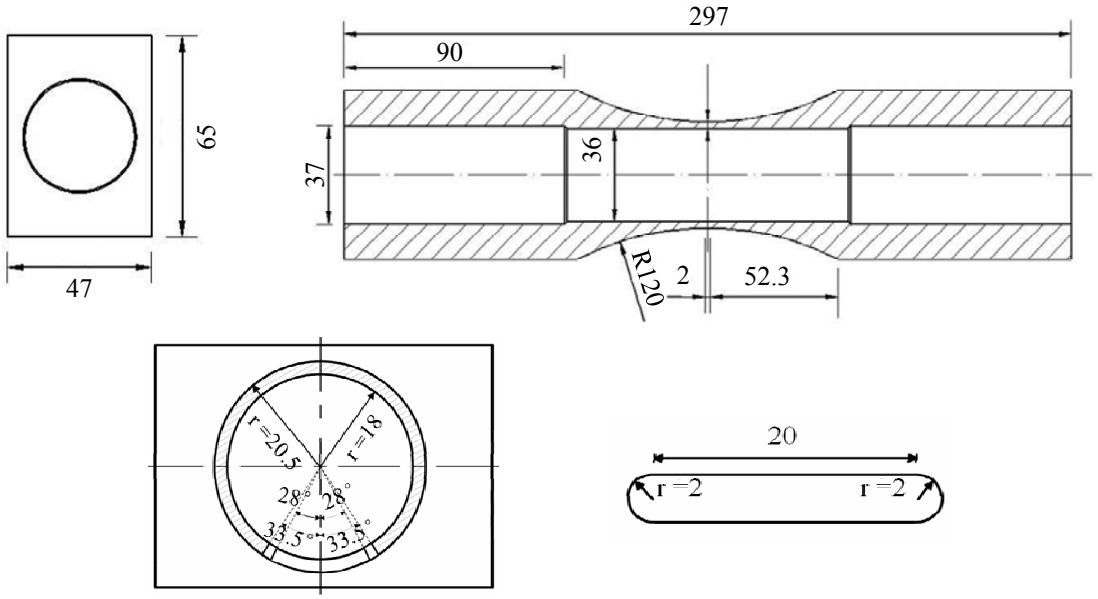

Figure 1. Specimen and notch geometry (dimensions in millimetres)

The algorithm consists of three main modules: (a) determination of the crack initiation position; (b) calculation of the maximum equivalent stress intensity factor K_{eq} in one loading cycle, which is taken as the crack driving force parameter; (c) crack growth process. Module (b) and (c) are repeated until the crack growth path can be presented clearly. Brief expression of each module is introduced in the following sections, more details can be found in reference [8].

2.1. Location of crack initiation

The crack initiation will occur in the notch root at the position where the locally uniaxial notch stress is maximum in one loading cycle. A 3-dimensional finite element model was created using ABAQUS software for stress analysis. Refined mesh was applied in the crack growth region as shown in Fig 2 (a). Along the notch root, there are four potential crack initiation sites numbered 1, 2, 3 and 4 clockwise, shown in Fig 2 (b). The analysis indicated that the maximum tangential stress in one loading cycle along the notch root on the inside edges is almost 2 times larger than the tangential stress on the outside edge, therefore a corner crack is considered to be a reasonable shape to initial crack simulation. As can be expected, the initial corner crack will propagate through the thickness of the notch and extend to the outside surface of the specimen in the crack growth process.

An incipient corner crack was inserted into the inside edge of the notch root where tangential stress is maximum by program Fracture Analysis Code 3D (FRANC3D). This program package is designed to simulate crack growth in engineering structures or components with arbitrary crack

geometry under different loading and boundary conditions. FRANC3D adaptively remeshes an existing finite element model with the inserted initial crack to generate a cracked model. Furthermore, FRANC3D is also used to calculate stress intensity factor (SIF) for an entire crack front.

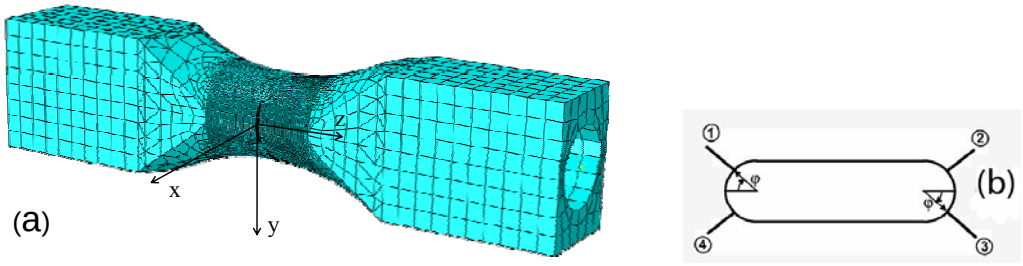

Figure 2. (a) Finite element model, (b) Crack initiation sites

2.2. Crack driving force calculation

In the present paper, mode I and mode II SIFs, K_{I} and K_{II} in one cycle under non-proportional tension combined with torsion loading are computed for the sake of obtaining the equivalent SIF, K_{eq}. Erdogan and Sih proposed that the equivalent stress intensity factor according to the maximum tangential stress criterion can be described by:

$$K_{eq}=\frac{1}{4}\left(3\cos\frac{\theta^{*}}{2}+\cos\frac{3\theta^{*}}{2}\right)K_{\mathrm{I}}-\frac{3}{4}\left(\sin\frac{\theta^{*}}{2}+\sin\frac{3\theta^{*}}{2}\right)K_{\mathrm{II}} \tag{1}$$

θ^{*} is a function of K_{I} and K_{II}, representing the direction where the tangential stress $\sigma_{\theta\theta}$ in the vicinity of the crack tip is maximum. And also the shear stress $\tau_{r\theta}$ vanishs along this direction on the basis of MTS criterion.

$$\theta^{*}=2\arctan\left(\frac{1}{4}\frac{K_{\mathrm{I}}}{K_{\mathrm{II}}}\pm\frac{1}{4}\sqrt{\left(\frac{K_{\mathrm{I}}}{K_{\mathrm{II}}}\right)^{2}+8}\right) \tag{2}$$

The stress intensity factors for mode I and mode II are calculated by FRANC3D software for tension F=1 and torsion M_{T} =1. The combined tension and torsion mixed mode stress intensity factors K_{I} and K_{II} are obtained from the superposition according to equation (3):

$$\begin{aligned}K_{\mathrm{I}}(\mathrm{t})&=K_{\mathrm{I},F}\cdot F(\mathrm{t})+K_{\mathrm{I},M}\cdot M_{T}(\mathrm{t})\\ K_{\mathrm{II}}(\mathrm{t})&=K_{\mathrm{II},F}\cdot F(\mathrm{t})+K_{\mathrm{II},M}\cdot M_{T}(\mathrm{t})\end{aligned} \tag{3}$$

The combined SIFs computed from equation (3) are inserted to equation (2) to find the angle θ^{*}, which is put into equation (1). The equivalent stress intensity factor K_{eq} is calculated for a full loading cycle. Among all the equivalent stress intensity factors, the peak value $K_{eq,\max}$ is taken as the crack driving force, which means the loads at this instant $t_{\max}$, $F(t_{\max})$ and $M_{\mathrm{T}}(t_{\max})$ are used for

crack propagation simulation.

2.3. Crack growth process

The load corresponding to the $K_{eq,\max}$, $F(t_{\max})$ and $M_T(t_{\max})$ are applied to the cracked finite element model. Stress analysis is carried out in ABAQUS. The SIF solutions for the cracks are again obtained from FRANC3D based on the stress analysis. Although the solutions for K_I, K_{II} and K_{eq} are already at hand for $t = t_{\max}$, the re-evaluation of this loading case combination can now be used to let the FRANC3D software create the crack propagation increment Δa. The ABAQUS/FRANC3D interface was implemented to perform the crack growth analysis. The finite element modeling and the stress analysis are performed in ABAQUS, FRANC3D is used to calculate crack growth parameters and updates the crack geometry and mesh. This process is continued until the crack has grown to a certain length.

As referred before, on one hand the MTS criterion is used as the rule for estimating crack propagation direction in most cases, on the other hand as will be shown later that under certain loading conditions, the simulated crack growth path deviated from the experimental crack path when the length of the crack is long enough. In order to investigate the crack growth path behavior under these complicated loading cases, a modification is essentially to keep the deviation between experimental results and simulation in an acceptable extent. Due to an extremely inadequate hypothesis about the criterion which is suitable for fatigue crack growth direction prediction under non-proportional mixed mode loading, the modification is implemented manually to adjust the position of newly generated crack front in order to make the simulated crack increment direction coincident with the experimental results. As a result, although the simulated crack growth path is not perfectly identical with the experimental data, a close match is enforced.

3. Results

3.1. AlMg4.5Mn specimens

In the experiment, specimen A7 (amplitude load values: F=8kN; M_T=96Nm) was tested under a non-proportional loading with an out of phase angle of 90°, while specimen A8 (amplitude load values: F=6.5kN; M_T=72Nm) was subjected a loading with a out of phase angle of 45°. The crack growth paths are shown in Figure 3. According to the stress analysis for the uncracked specimen, the local tangential stress along the notch root in site 1 and 3 are approximately 1.6 times larger than the stresses in site 2 and 4, therefore cracks should occur in site 1 and 3. Very curvilinear paths were displayed in specimen A7, furthermore in the experiment, crack branching appeared and then the crack growth path continues nearly perpendicularly to the previous propagation direction. The simulation algorithm at present does not contain a condition for crack branching, only the first curvilinear paths are presented. For specimen A8, the crack propagates along an angle of nearly 45° with the longitudinal axis. After the crack reaches a certain length, it has a tendency to turn into a plane, which is perpendicular to the longitudinal axis.

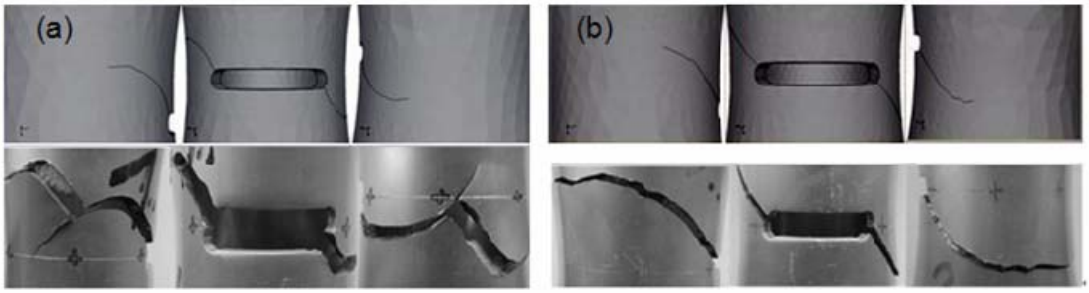

Figure 3. (a)A7 crack growth path, (b) A8 crack growth path [8]

3.2. S460N specimens

Specimen S7 (amplitude load values: F=27kN; M_T=408Nm) under the loading with a out of phase angle of 90° and the corresponding loading phase angle for specimen S13 (amplitude load values: F=22.5kN; M_T=272Nm) is 45°. 4 initial corner cracks are inserted into the notch root in specimen S7 because the maximum local tangential stresses are almost equal for sites 1-4. The crack propagation trend for specimen S13 is similar with specimen A8 as shown in Figure 4(b).

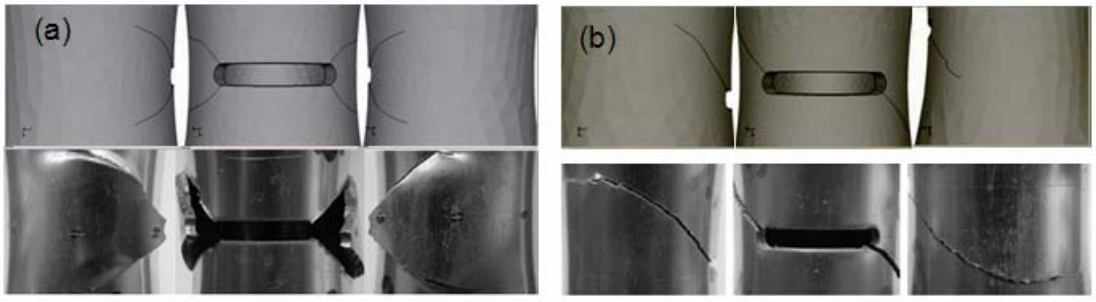

Figure 4. (a) S7 crack growth path, (b) S13 crack growth path [8]

Besides crack growth paths, the fatigue life for each specimen was also calculated based on Paris law. More details and the curves for crack length versus number of cycles are shown in reference [8].

4. Discussion

4.1. Crack propagation behavior of specimen A7

Crack paths are marked as ①, ②, ③ and ④ corresponding to the crack initiation sites as shown in Figure 2(b). The coordinate system is illustrated in Figure 2(a), the centre point of specimen is considered as the origin. The crack propagation trajectory (path ①) for specimen A7 is plotted in Figure 5(a). The solid line represents the simulated crack growth path in FRANC3D. The path labelled by squares is calculated based on the MTS criterion. It can be seen that when the crack reaches to a certain length (the length of this crack is from the notch root to point A), the crack growth path will deviate from the prediction of MTS criterion. From point A, MSS criterion predicted path is marked by triangle symbols. Obviously, the crack path starting from point A does

not follow the route estimated by either MTS criterion or MSS criterion. A path between the prediction of MTS and MSS criteria seems more reasonable compared with the experiment results. From point B, the simulated crack path seems to be controlled by MSS criterion, a negligible deviation can be found in Figure 5(a). In the contrary, large divergence is shown for the crack path estimated by MTS criterion. Based on the LEFM analysis, MTS criterion is valid in tension mode fracture and MSS criterion is used in shear mode problem, both of these two criteria are supported by a large quantity of corresponding experiments. The simulated crack path from point A to point B which keeps the same trend with the experimental result between tensile mode and shear mode is defined as the so called transition mode fracture [10]. Comparing to common investigated tension mode and shear mode, the transition mode is an occasional situation, appearing under very complex and dynamic loading, for instance for the present cyclic non-proportional mixed mode loading.

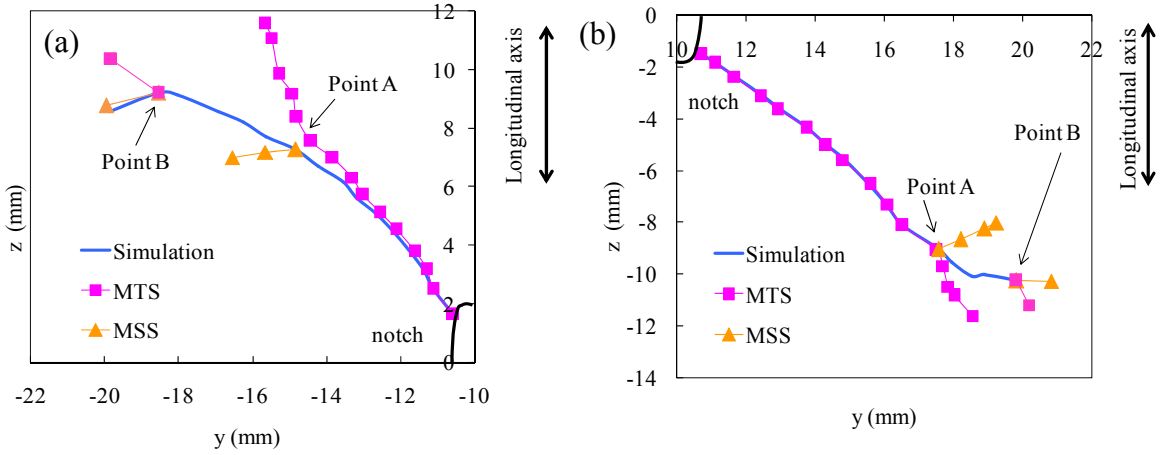

Figure 5. Crack growth path of (a) specimen A7, (b) specimen A8

4.2. Crack propagation behavior of specimen A8

Figure 5(b) shows the propagation crack path ③ for specimen A8. The symbols for different crack growth paths are defined as the same for specimen A7. The crack path starting from the notch root to point A complied perfectly with the prediction of MTS criterion. Beginning with point A, the crack path estimated by MTS criterion propagated almost along with the total previous crack path angle with no obvious transforming for the direction of crack extension. When the MSS criterion predicted crack growth path is contrasted with the MTS one from point A, the difference is very apparent as shown with the triangle diagram in Figure 5(b). The MSS path displayed a sharp deflection with the previous crack path direction and extended nearly in an opposite orientation, which is upward compared to the previous crack path. Obviously, these two crack growth paths do not conform to the experiment result. A path between the prediction of MTS criterion and MSS criterion gradually routed the crack to grow perpendicularly to the longitudinal axial. A transition fracture mode occurred in this specimen. As well as specimen A7, the transition fracture mode is followed by a shear fracture dominant crack path from point B. The MSS criterion predicted crack path could be considered to be perpendicular to the longitudinal axial of specimen. As can be seen from Figure 3(b), in the experiment once the crack changed propagating direction normal to the longitudinal axial, the coplanar shear crack growth is persistent until to the final fracture.

4.3. Crack propagation behavior of specimen S13 and S7

The crack growth path (path ①) for specimen S13 is plotted in Figure 6(a). An acceptable crack path compared with the experimental result from the notch root to point A was predicted by the MTS criterion. The transition fracture mode is expected following tension mode fracture. The simulated crack growth path for this specimen is not long enough to show a complete transition path. Nevertheless, it could be inferred that a shear mode fracture would occur as well as in specimen A8. The crack propagation path of specimen S13 is similar with specimen A8 (see Figure 3(b), Figure 4(b)), the final fracture is a coplanar crack extension perpendicular to the longitudinal axis which can be predicted by MSS criterion. Figure 6(b) illustrates one crack growth path (path ①) for specimen S7. It is found that the presented crack path has good agreement with the predicted crack path using MTS criterion. From the experimental result as shown in Figure 4(a), the crack growth paths did not deflect to the plane perpendicular to the longitudinal axis for coplanar shear crack extension, which means no shear mode fracture occurred in this specimen.

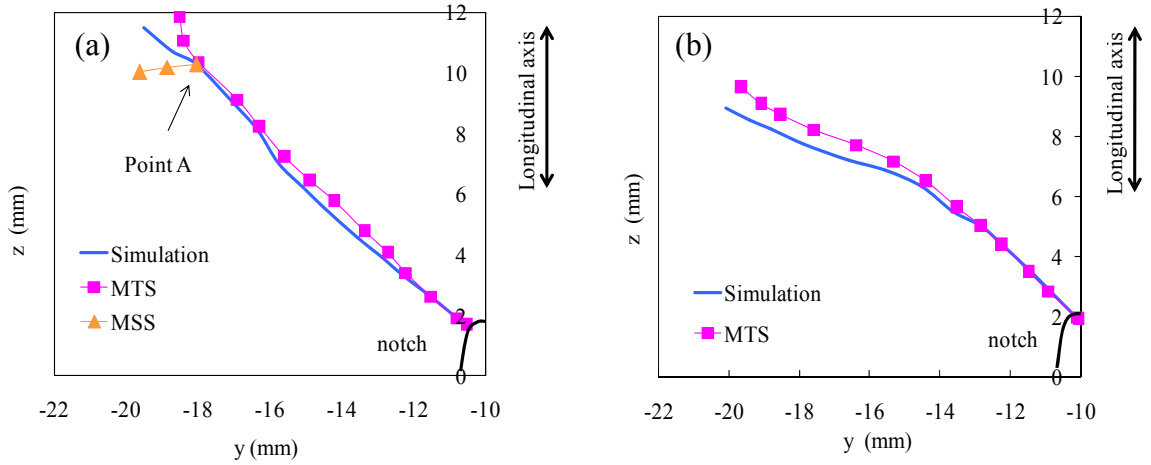

Figure 6. Crack growth path of (a) specimen S13, (b) specimen S7

4.4. Mode transition analysis

The tension mode and shear mode competition under non-proportional mixed mode loading reflects the variation of K_I and K_{II} values. Figure 7 illustrates the K_I and K_{II} values in one loading cycle under combined tension and torsion with a phase angle of 90°. The equivalent stress intensity factors K_{eq} reaches its peak values $K_{eq,\max}$ at time $t_{\max}$, which is taken as the crack growth driving force. The corresponding K_I, K_{II} components are marked as K^*_I and K^*_{II}. The K^*_{II} values of each crack propagation step for the four different specimens are shown in Figure 8 (①, ③ represent the corresponding crack paths) based on the calculation results from FRANC3D. The ordinate represents K^*_{II} values (absolute value), the abscissa represents the crack growth step. For all specimens the same tendency of increasing K^*_{II} with crack length is observed. From step 13 for specimen A7, step 15 for specimen A8 and S13, the transition mode started. It can be inferred that a threshold value $K^*_{II\ th}$ exists in the transition mode. If the mode II component of the maximum equivalent stress intensity factor $K_{eq,\max}$ in a loading cycle, K^*_{II}, is less than the threshold value,

tension mode dominated crack propagation prevails, if a threshold value is exceeded, transition mode dominated crack propagation is a reasonable crack growth pattern. The threshold $K^*_{\mathrm{II\ th}}$ is a function of several parameters, such as material property, the R ratio or the mode I threshold value and so on. Further research is needed to complete the concept.

$$K^*_{\mathrm{II}} > K^*_{\mathrm{II\ th}} \tag{4}$$

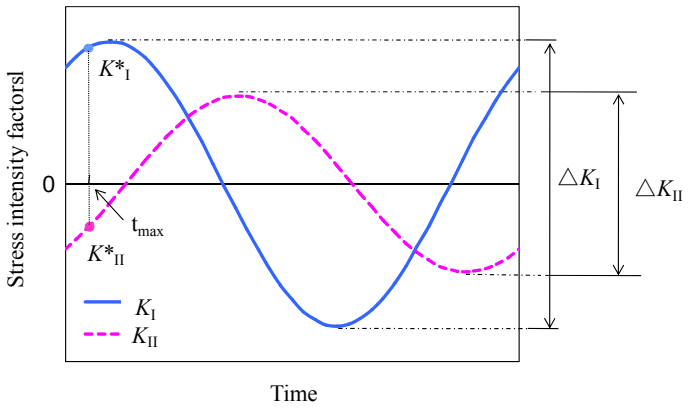

Figure 7. Variation of stress intensity factors

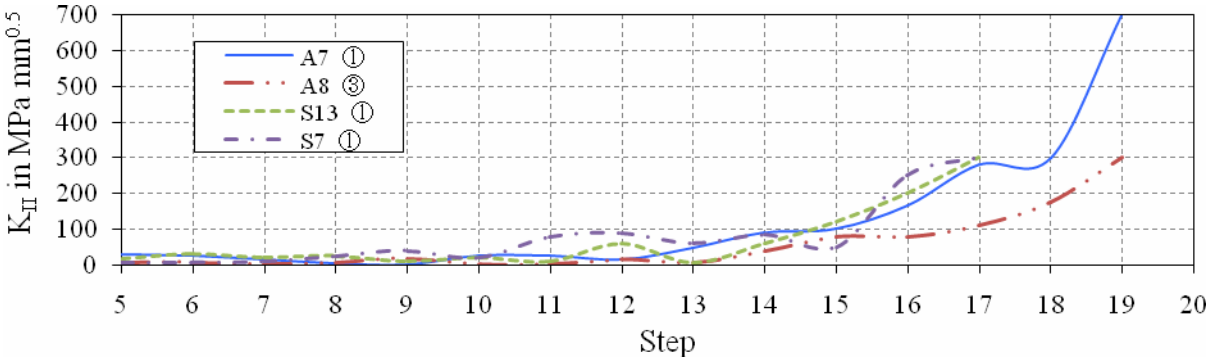

Figure 8. K^*_{II} values

Only for specimen S7 transition and shear modes did not appear. However, the K^*_{II} increased in the same way as for the other specimens. This implies that the crack growth path behaviour is not just controlled by K^*_{II}. Considering one loading cycle, the stress intensity range is defined as: (see Figure 7)

$$\triangle K_i = K_{i\ \max}(1\text{-}R) \quad (i\text{=I, II}) \tag{5}$$

The ratios of $\triangle K_{\mathrm{II}}$ to $\triangle K_{\mathrm{I}}$ in one loading cycle are shown in Figure 9. Similar with K^*_{II} versus crack growth step curve, an ascending tendency is revealed in the ratio of mode II range to mode I range especially for specimen A7 and A8. The transition mode started at step 13 for specimen A7 and at step 15 for specimen A8, the ratio of stress intensity range corresponding to these two steps are larger than 0.4, which could be considered as an assumed threshold value. Although the ratios from step 8 to 11 are also larger than 0.4 in specimen A7, the K^*_{II} values are too small to induce transition mode crack growth. In specimen A7 and A8 shear mode was subsequent from step 18,

step 19, the ratio values are larger than 1.3. It implies that transition mode is not a stable crack growth pattern; a critical ratio of stress intensity factor range is proposed between transition mode and shear mode. Once the proportion of $\triangle K_{II}$ in one loading cycle is large enough, shear mode crack growth occurred.

$$(\triangle K_{II}/\triangle K_I)_{th} < \triangle K_{II}/\triangle K_I < (\triangle K_{II}/\triangle K_I)_{cr} \tag{6}$$

The curves for specimen S13 and S7 are much smoother compared to the curve of A7 and A8. The different loading type may be a main reason to explain this phenomenon. Even so, it can be observed that from step 15 curve S13 increased persistently and the values are larger than 0.25. The curve of S7 does not show a rising trend but a relative downward tendency. It means that the mode I stress intensity range increased faster than the mode II range in this specimen. Transition and shear mode crack propagation is suppressed by this rapidly growing mode I component. The assumed transition mode threshold ratios for specimen A7 and A8, S13 are 0.6, 0.45 and 0.25 respectively. Beside the different material property, plasticity plays an important role in reducing the threshold value for specimen S13. Depending on the loading level, more plasticity compared to A7, A8 is displayed in specimen S13, accelerating the transformation of tension mode to transition mode or even to shear mode.

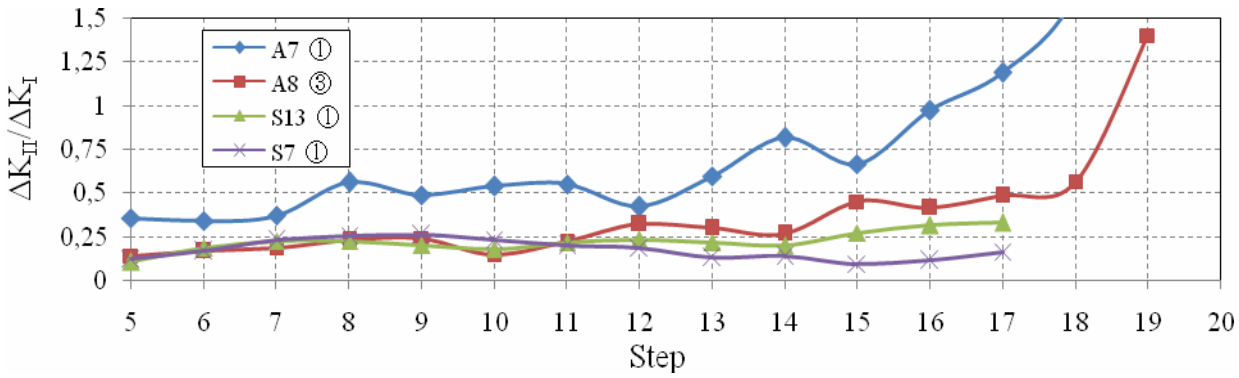

Figure 9. Ratio of stress intensity factors range

5. Conclusions

In the present paper, 3-dimensional crack growth simulation is implemented by using the LEFM-based algorithm. The simulation for two different materials AlMg4.5Mn, S460N, two phase angles 45° and 90°, different loading levels and M_T/F ratio have been presented. The M_T/F ratio has a great influence on the number of cracks, 4 cracks will occur when torsion loading M_T reaches a certain percentage of the total loading. The loading phase angle affects the crack growth path behaviour and also numbers of initiated cracks. Compared to the phase angle of 45°, specimens under out of phase loading with a phase angle of 90°, demonstrate more variations in crack initiation and crack growth path, depending on different load levels and M_T/F ratios.

Under non-proportional mixed mode loading, three distinct features of the crack growth path behaviour are observed which are tension mode, transition mode and shear mode. Based on the

analysis of specimen A7, A8 and S13, crack growth followed tension mode in most cases until the crack reaches a certain length corresponding to:
(1) The mode II component of the maximum equivalent $K_{eq,\max}$ in one loading cycle exceeds a threshold value and in the meantime;
(2) The ratio of mode II stress intensity factor range to mode I stress intensity factor range in one loading cycle is higher than a corresponding threshold value and;
(3) Shear mode crack growth occurs when the latter ratio exceeds a critical value.

Considering that no theoretical hypotheses can be applied to confirm the two threshold values to the transition mode at present, further research is needed to explain the crack growth path behavior under non-proportional loading cases. Further investigations especially in the field of micromechanics may provide more indications for this problem and improve the proposal of the present paper.

Acknowledgements

The authors wish to thank the Senior Research Associate in Cornell Fracture Group, Carter Bruce, for technical advice in FRANC3D operating.

References

[1] Erdogan, F., Sih, G.C., On the Crack Extension in Plates Under Plane Loading and Transverse Shear. J. Basic Engineering, 85D (1963) 519-527.
[2] Sih, G.C., Strain-energy-density factor applied to mixed mode crack problems. Int. J. Fracture, 10 (1974) 305-321.
[3] R. J. Nuismer, An energy release rate criterion for mixed mode fracture. Int. J. Fracture, 11 (1975) 245-250.
[4] Chambers. A. C., Hyde. T. H., Webster. J. J., Mixed mode fatigue crack growth at 550°C under plane stress conditions in Jethete M152. Engng. Frac. Mech, 39 (1991) 603-619.
[5] Hussain, M.A., Pu, S.L., Underwood, J.H., Strain energy release rate for a crack under combined mode I and II. Fracture Analysis, (1974) 2-28. ASTM STP 560, Philadelphia.
[6] Highsmith Jr., S., Crack path determination for non-proportional mixed-mode fatigue. PhD Thesis, Georgia Institute of Technology, USA, (2009).
[7] M. Vormwald, P. Zerres, Review of fatigue crack growth under non-proportional loading. Proceedngs of the 4th international conference on CRACK PATHS, (2012) 1-14.
[8] Y. Yang, M. Vormwald, LEFM-based simulation of fatigue crack growth under non-proportional mixed-mode loading. Proceedngs of the 4th international conference on CRACK PATHS, (2012) 465-472.
[9] Brüning, J., Untersuchungen zum Rissfortschrittsverhalten unter nichtproportionaler Belastung bei elastisch-plastischem Materialverhalten-Experimente und Theorie, Instituts für Stahlbau und Werkstoffmechanik der Technischen Universität Darmstadt, report 85 ISBN 978-3-939195-14-6, Germany. (2008)
[10] D. Haboussa, T. Elguedj, B. Leblé, A. Combescure, Simulation of the shear-tensile mode transition on dynamic crack propagations. Int. J. Fracture, 178 (2012) 195-213.

Effect of Levels of Residual Stress at Notch on Fatigue Crack Growth

M. Benachour[1,*], M. Dahaoui[1], N. Benachour[1,2], A. Cheikh[1], M. Benguediab[3]

[1] IS2M Laboratory, Department of Mechanical Engineering, Tlemcen University, Tlemcen 13000, Algeria
[2] Faculty of Sciences, Physics Department, Tlemcen University, Tlemcen 13000, Algeria
[3] LMSR, Department of Mechanical Engineering, Sidi Bel Abbes University, Sidi Bel Abbes 22000, Algeria
* Corresponding author: bmf_12002@yahoo.fr

Abstract In this paper, fatigue crack growth of finite plate with hole under constant amplitude loading through compressive residual stress at notch of aluminum alloys was investigated. Residual stress fields were generated by plastic deformation using finite element method. Based on fatigue crack growth rates (FCGRs) experimental data without residual stress, fatigue life and FCGR were predicted using AFGROW code. It was shown that the fatigue crack growth was affected by level of residual stress at notch for different level of plastic deformation. In this investigation, the presence of compressive residual stresses increase the total fatigue life and reduces the FCGRs. In addition stress ratio effect on fatigue behavior was studied.

Keywords Fatigue crack, Compressive residual stress, Al-alloy, notch, stress ratio

1. Introduction

Fatigue crack growth behavior is a significant issue in the establishment of inspection and maintenance procedures in variety industries such as aerospace, automotive, oil industries, rail...etc. This behavior is divided in three stages [1]: fatigue crack initiation, stable crack propagation and unstable crack propagation. Generally, mechanical components and structures contain geometrical discontinuities and notches. Stress concentration will be produced in theses discontinuities as a result of external force and depend of notch radius. The stresses are generally higher than the nominal values, and if precautions (good quality of machining of notch, induction of residual stress …etc.) are not taken into account, notches could be sites of crack initiation. Residual fatigue life of materials and structures depends on several parameters. In stable stage, fatigue life is linked strongly geometrical, loading parameters and residual stress. However, the stresses resulting from applied service loading are not the only stresses of significance for fatigue. Many components also contain residual stresses that were established prior to placing the component into service and which remain in place during the service life. These residual stresses are static load and influence the mean or maximum value of the load in each fatigue cycle. The residual stresses present diverse origin and several shapes [2-11] namely shot-penning, expansion of hole, overloads, underload, pre-strain or pre-deformation, welding, machining process… The stress field is beneficial if the stress is in compressive state [12, 15]. Contrary to this, the fatigue crack is accelerated [16]. Pre-strain is a process when preload induced plastic deformation, induced intentionally or not and create a residual stress field. The level and nature of these residual stresses depend on the amplitude and direction of applied load.

In the investigation of Kamel et al. [17] effects of tensile and compressive residual stress in fracture mechanics specimens by the application of a mechanical pre-load were studied using ‘C’ shape specimen. Finite element analysis is performed to simulate the pre-loading and the subsequent fracture loading of the cracked specimen. Recently, effect of residual stress on the fatigue behavior

of 2024 Al-alloy was studied experimentally and numerically using FEM by Al-Khazraji et al. [18]. Effect of plastic predeformation by bending to create deep residual compressive stresses on the fatigue strength of steel specimens and compressor blades was studied by Ezhov and Sidyachenko [19]. It was found that plastic predeformation increases the fatigue strength by about 20%. In other work, effect of residual stress induced by plastic predeformation was investigated by Mokhdani [20] on API 5L pipeline steel and Benachour [21] and Jones [22] on 2024 T351 Al-alloy using Four bent specimen. It was found that the fatigue life was influenced by the plastic preload. An increasing in fatigue life was shown by increasing of the level of plastic preload. The fatigue crack growth rates at low stress intensity factor were decreased by the presence of compressive residual stress. In study conducted by Jones and Dunn [23], fatigue crack growth from a hole with residual stress introduced by tensile preload was predicted using linear elastic fracture mechanics and the principle of superposition. O'Dowd et al. [24] introduced residual stresses in compact tension (CT) specimen by mechanical compression. The level of the compressive load was determined by finite element method (FEM). The compressive residual stresses present a beneficial effect on fatigue lifetime. Additionally fatigue life and fatigue crack growth rate (FCGR) were affected by stress ratio. Many researchers [25-28] have studied effect of this parameter on some Al-alloy with and without residual stress.

The main aims of the present investigation is to studied effect of residual stress on fatigue life and fatigue crack growth around hole, determined by plastic preload in tension of samples using finite element method.

2. Finite element model and analysis procedure

2.1. Modeling

The FE model used in simulation of plastic preload (PP) was a plate assumed to be made from Al-alloy 2024 T351 and 6061 T6. The mechanical properties of the both materials are shown in Table 1. In order to analyze the respect of elasto-plastic behavior, a true stress–true strain curve as shown in Figure 1 was used as an input property of FE analysis. As shown in Figure. 2, the dimensions of the plate containing Ø 6 diameter holes and thickness (t) = 4 mm. I have varied the level of applied preload characterized by non dimensional ratio σ_p/σ_y, where σ_p is applied preload and σ_y is yield stress for specified material, in order to investigate the level of the residual stress variation on fatigue crack growth behavior. The finite element mesh is shown in Figure 3. Only four quart of the entire plate has been modeled considering of the symmetry. More finite elements than those in other regions are put closer to the boundary of holes. Since we are interested of the residual stress variation according to the X axis from hole edge to free surface, two-dimensional analysis has been carried out with uniform distributed plastic preload σ_p. The program used in the FE analysis was ANSYS, Ver. 11. The mesh element type was “PLANE183”.

Table 1. Mechanical properties for Al-alloys

Al-alloys	E (GPa)	σy (MPa)	UTS (MPa)	ν
2024 T351 [44]	74.08	363	477	0.33
6061 T6 [45]	69.04	252	360	

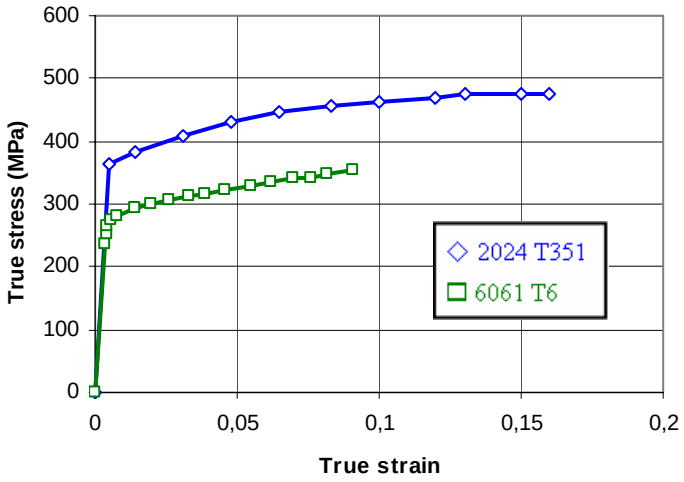

Figure 1. True stress–true strain curves of Al-alloy 6061-T6 and 2024 T351

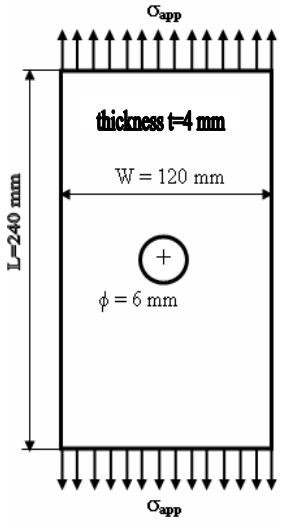

Figure 2. Analysis model

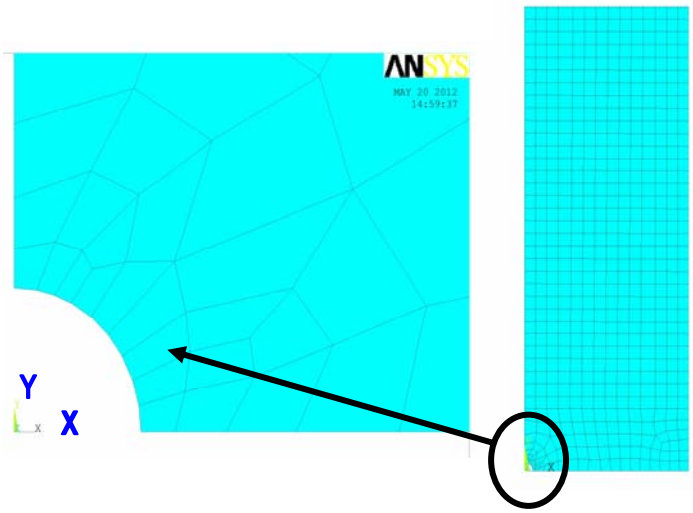

Figure 3. Quarter of finite element mesh with central hole

To generate a residual stress field, the applied load must exceed the elastic limit is to say that the force generated during the loading phase of plastic deformation where the isotropic plasticity model of Von Mises was used to account of the plasticity of material. The applied loading and unloading sequence (i.e. 2024 T351 Al-alloy) to generate residual stress by preload is shown in figure 4. The levels of preload is characterized by ratio σ_p/σ_y for both materials are shown in Table 2.

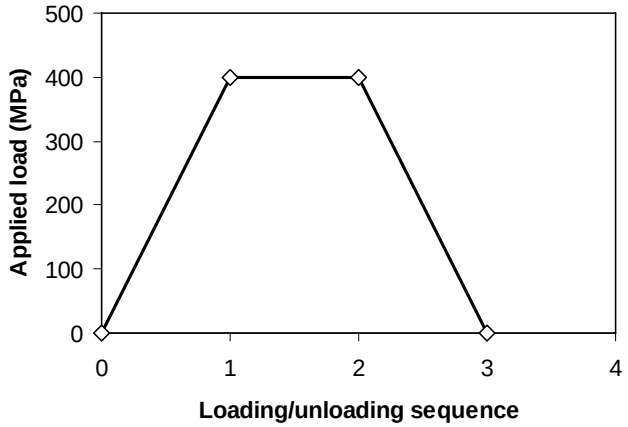

Figure 5. Loading sequence to generate residual stress

Table 2. Levels of preload for both materials

Al-Alloy	2024 T351	6061 T6
σp/σy	1.047	1.19
	1.102	1.23
	1.212	1.39
	1.350	

2.2. Generated residual stress

Under levels shown in Table 2, respective residual stress fields were generated. Figures 6 and 7 shown residual stress distribution around hole σ_{yy} for different applied preload for 2024 T351 and 6061 T6 Al-alloy respectively for specified levels. Interesting distributions of these residual stresses are along X-axis. X-axis is a planned path for crack propagation in mode I. Figure 8 shows variation of residual stress distribution σ_{yy} along X-axis for 2024 Al-alloy for different preload levels. It shows an increasing of compressive residual stress with increasing of preload levels at hole. was shown

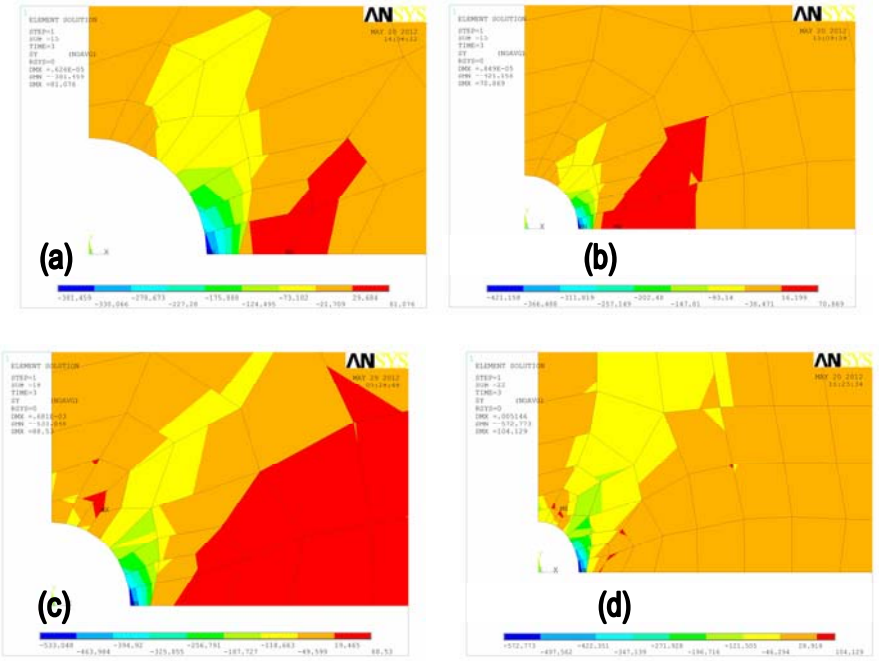

Figure 6. Stress contour for preload levels σ_p/σ_y for 2024 T351: (a) 1.047; (b) 1.102; (c) 1.212 (d) 1.350

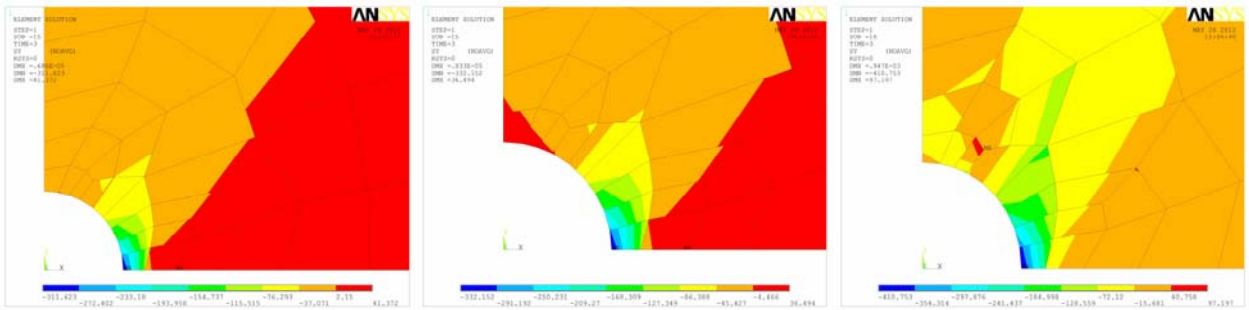

Figure 7. Stress contour for preload levels for 6061 T6 σ_p/σ_y: (a) 1.19 ; (b) 1.23 ; (c) 1.39

Figure 8 shows variation of residual stress distribution σ_{yy} along X-axis for 2024 Al-alloy at different preload levels. Residual stresses are in compression state up to a depth of 1.57 to 1.72 mm from the edge of the hole. It shows an increasing of compressive residual stress with increasing of preload levels at hole. Around distance of 4.5 mm, residual stresses become tensile stresses and difference is negligible. Distributions of residual stresses σ_{yy} along X-axis for 6061 T6 Al-alloy at specified preload levels, are shown in figure 9. No high difference of residual stress at edge of hole was shown. The residual stress in tension is maximal at 2 mm deep from the edge of the hole still; it is of the order of 30 MPa.

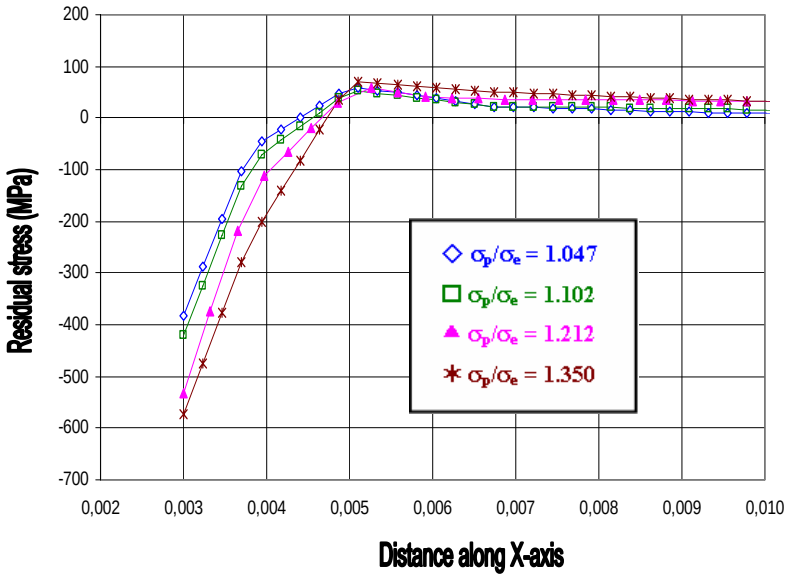

Figure 9. Residual stress along X-axis for 2024 T351 Al-alloy

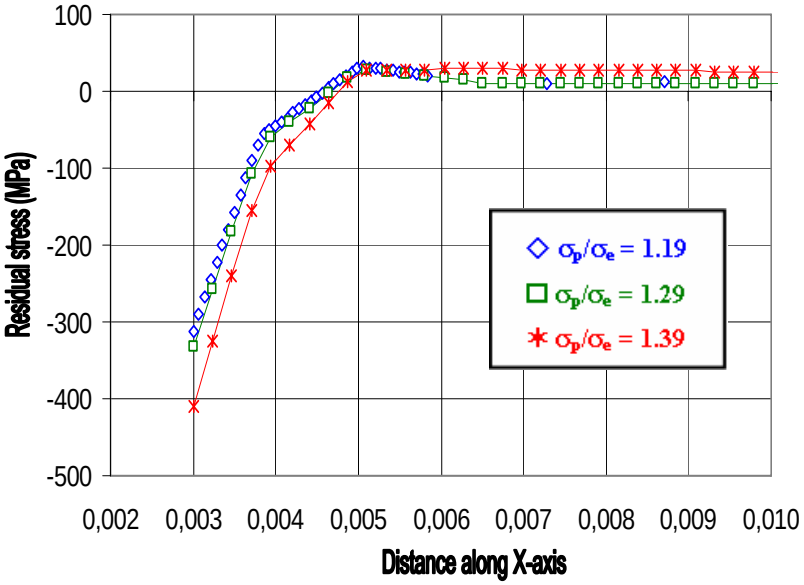

Figure 10. Residual stress along X-axis for 6061 T6 Al-alloy

3. Results and discussion

3.1. Fatigue crack growth modeling

The stress intensity factor for the studied specimen implemented in AFGROW code depends on several parameters and is given by Eq. 1.

$$\Delta K = \sigma\sqrt{\pi.a}.\beta\left(\frac{a}{r}\right) \tag{1}$$

where β is the geometry correction factor is expressed below (Eq. 2):

$$\beta\left(\frac{a}{r}\right) = 1 - 0.15\lambda + 3.46\lambda^2 - 4.47\lambda^3 + 3.52\lambda^4 \tag{2}$$

where: $\lambda = 1/(1 + (a/r))$

The interest model is NASGRO model when totality of fatigue crack growth curves is considered. Nasgro model are expressed bellow (Eq. 3):

$$\frac{da}{dN} = C\left[\left(\frac{1-f}{1-R}\right)\Delta K\right]^n \frac{\left(1 - \frac{\Delta K_{th}}{\Delta K}\right)^p}{\left(1 - \frac{K_{\max}}{K_{crit}}\right)^q} \tag{3}$$

f present the contribution of crack closure and the parameters C, n, p, q were determined experimentally and ΔK_{th} is the crack propagation threshold value of the stress–intensity factor range. For constant amplitude loading, the function f was determined by Newman [28] (see Eq. 4).

$$f = \frac{K_{op}}{K_{\max}} = \begin{cases} \text{Max}\left(R, A_0 + A_1 R + A_2 R^2 + A_3 R^3\right) & R \geqslant 0 \end{cases} \tag{4}$$

Crack growth parameters of Nasgro model for both materials are presented in Table 3.

Table 3. Parameters of Nasgro model for Al-alloys

Al-Alloy	ΔK_{tho} $MPa\sqrt{m}$	K_{IC} $MPa\sqrt{m}$	K_C $MPa\sqrt{m}$	n	p	q	C
2024 T351	2.857	37.36	74.72	3	0.5	1	1.707×10^{-10}
6061 T6	3.846	28.57	50.0	2.3	0.5	0.5	0.840×10^{-10}

3.2. Residual stress effect on fatigue crack growth

The variation of the fatigue crack growth rate (FCGR) as a function of the amplitude of the stress intensity factor ΔK through residual stresses fields obtained for different preload levels for 2024 T351 Al-alloy is shown in Figure 11. The result shows that FCGR depends on the magnitude of the compressive residual stresses developed at edge of hole.

We note that the FCGR increases while decreasing the preload level. At preloading level σ_p/σ_y equal 1.350, FCGR is about 1.6×10^{-9} m/cycle to crack initiation; against by a low level ie at σ_p/σ_y= 1.047, the FCGR is 1.75×10^{-7} m/cycle. This reduction is influenced by the decrease in residual stress intensity factor K_r whose variation is shown in Figure 12. Factor K_r past from -13.83 $MPa\sqrt{m}$ to -4.65 $MPa\sqrt{m}$. In absence of residual stress, FCGR is about 3.83×10^{-7} m/cycle.

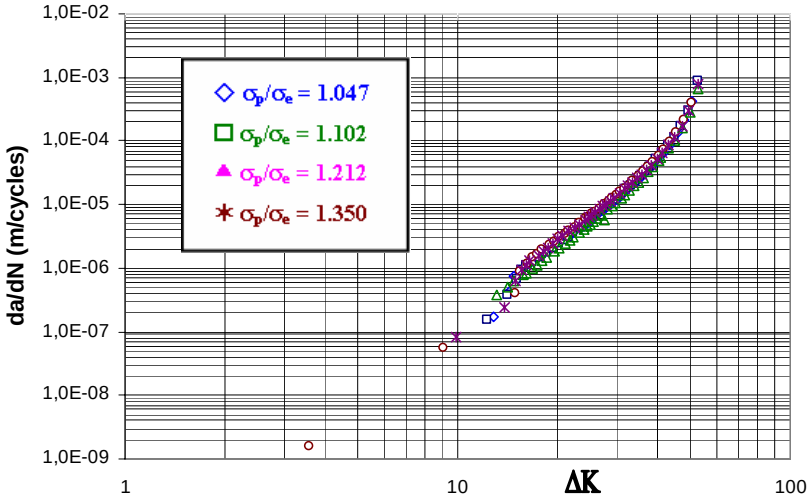

Figure 11. Preload levels effect on FCGR for 2024 T351 Al-alloy at R=0.25

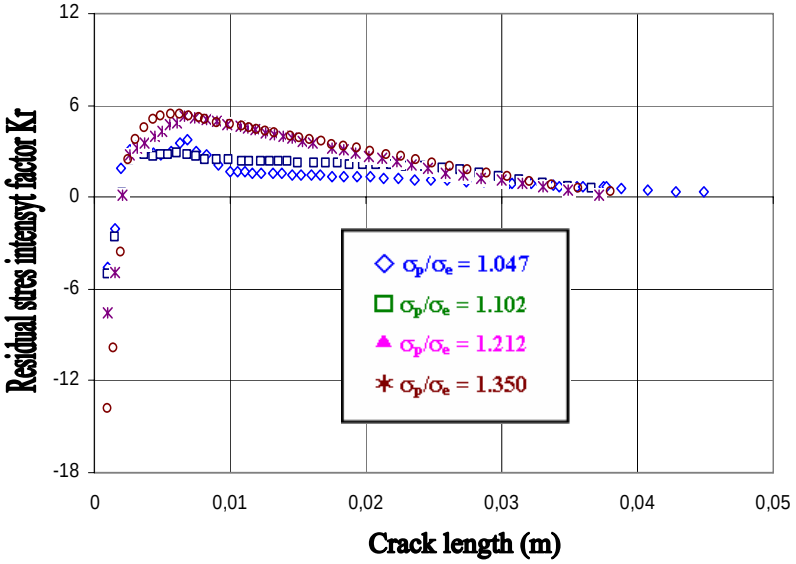

Figure 12. Variation of residual stress intensity factor Kr for preload levels of 2024 T351 Al-alloy

Residual stress effect on FCGR for 6061 Al-alloy is shown in figure 13. Their effect was significant at early cracking when residual stresses are is compressive state. Comparatively to state without residual stress, FCGR for level σ_p/σ_y equal to 1.19 was increased by 30%. For high preload level, σ_p/σ_y=1.37, FCGR was increased by 28.6%. The increasing of FCGR was linked to the decreasing of factor Kr when his variation was shown in figure 14. From 3.37 mm of crack length, residual stress intensity factor at σ_p/σ_y=1.37 is greatest to the other levels. This increasing was due to the presence of tensile residual stress at this area from 3.37 to 20 mm. The effect of residual stress was explained by the variation of stress ratio at any cycles for specified crack length.

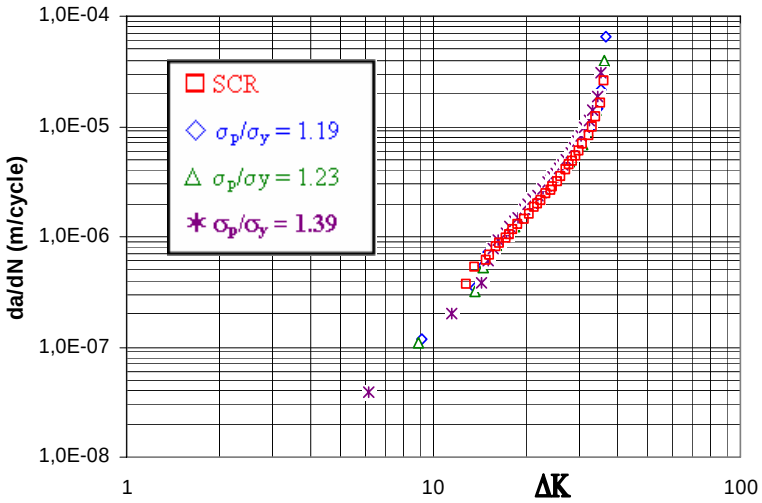

Figure 13. Preload levels effect on FCGR for 6061 T6 Al-alloy at R=0.25

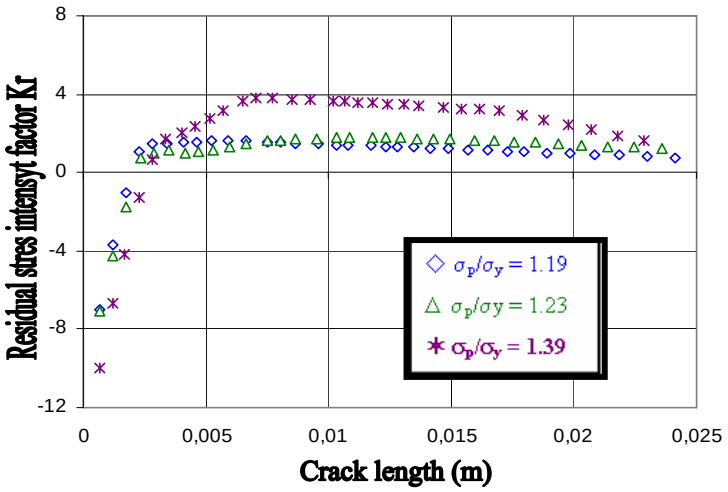

Figure 14. Variation of residual stress intensity factor Kr for preload levels of 6061 T6 Al-alloy

4. References

[1] G. Glinka, "Residual stress in fatigue and fracture: Theoretical analyses and experiments". In Niku-Lari A., Editor, Advances in Surfaces Treatments, Pergamon Press, 1987, 413-454.

[2] Pavier, M.J., Poussard, C.G.C. and Smith, D.J., "Effect of residual stress around cold worked holes on fracture under superimposed mechanical load", Engineering Fracture Mechanics, 63 (1999), 751-773.

[3] Makabe, C., Purnowidodo A. and McEvily, A.J., "Effect of surface deformation and crack closure on fatigue crack propagation after overloading and under-loading", International Journal of fatigue, 26 (2004), 1341-1348.

[4] John, R., Jata K.V., and Sadananda, K., "Residual stress effects on near-threshold fatigue crack growth in friction stir welds in aerospace alloy", International Journal of fatigue, 25 (2003), 939-948.

[5] H. Wang, F.G. Buchholz, H.A. Richard, S. Jägg, B. Scholtes, Numerical and experimental analysis of residual stress for fatigue crack growth., Computational Materials Science 16 (1999), 104-112.

[6] J. Barralis, L. Castex, G. Maeder, Précontraintes et traitements superficiels. Technique de l'Ingénieur, traité matériaux métalliques M1 180.

[7] P.J. Withers, H.K.D.H. Bhadeshia, "Residual stress - Part 2: Nature and Origins". Materials Sciences and Technology, 17, April 2001.

[8] Lim Won-Kyum, Jeong-hoon Song, B.V. Sankar, Effect of ring indentation on fatigue crack growth in an aluminum alloy plate. International Journal of Fatigue, 51 (1981), 61-69.

[9] M. Benedetti, T. Bortolamedi, V. Fontanriand, F. Frendo, Bending fatigue behavior of differently shot penned Al 6082 T5 alloy. International Journal of Fatigue, 26 (2004), 889-897.

[10] T. Fett, Residual crack profiles under weak phase transformation conditions. Engineering Fracture Mechanics, 56 (1997), 275-284.

[11] V.V. Silberschmidt, E. Werner, Analysis of thermal residual stresses in duplex-type materials, Computational Material Science, 16 (1999), pp 39-52.

[12] Y.C. Lam, K.S. Lian, The effect of residual stress and its redistribution on fatigue crack growth. Theoretical and Applied Fracture Mechanics, 12 (1989), 59-66.

[13] M. Beghini, L. Bertini, Fatigue crack propagation through residual stress fields with closure phenomena. Engineering Fracture Mechanics, 36 (1990), 379-387.

[14] L. Wagner, G. Lütjering, V. Sedlàcek, Fatigue crack growth retardation in an Al alloy 2024 in a residual compressive stress field. International Conference on Residual Stresses: ICRS2, 23-25 November (1988), 803-808.

[15] M.A. Wahab, G.R., Rohrsheim, J.H. Park, Experimental study on the influence of overload induced residual stress field on fatigue crack growth in aluminum alloy. Journal of Materials Processing Technology, 153-154 (2004), 945-951.

[16] S. Suresh, R.O. Ritchie, On the influence of fatigue underload on cyclic crack growth at low stress intensities. Materials Sciences and Engineering, 51 (1981), 61-69.

[17] S. Kamel, Robert C. Wimpory, Michael Hofmann, Kamran M. Nikbin, N.P. O'Dowd, Advanced Materials Research, 89-91 (2010), 275.

[18] A.N. Al-Khazraji, F.M. Mohammed, R.A. Al-Taie, Eng. Tech. Journal, 29(3) (2011).

[19] V. N. Ezhov, V.M. Sidyachenko, Influence of plastic predeformation on the fatigue strength of compressor blades with defects. Strength of Materials, Vol. 26, Issue 10, (1994), 772-782

[20] C. Mokhdani, Amorçage et propagation de fissures de fatigue dans un acier pour tubes de transport de gaz : Identification des lois de d'endommagement et application aux structures tubes sous pression interne. Thesis in french Doctorat Es-sciences, Mines ParisTech, France, 1995.

[21] M. Benachour, Simulation of fatigue crack growth through residuals stresses field. Thesis in French Doctorat Es-Sciences, University of Sidi Bel Abbes, Algeria, 2008.

[22] Jones K.W., Dunn M.L. (2008) Fatigue crack growth through a residual stress field introduced by plastic beam bending. Fatigue Fracture Engineering Materials Structures 31, 863-875.

[23] Keith W. Jones, Martin L. Dunn. Predicting fatigue crack growth from a preyielded hole. International Journal of Fatigue 31 (2009), pp 223–230.

[24] N.P. O'Dowd, K.M. Nikbin, R.C. Wimpory, F.R. Biglari, M.P. O'Donnell, Computational and experimental studies of high temperature crack growth in the presence of residual stress, PVP2006-ICPVT-11, ASME Pressure Vessels and Piping Division Conference. July 23-27 (2006), Vancouver, BC, Canada.

[25] M. Benachour, A. Hadjoui, M. Benguediab and N. Benachour. Stress ratio effect on fatigue behavior of aircraft aluminum alloy 2024 T351. MRS Proceedings, 1276, 7 (2010).

[26] O.P. Ostash, R.V. Chepil, V.V. Vira. Fatigue crack initiation and propagation at different stress ratio values of uniaxial pulsating loading. Fatigue Fract Engng Mater Struct 34, (2010), pp 430–437.

[27] C.A. Rodopoulos, J.H. Choi, E.R. de los Rios, J.R. Yates. Stress ratio and the fatigue damage map-Part II: The 2024-T351aluminium alloy. International Journal of Fatigue 26 (2004), pp 747–752.

[28] R. Kumar, S.B.L. Garg. Influence of stress ratio and material properties on effective stress range ratio and crack growth. Engineering Fracture Mechanics 32(2), (1989), pp. 195-202.

[29] J.C. Newman, International Journal of Fracture, 24(3), 1984, 131

Determination of fatigue crack propagation limit curves for high strength steels, and their applicability for structural elements having crack like defects

János Lukács[1,*]

[1] Department of Mechanical Engineering, University of Miskolc, H-3535 Miskolc-Egyetemváros, Hungary
* Corresponding author: janos.lukacs@uni-miskolc.hu

Abstract There are different documents and standards containing fatigue crack propagation limit or design curves and rules for the prediction of crack growth. The research work aimed to characterise the fatigue crack propagation resistance of different steels using limit curves, based on statistical analysis of test results and fatigue crack propagation law, and to determine fatigue crack propagation limit curves for different structural steels and wide-spreading high strength steels, and their welded joints, under mode I and mixed mode I + II loading conditions. Experiments were performed on different (high strength) steels and partially their welded joints. The specimens were cut parallel and perpendicular to the characteristic directions of the materials; therefore the specimens represent the different possible locations of cracks in the base materials and welded joints. Fatigue crack growth experiments were performed by *ΔK*-decreasing and constant load amplitude methods. The evaluation process consists of six steps and by means of the evaluated and selected values a simplified method can be proposed for determination of fatigue crack propagation limit curves. The determined limit curves represent a compromise of rational risk and acceptable safety.

Keywords fatigue crack growth, limit curve, high strength steel, engineering critical assessment

1. Introduction

Reliability of a structural element having crack or crack-like defect under cyclic loading conditions is determined by the geometrical features of the structural element and the flaws, the loading conditions, as well as the material resistance to fatigue crack propagation. There are different documents [1-3], standards and recommendations [4-6] containing fatigue crack propagation limit or design curves and rules for the prediction of crack growth [6, 7]. The background of the fatigue crack propagation limit curves and the calculations consist of two basic parts: statistical analysis of numerous experiments (fatigue crack propagation tests) and fatigue crack propagation law, frequently the Paris-Erdogan law [8],

$$\frac{da}{dN} = C\Delta K^n, \tag{1}$$

where *da/dN* is the fatigue crack growth rate, *ΔK* is the stress intensity factor range, furthermore *C* and *n* are material constants.

The research work aimed
- to characterise the fatigue crack propagation resistance of different steels using limit curves [9], [10], based on statistical analysis of test results and the Paris-Erdogan law;
- determination of limit curves for different structural steels and wide-spreading high strength steels [11], and their welded joints, under mode I (tension) and mixed mode I + II (tension and shear) loading conditions.

2. Examinations

2.1. Materials and welding characteristics

The most important characteristics of the investigated structural steels and high strength steels, and used welding technologies are summarized in Table 1.

Table 1. Main characteristics of the investigated materials and used welding technologies

Steel type	Grade/Mark	Welding method	Shielding gas	Filler material
micro-alloyed	37C	gas metal arc	100 CO_2	VIH-2
low-alloyed DP	DP-25156	–	–	–
micro-alloyed	E420C	gas metal arc	80 Ar + 20 CO_2	Union K56
high strength TRIP	TRIP-28670	–	–	–
high strength	X80TM	gas metal arc	82 Ar + 18 CO_2	X-90 IG
high strength	QStE690TM	–	–	–
high strength	S960QL	under development (see 5. Conclusions, too)		
high strength	XABO 1100	–	–	–

The measured mechanical properties (R_y, R_m, A_5) and the therefrom calculated values (R_y/R_m, R_m*A_5) of the investigated base materials and weld metals are summarized in Table 2.

Table 2. Mechanical properties and characteristic calculated values of the investigated materials

Grade/Mark	R_y [(1)] N/mm^2	R_m N/mm^2	R_y/R_m –	A_5 %	$R_m * A_5$ $N/mm^2 * \%$
37C base material	270	405	0,666	33,5	13567
VIH-2 weld metal	410-485	535-585	0,766-0,829	22,0-24,8	≥11770
DP-25156 base material	350-380	790-820	0,427-0,481	12,5-19,8[(2)]	≥9875[(2)]
E420C base material	450	595	0,756	30,7	18266
Union K56 weld metal	≥500	560-720	0,694-0,893	≥22,0	≥12320
TRIP-28670 base material	430-490	730-745	0,577-0,671	24,2-28,6[(2)]	≥17666[(2)]
X80TM base material	540	625	0,864	25,1	15687
QStE690TM alapanyag	780	850	0,918	18,3	15555
Böhler X90-IG weld metal	≥890	≥940	≈0,947	≥16,0	≥15040
S960QL base material	1007	1045	0,964	16,0	16112
XABO 1100 base material	1125	1339	0,840	11,0[(3)]	14729[(3)]

(1) R_y means R_{eH} or $R_{p0,2}$.
(2) For these material A_{80} instead of A_5.
(3) For these material A_{97} instead of A_5.

Fig. 1 shows the ultimate tensile strength vs. elongation (fracture strain) diagram [12] and the location of the investigated base materials based on the data can be found in Table 2.

2.2. Fatigue crack growth examinations

Compact tension (*CT*), three point bending (*TPB*) and single edge notched tension (*SENT*) specimens were tested for base materials and welded joints, while for testing of weld metal *TPB* type specimens were used. *CT* and *TPB* type specimens were cut from the sheets parallel and perpendicular to the rolling direction, so the directions of fatigue crack propagation were the same. For testing of weld metals cracks, which propagate parallel or perpendicular to the axis of the joint were also distinguished. Compact tension shear (*CTS*) specimens were used for tests under mixed mode I + II loading condition. The specimens were cut parallel to the rolling direction; the ratio of the two loading modes (I and II) was varied using a special specimen holder [13], so the cracks were propagated in different angles according to the rolling direction.
Tests were carried out according to the ASTM prescription [14] by an universal electro-hydraulic MTS testing machine. Experiments were performed by ΔK-decreasing and constant load amplitude methods, at room temperature, in air, following sinusoidal loading wave form. Stress ratio was constant ($R = 0,1$), and the crack propagation was registered by compliance and/or optical method.

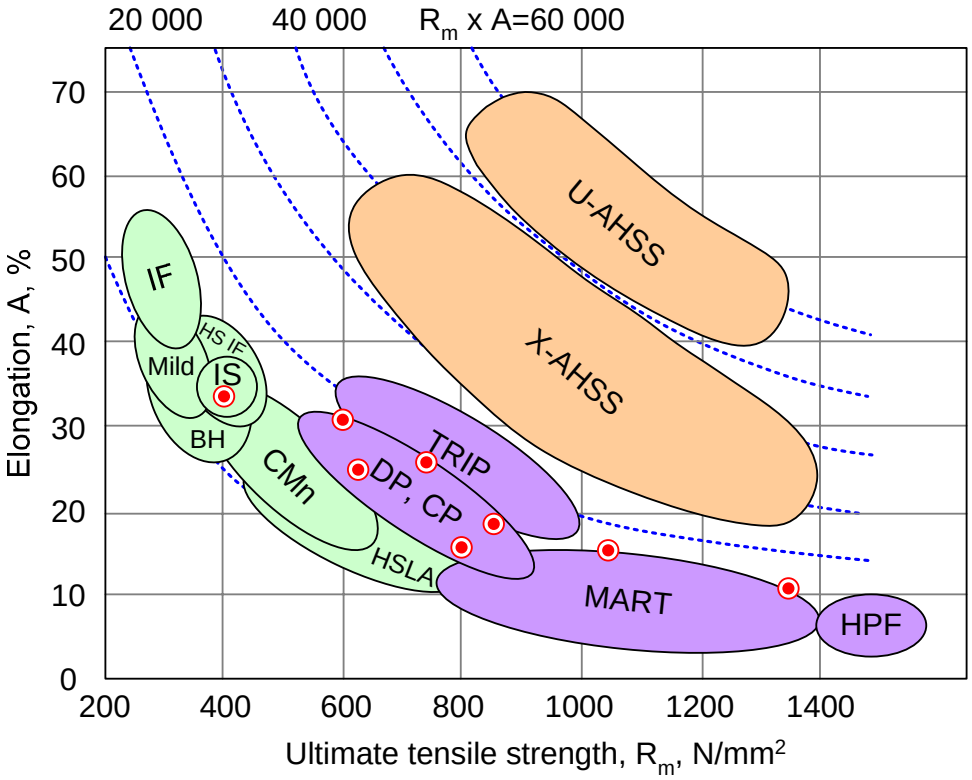

Figure 1. The investigated base materials in the ultimate tensile strength vs. elongation diagram

Fig. 2, Fig. 3 and Fig 4 show the calculated kinetic diagrams (fatigue crack propagation rate vs. stress intensity factor range curves) of tested DP-25156 and TRIP-28670 steels using *SENT* specimens, and S960QL steel using *TPB* specimens, respectively.

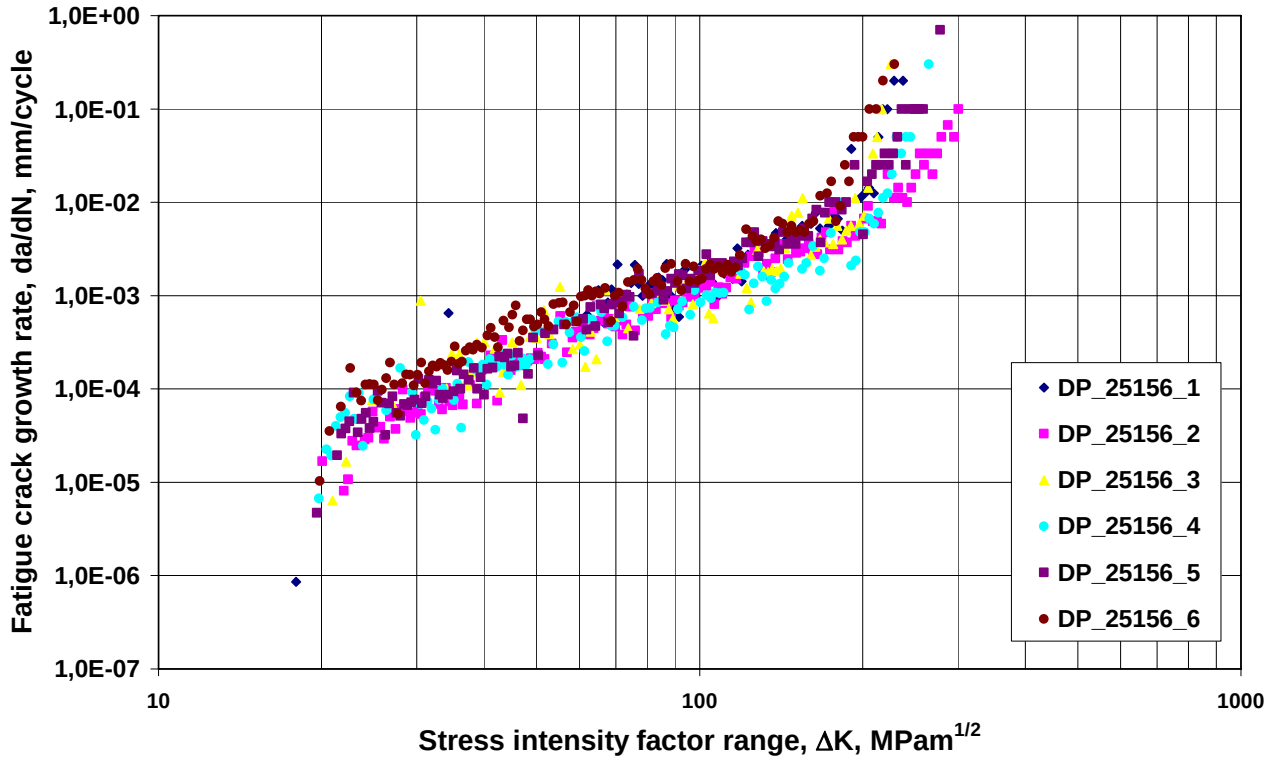

Figure 2. Kinetic diagrams of fatigue crack propagation from tested DP-25156 steel (*SENT* specimens)

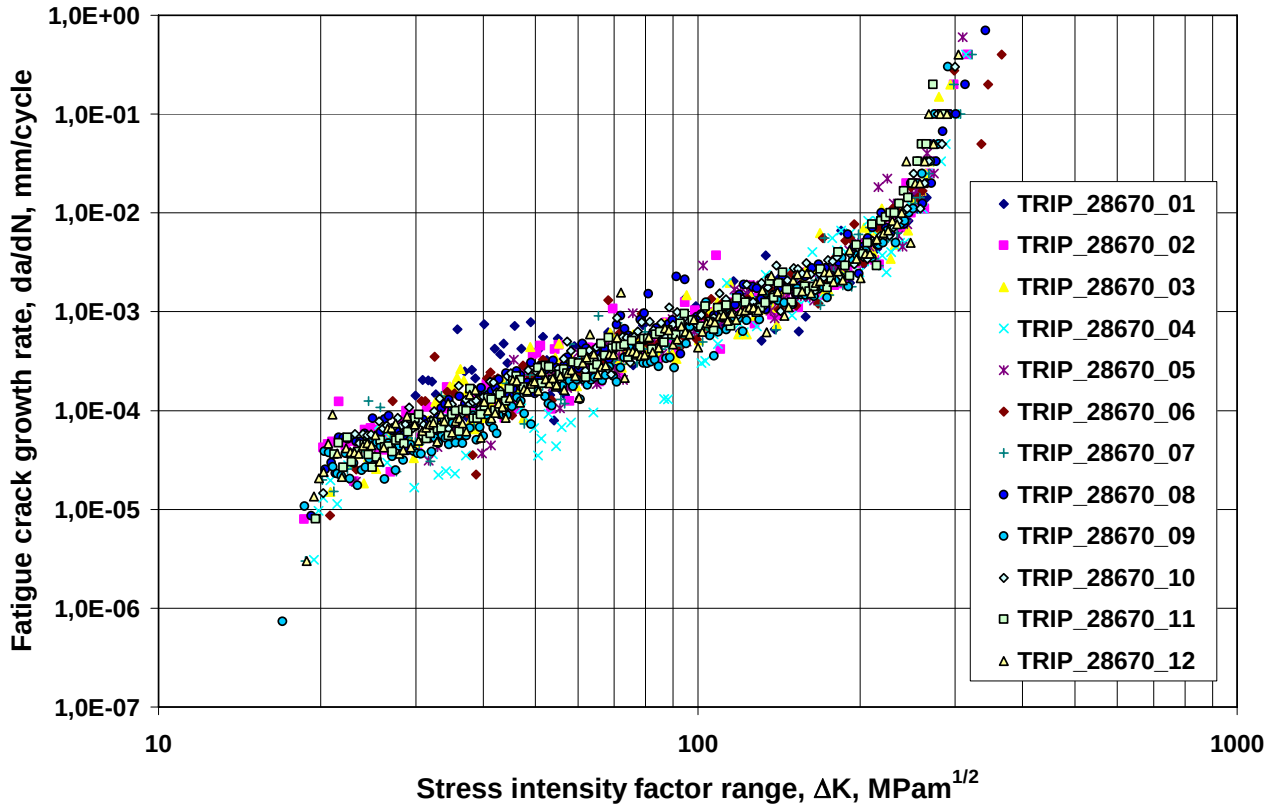

Figure 3. Kinetic diagrams of fatigue crack propagation from tested TRIP-28670 steel (*SENT* specimens)

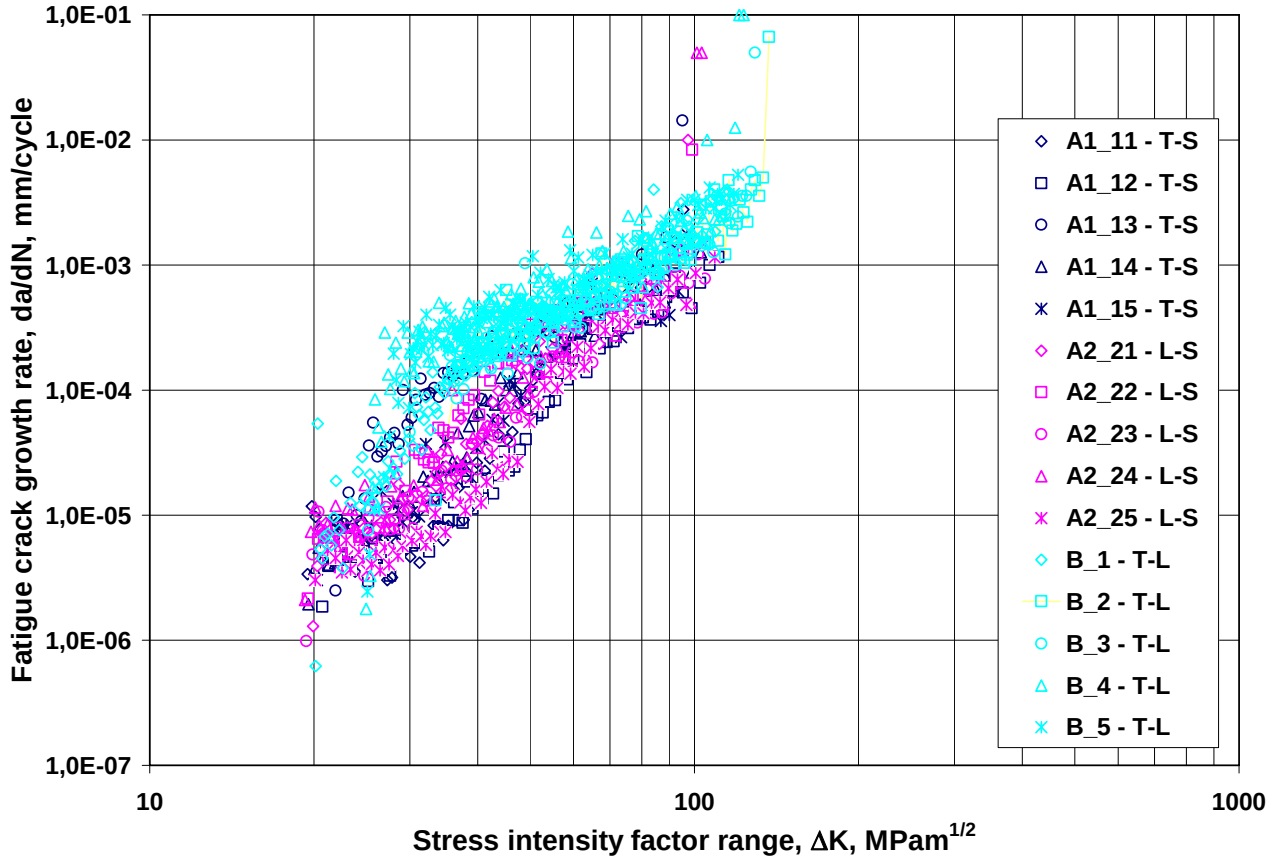

Figure 4. Kinetic diagrams of fatigue crack propagation from tested S690QL steel (*TPB* specimens)

3. Determination of fatigue design limit curves

The determination of the fatigue design limit curves consists of six steps.

First step: determination of measuring values. Values of threshold stress intensity factor range (ΔK_{th}) and two parameters of Paris-Erdogan law (C and n) were calculated according to ASTM prescriptions [14]. Fatigue crack propagation rate was determined by secant method or seven point incremental polynomial method. Values of fatigue fracture toughness (ΔK_{fc}) were calculated from crack size determined on the fracture surface of the specimens by the means of stereo-microscope.

Second step: sorting measured values into statistical samples. On the basis of calculated test results, mathematical-statistical samples were examined for each testing groups. As its method, Wilcoxon-probe was applied [15], furthermore statistical parameters (average, standard deviation and standard deviation coefficient) of the samples were calculated. Standard deviation coefficients (standard deviation/average) of the samples were generally less than *0,2*, which means reliable and reproducible testing and data processing methods. Table 3 summarizes the mathematical-statistical samples and their characteristics of experimental results on S690QL steel, as an example.

Table 3. Mathematical-statistical samples and their characteristics of experimental results on S690QL steel

Orientation	Element number of the sample	Parameter	Unit	Average	Standard deviation	Standard deviation coefficient
T-S	5	n	–	3,959	0,946	0,2390
L-S	5			3,735	0,273	0,0731
T-S and L-S	10			3,847	0,667	0,1734
T-L	5			2,441	0,615	0,2519
T-S	5	ΔK_{fc}	$MPam^{1/2}$	100,22	6,685	0,0667
L-S	5			102,68	4,574	0,0446
T-S and L-S	10			101,45	5,553	0,0547
L-T	5			125,11	8,385	0,0670

Third step: selection of the distribution function. Afterwards it was examined, what kind of distribution functions can be used for describing the samples. For this aim Shapiro-Wilk, Kolmogorov, Kolmogorov-Smirnov and χ^2 statistical probes were used at a level of significance $\varepsilon = 0,05$ [15-17]. It was concluded, that three parameter Weibull-distribution is the only function suitable for describing all the samples.

Fourth step: calculation of the parameters of the distribution functions. Parameters of three parameter Weibull-distribution function were calculated for all the samples:

$$F(x) = 1 - \exp\left[-\left(\frac{x - N_0}{\beta} \right)^{1/\alpha} \right] \tag{2}$$

where N_0 is the threshold parameter, α is the shape parameter and β is the scale parameter of the three parameter Weibull distribution function.

Fifth step: selection of the characteristic values of the distribution functions. Based on the calculated distribution functions, considering their influencing effect on life-time, characteristic values of ΔK_{th}, n and ΔK_{fc}, were selected. With the help of these values a reliable method can be proposed for determination of fatigue crack propagation limit curves:

– the threshold stress intensity factor range, ΔK_{th}, is that value which belongs to the *95 %*

probability of the Weibull-distribution function;
- the exponent of the Paris-Erdogan law, n, is that value belonging the *5 %* probability of Weibull-distribution function;
- the Paris-Erdogan constant, C, is calculated on the basis of the correlation between C and n;
- the critical value of the stress intensity factor range or fatigue fracture toughness, ΔK_{fc}, is that value which belongs to the *5 %* probability of the Weibull-distribution function.

Sixth step: calculation of the parameters of the fatigue crack propagation limit curves. Simplified method was used for the calculation of the design curves, based on simple crack growth law, using the above mentioned five steps. The details of the curves can be found in the Table 4. and on Fig. 5.

Table 4. Details of determined fatigue crack propagation limit curves (simple law)

Grade/Mark	ΔK_{th}	n	C	ΔK_{fc}
	$MPam^{1/2}$	$MPam^{1/2}$ and mm/cycle		$MPam^{1/2}$
37C base material	10,4	2,98	8,22E-09	53
37C welded joint	–[(1), (2)]	3,16	2,42E-09	70
DP-25156 base material	–	2,02	1,68E-07	95
E420C base material	8,0	2,26	9,78E-08	92
E420C welded joint	–[(1), (3)]	2,74	1,16E-08	101
TRIP-28670 base material	–	1,84	3,06E-07	250
X80TM base material	–	1,78	3,74E-07	129
X80TM welded joint	–[(1)]	1,86	3,13E-07	–
QStE690TM base material	–	1,82	3,27E-07	–
QStE690TM base material[(4), (5)]	–	2,15	1,09E-07	–
S960QL base material	–	1,80	3,50E-07	94
XABO 1100 base material	–	1,76	4,00E-07	104

(1) It can be derived from data concerning to the base metal after the evaluation of characteristic and assessment of magnitude of residual stresses.

(2) Average value of *16* tests under compressive residual stress: $\Delta K_{th} = 16{,}9\ MPam^{1/2}$.

(3) Average value of *4* tests under compressive residual stress: $\Delta K_{th} = 16{,}3\ MPam^{1/2}$.

(4) Under mixed mode I + II (tension and shear) loading condition.

(5) ΔK should be replaced by ΔK_{eff}.

4. Discussion

For the investigated steels and their welded joints both the tendency of threshold stress intensity factor range (ΔK_{th}) and the tendency of the Paris-Erdogan exponent (n) decrease with the increase of the strength of material; while the tendency of fatigue fracture toughness (ΔK_{fc}) has not unambiguous dependence on the strength of material.

For the investigated steels both the Paris-Erdogan exponent (n) and the fatigue fracture toughness (ΔK_{fc}) for welded joints are higher than those of base materials.

The proposed method is suitable for determination of fatigue crack propagation design curves under mixed mode I + II (tension and shear) loading condition, too. For this case stress intensity factor range (ΔK) should be replaced by effective stress intensity factor range (ΔK_{eff}).

The design curves of welded joints in the near threshold region are open. On the one hand, if the threshold stress intensity factor range value (ΔK_{th}) is not known, values can be found in the

literature (e.g. [18]) are usable. On the other hand, the threshold stress intensity factor range, ΔK_{th}, must be reduce by tensile residual stress field and may be increase by compressive residual stress field (e.g. welding residual stresses).

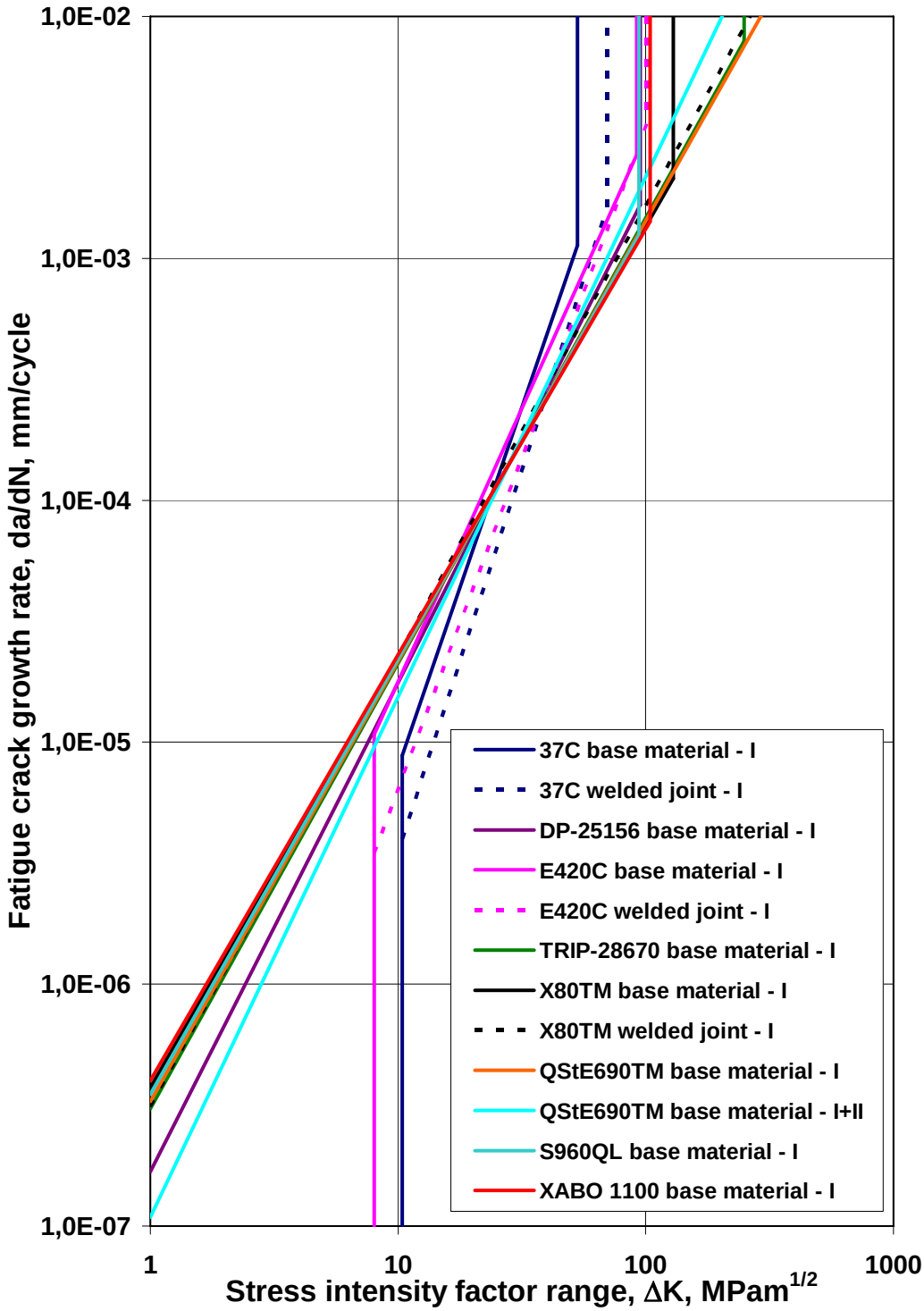

Figure 5. Fatigue design limit curves for the investigated steels, and their welded joints

The calculated fatigue crack propagation limit curves of base materials locate among the design curves determined by various procedures. Table 5. summarizes our measured average data and measured individual data can be found in the literature [19]. It can be concluded that our average values are in harmony with the individual values.

Table 5. Comparison of measured data with data from the literature

Grade/Mark	R_y	R_m	ΔK_{th}	n	ΔK_{fc}
	N/mm^2	N/mm^2	$MPam^{1/2}$	$MPam^{1/2}$ and mm/cycle	$MPam^{1/2}$
37C	270	405	7,69	3,60	62,70
St38b-2	280	440	5,5	3,7	45
DP-25156	350-380	790-820	–	2,20	261,01
E420C	450	595	5,72	2,55	100,41
H60-3	500	630	5,9	3,8	50
TRIP-28670	≥500	560-720	–	2,06	320,73
X80TM	540	625	–	2,49	136,57
H75-3	600-680	–	4,3-5,2	2,5-2,7	70-75
QStE690TM	780	850	–	2,39	–
N-A-XTRA 70	810	850	2,7	2,7	88
S960QL	1007	1045	–	2,44	125,11
XABO 1100	1125	1339	–	2,00	116,41

5. Conclusions

Based on the results of our experimental tests, evaluated samples and data can be found in the literature the following conclusions can be drawn.

- The proposed method can be generally applied for determination of fatigue crack propagation limit curves for steels and high strength steels, and their welded joints under mode I (tension) and mixed mode I + II (tension and shear) loading conditions. Additional information of applications of the proposed method for metallic materials (e.g. pressure vessel steels, aluminium alloys, austempered ductile iron) and non-metallic materials (e.g. silicon nitride ceramics, polymers, reinforced polymer matrix composites) see in our earlier works in the literature [10, 21-23].
- The limit curves calculated by both methods represent a compromise of rational risk (not the most disadvantageous case is considered) and striving for safety (uncertainty is known).
- Based on the determined fatigue design limit curves integrity assessment calculations can be done for operating structural elements and structures having cracks or crack-like defects:
  - = determination of propagable an critical crack sizes;
  - = calculation of lifetime determined by the propagable crack size;
  - = calculations of remaining lifetime functions, influences on the lifetime values and lifetime function (parameter study);
  - = reliability of remaining lifetime estimation;
  - = calculation of damage parameter and damage function [24].
- The examinations of the welded joints should be continued. The welding technologies, the welding parameters and their influences should be investigated, on the basis of their influences on the properties and the adequacy of the welded joints [25, 26].

Acknowledgements

Author wishes to acknowledge the assistance given by the National Scientific Research Foundation (OTKA F4418, OTKA T022020, OTKA T034503 and OTKA T049126), furthermore the Agency for Research Fund Management and Research Exploitation (GVOP-3.1.1.-2004-05-0215/3.0) for supporting the earlier executed research. The research work has continued as a part of the TAMOP-4.2.1.B-10/2/KONV-2010-0001 project, and will be continued as a part of the

TAMOP-4.2.2.A-11/1/KONV-2012-0029 project, with support by the European Union, co-financed by the European Social Fund.

References

[1] R. J. Allen, G.. S. Booth, T. Jutla, A review of fatigue crack growth characterisation by linear elastic fracture mechanics (LEFM). Part I – Principles and methods of data generation. Fatigue and Fracture of Engineering Materials and Structures, 11/1 (1988) 45-69.

[2] R. J. Allen, G.. S. Booth, T. Jutla, A review of fatigue crack growth characterisation by linear elastic fracture mechanics (LEFM). Part II – Advisory documents and applications within national standards. Fatigue and Fracture of Engineering Materials and Structures, 11/2 (1988) 71-108.

[3] A. Ohta, Y. Maeda, M. Kosuge, S. Machida, H. Yoshinari, H., Fatigue Crack Propagation Curve for Design of Welded Structures. Transactions of the Japan Welding Society, 20/1 (1989) 17-23.

[4] Merkblatt DVS 2401 Teil 1: Bruchmechanische Bewertung von Fehlern in Schweissverbindungen. Grundlagen und Vorgehensweise (Oktober 1982).

[5] Det norske Veritas, Classification Notes, Note No. 30.2: Fatigue strength analysis for mobile offshore units (August 1984).

[6] BS 7910: Guide on methods for assessing the acceptability of flaws in fusion welded structures (1999).

[7] Merkblatt DVS 2401 Teil 2: Bruchmechanische Bewertung von Fehlern in Schweissverbindungen. Praktische Anwendung (April 1989).

[8] P. Paris, F. Erdogan, A critical analysis of crack propagation laws. Journal of Basic Engineering, Transactions of the ASME, (1963) 528-534.

[9] J. Lukács, Reliability of Cyclic Loaded Welded Joints Having Cracks, CSc dissertation, Miskolci Egyetem, Miskolc and Budapesti Műszaki Egyetem, Budapest (1992). (In Hungarian: Repedést tartalmazó hegesztett kötések megbízhatósága ismétlődő igénybevétel esetén.)

[10] J. Lukács, Fatigue crack propagation in steels and their welded joints, Publications of the University of Miskolc, Series C, Mechanical Engineering, 46/1 (1996) 77-91.

[11] A. Balogh, I. Török, M. Gáspár, D. Juhász, Present state and future of advanced high strength steels, Journal of Production Processes and Systems, 6/1 (2012) 79-90.

[12] M. Tisza, Materials science and technological developments in metal forming, in: L. Pokorádi (Ed.), Műszaki Tudomány az Észak-alföldi Régióban 2010 Konferencia előadásai, Debreceni Akadémiai Bizottság Műszaki Albizottsága, Debrecen, 2010, pp. 1-8. (In Hungarian: Anyagtudományi és technológiai fejlesztések a képlékenyalakításban.)

[13] J. Lukács, Fatigue crack propagation in railway rails under I and I+II loading conditions, in: G. Lütjering, H. Nowack (Eds.), Proceedings of the Sixth International Fatigue Congress (FATIGUE'96), Elsevier Science Ltd., 1996, Vol. II, pp. 1189-1194.

[14] ASTM E 647: Standard test method for measurement of fatigue crack growth rates (1988).

[15] D. B. Owen, Handbook of statistical tables, Vychislitel'nyjj Centr AN SSSR, Moskva, 1973. (In Russian: Sbornik statisticheskikh tablic.)

[16] I. Vincze, Mathematical statistics with industrial applications, Műszaki Könyvkiadó, Budapest, 1975. (In Hungarian: Matematikai statisztika ipari alkalmazásokkal.

[17] A. Balogh, F. Dukáti, L. Sallay, Quality control and reliability, Műszaki Könyvkiadó, Budapest, 1980. (In Hungarian: Minőségellenőrzés és megbízhatóság.

[18] D. Taylor, A Compendium of Fatigue Thresholds and Growth Rates, EMAS Ltd., Warley, 1985.

[19] Bruchmechanische Werkstoffcharakterisierung, H. Blumenauer (Ed.), Deutscher Verlag für Grundstoffindustrie, Leipzig, 1991.

[20] J. Lukács, Determination of fatigue crack propagation limit curves and their application for pipelines having crack like defects, in: R. Denys (Ed.), Pipeline Technology, Elsevier Science B. V., 2002, Vol. 2, pp. 127-140.

[21] I. Török, Factors affecting the properties of welded joints of aluminium and its alloys, Publications of the University of Miskolc, Series C, Mechanical Engineering. 46/1 (1996) 33-44.
[22] J. Lukács, Determination of fatigue crack propagation limit curves for metallic and non-metallic materials, in: A. F. Blom (Ed.), Proceedings of the Eighth International Fatigue Congress (FATIGUE 2002), EMAS, West Midlands, 2002, Vol. 2/5, pp. 1179-1186.
[23] J. Lukács, Fatigue crack propagation limit curves for different metallic and non-metallic materials, Materials Science Forum, 414-415 (2003) 31-36.
[24] J. Lukács, Determination of fatigue crack propagation limit curves and one possibility of their application, in: K. Jármai, J. Farkas (Eds.), Metal Structures – Design, Fabrication, Economy, Millpress, Rotterdam, 2003. pp. 33-38.
[25] M. Gáspár, A. Balogh, Experimental investigation on the effect of controlled linear energy applied to the welding of high strength steels, in: The Publications of the XXVI. microCAD International Scientific Conference, Miskolci Egyetem, Miskolc, CD-ROM, pp. 1-6.
[26] M. Gáspár, A. Balogh, Optimum range of the linear energy to the welding of tempered high strength steels, in: 26. Hegesztési Konferencia és Hegesztéstechnikai Kiállítás Kiadványa, Óbudai Egyetem, Budapest, 2012, pp. 173-178. (In Hungarian: A vonalenergia optimális tartománya nemesített nagyszilárdságú acélok hegesztésekor.)

Thermal Mechanical Fatigue of Coke Drum Materials

Jie Chen[1], Zihui Xia[1*]

[1] Department of Mechanical Engineering, University of Alberta, Edmonton T6G 2G8, Canada

* Corresponding author: zihui.xia@ualberta.ca

Abstract Coke drums are vertical pressure vessels used in the delayed coking process in petroleum refineries. Significant temperature variation during the delayed coking process causes damage in coke drums in the form of bulging and cracking. There were some studies on the fatigue life estimation for the coke drums, but most of them were based on strain-fatigue life curves at constant temperatures which do not consider simultaneous cyclic temperature and mechanical loading conditions. In this study, a thermal-mechanical material testing system is successfully designed and implemented. A selected set of base and clad materials of coke drums are investigated under isothermal cyclic loadings. In addition, a comparative study between isothermal and thermal mechanical fatigue lives of clad materials is conducted. Some of these fatigue tests are similar to the actual loading scenario experienced by the coke drums. The experimental findings lead to better understanding of the damage mechanisms occurring in coke drums and more accurate prediction of fatigue life of coke drum materials.

Keywords: Coke drums, Low cycle fatigue, Isothermal mechanical fatigue, Thermal mechanical fatigue

1. Introduction

Coke drums are vertical pressure vessels used in the delayed coking process in petroleum refineries and oil sands plants. They are normally constructed of carbon or low carbon alloy steels and internally clad with SA 240 Type 410S or Type 405 stainless steel to protect the coke drums from corrosion. They range in size from 4 to over 9 meters in diameter and 25 to over 40 meters in height. The maximum shell thickness varies from 14 to 42 millimeters. The maximum operating temperature ranges from 427 to 482°C [1].

First, heavy residual is imported into a coker heater and heated to approximately 482°C. Before direct the heavy oil into the coke drum, the drum is preheated by flowing vapour from the bottom of the drum to the top. (Temperature rises from approximate 150 °C to 360 °C). Then, the hot heavy oil is directed into the coke drum to begin the fill cycle. The fill cycle usually takes 14-18 hours. When the filling is completed, light hydrocarbon from the coke produced during the thermal cracking process is removed by steam stripping. (Temperature drops from 450 °C to 250 °C approximately) After that, high rate of quench water is injected into the coke drum cooling the vessel and possibly extracting the solid coke. After soaking, the solid coke is cut by applying the high-pressure water steams. After all the coke is removed from the drum, the coke drum is reheated and checked in order to prepare for a new operation cycle. [1]

The severe cyclic thermal-mechanical load makes coke drums susceptible to damage. It is also found that shell bulging is one of the causes contributing to cracking and failure in the vessel shell

of coke drums. There are studies on the fatigue life estimation for the coke drums [2-4], these are based on base metal under uniaxial isothermal fatigue lives which do not consider cyclic temperature conditions. Xia et al. [5, 6] conducted a finite element study on heat transfer and stress analysis of coke drum for a complete operating cycle. It is found that significant stress and strain values are observed at the clad of the coke drum, which can exceed the yield limit of the material. Therefore, the fatigue life evaluation of coke drum based only on base material is not sufficient. The more accurate evaluation of the fatigue life behavior should be carried out under loading conditions similar to the operational condition, such as under thermal-mechanical cyclic loading.

In this paper, a successfully-developed thermal-mechanical fatigue testing system is presented. A selected set of base and clad materials of coke drums are investigated under isothermal cyclic loadings. In addition, in addition, a comparative study between isothermal and thermal mechanical fatigue lives of clad materials is conducted.

2. Experimental Setup

In order to experimentally investigate fatigue life of coke drum materials under thermal-mechanical cyclic loading, a thermal-mechanical fatigue (TMF) testing system has been successfully installed in our lab. The system mainly consists of a closed-loop servo-controlled hydraulic MTS testing machine which is used as a principal loading frame, a heating device, a control system, and gripping fixtures.

2.1. Heating Device

The TMF testing involves a temperature cycling. Therefore, a relatively fast heating and cooling is essential for conducting a fatigue test. There are various techniques including induction, direct resistance, radiant, or forced air heating. By evaluating the scope of this research and the interested regime of fatigue life, an induction heating with power rated at 5 kW is selected as a effective heating source. The induction unit mainly consists of a power unit, a working coil, and a cooling system. By positioning the conductive material such as metal specimen inside the working coil, the specimen can be heated up at adjustable rate. Because the working coil provides an open environment, this approach also offer an opportunity to install active specimen cooling (for example, forced air) to achieve desired cooling rate.

One of the difficulties using this system is to minimize the dynamic thermal gradient along the axial-direction of the specimen. The configuration of working coil plays an important role affecting the thermal gradient along the axial direction. Variables such as number of coil turns and patterns can have significant effect on the thermal gradients. There are several researchers [7-10] investigated the effect of working coil configuration on the thermal gradient of the specimen. In reference [7] it was found that by using ten-turns one direction helical configuration of the working coil, the thermal gradient along the gauge length of a solid cylindrical specimen could be within ±10°C at 800°C. In reference [9] an investigation on the effect of working coil configuration on

solid flat specimen was carried out. It concludes that an elliptical coil with its centre axis perpendicular to the middle axis of the specimen gives a smallest thermal gradient on the solid flat specimen. In addition, it was recommended in [10] that a longitudinal opposite direction working coil is for better axial temperature gradients. An experimental investigation of effect of working coil configurations on thermal gradient along a flat specimen was first carried out, as shown in Fig. 3-3.

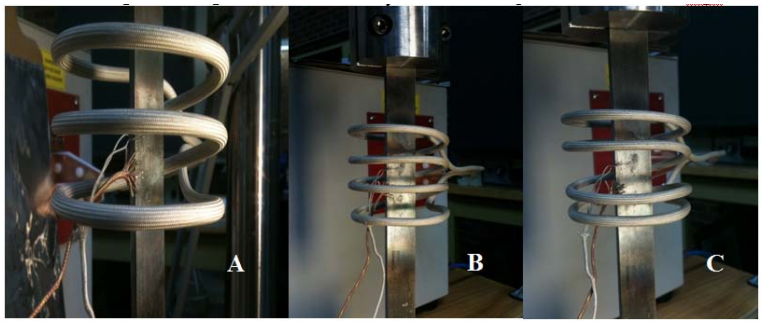

Figure 1 Configuration of working coil on flat specimen

Fig. 1 A-C shows the one direction longitudinal configuration with different turns. The temperature increases up to 500°C, and the dynamic temperature was recorded. The results shows that the working coil configuration C (4 turns with 25 mm gap in the middle) gives the minimal thermal gradients (10°C) at 500°C.

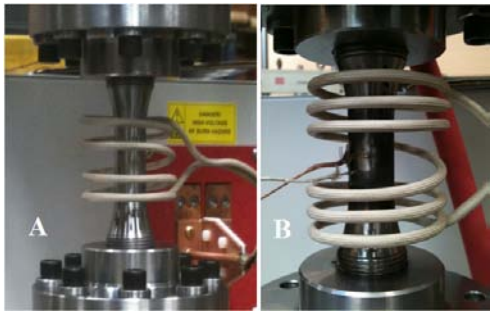

Figure 2 Configuration of working coil on thin-walled tubular specimen

Fig. 2 shows the two different working coil configurations on thin-walled tubular specimen. The temperature increases up to 500°C, and the dynamic temperatures were recorded. The results shows that the working coil configuration A (4 turns with gap in the middle) gives larger thermal gradients (50°C) at 500°C. If the number of turns increases to 6 with gap in the middle, the thermal gradients greatly reduced to 10°C at 500°C.

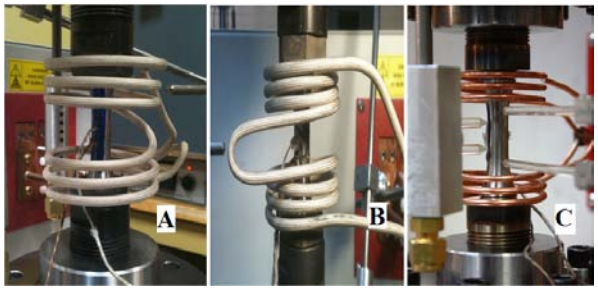

Figure 3 Configuration of working coil on cylindrical solid specimen

Figure 3 shows the three different working coil configurations on cylindrical solid specimen. The results showed that the working coil configuration A (6 turns with gap in the middle) gives larger thermal gradients (30~40°C) at 500°C. A configuration of longitudinal opposite-direction working coil (Fig. 3-5 B) was then tested, the result showed oppose thermal gradient (500°C in the center, 520~530°C at 12.7 mm away from the center). After several trial and error experimentations, the third configuration C was designed. Two separate working coils were attached on the power unit, and each with three turns. From the experimental result of this configuration, the dynamic thermal gradient almost disappears (within 5~10°C) along the axial direction at 500°C. Therefore, through this series of experimentations of working coil configuration, two separate working coil gives the minimal thermal gradient in axial direction.

2.2. Control System

To conduct in-phase strain-controlled TMF test, a program was written in the control system to accurately manage all the components. The dynamic temperature of the specimen is measured by the spot-welded thermocouple in the center of the gage length, and the temperature controller sends the measurement to the signal controller synchronistically. The signal controller send the commands to the heater and air jet during the heating and cooling phases, and it also controls the axial strain to feedback the hydraulic piston to apply the load. All the data is stored by the data acquisition on timed-basis. The strain is controlled by the dynamic temperature signal as shown in Fig. 4. The thermal cycling is carried out at beginning of each test, and thermal strains at T_{max} and T_{min} are recorded. The total strains at T_{max} and T_{min} are calculated:

$$\varepsilon_{Tot}^{T_{\max}} = \varepsilon_{Thermal}^{T_{\max}} + \varepsilon_{mech} \tag{1}$$

$$\varepsilon_{Tot}^{T_{\min}} = \varepsilon_{Thermal}^{T\min} + (-\varepsilon_{mech}) \tag{2}$$

A strain-temperature range ratio δ is defined as:

$$\delta = \frac{\Delta\varepsilon}{\Delta T} = \frac{\left(\varepsilon_{Tot}^{T_{\max}} - \varepsilon_{Tot}^{T_{\min}}\right)}{\left(T_{\max} - T_{\min}\right)} \tag{3}$$

both ε and T in voltages.

The ratio of input to output voltages of the gain amplifier and attenuator is then adjusted to the ratio of δ. The temperature cycling between T_{max} and T_{min} will also generate a voltage which is equal to total strain at the corresponding temperature. After the test, thermal strain is fitted as a function of temperature in a polynomial equation. The mechanical strain can be obtained by subtracting the thermal strain from the total strain.

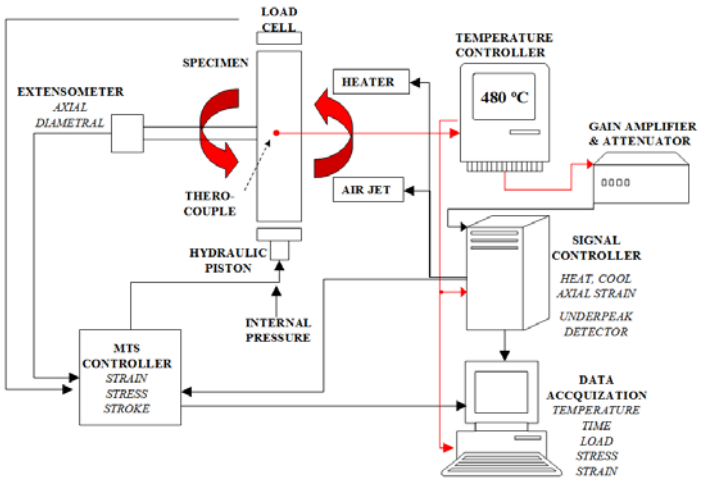

Figure 4 Demonstration of temperature-dependent strain-controlled mode

2.3. Strain Control and Measurement

A new strain control and measurement technique is introduced for high temperature fatigue testing. For high temperature strain-controlled fatigue tests, implementation of punching dimples or knife-edges within gauge length of specimen are common practices for mounting extensometers. Premature failure on the test section of the specimens were introduced at the punch dimple or knife-edge contact area by implementing these techniques as shown in Fig. 5 A and B, respectively.

Figure 5 Photos of premature failure caused by dimple and knife-edge

Alternatively, a pair of dimples is punched outside the gauge length of the specimen as shown in Fig. 6. The punched dimples are located on the thicker cross sections which are outside the effective gauge length of the test sections. Therefore, the premature failure will not be introduced by these dimples. However, since the controlled strain is from outside of gage length, a correlation between measured strain and strain within gauge length should be carefully calibrated and verified. The correlation coefficient is defined as (in this case):

$$C = \frac{\varepsilon_{0.6"}}{\varepsilon_{1"}} \tag{4}$$

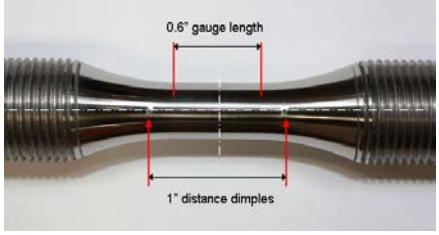

Figure 6 Picture of the specimen with dimples

Two approaches, analytical analysis and finite element analysis are implemented to establish the strain correlation at elevated temperature for each material. The results are then compared with the experiments to verify the established correlations at each temperature.

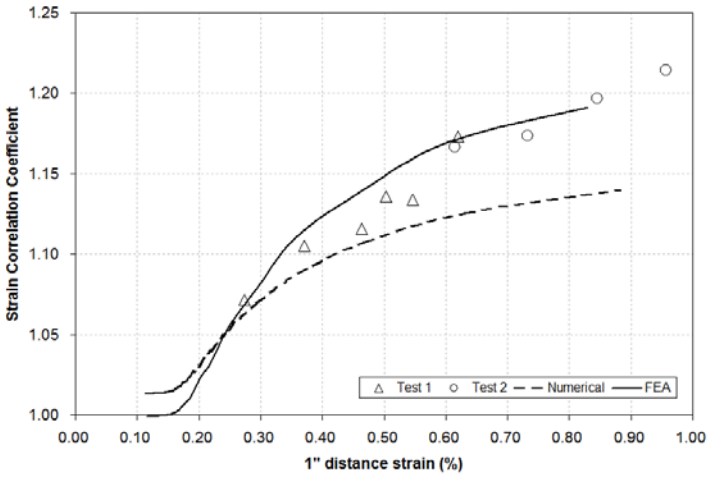

Figure 7 Comparison of room temperature correlation coefficients

The correlation coefficients between the experiment and the two analysis methods are shown in Fig. 7. It can be seen that the experimental points are mainly fallen in the range between the two correlation curves by the analytical and FEA methods. At higher strain range, those points are closer to the FEM correlation curve. However, the difference of the correlation coefficients predicted by the analytical and FE methods is about only 4% when the strain is up to 0.8%. Therefore, a mean curve of the two predictive curves is suggested to be used. In addition, the strain correlation technique can also be applied to thermal-mechanical fatigue tests.

2.4. Materials and Test program

Table 1 Tested coke drum materials

Name	Nominal Chemical Comp.	Plate
SA387 Gr. 22 CL2	2 ¼Cr-1 Mo	Base
SA 240 TP410S	13Cr	Clad

In this paper, low cycle fatigue tests conducted for the following materials: SA387 Gr. 22 CL2 and 410S. Uni-axial isothermal low cycle fatigue tests were carried out as benchmark tests. The tests are under strain-controlled condition at rate of 0.005/Sec. The tests were conducted at fully-reversed cyclic loading condition ($R=\varepsilon_{min}/\varepsilon_{max}$ = -1) at both 100 and 480°C. In addition, TMF tests were conducted on 410S. The tests are under temperature-dependent strain-controlled condition, and in-phase thermal-mechanical loading was applied.

3. Results

Isothermal fatigue lives of SA387 Gr.22 CL 2 at 100 and 480^{o}C are shown in Fig 8. From the results,

it is shown that as the temperature increases, the fatigue life decreases. One also see that the linear lines can fit the data points quite well, in addition the two fatigue lines at two different temperature are almost parallel to each other in the log-log scale graphs. Therefore, the isothermal fatigue data can be fit by the following equation:

$$\frac{\Delta\varepsilon}{2} = A(T)(N_f)^c \tag{5}$$

where $\Delta\varepsilon/2$ is the strain amplitude (mechanical strain), N_f is the number of cycle to failure, c is a constant and A is a temperature dependent constant,

where
$$A(T) = A_{T_{\max}} - \frac{(T_{\max} - T)(A_{T_{\max}} - A_{T_{\min}})}{(T_{\max} - T_{\min})} \tag{6}$$

T_{max} = 480°C and T_{min} =100°C in this case.

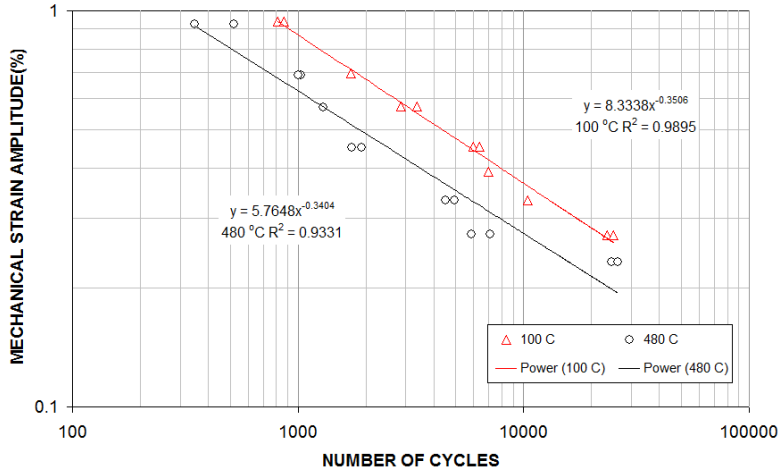

Figure 8 Isothermal fatigue Lives of SA387 GR.2 CL2 at 100 and 480°C

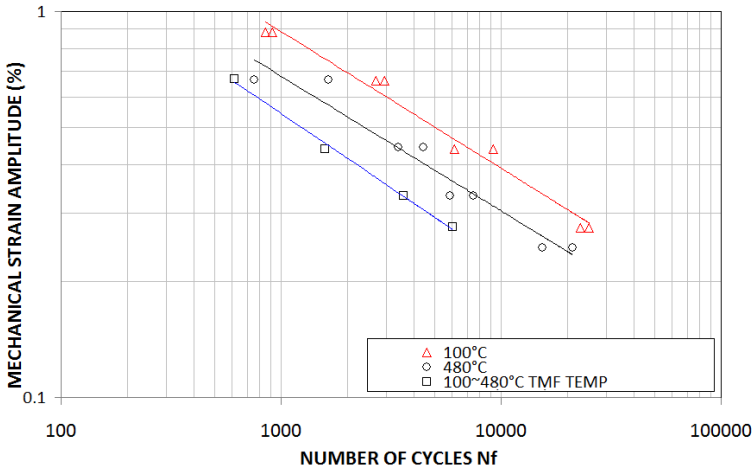

Figure 9 Isothermal and TM fatigue lives of 410S

Isothermal and thermal-mechanical fatigue lives of 410S are shown in Fig 9. From the results, it is shown the same trend as that of the isothermal fatigue tests for the material SA387 Gr. 22 CL2. Therefore the same form of the above equations (5) and (6) can be used to fit the fatigue life data

for the material 410S. In Fig. 9, four data points from the in-phase TMF tests with temperature cycling between 100 and 480°C are provided. It is found that the fatigue life of 410S under TMF loading is even shorter than the life at constant temperature of 480°C, though in the TMF loading the maximum temperature is 480°C. Due to the insufficient amount of data conducted, more data points are required to verify the trend of this observation.

4. Summary

In this paper, newly-developed thermal-mechanical fatigue testing system is presented. The developed system can successfully simulate in-phase thermal-mechanical loading which is similar to the loading experienced by the coke drums. Some key developments of this system are introduced such as heating device and control system. In addition, an alternative strain control and measurement technique was developed for both isothermal and TMF fatigue tests Furthermore, some preliminary fatigue tests results were presented. For isothermal fatigue tests, it is shown that as temperature increases, the fatigue lives of SA387 and 410S decrease significantly. Additionally, by comparing lives between isothermal and thermal-mechanical fatigue, it is found that the fatigue life of 410S under TMF loading is shorter than the life at 480°C. Therefore, it is inaccurate to estimate the service life of coke drums based on isothermal fatigue data. Due to the insufficient amount of experimental data, this trend need to be further verified and the mechanisms of this observation need to be explored. More tests are still carrying on in our lab. Based on the comprehensive experimental investigation, reasonable fatigue life models will be developed for the coke drum materials.

Acknowledgements

This research is supported by a Collaborative Research and Development (CRD) Grants of The National Science and Engineering Research Council (NSERC) of Canada (CRD #350634-07 and CRDPJ 403054-10).

References

[1] Penso, J. A., Lattarulo, Y. M., Seijas, A. J., Torres, J., Howden, D., and Tsai, C. L., 1999, “Understanding Failure Mechanisms to Improve Reliability of Coke Drum,” ASME, New York, PVP-Vol. 395, pp. 243–253.

[2] Ramos, A., Rios, C., Vargas, J., Tahara, T., and Hasegawa, T., 1997, “Mechanical Integrity Evaluation of Delayed Coke Drums,” *Fitness for Adverse Environments in Petroleum and Power Equipment*, ASME, New York, Vol. 359, pp.291–298.

[3] Ramos, A., Rios, C., Johnsen, E., Gonzalez, M., and Vargas, J., 1998, “Delayed Coke Drum Assessment Using Field Measurements and FEA,” *Analysis and Design of Composite, Process, and Power Piping and Vessels*, ASME, New York, Vol. 368, pp. 231–237.

[4] Ramos, A. J., Rios, C. and Vargas, J.A.R., 1999, “Fatigue Life Prediction of Delayed Coke Drums”, *Vision Techenologica*, Vol.6, pp. 93-100

[5] Z. Xia, F. Ju, and P. D. Plessis, 2010, Heat Transfer and Stress Analysis of Coke Drum for a Complete Operating Cycle, Journal of Pressure vessel technology, 132.

[6] F. Ju, J. Aummuler, Z. Xia, and P. D. Plessis, 2011, Global and Local Elastic-Plastic Stress Analysis of Coke Drum Under Thermal-Mechanical Loadings, Journal of Pressure vessel technology, 133.

[7] C. J. Hyde, W. Sun, S. B. Leen, 2010, Cyclic thermo-mechanical material modelling and testing of 316 stainless steel, International journal of pressure vessels and piping, 87, 365-372.

[8] E. E. Affeldt, J. Hammer, U. Huber, H. Lundblad, 2003,Analysis of thermal gradients during cyclic thermal loading under high heating rates, Thermomechanical fatigue behavior of materials, 4, 312-324.

[9] T. Brendel, E. Affeldt, J. Hammer, C. Rummel, 2008, Temperature gradients in TMF specimens. Measurement and influence on TMF life, International Journal of Fatigue, 30, 234-240.

[10] P. Haehner, E. Affeldt,T.Beck,H. Klingelhoeffer, M. Loveday,C. Rinaldi, 2006, Validated code-of-practice for strain controlled thermo-mechanical fatigue testing, ECReport EUR 22281 EN, ISBN92-79-02216-6.

Application of a non local fatigue stress gradient- weigth function approach to predict the crack nucleation risk induced by Fretting Fatigue

Siegfried Fouvry*, Bruno Berthel

LTDS, Ecole Centrale Lyon, 69134 Ecully, France
* Corresponding author: siegfried.fouvry@ec-lyon.fr

Abstract

Fretting-Fatigue problems are very complex to address due to the multiaxiality and the very sharp stress gradients imposed below the interfaces. Hence, multiaxail and non local fatigue approach must be considered. An experimental cylinder/plane fretting fatigue and plain fretting analysis a 35 Ni Cr Mo 16 low alloyed steel at 10^6 cycles has been performed to investigate the incipient crack nucleation response for various stress gradient conditions. Imposing elastic stress conditions, the Crossland's approach is applied to predict the crack nucleation risk. This analysis confirms that a local stress analysis at the "hot spot" stress located at surface trailing contact border is not suitable. The non local "critical distance" approach which considers the stress loading path at a fixed distance from the "hot spot" improves the prediction but still induce a large discrepancy. Finally, the best predictions are achieved using an alternative non local "weight function" approach where the crack nucleation risk computed at the "hot spot" is weighted by a function expressed as as a linear decreasing expression of the hydrostatic stress gradient operating around the "hot spot" location. The stability of this approach regarding the contact stress field resolution and related application for FEM application is discussed.

Keywords Fretting Fatigue crack nucleation, Stress gradient, Non local fatigue approach, Crossland

1. Introduction

Fretting is a small amplitude oscillatory movement, which may occur between contacting surfaces that are subjected to vibration or cyclic stress. Combined with cyclic bulk fatigue loading, the so-called fretting-fatigue loading can induce catastrophic cracking phenomena which critically reduce the endurance of assemblies [1]. Fretting Fatigue loading can be characterized by the superposition of a heterogeneous cyclic stress gradient related to the contact loading, and a quasi-homogeneous fatigue bulk loading (Fig. 1). The crack nucleation phenomenon is commonly addressed by transposing conventional multi-axial fatigue criteria [2] taking into account or not the stress gradient effects [3, 4]. Indeed, as illustrated in Figure 2, the fretting stressing conditions are characterized by very severe stress gradients which could be one order of magnitude higher than common notch fatigue stress configurations. Non local fatigue approaches are therefore required to predict the cracking risk. Stress averaging approaches [3, 5], or equivalent critical distance methods [4] which consist to consider the stress state at a "critical distance" from the stress "hot spot" are commonly applied to capture the stress gradient effect. However, these approaches, which consider a fixed length scale value are limited when large stress gradient fluctuations are operating. To palliate such limitation, an alternative strategy which consists to weight the prediction given at the "hot spot" location using a linear decreasing function expressed as a function of the gradient of the hydrostatic stress around the hot spot stress location is considered. Introduced by Papadopoulos [6], this approach was simplified by Amargier et al. to predict plain fretting crack nucleation conditions

[7]. The purpose of this research work is to extend this approach for partial slip fretting fatigue situations. This analysis also addresses the influence of the size domain over which the hydrostatic stress gradient is computed thus to establish the stability of this approach regarding the spatial contact stress resolution.

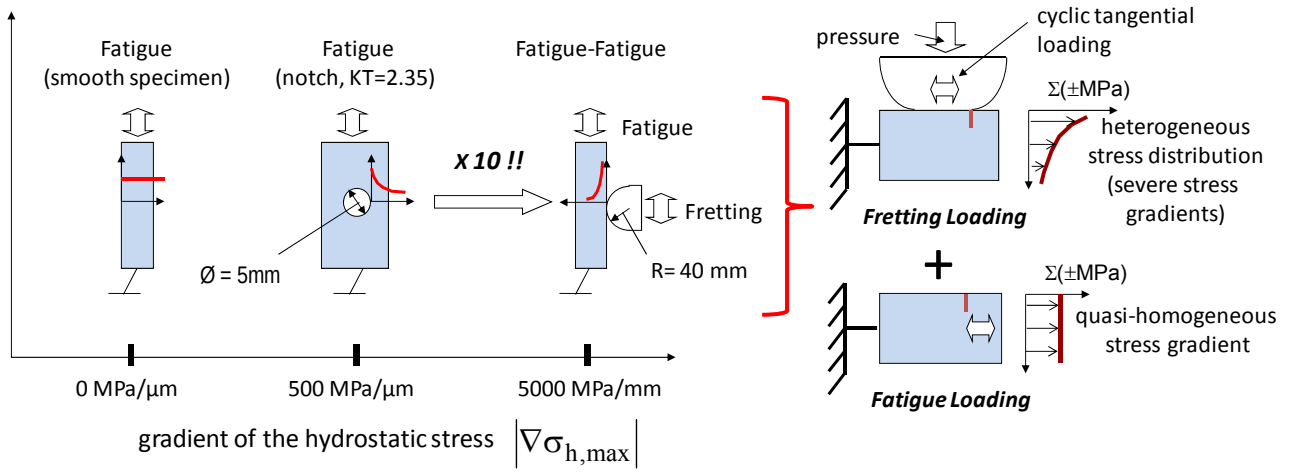

Figure 1. Illustration of the stress condition characterizing the fretting fatigue loading.

2. Materials and experimental procedure

2.1. Materials

The studied material is a tempered a 35 Ni Cr Mo 16 low alloyed steel displaying a tempered Martensitic structure. The original austenite grain size is about Ø =20 µm. The mechanical and fatigue properties of this steel, are summarized in the following table 1.

Table 1. Mechanical and fatigue properties of the studied 35 Ni Cr Mo 16 low alloyed steel.

E(MPa)	ν	$\sigma_{y0.2\%}$ (MPa)	σ_u (MPa)	σ_d (MPa)	τ_d (MPa)	ΔK_{th} (MPa$\sqrt{m}$)
205000	0.3	950	1130	575	386	3.2

E: Young's modulus; ν: Young's modulus, $\sigma_{y0.2\%}$: Yield stress (0.2%); σ_u: ultimate stress; σ_d : traction – compression fatigue limit ($R\sigma = \sigma min/\sigma max = -1$ for 10^7 cycles); τ_d : shear fatigue limite ($R\tau = -1$ for 10^7 cycles); ΔK_{th} : long crack threshold (R=-1).

Chromium 52100 steel was chosen for the cylindrical pads in order to maintain elastically similar conditions whilst simultaneously ensuring that cracks arose only in plane and fatigue 35NiCrMo16 specimens. Both plane and cylindrical pad surfaces were polished to achieved a small Ra=0.05 µm surface roughness.

2.2. Test conditions

As illustrated in Figure 3, two different test apparatuses were involved to quantify respectively the fretting and the fatigue influences in cracking processes.

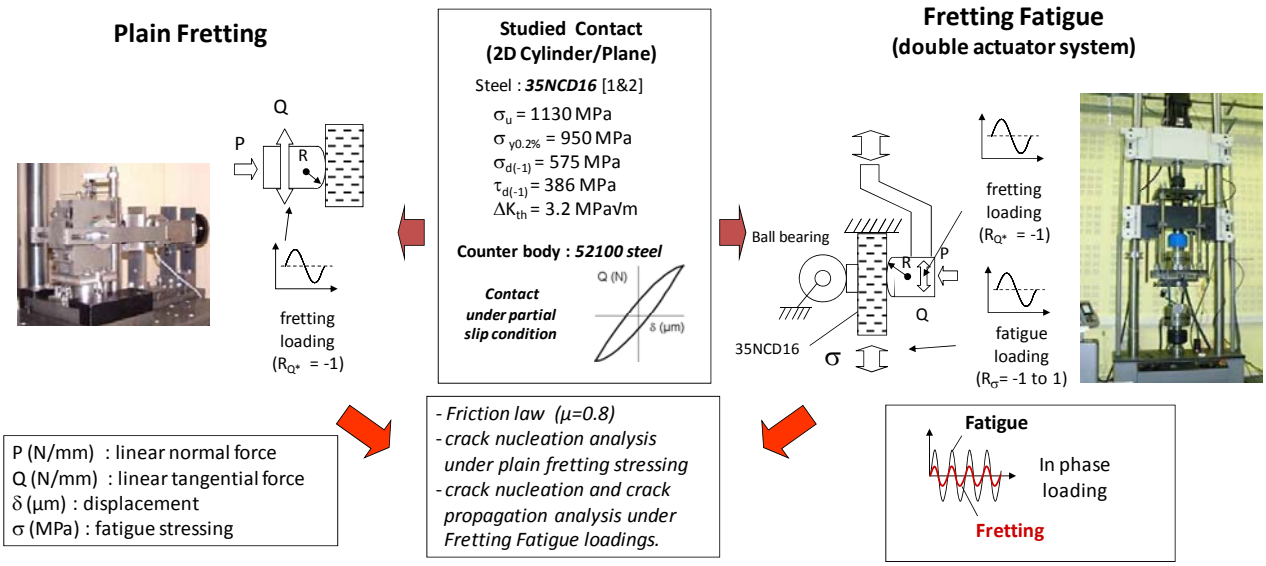

Figure 2. Illustration the experimental strategy based a combined plain fretting and fretting fatigue analysis involving similar contact configurations.

Plain Fretting tests were applied by imposing a nominally static normal force P, followed by a purely alternating cyclic displacement amplitude (δ*), so that an alternating cyclic tangential load Q was generated on the contact surface. During a test, P, Q and δ are recorded, from which the δ - Q fretting loop can be plotted. The studied plane specimen is not subjected to any fatigue stressing.
The fretting fatigue experiments were performed using a dual actuator device inspired by Fellows et al. [8]. This test system allows the separate application and control of fretting and fatigue loadings. Like for the plain fretting, the system is instrumented to measure the contact loading (P, Q*, δ*) but also the fatigue stressing (σ, $R_\sigma=\sigma_{min}/\sigma_{max}$).
In order to analysis both contact pressure, fatigue stress and stress gradient effects, various cylinder radius from R= 20 to 80 mm, Hertzian contact pressures from p_{max}=600 to 1000 MPa and fatigue stress conditions from σ_{max}= 0 and 400 MPa considering two stress ratio Rσ=0.1 and 1.0 were investigated. The details of the studied conditions are compiled in table 2. Note that the lateral width of the cylinder pads (W) was chosen to satisfy plain strain conditions.

3. Experimental results

3.1. Friction analysis

Because the partial contact stress field depends on the coefficient of friction, it is important to establish this value. H. Proudhon et al. show in [10] that the friction coefficient measured at the transition between partial and gross slip conditions (μ_t) may be used to provide a representative value of the friction under partial slip conditions (i.e. $\mu_{PS}=\mu_t$). Figure 3b compares the obtained μ_t

values as a function of the Hertzian contact radius for different contact pressures. A quasi constant evolution is observed which allows us to consider a constant friction value (i.e. $\mu=\mu_{PS}=\mu_t=0.8$).

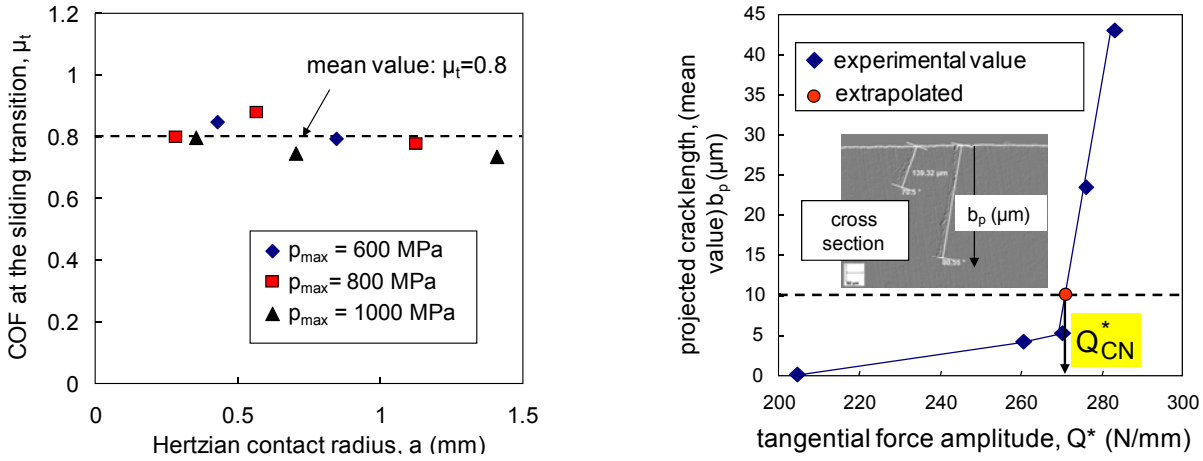

(a) (b)

Figure 3. a) Evolution of the coefficient of friction (COF) at the sliding transition as a function of the contact radius and the maximum Hertzian pressure for the studied interfaces - b) Illustration of the destructive methodology used to identify the crack nucleation condition for plain fretting and fretting fatigue conditions.

Table 2. Compilation of the studied test conditions (PF : plain fretting, FF: fretting fatigue)

	R (mm)	W (mm)	P (N/mm)	σ_{max} (MPa)	$R\sigma$	p_{max} (MPa)	a (mm)	μ_t	Q^*_{CN} (N/mm)	$k=\frac{c}{a}$	e (mm)	$\frac{\sigma_{VM}}{\sigma_Y}$
PF_1	20	3	353	0	0	800	0.28	0.8	186	0.58	-	0.97
PF_2	20	3	552	0	0	1000	0.35	0.8	218	0.71	-	1.05
PF_3	40	5	398	0	0	600	0.42	0.85	271	0.38	-	0.83
PF_4	40	5	707	0	0	800	0.56	0.88	287	0.70	-	0.85
PF_5	40	5	1100	0	0	1000	0.70	0.75	310	0.80	-	0.89
PF_6	80	8	795	0	0	600	0.84	0.79	305	0.72	-	0.62
PF_7	80	8	1414	0	0	800	1.12	0.78	399	0.80	-	0.71
PF_8	80	8	2209	0	0	1000	1.40	0.74	470	0.85	-	0.77
FF_1	80	8	795	100	0.1	600	0.84	-	273	0.75	0.02	0.69
FF_2	80	8	795	200	0.1	600	0.84	-	261	0.76	0.04	0.78
FF_3	80	8	795	400	0.1	600	0.84	-	137	0.88	0.08	0.87
FF_4	40	8	398	100	0.1	600	0.42	-	210	0.58	0.01	0.83
FF_5	40	8	398	200	0.1	600	0.42	-	192	0.62	0.02	0.90
FF_6	40	8	398	400	0.1	600	0.42	-	100	0.83	0.04	0.93
FF_7	80	8	795	200	1	600	0.84	-	300	0.72	-	0.80
FF_8	80	8	795	400	1	600	0.84	-	280	0.74	-	0.97

3.2. Crack nucleation analysis

The cracking investigation consists in identifying the partial fretting loading (i.e. $Q^*<\mu P$) inducing

a threshold crack length after 10^6 cycles. The following methodology is applied: After each fretting test, the plane specimen is cut along the median axis of the fretting scar. Cross section observations are performed to determine the projected crack length (b_p) along the normal of the surface. The polishing process is then repeated twice so that the crack measurement is performed on 6 different planes located along the median axis of the fretting scar. From these six measurements, the maximum projected crack length (b_{pmax}) is determined. This crack analysis is generalized to various tangential force amplitudes in order to plot the evolution of b_{pmax} versus the applied tangential force amplitude (Fig. 3b). Finally, the threshold crack nucleation is determined by extrapolating the tangential force amplitude related to a b_{pth} = 10 µm projected crack length. This strategy was systematically applied for all the studied conditions. The corresponding Q^*_{CN} values are compiled in table 2. The expertise shows that the incipient crack nucleation is systematically observed at the trailing contact borders. Note that under established partial slip conditions, the surface wear is negligible and the contact geometry assumed unchanged during the fretting tests.

4. Contact stress analysis

4.1. Fretting Fatigue Stress field computation

The contact stress analysis of studied plain fretting and fretting fatigue experiments is performed by applying an analytical formulation which consists to combine the Mindlin's analytical description of partial slip contact (Fig. 4a) [9] with an adequate application of the McEven formalism's [9].

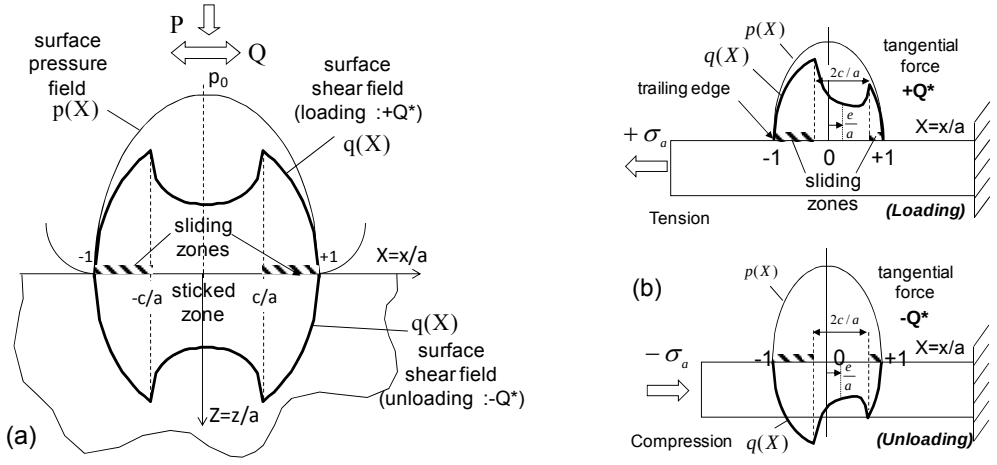

Figure 4. Pressure and Shear surface profiles under partial slip conditions a) plain fretting – b) fretting fatigue

The McEven formalism allows us to establish the stress state below the surface related to elliptical surface pressure or shear profiles. By summing the contribution of various elliptical shear distributions, the partial slip loading path can be determined. Note that the offset or eccentricity "e" of the stick zone, which induced by the fatigue strain deformation of the fatigue specimen, is considered by applying the Nowel's formalism [11] (Fig. 4b). This approach is justified if the

Hertzian hypotheses are satisfied which implies elastic stress conditions, smooth surfaces, plain strain hypothesis and thick enough specimen to satisfy the semi infinite contact configuration. The low surface roughness of specimens, the large lateral width of cylinder pads and the 10 mm specimen thicknesses support such hypothesis. Besides, a posteriori stress analysis shows that all the crack nucleation conditions correspond to elastic stress conditions ($\sigma_{VM}/\sigma_y < 1$). A major interest of this analytical stress description is the very fast computation of the cyclic stress path which allows an extensive non local multiaxial fatigue stress analysis.

4.2. Crossland's Multiaxial Fretting criterion

The stress loadings operating below the surface are multiaxial and therefore a multixial fatigue analysis is required. The Crossland's multiaxial fatigue approach [12], well adapted to describe the fatigue response of the studied alloy, is considered. The crack risk is expressed as a linear combination of the maximum amplitude of the second invariant of the stress deviator $\sqrt{J_{2,a}}$, and the maximum value of the hydrostatic pressure ($\sigma_{h,max}$) (Fig. 5a).

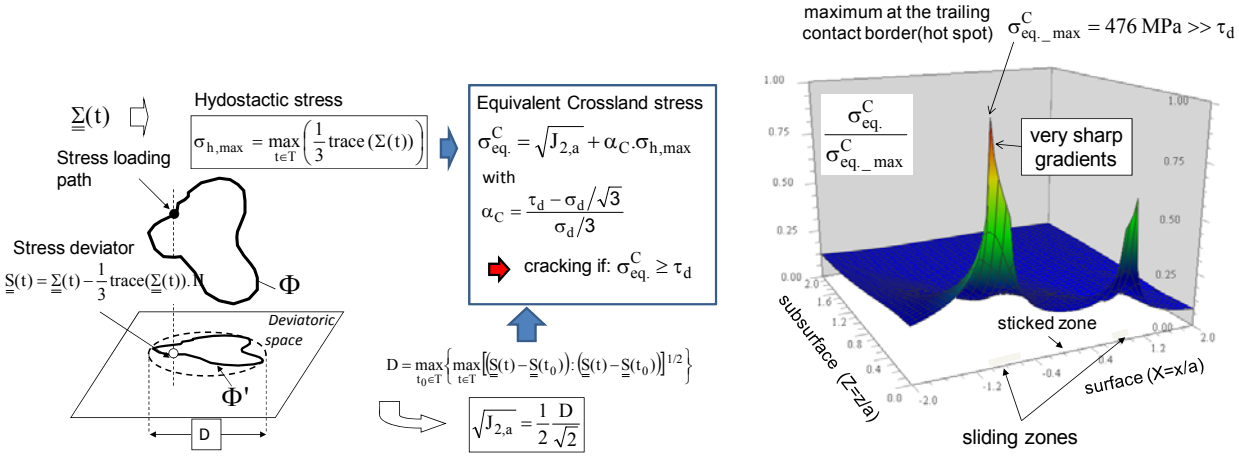

Figure 5. a) Illustration of the Crossland criterion – b) Crossland distribution of the FF2 condition (local stress analysis) (Table 2)

The crack nucleation condition is verify if the equivalent Crossland fatigue stress is becoming larger than the shear fatigue limit :

$$\sigma_{eq.}^{C} = \sqrt{J_{2,a}} + \alpha_C.\sigma_{h,max} \geq \tau_d \quad \text{with for the studied alloy} \quad \alpha_C = 0.28 \qquad (1)$$

Figure 5b shows the distribution of Crossland criterion computed for a representative Fretting Fatigue crack nucleation condition (i.e. FF2 test, Table 2) applying a local stress analysis. Confirming the experimental results, the maximum risk value is localized at the trailing contact border. The distribution shows very sharp gradients and a dissymmetry of the profile induced by stick zone offset generate by the fatigue mismatching strain deformation within the interface.

5. Comparison between experiments and fatigue modeling

5.1. Local « hot spot » fatigue analysis

The multaxial fatigue analysis is applied using a local stress description at the hot spot stress location (i.e. trailing contact border). The analysis is performed for each plain fretting and fretting fatigue crack nucleation conditions and reported in a $\sqrt{J_{2,a}}$ - $\sigma_{h,max}$ diagram (Fig. 6).

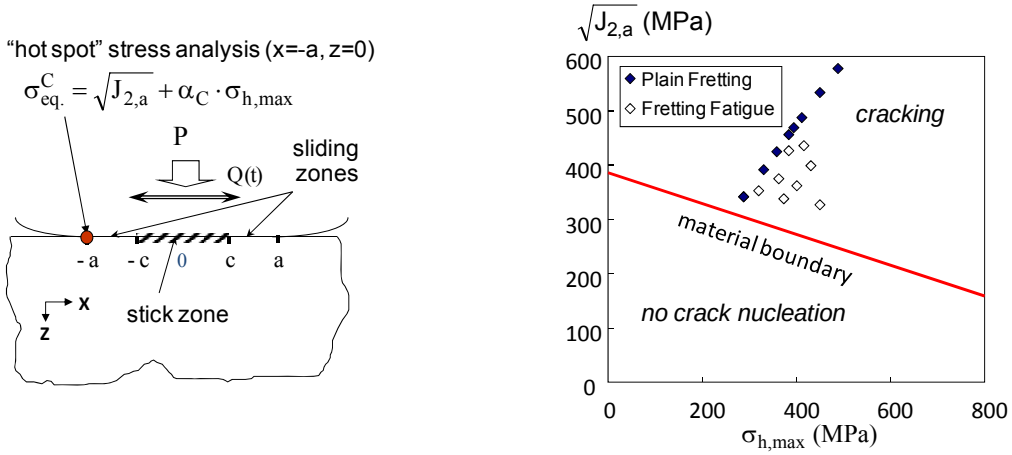

Figure 6. Local Crossland analysis at the "hot spot" trailing contact border.

As expected, the experimental data are highly dispersed and systematically above the material boundary. This local Crossland fatigue approach does not integrate the severe stress gradients operating next to the "hot spot" and therefore is not suitable to predict the fretting cracking risk. To quantify the stability of the prediction, the mean value and the square root variance of the equivalent Crossland stress obtained for the 16 test conditions are computed.

$$\overline{\sigma}_{eq.}^{C.} = \frac{1}{N}\sum_{i=1}^{N}\sigma_{eq.}^{C.}(i)\,,\quad \%E\overline{\sigma}_{eq.}^{C.} = \left(\frac{\overline{\sigma}_{eq.}^{C.} - \tau_d}{\tau_d}\right)x100\,,\quad V\sigma_{eq.}^{C.} = \sqrt{\frac{\sum_{i=1}^{N}\left(\sigma_{eq.}^{C.}(i) - \overline{\sigma}_{eq.}^{C.}\right)}{N-1}}\,,\quad \%V\overline{\sigma}_{eq.}^{C.} = \left(\frac{V\overline{\sigma}_{eq.}^{C.}}{\overline{\sigma}_{eq.}^{Cross.}}\right)x100 \qquad (2)$$

The $\%E\overline{\sigma}_{eq.}^{C}$ allows to estimate the global error of prediction versus the theoretical material prediction, whereas the $\%V\overline{\sigma}_{eq.}^{C}$ variable provides a relative estimation of the dispersion. For the given local fatigue description, we found $\%E\overline{\sigma}_{eq.}^{C}$ = +36 % and $\%V\overline{\sigma}_{eq.}^{C}$ = 16% which correspond to a critical overestimation and a high dispersion.

5.2. Non local « critical » distance fatigue approach

The critical distance method which consists to define the stress state at a certain distance below the contact "hot spot" (Fig. 7a) is applied. Using the Taylors's theory [13] which approximates the critical distance as the half value of the long crack propagation transition b_0, we deduced :

$$\lambda_T = \frac{b_0}{2} \approx \frac{1}{2\pi}\left(\frac{\Delta K_{th}}{\sigma_d}\right)^2 \approx 5\mu m \tag{3}$$

This strategy previously applied par Araujo et al. in [4] is now considered for the given Crossland's fatigue analysis (Fig. 7).

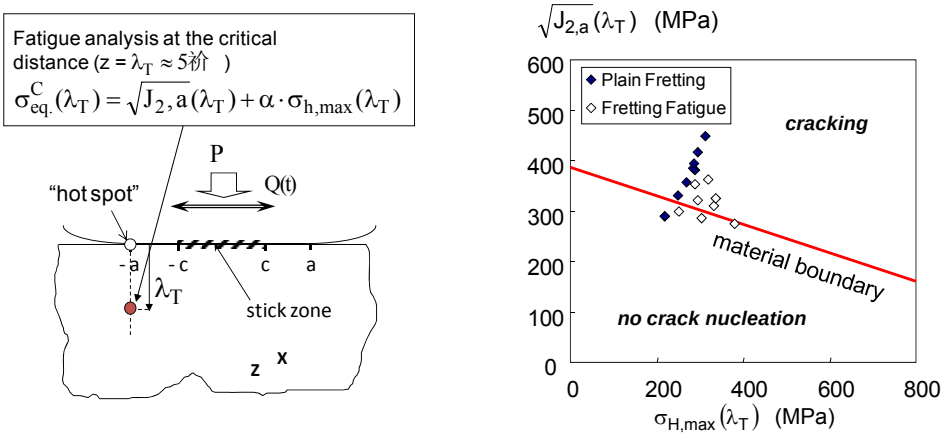

Figure 7: Critical distance approach assuming a constant length scale value ($\lambda_T = b_0/2 = 5\mu m$).

The experimental results are closer to the material boundary and the dispersion is reduced. The statistical analysis gives $\%E\overline{\sigma}^C_{eq.}(\lambda_T) = 11\%$ and $\%V\overline{\sigma}^C_{eq.}(\lambda_T) = 12\%$. The global predictions are less conservative but still dispersed. This suggests that the "critical distance" approach which consider a single "material" length scale parameter is not sufficient to fully capture the stress gradient for such very large stress gradient range.

5.3 Weigth function approach

An alternative non local approach which consists to consider the "hot spot" fatigue stress value weighted by a linear decreasing function (w) of the hydrostatic stress gradient surrounding the hot spot location is now considered [6, 7]:

$$\sigma^{C*}_{eq.} = \sigma^{C}_{eq.}.w\left(\left|\overline{\nabla}_\lambda(\sigma_{h\,max})\right|\right) \quad \text{where} \quad w = 1 - k.\left|\overline{\nabla}_\lambda(\sigma_{h\,max})\right| \tag{4}$$

With $\left|\overline{\nabla}_\lambda(\sigma_{h\,max})\right|$ the mean stress gradient of the hydrostatic stress over a cubic volume defined by the length scale λ. Hence for plain strain conditions it leads to

$$\left|\nabla(\sigma_{h,max}(x,z))\right| = \sqrt{\left(\frac{\partial\sigma_{h,max}}{\partial x}\right)^2 + \left(\frac{\partial\sigma_{h,max}}{\partial z}\right)^2} \tag{5}$$

which for the studied fretting conditions infers :

$$\left|\overline{\nabla}_\lambda(\sigma_{h\,max})\right| = \sqrt{\left(\frac{\sigma_{h,max}(-a,0) - \sigma_{h,max}(-a,\lambda)}{\lambda}\right)^2 + \left(\frac{\sigma_{h,max}(-a,0) - \sigma_{h,max}(-a+\lambda,0)}{\lambda}\right)^2} \tag{6}$$

The length scale λ is usually related to the grain size so that $\lambda = Ø/2 = 10\ \mu m$ which presently gives $k = 0.0142\ (MPa/\mu m)^{-1}$

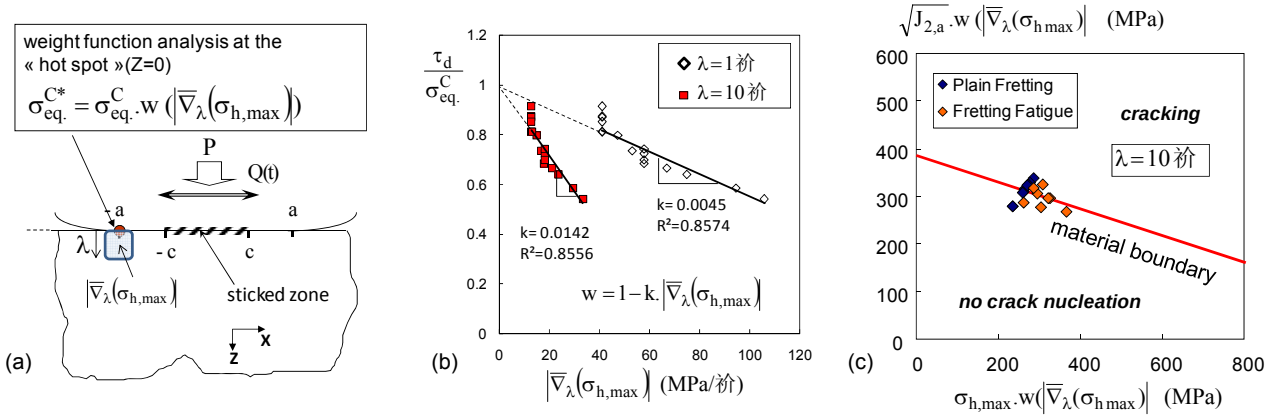

Figure 7: Weight function approach: a) illustration of the methodology- b) identification of the weight function – c) Application of the methodology (ℓ=Ø/2=10µm).

Using this weight function approach the predictions are highly improved. The statistical analysis gives $\%E\bar{\sigma}_{eq.}^{C*} = 1\%$ and $\%V\bar{\sigma}_{eq.}^{C*} = 6\%$. However, as shown in Fig. 7b, the "k" coefficient highly depends on the volume dimension over which the hydrostatic stress gradient is computed. The smaller the ℓ value, the higher the stress gradients, and smaller the k factor is. This suggests that the methodology must be calibrated keeping constant the ℓ dimension from the identification of the weight function to the structural fatigue analysis. By contrast, the R^2 coefficient is very stable which indirectly support the stability of this approach. Theses tendencies are confirmed by Figure 8, where using extensive computations, both "k and R^2" variables are plotted versus ℓ variable. The k variable can be expressed using a very simple power function at least for the studied cylinder/plane contact:

$$k = 5.10^{-3} \cdot \sqrt{\lambda} \tag{7}$$

Besides, the related R^2 coefficient remains unchanged around 0.85 whatever the ℓ value. Hence, it can be intuited that such approach could be transposed for any low spatial stress field resolution like observed in industrial FEM contact analysis. Fixing the ℓ variable equal for instance to the FEM contact mesh size and calibrating the related k weight function factor, very good prediction of the crack risk are expected.

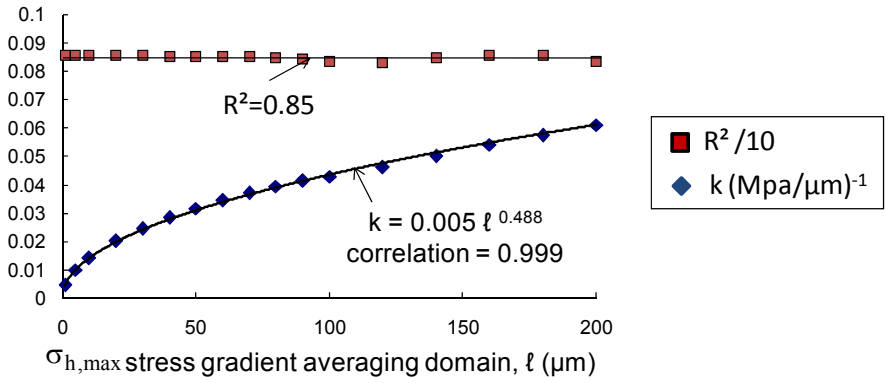

Figure 8: evolution of the k coefficient and related R^2 correlation factor as a function of the length scale ℓ.

5. Conclusion

A combined experimental and Crossland multiaxail fatigue approach is developed to rationalise the crack nucleation risk induced by plain fretting and fretting fatigue loadings. It shows that due to the very stress grading imposed by the contact stressing, a local “hot spot” fatigue stress analysis is not suitable. The application of the critical distance approach based on the Taylor’s formalism improves the prediction but still display high dispersion. Finally, the non local “weight function” approach provides very consistent and stable predictions. This analysis shows that the “k” factor defining weight function is highly dependent on the ℓ length scale variable over which the hydrostatic stress gradient is computed. We show a variation of the k factor versus the ℓ length variable. Finally, we confirm that the stability of this approach according that the related R^2 correlation factor remains high and constant (i.e. above 0.85) over the whole studied ℓ length (i.e. up to 200μm). This stability regarding the spatial stress resolution suggests that, this approach could efficiently be transposed in coarse industrial FEM contact meshing to achieve pertinent fretting cracking predictions.

References

[1] R.B. Waterhouse, Fretting Fatigue, Applied Science publishers, 1981.
[2] M.P. Szolwinski, T.N. Farris, Mechanics of fretting crack formation. Wear 1996;198:93-107.
[3] S. Fouvry, Ph. Kapsa, F. Sidoroff, L. Vincent, Identification of the characteristic length scale for fatigue cracking in fretting contacts. J. Phys. IV France 1998; 8: 159-166.
[4] J.A. Araújo, D. Nowell, The effect of rapidly varying contact stress fields on fretting fatigue. International Journal of Fatigue 2002; 24 (7): 763-775.
[5] S. Fouvry, K. Kubiak, Development of a fretting–fatigue mapping concept: The effect of material properties and surface treatments, Wear, 267(2009) 2186–2199
[6] IV. Papadopoulos. Int J Fatigue 2001;23:839–49.
[7] R. Amargier, S. Fouvry, L. Chambon, C. Schwob, C. Poupon, , Int. J of Fatigue,2010, 32 (12) : 1904-1912.
[8] L.J. Fellows, D. Nowell, DA. Hills, On the initiation of fretting fatigue cracks. Wear 1997;205:120–9.
[9] KL. Johnson, Contact Mechanics, Cambridge University Press,1985.
[10] H. Proudhon, S. Fouvry, J.-Y. Buffière, A fretting crack initiation prediction taking into account the surface roughness and the crack nucleation process volume. International Journal of Fatigue,2005; 27(5):569-579.
[11] D. Nowell, D.A. Hills,Mechanics of fretting fatigue tests, Int. Jnl. Mech. Sci., 1987, 29, 5: 355-365
[12] B. Crossland, Proceeding of the Inter. Conf. On Fatigue of Metals, Inst. of Mechanical Engineers, London, 1956, pp. 138-149.
[13] D. Taylor D. Analysis of fatigue failures in components using the theory of critical distances. Engng Fail Anal 2005;12:906–14.

Analysis of the multiaxial fatigue strength at the mesoscopic scale using 3D microstructure modeling and extreme value statistics

Anis Hor[1,*], Nicolas Saintier[1], Camille Robert[2], Thierry Palin-Luc[1], Franck Morel[2]

[1] Arts et Métiers ParisTech, I2M - CNRS, Esplanade des Arts et Métiers 33405 Talence, France
[2] Arts et Métiers ParisTech, LAMPA, 2 bd du Ronceray 49035 Angers, France
* Corresponding author: anis.hor@ensam.eu

Abstract Fatigue life computing methods are generally based on putting into equation the mechanical quantities calculated at the micro or meso scale, the relevance of these selected quantities being validated by the capacity of the models to reproduce experimental results at the macroscopic scale. Although the scaling of the damage mechanisms involved in fatigue crack initiation processes are relatively well identified (grain scale, slip bands), their explicit consideration in fatigue criteria is still not well-developed. Furthermore, the existing methods do not consider the microstructure-sensitivity. The aim of this paper is to present the computational strategies developed to account for the microstructure-sensitivity in the calculation of fatigue strength. This work is based on three parts: (1) the development of 3D microstructure modeling tools (2) the analysis of the dispersion induced by the microstructure heterogeneities on the critical fatigue damage indicators and (3) the development of a statistical approach which provides a framework for analyzing calculation results in the HCF (High Cycle Fatigue) regime.
In this context, a method based on the construction of statistical extreme value distributions from FEA calculation results was developed. The evolution of the scaling parameters of these distributions for different loading conditions is related to the effect of non-proportional loading and microstructure. A design method based on these extreme value statistics is presented to obtain a new mesoscopic criterion sensitive to microstructure parameters. Finally, surface effects are discussed.

Keywords HCF, crystal plasticity, extreme value probability, FE simulation.

Abbreviation and designation

HCF:	*High Cycle Fatigue*
FIP:	*Fatigue Indicator Parameter*
RVE:	*Representative Volume Element*
SVE:	*Statistical Volume Element*
GEV:	*Generalized Extreme Value distribution*
Microscopic length scale:	*corresponding to the integration points*
Mesoscopic length scale:	*Corresponding to the average density in a grain*
Macroscopic length scale:	*Corresponding to the elementary volume average*

1. Introduction

In literature, methods for determining the fatigue behavior based on multiscale modeling estimate that the fatigue strength of metals depends on the extreme value statistics of a single microstructure

attribute [1] (for example inclusion size). This is only valid when the considered element of microstructure is a representative volume element (RVE) with regards to fatigue. Although the definition of the RVE is possible for some deterministic behaviour aspects (such as elastoplastic behaviour), it is difficult to evaluate a RVE for the HCF strength which is macroscopically highly dispersed. Therefore the use of a single microstructure element (with a smaller volume than the RVE with regards to the fatigue behaviour but equal to the RVE size with regards to the elastoplastic behaviour) does not make it possible to take into account the contribution of the microstructure heterogeneities in the HCF response. To solve this issue, Liao [2] used the Monte Carlo method to build statistical volume element (SVE) of a microstructure with a random distribution of grain sizes and crystallographic orientations. Despite considering elastic behaviour of crystal only, Liao showed a good correlation between the results obtained by modeling the extreme value probability with a Fréchet distribution and experimental results. Recently, Przybyla et al. [3, 4] introduced a new framework taking into account the effects of neighborhood through the extreme values of the marked correlation functions to quantify the influence of microstructure on the fatigue limit and the contribution of interactions in the microstructure in the case of uniaxial loading. Przybyla used Gumbel distribution function to describe the extreme value probability of the studied parameters.

The purpose of this work is, first, to analyze the microstructure sensitivity (morphology and orientation) of the fatigue indicator parameter (FIP) corresponding to the adaptation of multiaxial fatigue strength criteria at the mesoscopic length scale. Then a statistical study is used to define new mesoscopic thresholds for the FIPs, different from the original thresholds of the macroscopic criteria. Finally, the capability of the macroscopic criteria to take into account the microstructure sensitivity will be discussed through a comparison between the thresholds determined by the statistical response of the microstructure at the grain scale (called mesoscopic) and the original macroscopic thresholds. Free surface effects are also discussed with the comparison between FIPs determined from different FE models: 2D, 3D and 3D taking into account the grain surface only.

2. Numerical model

2.1. Constitutive relations

The material parameters considered in this work are those of pure copper. This material has a face-centered cubic crystal structure with 12 slip systems (<111> {110}). The behaviour is modeled by cubic elasticity and crystal plasticity constitutive law. The crystal plasticity model used in this work is the one introduced by Meric and Cailletaud [5]. The cubic elasticity constants, the material parameters and the coefficients of the interaction matrix have been identified on a high purity copper by Gérard et al. [6].

2.2. Grain morphology and crystallographic texture

The simulations performed in this study were done using 3D semi-periodic microstructures (periodicity along X_1 and X_2 directions). The Voronoï polyhedra method was used to model the morphology of the grains. The initial domain (with dimensions x_1=1, x_2=1 and x_3=0.5) is filled by

randomly positioned and oriented germs so as to have a distance greater than or equal to 0.02 between two germs. The CAD model was discretized by around to 5.10^5 linear tetrahedral finite elements (figure 1-(b)). Computed microstructure contains 200 equiaxed grains (figure 1-(a)) with an average of 2500 finite elements per grain. In addition to loading, periodicity conditions were applied on the planes corresponding to X_1min, X_1max, X_2min and X_2max. To take into account the free surface effect, the symmetry conditions were applied on the face corresponding to X_3min. The grain number on the free surface (corresponding to X_3max) is about 50. Finally, the random selection of 200 crystal orientations was carried out in the Euler space defined by the three angles $(\varphi_1, \phi, \varphi_2)$ assuming cubic crystal symmetry and triclinic sample symmetry. Figure 1-(c) shows the {100} and {110} pole figures of these 200 orientations. Given the low number of orientations, this crystallographic aggregate can be considered as having no preferential orientations.

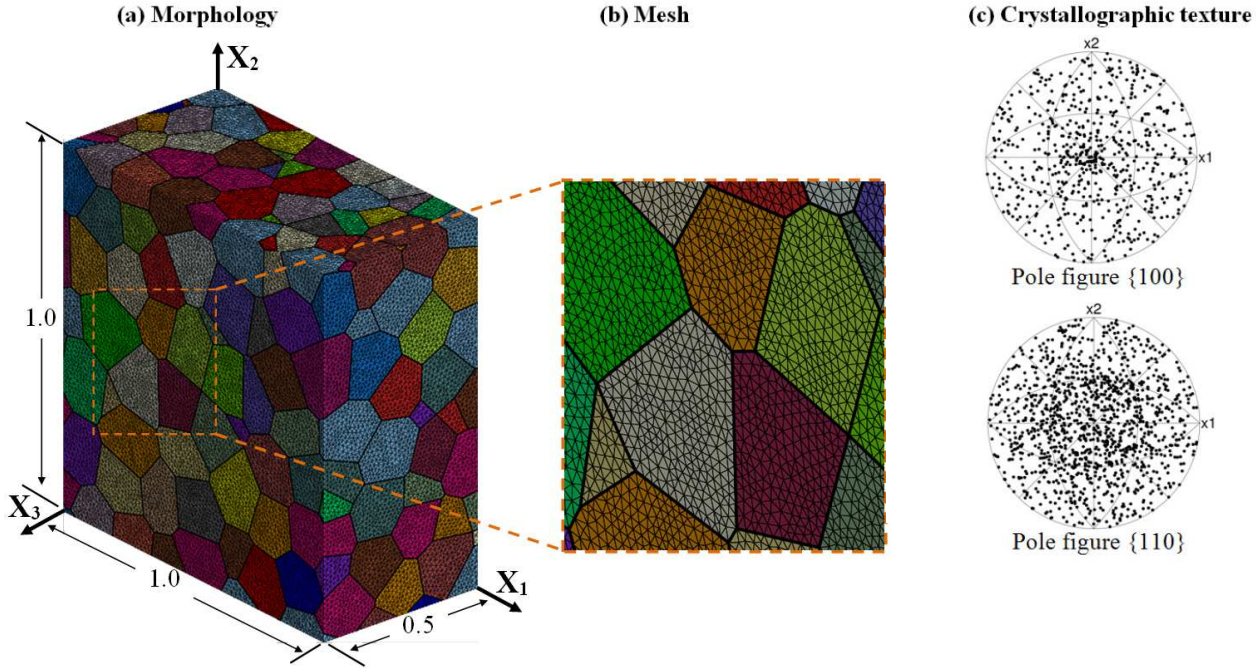

Figure 1. (a) Grain morphology, (b) Mesh and (c) {100} and {110} pole figures showing the selected crystallographic orientations

2.3. Fatigue loading conditions

Different loading conditions are investigated in this section: uniaxial loading, and tension /torsion loadings with different biaxiality ratios $k = \sigma_a / \tau_a$ and different phase shifts. The selected loading ratio is $R_\Sigma = \sigma_{a,\min} / \sigma_{a,\max} = -1$. The combined loading levels equivalent to the median fatigue limit at 10^7 cycles are determined using the Crossland criterion [9]. These load levels are given in Table1.

Table 1. Tension (σ_a) and torsion (τ_a) stress amplitude used for different load conditions

	loading	**Tension**	**Torsion**	**Combined loading** $\sigma_a[MPa]/\tau_a[MPa]$		
Phase shift	biaxiality	$k=0$	$k=\infty$	$k=0.5$	$k=1$	$k=2$
	$\varphi=0°$	56/0	0/36	43.5/22	30/30	17/34
	$\varphi=45°$			47/23	31/31	17/34.5
	$\varphi=90°$			56/28	34/34	17.5/35

3. Mesoscopic fatigue indicator parameters

The studied fatigue indicator parameters (FIPs) were selected from stress criteria widely used in the literature. The multiaxial HCF criteria considered here are Crossland [9], Matake [10] and Dang Van [11]. These fatigue criteria are generally defined in the context of continuum mechanics. In order to evaluate the fatigue criterion on each computed microstructures, the usual HCF criteria are projected on the slip systems of the crystals. This procedure is repeated for each crystal considering its local orientation (φ_1,ϕ,φ_2) and local stress state computed by FE for each loading case. For instance, the shear stress vector in a given plane is transformed into a resolved shear stress vector over a slip system. The rotation of the crystal in space (defined by the Euler angles (φ_1,ϕ,φ_2)) covers all the planes and directions of space, which enables to find the same critical planes and directions (planes and directions maximizing the criterion) than those obtained by the original criterion (with continuous formulation). Table 4 gives FIP expressions adapted to the crystal scale.

Table 2. Expression of Fatigue Indicator Parameters (FIPs) of the studied criteria

Criterion	I_i	α_i
Crossland	$I_c=\tau^s_{oct,a}+\alpha_c\sigma_{hyd,\max}\le\beta_c$	$\alpha_c=\dfrac{t_{-1}-\left(s_{-1}/\sqrt{3}\right)}{\left(s_{-1}/3\right)}$
Matake	$I_m=\max\limits_{s=1,12}(\tau^s_a)+\alpha_m\sigma_{s,\max}\le\beta_m$	$\alpha_c=2\dfrac{t_{-1}}{s_{-1}}-1$
Dang Van	$I_{dv}=\max\limits_{s=1,12}(\max\limits_t[\left\|\hat{\underline{\tau}}^s(s,t)\right\|+\alpha_{dv}\sigma_{hyd}(t)])\le\beta_{dv}$	$\alpha_{dv}=\dfrac{t_{-1}-\left(s_{-1}/2\right)}{\left(s_{-1}/3\right)}$

Finally, the parameters α_i and β_i describing the median macroscopic threshold of the considered criteria are identified from two median fatigue limits for 10^7 cycles of the considered material on smooth specimens under fully reversed loadings: tension ($s_{-1}=56\ MPa$) and torsion ($t_{-1}=36\ MPa$)

from the work of Lukas and Kunz [12]. The parameters β_i are identical for the three criteria ($\beta_c = \beta_m = \beta_{dv} = t_{-1}$). The expression of α_i are given in Table 2.

A comparison between the mesoscopic FIPs predictions and the macroscopic (original) criteria is shown in Figure 2. This comparison shows the existence of grains at the surface (highlighted in light blue) or in the bulk of the volume element from which the FIP exceeded the macroscopic threshold. The macroscopic threshold is not applicable at the grain scale. This is especially true for the Crossland criterion where most of the grains are above the threshold. For other criteria, only a small number of grains exceeded the macroscopic threshold. A statistical analysis of the microstructure-sensitivity of the different FIPs will be presented in the next section. This statistical analysis will determine a new mesoscopic threshold to take into account the microstructure heterogeneities.

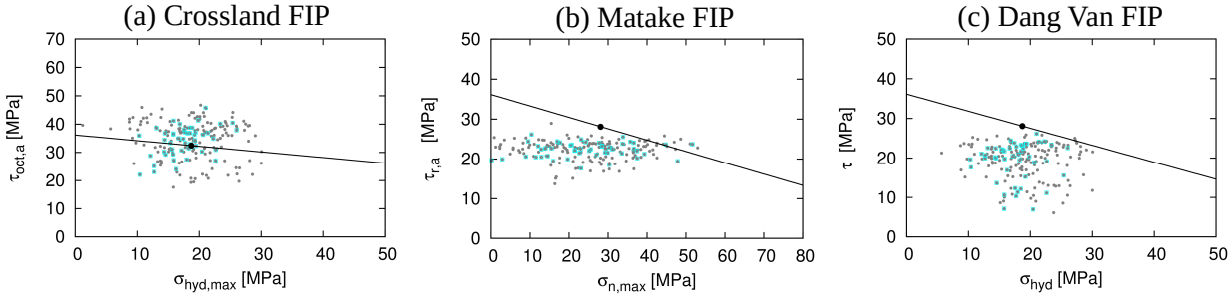

Figure 2. Locus of the 200 FIPs at the grain length scale (gray dots), and macroscopic criterion (black dot) in the case of tension loading ($R_\Sigma = -1$). The FIPs corresponding to the surface grains are highlighted (in light blue) and the black straight line is the experimental macroscopic threshold

4. Microstructure sensitivity

The HCF strength is related to the critical grain whose response leads to the maximum value of the FIP. These extreme values are located at the tails of the probability density functions of mesoscopic responses (see Figure 3) and are highly sensitive to the microstructure attributes. To study these critical grains, several statistical approaches are possible. The method selected for this work was based on the extreme value probability. This method involves the statistical analyze of the maximum values of the mesoscopic FIP, corresponding to the various studied volume element, by considering a single value for each aggregate.

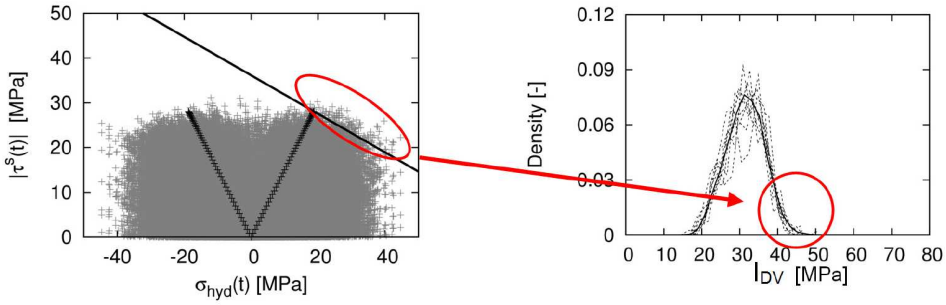

Figure 3. Localization of the extreme values in the tails of the Dang Van FIP distribution

The extreme value database was constructed by identifying the maximum value of FIP for each statistical volume element (SVE). The number of SVEs was between 25 and 35: they were obtained by the combination of 7 random morphologies (Figure 4-(a)) and 5 isotropic textures (Figure 4-(b)). This sample size is sufficient to determine the extreme values distribution function. Indeed Przybyla showed that from a number of SVEs greater than 20, the difference between the empirical distribution and the experimental sample becomes negligible [3, 4]. The maximum value of FIP has been determined on the one hand from the FIP concerning all the grains of the SVE and on the other hand by separating only the surface grains of the aggregate.

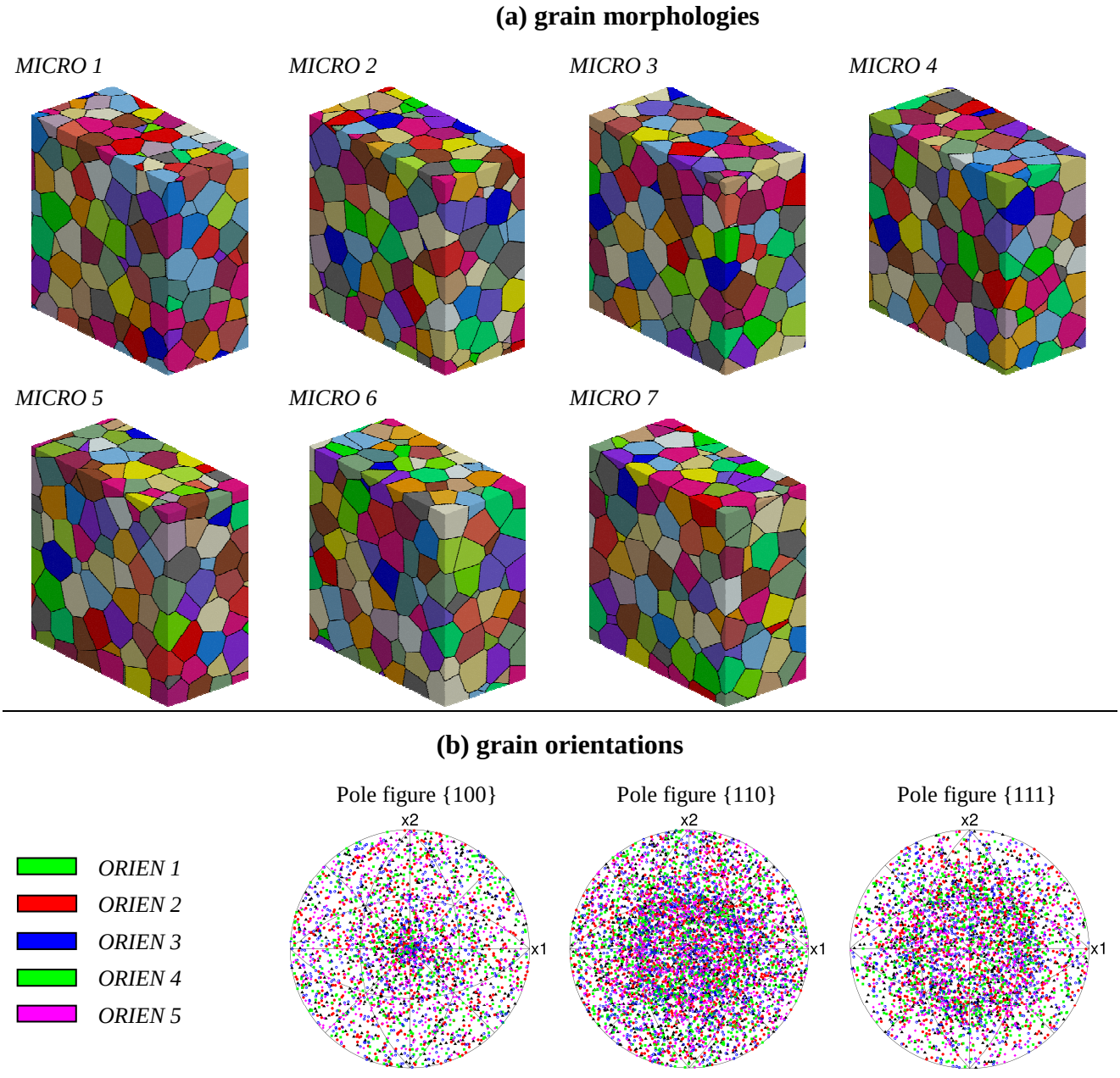

Figure 4. (a) random morphologies and (b) isotropic textures used to create the extreme values database

5. Generalized extreme values probability

Let us consider a random variable x with the distribution function $F_X(x)$. The n extreme realizations in n samples of the random variable can be defined as:

$$Y_n = \max(X_1, X_2, ..., X_n) \tag{1}$$

The distribution function of Y_n is defined as:

$$F_{Y_n}(y) \equiv P(Y_n \le y) = P(X_1 \le y, X_2 \le y, ..., X_n \le y) \tag{2}$$

According to the *Fisher-Tippet theorem*, if there exist two real normalizing sequences $(a_n)_{n\ge1}$, $(b_n)_{n\ge1}$ and a non-degenerated distribution (not reduced to a point) G so that:

$$P\left(\frac{Y_n - b_n}{a_n} \le x\right) = F^n(a_n x + b_n) \underset{n\to+\infty}{\longrightarrow} G(x) \tag{3}$$

G is necessarily one of the three types of distributions: Fréchet, Weibull or Gumbel.
Jenkinson [13] combined the three limit distributions in a single parametric form called Generalized Extreme Value (GEV) distribution depending on a single parameter ξ:

$$G_\xi(x) = \begin{cases} \exp\left(-(1+\xi x)^{-\frac{1}{\xi}}\right) & si\ \xi \ne 0, \forall x / 1+\xi x > 0 \\ \exp(-\exp(-x)) & si\ \xi = 0 \end{cases} \tag{4}$$

The ξ parameter is called extreme index. Its sign indicates the type of asymptotic distribution: Weibull ($\xi < 0$), Gumbel ($\xi = 0$) or Fréchet ($\xi > 0$). The variable $(Y_n - b_n)/a_n$ is called normalized maximum of the random variable x.The parameters a_n and b_n are also called shape factors of the distribution.

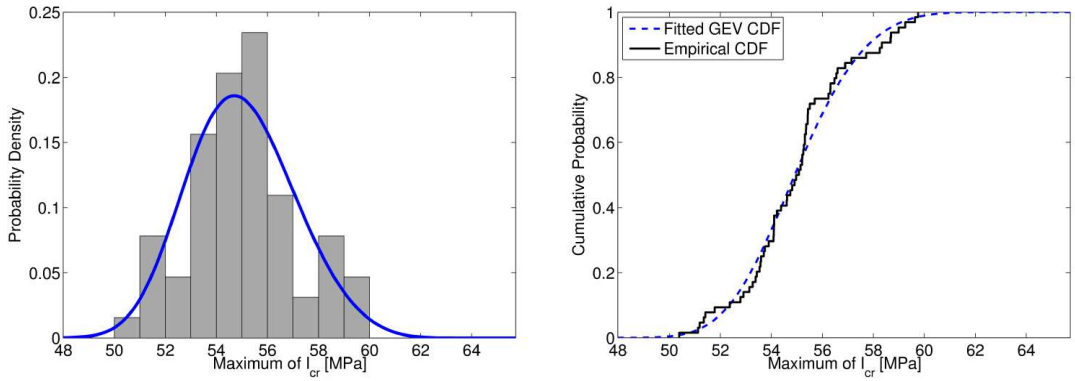

Figure 5. Probability density and cumulative probability determined using the maximum likelihood method from the extreme values of Crossland FIP for tensile loading ($R_\Sigma = -1$)

We are interested in the maximum values of different FIPs listed in Table 2. Scale factors (a_n and b_n) and extreme index ξ are determined using the maximum likelihood method with a confidence interval of 99%. Figure 5 shows a comparison between the determined distributions and the samples for the Crossland FIP. The identified GEV density function and distribution function showed a good correlation with the probability density and the cumulative probability determined from the extreme values of FIPs database.

6. Results and discussions

Figure 6 represents the mesoscopic thresholds (medians and also the values of 0.1 and 0.9 quantiles) for each loading condition. The mesoscopic thresholds are statistically determined from the FIPs at the grain scale considering the local stress state. This local stress state is computed by a finite element (FE) simulation. A comparison between the mesoscopic thresholds obtained by considering a 3D FE model (described above) and a 2D FE model [14] is presented in this figure.

The mesoscopic thresholds are normalized by the macroscopic threshold to analyze the effect of microstructure variability. Referring to figure 6, for all studied loading conditions and studied FIPs, the normalized mesoscopic thresholds were always larger than 1 in the case of the local stress state computed by 2D FE model [14]. When the local stress state is determined by a 3D model, the mesoscopic threshold determined from all grains decreases for Matake and Dang Van criteria, and increases slightly in the case of Crossland criterion. When considering all the grains (bulk + surface), this threshold is higher for Crossland criterion and is close to 1 for Matake criterion and especially for Dang Van criterion. The mesoscopic threshold determined by considering only the surface grains becomes lower than the macroscopic threshold for Dang Van criterion. This is not verified for the other two criteria. This comparison highlights the ability of the Dang Van criterion to reflect the microstructural heterogeneities compared to the two other criteria.

On the other hand, the mesoscopic thresholds, defined as the medians of the extreme value distribution of the studied FIPs depend on the loading case. This gap depends on the studied FIP: it is low in the case of the Crossland and Dang Van FIPs (Figure 6-(a) and (c)) and significant in the case of the Matake FIP (Figure 6-(b)). For this last FIP, the change in mesoscopic thresholds was observed especially for the biaxial loading with a phase shift of 90°.

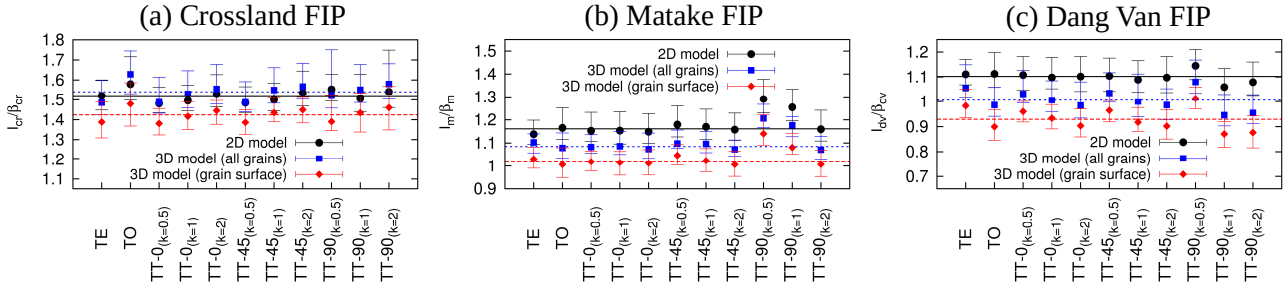

Figure 6. Evolution of the median (a probability of 0.50) of the extreme value distributions of (a) Crossland, (b) Matake and (c) Dang Van FIPs, as a function of loading conditions determined by 2D (in black), and 3D (in blue and red) FE model. The two limits of the interval correspond to a probability of 0.10 and 0.90.

Finally, the mesoscopic threshold, common to all the loading cases was determined as the average of the thresholds associated to each loading conditions. This mesoscopic average threshold is shown in Figure 6 by the dashed horizontal lines passing through all intervals bounded by the values of 0.1 and 0.9 quantiles in the case of Crossland and Van Dang FIPs. For Matake FIP, this was also true except for the case of biaxial loadings with a phase shift of 90° due to the reasons mentioned above.

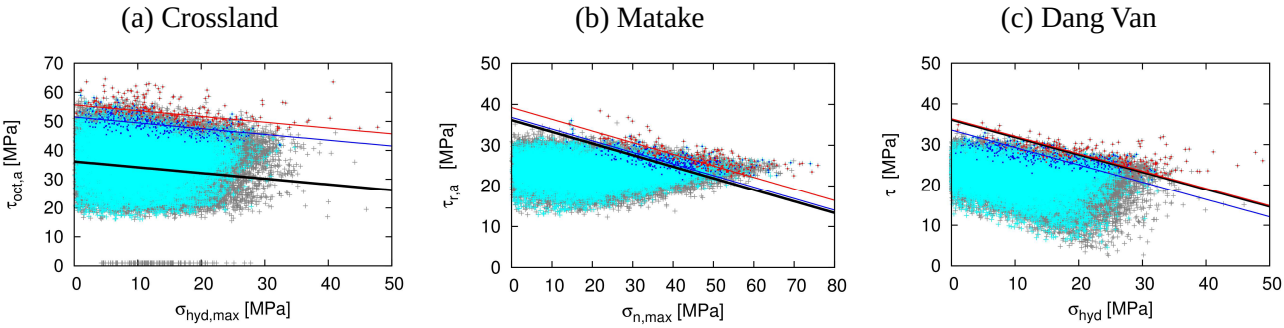

Figure 7. Predictions from (a) Crossland, (b) Matake and (c) Dang Van at the macroscopic length scale (black line) and the mesoscopic length scale considering all grains (gray dots) and surface grains (gray dots).

The mesoscopic threshold of different FIPs is the average (over the different loading conditions) of the medians of the extreme value distributions. Keeping the same value for the α_i parameter, the new criterion containing microstructural heterogeneities contribution at the mesoscopic length scale is plotted in Figure 7. This Figure illustrates for each criterion two mesoscopic thresholds : the first was determined from all the grains of the aggregate (red line) and the second was computed by considering only the surface grains. When the mesoscopic threshold is close to the macroscopic one (black line), the microstructure heterogeneities are taken into account by the original criterion. This is especially the case of Dang Van criterion, when the mesoscopic threshold determined for all the aggregate grains is equal to the macroscopic thresholds, and to a lesser extent the case of Matake criterion (Table 3). For the Crossland criterion, the distance between the two straight lines is important in the case of thresholds determined from all the grains and from the surface grains (table 3). This comparison shows that critical plane type approaches can capture the microstructure heterogeneity despite simplifying assumptions [11].

Table 3. Values of macroscopic thresholds and mesoscopic thresholds obtained by 2D and 3D FE modeling

Criterion	**Macroscopic Thresholds**	**Mesoscopic Thresholds**		
		2D model (all grains)	3D model (all grains)	3D model (surface grains)
Crossland	36.15	54.78	55.68	51.48
Matake	36.15	41.97	39.21	36.82
Dang Van	36.15	39.81	36.36	33.59

7. Conclusion

From polycrystalline modeling of pure copper coupled with a statistical study of the critical grains, we analyzed the mesoscopic responses of the multiaxial fatigue criteria, widely studied in the literature (Crossland, Matake and Dang Van). This statistical study allows us to introduce microstructural heterogeneities effect in the variability of the fatigue strength.

The comparison between the mesoscopic predictions of these criteria and the macroscopic (original) ones shows that they are not conservative at the grain scale. Indeed the identification of macroscopic parameters of these criteria does not take into account variations of the strain field at the microstructure scale. The proposed method, based on extreme value statistics, consists in readjusting these parameters on the most critical grain computed from FE calculations. These critical grains are located in the tails of the aggregate response distributions. The determination of the different distributions allowed us to define a new mesoscopic threshold for the studied criteria.

These thresholds are the average of the medians of the extreme value distributions related to the different loading conditions. These thresholds are different or similar to the macroscopic thresholds depending on the considered criterion. For Dang Van, the mesoscopic threshold is equal to the macroscopic value of the fatigue indicator parameter. At the opposite, for Crossland, the ratio between meso and macro thresholds is greater than 1.4. Matake criterion has a ratio of around 1.1.

Finally, except for the biaxial loading with a phase shift of 90° where FIP median values are very different from one criterion to another, the mesoscopic thresholds is almost the same for all the loading conditions. Thus, these new mesoscopic thresholds can therefore be determined by applying a single loading case.

References

[1] H.V. Atkinson and G. Shi. Prog. in Mater. Sci., 48: 457-520, 2003.
[2] M. Liao. Eng. Frac. Mech., 76: 668-680, 2009.
[3] C. P. Przybyla, R. Prasannavenkatesan, N. Salajegheh, and D. L. Mc-Dowell. Int. J. of Fatigue, 32(3): 512-525, 2010.
[4] C. P. Przybyla and D. L. McDowell. Int. J. of Plasticity, 26(3): 372-394, 2010.
[5] L. Meric and G. Cailletaud. J. of Eng. Mater. and Tech., 113(1): 171-182, 1991.
[6] C. Gérard, F. N'Guyen, N. Osipov, G. Cailletaud, M. Bornert, and D. Caldemaison. Comput. Mater. Sci., 46(3): 755-760, 2009.
[7] C. Robert, N. Saintier, T. Palin-Luc, and F. Morel, Méca. et Indus., 209-214, 2011.
[8] C. Robert, N. Saintier, T. Palin-Luc, and F. Morel, Mech. of Mater., 55: 112-129, 2012.
[9] B. Crossland. Proceedings of the Inter.Conf. on Fatig. of Met., 138-149, London 1956.
[10] T. Matake. Bulletin of the JSME, 141:257–263, 1977.
[11] K. Dang Van, B. Griveau, and O. Message. Mech. Eng. Publi. London, 479-496, 1989.
[12] P. Lukás and L. Kunz. Int. J. of Fatigue, 11(1): 55-58, 1989.
[13] A.F. Jenkinson. Quaterly Journal of the Royal Meteorological Society, 81, 1955.
[14] A. Hor**,** N. Saintier, C. Robert, T. Palin-Luc and F. Morel, 19TH European Conference on Fracture (ECF19), kazan (Russia), 2012.

Fretting fatigue analysis on nuclear fuel cladding tubes

Lichen Tang, Shurong Ding, Yongzhong Huo*

Department of Mechanics and Engineering Science, Fudan University.
220 Handan Road, Shanghai 200433, China.
* Corresponding author: yzhuo@fudan.edu.cn

Abstract

Grid-to-rod fretting failure due to fuel rod vibration remains as a significant cause of nuclear fuel failure in pressurized water reactors (PWRs). In order to carry out fretting fatigue tests to tube shaped specimens, a special designed apparatus was developed. The strain-life curve of the Zr-4 tube specimen under some given fretting contact pressure is obtained. It is found that the fatigue life of the Zr-4 tube under fretting contact conditions can be substantially lower than its life without fretting. The fretting wear scars and fatigue cracks were analyzed by microscope. The results show that the initial crack does not occur at the middle of the contact area where the wear depth reached the maximum, but at the edge of the initial contact area. where the amplitude of stress is confirmed to reach the maximum by FEM simulation. The position of crack nucleation can be predicted by half-length of the initial contact region and the slip displacement.

Keywords: Fretting fatigue test, Tube specimen, Nuclear fuel cladding tube, Fretting fatigue nucleation.

1. Introduction

Fretting is a special wear process that occurs at the contact area between two materials under loads and subject to minute relative motions by vibrations or some other forces. Fretting decreases the fatigue strength of materials operating under cycling stresses [1, 2]. The fretting fatigue phenomenon is very complex because there are too many factors that can affect the fretting behavior of materials [3]. A number of studies were taken to analyze the effects of various parameters on the fretting damage, such as the contact pressure [4-6], the amplitude of slip displacement [4], the coefficient of friction [5] and the nature of contact [7, 8]. For various materials, both experimental and numerical methods are taken to analyze the fretting damage [6, 9-11, 15]. Bridge-type fretting pads were used in many fretting fatigue experiments to produce contact in two places on each side of the specimen [6, 13, 14]. The pair of bridges and its load cell had to be hung on the specimen during the test by friction, thus a large clamping force and a flat contact were a must. Petiot [9] bolted one foot of the bridge to the end of the specimen and reduced the clamping force to a value of 100N. Similar apparatus were developed for the cases of point contact, such as cylinder-cross-cylinder and sphere-on-flat. The advantages of two arrangements of specimens and fretting bridges were discussed by Waterhouse [17].

Grid-to-rod fretting failure due to fuel rod vibration remains as a significant cause of nuclear fuel failure in pressurized water reactors (PWRs) [16]. The fuel rods are supported by the friction forces between the fuel rods and the springs or dimples of the grids in a fuel assembly as shown in Fig.1. When the reactor operates, the coolant flows through the surface of the fuel rods, and causes a flow-induced vibration (FIV) phenomenon, which is considered as the main driving force for fretting damage of the fuel rods. Fretting wear experiments of nuclear fuel cladding tubes were carried out by Kim [7] to study the effects of contact forces and slip displacements on fretting wear

under environment of air as well as water.

In this paper, both experimental and numerical researches are taken for fretting fatigue analysis on Zr-4 tube specimen. In section 2, fretting fatigue experiment device, design and results will be introduced. In section 3, a similar structure as experiment is analysis by FEM. Initial crack nucleation can be predicted.

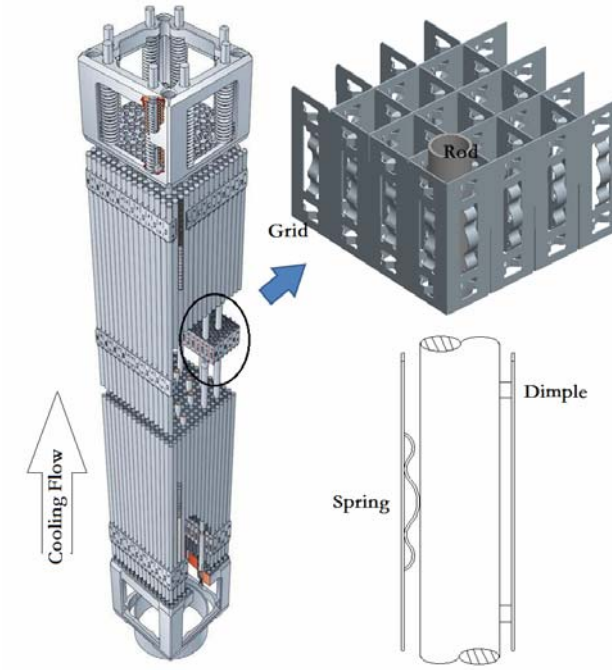

Figure 1. Grid-to-rod assembly

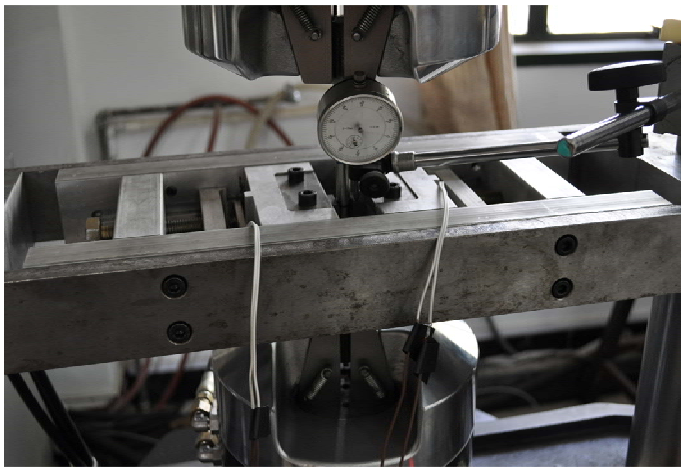

Figure 2. Fretting fatigue experiment device

2. Fretting Fatigue Experiment

2.1. Experiment Design

An experiment device is designed and added to a MTS fatigue testing machine, as shown in Fig. 2. It is assembled by several separated parts, and every part can be replaced for different experimental conditions. Compared with the bridge-type fretting apparatus, this kind of device is supported on the MTS machine directly but not hung on the specimen. A much smaller and stable contact force could be supplied. By using this device, fretting fatigue experiments can be made directly on tube specimens.

In our case, Zr-4 fuel rod cladding tubes (size Φ10mm×0.7mm×250mm) which are used in Chinese 300MWe reactors were tested as specimens. Its chemical composition is given in Table 1. As shown in Fig. 3, some necessary preventive measures were taken to make sure that there was no radial deformation neither any surface scars inside or outside the tube except the fretting point we expected. The contact force was set as 150N, and a constant amplitude displacement loading ($R_e=\varepsilon_{min}/\varepsilon_{max}$ =0.1) at a frequency of 10 Hz was applied. The contact geometry is a cylinder-cross-cylinder type. The pads are made of Cr12MoV Steel. The slip displacements (δ) between the pads and the specimen are determined by the imposed strain in specimen and the vertical motion of the pads during the tests measured by a dial indicator. For a maximum strain ε_{max} =0.4%, the slip displacement is 200 μm.

Table 1. Chemical composition of Zr-4 tube

Sn	Fe	Cr	O	Si	Al	C	Hf	N	Pb
1.30	0.22	0.11	0.13	0.0096	0.0051	0.0130	0.0053	0.0040	<0.0025

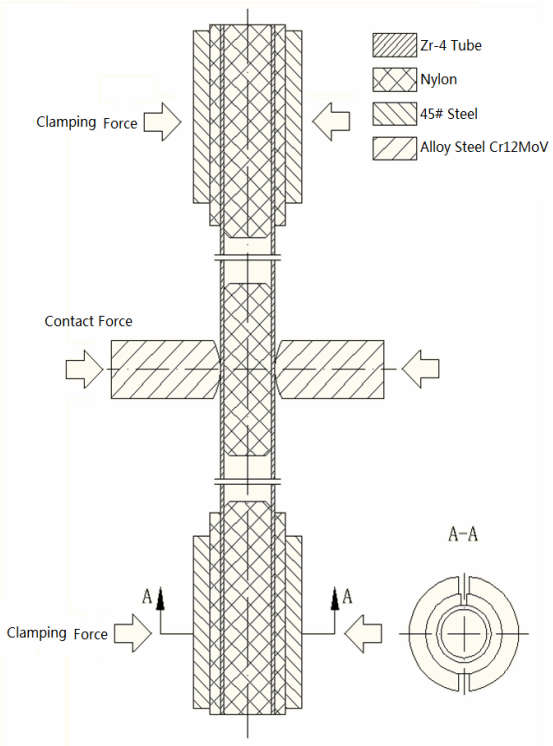

Figure 3. Geometry of assembled specimen

2.2. Experiment Results

Fig. 4 shows the fretting scars and cracks of two specimens for cases of maximum strain ε_{max}=0.6%. Ellipse fretting scars are made after 10^4 cycles. And the crack does not occur at the middle of the contact area where the wear depth reached the maximum, but at the edge of the initial contact area. Fig. 5 shows the comparison between fatigue S-N curve of the standard specimens and fretting fatigue S-N curve of the tube specimens. σ_{max} is the maximum engineering stress calculated by the measured force and the area of the section, σ_{min} is the minimum one, and $\Delta\sigma=\sigma_{max}-\sigma_{min}$ is the amplitude of the stress. N_f is the number of cycles when the specimen cracks. It is illustrated that the influence of fretting on the fatigue resistance occurs above 10^4 cycles and becomes stronger in higher cycle fatigue situation. The fretting decreases fatigue strength of material above 50% after 10^5 cycles. For cases of ε_{max}=0.4~0.8% (specimen no.6~15), the results are listed in Table 2. l_1 and l_2 is the length of the fretting scars on two sides of the specimen, and d_1 and d_2 are the corresponding distances from the crack to the middle of the fretting wear scar. The mean value of d equals 0.52834mm, and variance of d equals 0.0416mm^2.

Figure 4. Fretting scars and cracks of specimen no.9 and no.10

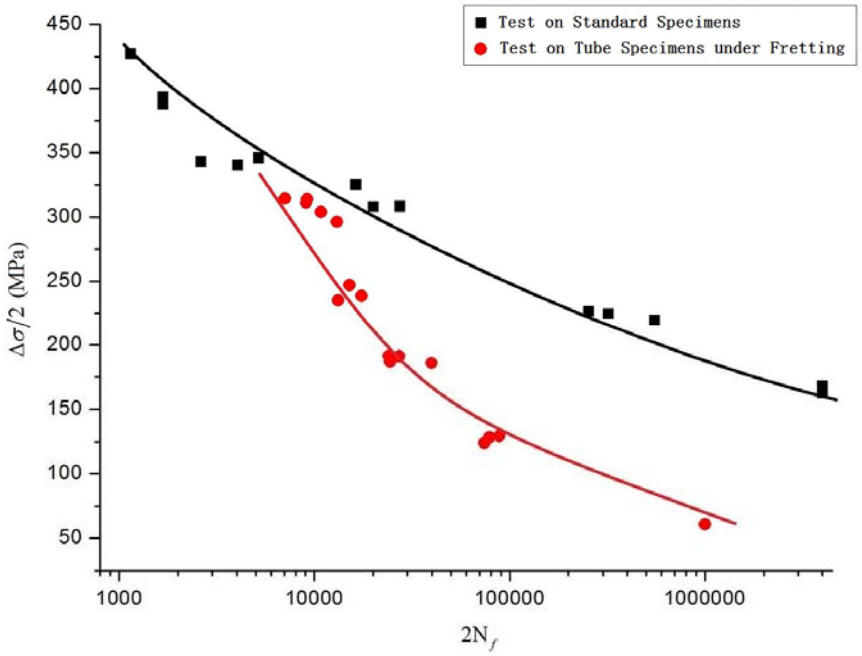

Figure 5. Comparison between fatigue S-N curve of the standard specimens and fretting fatigue S-N curve of the tube specimens

Table 2. Length of the wear scars and distance from the crack to the middle of the fretting wear scar

Specimen No.	l_1 (mm)	d_1 (mm)	l_2 (mm)	d_2 (mm)
6	2.3346	0.7933	2.4620	0.0726
7	2.6682	0.7525	2.3803	0.5883
8	2.4273	0.3545	2.3914	0.4456
9	2.4506	0.7165	2.5363	0.0740
10	2.5883	0.7197	2.5820	0.7666
11	2.5391	0.6570	2.4372	0.4760
12	2.7890	0.6986	2.5711	0.4131
13	2.2308	0.5218	2.3587	0.3494
14	2.2524	0.5993	2.1378	0.5708
15	2.3581	0.3850	2.2173	0.6122

3. FEM simulation

3.1 FEM model

Because of the symmetry of the structure, a quarter model of pad-on-tube structure is employed as shown in Fig. 6. The size of the tube is Φ10mm×0.7mm×100mm. Symmetrical boundary condition is applied on plane XoZ and XoY. Clamped boundary condition is applied on plane YoZ. P is the applied contact pressure on the back of the pad. Dload is the displacement load on the top end of the tube. Fig. 7 shows that the applied contact pressure keeps 7.5MPa during the displacement load

cycles and Dload with an range of 0.04~0.4mm is applied, which can make a similar fretting situation as the test (ε_{max} =0.4%, δ=200 μm, Re=0.1). Both tube and pad are considered as isotropic linear elastic material. The material parameters are listed in Table 3. Several cycles' loading is necessary because of plasticity.

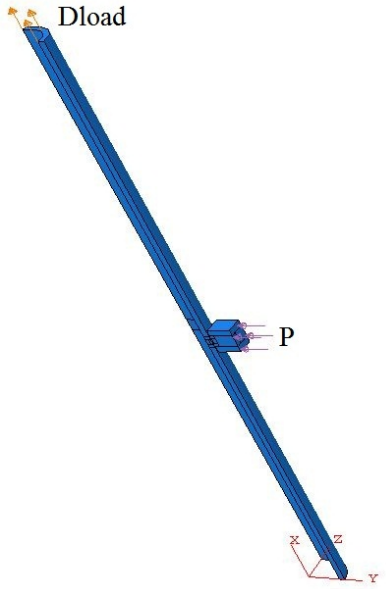

Figure 6. Quarter FEM model of pad-on-tube

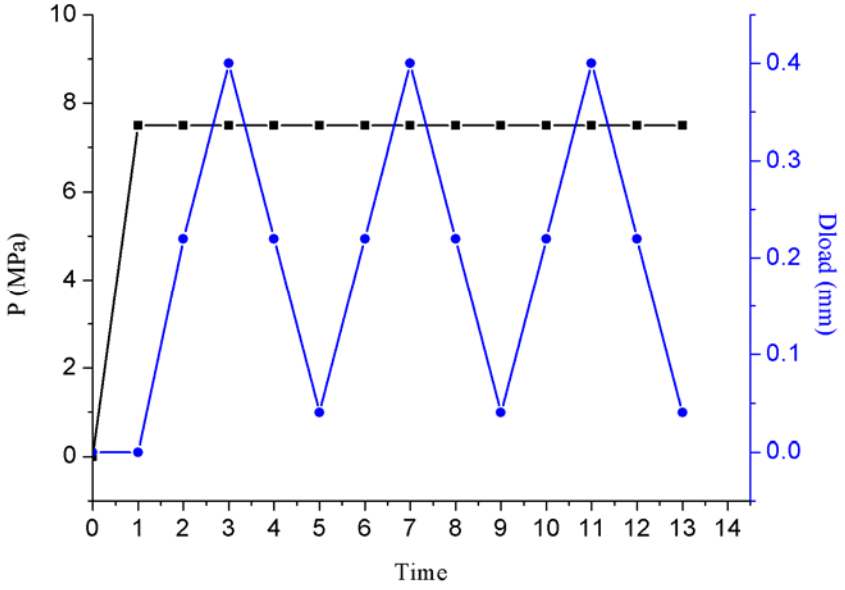

Figure 7. Applied contact pressure and displacement load

Table 3. Material Parameter

	Young's module	Passion's ratio
Tube	96GPa	0.43
Pad	206GPa	0.3

3.2 Simulation results

The contours of the contact pressure on the tube are plotted in Fig. 8 for different time steps. Fig. 8(a) shows that the initial contact region is an ellipse with a length of 600μm and a width of 480μm. Comparison of Fig. 8(a) and 8(b) shows that the contact region is moving with the increasing of the applied load. Fig. 9(a) and 9(b) shows the contact shear stress on the tube surface for the same Dload, but one is increasing and the other is decreasing. It is illustrated that the absolute value of the contact shear stress for the two cases are almost the same, but the directions of the friction force are the opposite. The contact pressures of path 1 for different times are shown in fig. 10. The contact region on the surface of the tube can be separated into two parts. One is always under the contact (noted as Region I in Fig. 10) and the other is scanned by the edge of the contact region during the cycles (noted as Region II in Fig. 10). The rest region of the tube surface is not under contact during the cycles (noted as Region III in Fig. 10). The separation of the contact surface is shown in fig. 11. σ_x is a periodic function with a same frequency of applied load. σ_x of three point from these three separated regions are shown in Fig.12. σ_x of point A keeps increasing in the loading process and decreasing in the unloading process. For the point B, the increasing of σ_x in the loading process is faster than in region I and reaches a maximum value when the edge of the contact region scans over it. And the decreasing of σ_x in unloading process is also faster than point A and reaches a minimum

value when the edge of the contact region scans over it again. For the point C, σ_x keeps negative during the loading and unloading process. Apparently, the amplitude of σ_x of the point B is much larger than the point A and the point C because of the scanning of the contact edge.

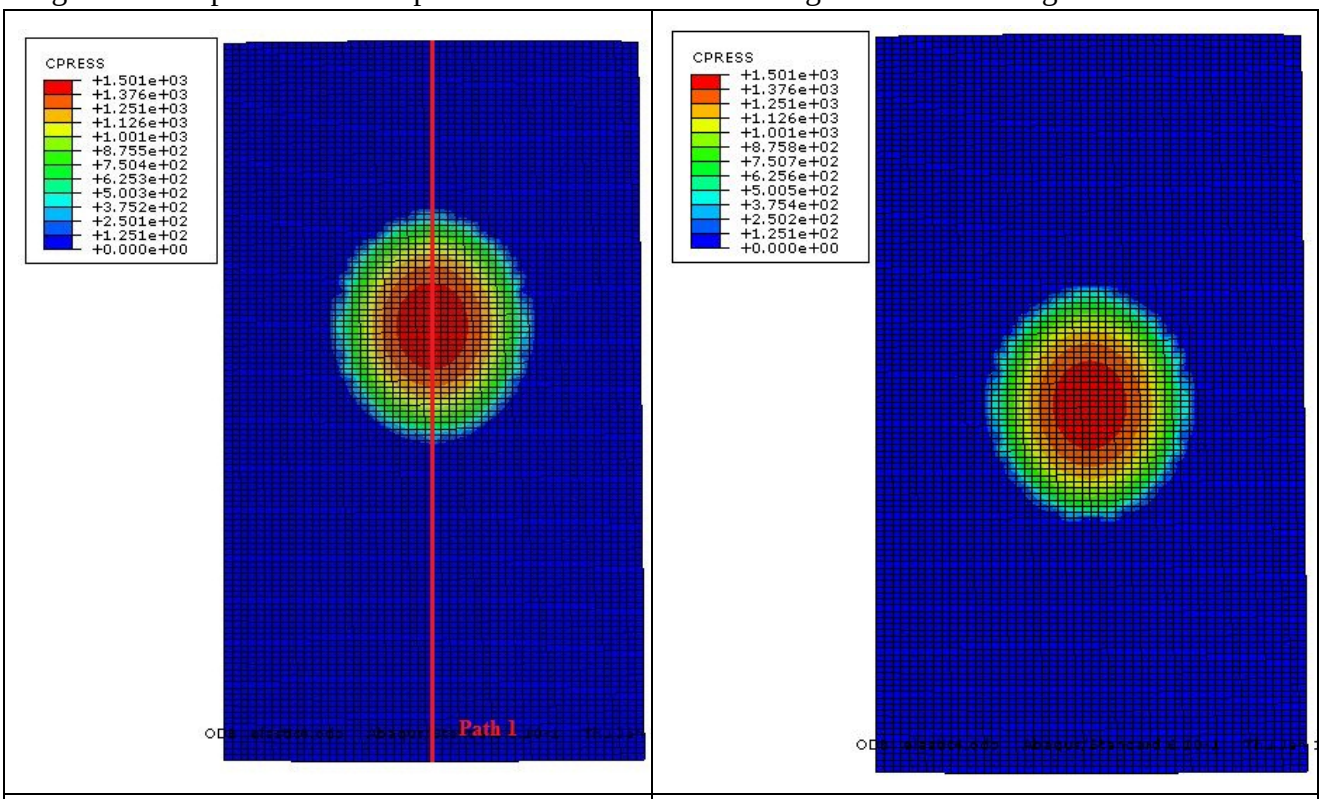

(a) (b)

Figure 8. Contact pressure on the tube surface for (a)time=1.0; (b)time=3.0

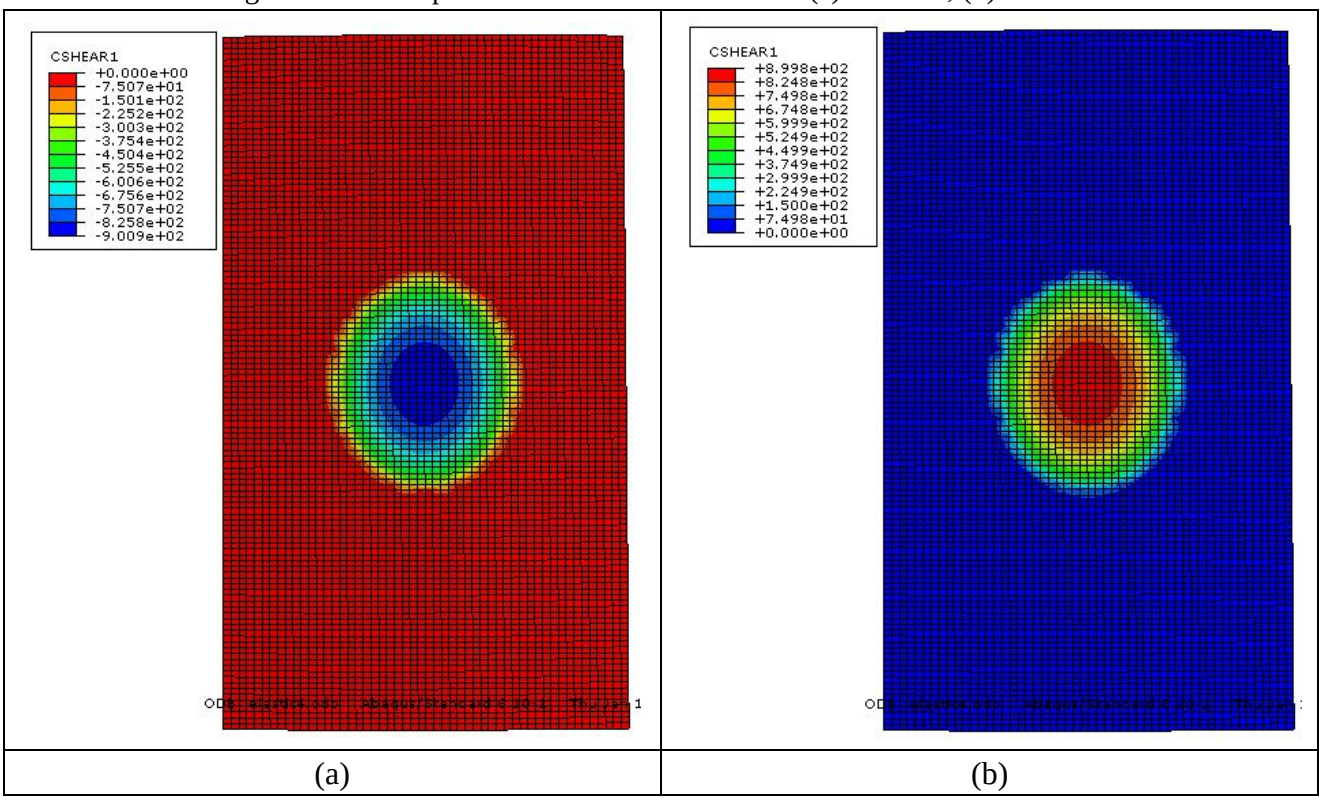

(a) (b)

Figure 9. Contact shear stress on the tube surface for (a) time=2.9; (b) time=3.1.

σ_{max} and σ_{min} are of path 1 are shown in Fig. 13, where

$$\sigma_{max}(x) = \max_t(\sigma_x(x,t)), \qquad \sigma_{min}(x) = \min_t(\sigma_x(x,t)), .$$

It is illustrated that the σ_{max} of nodes in region II are larger than the nodes in region I and region III. σ_{max} reaches a maximum value when the contact region moves to the red region in Fig. 11 because of the cumulated effect of contact shear stress and maximum applied load. $\Delta\sigma = \sigma_{max} - \sigma_{min}$ is shown in Fig. 14. It gives a different property with the stress amplitude of a standard specimen as shown in Fig 15. It may clarify that the crack does not occur at the middle of the contact area where the wear depth reached the maximum, but at the edge of the contact area.

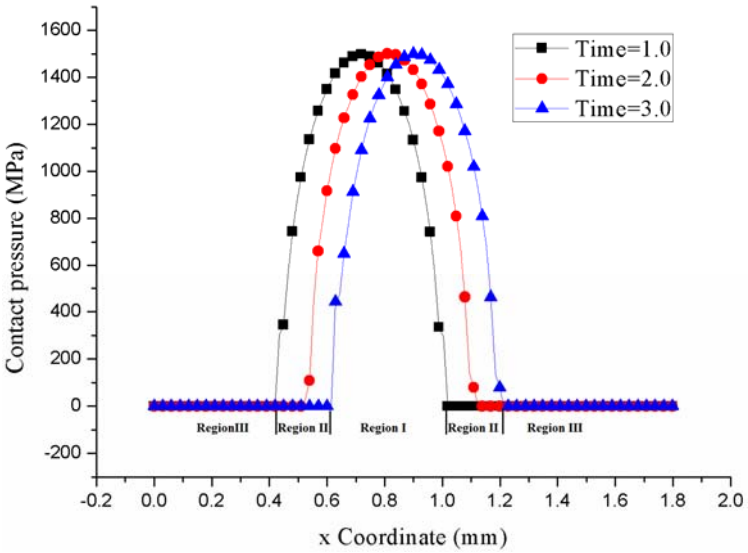

Figure 10. The contact pressures of path 1 for different times.

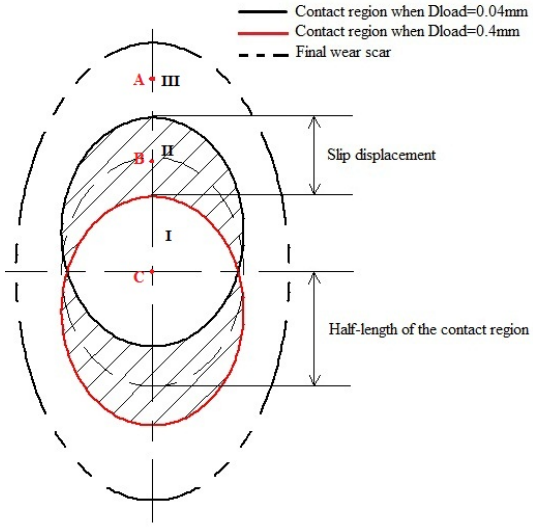

Figure 11. The regions on the surface of the tube.

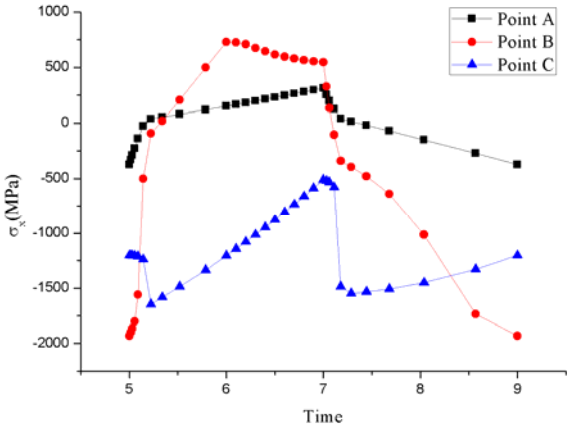

Figure 12. Stress of the elements in the three different regions

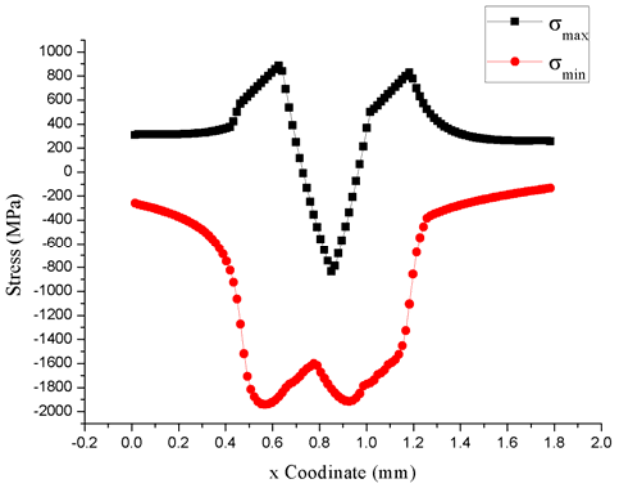

Figure 13. The maximum and minimum stress of nodes on path 1 during one cycle.

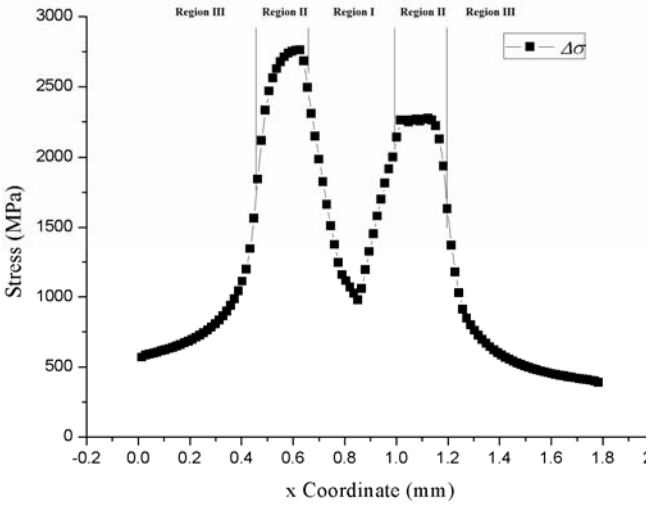

Figure 14. The stress amplitude of nodes on path 1 during one cycle.

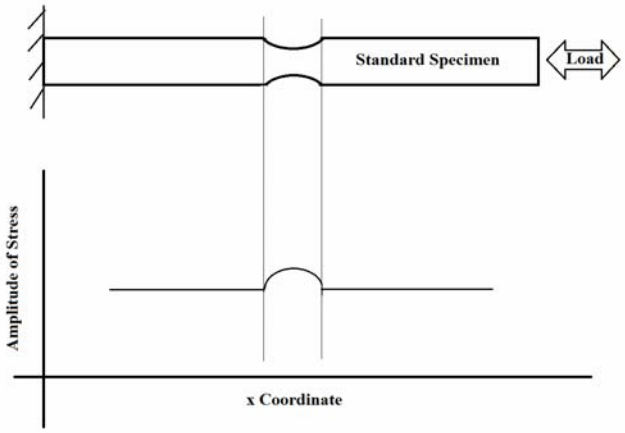

Figgure 15. The stress amplitude of a standard specimen.

4. Conclusion and discussions

(1) The fretting fatigue experiment taken on tube specimen gives a S-N curve of nuclear fuel cladding tube material. It is illustrated that the influence of the fretting on the fatigue resistance occurs above 10^4 cycles and becomes stronger in higher cycle fatigue situations. The fretting decreases fatigue strength of material above 50% after 10^5 cycles.

(2) The fretting fatigue experiment shows that crack does not occur at the middle of the contact area where the wear depth reached the maximum, but at the edge of the initial contact region. The mean value of distances from the crack to the middle of the fretting wear scar (d) equals 0.52834mm, and variance of d equals 0.0416mm^2.

(3) An FEM simulation is employed to analyze the crack nucleation on the tube surface. It is predicted that the region scanned by the edge of the contact region during the cycles will be the region of crack nucleation. The region II in Fig. 10 can be predicted by initial contact region and slip displacement. The distance from the crack to the middle of the fretting wear scar $d=a\pm\delta/2$, where a is the half-length of the initial contact region.

(4) Elastic materials are used in this simulation, which leads a smaller contact region and a larger contact stress. For the case in Section 3.1, a=0.455mm and δ=0.2mm if linear elastoplastic materials are employed in the simulation. This fits the tests of the specimen no.13~15 better.

Acknowledgements

This work was supported by the National Natural Science Foundation of China(No.11072062, 11172068 and 11272092), the Research Fund for the Doctoral Program of Higher Education of China (20110071110013), the High Technology Develop Program of China (863 Program: 2009AA04Z408) and the Graduate Innovation Fund of Fudan University.

References

[1] P.L. Hurricks, Mechanism of fretting. Wear, 15 (1970) 389-409.

[2] R.B. Waterhouse, Fretting fatigue. International Materials Reviews, 37(1992) 77-98.
[3] J.M. Dobromirski, Variables of fretting process: are there 50 of them? AETM STP 1159, American Society for Testing and Materials, Philadelphia, 1992,pp. 60-66.
[4] H. Mohrbacher, J.P. Celis, J.R. Roos, Laboratory testing of displacement and load induced fretting. Tribology International, 28(1995) 269-278.
[5] H.A. Fadag, S. Mall, V.K. Jain, A finite element analysis of fretting fatigue crack growth behavior in Ti-6Al-4 V. Engineering Fracture Mechanics, 75(2008) 1384-1399.
[6] N.K.R. Naidu, S.G.S. Raman, Effect of contact pressure on fretting fatigue behaviour of Al-Mg-Si alloy AA6061. International Journal of Fatigue, 27(2005) 283-291.
[7] H.K. Kim, Y.H. Lee, S.P. Heo, Mechanical and experimental investigation on nuclear fuel fretting. Tribology International, 39(2006) 1305-1319.
[8] J.A. Pape, R.W. Neu, Influence of contact configuration in fretting fatigue testing. Wear, 225-229(1999) 1205-1214.
[9] C. Petiot, et al. An analysis of fretting-fatigue failure combined with numerical calculations to predict crack nucleation. Wear, 181-183(1995) 101-111.
[10] A.L. Hutson, T. Nicholas, R. Goodman. Fretting fatigue of Ti-6Al-4V under flat-on-flat contact. International Journal of Fatigue, 21(1999) 663-669.
[11] J.M. Wallace, R.W. Neu. Fretting fatigue crack nucleation in Ti-6Al-4V. Fatigue Fract Engng Mater Struct, 26(2003)199-214.
[12] M.P. Szolwinski, T.N. Farris. Mechanics of fretting fatigue crack formation. Wear, 198(1996) 93-107.
[13] T. Hattori, M. Nakamura, et al., Simulation of fretting-fatigue life by using stress-singularity parameters and fracture mechanics. Tribology International, 36(2003) 87-97.
[14] Y. Liu, J.Q. Xu, Y. Mutoh, Evaluation of fretting wear based on the frictional work and cyclic saturation concepts. International Journal of Mechanical Sciences, 50 (2008) 897-904.
[15] D.A. Hills, Mechanics of fretting fatigue. Wear, 175(1994) 107-113.
[16] W. Klinger, IAEA-TECDOC-1345, 2002, pp 21-29.
[17] R.B. Waterhouse. The Problems of Fretting Fatigue Testing, Standardization of Fretting Fatigue Test Methods and Equipment, ASTM STP 1159. American Society for Testing and Materials, Philadelphia, 1992: 13-19.

A Model Allowing for the Influence of Geometry and Stress in the Assessment of Fatigue Data

Constanze Przybilla[1,2,*], Roland Koller[2], Alfonso Fernández-Canteli[1], Enrique Castillo[3]

[1] Department of Construction and Manufacturing Engineering, University of Oviedo, 33203 Gijón, Spain
[2] Laboratory for Mechanical Systems Engineering, EMPA, 8600 Dübendorf, Switzerland
[3] Department of Applied Mathematics and Computational Sciences, University of Cantabria, 39005 Santander, Spain
* Corresponding author: przybillaconstanze@uniovi.es

Abstract Usually, the Wöhler field of a material is obtained from fatigue lifetime data resulting from testing specimens of reduced size in the laboratory. This basic information finds subsequent application in lifetime prediction of larger structural and mechanical components. Thus, an important question arises: how can the S-N field be transformed into an ideal one referred to a characteristic size (length, area or volume) subjected to a constant stress distribution in order to achieve a safe structural integrity design?
In this work, the influence of specimen geometry and variable stress state on the fatigue lifetime distribution for constant amplitude fatigue tests is investigated. An experimental program has been carried out with unnotched specimens of nominally the same material but differing in length, diameter, and shape.
The experimental data is fitted to a newly developed fatigue model, capable of describing the S-N-field in a probabilistic manner accounting for both the specimen geometry and the variable stress state of the specimens. As the estimated Wöhler field is referred to an elemental surface, loaded by a constant stress level $\Delta\sigma$, the extrapolation of the fatigue resistance to different specimen geometries is possible. Additionally, problems encountered due to scatter of the material properties are discussed.

Keywords SN curves, Size effect, Probabilistic modelling, Transferability, Specimen geometry

1. Introduction

It has been observed that fatigue lifetime depends on the size of the structural element, whereby larger specimens present lower fatigue lifetime than smaller ones when loaded by the same stress range. This so-called size effect stems from the higher probability of larger specimens to contain a critical crack, capable of initiating the fatigue process, compared to smaller specimens. Investigations on the size effect in fatigue have been done, amongst others, by Weibull [1] on ball bearing steel, by Picciotto [2] on yarn, by Köhler [3] on wires and flat specimens, by Fernández-Canteli et al. [4] on prestressing wires and by Shirani et al. [5] on wind turbine castings.
Understanding the size effect is crucial to extrapolate fatigue data from small specimens tested in the laboratory to real structures. Additionally, specimen geometries used in fatigue experiments sometimes present a cross-section with varying diameter along their lengths (see Fig. 2). The experimental results ($\Delta\sigma$ versus lifetime N) obtained from testing these specimens are usually evaluated considering the maximum nominal stress range $\Delta\sigma_0$ acting in the smallest cross section and the stress ratio $R=\sigma_{min}/\sigma_{max}$. While the stress ratio R is the same for all cross sections, $\Delta\sigma$ varies along the specimen length. Thus, even if a specimen is likely to fail in the section with the highest $\Delta\sigma$, the remaining sections with lower $\Delta\sigma$ influence the overall failure probability. That is why for a specimen as depicted in Fig. 2 it is statistically not correct to refer the results only to the surface or volume with the smallest radius (central section). Though there are models to account for the pure length effect, e.g. [6], the variable stress in the specimen is in general not accounted for.
The present investigation proposes a new model to evaluate fatigue test data considering both size effect and variable stress state of the test specimens. This allows, on one hand, a comparison of fatigue data obtained for different specimen sizes and, on the other hand, to establish a new method to extrapolate fatigue life results from laboratory tests to different specimen sizes and real structures. The applicability of the model is checked by evaluating three experimental fatigue data

sets corresponding to three specific specimen geometries of the same material: the aluminium alloy AlMgSi1-6082.

2. Model proposal

In this section a new method to evaluate fatigue data is presented which extends the applicability of the probabilistic fatigue model presented by Castillo and Fernández-Canteli [6] for a more general description of the fatigue behaviour considering specimen geometry, i.e. size effect and variable stress state.

2.1. Probabilistic model

The Weibull regression model described in [6] is based on physical and statistical assumptions. The compatibility condition between the probability distributions present in the Wöhler field, i.e. the probability distribution $P_f(\Delta\sigma|N)$ of $\Delta\sigma$ for constant N and the probability distribution $P_f(N|\Delta\sigma)$ of N for constant values of $\Delta\sigma$, plays an important role, manifesting that the values of the failure probability for every combination of $\Delta\sigma$ and N must be equal for $P_f(\Delta\sigma|N)$ and $P_f(N|\Delta\sigma)$. The model describes the Wöhler field in a probabilistic way by means of percentile curves, i.e. curves representing a constant failure probability, and computes the failure probability $P_f(N, \Delta\sigma)$ for a combination of stress range $\Delta\sigma$ and number of cycles N by

$$P_f(N,\Delta\sigma) = 1 - \exp\left[-\left(\frac{\left((\ln N - B)(\ln \Delta\sigma - C) - \lambda\right)}{\delta}\right)^{\beta}\right], \tag{1}$$

which corresponds to a three-parameter Weibull distribution of the variable $V = (\ln N - B)(\ln \Delta\sigma - C)$ with location parameter λ, shape parameter β, and scale parameter δ [7]. V represents a normalizing variable and could be interpreted as a damage parameter. B and C are the threshold parameters for lifetime and stress range, respectively. Fig. 1 gives an example of the model depicting the SN field on the left and the normalized variable on the right. A detailed description of the model can be found in [6].

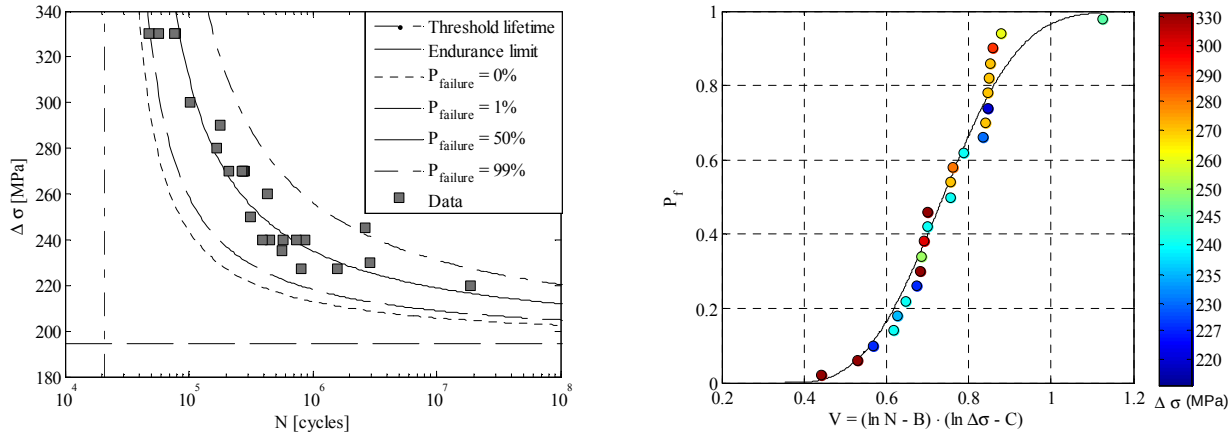

Figure 1. SN field and normalized variable V

2.2. Consideration of size effect and variable stress state

In principle the fatigue life depends not only on the material, the stress range, and the stress ratio, but also on the specimen length, as found for example in [4]. This means that the longer a specimen the higher the failure probability if the same stress range $\Delta\sigma$ is applied. This phenomenon, called statistical size effect, is due to the fact that a larger specimen is more likely to contain a large critical crack than a smaller specimen, cracks being considered to originate fatigue failure. Furthermore, specimen geometries used in fatigue experiments frequently present a cross-section with varying diameter along their lengths (see Fig. 2). The experimental results ($\Delta\sigma$ versus lifetime N) stemming from testing these specimens are usually evaluated considering only the maximum stress range $\Delta\sigma_0$, acting on the smallest cross section, and the stress ratio $R=\sigma_{min}/\sigma_{max}$. While the stress ratio R is the same for all cross sections, $\Delta\sigma$ is varying along the specimen length. To extrapolate from those test results to structural elements or specimens of different size it is advantageous to obtain a "normalized" Wöhler field. To accomplish this task a new method is developed, based on the following assumptions:

a) Fatigue failure initiates from surface flaws. Therefore the size effect is related to the stressed surface area, i.e. the larger the stressed surface the higher is the failure probability for the same combination of $\Delta\sigma$ and N.

b) Validity of statistical independence and weakest-link principal implying that the survival probability $P_{s,S}$ of a surface $S = n \cdot S_i$ composed of n surface elements of size S_i is given by the product of the individual survival probabilities P_{s,S_i} of the subelements each loaded by a stress range $\Delta\sigma_i$, i.e.

$$P_{s,S}(N,\Delta\sigma) = \prod_{i=1}^{n} P_{s,S_i}(N,\Delta\sigma_i). \tag{2}$$

Accordingly, if all surface elements have the same size S_i and are loaded by the same stress range $\Delta\sigma_i$ one gets

$$P_{s,S}(N,\Delta\sigma) = \left(P_{s,S_i}(N,\Delta\sigma_i)\right)^{S/S_i}. \tag{3}$$

c) For the moment, only the uni-axial load case is considered, so that Eq. (1) describes the failure probability $P_{f,\Delta S}$ for a uni-axially tensioned surface element ΔS.

With those assumptions and $P_{s,\Delta S} = 1 - P_{f,\Delta S}$ we can combine Eqs. (1) and (3) to obtain the survival probability for a uni-axially tensioned surface element of size $S_i = n_i \cdot \Delta S$ as

$$P_{s,S_i}(N,\Delta\sigma) = \left(1 - P_{f,\Delta S}(N,\Delta\sigma)\right)^{S_i/\Delta S} = \exp\left[-\frac{S_i}{\Delta S}\left(\frac{(\ln N - B)(\ln\Delta\sigma - C) - \lambda}{\delta}\right)^{\beta}\right] \tag{4}$$

Thus, for an arbitrary structure under fatigue load with tensioned surface $S = n \cdot S_i$ composed of n surface elements of size S_i, each loaded by a different stress level $\Delta\sigma_i$, combining Eqs. (2) and (4) one gets

$$P_f(N,\Delta\sigma_0) = 1 - \prod_{i=1}^{n} \exp\left[-\frac{S_i}{\Delta S}\left(\frac{(\ln N - B)(\ln \Delta\sigma_i - C) - \lambda}{\delta}\right)^{\beta}\right]$$
$$= 1 - \exp\left[-\sum_{i=1}^{n} \frac{S_i}{\Delta S}\left(\frac{(\ln N - B)(\ln \Delta\sigma_i - C) - \lambda}{\delta}\right)^{\beta}\right] \quad (5)$$

For a specimen with circular cross section and variable diameter $d(x)$ over its length, being d_0 the minimal diameter in the section loaded by the maximum stress level $\Delta\sigma_0$, the summation can be extended to an integral. With $S_i = \pi\, d(x)\, dx$, we get

$$P_f(N,\Delta\sigma_0) = 1 - \exp\left[-\frac{2\Pi}{\Delta S}\int_0^{UB}\left(\frac{(\ln N - B)\left(\ln\left(\Delta\sigma_0 \frac{d_0^2}{d(x)^2}\right) - C\right) - \lambda}{\delta}\right)^{\beta} d(x)dx\right]. \quad (6)$$

Due to symmetry, the integration is carried out over half the specimen length starting in the centre of the specimen, being the upper integration bound UB the x-coordinate, where $(\ln N - B)(\ln(\Delta\sigma(x)) - C) = \lambda$.

2.3. Effective surface area

For a specimen under variable stress state an effective specimen surface S_{eff} can be defined having the same failure probability as the whole specimen but subjected to a constant stress range $\Delta\sigma$. The normalizing variable for the nominal maximum stress $\Delta\sigma_0$ acting in the central section of the specimen with diameter d_0 is represented by $V_0 = (\ln N - B)(\ln \Delta\sigma_0 - C)$. For different specimen sections with diameter $d(x)$ we have $V(x) = (\ln N - B)(\ln(\Delta\sigma_0 \cdot d_0^2/d(x)^2) - C)$. An analytical expression for S_{eff} is obtained equating Eqs. (5) (with $S_i = S_{eff}$) and (6):

$$S_{eff} = \frac{2\,\Pi \int_0^{UB} (V(x) - \lambda)^{\beta} d(x)\mathrm{d}x}{(V_0 - \lambda)^{\beta}}. \quad (7)$$

As can be observed from Eq. (7) S_{eff} is independent of δ but depends on the parameters B, C, λ and β of the Weibull model and also on the number of cycles N and the stress range $\Delta\sigma$. For given values of N and $\Delta\sigma_0$ and known material parameters B, C, λ and β the effective surface and the failure probability can be computed. However, for a specific specimen S_{eff} cannot be calculated directly from the failure data, since the Weibull parameters are still unknown. Thus, an iterative process, as explained in [8], is used for the parameter estimation. Firstly, the n test data are fitted to the model given by Eq. (1), then the normalized values V_0 are assigned their accumulated failure probabilities by $P_f = (i - 0.3)/(n + 0.4)$. To refer the data to the surface element ΔS, those failure probabilities are shifted by using $P_{f,i,\Delta S} = 1 - \left(1 - P_{f,i,S_{eff}}\right)^{\Delta S/S_{eff,i}}$. The $V_{0,i}$ and their corresponding $P_{f,i,\Delta S}$ are fitted to a three-parameter Weibull distribution. The obtained values for λ and β are used to update the effective surface given by Eq. (7) in each iteration loop. Those steps are repeated until the Weibull parameters converge.

3. Material and experimental programme

To investigate the influence of the size effect and the variable stress state on the fatigue behaviour, specimens with different geometries have been tested until complete fracture at EMPA-Dübendorf (Swiss Federal Material Testing and Research Laboratories). All specimens whose dimensions are given in table 1 and refer to Fig. 2 have been machined by the same manufacturer from rods of the aluminium alloy AlMgSi1 6082-T6 with chemical composition given in table 2. The d3 and d8 specimens were machined from rods of diameter 25 mm and the d22 specimens from rods with diameter 45 mm. The corresponding yield and ultimate strengths are given in table 2 as the mean of three values obtained from static strength tests using normalized specimens.

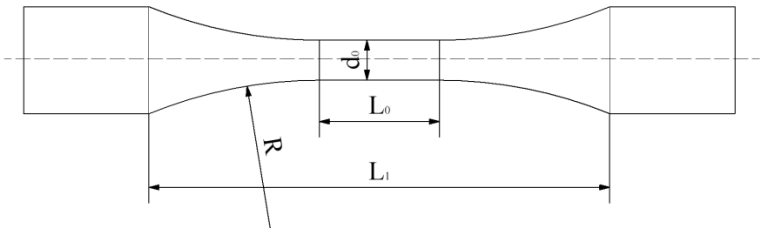

Figure 2. Specimen geometry

Table 1. Tested specimen geometries

Name	d_0 [mm]	L_0 [mm]	L_1 [mm]	R [mm]
d3	3	0	22.4	24
d8	8	24	88.6	90
d22	22	240	385.0	245

Table 2. Chemical composition and strength of AlMgSi1 6082-T6

d [mm]	Si [%]	Fe [%]	Cu [%]	Mn [%]	Mg [%]	Cr [%]	Zn [%]	Ti [%]	Pb [%]	R_m [MPa]	$R_{p0.2}$ [MPa]
25	1.002	0.499	0.091	0.749	0.831	0.032	0.186	0.063	0.026	410	402
45	0.850	0.280	0.060	0.430	0.710	0.050	0.050	0.030	N/A	369	350

Since the static strength of the specimens differs for the different rods, additionally micrographies were taken (one from each rod) as shown in Fig. 3. It can be observed that the microstructure happens to be quite similar for both samples, thus, justifying a direct comparison of the fatigue test data.

The constant amplitude fatigue tests were carried out in pure tension with a stress ratio R=0.1. For the tests of the d3 and d8 specimens resonance frequency machines (Rumul) equipped with 5 kN and 100 kN load cells, respectively, were used, whereas the d22 specimens were tested by a servo-hydraulic machine (Schenck) with 630 kN load cell. The forces were calculated taking into account the measured diameters in the central section of each specimen and the stress ranges $\Delta\sigma$, to be applied in this section. For all specimens the difference between measured and nominal diameter was less than 0.03 mm. The predominant role of the surface flaws has been corroborated by ocular

and microscopic inspection of the failure sites revealing that the practical totality of the fatigue failures started from the specimen surface. In the exceptional case that a failure could be identified to have its origin in a volume defect, it was not considered in the present analysis.

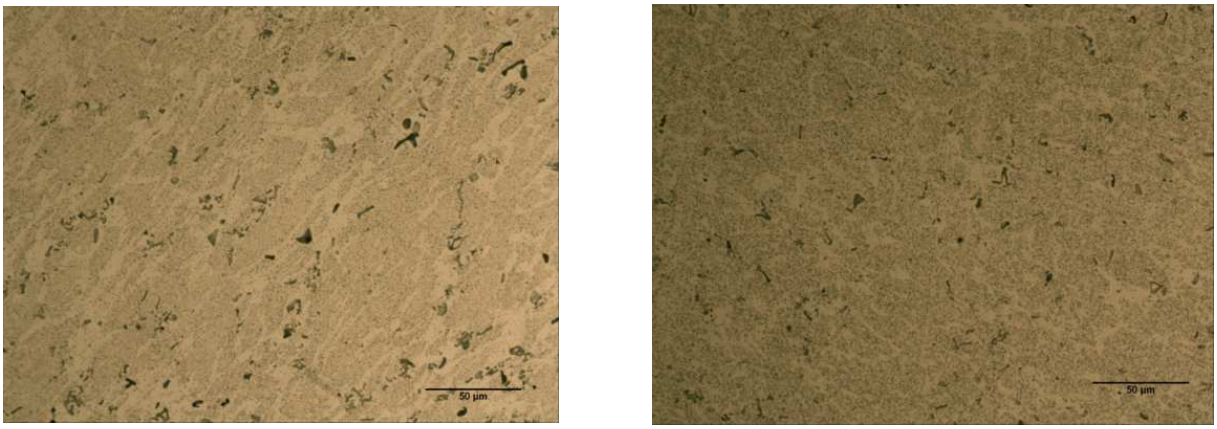

a) Rod d=25 mm (used for d3 and d8 specimens) b) Rod d=45 mm (used for d22 specimens)

Figure 3. Microstructure of AlMgSi1

4. Results and model application

The experimental data sets for each specimen geometry were individually fitted to the model given by Eq. (6) of section 2.2. to obtain the parameters referred to ΔS=9 mm^2 as shown in table 3. The choice of ΔS is free, so that larger values of ΔS will only result in smaller values of δ, remaining the other parameters unchanged.

Table 3. Parameter estimates for each data set

d_{min} [mm]	ΔS [mm^2]	B	exp(B) [cycles]	C	exp(C) [MPa]	λ	β	δ
3	9	11.57	105873	5.40	221	0.01	2.42	0.16
8	9	9.95	20952	5.27	194	0.21	4.31	1.65
22	9	10.63	41357	5.27	194	0.00	3.41	4.09

The fatigue test data and their corresponding Wöhler fields are represented in Fig. 4 for the specimen geometries d3, d8, and d22. The percentiles are computed replacing into Eq. (6) the parameter estimates referred to the area ΔS given in table 3 and the specimen geometries of table 1.
In a second step, the SN fields for the d3 and d22 specimens are predicted based on the parameter estimates, found by fitting the data of another specimen geometry, by substituting the corresponding radii and lengths in Eq. (2). Figs. 5a and b show the Wöhler fields for the d3 and d22 specimens using the parameter estimates obtained by fitting the d8 data. The extrapolations from the d3 to the d22 specimen and from the d22 to the d3 specimen are given in Figs. 5c and d, respectively.

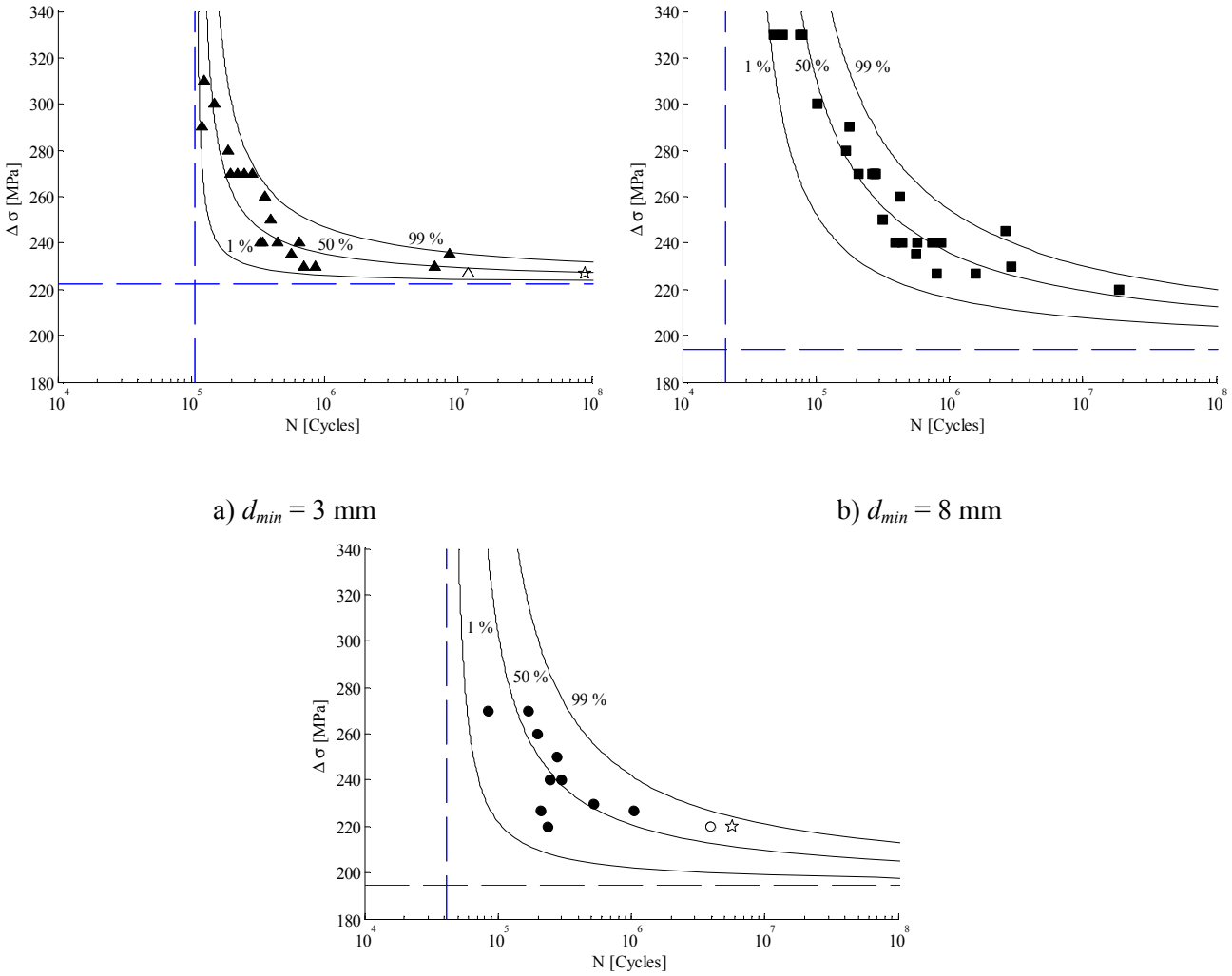

a) d_{min} = 3 mm

b) d_{min} = 8 mm

c) d_{min} = 22 mm

Figure 4. AlMgSi1 fatigue data and percentile curves for 1, 50 and 99 % failure probability

5. Discussion

As can be observed in Fig.4, the percentile curves for all three specimen geometries provided by the model describe the fatigue data well, both in terms of median curve and data scatter. As the estimated parameters for each data set are referred to the same surface area ΔS, they should coincide for all three data sets. Nevertheless, as can be seen in table 3, this is only the case for the threshold parameter C for the d8 and d22 specimens. According to the model, a comparison of the Weibull parameters λ, β and δ requires the parameters B and C to be coincident to compute the normalized variable V.

The extrapolation from the d8 estimates to the d3 Wöhler field overestimates both the median curve of fatigue life for constant stress levels and the data scatter. A possible reason could be that for such small specimens statistical independence, as is an assumption of the model, is not fulfilled in this case. As reference for other practical cases, in [6] it was also observed that the fatigue behaviour of the shortest prestressing wires could not be described based on the estimates for the longer wires. Therefore, the statistical dependence [9] based on considerations related to the defects from which fatigue initiation arises together with experimental work should be further investigated in order to

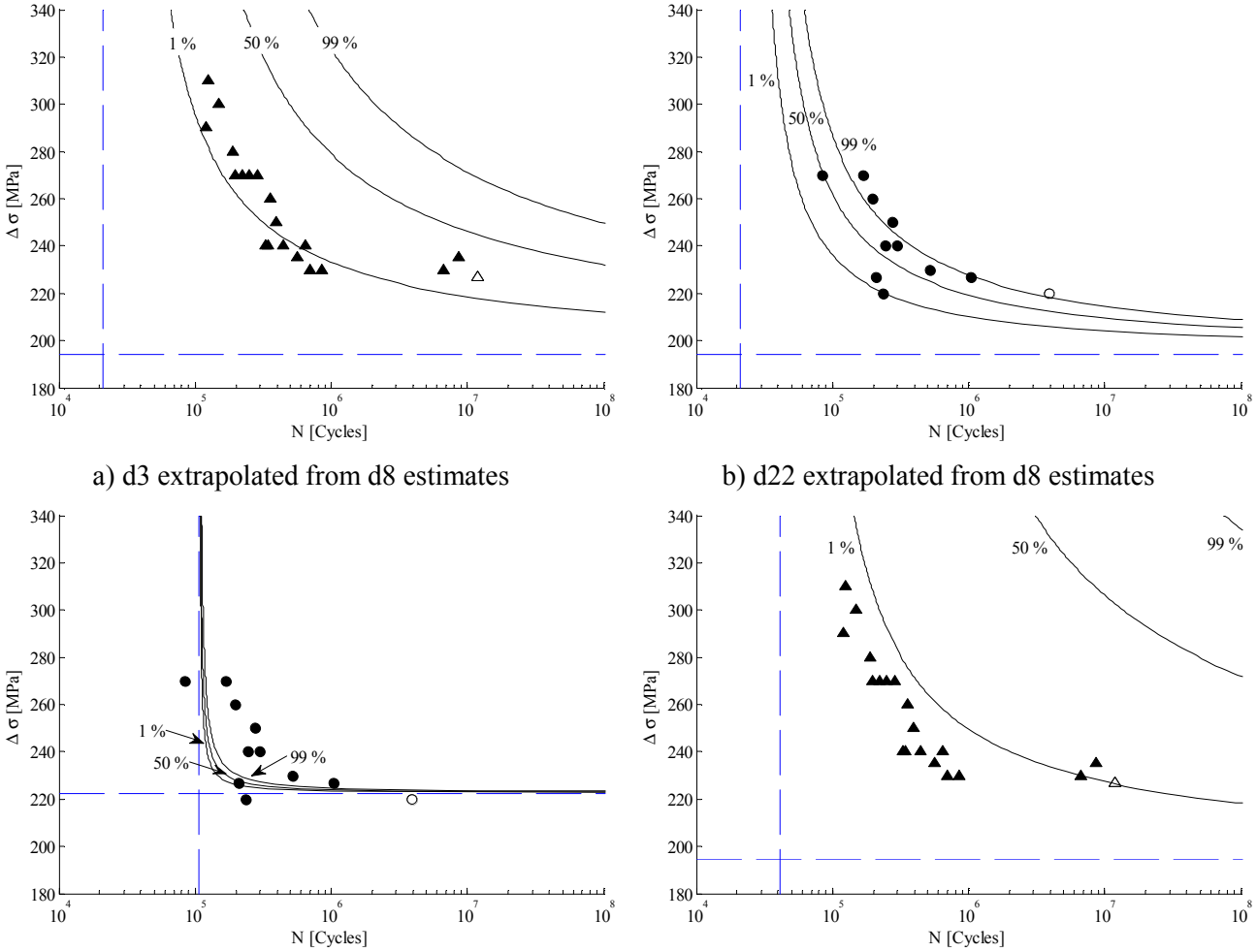

a) d3 extrapolated from d8 estimates

b) d22 extrapolated from d8 estimates

c) d22 extrapolated from d3 estimates

d) d3 extrapolated from d22 estimates

Figure 5. Extrapolation to different specimen geometries (1, 5 and 99 % percentile curves)

improve the model. Different surface quality can also be excluded, as all specimens were machined in the same workshop, therefore supposedly having undergone the same surface treatment. In particular, both the d3 and d8 specimens were fabricated from 25 mm diameter rods. Although, this implies that the surface of the d3 specimens is closer to the centre of the rods than the surface of the d8 specimens and possibly having experienced both different cooling rates, the difference is negligible bearing in mind the original rod diameter.

One could also question the existence of a size effect. Though this assumption might be true for the d3 and d8 specimens, it is obvious from Fig. 6 that the d22 specimens have lower lifetimes than the d3 and d8 specimens for the same stress ranges. Nevertheless, in the region of low stress ranges, the d3 specimens tend to present higher fatigue lifetimes than the d8 specimens.

On the other hand, the prediction for the d22 specimens based on the d8 estimates (Fig. 5b) is quite good lying almost all failure data for the d22 specimens between the 1 and 99 % - percentiles. However, a tendency to underestimate the fatigue strength is noticeable since by the extrapolation the data with highest lifetime are assigned to failure probabilities higher than 99 %.

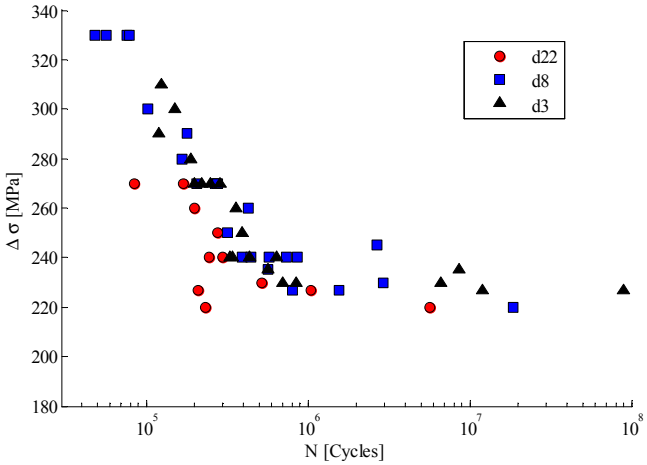

Figure 6. AlMgSi1 fatigue data for the tested specimen geometries

The extrapolation to the d22 specimen geometry based on the d3 estimates (Fig. 5c) leads to an underestimation of the data scatter and of the median curve. In this context, it has to be noted that the threshold parameters for the d3 data set were estimated in higher values than those for the d8 and d22 data sets. In fact, the threshold stress exp(C) for the d3 specimens results in 221 MPa which represents a higher value than the lowest stress range in the fatigue results for the d8 and d22 specimens equal to 220 MPa. Therefore, failure data lying below the threshold stress of the estimated model cannot be represented by the model. In contrast, the prediction of the SN field for the d3 geometry based on the d22 estimates (Fig. 5d) results in a noticeable overestimation of mean curve and data scatter.

6. Conclusions

A new model for the evaluation of fatigue test results under simultaneous consideration of size effect and variable stress state along the specimens is presented. The model, describing the SN field by means of percentiles, has been applied to three sets of fatigue data for AlMgSi1, each set obtained on specimens with different size. The estimated SN fields fit the experimental data well. As the parameters of the fatigue model are referred to a uni-axially and uniformly tensioned surface element, extrapolation to different specimen geometries can be performed. However, extrapolation to different specimen geometries is only satisfactory from the d8 to the d22 specimens. For the other presented cases, an extrapolation of the model from larger to smaller specimens overestimates the lifetimes of the smaller specimens and vice versa, an extrapolation from smaller to larger specimens tends to underestimate the fatigue behaviour. Thus, further research will be undertaken to get a deeper understanding of the size effect, and the role played by the defect distribution and the statistical independence assumption in order to improve the model.

Acknowledgements

The authors are indebted to the MICINN (Ministry of Science and Innovation) (Project BIA2010-19920) for financial support of this work. Furthermore, we thank Ing. Ana Teresa Vielma Mendoza for her help in the preparation of the micrographies.

References

[1] W. Weibull. A statistical representation of fatigue failures in solids. Technical report, Royal Institute of Technology of Sweden, 1949.
[2] R. Picciotto. Tensile fatigue characteristics of sized polyester/viscose tarn and their effect on weaving performance. PhD thesis, North Caroline State University, 1970.
[3] J. Köhler. *Statistischer Größeneinfluss im Dauerschwingverhalten ungekerbter und gekerbter metallischer Bauteile*. PhD thesis, TU München, 1975.
[4] A. Fernández-Canteli, V. Esslinger, and B. Thürlimann. Ermüdungsfestigkeit von Bewehrungs- und Spannstählen. Technical report, Institut für Baustatik und Konstruktion ETH Zürich, 1984.
[5] M. Shirani and G. Härkegård. Fatigue life distribution and size effect in ductile cast iron for wind turbine components. *Engineering Failure Analysis*, 18(1):12 – 24, 2011.
[6] E. Castillo and A. Fernández-Canteli. *A Unified Statistical Methodology for Modeling Fatigue Damage*. Springer, 2009.
[7] W. Weibull. A statistical theory of the strength of materials. *Proc Roy Swed Inst Eng Res*, (151):1 – 45, 1939.
[8] C. Przybilla, A. Fernández-Canteli, and E. Castillo. Deriving the primary cumulative distribution function of fracture stress for brittle materials from 3- and 4-point bending tests. *Journal of the European Ceramic Society*, 31:451–60, 2011.
[9] E. Castillo, A. Fernández-Canteli, J. Ruiz-Tolosa, and J. Sarabia. Statistical models for analysis of fatigue life of long elements. *Journal of Engineering Mechanics*, 116(5):1036–1049, 1990.

Property for Fatigue Crack Propagation of Friction Stir Welded 2024-T3 Aluminum alloy

Masakazu Hirose[1,*], Motoo Asakawa[2], Takao Okada[3], Shigeru Machida[3], Toshiya Nakamura[3], Shuji Kishishita[4], Kazuya Kuwayama[5], Shinya Fujita[5], Takuya Noguchi[1]

[1] The Graduate School of Science and Engineering, Waseda University, Tokyo 169-8555, Japan
[2] Department of Applied Mechanics and Aerospace Engineering, Waseda University, Tokyo 169-8555, Japan
[3] Japan Aerospace Exploration Agency, Tokyo 181-0015, Japan
[4] Advanced Engineering Services, Tsukuba 305-0032, Japan
[5] Alumnus of the Graduate School of Waseda University, Tokyo 169-8555, Japan
* Corresponding author: m_hirose1989@ruri.waseda.jp

Abstract
In this study, crack propagation tests were conducted to clarify property for the fatigue crack propagation of Friction Stir Welded (FSW) 2024-T3 aluminum alloy. FSW panel has residual stress around weld line and the longitude residual stress is higher around it. The peak tensile residual stress is about 180 MPa in this case. To understand fatigue crack growth property on FSW panel, crack opening stress measurement of the base material and FSW joint using an extensometer with the modified tool is also conducted during the crack growth test. The modified tool is jig to mount the extensometer to the specimen with magnets. The test results indicate that the accuracy of crack opening stress measurement is improved. In addition, the crack growth acceleration and decelerate around the FSW line under the low applied stress range (25 MPa) is bigger than that under high applied stress range (50 MPa). This means the effect of residual stress under low stress range is relatively larger than that under high stress range.

Keywords: Friction Stir Welding, Fatigue Crack Growth Propagation, Residual Stress, Crack Opening Stress

1. Introduction

Friction stir welding (FSW) is one of recently developed welding process[1] as shown in figure 1. It has the capability of welding high strength Aluminum alloys of 2xxx and 7xxx type which are difficult to weld by conventional welding. FSW has applied many structures such as trains, rockets and ships. From point of reducing production cost and structural weight, FSW is expected to be applied to commercial aircraft primary structures as an alternative to riveted joints. FSW was firstly used on a normal category aircraft “Eclipse 500” by Eclipse Aviation in 2006. However, the safety factor of FSW joint is estimated high in this aircraft. So far the study of FSW has been not sufficient to meet a damage tolerance. The Federal Aviation Regulations (FARs) on damage tolerance and fatigue evaluations of aircraft structures require understanding of the locations of fracture origin and the fatigue crack propagation property of the materials for aircrafts. To apply the structures jointed by FSW on aircrafts, the investigation of relationship between fatigue crack propagation property and residual stress on FSW panel is particularly significant. In case of FSW, the fatigue crack propagation rate is accelerated by the tensile residual stress around weld line as a result of non-uniform deformation caused by welding heat. Therefore, the explanation is required to determine an effect of residual stress on the crack propagation in the FSW panel. The aim of this study is to accurately evaluate the crack growth rate on FSW panel. The significance of this study is to focus on the crack opening stress to predict crack growth rate on FSW panel.
Our final goal of this research is to accurately predict the crack growth rate using FEM analysis. To achieve this goal, we have conducted the crack growth test[2-5]. In this paper we report the crack growth test results of the FSW panel with different applied stress and crack opening stress of the base material and FSW joint using an extensometer with the modified tool.

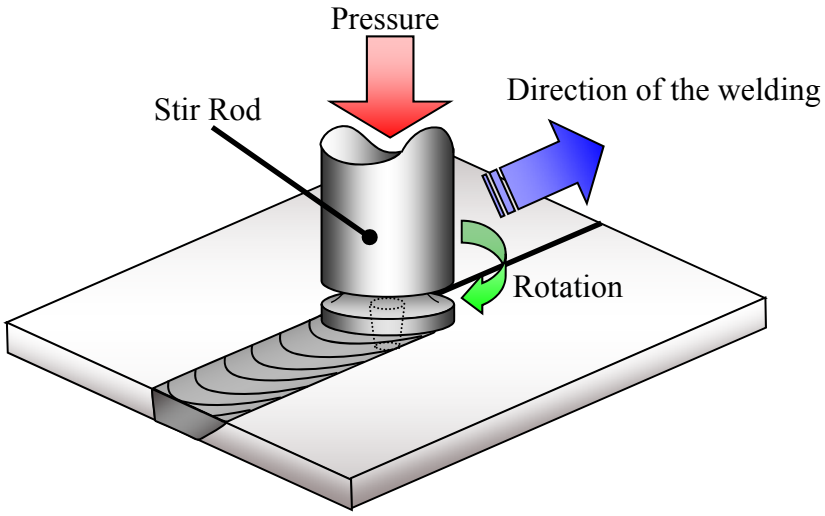

Figure 1. Schematic scheme of Friction Stir Welding

2. Material, specimen and method

The crack propagation tests were conducted, in accordance to the procedure in ASTM E647-08[6] standard test method. Sheet of 2024-T3 with a thickness of 2 mm were joined by FSW to form a butt joint. It is fabricated by Japanese aircraft manufacturer. The situations of Base metal panels and FSW panels are shown as Figure 2. Table 1 shows the list of specimens. All specimens have a center hole and notches as the initial flaw. All FSW panels have been welded by same welding procedures. So the level of residual stress is presumed to become same as each FSW panels. Figure 3 shows the result of measuring the residual stress in the vicinity of the weld line.

The crack growth test is subject to cyclic load with stress range: $\Delta\sigma$ = 25, 50, 75 MPa, stress ratio: R = 0.1 and load frequency: f = 5 Hz. The crack length was measured using a CCD camera. And we have installed the extensometer on specimens to measure crack opening displacement in order to evaluate the crack opening stress based on the compliance method which is improved by Chung et. al.[7]. In this test, the displacement above and below the hole was measured by an extensometer; the crack opening stress was determined on the basis of the change in the compliance of the specimen. We had installed the extensometer with bolts. In this study, the extensometer has been installed with modified tools. The modified tool is jig to mount the extensometer to the specimen with magnets.

Table 1. The list of specimens

No.	Base metal or FSW panel	Specimen size	stress range Δσ MPa
1	Base metal	Large size	50
2		Small size	25
3	FSW panel	Large size	75
4		Large size	50
5		Small size	25

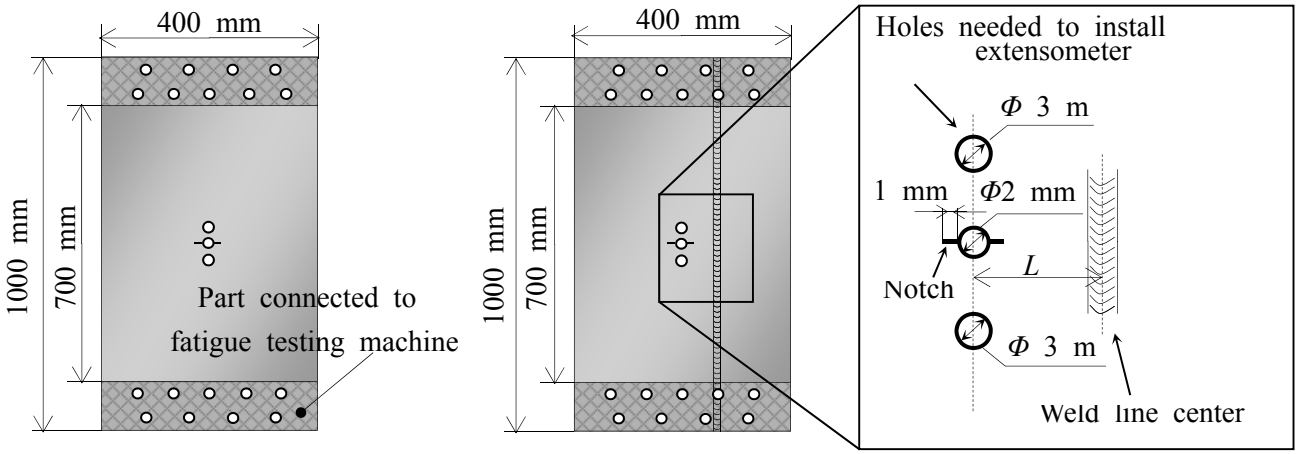

(a) Base metal (b) FSW panel (Large size specimen)

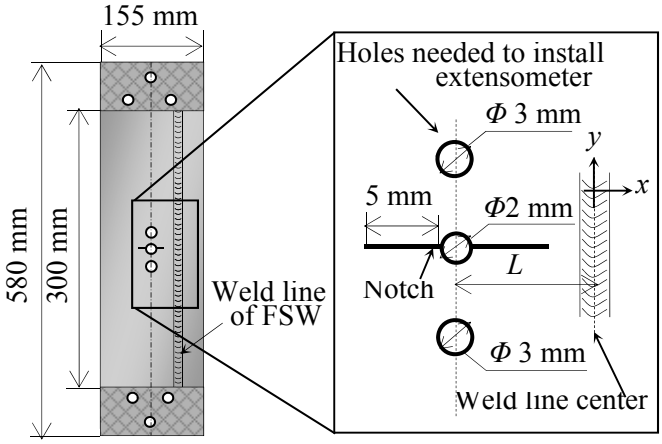

(c) FSW panel (Small size specimen)

Figure 2. Specimen's dimensions

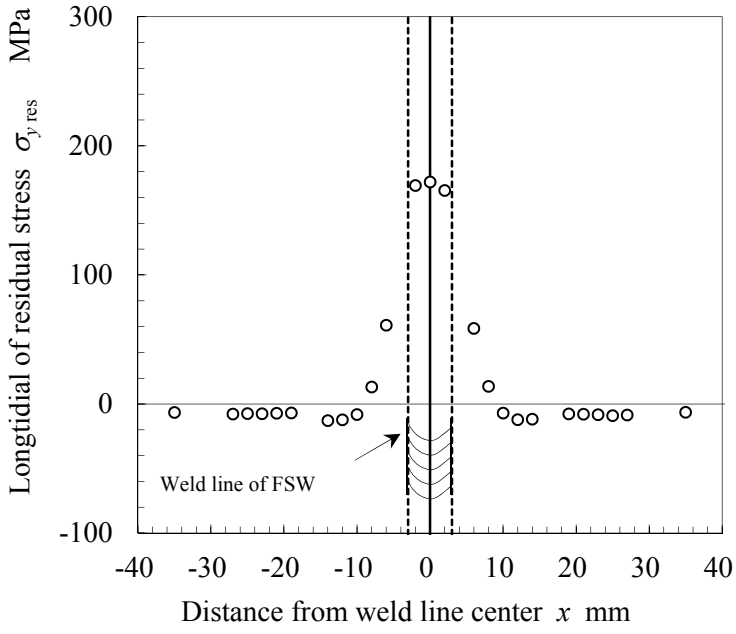

Figure 3. Relationship between longitudinal of residual stress and distance from weld line center

3. Result and discussion

3.1. Improvement of the jig

We need to mount an extensometer on specimens when we measure the crack opening stress. In case of $\Delta\sigma$ = 50 and 75 MPa, the extensometer was installed on specimen with bolt jig as shown in Figure 3(a) and measure the crack opening displacement. However, if tightening torque of bolts is not appropriate, the extensometer is not fixed on specimen and it is drifted. Therefore, we improved jig to mount the extensometer to the specimen tightly with magnets as shown in Figure 3(b).
To verify that the magnet jig can measure the crack opening stress, we measured the crack opening stress of base metal and compare the result of both jigs. In this study, we decided that crack is opening completely when the relative compliance offset become 5 %. This method is based on Chung's research[7]. In case of using bolt jig, the result of relative compliance offset is unstable and become greater than 5 % when the crack tip is not opening. So judgment of crack opening had been difficult. In case of using magnet jig, the relative compliance offset is stable and become less than 5 % when the crack tip is not opening. Therefore, the accuracy of crack opening stress measurement is improved by the magnet jig.

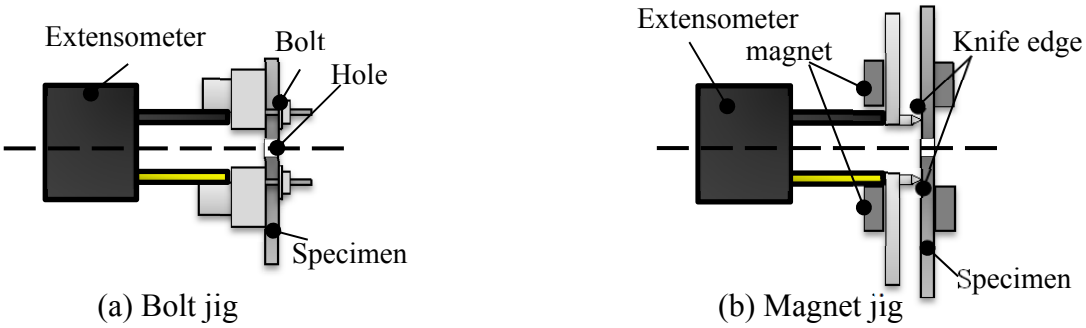

(a) Bolt jig (b) Magnet jig

Figure 3. Installing extensometer

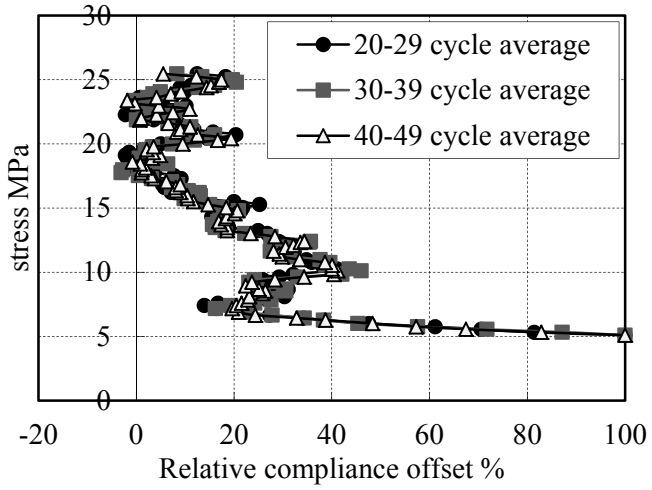

Figure 4. Determination of crack opening stress (bolt, a = 25.93 mm)

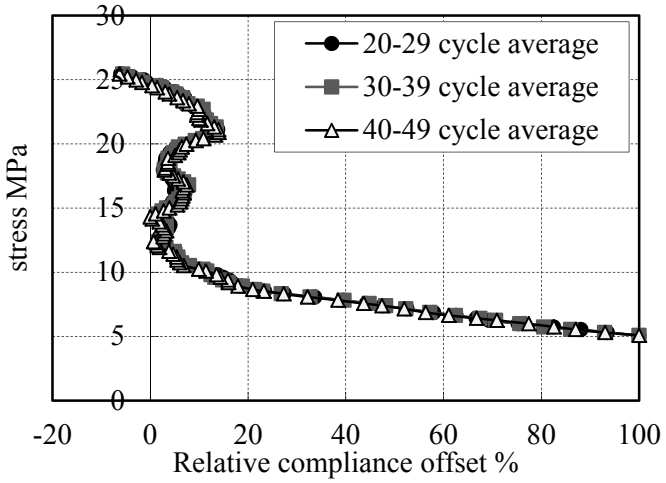

Figure 5. Determination of crack opening stress (magnet, a = 25.93 mm)

3.2. The result of crack opening stress measurement

The effective stress range, $\Delta\sigma_{eff}$, which is calculated using the maximum stress, σ_{max}, has one to one correlation to the crack growth rate. Here, $\Delta\sigma_{eff}$ is calculated by the following equation 1.

$$\Delta\sigma_{eff} = \sigma_{max} - \sigma_{op} \tag{1}$$

Elber[8] shows in full detail that The rate of crack propagation can be evaluated uniformly by using the effective stress range.

So the crack growth rate can be predicted by crack opening stress. To use the effective stress range, we have to accurately measure the crack opening stress of FSW panel.

There are some studies calculating crack opening stress of base metal by using empirical equations. Some of them, we have used empirical equations for 2024-T3 proposed by schijive[9] as eq. 2 and eq. 3.

$$U = 0.55 + 0.3R + 0.1R^2, \tag{2}$$

$$\therefore \sigma_{op} = \sigma_{max} - \left(0.55 + 0.3R + 0.1R^2\right)\Delta\sigma. \tag{3}$$

Figure 6 shows the result of crack opening stress measurement in each crack length. In addition, the calculated values obtained by the Schijive's equation and the experimental result of base metal ($\Delta\sigma$ = 75 MPa) are shown together.

In case of $\Delta\sigma$=75 MPa, the unti-buckling pate which suppress the out of plane deformation was used and measured with bolt jig. However, in case of $\Delta\sigma$ = 25 MPa, the unti-buckling plate was not used and measured with magnet jig. Therefore, the width of the variability of the measurement results is reduced by about 58%. Moreover, the result of measurement is same as the calculated values obtained by Schijive equation. For that reason, the validity of this measurement was confirmed and the test results indicate that the accuracy of crack opening stress measurement is improved.

Next, focus on the result of FSW panel as shown part A in figure 6. After crack tip invasion into weld line, crack opening stress is reduced substantially. Then, crack opening stress is asymptotic to the result of base metal as go away from weld line. From this result, the effect of residual stress is reduced when a position of crack tip is taken enough away from the weld line.

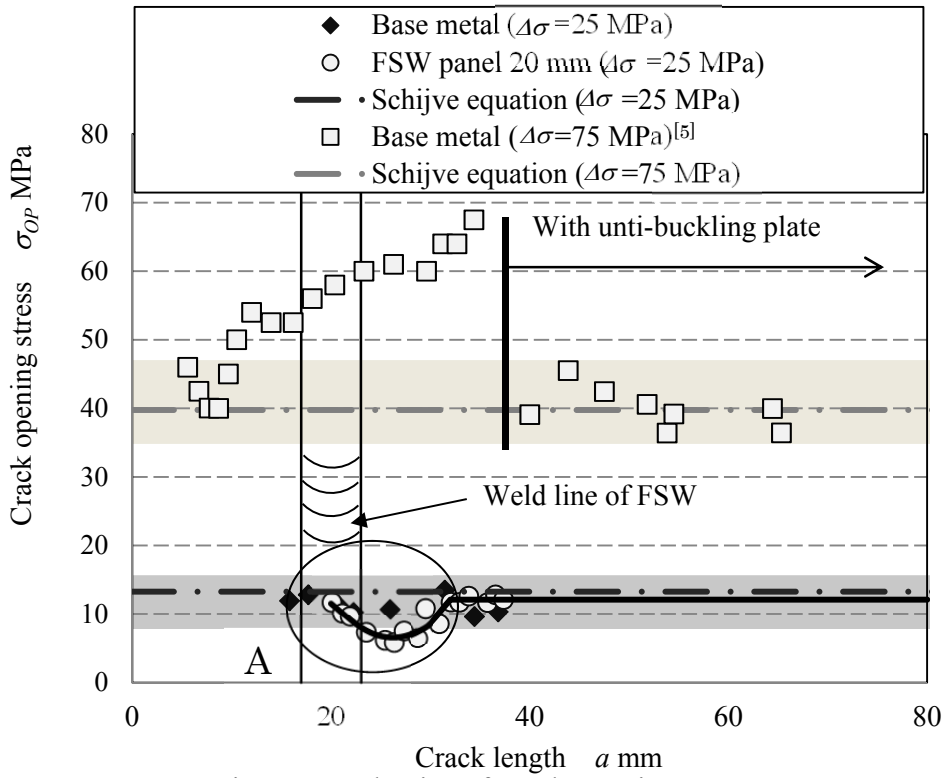

Figure 6. Behavior of crack opening stress

3.3. Effect of residual stress on crack propagation rate

We conducted crack growth tests with three types of external load conditions; $\Delta\sigma$ = 25, 50, 75 MPa. First, The results of $\Delta\sigma$ = 50, 75 MPa are shown in Figure 8. The stress intensity factor range is calculated by equation 4.

$$\Delta K = \Delta\sigma\sqrt{\pi a}\cdot F(a) \tag{4}$$

Here, F(a) is a correction factor. The reason why the position of weld line of FSW is different is because these two tests are different in stress range $\Delta\sigma$.

The maximum of the acceleration ratio of the crack growth rate for the FSW panel against the base material is 1 to 2 mm far away from the weld line after crack tip passes it. In case of $\Delta\sigma$ = 50 MPa, the acceleration ratio is 2.1, and $\Delta\sigma$ = 75 MPa the ratio is 2.3. The residual stress influences the crack growth rate. The FSW panels have the same level of residual stress distribution. So in case of external stress is high, the effect of residual stress is expected relatively low. This means the acceleration of crack growth rate for that situation is also low. However in this experiment, the difference on the acceleration ratio for crack growth rate is almost same at this two stress level; $\Delta\sigma$ = 50, 75 MPa.

The result of $\Delta\sigma$ = 25 MPa is shown in Figure 9. From the figure, it is observed that the crack propagation rate is decelerated by the compressive residual stress when the crack tip is located before the weld line. After the crack tip had moves on the weld line, the crack propagation rate is accelerated by the tensile residual stress. Finally, when the crack tip is located after the weld line, the crack growth rate is gradually approached to that of the base metal. In case of $\Delta\sigma$ = 25 MPa, the acceleration ratio of the crack growth rate for the FSW panel against the base material is 3.7.

The acceleration ratio of each stress range is shown in Figure 10. In summary, the crack propagation rate is affected by the residual stress and stress range $\Delta\sigma$. All FSW panel using in this study is made

under the same FSW condition. Therefore, residual stress of all specimens is identical. So, in the case of $\Delta\sigma$ = 25 MPa, the effect of residual stress is relatively high. This means the acceleration and deceleration of crack growth rate for that situation is also high.

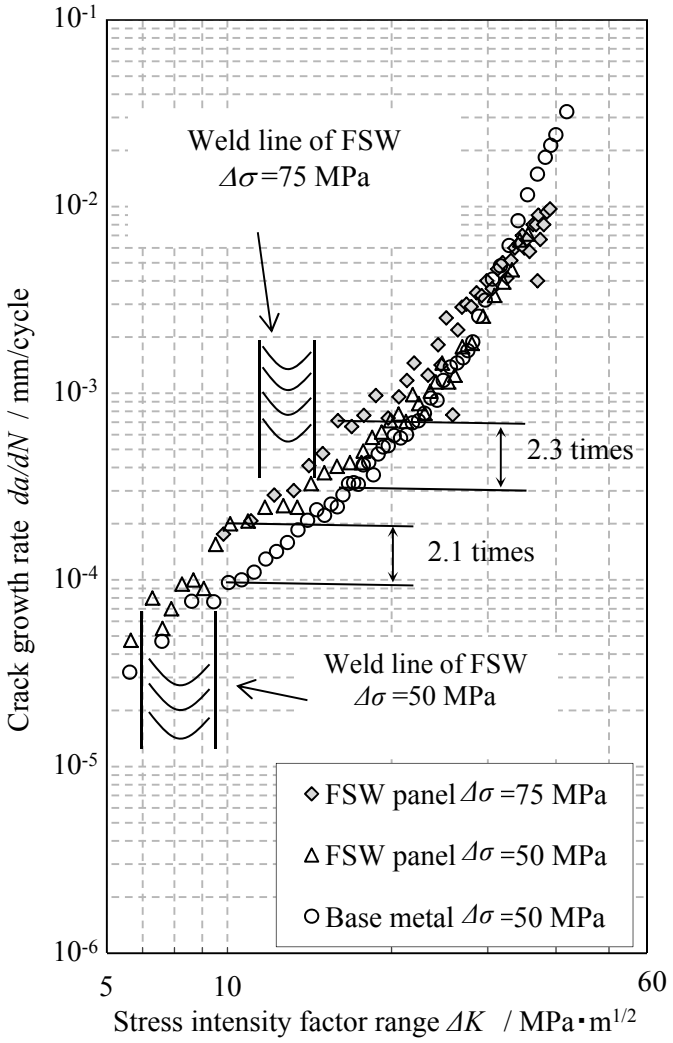

Figure 8. da/dN-ΔK curves for different external stress

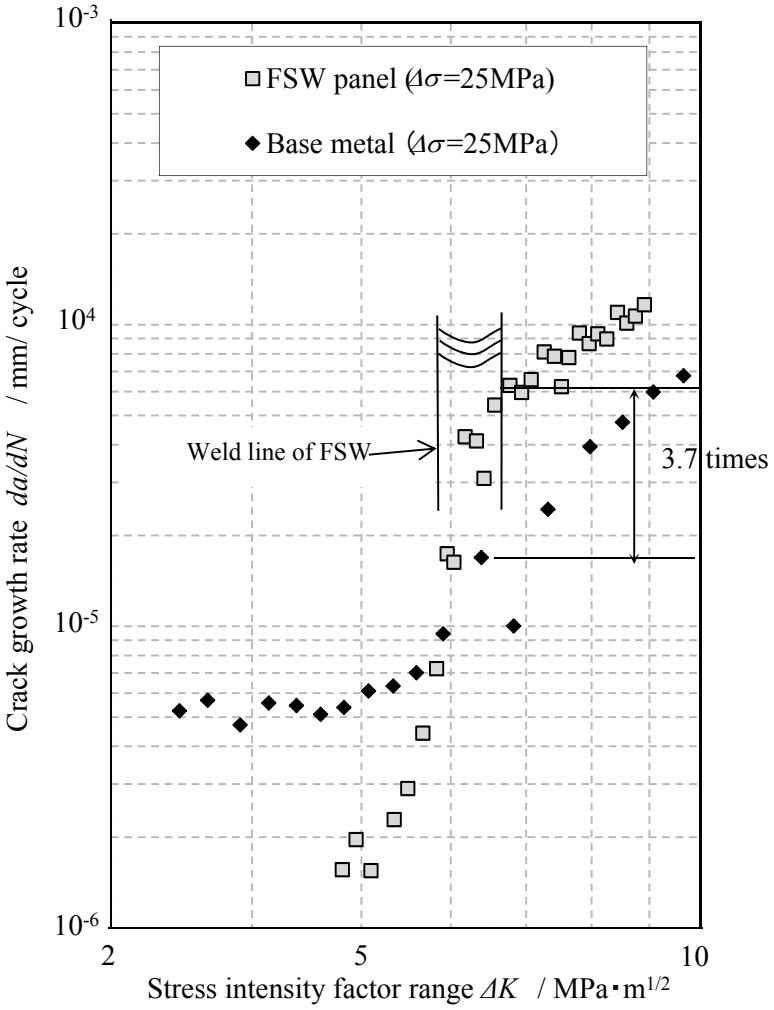

Figure 9. da/dN-ΔK curves ($\Delta\sigma$ = 25 MPa)

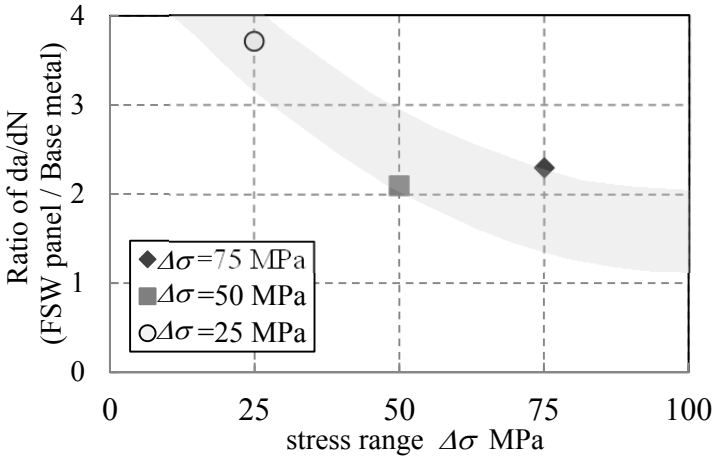

Figure 10. Comparison of fatigue crack growth rate

4. Conclusions

Fatigue crack growth test were conducted in order to evaluate the effect of residual stress field on crack growth propagation. The results are as follows:

(1) The extensometer can be installed tightly on the specimen by using the modified jig with magnet. The test results indicate that the accuracy of crack opening stress measurement is improved.
(2) Stress ranges between 50 MPa and 75 MPa does not clearly affect the acceleration ratio for crack growth rate against the base material. On the other hand, in the case of $\Delta\sigma$ = 25 MPa, the effect of residual stress on the acceleration ratio for crack growth rate against the base material is relatively high. This means the acceleration and deceleration of crack growth rate for that situation is also high. In this test, the acceleration ratio of the crack growth rate for the FSW panel against the base material is 3.7.

References

[1] G. Bussu, P E. Irving, Static and fatigue performance of Friction Stir Welded 2024-T351 aluminum joints, Proceedings of 1st International Symposium on Friction Stir Welding, 1999.
[2] K. Kuwayama, M. Asakawa, T. Okada, T. Nakamura, S. Machida, S. Fujita, Fatigue crack propagation property of friction stir welded 2024-T3 aluminum alloy, APISAT 2009, CD.
[3] T. Okada, K. Kuwayama, S. Fujita, M. Asakawa, T. Nakamura, Properties of fatigue crack propagation in friction stir welded 2024-T3 aluminum alloy, ICAF 2009, pp. 899-908
[4] S. Fujita, M. Asakawa, T. Okada, T. Nakamura, S. Machida, K. Kuwayama, Evaluation of FSW Fatigue Crack Growth Rate Based on Crack Closure Phenomenon, APISAT 2010, CD.
[5] T. Noguchi, M. Asakawa, T. Okada, T. Nakamura, S. Machida, K. Kuwayama, S. Fujita, Property for Fatigue Crack Propagation of Friction Stir Welded 2024-T3 Aluminum Alloy, APISAT 2012; CD.
[6] American Society for Testing and Material, Standard Test Method for Measurement of Fatigue Crack Growth Rates, ASTM E647-08, 2008
[7] Y. Chung, J. Song, Improvement of ASTM compliance offset method for precise determination of crack opening load, International Journal of Fatigue 31, 2009, pp.809-819
[8] W. Elber, The Significance of Fatigue Crack Closure, ASTM STP 486, 1971
[9] J.Schijve, Some Formulas for the Crack Opening Stress Level, Engineering Fracture Mechanics, 1981, pp.461-465.

Development and Several Additional Performances of Dual-Spindle Rotating Bending Fatigue Testing Machine GIGA QUAD

Taizoh Yamamoto[1,*], Akio Kokubu[1], Tatsuo Sakai[2], Yuki Nakamura[3]

[1] Yamamoto Metal Technos Co. Ltd., 4-7 Setoguchi 2-chome, Hirano-ku, Osaka, 547-0034 Japan
[2] Ritsumeikan University, 1-1-1 Nojihigashi, Kusatsu, Shiga, 525-8577 Japan
[3] Toyota National College of Technology, 2-1 Eiseicho, Toyota, Aichi, 471-8525 Japan
* Corresponding author: yamakin@mx1.alpha-web.ne.jp

Abstract In order to investigate the fatigue characteristics of metallic materials experimentally, a long period of time is required to get sufficient number of S-N data. In recent years, in order to overcome this difficulty, multi-type rotating bending fatigue testing machine whose name is GIGA QUAD have been developed by Yamamoto Metal Technos Co., Ltd., in which four specimens can be tested simultaneously.
In this time, some additional new functions have been developed as follows;
(1) 'high and low temperature environmental testing unit' whose target temperature is in a range of 600℃ and -150deg.C, (2) 'constant temperature/humid environmental testing unit' combined with the conventional corrosive cell, (3) ‘fracture alarm unit’, and (4) ‘2-step variable loading unit’.
By combining these new functions with the machine of GIGA QUAD, one can perform the fatigue tests efficiently corresponding to the respective requirements for researchers in both of academic and industrial sectors.
Keywords High temperature environmental testing unit, Low temperature environmental testing unit, Constant temperature/humid environmental testing unit, Fracture alarm unit, 2-step variable loading unit

1. Introduction

One of difficulties in fatigue tests for structural materials is to take a long time to perform the fatigue test. Fatigue tests are usually conducted toward the loading cycles of $N=10^7$, but the fatigue property in gigacycle regime is also focused as an important subject in recent years[1]-[8]. In such a long life region, a tremendous long period is required to perform fatigue tests. If the fatigue test is performed at the loading frequency of 50Hz, it takes more than 200 days to reach 10^9 cycles of the load application. It means that it takes very long term for us to obtain one S-N curve.
In addition, since the fatigue life of any metallic material has a distinct scatter, sufficient number of specimens should be tested to obtain the reliable fatigue property. An example of such fatigue test data for a bearing steel in very high cycle regime are shown in Figure 1 as an S-N diagram[5]. Type I indicates the conventional bearing steel, whereas Type II indicates the high purity bearing steel.

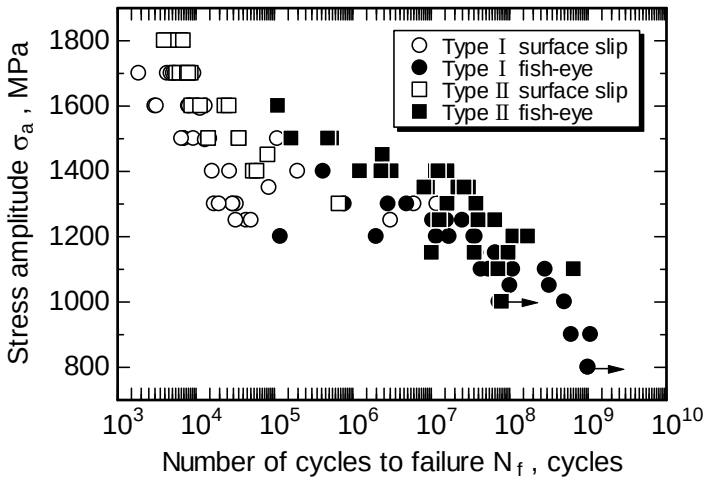

Figure 1. Typical example of fatigue test data for bearing steel in very high cycle regime

Open marks indicate the data in the surface initiated fracture, while solid marks give those data in the interior inclusion initiated fracture. In order to complete a series of fatigue tests to obtain all the data in Fig.1, it takes several years for one kind of metallic material. This circumstance introduces a serious difficulty to every researcher in the area of "*Metal Fatigue*" from technological and economical backgrounds.

If the high loading frequency such as ultrasonic fatigue test was accepted to save the testing time, temperature raising of the specimen due to the internal friction would take place and some cooling system or intermittent loading system should be furnished to examine the original fatigue property[9-12]. Thus, the acceleration fatigue test by ultrasonic technology would cause new difficult subjects as the fatigue testing method to obtain the fatigue property at the usual frequency.

In order to overcome these difficulties, authors have developed special types of fatigue testing machines in rotating bending, in which four specimens can be tested simultaneously[13,14]. Thus a series of fatigue tests even in gigacycle regime can be carried out within a reasonable time period. Based on this advantageous performance, the name of "GIGA QUAD" was accepted for this new machine. By using this machine of GIGA QUAD, fatigue tests can be performed much quickly comparing with the conventional testing machines, even if it is used with various environment options. Accordingly, this machine is useful to file up a number of fatigue test data in gigacycle regime for various kinds of metallic materials, and such databases can provide the fundamental design data for mechanical structures in the wide variety of the engineering application.

2. DUAL-SPINDLE ROTATING BENDING FATIGUE TESTING MACHINE

This machine has two spindles and two specimens can be mounted at both ends of each spindle as indicated in Fig.2 and Fig.3. Each spindle is driven by an electric motor via a V belt and the number of revolution is counted by means of photo-sensor. Thus, this machine can perform fatigue tests for 4 specimens simultaneously. In order to apply the testing load, the corresponding weight is suspended through a helical spring attached to the outer bearing block. The rotating speed of the spindle, that is, the testing speed is 3,150rpm (52.5Hz)

GIGA QUAD has two types of 'YRB200' and 'YRB200L' according to the loading capacity (Maximum load). The maximum load of YRB200 is 20kg, whereas the load of YRB200L is 80kg.

Table 1. Specification of the Device

	YRB200	YRB200L
Motor	0.2kw-4P	0.4kw-4p
Capacitance	380V	380V
Collet Chuck	φ2.5～13	φ2.5～20
Max Load	20kg x 4	80kg x 4
Spindle Speed	3,150rpm	3,150rpm
Weight	140kg	170kg
Size	470x400x1050	800x660x1100
Spindle Number	2	2

Figure 2. GIGA QUAD YRB200

Figure 3. GIGA QUAD YRB200L

Hourglass type of specimen as shown in Fig.4 is accepted as a formal test piece. Diameter of the critical section 'φβ' is designed as to give the reasonable stress level for the each material, while the diameter of the specimen grip 'φγ' may be decided by user freely. Collet chucks with different diameters such as 6mm, 8mm and 10mm are prepared in advance. Among them, the user can choose the most preferable collet chuck depending on the individual circumstance for the testing material.

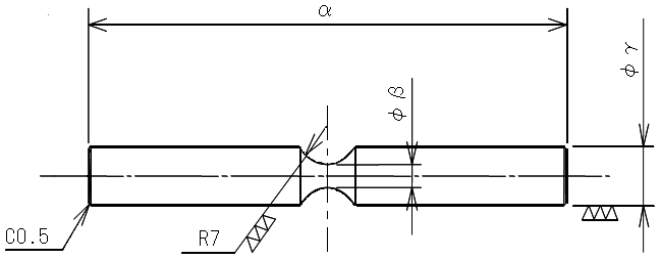

Figure 4. The shape and dimensions of the specimen

3. Support for environmental testing

3.1. High temperature environmental testing unit

In order to perform the rotating bending fatigue test at high temperature, a special chamber and a

temperature controlling system have been developed.
By using such an unit, one can carry out the fatigue test within a temperature range of room temperature (RT) to 600deg.C. Accuracy of the temperature controlling is within ±2deg.C. As fatigue test data are distinctly affected by the testing temperature, it is important to perform the fatigue tests at the accurate temperature. In such a case, this unit is useful to obtain the correct S-N property of the material at the definite temperature.

Specification
Temperature controlling range: room temperature to 600deg.C
Size of control panel box: 170mm x 220mm x 280mm
Specimen type : our standard specimen (φ10)
Power: AC100V 1set

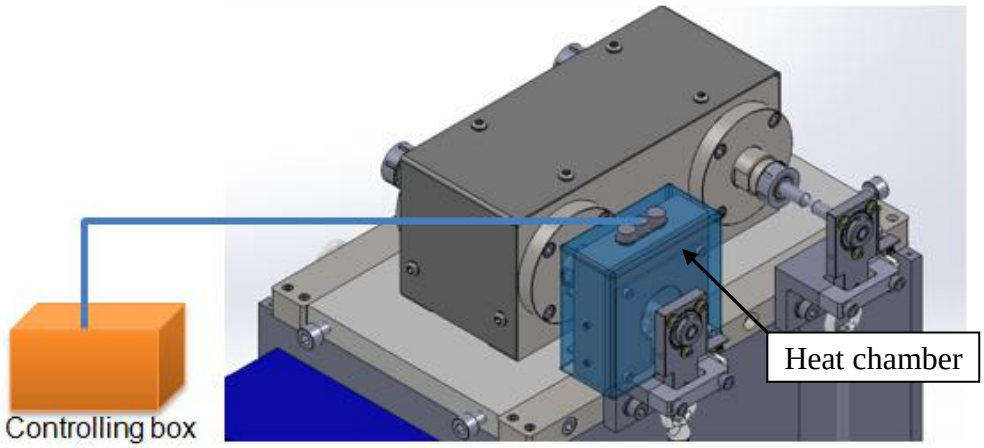

Figure 5. High temperature environmental testing unit

3.2. Low temperature environmental testing unit

A special unit to spray liquid nitrogen into the chamber has been developed to conduct the rotating bending fatigue test at low temperature environment.
By using this unit, one can carry out the fatigue test within the temperature range of RT to -150deg.C with the accuracy of ±2deg.C.

Specification
Temperature controlling range : -150 deg.C to room temperature
Size of control panel box : 170mm x 220mm x 280mm
Specimen type : our standard specimen (φ10)

3.3. Constant temperature/humid environmental testing unit

A special unit to control the temperature and humidity inside the chamber has been developed to perform the rotating bending fatigue test under such a corrosive environment.
In the case of corrosive environment, the control of temperature and humidity is the most important requirement to obtain reliable experimental data.

By means of this unit, a variety of environment varying cycles such as dried and humid environment after dropping the corrosive solution can be created easily.

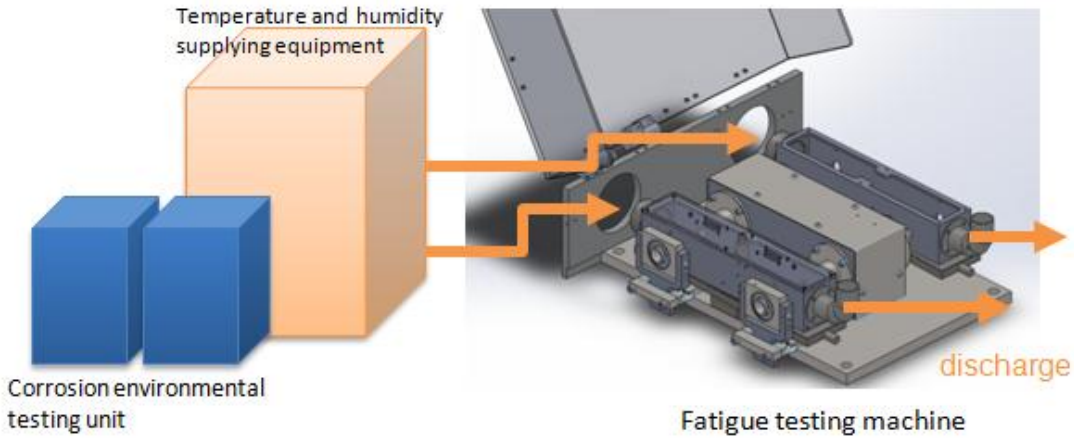

Figure 6. High temperature environmental testing unit

3.4. 2-step variable loading unit

A special loading unit has been developed to perform the rotating bending fatigue test under the condition of 2-step variable loading. Stress applied to the specimen is provided by suspending the appropriate weight in the structure of the machine. In this unit, 2-step loading is applied by lifting a part of weight with air cylinder periodically in testing. By setting any value of the weight and the lifting period, one can perform fatigue tests in a wide variety of the testing environments close to real machines in the practical use.

3.5. Fracture alarm unit

A fracture alarm unit which can detect fracture of specimen and inform the fracture to researchers via e-mail has been developed. In the case of fatigue test to obtain the S-N property, the test is repeatedly conducted by using a lot of specimens. In some cases, stress is changed with a definite time span in order to simulate the actual service loading. Since the fatigue life of each specimen has a distinct scatter, it is impossible to know the fatigue life exactly before the fatigue test. Due to this difficulty, every researcher has to come to the testing machine to confirm whether the specimen has failed or not.

If the person does not notice the fracture of the specimen, he/she wastes much time to find the fatigue failure even though the number of cycles to failure is recorded. In order to prevent such a time consumption, this unit was originally developed here.

Adopting this unit, the researcher can get the prompt information on the failure immediately after the specimen has failed. Thus, the next fatigue test can be started soon and the above time consumption can be effectively solved. In addition to this advantage, researchers' mental stress to check the fatigue failure can be also reduced.

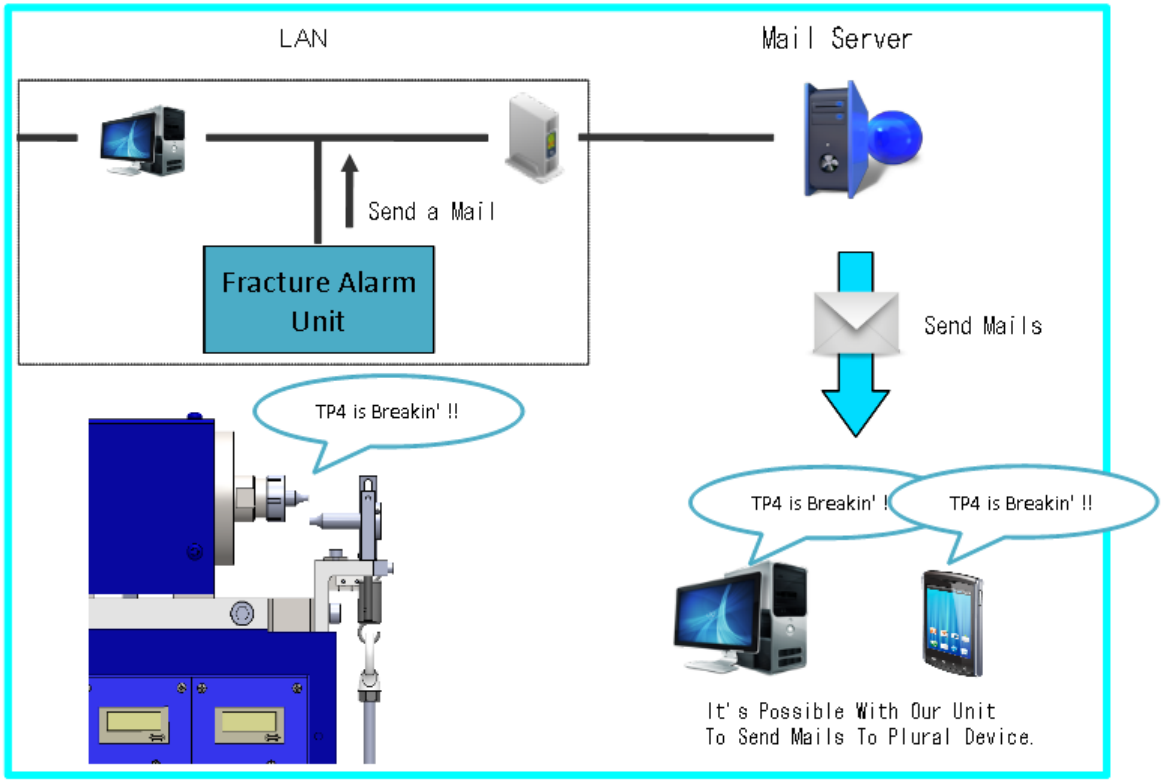

Figure 7. Fracture alarm unit

4. CONCLUDING REMARKS

Conventional fatigue tests take a long time more than 200days to reach $N=10^9$, and a number of fatigue test data are required as the fundamental data in the mechanical design. In order to solve such difficulties, the high performance fatigue testing machine in rotating bending "GIGA QUAD" has been developed in this work.

Based on a lot of experimental results, the fundamental performance of this testing machine was confirmed. Actually these machines are already being used at many laboratories in universities and industries. Thus, conventional customers and new customers have informed that this testing machine is successfully used to obtain a number of fatigue data within a reasonable short period.

5. REFERENCES

[1] Sakai T. Review and Prospects for Current Studies on Very High Cycle Fatigue of Metallic Materials for Machine Structural Use. Proc. of VHCF-4, Ann Arbor, MI, USA, (2007), 3-12.

[2] Bathias, C., P. C. Paris. Gigacycle Fatigue in Mechanical Practice, Marcel Dekker, 2005.

[3] Sakai T., Ochi Y., Jones J. W. Special Issue on the Third International Conference on Very High Cycle Fatigue held in Kyoto/Kusatsu, Japan on 16-19 September, 2004, International Journal of Fatigue, 2006; 28: 1437.

[4] T. Sakai, Review and Prospects for Current Studies on Very High Cycle Fatigue of Metallic Materials for Machine Structural Use, Journal of Solid Mechanics and Materials Engineering, Vol.3, No.3, (2009), 425-439.

[5] N. Oguma, B. Lian, T. Sakai, K. Watanabe, and Y. Odake, Long Life Fatigue Fracture Induced by Interior Inclusions for High Carbon Chromium Bearing Steels under Rotating Bending, Journal of ASTM International, Vol.7, No.9, (2010), 1-9.
[6] W. Li, T. Sakai, Q. Li, L.T. Lu and P. Wang, Effect of Loading Type on Fatigue Properties of High Strength Bearing Steel in Very High Cycle Regime, Materials Science and Engineering, A, Vol.528, No.15, (2011), 5044-5052.
[7] H. Mughrabi, Zur dauerschwingfestigkeit im bereich extrem hoher bruchlastspielzahlen: Mehrstufige lebensdauerkurven, Harterei-technische Mitteilungen, 56 (2001), 300-303.
[8] T. Sakai, B. Lian, M. Takeda, K. Shiozawa, N. Oguma, Y. Ochi, M. Nakajima, T. Nakamura, Statistical duplex S–N characteristics of high carbon chromium bearing steel in rotating bending in very high cycle regime, Int J Fatigue, 32 (2010), 497-504.
[9] R. Ebara, The Present Situation and Future Problems in Ultrasonic Fatigue Testing – Mainly reviewed on Environmental Effects and Materials' Screening, International Journal of Fatigue, 28, (2006), 1465-1470.
[10] H. O. K. Kirchner, W. Kromp, F. B. Prinz, P. Trimmel, Plastic Deformation under Simultaneous Cyclic and Unidirectional Loading at Low and Ultrasonic Frequencies. Mat. Sci. Eng., 68, (1985), 197-206.
[11] S. Stanzl-Tschegg, Fatigue Crack Growth and Thresholds at Ultrasonic Frequencies, International Journal of Fatigue, 28, (2006), 1465-1470.
[12] H. Ishii, T. Yamada, Y. Okada, Very High Cycle Fatigue Strengths of Thin Sheet Metals, Proceedings of VHCF-3, (2004), 420-426.
[13] T. Sakai, T. Furusawa, R. Takizawa, M. Nakajima, K. Shiozawa, N. Oguma, K. Okada, Y. Ochi, A. Sugeta, N. Kawagoishi, A. Sakaida, H. Sakamoto, Development of Multi-type Fatigue Testing Machine in Axial Loading and Some Fatigue Test Results on A Bearing Steel, Proceedings of VHCF-3, (2004), 484-491.
[14] T. Sakai, T. Furusawa, R. Takizawa, N. Oguma, H. Hohjo, H. Ikuno, Development of Multi-type High Efficiency Fatigue Testing Machines in Rotating Bending and Axial Loading, Proceedings of the Hael Mughrabi Honorary Symposium, TMS Annual Meeting, (2008), 241-246.

High Cycle Fatigue Simulation using Multi-temporal Scale Method coupled with Continuum Damage Mechanics

Dong Qian[1,*], Sagar Bhamare[2]

[1] Department of Mechanical Engineering, University of Texas at Dallas, Richardson, TX 75080, USA
[2] Innova Engineering, Inc., Irvine, CA 92614, USA
* Corresponding author: dong.qian@utdallas.edu

Abstract A multiple temporal scale computational approach for assessing the fatigue life of engineering materials and components is presented. This full-scale simulation approach is developed in light of the challenges in employing the traditional computational method based on Finite Element Method (FEM)) and semi-discrete schemes for fatigue design and analysis. Simulating loading conditions with cycles on the order of hundreds of thousands and beyond is generally an impractical task for FEM even with the high-performance computing platform. Two critical aspects are addressed, i.e., the multiple time scales associated with the fatigue loading condition and the fatigue initiation/growth representations. Detailed implementation of integrating a multiscale space-time representation with a robust material model for the fatigue failure is outlined and demonstrated in the context of a common choice of industrial metal.

Keywords Space-time FEM, High Cycle Fatigue, Multi-temporal Scale Method, Enrichment

1. Introduction

In fatigue-based design of mechanical components and structures, safe-life and damage-tolerance approaches have been widely employed in practice. In safe-life approach, stress or strain are related to the number of cycles to failure under fatigue loading. Empirical curves developed from such a kind of relation are utilized to predict the life or acceptable level of fatigue load. Damage-tolerance approach based itself on the fracture mechanics concepts established by Griffith [1] and Irwin [2]. Using these concepts, Paris [3] proposed the relationship between the rate of crack growth and the range of applied stress intensity factor, which is used to predict the fatigue crack growth under cyclic loading history. While both methodologies have been widely used by the industry, they have significant limitations due to the empirical nature of the method. In addition, there can be significant scatterings in the fatigue test, which makes the curve-fitting unreliable. Further, the extrapolation of constant amplitude (CA) test data to predict life under variable amplitude (VA) and random loading conditions is a challenging task [4].

Motivated by these limitations, a multiple temporal scale computational approach is developed to assess the fatigue life of structural components. Examples include columns, beams, plates, and shells that are extensively used in assembly of mechanical components. This full-scale simulation approach is established in light of the challenges in employing the traditional computational method based on Finite Element Method (FEM) and semi-discrete schemes for fatigue design and analysis. Semi-discrete schemes such as the popular central difference or Newmark-β methods are known to suffer from either the time-step constraints or lack of convergence due to the oscillatory nature of the fatigue loading condition. As such, simulating loading conditions with cycles on the order of hundreds of thousands and beyond is generally an impractical task for FEM even with the high-performance computing platform. On the other hand, there is a great demand for such a computational capability as factors such as stress history and triaxiality, nonlinear coupling among the loads, complex geometry are known to critically influence the fatigue failure and generally not

fully accounted for in the empirical design approaches that are in practice today.

More specifically, an enriched space-time finite element method (XTFEM) based on the time discontinuous Galerkin formulation is developed to handle the multiple temporal scales in fatigue problems. XTFEM is coupled with the two-scale continuum damage mechanics model for evaluating fatigue damage accumulation, with a damage model governing the fatigue crack-initiation and propagation as the simulation progresses. High Cycle Fatigue (HCF) simulations are performed using the developed methodology on a notched specimen of AISI 304L steel to predict total fatigue life under cyclic conditions.

2. Technical Approach

2.1 A Computational Framework of Enriched Space-time FEM

As the name suggests, space-time method introduces discretization both in the spatial and time domains. The main advantage of the space-time method over the semi-discrete scheme based methods is reflected in the ability to introduce approximations in the temporal domain. Space-time methods are also known for their capability of reducing artificially oscillations and handling loads with sharp gradients. These features of space-time method make it an attractive platform for fast and accurate simulation of the fatigue loading. In the semi-discrete scheme, approximations are established in space **x** for each time instance *t*. In the space-time formulation, the approximations are built simultaneously with both space **x** and time *t*. If finite element method is used, we have the following approximation in the space/time description for a general three-dimensional case

$$\mathbf{u}(\mathbf{x},t)=\sum_{I} N_{\mathbf{I}}(\mathbf{x},t)\mathbf{d}_{\mathbf{I}} \tag{1}$$

in which $N_I(\mathbf{x},t)$ is the finite element shape functions at nodes indexed by I and $\mathbf{d}_I$ is the corresponding nodal displacement vector. Note that although N_I and $\mathbf{d}_I$ look similar to the ones in the semi-discrete scheme, they are defined on a space/time grid as opposed to space only.

To describe our approach what is also known as the time discontinuous Galerkin method (TDG) [5], the 2D space/time grid plotted in Figure 1 will be used as a reference. We consider a space/time domain Q, which is the Cartesian product of space domain Ω and time duration $(0,\mathrm{T})$, i.e., $Q=\Omega\times(0,\mathrm{T})$.

As can be seen from Figure 1, the time domain is subdivided into time slabs with the n-th time slab given as $Q_n=\Omega\times(t_{n-1},t_n)$. In the current method, we will restrict the presence of discontinuities to the mechanical field only. We define a jump operator $[\ ]$, given as

$$[w(t)]=w(t^+)-w(t^-) \ \text{ and } \ [w(\mathbf{x})]=w(\mathbf{x}^+)-w(\mathbf{x}^-) \tag{2}$$

with $w(t^\pm)=w(t\pm\varepsilon)$, $w(\mathbf{x}^\pm)=w(\mathbf{x}\pm\varepsilon\mathbf{n})$, ε represents infinitesimal perturbation, **n** is the

normal to the surface of discontinuity.

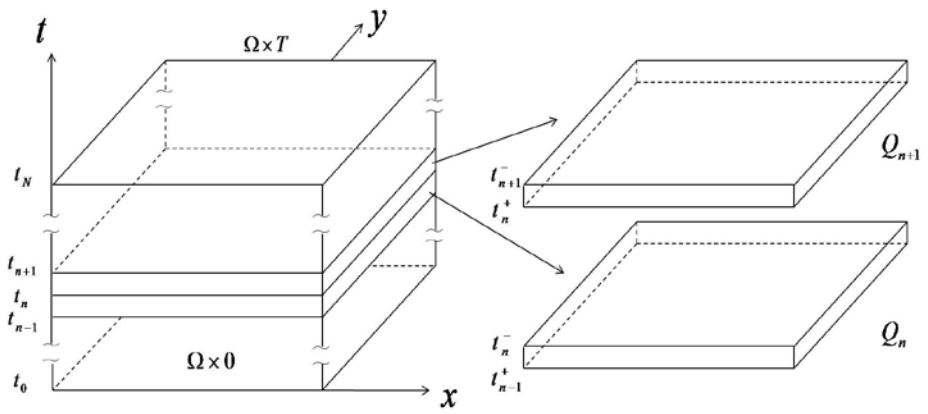

Figure 1: Illustration of TDG discretization of space-time finite elements.

By applying the variational principle to the governing equations of momentum within each time slab, we develop the so-called weak form that serves as the basis for computational implementation. For the the *n*-th time slab, we have the following bilinear form:

$$B_{DG}\left(\mathbf{w}^h,\mathbf{u}^h\right)_n = L_{DG}\left(\mathbf{w}^h\right)_n \tag{3}$$

with

$$B_{DG}\left(\mathbf{w}^h,\mathbf{u}^h\right)_n = \int_Q \dot{\mathbf{w}}^h\cdot\rho\ddot{\mathbf{u}}^h dQ_n + \int_Q \nabla\dot{\mathbf{w}}^h\cdot\boldsymbol{\sigma}\left(\nabla\mathbf{u}^h\right)dQ_n + \int_\Omega \dot{\mathbf{w}}^h\left(t_{n-1}^+\right)\cdot\rho\dot{\mathbf{u}}^h\left(t_{n-1}^+\right)d\Omega + \int_\Omega \nabla\mathbf{w}^h\left(t_{n-1}^+\right)\cdot\boldsymbol{\sigma}\left(\nabla\mathbf{u}^h\left(t_{n-1}^+\right)\right)d\Omega$$

$$L_{DG}\left(\mathbf{w}^h\right)_n = \int_Q \dot{\mathbf{w}}^h\cdot\rho\,\mathrm{b}dQ_n + \int_\gamma \dot{\mathbf{w}}^h\cdot\mathrm{t}d\left(\gamma_t\right)_n + \int_\Omega \dot{\mathbf{w}}^h\left(t_{n-1}^+\right)\cdot\rho\dot{\mathbf{u}}^h\left(t_{n-1}^-\right)d\Omega + \int_\Omega \nabla\mathbf{w}^h\left(t_{n-1}^+\right)\cdot\boldsymbol{\sigma}\left(\nabla\mathbf{u}^h\left(t_{n-1}^-\right)\right)d\Omega + \int_\gamma \dot{\mathbf{w}}^h\cdot\left[\mathrm{n}\cdot\boldsymbol{\sigma}\right]d\left(\gamma_i\right)_n \tag{4-5}$$

in which $\mathbf{u}^h$ and $\mathbf{w}^h$ are respectively the trial and test function for displacement. In Eqs.(4) and (5), the combination of the first two terms represents the momentum balance and traction boundary conditions. The 3rd and 4th terms in Eqs.(4) and (5) combined gives the continuity conditions between the time slabs. The last term in Eq.(5) is due to internal discontinuity.

In addressing the multiple temporal scales, we propose that the space-time approximation from Eq.(1) can be further improved by introducing enrichment [6-8]. In the enrichment formulation, the displacement field is approximated as

$$\mathbf{u}^h\left(\mathbf{x},t\right) = \sum_{I\in\bar{N}} N_I\left(\mathbf{x},t\right)\mathbf{d}_I + \sum_{J\in\bar{N}} N_J\left(\mathbf{x},t\right)\left(\phi\left(\mathbf{x},t\right)-\phi\left(\mathbf{x}_J,t_J\right)\right)\mathbf{a}_J \tag{6}$$

in which $N_I\left(\mathbf{x},t\right)$ is the regular space/time finite element shape functions, $\phi\left(\mathbf{x},t\right)$ is the called an enrichment function and is selected based on the physics of the problem. Correspondingly, $\mathbf{d}_I$ is the nodal displacement, and $\mathbf{a}_J$ is the enriched degree of freedom. The multiscale

decomposition in Eq.(6) can be further written in direct notation, i.e., $\mathbf{u}^h(\mathbf{x},t) = \mathbf{N}\mathbf{u} = \bar{\mathbf{N}}\mathbf{d} + \tilde{\mathbf{N}}\mathbf{a}$ where $\bar{\mathbf{N}}$ is the FEM shape function matrix and $\tilde{\mathbf{N}}$ is the enrichment shape function matrix. $\mathbf{N} = \left[\bar{\mathbf{N}}, \tilde{\mathbf{N}}\right]$ and $\mathbf{u} = [\mathbf{d}, \mathbf{a}]^T$ with $\mathbf{d}$ the nodal displacement vector and $\mathbf{a}$ the vector for the enriched degree of freedom. Note that the way that the enrichment function $\phi(\mathbf{x},t)$ being built in Eq.(6) is an equivalent statement of the "partition-of-unity" concept. It ensures the consistency of the approximation. An example of regular and enrichment space-time shape functions is shown in Figure 2. In this case, we have used a fine scale harmonic function for $\phi(\mathbf{x},t)$ with a temporal scale that is smaller than the temporal element size of the regular space-time FEM.

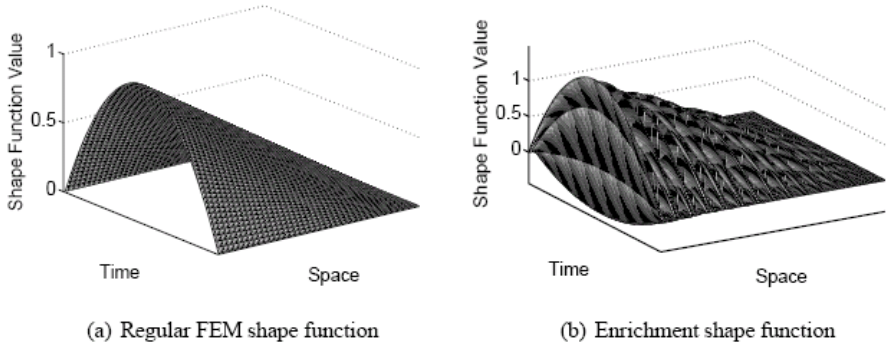

(a) Regular FEM shape function (b) Enrichment shape function

Figure 2: Examples of regular and enrichment shape functions.

We have employed *harmonic* enrichment function considering the fine scale harmonic components of the loading and the solution (displacement) in the case of HCF. i.e., $\phi(\mathbf{x},t) = \sum_k \sin(\omega_k t)$ in which ω_k represents the *k*-th characteristic frequency. Complete spatial domain will be enriched with the time enrichment function as the whole structure is subjected to fatigue loads. With the addition of the enrichment, the final discretized equation is in the form of

$$\begin{bmatrix} \mathbf{K}_{rr} & \mathbf{K}_{re} \\ \mathbf{K}_{er} & \mathbf{K}_{ee} \end{bmatrix} \begin{Bmatrix} \mathbf{d} \\ \mathbf{a} \end{Bmatrix} = \begin{Bmatrix} \mathbf{F}_r \\ \mathbf{F}_e \end{Bmatrix} \tag{7}$$

with subscripts "r" and "e" representing the contribution from the regular and enrichment components, respectively.

2.2 Modeling of Material Failure under Cyclic Loading

Modeling damage under fatigue loading is challenging due to the strong coupling to the loading path. Many techniques have been developed, including fracture mechanics, porous plasticity and continuum damage mechanics (CDM). In HCF, we introduce the two-scale CDM approach proposed by Lemaitre et al. [9] and Desmorat et al. [10]. This approach assumes that material behavior at mesoscale is elastic and damage can be treated as quasi-brittle in HCF. This quasi-brittle damage is modeled by introducing damage variables that represent the microcracks and microvoid

due to HCF at microscale. These microdefects cause the plasticity at microscale but the mesoscale behavior remains elastic. In light of the the basic features of HCF, a two-scale damage model is developed. A schematic of the model is shown in Figure 3. All the quantities with subscript μ are defined at the microscale.

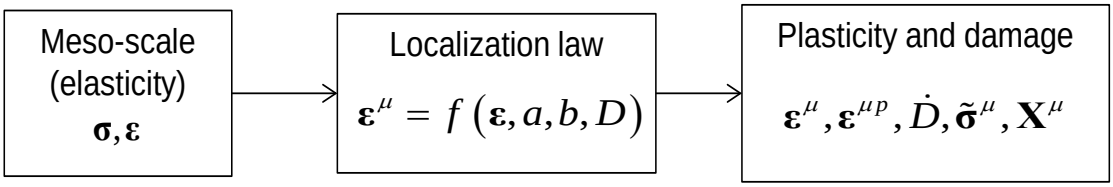

Figure 3: A schematic for the two-scale damage model.

The development of the model can be described by three steps. First of all, stress-strain $\left(\boldsymbol{\sigma}-\boldsymbol{\varepsilon}\right)$ data at mesoscale can be obtained using the elastic material properties such as Young's modulus and Poisson's ratio $\left(E,\nu\right)$. Secondly, the scale transition from the meso to micro will be described by a localization law based on the modified Eshelby-Kroner law. Localization law relates the microscale strain $\boldsymbol{\varepsilon}^{\mu}$ to the mesoscale strain $\boldsymbol{\varepsilon}$ through material parameters *a*, *b* and damage *D* given in the second box in Figure 3. Here *a*, *b* are functions of ν based on Eshelby's inclusion theory. Finally we will formulate a plasticity-damage model at the microscale as shown in the third box of Figure 3. The key component of this model is the damage evolution law, which assumes that the damage rate is proportional to the effective plastic strain rate $\dot{p}^{\mu}$, given as

$$\dot{D} = \left(\frac{Y^{\mu}}{S}\right)^{s} \dot{p}^{\mu} \quad \text{if } \dot{p}^{\mu} \geq \dot{p}_{D}^{\mu} \text{ or } w_s \geq w_d \tag{8}$$

Here s, S are the material parameters to be calibrated from available experimental data on fatigue, Y^{μ} is the damage energy release rate and w_s is the stored energy in the material, w_d is the damage threshold energy, $\dot{p}_{D}^{\mu}$ is the threshold effective plastic strain. Threshold values act as a barrier for damage initiation. Once these conditions are met, damage accumulation begins. Threshold values depend on the material and the type of loading condition. The major advantage of employing Eq.(8) is from the fact that fatigue failure is regarded as a function of increment in strain or stress as opposed to function of the load cycles.

A constitutive solver has been developed for the two-scale damage model outlined here and integrated with the space-time FEM framework. The specific algorithm will be similar to that of a standard rate-dependent plasticity-damage model. A mixed explicit-implicit scheme has been implemented.

3. Numerical Example

The developed methodology is applied to the simulation of fatigue response of a single notched rectangular steel plate subjected to cyclic load. The geometry and boundary condition are shown in Figure 4. A fully reversed fatigue load at $\omega = 20Hz$ is applied to the top face of the plate in a form of uniformly distributed pressure of 70 MPa while the bottom surface is fixed, which replicates the loading conditions during the actual fatigue test where the bottom surface is clamped in grips and top surface is subjected to push-pull loading. The plate thickness is taken as $2mm$. The problem is modeled as plane stress problem. Motivation behind this problem is to simulate the complete fatigue loading history using the presented formulation, calculate damage at gauss points during the simulation, and predict the fatigue crack initiation and propagation. Mode I crack growth is expected in this loading situation.

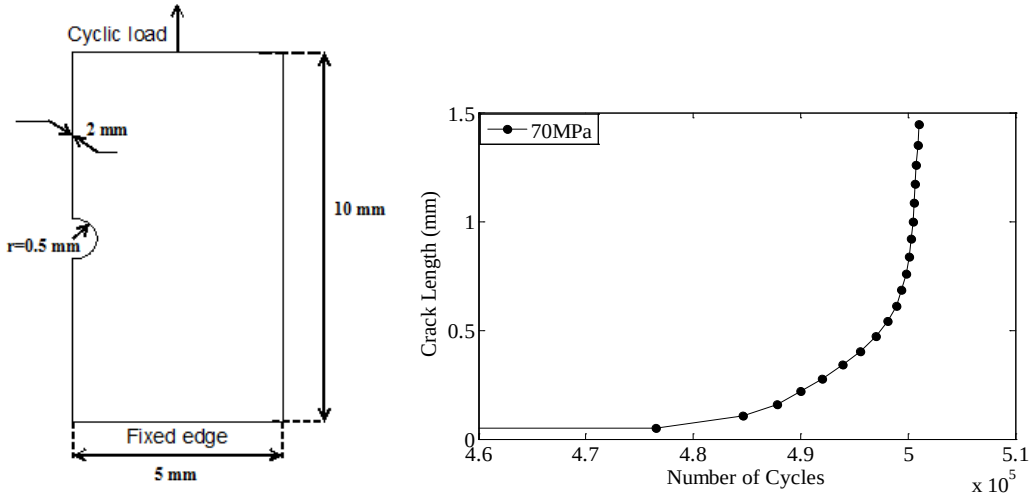

Figure 4: (a) Configuration of the fatigue simulation of a single notched plate. (b) Crack growth vs. number of cycles for the case of completely reversed load of 70 MPa

The space-time discretization employs a multiplicative form of the shape function so that the spatial discretization is independent of the temporal discretization. Advantage of this treatment is that the existing meshing scheme widely used in the case conventional FEM can be directly adopted. In the present case, the plate is discretized by quadrilateral mesh with non-uniform mesh density. Fine mesh is prescribed close to the notch in order to capture crack initiation and growth. In the temporal dimension, quadratic shape function is employed for each space-time slab. The regular space-time shape functions are enriched with a harmonic function with frequency of $20\,Hz$. With the two-scale damage model introduced here, crack initiation and propagation are governed by the evolution of the damage. Numerically, once the damage-based the crack criteria is met, the corresponding space element is eliminated. The material parameters chosen correspond to 304L steel and are based on the earlier work by Lemaitre and Desmorat [9-12]. Detailed implementations of the model is documented in an upcoming paper [13] and will not be presented here due to page limitation.

Crack growth as a function of the load cycles predicted by the simulation is shown in Figure 4. It is worth noting that up to half-million load cycles are successfully simulated with the proposed numerical approach. In addition, the nature of the crack growth data is similar to that obtained from the experiments. This suggests that, with the calibrated material model accurate fatigue simulation for the HCF loading can be performed using the methodology outlined in this paper.

4. Conclusions

In summary, the proposed multiscale space-time formulation with harmonic enrichment function successfully simulates the practical fatigue loading histories. To capture the fatigue crack initiation and propagation, a two-scale damage model algorithm is implemented. Damage model algorithm is integrated with the multiscale space-time FEM formulation. Standard techniques of *element deletion* are used to predict the fatigue crack initiation and propagation. HCF simulations are performed on the notched plate without any *ad hoc* procedure to predict the total fatigue life. Based on the simulations, crack length verses number of cycles curve is generated. The trend of the results is similar to what is observed in the experiments. Mode I crack growth is successfully using XTFEM. Future plan is to verify the predictions by comparing with either literature data or analytical model (e.g., Paris law crack growth predictions). In addition, different fatigue-based material model can be integrated with the framework presented.

Acknowledgements

The authors gratefully acknowledge the financial support of the start-up fund from the University of Texas at Dallas and the ASEE Air Force Summer Faculty Fellowship. This work was also supported in part by an allocation of computing time from the Ohio Supercomputer Center.

References

[1] A. Griffith, "The Phenomena of Rupture and Flow in Solids," *Philosophical Transactions of the Royal Society of London*, vol. 221, pp. 163-198, 1920.

[2] G. Irwin, "Analysis of stresses and strains near to the end of crack traversing a plate," *ASME Journal of Applied Mechanics*, vol. 24, pp. 361-364, 1957.

[3] P. C. Paris and F. Erdogan, "A critical analysis of crack propagation laws," *J basic Eng*, vol. 85, pp. 209-219, 1963.

[4] L. Molent, M. McDonald, S. Barter, and R. Jones, "Evaluation of spectrum fatigue crack growth using variable amplitude data," *International Journal of Fatigue*, vol. 30, pp. 119-137, 2008.

[5] G. M. Hulbert and T. J. R. Hughes, "Space-Time Finite-Element Methods For 2nd-Order Hyperbolic-Equations," *Computer Methods In Applied Mechanics And Engineering*, vol. 84, pp. 327-348, Dec 1990.

[6] S. U. Chirputkar and D. Qian, "Coupled atomistic/continuum simulation based on extended space-time finite element method," *Cmes-Computer Modeling In Engineering & Sciences*, vol. 24, pp. 185-202, Feb 2008.

[7] J. Chessa and T. Belytschko, "Arbitrary discontinuities in space-time finite elements by level sets and X-FEM," *International Journal for Numerical Methods in Engineering*, vol. 61, pp. 2595-2614, 2004.

[8] Y. Yang, S. Chirputkar, D. N. Alpert, T. Eason, S. Spottswood, and D. Qian, "Enriched space-time finite element method: a new paradigm for multiscaling from elastodynamics to molecular dynamics," *International Journal for Numerical Methods in Engineering*, vol. 92, pp. 115-140, Oct 12 2012.

[9] J. Lemaitre, J. P. Sermage, and R. Desmorat, "A two scale damage concept applied to fatigue," *International Journal of Fracture*, vol. 97, pp. 67-81, 1999.

[10] R. Desmorat, A. Kane, M. Seyedi, and J. P. Sermage, "Two scale damage model and related numerical issues for thermo-mechanical High Cycle Fatigue," *European Journal of Mechanics - A/Solids,* vol. 26, pp. 909-935, 2007.

[11] J. Lemaitre, *A Course of Damage mechanis,* 2nd ed. Berlin: Springer-Verlag, 1996.

[12] J. Lemaitre and I. Doghri, "Damage 90: a post processor for crack initiation," *Computer Methods in Applied Mechanics and Engineering,* vol. 115, pp. 197-232, 1994.

[13] S. Bhamare, T. Eason, M. Spottswood, S. R. Mannava, V. K. Vasudevan, and D. Qian, "High Cycle Fatigue Simulation using Extended Space-Time Finite Element Method coupled Coupled with Continuum Damage Mechanics (submitted)," 2013.

Study on the fatigue crack growth behavior of 30CrMnSiA Straight Attachment Lugs

LiMing Wu[1], YuTing He[1,*], HaiWei Zhang[1], Teng Zhang[1], Qing Shao[1]

[1] Aeronautics and Astronautics Engineering College, Air Force Engineering University, 710038, China
* Corresponding author: hyt666@tom.com

Abstract The finite element model of straight attachment lug subjected to axial or oblique loading is built by using finite element software, a cosine pin-bearing pressure distribution is applied on the pin-hole squeeze surface as a boundary condition. The stress intensity factor (SIF) expressions for single through-the-thickness crack in straight attachment lug that subjected to axial or oblique pin-load less than 45 degrees are determined and validated. The fatigue crack growth rate da/dN and the stress intensity factor range ΔK are obtained by using the fatigue crack growth test data and the SIF expressions. The fatigue crack growth model of the typical straight lugs is established by using the Paris law, offering an analytical as well as experimental method for assessing and designing damage tolerant attachment lugs.

Keywords attachment lug, finite element method, fatigue crack growth, stress intensity factor, the Paris law

1. Introduction

Attachment lugs are one of the most fatigue-and fracture-critical components in modern engineering structures[1]. In aircraft structures, lug-type joints are frequently used to connect major structural components or in linkage structure, theirs failure can result in disastrous accidents. In the study of fatigue crack growth and fracture behavior of attachment lugs, an accurate calculation of the stress intensity factor is essential. There are a number of different methods for determining SIF, K, for crack in aircraft attachment lug.

Over the years, several extensive studies have been made on lug fatigue performance, involving both experimental and analytical means. Liu and Kan[2] and Kirkby and Rooke[3] used the simple compounded solution method which involves superimposing known solutions, such as in Reference [4] to estimate the stress intensity factors. Schijve and Hoeymakers[5] and Wanhill[6] derived empirical K-solutions from the growth rate data for through cracks under constant amplitude loading using a backtracking method such as that proposed by James and Anderson[7]. Pian, et al[8], used the hybrid finite element method to compute the K-values for cracks oriented in various angles from the axial direction of straight lugs. Aberson and Anderson[9] used a special crack-tip singularity element to compute the stress intensity factors for a crack in a nonsymmetrical aircraft lug of an engine pylon. Impellizzeri and Rich[10] modified the exact weight function derived by Bueckner[11], for an edge crack in a semi-infinite plate, to include a series of geometry correction factors. Then they computed the K-values using the weight function method. However, at the aspect of damage tolerance design and analysis, only the situation of straight lug subjected to axial pin loading can be solved. For the straight lug and symmetric tapered lug, which are subjected to axial, oblique and transverse pin loadings, there is a lack of methods for ascertaining the crack propagation characteristics and residual strength. So, it is important to develop analytical as well as experimental procedures for assessing and designing damage tolerant attachment lugs to ensure the operational safety of aircraft[12], and to calculate the stress intensity factors (SIFs) in different geometric parameters and load conditions.

Most of the researches made the assumption that the assumed or computed pin-bearing pressure distribution for an uncracked case remains unchanged even after the crack has initiated and propagated. Based on the parametric study conducted in Reference [8], it was found that, for any given crack length, the difference in the SIF computed using the uniform and cosine pin-bearing pressure distributions was as much as 30 percent. Therefore, it is salient that the correct representation of the pin-bearing pressure distribution during the crack growth process is essential to the calculation of accurate stress intensity factors.

This paper presents a systemic study of the 30CrMnSiA straight attachment lug's fatigue crack growth behavior using the finite element software ANSYS. The finite element model of the lug is established

and the effect of geometric parameters on SIF is calculated and analyzed by the finite element method (FEM) with linear elastic assumptions, as in essence, the fatigue crack growth is brittle and it is often based on Linear Elastic Fracture Mechanics (LEFM) assumption[13]. The fatigue crack growth test and residual strength test are carried out by the material test system MTS-810, the test data validate the finite element analysis and are used to determine the constants C&m of the Paris Law. The fatigue crack growth model of the typical straight lugs is established, offering an analytical as well as experimental method for assessing and designing damage tolerant attachment lugs.

2. Finite Element Modeling and Analyzing

2.1. Finite element modeling and meshing

Figure 1 shows the size of the straight lug discussed in this paper, millimeter is used as the length unit. The length of the single through-the-thickness crack is *a*. The model is meshed with PLANE 183 triangular element, the real constant for "plane stress with thickness" is set to 6.7. The elastic modulus is 200Gpa and the Poisson ratio is 0.3. The node at the crack tip is defined as a singular point and there are 12 triangular elements around it. The radius of the 1st row of elements is *a*/10. The global elements edge length is set to 2. Figure 2 & Figure 3 show the mesh result.

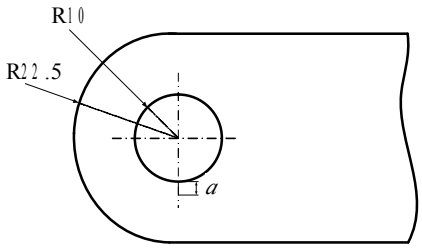

Figure 1. Size of the straight lug

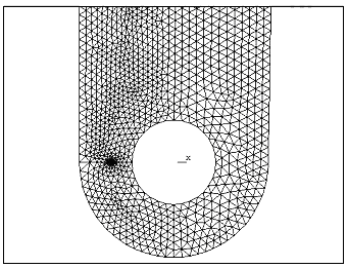
Figure 2. Mesh of the straight lug

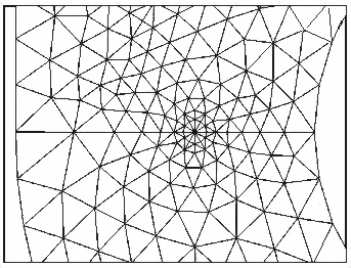
Figure 3. Mesh of the crack tip

2.2. Setting boundary conditions and applying cosine distributed load

Pin load is transferred by squeezing between the lug and the pin matched. Load and stress are supposed to keep unchangeable along the thickness of the hole. The pressure distributed on the squeeze surface follows the cosine distribution law, and the radial load P_i at the point i on the squeeze surface is equal to $P_0 \cos\gamma_i$ [14], as shown in Figure 4.

The x and y axis components of the load P_i are as follows.

$$P_{ix} = P_i \sin\gamma_i \,, \tag{1}$$

$$P_{iy} = P_i \cos\gamma_i \,. \tag{2}$$

The resultant force along y axis is shown as follow.

$$P = \sum P_{iy} = \sum P_i \cos\gamma_i = \sum P_0 \cos^2\gamma_i \,. \tag{3}$$

The cosine distributed nodal force is applied on the nodes on the surface ABC. All the nodes on the symmetry plane of the lug are selected and the displacement values are set to zero. Figure 5 shows the boundary conditions.

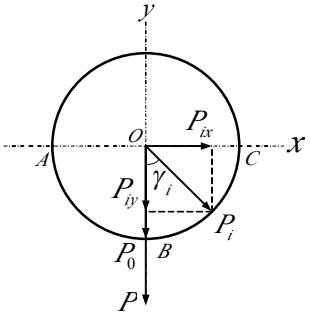

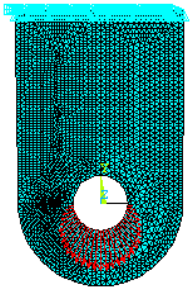

Figure 4. Pin-loading on the squeeze surface

Figure 5. Boundary conditions

2.3. Results analysis

Figure 6 and Figure7 respectively show the Von Mises stress distribution around the lug's hole and the crack tip.

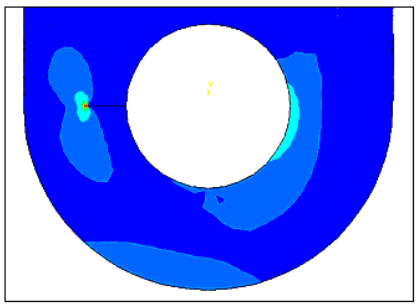

Figure 6. Stress distribution around the lug's hole

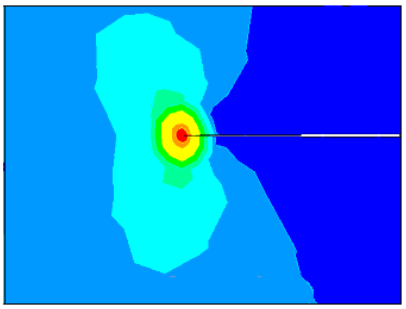

Figure 7. Stress distribution around the crack tip

SIFs of cracks with different lengths are calculated by three methods. Case 1 uses the equation that is used for estimating the straight lugs' critical load in [15] (see formula (4)) to calculate the SIFs. Case 2 uses the configuration factor J_{41L} in [15] (see Figure 8) to get the SIFs' values. This paper calculates the SIFs by finite element method, and the results are shown as case 3 in Figure 9 to compare with the other two cases.

In reference [15] (page 270), it is indicated that the critical load $[P]_c$ of the attachment lug subjected to axial pin-load is

$$[P]_C = \frac{2R_2 tK_C}{\beta\sqrt{\pi a}}. \tag{4}$$

Where

$$\beta = \left(\frac{2W}{1.971D}\beta_1 + \frac{1}{2}\beta_2\right)\cdot\beta_{fw}, \tag{5}$$

$$\beta_1 = \frac{0.31711}{\left(0.3857 + \frac{a}{R_1}\right)^{1.33734}}, \tag{6}$$

$$\beta_2 = \frac{0.8734}{0.3246 + \frac{a}{R_1}} + 0.6762, \tag{7}$$

$$\beta_{fw} = \sqrt{\sec\left(\frac{\pi}{2}\cdot\frac{2R_1 + a}{2R_2 - a}\right)}. \tag{8}$$

In reference [15] (page 139), the SIF of attachment lug subjected to axial pin-load is equal to

$$K = J_{41Z}\cdot\sigma\cdot\sqrt{\pi a}. \tag{9}$$

where the configuration factor J_{41L} can be determined by using Figure 8.

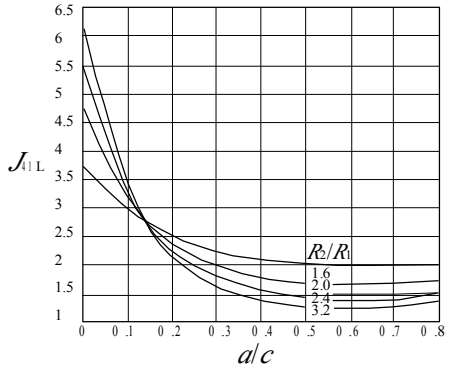

Figure 8. The configuration factor J_{41L} curves

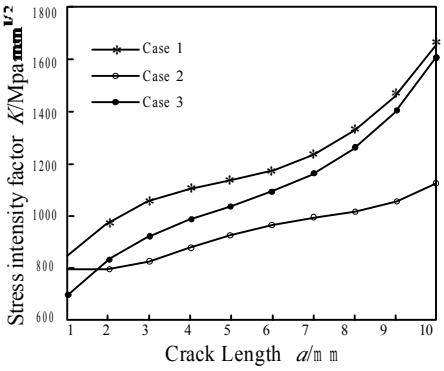

Figure 9. Comparison of the stress intensity factors

3. Calculation of the SIF equations

The geometric parameters of the lug are wrote to the APDL program text file and executed by ANSYS to solve the SIFs automatically and efficiently. The case of the straight attachment lug subjected to axial pin-load is taken as an example for illustrating the approach. Figure 10 shows the parameterized geometry of the lug.

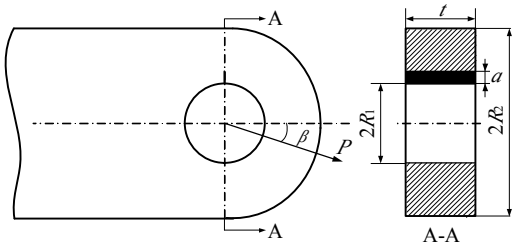

Figure 10. Geometry of the straight attachment lug

The influence law of the dimensionless crack length (a/R_1), the ratio of outer radius to inside radius (R_2/R_1) and the inside radius (R_1) on the SIF are studied, and then, the equation (4) is modified to fit the SIF equation for the straight attachment lug with a single through-the-thickness crack.

Table 1 shows the solving idea. K, K_1, K_2, K_3 stand for the SIFs calculated by equation (4) and represent the values that need to be modified by the influence law of a/R_1, R_2/R_1 and R_1 respectively. K' stands for the SIF calculated by ANSYS as the reference exact value for modifying K_1, K_2, K_3.

Table 1. Solving the SIF equation of the straight lug subjected to axial pin-load

Variate	Invariants	K	K'	$(K')_i/K_i$	Calculating process
$(a/R_1)_1$	R_2/R_1, R_1	$(K_1)_1$	$(K')_1$	$(K')_1/(K_1)_1$	$(a/R_1)_i$ is set as the variate, while $(K')_i/(K_1)_i$ as the dependent variable, function $g(a/R_1)$ can be fitted as below.
⋮	⋮	⋮	⋮	⋮	
$(a/R_1)_n$	R_2/R_1, R_1	$(K_1)_n$	$(K')_n$	$(K')_n/(K_1)_n$	$K_2=K_1\cdot g(a/R_1)$ (10)
$(R_2/R_1)_1$	a/R_1, R_1	$(K_2)_1$	$(K')_1$	$(K')_1/(K_2)_1$	$(R_2/R_1)_i$ is set as the variate, while $(K')_i/(K_2)_i$ as the dependent variable, function $f(R_2/R_1)$ can be fitted as below.
⋮	⋮	⋮	⋮	⋮	
$(R_2/R_1)_n$	a/R_1, R_1	$(K_2)_n$	$(K')_n$	$(K')_n/(K_2)_n$	$K_3=K_2\cdot f(R_2/R_1)= K_1\cdot g(a/R_1)\ f(R_2/R_1)$ (11)
$(R_1)_1$	a/R_1, R_2/R_1	$(K_3)_1$	$(K')_1$	$(K')_1/(K_3)_1$	$(R_1)_i$ is set as the variate, while $(K')_i/(K_3)_i$ as the dependent variable, function $h(R_1)$ can be fitted.
⋮	⋮	⋮	⋮	⋮	Finally the straight attachment lug's SIF equation can be obtained as below.
$(R_1)_n$	a/R_1, R_2/R_1	$(K_3)_n$	$(K')_n$	$(K')_n/(K_3)_n$	$K=K_3\cdot h(R_1)=K_1g(a/R_1)\cdot f(R_2/R_1)\cdot h(R_1)$ $=K_1\mathrm{F}(a/R_1,R_2/R_1, R_1)$ (12)

The value of a/R_1 is increased from 0.1 to 1.6 by 0.1 while the others are fixed, K_1 can be modified as $K_2=K_1*g(a/R_1)$, where

$$g(a/R_1)=-0.1285*(a/R_1)^2+0.3059*(a/R_1)+0.8228 \tag{13}$$

The value of R_2/R_1 is increased from 1.5 to 3 by 0.1 while the others are fixed, K_2 can be modified as $K_3=K_2*f(R_2/R_1)$, where

$$f(R_2/R_1)=-0.1654*(R_2/R_1)^4+1.6326*(R_2/R_1)^3-6.0293*(R_2/R_1)^2+9.9046*(R_2/R_1)-5.1399 \tag{14}$$

The value of R_1 is increased from 5 to 20 by 1 while the others are fixed, the function $h(R_1)$ can be obtained as $h(R_1)= 0.99$, it is obvious that the effect of R_1 on SIF is less than the other parameters. Finally we can obtain the modified straight attachment lug's SIF equation as $K=K_3*h(R_1)$, the SIF equation of straight lug (Figure 10) is obtained as blows.

$$K = F\cdot\sigma\cdot\sqrt{\pi\cdot a}. \tag{15}$$

Where

$$\sigma = \frac{P}{2ct}, \tag{16}$$

$$c = R_2 - R_1, \tag{17}$$

$$F = f_{ar}\cdot f_{fw}\cdot f_r, \tag{18}$$

$$f_{ar} = \frac{1.98R_2}{1.971R_1}\cdot\frac{0.31711}{\left(0.3857+\frac{a}{R_1}\right)^{1.33734}}+\frac{1}{2}\cdot\left(0.8734/\left(0.3246+a/R\right)+0.6762\right), \tag{19}$$

$$f_{fw} = \sqrt{\sec\left(\frac{\pi}{2}\cdot\frac{2R_1+a}{2R_2-a}\right)}, \tag{20}$$

$$f_r = \left(-0.1654\cdot\left(\frac{R_2}{R_1}\right)^4+1.6326\cdot\left(\frac{R_2}{R_1}\right)^3-6.0293\cdot\left(\frac{R_2}{R_1}\right)^2+9.9046\cdot\left(\frac{R_2}{R_1}\right)-5.1399\right)\cdot \tag{21}$$

Scope of application：

$$0.1\le\frac{a}{R_1}\le 1.6,\quad 1.5\le\frac{R_2}{R_1}\le 3,\quad 5\le R_1\le 20.$$

In the same way, considering the load degrees β additionally, the SIF equation of the straight attachment lugs subjected to oblique pin-load less than 45 degrees can be obtained as below.

$$K = F\cdot\sigma\cdot\sqrt{\pi\cdot a} \tag{22}$$

where

$$\sigma = \frac{P}{2ct}, \tag{23}$$

$$c = R_2 - R_1, \tag{24}$$

$$F = f_\beta\cdot f_{ar}\cdot f'_{ar}\cdot f_{fw}\cdot f_{rr}, \tag{25}$$

$$f_\beta = -3.7107\times10^{-6}\cdot\beta^3+8.4026\times10^{-5}\cdot\beta^2+0.0092469\cdot\beta+1.05, \tag{26}$$

$$f_{ar} = \frac{1.98R_2}{1.971r_1}\cdot\frac{0.31711}{\left(0.3857+a/R_1\right)^{1.33734}}+\frac{1}{2}\cdot\left(0.8734/(0.3246+a/R_1)+0.6762\right), \tag{27}$$

$$f'_{ar} = -0.063305\cdot\left(\frac{a}{R_1}\right)^2+0.067224\cdot\frac{a}{R_1}+0.94853, \tag{28}$$

$$f_{fw}=\sqrt{\sec\left(\frac{\pi}{2}\cdot\frac{2R_1+a}{2R_2-a}\right)}\ , \tag{29}$$

$$f_{rr}=\left(-0.1654\left(\frac{R_2}{R_1}\right)^4+1.6326\left(\frac{R_2}{R_1}\right)^3-6.0293\left(\frac{R_2}{R_1}\right)^2+9.9046\left(\frac{R_2}{R_1}\right)-5.1399\right)\cdot \tag{30}$$

Scope of application：

$$5°\le\beta\le45°,\ \ 0.1\le\frac{a}{R_1}\le1.6,\ \ 1.5\le\frac{R_2}{R_1}\le3,\ \ 5\le R_1\le20\ .$$

4. Fatigue crack growth test and residual strength test

4.1 Test pieces

Figure 11 shows the dimensional drawing of the straight attachment lug piece. There is a small slot made by electrical discharge machine (EDM) besides the lug hole with an angle of θ=90° or θ=60°. The slot length a_0 is approximately equal to 1mm. The lugs pieces subjected to axial (θ=90°) or 30 degrees oblique (θ=60°) pin-load are all made of 30CrMnSiA material, 4 pieces for each case.

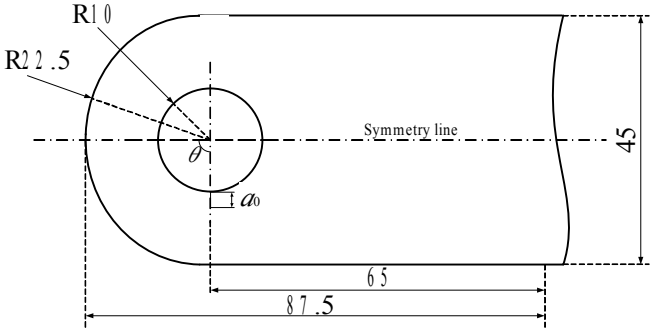

Figure 11. Geometry of the test piece

4.2 Test equipments and loading requirement

The tests are carried out on the material test system MTS-810 (load relative error <±2%) with a constant amplitude loading spectrum of sine waveform. The length of the crack is observed and measured by JXD-250mm scale microscope with a precision of 0.01mm.

Surface around test piece's wire-cutting slot tip is polished by a sand paper along the direction perpendicular to the slot direction. Peak load P_{pp} in the crack growth preparation test is 13.85KN, valley load P_{pv} is 0.83KN, R=0.06, load frequency is 5Hz. A crack with a length of 0.314mm was observed when fatigue cycle reaches about 15000, and grows to 0.612mm when 21000 cycles. The a-N data shows that the crack is growing steadily under the peak load of the fatigue crack growth test P_p=20.77KN and the valley load P_v=1.246KN.

Table 2 shows values of the test load.

Table 2. The test load values

Case	P_{pp}/(KN)	P_{pv}/ (KN)	P_p/(KN)	P_v/(KN)
θ=90°	13.85	0.83	20.77	1.25
θ=60°	13.85	0.83	20.77	1.25

4.3 Fatigue crack growth test

Figure 14 & Figure 15 show the experimental scene.

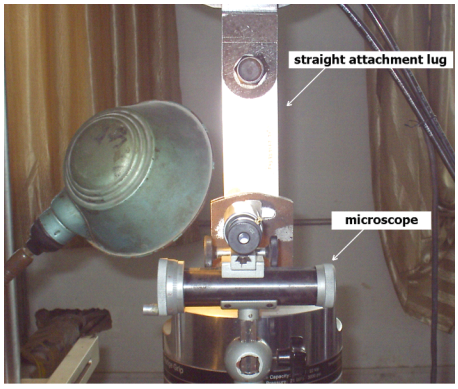

Figure 14. Experimental field of the case of θ=90°

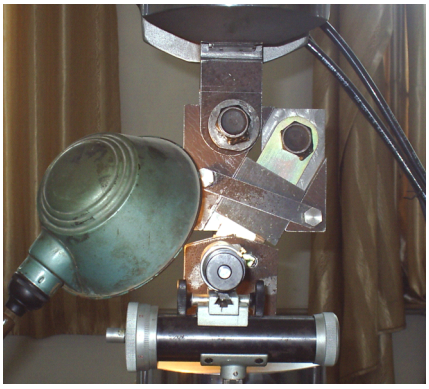
Figure 15. Experimental field of the case of θ=60°

The micro objective is aimed at the wire-cutting slot tip for detecting the fatigue crack in time. The frequency is changed to 1Hz every other 1000~2000 cycles in order to observe the crack length and record the *a*-*N* data.

4.5 Residual strength test

After obtaining enough *a*-*N* data, the test pieces with different residual fatigue crack lengths are loaded with a sustained increasing load till the test pieces fracture, the corresponding residual strength data are recorded in Table 3 & Table 4.

Table 3. The residual strength test results of the lugs subjected to axial pin-load

test piece num.	No.1	No.2	No.3	No.4
crack length *a*/(mm)	7.109	8.127	8.972	10.115
residual strength *P*/(KN)	91.456	83.242	78.051	72.947

Table 4. The residual strength test results of the lugs subjected to 30 degrees oblique pin-load

test piece num.	No.1	No.2	No.3	No.4
crack length *a*/(mm)	10.58	10.99	11.45	9.98
residual strength *P*/(KN)	58.54	42.38	40.24	58.8

The data of crack length *a* and corresponding residual strength *P* in Table 4 & Table 5 are used to substitute the *a*&*P* in formula (15) and formula(22) to calculate the SIFs. The SIFs of the axial pin-load case are: 164.30, 162.47, 166.37, 184.04, while the other case's SIFs are: 214.91, 162.08, 171.77, 179.69, the unit is $MPa\cdot\sqrt{m}$. As the fracture toughness of the material 30CrMnSiA with thickness 6.7mm is around 180 $MPa\cdot\sqrt{m}$ [16], it shows the SIFs calculated by formula (15) and formulas (22) are consistent with the true values.

5. Establishment of the fatigue crack growth model

The fatigue crack growth data are fitted by using least square method, the curves are shown in Figure16 and Figure 17.

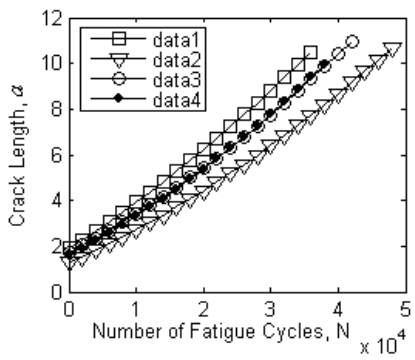

Figure 16. *a*-*N* curves of the case of axial pin-load

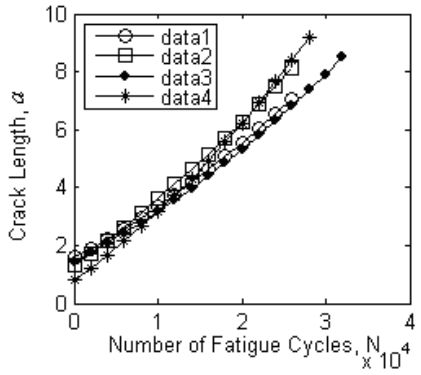

Figure 17. *a*-*N* curves of the case of 30° pin-load

The *a*-*N* data are calculated by the seven points incremental polynomial method[16]. The SIF range value ΔK and da/dN can be obtained by the fitted crack length value a^*. Table 5 shows the data processing of the test piece No.1.

Table 5. Data processing of the test piece No.1

N/(cycle)	a /(mm)	a^*/(mm)	da/dN	ΔK/(MPa·m$^{1/2}$)	lg(da/dN)	$lg(\Delta K)$
0	1.539					
2000	1.967					
4000	2.276					
6000	2.506	2.579	1.79E-7	26.556	1.424	-6.746
8000	2.958	2.927	1.85E-7	27.292	1.436	-6.732
10000	3.307	3.316	2.01E-7	28.026	1.447	-6.697
12000	3.767	3.752	2.14E-7	28.781	1.459	-6.669
14000	4.159	4.186	2.16E-7	29.497	1.469	-6.665
16000	4.652	4.629	2.24E-7	30.218	1.480	-6.649
18000	5.091	5.074	2.31E-7	30.956	1.490	-6.636
20000	5.503	5.543	2.43E-7	31.771	1.502	-6.614
21800	5.981	5.976	2.47E-7	32.577	1.512	-6.608
23000	6.291	6.278	2.59E-7	33.180	1.520	-6.585
24000	6.578					
25000	6.756					
26000	7.109					

The da/dN data of the other three test pieces can be obtained by the same method. The data points of region II are fitted by the least square method to get the lg(da/dN)~lg(ΔK) curve. Figure18 shows the fitted line of the data points.

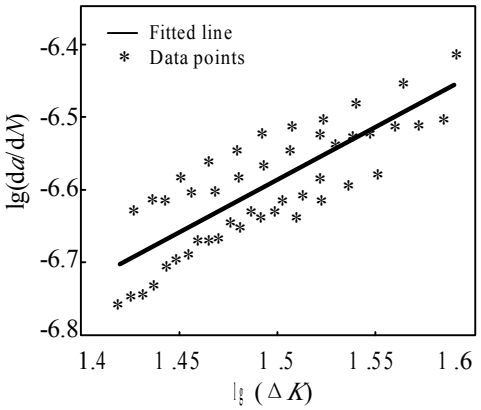

Figure 18. lg(da/dN)~lg(ΔK) curve of the axial pin-load case

The equation of the line is shown as below.

$$\lg(da/dN) = 1.4231 \cdot \lg(\Delta K) - 8.7221. \tag{31}$$

The Paris equation is

$$da/dN = C(\Delta K)^m. \tag{32}$$

In order to get the values of C and m, the paper takes the logarithm on both sides of the equation (32).

$$\lg(da/dN) = m \cdot \lg(\Delta K) + \lg C. \tag{33}$$

The values of the Paris constants C and m are obtained by comparing the equation (31) with (33).

C=1.896E-09, m=1.4231.

The lg(da/dN)~lg(ΔK) curve of region II of the lugs subjected to 30 degrees oblique pin-load can be got by the same method. Figure 19 shows the lg(da/dN)~lg(ΔK) curve.

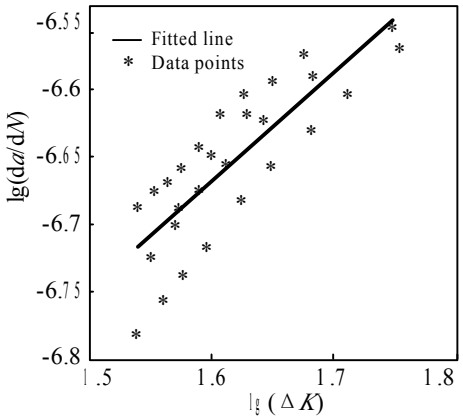

Figure 19. lg(da/dN)~lg(ΔK) curve of the 30 degrees oblique pin-load case

The equation of the line and the values of the Paris constants C and m are shown as below.

$$\lg(da/dN) = 0.7649 \cdot \lg(\Delta K) - 7.8902 \tag{34}$$

C=1.2877E-08, m=0.7649.

6. Conclusions

Analytical and experimental investigations for fatigue crack growth behavior of 30CrMnSiA straight attachment lugs were performed. From this investigation followings are concluded.

1. The boundary conditions of the finite element model is consistent with the true condition, cosine distributing load is the key of ensuring precision of FEM analysis.
2. The expressions of the SIFs of straight lugs subjected to axial or less than 45 degrees oblique pin-load are determined and validated. Based on this, the stress intensity factor range (ΔK) can be calculated.
3. The fatigue crack growth model of the typical straight lugs is established, offering an analytical as well as experimental method for assessing and designing damage tolerant attachment lugs in engineering.

References

[1] R. Rigby, M.H. Aliabadi. Stress intensity factors for cracks at attachment lugs. Eng. Failure Anal. 1997;4(2):133-146.
[2] Liu, A. F., Kan, H. P.. Test and Analysis of Cracked lugs. Frac. 1977;3: 567-664.

[3] Kirkby, W. T., and Rooke, D. P.. A Fracture Mechanics Study of Residual Strength of Pin-Lug Specimens. Frac. Mech. in Eng. Practice. 1977: 339.
[4] Cartwright, D. J., and Rooke, D. P.. Approximate Stress Intensity Factors Compounded from Known Solutions. Eng. Frac. Mech. 1974;6:563-571.
[5] Schijve, J., and Hoeymakers, A.H.W.. Fatigue Crack Growth in Lugs and the Stress Intensity Factor. Report LR-273, Delft University of Technology, Delft, the Netherlands, July 1978.
[6] Wanhill, R.J.H., and Lof, C.F.. Calculation of Stress Intensity Factors for Corner Cracking in a Lug. Frac. Mech. Design Methodology. ARGARD CP221, February 1977, Paper No. 8.
[7] James, L. A., and Anderson, W. E.. A Simple Experimental Procedure for Stress Intensity Factor Calibration. Eng. Frac. Mech. 1969;1:565-568.
[8] Pian, T. H. H., Mar, J. W., Orringer, O., and Stalk, G.. Numerical Computation of Stress Intensity Factors for Aircraft Structural Details by the Finite Element Method. AFFDL-TR-76-12, Air Force Flight Dynamics Laboratory, May 1976.
[9] Aberson, J. A., Anderson, J. M.. Cracked Finite-Elements Proposed for NASTRAN. Third NASTRAN Users' Colloquium, NASA TMX-2893, 1973:531-550.
[10] Impellizzeri, L. F., and Rich, D. L.. Spectrum Fatigue Crack Growth in Lugs. Fatigue Crack Growth Under Spectrum Loads, ASTM STP 595, 1976:320-336.
[11] Bueckner, H. F.. Weight Functions for the Notched Bar. Zeitschrift for Angewandte Mathematik und Mechanik. 1971;51: 97-109.
[12] Jong-Ho Kim, Soon-Bok Lee, Seong-Gu Hong. Fatigue crack growth behavior of Al7075-T7451 attachment lugs under flight spectrum variation. Eng. Fract. Mech. 2003;40:135-144.
[13] S.Baster, L. Molent, N.Goldsmith, R.Jones. An experimental evaluation of fatigue crack growth. Eng. Fail. Anal. 2005;12:99-128.
[14] Xue Jingchuan. Bolt and Lug Strength Analysis Handbook. Beijing: Aviation Industry Press;1998.
[15] Zheng Xiaoling. Civil Aircraft Durability and Damage Tolerance Design Handbook. Beijing: Aviation Industry Press;2003.
[16] Interpreted by Scientific and Technical Research Institute of Ministry of Aero-space Industry. USAF Damage Tolerance Design Handbook. Xi'an: Northwest Polytechnical University Press;1989.

Fatigue damage indicators based on the infrared thermographic method

Pei.J.Hou [1], Xing.L. Guo [2,*], Fang.Han[3], Jun.L.Fan [4]

[1,2,3,4]State Key Laboratory of Structural Analysis for Industrial Equipment, Dalian University of Technology, Dalian 116023, China

* Corresponding author: xlguo@dlut.edu.cn

Abstract It is a new and valuable research that studying the influence of heat treatments on fatigue performance of materials by the infrared thermographgic method. Based on three theoretical models of fatigue indicators, this paper studied mechanical properties of the virgin and heat-treated FV520B steels. With the three indicators and the energy theory, comparison analysis of macro-phenomenon and microstructure evolution during fatigue of the two type specimens was performed. Using the intrinsic dissipation, fatigue limits were fast determined. Influence of heat treatments on mechanical properties and fatigue life was discussed. The research shows that the accuracy of the lock-in thermography could satisfy the needs of engineering design.

Keywords Infrared thermographic method, Fatigue indicator, Heat treatment, Energy Approach

1. Introduction

Fatigue design requires statistical processing of numerous tests. However, the traditional evaluation methods are often difficult to be performed for their time-consuming and expensive costing[1,2]. The infrared thermographic method was first proposed by Risitano et al. [3] by using the surface temperature increments as the major fatigue indicator. The infrared thermographic method, based on the analysis of the heat during a loading fatigue test, was developed over the last 30 years. Fargione et al. [4] obtained the connection between the quantity of heat dissipated in taking a given element to failure based on the physical hypothesis, which the failure of materials through fatigue occurs when the energy of plastic deformation reaches a constant limiting value, and the fatigue limit by applying fatigue tests.

Suitable heat treatments can improve the static tensile strength and fatigue resistance of materials [5,6]. Now it is still a new task to investigate effect of heat treatments on fatigue behavior of materials using the infrared thermographic method. The purpose of this paper is to study the relationship between the internal microstructure and mechanical properties using different fatigue indicators. FV520B steel is a kind of martensite steel developed by Firth-Vickers Materials Lab in British. The steel is widely used in aerospace engineering and medical instruments, etc. due to its high strength, corrosion resistance and weldability [5,7]. However, heat treatments, used in practical engineerings, play an important role in determining the internal microstructure which governs mechanical responses of FV520B. Therefore, it is necessary to investigate the correlation between heat treatments and mechanical behavior useful for directing the mechanical design.

In the present paper, the infrared thermographic method was employed to explore influence of different heat treatments on FV520B steel. Fatigue limits of two type steels were determined by the intrinsic dissipation. The internal microstructural changes were studied to understand the fatigue process.

2. Theoretical models of fatigue damage indicators

Relative temperature increment. Fatigue damage is known as energy dissipation accompanied by temperature changing. The temperature linked with energy dissipation enables us to understand the energy transformation, toughness reduction and damping vibration of materials. Therefore, the fatigue process can be qualitatively evaluated using the relative temperature increment.

During fatigue tests, to avoid any possible errors induced by the environmental perturbation and the experimental system sensitivity, the relative temperature increment ΔT on the hot-spot zone of the specimen surface is used to describe fatigue damage status:

$$\Delta T = T_m - T_0 \tag{1}$$

where T_m is the average temperature on the zone; and T_0 is the initial temperature.

Standard deviation of stress. Microcracks often initiate from local points due to the stress concentration. The fatigue damage distribution is not uniform when a material suffers from cyclic loading. The distribution of the local stress can be described by the standard deviation. The stress state on the hot-spot zone, due to the local high stress, enables us to qualitatively identify the critical location responsible for the final fracture. Accordingly, the economic losses caused by the sudden fatigue fracture might be greatly decreased by analyzing this damage indicator.

The stress level used here is the thermoelastic stress calculated by the equation below:

$$\Delta T = -\frac{\alpha}{\rho C_p} \cdot T \cdot \Delta\sigma \tag{2}$$

where α is the coefficient of linear expansion; C_p is the specific heat capacity; ρ is the material density; T is the absolute temperature; Δσ is the change in the sum of principal stresses; and ΔT is the change in temperature.

The stress pattern can be visibly obtained using the infrared camera, and each pixel stands for a point in the selected zone Ω. Thus, the standard deviation of the stress can be written as:

$$\sigma_{SDS} = \sqrt{\frac{1}{N}\sum_{x,y\in\Omega}(\sigma(x,y)-\sigma_m)^2} \tag{3}$$

Where σ_m denotes the average stress in the zone Ω; σ(x, y) denotes the stress value at the point (x, y); and N denotes all the points in the zone Ω.

Intrinsic dissipation. Based on the small perturbation hypotheses, fatigue test is considered as a quasi-static dissipation process. The local coupled thermomechanical equation is derived [8]:

$$\rho C_p \dot{T} - k\nabla^2 T = (\sigma - \rho\frac{\partial\psi}{\partial\varepsilon}) : \dot{\varepsilon} - \rho\frac{\partial\psi}{\partial\alpha}\cdot\dot{\alpha} + \rho T\frac{\partial^2\psi}{\partial T\partial\varepsilon} : \dot{\varepsilon} + \rho T\frac{\partial^2\psi}{\partial T\partial\alpha} : \dot{\alpha} + \gamma^e \tag{4}$$

where k is the heat conduction coefficient; σ denotes the stress tensor; ψ is Helmholtz free energy; ε is the strain tensor; α is internal variables; and γ^e is the external heat resource.

The intrinsic dissipation is defined as:

$$d = (\sigma - \rho\frac{\partial\psi}{\partial\varepsilon}) : \dot{\varepsilon} - \rho\frac{\partial\psi}{\partial\alpha}\cdot\dot{\alpha} \tag{5}$$

In fact, the intrinsic dissipation describes the dissipated energy due to inelastic effects, and it is an important part of the non-linear energy dissipation for materials and components subjected to fatigue loading. The infrared thermographic method can be used to quantitatively evaluate fatigue

damage status, and accordingly the fatigue limit can be fast determined.

3. Experiment investigations

Material and specimen. The studied material is FV520B [7]. Its mechanical properties are greatly affected by heat treatments. Thus, two type specimens (Figure 1. Size of the specimen) were machined from two plates. One plate was just annealed (type A), and the other was treated with treatments in Ref.[9] (type B).

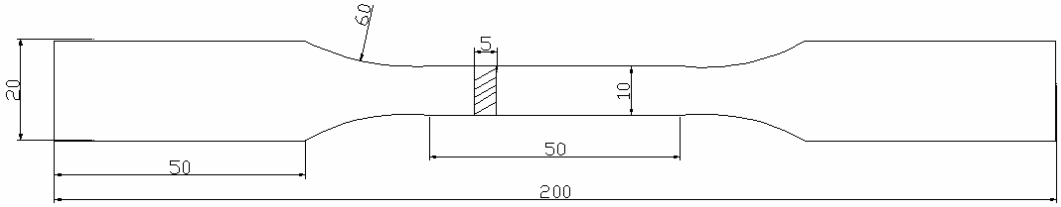

Figure 1. Size of the specimen (unit: mm)

Experimental procedures. Fatigue tests were carried out at room temperature without disturbance of the external heat resource. The testing system is composed of MTS810 system, infrared camera, lock-in module, computers and corresponding softwares [9].

Before tests, all the specimens were polished with fine grit papers, and then painted the specimens black to improve the heat radiation. The stress ratio is set as R=-1 with a frequency of 20Hz. The stepwise loading procedure was applied to the same specimen. To avoid fatigue damage accumulation, the stress was applied from 100MPa with steps of 50MPa until fracture. The thermal images on the hot-spot zone were recorded by the infrared camera to perform the subsequent data analysis.

3. Results and discussion

Qualitative identification of the fatigue damage. Temperature evolution is mainly attributed to the thermoelastic effect, plastic effect and heat conduction. The fluctuating temperature is due to the thermoelastic effect. The temperature amplitudes increase with the increasing cyclic loading. However, the thermoelastic effect has no contribution to the average temperature [8]. Figure.2 exhibits the relative temperature evolution of the two type specimens, showing the almost same trend.

The elastic stress controls mechanical responses of tested specimens when the stress is less than 300MPa. At this term, the specimen mainly takes place elastic deformation, and the temperature increment are mainly induced by non-plastic effects, i.e. viscosity effect etc. If the stress is higher than the fatigue limit, microcracks will initiate from the specimen boundaries, such as: the corner and the free surface. They initiate along the axial direction of 45^{o}, and then coalesce to form a main crack. The main crack propagates perpendicular to the principal stress direction. The plastic strain energy accumulates with the fatigue evolution. Most of the mechanical energy is dissipated as heat energy heating up the specimen. There are，however, still some different between the two type steels. The temperature increment of the type B is generally less than that of the type A. That is attributed to the slow evolution of internal microstructures of the type B, indicating its better fatigue resistance.

As a consequence, heat treatments [9,10] improve the microstructure of the type B (such as dislocation distribution and defect density, etc.), and accordingly enhance its mechanical properties. Figure.3 presents variations of the stress standard deviation of the two type steels. There is no obvious plastic deformation when the applied stress is lower. Accordingly the standard deviation is relatively small. If the stress is higher than the fatigue limit, it sets to increase sharply in the local zone due to stress concentration. The break point indicates that the mechanisms related to fatigue failure have changed into plastic effect. Local stress concentration, due to pores and impurities, governs the stress distribution. The damage status can be qualitatively identified by the standard deviation to avoid the sudden fracture. From Figure.3, the standard deviation of the type B is small relative to the type A since the grain refinement due to heat treatments improves the arrangement of the internal microstructure, which makes the type B take on better fatigue resistance.

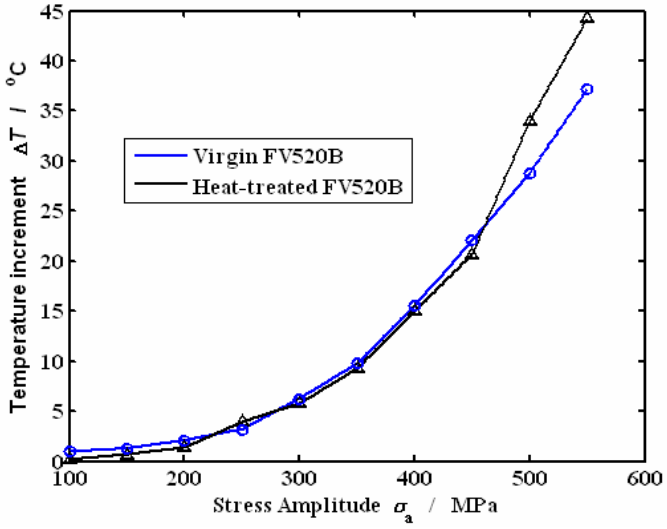

Figure.2 Relative temperature increment

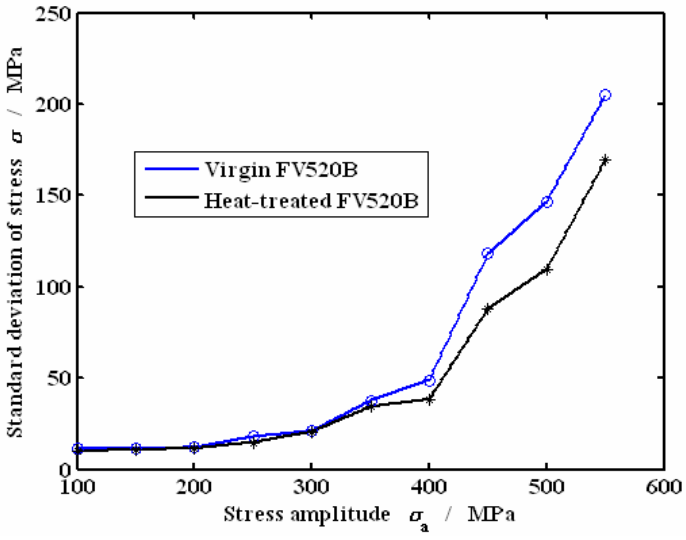

Figure.3 Standard deviation of stress

Fatigue limit evaluation. From Figure.2 and 3, the fatigue limit of the type B should be higher than that of the type A. In this part, the intrinsic dissipation shown in Figure.4 was utilised to get their fatigue limits. The break points are in the range of 250MPa~350MPa. The intersection of the two straight lines denotes the corresponding fatigue limit [11]. Thus the fatigue limit of the type A is

291MPa, and 319MPa for the type B. Fortunately, using the traditional method, the fatigue limits of the type A and B are 274MPa and 310MPa, respectively. The low values of errors, 6.2% and 2.9%, confirm the reliability of the infrared thermographic method in predicting fatigue parameters of materials with different heat treatments. To verify that the fatigue limit of the type B is higher, two fatigue tests, with the same cyclic stress 400MPa, were carried out to compare their fatigue life. The life of the type A is 141606 cycles, and 300748 cycles for the type B, confirming our results.

It is different for the variation of energy accumulation and heat dissipation during different fatigue process. The above fatigue tests can be divided into three phases. At lower stress, i.e. 100MPa~300Mpa, the temperature increases slowly, and the intrinsic dissipation is practically null. The internal microstrucutre evolution is reversible under the elastic stress. However, when the stress is close to the fatigue limit, the local stress may be beyond the yield limit due to the stress concentration in micro-scale. Consequently, the slip band begins to form, and numerous microcracks initiate here. Fatigue damage sets to accumulate continuously. If the stress is higher than 450MPa, all the three damage indicators, related to the final failure, increase drastically.

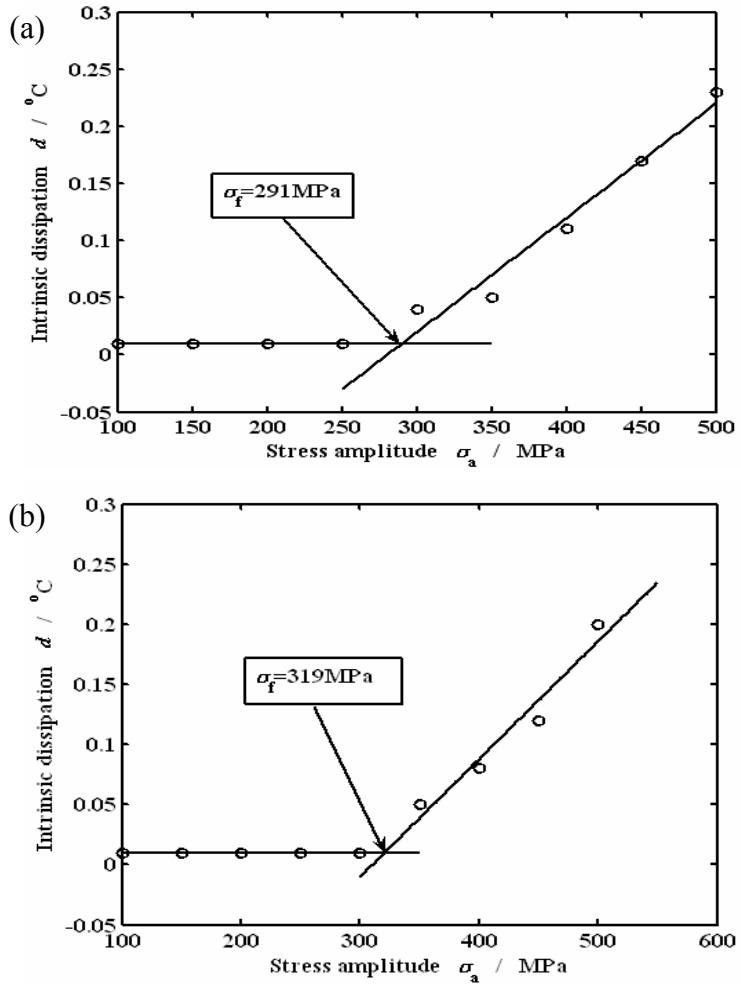

Figure. 4 Fatigue limit by the infrared thermographic method: (a) the type A; (b) the type B

4. Conclusions

[1] The infrared thermographic method enables us to qualitatively and quantitatively evaluate fatigue behavior of materials with different heat treatments.

[2] All the three fatigue damage indicators can describe the fatigue damage process. The macro-phenomenon and internal microstructure evolution are associated by the energy theory.
[3] The low errors of the predicted fatigue limits demonstrate the reliability of the infrared thermographic method in predicting fatigue parameters of materials and components.
[4] It is a fast and accurate technique for fatigue evaluation using various damage indicators resorting to the infrared technique. Consequently, the method may be used to identify the fatigue damage status of structures in service in the future.

Acknowledgements

The financial supports of Natural Science Foundation of China (No.11072045) and National Basic Research Program of China (No.2011CB706504) are gratefully acknowledged.

References

[1] W.Fricke, Fatigue analysis of welded joints: state of development. Mar.Struct.16 (2003) 185-200.

[2] V.Crupi, E.Guglielmino, M.Maestro, et al., Fatigue analysis of butt welded AH36 steel joints: Thermographic Method and design S－N curve. Mar. Struct. 22 (2009) 373-386.

[3] G.La Rosa, A.Risitano, Thermographic methodology for rapid determination of the fatigue limit of materials and mechanical components. Int. J. Fatigue, 22 (2000) 65-73.

[4] G.Fargione, A.Geraci, G.La Rosa, A.Risitano, Rapid determination of the fatigue curve by the thermographic method. Int. J. Fatigue, 24 (2002) 11-19.

[5] J. Nowacki, Weldability of 17-4 PH stainless steel in centrifugal compressor impeller applications. Process Tech. 157-158(2004) 578-583.

[6]M.I. Khan, M.L. Kuntz, and E. Biro, Y.Zhou, Microstructure and Mechanical Properties of Resistance Spot Welded Advanced High Strength Steels. Mater. Trans. 49 (2008) 1629-1637.

[7]J.L.Fan, X.L.Guo, C.W.Wu, et al, Effect of Heat Treatments on Fatigue Properties of FV520B Steel Using Infrared Thermography. Chin. J. Mater. Res. 26(2012), 61-67.

[8]T. Boulanger, A. Chrysochoos, C. Mabru, et al, Calorimetric analysis of dissipative and thermoelastic effects associated with the fatigue behavior of steels.: Int. J. Fatigue. 26(2004) 221-229.

[9]J.L. Fan, X.L. Guo, C.W. Wu, et al, Research on fatigue evaluation and fatigue fracture mechanism of cruciform welded joints. Mater. Sci. & Eng. A. 528(2011) 8417-8427.

[10]J.Fan, X. Guo, C.Wu, A new application of the infrared thermography for fatigue evaluation and damage assessment. Int. J. Fatigue. 44(2012) 1-7.

[11]F. Curà, G. Curti, R. Sesana, A new iteration method for the thermographic determination of fatigue limit in steels. Int. J. Fatigue. 27(2005) 453-459.

Fatigue Cracking Paths and Compliance Analysis in Round Bars under Tension and Bending

Jesús Toribio[1,*], Juan-Carlos Matos[2], Beatriz González[1], José Escuadra[2]

[1] Department of Materials Engineering, University of Salamanca, E.P.S. Zamora, Spain
[2] Department of Computing Engineering, University of Salamanca, E.P.S. Zamora, Spain
* Corresponding author: toribio@usal.es

Abstract The aim of this paper is to calculate how the surface crack front and the dimensionless compliance evolve in cracked cylindrical bars subjected to cyclic tension or bending with different initial crack geometries (crack depths and aspect ratios). To this end, a computer application (in the Java programming language) that calculates the crack front's geometric evolution and the dimensionless compliance was made by discretizing the crack front (characterized with elliptical shape) and assuming that every point advances perpendicularly to the crack front according to the Paris law, and using a three-parameter stress intensity factor (SIF). The results show that in fatigue crack propagation, relative crack depth influences more on dimensionless compliance than the aspect ratio, because the crack front tends to converge when the crack propagates from different initial geometries, the compliance showing greater values for tension than for bending. Furthermore, during fatigue crack growth, materials with higher values of the exponent of the Paris law produce slightly greater dimensionless compliance and a better convergence between the results for straight-fronted and circular initial cracks.

Keywords Numerical modelling, Cracked round bar, Fatigue crack growth, Dimensionless compliance

1. Introduction

The problem of fatigue crack propagation in round bars is of great interest in fracture mechanics, applied to linear structural elements. These components, usually subjected to oscillating load, may fracture after surface fatigue crack growth, frequently with semi-elliptical flaws contained in a plane perpendicular to the loading axis.

Several criteria have been stated in the past to characterize fatigue crack growth in these geometries, e.g., prediction of the 90º intersecting angle of the crack with the surface or the iso-K criterion along the crack front [1]. The most used are those based on the Paris-Erdogan law [2-7], requiring the knowledge of the dimensionless stress intensity factor (SIF), Y, along the crack front in the round cracked bar. It has been deducted by several authors following different procedures: compliance methods, finite element analysis, boundary integral equation methods, experimental techniques, etc. [1, 8-11].

Dimensionless compliance in round cracked bars under tension or bending depends on the crack geometry. If the crack is characterized by an elliptical shape, there are two factors exerting influence: the relative crack depth (crack depth divided by the diameter), which causes an increase of its value, and the aspect ratio (ratio of the crack depth to the other semiaxis of the ellipse), which causes a decrease of its value [3, 12]. Thus, there is a relation between the change in compliance during fatigue crack growth and the crack geometry evolution, depending on the specimen material, the initial crack geometry and the type of applied load [11, 13].

The aim of the present paper is the numerical modelling of crack front evolution for semielliptical surface cracks (under the hypothesis that every point at the crack front advances according to a Paris-Erdogan law), as well as analyzing how dimensionless compliance evolves during fatigue of round bars of different materials (Paris coefficient m of 2, 3 and 4), with different initial crack geometries (circular and quasi-straight, both crack shapes linked with initial relative depth $(a/D)_0$ of 0.1, 0.3 and 0.5) and applying tensile load or bending moment.

2. Numerical Modelling

A computer program in the Java programming language was developed to determine the geometrical evolution of the crack front according to the Paris law, for a transverse surface crack in a cylindrical geometry subjected to tensile loading or bending fatigue moment (Fig. 1). This would be the basis to determine the change taking place in the dimensionless compliance of the round bar during the fatigue crack propagation process.

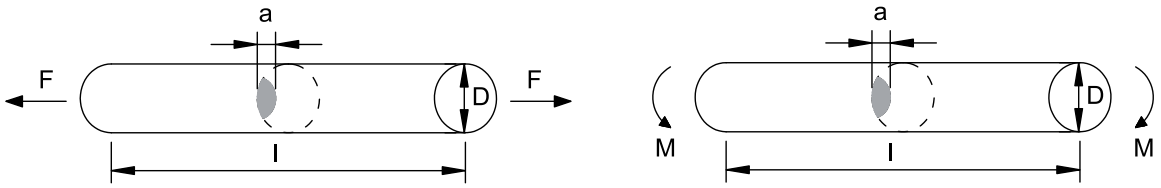

Figure 1. Cracked bar under tension loading (left) and bending moment (right)

2.1. Aspect Ratio

The basic hypothesis of the modelling consisted of assuming that the crack front can be modelled as an ellipse with centre on the bar surface [13] and the fatigue propagation takes place in a direction perpendicular to this crack front, following a Paris Erdogan law [14],

$$\frac{\mathrm{d}a}{\mathrm{d}N} = C\Delta K^{\mathrm{m}} \tag{1}$$

Every elliptical arc of the crack front was divided in z segments with exactly the same length using the Simpson's rule in order to discretize the front. The point on the round bar surface was not taken into account, since it presents some difficulties regarding the computation of the dimensionless SIF (there is a plane stress state on the crack surface).

After that, every single point was shifted according to the Paris-Erdogan law perpendicular to the front and so as to keep constant the maximum crack depth increment, $\Delta a(\max) \equiv \max \Delta a_{\mathrm{i}}$, all over the process [7]. The advance of every front point, Δa_{i}, can be obtained from the maximum crack increment and the ratio of the SIF at that point to the maximum SIF over the crack front,

$$\Delta a_{\mathrm{i}} = \Delta a(\max)\left[\frac{Y_{\mathrm{i}}}{Y(\max)}\right]^{\mathrm{m}} \tag{2}$$

The newly obtained points, fitted by the least squares method, generate a new ellipse with which the process is repeated iteratively until the desired crack depth is reached. Due to the existing symmetry, only half of the problem was used for the computations.

2.2. Dimensionless SIF

The dimensionless SIF, Y, depends on three-parameters for the crack modelled as an ellipse with centre on the round bar surface and its value depends on the crack geometry (depth and aspect ratio) and on the point on the front where it is calculated. The dimensionless SIF used in the computations is that proposed by Shin and Cai [11] obtained by the finite element method and the virtual crack extension technique, whose value is function of the relative crack depth a/D, the crack aspect ratio a/b, and the position of the point considered on its front x/h (Fig. 2).

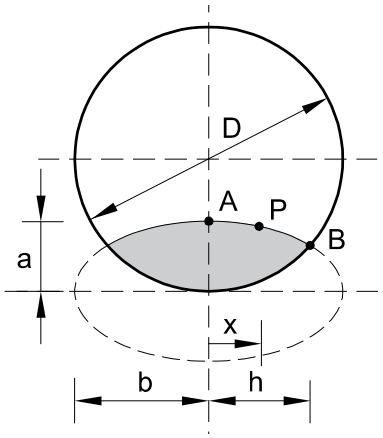

Figure 2. Elliptical crack model used by Shin and Cai [6]

The fitting of the results provides a three-parametrical expression which is defined as a function of the coefficients M_{ijk} for tension with free sample ends [11], i.e., unrestrained bending during tension,

$$Y = \sum_{i=0}^{2}\sum_{j=0}^{7}\sum_{k=0}^{2} M_{ijk}\left(\frac{a}{b}\right)^{i}\left(\frac{a}{D}\right)^{j}\left(\frac{x}{h}\right)^{k} \tag{3}$$

and the coefficients N_{ijk} for bending [11],

$$Y = \sum_{i=0}^{2}\sum_{j=0}^{6}\sum_{k=0}^{2} N_{ijk}\left(\frac{a}{b}\right)^{i}\left(\frac{a}{D}\right)^{j}\left(\frac{x}{h}\right)^{k} \tag{4}$$

2.3. Dimensionless Compliance

Experimentally the geometrical evolution of the crack front in a cylindrical bar can be observed *post mortem* (once fractured) and there are several techniques to mark the front according to the material studied. It is possible to relate the crack front geometry with compliance, one of the few characteristics which can be measured during the crack propagation [15].

If tensile load is applied, it is obtained that the local displacement u is related to the applied force F through compliance as follows:

$$u = \lambda F \tag{5}$$

If bending is applied, in this case the angle φ is related to the applied moment M through compliance as follows:

$$\varphi = \lambda M \tag{6}$$

The strain energy U can be expressed taking into account the equivalence between the energy release rate G and the stress intensity factor in plane strain K,

$$\mathrm{d}U = G\mathrm{d}A = \frac{K^2(1-\nu^2)}{E}\mathrm{d}A \tag{7}$$

where ν is the Poisson coefficient and dA the differential of the cracked area.

On the other hand, the strain energy for a cracked bar subjected to tensile load is, introducing the value du from eq. (5),

$$\mathrm{d}U = \frac{1}{2}F\mathrm{d}u = \frac{1}{2}F^2\mathrm{d}\lambda \tag{8}$$

and the strain energy for a cracked bar subjected to bending is, introducing the value du from the eq. (6),

$$\mathrm{d}U = \frac{1}{2} M \mathrm{d}\varphi = \frac{1}{2} M^2 \mathrm{d}\lambda \tag{9}$$

The SIF in plane strain for the geometry of the study can be obtained as follows:

$$K = Y\sigma\sqrt{\pi a} \tag{10}$$

where the stress σ for axial tension is calculated as:

$$\sigma = \frac{4F}{\pi D^2} \tag{11}$$

and the maximum stress σ for bending is calculated as:

$$\sigma = \frac{32M}{\pi D^3} \tag{12}$$

If equations for strain energy are made equal and introducing values K and σ, the isolated compliance is obtained for tension loading:

$$\lambda = \frac{32\left(1-\nu^2\right)}{\pi D^4 E} \int_0^a Y^2 a \mathrm{d}A \tag{13}$$

and for bending moment,

$$\lambda = \frac{2048\left(1-\nu^2\right)}{\pi D^6 E} \int_0^a Y^2 a \mathrm{d}A \tag{14}$$

Solving the integral which appears in eqs. (13) and (14) is not trivial. In order to achieve that, the Cartesian coordinates (x, y) were change into parametrical coordinates (a, θ), relating themselves through the expressions:

$$x = b\cos\theta \tag{15}$$

$$y = a\sin\theta \tag{16}$$

where the correspondence between angles δ and θ, deducted from Fig. 3, is as follows,

$$\tan\delta = \frac{y}{x} = \frac{a}{b}\tan\theta \tag{17}$$

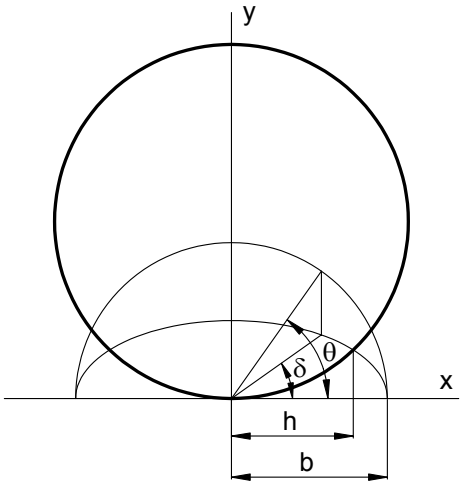

Figure 3. Relationship between δ and θ angles

The differential of the ellipse area modelling the crack advance is:

$$\mathrm{d}A = \mathrm{d}x \wedge \mathrm{d}y \tag{18}$$

differentiating the coordinates (x, y) according to the new coordinates (a, θ),

$$\mathrm{d}x = b'(a)\cos\theta\,\mathrm{d}a - b\sin\theta\,\mathrm{d}\theta \tag{19}$$

$$\mathrm{d}y = \sin\theta\,\mathrm{d}a + a\cos\theta\,\mathrm{d}\theta \tag{20}$$

and substituting these expressions on the eq. (18), it is obtained:

$$\mathrm{d}A = \left(ab'(a)\cos^2\theta + b\sin^2\theta\right)\mathrm{d}a \wedge \mathrm{d}\theta \tag{21}$$

The problem that arises in calculating eq. (21) can be found in the previous knowledge of the variation of the parameter b with the crack depth a. The definition of the derivative at a point can be used to this purpose,

$$b'(a) \approx \frac{b(a+\Delta a) - b(a)}{\Delta a} \tag{22}$$

Introducing eq. (21) in eq. (13), that allows the computation of the compliance in a cracked round bar subjected to axial tensile loading, it is obtained:

$$\lambda = \frac{64\left(1-\nu^2\right)}{\pi D^4 E}\int_0^a \int_{\arccos\frac{h}{b}}^{\pi/2} Y^2 a\left(ab'(a)\cos^2\theta + b\sin^2\theta\right)\mathrm{d}\theta\,\mathrm{d}a \tag{23}$$

Introducing eq. (21) in eq. (14), which allows calculating compliance in a cracked round bar subjected to bending loading, it is obtained:

$$\lambda = \frac{4096\left(1-\nu^2\right)}{\pi D^3 E}\int_0^a \int_{\arccos\frac{h}{b}}^{\pi/2} Y^2 a\left(ab'(a)\cos^2\theta + b\sin^2\theta\right)\mathrm{d}\theta\,\mathrm{d}a \tag{24}$$

where f is defined as the dimensionless compliance due to tensile or bending load:

$$f = \int_0^a \int_{\arccos\frac{h}{b}}^{\pi/2} Y^2 \frac{a}{D^3}\left(ab'(a)\cos^2\theta + b\sin^2\theta\right)\mathrm{d}\theta\,\mathrm{d}a \tag{25}$$

The dimensionless compliance value can be calculated incrementally with the crack growth, where the integral,

$$f = \sum_i \int_{a_i}^{a_{i+1}} \int_{\arccos\frac{h}{b}}^{\pi/2} R\,\mathrm{d}\theta\,\mathrm{d}a \tag{26}$$

it is solved using the trapezoidal rule (where R is the corresponding expression according to eq. (25)), following the scheme on Fig. 4, dividing every crack increment in eight parts for half of the problem, so they correspond with the coordinate's isolines (a, θ).

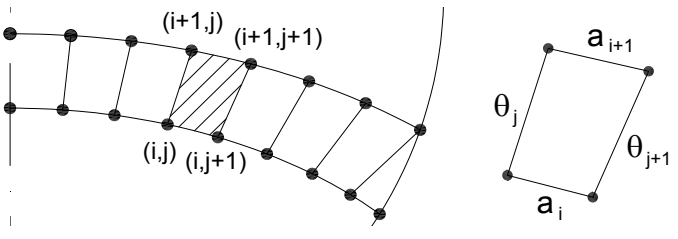

Figure 4. Divisions with the isolines used in the trapezoidal rule

The compliance increment in every crack advance is calculated using the following expression,

$$f = \sum_{i} \left(a_{i+1} - a_{i} \right) \left(\sum_{j=0}^{7} \left(\theta_{j+1} - \theta_{j} \right) \frac{\left(R(i,j) + R(i,j+1) + R(i+1,j) + R(i+1,j+1) \right)}{4} + \right.$$
$$\left. + \frac{\left(\theta_{8} - \theta_{7} \right)}{2} \frac{\left(R(i,7) + R(i+1,7) + R(i,8) \right)}{3} \right) \tag{27}$$

In order to obtain the dimensionless compliance of the initial crack, the process is similar to that just described, but easier, because it considers that every previous crack front has the same aspect ratio as the initial one. Furthermore, cracks smaller than the minimum ones used by Shin and Cai (a/D=0.067) were not taken into account in the compliance calculation.

3. Numerical Results and Discussion

3.1. Fatigue Cracking Paths

The study of the convergence was performed to obtain the number of segments in which each ellipse is divided, z=14, and the value of the maximum crack increase, $\Delta a(\max)=D/1000$. The geometrical evolution of the crack front, characterized as part of the ellipse, was determined for every relative crack depth, a/D, through the aspect ratio, a/b, for materials with Paris exponent m=2, 3 and 4, starting from different initial crack geometries (corresponding to the beginning of each curve, i.e., the point of minimum crack depth a/D) under tension loading and bending moment (Figs. 5 to 7).

Under fatigue loading, different initial crack configurations tend to a preferential path (in a plot a/b-a/D), the convergence (proximity between the curves representing the crack advance from different initial crack shapes) being faster for higher values of the m coefficient of the Paris law and greater for the bending loading than for the tensile loading. When subjected to bending, growth curves generally present lower values for the a/b parameter than under tension, with the exception of the deepest cracks growing from an initial crack aspect ratio $(a/b)_0 \cong 0$. If the initial crack is circular (i.e., $(a/b)_0=1$), the aspect ratio a/b diminishes with the crack growth, whereas when the initial crack is quasi-straight (i.e., $(a/b)_0 \cong 0$), the aspect ratio a/b increases at the beginning and decreases later (with the exception of initially deep cracks with $(a/D)_0 \cong 0.5$, where the aspect ratio a/b always increases), cf. Figs. 5 to 7.

It is observed that results depend on the exponent of the Paris law (Paris coefficients), so that for m=2 and m=3 the crack fronts are more distant between them than for m=3 and m=4, where the m=3 front is between m=2 and m=4. In the case of growth from *circular initial cracks* (i.e., $(a/b)_0=1$), the maximum discrepancy with regard to the crack fronts appears for intermediate cracks (a/D~0.5), a/b being lower for higher values of m-exponent in the Paris law.

In the case of growth from *quasi-straight initial cracks* (i.e., $(a/b)_0 \cong 0$), the maximum discrepancy in the matter of the crack fronts appears for short ($(a/b)_0$~0.3) and long ($(a/b)_0$~0.7) cracks, whereas for intermediate ($(a/b)_0$~0.5) cracks the results for different Paris coefficient m almost match. For short cracks a/b is higher for greater m; whereas for long cracks a/b is higher for lower values of m (again with the exception of initially deep cracks with $(a/D)_0 \cong 0.5$).

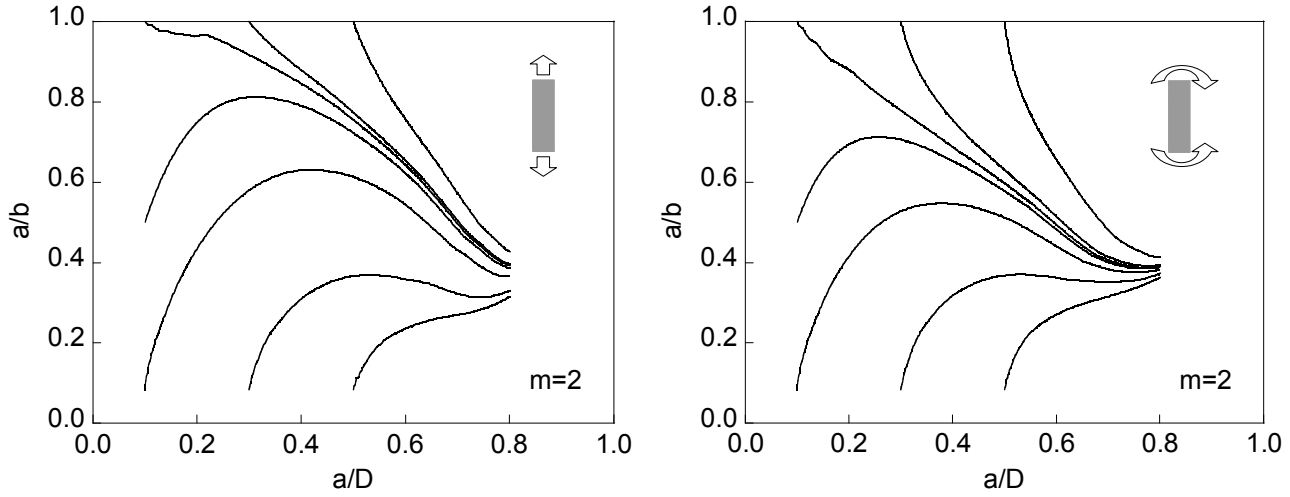

Figure 5. Evolution of the aspect ratio a/b with crack growth (represented by the relative crack depth a/D) for m=2, starting from different initial crack geometries under tension loading (left) and bending moment (right)

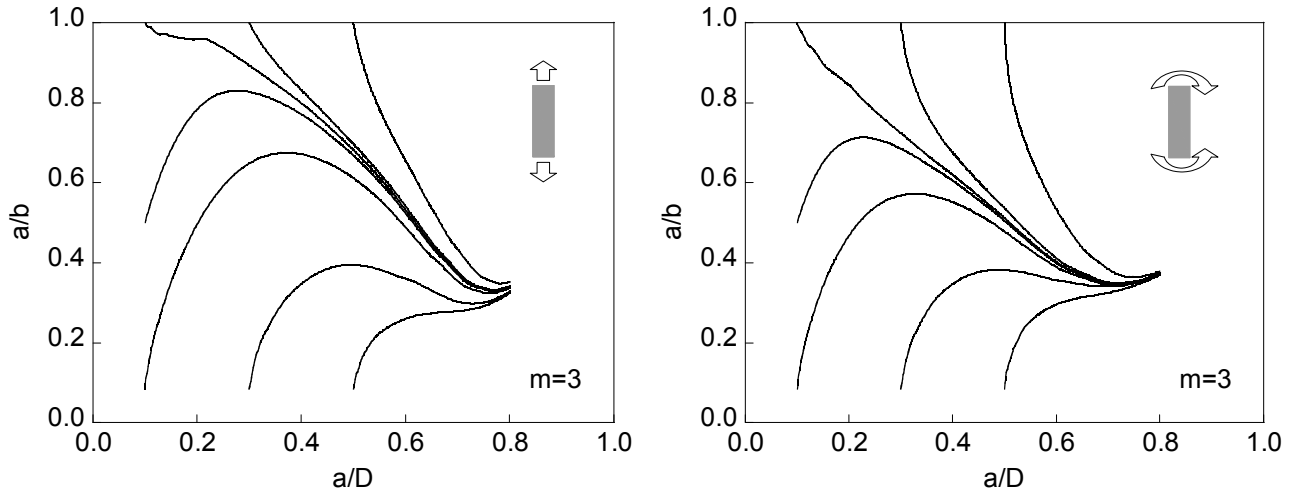

Figure 6. Evolution of the aspect ratio a/b with crack growth (represented by the relative crack depth a/D) for m=3, starting from different initial crack geometries under tension loading (left) and bending moment (right)

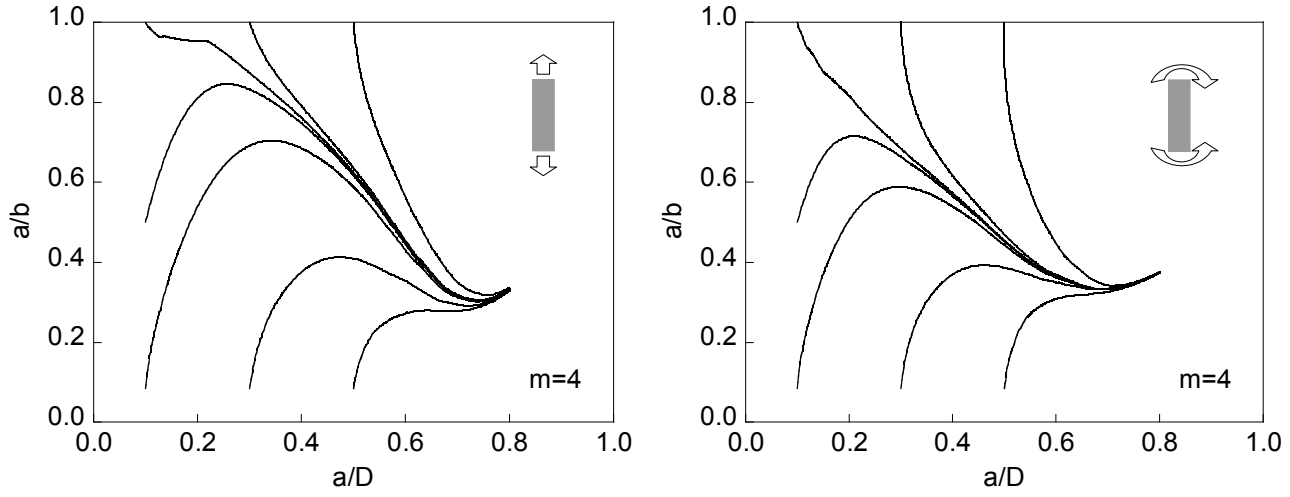

Figure 7. Evolution of the aspect ratio a/b with crack growth (represented by the relative crack depth a/D) for m=4, starting from different initial crack geometries under tension loading (left) and bending moment (right)

3.2. Dimensionless Compliance

The evolution of the dimensionless compliance f during fatigue crack propagation is shown in Figs. 8 to 10, for different initial crack depths ($(a/D)_0$={0.1, 0.3, 0.5}), initial crack aspect ratios $(a/b)_0$=0.08 (quasi-straight front) and $(a/b)_0$=1.00 (circular front), and different loading conditions (tension under free ends and bending).

In cracked cylindrical bars, dimensionless compliance f depends on the loading conditions, on the relative crack depth a/D and on the crack aspect ratio a/b. During fatigue crack growth starting from different initial crack geometries, it is observed how the dimensionless compliance f increases with the relative crack depth a/D and how the influence of the crack aspect ratio a/b is lower as the crack grows, due to the marked geometrical convergence taking place for the deepest cracks, in which the compliance reaches the highest values. The dimensionless compliance f for initially quasi-straight cracks is approximately twice than that for initially circular crack, both being really small at the beginning (initial cracks) and increasing clearly and approaching between them under fatigue.

The dimensionless compliance f in the cracked bars is higher under tensile loading (with free ends) than under bending moment, the ratio being as high as five for the deepest cracks of the present analysis (a/D=0.7). The f-a/D plots starting from an initially circular crack front $(a/b)_0$=1 and from an initially quasi-straight crack front $(a/b)_0$=0.08 are closer when (i) the applied load is bending instead of tension, (ii) the exponent m of the Paris law is higher, (iii) the initial crack depth $(a/D)_0$ is lower. Furthermore, during fatigue crack growth, materials with higher values of the Paris parameter m produce slightly greater dimensionless compliance.

4. Conclusions

According to the Paris-Erdogan law, in fatigue propagation the different initial crack geometries tend to a unique path on the a/b *vs*. a/D plot, this convergence (proximity between the curves representing the crack advance from different initial crack shapes) being faster for higher coefficients m of Paris and quicker for bending moment than for tensile loading.

With quasi-circular initial geometries (i.e., $(a/b)_0$=1), the crack aspect ratio a/b always diminishes with the crack growth, whereas when the initial crack is quasi-straight (i.e., $(a/b)_0$=0.08), the aspect ratio a/b increases at the beginning and decreases at the end (with the exception of initially deep crack with $(a/D)_0 \cong 0.5$).

In fatigue crack propagation, relative crack depth a/D influences more on dimensionless compliance f than the aspect ratio a/b, because the crack fronts tend to converge as the cracks propagate from different initial geometries, the convergence being quicker for initially short cracks than initially long cracks.

The f-a/D plots starting from an initially circular crack front $(a/b)_0$=1 and from an initially quasi-straight crack front $(a/b)_0$=0.08 are closer when the applied load is bending, the exponent m of the Paris law is higher or the initial crack depth $(a/D)_0$ is lower. Materials with higher values of the Paris parameter m produce slightly greater dimensionless compliance during fatigue crack growth.

The greater the m coefficient of the Paris law, the greater the convergence of the different initial crack conditions: geometry of the crack front (a/b) and dimensionless compliance f. The difference between the results for the different values of m is always bigger between m=2 and m=3 than between m=3 and m=4, which implies that, as this parameter increases, there is less dependence of results on it.

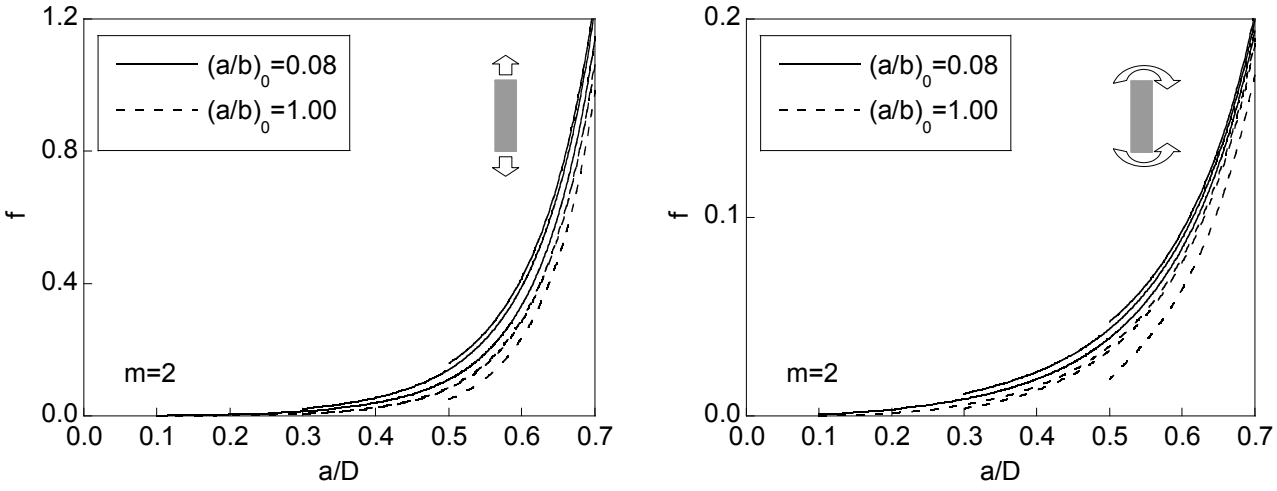

Figure 8. Evolution of the dimensionless compliance f with crack growth (represented by the relative crack depth a/D) for m=2, starting from different initial crack geometries under tension loading (left) and bending moment (right)

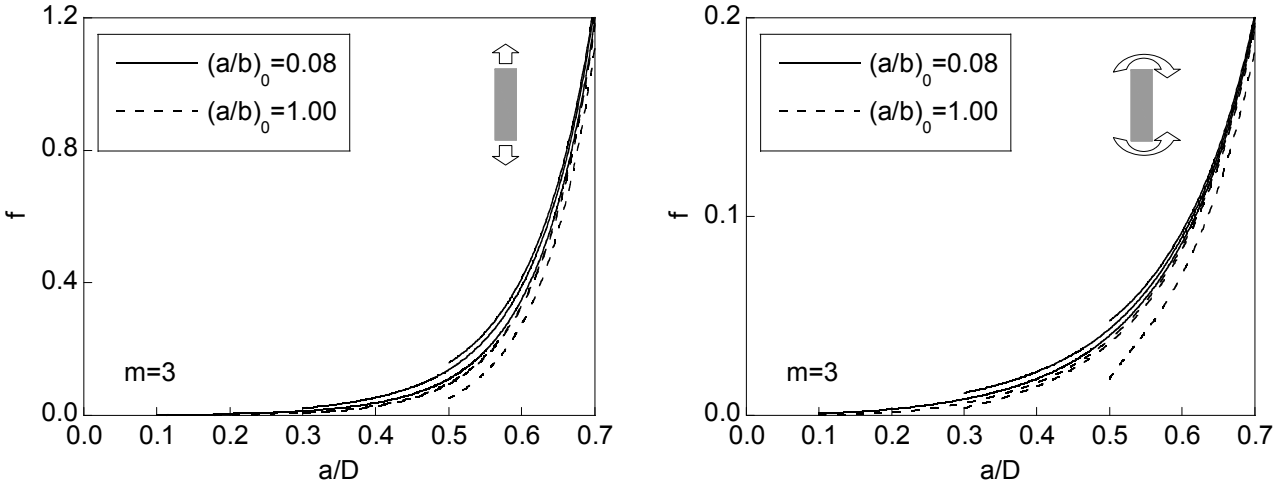

Figure 9. Evolution of the dimensionless compliance f with crack growth (represented by the relative crack depth a/D) for m=3, starting from different initial crack geometries under tension loading (left) and bending moment (right)

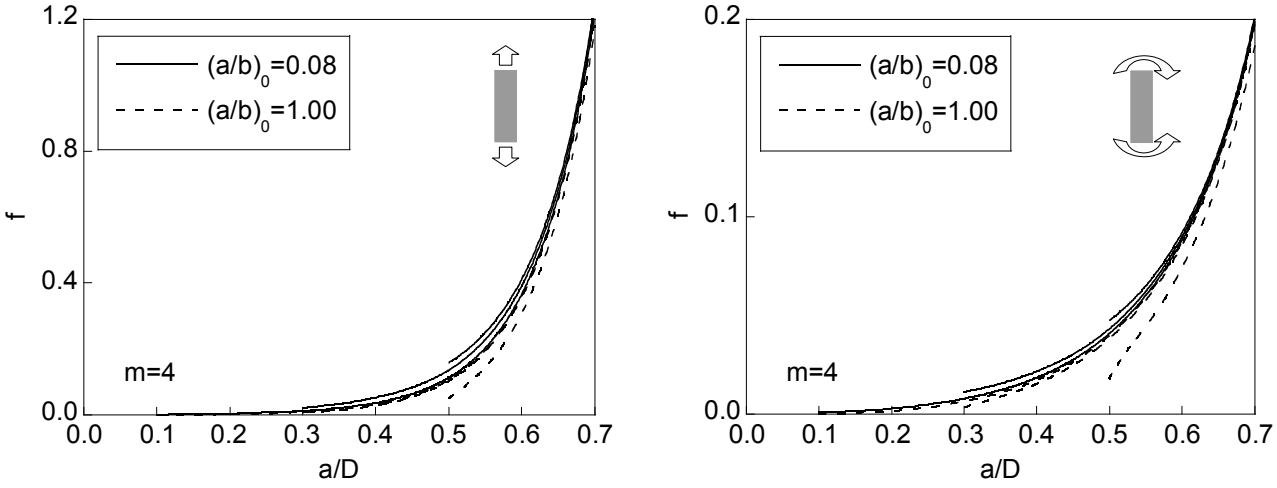

Figure 10. Evolution of the dimensionless compliance f with crack growth (represented by the relative crack depth a/D) for m=4, starting from different initial crack geometries under tension loading (left) and bending moment (right)

Acknowledgements

The authors wish to acknowledge the financial support provided by the following Spanish Institutions: Ministry for Science and Technology (MCYT; Grant MAT2002-01831), Ministry for Education and Science (MEC; Grant BIA2005-08965), Ministry for Science and Innovation (MICINN; Grants BIA2008-06810 and BIA2011-27870), Junta de Castilla y León (JCyL; Grants SA067A05, SA111A07 and SA039A08).

References

[1] A. Carpinteri, Shape change of surface cracks in round bars under cyclic axial loading. Int J Fatigue, 15 (1993) 21–26.
[2] Y.-S. Shih, J.-J. Chen, Analysis of fatigue crack growth on a cracked shaft. Int J Fract, 19 (1997) 477–485.
[3] N. Couroneau, J. Royer, Simplified model for the fatigue growth analysis of surface cracks in round bars under mode I. Int J Fatigue, 20 (1998) 711–718.
[4] X.B. Lin, R.A. Smith, Shape growth simulation of surface cracks in tension fatigued round bars. Int J Fatigue, 19 (1997) 461–469.
[5] X.B. Lin, R.A. Smith, Fatigue growth simulation for cracks in notched and unnotched round bars. Int J Mech Sci, 40 (1998) 405–419.
[6] C.S. Shin, C.Q. Cai, Evaluating fatigue crack propagation properties using a cylindrical rod specimen. Int J Fatigue, 29 (2007) 397–405.
[7] J. Toribio, J.C. Matos, B. González, J. Escuadra, Numerical modelling of crack shape evolution for surface flaws in round bars under tensile loading. Eng Fail Anal, 16 (2009) 618–630.
[8] M.A. Astiz, An incompatible singular elastic element for two- and three-dimensional crack problems. Int J Fract, 31 (1986) 105–124.
[9] A. Carpinteri, Elliptical-arc surface cracks in round bars. Fatigue Fract Eng Mat Struct, 15 (1992) 1141–1153.
[10] A. Levan, J. Royer, Part-circular surface cracks in round bars under tension, bending and twisting. Int J Fract, 61 (1993) 71–99.
[11] C.S. Shin, C.Q. Cai, Experimental and finite element analyses on stress intensity factors of elliptical surface crack in a circular shaft under tension and bending. Int J Fract, 129 (2004) 239–264.
[12] L. Rubio, B. Muñoz-Abella, G. Loaiza, Static behaviour of a shaft with an elliptical crack. Mech Syst Signal Process, 25 (2011) 1674–1686.
[13] J. Toribio, J.C. Matos, B. González, J. Escuadra, Compliance evolution in round cracked bars under tensile fatigue. Eng Fract Mech, 78 (2011) 3243–3252.
[14] P.C. Paris, F. Erdogan, A critical analysis of crack propagation laws. J Basic Eng, 85D (1963) 528–534.
[15] C.Q. Cai, C.S. Shin, A normalized area-compliance method for monitoring surface crack development in a cylindrical rod. Int J Fatigue, 27 (2005) 801–809.

Role of Surface Defects in the Initiation of Fatigue Cracks in Pearlitic Steel

Jesús Toribio[1,*], Juan-Carlos Matos[2], Beatriz González[1]

[1] Department of Materials Engineering, University of Salamanca, E.P.S. Zamora, Spain
[2] Department of Computing Engineering, University of Salamanca, E.P.S. Zamora, Spain
* Corresponding author: toribio@usal.es

Abstract In this paper, tensile fatigue tests were performed under load control, with constant stress amplitude, on pearlitic steel wires with different cold drawing degree, from the hot rolled bar (not cold drawn at all) to the commercial prestressing steel wire (which has undergone seven cold drawing steps and a stress relieving treatment). Results show that fatigue cracks in pearlitic steels initiate at the wire surface starting from small defects, whose size decreases with the drawing process, as the cross sectional area of the wire does. Some of these defects appear during the drawing process itself. Fatigue cracks created from defects (initiation phase) exhibit a fractographic appearance consisting of ductile microtearing events which can be classified as tearing topography surface or TTS. Such microtearings are more planar in the initiation period than in the propagation phase and exhibit a spacing remarkably lower in the pretressing steel wire than in the hot rolled bar, so that their size decreases with cold drawing as the steel microstructure does.

Keywords Pearlitic steel, Cold drawn steel wire, Initiation of fatigue cracks, Surface defects

1. Introduction

Fatigue life of steel wires depends on their surface state and the existence of defects (such as microcracks, inclusions, etc.) present in the material. In wires made of eutectoid cold drawn steel, the fatigue process initiates in surface defects [1-3], broken martensite layers (due to a overheating during the wire drawing process), longitudinal groves and holes mainly caused by surface inclusions [1]. Many times surface defects are caused by the drawing process itself [4].

Surface defects present in the material before wire drawing can be eliminated by such a mechanical treatment. A scratch on the wire surface can be removed by repeated drawing; however, the flaw remains inside the wire because of the development of an overlap, and it is thus difficult to completely remove the flaw [5]. In corrosion-fatigue the aggressive environment can blunt the surface defects due to material dissolution, increasing the number of cycles required to initiate cracking [6].

The main cause of failure in steel wires is the presence of non-metallic inclusions during wire drawing or service [7]. The existence of non-metallic inclusions in cold drawn pearlitic steel affects its fatigue properties [8] by modifying the local stress state surrounding the inclusions, depending on the size, localization, composition and geometry of the inclusion [9].

This paper studies the defects able to initiate the fatigue phenomenon in pearlitic steel applied in two forms —i.e., as a hot rolled bar and as a commercial prestressing steel wire— by analyzing the effects of cold drawing on such defects and the microstructural arrangement and how these changes affect the fatigue performance of prestressing steel.

2. Experimental Procedure

2.1. Material

The material used was eutectoid pearlitic steel (chemical composition 0.789% C, 0.681% Mn, 0.210% Si, 0.010% P, 0.218% Cr, 0.061% V). It was studied in two forms: firstly, as a hot rolled bar

(non cold drawn at all) and, secondly, as a commercial prestressing steel wire which has undergone seven cold drawing steps up to reaching a cumulative plastic strain ε^P=1.6 and a posterior stress-relieving treatment to eliminate, or at least diminish, residual stresses. Steel was supplied in form of wires with circular section, the diameter ranging respectively between 11 and 5 mm for the hot rolled bar and the prestressing steel wire.

Cold drawing produces a clear improvement of conventional mechanical properties (Table 1) obtained from a standard tension test: both the yield strength (σ_Y) and the ultimate tensile strength (UTS, σ_R) increase with cold drawing, while the Young's modulus (E) remains constant and the strain at UTS (ε_R) decreases with it.

Table 1. Mechanical properties of the material in both conditions, i.e. as a hot rolled bar and as a prestressing steel (cold drawn) wire

Steel	E (GPa)	σ_Y (MPa)	σ_R (MPa)	ε_R
Hot rolled bar	202	700	1220	0.078
Prestressing steel wire	209	1480	1820	0.060

Cold drawing also improves the fatigue and fracture behaviour of eutectoid steel. The fracture toughness K_{IC} was obtained by means of fracture test on precracked wires under tensile loading, as described in [10]. The K_{IC} value increases from 53 MPa·m$^{1/2}$ in the hot rolled bar to 137 MPa·m$^{1/2}$ (for θ=0º, fracture toughness in the transverse direction) in the prestressing steel wire, where cold drawing also induces an important strength anisotropy with a directional fracture toughness whose value is dependent on the particular axis of analysis. Values C and m (constants of the Paris law) were obtained by means of tensile fatigue tests, as explained in ref. [11]. The m coefficient in the Paris law (slope of the line) is the same for the two steels and rounds the value 3, whereas the C parameter decreases with cold drawing, changing form $5.3\cdot10^{-12}$ in the hot rolled bar to $4.1\cdot10^{-12}$ in the cold drawn wire (units for C and m are the adequate to measure da/dN in m/cycle and ΔK in MPa·m$^{1/2}$).

2.2. Test Procedure

Wöhler fatigue tests were performed under tensile load control with constant $\Delta\sigma$, sinusoidal wave shape, frequency of 10 Hz, R-ratio R=0 and a maximum stress lower than the yield stress σ_Y (some S-N tests were performed under a stress range of about half the yield strength). The specimens were in the form of 30 cm long bars of circular cross section and the same diameter as the supplied wires. A total number of 20 tests were performed. Fracture surfaces were analyzed by scanning electron microscopy (SEM).

3. Experimental Results

3.1. Microstructure

Figs. 1 and 2 show the microstructure of both steel forms, hot rolled bar and prestressing steel wire, in both transverse and longitudinal section, where the horizontal side of the micrograph corresponds to the radial direction and the vertical side is associated with the axial direction in the longitudinal cut and with the circumferential one in the transverse cut.

Cold drawing produces important microstructural changes in the pearlitic steel [12, 13] in the form of slenderizing of pearlitic colonies, decreases of interlamellar spacing of pearlite and progressive orientation with cold drawing of both colonies and lamellae. Thus, the transverse section (Fig. 1) shows that the lamellae evolve towards a structure with increased packing closeness while at the same time adopting a curved appearance (*curling* phenomenon) from the very beginning of the cold drawing

process (very common when drawing metals with bcc structure). With regard to the longitudinal section (Fig. 2), both decrease of interlamellar spacing and lamellar orientation in axial direction are observed.

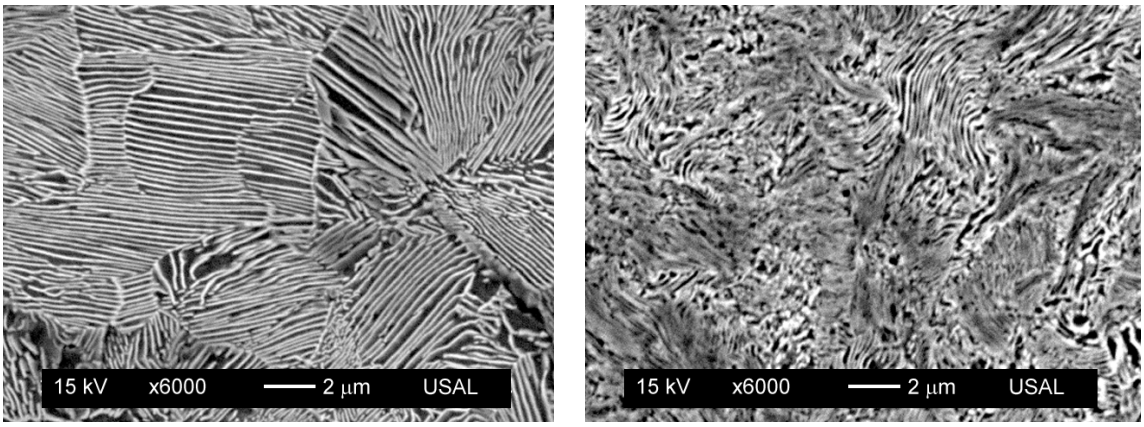

Figure 1. Microstructure in the transverse section: hot rolled bar (left) and prestressing steel wire (right)

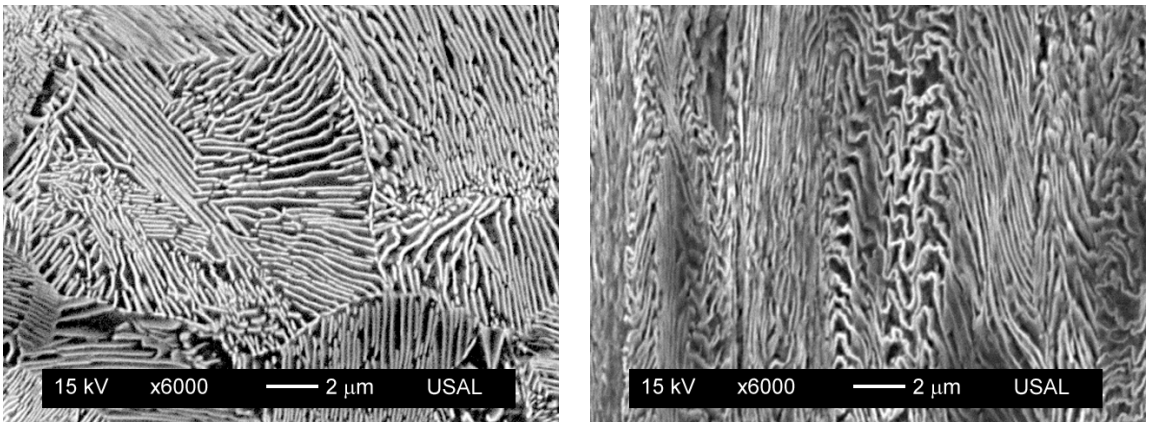

Figure 2. Microstructure in the longitudinal section: hot rolled bar (left) and prestressing steel wire (right). In both micrographs the vertical side is associated with the wire axis or cold drawing direction

3.2. Initiation of Fatigue Cracks from Surface Defects

The surface quality of both commercial products, hot rolled bar and prestressing steel wire, is very different (Fig. 3). While in the first (which comes from a hot rolling process) some material losses and irregularities can be observed on its uneven surface, in the prestressing steel wire (heavily drawn) longitudinal grooves are observed (typical surface features in drawn steel wires [1]), the roughness being higher in the hot rolled bar than in the prestressing steel wire. The defects (pre-existent in the hot rolled bar) change the geometry with the drawing process, their depth decreasing up to the total disappearing in some cases [5]. In addition, the analyzed material (in the two forms as a hot rolled bar or a prestressing steel wire) has frequent inclusions (sulphides, oxides, silicates…), some of which can be found on the wire surface, provoking voids on the material (Fig. 4).

Results show that fatigue cracks in pearlitic steels begin at the wire's surface starting from some of these small defects (Fig. 5). The defect size decreases with the drawing process, as the cross sectional of the wire does. In the hot rolled bar the fatigue initiators are mainly the surface defects with small aspect ratio (material losses at the peripheral zones) while in the prestressing steel wire such initiators are principally the voids created by, probably, the existence of particles near the wire surface (cf. Fig. 5). Depth of maximum surface defects is about 120 μm in the hot rolled bar and about 25 μm in the cold drawn wire. Initiation of fatigue cracks from surface defects is due to the fact that the latter act as stress concentrators.

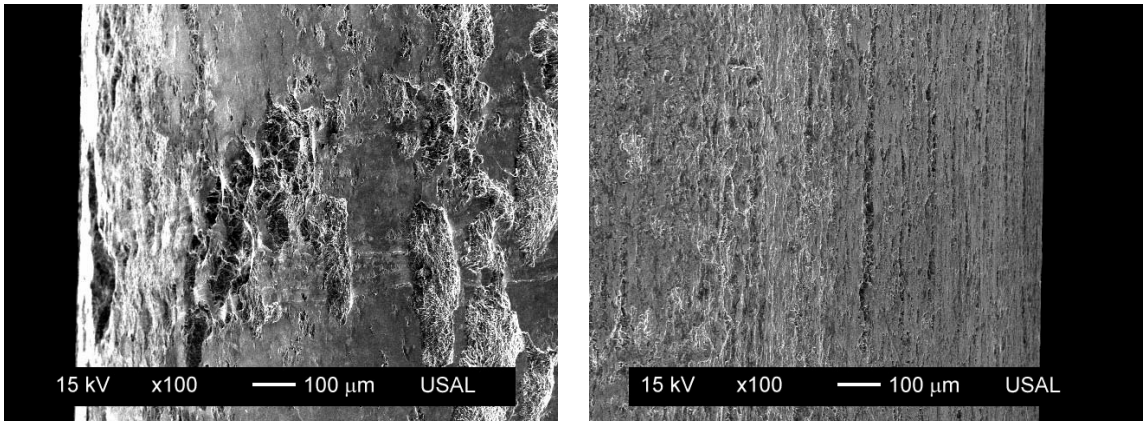

Figure 3. Surface of the material in the two forms: hot rolled bar (left) and prestressing steel wire (right). In both pictures the vertical side is aligned with the wire axis or cold drawing direction

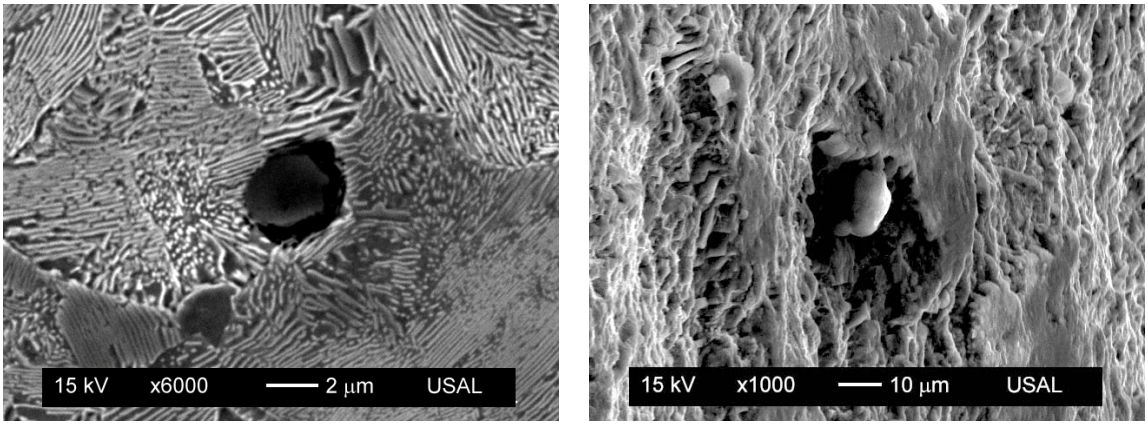

Figure. 4. Inclusions in hot rolled bar: inside the wire (left) and on the wire surface (right). In both pictures the vertical side is aligned with the wire axis or cold drawing direction

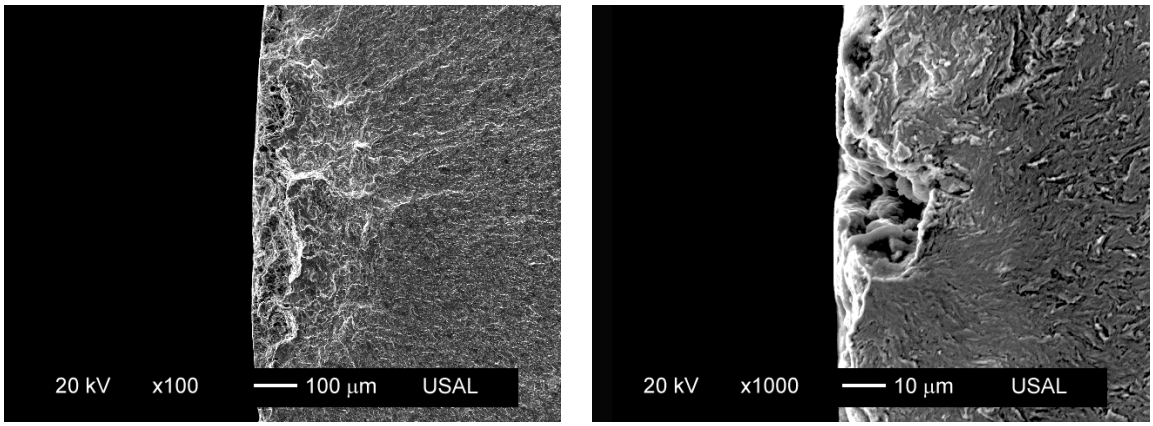

Figure. 5. Initiation of fatigue crack growth from a surface defect: hot rolled bar (left) and prestressing steel wire (right). Both images represent the transverse fatigue fracture surface (circular section perpendicular to the wire axis or cold drawing direction) and crack growth direction takes place from left to right in the fractographs

With regard to fatigue crack initiation from the surface defects in the material supplied as a hot rolled bar and a prestressing steel wire, Fig. 6 shows the same information as Fig. 5 but includes arrows to identify the fatigue crack growth from the aforesaid defect. It is seen that the defect appearance is different in the two material forms. In the hot rolled bar the surface defect looks like an extremely shallow flaw with an approximate aspect ratio of 0.2 whereas the prestressing steel wire such a defect looks like a relatively small circumferential flaw with an approximate aspect ratio equal to the unity. In the matter of the initiation of fatigue crack growth, it is important to say

that, apparently, there is no single initiation point over the defect boundary, but instead of it a line (i.e. a set of points can be viewed) defining the emerging fatigue crack front at the early stages of cracking and diverging fatigue propagation lines emanating from the defect: lack of material previously lost during the manufacturing process in the case of the hot rolled bar and voids created by a previous inclusion in the prestressing steel wire.

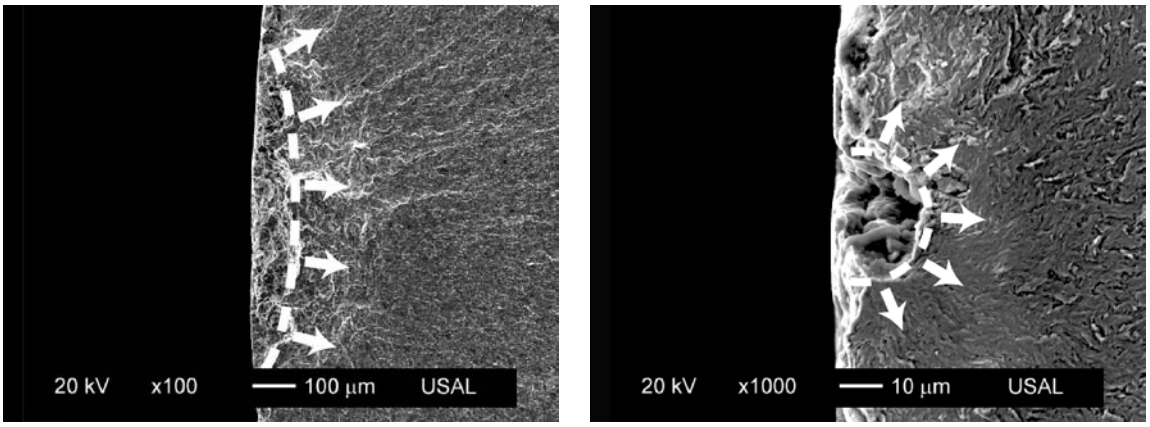

Figure 6. Initiation of fatigue crack growth from a surface defect: hot rolled bar (left) and prestressing steel wire (right), including arrows to identify the fatigue crack growth from defect

In high strength eutectoid steels fatigue crack growth can start from defects caused by the drawing process itself. Fig. 7 shows a surface defect possibly generated by a hard particle in the wire surface during the drawing process, because a longitudinal track, aligned in the drawing direction, appears in the wire surface. A sort of plastic deformation can be observed surrounding the hole (Fig. 7; left) with a very regular geometry. Fig. 7 also includes a magnification (right) of the surface defect (and consequent fatigue crack growth) viewed from different angle, showing the longitudinal scratching marks, an evidences of the pre-damage created by an inclusion (hard particle) during the plastic straining as a consequence of the manufacturing process by cold drawn.

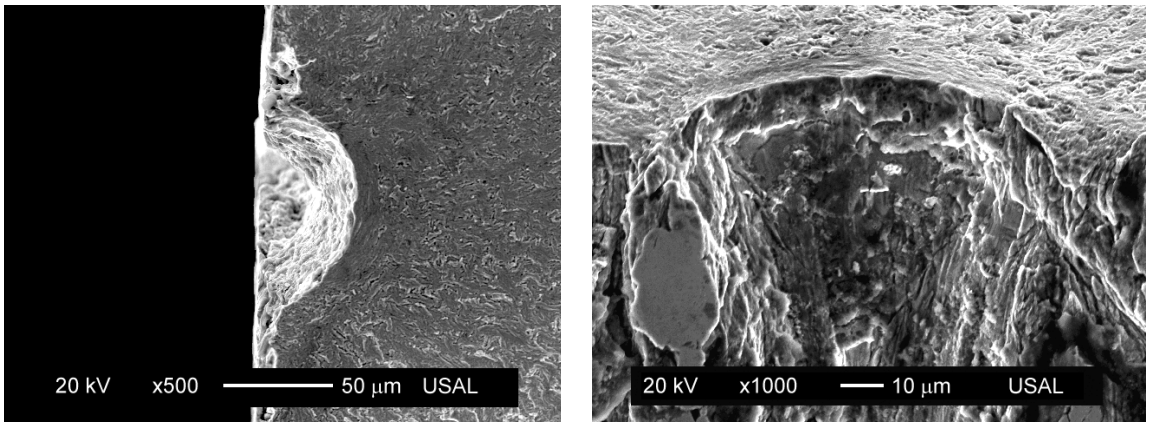

Figure 7. Surface defect caused by cold drawing producing transverse cracking in the prestressing steel wire (left) and magnification of the surface defect (and consequent fatigue crack growth) viewed from different angle (right)

Fatigue cracks created from defects exhibit a fractographic appearance consisting of ductile microtearing events (Fig. 8), which can be classified as *tearing topography surface* or TTS [14]. Such microtearings are less rough in the initiation period (Fig. 8) than in the propagation phase (Fig. 9) and exhibit a spacing remarkably lower in the prestressing steel wire than in the hot rolled bar, so that their size decreases with cold drawing as the steel microstructure does, and a sort of materials science relationship appears between microstructural unit size and fatigue microfracture event. The aforesaid TTS microfracture mode has been associated with hydrogen embrittlement in

pearlitic steel [15] and it can be considered a slow propagation mode in hydrogen-assisted fracture processes linked with subcritical cracking at one micrometer per second or less [16].

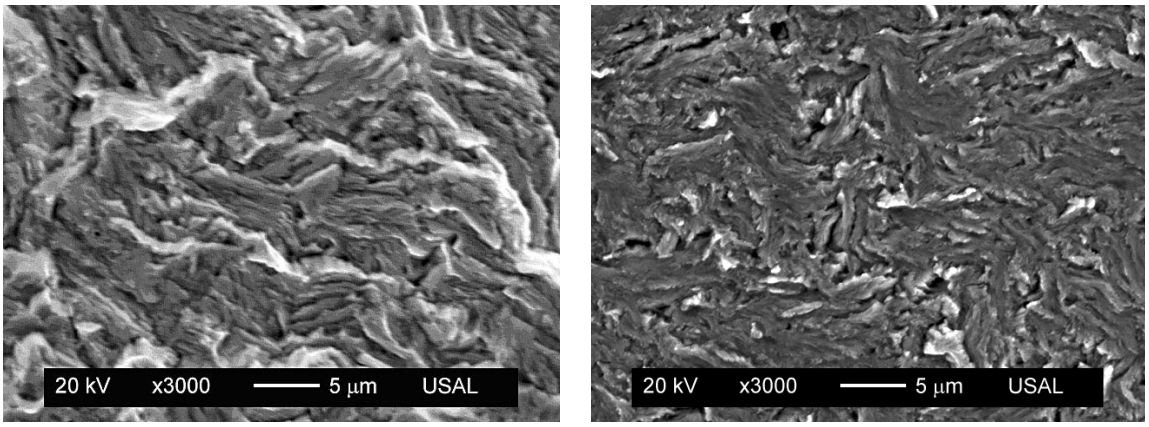

Figure 8. Fractograph corresponding to fatigue initiation phase: hot rolled bar (left) and prestressing steel wire (right). In both images the fatigue crack growth direction is from left to right

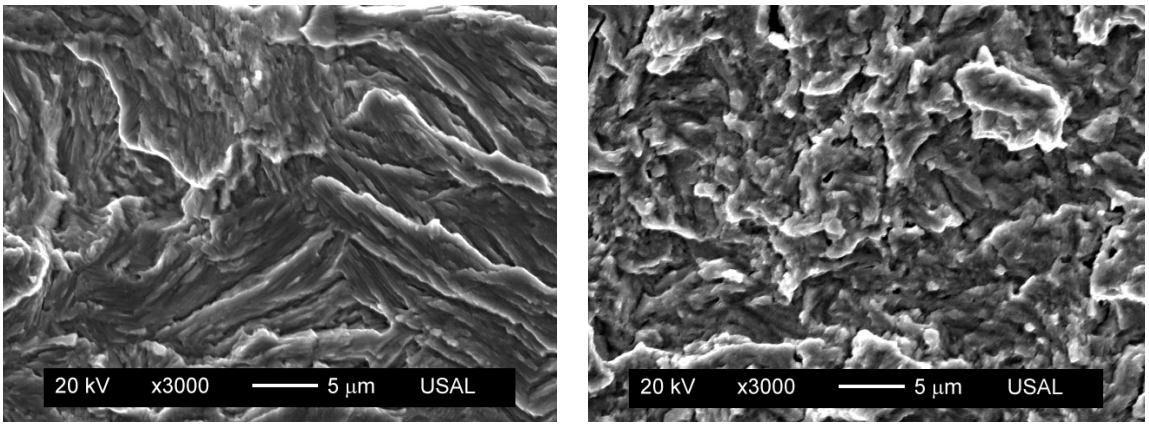

Figure 9. Fractograph corresponding to fatigue propagation phase: hot rolled bar (left) and prestressing steel wire (right). In both images the fatigue crack growth direction is from left to right

4. Simulations

In the Whöler tests, a smooth specimen (samples of the as-supplied wire) was subjected to fatigue loading under constant amplitude, stress level of about half of the yield strength ($\Delta\sigma=\sigma_Y/2$), up to fracture due to initiation and propagation of a fatigue crack reaching its critical value (Fig. 10).

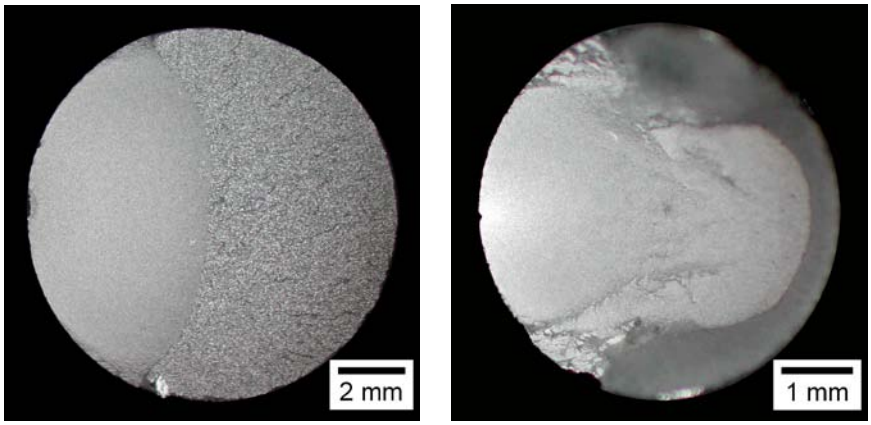

Figure 10. Fracture surface in the specimens after the Whöler tests: hot rolled bar (left) and prestressing steel wire (right). In both images the fatigue crack growth direction is from left to right

Fatigue life N_f was experimentally obtained by means of Whöler tests. The experimental results corresponding to prestressing steel are similar as those previously obtained by Beretta and co-workers [3, 4]. In addition, a numerical estimation was made of the number of cycles needed for crack propagation N_p, on the basis of a simple model previously used by other authors in the scientific literature [17, 18], considering that it follows the Paris law [19],

$$\frac{da}{dN} = C\Delta K^m \tag{1}$$

and the stress intensity range ΔK is given by,

$$\Delta K = Y\Delta\sigma\sqrt{\pi a} \tag{2}$$

where Y is the dimensionless stress intensity factor (SIF).

The number of cycles for propagation was calculated by following expression derived from the Paris law,

$$N_p = \frac{1}{C\Delta\sigma^m \pi^{m/2}} \int_{a_0}^{a_C} \frac{da}{Y^m a^{m/2}} \tag{3}$$

where a_0 and a_C are respectively the initial and the final crack sizes, the first associated with the fatigue threshold [2] and the latter with the critical instant of failure ($K_{Imax}=K_{IC}$, according to the local fracture criterion) and the path followed by the crack during propagation is that plotted in Fig. 11. During its growth, the fatigue crack exhibits an elliptical shape in the Paris regime.

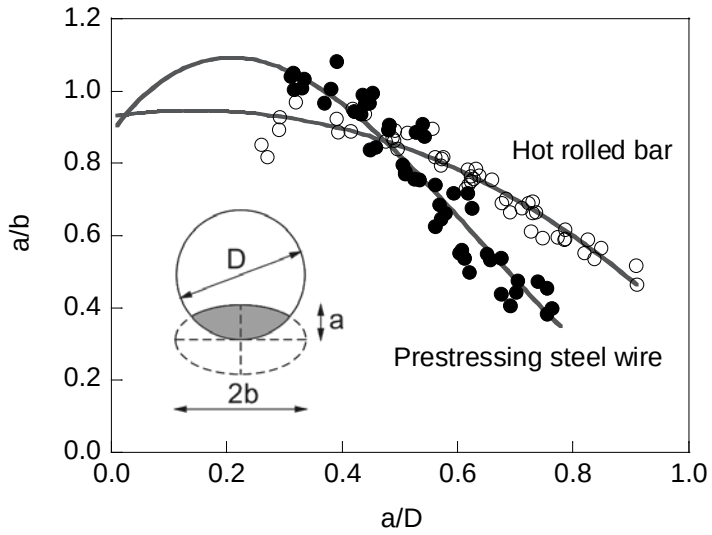

Figure 11. Geometrical changes in the crack front during fatigue crack propagation

The crack front was characterized as an ellipse with semiaxes a (crack depth) and b, its centre been at the wire surface. On the basis of the experimental tests [11] and extrapolating for small crack sizes where the crack front exhibits a quasi-circular appearance (Fig. 12), a relationship was obtained between the relative crack depth (crack depth divided by the diameter, a/D) and the aspect ratio (ratio between the semiaxes of the ellipse, a/b), Fig. 11.

The size effect appearing in the steel samples was taken into account during the propagation phase because it changes the geometric evolution during fatigue. In a previous research work, Shin and Cai [20] observed how when the sample diameter decreases, the fatigue crack growth rate (FCGR) changes at the crack surface when compared with the same value at the crack centre, whereas for higher diameters the FCGR (represented by the Paris law) is the same at the centre and the surface. The aforesaid size effect affects how the crack front evolves (and thus the crack aspect ratio).

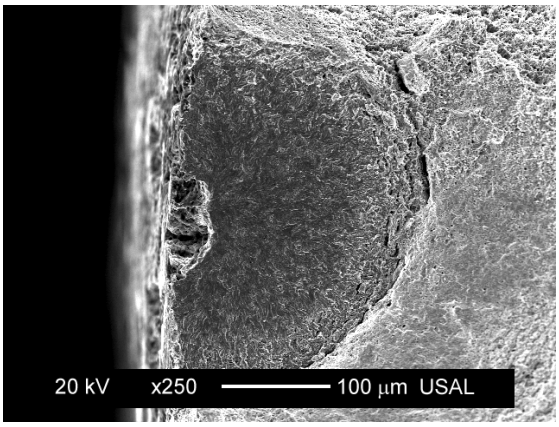

Figure 12. Short crack emanating from a surface defect in the form of void created by a previous inclusion in cold drawn steel. Fatigue crack propagation from left (surface defect) to right

The dimensionless SIF Y employed is that calculated by Astiz [21], for the central point of the crack front by using the finite element method, which depends on the relative crack depth a/D and the aspect ratio a/b through the coefficients C_{ij} (Table 2),

$$Y = \sum_{\substack{i=0 \\ i\neq 1}}^{4} \sum_{j=0}^{3} C_{ij} \left(\frac{a}{D}\right)^{i} \left(\frac{a}{b}\right)^{j} \tag{4}$$

Table 2. Coefficients C_{ij} of Eq. (4) taken from ref. [21]

i	*j=0*	*j=1*	*j=2*	*j=3*
0	1.118	-0.171	-0.339	0.130
2	1.405	5.902	-9.057	3.032
3	3.891	-20.370	23.217	-7.555
4	8.328	21.895	-36.992	12.676

Solution of equation (3) was obtained in incremental form, the convergence being guaranteed by the adequate choice of the crack increment Δa (sufficiently low).

The number of cycles associated with crack initiation N_i can also be estimated as follows [17, 18],

$$N_i = N_f - N_p \tag{5}$$

where the common definition of initiation in reality pertains to both nucleation and propagation of microcracks [22].

Table 3 shows the fatigue life N_f experimentally obtained for a stress range about half of the yield strength of each material. In both the hot rolled bar and the cold drawn wire the life is around 300000 cycles, which indicates that the cold drawing process improves the fatigue performance in a similar way that the increase of material strength. In addition, the main part of the fatigue life (measured as number of cycles) is associated with the propagation phase in the hot rolled bar and with the initiation phase in the cold drawn wire.

Table 3. Fatigue life N_f (experimental, average of five tests), number of cycles for propagation N_p (obtained by simulations) and number of cycles for initiation N_i ($N_i = N_f - N_p$)

Steel	$\Delta\sigma$ (MPa)	N_f (cycles)	N_p (cycles)	N_i (cycles)
Hot rolled bar	347	308200	253700	54500
Prestressing steel wire	790	312910	57655	255255

The prestressing steel wire exhibits a Paris curve below that of the hot rolled bar (lower parameter *C*) [11], thus producing a retardation in fatigue crack propagation with the cold drawing process. In addition the fracture toughness is also higher in the cold drawn wire than in the hot rolled bar [23]. This indicates that cold drawing is beneficial since it improves both the fatigue and the fracture performance by dropping the Paris law [11] and elevating the fracture toughness [10], a clear implication for structural engineers. Moreover, the prestressing steel wire is again the best option on the basis of a clear reduction of the size of the surface defects (acting as crack initiators) and the microstructural changes induced by the drawing process (e.g., orientation of the cementite layers acting as barriers to dislocational movement). Both characteristics, small surface defects and special microstructural arrangement, contribute to a delay of the initiation of fatigue crack growth.

5. Conclusions

The following conclusions may be drawn from the experimental results of fatigue crack growth from surface defects in pearlitic steel:

(i) Fatigue cracks in pearlitic steels are initiated at the wire surface starting from small defects. In the hot rolled bar the fatigue initiators are mainly the surface defects (material losses) while in the prestressing steel wire such initiators are principally the voids created by the existence of particles near the wire's surface.

(ii) Fatigue cracks created from defects exhibit a fractographic appearance consisting of ductile microtearing events which can be classified as *tearing topography surface* or TTS, and exhibit a spacing remarkably lower in the prestressing steel wire than in the hot rolled bar.

(iii) The number of cycles necessary for fatigue crack initiation in the prestressing steel wire is quite higher than that of the hot rolled bar (for $\Delta\sigma=\sigma_Y/2$) and thus changes in surface defects and microstructural arrangement produced by the drawing process considerably improves its fatigue performance.

Acknowledgements

The authors wish to acknowledge the financial support provided by the following Spanish Institutions: Ministry for Science and Technology (MCYT; Grant MAT2002-01831), Ministry for Education and Science (MEC; Grant BIA2005-08965), Ministry for Science and Innovation (MICINN; Grant BIA2008-06810 and BIA2011-27870), *Junta de Castilla y León* (JCyL; Grants SA067A05, SA111A07 and SA039A08), and the steel supplied by EMESA TREFILERÍA (La Coruña, Spain).

References

[1] I. Verpoest, E. Aernoudt, A. Deruyttere, M. de Bondt, The fatigue threshold, surface condition and fatigue limit of steel wire. Int J Fatigue, 7 (1985) 199–214.
[2] J. Llorca, V. Sánchez-Gálvez, Fatigue threshold determination in high strength cold drawn eutectoid steel wires. Eng Fract Mech, 26 (1987) 869–882.
[3] S. Beretta, S. Matteazzi, Short crack propagation in eutectoid steel wires. Int J Fatigue, 18 (1996) 451–456.
[4] S. Beretta, M. Boniardi, Fatigue strength and surface quality of eutectoid steel wires. Int J Fatigue, 21 (1999) 329–335.
[5] T. Shinohara, K. Yoshida, Deformation analysis of surface flaws in stainless steel wire drawing. J Mater Process Technol, 162–163 (2005) 579–584.
[6] N. Singh, V. Sánchez-Gálvez, Effect of $Ca(OH)_2$+NaCl environment corrosion fatigue crack growth in cold drawn eutectoid steel rods. Br Corros J, 26 (1991) 117–121.

[7] M. Yilmaz, Failures during the production and usage of steel wires. J Mater Process Technol, 171 (2006) 232–239.
[8] G.J. Fowler, The influence of non-metallic inclusions on the threshold behavior in fatigue. Mater Sci Eng, 39 (1979) 121–126.
[9] K. Lambrighs, I. Verpoest, B. Verlinden, M. Wevers, Influence of non-metallic inclusions on the fatigue properties of heavily cold drawn steel wires. Procedia Engineering, 2 (2010) 173–181.
[10] B. González, Influencia del proceso de fabricación en el comportamiento plástico y en fractura de aceros de pretensado, PhD Thesis, University of Salamanca, Zamora, Spain, 2007.
[11] J. Toribio, J.C. Matos, B. González, Micro- and macro-approach to the fatigue crack growth in progressively drawn pearlitic steels at different R-ratios. Int J Fatigue, 31 (2009) 2014–2021.
[12] J. Toribio, E. Ovejero, Effect of cumulative cold drawing on the pearlite interlamellar spacing in eutectoid steel. Scripta Mater, 39 (1998) 323–328.
[13] J. Toribio, E. Ovejero, Effect of cold drawing on microstructure and corrosion performance of high-strength steel. Mech Time-Depend Mater, 1 (1998) 307–319.
[14] A.W. Thompson, J.C. Chesnutt, Identification of a fracture mode: the tearing topography surface. Metall Trans A, 10 (1979) 1193–1196.
[15] J.E. Costa, A.W. Thompson, Hydrogen cracking in nominally pearlitic 1045 steel. Metall Trans A, 13 (1982) 1315–1318.
[16] J. Toribio, A.M. Lancha, M. Elices, Characteristics of the new tearing topography surface. Scripta Metall Mater, 25 (1991) 2239–2244.
[17] A. Sonsöz, A.E. Tekkaya, Service life estimation of extrusion dies by numerical simulation of fatigue-crack-growth. Int J Mech Sci, 38 (1996) 527–538.
[18] D.O. Olowokere, D.I. Nwosu, Numerical studies on crack growth in a steel tubular T-joint. Int J Mech Sci, 39 (1997) 859–871.
[19] P.C. Paris, F. Erdogan, A critical analysis of crack propagation laws. J Basic Eng, 85D (1963) 528–534.
[20] C.S. Shin, C.Q. Cai, Fatigue crack propagation properties from small sized rod specimens. Nucl Eng Des, 236 (2006) 2574–2579.
[21] M.A. Astiz, An incompatible singular elastic element for two- and three-dimensional crack problems. Int J Fract, 31 (1986) 105–124.
[22] D.L. McDowell, An engineering model for propagation of small cracks in fatigue. Eng Fract Mech, 56 (1997) 357–377.
[23] J. Toribio, A. Valiente, Failure analysis of cold drawn eutectoid steel wires for prestressed concrete. Eng Fail Anal, 13 (2006) 301–311.

Impact Fatigue Life Prediction of the Wind Tunnel Balance

CHEN Ding*, Bu JunHui, SHEN FengJing
LIU Peng, ZHANG Yan
China Academy of Aerospace Aerodynamics, 100074, Beijing, China
* Corresponding author: ringing282@163.com

Abstract Impact fatigue damage is the main factor which influenced the life of a wind tunnel balance. It is necessary to predict impact fatigue life of a balance especially in the key points of a balance after static analysis. It is unpractical to implement the impact fatigue experiment in the laboratory while wind tunnel balance is a special transducer which would not be manufactured in batches. Generally, balance designers didn't do this analysis for its special use. In fact, accidents of this sort which is in the testing are happening with increasing frequency. This paper provided a method to predict impact fatigue life of a balance which based on the finite element analysis. We used finite element analysis tools to modeling the wind tunnel balance, and then we meshed the whole model as fine as possible. After that, stress of the wind tunnel balance under static loading was figured out, as well as the key points of the balance. The fatigue analysis tools were used to estimate the stress of the balance which was bearing the impact loading. These analysis results would much valuable to the wind tunnel testing.
Keywords wind tunnel balance, fatigue damage, finite element analysis

1. Introduction

Wind tunnel balance is used in the wind tunnel widely by the enlargement of the wind tunnel testing, thus the performance of the balance is more attractive to the researchers. These researchers focused on the failure and accident of the wind tunnel balance, because they doubt that the fatigue of the balance is the main factor of these accidents. But what is the fatigue? Maybe this is the first thing which the wind tunnel balance researchers want to know eagerly. Here quote a definition of ASTM E206-72: The process of progressive localized permanent structural change occurring in a material subjected to conditions which produce fluctuating stresses and strains at some point or points and which may culminate in crack or complete fracture after a sufficient number of fluctuations. The actual mechanization of the material fatigue and its scientific describe are not reported at present. Analysis method of fatigue life prediction is the main aspect of fatigue, and this content was concluded throughout of the history of fatigue. For the cost of the fatigue testing is so large that most researchers tend to using finite element analysis to acquire the data of the material which they concerned. Finite element analysis is the most important method for the researcher to develop a new balance for the wind tunnel balance is special research equipment which is unpractical to proceed the fatigue testing.

The purpose of a wind tunnel balance is to measure the aerodynamic forces and moments, which load a model during wind tunnel tests. The balance measures the aerodynamic forces and moments by the wheatstone bridge which consist of strain gauges adhere to the sensitive elements. The sensitive elements suffered pull、torsion、torsion and bend，and even the combination of them. A slot partition a balance into two parts, the axial force elements combined these as a parallelogram. The forces and moments will transfer from model to the balance. The balance used in the airplane was show in figure1.

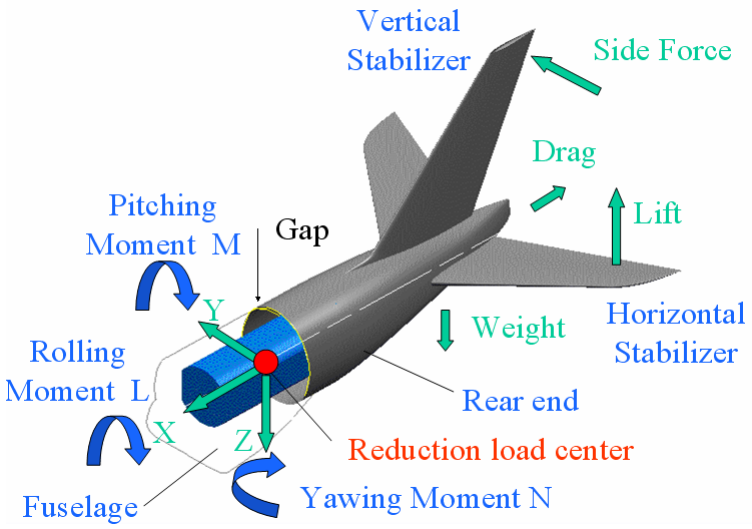

Figure 1. sketch of the six components of wind tunnel balance

Wind tunnel balance is special testing equipment for the wind tunnel testing. They are many rigorous procedures before and after the manufacture of a wind tunnel balance to ensure the balance to be qualified testing equipment. Wind tunnel balance flourishing many years accompany with the new structure and new application domain while the fatigue performance of the balance was ignored by most wind tunnel balance researchers. But this is a question which we could not inevitable, and this is the purpose of this paper also.

2. Fatigue Life Prediction of wind tunnel balance

Fatigue Life Prediction of wind tunnel balance is the responsibility of every balance researcher as other engineering's. Balance users would utilize balance reasonably after fatigue life prediction, and exception handles would also more easier.

Supersonic wind tunnel balance usually bear impact load and steady load and even other complexity situations. Sensitivity of the wind tunnel balance is so excellent that even any relative collection data of the balance would show the trouble of the balance. All of these factors complexes the designing of a wind tunnel balance. Utilizing analysis method to replace the testing method is the goal of the finite element analysis for the balance, and this will decrease the workload and cut down the cost. Utilizing analysis method would get the accurate fatigue life data for the ability of complex geometry processing and anomalous load curse.

Fatigue Life Prediction of wind tunnel balance included several steps. Firstly, we analysis the static stress of the wind tunnel balance, we obtained the dangerous sections or key points of the balance. After that, we take the process of the fatigue analysis until acquire the fatigue life data.

2.1. static stress analysis

The first step of the fatigue life prediction is the static stress analyses, which will also the very important step in the whole curse. Static stress analyzes means that we load the balance by every possible load or rated load. The purpose of static stress analyzes is obtain the dangerous sections by various loading condition. The results of this analysis would play important role to the designing of a wind tunnel balance.

Static stress analyses include several steps: modeling the balance; meshing, loading and solving the problem.

2.2. fatigue analysis

Fatigue analysis should according to the actual working condition, which means every balance designer should find out the actual load curve of the balance. It is useful to predict the true life of a balance by analysis the balance in a real loading condition and real working frequency.

It is more suitable to use the Miner assumption when the curse contains various fatigue stress breadth. Miner on the assumption that: if the cycle stress were a serials breadth denote as S1,S2,S3,….and corresponding destroy life of this material were Nf1,Nf2,Nf3,… then, the life of every stress breadth will be express as the quotient of the actual cycles Ni and life Nfi. We can assumption that the damage cumulate as above method, see Eq. (1)

$$\frac{N_1}{N_{f1}}+\frac{N_2}{N_{f2}}+\frac{N_3}{N_{f3}}...+\frac{N_i}{N_{fi}}=1, \qquad (1)$$

Life will come to the end while the cycles up to the failure times Nfi under a specified stress breadth.

It has many reproaches when we regard the Miner assumption as a effectively designing rule for the testing results are very decentralization. It is widely used in many fields for its simpleness and other strongpoint.

2.3. process of fatigue life prediction

The process of fatigue life prediction listed as follows:

(1) create the frame of fatigue life prediction, define the characteristic of material, set up the parameter of analysis；
(2) define the mode of contact;
(3) using solution combination or specify special stress curve。
(4) solve this problem；

3. example of the fatigue Life Prediction of wind tunnel balance

This section analysis the fatigue life of the B630Q wind tunnel balance which was used in the supersonic wind tunnel.

B630Q wind tunnel balance is a usual balance used for the force and moment measurement. The rated load of this balance listed in the table 1.

Table 1. rated load of B630Q

	My （N.M）	Z （N）	Mz （N.M）	Y （N）	Mx（N.M）	Q（N）
Rated load	50	600	100	2000	30	600

B630Q wind tunnel balance connected with the model by a structure which looked like a cone, which means the contact region is a cone. The finite element model which contains the load equipment showed in the figure 2.

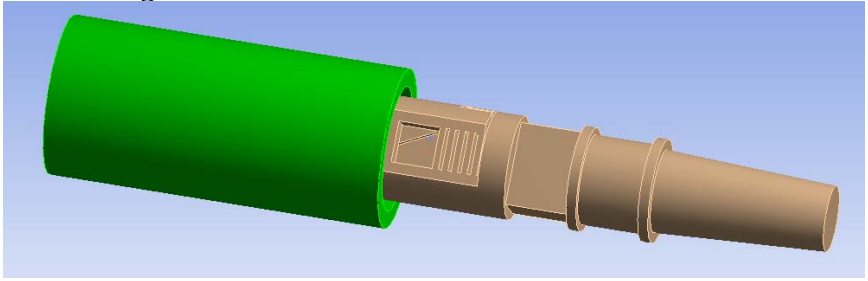

Figure 2. finite element analysis model

3.1. static stress analysis of B630Q balance

This paper analyzed the B630Q wind tunnel balance by finite element analysis. We modeled the balance after the theoretic analysis of this balance. After that, meshing the model was conducted by the software. We can conclude from the meshing contour that the compute node is 172545 and the number of element is 105639. Meshing results of B630Q balanc was showed in figure3. Figure4 showed the contact region of the balance and loading equipment.

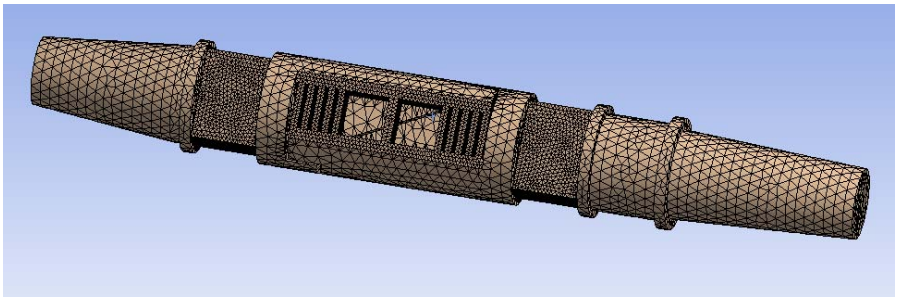

Figure 3. meshing results of the balance

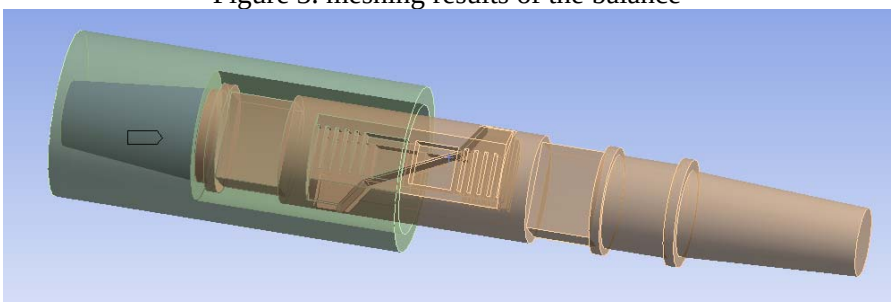

Figure 4. Contact Region

The processing was conducted after the process of meshing the model was completed. The static stress contour and dangerous sections were obtained after six component's load was imposed on the balance and also the integrative load. Figure 5 showed the stress contour of that the six component rated load was loaded integrative. We can conclude that the maximum stress was only 410.7MPa which was lower than the tensile ultimate strength and the location was lie on the root of the supporting beam. Figure 6 showed the each life contour of six components's loading. These figures informed that the dangerous sections were in the root of the supporting beam and the root of the axial force element indeed.

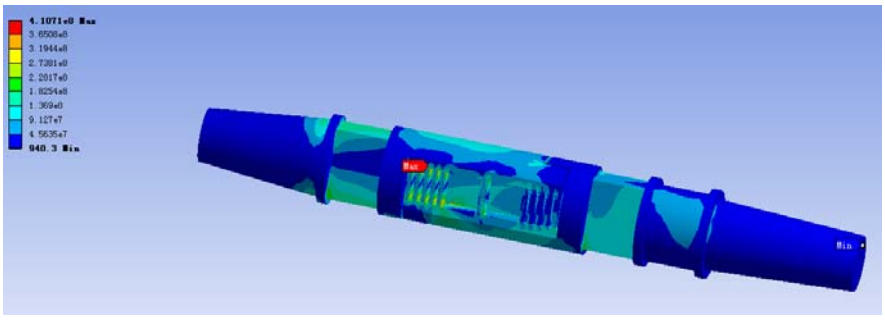

Figure5. Contour of stress

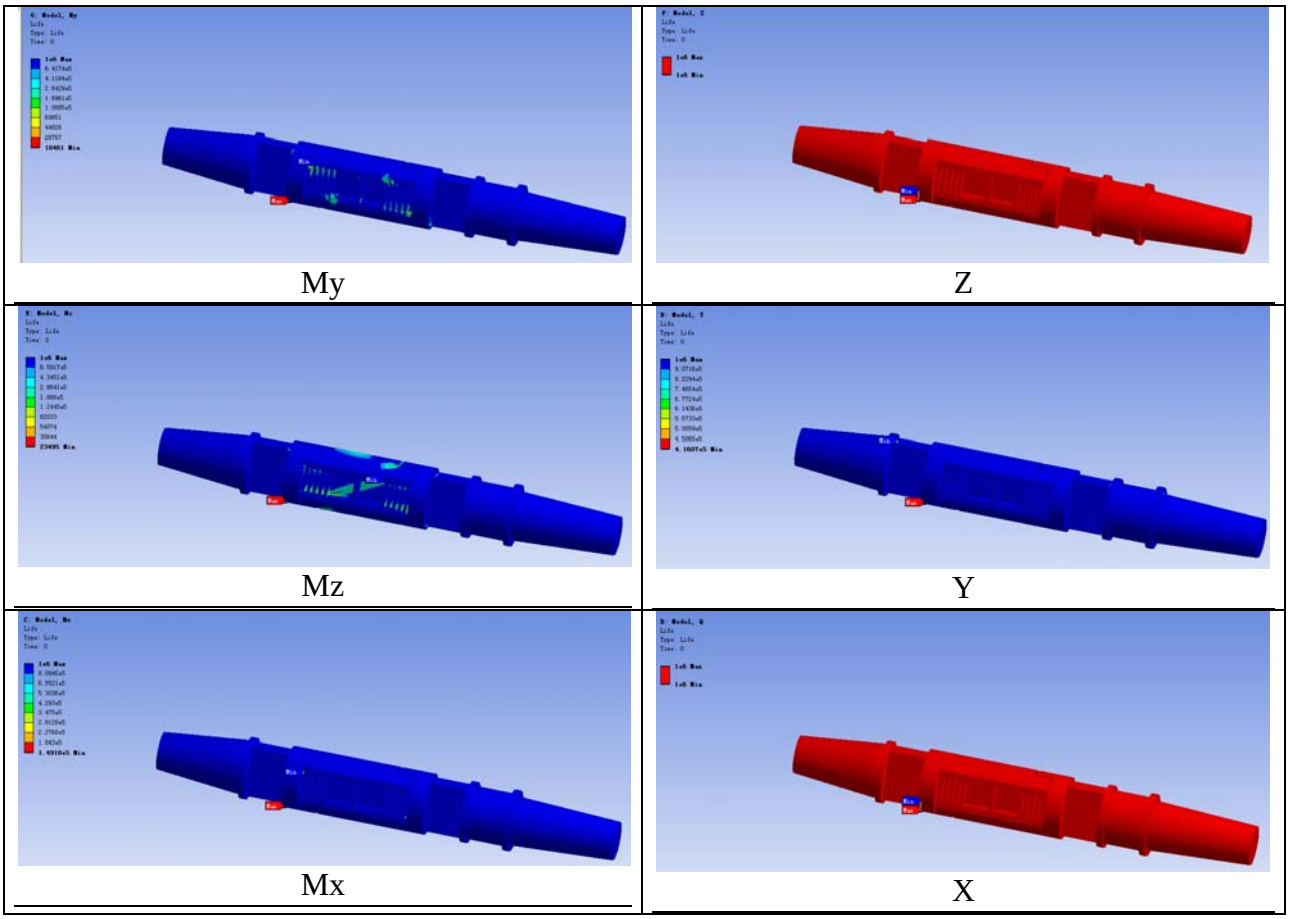

Figure6. Life contour of six component load alone

3.2. fatigue Life Prediction of B630Q balance

We defined the characteristic of the material which was used to manufacture balance. The material was used the structural steel. Detailed parameter were showed subsequently， Poisson's Ratio is 0.3,Young's Modulus is 2.0e+011Pa.Tensile Yield Strength is 2.5e+008 Pa, Compressive Yield Strength is 2.5e+008 Pa. Tensile Ultimate Strength is 4.6e+008 Pa, N-S curve showed in the figure 7.

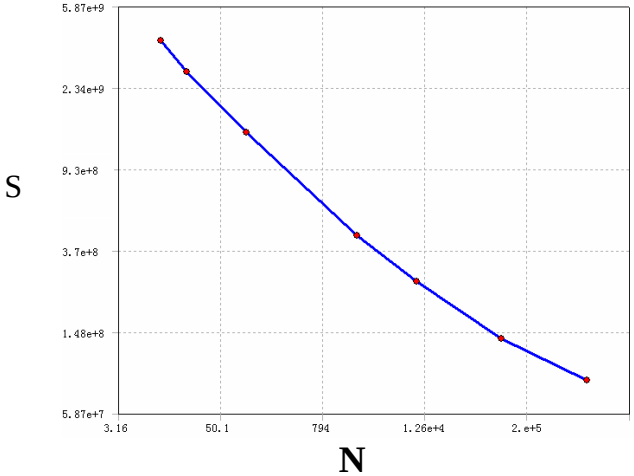

Figure7. N-S curve of structural steel

First, we used history data to simulate the balance. For simplification, the fatigue life prediction curse concerned on the impact on the balance while the wind tunnel startup and steady flow after that and the course of shut down the wind tunnel. We defined the load curve after colligate the

above situation. The load curve was showed in figure8.

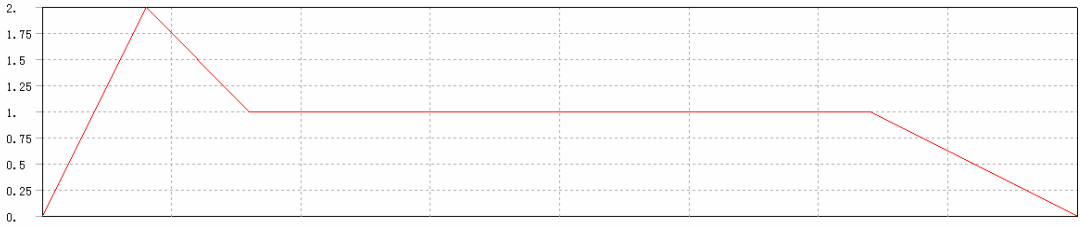

Figure8. load curve of the B630Q balance

Life contour of balance B636Q bearing the combination load was showed in figure 9. We can conclude that the minimum life of balance is 2616 cycles, and the dangerous section was in the root of the supporting beam.

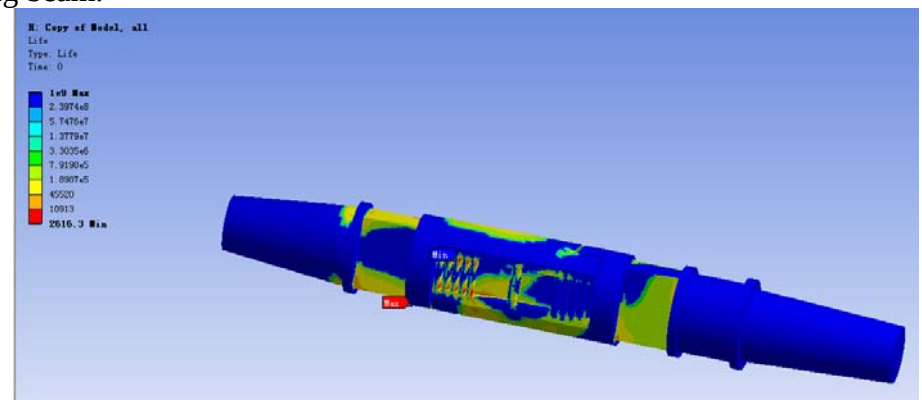

Figure9 Life contour of balance B630Q bearing the combination load

Second, we used solution combination methods to solve this problem. We combined the lift force、pitching moment and axial force according the actual using setting.Life contour of balance B630Q subjected the combination load was showed in figure 10. We can conclude that the minimum life of balance is 15388 cycles, and the dangerous section was not in the root of the axial force element but in the root of the rectangular section. These results maybe arise from the actual load curve didn't contain the side force and yawing moment.

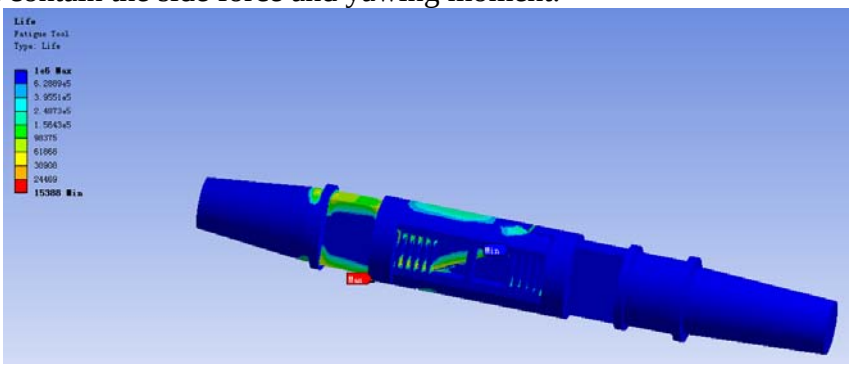

Figure10 Life contour of balance B630Q bearing the combination load

4. conclusions

This paper developed a method to predict the fatigue life of a wind tunnel balance, which was verified by a B630Q balance.

References

[1] J.T.barnby, Fatigue, science Press, 1984.
[2] QIAN Yi,CUI Wei-cheng, An approach for prediction fatigue crack growth based on the cumulative damage theory and elasto-plastic stress field of crack tip, Journal of Ship Mechanics, 2012 ,Vol.16 No.8, 954-961.
[3] He DeXin， Wind Tunnel Balance. Press of Defense Industry China, 2011

Fatigue performance analysis of frictional type high strength bolts of overlapped joints

Huili Wang[1,*], Hongjian Yin[1], SIfeng Qin[2]

[1] Bridge Science Research Institute Dalian University of Technology, Dalian, 116023,China

[2] Research Center for Numerical Tests on Material Dalian University, Dalian, 116022,China

* Corresponding author:: whl7997@163.com

Abstract: According to the fatigue crack extension theory of the fracture mechanics, this paper analysis the relationship between the property of the high-strength bolts and the connection surface friction coefficient, as well as the relationship between the property of the high-strength bolts and temperature. The fatigue life and fatigue damage degree under different anti-friction coefficient and different temperature are calculated by high-strength bolt three-dimension FEM model. After recycling for the same times, the fatigue life will decrease with the increase of the anti-fiction coefficient as well as the temperature. The bigger the anti-friction coefficient is, the more serious the fatigue damage is. The higher the temperature is, the more serious the fatigue damage degree is. With the increase of the anti-friction coefficient, the structure safety factor will decrease, for the increased anti-friction coefficient makes the connection surface geometric discontinuities degree become serious, then the crack extension rate will be faster. With the increase of the temperature, the structure safety factor will also decrease. The conclusions can be used as a reference for the afterwards fatigue design about such components.

Keywords: Fatigue Life, Fatigue Damage, Safe factor, Fracture mechanics

1. Introduction

Because of convenient installation, high-strength material of steel bridge, it was adapted by engineer, as the main form of the structure of large- span bridge design. Factory welding and construction site bolt connection as the general connection between Steel components. As welding connection mode restrictions by welding process and construction environmental, it was difficult to ensure the construction quality when the construction site in the way. So components on site installation connected often use high strength bolt connection. Because bridge often bears car live load function etc, as a result the bridge always under repeated load, will eventually cause fatigue damage of steel bridge. Now a lot of research on the fatigue of the connection method for welding, but for the high strength bolts of fatigue performance opposite less, but bolt-connection structure also had fatigue problems. In this article we use three dimension finite element model of double plate joints connected by high strength friction type bolt, and analysis the node fatigue performance under different temperature and different interface handle methods.

2 Fatigue crack expansion and estimate fatigue life of structure

Fatigue phenomenon produced when the cyclic stress impact on the structure, caused by the subtle crack and steady state expansion, most components considered having the internal defects, having the propagation of the crack which eventually leads to fatigue damage. The maximum stress reached probably in t elastic deformation range in the entire stress object, so effective prediction of fatigue life is the key to guarantee the safety of component. Fracture mechanics applied to solve the problem of the fatigue crack propagation law made well. Etc of variable load in the fatigue crack propagation characteristics can be made by Pairs formula says:

$$\frac{da}{dN} = A \bullet (\Delta K)^n \qquad (\ )$$

a—Crack length,N—Cycle, ΔK —Stress intensity factor range, A, n material constants

From the formula, we can see the fatigue crack growth rate has a close relationship with the stress intensity factor of the materials. Stress intensity factor can be used to characterize crack toughness of the materials that the ability of gap materials to bear loads and plastic deformation under slow loading and linear elastic properties. Generally the critical stress intensity factor (K_C) is used to describe it. Generally speaking, the structure crack toughness, especially steel, increased with temperature, the destroyed stress intensity factor will increase the range and will increase the crack growth rate.

Another factor of fatigue crack propagation is stress concentration .The influence of the geometric not continuity will increase the nominal stress value of bearing structure parts. For fatigue crack with stress concentration expansion laws can be shown as (2) formula express:

$$\frac{da}{dN} = A \bullet (\Delta K_{eff})^n \qquad (2)$$

In the formula： A ， n ——material constant, $\Delta K_{eff} \propto K_t(a)\Delta\sigma\sqrt{a}$, $\Delta\sigma$ —Nominal stress range, a ——Crack length, $K_t(a)$ ——The stress concentration factor.

The strength problem of engineering structure , often need to estimation fatigue life of the dangerous parts in the structure. If knowing the material fatigue performance data, fatigue load spectrum, in principle we can estimation life by cumulative damage theory.

In this article, the circulation of the cumulative damage as circulation method, namely to crack length as the measure of the damage, the initial damage is described by initial crack length, the critical damage is described by critical crack length,the cumulative damage produced by each load cycles is described wit the crack propagation incremental produced by one load cycles. So damage accumulation formula can express into (3) type:

$$a_c = a_0 + \sum_{i=1}^{N_c} \Delta a_i = a_0 + \sum_{i=1}^{N_c} \Delta\left(\frac{da}{dN}\right)_i \qquad (3)$$

a_c—Critical crack length, a_0—Initial crack length, Δa_i—Crack propagation incremental, i — Cycle time, N_c — Cycle times reached the critical crack length.

Through the cycle by the expression of the total circulation damage theory we can see, the fatigue life of the component has a close relationship to the crack growth rate In practical engineering, the maximum length of fatigue crack propagation general is considered to be certain value, we usually think the maximum length of bolt connection is the pure distance between two bolt hole. So the crack's growth rate directly affects the fatigue life of components.

3 The finite element analysis

3.1 Calculation model size and material parameters

In this paper the calculation model is a double board lap connected by high strength bolt with tension load impacting on the axis of it. The joints has a top and a bottom board and one middle connection plate And thickness of joining board is 12 mm &Q345q steel, the connecting slab is 24 mm. the magnitude of bolt is 10.9 specification.&M20. Friction type aperture of the high strength bolts is 1.5~2mm more than bolt stem nominal diameter .During the calculation process bolt aperture takes 22 mm. In the process of computation, steel plate and bolts are assumed for isotropic elastic material, characteristic parameters of material see table 1. For material fatigue properties, there are many scientific research data as a reference, material fatigue properties in this paper using literature [5], [6] research data.

Table 1 Material parameter table

Member	$E(Ngmm^{-2})$	$\rho(kggn^{-3})$	μ	$f_y(Ngmm^{-2})$	$\alpha(^{o}C^{-1})$
Gusset plate	201	7850	0.3	420	1.4e-7
Connected plate	201	7850	0.3	420	1.4e-7
High-strength bolts	206	7850	0.3	942	1.4e-7

3.2 Unit selection and boundary conditions

Because screw, nut, washer are the same material, in order to reduce the contact surface analysis and unit number to increase the simulation efficiency ,the bolt model ignored the contact among screw, nut and washer ,built whole bolt. This paper we simulated high strength bolt and ignored the impact of tightening the nut on the bolt lever torque. The cell division of the finite element model is shown in Figure 1. The model is divided into seven entities part by regular hexahedron unit . the Meshing number is 1333 unit. Bolts and nuts adopted bound connection contact , reaction in the form of a confrontation between two binding contact area designated as the two roles are equal and opposing. Nut with connecting plate and connected to the backplane, connected to the base plate and connecting plate using frictional contact, this contact before the relative sliding can assume a certain level of shear stress in the two contact surfaces. Freedom at one end of the adapter plate, the intermediate connecting both DON stress is applied at one end of the freedom of the upper and lower splicing plates fixed constraints. The simulation consider different temperatures, temperature load is applied at the same time.

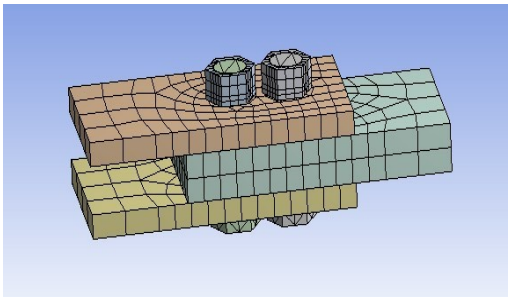

Fig 1 3D Single lap connecting slab model finite element grid partition

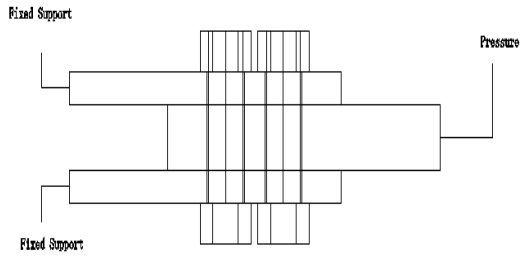

Fig 2 Boundary condition and the load

Different friction coefficients were chosen 0.35,0.40,0.55, many studies were studied for the effects of temperature, this taking into account the temperature difference between the bridge actual working environment, respectively, of -45 a working temperature of -25, 0, 25, 45, etc., fatigue performance simulation.

4 Results analysis

This paper the finite element model of the design life of the times, a major concern under constant stress amplitude fatigue damage D (design life and the useful life of the ratio), the expression can be expressed as (4). Safety factor S (in a given design life, the failure probability), the fatigue life of F (member fatigue failure when the number of load cycles).

$$D = \frac{L_A}{L_D} \qquad (4)$$

D —Fatigue damage, L_D —Fatigue design life, L_A —Available fatigue life.

As can be seen from Figure 3 to 5 leads to the difference in coefficient of the contact surface of the anti-friction, after the same number of times in the cycle as the anti-friction coefficient increases effective fatigue life is gradually reduced, resulting in increased fatigue damage due to the contact surface of the processing in different ways, The safety factor is gradually reduced.

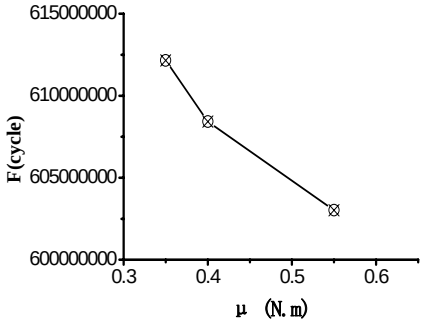

Fig 3 Fatigue life under different friction factor

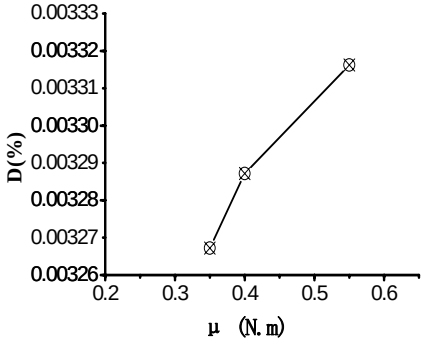

Fig 4 Fatigue damage under different friction coefficient

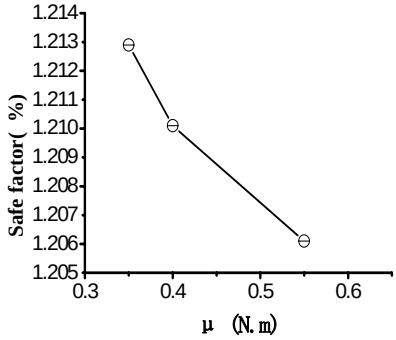

Fig 5 Safe factor with different friction factor

The different friction coefficients reflect the different processing side, the increase in friction coefficient can effectively reduce the relative slippage between the connecting plate, but so that the contact surface between the geometric discontinuity degree increases, resulting in a discontinuous area near the nominal stress value increases, The fatigue crack growth faster, reduce the safety factor of the structure[9].

As can be seen from Figure 6 to 8 with the temperature increasing the effective life of the same times in the cycle after the fatigue decreased, resulting in increase in the fatigue damage in the function of temperature, the safety factor of the structure decreases.

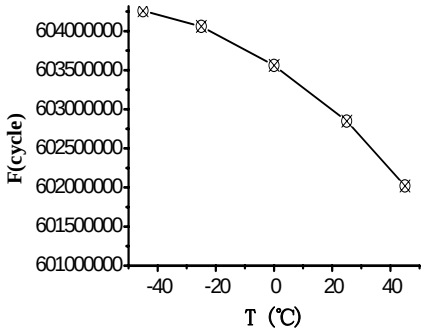

Fig 6 Fatigue life under different temperature

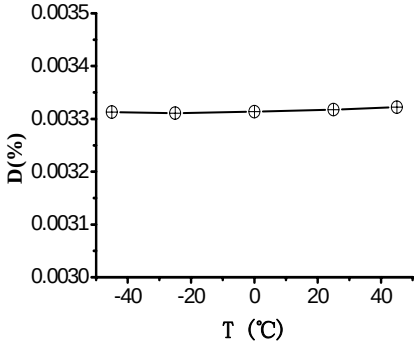

Fig 7 Fatigue damage under different temperature

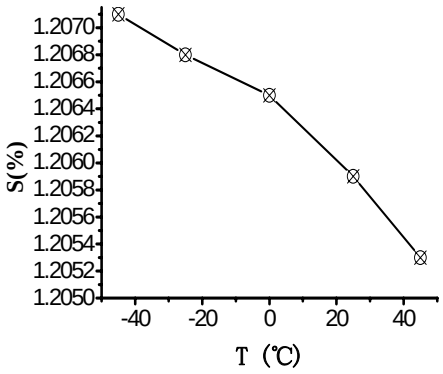

Fig 8 Safe factor with different temperature

5 Conclusion

By the theoretical analysis and finite element analysis, we can get about fatigue life and fatigue damage as well as the structure of the safety factor, the following conclusions:

(1) the effective life of the cycle the same number of times of fatigue due to the approach, in the contact surface between the structure of the different working environment varies, the contact surface more rough lower fatigue life, the lower the higher the fatigue life of the temperature of the working environment.

(2) of the contact surface of the node using a different approach and structure in a different working environment showed a different degree of damage. Contact surface more rough structure of fatigue damage is more severe, and the greater the higher the temperature of the work environment the structure of the fatigue damage.

(3) The different treatment of the contact surface causes the contact surface of the geometric discontinuity degree is increased, resulting in crack growth rate is accelerated to the structure of the lower safety coefficient; increase the safety of the structure with the elevated temperature of the fatigue crack growth rate coefficient is reduced.

6 References

[1] Wang Tianliang, the overall steel truss node test study [J] bridge construction, 1999, 4: 32 to 40.

[2] the Fu Xiangjiong, structural fatigue and fracture [M], Northwest Industrial Press, Xi'an, 1995:114 ~

120.

[3] ST Rolf JM Pakistan Morrison mother was, Wen-Ting Liu translated structure Fracture and Fatigue Control - fracture mechanics applications [M], Mechanical Industry Press, Beijing ,1997:101-285.

[4]H.E.M.Sallam，A.E.A.EI-Sisi，E.B.Matar，O.M.EI-Hussieny，Effect of clamping force and friction coefficient on stress intensity factor of crack lapped joints[J]，Engineering Failure Ansyis18(2011):1550~1558 .

[5] Lei Honggang, M20 high-strength bolts amplitude fatigue test study and fatigue life estimation [J], Steel Structure Engineering, 2002 Supplement: 256 to 261.

[6] Fang Donghui, Liu Yongjie, CHEN Yi-yin, Q345 bridge steel long life fatigue performance research [J], Chinese scientific papers online, 2009, 7 :480-484.

[7] Duyun Xing Huan Hui-ling, Huo Jingsi bearing type of high-strength bolts connected component intensity control study [J] Hunan University of Science and Technology (Natural Science), 2011, 38: 8 to 12.

[8] RH Oskouei, RN Ibrahim, The effect of clamping compressive stresses on the fatigue life of Al 7075-T6 bolted plates at different temperatures [J], Materials and Design 34 (2012): 90-97.

[9] Zhang Gang, Liu Jun, Liu Yongshou, Yue Everest, the surface roughness of the surface stress concentration factor and fatigue life analysis [J], mechanical strength, 2010,32 (1) :110-115.

Elastodynamic analysis of a finite crack at an arbitrary angle in the functionally graded material under in-plane impact loading

Sheng-Hu Ding*, Xing Li
School of Mathematics and Computer Science, Ningxia University, Yinchuan, 750021, China
*Corresponding author:Email:dshsjtu2009@163.com

Abstract The plane problem for a infinite functionally graded material containing a finite crack subjected to the dynamic impact loads is investigated. The crack arbitrarily oriented with respect to the direction of property gradient is considered. Based on the use of Laplace and Fourier integral transforms, formulation of the transient crack problem is reduced to solving a system of Cauchy-type singular integral equation in the Laplace transform domain. The crack-tip response in the physical domain is recovered via the inverse Laplace transform and the values of dynamic stress intensity factors are obtained as a function of time. The effects come from the crack orientation and the nonhomogeneous material parameter on the dynamic stress intensity factors are discussed graphically.

Keywords Functionally graded material, Arbitrarily oriented crack, Singular integral equations, Dynamic stress intensity factors

1. Introduction

With the application of functionally gradient materials in engineering, most of the current researches [1-5] on the fracture analysis of the FGMs interface have been devoted to the FGMs interlayer and the interface between the functionally graded material (FGM) coating and the homogeneous substrate. However, to date, only a few articles were devoted to the dynamic fracture mechanics of FGMs. Among these limited work, Atkinson [6] first studied the crack propagation in media with spatially varying elastic properties. Li and Wen [7] investigated the dynamic stress intensity factor of a cylindrical interface crack located between two coaxial dissimilar homogeneous cylinders that are bonded with a functionally graded interlayer and subjected to a torsional impact loading. The transient response of a functionally graded coating-substrate system with an internal or edge crack perpendicular to the interface [8] has been studied under an in-plane impact load. Recently, the dynamic fracture problem of the weak-discontinuous interface between a FGM coating and a FGM substrate have been studied by Li and his coauthors [9]. Ding and Li [10] studied the dynamic stress intensity factor of collinear crack-tip fields in bonded functionally graded finite strips.

For the arbitrarily oriented crack, Bogy [11] studied the problem of an arbitrarily oriented crack terminated at the bonded interface. For FGMs, till 1994 when Konda and Erdogan [12] considered the mixed mode crack problem in a nonhomogeneous elastic medium. Under the condition of antiplane shear impact, the corresponding dynamic stress intensity factors for a crack in a homogeneous material when a graded stip between dissimilar half-planes was evaluated by Choi [13].

The objective of the present paper is to provide a theoretical analysis of the dynamic behavior of a finite crack in the functionally graded material subjected to in-plane impact loading. To solve the proposed crack problem, the Fourier integral transform method is employed together with Laplace transform, leading to the derivation of a singular integral equation with a generalized Cauchy kernel. It is a simple and convenient method for solving this problem. In the numerical results, the values of mixed-mode stress intensity factors (SIFs) are provided as a function of crack orientation angle. The effects come from the crack orientation and the nonhomogeneous material parameter on the dynamic stress intensity factors (DSIFs) are discussed graphically.

2. Formulation of the problem

As shown in Fig.1, consider the plane problem of an arbitrarily oriented crack located in a functionally graded material. Two rectangular Cartesian coordinate systems, (x, y, z) and (x_1, y_1, z_1), are defined to describe the direction of the material gradient and crack orientation, respectively. The system (x_1, y_1, z_1) is obtained by rotating counterclockwise to the system (x, y, z) with angle θ .The crack is assumed to occupy the region $a \le x_1 \le b$, $y_1 = 0$, $|z_1| < \infty$. The shear modulus μ and mass density ρ in (x_1, y_1, z_1) and (x, y, z) coordinate can be written, respectively, as follows [12]

$$\mu(x_1, y_1) = \mu_0 \exp(\beta_1 x_1 + \beta_2 y_1), \quad \rho(x_1, y_1) = \rho_0 \exp(\beta_1 x_1 + \beta_2 y_1), \tag{1}$$

$$\mu(y) = \mu_0 \exp(\beta y), \quad \rho(y) = \rho_0 \exp(\beta y), \tag{2}$$

where β, μ_0 and ρ_0 are material constants, and $\beta_1 = \beta \sin(\theta), \beta_2 = \beta \cos(\theta)$.

The mixed boundary value problem shown in Fig.1 will be solved under the following conditions

$$\sigma_{y_1 y_1}(x_1, 0^+, t) = \sigma_{y_1 y_1}(x_1, 0^-, t), \quad \sigma_{x_1 y_1}(x_1, 0^+, t) = \sigma_{x_1 y_1}(x_1, 0^-, t), \quad -\infty < x_1 < \infty, \tag{3}$$

$$u(x_1, 0^+, t) = u(x_1, 0^-, t), \quad v(x_1, 0^+, t) = v(x_1, 0^-, t), \quad x_1 < a, \quad \text{or} \quad x_1 > b, \tag{4}$$

$$\sigma_{y_1 y_1}(x_1, 0^+, t) = \sigma_1 H(t), \quad a < x_1 < b, \tag{5}$$

$$\sigma_{x_1 y_1}(x_1, 0^+, t) = \sigma_2 H(t), \quad a < x_1 < b, \tag{6}$$

where $\sigma_1 H(t)$ and $\sigma_2 H(t)$ are the negative of dynamic normal stress and shear stress at the crack plane under external loading in an uncracked specimen. $H(t)$ is the Heaviside function of time t. When $t < 0$, $H(t) = 0$, and when $t \ge 0$, $H(t) = 1$.

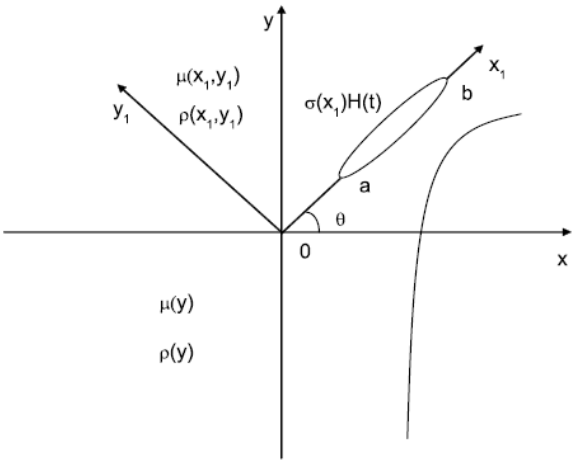

Figure 1. Geometry of the functionally graded material with an arbitrarily oriented crack

3. Method of solutions

The general expressions for displacements components can be written as

$$\hat{u}(x_1, y_1^+, p) = \frac{1}{2\pi}\int_{-\infty}^{\infty}\left[G_1(\xi, p)C_1(\xi, p)e^{\lambda_1(\xi,p)y_1} + G_2(\xi, p)C_2(\xi, p)e^{\lambda_2(\xi,p)y_1}\right]e^{i\xi x_1}\mathrm{d}\xi,$$
$$\hat{v}(x_1, y_1^+, p) = \frac{1}{2\pi}\int_{-\infty}^{\infty}\left[C_1(\xi, p)e^{\lambda_1(\xi,p)y_1} + C_2(\xi, p)e^{\lambda_2(\xi,p)y_1}\right]e^{i\xi x_1}\mathrm{d}\xi, \tag{7}$$

$$\hat{u}(x_1, y_1^-, p) = \frac{1}{2\pi}\int_{-\infty}^{\infty}\left[G_3(\xi, p)C_3(\xi, p)e^{\lambda_3(\xi,p)y_1} + G_4(\xi, p)C_4(\xi, p)e^{\lambda_4(\xi,p)y_1}\right]e^{i\xi x_1}\mathrm{d}\xi,$$
$$\hat{v}(x_1, y_1^-, p) = \frac{1}{2\pi}\int_{-\infty}^{\infty}\left[C_3(\xi, p)e^{\lambda_3(\xi,p)y_1} + C_4(\xi, p)e^{\lambda_4(\xi,p)y_1}\right]e^{i\xi x_1}\mathrm{d}\xi, \tag{8}$$

where $C_j(\xi, p)(j = 1-4)$ are unknown functions, and $\lambda_j(\xi, p)(j = 1-4)$ are the roots of the characteristic equation

$$\lambda^4 + \Omega_1\lambda^3 + \Omega_2\lambda^2 + \Omega_3\lambda + \Omega_4 = 0, \tag{9}$$

where

$$\Omega_1 = 2\beta_2, \quad \Omega_2 = -2\xi^2 + 2i\xi\beta_1 + {\beta_2}^2 + \frac{(\kappa-3){\beta_1}^2}{1+\kappa} - 2\frac{\kappa\rho_0 p^2}{(1+\kappa)\mu_0}, \tag{10}$$

$$\Omega_3 = -2\xi^2\beta_2 + \frac{8i\beta_2\beta_1\xi}{1+\kappa} - 2\frac{\beta_2\kappa\rho_0 p^2}{\mu_0(1+\kappa)}, \tag{11}$$

$$\Omega_4 = \xi^4 - 2i\xi^3\beta_1 - \xi^2{\beta_1}^2 + \frac{(3-\kappa){\beta_2}^2\xi^2}{1+\kappa} + 2\frac{\kappa\rho_0 p^2\xi^2}{\mu_0(1+\kappa)} - \frac{2i\beta_1\rho_0 p^2\kappa\xi}{\mu_0(1+\kappa)} + \frac{-{\rho_0}^2 p^4 + {\rho_0}^2 p^4\kappa}{(1+\kappa){\mu_0}^2}. \tag{12}$$

Here, $G_j(\xi, p)(j = 1-4)$ can be expressed as

$$G_j(\xi, p) = -\frac{[2i\xi + \beta_1(3-\kappa)]\lambda_j + i\xi\beta_2(\kappa-1)}{(\kappa-1)\lambda_j^2 + \beta_2(\kappa-1)\lambda_j + (i\xi\beta_1 - \xi^2)(\kappa+1) - \rho_0(\kappa-1)p^2/\mu_0}. \tag{13}$$

4. Singular integral equation

Now, we define the following new unknown functions

$$\hat{g}_1(x_1, p) = \frac{\partial}{\partial x_1}[\hat{u}(x_1, 0^+, p) - \hat{u}(x_1, 0^-, p)], \quad a < x_1 < b,$$
$$\hat{g}_2(x_1, p) = \frac{\partial}{\partial x_1}[\hat{v}(x_1, 0^+, p) - \hat{v}(x_1, 0^-, p)], \quad a < x_1 < b. \tag{14}$$

From (3-6), we obtain

$$\int_a^b \frac{\hat{g}_2(t, p)}{t - x_1}\mathrm{d}t + \int_a^b K_{11}(x_1, t, p)\hat{g}_1(t, p)\,\mathrm{d}t + \int_a^b K_{12}(x_1, t, p)\hat{g}_2(t, p)\,\mathrm{d}t = \frac{(\kappa+1)\sigma_1}{2\mu_0 p e^{\beta_1 x_1}},$$
$$\int_a^b \frac{\hat{g}_1(t, p)}{t - x_1}\mathrm{d}t + \int_a^b K_{21}(x_1, t, p)\hat{g}_1(t, p)\,\mathrm{d}t + \int_a^b K_{22}(x_1, t, p)\hat{g}_2(t, p)\,\mathrm{d}t = \frac{(\kappa+1)\sigma_2}{2\mu_0 p e^{\beta_1 x_1}}, \tag{15}$$

where

$$K_{11}(x_1, t, p) = \frac{\kappa+1}{4(\kappa-1)}\left\{\int_0^A (k_{11} + k_{11c})\cos[\xi(t - x_1)]d\xi + \int_A^\infty (k_{11} + k_{11c} - \frac{2(\kappa-1)\beta_2}{\xi(1+\kappa)})\cos[\xi(t - x_1)]d\xi\right.$$
$$\left. + \int_A^\infty \frac{2(\kappa-1)\beta_2}{\xi(1+\kappa)}\cos[\xi(t - x_1)]d\xi - \int_0^\infty (k_{11} - k_{11c})i\sin[\xi(t - x_1)]d\xi\right\}, \tag{16}$$

$$K_{12}(x_1,t,p)=\frac{\kappa+1}{4(\kappa-1)}\Big\{\int_0^A(k_{12}+k_{12c})\cos[\xi(t-x_1)]d\xi+\int_A^\infty(k_{12}+k_{12c}-\frac{2(\kappa-1)\beta_1}{\xi(1+\kappa)})\cos[\xi(t-x_1)]d\xi$$
$$+\int_A^\infty\frac{2(\kappa-1)\beta_1}{\xi(1+\kappa)}\cos[\xi(t-x_1)]d\xi-\int_0^\infty(k_{12}-k_{12c}-\frac{4i(\kappa-1)}{\kappa+1})i\sin[\xi(t-x_1)]d\xi\Big\},\tag{17}$$

$$K_{21}(x_1,t,p)=\frac{\kappa+1}{4}\Big\{\int_0^A(k_{21}+k_{21c})\cos[\xi(t-x_1)]d\xi+\int_A^\infty(k_{21}+k_{21c}-\frac{2\beta_1}{\xi(1+\kappa)})\cos[\xi(t-x_1)]d\xi$$
$$+\int_A^\infty\frac{2\beta_1}{\xi(1+\kappa)}\cos[\xi(t-x_1)]d\xi-\int_0^\infty(k_{21}-k_{21c}-\frac{4i)}{\kappa+1})i\sin[\xi(t-x_1)]d\xi\Big\},\tag{18}$$

$$K_{22}(x_1,t,p)=\frac{\kappa+1}{4}\Big\{\int_0^A(k_{22}+k_{22c})\cos[\xi(t-x_1)]d\xi+\int_A^\infty(k_{22}+k_{22c}+\frac{2\beta_2}{\xi(1+\kappa)})\cos[\xi(t-x_1)]d\xi$$
$$-\int_A^\infty\frac{2\beta_2}{\xi(1+\kappa)}\cos[\xi(t-x_1)]d\xi-\int_0^\infty(k_{22}-k_{22c})i\sin[\xi(t-x_1)]d\xi\Big\},\tag{19}$$

$$k_{11}=\frac{i}{\xi}\frac{E_1J_4-E_2J_3}{J_3J_2-J_1J_4},\quad k_{12}=\frac{i}{\xi}\frac{E_2J_1-E_1J_2}{J_3J_2-J_1J_4},\tag{20}$$

$$k_{21}=\frac{i}{\xi}\frac{F_1J_4-F_2J_3}{J_3J_2-J_1J_4},\quad k_{22}=\frac{i}{\xi}\frac{F_2J_1-F_1J_2}{J_3J_2-J_1J_4},\tag{21}$$

$$J_1=G_1+\frac{G_3\left(E_4F_1-E_1F_4\right)}{E_3F_4-F_3E_4}-\frac{G_4\left(E_3F_1-F_3E_1\right)}{E_3F_4-F_3E_4},\tag{22}$$

$$J_2=G_2-\frac{G_4\left(E_3F_2-F_3E_2\right)}{E_3F_4-F_3E_4}+\frac{G_3\left(E_4F_2-E_2F_4\right)}{E_3F_4-F_3E_4},\tag{23}$$

$$J_3=1+\frac{E_4F_1-E_1F_4}{E_3F_4-F_3E_4}-\frac{E_3F_1-F_3E_1}{E_3F_4-F_3E_4},\tag{24}$$

$$J_4=1+\frac{E_4F_2-E_2F_4}{E_3F_4-F_3E_4}-\frac{E_3F_2-F_3E_2}{E_3F_4-F_3E_4}.\tag{25}$$

and $k_{ijc}(i,j=1,2)$ are the complex conjugates of k_{ij}.

The solutions of the singular integral equations Eq.(15) are [14]

$$\hat{g}_1(u,p)=G_1(u,p)/\sqrt{1-u^2},\quad \hat{g}_2(u,p)=G_2(u,p)/\sqrt{1-u^2}.\tag{26}$$

The stress intensity factors in Laplace domain can be defined as

$$\hat{K}_I(a,p)=\lim_{x_1\to a}\sqrt{2(a-x_1)}\sigma_{y_1y_1}(x_1,0)=\frac{2\mu_0e^{\beta_1a}}{\kappa+1}\sqrt{(b-a)/2}G_2(-1,p),\tag{27}$$

$$\hat{K}_I(b,p)=\lim_{x_1\to b}\sqrt{2(x_1-b)}\sigma_{y_1y_1}(x_1,0)=-\frac{2\mu_0e^{\beta_1b}}{\kappa+1}\sqrt{(b-a)/2}G_2(1,p),\tag{28}$$

$$\hat{K}_{II}(a,p)=\lim_{x_1\to a}\sqrt{2(a-x_1)}\sigma_{x_1y_1}(x_1,0)=\frac{2\mu_0e^{\beta_1a}}{\kappa+1}\sqrt{(b-a)/2}G_1(-1,p),\tag{29}$$

$$\hat{K}_{II}(b,p)=\lim_{x_1\to b}\sqrt{2(x_1-b)}\sigma_{x_1y_1}(x_1,0)=-\frac{2\mu_0e^{\beta_1b}}{\kappa+1}\sqrt{(b-a)/2}G_1(1,p).\tag{30}$$

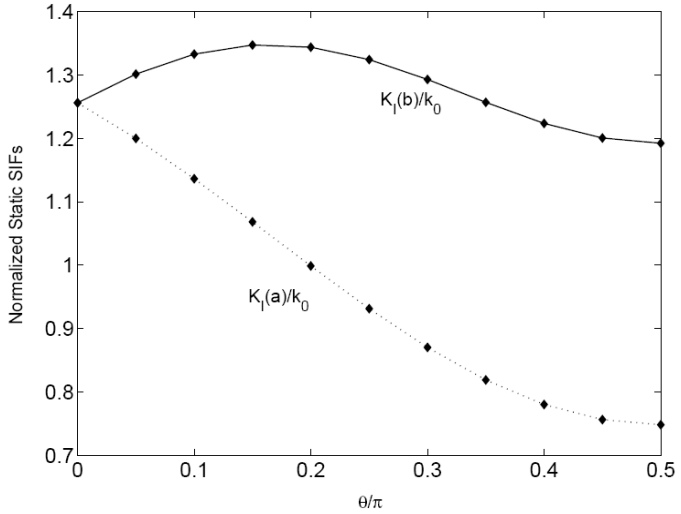

Figure 2. The variation of static SIFs with crack orientation angle θ under crack surface pressure ($\beta a_0 = 1.0$)

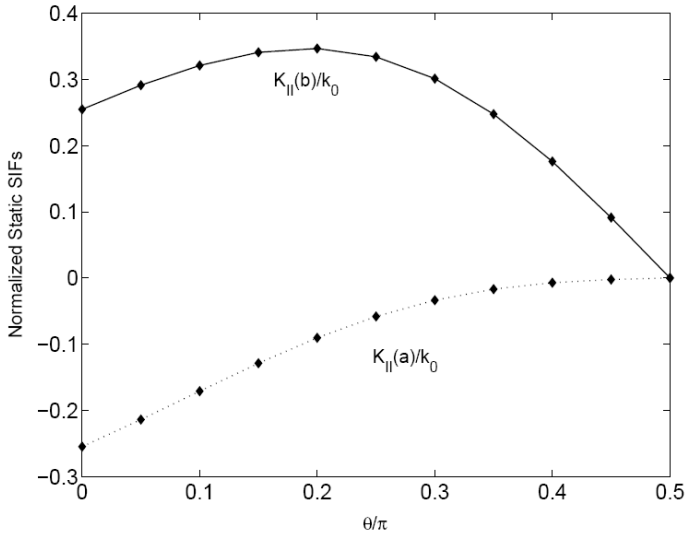

Figure 3. The variation of static SIFs with crack orientation angle θ under crack surface pressure ($\beta a_0 = 1.0$)

The stress intensity factor in the time domain can be obtained from Eqs.(27-30) by using Laplace numerical inversion by Miller and Guy [15].

5. Numerical results and discussion

The following analysis will be conducted under the plane strain state. The surface of the crack loaded by $\sigma_{10}H(t)$ and $\sigma_{20}H(t)$ respectively, where σ_{10} and σ_{20} are constant tractions. Poisson's ratio is taken as $\nu = 0.3$. The dynamic stress intensity factors are normalized by $k_0 = \sigma_{10}\sqrt{a_0}$ and $k = \sigma_{20}\sqrt{a_0}$ for different loads respectively, where $a_0 = (b-a)/2$. $c_2 = \sqrt{\mu_0 / \rho_0}$ is the shear wave velocity, $c_2 t / a_0$ is the non-dimensional time.

Before the analysis, the validity of the analytical solution must be verified. First, we restrict our attention to the crack problem in FGM under static loading. The corresponding static problem was

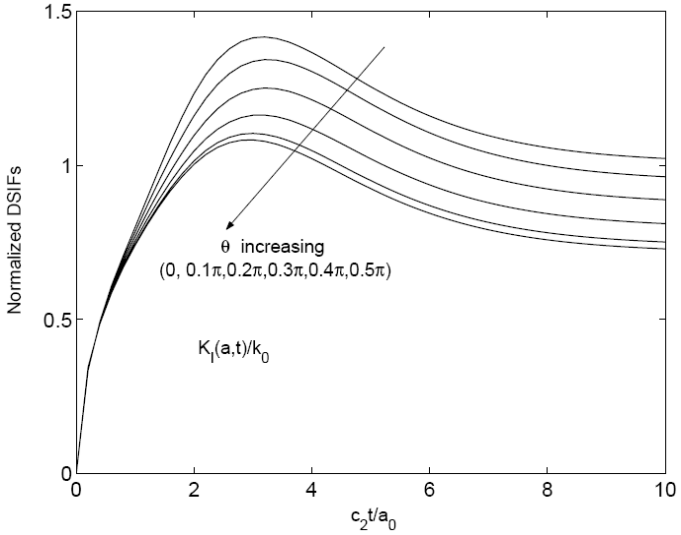

Figure 4. The variation of DSIFs with crack orientation angle θ under crack surface pressure ($\beta a_0 = 0.5$)

studied in [12]. Figs. 2-3 show the variations of the normalized SIFs with the angle θ under the uniform normal traction. These results are very similar to Konda's results [12].

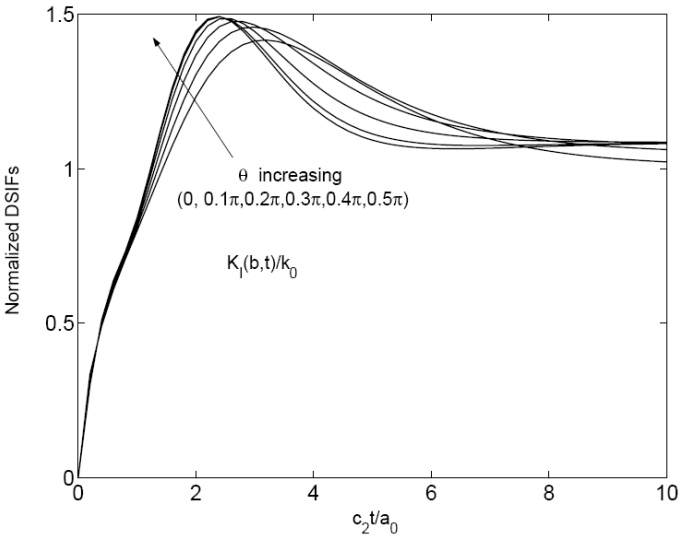

Figure 5. The variation of DSIFs with crack orientation angle θ under crack surface pressure ($\beta a_0 = 0.5$)

Figs.4-5 show the influence of θ on the DSIFs. It can be found that the peak value of $K_I(a,t)/k_0$ decreases with an increase of θ regardless of the value of βa_0. For $\beta a_0 = 0.5$, the peak value of $K_I(b,t)/k_0$ increases with the increasing of θ. And meanwhile, the emergence of time for the DSIFs gradually delays with the decreasing of θ.

Figs.6-7 depict the variations of the normalized mode II DSIFs with the crack direction angle under

uniform shear stress when $\beta a_0 = 0.5$. It can be found that the normalized DSIFs increases quickly with time up to the peak, and then the oscillations gradually decay until corresponding steady-state value. The peak time of DSIFs appears more or less for $c_2 t / a_{01} = 1.5$, and then exhibit a slight oscillation after reaching a peak. The peak values of $K_{II}(a,t)/k_0$ and $K_{II}(b,t)/k_0$ increase or decrease with an decrease of θ regardless of the value of βa_0.

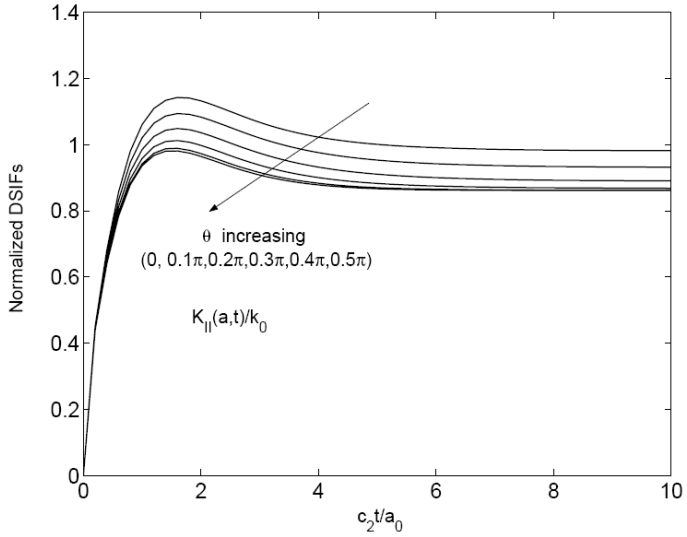

Figure 6. The influence of crack orientation angle θ on the DSIFs under crack surface shear ($\beta a_0 = 0.5$)

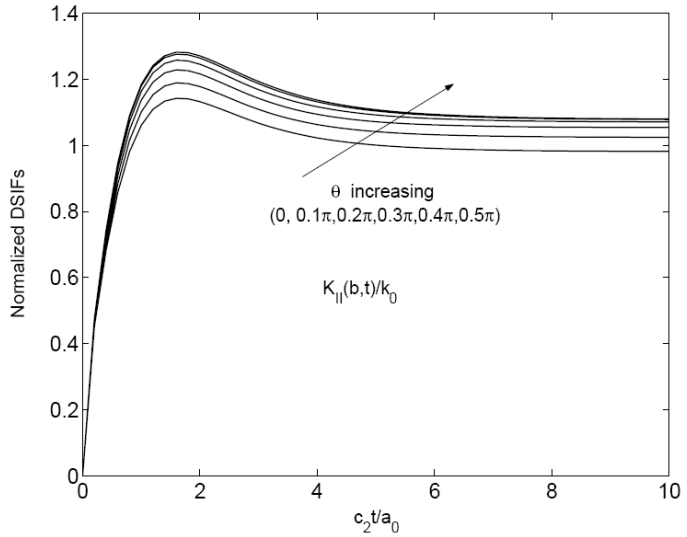

Figure 7. The influence of crack orientation angle θ on the DSIFs under crack surface shear ($\beta a_0 = 0.5$)

Based on the premise that the peak dynamic stress intensity factors may induce brittle fracture, such peaks are plotted in the sequel as a function of the crack orientation angle θ in Figs. 8-9. For $\beta a_0 = 0.5$, as shown in Fig.8, the peak value of the mode I DSIFs in crack tip a increases with an decrease of θ, while the peak value of the mode I DSIFs in crack tip b increases with an increase of θ. For $\beta a_0 = 1.0$ or 1.5, the peak value of the mode I DSIFs in crack tip b increases with θ, going through the maxima at some angle, and then begin to decrease at the enlarged crack obliquity,

e.g., $\theta = 0.1\pi$ or 0.15π. The peak value of the mode I DSIFs in crack tip a decreases with an increase of θ. Of interest in the figure is that for the crack angle more than 0.4π, the variation of θ appears to hardly affect the peak stress intensification at the crack tips. From Fig.9, it can be seen that the peak values of crack tips a and b decrease or increase with an increase of θ.

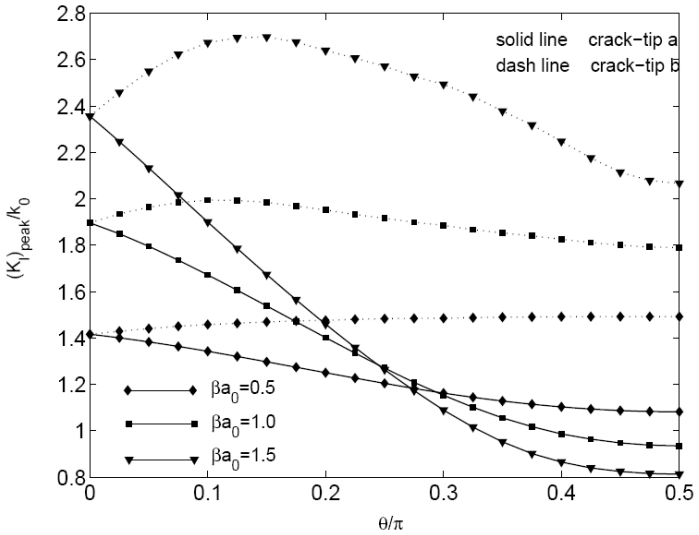

Figure 8. The influence of crack orientation angle θ on the peak values of the DSIFs under crack surface pressure

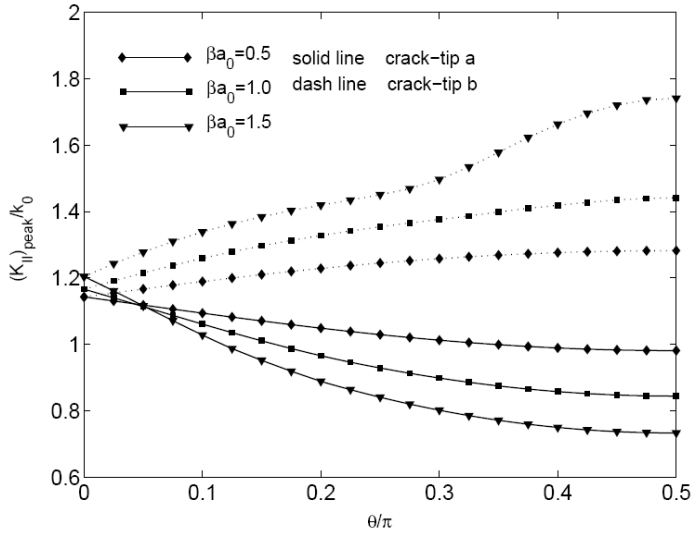

Figure 9. The influence of crack orientation angle θ on the peak values of the DSIFs under crack surface shear

6. Conclusion

The elastodynamic response of an arbitrarily oriented crack in functionally graded materials has been investigated with the aid of the basic plane elasticity equations. The mixed-mode DSIFs evaluated for an arbitrarily oriented crack were shown to be strongly affected by the geometric and loading configuration of the media in conjunction with the material gradations in the

nonhomogeneous constituent. The integral transform techniques were employed in conjunction with the coordinate transformations of relevant field variables and a resulting Cauchy-type singular integral equation was solved in the Laplace transform domain. Following the inversion of the Laplace transforms, the evolution of the dynamic mixed-mode DSIFs stress intensity factors with time was evaluated.

Acknowledgements

This work is supported by the National Natural Science Foundation of China (51061015,11261045) and research fund for the doctoral program of higher education of China (20116401110002).

References

[1] Delale, F., Erdogan, F., On the mechanical modeling of the interfacial region in bonded half-planes. J. Appl. Mech., 55(1988) 317-324.
[2] Chen, Y.F., Erdogan, F., The interface crack problem for a nonhomogeneous coating bonded to a homogeneous substrate. J. Mech. Phys. Solids, 44(1996) 771-787.
[3] Huang, G.Y., Wang, Y.S., Yu, S.W., Fracture analysis of a functionally graded interfacial zone under plane deformation. Int.J. Solids Struct., 41(2004) 731-743.
[4] Ding, S.H., Li, X., Anti-plane problem of periodic interface cracks in a functionally graded coating-substrate structure. Int. J.Fract., 153(2008) 53-62.
[5] Ding, S.H., Li, X., Thermal stress intensity factors for an interface crack in a functionally graded layered structures. Archive of Applied Mechanics., 7(2011) 943-955.
[6] Atkinson, C., Some results on crack propagation in media with spatially varying elastic properties. Int. J. Fract. ,11(1975)619-628.
[7] Li, C.Y., Weng, G.J., Dynamic stress intensity factor of a cylindrical interface crack with a functionally graded interlayer. Mech. Mater., 33(2001) 325-333.
[8] Guo, L.C., Wu, L.Z., Ma, L., Zeng, T., Fracture analysis of a functionally graded coating-substrate structure with a crack perpendicular to the interface - Part II: Transient problem. Int. J.Fract., 127(2004)39-59.
[9] Li, Y.D., Lee,K.Y., Yao D., Dynamic stress intensity factors of two collinear mode-III cracks perpendicular to and on the two sides of a bi-FGM weak-discontinuous interface. Eur. J. Mech. A-Solids, 27(2008)808-823.
[10] Ding, S.H., Li, X., Zhou Y.T., Dynamic Stress Intensity Factors of Mode I Crack Problem for Functionally Graded Layered Structures.CMES: Computer Modeling in Engineering & Sciences., 56(2010)43-84.
[11] Bogy, D.B., On the plane elastostatic problem of a loaded crack terminating at a material interface. ASME. J. Appl. Mech., 38 (1971) 911-918
[12] Konda, N., Erdogan, F., The mixed-mode crack problem in nonhomogeneous elastic plane. Eng. Fract. Mech., 47(1994)533-545.
[13] Choi, H.J., Impact behavior of an inclined edge crack in a layered medium with a graded nonhomogeneous interfacial zone: antiplane deformation. Acta Mech., 193(2007)67-84.
[14] Muskelishvili, I. N., Singular integral equations, Groningen: Noordhoff, The Netherlands,1953.
[15] Miller, M. K., Guy, W. T., Numerical inversion of the Laplace transform by the use of Jacobi polynomials. SIAM J. Numer. Anal., 3(1966)624-635.

STUDY OF PARAMETERS AFFECTING FRACTURE OF TITANIUM NITRIDE FILMS (TiN)

Marcos F. Odorczyk[1,*], José D. Bressan[1], Luiz C. Fontana[1]

[1]PGCEM, University of Santa Catarina State, Joinville-SC- 89219-710, Brasil

* Corresponding author: Dem6mdo@joinville.udesc.br

ABSTRACT: Present work examines theoretically the relationship between micro-cracks and failure criteria for fracture modes I and II in coating films. TiN films deposited by magnetron sputtering on substrates of steel or aluminum, with homogeneous (HMG) or functionally graded (FGM) structure were considered. The stress field in the film and substrate was generated from the Hertzian normal pressure and tangential force due to the friction from loading displacement at constant sliding velocity on the film surface. At the interface of the film and substrate, there are substantial differences among material properties. These differences, together with the film deposition conditions, can induce the formation of imperfections in the film condensation front, thus, becoming a region of potential micro-cracks formation. Stress-intensity factors at crack tip and a fracture criterion for combined rupture modes I and II in function of TiN film thickness, structure type (FGM x HMG), friction coefficient μ and substrate, were analyzed. A variance study by ANOVA has indicated that for both fracture failure mode I and II, the material factors, substrate and film structure, have higher significance than other factors analyzed. Film thickness is a significant factor, but not at the same level as material factors. Aluminium substrate with HMG coating has a higher risk level than steel substrate. FGM films reduce drastically the fracture failure risk mode I and II, when compared with HMG films,for both substrate. On FGM films, and HMG thin films over steel substrate, the mode II is more importante than the mode I, although the values are not high. For other cases, the mode I is more significative. The friction, altough is a important fator, has not the same significance level when compared with the others investigated.

Key-words: FGM, micro-cracks, TiN film, fracture criterion, combined fracture mode I and II.

1. Introduction

The use of coating films is based on the idea to combine materials with different properties, in order to obtain the benefit of both constituents. However, such differences lead to a non-continuous mechanical behavior at the interface film and substrate. To reduce this functional discontinuity, materials were developed whose properties vary gradually through the thickness direction and are called Functionally Gradade Materials (FGM). One consequence of this properties discontinuity is delamination of the film at the interface with the substrate due to load applications. This behavior depends on load factors, geometry, surface roughness and material of the film and substrate. The variation of the properties in films FGM can follow linear or exponential laws, making the transition smoother interface than the homogeneous films. Several works have been presented in this area. Shodja [1] presented a study with analytical solutions for the temperature field and stress of a tribological pair under thermomechanical loading. Odorczyk [2] presented a study with numerical solutions for the same case. The tribological pair study consists of a displacement normal force over the surface of a TiN film HMG or FGM deposited on a steel or aluminum substrate. The stress intensity factors KI and KII were analyzed in relation to the main normal and shear stresses at the interface. By analysis of variance, it was evaluated the significance of the factors friction, thickness, substrate material and film strucutre on a mixed KI/KIc and KII/KIIc criteria.

2. Methods

Titanium Nitride (TiN) is typically used in coating films due to their high elastic modulus E, low thermal conductivity *k* and low coefficient of thermal expansion α compared to steel or aluminum substrates. A normal force is applied in the form of Hertzian pressure that combined with the friction and displacement between the surfaces, generates a normal and a tangential mechanical and thermal loading, shown in Fig 1.

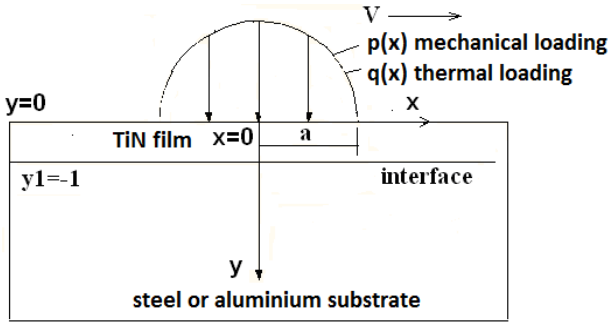

Figure 1. Tribological pair under thermomechanical loading.

The film coating was considered isotropic, following the laws of functional gradation according to Eqs (1) and (2)

$$P_c(y_c) = P_0 e^{\beta y^M} \tag{1}$$

$$\beta = \frac{1}{y_s^M} \ln \frac{k_s}{k_0} \tag{2}$$

where P is the property studied (α, k E), the index M = 0 is for HMG and M = 1 for FGM film structure, the subscripts s, c and 0 respectively identify the values at the interface between the film and the substrate, within the film and at the surface of the coating film and y is the direction across the film. The properties of the substrates, Poisson's ratio and the thermal diffusivity of the film coating were considered constant. It is assumed that the substrate is an elastic solid homogeneous, isotropic and dimensions enough large to be considered as infinite. The normal and tangential Hertzian pressure due to mechanical loading and the friction between the sliding surfaces generates normal and shear stress and heat. The normal pressure loads p(x), shear $p_{tan}(x)$ and heat flux are defined by Eqs (3) to (5)

$$p(x) = p_0 \sqrt{(1-x^2)} H(1-|x|) \tag{3}$$

$$p_{tan}(x) = p(x)\mu \tag{4}$$

$$q_p(x) = p(x)v\mu \tag{5}$$

where p_0 is the load at x = 0, H is the Heaviside function, μ is the film friction coefficient, q_p is the heat flux generated at the film surface and v is the load displacement velocity on x direction.
The flexural tensile and shear stress at film and substrate interface, responsible for failure adhesion, are defined by Eqs (6) and (7)

$$\tau_{xy(adim)} = \frac{\tau_{xy(max)}}{p_0} \tag{6}$$

$$\sigma_{xx(adim)} = \frac{\sigma_{xx(max)}}{p_0} \tag{7}$$

where $\tau_{xy(adim)}$ is the maximum shear stress normalized, $\tau_{xy(max)}$ is the maximum shear stress, $\sigma_{xx(adim)}$ is the maximum flexural stress normalized, $\sigma_{xx(max)}$ is the maximum normal stress, all at the interface. The stresses do not occur at the same point at the interface.

A variance study ANOVA presented by Odorczyk [4] indicated film thickness, friction coefficient and its interaction are factors of high significance for shear stresses. For tensile flexural stresses, material of substrate, thickness and structure and its interactions are highly significant. The velocity is not significant for both stress cases.

From the stresses calculated in Eqs.(6) and (7), were calculated the principal stresses, tensile flexural and shear for the same points. With the principal stresses, assuming the greatest stress state at the interface, were calculated values for stress intensity factors KI and KII for brittle fracture failure modes I and II.

Considering that a crack can propagate in any direction, the KI and KII parameters for the principal stress directions were investigated. It was considered a crack length of about 0.4 film thickness. The stress intensity factors KI and KII were obtained by Eq. (8)

$$\begin{Bmatrix} K_I \\ K_{II} \end{Bmatrix} = \begin{Bmatrix} \sigma \\ \tau \end{Bmatrix} \sqrt{\pi a_t} \tag{8}$$

It was adopted a mixed fracture criterion [6] considering KI and KII according to Eqs (9) and (10)

$$\left(\frac{K_I}{K_{IC}}\right)^m + \lambda \left(\frac{K_{II}}{K_{IC}}\right)^n = 1 \tag{9}$$

$$\lambda = \left(\frac{K_{IC}}{K_{IIC}}\right)^n \tag{10}$$

assuming m = n = 2.

Also, it were considered the values of fracture toughness KIc = 1 and KIIc = 2, since the present study investigates just the competition between modes of fracture I and II.

It were obtained KI and KII values for combinations of thickness, μ, type of substrate (steel and aluminum), and TiN film structure FGM x MGF. A variance study ANOVA was performed to investigate the influence of the parameters mentioned on the mixed fracture criteria shown in Eq. (9), to the main directions normal and shear. The experiment structure is shown in Table (1).

Table 1. Influence of parameters on KI/KIc and KII/KIIc.

SUBSTRACT MATERIAL	AL(-1)						STEEL (+1)					
FILM STRUCTURE	FGM (-1)			HMG (+1)			FGM (-1)			HMG (+1)		
THICKNESS	0,5	1	2	0,5	1	2	0,5	1	2	0,5	1	2
FRICTION	0,05	0,25	0,50	0,05	0,25	0,50	0,05	0,25	0,50	0,05	0,25	0,50

3. Results

The variance study ANOVA results are show in Figs. (2) and (3). The values in Italic have high significance.

ANOVA; Var.:KI/KIc; R^2 =0,89576; R Adj=0,77198 Experiment with 2 factors at 2 levels combined with 2 factors at 3 levels, 36 runs ; MS Residual=0,4254813					
Factors	SS	df	MS	F (fisher)	p
(1)Substrate (L)	14,42	1	14,42	***33,88***	***0,000026***
(2)Film structure (L)	16,68	1	16,68	***39,21***	***0,000011***
(3)Film thickness (L+Q)	3,27	2	1,63	***3,84***	***0,043463***
(4) µ Friction coef (L+Q)	0,64	2	0,32	0,75	0,488018
Interaction 1 x 2	14,35	1	14,35	***33,73***	***0,000027***
Interaction 1 x 3	3,70	2	1,85	***4,35***	***0,030995***
Interaction 1 x 4	0,67	2	0,34	0,79	0,470006
Interaction 2 x 3	3,29	2	1,65	***3,87***	***0,042603***
Interaction 2 x 4	0,65	2	0,32	0,76	0,483810
Interaction 3 x 4	0,83	4	0,21	0,49	0,745476
Error	6,81	16	0,46		
Total SS	65,31				

Figure 2. ANOVA results for KI/KIc.

ANOVA; Var.:KII/KIIc; R^2 =0,89293; R Adj=0,76579 Experiment with 2 factors at 2 levels combined with 2 factors at 3 levels, 36 runs ; MS Residual=0,0210749					
Factors	SS	df	MS	F (fisher)	p
(1)Substrate (L)	0,67	1	0,67	***31,83***	***0,000037***
(2)Film structure (L)	0,80	1	0,80	***38,16***	***0,000013***
(3)Film thickness (L+Q)	0,21	2	0,10	***4,89***	***0,021926***
(4) µ Friction coef (L+Q)	0,04	2	0,02	0,91	0,421088
Interaction 1 x 2	0,60	1	0,60	***28,49***	***0,000067***
Interaction 1 x 3	0,18	2	0,09	***4,31***	***0,031890***
Interaction 1 x 4	0,04	2	0,02	1,02	0,381568
Interaction 2 x 3	0,17	2	0,08	***4,17***	***0,034908***
Interaction 2 x 4	0,04	2	0,02	0,97	0,398810
Interaction 3 x 4	0,05	4	0,01	0,60	0,670521
Error	0,34	16	0,02		
Total SS	3,15				

Figure 3. ANOVA results for KII/KIIc

The results on Fig.(2) and (3) shows that the film structure (FGM x HMG) and his interactions, followed by the substrate material, are the most important factors to prevent fracture failure, on mode I and II. The film thickness is a significant factor, but lower (about 10 times) than the material factors significance. The friction is not significant for mode I and II. On Fig. (4), it is possible to compare the significance of the factors and their interactions.

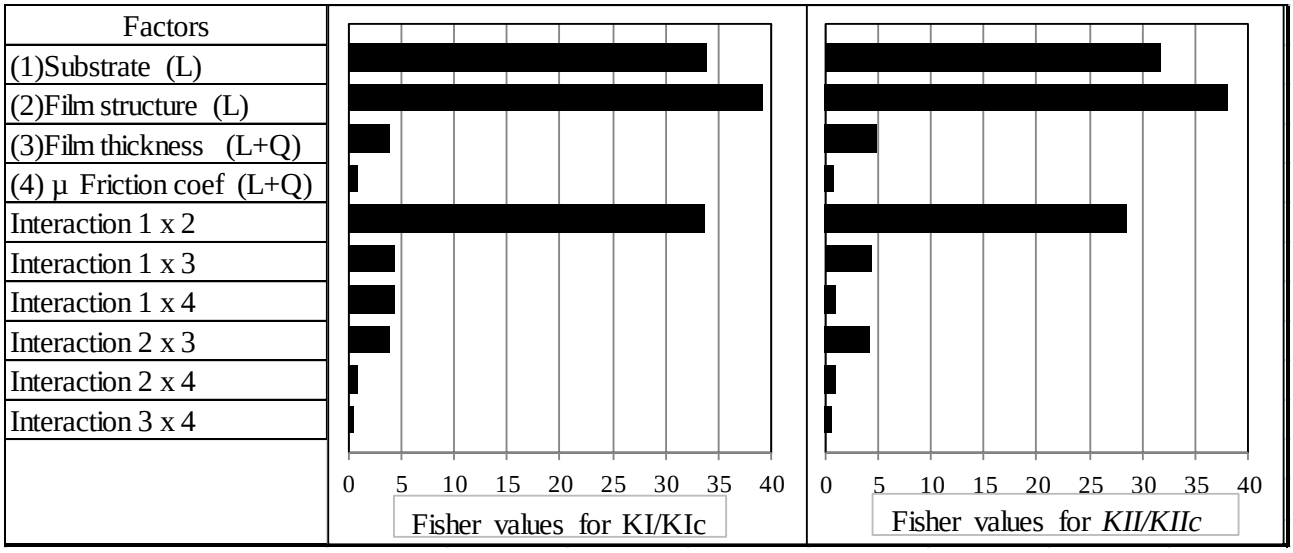

Figura 4. Fisher distribution values of influence factors on KI/KIc and KII/KIIc modes.

The results of KI/KIc and KII/KIIc obtained by Eq.(9) corresponding to the principal directions, for μ=0.25, for film thickness thin, medium, large, for TiN film FGM and HMG over steel and aluminium substrate, are shown in Fig. (5a), (5b), (6a), (6b).

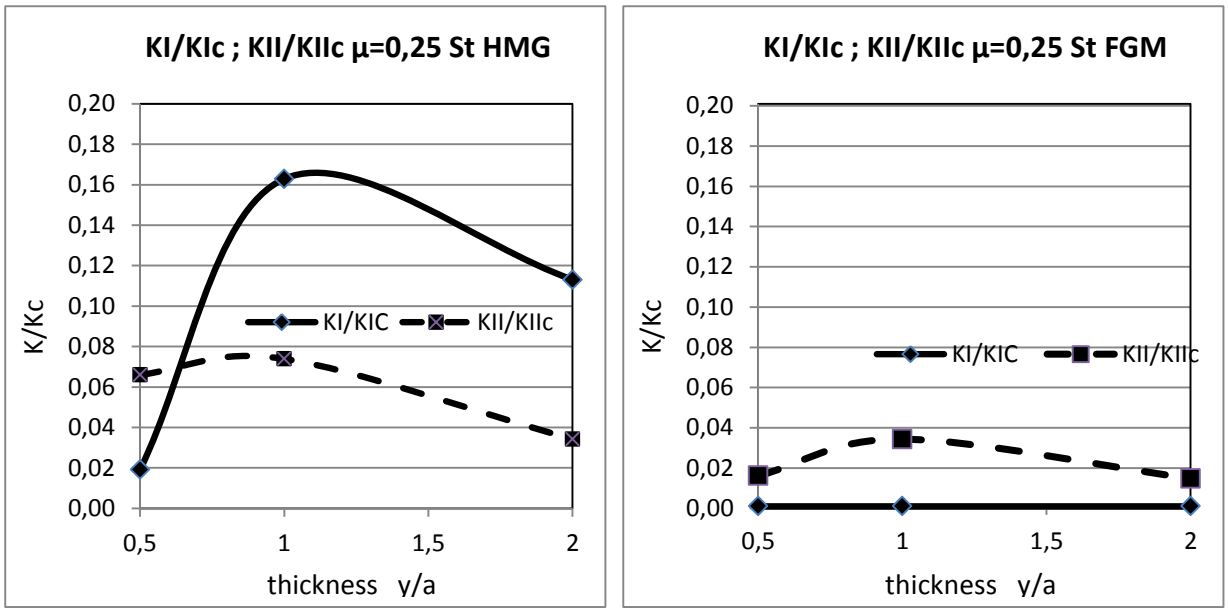

(a) (b)

Figure 5. KI/KIc and KII/KIIc for μ=0.25 Steel, (a) TiN HMG, (b) TiN FGM.

In Fig. (5) is possible to see that for TiN film HMG over steel substrate, the fracture mode I is more important than the mode II, except for thin films, although these values for thin films are not high when compared with other film thickness. For TiN film FGM over steel substrate, the mode of fracture II is more important than the mode I for all thickness, although the values are not high when compared with TiN HMG steel cases.

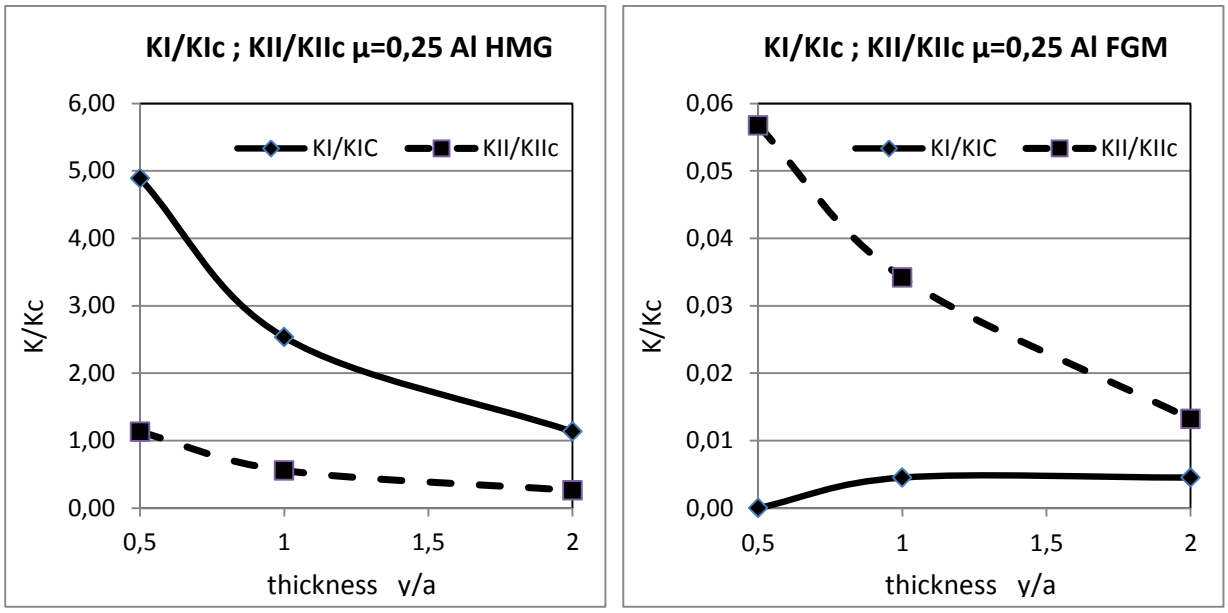

(a) (b)

Figure 6. KI/KIc and KII/KIIc for μ=0.25 and aluminium: (a) TiN HMG, (b) TiN FGM.

In Fig. (6) is possible to see that for TiN film HMG over aluminium substrate, the fracture mode I is more importante than the mode II and the values are significativelly higher compared with TiN steel cases. For TiN film FGM over aluminium substrate, the mode of fracture II is more important than the mode I, although the values are not high compared with TiN HMG Al and similar to TiN FGM steel cases.

4. Conclusions

From the theoretical analysis using ANOVA variance study to investigate the influence of factors such as friction, thickness, substrate material and film structure and the relationship between micro-cracks and failure criteria for fracture modes I and II in coating films, the following conclusions can be drawn.

For both fracture failure modes I and II, the material factors, substrate and film structure, have higher significance than other factors analyzed. Film thickness is a significant factor, but not at the same level as material factors. Aluminium substrate with homogeneous structure, HMG, coating has a higher risk level than steel substrate. The functionally graded structure, FGM, films reduce drastically the fracture failure risk mode I and II, when compared with HMG films, for both substrate. On FGM films, and HMG thin films over steel substrate, the mode II is more important than the mode I, although the values are not high. For other cases, the mode I is more significant. The friction, altough is an important factor, has not the same significance level when compared with the others investigated.

Acknowledgements

Prof. Dr. José D. Bressan, for his contributions on Fracture Mechanics.
Prof. Dr. Luis César Fontana, for his contributions on thin films.
University of Santa Catarina State – UDESC, PGCEM, FAPESC and CNPq for financial support.

References

[1] H.M. Shodja, A. Ghahremaninejad, An FGM coated elastic solid under thermo-mechanical loading : a two dimensional linear elastic approach, Surface & Coatings Technology, 200, pp. 4050–4064 , 2006.

[2] M.F. Odorczyk, Uma estratégia numérica para análise termoelástica de sólidos recobertos com filmes de material funcionalmente gradado (FGM). Dissertação de mestrado na UDESC – PGCEM, 2011.

[3] M.F. Odorczyk, Variance analysis of influence factors on TiN film coating stress field, CEBECIMAT 2012.

[4] D.C. Montgomery, Design and Analysis of Experiments, John Wiley & Sons Inc, 5th. Edition, 2008.

[5] H. Tada, P.C. Paris, G.R. Irwin, The Stress Analysis of Cracks Handbook, ASME, 2000 edition.

[6] J. Mencik, Mechanics of components with treated or coated surfaces, Kluwer Academic Publishers, 1996.

A Periodic Array of Parallel Edge Cracks in a Functionally Graded Plate Subjected to Finite Cooling Rates

Yuezhong Feng[1,*], Zhihe Jin[2]

[1] School of Mechanical Engineering, Purdue University, 47907, USA
[2] Department of Mechanical Engineering, University of Maine, 04469, USA
* Corresponding author: feng81@purdue.edu

Abstract This work investigates the effects of cooling rate on the thermal fracture behavior of a functionally graded plate (FGM plate) with a periodic array of parallel edge cracks of alternating lengths. The thermal properties of the FGM are assumed to be continuous and piecewise differentiable functions of the coordinate in the plate thickness direction. A linear ramp function describes the rate of boundary temperature variation at the surfaces of the FGM plate. The integral equation method is used to analyze the thermal stress intensity factors (TSIFs) at the crack tips. The asymptotic solutions of TSIF are obtained using a closed form, short time solution of temperature field in the FGM plate. The effects of cooling rate and crack length ratio on the TSIF are examined using an Al_2O_3/Si_3N_4 FGM. Numerical results show that for given material gradation profile and crack morphology parameters, a lower cooling rate leads to a lower peak TSIF. For a given cooling rate, an appropriate material gradation profile reduces peak TSIFs. Finally, the variations of the TISF for the long and short cracks with the cooling rate and crack length ratio exhibit a complex pattern due to the interactions between the long and short cracks.

Keywords functionally graded material, heat conduction, cooling rate, thermal stress intensity factor, periodic cracks

1. Introduction

Functionally graded ceramics suffer multiple surface cracking when subjected to thermal shocks [1, 2]. These surface cracks greatly influence the thermal fracture behavior of the materials. FGMs with multiple surface cracks under thermal loading were considered by Rangaraj and Kokini [3], Han and Wang [4], and Jin and Feng [5]. Jin and Feng [6] further investigated thermal shock residual strength of an FGM with multiple surface cracks. The existing analytical and computational studies on multiple surface cracking in FGMs have assumed that the cracks have equal length. However, FGMs when subjected to thermal shocks may develop multiple cracks of unequal lengths as in the case of monolithic ceramics. An improved model is a periodic array of parallel cracks with alternating lengths. For monolithic ceramics, Nemat-Nasser et al. [7] considered a periodic array of parallel cracks with alternating lengths in a half plane and studied the stability problem of crack growth. Using a boundary element method and an energy release fracture criterion, Bahr et al. [8] studied the same crack geometry in a plate of finite thickness. Jin and Feng [9] considered an array of parallel edge cracks with alternating lengths in an elastic strip subjected to a thermal shock and presented detailed results on the effects of crack length ratio and crack spacing on the thermal stress intensity factors (TSIFs). For functionally graded ceramics, Feng and Jin [10, 11] investigated the effects of crack length ratio on the TSIFs at the tips of long and short cracks and thermal shock residual strength using a singular integral equation technique.

All of the analytical studies above assume that the FGM specimens are subjected to a sudden cooling condition at their surfaces, i.e., the boundary temperature immediately attains the ambient temperature. In practical applications, however, the cooling rates on the material surfaces are finite.

The objective of this work is to investigate the effects of cooling rate on the TSIFs for an array of parallel edge cracks with alternating lengths in a functionally graded ceramic plate. A linear ramp function is used to describe the rate of boundary temperature variations at the surfaces of the FGM plate. The remainder of the paper is organized as follows. Section 2 reviews a closed-form, asymptotic solution of temperature field for short times and the thermal stresses in the periodically cracked FGM plate. Section 3 describes an integral equation method to obtain the TSIFs at the tips of long and short cracks. Section 4 presents numerical results of TSIFs for an Al_2O_3/Si_3N_4 FGM. Section 5 provides concluding remarks.

2. Temperature and Thermal Stress Fields

This section reviews the temperature and thermal stress solutions for a long FGM plate with an array of parallel edge cracks with alternating lengths as shown in Fig. 1, where a_1 is the length of the long cracks, a_2 is the length of the short cracks, h is the crack spacing, and b is the plate thickness. The thermal properties of the FGM plate are arbitrarily graded in the thickness direction (x-direction). Initially the temperature of the plate is a constant T_0 which can be assumed to be zero without loss of generality. The temperature then gradually changes to $-T_a$ and $-T_b$ at the surfaces $x = 0$ and $x = b$ of the plate, respectively. We use a linear ramp function to describe the variations of the boundary temperatures. The initial and boundary conditions for the heat conduction problem are thus

$$T(x,0) = 0, \qquad 0 \le x \le b, \tag{1}$$

$$T(0,t) = \begin{cases} -T_a\left(t/t_a\right), & 0 \le t \le t_a \\ -T_a, & t > t_a \end{cases}, \tag{2a}$$

$$T(b,t) = \begin{cases} -T_b\left(t/t_b\right), & 0 \le t \le t_b \\ -T_b, & t > t_b \end{cases}, \tag{2b}$$

where $T = T(x, t)$ is the temperature, t is time, and t_a and t_b are two temporal parameters describing the rates of temperature variation (cooling/heating rates) at the plate surfaces. The one-dimensional heat conduction in the plate is governed by the following basic equation

$$\frac{\partial}{\partial x}\left[k(x)\frac{\partial T}{\partial x}\right] = \rho(x)c(x)\frac{\partial T}{\partial t}, \tag{3}$$

where $k(x)$ is the thermal conductivity, $\rho(x)$ the mass density, and $c(x)$ the specific heat.

Jin [12] obtained a closed form solution of the temperature field for short times in the FGM plate with continuous and piecewise differentiable properties as follows

$$\frac{T(x,\tau)}{T_a} = T^{(1)}(x,\tau) + \left(\frac{T_b}{T_a}\right) T^{(2)}(x,\tau), \tag{4}$$

where $T^{(1)}(x,\tau)$ and $T^{(2)}(x,\tau)$ are given by

$$\begin{aligned} T^{(1)}(x,\tau) = &-\frac{1}{\tau_a}\left[\frac{\rho_0 c_0 k_0}{\rho(x)c(x)k(x)}\right]^{1/4} \\ &\times\left\{\left[\tau + \frac{1}{2}\Omega_1^2(x)\right] erfc\left(\frac{\Omega_1(x)}{2\sqrt{\tau}}\right) - \frac{\Omega_1(x)}{\sqrt{\pi}}\sqrt{\tau}\exp\left[-\frac{\Omega_1^2(x)}{4\tau}\right]\right\}, \quad \tau \le \tau_a, \end{aligned} \tag{5a}$$

$$T^{(1)}(x,\tau)=-\frac{1}{\tau_a}\left[\frac{\rho_0 c_0 k_0}{\rho(x)c(x)k(x)}\right]^{1/4}\left\{\left[\tau+\frac{1}{2}\Omega_1^2(x)\right]erfc\left(\frac{\Omega_1(x)}{2\sqrt{\tau}}\right)-\frac{\Omega_1(x)}{\sqrt{\pi}}\sqrt{\tau}\exp\left[-\frac{\Omega_1^2(x)}{4\tau}\right]\right.$$
$$\left.-\left[\tau-\tau_a+\frac{1}{2}\Omega_1^2(x)\right]erfc\left(\frac{\Omega_1(x)}{2\sqrt{\tau-\tau_a}}\right)+\frac{\Omega_1(x)}{\sqrt{\pi}}\sqrt{\tau-\tau_a}\exp\left[-\frac{\Omega_1^2(x)}{4(\tau-\tau_a)}\right]\right\},\quad \tau>\tau_a, \tag{5b}$$

and

$$T^{(2)}(x,\tau)=-\frac{1}{\tau_b}\left[\frac{\rho(b)c(b)k(b)}{\rho(x)c(x)k(x)}\right]^{1/4}$$
$$\times\left\{\left[\tau+\frac{1}{2}\Omega_2^2(x)\right]erfc\left(\frac{\Omega_2(x)}{2\sqrt{\tau}}\right)-\frac{\Omega_2(x)}{\sqrt{\pi}}\sqrt{\tau}\exp\left[-\frac{\Omega_2^2(x)}{4\tau}\right]\right\},\quad \tau\le\tau_b, \tag{6a}$$

$$T^{(2)}(x,\tau)=-\frac{1}{\tau_b}\left[\frac{\rho(b)c(b)k(b)}{\rho(x)c(x)k(x)}\right]^{1/4}\left\{\left[\tau+\frac{1}{2}\Omega_2(x)\right]erfc\left(\frac{\Omega_2(x)}{2\sqrt{\tau}}\right)-\frac{\Omega_2(x)}{\sqrt{\pi}}\sqrt{\tau}\exp\left[-\frac{\Omega_2^2(x)}{4\tau}\right]\right.$$
$$\left.-\left[\tau-\tau_b+\frac{1}{2}\Omega_2^2(x)\right]erfc\left(\frac{\Omega_2(x)}{2\sqrt{\tau-\tau_b}}\right)+\frac{\Omega_2(x)}{\sqrt{\pi}}\sqrt{\tau-\tau_b}\exp\left[-\frac{\Omega_2^2(x)}{4(\tau-\tau_b)}\right]\right\},\quad \tau>\tau_b, \tag{6b}$$

respectively, and τ, τ_a and τ_b are the nondimensional times defined by

$$\tau=t\kappa_0/b^2,\qquad \tau_a=t_a\kappa_0/b^2,\qquad \tau_b=t_b\kappa_0/b^2, \tag{7}$$

in which $\kappa_0=\kappa(0)$ and $\kappa(x)=k/(\rho c)$ is the thermal diffusivity. In Eqs. (5) and (6), *erfc*( ) is the complementary error function and $\Omega_1(x)$ and $\Omega_2(x)$ are defined by

$$\Omega_1(x)=\frac{1}{b}\int_0^x\sqrt{\frac{\kappa_0}{\kappa(x')}}\,dx',\qquad \Omega_2(x)=\frac{1}{b}\int_x^b\sqrt{\frac{\kappa_0}{\kappa(x')}}\,dx'. \tag{8}$$

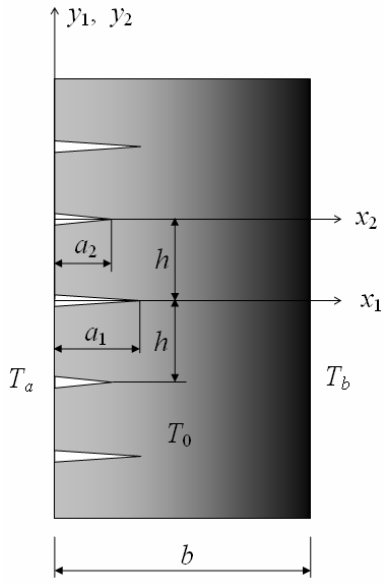

Figure 1. An FGM plate containing an array of periodic edge cracks with alternating lengths subjected to a thermal shock

The above temperature filed induces thermal stresses in both longitudinal (perpendicular to the crack direction) and transverse (perpendicular to the *x*-*y* plane) directions in the FGM plate. The

growth of the periodic edge cracks, however, is caused by the longitudinal stress which has the following form when the cracks have not been considered

$$\sigma_{yy}^{T}(x,\tau)=-\frac{E\alpha\theta(x,\tau)}{1-\nu}+\frac{E}{1-\nu}\left[\left(4-6\frac{x}{b}\right)\frac{1}{b}\int_0^b\alpha\theta(x,\tau)dx-\left(6-12\frac{x}{b}\right)\frac{1}{b^2}\int_0^b\alpha x\theta(x,\tau)dx\right], \quad (9)$$

where $\theta(x,\tau) = T(x,\tau)-T_0$, E is Young's modulus, ν is Poisson's ratio, and $\alpha = \alpha(x)$ is the coefficient of thermal expansion. Here we assume that the FGM plate is thermally nonhomogeneous but elastically homogeneous, i.e., the Young's modulus and Poisson's ratio are constant. While this assumption imposes limitations on the application of the present model, there exist some FGM systems for which the Young's modulus remains approximately constant. Examples include TiC/SiC, $MoSi_2/Al_2O_3$, Al_2O_3/Si_3N_4, and ZrO_2/Nickel FGM systems.

3. Thermal Stress Intensity Factors

This section uses the asymptotic temperature solution (4) – (6) to calculate the thermal stress intensity factor (TSIFs) at the tips of long and short crack in an elastically homogeneous but thermally graded FGM plate (see Fig. 1). The integral equation method is employed and the singular integral equations of the crack problem are given as follows

$$\int_{-1}^{1}\left[\frac{1}{s_1-r_1}+\frac{a_1}{2}k_{11}(r_1,s_1)\right]f_1(s_1)ds_1+\int_{-1}^{1}\frac{a_2}{2}k_{12}(r_2,s_2)\,f_2(s_2)ds_2 = -\frac{2\pi(1-\nu^2)}{E}\sigma_{yy}^{T}(r_1,t), \qquad -1\le r_1\le 1, \quad (10a)$$

$$\int_{-1}^{1}\left[\frac{1}{s_2-r_2}+\frac{a_2}{2}k_{22}(r_2,s_2)\right]f_2(s_2)ds_2+\int_{-1}^{1}\frac{a_1}{2}k_{21}(r_1,s_1)\,f_1(s_1)ds_1 = -\frac{2\pi(1-\nu^2)}{E}\sigma_{yy}^{T}(r_2,t), \qquad -1\le r_2\le 1, \quad (10b)$$

where the basic unknown variables $f_1(x_1)$ and $f_2(x_2)$ are defined by

$$f_1(x_1)=\frac{\partial v^{(1)}(x_1,0^+)}{\partial x_1}, \quad f_2(x_2)=\frac{\partial v^{(2)}(x_2,0^+)}{\partial x_2}, \quad (11)$$

with $v^{(1)}(x_1, y_1)$ and $v^{(2)}(x_2, y_2)$ being the displacements in the y-direction, x_1, y_1, x_2 and y_2 are coordinates defined by

$$x_1 = x, \quad y_1 = y, \qquad x_2 = x, \quad y_2 = y - h. \quad (12)$$

r_1, s_1, r_2, and s_2 are the normalized coordinates

$$x_1=\frac{a_1}{2}(1+r_1), \quad x_1'=\frac{a_1}{2}(1+s_1), \qquad x_2=\frac{a_2}{2}(1+r_2), \quad x_2'=\frac{a_2}{2}(1+s_2). \quad (13)$$

k_{11}, k_{12}, k_{21} and k_{22} are known kernels given by Feng and Jin[10], and σ_{yy}^{T} is given in Eq. (9).

According to the singular integral equation theory [13], the solutions of Eq. (7) have the following form

$$f_1(r_1)=\frac{F_1(r_1)}{\sqrt{1-r_1}},\qquad f_2(r_2)=\frac{F_2(r_2)}{\sqrt{1-r_2}}, \tag{14}$$

where $F_1(r_1)$ and $F_2(r_2)$ are continuous and bounded functions. Once the solutions of the above integral equations are obtained, the TSIFs at the periodic crack tips can be computed from

$$\begin{aligned} K_I^{(1)*}&=\frac{(1-\nu)K_I^{(1)}}{E\alpha_0\Delta T\sqrt{\pi\, b}}=-\frac{1}{2}\sqrt{\frac{a_1}{b}}F_1(1),\\ K_I^{(2)*}&=\frac{(1-\nu)K_I^{(2)}}{E\alpha_0\Delta T\sqrt{\pi\, b}}=-\frac{1}{2}\sqrt{\frac{a_2}{b}}F_2(1), \end{aligned} \tag{15}$$

where $K_I^{(1)}$ and $K_I^{(2)}$ denote the TSIFs at the tips of the long and short cracks, respectively, $K_I^{(1)*}$ and $K_I^{(2)*}$ are the corresponding nondimensional TSIFs, $\Delta T = T_a$, and α_0 is the coefficient of thermal expansion at $x = 0$. In Eq. (15), $F_1(1)$ and $F_2(1)$ have been normalized by $(1+\nu)\alpha_0\Delta T$.

4. Numerical Results and Discussion

In the numerical examples, we use a graded system of alumina/silicon nitride (Al_2O_3/Si_3N_4) FGM for cutting tools applications to examine the effects of cooling rate on the TSIFs. The FGM is assumed to be a two-phase composite material with graded volume fractions of its constituent phases. The volume fraction of Si_3N_4 is assumed to follow a simple power function

$$V(x)=(x/b)^p, \tag{16}$$

where p is the exponent determining the volume fraction profile. The material properties of the FGM are calculated using conventional micromechanics models [14] and the properties of Al_2O_3 and Si_3N_4 are given in Table 1 [15]. In the numerical calculations, we only consider the loading case of $T_b = 0$ (the initial temperature), which means that only the cracked surface $x = 0$ of the FGM plate is subjected to a temperature drop.

Fig. 2a shows the normalized TSIF $K_I^{(1)*}$ at the tips of the long cracks versus nondimensional time τ for various values of the cooling rate parameter τ_a. The crack spacing is $h/b = 1$, the length of the long cracks is $a_1/b = 0.1$, the crack length ratio is $a_2/a_1 = 0.2$, and the material gradation profile index is $p = 0.5$. The TSIF under the sudden cooling condition ($\tau_a = 0$, and hence infinite cooling rate) is also included. For a given cooling rate (T_a/τ_a), the TSIF initially increases with time, rapidly reaches the peak value and then decreases with time. The peak TSIF decreases dramatically with a decrease in the cooling rate (increasing τ_a). Moreover, the time at which the TSIF reaches its peak increases with a decrease in the cooling rate.

Fig. 2b shows the normalized TSIF $K_I^{(2)*}$ at the tips of the short cracks versus nondimensional time τ. All the geometrical and material gradation parameters are the same as those in Fig. 2a. The TSIF versus time response exhibits similar trend to that at the tips of the long cracks shown in Fig. 2a. Comparing the results in Figs. 2a and 2b, we can see that the peak TSIF at the short crack tip under the sudden cooling condition is about the same as the corresponding value for the long cracks. The peak TSIFs under finite cooling rates (nonzero τ_a), however, are significantly lower than the

corresponding values at the tips of the long cracks.

Table 1. Material properties of Al_2O_3 and Si_3N_4

	Young's modulus (GPa)	Poisson's ratio	CTE (10^{-6}/K)	Thermal conduc-tivity (W/m-K)	Mass density (g/cm^3)	Specific heat (J/g-K)	Fracture toughness (MPa-m$^{1/2}$)
Al_2O_3	320	0.25	8.0	20	3.8	0.9	4
Si_3N_4	320	0.25	3.0	35	3.2	0.7	5

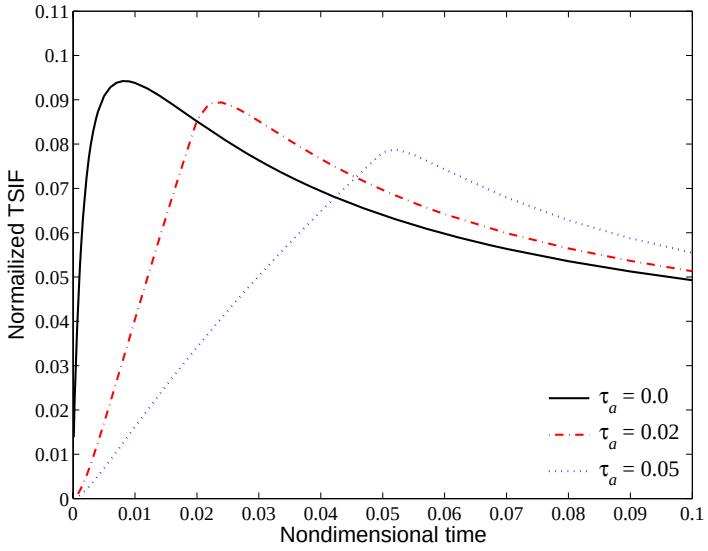

Figure 2a: Normalized TSIF versus nondimensional time at the tips of the long cracks (a_1/b = 0.1, a_2/a_1 = 0.2, h/b = 1.0, p = 0.5)

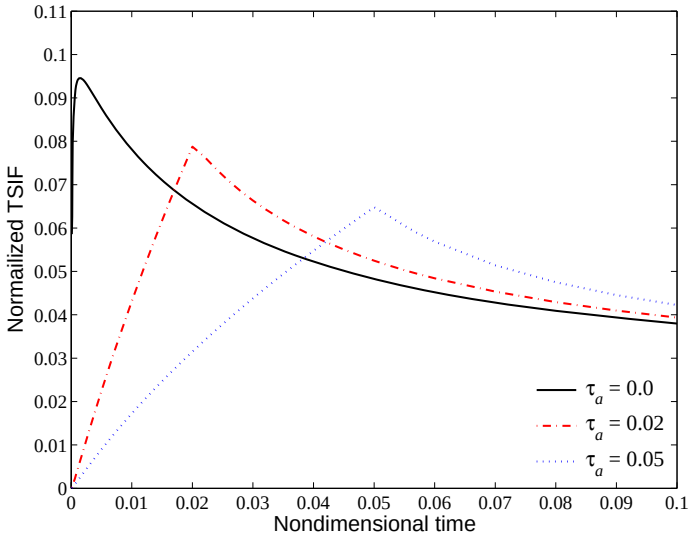

Figure 2b: Normalized TSIF versus nondimensional time at the tips of the short cracks (a_1/b = 0.1, a_2/a_1 = 0.2, h/b = 1.0, p = 0.5)

Figs. 3a and 3b show the normalized TSIFs at the tips of the long and short cracks, respectively, versus nondimensional time τ for a different crack length ratio a_2/a_1 of 0.6. All other parameters are the same as those in Fig. 2. It is seen that the trend of the TSIF versus time is similar to the case of a_2/a_1 = 0.2 shown in Figs. 2a and 2b. The peak TSIFs for the long cracks now are lower than those for a_2/a_1 = 0.2. However, the peak TSIFs for the short cracks are higher than those for a_2/a_1 = 0.2. The decreased peak TISF for the long cracks and the increased peak TSIFs for the short cracks are the results of enhanced interaction between the long and short cracks as the difference in the crack lengths is now smaller.

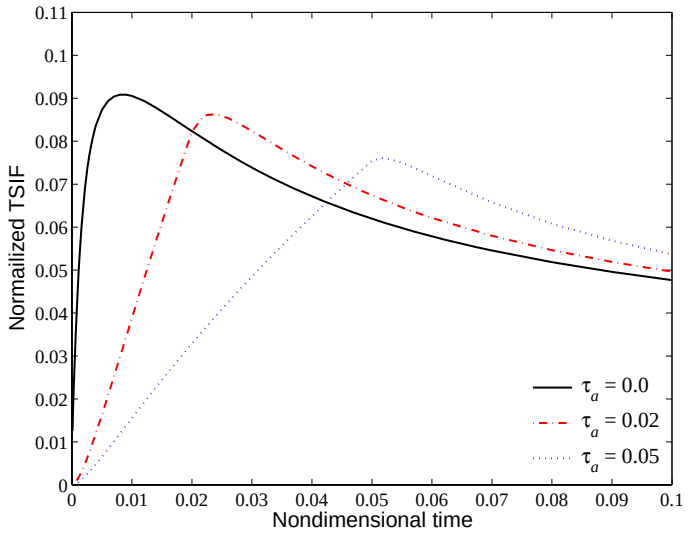

Figure 3a: Normalized TSIF versus nondimensional time at the tips of the long cracks (a_1/b = 0.1, a_2/a_1 = 0.6, h/b = 1.0, p = 0.5)

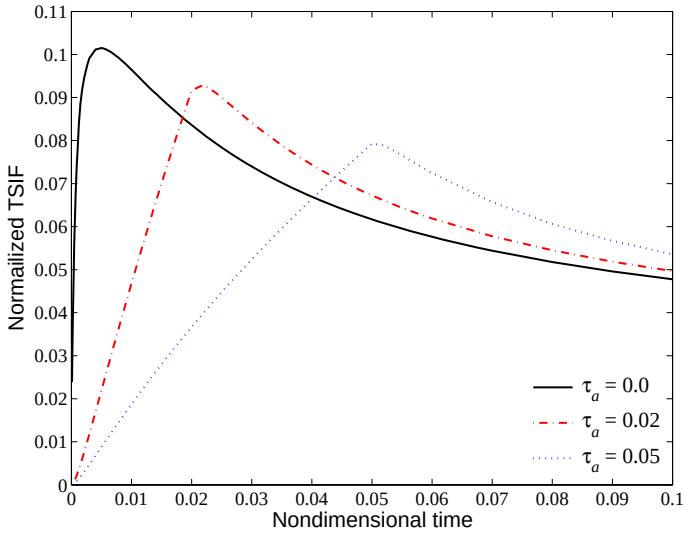

Figure 3b: Normalized TSIF versus nondimensional time at the tips of the short cracks (a_1/b = 0.1, a_2/a_1 = 0.6, h/b = 1.0, p = 0.5)

5. Concluding Remarks

This work is focused on the effects of cooling rate on the thermal stress intensity factors (TSIFs) at the tips of parallel edge cracks of alternating lengths in an FGM plate. The cooling rates at the surfaces of the FGM plate are described by a linear ramp function. The TSIFs are obtained using a closed-form, short-time temperature solution and an integral equation method. Numerical results for an Al_2O_3/Si_3N_4 FGM system show that the peak TSIFs at the tips of both long and short cracks decrease with a decrease in cooling rate. The variations of the peak TISF for the long and short cracks with the cooling rate and crack length ratio exhibit a complex pattern due to the interactions between the long and short cracks.

References

[1] A. Kawasaki, R. Watanabe, Fabrication of disk-shaped functionally gradient materials by hot pressing and their thermomechanical performance, in: J.B. Holt, M. Koizumi, T. Hirai, Z.A. Munir (Eds.), Ceramic Transactions, Vol. 34, American Ceramic Society, Westerville, OH, 1993, pp. 157–164.

[2] K. Kokini, J. DeJonge, S. Rangaraj, B. Beardsley, Thermal shock of functionally graded thermal barrier coatings, in: K. Trumble, K. Bowman, I. Reimanis,S. Sampath (Eds.), Ceramic Transactions, Vol. 114, American Ceramic Society, Westerville, OH, 2001, pp. 213-221.

[3] S. Rangaraj, K. Kokini, Multiple surface cracking and its effect on interface cracks in functionally graded thermal barrier coatings under thermal shock. ASME Journal of Applied Mechanics, 70 (2003) 234-245.

[4] H.C. Han, B.L. Wang, Thermal shock resistance enhancement of functionally graded materials by multiple cracking. Acta Materialia, 54 (2006) 963-973.

[5] Z.H. Jin, Y.Z. Feng, Thermal fracture resistance of a functionally graded coating with periodic edge cracks. Surface & Coatings technology, 202 (2008) 4189-4197.

[6] Z.H. Jin, Y.Z. Feng, Effects of multiple cracking on the residual strength behavior of thermally shocked functionally graded ceramics. International Journal of Solids and Structures, 45 (2008) 5973-5986.

[7] S. Nemat-Nasser, L.M. Keer, K.S. Parihar, Unstable growth of thermally induced interacting cracks in brittle solids. International Journal of Solids Structures, 14 (1978) 409-430.

[8] H.A. Bahr, H.J. Weiss, H.G. Maschke, F. Meissner, Multiple crack propagation in a strip caused by thermal shock. Theoretical and Applied Fracture Mechanics, 10 (1988) 219-226.

[9] Z.H. Jin, Y.Z. Feng, An array of parallel edge cracks with alternating lengths in a strip subjected to a thermal shock. Journal of Thermal Stresses, 32 (2009) 431-447.

[10] Y.Z. Feng, Z.H. Jin, Thermal fracture of a functionally graded plate with parallel surface cracks. Acta Mechanica Solida Sinica, 22 (2009) 453-464.

[11] Y.Z. Feng, Z.H. Jin, Thermal shock damage and residual strength behavior of a functionally graded plate with surface cracks of alternating lengths. Journal of Thermal Stresses, 35 (2012) 30-47.

[12] Z.H. Jin, Heat conduction in a functionally graded plate subjected to finite cooling/heating rates: An asymptotic solution. Materials, 4 (2011) 2108-2118.

[13] F. Erdogan, G.D. Gupta, T.S. Cook, Numerical solution of singular integral equations, in: G.C. Sih (ed.), Mechanics of Fracture, Vol. 1: Methods of Analysis and Solutions of Crack Problems, Noordhoff International Publishing, Leyden, The Netherlands, 1973.
[14] R.M. Christensen, Mechanics of Composite Materials, John Wiley & Sons, New York, 1979.
[15] D. Munz, T. Fett, Ceramics, Springer, Berlin, 1999.

The Higher Order Crack Tip Fields for FGMs Spherical Shell with Reissner's Effect

Yao Dai[1], Xiao Chong[1,*], Lei Zhang[1]

[1] The department of mechanical engineering, the academy of armored force engineering, Beijing, 100072, China
* chongxiao2005@163.com

Abstract Based on the theory of shells considering the transverse shear deformation or Reissner's effect, the crack tip fields are investigated for a cracked spherical shell made of isotropic functionally graded materials (FGMs). The elastic modulus and Poisson's ratio of the FGMs are assumed to be the linear function of x and a constant, respectively. The governing equations, i.e. the system of the tenth order partial differential equations with variable coefficients are first derived. Then, the eigen-expansion method is employed to the system, and the higher order crack tip fields of the cracked spherical shell are obtained. As the in-homogeneity parameter approaches to zero, the solutions degenerate to the corresponding fields of isotropic homogeneous spherical shell with Reissner's effect.

Keywords crack tip fields, Reissner's effect, spherical shell, FGMs

1. Introduction

As the gradient can be tailored to meet specific needs and the macroscopic interfaces of traditional composites are eliminated, the functionally graded materials have been widely applied in engineering. However, due to the limitations of the manufacture technology, a large number of micro-cracks cannot be avoided in functionally graded plates and shells, which would seriously endanger the security of these structures. Therefore, the fracture analysis for functionally graded shells is necessary.

It is well known that Kirchhoff classical theory does not consider the transverse shear deformation and has some limitations in the fracture analysis [1], so Reissner's theory [2] is often adopted.

Considering the effect of transverse shear, F.Delale[3] investigated the problem for spherical cap containing a through crack. For the plates and shells of homogeneous materials, the higher order crack tip fields are obtained based on Reissner's theory by Liu Chuntu[4]. The corresponding field for FGMs shell has been given only for which the material gradient is along thickness direction [5]. In this paper, the crack tip fields are studied for functionally graded spherical shell with Reissner's effect by the eigen-expansion method.

2. Basic equations

The effect of Poisson's ratio on stress intensity factor (SIF) is far less than that of elastic modules [6]. Therefore, Poisson's ratio is assumed as a constant, and the elastic modules is assumed as the linear function of spatial coordinates x as

$$E = E(x) = E_0(1+\beta x), \quad \mu = const \tag{1}$$

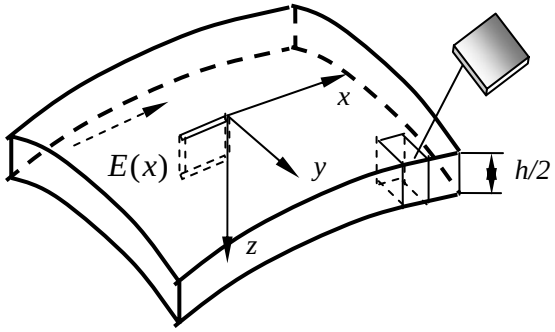

Fig.1 The functionally graded spherical shell

where, E_0 is elastic modulus at $x=0$, β is non-homogeneous coefficients. *Z*–axis is along the thickness direction, the radius is *R* and the thickness is *h* as shown in Fig.1.

The basic equations for Reissner's spherical shell are

$$\begin{cases} \beta(\mu\dfrac{\partial\varphi_y}{\partial y}+\dfrac{\partial\varphi_x}{\partial x})h^3+(1+\beta x)(\mu\dfrac{\partial^2\varphi_y}{\partial x\partial y}+\dfrac{\partial^2\varphi_x}{\partial x^2})h^3-\dfrac{1}{2}(1+\beta x)(\mu-1)(\dfrac{\partial^2\varphi_x}{\partial y^2}+\dfrac{\partial^2\varphi_y}{\partial x\partial y})h^3 \\ -5(1+\beta x)(\mu-1)h(\dfrac{\partial w}{\partial x}-\varphi_x)=0 \\ -\dfrac{1}{2}\beta(\mu-1)(\dfrac{\partial\varphi_x}{\partial y}+\dfrac{\partial\varphi_y}{\partial x})h^3-\dfrac{1}{2}(1+\beta x)(\mu-1)(\dfrac{\partial^2\varphi_x}{\partial x\partial y}+\dfrac{\partial^2\varphi_y}{\partial x^2})h^3+(1+\beta x)(\mu\dfrac{\partial^2\varphi_x}{\partial x\partial y} \\ +\dfrac{\partial^2\varphi_y}{\partial y^2})h^3-5(1+\beta x)(\mu-1)h(\dfrac{\partial w}{\partial y}-\varphi_y)=0 \\ 5hE_0(1+\beta x)(\nabla^2 w-\dfrac{\partial\varphi_x}{\partial x}-\dfrac{\partial\varphi_y}{\partial y})+12\kappa(1+\mu)\nabla^2\psi+5E_0\beta h(\dfrac{\partial w}{\partial x}-\varphi_x)=0 \\ (1+\beta x)^2\nabla^4\psi+\kappa E_0 h(1+\beta x)^3\nabla^2 w-2\beta(1+\beta x)\dfrac{\partial(\nabla^2\psi)}{\partial x}-2\beta^2\mu\dfrac{\partial^2\psi}{\partial y^2}+2\beta^2\dfrac{\partial^2\psi}{\partial x^2}=0 \end{cases} \tag{2}$$

where, φ_x, φ_y are the angle displacement, w is the deflection, κ is the curvature, ψ is the stress function.

3. The boundary conditions

As the crack surface is free, the boundary conditions are

$$\begin{cases} M_y=0,\ M_{xy}=0,\ Q_y=0 \\ N_y=0,\ N_{xy}=0 \end{cases} \tag{3}$$

Further, they can be expressed as

$$\begin{cases} \mu\dfrac{\partial\varphi_x}{\partial x}+\dfrac{\partial\varphi_y}{\partial y}=0, & \dfrac{\partial\varphi_x}{\partial y}+\dfrac{\partial\varphi_y}{\partial x}=0 \\ \dfrac{\partial w}{\partial y}-\varphi_y=0, & \dfrac{\partial^2\psi}{\partial x^2}=0, \quad \dfrac{\partial^2\psi}{\partial x\partial y}=0 \end{cases} \tag{4}$$

The crack tip stress field would be equipped with the same square root singularity as that of homogeneous materials when the material properties of different composite materials at the interfaces are continuous [7,8]. Therefore, the generalized displacements $\varphi_r, \varphi_\theta, w$ and the stress function ψ can be expressed as follows [9]

$$\varphi_x=\sum_{i=1}^{\infty}\varphi_{xi}(\theta)r^{i/2},\ \varphi_y=\sum_{i=1}^{\infty}\varphi_{yi}(\theta)r^{i/2},\ w=\sum_{i=1}^{\infty}w_i(\theta)r^{i/2},\ \psi=\sum_{i=1}^{\infty}\psi_i(\theta)r^{1+i/2} \tag{5}$$

where, $\varphi_{xi}(\theta)$、$\varphi_{yi}(\theta)$、$w_i(\theta)$ are the eigen-functions of the generalized displacement components, $\psi_i(\theta)$ are the eigen-functions of the stress function.

Substituting Eq. (5) into Eq. (4) and considering the linear independence of $r^{-3/2}$, r^{-1}, $r^{-1/2}$,…, $r^{i/2-2}$,…, the boundary conditions are

$$\begin{cases} i\mu\cos\theta\varphi_{xi}(\theta)-2\mu\sin\theta\varphi'_{xi}(\theta)+i\sin\theta\varphi_{yi}(\theta)+2\cos\theta\varphi'_{yi}(\theta)=0 \\ i\sin\theta\varphi_{xi}(\theta)+2\cos\theta\varphi'_{xi}(\theta)+i\cos\theta\varphi_{yi}(\theta)-2\sin\theta\varphi'_{yi}(\theta)=0 \\ \begin{cases} i\sin\theta w_{i+2}(\theta)+2\cos\theta w'_{i+2}(\theta)-2\varphi_{yi}(\theta)=0, & i=1,2,3,\mathrm{L} \\ i\sin\theta w_{i+2}(\theta)+2\cos\theta w'_{i+2}(\theta)=0, & i=1,2. \end{cases} \\ 4\psi''_i(\theta)\sin^2\theta-2i\psi'_i(\theta)\sin 2\theta+\psi_i(\theta)(i^2\cos^2\theta+4\sin^2\theta+2i)=0 \\ -4\psi''_i(\theta)\sin 2\theta+4i\psi'_i(\theta)\cos 2\theta+\psi_i(\theta)\sin 2\theta(i^2-4)=0 \end{cases} \tag{6}$$

where, $(\ )'=d(\ )/d\theta$, $(\ )''=d^2(\ )/d\theta^2$.

4. The higher order crack-tip field

Substituting Eq. (5) into Eq. (2) and Eq. (6) and utilizing the linear independence of $r^{-3/2}$, r^{-1}, $r^{-1/2}$,…, $r^{i/2-2}$,…, the system of ordinary differential equations are obtained. Solving the system, we can obtain the results

$$
\begin{cases}
\varphi_{x1}(\theta)=C_{11}\sin\dfrac{\theta}{2}+C_{12}\cos\dfrac{\theta}{2}+C_{13}\sin\dfrac{3\theta}{2}+C_{14}\cos\dfrac{3\theta}{2} \\
\varphi_{x2}(\theta)=C_{23}\sin\theta+C_{24}\cos\theta \\
\varphi_{x3}(\theta)=\dfrac{1}{12h^2(\mu+1)^2}[-3\beta h^2(\mu+1)^2C_{13}\sin\dfrac{5\theta}{2}-3\beta h^2(\mu+1)^2C_{14}\cos\dfrac{5\theta}{2}+(48\beta\mu^2h^2C_{13}- \\
\quad 96\beta\mu h^2C_{13}+112\beta h^2C_{13}-16\beta h^2C_{11}+16\beta\mu^2h^2C_{11}+12h^2C_{32}+16\mu^2h^2C_{33}-48h^2C_{33} \\
\quad +80\mu^2B_{11}+12\mu^2h^2C_{32}+24\mu h^2C_{32}-32\mu h^2C_{33}-80B_{11})\sin\dfrac{3\theta}{2}+(96\beta\mu h^2C_{14}-80B_{11} \\
\quad -48\beta\mu^2h^2C_{14}-112\beta h^2C_{14}-16\beta h^2C_{12}+16\beta\mu^2h^2C_{12}-12h^2C_{31}-48h^2C_{34}+80\mu^2B_{11} \\
\quad +16\mu^2h^2C_{34}-12\mu^2h^2C_{31}-24\mu h^2C_{31}-32\mu h^2C_{34})\cos\dfrac{3\theta}{2}+(24\beta h^2C_{13}+24\beta\mu^2h^2C_{13} \\
\quad +48\beta\mu h^2C_{13}-12h^2C_{33}-12h^2\mu^2C_{33}-24h^2\mu C_{33})\sin\dfrac{\theta}{2}+(24\beta h^2C_{14}+24\beta\mu^2h^2C_{14}+ \\
\quad 48\beta\mu h^2C_{14}+12h^2C_{34}+12h^2\mu^2C_{34}+24h^2\mu C_{34})\cos\dfrac{\theta}{2}] \\
\varphi_{x4}(\theta)=(-12h^2C_{42}+4h^2C_{44}+20\mu B_{21}+4\mu h^2C_{44}+2\beta\mu h^2C_{22}-20B_{21}-2\beta h^2C_{22}+4\mu h^2C_{42} \\
\quad -2\beta h^2C_{23}+2\beta\mu h^2C_{23})\sin2\theta+(-12h^2C_{41}-h^2C_{43}-\mu^2h^2C_{43}-\beta\mu^2h^2C_{21}-\beta\mu h^2C_{24} \\
\quad +5\mu^2B_{22}-8\mu h^2C_{41}-2\mu h^2C_{43}+4\mu^2h^2C_{41}-\beta h^2C_{24}-\beta\mu h^2C_{21})\cos2\theta-\mu^2h^2C_{43}- \\
\quad \beta h^2C_{24}-5B_{22}+4h^2C_{41}-\beta\mu^2h^2C_{21}-\beta\mu h^2C_{24}-\beta\mu h^2C_{21}+5\mu^2B_{22} \\
\quad \cdots\cdots
\end{cases}
\tag{7}
$$

$$
\begin{cases}
\varphi_{y1}(\theta)=-\dfrac{1}{\mu+1}[-(C_{14}+\mu C_{14})\sin\dfrac{3\theta}{2}+(C_{13}+\mu C_{13})\cos\dfrac{3\theta}{2}+(-4\mu C_{14}+12C_{14} \\
\quad +C_{12}+\mu C_{12})\sin\dfrac{\theta}{2}+(-4\mu C_{13}+12C_{13}-C_{11}-\mu C_{11})\cos\dfrac{\theta}{2}] \\
\varphi_{y2}(\theta)=C_{21}\sin\theta+C_{22}\cos\theta \\
\varphi_{y3}(\theta)=C_{34}\sin\dfrac{\theta}{2}+C_{33}\cos\dfrac{\theta}{2}+C_{31}\sin\dfrac{3\theta}{2}+C_{32}\cos\dfrac{3\theta}{2}-\dfrac{1}{4}\beta C_{14}\sin\dfrac{5\theta}{2}+\dfrac{1}{4}\beta C_{13}\cos\dfrac{5\theta}{2} \\
\varphi_{y4}(\theta)=C_{43}\sin2\theta+C_{44}\cos2\theta+C_{42} \\
\quad \cdots\cdots
\end{cases}
\tag{8}
$$

$$
\begin{cases}
\psi_1(\theta)=A_{11}\sin\dfrac{\theta}{2}+A_{12}\cos\dfrac{\theta}{2}+A_{13}\sin\dfrac{3\theta}{2}+A_{14}\cos\dfrac{3\theta}{2} \\
\psi_2(\theta)=A_{21}+A_{24}\cos2\theta \\
\psi_3(\theta)=A_{31}\sin\dfrac{\theta}{2}+A_{32}\cos\dfrac{\theta}{2}+\dfrac{A_{11}}{4}\beta\sin\dfrac{3\theta}{2}+\dfrac{A_{12}}{4}\beta\cos\dfrac{3\theta}{2}+A_{34}\cos\dfrac{5\theta}{2}+A_{33}\sin\dfrac{5\theta}{2} \\
\psi_4(\theta)=A_{41}\sin3\theta+A_{42}\cos3\theta+A_{43}\sin\theta+A_{34}\cos\theta \\
\quad \cdots\cdots
\end{cases}
\tag{9}
$$

$$
\begin{cases}
w_1(\theta) = B_{11}\sin\dfrac{\theta}{2}, \\
w_2(\theta) = B_{22}\cos\theta, \\
w_3(\theta) = \dfrac{1}{20E_0h(\mu+1)}[(-40E_0hC_{13} + 5E_0\beta hB_{11} - 96\kappa\mu A_{11} - 48\kappa\mu^2 A_{11} - 48\kappa A_{11} + 5E_0\beta h\mu B_{11} \\
\qquad +40E_0h\mu C_{13})\sin\dfrac{\theta}{2} + (-96\kappa\mu A_{12} - 48\kappa\mu^2 A_{12} - 48\kappa A_{12} - 40E_0hC_{14} + 40E_0h\mu C_{14})\cos\dfrac{\theta}{2} \\
\qquad +(20hE_0B_{32} + 20hE_0\mu B_{32})\sin\dfrac{3\theta}{2} + (20hE_0B_{31} + 20hE_0\mu B_{31})\cos\dfrac{3\theta}{2}] \\
w_4(\theta) = B_{42}\sin 2\theta + B_{41}\cos 2\theta + \dfrac{5hE_0(C_{21} + C_{24} - \beta B_{22}) - 48A_{21}(\mu+1)\kappa}{2E_0h} \\
\qquad \text{.....}
\end{cases}
\tag{10}
$$

where: A_{ij} , B_{ij} , C_{ij} are the undetermined coefficients.

Substituting Eq. (7)-(10) into Eq.(5), the generalized displacement fields of FGMs spherical shell are obtained.

5. Conclusion

For a functionally graded spherical shell with Reissner effect, the higher order crack tip fields which are similar to the Williams' solutions of crack problems in homogenous materials are obtained. As the in-homogeneity parameter $\beta \to 0$, the solutions degenerate to the corresponding fields of isotropic homogeneous spherical shell with Reissner's effect. Obviously, these results provide the theoretical basis for experimental investigation and engineering application.

Acknowledgements

The research is supported by the National Natural Science Foundation of China (No.11172332., No. 90305023)

References

[1] Y.Z. Li, C.T. Liu, Analysis of Reissner plate bending fracture problem. Acta Mechanica Sinica, 4 (1983) 366–374.

[2] E. Reissner, The effect of transverse shear deformation on the bending of elastic plates. ASCE.J.Appl.Mech, (1945) 69–78.

[3] F.Delale, Erdagan, Effect of transverse shear and material orthotropy in a cracked spherical

cap. Snlrd Struct. 15 (1979) 907–926.
[4] Liu Chuntu, Jiang Chiping, Fracture Mechanics for plates and shells. Defense Industry Press. Beijing, 2000.
[5] Y.Dai, L. Zhang, S.M.Li, X.Chong, J.F.Liu, The higher order crack-tip field of functionally graded Reissner's spherical shell. 2011 International Conference on Electronic and Mechanical Engineering and Information Technology, Harbin, 8 (2011) 2699–2701.
[6] F. Delale, F.Erdogan, The Crack Problem for a Nonhomogeneous Plane. Journal of Applied Mechanics, 50 (1983) 609–614.
[7] F.Delale, F.Erdogan, Interface Crack in a nonhomogeneous elastic Medium. International Journal of Engineering Science, 26 (1988) 559–602.
[8] Z. H. Jin, N. Noda, Crack-tip singular fields in nonhomogeneous materials. Journal of Applied Mechanics, 61(1994) 738–740.
[9] Y.Dai, L. Zhang, P. Zhang, S.M.Li, J.F.Liu, X.Chong, The eigen-functions of anti-plane crack problems in non-homogeneous materials. Science China, 8(2012) 852–860.

Three dimensional finite element study of crack in functionally graded material under thermal loading

Parya Aghasafari[1*], Vahid Arabzadeh[1],Ali Daraei[1] ,Mahmoud Salimi[2]

[1] Department of Mechanical Engineering, IUT University, 8415683111, Iran
[1] International Petro-Structure Co, 8015673611, Iran
[1] Department of Physics, UI University, 8174673441, Iran
[2] Faculty of mech.Eng dept, Institute of IUT, 8415683111, Iran
* Corresponding author: p.aghasafari@me.iut.ac.ir

Abstract

This article focused on three-dimensional analyses of a functionally graded material plate which contains a semi-elliptical surface crack and subjected to transient thermal loading. Strain singularity around the crack front is simulated using collapsed 20 – node quarter – point brick elements. Three –dimensional displacement correlation technique is utilized to extract the mixed mode stress intensity factors around the crack front for different inclination angles of the semi-elliptic surface crack. Comparisons between current results and those from analytical and other numerical methods yield good agreement. Thus, it is concluded that the applied three-dimensional enriched finite elements are capable of accurately computing mixed-mode fracture parameters for cracks in FGMs.

Keywords: FGM, semi–elliptical inclined surface crack, displacement correlation technique, mixed modes stress intensity factors, finite element method

1. Introduction

Numerical simulations of crack initiation, propagation and branching are a computationally intensive process. Traditional finite element packages simulate the crack propagation problem either by using singularity elements or by using line spring elements with built-in fracture criteria. Recently, a popular method to do this task is the cohesive surface modeling of the fracture zone. Following the work of Baren blatt[2], Dugdale [3] ,and Willis [4], many researchers have addressed the issue to this approach. Nee-dleman[5] provided a framework for these parathion process starting from initial de-bonding in the cohesive zone. Larsson [6] used this approach to simulate crack growth in brittle materials, while Xia and Shih[7] simulated fracture inductile material sunder static loading. Camacho and Ortiz[8] have used cohesive surface modeling to study material fragmentation, while Xu and Needleman[9] used it to study dynamic crack tip in stabilities by allowing cracks to formal on element boundaries. The method by Xu and Needleman involves introducing special boundary elements between regular elements, where the boundary Elements obey a cohesive law. Three factors influence the cohesive law behavior, namely the cohesive Strength, the critical separation at cohesive strength and the fracture energy in the separation process. These Models obviate the need for a separate external fracture criterion in fracture simulations. The effects of Plasticity inside volumetric elements have been investigated using the embedded-process-zone cohesive Fracture model by Tvergaard and Hucthinson[10,11]. Gullerud and Dodds [12] have used 3-D cohesive Elements for modeling ductile crack growth. More recently Foulketal.[13] presented a procedure for Implementing the cohesive zone modeling a 3-D finite

element framework where zones of cracking are Known a-priori and cohesive zone elements are placed along these element boundaries.
Gao [14,15] proposed that materials undergoing brittle fracture have large non-linear elastic deformations and that a hyper elastic description of the crack tip behavior provides a better explanation of dynamic Crack tip in stabilities. Gao and Klein[16] developed a method, called the virtual internal bond(VIB)model ,In which a cohesive type law is directly incorporated in to the constitutive model. This is done by treating the Body as a collection of randomly distributed material points inter connected by a network of cohesive bonds.
The Cauchy–Bornrule of crystal elasticity is used to derive the overall constitutive relations. This is done by equating the strain energy of the bonds to the potential energy stored in the continuum due to applied loads and deformations. As this is implemented in a hyper elastic frame work deformation continuum mechanics, the Green–Lagrange strain tensor can be evaluated from deformation gradient, and the second Piola–Kirchoff stress tensor can be computed from the potential energy expression. The main advantage of this method is that, as in the cohesive boundary element approach [9], no separate fracture criterion is needed. Furthermore, the cohesive law is now embedded directly into the constitutive equations, thus no special boundary elements between regular elements are needed.
This study implements a finite element model to study the thermal fracture behavior of functionally graded materials. Stress intensity factors (SIF) are evaluated using a thermo mechanics and fracture mechanics approach. The results show that the components gradation of the FGM composites has significant influence on the specimens' thermal behavior.

2. Thermo-mechanical finite element modeling of FGM

A problem which is encountered in three-dimensional finite element analyses is the large number of elements and as a result, a remarkable and time consuming computation. Also, because of very rapid changes in the geometrical parameters around the crack front region, mesh generation of this region must be done with a great care. This may lead to increase the run time which makes it difficult to reach valid results and conclusion [17].
The main objective of this study is to model and analyze a three dimensional inclined semi-elliptic surface crack in a plate made of Functionally Graded Material (FGM). FGM is 100% zirconia-yttria (ZrO2-8wt%-Y2O3) at x=0 and 100% nickel-chromium–aluminum– zirconium (NiCrAlY) at x= t. The thermo mechanical properties of the FGM structure are assigned according to variation function by using the centroid of each finite element. This procedure is developed by utilizing ANSYS codes. A unique material property is assigned to each element with the help of this method.
In this study three different ratio regarding to modulus of elasticity (E) are considered as E2/E1= 20, E2/E1= 0.05 and homogeneous material case.E1and E2 are the values of the elastic module at x= 0 and x=t, respectively. Except elastic module a total of five material parameters are required to be known in order to carry out the transient thermal fracture analysis. These parameters are Poisson's ratio υ, thermal expansion coefficient αt, thermal conductivity k and density multiplied by specific heat (ρc_t). (ρc_t) can be evaluated using the relationship $D = {}^{k}/_{\rho c_t}$ where D is the thermal diffusivity.

$$E(x) = Ee^{\beta x} \quad 0 < x < t \qquad \textit{(Eq. 1)}$$
$$v(x) = ve^{\beta x} \quad 0 < x < t \qquad \text{(Eq. 2)}$$
$$\alpha(x) = \alpha e^{\beta x} \quad 0 < x < t \qquad \textit{(Eq. 3)}$$
$$k(x) = ke^{\beta x} \quad 0 < x < t \qquad \text{(Eq. 4)}$$
$$\rho c_t(x) = \rho c_t e^{\beta x} \quad 0 < x < t \qquad \text{(Eq. 5)}$$

β is material constant and

$$\beta = {}^{1}/_{t}\, Ln\left({}^{E_2}/_{E_1}\right) \qquad \text{(Eq. 6)}$$

Table 1

Table 1

Material	Modulus Of Elasticity (GPa)	Poisson's ratio	Coefficient of thermal expansion ($^{\circ}C^{-1}$)	Coefficient of thermal conductivity (W/mK)	thermal diffusivity (m^2/s)
Substrate (Ni)	175.8	0.25	13.91×10^{-6}	7	2×10^{-6}
Bond Coat (NiCrAIY)	137.9	0.27	15.16×10^{-6}	25	8×10^{-6}
Zirconia-Yttria	27.6	0.25	13.91×10^{-6}	1	5×10^{-6}

In this paper combined thermal-structural analysis is studied. In the thermal analysis, first transient heat conduction in the FGM structure is conducted and consequently temperature distribution within the structure is computed. Afterwards, this temperature distribution is utilized as an input for the structural problem. While performing the analyses, it is assumed that the crack surfaces are completely insulated and the medium is free of any mechanical constraints. Furthermore, coupling of the thermal and structural problems are assumed to be through the calculated temperature distribution only since the inertia effects are not taken into account. During the solution, minimum and maximum time step sizes are entered. In order to overcome oscillations in the distribution of temperature, minimum time step size is taken to be very small and maximum time step size is chosen as not to be very large. By imposing temperature of the environment and applying free and forced convection coefficients on related surfaces of the FGM structure in time steps the problem is solved and calculated at each node. Then after computing the mixed mode stress intensity factors at the crack front nodes by utilizing the displacement correlation technique, the procedure of solving is repeated for each required time until the end time is reached.

3. The Displacement Correlation Technique (DCT)

Since the problem considered in this study is related to the inclined cracks (unsymmetrical), a complete crack model is needed to calculate the stress intensity factors. The figure below shows the full model which is to be used for mode I stress intensity factor calculation of an inclined crack.

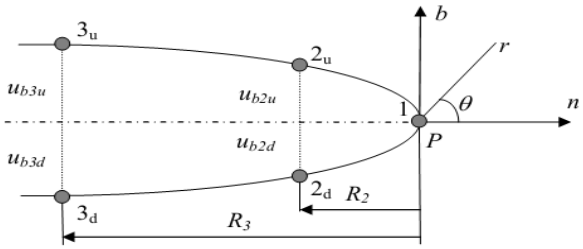

Fig 1- Deformed shape of the crack surface (non-symmetric)

The displacement component, which is required to calculate KI, at point P on the crack front can be expressed as

$$u_{\Delta}(r,\theta)=\left(\frac{1+\nu}{E}\right)\sqrt{\frac{2r}{\Pi}}\left\{k_{\imath}(s)\sin\left(\frac{\theta}{2}\right)\left[2(1-\nu)-\cos^2\left(\frac{\theta}{2}\right)\right]\right.$$

$$\left.-k_{\imath\imath}(S)\cos\left(\frac{\theta}{2}\right)\left[(1-2\nu)-\sin^2\left(\frac{\theta}{2}\right)\right]\right\} \qquad \text{(Eq. 1)}$$

$u_{\Delta}(r,\Pi)$is calculated by using equation (4.1). For the non-symmetric crack model, $u_{\Delta}(r,-\Pi)$ is also required. Thus, substituting $\theta=-\Pi$ into equation:

$$u_{\Delta}(r,-\Pi)=-\left(\tfrac{1+\nu}{E}\right)\sqrt{\tfrac{2r}{\Pi}}k_1 2(1-\nu) \qquad \text{(Eq. 2)}$$

Kı can be obtained as

$$k_1=\frac{\sqrt{2\Pi}\cdot E}{8(1-\nu^2)}\cdot\left[\lim_{r\to 0}\left\{\frac{u_{\Delta}(r,\Pi)-u_{\Delta}(r,-\Pi)}{\sqrt{r}}\right\}\right] \qquad \text{(Eq. 3)}$$

At the crach tip (i.e. $r\to 0$) , $\lim_{r\to 0}\left\{\frac{u_{\Delta}(r,\Pi)-u_{\Delta}(r,-\Pi)}{\sqrt{r}}\right\}=X$.Hence, equation

$$k_1=\frac{\sqrt{2\Pi}\cdot E}{8(1-\nu^2)}\cdot X \qquad \text{(Eq. 4)}$$

$$x=\frac{R_3^{3/2}(u_{\Delta\,2,0}-u_{\Delta\,2,3})-R_2^{3/2}(u_{\Delta\,3,0}-u_{\Delta\,3,3})}{\sqrt{R_2}\sqrt{R_3}(R_3-R_2)} \qquad \text{(Eq. 5)}$$

For r=R_2 → $\frac{u_{\Delta}(R_2,\Pi)-u_{\Delta}(R_2,-\Pi)}{\sqrt{R_2}}=\frac{u_{\Delta\,2,0}-u_{\Delta\,2,3}}{\sqrt{R_2}}=x+YR_2$

And

For r=R_3 → $\frac{u_{\Delta}(R_3,\Pi)-u_{\Delta}(R_3,-\Pi)}{\sqrt{R_3}}=\frac{u_{\Delta\,3,0}-u_{\Delta\,3,0}}{\sqrt{R_3}}=x+YR_3$

$$k_{\imath\imath}=\frac{\sqrt{2\Pi}\cdot E}{8(1-\nu^2)}\cdot\left[\lim_{r\to 0}\left\{\frac{u_0(r,\Pi)-u_0(r,-\Pi)}{\sqrt{r}}\right\}\right] \qquad \text{(Eq. 6)}$$

For r=R_2 → $\frac{u_0(R_2,\Pi)-u_0(R_2,-\Pi)}{\sqrt{R_2}}=\frac{u_{0\,2,0}-u_{0\,2,3}}{\sqrt{R_2}}=x+YR_2$

And

For r=R_3 → $\frac{u_0(R_3,\Pi)-u_0(R_3,-\Pi)}{\sqrt{R_3}}=\frac{u_{0\,3,0}-u_{0\,3,3}}{\sqrt{R_3}}=x+YR_3$

$$x = \frac{R_3^{3/2}(u_{0\,2,0}-u_{0\,2,3})-R_2^{3/2}(u_{0\,3,0}-u_{0\,3,3})}{\sqrt{R_2}\sqrt{R_3}(R_3-R_2)} \quad \text{(Eq. 7)}$$

$$k_{II} = \frac{\sqrt{2\Pi}\cdot E}{8(1-\nu^2)} \cdot X \quad \text{(Eq. 8)}$$

KIII can be calculated by the tangential displacement component at point P on the crack front. The tangential displacement component at this point is

$$u_c(r,\theta) = 2\left(\frac{1+\nu}{E}\right)\sqrt{\frac{2r}{\Pi}}k_m(s)\sin\left(\frac{\theta}{2}\right) \quad \text{(Eq. 9)}$$

For r=R_2 → $\frac{u_c(R_2,\Pi)-u_c(R_2,-\Pi)}{\sqrt{R_2}} = \frac{u_{c\,2,0}-u_{c\,2,3}}{\sqrt{R_2}} = x + YR_2$

And

For r=R_3 → $\frac{u_c(R_3,\Pi)-u_c(R_3,-\Pi)}{\sqrt{R_3}} = \frac{u_{c\,3,0}-u_{c\,3,3}}{\sqrt{R_3}} = x + YR_3$

$$x = \frac{R_3^{3/2}(u_{c\,2,0}-u_{c\,2,3})-R_2^{3/2}(u_{c\,3,0}-u_{c\,3,3})}{\sqrt{R_2}\sqrt{R_3}(R_3-R_2)} \quad \text{(Eq. 10)}$$

$$k_{III} = \frac{\sqrt{2\Pi}\cdot E}{8(1-\nu^2)} \cdot X \quad \text{(Eq. 11)}$$

$$\mu = \frac{E}{2(1+\nu)} \quad \text{(Eq. 12)}$$

Therefore, the total strain energy release rate under mixed mode loading is

$$G_T = G_1 + G_{II} + G_{III} = \frac{(1-\nu^2)}{E}\left\{k_1^2 + k_{II}^2 + \frac{k_{III}^2}{1-\nu}\right\} \quad \text{(Eq. 13)}$$

After the accuracy of the finite element model is checked out, the same model is used for the analyses of semi-elliptic inclined surface crack embedded in the FGM coating of composite structure. The finite element analyses of FGM coating- bond coat-substrate structure are carried out and the numerical results are calculated for various inclinations of three dimensional semi-elliptic surface crack, coating types, crack front angles and relative dimension of the crack with respect to FGM coating thickness.

4. Numerical results

There is a semi-elliptic inclined surface crack which has a length of 2c and a depth of a. The semi-elliptic crack has an inclination angle α, on the surface of the FGM at x=0. In the numerical analysis conducted, crack depth/ FGM thickness $^a/_t$ ratios and aspect ratio are used. These are as follows:

$$^a/_t = 0.2 \; and \; ^a/_c = {}^1/_2 \quad \text{(Eq. 14)}$$

In this analysis, the stress intensity factors are normalized by,

$$k_R = \sigma_0\sqrt{\frac{\Pi a}{Q}} \quad \text{(Eq. 15)}$$

Q is defined by,

$$Q = \begin{cases} 1 + 1.464(a\ /\ c)^{1.65} & \text{if } (\frac{a}{c}) \le 1 \\ 1 + 1 \cdot 464(c\ /\ a)^{1.65} & \text{if}(\frac{a}{c}) > 1 \end{cases} \qquad \text{(Eq. 16)}$$

The schematic of the crack front can be seen at Figure 2. The validation of the model is done by modeling and analyzing the plate, which contains a semi-elliptic inclined surface crack, with finite dimensions subjected to uniform tension (figures 3 and 4). As it can be seen from these figures, the results of this study are plotted for $\alpha = 0\ and\ \alpha = 30$. it can be said that the obtained results are in good agreement with that of Ayhan et al. [11]

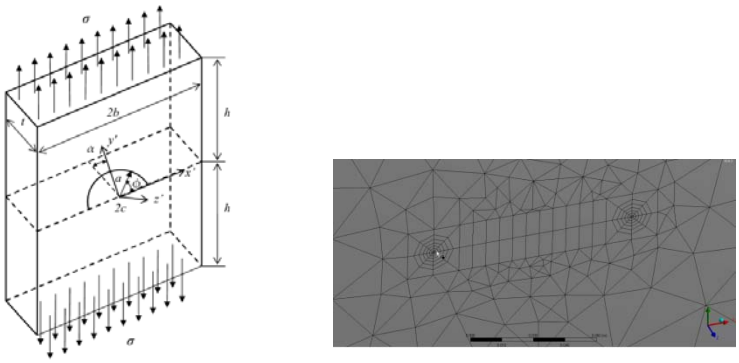

Fig 2- semi-elliptic inclined surface crack in a plate under uniform tensile remote stresses

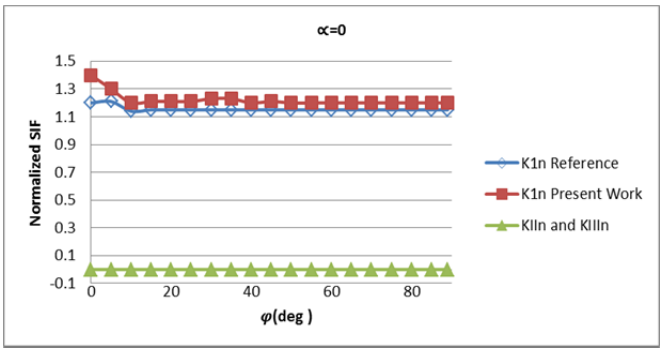

Fig 3- Comparisons of normalized mixed mode stress intensity factors for 0^o inclination angle

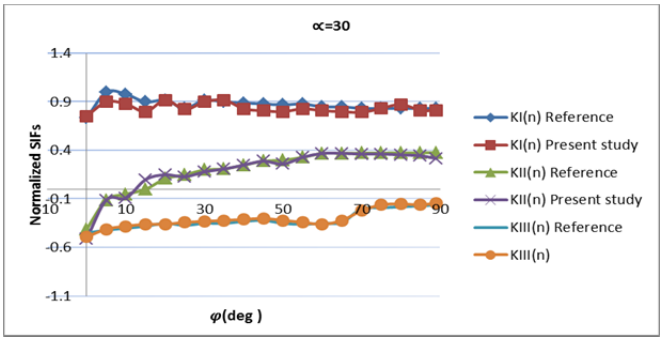

Fig 4- Comparisons of normalized mixed mode stress intensity factors for 30^o inclination angle

Transient Thermal Loading

The boundary conditions for this loading case are depicted in Figure 5.

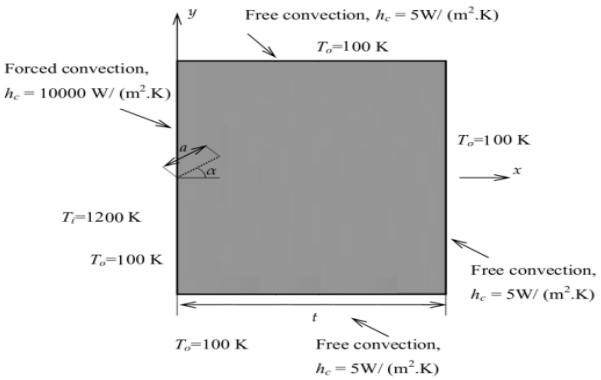

Fig 5- Thermal boundary conditions for the FGM coating, bond coat and substrate structure

It is assumed that the composite medium is initially stress-free at a high processing temperature of T_i = 1200 K. Then, the other face of solid is left in an environment which has a temperature of T_o = 100 K. The boundary conditions for this loading case are depicted in Figure 5. The thermo mechanical parameters used in the transient thermal analyses are described before. For the transient thermal analyses, inclination angles of 45^osemi-elliptic surface crack are considered. It is seen that the normalized stress intensity factors rates go through a maximum in a short time period and then starts to decrease (Figures 6, 7 and 8) for different ratio of E_2/E_1. Figures 9 show the distribution of energy release around the crack front.

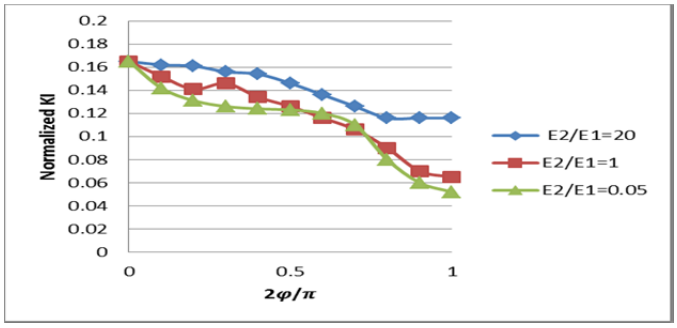

Fig 6- Distribution of normalized mode I stress intensity factors around crack front

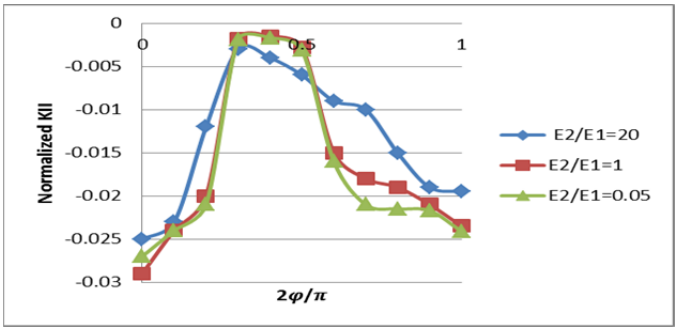

Fig 7- Distribution of normalized mode II stress intensity factors around crack front

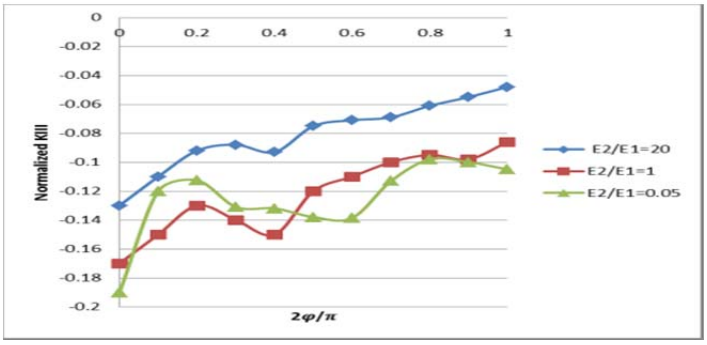

Fig 8- Distribution of normalized mode III stress intensity factors around crack front

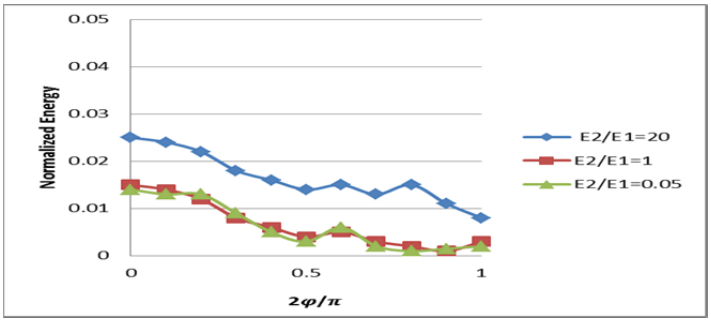

Fig 9- Distribution of normalized energy release rates around crack front

Figures 10 shows the distribution of temperature around the crack front at the time maximum values of normalized SIFs and energy release rates are reached.

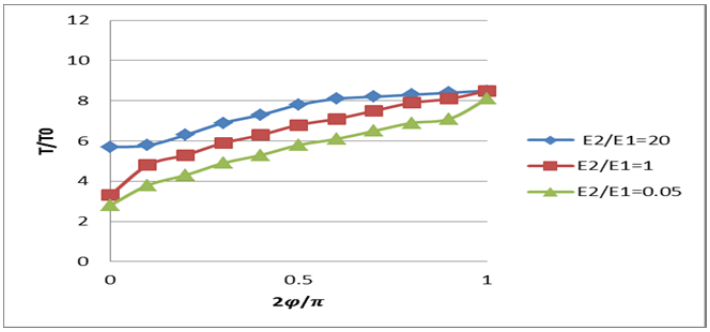

Fig 10- Distribution of temperature around crack front

In this study, an inclined semi-elliptical surface crack in an FGM structure is modeled in three dimension and fracture analyses are carried out by implementing finite element technique. For the model generations and finite element analyses, the multi-purpose finite element code ANSYS is used. The behavior of three dimensional inclined semi-elliptical surface cracks is examined under transient thermal loading for different ratios of material gradient. The mixed mode stress intensity factors and energy release rates around the crack front are calculated by utilizing displacement correlation technique.In order to verify the model and technique utilized in FGM structure, first of all, a plate and a semi-infinite solid with homogeneous material properties are modeled and analyzed under uniform tension. Then, the results obtained are compared to those given by Ayhan et al. [1 1]. It is observed that the figures generated for comparisons are in good agreement and therefore, it is concluded that this model can also be used for the finite element

analyses of the composite medium. The transient thermal analyses of the FGM structure are carried out for three different material gradients. It is assumed that the composite medium is initially at a high processing temperature. Then, this structure is left in an environment which is at a low temperature. Due to the high temperature difference, thermal stresses are induced at the composite structure containing an inclined semi-elliptical surface crack. Mixed mode SIFs and energy release rates are calculated along the crack front. It is observed that as the inclination angle increases, the normalized modes stress intensity factors decrease. The normalized energy release rates also decrease as the inclination angle increases. It is seen that for all inclination angles the normalized temperature increases as the crack front angle increases. It is could be concluded that material gradation has considerable effect on mode-II and mode-III stress intensity factors also. Thus, it is concluded that the 3D elements can be applied to calculate mixed-mode cracks in FGMs accurately and efficiently without needing special meshes near the crack front and detailed post-processing of the finite element solution.

References

[1] Andrews EW, Kim KS. Threshold conditions for dynamic fragmentation of ceramic particles. Mech Mater1998; 29:161–80.

[2] Barenblatt GI. The formation of equilibrium cracks during brittle fracture: general ideas and hypotheses, axially symmetric cracks. Appl Math Mech (PMM) 1959;23:622–36.

[3] Dugdale DS. Yielding of steel sheets containing slits . J Mech Phys Solids 1960;8:100–8.

[4] Willis JR . A comparison of the fracture criteria of Griffth and Barenblatt . J Mech Phys Solids 1967;15:151–62.

[5] Needleman A. A continuum model for void nucleation by inclusion debonding . J Appl Mech 1987;54:525–31.

[6] Larsson R.A generalized fictitious crack model based on plastic localization and discontinuous approximation. Int Journal Meth Eng.1995;38:3167–88.

[7] XiaL , Shih FC.Ductile crack growth—I. A numerical study using computational cells with micro structurally based length scales.J Mech Phys Solids 1995;43:233–59.

[8] Camacho GT, Ortiz M. Computational modeling of impact damage in brittle materials . Int J Solids Struct 1996;33:2899–938.

[9] Xu XP, Needleman A. Numerical simulation of fast crack growth in brittle solids. J Mech Phys Solids 1994;42(9):1397–434.

[10] Tvergaard V, Hutchinson JW. The relation between crack growth resistance and fracture process parameters in elastic–plastic solids. J Mech Phys Solids 1992;41:1377–97.

[11] Tvergaard V, Hutchinson JW. The influence of plasticity on mixed mode interface toughness. J Mech Phys Solids 1993;41:1119–35.

[12] Gullerud A, DoddsR.3-D modeling of ductile crack growth in thin sheet metals. Engng Fract Mech 1999;63:347–74.

[13] Foulk JW , Allen DH, HelmsKLE. Formulation of a three dimensional cohesive zone model for application to a finite element algorithm. Comput Meth Appl Mech Engng 2000;183:51–66.

[14] Gao H. A theory of local limiting speed in dynamic fracture . J Mech Phys Solids 1996;44:1453–74.

[15] Gao H. Elastic waves in a hyper elastic solid near its plane strain equibiaxial cohesive limit. PhilosMagLett1997;76:307–14.
[16] Gao H, Klein P. Numerical simulation of crack growth in an isotropic solid with randomized internal cohesive bonds .J Mech Phys Solids 1998;46:187–218.
[17] Wang QZ, Jia XM. More accurate stress intensity factor derived by finite element analysis for the ISMR suggested rock fracture toughness specimen-CCNBD. Int J Rock Mech Min Sci 2003;40:233e 41.

The thermal effect of anti-plane crack in a functionally graded piezoelectric strip under electric shock

Xing Li*, Yongyi Long, Pengpeng Shi

School of Mathematics and Computer Science, Ningxia University, 750021, China
* Corresponding author: email@li_x@nxu.edu.cn

Abstract The thermal effect of mode III crack in a functionally graded strip under the electric shock is investigated. This fracture analysis can be expressed through the superposition of two problem solutions. The first solution is the dynamic behaviors of a functionally graded piezoelectric material with central crack subjected to the electric shock. The second solution means the temperature field by calculating the power of point heat source around the crack tip. Based on the Laplace transform and Fourier transform technique, this mixed boundary value problems is reduced to a Cauchy singular integral equation, which is solved numerically by the Cauchy-Chebyshev quadrature technique. Numerical results are presented to show the effects of geometrical of crack and graded quantities of material on the stress intensity factors.

Keywords Anti-plane crack, Functionally graded piezoelectric materials, Electric shock, Thermal effect

1. Introduction

Piezoelectric materials (PMs) have been widely used as a smart material in electromechanical devices due to the demand of transform from mechanical to electrical loadings, and vice versa. To improve the reliability and durability problems arising largely from high residual and thermal stress, poor interfacial bonding strength, the functionally graded piezoelectric materials (FGPMs) as a new class of advanced composites have been developed.

Recently, some researchers start to investigate the fracture behavior in FGPMs. Wang and Node [1] firstly studied the thermo-piezoelectric fracture problem of a functionally graded piezoelectric layer bonded to a metal. They obtained the thermal flow, stress and electric displacement intensity factors and predict the direction of crack extension by using the energy density theory. Wang considered the mode III crack problem in FGPM, where the material properties are assumed in a class of functional form such that an analytic solution is possible. Recently, Li and Lee [2] investigated the fracture behavior of a weak discontinuous interface between two piezoelectric strips under electro-mechanical loads by using the methods of Fourier integral transform and Cauchy singular integral equation. Ding and Li [3] studied the problem of periodic interface cracks in a functionally graded coating-substrate structure. Recently, based on the methods of variable separation and singular integral equation, Ref. [4] investigated the arc-shaped interfacial cracking problem in a hollow cylinder that consists of an inner orthotropic dielectric layer and an outer functionally graded piezoelectric layer.

Although a variety of challenging issues related to certain crack problems in the functionally graded piezoelectric materials have been addressed, one of the remaining problems that need to fully understand is that FGPMs belongs to the dielectric material. Research of Bilyk et al [5] revealed that applying high current on the conductor, the temperature of conductor is lager than the temperature just under force load. To the authors' knowledge, few papers considered the solution for the problem of the heating effect of the crack tip in FGPM under electric shock. Then, this paper discusses the heating effect of the crack tip on piezoelectric medium under the high electric shock load.

2 Formulation of the problem

2.1 Theoretical model

The thermal effect of mode III crack in a functionally graded strip under the electric shock is investigated. This fracture analysis can be expressed through the superposition of two problem solutions. The first solution refers to the dynamic behaviors of a functionally graded piezoelectric material with central crack subjected to the electric shock. The second solution means the temperature field by calculating the power of point heat source around the crack tip. Illustrated in Fig.1 is the fracture model of a functionally graded piezoelectric strip which is assumed to contain a center crack. The crack of length and the thickness of strip are defined as $2c$ and $2h$. In addition, the rectangular coordinate system is established as fig 1. Since the poling directions of piezoelectric materials are orientated along z-axis, the antiplane mechanical field and inplane electric field are coupled. Here, the fundamental solution of crack under a pair of the equivalent electric shock $-D_0H(t)$ and shear traction $-\tau_0H(t)$ acting on the crack surface is considered. $H(t)$ is Heaviside function, and τ_0, D_0 are the range of the impact load of force field and electric field.

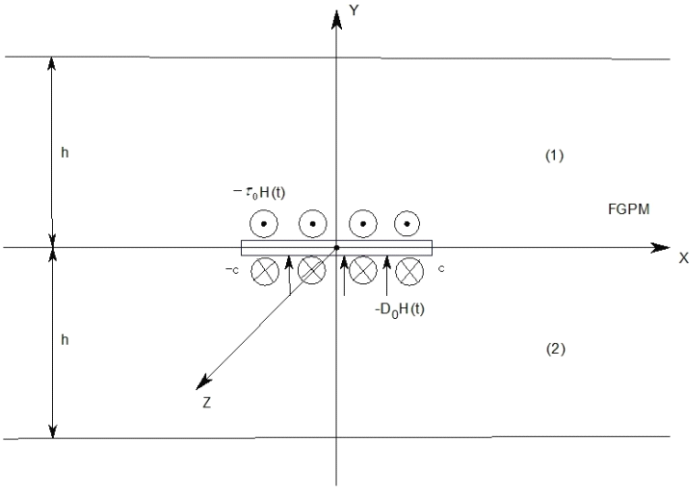

Figure 1. Functionally graded piezoelectric strip with central crack subjected to the electric shock

In fracture analysis of functionally graded piezoelectric strip, for the convenience of employing some standard methods such as Fourier transforms and integral equations, material properties are always assumed to be continuous functions of spatial coordinates, among which the most widely used one is exponential function [4]. Therefore, like many previous literatures, the properties of the functionally graded piezoelectric strip are assumed in power forms along y axis as follows:

$$c_{44} = c_0 e^{\beta y}, \quad e_{15} = e_0 e^{\beta y}, \quad \kappa_{11} = \kappa_0 e^{\beta y}, \quad \rho = \rho_0 e^{\beta y} \tag{1}$$

where $c_0, e_0, \kappa_0, \rho_0$ are the coefficient of the functionally graded strip at $y=0$, such as shear modulus, piezoelectric coefficient, dielectric permittivity and density permeability, respectively. β is the non-homogeneity parameters controlling the material coefficient in the graded layer.

2.2 Governing equations

Firstly, without considering the related effect of temperature field, a theoretical model is developed for the dynamic fracture analysis of a functionally graded piezoelectric material of a finite dimension with central crack subjected to the electric shock. Under axial shear deformation, the constitutive relations can be expressed in terms of polar coordinate system in the form

$$\sigma_{xz} = c_{44}(y)\frac{\partial \omega}{\partial x} + e_{15}(y)\frac{\partial \phi}{\partial x}, \sigma_{yz} = c_{44}(y)\frac{\partial \omega}{\partial y} + e_{15}(y)\frac{\partial \phi}{\partial y}$$
$$D_x = e_{15}(y)\frac{\partial \omega}{\partial x} - \kappa_{11}(y)\frac{\partial \phi}{\partial x}, D_y = e_{15}(y)\frac{\partial \omega}{\partial y} - \kappa_{11}(y)\frac{\partial \phi}{\partial y} \quad (2)$$

where ϕ and w denote the electric potential and anti-plane mechanical displacement, D and σ are the electric displacement and anti-plane stresses, respectively.
The geometric equation can be written as

$$2\varepsilon_{xz} = \frac{\partial \omega}{\partial x}, \quad 2\varepsilon_{yz} = \frac{\partial \omega}{\partial y}, \quad E_x = -\frac{\partial \phi}{\partial x}, \quad E_y = -\frac{\partial \phi}{\partial y}, \quad E_z = -\frac{\partial \phi}{\partial z} \quad (3)$$

Under the static condition, when body forces and body charges are omitted, the stress, electric displacement should satisfy the following equations

$$\frac{\partial \sigma_{xz}}{\partial x} + \frac{\partial \sigma_{yz}}{\partial y} = \rho \frac{\partial^2 \omega}{\partial t^2}, \quad \frac{\partial D_x}{\partial x} + \frac{\partial D_y}{\partial y} = 0 \quad (4)$$

Introduce an auxiliary function by

$$\psi = \phi - \frac{e_0}{\kappa_0}\omega \quad (5)$$

Substituting Eqs. (1-3) into Eq. (4) yields the decoupled governing equations in the piezoelectric strip

$$\nabla^2 \omega + \beta \frac{\partial \omega}{\partial y} = s_0 \frac{\partial^2 \omega}{\partial t^2}, \nabla^2 \psi + \beta \frac{\partial \psi}{\partial y} = 0 \quad (6)$$

where

$$s_0 = \rho_0 / (c_0 + \frac{e_0^{\ 2}}{\kappa_0}) \quad (7)$$

2.3 Boundary conditions

The upper region $y \in [0, h]$ and lower region $y \in [-h, 0]$ is symmetric with respect to the x axis. Therefore, in the following we confine our attention to the upper region $y \in [0, h]$. Then, based on the symmetry, the corresponding boundary conditions are imposed

$$\omega(x,0,t) = 0, \quad \phi(x,0,t) = 0 \ (|x| > c) \quad (8)$$

Here, the fundamental solution of crack under a pair of the equivalent electric shock $-D_0 H(t)$ and shear traction $-\tau_0 H(t)$ acting on the crack surface is considered. The corresponding mechanical boundary conditions on the crack surface are imposed

$$\sigma_{yz}(x,0,t) = -\tau_0 H(t), \quad D_y(x,0,t) = -D_0 H(t) \ (-c < x < c) \quad (9)$$

Assume that the upper surface $y = h$ is free of loading. Therefore, the electric displacement and anti-plane stresses on the upper surface is taken as zero,

$$\sigma_{yz}(x,h,t) = 0, \quad D_y(x,h,t) = 0 \ (-\infty < x < +\infty) \quad (10)$$

3. Solution

3.1 Basic solution expression

Using the Laplace transform and Fourier transform technique, ones can transform Eqs. (6) into a system of decoupled differential equations

$$(-s^2)F(s,y,p)+\frac{\partial^2}{\partial y^2}F(s,y,p)+\beta\frac{\partial}{\partial y}F(s,y,p)=s_0p^2F(s,y,p) \tag{11}$$

$$(-s^2)G(s,y,p)+\frac{\partial^2}{\partial y^2}G(s,y,p)+\beta\frac{\partial}{\partial y}G(s,y,p)=0 \tag{12}$$

where

$$\psi^*(x,y,p)=\int_0^{+\infty}\psi(x,y,t)e^{-pt}dt,\psi(x,y,t)=\int_{Br}\psi^*(x,y,p)e^{pt}dp \tag{13}$$

$$\omega^*(x,y,p)=\int_0^{+\infty}\omega(x,y,t)e^{-pt}dt,\omega(x,y,t)=\frac{1}{2\pi i}\int_{Br}\omega^*(x,y,p)e^{pt}dp \tag{14}$$

$$\omega^*(x,y,p)=\frac{1}{2\pi}\int_{-\infty}^{+\infty}F(s,y,p)e^{-isx}ds,F(s,y,p)=\int_{-\infty}^{+\infty}\omega^*(x,y,p)e^{isx}dx \tag{15}$$

$$\psi^*(x,y,p)=\frac{1}{2\pi}\int_{-\infty}^{+\infty}G(s,y,p)e^{-isx}ds,G(s,y,p)=\int_{-\infty}^{+\infty}\psi^*(x,y,p)e^{isx}dx \tag{16}$$

where $\omega^*(x,y,p),\psi^*(x,y,p)$ are the Laplace transform of $\omega(x,y,t),\psi(x,y,t)$, Br means path integral Bromwich formulation. And $F(s,y,p),G(s,y,p)$ are the Fourier transform of $\omega^*(x,y,p),\psi^*(x,y,p)$.

Afterwards, solving Eqs. (11-12), one can finally express the mechanical displacement, electric potential of the strip in the Laplace domains below

$$\omega^*(x,y,p)=\frac{1}{2\pi}\int_{-\infty}^{+\infty}[A_1(s,p)e^{t_1y}+A_2(s,p)e^{t_2y}]e^{-isx}dx \tag{17}$$

$$\psi^*(x,y,p)=\frac{1}{2\pi}\int_{-\infty}^{+\infty}[A_3(s,p)e^{t_3y}+A_4(s,p)e^{t_4y}]e^{-isx}dx \tag{18}$$

$$\begin{aligned}\phi^*(x,y,p)=&\frac{1}{2\pi}\int_{-\infty}^{+\infty}\frac{e_0}{\kappa_0}[A_1(s,p)e^{t_1y}+A_2(s,p)e^{t_2y}]e^{-isx}dx\\&+\frac{1}{2\pi}\int_{-\infty}^{+\infty}[A_3(s,p)e^{t_3y}+A_4(s,p)e^{t_4y}]e^{-isx}dx\end{aligned} \tag{19}$$

There are four unknown functions $A_i(s,p),i=1,2,3,4$ which can be solved by considering the boundary conditions and continuity conditions which are formulated by Eqs. (8-10).

$$t_1=-\frac{\beta}{2}+\sqrt{(\frac{\beta}{2})^2+s^2+s_0p^2},t_2=-\frac{\beta}{2}-\sqrt{(\frac{\beta}{2})^2+s^2+s_0p^2},t_3=-\frac{\beta}{2}+\sqrt{(\frac{\beta}{2})^2+s^2},t_4=-\frac{\beta}{2}+\sqrt{(\frac{\beta}{2})^2+s^2} \tag{20}$$

3.2 Transformation to singular integral equation

In order to derive the singular integral equation, two dislocation density functions are introduced as

$$f^*(x,p)=\begin{cases}\dfrac{\partial\omega^*(x,0,p)}{\partial x} & |x|\le c\\ 0 & |x|>c\end{cases} \tag{21}$$

$$g^*(x,p)=\begin{cases}\dfrac{\partial\phi^*(x,0,p)}{\partial x} & |x|\le c\\ 0 & |x|>c\end{cases} \tag{22}$$

Substituting Eqs. (17-19) into Eq. (8), and considering Eqs. (21-22), one can obtain the following relation

$$A_1(s,p)+A_2(s,p)=\frac{1}{-is}\int_{-c}^{c}f^*(t,p)e^{ist}dt \tag{23}$$

$$A_3(s,p)+A_4(s,p)=(-\frac{e_0}{\kappa_0})\cdot(\frac{1}{-is}\int_{-c}^{c}f^*(t,p)e^{ist}dt)+\frac{1}{-is}\int_{-c}^{c}g^*(t,p)e^{ist}dt \tag{24}$$

Substituting Eqs. (2) (17-19) into Eq. (10), it yields

$$(c_0+\frac{e_0^{\ 2}}{\kappa_0})e^{\beta h}[t_1A_1(s,p)e^{t_1h}+t_2A_2(s,p)e^{t_2h}]+e_0e^{\beta h}[t_3A_3(s,p)e^{t_3h}+t_4A_4(s,p)e^{t_4h}]=0 \tag{25}$$

$$2e_0e^{\beta h}[t_1A_1(s,p)e^{t_1h}+t_2A_2(s,p)e^{t_2h}]+\kappa_0e^{\beta h}[t_3A_3(s,p)e^{t_3h}+t_4A_4(s,p)e^{t_4h}]=0 \tag{26}$$

One can finally obtain the following relations form Eqs. (23-26)

$$A_1=\frac{-t_2e^{t_2h}}{t_1e^{t_1h}-t_2e^{t_2h}}f,\quad A_2=\frac{t_1e^{t_1h}}{t_1e^{t_1h}-t_2e^{t_2h}}f \tag{27}$$

$$A_3=\frac{-t_4e^{t_4h}}{t_3e^{t_3h}-t_4e^{t_4h}}(-\frac{e_0}{\kappa_0}f+g),\quad A_4=\frac{t_3e^{t_3h}}{t_3e^{t_3h}-t_4e^{t_4h}}(-\frac{e_0}{\kappa_0}f+g) \tag{28}$$

where

$$f=\frac{1}{-is}\int_{-c}^{c}f^*(t,p)e^{ist}dt,\quad g=\frac{1}{-is}\int_{-c}^{c}g^*(t,p)e^{ist}dt \tag{29}$$

Then, substituting Eqs. (2) (27-29) into Eqs. (2), the basic solution expression of the electric displacement and anti-plane stresses is obtained. And then, substituting the electric displacement and stress component into Eq. (8), one arrives at an integral equation in the form [6]

$$\frac{1}{\pi}\int_{-c}^{c}\frac{f^*(t,p)}{t-x}dt+\frac{e_0}{\pi}\int_{-c}^{c}\frac{g^*(t,p)}{t-x}dt+\frac{1}{\pi}\int_{-c}^{c}K_{11}(x,t,p)f^*(t,p)dt$$
$$-\frac{e_0}{\pi}\int_{-c}^{c}K_{12}(x,t,p)g^*(t,p)dt=-\frac{\tau_0}{p} \tag{30}$$

$$-\frac{e_0}{\pi}\int_{-c}^{c}\frac{f^*(t,p)}{t-x}dt+\frac{\kappa_0}{\pi}\int_{-c}^{c}\frac{g^*(t,p)}{t-x}dt-\frac{e_0}{\pi}\int_{-c}^{c}K_{21}(x,t,p)f^*(t,p)dt$$
$$+\frac{\kappa_0}{\pi}\int_{-c}^{c}K_{22}(x,t,p)g^*(t,p)dt=-\frac{D_0}{p} \tag{31}$$

where

$$K_{11}=\int_0^{+\infty}[U_1(s,p)-1]\sin s(t-x)ds,\quad K_{12}=\int_0^{+\infty}[U_2(s,p)+1]\sin s(t-x)ds,$$
$$K_{21}=K_{22}=\int_0^{+\infty}[U_2(s,p)-1]\sin s(t-x)ds \tag{32}$$

$$U_1=\frac{1}{s}[\frac{e_0^{\ 2}}{\kappa_0}\cdot\frac{t_3t_4e^{t_3h}-t_3t_4e^{t_4h}}{t_3e^{t_3h}-t_4e^{t_4h}}-(c_0+\frac{e_0^{\ 2}}{\kappa_0})\cdot\frac{t_1t_2e^{t_1h}-t_1t_2e^{t_2h}}{t_1e^{t_1h}-t_2e^{t_2h}}],\ U_2=\frac{1}{s}\cdot\frac{t_3t_4e^{t_3h}-t_3t_4e^{t_4h}}{t_3e^{t_3h}-t_4e^{t_4h}} \tag{33}$$

Because of the symmetry of fracture analysis, the dislocation density function $F(u,p),(u,p)$ must be an odd function of u. Then, it is automatically satisfied

$$f^*(0,p)=0,g^*(0,p)=0 \tag{34}$$

3.3 Numerical solution

Introducing $t=uc,x=rc$, $f^*(t,p)=F(u,p),g^*(t,p)=G(u,p)$, $K_{ij}(x,t,p)=K_{ij}^{\ *}(u,r,p)(i,j=1,2)$, Eqs. (30-31) and (34) can be transformed into the standard form of the first kind Cauchy singular integral equations as

$$\frac{1}{\pi}\int_{-1}^{1}\frac{F(u,p)}{u-r}du+\frac{e_0}{\pi}\int_{-1}^{1}\frac{G(u,p)}{u-r}du+\frac{c}{\pi}\int_{-1}^{1}K_{11}^{*}(r,u,p)\cdot F(u,p)du$$

$$-\frac{e_0 c}{\pi}\int_{-1}^{1}K_{12}^{*}(r,u,p)G(u,p)du=-\frac{\tau_0}{p} \tag{35}$$

$$-\frac{e_0}{\pi}\int_{-1}^{1}\frac{F(u,p)}{u-r}du+\frac{\kappa_0}{\pi}\int_{-1}^{1}\frac{G(u,p)}{u-r}du-\frac{e_0 c}{\pi}\int_{-1}^{1}K_{21}^{*}(r,u,p)\cdot F(u,p)du$$
$$+\frac{\kappa_0 c}{\pi}\int_{-1}^{1}K_{22}^{*}(r,u,p)G(u,p)du=-\frac{D_0}{p} \tag{36}$$

$$F(0,p)=0\,,\ G(0,p)=0 \tag{37}$$

According to the theory of singular integral equation, the solution of $F(u,p)$ 和 $G(u,p)$ may be expressed as [6]

$$f^{*}(t,p)=F(u,p)=\frac{R(u,p)}{\sqrt{1-u^2}}\,,\quad R(u,p)=\sum_{n=0}^{\infty}C_n T_n(u,p) \tag{38}$$

$$g^{*}(t,p)=G(u,p)=\frac{S(u,p)}{\sqrt{1-u^2}}\,,\quad S(u,p)=\sum_{n=0}^{\infty}D_n T_n(u,p) \tag{39}$$

Based on the Cauchy-Chebyshev collocation method, Eqs. (35-37) are reduced into a system of algebraic equations [6]

$$\sum_{l=1}^{N}\left[\frac{1}{u_l-r_m}+cK_{11}^{*}(r_m,u_l,p)\right]\frac{R(u_l,p)}{N}+\sum_{l=1}^{N}\left[\frac{e_0}{u_l-r_m}+e_0 cK_{12}^{*}(r_m,u_l,p)\right]\frac{S(u_l,p)}{N}=-\frac{\tau_0}{p} \tag{40}$$

$$\sum_{l=1}^{N}\left[-\frac{e_0}{u_l-r_m}+e_0 cK_{21}^{*}(r_m,u_l,p)\right]\frac{R(u_l,p)}{N}+\sum_{l=1}^{N}\left[\frac{\kappa_0}{u_l-r_m}+\kappa_0 cK_{22}^{*}(r_m,u_l,p)\right]\frac{S(u_l,p)}{N}=-\frac{D_0}{p} \tag{41}$$

$$\sum_{l=1}^{N}\frac{R(u_l,p)}{N}=0\,,\sum_{l=1}^{N}\frac{S(u_l,p)}{N}=0 \tag{42}$$

where

$$u_l=\cos\left(\frac{2l-1}{2N}\pi\right)\ (l=1,2,\cdots,N)\,,\ r_m=\cos\left(\frac{m}{N}\pi\right)\ (m=1,2,\cdots,N-1) \tag{43}$$

Solving Eqs. (40-41) and taking (42) into account, the numerical values of the function $R(u_l,p)$ and $S(u_l,p)$ can be obtained. Furthermore, the values of the function $F(u,p)$ and $G(u,p)$ can be obtained numerically. Thus, after obtaining the solutions $f\,,g$ from the Eqs. (19), we may obtain the four unknown functions $A_i(s,p),i=1,2,3,4$ from Eqs. (27-28), furthermore, the mechanical displacement, electric potential of the strip in the Laplace domains will be obtained from Eqs. (17-19).

3.4 Temperature field of the crack tip

Research of Bilyk et al [5] revealed that applying high current on the conductor, the temperature of conductor is lager than the temperature just under force load. Then, this paper discusses the heating effect of the crack tip on piezoelectric medium under the high electric shock load. Secondly, within supposing that it is a heat insulation process in a short time, and thermal field and electromechanical filed is decoupled, the thermal effect is calculated. according to ref. [5] which shows that electromagnetic field diffusion time scale is far less than the heat conduction time scale under action current load, the this process can be approximated as adiabatic process, so this assumption is established.

In accordance with the above assumptions, under the adiabatic conditions, the first approximation of heat conduction equation of the piezoelectric materials is

$$p = c_0 \frac{\partial T}{\partial t} \tag{44}$$

where c_0 denotes specific heat capacity.

For there is no external heat source, according to the ref. [7] of the electric shock which can retard effectively crack propagation, the heat source power can be introduced to the function of equivalent external point heat source

$$p = E \cdot J \tag{45}$$

where J denotes the electric current density vector field of the dielectric materials.

Current density vector of the dielectric material can be expressed as

$$J = \frac{\partial D}{\partial t} \tag{46}$$

Functionally graded piezoelectric material belongs to the dielectric material. Similarly, introducing power of heat source, temperature field of piezoelectric medium is obtained from the time integration of expression which can be obtained by substituting (45-46) into expressions of (44),

$$T(x,y,t) = \frac{1}{c_0}\int_0^t E(x,y,\tau)\frac{\partial D(x,y,\tau)}{\partial \tau}d\tau \tag{48}$$

For the geometric Eq. (3), constitutive Eq. (2) and fundamental solution (17-19), we get

$$\begin{aligned} E_x^*(x,y,p) = {} & \frac{1}{2\pi}\int_{-\infty}^{+\infty} is\cdot\frac{e_0}{\kappa_0}[A_1(s,p)e^{t_1 y} + A_2(s,p)e^{t_2 y}]e^{-isx}ds \\ & + \frac{1}{2\pi}\int_{-\infty}^{+\infty} is\cdot[A_3(s,p)e^{t_3 y} + A_4(s,p)e^{t_4 y}]e^{-isx}ds \end{aligned} \tag{49}$$

$$\begin{aligned} E_y^*(x,y,p) = {} & -\frac{1}{2\pi}\int_{-\infty}^{+\infty}\frac{e_0}{\kappa_0}[t_1 A_1(s,p)e^{t_1 y} + t_2 A_2(s,p)e^{t_2 y}]e^{-isx}ds \\ & - \frac{1}{2\pi}\int_{-\infty}^{+\infty}[t_3 A_3(s,p)e^{t_3 y} + t_4 A_4(s,p)e^{t_4 y}]e^{-isx}ds \end{aligned} \tag{50}$$

$$\begin{aligned} D_x^*(x,y,p) = {} & (e_{15} - \kappa_{11}\cdot\frac{e_0}{\kappa_0})\frac{1}{2\pi}\int_{-\infty}^{+\infty}(-is)\cdot[A_1(s,p)e^{t_1 y} + A_2(s,p)e^{t_2 y}]e^{-isx}ds \\ & - \kappa_{11}\cdot\frac{1}{2\pi}\int_{-\infty}^{+\infty}(-is)\cdot[A_3(s,p)e^{t_3 y} + A_4(s,p)e^{t_4 y}]e^{-isx}ds \end{aligned} \tag{51}$$

$$\begin{aligned} D_y^*(x,y,p) = {} & (e_{15} - \kappa_{11}\cdot\frac{e_0}{\kappa_0})\frac{1}{2\pi}\int_{-\infty}^{+\infty}[t_1 A_1(s,p)e^{t_1 y} + t_2 A_2(s,p)e^{t_2 y}]e^{-isx}ds \\ & - \kappa_{11}\cdot\frac{1}{2\pi}\int_{-\infty}^{+\infty}[t_3 A_3(s,p)e^{t_3 y} + t_4 A_4(s,p)e^{t_4 y}]e^{-isx}ds \end{aligned} \tag{52}$$

Furthermore, the solution of electric field strength and electric displacement intensity in the Laplace transform domain is

$$E_x^*(x,y,p) = c[\sum_{l=1}^{N} K_{ex1}(u_l,x,y,p)\frac{R(u_l,p)}{N} + \sum_{l=1}^{N} K_{ex2}(u_l,x,y,p)\frac{S(u_l,p)}{N}] \tag{53}$$

$$E_y^*(x,y,p) = c[\sum_{l=1}^{N} K_{ey1}(u_l,x,y,p)\frac{R(u_l,p)}{N} + \sum_{l=1}^{N} K_{ey2}(u_l,x,y,p)\frac{S(u_l,p)}{N}] \tag{54}$$

$$D_x^*(x,y,p) = c[\sum_{l=1}^{N} K_{dx1}(u_l,x,y,p)\frac{R(u_l,p)}{N} + \sum_{l=1}^{N} K_{dx2}(u_l,x,y,p)\frac{S(u_l,p)}{N}] \tag{55}$$

$$D_y^*(x,y,p)=c[\sum_{l=1}^{N}K_{dy1}(u_l,x,y,p)\frac{R(u_l,p)}{N}+\sum_{l=1}^{N}K_{dy2}(u_l,x,y,p)\frac{S(u_l,p)}{N}] \tag{56}$$

where

$$K_{ex1}(u,x,y,p)=\int_0^{+\infty}\frac{e_0}{\kappa_0}[\frac{t_2e^{t_2h+t_1y}-t_1e^{t_1h+t_2y}}{t_1e^{t_1h}-t_2e^{t_2h}}+\frac{t_3e^{t_3h+t_4y}-t_4e^{t_4h+t_3y}}{t_3e^{t_3h}-t_4e^{t_4h}}]\cos[s(cu-x)]ds \tag{57}$$

$$K_{ex2}(u,x,y,p)=\int_0^{+\infty}\frac{t_4e^{t_4h+t_3y}-t_3e^{t_3h+t_4y}}{t_3e^{t_3h}-t_4e^{t_4h}}\cos[s(cu-x)]ds \tag{58}$$

$$K_{ey1}(u,x,y,p)=\int_0^{+\infty}\frac{e_0}{\kappa_0}[\frac{t_1t_2e^{t_1h+t_2y}-t_1t_2e^{t_2h+t_1y}}{t_1e^{t_1h}-t_2e^{t_2h}}+\frac{t_3t_4e^{t_4h+t_3y}-t_3t_4e^{t_3h+t_4y}}{t_3e^{t_3h}-t_4e^{t_4h}}]\sin[s(cu-x)]ds \tag{59}$$

$$K_{ey2}(u,x,y,p)=\int_0^{+\infty}\frac{t_3t_4e^{t_3h+t_4y}-t_3t_4e^{t_4h+t_3y}}{t_3e^{t_3h}-t_4e^{t_4h}}\sin[s(cu-x)]ds \tag{60}$$

$$K_{dx1}(u,x,y,p)=\int_0^{+\infty}(e_{15}-\kappa_{11}\frac{e_0}{\kappa_0})\frac{t_1e^{t_1h+t_2y}-t_2e^{t_2h+t_1y}}{t_1e^{t_1h}-t_2e^{t_2h}}+\kappa_{11}[\frac{t_3e^{t_3h+t_4y}-t_4e^{t_4h+t_3y}}{t_3e^{t_3h}-t_4e^{t_4h}}]\cos[s(cu-x)]ds \tag{61}$$

$$K_{dx2}(u,x,y,p)=\int_0^{+\infty}\kappa_{11}\frac{t_4e^{t_4h+t_3y}-t_3e^{t_3h+t_4y}}{t_3e^{t_3h}-t_4e^{t_4h}}\cos[s(cu-x)]ds \tag{62}$$

$$K_{dx1}(u,x,y,p)=\int_0^{+\infty}(e_{15}-\kappa_{11}\frac{e_0}{\kappa_0})\frac{t_1t_2e^{t_2h+t_1y}-t_1t_2e^{t_1h+t_2y}}{t_1e^{t_1h}-t_2e^{t_2h}}-\kappa_{11}[\frac{t_3t_4e^{t_3h+t_4y}-t_3t_4e^{t_4h+t_3y}}{t_3e^{t_3h}-t_4e^{t_4h}}]\sin[s(cu-x)]ds \tag{63}$$

$$K_{dx2}(u,x,y,p)=\int_0^{+\infty}-\kappa_{11}\frac{t_3t_4e^{t_4h+t_3y}-t_3t_4e^{t_3h+t_4y}}{t_3e^{t_3h}-t_4e^{t_4h}}\sin[s(cu-x)]ds \tag{64}$$

The solution of electric field strength and electric displacement intensity in the time domain are calculated by Laplace numerical inversion method. Furthermore using Eq. (48), the temperature field of the crack tip is obtained.

4. Numerical Examples and discussions

In the numerical computation, the functionally graded piezoelectric strip layer is assumed to be a non-homogeneous $BaTiO_3$ composite and the material constants of $y=0$ are

$$c_{44}=44Gpa,\quad e_{15}=11.4C/m^2,\quad \kappa_{11}=128.3\times10^{10}C/Vm,\quad \rho=5700Kg/m^3 \tag{65}$$

Here, the fundamental solution of crack under a pair of the equivalent electric shock $-D_0H(t)$ acting on the crack surface is considered strongly, so it assume that $\tau_0=0$.

Fig. 2 show the the temperature field around the crack tip versus the value of time. It is indicated that the effect of time on the temperature field is simple, i.e., when $c/h=1/2,1/3,1/4$ are specified, the temperature field increases drastically as time increases from 0 to 3. However, when time is larger than 3, the temperature field gradually decrease with time, finally, stabilized. It is also observed that the temperature field increases with the c/h increasing.

Fig. 3 depict the variation of the the temperature field around the crack tip versus the non-homogeneity parameter β. When time is small (t<2), the temperature field decreases as β increases; but when time is larger than 2, the temperature field increases drastically as β increases. Meanwhile, it is obviously indicated that when time is larger (t>2), the effect is larger than that when time is small (t<2). The above results show that the crack tip will cause high temperature change under high electric shock load. In this case, the crack tip temperature effect cannot be ignored

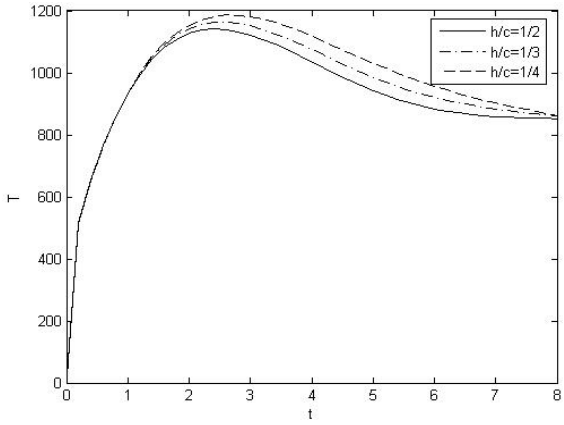

Figure 2. The temperature field around the crack tip versus time（$\beta = 0.5$ $\tau_0 = 0$， $D_0 = 5\times10^4$）

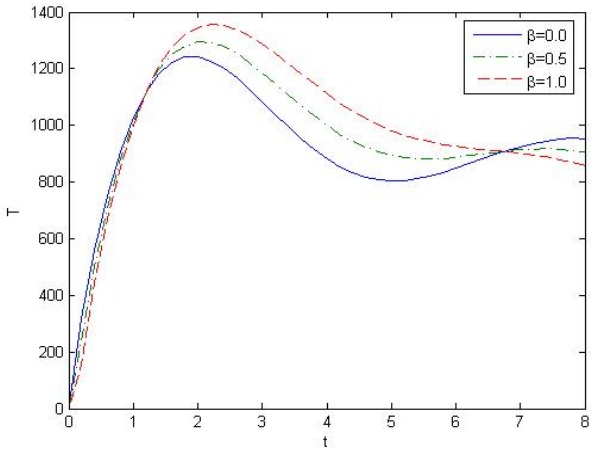

Figure 3. The temperature field around the crack tip versus parameter β （$h = 0.5c$，$\tau_0 = 0$，$D_0 = 5\times10^4$）

5. Conclusions

Research of Bilyk et al [5] revealed that applying high current on the conductor, the temperature of conductor is lager than the temperature just under force load. Then, this paper discusses the heating effect of the crack tip on piezoelectric medium under the high electric shock load. The thermal effect of a mode III crack in a functionally graded strip under the electric shock is investigated. This fracture analysis can be expressed through the superposition of two problems. The first problem refers to the dynamic behaviors of a functionally graded piezoelectric strip with central crack subjected to the electric shock. The second problem means the temperature field by calculating the power of point heat source around the crack tip.

Firstly, without considering the related effect of temperature field, a theoretical model is developed for the dynamic fracture analysis of a functionally graded piezoelectric strip of a finite dimension with central crack subjected to the electric shock. The Laplace transformation and the Fourier transforms are applied to make the transient problem tractable, and singular integral equations is derived with the dislocation density functions of crack as the unknown functions. In particular, the closed-form expressions for the electric field intensity and electric displacements intensity in terms of fundamental functions are derived, which provide a scientific basis for the interpretation of the thermal effect. Secondly, within supposing that it is a heat insulation process in a short time, the thermal effect is calculated. For this problem, thermal field and electromechanical filed is decoupled. So the heat conduction equation contains no electromechanical quantity. Based on that the

temperature of conductors increases when high voltage is applied and that the electric field intensity and electric displacements intensity is obtained in the first solution. The power of point heat source of functionally graded piezoelectric strip is deduced. Therefore, from the time integration of power equations of point heat source, the temperature field around the crack tip is calculated.
It is worth noting that the problem of a cracked functionally graded piezoelectric strip under electric shock is a mix mode crack problem. The first problem is an electromechanical coupling problem. And the second problem is the temperature field around the crack tip, which is the basis problem of mode I or II heat crack analysis.

Acknowledgements

The work is supported by the National Natural Science Foundation of China (10962008; 51061015; 11261045) and Research Fund for the Doctoral Program of Higher Education of China (20116401110002).

References

[1] B.L. Wang, N. Node. Thermally induced fracture of a smart functionally graded composite structure. Theoretical and Applied fracture Mechanics 35 (2001) 93-109.
[2] Y.D. Li, K.Y. Lee. Anti-plane fracture analysis for the weak-discontinuous interface in a non-homogeneous piezoelectric bi-material structure. European Journal of Mechanics A/Solids 28 (2009) 241-247.
[3] S.H. Ding, X. Li. Crack problem for a functionally graded piezoelectric strip bonded to a functionally graded piezoelectric material. Journal of Lanzhou University (Natural Sciences), 44 (2008) 102-107. (in Chinese)
[4] P.P. Shi, S. Sun, X. Li. Arc-shaped interfacial crack in a non-homogeneous electro-elastic hollow cylinder with orthotropic dielectric layer. Meccanica 2012; doi: 10.1007/s11012-012-9610-x
[5] S. B. Bilyk, K. T. Ramesh, T. W. Wright. Numerical modeling of electro-mechanical interactions in mental cylinders, Mechanics of Electro-magnetic Materials and Structures, Eds: J.Y. Yang, G.A. Maugin. (2000)1-16
[6] Li X. Integral equation. Beijing: Science Press; 2008.
[7] Y.D. Hu, X.Z. Bai. Stress field around crack tips in a thin current carrying plate. Journal of Mechanical Strength 24 (2002) 98-100 (in Chinese)

Experimental investigations on the crack growth behavior in graded ferritic martensitic steel

Tobias Stein[1,*], Frank Zeismann[1], Angelika Brückner-Foit[1]

[1] Institute of Materials Engineering, Quality and Reliability Group, University of Kassel, Moenchebergstrasse 3, D-34109 Kassel, Germany
* Corresponding author: stein@uni-kassel.de

Abstract
An experimental approach is presented for characterizing the fatigue behavior of a functionally graded flange shaft. Micro-specimens are defined based on the inhomogeneous phase distribution and microstructure of the flange. Subsequently the experimental setup is described for the investigation of the phase dependent fatigue behavior, and some results are presented. It was found that there is a significant amount of crack retardation in the transition zone in the flange which is located between the soft ferritic phase and the hard martensitic phase. This is verified using a two-sided observation of the propagating crack with two travelling microscopes.
Keywords Graded material, crack growth, fatigue, edge crack

1. Introduction

Functionally graded steel components can play a key-role in the on-going challenges about increase of productivity and saving of resources as they can be tailor-made to the specific requirements in a given application case. However, standard testing and design procedures based on results obtained with homogenous materials may not be sufficient to ensure reliable operation of such components as the interaction of the different regions in the graded component can induce additional damage mechanisms. This is especially true for microstructure-based failure processes such as fatigue failure.

A simple example for a functional gradation is the surface hardening process of a steel component in order to achieve a soft, ductile core and a hard, wear resistant surface. The fatigue behavior of case or surface hardened steel component has investigated (e.g. [1, 2]) recently, and it was found that the failure behavior could not be predicted by just superimposing the results obtained with the constituents in standard tests.

Another, more complex way to produce a functionally graded component is an integrated thermo-mechanical treatment on a steel shaft to form a flange shaft. [3] Such a flange shaft is characterized by a defined local distribution of at least three phases – the soft ferritic-pearlitic base material in an untreated and a deformed state, a hard martensitic phase and a small, mainly bainitic transition zone in between. Under fatigue loading, crack may initiate in the soft phase and propagate towards the hard phase leading to catastrophic failure. In this case, crack initiation and propagation depends not only on the fatigue properties of each phase, but also on their spatial distribution. Obviously, conventional fatigue testing with homogenous specimens will not capture these specific features of the damage accumulation process in a graded component, and may therefore lead to erroneous results. Instead, specimens have to be defined which can directly be cut from the component and contain the phases of interest together with the component specific grading [4, 5].

This paper deals with obtaining valid crack growth data in the flange-shaft mentioned above [3].

The material and the microstructure obtained by the thermo-mechanical forming process are described in the first section. Then the experimental set-up is described which has been developed for obtaining microstructure-dependent crack growth rates. Finally the experimental results are compared with findings of a FE simulation.

2. Material and graded microstructure

The tested material is a low-alloy steel in tempered condition (German designation 51CrV4) with the chemical composition given in Table 1. It has a ferritic-perlitic microstructure and a yield strength of 520 MPa.

Table 1. Chemical composition of 51CrV4

Element	C	Si	Mn	Cr	V	P	S
Weight %	0,47-0,55	≤0,40	0,70-1,10	0,90-1,20	0,10-0,25	≤0,035	≤0,035

An integrated thermo-mechanical forming process, as shown in Fig. 1, was applied to a shaft resulting in a flange shaft with a graded microstructure [3]. First the shaft was heated up above austenitization temperature by induction heating and then put into the molding press to form the flange, which lead to a local martensitic transformation of the original ferritic-perlitic phase.

Figure 1: Integrated thermo-mechanical forming process of the flange shaft [6]

Due to the high natural strain during the forming process a fine grained microstructure is formed, which contains dispersed small defects like inclusions and carbides. The resulting phase distribution is given in the etched micrograph in Fig. 2. It is characterized by the ferritic-perlitic base cold-worked material (grey) in a in the core of the flange shaft and a martensitic phase (dark) at the outside of the flange. The phases are linked by a transition zone (white) of varying width and material properties. For an unambiguously phase identification micro-hardness measurements are used. As shown in Fig. 3, the martensite possesses hardness values above 650 HV (Pos. 1), the transition zone about 450 HV (Pos. 2) and the deformed base material has hardness values below 300 HV (Pos. 1).

Figure 2. Micrograph of the flange shaft, etched

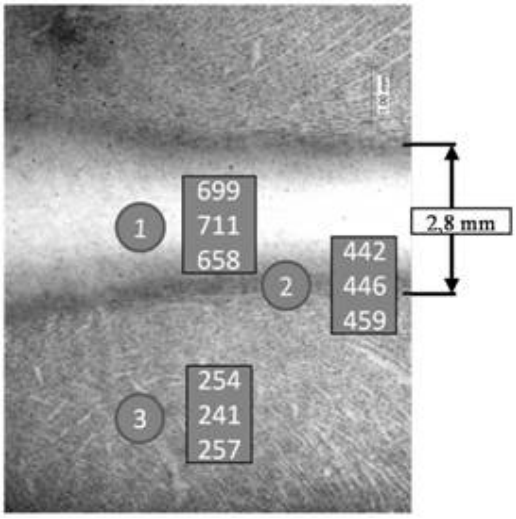

Figure 3. Vickers hardness of the different phases

In order to optimize the local phase distribution and its properties in the flange shaft several pre-heating strategies were developed. Beside the standard flange shaft having room temperature at the start of the forming process four pre-heating temperatures were used for the flange. Therefore the flanges were heated up to 300, 400, 500 or 600°C in a convection oven. Then the local induction heating above the austenitization temperature was carried out before forming. The corresponding phase distribution in the flange shaft for each pre-heating temperature is given in Fig. 4 a-d).

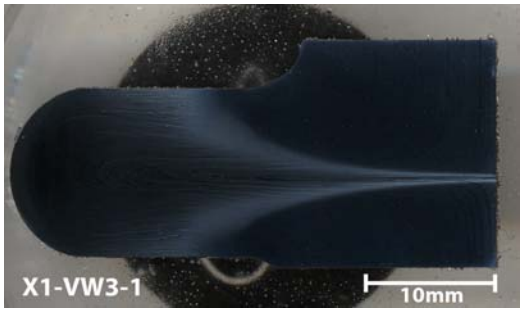

a) pre-heating temperature 300°C

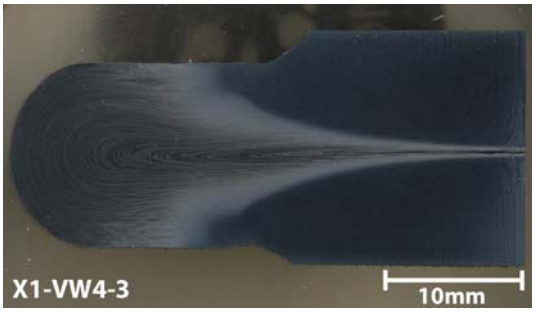

b) pre-heating temperature 400°C

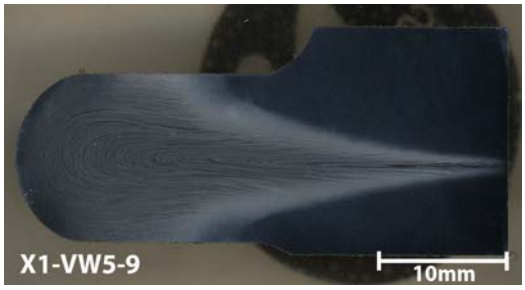

c) pre-heating temperature 500°C

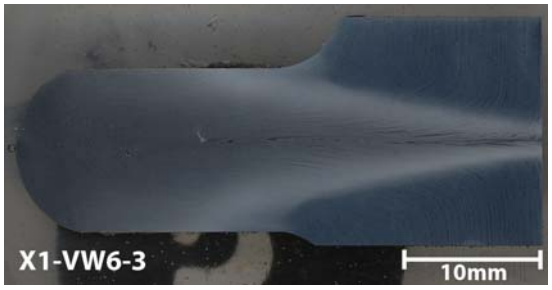

d) pre-heating temperature 600°C

Figure 4. Micrographs of the flange shafts with various pre-heating temperatures, etched

The etched micrographs of the flange shafts, given in Fig. 4 a)-d), reveal that an increasing pre-heating temperature leads to an increasing amount of the transformed phase at the outer part of the flange. The width of the transition zone (white area) increases as well. A second observation of

the micrographs is that the etched micrograph becomes brighter in the transformed phase with an increasing pre-heating temperature. This indicates an increasing amount of bainite in the martensitic zone caused by a lower cooling rate during the phase transformation. Verification of this observation can be given by a micro-hardness indentation only, which is shown in Fig. 5 a-b).

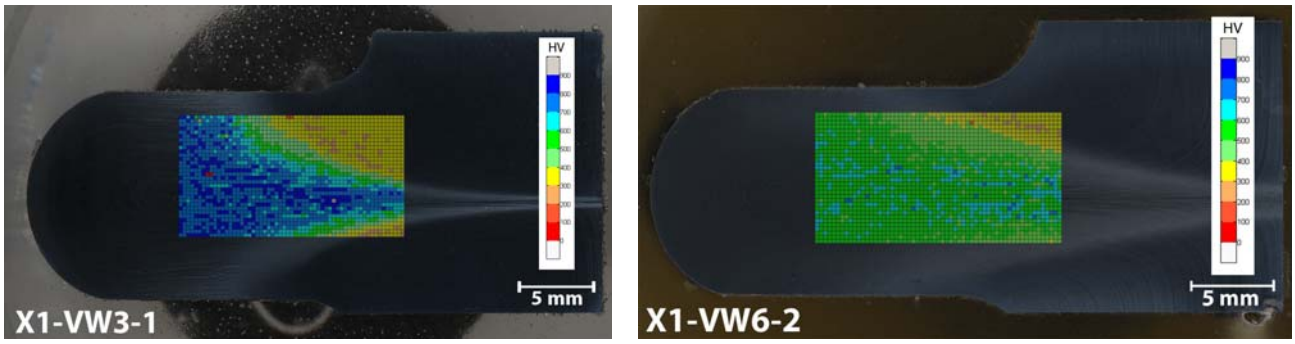

a) pre-heating temperature 300°C b) pre-heating temperature 600°C

Figure 5. Micro hardness indentations on 300°C and 600°C pre-heated flange shafts

Pre-heating the flange shaft with a temperature of 600°C decreases the hardness gradient in the flange as expected. As presented in Fig. 5 b), the difference in the Vickers hardness between transition zone and the martensitic zone becomes marginal compared to a 300°C pre-heated flange shaft, given in Fig. 5 a).

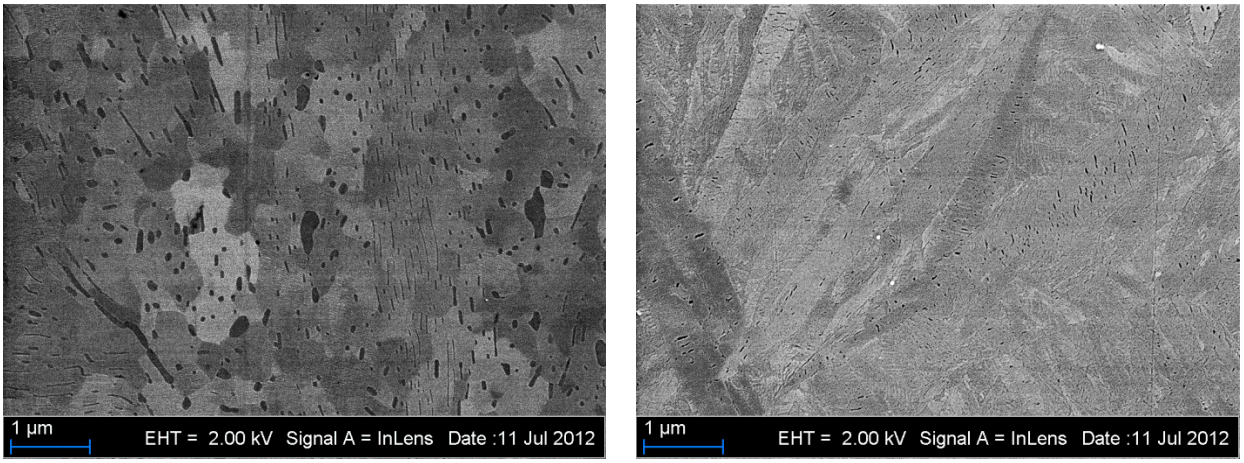

c) deformed base material b) martensite

Figure 6. SEM-images from the microstructure of a 500°C pre-heated flange-shaft

Due to the high degree of deformation combined with the high temperature during the forming process a very fine grained and complex microstructure exists in the flange shaft. SEM micrographs show that the grain size is of the order of 1 micron, see Fig. 6 for a 500°C pre-heated flange shaft. The deformed base material, shown in Fig. 6 a), still has its ferritic-pearlitic microstructure, but the original lamellar structure of the pearlite is mainly destroyed. The former cementite lamellae now mostly have a globular shape while the remaining ones are highly deformed. The martensite, shown in Fig. 6 b), is characterized by small carbides in the martensitic needles. It has been observed, that with an increasing pre-heating temperature the amount of carbides increases as well. This observation may support the assumption of a hardness decreasing tempering effect which is caused by significantly slower cooling rate after the phase transformation [7].

Both the increase of the transition zone width and the decrease of the hardness in the transformed phase are desired effects of the pre-heating strategy, but will lead to a variation in the fatigue behavior of the flange shaft. So, a comparison of the fatigue crack propagation in the flange shafts for all four pre-heating temperatures is necessary.

3. Experimental set-up

For analyzing the fatigue behavior of the transition zone micro-specimens were cut out from the flange using high precision spark erosion. A dog-bone shaped micro-specimen (32.5 mm long and about 2.4 mm thick), shown in Fig. 8, was developed with the purpose of performing microstructure specific fatigue tests. As shown in Fig. 8, the center of the specimen consists of martensite (dark) while the white areas mark the transition zone and the deformed base material is in grey again. The preparation of the specimens consisted of mechanical polishing and mechanical-chemical polishing with OPS in the final step.

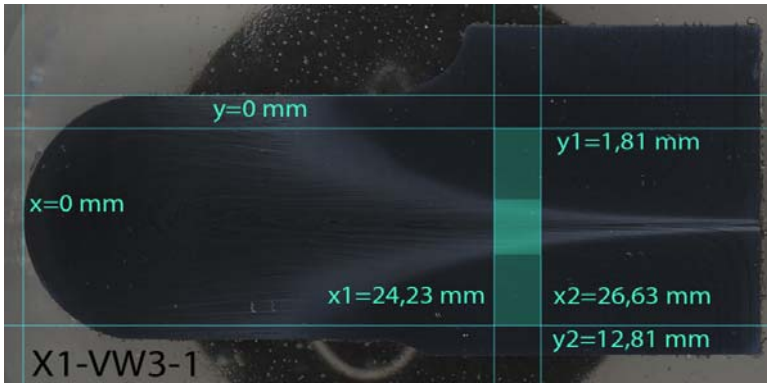

Figure 7. Micrograph taken from a flange shaft to determine the exact specimen position, etched

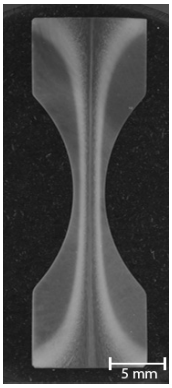

Figure 8. Micro specimen, etched

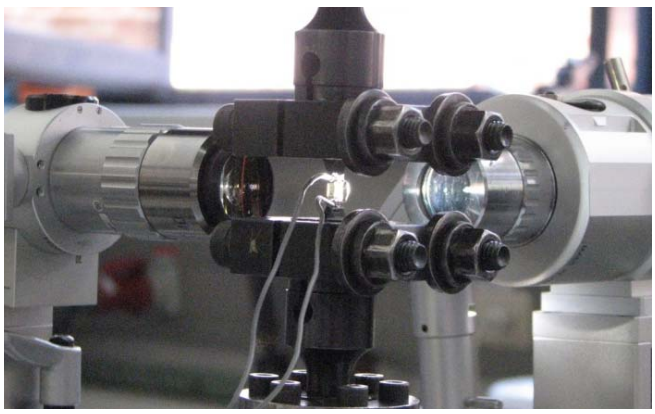

Figure 9. Experimental setup with two long distances microscopes in front of the micro-specimen

All fatigue tests were carried out as uniaxial tests at room temperature on a servo-hydraulic testing machine. The stress ratio was set to R = -1 (i.e. fully reversed) with 500 MPa were chosen as load amplitude. Tests with smooth specimens were monitored using one travelling long distance

microscope, whereas two long distance microscopes sitting on motorized three-axis stages were mounted on the rig of the fatigue testing machine to observe the fatigue crack growth at the edge-notched micro-specimen in horizontal and vertical direction, as shown in Fig. 9.
The test procedure itself starts with a scan of the unloaded surface of the micro-specimen. Then the micro-specimen is subjected to fatigue loading with a pre-defined number of load cycles and the surface is scanned again. Repeating this procedure allows monitoring the damage accumulation process on the surface of the micro-specimen and determining the local crack growth rates.

4. Results

Under fatigue loading, microcracks were initiated at inclusions in the base material on the surface of smooth specimens. However, these cracks showed only limited crack extension and never caused failure. Instead, one or two edge cracks were initiated in the vicinity of the notch root. A typical example is shown in Figure 10. It can be seen that the crack paths are fairly rough in spite of the fine microstructure and that the averaged crack line is not exactly perpendicular to the loading direction. These effects can be attributed to texture effects in the deformed base material. First of all, the rods used in the forming process possessed a rather pronounced manufacturing texture and showed lines of enhanced chromium content (dark lines in the shaft in Figure 2). These lines are still visible in the flange after the thermo-mechanical forming process. SEM analyses indicated that crack kinking can also be correlated with local bands of pearlite which survived the forming process. Moreover, there are regions in which the grains in the deformed base material are strongly correlated in their crystallographic orientations (e.g. areas highlighted with white dashed lines Figure 11), i.e. the grain structure shown in Figure 6 is replaced by set of subgrains separated by low angle boundaries. A crack passing through such an area is deviated from its original path due to the local anisotropy of the microstructure (yellow dashed line in Figure 11).
The growth rate of crack #1 is depicted in Figure 12. Apparently, the crack was slowed down after it had reached a length of about 1mm, and picked up considerable speed at about 1.3mm. Comparison with Figure 10 indicates that these changes in the crack growth rate may be related to the graded microstructure. This conjecture was verified using micro-hardness indentation along the crack faces as shown in Figure 13. Figure 12 indicates that there is a clear correlation between an increase in the hardness (corresponding to the transition region) and a decrease in the crack growth rate, and that the sudden rise in the crack growth rate occurs at the maximum of the hardness curve (martensite).

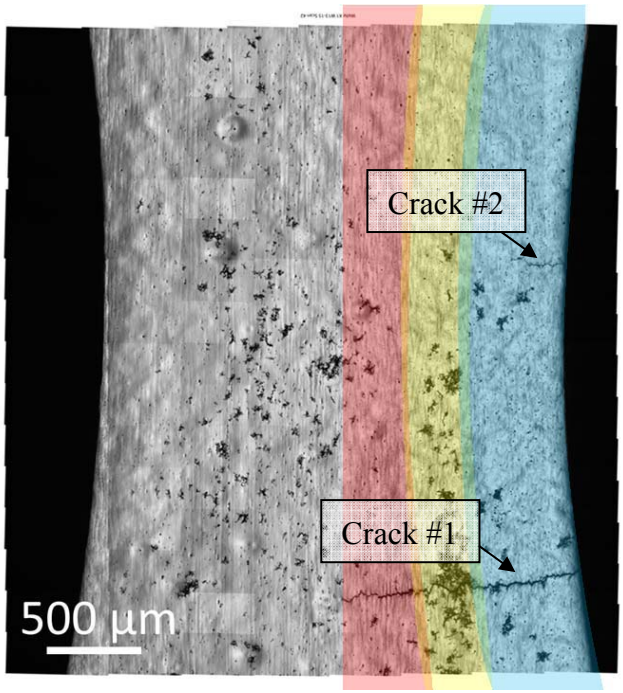

Figure 10. Typical crack paths on the surface of a micro-specimen; phase boundaries are indicated in color

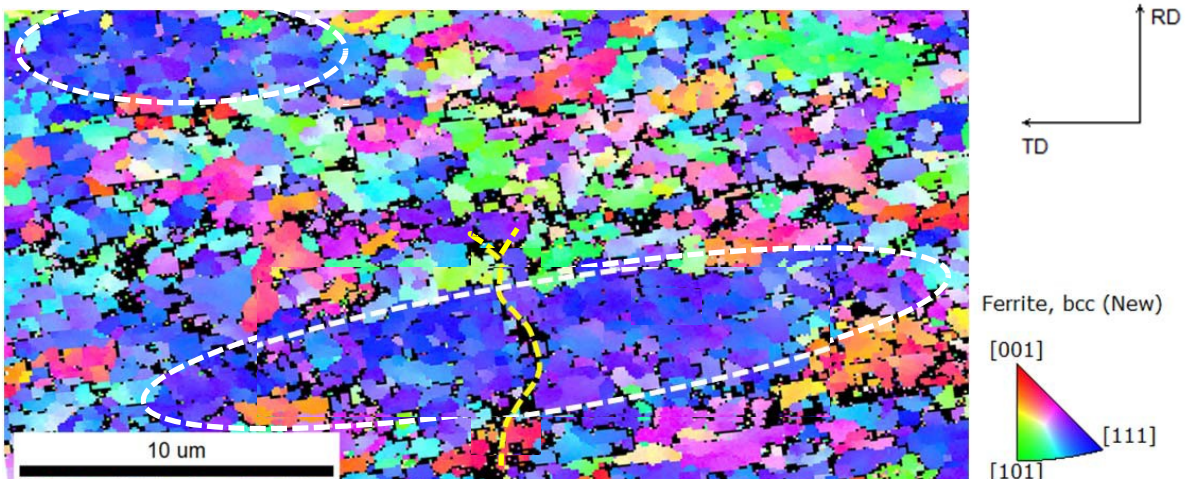

Figure 11. Interaction of crack with areas of local anisotropy

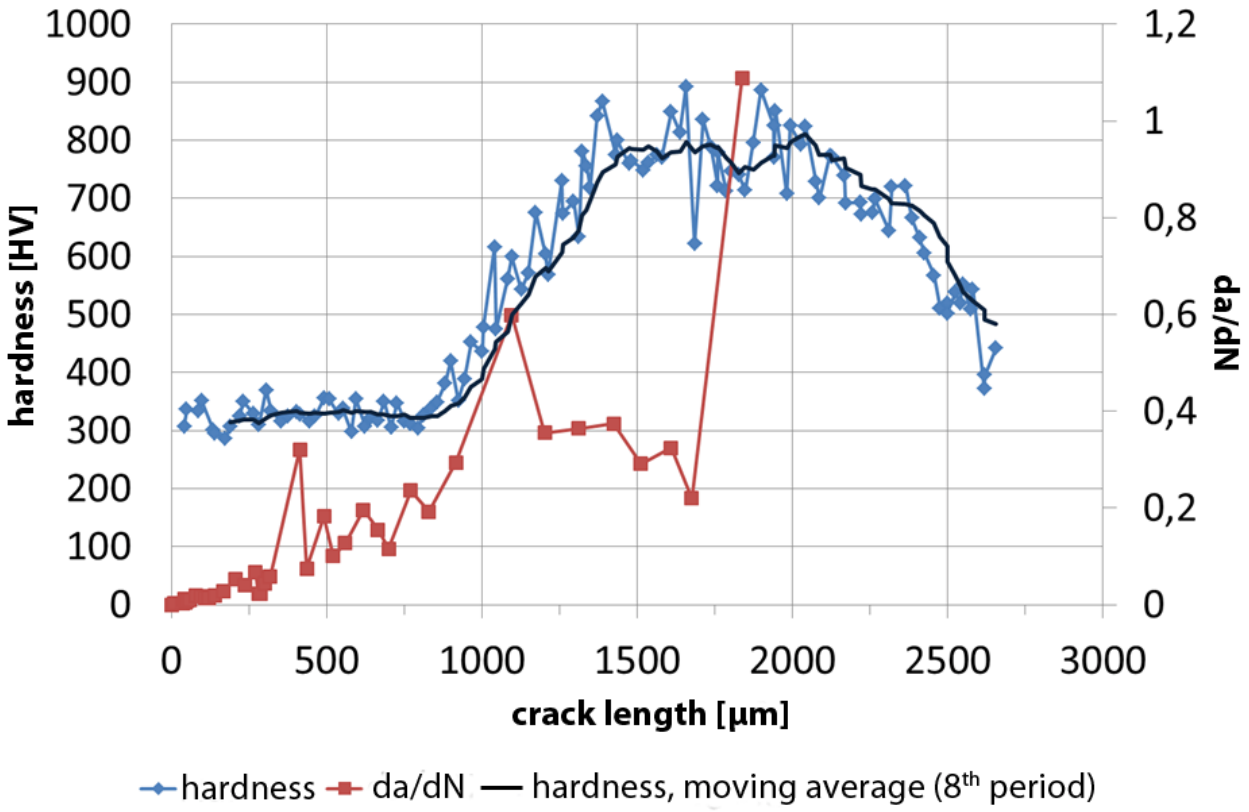

Figure 12. Microstructure dependent growth rate of crack #1

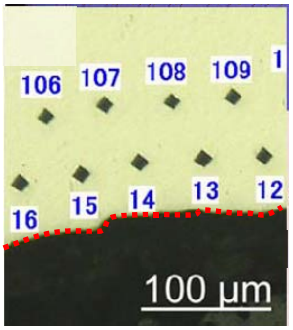

Figure 13. Micro-hardness indentations along section of crack face (dotted red line)

Even though the correlation between the distribution of the phases in the specimen and the acceleration and deceleration of the crack extension process is quite good, it has to be kept in mind that extension of an edge crack is a three-dimensional process, and that conclusions based only on surface observation may be misleading. Therefore a micro-specimen was prepared with an artificial edge notch, and the crack extension from the notch was monitored using the experimental set-up with two travelling microscopes as shown in Figure 9. The initial scans were made in the unloaded state and are given in Fig. 14 a) for the side view (vertical direction) of the micro-specimen and in Fig. 14 b) for the front view (horizontal direction). The fatigue crack initiated at the notch as expected and propagated in both directions. After a total of 45.000 load cycles, which represents approx. 96 % of the lifetime, the fatigue crack has reached a length of 1693.75 µm in the vertical direction (see Fig. 14 c)) and 1002.62 µm in the horizontal direction (see Fig. 14 d)). It seems that

the fatigue crack extends more rapidly in the vertical direction than in the horizontal direction. This effect may be related to an inhomogeneous phase distribution in the specimen. This will be clarified by a phase analysis of the fracture surface which is under way.

a) side view with edge-notch in unloaded state

b) front view with edge-notch in unloaded state

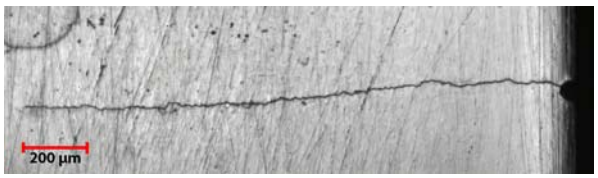

c) side view with fatigue crack after 45.000 load cycles

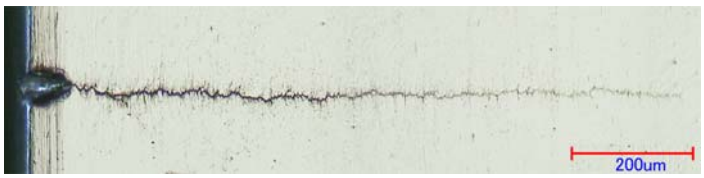

d) front view with fatigue crack after 45.000 load cycles

Figure 14. Data of the test setup gained from the long-distance microscopes with an edge-notched micro-specimen

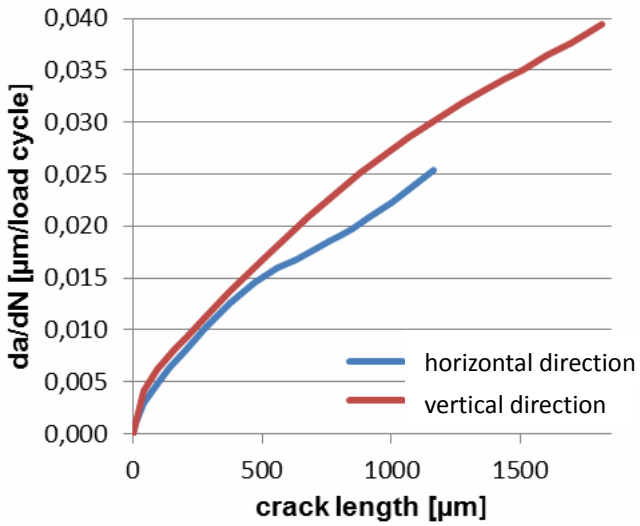

Figure 15. Local crack growth rate of the fatigue crack in horizontal direction (blue) and vertical direction (red)

5. Summary and outlook

The fatigue damage accumulation process in a flange shaft made by a thermo-mechanical forming is dominated by single cracks which are initiated in the soft ferritic phase. Even though in those cases where these cracks are very small they do not propagate as microscopically small cracks as the microstructure is greatly refined due to the forming process with grain sizes of the order of 1 micron or even less. However there is a strong influence of the texture of the material on the crack path leading to pronounced deviations from straightforward mode-I crack propagation. A significant retardation in the crack growth rate was observed when the crack crosses the transition zone between the ferritic and the martensitic phases. This effect will be studied by using different

pre-heating strategies which greatly influence the phase distribution in the flange shaft.

Acknowledgements

The study is carried out by the transregional collaborative research centre SFB/TR TRR 30, which is kindly supported by the German Research Foundation (DFG).

References

[1] D. Firrao, P. Matteis, P. Russo Spena, G.M.M. Mortarino, Fatigue crack growth in inhomogeneous steel components, Int. J. of Fatigue (2010) 864-869.

[2] L. T. Sandor, I. Politori, C.S. Goncalves, A.Y. Uehara, C.V. Leal, M. Sato, I. Ferreira, Fatigue Crack Propagation in Nine Steels, Type SAE 43XX, from 0.20 to 1.00 %, for the Simulation of the Fatigue Behavior in a Carburized Layer of the SAE 4320, Proc. Eng. 2 (2010) 735-742.

[3] K. Steinhoff, U. Weidig, N.Saba, Investigation of Plastic Forming Under the Influence of Locally and Temporally Variable Temperature and Stress States, in: K. Steinhoff, H.J. Maier, D. Biermann (Eds.), Functionally Graded Materials in Industrial Production, Verlag Wissenschaftliche Skripten, Auerbach, Germany, 2009, pp. 35-52.

[4] M. Besel, A. Brueckner-Foit, Surface damage evolution of engineering steel, Fatigue & Fracture of Engineering Materials Structures 31 (2008) 885-891.

[5] A. Brueckner-Foit, F. Zeismann, B. Bode, Y. Xue, Fatigue cracks in a thermal-mechanically processed high-strength steel, Proc. Eng. 2 (2010) 2075-2084.

[6] N. Saba, Untersuchung der plastischen Formgebung unter Einfluss örtlich und zeitlich veränderlicher Temperatur- und Spannungszustände, Dissertation, Kassel University Press, Kassel, Germany (2011).

[7] H. Oettel, H. Schumann, Metallografie - mit einer Einführung in die Keramographie, 15th ed. Wiley-VCH-Verlag, Weinheim, Germany, 2011.

A PARTIALLY PERMEABLE MIXED-MODE CRACK EMBEDDED IN A FUNCTIONALLY GRADED MAGNETO ELECTRO ELASTIC LAYER

M. Rekik[1], S. El-Borgi[1,2*] and Z. Ounaies[3]
[1]*Applied Mechanics and Systems Research Laboratory, Tunisia Polytechnic School, University of Carthage, B.P. 743, La Marsa 2078, Tunisia*
[2]*Texas A&M University at Qatar, Engineering Building, Mechanical Engineering Program, PO. Box 23874 Education City, Doha, Qatar*
[3]*Department of Mechanical Engineering, The Pennsylvania State University, 157B Hammond Building, University Park, PA 16802, USA*

mongi.rekik@hotmail.com, *sami.el_borgi@qatar.tamu.edu*, *zxo100@engr.psu.edu*

Abstract

This ~~work~~ paper considers the problem of a partially permeable mixed-mode crack embedded in a graded magneto electro elastic layer subjected to magneto electro mechanical loads. The medium is graded in the direction orthogonal to the crack plane and is modeled as a non homogeneous medium with anisotropic constitutive laws. Using Fourier transform, the resulting magneto electro elasticity equations are converted analytically into singular integral equations which are then solved numerically to yield the crack-tip mode I and II stress, electric displacement and magnetic induction intensity factors. The main objective of this work is to study the influence of material non homogeneity, crack position and magneto electric permeabilities on the fields' intensity factors for the purpose of gaining better understanding on the behavior of fractured graded magneto electro elastic layers. Results showed that fields' intensity factors increase with nonhomogeneity, and decrease with magnetic and electric permeabilities, and as the crack become closer to the layer's center.

Introduction

Smart structures possessing the ability of magneto electro mechanical energy conversion have found increasing application in several engineering fields such as magnetic field probes, electric packaging, acoustic, hydrophones, medical ultrasonic imaging, microwave electronics, optoelectronics, electronic instrumentation, transducers, sensors and actuators. Research has focused on the use of Functionally Graded Magneto Electro Elastic Materials (FGMEEM) in smart structures to improve their performance. But, the manufacturing of FGMEEMs may lead to cracks that can eventually propagate and cause premature failure. Therefore, it is of a great importance to study the fracture behavior of magneto electro elastic composites.

A number of authors considered FGMEEM crack problems. Ma et al (2007) studied the mode III crack problem in a functionally graded magneto electro elastic strip accounting for ideal crack surface magneto electric permeability. Ma et al (2009) considered the problem of a surface crack in a functionally graded magneto electro elastic coating homogeneous elastic substrate subjected to anti-plane mechanical and in plane magneto electrical loading for the ideal crack surface magneto electric permeability. Zhou et al (2004) examined the problem of two parallel symmetric permeable cracks in functionally graded materials under anti-plane shear loading. Feng et al (2007) analyzed the dynamic behavior of magneto electrically impermeable cracks in functionally graded magneto electro elastic plates. Feng et al (2006) studied the dynamic problem of a crack embedded in a graded magneto electro elastic strip assuming ideal crack surface permeability. Jun (2007) examined the scattering of harmonic anti-plane shear stress waves by a crack in functionally graded magneto electro elastic materials assuming purely permeable crack surfaces. Zhou et al (2008) solved the mode I crack problem in a FGMEEM infinite medium assuming air permeability within the crack. Li et al (2008) considered the anti-plane problem of a permeable crack intersecting the interface between two FGMEEM layers. Li et al (2008) analyzed the anti-plane problem of a crack in the interface of tow symmetrically bonded FGMEEM assuming a linear variation of the magneto electromechanical properties. Guo et al (2009) solved the anti-plane problem of a crack in bonded FGMEEM strip sandwiched between two functionally graded strips assuming ideal magneto electrical permeability on the crack faces. Rekik et al (2012) considered the problem of magneto electrically impermeable crack embedded in a graded infinite medium subjected to magneto electro mechanical loading.

The present work consists of studying the plane problem of a partially magneto electrically permeable crack embedded in a graded magneto electro elastic layer. The applied magneto electro mechanical loading will give rise to coupled fields intensity factors; namely, mode I and II stress, electric

displacement and magnetic induction intensity factors denoted respectively k_1, k_2, k_D and k_B. To the best of the authors' knowledge, this problem was not considered in the open literature to-date.

Problem description and formulation

As shown in Figure 1, the problem under consideration consists of a functionally graded magneto electro elastic layer containing an embedded crack of length *2a* along the *x*-axis. The crack surfaces are assumed to be partial magneto electrically permeable using the magnetic and electric permeability parameters k_m and k_e varying in between 0 and 1 representing the cases of completely impermeable and completely permeable crack surfaces, respectively. Consequently, crack faces are subjected to mechanical tangential and normal tractions $\omega_1(x)$ and $\omega_2(x)$, electric displacement $(1-k_e)E(x)$, and magnetic induction $(1-k_m)B(x)$. The graded layer is modeled as a nonhomogeneous elastic medium with magneto electromechanical properties varying in the depth direction (y-coordinate) as follows:

$$\left(c_{11}, c_{13}, c_{33}, c_{44}\right) = \left(c_{110}, c_{130}, c_{330}, c_{440}\right) \mathrm{e}^{\beta y}, \quad \left(e_{15}, e_{31}, e_{33}\right) = \left(e_{150}, e_{310}, e_{330}\right) \mathrm{e}^{\beta y}, \quad \forall y, \qquad (1a,b)$$

$$\left(f_{15}, f_{31}, f_{33}\right) = \left(f_{150}, f_{310}, f_{330}\right) \mathrm{e}^{\beta y}, \quad \left(\varepsilon_{11}, \varepsilon_{33}\right) = \left(\varepsilon_{110}, \varepsilon_{330}\right) \mathrm{e}^{\beta y}, \quad \forall y, \qquad (1c,d)$$

$$\left(g_{11}, g_{33}\right) = \left(g_{110}, g_{330}\right) \mathrm{e}^{\beta y}, \quad \left(\mu_{11}, \mu_{33}\right) = \left(\mu_{110}, \mu_{330}\right) \mathrm{e}^{\beta y}, \quad \forall y. \qquad (1e,f)$$

where $c_{ij0}, e_{ij0}, f_{ij0}, \varepsilon_{ij0}, g_{ij0}, \mu_{ij0}$ are the value of the magneto electromechanical coefficient in the FGMEEM layer along the axis $y = 0$ and β is the nonhomogeneity parameter controlling the variation of these coefficient in the graded layer.

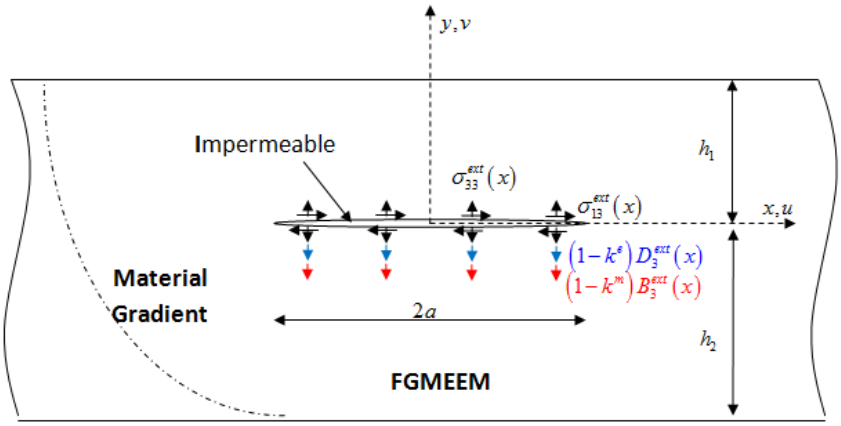

Figure 1. Geometry and loading of the crack problem

Neglecting body forces and local electric charge, assuming small deformations and considering linear constitutive laws, the basic equations consisting of equilibrium equations and Gauss's laws for electricity and magnetism can be combined, resulting in the following governing magneto electro elasticity equations:

$$c_{11}\frac{\partial^2 u}{\partial x^2} + c_{33}\left(\frac{\partial^2 u}{\partial y^2} + \beta\frac{\partial u}{\partial y}\right) + c_{12}\frac{\partial^2 v}{\partial x \partial y} + c_{33}\left(\frac{\partial^2 v}{\partial x \partial y} + \beta\frac{\partial v}{\partial x}\right) + e_{21}\frac{\partial^2 \phi}{\partial x \partial y} + e_{13}\left(\frac{\partial^2 \phi}{\partial x \partial y} + \beta\frac{\partial \phi}{\partial x}\right) + f_{21}\frac{\partial^2 \psi}{\partial x \partial y} + f_{13}\left(\frac{\partial^2 \psi}{\partial x \partial y} + \beta\frac{\partial \psi}{\partial x}\right) = 0, \qquad (2a)$$

$$c_{33}\frac{\partial^2 u}{\partial x \partial y} + c_{12}\left(\frac{\partial^2 u}{\partial x \partial y} + \beta\frac{\partial u}{\partial x}\right) + c_{33}\frac{\partial^2 v}{\partial x^2} + c_{22}\left(\frac{\partial^2 v}{\partial y^2} + \beta\frac{\partial v}{\partial y}\right) + e_{13}\frac{\partial^2 \phi}{\partial x^2} + e_{22}\left(\frac{\partial^2 \phi}{\partial y^2} + \beta\frac{\partial \phi}{\partial y}\right) + f_{13}\frac{\partial^2 \psi}{\partial x^2} + f_{22}\left(\frac{\partial^2 \psi}{\partial y^2} + \beta\frac{\partial \psi}{\partial y}\right) = 0, \qquad (2b)$$

$$e_{13}\frac{\partial^2 u}{\partial x \partial y} + e_{21}\left(\frac{\partial^2 u}{\partial x \partial y} + \beta\frac{\partial u}{\partial x}\right) + e_{13}\frac{\partial^2 v}{\partial x^2} + e_{22}\left(\frac{\partial^2 v}{\partial y^2} + \beta\frac{\partial v}{\partial y}\right) - \varepsilon_{11}\frac{\partial^2 \phi}{\partial x^2} - \varepsilon_{22}\left(\frac{\partial^2 \phi}{\partial y^2} + \beta\frac{\partial \phi}{\partial y}\right) - g_{11}\frac{\partial^2 \psi}{\partial x^2} - g_{22}\left(\frac{\partial^2 \psi}{\partial y^2} + \beta\frac{\partial \psi}{\partial y}\right) = 0, \qquad (2c)$$

$$f_{13}\frac{\partial^2 u}{\partial x\partial y}+f_{21}\left(\frac{\partial^2 u}{\partial x\partial y}+\beta\frac{\partial u}{\partial x}\right)+f_{13}\frac{\partial^2 v}{\partial x^2}+f_{22}\left(\frac{\partial^2 v}{\partial y^2}+\beta\frac{\partial v}{\partial y}\right)-g_{11}\frac{\partial^2\phi}{\partial x^2}-g_{22}\left(\frac{\partial^2\phi}{\partial y^2}+\beta\frac{\partial\phi}{\partial y}\right)-\mu_{11}\frac{\partial^2\psi}{\partial x^2}-\mu_{22}\left(\frac{\partial^2\psi}{\partial y^2}+\beta\frac{\partial\psi}{\partial y}\right)=0, \qquad (2d)$$

where u and v are, respectively, the x and y components of the mechanical displacement vector, ϕ and ψ are, respectively, the electric and magnetic potentials.

The above magneto electro elasticity equations are subjected to the following boundary conditions:

$$\sigma_{13}\left(x,0^+\right)=\sigma_{13}^{ext}\left(x\right), \qquad \sigma_{33}\left(x,0^+\right)=\sigma_{33}^{ext}\left(x\right), \qquad \left|x\right|\le a, \qquad (3a,b)$$

$$D_3\left(x,0^+\right)=\left(1-k^e\right)D_3^{ext}\left(x\right), \qquad B_3\left(x,0^+\right)=\left(1-k^m\right)B_3^{ext}\left(x\right), \qquad \left|x\right|\le a, \qquad (3c,d)$$

$$\sigma_{13}\left(x,0^+\right)=\sigma_{13}\left(x,0^-\right), \qquad \sigma_{33}\left(x,0^+\right)=\sigma_{33}\left(x,0^-\right), \qquad \forall x, \qquad (4a,b)$$

$$D_3\left(x,0^+\right)=D_3\left(x,0^-\right), \qquad B_3\left(x,0^+\right)=B_3\left(x,0^-\right), \qquad \forall x, \qquad (4c,d)$$

$$u\left(x,0^+\right)=u\left(x,0^-\right), \qquad v\left(x,0^+\right)=v\left(x,0^-\right), \qquad \left|x\right|\ge a, \qquad (5a,b)$$

$$\phi\left(x,0^+\right)=\phi\left(x,0^-\right), \qquad \psi\left(x,0^+\right)=\psi\left(x,0^-\right), \qquad \left|x\right|\ge a, \qquad (5c,d)$$

$$\sigma_{13}\left(x,h_1\right)=0, \qquad \sigma_{33}\left(x,h_1\right)=0, \qquad \forall x, \qquad (6a,b)$$

$$D_3\left(x,h_1\right)=0, \qquad B_3\left(x,h_1\right)=0, \qquad \forall x, \qquad (6c,d)$$

$$\sigma_{13}\left(x,-h_2\right)=0, \qquad \sigma_{33}\left(x,-h_2\right)=0, \qquad \forall x, \qquad (7a,b)$$

$$D_3\left(x,-h_2\right)=0, \qquad B_3\left(x,-h_2\right)=0, \qquad \forall x, \qquad (7c,d)$$

Eqs. (3a-d) describe the applied magneto electro mechanical loadings on the crack faces. Eqs. (4a-d) represent the continuity of stresses, electric displacement and magnetic fields along the crack plane. Eqs. (5a-d) describe the continuity of the mechanical displacement and the magnetic and electric potentials outside the crack. Eqs. (6a-d) and (7a-d) represent the free layer' surfaces boundary conditions.

Singular integral equations and their solutions

The magneto electro elasticity equations (2a-d) are solved using Fourier transform to yield the mechanical displacement and electric and magnetic potentials in the composite medium. The density functions which represent the discontinuity of the mechanical displacement, electric and magnetic fields across the crack are now introduced

$$\varphi_1\left(x\right)=\frac{\partial\left(u^+-u^-\right)}{\partial x}, \qquad \varphi_2\left(x\right)=\frac{\partial\left(v^+-v^-\right)}{\partial x}, \qquad (8a,b)$$

$$\varphi_3\left(x\right)=\frac{\partial\left(\phi^+-\phi^-\right)}{\partial x}, \qquad \varphi_4\left(x\right)=\frac{\partial\left(\psi^+-\psi^-\right)}{\partial x}. \qquad (8c,d)$$

Applying the boundary conditions and after a lengthy analysis, we obtain four coupled singular integral equations in which the unknowns are the density functions $\varphi_1,\varphi_2,\varphi_3$ and φ_4. After extracting the Cauchy and logarithmic singularities from the kernels, the four equations take the following form:

$$\frac{k_{11}^0}{\pi}\int_{-a}^{a}\frac{1}{t-x}\omega_u\left(t\right)dt+\frac{1}{\pi}\int_{-a}^{a}k_{11}\left(t,x\right)\omega_u\left(t\right)dt-\frac{k_{12}^1}{\pi}\int_{-a}^{a}\beta\ln\left|t-x\right|\omega_v\left(t\right)dt+$$
$$\frac{1}{\pi}\int_{-a}^{a}k_{12}\left(t,x\right)\omega_v\left(t\right)dt-\frac{k_{13}^1}{\pi}\int_{-a}^{a}\beta\ln\left|t-x\right|\omega_\phi\left(t\right)dt+\frac{1}{\pi}\int_{-a}^{a}k_{13}\left(t,x\right)\omega_\phi\left(t\right)dt-$$
$$\frac{k_{14}^1}{\pi}\int_{-a}^{a}\beta\ln\left|t-x\right|\omega_\psi\left(t\right)dt+\frac{1}{\pi}\int_{-a}^{a}k_{14}\left(t,x\right)\omega_\psi\left(t\right)dt=\sigma_{13}^{ext}\left(x\right), \qquad \left|x\right|\le a, \qquad (9a)$$

$$-\frac{k_{21}^{1}}{\pi}\int_{-a}^{a}\beta\ln|t-x|\,\omega_u(t)\,dt+\frac{1}{\pi}\int_{-a}^{a}k_{21}(t,x)\,\omega_u(t)\,dt+\frac{k_{22}^{0}}{\pi}\int_{-a}^{a}\frac{1}{t-x}\omega_v(t)\,dt+$$
$$\frac{1}{\pi}\int_{-a}^{a}k_{22}(t,x)\,\omega_v(t)\,dt+\frac{k_{23}^{0}}{\pi}\int_{-a}^{a}\frac{1}{t-x}\omega_\phi(t)\,dt+\frac{1}{\pi}\int_{-a}^{a}k_{23}(t,x)\,\omega_\phi(t)\,dt+$$
$$\frac{k_{24}^{0}}{\pi}\int_{-a}^{a}\frac{1}{t-x}\omega_\psi(t)\,dt+\frac{1}{\pi}\int_{-a}^{a}k_{24}(t,x)\,\omega_\psi(t)\,dt=\sigma_{33}^{ext}(x),\qquad |x|\le a, \tag{9b}$$

$$-\frac{k_{31}^{1}}{\pi}\int_{-a}^{a}\beta\ln|t-x|\,\omega_u(t)\,dt+\frac{1}{\pi}\int_{-a}^{a}k_{31}(t,x)\,\omega_u(t)\,dt+\frac{k_{32}^{0}}{\pi}\int_{-a}^{a}\frac{1}{t-x}\omega_v(t)\,dt+$$
$$\frac{1}{\pi}\int_{-a}^{a}k_{32}(t,x)\,\omega_v(t)\,dt+\frac{k_{33}^{0}}{\pi}\int_{-a}^{a}\frac{1}{t-x}\omega_\phi(t)\,dt+\frac{1}{\pi}\int_{-a}^{a}k_{33}(t,x)\,\omega_\phi(t)\,dt+$$
$$\frac{k_{34}^{0}}{\pi}\int_{-a}^{a}\frac{1}{t-x}\omega_\psi(t)\,dt+\frac{1}{\pi}\int_{-a}^{a}k_{34}(t,x)\,\omega_\psi(t)\,dt=\left(1-k^{e}\right)D_3^{ext}(x),\qquad |x|\le a, \tag{9c}$$

$$-\frac{k_{41}^{1}}{\pi}\int_{-a}^{a}\beta\ln|t-x|\,\omega_u(t)\,dt+\frac{1}{\pi}\int_{-a}^{a}k_{41}(t,x)\,\omega_u(t)\,dt+\frac{k_{42}^{0}}{\pi}\int_{-a}^{a}\frac{1}{t-x}\omega_v(t)\,dt+$$
$$\frac{1}{\pi}\int_{-a}^{a}k_{42}(t,x)\,\omega_v(t)\,dt+\frac{k_{43}^{0}}{\pi}\int_{-a}^{a}\frac{1}{t-x}\omega_\phi(t)\,dt+\frac{1}{\pi}\int_{-a}^{a}k_{43}(t,x)\,\omega_\phi(t)\,dt+$$
$$\frac{k_{44}^{0}}{\pi}\int_{-a}^{a}\frac{1}{t-x}\omega_\psi(t)\,dt+\frac{1}{\pi}\int_{-a}^{a}k_{44}(t,x)\,\omega_\psi(t)\,dt=\left(1-k^{m}\right)B_3^{ext}(x),\qquad |x|\le a, \tag{9d}$$

where the functions $k_{ij}(t,x)$, where $i,j=1...4$, are known continuous and bounded kernels that depend on the nonhomogeneity parameter β.

The solution of (9a-d) subject to the single-valuedness conditions may be expressed as $\varphi_i(t)=w(t)\vartheta_i(t)$, $(i=1..4)$. In this solution, $w(t)=1/\sqrt{1-t^2}$ is the weight function which is obtained from the nature of the singularity at the crack tips and which is associated with the Chebyshev polynomial of the first kind $T_n(t)=\cos(n\arccos(t))$. The functions $\vartheta_i(t)$, $(i=1..4)$ are continuous and bounded functions in the interval $[-1,1]$ which may be expressed as truncated series of Chebyshev polynomial of the first kind. Using a suitable collocation method, a linear algebraic system of the unknown coefficients of the density functions is obtained. As a result, the stress intensity factors, the electric displacement intensity factor and the magnetic induction intensity factor can be expressed as:

$$k_1(1)=-\sum_{n=1}^{N}\left(k_{22}^{0}\tilde{b}_n+k_{23}^{0}\tilde{c}_n+k_{24}^{0}\tilde{d}_n\right),\qquad k_1(-1)=-\sum_{n=1}^{N}(-1)^n\left(k_{22}^{0}\tilde{b}_n+k_{23}^{0}\tilde{c}_n+k_{24}^{0}\tilde{d}_n\right), \tag{10a,b}$$

$$k_2(1)=-k_{11}^{0}\sum_{n=1}^{N}\tilde{a}_n,\qquad k_2(-1)=-k_{11}^{0}\sum_{n=1}^{N}(-1)^n\tilde{a}_n, \tag{10c,d}$$

$$k_D(-1)=-\sum_{n=1}^{N}\left(k_{32}^{0}\tilde{b}_n+k_{33}^{0}\tilde{c}_n+k_{34}^{0}\tilde{d}_n\right),\qquad k_D(-1)=-\sum_{n=1}^{N}(-1)^n\left(k_{32}^{0}\tilde{b}_n+k_{33}^{0}\tilde{c}_n+k_{34}^{0}\tilde{d}_n\right), \tag{10e,f}$$

$$k_B(-1)=-\sum_{n=1}^{N}\left(k_{42}^{0}\tilde{b}_n+k_{43}^{0}\tilde{c}_n+k_{44}^{0}\tilde{d}_n\right),\qquad k_B(-1)=-\sum_{n=1}^{N}(-1)^n\left(k_{42}^{0}\tilde{b}_n+k_{43}^{0}\tilde{c}_n+k_{44}^{0}\tilde{d}_n\right). \tag{10g,h}$$

Results and discussion

The formulation using singular integral equations to determine the stress intensity factors of cracked functionally graded magneto electro elastic materials was established. For validation, the results for the case of a sufficiently thick layer, were compared to those of infinite medium (Rekik et al 2012) and a good agreement was obtained (Fig. 2).

Then, a number of simulations, for different magneto electro mechanical load cases, were performed by varying the nonhomogeneity parameter, crack position, crack length and permeability parameters. The considered material is a bimorph composed of the Barium Titanium Oxide, BaTiO3 and the Cobalt Iron Oxide, CoFe2O4.

Fig. 3 illustrates the effect of varying the nonhomogeneity parameter βa on the fields' intensity factors for normal tractions, tangential tractions, magnetic and electric loadings in case of a central crack as large as the layer thickness and electromagnetic permeability of 25%. For each loading case, the corresponding field''s intensity factors showss lower sensibility to material's nonhomogeneity while remaining fields' intensity factors increase ~~monotonously~~monotonically.

Fig. 4 illustrates the effect of varying the crack position on the fields' intensity factors for the same loading cases in the case of a crack as large as the layer thickness and electromagnetic permeability of 25%. In case of normal traction, electric or magnetic loadings, k_1, k_B and k_D show parabolic variation with crack position while k_2 varies oddly. Similarly, in case of tangential traction loading, k_2 varies ~~parbolically~~parabolically while the k_1, k_B and k_D vary oddly.

Fig. 5 illustrates the effect of varying magneto electric permeabilities parameter in case of a central crack as large as the layer thickness. Fields' intensity factors vary linearly with increasing impermeability.

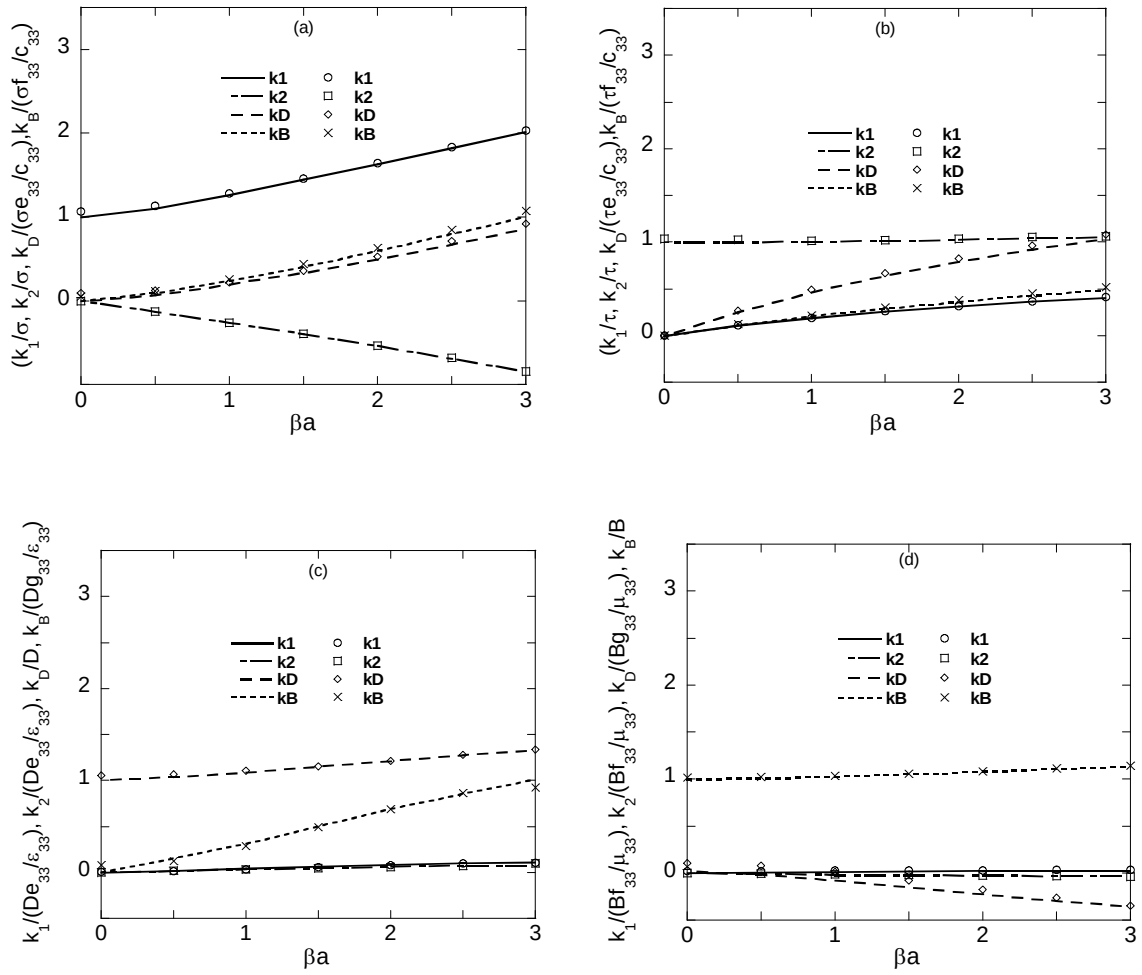

Figure 2: Comparison of normalized fields' intensity factors (markers) with those published by Rekik et al (2012) (continuous lines) for the case of a central crack, magneto electrically impermeable, embedded in an FGMEEM layer four times as thick as the crack length, subjected to uniform normal tractions (a), tangential tractions (b), electric displacement (c), and magnetic induction (d)

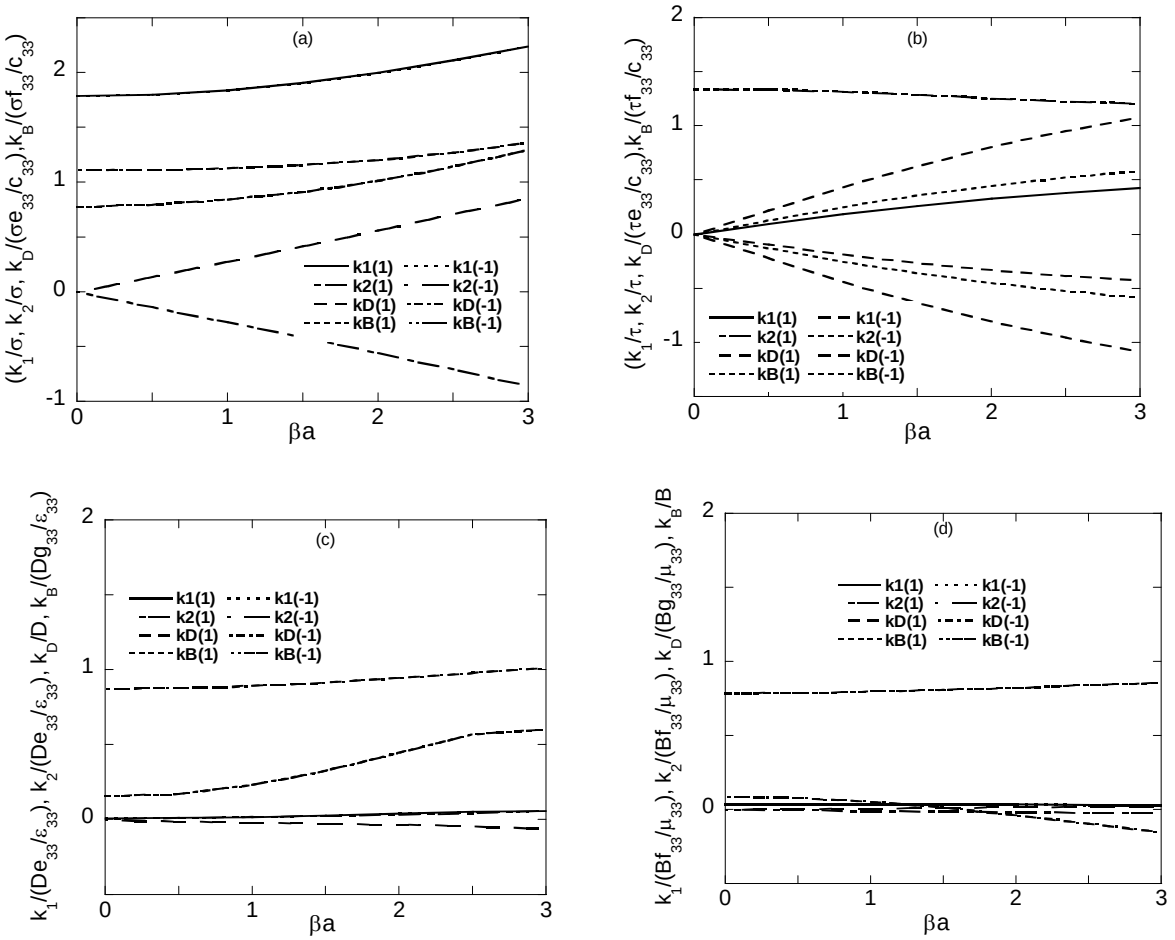

Figure 3: Effect of the non homogeneity parameter βa on the normalized fields' intensity factors under constant normal (a) and tangential (b) crack surface tractions in addition to constant electric displacement (c) and magnetic induction (d) in the case of central crack with $h_1 = h_2 = a$, and $k^e = k^m = 0.25$.

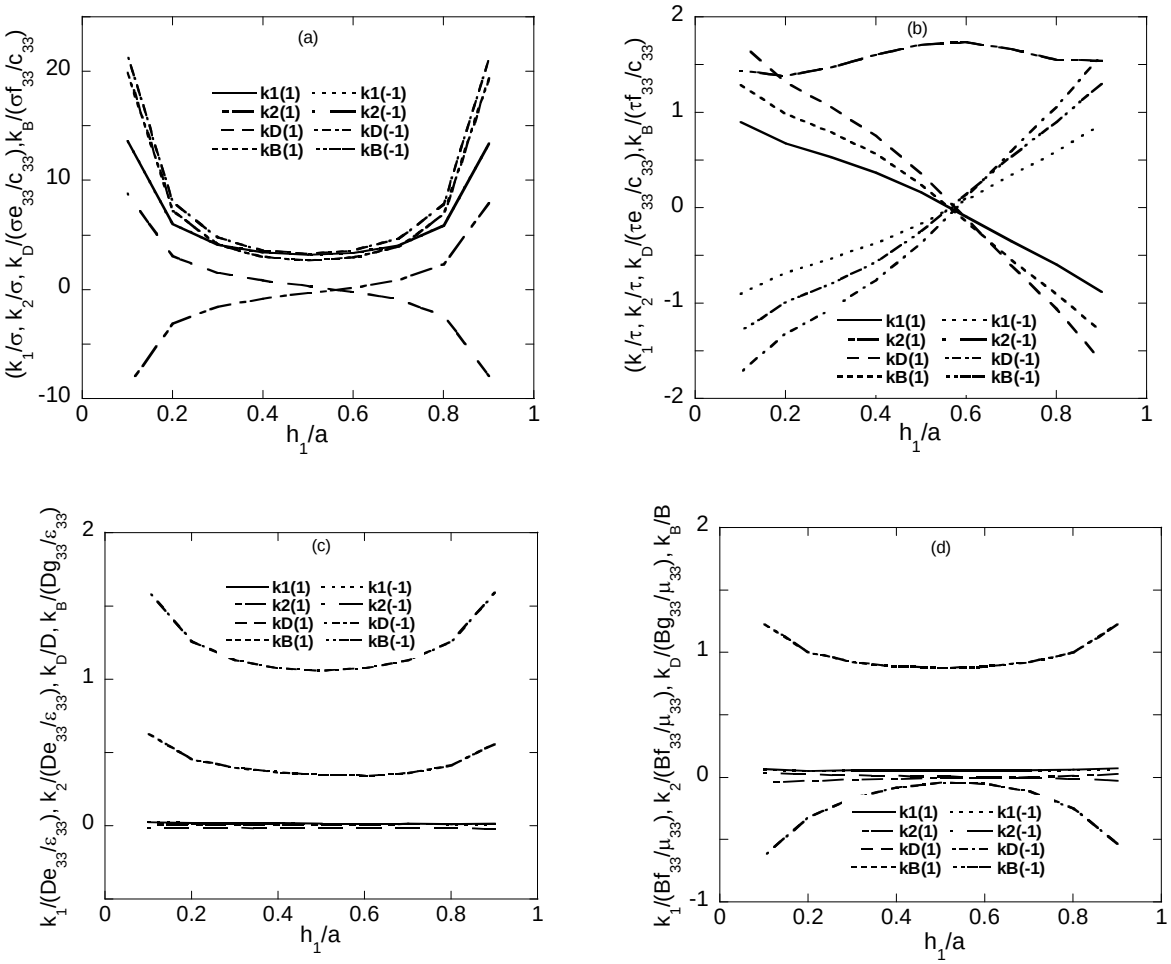

Figure 4: Effect of the crack position on the normalized fields' intensity factors under constant normal (a) and tangential (b) crack surface tractions in addition to constant electric displacement (c) and magnetic induction (d) in the case of $\left(h_1+h_2\right)=a$, $\beta a=1$ and $k^e=k^m=0.25$.

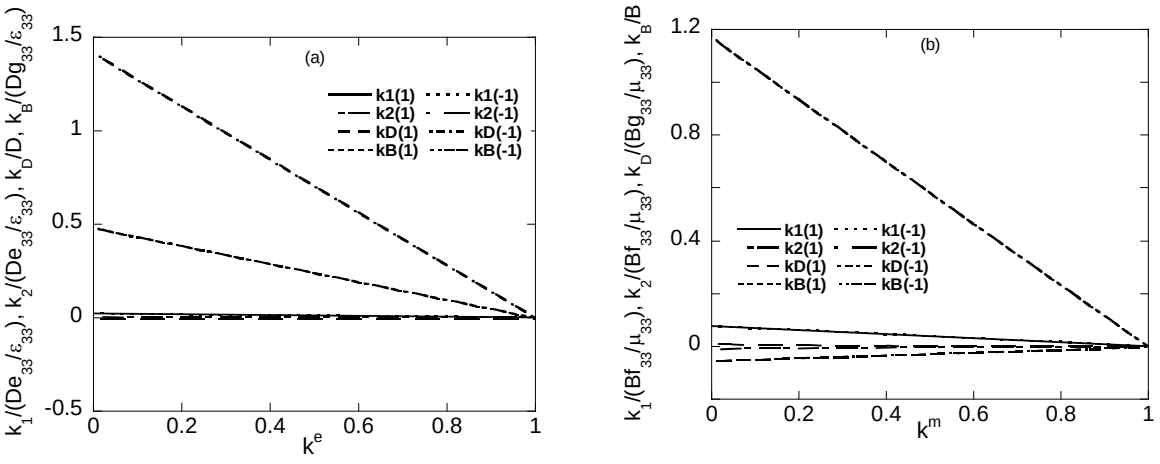

Figure 5: Effect of the magneto electric partial permeability parameters on the normalized fields' intensity factors under constant electric displacement (a) and magnetic induction (b) loadings in the case of central crack, $h = a$ and $\beta a = 1$.

Acknowledgement

The first two authors are grateful for the funding provided to their laboratory by the Tunisian Ministry of Higher Education and Scientific Research. This work was performed within the framework of the International Institute for Multifunctional Materials for Energy Conversion which is funded by the US National Science Foundation.

References

Mode III crack problem in a functionally graded magneto-electro-elastic strip Li Ma, Jia Li, Radhi Abdelmoula, Lin-Zhi Wu, International Journal of Solids and Structures 44 (2007) 5518–5537

Surface crack problem for functionally graded magneto electro elastic coating homogeneous elastic substrate system under anti-plane mechanical and in-plane electric and magnetic loading, Li Ma, Lin-Zhi Wua, Lin-Ping Feng , Engineering Fracture Mechanics 76 (2009) 269–285

Two parallel symmetry permeable cracks in functionally graded piezoelectric/piezomagnetic materials under anti-plane shear loading, Zhen-Gong Zhou, Biao Wang, International Journal of Solids and Structures 41 (2004) 4407–4422

Dynamic fracture behaviors of cracks in a functionally graded magneto-electro-elastic plate, Feng Wenjie, Su Raykaileung, European Journal of Mechanics A/Solids 26 (2007) 363–379

Dynamic internal crack problem of a functionally graded magneto-electro-elastic strip W.J. Feng, R.K.L. Su, International Journal of Solids and Structures 43 (2006) 5196–5216

Scattering of harmonic anti-plane shear stress waves by a crack in functionally graded piezoelectric/piezomagnetic materials, Liang Jun, Acta Mechanica Solida Sinica, Vol. 20, No. 1, March, 2007

Basic solution of a Mode-I limited-permeable crack in functionally graded piezoelectric/piezomagnetic materials, Zhen-Gong Zhou, Zeng-Tao Chen, International Journal of Solids and Structures 45 (2008) 2265–2296

Anti-plane crack intersecting the interface in a bonded smart structure with graded magneto electro elastic properties, Y.D. Li, K.Y. Lee, Theoretical and Applied Fracture Mechanics 50 (2008) 235–242

Fracture analysis and improved design for a symmetrically bonded smart structure with linearly non-homogeneous magneto electro elastic properties, Yong-Dong Li, Kang Yong Lee, Engineering Fracture Mechanics 75 (2008) 3161–3172

Crack in a bonded functionally graded magneto-electro-elastic strip, Li-Fang Guo, Xing Li, Sheng-Hu Ding, Computational Materials Science 46 (2009) 452–458

An embedded mixed-mode crack in a functionally graded magnetoelectroelastic infinite medium, Rekik M., El-Borgi S., Ounaies Z., 2012 International Journal of Solids and Structures 49 (2012) 835–845

Subcritical Crack Propagation and Coalescence Induced by the Oil-Gas Transformation

Zhi-Qiang Fan[1], Zhi-He Jin[1*] , Scott. E. Johnson[2]

[1]Department of Mechanical Engineering, University of Maine, Orono, ME 04469, USA
[2]School of Earth and Climate Sciences, University of Maine, Orono, ME 04469, USA
* Corresponding author: zhihe.jin@maine.edu

Abstract The present work develops a multi-physics model to investigate subcritical propagation of initially oil-filled, sub-horizontal collinear microcracks driven by the excess pressure induced during the conversion of oil to gas in a petroleum source rock under continuous burial. The crack propagation distance, propagation duration, crack coalescence and overpressure in the crack are determined using a finite difference scheme that couples linear elastic fracture mechanics, oil-gas transformation kinetics and an equation of state for the gas. The numerical results for a source rock with typical properties show that when the crack spacing is greater than $b/a_0 = 3$ (where a_0 is the half crack length and b the half distance between crack centers) the cracks do not coalesce and the duration of gas-driven crack propagation is governed by the transformation kinetics because the subcritical crack propagation rate is much faster than the oil-gas conversion rate. The collinear cracks coalesce for smaller crack spacing and the crack propagation duration may be reduced significantly due to crack interactions. The multi-physics model developed in this work together with our previous model for crack propagation during conversion of solid kerogen to oil indicates that microcracks resulting from buildup of excess fluid pressure during hydrocarbon generation may serve as an effective pathway for primary petroleum migration.

Keywords: Collinear cracks, Migration, Oil-gas conversion, Overpressure, Subcritical growth

1. Introduction

Overpressures widely observed in the deep part of sedimentary basins coincident with primary zones of gas generation are commonly attributed to thermal cracking of kerogen to oil/gas and oil to gas. Microfractures are a common feature of petroleum source rocks in these basins interpreted to serve as migration conduits for oil and gas [1]. Understanding the dominant mechanisms responsible for the microfracture initiation and development in petroleum source rocks at great depth is crucial for hydrocarbon exploration and safe drilling.

Fine grained source rocks like shales rich in kerogen undergo progressive burial, which leads to an increase in bulk density and loss of porosity. With increasing depth of burial, there is also a marked decrease in permeability. As temperatures and pressures increases, kerogen breaks down to release oil when it becomes mature. Conversion of kerogen to oil results in significant volume increase due to the density difference between the precursors and the products. Meanwhile, part of the overburden load will be transferred to the newly generated oil. As a natural result, overpressure is generated [2, 3]. Clay-sized minerals within source rocks functioning as effective seals enable local overpressure build-up [1]. When the overpressure exceeds the mechanical strength of the source rocks, microfractures around kerogen particles are initiated, thus creating a migration pathway for oil [4, 5].

As burial proceeds, temperatures continue to increase. When the gas window is reached, oil retained in the microfractures will be subjected to thermal cracking to form gas, which consists predominantly of methane [2-3]. The volume increase associated with transformation of oil to gas is more appreciable. According to Barker [6], less than two percent of oil conversion to gas would

readily create overpressure in excess of lithostatic pressure and cause microfracturing in an effectively sealed reservoir. As a result, microfractures driven by the overpressure may grow and coalesce to form interconnected fracture networks, which may facilitate further migration of hydrocarbons [2, 7].

Convincing evidence from field observations has been presented to support the concept that microfractures induced by overpressure from hydrocarbon generation serve as migration conduits for hydrocarbons. Examples include the Bakken shale in Williston Basin [8], La Luna source rocks in the Maracaibo Basin [9], Woodford Formation in Oklahoma and Arkansas [10], fractured source rocks from the Oligocene Frio Formation, Texas [11], mature shales in the Hils area in Germany [12] and Alberta Basin in Canada [13]. Detailed observations by Lash and Engelder [14] showed that layer parallel microcracks filled with bitumen in organic-rich Dunkirk shale of Catskill delta, New York resulted from hydrocarbon generation. Common features of these microfractures in overpressured source rocks are summarized as follows: (1) the microcracks are of opening mode, i.e. mode I; (2) the preferred orientation of microfractures is parallel or sub-parallel to bedding plane; (3) most microcracks contain bitumen or calcite, showing the characteristic of petroleum generation; and (4) microfractures are found in organic-rich source rocks at high maturity level.

More recently, Jin et al. [4] developed a model of primary migration of oil by collinear microcrack coalescing during the main stage of oil generation and found that microfractures propagate subcritically since excess pressure resulted from kerogen conversion to oil is not high enough to drive critical crack growth. In the present paper we extend our previous work to investigate subcritical growth of a series of periodically spaced subhorizontal collinear microfractures driven by excess fluid pressure due to thermal cracking of oil to gas. As a special case, the propagation of a single crack is also studied. We focus on the effects of gas compressibility and crack spacing on the crack propagation behavior including crack propagation distance and duration, as well as excess pressure evolution.

2. Formulation of theoretical model of crack propagation during gas generation

2.1. Thermal cracking of oil to gas

Transformation of oil to gas satisfies the following first order differential equation [15]

$$\frac{dM}{dt} = -BM \exp\left[-\frac{E_A}{RT(t)}\right] \tag{1}$$

where M is the mass of convertible oil at time t, B is a pre-exponential constant, E_A is the activation energy of the transformation, R is the universal gas constant, and T is the absolute temperature. We assume a constant burial rate S and a constant geothermal gradient G so that the depth of burial z and time-varying temperature T can be written as

$$z(t) = H_0 + St\,, \quad T(t) = T_0 + G(z - H_0) = T_0 + GSt \tag{2}$$

where H_0 is the initial burial depth at which the oil-filled cracks are located, T_0 is the corresponding temperature at H_0. By integrating Eq. (1) with Eq. (2) and using mass conservation, Fan et al. [7] obtained the volumes of oil and gas at time t as follows

$$V_{oil}^t = M_0 \exp\left[-\Phi(t)\right]/\rho_{oil}\,, \quad V_{gas}^t = M_0\left\{1 - \exp\left[-\Phi(t)\right]\right\}/\rho_{gas} \tag{3}$$

where M_0 is the initial mass of oil, ρ_{oil} is the density of oil, ρ_{gas} is the gas density which is a function of pressure and temperature determined by the equation of state (EOS), and $\Phi(t)$ is given by

$$\Phi(t)=\frac{B(T_0+GSt)}{GS}\exp\left[-\frac{E_A}{R(T_0+GSt)}\right]-\frac{BT_0}{GS}\exp\left(-\frac{E_A}{RT_0}\right)+\frac{BE_A}{RGS}\left[E_i\left(-\frac{E_A}{R(T_0+GSt)}\right)-E_i\left(-\frac{E_A}{RT_0}\right)\right] \tag{4}$$

in which $E_i(\ )$ is the exponential integral defined by

$$E_i(x)=\int_{-\infty}^{x}\frac{e^{x'}}{x'}dx' \tag{5}$$

2.2. An equation of state (EOS) for gas

To account for the compressibility of gas under subsurface conditions, we adopt an EOS for methane developed by Duan et al. [16], since natural gas consists primarily of methane. The EOS, which is capable to describe the behavior of methane with high accuracy over wide temperature and pressure range (0 - 1000 ^{o}C and 0 - 800 MPa, respectively), takes the form

$$\frac{P_rV_r}{T_r}=1+\frac{C_1}{V_r}+\frac{C_2}{V_r^2}+\frac{C_3}{V_r^4}+\frac{C_4}{V_r^5}+\frac{C_5}{V_r^2}\left(\beta+\frac{\gamma}{V_r^2}\right)\exp\left(-\frac{\gamma}{V_r^2}\right) \tag{6}$$

where $P_r=P/P_c$, $T_r=T/T_c$, $V_r=V/V_c$, P and T are the pressure and temperature of the gas, respectively, $V = m/\rho_{\text{gas}}$ is the molar volume with m denoting the molar mass, T_c is the critical temperature above which methane can not be liquefied regardless of the pressure applied, P_c is the critical pressure required to liquefy methane at the critical temperature T_c, $V_c = RT_c/P_c$, and

$$C_1=a_1+\frac{a_2}{T_r^2}+\frac{a_3}{T_r^3}\quad C_2=a_4+\frac{a_5}{T_r^2}+\frac{a_6}{T_r^3},\ C_3=a_7+\frac{a_8}{T_r^2}+\frac{a_9}{T_r^3},\ C_4=a_{10}+\frac{a_{11}}{T_r^2}+\frac{a_{12}}{T_r^3},\ C_5=\frac{\alpha}{T_r^3} \tag{7}$$

The EOS contains 15 material constants: a_i (i = 1, 2… 12), α, β and γ， which can be found in [16].

From Eq. (6) we can express gas pressure in terms of gas density and temperature as follows

$$P=P(\rho_{gas})=\frac{P_cT_rV_c\rho_{gas}}{m}\left[1+\frac{BV_c\rho_{gas}}{m}+\frac{CV_c^2\rho_{gas}^2}{m^2}+\frac{DV_c^4\rho_{gas}^4}{m^4}+\frac{EV_c^5\rho_{gas}^5}{m^5}+\frac{FV_c^2\rho_{gas}^2}{m^2}\left(\beta+\frac{\gamma V_c^2\rho_{gas}^2}{m^2}\right)\exp\left(-\frac{\gamma V_c^2\rho_{gas}^2}{m^2}\right)\right] \tag{8}$$

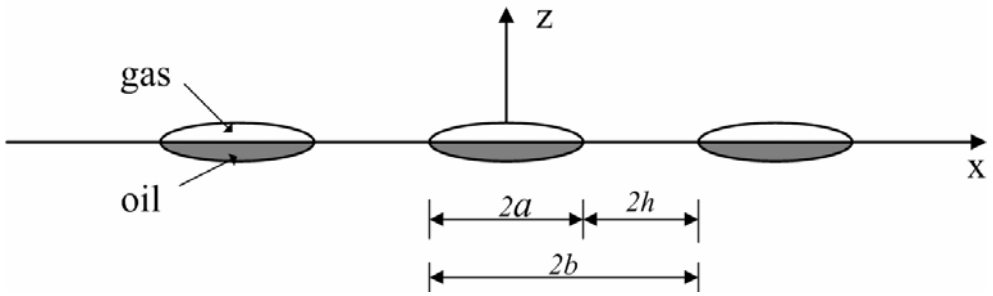

Figure 1. Subhorizontal periodically spaced collinear microcracks filled by oil and gas

2.3. Fracture mechanics model

Consider a row of periodic collinear microcracks initially filled by oil within a source rock under continuous burial as shown in Figure 1, where $2a = 2a\ (t)$ denotes the crack length at time t and

$2h$ is the crack spacing. Initially the crack is subjected to uniform oil pressure on the crack surface. The initial excess pressure is denoted by Δp_0 which is the oil pressure beyond the overburden pressure. The excess pressure increases as oil to gas conversion proceeds. At time t, the excess pressure can be obtained as follows

$$\Delta p = P(\rho_{gas}) - \rho_s g z = P(\rho_{gas}) - \rho_s g\left(H_0 + St\right) \tag{9}$$

where ρ_s is the average sediment density, g = 9.8 m/s^2 is gravitational acceleration, and $P(\rho_{gas})$ is the gas pressure given by Eq. (8).

The stress intensity factor (SIF) at the crack tips is given by

$$K_I = \Delta p\sqrt{2b\tan\left(\frac{\pi a}{2b}\right)} \tag{10}$$

where $b = a + h$. The volume per unit thickness in the y direction of the crack is

$$V_{crack}^{t} = \frac{16b^2\Delta p\left(1-\nu^2\right)}{\pi E}\ln\left[\sec\left(\frac{\pi a}{2b}\right)\right] \tag{11}$$

where E and ν are Young's modulus and Poisson's ratio of the source rock, respectively. Since the crack is fully saturated with oil and gas, the volume of the crack must equal the sum of oil and gas volumes, that is,

$$V_{oil}^{t} + V_{gas}^{t} = V_{crack}^{t} \tag{12}$$

From Eq. (11), we can get the initial mass of oil within the crack

$$M_0 = \frac{16b^2\rho_{oil}\Delta p_0\left(1-\nu^2\right)}{\pi E}\ln\left[\sec\left(\frac{\pi a_0}{2b}\right)\right] \tag{13}$$

where a_0 is the half initial crack length. Clearly the SIF increases with the increasing excess pressure.

Subcritical crack propagation will be initiated once the SIF reaches a threshold value K_{Ith}, but less than the rock fracture toughness K_{Ic}. Generally, the subcritical crack growth can be described by the Charles power law [17]

$$v = \frac{da}{dt} = A\left[K_I(a)\right]^n \tag{14}$$

where ν is the subcritical propagation velocity, n is the subcritical crack growth index and A is a material constant. It follows from Eq. (10) that the excess fluid pressure corresponding to the onset of subcritical crack growth is

$$\Delta p_{th} = K_{\mathrm{I}th} / \sqrt{2b\tan\left(\frac{\pi a_0}{2b}\right)} \tag{15}$$

The corresponding crack volume is

$$V_{crack}^{0} = \frac{16b^2\left(1-\nu^2\right)K_{\mathrm{I}th}}{\pi E\sqrt{2b\tan\left(\frac{\pi a_0}{2b}\right)}}\ln\left[\sec\left(\frac{\pi a_0}{2b}\right)\right] \tag{16}$$

The time needed for the excess pressure to reach Δp_{th} from the start of oil-gas transformation, denoted by t_0, can be determined by solving the following two equations

$$P\left(\rho_{gas}^{th}\right) - \rho_s g(H_0 + St_0) = K_{\mathrm{I}th} / \sqrt{2b\tan\left(\frac{\pi a_0}{2b}\right)} \tag{17}$$

$$\frac{M_0\left\{1-\exp\left[-\Phi\left(t_0\right)\right]\right\}}{\rho_{gas}^{th}}+\frac{M_0\exp\left[-\Phi\left(t_0\right)\right]}{\rho_{oil}}=\frac{16b^2\left(1-\nu^2\right)\Delta p_{th}}{\pi E}\ln\left[\sec\left(\frac{\pi a_0}{2b}\right)\right] \tag{18}$$

where ρ_{gas}^{th} is the corresponding gas density at time t_0.

2.4. Simulation of subcritical crack propagation and coalescence using finite difference

A finite difference formulation is used to study the coupling between gas generation from oil degradation and gas expulsion through microfracture propagation and coalescence. Consider the microcrack propagation from time t_0 to current time t. We subdivide the time domain into N intervals to construct a mesh of equally-spaced grids: $t_0, t_1,\ldots, t_{N-1}, t_N$ with $t_N=t$. The following notations are adopted. $a_i=a(t_i)$ and $\rho_{gas}^i=\rho_{gas}(t_i)$ represent the half crack length and the corresponding gas density at time step t_i , respectively. Replace the derivative in Eq. (14) by a forward difference approximation at time t_i, then we obtain the following expression for the half crack length at t_{i+1}

$$a_{i+1}=a_i+A[P(\rho_{gas}^i)-\rho_s g\left(H_0+St_i\right)]^n(2b)^{n/2}\left[\tan\left(\frac{\pi a_i}{2b}\right)\right]^{n/2}(t_{i+1}-t_i) \tag{19}$$

Neglecting the mutual solubility of gas and oil, we obtain the oil and gas volumes at t_{i+1} as follows

$$V_{oil}^{i+1}=\frac{M_0\exp\left[-\Phi\left(t_{i+1}\right)\right]}{\rho_{oil}},\qquad V_{gas}^{i+1}=\frac{M_0\left\{1-\exp\left[-\Phi\left(t_{i+1}\right)\right]\right\}}{\rho_{gas}^{i+1}} \tag{20}$$

where ρ_{gas}^{i+1} is the gas density at time step t_{i+1}. The volume of the crack at t_{i+1} is by Eq. (11) applied at step t_{i+1}.

The requirement that crack volume must be equal to the sum of oil and gas volumes yields the excess pressure Δp_{i+1} at t_{i+1},

$$\Delta p_{i+1}=M_0\left[\frac{\exp\left[-\Phi\left(t_{i+1}\right)\right]}{\rho_{oil}}+\frac{\left\{1-\exp\left[-\Phi\left(t_{i+1}\right)\right]\right\}}{\rho_{gas}^{i+1}}\right]\Bigg/\left\{\frac{16b^2\left(1-\nu^2\right)}{\pi E}\ln\left[\sec\left(\frac{\pi a_{i+1}}{2b}\right)\right]\right\} \tag{21}$$

Note that $\Delta p_{i+1}=P(\rho_{gas}^{i+1})-\rho_s g\left(H_0+St_{i+1}\right)$, and then we can solve this equation for the unknown gas density ρ_{gas}^{i+1}. Consequently the excess pressure Δp_{i+1} at t_{i+1} can be obtained using Eq. (21). To drive the crack growth subcritically, Δp_{i+1} must satisfy the following condition

$$\Delta p_{i+1}\geq K_{1th}/\sqrt{2b\tan\left(\frac{\pi a_{i+1}}{2b}\right)} \tag{22}$$

Otherwise, we need to adjust time t_{i+1} by solving Eq. (17) and (18) with a_0, t_0 and ρ_{gas}^{th} replaced by a_{i+1}, t_{i+1} and ρ_{gas}^{i+1}, respectively.

3. Numerical Results and Discussions

This section presents numerical examples to illustrate effects of initial burial depth and crack spacing on the excess pressure evolution with time and crack propagation distance for a single crack, and propagation and coalescence of collinear cracks. Since shales are major source rocks for oil and natural gas, in our simulation we study shales for illustration purpose. Typically thermal cracking of oil is initiated at temperatures of 120-160 ^oC, and ultimate conversion to methane may occur at

temperatures in excess of 200 ^{o}C, at depth of burial ranging between 3000m and 7000m [19]. We examine the sensitivity of crack propagation to variations of initial depth of burial in the range of 3500-5000m. The initial temperature is assumed as T_0 = 150 ^{o}C. We also assume that $\Delta p_0 = \Delta p_{th}$ and the stress intensity factor equals the threshold value K_{Ith} due to the excess oil pressure at the initial state. Other physical and geometrical parameters used in our simulation are summarized in Table 1[14, 16-19].

Table 1 Physical and geometrical parameters used in the numerical simulation

Symbols	Definition	Value(unit)
Rock Matrix		
E	Young's modulus	2.0 GPa
ν	Poison's ratio	0.4
ρ_s	Average sediment density	2350 kg/m^3
K_{Ith}	Threshold stress intensity factor	0.06 MPa-m$^{1/2}$
A	Subcritical crack growth constant	10^7 m/s/(MPa-m$^{1/2}$)^{10}
n	Subcritical crack growth index	10
a_0	Initial half crack length	50 μm
H_0	Initial depth of burial	4000 m
T_0	Initial temperature	150 ^{o}C
G	Geothermal gradient	30 ^{o}C/km
S	Burial rate	0.1 km/M.y.
Oil		
ρ_{oil}	Oil density	850 kg/m^3
Methane		
m	Molar mass	16 g/mol
T_c	Critical temperature	191.1 K
P_c	Critical pressure	4.64 MPa
Kinetics		
B	Pre-exponential constant	1.744×10^{13} sec^{-1}
E_A	Activation energy	217.6 kJ/mol
R	Universal gas constant	8.314 J/mole/K

3.1 Single crack case

When $b/a_0 \rightarrow \infty$ the crack interaction disappears and the problem reduces to the single crack case. Figures 2 shows crack propagation distance versus time corresponding to three different values of H_0 for a single crack. The corresponding excess pressure profiles are shown in Figure 3. Similar to the kerogen conversion to oil case [4], subcritical crack propagation rate is much faster than the oil-gas conversion rate, so the crack propagation duration is governed by the oil-gas transformation kinetics. The excess pressure decreases monotonically as crack propagation distance increases with time, which is indicated by Eq. (10). It is seen from Figure 2 that the final crack length increases with decreasing initial depth of burial. It can be explained by considering the gas compressibility in Eq. (8). Gas density increases monotonically with increasing depth of burial, so the density difference between the transformation precursor and end product becomes smaller. Therefore, the crack propagation distance becomes smaller at greater depth of burial. From Figure 3 we can see that at a given time, the excess pressure within the crack is lower at a shallower depth of burial because longer cracks require smaller overpressure to grow as suggested by Eq. (10).

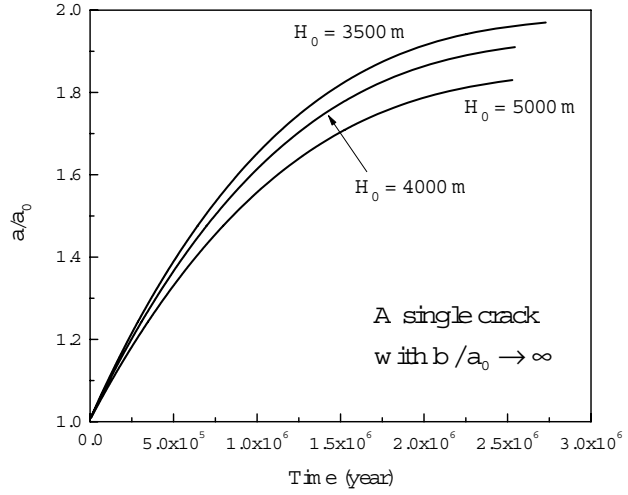

Figure 2. Crack propagation distance versus time for a single crack corresponding to different initial depths of burial

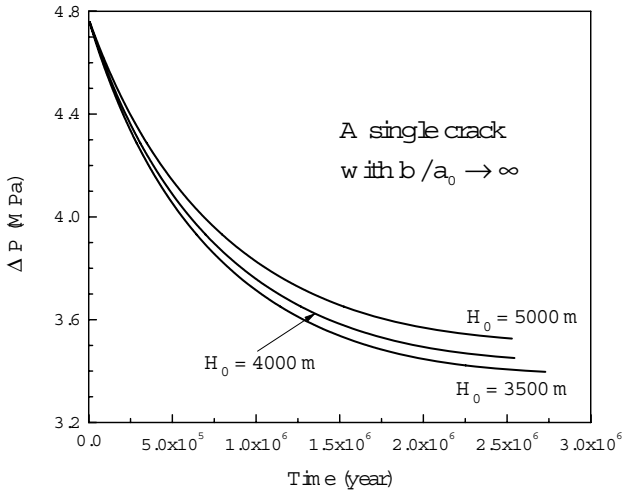

Figure 3. Excess pressure evolution over time for a single crack corresponding to different initial depths of burial

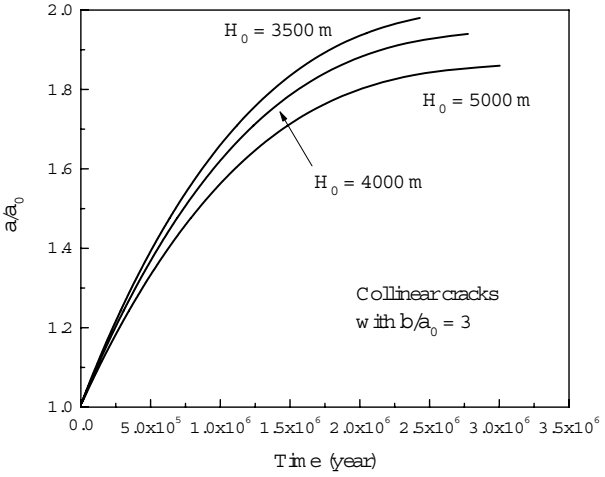

Figure 4. Effect of initial depth of burial on the crack propagation distance for collinear cracks with initial crack spacing $b/a_0 = 3$

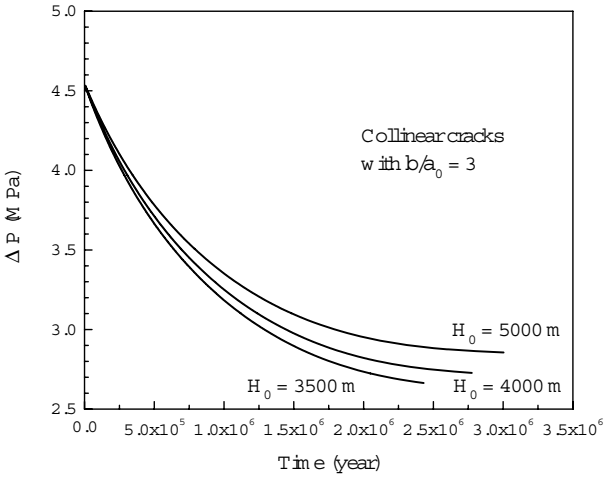

Figure 5. Effect of initial depth of burial on the excess pressure for collinear cracks with initial crack spacing $b/a_0 = 3$

3.2 Collinear cracks case

The effects of initial burial depth on crack propagation distance and excess pressure evolution for b/a_0=3 are shown in Figures 4 and 5, respectively. The general trends in the variation of crack propagation distance and excess pressure with time corresponding to different H_0 are quite similar to those observed in Figures 2 and 3, respectively. A particularly noteworthy feature is sharp differences on the crack propagation duration between a single crack and collinear cracks at shallow burial depth. For example, Figure 2 shows that it takes about 2.74 million years for the single crack to grow to 1.97 times its original length when all the oil within the crack converts to gas completely. For collinear cracks, it takes about 2.42 million years to grow to 1.98 times its original length and the microcracks are almost to coalesces (b/a_0=3 and h/a_0=2) to form macroscopic cracks. The

marked decrease in crack propagation duration is due to rapid acceleration of crack growth associated with drastic increase in stress intensity factor as crack spacing decreases.

We also examine the sensitivity of crack propagation distance and excess pressure to the changes of crack spacing, as shown in Figures 6 and 7, respectively. Our numerical calculation shows that when $b/a_0 > 3$, no crack coalescence is found for typical burial depth in the range of 3000-7000m where thermal cracking of oil to gas occurs. For $b/a_0 = 2.0$, the excess pressure decreases with time and drops sharply when the cracks are about to coalesce. Due to crack interaction, the threshold excess pressure to initiate subcritical crack growth increases with increasing crack spacing. The crack propagation reduces significantly for smaller crack spacing. For example, the crack propagation duration is about 3.39 million years for $b/a_0=5$. It reduces to about 1.09 million years when $b/a_0=2$.

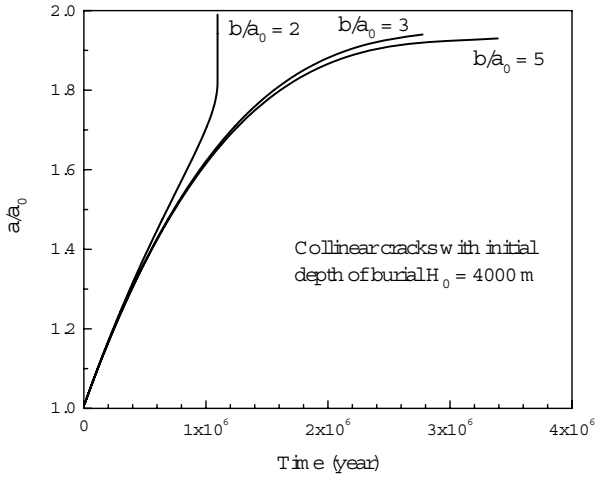

Figure 6. Effect of crack spacing on the crack propagation distance for collinear cracks with initial depth of burial $H_0 = 4000$ m

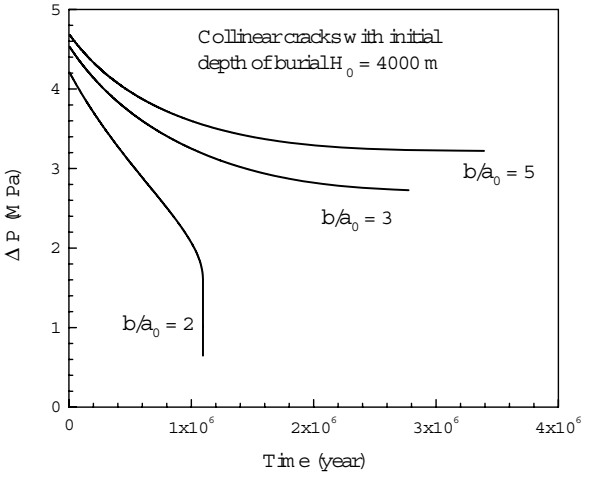

Figure 7. Effect of crack spacing on the crack propagation distance for collinear cracks with initial depth of burial $H_0 = 4000$ m

Concluding Remarks

To address the coupling between gas generation and expulsion, we develop a theoretical model to study the gas migration through propagation and coalescence of collinear microfractures initially filled by oil incorporating fracture mechanics of source rocks, geochemistry of thermal cracking of oil to gas, and an equation of state for gas. Based on our numerical simulation, the following conclusions can be reached, which may provide some insight into gas migration process.

(1) Gas expulsion through self-propagating microfractures is an effective mechanism for primary migration within well-sealed source rocks and excess pressure caused by thermal cracking of oil to gas serves as driving force for microfracture propagation.

(2) Increasing depth of burial leads to decreasing crack propagation distance due to gas compressibility. Therefore cracks at shallower depth are more likely to form interconnected fracture network.

(3) Crack spacing has a significant effect on crack propagation duration for collinear cracks with smaller crack spacing leading to shorter crack propagation duration.

References

[1] Momper, J. A., Oil migration limitations suggested by geological and geochemical considerations, *AAPG Course Note Series*, 8**(**1978), B1–B60.
[2] Hunt, J. M., *Petroleum geochemistry and geology*, Freeman, San Francisco, 1979.
[3] Tissot, B.P. & Welte D.H., Petroleum formation and occurrence, *A New Approach to Oil and Gas Exploration*, Springer, Berlin, 1984.
[4] Jin, Z.-H., Johnson, S.E. & Fan, Z.Q., Subcritical propagation and coalescence of oil-filled cracks: getting the oil out of low-permeability source rocks, *Geophys. Res. Lett.*, 37 (2010), L01305.
[5] Fan, Z. Q., Jin, Z.-H. & Johnson, S. E., Subcritical propagation of an oil-filled penny-shaped crack during kerogen–oil conversion, *Geophys. J. Int.*, 182 (2010), 1141–1147.
[6] Barker, C, Calculated volume and pressure changes during the thermal-cracking of oil to gas in reservoirs. AAPG Bull, 74(1990): 1254-1261.
[7] Fan, Z. Q., Jin, Z.-H. & Johnson, S. E., Gas-driven subcritical crack propagation during the conversion of oil to gas, *Petrol. Geosci.*, 18(2012): 191-199.
[8] Meissner, F. F., Petroleum geology of the bakken formation williston basin, north Dakota and Montana. Williston Basin Symposium, Montana Geological Society, 24th Annual Conference, 1978
[9] Talukdar, S., Observations on the primary migration of oil in the la luna source rocks of the maracaibo basin, venezuela. in. Doligez B., (Ed). Migration of hydrocarbons in sedimentary basins, Editions Technip. Paris, 1987, pp59-77
[10] Comer, J.B. & Hinch, H.H., Recognizing and quantifying expulsion of oil from the Woodford Formation and age-equivalent rocks in Oklahoma and Arkansas, *AAPG Bull.*, 71 (1987) 844–858.
[11] Capuano, R.M., Evidence of fluid flow in microcracks in geopressured shales, *AAPG Bull.*, 77 (1993), 1303–1314.
[12] Littke, R., D. R. Baker and D. Leythaeuser , Microscopic and sedimentologic evidence for the generation and migration of hydrocarbons in toarcian source rocks of different maturities. Org. Geochem., 13(1988), 549-559.
[13] Marquez, X.M. & Mountjoy, E.W., Microcracks due to overpressure caused by thermal cracking in well-sealed Upper Devonian reservoirs, deep Alberta basin, *AAPG Bull.*, 80 (1996), 570–588.
[14] Lash, G.G. & Engelder, T., An analysis of horizontal microcracking during catagenesis: an example from the Catskill delta complex, *AAPG Bull.*, 89 (2005), 1433–1449.
[15] Berg, R.R. & Gangi, A.F., Primary migration by oil-generation microfracturing in low-permeability source rocks: application to the Austin Chalk, Texas, *AAPG Bull.*, 83 (1999), 727–756.
[16] Duan, Z. H., Moller, N. & Weare, J. N., An equation of state for the CH_4-CO_2-H_20 system: I. Pure systems from 0 to 1000^{o}C and 0 to 8000 bar, *Geochim. Cosmochim. Acta*, 56 **(**1992), 2605-2617.
[17] Atkinson, B.K., Subcritical crack growth in geological materials, *J. geophys. Res.*, **89**(1984), 4077–4144.
[18] Pepper A. S. & Corvi P. J., Simple kinetic models of petroleum formation. Part I: oil and gas generation from kerogen, *Mar. Petrol. Geol.*, 12 (1995), 291–319.
[19] Schmidt, R. Fracture mechanics of oil shale-unconfined fracture toughness, stress corrosion cracking, and tension test results. The 18th US Symposium on Rock Mechanics (USRMS), Golden, Colorada, Colorado School of Mines, 1977.

On Incorrectness in Elastic Rebound Theory for Cause of Earthquakes

Zhong-qi Quentin Yue[1,*]

[1] Department of Civil Engineering, The University of Hong Kong, Hong Kong, China
* Corresponding author: yueqzq@hku.hk

Abstract The elastic rebound theory was developed 100 years ago from the observations of co-seismic surface ruptures induced by the 1906 California Earthquake. It is only partially correct because it associates earthquakes with geological faults. However, it is inconsistent and even violates many other phenomena that were present before, during and after earthquakes. Numerous failures have been encountered and experienced in the tremendous efforts using the elastic rebound theory in the prediction of earthquakes over the past 100 years. Many current seismo-geologist and seismologists have lost their original goals to predict earthquakes and turned to believe that earthquakes are unpredictable with present techniques. All these problems are due to the fact that the incorrect elastic rebound theory for cause of earthquakes was used in the investigation and prediction of earthquakes. The paper also shows that the energy released during earthquake is not the elastic stress and strain energy accumulated in brittle crustal rock solids during relative movements of tectonic plates. The released energy is the volumetric expansion energy of highly compressed and dense natural gas rapidly escaped from its deep crustal traps via fault channels. This gas hypothesis for the cause of earthquakes would make earthquake predicable in the near future.

Keywords Earthquake, Energy, Fault, Heat, Natural Gas

1. Introduction

Earthquake occurs every day. Seismologists have developed and used seismometers to report the locations and magnitudes of earthquakes within minutes of their occurrence. But, they cannot predict earthquakes. Earthquake prediction is to predict where and when the next damaging earthquake will occur and what will be its magnitude. For last hundred and thousand years, earthquakes have frequently hit us without notice and wreaked terrible disasters and numerous fatalities. In addition, there were many false prediction cases and only a few successful prediction cases. Due to numerous failure cases, seismologists have reached a consensus that the next strong earthquake can NOT be predicted.

For example, Chen and Wang [1] wrote, “Few seismologists believe that it is presently possible or forever impossible to predict an earthquake with the time, location, and size specified accurately enough to guide plans for evacuation. Regardless of its scientific merit and future development, governments of most industrial countries consider earthquake prediction to be presently impractical.” Hough [2] also wrote, “Are earthquake predicable? The title of this book implies an answer and suggests a paradox. We cannot say it will always be the case, but, given the state of earthquake science at the present time, earthquakes are unpredictable.” Therefore, the following issue must be asked and addressed: Why are the next damaging earthquakes unpredictable?

In this paper, the author tries to point out the core reason for this earthquake unpredictability issue. The core reason is the inadequacy of the existing theory in explaining the cause of earthquakes. It is the elastic rebound theory developed one hundred years ago in 1910 [3, 4]. It has been regarded as “one of the most fundamental tenets of earthquake science” [2]. The prediction efforts over the last one hundred years have been based on the incorrect cause theory of tectonic earthquakes. Hence, a majority of their results have been unsatisfactory. Furthermore, the theory of plate tectonics, developed in later 1950s and early 1960s, used this elastic rebound theory as one of the foundations. On the other hand, the plate tectonic theory gives the reasons why and how the elastic stress can be built up in crustal fault rocks for cause of earthquakes associated with the elastic rebound theory [5].

The plate tectonic theory has become the dominant theory for the Earth system in geosciences including seismogeology and seismology. Consequently, the belief and/or consensus that earthquakes are unpredictable have become much widely acceptance in recent 40 years.

In the ensuing, the author will give a brief account of the elastic rebound theory, and then show its incorrectness. At the end, the author will put forward his gas hypothesis to explain the cause of earthquakes [6-10].

2. The Elastic Rebound Theory

2.1. The origin

The 1906 California Earthquake was investigated by the State Earthquake Investigation Commission. The two reports [3, 4] are the first comprehensive and systematical documentations of damage earthquakes in modern science. In particular, co-seismic surface ruptures were frequently observed along the northern segment of San Andreas Fault and evidenced the fault motion of right-lateral strike-slip (horizontal motion), as shown by the red arrows in Figure 1. Accordingly to plate tectonics, this fault forms the tectonic boundary between the Pacific Plate and the North American Plate.

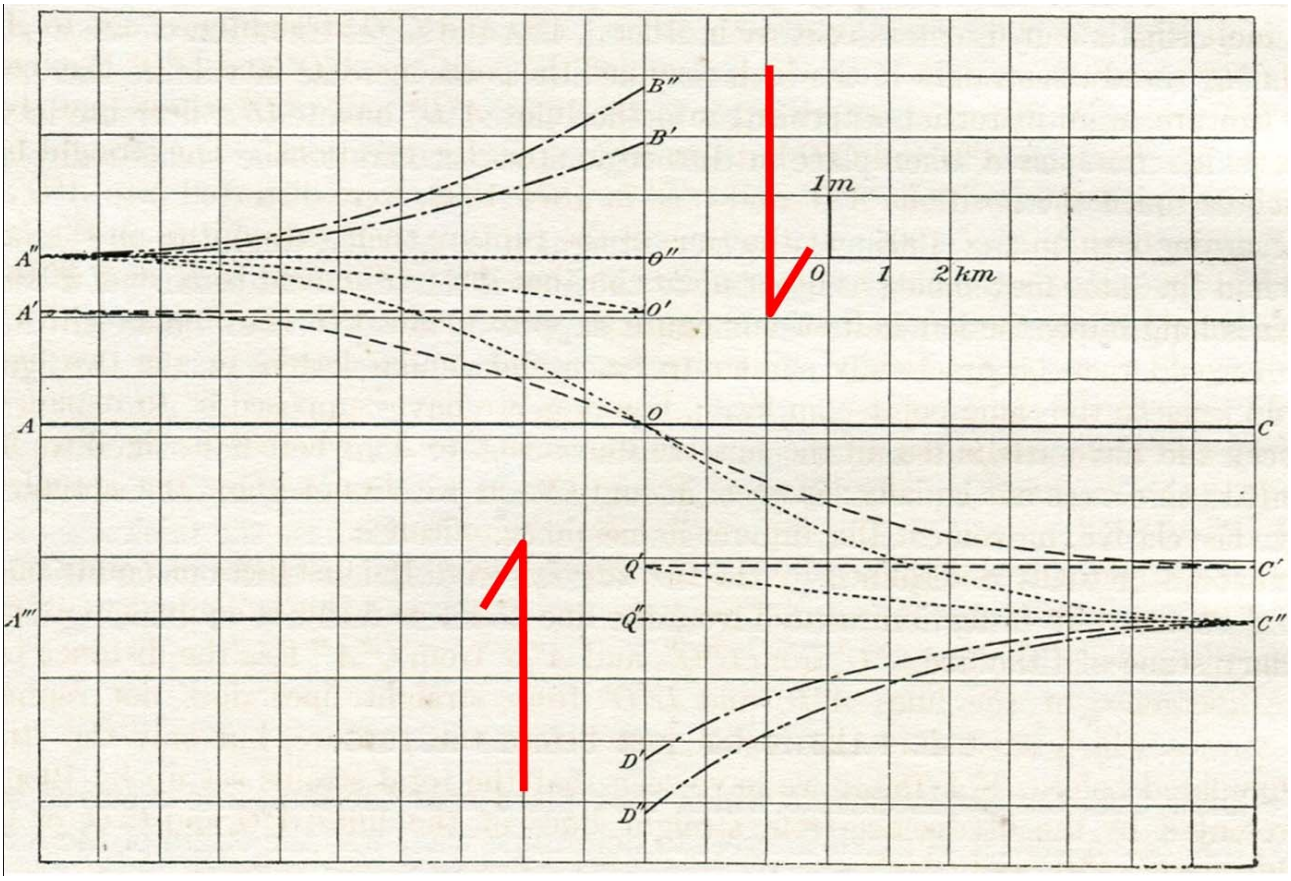

Figure 1. Illustration for elastic rebound for the cause of the 1906 California earthquake [4]

The ruptured fault traversed a part of the region where accurate ground topography surveys were made by the U. S. Coast and Geodetic Survey at various times before and after the earthquake [3, 4]. A summary of the survey results on ground plane is given in Figure 1. The central line passing through the points B'', B', O'', O', O, Q', Q'', D' and D'' is the fault line. The side with the

points A'', A', A, and A''' is the Pacific Plate on the west. The side with the points C, C', and C'' is the North American Plate on the east. It was pictured the displacements and the strains experienced at the region before, during and after the earthquake as follows [4].

"Let AOC be a straight line at some early data when the region was unstrained. By 1874-1892, A had been moved to A' and C to C', and AOC had been distorted into $A'OC'$; By the beginning of 1906, A had been further displaced to A'' and C to C'', then the sum of the distances AA'' and CC'' being about 6 meters; and AOC had been distorted into $A''OC''$."

"When the rupture came, the opposite sides of the fault slipt about 6 meters past each other; $A''O$ and $C''O$ straightened out to $A''O''$ and $C''O''$; and the straight lines which occupied the positions $A''O''$ and $C''Q''$ just before the rupture, were distorted afterwards into the lines $A''B''$ and $C''D''$, these lines being exactly like the lines $A''O$ and $C''O$ but turned in opposite directions."

"The straight lines, which occupied the positions $A'O'$ and $C'Q'$ in 1874-1892, were distorted into $A''O'$ and $C''Q'$ in the beginning of 1906; at the time of the rupture their extremities on the fault-line had the same movements as other points on that line; O' moved to B' and Q' moved to D'."

Subsequently, the elastic rebound theory for the cause of earthquake was developed, established and used by many others. It has been the main stream theory for the past one hundred years.

2.2. Brief description

Correspondingly, the existing elastic rebound theory in association with the plate tectonics for the cause of tectonic earthquakes can be briefly described below. The Earth's crust can be divided into a number of large and/or small tectonic plates. There edges are deep faults. The slow motion of convection currents in the plastic hot material of the mantle drives, pushes and pulls the plates. The tectonic plates can have relative motions in the order of several cm per year. Deep faults with brittle and locked zones can be present in the crust rocks. As the plates move slowly, their fault edges can stay locked, the surrounding crustal rocks can gradually deform for a long time. The elastic stress-strain energy can be built up and stored in rock masses. When the stress on the locked fault zone exceeds its breaking strength, a sudden rupture of the brittle fault part would occur, which causes an earthquake. Its side rocks can abruptly slip into new positions. Such sudden rupture can occur along pre-existing faults or newly formed faults. The larger the earthquake magnitude, the larger the ruptured fault length and the larger the slip offset. They take place at either tectonic plate boundaries or inside plates. So, there are interplate and intraplate earthquakes. The sudden rupture can occur along pre-existing faults or newly formed faults.

2.3. Work and energy

The work (W) done at the time of rupture was given by the following equation [4]:

$$W = \frac{1}{2} FDA, \tag{1}$$

where F is the force per unit area of the fault-plane, A the area of the fault plane and D the slip.

For the 1906 California earthquake, the fault depth was 25 km, the length 435 km, the average shift 4 meters, and the force 1×10^8 dynes per square centimeter. The work was estimated 1.75×10^{24} ergs (or 1.75×10^{17} joules). "This energy was stored up in the rock as potential energy of elastic strain

immediately before the rupture; when the rupture occurred, it was transformed into the kinetic energy of the moving mass, into heat and into energy of vibrations; the first was soon changed into the other two. When we consider the enormous amount of potential energy suddenly set free, we are not surprised, that, in spite of the large quantity of heat which must have been developt on the fault-plane, an amount was transferred into elastic vibrations large enough to accomplish the great damage resulting from the earthquake and to shake the whole world so that seismographs, almost at the antipodes, recorded the shock."[4]

Modern seismology has adopted the fault rupture and/or slip model in the quantitative analysis of seismic waves [5]. A quantitative measure of the size and strength of a seismic shear source is the scalar seismic moment M_0 with the unit Nm (or Joule). M_0 is a measure of the irreversible inelastic deformation in the rupture area and can be expressed as follows [5]:

$$M_0 = \mu \overline{D} A, \tag{2}$$

where μ the rigidity or shear modulus of the rock mass, $\overline{D}$ the average final displacement after the rupture, A the surface area of the rupture. M_0 has the following relations with the surface-wave magnitude scale M_S (or the moment magnitude M_W) and the radiated seismic strain energy E_S (Joule):

$$\log M_0 = 1.5M_S + 9.1, \tag{3}$$

$$\log E_S = 4.8 + 1.5M_S \tag{4}$$

Furthermore, the total energy release E_T can be expressed by:

$$E_T = E_S + E_f, \tag{5}$$

where E_f is the friction energy to power the growth of the earthquake fracture ($E_{fracture}$) and the production of heat (E_{heat}).

The ratio E_S/E_T (i.e., the seismic efficiency) is perhaps only about 0.01 to 0.1, depending both on the stress drop during the rupture as well as on the total stress in the source region. In other words, only a small fraction of E_T goes into producing seismic waves. For instance, the 2011 off the Pacific Coast of Tohoku Earthquake may have $M_W = 9.0$, Mo = 4.5×10^{22} Nm, and $E_S = 2.0\times10^{18}$ Joule. The 2001 Kunlun Pass W. Earthquake may have $M_S = 8.1$, Mo = 1.8×10^{21} Nm, and $E_S = 8.9\times10^{16}$ Joule.

3. Observations and Comments

Based on the above brief, the existing elastic rebound theory for the cause of earthquakes looks quite simple and straightforward. Accordingly, the classical theories of elasticity, elastodynamics, fracture mechanics and plasticity have been extensively applied to mechanically examine the mechanism of earthquakes and to quantitatively predict the earthquakes since the crustal rocks and soils can be considered as solid materials [5, 11, 12]. Furthermore, the monitoring, testing and modeling techniques and methods have been rapidly developed and used. A huge amount of accurate data such as GPS, satellite images and seismographs have been monitored and measured for the movement of tectonic plates and faults.

Hence, if the elastic rebound theory had been correct or along the right track, the movement and deformation of the massive solid rocks and soils associated with the tectonic plates and faults would have had many regularities and phenomena following the guidance of the classical theories of solid mechanics. The earthquake unpredictable statement would not have become a mainstream consensus in modern seismology and seismo-geology. However, many devastating damage earthquakes still occurred suddenly without pre-warning or pre-notice by human beings. Recent examples are the 2008 Wenchuan Earthquake [1] and the 2011 off the Pacific Coast of Tohoku Earthquake [13-15].

The author has actively participated in the field investigation of the Wenchuan Earthquake of May 12, 2008. He has found many natural phenomena that happened before, during and after Wenchuan Earthquake. These phenomena cannot be logically and consistently explained with the existing elastic rebound theory in association with the plate tectonics. Mostly importantly, the elastic rebound theory violates many phenomena. He has further actively investigated many other earthquakes including the 1976 Tangshan Earthquake, the 2001 Kunlun Pass W. Earthquake and the 2011 off the Pacific Coast of Tohoku Earthquake. The same observations can be made. The existing elastic rebound theory cannot describe many earthquake phenomena and sometimes violates the phenomena [6-10].

As discussed in Section 2, the elastic rebound theory claims that a large amount of heat must be developed on the rupture-plane [4]. The friction energy to power the growth of the earthquake fracture and the production of heat is about 90% to 99% of the total energy release during earthquake [5]. The rupture speed is very fast and can be 2 to 3 km/s over hundred kilometers crustal rock faults according to analysis of seismograph records. Accordingly, the heat must cause some substantial increases in temperatures of the ruptured rocks and soils and the ground air at epicenters. However, field observations did not show any expected increase in temperatures of the ground rocks, soils and air. For example, Rice [16] stated the observations of “low heat outflow from major faults and a scarcity of glass (pseudotachylyte) that would be left from rapid recooling of silicate melts”. The author has further found that temperatures of the ground rocks, soils and air can suddenly drop during and immediately after ground shocking. An example is given below to show the inconsistency between the observed phenomena and the elastic rebound theory.

4. The 2001 Kunlun Pass W. Earthquake

4.1. Brief description

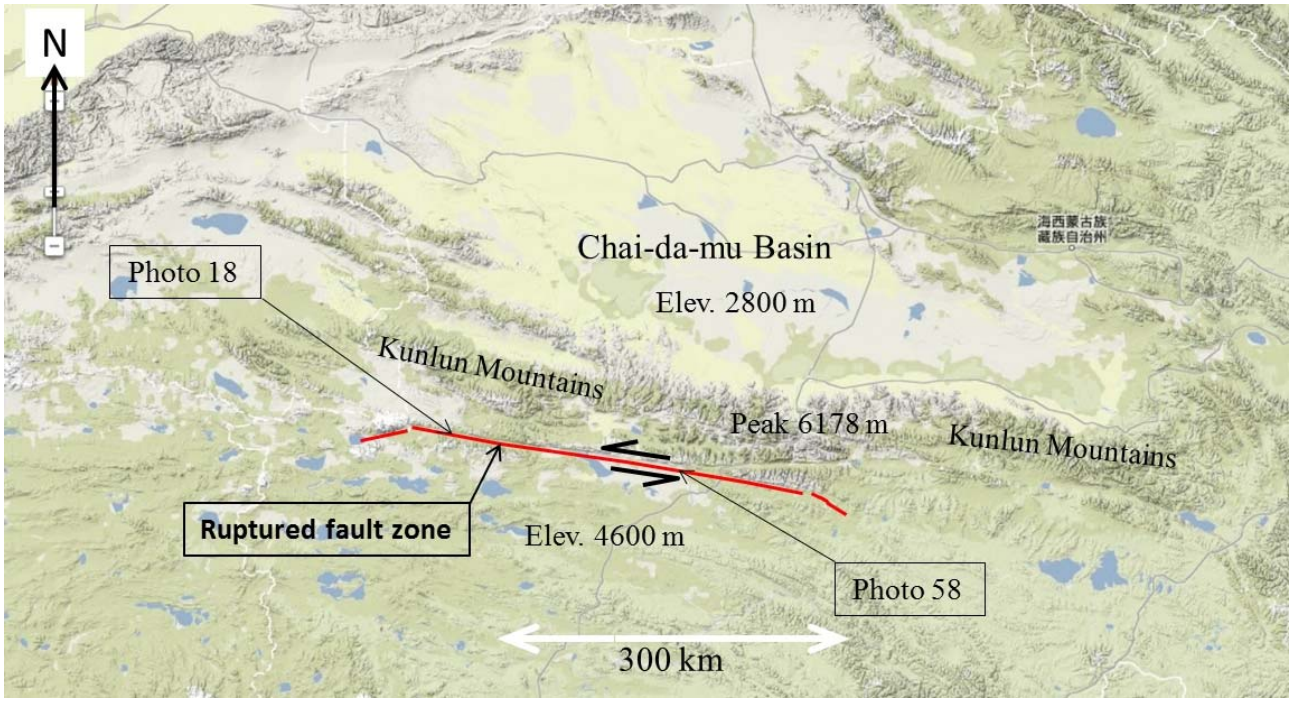

Figure 2. Google topography based seismic rupture zone for 2001 Kunlun Pass W. Earthquake

The Kunlun Pass W. Earthquake of magnitude 8.1 suddenly occurred along the western segment of

the Kunlun Mountain Fault at 17 hours and 26 minutes and 14.7 seconds (Beijing time) in the afternoon of November 14, 2011. The epicenter was at (35.6°N, 94.1°E). The focal depth was 15 km. The total duration was about 120 seconds. It released a huge amount of energy and made the grand Kunlun Mountains rupturing and slipping. The released radiated seismic strain energy E_S might be 8.9×10^{16} Joule. It resulted in a surface rupture zone in the south slope of Kunlun Mountains. The seismic surface rupture zone was 426 km in total length and several hundred meters in width (as shown in Figure 2).

On November 16, 2001, a group of scientists from China Seismological Bureau went to the epicenter area for seismological and damage investigation. They observed that the ground deformation and destruction were serious and great in scale. Their widths varied from several tens meters to several thousand meters along the 426 km long surface rupture zone. The maximum left-lateral displacement was 6 to 7 m.

4.2. Ruptured permafrost soils and ice

The Kunlun Mountain is part of the Qinghai-Tibet Plateau, a region of the largest-scale tectonic uplift. The ground elevations along the seismic surface rupture zone were about 4600 m to 5000 m above the sea level. The grounds that were ruptured by the seismic fault movement were dominantly permafrost grounds. Ice layers covered on the rivers were also ruptured. Album showing the seismic surface ruptures and destruction was published by China Seismological Bureau [17]. It contains 140 colored photographs showing the seismic rupture zone from the west to the east. Two photographs 18 and 58 from the Album [17] are represented in Figures 3 and 4, respectively. Their locations are identified in Figure 2.

Figure 3. A tent-shaped mole track typical of the frozen soil layer with a height of 2 m, north of Wuxue Peak (after photograph 18 of [17])

From the site photograph 18 in Figure 3, it can be evidently observed that the frozen soil layer was largely uplifted, bended and then cracked in tension and shear. The broken frozen soil layer was relatively rigid. Their fractured sides and edges were fresh, sharp and angular. There were no signs

of melting, thawing, plastic flow, muds, and/or re-freezing. In other words, the seriously broken frozen soil layer maintained its frozen state during and a few days after the ground rupture and shock.

From the site photograph 58 in Figure 4, it can be evidently observed that the frozen soil layer and the ice cover in a gully were largely uplifted, bended and then dislocated in tension and shear. The broken ice plates had fresh, sharp and angular sides and edges. There were no signs of melting, thawing, plastic flow, muds, and/or refreezing in the gully ice plates and frozen soils. In other words, the seriously broken frozen soils and ice plates maintained their frozen states during and a few days after the ground rupture and shock.

Figure 4. The ice in a gully was displaced 1.4 m in left-lateral sense 25 km east of Kusai Lake (after photograph 58 of [17])

The above no melting and thawing phenomena in the broken and deformed permafrost soils and ice covers are typical and can be observed in almost all the 140 photographs collected in the Album [4]. Chen et al. [18] also observed that the earthquake ruptures in frozen soils mainly showed brittle deformation, were composed of shear fractures, tension fracture and seismic ridges.

4.3. Energy analysis for melting frozen soils

Xu and Chen [19] carried out a temporal and spatial rupture process analysis of the earthquake by back-calculating the high signal-to-noise-ratio P-waveform data of vertical components of 20 stations with epicentral distances less than 900 km. Their back-calculated results showed that the earthquake had three sub-rupture events forming 220 km, 120 km and 270 km long fault ruptures. The six rupture speeds were 2.2 km/s to 5.8 km/s.

Secondly, according to fracture mechanics, the energy required for the growth of the earthquake fracture ($E_{fracture}$) in the rocks and soils may be estimated with the following equation.

$$E_{fracture} = \frac{AK_c^2}{E}, \quad (6)$$

where A is the total fractured area along the fault plane (m^2), K_c is the rock fracture toughness with the unit MPa $m^{1/2}$, and E is the rock elastic modulus (MPa). If E = 20,000 MPa, K_c = 1 MPa $m^{1/2}$, and A = 6.39 ×10^9 m^2 (=426 km × 15 km), then, $E_{fracture}$ = 3.2 ×10^{11} Joule. So, $E_{fracture}$ (3.2 ×10^{11} Joule) is far less than the E_S (8.9×10^{16} Joule).

Thirdly, the specific heat capacity c_p^{frozen} for completely frozen soil can be determined with the following equation:

$$c_p^{frozen} = \frac{c_p^{soil} + w_0 c_p^{ice}}{1 + w_0}, \quad (7)$$

where c_p^{soil} is the specific heat capacity for soil and is equal to 800 Joule/(kg °C), c_p^{ice} is the specific heat capacity for ice and is equal to 2060 Joule/(kg °C), and w_0 is the water (ice) content in the complete frozen soil. Normally, c_p^{frozen} is between 800 and 2060 Joule/(kg °C). The temperature increase ΔT of the frozen soil has the following relation with its mass M_{soil} and the heat increase ΔQ:

$$\Delta T = \frac{\Delta Q}{c_p^{frozen} M_{soil}}, \quad (8)$$

Assuming, w_0 is 15% and its degree of saturation 100%, then c_p^{frozen} 964 Joule/(kg °C) and the unit weight of the frozen soil is about 2209 kg/m^3. Assuming, for a total frozen soil along the ruptured zone, its thickness is 20 m, its length 426 km and its width 100 m. Its total mass is 1.9×10^{12} kg. It might have the temperature from –1°C to –20°C. The heats for the total frozen soil temperature increases 1°C and 20°C are 1.8×10^{15} Joules and 3.6×10^{16} Joules, respectively. The frozen soil has a total of 2.4×10^{11} kg ice. As the latent heat of ice is 3.34×10^5 Joule/kg, the total latent heat required for melting all the ice at 0°C in all the permafrost soil into liquid water is 8.2×10^{16} Joules.

As a result, the total heat required for melting all the frozen soil is between 8.3×10^{16} Joules and 11.8×10^{16}, which is similar to the released radiated seismic strain energy E_S 8.9×10^{16} Joule. Furthermore, if E_S is perhaps only about 0.01 to 0.1 of the total released energy E_T [5], there would be enough heat energy to melt and thaw the entire frozen soils along the surface ruptured zone. But, no melting or thawing phenomena were observed in the 140 site photographs [17]. The theoretical results and field observations can demonstrate that the elastic rebound theory is incorrect.

5. The Gas Cause of Earthquakes

A further question may be asked: what type of loading can rapidly crack the crustal fault for tens to hundreds km long and tens km deep, generates the strong seismic waves, but does not produce heat? One most possible and feasibility loading is the rapid expansion and migration of highly compressed natural gas from deep crustal traps via tectonic fault channel. This is the internal loading associated with the gas hypothesis for cause of earthquakes [6-10]. The hypothesis can be briefly described below.

An earth quaking is an adiabatic process of interaction between rapid upward expansion and migration of compressed natural gas and its surrounding crustal rocks and ground soils. The natural gas is produced in core and/or mantle and gradually accumulated in the traps below crustal fault rocks. It escapes from its traps in deep fault zones of the lower crustal rocks. Because of the

extremely high pressure drops in front of the moving gas mass, the gas migration speed in the fault zone can be several km/s. The interaction is instantaneous and flashing. It can be complete within few to tens and to hundreds seconds. The gas expansion and migration are confined and constrained by the inward gravity, the tectonic stresses and the rigidness and strengths of the crustal rocks. The energy of earth quaking is mainly the physical expansion energy of the highly compressed methane gas. The gas expansion is a cooling process, which reduces the temperatures of ground rocks and soils and air during and immediately after the shock. All the earthquake phenomena can be logically and consistently explained and predicted with the gas hypothesis. Specially, the broken permafrost soils and ices along the 426 km long surface rupture zone in south slope of Kunlun Mountains could keep sharp, angular and fresh immediately after the earthquake on November 14, 2001.

6. Concluding Remarks

The author would like to recall the four rules of reasoning in philosophical inquiries of nature summarized by Sir Isaac Newton about 300 years ago [20].

- RULE I. *We are to admit no more causes of natural things than such as are both true and sufficient to explain their appearances*.
- RULE II. *Therefore to the same natural effects we must, as far as possible, assign the same causes*.
- RULE III. *The qualities of bodies, which admit neither intensification nor remission of degrees, and which are found to belong to all bodies within the reach of our experiments, are to be esteemed the universal qualities of all bodies whatsoever*.
- RULE IV. *In experimental philosophy we are to look, upon propositions inferred by general induction from phenomena as accurately or very nearly true, notwithstanding any contrary hypotheses that may be imagined, till such time as other phenomena occur, by which they may either be made more accurate, or liable to exceptions*.

We may have to follow these four rules in our scientific inquiry of the nature of earthquakes. The elastic rebound theory was developed one hundreds year ago from the observations of co-seismic surface ruptures induced by the 1906 California Earthquake. It is only partially correct because it associates earthquakes with faults. It is inconsistent and even violates many other phenomena that were present before, during and after earthquakes.

Numerous failures have been encountered and experienced in our tremendous efforts using the elastic rebound theory in the prediction of earthquakes. Many current seismo-geologist and seismologists have lost their original goals to predict earthquakes and turned to believe that earthquakes are unpredictable with the present techniques. All these problems are due to the fact that the incorrect elastic rebound theory for the cause of earthquakes was used in the investigation and prediction of earthquakes.

It is evident that the energy released during earthquake is not the elastic stress and strain energy accumulated in brittle crustal rock solids during relative movements of tectonic plates. The released energy is the volumetric expansion energy of highly compressed and dense natural (methane) gas. The gas rapidly escaped from its deep crustal traps and was migrating via deep faults into shallow grounds and the sky. The author trusts that this gas hypothesis for the cause of earthquakes would make earthquake predicable in the near future.

Acknowledgements

The author would like to thank many friends and colleagues for their invaluable advices, assistances, discussions, information, data and supports during his independent investigations of the nature of

earthquakes and the Earth system.

References

[1] Q.F. Chen, K. L. Wang, The 2008 Wenchuan Earthquake and earthquake prediction in China. Bulletin of the Seismological Society of America, 100(5B), 2010, 2840–2857
[2] S. E. Hough, Predicting the Unpredictable, the Tumultuous Science of Earthquake Prediction, Princeton University Press, New Jersey. 2010.
[3] A.C. Lawson, The Mechanics of the Earthquake, The California Earthquake of April 18, 1906, Report of the State Earthquake Investigation Commission, Vol.1, Parts I and II, Carnegie Institution of Washington, Washington, D.C., USA. 1908, p. 451
[4] H.F. Reid, The Mechanics of the Earthquake, The California Earthquake of April 18, 1906, Report of the State Earthquake Investigation Commission, Vol.2, Carnegie Institution of Washington, Washington, D.C., USA. 1910, p. 192
[5] P. Bormann (Ed.), New Manual of Seismological Observatory Practice (NMSOP-2), IASPEI, GFZ German Research Centre for Geosciences, Potsdam; 2012, http://nmsop.gfz-potsdam.de; DOI: 10.2312/GFZ.NMSOP-2, urn:nbn:de:kobv:b103-NMSOP-2
[6] Z.Q. Yue, “What caused the catastrophic landslides during the May 12 Wenchuan Earthquake in Sichuan, China.” Abstract and oral presentation at The 12th International Conference of International Association for Computer Methods and Advances in Geomechanics (IACMAG), 1-6 October, 2008, Goa, India: 135.
[7] Z. Q. Yue, The source of energy power directly causing the May 12 Wenchuan Earthquake: Huge extremely pressurized natural gases trapped in deep Longmen Shan faults, News Journal of China Society of Rock Mechanics and Engineering, 86 (2009 (2)), 45-50.
[8] Z. Q. Yue, Features and mechanism of coseismic surface ruptures by Wenchuan Earthquake. In Rock Stress and Earthquake, edited by Furen Xie, Taylor & Francis Group, London, ISBN 978-0-415-60165-8, 2010, 761-768.
[9] Z. Q. Yue, On the common energy and gas source for causing earthquakes and natural gas. Bulletin of Earth Sciences & Philosophy, No.1 in 2011 and Total No.50: 21-64 (in Chinese)
[10] Z. Q. Yue, The cause and mechanism of earthquakes by extremely compressed natural gas in deep fault zones of the crust. Proceedings of Symposium of Earthquake Genesis and Prediction in Continents, Wuhan, China, Nov. 5-6, 2010, 94-100 (in Chinese).
[11] R. Wang, G .Q. He, Y. Q. Yin, Y. E. Cai, A mathematical simulation for the pattern of Seismic transference in North China, Acta Seismologica Sinica, 2(1), 1980, 32-42 (in Chinese)
[12] S. M. Wang, R. Wang, Joint inversion of the kinematics and dynamics of the North American plate, Tectonophysics, 302(3-4), 1999, 173-201
[13] D. Normile, Devastating earthquake defied expectations, Science, 33 (2011) 1375-1376
[14] R. J. Geller, Shake-up time for Japanese seismology, Nature, Nature 472 (2011) 407–409
[15] R. Monastersky, Giant shock rattles ideas about quake behavior, Nature, 471 (2011) 274
[16] J. R. Rice, Heating and weakening of faults during earthquake slip, Journal of Geophysical Research – Solid Earth, 111(B05311), 2006, 1-29
[17] R. X. Song (Editor-in-Chief), Album of the Kunlun Pass W. Ms 8.1 Earthquake, China, Seismological Press, Beijing, 2003, ISBN 7-5028-2215-1
[18] Y. M. Chen, L. M. Wang, W. Dai, W. F. Wang, H. G. Dai, The frozen soils and devastating characteristics of west Kunlun Mountains Pass Ms 8.1 Earthquake Area in 2001, Earthquake Research in China, 20(2), 2004, 161-169
[19] L. S. Xu, Y. T. Chen, Temporal and spatial rupture process of the great Kunlun Mountain Pass earthquake of November 14, 2001 from the GDSN long period waveform data, Science in China Series D-Earth Sciences, 48(1), 2005, 112-122
[20] Sir Isaac Newton, Mathematical Principles of Natural Philosophy, 1725, Translated into English by Andrew Motte,1846, New York, published by Daniel Adee

Effects of a newly incorporated with a stress-weakening term in a revised RSF on earthquake nucleation

Nobuki Kame[1,*], Satoshi Fujita[1], Masao Nakatani[1], Tetsuya Kusakabe[1]

[1] Earthquake Research Institute, the University of Tokyo, Tokyo 113-0032, Japan
* Corresponding author: kame@eri.u-tokyo.ac.jp

Abstract Quasi-static nucleation on a frictional fault embedded in an elastic medium is known to be sensitive to the frictional properties. Earlier works have employed 'aging' and 'slip' versions of rate- and state-dependent friction (RSF) law, but some clear flaws have been known; the aging law wrongly predicted linearly increasing slip-weakening distance with the amount of strength reduction, whereas the slip law could not reproduce observed time-dependent healing at very low velocities. Recently Nagata et al. [1] proposed a revised version of RSF by incorporating a stress-weakening effect newly found in laboratory experiments and by correcting the frictional parameters '*a*' and '*b*' largely, where '*a*' and '*b*' are the coefficients of RSF. It seems to be free from the previously known flaws and we here reexamined nucleation by using the revised RSF. From numerical simulations, two major differences were found. 1) For weakly velocity-weakening range of $0.85<a/b<1$, nucleation has characteristics of both unidirectional slip-pulse regime found in the slip law case and crack-like expansion regime in the aging law case. 2) Fixed-length patch regime occurs over a wider condition of a/b up to 0.85 in contrast with the previously reported range of $a/b<0.5$ implying strongly velocity-weakening faults.

Keywords Nucleation, Earthquake, Fault, Rate and State Friction

1. Introduction

On the basis of laboratory rock friction experiments the rate- and state-dependent friction law (RSF) was introduced [2]. It has been widely used in modeling of earthquake occurrence and successfully explained the mechanics of seismic cycles [3], aftershock activities [4] and many others. In the present paper, we focus on the modeling of earthquake nucleation by careful attention to the RSF formulae.

Quasi-static nucleation on a frictional fault buried in an elastic continuum is known to be sensitive to the frictional properties. Earlier works studied spontaneous nucleation under slow tectonic loading using 'aging' and 'slip' versions of rate- and state-dependent friction (RSF) law [5-7]. For strongly velocity-weakening faults characterized by $a/b<0.5$ ('*a*' and '*b*' are the coefficients of RSF), nucleation occurs in a 'fixed-length patch' regime, where regions of quasi-static slip remains relatively small. For weakly velocity-weakening faults ($0.5<a/b<1$), nucleation must propagate spatially (Fig. 1). Propagation occurs in a form of an expanding crack in the aging law case and in a form of a migrating slip pulse in the slip law case.

Both versions of RSF were proposed as descriptions of laboratory friction experiments, but some clear flaws are known; aging law's slip-weakening distance increases linearly with the amount of strength reduction, while slip law does not reproduce time-dependent healing at very low velocities. Recently Nagata et al. [1] proposed a revised version of RSF by incorporating a stress-dependent term with a coefficient '*c*' and by correcting the RSF parameters '*a*' and '*b*' largely. This new version of RSF seems to be free from the previously known flaws and is here employed to reexamine nucleation.

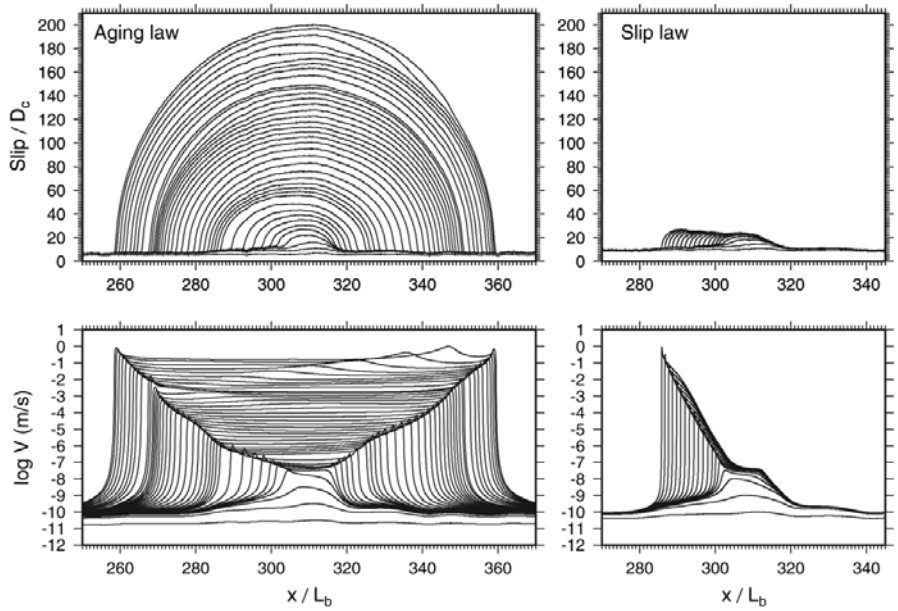

Figure 1. Snapshots of normalized slip (top panels) and slip rate (bottom) for two simulations identical in all respects except that the left panels use the aging law and the right panels the slip law. *a/b*=0.95, $D_c = 0.4 \times 10^{-3}\,\mathrm{m}$, $V_0 = 10^{-9}\,\mathrm{m/s}$, $\tau_r = 10^{-2}\,\mathrm{Pa/s}$, the normalizing length scale $L_b \equiv \mu_* D_c/(b\sigma) = 4.6\mathrm{m}$. From figure 2 of Ampuero and Rubin [7] (in the present paper, the notation D_c is replaced by L).

1-1. Existing and revised RSFs

RSF consists of two equations bearing logically separate roles [8]. One is the constitutive law, which describes the relationship between applied shear stress τ and slip rate V as

$$V = V\exp\left(\frac{\tau-\Phi}{a\sigma}\right), \text{ or } \tau = \Phi + a\ln\left(\frac{V}{V_*}\right), \tag{1}$$

where Φ is the state variable specifying the internal physical state of the interface, which may reflect the real contact area [9], a is called direct effect coefficient and play an important role in the constitutive law for which the physical mechanism has been attributed to thermally activated creep [8,10], σ is a normal stress and V_* is a reference velocity. Another equation is the evolution law, which phenomenologically describes variations of the state Φ. Two empirical evolution equations for the evolution of Φ, first formalized by Ruina [11], are common use. These are

$$\frac{d\Phi}{dt} = \frac{b\sigma}{L}V_*\exp\left(-\frac{\Phi-\Phi_*}{b\sigma}\right) - \frac{b\sigma}{L}V \quad \text{(Aging law)}, \tag{2}$$

$$\frac{d\Phi}{dt} = -\frac{V}{L}\left(\Phi - \Phi_* - b\sigma\ln\left(\frac{V}{V_*}\right)\right) \quad \text{(Slip law)}\,, \tag{3}$$

where b is a RSF parameter relating change in state, L is a length scale related with slip, Φ_* is a reference state. The first and second terms of eq. (2) represent logarithmic time-dependent healing and linear slip weakening with a constant rate b/L per unit slip, while eq. (3) represents exponential slip weakening with a fixed distance L [8]. The aging law has trouble in reproducing a symmetric exponential change of friction over a fixed slip distance subsequent to stepwise velocity jumps to opposite signs observed in velocity-step tests (Fig. 2a) though it explains time-dependent healing in hold-slide tests very well as observed [8,11]. The slip law does explain the slip weakening (Fig. 2b), but has a well-known difficulty in reproducing time healing at low slip rate [12-13].

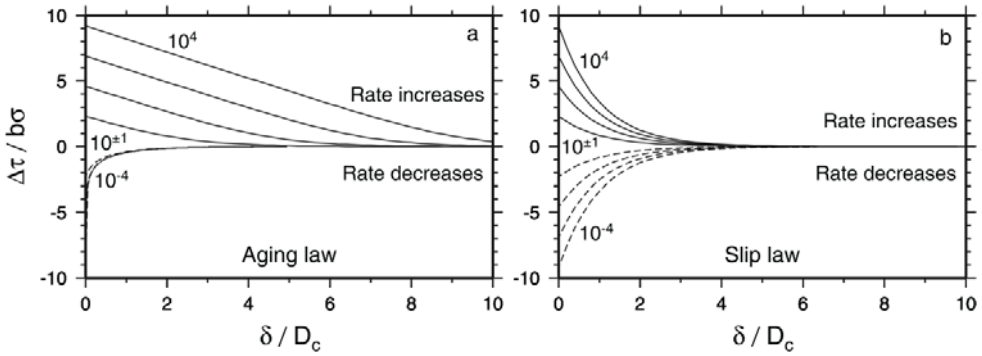

Figure 2. Plots of normalized stress as a function of normalized slip, for step velocity increases (solid lines) and decrease (dashed lines) of 1-4 orders of magnitude, for (a) the aging law and (b) the slip law. Stresses are relative to the future steady state value. For the aging law the curves for step decreases of 2-4 orders of magnitude appear indistinguishable, but they intersect the vertical axis at the same values of $\Delta\tau$ as the slip law. From figure 3 of Ampuero and Rubin [7] (in the present paper, the notation D_c is replaced by L).

Recently Nagata et al. [1] proposed a revised RSF, using new rigorous methods of laboratory data analysis. Firstly, the direct effect coefficient a was constrained to be 0.05, about five times larger than previously believed. The difference came from their new method to constrain a without using any evolution laws, contrasting to conventional methods where the state change from imperfection of real-world 'step' tests was inferred by assuming 'flawed' evolution law. This large a immediately led to similarly large $b \sim 0.05$ because $(b-a) \sim 0$ was reliably constrained from velocity dependence of steady-state friction without any evolution laws. Secondly, a strong linear negative dependence of $d\Phi/dt$ on $d\tau/dt$ was newly found from the misprediction analysis of Φ between the observed $\Phi(=\tau - a\ln(V/V_*))$ and the predicted Φ by using eq. (2). The shear-stress weakening effect was incorporated as

$$\frac{d\Phi}{dt} = \frac{b\sigma}{L} V_* \exp\left(-\frac{\Phi - \Phi_*}{b\sigma}\right) - \frac{b\sigma}{L} V - c\frac{d\tau}{dt} \quad , \tag{4}$$

where c is the stress weakening parameter. The term $-cd\tau/dt$ works to resolve the artifact of varying slip-weakening distance in the aging law as clearly seen in Fig. 3; when c=0, eq. (4) coincides with eq. (2) and the artifact remains unsolved, but with increasing c, the symmetric response in opposite sign of velocity-step tests was attained and the prediction curves became more symmetric like the slip law, keeping with the time-dependent healing term [14]. From the above misprediction analysis, the best-fit value of c was determined about 2.0. Nagata et al. [1] confirmed that the revised RSF could correctly reproduce both hold-slide and velocity-step tests with the same values of frictional parameters, which had never been attained in the existing RSFs. Very recently the revised RSF was employed to simulate earthquake cycle [15] and aftershock triggering [16].

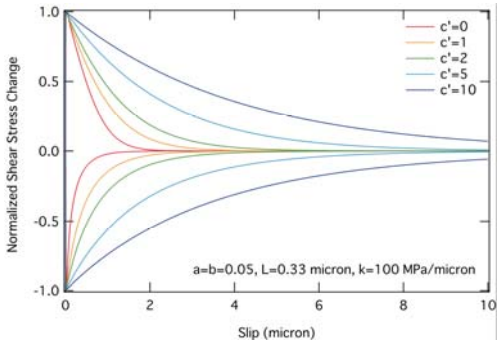

Figure 3. Normalized change of shear stress in velocity step-up and step-down tests predicted for different c. Slip rate is increased or decreased tenfold. From figure 5.21 of Nagata [14].

1-2. Nucleation regimes and lengths

We here briefly summarize nucleation regimes and their lengths in the previous studies [5-7] examined both numerically and analytically.

For strongly velocity-weakening faults characterized by $a/b<0.5$, nucleation occurs in a 'fixed-length patch' regime, where regions of quasi-static slip remains relatively small. In the patch regime, the state along patch kept well above steady state with insignificant healing. With a no-healing approximation, Rubin and Ampuero [6] analytically estimated the patch half-length as

$$L_\nu = 1.3774 L_b \qquad (L_b \equiv \frac{\mu_* L}{b\sigma}), \tag{5}$$

where $\mu_* = \mu/(1-\nu)$ is the stiffness of a medium for edge dislocation, μ is the rigidity, and ν is the Poisson's ratio. For the slip law, the patch length is slightly smaller than L_ν [7].

For weakly velocity-weakening faults ($0.5<a/b<1$), nucleation must propagate spatially. Propagation occurs in a form of an expanding crack ('crack-like expansion' regime) in the aging-law case (Fig. 1a) and in a form of a migrating slip pulse ('unidirectional slip-pulse' regime) in the slip-law case (Fig. 1b). In the crack regime, the state along expanding portion instead kept steady state for increasing slip, that is, healing effect was not negligible. The nucleation half-length was estimated with a steady-state approximation as

$$L_\infty = \left(\frac{b}{b-a}\right)^2 \frac{L_b}{\pi} \qquad (b-a>0). \tag{6}$$

Ampuero and Rubin [7] attributed the crack-like expansion to the slip-weakening curves predicted with the aging law in response to velocity step ΔV (Fig. 2a), which would be experienced at the expanding nucleation front where the concentrated stress yields with a sudden jump in the slip rate. In their analysis, nucleation zone was proven to be approximated by a crack; stress uniformly drops by $\Delta\tau$ on the crack and locally concentrates at the tips by peak-to-residual stress drop $\Delta\tau_{p\text{-}r}$. Fracture mechanics tells us the energy release rate G in terms of the crack length l and fracture energy G_c at the crack tip, which were then connected to slip rate V on RSF faults as

$$G = \frac{\pi}{2}\frac{l}{\mu_*}(\Delta\tau)^2 \propto (\ln V)^2 \qquad (\Delta\tau \sim \sigma(b-a)\ln(V/V') - b\varepsilon) \tag{7}$$

$$G_c = \frac{\Delta\tau_{p-r}\delta_c}{2} = \frac{L}{2b\sigma}(\Delta\tau_{p-r})^2 \propto (\ln V)^2 \qquad (\Delta\tau_{p-r} \sim b\sigma\ln(V/V'') - \varepsilon) \tag{8}$$

where V' and V'' are nearly constant slip rates, δ_c is the effective slip-weakening distance following the linear slip-weakening rate *(b/L)*, and $\varepsilon \sim 0$. Setting $G = G_c$ and solving for the instantaneous nucleation length l lead to

$$l = \frac{L_b}{\pi}\left(\frac{\Delta\tau_{p-r}}{\Delta\tau}\right)^2 = l(V). \tag{9}$$

At every moment in accelerating V, the energy balance $G=G_c$ is satisfied; this is why the nucleation can be the crack-like expansion. By considering the ratio $\Delta\tau_{p\text{-}r}/\Delta\tau$ approaching *b/(b-a)* in the limit of large slip rate V, the nucleation size L_∞ in eq. (6) was derived. However, the prediction curves with increasing slip-weakening distances are an artifact due to the linear slip-weakening rate and contradict with laboratory experiments [8].

On the contrary, following the slip-weakening curves of the slip law (Fig. 2b), the fracture energy becomes $G_c \propto (\Delta\tau_{p-r})^1 \propto (\ln V)^1$ due to the constant slip-weakening distance, keeping $G \propto (\ln V)^2$ remain the same extent. The energy balance suggests that the accelerating V is incompatible with the crack-like expansion of the nucleation zone and numerical simulation demonstrated that the nucleation instead takes the form of unidirectional slip pulse (Fig. 1b). It must be noted that the nucleation was, however, wrongly predicted at the very beginning where the slip rate was very low and healing should have dominated. A genuine regime following laboratory experiments should be investigated by using the revised RSF.

2. Simulation method and choice of parameters

Following Dieterich [5], quasi-static nucleation is modeled here by adopting the revised RSF. A fault is divided by n equally spaced segment with a length Δs and loaded by a constant stressing rate τ_r:

$$\tau_i = \tau_i^0 + \tau_r t + \Delta\tau_i \quad (i = 1, 2, \quad , n), \tag{5}$$

where τ_i is the shear stress, τ_i^0 is the initial stress, $\Delta\tau_i (= \Sigma S_{ij}\delta_j)$ is the change of stress resulting from the slip δ_j over the fault, and S_{ij} is stress kernel obtained from elastic dislocation solution [5]. By equating eq. (5) with eq. (1) and by substituting the revised law of eq. (4) to eliminate Φ, we obtain a couple of nondimensional differential equations:

$$d\tau_i'/dt' = \tau_r' + S_{ij}' V_j' \tag{1.1}$$

$$d\left(\ln V_i'\right)/dt' = \left(a/b\right)^{-1}\left\{(1+c)d\tau_i'/dt' - \exp[-(\tau_i' - (a/b)\ln V_i')] + V_i'\right\} \tag{1.2}$$

where $\tau_i' = (\tau_i - \tau_*)/(b\sigma)$, $V_i' = V_i/V_*$, $t' = t/(L/V_*)$, $\tau_r' = \tau_r/(b\sigma/(L/V_*))$, $S_{ij}' = S_{ij}/(b\sigma)$ and frictional parameters (a,b,c,L) are assumed the same at all points on the fault. A factor (1+c) is newly appeared by the shear-stress dependent term. Nagata et al. [1] obtained a best fit parameter set (a,b,c,L)=(0.051, 0.0565, 2.0, 0.33micron) and this is the only set ever constrained by laboratory experiments. It leads to a/b=0.90 and (1+c)=3.0 in simulating nucleation.

In our controlled numerical experiments, c is chosen for a tuning parameter: no stress weakening c=0.0 is for the aging law, the optimum c=2.0 for the revised law, and an excessed c=4.0 for comparison. a/b is chosen as 0.95, 0.90, 0.85, 0.80, 0.75, implying that smaller a/b corresponds to stronger velocity weakening. Except for a/b and c, all simulations are identical in all respects. Fault discretization is done with n=2400 and $\Delta s = L_b/10$, small enough to resolve nucleation length. Initial velocity is assumed to be uniformly distributed $V_i'^0 = 1.0 (= V_*')$ and initial stress $\tau_i'^0$ is assumed to be randomly distributed between [-1,0] in order to start nucleation from below-steady state where the time-healing term dominates the slip-weakening term. $\tau_r' = 0.1$ and $\mu_*' = 11.56 \times 10^3$ are chosen the same as in Ampuero and Rubin [7]. If $V_* = 10^{-9}$m/s is taken, our simulation results are directly comparable with Fig. 1. Time integration is numerically done by using the Runge-Kutta method until $V_{\max}' = 10^9$.

3. Result

We conducted nucleation simulations with the total 15 sets of the revised RSF parameters (*a/b*, *c*) and found systematic changes in the results. Figure 4 shows the results with variation of *c*=0.0, 2.0, 4.0 under a fixed *a/b*=0.95, the snap shots of slip and slip rate evolution. When *c*=0.0 (the aging law) was adopted, a crack-like expansion occurred similar to Fig. 1a. Contrasting to this, when *c*=2.0, 4.0 were adopted, the crack-like propagation was completely disappeared. A narrow zone of peak slip velocity appears at the edge of the nucleation front propagating outwards like in the slip-law case, but the wide (and growing) region behind the front remains slipping at a velocity more than the 1/3 of the peak velocity, resulting in a slip distribution similar to that of an expanding crack as in the aging law case. Namely, the nucleation regime with the revised RSF was found to have both pulse feature in the spatial propagation and the crack feature in the slip rate distribution. The result may be understandable by comparing the revised law and the slip law. The revised law, as in the slip law favoring pulse, yields a slip-weakening distance nearly independent of the amount of strength reduction (Fig. 3), but it differs from the slip law in that it involves a time-dependent healing term, which should contribute significantly where the slip is proceeding near steady state. Crack-like extension would be no longer incompatible with the energy balance for instantaneous nucleation length *l* as pointed out in the section 1.2.

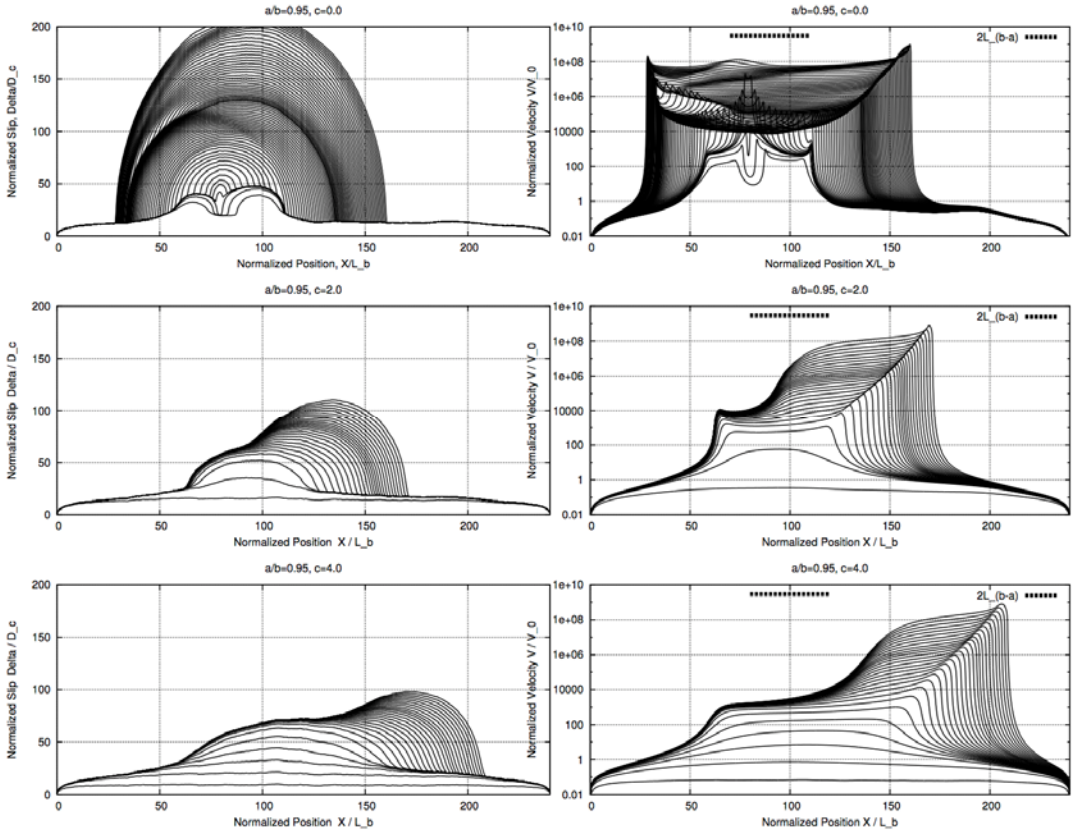

Figure 4. Snapshots of normalized slip (left panels) and slip rate (right panels) simulated by using the revised RSF for *a/b*=0.95 with three variations in the *c* parameter: (top) case with *c*=0.0, (middle) case with *c*=2.0, and (bottom) case with *c*=4.0.

Figure 5 shows the results with variation of *a/b*=0.90, 0.85, 0.80, 0.75 under fixed *c*=2.0 (the optimum) and *c*=4.0. Only snap shots of the slip rate are shown for brevity. For both *c*, transition from a pulse regime to a patch regime was observed as *a/b* was decreased. The transition was around *a/b*=0.80 for *c*=2.0 and *a/b*=0.85 for *c*=4.0, which are much larger than *a/b*=0.5 in the previous studies as schematically summarized in Fig. 6. The condition for the patch regime widens

as we increase a stress-weakening parameter *c*. As to the patch length with the revised RSF, it is obviously larger than the theoretical length $2L_\nu$ with the aging law in eq. (5) that is just a few digits $(\sim 2.7L_b)$ in the normalized position in Fig. 5. The newly incorporated stress dependent term brought significant effects on the fixed-length path regime: the wider *a/b* range and the larger patch length. As to these results, a clear explanation has not been come up with.

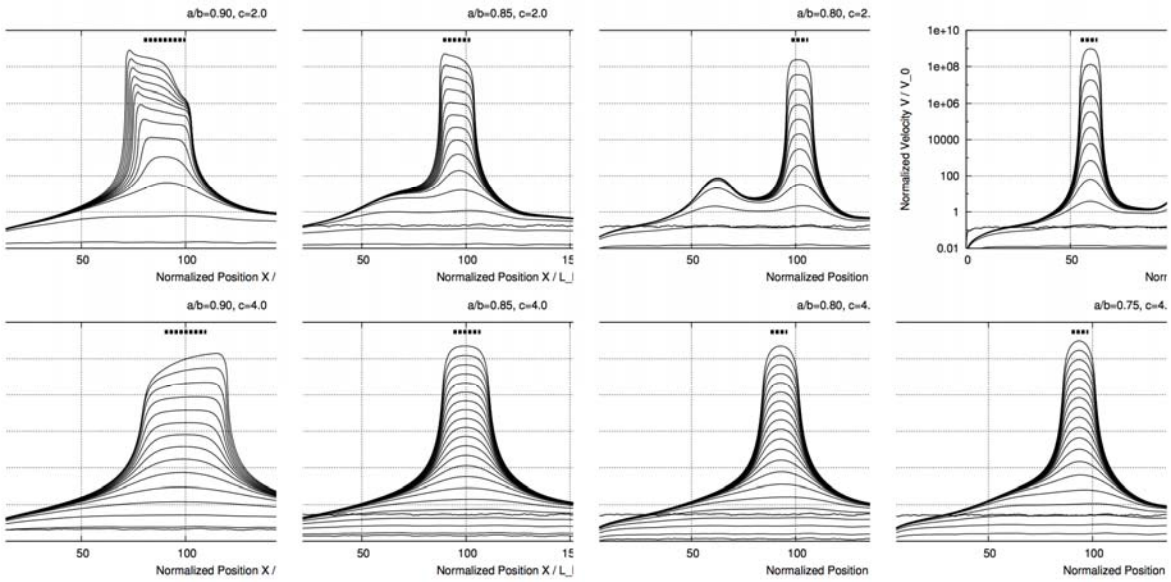

Figure 5. Snapshots of slip rate simulated with the revised RSF: (upper panels) cases with *c*=2.0, and (lower) cases with *c*=4.0 (from left to right: *a/b*=0.90, 0.85, 0.80, 0.75). All the vertical axes are in the same scale. A length scale $2L_{b\text{-}a}$ is plotted for reference by thick dashed line.

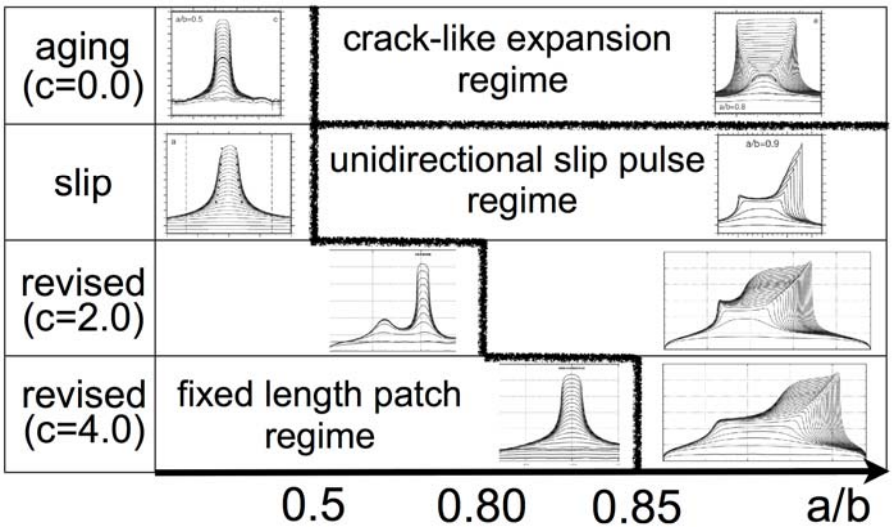

Figure 6. Nucleation regimes in 2-D simulation of quasi-static nucleation on RSF faults. The nucleation icons are from figure 1 of Rubin and Ampuero [6] in the aging law and figures 5 and 7 of Ampuero and Rubin [7] in the slip law.

4. Discussion

The simulated nucleation length was compared with the theoretically predicted value $2L_\nu$ and was

found to be larger than $2L_v$. Seeking for a characteristic patch length with the revised RSF, we then compare it with another length scale

$$L_{b-a} \equiv \frac{\mu_* L}{(b-a)\sigma}, \tag{6}$$

where L_{b-a} is a characteristic nucleation length based on long-tem stick-slip instability [6]. $2L_{b-a}$ is plotted for reference by thick dashed line in Fig. 5. It seems to show a better agreement than $2L_v$ and may be a possible reference length at the moment. It is a tentative scale as a matter of course and future analytic work will be absolutely necessary to quantify the nucleation patch length explicitly including *c* parameter [17].

4. Conclusion

Nucleation on frictional faults was reexamined by using the revised RSF which seems to be free from previously known flaws. Our simulation results with systematic changes in the frictional parameter sets (*a/b*,*c*) comprehensively disclosed two major differences. 1) For weakly velocity-weakening range of $0.85<a/b<1$, nucleation had characteristics of both unidirectional slip-pulse regime found in the slip law case and crack-like expansion regime in the aging law case. 2) Fixed-length patch regime occurred over a wider condition of *a/b* up to 0.85 in contrast with the previously reported range of $a/b<0.5$ implying strongly velocity-weakening faults, and its patch length was larger than that predicted by the aging law.

Acknowledgements

N. Kato provided his numerical code. N.K. was supported by MEXT Grant-in-Aid for Scientific Research on Innovative Areas Number 21107007. This study was also supported by MEXT, under its Observation and Research Program for Prediction of Earthquakes and Volcanic Eruptions.

References

[1] K. Nagata, M. Nakatani, S. Yoshida, A revised rate- and state-dependent friction law obtained by constraining constitutive and evolution laws separately with laboratory data, J Geophys Res, 117 (2012) B02314 doi:10.1029/2011JB008818.
[2] J.H. Dieterich, Modeling of rock friction 1. experimental results and constitutive equations, J Geophys Res, 84 (1979) 2161-2168.
[3] S.T. Tse, J.R. Rice, Crustal earthquake instability in relation to the depth variation of frictional slip properties, J Geophys Res, 91 (1986) 9452-9472.
[4] J.H. Dieterich, A constitutive law for rate of earthquake production and its application to earthquake clustering, J Geophys Res, 99 (1994) 2601-2618.
[5] J.H. Dieterich, Earthquake nucleation on faults with rate- and state-dependent strength, Tectonophysics, 211 (1992) 115-134.
[6] A.M. Rubin, J.-P. Ampuero, Earthquake nucleation on (aging) rate and state faults, J Geophys Res, 110 (2005) B11312 doi:10.1029/2005JB003686.
[7] J.-P. Ampuero, A.M. Rubin, Earthquake nucleation on rate and state faults - Aging and slip laws, J Geophys Res, 113 (2008) B01302 doi:10.1029/2007JB005082.
[8] M. Nakatani, Conceptual and physical clarification of rate and state friction: Frictional sliding as a thermally activated rheology, J Geophys Res, 106 (2001) 13347-13380.
[9] J.H. Dieterich, B.D. Kilgore, Imaging surface contacts: power law contact distributions and contact stresses in quartz, calcite, glass and acrylic plastic, Tectonophysics, 256 (1996) 219-239.

[10] F. Heslot, T. Baumberger, B. Perrin, B. Caroli, C. Caroli, Creep, stick-slip, and dry-friction dynamics: Experiments and a heuristic model, Physical review E, 49 (1994) 4973-4988.
[11] A. Ruina, Slip instability and state variable friction laws, J Geophys Res, 88 (1986) 10359-10370.
[12] C. Marone, Fault zone strength and failure criteria, Geophys Res Lett, 22 (1995) 723-726.
[13] N. Kato, T.E. Tullis, A composite rate- and state-dependent law for rock friction, Geophys Res Lett, 28 (2001) 1103-1106.
[14] K. Nagata, Experimental study of friction behaviors using acoustic in-situ monitoring of frictional interface, Dr. Sc. Thesis, the University of Tokyo, 2008.
[15] N. Kame, S. Fujita, M. Nakatani, T. Kusakabe, Earthquake cycle simulation with a revised rate- and state-dependent friction law, Tectonophysics, (2012) doi: 10.1016/j.tecto.2012.11.029.
[16] N. Kame, S. Fujita, M. Nakatani, T. Kusakabe, Effects of a revised rate- and state-dependent friction law on aftershock triggering model, Tectonophysics, (2012) doi: 10.1016/j.tecto.2012.11.028.
[17] P. Bhattacharya, A.M. Rubin, Numerical and analytical study of rupture nucleation on 1D and 2D faults under a new state evolution law, AGU 2012 Fall Meeting abstract, S21B-2466, San Francisco.

XFEM modelling of degradation-permeability coupling in complex geomaterials

B. Sonon[1], B. François[1], A.P.S. Selvadurai[2], T.J. Massart[1,*]

[1] Building, Architecture and Town Planning CP 194/2, Université Libre de Bruxelles (ULB), Avenue F.D. Roosevelt 50, 1050 Brussels, Belgium
[2] Department of Civil Engineering and Applied Mechanics, McGill University, 817 Sherbrooke Street West, Montreal, Canada, H3A 2K6
* Corresponding author: thmassar@ulb.ac.be

Abstract The theory of poromechanics is widely used to examine problems in the environmental geosciences. In classical poromechanics, the material parameters such as the elastic stiffness or the permeability are assumed to remain constant. The porous fabric can, however, experience micromechanical processes that can lead to alterations in the stiffness and fluid transport characteristics. Experiments on rocks indicate permeability increases even at deviatoric stress states well below peak stress levels, which can contribute to errors in predicting the progress of transient phenomena. This paper presents a multi-scale approach for investigating permeability evolution in a heterogeneous geomaterial. The complex microstructure of geomaterials is modelled using a level set-based extended finite element description (XFEM) that allows uncoupling the meshing operations from the presence of the fine scale material interfaces. A dedicated tool for the generation of representative volume elements based on similar concepts is exploited. Fine scale plastic constitutive laws are used to model the progressive mechanical degradation under stress. The local (fine-scale) permeability evolution can then be coupled to the local plastic dissipation quantities. These fine-scale developments are combined with a versatile computational homogenization technique to upscale mechanical and transport properties corresponding to heterogeneous microstructures. Using this procedure, the effect of progressive degradation on the averaged permeability properties of geomaterials is investigated. These procedures are illustrated by estimating the variation of permeability with the confining pressures and deviatoric stresses applied in triaxial testing.

Keywords Mechanical Degradation, Degradation-induced permeability, Level Set functions, XFEM modelling

1. Introduction

Heterogeneous geomaterials possess complex microstructures. The computational homogenisation of such microstructures requires specific tools to take this complexity into account, both from the point of view of the availability of representative volume elements, and from the point of view of the discretisation technique. This paper presents a level set-based extended finite element description (XFEM), that allows uncoupling the meshing operations from the modelling of the fine scale material interfaces. A dedicated tool for the generation of representative volume elements based on similar concepts is also exploited. Fine-scale plastic constitutive laws are used to model the progressive mechanical degradation under stress. The local (fine-scale) permeability evolution is assumed to be coupled to the local plastic dissipation. Using this procedure, the effect of progressive degradation on the averaged permeability properties of geomaterials is investigated. These procedures are illustrated by estimating the alteration of permeability with the confining pressures and deviatoric stresses applied in triaxial testing.

2. Computational homogenisation of mechanical and transport properties

The upscaling framework described in detail in [1] can be used to extract the homogenised behaviour of a heterogeneous material, starting from its microstructure. The essential features of this approach are summarized below. For completeness, a detailed derivation of the averaging relationships can be found in [1] and references therein.

2.1. Averaged mechanical response of a RVE

The averaged mechanical properties of a heterogeneous material can be deduced by loading a RVE containing the main microstructural features of the material, and solving the corresponding equilibrium problem. When a macroscopic strain $\mathbf{E}$ is applied to a RVE, the displacement of a point inside the RVE is given by

$$\vec{u}(\vec{x}) = E.\vec{x} + \vec{u}_f(\vec{x}) \tag{1}$$

where $\vec{x}$ is the position vector within the RVE and $\vec{u}_f$ is a fluctuation field caused by the heterogeneity of the material. Assuming that the macroscopic strain is the volume average of the fine-scale strain field ε resulting from the above equation, and accounting for a periodic fluctuation, the Hill-Mandel condition (energy equivalence between the fine-scale and macroscopic descriptions)

$$\Sigma : \delta E = \frac{1}{V}\int_V \sigma : \delta\varepsilon \, dV \tag{2}$$

implies that the macroscopic stress tensor is obtained as the volume average of the microstructural stress tensor. Considering the periodicity of the fluctuation field, the macroscopic stress tensor can next be identified based on the cell tying forces at nodes controlling the macroscopic loading as

$$\Sigma = \frac{1}{V}\int_V \sigma \, dV = \frac{1}{V}\sum_{a=1}^{4} \vec{f}^{(a)}\vec{x}^{(a)} \tag{3}$$

where the summation spans the nodes controlling the RVE loading. Any type of material behaviour can be postulated at the fine scale, and the periodicity of the microfluctuation field can be enforced by homogeneous linear connections between corresponding faces. In a three-dimensional body, four controlling points (denoted 1 to 4 in Fig. 1a) are used to apply the macroscopic stress or deformation modes of the boundary of the RVE, provided identical meshes are used on the opposite faces of the RVE.

The RVE equilibrium problem under the macroscopic stress loading is then solved by imposing forces $\vec{f}^{(a)}$ at the controlling points, which represent the action of the neighboring continuum on the RVE. The displacements of the controlling points, energetically conjugated to the imposed controlling forces, can be used to extract the macroscopic strain.

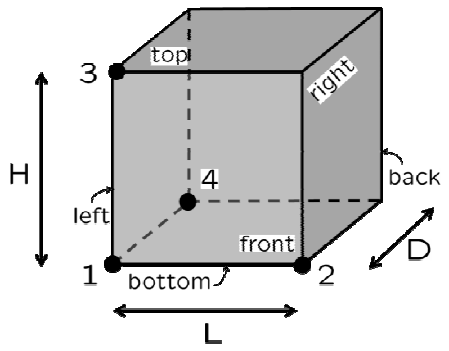

Figure 1. Control points for macroscopic quantities control on a RVE for upscaling principles

2.2. Averaged permeability of a RVE

The homogenised permeability for a given local permeability distribution within the RVE can be evaluated using an upscaling scheme similar to the one developed for heat conduction in [2]. For fluid flow, the mass conservation equation at the scale of the components has to be solved. Expressing the fine scale flux is expressed in terms of the local permeability distribution $K_m(\vec{x})$ and with a fluid of dynamic viscosity μ, mass conservation reads

$$\vec{\nabla}_m \left(-\frac{K_m(\vec{x})}{\mu} \vec{\nabla}_m p_m \right) = 0 \tag{4}$$

A periodic fluctuation $p_f(\vec{x})$ of the pressure field is assumed [1,2] to describe the pressure variation inside the RVE according to

$$p_m(\vec{x}) = p_m^k + \vec{\nabla}_M p_M . \left(\vec{x} - \vec{x}^k \right) + p_m(\vec{x}) \tag{5}$$

where $\vec{\nabla}_M p_M$ is the macroscopic pressure gradient to be applied in an average sense on the RVE, and where p_m^k is the pressure of an arbitrary point in the RVE. An averaging relation for the pressure gradient is required as

$$\vec{\nabla}_M p_M = \frac{1}{V} \int_V \vec{\nabla}_m p_m dV \tag{6}$$

Assuming the periodicity of the pressure field fluctuation and using the Green-Gauss theorem, the average of the fine-scale pressure gradient can be expressed as

$$\frac{1}{V} \int_V \vec{\nabla}_m p_m dV = \vec{\nabla}_M p_M + \frac{1}{V} \oint p_f \vec{n} \, dS \tag{7}$$

With the periodicity of $p_f(\vec{x})$, the last integral of this relationship vanishes and the relationship prescribing the consistency between the macroscopic and fine scale pressure gradients is satisfied. In a computational treatment, the periodicity constraint on the pressure fluctuation field requires that relationships of the form

$$p_m^S - p_m^M = \vec{\nabla}_M p_M . (\vec{x}^S - \vec{x}^M) \tag{8}$$

be satisfied between the master M and slave S nodes of opposite faces of the RVE. An additional averaging relationship is used to impose consistency between scales of the product of the pressure gradient by the flux

$$\vec{\nabla}_M p_M . \vec{q}_M = \frac{1}{V} \int_V \vec{\nabla}_m p_m . \vec{q}_m \, dV \tag{9}$$

Combining the pressure gradient averaging with this relationship, it can be shown that the macroscopic flux is automatically obtained as the RVE average of the fine-scale fluxes [2]

$$\vec{q}_M = \frac{1}{V} \int_V \vec{q}_m \, dV \tag{10}$$

Details of the derivation of this last averaging relationship can be found in [1]. The constraints on the pressures at the boundary can be enforced using control nodes to apply the macroscopic pressure gradients to the RVE. The averaged permeability tensor of the RVE can be identified from the link between the applied macroscopic pressure gradient and the fluxes developing as a reaction

to them. At equilibrium, the discretized system of equations for the transport problem can be condensed at the control nodes

$$q_{m_n}^{(a)} = \sum_{b=1}^{4} k_{disc}^{(ab)} \left(\nabla_j p \; x_j\right)^{(b)} \tag{11}$$

where $k_{disc}^{(ab)}$ results from the condensation of the entire RVE stiffness values. Using periodicity, the averaged flux is obtained from the 'reaction' fluxes at the controlling nodes as

$$q_{M_i} = \frac{1}{V} \oint_S q_{m_n} x_i dS = \frac{1}{V} \sum_{a=1}^{a=4} q_{m_n}^{(a)} x_i^{(a)} \tag{12}$$

Upon substitution of the two previous relationships, one identifies the (averaged) permeability as

$$K_{M_{ij}} = \frac{\mu}{V} \sum_{a=1}^{a=4} \sum_{b=1}^{b=4} x_i^{(a)} k_{disc}^{(ab)} x_j^{(b)} \tag{13}$$

As in the mechanical case, any modelling choice (constitutive laws, discretisation technique) can be adopted for the fine-scale modelling.

3. Representative volume element generation

The RVE generator tool is mainly designed based on distance fields and level set functions as presented in [3] for 2D RVEs, and extended in [4] for 3D simulations. A random distribution of inclusions is first generated, which is subsequently morphed to produce a grain-like structure.

3.1. Inclusion packing

The inclusion packing is the first step of the RVE generation method that gives the basis for the microstructural spatial arrangement. It allows incorporating prescribed volume fractions and/or grain size distributions as input parameters. The geometry used for the shape of inclusions is arbitrary and can be randomly generated through a parameterization, or explicitly defined from existing data (e.g. in order to use data from Computed X-Ray Tomography).

The problem of filling a container with a given volume fraction of inclusions while respecting prescribed size distributions and grain shapes is achieved here using a sequential addition of inclusions, improved by the use of distance fields. In the classical RSA algorithm, each loop generates randomly a trial position in the RVE for the next inclusion to be added. This inclusion is then verified to ensure no interpenetration with previously added inclusions when placed at the trial position, in which case it is rejected and another trial position is generated. Costly computational operations (overlap and distance evaluation) are required at each trial, but few trials lead to a successful inclusion addition, especially when dense packing must be reached.
This original sequential addition methodology can be dramatically improved using distance fields. Instead of a purely random trial position, a set of discrete positions satisfying a priori the non-overlapping and neighboring distance conditions is used to select new inclusion locations. This set is built using the nearest neighbor distance function $LS_1(x)$ (see Fig. 2a) which is maintained on a structured grid of points x_n at each inclusion addition. The radius *r* of the smallest enclosing circle (or sphere) of the new inclusion is used as an indicator of its size.

The positions on the grid leading to overlap with existing inclusions can be excluded for the random inclusion positions by allowing selection only among the points satisfying the condition (Fig.2a)

$$LS_1(x_n) > r \tag{14}$$

This allows the addition of a new inclusion at each trial, and the generation cost is therefore not linked to any probability relative to the actual density, but rather to the number of added inclusions. Additional neighboring distance conditions can be enforced using $LS_1(x)$ such as for instance

$$nn_{min} + r < LS_1(x_n) < nn_{max} + r \tag{15}$$

where $nn_{min}$and $nn_{max}$are the minimum and maximum distance imposed from the first neighbor of the added inclusion (Fig. 2a). To increase packing density, the spatial organization has to be optimized by minimizing the distances of the added inclusion to its second nearest neighbor in 2D and its third nearest neighbors in 3D. The corresponding distance functions $LS_2(x_n)$ and $LS_3(x_n)$ are used for this purpose with the same type of condition (Fig. 2b).

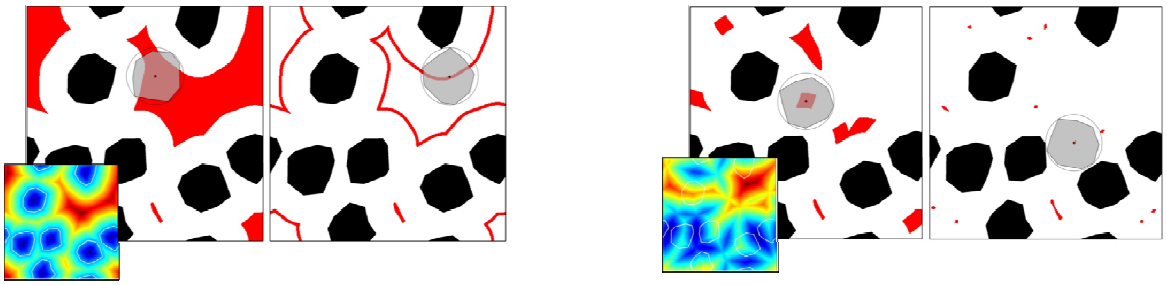

(a) (b)

Figure 2. (a) Non-overlap and first neighbor distance criteria to restrict the random position of the new inclusion to be added (the function $LS_1(\mathbf{x})$ is represented in the insert), (b) First and second neighbor distance criteria to optimize spatial organization to obtain dense packings (the function $LS_2(x_n)$ is represented in the insert)

3.2. Inclusion morphing

Marginal corrections required to adjust the inclusion volume fraction or shapes and more substantial modifications allowing to produce polycrystalline or cellular microstructures motivate the development of a tool enabling the morphing of inclusions once their population is entirely generated by sequential addition. At this stage, the inclusions neighborhood is completely determined and can be used to modify their shape according to inter-inclusion distance rules. A complete expansion of inclusions until vanishing the inter-grain joint thickness allows forming polycrystal-like microstructures.

The morphing technique is strongly based on level set functions. The $LS_1(x_n)$ and $LS_2(x_n)$ functions built during the sequential addition process are used to construct a function $O(x_n)$ that can be contoured to extract updated shapes of the inclusions. The case of complete expansion of inclusions to form a polycrystal morphology is used here to illustrate the methodology. The function

$$O(x_n) = LS_1(x_n) - LS_2(x_n) \tag{16}$$

vanishes at points of equal distance between two nearest inclusions and is negative elsewhere. The zero level set of this function thus determines a Voronoï-like diagram, each cell enclosing an inclusion and points closer to it than to other inclusions. If the initial inclusion distribution is a

dense arrangement of mono-sized spheres, the produced grains are convex and the result is exactly a Voronoï diagram (see Fig. 3a). The use of multi-sized arbitrary shaped polyhedra leads to disordered microstructures (see Fig. 3b). A constant thickness w joint between the grains can be obtained by considering the function $O(x_n) = LS_1(x_n) - LS_2(x_n) + w$.

4. LS-XFEM discretisation for material heterogeneities

The complexity of generating finite element meshes for the generated RVEs motivates the use of an alternative discretisation method. The eXtended Finite Element Method [5], that does not require meshes conforming with the material boundaries, is therefore used. In addition to be defined as an extension of the standard finite element scheme, this method uses the level set formalism to describe the RVE geometry, which allows its seamless integration with the RVE generator.

(a) (b)

Figure 3. (a) convex Voronoï-like cells produced by a circle packing, (b) disordered cells produced by an arbitrary shaped multi-sized inclusion packing

The principle of XFEM is to use a non conforming regular mesh with additional degrees of freedom related to additional shape functions (denoted the enrichment) introducing the strain jumps induced by material heterogeneities. This treatment, concentrated on finite elements intersected by a material interface (e.g. inclusion/matrix boundary), uses signed distance functions to construct the enrichment and to subdivide elements by material at the stiffness integration stage. The interpolation of each displacement field components therefore reads

$$u_{XFEM}(x) = \sum_i N_i(x)\, d_i + \sum_j N_j(x)\, \Psi(x)\, a_j \tag{17}$$

where the first term represents the usual finite element polynomial interpolation containing the standard shape functions as a partition of unity. The second term introduces the XFEM enrichment with a_j the additional unknowns and $\Psi(x)$ the enrichment functions. For heterogeneous materials, the LS_1 level set (distance) function was shown to introduce the required strain jump at the material boundary. This principle is illustrated in Fig. 4 for the 1D case.
Likewise, the pressure field within the heterogeneous microstructure can be described using a similar principle.

$$p_{XFEM}(x) = \sum_i N_i(x)\, p_i + \sum_j N_j(x)\, \Psi(x)\, d_j \tag{18}$$

The XFEM methodology was implemented in a 3D setting, and was coupled with periodic homogenization. The result of the mechanical loading of a RVE can subsequently be used in the

fluid transport simulation, thereby enabling a one-way coupling between the local mechanical degradation of the material and its local permeability.

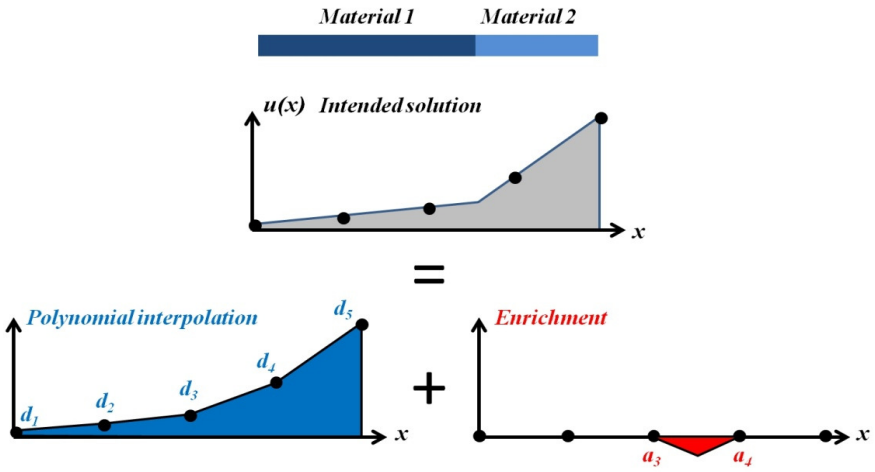

Figure 4. Principle of XFEM enrichment by level set function

5. Application to rock-type materials

The concepts presented previously are now illustrated using two RVEs generated with the tools described in Section 3 and in [4]. The first RVE used for fluid transport homogenisation is produced starting from an initial distribution of elongated inclusions that are subsequently morphed into grains separated by joints. Considering the aspect ratio of the grains, if different permeability properties of the constituents are selected, the resulting average permeability should be anisotropic, as will be illustrated in Section 5.1. The second RVE contains grains without any preferential orientation. The evolving macroscopic permeability resulting from the local plasticity-induced permeability evolution in the joints is analysed in Section 5.2.

5.1. Averaged anisotropic permeability properties

As a first illustration of the proposed level set based homogenisation of heterogeneous materials, the permeability of a anisotropic grain-based material is considered. An anisotropic RVE is generated with a 69% volume fraction of grains (Fig. 5). A grain permeability $k_{grains} = 10^{-13}m^2$ is used, while the joints are assumed 10 times more permeable ($k_{joints} = 10^{-12}m^2$). Since the inclusions are parallel and elongated along the vertical direction, the macroscopic averaged vertical permeability should be higher than for the transverse directions. This is indeed the case as the obtained permeability properties read

$$k_{vertical} = 3\ 10^{-13}m^2 \text{ and } k_{horizontal} = 2{,}3\ 10^{-13}m^2$$

This is further illustrated in Fig. 5 where the fluid flow is illustrated for a unit pressure gradient along the horizontal and vertical directions. As can be seen the preferential orientation of the inclusions clearly favors the fluid flow along the vertical direction, leading to a higher vertical permeability.

5.2. Plasticity-induced permeability evolution in a triaxial test

The coupling between the local mechanical degradation and the fluid transport properties is

illustrated based on a RVE made of grains and large joints with a grain volume fraction of 58%, and subjected to triaxial loading. The RVE is assumed to have dimensions of 10 mm along each direction.

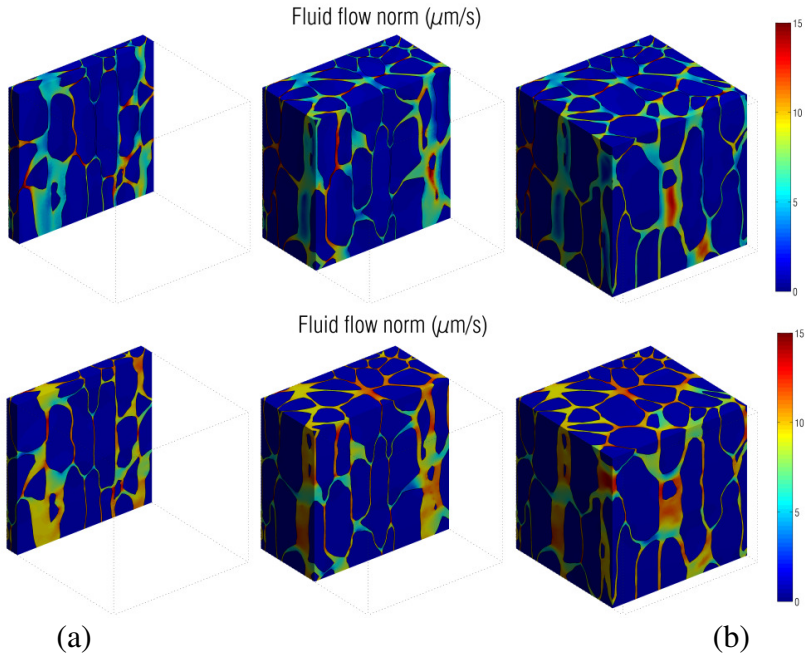

Figure 5. Norm of flow vector for (top) horizontal pressure gradient and (bottom) vertical pressure gradient in anisotropic medium

The grains do not present any preferential orientation as illustrated in Fig. 7. They are assumed purely elastic, whereas a plastic behaviour is assumed in the joints (${}^4H$ is the 4th order elasticity tensor)

$$\sigma = {}^4H : \left(\varepsilon - \varepsilon^{pl}\right) \tag{19}$$

with a Drucker-Prager criterion and an associated flow rule

$$f(p,q) = q - Ap - s(\kappa) \qquad \text{and} \qquad d\varepsilon^{pl} = d\kappa \frac{\partial f}{\partial \sigma} \tag{20}$$

with

$$p = \frac{I_1}{3}$$
$$q = \sqrt{3J_2}$$

where I_1 and J_2 are respectively the first invariant of the stress tensor and the second invariant of the stress deviator. The initial A and s can be expressed as a function of the cohesion c and of the friction angle φ of the material as

$$s = \frac{6c\cos\varphi}{3-\sin\varphi}, \qquad A = \frac{6\sin\varphi}{3-\sin\varphi} \tag{21}$$

To avoid numerical difficulties often met with perfect plasticity, a linear evolution of the yield limit with the plastic strain is introduced through

$$s = s_0 + s_1\kappa \tag{22}$$

Assuming a dilatant behaviour of the joints as defined by an associated plastic flow rule, the volumetric plastic strain increases during the deviatoric loading phase. This increase is used to update the local permeability in plastified joints according to

$$k = k_0\left(1 + B\varepsilon_{vol}^{pl}\right) \tag{23}$$

The set of parameters used in the computations is defined in Table 1. The applied loading follows a typical triaxial test with a strong confinement. A confinement of 100 MPa is first applied in all directions, followed by an increased of the axial stress, the other stress components remaining fixed. This high confining stress is used to avoid any convergence problem in the mechanical problem, and to keep the local strain distribution consistent with a small strain description.

Table 1. Material parameters used in mechanical and fluid transport homogenisation

Material	E	ν	c	φ	s_1	k_0	B
	GPa		MPa	°	GPa	(m²)	
Grains	60	0.1	-	-	-	10^{-13}	0
Joints	30	0.3	40	17	1	10^{-13}	5.10^4

Based on these material and loading parameters, the simulation of the triaxial test is performed. Fluid transport homogenisation is then performed for the mechanical degradation states of the RVE corresponding to successive deviatoric stress levels. The mechanical response of the RVE is depicted in Fig. 6a.

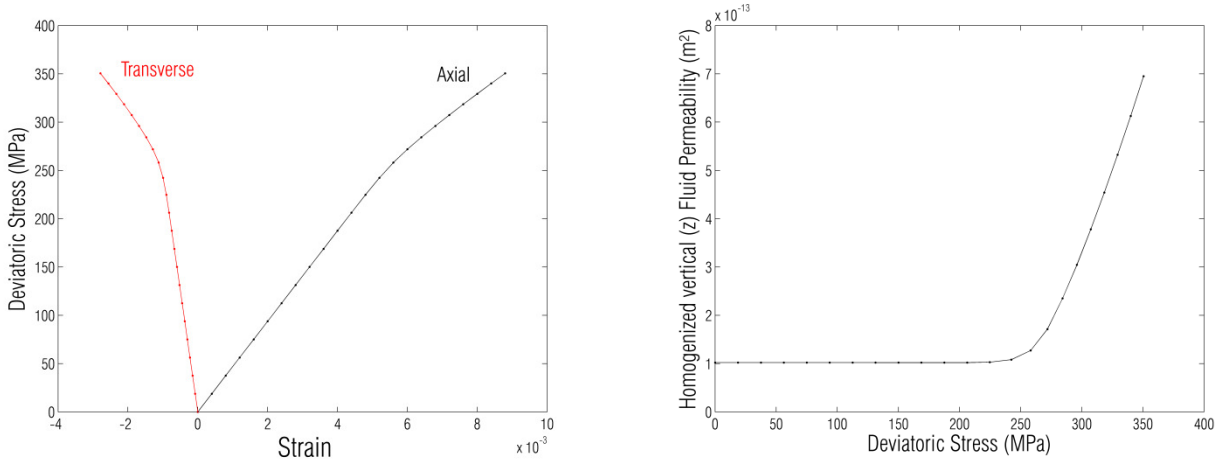

(a) (b)

Figure 6. Homogenised response of the RVE: (a) Mechanical response under triaxial conditions depicting the average deviatoric stress applied as a function of the axial and transverse strains, (b) Axial permeability evolution as a function of the applied deviatoric stress

The corresponding vertical averaged permeability evolution as a function of the deviatoric stress is depicted in Fig. 6b. A permeability increase of almost one order of magnitude is obtained based on the chosen value of the parameter B for the strong confinement applied (100 MPa). The volumetric strain distribution, that directly controls the local permeability evolution inside the RVE, is depicted in Fig. 7. As can be noted from these plots, local permeability can be magnified by a factor up to 500 at a macroscopic deviatoric stress of 350 MPa. The averaged permeability increase for the RVE however remains more restricted as a result of the absence of continuous pathways with high local permeability values inside the microstructure.

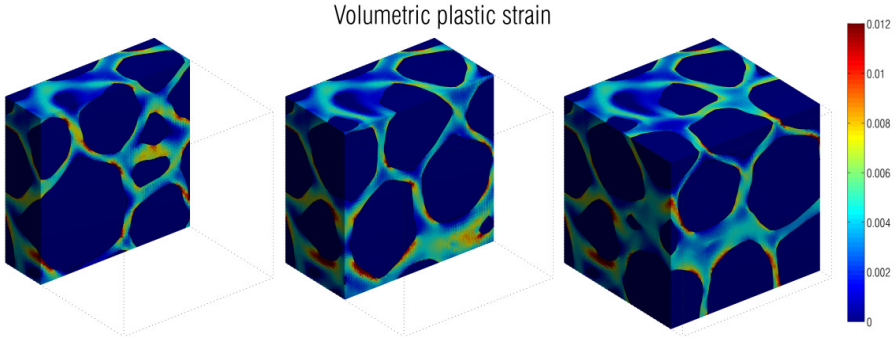

Figure 7. Local volumetric strain distribution inside the RVE at a deviatoric stress of 350 MPa

6. Concluding remarks

Based on the results presented, XFEM discretisation techniques can be efficiently combined with the proposed RVE generation approach to investigate the permeability and mechanical properties of heterogeneous geomaterials. From a fluid transport perspective, this modelling tool could be used in order to identify microstructural features responsible for average (fixed) permeability properties of rocks, in combination with kridging type approaches combined with surface permeability experimental tests [6].

With respect to stress induced permeability evolution, a moderate increase of permeability was obtained as a result of local plastic degradation. Complementary investigations should be performed to analyse the confinement dependency of the permeability evolution, as well as to compare quantitatively such computational results with experimental data. Further developments could incorporate cracking in addition to the plastic dissipation mechanisms contributing to the local permeability evolutions, as well as more advanced plasticity formulations.

Acknowledgements

The first author gratefully acknowledges F.R.S-FNRS Belgium for funding through the FRIA grant 5.0.011.12.F. The Marie Curie International Outgoing fellowship supporting the MULTIROCK project and funded by EU is also acknowledged by the third and last authors.

References

[1] T.J. Massart, A.P.S. Selvadurai, Stress-induced permeability evolution in a quasi-brittle geomaterial, J. Geophys. Res., 117 (2012) B07207.

[2] I. Ozdemir I, W.A.M. Brekelmans, M.G.D. Geers. Computational homogenization for heat conduction in heterogeneous solids. Int. J. Numer. Meth. Engng. 2008; 73:185-204.

[3] B. Sonon, B. François, T.J. Massart, A unified level set based methodology for fast generation of complex microstructural multi-phase RVEs, Comp. Meth. Appl. Mech. Engng., 223-224 (2012) 103-122.

[4] B. Sonon, B. François, T.J. Massart, Generation of complex three-dimensional RVEs for computational homogenisation, In preparation, 2013.

[5] N. Moes, M. Cloirec, P. Cartraud, J.F. Remacle, A computational approach to handle complex microstructure geometries, Comp. Meth. Appl. Mech. Engng. (2003), 192(28-30):3163-3177.

[6] A.P.S. Selvadurai, P.A. Selvadurai, Surface permeability tests: experiments and modelling for estimating effective permeability, Proc. R. Soc. A (2010), 466:2819-2846

Boundary Fractures and Indentation Tests

A.P.S. Selvadurai[1]

[1] Department of Civil Engineering and Applied Mechanics, McGill University, Montréal, QC, Canada H3A 0C3

Abstract
The paper presents an evaluation of the factors influencing fracture initiation at the boundary of a rigid test plate that are used to estimate the in-situ deformability characteristics of a geologic medium. The paper outlines the techniques that are used to perform in situ plate load tests and focuses on the problem of boundary fracture generation at the edges of the geologic medium. If the mechanical behaviour of the rock mass can be assumed to display brittle elastic behaviour, computational methods based on boundary element techniques can be used to examine the mode of crack extension within the elastic geomaterial. The process of fracture generation can influence the extent of the region being evaluated and, more importantly, this can adversely affect the theoretical relationships for the interpretation of test plate data. In most instances the boundary crack may not be visible; this is especially true if the plate load test is conducted with some nominal embedment. This paper discusses issues associated with the interpretation of plate load tests conducted as a validation of experimental data determined from plate load tests. The methodology for the correct interpretation of plate load tests conducted on brittle elastic materials requires knowledge of additional parameters governing the mechanical behaviour of the rock; this involves laboratory evaluation of fracture toughness data. The paper presents results concerning the influence of axisymmetric boundary fractures on the estimated deformability characteristics of the rock mass.

Keywords plate load tests, brittle edge fracture, boundary elements, interpretation of fields tests

1. Introduction

The evaluation of the effective geomechanical characteristics of complex and heterogeneous geological materials is best accomplished through static load tests that are conducted in-situ. A technique that has been used extensively in this connection is the plate loading test where a plate of known dimensions and flexural rigidity is maintained in contact with the surface of the geological medium under examination and is then subjected to an axial loading [1,2]. As the elastic stiffness of the geomaterial increases large loads are required to attain measurable test plate deflections. When plate load tests are conducted in galleries and adits, the loads needed to indent the test plate can be achieved through reaction against the walls of the gallery or enclosure. When plate load tests are performed on large open surfaces this facility is not available and recourse must be made to provide the test loads through a self stressing reaction system. The method of cable jacking introduces the reactive loads through an anchor region located in the medium that is being tested. The method was first proposed by Zienkiewicz and Stagg [3] and presents a simpler test configuration than that involving anchor piles and a bracing frame to accommodate the remoteness of the anchoring loads from the plate location. The influence of the anchor load on the resulting net settlement of the test plate was first examined by Selvadurai [4], who examined the problem of the interaction between a smoothly indenting plate and a Mindlin force [5] located at a finite depth from test plate. The analysis was subsequently extended to cover distributed anchor loads [6], transverse isotropy of the rock mass [7], flexibility of the test plate [8-11] and creep effects of the geologic medium [12].
In this paper we examine the problem of crack extension in a brittle elastic geologic medium during the indentation of the brittle elastic half-space by a cylindrical punch with a smooth flat contact surface. The paper discusses a procedure for locating the point of nucleation of the crack within the brittle elastic solid and employs a boundary element technique to locate the progress of crack evolution as the force on the loading device is increased [13]. The numerical results illustrate how the extent of crack development influences the load vs. displacement relationship for the rigid test plate. The development of boundary fracture is characteristic of any indentation problem involving brittle elastic materials and sharp-edged indenters. Results are developed for geomechanical investigations that are carried out both at the surface of a geomaterial and at depth. The work can also be extended to include flexibility of the plate that is applying the indentation loads.

2. Theoretical Results-Indentation

The theoretical concepts that are used in the interpretation of plate loading tests conducted on brittle elastic geologic media are invariably based on the validity of the theory of elasticity. The analysis is frequently restricted to assumptions of isotropy of the rock mass, While this is considered to be a limitation for in situ testing, the characterization of elastic materials that are generally anisotropic (with 21 independent elastic constants), orthotropic (with 9 independent elastic constants), or transversely isotropic (with 5 independent elastic constants) [14, 15] is regarded as a difficult exercise even under highly controlled laboratory conditions [16]. The best that can be accomplished in an in situ plate loading test is to arrive at an effective deformability modulus of the region in which the plate load test is conducted. The simplest idealization that permits the use of an effective property is the assumption of isotropy of the tested region. It is relatively clear that if the geologic medium possesses dominant stratification then the deformability should be interpreted appropriately. The theoretical concepts can also be extended to include both transverse isotropy of the rock mass and elastic inhomogeneity of the geologic medium [17-20]; however, the inverse analysis for the elasticity parameter identification in these situations cannot be conducted using only the results of plate load tests. Even with the restrictions of isotropic and homogeneous behaviour of the rock mass, the results of a plate load test can only provide an overall estimate for the deformability of the rock mass that can include both the elastic constants encountered in the isotropic elastic model. The theoretical analysis of the plate load test involving no reactive anchor forces can be conducted by formulating the mixed boundary value problem of the indentation of an isotropic elastic halfspace by a rigid test plate. In order to formulate the mathematical problem, it is also necessary to identify the contact conditions that can be present at the interface between the test plate and the geomaterial. This largely depends on the condition of the test plate and the procedures used to either make the interface completely smooth or completely frictional, which will inhibit relative slip between the plate and the geomaterial. Finally, the extent of the geomaterial region that is tested is assumed to be large in comparison to the dimensions of the plate, enabling the region to be approximated by an elastic halfspace region. Reviews of contact problems of special interest to in situ plate loading tests are given in [21-25]. The axisymmetric mixed boundary value problem associated with the smooth indentation of a halfspace by a rigid circular test plate (Figure 1) is described by the boundary conditions

$$u_z(r,0)=\Delta, \quad \forall r\in(0,a); \quad \sigma_{zz}(r,0)=0, \quad \forall r\in[a,\infty); \quad \sigma_{rz}(r,0)=0, \quad \forall r\in(0,\infty) \tag{1}$$

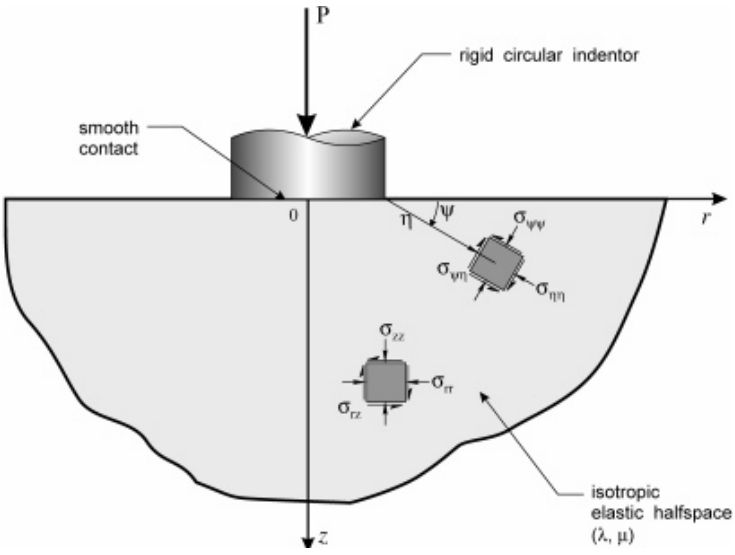

Figure 1. The classical indentation problem for a geomaterial halfspace.

where $\mathbf{u}(=(u_r,0,u_z))$ and $\boldsymbol{\sigma}$ are, respectively, the axisymmetric versions of the displacement vector and the stress tensor referred to the cylindrical polar coordinate system (r,θ,z) and Δ is the displacement of the test plate. In addition, the regularity conditions require that $\mathbf{u}$ and $\boldsymbol{\sigma}$ reduce to zero as either r or $z\to\infty$. The mixed boundary value problem in elasticity defined by the set of equations (1) is a classical problem solved by Boussinesq [26] employing results of potential theory and by Harding and Sneddon [27] using the theory of dual integral equations. Details of the methods of solution are also given in [21-25] and [28, 29]. The result of interest to geomechanics is the relationship between the indentation displacement (Δ) and the corresponding axial load (P) required to achieve the indentation. This can be obtained in exact closed form as

$$\Delta=\frac{P(1-\nu)}{4\mu a} \tag{2}$$

where μ and ν are, respectively, the linear elastic shear modulus and Poisson's ratio of the geomaterial. As is evident from (2), the classical analysis of the plate load test provides only an estimate of $\mu/(1-\nu)$ and additional information is needed to determine the parameters separately. When the plate adheres to the surface of the geomaterial, the resulting boundary value problem is described by the following boundary conditions:

$$\begin{aligned} &u_z(r,0)=\Delta,\ \forall r\in(0,a)\ ;\quad \sigma_{zz}(r,0)=0,\quad \forall r\in[a,\infty);\\ &u_r(r,0)=0,\ \forall r\in(0,a)\ ;\quad \sigma_{rz}(r,0)=0,\quad \forall r\in(a,\infty) \end{aligned} \tag{3}$$

This mixed boundary value problem can be examined by appeal to the theory of integral equations where the problem can be reduced to the solution of the Hilbert problem involving singular integral equations. The elasticity problem of adhesive contact between a plate and an elastic halfspace region was examined by Mossakovskii [30] and Ufliand [31] and the exact closed form result is given by

$$\Delta=\frac{P(1-2\nu)}{4\mu a\ln(3-4\nu)} \tag{4}$$

The Hilbert problem approach accounts for the oscillatory form of the stress singularity at the boundary of the rigid plate. Selvadurai [32] also examined the mixed boundary value problem defined by (3) but by replacing the oscillatory form of the stress singularity by a regular $(a^2-r^2)^{-1/2}$ type singularity, thus reducing the problem to the solution of a Fredholm integral equation of the second-kind. It was shown that the difference between the exact result based on the Hilbert problem formulation and the Fredholm integral equation formulation is less than 0.5% when $\nu=0$ and the results converge when $\nu=1/2$. A further classical development is to consider that the entire surface of the halfspace is composed of an inextensible membrane, in which case the bonded boundary condition is automatically satisfied in the indentation zone and the shear tractions are non zero beyond the indented zone. The load-displacement relationship of the indenter can be obtained from the result for the problem of a rigid disc embedded in an elastic infinite space [33, 34]: i.e.

$$\Delta=\frac{P(3-4\nu)}{16\mu a(1-\nu)} \tag{5}$$

It should be noted that in the limit of material incompressibility, (2) and (4) reduce to the same result. The analysis can be extended to include Coulomb friction at the contact zone [35] and the influence of depth of embedment of the test plate [36, 37].

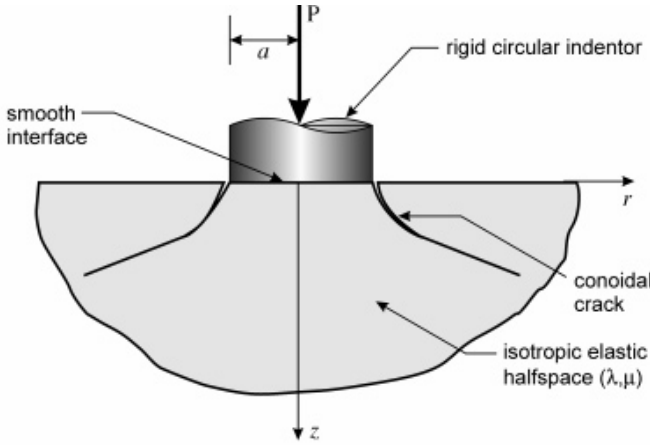

Figure 2. Conoidal boundary fractures emanating from the edge of the indented region.

3. Computational Results-Indentation Fracture

The region at the outer boundary of the test plate is subjected to singular stress fields due to the mixed boundary conditions imposed by the indentation. It can be shown that even when indentation is made by flexible flat test plates, the edges of the indented geomaterial will experience stress concentrations that are singular. The boundary of the indenter is therefore a location where indentation fracture can initiate. The objective of this paper is to demonstrate the influences of fracture development on the load displacement relationship for a rigid test plate. We consider the axisymmetric indentation of the surface of an isotropic elastic half-space region by a smooth flat rigid indenter of radius *a* (Figure 2). The process of crack initiation and crack extension is most conveniently handled using a computational approach that can model the quasi-static crack extension process. The analysis of crack extension during indentation can be performed via a variety of computational schemes. These can include either finite element methods or boundary integral equation methods or combinations of these. The application of finite element techniques to fracture extension is well established; it requires the specification of criteria both for the initiation of crack extension and for the location of the orientation of the crack path. These relationships applicable to brittle elastic fracture initiation and extension are available in the literature on fracture mechanics [38]. In modelling crack extension via the finite element method, re-meshing is an important feature that ensures accuracy of both the local and global stress fields. Adaptive re-meshing techniques have been used quite effectively to examine crack extension in brittle geomaterials such as concrete and rock [39]. An alternative to re-meshing involves extensive graded mesh refinement in the vicinity of the singular crack tip element and allows crack extension to take place at element boundaries. Alternative schemes, such as the boundary element method, provide greater flexibility when examining the crack extension process. The primary advantage of integral equation-based concepts such as the boundary element method or the displacement discontinuity method is that the domain rearrangement resulting from the crack extension process requires only an incremental change in the boundary element mesh or along the displacement discontinuity line of the crack extension. We shall illustrate here the application of the boundary element scheme to examine the process of quasi-static conoidal crack extension in the geomaterial originating at the boundary indenter. The application of boundary element schemes to problems in fracture mechanics originated with the work of Cruse and Wilson [40] and has been extended by a number investigators [41-43] to include a variety of problems including cracks with frictional interfaces. The review [44] gives a comprehensive survey of research related to boundary element formulations in fracture mechanics. Further details of the application of boundary element techniques to crack indentation problems are given in [13] and summarized here for completeness.

3.1. Governing Equations

We examine the class of axisymmetric problems where fracture extension in brittle elastic media satisfies Hooke's Law and the corresponding Navier equations: i.e.

$$\sigma_{ij} = \lambda\varepsilon_{kk}\delta_{ij} + 2\mu\varepsilon_{ij} \quad ; \quad \mu\nabla^2 u_i + (\lambda+\mu)u_{k,ki} = 0 \tag{6}$$

and λ and μ are Lamé's constants and ∇^2 is Laplace's operator. The boundary integral equation governing axisymmetric deformations of the geomaterial region can be written as

$$c_{lk}u_k + \int_\Gamma \left\{ P^*_{lk}u_k + u^*_{lk}P_k \right\} \frac{r}{r_i} d\Gamma = 0 \tag{7}$$

where Γ is the boundary of the domain; u_k and P_k are, respectively, the displacements and tractions on Γ and u^*_{ik} and P^*_{ik} are the fundamental solutions [45,46]. In (7), c_{lk} is a constant, which can take values of either zero (within the domain), $\delta_{ij}/2$ (if the point is located at a smooth boundary) or is a function of the discontinuity at a corner and of Poisson's ratio. For axial symmetry, the displacement fundamental solutions take the forms

$$u^*_{rr} = C_1 \left\{ \frac{4(1-\nu)(\rho^2+\overline{z}^2)-\rho^2}{2r\overline{R}} \right\} K(\overline{m}) - \left\{ \frac{(7-8\nu)\overline{R}}{4r} - \frac{(e^4-\overline{z}^4)}{r\overline{R}^3 m_1} \right\} E(\overline{m}) \tag{8}$$

$$u^*_{rz} = C_1\overline{z} \left\{ \frac{(e^2+\overline{z}^2)}{2\overline{R}^3 m_1} E(\overline{m}) - \frac{1}{2\overline{R}} K(\overline{m}) \right\} \tag{9}$$

…etc., where

$$\begin{aligned} &\overline{z} = (z - z_i); \quad \overline{r} = (r + r_i); \quad \rho^2 = (r^2 + r_i^2); \quad m_1 = 1 - \overline{m} \\ &e^2 = (r^2 - r_i^2); \quad \overline{R}^2 = \overline{r}^2 + \overline{z}^2; \quad \overline{m} = \frac{4rr_i}{\overline{R}^2}; \quad C_1 = \frac{1}{4\pi\mu(1-\nu)} \end{aligned} \tag{10}$$

and $K(\overline{m})$ and $E(\overline{m})$ are complete elliptic integrals of the first and second-kind and (r, z) and (r_i, z_i) correspond to the coordinates of the field and source points respectively. The relevant fundamental solutions for P^*_{lk} can be obtained by manipulating results of the types (8) and (9). Upon discretization of the boundary Γ, the integral equation can be expressed in the form of a boundary element matrix equation

$$[\mathbf{D}]\{\mathbf{U}\} = [\mathbf{T}]\{\mathbf{P}\} \tag{11}$$

where $[\mathbf{D}]$ and $[\mathbf{T}]$ are obtained, respectively, by integration of the displacement and traction fundamental solutions. When considering the discretization of the boundary Γ of the domain, quadratic elements can be employed quite effectively; the variations of the displacements and tractions within an element can be described by

$$\left.\begin{matrix} u_i \\ P_i \end{matrix}\right\} = \sum_{n=0}^{3} a_n \zeta^n \tag{12}$$

where ζ is the local coordinate.. Then modeling cracks that occur at the boundaries or within the interior of the elastic geomaterial, it is necessary to modify (12) to take into consideration the $1/\sqrt{\zeta}$ type locally two-dimensional stress singularity at the crack tip. In contrast to finite element approaches that use quarter-point elements, here we utilize the singular traction quarter-point boundary elements [40] where the tractions can be expressed in the form

$$P_i = \frac{c_0}{\sqrt{r}} + c_1 + c_2\sqrt{r} \tag{13}$$

where $c_i (i = 0,1,2)$ are constants. The Mode I and Mode II stress intensity factors that will be used in the estimation of crack growth can be determined by applying a displacement correlation technique, which makes use of the nodal displacement at four locations A, B, E and D and the crack tip (Figure 3).

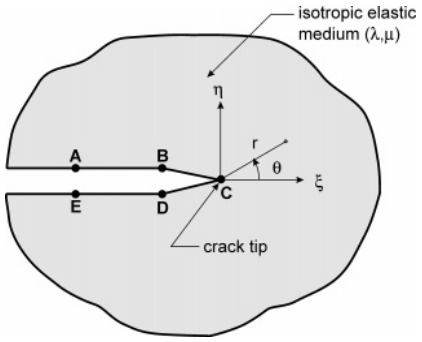

Figure 3. The crack tip geometry and the node locations.

The stress intensity factors are given by

$$\left.\begin{matrix} K_{\mathrm{I}} \\ K_{\mathrm{II}} \end{matrix}\right\} = \frac{\mu}{(k+1)}\sqrt{\frac{2\pi}{l_0}} \left\{\begin{matrix} 4[u_\eta(B) - u_\eta(D)] + [u_\eta(E) - u_\eta(A)] \\ 4[u_\xi(B) - u_\xi(D)] + [u_\xi(E) - u_\xi(A)] \end{matrix}\right. \tag{14}$$

where $k = (3 - 4\nu)$ and l_0 is the length of the crack tip element ξ and η are the local coordinates at the crack tip.

3.2. Modelling of Crack Extension

The boundary element approach can be used to examine the crack extension during indentation. The stress state necessary to initiate crack nucleation can be obtained by using integral results for the stress state associated with the mixed boundary value problem defined by (1). The results presented by Harding and Sneddon [27] can be used for this purpose. The axisymmetric stress state is

$$\begin{aligned}
\sigma_{zz}(r,z) &= -\frac{4\mu\Delta}{\pi a}\left(\frac{\lambda+\mu}{\lambda+2\mu}\right)\left\{J_1^0 + \xi J_2^0\right\} \\
\sigma_{\theta\theta}(r,z) &= -\frac{4\lambda\mu\Delta}{\pi a(\lambda+2\mu)}\left\{J_1^0\right\} - \frac{4\mu^2\Delta}{\rho(\lambda+2\mu)}\left\{J_0^1 - \frac{(\lambda+\mu)}{\mu}J_1^1\right\} \\
\sigma_{rz}(r,z) &= -\frac{4\mu\Delta}{\pi a}\left(\frac{\lambda+\mu}{\lambda+2\mu}\right)\xi J_2^1
\end{aligned} \tag{15}$$

etc…., where

$$\begin{aligned}
J_n^m &= \int_0^\infty p^{(n-1)}\sin(p)e^{-p\xi}J_m(\rho p)\,dp \\
r^2 &= 1+\xi^2; \quad \tan\theta = \xi^{-1}; \quad R^2 = (\rho^2 + \xi^2 - 1)^2 + 4\xi^2 \\
\tan\phi &= \frac{2\xi}{(\rho^2 + \xi^2 - 1)}
\end{aligned} \tag{16}$$

$J_m(x)$ is the Bessel function of the first kind of order m and the dimensionless coordinates are $\rho = r/a$ and $\xi = z/a$. The maximum local tensile stress within the elastic geomaterial, in the

vicinity of the boundary of the indenter (Figure 1) can be obtained through a computer based search technique. The location of the point of maximum tensile stress will be characterized by the local coordinates η_0 and ψ_0 and will depend only on Poisson's ratio. This technique allows the location of the orientation and length of a starter crack and the boundary element meshing is structured to accommodate this starter crack and a semi-infinite domain (Figure 4).

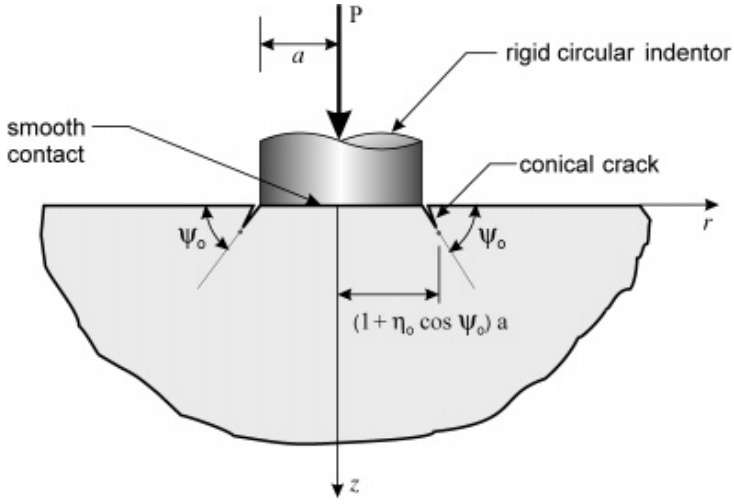

Figure 4.The location and orientation of starter crack.

3.2. Onset and Orientation of Crack Extension

The onset of crack extension can be based on a number of criteria applicable to brittle geomaterials. An elementary criterion for onset of crack extension is the attainment of a critical value of the Mode I stress intensity factor; i.e.

$$K_{\mathrm{I}} = K_{\mathrm{IC}} \tag{17}$$

The orientation of crack extension has to take into account the influence of both stress intensity factors. The criterion used is that proposed by Erdogan and Sih [47]. The maximum stress criterion assumes that the crack will extend in the plane that is normal to the maximum stress $\sigma_{\psi\psi}$ shown in Figure 4b and according to

$$K_{\mathrm{I}} \sin\psi + K_{\mathrm{II}}(3\cos\psi - 1) = 0 \tag{18}$$

Other criteria, such as crack extension along paths where $K_{\mathrm{II}} = 0$, are possible [48] but in this study the criterion (18) is used.

4. Numerical Results

The objective of the study is to examine the extent to which the load displacement of the rigid indenter is influenced by the development of boundary fracture. The results can be presented in relation to a load-displacement relationship for the rigid indenter, taking into account the parameters that control the crack initiation and extension process described previously and documented in detail in [13]. Figure 5a illustrates the results for the load-displacement relationship for the case where the orientation of the starter crack is determined from procedures outlined in Section 3.2. Figure 5b illustrates similar results derived by assuming a priori that the starter crack is oriented normal to the boundary of the indented surface. Results for the load-displacement relationships for

the uncracked situations are also presented for purposes of comparison. In both instances, cracking of the halfspace region will lead to a reduction in the elastic stiffness of the rigid indenter.

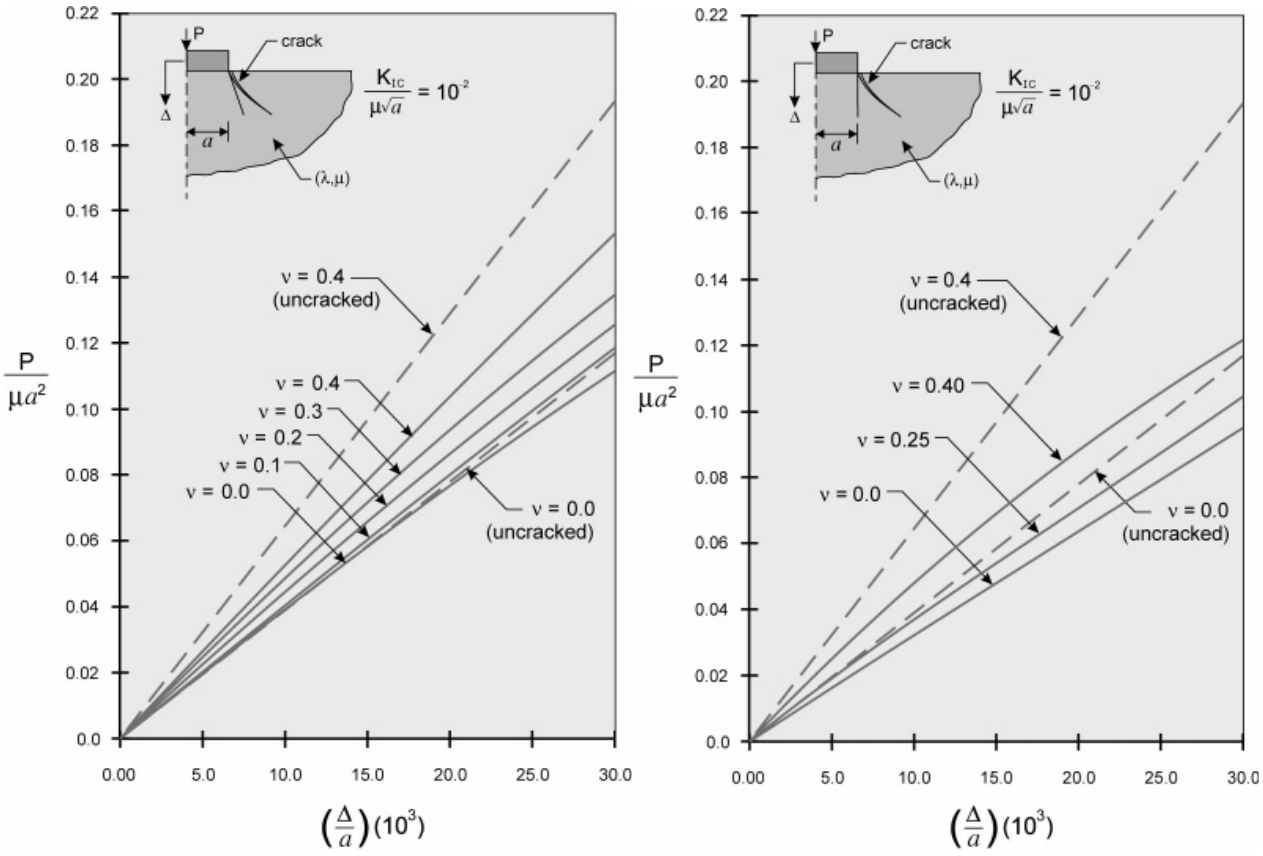

Figure 5. Influence of geomaterial cracking on the stiffness of the rigid indenter

5. Concluding Remarks

The objective of the study is to examine the extent to which the load displacement of the rigid indenter is influenced by indentation fracture that can occur beneath the surface of the region that is being indented. In a geomechanics context, indention testing is carried out in order to determine the in situ properties of the geomaterial. Studies of this type serve two purposes; first it will alert the user to the stress levels that can lead to the development of cracking in the indented region. Modern acoustic emissions monitoring could be used to supplement the experiments. Secondly, if fractures occur it will influence the interpretation of the in situ deformability characteristics of the geomaterial region. The boundary cracking will generally lead to a lower estimate of the in situ modulus. The methodology described here is not without constraints, the most important of which is the assumption that some estimates can be made of the fracture toughness of the geomaterial as interpreted through the critical Mode I stress intensity factor. This pre-supposes that this parameter can be estimated from either laboratory tests or preferably in situ fracture tests conducted by flat jack expansion testing of surface slots cut into the rock surface.

Acknowledgements
The work described in this paper was supported in part by the *James McGill Professorship*, awarded by McGill University and in part by a *Discovery Grant* awarded by the Natural Sciences and Engineering Research Council of Canada.

References

[1] Ch. Jaeger, Rock Mechanics and Rock Engineering, Cambridge University Press, Cambridge, 1972.
[2] F.G. Bell (Ed.), Ground Engineer's Reference Book, Butterworths, London, 1987.
[3] O.C. Zienkiewicz, K.G. Stagg, Cable method of in-situ rock testing, Int. J. Rock Mech. Mining Sci., 4(1967) 273-300.
[4] A.P.S. Selvadurai, (1978) The interaction between a rigid circular punch on an elastic halfspace and a Mindlin force. Mech Res Comm, 5 (1978) 57-64.
[5] R.D. Mindlin, Force at a point in the interior of a semi-infinite solid, Physics, 7(1936) 195-202
[6] A.P.S. Selvadurai, The displacement of a rigid circular foundation anchored to an isotropic elastic halfspace. Géotechnique, 29 (1979) 195-202.
[7] A.P.S. Selvadurai, The interaction between a rigid circular foundation and an anchor region located in a transversely isotropic elastic rock mass, in: P.J.N. Pells Ed. Proceedings of the International Conference on Structural Foundations on Rock, Sydney, A.A. Balkema, The Netherlands, Vol.1 (1980) 23-28.
[8] A.P.S. Selvadurai, Elastic contact between a flexible circular plate and a transversely isotropic elastic halfspace, Int J Solids Struct, 16 (1980) 167-176.
[9] A.P.S. Selvadurai, N.A. Dumont, Mindlin's problem for a halfspace indented by a flexible plate, J Elast, 105 (2011) 253-269.
[10] A.P.S. Selvadurai A contact problem for a Reissner plate and an isotropic elastic halfspace, J Theor Appl Mech, 3 (1984) 181-196.
[11] A.P.S. Selvadurai, An energy estimate of the flexural deflections of a circular foundation embedded in an elastic medium, Int J Num Analyt Meth Geomech, 3 (1979) 285-292.
[12] A.P.S. Selvadurai, Some results concerning the viscoelastic relaxation of prestress in a near surface rock anchor, Int J Rock Mech, Min Sci Geomech Abst, 16 (1979) 309-317
[13] A.P.S Selvadurai, Fracture evolution during indentation of brittle elastic solid, Mech Cohesive-Frict Mat, 5 (2000) 325-339.
[14] S.G. Lekhnitskii, Anisotropic Elasticity, Holden-Day, San Francisco, 1963.
[15] A.J.M. Spencer, Continuum Mechanics, Dover Publ, Mineola, New York, 2004.
[16] R.O. Davis, A.P.S. Selvadurai, Elasticity and Geomechanics, Cambridge University Press, Cambridge, 1996.
[17] H.A. Elliott, Axially symmetric stress distributions in aelotropic hexagonal crystals, Proc Camb Phil Soc, 45 (1949) 621-630.
[18] R.T. Shield, R.T. 1951. Notes on problems in hexagonal aelotropic materials, Proc Camb Phil Soc, 47 (1951) 401-409
[19] V.A. Sveklo, The action of a stamp on an elastic anisotropic halfspace, Prikl Math Mech, 34 (1970) 165-171.
[20] A.P.S. Selvadurai, The settlement of a rigid circular foundation resting on a halfspace exhibiting a near surface elastic non-homogeneity, Int J Num Analyt Meth Geomech, 20 (1996) 351-364.
[21] A,P.S. Selvadurai, Elastic Analysis of Soil-Foundation Interaction, Developments in Geotechnical Engineering 17, Elsevier Sci. Publ Co, 1979.
[22] G.M.L. Gladwell, Contact Problems in the Classical Theory of Elasticity, Sijthoff-Noordhoff, Alphen Aan den Rijn, The Netherlands, 1980.
[23] A.P.S. Selvadurai, On the mathematical modelling of certain fundamental elastostatic contact problems in geomechanics, in: Modelling in Geomechanics, (M. Zaman, G. Gioda, J.R. Booker Eds.) Ch. 13 (2000) 301-328.
[24] A.P.S. Selvadurai, The analytical method in geomechanics, Appl Mech Rev, 60 (2007) 87-106.
[25] S.M. Aleynikov, Spatial Contact Problems in Geotechnics. Boundary Element Method,

Springer-Verlag, Berlin, 2011.
[26] J. Boussinesq, Application des Potentiels á l'Étude de l'Équilibre et du Mouvement des Solides Élastiques, Gauthier-Villars, Paris, 1885.
[27] J.W. Harding, I.N. Sneddon, The elastic stresses produced by the indentation of the plane surface by a rigid flat indenter, Proc Camb Phil Soc, 41 (1945) 16-26.
[28] I.N. Sneddon, Fourier Transforms, McGraw-Hill, New York, 1951.
[29] A.P.S. Selvadurai, Partial Differential Equations in Mechanics, Vol. 2, The Biharmonic Equation, Poisson's Equation, Springer-Verlag, Berlin, 2000.
[30] V.I. Mossakovskii, The fundamental mixed boundary value problem of the theory of elasticity for a halfspace with a circular line separating the boundary condition, Prikl Math Mekh, 18 (1954) 187-196.
[31] Ia. S. Ufliand, The contact problem of the theory of elasticity for a die, circular in its plane, in the presence of adhesion, Prikl Math Mekh, 20 (1956) 578-587.
[32] A.P.S. Selvadurai, The influence of a boundary fracture on the elastic stiffness of a deeply embedded anchor plate, Int J Num Analyt Meth Geomech, 13 (1989)159-170.
[33] A.P.S Selvadurai, The load-deflexion characteristics of a deep rigid anchor in an elastic medium, Géotechnique, 26 (1976) 603-612.
[34] A.P.S. Selvadurai, T.J. Nicholas, A theoretical assessment of the screw plate test, 3rd International Conference on Numerical Methods in Geomechanics, (W. Wittke, Ed.), Aachen, Vol.3, A.A. Balkema, The Netherlands (1979) 1245-1252.
[35] D.A. Spence, Self-similar solutions to adhesive contact problems with incremental loading, Proc Roy Soc, Ser A, 305(1968) 55-80.
[36] S.C. Hunter, D. Gamblen, The theory of a rigid disc ground anchor buried in an elastic soil either with adhesion or without adhesion, J Mech Phys Solids, 22 (1975) 371-399.
[37] A.P.S. Selvadurai, The axial loading of a rigid circular anchor plate embedded in an elastic halfspace, Int J Num Analyt Meth Geomech, 17(1993) 343-353.
[38] B. R. Lawn, Fracture of Brittle Solids, Cambridge University Press, Cambridge, 1993.
[39] S.P. Shah, S.E. Swartz (Eds.), Fracture of Concrete and Rock, SEM-RILEM Int Conf. Springer-Verlag, Berlin, 1989.
[40] T. Cruse, R.B. Wilson, Boundary Integral Equation Methods for Elastic Fracture Mechanics, AFOSR-TR-0355, 1977.
[41] C.A. Brebbia, J.C.F. Telles, L.C. Wrobel, Boundary Element Techniques, Springer-Verlag, Berlin, 1984.
[42] A.P.S. Selvadurai, Matrix crack extension at a frictionally constrained fiber, J Engng Mat Tech, Trans ASME, 116 (1994) 398-402.
[43] A.P.S. Selvadurai, A. ten Busschen, Mechanics of the segmentation of an embedded fiber. Part II. Computational modelling and comparisons, J Appl Mech, Trans ASME, 62 (1995) 98-107.
[44] M.H. Aliabadi, Boundary element formulations in fracture mechanics, Appl Mech Rev, 50 (1997) 83-96.
[45] Th. Kermanidis, Numerical solution for axially symmetric elasticity problems, Int J Solids Struct, 11(1975) 495-500.
[46] M.F.F. Oliveira, N.A. Dumont, A.P.S. Selvadurai, Boundary element formulation of axisymmetric problems for an elastic halfspace, Eng Anal Bound Elem, 36 (2012)1478-1492.
[47] F. Erdogan and G.C. Sih, On the crack extension in plates under plane loading and transverse shear, J. Basic Engng, Trans ASME, 85 (1963) 297-312.
[48] A.P.S. Selvadurai, The modeling of axisymmetric basal crack evolution in a borehole indentation problem, Eng Anal Bound Elem, 21 (1998)377-383.

Applications of Fracture Theory to Instability Co-seismic Fault Problem

TianYou Fan[1,*], ZhuFeng Sun[1], ZhongLei Du[1], YaoLin Shi[2] , BoJing Zhu[2,3,*]

[1] Beijing Institute of Technology, Beijing 100081,CHINA

[2] Key Laboratory of Computational Geodynamics of CAS, University of Chinese Academy of Sciences, Beijing 100049, CHINA

[3] Rock Mechanics Laboratory, University of Durham, Durham DH1 3LE, UK

* Corresponding author: tyfan2006@yahoo.com.cn(T.Y.Fan); cynosureorion@ucas.ac.cn (B.J.Zhu)

Abstract: Co-seismic earthquake faults can be treated as cracks of fracture theory in the framework of continuum mechanics. It is well known that the instability of the faults leads to earthquakes, and the relevant problem can be explored through the fracture theory. There are many factors influencing the instability such as tectonic stresses, geology structure and so on. In this work, we discuss the effects of geometry, interaction between faults and the speed of nucleation and co-seismic process. For single fault, the closed formulations of fracture theory is simpler; for two collinear faults, the analytic solution is available; while for two parallel faults the semi-analysis is approximate with finite element/boundary element method. The theoretical prediction is compared with the observation data of Xingtai earthquake 1966, Hejian earthquake 1967, Tangshan-Luanxian earthquake 1976 and Wenchuan earthquake 2008.

Keywords Fault, Strong Earthquake, Block and Plate, Instability, Fracture theory

1. Introduction

In China, some strong earthquakes happened in plate rather than in boundary between plates. These strong earthquakes are called in plate strong earthquake, or land strong earthquakes. The typical examples are the Ms7.3 Xingtai earthquake on March 8, 1966, the Ms7.8 Tangshan earthquake on July 28, 1976, the Ms8.0 Wenchuang earthquake on May 8, 2008, etc., which resulted in serious destroy and killed a lot of people.

Why did the strong earthquakes happen in plate? To explain the phenomenon, geologists, geophysicists and seismologists in China put forward the block hypothesis of the land strong earthquakes [1-5]. They observed that these earthquakes appeared in the boundaries between blocks. In China land the blocks are very developed, some blocks have quite big sizes though they are smaller compared with plates. For example, the Wenchuang earthquake is in Wenchuang-Beichuang fault, which is located in the boundary between the Tibet Block and the South China Block that have huge sizes. The land strong earthquake presents some natures themselves different from those of earthquakes in boundary between plates.

In this work, we focus on the block characters and apply fracture theory doing some analysis, and preliminarily explain phenomena concerning Xingtai Earthquake, Tangshan earthquake and Wenchuang earthquake those happening in China land.

2. Physics modeling

The land strong earthquakes occurred along some faults in the boundary between blocks, a crack

model concerning fault instability has been developing since the 1970s and numerous work has been done since then, e.g. refs. [1-6]. Thus studies may be beneficial for investigating the land strong earthquakes in China. Due to the dependence of the earthquakes with blocks, the complex system consisting of blocks and faults are studied. For this system a characteristic size is needed. For this purpose we consider the model shown in Fig.1. The configuration concerning a strike slip fault is only an example, if the applied shear stress in plane instead by a shear stress out of plane, then it represents an inverse fault. The boundary between blocks is a transitional region with thickness *2H*, and the fault with length *a*, we takes *a/H* as a characteristic size of the complex system. The tip of the fault is often the earthquake source, it has some intra-structures, one among them is the so-called the slip weakening zone (or breakdown zone), which can be described by a size *R*, so that have another characteristic size *R/H*.

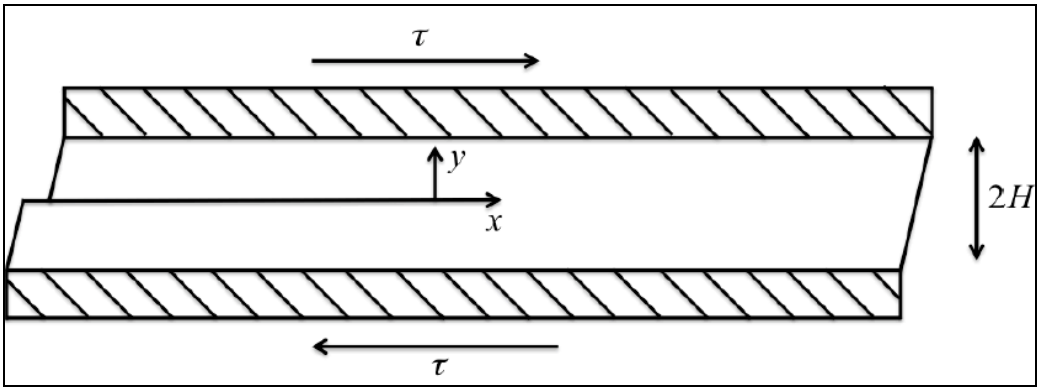

Fig. 1. The cracked strip model on fault

The tectonic shear stress τ acting at the external boundary of the body is removed, whereas the two faces of the fault are subjected to the stress τ over the length an extending back from the fault tip; the quantity a may simulate a finite fault. The fact that tectonic stress acts at fault plan has been proved by quite a lot of geological and geophysical observations, which comes from the interaction between blocks. Because of the roughness of rock materials, there is the frictional stress τ_f at the fault plane, so that the total stress applied at the fault faces should be $(\tau-\tau_f)$.

There is a breakdown zone with length *R* near the fault tip mentioned above, whose magnitude is unknown so far, whereas it will be determined in the successive analysis. At the break down zone another stress drop $(\tau_b-\tau_f)$ acts as well, in which τ_b denoting the breakdown limit of the rock material, should be a material constant. The introduction of the breakdown zone is consistent with the slip-weakening model adopted in the above-mentioned references, or say, it is a concrete application of the slip-weakening model. Fig. 2 shows the model schematically. According to the terminology of the fracture theory, $(\tau_b-\tau_f)$ is also named the cohesive stress.

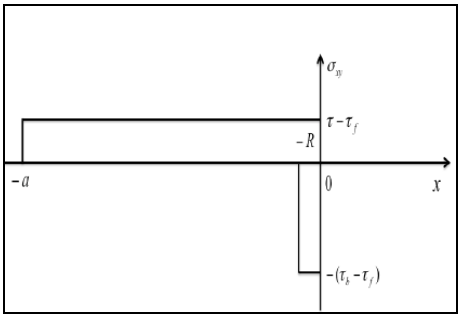

Fig.2 Breakdown zone and the stress distribution in the neighborhood of the fault tip

Reference [6] used this model, but the analysis there is preliminary only for the static case. The present analysis develops the study of Ref [6] in a quite wide range, i.e. it not only studies the static problem, but also the dynamic problem.

2.1 Fault extension initiation

The initiation of fault extension is a static problem. Assume that the fault body is anisotropic homogeneous elastic body. We define Airy stress function as $U(x, y)$, and then the strike slip process of the fault is governed by equation

$$\nabla^2\nabla^2 U = 0 \tag{1}$$

where $\nabla^2 = \partial^2/\partial x^2 + \partial^2/\partial y^2$ denotes the two-dimensional Laplace operator, and the stress component, σ_{ij} , can be written as

$$\sigma_{xx} = \frac{\partial^2 U}{\partial^2 y^2} \quad \sigma_{yy} = \frac{\partial^2 U}{\partial^2 x^2} \quad \sigma_{xy} = \frac{\partial^2 U}{\partial^2 xy} \tag{2}$$

The problem of inverse fault is governed by

$$\nabla^2 u_z = 0 \tag{3}$$

The problem of the fault extension initiation induced by stress drop ($\tau_b - \tau_f$) (the tectonic stress) is described by the following boundary condition:

$$\left.\begin{aligned} &y = \pm H, -\infty < x < \infty : \sigma_{yy} = \sigma_{xy} = 0, \\ &y = \pm\infty, -H < x < H : \sigma_{xx} = \sigma_{xy} = 0, \\ &y = \pm 0, -\infty < x < a : \sigma_{yy} = \sigma_{xy} = 0, \\ &y = \pm 0, -a < x < 0 : \sigma_{yy} = 0, \sigma_{xy} = -\left(\tau - \tau_f\right) \end{aligned}\right\} \tag{4}$$

The most effective tool for solving boundary value problem (1), (4) is complex analysis, i.e., take the solution

$$U(x, y) = Re\left[\bar{z}\phi_1(z) + \int \psi_1(z)dz\right] \tag{5}$$

where $\phi_1(z)$ and $\psi_1(z)$ represents any analytic functions of complex variable $z = x + iy, i = \sqrt{-1}$. The author suggested a conformal mapping approach to solve the boundary value problem (4) of eq. (1),

i.e. by taking the function

$$z=\omega(\zeta)=\frac{H}{\pi}\ln\left[1+\left(\frac{1+\zeta}{1-\zeta}\right)^2\right] \tag{6}$$

and mapping the region of the physical plane (z=x+iy plane) onto the interior of the unit circle γ in the $\zeta(=\zeta+\mathrm{i}\eta)$ plane, the solution in closed form is found[9-11]

$$\phi'(\xi)=\frac{Hp}{2\pi^2 i}\left\{\frac{1}{1\text{-}\xi}\ln(\sigma-1)\text{-}\frac{1+\xi}{(1\text{-}\xi)(1+\xi^2)}\ln(\sigma-\xi)\ -\frac{\xi}{2(1+\xi^2)}\ln(1+\sigma^2)+\frac{i}{2(1+\xi^2)}\ln\left(\frac{\sigma-i}{\sigma+i}\right)\right\}_{\sigma_{-a}}^{\overline{\sigma_{-a}}} \tag{7}$$

in which

$$\left.\begin{aligned}\sigma_{-a}&=\frac{-e^{\pi a/H}+2i\sqrt{1-e^{-\pi a/H}}}{2-e^{-\pi a/H}}\\ \overline{\sigma_{-a}}&=\frac{-e^{\pi a/H}-2i\sqrt{1-e^{-\pi a/H}}}{2-e^{-\pi a/H}}\end{aligned}\right\} \tag{8}$$

and

$$\phi(\zeta)=\phi_1(z)=\phi_1[\omega(\zeta)],\psi(\zeta)=\psi_1(z)=\psi_1[\omega(\zeta)] \tag{9}$$

The corresponding stress intensity factor is determined as

$$K_{\tau-\tau_f}^{static}=\frac{\sqrt{2}(\tau-\tau_f)\sqrt{H}}{2\pi}\ln\left(\frac{2\exp(\pi a/H)-1+2\exp(\pi a/H)\sqrt{1-\exp(-\pi a/H)}}{2\exp(\pi a/H)-1-2\exp(\pi a/H)\sqrt{1-\exp(-\pi a/H)}}\right) \tag{10}$$

The initiation of fault growth induced by stress drop (τ_b - τ_f) (the cohesive stress) is interpreted by the boundary condition as follows:

$$\left.\begin{aligned}&y=\pm H,-\infty<x<\infty:\sigma_{yy}=\sigma_{xy}=0,\\ &y=\pm\infty,-H<x<H:\sigma_{xx}=\sigma_{xy}=0,\\ &y=\pm 0,-\infty<x<-R:\sigma_{yy}=\sigma_{xy}=0,\\ &y=\pm 0,-R<x<0:\sigma_{yy}=0,\sigma_{xy}=\tau_B-\tau_f\end{aligned}\right\} \tag{11}$$

Boundary value problem (11) of eq. (1) can be solved similarly as above. And the corresponding stress intensity factor is determined as

$$K_{\tau_b-\tau_f}^{static}=-\frac{\sqrt{2}(\tau_b-\tau_f)\sqrt{H}}{2\pi}\ln\left(\frac{2\exp(\pi a/H)-1+2\exp(\pi a/H)\sqrt{1-\exp(-\pi a/H)}}{2\exp(\pi a/H)-1-2\exp(\pi a/H)\sqrt{1-\exp(-\pi a/H)}}\right) \tag{12}$$

Because the stresses over the breakdown zone are refer to (11), it means that there is no stress singularity at the fault tip, i.e. the total stress intensity factor must vanish:

$$K_{\text{total}}^{\text{static}}=K_{\tau-\tau_f}^{\text{static}}+K_{\tau_b-\tau_f}^{\text{static}}=0 \tag{13}$$

Substituting (5) and (12) into (13) determines the size R of the breakdown zone. Actually, $R/a\ll 1$; this and (13) offer a very simple expression for R. For explicitly, we here

denote it by R^{static}, i.e.

$$R^{\text{static}} = \frac{\pi}{8}\left(\frac{K_{\tau-\tau_f}{}^{\text{static}}}{\tau_b - \tau_f}\right) \tag{14}$$

where $K_{\tau-\tau_f}^{\text{static}}$ is given by (11). At the end of the breakdown zone, i.e. at y=0, x=-R, the slip of the fault is

$$u_x(-R,+0) - u_x(-R,-0) \equiv \delta^{\text{static}} = \frac{\left(K_{\tau-\tau_f}^{\text{static}}\right)}{E'(\tau_b - \tau_f)} \tag{15}$$

in which

$$E' = \begin{cases} E & (\text{plane stress state}) \\ E/(1-\nu^2) & (\text{plane strain state}) \end{cases} \tag{16}$$

E and v represent Young's modulus and Poisson's ratio of the rock material, respectively. The physical quantity (15) may be taken as a control parameter in checking the fault instability. According to the fracture theory, there is a critical value of δ^{static} denoted by $\delta_{\text{c}}^{\text{static}}$, which should be a material constant, while

$$\delta^{\text{static}} = \delta_{\text{c}}^{\text{static}} \tag{17}$$

It can be considered as a criterion for judging the instability. By the criterion one can determine the critical shear stress τ_{c} of the initiation of fault growth. Inserting (11) into (15) and then into (17) yields

$$\tau_{\text{c}} - \tau_{\text{f}} = \frac{2\pi}{\sqrt{2H}}\sqrt{E'(\tau_b - \tau_{\text{f}})\delta^{\text{static}}} \Big/ \ln\left(\frac{2\exp(\pi a/H) - 1 + 2\exp(\pi a/H)\sqrt{1-\exp(-\pi a/H)}}{2\exp(\pi a/H) - 1 - 2\exp(\pi a/H)\sqrt{1-\exp(-\pi a/H)}}\right) \tag{18}$$

The initiation will occur as $\tau > \tau_b$. At H/a $\to\infty$, it follows from (10) that

$$(K_{\tau-\tau_f}{}^{\text{static}})_{H/a\to\infty} = (\tau_b - \tau_f)\sqrt{8a/\pi} \tag{19}$$

Which is identical with the well-known exact solution[12,13]. In this way, as H/a $\to$0, it follows from (10) that

$$(K_{\tau-\tau_f}{}^{\text{static}})_{H/a\to 0} = \sqrt{2}(\tau_b - \tau_f)a/\sqrt{H} \tag{20}$$

This is a completely new result. Ref. [6] shows that one can find a similar result by using J-integral, in which it contains an unknown constant which could not be determined by the method itself. According to formula (10) the constant=$\sqrt{2}$. Formulae (19) and (20) give an examination of the correctness of the above derivation.

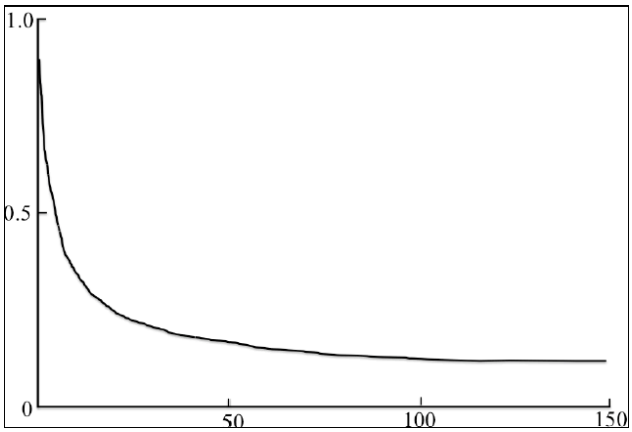

Fig.3.The effect of size of fault and the low-stress drop

Substituting (19) into the left-hand side of (17) determines the critical shear stress corresponding to the infinite fault body, and marked by $(\tau_c - \tau_f)_{H/a\to\infty}$, the ratio $(\tau_c - \tau_f)/(\tau_c - \tau_f)_{H/a\to\infty}$ is the normalized critical shear stress, the variation of which versus the characteristic size *a/H* of fault body describes the effect of fault body size on the fault instability, as description in Fig. 3. This result is identical with that obtained in ref. [2], and gives a quantitative description of the low-stress drop observed in earthquake source.

2.2 Fast propagation of fault

After the initiation of fault growth, it may experience a stable but further unstable growth, or it may become unstable growth directly after the initiation. Before and after the unstable propagation, there is another possibility that the propagation is arrested. Since the velocity of the unstable growth may reach the order of magnitude of elastic wave velocity, it may lead to an earthquake. We here discuss the case in which earthquake rather than arrest may be caused.

As pointed out just now, the state corresponding to the fast fault propagation is quite different from that corresponding to static case. It is necessary to carry out a fully dynamic analysis, which is governed by the following equations:

$$\nabla^2\phi = \frac{1}{c_1^2}\frac{\partial^2\phi}{\partial t^2}, \nabla^2\psi = \frac{1}{c_2^2}\frac{\partial^2\psi}{\partial t^2} \tag{21}$$

for strike slip fault; while for inverse fault

$$\nabla^2 u_z = \frac{1}{c_2^2}\frac{\partial^2 u_z}{\partial t^2} \tag{22}$$

where c_1 and c_2 represent the speeds of longitudinal and transverse waves, respectively. The dynamics analysis reveals the low stress drop effect again.

3. Interaction between co-linear faults

The principle discussed in the previous section can be used to the interaction between co-linear faults. The Ms7.2 Xingtai earthquake happened on March 8, 1966 in North China Block, immediately after the event, Prof. Li Shi-Guang, pointed out the earthquake transmission was going

along the north-east direction [5] ， and the fact of the happening of Ms6.3 Hejian earthquake on March 2, 1967 proved the prediction of Prof. Li Shi-Guang. This shows the interaction between earthquake faults.

3.1 The static fracture analysis

We take the physical model for the interaction between co-linear faults shown in Fig.4

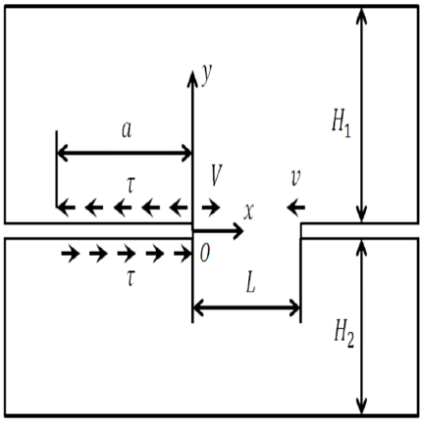

Fig.4 Model for co-linear faults in North China Block

The static fracture analysis on the interaction between co-linear strike slip faults can be based on the equation (1) and (2), but the boundary conditions are given as follows

$$\left.\begin{aligned} &y = H_1, -H_2, -\infty < x < +\infty : \sigma_{yy} = \sigma_{xy} = 0 \\ &y = 0, -a < x < 0 : \sigma_{yy} = 0\ ,\ \sigma_{xy} = -\tau \\ &x < -a : \sigma_{yy} = 0\ ,\ \sigma_{xy} = 0 \\ &x > L : \sigma_{yy} = 0\ , \sigma_{xy} = 0 \\ &H_1 > y > -H_2\ ,\ x = \pm\infty : \sigma_{xx} = 0\ , \sigma_{xy} = 0 \end{aligned}\right\} \tag{23}$$

The complex analysis is still effective for the present problem, but we should use the following conformal mapping

$$U(x,y) = Re\left[\overline{z}\phi_1(z) + \int \psi_1(z)dz\right] \tag{24}$$

$$z = \omega(\zeta) = \frac{H}{\pi}\ln\frac{1+\alpha\left(\dfrac{1-\zeta}{1+\zeta}\right)^2}{1+\gamma\alpha\left(\dfrac{1-\zeta}{1+\zeta}\right)^2} \tag{25}$$

$$\zeta = \xi + i\eta \qquad \alpha = \frac{1-e^{-\pi a/H}}{1-e^{-\pi(a+L)/H}} \qquad \gamma = e^{-\pi L/H} \tag{26}$$

and find the solution

$$\phi'(\zeta) = \frac{2\tau H}{\pi^2}\left[\frac{\sqrt{\gamma\alpha}M}{(1+\zeta)^2+\gamma\alpha(1-\zeta)^2} - \frac{\sqrt{\alpha}A}{(1+\zeta)^2+\alpha(1-\zeta)^2}\right] - \frac{2\tau H}{\pi^2}\frac{i\alpha(1-\gamma)(1-\zeta^2)}{[(1+\zeta)^2+\gamma\alpha(1-\zeta)^2][(1+\zeta)^2+\alpha(1-\zeta)^2]} \times \ln\frac{i-\zeta}{1-i\zeta} \tag{27}$$

where

$$\phi(\zeta)=\phi_1(z)=\phi_1[\omega(\zeta)],\psi(\zeta)=\psi_1(z)=\psi_1[\omega(\zeta)] \tag{28}$$

and

$$A=\ln(1+\sqrt{\alpha})/(1-\sqrt{\alpha}) \qquad M=\ln[1+\sqrt{\gamma\alpha}/(1-\sqrt{\gamma\alpha})] \tag{29}$$

so that

$$K\equiv K_{\mathrm{I}}-iK_{\mathrm{II}}=\lim_{\zeta\to\zeta_1}2\sqrt{\pi}\frac{\phi'(\zeta)}{\sqrt{\omega''(\zeta)}} \tag{30}$$

$$\zeta=\omega^{-1}(z)=\left[\sqrt{\alpha}-\sqrt{\frac{e^{\pi z/H}-1}{1-\gamma e^{\pi z/H}}}\right]/\left[\sqrt{\alpha}+\sqrt{\frac{e^{\pi z/H}-1}{1-\gamma e^{\pi z/H}}}\right] \tag{31}$$

$$K_{\mathrm{II}}^{(0,0)}=\frac{\sqrt{2H}\tau}{\pi\sqrt{1-\gamma}}[\ln\frac{1+\sqrt{\alpha}}{1-\sqrt{\alpha}}-\sqrt{\gamma}\ln\frac{1+\sqrt{\gamma\alpha}}{1-\sqrt{\gamma\alpha}}] \tag{32}$$

$$K_{\mathrm{II}}^{(\mathrm{L},0)}=\frac{\sqrt{2H}\tau}{\pi\sqrt{1-\gamma}}[\sqrt{\gamma}\ln\frac{1+\sqrt{\alpha}}{1-\sqrt{\alpha}}-\ln\frac{1+\sqrt{\gamma\alpha}}{1-\sqrt{\gamma\alpha}}] \tag{33}$$

The fracture criterion

$$K_{\mathrm{II}}^{(\mathrm{L},0)}=K_{\mathrm{IIC}} \tag{34}$$

Is used, in which $K_{\mathrm{IIC}}\approx K_{\mathrm{IC}}=2.81MPa\bullet m^{1/2}$

3.1.1 Earthquake example 1: *Interaction between Xingtai fault and Hejian fault*

The Xingtai fault and Hejian fault with $a=55km, L\approx 400km, H\approx 300km$ and Ms7.1 Xingtai earthquake in N37.5^0, E115.1^0 happened on March 8, 1966 with the stress drop $\tau=42$ bar. Substituting $a=55km, L\approx 400km, H\approx 300km$ into (34) can determine the critic stress τ_c which is $\tau_c=3.4$ bar. Because $\tau_c=3.4\,\mathrm{bar}\le\tau=42$ bar, this means the Xingtai earthquake can induce the Hejian fault to occur earthquake. In fact, the Ms 6.3Hejian earthquake happened on March 2, 1967.

3.1.2 Earthquake example 2: *Interaction between Tangshan fault and Luanxian fault*

The Tangshan fault and Luanxian fault with $a=115km, L\approx 10km, H\approx 150km$ and Ms 7.8 Tangshan earthquake in N38.5^0, E118.7^0 happened on July 28, 1976 with the stress drop $\tau=8$ bar. Substituting $a=115km, L\approx 10km, H\approx 150km$ into (25) can determine the critic stress τ_c that is $\tau_c=0.35$ bar. Because $\tau_c=0.35\,\mathrm{bar}\le\tau=8$ bar, this means the Tangshan earthquake can induce the Luanxian fault to occur earthquake. In fact, the Ms7.1 Luanxian earthquake happened on July 29, 1976 (only 15 hours after the main shock of Tangshan earthquake).

3.2 The dynamic fracture analysis

The dynamic fracture analysis is also carried out in which the wave equations (21~22) are used, and the initial and boundary value conditions are as follows

$$t=0: u_x=u_y=0\ ,\ \frac{\partial u_x}{\partial t}=\frac{\partial u_y}{\partial t}=0 \tag{35}$$

$$\left.\begin{array}{l}\sqrt{x^2+y^2}\to\infty:\sigma_{ij}=0\\ y=0\ ,-\infty<x<-a:\sigma_{yy}=\sigma_{xy}=0\\ -a<x<0:\sigma_{xy}=-\tau\ ,\sigma_{yy}=0\\ L<x<+\infty:\sigma_{yy}=\sigma_{xy}=0\\ -H_2<x<H_1:x=\pm\infty:\sigma_{xx}=\sigma_{xy}=0\end{array}\right\} \tag{36}$$

We developed a complex analysis method, in which the approximate conformal mapping

$$z_1/\alpha_1\ ,z_2/\alpha_2=\omega(\zeta)=\frac{H}{\pi}\ln\frac{1+\alpha\left(\dfrac{1-\zeta}{1+\zeta}\right)^2}{1+\gamma\alpha\left(\dfrac{1-\zeta}{1+\zeta}\right)^2} \tag{37}$$

Which is used with parameters $\alpha=\dfrac{1-e^{-\pi a/H}}{1-e^{-\pi(a+L)/H}}$, $\gamma=e^{-\pi L/H}$ and determine the approximate dynamic stress intensity factors $\alpha=\dfrac{1-e^{-\pi a/H}}{1-e^{-\pi(a+L)/H}}$, $\gamma=e^{-\pi L/H}$

$$\left.\begin{array}{l}K_{\mathrm{II}}^{(0,0)}(t)=\dfrac{\sqrt{2H}\tau}{\pi\sqrt{1-\Gamma}}[\ln\dfrac{1+\sqrt{A}}{1-\sqrt{A}}-\sqrt{\Gamma}\ln\dfrac{1+\sqrt{\Gamma A}}{1-\sqrt{\Gamma A}}]\\ K_{\mathrm{II}}^{(\mathrm{L},0)}(t)=\dfrac{\sqrt{2H}\tau}{\pi\sqrt{1-\Gamma}}[\sqrt{\Gamma}\ln\dfrac{1+\sqrt{A}}{1-\sqrt{A}}-\ln\dfrac{1+\sqrt{\Gamma A}}{1-\sqrt{\Gamma A}}]\end{array}\right\} \tag{38}$$

With $A=\dfrac{1-e^{-\pi a/\alpha_1 H}}{1-e^{-\pi(a+L)/\alpha_1 H}}$, $\Gamma=e^{-\pi L/\alpha_1 H}$, $\alpha_1=\sqrt{1-V^2/c_1^2}$, in which V is the fault propagating speed, and c_1 the longitudinal wave speed. We use the fracture criterion for fault propagation

$$K_{\mathrm{II}}^{(\mathrm{L},0)}(t)=K_{\mathrm{IIC}} \tag{39}$$

and $K_{\mathrm{IIC}}\approx K_{\mathrm{IC}}=2.81MPa\bullet\ m^{-1/2}$.

3.2.1 Earthquake example 1 *Interaction between Xingtai fault and Hejian fault*

The Xingtai fault and Hejian fault with *a=55km/s, L≈400km/s, H≈300km* and 1966 Ms 7.1 Xingtai earthquake (N37.5°, E115.1°) with the stress drop $\tau=42$ bar and $c_1=6\mathrm{km/s}$ $V=3$ km/s. Substituting the earthquake geometry parameters and $c_1=6\mathrm{km/s}$ $V=3$ km/s into (39) can determine the critic stress τ_c which can induce the Hejian earthquake is $\tau_c^{dyn}=0.39$ bar。Because $\tau_c^{dyn}=0.39\,\mathrm{bar}\le\tau=42$ bar, this means the Xingtai earthquake can induce the Hejian fault to occur earthquake. In fact, the Ms 6.3Hejian earthquake happened on March 2,1967.

3.2.2 Earthquake example 2 Interaction between Tangshan fault and Luanxian fault

The Tangshan fault and Luanxian fault with *a=111km/s, L≈115km/s, H≈150km* and 1976 Ms7.8 Tangshan earthquake (N38.5°, E118.7°) with the stress drop $\tau=8$ bar, and c_1*=6km/*s,$V=2.7$ km/s.

Substituting the earthquake fault geometry parameters and $c_1 = 3\text{km/s}$, $V = 2.7$ km/s into (39) can determine the critic stress τ_c which can induce the Luanxian earthquake is $\tau_c = 0.024$ bar. Because $\tau_c = 0.024\,\text{bar} \le \tau = 8$ bar, this means the Tangshan earthquake can induce the Luanxian fault to occur earthquake. In fact, the Ms7.1 Luanxian earthquake happened on July 29, 1976 (only 15 hours after the main shock of Tangshan earthquake).

4. Interaction between parallel faults

The zone of 2008 Ms8.0 Wenchuan earthquake and the simplified mathematical model are shown in Fig.5.The zone is located in the Longmenshan earthquake region that is the boundary between Tibet Block and South China Block. The line AB in Fig 5 represents Maoxian fault, which does not appear earthquake during the Wenchuan earthquake event 0f 2008, and can be treated as a free boundary. The line $\mathrm{A_2B_2}$ represents the main shock fault, the Yingxiu-Beichuan fault, the epicenter is the Yingxiu Town, and line $\mathrm{A_1B_1}$ the Pengxian-Guangxian fault, where the strong earthquake happened induced by the main shock, and line CD the boundary of South China Block, which can be seen as a fixed boundary. The main shock and induced shock are mainly the inverse motion rather than strike slip motion. This complicated configuration is not available for analytic solving. We have done the numerical analysis by finite element for initiation of fault growth only; the fast fault propagation has not been completed yet. At meantime, for the main shock fault (fault $\mathrm{A_2B_2}$) an approximate solution is given as below

$$K^{static}_{\tau-\tau_f}\Big|_{yingxiu} = \frac{\sqrt{2}\left(\tau_1-\tau_f\right)\sqrt{H_0}}{2\pi}\ln\left(\frac{2\exp(\pi a_{20}/H_0)-1+2\exp(\pi a_{20}/H_0)\sqrt{1-\exp(-\pi a_{20}/H_0)}}{2\exp(\pi a_{20}/H_0)-1-2\exp(\pi a_{20}/H_0)\sqrt{1-\exp(-\pi a_{20}/H_0)}}\right) \tag{40}$$

The analytic solution for fault $\mathrm{A_1B_1}$ in general cannot be obtained, we introduce an approximate formula [11]

$$K^{static}_{\tau-\tau_f}\Big|_{pengxian} = \frac{2\left(\tau_1-\tau_f\right)}{\pi}\sqrt{H_0\tanh\frac{\pi a_{20}}{H_0}}\arcsin\left(\frac{\sinh\frac{\pi(a_2-a_{20})}{H_0}}{\sinh\frac{\pi a_{20}}{H_0}}\right) \tag{41}$$

For the dynamic analytic solution cannot be obtained even if for approximate study. The comparison between numerical and approximate analytic solutions, we find that

$$\frac{K^{static}_{\tau-\tau_f}\Big|_{yingxiu}}{K^{static}_{\tau-\tau_f}\Big|_{pengxian}} \approx 3.0 \sim 8.0 \tag{42}$$

This means the accuracy of the approximate analytic solution and numerical solution is in the same order of magnitude. This also shows the main shock induces the shock of Pengxian-Guanxian. The shock is propagates in elastic wave speed, after happening of the main shock, the induced shock occurred immediately, because the distance between the two faults is only 10 to 20 kilometers.

5. Conclusion and discussion

The block hypothesis on the strong earthquake in plate in China land is explained with fracture theory, the single fault analysis explained the low stress drop phenomena, in the co-linear faults analysis the theoretical prediction is in good agreement to the observation results for Xingtai-Hejianfault interaction and Tangshan-Luanxia fault interaction. However the analysis on parallel faults is as just a preliminary work, which must be down the further analysis.

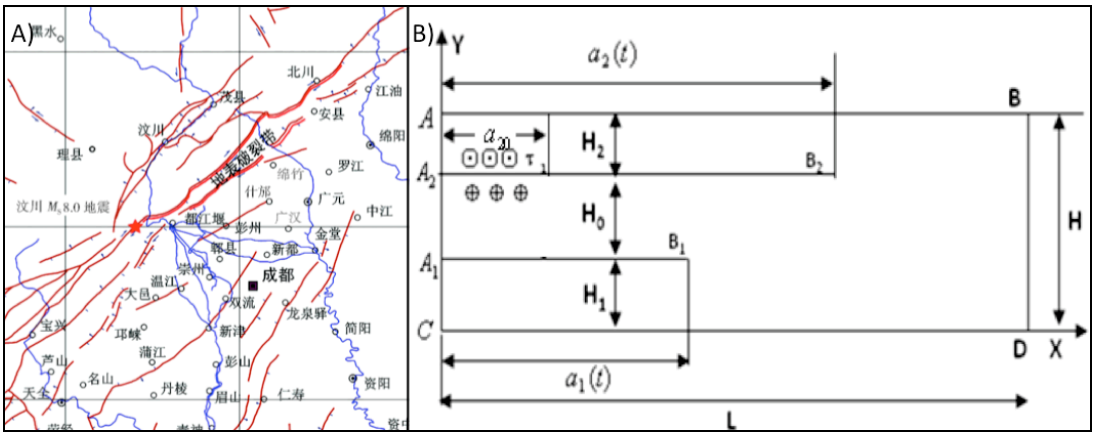

Fig.5 Yinxiu fault and Pengxian fault in Wenchuan Earthquake

Acknowledgements

The work was supported by National Natural Science Foundation of China (NOD0408/4097409), Chairmen Foundation of UCAS [A](D0408/4097409) and Deep exploration in China-Sinoprobe-04 (0819011A90).

References

[1] Zhang W Y,Introduction to Faulting Blocks, Beijing, Petro Industry Press, 1984 (in Chinese).
[2] Ma Jin, Transition from fault theory to block theory on China strong earthquakes, Earth Science Front, 1999, 6, 33-370 (in Chinese).
[3] Ma Xin Yuan, Dynamics Figures of China Lithosphere, Beijing, Geography Press, 1989 (in Chinese).
[4]Ding Guo Yu, Introduction to China Lithosphere Dynamics,Seismological Press, 1991(in Chinese).
[5] Ma S L, Annual Spectrum of Professor Li Shi Guang, Beijing,Geological Press, 1989 (in Chinese)
[6] Maruyama T, Fan T Y，A breakdown zone model of a fault in a strip, J Phys Earth, 1993,41, 21-39.
[7] Fan T Y, Exact solution of semi-infinite crack in a strip, Chin PhysLett, 1991, 7, 402-404.
[8] Shen D W and Fan T Y,Exact solutions of two semi-infinite cracks in a strip, Eng Fract Mech, 2003, 70, 813-822.
[9] Fan T Y, Fracture Dynamics—Principle and Applications, 2006, Beijing, Beijing Institute of Technology (in Chinese).
[10] Sun Z F, Fan T Y, Tectonic stress field of Ms 8.0 Wenchuan earthquake of May 8, 2008, J Beijing Inst Tech, 2010, 30, 253-257.
[11] Tada H, Paris P C, Irwin G R, The Stress Analysis of Cracks Handbook, Del Research Cooperation, Hellertown,1973.

Dynamic Fracture Associated with Shallow Dip-Slip Seismic Faulting

Koji Uenishi[1,*], Keisho Yamagami[1], Fukutaro Ishida[1], Koji Fujimoto[1]

[1] Department of Aeronautics and Astronautics, The University of Tokyo, Tokyo 113-8656 Japan
* Corresponding author: uenishi@mat.t.u-tokyo.ac.jp

Abstract Unlike strike-slip earthquakes, the physical properties of shallow dip-slip quakes remain unexplored because of the insufficient number of near-field seismological recordings and analytical difficulties at the tip of a surface-breaking fault. Here, based on the finite difference technique and dynamic photoelasticity in conjunction with high speed digital cinematography, we numerically and experimentally simulate the source dynamics of dip-slip faulting. Our two-dimensional model may contain a flat fault plane (interface) dipping either vertically or at some angle in a monolithic linear elastic medium. We record the evolution of wave field related to the crack-like rupture along this fault. The observations suggest if the fault rupture, initiated at some depth, arrests just below or reaches the free surface, four Rayleigh-type waves are generated: two propagating along the free surface into the opposite directions to the far field, the other two moving back along the fractured interface downwards into depth. These downward interface waves may largely control the stopping phase of the dynamic rupture. In the case of an inclined fault plane, the interface and Rayleigh waves interact with each other and a shear wave carrying concentrated kinematic energy (corner wave) is induced to generate enormously strong particle motions in the hanging wall.

Keywords Earthquake dynamics, Earthquake ground motions, Fracture dynamics, Experimental mechanics, Computational seismology

1. Introduction

After the reasonable agreement between the theoretical and observational near-field seismograms related to the 1966 strike-slip Parkfield, California, earthquake [1], the techniques to evaluate the near-field generated by strike-slip faulting have become remarkably refined. At present it is common to invert seismological recordings for estimating fault slip distribution, rupture history and their effects for large, shallow strike-slip earthquakes [1–4]. However, the situation is different for shallow dip-slip earthquakes since only few seismic events of this type have been well recorded in the near-field and the mechanical characteristics have not been fully clarified owing to analytical difficulties at the tip of a surface-breaking fault [4–15]. Hazard risk due to such dip-slip earthquakes may be higher in the tectonically compressive regions like Los Angeles, Japan and Taiwan, Central and South America, and in extensional regimes such as the Mediterranean and the Great Basin of Nevada, Utah, and Idaho [5], and an extensive effort has been made to model dip-slip events and the strong motion (particle motion) generated by them [4–15]. Earlier study of shallow dip-slip faulting is based on kinematical models, using the Cagniard-de Hoop [12] or a numerical spectral method [13]. But the analysis becomes very sophisticated and often it does not work correctly, because of analytical singularities, when the fault rupture reaches the free surface. Nevertheless, the previous works posed questions regarding the effect of the free surface near the shallow dipping fault, which require careful study [4].

One noteworthy observation in shallow dip-slip earthquakes is the asymmetric ground motion in the vicinity of the fault: Generally, strong motion is much larger in the hanging wall than in the footwall. For example, the 1971 San Fernando and the 1994 Northridge earthquakes caused systematically severer damage or larger ground motion on the hanging wall [5]. The more recent earthquakes, the 1999 Chi-Chi in Taiwan [6, 7] and the 2004 Niigata-ken Chuetsu [16] and 2008 Iwate-Miyagi Inland [17] in Japan, seem to support this viewpoint. This observed effect is considered to be caused by the strong disturbance in the proximity of the propagating rupture front (rupture front wave) [4], the trapped wave in the hanging wall [5], or the asymmetric mass distributions on each wall and the

normal stress acting perpendicular to the fault surface [5, 7–9]. However, the dynamic properties of shallow dip-slip faulting are not fully understood yet.

Here, in order to give a possible physical explanation of the abovementioned observation, we numerically and experimentally study rupture (fracture) dynamics of a dip-slip fault (interface) situated in a two-dimensional, monolithic linear elastic medium. We employ the finite difference technique for numerical simulations on a PC basis, and in a series of experiments, we initiate rupture in the birefringent linear elastic material using a Q-switched Nd:YAG laser system or a projectile launched by a gun. We record the time-dependent evolution of the wave field induced by the crack-like rupture along the fault, and also monitor the particle motions on the free surface of the model.

2. Geometry and setting

Our model contains a fault plane dipping either 90° (vertical) or 45° (nonvertical case) (Fig. 1) and in each case, the initial static shear stresses acting on the fault plane are set to be equal: For the vertical case (Fig. 1a), remote shear loading which increases linearly with depth is assigned; In the nonvertical case (Fig. 1b), compressive normal stress increasing with depth is given so that linearly increasing static shear stress acts on the fault plane (Fig. 1b). Using the finite difference technique [18], we study the seismic wave field (isochromatic fringe patterns) produced by rupture of this straight fault and try to gain insight into the free surface effect on dip-slip faulting.

As we consider the problem in the framework of linear elasticity, we may assume, without loss of generality, the longitudinal (P) wave speed c_P in the medium is 1. If Poisson's ratio is 0.25, then the shear (S) wave speed c_S becomes $1/\sqrt{3}$ (~ 0.58) and the Rayleigh (R) wave speed c_R is about 0.53. We use the orthogonal 201 times 201 grid points and calculate displacements at each grid point with the second order accuracy. The uniform spacing between each orthogonal grid is 0.05, and the time step is also constant to be 0.025. We further assume the energy absorbing boundary conditions to the outer boundaries except for the upper free surface where the vertical normal and the tangential shear stresses are always zero.

We simulate three different situations: finite fault that ruptures only at depth (Fig. 2); fault rupture (interface crack) starting at depth and arrested well below the free surface (Fig. 3); and fault rupture initiated at depth and reaching the free surface (Fig. 4). By showing the time-dependent dynamic (maximum in-plane shear) stress field, we suggest that the magnitudes of the stresses induced in the

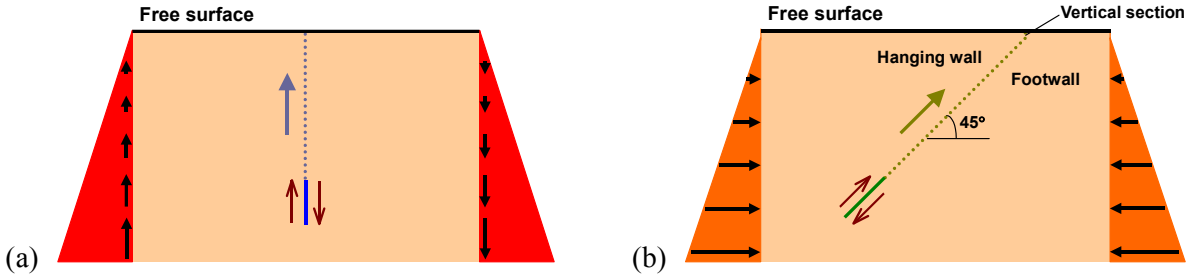

Figure 1. Schematic diagram of the geometry of the dip-slip fault model. For both (a) vertical and (b) nonvertical (45° dipping) situations, we assume a monolithic, linear elastic medium. The fault rupture (interface crack) starts at the bottom and in later simulations it propagates towards the free surface. While the geometrical symmetry is preserved in (a), the symmetry between the free surface and the two sides of the fault (hanging wall and footwall) is broken in (b).

hanging wall and in the footwall may become completely dissimilar for the three cases. Note, in all numerical simulations, we assume crack-like rupture, i.e., once a fault segment is ruptured, the accumulated static shear stress on that segment is released and that section of the fault remains broken without being healed. As shown in Fig. 1, fault slip (displacement discontinuity) is oriented so that the fault behaves as a thrust one, but the results shown below are valid also for normal dip-slip faulting. In the following, snapshots of the isochromatic fringe patterns, i.e., contours of the (dynamic) maximum in-plane shear stress (τ_{max}), are exhibited where the fringe order is proportional to τ_{max} (≥ 0) and all types of elastic waves may be displayed.

3. Numerical case studies

3.1. Finite fault buried at depth

Figure 2 shows the dynamic rupture-induced stress field for the case of a finite dip-slip fault located at depth (length $L = 0.05$, depth $h = 2$ and $L = 0.05\sqrt{2}$, $h = \sqrt{2}$ for the vertical and nonvertical cases, respectively). This problem is rather classical in seismology: The entire (short) fault segment breaks instantaneously at time $t = 0$ to radiate body waves. At time $t = 1.5$, we recognize weak shear waves radiated from the hypocenter (identified as S in the figure). In the geometrically symmetrical case (Fig. 2a), at $t = 3.9$, clear but weak surface reflected *SS* wave and two Rayleigh surface pulses (R) are visible. We also find weak *PS* waves, the *P* waves diffracted by the free surface and converted into *S* waves, but the *P* wave front propagating from the hypocenter is invisibly weak. These *PS* waves interact with the outgoing *S* waves, but their effects seem, again, negligible. At later stages ($t = 6.3$ and 8.7), both surface pulses *R* follow the *S* waves and propagate into the far-field (without decay in these two-dimensional simulations), but the reflected shear wave *SS* attenuates upon propagation and its interaction with the seismic source (hypocenter), now showing static stress singularities, is very small. Similar discussion holds in the asymmetrical case (Fig. 2b) except that here Rayleigh pulse (R_h) and shear wave (S_h) in the hanging wall are stronger than those (R_f and S_f) in the footwall. It is important to note that in seismology an approximate (kinematic) approach, stacking the finite fault segments and rupturing these segments sequentially, is usually employed to inversely obtain a progressive fault rupture related to an earthquake (seismograms). However, from dynamics point of view this approach may not be valid because, as we see below, the wave field generated in the finite fault segments approach (Fig. 2) has a characteristic radiation pattern very different from the one associated with the continuously rupturing fault (Figs. 3 and 4). This situation is akin to blasting simulations of a progressively detonating column charge: The characteristic dynamic wave patterns in the approximate approach that is based on stacking spherical charges and detonating these charges sequentially are very dissimilar compared with the radiation patterns of continuously exploding charge [19, 20].

3.2. Fault rupture starting at depth and arresting well below the free surface

In Fig. 3, the fault rupture is initiated at depth ($h = 2$ and $\sqrt{2}$ for Figs. 3a and 3b, respectively), propagated upwards but suddenly arrested well below the free surface. At time $t = 0$, fracture starts moving along the prescribed fault plane with a constant speed c, and after a certain time $t = L/V$ it arrests, leaving a final rupture zone of length $L = 1$. For this crack-like fault model, we assume the constant rupture speed is in the subsonic range, 0.4 c_P (~ 0.7 c_S; smaller than the Rayleigh wave speed c_R). The noteworthy phenomenon observed here is the strong rupture front wave ($t = 1.5$). In the vertical case (Fig. 3a), the problem is still geometrically symmetrical and the induced particle motions are symmetrical with respect to the rupturing fault plane: Upon arrest, a relatively strong shear wave (S_1) is radiated from the upper tip of the ruptured fault plane (interface) ($t = 3.9$) and

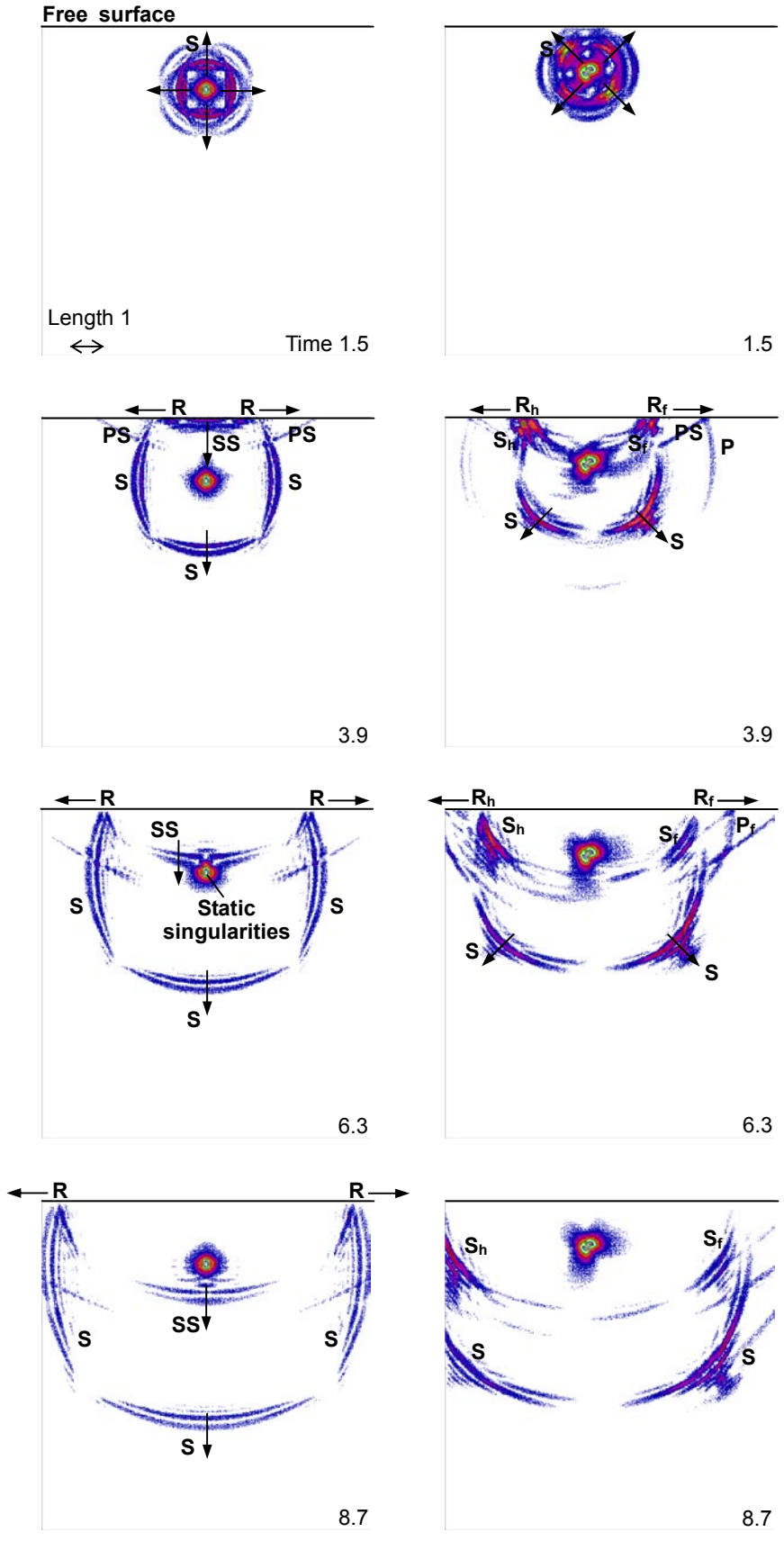
Free surface
S
Length 1
Time 1.5
1.5
R
R
PS
SS
PS
S
S
S
3.9
R_h
R_f
S_h
S_f
PS
P
S
S
3.9
R
R
SS
S
Static
singularities
S
S
6.3
R_h
R_f
S_h
S_f
P_f
S
S
6.3
R
R
SS
S
S
S
8.7
S_h
S_f
S
S
8.7

(a) (b)

Figure 2.

interacts with the free surface. The reflected shear wave (SS) and another shear (S_2) wave generated by the stopping phase of the rupture process interact with the ruptured interface but their influence on the interface seems relatively small. Rayleigh pulses propagating along the free surface are much stronger than those in Fig. 2a. When the fault plane is nonvertical (Fig. 3b), the geometrical symmetry is totally broken: The induced stress is much larger in the footwall than in the hanging wall, with a much stronger shear S_f wave recognizable in the footwall. It is contrary to the previous and the following observations (Figs. 2b and 4b) where the dynamic disturbances are stronger in the hanging wall than in the footwall, and it may be due to the strong rupture front wave that is diffracted at the upper tip of the ruptured interface and flows into the footwall across the unbroken (extended) section of the fault plane.

3.3. Fault rupture approaching the free surface from bottom

The wave field where the fault breaks the free surface is shown in Fig. 4. As in the previous case (Fig. 3), the crack-like rupture, starting at $t = 0$, propagates along the fault plane with a constant speed $c = 0.4\ c_P$ for a length $L = 2$ until it surfaces. In both vertical and nonvertical cases, when the rupture front approaches the free surface, four Rayleigh-type pulses are generated: two propagating along the free surface into the opposite directions to the far-field (labeled as R or R_h, R_f), the other two moving back along the ruptured interface downwards into depth (I). This downward surface-type pulse can be observed also in the numerical simulations of borehole blasting in a rock mass where the explosive charge is detonated at the bottom and a detonation front moves along an explosive column toward the free surface (bottom-to-top blasting); Rayleigh pulses are generated when the detonation front reaches the surface and they may move downwards along the explosive column [19, 20]. If the fault is vertical and geometrically symmetrical (Fig. 4a), the downward interface pulses may largely control the stopping phase of the dynamic rupture on the fault. If the fault is nonvertical and asymmetrical (Fig. 4b), the downward interface pulse and the outward-moving surface pulse (R_h) interact with each other to induce a specific shear wave, corner wave (C), in the hanging wall. This corner wave carries concentrated wave energy and generates strong particle motions in the hanging wall. In the footwall, on the contrary, the weaker surface pulse (R_f) dominates the ground (free surface) motion and the interaction of this surface pulse with the interface pulse moving in the opposite direction (I) is also small. Thus, the asymmetric ground motion, abovementioned and often observed in shallow dip-slip earthquakes, may be caused. The *P* and *S* waves generated in the footwall upon fault surfacing (P_f, S_f) is also relatively strong, but they are much weaker than the corner wave in the hanging wall. The generation of the interface pulse and the corner wave has not been well recognized so far, partly because these waves may not be expected for a fault fracturing only at depth (Figs. 2 and 3), but we should note that similar rupture pattern (downwards rupture after initial upward one) has been reported for the rupture development related to the 2011 off the Pacific coast of Tohoku, Japan, earthquake [21]. In the simulation of the surfacing nonvertical fault, the shallowest part (length 0.15, i.e., three times the grid spacing; see Fig. 1b) is assumed vertical so that we can numerically treat the corner effect appropriately in the framework of the finite difference method: This geometry is selected so as to avoid the problems related to analytical singularities. However, further computations may indicate that qualitatively same phenomena can be observed without this short vertical section, i.e., even when the nonvertical fault rupture stops just below the free surface (at a very shallow depth of 0.15). However, the amplitudes of the induced surface, interface pulses and the corner waves become smaller.

Figure 2 (continued). Snapshots of the dynamic stress field (isochromatic fringe patterns) associated with the rupture of the (a) vertical and (b) nonvertical finite dip-slip seismic sources at depth. The fringe order is proportional to the magnitude of the maximum in-plane shear stress (τ_{max}). Rupture is initiated at time $t = 0$. Weak Rayleigh surface pulses as well as the waves reflected at the free surface can be recognized.

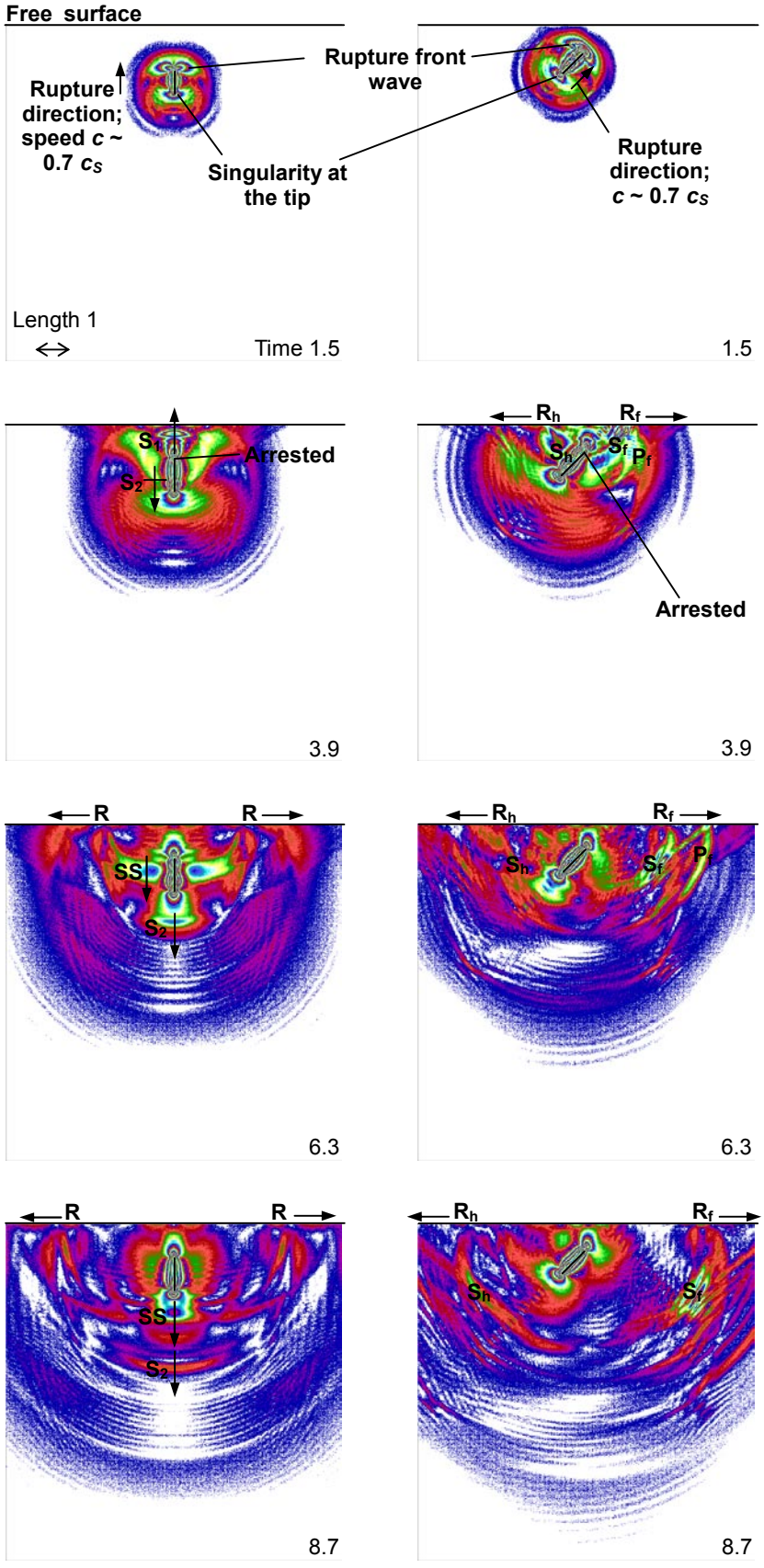
Free surface
Rupture direction; speed c ~ 0.7 cS
Singularity at the tip
Rupture front wave
Rupture direction; c ~ 0.7 cS
Length 1
Time 1.5
1.5
S1
S2
Arrested
3.9
Rh
Rf
Sh
Sf
Pf
Arrested
3.9
R
SS
S2
6.3
Rh
Rf
Sh
Sf
Pf
6.3
R
SS
S2
8.7
Rh
Rf
Sh
Sf
8.7

(a) (b)

Figure 3.

4. Preliminary experimental results

Next, in order to try to confirm the numerical results, we perform laboratory photoelastic fracture experiments using a birefringent linear elastic material as well as a Q-switched Nd:YAG laser system or a projectile launched by a gun. We prepare a pre-cut interface in a polyurethane plate (50 mm × 25 mm × 12 mm), which is essentially under no static stresses. Dynamic fracture may be induced upon initiation of irradiation of laser pulses or incidence of a projectile (at a speed of 55.5 m/s) and propagated along the interface that is vertical or inclined at an angle of 45 degrees. We record the development of dynamic wave field with a high speed digital video camera system at a frame rate of 100,000 fps (e.g., Fig. 5 for incidence of a projectile), and at the same time, we monitor the particle motions on the free surface using a laser displacement meter (at positions 6 mm away from the surface-breaking point). The observations show that the experimental dynamic isochromatic fringe patterns are similar to the wave patterns generated by the numerical simulations, and if the inclined fault rupture reaches the free surface, the maximum vertical surface displacement on the hanging wall is about 4.6 times as large as that on the footwall (Fig. 6). On the contrary, as is expected from Fig. 3, when the fracture of the interface is arrested well below the free surface (arrested depth equal to a half of the plate height), the vertical motion on the footwall becomes about 1.2 times as large as that on the hanging wall.

5. Conclusions

We have studied the dynamic model of the seismic wave field radiated by rupture of a dip-slip fault located near Earth's free surface. The results of the numerical simulations and preliminary experiments suggest that the dynamic stresses and surface particle motions in the hanging wall, induced by nonvertical dip-slip faulting, may become larger or smaller than those in the footwall, depending on the depth of the arresting point of the fault rupture. We have also indicated that if the fault rupture starting at some depth approaches the free surface, four Rayleigh-type pulses (waves) may be produced: two moving along the free surface and the other two propagating back downwards along the ruptured interface. The downward interface pulses may considerably affect the stopping phase of the dynamic fracture process, and indeed, they might have governed the seismic rupture associated with the 2011 off the Pacific coast of Tohoku earthquake in Japan. If the fault plane is inclined, the interface pulse may interact with the Rayleigh pulse to generate a strong corner shear wave in the hanging wall. In the footwall, the interaction between the Rayleigh and interface waves is much smaller and the ground (free surface) motion is dominated simply by a weaker Rayleigh wave propagating along the free surface. The existence of downward interface waves and corner wave, which is not expected from a conventional seismological analyses where a fault ruptures only at depth, may play a crucial role in understanding the effect of the geometrical asymmetry on the strong motion induced by shallow dip-slip faulting. As stated above, the seismological recordings of recent earthquakes seem to support this idea, and there is certainly a need for careful consideration of dynamic fracture process along a shallow dip-slip fault plane. Although the model employed here is simple, they may provide a dynamic physical explanation of the observations associated with shallow dip-slip earthquakes.

Figure 3 (continued). The τ_{max} stress field induced by the (a) vertical and (b) nonvertical crack-like dip-slip faulting. Rupture starts at depth at time $t = 0$ and moves upward at a constant speed to suddenly arrest well below the free surface. The rupture propagation speed is assumed to be below the Rayleigh wave speed. In both cases, the rupture front wave, a strong disturbance in the proximity of the propagating rupture front, can be identified. In (b), the amplitude of the shear wave is larger in the footwall than in the hanging wall, because much of the energy carried by the rupture front wave in the hanging wall is diffracted at the tip of the broken fault segment and flows into the footwall.

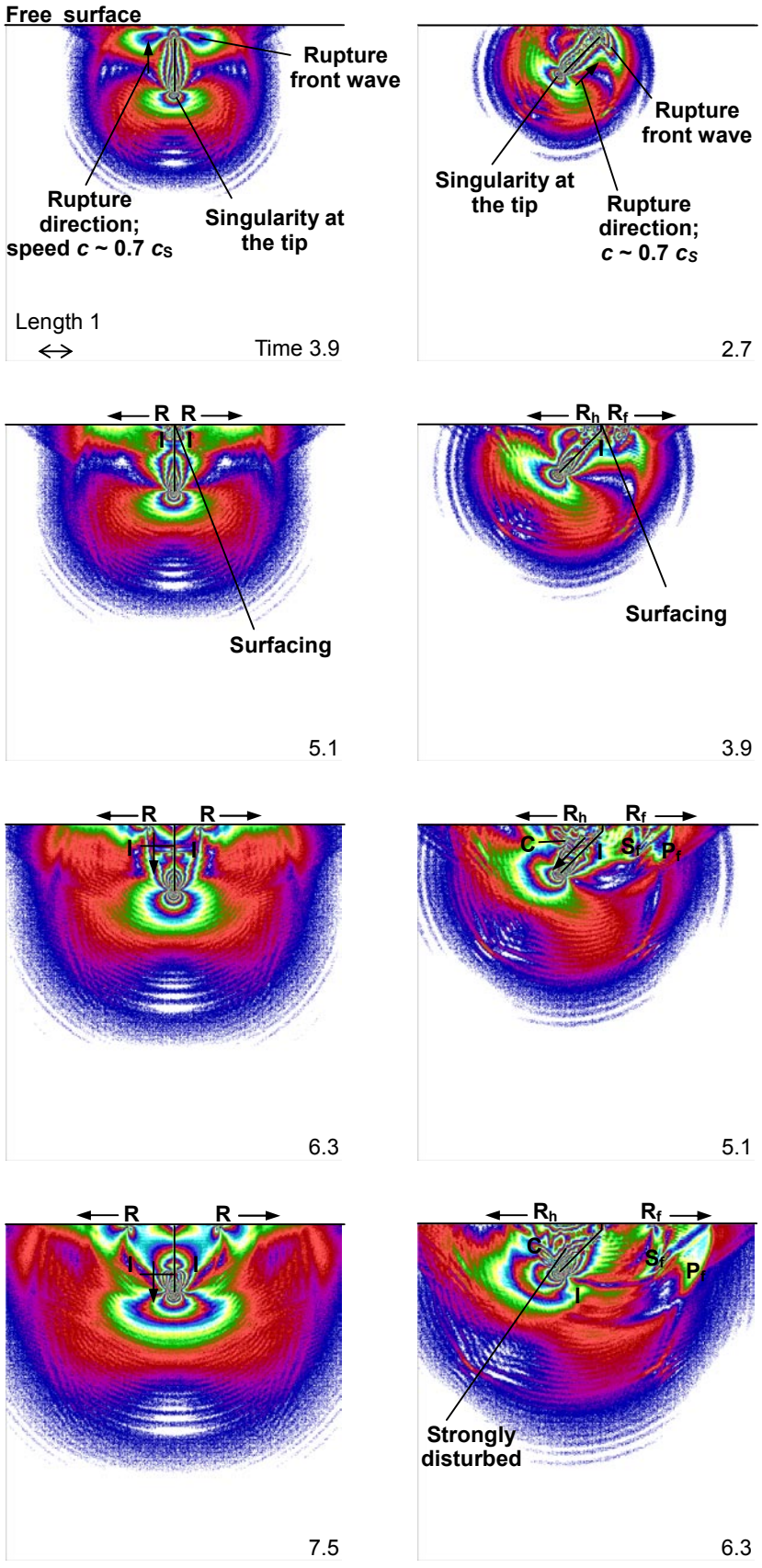
Free surface
Rupture front wave
Rupture direction; speed $c \sim 0.7\ c_S$
Singularity at the tip
Length 1
Time 3.9
2.7
Rupture front wave
Singularity at the tip
Rupture direction; $c \sim 0.7\ c_S$
R R
I I
Surfacing
5.1
R_h R_f
I
Surfacing
3.9
R R
I I
6.3
R_h R_f
C I S_f P_f
5.1
R R
I I
7.5
R_h R_f
C I S_f P_f
Strongly disturbed
6.3

(a) (b)

Figure 4.

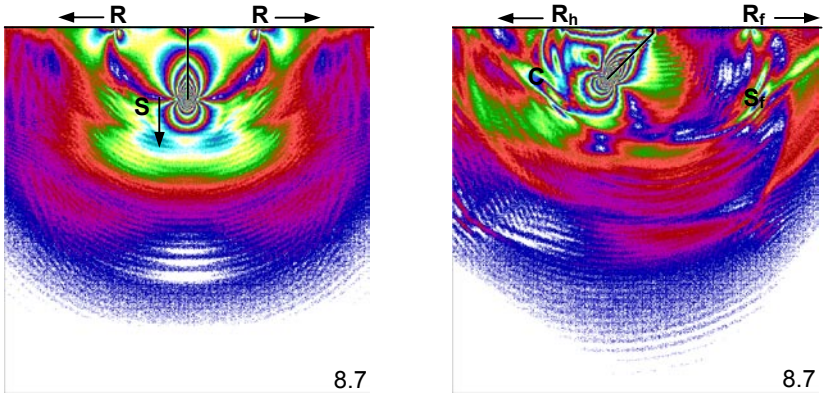

(a) (b)

Figure 4 (continued). The sequence of snapshots of the τ_{max} stress field induced by the (a) vertical and (b) nonvertical dip-slip faulting. As in Fig. 3, the rupture, initiated at depth at $t = 0$, propagates upwards but now it breaks the free surface. In (a), upon fault surfacing, four surface-types waves are generated: The Rayleigh pulses (waves) (marked as R) move along the free surface into the far-field and the interface pulses (I) propagate downwards along the ruptured fault surfaces. At a later stage ($t = 8.7$), the interface pulses merge into a shear wave. In (b), the wave energy trapped in the hanging wall is identifiable as a Rayleigh pulse R_h and the corner wave C. Strong dynamic disturbance may be found in the hanging wall behind the corner wave while in the footwall the induced stresses are relatively small.

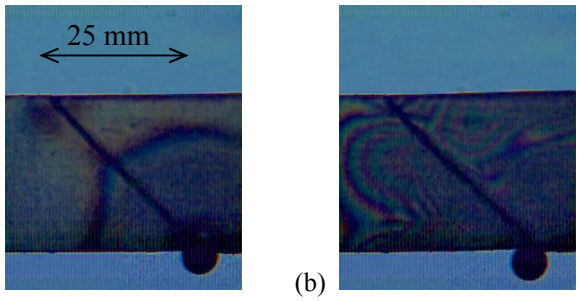

(a) (b)

Figure 5. The experimentally obtained snapshots of isochromatic fringe patterns showing the typical dynamic wave field induced by fracture of an interface inclined at an angle of 45 degrees to the free surface. The photographs are taken at (a) 40 and (b) 280 μs after the incidence of the projectile, respectively.

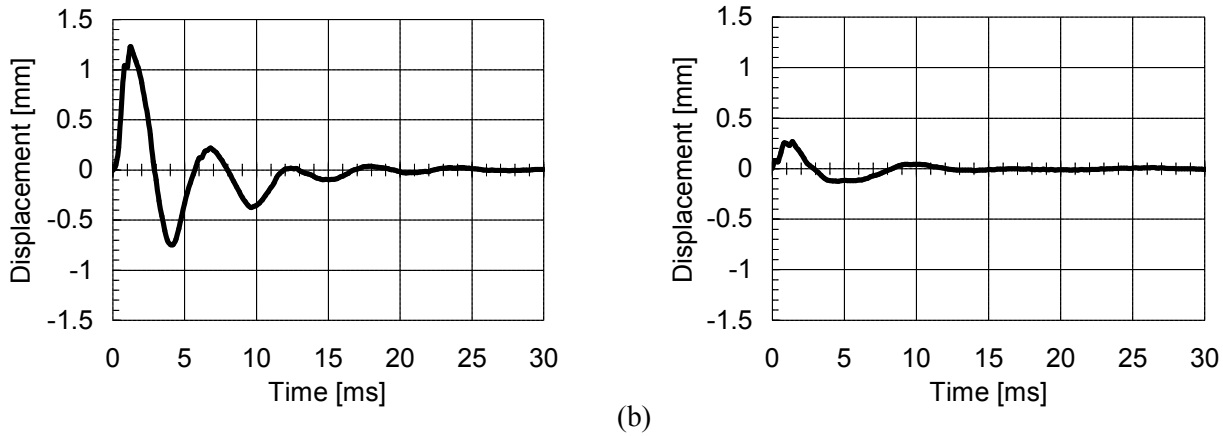

(a) (b)

Figure 6. Typical particle displacements measured on the free surface associated with surface-breaking interface fracture, (a) on the hanging wall and (b) on the footwall (nonvertical case, time is zero when dynamic motion is detected for each diagram).

References

[1] K. Aki, Seismic displacements near a fault. J Geophys Res, 73 (1968) 5359–5376.
[2] K. Olsen, R. Madariaga, R. Archuleta, Three-dimensional dynamic simulation of the 1992 Landers earthquake. Science, 278 (1997) 834–838.
[3] K. Uenishi, H. P. Rossmanith, A. E. Scheidegger, Rayleigh pulse – Dynamic triggering of fault slip. Bull Seismol Soc Am, 89 (1999) 1296–1312.
[4] R. Madariaga, Radiation from a finite reverse fault in a half space. Pure Appl Geophys, 160 (2003) 555–577.
[5] D. D. Oglesby, R. J. Archuleta, S. B. Nielsen, Earthquakes on dipping faults; the effects of broken symmetry. Science, 280 (1998) 1055–1059.
[6] H. Kao, W.-P. Chen, The Chi-Chi earthquake sequence: Active, out-of-sequence thrust faulting in Taiwan. Science, 288 (2000) 2346–2349.
[7] D. D. Oglesby, S. M. Day, Fault geometry and the dynamics of the 1999 Chi-Chi (Taiwan) earthquake. Bull Seismol Soc Am, 91 (2001) 1099–1111.
[8] P. M. Davis, L. Knopoff, The dipping antiplane crack. Geophys J Int, 106 (1991) 581–585.
[9] D. D. Oglesby, R. J. Archuleta, S. B. Nielsen, Dynamics of dip-slip faulting; Explorations in two dimensions. J Geophys Res, 105 (2000) 13,643–13,653.
[10] R. Burridge, G. Halliday, Dynamic shear cracks with friction as models for shallow focus earthquakes. Geophys J R Astron Soc, 25 (1971) 261–283.
[11] D. M. Boore, M. D. Zoback, Near-field motions from kinematic models of propagating faults. Bull Seismol Soc Am, 64 (1974) 555–570.
[12] A. Niazi, An exact solution for a finite, two-dimensional moving dislocation in an elastic half space with applications to the San Fernando earthquake of 1971. Bull Seismol Soc Am, 65 (1975) 1797–1826.
[13] M. Bouchon, K. Aki, Discrete wave number representation of seismic-source wavefields. Bull Seismol Soc Am, 67 (1977) 259–277.
[14] B. Shi, J. N. Brune, Y. Zeng, A. Anooshehpoor, Dynamics of earthquake normal faulting: Two-dimensional lattice particle model. Bull Seismol Soc Am, 93 (2003) 1179–1197.
[15] K. Uenishi, R. I. Madariaga, Surface breaking dip-slip fault: Its dynamics and generation of corner waves. Eos Trans AGU, 86 (2005) Fall Meet Suppl, Abstract S34A-03.
[16] The accelerograms obtained by the K-NET (Kyoshin Net) have shown the same tendency. The K-NET by the National Research Institute for Earth Science and Disaster Prevention of Japan provides the strong-motion data on the Internet (http://www.k-net.bosai.go.jp/). At that time, the seismic data were systematically collected at 1,000 observatories deployed all over Japan, with the average interval of some 25 km. For the distributions of the hypocenters of the main and aftershocks, see e.g., A. Kato et al., Imaging the Source Region of the 2004 Mid-Niigata Prefecture Earthquake and the Evolution of a Seismogenic Thrust-Related Fold, Geophys. Res. Lett., 32, doi:10.1029/2005GL022366, 2005.
[17] S. Aoi, T. Kunugi, H. Fujiwara, Trampoline effect in extreme ground motion. Science, 322 (2008) 727–730.
[18] The numerical simulations have been performed using the finite difference technique originally developed in K. Uenishi, H. P. Rossmanith, SWIFD Finite Difference Wave Simulator and User Manual, Vienna University of Technology, Vienna, 1995.
[19] H. P. Rossmanith, K. Uenishi, N. Kouzniak, Blast wave propagation in rock mass – Part I: Monolithic medium. Fragblast, 1 (1997) 317–359.
[20] K. Uenishi, H. P. Rossmanith, Blast wave propagation in rock mass – Part II: Layered media. Fragblast, 2 (1998) 39–77.
[21] S. Ide, A. Baltay, G. C. Beroza, Shallow dynamic overshoot and energetic deep rupture in the 2011 M_w 9.0 Tohoku-oki earthquake. Science, 332 (2011) 1426–1429.

Fracture damage identification of pile using element strain energy method based on sensitive modals

Wenjuan Yao[1,*], Xiaozhong Zhang[1,2]

[1] Department of Civil Engineering, Shanghai University, Shanghai 200072, China
2 School of Architectural Engineering ,Quzhou University,ZheJiang,Quzhou,324000,China
* Corresponding author: wenjuan@mail.shu.edu.cn

Abstract A sensitive identification method for fracture damage identification of pile was established using the rate of change of natural frequency, element modal strain energy method and fracture mechanics theory. According to the structural vibration equation of damaged pile, a structural damage identification equation was deduced which containing modal damage sensitivity factor, fracture injury factor of pile and element modal strain energy change ratio. Sensitive damage identification modals were selected applying modal damage sensitivity factor, then damage warning indicators of pile were established according to the strain energy changes ratio, and the fracture damage location identification of pile was implemented using wavelet analysis techniques. On the basis of the damage location identification, the pile fracture damage size was identified using structural damage identification equation. Pile damages of Wenzhou City Stadium were identified applying the proposed method. The comparation of the results using proposed method and low strain test results verified the correctness and practicability of the proposed method. This study provided a new and efficient method for structural damage identification for pile.

Keywords sensitive modals; element modal strain energy method; Fracture damage identification of pile; low strain test

1. Introduction

In service process, pile foundation's quality is influenced by factors related to the conditions of geotechnical engineering, structural design, construction quality, and the external environment, it is difficulty to found quality problems and hard to deal with the accident. For pile foundation, the characteristics of hidden and complexity, the limitations of the existing identification methods, and some other uncertainty factors make its damage detected in both theory and practice to face many problems[1-4]. How to early detect the crack damage of the pile foundation and how to develop the relevant prevention measures become a challenging topics for the structural health evaluators.

A variety of pile detection technology at home and abroad have been developed to solve the pile quality problems in the construction. Chen studied the application of core drilling method for testing the damage of piles[5], but the core drilling method can not accurately judge the fracture and the development of piles foundation in service. Xiao studied the application of ultrasonic transmission method for the pile foundation defect detection[6]. Liu et al. [7]applied the low strain method to detect the defects of piles. Wu et al.[8] proposed a approach of foundation piles test which combines application of core drilling method , ultrasonic transmission method and low strain integrity testing. Actually the results demonstrated the reliability of the technical advantages and the measures. The above studies are directed in the pile foundation detection of bridges or buildings under construction. Pile foundation construction of bridges or buildings, when the need to determine its integrity, due to the limitations of the superstructure, the usual pile testing methods are not fully applicable.

Johnson et al. [9] and Luo et al.[10]gradually proposed the low strain dual velocity method, super shock, equality seismic detection methods to detect damage of the pile foundation in service. In 1995, Japanese scientists explore the application hole camera technology roughly detect the foundation piles cracking and damage after southern Hyogo earthquake, but they did not achieve good results for various reasons[11]. Yuan et al. [12] determined the integrity of the bridge piles in service, applying combined horizontal impact load displacement signal collected under static

loading. Qi proposed the application of full-bore wall imaging technology to detect damage of the pile foundation in service, and achieved very good detection accuracy[13]. But the piles will produce some damage when the cores of piles are drilling. In order to weaken the flat-slab superstructure on the foundation pile test signal, Zhang et al. [14] used wavelet analysis method to eliminate the interference signal, and the applied wavelet analysis technology to detect the high-pile integrity.

In summary, scientists at home and abroad have done a series of studies on the pile injury, and they have achieved a certain amount of research. However, the in-service structure damage identification of pile foundation is only in the exploratory stage, a lot of work needs to be further in-depth research if the methods would be used in engineering practice. Especially for the small initial crack damage detection of pile foundation, it need more theoretically further analysis and further explore in practice. This article established a recognition method of small injury on the pile positioning and degree. The method take full use the advantage of the natural frequency on the integrity of the damage to determine, the sensitivity of the element modal strain energy method on small injuries, the efficient local analysis capabilities of time domain wavelet analysis. Finally, the engineering application examples are used to verify the accuracy and efficiency of the damage identification method for the piles in service.

2. Basic theory

2.1. Structural vibration eigenvalue equation with fracture damage

The general performance of the structure fracture damage is that the local stiffness of the structure reduced, and it has nothing to do with the quality of the structure. Therefore, according to the perturbation theory, the structural vibration injury eigenvalue equation is as follows[15]:

$$[(K+\Delta K)-(\lambda_i+\Delta\lambda_i)M)](\phi_i+\Delta\phi_i)=0 \tag{1}$$

Where,
$$\Delta K=\sum_{j=1}^{n}\Delta K_j=-\sum_{j=1}^{n}\alpha_j K_j \quad (0\le\alpha_j\le 1) \tag{2}$$

$$\Delta\lambda_i=\Delta\omega_i^2=\phi_i^T\Delta K\phi_i \tag{3}$$

M, K represent the mass matrix and stiffness matrix of the structure respectively; ϕ_i represents the i^{th} order modal vector of the structure; λ_i represents the eigenvalue of i^{th} modal of the vibration system, $\lambda_i=\omega_i^2=(2\pi f)^2$; ΔK represents Changes of structural stiffness; α_j represents j^{th} element damage factor of the structure; K_j represents structural stiffness matrix of the j^{th} element before damage; n represents the total number of elements of the structure.

Expand the Eq.(1) and finish structural vibration eigenvalue equation, the Eq.(1) of the structure can be expressed as:

$$\phi_i^T\Delta K\phi_i+\delta_i\phi_i^T K\phi_i+\phi_i^T\Delta K\Delta\phi_i+\delta_i\phi_i^T K\Delta\phi_i=0 \tag{4}$$

Where, $\delta_i=-\Delta\lambda_i/\lambda_i$ is structure Eigenvalue change rate, it is used to determine sensitivity of the i^{th} modal structural damage detection for the structure; therefore, it is called modal damage sensitivity factor.

2.2. Structural damage identification equation

According to the principle of energy balance, cracks release of elastic strain energy into plastic strain energy and surface energy when the pile cracks, thus contributing to the crack propagation, eventually lead to structural strain can be reduced. Based on this, the Eq. (4) can be expressed in the form of the strain energy. For piles structures, define the i^{th} modal j^{th} element strain energy as:

$$MSE_{ij} = \phi_i^T K_j \phi_i \tag{5}$$

$$MSE_{ij}^d = (\phi_i^d)^T K_j^d \phi_i^d = (1-\alpha_j)(\phi_i^d)^T K_j \phi_i^d \tag{6}$$

Where, the superscript "d" represents the damaged structure.
According to the above formulas we can get:

$$\phi_i^T K \phi_i = \sum_{j=1}^{n} \phi_i^T K_j \phi_i = \sum_{j=1}^{n} MSE_{ij} = MSE_i \tag{7}$$

$$\phi_i^T \Delta K \phi_i = \sum_{j=1}^{n} \phi_i^T \Delta K_j \phi_i = -\sum_{j=1}^{n} \alpha_j \phi_i^T K_j \phi_i = -\sum_{j=1}^{n} \alpha_j MSE_{ij} \tag{8}$$

Ignore second-order or more high-end items, we can get:

$$\phi_i^T K \Delta\phi_i = \sum_{j=1}^{n} \phi_i^T K_j \Delta\phi_i = \sum_{j=1}^{n} [(\phi_i^d)^T K_j \phi_i^d - \phi_i^T K_j \phi_i + (\phi_i^d)^T \Delta K_j \phi_i^d] \tag{9}$$
$$= \sum_{j=1}^{n} [(1-\alpha_j)(\phi_i^d)^T K_j \phi_i^d - \phi_i^T K_j \phi_i] = \sum_{j=1}^{n} (MSE_{ij}^d - MSE_{ij})$$

$$\phi_i^T \Delta K \Delta\phi_i = \sum_{j=1}^{n} \phi_i^T \Delta K_j \Delta\phi_i = -\sum_{j=1}^{n} \alpha_j \phi_i^T K_j \Delta\phi_i = -\sum_{j=1}^{n} \alpha_j (MSE_{ij}^d - MSE_j) \tag{10}$$

Eq.(7), Eq. (8), Eq. (9) and Eq. (10) substituted into Eq. (4), Eq. (4) can be expressed as:

$$\delta_i \cdot MSE_i^d = \sum_{j=1}^{n} (\alpha_j \cdot MSE_{ij}^d) \tag{11}$$

Where, $MSE_i^d = \sum_{j=1}^{n} MSE_{ij}^d$, the total strain energy of the i^{th} modal of Injury structure.

The formula (11) is structural damage identification equation, which is composed by modal damage sensitivity factor, modal strain energy of injury structure and the element damage factor.The strain energy is more sensitive to the small damage of the structure[16], Measuring modal the damage sensitivity factor is relatively easy, and it has a high measuring accuracy[17]. So the Eq.(11) can be used to identify small damage of the pile structure with higher accuracy.

δ_i is the indicator used to determine the modal sensitivity of structural damage, the value of δ_i is the larger, the modal damage identification of structural damage is the more sensitive, or vice versa. Therefore, according to the modal damage sensitivity factor δ_i, we can select the mode used for structural damage identification. Practical application is setting a threshold based on the environment and damage of the structure, it is the efficient mode when the threshold value greater than the set threshold value.

2.3. Element modal strain energy calculation

For the pile structure, in the case of element is sufficiently small, element modal strain energy can be represented by the formula as follow:

$$MSE_{ij} = \phi_i^T K_j \phi_i = \frac{1}{2}\int_{b_j}^{b_{j+1}} (EI)_j (\frac{\partial^2 \phi_i}{\partial z^2})^2 dz \quad (15)$$

$$MSE_{ij}^d = (1-\alpha_j)(\phi_i^d)^T K_j \phi_i^d = \frac{1}{2}\int_{b_j}^{b_{j+1}} (EI)_j^d (\frac{\partial^2 \phi_i^d}{\partial z^2})^2 dz \quad (16)$$

$(EI)_j$ and $(EI)_j^d$ represent the structural flexural rigidity of j^{th} element before and after damage respectively. b_j and b_{j+1} represent z coordinates of node j and node $j+1$ respectively.

The bending stiffness $(EI)_j^d$ of structure with damage is unknown for experimental modal analysis, it can be substituted by bending stiffness before injury ($(EI)_j$)in the case of small injuries. Consider the selected elements is relatively small, the bending stiffness $(EI)_j$ of the j^{th} element can be approximated as a constant, it can be mentioned the integral sign. Eq. (15) and (16) can be rewritten as:

$$MSE_{ij} = \frac{1}{2}(EI)_j \int_{b_j}^{b_{j+1}} (\frac{\partial^2 \phi_i}{\partial z^2})^2 dz \quad (17)$$

$$MSE_{ij}^d = \frac{1}{2}(EI)_j \int_{b_j}^{b_{j+1}} (\frac{\partial^2 \phi_i^d}{\partial z^2})^2 dz \quad (18)$$

$(\frac{\partial^2 \phi_i}{\partial z^2})^2$ in Eq. (17) can be instead by the mean value of $(\phi_{ij}^{''})^2$ and $(\phi_{i(j+1)}^{''})^2$, so Eq.(17) can be expressed as:

$$MSE_{ij} = \frac{1}{4}(EI)_j [(\phi_{ij}^{''})^2 + (\phi_{i(j+1)}^{''})^2](b_j + b_{j+1}) \quad (19)$$

Similarly, the equation (18) can be rewritten as:

$$MSE_{ij}^d = \frac{1}{4}(EI)_j \{[(\phi_{ij}^d)'']^2 + [(\phi_{i(j+1)}^d)'']^2\}(b_j + b_{j+1}) \quad (20)$$

Where, $(\phi_{ij}^{''})^2$、$(\phi_{i(j+1)}^{''})^2$、$[(\phi_{ij}^d)'']^2$ and $[(\phi_{i(j+1)}^d)'']^2$ can be got by measuring displacement mode shapes.

2.4.Damage location determination

The original signal of injury can be got by the difference of element modal strain energy of the before and after damage:

$$f_j(z) = MSE_{ij}^d - MSE_{ij} \quad (21)$$

Fitting signal $f_j(z)$ using cubic spline interpolation, the signal are transformed by wavelet function, we get the transform coefficients which can be used to detect the damage location.

$$DI_{ij} = C(a,b)_{i,j} \quad (22)$$

$C(a,b)_{i,j}$ represents the j^{th} element transform coefficient, DI_{ij} represent element injury positioning indicators. So index DI_{ij} can be used to determine the damage element, if the index DI_{ij} is a large value, we can judge the j^{th} element occur injury.

In order to reduce the impact of random noise from the test mode shapes , multi-order efficient modality are used to diagnose structural damage location:

$$DI_j = \frac{1}{N}\sum_m DI_{ij} \qquad (23)$$

Where, N is the efficient modal number of selection. A given threshold value of DI_j to determine whether the structure has occurred injury can be applied in practical applications.

2.5.Degree of damage calculation

After the injury element is determined, the formula (11) can be used to calculated the degree of element damage. The element damage factor α_j can be used to represent the degree of damage. If there is only one location injury, assuming k element injury, then $\alpha_j = 0(j \neq k)$, only $\alpha_k \neq 0$. The Eq.(11) can be expressed:

$$\alpha_k = \frac{\delta_i \cdot MSE_i^d}{MSE_{ik}^d} \qquad \textbf{(24)}$$

If there are multiple locations injury, assuming m element（k_1、k_2、$\cdots k_m$） injury $(m \le n)$, then need m efficient mode（q_1、q_2、$\cdots q_m$）to be calculated. m equations can solve the corresponding damage factor α. The equations are as follows:

$$\overline{\delta} \cdot MSED = \overline{\alpha} \cdot MSEDD \qquad (25)$$

Where,

$$\overline{\delta} = \begin{bmatrix} \delta_{q_1} & \delta_{q_2} & \delta_{q_3} & \ldots & \delta_{q_m} \end{bmatrix}$$

$$MSED = \begin{bmatrix} MSE_{q_1}^d \\ MSE_{q_2}^d \\ MSE_{q_3}^d \\ \ldots \\ MSE_{q_m}^d \end{bmatrix}$$

$$\overline{\alpha} = \begin{bmatrix} \alpha_{k_1} & \alpha_{k_2} & \alpha_{k_3} & \ldots & \alpha_{k_m} \end{bmatrix}$$

$$MSEDD = \begin{bmatrix} MSE_{q_1k_1} & MSE_{q_2k_1} & MSE_{q_3k_1} & \ldots & MSE_{q_mk_1} \\ MSE_{q_1k_2} & MSE_{q_2k_2} & MSE_{q_3k_2} & \ldots & MSE_{q_mk_2} \\ MSE_{q_1k_3} & MSE_{q_2k_3} & MSE_{q_3k_3} & \ldots & MSE_{q_mk_3} \\ \ldots & \ldots & \ldots & \ldots & \ldots \\ MSE_{q_1k_m} & MSE_{q_2k_m} & MSE_{q_3k_m} & \ldots & MSE_{q_mk_m} \end{bmatrix}$$

If $p < m$, extended modal can be applied to the calculation.

3. Instance of verification

3.1. Project overview

Artificial hollowed piles are used to pile foundation of Ouhai Sports Center Stadium. Effective pile length is 4.00m ~ 30m, pile diameter is 600mm ~ 1000mm, the pile concrete is C25. The project total pile is 129, according to the verify results of low strain detection and excavation, 9.6% of the damage occurred at 7.4m from the top of the pile of NO.71 piles. No. 71 piles pile length is 21m, diameter is 1m. Real damage of No.71 pile is shown in Fig.1.

3.2.Finite Element Modeling

Applying of finite element software ANSYS, according to the design drawings, we establish finite element model of the role of interaction between pile and soil for NO.71 pile (Fig.2(a)). According to actual damage on the No. 71 pile, pile model with cracks was established at 7.4 meters from the top of the pile. Crack depth is 9.6% of the diameter of pile foundation (Fig.2(b)). The element type of pile foundation model is SOLID45. Pile-soil interaction applies the nonlinearity the spring element COMBIN139 to simulate. In order to establish the finite element computation model which are in line with the environment of the actual engineering, model updating technology based on the measured data was used to improve the finite element model.

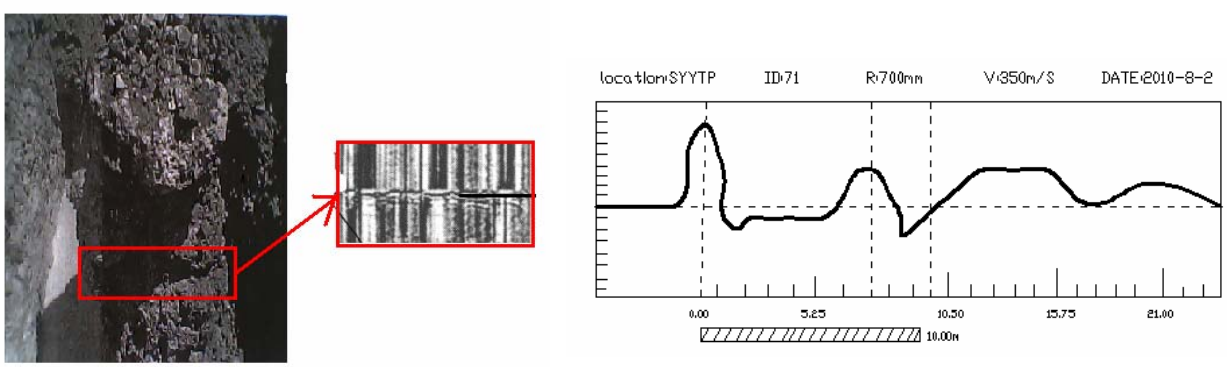

（a）Site excavation detection　　（b）Detection of low strain

Figure 1 The actual damage location of No. 71 piles

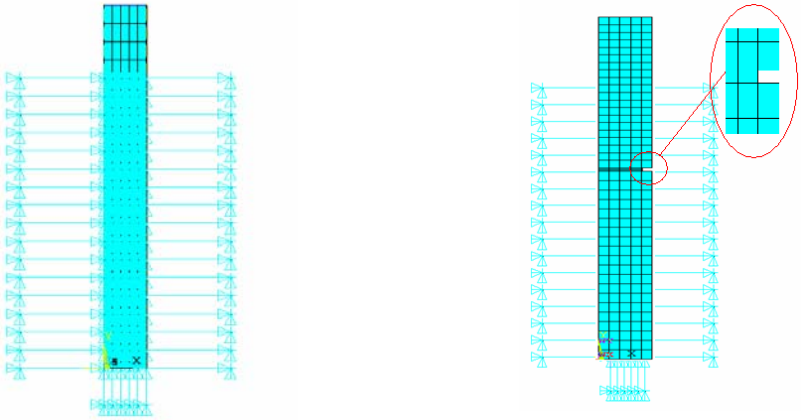

（a）Before damage　　（b）After damage

Figure 2 Finite element model of pile-soil interaction

3.3.Efficient mode selection

The rate of change of the natural frequencies before and after the injury is shown in Fig. 3, efficient frequency threshold is set as $\delta_i \geq 0.4\%$. As Fig. 3 shows, the damage determination efficient modes are mode 1 and mode 4.

3.4. Damage location identification

Information function is established using the changes of element strain energy before and after injury, wavelet transform is used to determine the parameters (DI) for the location of damage. DI_j of efficient modal shown in Fig. 4. By setting the threshold （ $DI > 2$ ）, we can clearly determine that the element 55 to 59 crack damage occurs. This is is very consistent with the actual damage location. Results of location damage identification shown as table 1. Identification error is 3%, it proved that the method of damage location identification has a higher accuracy.

3.5. Identification of injury severity

Element damage factor is calculated applying Eq.25, the results of calculation shown as table 1. As shown in Table 1, actual injury and calculation of injury is very close. Identification error is 6.2%, it proved that the method of damage severity identification has a higher accuracy.

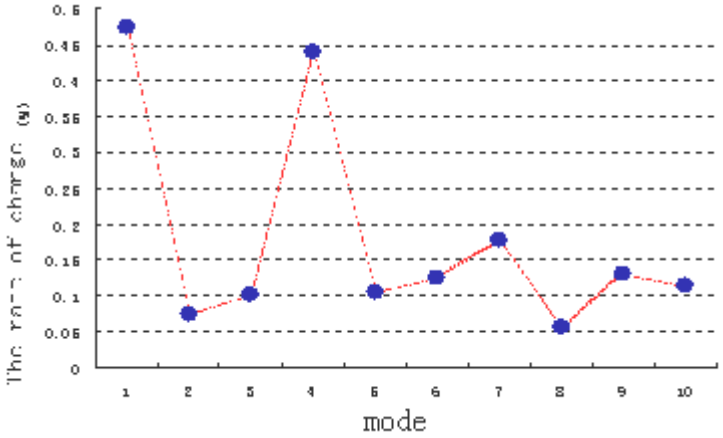

Figure 3 The rate of change of the natural frequency

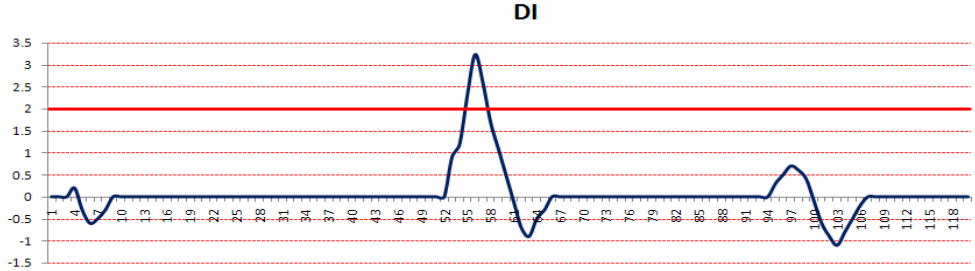

Figure 4　DI value for each element applying of efficient modal

Table 1 Results of damage identification

	Actual injury	Low strain method/error	New method/error
damage location	7.4m	6.71m/9.3%	7.08m/4.3%
damage severity	9.6%	Small damage	10.2%/6.2%

4 Conclusion

This paper selected efficient modal for damage identification applying the change rate of eigenvalues firstly, then established the small injury accurate recognition method based on the application of sensitivity of element modal strain energy to small structural injury and efficient local analysis capabilities of wavelet analysis. The efficiency and accuracy of the proposed method is verified by small cracks damage identification of the pile of Ouhai Sports Center. The concrete conclusions are as follows:

(1) Fracture identification method proposed in this paper for the pile foundation can effectively identify the fracture damage location of the hidden structures in service, this method has a high recognition accuracy.

(2) Fracture identification method proposed in this paper for the pile foundation can effectively identify the fracture damage severity of the hidden structures in service; it is able to quantify the degree of damage; it provides an important reference for the pile foundation fracture injury assessment.

(3) The method presented in this paper provides a new approach to concealed structure damage identification.

Acknowledgements

This work was financially supported by Zhejiang Provincial Education Department's research projects, the project name: Synchronous Identification Method of Structural damage and load under ambient excitation, project number: Y201223039.

References

[1]H.W. Zhou, W.T. Weng, Y. Wang. Several methods of the bridge pile testing. Highway and Transportation Research (Applied Technology Edition), 4(2012) 222-225.

[2]X.L. Han, Y.X. Han, X.M. Tang. Numerical analysis of wave propagation in platform-pile system. Chinese journal of geotechnical engineering 6(2001) 105-107.

[3]H.Y. Chai, M.G. Liu, S.W. Bai. Numerical analysis of wave propagation in platform-pile system. Chinese journal of geotechnical engineering, 5(2003) 624-628.

[4]C.H. Zhang, J.L. Zhang, J.H. Xie, et al.. The multi-reflected wave analysis on the low strain integrity testing of pile foundation. Journal of xiamen university： natural science, 3(2005)214-216.

[5]Y.M. Chen. Got Method Drills in Pile Foundation Inspection About the Application Analysis. Construction and Design for Project, 7(2011)129-131.

[6]C.X. Xiao. Application of ultrasonic transmission method to detecting integrity of large-diameter bored cast-in-place piles[J]. Rock and Soil Mechanics, S1(2003)169-171.

[7]F.C. Liu，W. Wang，Z.S. Zhang，W.Q. Liu. Wave Analysis of Pile Foundation Low Strain Detection and Determination of Pile Body Integrity. Port Engineering Technology, 2(2012)46-48.

[8]H.Q. Wu, R.Y. Ma，L.Y. Huang，J. Peng，L. Chen. General application and analysis of several detection methods in the engineering foundation piles. Concrete, 4(2012)119-121.

[9] M. Johnson, F. Rausche. Low strain testing of piles utilizing tow acceleration signa. Stress Wave, 3(1996)859-869.
[10] X. Luo, H. Haya, T. Inaba, T. Shiotani, Y. Nakanishi. Damage evaluation of railway structures by using train-induced AE. Construction and Buiding Materials, 3(2004)215-223.
[11]X.S. Hao . Outline of on-the-spot investigation on the earthquake occurring in the south of hyogo prefecture, Japan on January 17,1995. Recent Developments in World Seismology, 7(1995)12-16.
[12]W.C. Yuan, F. Cui, Q.W. Zhang. Current research and development of structural health monitoring and condition assessment for bridges[J]. Journal of Tongji University, 2 (1999):184-188
[13]Y.Z. Qi. Hole wall imaging technology in old bridge pile foundation inspection. Highway, 3(2012)16-19.
[14]Y. Zhang，S.Z. Tian. Application of wavelet analysis in high-piled wharf pile integrity testing. Journal of Waterway and Harbor, 2(2012)163-168.
[15] L.J. Hadjileontiadis, E. Douka, A. Trochidis, Fractal dimension analysis for crack identification in beam structures, Mechanical Systems and Signal Processing , 3(2005) 659–674.
[16]W. Fan , P. Z. Qiao. A strain energy-based damage severity correction factor method for damage identification in plate-type structures. Mechanical Systems and Signal Processing, 28(2012):660-678.
[17]H.W. Hu, C.B. Wu, W.J. Lu . Damage detection of circular hollow cylinder using modal strain energy and scanning damage index methods. Computers and Structures ,1-2(2011)149－160.

Theoretical and Numerical Study of Symmetric, In-plane, Free Vibration of Timoshenko Portal Frame with Open Crack

Nikam M Satyavan, Sandeep Kumar and S.M. Murigendrappa*

Department of Mechanical Engineering, National Institute of Technology Karnataka, Surathkal-575025, India
*Corresponding author: smm@nitk.ac.in

Abstract The local flexibility introduced by cracks changes the vibration behaviour of the structure and by examining this change, crack severity can be identified. This paper presents the natural frequencies of symmetric, in-plane free-vibrations of Timoshenko portal frame with and without open crack for different boundary conditions. Cracked segment is modelled as two segments connected by a massless torsional spring. Considering appropriate compatibility requirements at the crack section in any one of segments and at the junction of two segments, the characteristic equations are established for corresponding boundary conditions and solved for natural frequencies by numerically. Crack location ranging from 20% to 70% of length of segment and crack size ranging from 20% to 60% of depth have been considered. Results obtained analytically are compared numerically using standard commercially available finite element software. The frame has been modelled by using quadratic quadrilateral shell elements and quarter-point singular elements are employed around the crack-tip. It is observed that as expected, with increase in crack depth the change in frequencies of the frame with and without crack increases. The maximum difference between the analytical and numerical results is 7.09% for all the cases considered, which proves usefulness of the data.

Keywords Timoshenko Portal Frame, Open Crack, Massless Torsional Spring, In-plane Free Vibration, FEM

1. Introduction

The problem of Timoshenko portal frames with defect is of importance in many fields of engineering. Defects are almost unavoidable in such frames and their existences will decrease stiffness, strength and safety. Although, a number of accurate, effective and reliable on-line damage detection methods based on either X-ray, ultrasonic tests etc., are available, their adoption require scanning of the whole length of frame. This process is a very time consuming, labour-intensive and expensive. In view of these limitations there is a need to develop Non-Destructive Testing methods which can detect damages in a component from the measurement of vibration responses, which may be collected from at a single point, or at the most, a few points, on the component.

The most significant vibration parameter applied in damage identification methods is change in natural frequencies of vibrations of structures caused by the crack. Hence, it may be possible to predict the presence of a crack from the measurements of natural frequencies of the damaged component. A wide variety of beam structures modelled by Euler-Bernoulli or Timoshenko beam theory have been considered for crack detection by representing the crack with massless torsional spring[1-9] etc. Experimental results, though not very exhaustive, are also reported.

Most of the studies on frames consider them to be free from defects [10-16]. A few investigators have reported inverse problem of determination of crack details from the natural frequencies or mode shapes (e.g.,[17-19]) for frame modelled by Euler-Bernoulli beam theory. Frames modelled by Timoshenko beam theory with crack have not yet been studied. This paper presents, a method of solving a forward problem i.e., determination of natural frequencies knowing the crack details of symmetric, in-plane vibrations of Timoshenko portal frame with crack. Associated cracked segment in the portal frame is modelled as two segments connected by a massless torsional spring. The characteristic equations are established using boundary conditions, compatibility conditions at

junctions of two segments and continuity conditions at the crack location. These characteristic equations are used to compute the natural frequencies of Timoshenko portal frame by numerically. Finally, these computed natural frequencies are compared with that of natural frequencies obtained from finite element method for fixed-hinged, hinged-hinged and fixed-fixed end conditions.

2. Theoretical formulation

For in-plane free vibration analysis of Portal frame without and with crack, initially a beam with crack has been studied and natural frequencies have been compared with available literature. For the In-plane free vibration analysis of portal frame, transverse and longitudinal motions of each member are taken into consideration. In analytical modelling of frame, Timoshenko beam theory approach is used for analysis of transverse vibration, while axial vibration of rod is considered for analysis of longitudinal vibration of each member.

A portal frame containing a part through-the-thickness edge crack undergoing free transverse vibration, gives rise to a deformation pattern corresponding to natural frequencies. This in turn will change the slope-mode shape, curvature mode shape, etc. The forward problem of determination of natural frequencies knowing the crack details for fixed-hinged, hinged-hinged and fixed-fixed end conditions have been examined. Accuracy obtainable in connection with natural frequencies is compared numerically using commercially available FE tool for different boundary conditions.

2.1. Formulation for portal frame without crack

For a free, in-plane, symmetric transverse and axial motions of each segments in portal frame without any crack is modelled by using Timoshenko beam theory i.e., taking the effects of shear deformation and rotational inertia. Neglecting damping effect, the mode shape equations of each segments are governed by (Fig. 1)[11]

Transverse motion:

$$v_i''''(\eta_i) + (\sigma+\tau)\, v_i''(\eta_i) - (\alpha - \sigma\tau) v_i(\eta_i) = 0, \qquad 0 < \eta_i < \beta_i \quad \text{for } i = 1,2,3 \tag{1}$$

Slope due to bending:

$$\phi_i''''(\eta_i) + (\sigma+\tau)\, \phi_i''(\eta_i) - (\alpha - \sigma\tau) \phi_i(\eta_i) = 0, \qquad 0 < \eta_i < \beta_i \quad \text{for } i = 1,2,3 \tag{2}$$

Longitudinal motion:

$$u_i''(\eta_i) + \gamma^2\, v_i(\eta_i) = 0, \qquad 0 < \eta_i < \beta_i \quad \text{for } i = 1,2,3 \tag{3}$$

where v_i is transverse displacement, u_i is axial displacement, ϕ_i is the rotation due to bending of the segments, these are function of non-dimensional position, η_i along the length of segment in a particular mode for the segment i, a prime indicates differentiation with respect to η_i and additional parameters given by

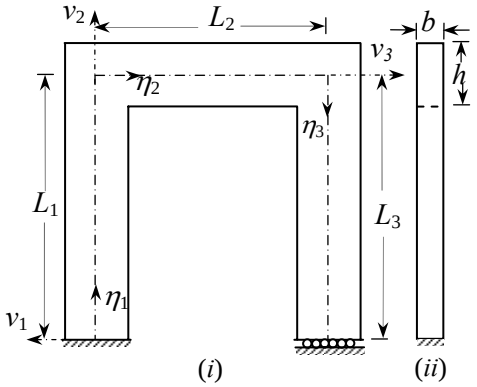

Figure 1. Schematic of Timoshenko portal frame: (*i*) front view and (*ii*) side view.

$$\sigma=\frac{\rho L^2\omega^2}{E},\ \tau=\frac{\rho L^2\omega^2}{\kappa G},\ \alpha=\frac{\rho L^4\omega^2 A}{EI},\ \gamma^2=\frac{\rho L^2\omega^2}{E},\ \beta_i=\frac{L_i}{L},\ L=L_1+L_2+L_3 \tag{4}$$

E is modulus of elasticity, I is second moment of inertia, A is cross sectional area, G is shear modulus, ρ is density of material, κ is Timoshenko's shear coefficient and its value is 5/6 for rectangular cross-section, L is total length of portal frame.

The solutions of Eq. (1-3) are given by

$$v_i(\eta_i)=A_i\cosh\lambda_1\eta_i+B_i\sinh\lambda_1\eta_i+C_i\cos\lambda_2\eta_i+D_i\sin\lambda_2\eta_i,\quad 0<\eta_i<\beta_i\quad \text{for } i=1,2,3 \tag{5}$$

$$\phi_i(\eta_i)=q_1A_i\sinh\lambda_1\eta_i+q_1B_i\cosh\lambda_1\eta_i+q_2C_i\sin\lambda_2\eta_i-q_2D_i\cos\lambda_2\eta_i,\quad 0<\eta_i<\beta_i\quad \text{for } i=1,2,3 \tag{6}$$

$$u_i(\eta_i)=E_i\sin\gamma\eta_i+F_i\cos\gamma\eta_i,\qquad 0<\eta_i<\beta_i\quad \text{for } i=1,2,3 \tag{7}$$

where $\lambda_1=\sqrt{\sqrt{\left(\frac{\sigma-\tau}{2}\right)^2+\alpha}-\frac{\sigma+\tau}{2}}$, $\lambda_2=\sqrt{\sqrt{\left(\frac{\sigma-\tau}{2}\right)^2+\alpha}+\frac{\sigma+\tau}{2}}$, $\lambda_3=\sqrt{\frac{\rho L^2\omega^2}{\kappa G}}$, $q_1=\frac{\lambda_1^2+\lambda_3^2}{\lambda_1}$, $q_2=\frac{\lambda_3^2-\lambda_2^2}{\lambda_2}$,

A_i, B_i, C_i, D_i, E_i and F_i are arbitrary constants evaluated from the boundary conditions.
The boundary and compatibility conditions for a fixed-hinged frame (Fig. 1) are as follows.

$$\left.\begin{aligned}&\text{at}\quad \eta_1=0;\qquad v_1(0)=0,\quad \phi_1(0)=0,\quad u_1(0)=0\\&\text{at}\quad \eta_3=\beta_3;\qquad v_3(\beta_3)=0,\quad \phi_3'(\beta_3)=0,\quad u_3(\beta_3)=0\end{aligned}\right\} \tag{8}$$

$$\left.\begin{aligned}&\text{at}\quad \eta_1=\beta_1,\quad \eta_2=0;\quad v_2(0)=u_1(\beta_1),\quad -v_1(\beta_1)=u_2(0),\quad v_2'(0)=v_1'(\beta_1),\quad \phi_2'(0)=\phi_1'(\beta_1)\\&\qquad\qquad \kappa G\left[v_2'(0)-\phi_2(0)\right]=Eu_1'(\beta_1),\quad \kappa G\left[v_1'(\beta_1)-\phi_1(\beta_1)\right]=-Eu_2'(0)\end{aligned}\right\} \tag{9}$$

$$\left.\begin{aligned}&\text{at}\quad \eta_2=\beta_2,\quad \eta_3=0;\quad v_3(0)=u_2(\beta_2),\quad -v_2(\beta_2)=u_3(0),\quad v_3'(0)=v_2'(\beta_2),\quad \phi_3'(0)=\phi_2'(\beta_2)\\&\qquad\qquad \kappa G\left[v_3'(0)-\phi_3(0)\right]=Eu_2'(\beta_2),\quad \kappa G\left[v_2'(\beta_2)-\phi_2(\beta_2)\right]=-Eu_3'(0)\end{aligned}\right\} \tag{10}$$

By substituting Eqs. (5-7) in to Eqs. (8-10) results in following 18 homogeneous equations.

$$A_1+C_1=0 \tag{11}$$

$$q_1B_1-q_2D_1=0 \tag{12}$$

$$F_1=0 \tag{13}$$

$$A_3\cosh\lambda_1\beta_3+B_3\sinh\lambda_1\beta_3+C_3\cos\lambda_2\beta_3+D_3\sin\lambda_2\beta_3=0 \tag{14}$$

$$A_3\lambda_1q_1\cosh\lambda_1\beta_3+B_3\lambda_1q_1\sinh\lambda_1\beta_3+C_3\lambda_2q_2\cos\lambda_2\beta_3+D_3\lambda_2q_2\sin\lambda_2\beta_3=0 \tag{15}$$

$$E_3\sin\gamma\beta_3+F_3\cos\gamma\beta_3=0 \tag{16}$$

$$E_1\sin\gamma\beta_1+F_1\cos\gamma\beta_1-A_2-C_2=0 \tag{17}$$

$$A_1\cosh\lambda_1\beta_1+B_1\sinh\lambda_1\beta_1+C_1\cos\lambda_2\beta_1+D_1\sin\lambda_2\beta_1+F_2=0 \tag{18}$$

$$A_1\lambda_1\sinh\lambda_1\beta_1+B_1\lambda_1\cosh\lambda_1\beta_1-C_1\lambda_2\sin\lambda_2\beta_1+D_1\lambda_2\cos\lambda_2\beta_1-\lambda_1B_2-\lambda_2D_2=0 \tag{19}$$

$$A_1\lambda_1q_1\cosh\lambda_1\beta_1+B_1\lambda_1q_1\sinh\lambda_1\beta_1+C_1\lambda_2q_2\cos\lambda_2\beta_1+D_1\lambda_2q_2\sin\lambda_2\beta_1-\lambda_1q_1A_2-\lambda_2q_2C_2=0 \tag{20}$$

$$\gamma E\left(E_1\cos\gamma\beta_1-F_1\sin\gamma\beta_1\right)-\kappa G\left[B_2\left(\lambda_1-q_1\right)+D_2\left(\lambda_2+q_2\right)\right]=0 \tag{21}$$

$$\kappa G\left[A_1\left(\lambda_1-q_1\right)\sinh\lambda_1\beta_1+B_1\left(\lambda_1-q_1\right)\cosh\lambda_1\beta_1-C_1\left(\lambda_2+q_2\right)\sin\lambda_2\beta_1+D_1\left(\lambda_2+q_2\right)\cos\lambda_2\beta_1\right]+E\gamma E_2=0 \tag{22}$$

$$E_2\sin\gamma\beta_2+F_2\cos\gamma\beta_2-A_3-C_3=0 \tag{23}$$

$$A_2\cosh\lambda_1\beta_2+B_2\sinh\lambda_1\beta_2+C_2\cos\lambda_2\beta_2+D_2\sin\lambda_2\beta_2+F_3=0 \tag{24}$$

$$A_2\lambda_1\sinh\lambda_1\beta_2+B_2\lambda_1\cosh\lambda_1\beta_2-C_2\lambda_2\sin\lambda_2\beta_2+D_2\lambda_2\cos\lambda_2\beta_2-\lambda_1B_3-\lambda_2D_3=0 \tag{25}$$

$$A_2\lambda_1q_1\cosh\lambda_1\beta_2+B_2\lambda_1q_1\sinh\lambda_1\beta_2+C_2\lambda_2q_2\cos\lambda_2\beta_2+D_2\lambda_2q_2\sin\lambda_2\beta_2-\lambda_1q_1A_3-\lambda_2q_2C_3=0 \tag{26}$$

$$\gamma E\left(E_2\cos\gamma\beta_2-F_2\sin\gamma\beta_2\right)-\kappa G\left[B_3\left(\lambda_1-q_1\right)+D_3\left(\lambda_2+q_2\right)\right]=0 \tag{27}$$

$$\kappa G\left[A_2\left(\lambda_1-q_1\right)\sinh\lambda_1\beta_2+B_2\left(\lambda_1-q_1\right)\cosh\lambda_1\beta_2-C_2\left(\lambda_2+q_2\right)\sin\lambda_2\beta_2+D_2\left(\lambda_2+q_2\right)\cos\lambda_2\beta_2\right]+E\gamma E_3=0 \tag{28}$$

These can be expressed conveniently in the following form.

$$\left[\Delta(\omega)\right]_{18\times18}\left\{C\right\}_{18\times1}=\left\{0\right\}_{18\times1} \tag{29}$$

where $\{C\}=\{A_1,B_1\ldots F_3\}^T$ are unknown arbitrary constants.

For non-trivial solution,

$$\left|\Delta(\omega)\right| = 0 \tag{30}$$

which gives the characteristic equations. Solving this equation numerically, the natural frequencies of portal frame without crack are obtained.

2.2. Formulation for portal frame with crack located in left vertical segment

One of the convenient methods of modelling the vibration of a beam segment with a crack is to split the segment into two around the crack section and connect them by massless spring element, whose flexibility is given by a matrix of size 6×6 [20,21]. When the various modes of vibration become uncoupled, the size of the flexibility matrix reduces. Particularly, for a pure transverse vibration the matrix is of size 1×1. That is, there is only one spring element, which is a torsional spring. A typical representation of a portal frame with a crack located in left vertical segment is shown in Fig. 2. The governing mode shape equations of each segment are of the form:

$$v_i''''(\eta_i) + (\sigma+\tau)\, v_i''(\eta_i) - (\alpha - \sigma\tau) v_i(\eta_i) = 0, \qquad 0 < \eta_i < \beta_i \quad \text{for } i = 1,2,3,4 \tag{31}$$

$$\phi_i''''(\eta_i) + (\sigma+\tau)\, \phi_i''(\eta_i) - (\alpha - \sigma\tau) \phi_i(\eta_i) = 0, \qquad 0 < \eta_i < \beta_i \quad \text{for } i = 1,2,3,4 \tag{32}$$

$$u_i''(\eta_i) + \gamma^2\, v_i(\eta_i) = 0, \qquad 0 < \eta_i < \beta_i \quad \text{for } i = 1,2,3,4 \tag{33}$$

where values of β_i are as follows.

$$\beta_1 = \delta L_1/L,\ \beta_2 = (1-\delta) L_2/L,\ \beta_3 = L_3/L,\ \beta_4 = L_4/L \text{ and crack location, } 0 \le \delta \le 1 \tag{34}$$

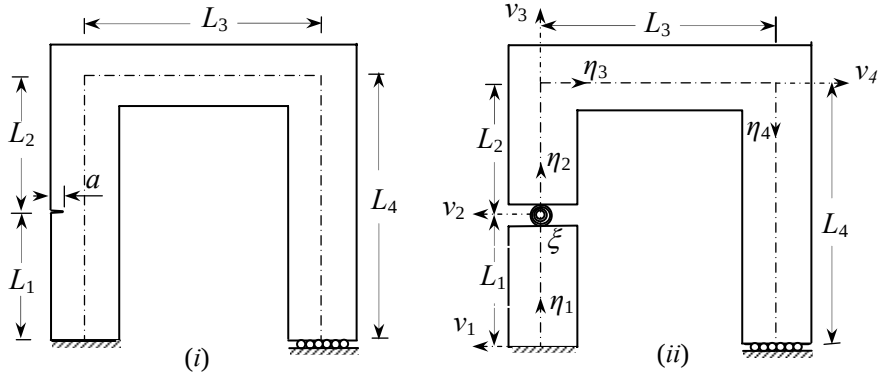

Figure 2. (*i*) Schematic of Timoshenko portal frame with crack in left vertical segment and (*ii*) Representation by rotational spring.

The general solutions of Eq. (31-33) are of the form Eqs. (5-7). Boundary and compatibility conditions at the junctions are as follows.

$$\left.\begin{array}{ll} \text{at} \quad \eta_1 = 0; & v_1(0) = 0, \quad \phi_1(0) = 0, \quad u_1(0) = 0 \\ \text{at} \quad \eta_4 = \beta_4; & v_4(\beta_4) = 0, \quad \phi_4'(\beta_4) = 0, \quad u_4(\beta_4) = 0 \end{array}\right\} \tag{35}$$

$$\left.\begin{array}{l} \text{at} \quad \eta_2 = \beta_2, \quad \eta_3 = 0; \quad v_3(0) = u_2(\beta_2), \quad -v_2(\beta_2) = u_3(0), \quad v_3'(0) = v_2'(\beta_2), \quad \phi_3'(0) = \phi_2'(\beta_2) \\ \qquad\qquad \kappa G\left[v_3'(0) - \phi_3(0)\right] = E u_2'(\beta_2), \quad \kappa G\left[v_2'(\beta_2) - \phi_2(\beta_2)\right] = -E u_3'(0) \end{array}\right\} \tag{36}$$

$$\left.\begin{array}{l} \text{at} \quad \eta_3 = \beta_3, \quad \eta_4 = 0; \quad v_4(0) = u_3(\beta_3), \quad -v_3(\beta_3) = u_4(0), \quad v_4'(0) = v_3'(\beta_3), \quad \phi_4'(0) = \phi_3'(\beta_3) \\ \qquad\qquad \kappa G\left[v_4'(0) - \phi_4(0)\right] = E u_3'(\beta_3), \quad \kappa G\left[v_3'(\beta_3) - \phi_2(\beta_3)\right] = -E u_4'(0) \end{array}\right\} \tag{37}$$

The compatibility conditions at crack location are given by

$$\left.\begin{array}{l} \text{at} \quad \eta_1 = \beta_1, \quad \eta_2 = 0; \quad v_2(0) = v_1(\beta_1),\ \phi_2'(0) = \phi_1'(\beta_1),\ v_2'(0) - \phi_2(0) = v_1'(\beta_1) - \phi_1(\beta_1), \\ \qquad\qquad v_2'(0) - v_1'(\beta_1) = \xi \phi_1'(\beta_1),\ u_2(0) = u_1(\beta_1),\ u_2'(0) = u_1'(\beta_1) \end{array}\right\} \tag{38}$$

where ξ is the non-dimensional flexibility of the torsional spring representing the crack and the relation through crack size can be written in the following form[6]:

$$\xi = 6\pi\, r^2 \frac{h}{L} f \tag{39}$$

where r is crack size a to segment depth h ratio and f is crack geometry parameter defined by

$$f(r) = 0.6384 - 1.035r + 3.7201r^2 - 5.1773r^3 + 7.533r^4 - 7.332r^5 + 2.4909r^6 \tag{40}$$

By inserting general solutions of type (5-7) into Eqs. (35-38) results in following 24 homogeneous equations.

$$A_1 + C_1 = 0 \tag{41}$$
$$q_1 B_1 - q_2 D_1 = 0 \tag{42}$$
$$F_1 = 0 \tag{43}$$
$$A_4 \cosh\lambda_1\beta_4 + B_4 \sinh\lambda_1\beta_4 + C_4 \cos\lambda_2\beta_4 + D_4 \sin\lambda_2\beta_4 = 0 \tag{44}$$
$$A_4\lambda_1 q_1 \cosh\lambda_1\beta_4 + B_4\lambda_1 q_1 \sinh\lambda_1\beta_4 + C_4\lambda_2 q_2 \cos\lambda_2\beta_4 + D_4\lambda_2 q_2 \sin\lambda_2\beta_4 = 0 \tag{45}$$
$$E_4 \sin\gamma\beta_4 + F_4 \cos\gamma\beta_4 = 0 \tag{46}$$
$$A_1 \cosh\lambda_1\beta_1 + B_1 \sinh\lambda_1\beta_1 + C_1 \cos\lambda_2\beta_1 + D_1 \sin\lambda_2\beta_1 - A_2 - C_2 = 0 \tag{47}$$
$$A_1\lambda_1 q_1 \cosh\lambda_1\beta_1 + B_1\lambda_1 q_1 \sinh\lambda_1\beta_1 + C_1\lambda_2 q_2 \cos\lambda_2\beta_1 + D_1\lambda_2 q_2 \sin\lambda_2\beta_1 - \lambda_1 q_1 A_2 - \lambda_2 q_2 C_2 = 0 \tag{48}$$
$$A_1(\lambda_1 - q_1)\sinh\lambda_1\beta_1 + B_1(\lambda_1 - q_1)\cosh\lambda_1\beta_1 - C_1(\lambda_2 + q_2)\sin\lambda_2\beta_1 + D_1(\lambda_2 + q_2)\cos\lambda_2\beta_1 - B_2(\lambda_1 - q_1) - D_2(\lambda_2 + q_2) = 0 \tag{49}$$
$$\left.\begin{aligned} &A_1(\lambda_1 \sinh\lambda_1\beta_1 + \xi\lambda_1 q_1 \cosh\lambda_1\beta_1) + B_1(\lambda_1 \cosh\lambda_1\beta_1 + \xi\lambda_1 q_1 \sinh\lambda_1\beta_1) \\ &+ C_1(\xi\lambda_2 q_2 \cos\lambda_2\beta_1 - \lambda_2 \sin\lambda_2\beta_1) + D_1(\lambda_2 \cos\lambda_2\beta_1 + \xi\lambda_2 q_2 \sin\lambda_2\beta_1) - B_2\lambda_1 - D_2\lambda_2 = 0 \end{aligned}\right\} \tag{50}$$
$$E_1 \sin\gamma\beta_1 + F_1 \cos\gamma\beta_1 - F_2 = 0 \tag{51}$$
$$E_1 \cos\gamma\beta_1 - F_1 \sin\gamma\beta_1 - E_2 = 0 \tag{52}$$
$$E_2 \sin\gamma\beta_2 + F_2 \cos\gamma\beta_2 - A_3 - C_3 = 0 \tag{53}$$
$$A_2 \cosh\lambda_1\beta_2 + B_2 \sinh\lambda_1\beta_2 + C_2 \cos\lambda_2\beta_2 + D_2 \sin\lambda_2\beta_2 + F_3 = 0 \tag{54}$$
$$A_2\lambda_1 \sinh\lambda_1\beta_2 + B_2\lambda_1 \cosh\lambda_1\beta_2 - C_2\lambda_2 \sin\lambda_2\beta_2 + D_2\lambda_2 \cos\lambda_2\beta_2 - \lambda_1 B_3 - \lambda_2 D_3 = 0 \tag{55}$$
$$A_2\lambda_1 q_1 \cosh\lambda_1\beta_2 + B_2\lambda_1 q_1 \sinh\lambda_1\beta_2 + C_2\lambda_2 q_2 \cos\lambda_2\beta_2 + D_2\lambda_2 q_2 \sin\lambda_2\beta_2 - \lambda_1 q_1 A_3 - \lambda_2 q_2 C_3 = 0 \tag{56}$$
$$\gamma E(E_2 \cos\gamma\beta_2 - F_2 \sin\gamma\beta_2) - \kappa G[B_3(\lambda_1 - q_1) + D_3(\lambda_2 + q_2)] = 0 \tag{57}$$
$$\kappa G[A_2(\lambda_1 - q_1)\sinh\lambda_1\beta_2 + B_2(\lambda_1 - q_1)\cosh\lambda_1\beta_2 - C_2(\lambda_2 + q_2)\sin\lambda_2\beta_2 + D_2(\lambda_2 + q_2)\cos\lambda_2\beta_2] + E\gamma E_3 = 0 \tag{58}$$
$$E_3 \sin\gamma\beta_3 + F_3 \cos\gamma\beta_3 - A_4 - C_4 = 0 \tag{59}$$
$$A_3 \cosh\lambda_1\beta_3 + B_3 \sinh\lambda_1\beta_3 + C_3 \cos\lambda_2\beta_3 + D_3 \sin\lambda_2\beta_3 + F_4 = 0 \tag{60}$$
$$A_3\lambda_1 \sinh\lambda_1\beta_3 + B_3\lambda_1 \cosh\lambda_1\beta_3 - C_3\lambda_2 \sin\lambda_2\beta_3 + D_3\lambda_2 \cos\lambda_2\beta_3 - \lambda_1 B_4 - \lambda_2 D_4 = 0 \tag{61}$$
$$A_3\lambda_1 q_1 \cosh\lambda_1\beta_3 + B_3\lambda_1 q_1 \sinh\lambda_1\beta_3 + C_3\lambda_2 q_2 \cos\lambda_2\beta_3 + D_3\lambda_2 q_2 \sin\lambda_2\beta_3 - \lambda_1 q_1 A_4 - \lambda_2 q_2 C_4 = 0 \tag{62}$$
$$\gamma E(E_3 \cos\gamma\beta_3 - F_3 \sin\gamma\beta_3) - \kappa G[B_4(\lambda_1 - q_1) + D_4(\lambda_2 + q_2)] = 0 \tag{63}$$
$$\kappa G[A_3(\lambda_1 - q_1)\sinh\lambda_1\beta_3 + B_3(\lambda_1 - q_1)\cosh\lambda_1\beta_3 - C_3(\lambda_2 + q_2)\sin\lambda_2\beta_3 + D_3(\lambda_2 + q_2)\cos\lambda_2\beta_3] + E\gamma E_4 = 0 \tag{64}$$

Eqs. (41-64) can be expressed conveniently in the following matrix equation.

$$[\Delta(\omega,\xi)]_{24\times24}\{C\}_{24\times1} = \{0\}_{24\times1} \tag{65}$$

where $\{C\}=\{A_1, B_1 \ldots F_4\}^T$ are unknown arbitrary constants.
For non-trivial solution

$$|\Delta(\omega,\xi)| = 0 \tag{66}$$

Evaluation of Eq. (66) numerical method yields natural frequencies of portal frame with crack.

2.3. Formulation for Portal frame with crack located in horizontal segment

The modelling of portal frame with crack located in horizontal segment (Fig.3) is done in the similar way as explained in the preceding section. The characteristic equations of type (66) can be obtained by incorporation of the following compatibility conditions at two junctions and crack location with associated boundary conditions.

$$\left.\begin{aligned} &\text{at}\quad \eta_1 = \beta_1,\quad \eta_2 = 0;\quad v_2(0) = u_1(\beta_1),\quad -v_1(\beta_1) = u_2(0),\quad v_2'(0) = v_1'(\beta_1),\quad \phi_2'(0) = \phi_1'(\beta_1) \\ &\qquad \kappa G[v_2'(0) - \phi_2(0)] = Eu_1'(\beta_1),\quad \kappa G[v_1'(\beta_1) - \phi_1(\beta_1)] = -Eu_2'(0) \end{aligned}\right\} \tag{67}$$

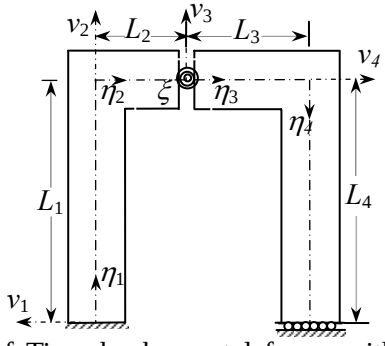

Figure 3. Schematic of Timoshenko portal frame with crack located in horizontal segment represented by torsional spring.

$$\text{at} \quad \eta_3=\beta_3, \quad \eta_4=0; \quad \left.\begin{array}{l} v_4(0)=u_3(\beta_3), \quad -v_3(\beta_3)=u_4(0), \quad v_4'(0)=v_3'(\beta_3), \quad \phi_4'(0)=\phi_3'(\beta_3) \\ \kappa G\left[v_4'(0)-\phi_4(0)\right]=Eu_3'(\beta_3), \quad \kappa G\left[v_3'(\beta_3)-\phi_2(\beta_3)\right]=-Eu_4'(0) \end{array}\right\} \tag{68}$$

$$\text{at} \quad \eta_2=\beta_2, \quad \eta_3=0; \quad \left.\begin{array}{l} v_3(0)=v_2(\beta_2),\ \phi_3'(0)=\phi_2'(\beta_2),\ v_3'(0)-\phi_3(0)=v_2'(\beta_2)-\phi_2(\beta_2), \\ v_3'(0)-v_2'(\beta_2)=\xi\phi_2'(\beta_2),\ u_3(0)=u_2(\beta_2),\ u_3'(0)=u_2'(\beta_2) \end{array}\right\} \tag{69}$$

For other end conditions; hinged-hinged and fixed-fixed, of portal frame with crack are as follows.
For hinged-hinged ends:

$$\left.\begin{array}{ll} \text{at} \quad \eta_1=0; & v_1(0)=0, \quad \phi_1'(0)=0, \quad u_1(0)=0 \\ \text{at} \quad \eta_4=\beta_4; & v_4(\beta_4)=0, \quad \phi_4'(\beta_4)=0, \quad u_4(\beta_4)=0 \end{array}\right\} \tag{70}$$

For fixed-fixed ends:

$$\left.\begin{array}{ll} \text{at} \quad \eta_1=0; & v_1(0)=0, \quad \phi_1(0)=0, \quad u_1(0)=0 \\ \text{at} \quad \eta_4=\beta_4; & v_4(\beta_4)=0, \quad \phi_4(\beta_4)=0, \quad u_4(\beta_4)=0 \end{array}\right\} \tag{71}$$

3. Finite element computation for natural frequencies

The natural frequencies of portal frame with and without crack are computed for a numerical verification of the solution to forward problem by a standard finite element software (i.e., ANSYS-11[22]). A frame is discretized by Eight-node quadrilateral shell elements and quarter-point singular elements employed around the crack-tip is as shown in Fig. 4.

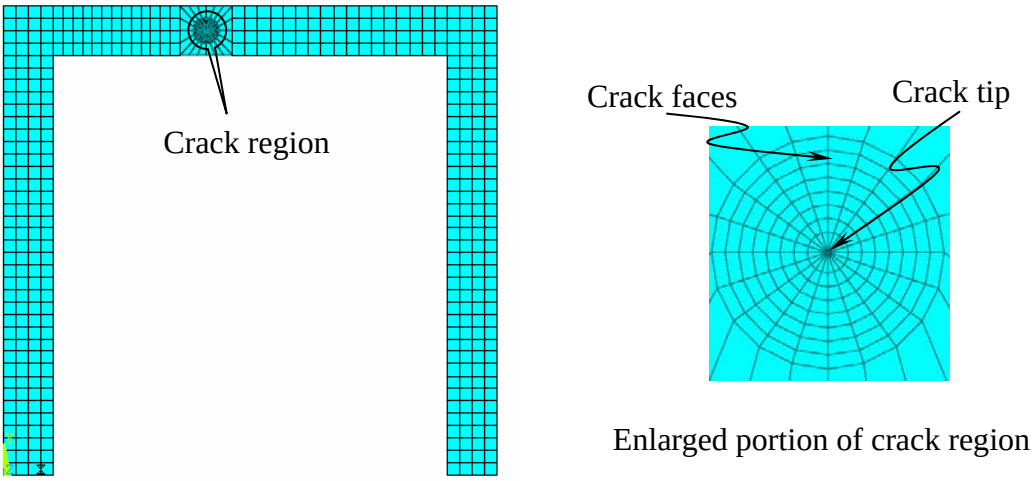

Figure 4. Schematic of finite element modelling of Timoshenko portal frame with crack located in horizontal segment.

4. Results and Discussions

In this study, non-destructive direct solutions for the estimation of the natural frequency of a portal frame with and without crack have been presented. Changes in the natural frequencies of a portal frame due to the presence of a crack may provide additional information for damage detection of these structures. The presence of crack has been theoretically considered by an equivalent torsional spring. To take into account the effects of rotational inertia and shear deformation, Timoshenko beam theory has been employed. The three set of end conditions, fixed-hinged, hinged-hinged and fixed-fixed, have been considered. Crack locations ranging from 20% to 70% of length of segment and crack sizes ranging from 20% to 60% of depth are considered. By means of these boundary conditions and applying suitable compatibility conditions at the cracked section, the characteristic equations have been derived explicitly, whose solution provides the natural frequencies of the portal frame. A MATLAB code has been written to compute the frequencies numerically. The computed natural frequencies have been compared with those obtained by the finite element tool. The geometry of the portal frame with following cross-sectional dimensions and material properties are considered: Length of each no-crack segments (L_i)=0.225m, width (b)=0.0125m and depth (h)=0.025m. The material data employed are: mass density (ρ)= 7800kg/m^3, modulus of elasticity E=210GPa, Poisson's ratio μ=0.3 and Timoshenko shear coefficient κ =5/6. The first three natural frequencies calculated by forward analysis are presented in Tables 1 and 2. The percentage difference in the frequencies taking finite element results as the reference is shown in the Tables 1 and 2. The maximum difference among all results is 7.09% which proves usefulness of proposed method. As expected, the trend of natural frequencies of portal frame with crack, decreases as the crack size increases in comparison with natural frequencies of portal frame without crack (Fig. 5).

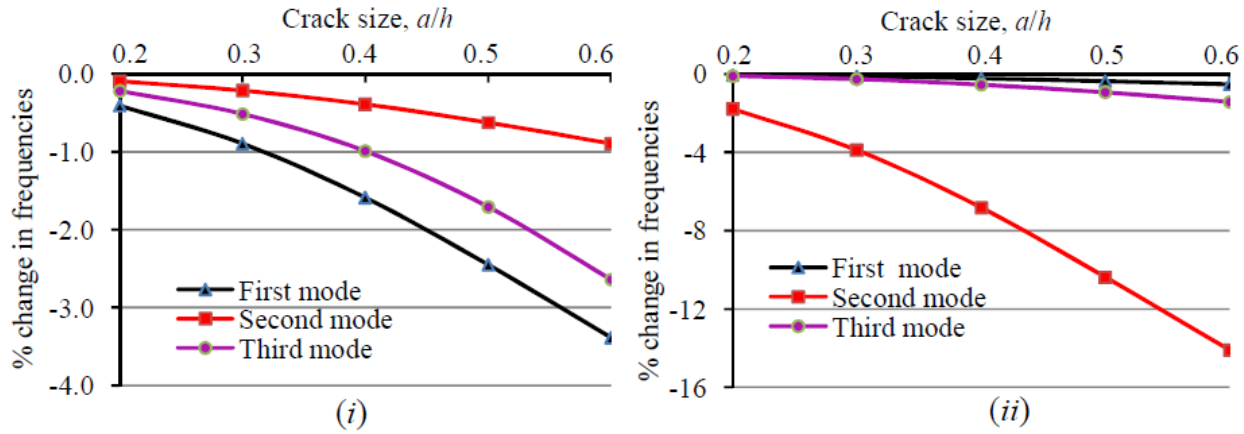

Figure 5. Plot of percentage change in natural frequencies vs. crack size: (*i*) Fixed-hinged ends of frame with crack located in vertical segment at δ=0.4 and (*ii*) Fixed-fixed ends of frame with crack located in horizontal segment at δ=0.4.

5. Conclusion

Solution to forward problems i.e. determination of natural frequencies knowing the crack details in Timoshenko portal frame has been studied. The presence of crack has been modelled by an equivalent torsional spring. It is found that the maximum percentage differences between the natural frequencies computed by analytical approach are less than 7.09% as compared to the finite element result. Changes in the natural frequencies of the portal frame due to the presence of a crack may provide additional information for damage detection of these structures.

Table 1. Comparison of natural frequencies computed by analytical method and finite-element method for Timoshenko portal frame with crack located in left vertical segment.

End cond	Crack loc. δ	a/h	Natural frequencies (Hz)								
			Analytical method			Finite element method			% Difference		
			ω_1	ω_2	ω_3	ω_1	ω_2	ω_3	ω_1	ω_2	ω_3
F-H	nocrack		278.97	1247.63	1874.68	284.72	1253.30	1915.70	2.02	0.45	2.14
	0.2	0.2	273.59	1246.07	1874.27	278.67	1250.30	1914.10	1.82	0.34	2.08
		0.4	259.76	1242.22	1873.25	263.04	1241.50	1909.00	1.25	-0.06	1.87
		0.6	242.61	1237.76	1872.06	239.40	1226.50	1898.60	-1.34	-0.92	1.40
	0.4	0.2	277.82	1246.41	1870.52	283.40	1252.70	1912.40	1.97	0.50	2.19
		0.4	274.53	1242.68	1855.99	279.40	1251.40	1901.20	1.74	0.70	2.38
		0.6	269.52	1236.45	1825.18	271.45	1249.70	1851.60	0.71	1.06	1.43
	0.7	0.2	278.39	1238.80	1866.35	284.15	1245.80	1908.50	2.03	0.56	2.21
		0.4	276.67	1212.19	1842.10	282.47	1225.10	1888.50	2.05	1.05	2.46
		0.6	273.87	1169.33	1806.42	279.38	1186.20	1846.20	1.97	1.42	2.15
H-H	nocrack		171.26	1127.17	1699.66	175.89	1127.60	1725.90	2.63	0.04	1.52
	0.2	0.2	171.05	1121.54	1684.13	175.73	1123.00	1707.30	2.66	0.13	1.36
		0.4	170.33	1100.86	1631.91	175.24	1106.70	1635.10	2.80	0.53	0.20
		0.6	168.74	1049.62	1536.78	174.02	1044.30	1435.10	3.03	-0.51	-7.09
	0.4	0.2	170.47	1112.51	1669.77	175.15	1114.30	1691.40	2.67	0.16	1.28
		0.4	167.87	1062.04	1590.26	172.84	1068.80	1590.50	2.88	0.63	0.02
		0.6	162.52	963.96	1501.23	167.14	944.69	1438.70	2.76	-2.04	-4.35
	0.7	0.2	169.22	1116.83	1695.43	173.83	1118.50	1721.50	2.65	0.15	1.51
		0.4	162.97	1086.81	1684.06	167.78	1093.50	1707.90	2.87	0.61	1.40
		0.6	152.36	1041.43	1669.02	155.49	1047.50	1680.50	2.01	0.58	0.68
F-F	nocrack		371.92	1412.93	2299.39	379.70	1426.70	2333.60	2.05	0.97	1.47
	0.2	0.2	367.23	1411.38	2298.55	374.29	1423.10	2332.90	1.89	0.82	1.47
		0.4	355.35	1407.55	2296.43	360.43	1412.50	2329.90	1.41	0.35	1.44
		0.6	340.98	1403.10	2293.85	339.92	1393.40	2323.80	-0.31	-0.70	1.29
	0.4	0.2	371.14	1410.18	2275.30	378.75	1425.20	2306.00	2.01	1.05	1.33
		0.4	368.89	1401.69	2193.73	375.81	1421.60	2197.10	1.84	1.40	0.15
		0.6	365.49	1387.23	2076.01	369.81	1415.80	1963.20	1.17	2.02	-5.75
	0.7	0.2	371.08	1399.78	2285.05	378.86	1415.70	2318.50	2.05	1.12	1.44
		0.4	368.56	1361.07	2243.52	376.45	1386.10	2286.90	2.10	1.81	1.90
		0.6	364.46	1301.56	2186.91	372.01	1331.50	2155.50	2.03	2.25	-1.46

Note: F-H - Fixed-hinged, H-H – Hinged-hinged and F-F – fixed-fixed end conditions.

Table 2. Comparison of natural frequencies computed by analytical method and finite-element method for Timoshenko portal frame with crack located in horizontal segment.

End cond.	Crack loc. δ	a/h	Natural frequencies (Hz)								
			Analytical method			Finite element method			% Difference		
			ω_1	ω_2	ω_3	ω_1	ω_2	ω_3	ω_1	ω_2	ω_3
F-H	nocrack		278.97	1247.63	1874.68	284.72	1253.30	1915.70	2.02	0.45	2.14
	0.2	0.2	276.55	1246.04	1865.88	282.13	1252.10	1905.40	1.98	0.48	2.07
		0.4	269.46	1241.25	1839.67	275.00	1248.90	1874.90	2.01	0.61	1.88
		0.6	258.46	1233.46	1798.69	262.03	1242.80	1816.40	1.36	0.75	0.98
	0.4	0.2	278.33	1233.51	1855.02	284.05	1240.20	1893.60	2.01	0.54	2.04
		0.4	276.38	1190.17	1804.91	282.21	1201.00	1834.20	2.07	0.90	1.60
		0.6	273.01	1119.64	1746.49	278.46	1119.40	1739.40	1.96	-0.02	-0.41
	0.7	0.2	278.82	1231.95	1874.48	284.52	1238.60	1915.60	2.00	0.54	2.15
		0.4	278.37	1186.61	1873.94	283.86	1197.80	1913.80	1.93	0.93	2.08
		0.6	277.61	1118.15	1873.15	282.40	1123.20	1908.10	1.70	0.45	1.83
H-H	nocrack		171.26	1127.17	1699.66	175.89	1127.60	1725.90	2.63	0.04	1.52
	0.2	0.2	170.06	1121.71	1689.28	174.53	1123.00	1714.70	2.56	0.11	1.48
		0.4	166.48	1105.35	1660.88	170.61	1110.50	1685.60	2.42	0.46	1.47
		0.6	160.72	1079.11	1622.47	162.97	1087.80	1638.10	1.38	0.80	0.95
	0.4	0.2	171.12	1112.64	1698.17	175.71	1114.20	1724.10	2.61	0.14	1.50
		0.4	170.71	1069.01	1693.32	175.24	1075.70	1718.60	2.59	0.62	1.47
		0.6	169.97	999.73	1684.19	174.22	999.78	1701.00	2.44	0.01	0.99
	0.7	0.2	170.72	1116.71	1694.33	175.29	1118.20	1720.20	2.61	0.13	1.50
		0.4	169.08	1085.34	1678.86	173.48	1091.70	1703.30	2.54	0.58	1.43
		0.6	166.31	1035.35	1655.99	169.74	1040.60	1669.40	2.02	0.50	0.80
F-F	nocrack		371.92	1412.93	2299.39	379.70	1426.70	2333.60	2.05	0.97	1.47
	0.2	0.2	370.06	1408.26	2284.20	377.59	1422.60	2317.40	1.99	1.01	1.43
		0.4	364.63	1394.43	2240.90	371.73	1410.90	2274.90	1.91	1.17	1.49
		0.6	356.26	1372.69	2179.08	361.01	1388.60	2202.70	1.32	1.15	1.07
	0.4	0.2	371.71	1387.86	2296.75	379.42	1402.20	2330.50	2.03	1.02	1.45
		0.4	371.06	1316.61	2286.83	378.70	1333.30	2318.10	2.02	1.25	1.35
		0.6	369.92	1213.84	2266.57	377.13	1207.20	2265.20	1.91	-0.55	-0.06
	0.7	0.2	371.08	1397.73	2290.78	378.77	1412.20	2324.10	2.03	1.02	1.43
		0.4	368.54	1353.49	2265.65	376.00	1371.00	2295.40	1.98	1.28	1.30
		0.6	364.36	1286.74	2229.64	370.48	1292.60	2234.50	1.65	0.45	0.22

Note: F-H - Fixed-hinged, H-H – Hinged-hinged and F-F – fixed-fixed end conditions.

References

[1] R.Y. Liang, J. Hu, F.K. Choy, Detection of crack in beam structures using measurement of natural frequencies, Journal of Franklin Institute, 328 (1991) 505-518.

[2] W.M. Ostachowicz, M. Krawczuk, Analysis of the effect of cracks on the natural frequencies of a cantilever beam, Journal of Sound and vibration, 150 (1991) 191-201.

[3] O.S. Salawu, Detection of structural damage through changes in frequency: a review, Engineering structures, 19 (1997) 718-723.

[4] B.P. Nandwana, S.K. Maiti, Detection of location and size of a crack in stepped cantilever beam based on natural frequencies, Journal of Sound and Vibration, 203(1997) 435-446.
[5] S.H.S. Carneiro, D.J. Inman, Continuous model for the transverse vibration of cracked Timoshenko beams, Transactions of ASME, 124 (2002) 310-320.
[6] N. Khaji, M. Shafiei, M. Jalalpour, Closed form solution for crack detection problem of Timoshenko beams with various boundary conditions, International Journal of Mechanical Science, 51 (2009) 667-682.
[7] S.P. Lele and S.K. Maiti, Modelling of transverse vibration of short beams for crack detection and measurement of crack extension, Journal of Sound and Vibration, 257 (2002) 559-583.
[8] J.A. Loya, L. Rubio, J. Fernandez-Saez, Natural frequencies for bending vibration of Timoshenko cracked beams, Journal of Sound and Vibration, 290 (2006) 640-653.
[9] D.Y. Zheng, S.C. Fan, Natural frequency changes of a cracked Timoshenko beam by modified Fourier series, Journal of Sound and Vibration, 246 (2001) 297–317.
[10] C.M. Albarracin, R.O. Grossi, Vibrations of elastically restrained frames, Journal of Sound and Vibration, 285 (2005) 467-476.
[11] H.P. Lin J.D. Wu, Dynamic analysis of planar closed frame structures, Journal of Sound and Vibration, 282 (2005) 249-264.
[12] H.P. Lin, J. Ro, Vibration analysis of planar serial-frame structures, Journal of Sound and Vibration, 262 (2003) 1113-1131.
[13] C.H. Chang, P.Y. Wang, Y.W. Lin, Vibration of X-braced portal frames, Journal of Sound and Vibration, 117(1987) 233–248.
[14] C.P. Filipich, P.A.A. Laura, In-plane vibrations of portal frames with end supports elastically restrained against rotation and translation, Journal of Sound and Vibration, 117(1987) 467–474.
[15] G.M.L. Gladwell, The vibration of frames, Journal of Sound and Vibration, 1(1964) 402-425.
[16] T.M. Wang, T.A. Kinsman, Vibrations of frame structures according to the Timoshenko theory, Journal of Sound and Vibration, 14 (1971) 215-227.
[17] S. Hassiotis, G.D. Jeong, Assessment of structural damage from natural frequency measurement, Computers and Structures, 49 (1993) 679-691.
[18] P.G. Nikolakopoulos, D.E. Katsareas, C.A. Papadopoulos, Crack identification in frame structures, Computers and Structures, 64 (1997) 389-406.
[19] S.M. Murigendrappa, S.K. Maiti, H.R. Srirangarajan, Detection of crack in L-shaped pipes filled with fluid based on transverse natural frequencies, Structural Engineering and Mechanics-An International Journal, 21 (2005) 635-658.
[20] G. Gounaris, A.D. Dimarogonas, A finite element of a cracked prismatic beam for structural analysis, Computers and Structures, 28 (1988) 309-313.
[21] T.G. Chondros, A.D. Dimarogonas, Dynamic sensitivity of structures to cracks, Transaction of the ASME Journal of Vibration, Acoustics, Stress and Reliability in Design, 111 (1989) 251-256.
[22] ANSYS-11.0, User’s Manual, 2007.

Accuracy of Acoustic Emission Localization for Masonry Structures Monitoring

Jie Xu[1*], Qinghua Han[1], Giuseppe Lacidogna[2], Alberto Carpinteri[2]

[1] School of Civil Engineering, Tianjin University, Tianjin, 300072, China
[2] Department of Structural, Geotechnical and Building Construction, Politecnico di Torino, Turin, 10129, Italy
* Corresponding author: jie.xu@polito.it

Abstract Acoustic Emission (AE) is a promising non-destructive monitoring technique to investigate the damage location and to evaluate the structural health conditions. Based on the tests performed on a masonry bridge, three ingredients –sensor distribution, onset time determination and degree of inhomogeneity– affecting the accuracy of AE localization are discussed. The test result shows a reasonable sensor arrangement is of great importance for the localization capability. The highest accuracy can be achieved for damage sources localized among the sensor distributions. Distances of sources far from the sensor network are less accurate. Onset time determination of an AE signal is another important factor in this technique. A widely used approach, based on the Akaike Information Criterion (AIC), is confirmed to provide more reliable onset time determination of AE signals. Moreover, the inhomogeneity of the test object may lead to errors in the ultrasonic wave travelling model. Different-scale fluctuations and structure variations in the composite structure can result in random variations of the propagation velocity and systematic errors. A new proposed parameter, the degree of inhomogeneity ξ, introduced into the classical method, can effectively decrease the crack localization unavoidable errors due to inhomogeneities in masonry material.

Keywords Acoustic emission, masonry structures, crack localization, structural health monitoring.

1. Introduction

Various masonry structures, such as towers, bridges and historical buildings are widely distributed all over the world. As a consequence of building with old techniques, long-time exposing to the environmental conditions and changing loading regimes, many of these masonry structures are placed in repair and strengthening programs [1, 2]. Prior to repair and rehabilitation, inspections of the structures to estimate the current state in service are essentially required. As one of the non-destructive evaluation and diagnostic techniques, Acoustic Emission (AE) technique is gradually employed in the masonry monitoring [2-5].

Within civil engineering practice, the AE technique is a widely applied non-destructive technique for the detection of damage onset and growth [6, 7]. AE is the class of phenomena whereby transient elastic waves are generated by the rapid release of strain energy when damage occurs within a material. By investigating onset times and other characteristics of acoustic signals, AE techniques provide an insight into the deterioration processes of a tested object [8]. As the onset times of AE signals at different sensors are linked to the propagation speed inside the material, algorithm can be used to locate the emitting sources and to predict their subsequent development [1, 9]. AE is widely used for monitoring metallic [10], rock [11, 12] and concrete structures [13, 14], because AE is well suited for homogeneous or qusai-homogeneous materials with good acoustic transmission. However, its application in heterogeneous materials such as masonry is much problematic [15].

This paper presented the recent research about the accuracy of the crack localization of AE technique in masonry structure, which is one of the most important and challenged topics in AE

applications. The application of AE monitoring in masonry structure is highly complicated, as attenuation and wave propagation are dependent on the heterogeneity of the material. Besides, the presence of voids, cracks and cavities does also influence the AE detection itself. The AE waves, generated at the other side of a large crack to which the sensors are placed, will generally not be detected by AE sensors. This, for example, would be the case between the disconnected layers of a multiple-leaf wall, which is often encountered in historical masonry structures. All these ingredients make the source localization in masonry structure rather difficult [9].

In order to address these issues regarding damage region assessment in masonry, a series of tests were designed and carried out on a masonry model bridge. The results for the tests are discussed in this paper.

2. Source location of AE events and classical localization method

Localization of AE sources is important to assess the regions of active damage in the monitoring technique. Location problems are usually solved by various triangulation techniques based on mathematical analysis of acoustic wave trajectories [16]. This analysis cannot be simply performed if the structure of tested specimen is geometrically complicated. Generally, these techniques depend on the mode of propagation, the elasticity modulus, and signal attenuation due to the heterogeneity and anisotropy of material. In this Section, a general overview on the classical localization method and the corresponding knowledge is depicted.

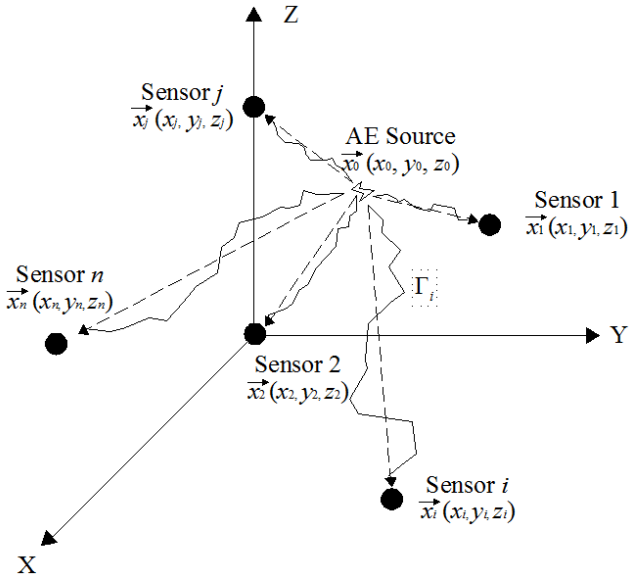

Figure 1. Localization of point AE source involving a generic array of *n* sensors.

As shown in Fig. 1, in a theoretical model with wave propagation velocity v_{Pi}, the onset time t_i^* at sensor $\vec{x}_i$, unknown crack coordinates $\vec{x}_0$ and origin time t_0 can be estimated by an integral along the actual ray path Γ_i:

$$t_i^* = t_0 + \underbrace{\int_{\Gamma_i} (d\Gamma_i / v_{Pi}(\mathrm{r}))}_{\mathrm{I}}, \tag{1}$$

where $v_{Pi}(\mathrm{r})$ is the wave velocity field in the specimen or structure. If the material is homogeneous, Eq. (1) can be simplified as:

$$t_i^* = t_0 + \frac{|\vec{x}_0 - \vec{x}_i|}{v_p} = t_0 + \frac{\vec{x}_{i0}}{v_p}. \tag{2}$$

For each sensor *i* there will be residual r_i between the detected onset time t_i and the calculated onset time t_i^*:

$$r_i = t_i - t_i^*. \tag{3}$$

If t_j is the onset time at another sensor $\vec{x}_j$, the measured onset time difference between sensors *i* and *j* is used. Usually we have:

$$r_{ij}^* = \Delta t_{ij} - \frac{\left(\vec{x}_{i0} - \vec{x}_{j0}\right)}{v_p}, \qquad (i \neq j). \tag{4}$$

If there are more than four onset times available for one event, the problem is overdetermined. These residuals are minimized using the least square method, in which the total error for (*n*-1) equations is simply the sum of all squared time-residuals:

$$\chi^2 = \sum_{i=2}^{n} (r_i^*)^2. \tag{5}$$

Residuals are reduced by applying corrections $\Delta\vec{x}$ and Δv_p to the source parameters, which can be written as:

$$A^T A\vec{r} = -\mathrm{A}(\Delta\vec{x},\ \Delta v_p)^T. \tag{6}$$

Thereby, $\vec{r}$ is the data vector with the residuals for *n* observations of one event. **A**, which is a $(n-1)\times 4$-matrix, contains the partial derivatives of the calculated travel times with respect to the source coordinates, calculated at $\vec{x}_0$:

$$A = \begin{pmatrix} \frac{\partial r_2^*}{\partial x} & \frac{\partial r_2^*}{\partial y} & \frac{\partial r_2^*}{\partial z} & \frac{\partial r_2^*}{\partial v_p} \\ \vdots & \vdots & \vdots & \vdots \\ \frac{\partial r_n^*}{\partial x} & \frac{\partial r_n^*}{\partial y} & \frac{\partial r_n^*}{\partial z} & \frac{\partial r_n^*}{\partial v_p} \end{pmatrix}_{\vec{x}_0}. \tag{7}$$

Due to the linearization of Eq. (6) the problem is solved iteratively until convergence, starting with an initial guess for the crack source location.

3. Experimental setup and operation

According to the aforementioned crack source localization problem in masonry structure, several tests based on a two-arch masonry model bridge are operated in this research.

3.1. Wave velocity test

A series of pencil-lead break tests are performed on the central pier of the bridge to study the attenuation and the velocity properties. The size of the central pier is of 160×50×28 cm, shown in Fig. 2, and it can be considered as a representative masonry solid structure.

Six sensors (S_0~S_5) are used to detect AE signals and the distance between two adjacent sensors increased from $S_{1\text{-}0}$ to $S_{5\text{-}4}$ with an increment of 5 units, shown in Fig. 2. The pencil is broken beneath the sensor S_0 with 5cm distance away in the same surface to study the surface velocity propagation, which is the scenario shown in Fig. 2.

Figure 2. Wave velocity test: (Left) the sketch of the pencil-lead break point and the sensor distribution; (Right) scenario of the velocity test.

The results of the measured velocities are shown in Fig. 3. The velocity named V-homogeneous, is calculated assumed the material is homogeneous [6]. The V-average is the average velocity value of all the calculated velocities in the corresponding test.

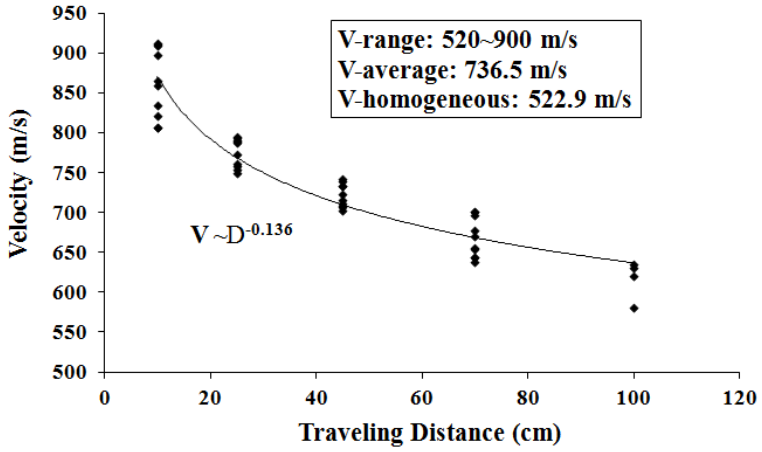

Figure 3. Wave velocity of the AE on the surface of masonry model bridge.

3.2. Sensor distribution and source localization tests

Ad hoc tests are performed to reproduce AE source using pencil-lead break on the right-side surface of the masonry abutment. Six sensors are attached to the surfaces, shown in Fig. 4. In particular, 19 different pencil-lead break points (artificial source) are drawn on this surface, and for each point the tip of a pencil is broken 8 times, so a total of 152 measurements are recorded. For this test 912 AE events from the six sensors are obtained and then sensor distribution and the source localizations of all the 19 points are analyzed in the following sections.

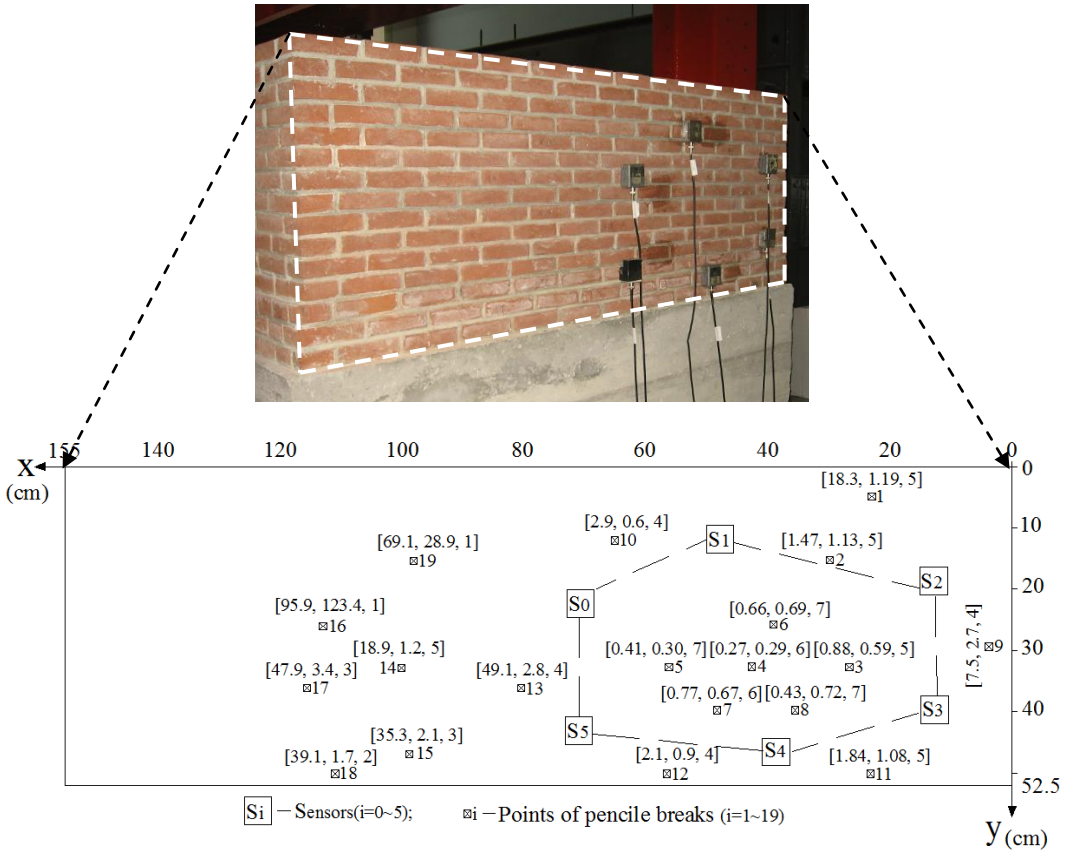

Figure 4. Results of the source localization calculated from the classical and the modified methods. In [*a*, *b*, *c*], *a* is the average error of all the available breaks from the classical method, and *b* is the average error of all the available breaks from the modified method, and *c* is the available breaks which can be used for each point.

4. Accuracy analysis of AE locations based on the test

4.1. Degree of inhomogeneity

The classical localization method can be used in the concrete structures according to the experiences [6-8]. But the localization of AE source in masonry structures is highly complicated, as attenuation and wave velocity are dependent on the heterogeneity of the material (not only the interface between bricks and mortar, but also cracks and cavities in existing structures). The theoretical analysis in Section 2 and the test result in Section 3.1 both illustrate that the classical localization method based on Eq. (2) cannot be used directly in masonry. A modified method based

on the classical method is introduced in the following part.

The basic idea of the localization in masonry is the same as that in concrete. But propagation delay due to the layers in the masonry structures makes the homogeneous assumption is unavailable here. Modifications for propagation delay are implemented.

The geometry distance *ds* is still taken as the calculated path, since the detailed knowledge of the actual wave path Γ, is not possible to be known. But modification can be made for the time-delay according to the velocity property in Fig. 3 to reduce the effect of inhomogeneous property. In the modified model, the classical model result in Eq. (5) is modified into:

$$\chi^2 = \sum_{i=2}^{n} {r_{i1}}^2 = \sum_{i=2}^{n} \left[\vec{x}_{10} - \vec{x}_{i0} - (k_i t_i - t_1) v_1 \right]^2 , \tag{8}$$

where $k_i = \left(d_1 / d_i \right)^{\xi}$ is the modified factor, which is used to modify the effects of the inhomogeneity or propagation delay. The parameter ξ, denoted as degree of the inhomogeneity, in k_i reflects the inhomogeneous degree of the material. The degree of the inhomogeneity ξ is determined from the result of the pencil-lead break wave velocity test, shown in Fig. 3. It reflects the relationship between the calculated velocity and the wave propagation distance. In strictly homogeneous materials, the value ξ is 0 since the wave velocity is a constant value and does not changes with travelling distance. If the material is not homogeneous, value ξ will theoretically increases with the degree of the heterogeneity. The degree of the inhomogeneity ξ in our research is 0.14, which is taken from the relation between the velocity and travelling distance shown in Fig. 3.

4.2. Sensor distribution

The results of the locations are shown in Fig. 4 for both the modified and classical methods. It can be noted that the location accuracy varies with the position of the breaks. The break points can be approximately divided into three groups. The points 3~8 inside the central area of the sensor covered region (the dashed line in Fig. 4) have the best crack source monitoring result for both classical and the modified methods. In the second group, including points 2, 9, 10, 11, 12, points are distributed on the nearby region of the sensor covered region. The rest of the points, far from the sensor network, are in the third group.

For points in the first group, both methods give the ideal result, all the errors are smaller than 6 mm, and most of the crack events can be monitored. For the second group, the modified model shows better results than the classical method. The errors (*a* value in Fig. 4) in the classical method are about 15~75 mm, whereas the counterparts (*b* value in Fig. 4) can be reduced to about 6~27 mm in the modified method. In this condition, about half of the break events can be detected according to the *c* value in Fig. 4. The result from the classical method for the third group is barely acceptable for its exaggerated errors, whereas modified method is still in good conditions. Although the errors were slightly large, about three or four centimeters, the results are still acceptable considering the entire size scale of the surface. Three representative points, 4, 10 and 17 respectively, of the three

groups are selected to give the detailed results in Fig. 5.

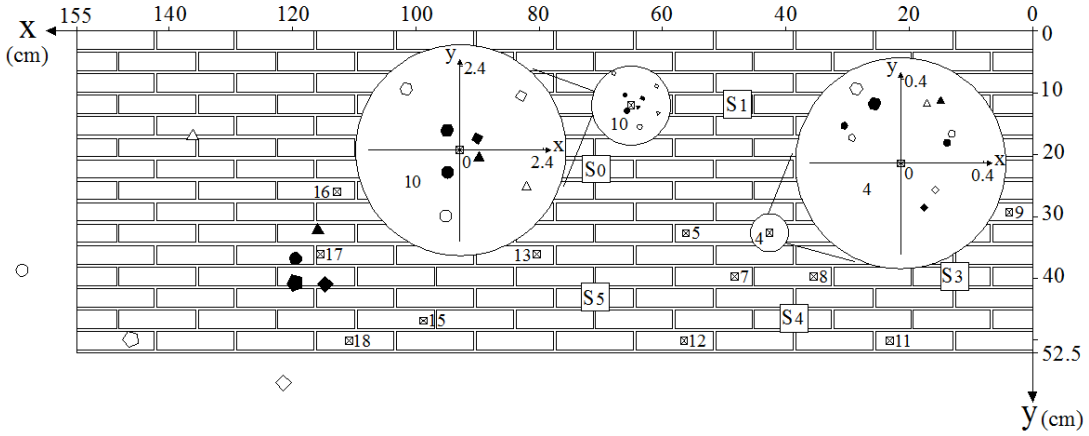

Figure 5. Detailed localization results of the point 4, point 10 and point 17. The solid points represent the results of the modified method and the empty points of the classical method.

4.3. Onset time determination

Source localization is based on the onset times or arrival times of the direct body waves. Theoretically, onset times of the direct body waves, *P*-wave and *S*-wave both can be used for source localization. However, only first wave onset times (*P*-times) are usually measurable, since multiple side reflections, structural noise and sensor response will interfere the later phases.

The true onset time of a crack AE event could be described as the moment when the first energy of a particular signal phase reaches the sensor positions [17]. In signal analysis, the onset time is usually picked as the point where the first difference between the signal and the noise takes place [18]. Determination of the onset time of AE signals is crucial for the whole localization process and is the major premise to affect the localization accuracy [6].

Manually picking is the preferred choice if there are only few events available. It is still necessary to have reliable automatic picking tools, because human analysts cannot manage the vast amount of data recorded in the monitoring. In concrete monitoring, many algorithms have been proposed for automatic detection of onset times and the detailed description can be found in [19]. Two mostly used methods, STA/LTA (STA Short Term Average, LTA Long Term Average) picker by [20] and AIC-picker [6, 21] are employed and investigated for the AE signals in masonry structures. The picking accuracy of the STA/LTA-picker and AIC-picker was quantified by a comparison with picks that were set manually.

For 1122 signals of AE events recorded at the pencil-lead break tests in Sections 3, the differences Δt between the automatic and the manual picks are examined. Fig. 6 shows the results for the STA/LTA-picker and for the AIC-picker, compared to manually picked onset times.

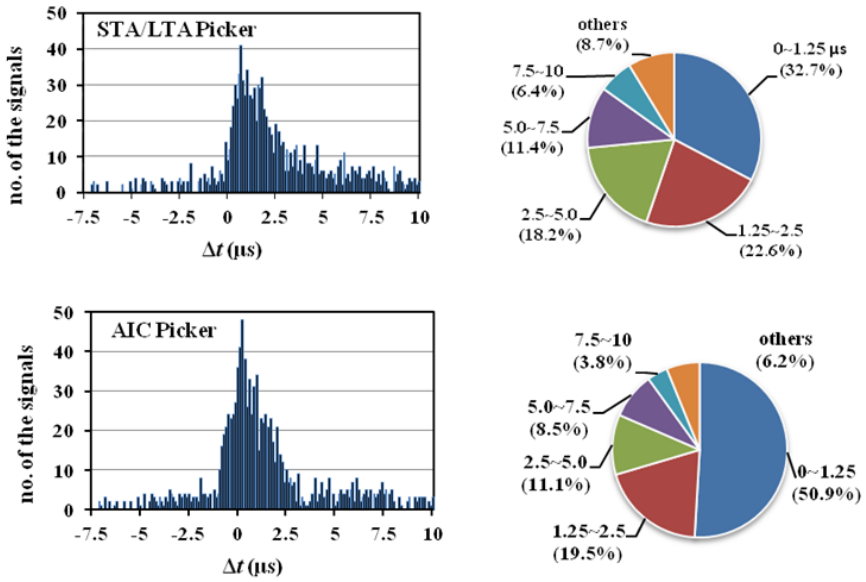

Figure 6. Differences Δt between automatically and manually picked arrival times for the STA/LTA (top) and the AIC-picker (bottom). The pie charts show the performance of both automatic pickers.

The signals have different reading precisions of their onsets, depending on the signal to noise ratio and how impulsive onsets are. The results from the two methods are both acceptable, although the STA/LTA-picker obviously shows a trade-off. With the AIC-picker almost twice as many signals than the STA/LTA-picker are picked in a very good correlation, $\Delta t \leqslant 1.25\mu s$. Also, the number of mispicks with $\Delta t \geqslant 5\mu s$ in the noise and picks too late in the signal could be reduced from 26.5% of that in STA/LTA-picker to 18.5%. Accordingly, the AIC-picker can be suggested as a reliable and accurate algorithm to determine the onset times of AE signals in masonry structures.

5. Discussion and conclusion

With wide existence of masonry structures, the monitoring techniques have received considerable attention due to the increasing demand of the structural retrofit and strengthening. As one of the non-destructive monitoring techniques, acoustic emission technique is employed for the masonry cracking analysis.

For AE applications in monitoring, localization of AE sources is important to offer the information of the active damage region. The investigation of the localization accuracy has shown that monitoring results are greatly influenced by the material of structures. Classical localization method is mostly adopted to realize the localization operation in metal and concrete structures. However, for the masonry structures, the complicated material properties make the classical localization method cannot be applied directly.

The modified localization method proposed in this paper allows giving a reasonable location results. In the modified method, a modified factor k_i related to inhomogeneous or propagation delay is introduced. The degree of the heterogeneity ξ in k_i plays a key role to eliminate the effect of the inhomogeneous of the material. Accordingly, the pencil-lead break velocity tests on the masonry

structure to measure the relation between the wave velocity and travelling distance should be fulfilled before the monitoring. Based on this test result, the value ξ can be obtained and employed in the monitoring process.

The sensor arrangement is another task which should be carefully considered. The investigation of the localization accuracy has shown that the sensor distribution is essential for monitoring AE activity in the specimen. The ideal condition is to ensure that all relevant regions are covered by enough sensors before the monitoring starts. Detected events are only a fractional amount of all recorded AE signals and, again, only a limited number of all detected events can be localized with a sufficient accuracy. For a good imaging of crack progression it is necessary that enough events could be localized. Therefore the proper arrangement of the sensors can give us more available points, which is well testified by the *c* value in Fig. 4.

In conclusion, with the assistance of the reliable onset time picker (AIC-picker) and proper sensor distribution, the source localization in masonry can be realized properly by the modified model.

References

[1] A. Carpinteri, G. Lacidogna, G. Niccolini, Acoustic emission monitoring of medieval towers considered as sensitive earthquake receptors. Natural Hazards and Earth System Sciences, 7 (2007) 251-261.

[2] C. Melbourne, AK. Tomor, Application of Acoustic Emission for Masonry Arch Bridges. Strain, 42 (2006) 165-172.

[3] A. Carpinteri, G. Lacidogna, Damage monitoring of an historical masonry building by the acoustic emission technique. Materials and Structures, 39 (2006) 161-167.

[4] J. Xu, G. Lacidogna, Modified Acoustic Emission source localization method to determine crack locations for masonry arch bridge. Applied Mechanics and Materials, 71-78 (2011) 4823–4826.

[5] E. Verstrynge, L. Schueremans, DV. Gemert, M. Wevers, Application of the acoustic emission technique to assess damage in masonry under increasing and sustained axial loading, in: NDTCE'09, Non-Destructive Testing in Civil Engineering. Nantes, France, 2009.

[6] A. Carpinteri, J. Xu, G. Lacidogna, A. Manuello, Reliable onset time determination and source location of acoustic emissions in concrete structures. Cement & Concrete Composites, 34 (2012) 529-537.

[7] CU. Grosse, M. Ohtsu, Acoustic Emission Testing: Basics for Research - Applications in Civil Engineering, Springer, 2009.

[8] B. Schechinger, T. Vogel, Acoustic emission for monitoring a reinforced concrete beam subject to four-point-bending. Construction and Building Materials, 21 (2007) 483-490.

[9] E. Verstrynge, L. Schueremans, D. Gemert, M. Wevers, Monitoring and predicting masonry's creep failure with the acoustic emission technique. NDT & E International, 42 (2009) 518-523.

[10] D. Dutta, H. Sohn, KA. Harries, P. Rizzo, A Nonlinear Acoustic Technique for Crack Detection in Metallic Structures. Structural Health Monitoring, 8 (2009) 251-262.

[11] G. Niccolini, J. Xu, A. Manuello, G. Lacidogna, A. Carpinteri, Onset time determination of acoustic and electromagnetic emission during rock fracture. Progress In Electromagnetics

Research Letters, 35 (2012) 51-62.

[12] E. Eberhardt, D. Stead, B. Stimpson, Quantifying progressive pre-peak brittle fracture damage in rock during uniaxial compression. International Journal of Rock Mechanics and Mining Sciences, 36 (1999) 361-380.

[13] SC. Lovejoy, Acoustic Emission Testing of Beams to Simulate SHM of Vintage Reinforced Concrete Deck Girder Highway Bridges. Structural Health Monitoring, 7 (2008) 329-346.

[14] A. Carpinteri, G. Lacidogna, G. Niccolini, S. Puzzi, Critical defect size distributions in concrete structures detected by the acoustic emission technique. Meccanica, 43 (2008) 349-363.

[15] A. Anzani, L. Binda, RG. Mirabella, The effect of heavy persistent actions into the behaviour of ancient masonry. Materials and Structures, 33 (2000) 251-261.

[16] T. Kosel, I. Grabec, P. Muzic, Location of acoustic emission sources generated by air flow. Ultrasonics, 38 (2000) 824-826.

[17] CU. Grosse, F. Finck, Quantitative evaluation of fracture processes in concrete using signal-based acoustic emissions techniques. Cement & Concrete Composites, 28 (2006) 330-336.

[18] J. Kurz, CU. Grosse, HW. Reinhardt, Strategies for reliable automatic onset time picking of acoustic emissions and of ultrasound signals in concrete. Ultrasonics, 43 (2005) 538-546.

[19] J. Xu, Energy emissions from critical phenmena and applications to structural health monitoring. Politecnico di Torino, Structural Engineering Department, 2012.

[20] M. Baer, U. Kradolfer, An automatic phase picker for local and teleseismic events. Bulletin of the Seismological Society of Ameria, 77 (1897) 1437-1445.

[21] J. Xu, An Effective Way to Validate Signal Arrival Time in AE Structural Monitoring. Advanced Materials Research, 163-167 (2010) 2471-2476.

Multiscale strain investigation of stressed carbon fiber reinforced composites based on data of strain gauging, digital image correlation, acoustic emission

Sergey Panin[1,2,*], Mikhail Burkov[1], Anton Byakov[1], Pavel Lyubutin[1], Vladimir Titkov[1], Alexander Eremin[2]

[1] Institute of Strength Physics and Materials Science SB RAS, Tomsk, Russia
[2] National Research Tomsk Polytechnic University, Russia
* Corresponding author: svp@ispms.tsc.ru

Abstract. A combined method for investigation of localized deformation processes in carbon fiber reinforced composite specimens is applied in order to reveal characteristic stages of strain and fracture. Stress concentrators have the shape of a circular hole and edge crack of various sizes. Use of simultaneous strain data registration has allowed us to register and compare parameters under analysis during entire time of the experiments. The reasons of similarity and difference of the results are shown and discussed. It is offered to apply the obtained results for the aims of non-destructive testing of structural materials being based on revealing characteristic stages of strain development and a particularly prefracture stage.

Keywords: strain gauging; digital image correlation; acoustic emission; carbon fiber composite, non-destructive testing, health monitoring of structures.

1. Introduction

In compliance with literary data and results of our previous investigations [1, 2] the stage character of deformation development can be registered with various methods of studying and estimation of strain. Each method due to operation principle is sensitive to particular scale level. In situ application of 3 methods: strain gauging, acoustic emission (AE) and digital image correlation (DIC) allows one to obtain complete pattern of deformation and fracture of stressed structural materials. Application of stain gauging and AE is described in papers [3, 4] while use of DIC method is explained in [5, 6].

Thus depending on physical principle of a method used it is possible with high sensitivity to register and characterize quantitatively the deformation processes at each scale. Strain gauging characterizes macroscale level or response of a specimen as a whole on applied stress. DIC (Meso II) describes level which is comparable with macrolevel, because in DIC the area of observation considers with whole width of a specimen under testing. AE (Meso I) complies level generally of debonding on matrix-fiber interface. AE characterizes changes inside material, while DIC method is revealing processes in outer ply of a specimen, that is critical to composite materials with different fiber layers orientation.

For numerical analysis of data information parameters for 3 methods were chosen. For the AE method count rate dN_{AE}/dt was calculated; for DIC - γ shear strain intensity, for strain gauging - $d\sigma/dt$ (time derivative of the external applied stress).

2. Materials and investigation technique

CFRC is pseudo-isotropic composite made of unidirectional carbon fiber layers [0°, 45°, -45°, 90°] sintered in carbon matrix. Dimensions of specimens were taken according to ASTM D5766/5766M. Strain localization degree is varied by different dimensions of stress concentrators (central hole diameter 7; 10; 13 mm; depth of edge crack 14,5; 18; 21,5 mm).

Dimensions of the specimens are presented on Fig.1.

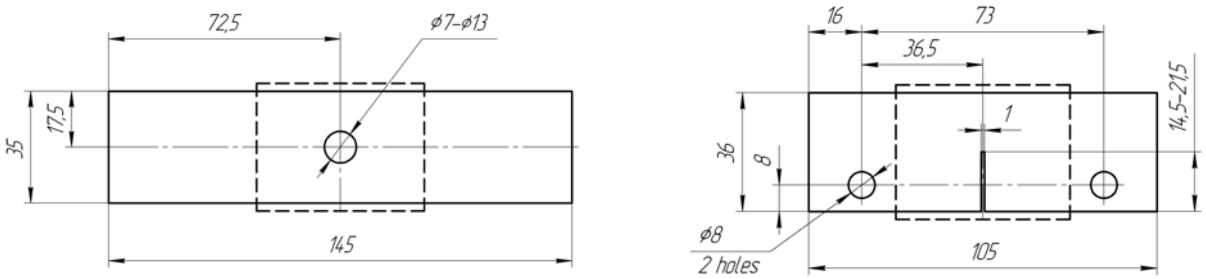

Fig. 1. Scheme of the specimens, thickness 4 mm: a) specimen with central hole; b) specimen with edge crack.

Specimens were stretched under static loads at electro-mechanical testing machine Instron 5582. Strain gauging data was registered using integrated transducer of the testing machine.

Registration of acoustic emission (AE) signals was performed by PC-based hard-software measuring technique [7]. For analysis of acoustic emission data, the derivative on AE events accumulation over loading time (acoustic emission count rate) was calculated as the basic informative attribute of AE data.

Surface imaging was carried out by Canon EOS 550D DSLR camera. The camera has been equipped by telephoto lens Canon EF-S 100-400 mm 1/4-5.6 IS. A certain region of the image was determined for calculation of the average value of shear strain intensity. For example, specimen with central holes the area of the image with the size of 3300×4950 pixels (the physical sizes ~32×52,5 mm) was taken. The sizes of the regions for strain estimation were chosen in order to ensure observation of formation and development of macro scale shear–bands for various types of specimens.

Use of simultaneous registration has allowed us to register and compare parameters under analysis during entire time of the experiments

3. Experimental results

3.1. Macroscale level. Analysis of strain gauging data

Loading diagrams of specimens with central holes and edge cracks are resulted in fig. 2. With increase of the notch dimension for both types of specimens the elongation and ultimate strength at fracture are decreased. The derivative dσ/dt was calculated and is shown on fig. 3.

Further, for comparison of the deformation behavior of specimens with central holes and edge cracks, the results obtained by 3 methods for the composite specimen with ∅7 mm hole and 14,5 mm edge crack are described.

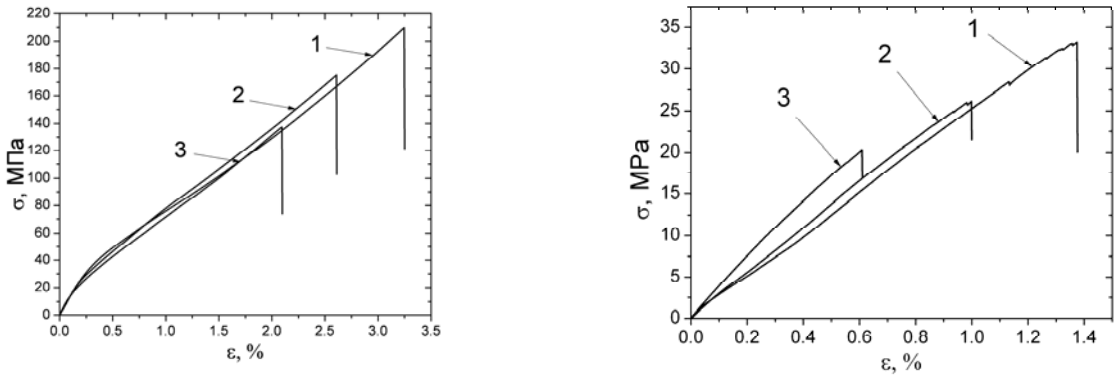

Fig. 2. «σ-ε» graphs: a) specimens with open holes: 1) ∅7mm, 2) ∅10mm, 3) ∅13mm); b) specimens with edge cracks: 1) 14,5mm, 2) 18 mm, 3) 21,5 mm

3.2. Meso I level. Analysis of AE registration data

Dependences of AE count rate versus loading time dN_{AE}/dt for specimens are shown in fig. 3. This parameter was chosen for the analysis as being most "sensitive" to change of a leading scale level of deformation in a specimen under loading. The point graphs of AE count rate were smoothed by average curves. For both types of specimens it is visible, that generation of AE pulses begins practically from the beginning of loading. However appreciable increment of the AE count rate starts at time related to transition of key role of deformation to the meso-scale level.

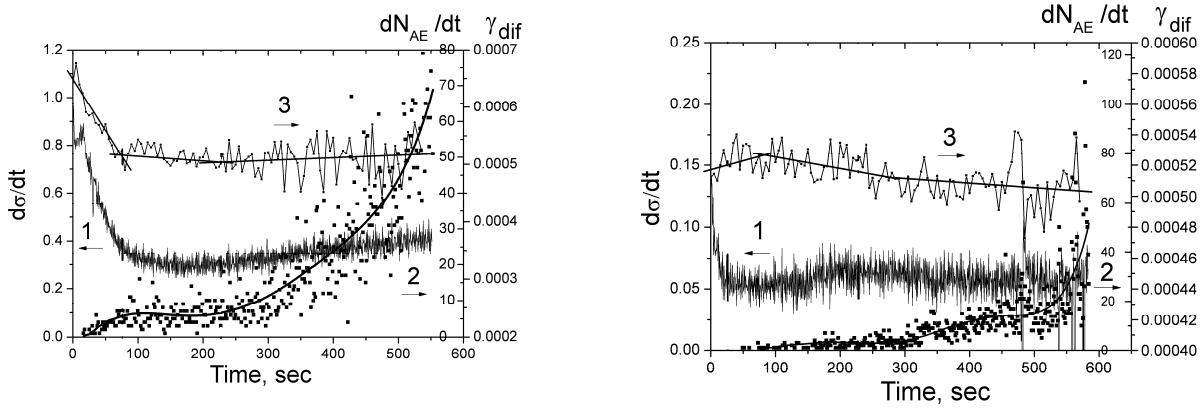

Fig. 3. Combined $d\sigma/dt$ - γ_{dif} - dN_{AE}/dt graphs: a) specimen with central hole: ∅7 mm; b) specimen with edge crack: 14,5 mm.

3.3. Meso II level. Shear strain intensity

The analysis of strain evolution at the meso II level was made by 2 methods of image processing: integral and differential (detailed description of the technique is given in paper [8]). In the first case displacement vectors were mapped by comparison of a first (initial) image with each current ones, while at the differential method of calculation a current and a subsequent images of a deformed specimen surface were compared.

Dependences of the shear strain intensity calculated by the differential method of the image processing which is more sensitive to local strain changes, for both types of specimens are presented in fig. 3. These dependences are sectionally-linear approximated.

4. Conclusions

Combination of DIC and AE data used in the research allows us to examine stage patterns for deformation development at various scale levels. In our previous investigations aluminum specimens were tested [9]. For aluminum specimens at the initial stages of loading the AE method seems to be the most sensitive to deformation processes. At greater degrees of deformation the method of digital images correlation (DIC) more precisely characterizes the change of the key role from meso- to macroscopic scale of the deformation development.

For CRFC specimens AE method have high sensitivity and ability to describe processes inside material, strain gauging characterizes response of specimen on applied stress and allows to identify transition between stages, DIC method can be used to visualize deformation processes with their numerical estimation.

The results are offered to be applied for the aims of non-destructive testing of structural materials being based on revealing characteristic stages of strain development and particularly prefracture stage.

References

[1] C.C. Chamis, S.K. Mital Mesomechanics applied to composites – a matter of scale //Mesomechanics 2000. Proc. of the 3rd Int. Conf for Mesomechanics. V.2,- Xi'an, China, 2000, pp. 623-630.
[2] Panin S.V., Byakov A.V., Grenke V.V., Yussif S.A.K. Multiscale research of stage patterns of localized plastic deformation under tension of AA2024 alloy specimens with notches by acoustic emission and television–optical methods. Physical mesomechanics. 2009. V. 12. No. 6. P. 63-72.
[3] A. Bussiba, M. Kupiec, S. Ifergane, R. Piat, T. Bohlke. Damage evolution and fracture events sequence in various composites by acoustic emission technique. Composite science and technology, 2008, №69, p. 1144-1155.
[4] G. Kotsikos, J.T. Evans, A.G. Gibson, J.M. Hale. Environmentally enhanced fatigue damage in glass fibre reinforced composites characterised by acoustic emission. Composites, 2000, Part A, № 31, p. 969-977.
[5] Olivier De Almeida, Fabienne Lagattu, Jean Brillaud. Analysis by a 3D DIC technique of volumetric deformation gradients: Application to polypropylene/EPR/talc composites. Composites, 2008, Part A, № 39, p. 1210-1217.
[6] A. Godara, D. Raabe, I. Bergmann, R. Putz, U. Müller. Influence of additives on the global mechanical behavior and the microscopic strain localization in wood reinforced polypropylene composites during tensile deformation investigated using digital image correlation. Composite science and technology, 2009, №69, p. 139-146.
[7] Panin S.V., Byakov A.V., Kuzovlev M.S. et al. «Testing of automatic system for registration, processing and analysis of acoustic emission data by model signals». Proceedings IFOST'2009, 21-23 October, 2009, Ho Chi Ming City, Vietnam, Vol. 3, p. 202-206.
[8] Panin S.V., Lyubutin P.S., Buyakova S.P. and Kulkov S.N. Investigation of porous ceramics behavior under loading by calculation of mesoscopic deformation characteristics. Phys. Mesomech. – 2008. – V. 11. – N 6. – P. 77-86.
[9] Panin S.V., Burkov M.V., Byakov A.V., Lyubutin P.S. Multiscale technique for localized strain investigation in metal alloys and carbon fiber reinforced composites based on data of strain gauging, digital image correlation and acoustic emission. Mesomechanics-2011, 13th International Conference, Vicenza, Italy 6-8 July, 2011, p. 44-47

Dynamic Monitoring of Fatigue Crack Process of Orthotropic Steel Bridge Structure with Acoustic Emission

Yuling Zhang[1], Qiao Rong[1], Delian Kong[2], Wenyou Wang[2]
Fengjing Xu[2], Weiping Dong[2,*]

[1]Railway Engineering Research Institute, CARS, Beijing 100081, China
[2]Physical Acoustics Beijing, Beijing 100029, China
*Corresponding author: Jason.dong@mistrasgroup.com

Abstract This paper introduces how to use acoustic emission (AE) technology to monitor dynamic process of crack growth of a segment model of a full size orthotropic steel bridge structure during a 30 day fatigue test. The dimension of the test model is 12.54x2.99x0.6 (LxWxH) meter. Multiple AE sensors were located on different places of the structure. Crack initiation, location and development process were dynamically monitored and recorded. This paper discusses how AE technology is used in the fatigue test of large structure, how is burst crack signal captured, how is crack location identified, what are the behavior of crack developments and how is the result of visual inspection in comparison with the AE technology. The results of the fatigue test monitored with AE have shown that AE is a very valuable technology for monitoring dynamic process of crack development. It can be used not only for various tension, compression and fatigue tests in labs, but also for structure health monitoring in the fields.

Keywords Fatigue Crack, Fracture, Damage, Acoustic Emission, Dynamic Monitoring

1. Introduction

Although orthotropic steel bridge structure is getting more and more widely used, fatigue cracks on the welds and the structure material are still concerns due to the complexity the orthotropic structure and stress concentration in the welds under repeated loadings of the structure[1-2]. It is not uncommon that cracks were found in an orthotropic steel structure that is younger than its design or predicated life age. The actual fracture behavior of orthotropic steel structure were not fully studied and experimentally tested yet.

In fatigue tests of structures or materials, strain or stress measurement is usually a very common way for fatigue crack detection. But, not only the strain measurement cannot tell the development process of the crack growth, but also for a big or complex structure, e.g. a full size orthotropic steel deck, it is hard to predict where the cracks are going to occur and where are the optimum positions that strain gauges should be installed. Each strain gauge can only measure the stress where the strain gauge sticks to and its vicinity, it is not possible to show

crack stresses which are certain distance away from the strain gauge.

On the other hand, it is quite common that cracks were visually inspected in fatigue tests. However, disadvantages of visual inspection are also obvious. First of all, a fatigue test process might need to be stopped in order to have a reliable visual inspection. Secondly, crack initiation is not possible to be visualized due to its microscopic size. Thirdly, if a structure size is big or cracks are located in blocked or inaccessible areas of the structure, the cracks are not able to be picked up by visual inspection. Actually, it is relatively feasible to visually check crack development during fatigue test of small samples, but it is very difficult to know overall crack growing process from a fatigue test of a big structure, e.g. how many active cracks exist in one time? when is each crack initiated? where are cracks located? what are the behaviors of crack growth? This is particular true for a big steel bridge structure test that lasts for days and months.

Although, in some instances, NDT technology, e.g. dye penetration, ultrasonic, eddy current and radiology methods is also used to inspect fatigue cracks, they are actually not real time monitoring technologies, the fatigue testing process has to be stopped in order to perform the NDT tests. Not only it interrupts the fatigue testing process, but also it takes a lot extra time to prepare the NDT test. If the tested part is not a small object, but a very big object like the full size orthotropic steel deck, it would be impossible to inspect the complete structure or to inspect all potential crack areas within a limited time.

In the recent years, acoustic emission (AE) technology is getting more and more widely used in not only fatigue tests in the laboratories, but also active crack detection of bridge structures[3-7]. There are quite a few unique advantages in using AE for crack detection and structure health monitoring, such as

- Real time on-line structure health monitoring
- Very sensitive to crack development or active crack growth
- Global area monitoring with sensors away from exact crack locations
- Location of one or more crack sources
- Suitable for long term Ethernet or wireless remote monitoring

With these advantages, it is possible to answer the questions regarding crack initiation and development of full size steel structures during a fatigue test or actual structure health monitoring. Wang et al[2] has used AE to test a full size orthotropic steel bridge deck, but it only monitored very short time when a crack has already been found before AE applied, there was no crack development process studied.

In this paper, a fatigue test process of a full size orthotropic steel bridge deck with dimension 12.54x2.99x0.6 (LxWxH) meters is studied. Initially, the objective of this test is pretty straight forward, i.e. to find out all fatigue cracks with visual inspection and their corresponding fatigue cycles

when the test is done. However, it was soon realized that this is not a simple task as the structure is too big and it would be not possible to identify real initial crack with its location and actual fatigue cycles with visual inspection. Therefore, AE technology is introduced in the test, it tries to identify in what fatigue cycle that a crack is initiated? How earlier that a crack can be detected by AE than by visual inspection? Can AE locate the crack sources? What is the behavior of crack growth during the fatigue process? Where are the tangible crack locations in the orthotropic steel bridge deck etc.. Experimental results have shown that AE is a very effective tool for monitoring the dynamic process of fatigue crack growth of larger structures.

2. Cracking monitoring with acoustic emission

AE is a phenomenon of rapid energy release of stress concentration in the material. Cracking is associated with stress relief and therefore generation of burst AE signal. AE does not depend on the length and width of the existing crack, but on if the crack is actively opening or growing, no AE exists if there is no active cracking. As such, AE can be effectively used for monitoring crack growth processes.

The frequency range of crack induced AE is usually in between 20 – 1000 KHz which is above the frequency range of auditable sound range. The detectable fracture related AE signal level varies considerably in accordance with materials and cracking status. In a very quiet lab environment, AE induced by material crystal dislocation can be detected with a signal level in 20 dB. On the other hand, AE can also be detected in macro fracture or sudden break of a structure with a signal level in 120 dB with the same AE system without gain adjustment. Figure 1 depicts an active cracking process with AE monitoring. When a crack is growing microscopically or macroscopically, burst type AE is generated at the crack tip with acoustic wave energy travels along the structure with a velocity that is inherent with particular type of material. AE sensors installed in surrounding areas would pick up the acoustic wave energy in a time order depending on the distance between the crack source to the sensors. AE system does the data acquisition and signal processing with filtering, AE feature extraction, crack identification and source location to determine if a crack is in active growing and where is the crack located.

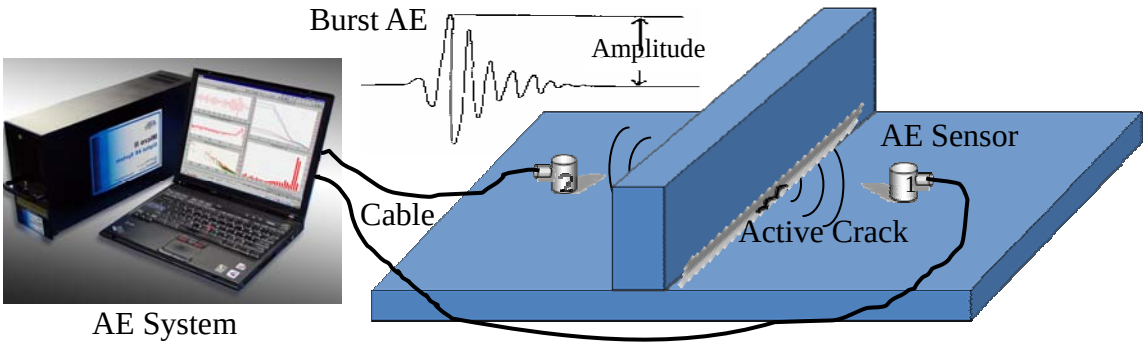

Figure 1. Illustration of active crack monitoring with AE

3. Setup of fatigue test of orthotropic steel bridge deck and AE monitoring

A fatigue test and AE monitoring were conducted on a segment model f a full size orthotropic steel bridge deck. A sketch drawing of the tested model is shown in Figure 2. The dimension of the deck model is 12.54x2.99x0.6 (LxWxH) meter, it consists of 5 U ribs and 4 webs. The deck was alternatively loaded with two actuators at 1 Hz fatigue cycle. The locations of the two actuators are indicated in Figure 2. The intersection areas of the U ribs and the first two webs were monitored with AE. Figure 3 shows photos of the orthotropic steel bridge deck and AE sensors installed. 150 KHz integral preamplifier AE sensors R15I made by Physical Acoustics Corporation were installed on the U ribs in front of the first two webs.

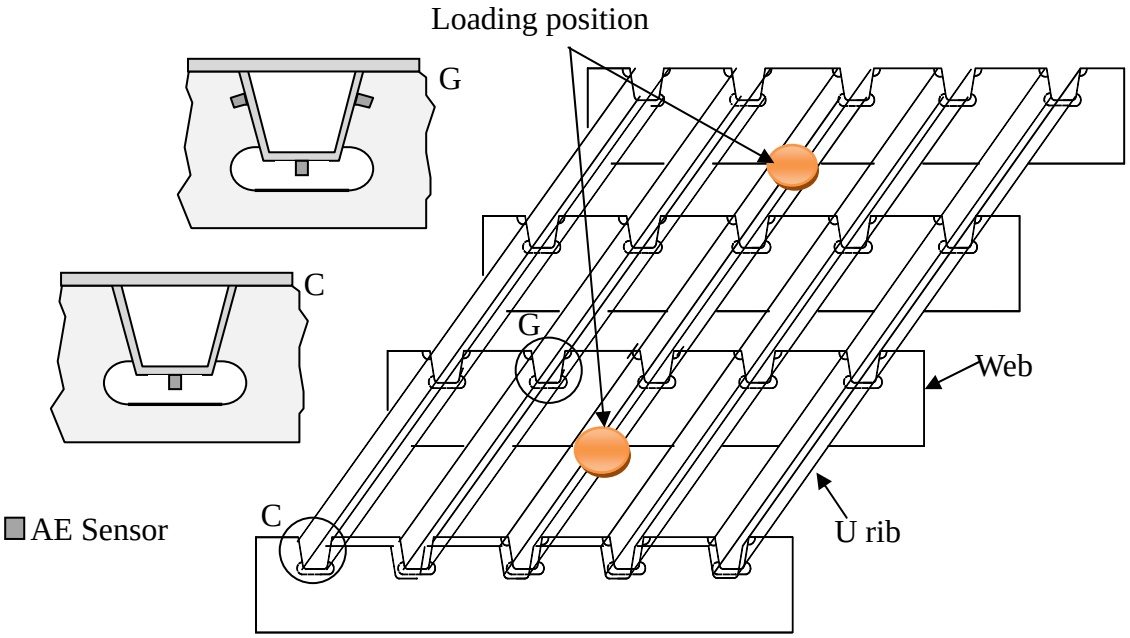

Figure 2. Drawing of the orthotropic steel bridge deck and actuator locations

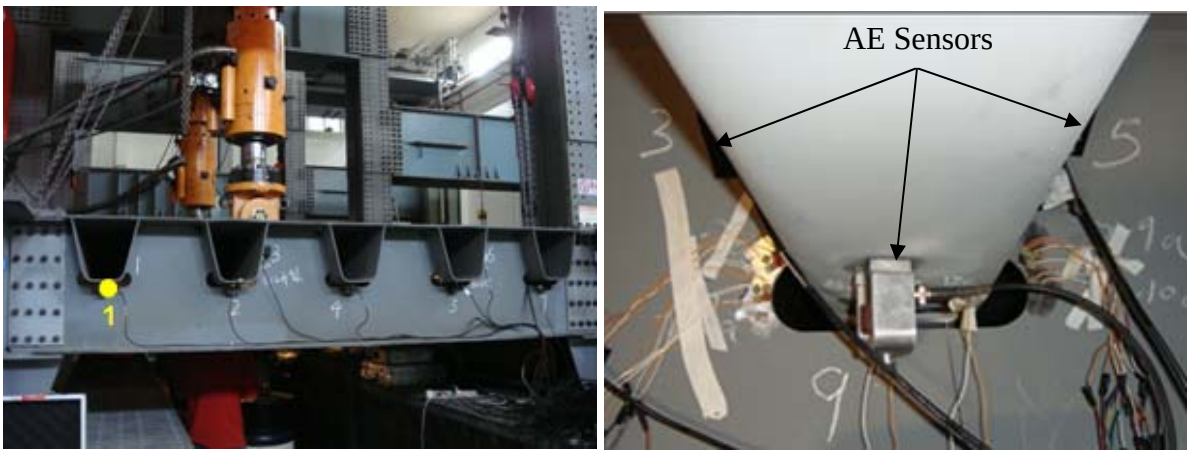

(a) Photo of an orthotropic steel bridge deck (b) Area monitored with 3 AE sensors

Figure 3. Fatigue test and AE monitoring photos

Figure 1 also shows illustrations of sensor installations with one AE sensor and three AE sensors. In the latter case, one sensor is installed at the bottom of the U rib, two more sensors were installed at the left and right side of the U rib respectively to perform crack source location. A 16 channel smart AE monitoring system MicroII made by Physical Acoustics Corporation was used for continuous monitoring of the fatigue test process. The fatigue test lasted for 30 days, the AE sensors were not installed until 7 days or 504 thousands load cycles of the fatigue test.

4. Behavior of acoustic emission in fatigue crack development

During the 30 day fatigue test, visual inspections on the deck were conducted from time to time in each day in order to find out if there is crack initiation or crack growing. Specifically, the visual inspection is focused on

a). areas that AE has indicated crack activity so that to find out if the observed crack matches with the AE indication;
b). if there is a crack in somewhere that AE hasn't picked it up before it is visualized.

In the end of the 30 day fatigue test, the orthotropic steel bridge deck was thoroughly inspected and cracks were found in 12 locations. Among them, 10 of the locations are at the intersections of the U ribs and the lateral webs where AE sensors were installed. 2 of the locations are not in the web area, but in the middle of two webs with crack direction along with the rib length. At all 10 locations where the AE sensors were installed nearby, crack initiations were found by AE well before the visual inspection. However, since there was no AE sensors installed in middle of the webs, the 2 cracks located in the midway of the U ribs were not found by AE because the AE sensors were too far from the crack positions so that the AE signal was greatly attenuated before it reaches to the AE sensor.

In order to illustrate how AE behaviors during crack initiation and development, the AE data in the two of the seven crack locations where AE sensors were installed were analyzed here. The two crack positions are labeled as C and G as shown in Figure 2.

4.1 Case study 1: AE activities at position C

Take the position C as the first example, the elapsed time and the fatigue cycles along with AE monitoring and visual inspection results at location C are shown in Table 1. As is seen in the table, crack initiation was observed about 142.3 fatigue hours or 513 thousand fatigues cycles by the AE. The crack was not visually found until 182.6 fatigue hours or 657.5 thousand fatigue cycles when a 20 mm crack was observed. So, in this example, the AE was able to report the crack initiation in about 40 hours before visual inspection.

On the other hand, the crack initiation and development process can be clearly identified from a time history graph of AE hit activity as shown in Figure 4(a). In this figure, the vertical axis

is the AE hit rate per second, the horizontal axis is the fatigue testing time from 139.9 to 160.2 elapsed fatigue hours. Crack was initiated in about 513 thousand fatigue cycles or 142.3 hours after the fatigue test started, then the AE activity keeps relatively quite which implies that the crack was rest for a while after initiation. In about 6 hours later or 535 thousand overall fatigue cycles, significant crack activity or crack growth that was lasting for about 4 hours was observed. The AE amplitude in this period is shown in Figure 4(b), each dot in the figure represents the amplitude of each AE hit. Trending of the AE amplitudes around 40 dB is clearly seen in the figure, this indicates continuous crack growth in this period though occasionally the amplitude drops below 35 dB. By further zooming the instant signal around 12:00 am of August 3rd in Figure 4(b), the AE amplitudes in less than one minute span are shown in Figure 4(c). The amplitudes are scattered in fairly regular interval which coincides to the fatigue cycle, i.e. one per second. In other words, there is one AE hit or one crack event in every fatigue cycle in this period.

Table 1. Remarks of crack monitoring alone with elapsed fatigue time & cycles at location C

Date	Time of the Day	Elapsed Time (Hours)	Fatigue Cycles (Thousands)	Remarks
2/Aug	14:07	139.9	504	AE monitoring started.
	16:32	142.3	513	AE activity that indicates crack initiation was observed in the first time.
	20:17	146.1	526	AE activity lasting for about 10 minutes was observed.
	22:42	148.5	535	Significant AE activity that indicates continuous fatigue crack development in about 4 hours was observed in the AE.
3/Aug	08:30	158.3	570	**Visual inspection didn't find crack.**
	14:24	164.2	592	**Visual inspection didn't find crack.**
	16:05	165.9	598	Stepwise AE activity that indicates crack growing and resting was observed.
4/Aug	05:50	179.6	647	Long lasted AE activities were observed.
	08:50	182.6	658	**Visual inspection found crack with 20mm long, in 40 hours later than that AE reported crack initiation.**

Besides the continuous cracking activity observed, a stepwise cracking activity was also observed in location C. Figure 5 shows the AE amplitude in about 598 thousand fatigue cycles or 165.9 elapsed fatigue hours. Not only the amplitude shows an increasing trend, but also the amplitude drops down to a lower level and then it increases again. This phenomenon implies crack growing and stress relief during the fatigue process. When micro cracking is build up, the AE amplitude is increased until the stress concentration is big enough to

generate macro cracking which results in stress relief and therefore decrease of the AE amplitude. Then the micro cracking would rebuild up again so that stepwise AE amplitude is observed. Obviously, the micro cracking or stress concentration build up didn't show regular trend, occasionally, sometimes it builds up quickly, sometimes it takes a long resting time before micro cracking is rebuild up again.

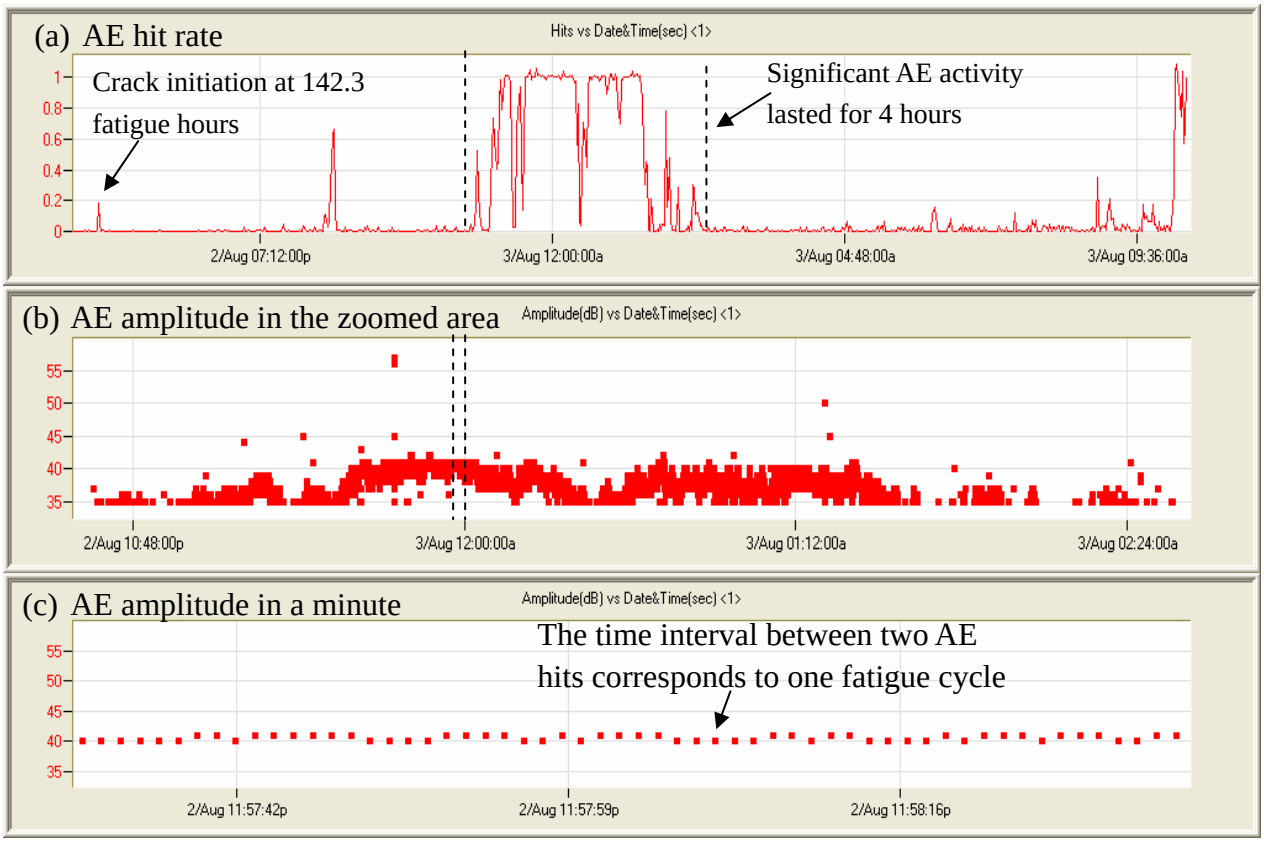

Figure 4. AE hit rate and amplitude at location C from 139.9 elapsed fatigue hours

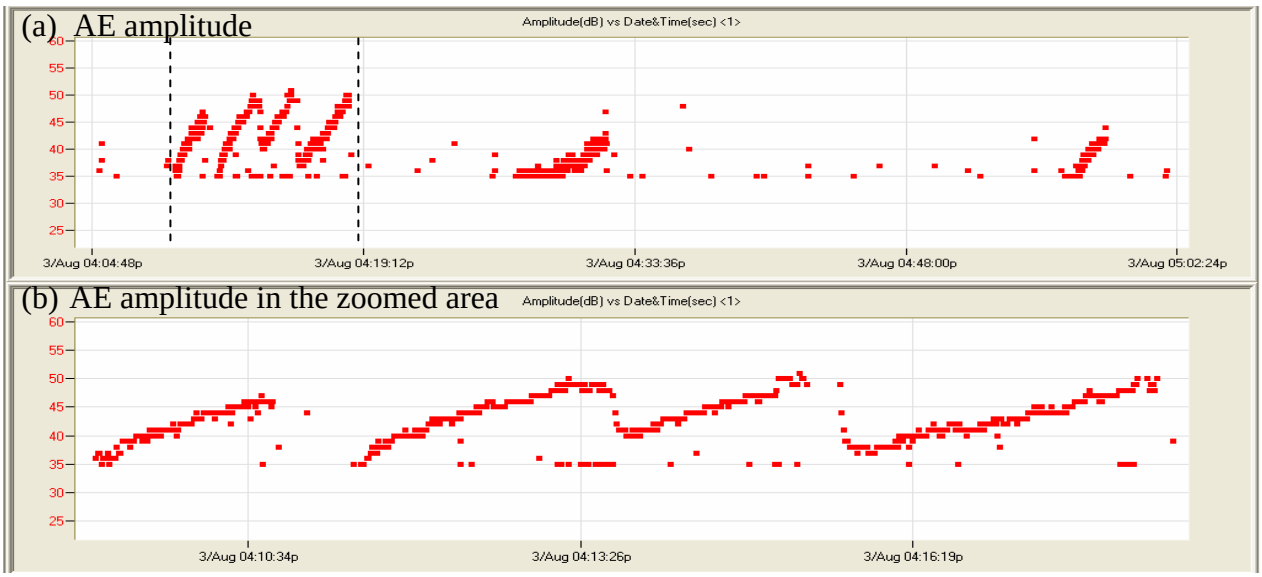

Figure 5. AE hit amplitude versus testing time that shows stepwise crack growth.

4.2 Case study 2: AE activities at position G

The second example is for the crack monitoring of position G of Figure 2. The elapsed time and the fatigue cycles along with AE monitoring and visual inspection results at this position are shown in Table 2. Figure 6 shows the AE hit rate from 139.9 to 237.8 elapsed fatigue hours. AE activity or crack initiation started from 148.4 elapsed fatigue hours or 534 thousand fatigue cycles, then continuous AE activities lasting for over 12 hours were observed, there is also long resting period that no or very rare AE activity was observed after the crack initiation. Since three sensors, numbered as 1, 8 and 2, were installed in position G, crack locations are able to be picked up with the linear location algorithm applied to the AE hits detected by the three sensors. Figure 7(a) shows a distribution of the located crack events along with the linear coordinate of the sensors, it shows two clustered location groups around the sensor 8, one is in between sensors 1 and 8 and another one is in between sensors 8 and 2. These two clustered location groups indicate that two cracks exist in these two areas. However, as is seen in Table 2, visual inspection couldn't find cracks in the following 21 days which it challenged the findings of the acoustic emission.

Table 2. Remarks of crack monitoring alone with elapsed fatigue time & cycles at location G

Date	Time of the Day	Elapsed Time (Hours)	Fatigue Cycles (Thousands)	Remarks
2/Aug	16:07	139.9	504	AE monitoring started.
	22:35	148.4	534	AE activity that indicates crack initiation was observed in the first time.
3/Aug	9:30	159.3	574	Visual inspection didn't find crack.
	13:47	163.6	589	Visual inspection didn't find crack.
4/Aug	8:50	182.6	658	Visual inspection didn't find crack. AE activity was relatively quiet in this period.
5/Aug	8:45	206.5	744	Visual inspection didn't find crack. Significant AE activities with locations were observed in next few days which indicate long lasted continuous fatigue crack development.
	13:07	210.9	760	Visual inspection didn't find crack.
6 – 23 /Aug				AE kept indicating crack activities, but no crack was found with visual inspection at this location in this period.
24/Aug	9:00	662.8	2880	After applying higher load and faster fatigue frequency up to 2 Hz, visual inspection eventually found two cracks in 220mm and 15 mm long respectively.

With continued fatigue cycles, although AE kept indicating crack activities, no crack was found at this monitoring area for over 21 days after the crack initiation was detected with AE.

Before finishing the 30 day fatigue test, accelerated fatigue test parameters, e.g. higher load and faster fatigue test frequency up to 2 Hz, were applied to the structure to speed up the damage process. Then two cracks were eventually visualized in about 22 days after AE detected crack initiation. A photo of the crack location after the overall 30 day fatigue test is shown in Figure 7(b), one crack in 220mm long is located at the web in between sensors 1 and 8, another crack in 15mm long is located along with the weld of the rib in between sensors 8 and 2, these two cracks are located at the same positions that AE technology has reported in about 22 days ago. This illustrates that either the microscopic initial crack was too small to be visualized or the crack was not in the surface of the visible area in early stage of fatigue crack growth. However, AE not only detected the crack initiation and growing process, but also it located crack positions in so many days before visual inspection found the cracks. The visual inspection results eventually proved the effectiveness of the AE technology for dynamic monitoring of fatigue crack process of large structures.

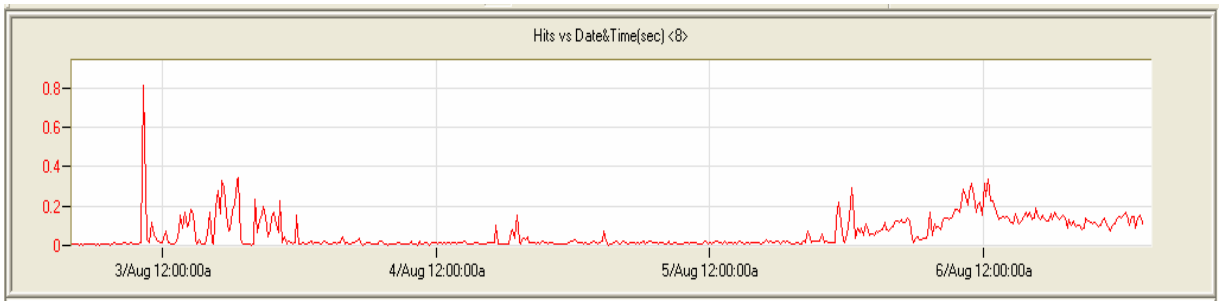

Figure 6. AE hit rate at position G from 144.4 elapsed fatigue hours

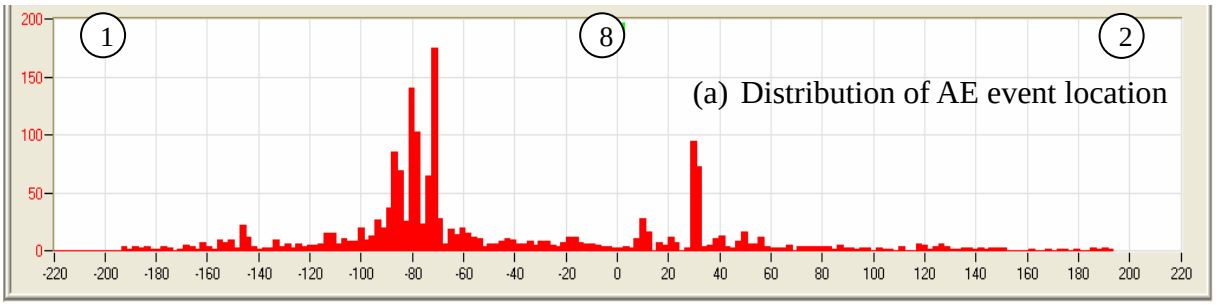

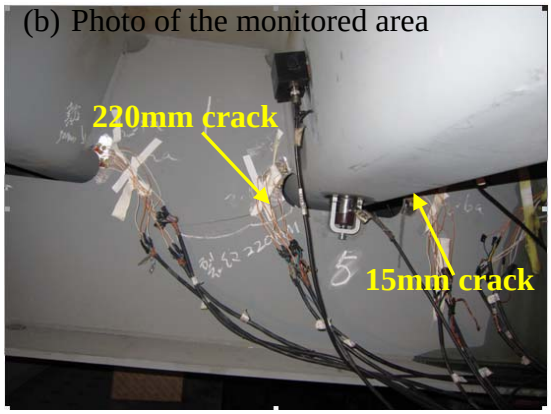

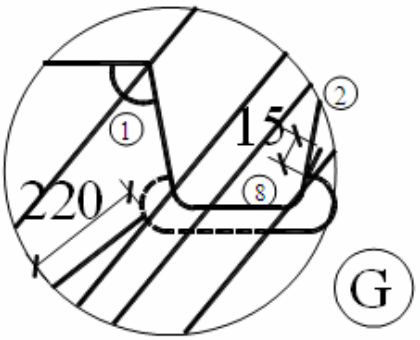

(c) Sketch drawing of crack location

Figure 7. AE crack event location and indications of the cracks found

5. Conclusions

This paper has applied acoustic emission technology for monitoring the dynamic process of fatigue crack initiation and growing of a full size orthotropic steel bridge deck. Experimental results have proven:

1). AE is an effective technology for structure health monitoring, specially AE can monitor the whole dynamic development process from crack initiation and growth to structure fracture. Not only AE can tell when a crack is initiated, but also it can tell where the crack is located and how it develops.

2). AE has much higher sensitivity for active crack identification than any other NDT technologies. It can detect microscopic crack activity and is able to report crack initiation in hours or days in advance of visual inspection and other technologies. This actually draws another inference, i.e. a fatigue test may not be able to find correct material life cycle without using AE for crack detection.

3). In the experiment, it was found that the cracks of the tested deck are not necessarily found in welds, but also it existed in other weak locations of the structure material.

Acknowledgement

The authors would like to thank Ed Zhou from URS Corporation in US for his help and suggestive discussions in implementing this project.

References

[1] S.T. de Freitas, H. Kolstein, F. Bijlaard, Structural monitoring of a strengthened orthotropic steel bridge deck using strain data, Structural Health Monitoring, Vol. 11, No. 5, September 2012, 558 – 576.

[2] C. Wang, L. Tian, B. Fu, Fatigue cracking monitoring and evaluation using smart sensors for steel bridge decks, Bridge Maintenance, Safety Management, Resilience and Sustainability, Biondini & Frangopol (Eds), 2012 Taylor & Francis Group, London, ISBN 978-0-415-62124-3.

[3] Inspecting Bridges with Acoustic Emission, Technical Report TR-103-12, Physical Acoustics Corporation, 1996.

[4] J. A. Mckeefry and C. K. Shield, Acoustic Monitoring of Fatigue Cracks in Steel Bridge Girders, Minnesota DOT Report MN/RC-1999-36, September, 1999.

[5] A. Schultz, Development of An Advanced Structural Monitoring System, Minnesota DOT Report MN/RC 2010-39, November, 2010.

[6] M.B. Johnson, D. Ozevin, G.A. Washer, K. Ono, R.S. Gostautas, T.A. Tamutus, Real time steel fatigue crack detection in eyebar using acoustic emission method. Journal of the Transportation Research Board, accepted in 2012.

[7] T.M. Roberts, M. Talebzadeh, Acoustic emission monitoring of fatigue crack propagation, Journal of Constructional Steel Research 59 (2003) 695 – 712.

Development of a Wireless Sensor for Simultaneous Measurement of Fatigue and Corrosion

Fang Yuan[1,*], Takayuki Shiraiwa[1], Manabu Enoki[1] and Tadashi Shinohara[2]

[1] Department of Materials Engineering, The University of Tokyo, 7-3-1 Hongo, Bunkyo-ku, Tokyo 113-8656, Japan
[2] Environment and Energy Materials Division, National Institute for Materials Science, 1-2-1 Sengen, Tsukuba, Ibaraki, 305-0047, Japan
* Corresponding author's e-mail address: yuanfang@rme.mm.t.u-tokyo.ac.jp

Abstract In previous study, it was demonstrated that smart stress-memory patch and ACM (Atmospheric Corrosion Monitor) sensor are suitable and effective for fatigue and corrosion monitoring, respectively. However, some problems still exist on the smart patch and ACM sensor. First, although "sputtered smart patch", which can estimate crack length wirelessly, has been developed, the crack length could not be estimated accurately sometimes because the resistance of the metal film on it was unstable. Second, it has not been figured out whether the existing patch is applicable to some fatigue condition such as the landing gears of the airplanes. Third, until now the wireless monitoring by ACM sensor has not been developed, and the communication distance of smart stress-memory patch via RFID tag (30 mm) is not sufficient. Therefore, in this research, 1) the measurement accuracy of the ion-sputtered metal film was improved through FEM; 2) whether the existing smart patch is applicable to high-stress low-cycle fatigue environment or not has been figured out; 3) a new wireless device equipped with ZigBee has been developed. By using this device, the wireless monitoring by ACM sensor was realized and the communication distance has been improved to more than 30 m.

Keywords Structural health monitoring, Fatigue, Corrosion, Wireless, Smart stress-memory patch

1. Introduction

Many construction accidents, which are due to the degradation progress, occur to structures, such as bridges, ships, trains, aircraft, power plants and buildings every year. Since these failure accidents brought much risk to our daily lives and industry production, it is important to prevent them in advance. Moreover, it has been well known that fatigue and corrosion are fate factors of such failure. Thus, a sensor which is able to monitor fatigue and corrosion effectively at the same time for a long-term performance is desired. In previous study, it was demonstrated that smart stress-memory patch and ACM (Atmospheric Corrosion Monitor) sensor are suitable and effective for fatigue and corrosion monitoring respectively.

Smart stress-memory patch (hereinafter called "smart patch") is consists of a thin copper specimen with a pre-crack can estimate fatigue damage parameters such as number of cycles, stress amplitude of structures[1-5], which can be estimated from the fatigue crack growth of smart patch fixed on the structure by using two smart patches with different characteristics. Moreover, "sputtered smart patch", which has ion-sputtered metal film and insulating layer on smart patch as a thin crack gage, can estimate crack length by measuring electrical resistance change of the ion-sputtered metal film wirelessly via RFID tag.[6] However, some problems still exist for this application. First, the crack length could not be estimated accurately because sometimes the resistance of the ion-sputtered metal film was unstable and did not increase monotonically as the crack length increased. Second, the communication distance of smart patches via RFID tags only (30 mm) is not sufficient for wireless network system. Third, to prevent the fatigue failure of the landing gears of the airplanes, a sensor which is applicable for high-stress low-cycle fatigue environment is also necessary. It has not been figured out whether the existing smart patch is applicable to such fatigue condition or not.

For corrosion monitoring, ACM sensor consisting of a Fe-Ag galvanic couple was developed and

applied for the evaluation of corrosion of atmospheric environments for long-term performance. By analyzing the magnitude and time variation of the sensor output, I, the occurrence and duration of rain, dew and dry periods, T_{rain}, T_{dew} and T_{dry}, could be distinguished and determined, respectively. And by referencing to the calibrating curve between output of ACM sensor (I) and relative humidity (RH) - empirical I-RH calibrating curve, the amount of deposited sea salt could also be estimated.[7] However, because ACM sensor was powered by battery, AC power or solar battery and the output data of ACM sensor was recorded by a microcomputer, the setting-up places has been restricted and the data collecting costs time and labor. Thus, it is necessary to develop a wireless monitoring method for ACM sensor which can be used for long-term performance as well as smart patch.

In this study, (1) the measurement accuracy of the ion-sputtered metal film on "sputtered smart patch" was improved by changing the shape of the ion-sputtered metal film through FEM; (2) a new wireless device was developed to improve the communication distance between smart patches; (3) fatigue experiments have been executed to figure out whether the existing smart patch is applicable to high-stress low-cycle fatigue environment or not; (4) the wireless monitoring by ACM sensor was realized by using the new wireless device as well as smart patch.

2. Principle

2.1. Estimation of cyclic number and stress amplitude by RFID-based smart patch

A schematic image of the sputtered smart patch is shown in Figure 1. This sensor is composed of an ion-sputtered metal film deposited on the smart patch (a thin copper specimen with a pre-crack).

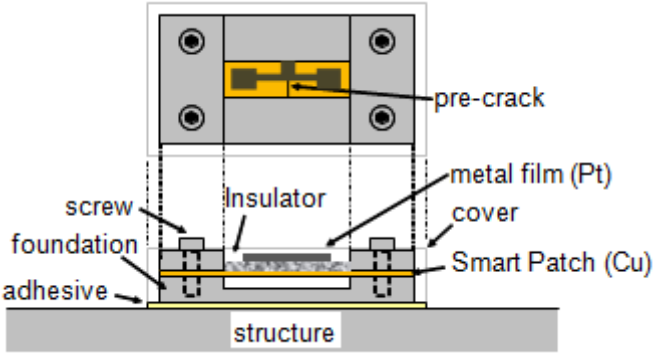

Figure 1. Schematic image of the sputtered smart patch. [6]

The details of the principle of smart patch is described in the previous paper.[1] The cyclic number (N) and stress amplitude ($\Delta\sigma$) of structures can be estimated from the crack length values detected from the two smart patches with different characteristics using the following equations:

$$\Delta\sigma = [C_2 \cdot C_1^{-1} \cdot W_1 \cdot W_2^{-1} \cdot (\pi W_2)^{-m_2/2} \cdot (\pi W_1)^{-m_1/2} \int_{\alpha_0}^{\alpha_1} \{\sqrt{\alpha} f(\alpha)\}^{-m_1} d\alpha \Big/ \int_{\alpha_0}^{\alpha_2} \{\sqrt{\alpha} f(\alpha)\}^{-m_2} d\alpha]^{1/(m_1-m_2)} \quad \cdots\cdots(1)$$

$$N = [C_2^{m_1} \cdot C_1^{-m_2} \cdot W_1^{m_2} \cdot W_2^{-m_1} \cdot (W_2/W_1)^{m_1 m_2/2} \{\int_{\alpha_0}^{\alpha_1} \{\sqrt{\alpha} f(\alpha)\}^{-m_1} d\alpha\}^{m_2} \Big/ \int_{\alpha_0}^{\alpha_2} \{\sqrt{\alpha} f(\alpha)\}^{-m_2} d\alpha\}^{m_1}]^{1/(m_2-m_1)} \quad \cdots\cdots(2)$$

where W is the width of specimen, α_0 is the normalized initial crack length, α is the normalized

initial crack length, C and m are empirical constants of Paris law and $f(\alpha)$ is the shape factor of the stress intensity factor. Indexes 1 and 2 represent smart patch 1 and 2, respectively. By substituting the normalized crack lengths α_1 and α_2 detected from two smart patches into Eqs. (1) and (2), the cyclic number and the stress amplitude can be estimated as shown in Figure 2. Furthermore, fatigue life will be assessed by substituting the estimated cyclic number and stress amplitude into Miner's rule.[8]

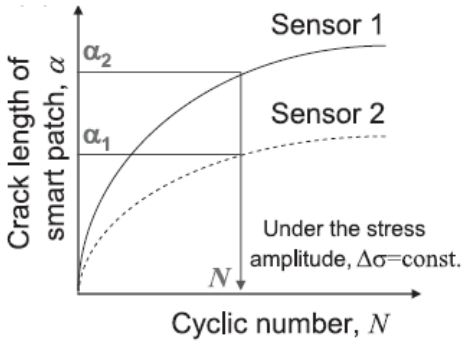

Figure 2. Principle of estimation of cyclic number from crack lengths in two smart patches.[6]

2.2. Estimation of corrosivity in atmospheric environment by ACM Sensor

An ACM (Atmospheric Corrosion Monitor) type corrosion sensor, consisting of a Fe-Ag galvanic couple was developed and applied for the evaluation of corrosivity of atmospheric environments. The sensor was designed considering mass-production and good reproducibility of results, making it convenient for long-term corrosion data acquisition. Besides the sensor output, I, temperature, relative humidity (RH) were also recorded by a microcomputer. By analyzing the magnitude and time variation of I, the occurrence and duration of rain, dew and dry periods, T_{rain}, T_{dew} and T_{dry}, could be distinguished and determined, respectively. And by referencing to the empirical I-RH calibrating curve, the amount of deposited sea salt, Ws, could also be estimated. It was also found that the corrosion loss could be estimated in both indoor and outdoor sites by analyzing sensor output. Corrosivities of some kinds of exposure sites, not only outdoor environments but also indoor environments, were evaluated by using the ACM sensor.

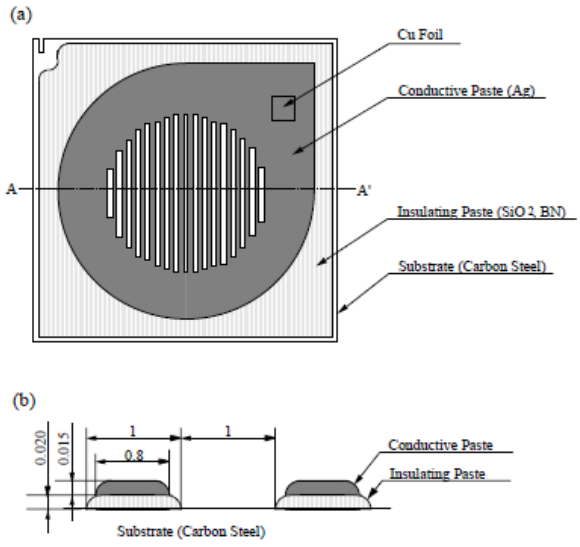

Figure 3. Schematic representation of the sensor.[7]

The sensor is shown schematically in Figure 3. A 0.8 mm thick carbon steel sheet was machined to the size of 64 mm x 64 mm to work as the substrate. After ultrasonically degreasing the substrate in acetone, an insulating paste with BN filler and epoxy resin, was printed on the substrate with a thickness of 20 μm. A conductive paste with Ag filler and epoxy resin was then printed on top of the insulating layer with a thickness of 15 μm. This conductive paste acted as the cathode, and the exposed area of steel substrate, as the anode.

3. Experiment and Simulation

3.1. FEM model to evaluate the measurement accuracy of the metal film

As showed in Figure 4, the crack length could not be estimated accurately because sometimes the resistance of the existing ion-sputtered metal film was unstable and did not increase monotonically as the crack length increased.

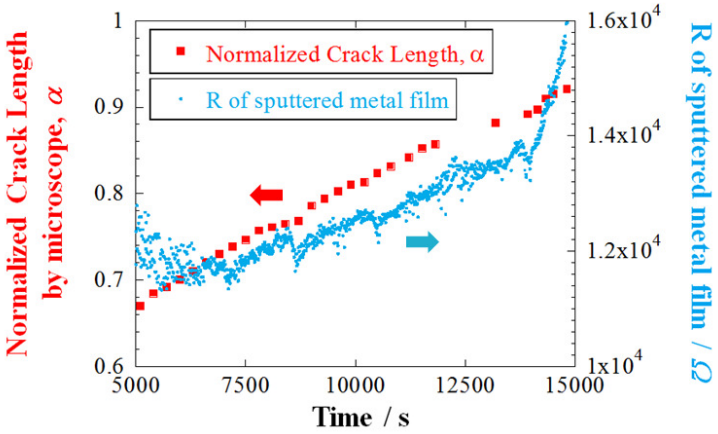

Figure 4. The correlation between normalized crack length observed by microscope and the resistance of sputtered metal film measured by digital multimeter (DMM).

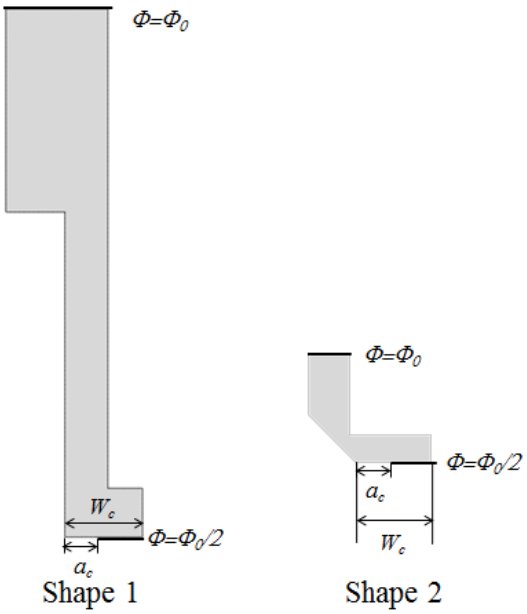

Figure 5. Definition of a_c and W_c in the ion-sputtered metal film, and the boundary condition on FEM.[6]

In order to figure out the optimum shape of the conductive film, electrical potential analysis by FEM was performed by changing the crack length a_c=0 to 1.9 mm under the fixed voltage. Because

the shape of the ion-sputtered film is always laterally zygomorphic, it is suitable to calculate the electric current by adding half of the voltage to half shape of the film. The definition of a_c and W_c (W_c=1.9 mm) of the ion-sputtered film and the boundary condition for FEM are shown in Figure 5. The electric current of metal film was calculated by the integration of current density in analytical results, and the resistance was derived from Ohm's law.

3.2. Wireless Communication

3.2.1 . Using RFID tag

RFID (Radio Frequency Identification) is a technology that transmits information between a reader and tags attached to an object using electromagnetic induction for the purpose of identification. It is widely used as IC tag or IC card. The RFID system is well known for its benefits of low cost, simple measurement, easy configuration and so on. Since tag is powered by electromagnetic induction from the reader, tag itself does not need battery for sensing and data transmission. By using RFID tags, evaluating the fatigue damage has been realized in previous research.[5] The schematic of wireless system for measuring crack length using RFID tag is shown in Figure 6.

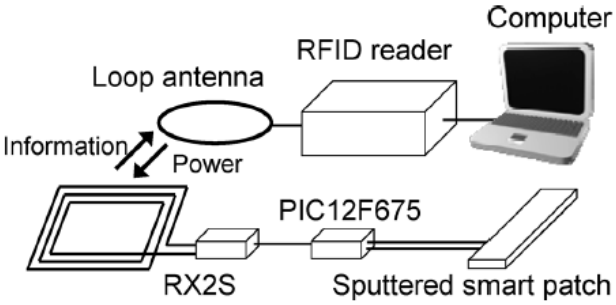

Figure 6. Schematic of wireless system for measuring crack length using RFID tag and reader.[6]

The wireless system composed of sputtered smart patch, RFID tag (RX2S, Yoshikawa RF Systems Co., Ltd.) and microprocessor (PIC12F675, Microchip Technology Inc.), in which the electrical resistance of the ion-sputtered metal film was converted to digital value and transmitted to the RFID reader (RX2100, Yoshikawa RF Systems Co., Ltd.). The RFID reader plays two roles of supplying power to RFID tag and acquiring the measured value from RFID tag by a unique protocol.

3.2.2. Using ZigBee

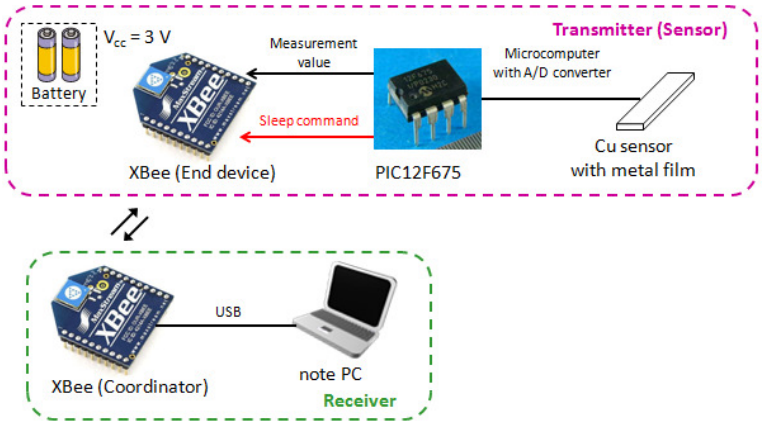

Figure 7. Schematic of new wireless system

To improve the communication distance, a new wireless device equipped with ZigBee (IEEE

802.15.4) was developed. The schematic of new wireless system for measuring crack length using ZigBee is shown in Figure 7. The transmitter contains sputtered smart patch and microprocessor (PIC12F675, Microchip Technology Inc.) as the same as the method.

Moreover, several wireless devices need to transmit with one receiver at the same time, to build the wireless system. The wireless communication among 1 receiver and 4 wireless transmitters has been tested as shown in Figure 8. The distance from transmitters to receiver are 20 m, 30 m, 30 m, 20m, respectively. Moreover, two transmitters were put at about 1 m above the ground, and two were on the ground.

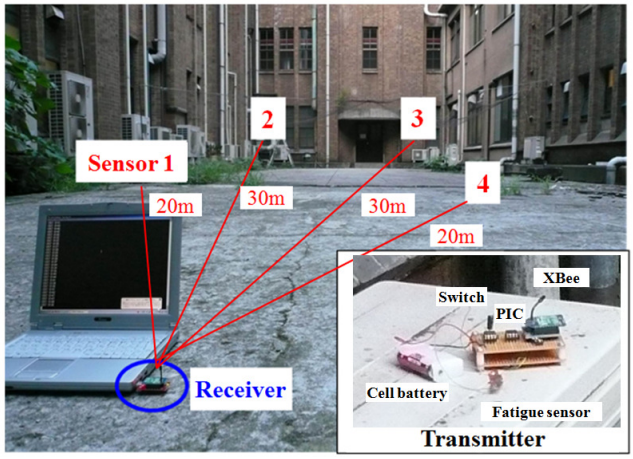

Figure 8. The wireless communication among 1 receiver and 4 new wireless devices and the composition of the new wireless device.

3.3. Fatigue experiment

To figure out whether the existing smart patch is applicable to high-stress low-cycle fatigue environment or not, fatigue experiments have been executed. Smart patch was clamped at both ends on fatigue testing machine with an electro-magnetic actuator (MMT-500N, Shimadzu), and fatigue pre-crack was introduced under maximum strain of 0.002 and strain ratio of 0.5 until total crack length reached about 2.7 mm. Afterwards, fatigue experiments were carried out under constant amplitude strain with maximum strain of 0.004 twice and 0.006 once respectively, strain ratio of 0.5 and frequency of 19 Hz. During fatigue experiments, the crack length of the sputtered smart patch was observed by optical microscope from the ion-sputtered side.

3.4. Wireless monitoring of ACM sensor

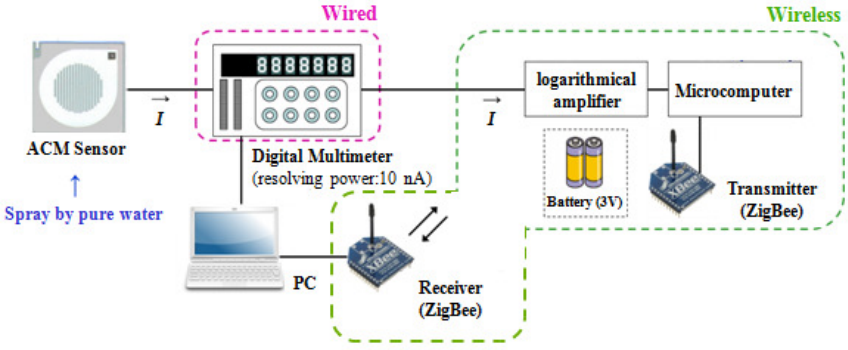

Figure 9. The schematic of the wireless system for ACM sensor

The wireless monitoring by ACM sensor was tested by using new wireless device. Because the output I from ACM sensor is galvanic electric current, and is so small that it is easy to be affected by noises while wireless communication, a wireless device which combines the new wireless device

and logarithmical amplifier (AD8304) was proposed. The schematic of the wireless system for ACM sensor is shown in Figure 9.

The accuracy was evaluated by two measurement systems. One is wired, consisted of digital multimeter. The other one is wireless, consisted of logarithmical amplifier (AD8304), microprocessor (PIC12F675, Microchip Technology Inc.), Battery (3 V), transmitter ZigBee (IEEE 802.15.4) and receiver ZigBee. To imitate different corrosion conditions in the atmosphere (Rain, Dew, Dry), pure water was sprayed to ACM sensor by different times.

4. Results and Discussion

4.1. Evaluation of the measurement accuracy of the metal film by FEM

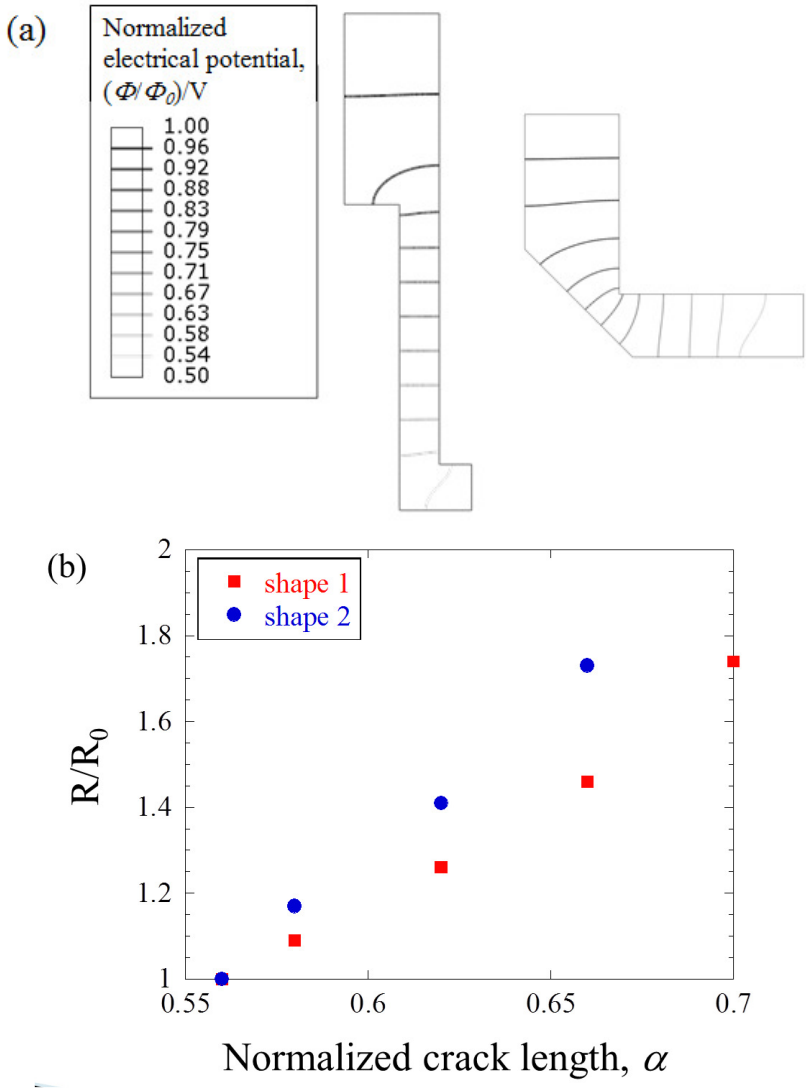

Figure 10. (a) Electrical potential distributions in the ion-sputtered metal film calculated by FEM (a_c=1.3 mm); (b) Relationship between the normalized crack length in sputtered smart patch and the normalized resistance of the ion-sputtered metal film through FEM.

The examples of analytical results about the normalized electrical potential (Φ/Φ_0) distribution are shown in Fig. 10 (a). The relationship between the normalized crack length in sputtered smart patch and the normalized resistance of the ion-sputtered metal film is shown in Fig.10 (b). By changing the shape of the ion-sputtered metal film from shape 1 to shape 2, the increase amount of

normalized resistance R/R_0 at the beginning of crack growth has been improved to about 1.5 times as the conventional. As a result, it is supposed to be an effective way to solve the unstable phenomenon at the beginning of crack growth shown in Figure. 4.

Therefore, the measurement accuracy of the ion-sputtered metal film on "sputtered smart patch" was improved by changing the shape of the ion-sputtered metal film through FEM. Fatigue experiments will be conducted to verify the effectivity of this shape.

4.2. Wireless communication

4.2.1. Using RFID tag

The conventional wireless measuring system, which composed of the ion-sputtered metal film, AD converter and RFID tag, was successfully applied to measure the crack length of sputtered smart patch during fatigue test. However, the communication distance was only 30 mm, and is not sufficient for wireless network system.

4.2.2. Using ZigBee

By using the new wireless device, the communication distance was improved to more than 20 m. The wireless communication was proved to be possible among 1 receiver and 4 wireless devices. Moreover, within 20 m, the loss rate was almost 0, and more than 30 m, the loss rate was near to 5 percent. It could be expected to build a wireless fatigue monitoring system, which will be applied to the real structure such as bridge and ships, by using these new wireless devices.

4.3. Fatigue experiment

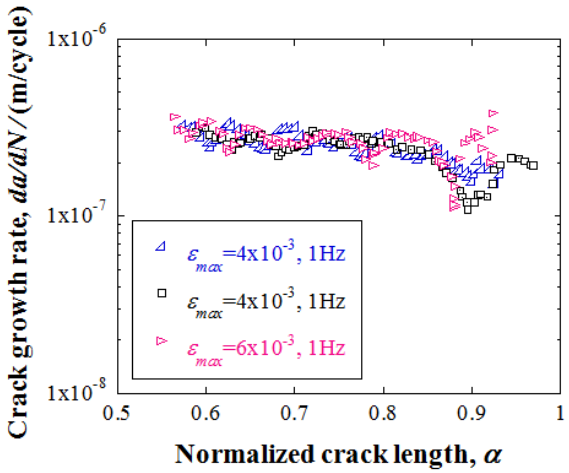

Figure 11. Relationships between the normalized crack length and the crack growth rate

In the high-stress low-cycle fatigue environment, the fatigue crack path of the sensor exhibited a straight line and is possible to measure the crack length easily. Figure 11 shows the relationships between the normalized crack length and the crack growth rate calculated by the incremental polynomial technique under each test condition. Tests performed two times under the same condition (ε_{max}=4x10^{-3}) showed good repeatability. The crack growth rate was almost constant with fatigue cycles in the range of α=0.54 to 0.86, and it decreased slightly before increasing in the range of α>0.86. The crack growth rate did not change a lot even through the maximum strain changed. This tendency is quite different from that of the low-stress fatigue environment. Further research is

needed to figure out the reason for this result.

4.4. Wireless monitoring of ACM sensor

It was possible to make ACM sensor wireless by using the new wireless device and logarithmical amplifier. Figure 12 shows the output of ACM sensor estimated by wireless and wired systems. Both of them show very good coincidence during three periods (Rain, Dew, and Dry). Moreover, by using the logarithmical amplifier, the electricity in the dry period could be distinguished more remarkably than by multimeter. Thus, it was confirmed that the output of ACM sensor can be transmitted wirelessly by the combination of the new wireless device and logarithmical amplifier.

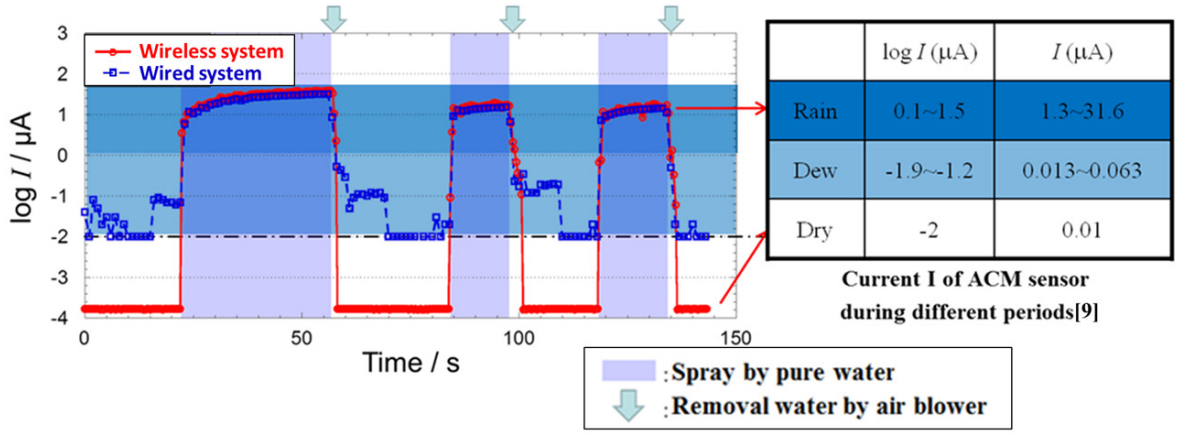

	log *I* (μA)	*I* (μA)
Rain	0.1~1.5	1.3~31.6
Dew	-1.9~-1.2	0.013~0.063
Dry	-2	0.01

Current I of ACM sensor during different periods[9]

Figure 12. The output of ACM sensor estimated by wireless and wired systems

5. Conclusion

In this study, (1) the measurement accuracy of the ion-sputtered metal film on "sputtered smart patch" was improved by changing the shape of the ion-sputtered metal film through FEM. (2) a new wireless device equipped with RFID and ZigBee was developed. By using this device, the communication distance between smart patches was improved to more than 20 m. The wireless communication among 1 receiver and 4 transmitters has been tested and proved to be possible. (3) the existing smart patch was proved to be not applicable to high-stress low-cycle fatigue environment through fatigue experiments because the crack growth rate did not change a lot even through the maximum strain changed, which tendency is quite different from that of the low-stress fatigue environment. Further research is needed to figure out the reason for this result. (4) the wireless monitoring by ACM sensor was realized by combining new wireless device and logarithmical amplifier.

References

[1] S. Nambu, M. Enoki, Smart Stress-Memory Patch for Fatigue Damage of Structure. Mater. Trans., 48 (2007) 1244-1248.
[2] S. Nambu, M. Enoki, Scattering in Fatigue Crack Growth of Thin Pure Copper Sheet for Smart Stress Memory Patch. ISIJ Int., 47 (2007) 1687-1691.
[3] Y. Fujino, S. Nambu, M. Enoki, AE behavior of smart stress memory patch after variable amplitude loading. Mod. Phys. Lett. B, 22 (2008) 1105-1110.
[4] S. Nambu, M. Enoki, Monitoring of Acoustic Emission Activity of Smart Stress Memory Patch to Estimate Maximum Fatigue Stress for Structural Health Monitoring. ISIJ Int., 51 (2011) 88-92.
[5] T. Shiraiwa, M. Enoki, Evaluation of Fatigue Properties of Steel Bar by Smart Stress-memory Patch. ISIJ Int., 51 (2011) 250-255.

[6] T. Shiraiwa, M. Enoki, Fatigue Crack Length Measurement of Sputtered Metal Film for RFID-based Smart Stress Memory Patch. ISIJ Int., 51 (2011) 1480-1486.
[7] T. Shinohara, Evaluation of corrosivity in atmospheric environment by ACM (Atmospheric Corrosion Monitor) type corrosion sensor. 5th Pacific Rim International Conference on Advanced Materials a Materials Science Forum, (2005) 61-64.
[8] M. A. Miner, Cumulative damage in fatigue. J. Appl. Mech., 12 (1945) A159-A164.
[9] T. Shinohara, S. Motoda, W. Oshikawa, Evaluation of Corrosivity of Atmosphere by ACM Type Corrosion Sensor. Zairyo-to-Kankyo, 54 (2005) 375-382.

Near-threshold Fatigue Crack Behavior of Thin Copper Sheet and its Application for Structural Health Monitoring

Takayuki Shiraiwa[1,*], **Manabu Enoki**[1]

[1] Department of Materials Engineering, The University of Tokyo, Tokyo 113-8656, Japan
* Corresponding author: shiraiwa@rme.mm.t.u-tokyo.ac.jp

Abstract Smart stress-memory patch is a novel sensing method in structural health monitoring for evaluating fatigue damage. The patch can estimate the number of cycles and stress amplitude using fatigue crack growth properties in Paris region of thin metal sheets. In this study, near-threshold fatigue crack growth behavior in thin pure copper sheet was investigated under strain-controlled testing to improve the measuring range and accuracy. Using a function describing the initiation as well as the stable growth of fatigue cracks, the relationship between stress intensity factor range and crack growth rate was successfully fitted to one equation regardless of strain amplitude. Based on these experimental results, a new equation for estimating fatigue cycles and stress amplitude from fatigue crack length of two specimens was derived. This equation overcame the limitation that the patch requires two or more materials with different fatigue characteristics. The new equation needs only one material for simultaneous estimation of fatigue cycles and stress amplitude, and the measuring range can be controlled by geometry of specimen. Since this patch needs neither power supply nor wiring, it provides a great potential for long-term structural health monitoring with easy maintenance and low cost.

Keywords Fatigue crack growth, Finite element method, Copper, Structural health monitoring, Smart stress-memory patch

1. Introduction

Structural health monitoring (SHM) is highly required to ensure the reliability of bridges, ships, trains, aircraft, power plants and industrial machines. Especially, a long-term sensing method of fatigue damage is very important to avoid the fracture caused by cyclic loading. Strain gauge, FBG (Fiber Bragg Grating) sensor and wireless strain sensing systems are utilized to monitor strain and to evaluate fatigue damage. However, there are several problems on the practical use such as necessity of wiring, electrical power supply and complicated measuring devices. Concept of smart stress-memory patch (hereinafter called "smart patch") was proposed to overcome above problems in the previous papers [1-6]. Sensor in smart patch consists of a thin metal sheet with a pre-crack, and the number of fatigue cycles and stress amplitude on structure can be estimated from fatigue crack growth in the sensor. Smart patch is a promising technique for long-term SHM because it needs neither power supply nor wiring. Furthermore, the patch is successfully applied to batteryless wireless system to measure the crack length in the sensor using RFID [4].

The fatigue crack growth behavior in the sensor under stress-controlled fatigue test has been investigated to estimate stress amplitude and fatigue cycles [1, 2]. However, when the patch is attached to structure, the sensor is subjected to strain-controlled loading under the change in strain of the structure. Therefore, it is necessary to evaluate fatigue behavior in the sensor under strain-controlled conditions for application of smart patch to structure. While most studies about fatigue in thin metal sheet have focused on stress-life (S-N) and strain-life (ε-N) curves for reliability of microelectronic products [7-10], the fatigue crack growth behavior under strain-controlled testing has not been enough explored in detail.

In this study, fatigue crack growth behavior of the sensor (thin pure copper sheet) was evaluated under uniaxial strain-controlled fatigue testing in order to obtain the characteristics of the attached sensor to structure. The scattering in crack growth was also examined by a stochastic model to assess the error in estimation of fatigue cycles and stress amplitude. From these observations, a method to evaluate fatigue cycles and residual fatigue life of structure using smart patch was proposed.

2. Principle of smart stress-memory patch

The details of the principle were described in the previous paper [5]. A schematic image is shown in Fig. 1 (a). Sensor in the patch consists of a thin metal sheet with a pre-crack. Since fatigue damage in structure tends to occur in structural component, more than one sensor is attached, for example, close to the welded part. When the structure is subjected to cyclic loading, the sensor is also cyclically loaded in response to the change of strain in the structure. Then, fatigue crack growth from pre-crack in the sensor will occur according to the cyclic loading. After a certain period, the crack length in each sensor will be measured by optical microscope or wireless measurement of electrical resistance change. The number of fatigue cycles (N) and stress amplitude ($\Delta\sigma$) on the structure can be estimated from the crack length detected from two sensors with different characteristics as shown in Fig. 1 (b).

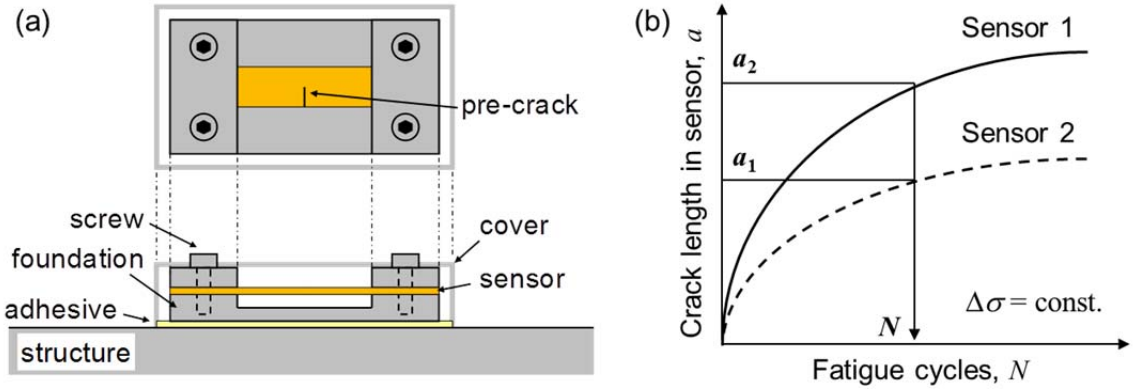

Figure 1. (a) Schematic image of smart stress-memory patch and (b) principle to estimate cyclic number from crack length.

3. Experimental procedure

3.1. Materials

The sensors were made of electrodeposited (ED) copper and nickel. These electrodeposited materials tend to have a very small grain size and provides stable crack propagations [11, 12]. The ED-Cu sheet with a thickness of 0.1 mm was cut to rectangular coupons with a dimension of 40 mm × 5 mm, 40 mm × 10 mm and 60 mm × 10 mm, and the ED-Ni sheet with a thickness of 0.05 mm was cut to 40 mm × 5 mm. Specimen geometries are shown in Fig. 2. A single notch with a length of 2.5 mm and a width of 0.3 mm was induced at the center from one side of the coupon. The notch tip was a round-shaped with a radius of approximately 150 μm. Additionally, the notch tip was sharpened to curvature radius of about 30 μm by the blade (High-stainless 100 μm, Feather Safety Razor Co., Ltd.). One side of the coupon was polished to a mirror finish using 3 μm and 1 μm alumina slurry to observe crack length clearly. Afterward, fatigue pre-crack was introduced.

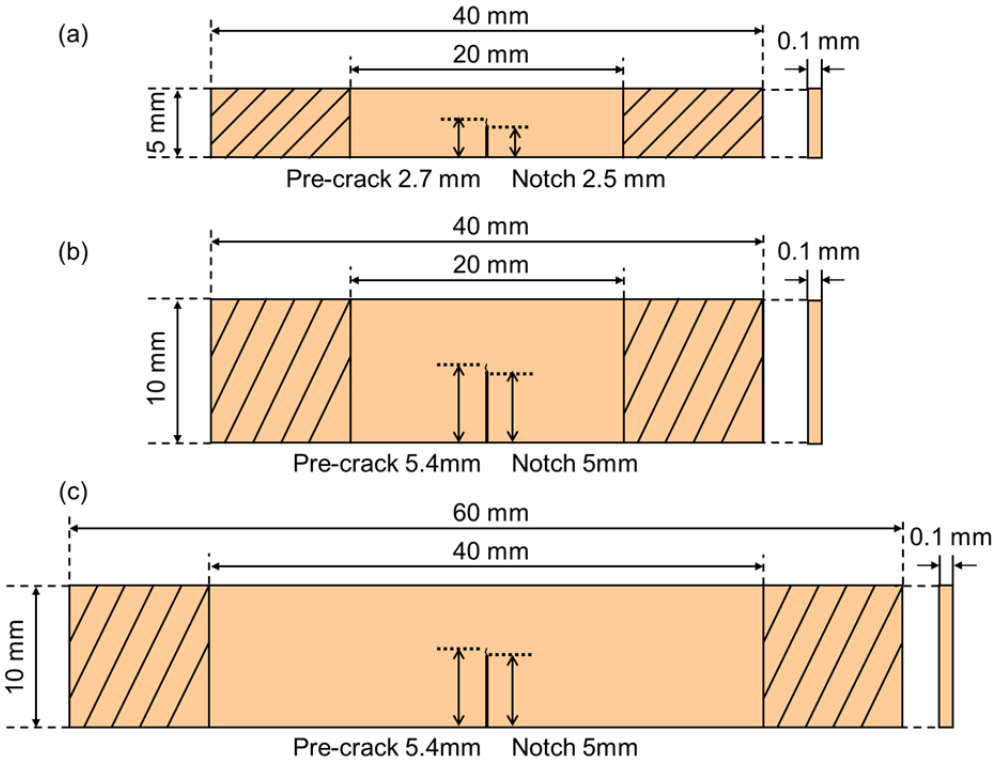

Figure 2. Specimen geometry. (a) Standard type, (b) High-cycle type, (c) High-sensitive type.

3.2. Fatigue test

Both ends of the sensor were clamped in jigs mounted in a fatigue testing machine (MMT-100N, Shimadzu), and the gauge length between the upper and lower jigs is adjusted to 20 mm. Fatigue tests were performed under maximum crosshead displacement (u_{max}) of 20, 25 and 30 μm, displacement ratio of R = 0.1 to 0.5, and frequency of 19 Hz. The strain ratio (R) was 0.1 and maximum strain (ε_{max}) was changed from 0.05 to 0.2 % where the strain is defined as a crosshead displacement divided by gauge length of specimen. The crack length was measured optically with digital microscope (VHX-600, Keyence).

3.3 Stress intensity factor

A proper shape factor, $f(\alpha)$, for the present sensor geometry is necessary to characterize the fatigue crack growth behavior as a function of stress intensity factor range, ΔK. It is commonly known that the stress intensity factor of single edge-cracked tension specimen with prescribed end displacements can be expressed by

$$K = \sigma\sqrt{\pi a}\cdot f(\alpha,\beta),\quad \sigma = \frac{Eu}{L},\quad \alpha = \frac{a}{W},\quad \beta = \frac{L}{W}, \tag{1}$$

where W is width of the specimen, L is gauge length of the specimen, a is crack length, E is Young's modulus, u is displacement on the specimen, α is normalized crack length and β is ratio of the gauge length to the width. Although the shape factor has been investigated in the range of β = 0.5 to 1 [13], the present sensor has the higher value of β = 2.0 to 4.0.

In order to evaluate shape factor of the sensor, linear elastic stress analysis was performed by finite element method (FEM). Geometry and boundary conditions for the simulation are shown in Fig. 3 (a), where Young's modulus was 120 GPa, Poisson ratio was 0.34 and L, W and u was changed as the same as experimental conditions. The model was sectioned into quadrilateral plane stress elements

with size of 0.05 mm × 0.05 mm. In the analysis, ten integration paths were defined from the crack tip to the outside, and the *J*-integral was calculated for normalized crack length ($\alpha = a/W$) ranging from 0.1 to 0.9. Since the *J*-integral reached a constant value from the fifth path in each condition, the constant value was used for calculation of stress intensity factor. Under plane stress conditions, the stress intensity factor can be described by

$$J = K^2/E, \tag{2}$$

and the shape factor was solved using eq. (1) and (2) as a function of stress intensity factor range, as shown in Fig. 3(b). The shape factors can be fitted as follows:

$$f(\alpha) = 1.002 - 0.040\alpha - 1.52\alpha^2 + 1.09\alpha^3 \quad (\beta = 2), \tag{3}$$

$$f(\alpha) = 0.896 - 1.43\alpha - 2.71\alpha^2 + 1.02\alpha^3 \quad (\beta = 4), \tag{4}$$

The calculated shape factor of β = 0.5 to 1 showed good agreement with the results by boundary element method (BEM) [13].

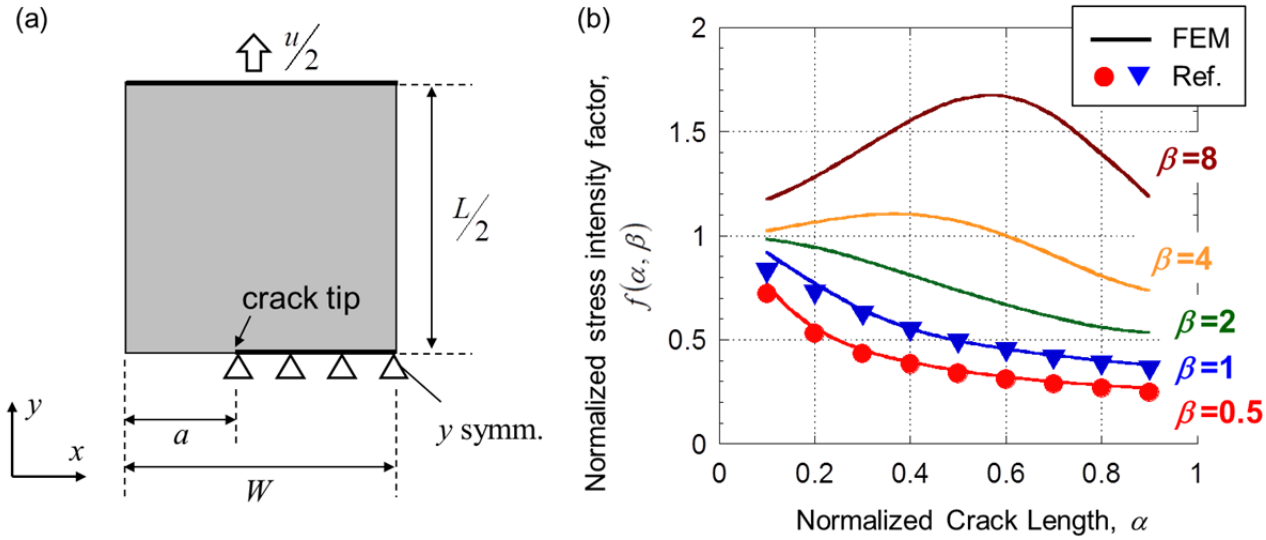

Figure 3. (a) Rectangular plate with prescribed end displacement, (b) Normalized stress intensity factor under plane stress condition.

4. Results

4.1. Fatigue crack growth behavior of ED-Cu

Near-threshold fatigue crack growth behavior in thin pure copper sheet with pre-crack was evaluated under strain-controlled fatigue testing. Fatigue crack path of the sensor exhibited the significantly straight line as shown in Fig. 4 (a). The relationships between the crack growth rate and stress intensity factor range is shown in Fig. 4 (b). The fit curve was analyzed by the following Kohout equation[14]:

$$\frac{da}{dN} = C\left[\left\{\frac{\Delta K}{(1-R)^{1-\beta_w}}\right\}^m - \Delta K_{th0}^m\right] \tag{5}$$

where, C, m, β_w are material constants and ΔK_{th0} is the threshold value of stress intensity factor range with R = 0. The fit is relatively good and the calculated values of the parameters are $C = 1.16 \times 10^{-11}$, m = 2.87, ΔK_{th0} = 4.41 MPa·m$^{1/2}$, β_w = 0.198.

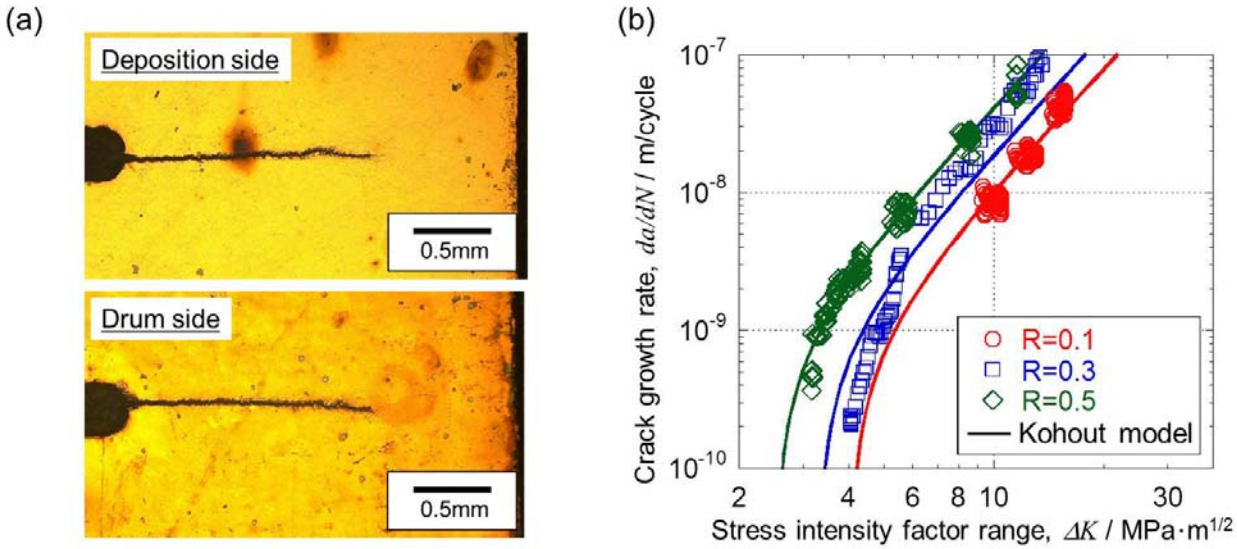

Figure 4. (a) Fatigue crack path of ED-Cu sheet. (b) Relationship between stress intensity factor range calculated from FEM and experimental crack growth rate.

4.2. Fatigue crack growth behavior of ED-Ni

Fatigue tests with ED-Ni were also performed to obtain the sensor characteristics of smart patch. The fatigue crack path observed from the drum side was smooth while the opposite side was relatively rough. The fatigue crack growth behavior of ED-Ni is shown in Fig 5 (b). The experimental results were within Paris region and the effect of strain ration was observed. Therefore, the fit curve was analyzed by the Walker equation:

$$\frac{da}{dN} = C\left[\frac{\Delta K}{(1-R)^{1-\beta_W}}\right]^m \tag{6}$$

The calculated parameters were m =3.26, C =4.54×10^{-12}, β_w =0.556.

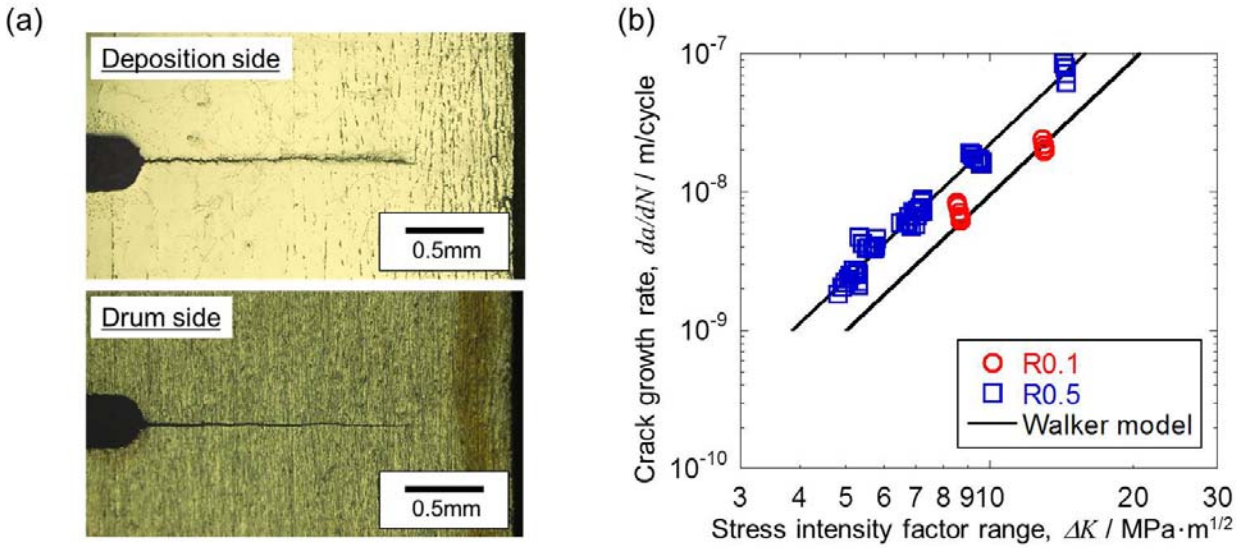

Figure 5. (a) Fatigue crack path of the ED-Ni sheet. (b) Relationship between stress intensity factor range and fatigue crack growth rate in ED-Ni specimen.

4.3. Effect of specimen geometry on fatigue crack growth

Three different specimen geometries were used in the present study. All specimens were made of ED-Cu. The fatigue crack growth rate is shown in Fig. 6 (a). The relationship between stress intensity factor range calculated from FEM and experimental crack growth rate is fitted on one curve regardless of the geometries as shown in Fig. 6 (b).

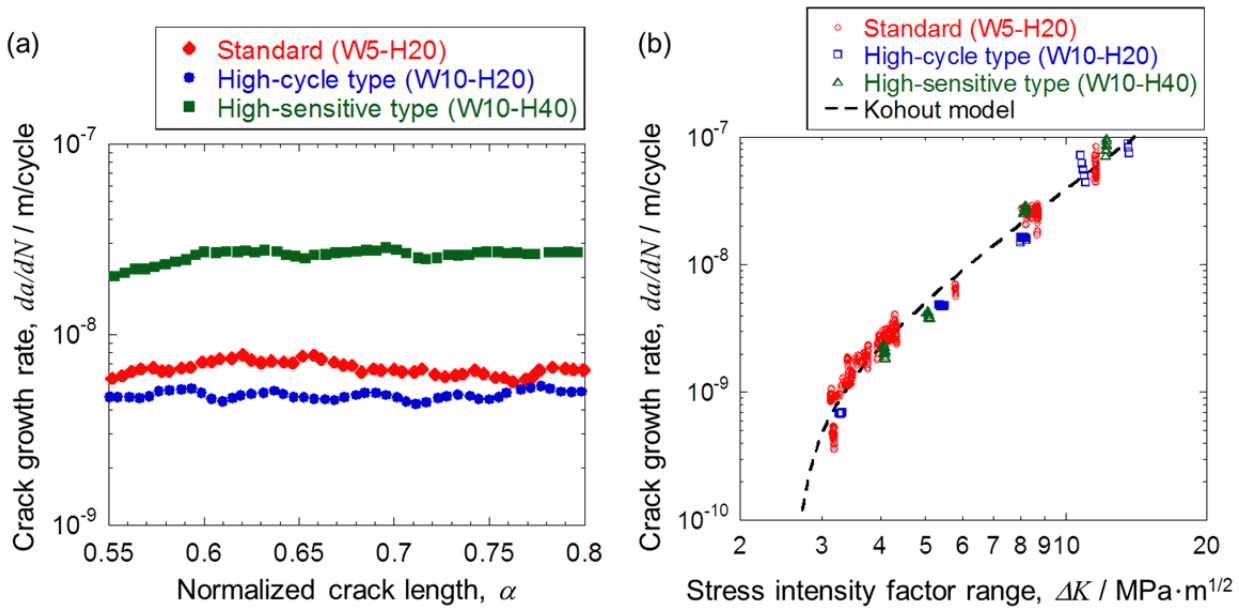

Figure 6. (a) Fatigue crack growth rate of ED-Cu specimens with three geometries. (b) Relationship between stress intensity factor range and fatigue crack growth rate of ED-Cu specimens with three geometries.

5. Discussion

5.1. Fatigue crack growth behavior

Many studies about fatigue behavior in thin metal sheet have shown that fatigue life is associated with the grain structure and specimen thickness using smooth specimen [7-10]. In the present study, fatigue crack propagation experiments were performed with notched specimen under strain-controlled condition. The crack path of the specimen exhibited almost straight line as shown in Fig. 4 (a) and Fig. 5. (a). It allows us to measure the crack length in the sensor easily. Among them, the path observed from the deposition side in ED-Ni was relatively rough due to the development of columnar grains during electrodepositing process. The relationship between stress intensity factor range calculated from FEM and experimental crack growth rate is fitted to one equation regardless of strain amplitude, strain ratio and specimen geometry. Therefore, two specimens made of different materials are needed to apply the principle of smart stress-memory patch. The threshold value of stress intensity factor range was determined by Kohout equation, which is related to the minimum value of detectable stress amplitude.

5.2. Estimation of fatigue damage using two materials

Based on fatigue testing results, a method to evaluate fatigue damage of structure using smart patch will be discussed. When the patch is attached to structure, the sensor is subjected to strain-controlled loading under the change in strain of the structure. A simple model for the attached sensor to structure is depicted in Fig. 7. It is assumed that the far-field stress in the plate is a uniaxial tension ($\sigma_{structure}$) in

elastic region and the sensor is perfectly bonded on the plate. If thickness of the sensor is enough thin, strain distribution in the plate is uniform regardless of the presence of the sensor, and $\sigma_{structure}$ is described as follows:

$$\sigma_{\text{structure}} = E_{\text{strucutre}} \frac{u}{L}, \tag{7}$$

where $E_{\text{strucuture}}$ is Young's modulus of structure, u is the displacement on the sensor and L is gauge length of the sensor, respectively. Using Walker equation, the fatigue cycles, N, is represented as the function of the normalized crack length, α, and the maximum strain, $\varepsilon_{\max}$, as:

$$N = \frac{W_2}{C_2}\left\{E_2\varepsilon_{\max}(1-R)^{\beta_{W2}}\sqrt{\pi W_2}\right\}^{-m_2}\int_{\alpha_{0,2}}^{\alpha_2}\left\{\sqrt{\alpha}f(\alpha)\right\}^{-m2}\mathrm{d}\alpha. \tag{8}$$

Furthermore, when two sensors of different properties are employed, simultaneous equation are given as follows,

$$N = \frac{W}{C_1}\left\{E_1\varepsilon_{\max}(1-R)^{\beta_{W1}}\sqrt{\pi W_1}\right\}^{-m_1}\int_{\alpha_{0,1}}^{\alpha_1}\left\{\sqrt{\alpha}f(\alpha)\right\}^{-m_1}\mathrm{d}\alpha,$$

$$N = \frac{W_2}{C_2}\left\{E_2\varepsilon_{\max}(1-R)^{\beta_{W2}}\sqrt{\pi W_2}\right\}^{-m_2}\int_{\alpha_{0,2}}^{\alpha_2}\left\{\sqrt{\alpha}f(\alpha)\right\}^{-m2}\mathrm{d}\alpha. \tag{9}$$

Indexes 1 and 2 represent sensor 1 and 2, respectively. From these equations, the fatigue cycles and the stress amplitude of structure, $\sigma_{\text{strucuture}}$, are obtained as:

$$N = \left[\frac{{C_2}^{m_1}}{{C_1}^{m_2}}\cdot\frac{{W_1}^{m_2}}{{W_2}^{m_1}}\cdot\left\{(1-R)^{\beta_{W2}-\beta_{W1}}\frac{E_2}{E_1}\sqrt{\frac{W_2}{W_1}}\right\}^{m_1m_2}\cdot\frac{F_1(\alpha_1)}{F_2(\alpha_2)}\right]^{\frac{1}{m_2-m_1}},$$

$$\Delta\sigma_{\text{structure}} = E_{\text{structure}}(1-R)\left[\frac{C_2}{C_1}\cdot\frac{W_1}{W_2}\cdot\frac{\left\{E_2(1-R)^{\beta_{W2}}\sqrt{\pi W_2}\right\}^{m_2}}{\left\{E_1(1-R)^{\beta_{W1}}\sqrt{\pi W_1}\right\}^{m_1}}\cdot\frac{F_1(\alpha_1)}{F_2(\alpha_2)}\right]^{\frac{1}{m_1-m_2}}. \tag{10}$$

In the case that the steel structure ($E_{\text{strucuture}}$ = 200 GPa) is subjected to cyclic loading with the stress ratio of 0.1, the fatigue cycles and the stress amplitude were calculated by eqs. (10) and experimental parameters of ED-Cu and ED-Ni, as shown in Fig. 8. Stress amplitude can be estimated from crack length detected from two sensors with different characteristics. Therefore, it was shown that fatigue cycles on structures can be estimated using smart patch.

Evaluation of fatigue damage of structure is important to avoid the rapture caused by cyclic loading. Cumulative fatigue damage is commonly determined using the Palmgren-Miner rule [15]. In this rule, the amount of fatigue damage, D, is given as the ratio of cyclic number of N / N_{f}, where N_{f} is the number of cycles to failure. Based on many studies about fatigue life of structural components, relationship between stress amplitude and the number of cycles to failure is generally characterized by S-N curve in high-cycle fatigue situations as:

$$N_f = C_{SN}\Delta\sigma^{-m_{SN}}, \tag{11}$$

where C_{SN} and m_{SN} is material constants and $\Delta\sigma$ is stress amplitude [16]. Using the fatigue cycles calculated by smart patch and S-N curve (as shown in Fig. 9(a)), the amount of fatigue damage can be evaluated as shown in Fig. 9 (b). Therefore, it was demonstrated that the health of structure can be estimated using smart patch.

5.3. Estimation of fatigue damage using single material

Another equation for estimating fatigue cycles and stress amplitude from fatigue crack length of two specimens can be derived using near-threshold fatigue crack behavior as shown in Fig. 10. Using Kohout equation, the fatigue cycles, N, is represented as:

$$N = \frac{W_1}{C}\int_{\alpha_0}^{\alpha_1}\left[\frac{d\alpha}{\left\{\varepsilon_{\max}E(1-R)^{\beta_w}\sqrt{\pi W\alpha}\,f_1(\alpha)\right\}^m - \Delta K_{th0}{}^m}\right]. \tag{11}$$

This equation overcame the limitation that the patch requires two or more materials with different fatigue characteristics. Estimation map of fatigue cycles and stress amplitude of steel structure as a function of normalized crack length in two sensors made of same material are shown in Fig. 11. The new equation needs only one material for simultaneous estimation of fatigue cycles and stress amplitude, and the measuring range can be controlled by geometry of specimen. Since this patch needs neither power supply nor wiring, it provides a great potential for long-term structural health monitoring with easy maintenance and low cost.

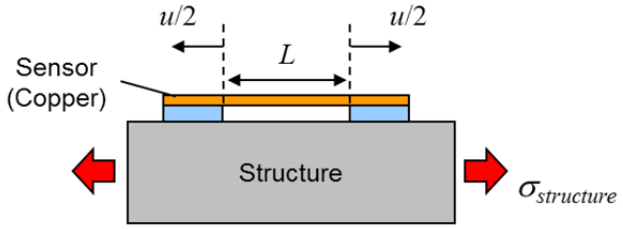

Figure 7. Schematic of simple model for the attached sensor to structure.

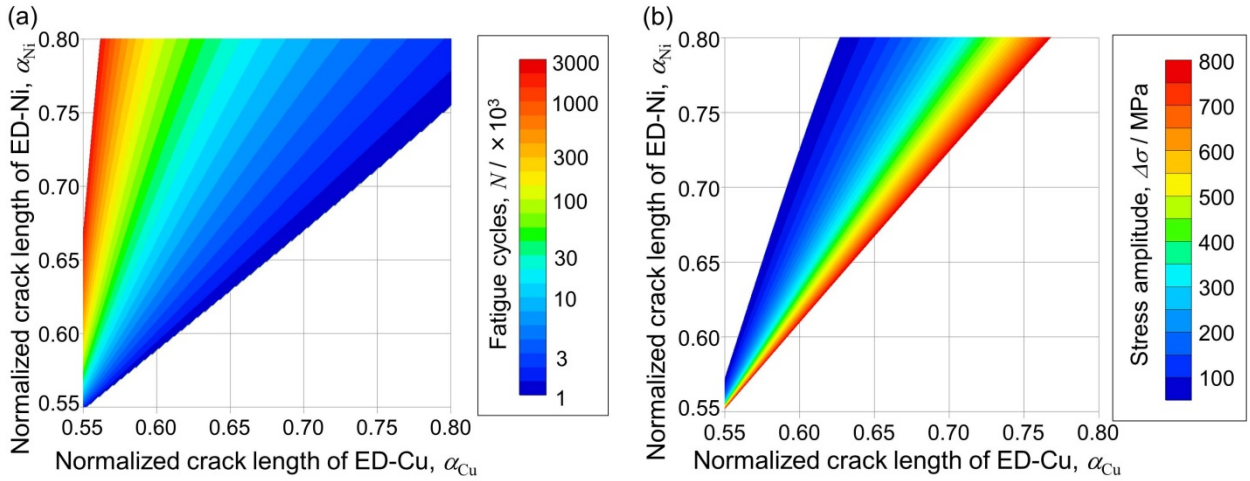

Figure 8. Estimation map of (a) fatigue cycles and (b) stress amplitude of steel structure as a function of normalized crack length in two sensors consisted of different materials.

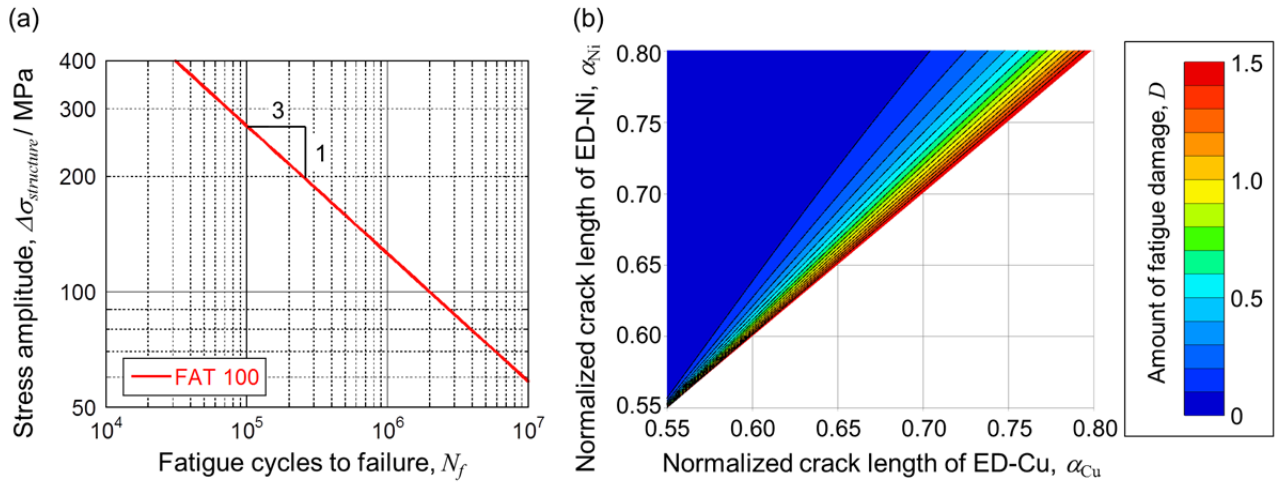

Figure 9. (a) S-N curve of FAT100 (Fatigue strength at two million cycles is 100 MPa), (b) Estimation map of the amount of fatigue damage as a function of normalized crack length in two sensors.

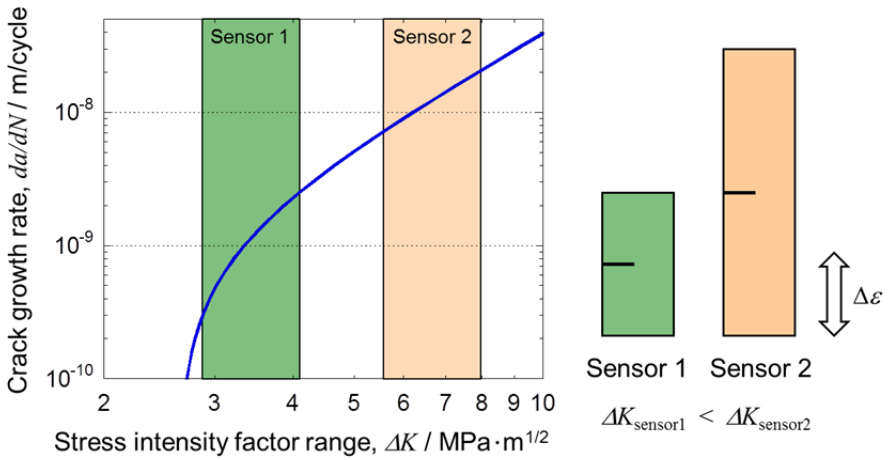

Figure 10. Schematic of estimation method of fatigue damage using single material.

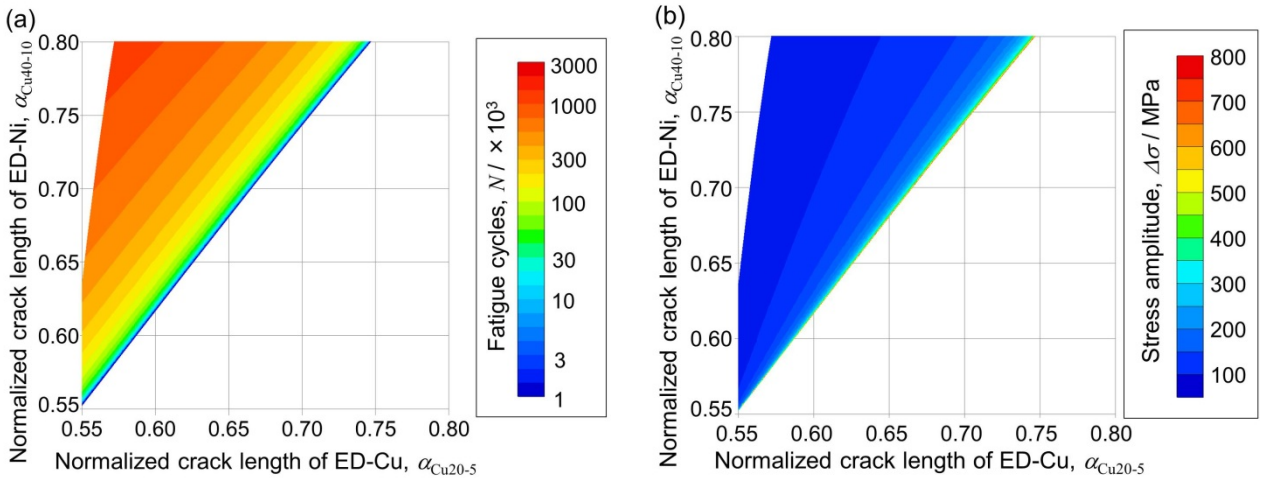

Figure 11. Estimation map of (a) fatigue cycles and (b) stress amplitude of steel structure as a function of normalized crack length in two sensors made of same material.

5. Conclusions

In the present study, near-threshold fatigue crack growth behavior in thin pure copper sheet with pre-crack was evaluated under strain-controlled fatigue testing in order to obtain the sensor characteristics of smart stress-memory patch and the following conclusions were obtained.

(1) Using a function describing the initiation as well as the stable growth of fatigue cracks, relationship between stress intensity factor range and crack growth rate of ED-Cu was successfully fitted to one equation regardless of strain amplitude, strain ration and specimen geometry.

(2) It was shown that the stress amplitude and the cyclic number can be estimated from the crack lengths of two sensors made of ED-Ni and ED-Cu. Furthermore, using S-N curve of structural material, the cumulative fatigue damage could be evaluated as a function of crack length of smart patch.

(3) Based on these experimental results, a new equation for estimating fatigue cycles and stress amplitude from fatigue crack length of two specimens was derived. This equation overcame the limitation that the patch requires two or more materials with different fatigue characteristics.

Acknowledgements

This study was partially supported by research fellowship program (No. 22･10020) of Japan Society for the Promotion of Science (JSPS).

References

[1] S. Nambu, M. Enoki, Scattering in fatigue, crack growth of thin pure copper sheet for smart stress memory patch. ISIJ Int., 47 (2007) 1687-1691.
[2] S. Nambu, M. Enoki, Monitoring of Acoustic Emission Activity of Smart Stress Memory Patch to Estimate Maximum Fatigue Stress for Structural Health Monitoring. ISIJ Int., 51 (2011) 88-92.
[3] T. Shiraiwa, M. Enoki, Evaluation of Fatigue Properties of Steel Bar by Smart Stress-memory Patch. ISIJ Int., 51 (2011) 250-255.
[4] T. Shiraiwa, M. Enoki, Fatigue Crack Length Measurement of Sputtered Metal Film for RFID-based Smart Stress Memory Patch. ISIJ Int., 51 (2011) 1480-1486.
[5] S. Nambu, M. Enoki, Smart stress-memory patch for fatigue damage of structure. Mater. Trans., 48 (2007) 1244-1248.
[6] Y. Fujino, S. Nambu, M. Enoki, AE behavior of smart stress memory patch after variable amplitude loading. Mod. Phys. Lett. B, 22 (2008) 1105-1110.
[7] H. D. Merchant, M. G. Minor, Y. L. Liu, Mechanical Fatigue of Thin Copper Foil. J. Electron. Mater., 28 (1999) 998-1007.
[8] M. Hommel, O. Kraft, E. Arzt, A new method to study cyclic deformation of thin films in tension and compression. J. Mater. Res., 14 (1999) 2373-2376.
[9] M. Judelewicz, H. U. Künzi, N. Merk, B. Ilschner, Microstructural development during fatigue of copper foils 20–100 μm thick. Mater. Sci. Eng. A, 186 (1994) 135-142.
[10] M. Gonzalez, F. Axisa, M. V. Bulcke, D. Brosteaux, B. Vandevelde, J. Vanfleteren, Design of metal interconnects for stretchable electronic circuits. Microelectron. Reliab., 48 (2008) 825-832.
[11] S. Nambu, M. Enoki, Scattering in fatigue crack growth of thin pure copper sheet for smart stress memory patch. ISIJ Int., 47 (2007) 1687-1691.
[12] T. Hanlon, E. D. Tabachnikova, S. Suresh, Fatigue behavior of nanocrystalline metals and alloys. Int. J. Fatigue, 27 (2005) 1147-1158.
[13] P. J. Torvik, On the Determination of Stresses, Displacements, and Stress-Intensity Factors in Edge-Cracked Sheets With Mixed Boundary Conditions. J. Appl. Mech. , 46 (1979) 611-617.
[14] J. Kohout, A new function describing fatigue crack growth curves. International Journal of Fatigue, 21 (1972) 813–821.
[15] M. A. Miner, Cumulative Damage in Fatigue. J. Appl. Mech., 12 (1945) A159-A164.
[16] S. Suresh, Fatigue of Materials, Cambridge University Press, Cambrige, 1998.

A validation study for a new SHM technology (ICM) under operational environment

Zhi Wang[1,*], Jiakun Cai[1], Jinshan Li[1], Mabao Liu[2]

[1]Beijing Aeronautical Technology Research Center (BATRC), Beijing 100076,China
[2] Xi'an Jiaotong University, Xi'an, 710049, China
* Corresponding author: wangzhi6022@sohu.com

Abstract A new invented SHM technology, named as Intelligent Coating Monitoring (ICM), was verified by various lab-scale experiments as along with full-scale fatigue tests to inspect ICM capability for monitoring crack initiation and propagation in metal substance. In order to apply the technology to fighter aircrafts, ICM system was validated at real service condition. Firstly, ICM is briefly introduced, including the principle of sensor, the make-up of the system and various lab-scale experiments as well as full-scale fatigue tests for verification and application. Then the installation of ICM system on an operational aircraft structure was given which includes the determination of critical locations that needs monitoring, the selection of sensors corresponding to each monitoring point with certain geometry, the method of sensors splicing and main-/sub-interrogation units fixing and the connection of the above hardware through wires laying to form a ICM system. Finally, the operating situation and the effectiveness of the ICM system under operational environment were validated and summarized.

Keywords Crack monitoring, Aircraft Structure Health, Intelligent coating, Fracture

1. Introduction

At present, the safety of aircraft structures in most of countries is generally maintained by periodic inspection utilizing traditional nondestructive testing (NDT) techniques such as eddy-current, ultrasound, radiography, thermograph etc. However, these inspections often require the disassembly of the structure, which is a difficult and time-consuming procedure. As many locations of fighter aircraft in which cracks are prone to generate or form during full-scale fatigue in aging airframes are hidden in the structure, it is impossible to access for some certain areas. It is reported that recent aircraft crashes such as C-130A and F-15C in USA were resulted from catastrophic structural failure [1], suggesting that the current NDT is not reliable and is not adequate for aircraft safety. Moreover, the catastrophic risk of critical components also increases with the continued operation of aging fighter aircraft beyond its initial design life and in more severe service environments. Consequently, a desired solution is to implant a structural health monitoring (SHM) system on fighter aircraft which have the huge potentials to improve aircraft safety and reduce operational and maintenance cost.

Currently, several candidates of sensors suitable for SHM application have been widely investigated through lab-scale experiments, which include piezoelectric, fiber-optic, MEMS, strain-gages, CVM etc. To validate the effectiveness, some technologies based on different sensors have already installed in the service civil airplanes. For example, Bragg Fibre Gratings, impact and crack monitoring facilities, such as acoustic emission, eddy current and CVM sensors have installed in an AIRBUS A320 and an AIRBUS A340-600. In addition, diverse SHM technology such as crack wires, CVM or acoustic emission sensors were used during the full-scale fatigue test of the fuselage of the Airbus A380 [2]. Moreover, some structural health monitoring (SHM) systems have matured in recent years, allowing SHM systems to be tested on experimental flight tests [3-6]. However, there is a huge gap for SHM technology to translate these laboratory outcomes to practical application on the fighter aircrafts.

Although the effectiveness of detecting crack, the reliability and the durability for many sensors /actuators of SHM have been valiated in the lab-scale experimental condition, it should overcome many barriers in the practical applications, for instance, how to integrate the sensors /actuators to an already “overcrowded” aircraft structures effectively, how to connect them by wires to form a SHM net system which do not conflict with current systems in aircraft, how to optimize the number and location of sensors and how to enhance the reliability of the sensors in order to survive in the severe environments. It is no doubt that the gulf may exist between what has been demonstrated in the laboratory and what has been rigorously validated for operational use, since most of sensors are tested by a limited number of components with simple geometric shape such as plates, shells or shafts with possible some notches. But the real aircraft components usually are heavy-loaded and light weight with more complex geometric and shape. Moreover, it is inevitable to increase the costs and complexity when a prototype concept translates into service.

It is an indispensable step to carry out validating tests for any type of SHM systems under operational environments before they become the application-ready products. Canada Institute for Aerospace Research (IAR) developed a novel National Research Council (NRC)-developed crack detection system called the “Surface Mountable Crack Sensor (SMCS)” which had shown promising results as a means of detecting cracks proved by lab-experiments. In order to put SMCS into real application, a prototype installation of the SMCS was carried out on an operational aircraft [7] which showed that was a very important step in verifying its operation effectiveness.

A new SHM technology called ICM (Intelligent Coating Monitoring) which is mainly based on the intelligent coating sensors has been invented in China [8, 9]. ICM has shown the capability of monitoring crack initiation and propagation verified by a series of coupons with different material and dimensions under fatigue loading. Furthermore various experiments under environmental loading (temperature extremes, thermal shock, high humidity, fluid susceptibility, altitude/pressure) were carried out to test the durability and reliability of ICM system. It should be noted that ICM technology has been applied on several full scale fatigue tests [10]. Besides the achievements mentioned above, the sensors and interrogation units of the ICM system added on an aircraft have very small size and light weigh. Those superiorities make it easier to implant ICM instruments on aircraft structure on the active service as a part of an SHM system than most of other available SHM technologies which usually require heavy instruments.

The goal of the present study is to validate the durability, reliability, longevity and crack detecting capability of the ICM system under real flight conditions and improve various properties. An active service fighter aircraft which was in the overhauling was selected for the study. Total 78 sensors monitoring 42 sites were distributed in different areas of the aircraft such as wing, landing gear, horizontal tail and airframe etc, 12 sub-interrogators connecting all sensors and 2 main-interrogators connecting all sub-interrogators were installed on the aircraft. The aircraft returned to service after installing all the instruments of ICM system on the aircraft. So far, the aircraft with ICM system has been on active service more than 2 years, the data recorded by the system during the period were collected and analyzed once per month. ICM system provides more valuable information in the future applications.

This paper briefly introduce ICM system including the principle of sensor, the make-up of the system and various lab-experiments as well as full-scale fatigue tests for verification, give information about the installation of ICM system on an operational aircraft structure including the determination of critical locations that needs monitoring, the selection of sensors corresponding to each monitoring point with certain geometry, the method of sensors splicing and main-/sub-interrogation units fixing and the connection of the above hardware through wires laying to form a

ICM system, valiate the effectiveness of the ICM system under operational environment and summarize on the experiences and lessons from the study.

2. Description of ICM Technology

2.1. Principle of sensor

The core of ICM technology is intelligent coating sensor which comprises of three layers: the driving layer, the sensing layer and the protective layer，as shown in Figure 1. The driving layer is made of bifunctional nonconductive materials: one function is that crack will also form on the driving layer once cracks generate on the substrate, and further makes the sensing layer split at the same time; secondly the driving layer spaces out the substrate and the sensing layer with good insulating efficiency in conformity to the design requirement. The sensing layer is made up of conductive materials such as Cu, Ag, C, etc and can detect the crack length in the substrate by the variation of electric resistance. As the ICM sensor is about several tens of micrometers, a small surface crack will cause the sensor cracking and the electric resistance rise accordingly, as shown in Figure 2. The increase of electric resistance of the sensor corresponds to the crack growth. The method of ICM is very simple and stable measurement system, which consists of a DC power source, an electric resistor and a data recorder.

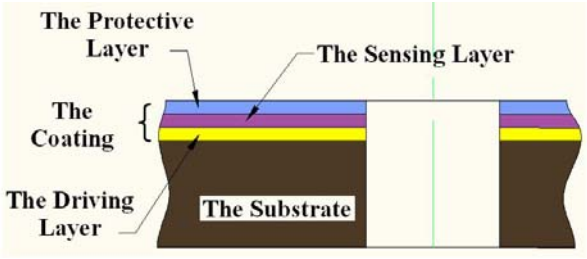

Figure 1 A formation of the intelligent coating sensor

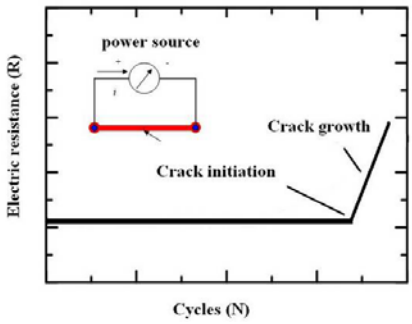

Figure 2 The relationship of eletricc resistance and crack length

2.2. ICM system construction

A typical ICM system consists of hardware and software. The on-board hardware parts include virus sensors, sub-interrogators and main-interrogators, see figure 3. Each sub-interrogator, a chip microcomputer system, consists of switches for signal channel of multi path sensors, conversion circuits for A/D modulus, central process units, digital communication circuits and power circuit and other auxiliary circuits. The sub-interrogators can realize the online measuring and processing of the electric resistance value detected by each cable-connected sensor and transmit the digital

signals to the main interrogator by cables. One sub-interrogator can connect with as many as 8 sensors. A main interrogator comprises of following units: 1) communication unit for sending and receiving the message from each sub-interrogator; 2) storage unit for saving all working parameters and data; 3) date-time unit for recording the date and the time as the resistance value changes of each sensor; 4) man-machine interaction for monitoring working conditions of all sensors through the lights in the main-interrogator and downloading the message to a ground–portable computer through the USB interface for further processing; 5) central process unit for managing all the above units and 6) DC power converting module with wide inputting voltage.

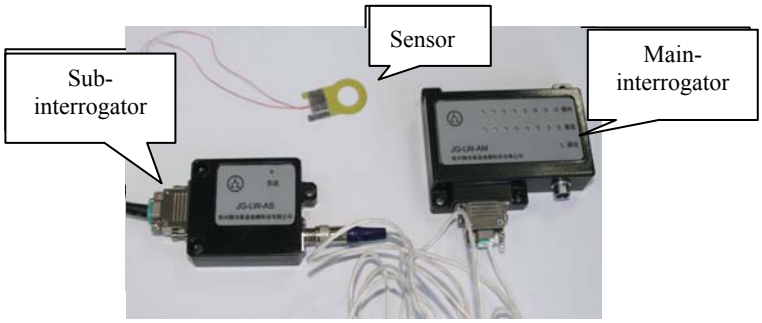

Figure 3 The construction of ICM system hardware

The weight of sensor can be ignored and the weights for a typical sub-interrogator and main interrogator are less than 180g and 80g, respectively. The dimensions of a normal sub-interrogator are 67mmx50mmx16.5mm and the dimensions of a normal main interrogator are 110mmx50mmx 20mm.

The software component is a special developed program for managing the ICM system which can be installed on a portable computer. The program can download and process all the data recorded and saved by the ICM system. Since the system has a huge internal memory, it can store up all recorded data by existing sensors during their lifetime, the intervals for off-board downloading and processing the data can be conducted by users according to their own needs. The possessed data can help users determine whether the ICM integrity has been compromised or real damage like cracks has been appeared on the monitored locations. In addition, the program can also realize real-time monitoring.

2.3. Verification tests

2.3.1. Coupon tests

Figure 4a Five types of specimens

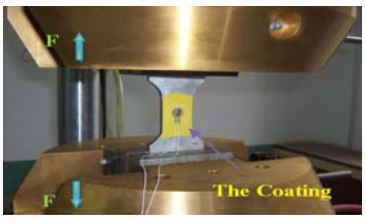

Figure 4b The picture of coupon testing

Fatigue tests were carried out on five types of specimens including riveted lap joint and screwed connection made of 4340M steel, 7074 aluminum alloy and TC4 titanium alloy, as shown in Figures. 4 and 5. All specimens were fatigue loaded with 15 Hz, load ratio R=0.2 and the maximum tension

load P=18KN. As one example, Figure 5 is the relationship between resistance variations measured by sensor spliced on one 7074Al specimen and test load cycles. As the set alarm value was $\Delta R = 0.05\Omega$ in the test, the crack was detected at approximate $5.8x10^4$ cycles. The crack length was about 0.3mm corresponding to $\Delta R=0.05\Omega$ which was measured on the fracture surface by stereoscope analysis.

ICM under different loading ways, such as tension-tension, tension-push and three point bending, has the similar results for crack detection, as depicted in Figure 6. Particularly, ICM sensors are able to monitor the riveted lap and butt joints where fatigue cracks likely commence at holes edges. From above coupon results, it is thought that ICM is suitable to detect small fatigue cracks and monitor their growth.

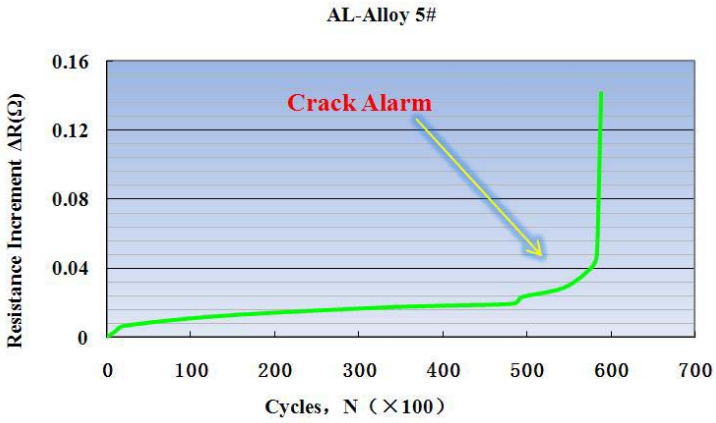

Figure 5 The curve of resistance and load cycle from 7074Al specimen test results

2.3.2. Component tests

Full-scale fatigue tests were carried out using real horizontal tail shafts as specimens. Taking this advantage, ICM system with 5 special sensors spliced on the fatigue critical areas of the shaft determined by finite element analysis has been used during the test, as shown in figure 6. The histories of cracks from initiation, growth till fracture in the shafts were monitored by ICM system during tests. Figure 7 is a resistance-hour curve recorded by ICM system for one of shafts which can verify the effectiveness of crack detection for ICM system in real component.

Figure 6 Some works done for extending the fatigue life of the shaft in a type of fighter aircraft

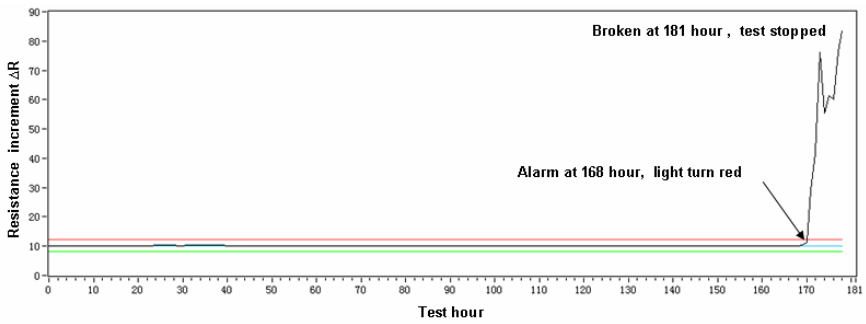

Figure 7 The history of crack length increasing with test time

2.3.3. Full-scale aircraft structure tests

Based on the above coupon and component verification experiments, ICM system has been verified in several full-scale aircraft structure fatigue tests with most sensors spliced at fatigue critical locations where are hidden in the structure and hard to access by the conventional non-destruction inspection methods. For example, ICM sensors were mounted on a full scale central wing fatigue testing aircraft. Figure 8 shows the sensor splicing between two repaired Al-alloy parts with a piece region of rivets which can give alarm signals when the cracks appear at this location. The other example is a full-scale fatigue test for a fighter structure. Total 110 sensors were fixed in 80 key locations inside structures including fuselage frames, wings, empennages and landing gears which formed a net after connected with interrogators for monitoring all locations prone to crack. With the aid of ICM system, some cracks were detected in time. Figure 9a shows sensors distributed in one frame and figure 9b gives the history of crack length increasing with test time in the fractured locations of the frame.

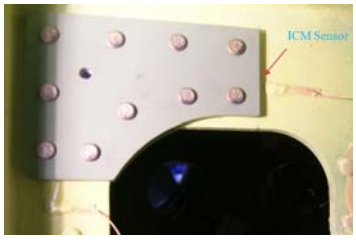

Fig.8. ICM Sensors Monitoring on Central Wing

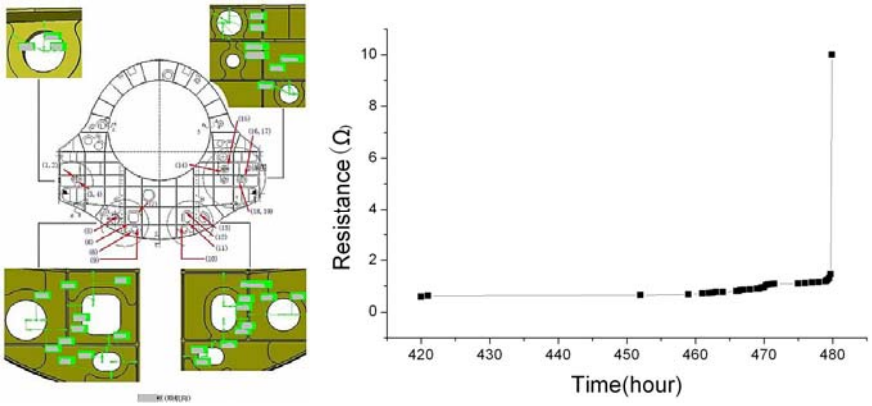

Figure 9 Sensors distributed in one frame (a) and the history of crack length increasing with test time in the fractured location of the frame (b)

At present, ICM system has become an indispensable measure for monitoring damage in most full

scale aircraft fatigue tests carried out in China.

3. Validation study on ICM system under operational environment

From various levels tests mentioned above, it can verify that ICM system can detect damage in the aircraft structure. Furthermore, ICM product have excellent electromagnetic compatibility and environmental adaptability, which were tested by various harsh environmental loading experiments such as high/low temperature extremes, thermal shock, high humidity, fluid susceptibility, altitude/pressure etc. Hence, it is believed that that ICM system is reliable, robust, immune to radio frequency and electromagnetic interferences, easily networked to on-board preprocessing, capable of withstanding environmental conditions and low power which make it easier to obtain approve for installation of ICM hardware on aircraft structure in service. In order to put ICM into the oncoming real application, a study was carried to validate durability, reliability, longevity and crack detecting capability of the ICM system under actual flight condition and improve various properties accordingly.

3.1. Installation of ICM hardware

One of overhauling fighter aircrafts was selected as the subject for the study.Total 78 sensors monitoring 42 fatigue critical sites distributed in different locations of the aircraft including wing, fuselage, horizontal tail and landing gear which were distributed symmetrically along the yaw axes of the aircraft, as listed in Table 1. All those sites determined by full-scale fatigue test and finite element analysis were impossible to access by conventional NDT methods. Each side of sensors was connected by 6 sub-interrogators which were connected by one main-interrogator. Actually two independent ICM systems are responsible for two sides of the aircraft. Figure 10 shows the distribution of ICM hardware in a whole aircraft.

Table 1 Sensors and locations in different structural components (one side of aircraft)

Structural component	The number of locations	The number of sensors
Central Wing	8	15
Forward Fuselage	1	1
Outboard Wing	7	14
Horizontal Tail	2	5
Rear Fuselage	3	4
Total	21	39

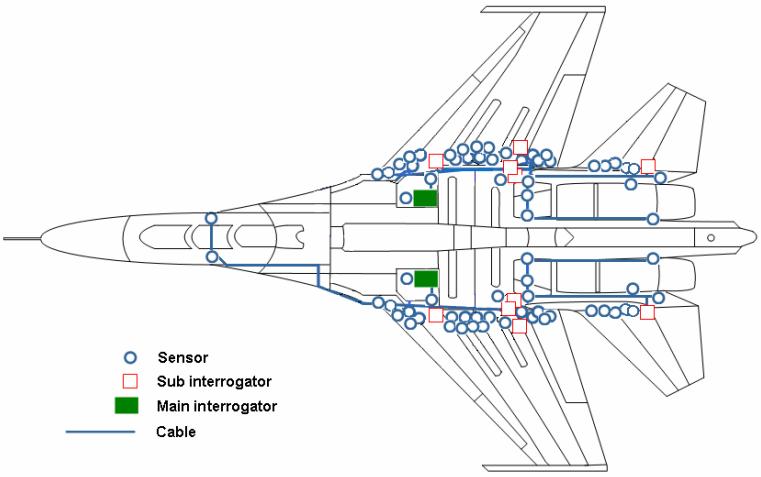

Figure 10 Laying-out of ICM hardware

Different shapes of sensors were designed according to their geometries of monitored sites. Figure 11 gives 3 kinds of sensors for monitoring hole, lug and surface cracking which were spliced in different sites on the aircraft. Figure 12 are main interrogator and 6 subinterrogators fixed at the different locations.

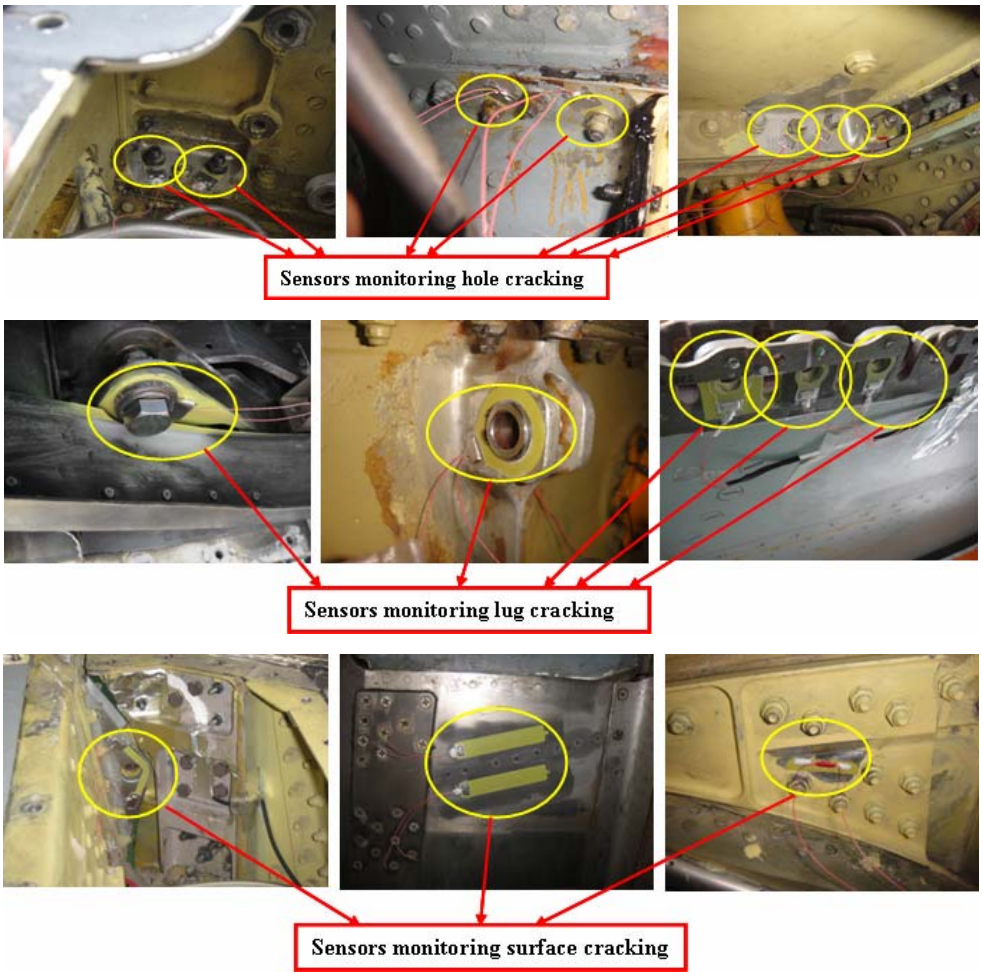

Figures 11 Typical sensors spliced in different sites

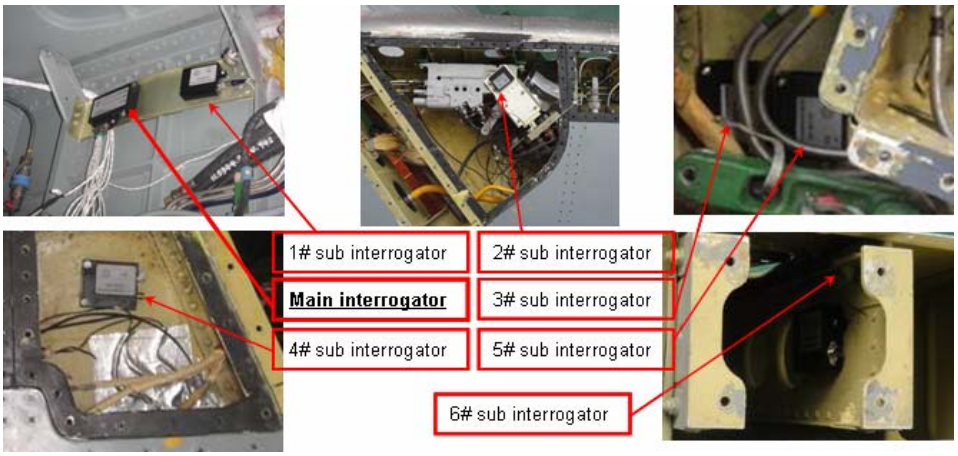

Figure 12 Main interrogator and 6 subinterrogators fixed at the different locations.

3.2. Working situation of ICM system under operational environment

There are two rows of lights on one main interrogator, with each row of 8 lights as shown in figure 13. Therefore one main interrogator can connect with as many as 8 sub interrogators and 64 sensors accordingly. When the ICM system is in working condition, the main interrogator continually checks its sub interrogators one by one with each taking 2~3 seconds for checking its subordinating sensors. During the process, only one light in the first row is on at each turn, which indicates the state of the sub interrogator being checked. If the light is “green”, then the lights in the second row will be “green”, which indicates that all sensors subordinated to this sub interrogator are in good conditions. If the light is “red”, there must be one or more “red” lights in the second row, which indicates that the corresponding sensors are in bad conditions, suggesting that either cracks appear or sensors including wires are broken.

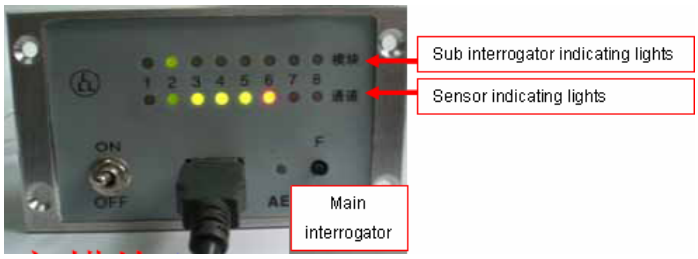

Figure 13 The front view of main interrogator

After installating ICM system, the aircraft returned to the service. In comparison with other same type aircrafts, the only additional thing for the mechanician of the aircraft is to check the lights on the main interrogators fixed in the landing gear cabin shown in Figure 12 before and after every flight. The mechanician can obtain the message immediately once he finds any “red” light based on the data analysis from the system. Besides the data recorded by the ICM system were collected and analyzed once per month. Up to now the aircraft with ICM system has been used more than 2 years, during this period, the working situations for both the aircraft and the ICM system run well as expected except some broken sensors transmit false signals.

4. Summaries

It can prove by the present investigation that ICM system installed on the aircraft structure can monitor cracks which might occur at any specified location, and most sensors along with other hardware can operate normally and effectively under actual condition.

Meanwhile, it is regrettable that some sensors located in the areas of high strain failed in short-time running, thus resulting in false signals. Therefore, more research is needed to design special sensors and corresponding splicing process for those high strain areas. Fortunately, a large progress has been made on this field which will be verified soon.

In a word, ICM prototype installation is a significant first step in validating its effectiveness in operations and putting it into practical applications. Field data including false signals collected from operations provides useful results of the environmental effects on the ICM system and valuable information for ICM improvements.

Acknowledgments

This work was supported by the Chinese NSFC with grants of 51175404.

References

[1] S.S. Kessler. “Certifying a Structural Health Monitoring System: Characterizing Durability, Reliability and Longevity”. In Proceedings of the 1st International Forum on Integrated Systems Health Engineering and Management in Aerospace, Napa, CA, 7-10 November 2005.

[2] S.S. Kessler and D.J. Shim. “Validation of a Lamb Wave-Based Structural Health Monitoring for Aircraft Applications”. In Proceedings of the SPIE’s 12th International Symposium on Smart Structures and Materials, pages 293-301, San Diego, CA, 7-10 March 2005.

[3] F-K Chang. “Structural Health Monitoring: A Summary Report”. In Proceedings of the 2nd International Workshop on Structural Health Monitoring, Stanford, CA, 8-10 September 1999.

[4] V. Giurgiutiu. “Tuned Lamb-Wave Excitation and Detection with Piezoelectric Wafer Active Sensors for Structural Health Monitoring”. Journal of Intelligent Material Systems and Structures, v.16:291-306, 16 April 2005.

[5] D.Cope, J.Cronenberger, K.Schrader, L.Smith and C.Thwing, Integration of Remote Sensing and Risk Analysis for Airframe Structural Integrity Assessment, 2010 Aircraft Airworthiness & Sustainment Conference ,Austin, TX , May 10-20, 2010

[6] H. Speckmann, International Maintenance Review Board Policy Board (IMRBPB) Meeting, EASA, April 22, 2007, Cologne 2007.

[7] B.P.Y. Tang, M. Martinez, T. Marincak, T. Benak and N.C. Bellinger, PROTOTYPE INSTALLATION OF A SURFACE MOUNTABLE CRACK SENSOR, Presented in the 11th Joint NASA/FAA/DOD Conference on Aging Aircraft ,Phoenix, Arizona, April 21-24, 2008,

[8] Z. Lü, M. Liu, China Patent, No.200610104559.4.

[9] Z. Lü, M. Liu, China Patent, No.200620079776.8.

[10] Feng Hu, Mabao Liu, Zhigang Lü. “The flaw-detected coating and its applications in R&M of aircrafts”, Proc. of SPIE, Vol. 7493, 2009, Page(s):1-7

In-situ monitoring of fatigue of metastable austenitic steels with electromagnetic acoustic transducers, EMATs

Andreas Sorich*, Marek Smaga, Dietmar Eifler

Institute of Materials Science and Engineering,
University of Kaiserslautern, P.O. Box 3049, D-67653 Kaiserslautern, Germany
*Corresponding author: sorich@mv.uni-kl.de

Abstract In this research work an in-situ method for the characterization of fatigue processes in metastable austenitic steels with electromagnetic acoustic transducers (EMATs) was developed. The austenitic steel AISI 347 (1.4550, X6CrNiNb1810) was investigated in isothermal total strain-controlled tests in the LCF-range at ambient temperature and 300 °C. By means of cross effects between physically based mechanical- and EMAT-measurements, a detailed characterization of cyclic hardening and softening processes as well as fatigue induced phase transformations and changes of specimens topography and crack initiation were performed.

Keywords Austenitic stainless steel, fatigue, phase transformation, α´-martensite, NDT, EMAT

1. Introduction

In power plants as well as in chemical plants, metastable austenitic steels are subjected to monotonic and cyclic thermo-mechanical loading [1-2]. The cyclic deformation behavior of metastable austenitic steels at ambient temperature (AT) and elevated temperature strongly depends on the deformation induced α´-martensite formation. This phase transformation from paramagnetic austenite (fcc) into ferromagnetic α´-martensite (bcc) leads to cyclic hardening and thus to an increase of the fatigue strength [2-4, 8]. At elevated temperatures no α´-martensite formation was observed in the LCF-range. Therefore the fatigue behavior at elevated temperatures depends basically on cyclic hardening processes due to an increase of dislocation density, followed by cyclic saturation and/or softening processes due to changes in dislocation arrangement and density and finally the formation and propagation of fatigue cracks [5-8]. The investigations are focused on the characterization of the fatigue processes at AT and 300 °C and the development of in-situ monitoring methods on the basis of electromagnetic acoustic measurements. EMATs, which generate ultrasonic waves directly in electrically conductive materials without the use of a couplant, were developed at the Fraunhofer Institute for Non-Destructive Testing (IZFP) Saarbrücken in Germany and calibrated to defined fatigue states in collaboration with the Institute of Materials Science and Engineering (WKK) at the University of Kaiserslautern in Germany [8]. The activities at WKK are focused on the characterization of the materials science aspects of the fatigue processes, while IZFP develops electromagnetic acoustic transducers.

2. Experimental procedures

2.1. Experimental setup

The fatigue tests were performed at different constant total strain amplitudes ($\varepsilon_{a,t}$ = 0.8, 1.0, and 1.2 %) at ambient temperature and 300 °C on a servo-hydraulic testing system with a strain ratio of R_ε = -1 using triangular load-time functions and a frequency of 0.01 Hz. Figure 1 shows schematically the experimental setup for both temperatures. Besides electromagnetic non-destructive testing methods using EMAT and a Feritescope® sensor, full mechanical strain-stress hysteresis measurements were performed to allow a microstructure-related description of the cyclic deformation behavior of the metastable austenite. Electromagnetic acoustic transducers use electromagnetic fields to excite ultrasonic waves and therefore have the great advantage that

they can be used for ultrasonic measurements without a coupling medium between the transmitter/receiver and the test object. This set-up allows measurements on sensitive surfaces and objects also at elevated temperatures. Another advantage of EMATs is their very efficient generation of shear waves with both vertical and horizontal polarization for oblique angles of incidence as well as the generation of linearly, radially and elliptically polarized shear waves for the normal incidence [9].

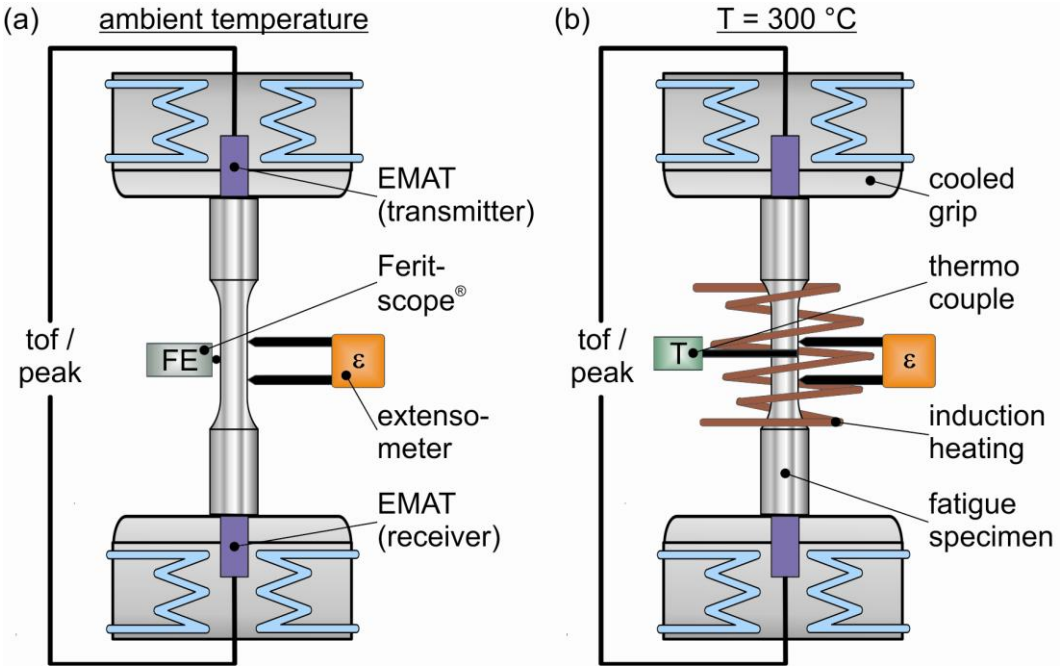

Figure 1. Schematic drawing of the experimental setup:
ambient temperature (a) and T = 300 °C (b)

EMATs generate ultrasonic waves by means of Lorentz forces, magnetostriction or by magnetic forces. Ultrasound generation by means of magnetostriction or magnetic forces requires ferromagnetic materials. Thus, since the investigated material in this project is a paramagnetic austenitic steel, the ultrasonic waves are generated only by Lorentz forces. The excitation of ultrasound by EMATs is performed by the superposition of high frequency eddy currents, induced by a coil with a geometry matched to the wave pattern, and a static or low-frequency magnetic field (Figure 2). The waves are picked up by a receiving coil geometrically identical to the transmitter coil. In this project radially polarized shear waves are generated by the transmitter at the one end and the receiver at the other end [9].

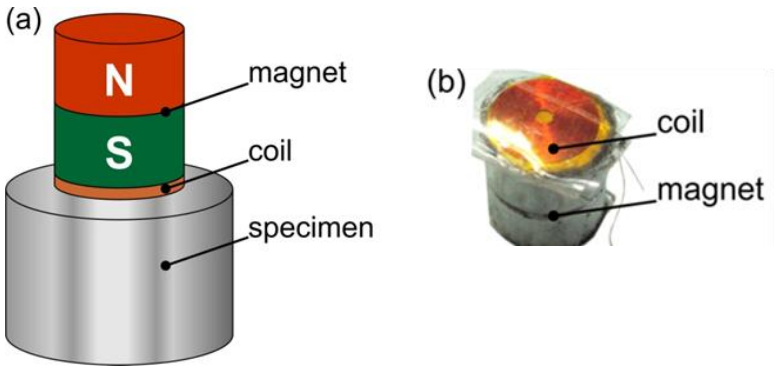

Figure 2. Assembling of an electromagnetic acoustic transducer for radially polarized shear waves: schematic picture (a), photo of a probe (b)

2.2. Material

The investigated material was the Nb-stabilized metastable austenitic stainless steel AISI 347 (1.4550, X6CrNiNb1810). The chemical composition is given in Table 1. The calculation of the austenite stability parameters (e.g. M_{d30} = 26 °C by Angel) results in a metastable state of the test material at ambient temperature. This calculation gives an approximate value, which means, that at a sufficient plastic deformation at ambient temperature an austenite-martensite-transformation can be expected. The initial microstructure (Figure 3) of the investigated steel has a mean grain size of 120 µm and a HV10 hardness of 140 HV. Also Nb-carbides were observed. The chemical composition of these carbides was analyzed via EDX-mapping. As expected the tensile strength, ultimate strain and reduction in area decrease with increasing temperature. At ambient temperature, at a plastic deformation of 66 %, 4.41 FE-% α´-martensite was formed. The α´-martensite formation starts at a total strain of 22 %. Magnetic measurements and micrographs after tensile tests at 300 °C indicated no α´-martensite formation.

Table 1. Chemical composition in weight-%

C	Cr	Ni	Nb	N	Si	Mn	P	S	Al
0.040	17.600	10.640	0.620	0.007	0.410	1.830	0.020	0.007	0.016
Ti	Sn	Mo	W	Cu	Co	V	Pb	B	Fe
0.020	0.008	0.290	0.030	0.060	0.010	0.070	< 0.008	< 0.005	bal.

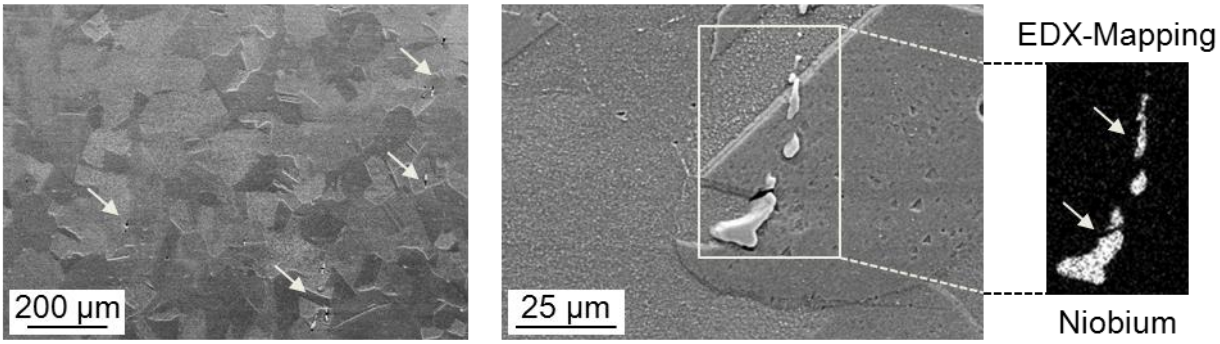

Figure 3. SEM-micrograph and EDX-analyses of AISI 347 in solution annealed state

3. Results and discussion

3.1. Evaluation of the fatigue behavior with deformation induced α´-martensite formation

Figure 4 shows the development of the stress amplitude σ_a and ferromagnetic martensite fraction ξ (Figure 4a), the change in the mean value of time of flight Δtof_{mean} (Figure 4b) and the change in the mean value of the electromagnetically activated ultrasonic amplitude $\Delta peak_{mean}$ (Figure 4c) versus the number of cycles N in fatigue tests at ambient temperature.

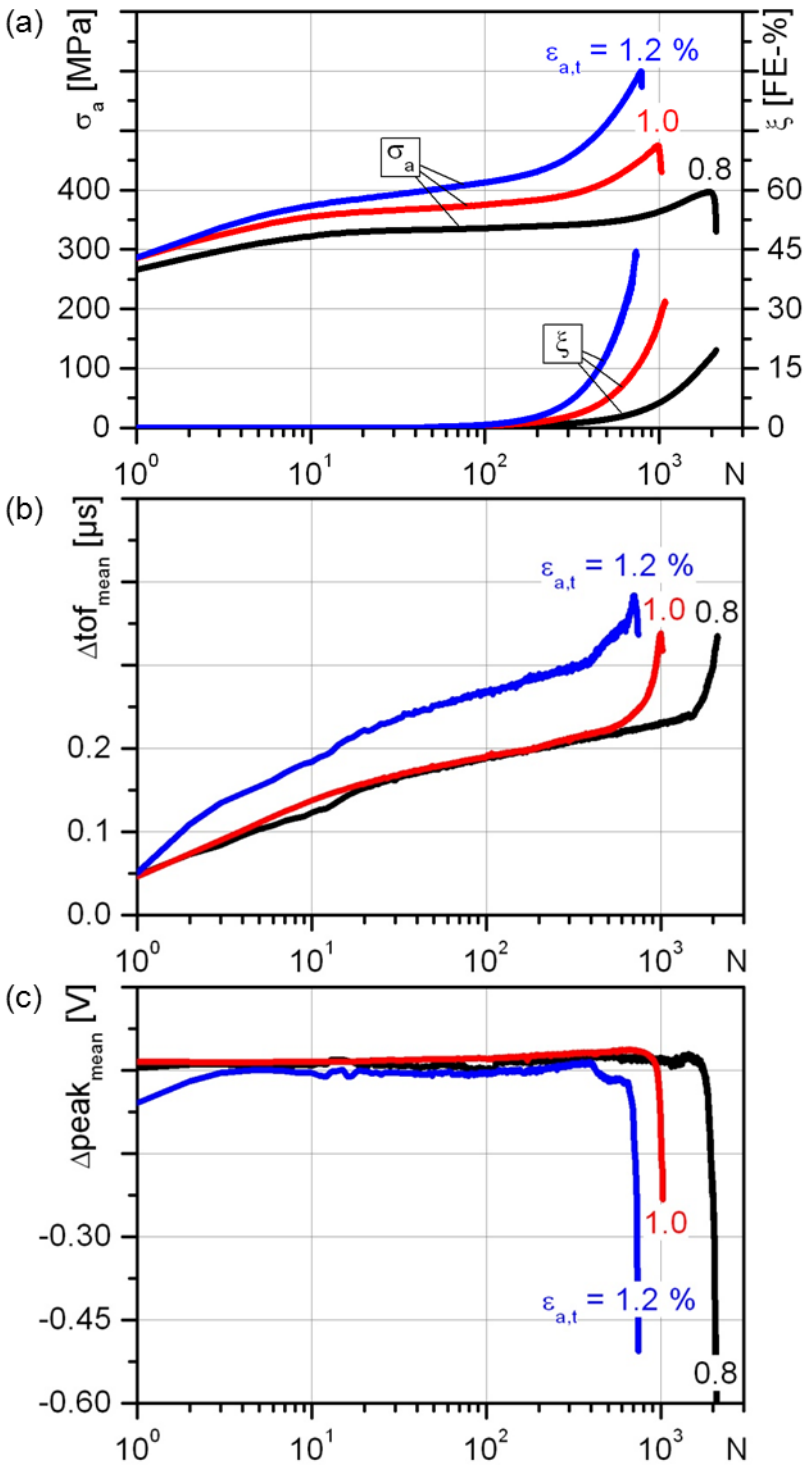

Figure 4. Stress amplitude σ_a and ferromagnetic martensite fraction ξ (a), change in Δtof_{mean} (b) and change in $\Delta peak_{mean}$ (c) vs. number of cycles N at ambient temperature

Due to the change of tof and peak within one cycle, caused by the elongation of the specimen and change of the stress state of the specimen (Figure 7), an arithmetic mean value per load cycle for tof and peak was chosen to characterize the fatigue behavior [8]. The cyclic deformation behavior of the investigated austenite at ambient temperature is predominantly determined by the deformation induced austenite-martensite transformation. After a load dependent number of cycles N, the formation of α'-martensite starts and increases continuously with increasing number of cycles until specimen failure (Figure 4a). The σ_a, N-curves illustrate the cyclic hardening processes, which lead

for $\varepsilon_{a,t}$ = 1.2 % to a maximum stress amplitude in the range of the tensile strength σ_f = 569 MPa of the solution-annealed austenite. Due to an increase of the dislocation density, formation of deformation-induced α´-martensite, development of intrusion and extrusions at the specimen surface and finally the formation of micro- and macro-cracks a continuous increase of the change in the mean value of time of flight Δtof_{mean} from the beginning of the fatigue loading up to specimen failure was observed at ambient temperature (Figure 5). However the electromagnetically activated ultrasonic amplitude $\Delta peak_{mean}$ shows no significant changes until the formation and propagation of micro- and macro-cracks (comp. Figure 4c with Figure 5). Because Δtof_{mean} is more sensitive to microstructural fatigue effects, which lead to an increase of Δtof_{mean} until specimen failure, it isn't possible to detect the state of macro-crack formation and propagation. The change in the mean value of the ultrasonic amplitude $\Delta peak_{mean}$ shows in contrast to Δtof_{mean} a decrease at the fatigue state of macro-crack formation and propagation. Thus it is possible to detect specimen failure at an earlier fatigue state.

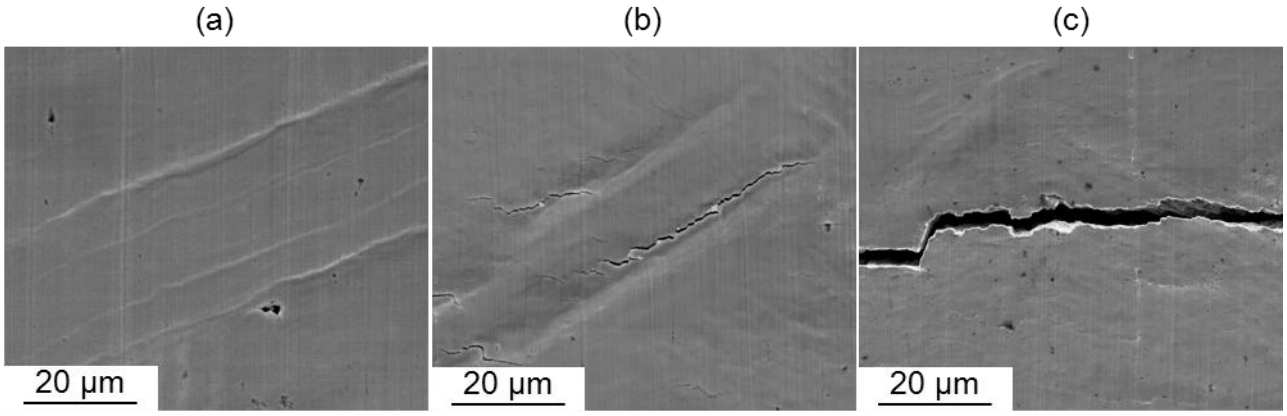

Figure 5. Changes in specimen surface topography at defined fatigue states at ambient temperature: N = 100 slip bands (a), N = 400 micro-cracks (b) and N = 900 macro-crack (c)

3.2. Evaluation of the fatigue behavior without deformation induced α´-martensite formation

Figure 6 shows the development of the stress amplitude σ_a (Figure 6a), the change in the mean value of time of flight Δtof_{mean} (Figure 6b) and the change in the mean value of the electromagnetically activated ultrasonic amplitude $\Delta peak_{mean}$ (Figure 6c) versus the number of cycles N for fatigue tests at 300 °C. The cyclic deformation behavior of the investigated metastable austenite at this temperature is characterized by initial cyclic hardening, followed by cyclic softening before the final stress amplitude drop, associated with the propagation of a fatigue crack. At 300 °C no martensite formation occurs and compared to ambient temperature the stress amplitude is significantly lower. In the Δtof_{mean}, N-curves generally three sections over the fatigue life were observed. In the first section Δtof_{mean} shows similar to σ_a and tests at ambient temperature an initial increase caused by dislocation hardening. The second section follows with a decrease of Δtof_{mean} due to cyclic softening. The third one shows a secondary increase of Δtof_{mean}, which is mainly affected by the development of intrusions and extrusions at the specimen surface and finally the inititation and propagation of fatigue cracks (Figure 6b). In analogy to the investigations at ambient temperature, the change in the mean value of the ultrasonic amplitude $\Delta peak_{mean}$ shows in contrast to Δtof_{mean} a decrease at the fatigue state of macro-crack formation and propagation.

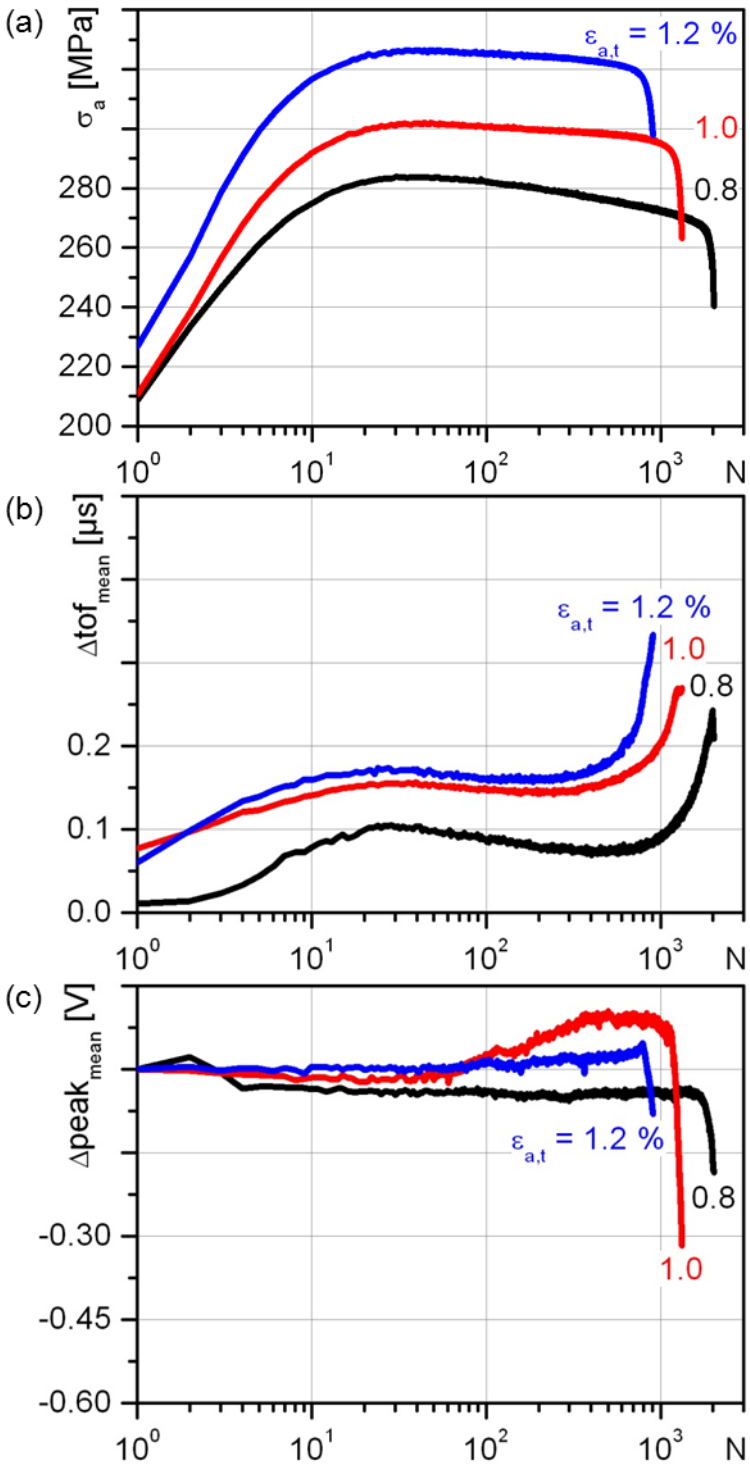

Figure 6. Stress amplitude σ_a(a), change in Δtof_{mean} (b) and change in $\Delta peak_{mean}$ (c) vs. number of cycles N at T = 300 °C

3.3. In-situ monitoring of fatigue damage by means of cross effects between mechanical and EMAT data

Besides the conventional characterization of the cyclic deformation behavior using stress-strain-hysteresis measurements, far-reaching cross effects of physically based data from electromagnetically activated ultrasonic measurements and mechanical strain measurements can be used for in-situ monitoring of fatigue processes. Figure 7 shows stress-strain-hysteresis at defined

number of cycles (N) during total-strain-controlled LCF-fatigue tests with $\varepsilon_{a,t}$ = 1 % at ambient temperature (Figure 7a) and at 300 °C (Figure 7b). The development of stress amplitude and/or plastic strain amplitude is used usually for the characterization of cyclic softening or hardening processes (comp. Figure 4a and 6a). The change of the shape (A) of σ-ε-hysteresis loop occurs due to macro-crack formation at N = 1020 at ambient temperature and at N = 1300 in the test at 300 °C.

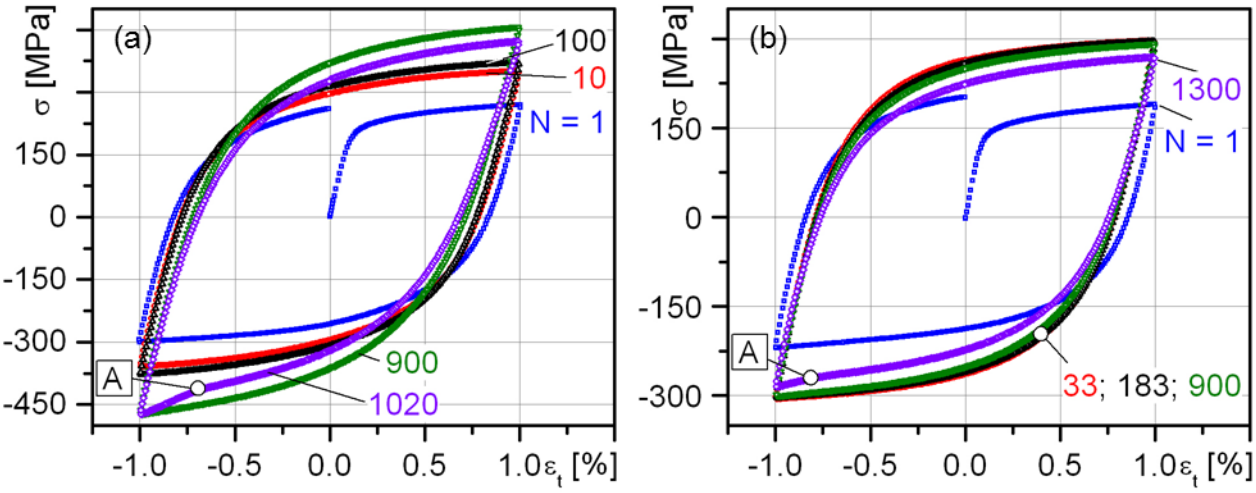

Figure 7. Stress-strain-hysteresis at ambient temperature (a) and T = 300 °C (b)

The time of flight-total-strain-relationship (tof-ε_t) provides, in analogy to the stress-strain hysteresis, information about the actual state of fatigue of the austenitic steel. In the range of elastic-plastic material behavior, the tof-ε_t relation leads to a hysteresis-relationship (Figure 8a) for fatigue tests at ambient temperature and 300 °C (Figure 8b). It can be seen, that an increase/decrease of total-strain (ε_t) leads to increase/decrease of the tof signal. Due to elastic-plastic material behavior, microstructural changes like e. g. increase of dislocation density lead to an increase of the mean value of tof and shift the hysteresis-loop to higher values with increasing number of cycles. In tests at ambient temperature further cycling leads to deformation-induced α´-martensite (Figure 4a), which correlates with an increase of the mean value of tof. Due to changes in dislocation arrangement in tests at 300 °C cyclic softening occurs after N = 183 cycles, which leads to a decrease of the mean value of tof. Furthermore the tof-ε_t-relationship depends on micro and macro-crack initiation and propagation, which also shifts the hysteresis-loop to higher values along the ordinate. In comparison to the σ-ε-hysteresis (Figure 7), a significant change in the shape of the tof-ε_t-hysteresis loop occurs.

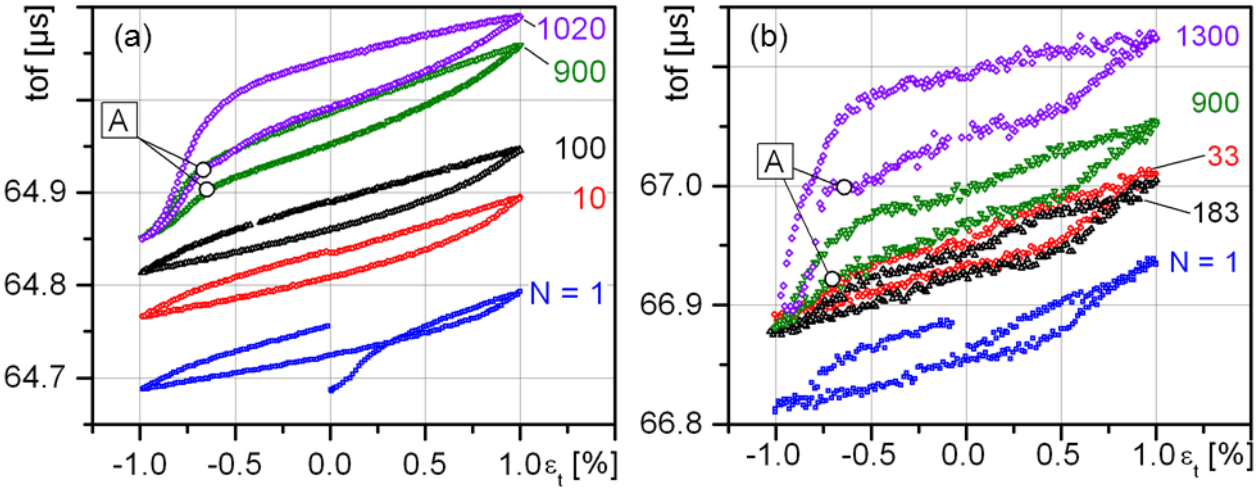

Figure 8. Correlation between time of flight (tof) and total-strain (ε_t) at ambient temperature (a) and T = 300 °C (b)

In analogy to σ-ε_t-, and tof-ε_t-hysteresis, the relationship between the electromagnetically activated ultrasonic amplitude (peak) and total-strain (ε_t) was investigated in fatigue tests at ambient temperature (Figure 9a) and 300 °C (Figure 9b). Generally an increase/decrease of ε_t leads to decrease/increase of peak. The peak is a physically based data, which in comparison to the above mentioned values, describes most sensible the occurrences of macro-crack and less sensible the change in dislocation density and arrangement or initiation of micro-cracks. Hence critical values of the change in the electromagnetically activated ultrasonic amplitude can be defined for structural health monitoring applications, which correlate with macro-cracks.

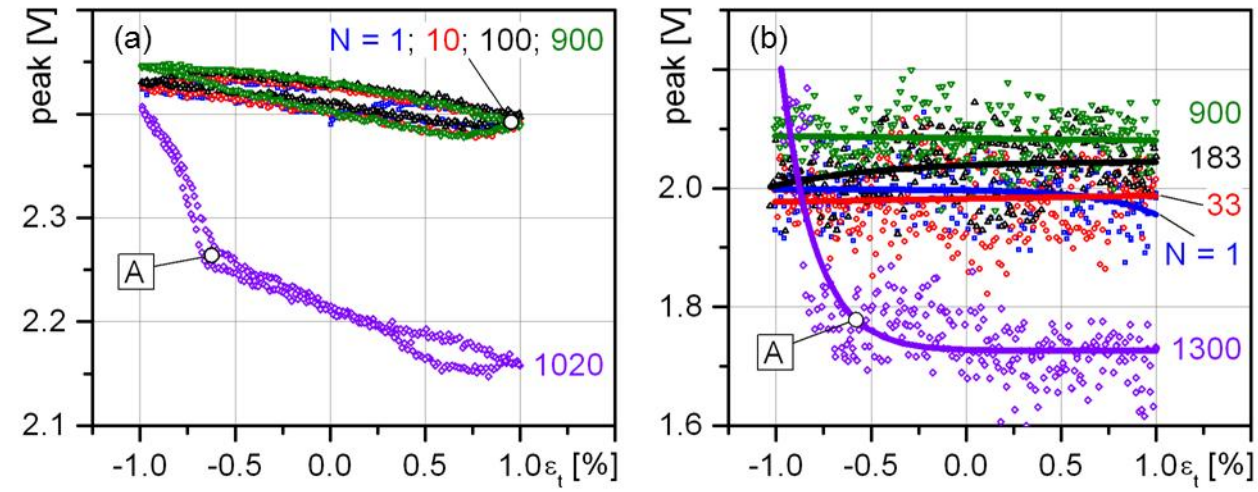

Figure 9. Correlation between electromagnetically activated ultrasonic amplitude (peak) and total strain (ε_t) at ambient temperature (a) and T = 300 °C (b)

3. Conclusions

In total strain controlled fatigue tests at ambient temperature and T = 300 °C the fatigue behavior of the austenitic steel AISI 347 was investigated by conventional stress-strain-hysteresis (σ-ε) measurements and by continuous, in-situ ultrasonic measurements generated with electromagnetic acoustic transducers (EMATs). Far reaching cross effects of EMAT and mechanical strain

measurements enable the recording of a hysteresis relation between time of flight (tof) and total-strain (ε_t) as well as relationship between the electromagnetically activated ultrasonic amplitude (peak) and total-strain (ε_t). The tof-ε_t-hysteresis gives, in analogy to the stress-strain-hysteresis, information about the cyclic hardening and/or softening processes, micro- and macro-crack initiation and propagation. Due to the occurrence of micro-cracks a significant change in the shape of the tof-ε_t-hysteresis curve can be detected earlier compared to σ-ε-hysteresis measurements. The significant changes in the peak values correlate with the development of macro-cracks. This effect can be used for the early detection of critical fatigue states before final failure in the sense of structural health monitoring.

Acknowledgements

This research work was carried out within the framework of the R&D in the Nuclear Safety Research Program, financed by Federal Ministry of Economy and Technology (BMWi), project number: 1501379, Germany. We also thank the German Research Foundation for financial support of the work. The used EMAT probes were developed at the Fraunhofer Institute for Non-Destructive Testing (IZFP), Saarbrücken, Germany. We thank the director of the IZFP, Prof. C. Boller and his coworkers, R. Tschuncky, I. Altpeter and G. Dobmann for their very helpful support.

References

[1] J. Rudolph, S. Bergholz, A. Willuweit, M. Vormwald, K. Bauerbach, Methods of detailed thermal fatigue evaluation of nuclear power plant components, Mat.-wiss. u. Werkstofftech. 42, (2011) 1082-1092.

[2] K.H. Lo, C.H. Shek, J.K.L. Lai, Recent developments in stainless steels, Mater. Sci. Eng. R-Rep R65 (2009) 39-104.

[3] M. Bayerlein, H.J. Christ, H. Mughrabi, Plasticity-induced martensitic-transformation during cyclic deformation of AISI 304L stainless-steel, Mat. Sci. Eng. A 114, (1989) L11-16.

[4] M. Smaga, F. Walther, D. Eifler, Deformation-induced martensitic transformation in metastable austenitic steels, Mat. Sci. Eng. A 483-484, (2008) 394-397.

[5] M. Smaga, F. Hahnenberger, A. Sorich, D. Eifler, Cyclic deformation behavior of austenitic steels in the temperature range -60 °C ≤ T ≤ 550 °C, KEM 465, (2011) 439-442.

[6] V.S. Srinivasan, M. Valsan, R. Sandhya et al., High Temperature Time-Dependent Low Cycle Fatigue Behaviour of a Type 316L(N) Stainless Steel, International Journal of Fatigue 21, (1999) 11-21.

[7] H. Mughrabi, H.J. Christ, Cyclic Deformation and Fatigue of Selected Ferritic and Austenitic Steels: Specific Aspects, ISIJ International 37, (1997) 1154-1169.

[8] I. Altpeter, G. Dobmann, C. Boller et al. and M. Smaga, A. Sorich, D. Eifler, Early detection of damage in thermo-cyclically loaded austenitic materials, Electromagnetic Nondestructive Evaluation XV, IOS Press, 36, (2012) 130-139.

[9] H.J. Salzburger, EMAT's and its Potential for Modern NDE - State of the Art and Latest Applications, IEEE International Ultrasonics Symposium 1 (2009), 621-628.

Correlation between Acoustic Emission and Seismicity in the Sacred Mountain of Varallo Renaissance Complex in Italy

Alberto Carpinteri[1], Giuseppe Lacidogna[1], Amedeo Manuello[1], Gianni Niccolini[1], Federico Accornero[1,*]

[1] Department of Structural, Geothecnical and Building Engineering, Politecnico di Torino, 10129 Torino, Italy
* federico.accornero@polito.it

Abstract In this work, we examine an application of AE technique for a probabilistic prediction of the time and place of earthquakes, in order to preserve the inestimable Italian Renaissance Architectural Complex named "The Sacred Mountain of Varallo". This historical site is composed of 45 Chapels, some of which are isolated, while others are part of monumental groups. The Chapels contain over 800 life-size wooden and multicoloured terracotta statues, which represent the Life, Passion and Death of Christ. The site is considered the most notable example in the group of Sacred Mounts of Piedmont, a complex that has been included in the UNESCO World Heritage List since 2003.
The structure of the Chapel XVII of this Renaissance Complex is at risk for its poor structural health and on account of the intensity of the stresses it is subjected to, due to the level of regional seismicity. For the reliability and safety of this masterpiece of cultural heritage, a life-time assessment should take into account the evolution of damage phenomena. Therefore a continuous AE monitoring is performed to assess the structural behavior of the Chapel.
Earthquakes always affect structural stability: the amount of energy released in a seismic event can cause catastrophic damage in a wide variety of ways. Beside this well-known point of view, in this paper it is claimed that the structures of the "Sacred Mountain of Varallo" behave as sensitive earthquake receptors, since the stress propagation through the Earth's crust, which can be considered as an earthquake precursor, can be effectively monitored by means of the AE technique.
In some works, a burst of AE activity is considered as representative of a large amount of stress which is crossing some large crustal area surrounding the AE recording site. Such AE crises are observed some time in advance compared to the earthquake, leading to consider AE records like earthquake precursors.
During the monitoring period, a correlation between peaks of AE activity in the masonry of the "Sacred Mountain of Varallo" and regional seismicity is found. These two classes of phenomena, AE in materials and earthquakes in Earth's crust, though they take place on very different scales, are very similar due to the release of elastic energy from localized sources inside the medium: opening microcracks and hypocenters of earthquakes.

Keywords Acoustic Emission, Structural Monitoring, Cultural Heritage, Earthquake, Seismic Precursors.

1. Introduction: The historic site of the Sacred Mountain of Varallo

The Sacred Mountain of Varallo is located in the italian province of Vercelli. Set on a cliff above the town of Varallo, it is the oldest and most important Sacred Mountain of the Alps (Fig.1). His story began in the late fifteenth century when the Franciscan friar Bernardino Caimi of Milan, returning from the Holy Land where he was guardian of the Holy Sepulchre, decided to reproduce in Varallo the holy places of Palestine [1].

The "New Jerusalem", as it is called the Sacred Mountain, initially intended to represent the distant sites of the Christian tradition for all those people who could never go there (Fig.2). Inside these places are, instead of pictures, paintings and sculptures to evoke the corresponding event in the history of the life of Christ. Already in the early sixteenth century, thanks to the work of the

painter sculptor and architect Gaudenzio Ferrari, the scenes inside the chapels are represented in an ingenious and innovative merging of painting and sculpture, with a strong sense of reality, so that the devotee could feel himself deeply involved by the depicted scene of the Christ's Life and almost part of it (Fig.3). The work of Gaudenzio Ferrari will be taken as a model in the construction of many other Sacred Mountains. In the era of the Counter-reformation, the Sacred Mountain of Varallo assumed the appearance of a path, real but at the same time mystical, that the pilgrim completes following the telling of the story of Christ's Life. The Sacred Mountain is composed of a basilica and forty-five frescoed chapels, populated by over eight hundred statues. For the completion of this extraordinary monument worked important Piedmontese artists, among which there are Bernardino Lanino, Tanzio da Varallo, brothers D'Enrico, Morazzone, and Dionigi Bussola [1].

Fig.1. The Sacred Mountain of Varallo, Italy. Overview.

Fig.2. The Sacred Mountain of Varallo. The Square of Tribunals.

Fig.3. Chapel XXXIII. *Ecce Homo.*

Fig.4. Chapel XVII. *The Transfiguration of Christ on Mount Tabor.*

2. Chapel XVII monitoring set-up

The Acoustic Emission monitoring is conducted on the frescoed masonry walls of the Chapel XVII of the Sacred Mountain of Varallo: the Chapel of the Transfiguration of Christ on Mount Tabor (Fig.4). The construction of the Chapel XVII began in 1572, but the structure was completed only in 1647. In 1664 was built the lantern top as crowning.

The purpose of monitoring by means of AE sensors applied to the frescoed wall, is to detect the possible Acoustic Emission signals from a vertical crack and from a region of the wall in which the frescos show a detachment of plaster. The operations necessary for the AE sensors bonding to the wall are carried out by a group of restorers, which have prepared a film of Japanese paper, on the surface of which is coated a thin layer of "Paraloid".

The "Paraloid" is an acrylic resin (methyl acrylate soluble in ketones, esters, hydrocarbons and chlorinated hydrocarbons) and is used in the field of restoration as a consolidant at low concentrations (2,4%) or as an adhesive at higher concentrations. It allows an excellent waterproof performance and has the advantage of being reversible and long-term stable. The layer of "Paraloid" forms a good protective base for the AE sensors bonding with silicone glue. The sensors are applied to monitor both the vertical crack and the detachment of the plaster (Fig.5).

Fig.5. Chapel XVII. View of the Monitored Areas. Left Side: Sensors 5, 6, and the Frescos Detachment. Right Side: Sensors 1-4 and the Vertical Crack.

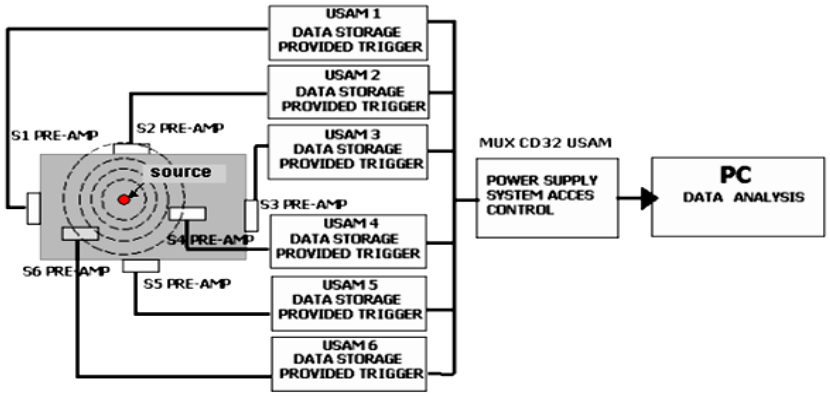

Fig.6. AE Acquisition System.

The Acoustic Emission acquisition system is shown schematically in Fig.6.

The piezoelectric transducers (PZT) are calibrated over a range of frequency between 50 kHz and 800 kHz. The USAM acquisition system consists of 6 pre-amplified sensors, 6 units of data storage provided of triggers, a central unit for the synchronization operations, internal clock and a trigger threshold. The obtained data are: progressive number of each signal, acquisition time, intensity, duration, number of oscillations over the threshold value [2,3].

4. AE and seismic events

Non-destructive testing methods are currently used to evaluate structural damage phenomena and to predict their development over time. In particular, the evaluation of damage in historic buildings is often a complex task [4,5]. It is essential to distinguish between stable damage patterns and damage in evolution toward a catastrophic collapse. Some structural damage can be triggered by

events such as earthquakes. Furthermore, the limited ductility of the masonry, combined with the large size of this type of construction, provides a structural behavior rather fragile [6]. For these reasons, the damage evolution in time can be effectively evaluated by means of the Acoustic Emission technique [7,8,9,10].

Moreover, the statistical distribution of earthquakes shows a complicated behavior space–time, that reflects the complexities of the Earth's crust. Despite this complexity, there is a scaling law universally valid: the statistical distributions of frequency-magnitude of an earthquake provided by the Gutenberg-Richter (GR) law [11].

On the other hand, AE in materials and earthquakes in the crust are very similar and correlated in time, even if they are phenomena that occur at different scales [12]. In both cases there is a release of elastic energy from a source located in the medium: respectively the opening of micro cracks and the seismic hypocenter [13]. This similarity suggests an interpretation in which the seismic events and the AE events can be related in space and time. In this view is therefore possible to search for a correlation between the parameters related to AE and the regional seismicity. As a matter of fact, this approach can be used to identify the warning signals that precede a catastrophic event for a structure since, in many cases, these warning signals can be detected well in advance with respect to the time at which the undesired event will occur [14,15].

Most earthquakes have precursors, ie phenomena that in the short or long term change their activity before the earthquake. In the past, many precursors have been proposed but it is still not clear what is really reliable. Surely any operative scheme of prediction must be based on a combination of more clues. Recently, major efforts in the field of earthquake prediction have focused on the fluctuations of the physical parameters of the crustal rocks of the seismically active continental areas, and on regular intervals in the space-time distribution of earthquakes [16]. The variation in the rate of the regional seismicity is considered as a precursor in the long term. A region which had a small earthquake activity for a remarkable number of years is called "seismic gap". The "seismic gaps" are considered as potential sites for major earthquakes. On the other hand, the increasing pressure in the rock surface in the region of the epicenter produces numerous cracks before the final collapse and, as a result, it causes changes in the properties of rocks. Therefore, the drop in speed of seismic waves caused by the expansion of the rock becomes a significant precursor. Other precursors linked to the expansion of the rocks and the opening of cracks are the crustal tilt and elevation changes, the decrease of the electrical resistivity of the rocks, and the release of radon gas in the atmosphere, which requires small pores to propagate. As the process of damage develops, the water diffuses from the surrounding rocks in pores and micro cracks of increasing size, which in the meantime are forming. The moment the water fills the cracks, the speed of seismic waves grows, the soil lifting stops, the emission of radon from the new cracks is relieved, and the electrical resistivity decreases. The next stage is the beginning of the earthquake, which is immediately followed by several aftershocks in the surrounding area [7,16].

When a crack in the Earth's crust increases, the corresponding AE show progressively lower frequencies, up to abandon eventually the ultrasound field reaching the sonic range: this represents the well known phenomenon of seismic roar. Thus, AE techniques have the potential for effectively monitoring the spread of tensions through the earth's crust. In fact, Italian researchers collected continue AE recordings for many years in the Gran Sasso massif. It was noted a peak of the AE about 400 km away from the epicenter, many months before the occurrence of the earthquake in

Assisi [14,15]. Progressively lower frequencies of detected AE seemed consistent with the theory that high-frequency AE can be associated with the progress of small lesions of the crust, which later coalesce to form defects growing bigger and bigger. In order to correlate the peaks of AE activity to seismic precursors mentioned earlier, it was observed that the fumes of radon occur almost simultaneously with the AE peaks about 7-8 months before the earthquake. Therefore, the potential of earthquake prediction related to the AE monitoring appears promising, since the AE signals may be picked up in advance [14].

4.1. Correlation algorithms between AE and seismic events

Among the various studies on the earthquakes space-time correlation, there is a statistical method that allows to calculate the degree of correlation both in space and time between a series of AE and the local seismic recordings, collected in the same period. This analysis is based on the generalization of the space-time correlation known as the integral of Grassberger-Procaccia [17], defined as follows:

$$C(r,\tau) \equiv \frac{1}{N_{EQ}N_{AE}} \sum_{k=1}^{N_{EQ}} \sum_{j=1}^{N_{AE}} \Theta(r - |x_k - x_j|)\Theta(\tau - |t_k - t_j|) \tag{1}$$

where N_{AE} is the number of peaks of AE activity registered in site and in a defined time window, N_{EQ} is the number of earthquakes recorded in the surrounding area during the same time window, and Θ is the step function of Heaviside ($\Theta(x) = 0$ if $x \le 0$, $\Theta(x) = 1$ if $x > 0$). The index k refers to the recorded seismic events $\{x_k, t_k\}$, while the index j refers to the recorded AE events $\{x_j, t_j\}$.

Therefore, between all possible pairs of recorded AE and seismic events, the sum expressed by the integral of Grassberger-Procaccia is valid for those having the epicentral distance $|x_k - x_j| \le r$ and the temporal distance $|t_k - t_j| \le \tau$. Hence, $C(r,\tau)$ is the probability of occurrence of two events, an earthquake and an AE event, whose mutual spatial distances are smaller than r and mutual temporal distances are smaller than τ.

Anyway, this approach does not consider the chronological order of the two types of event. Since the AE time series and the earthquake sequences are closely intertwined in the time domain, the problem of the predictive ability of the AE peaks is still open, and the records of noise could be the consequences of the progressive development of micro damage. However, a probabilistic response sought by considering the first AE events as precursors and later as aftershocks of an earthquake is utilized. This analysis is performed by using a modified correlation integral [7]:

$$C_{\pm}(r,\tau) \equiv \frac{1}{N_{EQ}N_{AE}} \sum_{k=1}^{N_{EQ}} \sum_{j=1}^{N_{AE}} \Theta\left(r - |x_k - x_j|\right)\Theta\left(\tau - |t_k - t_j|\right)\Theta\left(\pm (t_k - t_j)\right) \tag{2}$$

where "+" and "-" in the Heaviside function are used to take into account that the AE events could be respectively seismic precursors and aftershocks.

5. AE as seismic precursors in The Sacred Mountain of Varallo

5.1. AE monitoring periods

The AE collected data are grouped into two different time windows. The first time window starts from May 9, 2011 and finishes June 16, 2011. The second time window starts July 5, 2011 and finishes September 5, 2011. Both time windows shown in the following involve the monitoring of the vertical crack and of the frescos detachment [2,3].

5.2. Recognizing impending earthquakes by means of AE

In this section, referring to the theories introduced above, we obtain a correlation between seismic and acoustic events through the application of the modified integral of Grassberger-Procaccia.

The data series of AE analyzed are those related to the time periods listed above. The seismic events, taken from the website http://iside.rm.ingv.it/iside/standard/result.jsp?page=EVENTS#result (seismic catalog of INGV, National Institute of Geophysics and Volcanology), are selected introducing search parameters relating to the defined AE monitoring periods and to a radius of 100 km, close to the site of Sacred Mountain of Varallo (Fig.7).

Looking at the temporal distribution of earthquakes in relation to the cumulative AE trend, it can be seen a certain correspondence between AE peaks and earthquake events (Fig.8,9). By applying to the data series the modified correlation integral of Grassberger-Procaccia, we obtain the cumulative probabilities, depending on the radius of interest r and on the interval of occurrence t, considering the peak of Acoustic Emission both as earthquake precursor and as aftershock (Tables 1,2,3,4).

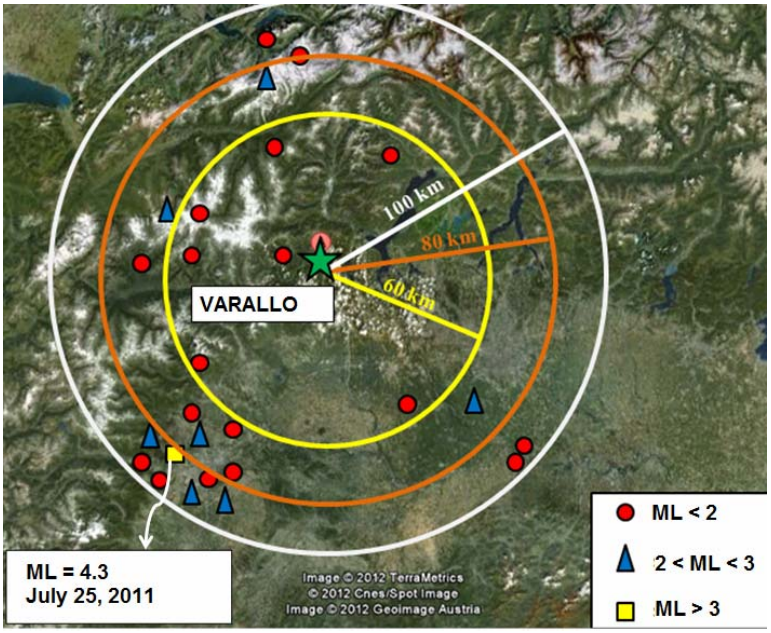

Fig.7. Seisimic Events around Varallo (Italy) from May, 2011 to September, 2011.

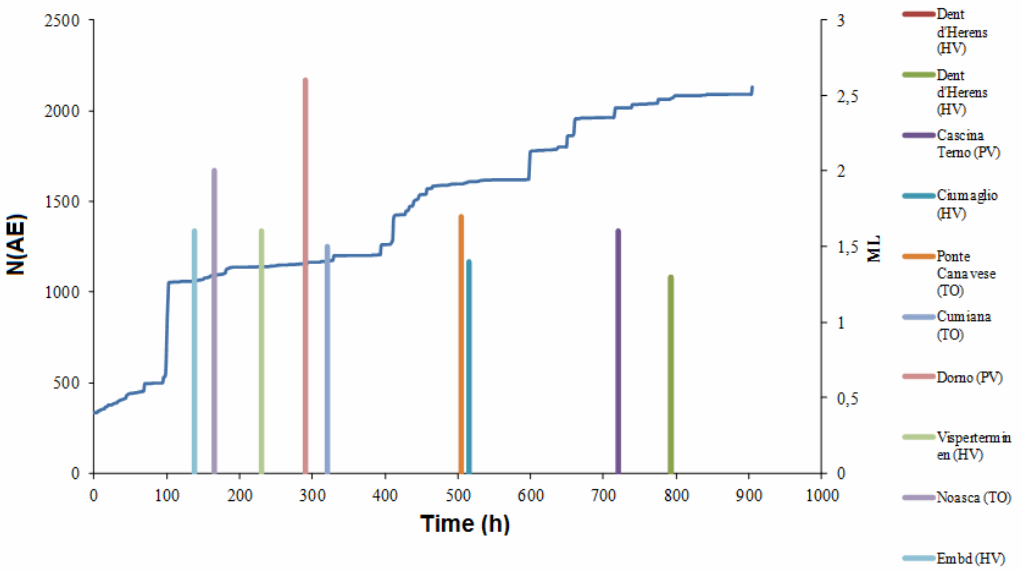

Fig.8. Sacred Mountain of Varallo: Cumulated AE and Seisimic Events from May 9, 2011 to June 16, 2011.

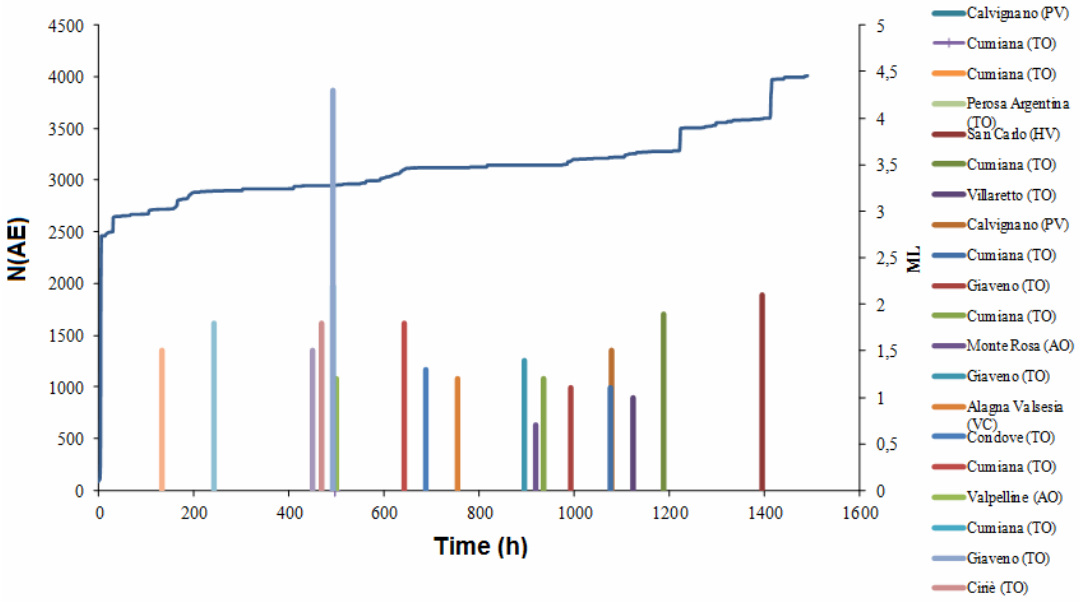

Fig.9. Sacred Mountain of Varallo: Cumulated AE and Seisimic Events from July 5, 2011 to September 5, 2011.

	60 km	**80 km**	**100 km**
1 week	0.0339	0.1121	0.2018
2 weeks	0.0772	0.2130	0.3661
3 weeks	0.1228	0.3018	0.4875
4 weeks	0.1487	0.3661	0.5549
5 weeks	0.1630	0.4321	0.6210

Table 1. Cumulative Probability C^{+}: AE as Precursor from May 9, 2011 to June 16, 2011.

	60 km	80 km	100 km
1 week	0.0254	0.0732	0.1437
2 weeks	0.0357	0.1196	0.2629
3 weeks	0.0371	0.1509	0.3362
4 weeks	0.0371	0.1652	0.3732
5 weeks	0.0371	0.1665	0.3768

Table 2. Cumulative Probability C^-: AE as Aftershock from May 9, 2011 to June 16, 2011

	60 km	80 km	100 km
1 week	0.0075	0.0278	0.0846
2 weeks	0.0184	0.0552	0.1896
3 weeks	0.0239	0.0833	0.3222
4 weeks	0.0346	0.1040	0.3841
5 weeks	0.0498	0.1210	0.4435
6 weeks	0.0557	0.1268	0.5130
7 weeks	0.0557	0.1268	0.5497
8 weeks	0.0557	0.1268	0.5607
9 weeks	0.0557	0.1268	0.5657

Table 3. Cumulative Probability C^+: AE as Precursor from July 5, 2011 to September 5, 2011

	60 km	80 km	100 km
1 week	0.0045	0.0298	0.1192
2 weeks	0.0132	0.0465	0.1916
3 weeks	0.0234	0.0717	0.2592
4 weeks	0.0301	0.0970	0.3251
5 weeks	0.0313	0.1114	0.3737
6 weeks	0.0313	0.1246	0.4164
7 weeks	0.0313	0.1299	0.4283
8 weeks	0.0313	0.1336	0.4333
9 weeks	0.0313	0.1341	0.4338

Table 4. Cumulative Probability C^-: AE as Aftershock from July 5, 2011 to September 5, 2011

Comparing the probability values obtained for the period May-June, it can be seen that, regardless of the distance and of the correlation time, the probability that a seismic event follows a peak of Acoustic Emission is always greater than the probability that the same AE peak is an effect of the damage caused by the earthquake (Tables 1,2). In practice, we see that the monitored structure behaves as a good seismic receptor.

It is interesting to note that, for both monitoring periods, within a radius of 60 km from the monitored site, the AE signal still plays its role as a seismic precursor. On the contrary at 80 km and 100 km, the AE behavior follows the variation of the time windows (Tables 3,4). In particular, we can observe a clear reversal of the AE signal behavior from precursor to aftershock for the second

monitoring period (July-September): at 60 km there was a tendency for AE to anticipate earthquakes even though they are effectively correlated only in the long term; at 80 km they are precursive signals only in the short term; at 100 km we see immediately the reversal outlined above, from precursor behavior to aftershock.

In any case, it is worth of the further investigations distinguishing environmental contributions to AE activity on the Chapel XVII due to crustal trembling (external source) from contributions due to structural damage (inner source).

To investigate the nature of these results, true progress can be realistically achieved by discriminating the signals recorded on the basis of a predetermined threshold both in frequency and amplitude, consistently with the physical nature of Acoustic Emissions detected by the sensors. Looking at the USAM data stored, a good choice to discriminate the signals nature, is setting a threshold frequency −for example 30 kHz, which divides the field VLF (Very Low Frequency) from the field LF (Low Frequency)− and a purposeful threshold signal amplitude.

It seems reasonable even from a theoretical point of view, that low frequencies allow the diffusion of the elastic waves in the masonry bulk, both intact or damaged. On the other side, low amplitudes are reasonably related to the fact that an event captured by AE sensors on the monitored structure may have originated from a source physically distant from the site monitored (seismic hypocenter) and therefore is subject to the laws of amplitude damping.

6. Conclusions

Besides the canonical use in Non-destructive Tests, the heuristic potential of AE monitoring of civil structures for earthquakes prediction appears very intriguing. Starting from the assumption that any structure should not be regarded as separated from its environoment, a method of correlating AE activity on the Renaissance Complex of the Sacred Mountain of Varallo subjected to a long-term monitoring with regional seismicity is investigated. Two qualitatively very similar phenomena such as Acoustic Emission and earthquakes become two aspects of a unique phenomenon which looks self-similar.

Furthermore, in this work by applying the modified Grassberger-Procaccia correlation algorithm −with the aim of explaining the correlation between regional seismicity and Acoustic Emission emerging from the Chapel XVII of the Sacred Mountain of Varallo− it is observed that the structure is a good sensitive receptors for earthquakes occurring within a radius of about 60 km.

In any case, it is worth of the further investigations distinguishing environmental contributions to AE activity on the Chapel XVII due to crustal trembling (external source) from contributions due to structural damage (inner source).

Acknowledgements

The financial support provided by the Piedmont Region (Italy) to the Project ‘‘*Preservation, Safeguard and Valorisation of Masonry Decorations in the Architectural Historical Heritage of Piedmont*” (RE-FRESCOS) is gratefully acknowledged.

The assistance of student Roberto Sodano in the processing of the data is gratefully acknowledged.

References

[1] E. De Filippis, *Sacro Monte of Varallo*. Borgosesia, 2009.

[2] F. Accornero, S. Invernizzi, G. Lacidogna, A. Carpinteri, Acoustic Emission and damage analysis of decorated surface structural supports. Proceedings of the 19th European Conference on Fracture, Kazan, Russia, 2012.

[3] A. Carpinteri, S. Invernizzi, G. Lacidogna, F. Accornero, Acoustic Emission monitoring of frescos degradation in a XVII Century chapel of the Sacred Mountain of Varallo (Italy). Structural Analysis of Historical Constructions, Jerzy Jasinko (ed), Wroclaw, Poland, 2012.

[4] A. Anzani, L. Binda, A. Carpinteri, G. Lacidogna, A. Manuello, Evaluation of the repair on multiple leaf stone masonry by acoustic emission. Materials and Structures 41 (2008) 1169-1189.

[5] A. Carpinteri, G. Lacidogna, S. Invernizzi, A. Manuello, L. Binda, Stability of vertical bearing structures of the Syracuse Cathedral: Experimental and numerical evaluation. Materials and Structures, 42 (2009) 877-888.

[6] A. Carpinteri, G. Lacidogna, Structural Monitoring and Integrity Assessment of Medieval Towers. Journal of Structural Engineering ASCE, 11 (2006) 1681-1690.

[7] A. Carpinteri, G. Lacidogna, G. Niccolini, Acoustic Emission monitoring of medieval towers considered as sensitive earthquake receptors. Natural Hazards and Earth System Sciences, 1 (2007) 1-11.

[8] A. Carpinteri, G. Lacidogna, N. Pugno, Structural damage diagnosis and life-time assessment by Acoustic Emission monitoring. Engineering Fracture Mechanics, 74 (2007) 273-289.

[9] A. Carpinteri, G. Lacidogna, Damage evolution of three masonry towers by Acoustic Emission. Engineering Structures, 29 (2007) 1569-1579.

[10] G. Niccolini, A. Carpinteri, G. Lacidogna, A. Manuello, Acoustic Emission monitoring of the Syracuse Athena Temple: Scale invariance in the timing of ruptures. Physical Review Letters, 106 (2011) 108503.

[11] C. Richter, Elementary Seismology, W. H. Freeman, San Francisco, 1958.

[12] A. Carpinteri, G. Lacidogna, N. Pugno, Richter's laws at the laboratory scal interpreted by Acoustic Emission. Magazine of Concrete Research, 58 (2006) 619-625.

[13] C. H. Scholz, The frequency-magnitude relation of microfracturing in rock and its relation to earthquakes. Bulletin of the Seismological Society of America, 58 (1968) 399-415.

[14] G.P. Gregori, G. Paparo, Acoustic Emission: A diagnostic tool for environomental sciences and for non destructive tests (with a potential application to gravitational antennas), in: Metereological and Geophysical Fluid Dynamics, Schroeder, Bremen, 2005.

[15] G. P. Gregori, G. Paparo, G. Poscolieri, A. Zanini, Acoustic Emission and released seismic Energy. Natural Hazards and Earth System Sciences, 5 (2005) 777-782.

[16] B. A. Bolt, Earthquakes, W. H. Freeman, San Francisco, 1978.

[17] P. Grassberger, I. Procaccia, Characterization of strange attractors. Physical Review Letters, 50 (1983) 346-349.

Measurement of Internal Stress and Internal Resistance Resulting from Creep of Type 316H Stainless Steel

Bo Chen[1,*], David J. Smith[1], Peter E.J. Flewitt[2, 3], Shu Yan Zhang[4]

[1] Department of Mechanical Engineering, University of Bristol, Bristol BS8 1TR, UK
[2] Interface Analysis Centre, University of Bristol, 121 St. Michael's Hill, Bristol BS2 8BS, UK
[3] H.H. Wills Physics Laboratory, University of Bristol, Tyndall Avenue, Bristol BS8 1TL, UK
[4] ISIS, Science and Technology Facilities Council, Rutherford Appleton Laboratory, Chilton, Didcot OX11 0QX, UK
* Corresponding author: b.chen@bristol.ac.uk

Abstract Descriptions of high temperature creep deformation often use the concept of the effective stress, which includes the presence of the internal stress. Many experimental techniques have been applied to measure the internal stress induced by creep deformation. However, there is still a debate about the validity of the measured values. This is partly because the distinction between internal stress and material internal resistance is unclear. In this paper, neutron diffraction measurements, undertaken using the spallation source at the Rutherford Appleton Laboratory, UK, are combined with in-situ loading to investigate the internal state of a Type 316H stainless steel. By undertaking measurements of the lattice strain for different grain families, before, during and after mechanical loading, the internal stress and internal resistance induced by prior creep were determined. The results show that these two parameters are important measures of the internal state, each changing during creep and influencing creep deformation rate. Additionally, internal stress is shown to be dependent on specific crystallographic planes of each grain family. The results are discussed with respect to the underlying mechanisms of creep deformation in stainless steel.

Keywords Internal Stress, Internal Resistance, Creep, Neutron Diffraction, Austenitic Stainless Steel

1. Introduction

Materials may deform by one of several different mechanisms depending upon the applied stress and temperature. It is convenient to present these mechanisms in the form of a deformation mechanism map [1]. More importantly, the use of engineering polycrystalline materials over the operational service life (typically $>10^5$ hours) produces a potential to change the initial microstructure, which can affect the controlling deformation mechanisms in creep [2, 3]. It has been recognised by Biberger and Gibeling [4] that creep deformation rate, $\dot{\varepsilon}_c$, relies on the state of the microstructure, temperature and applied stress. Thus, the deformation rate is described by a kinetic equation of the form:

$$\dot{\varepsilon}_c = f(\sigma_a, T, \hat{\sigma}_1, \hat{\sigma}_2 \cdots \hat{\sigma}_n) \quad (1)$$

where σ_a is the applied stress, T is the temperature, $\hat{\sigma}_1$, $\hat{\sigma}_2$ and $\hat{\sigma}_n$ represent a series of known and unknown internal state parameters which characterise the current state of the material. In addition, creep deformation leads to changes to the internal state parameters. Two of these parameters are considered here: (i) the creation of internal strains arising from strain incompatibility, for example due to the different creep deformation rates of individual grains in polycrystalline materials; (ii) a change in the material resistance. The first is called as internal stress and the second is called as internal resistance, as described by Chen et al. [5].

Many experimental techniques have been developed to provide a quantitative measure of these two terms, such as the widely accepted stress dip test technique [6], analysis of asymmetric X-ray diffraction peak profiles [7], dislocation density and geometrical arrangement obtained using transmission electron microscopy (TEM) [8]. In addition, creep deformation models, incorporating the term internal stress or internal resistance, have been developed to improve the prediction in creep deformation rate. These include models proposed by Estrin and Mecking [9],

Derby and Ashby [10], Esposito and Bonora [11]. However, there are two challenges remaining before those physically based creep deformation models can be adopted for the extension of life of existing power generation plants as well as the prediction of life for the future designs. First, the distinction between internal stress and internal resistance is often confusing and unclear [5]. Second, a reliable and simple measurement technique to quantify these two terms unambiguously is still required.

In this paper, we present a technique, based on neutron diffraction (ND) measurement combined with in-situ tensile deformation, to quantify the internal stress and internal resistance associated with high temperature creep deformation. The evolution of these two terms during creep deformation is measured quantitatively by this method. The crystallographic orientation dependence of the internal stress is discussed with respect to the underlying mechanisms of polycrystalline elasticity and plasticity. A newly developed self-consistent model has been established to interpret the measured results. The model is presented in the companion paper for this conference [12]. The ability of adopting this experimental technique to quantify internal state of the material is critically assessed, followed by concluding remarks.

2. Material and Experimental

2.1. Material

Type 316H austenitic stainless steel, provided by EDF Energy plc., with a chemical composition given in Table 1, was examined. The stainless steel had experienced 65,015 hours service at temperatures in the range of 763K to 803K and it was then subjected to a further thermal ageing at 823K for 22,100 hours. The grain size for this stainless steel was measured using the linear intercept method. The averaged grain size was 87±9μm.

Table 1. Chemical composition (wt.%) of Type 316H stainless steel

C	Si	Mn	P	S	Cr	Mo	Ni	Co	B	Fe
0.06	0.4	1.98	0.021	0.014	17.17	2.19	11.83	0.10	0.005	Bal.

Table 2. Summary of specimens subject to a prior deformation at high temperature (250MPa and 823K)

Specimen ID	Creep test duration	Plastic loading true strain, %	True creep strain, %
Specimen 1	No creep	0	0
Specimen 2	As loaded	1.88	0
Specimen 3	Primary, 160h	2.04	0.92
Specimen 4	Secondary, 1000h	1.98	4.86

2.2. Prior deformation at high temperature

To study systematically the influence of the prior deformation at high temperature on the internal state of the material, four prior deformation states were considered: (i) no creep, (ii) as loaded, (iii) primary creep, and (iv) secondary creep. Four specimens were prepared from the Type 316H austenitic stainless steel. Prior deformation tests at a temperature of 823K were then carried out. A summary is given in Table 2. Uniaxial round bar specimens with a 28.25mm gauge length and 5.65mm diameter were used. These specimens were deformed at 823K and at a constant stress of 250MPa to different stages of creep deformation. The left hand side in Fig. 1 (a) illustrates the strain history for a specimen, which was strained to reach primary creep. The specimen was heated to a temperature of 823K, step 1 in Fig. 1 (a). This was followed by the application of load

to reach the test stress of 250MPa at 823K, step 2 in Fig. 1 (a). Specimen was then creep deformed to a pre-defined creep duration, which was followed by cooling under the applied load to freeze the creep induced dislocation structure. Finally the specimen was unloaded and dismantled at room temperature. This procedure was adopted for each specimen shown in Table 2. Each specimen was then subject to incremental tensile deformation at room temperature and simultaneously measured using neutron diffraction. This is detailed in the next section.

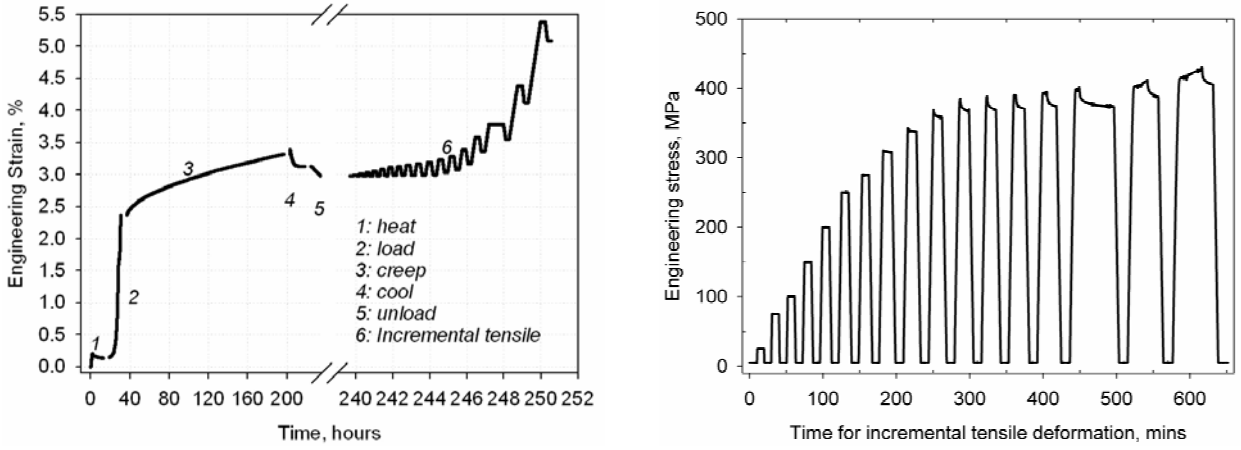

(a) (b)

Figure 1. A schematic diagram of the history applied to the specimen strained to the primary creep, followed by the room temperature incremental tensile deformation: (a) strain history and (b) stress cycles used in the incremental tensile deformation at room temperature combined with ND measurement

2.3. Incremental tensile deformation combined with neutron diffraction (ND)

The time-of-flight neutron diffractometer, at the Rutherford Appleton Laboratory, UK, is optimised to measure elastic strains at precise locations for the bulk material [13]. A pulsed beam of neutrons with a wide energy range travels to the specimen, see Fig. 2 (a), where a small fraction of the beam is diffracted to both detectors located at an angle of 2θ=90°. This arrangement provides a measure of axial strain vector from detector 1 and radial strain vector from detector 2, Fig. 2 (a). The wavelength, λ, of the detected neutrons is defined from their time-of-flight, t.

$$\lambda = \frac{h}{m(L_1 + L_2)} t \tag{2}$$

where h is the Planck constant, m is the neutron mass and L_1 and L_2 are the flight paths from the moderator to specimen and from the specimen to detector, respectively. A typical spectrum obtained from stainless steel is shown in Fig. 2 (b). Each diffraction peak, at a specific time-of-flight, according to Bragg's law, $\lambda_{hkl} = 2d_{hkl}\sin\theta$, represents a grain family with $\{hkl\}$ crystallographic orientation under a specific elastic strain. The evaluation of the elastic strain in each grain family of the material requires a measure of the lattice spacing of this grain family under the stress free condition. The elastic strain is determined from the change in the lattice spacing, as compared with the stress free lattice spacing:

$$\varepsilon_{hkl} = \frac{d_{hkl} - d^0_{hkl}}{d^0_{hkl}} \tag{3}$$

where ε_{hkl} is the elastic strain in the $\{hkl\}$ grain family, d_{hkl} is the lattice spacing at a specific strain state and d^0_{hkl} is the stress free lattice spacing. In this paper, four diffraction peaks are considered: {111}, {200}, {220} and {311} grain families, see Fig. 2 (b). In the time-of-flight instrument, the engineering strain can also be approximated from a Rietveld refinement of the

complete diffraction spectrum, see Fig. 2 (b) [13]. By knowing two principal strain vectors, the stress state in each grain family can be calculated from the generalized Hooke's law [14]. In our case, both axial and radial strain vectors have been measured from detectors 1 and 2.

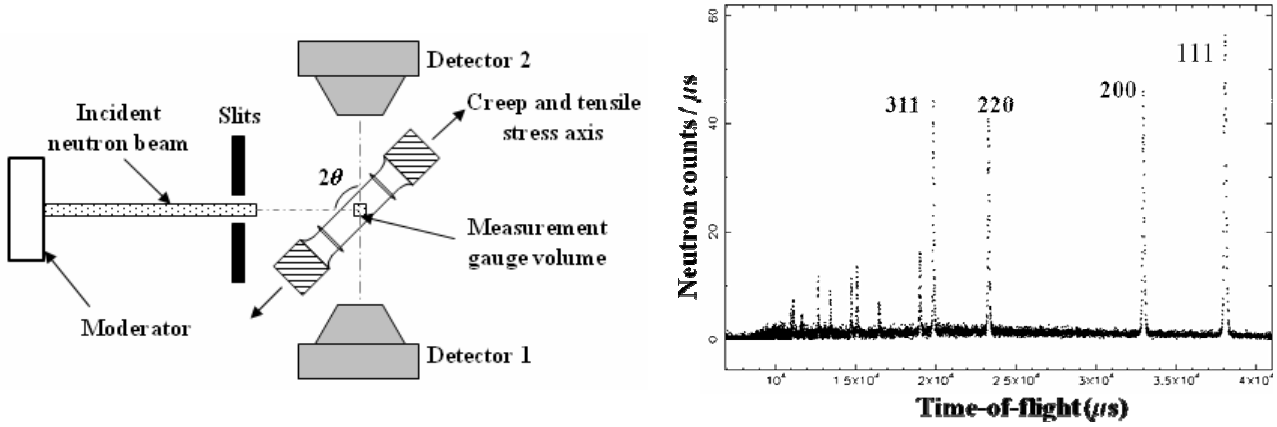

(a) (b)

Figure 2. Neutron diffraction: (a) arrangement of the in-situ tensile deformation specimen in the ENGIN-X neutron diffractometer; (b) typical time-of-flight diffraction spectrum for the investigated stainless steel

In-situ tensile deformation was performed at room temperature on the specimens, which had been subjected to a prior deformation at high temperature, see Figs. 1 (a) and (b). The arrangement of the neutron diffractometer in ENGIN-X with respect to the specimen is shown in Fig. 2 (a). The direction of applied loading for the prior creep deformation and the direction of the incremental tensile deformation were co-axial. As illustrated in Fig. 1 (a), room temperature incremental deformation may be considered to be a continuation of deformation in terms of the total strain accumulated. Fig. 1 (b) shows the applied stress history during the incremental tensile deformation, where the stress level was increased step by step. At the end of each load step, the specimen was held at either a constant stress (elastic region) or at a constant strain (plastic region) for the period of the neutron diffraction (ND) measurement time to provide a measure of d_{hkl}, see Figs. 1 (a) and (b) All the incremental tensile deformation tests were undertaken at a constant strain rate of 5×10^{-6}/s using the ENGIN-X 100kN servo-hydraulic stress rig. A fixed rate was selected because the yield point of stainless steel is very strain rate dependent. An extensometer was attached onto the specimen to measure the bulk axial strain of the material during loading.

A 3mm×3mm×4mm gauge volume was used for the neutron diffraction (ND) measurements to ensure the sampled gauge volume was fully contained within the specimen, as illustrated schematically in Fig. 2 (a). A typical measurement time of 540s was selected to ensure good counting statistics for the diffraction peaks. Some stress relaxation was observed when the stress was higher than 300MPa, Fig. 1 (b). To ensure the stress change was less than 3MPa when measurements were undertaken in the plastic region, a pre-defined delay for starting ND measurements, ranging from 180s to 360s, was adopted. Therefore all the neutron diffraction measurements were undertaken at a relatively constant stress.

2.4. Derivation of internal stress and internal resistance due to creep

The internal stress, due to the prior deformation at high temperature, was quantified directly by the change in the lattice spacing which was measured from each specimen (without being subjected to the incremental tensile deformation). Specimen 1 was not subjected to any prior deformation at high temperature, and therefore was considered to be a reference state that was free of internal

stress. The lattice spacings measured in the other three specimens, Table 2, were then compared with specimen 1:

$$\varepsilon_{hkl}^{i} = \frac{d_{hkl}^{i} - d_{hkl}^{1}}{d_{hkl}^{1}} \tag{4}$$

where ε_{hkl}^{i} is the internal strain in specimen i (i=1, 2, 3 or 4 based on Table 2), d_{hkl}^{1} is the lattice spacing in {hkl} plane measured from specimen 1 and d_{hkl}^{i} is the lattice spacing measured from specimen i (i=1, 2, 3 or 4 based on Table 2).

Internal resistance measurements were undertaken using a combination of loading and unloading steps to enhance the accuracy for the determination of the initial yield point in each specimen, Fig. 1 (b). In practice, the internal resistance is equal to the magnitude of applied stress that produced a deviation from linearity on a peak strain versus applied stress graph (ε_{hkl}-σ_a graph). The deviation from linearity was calculated from the difference between the measured elastic lattice strain and the predicted elastic lattice strain from diffraction elastic constants. It should be mentioned that the internal resistance measured using this method does not take into account the presence of internal stress. Thus the corrected internal resistance in each specimen was evaluated by deducting the magnitude of the pre-existing internal stress from the initially determined internal resistance.

A series of unloading steps to a nominally zero applied stress (5MPa) was adopted during the incremental tensile deformation, Fig. 1 (b). Using this approach it was possible to track the change in the internal stress introduced by room temperature tensile deformation. This can be then added to the pre-existing internal stress due to high temperature deformation to provide a measure of the evolution of internal stress introduced by the general plastic deformation, i.e. the sum of room temperature plastic deformation and high temperature plastic and creep deformations.

3. Results

3.1. Response of lattice strain responses and deviations from linearity

Fig. 3 (a) shows the ND measured lattice strains along the axial direction as a function of increasing applied stress for specimen 1, not subjected to a prior high temperature deformation. The diffraction elastic constants (DECs) for all four grain families were determined from the ND measurement data within the elastic region, the linear portion of the ε_{hkl}-σ_a graph, below the elastic limit illustrated by the dotted line in Fig. 3 (a). A linear least squares regression method was used to fit the data and obtain the DECs. From the region where the applied stress was above the elastic limit, the measured lattice strains for the {220}, {111} and {311} grain families diverged from linearity towards a lower strain value (to the left hand side of the prediction), whereas the {200} lattice strain diverged to a larger strain value (to the right hand side of the prediction). Fig. 3 (b) shows the calculated difference between the ND measured lattice strain and the predicted lattice strain using the DEC for each grain family. After reaching the applied stress of 375MPa, Fig. 3 (b), the difference was about -500×10^{-6} strain (compression) for the {220} grain family, however for the {200} grain family the difference was about $+500\times10^{-6}$ strain (tension). In addition the bulk plastic strain measured by the extensometer provided a consistent prediction of the deviation from linearity, Fig. 3 (b). This data analysis procedure was adopted for each specimen. The DECs and elastic limits of all four specimens are summarised in Table 3. Among the four grain families, {200} grain family was the most compliant and the {111} grain family was the stiffest. The progressive increase in the elastic limit from specimens 1 to 4 was consistent with the increase in the total strain introduced by the prior deformation at high temperature. The uncertainty for the

determination of the DECs is also given in Table 3 for each grain family.

Fig. 4 (a) and (b) show the influence of prior deformation at high temperature on the response of the lattice strains to the applied stress for the {200} and the {220} grain families, respectively. They are illustrated by the deviation from linearity. A negative value indicates the presence of a micro-yielding in a particular grain family and a positive value indicates the effects of sharing load due to yielding of other grain families. The uncertainties shown in the Figs. 4 (a) and (b) are based on the uncertainties in the determination of DECs, summarised in Table 3. This applies to all specimens shown in Figs. 4 (a) and (b). In terms of the {200} grain family, Fig. 4 (a), the magnitude of the deviation from linearity (positive values), decreased to a minimum value from specimen 1 to specimen 3, but increased slightly for specimen 4. The deviation from linearity observed in specimen 3 was typically less than 100×10^{6} and thus was less than the uncertainty. In terms of the {220} grain family, a very small decrease in the magnitude of the deviation from linearity (negative values) was observed from specimen 1 to specimen 3, Fig. 4 (b). However, specimen 4 showed a different lattice strain response, compared with the other three.

Table 3. Summary of diffraction elastic constants (DECs) and elastic limits of specimens

Specimen ID	Prior deformation	$E_{\{111\}}$, GPa	$E_{\{200\}}$, GPa	$E_{\{220\}}$, GPa	$E_{\{311\}}$, GPa	Elastic limit (measured at 0.01% bulk plastic strain), MPa
Specimen 1	No creep	225±12	167±5	209±16	170±16	184
Specimen 2	As loaded	255±21	155±4	211±8	172±8	333
Specimen 3	Primary	264±16	146±6	201±7	204±15	344
Specimen 4	Secondary	254±4	171±9	255±16	208±12	377
Averaged DECs		250±16	160±11	219±24	188±20	

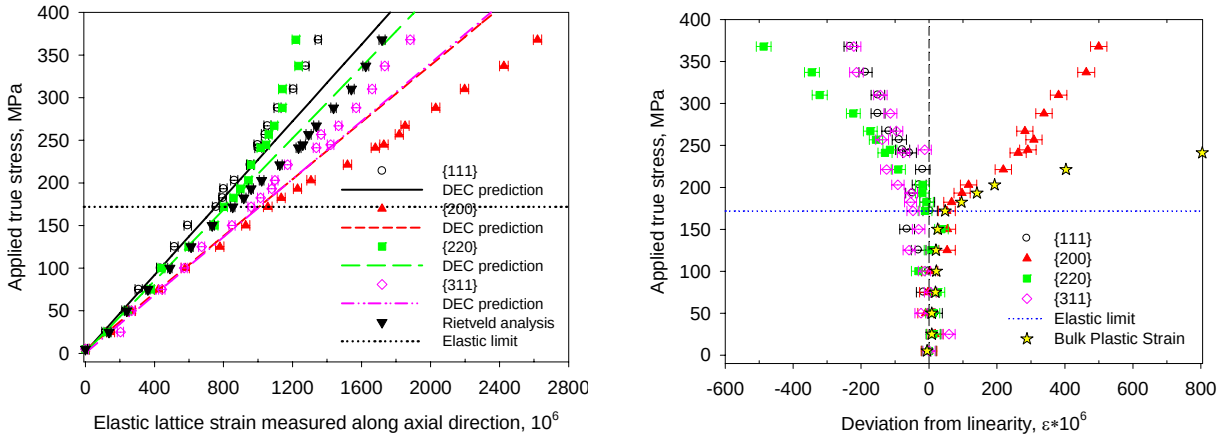

(a) (b)

Figure 3. (a) ND measured elastic lattice strain along the axial direction of specimen 1 for {111}, {200}, {220} and {311} grain families; (b) Deviation of the measured lattice strain from the extrapolated elastic lattice strain using DECs. Note: Measurement uncertainties are from the single peak fitting error

Neutron diffraction measurements undertaken at 5MPa after each step of unloading over the process of incremental tensile deformation at room temperature, see Fig. 1 (b), revealed the evolution of the residual elastic lattice strain. Figs. 5 (a) and (b) show the changes in the residual lattice strains with the increase in the bulk plastic strain measured by the extensometer attached on the specimen, for the {200} and {220} grain families, respectively. In terms of the {200} grain family, specimen 4 which was subjected to prior secondary creep deformation, had the highest compressive residual lattice strain, but specimen 1 had the highest tensile residual lattice strain. In terms of the {220}

grain family, very little residual elastic lattice strain (<150×10^{-6} strain) was accumulated during incremental tensile deformation of specimens subjected to prior deformation at high temperature.

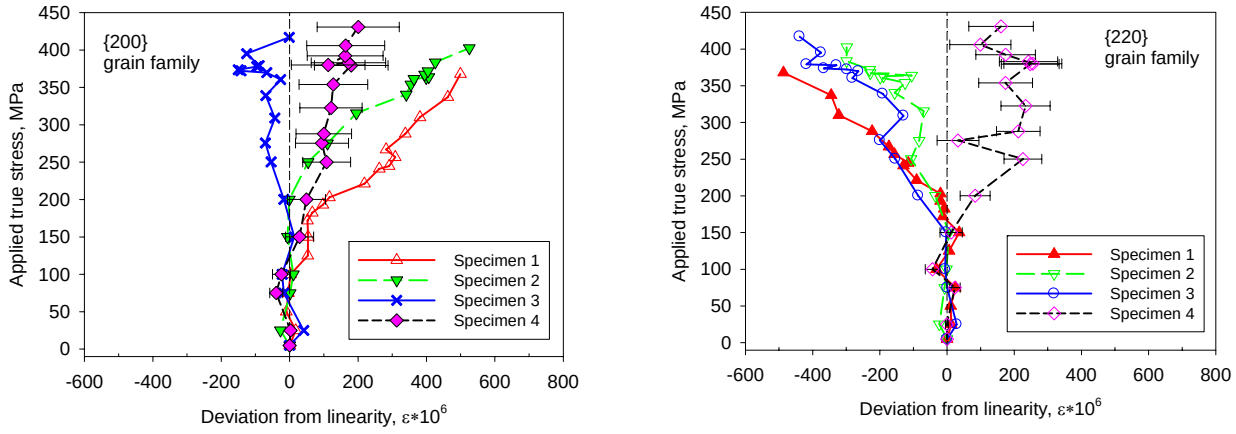

(a) (b)

Figure 4. Influence of prior deformation at high temperature on the subsequent elastic lattice strain response: (a) {200} grain family; (b) {220} grain family.

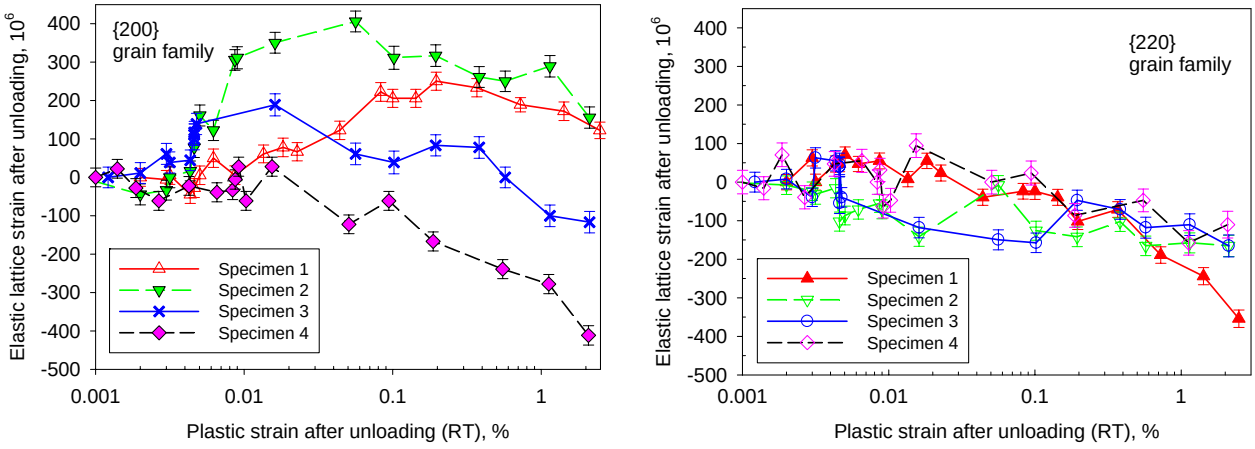

(a) (b)

Figure 5. ND measured elastic lattice strain after each step of unloading, measured at a stress of 5MPa, plotted against the accumulated plastic strain at room temperature: (a) {200} grain family; (b) {220} grain family

3.2. Internal stress

Figs. 6 (a) and (b) show the internal stresses along the axial and radial directions for specimens subjected to prior deformation. In general, an increase in the magnitude of the prior strain led to a higher internal stress. In addition, the internal stress was shown to have a crystallographic orientation dependence: internal stress in {200} grain family was tensile, whereas the other three were compressive. Of the three grain families the {220} grain family contained the highest compressive internal stress. Rietveld refinement predicted an averaged value for four grain families considered in Figs. 6 (a) and (b). It is interesting to note that {200} grain family in specimen 4 (highest total true axial strain) had a very similar value of internal stress compared with specimen 3. However, the {220} grain family in specimen 4 had an increased value of internal stress compared with specimen 3. These two phenomena are consistent with the in-situ observations shown in Fig. 4 (a) and (b), where a very similar lattice strain response was observed in the {200} grain family from specimens 3 and 4; this is different for the {220} grain family.

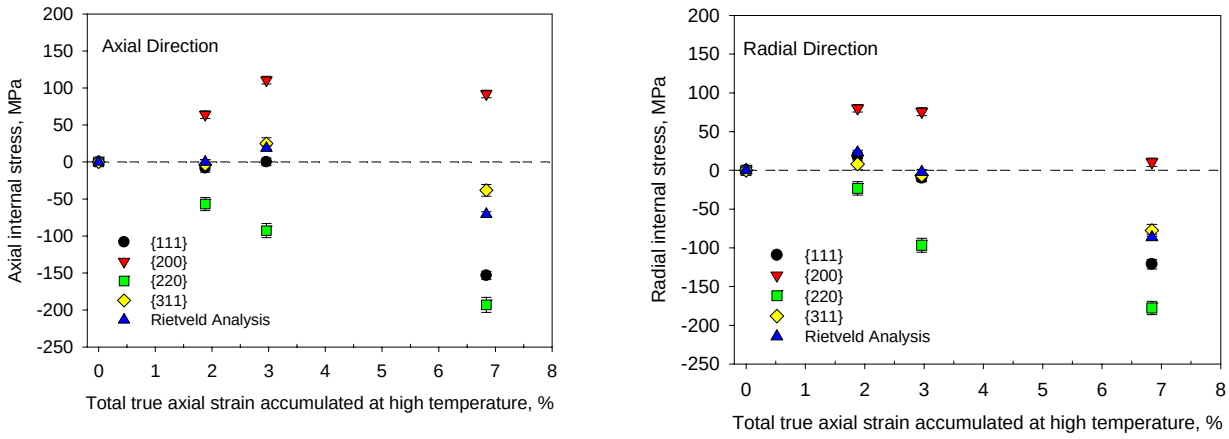

(a) (b)

Figure 6. Internal stresses in specimens 1 to 4, which were subjected to a prior deformation at high temperature: (a) axial direction and (b) radial direction

3.3. Internal resistance

Using the incremental tensile deformation for each specimen combined with neutron diffraction measurements, the magnitude of applied stress required to create room temperature plastic deformation was obtained. This is judged to be a measure of the internal resistance to material flow. Fig. 7 shows the internal resistance in the four specimens summarised in Table 2. Internal resistance obtained from the bulk stress-strain, {220} grain family is shown in Fig. 7. Here, the 0.01% plastic strain is used as a benchmark to determine the yield point for both macro-scale and grain family size-scale conditions. The internal resistance was determined using:

$$\sigma_{bulk}^{ir} = \sigma_a^{0.01\%,bulk} \tag{5}$$

$$\sigma_{220}^{ir} = \sigma_a^{0.01\%,\{220\}} \tag{6}$$

$$\sigma_{220}^{ir} = E_{220} \times \varepsilon_{220}^{0.01\%} \tag{7}$$

Equation 5 provides a measure of the macro-scale internal resistance, σ_{bulk}^{ir}, and was determined from the applied stress required to introduce 0.01% macro-scale plastic strain. Equation 6 provides a measure of the grain family size-scale internal resistance, σ_{220}^{ir}, determined from the applied stress that is required to introduce 0.01% micro-scale plastic strain. This is the deviation calculated in Fig. 4 (b). Equation 7 provides a second choice to measure σ_{220}^{ir}, determined from the 0.01% micro-scale plastic strain, using the DEC for {220} grain family given in Table 3.

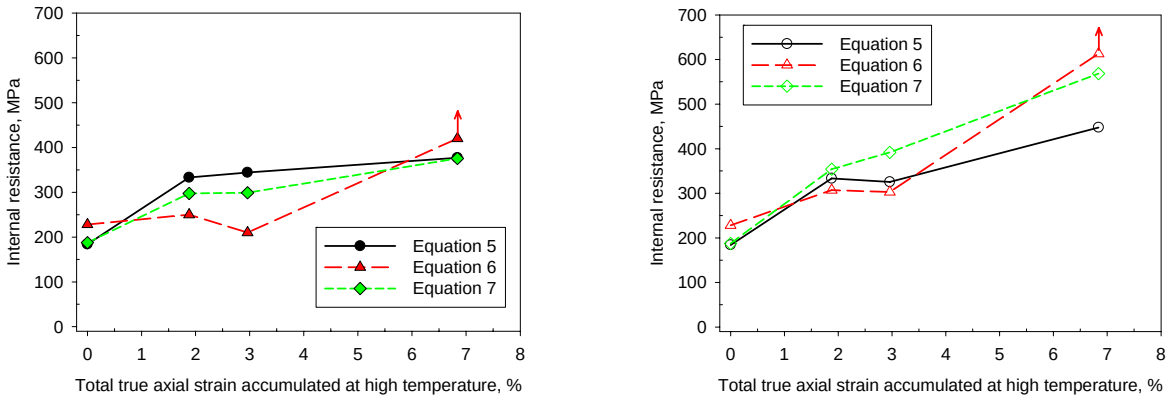

(a) (b)

Figure 7. Internal resistance in specimens subjected to prior deformation at high temperature: (a) internal resistance without knowledge of internal stress; (b) internal resistance with knowledge of internal stress

The evaluation of internal resistance without the knowledge of the pre-existing internal stress due to the prior high temperature deformation is shown in Fig. 7 (a). The combination of ND measured internal stresses in section 3.2 and the determined internal resistance produces the correct magnitude of the internal resistance, Fig. 7 (b). The internal stresses determined via Rietveld refinement was used to correct the macro-yield strength, read from each bulk stress-strain curve for the corresponding specimens. In general, the internal resistance of the material increased with an increase in the level of the prior strain induced at high temperature. The points with an upper arrow in Fig. 7 (a) and (b) indicates that the {220} grain family did not yield with the applied stress, as shown by specimen 4 in Fig. 4 (b).

4. Discussion and Concluding Remarks

Internal stress is a consequence of strain incompatibility between grains which deform differently due to their specific orientation. This deformation, arising from slip on {111} <110> system, is accommodated elastically within the various crystallographic grain families. Internal resistance is a reflection of the material internal microstructure that resists plastic deformation. These two terms have been measured using the present ND technique and the success is attributed to the separation of internal stress and internal resistance. The former can be measured after unloading from high temperature deformation by using a microstructure freezing technique. The latter can be measured with the applied stress to evaluate the flow stress. Mecking and Kocks [15], and Follansbee and Kocks [16] proposed a model and experimental method to measure the internal resistance (called a threshold strength) at temperatures of <300K. However, in this case the presence of the internal stress was not taken into account when the internal resistance was determined. The technique proposed in this paper measures the internal resistance and internal stress at both macro-scale and at the scale of grain families. The latter is very important when providing a crystal plasticity based self-consistent model, see Ref [12].

Using this approach it is found that the internal stress is dependent on the specific crystallographic orientation of each grain family, as shown in Fig. 6. The increase in the magnitude of the internal stress, {200} in tension and {220} in compression, corresponds to the increase in the inhomogeneous strain induced by high temperature deformation, summarised in Table 2. High temperature recovery may play a role in accommodating the strain incompatibility, and lead to a small decrease in the measured internal stress, see {200} grain family for specimens 3 and 4 shown in Fig. 6. This indicates that the creep deformation rate is grain orientation dependent, otherwise the accommodation will not decrease strain incompatibility in a polycrystalline material.

The crystallographic orientation dependence of the elastic lattice strain on the applied stress, Fig. 3 (a), is consistent with a previous study by Daymond and Bouchard [17]. The present work specifically explored the influence of the prior deformation at high temperature on the measured elastic lattice strain. It was shown that the {220} grain family no longer yielded after secondary creep deformation, see specimen 4 in Fig. 4 (b). The residual lattice strain, measured after each unloading step of the incremental tensile deformation, revealed a strong influence of creep deformation on the ability of the material to plastically deform in the {220} and {200} grain families, Fig. 5 (a) and (b).

Finally, we have described a method to distinguish between the internal stress and internal resistance based on neutron diffraction measurements combined with in-situ incremental deformation. This could be used to validate the threshold strength concept, proposed by Kocks, Mecking and their co-workers [9, 15, 16]. This has been discussed more fully in a review by Kocks and Mecking [18].

Acknowledgements

We acknowledge the ENGIN-X beamline allocation from ISIS, UK. Bo Chen thanks the financial support from EDF Energy and useful discussions with Mr Mike Spindler, EDF Energy. David Smith is supported by the Royal Academy of Engineering, EDF Energy and Rolls Royce plc. The authors also acknowledge the useful discussions and suggestions from Prof. Alan Cocks and Mr Jia Nan Hu at University of Oxford.

References

[1] H.J. Frost, M.F. Ashby, Deformation-mechanism Maps, Pergamon, Exeter, 1982.
[2] D.G. Morris, Creep in Type 316 stainless steel, Acta Metall., 26 (1978) 1143-1151.
[3] D.G. Morris, D.R. Harries, Metal Sci., 12 (1978) 525-531.
[4] M. Biberger, J.C. Gibeling, Analysis of creep transients in pure metals following stress changes, Acta Metall. Mater., 43 (1995) 3247–3260.
[5] B. Chen, P.E.J. Flewitt, D.J. Smith, A.C.F. Cocks, A review of the changes to internal state related to high temperature creep of polycrystalline metals and alloys, Int. Mater. Rev., (to be published).
[6] C.N. Ahlquist, W.D. Nix, The measurement of internal stresses during creep of Al and Al-Mg alloys, Acta Metall., 19 (1971) 373-385.
[7] S. Straub, W. Blum, H.J. Maier, T. Ungar, A. Borbely, H. Renner, Long-range internal stresses in cell and subgrain structures of copper during deformation at constant stress, Acta Mater., 44 (1996) 4337-4350.
[8] M.A. Morris, J.L. Martin, Microstructural dependence of effective stresses and activation volumes during creep, Acta Metall., 32 (1984) 1609-1623.
[9] Y. Estrin, H. Mecking, A unified phenomenological description of work hardening and creep based on one-parameter models, Acta Metall., 32 (1984) 57-70.
[10] B. Derby, M.F. Ashby, A microstructural model for primary creep, Acta Metall., 35 (1987) 1349-1353.
[11] L. Esposito, N. Bonora, A primary creep model for class M materials, Mater. Sci. Eng. A 528 (2011) 5496-5501.
[12] J.N. Hu, B. Chen, D.J. Smith, A.C.F. Cocks, A self-consistent model in the local residual stress evaluation of 316H stainless steel, 13th Int. Conf. Fract., Beijing, (2013).
[13] J.R. Santisteban, M.R. Daymond, J.A. James, L. Edwards, ENGIN-X: a third-generation neutron strain scanner, J. Appl. Cryst. 39 (2006) 812-825.
[14] M.R. Daymond, M.A.M. Bourke, R.B. Von Dreele, B. Clausen, T. Lorentzen, Use of Rietveld refinement for elastic macrostrain determination and for evaluation of plastic strain history from diffraction spectra, J. Appl. Phys., 82 (1997) 1554-1562.
[15] H. Mecking, U.F. Kocks, Kinetics of flow and strain hardening, Acta Metall., 29 (1981) 1865-1875.
[16] P.S. Follansbee, U.F. Kocks, A constitutive description of the deformation of copper based on the use of the mechanical threshold stress as an internal state variable, Acta Metall. 36 (1988) 81-93.
[17] M.R. Daymond, P.J. Bouchard, Elastoplastic deformation of 316 stainless steel under tensile loading at elevated temperatures, Metall. Mater. Trans. A 37 (2006) 1863-1873.
[18] U.F. Kocks, H. Mecking, Physics and phenomenology of strain hardening: the FCC case, Prog. Mater. Sci. 48 (2003) 171-273.

Creep fracture mechanism of polycrystalline Ni-based superalloy with diffusion coatings

Kang Yuan[1, *], Ru Lin Peng[1], Xin-Hai Li[2], Lennart Johansson[2], Sten Johansson[1], Yan-dong Wang[3]

[1]Department of Management and Engineering, Linkoeping University, SE-58183 Linköping, Sweden

[2]Siemens Industrial Turbomachinery AB, SE-61283 Finspång, Sweden

[3]Beijing Institute of Technology, Beijing 100081, China

[*]Corresponding author: kang.yuan@liu.se

Abstract: Diffusion coatings are widely used to increase oxidation and corrosion resistance of hot superalloy components for gas turbines. The aim of this study is to investigate the effect of coatings (NiAl and PtAl) on the creep fracture mechanism of samples with a substrate of IN792. The samples have been creep tested at two temperatures (850 °C and 950 °C) and different applied tensile stresses, until failure between 205 and 21000 hrs. The observation of cross-sections by SEM shows that the microstructural evolution in the coating is dependent on the diffusion of alloying elements in the sample. Furthermore the time and temperature induced growth of the coating is found to be controlled only by inward diffusion of Al. Grain-boundary cracking is the basic fracture mode in the substrate in all samples irrespective if the crack is initiated from coating or substrate. The analysis of microstructure shows that the diffusion coatings display two types of mechanical behavior - being easily plasticized or cracked - dependent on temperature and type of coating, and therefore can be considered as non-load carrying regions. After recalculating the creep stress to exclude the final effective coating thickness from the total sample thickness, the coated samples showed similar creep rupture behavior as the uncoated samples in the Larson-Miller diagram.

Keywords: Creep; Ni-based superalloy; Diffusion coating; Crack

1. Introduction

Due to their excellent high-temperature mechanical properties, superalloys are widely used as base material for components in advanced gas turbine operating at high temperatures [1]. Components with Al-rich coatings become much even more sustainable with better resistance against environmental attack from high-temperature oxidation and corrosion. Aluminide diffusion coatings are widely used to protect the superalloys in a gas turbine at temperatures lower than 1000 °C [2]. Due to the difference of mechanical properties compared to the base material, the effect of coatings on the mechanical behavior of the substrate needs to be considered. At higher temperatures creep of the material become an important issue. There have been some investigations on creep mechanism of superalloys with high temperature coatings, which suggest several effects of coatings: a change in microstructure of the base material; a change of load distribution; introduction of cracks [3,4]. Some valuable creep tests (generally < 1000 hrs) of diffusion coating-superalloy system have been made during the past decades [5-8]. However long-term creep test results (> 1000 hrs) are seldom presented in the best literature surveys. Furthermore in some specific situations, the coating has to be deposited onto the thin part of the component, which makes the effect of coating more critical. The industrial background to this research work actually emanates from problems in the walls of the cooling channels which can be as thin as in the order of millimeters. The aim of this paper is to investigate the mechanical effect of diffusion coatings on thin sectioned superalloy specimens (~ 1 mm) subjected to creep at the operating temperatures.

2. Experimental procedures

Creep samples in the form of sheet were produced from cast of nickel based polycrystalline superalloy Inconel 792 (IN792) with the nominal chemical composition of Ni-12.5Cr-9Co-4.175W-4.175Ta-3.975Ti-3.375Al-1.9Mo-0.08C-0.0175Zr-0.015B (wt.%). A drawing of the specimens is shown in Fig. 1. Two kinds of diffusion coatings - NiAl and PtAl - were deposited onto the specimen surface by the CVD process at 1050-1100 °C for 12-20 hrs. The specimens were solution treated at 1120 °C for 2 hrs and then aged at 845 °C for 24 hrs, followed by air cooling to room temperature. The main phases in the alloy are a solid solution of nickel based γ (disordered FCC) and an intermetallic γ' (FCC_$L1_2$). Four types of specimens were used in this study (Table 1). Specimens coated with only NiAl or PtAl, and specimens coated with NiAl on one side but PtAl on the other including an uncoated reference. The creep samples were tested under different static tensile loads at 850 °C or 950 °C in air until failure. The tested samples were cut as cross sections in their longitudinal direction (loading direction) and then carefully ground and mechanically polished pre, to study the microstructure below the fracture surface. The microscopic characterization was carried out by using a *FEG-SEM Hitachi SU-70* scanning electron microscope (SEM) with an INCA *Oxford Instruments* energy dispersive system (EDS).

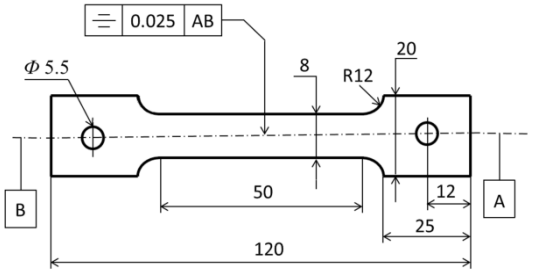

Figure 1. Dimensions of the sheet specimens with thickness of 1 mm (in millimeters).

Table 1. Sample type definition.

Sample type	Coating covering	
	One side	Another side
Uncoated	uncoated	uncoated
NiAl-NiAl	NiAl	NiAl
PtAl-PtAl	PtAl	PtAl
NiAl-PtAl	NiAl	PtAl

3. Results and discussion

3.1. Creep test and *effective coating thickness* (*ECT*)

Results from the creep tests are presented as applied stress versus creep life (Fig. 2). The creep lifetime varied largely between 205 hrs and 21000 hrs, depending on the testing temperature and applied stress. As expected, the resistances to creep rupture decreases with increasing test temperature, showing either a shorter creep life under the same applied stress or a lower applied stress for the same creep life. While the PtAl-PtAl at 850 °C shows scattered results and the

NiAl-PtAl has only two data points, a linear relationship between the applied stress and creep life, both plotted in logarithm scale, could be found for the other coated samples.

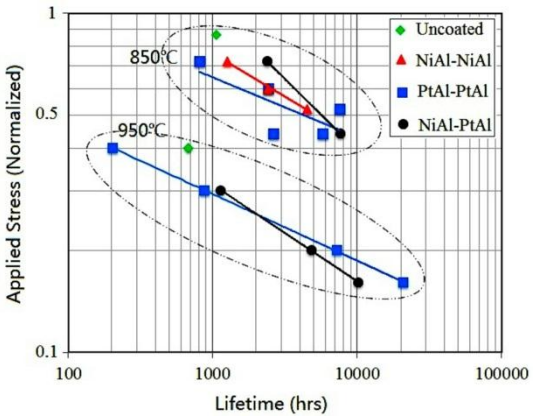

Figure 2. Creep lifetimes of specimens under different applied stresses (normalized) at 850 °C and 950 °C.

Based on their distinctive metallographic features, three characteristic zones are defined for the coatings (Fig. 3): outer zone (OZ), interdiffusion zone (IDZ) and second reactive zone (SRZ). The matrix phases in OZ, IDZ, SRZ and the substrate are respectively β, γ' (or β), γ' and γ. After long creep time at 900 °C the OZ shrinked in NiAl (Fig. 3(a)) but was well stabilized in PtAl (Fig. 3(b)), which indicates that Pt can restrict the β-to-γ' transformation by blocking the outward diffusion of Ti, Co, W and Ta. The enrichment of Cr, Mo and Co in those zones was responsible for the formation of some specific precipitates (i.e. TCP, Cr-α) which were observed in both NiAl and PtAl coatings. The phase identification in this research is achieved by comparing the EDS-detected composition with those given in literatures [1,9-11]. A more detailed analysis of the microstructural changes in the PtAl-PtAl samples could be found in [12].

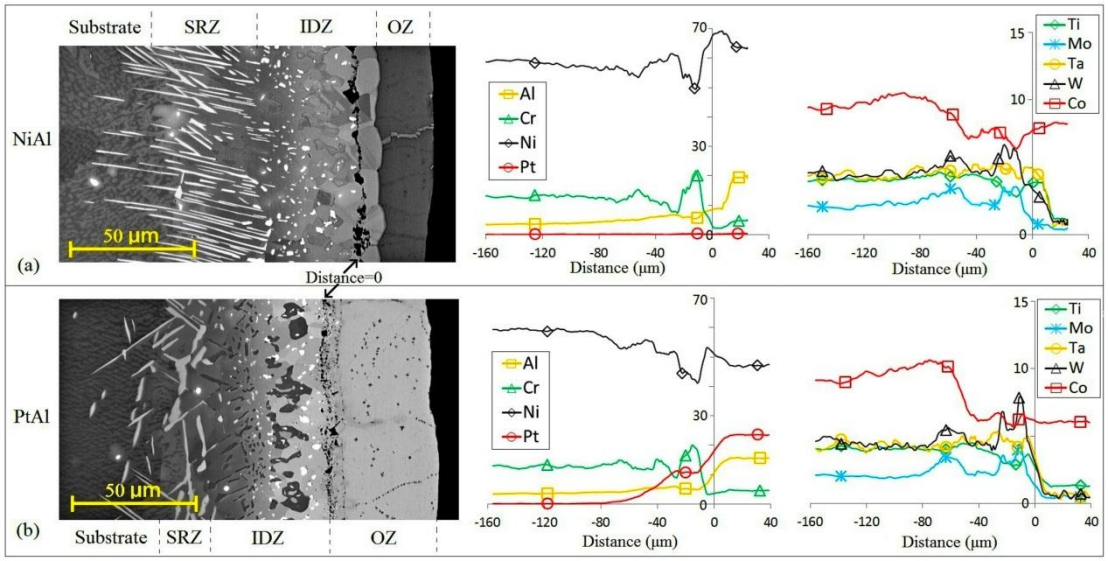

Figure 3. Microstructure and composition profiles (averaged from three different areas) on (a) NiAl side and (b) PtAl side in a NiAl-PtAl sample after creep test at 950 °C with lifetime 10244 hrs.

The micro-hardness tests of cross sections at room temperature show a variation along the diffusion coatings (Fig. 4(a)), verifying the difference in mechanical properties between coating and substrate. This means that the stress partitioning needs to be recalculated by considering the newly developed coating thickness. To encompass the growth of coating due to the diffusion of alloying elements

during the creep test an *effective coating thickness* (*ECT*) is defined, which is the total thickness of OZ, IDZ and SRZ. The inward diffusion of Al in the substrate is pre-assumed to control the movement of coating-substrate interface in both NiAl and PtAl coatings. The statistic results of the *ECT* in Fig. 4 (b) presents a linear correlation with $\sqrt{D^{Al} \times t}$, showing as

$$ECT = ECT_0 + C \times \sqrt{D^{Al} \times t} \quad (1)$$

In Eq. (1) ECT_0 is the original *effective coating thickness* and *C* is a constant. D^{Al} is the diffusion coefficient of Al in the substrate (IN792), calculated by using lower Hashin-Shrtikman bound [13]:

$$D^{Al} = D_{\gamma'}^{Al} + \frac{f_{\gamma}}{1/(D_{\gamma}^{Al} - D_{\gamma'}^{Al}) + f_{\gamma'}/(3D_{\gamma'}^{Al})} \quad (2)$$

In Eq. (2) D_{γ}^{Al} and $D_{\gamma'}^{Al}$ are the diffusion coefficient of Al in γ and γ' phases, f_{γ} and $f_{\gamma'}$ are the volume fraction of γ and γ' phases. The values of D_{γ}^{Al}, $D_{\gamma'}^{Al}$, f_{γ} and $f_{\gamma'}$ (listed in Fig. 4(b)) can be calculated by the software DICTRA [14] with Ni-based thermodynamic and kinetic database – TCNI5 and MOBNI2 [15]. The lower Hashin-Shrtikman bound [13] claims the easier-diffusion (high diffusivity) phase as the matrix phase which is likely the case in IN792 with the solid solution γ as the easier-diffusion and matrix phase. Actually applying another Hashin-Shrtikman bound (i.e. upper bound), which assumes the tougher-diffusion (lower diffusivity) phase as the matrix phase, gives the similar calculated results on diffusivity of Al in IN792 [12]. The paralleled curves in Fig. 4(b) give a coating-independent constant *C* (~ 2.54×10^5) in Eq. (1) for both NiAl and PtAl diffusion coatings, indicating that the coating thickening rate is controlled only by Al inward diffusion in the substrate. However this conclusion needs to be further checked since the statistic data scattering still exists in Fig. 4(b), especially when the $\sqrt{D^{Al} \times t}$ value is lower.

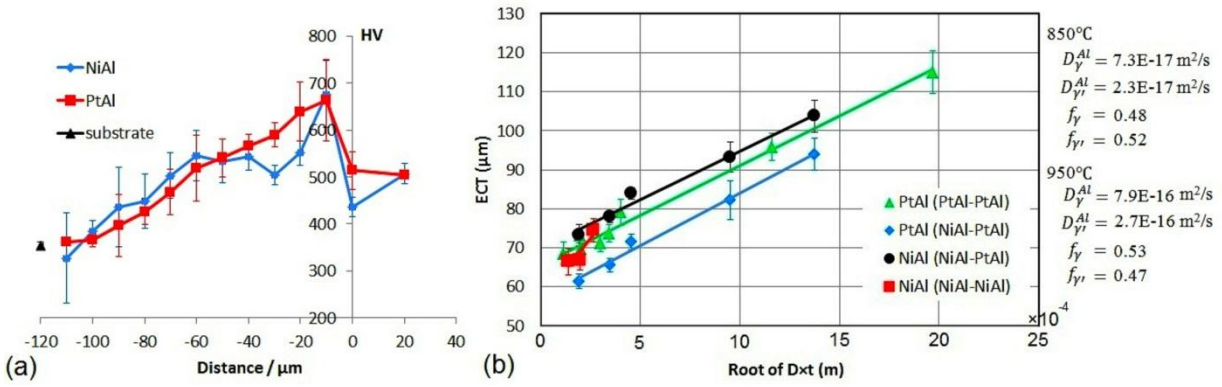

Figure 4. (a) Micro-hardness profiles (Vickers) in NiAl and PtAl measured at room temperature (in the same sample in Fig. 3) and (b) *Effective Coating Thickness* (*ECT*) near fracture surface vs. $\sqrt{D^{Al} \times t}$. The standard deviations (error bar) in both graphs are given by measurement at ~10 regions of the sample.

3.2. Morphology study of creep fracture

Because of heavy oxidation of the fracture surface fractographic analyses cannot be easily applied to study the creep rupture process. Instead, detailed microstructural examinations were carried out on polished lengthwise cross-sections cutting through the mid-width of the creep fractured specimens. The loading direction is in the length direction of the sample and is vertical in all the micrographs shown in this section.

3.2.1. Uncoated

Grain-boundary weakening is generally responsible for the creep failure of polycrystalline materials [16]. In the hot combustion and turbine sections of gas turbine the coarse-grained or even single-crystalline superalloys are commonly used to minimize the effect of grain boundary on creep behavior [1]. For polycrystalline superalloys (e.g. IN792) the addition of few ppm carbon, by forming carbides along grain boundaries, can improve the resistance of grain-boundary sliding [17]. Carbides detached from grain boundary of the superalloy by tensile force were observed by [18,19], which were also observed in the current study in the serrated crack path (Fig. 5(a)). According to the composition measurement by EDS two types of carbides were detected: (Cr,W)-rich $M_{23}C_6$ and (Ti,Ta)-rich MC. $M_{23}C_6$ was only observed along grain boundaries while MC was common both along grain boundaries and inside of the grains. The same microstructures have been reported in IN792 by other researchers [6,20]. The direction of the alignment of cracks is unsurprisingly perpendicular or near-perpendicular to the creep loading direction.

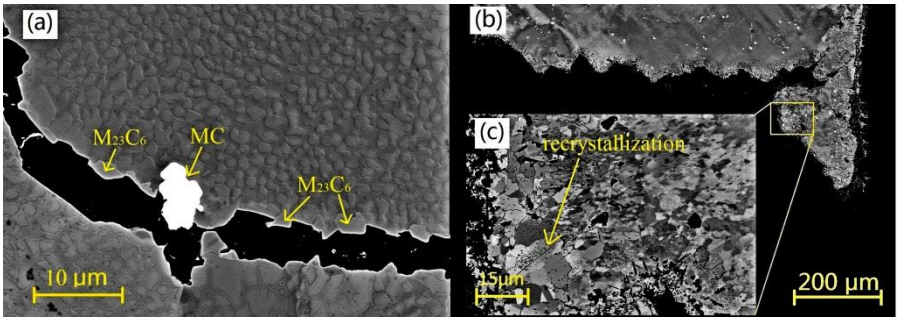

Figure 5. Fractured uncoated sample for 950 °C: (a) serrated grain-boundary crack with carbides, (b) morphology near fracture surface and (c) recrystallization near fracture surface.

The creep tests were conducted in air; consequently oxidation occurred at the sample' surface whether it was covered by coating or not. It has been reported that the surface oxide layer could lower the steady creep strain rate comparing with vacuum creep test (without surface oxidation) [21]. In this study oxidation was also present inside of material when the crack initiated from the surface. However such oxidation was reported to have little effect on the steady creep rate of the sample [6,20]. Fig. 5(b) shows the length-sectional morphology near the fracture surface of the uncoated sample. Since the crack propagates along the grain boundary, the roughness of the fracture surface is grain-size dependent. The appearance of recrystallization along the fracture surface indicates dynamic recrystallization caused by local plastic deformation during crack propagation at the creep testing temperature (Fig. 5(c)). Actually such recrystallization was also commonly observed along the fracture surface in other sample types.

3.2.2. NiAl-NiAl

Ductile-brittle transition temperature (DBTT) reflects the ductility of materials at high temperatures. The definition of DBTT is mainly based upon the amount of plastic deformation during failure. For instance Lowrie et al. [6,20] suggested the temperature above which the fracture strain of the

material was more than 0.6%. The coating can be even super-plastic at high enough temperature [22]. The DBTT of NiAl is 693 °C measured by [23]), which however should also be dependent upon the coating thickness according to the results of [24]. In this type of sample through-coating cracks were commonly found with the oxidation around (Fig. 6(a) and (b)). The formation of γ' in OZ may weaken the strength grain boundary and induce cracks (Fig. 6(c)). When a through-coating crack was meeting or is located near a grain boundary in the substrate, it could continue to penetrate into the substrate, being identified by the "L"-shape crack path near the coating part (Fig. 6(b)). The cracking of the coating makes it a non-load carrying member and leaves the substrate in a somewhat similar creep situation as the uncoated sample.

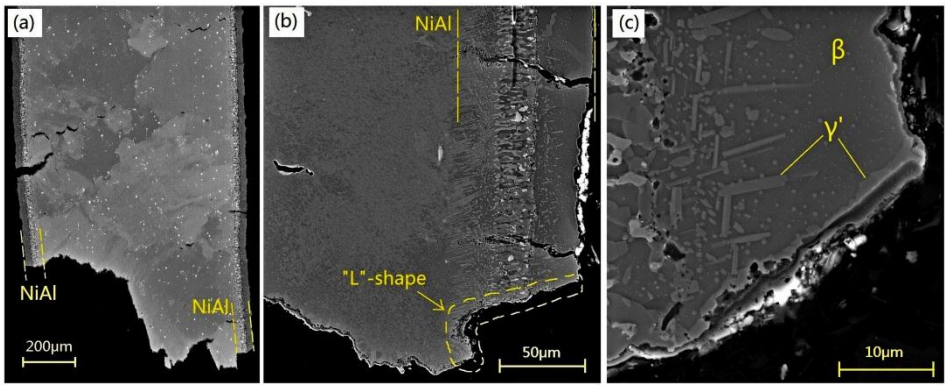

Figure 6. Fractured NiAl-NiAl sample for 850 °C: (a) morphology containing fracture surface, (b) "L"-shape path of though-coating cracks and (c) γ' precipitates in OZ. (The coating part is marked in Fig. 6-8).

3.2.3. PtAl-PtAl

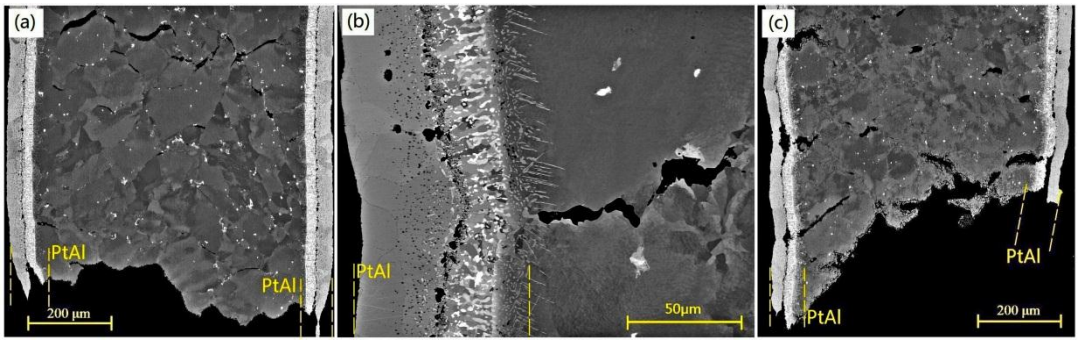

Figure 7. Fractured PtAl-PtAl sample: (a) morphology containing fracture surface (850 °C), (b) crack beneath PtAl (850 °C) and (c) morphology containing fracture surface (950 °C).

The addition of Pt into aluminide diffusion coating was initially intended to slow down the inward diffusion of Al. However the "diffusion barrier" effect by Pt has been demonstrated to be not so effective [25], which can be further supported by the results in Fig. 4 in this study. Although the PtAl coating has a higher DBTT (795 °C [26]) than NiAl (693 °C [24]), no significant through-coating cracks but some ductile deformation shapes were observed in PtAl at 850 °C (Fig. 7(a) and (b)). Addition of Pt prevents the conversion of β to γ' according to the analysing results in section 3.1, which is further demonstrated by the absence of γ' in OZ (Fig. 7(b)). This is probably the reason for the ductile behavior of the OZ in PtAl at 850 °C, different from the brittle behavior of

NiAl (Fig. 6(a) and (b)). Due to the difference of mechanical properties between two characteristic zones, e.g. OZ and IDZ or coating and substrate, some voids/cracks formed at their interface during the creep process at both temperatures (Fig. 7(b) and (c)) but more significant at 950 °C. Toshio [24] also observed such voids in SRZ in PtAl coatings under creep stress. Since the through-coating crack was not formed in PtAl, the "L"-shape crack near the coating part was not observed in this sample type. Either being easily plasticized or producing voids/cracks the coating part lost the ability to carry load during the creep process.

3.2.4. NiAl-PtAl

Comparison of the coating behavior of NiAl in NiAl-PtAl (Fig. 8(a)) with that in NiAl-NiAl (Fig. 6) shows no significant difference at 850 °C. The NiAl can be considered to be ductile at 950 °C since NiAl always shows plastic deformation along the whole cross section of the sample with a few cracks only observed near fracture surface (Fig. 8(b)). The behavior of PtAl looks similar as in PtAl-PtAl type samples at two temperatures: i.e. to be ductile but also to induce cracks beneath the coating or inside of coating.

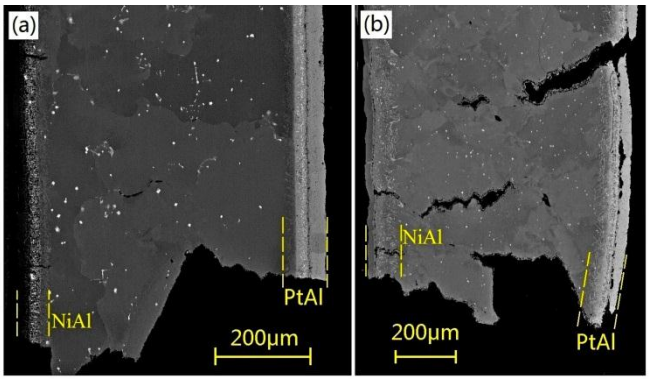

Figure 8. Fractured NiAl-PtAl sample of morphology near fracture surface for (a) 850 °C and (b) 950 °C.

3.3. Summary of creep fracture mechanism

Based on the experimental observations, the crack initiation and propagation mechanisms by which the coating affects the creep fracture behavior are proposed in Fig. 9. For the polycrystalline superalloy grain-boundary separation is always the failure mode in the substrate at 850 °C and 950 °C no matter that the crack initiates from the coating or the substrate. The grain-boundary carbides are beneficial for creep resistance. Due to formation of γ' along grain boundary in outer zone (OZ) at 850 °C NiAl coating can induce active through-coating cracks, which may further penetrate into the substrate along the nearest grain boundary beneath the coating. The γ' in OZ is somewhat restricted in NiAl at 950 °C and in PtAl at both 850 °C and 950 °C, which promotes ductile deformation occurring in the coatings. Even though, PtAl promotes the formation of the voids/cracks either beneath the coating or from inside of coating, caused by the difference of mechanical properties between different characteristic zones. The formed voids/cracks are more active to cause the sample failure at higher temperature.

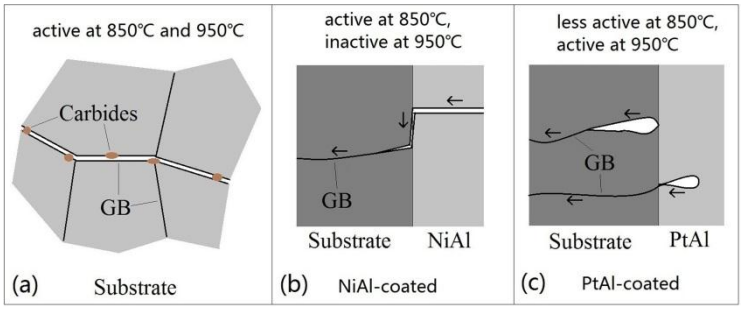

Figure 9. Summary for the crack initiation and propagation mechanism (a) in substrate and by coating's effect of (b) NiAl and (c) PtAl. (GB: grain boundary; Loading direction is vertical; small arrows show the cracking direction)

By using the Larson-Miller approach the creep results in Fig. 2 can be transferred as new ones presented in Fig. 10(a); the plot shows a somewhat negative effect of the coatings lowering the capacity to carry creep stress. Non-loading carrying by coating part above its DBTT was suggested according to some investigations [27]. Being encouraged by the analyses above the applied mechanical load in the creep sample is considered to be mainly carried by the substrate. After recalculating the creep stress by assuming the coating as load-free and excluding the final *effective coating thickness* (*ECT* in Fig. 4) from the total sample thickness, similar performance of coated and uncoated samples is achieved in Larson-Miller diagram (Fig. 10(b)).

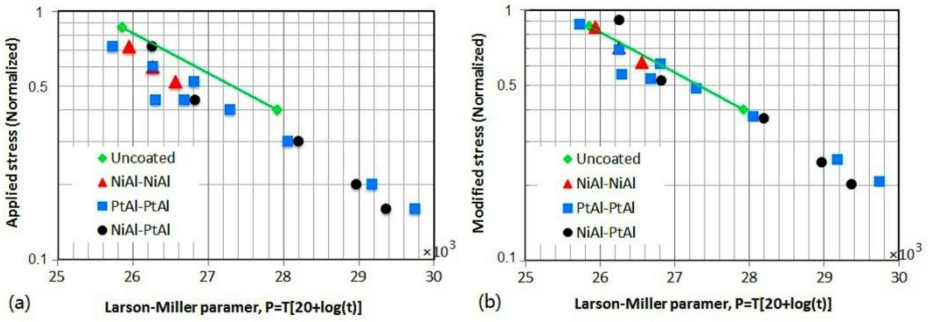

Figure 10. Creep stress (in log-scale and normalized) vs. Larson-Miller parameter (a) before and (b) after stress being modified.

4. Conclusions

In this study the effect of NiAl and PtAl diffusion coatings on the creep fracture mechanism of Ni-based polycrystalline superalloy IN792 is investigated at two temperatures, 850 °C and 950 °C. The following conclusions can be made from this study.

1) The microstructural development of the coating depends on the elemental diffusion during the creep process. The inward diffusion of Al controls the coating thickening rate which seems to be independent of the diffusion coating type.

2) Grain-boundary detachment, which is strengthened by carbides, is the basic cracking mode of the substrate in all samples whether the crack initiated from the coating or the substrate.

3) The diffusion coatings become easily-deformed or induce cracks dependent on coating type and temperature. NiAl is easily deformed at 950 °C but introduces through-coating cracks at 850 °C. PtAl induces voids/cracks in or beneath the coating at both creep temperatures. Those crack initiation modes by PtAl becomes more active when increasing temperature.

4) Based on the results from microstructure analysing, the creep stress of the sample is recalculated by taking the final coating part loading-free. By such stress modification the creep test results of the coated samples are similar with those of the uncoated samples presented in the Larson-Miller diagram. It can be concluded that the applied diffusion coating has a minor influence on the overall creep behavior of the superalloy, but just consuming the effective cross section of the superalloy to carry the creep load.

Acknowledgements

The Siemens Industrial Turbomachinery AB (Finspang, Sweden) is greatly acknowledged for its financial support and supply of materials in this research. The Swedish Energy Agency and GKN Aerospace Engine Systems are also acknowledged for their financial support.

References

[1] R.C. Reed, The Superalloys Fundamentals and Applications, Cambridge, New York, 2006.
[2] J.R. Nicholls, Designing oxidation-resistant coatings, JOM-J. Min. Met. Mat. S. 52 (2000) 28-35.
[3] S. Osgerby, B.F. Dyson, Modelling creep properties of coated superalloys in air and aggressive environments, Mater. Sci. Eng.: A. 120–121, Part 2 (1989) 645-650.
[4] H.J. Kolkman, Creep, Fatigue and Their Interaction in Coated and Uncoated Rene 80, Mater. Sci. Eng. 89 (1987) 81-91.
[5] R.R. Unocic, G.B. Viswanathan, P.M. Sarosi, S. Karthikeyan, J. Li, M.J. Mills, Mechanisms of creep deformation in polycrystalline Ni-base disk superalloys, Mater. Sci. Eng.: A. 483–484 (2008) 25-32.
[6] M.G. Hebsur, R.V. Miner, Stress Rupture and Creep Behavior of a Low Pressure Plasma-Sprayed NiCoCrAlY Coating Alloy in Air and Vacuum, Thin Solid Films. 147 (1987) 143-152.
[7] Y. Itoh, M. Saitoh, Y. Ishiwata, Influence of high-temperature protective coatings on the mechanical properties of nickel-based superalloys, J. of Mater. Sci. (UK). 34 (1999) 3957-3966.
[8] A. Sato, Y. Aoki, M. Arai, H. Harada, Effect of Aluminide Coating on Creep Properties of Ni-Base Single Crystal Superalloys, Journal of the Japan Institute of Metals. 71 (2007) 320-325.
[9] J. Angenete, K. Stiller, A comparative study of two inward grown Pt modified Al diffusion coatings on a single crystal Ni base superalloy, Mater. Sci. Eng. , A. 316 (2001) 182-194.
[10] J. Angenete, K. Stiller, Comparison of inward and outward grown Pt modified aluminide diffusion coatings on a Ni based single crystal superalloy, Surf. Coat. Technol. 150 (2002) 107-118.
[11] N. Vialas, D. Monceau, Effect of Pt and Al content on the long-term, high temperature oxidation behavior and interdiffusion of a Pt-modified aluminide coating deposited on Ni-base superalloys, Surf. Coat. Technol. 201 (2006) 3846-3851.
[12] K. Yuan, R.L. Peng, X.H. Li, L. Johansson, S. Johansson, Y.D. Wang, Analysis on

microstructural evolution of PtAl diffusion coating on Ni-based superalloy influenced by creep process, The 4th Conference on the Integrity of High Temperature Welds & 9th International Conference on Creep and Fatigue. (2012).
[13] Z. Hashin, S. Shtrikman, A Variational Approach to the Theory of the Effective Magnetic Permeability of Multiphase Materials, J. Appl. Phys. 33 (1962) 3125-3131.
[14] J. Agren, Numerical Treatment of Diffusional Reactions in Multicomponent Alloys, J. Phys. Chem. Solids. 43 (1982) 385-391.
[15] Thermo-Calc Software AB, Thermodynamic and Mobility Databases Overview, (2011).
[16] A. Lasalmonie, J.L. Strudel, Influence of Grain Size on the Mechanical Behaviour of Some High Strength Materials, J. Mater. Sci. 21 (1986) 1837-1852.
[17] F.T. Furillo, J.M. Davidson, J.K. Tien, L.A. Jackman, The Effects of Grain Boundary Carbides on the Creep and Back Stress of a Nickel--Base Superalloy, Mater.Sci.Eng. 39 (1979) 267-273.
[18] Q.Z. Chen, N. Jones, D.M. Knowles, The microstructures of base/modified RR2072 SX superalloys and their effects on creep properties at elevated temperatures, Acta Mater. (USA). 50 (2002) 1095-1112.
[19] Q.Z. Chen, C.N. Jones, D.M. Knowles, The grain boundary microstructures of the base and modified RR 2072 bicrystal superalloys and their effects on the creep properties, Mater. Sci. Eng., A. 385 (2004) 402-418.
[20] K. Aning, J.K. Tien, Creep and stress rupture behavior of a wrought nickel-base superalloy in air and vacuum, Mater. Sci. and Eng. 43 (1980) 23-33.
[21] J.M. Larson, Carbide Morphology in P/M IN-792, Metall.Trans.A. 7A (1976) 1497-1502.
[22] R. Lowrie, D.H. Boone, Composite coatings of CoCrAlY plus platinum, Thin Solid Films. 45 (1977) 491-498.
[23] K. Schneider, H.W. Grünling, Mechanical aspects of high temperature coatings, Thin Solid Films. 107 (1983) 395-416.
[24] M. Alam, D. Chatterjee, S. Kamat, V. Jayaram, D. Das, Evaluation of ductile-brittle transition temperature (DBTT) of aluminide bond coats by micro-tensile test method, Mater. Sci. Eng., A: Structural Materials: Properties, Microstructures and Processing. 527 (2010) 7147-7150.
[25] P. Hancock, H.H. Chien, J.R. Nicholls, D.J. Stephenson, In situ measurements of the mechanical properties of aluminide coatings, Surf. and Coat. Technol. 43–44, Part 1 (1990) 359-370.
[26] S. Bose, High Temperature Coatings, Butterworth-Heinemann, Oxford, 2007.
[27] T. Narita, A View of Compatible Heat-Resistant Alloy and Coating Systems at High-Temperatures, Proceedings of the International Workshop On Advanced Material For New and Renewable Energy. (2009) 63-67.
[28] T.K. Chaki, A.K. Singh, K. Sadananda, Effects of CoCrAlY coating on microstructural stability and creep behavior of a nickel-base superalloy, Thin Solid Films. 168 (1989) 207-220.

Creep and fracture behaviors of an advanced heat resistant austenitic stainless steel for A-USC power plant

Guocai Chai[1,2*] Patrik Kjellström[1] and Magnus Boström[1]

1 Strategy Research, Sandvik Materials Technology, 811 81 Sandviken, Sweden
2 Engneering Materials, Linköping University, 581 83 Linköping, Sweden
* Corresponding author: guocai.chai@sandvik.com

Abstract Creep and fracture behaviors in a newly developed austenitic stainless steel grade UNS S31035 (Sandvik Sanicro® 25) for use in A-USC power plant have been investigated. This new grade shows very good resistances to steam oxidation and hot corrosion, and higher creep rupture strength than other austenitic stainless steels available today. This makes it an interesting alternative for super-heaters and reheaters in future high-efficient coal fired boilers. This paper will mainly focus on the study of the creep and fracture behaviors of the material at temperatures from 600°C to 750°C by using SEM and TEM. The creep and fracture mechanisms at different temperature and loading conditions have been identified. The interactions between dislocations and precipitates and their contribution to the creep rupture strength have been discussed. In this paper, free temperature model has been used to evaluate the long-term creep behavior of the grade. A creep rupture strength near 100MPa at 700°C for 100 000h has been predicted.

Keywords Heat resistant austenitic stainless steel, Superheater, A-USC, Creep, Fracture

1. Introduction

The demand for electric power is continuously increasing around the world. Meanwhile the consciousness of the environmental impact from human action is growing. Although combustion processes generate carbon dioxide, coal-fired thermal power generation is still one of the most important methods in the medium to long-term future to satisfy this demand, since coal is available at a competitive price and often is the single domestic energy source [1]. However, the biggest challenge facing coal-fired power plants is to improve their energy efficiency. This can be accomplished by increasing the maximum steam temperature and the steam pressure. Conventionally, the heat efficiency of coal-fired power plants has stayed at around 41% in the super critical (SC) condition with a temperature of 550°C and pressure of 24.1MPa. In order to attain a power generating efficiency of about 43%, ultra super critical (USC) conditions with a steam temperature at about 600°C should be reached. By increasing the temperature up to 700°C (A-USC condition) and pressure of above 300 bars, a power plant efficiency of higher than 50% can be reached and CO_2 emission can be reduced by about 45% comparing with that of SC condition [2]. However, the steam data in practice will be limited by the material properties of the boiler tubes, especially tensile strength at elevated temperatures and creep strength combined with corrosion resistance.

A new austenitic stainless steel grade, UNS S31035 (Sandvik Sanicro 25), has recently been developed for the purpose of A-USC [3] in collaboration with a number of different industrial partners within the Thermie-project in Europe, intended for use in super-heaters and reheaters in advanced ultra-supercritical boilers at temperatures up to 700°C. They have been test-installed in different boilers in Europe and have run for more than five years, and are still in very good conditions [4]. In this paper the creep and fracture behaviors of this new grade are discussed.

2. Material and experimental

Since austenitic stainless steel grade, UNS S31035, was aimed for use in super-heaters and reheaters with metal temperatures up to 700°C, the design principles for this alloy were to achieve a stable microstructure, high strength by precipitation strengthening with stable nano precipitates and solution hardening, high corrosion resistance with high Cr content. Ni and N that can suppress the formation of sigma phase were added to reach sufficient structural stability and good fabricability. The chemical composition is shown in Table 1.

Table 1 Nominal composition of austenitic stainless steel grade, UNS S31035 (wt%)

C_{max}	Si	Mn	Cr	Ni	W	Co	Cu	Nb	N	Fe
0.1	0.2	0.5	22.5	25	3.6	1.5	3.0	0.5	0.23	Bal.

Figure 1 shows some fine precipitates observed in this newly developed austenitic stainless steel grade, UNS S31035 that can contribute to the improvement of the creep strength. Both intra- and intergranular $M_{23}C_6$ precipitates can be observed (Fig. 1a). In the grain boundaries, they have a $<100>_{\gamma}$ // $<100>_{M23C6}$ coherent relationship to the austenite matrix. Laves phase was observed both randomly within the grains but also ordered on what appears to be former twin boundaries (Fig. 1b). Both coherent Laves phase precipitates with a $[100]_{Laves}$ // $[100]_{\gamma}$ orientation relationship, and incoherent Laves phase precipitates were observed. In the aged material the Laves phase are needle shaped but rather small. In the creep tested materials, these particles are fine and isometric. Copper rich nanoparticles can also be observed. They are round with a size up to 50 nm (Fig. 1c). In this material, a dense distribution of about 10 nm large precipitates was observed (Fig. 1d). Due to the limitation of the TEM, these particles could not be identified, but they are probably MX carbides or carbonitrides. Similar particles have been identified in other analyses. These particles were rather stable [5].

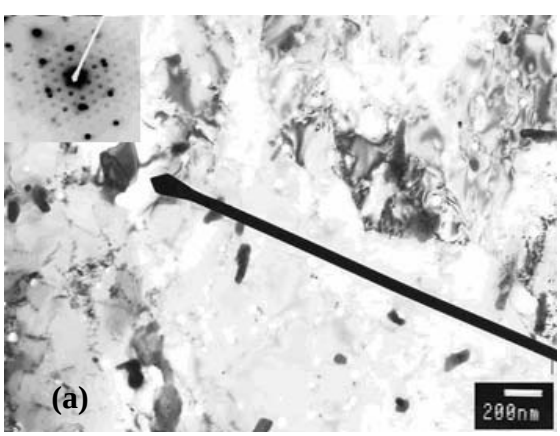

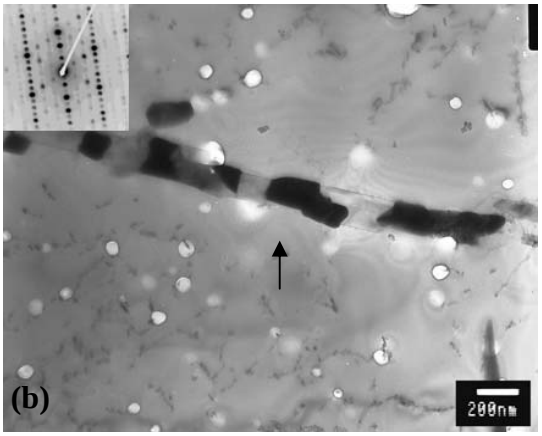

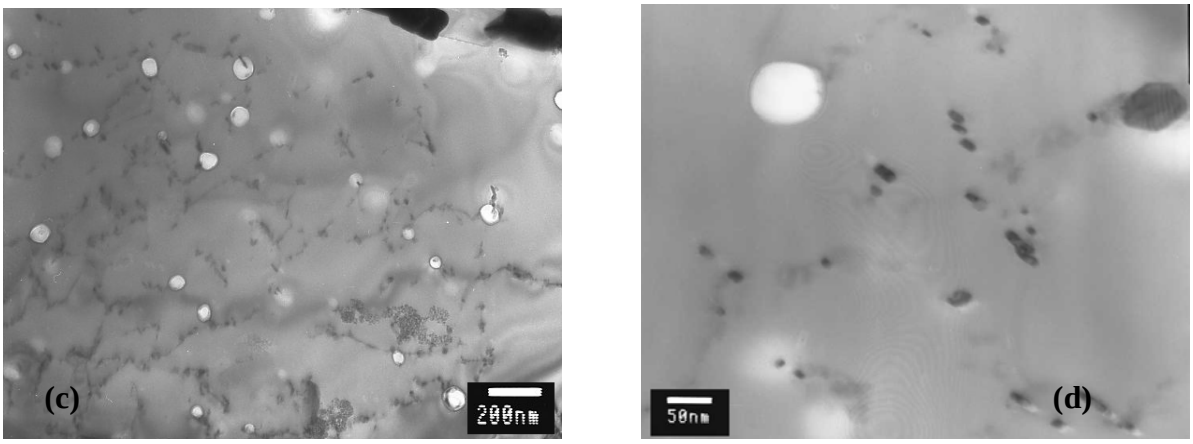

Figure 1. Fine precipitates that contribute to the creep strength of austenitic stainless steel grade, UNS S31035, (a) $M_{23}C_6$, 700°C for 1000 hours, (b) Laves phase, 700°C for 30 000 hours, (c) Copper-rich phase, 700°C for 30 000 hours, (d) Nanoparticles, 700°C for 30 000 hours.

The creep testing on UNS S31035 was performed from 550°C to 800°C. Both stress-rupture testing and creep-strain testing were done. The stress-rupture testing was performed in Escher Wyss (EW) creep testing machines. In these machines multiple samples can be tested simultaneously. The samples (Fig. 2) are mounted in the EW boxes. The tube in which the samples are located is then inserted into the furnace. The load from the compressed spring is applied after the samples have been heated in the furnace for one hour. The creep-strain testing was performed in Bofors machines. The sample was mounted in sample holders in the tube furnace and connected to thermocouples which can measure the temperature continuously. The strain was measured by two extensometers placed outside the furnace. The strain was logged manually regularly during testing to obtain creep curves.

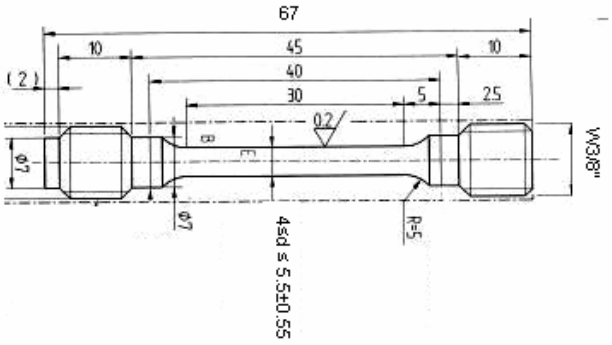

Figure 2. Schematic sample for the creep test.

The microstructure was studied using light optical microscope (LOM), scanning electron microscope (SEM) and transmission electron microscope (TEM). LOM and SEM were used to obtain information on features such as grain size, creep deformation, precipitates and how these changes with time, temperature and stress. TEM was used for phase identification and dislocation structure characterization.

3. Free temperature model

Pressure vessel components are normally designed for a long service time such as 200 000 h. Since creep is a very slow process, creep data for such a time are not available for design. They are therefore calculated by an extrapolation from the creep data of shorter time tests. One recently proposed procedure for extended extrapolation of creep rupture data is the free temperature model that allows for extrapolation by more than a factor of three in time [6, 7]. The procedure is based on a time-temperature parameter (TTP) which has the general mathematical form:

$$P_{TTP} = v(T)\log(t_r) + w(T) \tag{1}$$

where P_{TTP} is the time-temperature parameter, t_r is the time to rupture, and v(T) and w(T) are the functions of temperature. In the proposed procedure these functions are assumed to be polynomials in T. The TTP in Eq. 1 is referred as the free temperature model (FTM). The free temperature model is well suited for austenitic stainless steels where the temperature dependence of the creep rupture curve is non-monotonous [7].

The master curve is expressed by the creep stress as a function of polynomial in the TTP:

$$\log(\sigma) = \sum_{j=0}^{n_P} a_j TTP^j \tag{2}$$

The coefficients a_j are fitted to the creep rupture data and the stress – rupture time relations are derived. The reason for using a polynomial in log (t_r) rather than log (σ) which is the more common approach, is that it has been shown that this improves the accuracy in extended extrapolated values [7]. The extrapolation was performed in a Matlab program. The coefficients to the polynomials are derived by a non-linear least squares fit to the creep data.

To extrapolate the creep rupture data, the polynomials in Eq. 1 were both set to order 3 and the master curve, Eq. 2, was set to a second order polynomial. Figure 3 shows the master curve for the free temperature model of the austenitic stainless steel grade, UNS S31035, which is based on creep data at 550°C, 600°C, 650°C, 700°C and 800°C.

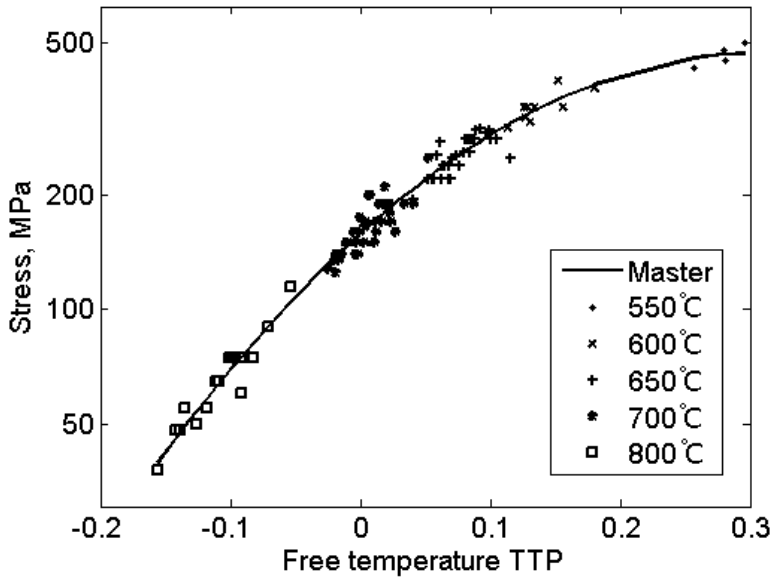

Figure 3 Master curve for austenitic stainless steel grade, UNS S31035, material.

4. Results and discussion

4.1 Creep strength

Up to now, the longest time to rupture from the creep test of this alloy is more than 74 000 h and some samples are still running. Figure 4 shows the results of the creep stress in rupture plots. With linear least squares regression (Larson-Miller relation) to extrapolate the creep rupture data, the predicted 10^5 h creep rupture strength at 700ºC is 104 MPa.

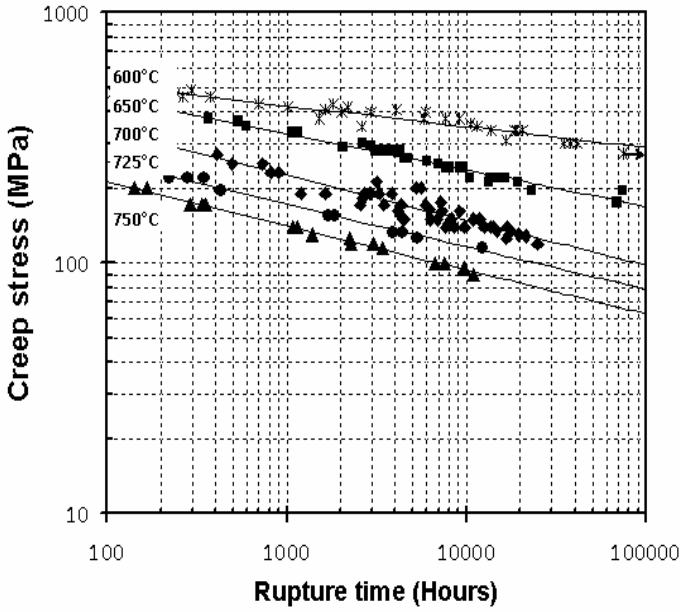

Figure 4 Creep stress versus rupture time of austenitic stainless steel and the linear regressions in the creep data.

The extrapolation was performed three times with rupture data up to 40000 h, 15000 h and 5000 h to verify the stability of the extrapolation. Figure 5a shows the result from the extrapolation. At both 700°C and 650°C the extrapolation overestimates the creep strength of the material when only short time creep data are used. This is common for many parametric methods and it is important that the deviation is not too large. The order of the polynomials and which temperature data sets the model is applied to will also influence the result. These factors are tested until a satisfactory result has been found. The predicted 10^5 h creep rupture strength at 700°C is about 99 MPa.

In Figure 5b, the correlation between the extrapolation and experimental data can be seen. The evaluation satisfies the post evaluation tests (PATs) and other criteria proposed by the European Collaborative Creep Committee (ECCC) [8].

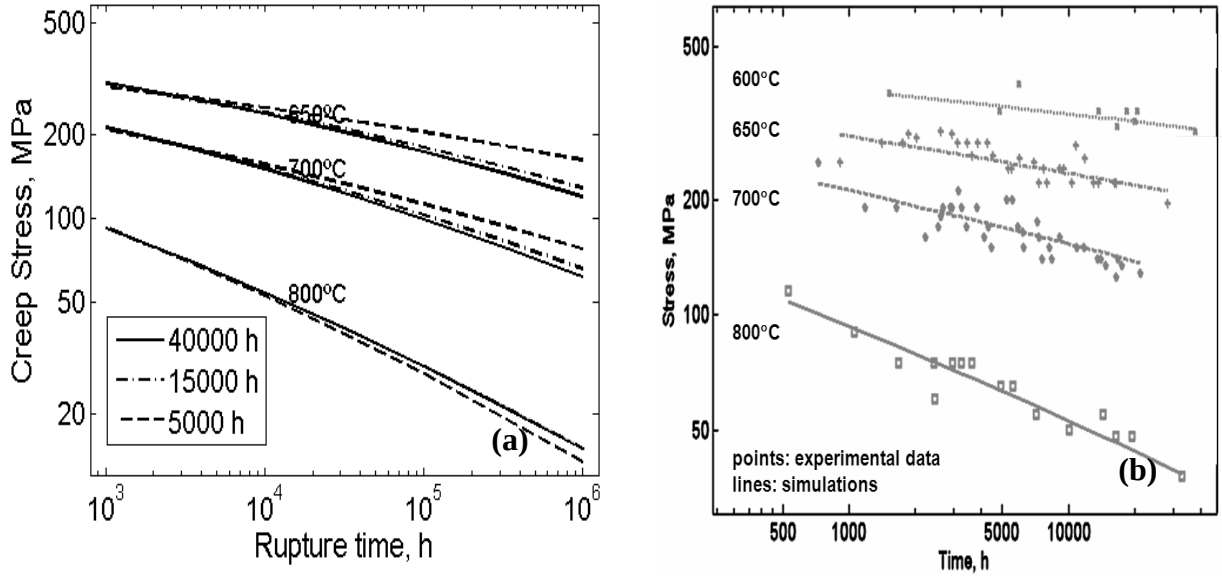

Figure 5 (a). Result from extrapolation with the free temperature model, performed three times with rupture data up to 5000 h, 15000 h and 40000 h, (b). Correlations between the extrapolation with rupture data up to 40000 h and the experimental data.

4.2 Strengthening mechanism

In the temperature range up to 700°C, one of the main creep strengthening mechanisms is the interaction between dislocations and precipitates [9]. Figure 6 shows two examples how interaction between the dislocations and precipitates in austenitic stainless steel grade, UNS S31035, creep specimen tested with 210 MPa at 700°C and with a rupture time of 3153 h. Moving dislocations at the nano-sized particles can be seen. Around the intergranular precipitates, the dislocation density is high which indicates that they function as obstacles for the dislocation movements. This increases the creep strength. Smaller nanoprecipitates such as copper rich particles and MX particles are more effective as obstacles for the dislocation movements. However, they have different mechanisms for dislocation crossing. For the copper rich nanoparticles, dislocations cross the particles mainly by climb / bypass of unit dislocations (Fig. 6a). For the MX nanoparticles, deformation might occur by

shearing of partial dislocations. The shadow around the particle in Figure 6b is believed to be dense dislocations. For MX particles, dislocation loops can be observed around the particles (Fig 6c and d).

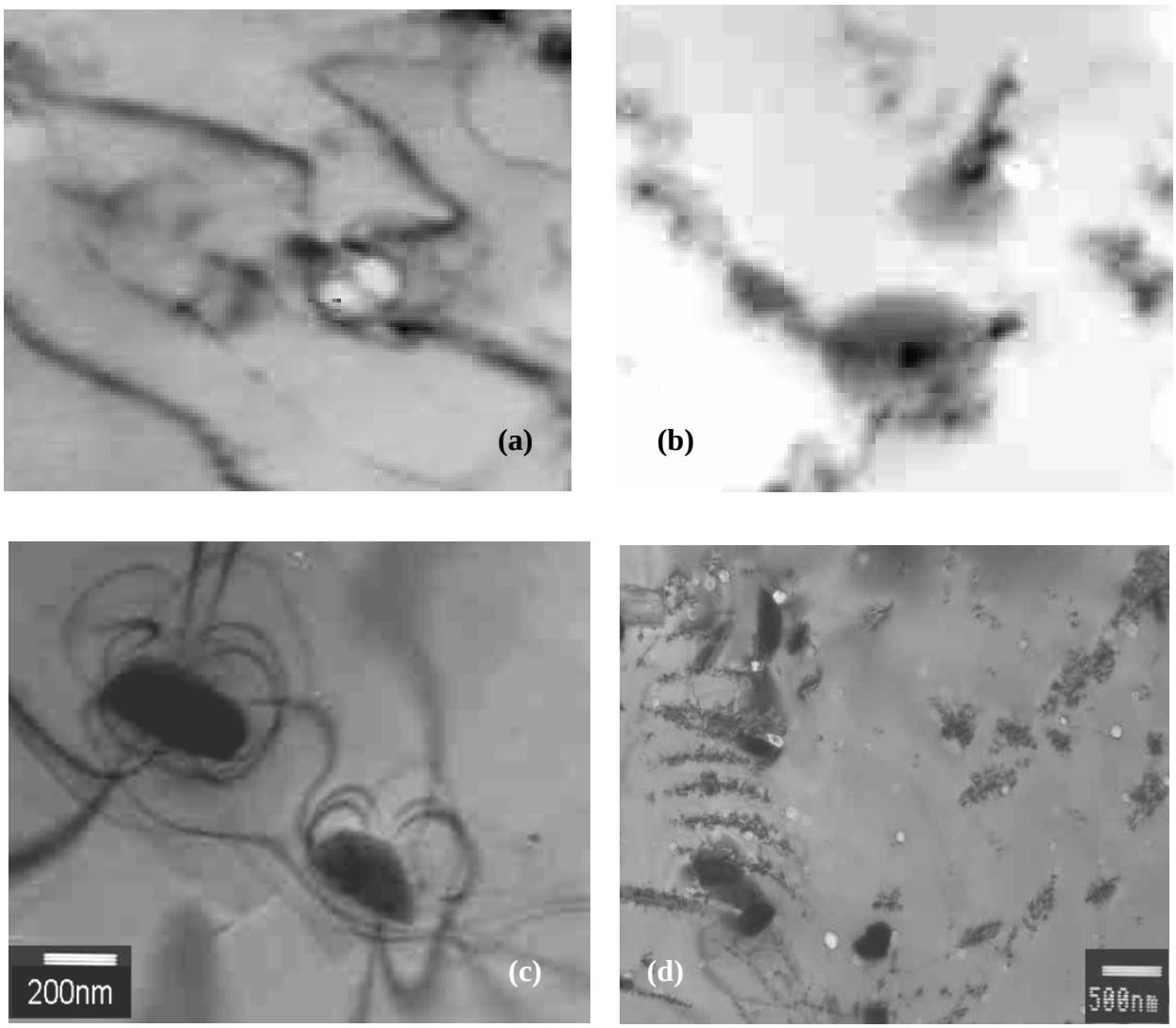

Fig. 6 Dislocation structures, (a). Interaction between dislocations and precipitates, (b). dislocation cloud or cluster near nona Cu-rich particles and MX particles

4.2 Rupture mechanisms

Figure 7 shows an investigation of the fracture modes such as transgranular or intergranular fractures and plastic deformation by creep in UNS S31035 material. A summary of the creep fracture modes are shown in Figure 8.

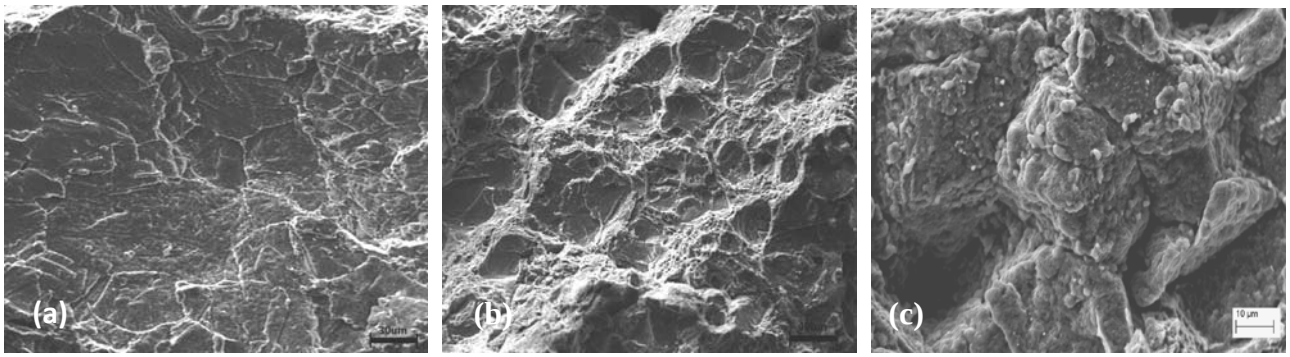

Figure 7 SEM micrograph of creep specimen near the fracture, (a). 700°C/240MPa, 1085h, transgranular cracking, (b). 700°C/210 MPa, 4203h, transgranular and intergranular mixed model, (c). 700°C/150 MPa, 14040 h, intergranular cracking

Plastic deformation and transgranular fracture is the main creep fracture mechanism in UNS S31035 material in the temperature ranges of interest (<700°C). The SEM analysis shows that the crack initiation area was mainly quasi cleavage and then cracks propagated with dimples. At intermediate stresses and temperatures a mixture of inter- and transgranular fracture occurs. The crack initiation often occurs at grain boundaries but propagate through the grains. At relatively low stresses and high temperatures, intergranular fracture could occur. However, plastic deformation can still be observed in these specimens.

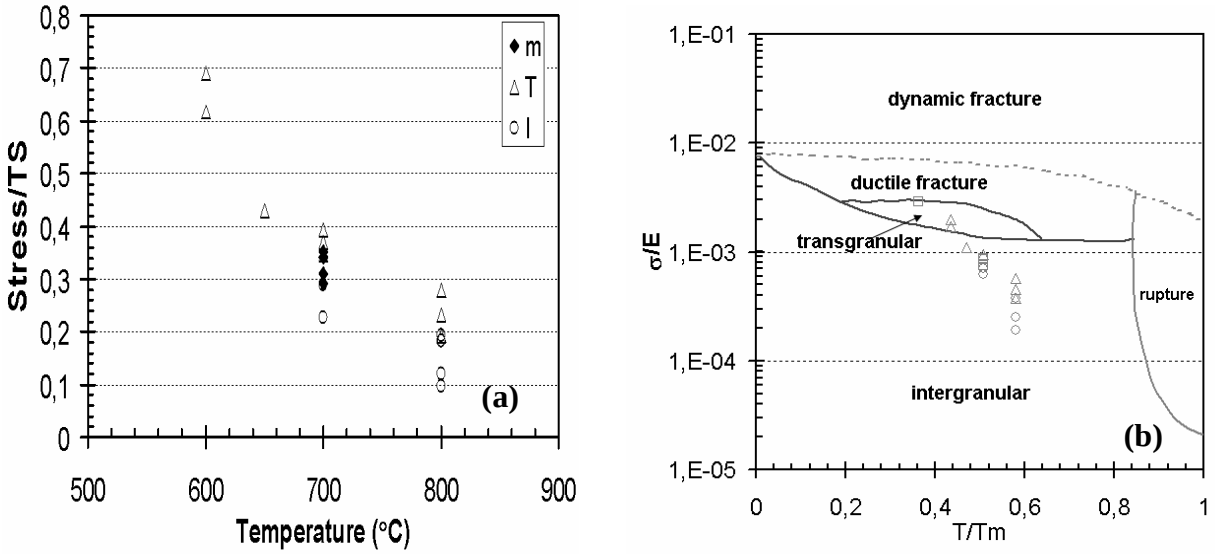

Figure 8 Fracture modes in UNS S31035 at different test conditions.

4. Conclusions

A new austenitic stainless steel grade, UNS S31035 (Sandvik Sanicro 25), has been developed intended for superheater and reheaters for A-USC. Extrapolation from creep data with two methods gives a creep strength of 99 ± 3 MPa at 700°C for 100 000 h, which is higher than that of other austenitic stainless steels available today.

The creep strength is related to intragranular precipitates and nano particles acting as obstacles for dislocation movement.

Plastic deformation and transgranular fracture is the main creep fracture mechanism in the creep test samples of UNS S31035 for high applied stresses, but trend to intergranular fracture with decreasing stresses and increasing temperature.

Acknowledgements

This paper is published by permission of Sandvik Materials Technology.

References

[1] IEA, 2009 energy statistics, http://www.iea.org/stats, (2010-02-25).
[2] R. Blum, R.W. Vanstone and C. Messelier-Gouze, Materials Development for Boilers and Steam Turbines Operating at 700 °C, Proc. 4th Int. Conf. on Adv. in Mater. Technol. for Fossil Power Plant, (2004) 116.
[3] R. Rautio, S. Bruce, Sandvik Sanicro 25, a new material for ultra supercritical coal fired boilers, Proc. 4th Inter Conf. on Adv. in Mater. Technol. for fossil power plants, (2004) 274.
[4] G. Chai, J.O. Nilsson, M. Boström, J. Högberg and U. Forsberg, Advanced Heat Resistant Austenitic Stainless Steels, Proc. of ICAS 2011 (2010) 56.
[5] G. Chai, M. Boström, M. Olaison and U. Forsberg, Creep and LCF behaviors of newly developed advanced heat resistant austenitic stainless steel for A-USC, Procedia Engineering 2012, in press
[6] R. Sandström, Journal of Testing and Evaluation, 31 (2003) 58-66.
[7] R. Sandström and L. Lindé, Precision in the extrapolation of creep rupture data, Journal of Testing and Evaluation Vol. 27, No3 (1999) 203-210.
[8] Generic recommendations and guidance for the assessment of full size creep rupture datasets, ECCC recommendations - volume 5 part in [issue 5], 2008.
[9] J. Högberg, G. Chai, P. Kjellström, M. Boström, U. Forsberg and R. Sandström, (2010), Creep behavior of the newly developed advanced heat resistant austenitic stainless steel grade UNS S31035, PVP2010-25727, Bellevue Washington, USA.

Damage and fracture behaviours in advanced heat resistant materials during slow strain rate test at high temperature

Mattias Calmunger[1,*], Guocai Chai[1, 2], Sten Johansson[1], Johan Moverare[1]

[1] Division of Engineering Materials, Department of Management and Engineering, Linköping University, SE-58183 Linköping, Sweden
[2] AB Sandvik Material Technology R&D center, SE-81181 Sandviken, Sweden
* Corresponding author: mattias.calmunger@liu.se

Abstract As a renewable energy resource, biomass or biomass co-firing in coal-fired power plants with high efficiency are desired which corresponding to elevated temperature and high pressure. An upgrade of the material performance to austenitic stainless steels is therefore required in order to meet the increased demands due to the higher temperature and the more corrosive environment. These materials suffer from creep and fatigue damage during the service. In this study, these behaviours are evaluated using slow strain rate testing (SSRT) with strain rate down to $1*10^{-6}$/s at temperature up to 700°C. The influence of temperature and strain rate on strength and ductility in one austenitic stainless steel and one nickel base alloys are investigated. The damage and fracture due to the interaction between moving dislocations and precipitates are studied using electron channelling contrast imaging (ECCI) and electron backscattering diffraction (EBSD). The deformation and damage mechanisms active during SSRT are essentially the same as under creep. The influence of dynamic strain ageing (DSA) phenomena that appears in the tested temperature and strain rate regime is also discussed, DSA is intensified by increased temperature and decreased strain rate.

Keywords Elevated temperature, slow strain rate, biomass power plant, austenitic stainless steel, nickel base alloy.

1. Introduction

Biomass or biomass co-firing in coal-fired power plants is a contribution to renewable energy resources for sustainable energy production. Also high efficiency which requires higher temperature and pressure is highly desired. However, the materials used in those power plants with increasing temperature and pressure also need to be resistant to the corrosive atmosphere connected to combustion of biomass fuel [1, 2].

In the operating temperature range of biomass or biomass co-firing coal-fired power plants, austenitic materials often show dynamic strain ageing (DSA). The temperature regime of DSA is from 200 to 800°C for austenitic materials [3, 4] and arises during plastic deformation from interaction between solute atoms related to bulk or pipe diffusion and mobile dislocations or forest junctions[5, 6]. Temperature and strain rate directly influence diffusing solute atoms and the mobility of dislocations respectively, which effects DSA [6]. At elevated temperatures (400°C to 650°C) nitrogen and/or substitutional chromium atoms are responsible for DSA [7, 8]. Portevin-Le Châtelier (PLC) effect which is serrated yielding in the stress-strain curve, characterizes DSA. The PLC effect is due to the pinning and unpinning of dislocations or formation of new dislocations [9].

These materials can undertake low deformation rate from 10^{-5}/s (low cycle fatigue) to 10^{-7}/s (creep) during service. This study was focused on damage and fracture mechanisms related to low strain rate and high-temperature in two austenitic materials. Using uniaxial slow strain rate tensile testing (SSRT) at high-temperatures, the influence of low strain rates on these mechanisms could be investigated. Also precipitation due to high-temperature and deformation could be coupled to the damage and fracture behaviour.

2. Materials and experimental details

2.1. Materials

The austenitic stainless steels, AISI 316L and the nickel-base alloys, Alloy 617 were used in this study. Both types were solution treated before testing. Table 1 shows the chemical composition of the materials.

Table 1. Nominal composition of the investigated materials in wt%.

Material	C	Si	Mn	Cr	Ni	W	Co	Cu	Nb	N	Mo	Fe
AISI 316L	0.04	0.4	1.7	17	12	-	-	-	-	-	2.6	Bal.
Alloy 617	0.1	-	-	22.5	53.8	-	12	-	-	0.5	9	1.1

2.2. Tensile deformation

For the slow strain rate tensile testing (SSRT) a Roell-Korthaus and an Instron 5982 tensile test machines were employed. The tensile test machines were equipped with a MTS 653 furnace and Magtec PMA-12/2/VV7-1 extensometer and ElectroHeat Sweden furnace and Epsilon extensometer respectively, both active in air environments. Round-bar specimens with 5 mm in diameter and 50 mm gauge length were used. The tensile tests were carried out at a strain rate of $2*10^{-3}s^{-1}$ down to $10^{-6}s^{-1}$. Three temperatures: room temperature (RT), 650°C and 700°C, were used. Alloy 617 was tested using strain rates $10^{-2}s^{-1}$, $2*10^{-3}s^{-1}$, $10^{-3}s^{-1}$, $10^{-4}s^{-1}$, $10^{-5}s^{-1}$ and $10^{-6}s^{-1}$, AISI 316L was tested using strain rates $2*10^{-3}s^{-1}$ and $10^{-6}s^{-1}$.

2.3. Scanning electron microscopy investigation

For the microstructural investigation of deformation and fracture behaviour the scanning electron microscopy (SEM) techniques electron channeling contrast imaging (ECCI) and electron backscatter diffraction (EBSD) were used. ECCI uses the interaction between backscattered electrons and the crystal planes to generate contrast resulting in an image where local orientation, defects and strain fields are shown as contrast variations [10].

3. Results

3.1. Strain rate and temperature influence on tensile deformation and damage

Low strain rates and elevated temperatures are increasing the probability of dynamic strain ageing (DSA), because the diffusion rate of the solute atoms increases and rate of dislocation movement decreases. During DSA the deformation mechanisms is shifting towards planar deformation [7]. None of the tested materials showed DSA at room temperature, but both materials showed DSA at elevated temperatures for all tested strain rates. For a strain rate of 10^{-6}/s at both elevated temperatures, AISI 316L and Alloy 617 show different types of PLC effects. AISI 316L display B-type and Alloy 617 shows C-type serrated yielding, see fig.1. B-type serrations means that the stress oscillates from a origin stress level and C-type of serration is characterized by a sudden drop in stress and then raises to the normal stress level [8, 9]. Alloy 617 show serrated yielding from low strain values until fracture for all tested strain rates at both elevated temperature except of strain rates 10^{-3}/s and 10^{-4}/s. At both elevated temperatures and strain rate 10^{-3}/s serrated yielding is present at low strain levels up to around 20% but DSA also appears just before fracture, see fig. 1a). For 10^{-4}/s at 650°C serrated yielding disappears after approximately 4% strain and after around 12%

with a few serration drops at 22% strain at 700°C. At room temperature the elongation to fracture increases with decreasing strain rate for AISI 316L, at a strain rate of $2*10^{-3}$/s it is 53% and 66% at 10^{-6}/s, see fig.1b). This behaviour is due to the lower deformation rate that causes the dislocation mobility to decrease and therefore resulting in a lower stress level when using a strain rate of 10^{-6}/s. At elevated temperatures and low strain rates AISI 316L show a decrease in the stress-level during tensile tests due to recovery that could be related to recovery-creep [11], see fig.1b), also features related to dynamic recrystallization can be found in the microstructure (fig.4) [12].

The strain rate influences the ductile response of Alloy 617, as shown in fig. 2 a). From 10^{-2}/s to 10^{-3}/s the ductility increases at both temperatures and continues to increase for strain rates of 10^{-4}/s at 650°C but decrease slightly at 700°C. With even slower strain rates the ductility decreases even more for both temperatures, 700°C have lower ductility than 650°C at a strain rate of 10^{-6}/s but have a higher tensile stress which can explain the differences in ductility. Alloy 617 has much higher ductility (A_{RT}=70.5%) and tensile stress (Rm_{RT}=709MPa) when it is deformed at room temperature than at elevated temperature ($A_{700°C}$=10.3% and $Rm_{700°C}$=489MPa) when using a strain of rate 10^{-6}/s, see fig.2. This behaviour is most likely due to grain boundary embrittlement coused by chromium rich precipitation in the grain boundaries, shown in fig.6.

In the DSA regime nano-twins can show up as a deformation mechanism [13]. AISI 316L material showed nano-twins close to the surface of the specimen. Other deformation mechanism in the microstructure of the SSRT tested samples was slip bands (SB) and planar slip. Fig.3 displays probable future damage due to interaction between slip bands and precipitates (fig.3 b)) and nano-twins and precipitates. Contrast differences that could be related to stress concentrations spots which is or will be future damage can be observed where these interactions appear in fig. 3 b) and c).

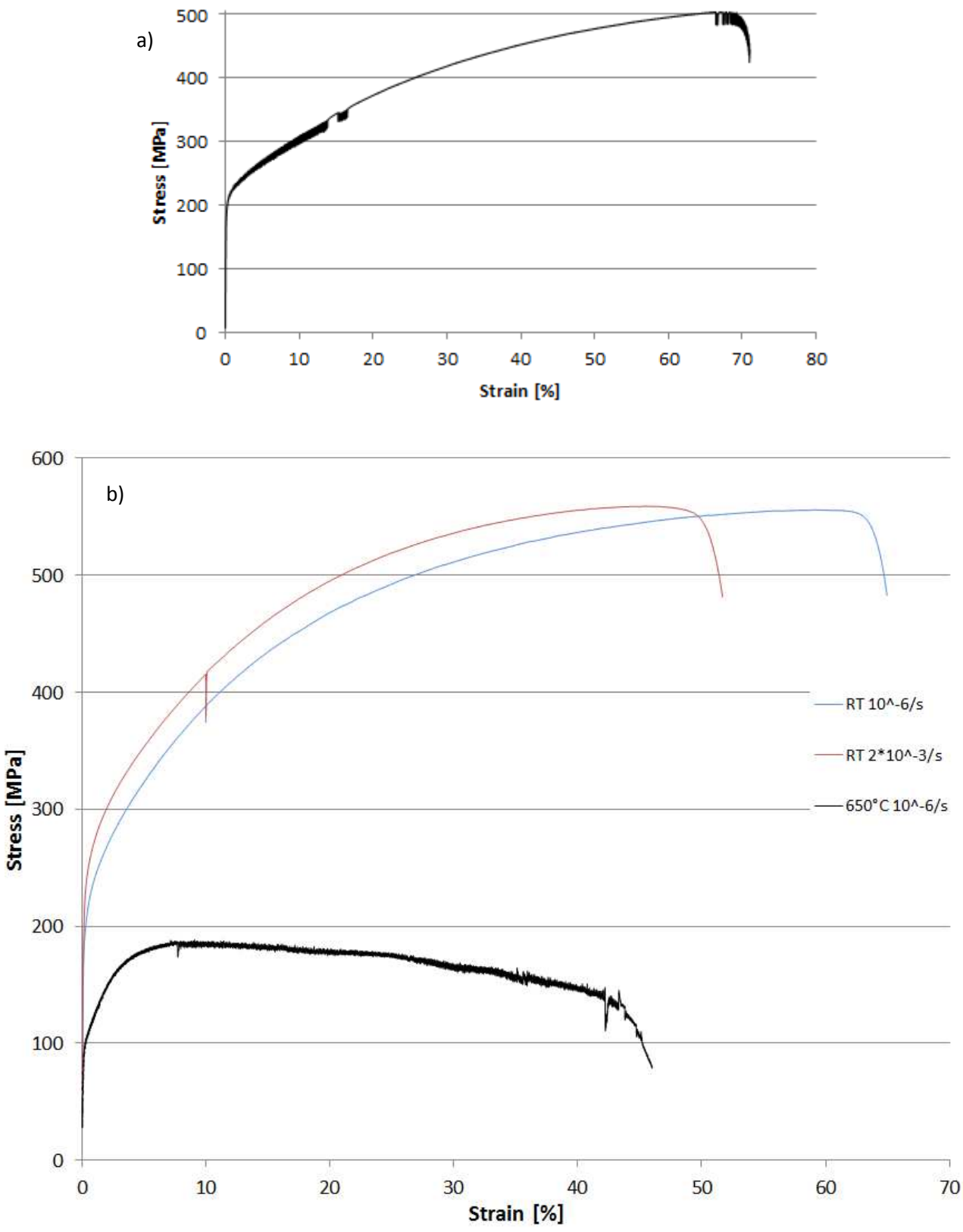

Figure 1. Engineering stress-strain curves showing a) C-type serration in Alloy 617 tensile tested at 700°C using strain rate 10^{-3}/s and b) B-serration in AISI 316L tensile tested at 650°C using strain rate 10^{-6}/s (black curve) and two curves showing AISI 316L tested at room temperature (RT) using strain rates 10^{-6}/s and $2*10^{-3}$/s (blue and red curve respectively).

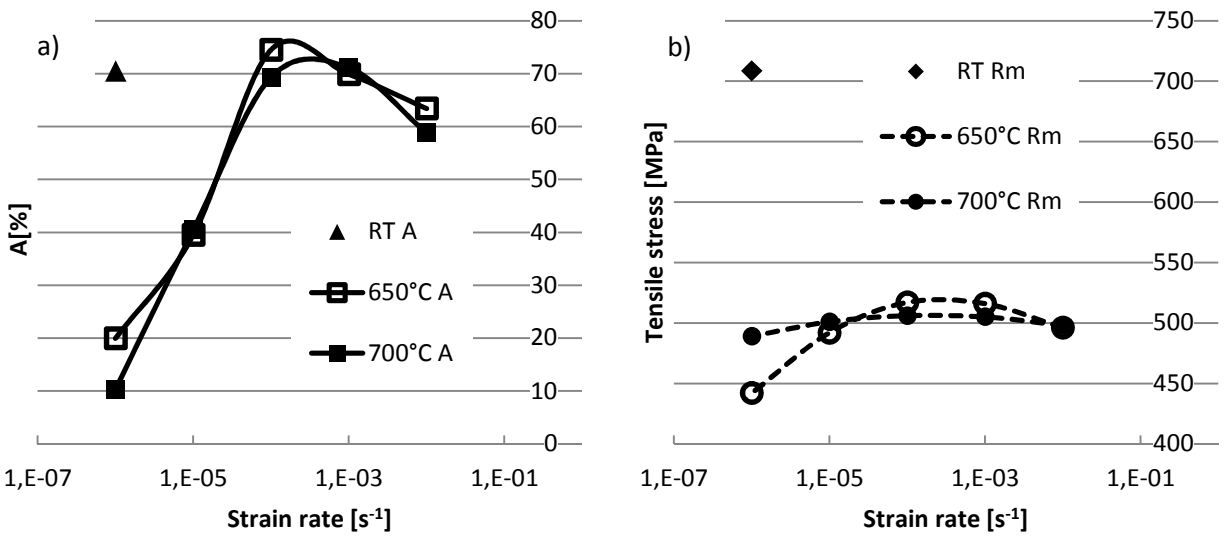

Figure 2. Influence of a) strain rate on ductility (A) and b) tensile stress (R_m) levels for Alloy 617.

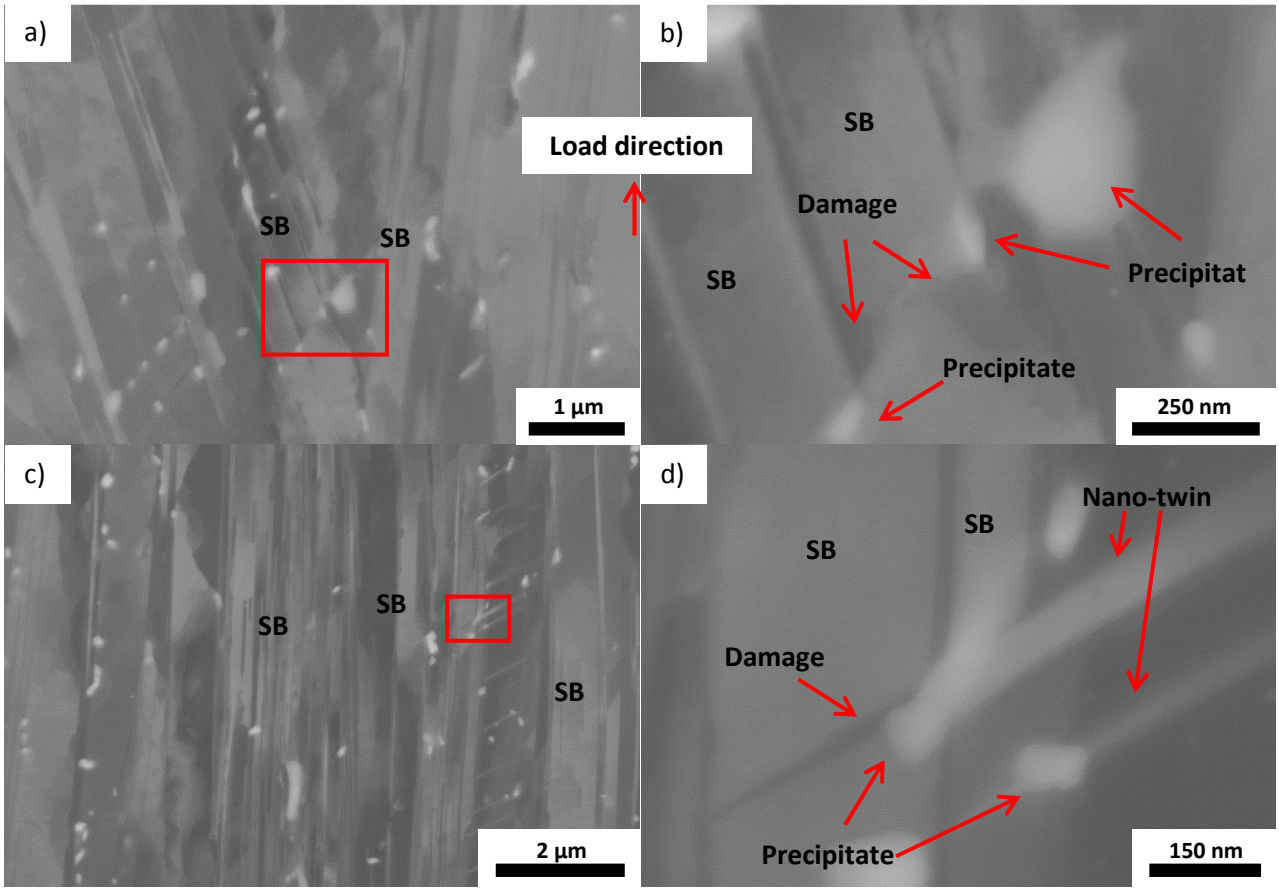

Figure 3. ECCI imaging of AISI 316L deformed to 46% strain, at a strain rate of 10^{-6}/s and 700°C, a) slip bands (SB) with two different directions interacting with precipitates, b) magnification of damage or probable future damage due to interaction between precipitate and slip bands, c) other location with slip bands and nano-twins interacting with precipitates and d) magnification of damage or probable future damage due to interaction between slip bands, nano-twins and precipitate. It is the same load direction in all the pictures.

Other damage behaviour in AISI 316L is shown in fig.4. At room temperature the deformation and damage behaviour is similar for strain rates of $2*10^{-3}$/s and 10^{-6}/s. Common damage appearing away from fracture zone is slip bands creating voids when intersecting with each other, grain boundaries or precipitates. Voids due to intersection between slip bands and grain boundaries, around 15mm away from the fracture surface are displayed in fig. 4 a). Voids also occur due to heavy deformation from shear bands as in fig.4 b). Near the fracture surface the microstructure is heavily deformed from multi-direction slip bands, shear bands and planar slip. Deformation bands with features looking like subcells appear near the fracture surface at room temperature for strain rates of $2*10^{-3}$/ and 10^{-6}/s. At elevated temperature the deformation bands look recrystallized as can be seen in fig. 4 c) and d). The EBSD analysis in fig.5 reveals that the areas that look like recrystallization has taken place (see fig.5 a)) don't show any new grains in AISI 316L at 650°C and a strain rate of 10^{-3}/s. Fig.5 b) shows the local misorientation in gray scale together with inversed pole figure (IPF) in color scale, and the brighter patterns correspond to local misorientation values above 4° and up to 5°. These brighter patterns have good correlation to some of the subcell or grains that can be seen in fig.5 a). The crystallographic orientation differs but doesn't give clear distinction between the supposed subcells or grains and the matrix and thus no evidence of recrystallization is found. The analysis in fig.5 is made in mostly one single grain or annealing twin, showing precipitates in the grain boundaries as white zero-solution in fig.5 b).

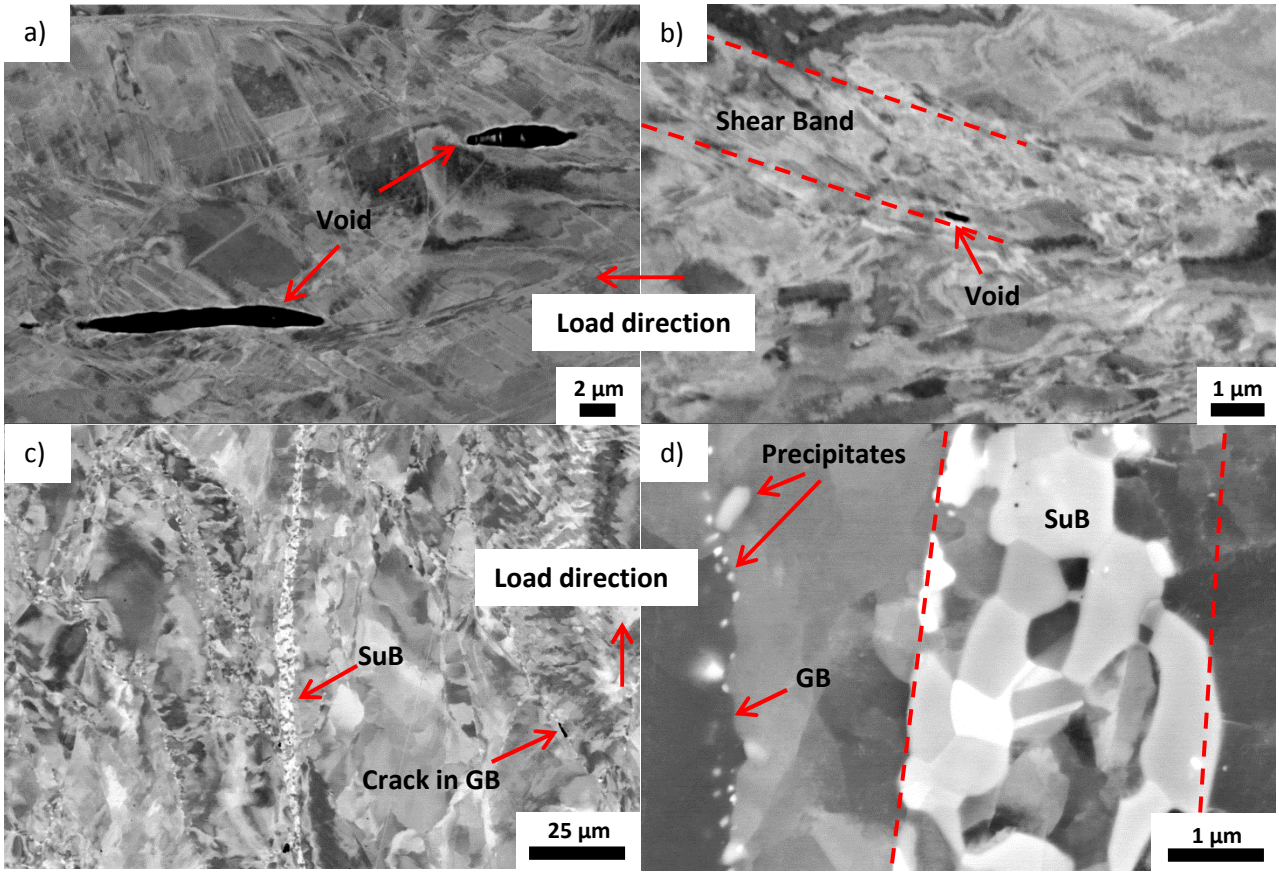

Figure 4. Deformation and damage behavior by ECCI in AISI 316L materials, a) voids from interaction between slip bands and grain boundaries (GB) at RT and strain rate $2*10^{-3}$/s, b) void due to deformation from shear band at RT and 10^{-6}/s, c) subcell band (SuB) at 650°C and 10^{-6}/s and d) magnification of subcell band.

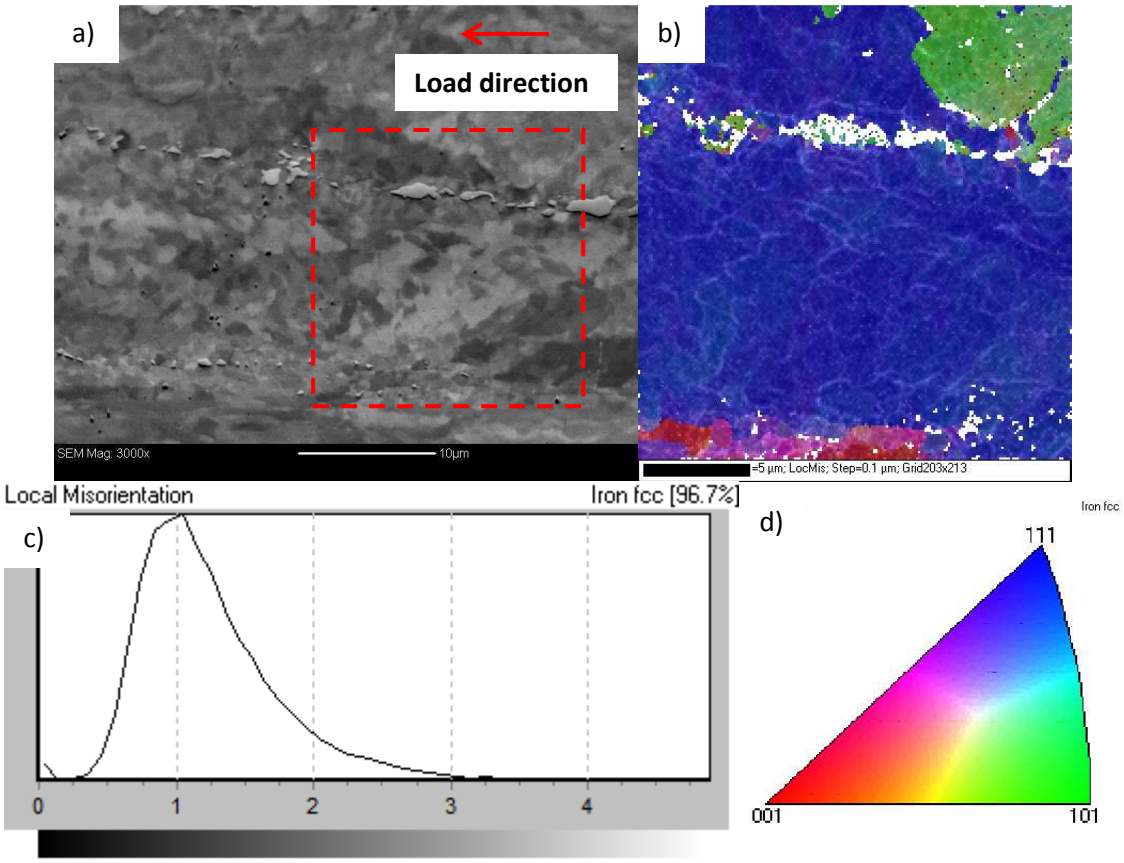

Figure 5. EBDS analysis showing recrystallization or subcell formation in AISI 316L after SSRT at 650°C to fractured using a strain rate of 10^{-6}/s, a) showing analyzed area, b) EBSD analysis displaying local misorientation (bright patterns) tighter with crystallographic orientation in a inversed pole figure (white color means zero-solution), c) local misorientation legend where the y-axis is frequency and x-axis is misorientation angle [°] and d) inversed pole figure legend showing crystallographic orientation.

3.2. Precipitates effect on damage

Both materials undergo precipitation due to the elevated temperature during the long deformation process. Alloy 617 has evenly distributed γ´ precipitates in the matrix and σ-phase in the grain boundaries [14]. AISI 316L get precipitates as Cr-rich carbides, that probably are $M_{23}C_6$ or M_6C, also σ-phase precipitate and they appear both in the matrix and grain boundaries [15]. The deformation time depends on material properties and strain rate, the deformation time varied from 1 minute to 130 hours. The size and amount of precipitates varied with the deformation time or strain rate and temperature, from no precipitate at high strain rates to more and bigger precipitates at the slower strain rates. Damage corresponding to the precipitation can be seen in fig.3 and fig. 6. At low strain rate and elevated temperature, the interaction between a moving dislocation and a precipitate can cause damage in the material. Fig. 6 display internal cracks that have initiate and propagate in the grain boundaries due to deformation and embrittlement from precipitates (Fig.6 c) and d)). Precipitates act as crack initiation points due to high local stress caused by the interaction between dislocations and precipitates.

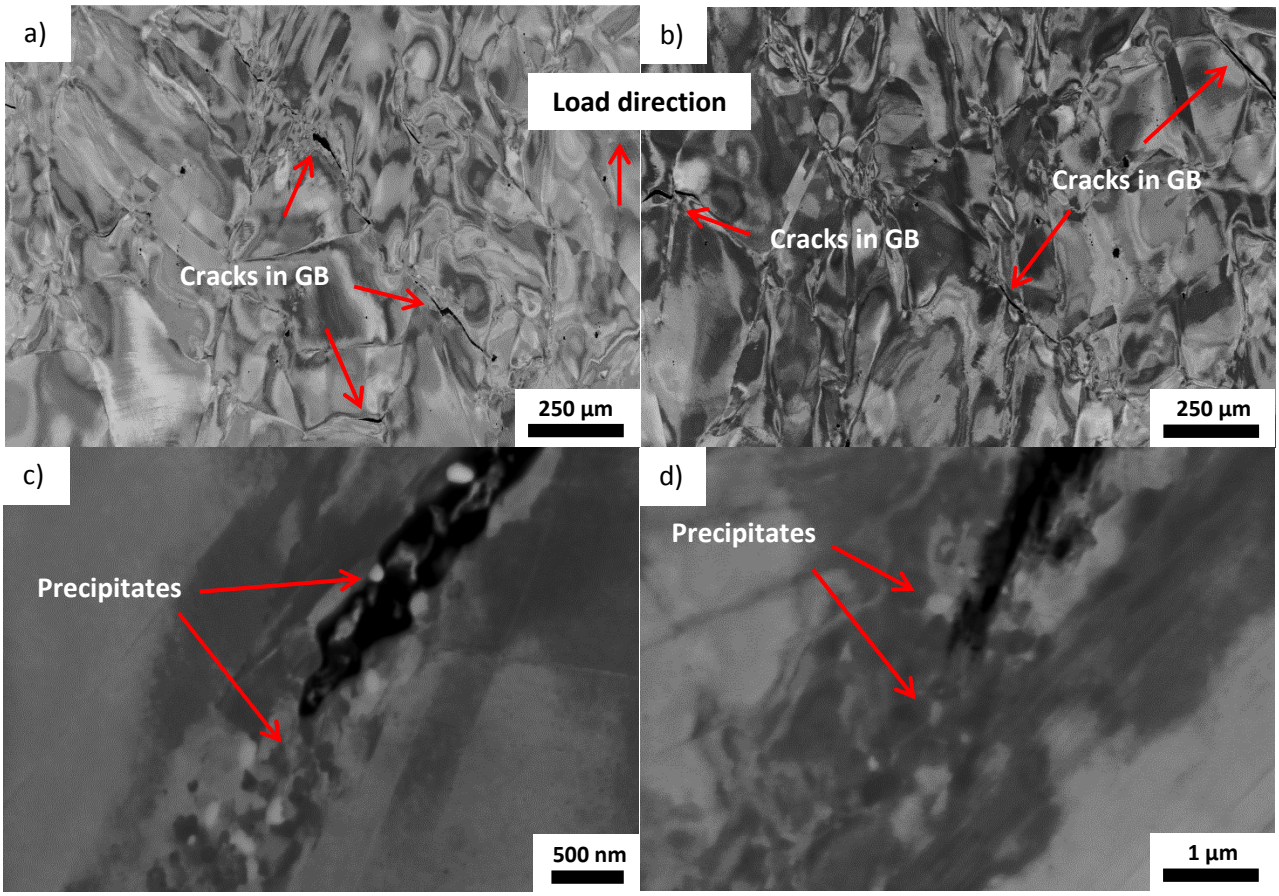

Figure 6. ECCI-picture showing internal cracks in the grain boundaries (GB) in Alloy 617, strain rate 10^{-5}/s and temperature a) 650°C, b) 700°C, c) crack tip, 650°C and b) crack tip, 700°C, tested to fracture. It is the same load direction in all the pictures.

4. Discussion

As known, DSA intensifies with increasing temperature and decreasing strain rate. However, in Alloy 617, DSA is present during the whole tensile deformation at elevated temperature when using a strain rate of 10^{-2}/s, but seems to disappear when the strain reach medium-high levels at an elevated temperature when using strain rates of 10^{-3}/s and 10^{-4}/s. DSA also appear again just before fracture when testing at elevated temperature using a strain rate of 10^{-3}/s. This behaviour could be described as a mismatch of the rates of solute atoms and moving dislocation, which could differ along the stress-strain curve and therefore serrations can appear just before fracture, where the local strain rate might be higher.

At room temperature the strain rate influencing the elongation in AISI 316L, when the strain rate decreases the elongation increases, also the stress level is lower at low strain rate. This is the result of the competition between hardening due to deformation and recovery due to the slow strain rate, where the recovery have more influence at slow strain rates than at higher. The recovery has a lager influence at lower deformations rates due to the fact that the moving dislocation rate decrease which affect the hardening to decrease. At high temperature the recovery probably can be an effect of creep, due to increasing diffusion rate and low deformation rate [11]. No clear microstructural signs as higher density of voids have been seen but they may be vanished due to high plastic deformation when the specimen is deformed to fracture. However, another sign that can be related to creep have been discovered, cell or subcell structure probably formed by creep deformation, from the EBSD-

analysis it is shown that the areas that look like recrystallization only have up to 5° misorientation which gives evidence for cell or subcell structures formed by creep deformation. According to the ECCI investigation there is areas and/or bands that display such cell or subcell structure, see fig.4c) and d). Further investigations are needed to confirm whether the cell or subcell structure is formed due to creep deformation in the AISI 316L material.

Elevated temperature and low strain rate decrease the ductility due to grain boundary embrittlement referred as sensitization and in some cases DSA. Sensitization is when chromium diffuses to the grain boundaries creating Cr-rich precipitates [16-19]. For sensitization the ageing time must be long enough for the precipitation to take place. According to literature sensitization occurs in AISI 316 material after less than 1h up to 100h depending on alloy content at 650°C and 700°C [17, 19]. After SSRT with a strain rate of 10^{-4}/s there are precipitates in the grain boundaries but they are too small to produce large scale embrittlement resulting in less internal cracks and larger elongation to fracture. For higher temperatures and long ageing times as in the case of SSRT tests with a strain rate of 10^{-6}/s and 700°C (fig.5 d)), desensitization probably can occur which means that chromium diffuses back into the interfacial region where the precipitate have grown [16, 19]. The desensitization seems to increase or keep the embrittlement of the material constant, see fig.2. In fig.2 b) the tensile stress increases which could refer to a hardening coupled to DSA that explain the large decrease in ductility. As known, precipitates in the matrix play two important roles for the life of the material, the first is to interact with moving dislocation and increase the strength or hardness of the material. The second is to cause stress concentration at the precipitate during dislocation accumulation that will in turn cause initiation of cracking by either precipitate cracking self or in the matrix.

5. Conclusion

After slow strain rate tensile testing at elevated temperatures and subsequent investigation of the microstructure using ECCI the following conclusions has been reached:

- Damage appears at interactions between moving dislocations and precipitates due to local stress concentration.

- DSA is present at all tested strain rates, but disappear at certain strain values for some deformation conditions. This is due to mismatches in the rates of moving dislocations and solute atoms at different strain intervals during the tensile deformation.

- Grain boundary embrittlement is causing damage as internal cracks and lowers the elongation to fracture. Therefore it is strongly affecting the material fracture behaviour at elevated temperature and is affecting for the high-temperature performances during deformation of the tested materials.

- AISI 316L show behaviour similar to creep at low strain rates (10^{-6}/s) and high temperatures.

Acknowledgements

Present study was financially supported by AB Sandvik Material Technology in Sweden and the Swedish National Energy Administration through the Research Consortium of Materials Technology for Thermal Energy Processes, Grant No. KME-501. Agora Materiae and Strategic Faculty Grant AFM at Linköping University are also acknowledged.

References

[1] J. Pettersson, H. Asteman, J. Svensson, L. Johansson, KCl Induced Corrosion of a 304-type Austenitic Stainless Steel at 600°C; The Role of Potassium, Oxidation of Metals. 64 (2005) 23-41.
[2] R. Viswanathan, K. Coleman, U. Rao, Materials for ultra-supercritical coal-fired power plant boilers, Int. J. Pressure Vessels Piping. 83 (2006) 778-783.
[3] L.H. de Almeida, I. Le May, P.R.O. Emygdio, Mechanistic Modeling of Dynamic Strain Aging in Austenitic Stainless Steels, Mater Charact. 41 (1998) 137-150.
[4] W. Karlsen, M. Ivanchenko, U. Ehrnstén, Y. Yagodzinskyy, H. Hänninen, Microstructural manifestation of dynamic strain aging in AISI 316 stainless steel, J. Nucl. Mater. 395 (2009) 156-161.
[5] M.A. Soare, W.A. Curtin, Solute strengthening of both mobile and forest dislocations: The origin of dynamic strain aging in fcc metals, Acta Materialia. 56 (2008) 4046-4061.
[6] A.W. Sleeswyk, Slow strain-hardening of ingot iron, Acta Metallurgica. 6 (1958) 598-603.
[7] S. Hong, S. Lee, Mechanism of dynamic strain aging and characterization of its effect on the low-cycle fatigue behavior in type 316L stainless steel, J. Nucl. Mater. 340 (2005) 307-314.
[8] K.G. Samuel, S.L. Mannan, P. Rodriguez, Serrated yielding in AISI 316 stainless steel, Acta Metallurgica. 36 (1988) 2323-2327.
[9] P. Rodriguez, Serrated plastic flow, Bulletin of Materials Science. 6 (1984) 653-663.
[10] I. Gutierrez-Urrutia, S. Zaefferer, D. Raabe, Electron channeling contrast imaging of twins and dislocations in twinning-induced plasticity steels under controlled diffraction conditions in a scanning electron microscope, Scr. Mater. 61 (2009) 737-740.
[11] R. Lagneborg, Recovery creep in materials hardened by a second phase, J. Mater. Sci. 3 (1968) 596-602.
[12] G.R. Stewart, A.M. Elwazri, S. Vue, J.J. Jonas, Modelling of dynamic recrystallisation kinetics in austenitic stainless and hypereutectoid steels, Materials Science and Technology. 22 (2006) 519-524.
[13] M. Calmunger, G. Chai, S. Johansson, J. Moverare, Influence of Dynamic Strain Ageing on Damage in Austenitic Stainless Steels, ECF19. (2012).
[14] M. Speicher, A. Klenk, K. Maile, E. Roos, Behaviour of Ni-based alloys for fossil-fired power plant components in the long-term creep regime, Advanced Materials Research. 278 (2011) 241-246.
[15] O.H. Ibrahim, I.S. Ibrahim, T.A.F. Khalifa, Effect of Aging on the Toughness of Austenitic and Duplex Stainless Steel Weldments, Journal of Materials Science & Technology. 26 (2010) 810-816.
[16] E.A. Trillo, R. Beltran, J.G. Maldonado, R.J. Romero, L.E. Murr, W.W. Fisher, A.H. Advani, Combined effects of deformation (strain and strain state), grain size, and carbon content on carbide precipitation and corrosion sensitization in 304 stainless steel, Mater Charact. 35 (1995) 99-112.
[17] S.K. Mannan, R.K. Dayal, M. Vijayalakshmi, N. Parvathavarthini, Influence of deformation on sensitization kinetics and its microstructural correlation in a nuclear grade 316 stainless steel, J. Nucl. Mater. 126 (1984) 1-8.
[18] N. Parvathavarthini, R.K. Dayal, Time–temperature-sensitization diagrams and critical cooling rates of different nitrogen containing austenitic stainless steels, J. Nucl. Mater. 399 (2010) 62-67.
[19] A.Y. Kina, V.M. Souza, S.S.M. Tavares, J.M. Pardal, J.A. Souza, Microstructure and intergranular corrosion resistance evaluation of AISI 304 steel for high temperature service, Mater Charact. 59 (2008) 651-655.

High temperature stress relaxation of a Ni-based single-crystal superalloy

Mikael Segersäll[1,*], Johan J. Moverare[1,2], Daniel Leidermark[1], Kjell Simonsson[1]

[1] Department of Management and Engineering, Linköping University, Linköping SE-58183, Sweden
[2] Siemens Industrial Turbomachinery AB, Finspång SE-61283, Sweden
* Corresponding author: mikael.segersall@liu.se

Abstract Nickel-based superalloys are often selected due to their remarkable mechanical and chemical properties at high temperatures. This makes the material suitable for high temperature applications such as gas turbines and aero engines. By use of single-crystal instead of poly-crystal material, both creep and fatigue properties are enhanced. Superalloys in single-crystal form exhibit an anisotropic behaviour and a tension/compression asymmetry. This makes it interesting to study different crystal orientations in both tension and compression. In this study, high temperature stress relaxation of a Ni-based single-crystal superalloy is investigated. Specimens with three different crystal orientations, ⟨001⟩, ⟨011⟩ and ⟨111⟩, were tested in both tension and compression. Results show an anisotropic stress relaxation behaviour, as well as a tension/compression asymmetry for all directions. During stress relaxation at 750°C, the creep properties decreases in the sequence ⟨001⟩, ⟨011⟩ and ⟨111⟩ in tension, while in compression ⟨001⟩ = ⟨011⟩, ⟨111⟩. However, at 950°C the creep properties are slightly better in the ⟨011⟩ direction compared to the ⟨001⟩ direction.

Keywords single-crystal superalloy, thermomechanical fatigue, stress relaxation

1. Introduction

Ni-based superalloys show remarkable mechanical and chemical properties at high temperatures, which make them a suitable as blade material in gas turbines and aero engines [1, 2]. The superalloys consist of the typical γ/γ′-microstructure, where the γ′-phase works as strengthener in a matrix of γ. The strengthening γ′-phase has an $L1_2$-ordered structure and is rich of Al, Ta and Ti. By using a single-crystal material instead of poly-crystal material both creep and fatigue properties are enhanced [3]. Gas turbine blades in single-crystal form are most common casted with the ⟨001⟩ crystallographic direction upwards, since this direction has the lowest stiffness of all crystal directions. Low stiffness implies good fatigue properties, which is of great importance for gas turbine blade components. Single-crystal superalloys exhibit an anisotropic behaviour and they also show a tension/compression asymmetry [4-7] .

Stress relaxation testing of superalloys is often associated with shorter hold times at high temperatures during thermomechanical fatigue (TMF) testing, for example hold times of 5 min during each cycle [8, 9]. However, Zhang et al. [10] applied a hold time of 1h at 900°C in compression at each cycle during TMF testing. In that study, three different stages of stress relaxation during the TMF tests were found, and each stage was connected to a specific microstructural behaviour. Other research showed that when applying hold times of 30-60 minutes during tensile loadings at temperatures from 700 to 1000°C, the stress relaxed to an asymptotic stress value after the hold time [11]. At high temperatures and loads a directional coarsening of the γ/γ′-microstructure is obtained. This phenomenon is called rafting and it is a diffusion controlled directional coarsening of the γ′-particles [12]. The orientation of the rafting is dependent on whether the alloy has a positive or negative lattice misfit [13]. Rafting doesn't always have to be negative for the material. For instance, research has shown how pre-rafting can improve creep properties [14]. Also isothermal high-temperature fatigue lives have proven to be enhanced by a pre-rafted

microstructure, instead of having the more common microstructure with γ′-cuboids in a γ-matrix [15, 16].

The aim of this study is to investigate the long-term stress relaxation behaviour of a Ni-based single-crystal superalloy. Due to anisotropy and the well-known tension/compression asymmetry, three different crystal orientations are tested in both tension and compression.

2. Experimental procedure

The Ni-based single-crystal superalloy MD2 with chemical composition Ni-5.1Co-6.0Ta-8.0Cr-8.1W-5.0Al-1.3Ti-2.1Mo-0.1Hf-0.1Si in wt.%, was used in this study. Prior testing, the material was solution heat treated at 1275°C for 8 h followed by a two-stage aging process with 3 h at 1100°C and 24 h at 850°C. Test specimens were machined from cast bars and the deviation from the ideal orientation was less than 10° for all specimens.

The tests were performed in an Instron servo-hydraulic TMF machine, and were conducted as strain controlled TMF cycles with a temperature range from 100°C to either 750°C or 950°C. During each cycle, a hold time of 100 h was applied at maximum temperature (T_{max}) and maximum strain. After the 100 h hold time, the temperature was lowered to 100°C and zero strain before the second cycle was initiated. Each specimen was subjected to two TMF cycles, and no specimens were cycled to fracture. Consequently, a hold time of total 200 h at T_{max} was applied for each specimen. Fig. 1 displays a plot of the TMF cycle. For a T_{max} of 750°C, the ⟨001⟩, ⟨011⟩ and ⟨111⟩ directions were tested. However, for a T_{max} of 950°C, only the ⟨001⟩ and ⟨011⟩ directions were tested. The total mechanical strain range ($\Delta\varepsilon_{mech}$) was chosen in order to obtain approximately the same inelastic strain for all specimens. Since the different crystal orientations have different Young's modulus, different $\Delta\varepsilon_{mech}$ were used for the different crystal directions. The ⟨001⟩ oriented specimens were subjected to a $\Delta\varepsilon_{mech}$ of 1%, the ⟨011⟩ specimens to 0.7%, and the ⟨111⟩ specimens were subjected to 0.6%. For each direction and T_{max}, one specimen was subjected to an in-phase TMF cycle (IP-TMF), and the other specimen was subjected to an out-of-phase TMF cycle (OP-TMF). An IP-TMF cycle implies tensile stress relaxation at T_{max} while OP-TMF implies compressive stress relaxation at T_{max}.

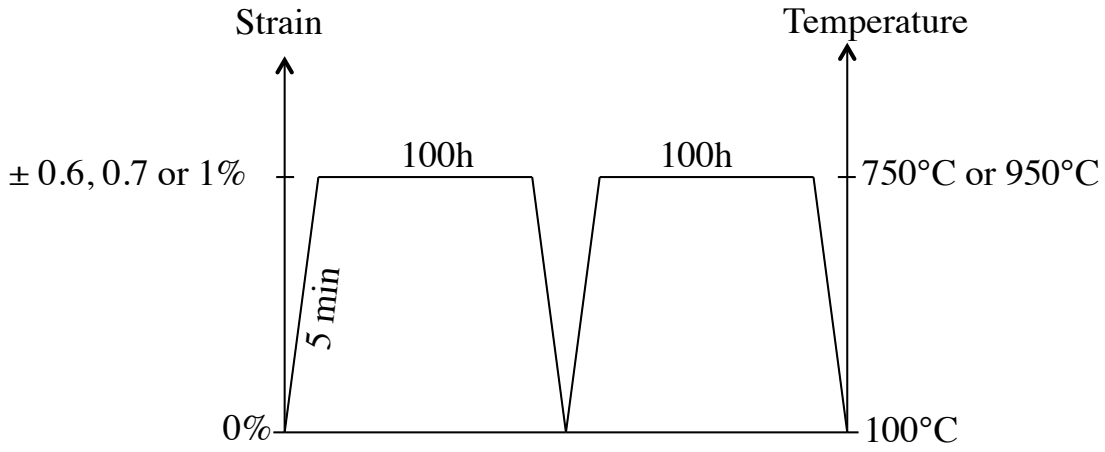

Figure 1. The TMF cycle used in the stress relaxation tests.

After the tests, all specimens were examined by stereomicroscopy before they were cut parallel to the loading direction for further microstructural investigation by scanning electron microscopy (SEM). The SEM samples were prepared by grinding and mechanical polishing, but no samples were etched. The microstructure investigation was performed in a Hitachi SU70 SEM, using voltages from 10 to 20 kV.

3. Results

3.1. Stress relaxation testing

Results from the tests with a T_{max} of 750°C show that the ⟨011⟩ oriented specimens demonstrates a serrated yielding behaviour during the loading phase. This was visible in both tension (IP) and compression (OP). However, the yielding for both the ⟨001⟩ and ⟨111⟩ directions during the loading phase was more stable, i.e. no serrated yielding was observed. In addition to the serrated yielding for the ⟨011⟩ direction, those specimens also demonstrated a clear noise during the loading phase. On the other hand, both the ⟨001⟩ and ⟨111⟩ directions were more quite. For the specimens subjected to stress relaxation at T_{max} of 950°C no serrated yielding and no noise was observed during the loading phase.

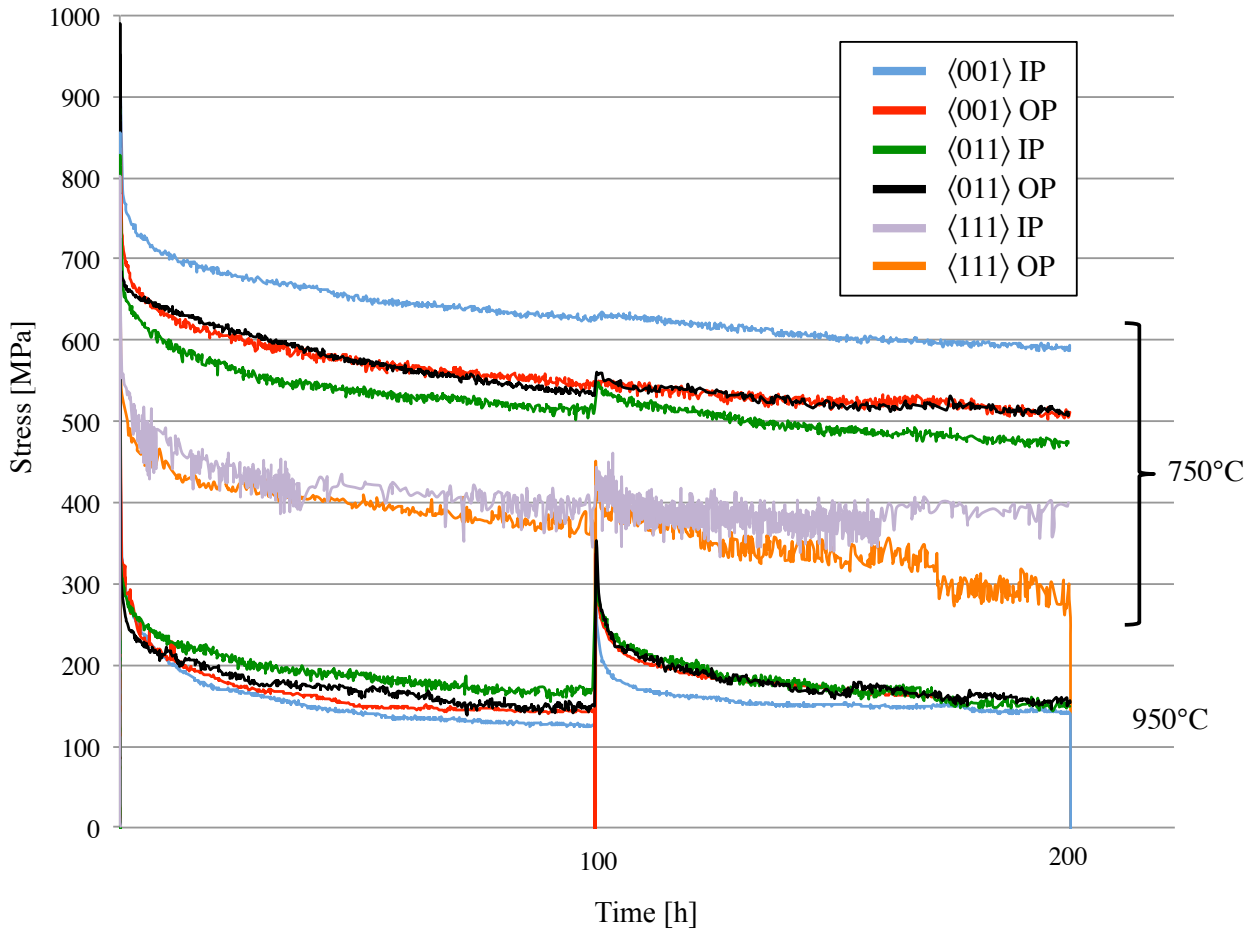

Figure. 2. Stress relaxation over 200 h for all crystal orientations tested.

Fig. 2 displays how the stress is relaxing during the 200 h hold time for all specimens. The figure shows that the stresses relax to lower stress states at 950°C compared to 750°C. The other significant differences in the stress relaxation behaviour are summarized below.

All crystal orientations show a tension/compression asymmetry. However, the asymmetry is most pronounced the ⟨001⟩ direction at 750°C. Here, tensile loading leads to a higher stress state compared to compressive loading, and the difference in stress is approximately 80 MPa after 200 h. The ⟨011⟩ oriented specimens show an opposite behaviour at this temperature; tensile loading leads to a lower stress state compared to compressive loading. Another difference at this temperature, is that the unloading after 100 h leads to an increase in stress state for the ⟨011⟩ direction when the material is loaded into the second 100 h TMF cycle. However, after some time the material relaxes and adapts into the pre-unloading behaviour. For the ⟨001⟩ direction the unloading after 100 h does not have an influence on the stress state.

Concerning the ⟨111⟩ oriented specimens, they relax to a significant lower stress state compared to both ⟨001⟩ and ⟨011⟩ directions. After the first 100 h TMF cycle, the stress is approximately 360 MPa for the ⟨111⟩ direction, while both ⟨001⟩ and ⟨011⟩ directions are well above 500 MPa. It should be noted that the stress relaxation in the ⟨111⟩ direction is very unstable compared to the other directions. The instability should be attributed to TMF machine instabilities, rather than any microstructural difference between the three directions. One reason can be that the high stiffness in the ⟨111⟩ direction makes it more difficult for the TMF machine to take care of instabilities.

At 950°C, only the ⟨001⟩ and ⟨011⟩ directions were tested. At this temperature, an opposite tension/compression asymmetry is observed compared to 750°C. The ⟨001⟩ direction is stronger in compression than tension, while the ⟨011⟩ direction is stronger in tension than compression. Here the unloading after 100 h also seems to influence the specimens to a greater extent compared to 750°C. A significant higher stress state is observed in the beginning of the second TMF cycle. This is the case for both ⟨001⟩ and ⟨011⟩ directions at 950°C, but only for the ⟨011⟩ direction at 750°C.

3.2. Microscopy

Crystallographic deformation bands across the specimens are found on the ⟨011⟩ oriented materials subjected to hold times at 750°C, both in tension (IP) and compression (OP). See Fig. 3a for the ⟨011⟩ oriented specimen subjected to 750°C in compression. Neither the ⟨001⟩ nor ⟨111⟩ oriented specimens show similar deformation bands at this temperature. However at 950°C, both ⟨001⟩ and ⟨001⟩ oriented specimens show crystallographic deformation bands (the ⟨111⟩ direction was not tested at this temperature). Another difference between the two temperatures is that the deformation bands become more distinct at 950°C compared to 750°C. All slip traces are consistent with slip along the {111}⟨110⟩ slip systems. In Fig. 3b, the more distinct deformation bands are visible. This figure shows the deformation bands on the ⟨011⟩ oriented specimen subjected to tensile stresses at 950°C. Here, slip traces on different {111} planes are found. In Fig. 3c, the deformation bands on the ⟨001⟩ oriented specimen subjected to tensile stresses are shown. In this case, in addition to the crystallographic deformation bands, also wavy deformation bands are found. This indicates that several slip systems are active during deformation in this direction at 950°C.

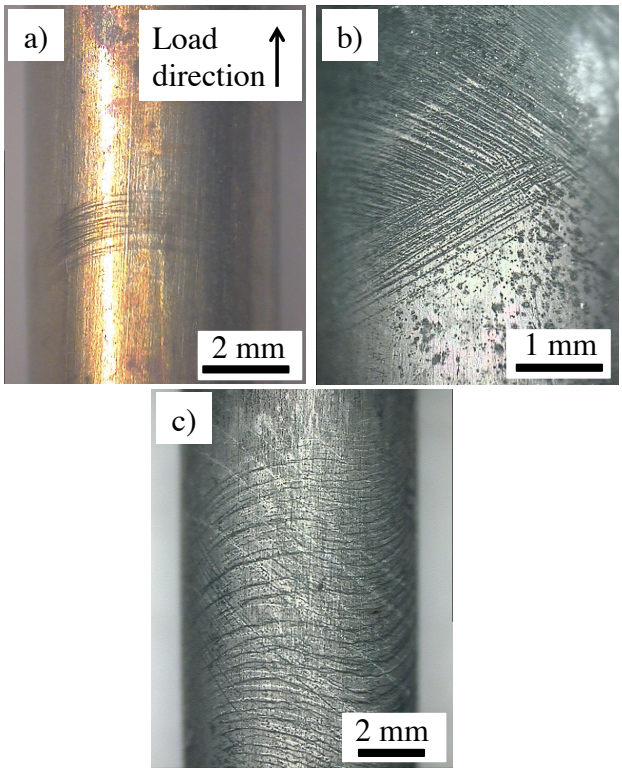

Figure. 3. Deformation bands on specimen surfaces, a) the ⟨011⟩ specimen subjected to 750°C in compression (OP), b) the ⟨011⟩ specimen subjected to 950°C in tension (IP), and c) the ⟨001⟩ specimen subjected to 950°C in tension (IP).

After cutting the specimens parallel to the loading direction all specimens were investigated by SEM. Fig. 4 provides a backscattered electron image where the deformation bands inside the specimen are clearly visible at low magnification. However, at higher magnification the crystallographic deformation bands are often difficult to detect. The SEM investigation shows that the deformation bands are neither twinning nor shearing of the γ/γ′-microstructure. Sometimes precipitation of topologically-close-packed (TCP) phases are visible within the deformation bands. Even though most deformation bands are difficult to detect at higher magnification, occasionally more distinct deformation bands are visible, see Fig. 5 for such a distinct deformation band. Most likely, both types of deformation bands are bundles of glide bands. Other than the crystallographic deformation bands, the specimens show very little deformation within the γ/γ′-microstructure. However, small amounts of twins are detected in the microstructure for the ⟨001⟩ specimen subjected to compression at 750°C, see Fig. 6. Here parallel twins propagates through the γ′-cuboids.

Rafting of the γ/γ′-microstructure is visible in specimens subjected to holdtimes at 950°C. The rafting direction is dependent on whether the superalloy has a negative or positive misfit between the γ′- and γ-microconstituents, and if the loading is tensile or compressive. The alloy used in this study (MD2) has a negative misfit which implies that tensile loaded specimens show a N-type of rafting, while material loaded in compression show a P-type of rafting. Fig. 7 displays N-type of rafting; the previously cuboidal γ′-particles are here coarsened and oriented Normal to the load direction. On the other hand, Fig. 5 shows P-type of rafting where the coarsened γ′-particles are oriented Parallel to the load direction.

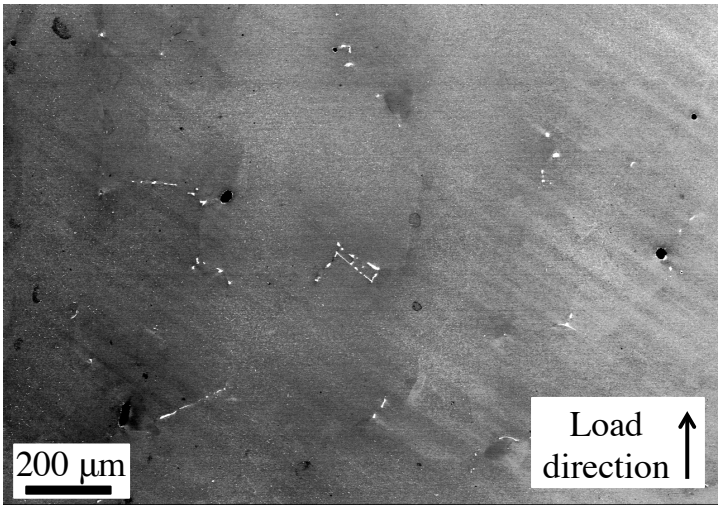

Figure. 4. Backscattered electron image of the ⟨011⟩ specimen subjected to stress relaxation tests at 950°C in tension (IP): crystallographic deformation bands at low magnification.

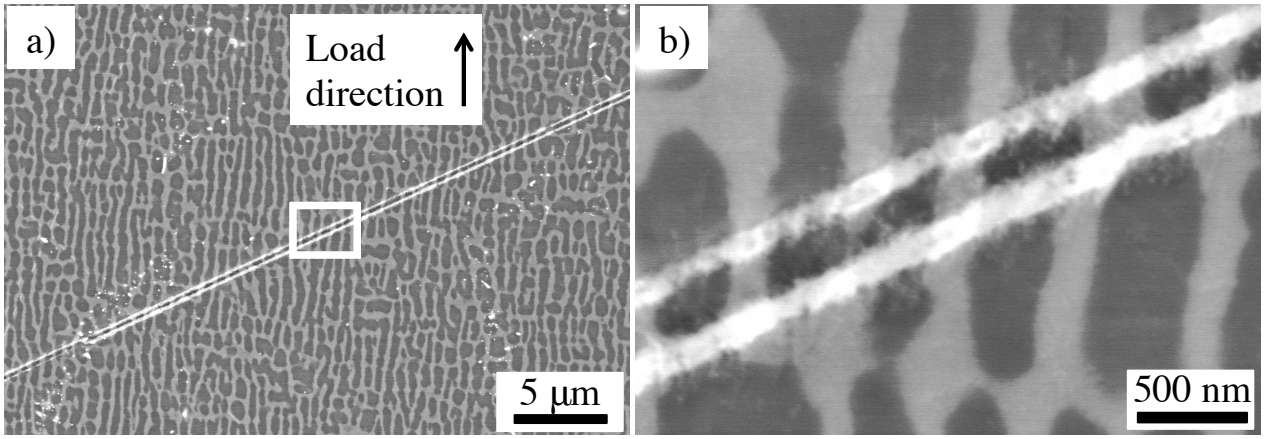

Figure. 5. Backscattered electron images of the ⟨011⟩ specimen subjected to stress relaxation tests at 950°C in compression (OP): a) distinct deformation band, b) magnification of a). P-type of rafting of the γ/γ′-microstructure.

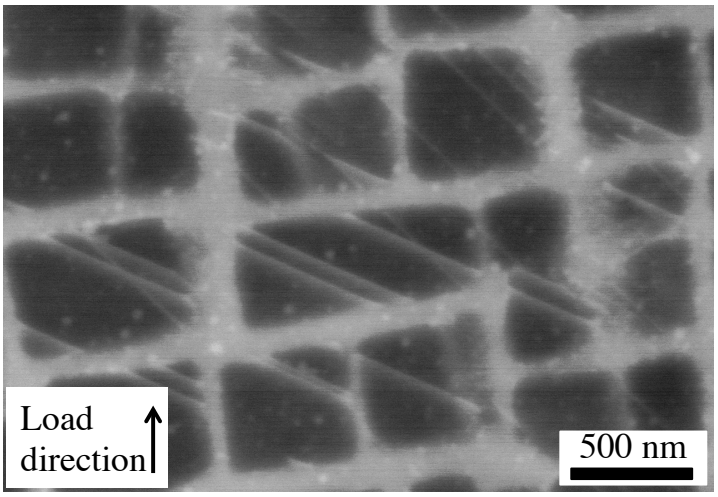

Figure. 6. Backscattered electron image of the ⟨001⟩ specimen subjected to stress relaxation tests at 750°C in compression (OP): twin formation in the γ/γ′-microstructure.

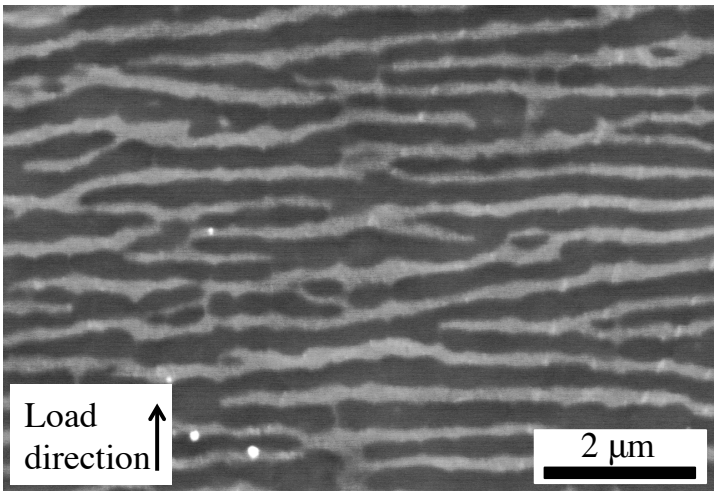

Figure. 7. Backscattered electron images of the ⟨001⟩ specimen subjected to stress relaxation test at 950°C in tension, N-type of rafting of the γ/γ′-microstructure.

4. Discussion

The MD2 alloy exhibits an anisotropic creep behaviour as well as a tension/compression asymmetry during stress relaxation, see Fig. 2. It can also be seen that the ⟨111⟩ direction has the worst creep properties at 750°C. This direction relaxes to a significant lower stress state compared to both ⟨001⟩ and ⟨011⟩ direction during the stress relaxation tests. At 750°C, the ⟨001⟩ and ⟨111⟩ specimens are stronger in tension than compression. However, for the ⟨011⟩ specimens the opposite behaviour is observed; compressive loading leads to a higher stress state compared to tensile loading. At 950°C, an opposite tension/compression asymmetry is observed: the ⟨001⟩ direction is stronger in compression than tension, and the ⟨011⟩ direction is stronger in tension than compression. It seems that there is a change in tension/compression asymmetry when going from 750°C to 950°C. That the tension/compression asymmetry changes with temperature has been showed by Ezz et al. [6] who studied the tension/compression asymmetry for the critical resolved shear stress (CRSS) for a single-crystal superalloy. They showed that the CRSS is higher in tension than compression at 750°C for orientations close to [001] in the stereographic triangle. On the other hand, for materials close to [011] and [111] in the stereographic triangle, there was a smaller asymmetry in CRSS at this temperature. At higher temperatures the asymmetry decreased. Present study shows that there is a change in tension/compression asymmetry also in stress relaxation behaviour, however the reason to this is still to be determined.

The ⟨011⟩ oriented specimens showed a serrated yielding behaviour during loading into the first TMF cycle in the tests at 750°C. This behaviour is attributed to two things; the fact that only one slip system is active during deformation in this direction and the effect of dynamic strain ageing (DSA). Serrated yielding behaviour of the ⟨011⟩ direction has previously been reported in the literature [17-20]. One explanation for this has been that only one slip system is active during deformation of the ⟨011⟩ direction while multiple slip systems are active during plastic deformation in the ⟨001⟩ direction [17]. The reason to single slip for the ⟨011⟩ direction is attributed to the lower symmetry, i.e. less equivalent slip systems, for this direction compared to the ⟨001⟩ and ⟨111⟩ directions. When several slip systems are active at the same time, there is always one slip system where the dislocations can propagate and a more stable yielding is observed. On the other hand, if

only one slip system is active, the dislocations are sometimes stopped if the stress is not large enough and a more serrated yielding is obtained. The fact that deformation bands are found only on the ⟨011⟩ specimens at 750°C can also be attributed to the fact that only one slip system is active in this direction and temperature. The deformation bands on the surfaces are topographic differences, which are more probable to obtain when only one slip system is active compared to the case when several systems are active. This since slip on several systems will lead to a more homogeneous surface. The serrated yielding behaviour of the ⟨011⟩ direction at 750°C can also be attributed to dynamic strain aging (DSA). Localized deformation bands are found on these specimens, and those deformation bands are likely glide bands with a high dislocation density. DSA is the interaction between solute atoms and moving dislocations, and is favoured in areas with a high dislocation density, i.e. within those localized deformation bands.

A clear noise was heard from the ⟨011⟩ oriented specimens when loading into the first TMF cycle for tests at 750°C. This behaviour of the ⟨011⟩ direction has been reported before when acoustic emission (AE) was used to measure noise during plastic deformation [21]. In that study, loading in the ⟨011⟩ direction led to higher AE signals and higher noise compared to ⟨001⟩. It is thus likely, that during loading of the ⟨011⟩ direction at this temperature, in which serrated yielding occurs, a high noise is created for each serration.

4. Conclusions

From this study it can be concluded that the Ni-based single-crystal superalloy MD2 shows an anisotropic creep behaviour as well as a tension/compression asymmetry during stress relaxation. At 750°C, the tensile creep properties is best for the ⟨001⟩ direction, followed by the ⟨011⟩ direction while the ⟨111⟩ direction has the worst creep properties. At the same temperature in compression, the ⟨001⟩ and ⟨011⟩ directions show similar creep properties, and also here the ⟨111⟩ direction shows the worst creep properties. During stress relaxation at 950°C, the creep properties are slightly better in the ⟨011⟩ direction compared to the ⟨001⟩ direction for both compressive and tensile loadings.

Acknowledgements

The work has been financially supported by Siemens Industrial Turbomachinery AB in Finspång, Sweden and the Swedish Energy Agency, via the Research Consortium of Materials Technology for Thermal Energy Processes, Grant No. KME-502.

References

[1] R.C. Reed, T. Tao, N. Warnken, Alloys-By-Design: Application to nickel-based single crystal superalloys. Acta Materialia, 57 (2009) 5898-5913.

[2] T.M. Pollock, S. Tin, Nickel-based superalloys for advanced turbine engines: Chemistry, microstructure, and properties. J. Propul, Power. 22 (2006) 361-374.

[3] R.C. Reed, The Superalloys - Fundamentals and Applications, Cambridge University Press, Cambridge, 2006.

[4] N. Tsuno, S. Shimabayashi, K. Kakehi, C.M.F. Rae, R.C. Reed, Tension/compression asymmetry in yield and creep strengths of Ni-based superalloys. Proceedings of the

International Symposium on Superalloys, (2008) 433-442.

[5] R.V. Miner, T.P. Gabb, J. Gayda, Orientation and temperature dependence of some mechanical properties of the single-crystal nickel-base superalloy René N4 III - Tension-compression anisotropy. Metallurgical Transactions A, 17 (1986) 507-512.

[6] S.S. Ezz, D.P. Pope, V. Paidar, The tension/compression flow stress asymmetry in Ni3(Al,Nb) Single crystals. Acta Metallurgica, 30 (1982) 921-926.

[7] D. Leidermark, J.J. Moverare, S. Johansson, K. Simonsson, S. Sjöström, Tension/compression asymmetry of a single-crystal superalloy in virgin and degraded condition. Acta Materialia, 58 (2010) 4986-4997.

[8] M. Segersäll, J.J. Moverare, K. Simonsson, S. Johansson, Deformation and damage mechanisms during thermomechanical fatigue of a single-crystal superalloy in the ⟨001⟩ and ⟨011⟩ directions. Proceedings of the International Symposium on Superalloys, (2012) 215-223.

[9] J.J. Moverare, S. Johansson, R.C. Reed, Deformation and damage mechanisms during thermal–mechanical fatigue of a single-crystal superalloy. Acta Materialia, 57 (2009) 2266-2276.

[10] J.X. Zhang, H. Harada, Y. Ro, Y. Koizumi, T. Kobayashi, Thermomechanical fatigue mechanism in a modern single crystal nickel base superalloy TMS-82. Acta Materialia, 56 (2008) 2975-2987.

[11] M. Dupeux, J. Henriet, M. Ignat, Tensile stress relaxation behaviour of Ni-based superalloy single crystals between 973 and 1273 K. Acta Metallurgica, 35 (1987) 2203-2212.

[12] H. Mughrabi, Microstructural aspects of high temperature deformation of monocrystalline nickel base superalloys: Some open problems. Materials Science and Technology, 25 (2009) 191-204.

[13] T.M. Pollock, A.S. Argon, Directional coarsening in nickel-base single crystals with high volume fractions of coherent precipitates, Acta Metallurgica et Materialia. 42 (1994) 1859-1874.

[14] U. Tetzlaff, H. Mughrabi, Enhancement of the High-Temperature Tensile Creep Strength of Monocrystalline Nickel-Base Superalloys by Pre-rafting in Compression. Proceedings of the International Symposium on Superalloys, (2000) 273-282.

[15] H. Mughrabi, U. Tetzlaff, Microstructure and high-temperature strength of monocrystalline nickel-base superalloys. Advanced Engineering Materials, 2 (2000) 319-326.

[16] M. Ott, H. Mughrabi, Dependence of the high-temperature low-cycle fatigue behaviour of the monocrystalline nickel-base superalloys CMSX-4 and CMSX-6 on the γ/γ′-morphology. Materials Science and Engineering: A, 272 (1999) 24-30.

[17] R.V. Miner, R.C. Voigt, J. Gayda, T.P. Gabb, Orientation and temperature dependence of some mechanical properties of the single-crystal superalloy René N4 Part I: Tensile behavior. Metallurgical Transactions A, 17 (1986) 491-496.

[18] T.S. Rong, Serrated yielding in the B2-ordered Nb–15Al–20V alloy. Intermetallics, 11 (2003) 151-155.

[19] X. Wu, J.H. Zhang, J.L. Liu, T. Jin, Y.B. Xu, Z.Q. Hu, Plastic deformation inhomogeneity in a single crystal nickel-base superalloy. Materials Science and Engineering: A, 325 (2002) 478-483.

[20] E.F. Westbrooke, L.E. Forero, F. Ebrahimi, Slip analysis in a Ni-base superalloy. Acta

Materialia, 53 (2005) 2137-2147.

[21] X. -H. Li, J. Moverare, The use of acoustic emission technology in coating ductility testing at various temperatures. Proceedings of ASME Turbo Expo (2004).

Modeling of Inclined Crack Growth under Creep Conditions

Vladimir I. Astafiev[1*], **Alexey N. Krutov**[2]

[1] Samara State Aerospace University, Samara 443086, Russia
[2] Samara State University, Samara 443011, Russia
* Corresponding author: vlast@ssu.samara.ru

Abstract The modeling of subcritical growth of inclined crack under creep condition is considered. In the first part of this paper the stress state near the tip of inclined crack for power creep law in the cases of plane stress and plane strain is calculated. To calculate the stress state near the tip of an inclined crack the Airy's stress function is used. The resulting nonlinear fourth order differential equation is formulated as two-point boundary value problem and is solved by shooting and Newton's methods.

The modeling of creep crack growth is based on Rabotnov-Kachanov damage theory and the criterion of crack growth ω=1 at the distance d from the crack tip, calculated for equivalent or maximum stress. The crack growth rate and the crack trajectory are calculated both for plane stress and plane strain and for n = 1, 3, 5, 7 and considered in the second part of this paper.

Keywords inclined crack, creep, stress distribution.

1. Introduction

Let us consider an infinite plate of a nonlinear elastic-creep material with a crack of the length 2a, located at the angle α to the axis *x* and loaded by the stress σ_∞ along the axis *y* (Figure 1). It is required to determine the stress state near the tip of inclined crack for the plane stress and the plane strain conditions. It should be noted that the problem of uniaxial tension of inclined crack is statically equivalent to the mixed tensile and shear loading by the stresses $\sigma_\infty \cos^2\alpha$ and $\sigma_\infty \cos\alpha \sin\alpha$, respectively (Fig. 1).

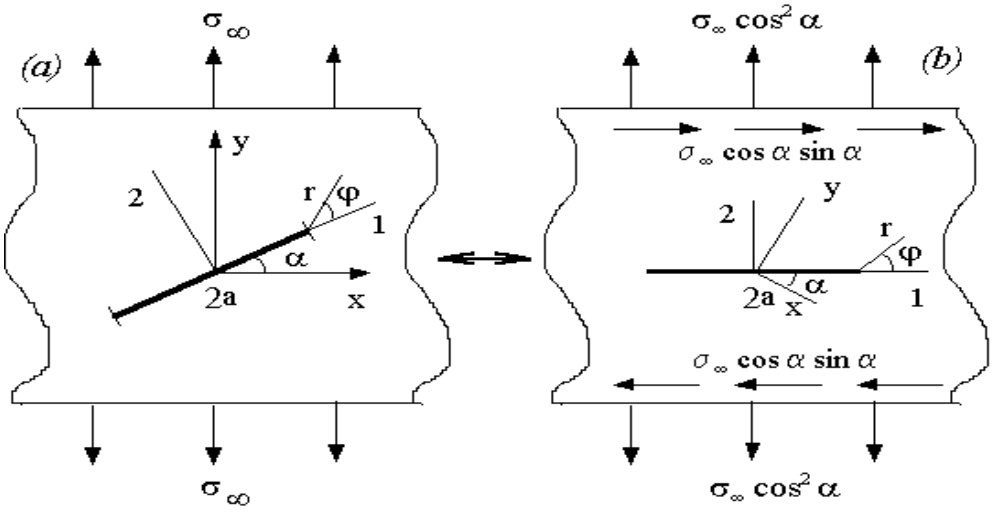

Figure 1. The geometry of the inclined crack.

2. Statement of the problem

2.1. Main equations

Let us consider the polar coordinate system (r, φ) associated with the tip of inclined crack (Fig. 1). The equilibrium equations and the Cauchy relations in the polar coordinate system for the plane strain or stress conditions are [1-3]:

$$\frac{\partial \sigma_{rr}}{\partial r}+\frac{1}{r}\frac{\partial \sigma_{r\varphi}}{\partial \varphi}+\frac{\sigma_{rr}-\sigma_{\varphi\varphi}}{r}=0,\quad \frac{1}{r}\frac{\partial \sigma_{\varphi\varphi}}{\partial \varphi}+\frac{\partial \sigma_{r\varphi}}{\partial r}+2\frac{\sigma_{r\varphi}}{r}=0. \tag{1}$$

$$\varepsilon_{rr}=\frac{\partial u_r}{\partial r},\quad \varepsilon_{\varphi\varphi}=\frac{u_r}{r}+\frac{1}{r}\frac{\partial u_\varphi}{\partial \varphi},\quad 2\varepsilon_{r\varphi}=\frac{1}{r}\frac{\partial u_r}{\partial \varphi}+\frac{\partial u_\varphi}{\partial r}-\frac{u_\varphi}{r}, \tag{2}$$

The constitutive equations for an incompressible material with a power creep law have the following form [1-2]:

$$\varepsilon_{ij}=(3/2)B\sigma_e^{n-1}s_{ij} \tag{3}$$

where ε_{ij} is the strain rate tensor, $s_{ij}=\sigma_{ij}-(1/3)\sigma_{kk}\delta_{ij}$ is the deviator of σ_{ij} stress tensor, $\sigma_e=\sqrt{(3/2)s_{ij}s_{ij}}$ is the equivalent stress, B is the material constant, n is the index of nonlinearity.

The equivalent stress σ_e for the plane stress and the plane strain is calculated as

$$\sigma_e=\sqrt{\sigma_{rr}^2-\sigma_{rr}\sigma_{\varphi\varphi}+\sigma_{\varphi\varphi}^2+3\sigma_{r\varphi}^2},\quad \sigma_e=\sqrt{(3/4)(\sigma_{rr}-\sigma_{\varphi\varphi})^2+3\sigma_{r\varphi}^2} \tag{4}$$

The strain compatibility equation in polar coordinates, resulting from Eq. (2), has the following form [1-3]:

$$\frac{1}{r}\frac{\partial^2}{\partial r^2}(r\varepsilon_{\varphi\varphi})+\frac{1}{r^2}\frac{\partial^2\varepsilon_{rr}}{\partial\varphi^2}-\frac{1}{r}\frac{\partial\varepsilon_{rr}}{\partial r}-\frac{2}{r^2}\frac{\partial}{\partial r}(r\frac{\partial\varepsilon_{r\varphi}}{\partial\varphi})=0. \tag{5}$$

Taking into account Eq. (1), Eq. (3) and Eq. (4), the strain compatibility Eq. (5) can be rewritten in the stress terms for the plane stress (a) and the plane stain (b) conditions as the follows:

$$\frac{1}{r}\frac{\partial^2}{\partial r^2}\left[\sigma_e^{n-1}r\left(\sigma_{\varphi\varphi}-\frac{1}{2}\sigma_{rr}\right)\right]+\frac{1}{r^2}\frac{\partial^2}{\partial\varphi^2}\left[\sigma_e^{n-1}\left(\sigma_{rr}-\frac{1}{2}\sigma_{\varphi\varphi}\right)\right]-$$
$$-\frac{1}{r}\frac{\partial}{\partial r}\left[\sigma_e^{n-1}\left(\sigma_{rr}-\frac{1}{2}\sigma_{\varphi\varphi}\right)\right]-\frac{3}{r^2}\frac{\partial}{\partial r}\left[r\frac{\partial}{\partial\varphi}\left(\sigma_e^{n-1}\sigma_{r\varphi}\right)\right]=0, \tag{6a}$$

$$\frac{1}{r}\frac{\partial^2}{\partial r^2}\left[\sigma_e^{n-1}r\left(\sigma_{\varphi\varphi}-\sigma_{rr}\right)\right]+\frac{1}{r^2}\frac{\partial^2}{\partial\varphi^2}\left[\sigma_e^{n-1}\left(\sigma_{rr}-\sigma_{\varphi\varphi}\right)\right]-$$
$$-\frac{1}{r}\frac{\partial}{\partial r}\left[\sigma_e^{n-1}\left(\sigma_{rr}-\sigma_{\varphi\varphi}\right)\right]-\frac{4}{r^2}\frac{\partial}{\partial r}\left[r\frac{\partial}{\partial\varphi}\left(\sigma_e^{n-1}\sigma_{r\varphi}\right)\right]=0, \tag{6b}$$

Thus, the main equations in stress terms for the power law constitutive equation (Eq. 4) are the equilibrium equations (Eq. 1) and the strain compatibility condition for the plane stress (Eq. 6a) or the plane stain (Eq. 6b), accordingly.

2.2. Airy's stress function

To solve the system of Eq. (1) and Eq. (6a) or Eq. (1) and Eq. (6b) it is often used the Airy's stress function $F(r, \varphi)$, defined as follows [1-3]:

$$\sigma_{rr} = \frac{1}{r}\frac{\partial F}{\partial r} + \frac{1}{r^2}\frac{\partial^2 F}{\partial \varphi^2}, \quad \sigma_{\varphi\varphi} = \frac{\partial^2 F}{\partial r^2}, \quad \sigma_{r\varphi} = \frac{1}{r^2}\frac{\partial F}{\partial \varphi} - \frac{1}{r}\frac{\partial^2 F}{\partial r \partial \varphi}. \tag{7}$$

Substituting Eq. (7) in the strain compatibility equation for plane stress and plane strain conditions (Eq. 6a or Eq. 6b, accordingly), we obtain the following nonlinear differential equation for the Airy's stress function $F(r, \varphi)$:

$$\frac{1}{r}\frac{\partial^2}{\partial r^2}\left[\sigma_e^{n-1}\left(r\frac{\partial^2 F}{\partial r^2} - \frac{1}{2}\left(\frac{\partial F}{\partial r} + \frac{1}{r}\frac{\partial^2 F}{\partial \varphi^2}\right)\right)\right] + \frac{1}{r^2}\frac{\partial^2}{\partial \varphi^2}\left[\sigma_e^{n-1}\left(\frac{1}{r}\frac{\partial F}{\partial r} + \frac{1}{r^2}\frac{\partial^2 F}{\partial \varphi^2} - \frac{1}{2}\frac{\partial^2 F}{\partial r^2}\right)\right] -$$
$$-\frac{1}{r}\frac{\partial}{\partial r}\left[\sigma_e^{n-1}\left(\frac{1}{r}\frac{\partial F}{\partial r} + \frac{1}{r^2}\frac{\partial^2 F}{\partial \varphi^2} - \frac{1}{2}\frac{\partial^2 F}{\partial r^2}\right)\right] - \frac{3}{r^2}\frac{\partial}{\partial r}\left[\frac{\partial}{\partial \varphi}\left(\sigma_e^{n-1}\left(\frac{1}{r}\frac{\partial F}{\partial \varphi} - \frac{\partial^2 F}{\partial r \partial \varphi}\right)\right)\right] = 0, \tag{8a}$$

where

$$\sigma_e^2 = \frac{\partial^2 F}{\partial \varphi^2}\left(\frac{2}{r^3}\frac{\partial F}{\partial r} + \frac{1}{r^4}\frac{\partial^2 F}{\partial \varphi^2} - \frac{1}{r^2}\frac{\partial^2 F}{\partial r^2}\right) + \frac{\partial F}{\partial r}\left(\frac{1}{r^2}\frac{\partial F}{\partial r} - \frac{1}{r}\frac{\partial^2 F}{\partial r^2}\right) -$$
$$-3\frac{\partial^2 F}{\partial r \partial \varphi}\left(\frac{2}{r^3}\frac{\partial F}{\partial \varphi} - \frac{1}{r^2}\frac{\partial^2 F}{\partial r \partial \varphi}\right) + \left(\frac{\partial^2 F}{\partial r^2}\right)^2 + \frac{3}{r^4}\left(\frac{\partial F}{\partial \varphi}\right)^2,$$

or

$$\frac{1}{r}\frac{\partial^2}{\partial r^2}\left[\sigma_e^{n-1}\left(r\frac{\partial^2 F}{\partial r^2} - \left(\frac{\partial F}{\partial r} + \frac{1}{r}\frac{\partial^2 F}{\partial \varphi^2}\right)\right)\right] + \frac{1}{r^2}\frac{\partial^2}{\partial \varphi^2}\left[\sigma_e^{n-1}\left(\frac{1}{r}\frac{\partial F}{\partial r} + \frac{1}{r^2}\frac{\partial^2 F}{\partial \varphi^2} - \frac{\partial^2 F}{\partial r^2}\right)\right] -$$
$$-\frac{1}{r}\frac{\partial}{\partial r}\left[\sigma_e^{n-1}\left(\frac{1}{r}\frac{\partial F}{\partial r} + \frac{1}{r^2}\frac{\partial^2 F}{\partial \varphi^2} - \frac{\partial^2 F}{\partial r^2}\right)\right] - \frac{4}{r^2}\frac{\partial}{\partial r}\left[\frac{\partial}{\partial \varphi}\left(\sigma_e^{n-1}\left(\frac{1}{r}\frac{\partial F}{\partial \varphi} - \frac{\partial^2 F}{\partial r \partial \varphi}\right)\right)\right] = 0, \tag{8b}$$

where

$$4\sigma_e^2 = \frac{\partial^2 F}{\partial \varphi^2}\left(\frac{6}{r^3}\frac{\partial F}{\partial r} + \frac{3}{r^4}\frac{\partial^2 F}{\partial \varphi^2} - \frac{6}{r^2}\frac{\partial^2 F}{\partial r^2}\right) + \frac{\partial F}{\partial r}\left(\frac{3}{r^2}\frac{\partial F}{\partial r} - \frac{6}{r}\frac{\partial^2 F}{\partial r^2}\right) -$$
$$-12\frac{\partial^2 F}{\partial r \partial \varphi}\left(\frac{2}{r^3}\frac{\partial F}{\partial \varphi} - \frac{1}{r^2}\frac{\partial^2 F}{\partial r \partial \varphi}\right) + 3\left(\frac{\partial^2 F}{\partial r^2}\right)^2 + \frac{12}{r^4}\left(\frac{\partial F}{\partial \varphi}\right)^2.$$

2.3. Near crack tip asymptotic

In the polar coordinate system the Airy's stress function $F(r, \varphi)$ near a crack tip has the following asymptotic representation [4-6]:

$$F(r,\varphi) = Kr^{\lambda} f(\varphi), \tag{9}$$

where $\lambda = (2n+1)/(n+1)$, $K = (J/BI_n)^{1/(n+1)}$, $J = \oint\left(\frac{n}{n+1}B\sigma_e^{n+1}\cos\varphi - \sigma_{ij}n_j\frac{\partial u_i}{\partial x}\right)ds$ is the path-independent contour integral (usually named as Cherepanov-Rice-integral or J-integral) and

$$I_n = \int_{-\pi}^{\pi}\left[\cos\varphi\left(\frac{n}{n+1}s_e^{n+1} - \frac{1}{n+1}\left(s_{rr}u_r + s_{r\varphi}u_\varphi\right)\right) - \sin\varphi\left(s_{rr}\left(u_\varphi - \frac{\partial u_r}{\partial\varphi}\right) - s_{r\varphi}\left(u_r + \frac{\partial u_\varphi}{\partial\varphi}\right)\right)\right]d\varphi$$

is the dimensionless constant.

Taking into account Eq. (7) and the asymptotic behavior (Eq. 9) of Airy's stress function $F(r, \varphi)$, the stress tensor σ_{ij} and the equivalent stress σ_e near a crack tip can be written as follows:

$$\begin{aligned}
\sigma_{rr} &= Kr^{\lambda-2}(\lambda f(\varphi) + d^2 f/d\varphi^2) = Kr^{\lambda-2}s_{rr}(\varphi),\\
\sigma_{\varphi\varphi} &= Kr^{\lambda-2}(\lambda(\lambda-1)f(\varphi)) = Kr^{\lambda-2}s_{\varphi\varphi}(\varphi),\\
\sigma_{r\varphi} &= Kr^{\lambda-2}(1-\lambda)(df/d\varphi) = Kr^{\lambda-2}s_{r\varphi}(\varphi),\\
\sigma_e &= Kr^{\lambda-2}s_e(\varphi),
\end{aligned}$$

where $s_e(\varphi)$ is the dimensionless function, written for the plane stress and the plane strain conditions, respectively, as the follows:

$$s_e^2 = \lambda^2(\lambda^2-3\lambda+3)f^2(\varphi) + 3(\lambda^2-2\lambda+1)(df/d\varphi)^2 + \lambda(3-\lambda)f(\varphi)(d^2f/d\varphi^2) + (d^2f/d\varphi^2)^2,$$

$$s_e^2 = \lambda^2(\lambda^2-4\lambda+4)f^2(\varphi) + 4(\lambda^2-2\lambda+1)(df/d\varphi)^2 + 2\lambda(2-\lambda)f(\varphi)(d^2f/d\varphi^2) + (d^2f/d\varphi^2)^2$$

Compatibility equations (8a) and (8b) for the asymptotic of Airy's stress function $F(r, \varphi)$ (Eq. 9) can be rewritten as non-linear ordinary differential equation for the unknown function $f(\varphi)$ [7-8]:

$$\begin{aligned}
&n(\lambda-2)s_e^{n-1}\left[((2-\lambda)n-3)(d^2f/d\varphi^2) + \lambda\left(2n\left(\lambda^2+3\right) + \lambda(3-7n) - 6\right)f(\varphi)\right] +\\
&+\frac{d^2}{d\varphi^2}\left[s_e^{n-1}\left(2d^2f/d\varphi^2 - \lambda(\lambda-3)f(\varphi)\right)\right] + 6(\lambda-1)((\lambda-2)(n-1)+\lambda-1)\frac{d}{d\varphi}\left[s_e^{n-1}df/d\varphi\right] = 0, \quad (10a)
\end{aligned}$$

$$\begin{aligned}
&n(\lambda-2)s_e^{n-1}\left[((2-\lambda)n-2)(d^2f/d\varphi^2) + \lambda(\lambda-2)(n(\lambda-2)+2)f(\varphi)\right] +\\
&+\frac{d^2}{d\varphi^2}\left[s_e^{n-1}\left(d^2f/d\varphi^2 - \lambda(\lambda+2)f(\varphi)\right)\right] + 4(\lambda-1)((\lambda-2)(n-1)+\lambda-1)\frac{d}{d\varphi}\left[s_e^{n-1}df/d\varphi\right] = 0. \quad (10b)
\end{aligned}$$

Thus, the equation (10a) or (10b) is a non-linear differential equation of fourth order for unknown asymptotic Airy's stress function $f(\varphi)$. To solve this equation and to determine the stress field near a crack tip it is necessary to add four boundary conditions.

2.4. Boundary conditions

The first two boundary conditions are the conditions of the free crack surfaces, i.e. $\sigma_{\varphi\varphi} = \sigma_{r\varphi} = 0$ at $\varphi=\pi$. Hence, two boundary conditions for asymptotic Airy's stress function $f(\varphi)$ are the follows:

$$f = df/d\varphi = 0\,,\ \varphi=\pi. \tag{11}$$

For mode I or mode II crack tip two additional boundary conditions are the symmetry conditions, i.e. $\partial\sigma_{rr}/\partial\varphi = \sigma_{r\varphi} = 0$ (mode I) or $\sigma_{\varphi\varphi} = \partial\sigma_{r\varphi}/\partial\varphi = 0$ (mode II) at $\varphi=0$. In this case two additional boundary conditions for asymptotic Airy's stress function $f(\varphi)$ are the follows:

$$df/d\varphi = d^3 f/d\varphi^3 = 0\,,\ \varphi=0 \text{ (mode I) or } \ f = d^2 f/d\varphi^2 = 0\,,\ \varphi=0 \text{ (mode II).} \tag{12}$$

Thus, for Eq. (10a) or Eq. (10b) with boundary conditions (Eq. 11) and (Eq. 12) it is obtained two-point boundary value problem for asymptotic Airy's stress function $f(\varphi)$. This problem can be solved by shooting method [9], when adding to symmetry conditions (Eq. 12) two additional boundary conditions

$$f = c_1, d^2 f/d\varphi^2 = c_2 \text{ (mode I) or } df/d\varphi = c_1, d^3 f/d\varphi^3 = c_2 \text{ (mode II) at } \varphi=0$$

the above-mentioned two-point boundary value problem reduces to the Cauchy problem. The Cauchy problem is usually solved by using the Runge-Kutta method [9], when choosing the values of additional boundary constants c_1, c_2 in such way as to satisfy the main boundary conditions at $\varphi=\pi$ (Eq. 11).

The boundary conditions (Eq. 12), followed from symmetry conditions, does not valid for mixed mode of loading or for inclined crack under tension (Fig. 1). In this case the boundary conditions at $\varphi=0$ can be represented as the follows [7-8]:

$$f = c_0, df/d\varphi = -\lambda c_0 tg\alpha, d^2 f/d\varphi^2 = c_1, d^3 f/d\varphi^3 = c_2\,,\ \varphi=0. \tag{13}$$

The constant c_0 is determined from some additional condition (named as normalization condition). Traditionally the normalization condition is selected in the form of $\max_{\phi} \sigma_e(\varphi) = 1$ [5-6].

The last two constants c_1, c_2 are sought by shooting method - to choose these constants, so that at $\varphi=\pi$ the boundary conditions (Eq. 11) are valid.

3. Method of solution

To solve this problem let us denote $f(\pi) = f_1(c_1, c_2)$, and $df(\pi)/d\varphi = f_2(c_1, c_2)$. In order to satisfy the main boundary conditions (Eq. 11) it is necessary to find the solution of the following system of two nonlinear algebraic equations:

$$f_1(c_1, c_2) = 0, \quad f_2(c_1, c_2) = 0. \tag{14}$$

It should be noted that the functions $f_1(c_1, c_2)$ and $f_2(c_1, c_2)$ are not given in analytical form, but are found numerically by solving the above-mentioned Cauchy problem for different values of c_1 and c_2. The system of nonlinear equations (Eq. 14) can be solved by the Newton's method. Newton's method is an iterative method for solving the system of nonlinear algebraic equations [9]. Rewrite the general formula of Newton's method for the system (Eq. 14) as the follows:

$$f_{1,1}^k c_1^{k+1} + f_{1,2}^k c_2^{k+1} = f_{1,1}^k c_1^k + f_{1,2}^k c_2^k - f_1^k,$$

$$f_{2,1}^k c_1^{k+1} + f_{2,2}^k c_2^{k+1} = f_{2,1}^k c_1^k + f_{2,2}^k c_2^k - f_2^k,$$

where c_i^k is the value of the parameter c_i at the *k*-th step of iteration, $f_{i,j}^k$ is the value of derivative of function f_i with respect to c_j, computed at the *k*-th step of iteration, *i,j=1,2; k= 1,2,3,…*

To calculate numerically the values of $f_{i,j}^k$ it is used the right finite difference scheme:

$$f_{1,1}^k = (f_1^k(c_1^k + \delta, c_2^k) - f_1^k(c_1^k, c_2^k))/\delta,$$
$$f_{1,2}^k = (f_1^k(c_1^k, c_2^k + \delta) - f_1^k(c_1^k, c_2^k))/\delta,$$
$$f_{2,1}^k = (f_2^k(c_1^k + \delta, c_2^k) - f_2^k(c_1^k, c_2^k))/\delta,$$
$$f_{2,2}^k = (f_2^k(c_1^k, c_2^k + \delta) - f_2^k(c_1^k, c_2^k))/\delta,$$

where δ *is* a small number.

Thus, to find the next approximation (c_1^{k+1}, c_2^{k+1}) of the parameters c_1 and c_2 it is necessary to integrate three time the Cauchy problem by Runge-Kutta method for the values of parameters (c_1^k, c_2^k), $(c_1^k + \delta, c_2^k)$ and $(c_1^k, c_2^k + \delta)$.

The above-described method of solving the nonlinear differential equation (Eq. 10a) or (Eq. 10b) has been tested for correctness and accuracy and compared with some known analytical or numerical results. Thus, in the case $n=1$ there exist analytical expressions for the stress tensor components for any inclined cracks [1-3]. For mode I ($\alpha = 0$) it is known the analytical result for the case $n=\infty$ and

the numerical results for $n>1$ [5-6]. Testing has shown that for $n=1$ the value of the relative error does not exceed 10^{-6}. The results of calculations based on above-described method as for the case $n=\infty$ as for $n>1$ practically coincided with the numerical results from [5-6].

4. Results of calculations

Some results of calculations for stress distribution around the crack tip for plane stress and plane strain conditions are shown on the Figures 2-5.

4.1. Plane stress

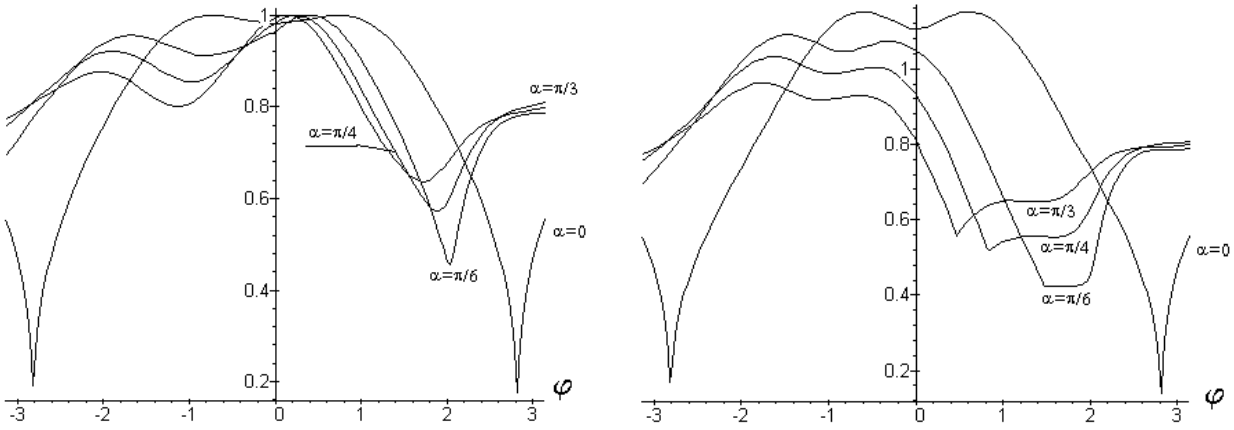

Figure 2. The distribution of the equivalent stress σ_e and the maximum stress $\sigma_{\max}$ around the crack tip for $n=3$ (plane stress).

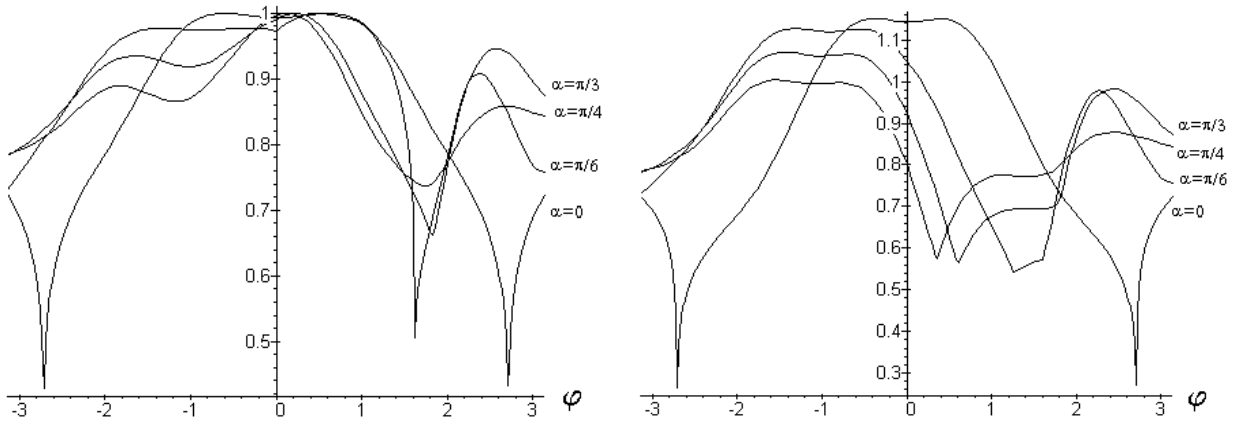

Figure 3. The distribution of the equivalent stress σ_e and the maximum stress $\sigma_{\max}$ around the crack tip for $n=7$ (plane stress).

4.2. Plane strain

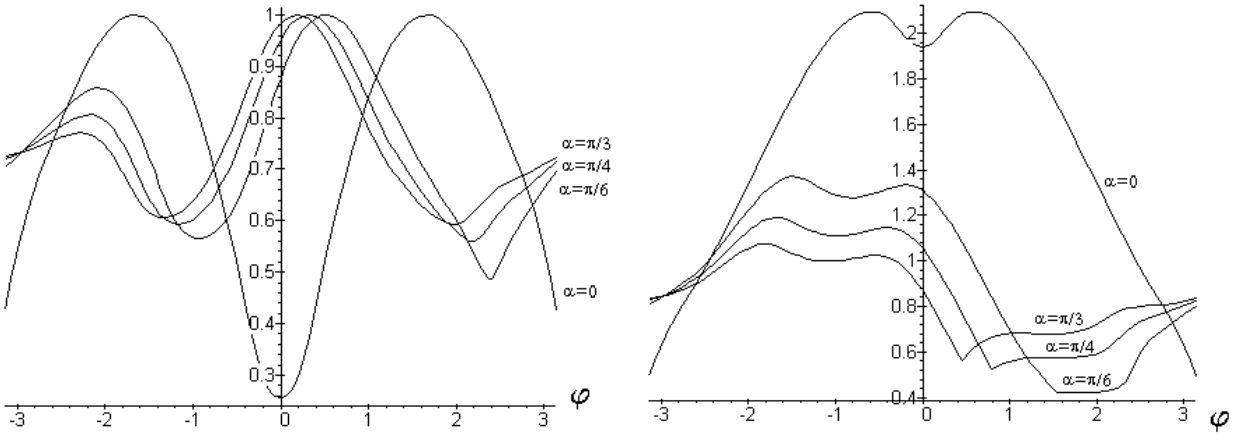

Figure 4. The distribution of the equivalent stress σ_e and the maximum stress $\sigma_{\max}$ around the crack tip for *n=3* (plane strain).

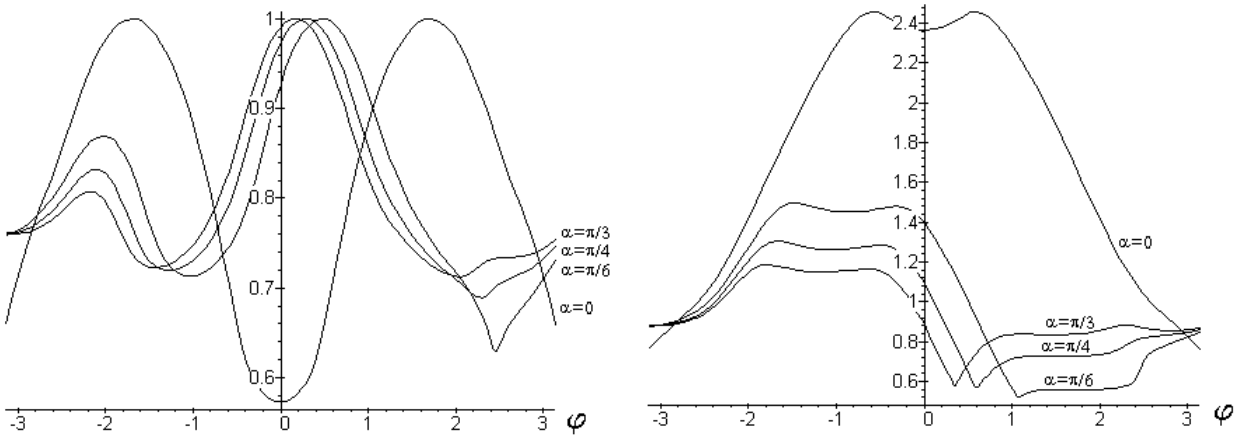

Figure 5. The distribution of the equivalent stress σ_e and the maximum stress $\sigma_{\max}$ around the crack tip for *n=7* (plane strain).

Acknowledgment

Authors are grateful the Russian Foundation for Basic Research for the financial support under Grant 12-08-00390-a.

References

[1] V.I. Astafiev, Yu.N. Radaev, L.V. Stepanova, Non-Linear Fracture Mechanics, Samara State University, Samara, 2001 (in Russian).

[2] L.V. Stepanova, Mathematical Methods in Fracture Mechanics, Fizmatlit, Moscow, 2009 (in Russian).
[3] V.M. Pestrikov, E.M. Morozov, Fracture Mechanics. Course of Lectures, EPS Professia, St. Petersburg, 2012 (in Russian).
[4] G.P. Cherepanov, Mechanics of brittle fracture, Nauka, Moscow, 1974 (in Russian).
[5] J.W. Hutchinson, Singular behavior at the end of tensile crack in a hardening material tip, J. Mech. Phys. Solids, 16, (1968) 13-31.
[6] J.R. Rice, G.F. Rosengren, Plane strain deformation near a crack tip in a power-law hardening material, J. Mech. Phys. Solids, 16, (1968) 32-48.
[7] V.I. Astafiev, A.N. Krutov, Stress distribution near a tip of inclined crack in nonlinear fracture mechanics, Vestnik SamGU, 14, (1999) 56-69 (in Russian).
[8] V.I. Astafiev, A.N. Krutov, Stress distribution near a tip of inclined crack in nonlinear fracture mechanics, Mechanics of Solids, 36, (2001) 101-108.
[9] N.S. Bakhvalov, N.P. Zhidkov, G.M. Kobelkov, Numerical Methods, Nauka, Moscow, 1987 (in Russian).

Effect of Notch Severity on Thermomechanical Fatigue Life of a Directionally-solidified Ni-base Superalloy

Patxi Fernandez-Zelaia[1] and Richard W. Neu[1,2*]

[1] Woodruff School of Mechanical Engineering, Georgia Institute of Technology, Atlanta, Georgia, 30332, USA
[2] School of Materials Science and Engineering, Georgia Institute of Technology, Atlanta, Georgia, 30332, USA
* Corresponding author: rick.neu@gatech.edu

Abstract The aim of this research is to understand the influence of notches under thermomechanical fatigue (TMF) in a directionally-solidified (DS) Ni-base superalloy. Experiments were performed utilizing linear out-of-phase (OP) and in-phase (IP) TMF loadings on longitudinally-oriented smooth and cylindrically-notched specimens. Several notch severities were considered with elastic stress concentrations ranging from 1.3 to 3.0. The local response of the notched specimens was determined using the finite element method with a transversely isotropic viscoplastic constitutive model. Comparing the analysis to experiments, the locations observed for crack nucleation in the notch, which are offset from the notch root in DS alloys, are consistent with the maximum von Mises stress. Various local and nonlocal methods are evaluated to understand the life trends under OP TMF. The results show that a nonlocal invariant area-averaging method is the best approach for collapsing the TMF lives of specimens with different notch severities.

Keywords notched specimens, thermomechanical fatigue, Ni-base superalloy, notch analysis

1. Introduction

Components in the high pressure turbine section of gas turbine engines undergo complex thermomechanical loads during engine cycle transients. Turbine blades contain stress elevating features such as cooling holes or fir-trees that can have a detrimental effect on component endurance and make endurance prediction difficult. The surrounding material around these stress elevators undergo cyclic inelastic deformation providing a source for fatigue crack nucleation [1, 2]. To improve component level endurance prediction methodologies, the effect of stress elevators on thermomechanical fatigue (TMF) needs to be addressed.

Few studies have targeted the problem of determining crack initiation of notched specimens under TMF. Presently, no accepted methods exist for predicting TMF crack initiation life at notches. Studies on the TMF of circumferentially-notched specimens fabricated from a rotor steel, 1CrMoV, found that uniaxial life results could be used to predict the notch endurance given that conditions at the notch root were comparable [3, 4]. Large spatial gradients were shown to reduce the driving force for creep damage and fatigue crack growth away from the notch root in notched specimens. For identical crack initiation criteria, this effect could potentially increase the measured endurance as physically small cracks grow slower in notched specimens.

A study on the TMF of notched specimens of Ni-base superalloys by Kupkovits and Neu [5] found that damage mechanisms present in notched specimens are identical to smooth specimens. Notched specimen geometries corresponding to theoretical elastic stress concentration factors of $k_t = 2$ and $k_t = 3$ were studied. Under $500°C \leftrightarrow 950°C$ OP TMF conditions loaded in the longitudinal (L) orientation, the reduction in life was identical for both of these notches in contrast to isothermal fatigue where the more severe notch had a greater knockdown factor [6]. The same held true under $500°C \leftrightarrow 750°C$ OP TMF. Fatigue-environmental damage mechanisms were observed in notched OP TMF $500°C \leftrightarrow 950°C$. All notched specimen experiments resulted in crack nucleation at the location of maximum Hills' or von Mises equivalent stress similar to isothermal fatigue studies [6].

This work identified the need to explore the TMF life behavior of less severe notches geometries to understand the transition in fatigue behavior from smooth specimens ($k_t = 1$) to the more severely notched specimens ($k_t \geq 2$).

This paper focuses on the role of notch severity on TMF life expanding the work described in Kupkovits and Neu [5] by considering milder notches. The notch response is evaluated using a transversely isotropic viscoplasticity model to further understand the gradients in the cyclic stress-strain response that influence of notch severity on life. Local and several nonlocal methodologies for life assessment are evaluated to determine which approaches exhibit the most promise for assessing notches under TMF.

2. Methods

2.1. Smooth and notched specimen experiments

One cylindrical smooth specimen ($k_t = 1$) and four different cylindrically-notched specimens (k_t = 1.3, 1.7, 2 and 3 based on isotropic elastic behavior) were utilized in TMF experiments. The net section diameter for all notched specimens was 6.35 *mm*, same as the diameter of the smooth specimen. The outside diameter for all notched specimens was 9.53 *mm*.

2.2. Material

The DS Ni-base superalloy, with primary alloying elements (in wt. %) 0.07C, 8.1Cr, 9.2Co, 9.5W, 3.2Ta, 0.5Mo, 5.6Al, 0.7Ti, 1.4Hf, was received in cast slabs consisting of columnar grains in the long direction of each slab with grain diameter varying from 200 μm to 1 *mm* with an average grain diameter of 0.5 *mm*. A standard heat treatment was applied to the slab to produce a microstructure representative of an in-service blade material. The microstructure consists of FCC matrix (γ) containing cuboidal γ' precipitates. The γ' in the as-received and heated-treated material had an average volume fraction of 60% and a bi-modal size distribution of cuboidal 500 *nm* and fine secondary precipitates in the γ channels of 75 *nm* in size.

All specimens were loaded in the longitudinal direction. All experiments were fully reversed with a minimum temperature of $T_{\min} = 500°C$. Maximum temperatures of $T_{\max} = 950°C$ and $T_{\max} = 750°C$ were utilized to study the effects of maximum temperature on damaging mechanisms and TMF life. A servohydraulic test frame with induction heating was used for all experiments. Axial displacements within the gage section were measured using a high temperature extensometer with 12.7 *mm* gage section. A 180 *s* cycle time was used with constant heating and cooling rates. K-type thermocouples spot welded to the ends of the gage section for the smooth specimens or near the notch on the notched specimens were utilized to provide a feedback signal for close-loop control of specimen temperature.

Experiments performed on smooth specimens were conducted in mechanical strain control in accordance with ASTM E2368-04 for thermomechanical fatigue testing. All notched specimen experiments were performed in force control and displacements across the gross notch section were measured using a high temperature extensometer with 12.7 *mm* gage length.

A crack initiation criterion was established to identify a crack depth of 0.5-1.0 *mm* for both mechanical strain-controlled and force-controlled experiments. For mechanical-strain controlled experiments (smooth specimens) a 10% load trend variation was used. As material hardening, softening or creep processes can result in a continuously changing load history, a 10% variation of the stabilized trend constitutes crack formation. For force-controlled experiments (notched specimens) an analogous method was implemented; initiation was defined when a 10% variation in the mechanical extensometer displacement signal occurred.

3. Results

3.1. Out-of-phase TMF 500°C↔950°C

OP TMF lives obtained in force control on smooth and circumferentially notched specimens are shown in Fig. 1. Notched specimens $k_t = 2$ and $k_t = 3$ follow the same life trend, indicating that increasing the notch severity beyond $k_t = 2$ is not more detrimental to OP TMF life. Experiments on the milder notch geometry $k_t = 1.3$ show that under the applied conditions, the effect of the notch is negligible as lives follow the smooth specimen life trend. Lives corresponding to $k_t = 1.7$ fall between the two bounds represented by the $k_t = 1/k_t = 1.3$ and $k_t = 2/k_t = 3$ trends.

Cracks that lead to final failure nucleated at a location away from the notch root, as shown in Fig. 2. Cracks nucleate furthest from the notch root in the bluntest notch, $k_t = 1.3$. The nucleation location approaches the notch root with increasing notch severity.

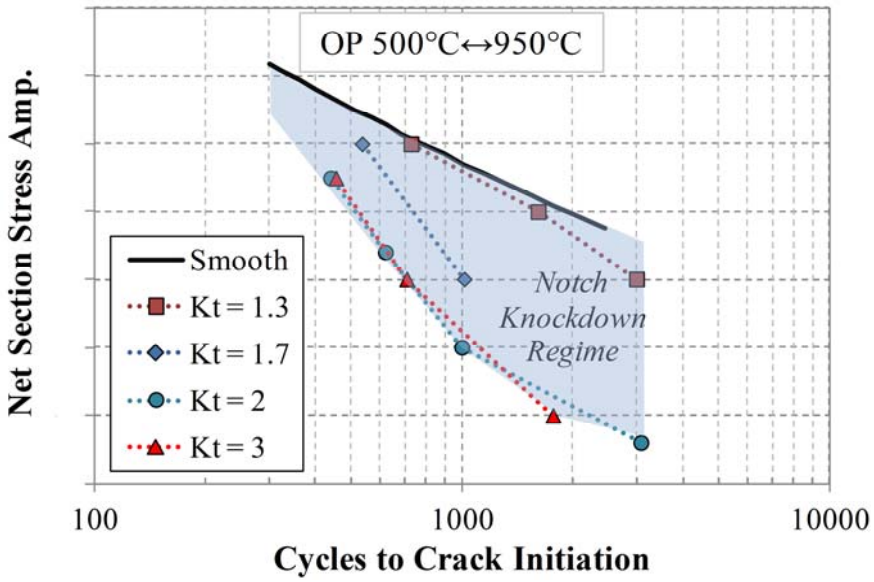

Figure 1. Crack initiation life under $500°C \leftrightarrow 950°C$ OP TMF for each notched specimen geometry.

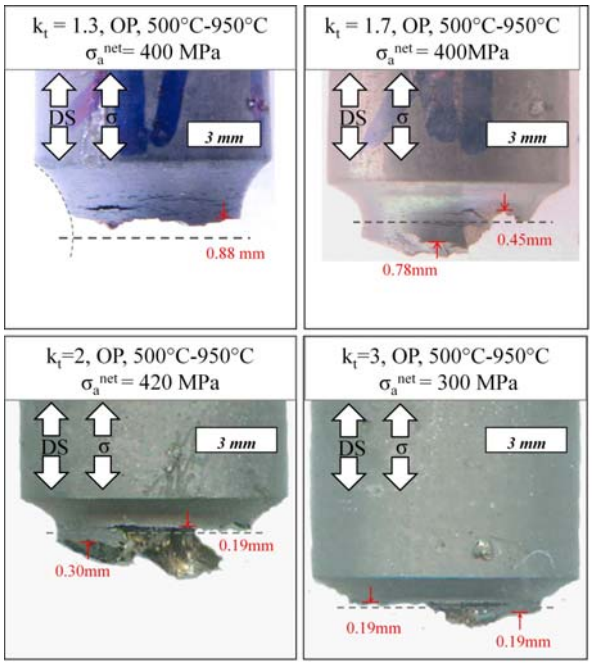

Figure 2. Fracture images indicating the location of crack initiation relative to the notch root.

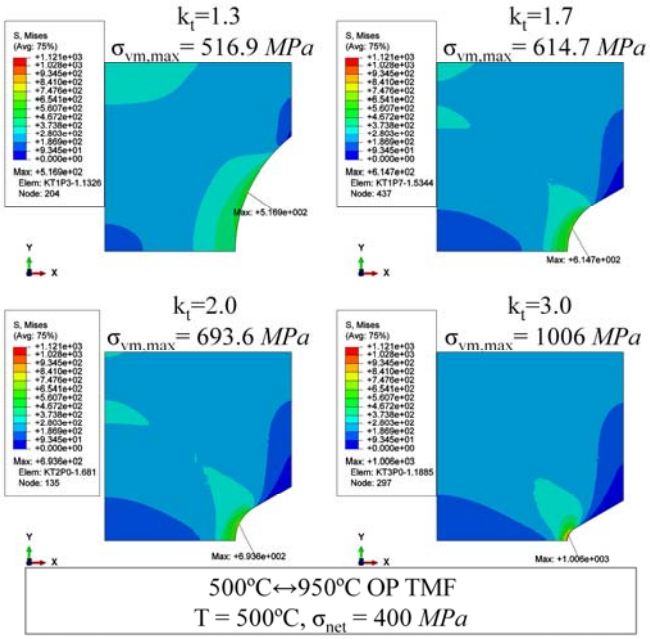

Figure 3. Von Mises equivalent stress at minimum temperature (tensile load).

The local notch response was predicted using a continuum based constitutive model within the ABAQUS finite element framework [7]. A model taking into account plasticity and creep was not available for the alloy studied and instead a transversely isotropic viscoplasticity model corresponding to another DS Ni-base superalloy was used [8]. The alloy studied exhibits higher yield strength in the virgin condition and a lower modulus. Nevertheless both superalloys exhibit the characteristic increase in yield strength around 750°C followed by a sharp decrease in strength. As such numerical results should be adequate for qualitative comparison.

The finite element meshes utilize linear quadrilateral elements throughout the domain. The cylindrically notched specimens were modeled using axisymmetric boundary conditions along with symmetry conditions at the net section to reduce the model to a quarter cross section of the extensometer gage section. A uniform pressure was applied to the top surface corresponding to the applied force. All TMF simulations of notched geometries were performed by first prescribing the mean temperature with no applied pressure. Then three reversals were applied, first loading to maximum temperature and applying the corresponding force for either OP or IP loading. Under the first peak force at elevated temperature, a great deal of initial yielding and hardening occurs. As such the cyclic response is taken as the final two reversals which better represent steady-state cyclic loading.

The stress responses at minimum temperature under the same OP TMF conditions are shown in Fig. 3. for an applied 400 *MPa* net section stress. The location of maximum von Mises stress during peak tension begins away from the notch root but approaches it with increasing notch severity. Similarly, the location of maximum equivalent inelastic cyclic strain approaches the notch root with increasing notch severity [9].

3.2. In-phase TMF 500°C↔950°C

Results from IP TMF are shown in Fig. 4 with the OP TMF knockdown regime region shown for

comparison. IP TMF lives of the $k_t = 1.3$ notch follow the smooth trend. This indicates that under IP TMF, as well as OP TMF, the $k_t = 1.3$ notch does not have a significant detrimental effect on TMF fatigue life.

3.3. Out-of-phase TMF 500°C↔750°C

The influence on initiation life from reducing the maximum temperature under OP TMF to $750°C$ is shown in Fig. 5. Even under the lower applied maximum temperature, notch geometries $k_t = 2$ and $k_t = 3$ follow the same life trend. Additional experiments within this temperature regime show that notch geometry $k_t = 1.3$ displays a small decrease in life compared to the smooth trend and $k_t = 1.7$ is slightly less damaging than exhibited by $k_t = 2 / k_t = 3$.

Under $T_{\max} = 750°C$ OP TMF, some oxidation is present along interdendritic regions and grain boundaries, but overall the contribution from environmental processes is small. Under higher temperature $T_{\max} = 950°C$ OP TMF, several secondary fatigue-environmental cracks oriented perpendicularly to the applied load are observed. There is no evidence of environmental-fatigue secondary cracks under IP TMF as seen under OP TMF.

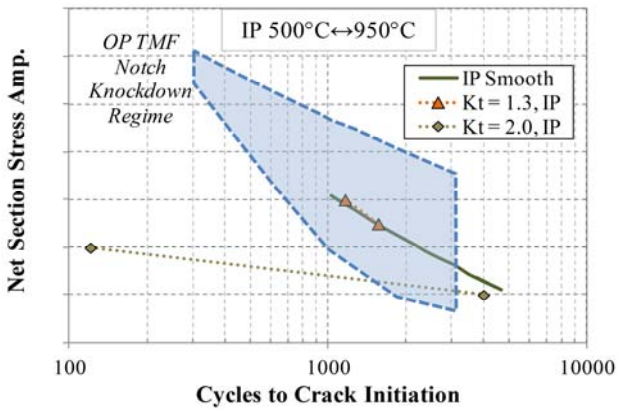

Figure 4. Crack initiation life under $500°C \leftrightarrow 950°C$ IP TMF for each notched specimen geometry.

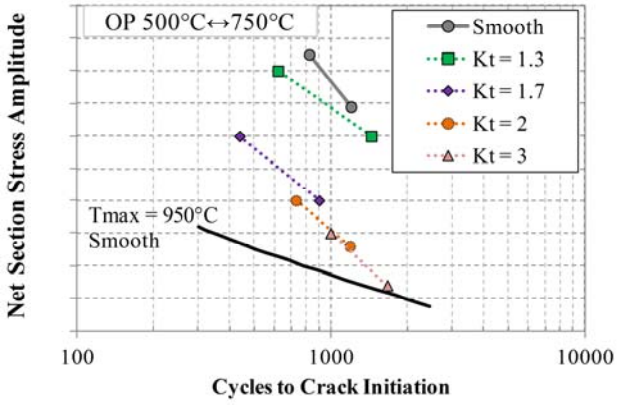

Figure 5. Crack initiation life under $500°C \leftrightarrow 750°C$ OP TMF for each notched specimen geometry.

4. Implications for life modeling

Most life modeling approaches tend to predict that increases in notch severity result in lower lives. It is apparent that a nonlocal approach will be needed to evaluate notched lives under TMF to predict the experimental results. In the next exercise, we evaluate some popular domain averaging schemes [10-14] to determine what methods work best in predicting the observed trends in lives. Here, we focus on OP TMF under $500°C \leftrightarrow 950°C$ to maintain a constant mechanism of damage. As shown earlier, the crack nucleation locations under OP TMF loading coincide well with the maximum von Mises stress and equivalent inelastic strain range. To keep the damage model simple for evaluation, a generalized energy-based damage parameter [15] that couples these two drivers is used,

$$D_O = \Delta\varepsilon_e^{in}\sigma_{e,\max} \tag{1}$$

where $\Delta\varepsilon_e^{in}$ is the equivalent inelastic strain range and $\sigma_{e,\max}$ is the maximum value of the von Mises equivalent stress over one cycle which occurs in tension for OP TMF. Since the loading is uniaxial, the loading in the vicinity of the notch is approximately proportional and hence using equivalent values is acceptable for this exercise for ease of computation.

As a baseline, the maximum D_O parameter for each geometry and applied load is shown in Fig. 6. As expected, this local approach gives high values for the D_O parameter and is highly conservative [3, 10-14, 16]. The local approach incorrectly predicts increasing damage with increasing notch severity, which is totally inconsistent with the observed experimental lives. A regression analysis using a power law relationship was used to attempt to correlate the maximum D_O parameter to lives, as shown in Fig. 7. This procedure does not collapse the life data.

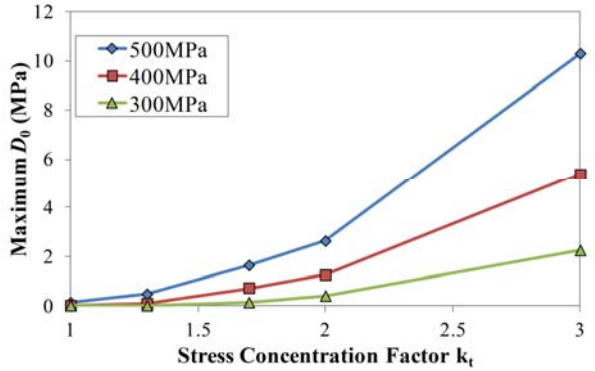

Figure 6. Maximum D_O parameter for all specimen geometries $500°C \leftrightarrow 950°C$ OP TMF.

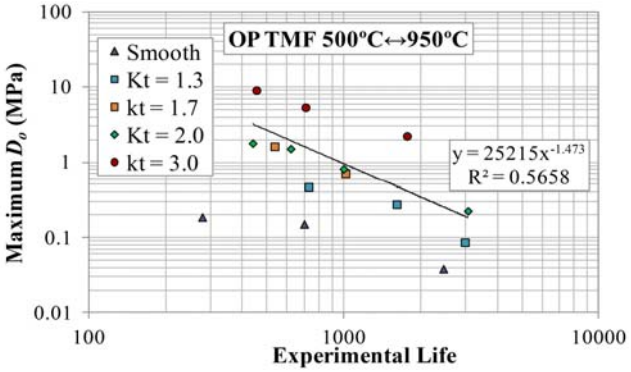

Figure 7. Correlation of maximum D_O parameter with experimentally determined OP TMF lives.

Rather than utilizing a local maximum quantity, nonlocal approaches utilize an averaged quantity over a domain or a point some distance away from the maximum. The simplest implementation is utilizing a point value some critical distance away from a key local quantity. Nonlocal quantities include averaging domains over a line, area or within a volume. The averaged generalized damage parameter can be defined as,

$$\bar{D}_O = \frac{1}{D}\int_D D_O \, dD \tag{2}$$

where D is the averaging domain; line, area or volume. Nonlocal approaches on isotropic materials typically utilize a line or point method as the response is centered about the notch root [10-12, 14]. However, for the transversely isotropic response of directionally-solidified (DS) alloys when loaded longitudinally, cracks are observed to initiate away from the notch root. Additionally the maximum equivalent inelastic strain range and maximum von Mises stress occur away from the notch root and the response changes during loading, with temperature, applied load level and across specimen geometries. Directions of relevant spatial gradients change with applied conditions and do not coincide with surface normals or crystallographic directions. As such an area averaging approach was used on the response predicted by the axisymmetric finite element method. As the domain represents an axisymmetric volume, in this case this is also equivalent to a volume averaging scheme.

A critical area approach [11, 13] was first evaluated for determining the integration domain. This method identifies the domain within which the damage quantity is a percentile of the maximum value,

$$A_{crit} = A\left(D_O \geq P \cdot \max\left\{D_O\right\}\right) \tag{3}$$

where A is the total area of the section of interest, A_{crit} is the critical area and P is a value between 0 and 1 that represents the percentile quantity used to define the critical domain. The critical area for all notch geometries based on 95-percentile (P = 0.95) under a 500 *MPa* applied net section stress is shown in Fig. 8. The size of the critical area decreases with increasing notch severity due to increases in the spatial gradients in the damage parameter.

The area averaged damage parameter using a 95-percentile area domain is shown in Fig. 9 for each notch geometry and three applied net section stresses. This method exhibits similar trends as using the local damage approach; increases in notch severity always produce additional damage in conflict with experimental observations.

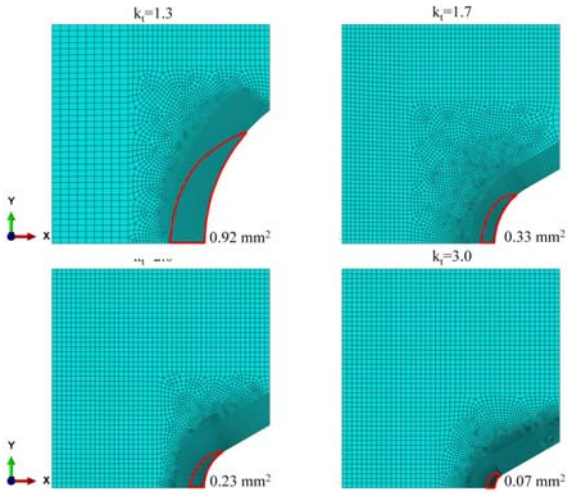

Figure 8. OP TMF $500°C \leftrightarrow 950°C$ 95-percentile critical areas based on D_O parameter.

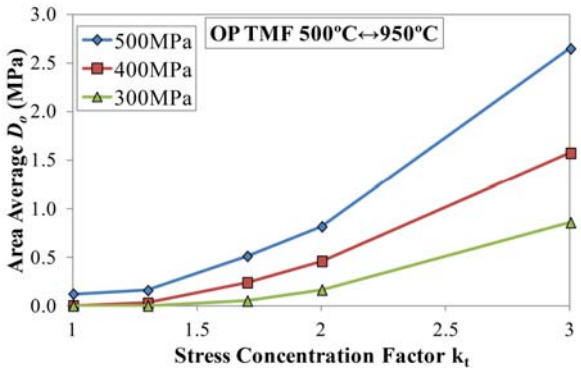

Figure 9. Nonlocal 95-percentile critical area $\bar{D}_O$ as a function of applied load and stress concentration.

Invariant averaging domains have been used successfully in notch and component analysis [11, 12, 16]. For evaluating this approach, two methods are implemented: (1) a surface-sweep of the notch surface into the component as seen in Fig. 10(a) and (2) a circular-sweep within the component centered about the location of the maximum damage parameter shown in Fig. 10(b). An iterative method was utilized to achieve the desired critical area domain for each component as the axisymmetric component areas are irregular. A bisection zero finding method was implemented to reduce the residual $R_i = \left|A_{crit} - A\left(L_i\right)\right|$ to a satisfactory tolerance by iterating on the critical length L.

The area scale was parametrically varied to achieve an optimum domain for the largest net section stress amplitude case as shown in Fig. 11. Increasing the averaging area decreases the area average damage parameter as one might expect. As the averaging area increases, the difference in the driver between $k_t = 2$ and $k_t = 3$ lives becomes indistinguishable which is consistent with

experimental observations. Hence, both experimentally observed notch life sensitivity trends at low and high notch severity values are captured simultaneously with a single parameter variation.

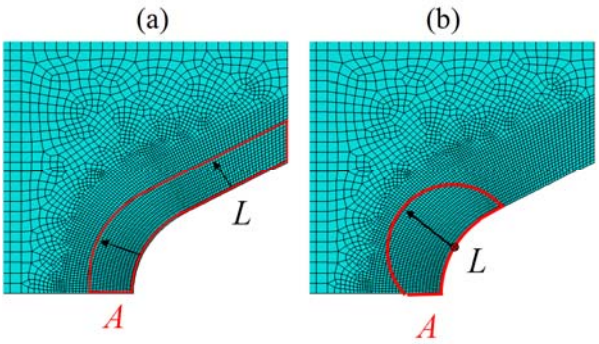

Figure 10. Domain for area averaging $k_t = 2.0$ notch using (a) surface-sweep method and (b) circular-sweep method.

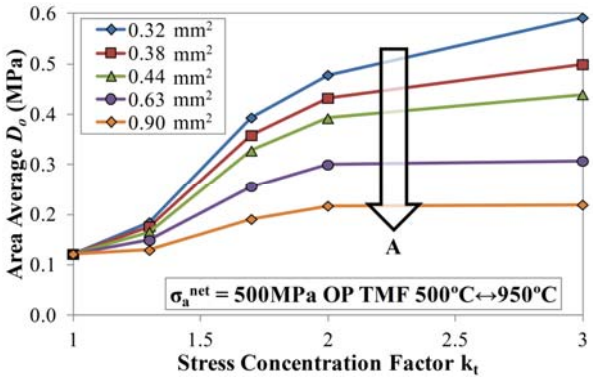

Figure 11. Surface-sweep nonlocal average $\bar{D}_O$ parameter for OP TMF under 500 *MPa* net section stress for increasing area domain.

Optimal areas for predicting $k_t = 1/k_t = 1.3$ and $k_t = 2/k_t = 3$ OP TMF notch life sensitivity trends were found to be 0.90 mm^2 and 0.77 mm^2 for surface-sweep and circular-sweep domains, respectively. The sweeping length scale, *L*, is shown for each method and notch geometry in Table 1.

Table 1. Sweeping Length Scales for Optimized Area Domains

Surface-Sweep		Circular-Sweep	
k_t	L (μm)	k_t	L (μm)
1.3	276	1.3	686
1.7	386	1.7	670
2	413	2	678
3	476	3	735

The surface-sweep scale is smaller than the circular-sweep scale as the sweeping area is performed over the entire notch surface length. The length scale changes to preserve the same size area for averaging the damage parameter in each notch geometry. Relevant length scales here are larger than the 200 μm length scale for point and line methods utilized by Moore and Neu for isothermal fatigue of the some notch geometry and material [16]. Naik et al. [14] found the line average domain to be between 20 μm and 100 μm for notched Ti-6Al-4V with stress concentrations varying between 2 and 4. For a notched Al alloy, Susmel and Taylor [12] utilized a 244 μm length scale for implementing a point method approach and a 154 μm length scale for a line method approach. In the same study Susmel and Taylor also investigated low-carbon steel and utilized 492 μm and 396 μm scales for point and line methods, respectively. It is critical to note however that the length scales obtained from the literature were determined from a line-method approach, whereas here an area method approach is utilized. As such it is expected that the scale will be larger here. Additionally, as the columnar grain size is fairly large in this alloy, and hence the relevant length scale can be expected to be on the same order as the grain size (0.2 *mm* to 1.0 *mm*).

The correlation of the area averaged damage parameter with experimental OP TMF life is shown in Fig. 12. Both averaging methods improve the life predictability as compared against the local method and critical area nonlocal approaches presented previously. With the exception of one life

value, all predictions are within a factor of two utilizing either averaging method.

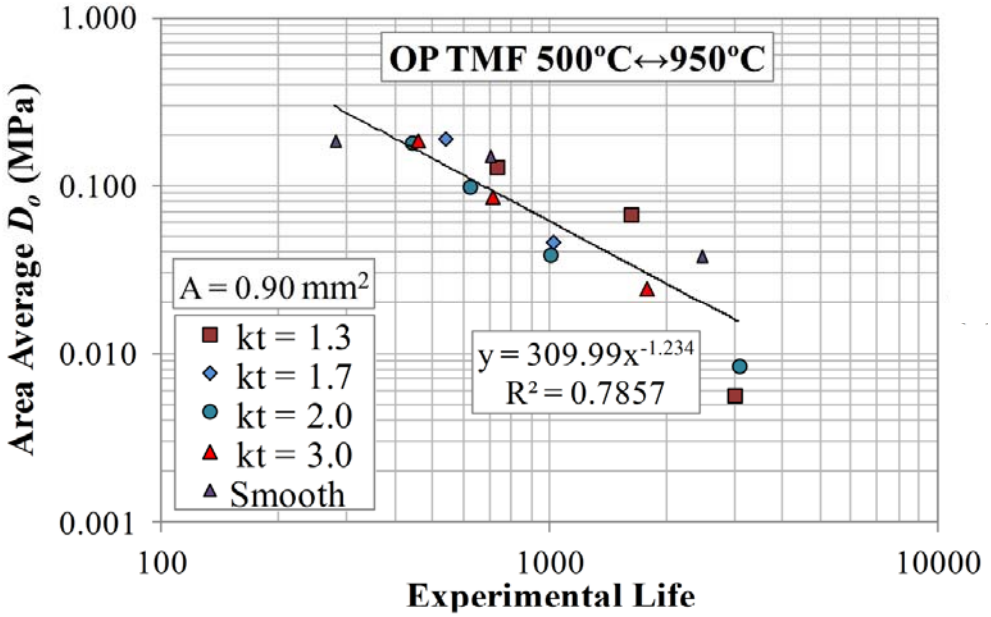

Figure 12. Correlated nonlocal $\bar{D}_O$ against experimentally determined OP TMF lives using the invariant area surface sweep method.

5. Conclusions

- For OP TMF $500°C \leftrightarrow 950°C$, the $k_t = 1.3$ notch represents the lower bound of fatigue notch sensitivity as there is no appreciable knock-down in life relative to the smooth life trend. For $k_t \geq 2$, the fatigue life is also insensitive to the severity of the notch. The $k_t = 1.7$ notch falls in between the $k_t = 1 / k_t = 1.3$ and $k_t = 2 / k_t = 3$ trends.
- In DS alloys loaded longitudinally, the OP TMF cracks in notched specimens nucleate away from the notch root. The nucleation location approaches the notch root with increasing notch severity and increasing applied force amplitude for a given notch geometry. These trends are captured in a computational stress-strain analysis using either von Mises equivalent stress or the cyclic inelastic equivalent strain range cyclic response parameters.
- For OP TMF with smaller maximum temperature, $500°C \leftrightarrow 750°C$, the $k_t = 1.3$ notch exhibits a small knock-down in life relative to the smooth life trend. The $k_t = 1.7$ notch falls in between the $k_t = 1.3$ and $k_t = 2 / k_t = 3$ life trends.
- Under IP TMF $500°C \leftrightarrow 950°C$, the $k_t = 1.3$ notch also follows the smooth specimen life trend similar to OP TMF.
- Neither local nor critical-domain nonlocal methods adequately collapsed notched and smooth OP TMF $500°C \leftrightarrow 950°C$ life data.
- A nonlocal invariant area-averaging method was utilized to collapse all experimental data that included variations in notch severity and force amplitude onto a single trend. Two schemes were implemented to define the invariant area-averaging domain; one based on the maximum value of the generalized damage parameter and a circular sweep of the surrounding domain and another based on the domain around the entire notch surface. Both methods worked reasonably well.

Acknowledgements

This effort was supported by Siemens Energy Inc., Orlando, FL. The interactions with Phillip Gravett, Sachin Shinde, and Saiganesh Iyer are appreciated.

References

[1] Z. Mazur, A. Luna-Ramirez, J.A. Juarez-Islas, A. Campos-Amezcua, Failure analysis of a gas turbine blade made of Inconel 738LC alloy. Eng Failure Analysis, 12 (2005) 474-486.

[2] R.C. Reed, The Superalloys - Fundamentals and Applications, Cambridge, 2006.

[3] E. Mazza, M. Hollenstein, S. Holdsworth, R.P. Skelton, Notched specimens thermo-mechanical fatigue of a 1CrMoV turbine steel. Nuclear Eng Design. 234 (2004) 11-24.

[4] F. Colombo, E. Mazza, S.R. Holdsworth, R.P. Skelton, Thermo-mechanical fatigue tests on uniaxial and component-like 1CrMoV rotor steel specimens. Int J Fatigue, 30 (2008) 241-248.

[5] R.A. Kupkovits, R.W. Neu, Thermomechanical fatigue of a directionally-solidified Ni-base superalloy: Smooth and cylindrically-notched specimens. Int J Fatigue, 32 (2010) 1330-1342.

[6] Z.J. Moore, R.W. Neu, Creep-fatigue of a directionally-solidified Ni-base superalloy – smooth and cylindrically notched specimens. Fatigue Fracture Eng Mater Struct, 34 (2010) 17-31.

[7] ABAQUS v6.9.Dassault Systèmes: Providence, RI, 2009.

[8] M.M. Shenoy, D.L. McDowell, R.W. Neu, Transversely isotropic viscoplasticity model for a directionally solidified Ni-base superalloy. Int J Plas, 22 (2006) 2301-2326.

[9] P. Fernandez-Zelaia, Thermomechanical Fatigue Crack Formation in Nickel-Base Superalloys at Notches, M.S. Thesis, Georgia Institute of Technology, Atlanta, GA, USA, 2012.

[10] R. Mucke, H. Kiewel, Nonlocal cyclic life prediction for gas turbine components with sharply notched geometries. J Eng Gas Turbines Power, 130(1) (2008) 012506.

[11] L. Susmel, D. Taylor, A novel formulation of the theory of critical distances to estimate lifetime of notched components in the medium-cycle fatigue regime. Fatigue Fracture Eng Mater Struct, 30 (2007) 567-581.

[12] L. Susmel, D. Taylor, An elasto-plastic reformulation of the theory of critical distances to estimate lifetime of notched components failing in the low/medium-cycle fatigue regime. J Eng Mater Technol, 132(2) (2010) 021002.

[13] D. Taylor, The theory of critical distances. Eng Fracture Mechanics, 75 (2008) 1696-1705.

[14] R.A. Naik, D.B. Lanning, T. Nicholas, A.R. Kallmeyer., A critical plane gradient approach for the prediction of notched HCF life. Int J Fatigue, 27 (2005) 481-492.

[15] W.J. Ostergren, A damage function and associated failure equations for predicting hold time and frequency effects in elevated temperature low cycle fatigue. J Testing Evaluation, 4 (1976) 327-339.

[16] Z.J. Moore, R.W. Neu, Fatigue life modeling of anisotropic materials using a multiaxial notch analysis. J Eng Mater Technol, 133(3) (2011) 031001.

Tensile mechanical behavior of as-cast AA7050 alloy in the super-solidus temperature range

T Subroto[1,2,*], A Miroux[1,2], D G Eskin[3], K Ellingsen[4], A Marson[5], M M'Hamdi[4], L Katgerman[2]

[1] Materials innovation institute (M2i), Mekelweg 2, Delft, 2628 CD, The Netherlands
[2] Dept. of Mat. Sci. and Engineering, Delft University of Technology, Mekelweg 2, Delft, 2628 CD, The Netherlands
[3] BCAST, Brunel University, Uxbridge, Middlesex, UB8 3PH, United Kingdom
[4] SINTEF Materials and Chemistry, NO-0314 Oslo, Norway
[5] SINTEF Materials and Chemistry, NO-7465 Trondheim, Norway
* Corresponding author: tsubroto@m2i.nl

Abstract Aluminum 7050 alloy is one of the primary alloys for the aviation industry owing to its excellent mechanical properties. However, this alloy has several poor physical properties that affect its solidification, such as relatively low thermal conductivity and large solidification range. These properties tend to increase the hot tearing susceptibility of the alloy, which makes it difficult to produce by direct-chill (DC) casting. Accurate knowledge of the mechanical behavior of the alloy during solidification is therefore crucial to ensure safe control of the casting process. Present work focuses on measuring the tensile mechanical properties of an as-cast AA7050 in the temperature range where hot tearing mainly occurs, i.e. from solid fractions of 0.85 to 1.0, or the solidus. Through these experiments, we extracted mechanical properties such as strain-rate sensitivity and ductility of the alloy in the super-solidus temperature range. The data obtained from this work will be useful in thermo-mechanical computer simulations aimed at reducing the hot tearing occurrence during DC casting, thus optimizing the production rate in the casting house.

Keywords AA7050, DC Casting, solidification, hot tearing, tensile mechanical properties

1. Introduction

AA7050 is one of the most used alloys for aerospace industries owing to its excellent mechanical properties such as high tensile strength, good fracture toughness and stress corrosion resistance [1, 2]. This alloy is usually produced via a vertical direct-chill (DC) casting method because of the robustness and relative simplicity of such process [3]. Despite its superior qualities, AA7050 is known to be susceptible to hot tearing due to its wide solidification range and relatively high thermal expansion coefficient [4]. Hot tearing usually occurs during DC casting, at the end of solidification when the alloy is in a semi-solid state but most of the liquid has been solidified and the remaining liquid resides at the grain boundaries [5]. The presence of such a defect causes the rejection of the ingot or lowers the quality of the cast product which subsequently affects its economical value [6]. In order to minimize the occurrence of hot tearing, it is critical to understand the mechanical properties in this solidification range [7]. Therefore, in this work, we investigated the tensile mechanical behavior of the alloy – which is the dominant stress mode related to hot tearing during DC casting, in the range of solid fractions of 0.85 and 1.0 (just before it is fully solidified), where hot tearing is most likely to occur. Such tensile mechanical properties will be useful input for a numerical process simulator aiming at minimizing the occurrence of hot tearing during DC casting, thus, optimizing the production rate in the aluminum cast house.

2. Experimental procedure

The tensile specimens used for the experiment were cut from an ingot produced via DC casting at Tata Steel (IJmuiden, The Netherlands). The ingot was DC cast using a conventional bore mold

from the melt that has been degassed in the furnace. The chemical composition of the alloy is given in Table 1.

Table 1. Chemical composition of AA7050.

Main alloying elements, wt pct					
Zn	Cu	Mg	Zr	Ti	Al
6.15	2.2	2.1	0.13	0.03	balance

The specimens were tested using a set-up developed at SINTEF Materials and Chemistry with an Instron 5944 series tensile test machine equipped with a 2-kN load cell. The specimen was heated up using an induction heating coil system which was controlled by a Eurotherm™ temperature controller. A quartz-glass tube coated with boron nitride aerosol on the inside, was used to enclose the center part of the sample in order to avoid liquid breakout during the fully melt phase. The coating was intended to prevent the sticking of the liquid aluminum onto the quartz tube which might affect the force measurement due to the added friction resistance. The experimental cycle (for both re-melt and mechanical testing temperature) is shown in Figure 1.

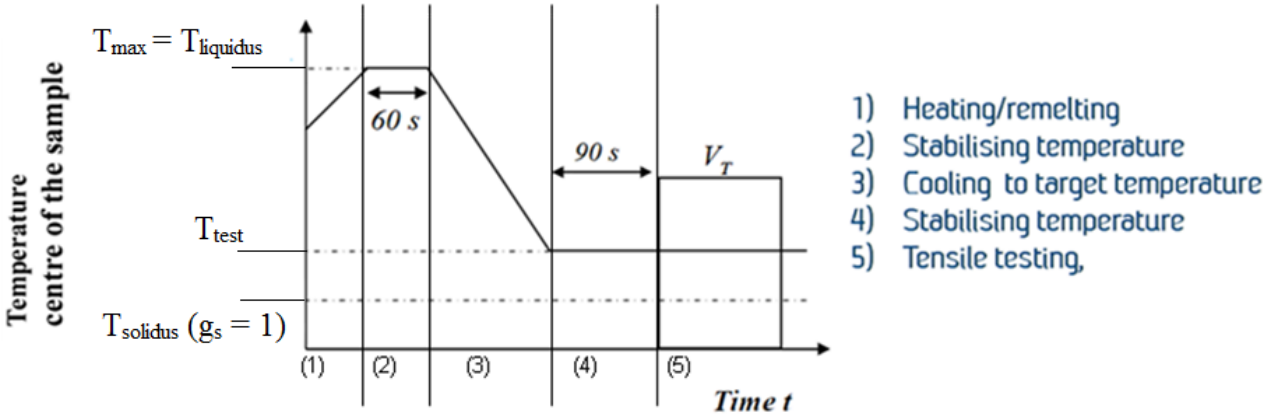

Figure 1. Experimental cycle of the tensile test.

The test cycle that we used in our experiment was as follows. First, we heated up the sample from room temperature up to T_{max} = 635 °C, which is the liquidus of an AA7050 alloy based on the JMat-Pro software (Figure 2). Then we held the sample at T_{max} for 60 seconds to assure that the central part of the specimen is fully liquid. Subsequently, we cooled down the sample to the test temperature with a cooling rate of 1 °C/s. We then held the sample at this test temperature for approximately 90 seconds to let the temperature in the specimen stabilize. Then we performed the mechanical tensile testing of the sample at a certain displacement rate until the force value was approximately zero after the fracture.

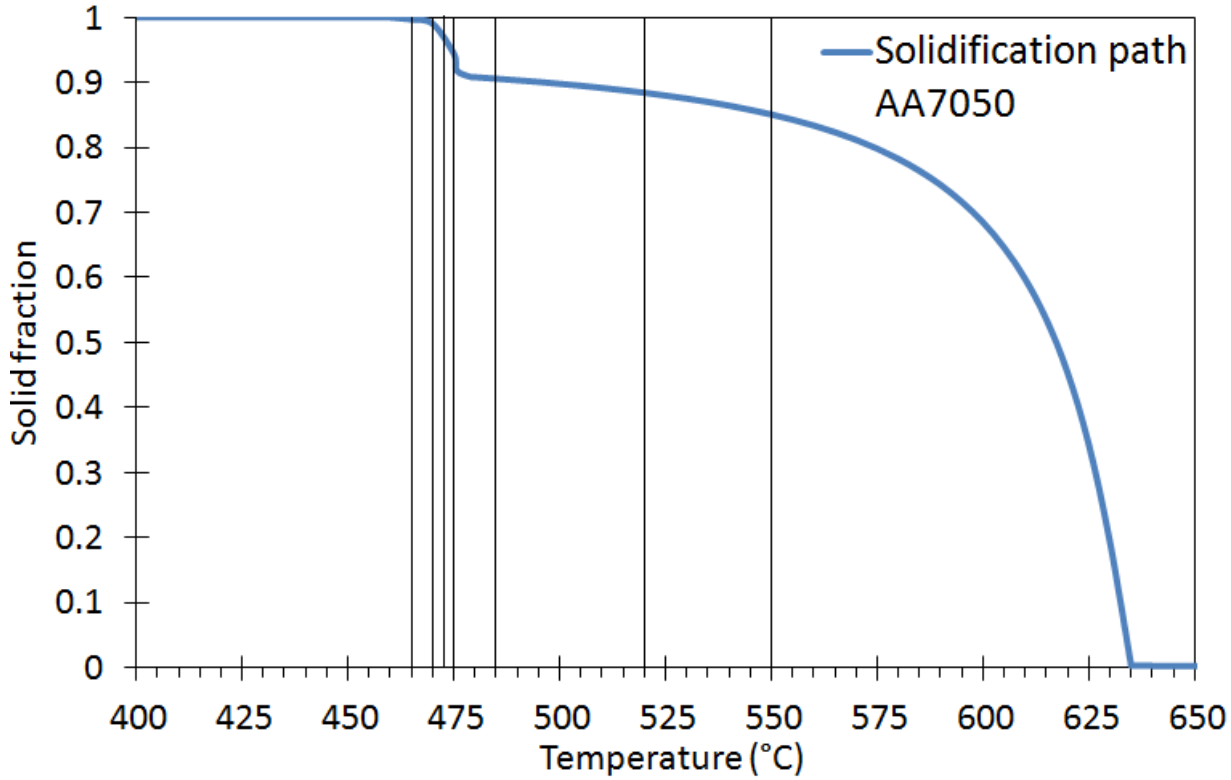

Figure 2. The solidification path of an AA7050 alloys as calculated by JMat-Pro software (Scheil calculation).

The test temperatures that we used in this work corresponded to solid fractions (f_s) between 0.85 and 1.0. We took data at several points within this range such as at 0.85, 0.88, 0.9, 0.94, 0.97, 0.99 and 1.0 or in terms of temperature – at 550, 520, 485, 475, 473, 470 and 465 °C, respectively. The solidification path of this alloy was calculated by JMat-Pro software and is shown in Figure 2, the vertical lines in such a figure show the temperature points where we performed the data acquisitions. To observe the displacement-rate sensitivity behavior of the alloy in this temperature range, we used two different displacement rates. For each combinations of the test (temperature–displacement rate), we repeated the test three to four times to obtain statistical information of the test. The fracture surface of the samples was observed in a Jeol JSM-6500F scanning electron microscope (SEM) at the tip of the failed specimens.

3. Results and discussion

3.1 Mechanical properties

From the tensile tests, we obtained force–displacement curves at different temperature points and displacement rates. The force–displacement curves with a displacement rate of 0.2 mm/min are shown on Figure 3 and with a displacement rate of 2 mm/min, on Figure 4. Due to the large scaling range of the force value, at the displacement rate 0.2 mm/min, we divided the entire data into two sets: The data from f_s = 1.0 down to f_s = 0.97 are shown in Figure 3a and the data from f_s = 0.97 down to f_s = 0.85 are shown in Figure 3b.

Figure 3 shows that at the displacement rate 0.2 mm/min, the height of the peak force in general

decreases as the solid fraction reduces. In addition, the shape of the curve also changes quite significantly from $f_s = 1.0$ (when the alloy is fully solid) to $f_s = 0.97$ (refer to Figure 3a) and then it changes again as the solid fraction decreases further, from $f_s = 0.97$ down to $f_s = 0.85$ (refer to Figure 3b). Such a transition in the force–displacement curve can be interpreted as a change in the mechanical behavior regime. From Figure 3, we observed two mechanical properties transitions. First, when the alloy behavior changes from ductile at $f_s = 1.0$ to brittle at $f_s = 0.97$. The sharp drop in ductility and strength at $f_s = 0.97$ informs us that the alloy fails in a brittle manner. The second transition in the mechanical behavior of the material occurs when the solid fraction of the alloy decreases from $f_s = 0.97$ to $f_s = 0.85$. As the solid fraction decreases, the end part of the curve (after peak force) changes, i.e. the slope of the curve is not as steep as for $f_s = 0.97$ and the slope gradually becomes shallower as the solid fraction decreases. Finally at the lowest solid fraction in this test ($f_s = 0.85$), the curve resembles a shallow symmetric hump with a long 'tail'. This might be caused by the sufficient liquid presence in the alloy, thus it is as if the alloy is dragging viscous liquid. Another possible explanation is, as suggested by Eskin *et al.* [8], that the main mechanism of deformation is grain boundary sliding thanks to the presence of sufficient interdendritic liquid surrounding the grain at such solid fraction.

Similar force–displacement curve shape change is also observed at a displacement rate of 2 mm/min. As shown in Figure 4, at $f_s = 0.99$, the force exhibits a sharp drop after the sample reaches fracture point which is interpreted as a brittle behavior of the alloy. As solid fraction decreases to $f_s = 0.94$, the peak force significantly decreases despite the similar curve shape with the preceding case. The main shape distinction is that the curve at $f_s = 0.94$ has a 'tail' after the sharp drop, which could be explained due to the additional amount of liquid at such solid fraction as compared to the higher solid fraction. At $f_s = 0.90$, the peak force is reduced even more and the shape of the force–displacement curve is significantly changed as compared to the two other curves at this displacement rate.

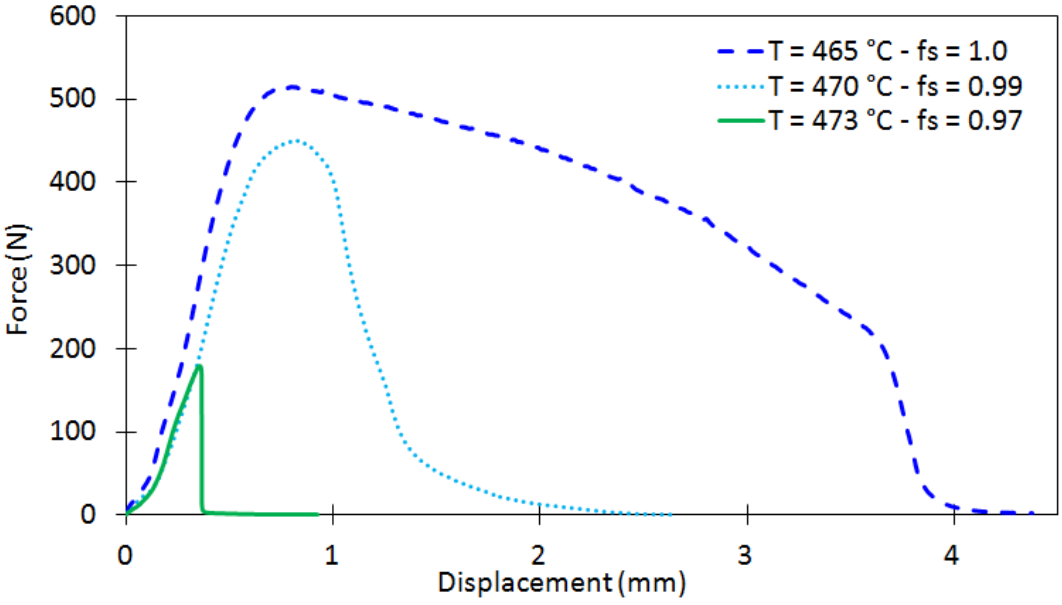

(a)

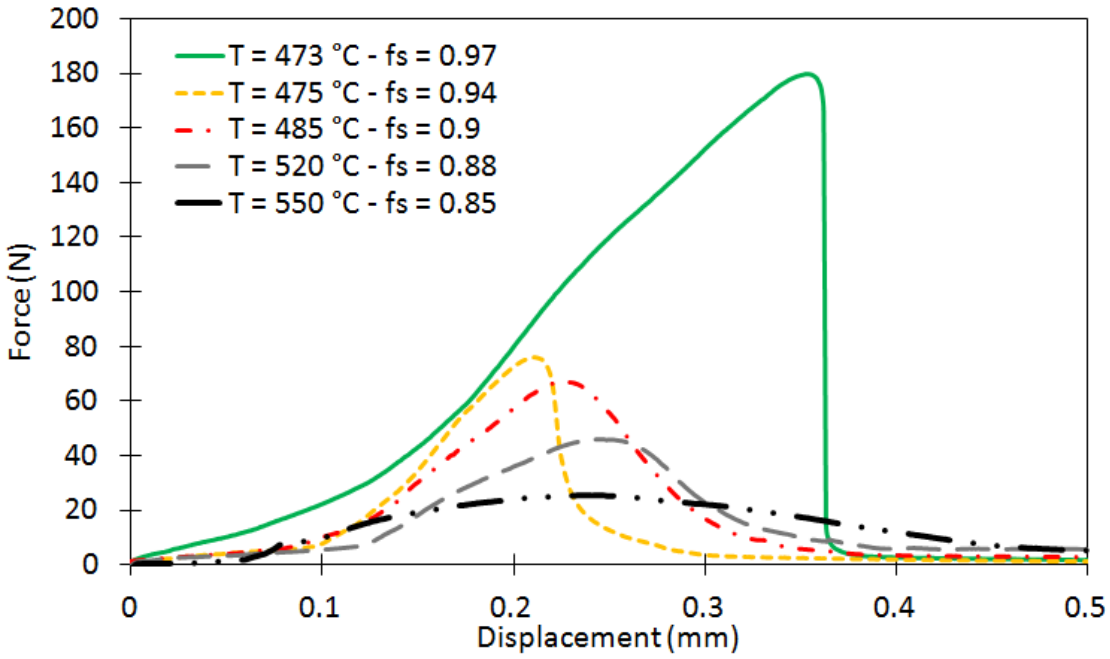

(b)

Figure 3. Force–displacement curves at a displacement rate of 0.2 mm/min for the solid fraction ranges from $f_s = 1.0$ – fully solid to $f_s = 0.97$ (a) and from $f_s = 0.97$ to $f_s = 0.85$ (b).

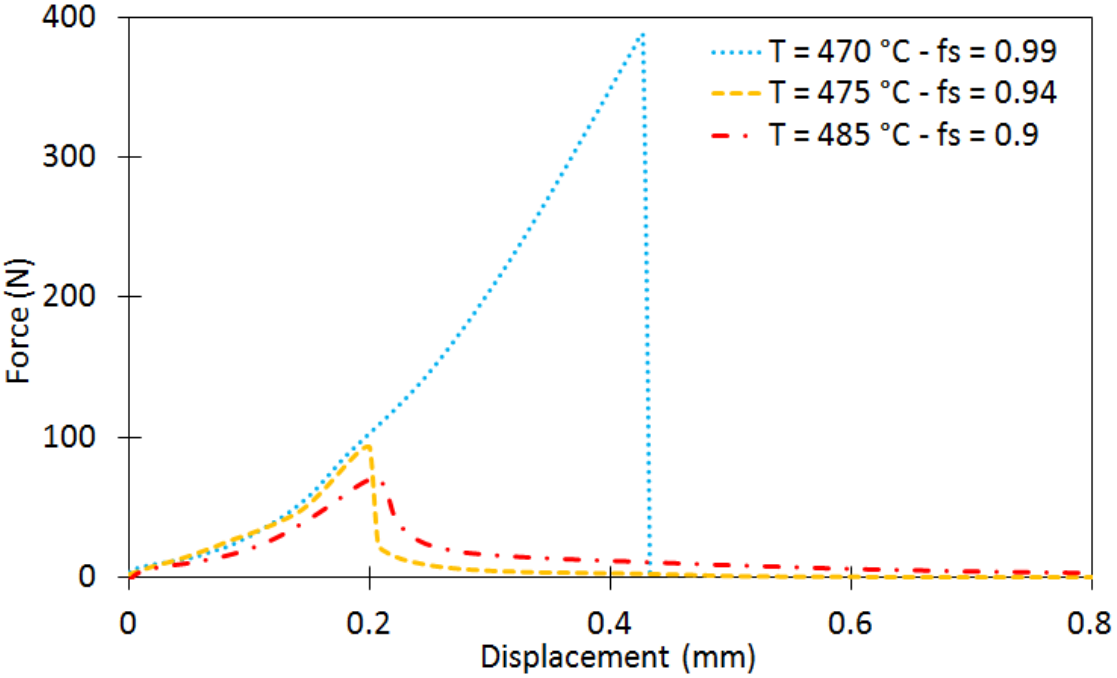

Figure 4. Force–displacement curves at a displacement rate of 2 mm/min for solid fractions from $f_s = 0.99$ to $f_s = 0.9$.

The evolution of the peak force of the alloy with respect to the temperature is shown in Figure 5. For both displacement rates, the peak force rapidly increases as the temperature is lowered below 475 °C. Therefore, we can argue that the grain coalescence occurs between $f_s = 0.94$ and $f_s = 0.97$. These values are supported by a few other works on different alloys [9, 10]. The temperature range

from 475 to 470 °C also coincides with the brittle fracture behavior and the eutectic solidification domain. One can also notice that the alloy starts to become sensitive with respect to displacement rate, the largest sensitivity at the lowest temperatures. In addition, one can observe that the error bars (standard deviation) are larger when the sample becomes brittle and smaller if it is ductile.

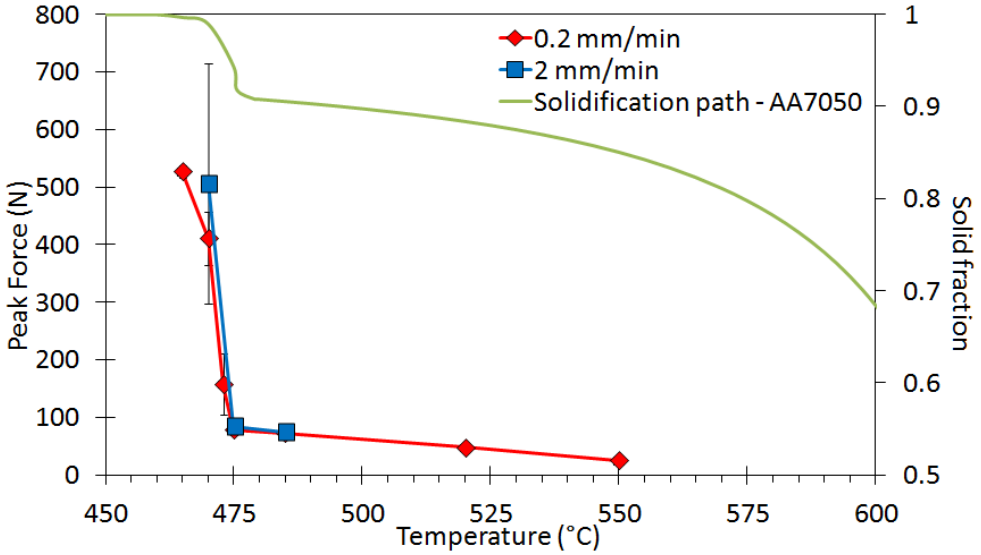

Figure 5. Comparison in peak forces between two different displacement rates at different temperature points (left vertical axis) and corresponding solid fractions (right vertical axis). The error bars are shown; when not visible they are smaller than the size of the data point.

The ductility of the alloy at different temperature points is shown in Figure 6. For both displacement rates, one can see that the ductility of the alloy starts to drop significantly as the temperature increases above 465 °C. The lowest ductility value for both displacement rates was found at a temperature of 475 °C or f_s = 0.94, which corresponds, according to the solidification path in Figure 2, to the beginning of the eutectic solidification. As the temperature increases further above 475 °C, the ductility starts to develop gradually up to 550 °C. If extrapolated to higher temperatures, the temperature dependence of the ductility points would resemble the shape of the classical brittle temperature range curve [8].

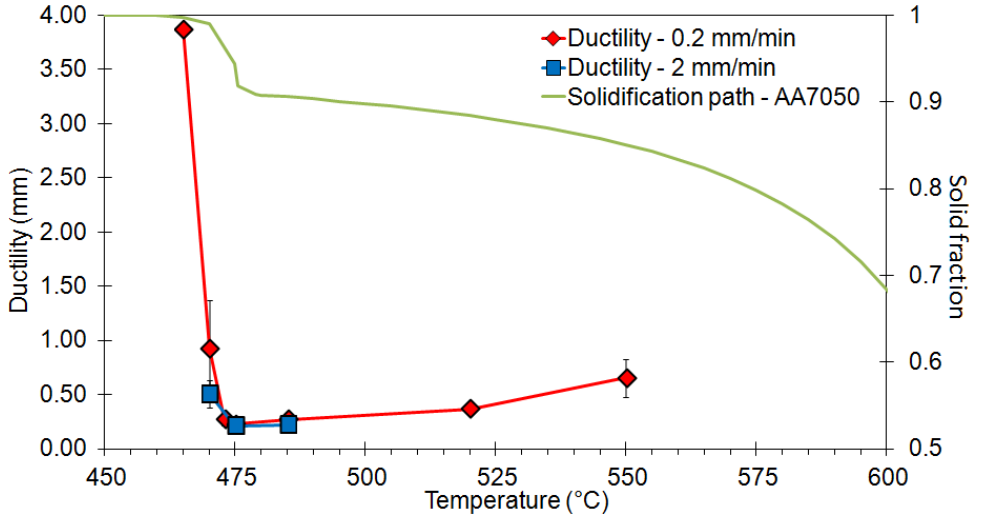

Figure 6. Comparison of the ductility of the alloy at different temperature points (left vertical axis) with respect to its respective solid fraction of the alloy (right vertical axis).

The displacement rate has a small effect on the mechanical behavior. The main difference is that at 470 °C the four tests at 2 mm/min gave a brittle behavior while at 0.2 mm/min two tests showed a brittle behavior the other two giving a ductile response. At temperature of 475 °C, there is a slight change in curve shape with different displacement rates. The most significant change is the shape of the curve after the peak force was reached. At lower displacement rate, the decrease is more gradual compared to the slope at 2 mm/min. This behavior is reasonable, because at 0.2 mm/min, the alloy has more time to compensate the deformation.

3.2 Fracture surface analysis

To analyze the behavior during fracture, we performed SEM analysis of the fracture surfaces at four different conditions, i.e. at two deformation rates and at solid fractions of 0.99 and 0.94, reflecting the transition from brittle to ductile behavior (see Figures 3–5). From all of the fracture analysis performed, we found that in general, the fracture mode is mixed between inter-granular (with dendritic morphology) and intra-granular. We observed such a mixed fracture mode at both solid fractions and displacement rates (figure 7). Moreover, features that possibly attest for broken dendrite arms (features within the dashed white ellipses in Figure 8a) were found for all conditions.

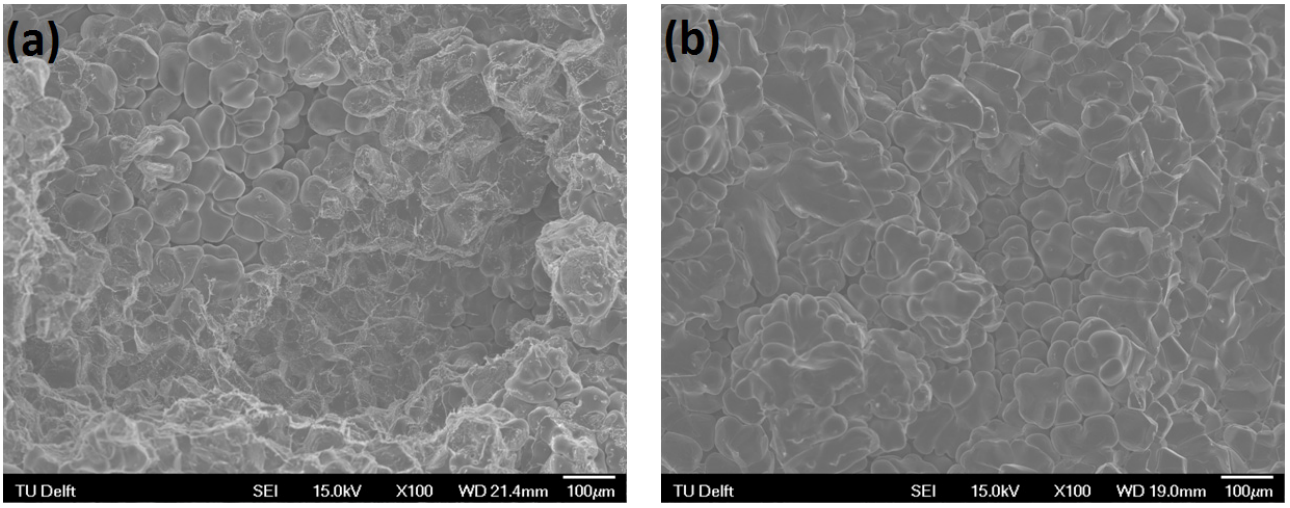

Figure 7. Examples of mixed-mode fracture surface at $f_s = 0.99$ with 0.2 mm/min displacement rate (a) and $f_s = 0.94$ with 2 mm/min displacement rate (b).

The higher solid fraction ($f_s = 0.99$) and lower displacement rate (0.2 mm/min) shows deformation of the solid and interdendritic liquid phases as evidenced in Figure 8b. While with a higher displacement rate (2 mm/min) and same solid fraction the interdendritic liquid phases have different shape (Figure 8c). The shape differences could be explained as the interdendritic liquid has more time to deform and rearrange at lower displacement rate compared to the higher one. At lower solid fraction ($f_s = 0.94$), for both displacement rates, the interdendritic liquid raptures [11] (features within the dashed white ellipses in Figure 8d) and the solid bridges fracture in a brittle fashion as illustrated in Figure 8d. Interestingly, such interdendritic liquid features are rarely found at the higher solid fraction.

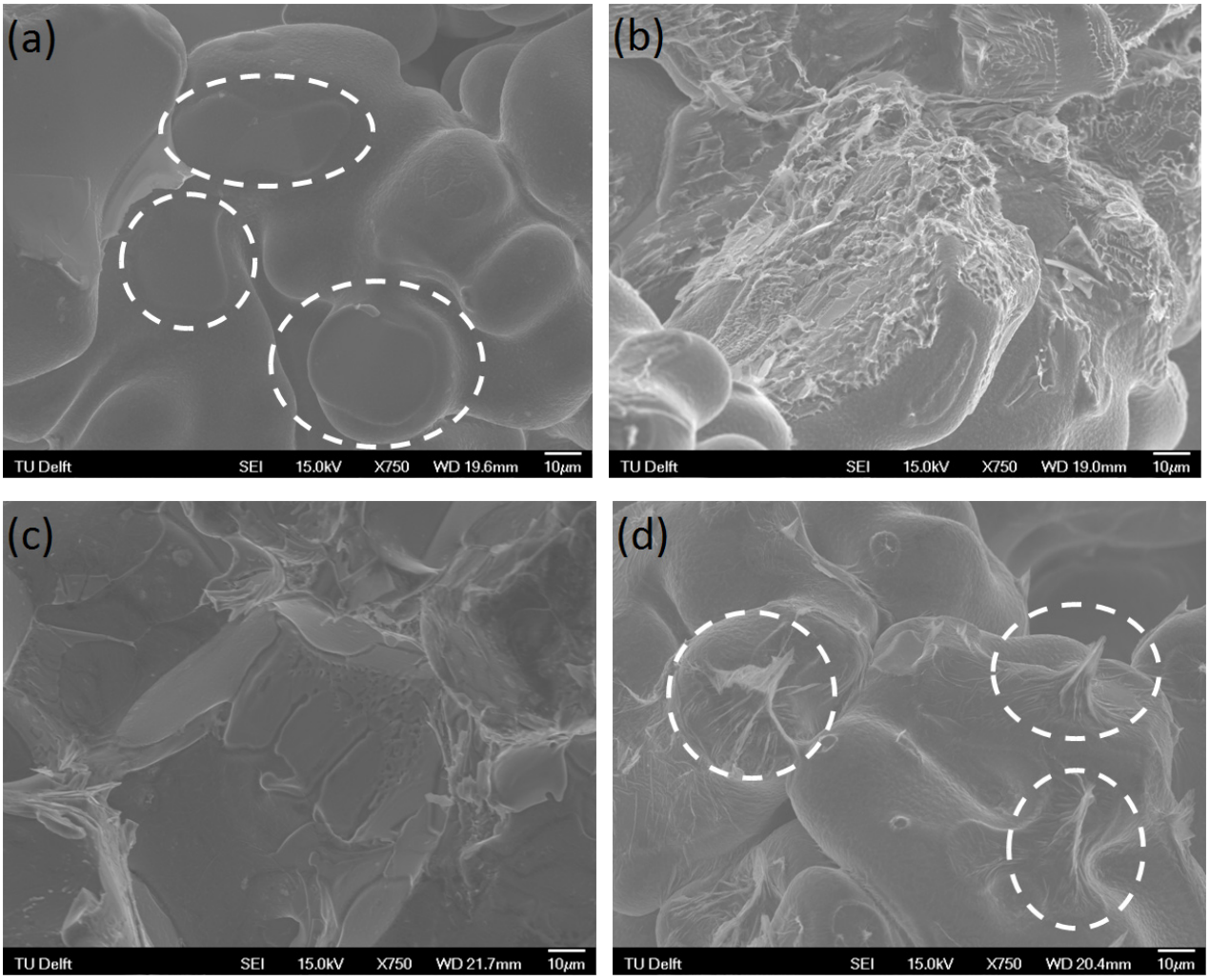

Figure 8. Pictures of fracture surface analysis using SEM: (a) Examples of broken dendrite arms, (b) example of extra-deformed eutectics, (c) example of layer-like eutectics and (d) examples of features that resemble necking of the interdendritic liquid stretched during fracture.

4. Summary

We can summarize the results obtained from the experiments as follows:

1. From the shape of the force–displacement curves, we found that in the range of f_s = 1.0 (fully solid) to f_s = 0.85, the alloy has three different mechanical behavior regimes; ductile (between f_s = 1.0 and f_s = 0.99), brittle (between 0.99 and 0.9) and then ductile again (between 0.9 and 0.85).
2. The grain coalescence in AA7050 occurs between f_s = 0.94 and f_s = 0.97. This is showed by the sharp increase in peak force between the mentioned solid fractions.
3. The alloy has almost no displacement rate sensitivity at high temperatures (below f_s = 0.94) but it has positive displacement rate sensitivity starting at f_s = 0.94 and at higher solid fractions.
4. The alloy produces a ‘classically’ shaped brittle temperature range curve with the minimum of ductility reached at 475 °C, and the alloy gains again ductility as the liquid fraction increases in the alloy.
5. From SEM fracture surface analyses at different data points showed in Figure 7, it is found

that in general the fracture mode is mixed between inter- and intra-granular. Additionally, at higher solid fraction, the morphology of eutectic is different at different displacement rates (Figure 8b and 8c). Sites that resemble necking of interdendritic liquid was observed at samples that were tested at lower solid fraction (Figure 8d), independent of displacement rate used during the test.

Acknowledgment

This research was carried out within the Materials innovation institute (www.m2i.nl) research framework, project number M42.5.09340. The establishment of the experimental set-up and testing procedure for the mechanical tensile testing in the semi-solid has been supported by the Norsk Hydro Fond for SINTEF. The authors would like to express their gratitude to Dr. Démian Ruvalcaba and Mr. Jacob van Oord (Tata Steel Research, Development & Technology, The Netherlands) and also to Mr. Hans I. Lange and Mr. Arne Nordmark (SINTEF Materials and Chemistry, Norway) for their support and inputs. Support from Modelling assisted INnovation for Aluminum DC Casting process (MINAC) community is highly appreciated.

References

[1] J.C. Williams, E.A. Starke Jr, Acta Materialia, 51 (2003) 5775-5799.
[2] L. Schra, W.G.J.t. Hart, Engineering Fracture Mechanics, 17 (1983) 493-507.
[3] M. Lalpoor, D.G. Eskin, L. Katgerman, Materials Science and Engineering A, 497 (2008) 186-194.
[4] M. Lalpoor, D.G. Eskin, L. Katgerman, Metallurgical and Materials Transactions A: Physical Metallurgy and Materials Science, 41 (2010) 2425-2434.
[5] D. Fabrègue, A. Deschamps, M. Suéry, W.J. Poole, Metallurgical and Materials Transactions A: Physical Metallurgy and Materials Science, 37 (2006) 1459-1467.
[6] A.B. Phillion, S.L. Cockcroft, P.D. Lee, Acta Materialia, 56 (2008) 4328-4338.
[7] M. Suéry, in: Conference of Advances in Metallic Materials and Manufacturing Processes for Strategic Sectors, 2012, pp. 35-42.
[8] D.G. Eskin, Suyitno, L. Katgerman, Progress in Materials Science, 49 (2004) 629-711.
[9] O. Ludwig, J.M. Drezet, C.L. Martin, M. Suéry, Metallurgical and Materials Transactions A: Physical Metallurgy and Materials Science, 36 (2005) 1525-1535.
[10] O. Ludwig, J.M. Drezet, P. Ménésès, C.L. Martin, M. Suéry, Materials Science and Engineering A, 413-414 (2005) 174-179.
[11] M. Rappaz, J.M. Drezet, P.D. Grasso, A. Jacot, in: 10th Modeling of Casting, Welding and Advanced Solidification Processes (MCWASP X), 2003, pp. 53-60.

Orientation and temperature dependences on fatigue crack growth (FCG) behavior of a Ni-base directionally solidified superalloy

Yangyang Zhang[1], Huiji Shi[1,*], Jialin Gu[2], Changpeng Li[3], Kai Kadau[4], Oliver Luesebrink[5]

([1]Department of Engineering Mechanics, Tsinghua University, Beijing 100084, China)

([2]Department of Material Science, Tsinghua University, Beijing 100084, China)

([3]Corporate Technology, Siemens Ltd. China, Beijing 100102, China)

([4]Siemens Energy Inc., Charlotte, USA)

([5]Siemens AG Energy, Mulheim an der Ruhr, Germany)

* Corresponding author. Email: shihj@mail.tsinghua.edu.cn

Abstract Fatigue crack growth (FCG) behaviors of a widely-used nickel-based directionally solidified (DS) superalloy were investigated. Direct-current potential drop method was employed to capture the crack length according to ASTM E647. Standard compact tension (CT) specimens in longitudinal, transverse and diagonal directions were cast and tested at T_0 and T_0+250^{0}C to reveal the orientation and temperature dependence. Moreover, the post-test fractography were observed through SEM and OM to understanding the underlying mechanism responsible for the fracture modes. Results suggested that cracks in all three orientations propagated transgranularly, no obvious differences were found between each other, and thus, the orientation dependence appeared to be very weak, all da/dN-DK curves in three orientations fell into one narrow band. However, temperatures showed significant dependence in diagonal directions, while in transverse direction the dependence became weak and even none in longitudinal orientation. Finally, methods for characterizing the FCG behaviors in different orientations and at both temperatures were proposed, which were able to explain the orientation and temperature dependences.

Key words Fatigue crack growth, directionally solidification, nickel-based superalloy

1. Introduction

Superalloys, either in the conventionally-cast (CC) or directionally solidified (DS) forms may contain porosity and shrinkage cracks, so that the life of rotating components, such as turbine blades, may be limited by crack propagation from these defects. It is therefore of interest to determine the resistance of the oriented grain structure, produced by DS, to the propagation of fatigue cracks [1]. Although lots of research have been focused on the fatigue crack growth behaviors of superalloys, few have shed light on those behaviors of directionally solidified superalloys[1-6]. In 1976, Scarlin [1] investigated the fatigue crack growth behaviors of nickel-based IN738 DS, and high cycle fatigue crack growth rates had been measured at room and high temperatures and for crack propagation both parallel and perpendicular to the solidification directions. However, comparable crack growth rate seemed to be found in his results. Okazaki et al [2] conducted low cycle fatigue tests to study the stage-I short crack growth behavior RENE80+Hf and CM247LC DS at 600^{0}C. Later, Highsmith et al [4, 6] and Yoon et al [5] studied the FCG behaviors of nickel-base GTD-111 DS, both in longitudinal and transverse directions, where the stress ratio effects and temperature effects were focused on, respectively. For DS material, it is seen that only crack growth in

longitudinal and transverse directions are interested and investigated. However, the diagonal direction is very often used as loading components during actual service; therefore more studies concerning this particular direction should be done.

The current DS material is a newly cast and wrought nickel-base directionally solidified (DS) superalloy, to meet the requirement for development of more efficient engine operation with higher operating temperatures and stresses. In the current paper, FCG behaviors of DS material have been evaluated at T_0 and T_0+250^{0}C, and in longitudinal, transverse and diagonal orientations. The effects of temperatures and grain orientations on the FCG behaviors are investigated in associated with fractographic analysis (For confidential, some of the test data are normalized).

2. Material and experimental procedure

The nominal chemical compositions of the material are listed in Table 1. The original slabs were directionally solidified to produce a longitudinal direction which corresponds to [001] crystal orientation. The directionally solidified direction along the axis of the bar was determined to be within 5^0 of dispersion using the X-ray diffraction technique.

Table 1. Nominal compositions of the current DS material (wt.%)

Al	B	C	Cr	Mo	Ta	Ti	W	Ni
3.40	0.0125	0.08	11.6	1.65	4.80	3.90	3.50	Bal.

FCG tests were conducted by using the direct-current electric potential drop method (DC-PDM) described in ASTM E647. Standard compact-tension (CT) specimens (48*50*10) were machined using electron-discharge machining techniques from the heat treated slabs. Prior to standard FCG tests, all specimens were pre-cracked at room temperature with a frequency of 10 Hz to eliminate the effect of machining notches. Lengths of all pre cracks were in a range of 2-3 mm. FCG tests were conducted in accordance with the requirements of ASTM E647 [7]. All tests were running loading control by a computer-control, closed-loop servo-hydraulic testing machine, with a fixed load ratio of 0.1 and frequency of 10 Hz. At both temperatures, two repeated specimens were tested in each grain orientation, one with standard FCG tests with constant loading, the other with threshold testing by decreasing loading, whose derating ratio is 0.1.

The crack length data in region II of each specimen, with or without threshold value test, are computed by two methods, i.e., the secant method (also known as point-to-point technique) as well as the seven-point incremental polynomial method, as described in [7]. Conventionally, the secant method gives a result that most reflects the actual conditions, such as crack growth rate change, fluctuation and so on, while the polynomial method produces a more smooth da/dN curve. In the subsequent analysis, results from the seven-point polynomial method will be used to compare the temperature as well as orientation effects.

For the standard C(T) specimens, the stress intensity factor ranges were calculated by the following equation as:

$$\Delta K = \frac{\Delta P}{B\sqrt{W}} \frac{(2+\alpha)}{(1-\alpha)^{3/2}} \left(0.886 + 4.64\alpha - 13.32\alpha^2 + 14.72\alpha^3 - 5.6\alpha^4\right) \quad (1)$$

where $\alpha = a/W$, a is computed crack length, W takes a constant value of 40, and P is the applied load.

3. Results and discussion

Three types of specimens with different orientations were machined from cast plates. Figure 1 indicates the schematic images of these three types of CT specimens, where the different-color cylinders indicate crystal grains. Totally 12 specimens were tested at T_0 and T_0+250^{0}C, with crack growth in longitudinal, transverse and diagonal directions, respectively.

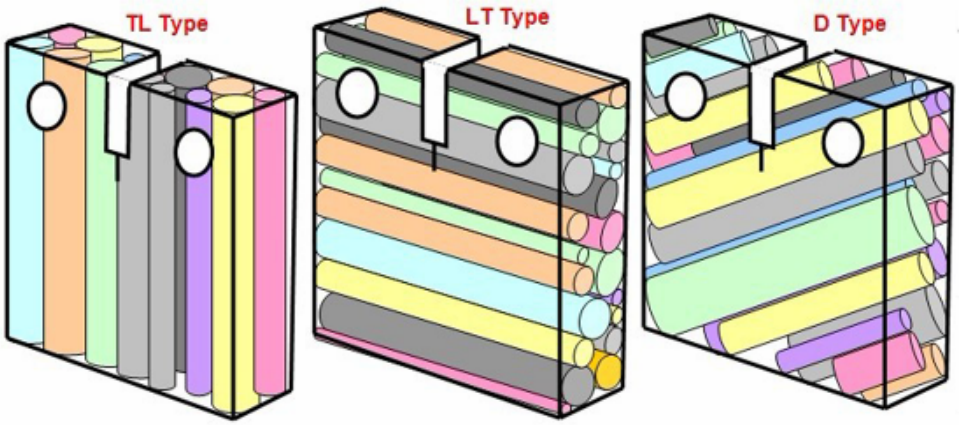

Figure 1. Schematic images of three types of C(T) specimens

3.1. Effect of orientation on FCG rates

The overall crack growth rate versus stress intensity factor values in Paris regime, i.e., $da/dN - \Delta K$ curves, are depicted in Figure 2, from which one can conclude that the orientation dependence is very weak, i.e., crack growth data in all orientations fall into one narrow [1/3, 3] band. Meanwhile, when using Paris law to obtain linear regression of all crack growth data, the correlation coefficient can be up to 0.88.

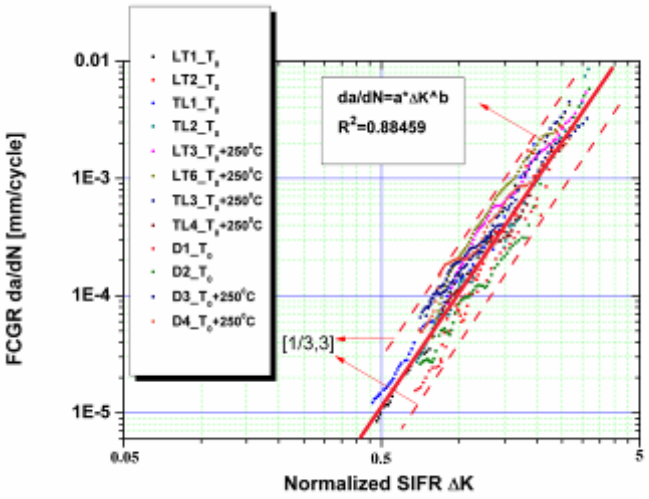

Figure 2. Fatigue crack growth behaviors for all DS specimens in Region II

Figure 3 shows the crack growth behaviors for the three types of specimens tested at T_0. Generally, comparable crack growth rate data can be found in longitudinal and transverse directions, while those in diagonal direction seem to be lower, especially in the high-ΔK regime. That's to say, there is no significant difference between crack growth rate in longitudinal and transverse directions, while specimens in diagonal direction have a much lower crack growth rate, and the difference becomes larger when it is up to the high-ΔK regime.

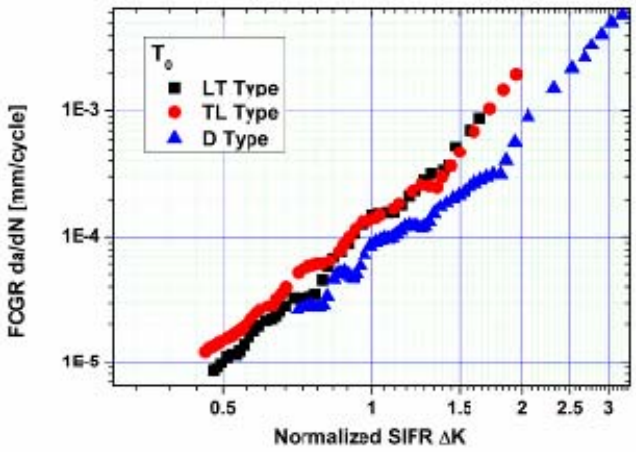

Figure 3. Crack growth behaviors of three types of specimens tested at T_0

However, at T_0+250^{0}C, the orientation dependence becomes even weaker, as can be seen in Figure 4. Cracks that travel in longitudinal and transverse directions also have a comparable crack growth rate; but different with those at T_0, cracks in diagonal directions still travel with a comparable rate, and no obvious difference can be found, even in the high-ΔK regime.

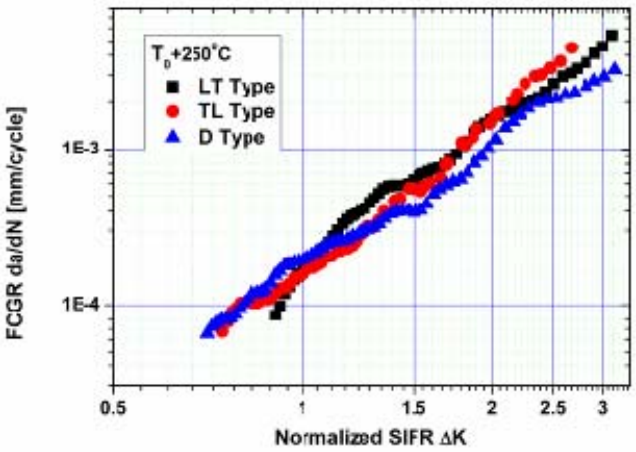

Figure 4. Crack growth behaviors of three types of specimens tested at T_0+250^{0}C

3.2. Effect of temperature on FCG rates

Figure 5 compares the growth rate of cracks traveling in longitudinal direction at both temperatures. In longitudinal direction, cracks seem to grow equally fast at both temperatures, and no obvious differences can be found between T_0 and T_0+250^{0}C.

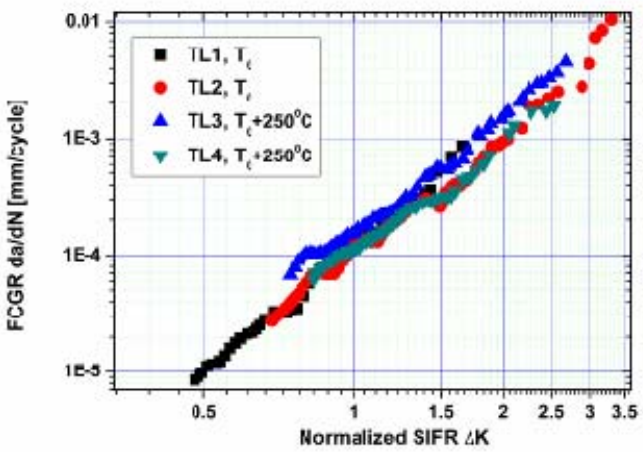

Figure 5. Crack growth behaviors of TL type specimens at T_0 and T_0+250^{0}C

In Figure 6, weak temperature dependence can be found on the LT type crack growth rate, i.e., cracks grow slightly faster at T_0+250^{0}C than at T_0.

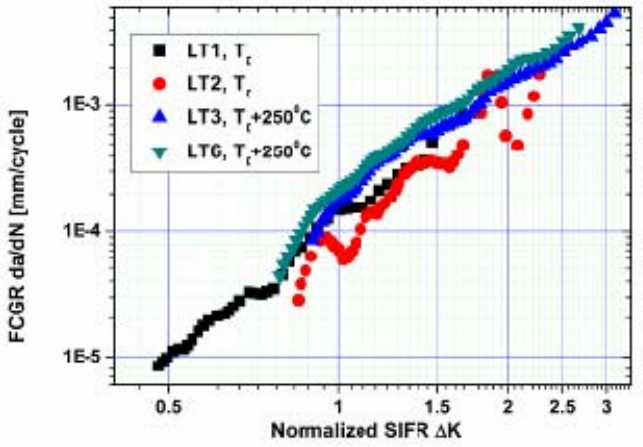

Figure 6. Crack growth behaviors of LT type specimens at T_0 and T_0+250^{0}C

Figure 7 compares the growth behaviors for diagonal cracks traveling both at T_0 and T_0+250^{0}C, from which one can conclude that apparent temperature effect can be found on the diagonal crack growth. Generally, cracks propagate much faster at T_0+250^{0}C than at T_0, especially in the low-ΔK regime. Subsequently, the growth rate at both temperatures become more and more close to each other as ΔK arise, and they take nearly the same value when normalized $\Delta K \approx 2.5$. After that, cracks at T_0 start to exceed those at T_0+250^{0}C, until the final break.

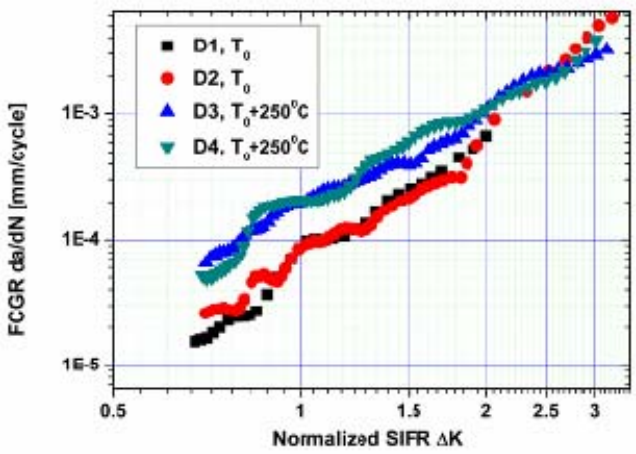

Figure 7. Crack growth behaviors of D type specimens at T_0 and T_0+250^{0}C

3.3. Fractography

All FCG tests were run until the specimen was separated into two parts. The fracture surfaces of all post-test specimens were observed through SEM and OM to understand the underlying mechanisms responsible for different damage modes. In regard to crack propagation behavior of single crystal superalloys, it is well known that cracks tend to propagate on <111> slip planes at low temperature, while cracks usually propagate normal to loading direction independent of crystal orientation at high temperature [8-11]. The former cracking behavior is called stage-I cracking, and the latter is called stage-II cracking. In current project, both stage-I and stage-II cracking modes can also be found, as can be seen by the side faces of fracture surfaces.

Table 2 lists the side faces of specimens tested at both temperatures, in which cracks propagated from left to right, and a black arrow in each figure corresponds to a machined notch tip. For TL type specimens (i.e., cracks propagate along the longitudinal direction), crack follow an angle of $\alpha \approx 14^0$ to the loading direction at T_0, which seems as a stage-I cracking mode, while both at T_0+250^{0}C show stage-II type of cracking modes. For LT type specimens (i.e., cracks travel along the transverse direction), trends are totally reversed, i.e., cracks at T_0 follow an angle of $\alpha \approx 8^0$ to the loading direction, while those at T_0+250^{0}C all travel along a constant angle of $\alpha \approx 25^0$; For diagonal specimens, stage-I cracking mode can also be seen at lower temperature ($\alpha \approx 27^0$), while at higher temperature, cracking surfaces show stage-II type cracking mode ($\alpha \approx 8^0$). To sum up, cracks in different orientations show different cracking modes, namely, cracks travel along longitudinal and diagonal directions show stage-I cracking at lower temperature and stage-II cracking at higher temperature, which is in accordance with literature. However, cracks travel in

transverse direction show a different trend.

Table 2. Side faces of post-test specimens at T_0 and T_0+250^{0}C

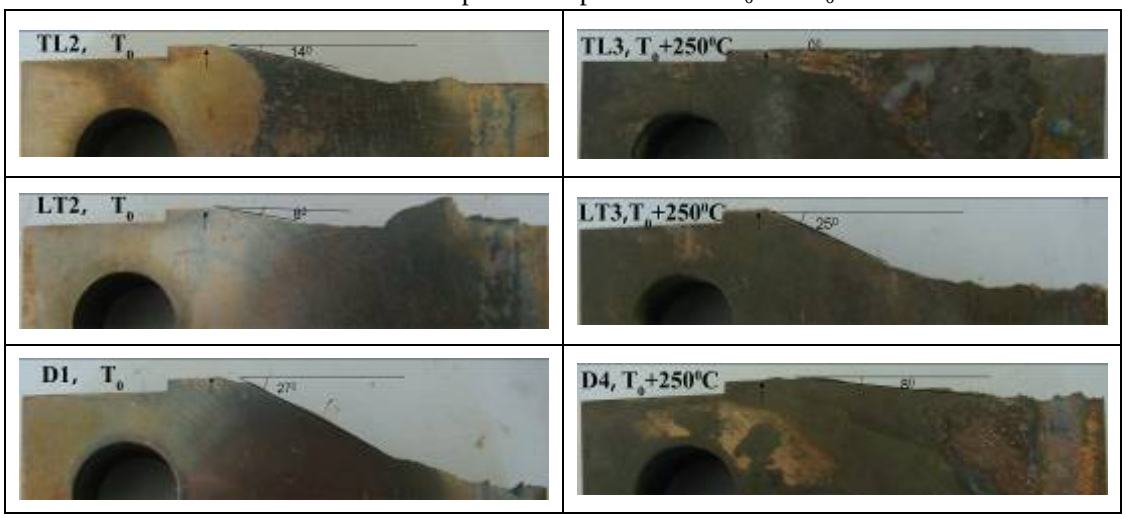

Note that for all the fracture surfaces, no angles were found through the thickness direction, i.e., all fracture surfaces are totally perpendicular to the specimen surfaces, and no inclinations were found.

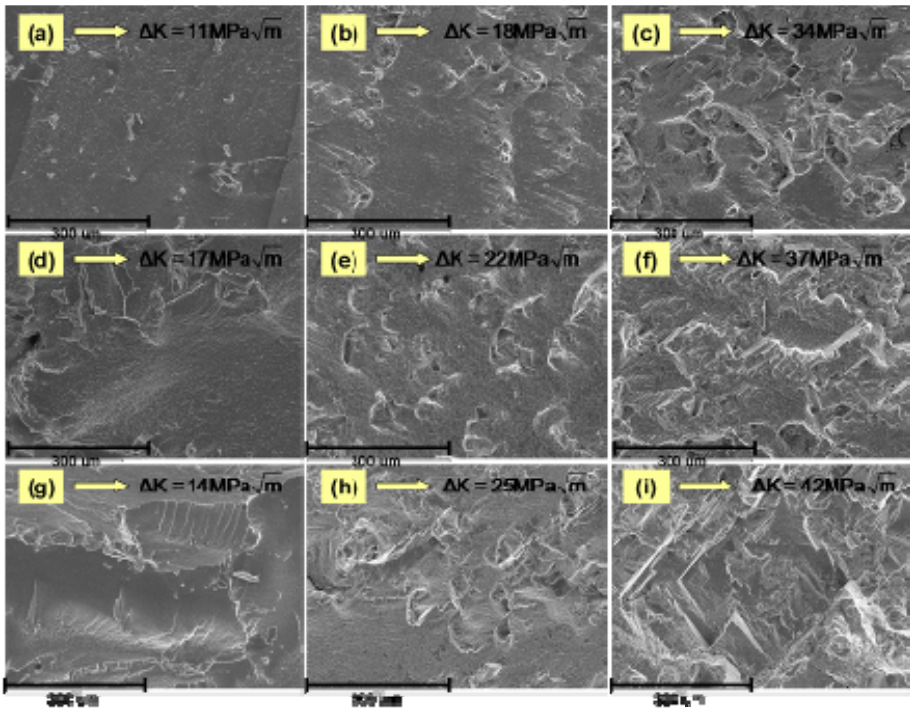

Figure 8. Fracture surfaces in various ΔK regimes at T_0 (a)-(c) TL type (d)-(f) LT type (a)-(c) D type

A more detailed examination results on the fracture surfaces in various ΔK regimes are presented in Figure 8. At low ΔK regimes, all fracture surfaces are smooth and very fine fatigue striations were observed on the fracture surfaces, indicating a slow but steady cracking stage, as can be seen in Figure 8 (a), (d) and (e); however, at higher ΔK regime a more textured fracture morphology with cracks was observed, and there were lots of claw-like barriers lying on the path (see Figure 8 (b), (e)

and (h)). This type of barrier is very common for most the specimens in all three orientations, and it is supposed that the effect of this kind of barrier on crack growth is much more important than the crystal boundaries. As ΔK arises, extensive crystal facet formations have been found for all three orientations. The reasons may be, as ΔK become so large that the local barriers can hardly produce any effective resistance, thus a predominant crack can easily and quickly travel though a crystal grain, and the appearance of crystal facet is attributed to the need for rapid energy dissipation by the advancing crack. Such energy dissipation is the fastest when cracks travel along the easiest path, i.e., the slip facets of each grain.

Figure 9 shows the typical claw-like barriers that have been widely found in the crack paths. It is suggested that when crack tip starts to reach these local barriers, it has been stopped due to the existence of these barriers, and as cyclic loading going on, new cracks start to re-initiate from these barriers; Subsequently, as the new cracks keeps growing and finally coalesce with the original crack, these barriers are seen to be passed through. Therefore it is inferred that these claw-like barriers do play an important role in cracks growth, and sometimes the effect of these barriers are so huge that the role of grain boundaries can hardly be seen. Besides, worth mentioning that in the previous pre-test procedure where some same C(T) specimens made of CM 247LC DS were conducted FCG tests, very few or no claw-like barriers had been found in their crack paths, so those specimens showed significant orientation dependence, and explanations associated with grain boundaries' resistance were made and it seemed that these explanation did work. As a result, there is reason to believe that due to the existence of numerous claw-like barriers in all three orientations, crack growth behaviors show weak orientation dependence for this DS material.

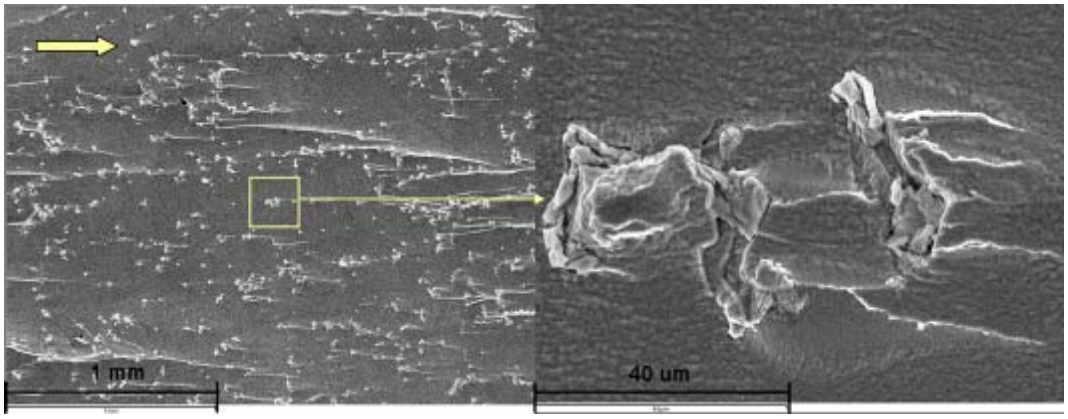

Figure 9. Typical claw-like barriers in the crack path

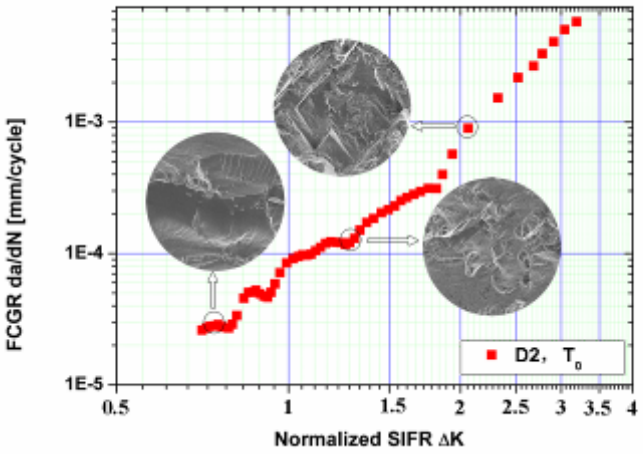

Figure 10. Crack growth rate corresponding to their typical microscopy

To sum up, cracks in all three orientations follow a similar propagation characteristic as ΔK arising. Figure 10 shows the typical microscopy corresponding to different ΔK regimes. It can be seen that as ΔK keeps increasing, the fracture surfaces become rougher and rougher. Meanwhile, more crystal facets appear when ΔK exceeds region II and runs into the fast-propagation region III.

4. Conclusions

Fatigue crack growth behaviors of a newly developed DS superalloy have been studied to investigate the effects of temperatures and orientations. Test specimens were subjected to two temperatures (T_0 and T_0+250^{0}C) and three crystal orientations (longitudinal, transverse and diagonal). Following conclusions can be drawn:

1) Weak orientation dependence have been found, and all $da/dN - \Delta K$ curves fall into a [1/3,3] narrow bond. Generally cracks in longitudinal and transverse directions have comparable crack growth rate, while those in diagonal direction propagate more slowly, especially in low-ΔK regimes;

2) Temperature dependence seems to vary in different orientations, i.e., cracks travel in longitudinal orientation show no temperature dependence, while those in transverse orientations show a little temperature dependence, and temperatures do have large effect on cracks travel in diagonal direction;

3) At lower temperatures, stage-I type cracking mode has been found in longitudinal and diagonal directions, while stage-II type cracking mode has been found in transverse direction; Besides, at higher temperatures, stage-II type cracking is preferred in longitudinal and diagonal directions, while stage-I type cracking is preferred in transverse direction.

Acknowledgement

The authors gratefully acknowledge Siemens Energy, Inc. for the support in completing this research; meanwhile, the financial support from National Natural Science Foundation of China (Grant NOs. 10872105 and 51071094) are also appreciated.

Reference

[1] R. B., Scralin. "Fatigue crack propagation in a directionally-solidified nickel-base alloy". Metallurgical Transactions A, 7A(1976) 1535-1541.

[2] M. Okazaki, T. Tabata, S. Nohmi. "Intrinsic Stage I crack growth of directioinally solidified ni-base superalloys during low-cycle faitgue at elevated temperature". Metallurgical Transactions A, 21A(1990) 2201-2208.

[3] B. Al-Abed, G. A. Webster. "Comparison of creep-fatigue crack growth in a conventionally cast and directionally solidified nickel base superalloy". Proceedings of the fifth international conference on creep and fracture of engineering materials and structures, B. Wilshire and R.W. Evans. Eds, The Institute of Materials, London, 1993(1993) 491-501.

[4] S. Highsmith. Jr., W. S. Johnson. "Scatter in fatigue crack growth rate in a directionally solidified nickel-base superalloy". Journal of ASTM International, 1(2)(2004) 1-12.

[5] K. B. Yoon, T. G. Park, A. Saxena. "Elevated temperatrue fatigue crack growth model for DS-GTD-111". Strength, Fractrue and Complexity, 4(2006) 35-40.

[6] S. Highsmith. Jr., W. S. Johnson. "Elevated temperature fatigue crack growth in directionally solidified GTD-111 superalloy". Fatigue and Fracture of Engineering Materials and Structures, 29(1)(2006) 11-22.

[7] Annual Book of ASTM Standards, E647, ASTM International.

[8] K. S. Chan, J. E. Hack, G. R. Leverant. "Fatigue crack propagation in Ni-base superalloy single crystals under multiaxial cyclic loads". Metallurgical Transactions A, 17A(1986) 1739-1750.

[9] K. S. Chan, J. E. Hack, G. R. Leverant. "Fatigue crack growth in MAR-M200 single crystals". Metallurgical Transactions A, 18a(1987) 581-591.

[10] K. S. Chan, G. R. Leverant. "Elevated-temperature fatigue crack growth behavior of MAR-M200 single crystals". Metallurgical Transactions A, 18a(1987) 593-602.

[11] H. Kagawa, Y. Mukai. "The effect of crystal orientation and temperatrue on fatigue crack growth of ni-based single crystal superalloy". Superalloy 2012: 12th international symposium on superalloys, 2012(2012) 225-233.

Analysis of Creep Crack Growth in Surface Cracked Specimens: Comparisons between Approaches of Fracture Mechanics and Continuum Damage Mechanics

Jian-Feng Wen, Shan-Tung Tu*

Key Laboratory of Pressure Systems and Safety (Ministry of Education), School of Mechanical and Power Engineering, East China University of Science and Technology, Shanghai 200237, PR China

*Corresponding author: sttu@ecust.edu.cn

Abstract The numerical approaches to simulate creep crack growth can be divided into two different categories. The first category is employing conventional fracture mechanics, in which the rate of crack growth is predicted by correlating it with a fracture mechanics parameter. The second category gaining much attention is on the basis of damage mechanics concept. In this paper, three dimensional analyses of creep crack growth are performed for 316 stainless steel specimens subjected to tension at high temperature with a semi-elliptical surface crack. Using two independent finite element analyses based on the fracture mechanics and continuum damage mechanics respectively, crack growth behaviors including crack profile development, crack size and propagation time are investigated and compared with each other and corresponding experimental data. The comparisons enable to show the different capabilities of the two approaches in predictions of creep crack growth.

Keywords Creep crack growth, Fracture mechanics, Continuum damage mechanics, Finite element analysis

1. Introduction

The increased computational power and programming capabilities have given impetus to the numerical prognoses of the structural integrity and service-ability throughout the lifetime of structures at high temperature. During the past decades, the numerical approaches to simulate creep crack growth have developed into two different groups. The first group is employing conventional fracture mechanics, in which the crack growth rate is predicted by correlating it with a fracture mechanics parameter such as stress intensity factor or C^*-integral [1-4]. The second group is based on damage mechanics concept [5]. When the creep damage variable reaches a critical value, material failure is considered to occur, and thus crack growth can be characterized by a completely damaged element zone ahead of the initial crack tip [6-9]. Alternatively, a node-release technique has been employed to simulate the separation of the crack face [10-14]. However, little research has been successfully conducted in applying the two approaches to three dimensional analysis of creep crack propagation. Furthermore, there is a need for a better understanding of the different capabilities of the two approaches in predictions of crack growth under creep conditions.

In this paper, three dimensional analyses of creep crack growth are performed for 316 stainless steel specimens subjected to tension at high temperature with a semi-elliptical surface crack. Section 2 briefly describes the conventional fracture mechanics models and a damage-based model recently proposed by the authors. The main idea of the two approaches in conjunction with the finite element (FE) method is demonstrated in Section 3. Subsequently, Section 4 shows the comparisons of

predictions using two independent analyses based on the two methods respectively. The conclusions are made in Section 5.

2. Mechanical model

2.1 Geometrical description

Thumbnail crack specimens tested at 600ºC by Hyde [15] subjected to static loads of tension are considered in the study, as shown in Fig. 1. The crack region can be divided into three parts: initial notch, fatigue crack and creep crack. In this work, attention is mainly paid to the creep crack region. Two specimens with extensive creep crack growth are chosen, of which test conditions are summarized in Table 1.

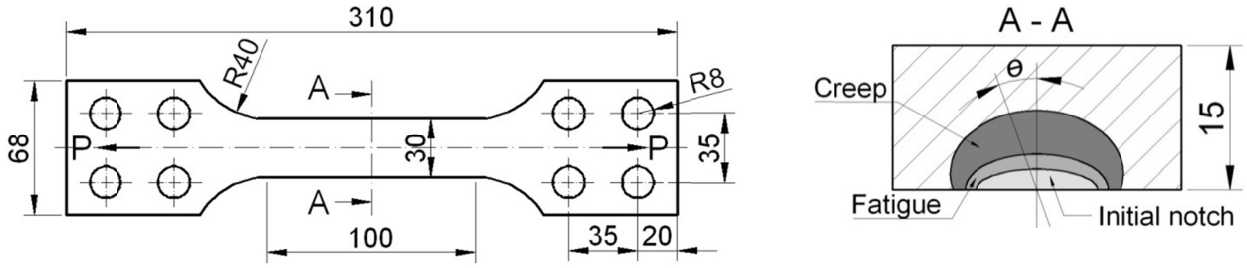

(a) (b)

Figure 1. Geometry of a thumbnail crack specimen: (a) a whole geometry; (b) an enlarged section view on A-A.

Table 1. Test conditions for the thumbnail crack specimens tested at 600 ºC.

Specimen No.	Initial creep crack size (mm)		Load (N)	Test duration (h)
	at $\theta = 0º$	at $\theta = 90º$		
5	2.88	4.33	90800	2760
6	3.50	4.37	90700	1200

2.2 Elasticity-secondary creep and creep fracture parameter

Basically, the time-dependent deformation characteristics for 316 stainless steel can be described by the following classical elastic-secondary creep constitutive relation

$$\dot{\varepsilon} = \frac{\dot{\sigma}}{E} + A\sigma^n, \tag{1}$$

where $\dot{\varepsilon}$ and $\dot{\sigma}$ denote the derivative of strain and stress corresponding to time; E is the Young's modulus; A and n are steady-state creep coefficient and steady-state creep exponent respectively. The material constants employed in FE analysis are listed in Table 2 [1, 9, 15].

For structures operated under creep regime, C^* is a proper fracture mechanics parameter to describe the crack growth. With regard to actual components such as plates and pipes, the values of C^* need to be determined by using FE methods. Then, with the transition time from small scale creep to the steady state ignored, the crack growth rate is represented in the following form:

$$\frac{da}{d\tau} = C(C^*)^q, \tag{2}$$

where τ, C and q denote the time, creep crack growth coefficient and exponent, respectively. Provided C^* has the unit of $Nmm^{-1}h^{-1}$, C and q for tests of compact tension (CT) specimens of 316 stainless steel at 600ºC [15] are also shown in Table 2.

Table 2. Material properties of the 316 stainless steel tested at 600ºC.

E (MPa)	ν	A ($MPa^{-n}h^{-1}$)	n	C	q	ε_f (%)
148000	0.3	1.47×10^{-29}	10.147	2.774×10^{-2}	0.958	27

2.3 Creep-damage model

The continuum damage mechanics model can trace its roots to Kachanov and Rabotnov's work [16, 17]. Since then there have been many attempts to develop an appropriate model [5, 18-20]. Recently, the authors presented a creep-damage model to simulate creep fracture, which is capable of characterizing the full creep curve and can reasonably reflect the influence of stress state on creep deformation and damage. More detailed description and validation of the proposed creep-damage model can be found in Refs. [21, 22]. The proposed model is as follows:

$$\dot{\varepsilon}_{ij}^c = \frac{3}{2} A\sigma_e^{n-1} s_{ij}\left[1+\beta\left(\frac{\sigma_1}{\sigma_e}\right)^2\right]^{\frac{n+1}{2}}, \tag{3}$$

and

$$\dot{\omega} = \frac{\dot{\varepsilon}^c}{\varepsilon_f^*}, \tag{4}$$

where A and n are material constants. ε_{ij}^c, s_{ij}, σ_e and σ_1 are the creep strain tensor, deviatoric stress tensor, equivalent stress and maximum principle stress, respectively. ω, $\dot{\varepsilon}^c$ and ε_f^* denote the damage variable, creep strain rate and multi-axial creep failure strain, respectively. β is a stress-independent function reflecting material behavior, having the form

$$\beta = \frac{2\rho}{n+1} + \frac{(2n+3)\rho^2}{n(n+1)^2} + \frac{(n+3)\rho^3}{9n(n+1)^3} + \frac{(n+3)\rho^4}{108n(n+1)^4}, \tag{5}$$

where the micro-crack damage parameter, ρ, depends primarily on the number of micro-cracks per unit volume and their average diameter. Suppose the damage variable is given as the reduction of the effective area in the cell, we can obtain

$$\rho = \frac{2(n+1)}{\pi\sqrt{1+3/n}}\omega^{3/2}. \tag{6}$$

It is known that the creep ductility significantly depends on the stress state. In this work, a modified multi-axial ductility model, which can describes the behavior of creep cavity growth more appropriately than the widely-used Cocks-Ashby model [23], is employed:

$$\frac{\varepsilon_f^*}{\varepsilon_f} = \exp\left[\frac{2}{3}\left(\frac{n-0.5}{n+0.5}\right)\right] \Big/ \exp\left[2\left(\frac{n-0.5}{n+0.5}\right)\frac{\sigma_m}{\sigma_e}\right], \tag{7}$$

where ε_f is the uniaxial creep failure strain and σ_m is the hydrostatic stress. In this work, the optimum value of ε_f for tests of uniaxial specimens of 316 stainless steel at 600ºC is found to be 0.27, as listed in Table 2.

3. Finite element framework

3.1 Using fracture mechanics approach

To predict the crack growth behavior of thumbnail crack specimens under creep conditions, fracture mechanics approach has been used in conjunction with the FE method. Numerical simulations of creep crack growth, which have been based on a step-by-step analysis procedure, are described as follows:

(a) Creating of the FE models. One quarter of the specimen containing a semi-elliptical surface crack has been created using the codes ABAQUS [24] and ZENCRACK [25] due to symmetry of both the geometry and loading. About 10,000 elements of type C3D8I for each model have been adopted. Note that extremely refined meshes are generated in the crack tip zone to obtain accurate results.

(b) Calculations of values of C^*. Values of C^* at a set of points which constitute the crack front can be calculated using the equivalent domain integral (EDI) method provided by the codes ABAQUS. In the study, the crack front has been divided into 16 sections, so values of C^* at 17 points are recorded in every step.

(c) Calculation of the increment of the crack size. The steady-state creep crack growth can be represented by Eq. (2), according to which, the creep crack growth increment at each point along the crack front, Δa_i, can be calculated as

$$\Delta a_i = \left(\frac{C_i^*}{C_{\max}^*}\right)^q \Delta a_{\max}, \tag{8}$$

where C_i^* and $C_{\max}^*$ are C^* at an arbitrary point and the maximum value along the crack front, respectively; $\Delta a_{\max}$ denote the maximum crack growth increment at the point where $C_{\max}^*$ occurs.

(d) Establishment of a new crack profile. Based on the creep crack increment at each point along the crack front, a set of new points can be determined. And then, a new crack profile can be created by using codes ZENCRACK.
(e) Returning to stage (a). The crack continued to extend through the stages from (a) to (d) until a termination condition is reached.

3.2 Using continuum damage mechanics approach

Creep damage modeling has been also carried out using the codes ABAQUS with the elastic-plastic-creep properties of 316 stainless steel tested at 600ºC [1, 9, 15]. The total strain can be calculated by

$$\varepsilon^{tol} = \varepsilon^{e} + \varepsilon^{p} + \varepsilon^{c}, \tag{9}$$

where $\varepsilon^{e}, \varepsilon^{p}$ and ε^{c} are elastic, plastic and creep strain components, respectively. The true stress-strain data beyond the yield point is used as input to FE analysis and a Mises flow rule with isotropic strain hardening is employed. To define the time-dependent and damage-coupled creep behavior, Eq. (3) is implemented into the ABAQUS user subroutine, CREEP. Eq. (4) is also embedded in CREEP to determine the damage accumulation. Creep damage variable, ω, is in the range of 0 to 0.99. When ω at a Gauss point reaches 0.99, all the stress components are sharply reduced to a small plateau and thus crack growth can be characterized by a completely damaged element zone ahead of the initial crack tip. Another user subroutine, USDFLD, is employed to embody this failure simulation technique.

Using this numerical method, three-dimensional creep damage analyses are performed to simulate the creep crack growth in thumbnail crack specimens. One quarter of the model consisting of about 10,000 eight-node C3D8R elements is modeled exploiting the symmetry conditions. The mesh size in the vicinity of the crack front is 200μm, which has been proved to provide excellent predictions in Ref. [21].

4. Results and discussion

4.1 Predictions using fracture mechanics approach

To achieve accurate predictions of crack growth using fracture mechanics approach, it is essential to choose a proper maximum crack growth increment, $\Delta a_{\max}$, in Eq. (8). Comparison of crack depth variations predicted using five different maximum crack growth increments, $\Delta a_{\max} = t/300$, $t/150$, $t/75$, $t/30$ and $t/15$, for the thumbnail crack in specimen 5 is shown in Fig. 2. It can be seen that the difference between the crack depth variations cannot be neglected when the maximum crack growth increment is relatively large ($\Delta a_{\max} = t/30$ and $t/15$). For $\Delta a_{\max} = t/300$, $t/150$ and $t/75$, however,

difference between predictions is extraordinarily hard to identify on the plot, which demonstrates the convergence of the relation between the crack depth and propagation time does exist. In this paper, the maximum crack growth increment is selected as $t/150$, which is small enough to achieve a required accuracy of crack growth time.

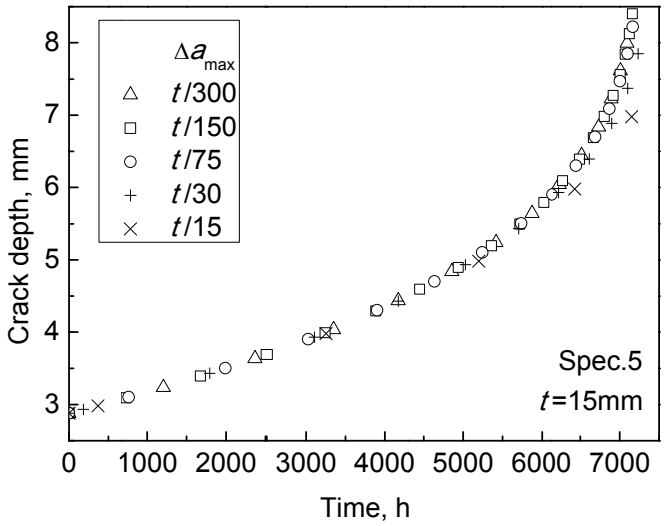

Figure 2. Comparison of crack depth variations predicted using five different maximum crack growth increments

Fig. 3 shows the predicted creep crack shape developments for thumbnail cracks in specimens 5 and 6 with the initial semi-elliptical crack front. It can be found that the increment along depth direction is always more considerable than that along surface direction at each step. As a result, the accumulative increment of crack depth is obviously larger than that of half crack length.

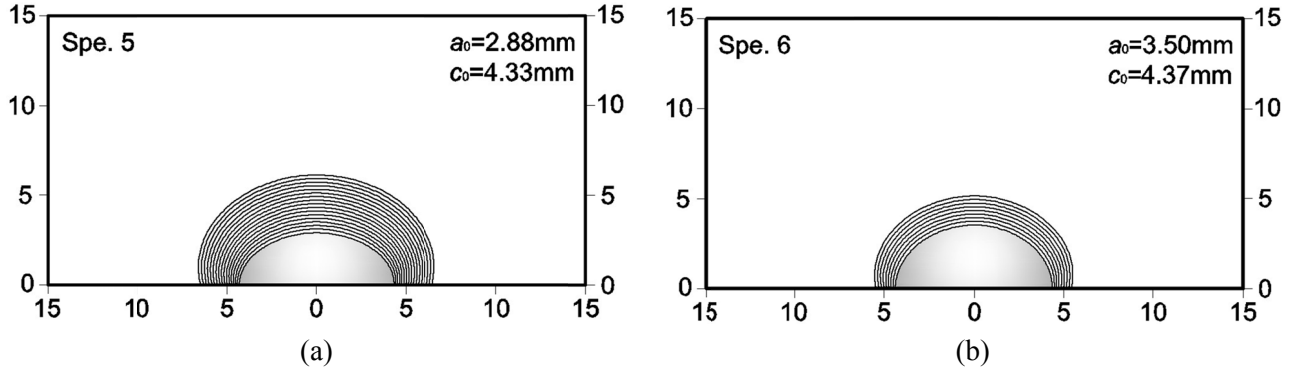

Figure 3. Predicted creep crack shape evolutions resulting from fracture mechanics approach: (a) specimen 5; (b) specimen 6

Fig. 4 depicts the tested specimen photos taken from Ref [9, 15] and predictions using fracture mechanics approach for specimens 5 and 6. It can be said that the predicted crack fronts are similar to the experimental results for both specimens. Nevertheless, the predicted propagations times are 2~3 times as long as the actual test durations. This is mainly because that creep crack growth coefficient and exponent, C and q, in Eq. (2) are obtained from the correlation of $\mathrm{d}a/\mathrm{d}t$ and C^* for tests of CT specimens instead of the investigated thumbnail crack specimens. For a given C^*, the

crack growth rate for a crack in a CT specimen can be considerably lower than in a thumbnail crack specimen due to the different constraint effect of varied types of specimens.

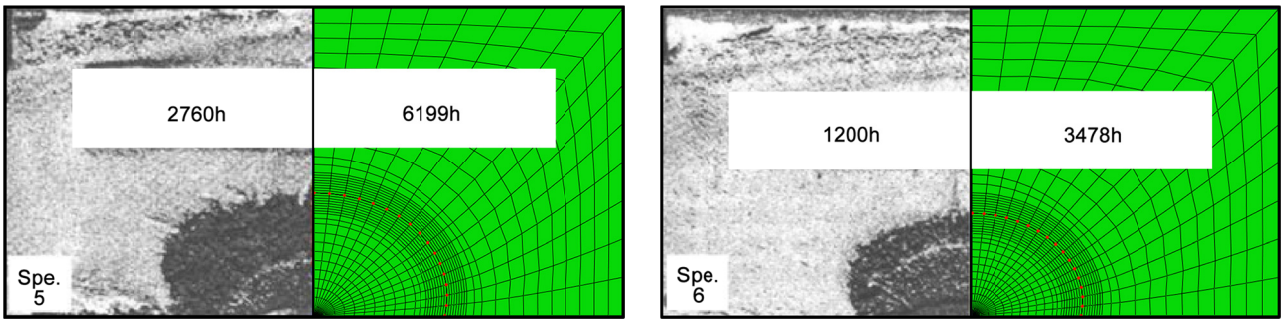

(a) (b)

Figure 4. Comparisons of tested specimen photos with predictions using fracture mechanics approach: (a) specimen 5; (b) specimen 6

4.2 Predictions using continuum damage mechanics approach

Predicted crack profiles using continuum damage mechanics approach are compared with the tested specimen photos in Fig. 5. Obviously, the FE predicted crack fronts match very closely to the experimental results. One can also find that the crack propagates with larger increment at $\theta = 0^{\circ}$ (approximately under plane-strain condition) than that at $\theta = 90^{\circ}$ (approximately under plane-stress condition) due to the constraint effect. Propagation times predicted by the numerical simulation are also in good agreement with the test durations. These encouraging results prove the validity and predictive capability of the proposed creep-damage model presented in Eqs. (3) and (4).

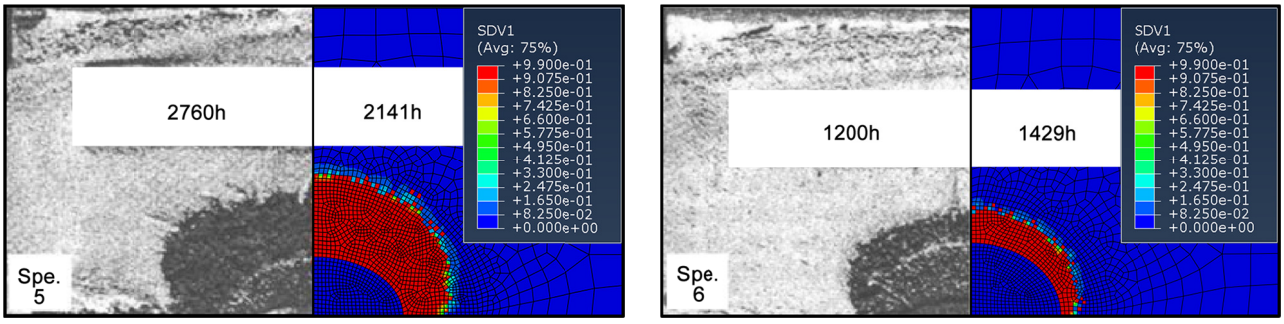

(a) (b)

Figure 5. Comparisons of tested specimen photos with predictions using continuum damage mechanics approach: (a) specimen 5; (b) specimen 6

Fig. 6 provides comparisons of crack depth variations predicted by using fracture mechanics and continuum damage mechanics approaches. It is clear that damage mechanics predictions are more closely to the experimental data. In addition, the crack initiation times, nearly 500 hours, can also be predicted by continuum damage mechanics approach. When C^*-type method is employed, no information regarding crack initiation can be obtained.

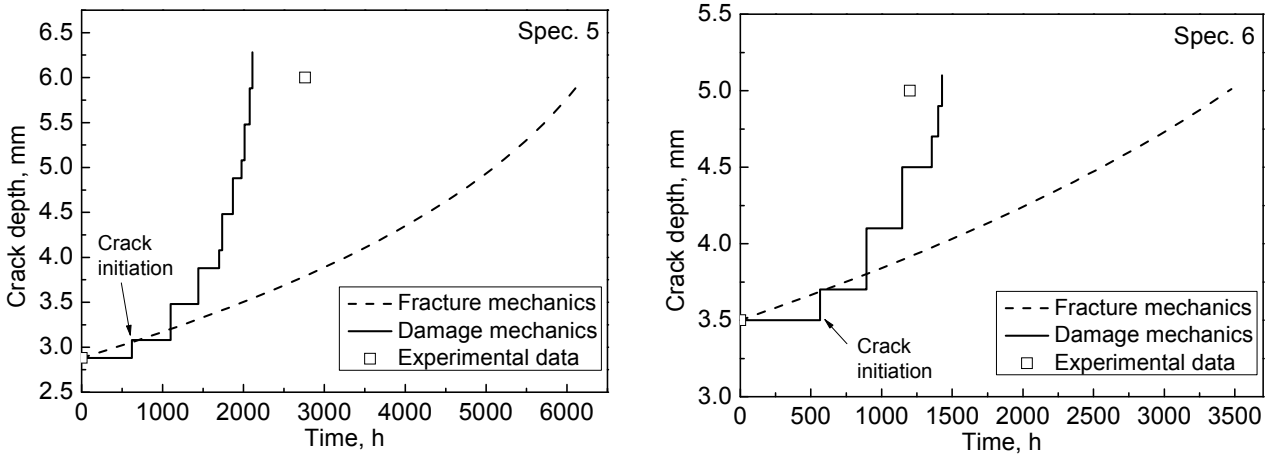

(a) (b)

Figure 6. Comparisons of crack depth variations predicted by using fracture mechanics and continuum damage mechanics approaches

5. Conclusions

The main conclusions drawn from the study are listed as follows:

(a) For fracture mechanics approach, the convergence of the relation between the crack depth and propagation time does exist if the maximum crack growth increment is small enough.

(b) Both fracture mechanics and continuum damage mechanics approaches in conjunction with the FE technique can give reasonable predictions of the crack profile when compared with the experimental results of thumbnail crack specimens tested under tension.

(c) The propagation time can also be appropriately predicted by the damage mechanics approach, while it is far from satisfactory when using the facture mechanics method. For the purpose of a more accurate prediction, the different constraint effects between the CT and thumbnail crack specimen need to be carefully considered.

(d) The crack initiation time can also be predicted by the damage-based approach presented in the study.

Acknowledgements

This work is financially supported by National Natural Science Foundation of China (Contract No. 50835003). The authors would also like to thank Prof. T.H. Hyde and Prof. W. Sun at University of Nottingham for the helpful discussion with them.

References

[1] Smith SD, Webster JJ, Hyde TH. Creep behaviour of a stationary, semicircular surface crack. Engng Fract Mech 1988;30:105-16.

[2] Yoon KB, Park TG, Saxena A. Creep crack growth analysis of elliptic surface cracks in pressure vessels. Int J Pres Ves Pip 2003;80:465-79.

[3] Kayser Y, Marie S, Poussard C, Delaval C. Leak Before Break procedure: Recent modification of RCC-MR A16 appendix and proposed improvements. Int J Pres Ves Pip 2008;85:681-93.
[4] Wen JF, Tu ST, Gong JM, Sun W. Creep fracture mechanics parameters for internal axial surface cracks in pressurized cylinders and creep crack growth analysis. Int J Pres Ves Pip 2011;88:452-64.
[5] Lemaitre J, Desmorat R. Engineering damage mechanics: ductile, creep, fatigue and brittle failures. Berlin: Springer-Verlag; 2005.
[6] Oh CS, Kim NH, Kim YJ, Davies C, Nikbin K, Dean D. Creep failure simulations of 316H at 550 degree C: Part I: method and validation. Engng Fract Mech 2011;78:2966-77.
[7] Oh CS, Kim NH, Min SH, Kim YJ. Finite element damage analysis for predictions of creep crack growth. Proceedings of the ASME 2010 Pressure Vessels & Piping Division / K-PVP Conference. Washington, USA. 2010.
[8] Hyde TH, Saber M, Sun W. Testing and modelling of creep crack growth in compact tension specimens from a P91 weld at 650 degree C. Engng Fract Mech 2010;77:2946-57.
[9] Hyde CJ, Hyde TH, Sun W, Becker AA. Damage mechanics based predictions of creep crack growth in 316 stainless steel. Engng Fract Mech 2010;77:2385-402.
[10] Yatomi M, Tabuchi M. Issues relating to numerical modelling of creep crack growth. Engng Fract Mech 2010;77:3043-52.
[11] Yatomi M, Davies CM, Nikbin KM. Creep crack growth simulations in 316H stainless steel. Engng Fract Mech 2008;75:5140-50.
[12] Yatomi M, O'Dowd NP, Nikbin KM, Webster GA. Theoretical and numerical modelling of creep crack growth in a carbon-manganese steel. Engng Fract Mech 2006;73:1158-75.
[13] Yatomi M, Bettinson AD, O'Dowd NP, Nikbin KM. Modelling of damage development and failure in notched-bar multiaxial creep tests. Fatigue Fract Engng Mater Struct 2004;27:283-95.
[14] Yatomi M, Nikbin KM, O'Dowd NP. Creep crack growth prediction using a damage based approach. Int J Pres Ves Pip 2003;80:573-83.
[15] Hyde TH. Creep crack growth in 316 stainless steel at 600 degree C. High Temp Technol 1988;6:51-61.
[16] Rabotnov YN. Creep problems in structural members. Amsterdam: North-Holland; 1969.
[17] Kachanov LM. Rupture time under creep conditions. Int J Fracture 1999;97:11-8.
[18] Liu Y, Murakami S. Damage localization of conventional creep damage models and proposition of a new model for creep damage analysis. JSME Int J Ser A 1998;41:57-65.
[19] Murakami S, Liu Y. Mesh-dependence in local approach to creep fracture. Int J Damage Mech 1995;4:230.
[20] Murakami S, Liu Y, Mizuno M. Computational methods for creep fracture analysis by damage mechanics. Comput Meth Appl Mech Engng 2000;183:15-33.
[21] Wen JF, Tu ST, Gao XL, Reddy JN. Simulations of creep crack growth in 316 stainless steel using a novel creep-damage model. Engng Fract Mech 2013; doi: http://dx.doi.org/10.1016/j.engfracmech.2012.12.014.
[22] Wen JF, Tu ST, Gao XL, Reddy JN. A new model for creep damage analysis and its application to creep crack growth simulations. 9th International Conference on Creep and Fatigue at Elevated Temperatures. London, UK. 2012.

[23] Cocks AF, Ashby MF. Intergranular fracture during power-law creep under multiaxial stresses. Metal Sci 1980;8:395-402.
[24] ABAQUS. Version 6.9-EF ed. Providence: Dassault Systèmes; 2009.
[25] ZENCRACK. Version 7.7 ed. London: Zentech International Limited; 2012.

Mechanical testing of a selective laser melted superalloy

Håkan Brodin[1,2,*], Olov Andersson[1] and Sten Johansson[2]

[1] Siemens Industrial Turbomachinery AB, Finspång, Sweden
[2] Linköping University, Department of Management and Engineering, Division of Engineering Materials, 581 83 Linköping, SWEDEN
* Corresponding author: hakan.brodin@liu.se

Abstract

Selective laser melting is an additive manufacturing technology where metal powder is melted by a laser source layer-wise, forming a solid, dense metallic component. With the selective laser meting process, near net shape components can be manufactured directly from a 3D-model. The model is sliced into thin layers and a powder is spread onto a build platform. In the next step, the powder is fused by a laser as dictated by the model. The laser energy is intense enough to permit full melting (welding) of the particles to form solid metal. The process is repeated layer by layer until the part is complete. A number of materials are available, including steel, aluminium, titanium and, in recent time, also superalloys. The material investigated in the current project is a nickel base superalloy composition-wise equivalent to Hastelloy X, a solution strengthened superalloy typically used in large welded components exposed to high temperatures in oxidizing as well as reducing environments.

Microstructurally, the material is different from both a hot-rolled, as well as a cast material due to the manufacturing process. Since the SLM process involves laser melting of powder particles in the size range of <50μm, the structure resembles of a weld structure, however on a smaller scale. Due to the layer-by-layer build strategy, the material will exhibit anisotropy.

In the current project, high temperature mechanical fatigue and creep tests are performed. The microstructure is evaluated and the influence on the mechanical properties is discussed. Anisotropy in mechanical properties is discussed and the underlying factors of the anisotropy are analyzed.

Keywords Additive manufacturing, Hastelloy X, fatigue, creep, anisotropy

1. Introduction

Selective laser melting (SLM), or, as the industry standard denotes the process, laser sintering, is an additive manufacturing process where metal powder is melted by a laser source layer-wise, forming a solid, dense metallic component. SLM belongs to a group of manufacturing processes recognized as rapid prototyping (RP). RP processes are well established for manufacturing of parts of plastic materials or metallic materials that can more or less easily be melted [1, 2]. Examples are 3D-printing [3] as patented by Massachusetts Institute of Technology, selective laser sintering (SLS) [4] developed at University of Texas at Austin and selective laser melting (SLM) [5] initially developed at the Fraunhofer Institute ILT in Aachen.

With the SLS process it is possible to melt materials like bronze [6]. Materials with a high melting point can be mixed with a lower melting point material in order to form a composite of, for instance, bronze as a matrix with embedded particles of steel or nickel [6].

With the SLM process, near net shape components can be manufactured directly from a CAD model. The model is sliced into thin (max 100µm thick) layers. Powder is spread onto a metallic build platform and the powder is fused in layers with a laser as dictated by the CAD model. The laser energy is intense enough to permit full melting (welding) of the particles to form solid metal. The process is repeated layer by layer until the part is complete. Examples of metallic materials commercially available for the SLM process are stainless steels AISI 304L [7] and 316L [8, 9], Aluminium alloys [10], Titanium Ti6Al4V [4] and also more temperature resistant materials such as Inconel 625 [4].

The laser melting manufacturing process can, as mentioned, be described as a layer-by layer process, where powder is distributed on a powder bed, Figure 1. After powder distribution, the powder is melted and a metal slice is formed on the powder bed.

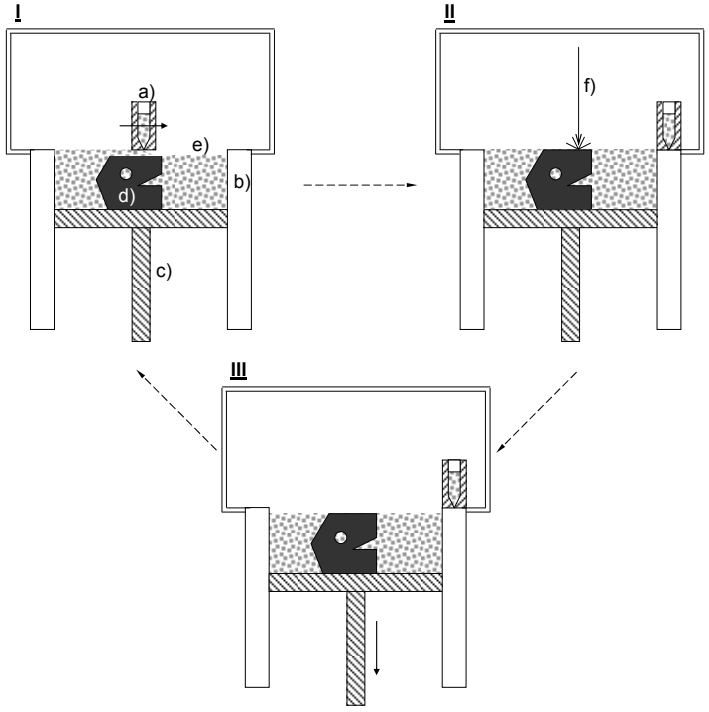

Figure 1. Schematic description of the SLM process. a) Powder is distributed on a powder bed, the build platform. b) The powder is melted by a laser beam and a slice of solid metal is formed. c) The powder bed is lowered and the process is repeated until a finished component is formed.

I: A powder distributer travels over the powder bed cavity contained by the build chamber walls b) and build plate c). Molten and solidified powder constitutes the component d) surrounded by unmolten powder e). II: A laser beam f) melts the powder layer and creates a new slice of solid material in the component d). III: A ram lowers the build platform c) and the process is repeated until

a finished geometry is formed. After finalization, the remaining loose powder is removed and the component is cut off from the build platform.

2. Experimental details

Since no harmonized nomenclature exists in the literature for specimen build / loading direction relative to build platform or build direction, it is necessary to give a reference to nomenclature used in the current paper. If the build platform is taken as reference, a specimen being built in the build platform plane (perpendicular to the build direction) the specimen build and loading direction is designated 0°. Any specimen build and loading direction tilted towards the normal of the build platform plane (i.e. a vector defining the machine global build direction) would be designated with a build angle $0° < \alpha \leq 90°$. Due to the nature of the SLM process, the layer-wise build-up of material is normally done with a scan strategy so that the material will be isotropic in the build plane. For each layer the scanning pattern is rotated and in a component the material will contain welds in many different directions. Any rotation of a specimen in the plane is considered to give corresponding results and the material can be considered as orthotropic [11]. The findings have been verified for 1.4404 [12]. The present definition of specimen build direction / loading direction is graphically visualized below, Figure 2.

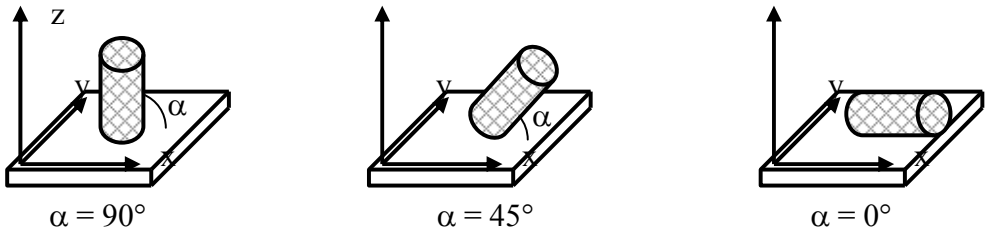

Figure 2. Definition of specimen build and loading direction relative to the build platform plane. A specimen "0°" would be a specimen in any direction in the build plane and a specimen "α°" ($0° < \alpha < 90°$) would be a specimen built out of the build platform. An angle $\alpha = 90°$ would indicate a specimen being built parallel to the SLM equipment build direction.

2.1. Process

Material manufacturing has been done in an Eosint M270 Dual Mode equipment. The atmosphere during building is Argon and the atmosphere is monitored by an oxygen probe throughout the entire process to ensure that the oxygen level is kept below a maximum level. A layer thickness of 20μm was used and for each new layer the laser beam rotated the scanning pattern and shifted the scanning pattern in order to avoid in-plane property variations.

2.2. Material11

For the material manufacturing, a nickel base superalloy in accordance to Hastelloy X (originally developed by Haynes International) has been used. The material is Ar gas atomized and sieved to a fraction suitable for selective laser melting applications, indicating a powder distribution from

10-45µm. The nominal composition of Hastelloy X is shown below as reference, Table 1.

Table 1. Nominal composition of Hastelloy X hot-rolled material.

Ni	Cr	Fe	Mo	Co	Si	Mn	W
Bal.	22	18	9	1.5	<1	<1	0.6

During SLM manufacturing the material is built up layer-wise with a layer thickness of 20µm. The typical powder morphology is shown below, Figure 3. The material is well atomized without large amounts of satellites, fused/bonded particles or inhomogenities.

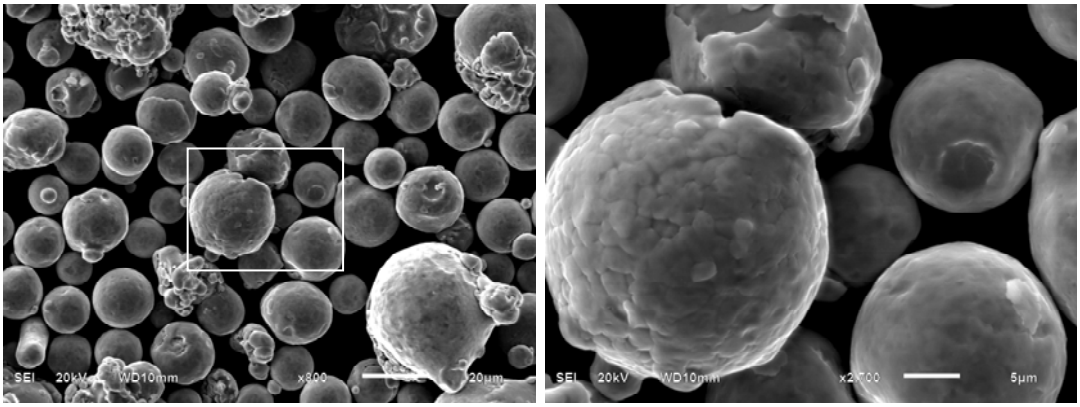

Figure 3. Scanning electron microscopy image of recycled Alloy X powder morphology. The powder is relatively free from satellites and sintered/bonded particles. Some coarse particles are present, a result of the powder being recycled.

Material has been built in different directions relative to the build plane as defined in Figure 2 above. Evaluations are done in the 0°, 45° and 90° directions. For testing of selective laser melted material properties presented in the current paper testing has been conducted on as-manufactured material. Reference material in hot-rolled condition is typically not available in any other condition than the standard solution heat treated material state. Therefore, comparative data for standard Hastelloy X material is included as reference. For Alloy X material manufactured by the SLM method, the best heat treatment route is not per say a standard solution heat treatment. In fact, the material is in the as-manufactured state very homogeneous with no segregations opposite to what could be expected from, for instance, a casting process. I.e., from a segregation point of view, a solution heat treatment would not necessarily be beneficial.

2.3. Mechanical testing and evaluation

Material testing has been performed at ambient and elevated temperature. At ambient temperature, the material has previously been shown to exhibit anisotropy in tensile properties [13, 14]. The current work tries to evaluate some of the high temperature properties of the selective laser melted Alloy X material with respect to thermomechanical fatigue (TMF) and creep loading. The resulting fracture surfaces and microstructures are evaluated by light optical and scanning electron microscopy. Etching of the material is done as electrolytic etching in 10% oxalic acid in distilled

water with a voltage of 6V and a time of 15-25s depending on specimen size. In the current paper, material properties are only evaluated for bulk material, i.e. all material was machined to final specimen dimensions and no influence from the rough surface is taken into consideration.

The thermomechanical data referenced below have been conducted as in-phase (IP) TMF between 50°C and 800°C and a hold time of 5 minutes at maximum temperature. Creep testing is performed at 816°C.

3. Results

3.1 Initial microstructure

The typical as-manufactured microstructure is shown below, Figure 4. The microstructural anisotropy is obvious. As seen in Figure 4, the material has a weld-like structure. Due to the conditions during manufacturing, the material will undergo rapid solidification. In the literature, in the melt pool solidification region, temperature gradients up to 3500 K/mm on the surface are indicated [15]. The resulting grain size will be fine-grained as seen in Figure 5.

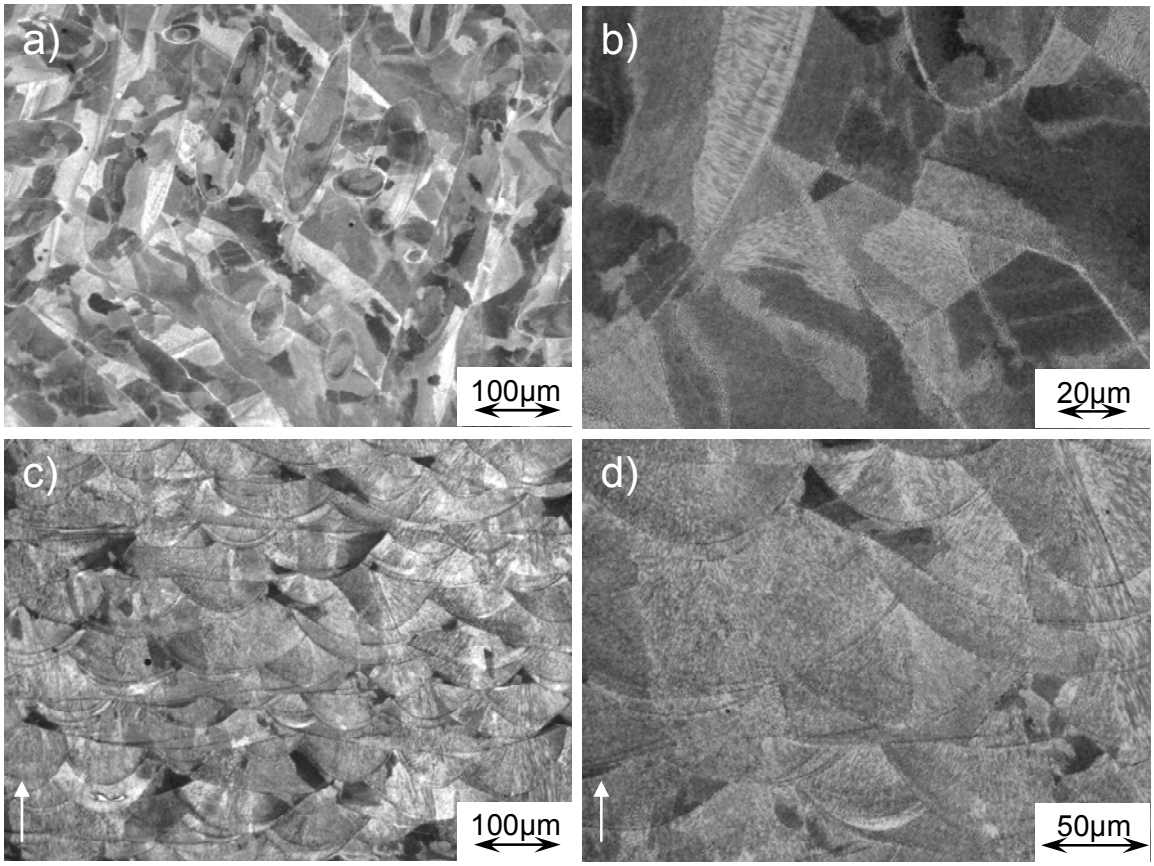

Figure 4. As manufactured microstructure. Top views (a, b) are light optical micrographs, bottom views (c, d) are corresponding scanning electron microscope images. Left views (a, c): Arrow indicates the build direction. The build plane is horizontal and below the bottom of the figure. Right views (b, d): The build direction is out of the plane, the build plane is in the plane of the figure.

From Figure 4 the micrographs a columnar structure can be observed. The grain structure is not

easily detected, therefore an EBSD analysis has been performed. An example of the results is shown below, Figure 5.

It is obvious that the structure is columnar and that the microstructure has a coupling to solidification. In the process, the build plate is kept at a constant temperature and the solidified material is surrounded by loosely packed metal powder, i.e. the metal powder will act as insulation for heat from the weld process. The columnar structure is an indication on conditions for heat transfer. Since the columnar structure is vertical in the image, the cooling gradient is mainly normal to the build platform.

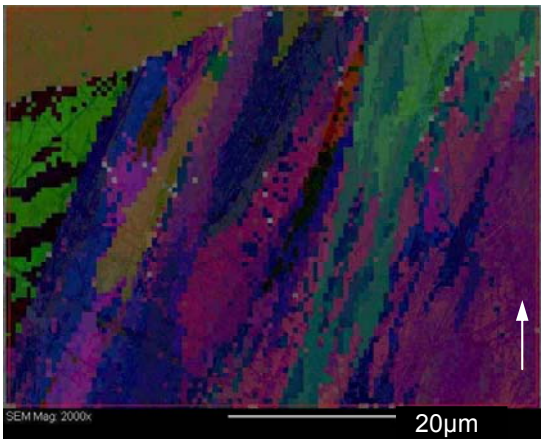

Figure 5. EBSD image of as-manufactured Alloy X. Build direction is indicated by an arrow in the figure.

3.2 Fatigue testing

Testing of the material at low temperature has been conducted as low cycle fatigue testing in strain control with a triangular wave shape and a strain ratio R_ε=1. Results are shown below, Figure 6.

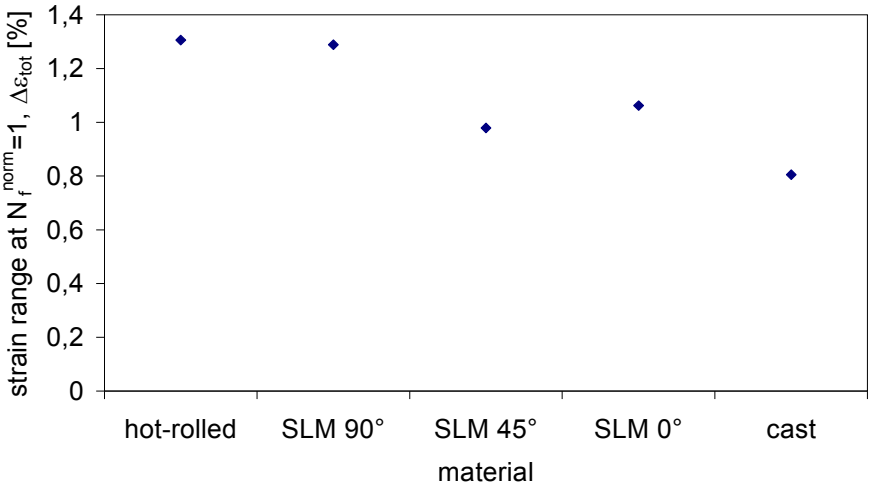

Figure 6. Normalized low cycle fatigue test results at ambient temperature.

Fracture surfaces of fatigue tested material have been evaluated by light optical microscopy and scanning electron microscopy. Corresponding typical micrographs are shown below, Figure 7 and

Figure 8.

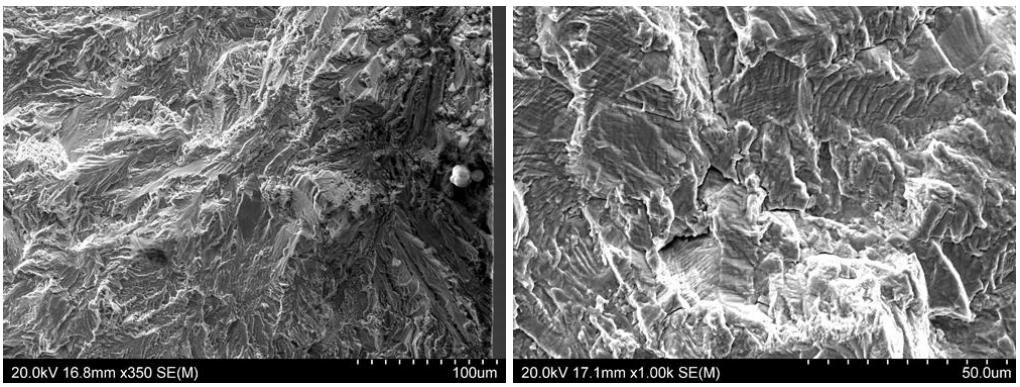

Figure 7. Fracture surface, low cycle fatigue testing, test temperature 20°C.

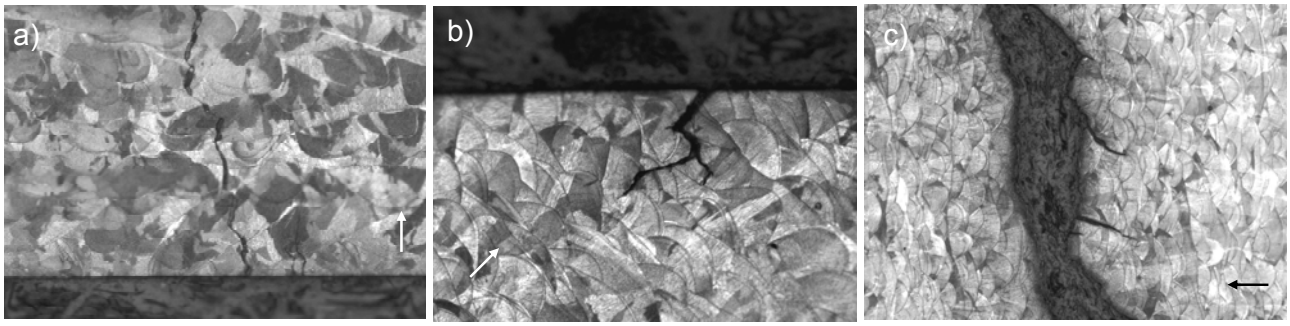

Figure 8. Crack patterns, low cycle fatigue, test temperature 20°C. In the figure, a) is 0° build direction, b) is 45° build direction and c) is 90° build direction. Loading direction is horizontal in the figure.

At high temperature, the testing has been performed as thermomechanical fatigue testing in strain control using a trapezoid wave form with hold time at T_{max} and a strain ratio R_ε=0. Normalized results from the thermomechanical testing are presented in Figure 9. In the figure, the relative strain value "1" indicates the normalized strain for a hot-rolled material to yield a certain fatigue life.

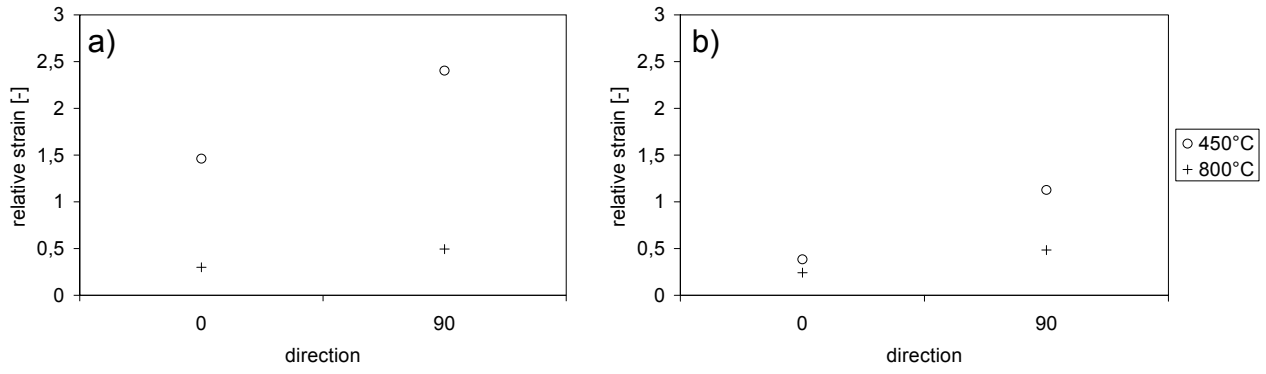

Figure 9. Normalized average data from thermomechanical fatigue test results. Strain measurements are relative to the strain that for a hot-rolled bar will yield a) 500 cycles and b) 1000 cycles.

For comparison, the fracture surfaces have been evaluated and typical fracture patterns at 450°C and 800°C are presented in Figure 10 and Figure 11 respectively.

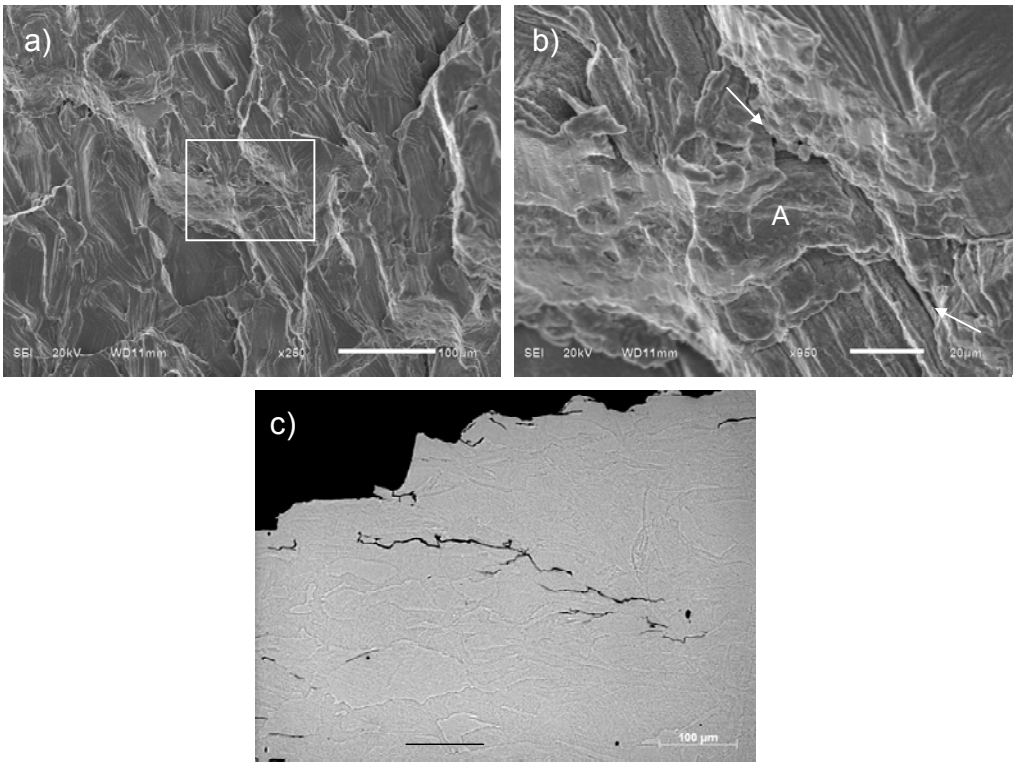

Figure 10. Fracture surface, elevated temperature 450°C, build direction 0°, thermomechanical fatigue testing. Fracture is intercrystalline with crack branching as indicated by arrows in right figure. Area "A" is an area with poor bonding.

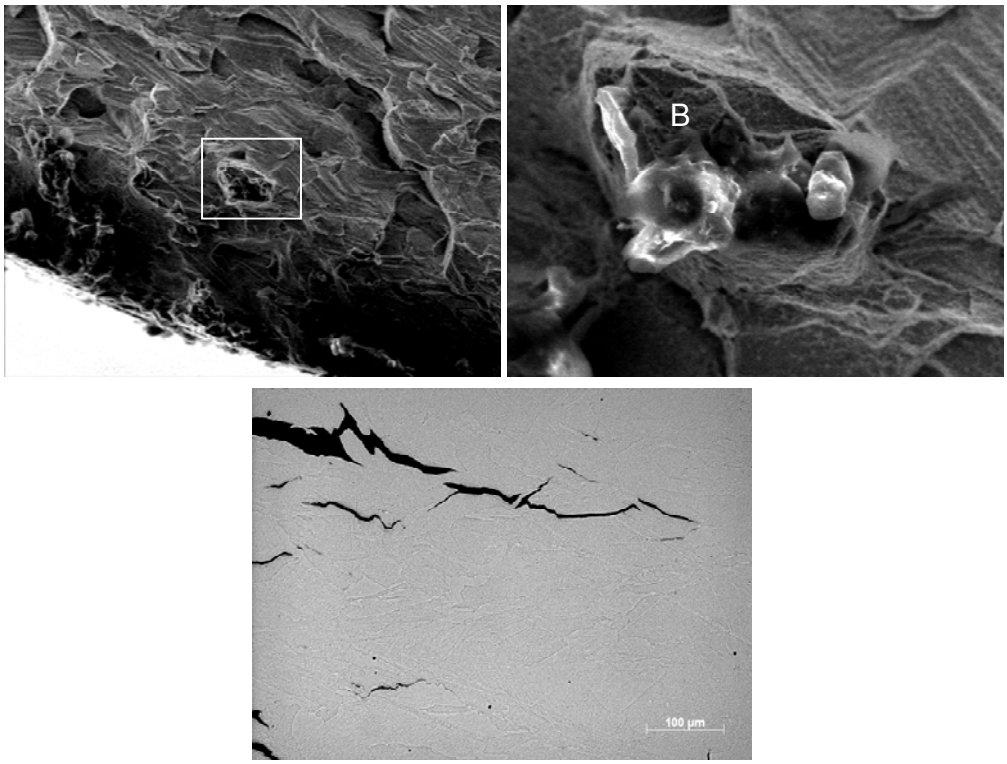

Figure 11. Fracture surface, elevated temperature 800°C, build direction 0°, thermomechanical fatigue testing. Fracture is intercrystalline with crack branching as indicated by arrows in right figure. Area "B" is an area containing an inhomogenity (partly molten particle).

3.3 Creep testing

Results from stress rupture testing of SLM material is presented below, Figure 12. In the figure, the relative creep rupture life "1" indicates the normalized life for a hot-rolled material to yield a certain creep life. Corresponding fracture surfaces and crack patterns are shown in Figure 13.

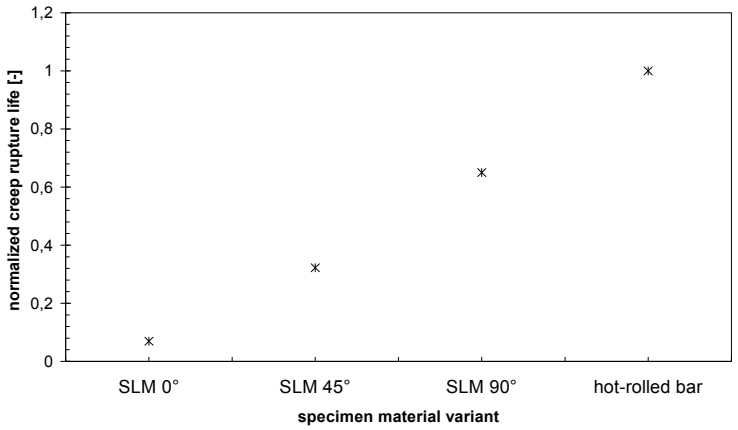

Figure 12. Stress rupture testing at 815°C. Comparison of SLM material and hot-rolled Hastelloy X.

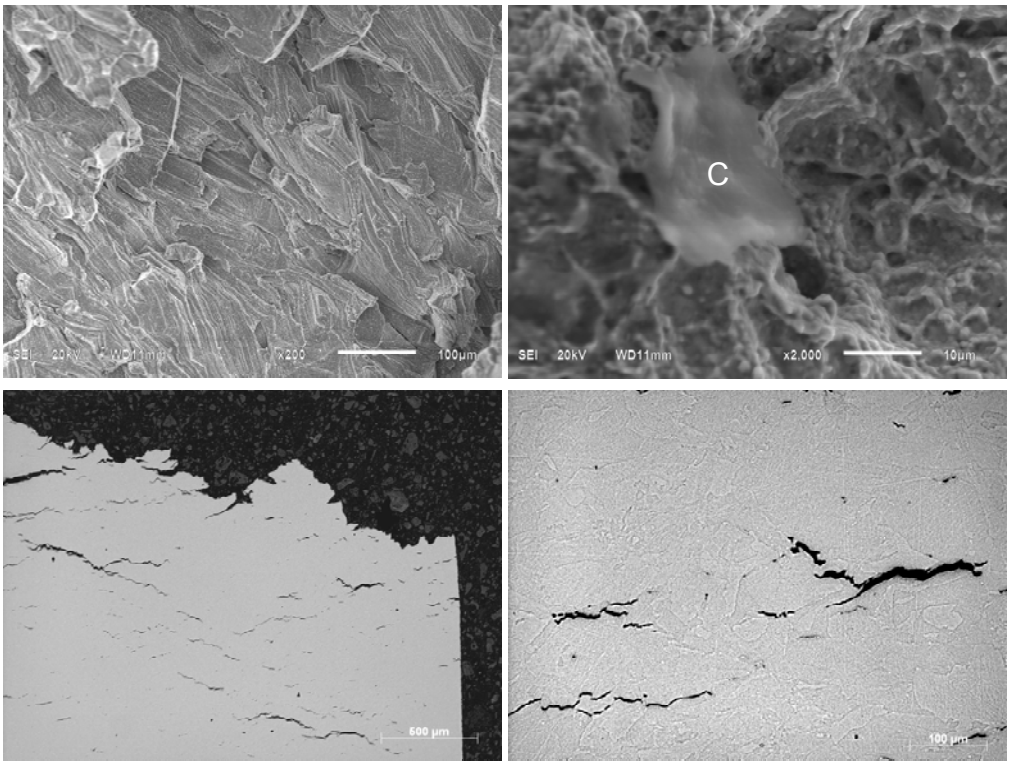

Figure 13. Fracture surface, test temperature 815°C, build direction 0°, creep testing. Fracture is intercrystalline with multiple crack sites. Area "C" is an area with poor bonding (internal flaw) to the surrounding.

4. Discussion

The tensile strength anisotropy has previously been indicated for Hastelloy X [13, 14, 16] and other alloys [11, 12, 17]. Here the anisotropy is obvious both in creep testing and in fatigue. The trend is that the 90 degree direction acts as the most fatigue and creep resistant direction. In this direction

the material will act as a less fine grained and creep properties are then likely to be improved due to a grain size effect. In fatigue the 90° direction is more ductile [13, 14]. This fact could be beneficial if, for instance the material contains a number of defects and individual defects play an important role in crack initiation. A more ductile material can possibly accommodate an increased stress field around an inclusion through a larger local plastic zone avoiding cracking. The microscopy evaluation shows that the material is isotropic from a microstructure point of view in a plane parallel to the build plane. In the 90° direction the microstructure is different, as shown in microstructure photos and EBSD. Taking both previous tensile, current fatigue and creep results into account, the conclusion is that the material is orthotropic.

Fracture surfaces indicate that both creep and fatigue testing at elevated temperature are very similar. Hence it cannot be excluded that creep play a role already at 450°C for this material, especially if the material is fine-grained.

5. Conclusions

A nickel-based superalloy manufactured by selective laser melting was investigated by mechanical testing and microstructural evaluations. The material is observed to have a layered weld-like structure. Due to the manufacturing process properties, a columnar grain structure is present. It is shown from mechanical testing that the material is orthotropic with respect to mechanical properties.

Fatigue properties in the 90° direction are comparable to hot rolled material at temperatures below temperatures where creep could be expected. However, in other directions < 90° the material is less resistant to crack initiation. The biggest concern with selective laser melted materials appears to be creep related. It is shown here that the creep properties are inferior to hot rolled material in all directions $0° \leq \alpha \leq 90°$ and that the material cannot compare to a standard hot-rolled material regarding creep. It is shown that the grain size is small, and it is well known that changes in grain size have a strong influence on both mechanical strength and creep properties.

6. References

[1] Chu J., Engelbrecht S., Graf G., and Rosen D.W., 2010. “A comparison of synthesis methods for cellular structures with application to additive manufacturing”. Rapid Prototyping Journal, 16, pp. 275-283.

[2] Rosen D.W., 2007. “Computer-aided design for additive manufacturing of cellular structures”. Computer-Aided Design and Applications, 4, pp. 585-594.

[3] Marchelli G., Prabhakar R., Storti D., and Ganter M., 2011. “The guide to glass 3D printing: developments, methods, diagnostics and results”. Rapid Prototyping Journal, 17(3), pp. 187 – 194.

[4] Das S., Beama J.J., Wohlert M., and Bourell D.L., 1998. "Direct laser freeform fabrication of high performance metal components". Rapid Prototyping Journal, 4(3), pp. 112 – 117.

[5] Kruth J.P., Froyen L., Van Vaerenberg J., Mercelis P., Rombouts M., and Lauwers B., 2004. “Selective laser melting of iron-based powder”. Journal of Materials Processing Technology, 149, pp. 616-622.

[6] Agarwala M., Bourell D., Beaman J, Marcus H., and Barlow J., 1995. "Direct selective laser sintering of metals". Rapid Prototyping Journal, 1(1), pp. 26 – 36.
[7] Abd-Elghany K., and Bourell D.L., 2012. "Property evaluation of 304L stainless steel fabricated by selective laser melting". Rapid Prototyping Journal, 18(5), pp. 420 – 428.
[8] Li R., Liu J., Shi Y., Du M., and Xie Z., 2010. "316L Stainless Steel with Gradient Porosity Fabricated by Selective Laser Melting". Journal of Materials Engineering and Performance, 19(5), pp. 666-671.
[9] Li R., Shi Y., Wang L., Liu J. and Wang Z., 2011. "Theory and technology of sintering, thermal and chemothermal treatment. The key metallurgical features of selective laser melting of stainless steel powder for building metallic part". Powder Metallurgy and Metal Ceramics, 50(3-4), pp. 141-151.
[10] Buchbinder D., Schleifenbaum H., Heidrich S., Meiners W., and Bültmann J., 2011. " High Power Selective Laser Melting (HP SLM) of Aluminum Parts" Physics Procedia, 12, pp. 271–278.
[11] Meiners, W., „Direktes Selektives Laser Sintern einkomponentiger metallisher Werkstoffe", RWTH Aachen, Shaker Verlag, 1999, Germany
[12] Rehme, O., „Cellular Design for Freeform Fabrication", TU Hamburg-Harburg, Cuvillier Verlag, 2010, Germany
[13] Brodin, H., Andersson, O., Johansson, S., ASME Turbo Expo, San Antonio TX, 2013
[14] Brodin, H., Saarimäki, J., "Mechanical properties of lattice truss structures made of a selective laser melted superalloy", International Conference on Fracture, Beijing, China, 2013
[15] Chivel, Y., Smurov, I., "On-line temperature monitoring in selective laser sintering/melting", Physics Procedia 5, (2010), pp. 515–521
[16] Wang F., 2012. "Mechanical property study on rapid additive layer manufacture Hastelloy® X alloy by selective laser melting technology". International Journal of Advanced Manufacturing Technology, 58, pp. 545-551.
[17] Wang Z., Guan K., Gao M., Li X., Chen X., and Zeng X., 2012. "The microstructure and mechanical properties of deposited-In718 by selective laser melting"., Journal of Alloys and Compounds, 513(5), pp. 518-523.

Creep-Fatigue Interactions in P91 Steel

Magdalena Speicher[1,*], Andreas Klenk[1], Kent Coleman[2]

[1] Materialpruefungsanstalt Universitaet Stuttgart, Stuttgart 70569, Germany
[2] Electric Power Research Institute, Charlotte NC 28262, USA
* Corresponding author: magdalena.speicher@mpa.uni-stuttgart.de

Abstract To determine and quantify the influence of creep-fatigue interactions on the crack behaviour of P91 steel creep-fatigue crack growth (CFCG) tests were carried out with holding times up to 60 minutes and compared to results from fatigue crack growth (FCG) and creep crack growth (CCG) tests.
It was found that the introduction of a holding time influences the crack initiation time but not the crack propagation. With holding times of 60 minutes, the difference between CCG and CFCG tests is very small.
To characterise the fracture mode metallographic analyses were performed on selected specimens after CFCG tests. The crack path is inter-granular and an area of high cavity density was identified around the crack tip in all specimens. By comparing CFCG, FCG and CCG results, it can be finally noticed that specimens with a holding time of 6 and 60 min show a similar crack growth rate as samples under creep loading.

Keywords martensitic steel, creep-fatigue, crack initiation, crack growth

1. Introduction

In components operated at high temperature, there is always some amount of interaction between fatigue, creep and the environment. This is typically the case in power plants where steam generating service start-ups or load changes produce changes in steam conditions and transient temperatures. In the last decades, it has been proven that in the creep-fatigue range, the lifetime of components is significantly shorter, particularly when hold periods are introduced between strain cycles. These interactions can be enhanced due to environmental effects such as for instance internal or surface oxidation. They are finally more pronounced for some materials, can be neglected for others. In this work, the crack behaviour of the steel P91 was investigated in creep-fatigue tests. The aim of this analysis is to gain information about how the crack behaviour of this steel is influenced by creep-fatigue-environment interactions at high temperature.

2. Experimental Details

2.1. Material

The base material P91 (X10CrMoVNb9-1) being under investigation, comes from a thick pipe with outer diameter of 492 mm and wall thickness of 85 mm. Its chemical composition is given in Table 1. These values are in accordance with the EN10216 requirements [1]. The P91 pipe was used in [2] for the investigation of similar welds under creep conditions. A classical Post Weld Heat Treatment (PWHT) was therefore used to relax the stresses that were induced by the welding process.

Table 1. Chemical composition of P91 used in this work

		Chemical composition in mass (%)										
		C	**Si**	**Mn**	**P**	**S**	**Cr**	**Mo**	**Ni**	**Al**	**Nb**	**V**
[1]	Min	0,08	0,20	0,30	-	-	8,0	0,85	-	-	0,06	0,18
	Max	0,12	0,50	0,60	0,02	0,010	9,5	1,05	0,40	0,04	0,10	0,25
this work	Meas.	0,104	0,27	0,46	0,014	0,003	8,17	0,9	0,16	0,02	0,064	0,194

In order to optimize the full-use of the already acquired database, the P91 samples investigated in this work where submitted to the same heat treatment as follows: austenitising at 1050°C for 10 min with air cooling, tempering at 750°C for 70 min and PWHT at 760°C for 2 h as it is often performed for components with welds.
The microstructure of P91 consists of tempered martensitic, see Fig. 1. During creep, fatigue or creep-fatigue interactions, the microstructure of such steels is instable. A drop in the dislocation density, an augmentation of the subgrain size leading to an equiaxial microstructure and a growth in the size of precipitates such as carbides $M_{23}C_6$ ($Cr_{23}C_6$) and carbonitrides MX (VN, VC, NbC) in the matrix are influencing the global deformation behaviour.

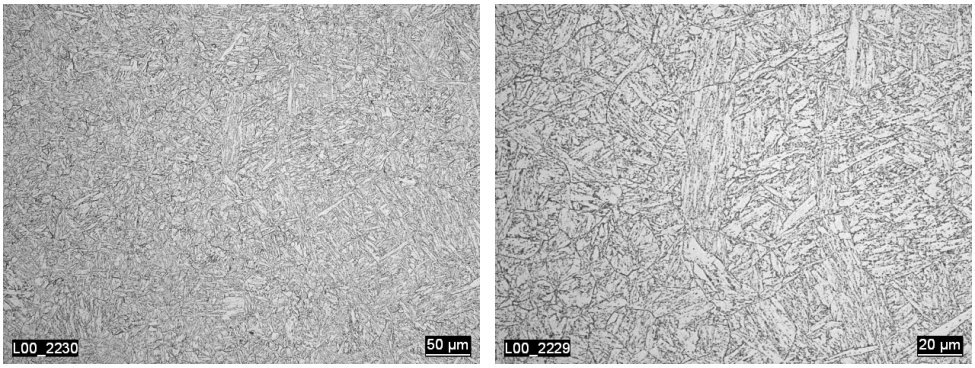

Figure 1. Microstructure of P91-steel, light optical images

2.2. Mechanical testing

For the crack growth tests side-grooved Compact Tension specimens C(T)-25 were used. The starter notch was realised by fatigue pre-cracking. All samples have an a_0/W-ratio in the range of 0.52 to 0.60. Creep Crack Growth tests (CCG) were performed according to ASTM E 1457-07 [3]. Creep-Fatigue Crack Growth tests (CFCG) were performed with a load ratio $R = F_{min}/F_{max}$ of 0.1 and with hold periods at maximum load of 6 and 60 min according to ASTM E 2760-10 [4]. Fatigue Crack Growth tests (FCG) were performed with a load ratio R = 0.1 and frequency of 0.5 Hz. All tests were carried out at 580°C and 600°C.
During the tests, the load line displacement was measured by means of capacitive high temperature strain gauges. The crack propagation was monitored online using the Alternating Current Potential Drop (ACPD) technique. At the end of each experiment, the potential drop signal was calibrated with the final crack length measured on the fractured specimens. For this, the specimen was broken up under liquid nitrogen after the test and the crack length was measured according to [3].

3. Description of crack initiation and crack propagation under creep and fatigue conditions

Crack initiation and crack propagation under creep conditions can be described by the usual fracture mechanics parameter C* and the stress intensity factor K_I.
- In linear-elastic fracture mechanics the stress intensity factor K_I is generally used for components with predominantly linear-elastic behaviour. Only a small plastic or creep zone at the crack tip can be assessed using this parameter. For side grooved C(T)-specimens the stress intensity factor is calculated as:

$$K_I = \frac{F}{\sqrt{B \cdot B_N \cdot W}} \cdot \left(2 + \frac{a}{W}\right) \cdot f\left(\frac{a}{W}\right) \quad (1)$$

$$f\left(\frac{a}{W}\right)=\frac{\left[0.886+4.64\cdot\left(\frac{a}{W}\right)-13.32\cdot\left(\frac{a}{W}\right)^2+14.72\cdot\left(\frac{a}{W}\right)^3-5.6\cdot\left(\frac{a}{W}\right)^4\right]}{\left(1-\frac{a}{W}\right)^{1.5}} \tag{2}$$

where F is load, B is specimen thickness, B_N is net thickness of side grooved specimens, a is crack length and W is test piece width.

- Components with stationary creep (not only at the crack tip) are assessed using the integral C*. In case of the experimental determination of the parameter C* approximation formulae can be used for a number of fracture mechanics specimens [5], which are basically functions of the load line displacement rate due to creep [3]:

$$C^* = \dot{v}_C \cdot \sigma_{net} \cdot \eta \tag{3}$$

with load line displacement rate $\dot{v}_C$, net section stress σ_{net} and the factor η depending on specimen geometry (η = [2+0.522•(1-a/W)] for C(T)-specimens).

For the evaluation of C(T)25-specimens the following equation was used:

$$C^* = \dot{v}\cdot\frac{F}{B_N\cdot c}\cdot\frac{h_1}{h_3}\cdot\frac{W/a-1}{\beta\cdot\eta} \tag{4}$$

where h_1 and h_3 are geometrical functions, c=W-a, and β: 1,071 for plain stress condition.

One of the validity criteria, which decide on the suitability of the relevant parameter, is the transition time t_1 [3]:

$$t_1 = \frac{K_I^2}{C^*\cdot(n+1)\cdot E'} \tag{5}$$

If t_1 is smaller than the crack initiation time $t_1 << t_i$ for the initiation criterion (Δa_i=0.5 mm) the parameter C* is more appropriate for the description of crack behaviour under creep conditions.

In order to describe the creep crack growth rate either the parameters C* or stress intensity factor K_I can be used, dependent on the situation in the component. Typically, the creep crack growth rate depending on the respective fracture mechanics parameter is presented as follows:

$$\frac{da}{dt} = C_1\cdot(K_I)^{m1} \tag{6}$$

$$\frac{da}{dt} = C_2\cdot(C^*)^{m2} \tag{7}$$

where C_1, C_2, m_1 and m_2 are material constants.

Fatigue crack behaviour can be described by threshold values for the beginning of cyclic crack growth and by the Paris-law [6] for the crack propagation:

$$\frac{da}{dN} = C_3\cdot(\Delta K)^{m3} \tag{8}$$

with C_3 and m_3 as material specific constants.

3. Results and Discussion

3.1. Crack initiation under creep-fatigue loading

The results of creep-fatigue crack growth tests as a function of stress intensity factor and initiation time are shown in Fig. 2 a compared to the creep crack growth tests and in Fig. 2 b compared to fatigue crack growth tests. In addition, the literature data from [7] are shown there.
An effect of holding time (HT) on the creep crack initiation time for the technical initiation criterion (Δa_i=0.5 mm) is observed, whereby the influence of HT of 6 min for both test temperatures is greatest. For lower loaded sample at 600°C (HT=6 min), the influence of the holding period on the initiation time is significantly lower than for the higher loaded specimen. This indicates the time-dependence during the holding period and the creep process seems to be dominant. If the holding time is one hour, the difference between the results of creep crack growth test and creep-fatigue crack growth test is small, especially at 600°C. The differences between the two specimens with short and long holding time at 580°C are not significant. This means that a reduction in time is expected due to cyclic stress for crack initiation. Literature data from [7] show no influence of the holding time on crack initiation time, so that these results can be described independently of the holding time by the creep curve in the investigated area (see Fig. 2 a).
Fig. 2 b shows the dependency of the cyclic stress intensity factor as a function of the number of cycles to crack initiation at Δa_i = 0.5 mm. It can be seen that the creep-fatigue specimens with short holding times are closer to the experiments under pure cyclic loading.

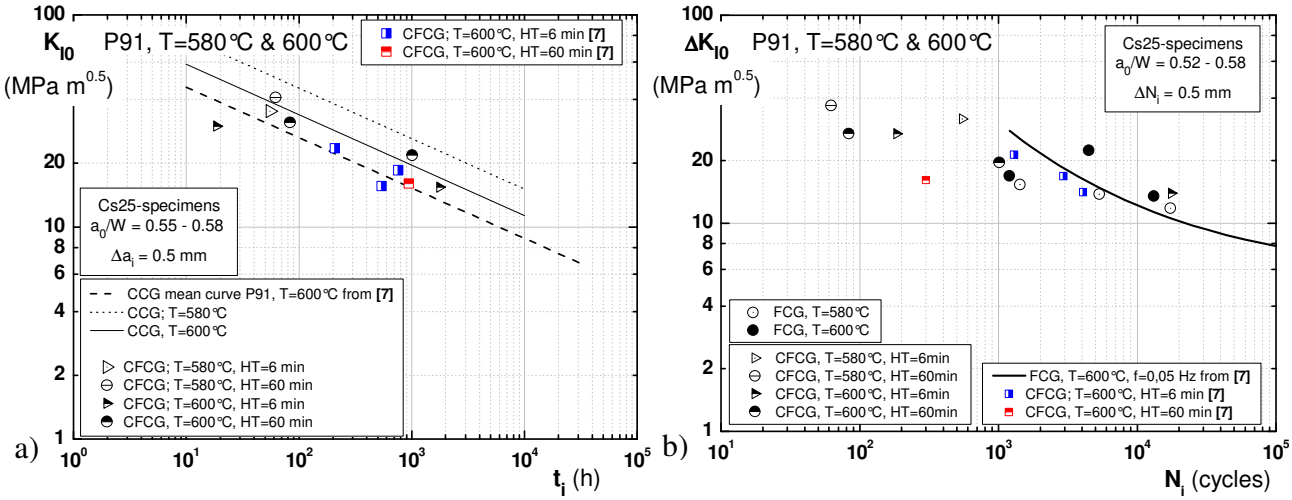

Figure 2. a) Stress intensity factor K_{I0} over time for Cs25-specimens (T=580°C & 600°C) under creep-fatigue loading compared to P91-steel mean curve for creep at 600°C from [7]; b) Cyclic stress intensity factor ΔK_{I0} over cycles for Cs25-specimens (T=580°C & 600°C) under creep-fatigue loading compared to the results under fatigue loading at 580°C and 600°C

In Fig. 3 the parameter C* is shown depending on the time to the crack initiation (determined at Δa=0.5 mm) under creep-fatigue condition. As expected, the creep-fatigue samples with longer holding periods are closer to the curve of creep crack growth tests.

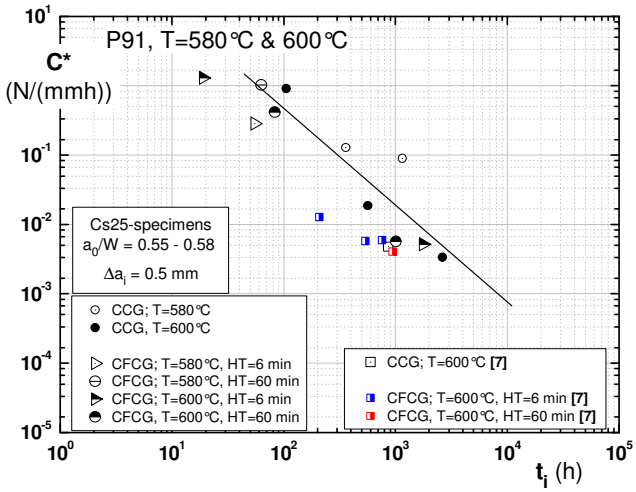

Figure 3. C* parameter over time for Cs25-specimens (T=580°C & 600°C) under creep-fatigue loading compared to P91-steel from [7]

3.2. Crack propagation under creep-fatigue loading

The comparison of CFCG- and CCG-experimental results shows (see Fig. 4 a and Fig. 4 b) that the specimens with a holding time of 6 min and 60 min have similar crack growth rates as samples without holding time, regardless of which of the two parameters describing the crack behaviour is used. No influence of holding time on crack initiation as described in the last section is observed for crack propagation. Thus, the cyclic loading has only an influence on the crack behaviour in the initial phase. In the holding time period the creep loading is dominant. Metallographic studies confirmed this observation so far (see next section).

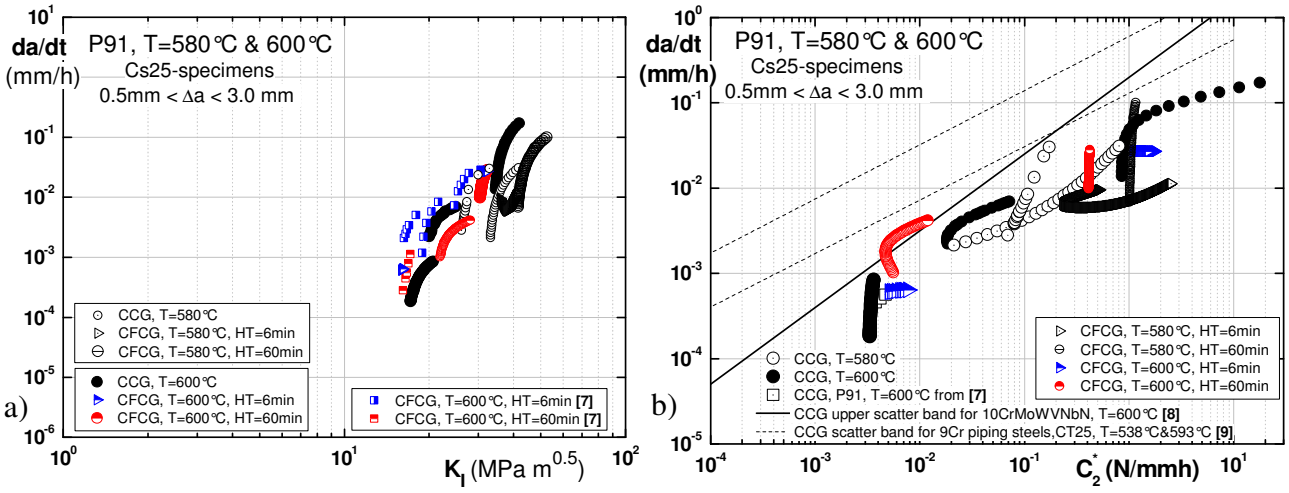

Figure 4. Creep-fatigue crack growth rate over a) stress intensity factor K_I and b) parameter C* for Cs25-specimens (T=580°C & 600°C) compared to literature data from [7-9]

In Fig.5 the results of fatigue crack growth tests at 580°C and 600°C are reported. The influence of temperature on the fatigue crack growth behaviour can be seen. The fastest crack growth rates are observed at 600°C. The results obtained in this work are similar to literature data from [9] for P91 at 565°C and a frequency f of 0.1 Hz. One sample at 600°C is slightly above the Paris-law curve, which can be explained by the different test temperature. It is also evident that results of CFCG-tests at 580°C and 600°C cannot be described by the Paris-law. The cyclic crack-growth rate increases if a hold time is imposed at maximum load. As the hold time increases, a change from cycle dependent to time dependent behaviour can be observed.

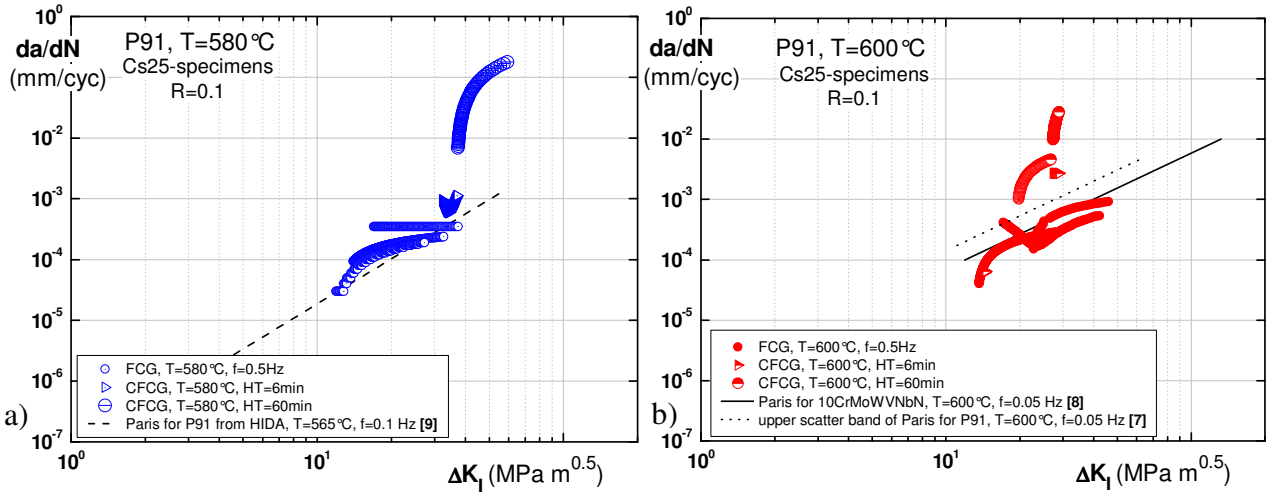

Figure 5. Creep-fatigue crack growth rate over ΔK_I for Cs25-specimens at a) T=580°C and b) T=600°C compared to literature data from [7-9]

3.4. Metallografic investigations

In Fig. 6 and Fig. 7, the crack paths for selected specimens of different crack growth tests are shown. A comparison of CCG-tests and CFCG-tests with a short and long holding time of 6 min and 60 min and under fatigue loading shows the different mechanisms that play a significant role in the crack propagation process.

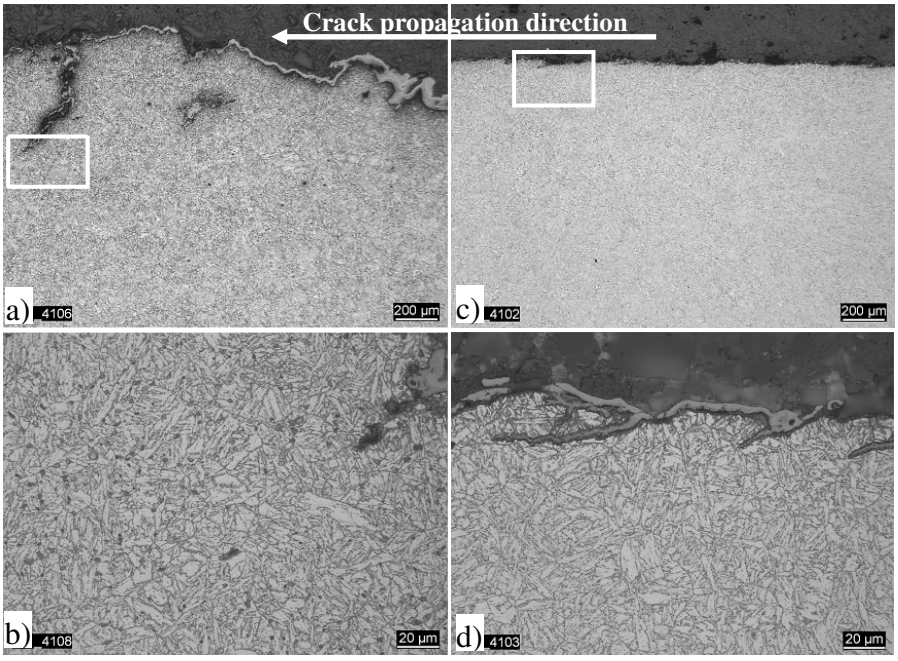

Figure 6: a) Specimen after CCG-test at 600°C, b) detail view from a); c) Specimen after FCG-test at 600°C, d) detail view from c)

A large amount of creep cavities is found on the prior austenite grain boundaries at the crack tip and along the crack path of a creep crack growth tested specimen (see Fig. 6a and b). Due to the strong oxidation of the crack surface, the crack cannot be clearly identified as inter-granular. Nevertheless, by comparing this specimen with the sample tested under pure fatigue loading (see Fig. 6 c and d), it is clear that the crack paths are different. This was already visible on the fracture surface. The surface of the specimen tested under fatigue loading was smooth, which suggests that the crack was

propagating trans-granular. This has been confirmed in an light-optical investigation of a cross section.

For the samples tested under creep-fatigue loading (see Fig. 7) the crack behaviour was found to be independent on the holding time similarly like specimens tested under creep loading (Fig. 6 a, b). Around the crack tip an area of high cavity density was identified and the crack path under creep-fatigue loading is comparable with the crack path under pure creep condition. Also along the crack path creep cavities were observed.

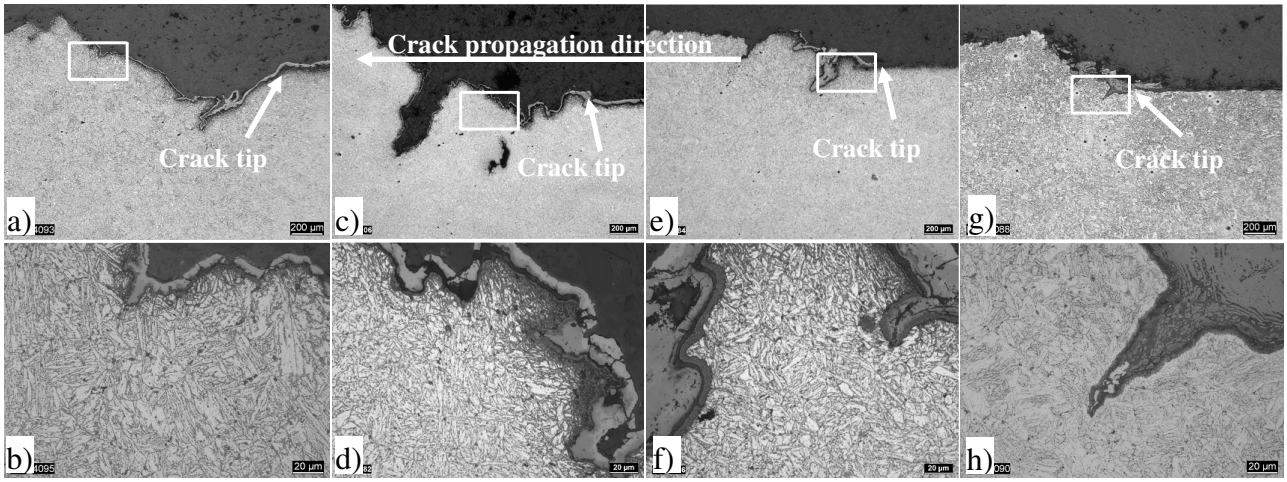

Figure 7: Specimen after CFCG-test at 580°C with a), b) HT=6 min (b) detail view from a)), c), d) HT=60 min (d) detail view from c)), at 600°C with e), f) HT=6 min (f) detail view from e)), g), h) HT=60 min (h) detail view from g))

3.3. Creep-fatigue interactions

The crack propagation rate da/dN under creep-fatigue loading is influenced by two failure mechanisms, and therefore depends on the load level, the mean stress, the stress ratio R and the temperature. Generally, there are three different areas [10]. At high frequencies, the crack growth per cycle is independent of frequency, because the cycle duration is so short that no time remains for creep crack growth. With decreasing frequency, the crack growth per cycle da/dN is greater. The time between two load cycles is then sufficiently large, so that fatigue crack growth and creep crack growth can overlap. With further decreasing frequency of the fatigue crack propagation loses its meaning. The crack propagation is now determined only by creep crack growth.

In literature [11, 12] different relationships exist to describe the crack growth under creep-fatigue loading, for example the following equation recommended for creep-ductile materials (see also [4]):

$$\frac{da}{dN} = C_0(\Delta K)^{n0} + \int_0^{t_h} C_1((C_t)_{avg})^q dt \tag{9}$$

According to [11] the final equation can be:

$$\frac{da}{dN} = C_0(\Delta K)^{n0} + C_1 K^{2m} t_h^{\,1-m} + C_2 C^{*m} t_h \tag{10}$$

with t_h as holding time. The first term is a pure-fatigue contribution reflecting no effect of hold time and corresponding to crack-growth behaviour at short hold times and high frequencies. This term can be evaluated if the Paris-law coefficients are available. For further evaluation, the coefficients from Table 2 will be used. The second term shows a nonlinear power-law dependence of

crack-growth rate on hold time and pertains to intermediate hold times and frequencies where creep-fatigue interaction is present. The coefficient C_1 was adopted from literature data for 1CrMoV-steel and 304 stainless steel [11]. A value between 10^{-7} and 10^{-6} for different materials at high temperature was found to be appropriate. For further evaluations a value of 10^{-6} was assumed, see Table 2. The third term including the C* parameter shows a linear dependence of crack growth on hold time and corresponds to purely creep-dominated crack growth occurring at long hold times and low frequencies [11]. Using the solutions for stress intensity factor K, and C* by appropriate Norton-law coefficients, the values from Table 2 are applied for the assessment.
With the accumulation rule according to Eq. (10) the results of creep-fatigue tests on P91-steel were evaluated under creep-fatigue loading and $R = F_{min} / F_{max}$=0.1. The assessment was carried out for C(T)-25 samples with a_0/W – ratio of 0.55.

Table 2. Material related parameters for describing the crack growth rates of P91

		Fatigue		Interaction		Creep	
		C_0	n_0	C_1	m	C_2	m
Eq. 10	580°C	8,85E-08	2,49	1E-06	0,66	4,21E-02	0,66
	600°C	8,85E-07	1,91				
Eq. 11	580°C	8,85E-08	2,49	-	-	6,17E-13	0,70
	600°C	8,85E-07	1,91	-	-		

The comparison between calculated and experimentally determined values is shown in Fig.8. The calculated values are overestimated for both temperatures and holding times. The creep portion is dominant in this case, so that the crack growth can be described based on creep only using C*. The biggest uncertainty here is the determination of C* with the Norton-approach, as the results are strongly influenced by changes in the Norton coefficients.

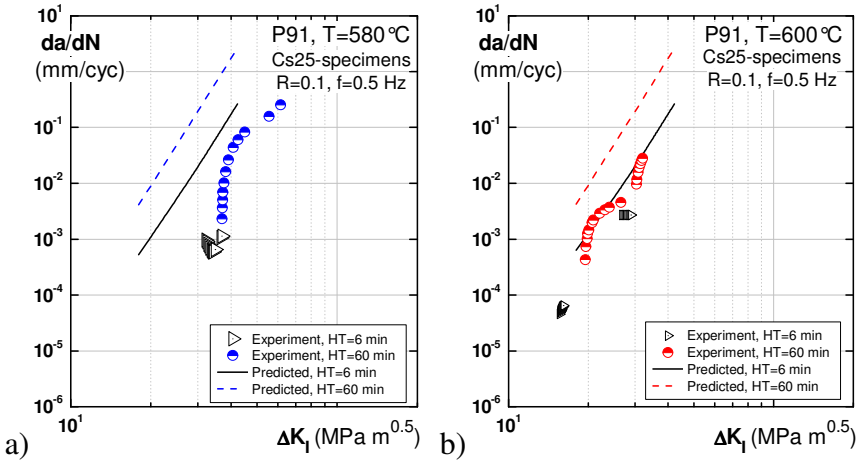

Figure 8. Creep-fatigue crack growth rate over ΔK_I for Cs25-specimens at a) T=580°C, b) T=600°C

Another commonly used approach based also on simple linear superposition of creep crack growth and fatigue crack growth is the model applying the fracture mechanics parameters ΔK for fatigue load and K for creep load [7]:

$$\frac{da}{dN}_{CFCG} = \frac{da}{dN}_{FCG} + \frac{1}{f} \cdot \frac{da}{dt}_{CCG} = C_0 (\Delta K)^{n0} + C_2 K^m \cdot t_h \qquad (11)$$

The results of the evaluation by this rule are shown in Fig. 9. It can be seen that this approach describes the behaviour under creep-fatigue loading much better, although the material is creep-ductile. At 580°C and the hold time of 6 min the influence of the fatigue proportion on the

crack growth can be recognize. For a holdtime of 60 min it is obviously that the behaviour is time dependent. At 600°C and both holding times, it is apparent that the rule describes the crack growth behaviour of creep-fatigue specimens quite well. Fig. 9e shows the dependence on the crack growth rate at 600°C on the holding time for a constant value of ΔK=27.2 MPam$^{0.5}$. In this case, the cycle/time dependent transition for this material can be expected at holding times greater than 0.1 minutes.

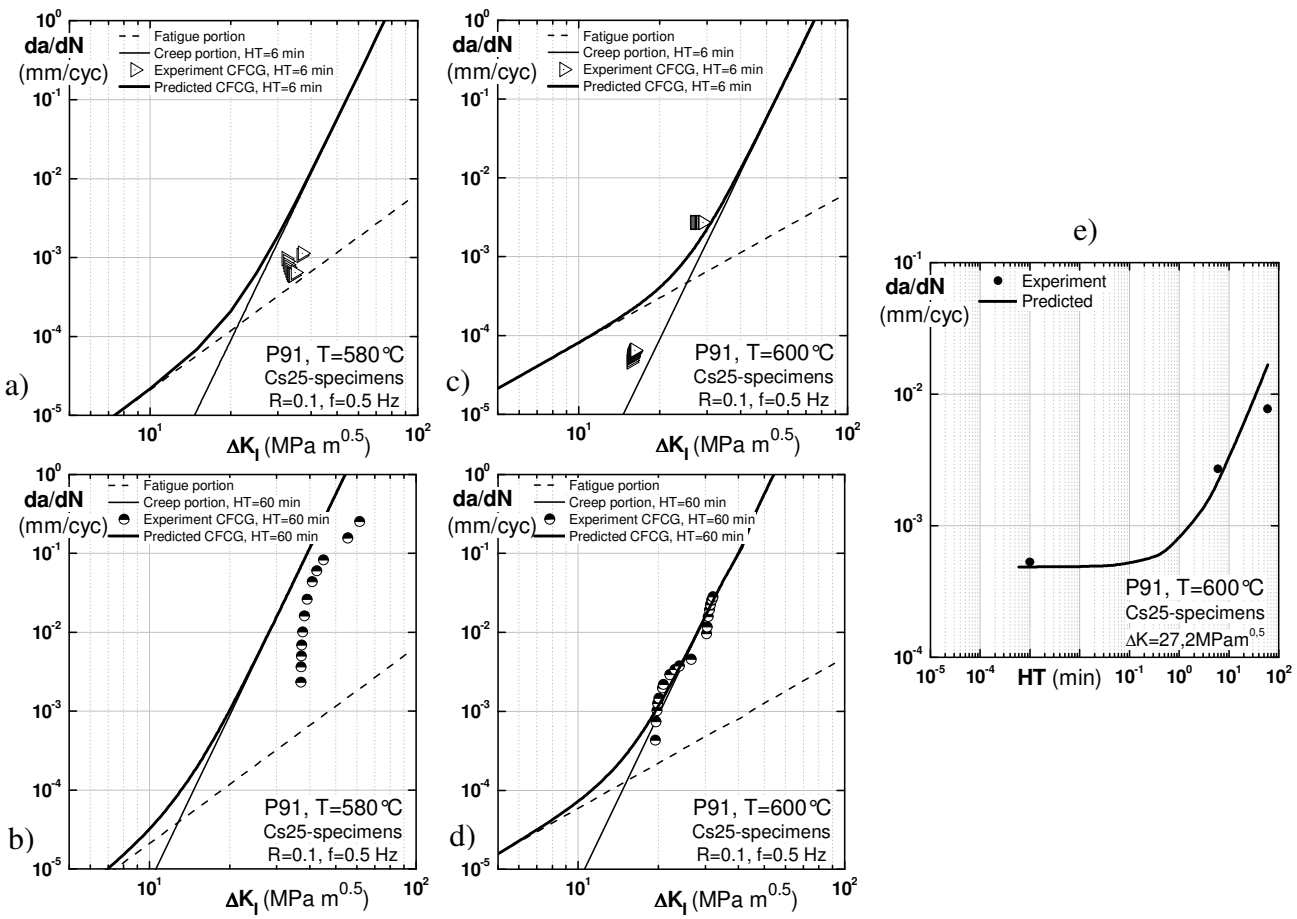

Figure 9. Creep-fatigue crack growth rate over ΔK_I for Cs25-specimens at a)&b)T=580°C, c)&d) T=600°C, e) Creep-fatigue crack growth rate over holding time for ΔK_I =27.2 MPam$^{0.5}$ at 600°C

4. Summary

The results of investigations on P91-steel show, that the creep crack initiation behaviour can be described by the parameter C* and by the stress intensity factor K_I. Due to the high creep ductility of P91 the C*-parameter is preferable. An effect of holding time (HT) on the creep crack initiation time is observed, whereby the influence of 6 min HT for both test temperatures is greatest. If the holding time is 60 min the difference between the creep crack growth test and creep-fatigue crack growth test is small, especially at 600°C. At 580°C the influence of short and long holding time on the crack initiation time for two creep-fatigue experiments is comparable. This means that a reduction in time is expected due to the cyclic stress for the crack initiation in the investigated range.

The crack propagation behaviour of P91-steel under creep conditions can be described both by the parameter C* and the stress intensity factor K_I. The Paris-law describes fatigue crack propagation. An influence of the temperature on crack propagation under fatigue loading can be observed, crack growth rate increases with increasing temperature. By comparing CFCG- and CCG-experimental

results, it can be noticed that specimens with a hold time of 6 min and 60 min have similar crack growth rate as samples without holding time, regardless of which of the two parameters describing the crack behaviour is used. Contrary to the influence of hold time on crack initiation almost no influence is observed on crack propagation. Hence, cyclic loading has only an influence on the crack behaviour in the initial phase. In the holding period creep loading is dominant.
Metallographic analyses show that the crack propagates inter-granularly under creep load and a large amount of cavities are found on the prior austenite grain boundaries near to the crack tip. Under fatigue loading trans-granular cracks without cavities were observed. For the samples tested under creep-fatigue loading the crack behaviour was found to be independent of the holding time. Around the crack tip an area of high cavity density was identified and the crack path under creep-fatigue loading is comparable to the crack path under creep condition.
The crack propagation under creep-fatigue loading is influenced by two failure mechanisms, and therefore depends on the load level, the mean stress and the temperature. With decreasing frequency the mechanisms changes from cycle dependent at high frequencies to time dependent at lower frequencies. In literature, different relationships exist to describe the crack growth under creep-fatigue loading, which were investigated in this study. It has been shown that the accumulation rule based on stress intensity parameter K_I better describes the crack growth behaviour of P91 under creep-fatigue loading. If the creep portion is described by parameter C*, the crack growth behaviour is overestimated. This may be the effect of the relatively large scatter of experiments data, or may result from uncertainties in the determination of C*.

Acknowledgements

The authors gratefully acknowledge the financial support provided by EPRI, Charlotte, USA.

References

[1] DIN EN10216: 09 Seamless steel tubes for pressure purposes - Technical delivery conditions - Part 1: Non-alloy steel tubes with specified room temperature properties; German version prEN 10216-1:2009.
[2] H. Theofel, K. Maile, Untersuchung einer artgleichen Schweißverbindung für 9%Cr1%Mo-Stähle unter besonderer Berücksichtigung des Langzeitkriechverhaltens, AiF Report Nr. 9300, 1997.
[3] ASTM E 1457-07, Standard Test Method for Measurement of Creep Crack Growth Rates in Metals, 2007.
[4] ASTM E 2760-10, Standard Test Method for Creep-Fatigue Crack Growth Testing, 2010.
[4] H. Riedel, Fracture at High Temperatures, Springer-Verlag, 1987.
[6] P.C. Paris, M.P. Gomez, W.E. Anderson, A Rational Analytic Theory of Fatigue, The Trend in Engineering, 13 (1961) 9-14.
[7] C. Berger, E. Roos, et al., Rissverhalten typischer warmfester Kraftwerksbaustähle im Kriechermüdungsbereich, Final report of AiF-Project Nr. 10395, 1999.
[8] E. Roos, C. Berger et al., Kriech- und Kriechermüdungsrissverhalten moderner Kraftwerkstähle im Langzeitbereich, Final report of AVIF-Project Nr. A178, 2006.
[9] Validation, Expansion and Standardisation of Procedures for High Temperature Defect Assessment (HIDA), Brite/Euram Project: BE1704, Final Report 1999.
[10] M. Pfaffelhuber, M. Rödig, F. Schubert, H. Nickel, Risswachstum unter überlagerter Kriech- und Ermüdungsbelastung in X10NiAlTi 32 20 (Alloy 800), Report of Kernforschungsanlage Jülich Nr. 2303, 1989.
[11] R. Viswanathan, Damage Mechanisms and Life Assessment of High-Temperature Components, AMS International, 1989.
[12] J.M. Larson, Th. Nicholas, Cumulative-Damage Modelling of Fatigue Crack Growth in Turbine Engine Materials, Engineering Fracture Mechanics, 22 (1985) 713-730.

A New Method of Introducing Long Range Residual Stresses to Study Creep Crack Initiation

A. M. Shirahatti*, Y. Wang, C. E. Truman, D. J. Smith

[1] Solid Mechanics Group, Department of Mechanical Engineering
University of Bristol, Bristol BS8 1TR, United Kingdom
* Corresponding author: anil.shirahatti@bristol.ac.uk

Abstract One of the many challenges in the behaviour of structures is to understand if the presence of residual stress plays an important role in contributing to failure of a structure operating at high temperature. A typical example is the reheat cracking, associated with the austenitic stainless steel welded components, where the presence of residual stress is seen as a major factor. A review of previous methods that introduce residual stresses into specimen indicated that a method that doesn't introduce microstructural changes during the generation of residual stresses should be sought. The purpose of this paper is to describe a new method of introducing long range residual stresses at high temperature. The method uses a three bar structure with an initial misfit introduced into the central bar to represent a long range residual stress. The rig was designed so that the induced residual stresses could be characterised easily without using time consuming residual stress measurement techniques. Initial results demonstrated that the magnitude and the interaction of the residual stress with the applied loading is a function of the initial misfit displacements and the relative stiffness of the components of the system. Additionally, the subsequent behaviour of the system, with and without the application of additional loading, is governed by (a) the degree to which the misfit is accommodated by plastic and creep strain and (b) the elastic follow-up provided by the system. The paper describes the design of a test rig and laboratory tests conducted to validate the method.

Keywords Residual stress, Creep, Elastic follow-up, 316H stainless steel

1. Introduction

Residual stress plays an important role in the component life assessment of the structures. Such stresses may arise usually as a consequence of the manufacturing process and final fabrication. Welding is a typical manufacturing process where, unless the component is subjected to post-weld heat treatment, the residual stress can attain a value close to or equal to the yield stress. Fabrication can also lead to additional locked-in stresses developed from the fitting-up of the different parts of an assembly [1]. Residual stresses are usually treated as secondary stresses. However, in certain circumstances they must be classed as primary. For example, in a cracked structure where the fit-up residual stresses do not self-equilibrate across a ligament, the residual stresses may provide a significant contribution to the plastic collapse of the ligament. Whether they do or not depends on how the residual forces change as a crack grows and plastic deformation accumulates in the structure. This in turn depends on the level of elastic follow-up (EFU). A typical practical case where we expect to see the effect of EFU is shown in fig 1 for a pressurized piping system. As shown schematically, the system and its welds can be treated as a series of springs with the pipe having stiffness K1, K3 and the weld with stiffness K2. When the pipe is built-in and welded we would expect that long range residual stresses to be present and are represented as an initial far field displacement X. The pipe will also be subjected to internal pressure and consequently the system is also subjected to external load P. Elastic follow-up is expected when part of a structure (the area around the welds) reduces its stiffness (either through creation of plasticity and/or the growth of crack) relative (i.e. EFU) to the surrounding material. This would result in additional strain accumulation and relaxation of the initial stresses created during the welding and fit-up.

Many methods have been proposed to generate well defined residual stress fields in laboratory test specimens. In the context of investigating the influence of residual stress on creep, the following

methods have been developed: pre-compression [2-6], quenching [7], side punching [8], Borland specimens [9], ring-weld specimens [10] and electron beam (EB) welding [1, 11, 12]. These methods produce either long-range or short-range residual stress fields. Quenching, Borland specimens and ring welding methods result in specimens with a residual stress field throughout the entire volume. On the other hand, side punching, in-plane compression and EB welding methods result in a residual stress field being set up in a very localised part of the specimen. The second group of methods rely on local, rather than global, incompatible displacements to set up the residual stress field.

Another important observation is that the in-plane compression and EB welded specimens require the introduction of a sharp notch by for example electro-discharge machining, prior to creep testing. Introducing such a notch redistributes the residual stresses and so, care must be taken to ensure that the required levels of residual stress remain in the specimen after this redistribution. Consider the in-plane compression method as an example. Here, a volume of material local to the semi-circular stress raiser deforms plastically and this plastic zone resists the relaxation of the surrounding material. If a long notch is introduced such that it extends through the plastic zone and into the surrounding elastic zone then the elastic zone is free to relax and the residual stress field is lost [11].

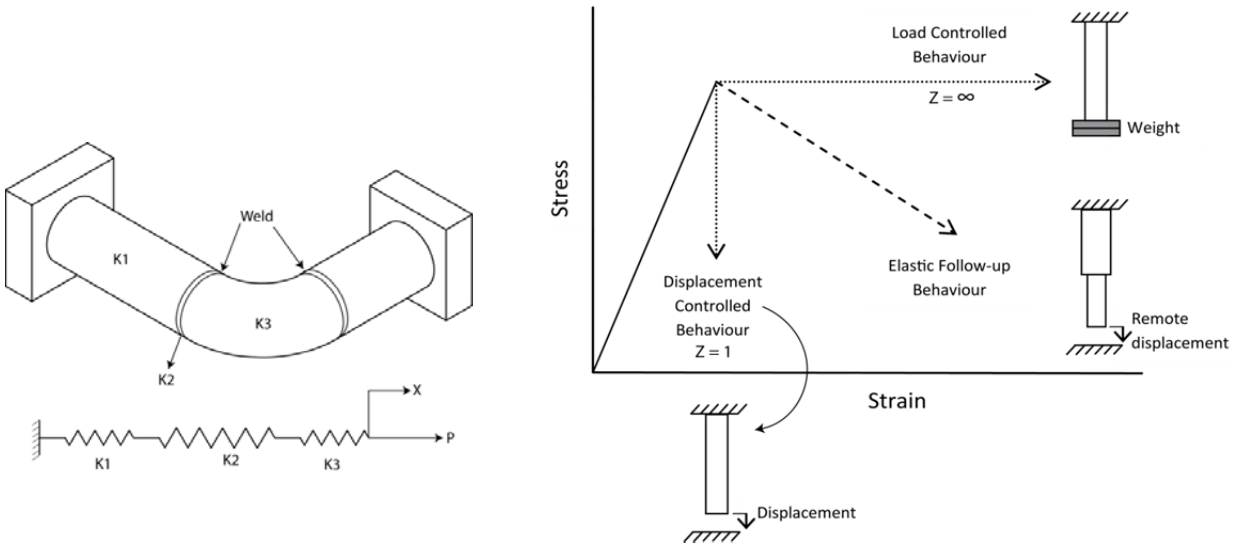

(a) (b)

Figure 1. (a) Built-in welded pipe bend (P is load, X is displacement) (b) Stress-strain behaviour of a local volume

In all the above methods the magnitude and distribution of residual stress are found by time consuming methods i.e. neutron diffraction. Also, in all the cases various and nominally identical specimens are manufactured to determine the stress distribution. For example in case of cylinder quenching by Hossain [7], three specimens were manufactured and the neutron diffraction method was used to measure the stress distribution after quenching, short term ageing (1.25 hrs) and long term ageing (1800 hrs). In all of the above methods, residual stress is introduced at room temperature and when the specimen is subjected to high temperature the magnitude of residual stress is reduced drastically (≈30% reduction) [2-8] due to the lower yield strength at high temperature. In all the cases, the residual stress at high temperature was determined using finite element analysis.

In order to study the effect of residual stress, it is desirable that the method chosen to induce residual stress in the specimen causes no other changes which might influence creep. It is also desirable that residual stress fields set up in the laboratory creep specimens are representative of the long range residual stress fields found in engineering structures.

Of the various methods reviewed only side punching, in-plane compression and EB welding have been used to study the effect of residual stress and applied load on creep under load control conditions. These techniques can also be used to carry out displacement controlled tests. In practical circumstances relaxation of residual stress in one section is compensated by changes in residual stress distribution in other sections to keep the complete structure in equilibrium, i.e. components are often subjected to combined displacement and load controlled situations as shown in fig 1b. It is not possible to study this effect using the reviewed samples and techniques.

A new method is presented that introduces residual stress in a controlled manner such that the stress can be calculated easily at any time and without the use of time consuming residual stress measurement techniques.

2. Three bar structure

The new method is based on a classical three bar model and is developed to introduce long range residual stresses through strain incompatibility. This model (or system) has several key features relevant to the high temperature problems of creep crack initiation and growth. The magnitude and the interaction of the residual stress with the applied loading are a function of the initial misfit displacements and the relative stiffness of the components of the system. The subsequent behaviour of the system, with and without the application of additional loading, is governed (a) by the degree to which the misfit is accommodated by plastic and creep strain and (b) the elastic follow-up provided by the system.

2.1. Model

Figure 2 shows the three bar structure model consisting of two outer bars ‘B’ and a central bar combination of bar ‘A’ and a compact tension, C(T) specimen. The bars A and B are able to deform elastically and have stiffness K_{in} and K_{out} respectively. An initial misfit, ‘X’ exists between the bars so that joining the bars together introduces fit-up residual stresses into the system, with tension in bar A and balancing compression in bar B. The residual force in the middle bar does not self equilibrate across a section but the tensile residual force in middle bar is in equilibrium with the net compressive force in the outer bars. The structure can be subjected to the applied load ‘P’ so that when plasticity, creep or crack growth occurs in the C(T) specimen and the overall EFU factor, Z is given by

$$Z = Z_{eff} Z_s \tag{1}$$

where,
$$Z_{eff} = \left(\frac{1+\alpha_{eff}}{\alpha_{eff}}\right) \text{ and } Z_s = \left(\frac{1+\beta}{\beta}\right)$$

$$\beta = \frac{K_{in}}{K_s}\ , \quad \frac{1}{\mathrm{K_{eff}}} = \frac{1}{\mathrm{K_S}} + \frac{1}{\mathrm{K_{in}}}\ , \quad \alpha_{eff} = \frac{2K_{out}}{K_{eff}} \tag{2}$$

and K_s is the stiffness of the specimen.

A detailed derivation of this is given in [13]. Figure 3 shows the overall elastic follow-up factor as a function of relative effective stiffness ratio. When the elastic follow-up factor is in excess of 6 (or 1/Z=0.167) these conditions essentially correspond to load controlled conditions, where as an elastic follow-up factor of more than 1.25 (or 1/Z=0.8), represents displacement controlled conditions.

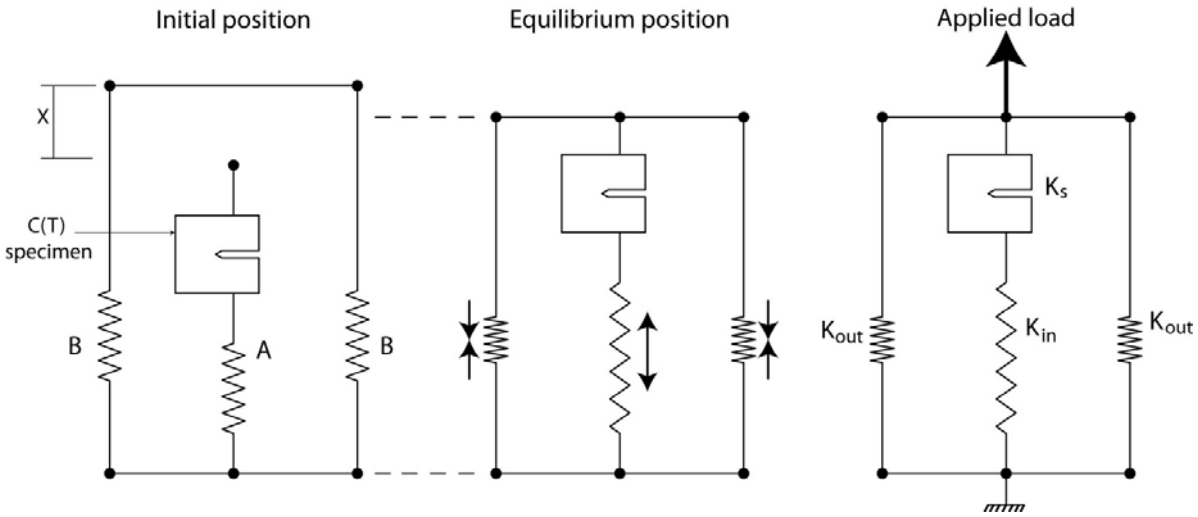

Figure 2. Three bar structure

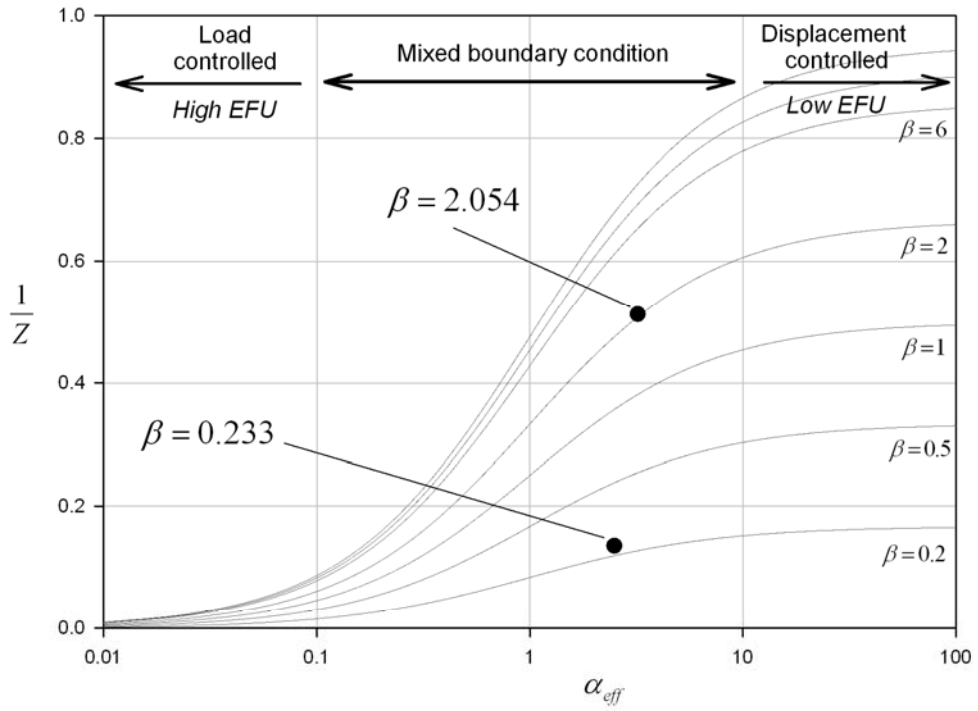

Overall EFU Z	1/Z	β	Diameter of bar (mm)		Overall length (mm)
			Middle	Side	
1.86	0.538	2.054	25.4	19.05	714
6.61	0.151	0.233	10	10	864

Figure 3. Variation of overall EFU with effective stiffness ratio in three bar structure

2.2. Behavior of the structure with applied load

Figure 4 shows loading conditions and relaxation during plasticity for a representative three bar structure. AA' gives the initial misfit, OB and OB' give the residual force in middle and outer bars respectively. When the structure is further subjected to external load, the force in the middle bar increases from B to C. At point C yielding of specimen starts and the specimen takes no further load and follows line CD while outer bar remains in the elastic range and follows path A'D'. Until yielding at point C, the initially induced residual force remains constant in the middle and outer bars and follows paths B-1 and B'1' respectively. As the applied load increases and the amount of plastic deformation in the specimen becomes equal to the initial misfit, the residual force reduces to zero. The rate of residual force relaxation for a mixed boundary condition follows path 1-2. The gradient of relaxation curves (1-3,1-2 or 1-4) depend upon the elastic follow-up factor. Structures having high EFU will follow path 1-4 while low EFU structures will follow path 1-3. Hence, the influence of initial residual stress present in a structure is dependent on the associated level of EFU.

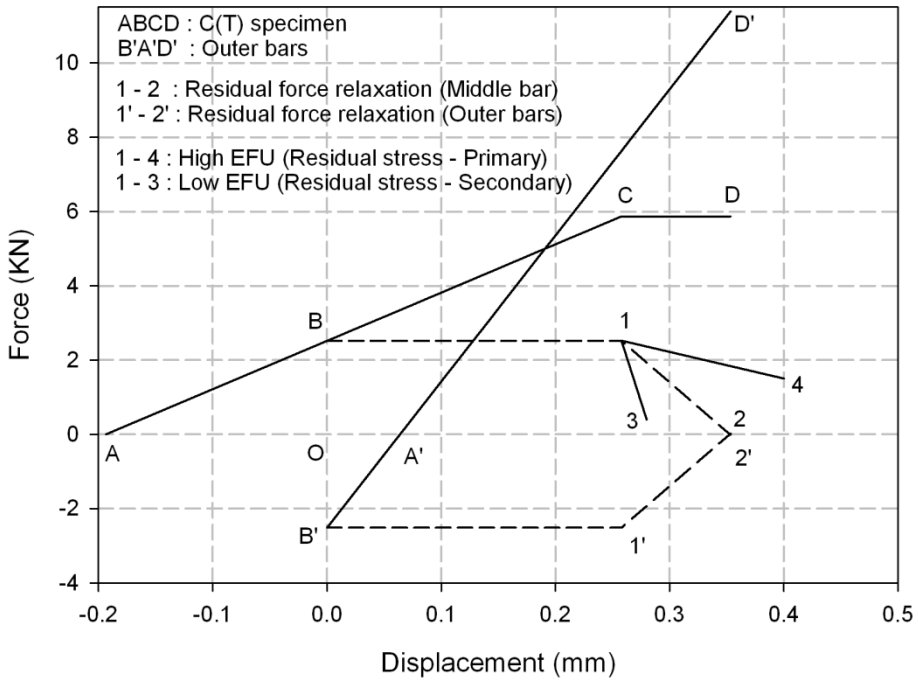

Figure 4. Loading and subsequent relaxation of a three bar

3. Experimental studies

3.1. Design of test rig

An experimental three bar test rig was designed based on the conceptual model discussed in the earlier section. Since the design was centered around a conventional cylindrical furnace with a maximum internal diameter of 130 mm for a creep test frame, the design was constrained to the available maximum diameter of the furnace, the overall length of the structure (1000 mm), the ease of assembly, the ability to introduce known residual stress at high temperature and then to apply a predetermined load to the assembly. The overall arrangement of the test rig is shown in fig 5 and the material properties of the components for the test rig are tabulated in table 1. The middle bar was a combination of 316H stainless steel C(T) specimen and a Nimonic bar of diameter 25.4 mm while the side bars were Nimonic bars of diameter 19.05 mm. These dimensions are selected to provide an EFU value of about 2 (as shown in fig 3). All bars were screwed to a top and bottom end piece

made from EN24T steel. Two linear voltage displacement transducers (LVDT) were mounted on each side of the upper and lower end to measure the total displacement of the structure. Also, two additional LVDTs were connected to the C(T) specimen to measure load line displacement. Four high temperature strain gauges (ZFLA-3-11) were mounted on the middle and side bars at 90^0 intervals to measure the residual force. In total seven thermocouples (3-specimen, 1-room, 3-strain gauge) were connected to measure the specimen temperature, room temperature and temperature at the point of application of strain gauges. A direct current potential drop (PD) system was connected to the C(T) specimen to measure crack initiation and growth. The overall arrangement was fitted into a creep test rig so that an external load was applied to the assembly via a lever arm arrangement.

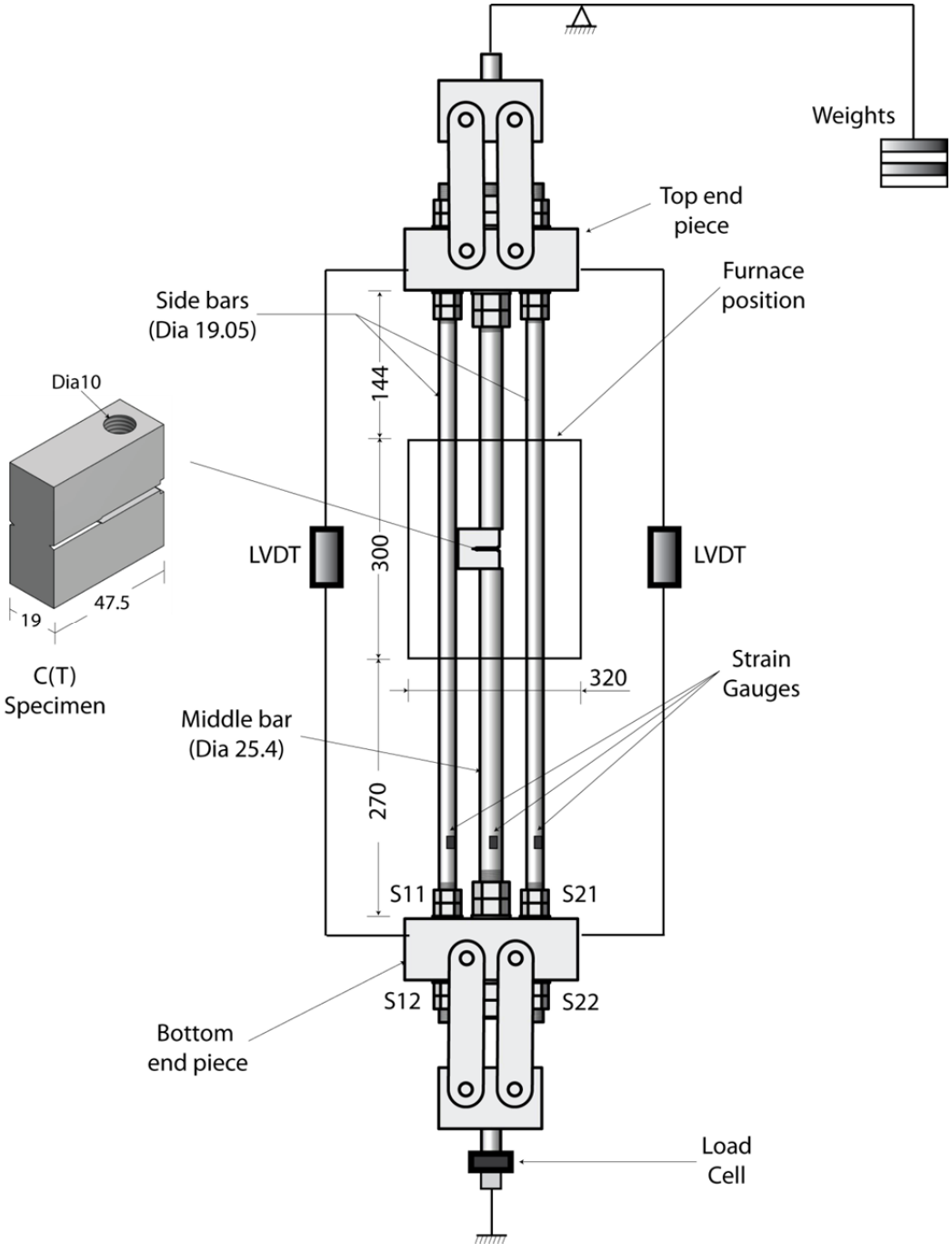

Figure 5. Three bar test rig (All dimensions in mm)

3.2. Calibration tests

A series of calibration tests were conducted and divided into two categories; preliminary tests and an load-unload test. Tests were carried out at high temperature and using a 316H stainless steel C(T) specimen. The C(T) specimen was manufactured as per ASTM 1457 but using a screw fitting arrangement rather than pins to load the specimen. This was adopted to ensure accurate measurement of stiffness rather than conventional pin loading. To restrict the crack growth, a 1 mm diameter hole was introduced at the end of standard 0.1 mm wide EDM notch.

Preliminary tests were conducted to determine the stiffness of bars, specimen and determine the overall elastic follow-up value for the rig experimentally. Two applied load tests, within the elastic region, were conducted such that in each case the temperature of the C(T) specimen was maintained at 550^0C. In the first test only the middle bar with the C(T) specimen was connected to both end pieces. In the second test both the side bars are connected to the top and bottom end bars but the middle bar with C(T) specimen was connected only to the top end piece such that it was free to move (i.e. used to record the C(T) specimen temperature). In each case, the load cell, the temperature at different locations, strain gauge, total displacement and CMOD were measured. The results from these tests are discussed later.

The second category of test was a load-unload test undertaken to understand the relaxation of residual force with applied load. First, a residual stress was introduced into the structure. The middle bar with the C(T) specimen was connected to both end pieces. Side bars were connected to only the top end piece and were free to move through the clearance holes in the bottom end piece. All instruments were then connected to the test rig and the furnace was heated to achieve 550 ^{0}C for the C(T) specimen. This arrangement permitted free thermal expansion of the bars and the specimen. When a stable temperature was achieved, nuts S11 and S21 (shown in fig 5) were screwed down, so that the top and bottom end pieces were forced apart. This resulted in the middle bar loaded in tension and the side bars carried the balancing compressive forces. The force in each bar was determined via the strain gauges. Finally when the desired residual force was introduced into the structure, nuts S12 and S22 on side bars were fixed. Having introduced the desired residual stress into the C(T) specimen, the entire assembly was repeatedly loaded and unloaded to progressively higher load levels. The residual force in all three bars, load line displacement of C(T) specimen, potential drop readings and overall extension of the rig were recorded for both load and unload path.

Table 1. Properties of materials for three bar structure

Material	Young's Modulus (GPa)	Yield Strength (MPa)	Tensile Strength (MPa)
316H stainless steel at 550^0C	151	172	444
Nimonic 80A at 550^0C	187	875	1210
EN24T Steel at room temperature	210	680	925

Table 2. Comparison of theoretical and experimental values

	K_s N/mm	K_{in} N/mm	K_{out} N/mm	K_{eff} N/mm	B	α_{eff}	Z_s	Z_{eff}	Z
Theoretical	69696	155047	85139	48083	2.23	3.54	1.45	1.28	1.86
Experimental	75781	155647	81761	50967	2.05	3.21	1.48	1.31	1.95

4. Results and discussion

The theoretical value of the overall elastic follow-up of the rig was calculated using the equations provided in [13]. Results from the preliminary tests consisted of measured strains, applied load, CMOD, overall displacement of the rig, accurate measurement of the diameters and length of the bars. The initial tensile tests measured the stiffness for each element of the assembly. Table 2 compares the experimental values obtained from preliminary test with theoretical values. It is evident from the results that a good agreement was found.

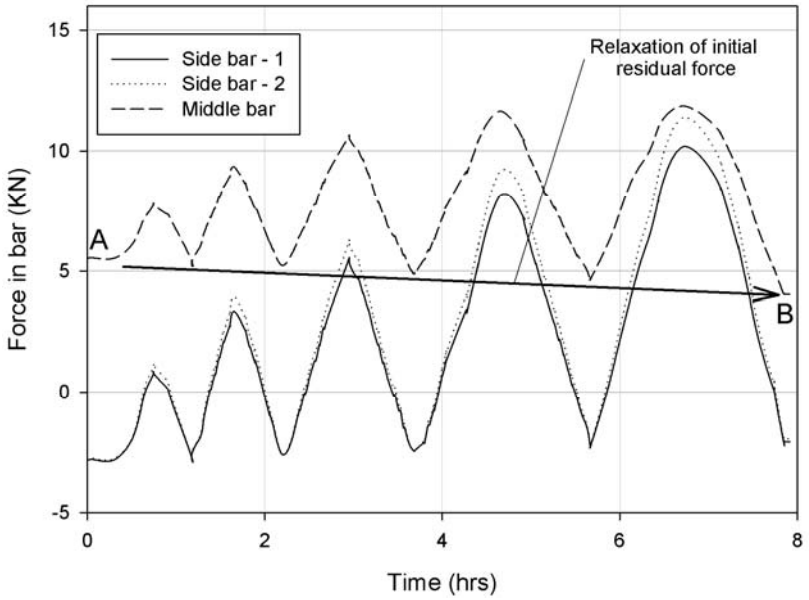

Figure 6. Variation of force in all bars with time

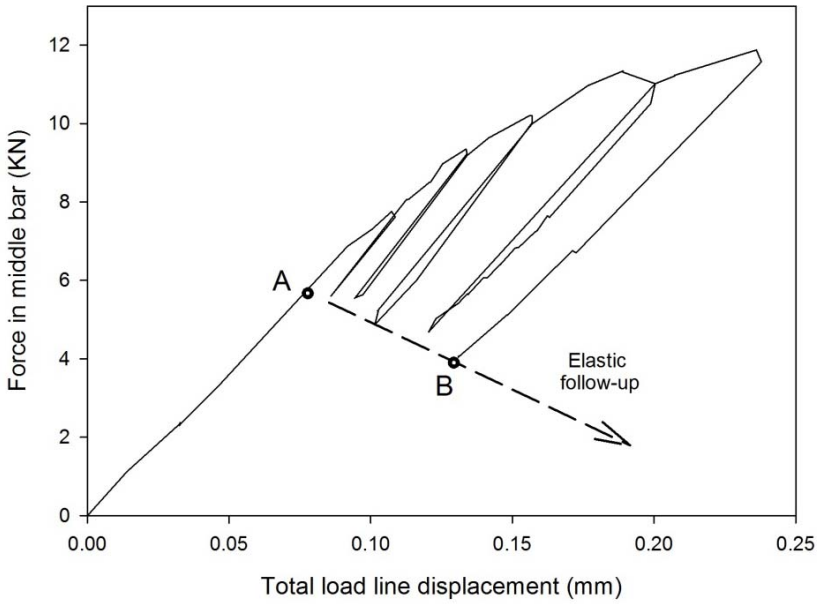

Figure 7. Load versus total load line displacement for C(T) specimen

The test results from the second category of tests are shown in fig 6, and give the details of variation of the residual force and its relaxation as the applied load increased. It is observed that under equilibrium condition, the total compressive residual force in the side bars was approximately equal

to the tensile residual force in middle bar. During the cyclic loading process, the tensile residual force in middle bar relaxed from 5.65 KN to 3.8 KN while the compressive residual force in the side bars relaxed from 2.8 KN and 1.9 KN.

Figure 7 shows the load acting on C(T) specimen against total load line displacement measured during the cyclic loading phase of the test. The following points should be noted. First at point 'A' the C(T) specimen was subjected to a tensile load of 5.65 KN while the total load applied to the assembly was zero. This tensile load corresponds to the initial level of preload in the assembly at the start of the cyclic loading phase of the test.

Second, five unloading lines did not return to the CMOD point 'A' from which the test started. This was due to the accumulation of plastic deformation in the specimen. It can be seen that about 0.06 mm of plastic CMOD had accumulated at the final unloading step. Also, the gradient of each of the unloading lines remained constant. This shows there has been no crack growth during cyclic loading and the same was recorded by PD system.

Third, the line AB corresponds to the locus of unloaded points and reveals that the initial preload relaxed, as plastic deformation accumulated in the specimen thereby reducing the misfit. At point B, with an applied load of zero, the 3.8 KN load on the C(T) specimen corresponds to the level of preload remaining in the assembly i.e. 33% reduction in the initial preload level. An important feature of the behaviour of this assembly is that the relaxation line AB has a slope dependent on the relative stiffness of the assembly and in turn corresponded to the EFU associated with the structure. To achieve different values of EFU, different combinations of diameters of the middle and the side bars can be used. For example, in the present rig if the dimensions are changed so that the middle and side bars diameter is 10 mm and overall height is 864 mm, one can achieve overall EFU of 6.61 (1/Z=0.151) as shown in fig 3.

5. Concluding remarks

Four methods of inducing residual stress in laboratory creep specimens were reviewed. These include quenching, side punching, in-plane compression and welding methods. It was found that the ability of these methods to provide insight into the effect of residual stress on creep in engineering structures is limited. These methods cause micro-structural changes to the material as well as inducing residual stress. Also, the short-range residual stresses produced by some of the methods do not accurately represent the long-range residual stresses found in many engineering structures. In each of these methods residual stress measured at room temperature before the start of test will change when the specimen is subjected to high temperature. None of the methods determine the effect of residual stress on creep and complete structure when the residual stress relaxes. We therefore conclude that new methods which can induce long-range residual stress without causing micro-structural change in the material and can represent combine boundary condition are required.

A new method based on a three bar structure illustrated that residual stresses can be induced into a specimen at high temperature in a controlled manner and can be characterised easily without the use of time consuming measurement techniques. The proposed method does not cause any micro-structural change in the specimen and provides details of residual stresses distribution in complete structure at any time. Calibration tests revealed that the structure replicates mixed boundary conditions. Different combinations of diameters of the middle and side bars can be used to achieve different elastic follow-up factors and can therefore study the influence of EFU on initial residual stress and structure as a whole. The new method and the test rig designed can be used for both cracked and uncracked specimens to carry out short and long term creep tests.

Acknowledgements

The authors gratefully acknowledge EDF Energy Limited for providing financial support for this work.

References

[1] P. Kapadia, C. M. Davies, D. W. Dean, and K. M. Nikbin, Numerical simulation of residual stresses induced in compact tension specimens using electron beam welding, in Proceedings of the ASME 2012 Pressure Vessels & Piping Conference, July 15-19, 2012, Toronto, Ontario, Canada.

[2] M. Turski, High temperature creep cavitation cracking under the action of residual stress in 316H stainless steel. PhD thesis, University of Manchester, UK, 2004.

[3] N. P. ODowd, K. M. Nikbin, R. C. Wimpory, F. R. Biglari, and M. P. ODonnell, Computational and experimental studies of high temperature crack initiation in the presence of residual stress, Journal of Pressure Vessel of Technology, vol. 130, pp. 0414031–0414037, 2008.

[4] N. P. ODowd, K. M. Nikbin, R. C. Wimpory, and F. R. Biglari, Creep crack initiation in a weld steels: Effects of residual stress, in Proceedings of Pressure Vessels & Piping Conference, PVP2005, July 17-21, 2005, Denver, Colorado USA.

[5] S. Kamel, C. Davies, H. Lee, and K. Nikbin, Effect of crack extension in a compact tension C(t) specimen containing a residual stress on the stress intensity factors, in Proceedings of the ASME 2010 Pressure Vessels & Piping Conference, PVP2010, July 18-22, 2010, Bellevue, Washington, USA.

[6] H. Y. Nezhad, N. P. ODowd, C. M. Davies, K. M. Nikbin, and R. C. Wimpory, Study of creep relaxation behaviour of 316h austenitic steels under mechanically induced residual stress, in Proceedings of the ASME 2011 Pressure Vessels & Piping Conference, PVP2011, July 17-21, 2011, Baltimore, Maryland, USA.

[7] S. Hossain, Residual stresses under conditions of high triaxiality. PhD thesis, University of Bristol, UK, 2005.

[8] S. Hossain, C. E. Truman, and D. J. Smith, Generation of residual stress and plastic strain in a fracture mechanics specimen to study the formation of creep damage in type 316 stainless steel, Fatigue & Fracture of Engineering Materials & Structures, vol. 34, pp. 654–666, 2011.

[9] M. W. Spindler, The use of borland specimens to reproduce reheat cracking in type 316H, Tech. rep., British Energy Generation Ltd., Report No. EPD/AGR/REP/0618/99 Issue 1, Feb 2000.

[10] R. J. Dennis, Detailed analysis of ring-weld creep test specimen, Tech. rep., British Energy Generation Ltd., Report No. BBGB/007/01 Issue 1, Feb 2008.

[11] C. M. Davies, R. C. Wimpory, D. W. Dean, G. Webster, and K. M. Nikbin, Effect of residual stresses on crack growth in 316h steel weldments, 3rd International Conference on Integrity of High Temperature Welds, pp. 333–344, 24-26 April 2007.

[12] C. M. Davies, D. Hughes, R. C. Wimpory, D. W. Dean, and K. M. Nikbin, Measurements of residual stresses in 316 stainless steel weldments, in Proceedings of the ASME 2010 Pressure Vessels & Piping Conference, PVP2010, July 18-22, 2010, Bellevue, Washington, USA.

[13] D. J. Smith, J. McFadden, S. Hadidimoud, A. J. Smith, A. J. Stormonth Darling, and A. A. Aziz, Elastic follow-up and relaxation of residual stresses, Proceedings of the Institution of Mechanical Engineers Part C: Journal of Mechanical Engineering Science, vol. 224, pp. 777–787, 2010.

PREDICTION OF CREEP CRACK INITIATION UNDER THE INTERACTION BETWEEN LONG RANGE RESIDUAL STRESS AND APPLIED LOAD

Yiqiang Wang[1,*], David J Smith[1], Christopher E Truman[1], A. M. Shirahatti[1]

[1] Department of Mechanical Engineering, University of Bristol, BS8 1TR, UK
* Corresponding author: yw9146@bristol.ac.uk

Abstract In this paper, a three bar structure is examined to simulate the behaviour of a component subjected to combined applied and residual stresses. This structure (or system) permits long-range residual stress to be created in a compact tension (CT) specimen through the introduction of a misfit. The magnitudes of the residual and applied stresses in the CT specimen are a function of the initial misfit displacements, applied load and the relative stiffness of the components of the system. The prediction of cracking initiation under combinations of residual and apply loads are investigated when the compact tension specimen creep according to a power law. We find that the creep crack initiation time is sensitive to the assumed creep constants and is significantly different under different loading conditions. The effect of residual stress on the crack initiation time is dependent on the ratio of the residual stress to the total stress. Overall, this study provides important insights into the assumptions adopted in structural analysis for creep crack initiation.

Keywords Crack initiation, Residual stress , elastic follow-up, 316H stainless steel

1. Introduction

Many components operating at high temperature are subjected to combinations of applied and residual stresses, especially welded steel sections. Evidence from industry is that the presence of residual stress is a contributing factor for initiation and growth of creep cracks, which has important consequences for the lifetime of components at high temperature. A typical practical example is reheat crack initiation observed in stainless steel welded components where the presence of residual stress is seen as a major factor [1]. In this paper, the purpose is to better understand whether the existence of residual stress plays an important role in contributing the crack initiation in components driven by a combination of applied and residual stress at elevated temperature. Previous work involved generating residual stresses directly into specimens using a variety of methods. A recent review of this work [2] concluded that in order to improve our understanding of the effects of residual stress on fracture new methods should be sought that do not introduce microstructural changes during the generation of residual stress. Therefore, in this paper we develop a simple method of introducing long range residual stress through strain incompatibility in a classical three bar model. An additional force can applied to the three bar structure system to simulate the behaviour of a component subjected to combined applied and residual stresses. The subsequent creep behaviour is governed by the materials properties and elastic follow-up provided by the system. Elastic follow-up is a consequence of the presence of a region of differing stiffness relative to the remainder of the structure. [3].

In parallel to a series of laboratory tests [4], an analysis is presented to predict creep crack initiation for different levels of elastic follow-up. We find is that the crack initiation time is sensitive to the assumed creep constants and is significantly different under different loading conditions. The effect of residual stress on the crack initiation time is dependent on ratio of the residual stress to the total stress. Overall, this study provides important insights into the assumptions adopted in structural analysis for creep crack initiation.

2. Response of the three bar system

In this analysis, the response of the three bar system will be determined for a system containing an initial misfit, (state 0). The system consists of 2 outer bars (Bar 3) and an inner bar (Bar 2) connected in series to a CT specimen. A long range residual stress is introduced in state 1. State 2 corresponds to the system subjected to external loading as shown in Fig. 1.

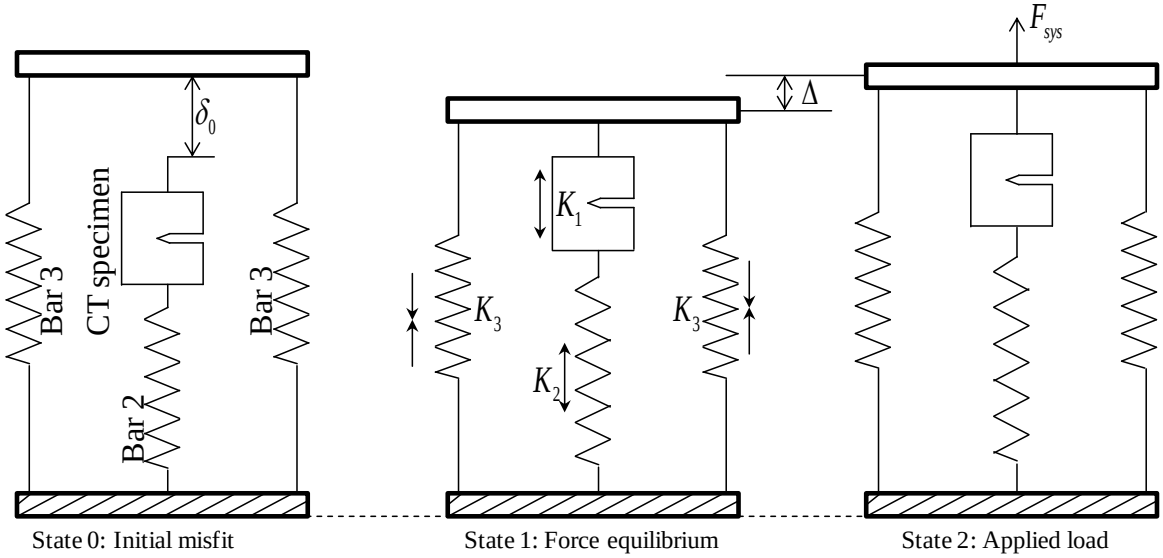

Figure 1. Parallel bars with an initial misfit subjected to an applied load.

In state 1, an initial residual stress field is introduced into system through the introduction of an incompatibility misfit. The displacements in the bars due to the misfit are:

$$\delta_1 = \left[\gamma/\left(\alpha_{eff}+1\right)\right]\delta_0 \qquad \delta_1+\delta_2 = \left[\alpha_{eff}/\left(\alpha_{eff}+1\right)\right] \qquad \delta_3 = -\left[1/\left(\alpha_{eff}+1\right)\right]\delta_0 \tag{1}$$

where δ_0 is the initial misfit, δ_1, δ_2 and δ_3 are the displacements in the CT specimen, and bars 2 and 3 respectively, K_1, K_2 and K_3 are the stiffness for the CT specimen, and bars 2 and 3 respectively. Various ratios for the stiffness of the components are given by

$$\beta = K_2/K_1 \qquad \gamma = 2K_3/K_1 \qquad \alpha_{eff} = 2K_3/K_{eff} \qquad 1/K_{eff} = 1/K_1 + 1/K_2 \tag{2}$$

The structure is then loaded through a rigid block (state 2) such that the displacement Δ for the whole system is given by:

$$\Delta = F_{Sys}/\left(K_{eff}+2K_3\right) \tag{3}$$

and the displacements in the bars are given by

$$\delta_1 = \left(\frac{\gamma}{\alpha_{eff}+1}\right)\delta_0 + \left(\frac{\beta}{\beta+1}\right)\Delta \qquad \delta_2 = \left(\frac{\alpha_{eff}}{\alpha_{eff}+1}\right)\delta_0 + \left(\frac{1}{\beta+1}\right)\Delta \qquad \delta_3 = -\left(\frac{1}{\alpha_{eff}+1}\right)\delta_0 + \Delta \tag{4}$$

The presence of elastic follow-up in the system results in a slower stress relaxation rate when compared to classical stress relaxation. There is also additional strain accumulation in the CT specimen. As an approximation, the creep strains accumulated in the CT specimen are considered to be a scalar factor Z times the creep strain which would be accumulated in the corresponding laboratory relaxation test (at the same initial stress, dwell time and temperature). Z is called the elastic follow-up factor and is given by [5].

$$Z = \left(\Delta\varepsilon_{\text{inc}} + \Delta\varepsilon_{\text{el}}\right)/\Delta\varepsilon_{\text{el}} \qquad \text{where} \qquad \Delta\varepsilon_{\text{el}} = \Delta\sigma_{ref}^{Total}/E_1 = \Delta F_1/L_{ref}K_1 \tag{5}$$

where $\Delta\varepsilon_{inc}$ is the incremental strain accumulation in specimen during creep stress relaxation; and $\Delta\sigma_{\text{ref}}^{\text{Total}}$ is the change of total reference stress on the CT specimen; ΔF_1 is the change in load on the CT specimen and L_{ref} is the reference length of the CT specimen.

For state 1 the incremental strain accumulation is given by

$$\Delta\varepsilon_{\text{inc}}^{\text{state-1}} = \left[\Delta F_1/2K_3 + \Delta F_1/K_2\right]/L_1 \tag{6}$$

In state 2, the strain accumulation in specimen has two different solutions. The first solution corresponds to the total reference stress on the CT specimen at any time being greater than the initial residual stress

$$\sigma_{ref-t}^{Total} \geq \sigma_{ref-0}^{Rs}, \text{ and } \Delta\varepsilon_{\text{inc}}^{\text{state-2}} = \Delta\varepsilon_{\text{inc}}^{\text{state-1}}; \tag{7}$$

The second solution corresponds to when the total reference stress at a given time is less than the initial reference stress from the residual stress, ie:

$$\sigma_{ref-t}^{Total} < \sigma_{ref-0}^{Rs} \qquad \Delta\varepsilon_{\text{inc}}^{\text{state-2}} = \left[\Delta F_1/\left(2K_3 + K_{eff}\right)\right]/L_1 \tag{8}$$

Combining Eqs. 5-8, the solutions for Z are as follows

State 1 :

$$Z_1 = 1 + 1/\gamma + 1/\beta = \left[\left(1+\alpha_{eff}\right)/\alpha_{eff}\right]\left[\left(1+\beta\right)/\beta\right] \tag{9}$$

State 2:

$$\sigma_{ref-t}^{Total} \geq \sigma_{ref-0}^{Rs} \qquad Z_2 = Z_1 \tag{10a}$$

$$\sigma_{ref-t}^{Total} < \sigma_{ref-0}^{Rs} \qquad Z_2 = 1 + \left[1/\left(\gamma + \beta/\left(\beta+1\right)\right)\right] \tag{10b}$$

Equations 9 and 10 show that Z for states 1 and 2 are the same if the current total reference stresses in the CT specimen is larger than the initial reference residual stress. When the current total reference stress is smaller than the initial reference residual stress, a new solution for Z for state 2 is given by Eq. 10. Those results are based on the assumption that only the CT specimen creeps while the reminder of the structure remains elastic. Z_1, Eq. 9, is independent of the initial stress and the creep deformation behavior of the CT specimen, i.e., Z is a constant geometrical value

dependent on the stiffness of the system. However, Z_2 is influenced by the stress in the CT specimen.

3. Creep of a three bar system

We now consider the behavior of states 1 and 2 with the aim of determining how the stress relaxes in the three bar system due to creep. The stress-strain and creep properties of the materials are required and hence the first part of this section presents relevant material properties for a Type 316H stainless steel. The solution for the stress relaxation of states 1 and 2 are given in the second part of this section.

3.1 Creep rupture and creep crack growth properties

Tensile, steady state creep rate and creep crack initiation properties of Type 316H Austenitic stainless steel at 550 ℃ are summarized in Table. 1. Tensile properties of Type 316H Austenitic stainless steel were measured at a strain rate of 1.5% per min [6]. The relevant creep data are taken from Douglas [7] and fitted using a simple power law as shown in Fig. 2a. The steady state creep rate is given by

$$\dot{\varepsilon} = D\sigma^m \tag{11}$$

where $\dot{\varepsilon}$ is the creep rate in $1/\mathrm{h}$, σ is the applied stress in MPa and D and m are material constants. A regression fit to data shown in Fig 2a provided values for the constants D and m. Values are shown in Table 1 for mean, upper and lower bound fits. The upper (UB) and lower bound (LB) curves correspond to ± 1 standard deviations on the mean, assuming the slope is constant.

Seven creep crack tests using CT specimens were completed with test times ranging from about 60 to 16600hrs [8, 9]. The relationship between the applied reference stresses and time t_i (h) to initiate a crack equal to 0.2mm is shown in Fig. 2b. The initiation time t_i is given by

$$t_i = C\sigma_{ref}{}^f \tag{12}$$

where σ_{ref} is the plane stress reference stress in MPa for pre-cracked CT specimens, and C and f are the corresponding material constants. A regression fit to data shown in Fig. 2b provided values for the constants C and f. These are shown in Table 1.

Table 1. Tensile, steady state creep rate and time corresponding to crack extension of 0.2mm properties of Type 316H Austenitic stainless steel at 550 ℃ [6].

Material properties (MPa)	Steady state creep rate properties	Creep crack initiation properties
Young's Modulus: 160000	n: 10.154	f: -5.45
Yield stress: 145	D: $10^{-29.54}$	C: 5×10^{15}
0.2% proof stress: 194	Upper bound (UB) and lower bound (LB) factor on D: 2.72	
UTS: 648		

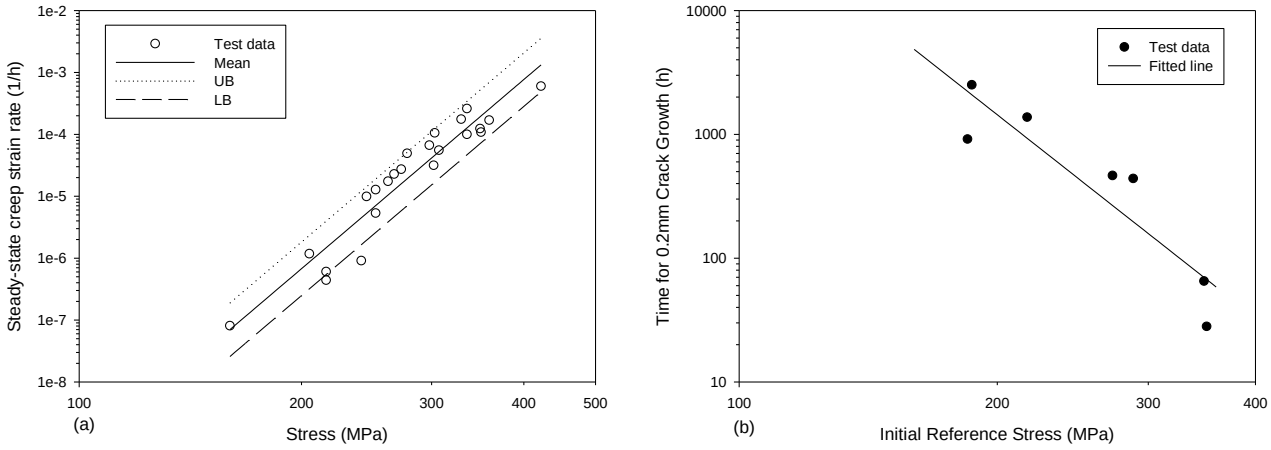

Figure 2. Material properties of Type 316H Austenitic stainless steel at 550 ℃ (a) Minimum creep strain rate, illustrating the mean, upper and lower bound regression fits ; (b) Time to crack initiation with respect to the reference stress.

3.2. Determination of stress relaxation in the three bar system

In order to simplify the analysis, the following three assumptions were made. a) The misfit and the applied load may be sufficient to cause plasticity in the CT specimen, but the surrounding structure remained elastic. The CT specimen was always at the creep temperature and creep only occurred in the specimen. b) For state 2, the applied force on the assembly was constant during the test period. Finally, c) the forces between the specimen and the elastic elements were always in equilibrium.

3.2.1 Relaxation of residual stress alone

Stress relaxation is a reduction of stresses with time due to the conversion of elastic strain to inelastic strain under constant total strain. For a material that follows a power creep law the reference strain rate in CT specimen can be expressed in terms of a reference stress, where

$$\dot{\varepsilon}_{ref} = D\sigma_{ref}^{\ n} \tag{13}$$

In a CT specimen the relationship between force, displacement, reference stress and strain, and stress intensity factor are given by [10]

$$\sigma_{ref} = F_1/B_n W m_L \qquad \varepsilon_{ref} = \delta/L_{ref} \qquad L_{ref} = E_1 B_n W m_L/K_1 \qquad F_1 = K_1\delta \qquad K_1 = BE_1/f(\alpha/W) \tag{14}$$

$$\text{where} \quad f(\alpha/W) = \left(\frac{1+\alpha/W}{1-\alpha/W}\right)^2 \left[\begin{array}{l} 2.163+12.219(\alpha/W)-20.065(\alpha/W)^2 \\ -0.9925(\alpha/W)^3+20.609(\alpha/W)^4-9.9314(\alpha/W)^5 \end{array}\right] \tag{15}$$

$$\text{and} \quad m_L = \sqrt{(1+\varphi)(1+\varphi(\alpha_0/w)^2)} - (1+\varphi(\alpha_0/w)) \qquad 0 \le \alpha_0/W \le 1 \tag{16}$$

where σ_{ref} is the plane stress reference stress, ε_{ref} L_{ref} are the reference strain and length respectively of a CT specimen, E_1 is the elastic modulus, δ is the load line displacement; a_0, B_n

and W are the initial crack depth, width, net thickness of a CT specimen respectively. The constant m_L given by Eq. 16 is for plane stress and a von-Mises yield criterion with $\varphi = 2/\sqrt{3}$. It can be shown that the change in reference stress with time for the three bar system in state 1 is given by

$$\tau^{Rs} = \left[1 \Big/ \left(1 + (1/Z_1)\, AE_1 (n-1) \left(\sigma_{ref-0}^{Rs}\right)^{n-1} t\right)\right]^{1/n-1} \qquad \text{where} \quad \tau^{Rs} = \sigma_{ref-t}^{Rs} \Big/ \sigma_{ref-0}^{Rs} \tag{17}$$

where σ_{ref-t}^{Rs} and σ_{ref-0}^{Rs} are the current and initial reference residual stresses respectively in the CT specimen.

For a time much greater than

$$t \gg 1 \Big/ (1/Z)\, AE_1 (n-1) \left(\sigma_{ref-0}^{Rs}\right)^{n-1} \tag{18}$$

Equation 17 is approximately independent of the initial reference stress. The influence of the magnitude of initial reference stress is greatest during the early stages of the relaxation process.

As an example; take an initial residual reference stress of 200MPa. Using equation 17 together with creep behavior described by equation 13, and the material constants in Table 1, the predicted residual stress relaxation using mean, upper and lower bound creep constants and different elastic follow-up factors are shown in Fig. 3. The results show that the stress relaxation behavior is sensitive to the creep constants and also significantly affected by the elastic follow-up. For Z=1, there is no strain accumulated in the specimen; therefore the total strain across the entire cross-section of specimen remains zero during the relaxation process. This is equivalent to the stress relaxation in a bolt that holds two rigid flanges together. For Z>1, there is slower stress relaxation and extra strain is accumulated in the CT specimen.

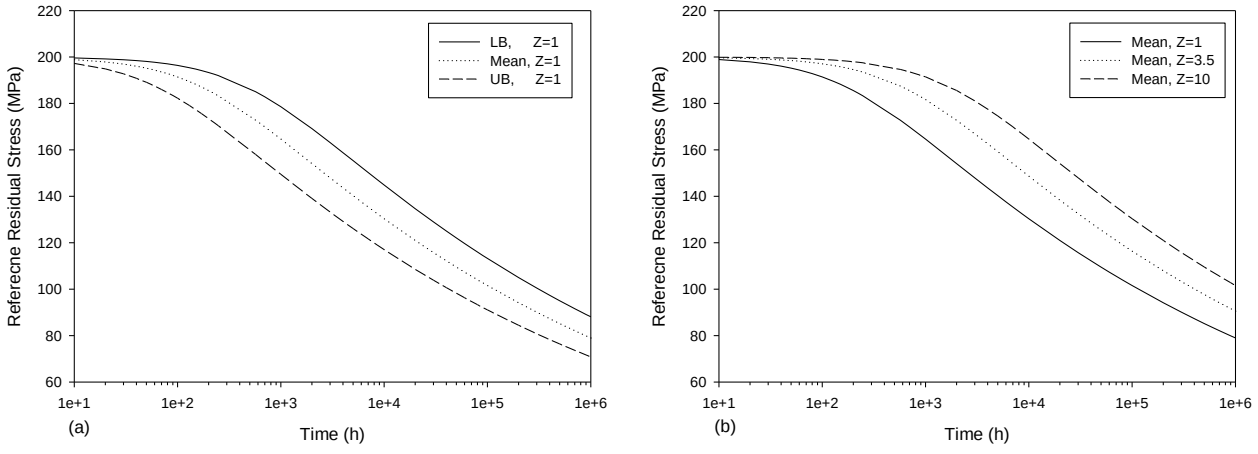

Figure 3. Prediction of reference residual stress relaxation from an initial value of 200MPa (a) using mean, and upper and lower bound creep constants and Z=1, (b) with mean creep data and different values of Z.

3.2.2 Relaxation of combined residual and applied stress

In state 2 the initial total reference stress (equal to residual plus applied stresses), and the elastic

follow-up factor change during total stress relaxation. The relaxation of the total reference stress for combinations of residual and applied loading is similar to Eq. 17, where

$$\tau^{Total} = \left[1 \Big/ \left(1 + \left(1/Z_2 \right) AE_1 (n-1) \left(\sigma_{ref-0}^{Total} \right)^{n-1} t \right) \right]^{1/n-1} \qquad \text{where} \quad \tau^{Total} = \sigma_{ref-t}^{Total} \Big/ \sigma_{ref-0}^{Total} \tag{19}$$

$$\eta = \sigma_{ref-0}^{Rs} \Big/ \sigma_{ref-0}^{Total} \qquad \sigma_{ref-0}^{Total} = \sigma_{ref-0}^{Rs} + \sigma_{ref-0}^{Applied} \qquad \sigma_{ref-t}^{Rs} = \sigma_{ref-0}^{Rs} - (\sigma_{ref-0}^{Total} - \sigma_{ref-t}^{Total}) \tag{20}$$

where τ^{Total} is the normalized total reference stress, η is the ratio of the initial residual to the total stress in the CT specimen. $\sigma_{ref-t}^{Total}, \sigma_{ref-0}^{Total}, \sigma_{ref-0}^{Rs}$ and σ_{ref-t}^{Rs} are the reference total stress and residual stresses at time t and 0 respectively. From Eqs. 7 to 10, the change from Z_1 to Z_2 occurs when $\tau^{Total} = 1 - \eta$. This corresponds to when the residual stress is relaxed to zero.

Therefore

$$t \le \frac{1-(1-\eta)^{n-1}}{\left(1/Z\right) AE_1 (n-1) \left(\sigma_{ref-0}^{Total} \right)^{n-1} (1-\eta)^{n-1}}, \text{ Z=Z}_1; \tag{21a}$$

$$t > \frac{1-(1-\eta)^{n-1}}{\left(1/Z\right) AE_1 (n-1) \left(\sigma_{ref-0}^{Total} \right)^{n-1} (1-\eta)^{n-1}}, \text{ Z=Z}_2 \tag{21b}$$

Now consider a three bar structure system with properties so that the relative stiffness ratios are $\beta = 0.25, \text{and } \gamma = 0.2$. From Eqs 9 and 10 $Z_1 = 10$ and $Z_2 = 3.5$. Assume an initial residual reference stress of 200MPa and subject the CT specimen to additional applied stress to give a total reference stress equal to 330MPa. For this case $\eta = 0.606$. The relaxation of the total and residual stresses is shown in Figure 4, again using the creep law given by Eqn 11 with creep constants given in Table 1. The change from Z_1 to Z_2 occurs when the total stresses relaxes to $(1-\eta)\, 330MPa = 130MPa$. This corresponds to a time where the residual stress relaxes to zero as shown in Figure 4a. Also Figure 4a shows that the residual stress decreases significantly due to the presence of the applied load.

Now consider the case when the total reference stress is 330MPa and residual stress is such that the ratio $\eta = 0.5 \; and \; 0.75$. The stress relaxation behaviour for these two different values of η is shown in Figure 4b. The solid line represents the stress relaxation path for $Z_1 = 10$ and the dashed line represents the stress relaxation for $Z_2 = 3.5$.

When $\eta = 1$ the residual stress accounts for 100% of total stress and stress relaxation corresponds to $Z_1 = 10$. When $\eta = 0$ this represents the case when there is no residual stress and the applied stress accounts for 100% of the total stress. Stress relaxation corresponds to $Z_2 = 3.5$.

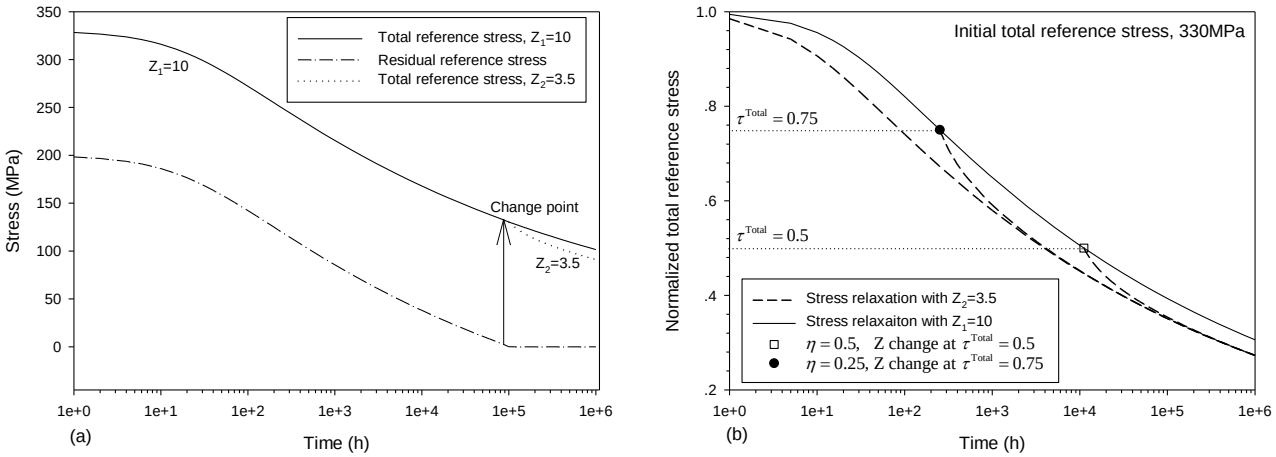

Figure 4. Initial total reference stress 330MPa (a) $\eta = 0.606$, the changing of residual reference stress with total reference stress (b) The relationship between total reference stress relaxation with different η.

4. Prediction of crack initiation

In this section crack initiation will be examined for two different cases. (1) Relaxation of a residual stress in the absence of any external stress. This represents stress relief cracking situations. (2) Relaxation in the presence of a superimposed applied stress. This simulates crack initiation for combined residual and applied stresses.

4.1 Prediction of crack initiation for residual stress alone

By combining Eqs 12 and 17 together with the creep deformation and crack initiation properties listed in Table. 1, the predicted time to crack initiation for a three bar system for state 1 is given by

$$\int_0^{t_i} \frac{1}{C}\left[(1/Z_1)(n-1)DE_1 t + (\sigma_{Spec-0}^{Rs})^{1-n}\right]^{f/(n-1)} dt = 1 \tag{22}$$

Equation 22 is solved numerically to obtain the initiation time. Predicted creep crack initiation times are shown in Fig 5, for initial residual stresses ranging from 75MPa to 400MPa.

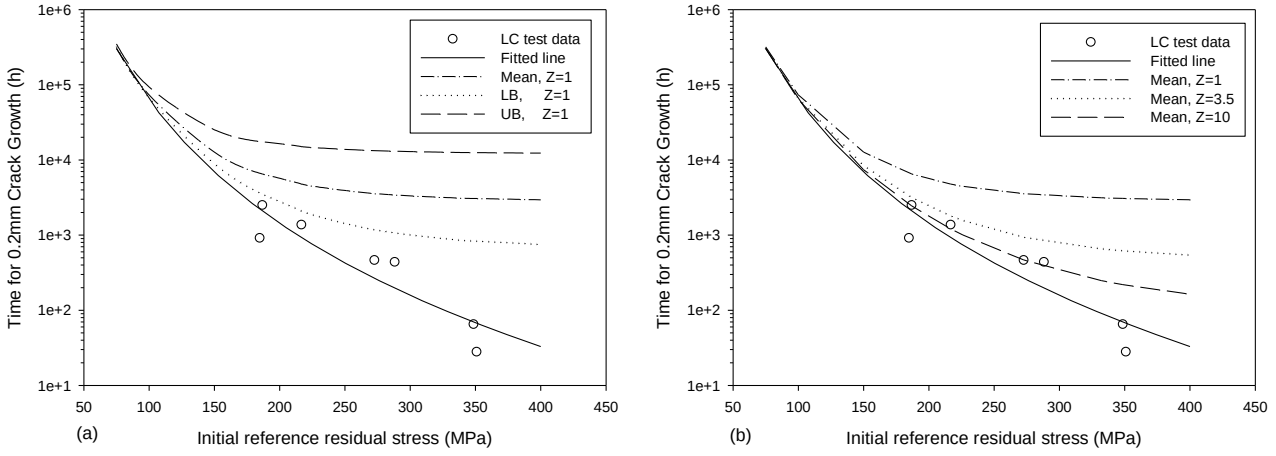

Figure 5. The prediction of crack initiation time with different initial reference residual stress, (a) illustrating the mean, upper and lower bound value (b) with different EFU factor with mean value.

Mean, lower and upper bound creep properties together with Z=1 were assumed for Fig 4a and mean creep properties and different elastic follow-up factors in Fig 4b. The results illustrate that the predictions are sensitive to the creep constants and elastic follow-up factors respectively. However, the initiation times for different constants and different Z tend to converge to similar initiation times for low initial reference stresses.

4.2 Prediction of crack initiation for combined residual and applied stress

By combining Eqs. 12 and 19 with the creep properties listed in table 1, the time for crack initiation can be obtained. If the initiation time is less than t_1 given by

$$t_1 \le \frac{1-(1-\eta)^{n-1}}{(1/Z)AE_1(n-1)\left(\sigma_{ref-0}^{Total}\right)^{n-1}(1-\eta)^{n-1}} \tag{23}$$

Then the initiation time is solved from Eqn. 22.

If, however, the initiation time is greater than t_1 then the initiation time is obtained by solving

$$\int_0^{t_1}\frac{1}{C}\left[(1/Z_1)(n-1)DE_1t+(\sigma_{Spec-0}^{Rs})^{1-n}\right]^{f/(n-1)}dt+\int_{t_1}^{t_i}\frac{1}{C}\left[(1/Z_2)(n-1)DE_1t+(\sigma_{Spec-t_1}^{Rs})^{1-n}\right]^{f/(n-1)}dt=1 \tag{24}$$

Solutions obtained by numerically solving equations 22 and 24 are shown in Figure 6. When the system is under load control the initiation time is 91 hours. If the same system is under displacement control (ie the initial stress is entirely residual and Z_2 ~1) the initiation time is 3132 hours. If was assumed that $\beta = 0.25, \text{and}\, \gamma = 0.2$ and therefore $Z_1 = 10$ and $Z_2 = 3.5$. When the stress (of 330MPa) on the CT specimen arises from applied loading along then Z=3.5 and the initiation time is 659 hours. In contrast if the CT specimen is subjected to a residual stress equal to 330MPa, the Z_1 =10. And the initiation time is 248 hours.

The influence of different ratios of residual to total stress (η) are shown in Fig 6b. Applied stress conditions lie to the left hand side while conditions where residual stress conditions dominate lie on the right hand side of the horizontal scale.

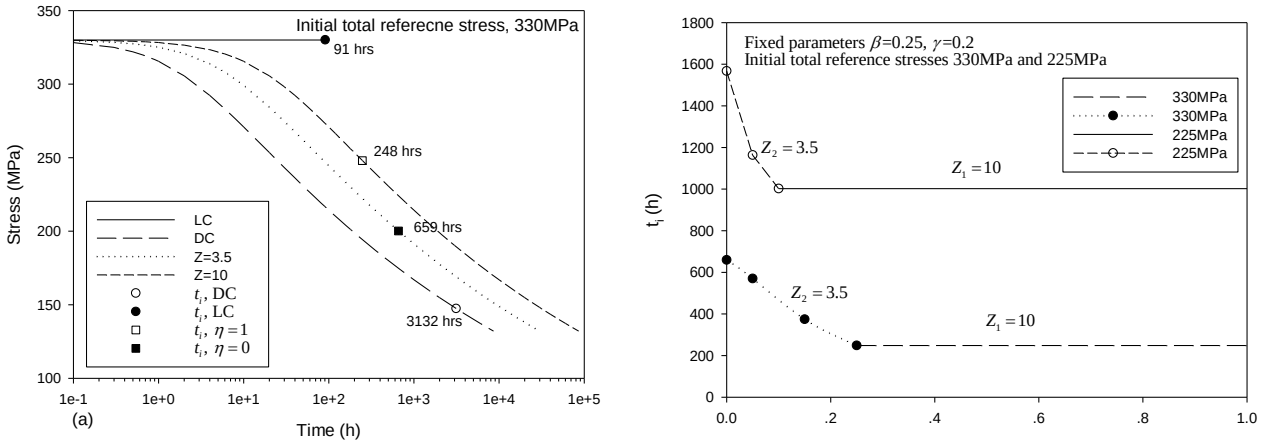

Figure 6. (a) The crack initiation time for initial total reference stress 330MPa under the displacement control, load control and mixed boundary control (b) the crack initiation time with different η and two different reference stresses.

4. Discussion and concluding remarks

A three bar structure has been designed to simulate the behaviour of a component subjected to combined applied and residual stresses. The properties of the three bar system are determined depending when the long range residual stress (state 1) is induced and following application of an external load (state 2). Closed form solutions of the elastic follow-up factor for states 1 and 2 are given and we find that the expression for elastic follow-up factor in state 2 changes when corresponding residual stress relaxes to zero.

Calculations performed to predict creep crack initiation in the presence of long range residual stress in Type 316H austenitic stainless steel provide results that yield significant insight to the behaviour of the system. Sensitivity studies have been included to determine the influence of changes in the material creep properties and the effects of elastic follow-up factor on stress relaxation. We find that the predictions of crack initiation are sensitive to both the creep constants and elastic follow-up factors respectively. However, the initiation times for different constants and different Z tend to converge to similar values for low initial reference stresses.

In state 2, the effect of residual stress on crack initiation is found to depend on the value of total stress (residual stress plus stress created by applied load) and the ratio of the residual stress to total stress. The elastic follow-up factor decreases significantly in state 2 when all of the residual stress has relaxed to zero.

Acknowledgements

The authors gratefully acknowledge the support provided by EDF Energy for this work.

References

1. P. J. Bouchard, P.J.W., S. A. McDonald, R. K. Heenam, *Quantification of creep cavitation damage around a crack in a stainless steel pressure vessel.* Acta Materialia, 2004. **52**.
2. Mahmoudi, A.H., Aird, C., Truman, C.E., Mirzaee-Sisan, A., Smith, D.J., , *Generating well defined residual stresses in laboratory specimens*, in *paper PVP2006-ICPVT11-93620, Proceedings of PVP2006: ASME Pressure Vessels and Piping Division Conference*2006: July 23-17, 2006, Vancouver, Canada.
3. Kasahara, N., *Strain concentrations at structural discontinuities and its prediction on characteristics of compliance change in structures.* JSME Int. J.,, 2001. **44**: p. 354-361.
4. A. M. Shirahatti, Y.W., C. E. Truman, D. J. Smith, *A new method of introducing long range residual stress to study creep crack initiaion*, in *13th International Conference on Fracture*2013: Beijing, China.
5. *R5-Assessment procedure for the high temperature response of structures, Revision3*, 2003: British Energy Generation Limited, Gloucester, UK.
6. M. Turski, P.J.B., A. Steuwer, P. J. Withers, *Residual stress driven creep cracking in AISI Type 316 stainless steel.* Acta Materialia, 2008. **56**: p. 3598-3612.

7. J. Douglas, M., Spinder, R. Dennis, *Development of an advance creep model for type 316 Stainless Steel*, in *Eighth international conference on creep and fatigue at elevated temperature*2007, ASME: San Antonio, Texas.
8. A. J. Fookes, D.J.S., *A new method for assessing high-temperature crack growth.* Fatigue Fract Enging Mater Struct, 2005. **28**: p. 769-778.
9. D. W. Dean, D.N.G., *Creep crack growth behaviour of Type 316H steels and proposed modifications to standard testing and analysis methods.* Int. J. Press. Vessels Pip.,, 2007. **84**: p. 378-395.
10. C. J. Aird, S.H.-M., C. E. Truman, and D. J. Smith, *Impact of residual stress and elastic folllow-up on fracture.* Journal of ASTM International, 2008. **5**: p. 1-14.

Creep-Fatigue Crack Growth Using Digital Image Correlation

Jeffrey L. Evans[1,*]

[1] Department of Mechanical and Aerospace Engineering, University of Alabama in Huntsville, Huntsville, Alabama 35899, USA
* Corresponding author: jeff.evans@uah.edu

Abstract Creep-fatigue crack growth tests are cyclic tests that have a hold period at the maximum load. This hold period, or dwell, is the period during the test when the time-dependent mechanisms operate. The length of the dwell period has been shown to affect the fatigue crack growth rate. During the hold period, crack tip blunting (due to creep deformation) and crack extension can be measured using 2-D digital image correlation (DIC). DIC requires a random speckle pattern on the flat surface being investigated. The speckle pattern is a unique pattern and, as the surface is strained, locations on the pattern will move to new positions relative to a previous strained condition. The images are compared and an algorithm calculates the strain. The camera can be positioned to view the crack tip and measure crack extension and crack opening displacement (COD). This provides a means by which the crack tip creep deformation can be determined during the hold period, providing valuable information regarding the crack tip kinetics and crack driving force. This paper will evaluate this technique for creep-fatigue crack growth measurements and provide preliminary data for a Ni-base alloy.

Keywords Creep-Fatigue, Crack Growth, Digital Image Correlation

1. Introduction

A number of important industrial applications require materials to be subjected to elevated temperatures, cyclic stresses, and potentially aggressive environments. Creep-fatigue occurs when a combination of these conditions are present. During the dwell period of a creep-fatigue cycle, several damaging effects at the crack tip can take place causing an increase in the crack growth rate. The crack tip driving force therefore could be influenced by a number of active processes, such as oxidation, oxygen diffusion, and creep deformation [1]. Understanding the kinetics of these various processes is essential to predicting the behavior of a material under creep-fatigue conditions [2]. Some studies and techniques have been proposed to evaluate the rates of these processes [3]. It is quite challenging to experimentally disassociate the different processes and arrive at the exact contribution provided by each process. Oxygen diffusion along the grain boundaries is clearly a culprit in embrittling some materials such as nickel-base alloys [4]. This diffusional process is, in part, driven by the crack tip stress. Rapid stress relaxation, therefore, has been proposed to reduce the crack growth rate [5]. Quantifying the re-distribution of stresses and strains at the crack tip is critical to predicting the crack growth rate during creep-fatigue.

One technique developed in the last 25 years that could be used to help interrogate the crack tip during creep-fatigue is digital image correlation [6]. This noncontact experimental technique allows for the observation of the strains using an image analysis technique [7]. The surface of a test specimen has to be prepared, having a unique speckle pattern. The random speckles are then used as reference points for determining amounts of displacement and strain measurements to be calculated with respect to a starting reference image. This technique has been used to determine crack tip displacements during creep crack growth as well as fatigue crack growth. This paper gives some preliminary results using a 2-D digital image correlation system to determine the crack tip displacements and crack growth rates for the nickel alloy Hastelloy X at elevated temperature with creep-fatigue conditions.

2. Experimental Procedure

The material used in this study was Hastelloy X (see Table 1 for the chemical composition), which was acquired in the annealed condition in the form of a cold finished plate with a thickness of 6.35mm. From this plate a sample was removed in the T-L orientation for the creep-fatigue test.

Table 1. Nominal chemical composition of Hastelloy X in weight %

Alloy	Ni	Fe	Cr	Mo	Cu	Co	W	Ti	C	Mn	Si	Al	Other
Hastelloy X	Bal.	18	22	9	<0.50	1.5	0.6	<0.15	0.1	<1	<1	<0.5	<0.08

From this plate a sample was removed in the T-L orientation for the creep-fatigue test with the geometry shown in Figure 1.

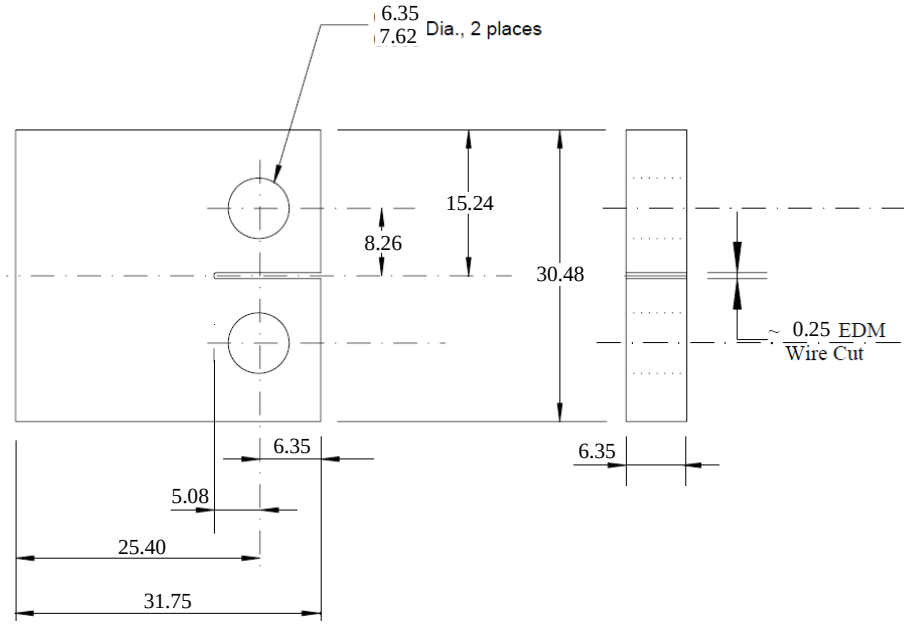

Figure 1. Creep-fatigue specimen geometry (dimensions are in mm)

The specimen was then prepared for the noncontact digital image correlation. A high contrast random, speckle pattern was applied in two steps. First a flat white high temperature ceramic based coating (VHT Flame Proof^{TM}) was applied to one surface of the specimen. After the coating had dried, a mist of a flat black high temperature coating was sprayed over the white coating layer to provide the contrasting speckle pattern.

The specimen was fatigue pre-cracked for ~2.5mm, ending with $\Delta K = 27.6$ MPam$^{1/2}$. The fatigue pre-cracking and creep-fatigue test were conducted using a 100kN MTS servo-hydraulic test system. The creep-fatigue test was performed using a trapezoidal waveform with a 1.5 second ramp up, a 120 second dwell at max load, and a 1.5 second ramp down. A loading ratio of R=0.05 was used. The test was conducted in laboratory air at 650ºC ± 3 ºC. The elevated temperature was applied using a 1.2kW Ameritherm induction heater and monitored using a two-color optical infrared thermometer.

The Correlated Solutions Vic-2D digital image correlation system was used to capture images and analyze crack tip displacements. Images were captured at a rate of ~6 images per second using a 5MP Point Grey camera. Images were captured for only a few cycles at a time collecting ~730 images per cycle.

3. Results and Discussion

3.1. Crack tip strain

The displacement measurements and strain calculations presented herein were performed for cycles number 9 and number 62 during the creep-fatigue test. The measurements were made with respect to an unloaded reference image. The strain measurements were made on a small region around the crack and crack tip as is shown in Figure 2.

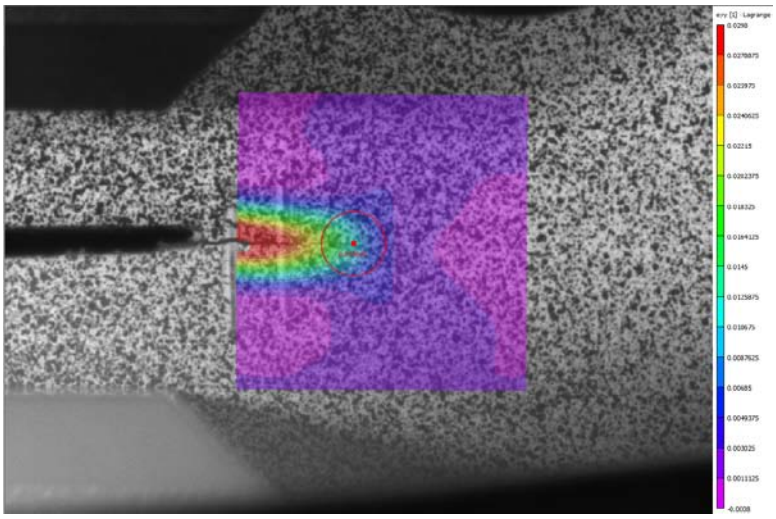

Figure 2. Representative image of the digital image correlation strain calculation. Inside the red circle is the region around the crack tip that was used for the strain measurements.

The crack tip strain was measured for the 120 second hold period of cycle 9 and cycle 62 of the creep-fatigue test using the region contained by the red circle in Figure 2. The strain was calculated for the y-direction using the Lagrange tensor, and the results for cycles 9 and 62 are shown in Figure 3.

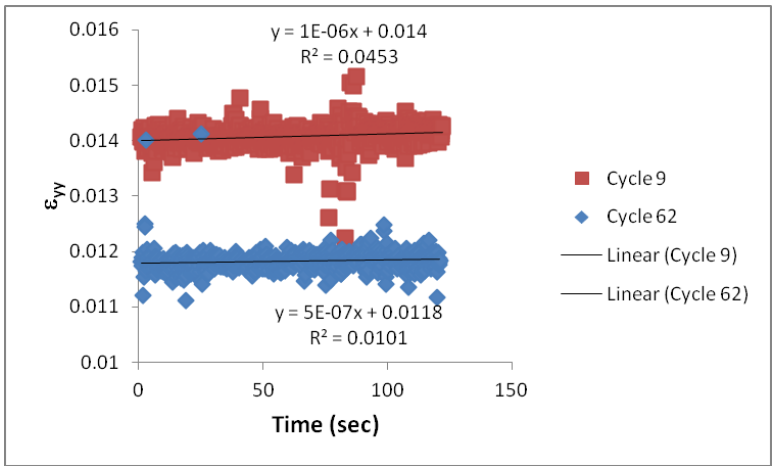

Figure 3. The crack tip strain during the creep-fatigue hold period for cycles 9 and 62.

During the hold period the strain measured had some noise present in the ~730 data points used for each cycle. This may be due to the thermal effect on the air between the camera and the sample. Nevertheless, a small positive slope was the trend for both cycles. Therefore a crack tip creep rate for this 120 second period was determined. During cycle 9 the creep rate was $1x10^{-6}$ and it was $5x10^{-7}$ during the hold period of cycle 62. This at least indicates that a crack tip creep rate can be measured on this material at 650ºC for a 120 second hold period using digital image correlation.

Also, the results showed that the magnitude of the strain is higher for cycle 9 than cycle 62. It is not clear what has produced this result. It may be that the images were taken with a resolution too low to accurately see the crack tip. Therefore, when the local selection was made to extract the data from the crack tip, the exact location may have differed between the two cycles.

3.2. Crack Opening Displacement (COD)

COD measurements were also measured for cycles 9 and 62. These measurements were made relative to the unloaded reference image. A linear measurement of COD was performed across a small region within the selected area shown in Figure 4.

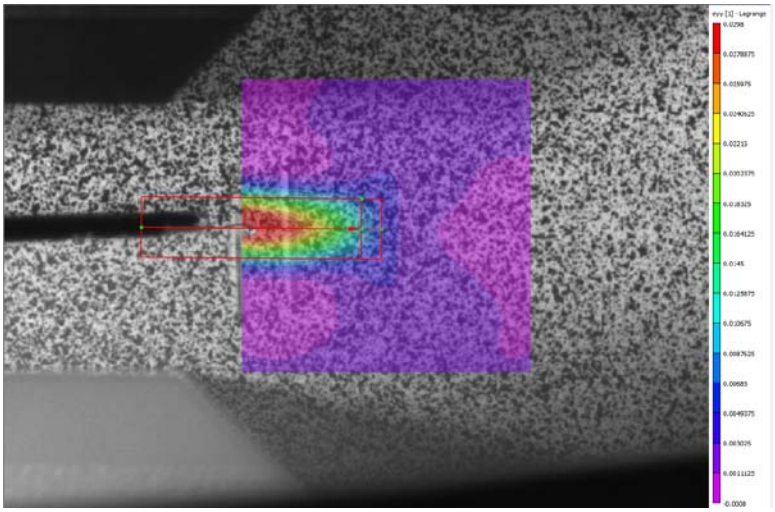

Figure 4. The crack opening displacement measurement was made along a linear region shown in the red rectangular box.

COD data (in pixels) was then extracted at a location across the EDM notch (i.e. the far left point in the red rectangle shown in Figure 4). The COD data was taken from the beginning (the first two seconds), the middle (seconds 60 and 61), and the end (seconds 119 and 120). The twelve data points at each location were then averaged. The results are shown in Figure 5.

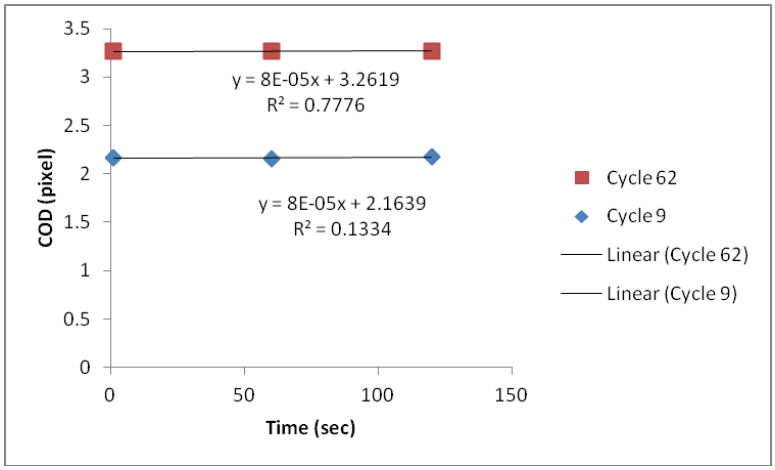

Figure 5. The COD measurements during the creep-fatigue hold period for cycles 9 and 62.

The COD measurements were clearly higher for cycle 62 than for cycle 9. This is what would be expected, since at a later point in the test the crack would have grown causing a larger COD measurement. Also, for both cycles the slope is positive, indicating that the crack opening increased during the hold period.

4. Conclusions

DIC was used to measure both the crack tip deformation and crack opening displacement during a 120 second hold period of a creep-fatigue crack growth cycle. The crack tip strain measurements can be used to determine crack tip creep rates during a creep-fatigue cycle. The results for both the strain measurements and the COD measurements showed that a positive slope existed over this 120 second period. The results shown herein are only for a very limited study, and it is expected that a greater understanding of the crack tip behavior could be gained by conducting these tests over many more cycles and different test conditions. Nevertheless these results suggest that creep and crack opening take place during the hold period studied for this material under these conditions and that they can be measured using the DIC system.

Acknowledgements

The author would like to thank graduate students Jason Ray, Milica Damjanovic, and Alex McCool for assistance in this work. Also, the in-kind support from AAR Precision, specifically Alan Ballenger and Willie Michaely, for machining the samples, is very much appreciated. This research was supported by NSF Contract #: DMR-1151109. That support is gratefully acknowledged.

References

[1] K.O. Findley, J.L. Evans, A. Saxena, A critical assessment of fatigue crack nucleation and growth models for Ni- and Ni,Fe-base superalloys, Int Mater Reviews, 25 (2011) 49-71.

[2] Evans, J.L. and Saxena, A., Elevated temperature crack growth rate model for Ni-base superalloys, in: Proceedings of the 12th International Conference on Fracture, Ottawa, Canada, July 12-17, 2009.

[3] J.L. Evans, Method for comparing the crack tip kinetics during creep-fatigue loading of nickel-base superalloys, Mater Sci Eng, A, 528 (2011) 5306-08.

[4] E. Andrieu, R. Molins, H. Ghonem, A. Pineau, Intergranular crack tip oxidation mechanism in a nickel-based superalloy. Mater Sci Eng A Struct Mater Prop Microstruct Process, A154 (1) (1992) 21-28.

[5] A. Pineau, S.D. Antolovich, High temperature fatigue of nickel-base superalloys – A review with special emphasis on deformation modes and oxidation, Eng Failure Analysis, 16 (2009) 2668-2697.

[6] D. Nowell, M.E. Kartal, P.F.P De Matos, Digital image correlation measurement of near-tip fatigue crack displacement fields: constant amplitude loading and load history effects, Fatigue Fract of Eng Mater Struct, 36 (2013) 3-13.

[7] G.J. Pataky, H. Sehitoglu, H.J. Maier, High temperature fatigue crack growth of Haynes 230. Mater Characterization, 75 (2013) 69-78.

[8] M.A. Sutton, J.J. Orteu, H. Schreier, Image Correlation for Shape, Motion and Deformation Measurements: Basic Concepts,Theory and Applications, Springer, New York, 2009.

Creep Strength of Dissimilar Welds for Advanced USC Boiler Materials

Masaaki Tabuchi[1,*], Hiromichi Hongo[1], Fujio Abe[1]

[1] National Institute for materials Science, Tsukuba Science City 305-0047, Japan
* Corresponding author: TABUCHI.Masaaki@nims.go.jp

Abstract The research project aiming to commercialize 700˚C class pulverized coal power system; advanced ultra-super critical (A-USC) pressure power generation has been conducted in Japan from 2008. In A-USC boilers, Ni base or Ni-Fe base alloys are used for high temperature parts at 650-700˚C and advanced high Cr ferritic steels are planning to be used at the temperatures lower than 650˚C. Because the high B-9Cr steel developed in National Institute for Materials Science (NIMS) has improved creep strength in welds, it is one of the candidate materials for A-USC boilers. In the present paper, the creep tests of the dissimilar welds between Ni base alloy and high B-9Cr steel for A-USC boilers were conducted at 650˚C. In the heat affected zone (HAZ) of the high B-9Cr steels, fine-grained microstructures were not formed and grain size of the base metal was retained. Free boron on the grain boundaries is considered to affect the mechanisms of the α-γ transformation during weld thermal cycle. Consequently, the Type-IV failure was not occurred in the present dissimilar welds and their creep rupture lives were 5-10 times longer than those of the conventional 9Cr steel welds at 650˚C.

Keywords A-USC boiler, High B-9Cr steel, Dissimilar weld, Creep

1. Introduction

Research project aiming to commercialize 700 ˚C class pulverized coal power system; A-USC power generation, with 46-48 % power generation efficiency, and to reduce CO_2 emissions more than 10 % has been conducted from 2008 in Japan. In the A-USC boiler, Ni base or Ni-Fe base alloys such as Alloy 617, Alloy 263 and HR6W are planning to be used for high temperature parts at 650-700 ˚C, and advanced high Cr ferritic steels are planning to be used at the temperatures lower than 650 ˚C. In the dissimilar weld between Ni base alloy and high Cr steel, Type-IV failure and thermal-fatigue (creep-fatigue) are the major concerns. Because the 9Cr-3W-3Co-VNb steel containing higher boron and lower nitrogen (high B-9Cr steel) developed in NIMS has improved creep strength in the HAZ and weld joint [1, 2], it is one of candidate materials for A-USC boilers [3].

In the present paper, creep tests of the dissimilar welds between high B-9Cr steels and Ni base alloys for A-USC boilers (Alloy 617 and Alloy 263) were conducted at 650 ˚C. Microstructures and creep damages in the welds were investigated.

2. Experimental procedure

Two kinds of the high B-9Cr steels; MARBN10 steel (9Cr-3W-3Co-VNb-0.01B-0.003N) and MARBN12 steel (9Cr-2.6W-3Co-VNb-0.01B-0.007N) were prepared. The chemical compositions are shown in Table 1. In the present steels, about 0.01% boron was added aiming to strengthen the grain boundaries. Nitrogen content was lower than 0.01 % to avoid the formation of boron nitride (BN) and to maximize the grain boundary strengthening effect of boron. MARBN12 steel contains higher nitrogen than MARBN10 steel. These steels were normalized at 1100 ˚C for 1 h and tempered at 800 ˚C for 1 h.

Four kinds of dissimilar welds between high B-9Cr steels (MARBN10 and MARBN12) and Ni base alloys for A-USC boilers (Alloy 617 and Alloy 263) were prepared by gas tungsten arc (GTA)

welding using the filler wire of Inconel 82 as shown in Fig. 1. The groove configuration of these welds was U with 20 ˚ of groove angle. After welding, all the weld joints were given post weld heat treatment (PWHT) at 740 ˚C for 4 h. Weld defects were not detected in the radiographic examination and magnetic particle testing. The distribution of micro Vickers hardness of the MARBN10 steel-Alloy 263 weld after PWHT and before creep condition is shown in Fig. 2.

Creep tests of the base metals were conducted using round bar-type specimens 6 mm in diameter and 30 mm in gauge length. Creep tests of the dissimilar weld joints were conducted at 650 ˚C using the smooth plate-type specimens 17.5 × 5 mm in section and 100 mm in gauge length as shown in Fig. 3.

Table 1. Chemical compositions of the present high B-9Cr steels (wt. %)

	C	Si	Mn	P	S	Cr	W	Mo	Co	Ni	V	Nb	N	O	B	Sol.Al
MARBN10	0.078	0.29	0.54	0.003	0.001	9.11	3.13	<0.01	3.03	<0.01	0.21	0.052	0.0030	0.003	0.010	0.001
MARBN12	0.081	0.30	0.53	0.001	0.001	9.09	2.62	<0.01	3.02	<0.01	0.21	0.052	0.0072	0.003	0.011	0.001

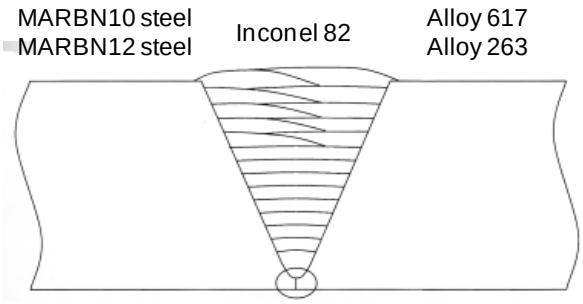

Figure 1. Dissimilar welds used in the present study

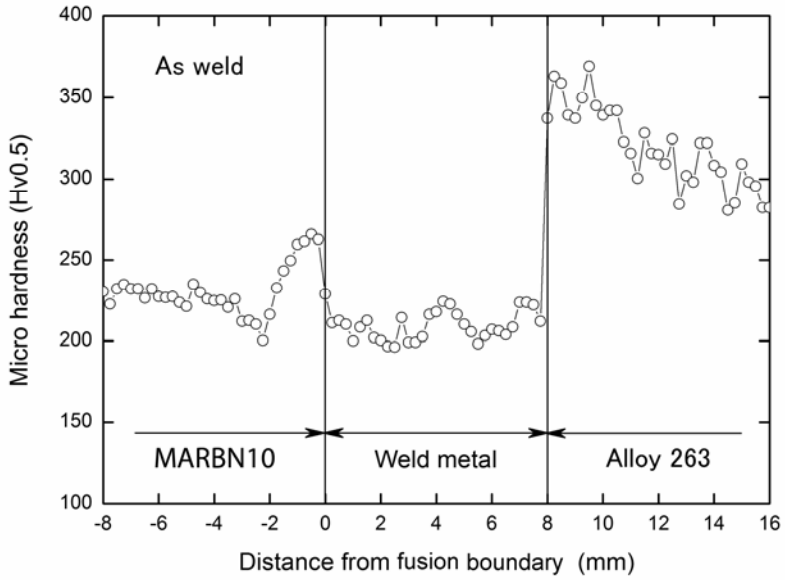

Figure 2. Hardness distribution in the present dissimilar weld joint (MARBN10 steel-Alloy 263 weld) after PWHT and before creep

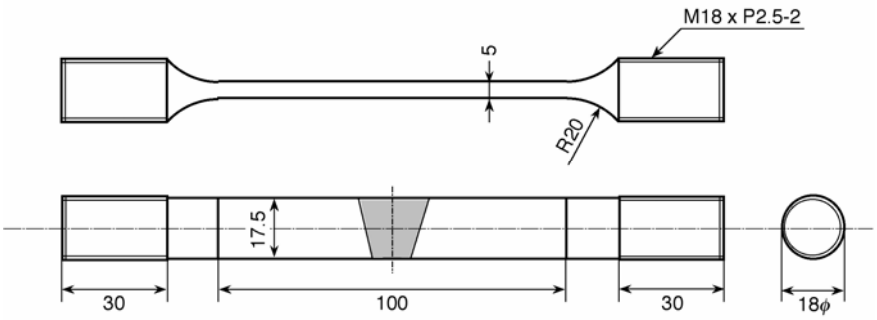

Figure 3. Creep test specimen for the dissimilar welds

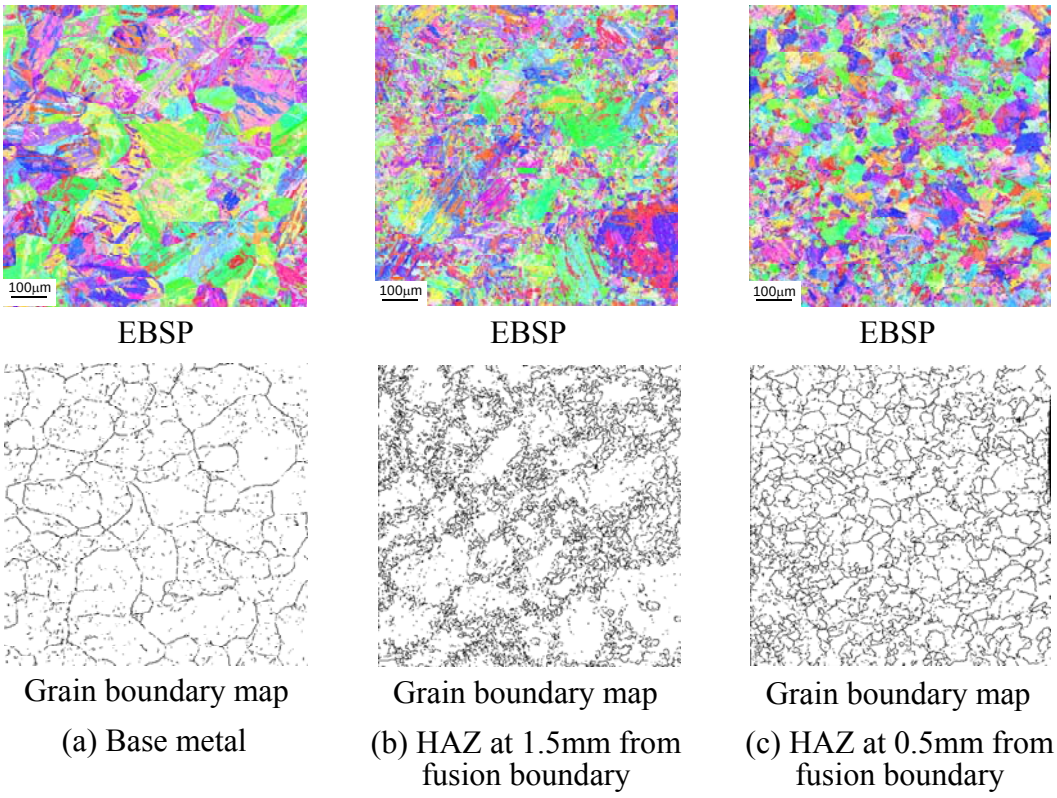

Figure 4. EBSP images and grain boundary mapping (15-48˚) for the base metal and HAZ of the high B-9Cr steel in the MARBN10 steel-Alloy 263 weld joint

3. Results and discussion

3.1. Microstructures of HAZ in the dissimilar welds

Figure 4 shows the EBSP (electron backscattered pattern) images and grain boundary maps of the base metal and HAZ of the high B-9Cr steel in the dissimilar welds between MARBN10 steel and Alloy 263. In the grain boundary map, grain boundaries with misorientation from 15 ˚ to 48 ˚ were drawn and their length was measured. We have reported that the fine-grained structures were not formed in HAZ of weld joints for the 9Cr-3W-3Co-VNb steel with boron and low nitrogen [1, 2]. The base metal of the present steel shows the tempered martensitic structures having the grain boundary length of 2.07 cm and KAM of 1.83 (Fig. 4(a)). The micro Vickers hardness of the

present base metal was 220-235 as shown in Fig. 2. In the conventional high Cr steels, fine-grained HAZ structures 5 μm in the average grain size were observed in the area at about 1.5 mm from the fusion boundary. In the present high B-9Cr steels, however, the fine-grained structures were not formed at a distance of 1.5 mm from the fusion boundary. In this region, the grain size of the base metal was retained and small grains formed only on the prior-austenite grain boundaries (Fig. 4(b)). The grain boundary length was 5.99 cm, KAM was 1.94, and hardness was 243 for the microstructure of Fig. 4(b). At a distance of 0.5 mm from the fusion boundary, recrystallization occurred; however their grain size was more than 10 μm (Fig. 4(c)). The grain boundary length was 4.94 cm, KAM was 2.22, and hardness was 266 for the microstructure of Fig. 4(c). The KAM corresponds well to the hardness.

In the conventional high Cr steel welds, Type-IV creep damages form in the fine-grained HAZ with average grain size of about 5 μm; consequently creep strength of welds decreases than base metal [4, 5]. These results mentioned above in Fig. 4 confirm that the HAZ microstructures of high B-9Cr steel are considerably different from those of the conventional high Cr ferritic steels, and soluble free boron is essential for suppression of grain refinement during weld thermal cycle. We consider that the free boron decreases the grain boundary energies, and suppresses the nucleation of γ phase from grain boundaries by diffusional transformation, and causes the martensitic reverse transformation. The similar phenomena of the martensitic reverse transformation that the original grain size and crystal orientation was retained after heating up to A_{C3} transformation temperature were also reported in the maraging steels [6] and 12Cr turbine rotor steels containing boron [7].

3.2. Creep strength of dissimilar weld joints

Figure 5 shows the relations between stress and creep rupture time of the base metal of high B-9Cr steels and four kinds of the present dissimilar weld joints at 650 ˚C. Open symbols show the rupture times of the base metal and dissimilar weld joints for the MARBN10 steel, and solid symbols show those for the MARBN12 steel. The creep strength of base metal of the high B-9Cr steels was higher than that of the conventional 9Cr steel (Gr.92 steel) due to the grain boundary strengthening effect of boron. The creep strength of base metal of MARBN12 steel with 0.007 % N was higher than that of MARBN10 steel with 0.003 % N.

The creep rupture tests of the dissimilar weld joints were conducted at 650 ˚C for 160, 140, 120 and 100 MPa. The dissimilar welds using the high B-9Cr steel show 5-10 times longer creep rupture times than the Gr.92 steel weld at 100 MPa. The differences of the creep strength between dissimilar welds and base metals are small up to 20000h at 650 ˚C, and we are now investigating the creep strength at lower stress conditions; 90 and 80 MPa.

The dissimilar welds fractured in the base metal of high B-9Cr steel for the short term test conditions and in the fusion boundary between high B-9Cr steel and Ni base filler wire (Inconel 82) for the long term test conditions. The failure in the fusion boundary was observed at the stresses lower than 120 MPa for the MARBN10 steel welds and lower than 140 MPa for the MARBN12 steel welds. All the present dissimilar weld joints using high B-9Cr steels did not show the Type-IV failure in HAZ and consequently the creep rupture lives were much longer than those of the conventional 9Cr steel welds that showed the Type-IV failure at the present creep test conditions. This means that the microstructures and creep strength of HAZ was considerably improved in the high B-9Cr steel, which contains 0.01 % boron and low nitrogen (<0.01 %), due to the effect of soluble boron.

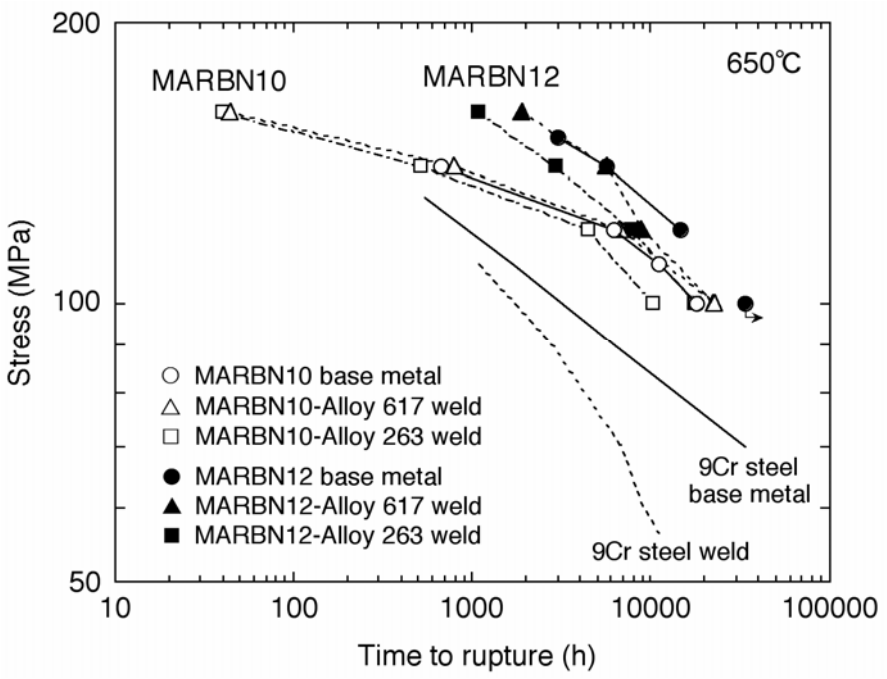

Figure 5. Creep rupture times of the base metals of the high B-9Cr steels and the dissimilar weld joints between high B-9Cr steels and Ni base alloys for A-USC boiler at 650 ˚C

(a) MARBN10 steel-Alloy 617 weld joint, 650 ˚C, 100MPa, 22766h

(b) MARBN12 steel-Alloy 617 weld joint, 650 ˚C, 100MPa, 22518h

Figure 6. Dissimilar weld joint specimens creep ruptured at 650 ˚C and 100MPa for 22000h

We have investigated the microstructures and creep damages in the crept welds. Figure 6 shows the dissimilar weld joint specimens creep ruptured at long-term test condition. It was observed that a creep crack initiated in the fusion boundary at the lower surface of U-groove and then propagated toward to the HAZ of the high B-9Cr steel.

Figure 7 shows microstructures and creep damages observed in the HAZ of the dissimilar welds between MARBN12 steel and Alloy 617 ruptured at 650 ˚C and 140 MPa for 5619h. In the HAZ at 1.5 mm from the fusion boundary, small amounts of creep voids were observed as shown in Fig. 7. This area corresponds to Fig. 4(b) where the grain size of the base metal was retained and small grains formed only on the prior-austenite grain boundaries. Creep voids in the HAZ of high B-9Cr

steel were observed on the prior-austenite grain boundaries with large grain size. It is considered that the void coalescence and crack formation, which causes Type-IV failure, is suppressed and consequently the life of weld is improved in these HAZ microstructures of high B-9Cr steel compared with the fine-grained HAZ microstructures of conventional high Cr steels.

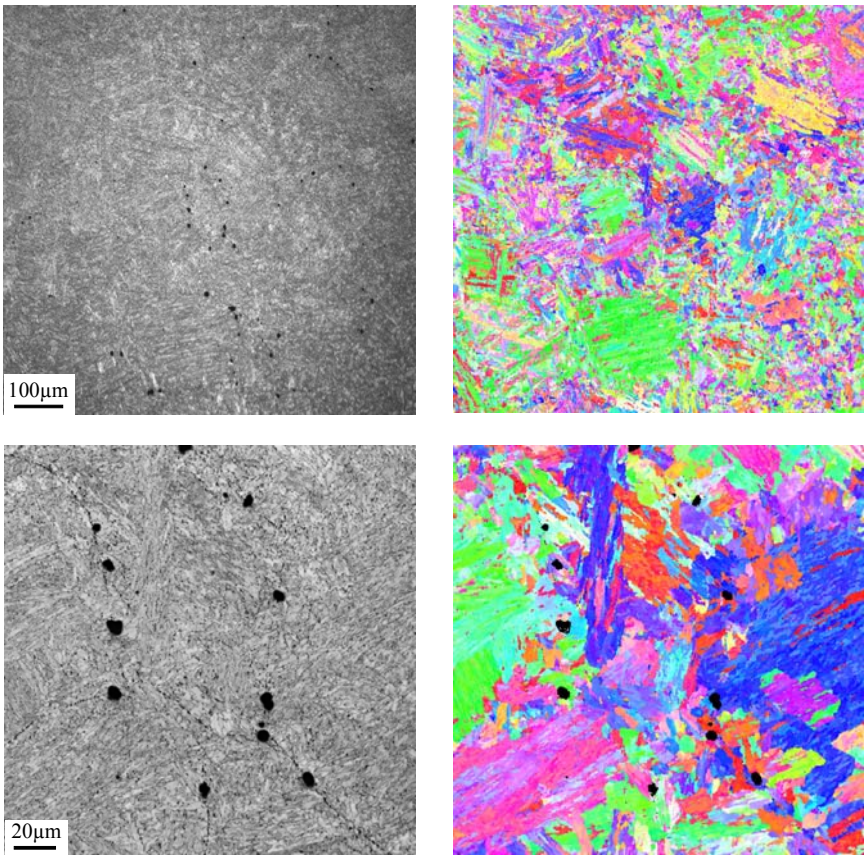

Figure 7. Microstructure and creep damage in the HAZ of the MARBN12 steel-Alloy 617 weld joint creep ruptured at 650 ˚C and 140 MPa for 5619 h

4. Conclusions

In the present paper, creep tests of the dissimilar welds between high B-9Cr steels and Ni base alloys, which are planning to be used in the 700 ˚C class pulverized coal power system (A-USC), were conducted. The results can be summarized as follows:

(1) For the high B-9Cr steels, fine-grained microstructures as shown in the conventional high Cr steels did not form in the HAZ. Free soluble boron is considered to decrease the grain boundary energy and change the mechanisms of the α-γ transformation during the weld thermal cycle.
(2) The creep rupture lives of the present dissimilar welds between high B-9Cr steels and Ni base alloys were 5-10 times longer than those of the conventional 9Cr steel welds at 650˚C.
(3) The failure locations of the dissimilar weld joints were base metal or fusion boundary. Small amounts of creep voids were observed in the HAZ with large grain size; however Type-IV failure did not occur for about 20000 h at 650˚C.

References

[1] M. Tabuchi, M. Kondo, H. Hongo, T. Watanabe, F. Yin, F. Abe, Improvement of creep properties of high Cr steel weldment by boron addition. Journal of the Society of Materials Science Japan, 54 (2005) 162-167.
[2] S.K. Albert, M. Kondo, M. Tabuchi, F. Yin, K. Sawada, F. Abe, Improving the creep properties of 9Cr-3W-3Co-NbV steels and their weld joints by the addition of boron. Metallurgical and Materials Transactions A, 36A (2005) 333-343.
[3] M. Fukuda, Advanced USC power generation technology. Journal of the Japan Society of Mechanical Engineers, 114 (2011) 244-247.
[4] H. Hongo, M. Tabuchi, T. Watanabe, Type IV creep damage behavior in Gr.91 steel welded joints. Metallurgical and Materials Transactions A, 43A (2012) 1163-1173.
[5] M. Tabuchi, H. Hongo, Evaluation of long-term creep damage in high Cr ferritic steel welds. Materials at High Temperatures, 28 (2011) 172-180.
[6] T. Maki, H. Morimoto, I. Tamura, Recrystallization of the austenite transformed reversely and structure of martensite in 18Ni maraging steel. Tetsu-To-Hagane, 65 (1979) 1598-1606.
[7] T. Azuma, K. Miki, Y. Tanaka, T. Ishiguro, Effect of B on the behavior of austenite formation and recrystallization in high Cr ferritic heat resistant steel. Tetsu-To-Hagane, 86 (2000) 667-673.

EPRI Initiatives related to Flexible Operation of High Temperature Power Plant

Jonathan Parker[1,*] and John Shingledecker[1]

[1] EPRI, 1300 West WT Harris Blvd, Charlotte NC 28262, USA
* Corresponding author: jparker@epri.com

Abstract

Variable demand and an increasing range of electricity supply methods are such that steam plant must perform under cyclic operation. Indeed, the multiplicity of generating options means that even defining a 'typical' cycle is difficult. Quantification of the range of potential damage mechanisms is even more complex. In response to the need for greater understanding of cyclic performance issues in high energy components, in 2006 EPRI initiated a series of Annual Expert Workshops on Creep Fatigue. These discussions identified key issues and areas for development related to the design and performance under transient operation. Summary documents, produced from each of the annual meetings, have helped guide this international effort in the field of creep-fatigue. It is apparent that a coordinated effort is critical to ensuring that outcomes are meaningful and effective. Excellence in science and engineering is necessary in aiding the electricity supply industry to meet current challenges associated with safe and reliable operation of plant. The present paper documents the current state of knowledge on creep fatigue behaviour and outlines achievements from the EPRI collaborative work. The overall goal of this effort is to provide the basis of a comprehensive approach to design and life management of components that are subject to creep-fatigue conditions.

Keywords Creep, Fatigue, Flexible Operation

1. Introduction

Utilities increasingly need to adopt generating practices that involve cycles. The number, magnitude, and complexity of the cycles associated with transient type operation have all increased. Thus, starts and stops as well as changes in generating output can lead to problems associated with thermal and /or mechanical loading as well as potential issues with water chemistry and corrosion. For components which operate at high-temperature, damage associated with transient operation is frequently called *creep-fatigue*. However, even in this group of components, specifics of damage mechanisms will vary widely. A schematic illustration of the primary options is shown in Fig 1.

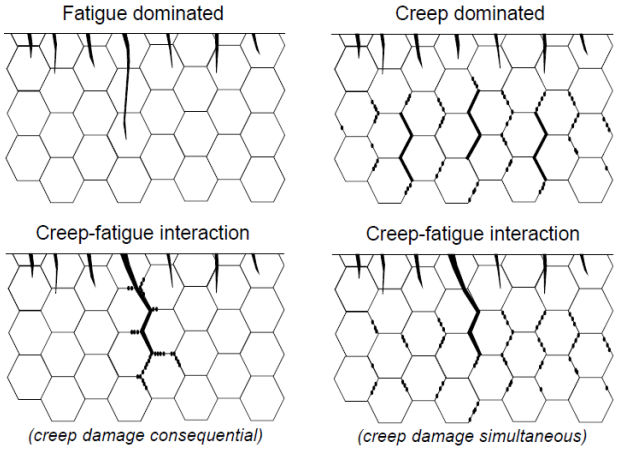

Figure 1. Schematic illustration of different forms of creep-fatigue type damage seen in high energy components.

While many examples of fatigue dominated and creep dominated in-service damage can be presented, the most problematic situation from a predictive point of view is when the effects are interactive. Under these conditions the primary concern is whether damage accumulates more quickly than would be expected for either mechanism alone. As power generating systems seek maximum flexibility from available plants, increasing numbers of components must operate in creep-fatigue conditions. Moreover, recent installation of combustion turbines and heat recovery steam generators have increased the number of materials and components that operate in high-temperature, cyclic conditions. In addition, high-efficiency coal plants operate with even higher steam and metal temperatures than those of traditional plants. Thus, creep-fatigue damage will occur more frequently and in more materials, including low-alloy ferritic steels, austenitic steels, nickel-based alloys, and creep-strength-enhanced steels.

The present paper documents the current state of knowledge on creep fatigue behaviour and outlines achievements from the EPRI collaborative work.

2. Achievements

EPRI's long-range research program (Technology Innovation) initiated a set of activities in 2006. The initial goals of the work were to:

- Examine how problems of Creep-Fatigue assessment are addressed internationally
- Identify deficiencies that exist with current knowledge and approaches, and
- Recommend improvements in application of the available technology and identify future Research and Development needs.

EPRI's overall approach to establishing solutions to assessing creep fatigue performance has involved facilitating discussion at annual expert workshops, preparation of critical reports and publications, facilitating the preparation and review of new ASTM standards for laboratory creep fatigue testing and establishing a platform and associated knowledge base of materials behavior. EPRI's Fossil Materials & Repair Program has funded many specific activities, but the overall success of this effort is due to broad international collaboration with participants bringing their own resources and expertise together including focusing their scopes of work for the benefit of the group. Key elements of these achievements are presented here.

2.1. Expert Workshops

A series of EPRI facilitated Formulative Expert Workshops has succeeded in presenting up-to-the-minute information concerning the current state-of-knowledge of creep-fatigue damage interaction. The meetings have been hosted at different global locations and the presentations made at these workshops have been published by EPRI, Table 1. In addition, the discussions held resulted in the development of an agreed listing of key issues for future consideration. These issues have been reviewed and updated as necessary and continue to be used to guide current and future work.

Table 1. Annual Expert Creep Fatigue Workshops

Year	Location	EPRI Reference
2006	Amsterdam, Holland	1014482
2007	Marco Island, USA	1018511
2008	Kyoto, Japan	1018512
2009	Paris, France	1020673
2010	San Antonio, USA	1024440

2011	Bussan, Korea	1024944
2012	Hilton Head, USA	EPRI Life Management Conference Proceedings (in publication)

Analytical evaluation of creep crack initiation has been considered using different methods. The most widely used overall approaches are ASME, Rules for the Construction of Nuclear Facility Components, Class 1 Components in Elevated Temperature Service, Boiler and Pressure Code, Section III, Division 1— Subsection NH [1], TRD 301, Annex I—Design: Calculation for Cyclic Loading due to Pulsating Internal Pressure or Combined Changes of Internal Pressure and Temperature [2], RCC-MR, Design and Construction Rules for Mechanical Components of FBR Nuclear Islands, Section I [3] and R5, An Assessment Procedure for the High Temperature Response of Structures,[4] .

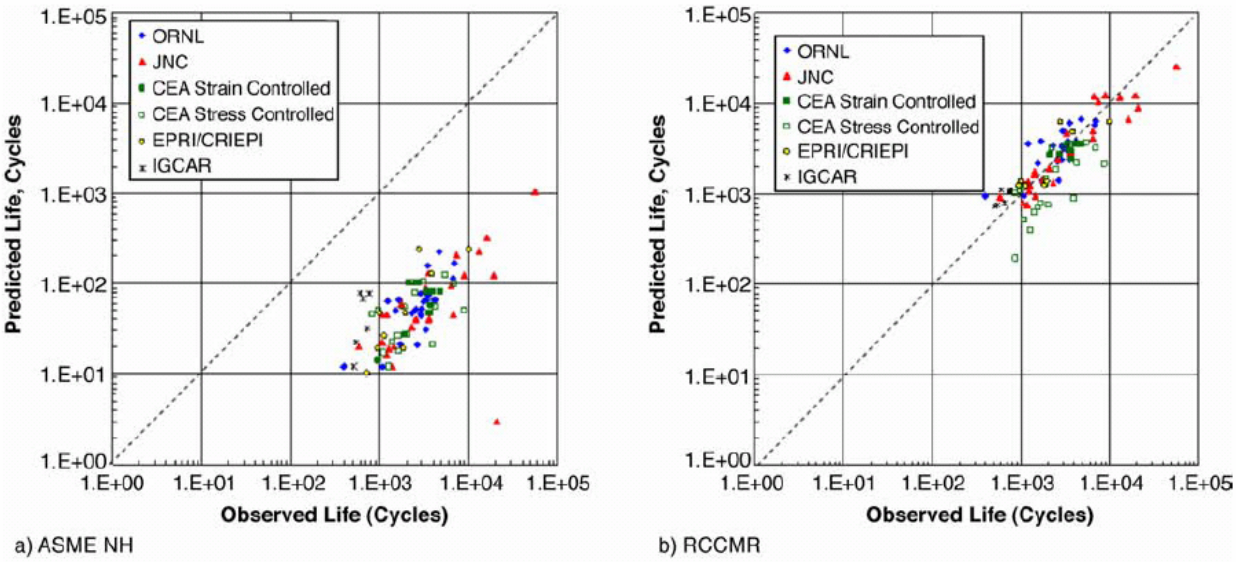

Figure 2. Comparison of the results of different methods of analysis of the same data set of creep fatigue data from Grade 91 steel, performed (a) using ASME NH [1] and (b) using RCCMR [3].

The difference in the approaches leads to very different predictions for creep fatigue behaviour. For example, the recommended interaction line for Grade 91 steel originally proposed in ASME – NH was very conservative. At least some of this excessive conservatism arises because this alloy exhibits complex behavior during cyclic tests at high temperature, and use of time fraction without considering stress-relaxation and strain-softening effects yields a very conservative outcome. The level of conservatism using the standard ASME NH approach is demonstrated by consideration of the results shown in Fig 2(a). Clearly, the calculated lives are at least 10 times less than the observed behavior. Application of an improved methodology, such as that developed in the French Code RCCMR, indicates that by accounting for the metallurgical complexities, the prediction comes into reasonable agreement with the observed behavior, see Fig 2(b).

2.2. Detailed Reports

The EPRI initiative has focused effort in specific agreed areas. One significant activity has been to facilitate preparation of State of Knowledge and other documents on Creep-Fatigue Damage

Interaction. A summary of these Milestone reports is provided in Table 2. It is apparent that the two main methods used to asses creep damage are:

- Time fraction
- Strain fraction (ductility exhaustion)

While these general terms describe the overall methodologies, there are also many variations in the detailed application. These variations and the assumptions that are often required to support the analysis frequently make definitive engineering judgments on accuracy difficult.

Table 2. Milestone Reports

Year	Title	Reference
2007	Creep-Fatigue Damage Accumulation and Interaction Diagram Based on Metallographic Interpretation of Mechanisms	1014837
2008	The State-of-Knowledge Report on Creep-Fatigue Interaction	1016489
2008	Review of Creep Deformation and Failure Models for Creep - Fatigue Assessment,	1018233
2008	Creep Fatigue Damage Interaction: Fatigue Deformation and Failure	1018439
2009	Plant Component Assessment for Creep-Fatigue Damage: Component Assessment Methodologies	1017608
2009	Plant Component Assessment for Creep-Fatigue Damage: Case Studies	1020511
2010	Creep-Fatigue Testing and Assessment Guideline: Material Property Data Requirements for Component Assessment	1019778
2012	Review and analyses of Creep-Fatigue data. Metallographic Atlas and examples of damage	In press

Whether time summation or strain summation is chosen, investigators have usually been at pains to demonstrate an agreement with experimental failure data to within a factor of two. This has generally been managed by increasing use of ‘partitioning’ rules or other degrees of sophistication so that the original models begin to lose their attractiveness – the most robust have proved to be those which are the easiest to use. By tracing some of the history of the damage laws, it appears that the time fraction rule originally took peak stress as the reference and was therefore conservative. Attempts to integrate down a relaxation curve and refine the appropriate time led to non-conservative predictions of life. Thus the interaction diagram was made bi-linear which restored conservatism.

There have been similar difficulties with analyzing ductility data for strain fraction. One basic question must be asked - which is the most physically correct ductility to take? The assumption of an average strain rate by taking ductility divided by time to failure is not necessarily an accurate reflection of secondary creep rate if both primary and tertiary stages of creep are large. Nevertheless, all models acknowledge the decreasing ductility (of whichever form) with decrease in strain rate, and there seems now to be a general acceptance that the ductility exhaustion approach is consistent and less prone to difficulties with scatter. In many cases, however, one may be forced to apply the time fraction rule because of data restrictions – it is highly unlikely that in long-term stress rupture

tests that specimens were fitted with extensometry to determine relevant strain rates, and further there is no guarantee that associated end-of-test ductility values are available.

2.3. Standardization

Many countries have established guidelines and procedures for creep fatigue testing. However, there were differences in detail between many of the recommendations. A key activity facilitated by the EPRI work was thus development of specific ASTM Creep - Fatigue Standards. Currently efforts have resulted in two standards:

- ASTM Standard: Test Method for Creep Fatigue Testing, ASTM E2714-09. This method covers the determination of mechanical properties pertaining to creep-fatigue crack formation in nominally homogeneous materials. It is primarily aimed at providing the material properties required for assessment of defect-free engineering structures containing features that are subject to cyclic loading at temperatures that are sufficiently high to cause creep deformation.
- ASTM Standard: Test Method for Creep-Fatigue Crack Growth Testing, ASTM E2760-10. This test method is concerned with developing creep-crack growth data under cyclic conditions which is used in some more sophisticated assessments of in-service materials when large flaws may be present.

As part of the review and acceptance process by ASTM, the provisional Standards listed above must be evaluated for a precision and bias statement through a round robin test program. A round robin testing program is now complete for ASTM E2714-09[5] (details below) and the precision and bias statement will be added in the next revision of the standard. Planning, preliminary testing, and specimen blank fabrication are now complete for ASTM E2760-10 with round robin testing expected in 2013.

The round robin test program for ASTM E2714-09 utilized Grade 91 steel test blanks (modified 9%Cr-1Mo-V) provided by EPRI. Sixteen laboratories around the world agreed to participate in the study with 13 eventually reporting their test results to EPRI and the ASTM Task Group on Creep-fatigue Crack Formation (E08.05.08). Strain controlled creep-fatigue tests were conducted at 625C at three stain amplitude. Each laboratory followed the provisional standard, but variations in specimen geometry, heating methods, and numbers of tests were acceptable. Statistical analysis of the inter- and intra-laboratory variability was conducted. EPRI highly recommends metallographic assessment as part of the post-test evaluation to see if creep or fatigue damage dominated the failure or if a true creep-fatigue interaction was found. Most laboratories did not do this, so additional post-test metallography was conducted.

Assessment of the data required development of an improved analytical method, not currently prescribed in the standard, to determine the cycles to crack formation. The analysis of the data found the variability factor for the 95% confidence interval bands increased at longer hold times and lower strains. One significant finding was that post-test inspection of specimens was necessary to determine if a test was valid (or not). Uneven heating due to the use of induction heating methods or failures due to bending were not identified by the testing laboratory, but post-test inspection and metallography resulted in some tests being rejected. Fig 3 shows an example of data before (a) and after post-test assessment for validity (b). The round robin (RR) research produced the following recommendations:

- From the results of the RR, the current precision and bias statements in the standard should be modified (this activity is underway)

- The current standard should be modified to include post-test metallographic analysis to ensure that the dominant crack(s) form within the gage length of the specimen and if bending and/or extensive bulging was present in the test specimen warranting rejection of the data.
- A cautionary note should be added in the standard to warn users of the possible effects of heating methods on the C-F lives of test specimens.
- A more in-depth test program should be considered using the available material to characterize the C-F properties of P91 steel and to also investigate the effects of heating methods on the C-F lives.

In addition to these standards, the experts group has produced a code of practice for short-crack growth under creep fatigue conditions [6].

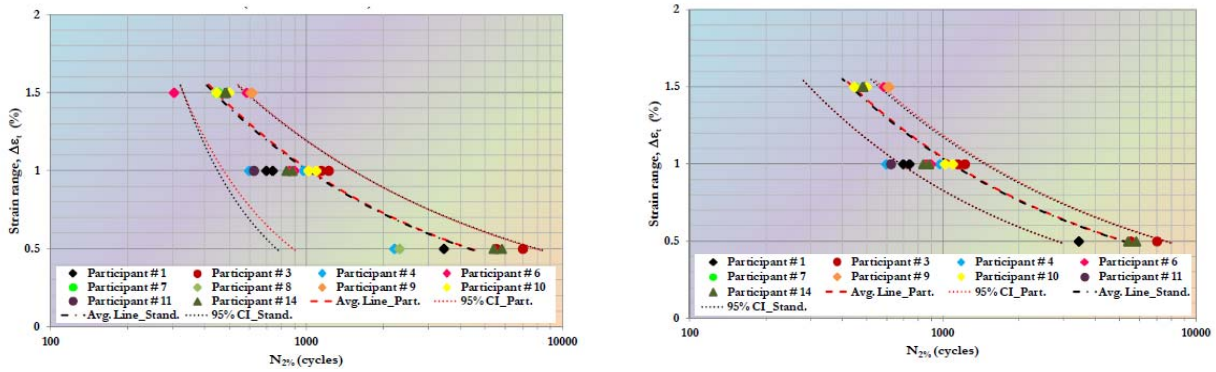

(a) (b)

Figure 3. Comparison of data produced as part of the creep-fatigue RR test program, (a) showing all the data while (b) shows the only data for tests which met the criteria for validity. The 95% confidence interval bands decrease significantly when post-test metallographic evaluation is used to eliminate invalid tests.

3. Discussion

It is clear that updated methodologies for estimating damage in service components should distinguish between sequential damage, for example, steady operation leading to creep followed by cyclic performance resulting in fatigue, and interactive damage, i.e. under conditions where the damage processes lead to rapid damage development. This is particularly important for alloys where time and/or cyclic microstructural changes occur. Damage accumulation in creep-fatigue should be described by a formulation that includes a term giving the influence of creep on fatigue and vice versa. In other words, where damage is truly interactive, the capacity for creep must be reduced due to the fatigue, and the capacity for fatigue must be reduced by creep.

Moreover, the challenges associated with using curve fitting approaches for parametric fitting of experimental data must be considered because although reasonable fits can be obtained to an existing data set, the accuracy of parametric data extrapolations may not be guaranteed. In all cases, there is a major requirement for the results of experimental and analytical programs to be supported by meaningful post test metallographic examination. Thus, post test examination should be performed to document the type, density and character of damage present recording at the very least whether the primary damage is intergranular or transgranular.

The practicality of using complex constitutive equations with many variables also needs to be considered. While design approaches, particularly for turbine components, may be carried out based on detailed knowledge, it is apparent that in-service assessment methods that are slightly conservative and can be applied without the need for extensive materials testing and/or complex stress analysis are required. This is particularly true for boilers and piping. This issue is illustrated by consideration of Fig 4. Here different analytical approaches have been applied to creep fatigue results from Grade 92 steel [7]. The relatively simple strain fraction method results in a consistently conservative prediction of behaviour. In contrast a more detailed modified strain fraction approach shows a much less conservative outcome. Indeed, with this analysis, experimental results and predictions are scattered on both sides of the line showing matching agreement, and all data are well within ±2. The continued validation of simple, sensibly conservative methods for at-risk plant components is necessary because of the implementation of new alloys and operating regimes.

Finally, it is important to note that the effect of Oxidation on Creep - Fatigue Damage interaction and Component Performance must be considered in specific circumstances of the component and details of the in-service environment. It is established that surface scales can lead to damage initiation in some component applications. Thus, when developing laboratory test programs it is important to ensure that the experimental damage mechanisms are relevant to in-service behavior.

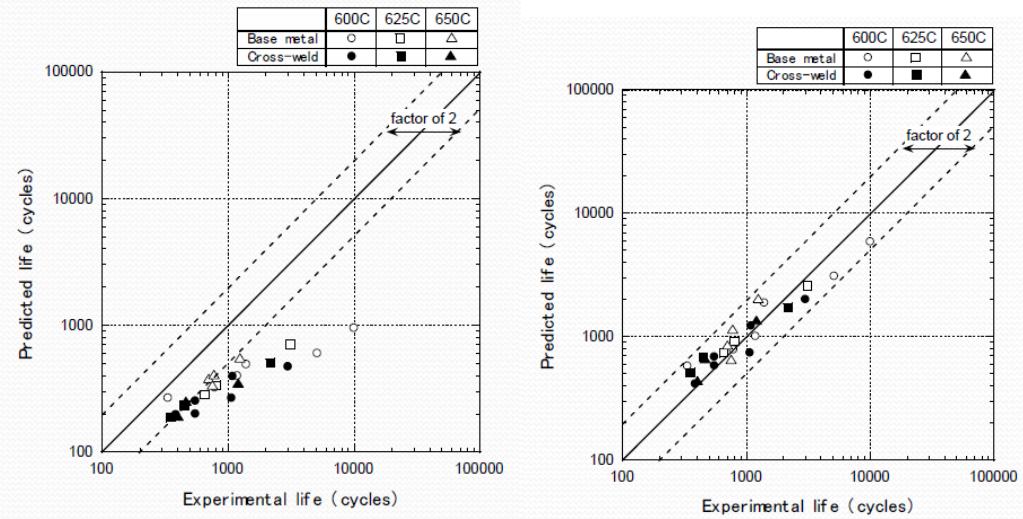

Figure 4. Comparison of Experimental and predicted Creep Fatigue lives for Grade 92 steel tested in the range 600 to 650°C. Analysis was performed using a strain fraction rule in (a) and a more complex Modified Strain Fraction rule in (b). **[7]**

4. On-going Commitment

There are relatively few examples where comprehensive data sets have been established without the need for significant assumptions and/or extrapolations. As an example, challenges with application of the strain fraction/ductility exhaustion methodology often occur because measurements of strain: time behavior are not available. In addition, there are many different suggestions for the appropriate value to use for Strain to Fracture. These variations include:

- Data averaged from available information for the alloy
- Simplified methods for total strain, for example, made using the product of the minimum creep rate and time to failure

- Estimates based on relationships describing creep strain with time for applicable stress/ temperature combinations
- Strain to Failure, Elongation/Reduction of Area, or other measured value for different conditions extrapolated to the conditions of interest

Moreover, although significant information exists for the most widely used boiler and turbine steels; in most cases testing has concentrated on generating parent properties. Thus, less laboratory data exist for weld metals, heat-affected zone (HAZ), or overall weldment performance, even though in many boiler applications, in-service damage in components operating at high temperature frequently occurs associated with welds.

EPRI is working with members of the expert group to establish comprehensive data compilations on the most widely used alloys. It is planned that analysis of the data sets compiled will result in published material data sheets suitable for base line type analysis. Alloys for which Data Compilation Books or 'Creep-fatigue data sheets' are planned include:

– Steels used in Boiler Headers and Piping, for example P22, P91 (X10CrMoV9-1), P92, E911,

– Alloys used in turbine rotors and discs (IN718, IN706, X12CrMoWVNbN10-1-1, IN617, etc.

An example of high temperature creep rupture, deformation and ductility data for Grade 91 steel is shown in Fig 5. The output analysis of this type of data would be included in the envisaged Creep-fatigue datasheets. The plan to produce master creep, fatigue, and creep-fatigue equations most relevant to plant operational conditions is critically important as the data input often becomes the most important source of uncertainty in life assessment calculations. Before releasing these summary equations and curves, the Creep-Fatigue datasheets will be provided to the EPRI expert working group for evaluation and approval. Adoption of standardized equations will aid current needs for creep-fatigue assessment as well as future developments in more sophisticated analytical approaches and in new materials.

5. Concluding Remarks

In general, creep-fatigue design considerations are intended to prevent crack initiation, where crack initiation is defined arbitrarily as the presence of cracks that can be detected visually, for example, 1 mm in length. The difference between crack initiation and failure life in a normal laboratory specimen is often a small proportion of the total life, and it can be argued that the failure endurance of a small specimen corresponds to the endurance at crack initiation in a large component. A recent discussion identified the following as primary classification of component types of concern:

- Thick sections, especially welds,
- Changes in section and complex geometries,
- Welds in low ductility (creep brittle) materials,
- Non-stress relieved welds,
- Thin section welds with defects.

The general consensus regarding methods of assessing crack initiation is the following:

- Time-fraction-type stress-based creep damage is insufficient for predicting life reduction due to creep holds. This is especially the case at the small strain ranges of practical interest. This effect cannot be properly described using creep-time fraction on an interaction diagram.

- Calculation of ductility-exhaustion-type strain-based creep damage tends to overestimate the creep fraction used per cycle when all inelastic strain during a hold period is counted. However, use of a modified stress ductility approach or equivalent appeared to provide the best method of assessment.
- As an initial approach to component assessment it seems that application of an easy to use conservative method offers a practical way of undertaking bounding type calculations. Use of these approaches must consider lower bound materials data and simplified stress analysis for both parent and welds.
- For second level assessments there are advantages to use of probabilistic assessment using validated inelastic analysis. Since this approach requires considerable effort on materials relationships and validation of models it will only be used for a very select number of components
- As Power plant operation now involves an increasing range of cyclic operation, issues of creep and cyclic damage increasingly a concern. The following questions summarize topics of focus for EPRI:
    - How to *predict field damage* using available models/ methodologies? Required accuracy? Important attributes?
    - *Monitoring*. Need for instrumentation in performing a component assessment?
    - Availability of relevant materials data to *assessment of an ageing plant (coal or HRSG pressure parts, rotors)*?
    - *Design*. Can we improve on the design for cyclic high temperature service? Should there be design life based on hours, cycles, and oxidation?
    - What is required for practical component assessment?

It is clear the groundwork laid by EPRI on creep-fatigue damage with the collaboration, assistance, and dedication of a large international experts group was a timely activity due to increased cyclic plant operation. While many tasks are now complete, more work is needed. The international group will continue to meet with key activities on completing standardization, developing creep-fatigue datasheets, and focusing on application case studies to improve component assessments.

Acknowledgements

Thanks to the support and contributions from the invited experts the discussions were successful in identifying key issues and perhaps more importantly developing solutions to these challenges. Support for this work has included the involvement of the following Bob Ainsworth, Dave Dean and Mike Spindler , British Energy (now EdF),UK; Ashok Saxina , Galgotias University, India (formerly University of Arkansas); Stuart Holdsworth, EMPA, Switzerland; Yukio Takahashi, CRIEPI, Japan; Bilal Dogan (formerly of GKSS and EPRI); Peter Skelton, consultant UK (formerly CEGB and Imperial College); Warwick Peyton, ANSTO, Australia; Toshimitsu A. Yokobori ,Tohoku University, Japan: Karl Maile and Andreas Klenk, MPA Stuttgart, Germany; Olivier Ancelet, CEA, France; Hellmuth Klingelhöffer, BAM, Germany; Fujimitsu Masuyama, Kyushu Institute of Technology, Japan; Andre Pineau, Ecole des Mines de Paris, France; Alfred Scholz, T.U. Darmstadt, Germany.

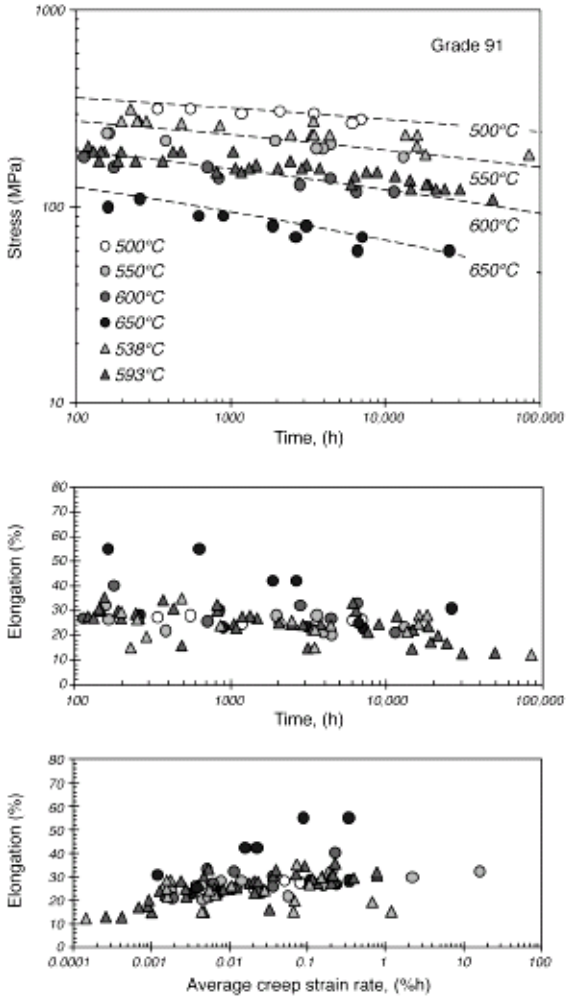

Figure 5. Summary of Properties for Grade 91 steel contained in the data workbook, EPRI report 1019778

References

[1]. ASME, "Rules for the Construction of Nuclear Facility Components, Class 1 Components in Elevated Temperature Service, Boiler and Pressure Code, Section III, Division 1— Subsection NH" (2001).

[2]. TRD 301, "Annex I—Design: Calculation for Cyclic Loading due to Pulsating Internal Pressure or Combined Changes of Internal Pressure and Temperature," *in Technical Rules for Steam Boilers* (1978).

[3]. RCC-MR, *Design and Construction Rules for Mechanical Components of FBR Nuclear Islands*, *Section I—Nuclear Islands Components* Edition. AFCEN (1985).

[4]. R. A. Ainsworth, et al. (eds.), R5, *An Assessment Procedure for the High Temperature Response of Structures*, Barnwood: British Energy Generation (2003).

[5]. Standard Test Method for Creep-Fatigue Testing, ASTM, Designation: E 2714 – 09.

[6]. S.R. Holdsworth, R.P. Skelton, B. Dogan. "Code of practice for the measurement and analysis of high strain creep-fatigue short crack growth." *Materials at High Temperature* **27**(4), 2010. 265-283.

[7]. *Program on Technology Innovation: Evaluation of the Creep-Fatigue Behavior of Grade 92 Steel and Its Predictability*. EPRI, Palo Alto, CA: 2011. 1024588.

Experimental requirements of small and large scale dynamic fracture mechanics testing

Wolfram Baer

BAM Federal Institute for Materials Research and Testing, Berlin, Germany
Corresponding email address: wolfram.baer@bam.de

Abstract The paper deals with experimental requirements of dynamic fracture mechanics tests in general with special focus on ductile cast iron materials. This is based on instructions for dynamic measurement techniques provided by the standards ASTM E 1820 and BS 7448-3 which were compared and rated.
The low blow multiple specimen technique using a drop tower was investigated for crack resistance curve determination on SE(B)25x25 specimens. It was shown that no detrimental effects should be expected from the second impact of the rebounded striker. Strain gage instrumentations for direct force measurement according to the standards provided different results. The ASTM position should be preferred. Important conclusions were drawn concerning hidden friction in drop towers from a comparison of electro-optically measured displacement and calculations from force-time record.
Full blow large scale tests on SE(B)140x280 specimens were performed using a servo-hydraulic test system to determine dynamic fracture toughness values. Different strain gage instrumentations were compared with respect to their force measurement capability. For displacement measurement only a non-contact electro-optical camera technique was applicable. An appropriate method of instrumentation was identified whose results show good agreement with numerical simulations of the tests.
It can be concluded that the recommendations of the test standards provide different results. Therefore, they must not simply be transferred to the own specific test requirements. It is regarded absolutely essential for dynamic fracture mechanics tests in general that all measuring techniques are being validated in advance.

Keywords dynamic fracture mechanics testing, ductile cast iron, measurement

1. Introduction

Design and safety assessment of components subjected to high strain rate or impact (dynamic) loading require adequate material data. Therefore, the focus of this paper is on the experimental determination of dynamic fracture mechanics material data.
The problem of how to measure basic quantities like force and displacement correctly and with sufficient precision in dynamic fracture mechanics tests has still been an experimental challenge, although such tests have been performed for at least 40 years. Advice given on that by test standards such as BS 7448-3 [1] or ASTM E 1820 [2] is fairly limited. The ISO standard 26843 [3] on the determination of dynamic fracture toughness using precracked Charpy specimens (PCVN) is still being drafted while comparable contents has recently been included in the very new annex 17 of [2].
A major lesson to be learned from experience is that the first step of experimental dynamic fracture mechanics investigations should always be to establish an appropriate test method. This seems to be trivial only in the first instance. In fact, the material behavior mainly governs the test techniques which are applicable. Many materials - such as the ductile cast iron (DCI) investigated here - substantially change their deformation, damage and fracture behavior from ductile to brittle by increasing loading rate, decreasing temperature and/or increasing stress triaxiality. Unfortunately, this does not happen suddenly so that the corresponding measuring techniques have to be adapted with deliberation.
As will be shown below, transferability of measuring techniques from one lab to another, from small to large scale tests or vice versa and of more or less common advice from standards to the own very special task cannot simply be taken for granted. In contrary, it is of vital importance to validate the basic measured quantities independently before using the data for further analyses and

to establish material characteristics. Basically this should be a matter of course. But it is time and money consuming and studying the literature often reveals an opposite practice.
Usually, conventional techniques as machine load cells and clip-on transducers cannot be applied to measure the true mechanical response of the specimen due to the short duration of dynamic fracture mechanics tests (microseconds up to milliseconds), inertial effects and resulting signal oscillations. The information which is given on that by relevant test standards [1,2] is shortly summarized in Table 1. Table 1 is limited to single edge bend specimens (SE(B)) since this type of specimen is primarily tested under dynamic loading at BAM.

Table 1. Standard information on force and displacement measurement in dynamic fracture mechanics tests on SE(B) specimens with thickness/width-ratios $1 \leq B/W \leq 4$

Informa-	BS 7448-3 [1]		ASTM E 1820 [2]		
tion on	Main body	Annex A	Annex A13	Annex A14	Annex A17
loading rate	$3 < \dot{K} < 3000$ MPa√m/s	$\dot{K} > 3000$ MPa√m/s	$\dot{K} > 2{,}75$ MPa√m/s, not for impact or quasi--impact testing (free-falling or swinging masses), minimum loading time 1 ms	$\dot{K} > 2{,}75$ MPa√m/s, minimum test time to be calculated to avoid presence of a significant kinetic energy component in the specimen relative to the internal energy and to assure applicability of static J-integral equations	no restriction on impact velocity provided the time to fracture is greater than the calculated minimum test time
force measurement	machine load cell	resistance strain gages attached to both sides of the specimen, wired as two quarter bridges, positions: W/2 from ligament and at W/2 in width	machine load cell as used for static plane strain fracture toughness test generally suitable, but response characteristic to be checked to avoid inertial effects	on-specimen force measurement recommended (remote load cells allowed if requirements are met), full bridge of 4 strain gages on the specimen midplane at the specimen span quarter points (on upper and lower specimen side)	strain gage instrumented striker
displacement measurement	direct load line displacement via horizontal comparator bar	approximation by test machine ram displacement	the same transducers as used for static plane strain fracture toughness test generally suitable, but response characteristic to be checked to avoid inertial effects	fibre-optic transducers	calculation from force/time record, no measurement
COD measurement	clip gage	-		cantilever beam displacement gages like in static fracture toughness testing down to loading times of 1 ms	-

Table 1 outlines the bottom line for a user when dynamic fracture mechanics tests have to be drafted. The first thing to note about Table 1 is that the recommendations of [1] and [2] regarding strain gage positions for force measurement are very different. This mirrors the status in the literature including for instance early basic studies of Ireland [4, 5] or Trudeau [6] which are still frequently cited. Some own experimental results will be discussed below.
With respect to load line displacement measurement BS [1] does not provide a convenient method for higher loading rates. The recommendation to approximate the test machine ram displacement is rated not sufficient. Compared with this, ASTM [2] at least indicates that non-contact optical methods are suited and inertial effects shall be avoided.

2. Experiments

The paper reports on experimental fracture mechanics impact investigations on bend type specimens of DCI materials. Depending on the DCI's material behavior [7], two types of tests have been investigated: a small scale low blow multiple specimen technique using a drop tower was investigated for crack resistance curve determination as well as large scale full blow tests on SE(B)140 specimens were performed. Different experimental aspects of the test methods are discussed here. Mechanical properties, microstructural aspects and the values of the fracture mechanics characteristics of the materials are not in the focus of this paper. They will be reported elsewhere.

2.1. Small scale low blow tests

When the DCI material exhibits R-curve behavior, it is still first choice to use the low blow multiple specimen technique for dynamic crack resistance curve determination. Unfortunately, single specimen techniques, as the key curve method, have not been proved successfully to be appropriate and to provide enough precision with DCI materials at dynamic loading conditions [8]. Primary goal of the investigations was to setup a multiple specimen test method to determine dynamic crack resistance curves in the temperature range from ambient to -40 °C. Series of small scale low blow tests on SE(B)25 specimens (length 138 mm, width 25 mm, thickness 25 mm, $a_0/W = 0.5$) were performed by use of a drop tower test system (Fig. 1) at stress intensity rates in the linear-elastic range of approximately $3 \cdot 10^5$ MPa$\sqrt{}$ms^{-1}.

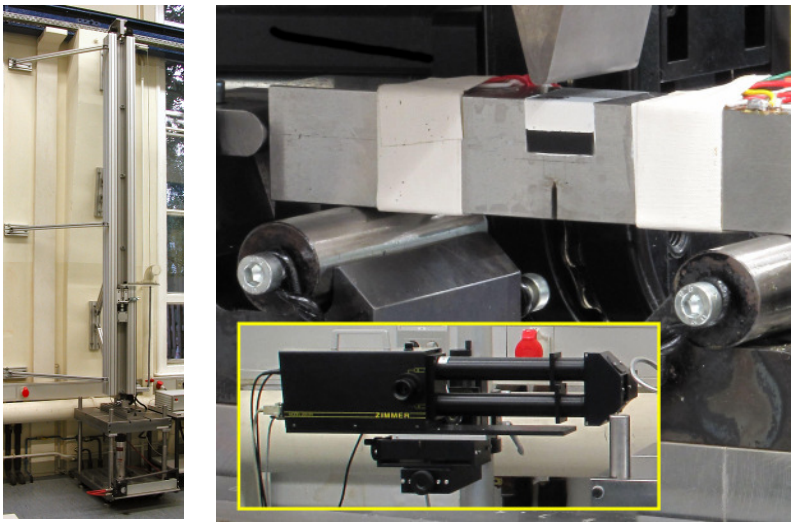

Figure 1. Left: BAM drop tower test system with $v_{0max} \approx 8$ ms^{-1}, max. energy $\approx$ 300 J, right: test setup with SE(B)25-specimen instrumented for opto-electronic measurement of load line displacement.

Fig. 2 shows different strain gage instrumentations which were compared with respect to their force measurement capability. All strain gages were statically calibrated before the tests.

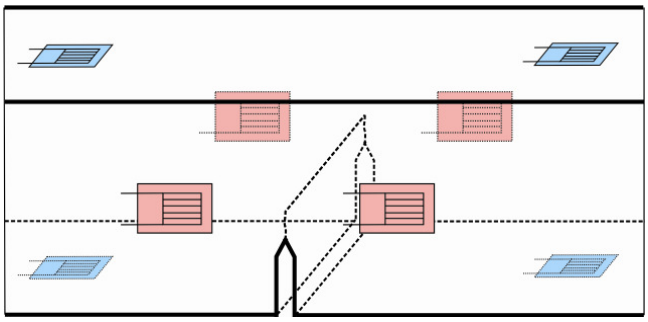

Figure 2. Strain gage instrumentations for direct force measurement on SE(B)25-specimens, blue: ASTM full bridge at specimen quarter points, red: 2 BS half bridges at W/2.

Basic principle of low blow tests is that a defined amount of energy is transferred to the specimen by a single hit of the striker causing deformation and stable crack growth. Therefore, it has either to be realized that second and following hits of the rebounded striker are prevented or that they are of such a magnitude that they will not cause crack growth in the specimen. Catching of the rebounded striker is practically impossible due to the low rebound height and the corresponding short time. Fig. 3 and Fig. 4 show force-time records of a low blow test on a DCI SE(B)25-specimen with $a_0/W = 0.5$ at -40 °C. The first hit of the striker causes the first force peak (low blow test) and the peaks (impulses) 2 to 4 are caused by the successively rebounding striker. After the test a stable crack growth of 0.62 mm was measured on the fracture surface ($a_E/W = 0.52$). As can be seen from comparison of the force signal height with the yield load of the specimen after the first hit ($a_E/W = 0.52$) or even assuming a maximum crack length of $a_{max}/W = 0.55$, the magnitude of the second and following impulses is clearly below the yield loads. This holds for BS- as well as ASTM-strain gage force measurement. The differences between ASTM- and BS-records will be discussed below. For the nonce, it can be concluded that second and following impulses cause only elastic deformation and do not contribute to crack growth so that they can be ignored.

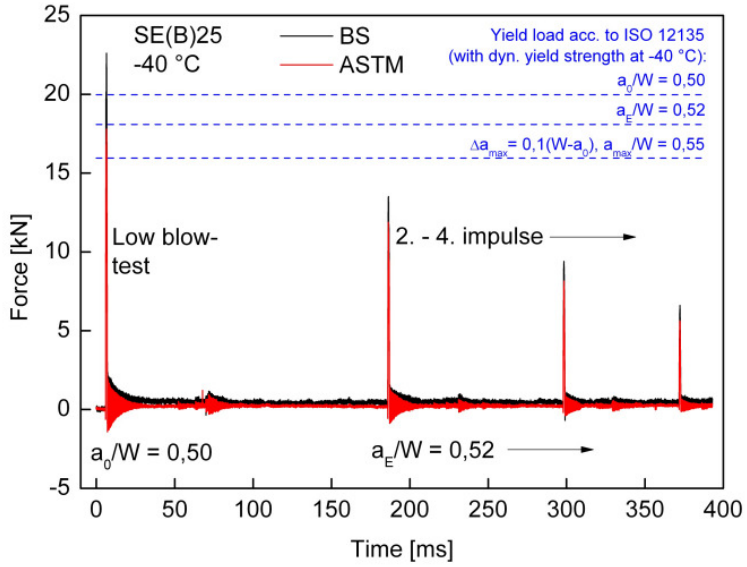

Figure 3. Force-time records of a low blow test, DCI, SE(B)25-specimen, $a_0/W = 0.5$, -40 °C.

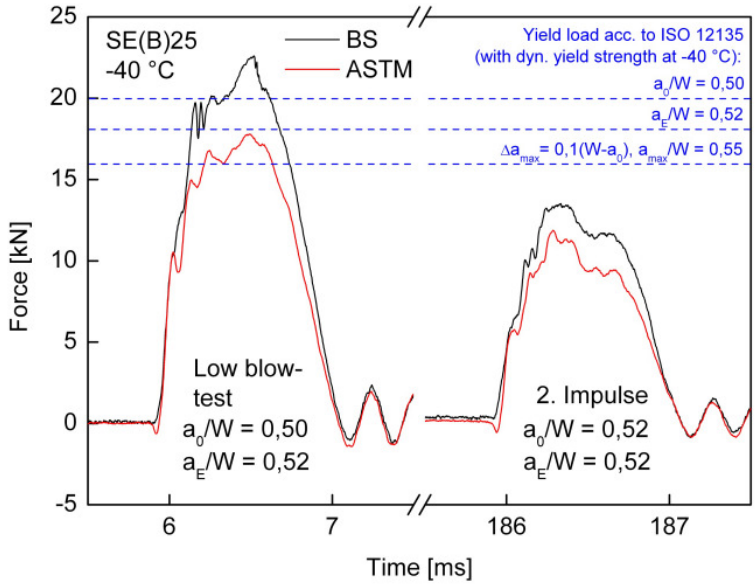

Figure 4. Details of force-time record from Fig. 3, DCI, SE(B)25-specimen, $a_0/W = 0.5$, -40 °C

As already indicated above, strain gage instrumentations according to ASTM and BS provide different results independent from temperature, Fig. 5, left. To clarify this, reference tests under quasistatic loading had been performed with the same instrumentation, Fig. 5, right. They revealed that the ASTM signal widely conforms to the reference while BS significantly differs and displays a remaining tensile force at the end of the test when the specimen is fully unloaded. In order to investigate if plasticity at the BS W/2 positions causes these differences (note: W = B and not W = 2B), a test with BS strain gages at a distance of W from the ligament was performed. A significant improvement could not be achieved. Therefore it is concluded for low blow tests that strain gages at ASTM positions work well with the investigated SE(B)25-specimens while BS positions cannot be recommended.

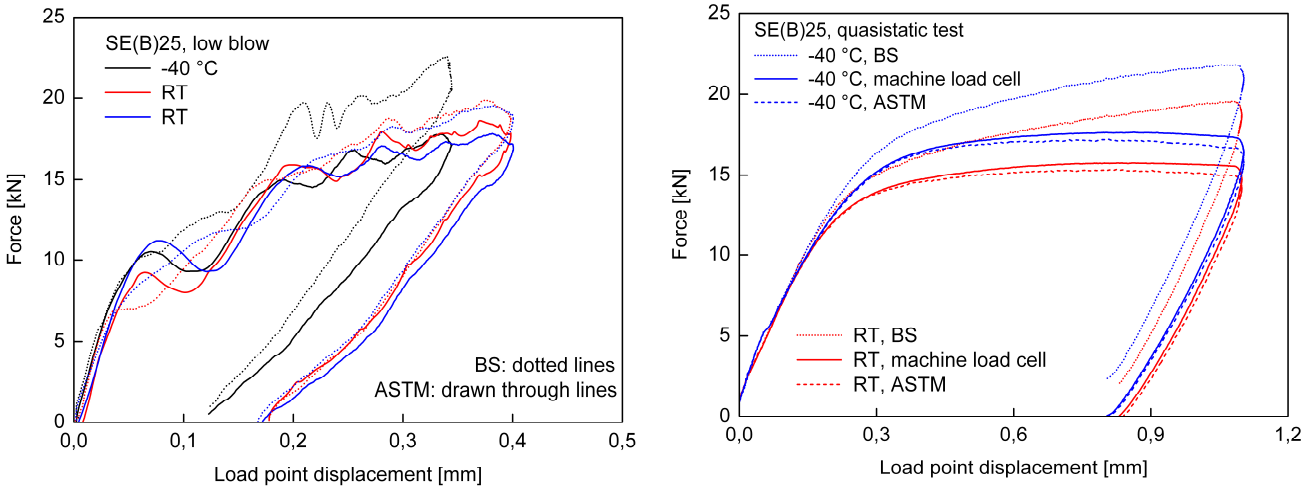

Figure 5. Comparison of ASTM and BS strain gage force measurements on SE(B)25-specimens in low blow tests (left) and quasistatic tests (right).

Basically, the load line displacement in tests using instrumented pendulum impact machines or drop towers can be determined by double integration of the force-time record. This is considered an attractive way to provide displacement data when expensive non-contact measuring equipment is not available or not applicable. However, as can be seen from Fig. 6, left, tremendous differences/errors may occur between the calculated values and the reference measured by an

independent and verified method. The errors were due to slight energy losses by hidden friction which may easily occur especially in larger drop towers. Therefore, the drop tower was constructively optimized and the tests were repeated, Fig. 6, right. The calculated and the measured displacement values are now nearly equal so that dynamic fracture mechanics tests could even be performed without having special equipment for displacement measurement available. But it must be considered an absolute essential prerequisite that this procedure can only be followed when the substance of Fig. 6 had been proven in advance. Further technical information on the camera and the validation of the corresponding measurement results is given at the end of chapter 2.2.

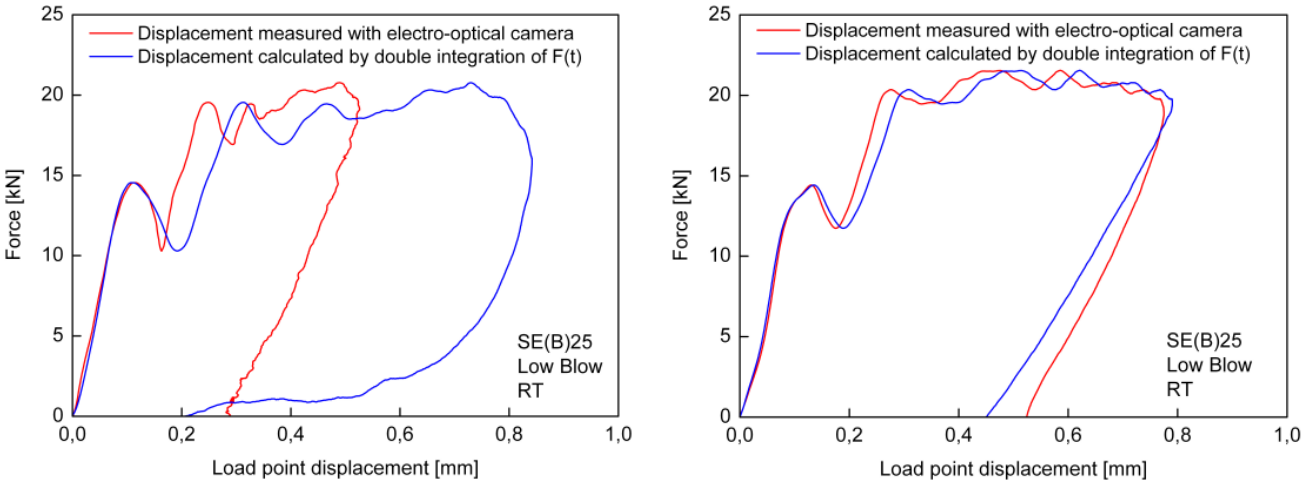

Figure 6. Force vs. calculated and measured displacement,
left: drop tower with friction losses, right: constructively optimized drop tower.

The question of how to detect initiation of stable crack initiation in dynamic fracture mechanics tests has not yet been resolved satisfyingly. Reported techniques like magnetic emission, acoustic emission or near crack tip strain gages seem to work in special cases but cannot be seen as robust methods nor generally be applicable. Additionally, they do not seem to work with DCI reproducibly enough. Therefore, an alternative technique based on the detection of stable crack initiation by failure of strands of a crack propagation sensor attached to the ligament was investigated here, Fig. 7. Two different sensor positions - (1) first strand right in front of the initial crack tip on the specimen surface (Fig. 8, left) as well as (2) sensor at the initial crack tip on the specimen surface (Fig. 8, right) - were investigated. It was observed that in both cases the crack sensors provide discrete signal jumps in quasistatic and dynamic tests on SE(B)25 specimens at RT and -40 °C. Nevertheless, with position (1) there is a large scatter of detected initiation forces F_{ini} of $0.5F_{max} \leq F_{ini} \leq 1.0F_{max}$. Material scatter may be a possible reason. But it seems more likely to

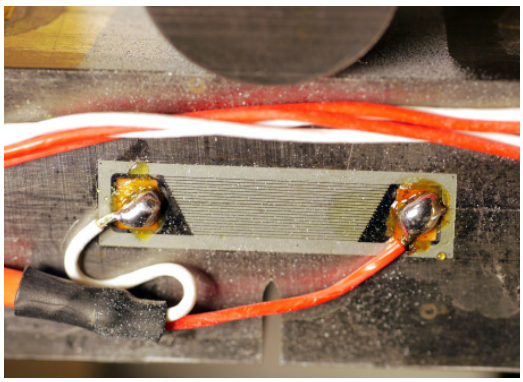

Figure 7. Crack sensor in front of the crack tip of a SE(B)25-specimen.

be due to the sensor position and analysis method. The sensor was placed only based on the nominal position of the precrack tip on the specimen surface. The real, measured initial crack length across the specimen thickness is not taken into consideration. Therefore, sensor position (2) on the crack was investigated. With (2) failure of the n-th strand positioned at the post-test measured mean initial crack length a_0 indicates crack initiation. Scatter of the crack initiation forces F_{ini} can still be observed with this procedure, $0.86F_{max} \leq F_{ini} \leq 1.0F_{max}$. But it is clearly lower than with method (1), although the tests were performed at -40 °C this time. Nevertheless, the data base for method (2) is still too small to finally rate the appropriateness of the technique.

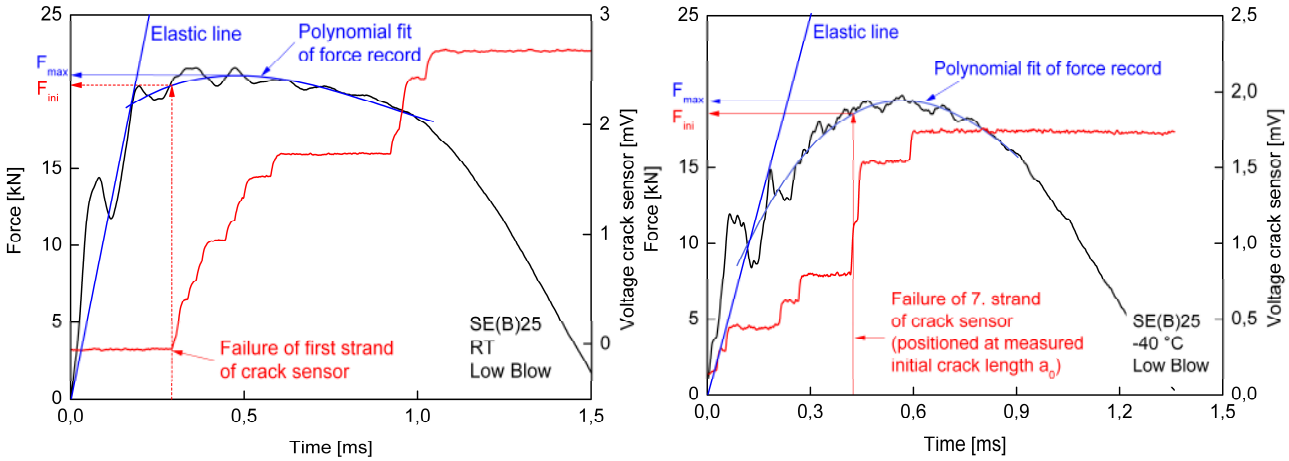

Figure 8. Principle of detection of stable crack initiation by failure of crack sensors, left: (1) crack sensor position at crack tip and failure of the first strand, right: (2) crack sensor position on the crack and failure of the n-th strand positioned at the measured initial crack tip.

2.2. Large scale full blow tests

A large wall thickness is typical for many applications of DCI such as casings or transport and storage cask for radioactive materials. In order to investigate how the fracture mechanics characteristics of small specimens, which could even be determined within quality assurance procedures, correspond to the results of large specimens with component-like thicknesses, series of large scale full blow tests were performed. Since large specimens do not show R-curve behavior under dynamic loading at -40 °C, a test method was developed for determination of dynamic fracture toughness values with SE(B)140 specimens (length 1350 mm, width 280 mm, thickness 140 mm, $a_0/W = 0.5$) at -40 °C by use of a servo-hydraulic impulse loading test system (max. 1 MN and 8 ms^{-1}). As with small scale testing, different strain gage instrumentations (Fig. 9) including as per BS and ASTM were compared with respect to their force measurement capability with SE(B)140 specimens at impact conditions and a stress intensity rate of $5 \cdot 10^4$ MPa$\sqrt{m}s^{-1}$. All strain gages were statically calibrated before the tests. Further details are reported for instance in [9].
Fig. 10 displays an example of force–time records and crack sensor signals. The test can roughly be assorted into 3 phases. During phase I, the rubber mat between striker and specimen is compressed and finally cut. After that, in phase II, the actual loading of the specimen takes place at a significantly higher but nearly constant loading rate compared to phase I. The stress intensity rate which is characteristic for the test is calculated as differential quotient in phase II.
Phase III is characterized by unstable cleavage crack growth until final fracture of the specimen. In phase III, the force signals F1–F4 and F2–F3 are not considered for further analysis with respect to the underlying test goal to determine dynamic fracture toughness at initiation of unstable cleavage fracture. The good agreement of the signals F1–F4 and F2–F3 illustrates the high symmetry of

loading. As expected, the machine load cell only provides a damped and less sensitive force signal which is delayed in time.

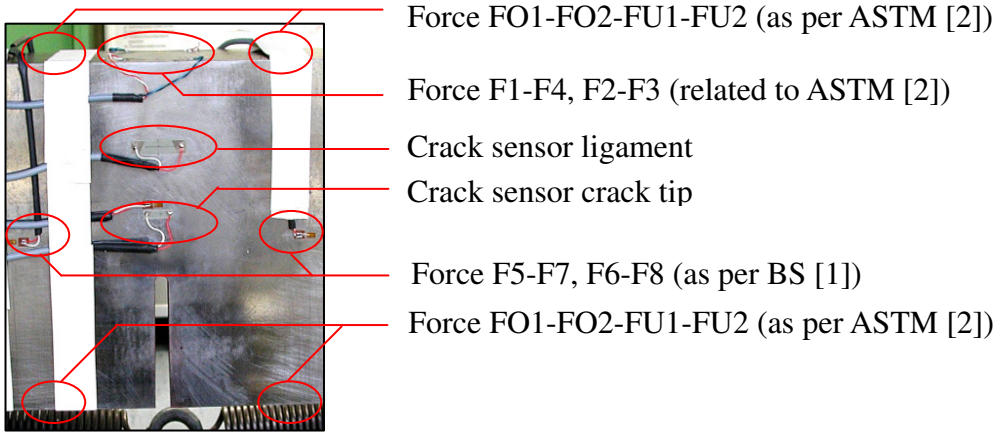

Figure 9. Strain gage instrumentation and crack sensors in and near the ligament of a SE(B)140-specimen.

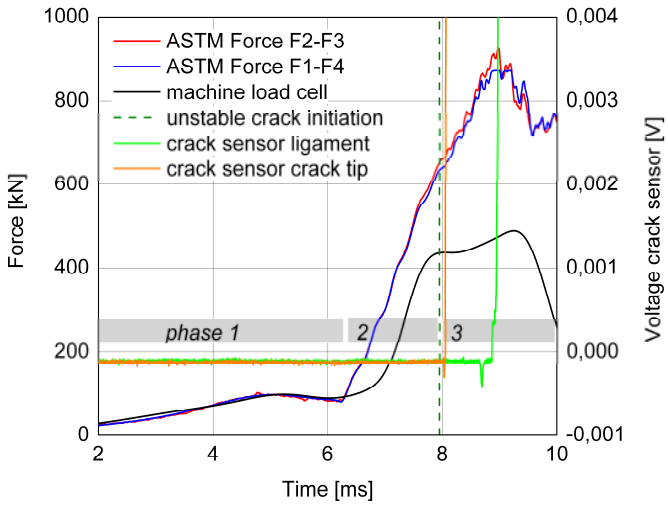

Figure 10, Signals from a dynamic SE(B)140 fracture mechanics test.

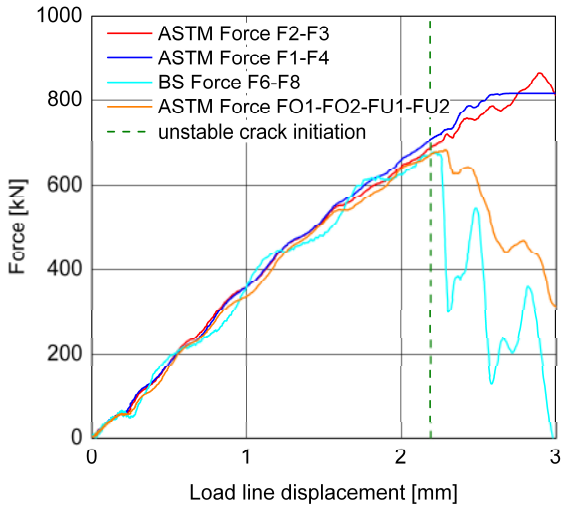

Figure 11a, Examples of force-displacement records of dynamic SE(B)140 fracture mechanics tests.

Finite element simulations of the SE(B)140 impact tests in [10] showed a good agreement between time dependent F1–F4 and F2–F3 force signals and numerically determined force-time data. The calculated crack tip loading in terms of K at the experimentally provided time of cleavage crack initiation corresponds very well to the experimental K_{Id} value.

Common feature of all test series is that the ASTM strain gage positions F1-F4 and F2-F3 show smallest dynamic effects, best sensitivity and reproducibility up to unstable crack initiation. Fig. 11 exemplarily shows the responses of different ASTM as well as BS force strain gage instrumentations for several specimens. As Fig. 11a reveals, the signals of ASTM and BS strain gage positions may nearly coincide. But in most of the cases the BS signals are below ASTM and show much more dynamic effects, Figs. 11b and 11c. Mostly, the ASTM half bridges F1-F4 and F2-F3 provide comparable signals to the ASTM full bridge FO1-FO2-FU1-FU2 up to unstable crack initiation. Nevertheless, the F1-F4 and F2-F3 signals show slight advantages in reproducibility and, very important, they offer valuable redundancy of measurement and simultaneously information on loading symmetry.

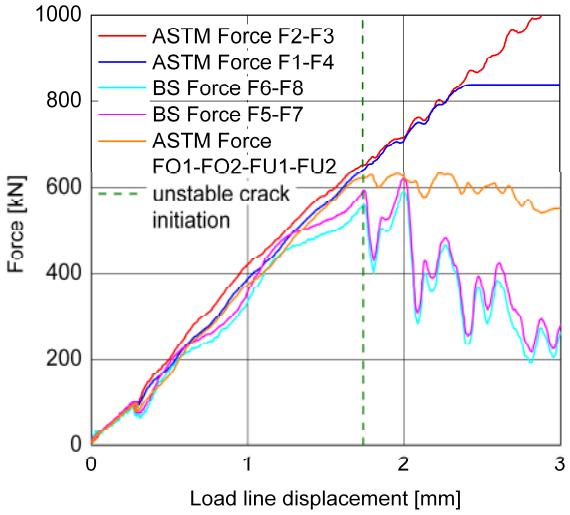

Figure 11b, Examples of force-displacement records of dynamic SE(B)140 fracture mechanics tests..

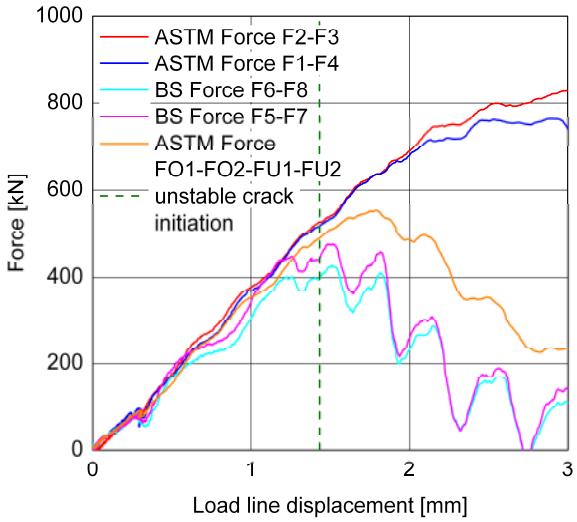

Figure 11c, Examples of force-displacement records of dynamic SE(B)140 fracture mechanics tests.

Generally, the F1-F4 and F2-F3 signals do not instantly show sharp drops at unstable crack initiation as it is known from Type I, II or III brittle behaviour of small PCVN specimens as per Annex 17 of [2] but keep rising until the crack has reached the crack sensor in the ligament, Fig. 10. This is not of concern when stable crack growth is absent and the test is only analyzed until unstable crack initiation. Nevertheless, this underlines the necessity of an adequate experimental method for detection of unstable crack initiation.

In this study, a method was elaborated where the initiation of unstable cleavage crack extension is indicated by fracture of the first strand of a crack sensor (Fig. 9) close to the crack tip (first steep signal rise in Fig. 10). However, since this crack sensor is not positioned at the crack tip directly but some millimeters in front of, a correction of the initiation time is necesssary. This is done by means of the crack velocity which is calculated from the known distance between the two crack sensors and the time measured between their responses. Since the distance between the crack tip and the first crack sensor is known too, the corrected time of unstable cleavage crack initiation can then be calculated. Due to the very limited plasticity in the ligament no problems related to sensors stripping away from the specimen surface were observed.

Since tactile displacement measurement devices are much too slow, the load line displacement was measured using an electro-optical camera, Fig. 12, as practiced with the small scale dynamic tests.

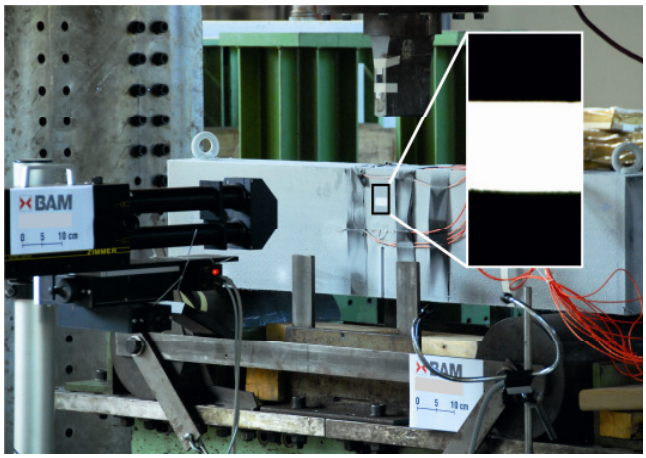

Figure 12. Electro-optical camera for measurement of load line displacement in dynamic SE(B)140-specimen tests.

The camera has two objective lenses, each of which tracing a black-white contrast on the specimen ligament so that two redundant displacement signals can be provided. The camera measurement technique is validated statically by gauge blocks and dynamically by comparison of the results of elongation measurement at rupture in dynamic tensile tests with the corresponding manually determined values.

3. Summary and conclusions

Experimental aspects of dynamic fracture mechanics tests on bend type specimens were discussed and different techniques for the measurement of force, displacement and crack initiation were investigated. It can be concluded that the fairly limited recommendations of the test standards may provide significantly different results. Therefore, they cannot simply be transferred to the own specific experimental tasks. It must be considered an absolute essential prerequisite that the used measuring techniques are validated in advance. The detection of unstable crack initiation by crack sensors in K_{Id} tests works well. Compared to that, the use of crack sensors to detect stable crack initiation in low blow R-curve tests needs further enlargement of the data base to finally rate the technique.

References

[1] BS 7448-3, Fracture mechanics toughness tests, Part 3: Method for determination of fracture toughness of metallic materials at rates of increase in stress intensity factor greater than 3 MPa √m/s, 2005.

[2] ASTM E 1820, Standard Test Method for Measurement of Fracture Toughness, 2011.

[3] ISO 26843, Metallic Materials – Measurement of fracture toughness at impact loading rates using precracked Charpy specimens, in preparation.

[4] D.R. Ireland, Procedures and Problems associated with Reliable Control of the Instrumented Impact Test, Instrumented Impact Testing, ASTM STP 563, 1974, pp. 3-23.

[5] D.R. Ireland, Critical review of instrumented impact testing, Dynamic Fracture Toughness: an International Conference arranged by the Welding Institute, London, 5-7 July 1976, published in 1977, pp. 47-62.

[6] Trudeau, L.P.: Dynamic toughness – its relevance and measurement, Research report R 275, Department of Energy, Mines and Resources, Mines Branch, Ottawa, Oct. 1974.

[7] W. Baer, A. Eberle, D. Klingbeil, The impact of ductile cast iron fracture behaviour on dynamic fracture mechanics R-curve testing using key curve methods, In: Fracture of Materials and Structures from Micro to Macro Scale, 18th European Conference on Fracture ECF18, Editors: D. Klingbeil, M. Vormwald and K.-G. Eulitz, ESIS European Structural Integrity Society, Dresden, Germany, Aug 30-Sep 03, 2010, 8 pages.

[8] W. Baer, D. Bösel, A. Eberle, D. Klingbeil, Determination of dynamic crack resistance of ductile cast iron using the compliance ratio key curve method, Engineering Fracture Mechanics 77 (2010), pp. 374-384.

[9] W. Baer, P. Wossidlo, B. Abbasi, M. Cassau, R. Häcker, R. Kossert, Large scale testing and statistical analysis of dynamic fracture toughness of ductile cast iron, Engineering Fracture Mechanics 76 (2009) 8, pp. 1074-1086.

[10] M. Enderlein, M. Kuna, A. Ricoeur, W. Baer, K. Müller, K. Klein, H.-P. Winkler, Numerische Analyse des Stossbiegeversuches zur Ermittlung der dynamischen Bruchzähigkeit, Proceedings der 35. Tagung des DVM-AK „Bruchvorgänge“, 18.-19.2. 2003, Freiburg, DVM-Bericht 235, 2003, pp. 251-260.

Metallic melt fracture and fragmentation under the high-current electron irradiation

Polina N. Mayer.[1,*], Alexander E. Dudorov[1], Alexander E. Mayer [1],

[1] Department of Physics, Chelyabinsk State University, 454001, Russia
* Corresponding author: polina.nik@mail.ru

Abstract Action of the high-current electron beam leads to an intensive heating of a surface layer of the irradiated metal. Rapid temperature increase can cause melting of the surface layer and generate intensive stresses in it. Release of these stresses induces fast expansion of the molten metal and, on the contrary, results in tension. Tension of the melt activates nucleation, growth and coalescence of vapor bubbles, it means, fracture and fragmentation of the metallic melt. In present work we numerically investigate kinetics of the liquid metal fracture and fragmentation under the dynamic tension initiated by the powerful electron irradiation. Metal is treated as a two-phase medium consisting of vapor bubbles in liquid metal at the first stage of the evolution and of liquid drops in vapor at the second stage. Two-level approach is used: on the macroscopic level, the irradiated metal is treated as a two-phase heterogeneous medium in the one-velocity approximation, while on the microscopic level, the exchange of energy, mass and volume between both phases are described including grow or decrease of size of the vapor bubbles or liquid drops. Generation of ultra-dispersed particles of copper at the high-current electron beam irradiation is numerically investigated.

Keywords Liquid metal, Dynamic fracture, Electron irradiation, Heterogeneous medium, Vapor bubbles

1. Introduction

Action of the high-current electron beam on the metals can be used for production of the ultrafine metal particles [1,2]. The process of particles formation passes through several stages. At the first stage, during the irradiation, fast beam electrons lose their energy in the substance, which leads to the metal heating and formation of the high pressure region inside the energy release zone [3-5]. The next stage is an expansion of the heated and "compressed" layer of metal, which generates tensile stresses (negative pressure) in it. Destruction of the expanded metal begins at the expense of nucleation and growth of cavities. The higher temperature of the surface layer leads to the lower threshold of the negative stress, required for the destruction [6,7].

Complete destruction of the liquid phase takes place when the cavities grow up thus much to coalescence with each other forming a singly connected vapor phase, while the remaining liquid is fragmented on drops. The following expansion of the vapor-drops mixture (aerosol) is accompanied by the metal evaporation and condensation on drops. At the sufficient level of the enclosed energy, the liquid drops can be fully evaporated with formation of pure vapor. In turn, the adiabatically expanding vapor can become oversaturated, which result in the nucleation of liquid drops in it. In the paper [8] the condensation of the metal particles from the pure vapor, obtained at the complete evaporation under the action of the high-current electron beam, was numerically investigated; it was shown, that the homogeneous nucleation and the coagulation of the drops determine the size of the produced metal nanoparticles.

Meanwhile, the electron beam irradiation leads to the incomplete evaporation in the most cases. A part of metal remains condensed in the form of liquid drops. During the adiabatic expansion these drops become the centers of condensation; their quantity determines the quantity and size of the formed ultrafine metal particles. In this report a mathematical model of the ultrafine metal particles formation in the case of incomplete evaporation is described. Kinetics of evaporation and condensation of metal irradiated by the high-current electron beam is numerically investigated.

Metastable version of the wide-range equations of state [9,10] has been used for the description of superheated liquid and supersaturated vapor.

2. Mathematical model of substance dynamics with evaporation and condensation

Metal was treated as a two-phase medium consisting of the vapor bubbles in liquid metal on the first stage and of the liquid drops in vapor thereupon. Size of bubbles and drops (about $0.1\ \mu\text{m}$) is less than the typical length scale of the problem (the last one is of the order of electron rage in substance about $10 \div 1000\ \mu\text{m}$). It allows using of the continuous approximation in which both phases are described by continuous fields of parameters: concentration and radius of bubbles (drops), pressure, temperature, density and volume fraction of liquid and vapor phases in each point of space. Estimations showed that the phases must have approximately the same velocities; therefore we have used a one-velocity approximation. Substance dynamics has been described by the continuum mechanics equations. The beam action has been taken into account through energy release of fast electrons. Generation and growth of vapor bubbles and consequent evolution of drops have been described by kinetic equations for phase transition [11]. A simple scheme of transition from the bubbles in liquid to the drops in vapor (a percolation problem) has been constructed.

We consider the 1D problem: substance moves along z-axis. At different stages of evolution the medium means: a) pure condensed metal (solid or liquid); b) liquid metal with trapped bubbles; c) vapor with trapped drops; and, maybe, d) pure vapor. The liquid (or solid) is a carrying agent at stages a) and b), while the vapor is carrying agent at stages c) and d). A dispersed phase consists of vapor bubbles at stage b) and of liquid drops at stage c); and this phase is clearly absent at stages a) and d).

The continuum mechanics equations for substance dynamics in Lagrangian coordinates are the next:

$$\frac{1}{\rho}\frac{d\rho}{dt} = -\frac{\partial v}{\partial z}, \tag{1}$$

$$\rho\frac{dv}{dt} = -\frac{\partial P_c}{\partial z}, \tag{2}$$

$$\rho\frac{dU}{dt} = -P_c\frac{\partial v}{\partial z} + \rho\cdot D, \tag{3}$$

where v is the z-component of substance velocity; P_c is a pressure in the carrying agent phase; D is the energy release function. Here and further the index c denotes the carrying agent phase, while the index d denotes the dispersed phase. Average density of the medium is $\rho = \rho_c\alpha_c + \rho_d\alpha_d$, where $\alpha_{c,d}$ is the volume fraction of corresponding phase. Average specific internal energy U is given by the next expression: $U = \left(U_c\alpha_c\rho_c + U_d\alpha_d\rho_d\right)/\rho$.

Eq. (2) determines the substance velocity v, which is equal for both phases. Eq. (1) and Eq. (3) must be supplemented by several assumptions for determination of the thermodynamic parameters of each phase. We have supposed that the dispersed phase volume is constant during the substance movement as a whole, and it changes only as a result of interaction between the phases; this interaction leads to the bubbles and drops growth or reduction. In these assumptions one can obtain the next equations:

$$\frac{d\alpha_c}{dt} = \alpha_d \frac{\partial v}{\partial z} - w, \tag{4}$$

$$\frac{d\alpha_d}{dt} = -\alpha_d \frac{\partial v}{\partial z} + w, \tag{5}$$

$$\frac{d\rho_c}{dt} = \frac{\rho_c}{\alpha_c}\left(-\frac{\partial v}{\partial z} + w\right) - \frac{J}{\alpha_c}, \tag{6}$$

$$\frac{d\rho_d}{dt} = -\frac{\rho_d}{\alpha_d} w + \frac{J}{\alpha_c}, \tag{7}$$

$$\rho_c \alpha_c \frac{dU_c}{dt} = P_c\left(-\frac{\partial v}{\partial z} + w\right) - Q, \tag{8}$$

$$\rho_d \alpha_d \frac{dU_d}{dt} = -P_c \cdot w + Q. \tag{9}$$

In the Eqs (4)-(9) w is the growth rate of the dispersed phase volume in a unit volume of the medium; it can be expressed as that follows:

$$w = n \cdot 4\pi R^2 \cdot \dot{R} + \left(4\pi/3\right) R_{cr}^3 \cdot \dot{n}, \tag{10}$$

where n is the concentration of the dispersed particles (bubbles or drops) in the medium, and R is radius of this particles; R_{cr} is the radius of critical (nucleating) bubbles.

In the Eq. (6), Eq. (7) J is the growth rate of the dispersed phase mass in a unit volume of substance:

$$J = n \cdot m_1 \cdot \dot{g} + \left(4\pi/3\right) R_{cr}^3 \cdot \rho_v \cdot \dot{n}, \tag{11}$$

where m_1 is the mass of one atom of the substance; g is a number of atoms in the bubble (or in the drop); ρ_v is a saturated vapor density. And, finally, the value Q characterizes the heat exchange between the phases, which tends to equal temperatures of the phases.

The next equation describes the bubbles growth in the liquid at the stage b) and a size change of the liquid drops at the stage c):

$$\ddot{R} = -\frac{3}{2}\frac{\dot{R}^2}{R} + \left[P_d - P_c - \frac{2\sigma}{R}\right] \cdot \frac{1}{R\rho} A - B\frac{8}{3}\frac{\eta}{\rho_c}\frac{\dot{R}}{R^2}, \tag{12}$$

where s is the surface tension and h is viscosity of the liquid metal; A and B are the numerical factors: $A = B = 1$ at the stage b), and $A = 5$, $B = 1,25$ at the stage c). Critical radius of the vapor bubble is equal to

$$R_{cr} = \frac{2\sigma}{P_v - P_c}, \tag{13}$$

where P_v is a saturated vapor pressure. The bubbles nucleation rate is

$$\dot{n} = \frac{c}{\left(2R_{cr}\right)^4} \cdot \exp\left(-\frac{W_{cr}}{kT_c}\right), \tag{14}$$

where c is a sound speed in liquid metal, T_c is a temperature, k is the Boltzmann constant, and is the formation work of the critical bubble:

$$W_{cr} = \frac{16\pi}{3}\frac{\sigma^3}{\left(P_v - P_c\right)^2}. \tag{15}$$

In the case of liquid drops, the condition $\dot{n} = 0$ has been supposed to hold, but the drops can

disappear if the number of atoms in it $g \le 2$ (the complete evaporation).

Number of atoms in each bubble is controlled by the next equation:

$$\frac{dg}{dt} = g\frac{2R}{c}\left[\exp\left(\ln\left\{\frac{P_v}{P_c}\right\} - \frac{4\pi R_1^2\sigma}{3kT_c \cdot g^{1/3}}\right) - 1\right], \tag{16}$$

where

$$R_1 = \left[\left(3m_1\right)/\left(4\pi\rho_v\right)\right]^{1/3}. \tag{17}$$

Pressure and temperature of the caring agent phase and of the dispersed phase have been obtained from the metastable equation of state: $P_{c,d} = P\left(\rho_{c,d}, U_{c,d}\right)$, $T_{c,d} = T\left(\rho_{c,d}, U_{c,d}\right)$. This equation of state has been used for determination of the density ρ_v and pressure of the saturated vapor as well.

Than the bubbles became large enough they merge and form a simply connected phase. On the contrary, the liquid divides on separate drops. These drops are the condensation centers in the expanding and cooling vapor. Number and sizes of the liquid drops are determined by the number and sizes of the vapor bubbles at the moment of merging. We have established this connection in a simplest case of equal distance between the bubbles centers. Bubbles merge then their diameters $2R$ reach the value of a distance between their centers. Single bubble occupy the volume $4\pi R^3/3$, liquid volume per one bubble at this time is $\left(8 - 4\pi/3\right)R^3$. We have assumed that the number of resulting drops is equal to the number of vapor bubbles, and then $\left(8 - 4\pi/3\right)R^3$ is the volume of one liquid drop. Due to the surface tension, the drops obtain a spherical form after the liquid phase division, and the radius of such spherical liquid drop can be estimated as $R_{\mathrm{L}} = \left(6/\pi - 1\right)^{1/3} R \approx R$. It follows, that the merging passes then the vapor volume fracture achieves the value $\alpha_c \approx 0.5$. A number of smaller drops can be formed during the vapor bubbles merging, but we neglect it here.

3. Numerical investigation of the metal fracture

We have numerically investigated the copper irradiation by the high-current pulsed electron beam with parameters: the energy of fast electrons is 1 MeV, the beam current density is 10 kA/cm^2, the pulse duration is 50 ns. The beam action causes the sharp heating of the substance (up to 4900 K) in the energy release zone (Fig. 1) and the formation of area of the high-pressure - up to 17 GPa (Fig. 2). The substance temperature exceeds the melting temperature up to the depth of 0.4 mm; in this layer the metal is melted. Release of the high pressure area results in formation of the compression wave with the amplitude up to 11.5 GPa. The compression wave front is becoming sharper with the time, and it transforms into the shock wave. Reflection from the free (irradiated) surface forms the rarefaction wave, following behind the shock wave. This rarefaction wave creates in the liquid metal the negative stress with the value up to 2.5 GPa, which initiates the fracture of the liquid phase through the generation and growth of the vapor bubbles. The generation and growth of the bubbles result in reduction of the liquid metal volume and, therefore, it releases the tensile stresses; the substance passes in the equilibrium two-phase state. This process restricts the tensile stresses; otherwise, the rarefaction wave amplitude would be the same as the amplitude of the compression wave.

It should be noted that the existence of metastable liquid state leads to propagation of the rarefaction (tensile) wave inside the metal behind the shock wave. Negative stresses in the rarefaction wave can reach 2.5 GPa. Thus, the structure of stresses in the metal differs from that in calculations [4,8],

where an approximation of the equilibrium two-phase state of the liquid and vapor was used for the description of the melted layers of metals. The rarefaction wave can substantially influence on the material modification [12] as well as on the spall fracture of solid metal near its back surface.

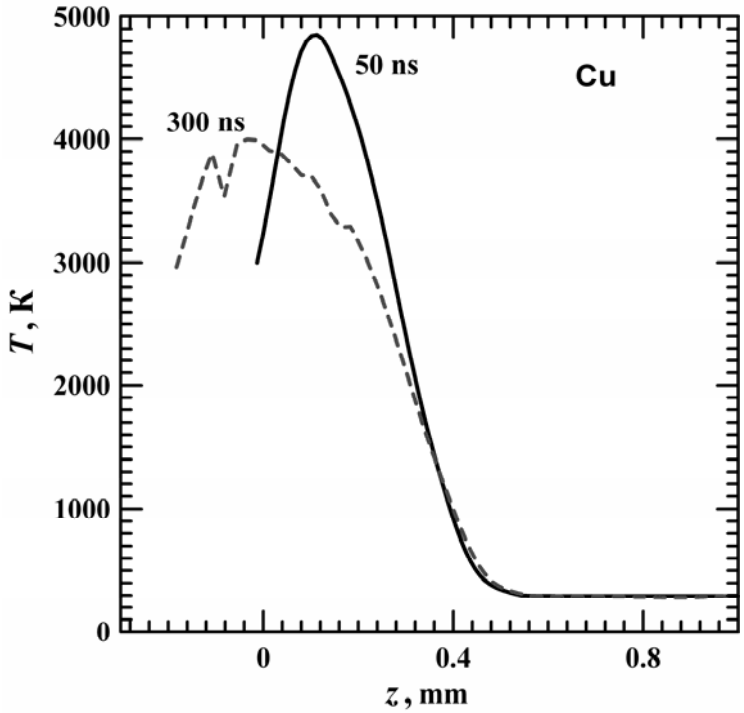

Figure 1. Temperature distributions in copper at the two time moments. Fast electrons energy is 1 MeV, the current density is 10 kA/cm^2, the pulse duration is 50 ns. At the moment of the pulse end, the temperature in the metal layer heated by the beam is maximal and it achieves 4900 K, after than, at the expansion of the "compressed" substance, the temperature becomes lower.

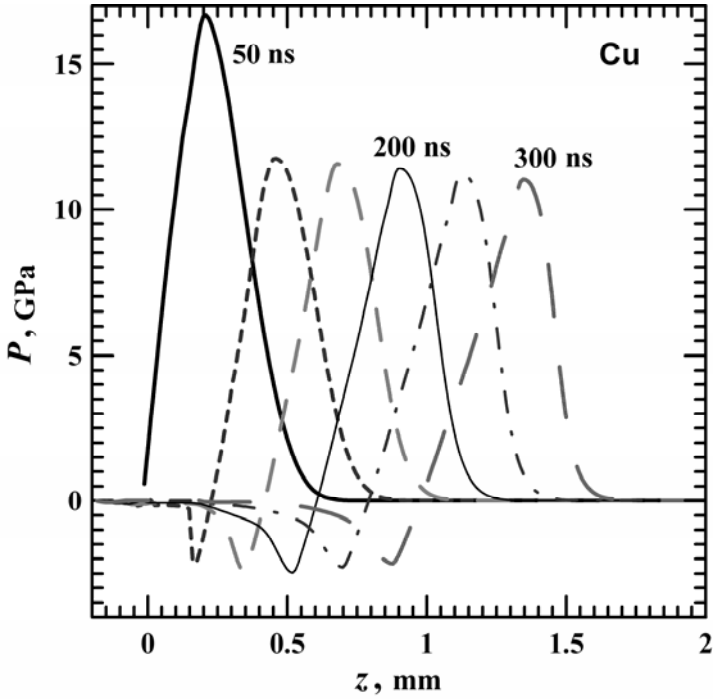

Figure 2. Distributions of pressure at consecutive time moments. High current electron beam irradiation of copper with the electrons energy 1 MeV, the current density 10 kA/cm^2, and the pulse duration 50 ns.

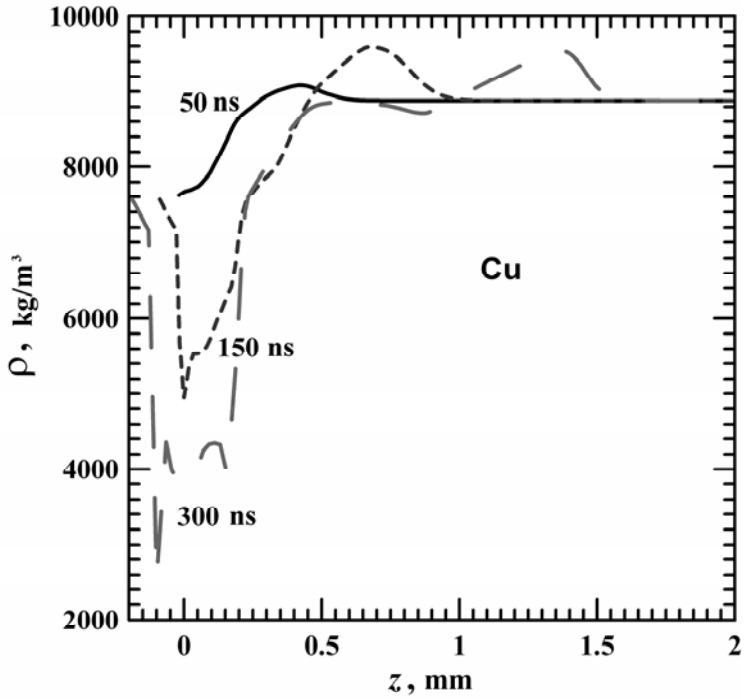

Figure 3. Distributions of the average density of the medium at consecutive time moments. High current electron beam irradiation of copper with the electrons energy 1 MeV, the current density 10 kA/cm^2, and the pulse duration 50 ns.

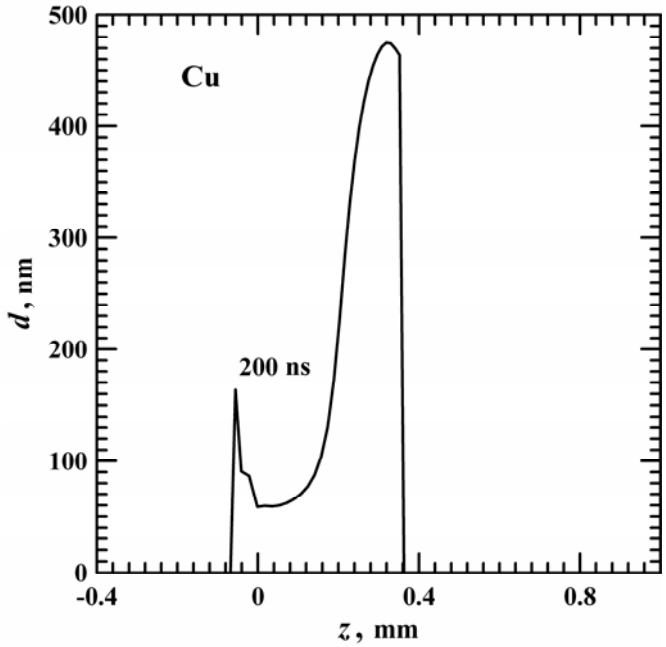

Figure 4. Depth distribution of the vapor bubbles diameters at the moment just before the fragmentation of the liquid phase. The lower bubbles diameters and, consequently, the larger concentrations correspond to the central region of the energy release zone, in which the tension occurs with the higher strain rate. Zero level corresponds here to the absence of the bubbles.

Appearance of the bubbles leads to the decrease of the average density of the two-phase medium (Fig. 3). Concentrations and diameters of vapor bubbles in different layers of the metal differ from

each other (Fig. 4); they depend on the strain rate of tension in the rarefaction wave and on the metal temperature in the layer. When the volume fraction of vapor exceeds the volume fraction of the liquid phase, the consolidation of bubbles begins in the layer; the liquid phase is destructed on the drops (Fig. 5). Gradually the liquid phase fracture takes place in all area, in which the bubbles were generated by the tension. Further evolution of the two-phase medium is reduced to the expansion of droplets accompanied by the droplets coalescence due to the Brownian motion.

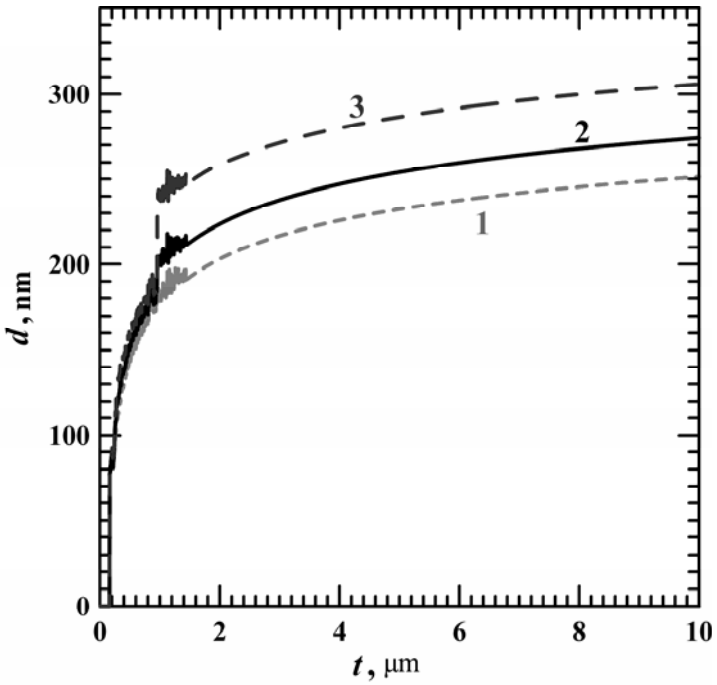

Figure 5. Time evolution of the average diameters of the drops: 1 – average on the number of drops, 2 – average on the drops surface areas, and 3 – average on the mass of the drops. The first drops are formed approximately 200 ns after the irradiation beginning in the layer with the maximal concentration of the vapor bubbles. A sharp increase of the average diameters is observed during the first 1 μs, it is connected with the gradual fracture of the liquid layers with lower concentration and, consequently, with the higher diameters of the vapor bubbles.

3. Conclusions

The mathematical model is proposed and the numerical investigation is performed of the metal fracture and fragmentation in the energy-release zone under the action of the high-current electron beam. The beam heats the metal and converts it in the metastable liquid state, which is destructed under the action of rarefaction wave propagating from the free (irradiated) surface of the metal. The tensile stresses of the value of about 2.5 GPa initiate the generation and growth of vapor bubbles. The following merging of the bubbles results in fragmentation of the simply connected liquid phase on the drops. Under the investigated conditions, the formation of the vapor bubbles begins 30 ns after the end of irradiation pulse. Concentration of the bubbles depends on the metal temperature and on the strain rate of tension in the rarefaction wave. This concentration determines the diameter of the resulting liquid drops, which varies from several tens up to several hundreds of nanometers in different parts of the energy release zone. Existence of the metastable state of expanded liquid results in propagation of the rarefaction wave with negative pressure of the value up to 2.5 GPa behind the shock wave in the deeper solid layers of the irradiated metal, which can substantially influence on the spallation of back surface in solid state as well.

Acknowledgements

The study was supported by The Ministry of education and science of Russian Federation, project 14.B37.21.0384, and by The Russian Foundation of Basic Research, project 12-02-31375/12.

References

[1] S.P. Bardakhanov, A.I. Korchagin, N.K. Kuksanov, A.V. Lavrukhin, R.A. Salimov, S.N. Fadeev, V.V. Cherepkov, Nanopowders obtained by evaporating initial substances in an electron accelerator at atmospheric pressure. Dokl Phys, 51 (2006) 353-356

[2] M.E. Balezin, V.V. Bazarnyi, E.A. Karbovnichaya, S.Yu. Sokovnin, Application of nanosecond electron beam for production of silver nanopowders. Nanotechn in Russia, 6 (2011) 757-762.

[3] V.V. Valchuk, S.V. Khalikov, A.P. Yalovets, Modeling of action of intensive charged particles beams on the slabs. Mat Model, 4 (1992) 112-124.

[4] S.A. Chistyakov, S.V. Khalikov, A.P. Yalovets, Investigation of the formation of elastoplastic waves in a metal target irradiated with charged particles. Techn Phys, 38 (1993) 5-9.

[5] E.F. Dudarev, O.A. Kashin, A.B. Markov, A.E. Mayer, A.N. Tabachenko, N.V. Girsova, G.P. Bakach, S.A. Kitsanov, M.F. Zhorovkov, A.B. Skosyrskii, G.P. Pochivalova, Deformation behavior and spalling fracture of a heterophase aluminum alloy with ultrafine-grained and coarse-grained structure subjected to a nanosecond relativistic high-current electron beam Russian Phys J, 54 (2011) 713-720.

[6] A.Yu. Kuksin, P.R. Levashov, V.V. Pisarev, M.E. Povarnitsyn, A.V. Yanilkin, A.S. Zakharenkov, Model of fracture of liquid aluminum based on atomistic simulations, in: Physics of Extreme States of Matter – 2011, IPCP RAS, Chernogolovka, 2011. pp. 57-59.

[7] A.Yu. Kuksin, G.E. Norman, V.V. Pisarev, V.V. Stegailov, A.V. Yanilkin, Theory and molecular dynamics modeling of spall fracture in liquids. Phys Rew B, 82 (2010) 174101.

[8] N.B. Volkov, E.L. Fen'ko, A.P. Yalovets, Simulation of generation of ultradisperse particles upon irradiation of metals by a high-power electron beam. Techn Phys, 55 (2010) 1389-1399.

[9] V.E. Fortov, K.V. Khishchenko, P.R. Levashov, I.V. Lomonosov, Wide-range multi-phase equations of state for metals. Nucl Instrum Meth Phys Res A, 415 (1998) 604–608.

[10] S.N. Kolgatin, A.V. Khachatur'yants, Interpolation equations of state of metals, Teplofiz Vys Temp, 20 (1982) 90-94.

[11] L.D. Landau, E.M. Lifshitz, Course of Theoretical Physics, Vol. 5, Statistical Physics, Part 1, New York, Pergamon, 1980.

[12] V.S. Krasnikov, A.E. Mayer, Numerical investigation of the change of dislocation density and microhardness in surface layer of iron targets under the high power ion- and electron-beam treatment. Surf Coat Techn, 212 (2012) 79-87.

Dynamics of Fragmentation of Fused Quartz Rods

Sergey Uvarov*, Marina Davydova, Oleg Naimark

Laboratory of PFC, ICMM UB RAS, Perm 614013, Russia
*Corresponding author: usv@icmm.ru

Abstract The dynamic fragmentation was studied in the impact experiments with quartz cylindrical rods using a gas gun. Impact leads to the formation of fracture surfaces, which produce an intensive light emission (mechanoluminescence). Mechanoluminescence was registered by two Photo Multiplayer Tubes (PMT) connected with the oscilloscope. Mechanoluminescence was in form of impulses with typical rise time 2-5 ns and fall time 5-50ns. It was found that the impulse frequency was not decreases monotonically but there was some kind of bursts or avalanches and fragmentation process time is 3-4 orders longer than acoustic time (time needed for compression wave to travel along the specimen). We found that the distribution of intervals between luminescence impulses is a power law distribution.

Keywords Fractoluminescence, scaling, power law, fragmentation

1. Introduction

Per Bak et al. in their paper “Self-Organized Criticality: An Explanation of 1/f Noise” mentioned: “The common feature for these systems is that the power-law temporal or spatial correlations extend over several decades where naively one might suspect that the physics would vary dramatically. Dynamical systems with extended spatial degrees of freedom naturally evolve into self-organized critical structures of states which are barely stable. We suggest that this self-organized criticality is the common underlying mechanism behind the phenomena described above. The combination of dynamical minimal stability and spatial scaling leads to a power law for temporal fluctuations. The noise propagates through the scaling clusters by means of a "domino" effect upsetting the minimally stable states. Long-wavelength perturbations cause a cascade of energy dissipation on all length scales” [2]. To confirm the fact that the fragmentation exhibits SOC, we need to establish the existence of a power law for temporal and spatial quantities. The evidence of the spatial scaling for the fragmentation of brittle materials under different loading conditions was given in paper [1] . For measurement of temporal scale we developed an experimental device to determine the time interval between the impulses of the light reflected from the newly created fracture surfaces. In our investigation (fragmentation of quartz rods under dynamic loading), SOC means that there exist:

•power law distribution of fragment size;
•power law distribution of time interval between the impulses of the light reflected from newly created surfaces.

2. Experiment

The fragmentation statistics was studied in recovery dynamic experiments with fused quartz cylindrical rods which have 10 mm diameter and 120 mm length.

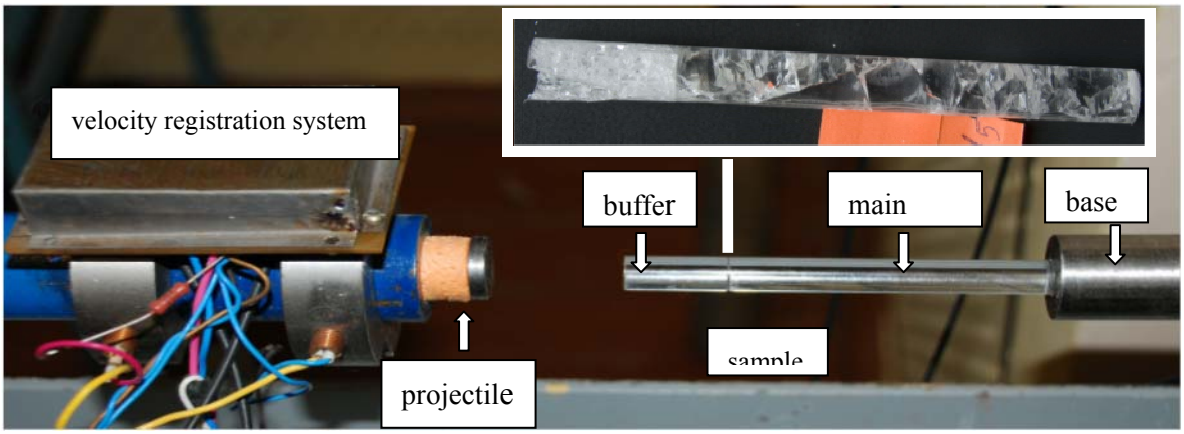

Figure 1. Ballistic set-up. An example of the fragmentation pattern is given in the upper right-hand corner.

Rods were loaded by ballistic set-up, which consisted of a gas gun with bore diameter of 19.3 mm, a velocity registration system and a base where the specimen was placed (Fig. 1). The sectional rod was composed of a buffer and the main part covered by an elastic shell. The buffer was used for realization of uniaxial loading produced by a cylindrical projectile of mass 13.9 g accelerated up to the velocities of 6-50 m/s.

In order to check influence of loading conditions on fragmentation statistics two types of boundary conditions at the rear end were checked. Rear end of the sample was glued to the steel rod and rear end was free [1]. We found that statistics of fragment distribution does not change significantly so next experiments were carried out with a free rear end of the sample. The mass of the fragments corresponding to the maximum of the probability density function is independent of the projectile energy. To obtain the fragment size distribution, the technique described in the previous experiments [1] was used, which made it possible to get the distribution obeying the scaling law. This experiments are presented in the talk "*Scaling Behavior in Quasi Static and Impact Fragmentation of Brittle Materials*" by Davydova M. and Uvarov S. at ICF13. The scheme given in Figure 2 illustrates the experimental technique used to measure the distribution of time quantities.

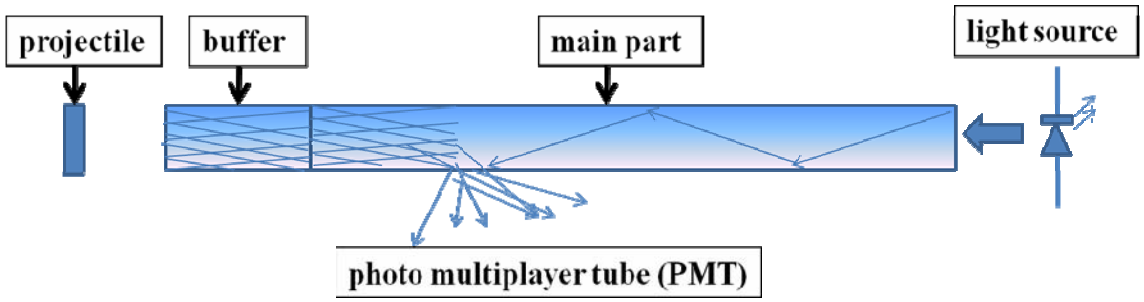

Figure 2. Scheme of the experiment. Light source was used for visualizing the cracks in the sample.

It is known [3] that cracking of quartz leads to emission of light known as a fractoluminescense or mechanoluminescence. The light intensity was registered by the Photo Multiplayer Tube connected

with the oscilloscope (oscilloscope sample rate is 1 GHz). The appearance of the new surfaces produces the impulses with a sharp front with typical rise time about 5 ns (Fig. 3).

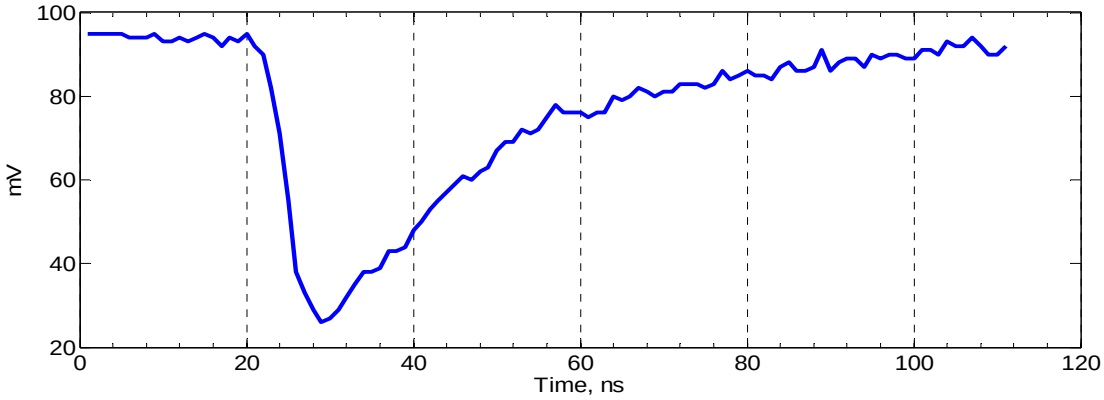

Figure 3. Typical fractoluminescence event.

Figure 4 shows the signal from the oscilloscope. One can note that fragmentation process lasts 2-3 decades longer than loading time (20 μs). Pulse rate does not decrease monotonically; instead of this one can note avalanches or bursts of pulses similar to the avalanches on the sand pile which is common illustration of SOC.

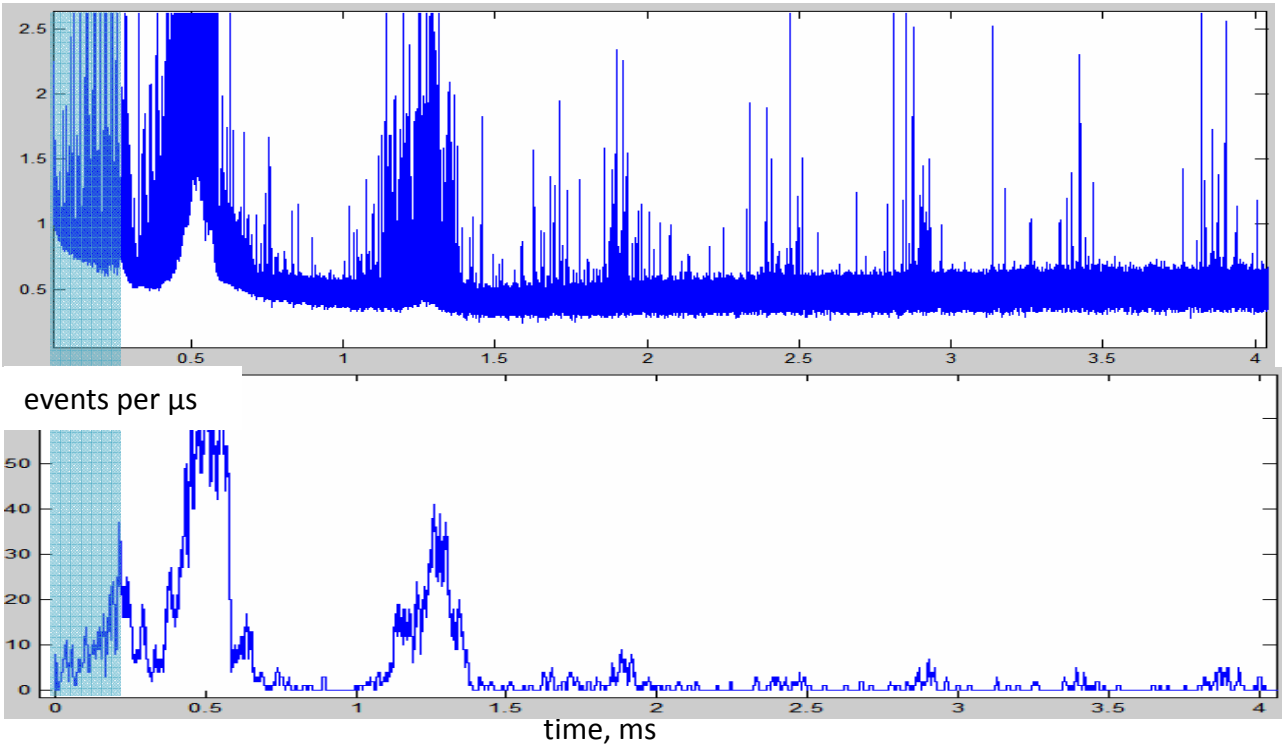

Figure 4. Signal from the oscilloscope (upper, polarity of pulses is reversed) and pulse rate (lower). Time scale is the same for both graphs.

1. Data analysis

The first step of data processing is signal filtration. Because the fractoluminescence pulses have a

very short rise time application of the high-pass filter to the original signal increase signal-to-noise ratio and makes possible to measure time intervals between events. The definition of the size of time interval between the impulses is shown at the Figure 5. The second step involves measuring the distance between the green bars showing a sharp rise in impulse. We consider only the impulses which are above some discrimination level (the red line). Discrimination level is determined by noise level in the way that not more than 1 false positive pulse was detected on the reference signal. Reference signal was taken before loading.

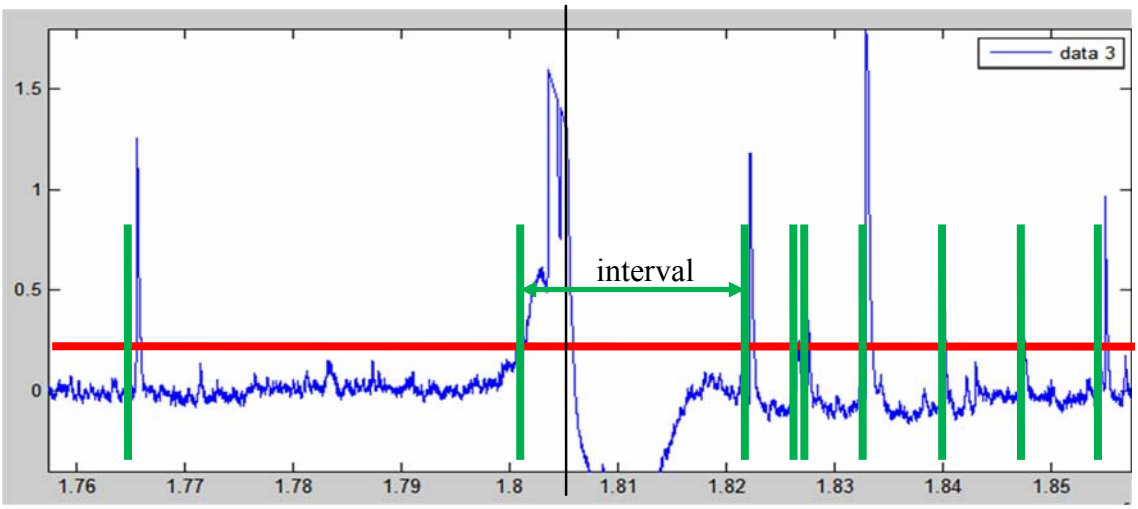

Figure 5. Determination of the size of time interval between the impulses of the light reflected from the fracture surfaces.

The cumulative distribution function of the time interval in the double logarithmic plot (Figure 6) is fitted by the straight line (total number of points 1073).

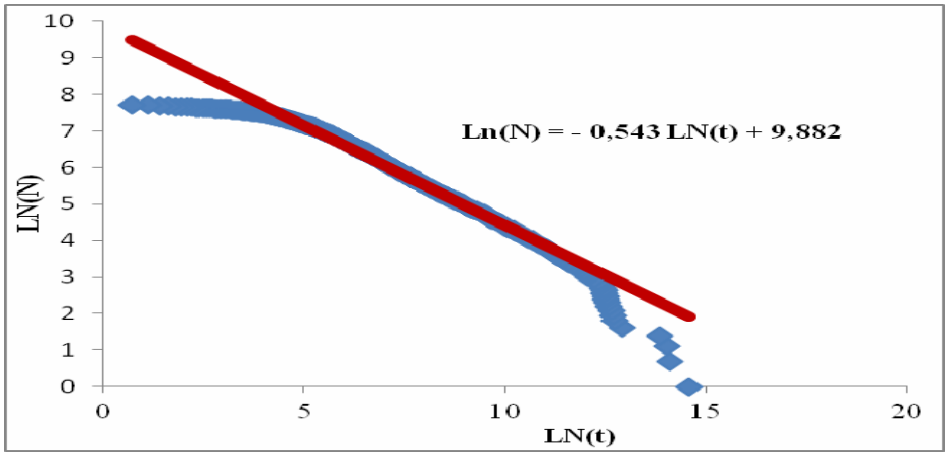

Figure 6. Cumulative distribution function of time interval in the double logarithmic plot.

At small sizes (77 points – 7.1761 % of the total number of points), the curve deviates from the straight line because the size of time interval is comparable with the oscilloscope sample rate (1 GHz). The falloff at the largest interval sizes (16 points – 1. 5% of the total number of points) is due to finite-size effects. In this case the time interval is comparable with the process time. The central

part is the line covering 91.3% of the total number of points. The process of light reflection looks like the process of avalanche spreading (Fig. 4). The lower plot represents the event frequency. The events are distributed in blocks. We have analyzed the time interval distribution in avalanches and found that the distribution at the initial stage (marked in blue in Fig. 4) cannot be described by the power law.

The left plot in Figure 7 illustrates the distribution at the initial stage in double logarithmic coordinates. In the right plot in Figure 7, only the vertical coordinate is logarithmic. The time interval distribution is subjected to the exponential law.

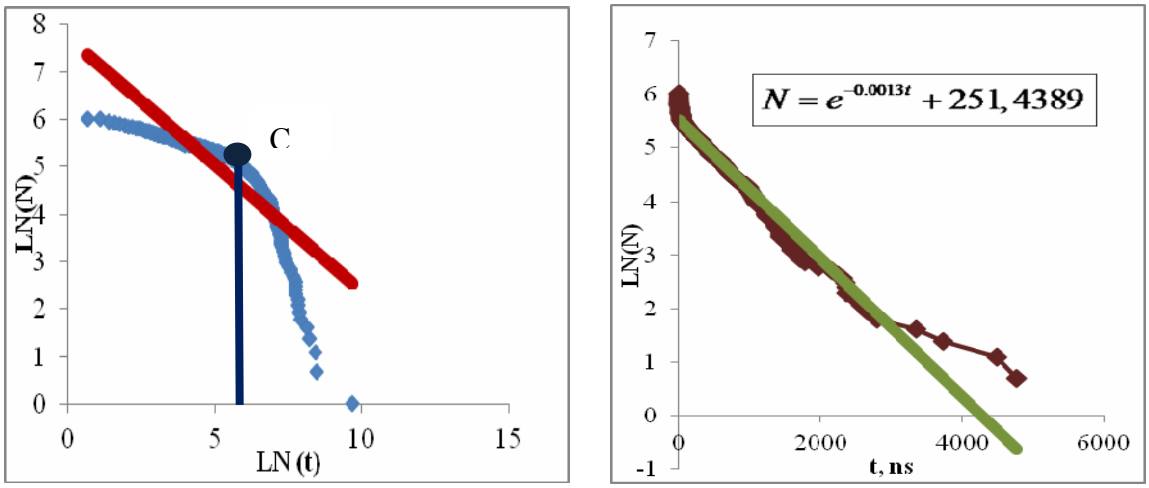

a) b)

Figure 7. a) Cumulative distribution function of time interval for initial stage in a double logarithmic plot. b) Cumulative distribution function of time interval for initial stage in a coordinate system Ln (N) –time t.

An exponential functional form requires a characteristic length scale which can be defined as

$$X_{ch} = tV \,, \tag{1}$$

where *Xch=2.6 mm* is the characteristic size, *t* is the x-coordinate of point C (t= 457 ns), and *V=5800 m/s* is the sound velocity in quartz. We suppose that this length scale correlates with the impactor thickness. The initial stage statistics does not change the total statistics, because only 10% of the points belong to the initial stage.

Investigation of the fragments by optical microscopy (Fig. 8.) reveals that surface of the fragments is not smooth so there is no simple relationship between pulse amplitude and crack size as in [3] where cracks are represented as smooth disk-shaped objects.

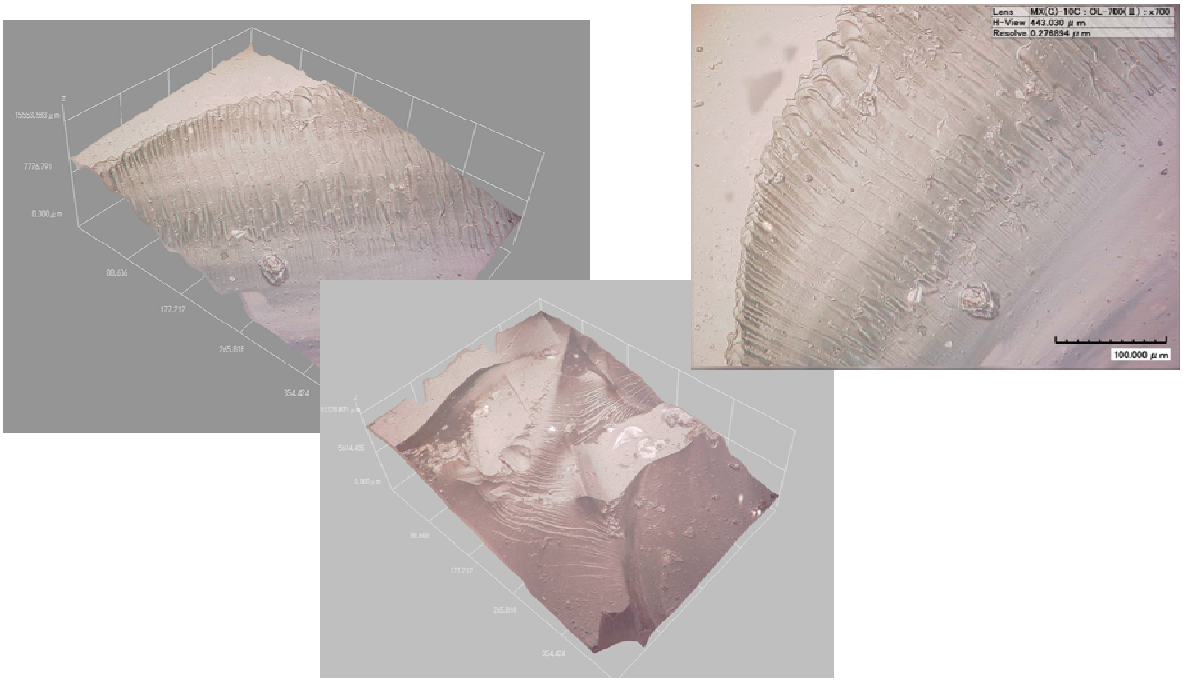

Figure 8. Fracture surface of quartz. Optical microscopy.

3. Conclusions

In our experiments we found that exist:

- Power law distribution of fragment size;
- Power law distribution of time interval between the impulses of the light reflected from newly created surfaces.

So we can suppose that self-organized criticality is the underlying mechanism of fragmentation except initial stage where exponential distribution is observed.

We suppose that the initial stage corresponds to the breaking of bulk specimen and formation of a granular media. The main stage at which most of the fragments was created corresponds to the fragmentation of the granular media formed at the first stage.

Acknowledgements

The author would like to acknowledge the Russian Foundation for Basic Research (grant RFBR 11-01-96010, grant RFBR 11-01-00712) and Russian Academy of Sciences (program #12-II-1-1021, #12-C-1-1013).

References

[1] M.M. Davydova, O.B. Naimark, V.A.Leontiev and S.V. Uvarov. Scaling properties of crack branching and brittle fragmentation. European Physical Journal Web of Conferences: 10, 00037p.1-00037p.4, 2010.

[2] P. Bak, C. Tang and K. Wiesenfeld, Self-organized criticality: an explanation of 1/f noise. Phys. Rev. Letters 59: 381-384, 1987.

[3] V. I. Vettegren', V. S. Kuksenko and I. P. Shcherbakov. Emission kinetics of light, sound, and radio waves from single-crystalline quartz after impact on its surface.
Technical Physics. V 56, N 4 (2011), 577-580, DOI: 10.1134/S1063784211040311

Threshold Fracture Energy for Differently Shaped Particles Impacting Halfspace (Erosion-Type Fracture)

Grigory Volkov[1,2,*], Yuri V Petrov[1,2], Nikolay Gorbushin[1]

[1] St. Petersburg State University, Research Center of Dynamics, St. Petersburg, Russia, 198504,
[2] Institute of Problems of Mechanical Engineering, St. Petersburg, Russia, 199178,
* Corresponding author: volkovgrig@mail.ru

Abstract Energetic aspects of erosion fracture are studied. Threshold (minimal) energy needed for initiation of fracture caused by a particle impact is estimated using the incubation time criterion. The dependences of the fracture threshold energy on impact duration are calculated for two different shapes of the impacting particle: sphere and cylinder. The difference in the threshold energy behavior between these two cases is demonstrated and discussed.

Keywords Incubation time criterion, erosion, threshold energy

Introduction

In the present work the problem of dynamic impact of spherical and cylindrical solid particle on elastic half-space is studied. This problem is considered within the framework of fracture mechanics by neglecting of the heat transfer process and wave-process origination. Also there is an assumption that the impact is quasistatic. It permits to use the solution of the problem of quasistatic of the indenter pressing in [1].

This problem plays an important role in practical application, since the short impacts are typical for such industry process as ultrasonic assisted machining [2,3].

Threshold Energy of a Sphere Particle

The normal impact of the spherical rigid particle on the elastic half-space is considered. Hertz solution for the contact problem gives the following temporal dependence of the contact force P on the distance h between the bodies approaching each other:

$$P(t) = k[h(t)]^{3/2}, \tag{1}$$

where $k = 4\sqrt{R}E/\left[3\left(1-\nu^2\right)\right]$, R - particle radius, E and ν - elastic constants of the half-space. If m is the mass of the particle and V is its initial velocity then the time dependence of the approach $h(t)$ can be determined by solving the equation of motion:

$$m\frac{d^2h(t)}{dt^2} = -P(t). \tag{2}$$

The solution of the differential equation (2) can be approximated with high precision by the following expression:

$$h(t) = h_0 \sin\left(\frac{\pi t}{t_0}\right), \tag{3}$$

where $h_0 = \left(\frac{5}{4k}mV^2\right)^{2/5}$ is maximum approach and $t_0 = 2.94\frac{h_0}{V} \approx 3.2\left(\frac{m^2}{Vk^2}\right)^{1/5}$ is the contact time.

Also Hertz solution gives the following expression for the tensile stresses originated on the half-space surface:

$$\sigma_r(t) = -\sigma_\theta(t) = \frac{1-2\nu}{2}\frac{P(t)}{\pi a^2(t)}, \tag{4}$$

$$a(t) = \left(3P(t)\left(1-\nu^2\right)\frac{R}{4E}\right)^{1/3} = \left(P(t)\frac{R^{3/2}}{k}\right)^{1/3}. \tag{5}$$

Parameter $a(t)$ defines the radius of the contact area and its value depends on the contact time. Values $\sigma_r(t)$ and $\sigma_\theta(t)$ correspond to maximum values of main stresses in cylindrical coordinates. Therefore, the radial component of stresses $\sigma_r(t)$ is considered, since usually tensile stresses lead to fracture. Below $\sigma_r(t)$ is denoted by $\sigma(t)$.

The expressions (3)-(5) can be used to determine the expression for the threshold energy of the spherical particle. By threshold energy we mean the minimum quantity of energy, which is necessary to spend on initiation of the threshold fracture pulse during impact intersection. In this work the incubation time criterion is applied for fracture prediction [4]:

$$\frac{1}{\tau}\max_t \int_{t-\tau}^{t} \sigma(R,V,s)ds = \sigma_c \ . \tag{6}$$

The static strength of the material σ_c can be experimentally measured. Parameter τ corresponds to incubation time of the fracture. It characterizes the time period for preparing the media to fracture or phase transformation. The incubation time is a material strength constant and its value can be measured experimentally or derived by computational and experimental methods. In the work [5] different interpretations of the incubation time are shown for various problems.

The application of the incubation time criterion caused by this criterion takes into account the process dynamics. The dynamic strength properties of materials appear when the loading duration has a similar value as the incubation time [6,7]. When the time of loading significantly exceeds the incubation time, the media resistance is specified by static strength properties.

After the substitution of the expressions (1), (3) and (5) into (4), the fracture criterion becomes:

$$\frac{1-2\nu}{2\pi}\frac{k}{R}\sqrt{h_0}\max_t \int_{t-\tau}^{t} \sqrt{\sin\left(\frac{\pi s}{t_0}\right)}ds = \tau\sigma_c \ . \tag{7}$$

The integral in the expressions (7) takes the maximum value at the time $t=(t_0+\tau)/2$. The impact duration, radius and velocity of the particle should be introduced in dimensionless form:

$$\lambda = \frac{\tau_0}{\tau}, \quad R_d = \frac{R}{c_p\tau}, \quad V_d = \frac{V}{c_p}.$$

From now on $c_p = \sqrt{E(1-\nu)/\rho_m(1+\nu)(1-2\nu)}$ is the propagation velocity of the dilatational wave in the elastic media with density ρ_m.

Then, the accepted criterion (7) gives the following expression for calculation of the threshold velocity in dimensionless form:

$$\alpha_d V_d^{2/5} \int_{\frac{\lambda-1}{2}}^{\frac{\lambda+1}{2}} \sqrt{\sin\left(\frac{\pi s}{\lambda}\right)}\left[H(s)-H(s-\lambda)\right]ds = 1, \tag{8}$$

where $\alpha_d = c_p^{2/5}\left(E^4\rho\right)^{1/5}(2\pi\sigma_{cr})^{-1}(1-2\nu)\left(4/3(1-\nu^2)\right)^{4/5}(5\pi/3)^{1/5}$ is dimensionless parameter, ρ is material density of the particle, $H(s)$ is the Heaviside function.

The value of the threshold radius can be calculated from following expression for the impact duration:

$$\lambda = \frac{t_0}{\tau} \approx 3.2\frac{1}{\tau}\left(\frac{\pi\rho(1-\nu^2)}{E}\right)^{2/5}\frac{R}{V^{1/5}}.$$

Then, the threshold radius is determined in dimensionless form by:

$$R_d = \frac{\lambda}{\beta_d} V_d^{1/5}, \tag{9}$$

where $\beta_d = 3.2\left(\pi\left(1-\nu^2\right)\rho c_p^2 / E\right)^{2/5}$ is dimensionless parameter. If the threshold velocity (8) and radius (9) are known, then the threshold energy of the particle can be calculated as:

$$W = \frac{2}{3}\pi\rho R^3 V^2. \tag{10}$$

In dimensionless form, (10) is given by the formula:

$$W_d = \frac{W}{\omega} = R_d^3 V_d^2, \tag{11}$$

where the parameter $\omega = 2\pi\rho\tau^3 c_p^5 / 3$ has the dimension of energy and is determined by material constants. Thus, the quantity W_d determines the minimum dimensionless value of particle energy required for half-space fracture. Figure 1 presents the graphs of dependence of the energy (11) on the impact duration (Fig. 1*a*) and radius (Fig. 1*b*), where the half-space material is zinc and parameters the value $\rho = 3200\,kg/m^3$.

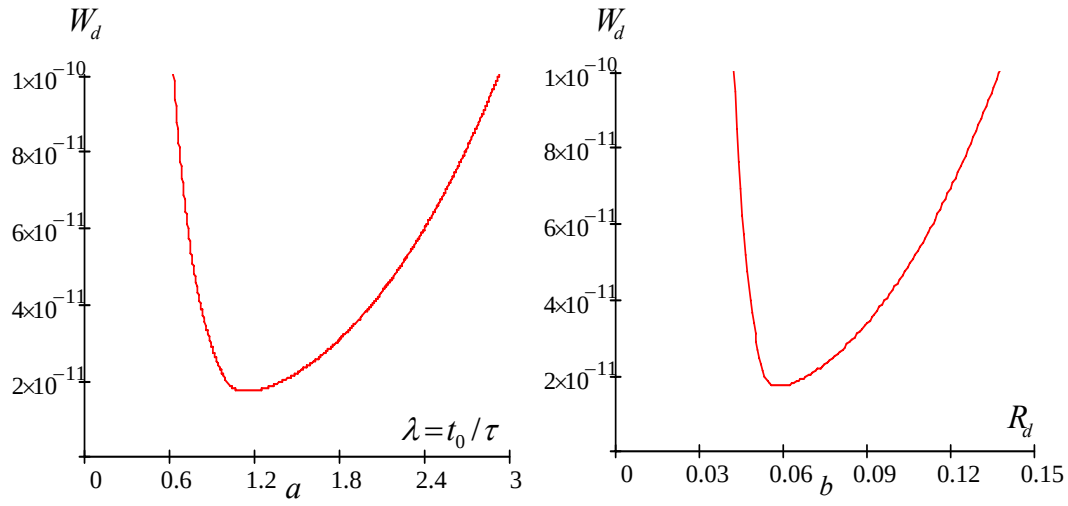

Figure 1. Dependence of the threshold energy of the spherical particle on: *a* – the impact duration, *b* – particle radius

These graphs show that the value of the threshold energy has the marked minimum distinct from equal zero. Hence, it is possible to decrease the energy costs for fracture by controlling such parameters as radius and velocity of particle.

Threshold Energy of a Cylindrical Particle

The similar analysis can be provided for cylindrical particles with a constant circle section of radius R. The cylinder height is equal to $H = 4R/3$, that follows from the assumption that the cylinder mass is equal to the ball mass. In the cylindrical case the contact force $P(t)$ and approach $h(t)$ are related as follows:

$$P(t) = kh(t), \tag{12}$$

where $k = 2RE/\left(1-\nu^2\right)$.

In this case the equation of motion (2) has the exact solution [8]:

$$h(t) = h_0 \sin\left(\frac{\pi t}{t_0}\right), \tag{13}$$

where $h_0 = \sqrt{\frac{mV^2}{k}}$ and $t_0 = \sqrt{\frac{m}{k}}$.

Also, there is the similar expression for maximum tensile stress:

$$\sigma(t) = \frac{1-2\nu}{2}\frac{P(t)}{\pi R^2}, \quad r \to R + 0 \tag{14}$$

After substituting the expression of tensile stress (14) into criterion (6), the integral attains its maximum value at time $t = (t_0 + \tau)/2$. The dimensionless quantities are introduced by analogy with the case of the spherical particle. And the following expressions of dimensionless velocity can be obtained by using criterion (8) and formulas (12) - (14):

$$\alpha_d V_d \int_{\frac{\lambda-1}{2}}^{\frac{\lambda+1}{2}} \sin\left(\frac{\pi s}{\lambda}\right)[H(s) - H(s-\lambda)]ds = 1, \tag{15}$$

where $\alpha_d = (1-2\nu)\left(8E\rho c_p^2 / 3\pi(1-\nu^2)\right)^{1/2}(2\sigma_{cr})^{-1}$ is dimensionless parameter, ρ - is material density of the particle. From the expression of the impact duration it is possible to calculate the value of radius in dimensionless form:

$$R_d = \frac{\lambda}{\beta_d}, \tag{16}$$

where $\beta_d = \pi\left(2\pi\rho c_p^2(1-\nu^2)/3E\right)^{1/2}$ is dimensionless parameter.

The threshold energy can be calculated by formula (10) and in dimensionless form by formula (11), where cylinder velocity and radius are determined by (15) and (16) respectively.

Figure 2 presents the graphs of dependence of the energy on impact duration (Fig. 2*a*) and radius (Fig. 2*b*), where the half-space material is zinc and parameters the value $\rho = 3200\,kg/m^3$.

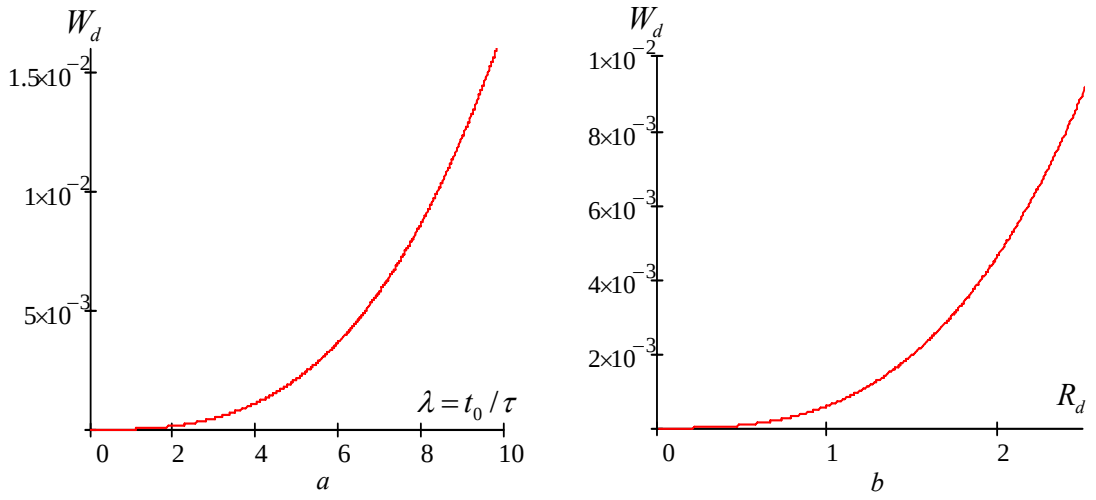

Figure 2. Dependence of the threshold energy of the cylindrical particle on *a* – the impact duration, *b* – particle radius

Fig. 2 shows that in case of cylindrical particle the threshold energy dependence is a monotone increasing function in contrast with the case of the spherical particle.

Results and Discussion

For the explanation of the difference in threshold energy behavior between both cases the following should be marked. The problems of the penetration with spherical and cylindrical indenters are fundamentally different. In case of the cylindrical particle, the contact area is a constant value during the penetration process, whereas for spherical particle, the contact area is a variable quantity. Also, in cylindrical case the points belonging to contact area border are singular and the stresses take out infinity in these points. But sphere indentation is attended with the finite values of stresses in all points of the contact region. The fact that the energy is zero for the zero impact duration and radius in the cylindrical case (Fig. 2) can be explained by the fact that the problem of penetration of a cylinder into a half-space is an idealized problem. When considering small particles, it is impossible to neglect the roundedness of the cylinder angles near the basis, and this model becomes unsuitable.

Acknowledgements

This work was financially supported with President of Russian Federation grant for young scientists.

References

[1] K.L. Johnson // Contact Mechanics, Cambridge University Press, 1987.
[2] Akbari J., Borzoie H., Mamduhi M.H. Study of Ultrasonic Vibration Effects on Grinding Process of Alumina Ceramic (Al2O3) // World Academy of Science, Engineering and Technology. 2008. N 17. P. 785–790.
[3] Li Z.C., Pei Z.J., Sisco T. et al. // In: Proceedings of the ASPE 2007 Spring Topical Meeting on Vibration Assisted Machining Technology, Chapel Hill, NC, USA, 2007. P. 52–57.
[4] Yu. V. Petrov, “On the ‘Quantum’ Nature of Dynamic Fracture of Brittle Solids,” Dokl. Akad. Nauk USSR 321 (1), 66–68 (1991) [Sov.Math. Dokl. (Engl. Transl.)].
[5] Yu. V. Petrov, “Incubation Time Criterion and the Pulsed Strength of Continua: Fracture, Cavitation, and Electrical Breakdown,”Dokl.Ross. Akad. Nauk 395 (5), 621–625 (2004) [Dokl. Phys. (Engl. Transl.) 49 (4), 246–248 (2004)]. Petrov Y.V. // Doklady Physics. 2004. Vol. 49. N 4. P. 246–249.
[6] Petrov Y., Morozov N. // ASME Journal of Applied Mechanics. 1994. Vol. 61. Issue 3. P. 710–712. Petrov Y.V., Morozov N.F., Smirnov V.I. // Fatigue and Fracture of Engineering Materials & Structures. 2003. Vol. 26. N 4. P. 363–372.
[7] Morozov N., Petrov Y. Dynamics of Fracture. Berlin–Hidelberg–NewYork: Springer–Verlag, 2000. 170 p.

Quantitative analysis of microcracks ensemble induced by shock-wave loading of metallic targets (vanadium and iron).

Elena Lyapunova*, Oleg Naimark, Sergey Uvarov

Institute of continuous media mechanics, 614013 1, Akademic Korolev St., Perm, Russia
* Corresponding author: lyapunova@ icmm.ru

Abstract Results of analysis of microstructure evolution of metallic samples (vanadium and iron) subjected to shock-wave loading are presented. The influence of loading velocity both on predominant mechanisms of structure deformation and fracture as well as regularities of microcracks ensemble evolution is investigated.

Keywords shock-wave loading, spall, microstructure analysis

1. Introduction

Understanding the material behavior under shock-wave loading has been paid a much attention for several decades because of its both practical and theoretical issues. Experimental results obtained till nowadays reveal highly complicated character of spall fracture. Changes of microstructure of material is one of the key factors among others, which reveals in nucleation, growing and coalescence of microcracks and microvoids, recrystallization processes, ets. It is not trivial problem to consider several microstructure mechanisms, for example nucleation and growing of recrystallized grains and evolution of defects (cracks, microvoids). Different kinetic models of metal behavior under dynamic loading usually use quantitative parameters characterizing size, shape or orientation of defects (microcracks or microvoids) in order to describe the role of microstructure. However there is still a big gap between experimental data and modeling results since the lack of complex information about kinetics of fracture and defect distribution corresponding to different loading rates. In the current work results of experiments on shock-wave loading of metallic targets are presented and microdefects evolution regularities during spall formation are discussed.

2. Experiment

Shock-wave loading of flat metallic samples was carried out one stage gas gun. Using of coarse-grained vanadium and polycrystalline iron as a target material allowed us to investigate deformation and fracture behavior of single crystallites (on vanadium samples) as well as typical polycrystalline metal behavior (iron samples). Dimensions of cylindrical samples and corresponding mean grain size are presented in table 1. In order to obtain different loading conditions, velocity of accelerated plate-projectile was varied in the interval 230… 375 m/s which is slightly above the velocity at which spallation occurs. Analysis of spall surface and inner microstructure changes was made with using of SEM (Quanda 600) and digital optical microscope Hyrox 7700. Preparation for investigation of inner microstructure included mechanical polishing and etching of sample sections made along the loading direction.

Table 1. Dimensions of samples

Material	Diameter, mm	Thickness, mm	Mean grain size
Vanadium	200	5	4 mm
Iron	200	10	50 mkm

3. Fracture surface analysis

Figure 1 represents the microphotographs of spall fracture surfaces of two materials under study. A highly coarse-grained structure of vanadium samples allowed one to define boundaries between crystallites (figure 1, left), and study the fracture regularities inside separate crystallites. It was shown that fracture surfaces of such crystallites consist of cleavage facets, ad the fraction of plastic deformation is significantly low (figure 2, left). Evidences of low fraction of plasticity in fracture of vanadium samples were obtained also from measurements of free surface velocity. In the central part of each cleavage facet a crack formation occurs, different stages of such cracks growing were observed. With increasing of projectile velocity relief of cleavage facets becomes smoother, which reflects higher fracture velocity, and the fraction of plastic deformation is getting lower.

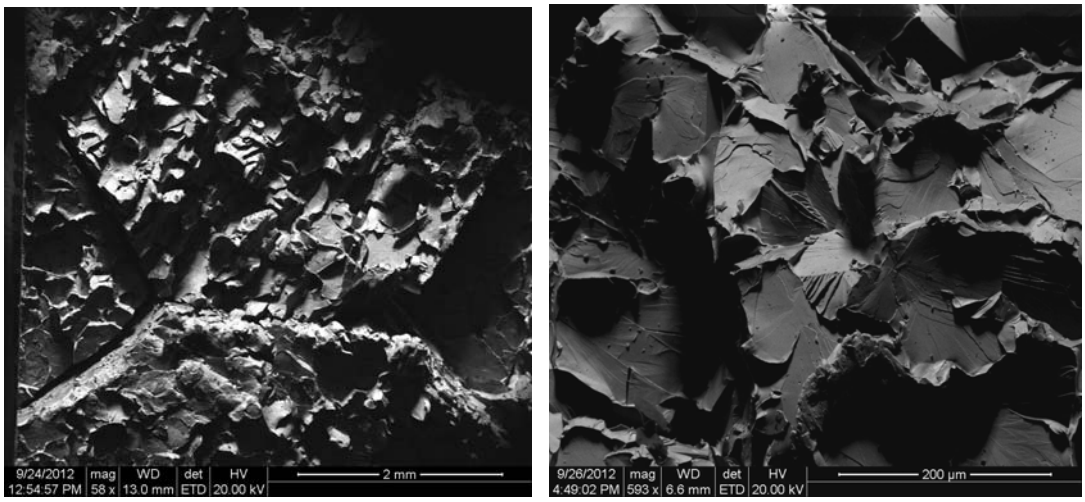

Figure 1. Microphotographs of fracture surfaces of two materials: left - coarse-grained vanadium (projectile velocity 280 m/s), right – polycrystalline iron (projectile velocity 300 m/s).

Fracture surfaces of polycrystalline iron-targets consist of intergranular cleavage facets with more inhomogeneous character because of much lower grain size (figure 1, right). In central part of facets, which size is corresponding to grain size scale, a formation of microvoid is usually occurs. Typical picture of such fracture surface elements is presented on figure 2, right. Increasing of projectile velocity in investigated interval didn't reveal any qualitative changes in fracture surface relief.

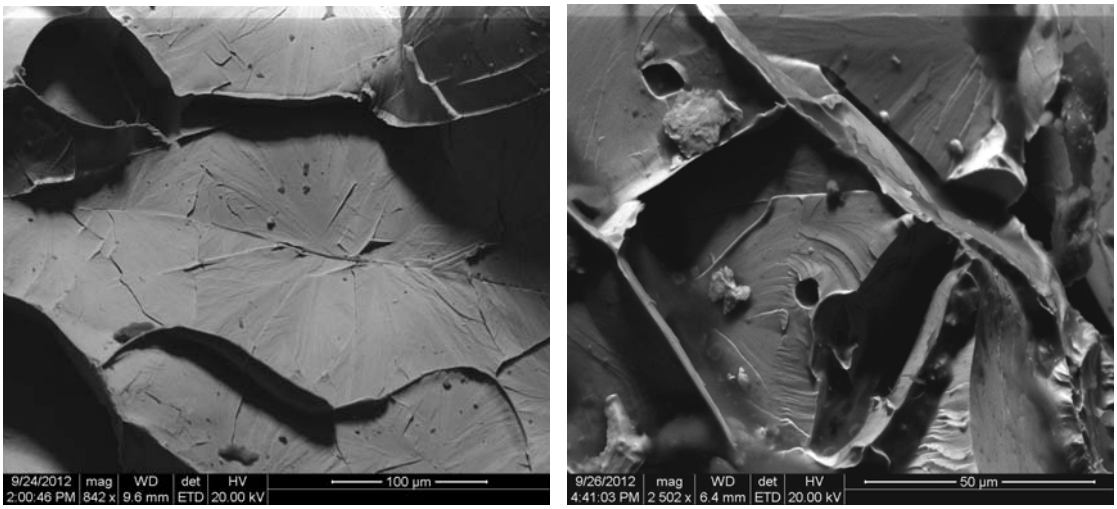

Figure 2. Elements of fracture surface relief on two materials: left picture – vanadium, right picture – polycrystalline iron.

3. Inner structure changes

Increasing of loading velocity for iron samples leads to qualitative changing of structure deformation: in the case of minimum developed projectile velocity there are some separately arranged highly deformed grains (fig. 3, left), whereas the number of such grains in target corresponding to maximum loading velocity is much bigger (fig. 3, right).

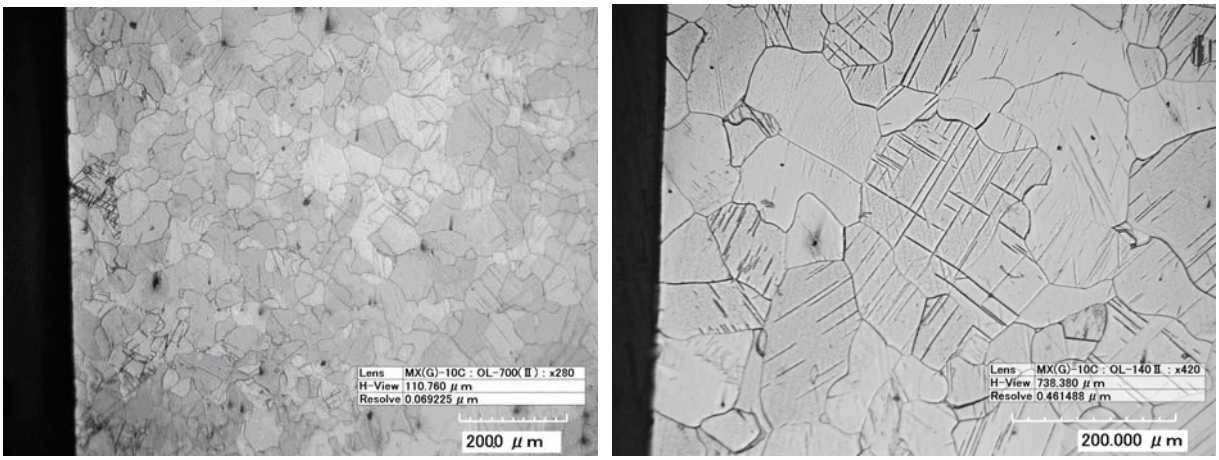

Figure 3. Microstructure near the loaded surface of deformed iron samples corresponding to different projectile velocity: left picture – 230 m/s, right picture – 260 m/s.

Shock-wave loading initiates dynamic recrystallization processes in iron targets. Near the loaded surface dynamic recrystallization usually takes place on grain boundaries, while near the spall area new grains can nucleate on microcracks (fig. 4). Besides, the higher projectile velocity the less deviation of grain size caused by intensive growing of recrystallized grains.

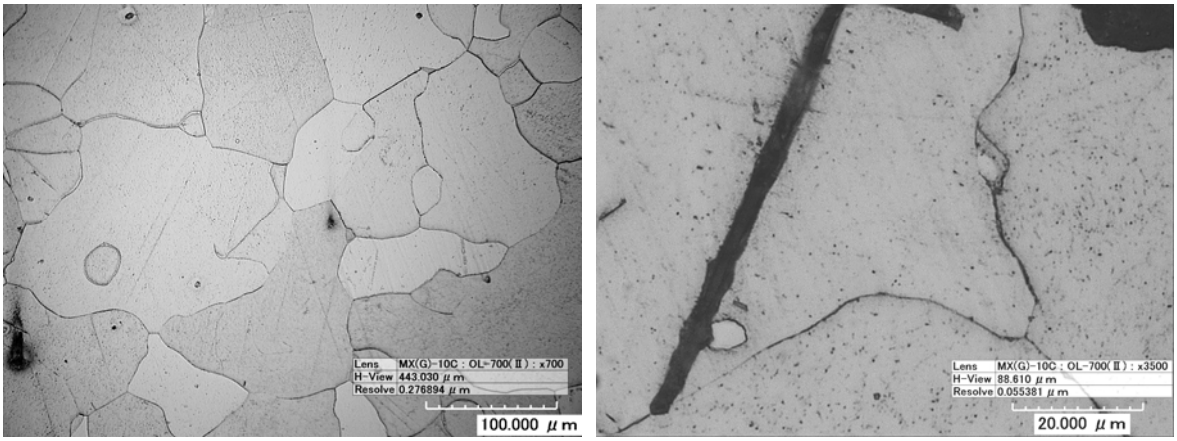

Figure 4. Microstructure of deformed iron samples corresponding to different projectile velocity: left picture – 230 m/s, right picture – 260 m/s.

Another feature of high-speed loading of targets is accumulation of misorientations in subgrain boundaries, resulting in fragmentation of initial grains. Far enough from spall region this transformation of low-angle boundaries to high-angle boundaries has crystallogeometrical character (fig. 5, left) whereas near the spall fracture surface presence of shear mode of deformation is observed (fig. 5, right).

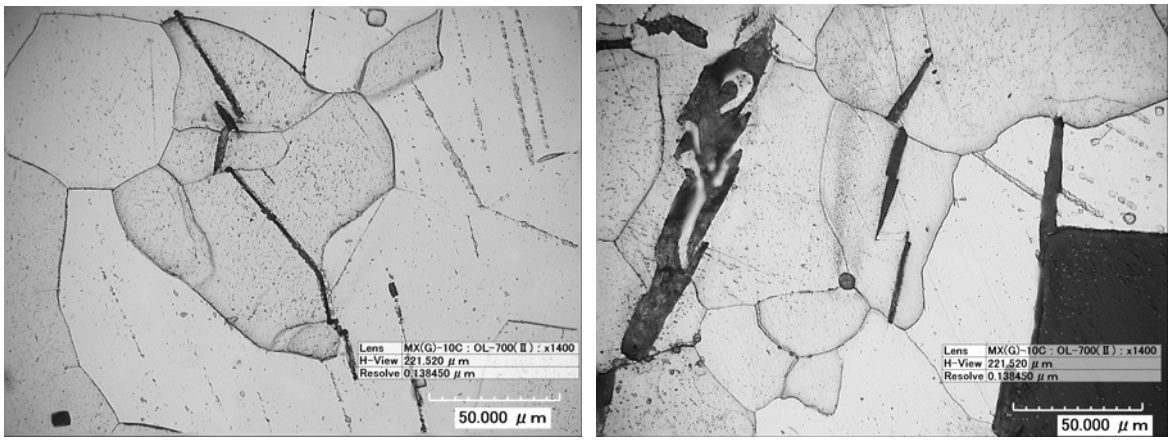

Figure 5. Fragmentation of initial grains: left picture – far from fracture surface, right picture – directly near the fracture surface. Projectile velocity 245 m/s

4. Conclusions

Results of microstructure analysis of metallic samples (coarse-grained vanadium and typical polycrystalline iron) subjected to shock-wave loading of different intensity are presented and structure relaxation mechanisms taking place during such loading in two investigated materials are discussed. An important role of dynamic fragmentation in the case of iron samples was established. Obtained data will be used for quantitative analysis of structure changes under high-speed loading of different intensity.

Acknowledgements

The authors would like to acknowledge the Russian Foundation for Basic Research (grant RFBR 09-01-92005, grant RFBR 12-01-31504, grant RFBR 11-01-96010, grant RFBR 12-01-92002) for support of this work.

Strain Rate Concentration Factor for Double-Edge-Notched Specimens Subjected to High Speed Tensile Loads

Nao-Aki NODA[1,*], Yoshikazu SANO[1], Makoto ANDO[1], Yoshihito KUROSHIMA[1], Takahiro SHINOZAKI[1], Hayato OHTSUKA[1] and Wenhai GUAN[1]

[1] Department of Mechanical and Control Engineering, Kyushu Institute of Technology,
1-1 Sensui-cho, Tobata-ku, Kitakyushu-city, Fukuoka, 804-8550, Japan
* Corresponding author: noda@mech.kyutech.ac.jp

Abstract Engineering plastics provide superior performance to ordinary plastics for wide range of the use. For polymer materials, dynamic stress and strain rate may be major factors to be considered when the strength is evaluated. Recently, high speed tensile test is being recognized as a standard testing method to confirm the strength under dynamic loads. In this study, therefore, high speed tensile test is analyzed by the finite element method; then, the maximum dynamic stress and strain rate are discussed with varying the tensile speed and maximum forced displacement. The strain rate concentration factor found to be constant independent of tensile speed, which is defined $K_{t\dot{\varepsilon}}$ as the maximum strain rate appeared at the notch root over the average nominal strain rate at the minimum section. The maximum strain rate is controlled by the tensile speed alone independent of the magnitude of the forced displacement. It is found that the difference between static and dynamic maximum stress concentration (σ_{max}-σ_{st}) at the notch root is proportional to the tensile speed when u/t$\leqq$5000mm/s.

Keywords Stress Concentration, Notch, Dynamic Stress, Strain Rate, Finite Element Method

1. Introduction

Engineering plastics are widely used in everyday products. Typically, a suitable engineering plastic is chosen for its range of enhanced physical properties. It is know that polycarbonate has superior impact and perforation resistance compared with other polymers, or indeed compared with some structural metals [1]. Most thermoplastics far below their glass transition temperature T_g give a brittle fracture when deformed in uniaxial tension. However, polycarbonate is an exception and deformed in a ductile manner. However, Izod impact studies of notched specimens show that the fracture mode changes from ductile to brittle below T_g. To investigate the brittle-ductile transition, which is affected by temperature and loading speed [2, 3], a high-speed tensile test is being recognized as a standard testing method in recent years. Generally, bluntly notched specimens failed in a fully ductile manner, and sharply notched specimens failed in brittle manner depending on the strain rate at the notch root.

It should be noted that Izod and Charpy impact tests are not suitable for evaluating the impact strength of real products because the impact speeds do not correspond to the real failure. In the high-speed tensile test, it is necessary to obtain the strain rate correctly to understand the impact strength of the polymer specimen. For smoothing specimens, the strain rate can be determined as $\dot{\varepsilon} = u/tl$ from the specimen length l and the tensile speed u/t. On the other hand, for notched specimens, it is necessary to measure the strain at the notch root by strain gauge measurement, for example. However, because only the average value of the strain concerning the gauge width can be measured. It is not easy to measure the strain at the notch root.

In the previous studies for dynamic stress concentration, circular holes [4] and elliptical holes [5] were investigated under step load [6, 7] and pulse load [7, 8]. In addition, several review papers for

impact problems are also available [9–11]. However, there are few studies on the strain rate concentration for notched specimens under various tensile speed. Therefore, in this paper, the finite element method is applied to analyze the notched specimens under various tensile speed. Then, the dynamic stress concentration factor and the strain rate factor will be discussed with varying tensile speed and maximum values of forced displacement.

2. Static stress concentration and specimen geometry

In this study, the material analyzed is assumed as polycarbonate, which has especially high impact strength among the polymeric materials. Young's modulus is assumed as E = 2.3GPa, Poisson's ratio ν = 0.37. Figure 1 shows the geometry of the double-edge-notched specimen, with dimensions of notch root radius $\rho = 0.03mm$ and $0.2mm$, notch depth t = 5mm, and opening angle 90º. The notch root radius $\rho = 0.03mm$ corresponds to the radius of fillet appearing at polymer products generally. The notch root radius $\rho = 0.2mm$ corresponds to the radius of the notched specimens used in the Izod and Charpy test. When the high-speed tensile test is performed, both ends of the specimen are gripped by rigid chuck, then forced displacement is applied to the end under constant speed. Figure 2 shows FE models for analysis. Here Model 1 has the notch radius $\rho = 0.03mm$, and Model 2 has $\rho = 0.2mm$. Figure 2(c) shows the notch root detail in Model 1, and Fig. 2(d) shows the notch root detail in Model 2. Minimum mesh size of the notch root is $e = \rho/243$ each model. Figure 3 shows the boundary conditions given to the end portion of the analysis models. Figure 3(a) shows boundary conditions in the rigid chucks, and Fig.3(b) shows a tensile stress boundary conditions

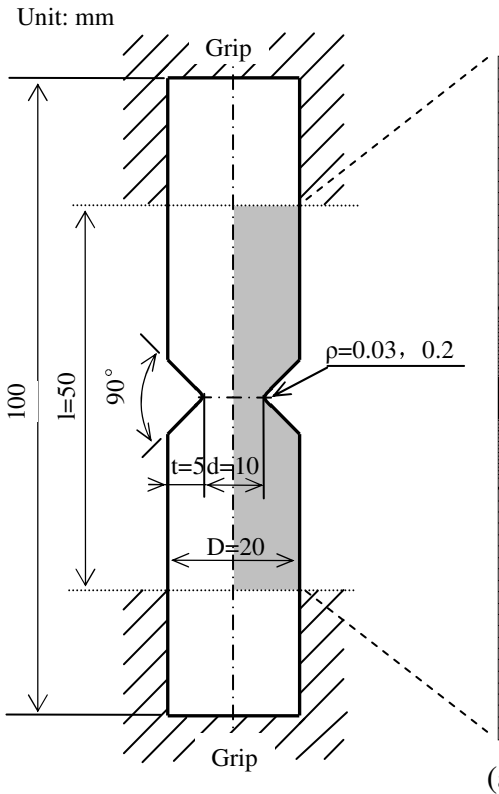

Figure 1. Geometry of specimen

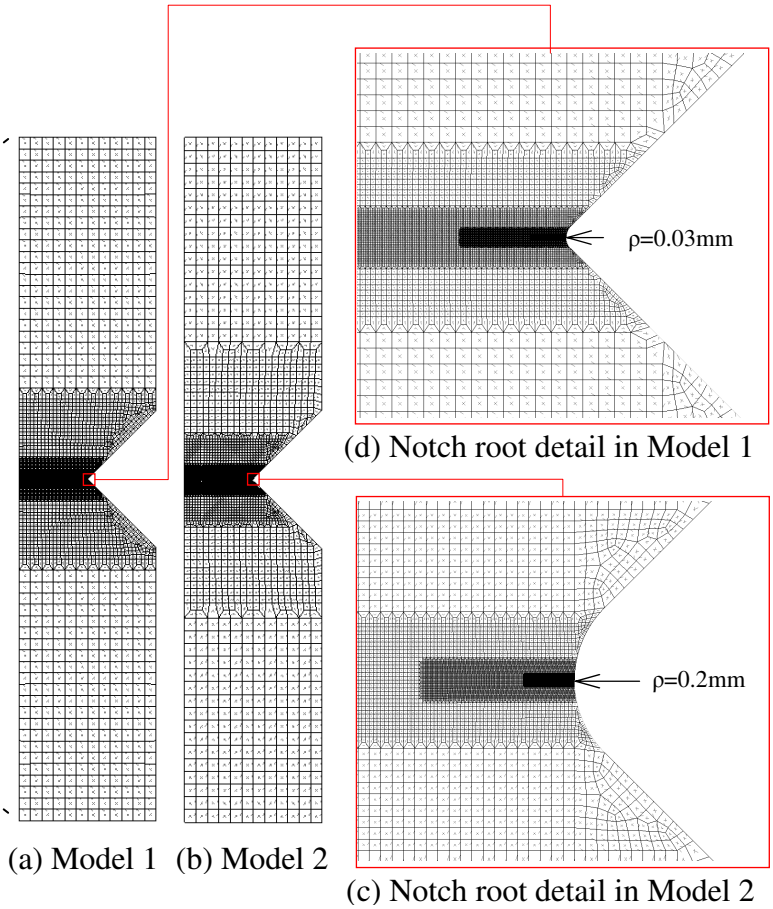

Figure 2. FE models

generally used. Table 1 shows the effect of boundary conditions on the static stress concentration factor. From Table 1, it is seen that the stress concentration factor is almost the same between the rigid grip tension and simple tension. Also, Table 1 shows the FE model in Fig. 2 shows less than 1% error compared to the exact stress concentration factor obtained by the approximate formula[12].

3. Dynamic stress concentration for high speed tensile test specimen

Figure 4 shows the forced displacement u given at the end of the specimen. The average stress σ_{gross} is also indicated, which is expressed as $\sigma_{gross}(t) = 0.867E \cdot u(t)/l$ from FEM. The stress at the

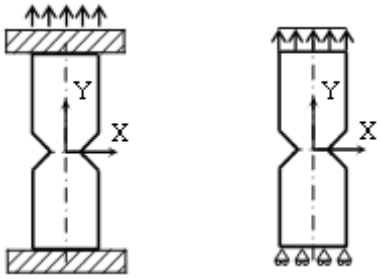

(a)Rigid grip tension (b)Simple tension

Figure 3. Boundary condition

Table 1. Static stress concentration factor by FEM

	K_t in Fig.3(a)	K_t in Fig.3(b)	Ref. [12] in Fig.3(b)
ρ=0.03, t=5	14.46	14.48	14.49
ρ=0.2, t=5	6.14	6.15	6.12

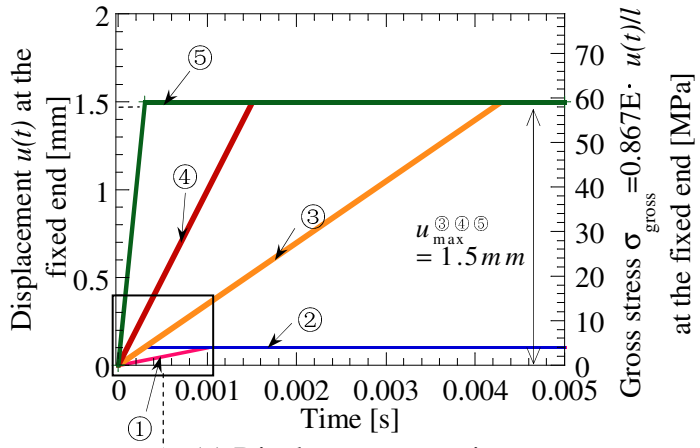

(a) Displacement vs. time

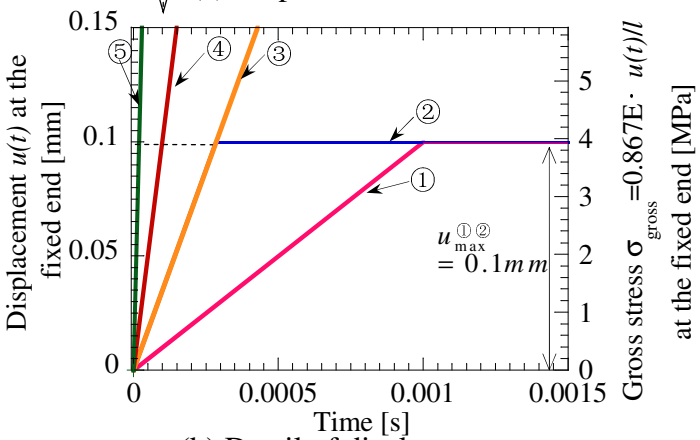

(b) Detail of displacement

Figure 4. Loading conditions

minimum section is expressed as $\sigma_{net} = (D/d)\sigma_{gross}$. Here, we consider 5 cases as shown in Table 2. Table 2 shows the tensile speed and the maximum forced displacement at the grip end with the time of that appear. In Case 5, the tensile speed $u/t = 5000\,mm/s$ corresponds to the impact speed when someone drops a call phone to the ground. The maximum displacement 1.5mm corresponds to the brittle fracture appears for high speed tensile test. The maximum displacement 0.1mm corresponds to an example of nondestructive case of for high speed tensile test.

Figure 5 shows the dynamic stress at the notch root A for Cases 1-5. Also Fig. 5 shows the detail of the dynamic stress oscillation with each case. From Fig. 4 and Fig. 5, it is seen that the maximum dynamic stress $\sigma_{\max}$ appears at almost the same time of the maximum forced displacement. Defined the maximum value of dynamic stress as $\sigma_{\max}$ in each case. After several oscillations due

Table 2. Maximum displacement and tensile speed given at the grip end

	Case		①	②	③	④	⑤
Condition	Maximum displacement	$u_{\max}$	0.1 mm t=0.00100s	0.1 mm t=0.00029s	1.5 mm t=0.00429s	1.5 mm t=0.00150s	1.5 mm t=0.00030s
	Tensile speed	u/t	100 mm/s t<0.00100s	350 mm/s t<0.00029s	350 mm/s t<0.00429s	1000 mm/s t<0.00150s	5000 mm/s t<0.00030s

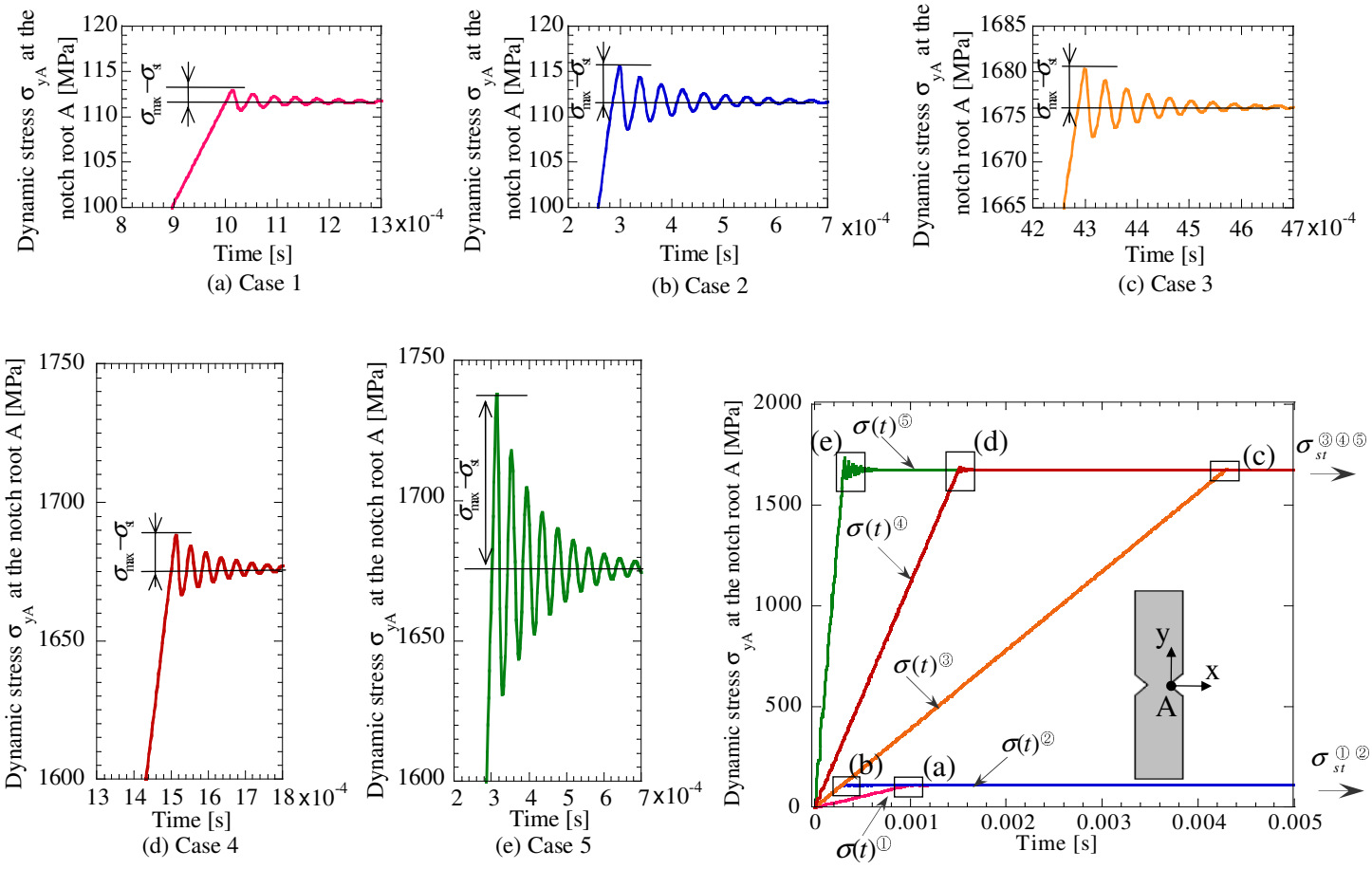

Figure 5. Dynamic stress at notch root A for ρ=0.03mm

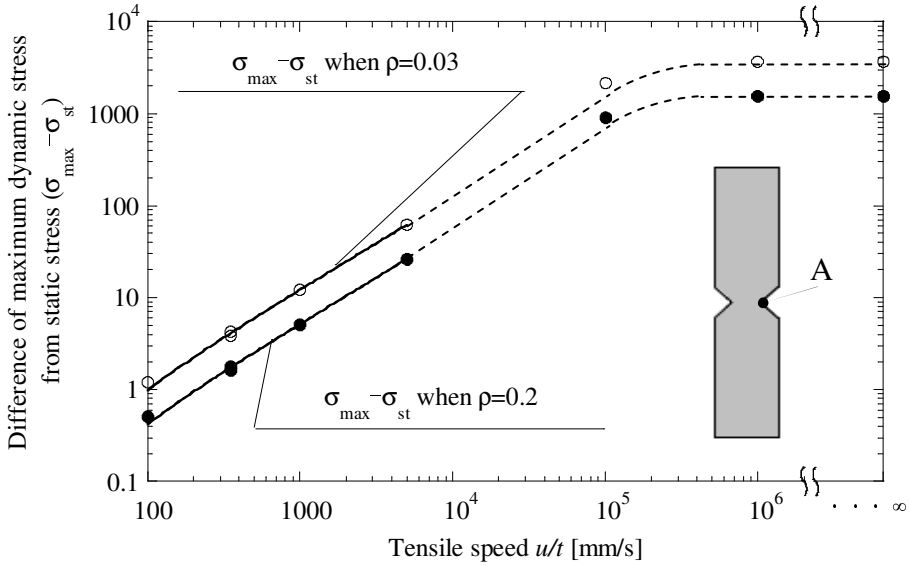

Figure 6. Difference between the static and dynamic maximum stress concentration ($\sigma_{\max} - \sigma_{st}$) vs. tensile speed

to the stress wave, dynamic stress approaches the static stress σ_{st}. From the comparison between Case 3 and Case 4, it is seen that of the maximum dynamic stress oscillation $(\sigma_{\max} - \sigma_{st})$ at the notch root A is always the same although the final displacement of Case 3 is 15 times larger than that in Case 2. It is may be concluded that the maximum dynamic stress oscillation $(\sigma_{\max} - \sigma_{st})$ is controlled by the tensile speed. Figure 6 shows the relationship between the tensile speed u/t and $(\sigma_{\max} - \sigma_{st})$ for $\rho = 0.03mm$ and $0.2mm$. Here the results for $u/t = 10^5, 10^6\ mm/s$ and step load $u/t = \infty$ are also indicated when the maximum displacement is 1.5mm. It is seen that $(\sigma_{\max} - \sigma_{st})$ is proportional to the tensile speed when $u/t \le 5000\,mm/s$. However, $(\sigma_{\max} - \sigma_{st})$ becomes constant when $u/t \ge 10^5\ mm/s$.

4. Strain rate concentration for high speed tensile test specimen

Figure 7 shows the strain rate at the notch root A for Cases 1-5. The strain rate increases dramatically at the start of applying forced displacement, Then, after several oscillations, the strain

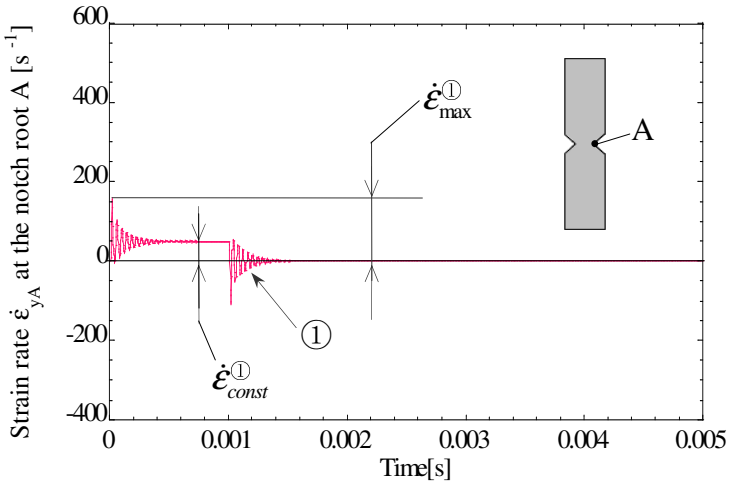

(a) Case 1

Figure 7. Strain rate at notch root A for ρ=0.03mm (Continued on next page)

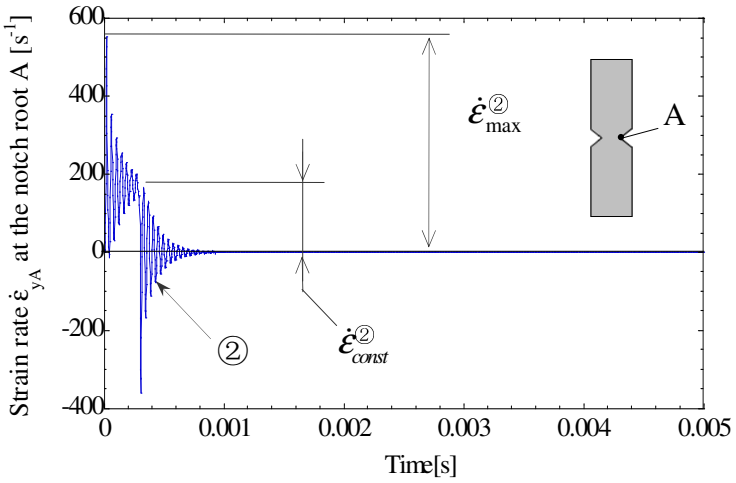

(b) Case 2

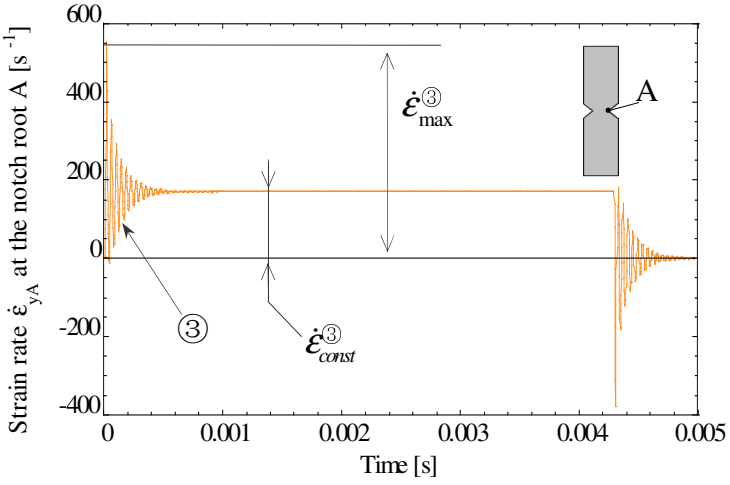

(c) Case 3

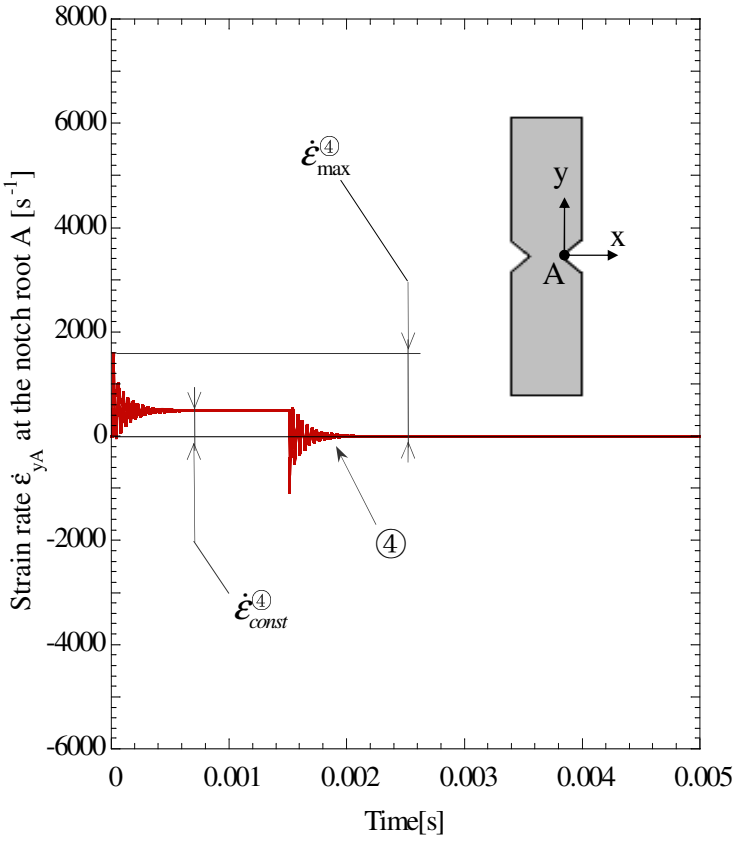

(d) Case 4

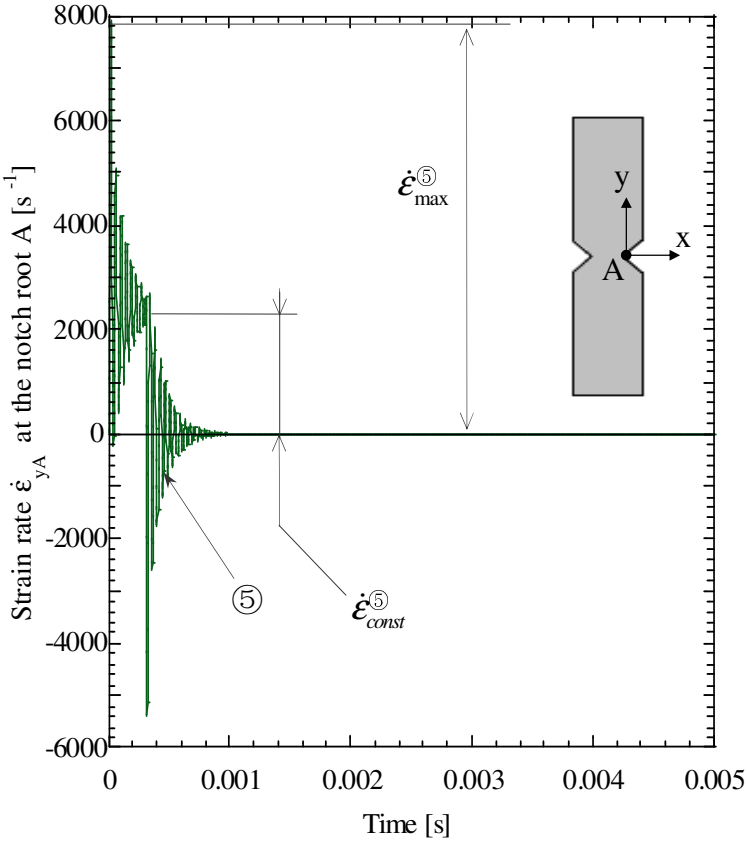

(e) Case 5

Figure 7. Strain rate at notch root A for ρ=0.03mm (Continued)

rate becomes constant. After stopping the forced displacement, several oscillations appear again, then it eventually converges to zero. From the comparison between Case 3 and Case 4, it is seen that the same maximum strain rate $\dot{\varepsilon}_{\max}$ and the same converged strain rate $\dot{\varepsilon}_{const}$ are observed although the final displacement $u_{\max}$ of Case 3 is 15 times larger than that in Case 2. It may be concluded that the strain rate concentration is controlled by the tensile speed. Figure 8 shows the

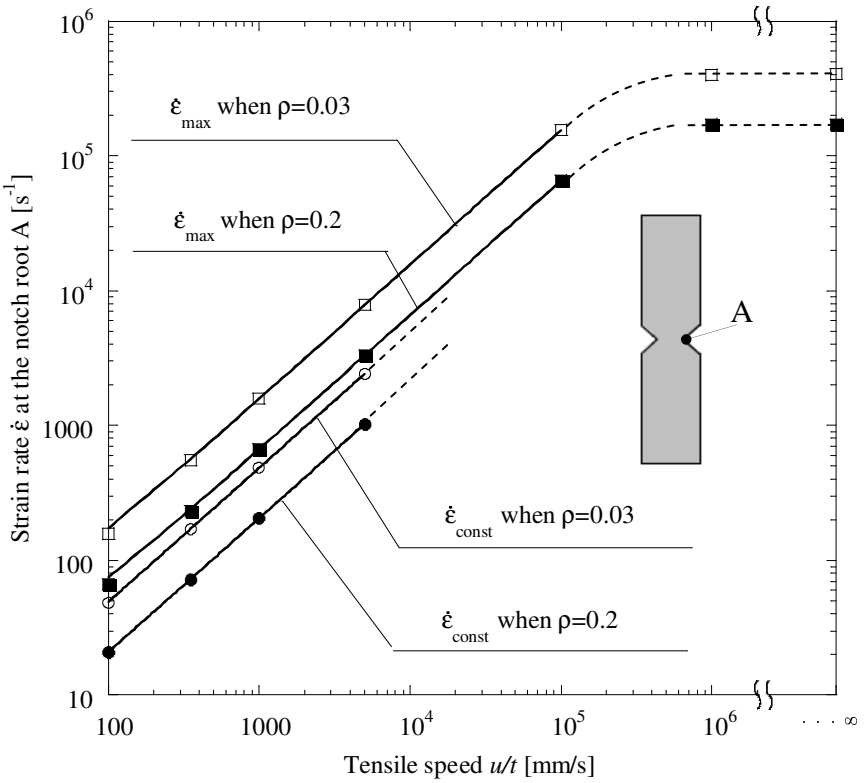

Figure 8. Maximum strain rate and converged strain rate vs. tensile speed

relationship between the tensile speed u/t and the strain rate for $\rho = 0.03mm$ and $0.2mm$. Here the results for $u/t = 10^5, 10^6\ mm/s$ and step load $u/t = \infty$ are also indicated when the maximum displacement is $1.5mm$. It is seen that the strain rate is proportional to the tensile speed when $u/t \le 5000\,mm/s$. However, the strain rate becomes constant when $u/t \ge 10^5\ mm/s$.

5. Dynamic stress and strain rate distributions of the minimum section

Figure 9(a) and Fig.10(a) show the dynamic stress distributions at the minimum section when the maximum dynamic stress appears. From Fig. 9(a), it is seen that the maximum dynamic stress $\sigma_{\max}(t)$ at the notch root when $\rho = 0.03mm$ is 14.48 times than that of the nominal stress $\sigma_{nom}(t)$ at the minimum section at each time for Case 1 –Case 5. On the other hand, from Fig. 10(a), it is seen that the maximum dynamic stress $\sigma_{\max}(t)$ at the notch root when $\rho = 0.2mm$ is 6.43 times than that of the nominal stress $\sigma_{nom}(t)$ at the minimum section at each time for Case 1 –Case 5. The stress concentration factor coincides with the static stress concentration factor obtained by Noda–Takase [12]. Figure 9(a) and Fig.10(a) show the strain rate distributions at the minimum section when the maximum strain rate appears. From Figure 9 (b), it is seen that the maximum strain rate $\dot{\varepsilon}_{\max}(t)$ at notch root when $\rho = 0.03mm$ is 22.87 times than that of the nominal strain rate $\dot{\varepsilon}_{nom}(t)$ at the minimum section for Case 1 –Case 5. From Fig. 10 (b), it is seen that the maximum strain rate $\dot{\varepsilon}_{\max}(t)$ at the notch root when $\rho = 0.2mm$ is 8.72 times than that of the nominal strain rate $\dot{\varepsilon}_{nom}(t)$ at the minimum section for Case 1 –Case 5.

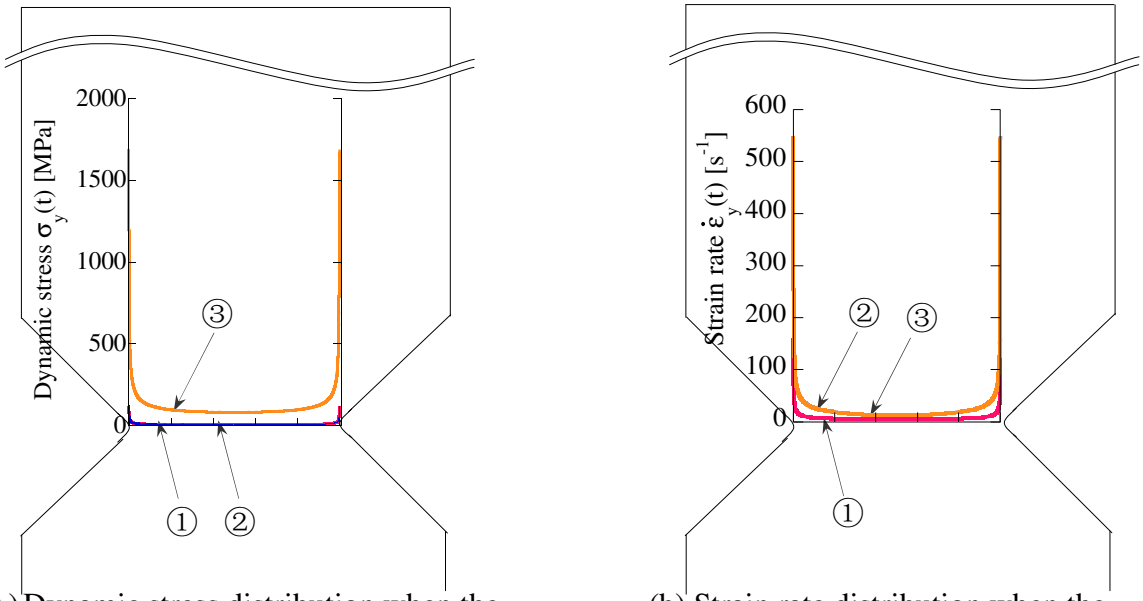

(A) Dynamic stress distribution when the maximum dynamic stress appeared

(b) Strain rate distribution when the maximum strain rate appeared

Figure 9. Stress and strain rate distribution around minimum section of ρ=0.03 mm

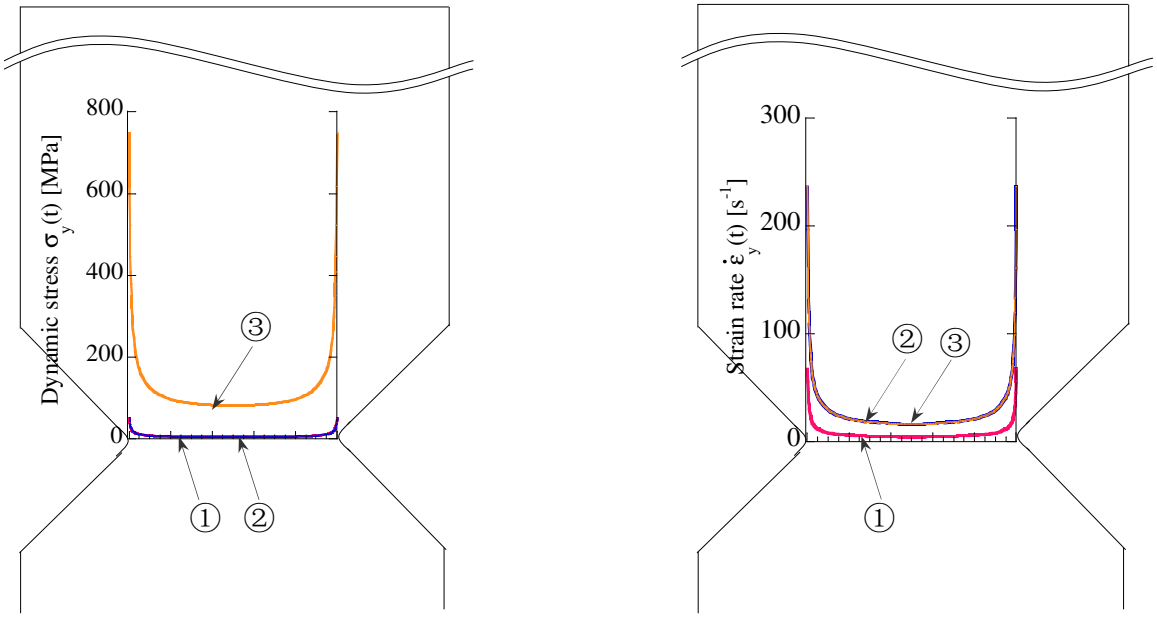

(A) Dynamic stress distribution when the maximum dynamic stress appeared

(b) Strain rate distribution when the maximum strain rate appeared

Figure 10. Stress and strain rate distribution around minimum section of ρ=0.2mm

6. Conclusion

Recently, high-speed tensile test is being used as a standard testing method to evaluate impact strength of the materials. For polymeric material, the strain rate and dynamic stress concentration is

significant factors, when we use this material as cellphone bumper. However, it is not easy to measure the dynamic stress or strain rate accurately at the notch root by experiment. In this study, therefore, dynamically and elastic FEM is applied to the high-speed tensile test for notched specimens. Then, the dynamic stress and strain rate concentrations have been discussed under various tensile speeds. The conclusions can be made the following way.

(1) It may be concluded that the strain rate concentration factor $K_{t\dot{\varepsilon}} = \dot{\varepsilon}_{\max}(t)/\dot{\varepsilon}_{nom}(t)$, which is defined by the maximum strain rate $\dot{\varepsilon}_{\max}(t)$ at the notch root over the average strain rate $\dot{\varepsilon}_{nom}(t)$ at the minimum section at each time, is always constant and controlled by the notch shape alone independent of the tensile speed.

(2) It is found that the difference between the static and dynamic maximum stress concentration ($\sigma_{\max} - \sigma_{st}$) at the notch root increases is proportional to the tensile speed when $u/t \le 5000\,mm/s$.

(3) It is found that the strain rate of the notch root increases is proportional to the tensile speed when $u/t \le 5000\,mm/s$.

References

[1] J. Radin, W. Goldsmith, Normal missile penetration and perforation of layered plates. Int. J. Impact Engng, 7, (1988) 229-259.

[2] T. Aya, T. Nakayama, Influence of Strain Rate on Elastic Modulus of Polymers. Journal of the Japan Society for Technology of Plasticity, Sosei-to-Kako, 36, 413 (1995) 665-670.

[3] S. Honma, Practical strength and durability of plastics (in Japanese). Plastics, 55, 1, (2004) 174-182.

[4] A. Chatani, S. Uchiyama, Dynamic stress concentration of notched strips. Material, 21, 226 (1972) 636-640.

[5] W. Altenhof, N. Zamani, W. North, B. Arnold, Dynamic stress concentrations for an axially loaded strut at discontinuities due to an elliptical hole or double circular notches. International Journal of Impact Engineering, 30, 3 (2004) 255-274.

[6] K. Kawata, S. Hashimoto, Dynamic stress concentration for notched elastic bar under dynamic load. University of Tokyo Institute of Space Aeronautical Report (in Japanese), 8, 2 (1972) 377-384.

[7] H. Matsumoto, I. Nakahara, Dynamic stresses in a hollow cylinder or a disc with a hole due to axially symmetric pressure variations. Transactions of the Japan Society of Mechanical Engineers, 32, 237 (1966) 709-717.

[8] H.G.. Georgiadis, A.P. Rigatos, N.C. Charalambakis, Dynamic stress concentration around a hole in a viscoelastic plate. Acta Mechanica, 111, 1-2 (1995) 1-12.

[9] S. Tanimura, Dynamic problems of materials and structures review of the studies. Transactions of the Japan Society of Mechanical Engineers, Series A, 63, 616 (1997) 2466-2471.

[10] N. Takeda, Impact damage and fracture of advanced composite materials/structures, Transactions of the Japan Society of Mechanical Engineers, Series A, 63, 616 (1997) 2472-2477.

[11] H. Inoue, K. Kishimoto, S. Aoki, Inverse analysis in impact problems. Transactions of the Japan Society of Mechanical Engineers, Series A, Vol. 63, No. 616 (1997), pp. 2478-2484.

[12] N.A. Noda, Y. Takase, Fatigue Notch Strength Useful for Machine Design (in Japanese), Nikkan Kogyo Shimbun Ltd, Tokyo, 2010.

Experimental observation of phase transformation front of SMA under impact loading

He Huang[1], Dominique Saletti[2], Stephane Pattofatto[1], Feifei Shi[1,4], Han Zhao[1,*]

[1] LMT-Cachan, ENS Cachan/CNRS 8535/UPMC, 61 Avenue du president Wilson, 94235 Cachan cedex, France
[2] Laboratoire de Biomécanique, Arts et Métiers ParisTech, 151, boulevard de l'Hôpital,75013 Paris, France
[3] School of Aeronautics, Northwestern Polytechnical university, 710072 Xi'an, China
* Corresponding author: zhao@lmt.ens-cachan.fr

Abstract Pseudoelasticity is one of the main characteristics of shape memory alloys (SMAs), allowing them to recover their initial state after undergoing large deformation. This is due to the martensitictransformation (MT) occurring in the material, turning the austenitic phase into a stress-induced martensitic phase when a mechanical load is experienced. Even if such an effect was largely studied in the past decades under quasi-static loading, the dependence of this effect of the loading rates was rather poorly documented. Only some studies have reported the strain rate dependence of the macroscopic behaviour of SMAs, but no detailed observation of the transformation process under impact loading is available.
This paper investigates the influence of the loading rate applied to a NiTi SMA at the level of the MT, providing experimental data of not only the macroscopic stress-strain curves, but also the corresponding observation of the heterogeneous strain field during the test. Main testing results are obtained under tensile loading. Experiments were conducted at three different levels of prescribed velocity : 0.01 mm/s, 1 mm/s and 5000 mm/s, using a classical loading machine for the quasi-static cases and a Split Hopkinson Tensile Bar (SHTB) for the dynamic cases. The observations of the heterogeneous strain field during the tests were made using a digital image correlation (DIC). Additional results under double shear test at various loading rate will be also presented.

Keywords Impact testing, Phase transition; NiTi shape memory alloy; Domain patterns and domain spacing; Strain rate.

1. Introduction

Shape memory alloys (SMA) have a great potential of applications in a lot of innovative technologies owing to two specific properties: the shape memory effect and pseudoelasticity [1]. In particular, NiTi-based SMA are widely used as biomaterials (to manufacture heart artery stents for instance) or in mechanical applications such as actuators, smart materials in the automotive industry, household appliances, and so on. The ability of NiTi alloys to undergo large strains is due to the transformation, under mechanical loading, of initial austenite to stress-induced martensite (SIM). This specific stress-induced martensitic transformation is associated to a mechanism of propagation of bands into the specimen as in localization phenomena (Luders bands, Portevin-Le Chatelier effect [2], compaction of foams ([3-4]), which leads to a non-homogeneous strain state ([5-7]).
Technically, the observation of the bands and the influence of strain rate on the propagation of the martensitic transformation has been initiated fifteen years ago ([6-8]). New measuring techniques, such as Digitial Image Correlation (DIC) that catches the measurable difference of strain between elastically loaded austenite and mechanically transformed martensite([9-10]), as well as the Infrared thermography (IRT) that takes advantage of the fact that the transformation of austenite into martensite is exothermic ([11-12]), have been used in the last decade. In the open literature, particular results are reported about the nucleation sites and the number of bands ([13]), the propagation of the transformation front, or the effect of stress concentration ([14]).

Under higher strain rates (more than 10 /s), some authors have studied the strain rate sensitivity of NiTi in compression ([15-19]) with Split Hopkinson Pressure Bars (SHPB), a system commonly used for accurate measurement of dynamic and macroscopic stress-strain responses of materials

([20-21]). It appears that SIM transformation is rate-dependent so that the stress triggering the transformation process increases with strain rate. There are also a few papers that present some experimental results with tensile Hopkinson bar tests (strain rate up to 1.67 /s in[22] and up to 1200 /s in [15]). Unfortunately, all these results under impact loading rate are only based on macroscopic measurements which are the nominal strain or stress. The observation of the transforming regions of NiTi alloys is not yet reported, probably due to the experimental difficulty to get these results at such strain rates. Thus, the description of nucleation sites, number of bands, transformation front velocity under higher strain rate are almost unknown. There is no available shear testing results under impact loading.

The present work wishes to provide a measurement of NiTi SMA behavior under tensile as well as shear loading up to an intermediate strain rate regime around 100 /s (3 decades higher than previous studies). In addition, heterogenous strain fields due to transforming regions is measured, coupled with a tensile Hopkinson bar system. For this purpose, strain fields of the sample are measured by Digital Image Correlation procedures using pictures captured with a high speed camera.

2. Experimental setup and macroscopic results

2.1 Tensile tests

2.1.1 NiTi specimens and quasi-static tests

The material of this study is taken from NiTi polycristalline cold-rolling sheets, in the cold-rolling direction. The metallurgical composition is 50.7 wt.% Ni and 49.3 wt.% Ti ([23]). All the experiments are performed at room temperature, clearly above the characteristic temperature A_f so that for stress-free condition the specimen is in a full austenite state. A single plate specimen, dog bone shaped, as schematically presented in the upper left corner of figure 1, is used for all the experiments. In its central part, the specimen is 60 mm long, 2.6 mm wide and 0.5 mm thick.

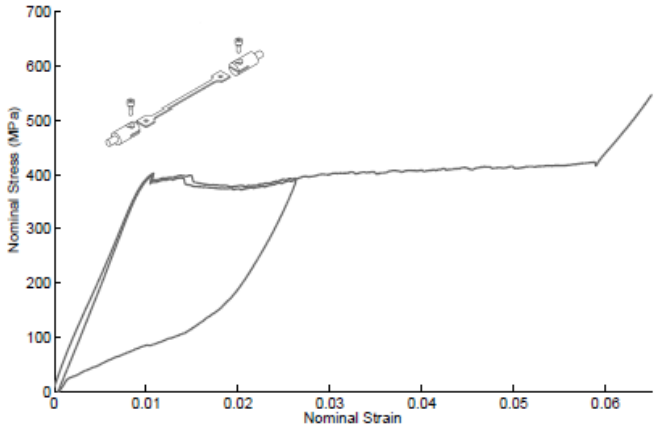

Fig. 1: Static strain-stress curve for a prescribed velocity of 0.01 mm/s ($1.4x10^{-4}$ /s), at room temperature

For the fixation in the grips, the width is 10 mm so that the fillet radius of 10 mm leads to a stress concentration. It is observed that this triggers the SIM transformation at both ends of the central part of the specimen. This is acceptable because the paper is focused on propagation of the transformation, not on its nucleation. For all the experiments, the specimen is fixed between two

tabs that can further be screwed (i) in the bars for dynamic tensile experiment, (ii) in a clamping system for static experiments. This allows to be more confident in the comparison of experimental results obtained with different devices. We could ensure that there is no sliding of the specimen during monotonic static or dynamic tension experiments due to the presence of a screw that fits into one hole machined into each end of the specimen. Quasi-static tensile tests were performed on an electromechanical Instron device so there was no heating of the specimen through the gripping system. Experiments were done at two different prescribed velocities : 0.01 mm/s ($1.4x\ 10^{-4}$/s) and 1 mm/s ($1.4x\ 10^{-2}$/s). Each experiment was repeated twice in order to check repeatability of the measurements. The nominal stress-strain curve obtained at 0.01 mm/s is shown in figure 1.
Three domains appear on the curve. First the elastic tension of the initial austenite phase for strains up to 0.01. Then the stress plateau associated to the pseudoelastic domain of interest in this study begins. It corresponds to the stress-induced martensitic (SIM) transformation for strains up to 0.06. One unloading-reloading cycle has been performed in the pseudoelastic domain in order to show that the reverse transformation is effectively reversible. It can be noticed that two serrations are visible at the beginning of the pseudoelastic domain. This phenomenon is due to the heterogeneity of the martensitic transformation ([12]). At a third stage, the supposed "fully" martensitic specimen is submitted to elastic tension. The vocabulary "fully martensitic" refers in fact to the end of the SIM transformation process even if it has been documented that probably all austenite has not been transformed yet ([24]). In this experiment, maximal strain is under 0.08 and there is no evidence of plastic deformation during tension.

2.1.2 The tensile Hopkinson bar experiment

The use of Hopkinson bars as a measurement technique has been introduced at the end of the 19th century and has led to many developments in the field of analysis of material behaviour under dynamic loading ([20], [25]). Hopkinson bar measurement allows to obtain an accurate measurement of dynamic forces and velocities at both ends of the specimen. The device used in this study is a Split Hopkinson Tensile Bar (SHTB) as schematized in figure 2. The apparatus is composed of two bars of 10 mm diameter, called the input and the output bars, made of maraging steel. The specimen (equipped with its end tabs) is tightly screwed at the end of each bar. The tabs are manufactured in the same material as the bars and designed so as to minimize any mass effect by matching the same acoustic impedance as the bars. The loading principle is the following: first a tensile elastic energy is stored in the input bar along a length L between points A and B of the input bar, then this energy is suddenly released from point B so that an incident tension pulse reaches the specimen ([26]). The initial elastic energy controls the subsequent strain and strain rate applied to the specimen. The initial load N_0 is applied with a hydraulic jack, and, to perform a test at an initial velocity of around 1000 mm/s, an initial load of around 5 kN is applied.

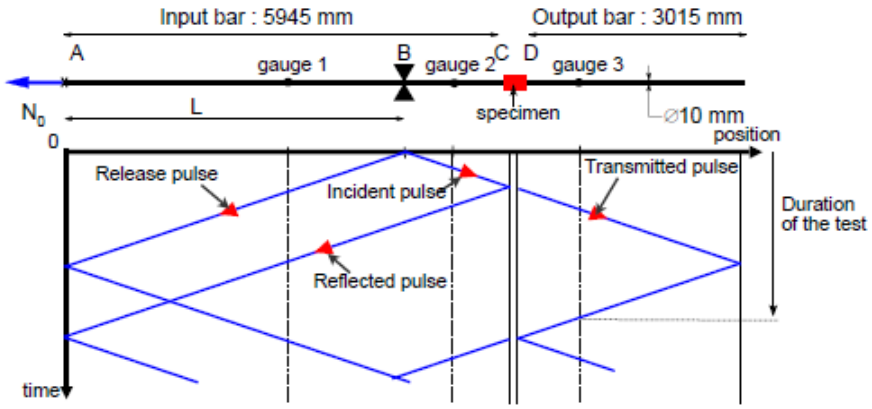

Fig. 2: Split Hopkinson Tensile Bar dimensions and corresponding lagrange diagram.

A significant increase of stress level is observed with impact strain rate, as shown in Figure 3.

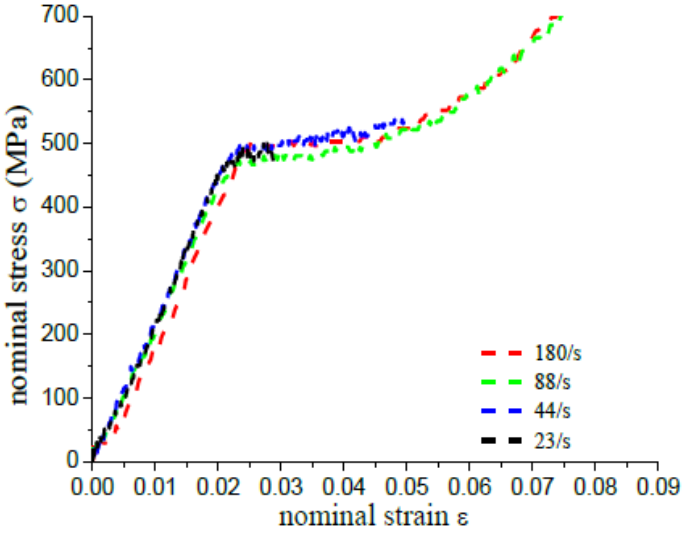

Figure 3 Stress strain curves at intermediate strain rates

2.2. Shear tests

Double shearing test can be realized which might prevent from geometrical instabilities. Divers versions of this test had been developed in the past decades [27-29]. A modified double shearing device to better fit with the 60mm-diameter Split Hopkinson pressure bar was developed by Merle [30]. Figure 4 shows the clamping device and specimen for the shearing tests. The specimen has two symmetric shearing zones of 3mm width and 20mm length. The clamping device is composed of the two moving coaxial pieces.

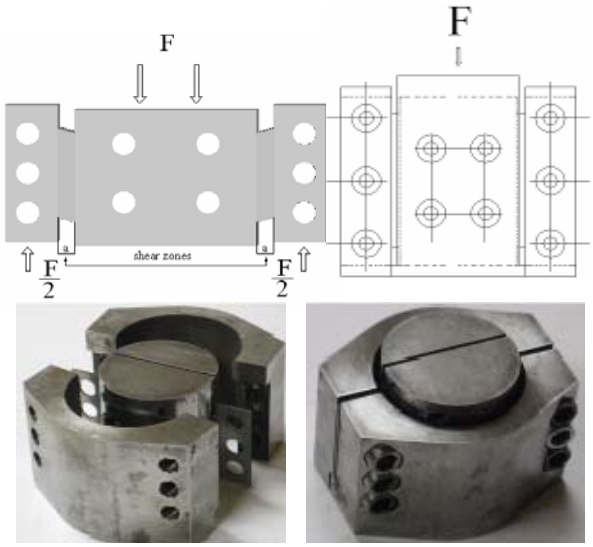

Fig. 4 Double shear specimen and shear device

Quasi-static tests were performed using a classical hydraulic testing machine with the device mentioned above. Dynamic tests were performed using the split Hopkinson of aluminum bars with a diameter of 60mm with 4m long incident bar and 2.5m long transmitted bar. The schematic drawing of the bars is shown in figure 5.

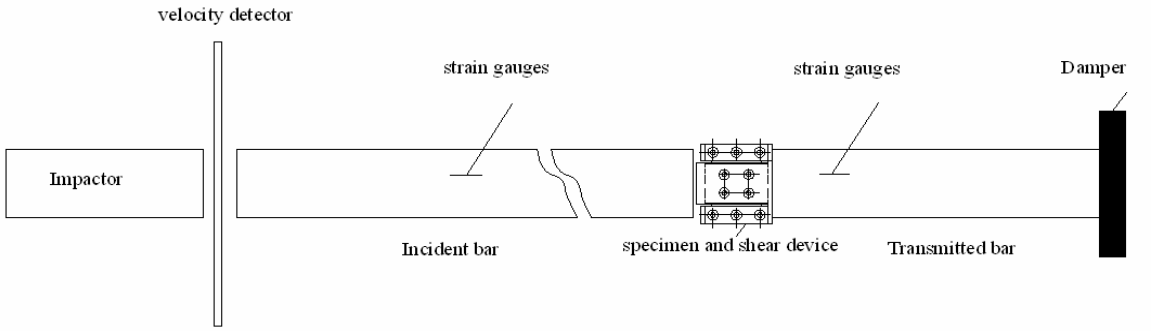

Fig.5 Schematic drawing of 60mm aluminum Hopkinson bar and device

Based on the plane shear assumption, the equivalent strain is calculated with measured displacement between the two clamping pieces d (Eqn 1.) and equivalent stress with the force F (Eqn 2).

$$\varepsilon_{eq} = \frac{\mathrm{d}}{l\sqrt{3}} \tag{1}$$

$$\sigma_{eq} = \tau\sqrt{3}\,,\ \tau = \frac{F}{S}. \tag{2}$$

Figure 6 shows first results at various strain rate. The same tendency of stress increases is also

observed.

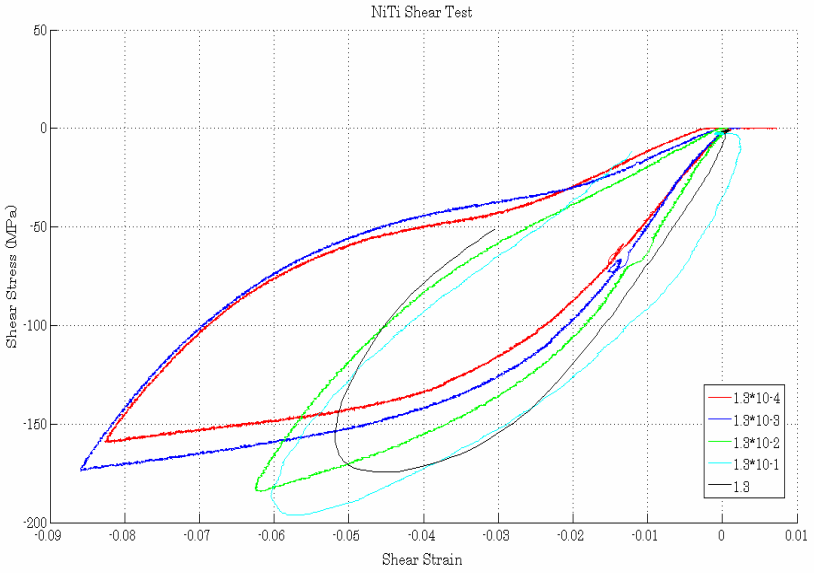

Figure 6 Shear stress-strain curves at various strain rates

3. Measurement of strain fields

3.1 Digital Image Correlation (DIC) setup

To acquire images, different devices were used, depending of the performed test. For low frequency acquisition, a reflex camera (Canon EOS) was used and for high frequency acquisition, fast cameras (PHOTRON) were used. The main difference between the two ways to get pictures is that for fast camera, the resolution is lower than for reflex camera. Subsequently, the spatial resolution is poorer for dynamic tests: the resolution of the fast camera is in inverse proportion to frame rate even if, for the last test, a more efficient camera was used in comparison with the previous test. This impact directly the accuracy of the optical measurement. In order to allow DIC computations, a speckle was applied on the observed surface of the specimen with black and white paint. Moreover, in order to avoid heating of the specimen surface, the lighting was done with LED lights during the quasi-static experiments and with short time light exposition of the specimen during the dynamic experiments. The principle of the used DIC computation program (CorreliQ4) is given in [31-32]. A first analysis of DIC results allows to give qualitative information on the phenomena taking place during the tests. Basic observation on figure 7, resulting from a quasi-static tensile test at 0.01 mm/s, shows that only two admissible strains are visible: a 1 % strain zone (supposed to be the austenitic phase) and a 6 % strain zone (supposed to be the stress-induced martensitic phase). An enlargement of the SIM region during the test can be observed.

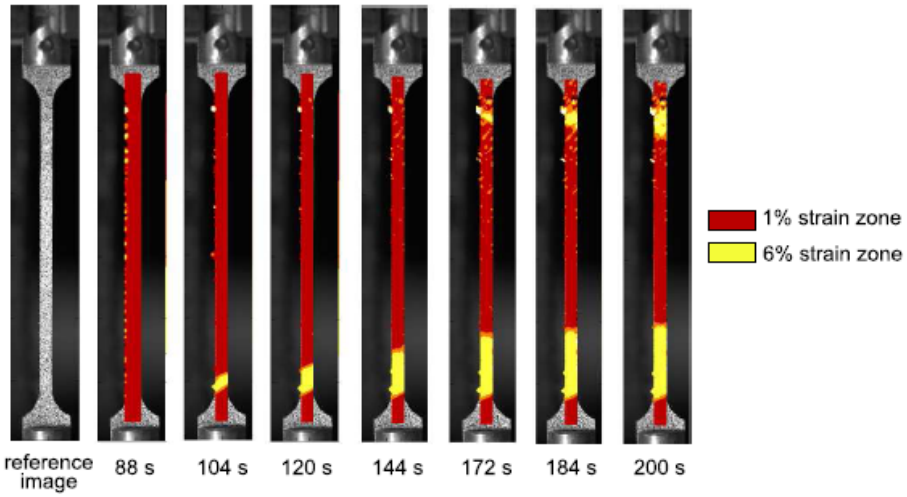

Fig. 7: Strain maps for quasi-static tensile test performed at 0.01 mm/s

The same image analysis can be also applied to the double shear tests. Figure 8 shows a strain map of shear tests. In contrast with tensile test, a rather homogeneous strain field was observed.

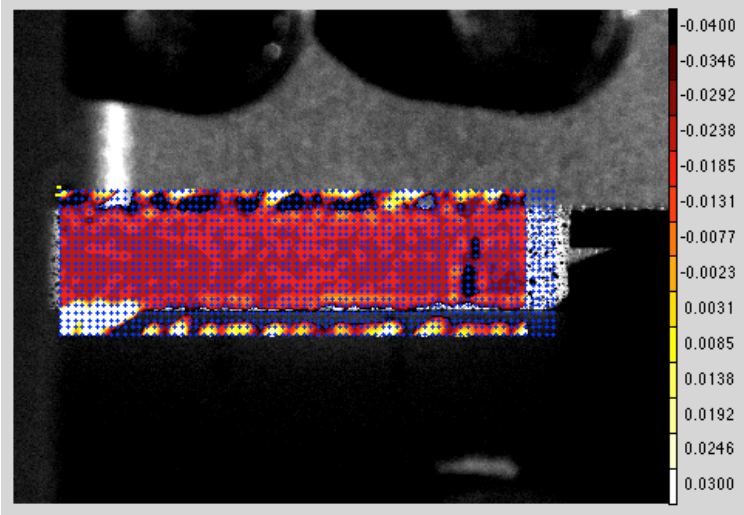

Figure 8, strain field measurement during shear tests

4 Conclusions

This paper used Split Hopkinson pressure bar system and high-speed testing machine to investigate the pseudoelastic deformation of a NiTi plate specimen at various strain rates. It provides original results of the strain rate dependence under not only tensile but shear loadings. In addition, the image analysis were used in all the testing which allows a measurement of strain fields.

Acknowledgements

Authors would like to express their thanks to the research team led by Prof. Sun Qingping of Hong Kong University of Science and Technology for his advice and supply of specimen used in all our experiments.

References

[1] Lagoudas D., Shape Memory Alloys, Springer (2008)
[2] Benallal A, Berstad T, Borvik T, Hopperstad OS, Nogueira de Codes R (2008) Effects of strain rates on the characteristics of PLC deformation bands for AA5083-H116 aluminium alloy. Philosophical Magazine 88(28)(29):3311-3338.
[3] El nasri I, Pattofatto S, Zhao H, Tsitsiris H, Hild F, Girard Y (2007) Shock enhancement of cellular stuctures under impact loading : Part I Experiments. Journal of the Mechanics and Physics of Solids 55:2652-2671.
[4] Pattofatto S, El Nasri I, Zhao H, Tsitsiris H, Hild F, Girard Y (2007) Shock enhancement of cellular stuctures under impact loading : Part II analysis. Journal of the Mechanics and Physics of Solids 55:2672-2686.
[5] Feng P and Sun QP (2006) Experimental investigation on macroscopic domain formation and evolution in polycrystalline NiTi microtubing under mechanical force. Journal of the Mechanics and Physics of Solids 54:1568-1603.
[6] Shaw JA and Kyriakides S (1998) Initiation and propagation of localized deformation in elasto-plastic strips under uniaxialtension. International Journal of Plasticity 13(10):837-871.
[7] Taillard K, Arbab Chirani S, Calloch S, Lexcellent C (2008) Equivalent transformation strain and its relation with martensite volume fraction for isotropic and anisotropic shape memory alloys. Mechanics of Materials 40:151-170.
[8] Shaw JA and Kyriakides S (1995) Thermomechanical aspects of NiTi. Journal of the Mechanics and Physics of Solids 43(8):1243-1281.
[9] Murasawa G, Yoneyama S, Sakuma T, TakashiM(2006) Influence of Cyclic Loading on Inhomogeneous Deformation Behavior Arising in NiTi Shape Memory Alloy Plate. Materials Transactions 47(3):1-7.
[10] Daly S, Ravichandran G, Bhattacharya K (2007) Stress-induced martensitic phase transformation in thin sheets of Nitinol. Acta Materialia 55:3593-3600.
[11] Pieczyska EA, Gadaj SP, Nowacki WK, Tobushi H (2006) Phase-Transformation Fronts Evolution for Stress- and Strain-Controlled Tension Tests in TiNi Shape Memory Alloy. Experimental Mechanics 46:531-542.
[12] Shaw JA and Kyriakides S (1997) On the nucleation and propagation of phase transformation fronts in NiTi alloy. Journal of the Mechanics and Physics of Solids 45(2):683-700.
[13] He YJ and Sun QP (2009) Scaling relationship on macroscopic helical domains in NiTi tubes. International Journal of Solids and Structures 46:4242-4251.
[14] Murasawa G, Yoneyama S, Sakuma T (2007) Nucleation, bifurcation and propagation of local deformation arising in NiTi shape memory alloy. Smart Materials and Structures 16:160-167.
[15] Adharapurapu RR, Jiang F, Vecchio KS, Gray III GT (2006) Response of NiTi shape memory alloy at high strain rate: A systematic investigation of temperature effects on tension-compression asymmetry. Acta Materialia 54:4609-4620.
[16] Chen W and Song B (2006) Temperature dependence of a NiTi shape memory alloy's superelastic behavior at high strain rate. Journal of Mechanics of Materials and Structures 1:339-356.
[17] Nemat-Nasser S and Choi JY (2005) Strain rate dependence of deformation mechanisms in a Ni-Ti-Cr shape-memory alloy. Acta Materialia 53:449-454.
[18] Nemat-Nasser S, Choi JY, GuoW-G, Isaacs JB (2005) Very high strain-rate response of a NiTi shape-memory alloy. Mechanics of Materials 37:287-298.
[19] Nemat-Nasser S and Guo W-G (2006) Superelastic and cyclic response of NiTi SMA at various strain rates and temperatures. Mechanics of Materials 38:463-474.
[20] Kolsky H (1949) An investigation of the mechanical properties of materials at very high strain

rates of loading. Proceedings of the Physical Society (London) 62-B:676-700.
[21] Zhao H and Gary G (1997) A new method for the separation of waves. Application to the SHPB technique for an unlimited duration of measurement. Journal of the Mechanics and Physics of Solids 45:1185-1202.
[22] Tobushi H, Shimeno Y, Hachisuka T, Tanaka K (1998) Influence of strain rate on superelastic properties of TiNi shape memory alloy. Mechanics of Materials 30:141-150.
[23] Qian L, Zhou Z, Sun QP, Yan W (2007) Nanofretting behaviors of NiTi shape memory alloy. Wear 63:501-507.
[24] Brinson LC, Schmidt I, Lammering R (2004) Stress-induced transformation behavior of a polycrystalline NiTi shape memory alloy: micro and macromechanical investigations via in situ optical microscopy. Journal of the Mechanics and Physics of Solids 52:1549-1571.
[25] Davies EDH and Hunter SC (1963) The dynamic compression testing of solids by the method of the split Hopkinson pressure bar. Journal of the Mechanics and Physics of Solids 11:55-179.
[26] Staab GH and Gilat A (1991) A direct-tension split Hopkinson bar for high strain rate testing. Experimental Mechanics 31(3):232-235.
[27] G.Gary, W.K.Nowacki, Essai de cisaillement plan appliqué à des tôle minces, Journal de physique Ⅳ. 4 (1994) C 8-65.
[28] J.R. Klepaczko, H. V. Nguyen, W.K. Nowacki, Quasi-static and dynamic shearing of sheet metals, J. Mech. A/solids. 18 (1999) 271-289.
[29] A. Rusinek, J.R. Klepaczko, Shear testing of a sheet steel at wide range of strain rates and a constitutive relation with strain-rate and temperature dependence of flow stress, International Journal of Plasticity. 17 (2001) 87-115.
[30] R. Merle, Mise en oeuvre et analyse d’un essai de double cisaillement en grandes déformations sous sollicitations dynamiques, France, 2003
[31] Hild F and Roux S (2006) Digital image correlation: from displacement measurement to identification of elastic properties, a review. Strain 42:69-80.
[32] Besnard G, Hild F, Roux S (2006) "Finite-element" displacement fields analysis from digital images: Application to Portevin-Le Chatelier bands. Experimental Mechanics 46(6):789-804.

Pre-kinking analysis of a cracked piezoelectric strip under impact loadings

Zengtao Chen[1,*], **Keqiang Hu**[1]

[1] Department of Mechanical Engineering, University of New Brunswick, Fredericton NB E3B 5A3, Canada
* Corresponding author: ztchen@unb.ca

Abstract An impermeable crack in a piezoelectric strip at arbitrary position under in-plane mechanical and electric impact loadings is considered. Due to the asymmetry of the geometry, this crack problem is a mixed-mode one. Fourier and Laplace transforms are applied to reduce the mixed boundary value problem of the crack to a system of singular integral equations. The asymptotic fields near the crack tip are obtained in explicit form and hoop and shear stress intensity factors are defined. Laplace inversion transforms are applied to get the dynamic hoop stress intensity factors. The crack kinking phenomena is investigated by applying the criterion of maximum hoop stress intensity factors. Numerical results show that the geometry of the cracked strip and the electric loadings have effects on the singular field distributions around the crack tip, and the hoop stress intensity factors are influenced by the material parameters, the electric loading and the geometric size ratios.

Keywords Mixed-mode crack, Piezoelectric Strip, Singular integral equations, Crack kinking; Hoop stress intensity factor

1. Introduction

Piezoelectric materials can be made into various functional devices, such as sensors and actuators, which are widely used in modern industrial fields. Due to the brittleness and low fracture toughness of piezoelectric materials, dynamic fracture analysis of piezoelectric materials has drawn considerable attentions. Dynamic anti-plane crack propagation in piezoelectric materials has been studied by Li and Mataga [1, 2]. Shindo et al. [3] obtained dynamic stress intensity factors of a cracked piezoelectric medium in a uniform dielectric field. The problem of a Griffith crack moving along the interface of two dissimilar piezoelectric materials was solved by Chen et al. [4] using the integral transform technique and it is shown that the stress and electric displacement are dependent on the speed of the crack and the material coefficients. Chen and Yu [5] investigated a semi-infinite crack in a piezoelectric medium subjected to antiplane impact loading. Mode-I transient response of a piezoelectric strip containing a center-situated crack under in-plane mechanical and electric impacts was investigated by Wang and Yu [6], and it was found that the intrinsic mechanical-electrical coupling plays a significant role in the dynamic fracture response of in-plane problems.

Crack kinking is an important phenomenon in the fracture of piezoelectric materials in response to electro-mechanical loading. Zhu and Yang [7] modeled the crack kinking in a piezoelectric solid by continuous distribution of edge dislocations and electric dipoles, and the solution was formulated via the Stroh formalism. The mixed-mode crack initiation in piezoelectric strip was studied by Wang and Noda [8] using the method of Fourier transform and singular integral equations. Hu and Zhong [9] considered a moving mode-III crack in a functionally graded piezoelectric strip. They found that the gradient of the material properties can affect the magnitudes of the stress intensity factors, and a high crack moving velocity can change the propagation orientation of the crack.

In this paper, the mixed-mode crack in a piezoelectric strip under in-plane electrical and mechanical impact loadings is studied. Fourier transform is employed to reduce the mixed boundary

value problem of the crack to solving a system of singular integral equations. The asymptotic fields near the crack tip are obtained in an explicit form and the hoop and shear stress intensity factors are then determined. The crack kinking phenomenon is investigated by applying the maximum hoop stress intensity factor criterion. The coupled electro-mechanical effects on the crack-tip fields are investigated and the influence of the geometric feature of the strip on the crack kinking is discussed.

2. Problem statement and method of solution

Consider a transversely isotropic, linear piezoelectric material and denote the rectangular coordinates of a point by (x, y, z). The constitutive equations can be written as

$$\begin{Bmatrix}\sigma_{xx}\\ \sigma_{zz}\\ \sigma_{xz}\end{Bmatrix}=\begin{bmatrix}C_{11} & C_{13} & 0\\ C_{13} & C_{33} & 0\\ 0 & 0 & C_{44}\end{bmatrix}\begin{Bmatrix}\partial u_x/\partial x\\ \partial u_z/\partial z\\ \partial u_x/\partial z+\partial u_z/\partial x\end{Bmatrix}+\begin{bmatrix}0 & e_{31}\\ 0 & e_{33}\\ e_{15} & 0\end{bmatrix}\begin{Bmatrix}\partial\phi/\partial x\\ \partial\phi/\partial z\end{Bmatrix}$$
$$\begin{Bmatrix}D_x\\ D_z\end{Bmatrix}=\begin{bmatrix}0 & 0 & e_{15}\\ e_{31} & e_{33} & 0\end{bmatrix}\begin{Bmatrix}\partial u_x/\partial x\\ \partial u_z/\partial z\\ \partial u_x/\partial z+\partial u_z/\partial x\end{Bmatrix}-\begin{bmatrix}\lambda_{11} & 0\\ 0 & \lambda_{33}\end{bmatrix}\begin{Bmatrix}\partial\phi/\partial x\\ \partial\phi/\partial z\end{Bmatrix} \quad (1)$$

where u_x, u_z are components of the displacement vector and ϕ is the electric potential, $C_{11}, C_{13}, C_{33}, C_{44}$ are elastic constants, e_{15}, e_{31} are piezoelectric constants, and $\lambda_{11}, \lambda_{33}$ are dielectric permittivities, σ_{ij} and D_i ($i, j = x, z$) are components of stress and electric displacement, respectively.

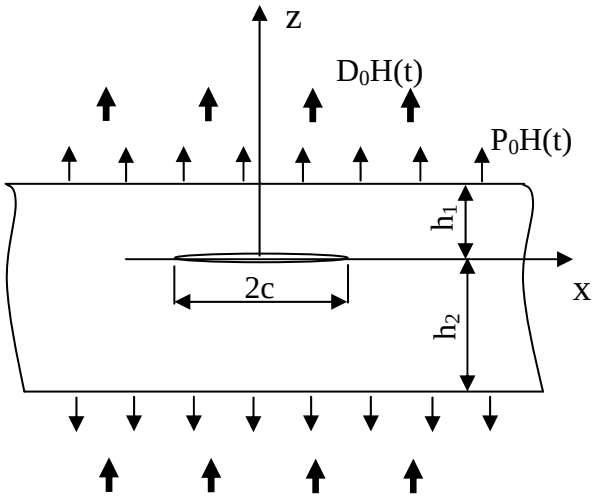

Figure 1. A cracked piezoelectric strip under in-plane mechanical and electric impact loadings

Studied in this paper is a Griffith crack of length $2c$ in a piezoelectric strip of width $h_1 + h_2$, with the poling direction perpendicular to the crack plane, as shown in Fig. 1. Uniform impact

normal stress $P_0\mathrm{H(t)}$ and impact electric displacement $D_0\mathrm{H(t)}$ are applied on the edges of the strip, where H(t) is the Heaviside step function. As shown in Fig. 1, symmetry conditions are used to allow for consideration of only the region ($x \geq 0,\ -h_2 \leq z \leq h_1$). In this paper the impermeable electric boundary condition on the crack faces is employed.

Application of Laplace transform leads to the governing equations in the Laplace domain as follows:

$$\begin{aligned} &C_{11}u^*_{x,xx} + C_{44}u^*_{x,zz} + (C_{13}+C_{44})u^*_{z,xz} + (e_{31}+e_{15})\phi^*_{,xz} = \rho p^2 u^*_x \\ &(C_{13}+C_{44})u^*_{x,xz} + C_{44}u^*_{z,xx} + C_{33}u^*_{z,zz} + e_{15}\phi^*_{,xx} + e_{33}\phi^*_{,zz} = \rho p^2 u^*_z \\ &(e_{31}+e_{15})u^*_{x,xz} + e_{15}u^*_{z,xx} + e_{33}u^*_{z,zz} - \lambda_{11}\phi^*_{,xx} - \lambda_{33}\phi^*_{,zz} = 0 \end{aligned} \tag{2}$$

where p is the Laplace transform parameter and the superscript * denotes the quantities in the Laplace transform domain.

The corresponding boundary conditions and continuity conditions in the Laplace domain are:

$$\sigma^*_{zz}(x,h_1,p) = \sigma^*_{zz}(x,-h_2,p) = P_0/p,\ \ \sigma^*_{xz}(x,h_1,p) = \sigma^*_{xz}(x,-h_2,p) = 0 \qquad (x \geq 0) \tag{3}$$

$$D^*_z(x,h_1,p) = D^*_z(x,-h_2,p) = D_0/p$$

$$\sigma^*_{zz}(x,0^+,p) = \sigma^*_{zz}(x,0^-,p),\ \ \sigma^*_{xz}(x,0^+,p) = \sigma^*_{xz}(x,0^-,p) \qquad (x \geq 0) \tag{4}$$

$$D^*_z(x,0^+,p) = D^*_z(x,0^-,p)$$

$$\sigma^*_{zz}(x,0,p) = 0,\ \ \sigma^*_{xz}(x,0,p) = 0,\ \ D^*_z(x,0,p) = 0 \qquad (0 \leq x < c) \tag{5}$$

$$u^*_z(x,0^+,p) = u^*_z(x,0^-,p),\ \ u^*_x(x,0^+,p) = u^*_x(x,0^-,p) \qquad (x \geq c) \tag{6}$$

$$\phi^*(x,0^+,p) = \phi^*(x,0^-,p)$$

Fourier transform is applied to Eq. (2) to obtain the solutions as

$$u^{*(n)}_x(x,z,p) = -\sum_{j=1}^{3}\int_0^\infty a_j\gamma_j\left[A^{(n)}_j(\xi,p)\sinh(\gamma_j\xi z) + B^{(n)}_j(\xi,p)\cosh(\gamma_j\xi z)\right]\sin(\xi x)d\xi \tag{7}$$

$$u^{*(n)}_z(x,z,p) = \sum_{j=1}^{3}\int_0^\infty \left[A^{(n)}_j(\xi,p)\cosh(\gamma_j\xi z) + B^{(n)}_j(\xi,p)\sinh(\gamma_j\xi z)\right]\cos(\xi x)d\xi + T_1 z/p \tag{8}$$

$$\phi^{*(n)}(x,z,p) = -\sum_{j=1}^{3}\int_0^\infty b_j\left[A^{(n)}_j(\xi,p)\cosh(\gamma_j\xi z) + B^{(n)}_j(\xi,p)\sinh(\gamma_j\xi z)\right]\cos(\xi x)d\xi + T_2 z/p \tag{9}$$

where T_j $(j=1,2)$ are constants and a_j, b_j $(j=1,2,3)$ are known functions defined in Appendix A, the superscripts $(n)=(1),\ (2)$ denote the fields quantities in the upper ($0 \leq y \leq h_1$) and lower ($-h_2 \leq y \leq 0$) parts of the piezoelectric strip, respectively, and $A^{(n)}_j(\xi,p)$, $B^{(n)}_j(\xi,p)$, $(n=1,2;\ j=1,2,3)$ are unknowns to be determined; γ_j ($j=1-3$) are the roots of the following characteristic equation:

$$\begin{vmatrix} C_{11}+\rho p^2/\xi^2-C_{44}\gamma^2 & (C_{13}+C_{44})\gamma & (e_{31}+e_{15})\gamma \\ (C_{13}+C_{44})\gamma & C_{33}\gamma^2-\rho p^2/\xi^2-C_{44} & e_{33}\gamma^2-e_{15} \\ (e_{31}+e_{15})\gamma & e_{33}\gamma^2-e_{15} & \lambda_{11}-\lambda_{33}\gamma^2 \end{vmatrix}=0 \tag{10}$$

Note that the sixth-order characteristic equation (10) has six roots which occur in pairs with the same magnitude but opposite signs, and for complex roots, they always appear in conjugate pairs. In Eqs. (7-9), the roots γ_j ($j=1-3$) with $\mathrm{Re}(\gamma_j)>0$ are chosen by requiring a positive internal energy for the system to be in a steady state, as stated by Suo et al. [10].

The stress and electric displacement components can be expressed as follows

$$\sigma_{xz}^{*(n)}=-\sum_{j=1}^{3}\int_0^\infty \xi f_j\left[A_j^{(n)}(\xi,p)\cosh(\gamma_j\xi z)+B_j^{(n)}(\xi,p)\sinh(\gamma_j\xi z)\right]\sin(\xi x)d\xi \tag{11}$$

$$\sigma_{zz}^{*(n)}=P_0/p-\sum_{j=1}^{3}\int_0^\infty \xi g_j\left[A_j^{(n)}(\xi,p)\sinh(\gamma_j\xi z)+B_j^{(n)}(\xi,p)\cosh(\gamma_j\xi z)\right]\cos(\xi x)d\xi \tag{12}$$

$$\sigma_{xx}^{*(n)}=\sigma_0/p-\sum_{j=1}^{3}\int_0^\infty \xi q_j\left[A_j^{(n)}(\xi,p)\sinh(\gamma_j\xi z)+B_j^{(n)}(\xi,p)\cosh(\gamma_j\xi z)\right]\cos(\xi x)d\xi \tag{13}$$

$$D_z^{*(n)}=D_0/p-\sum_{j=1}^{3}\int_0^\infty \xi m_j\left[A_j^{(n)}(\xi,p)\sinh(\gamma_j\xi z)+B_j^{(n)}(\xi,p)\cosh(\gamma_j\xi z)\right]\cos(\xi x)d\xi \tag{14}$$

where $\sigma_0=C_{13}T_1+e_{31}T_2$ and the coefficients f_j, g_j, q_j, m_j are defined in Appendix A. By applying the boundary conditions (3) and (4), the unknown functions $B_j^{(1)}(\xi,p)$, $A_j^{(2)}(\xi,p)$, $B_j^{(2)}(\xi,p)$ ($j=1-3$) can be expressed by the independent unknowns $A_j^{(1)}(\xi,p)$ ($j=1-3$) as

$$\begin{aligned} &B_j^{(1)}(\xi,p)=\sum_{i=1}^{3}R_{ji}^{(1)}(\xi,h_1,p)A_i^{(1)}(\xi,p),\quad B_j^{(2)}(\xi,p)=\sum_{i=1}^{3}Q_{ji}(\xi,h_1,h_2,p)A_i^{(1)}(\xi,p) \\ &A_j^{(2)}(\xi,p)=\sum_{i=1}^{3}T_{ji}(\xi,h_1,h_2,p)A_i^{(1)}(\xi,p) \end{aligned} \tag{15}$$

where $R_{ji}^{(1)}(\xi,h_1,p)$, $T_{ji}(\xi,h_1,h_2,p)$ and $Q_{ji}(\xi,h_1,h_2,p)$ are known functions. Introduce the auxiliary functions $\Phi_i(x,p)$ ($i=1-3$) such that

$$\begin{Bmatrix}\Phi_1(x,p)\\ \Phi_2(x,p)\\ \Phi_3(x,p)\end{Bmatrix}=\frac{\partial}{\partial x}\begin{Bmatrix}u_x^{*(1)}(x,0^+,p)-u_x^{*(2)}(x,0^-,p)\\ u_z^{*(1)}(x,0^+,p)-u_z^{*(2)}(x,0^-,p)\\ \phi^{*(2)}(x,0^-,p)-\phi^{*(1)}(x,0^+,p)\end{Bmatrix} \tag{16}$$

By applying the solutions (7-9) and using the Fourier inverse transform, the independent unknowns can be obtained as

$$\begin{Bmatrix} A_1^{(1)}(\xi,p) \\ A_2^{(1)}(\xi,p) \\ A_3^{(1)}(\xi,p) \end{Bmatrix} = -\frac{2}{\pi\xi}\begin{bmatrix} Y_{11}(\xi,p) & Y_{12}(\xi,p) & Y_{13}(\xi,p) \\ Y_{21}(\xi,p) & Y_{22}(\xi,p) & Y_{23}(\xi,p) \\ Y_{31}(\xi,p) & Y_{32}(\xi,p) & Y_{33}(\xi,p) \end{bmatrix}\begin{Bmatrix} \int_0^c \Phi_1(s,p)\cos(s\xi)ds \\ \int_0^c \Phi_2(s,p)\sin(s\xi)ds \\ \int_0^c \Phi_3(s,p)\sin(s\xi)ds \end{Bmatrix} \tag{17}$$

where $Y_{ij}(\xi,p)$ $(i,j=1-3)$ are known functions. Satisfaction of the mixed boundary conditions (5) and (6) on the crack face plane leads to the simultaneous singular integral equations

$$\begin{aligned} &\int_{-1}^{1}\left\{\kappa_{m1}(s,x,p)\Psi_1(s,p)+\sum_{j=2}^{3}\left[\frac{U_{mj}^0}{s-x}+\kappa_{mj}(s,x,p)\right]\Psi_j(s,p)\right\}ds=\frac{-\pi T_m}{p} \\ &\int_{-1}^{1}\left\{\left[\frac{U_{31}^0}{x-s}+\kappa_{31}(s,x,p)\right]\Psi_1(s,p)+\sum_{j=2}^{3}\kappa_{3j}(s,x,p)\Psi_j(s,p)\right\}ds=0 \end{aligned} \qquad (m=1,2) \tag{18}$$

where $T_1=P_0$, $T_2=D_0$, $\Psi_i(s,p)=\Phi_i(cs,p)$, $\kappa_{ij}(s,x,p)$ $(i=1,2,3)$ are known kernel functions, the constants U_{ij}^0 are defined as $U_{ij}^0=\lim_{\xi\to\infty}U_{ij}(\xi,p)$ and $U_{ij}(\xi,p)$ are known functions. The functions $\Psi_i(s,p)$ $(i=1-3)$ satisfy the single-valuedness condition:

$$\int_{-1}^{1}\Psi_i(s,p)ds=0, \quad (i=1-3) \tag{19}$$

and $\Psi_i(s,p)$ may be expressed as

$$\Psi_i(s,p)=H_i(s,p)\big/\sqrt{1-s^2} \tag{20}$$

where $H_i(s,p)$ $(i=1-3)$ are unknowns to be solved.

Use the Lobatto-Chebyshev method [11], singular integral equations (18) can be reduced to the following algebraic equations:

$$\sum_{i=1}^{n}A_i\left\{[\kappa_{m1}(x_k,s_i,p)]H_1(s_i,p)+\sum_{j=2}^{3}\left[\frac{U_{mj}^0}{s_i-x_k}+\kappa_{mj}(x_k,s_i,p)\right]H_j(s_i,p)\right\}=\frac{-\pi T_m}{p} \quad (m=1,2) \tag{21}$$

$$\sum_{i=1}^{n}A_i\left\{\left[\frac{U_{31}^0}{x_k-s_i}+\kappa_{31}(x_k,s_i,p)\right]H_1(s_i,p)+\sum_{j=2}^{3}[\kappa_{3j}(x_k,s_i,p)]H_j(s_i,p)\right\}=0 \tag{22}$$

$$\sum_{i=1}^{n}A_iH_j(s_i,p)=0 \qquad (j=1,2,3) \tag{23}$$

where,

$$s_i = \cos\left[\frac{(i-1)\pi}{n-1}\right], \quad (i=1,2,...,n); \quad x_k = \cos\left[\frac{(2k-1)\pi}{2(n-1)}\right], \quad (k=1,2,...,n-1)$$
$$A_i = \frac{\pi}{2(n-1)}, \quad (i=1,n); \quad A_i = \frac{\pi}{(n-1)}, \quad (i=2,3,...,n-1) \tag{24}$$

3. Asymptotic fields near the crack tip

Once functions $H_j(s,p)$ ($j=1,2,3$) are obtained from solving the algebraic equations (21-23), following the procedure in Li and Lee [12], the asymptotic expressions of the electro-elastic fields near the crack tip can be determined by introducing a polar coordinate system (r,θ) with the origin at the right crack tip, as follows

$$r = \sqrt{(x-c)^2 + z^2}, \quad \theta = \tan^{-1}\left[z/(x-c)\right] \tag{25}$$

The hoop and shear stresses at an angle θ near the right tip of the crack are obtained from the following relations in terms of the polar coordinates (r,θ)

$$\sigma^*_{\theta\theta}(r,\theta,p) = \sigma^*_{zz}(r,\theta,p)\cos^2\theta + \sigma^*_{xx}(r,\theta,p)\sin^2\theta - \sigma^*_{xz}(r,\theta,p)\sin 2\theta$$
$$\sigma^*_{r\theta}(r,\theta,p) = \sin 2\theta\left[\sigma^*_{zz}(r,\theta,p) - \sigma^*_{xx}(r,\theta,p)\right]/2 + \sigma^*_{xz}(r,\theta,p)\cos 2\theta \tag{26}$$

Define the hoop stress intensity factor and shear stress intensity factor associated with the hoop and shear stresses at an arbitrary angle θ as [13]

$$K^*_{\theta\theta} = \lim_{r\to 0}\left(\sqrt{2r}\,\sigma^*_{\theta\theta}\right), \quad K^*_{r\theta} = \lim_{r\to 0}\left(\sqrt{2r}\,\sigma^*_{r\theta}\right) \tag{27}$$

Substituting Eqs. (26) into (27), the hoop and shear stress intensity factors in the Laplace domain can be obtained as:

$$K^*_{\theta\theta} = \sqrt{c}\sum_{j=1}^{3}\left\{\begin{array}{l}(g_j^0\cos^2\theta + q_j^0\sin^2\theta)\left[(-1)^n H_1(1,p)Y^0_{j1}\Lambda_{1j}(\theta) + \sum_{k=2}^{3} H_k(1,p)Y^0_{jk}\Lambda_{2j}(\theta)\right] \\ -f_j^0\sin 2\theta\left[H_1(1,p)Y^0_{j1}\Lambda_{2j}(\theta) - (-1)^n\sum_{k=2}^{3} H_k(1,p)Y^0_{jk}\Lambda_{1j}(\theta)\right]\end{array}\right\} \tag{28}$$

$$K^*_{r\theta} = \sqrt{c}\sum_{j=1}^{3}\left\{\begin{array}{l}\frac{(g_j^0 - q_j^0)\sin 2\theta}{2}\left[(-1)^n H_1(1,p)Y^0_{j1}\Lambda_{1j}(\theta) + \sum_{k=2}^{3} H_k(1,p)Y^0_{jk}\Lambda_{2j}(\theta)\right] \\ +f_j^0\cos 2\theta\left[H_1(1,p)Y^0_{j1}\Lambda_{2j}(\theta) - (-1)^n\sum_{k=2}^{3} H_k(1,p)Y^0_{jk}\Lambda_{1j}(\theta)\right]\end{array}\right\} \tag{29}$$

where $0 \le \theta \le \pi$ when $n=1$ for the upper part and $-\pi \le \theta \le 0$ when $n=2$ for the lower part of the cracked layer, respectively; the angular functions $\Lambda_{1j}(\theta)$ and $\Lambda_{2j}(\theta)$ ($j=1,2,3$) are given in the following form

$$\Lambda_{nj}(\theta) = \sqrt{\frac{\sqrt{\cos^2(\theta) + \left[\gamma_j^0\sin(\theta)\right]^2} + (-1)^n\cos(\theta)}{2\left[\cos^2(\theta) + \left[\gamma_j^0\sin(\theta)\right]^2\right]}} \qquad (k=1,2) \tag{30}$$

in which the constants $g_j^0, q_j^0, f_j^0, Y_{ij}^0, \gamma_j^0$ are defined in Appendix A.

Note that by setting the angle θ equal to zero and using the relations in Eqs. (30), the common expressions for the Mode-I and Mode-II stress intensity factors can be obtained. The dynamic hoop and shear stress intensity factors can be obtained by performing the Laplace inverse transform to Eqs. (28) and (29) as

$$K_{\theta\theta}(\theta,t)=\frac{1}{2\pi i}\int_{Br}K_{\theta\theta}^{*}(\theta,p)\exp(pt)dp,\quad K_{r\theta}(\theta,t)=\frac{1}{2\pi i}\int_{Br}K_{r\theta}^{*}(\theta,p)\exp(pt)dp \tag{31}$$

where "Br" stands for the Bromwich path of integration. Different criteria have been proposed to predict the direction of crack branching [14]. Here we use the maximum hoop stress intensity factor criterion to predict crack kinking.

4. Numerical results and discussions

To study the effect of electro-elastic interaction on the stress field near the crack tip, the electric loading parameter $L_D=e_{33}D_0/(\lambda_{33}P_0)$ is introduced. The material constants of PCM-80 [15] are used in the following numerical calculation:

$$\begin{aligned}
&C_{11}=17.0\times10^{10}(\mathrm{N/m^2}),\ C_{13}=11.5\times10^{10}(\mathrm{N/m^2}),\ C_{33}=16.5\times10^{10}(\mathrm{N/m^2})\\
&C_{44}=3.05\times10^{10}(\mathrm{N/m^2}),\ e_{15}=13.7\ (\mathrm{C/m^2}),\ e_{31}=-5.99\ (\mathrm{C/m^2}),\\
&e_{33}=15.6\ (\mathrm{C/m^2}),\ \lambda_{11}=95.2\times10^{-10}(\mathrm{C^2/Nm^2}),\ \lambda_{33}=68.4\times10^{-10}(\mathrm{C^2/Nm^2})\\
&\rho=5.5\times10^{3}(\mathrm{Kg/m^3})
\end{aligned} \tag{32}$$

The variation of the normalized dynamic hoop stress intensity factors (HSIFs) $\frac{K_{\theta\theta}(t)}{P_0\sqrt{c}}$ with normalized time tV_s/c at different angles θ are displayed in Fig. 2. The shear wave velocity is defined as $V_s=\sqrt{c_{44}+\frac{e_{15}^2}{\lambda_{11}}\Big/\rho}$. Without loss of generality, the geometric size of the strip is taken to be $h_1/c=1,\ h_2/c=5$, and the applied electric loading parameter $L_D=+0.5$. Fig. 2 shows that the HSIFs increase as time increases, and reach their peak values at about $tV_s/c=3.5$, and then decrease and oscillate about their static values, until when $tV_s/c\to\infty$, HSIFs reduce to the static values. The peak values of the HSIF at $\theta=20$ degrees are bigger than that of $\theta=0$ degrees, which means that the crack tends to deviate from the original crack plane, provided that the material has the same fracture toughness in every direction.

Fig. 3 shows the variation of peak values of the dynamic hoop stress intensity factors versus angles θ when $L_D=+0.5$. For the case $h_1\neq h_2$, the maximum value of the HSIFs appears at an angle different from the original crack plane, which implies that the crack may kink in this particular direction. When $h_1/c=1,\ h_2/c=5$, the crack kinks at about $\theta=+20$ degrees, and in another case $h_1/c=5,\ h_2/c=1$, the crack kinks at about $\theta=-20$ degrees. It is evident that the

possible crack kinking direction is oriented toward the thinner side of the strip. This is in agreement with [16] and [8] for the static mixed mode crack problem. It also agrees with the physical phenomenon that surface cracking is more likely to happen, due to the mechanism the crack kinks into the direction toward the surface of the body. The maximum value of the HSIFs appear at the angle $\theta = 0$ in the symmetric case when $h_1 = h_2$, which implies that the crack may propagate along the extension of original crack plane.

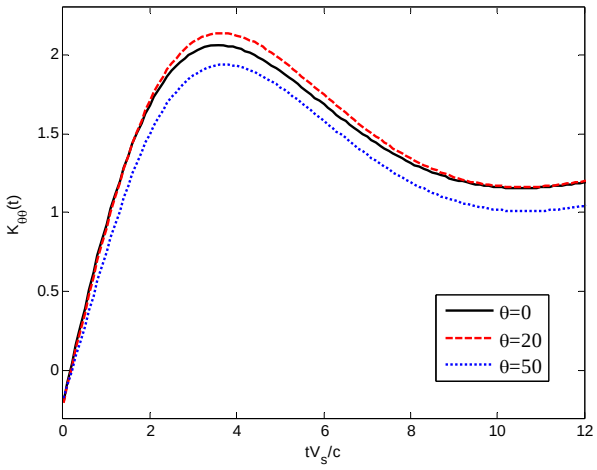

Figure 2. Dynamic hoop stress intensity factors for different angles

when $L_D = +0.5$, $h_1/c = 1$ and $h_2/c = 5$

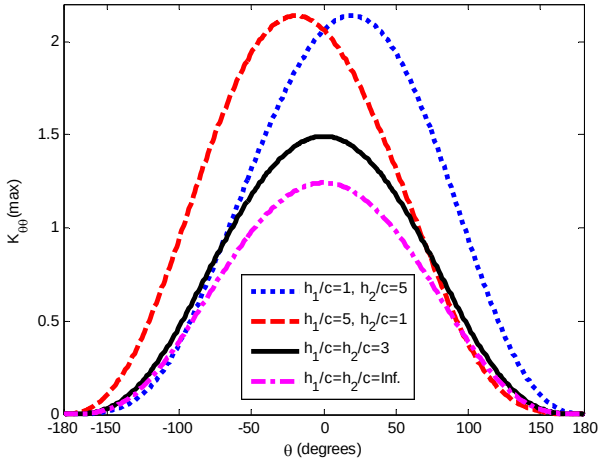

Figure 3. Maximum values of the normalized hoop stress intensity factors

versus angles when $L_D = +0.5$

Fig. 4 shows the effect of electric loading on the variation of normalized dynamic HSIFs at the angle $\theta = 20$ degrees. The electric loading parameter L_D affects the initial value and the peak value of the dynamic HSIFs. At the very beginning, a positive electric load leads to a lower initial value of the HSIF than negative electric load, whilst the peak value of the dynamic HSIFs induced by the positive electric load is higher than that for the negative electric load.

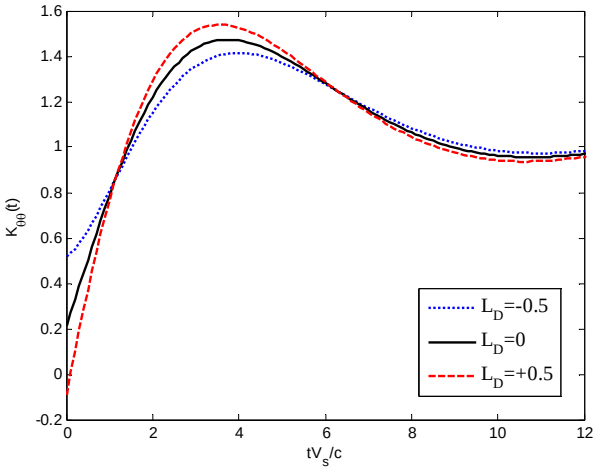

Figure 4. Dynamic hoop stress intensity factors for different electric loadings L_D

when $\theta = 20$ degrees and $h_2 = 2h_1 = 4c$

5. Concluding remarks

An impermeable crack in a piezoelectric strip under in-plane dynamic mechanical and electric loadings is studied. Fourier transforms are applied to reduce the mixed boundary value problem of the crack to dual integral equations, which are further expressed in terms of singular integral equations. Asymptotic fields near the crack tip are obtained in an explicit form and the corresponding field intensity factors are determined. The crack kinking phenomenon is investigated by applying the maximum hoop stress intensity factor criterion. Numerical results show that the geometry of the strip and the electric loading dominate the singular field distribution around the crack tip, and the hoop stress intensity factors are controlled by the material parameters, the electric loadings and the geometric size ratios.

Appendix A

The constants in Eqs. (14) and (15) are defined as

$$T_1 = (\lambda_{33}P_0 + e_{33}D_0)/(C_{33}\lambda_{33} + e_{33}^2), \quad T_2 = (e_{33}P_0 - C_{33}D_0)/(C_{33}\lambda_{33} + e_{33}^2) \tag{A.1}$$

$$\begin{Bmatrix} a_j \\ b_j \end{Bmatrix} = \begin{bmatrix} C_{11} + \rho p^2/\xi^2 - C_{44}\gamma_j^2 & e_{31} + e_{15} \\ (C_{13} + C_{44})\gamma_j^2 & e_{33}\gamma_j^2 - e_{15} \end{bmatrix}^{-1} \begin{Bmatrix} C_{13} + C_{44} \\ C_{33}\gamma_j^2 - C_{44} - \rho p^2/\xi^2 \end{Bmatrix} \tag{A.2}$$

$$f_j = C_{44}(a_j\gamma_j^2 + 1) - e_{15}b_j,\ \ g_j = (C_{13}a_j + e_{33}b_j - C_{33})\gamma_j$$
$$q_j = (C_{11}a_j + e_{31}b_j - C_{13})\gamma_j,\ \ m_j = (e_{31}a_j - \lambda_{33}b_j - e_{33})\gamma_j \tag{A.3}$$

$$g_j^0 = \lim_{\xi\to\infty} g_j,\ \ q_j^0 = \lim_{\xi\to\infty} q_j,\ \ f_j^0 = \lim_{\xi\to\infty} f_j,\ \ Y_{ij}^0 = \lim_{\xi\to\infty} Y_{ij}(\xi, p),\ \ \gamma_j^0 = \lim_{\xi\to\infty} \gamma_j(\xi, p) \tag{A.4}$$

References

[1] S.F. Li, P.A. Mataga, Dynamic crack propagation in piezoelectric materials-Part I: Electrode solution. J Mech Phys Solids, 44 (1996) 1799-1830.

[2] S.F. Li, P.A. Mataga, Dynamic crack propagation in piezoelectric materials-Part II: Vacuum solution. J Mech Phys Solids, 44 (1996) 1731-1866.

[3] Y. Shindo, H. Katsura, W. Yan, Dynamic stress intensity factor of a cracked dielectric medium in a uniform electric field. Acta Mech, 117 (1996) 1-10.

[4] Z.T. Chen, B.L. Karihaloo, S.W. Yu, A Griffith crack moving along the interface of two dissimilar piezoelectric materials, Int J Fract, 91(1998) 197-203.

[5] Z.T. Chen, S.W. Yu, Semi-infinite crack under anti-plane mechanical impact in piezoelectric materials. Int J Fract, 88 (1998) L53-56.

[6] X.Y. Wang, S.W. Yu, Transient response of a crack in piezoelectric strip subjected to the mechanical and electrical impacts: mode-I problem. Mech Mater, 33 (2001) 11-20.

[7] T. Zhu, W. Yang, Crack kinking in a piezoelectric solid. Int J Solids Struct, 36 (1999) 5013-5027.

[8] B.L. Wang, N. Noda, Mixed mode crack initiation in piezoelectric ceramic strip. Theor Appl Fract Mech, 34 (2000) 35-47.

[9] K.Q. Hu, Z. Zhong, A moving mode-III crack in a functionally graded piezoelectric strip. Int J Mech Mater Design, 2 (2005) 61-79.

[10] Z. Suo, C.-M. Kuo, D.M. Barnett, J.R. Willis, Fracture mechanics for piezoelectric ceramics. J Mech Phys Solids, 40 (1992) 739-765.

[11] P.S. Theocaris, N.I. Ioakimidis, Numerical integration methods for the solution of singular integral equations. Q Appl Math, 35 (1977) 173-183.

[12] X.F. Li, K.Y. Lee, Three-dimensional electroelastic analysis of a piezoelectric material with a penny-shaped dielectric crack. J Appl Mech, 71 (2004) 866-878.

[13] A. Azhdari, S. Nemat-Nasser, Hoop stress intensity factor and crack-kinking in anisotropic brittle solids. Int J Solids Struct, 33 (1996) 2023-2037.

[14] W. Yang, Mechatronic Reliability: Electric Failures, Mechanical-Electrical Coupling, Domain Switching, Mass-Flow Instabilities. Springer Verlag, New York, 2002.

[15] Y. Shindo, F. Narita, H. Mitsuru, Dynamic fatigue of cracked piezoelectric ceramics under electromechanical loading: Three-point bending test and finite element analysis. J Mech Mater Struct, 4 (2009) 719-729.

[16] J.W. Hutchinson, Z. Suo, Mixed mode cracking in layered materials. Adv Appl Mech, 29 (1992) 63-191.

Paper Template for Digital Speckle Interferometry Method for Research of Dynamic Processes

Michael N. Osipov[1], Anton N. Chekmenev[1], Yury D. Sheglov[1]

[1] Department of mathematic and mechanic, Samara State University, 443011, Ac. Pavlova str., 1, Russia
osipov@samsu.ru

Abstract The new digital speckle interferometry method for research of processes in mechanics of fracture, fatigue and strength of solid materials and structures in real time is considered. The new method is based on simultaneous registration of information by the standard digital speckle interferometry method and registration of distribution of intensity in the single speckle. Such decision allows to investigate fracture processes in real time; to increase sensitivity and accuracy of measurements; to expand a range of measured displacements. Besides, an offered method of the analysis of distribution of intensity in the single speckle allows will get rid of own noise inherent of interferometric methods of coherent optics.

In work theoretical and experimental results on realization of an offered method are presented. The optoelectronic scheme the digital speckle interferometer for registration at the same time speckle interferograms and intensity distribution in the single speckle is presented. The algorithm of processing of speckle interferograms on an offered method is presented.

It is shown that dynamic displacements can be measured with high resolution, in large range of measured value of displacements and in the large frequency range and in real time by this new method.

Keywords Experimental mechanics, Dynamic processes, Optical methods, Digital speckle interferometry, Processing and analysis of images and signals

1. Introduction

One of the main problems of solid mechanics, both fundamental, and the applied character, in many respects of a strength and durability of elements of designs, research of dynamic tasks is defining. Development of technique sets a task of increase of reliability of created and already working elements of designs subjecting to dynamic loadings. Existing mathematical models of the mechanics of fracture and settlement methods of forecasting don't allow to consider all real service conditions of designs fully. Experimental researches are necessary for confirmation of mathematical models of the mechanics of fracture and ensuring demanded parameters of designs at dynamic and static loadings. It demands development of the experimental measuring means, allowing to receive both qualitative, and quantitative data at dynamic and static loadings.

Optical contactless methods of researches gain now the increasing scientific and applied importance. Contactless methods have no impact on research elements of designs when carrying out experimental measurements that leads to increase of accuracy and reliability of received results. Considerable interest causes application of nondestructive interferometric methods for research of dynamic processes, both fundamental, and applied character. Optical, including laser interferometers, demand performance of a number of conditions which limit their practical application: the reflecting studied surface has to be optically smooth; the rigid mutual adjustment and fixing of elements of optical system is required. It should be noted also that interferometric methods, at practical application, demand use of lasers with a large spatial and time coherence that imposes additional restrictions when using data of systems in actual practice.

At the present stage it is necessary first of all to allocate from interferometric methods the digital holographic and speckle interferometry [1-4]. However, it is well known that at application of the

holographic and speckle interferometry there is a number of restrictions, which connected with existence of own noise (speckles), which lead to reduction of sensitivity and accuracy of measurements. Besides, speckle noise leads to restriction of measurement of displacements with great values of a gradient. Also we will note that existence of own noise (speckles) complicates processing of interferential pictures, both in the holographic, and the speckle interferometry and becomes impossible at research of high-frequency vibrations, because the contrast of interference fringes is falls. A problem of processing of the holographic and speckle interferograms the huge attention is paid [5-7]. Standard methods of the digital holographic and speckle interferometry, as a rule, don't allow to observe dynamic processes of solid mechanics in real time as at researches are generally used: averaging method in time; method of two expositions or pulse method.
In this work the new method of registration dynamic displacements of a research surface of object in large range of measured value of displacements and in the large frequency range on the basis of the analysis of distribution of intensity in the single speckle is considered. Such decision allows to overcome restrictions which are connected with existence of own noise (speckles) in the holographic and speckle interferometry and to register dynamic displacements in real time.

2. Speckle and practical application

2.1. Speckle pattern

When lighting by coherent radiation a rough surface because of scattering of a coherent radiation in space the complicated interference pattern, which is called speckle pattern, is formed. The characteristic kind of speckle pattern is presented in Fig. 1.

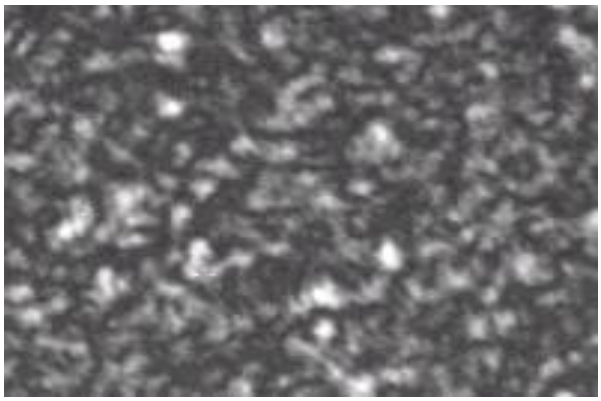

Figure 1. Photography of speckle patterns

Distinguish two kind of speckle patterns: a) the objective - formed in space at the expense of an interference of a large set of the reflected beams from a rough surface, and which can be registered directly without optical system on a photographic material; b) the subjective - formed and recorded on a photographic material by means of optical system in the plane of the image of a researched rough surface.
The sizes, longitudinal — L and transversal – H, of a speckle in objective and subjective speckle patterns are estimated on known formulas [1]:

$$L = \frac{4\lambda}{\alpha^2}, \tag{1}$$

$$H = 1{,}22\frac{\lambda}{\alpha}, \tag{2}$$

where λ is the wavelength of a laser, α – the relation of diameter of the lighted area of a research surface to distance from a research surface to a point of registration of the speckle for objective speckle pattern; α – the relation of diameter of an entrance aperture to focal length of optical system for subjective speckle pattern.
The dynamic processes arising on a surface of research object, lead to change of parameters speckle pattern (size and intensity) in space and in time that is connected with change of a phase of the reflected secondary spherical waves. Therefore, according to the analysis of existential behavior of the speckle pattern it is possible to investigate the dynamic and static processes of a research surface.

2.1. Proposed solution

As it was noted, parameters of the speckle pattern, changing in space and in time, are: longitudinal and transversal sizes; distribution of the intensity.
Let's estimate possibility of research of dynamic processes at the expense of measurement of parameters of the speckle pattern.
From Eq. (1) and (2) follows that the sizes of the subjective speckle pattern don't depend on dynamics of a research surface as α is a constant, and are therefore connected only with characteristics of optical system. Thus, the subjective speckle pattern doesn't allow to register displacements of a research surface, at the expense of measurement of the sizes speckle. On the other hand, registration subjective speckle pattern allows to tie rigidly its spatial arrangement in the image plane to a concrete point of a research surface. For registration of displacements in it cases are used methods of two expositions or averaging in time with the subsequent processing of interferograms.
Let's carry out a similar assessment for the objective speckle pattern. At dynamic displacements of a research surface of change of the sizes of a speckle for objective speckle pattern according to Eq. (1) and (2) will be defined by the following ratios:

$$L = \frac{4\lambda(r \pm \Delta r)^2}{D^2}, \tag{3}$$

$$H = 1{,}22\frac{\lambda(r \pm \Delta r)}{D}, \tag{4}$$

where r – distance from a research surface to a point of registration of the speckle; $\pm\Delta r$ – the value of displacement of a research surface; D – diameter of the lighted area of a research surface.
From the analysis of Eq. (1) and (2) follows that the transversal and longitudinal sizes of a speckle will change at very small value, as under real conditions of measurements $\Delta r/r \approx 0$. Therefore, as well as in a case with the subjective speckle pattern to define dynamics of a research surface at the expense of measurement of the sizes objective speckle pattern also it is almost impossible.
Let's consider possibility of definition of dynamics of a research surface, at the expense of registration of change of intensity of the speckle.
Change of intensity of a speckle occurs at the expense of change of its phase which depends on change of an optical way at displacement of a research surface. Change of value of a phase of the speckle on $\pm\pi$ $(2n+1)$, (where n=0,1,2. …) leads to change of intensity of the speckle from the minimum value to maximum or on a turn.
For registration of change of a phase of the speckle is necessary to use the reference beam of a laser radiation which is imposed on the speckle pattern, and therefore the secondary interference pattern in the form of fringe pattern is formed. Width of secondary interference fringes d is defined by well-known equation [8]:

$$d = \frac{\lambda}{2\sin(\frac{\Theta}{2})}, \tag{5}$$

where Θ – angle between the reference beam of a laser radiation and the focused scattered laser radiation from a research surface which forming image of this surface with speckle pattern in the plane of the photodetector.
The kind of speckle pattern with the secondary interference pattern is presented in Fig. 2.

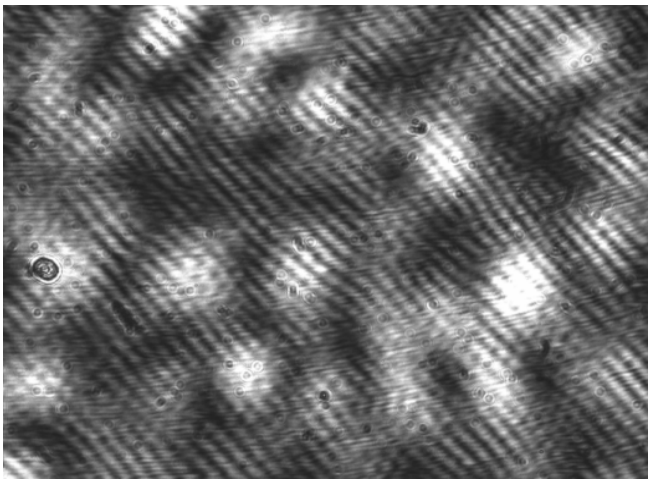

Figure 2. Photography of the speckle pattern with the secondary interference pattern

It is offered for effective registration of change of intensity of the single speckle to satisfy the following conditions: width of secondary interference fringes has to be agreed with the transversal size of the single speckle, and also with size of a sensitive cell of the photodetector.
For agreement of the transversal size of the single speckle with size of a sensitive cell of the photodetector it is necessary that the following ratio was carried out:

$$H \geq h, \tag{6}$$

where h – size of a sensitive cell of the photodetector.
Performance of this condition is achieved by sampling of the parameter α of a optical system, as appears from of Eq. (2).
In order that the sensitive cell of the photodetector could measure change of a phase of the single speckle it is necessary that width of secondary interference fringes d was more or equally of the size of a sensitive cell of the photodetector that is the following ratio was carried out:

$$d \geq h, \tag{7}$$

Performance of this condition is achieved by sampling of a angle of a convergence Θ between the reference beam and the focused scattered laser radiation from a research surface which forming image of this surface with speckle pattern in the plane of the photodetector, as appears from Eq. (5).
Performance of conditions – Eq. (6) and (7) – leads to that intensity of the single speckle, as whole, will change from minimum to the maximum value (or on the contrary) depending on displacements of a research surface.
Thus, measurement of intensity of the single speckle allows to investigate dynamic processes in a solid mechanics. Application in the offered method of high-speed photodiodes expands the frequency range of measured dynamic displacements.

2. 2 Measurement system

Realization of this method, based on the analysis of change of intensity of the single speckle, for measurement of dynamic processes in solid mechanics it is offered to carry out according to the optical scheme presented in Fig. 3.
By means of optical system L2 the rough surface of a research object O is lighted with laser radiation and is focused on the CCD TV. Let's emphasize, that as it was noted above, in the plane of a CCD matrix the image of object covered speckles is fixed. That allows to record on CCD TV a image of the research object with binding speckles to concrete points of this object.
If to direct the reference beam (in Fig. 3 it isn't shown) on a CCD matrix, as a result, we will receive standard the digital speckle interferometer which allows to make measurements of displacements with restrictions indicated in Introduction.

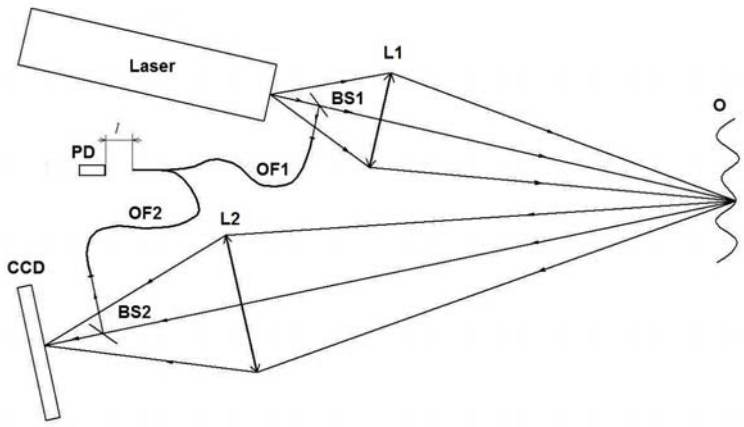

Figure 3. Optical scheme for dynamic measurement

Measurement of dynamic processes in solid mechanics is offered to be carried out according to the analysis of change of intensity of the single speckle. Standard CCD matrixes, as a rule, aren't the high-speed photodetector. Therefore they aren't capable to register of change of intensity of the single speckle in the wide frequency range. For overcoming of this restriction in the optical scheme it is offered to use in addition the high-speed photodetector PD, allowing to analyze of intensity of the single speckle in the wide frequency range.
For allocation single speckle, by means of the beam splitter BS2 the image of the single speckle goes on an entrance end face of an optical fiber OF2 which output end face is agreed with the high-speed photodetector PD. Diameter of a core of an optical fiber of OF2 has to be agreed with the transversal size of a speckle, that is the ratio (Eq. 6) has to be carried out.
For creation of a reference beam by means of the beam splitter BS1 the part of radiation of the laser L goes on an entrance end face of an optical fiber OF1 which output end face is also agreed with the high-speed photodetector FD. The output ends of optical fibers OF1 and OF1 are combined so that conditions (Eq. 6 and Eq. 7) were satisfied. The change of intensity of the single speckle is registered by the photodetector PD and is recorded in the PC for processing and visualization.

3. Theory

Let's consider for the offered optical scheme formation of distribution of intensity in the single speckle when performing conditions (Eq. 6 and Eq. 7). Let's write down values of vectors of electric intensity on the photodetector PD for waves passed through both optical fibers in the following kind:

$$\vec{E}_1 = \vec{E}_0 e^{i(kx_1 - \omega t + \varphi)}, \tag{8}$$

$$\vec{E}_2 = \vec{E}_0 e^{i(kx_2 - \omega t + \varphi)}, \tag{9}$$

where – E_0 amplitude of electric intensity of an electromagnetic field (we assume for simplification of calculations that it is identical in both optical fibers); $k=2\pi/\lambda$ – wave number; ω– circular frequency of laser radiation; φ– an initial phase which also is considered identical to both optical fibers; x_1 – distance from beam splitter BS1 to the photodetector PD on optical fiber OF1; x_2 – distance from beam splitter BS1 to the photodetector on optical fiber OF2.
Distance from beam splitter BS1 to the photodetector on an optical fiber OF2 recorded in the following kind:

$$x_2 = r_0 + r \pm 2\Delta r, \tag{9}$$

where r_0 – distance from beam splitter BS1 to a research object O; r – distance from a research object O to the photodetector PD on optical fiber OF2; $\pm\Delta r$ – the value of displacement of a research surface.
As the photodetector registers intensity, than the distribution of the intensity in an interference pattern of the single speckle will record in the following kind:

$$I(x,t) = \left|\left(\vec{E}_1 + \vec{E}_2\right)^{+}(\vec{E}_1 + \vec{E}_2)\right|^2 \approx 2E_0^2\left\{1 + \cos\left[k\left(x_1 - r_0 - r \mp 2\Delta r\right)\right]\right\}, \tag{10}$$

where the top index (+) means that vector value of electric intensity of an electromagnetic field is transposed and in a complex interfaced.
As appears from Eq. (10), and as it was noted above, intensity of a speckle changes from minimum to maximum values (or on the contrary) at change of value of a phase baked on $\pm\pi$ $(2n+1)$, (where n=0,1,2…) which is connected by dynamics of a research surface, that is with change Δr in time.
Change of intensity of the single speckle on an entrance of the photodetector it will be transformed to change of output signal of the photodetector which (see Eq. 10) can be expressed as follows:

$$u(t) = A + B\cos[\varphi(0) - \varphi(t)], \tag{11}$$

where $u(t)$ – the output voltage of the electrical scheme of the photodetector; A – the output bias voltage which is related to the average intensity of the single speckle; B – amplitude of useful output voltage which is defined by parameters of the optoelectronic scheme which related to a displacement of a research surface and kind of the optical scheme; $\varphi(0) = k(x_1 - r_0 - r)$ – initial value of a phase difference between the reference beam and the object beam forming speckle pattern in plane of a optical image. This phase difference can change but remains to constants in the time of measurements; $\varphi(t) = \pm 2k\Delta r$ is the change of a phase in single speckle related with change of the optical path in the object arm of a optical scheme at dynamic displacements of a research surface.
From the analysis of a Eq. (10) and (11) follows that change of output voltage of the photodetector depends on phase change $\varphi(t)$ characterizing dynamics single speckle related with movement of a research surface. As intensity single speckle changes from minimum to maximum or on the contrary, respectively and output voltage from the photodetector changes from the minimum value – $u(t)_{min}$ to the maximum value – $u(t)_{max}$ or on the contrary.
The theoretical results of behavior of the output voltage $u(t)$ in respect of vibrating displacements of the investigation surface are demonstrates in Fig. 4. The dashed curve represents the vibrations of

the investigation surface with amplitude increasing in time. The solid curve represents the theoretically calculated output voltage signal.

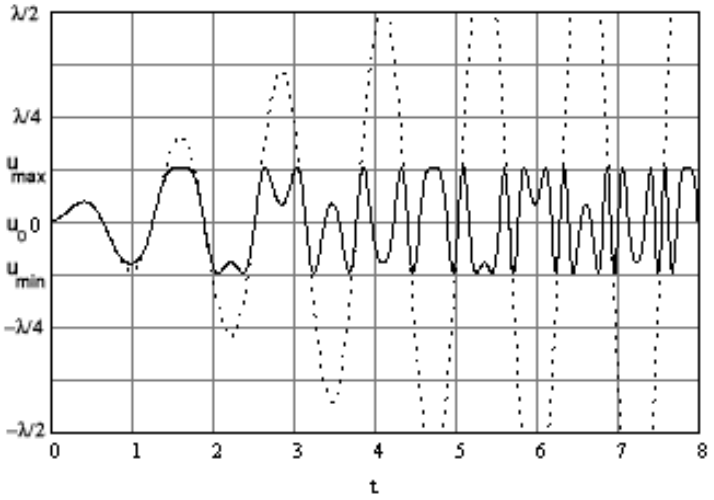

Figure 4. Theoretical curves of behavior output signal *u(t)* at the increasing amplitude of the investigation surface

3.1. Assessment of range of measurements

From the analysis of Eq. (10) and (11) follows that change of output voltage from minimum to the maximum corresponds to displacements of the investigation surface at a value equal $\lambda/4$.
Then, when demonstrate the constant direction - not sign-variable - for determination of value of full movement it is enough to define number of changes of the output single from maximum to the minimum. At sign-variable movements that corresponds to vibration loadings, character of an output signal of the photodetector has features.
The analysis of Eq. (10) and (11) shows that at vibrations of the investigation surface with amplitudes it is less or equally $\lambda/8$ the output voltage of the photodetector corresponds to a form of vibrations of this surface. With amplitudes of vibrations of the investigation surface more $\lambda/8$ the output voltage of the photodetector won't correspond to a form of vibrations of this surface that as it is visible in Fig. 4. In this case development of additional algorithm of interpretation of an output signal of the photodetector is required.
For registration of vibrations without additional processing of an output signal, as appears from Eq. (10) and (11), it is necessary to choose $\varphi(0)$ equal $\frac{\pi}{2}(2n+1)$ (where n=0,1,2…). This condition means that at the initial moment of measurements output voltage from the photodetector has to be established so that its value corresponded to value equal:

$$u(0) = \frac{u_{\max} + u_{\min}}{2} = A \tag{12}$$

It is reached by corresponding change of a phase of the reference beam. Under these conditions amplitude B of measured vibrations of the investigation surface will correspond to value equal $\lambda/8$.

4. Results and conclusion

Realization of this method, based on the analysis of change of intensity of the single speckle, was used for the investigation of wave processes in a plate subjected shock loading. Fig. 4 shows the

experimental behavior of the output voltage *u(t)* of the photodiode, which is obtained on high-speed storing oscillograph at the investigation of wave processes in a plate subjected shock loading. The comparison of the theoretical and experimental results allows us to make a conclusion that the represented above assumptions are valid.

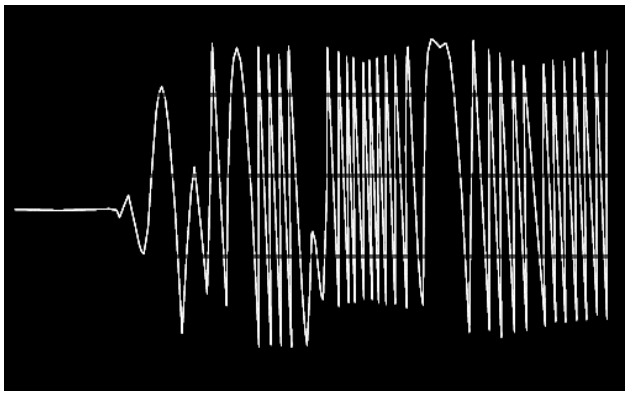

Figure 5. Experimental oscillogram of the output signal from the photodetector

In the experimental arrangement laser LCM-S-111-50-NP25 with wavelength λ = 532 nm and coherence length more 50 m is used. For the measurement of the dynamic displacements with very high frequency p-i-n photodiode with frequency range 20 MHz.

Thus, the new method of registration dynamic displacements of the investigation surface of object in large range of measured value of displacements and in the large frequency range on the basis of the analysis of distribution of intensity in the single speckle is considered.

Advantage of the offered method is that its use doesn't demand a careful adjustment of elements of optical system and allows to overcome restrictions which are connected with existence of own noise (speckles) in the holographic and speckle interferometry and to register dynamic displacements in real time.

References

[1] B.J.Thompson, Electronic speckle pattern interferometry principles and practice, Bellingham, Washington: SPIE Optical Engineering Press; 1996.

[2] Y. Arai, H. Hirai, S. Yokozeki, High-resolution dynamic measurement using electronic speckle pattern interferometry based on multi-camera technology, Optics and Lasers in Engineering, 46 (2008), 733– 738.

[3] L.X. Yang, M. Schuth, D. Thomas, Y.H. Wang, Stroboscopic digital speckle pattern interferometry for vibration analysis of microsystem, Optics and Lasers in Engineering, 47 (2009), 252– 258.

[4] Wang Wei-Chung, Jiong-ShiunHsu, Investigation of vibration characteristics of bonded structures by time-averaged electronic speckle pattern interferometry, Optics and Lasers in Engineering, 48 (2010) 958–965.

[5] E.M. Barj, M. Afifi, A.A. Idrissi, K. Nassim, S. Rachafi, Speckle correlation fringes denoising using stationary wavelet transform. Application in the wavelet phase evaluation technique, Optics & Laser Technology, 38, № 7, (2006) 506-511.

[6] R.A. Braga, W.S. Silva, T. Sáfadi, C.M.B. Nobre, Time history speckle pattern under statistical view, Optics Communications, 281 №9,1 (2008) 2443-2448.

[7] S. Mirza, P. Singh, R. Kumar, A.L. Vyas, C. Shakher, Measurement of transverse vibrations/visualization of mode shapes in square plate by using digital speckle pattern interferometry and wavelet transform, Optics and Lasers in Engineering, 44 № 1 (2006) 41-55.

[8] M. Born, E. Wolf, Principles of Optics, Pergamon Press, Oxford, London, New York, 1968.

Crack Propagation in PMMA Plates under Various Loading Conditions

Ivan Smirnov*, Yuri Sudenkov

St. Petersburg State University, 198504, Russia
* Corresponding author: ivansmirnov@math.spbu.ru

Abstract The experimental results of the dynamics of crack propagation in polymethylmethacrylate plates under quasi-static and dynamic loading are presented. Registration of the cracks was made by the method of slit-scanning of an image using a streak camera. Either a crack trajectory or caustic at the crack front was recorded in the experiments. It is shown that crack front extension has a stepwise character for any type of loading. However the average speed at the quasi-static loading increases smoothly up to the maximum value, and the average speed at pulsed loading takes the maximum value rather instantly. The value of the stress intensity factor at the moment of crack start under dynamic loading essentially exceeds the corresponding value for quasi-static loading. Furthermore, under dynamic loading, the crack speed depends on the thickness of the sample.

Keywords Crack propagation, Dynamic loading, Quasi-static loading

1. Introduction

Despite the fact that our knowledge constantly updates with experimental data about the process of fracture, questions about the conditions of initiation, propagation and stop of fracture remain actual. The problem is compounded by the fact that the data, which are used to develop the theoretical approaches, have been obtained at different scales, with different spatial and temporal resolution of recording equipment, under various load conditions and energy exchange of a sample and external environment.

Crack propagation in quasi-brittle and brittle materials has been studied for many decades. However, there is no complete understanding of the crack development process. Experimental results on quasi-static tensile of plates with a notch [see e.g. 1] lead to the conclusion that the speed of a crack is a monotonic function of time, and the relationship between the speed of a crack and the stress intensity factor can be described by an L-shaped curve. Studies of cracks in plates under dynamic load [2] showed that the speed of a crack is constant, but the corresponding stress intensity factor can change. In papers [3, 4] showed that the speed of a crack is unstable and stepwise. Such divergence of results suggests an idea about need of carrying out "systematizing" experiments which will allow to look at the behavior of strength characteristics of a material in terms of the scale factors, structural features and characteristics of energy input into the material.

In this work we have made an attempt to conduct the generalizing study of crack propagation process in brittle and quasi-brittle materials under quasi-static and dynamic loads. The loading schemes have been applied by analogy to the schemes in [1-4]. The quasi-static loading was carried out by slow uniaxial tension of plane samples with a starter notch. The dynamic load was carried out by means of electrical explosion of a wire between edges of a notch in a plane sample. Polymethyl methacrylate was chosen as the model material. PMMA shows quasi-brittle fracture and

its transparency gives the chance to see a crack extension and to control it by photo recording methods. Crack propagation was registered by a streak camera which allowed to receive the time sweep of crack trajectory with the resolution 40-400 ns.

2. Experimental Technique

Our experiments were performed on the samples of injection molding PMMA with the parameters: density ρ = 1180 kg/m^3, longitudinal sound velocity C_L = 2750±25 m/s, transverse sound velocity C_{TR} = 1400±25 m/s, modulus of elasticity E = 5.9 GPa.

The quasi-static loading was carried out on a tensile testing machine. The dumbbell-like plane samples with the dimensions of the working part of 93×35×5 mm were used. To initiate the crack, a notch was made by a razor blade in the middle of the working area. The notch depth was 0.4 - 1.3 mm.

The dynamic loading was realized by means of the setup for electrical explosion of conductors. The capacitor capacity was C = 1.0 μF; the charge voltage, $U \leq 25$ kV; the stored energy, $E \leq 312$ J. The samples were in the form of square plates (200×200 and 98×128 mm) with a side notch. The sample thickness was 5, 8 and 10 mm. The notch was 50 mm in length and 0.5 mm in width. The size of the greater samples was selected so that to remove the influence of reflected waves on the process of crack propagation during the registration time. The localized pressure pulse was generated by electrical explosion of a wire. The exploding wire (∅ 0.2 mm) was placed between the edges of the notch perpendicular to the plane of the plate at the distance of 24-31 mm from the notch base. A lavsan film was used to create the acoustic contact between the wire and notch edges. The same sample was used several times.

The registration of crack front extension was carried out by means of a streak camera (K008) using the method of slit-type scanning of an image. For this purpose, a beam of light was directed at the expected place of crack propagation at an angle to the plane of the sample. The camera recorded the space-time scan of the beam of light reflected from the surface of the growing crack. In the quasi-static tests, the synchronization of the camera was made on the change of intensity of a laser beam passing through the notch base. In the case of dynamic loading, the synchronization was carried out on the signal from a current sensor. The detailed diagrams of the experiments are presented in [5].

The registration of caustic near with a crack tip was carried out on the basis of schemes of receiving shadow optical images described in [6]. The change of caustic was registered by scanning the real image with help the streak camera. However, the diameter of caustic was registered along crack extension rather than across (as generally accepted). Note that it may affect quantitative estimates because of the large singularity at the back of caustic.

The calculation of the stress intensity factor was made according to the following formula [6]

$$KI(t) = \frac{2\sqrt{2\pi}F(v)}{3(3.17)^{5/2} z_0 cd} D(t)^{5/2},$$
$$F(v) = \frac{[4\alpha_1\alpha_2 - (1+\alpha_2^2)^2]}{[(\alpha_1^2 - \alpha_2^2)(1+\alpha_2^2)]},\ \alpha_j = (1 - \frac{v(t)^2}{c_j^2})^{1/2} \quad (j = 1,2) \tag{1},$$

where *KI* is the stress intensity factor of a crack in tension; $D(t)$ is the change in the diameter of the caustic; z_0 is the distance from the object to the image; c is the shadow optical constant; d is the thickness of the sample; c_1 and c_2 are the speeds of longitudinal and transverse waves respectively; $v(t)$ is the speed of the crack.

3. Results and Discussion

3.1. Quasi-static Tests

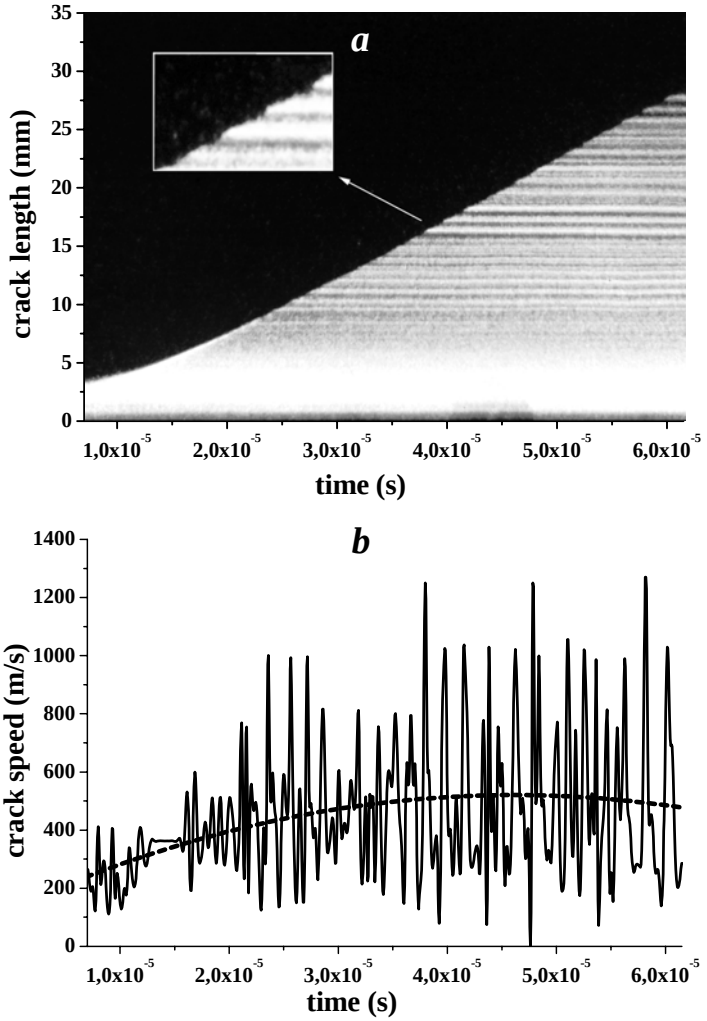

Figure 1. Crack propagation under quasi-static tension of plane samples of PMMA: a) slit scan of the crack tip trajectory; b) fluctuation of the crack front speed; dashed line is the mean speed (polynomial fitting).

Fig. 1a shows the typical trajectory of the crack front under quasi-static tensile of PMMA plates

with a notch. The speed of the crack front is shown in Fig. 1b. The speed was obtained by differentiating of the crack trajectory according to the formula of the central difference derivative. Note that the applied scheme synchronization does not allow you to capture the initial part of the crack trajectory.

Comparison of the crack trajectory and the fracture surface shows that the beginning of an unstable behavior of the crack corresponds to the beginning of the "ribbed" surface structure [3,7] with the distance between the ribs about 1 mm. The most pronounced oscillation frequency of the crack front speed is in range of 400-700 kHz. The similar dependence of crack propagation speed was also obtained in [3]. In this work, the speed of a crack was determined by change in electrical resistance of an aluminum layer deposited on the sample surface. It was shown that the crack front oscillations correlated with the profile of the fracture surface, and the critical speed of the transition to the unstable regime $V_c = 0.34C_R$ (C_R is the Rayleigh wave speed) does not depend on the geometry and thickness of a sample and the tensile rate.

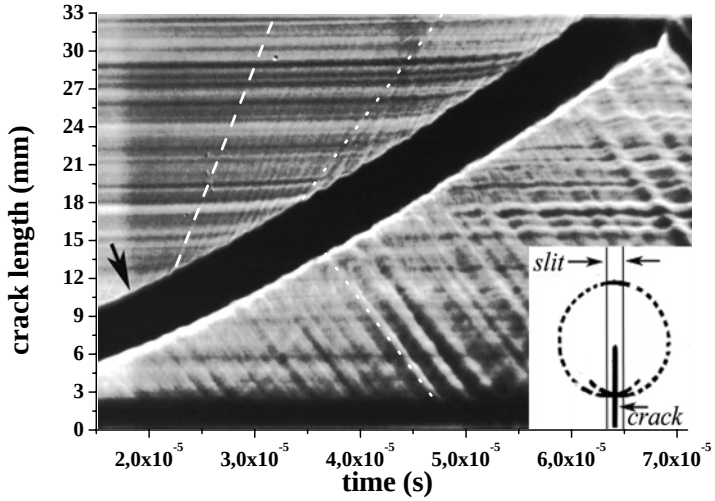

Figure 2. Slit scan of the stress-wave pattern at a crack tip under quasi-static tension of plane samples of PMMA.

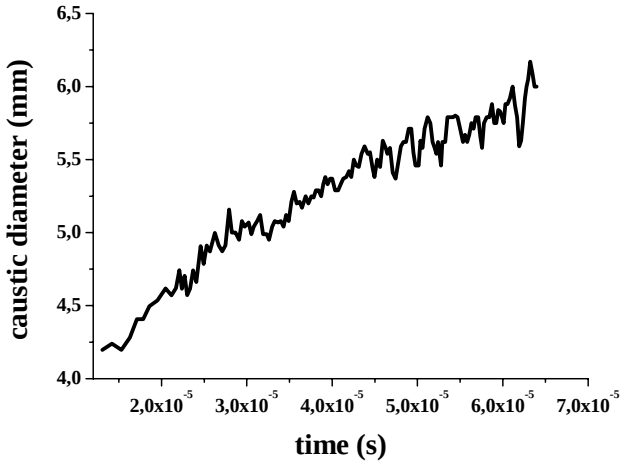

Figure 3. The caustic diameter at crack propagation in quasi-static tests.

The temporary scan of the caustic image was made to track change of stress fields in the process of crack propagation, Fig. 2. There is a clear qualitative picture, namely that elastic waves travel from the crack tip with a certain frequency. This frequency falls into the frequency range obtained during the registration of the crack trajectory (Fig. 1). The black arrow indicates the beginning of a distinct emission of elastic waves from the crack tip. There are two sets of lines that correspond to the longitudinal (dash line) and transverse speeds (dotted line). Fig. 3 shows the change of the caustic diameter at the crack propagation.

3.2. Dynamic Tests

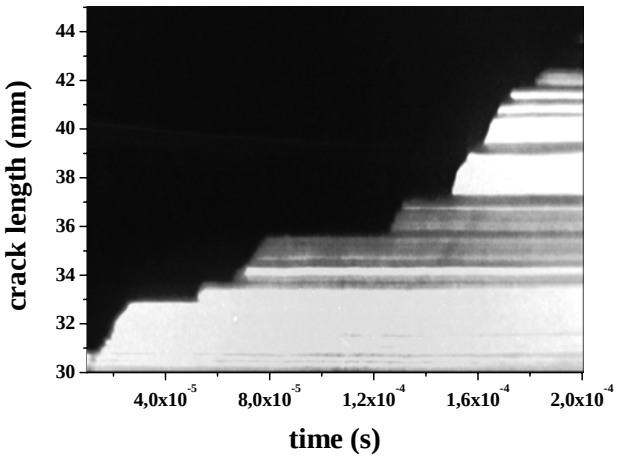

Figure 4. Crack propagation in case of dynamic loading of plates with a notch.

Fig. 4 shows the typical trajectory of crack extension obtained under pulsed pressure on the edges of the notch in the plates of PMMA. The stepped form of crack trajectory is associated with an arrival of elastic waves reflected from lateral faces of a sample. Therefore, the greatest interest is the first step of crack development without influence of reflected elastic waves. For this purpose the samples were made with such sizes that energy of reflected waves was not enough to re-start the crack. The typical trajectory of cracks obtained in these samples is shown in Fig. 5a; and the corresponding crack speed is shown in Fig. 5b.

The maximum fluctuations of the crack speed, as well as in the quasi-static tests, fall on the rougher area of the fracture surface. Unlike the quasi-static [3, 8] or the dynamic [9, 10] tests, here the return order of formation of characteristic zones of fracture surface is observed: fragmentary (large pieces), scaly, parabolic and mirror.

The scan of caustic in the dynamic tests is complicated by presence of elastic waves emanating from the point of application of pressure to the crack edges, and presence of "residual" caustic before and after crack propagation, Fig. 6. In Fig. 7 shows the characteristic change of the stress intensity factor at the crack tip and the corresponding change of the crack speed. It can be seen that the stress intensity factor, at which began the crack extension, substantially exceeds the static value K_{Ic} for a crack start.

The caustic at the crack tip begins to increase after the arrival of the Rayleigh wave; and the crack starts only through some microseconds. In general, the stress intensity factor decreases after the crack start together with the average speed of the crack.

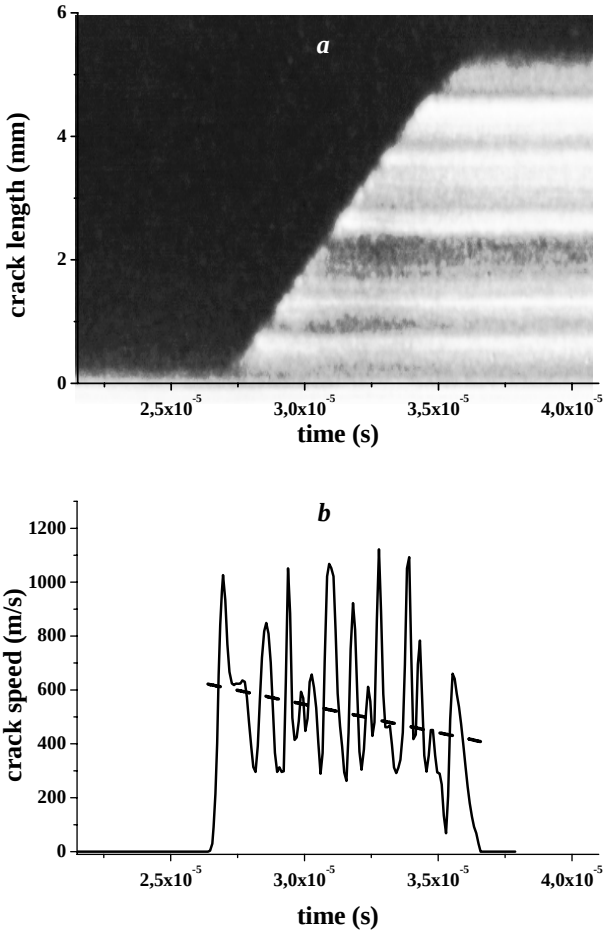

Fig. 5. Crack propagation under a localized pulse load on notch edges: a) slit scan of the crack tip trajectory; b) fluctuation of the crack front speed (dashed line - the mean speed).

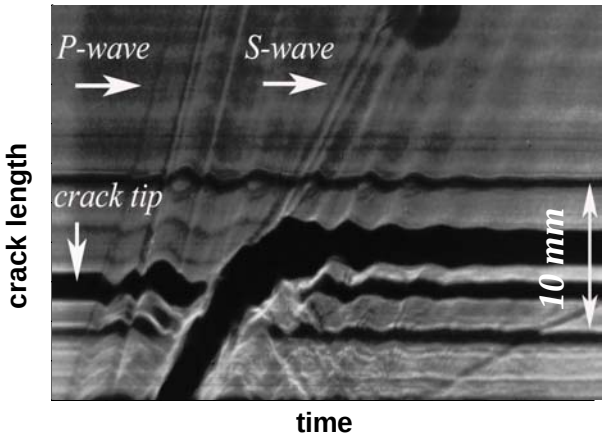

Figure 6. Stress waves in dynamic tests.

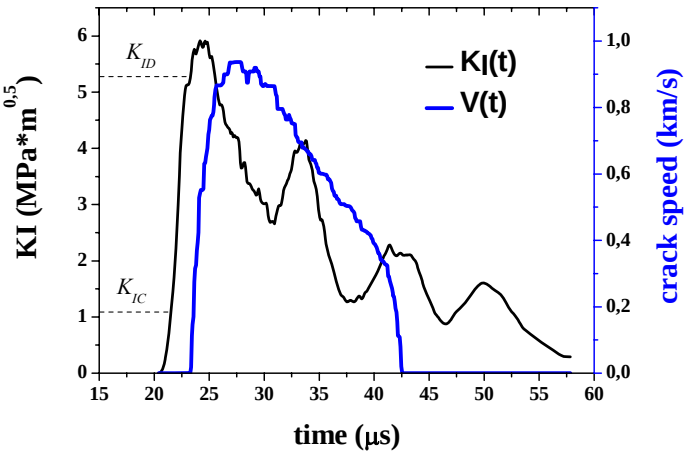

Figure 7. The dynamic stress intensity factor and the corresponding crack speed in dynamics tests.

3.3. Discussion

The results obtained by a single method for recording of dynamics of a crack in plates of PMMA allow to mark out similarities and differences in stages of a fracture process in fragile and quasi-fragile materials under quasi-static and dynamic loads. The slit scan of the development process of a crack front allows to estimate the crack speed on different time intervals, and thus the spatial scale (either the section of a crack front or the all front).

The experiments demonstrate the general property of spasmodic development of a crack front and qualitative agreement with the results obtained by other authors [3, 4]. The average speed of crack propagation in our experiments, both in the quasi-static and dynamic tests, did not exceed $0.5C_R$, but the instantaneous crack speed could approach the Rayleigh wave speed C_R on the "jumps".

The oscillations of the crack front speed correlate with changes of a profile of fracture surface. The observed dynamics of cracks may be related to a pre-fracture zone before the tip of a main crack [9-12], i.e. development of micro damages ensemble in the area of high stresses. The characteristic view of such pre-fracture zone, registered in the dynamic tests after stopping a crack, is shown in Fig. 8.

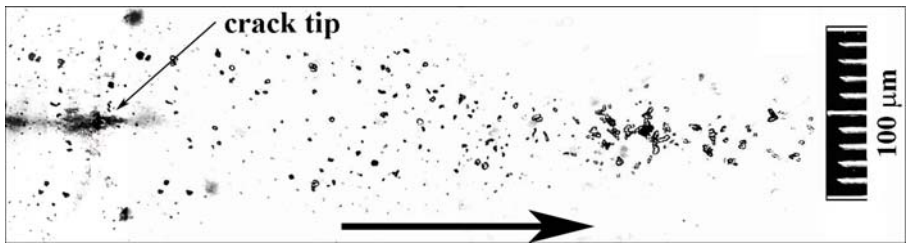

Figure 8. Magnified view of the pre-fracture zone before a crack tip. The photo was made after stopping the crack in dynamic tests. The arrow indicates the direction of crack propagation.

The principal difference between the two ways of loading is the behavior of the average speed of

cracks. Under quasi-static uniform extension of the plates, the average speed over smoothly reaches a maximum value. This fact is consistent with the results of [1]. In the case of pulse pressure on the notch edges, the average speed takes a maximum value almost instantly and then can be considered by a constant. That was observed in [4].

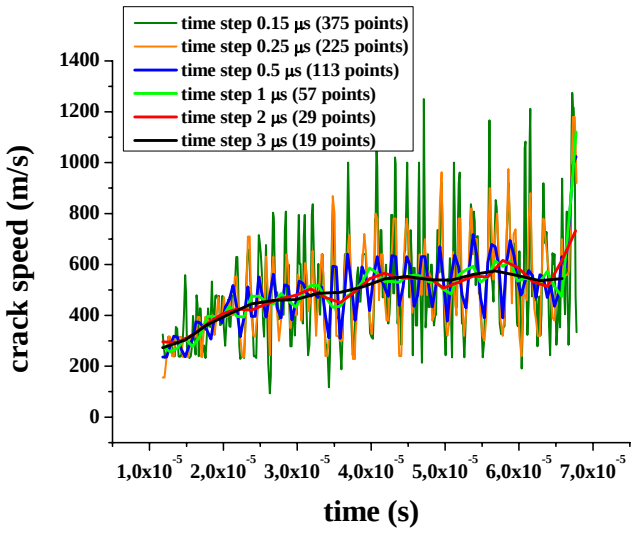

Figure 9. Speed of crack front extension depending on a time interval of registration of the crack front position.

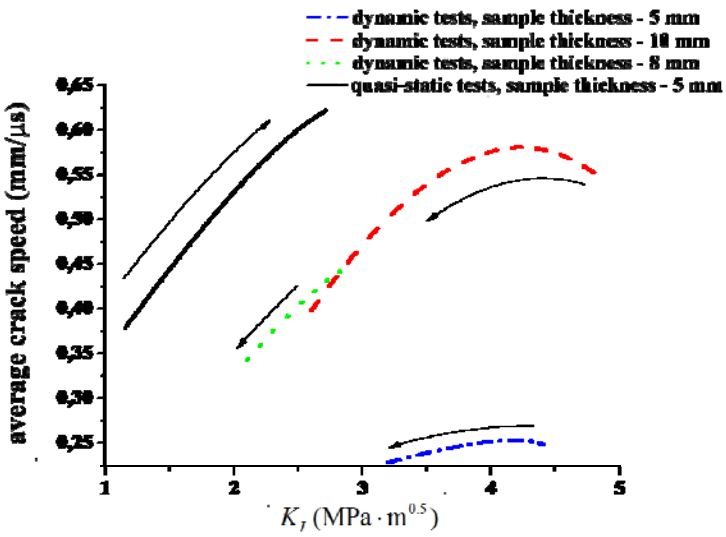

Figure 10. Average crack speed versus instantaneous stress intensity factor in plates of PMMA under different loading conditions.

The difference of experimental results for the same character of loading (see e.g. 1 and 2, 3 and 4) can be explained by resolution of recording equipment. Fig. 9 shows the crack speed in the quasi-static tests at different time intervals of the "fixing" moments of the crack locations. In [2, 4] "continuous" registration of a crack front position was applied (the electric signal from a resistive bridge or the slit scan of an image), while in [1, 3] single shooting with a given frame rate was used. Moreover, in [2, 4] the position of the crack front was registered, while in [1, 3] caustics or

isochromatics, which are integral characteristics of stress fields at the crack tip, were captured.

Another one important difference between the results at the different loading conditions is the values of the fracture characteristics. The stress intensity factor at the moment of the crack start in the dynamic tests significantly exceeds its analog in the quasi-static tests. Figure 10 shows dependence of the average speed of the crack on the dynamic stress intensity factor. It is clear that the shape of the curve depends on the method of obtaining mean values of the crack speed and the SIF. In this case, the average was obtained by means of polynomial approximation.

The dash curves were received in the dynamic tests at the same charge of the condenser, but at different thickness of the samples. It can be seen that the crack speed depends on the state of stress at the crack tip. Reduction of the thickness of the sample leads to reduction of the crack speed.

In contrast to the quasi-static tests, the stress intensity factor and the average crack speed in the dynamic tests decrease with crack growth that well correlates with change of a roughness of the fracture surface. This fact can be explained by the quantity of input elastic energy in the crack tip. In case of the quasi-static tests there is a constant supply of mechanical energy in the system "grips-sample". However, in the case of a dynamic load on the crack (such source of loading as a pulse laser, an explosion of explosives or a conductor, etc.), only the final quantity of energy injects in a sample; and the fracture characteristics are defined by the pulse energy and the possible rate of absorption of this energy in the area of the crack tip.

4. Summary

The study of the dynamics of crack propagation in plates of PMMA under quasi-static and dynamic loading was carried out.

It is shown that under both the quasi-static and dynamic testing conditions the change in the instantaneous crack front speed has a stepwise character. However the behavior of the mean speed depends on the type of loading. In the case of quasi-static loading, the crack accelerates to its maximum value smoothly. In the case of pulse loading, the crack accelerates to its maximum value almost immediately. At the same time the limiting value of the stress intensity factor under impact loading of a crack significantly exceeds its limit value for quasi-static loading.

The analysis shows that the differences observed in experimental results on study of crack propagation can be explained by the different time resolution of recording equipment. Moreover, results significantly depend on duration and intensity of loading, as well as on the stress state in the area of fracture.

References

[1] J.W. Dally, Dynamic photoelastic studies of fracture. Experimental Mechanics, (1979) 349-361.
[2] K. Ravi-Chandar, W.G. Knauss, An experimental investigation into dynamic fracture: 1 On steady-state crack propagation and crack branching. Int. J. of Fract. 26 (1984) 141-154.

[3] J. Fineberg, S.P. Gross, M. Marder, and H.L. Swinney, Instability in the propagation of fast cracks. Phys. Rewiew B 45 (1992) 5146-5154.
[4] Yu.A. Kostandov, A.N. Ryzhakov, and S.I. Fedorkin, Failure of solid polymers under pulse tension. Strength of Mater 42 (1992) 444-447.
[5] I.V. Smirnov, Yu.V. Sud'enkov, Crack dynamics in PMMA plates under quasi-static and dynamic loading. Technical Physics 56 (2011) 1811-1814.
[6] J.F. Kalthoff, The shadow optical method of caustics, in: A.S. Kobayashi (Ed), Handbook on Experimental Mechanics, Prentice Hall, Englewood Cliffs, New Jersey, 1986.
[7] R.P. Kusy and D.T. Turner, Influence of the molecular weight of PMMA on fracture morphology in notched tension. Polymer 18 (1976) 391-402.
[8] J.P., Berry, The morphology of polymer fracture surfaces. J. of Polymer Sci. C 3 (1963) 91-101.
[9] Yu.A. Kostandov and S. I. Fedorkin, Micromechanics of fracture of solid polymers in dynamic loading. Strength of Materials 22 (1990) 257-262.
[10] K. Ravi-Chandar and W.G. Knauss, An experimental investigation into dynamic fracture: II. Microstructural aspects. Int. J. of Fract. 26 (1984) 65-80
[11] O.B. Naimark, V.A. Barannikov, et al. Crack propagation: dynamic stochasticity and scaling. Tech. Phys. Lett. 26 (2000), p. 254.
[12] A.M. Leskovskii and B.L. Baskin, Some aspects of nucleation and evolution of microscopic and mesoscopic cracks and quasi-brittle fracture of homogeneous materials. Phys. Solid State 53 (2011) 1223-1233.

Equivalent dynamic mechanical properties of grid cylindrical structure

Lin Xiao-hu[1,*], Gao Xuan[1], Yang Er-meng[1], Xing Chun-lei[2]

1 Army Aviation Institute of PLA, Beijing 101123, China
2 Department of Engineering Mechanics, Beijing University of Technology, Beijing 100124, China
* Corresponding author: mmlinxiaohu@126.com

Abstract Grid cylindrical structure with infinite variety of cell shape and arrangement receives much concern, which results in many applications of these structural materials in aerospace and aviation engineering. However, the complexity of structure will bring high time-consuming in calculation and unanticipated self-contract in researching dynamic performance. Equations were used to get the equivalent material properties by theoretical derivation. Then dynamic mechanical properties of both equivalent structure and grid cylindrical structure were investigated. In detail, the dynamic deformation and energy absorption characteristics of the structure under different lateral impact velocities were analyzed by software LS-DYNA. The relative density and the relative thickness of the grid cylindrical structure to equivalent performance effect were taken into account. The results show that when relative density and relative thickness are defined in certain range, the equivalent method has high accuracy. This equivalent method provides a reference for the impact properties of complex grid cylindrical structure with arrangement periodically.

Keywords Grid structure, Homogenization, Deformation mode, Energy absorption, Effective property

1. Introduction

Grid structure has been widely used in aerospace, automotive industry, civil materials, biological engineering, transportation and other applications because of excellent energy absorption, high load carrying capacity, high specific strength, high specific stiffness and low structural weight [1,2]. It not only contains mesoscopic mechanics characteristics, but also has whole macro performance. These characteristics make the anti impact properties of structure greatly improved. In addition, the designability of cell geometric topological provides a broad platform for the development of grid structure. Therefore, the scientists and mechanical experts pay great attention to study grid structure in order to acquire better integrated design.

At present, impact resistance performance, energy absorption capability and dynamic mechanical properties of grid structure have been studied by many scholars. For example, The elastic response of triangular, hexagonal and quadrilateral grid structure has been obtained in by Hohe et al.[3,4].The deformation mode and load carrying capacity of hexagonal grid structure were studied by the numerical simulation in by Ruan et al. [5,6] and Zou et al.[7].The formulas of bearing capacity and energy absorption ability were deduced through the deformation model of hexagonal grid structure in the high speed impact, and the energy distribution was discussed in Hu et al.[8]. Researched in Hong[9] and Zarei et al.[10] is the impact direction angle on in-plane dynamics performance. The mechanical properties of grid structure filled with circle cells were researched through experiment and numerical simulation in Papka et al.[11,12].Nevertheless, all of the above researchers adopt discrete element method to solve the problem of the periodic grid structure, which not only costs a lot of computation resources, but also is infeasible sometimes [13].

In order to simplify performance research of grid structure, the equivalent elastic constants have been explored over the last few years. Gibson and Ashby [14] have investigated the equivalent elastic

constants of grid structure excluding the cell size factor. In other words, they calculated the equivalent elastic constants, which only considering the cell microstructure and volume fraction ratio. In addition, some correlative research works have been done by Andrews [15], Yan and Cheng [16]. Wei[17] deduced the basic equation of elasticity of grid structure according to the principle of minimum potential energy and FEM, gave the elastic matrix based on the equivalent of virtual strain energy, and got the equivalent of density based on the equivalent of the kinetic energy. It is verified that the method has a good precision and is appropriate for such kind of analysis in the engineering field.

The grid cylindrical structure is equivalent to an isotropic shell with homogeneous thickness through the equivalent of unit cell mechanics properties. The energy absorption capacity, deformation model of grid cylindrical structure and equivalent continuum cylindrical structure were studied under the impact load. Meanwhile, the influence of the relative density and relative thickness to equivalent accuracy of grid cylindrical structure were considered.

2. Calculation model and method

Finite element models of grid cylindrical structure filled with stagger-arranged triangular cell and equivalent to continuum cylindrical structure with the same thickness were established as shown in figure 1. The dimensions of the two structures are: radius R_1=100mm, length L_1=272mm, and thickness T_1. And the shape of cell is equilateral triangle with length L_2=15.7mm, height H=13.6mm and thickness T_2. The numbers of circumferential and axial cell are 40 and 20 respectively. For boundary conditions, all the nodes at upper and lower ends of cylindrical structure are constrained. Those two cylindrical structures are lateral impacted by rigid sphere with a certain speed, which radius R_2=30mm, horizontal direction X_1=100mm, vertical direction$Y_1=L_1/2$.

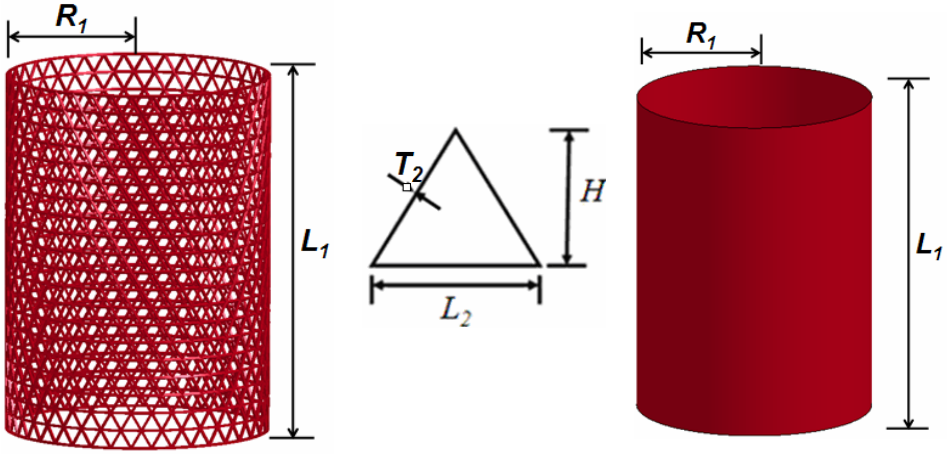

Grid structure Triangle Continuum structure

Figure 1. Finite element models of cylindrical structure

Cell-wall was modeled using Beam161 with Hughes-Liu element algorithm and rectangular cross section shape, and the material properties assumed to be perfect elastic. The number of the total elements is 24400 with each cell-wall divided into 10. In this numerical simulation, sphere was modeled using 3D Solid 164 , of which material property is plastic-kinematic, and yield stress is 76Mpa. All degree of sphere freedom was confined except lateral impact direction. The density of

both cell-wall and sphere is 2700 Kg/m^3, elastic modulus is 69Gpa, poisson's ratio is 0.3. Mesh sensitivity studies revealed that additional mesh refinements did not improve the accuracy of the calculations appreciably. The automatic single-surface contact type with the principle simple, rarely arouse the hourglass effect, no numerical noise and the momentum conservation accurate penalty function method is adopted.

3 Equivalent processing

Cell-wall was assumed to be 'two force rod' model as shown in Figure 2. Young's modulus and density of cell-wall matrix are E_s and ρ_s. The tensile load and internal force distribution on X_1 and X_2 direction can be found out through the force equilibrium condition. Then according to harmonize deformation of cell-wall, the relation of equivalent stress and strain can be established.

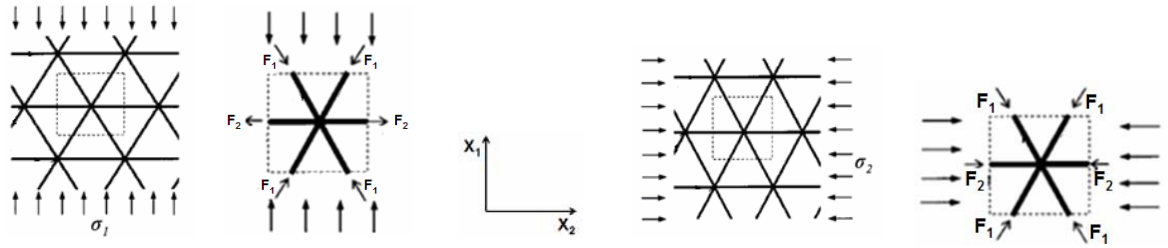

Figure 2. Triangle-grid structure under two cases of compression load [18]

The relative density is defined as $\rho = \rho^* / \rho_s$, where ρ^* is the equivalent density of grid structure, and ρ_s is the density of cell-wall matrix.

The material parameters of equivalent homogeneous shell [18] are:

Relative density: $\rho = \dfrac{\rho^*}{\rho_s} = \dfrac{3T_2}{L_2 \sin 60} = \dfrac{2\sqrt{3}T_2}{L_2}$, Young's modulus: $E_1 = E_2 = \dfrac{\rho}{3} E_s = \dfrac{2\sqrt{3}T_2}{3L_2} E_s$, Poisson's ratio: $\upsilon_{12} = \upsilon_{21} = \dfrac{1}{3}$, Shear modulus: $G_{12} = \dfrac{\rho}{8} E_s = \dfrac{\sqrt{3}T_2}{4L_2} E_s$

4 Result analysis and discussion

When structure is subjected to an impact load, the governing equations can be expressed as following [19]:

Equation of mass conservation:

$$\rho' V_{ij} = \rho_0 V_0 \tag{1}$$

where ρ' denotes the current density, V_{ij} represents the current volume, and ρ_0 denotes the initial density.

Equation of momentum conservation:

$$\sigma_{ij,j} + \rho' f_i = \rho' \ddot{u}_i \tag{2}$$

where σ_{ij} represents the Cauchy stress, f_i represents the body force density, and $\ddot{u}_i$ denotes the acceleration.

Equation of energy conservation:

$$\dot{E} = V s_{ij} \dot{\varepsilon}_{ij} - (p+q) \dot{V} \tag{3}$$

where s_{ij} and p denote the deviatoric stresses and hydrostatic pressure, respectively. q represents the bulk viscosity, δ_{ij} denotes the Kronecker delta (if i = j; otherwise δ_{ij} =0), and ε_{ij} denotes the strain rate tensor.

The proportion of hourglass energy has a crucial effect on energy conservation. Hughes-Liu integral was used in Beam element calculation, and full integral was adopted in the process of homogenization equivalent for continuous shell element. The relationship of internal energy and hourglass energy of grid cylindrical structure and equivalent continuum cylindrical structure are shown in figure 3(c-continuum cylindrical structure, g-grid cylindrical structure). It can be seen that the hourglass energy proportion is far less than 5%, which is required in simulation calculation. If the hourglass energy having a good control, we believe that energy is conservative, and calculation accuracy is high in the whole impact process.

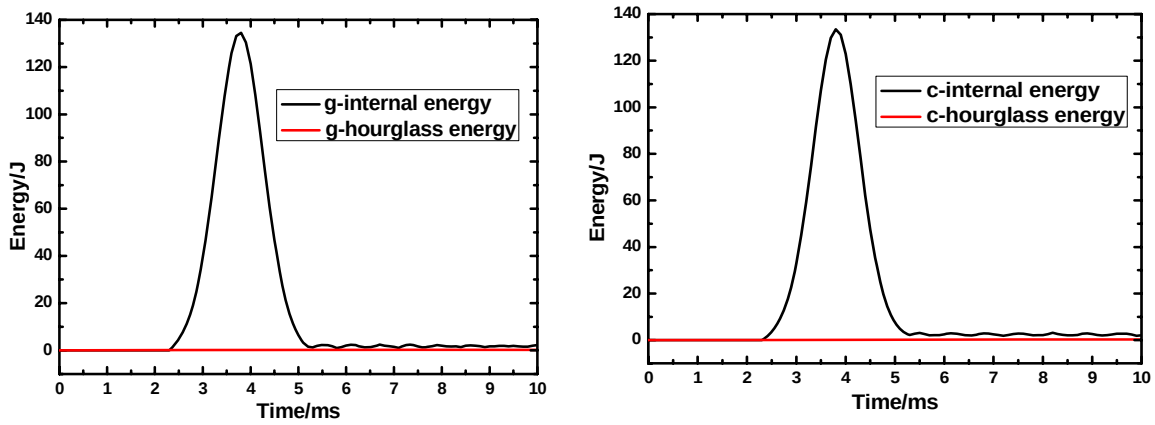

Figure 3. The relationship of internal energy and hourglass energy

4.1 The effect of the impact velocity

There are two main influence factors to impact resistant ability of cylindrical structure: structure deformation and energy absorption. When the sphere impacts to two kinds of structure at the velocity of 30 m/s, the displacement variation of structure is acquired before the sphere reflected back as shown in figure 4 (c-continuum cylindrical structure, g- grid cylindrical structure). It is obvious that the deformation of structure is basically identical before 3.1ms. With the increase of impact, the deformation error of structure is gradually increase. And the deformation of continuum cylindrical structure is larger about 6% than that of grid cylindrical structure at this stage.

This is because that the energy is absorbed through global deformation of the structure in the initial stage of impact. At this time, the difference of the two kinds of structure is not obvious and the deformations are approximately the same. With the proceeding of impact, the local deformation of structure becomes gradually obvious and concentrates to the impacted area. The influence of grid performance and arrangement mode to the impact resistance properties of structure is gradually reflected. Some energy is additionally absorbed by distortion of grid. Therefore, deformation of the continuum cylindrical structure is larger than that of grid cylindrical structure at this stage.

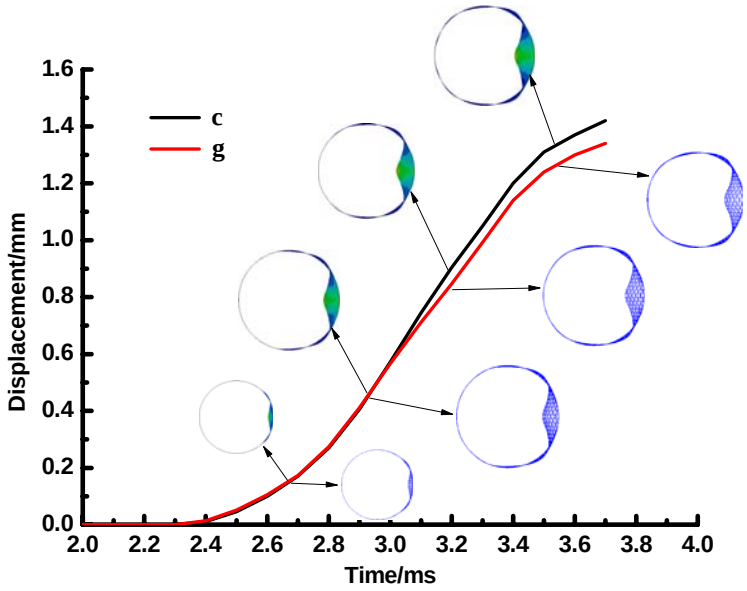

Figure 4. The deformation comparison of the two kinds of structures

Figure 5 depicts the deformation comparison of the two kinds of structure under different velocity. As can be seen from the graph, with the increase of impact velocity, deformation of structure is heightened, and deformation of continuum cylindrical structure is a little higher than that of grid cylindrical structure. It is obvious that the deformations of the two structures are agreement better at great impact velocity. The reason is that the coupled interaction between cells of grid cylindrical structure is small at the lower impact velocity. But cell shape and configuration mode has great influence on the structural deformation, which leads to the grid cylindrical structure can absorb more energy than the continuum cylindrical structure in small deformation. However, the coupling effect between grids will lead to the deformation more integrated and more closer to the deformation of the continuum cylindrical structure with the increase of impact velocity. So the deformation process is more similar and equivalent effect is better at higher velocity.

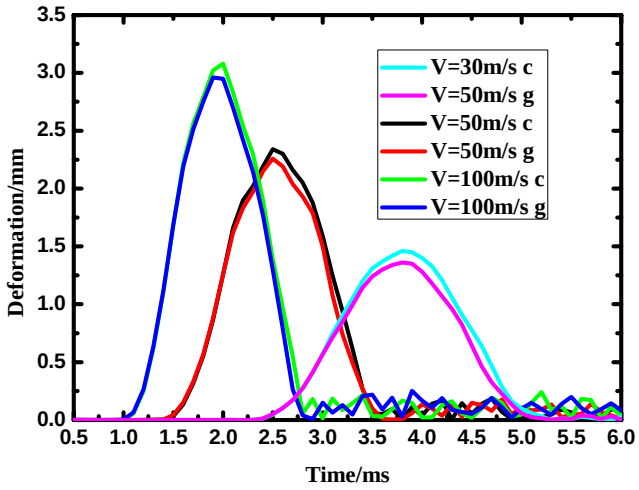

Figure 5. The deformation comparison of two kinds of structure under different velocities

4.2 The effect of the relative density

The relative density of grid cylindrical structure is changed by cell-wall thickness T_2, and other

parameters are constant. Take the relative density were 0.11, 0.22, 0.27, 0.3, 0.44, 0.88. When the impact velocity of the rigid ball is 10m/s, the deformation variation curve of structure is shown in figure 6.It is revealed that the homogenization equivalent method of grid structure is reasonable in a certain relative density range. When the relative density ranges from 0.2 to 0.4, the equivalent effect of structure is good, and the error is controlled within 10%. But, when the relative densities are 0.11 and 0.88, the errors are 30% and 104%, respectively. The impact performance of grid cylindrical structure has not been reflected really. Then, this kind of equivalent method is failure.

The relative density has a great influence on equivalent properties of structure. Grid cylindrical structure has a tendency to local deformation, and grid topology structure form has greater influence on deformation of structure. But the topology form has no influence on equivalent continuum cylindrical structure, which is the major reason to cause different deformations of structure.

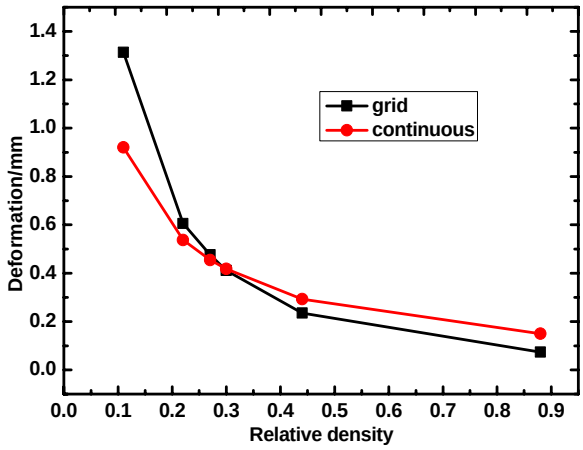

Figure 6. The relationship of relative density and deformation

4.3 The effect of the relative thickness

The relative thickness is defined as T_2/T_1, which is changed by thickness of the cylinder structureT_1. Take the relative density were 0.41、0.61、1.22、2.44 respectively. When the relative density is 0.27, the largest deformation change of structure with the increase of relative thickness is shown in figure 7.When the relative thickness less than 1.2, the maximum deformations of the two structure are almost to be equal. But the relative error has reached 23% at the relative thickness up to 2.44. It can be seen that with invariable thickness of grid cylindrical structure, the thicker the cylindrical structure is, the better the equivalent result is. However, the out-of-plane performance of grid cylindrical structure will gradually highlight with the increase of the thickness of the cylindrical structure, which will result in the failure of the equivalent method.

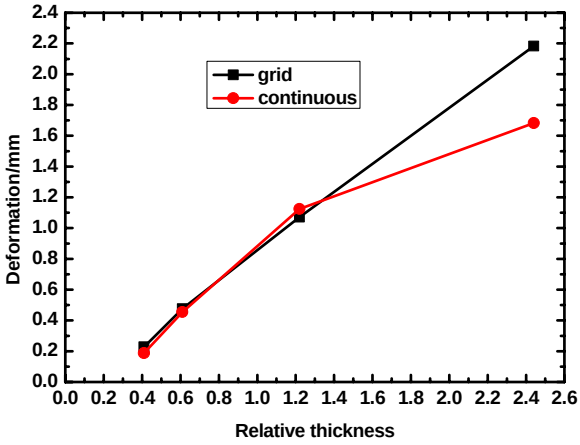

Figure 7. The relationship of the relative thickness and deformation

5. Concluding remarks

Based on the results obtained in the present work, the following main conclusions can be drawn:

(1) The relative density of grid cylindrical structure plays an important role in the homogenization process.

(2) It can be seen that the equivalent method is credible in a certain dimensionless parameter of relative density or relative thickness range.

(3) The deformation of grid cylindrical structure is smaller than that of the homogeneous equivalent for continuous shell structure under impacting, but the biggest error is controlled within 10%. So the equivalent method is reasonable in a certain range.

References

[1] J.L. Grenestedt, Effective elastic behavior of some models for 'perfect' cellular solids. International Journal of Solids and Structures, 1999, 36(10): 1471-1501.

[2] D. Slinchenko,V.E. Verijenko, Structural analysis of composite lattice shells of revolution on the basis of smearing stiffness. Composite Structures, 2001, 54(2-3): 341-348.

[3] J. Hohe, W. Becker, Effective elastic properties of triangular grid structures. Composite Structures 1999, 45: 131-145.

[4] J. Hohe, C Beschorner, W.Becker, Effective elastic properties of hexagonal and quadrilateral grid structures. Composite Structures, 1999, 46: 73-89.

[5] D. Ruan, G. Lu, B Wang, T X Yu, In-plane dynamic crushing of honeycombs-a finite element study. International Journal of Impact Engineering, 2003, 28(2):161-182.

[6] D. Ruan, G. Lu, In-plane static and dynamic properties of aluminum honeycombs. Australian Journal of Mechanical Engineering,2006,3:45-60

[7] Z. Zou, S.R. Reid, P J Tan, S Li, J J Harrigan, Dynamic crushing of honeycombs and features of shock fronts． International Journal of Impact Engineering 2009, 36(1):165-176.

[8] L.L. Hu，T.X. Yu, Dynamic crushing strength of hexagonal honeycombs. International Journal of Impact Engineering, 2010,37:467-474.

[9] S.T. Hong, Mechanical behavior of aluminum honeycombs under multi-axial loading conditions. Michigan: Michigan University, 2005.

[10] H. Zarei, M. Kroger, Optimum honeycomb filled crash absorber design. Materials and Design 2008, 29: 193-204.

[11] S.D. Papka， S. Kyriakides, Biaxial crushing of honeycombs Part I: Experiments. International Journal of Solids Structurals,1999,36(29):4367-4396.

[12] S.D Papka，S. Kyriakides, Biaxial crushing of honeycombs Part II: Analysis. International Journal of Solids Structurals,1999,36(29):4397-4423.

[13] W.B. Yu, T. Tang, Variational asymptotic method for unit cell homogenization of periodically heterogeneous materials. International Journal of Solids and Structures. 2007, 44(11-12): 3738-3755.

[14] L.J. Gibson， M.F. Ashby, Cellular Solids: Structure and Properties. Cambridge University Press，1997.

[15] E.W. Andrews，G. Gioux, P Onck, L G Gibson, Size Effects in Ductile Cellular Solids. Part II: Experimental Results. International Journal of Mechanical Sciences， 2001，43: 701－713.

[16] J Yan, G D Cheng, S T Liu, L Liu,. Prediction of equivalent elastic properties of truss materials with periodic microstructure and the scale effects. Acta Mechnica Solida Sinica. 2005，26 (4) :421－428.

[17] Z.G. Wei, C.W. Tang, Homogenization modeling of composite lattice structure for mode analysis. Acta Materiae Compositae Sinica. 2008, 25(2): 188-193.

[18] A. J. Wang, D. L. Mcdowell, In-plane stiffness and yield strength of periodic metal honeycombs. Journal of Engineering Materials and Technology, Transactions of the ASME. 2004, 126(2): 137-156.

[19] LS-DYNA Theoretical Manual, V.971, Livermore Software Technology Corporation, Livermore, CA, USA, 2006.

Mode I Fracture Toughness of Nanorubber Modified Epoxy under Wide loading Rate

Ying-Gang Miao[1,2], Hong-Yuan Liu [2]*, Yu-Long Li [1]*, Hsiu Hsien Wu [2], and Yiu-Wing Mai [2]

[1] School of Aeronautics, Northwestern Polytechnical University, Xi'an, Shaanxi Province, 710072, P.R.China

[2] Center for Advanced Materials Technology (CAMT), School of Aeronautics, Mechanical & Mechatronic Engineering J07, The University of Sydney, Sydney, NSW 2006, Australia

Corresponding Authors: hong-yuan.liu@sydney.edu.au (H-Y Liu);
liyulong@nwpu.edu.cn (Y-L Li)

Abstract

Dynamic mode I fracture toughness of nano-rubber modified epoxy were investigated using the split Hopkinson tension bar (SHTB) facility, with loading rates up to 3×10^4 MPa·√m/s. The quasi-static toughness of those nanocomposites were also measured with an Instron machine at two loading rates of ~0.04 MPa·√m/s and 5 MPa·√m/s, respectively. The materials tested are: neat epoxy; and 2, 6 and 10 wt.% nano-rubber particles, respectively, in epoxy. Special specimens with a single-edge crack in the finite width direction were designed for mode I toughness testing with the SHTB. In addition, pulse shaping technique was used to optimize the loading stress wave for accurate measurements with the SHTB. The results indicated that the presence of nano-rubber could improve the fracture toughness of the bulk composites in the range of loading rates studied. However, high loading rates might have degraded the cavitation capability of the nano-rubber and hence decreased the toughness of the rubber-modified epoxies compared to low loading rates.

Keywords Nano-rubber modified epoxy, fracture toughness, high strain rate, Hopkinson bar

1. Introduction

Epoxies have gained growing attention from industries for its specific properties, such as high modulus and strength. Epoxy products have also been widely used as structural materials, e.g., window of vehicles and helmet to resist impact and explosion. However, the low toughness of epoxy is always the disadvantage in its applications. The advent of nanoparticles has offered one excellent candidate for toughening epoxy to satisfy specific engineering requirements. To add soft or rigid nano-fillers to epoxy can significantly enhance the toughness of epoxy with no serious loss in strength and elastic modulus [1-2]. Owing to the expanded applications of epoxy products, their dynamic responses have drawn increasing attention from both industry and scientific communities, though some polymers have been investigated extensively under quasi-static loading. Sahraoui [3] studied the fracture behaviors of a modified epoxy resin by three different testing machines with loading rates in the range from 5×10^3 to 10^4 MPa·√m/s. Evora [4] measured dynamic fracture

toughness of polyester/TiO_2 nanocomposites with three-point bend specimens, which were higher than their quasi-static fracture toughness. However, there is little known on the dynamic fracture behaviors of epoxies filled with soft nano-rubber particles at high loading rates. But, such results are necessary to understand their performance and reliability as structural materials under those extreme conditions. In this study, ~100 nm diameter nano-rubber particles were used to process epoxy composites and prepare single-edge notched specimens for dynamic toughness measurements with a split Hopkinson tensile bar (SHTB) at a maximum loading rate of 3×10^4 MPa·√m/s. Toughness tests at lower quasi- static rates were also conducted on an Instron machine and the results were analyzed.

2. Materials and specimen

The resin selected was standard diglycidyl ether of bisphenol A(DGEBA) with an epoxide equivalent weight (EEW) of 185 g/mol and Araldite-F was supplied by Sigma-Aldrich in Australia. Spherical rubber particles ~100 nm with excellent dispersion were supplied with 25 wt.% (weight percent) concentration in bisphenol A resin by Kaneka Corporation, Japan. The curing agent was a cycloaliphatic secondary amine, Piperidine, obtained from Sigma-Aldrich.

Material formulations were prepared by mixing plain DGEBA resin with required amounts of nano-rubber master batch. Three weight fractions of nano-rubber particles were made, 2 wt.%, 6 wt.% and 10 wt.% nano-rubber particles in epoxy (denoted by R2, R6 and R10 hereafter), respectively. Samples with neat epoxy were also made to study the effect of nano- rubber. After adding the curing agent to the mixture, it was poured into two pre-heated moulds for curing at 120℃ for 16 h. One mould was fabricated for Compact Tension (CT) specimens following ASTM D5045-99 [5]; the other was for making bulk materials, which were cut into beams $4.5\times14\times65$ mm^3 for dynamic fracture tests. Figure 1 shows the TEM microstructures of R10, which indicates clearly nanoparticles dispersed uniformly in the epoxy matrix.

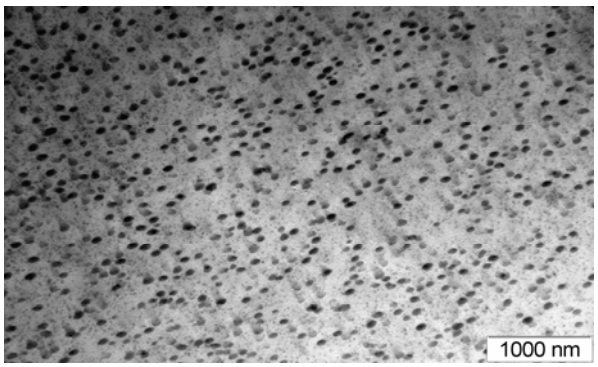

Figure 1. Nano-rubber dispersion of R10

All samples were first heated for 2 h at 80℃to remove any residual stress owing to surface polishing. A natural crack was then obtained by tapping a fresh razor blade at a specimen notch tip. The length a of the CT specimens was between 0.45W and 0.55W [5].

Figure 2. Quasi-static testing of CT specimen with the loading fixture

3: Experimental Work

3.1 Quasi-static fracture toughness tests with CT samples

Quasi-static tests were conducted on CT specimens in a screw-driven Instron 5567 machine with full control of loading rates in the range of 1 to 100 mm/min and full records of load and displacement (see Figure 2).

3.2 Dynamic fracture experiments

Dynamic fracture toughness tests were conducted on the SHTB facility to obtain the tensile stress-strain curves at high strain rates from 10^2 to 10^3 s^{-1} [6, 7]. SHTB consists basically of a striker tube, an incident bar and a transmitted bar (see Figure 3). The specimen was cemented between the incident and transmitted bars.

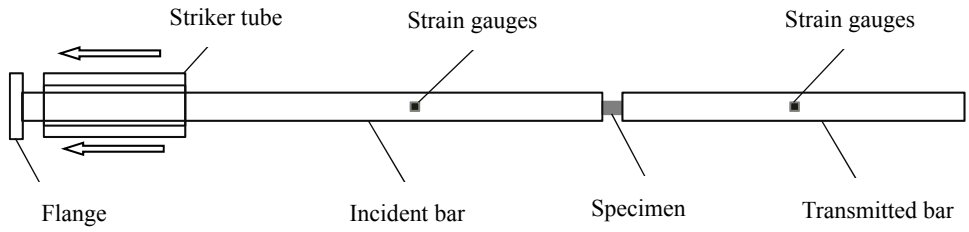

Figure 3. Schematic drawing of the SHTB test

While testing, the striker tube was projected towards the flange by a gas gun. Upon impacting, an incident wave $\varepsilon_i(t)$ was generated, and reflected at the flange free end, presenting tensile stress wave, and then propagated backwards to the interface between the incident bar and the specimen. At this interface, part of the incident wave, $\varepsilon_r(t)$ was reflected back into the incident bar. The rest went through the specimen and, finally developed the transmitted wave, $\varepsilon_t(t)$ in the transmitted bar. The incident, reflected and transmitted waves were recorded by the strain gauges and the dynamic strain recording machine.

From one-dimensional wave theory, the stress at the bar end is given by:

$$\sigma_I(t) = E(\varepsilon_i(t) + \varepsilon_r(t)) \tag{1}$$

$$\sigma_T(t) = E\varepsilon_t(t) \tag{2}$$

where E is Young's modulus of incident and transmitted bars; $\varepsilon_r(t)$ and $\varepsilon_t(t)$ are reflected and transmitted waves, respectively. Aluminum bars 15 mm diameter were used. Impact velocities of the striker tube were applied by controlling the pressure of the gas gun to achieve desired loading rates. Specimens were designed to suit the Hopkinson bars and essentially single-edge notched tension (SENT) geometry (see Figure 4).

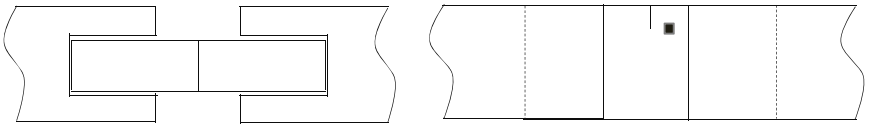

(a) Lateral view of fixed specimen (b) Top view of fixed specimen

Figure 4 Fixture of dynamic toughness specimen and arrangements of strain gauge and crack

The specimen, with the size of 4.5mm×14mm×65mm, was cemented and embedded 20 mm into the bars. The strain gauge glued near the crack-tip was used to ascertain the crack initiation time [8]. The pulse shaping technique was employed to trim and optimize the incident stress, and to achieve stress equilibrium in the specimen in a short time [9]. At least 3 repeated tests were conducted for each material.

4. Results and Discussion

4.1 Calculation of fracture toughness

For the CT tests, the fracture toughness is calculated by [5]

$$K_{IC} = \frac{P}{B\sqrt{W}} f(a/W) \tag{3}$$

where P is fracture initiation load, and

$$f(\frac{a}{W}) = f(\alpha) = \frac{2+\alpha}{(1-\alpha)^{3/2}}(0.886 + 4.64\alpha - 13.32\alpha^2 + 14.73\alpha^3 - 5.6\alpha^4) \tag{4}$$

For the SENT specimen under dynamic loading, the fracture toughness is obtained from [10]

$$K_{IC} = \sigma\sqrt{\pi a} \cdot F_I(\alpha), \alpha = \frac{a}{W} \tag{5}$$

where σ is fracture stress on the specimen width, and

$$F_I(\alpha) = 1.12 - 0.231\alpha + 10.55\alpha^2 - 21.72\alpha^3 + 30.39\alpha^4 \tag{6}$$

The fracture stress σ is calculated from the transmitted stress σ_T:

$$\sigma(t) = \frac{A_{Bar}}{A_{Specimen}} \sigma_{\mathrm{T}}(t) \tag{7}$$

In all the tests, the loading rate is defined by:

$$\dot{K}_I = \frac{K_{IC}}{t_c} \tag{8}$$

where K_{IC} is critical stress intensity factor and t_c is time interval from the start of loading to when the crack starts to propagate. A typical load-time curve recorded by the Instron machine for a CT specimen is shown in figure 5.

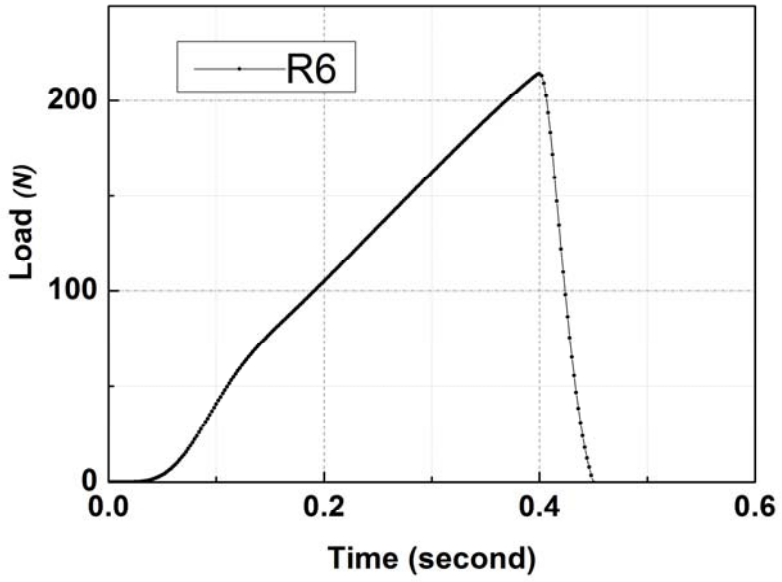

Figure 5 Load-time curve of a R6 CT specimen under a crosshead rate of 100 mm/min

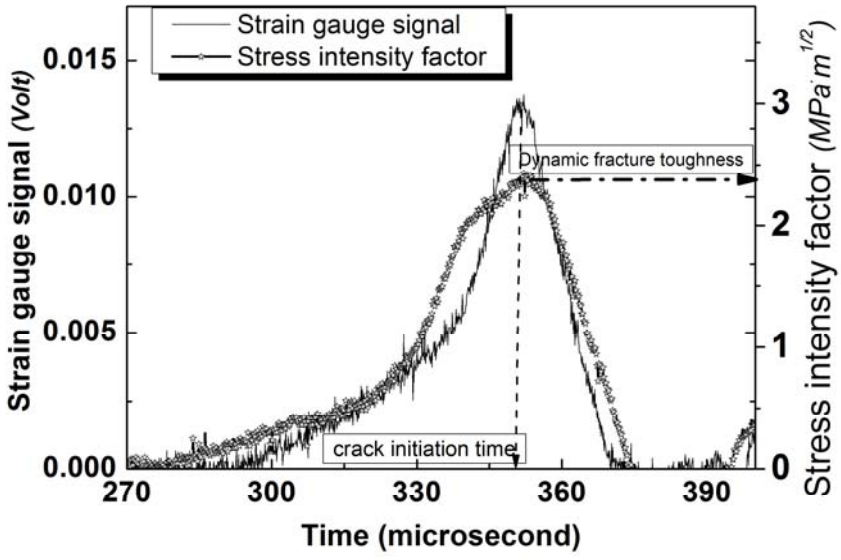

Figure 6 Toughness-time and strain signal-time curves of R6 from SHTB test

For the dynamic toughness tests, it is essential to ascertain the critical time at crack initiation. The strain measured from the strain gauge would drop dramatically when the crack was about to propagate because the strains accumulated around the crack-tip would be released once the crack moved away. Figure 6 shows the strain signal-time curve from which the stress intensity factor-time curve can be determined.

The quasi-static loading rates were 0.04 MPa·√m/s for the crosshead rate of 1 mm/min and 5 MPa·√m/s for 100 mm/min, respectively. The SHTB tests gave a much higher loading rate at ~3×10^4 MPa·√m/s. The results of all tested materials are shown in Figure 7.

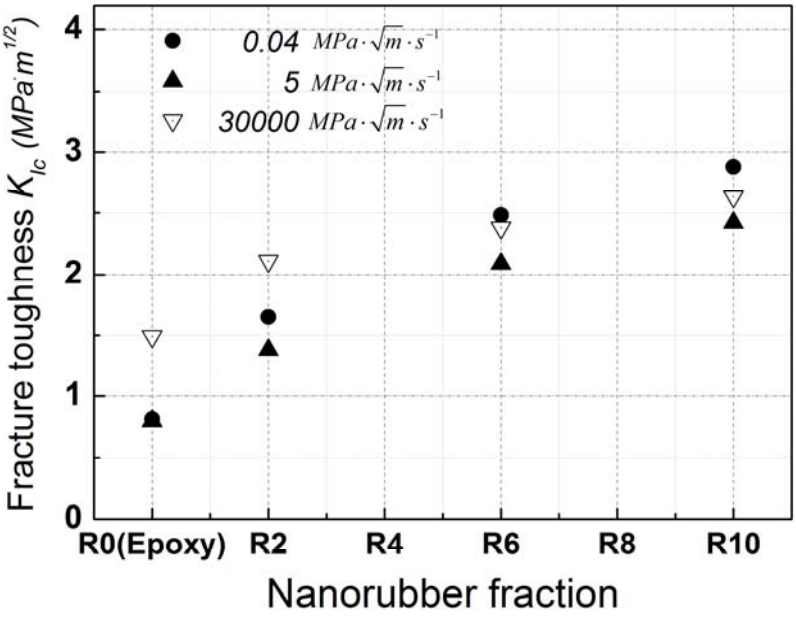

Figure 7 Effect of loading rate and nano-rubber weight fraction on fracture toughness

4.2 Nano-rubber fraction and loading rate effects

Figure 7 shows clearly the improving toughening effect with increasing nano-rubber fraction. This trend is true for all three loading rates implying nano-rubber particles can improve the toughness of epoxy even at a high loading rate. However, compared to the lower loading rates, 5 and 0.4 MPa√m/s, the toughness increased by the rubber content under high loading rate, 3×10^4 MPa√m/s, is less significant. For example, under quasi-static loading, 0.04 MPa√m/s, the toughness of R6 is more than 3.0 times the toughness of epoxy. But under high loading rate, 3×10^4 MPa√m/s, the toughness of R6 is only ~1.8 times the toughness of epoxy. It is possible that rubber particle cavitation is reduced due to the increased cavitation strength of the nanorubber under high loading rate. Future study will be conducted to clarify the rubber particle toughening mechanisms under different loading rates.

The results in Figure 7 show the crack growth responding to different loading rates. For neat epoxy, the toughness K_{ICm} is ~1.8 times larger at the dynamic loading rate of 3×10^4 MPa√m/s, compared to the quasi-static loading rates of 5 and 0.4 MPa√m/s, due to thermal blunting of the crack-tip

induced by adiabatic heating [11]. In rubber modified epoxy, R2, R6 and R10, although thermal blunting owing to localized adiabatic heating at the crack-tip may happen, its dependence at this high loading rate could be weak. Instead, the toughening mechanisms of rubber cavitation and matrix plastic deformation [2] are dominant and favored by the low loading rates, leading to the results displayed in Figure 7, especially when the rubber content is high. Again, further studies on the effects of loading rates on the relative amount of thermal blunting, cavitation and matrix plastic flow in these materials are essential to confirm the toughness results obtained.

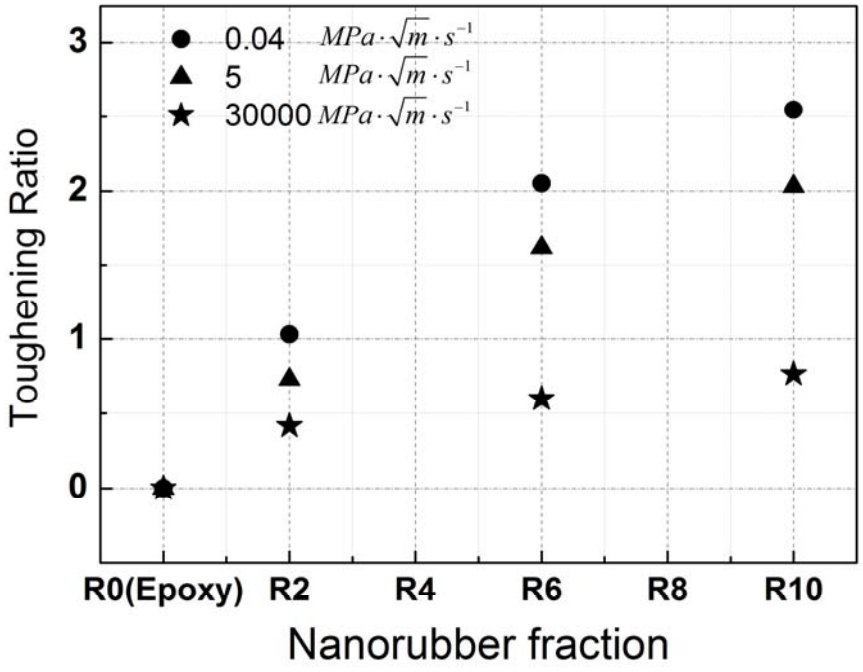

Figure 8 Normalized nano-rubber toughening efficiency of composites

A filler-toughening ratio parameter, η, can be used to evaluate the toughness increase associated with the nano-rubber particles. Thus, η is calculated from:

$$\eta = \frac{K_{IC} - K_{ICm}}{K_{ICm}} \tag{9}$$

where K_{IC}, K_{ICm} are the toughness values of nano-rubber filled epoxies and neat epoxy matrix, respectively. Hence, η is a ratio of the net toughness caused by the nano-rubber presence over the net toughness of the epoxy matrix. Figure 8 plots the toughening efficiency parameter η of nano-rubber based on equation (9). In Figure 8, the toughening ratio of R2, R6 and R10 at each loading rate was best fitted, and their slopes could be found to have a distinct trend: it drops with increasing loading rates. As explained in the above section, this may be due to the reduced rubber cavitation and matrix plastic flow under the high strain rate.

5. Summary and Conclusions

The fracture performance of nano-rubber filled epoxies under a wide range of loading rates from

quasi-static (0.04 MPa·√m/s) to Hopkinson bar (3×10^4 MPa·√m/s) tests were examined in terms of the fracture toughness and the toughening efficiency. Some important conclusions are summarized below:

1: The toughness of the nanocomposites increases with nano-rubber weight fraction.

2: The toughness of neat epoxy and 2 wt% rubber modified epoxy increases under dynamic loading due to thermal blunting.

3: The filler toughening efficiency drops with increasing loading rate. This is because increasing loading rates limit some toughening effects, such as cavitation and matrix plastic deformation, of rubber particles.

Acknowledgements

Y-G Miao would like to thank the Chinese Scholarship Council for supporting him to work on this project at the University of Sydney, and the financial support by National Natural Science Foundation of China (No. 10932008) and the 111 project (No. B07050). H-Y Liu wishes to thank the Australian Research Council (ARC) for the support of this project through a Future Fellowship awarded to her (FT0992081, 2009-2013) tenable at the University of Sydney. Thanks are also due to Y Zeng and XS Du of the CAMT for sample preparation and helpful discussions during the various stages of this work. Use of the SHTB facility funded by the ARC LIEF (LE100100045) is much appreciated.

References

1 H.-Y. Liu, G. T. Wang, Y.-W. Mai, Y. Zeng. Composites: Part B, 42(2011) 2170–2175.

2 S. W. Koh, J. K. Kim, Y.-W. Mai. Polymer, 34(1993) 3446-3455.

3 S. Sahraoui, J. L. Lataillade, J. Pouyet, N. Skhiri. Polymer testing, 7(1987) 269-278.

4 V. M. F. Evora, A. Shukla. Materials Science and Engineering: A, 361(2003) 358-366.

5 ASTM D5045-99. Standard test methods for plane-strain fracture toughness and stain energy release rate of plastic materials; 1999.

6 Y. L. Li, K. T. Ramesh, E. S. C. Chin, Materials Science and Engineering: A, 371(2004) 359-370.

7 Y. L. Li, K. T. Ramesh, International Journal of Impact Engineering, 34(2007) 784-798.

8 Z. J. Xu, Y. L. Li, F. L. Huang, Acta Mechanica Sinica, 28(2012) 424-431.

9 J. Zhu, S. S. Hu, L. L. Wang, International Journal of Impact Engineering, 36(2009) 61-72.

10 W. F. Brown, Jr. And J. E. Srawley, Plane strain crack toughness testing of high strength metallic materials,ASTM STP 410, 1966, pp.12.

11 I. M. Low, Y.-W. Mai, Journal of Materials Science, 24(1989) 1634-1644.

Low velocity perforation of an aluminum alloy: experiments and simulations

Léonard Antoinat[1,*], Régis Kubler[1], Guillaume Achard[1], Jean-Luc Barou[2], Philippe Viot[2], Laurent Barrallier[1]

[1] MSMP, Arts et Métiers ParisTech, 13617 Aix en Provence, France
[2] Arts et Métiers ParisTech, I2M, UMR 5295, 33405 Talence, France
* Corresponding author: leonard.antoinat@ensam.eu

Abstract Low velocity perforation of an aeronautical aluminum alloy sheet 2024 T3 subjected to impact is studied in this paper. The main objective is to compare experimental results and simulations by analysis of the failure. The perforation test is made with an instrumented 3 meter drop test. The striker has a large diameter (45 mm) and a conical shape. Sheets' thickness is 2 mm. The influence of the impact velocity is analyzed. A phenomenological behavior law of the sheet's material is implemented in the finite element code Abaqus/Explicit. Thus, 3D simulations of perforation are performed using a damage evolution law and a ductile failure criterion. To understand the phenomenon, the perforation force and the sticker velocity will be analyzed. Simulations are validated by experimental tests and compared with an analytical model.
Keywords Dynamic perforation, Aluminum, Experiments, FE Simulations, Analytical perforation model

1. Introduction

An increased attention in impact issues is paid by authors working on various engineering fields like aeronautic [1], naval [2], and automotive [3]. Impact on ductile material involves high strain rates effects [4] and temperature effects [5]. Thus, the knowledge of material dynamic behavior is necessary. Particular constitutive laws are known to be adapted for this type of issue [6]. The ductile target perforation is a specific case of impact studies. Perforation tests can be classified in categories according to the test velocity is high [7] or low [8], or according to the different striker's geometries (diameter, nose shape,…). An energetic approach is recommended to understand perforation issue. The energy absorbed by the target during impact E_a can be calculated using the difference between the initial kinetic energy and the final kinetic energy [8]. The ballistic limit V_{bl} is known to be the minimal initial velocity involving perforation. In order to have a better understanding of the rupture phenomenon and in order to compare with simulation results, it is necessary to know the force applied to the target and/or the striker displacement, during impact. This is the reason why some authors use the Hopkinson bar theory [9] [10] or an instrumented pneumatic accelerator or drop test [9] to be able to plot the curve of the force versus the time and/or the displacement. Low velocity perforation of an aeronautical aluminum alloy sheet 2024 T3 subjected to impact is studied in this paper. Unlike Rodriguez-Martinez [8] who studied the perforation of thin target (1 mm), the idea is here to work with thicker plates (2 mm) and with a larger striker (45 mm).

A two-pronged approach for perforation is proposed here: an experimental approach with the use of a drop test and a modeling approach including a finite element (FE) approach and an analytical approach. Results are compared and discussed.

2. Drop test: Perforation of 2024 T3 aluminum alloy sheets

2.1. Material

Aluminum alloys are known for their high mechanical characteristics against their density. The 2024 T3 aluminum alloy (2024 AA) is used in aeronautical structural parts as planes' fuselage or wings. The process route of this precipitation hardening material, alloyed with copper, is well known: a casting, a homogenizing, a hot rolling, a solute heat treatment at 495°C, a water quench, a cold work to obtain higher strain, and to finish a natural aging. This is the T3 heat treatment [11]. The chemical composition of the 2024 aluminum alloy is presented in Table 1.

Table 1. Chemical composition in %wt of the 2024 AA [12].

Al	Cu	Mg	Mn	Fe	Si	Zn	Ti	Cr
Bal.	4.76	1.38	0.65	0.22	0.08	0.07	0.03	0.01

2.2. Experimental setup

An instrumented drop test is used to perforate 2024 AA sheets (Fig. 1). A 5 kg test trolley slides on two bars from various height positions. Weights can be added to this trolley. Under the trolley a piezoelectric force sensor and a conical striker are fixed. This dynamic force sensor is calibrated for a range of validity from 0 to 100 kN and is used to measure the perforation force during impact with a relative error less than 5%. The striker is composed of a 60° conical nose and a 45 mm diameter cylindrical part. This cylindrical part is 10 mm long. A laser sensor (error of 0.5%) is used to measure the trolley's displacement. Two high speed cameras are used to measure the striker displacement and to take picture of the sheet's perforation. A mirror enables the observation beneath the sheet.

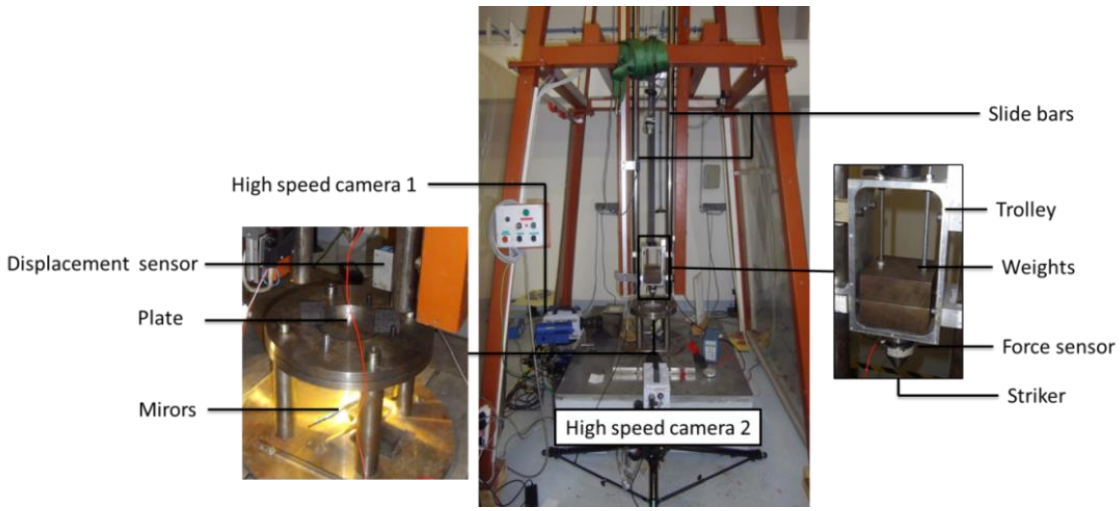

Figure 1. Instrumented drop test.

Twelve drop tests are performed to perforate a 2 mm 2024 AA sheet. The initial impact velocity and the striker total mass of each test are given in Table 2. If the striker perforates the sheet, values are in bolt font. The impact velocity evolves from 2.7 m/s to 6.9 m/s. The striker total mass is taken equal to 13 kg. The main objective is to find the ballistic limit velocity, to study the residual velocity and to analyze fracture and the force during impact.

2.3. Experimental results

2.3.1. Description of the perforation test

A 2 mm 2024 AA sheet is impacted by the striker. Thus, the striker nose induces plastic strain in the center of the sheet. More than four cracks appear, two in the laminated direction, two in the transversal direction, and sometimes in the 45° direction (Table 2). If the conical nose does not go through the plate, the striker bounces. If the conical nose goes through the sheet, the force sensor hits the sheet involving a bounce. All are analyzed before this bounce.

Table 2. Testing plan and main results.

Test number	1	2	3	4	5	6	**7**	**8**	**9**	**10**	**11**	**12**
Total mass (kg)	13	13	13	13	13	13	**13**	**13**	**13**	**13**	**13**	**13**
Drop test height (m)	0.4	0.4	1	1	1.5	1.5	**1.8**	**1.8**	**2**	**2**	**2.2**	**2.5**
Impact velocity (m/s)	2.79	2.71	4.24	4.20	5.00	4.81	**5.52**	**5.58**	**5.72**	**5.82**	**6.30**	**6.90**
Petals number	4	4	5	5	6	4	**6**	**5**	**4**	**4**	**6**	**5**
Residual velocity (m/s)	-1.4	-1.3	-1.3	-1.5	-1.3	-1.1	**2.6**	**3.2**	**2.6**	**2.6**	**4.0**	**4.6**
Absorbed Energy (J)	51	48	117	115	163	150	**155**	**160**	**168**	**152**	**157**	**170**
Peak Force (kN)	8.7	8.4	9.1	8.8	10.0	9.2	**9.3**	**9.5**	**9.5**	**9.2**	**9.2**	**Unknown**
Maximal Force (kN)	6.6	7.1	8.2	8.6	9.4	9.4	**9.6**	**9.4**	**9.9**	**9.6**	**9.6**	**Unknown**

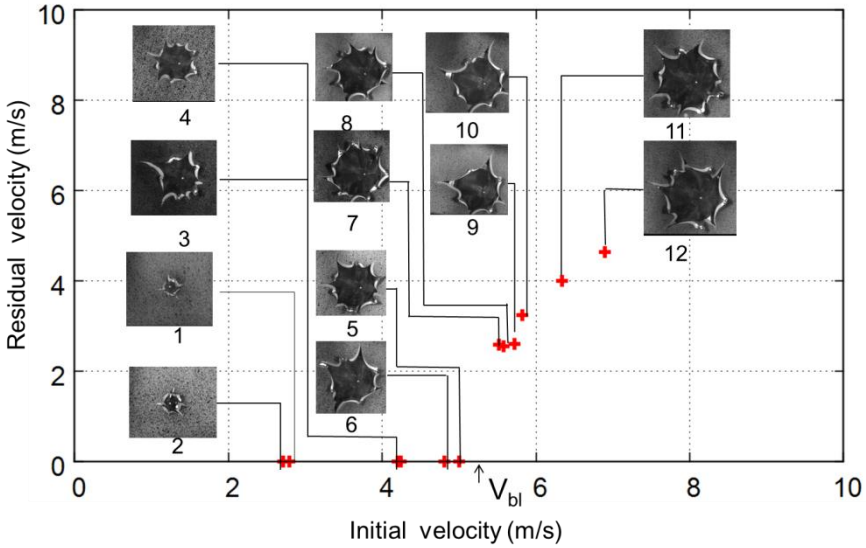

Figure 2. Residual velocity versus initial velocity.

2.3.2. Velocity results

It is usual to plot the residual velocity of the striker as a function of the initial velocity. In Fig. 2, if the striker does not perforate the sheet completely, the residual velocity is taken equal to 0. Classical results show that starting from the ballistic limit the velocity V_{bl} is a continuous growing curve [8]. Here this hypothesis is confirmed. In Fig. 2, pictures are taken at the end of the perforation (before the bounce). Thus it can be concluded, that using a 13 kg conical striker, the ballistic limit velocity to perforate a 2 mm sheet of 2024 AA is between 5 and 5.52 m/s. To obtain a better approximation of the ballistic limit velocity, the definition of the absorbed energy during perforation is used. This

energy is calculated as the difference between the initial kinetic energy and the final one and given in Table 2 for each test. The ballistic limit velocity V_{bl} can be estimated using the average absorbed energy E_a = 161 J as:

$$V_{bl} = \sqrt{\frac{2E_a}{m_{striker}}} \quad , m_{striker} = 13kg \tag{1}$$

It can be concluded that the ballistic limit velocity is equal to 5.0 m/s with an error of +/- 3%.

2.3.3. Force during impact

The force induced by the sheet on the striker can be plot during impact with the help of the force sensor (Fig. 6). Firstly, when the striker is reaching the sheet, a force peak can be observed. Secondly, cracks appear and so the force is continuously growing to be maximal when the striker cylindrical part is reached (test 7 to 12) or when the striker start to bounce back (test 1 to 6). After, the force is decreasing. If the conical nose goes through the sheet, the force sensor will hit the sheet involving a new increase of force.

2.4. Conclusion on experimental results

It can be concluded that the ballistic limit velocity is about 5 m/s +/- 3% using a 13 kg striker. Four or more than four petals always appear in the sheet during perforation. The perforation absorbed energy tends to be constant and equal to 161 J for impact velocity between 5 m/s and 7 m/s.

3. Modeling of perforation

Experimental tests are compared with two models: an analytical model based on energetic consideration and a shell finite elements model.

3.1 Perforation analytical model

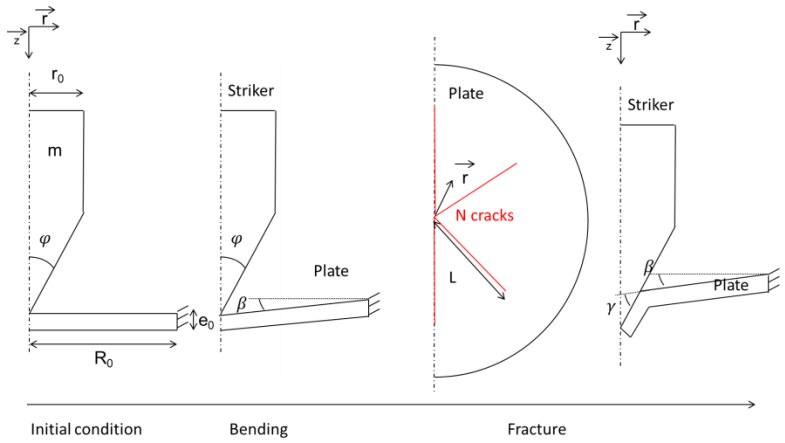

Figure 3. Analytical model.

An energetic approach for perforation is proposed by Nazeer [13]. A conical nose striker impacting thin plates involves bending deformation, stretching deformation and N cracks' propagation (fig 3).

The idea is to adapt this model in order to study the ballistic limit velocity and the residual velocity of the striker and with the hypothesis that the radius of the dimple is equal to the sheet radius. The elastic bending work is neglected. Thus, the total perforation work W is the sum of the bending plastic work W_b the stretching plastic work W_s, the petals' bending work W_{bf} and the fracture work W_f ($W = W_b + W_s + W_{bf} + W_f$). The perforation work is the absorbed energy and so with the definition of the absorbed energy, the residual velocity V_r is given as a function of the initial velocity V_0:

$$W = \frac{1}{2} m_{striker}(V_0^2 - V_r^2) \quad \rightarrow \quad V_r = \sqrt{V_0^2 - \frac{2W}{m_{striker}}} = \sqrt{V_0^2 - \frac{2(W_b+W_s+W_{bf}+W_f)}{m_{striker}}} \tag{2}$$

To obtain the ballistic limit velocity, the initial velocity is taken equal to V_{bl} and the residual velocity V_r equal to 0 m/s. Thus, we obtain:

$$V_{bl} = \sqrt{\frac{2W}{m_{striker}}} = \sqrt{\frac{2(W_b+W_s+W_{bf}+W_f)}{m_{striker}}} \tag{3}$$

where

- the bending work W_b is given as a function of the yield stress σ_y, the initial thickness e_0 the sheet's radius R_0 and the bending angle β (calculated as a function R_0 and the striker displacement z as $\tan(\beta) = \frac{z}{R0}$). by:
$$W_b = \pi \sigma_y e_0^2 R_0 \beta \tag{4}$$
- the stretching work W_s of the sheet is given as a function of the yield stress σ_y, e_0, R_0, and the stretching strain ε_s by $W_s = (\pi R_0)^2 \sigma_y e_0 \ \varepsilon_s$. The stretching strain can be defined thanks to the evolving surface area of the sheet and its original area $\left(\varepsilon_s = \ln\left(\sqrt{R_0^2 - z^2}/R_0\right)\right)$:
$$W_s = (\pi R_0)^2 \sigma_y e_0 \ \ln\left(\sqrt{\frac{R_0^2 - z^2}{R_0^2}}\right) \tag{5}$$
- the bending work W_{bf} involved by each petals can be written as a function of the number of petals N, the striker radius r_0, the thickness e, and γ the petals bending angle ($\gamma = \frac{\pi}{2} - \varphi - \beta$) as (see Fig. 3):
$$W_{bf} = \frac{\pi \sigma_y r_0 e^2 \gamma}{2} \frac{2+N}{1+N} \tag{6}$$
- the Fracture work W_f is due to crack propagation. It can be given as a function of the fracture toughness G, the thickness e and the length of fracture L by $W_f = NGeL$.The thickness e can be express with the stretching strain as $e = e_0/\sqrt{1 + z_b/R_0^2}$. L is taken equal to the projection of the striker on the bending sheet ($L = \sqrt{r_0^2 + z_b^2}$). The parameter z_b, is the ultimate bending striker displacement the parameter. Thus the fracture work is given by :
$$W_f = NGe_0 \ln\left(\sqrt{\frac{R_0^2 - z_b^2}{R_0^2}}\right)\sqrt{r_0^2 + z_b^2} \tag{7}$$

Here the angle of the conical striker is 60°, its mass is equal to 13 kg, and its diameter is 45 mm. The sheet thickness is 2 mm and its diameter is 148 mm. The static yield stress is $\sigma_y = 340\ MPa$, the number of petals is taken equal to 4 and the ultimate bending striker displacement z_b is 3 mm.

3.2 Finite element model for perforation

3.2.1 Material behavior law of 2024 T3 AA

A classical Johnson Cook behavior law [6] is used in the finite element code Abaqus [14] to model the viscoplastic behavior where A, B, n, m, C and $\dot{\varepsilon}_0$ are material parameters, Tmelt is the melt temperature and Troom is the room temperature. The stress σ can also be written as a function of the plastic strain ε^p , the plastic strain rate $\dot{\varepsilon}^p$, and the temperature T :

$$\sigma = \left(A + B\varepsilon^{p\,n}\right)\left(1 + Cln\left(\frac{\dot{\varepsilon^p}}{\dot{\varepsilon_0}}\right)\right)\left(1 - \left(\frac{T-T_{room}}{T_{melt}-T_{room}}\right)^m\right) \tag{8}$$

The elastic behavior is isotropic (E=74 GPa, ν=0.3). Above a plastic strain threshold, voids appear, grow and coalesce in the material, to produce the rupture [15]. To define this damage, a damage variable D is used in the model. The evolution of D can be written using the Johnson Cook dynamic damage model [16]. The damage D is dependent on the plastic strain rate, materials parameters m, D1, D2, D3¸D4 and D5, the hydrostatic pressure p, the equivalent stress σ_{eq}, the melt temperature Tmelt and the room temperature Troom :

$$\dot{D} = \frac{\dot{\varepsilon^p}}{\varepsilon_R} = \frac{\dot{\varepsilon^p}}{\left(D_1 + D_2\, e^{\frac{D_3 p}{\sigma eq}}\right)\left(1 + D_4 ln\left(\frac{\dot{\varepsilon^p}}{\dot{\varepsilon_0}}\right)\right)\left(1 - D_5\left(\frac{T-T_{room}}{T_{melt}-T_{room}}\right)^m\right)} \tag{9}$$

Lesuer [12] used an isotropic Johnson Cook hardening and a Johnson Cook rupture model for a 2024 AA with the parameters presented in Table 3. The strain rate parameter $\dot{\varepsilon}_0$ is taken equal to $1s^{-1}$, T_{room} equals 298 K and T_{melt} equals 775 K. Parameters D_1 and D_2 are determined to predict the residual velocity after impact, according to the presented experiment. Because of the temperature dependence, the specific heat cp is taken equal to 897 J/kg/K, the inelastic heat fraction equal β to 0.9 and the conductivity equal to 237 W/m/K.

Table 3. Johnson Cook hardening and fracture law parameters [12] (**modified in bolt fonts**)

A (MPa)	B (MPa)	n	C	m	D_1	D_2	D_3	D_4	D_5
369	684	0.73	0.0083	1.7	**0.035**	**0.035**	-1.5	0.011	0.0

3.2.2 3D finite element model.

A 3D finite element simulation is carried out using ABAQUS/Explicit. Shell elements are known to be well adapted for solving thin sheets' perforation issues [17]. Thus the 2024 AA sheet is modeled with 3200 S4RT elements and 1869 S3RT elements with the JC law presented above (Table 3.) For stability reason, five integration points are taken in the sheet's thickness. An analytical rigid surface is used to model the conical striker. The trolley mass is applied on the striker reference point. Interaction between the striker and the sheet is modeled by a perfect contact (hard contact and frictionless). Elements are deleted when the damage D is equal to 1. The sheet is clamped at the edges. The initial velocity is applied on the striker reference point. The striker moves only along the vertical direction. Temperature effects are taken into account but will not be discussed here. Initial

velocities of simulations are taken similar to experimental drop tests (2.7 m/s, 4.2 m/s, 5 m/s, 5.5 m/s, 5.8 m/s, 6.3 m/s and 6.9 m/s) and another one equal to 8 m/s.

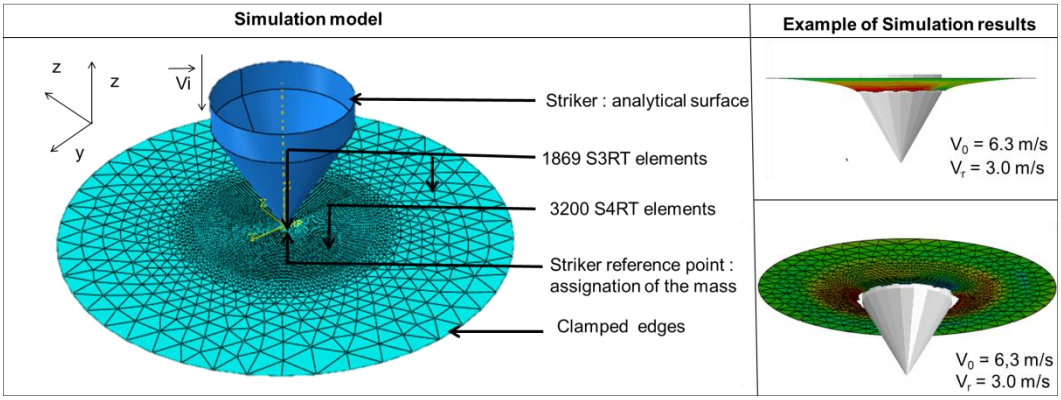

Figure 5. Shell finite elements model and simulation results.

4. Results and discussions

4.1. Perforation force

Drop tests force during impact is compared to numerical results. In Fig. 6, forces are plotted for an initial velocity of 5.8 m/s. Simulation's force is noised because of numerical instabilities. That's the reason why a centered average numerical force is plotted. It can be noticed that the first force peak is not simulated. The numerical model does not take in consideration friction effects and failure propagation and thus the numerical force underestimates the measured force. As the measured force, the numerical force rises during the perforation until a maximal force, equal to 8.8 kN, versus 9.6 kN for the measured force.

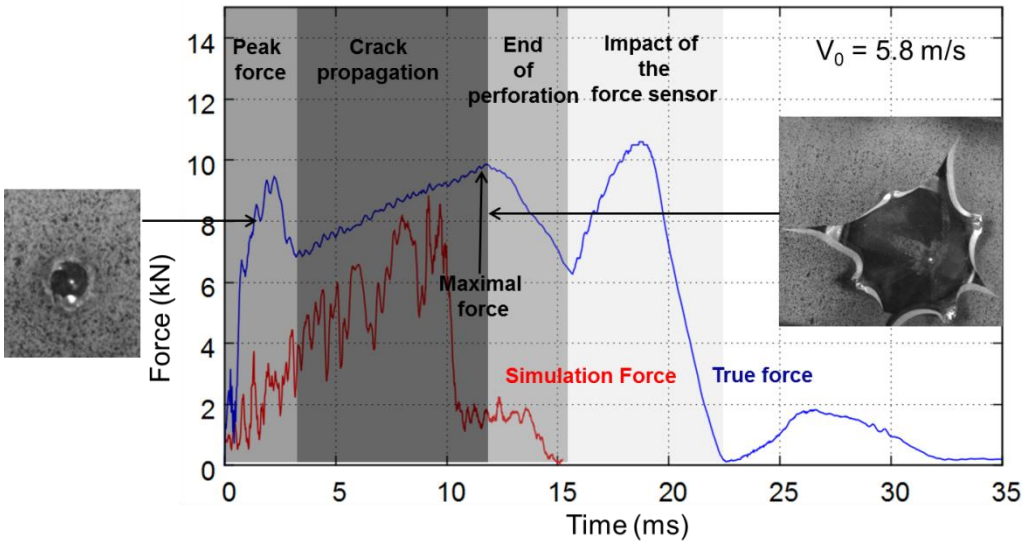

Figure 6. Force during impact versus time for an initial velocity of 5.8 m/s (test 9).

4.2. Discussion on the ultimate bending striker displacement before perforation

The ultimate bending striker displacement before perforation z_b, is used to calculate the residual velocity for the analytical model. It can be determined by drop tests' results and finite elements' results, and is equal to the displacement of the striker before rupture. For an initial velocity of 5.8 m/s, z_b is equal to 2.9 mm and 3.5 mm respectively for simulation and experiment. The hypothesis to take z_b equal to 3 mm for the analytical model is in good agreement.

4.3. Velocity discussions

Velocity's results are discussed by plotting the residual velocity as a function of the initial velocity (Fig. 7). Analytical model's results (N=4, z_b=3mm) are in good agreement with drop tests' results. Simulations tend to underestimate residual velocities, but results are close to experimental ones.

A good ballistic limit velocity correlation is found. With the analytical model, it is equal to 5.0 m/s. With the finite elements model, it is between 5 and 5.5 m/s. The experimental ballistic limit velocity is about 5.0 m/s.

Experimentally, the absorbed energy by the sheet during impact rises with the initial velocity until a maximal energy (about 161 J), reached for the ballistic limit velocity (Fig. 7). Drop tests' results give an average maximal absorbed energy for perforation of 161 J. In the analytical model, this maximal absorbed energy for perforation is the addition of plastic work and fracture work and is equal to 168 J. Because of the use of a rate dependent model, simulations show that the absorbed energy continues to rise beyond the ballistic limit velocity and exceeds 180 J.

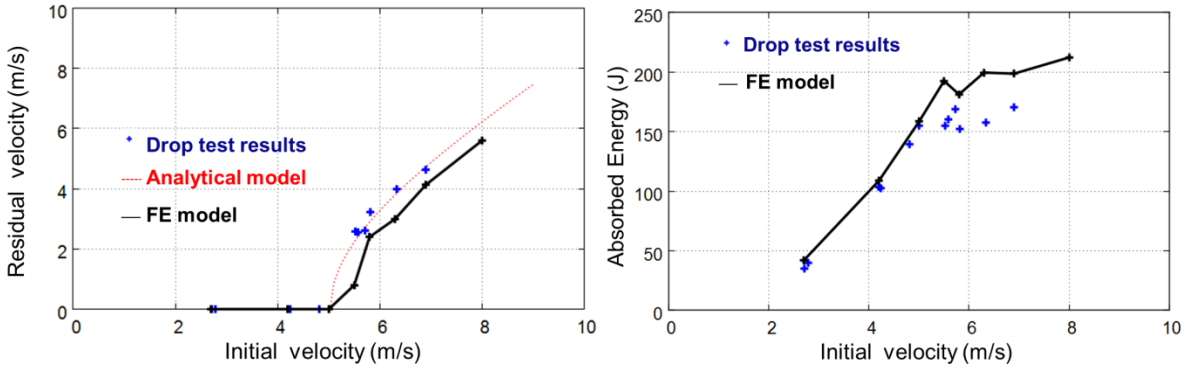

Figure 7. Residual velocity versus initial velocity and absorbed energy versus initial velocity.

4.4. Discussion on the number of petals.

More than four petals appear during perforation tests (Table 2). Because of the use of the "kill element" process, no petal is observed in FE simulations. It was already explained that results from the analytical model are number of cracks dependent. In this model, an evolution of the number of petals leads to an augmentation of the absorbed energy during impact and thus a decrease of the residual velocity. For example, for an initial velocity equal to 6.9 m/s the residual velocity is 4.7 m/s,

4.6 m/s and 4.5 m/s for respectively 4, 5 and 6 petals. This tendency is not confirmed by drop tests' results (Table. 2).

5. Conclusion and remarks

Thin sheets of 2024 AA were perforated, on a drop test, by a 60° and 45 mm diameter conical striker for a range of velocity from 2.7 m/s to 6.9 m/s. The energy needed to perforate is about 160 J. Four or more than four petals always appear in the sheet during perforation. A numerical model and an analytical model were proposed. Shell element model coupled with Johnson Cook viscoplastic and damage laws is adapted to simulate the perforation of thin sheet of aluminum alloy. The ballistic limit velocity, the residual velocity as well as the impact are in good agreement with experimental data. It can be shown that simulated force during impact is below the experimental force. The analytical model also predicts the residual velocity.

Simulations using an anisotropic material model for rolled sheets are underway and predict petals' formation during perforation (Fig. 8). Future analysis of pictures taken by high speed camera, beneath the sheet, will permit to perform image correlation for strain measurements in order to correlate the simulated strain field and the experimental strain field and therefore to better analyze the crack propagation (fracture criterion).

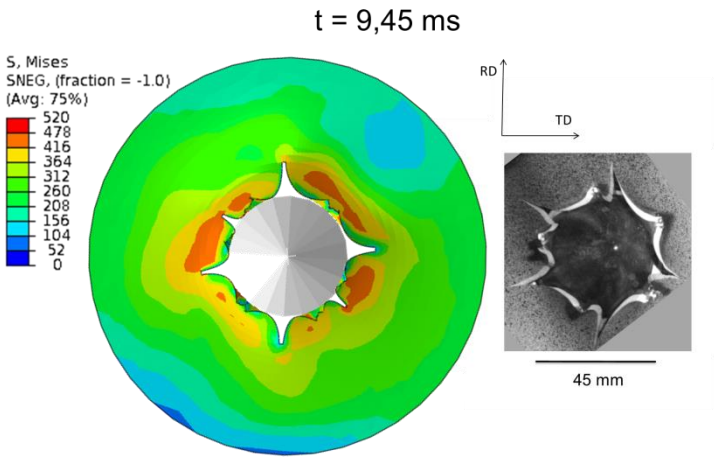

Figure 8. Simulation versus experiment for an initial velocity of 6.9 m/s using an anisotropic material model.

Acknowledgements

The financial support of this work from OSEO, a **s**tructure for the benefit of SMEs and innovation, is gratefully acknowledged.

References

[1] K. E. Jackson, R. L. Boitnott, E. L. Fasanella, L. E. Jones and K. H. Lyle, A History of Full-Scale Aircraft and Rotorcraft Crash Testing and Simulation at NASA Langley Research Center, 4th Triennial International Aircraft and Cabin Safety Research Conference, 2004.

[2] A. Tassin, Modélisation tridimensionnelle d'impacts hydrodynamiques pour l´étude du tossage des bulbes d´étrave., 2010.

[3] S. Hou, Q. Li, S. Long, X. Yang and W. Li, Multiobjective optimization of multi-cell sections for the crashworthiness design, International Journal of Impact Engineering, vol. 35, no. 11, pp. 1355-1367, 2008.

[4] G. Taylor, The Use of Flat-Ended Projectiles for Determining Dynamic Yield Stress. I. Theoretical Considerations, Proceedings of the Royal Society of London. Series A. Mathematical and Physical Sciences, vol. 194, no. 1038, pp. 289-299, 1948.

[5] R. J. Clifton, Response of materials under dynamic loading, International Journal of Solids and Structures, vol. 37, no. 1-2, pp. 105-113, 2000.

[6] G. R. Johnson and W. H. Cook, A constitutive model and data for metals subjected to large strains, high strain rates and high temperatures, Proceedings of the 7th International Symposium on Ballistics, vol. 547, no. 11, pp. 541-547, 1983.

[7] T. Borvik, A. H. Clausen, O. S. Hopperstad and M. Langseth, Perforation of AA5083-H116 aluminium plates with conical-nose steel projectiles : experimental study, International Journal of Impact Engineering, vol. 30, no. 4, pp. 367-384, 2004.

[8] J. Rodriguez-Martinez, A. Rusinek and A. Arias, Thermo-viscoplastic behaviour of 2024-T3 aluminium sheets subjected to low velocity perforation at different temperatures, Thin-Walled Structures, vol. 49, no. 7, pp. 819-832, 2011.

[9] F. Grytten, T. Borvik, O. Hopperstad and M. Langseth, Low velocity perforation of AA5083-H116 aluminium plates, International Journal of Impact Engineering, vol. 36, no. 4, pp. 597-610, 2009.

[10] M. Ramezani and Z. M. Ripin, Combined experimental and numerical analysis of bulge test at high strain rates using split Hopkinson pressure bar apparatus, Journal of Materials Processing Technology, vol. 210, no. 8, pp. 1061-1069, 2010.

[11] M. Stucky, Traitements thermiques des alliages d'aluminium, Les Techniques de l'Ingénieurs, vol. M 1 290v2, pp. 1-25, 1986.

[12] D. R. Lesuer, Experimentel Investigations of Material Models for Ti-6Al-4V Titanium and 2024-T3 Aluminum, Office of Aviation Research Washington, pp. 1-41, 2000.

[13] M. M. Nazeer, M. Khan, A. Naeem and A. u. Haq, Analysis of conical tool perforation of ductile metal sheets, International Journal of Mechanical Sciences, vol. 42, no. 7, pp. 1391-1403, 2000.

[14] Abaqus, Abaqus Analysis User's Manual, 2010.

[15] J. Lemaître and J. Chaboche, Mécanique des matériaux solides, Dunod, 1988.

[16] G. R. Johnson and W. H. Cook, Fracture characteristics of three metals subjected to various strains, strain rates, temperatures and pressures, Engineering Fracture Mechanics, vol. 21, no. 1, pp. 31-48, 1985.

[17] J. Dean, A. S-Fallah, P. Brown, L. Louca and T. Clyne, Energy absorption during projectile perforation of lightweight sandwich panels with metallic fibre cores, Composite Structures, vol. 93, no. 3, pp. 1089-1095, 2011.

Numerical Simulations on the Perforation of Metal Plates under Normal Impact by Conical-nosed Projectiles

Wu Qiaoguo[1,*], **Wen Heming**[2]

[1] National Technology Research Center on Pressure Vessel and Pipe Line Safety Engineering, Hefei General Machinery Research Institute, Hefei 230031, China
[2] CAS Key Laboratory for Mechanical Behavior and Design of Materials, University of Science and Technology of China, Hefei 230027, China
* Corresponding author: wuqiaoguo1015@163.com

Abstract This paper examines the perforation of Weldox460E steel plates struck normally by rigid conical-nosed projectiles through numerical simulations. The modified Johnson-Cook constitutive relation and the Gruneisen equation of state for metal plates are implemented in ABAQUS/Explicit as a user-defined material model by means of a subroutine (VUMAT). Numerical simulations are conducted on the perforation of Weldox460E steel plates struck normally by conical-nosed projectiles and flat-ended projectiles, it is shown that the numerical results are in good agreement with experiments. Finally, the effects of various cone angles of conical-nosed projectiles on the failure modes of metal plates and the energies absorbed for perforation are discussed.

Keywords Metal plates; Conical-nosed projectiles; Impact; Perforation; Numerical simulation

1. Introduction

An understanding of the response of structures subjected to intense dynamic loads which produce large inelastic deformation and failure is very important for safety calculations and assessment in various engineering such as nuclear, chemical, transport, offshore, naval, aerospace, and defense industries. In particular, the deformation and perforation behavior of plates is important for the design of offshore and protective structures against projectiles, fragments generated from explosion or dropped objects. The problem has been extensively studied in the past, and several studies are available in literature. Comprehensive reviews on the subject can be found in the papers by Backman and Goldsmith [1], Corbett et al. [2], and Goldsmith [3].

Borvik et al. [4-6] carried out experimental and axi-symmetric numerical investigation of Weldox steel plates struck normally by blunt, hemispherical and conical nosed projectiles. The effects of target strength and projectile nose shape on the failure modes and ballistic limits of steel plates are studied. Rosenberg et al. [7] examined the process of ductile plate perforation by sharp-nosed rigid projectiles through 2D numerical simulations, and the normalized resisting stress exerted by the plates can be simply related to the normalized thickness of the plates.

Iqbal et al. [8, 9] performed three-dimensional numerical simulations to study the behavior of ductile targets subjected to normal and oblique impact by sharp nosed cylindrical projectiles. Gupta et al. [10] dealed with the experimental and numerical investigations of aluminum target plates impacted by blunt, ogive and hemispherical nosed steel projectiles, and the effect of projectile nose shape, impact velocity and plate thickness on the deformation of the target plates was studied. Sun [11] carried out axi-symmetric numerical simulations of Weldox460E steel plates struck normally by flat-ended and conical-nosed projectiles using a viscoplastic constitutive model combined with ductile damage.

In this paper, numerical simulations are conducted on the perforation of Weldox460E steel plates struck normally by rigid conical-nosed projectiles and flat-ended projectiles. The modified Johnson-Cook constitutive relation and the Gruneisen equation of state which are valid for metals subjected to impact for large strains, high strain rates and high temperatures are implemented in ABAQUS/Explicit as a user-defined material model by means of a subroutine (VUMAT). Comparisons of the numerical results and the experiments show that the finite element models developed here are reliable. Based on the verified finite element model, numerical simulations are performed on the perforation of 6mm thick Weldox460E steel plates struck normally by conical-nosed projectiles with various cone angles, and the effects of various cone angles on the failure modes of metal plates and the energies absorbed for perforation are discussed.

2. Numerical simulation

In this section, numerical simulations are conducted on the perforation of Weldox460E steel plates struck normally by rigid conical-nosed projectiles and flat-ended projectiles, the cone angles of which are equal to 180^{o} as a special case of conical-nosed projectiles, using dynamic finite element code ABAQUS/Explicit. The targets was modelled using the modified Johnson-Cook constitutive relation which was implemented as a user-defined material model by means of a subroutine (VUMAT).

2.1. Finite element model

Finite element model in this section is based on the experiments of normal impact of Weldox460E steel plates by conical-nosed projectiles and flat-ended projectiles [4][12]. The projectiles have a nominal mass (G) and diameter ($d=2a$) of 197g and 20mm, respectively. The total length (L) and the cone angle (θ) of the conical-nosed projectile is 98mm and 33^{o}, and the total length (L) of the flat-ended projectile is 80mm. Projectiles were manufactured from Arne tool steel which has high strength and hardness, and it was observed that the plastic deformation of the projectiles was very small after perforation. In order to save CPU time and raise computational efficiency, projectiles are assumed to be rigid here. The target plates, having a span diameter ($S=2R$) of 500mm, were restrained at their periphery with respect to all degree of freedoms. Quarter models are used in the 3D finite element analysis, as seen in Fig. 1.

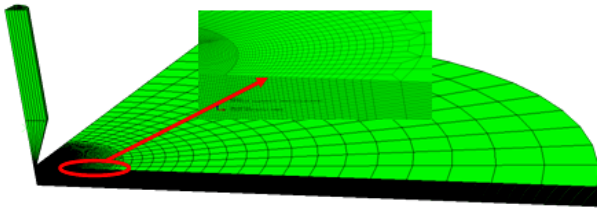

(a) Conical-nosed projectile

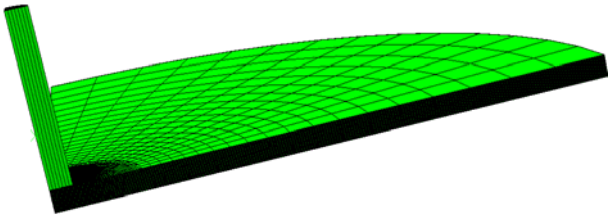

(b) Flat-ended projectile

Figure 1. Finite element model for Weldox460E steel plate struck normally by conical-nosed and flat-ended projectile.

As shown in Fig.1, the target was meshed with eight node brick elements, and all the meshes contained three regions: a finely zoned region which had noticeable effect on computational accuracy, a coarsely zoned region which did not have noticeable effect on computational accuracy, and a transitional region between the two regions above. The meshing method adopted here resolved the contradiction between mesh size and computational accuracy and efficiency to some extent. The element size in finely zoned region was taken to be 0.3mm×0.3mm×0.3mm approximately [5][9]. The diameter of the finely zoned region was 18mm (about 1.5 times as great as projectile diameter). The element size in transitional region and coarsely zoned region was increased from the central part to the outer part of the target. The element type used in the model was 8-node reduced integration elements (C3D8R). Contact between the projectile and target was assigned using the general contact algorithm. The value of coefficient of friction was hard to be measured accurately from experiments, and often taken to be 0~0.05 in literatures for penetration and perforation of metal plates by conical-nosed projectiles [5][7][11][13], and a coefficient of friction of 0.03 was considered here. For the perforation of Weldox460E steel plates by flat-end projectiles, a coefficient of friction of 0.0 was considered [10-12].

2.2. Constitutive relation

The modified Johnson-Cook constitutive relation is adopted for Weldox460E steel target [6]. The model includes linear thermoelasticity, the von Mises yield criterion, the associated flow rule, isotropic strain hardening, strain-rate hardening and softening due to adiabatic heating, and is valid for metals subjected to large strains, high strain rates and high temperatures. The equivalent stress is expressed as

$$\sigma_{eq} = \left(A + B\varepsilon^{n}{}_{eq}\right)\left(1 + \dot{\varepsilon}^{*}_{eq}\right)^{c}\left(1 - T^{*m}\right) \tag{1}$$

where A，B，C，n，m are material constants; ε_{eq} is the equivalent plastic strain; $\dot{\varepsilon}^{*}_{eq} = \dot{\varepsilon}_{eq}/\dot{\varepsilon}_{0}$ is the dimensionless strain rate, where $\dot{\varepsilon}_{0}$ is a user-defined reference strain rate; $T^{*} = \left(T - T_r\right)/\left(T_m - T_r\right)$ is the homologous temperature, where T is the absolute temperature, T_r is the room temperature, T_m is the melting temperature of the target material, respectively.

Johnson and Cook also developed a failure criterion that accounts for temperature, strain rate

and strain path in addition to the triaxiality of the stress state. The damage variable D has the basic form

$$D = \sum \frac{\Delta \varepsilon_{eq}}{\varepsilon_f} \tag{2}$$

where $\Delta\varepsilon_{eq}$ is the increment of accumulated plastic strain and ε_f is the fracture strain given as

$$\varepsilon_f = \left(D_1 + D_2 \exp\left(D_3 \sigma^*\right)\right)\left(1 + \dot{\varepsilon}^*_{eq}\right)^{D_4}\left(1 + D_5 T^*\right) \tag{3}$$

where D_1、D_2、D_3、D_4、D_5 are material constants, $\sigma^*=\sigma_H/\sigma_{eq}$ is the stress triaxiality ratio and σ_H is the mean stress. The temperature increment (ΔT) during perforation is calculated as

$$\Delta T = \int_0^{\varepsilon_{eq}} \chi \frac{\sigma_{eq} d\varepsilon_{eq}}{\rho_t C_p} \tag{4}$$

where ρ_t is the material density, C_p is the specific heat, χ is the coefficient that represents the proportion of plastic work converted into heat.

The damage variable D (Eq. 2) takes values between 0 (undamaged) and 1 (fully broken). When the damage variable D equals to 1, the damaged element will be removed from the mesh in the simulations. Meanwhile, the erosion strain (ε_c) of 2.0 is defined in the simulations in order to ensure that elements which are heavily deformed will not stop the computation process. The erosion strain (ε_c) of 2.0 is high enough to avoid any problems with mass erosion in the target [7]. When the equivalent plastic strain (ε_{eq}) is greater than the erosion strain (ε_c), the element will be removed.

The Gruneisen equation of state is employed, viz.

$$P = \rho_t C_0^2 \frac{\lambda}{(1 - s_1 \lambda)^2}\left(1 - \frac{\Gamma_0 \lambda}{2}\right) + \Gamma_0 \rho_t E_m \tag{5}$$

where P is hydrostatic pressure, C_0, S_1 and Γ_0 are material constants, E_m is specific internal energy of target material, and $\lambda = 1 - V/V_0$, where V is current volume and V_0 is initial volume.

The material parameters for Weldox460E steel target given in Table 1 are taken from Dey et al. [6]. E is the elastic moduli and ν is the Poisson's ratio of the target.

2.3. Simulation results

Fig.2 shows comparisons of the simulation results and the experimental data obtained by Borvik et al. [4] in terms of residual velocity for 12mm thick Weldox460E steel plates struck normally by conical-nosed projectiles with diameter (20mm), mass (197g) and cone angle (θ=33^o). Fig.3 shows comparisons of the simulation plot and the experimental image of the target after full perforation when the strike velocity of the projectile is 300.3m/s.

Table 1. Material parameters for Weldox460E steel targets [6]

E (GPa)	210	D_3	-2.969
ν	0.33	D_4	-0.014
ρ_t (kg/m^3)	7850	D_5	1.014
A (MPa)	499	C_p (J/kgK)	452
B (MPa)	382	χ	0.9
n	0.458	T_m (K)	1800
$\dot{\varepsilon}_0$ (s^{-1})	5×10^{-4}	T_r (K)	293
C	0.0079	C_0 (km/s)	3.574
m	0.893	S_1	1.920
D_1	0.636	Γ_0	1.69
D_2	1.936		

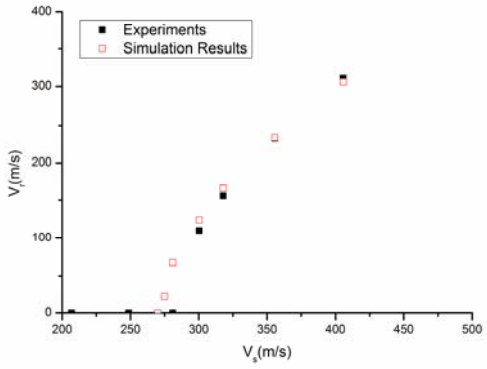

Figure 2. Comparisons of the simulation results with the experimental data [4] in terms of residual velocity for 12mm thick Weldox460E steel plates struck normally by conical-nosed projectiles.

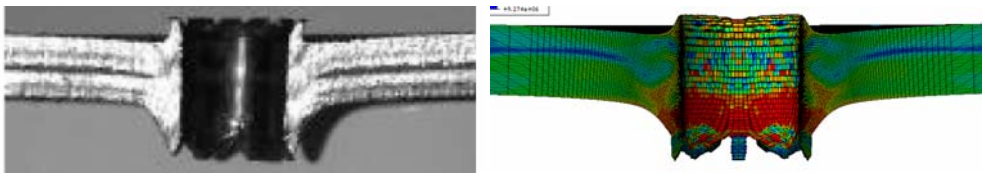

Figure 3. Comparisons of the simulation plot and the experimental image of 12mm thick Weldox460E steel plate after full perforation.

Fig.4 shows comparisons of the simulation results and the experimental data obtained by Borvik et al. [12] in terms of residual velocity for 6mm and 16mm thick Weldox460E steel plates struck normally by flat-ended projectiles with diameter (20mm), mass (197g). Fig.5 shows comparisons of the simulation plot and the experimental image of the plate after full perforation.

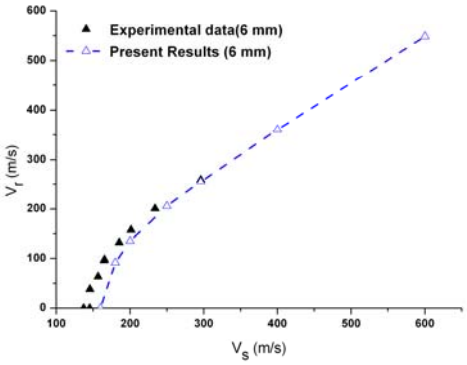

(a) 6mm thick Weldox460E steel plates

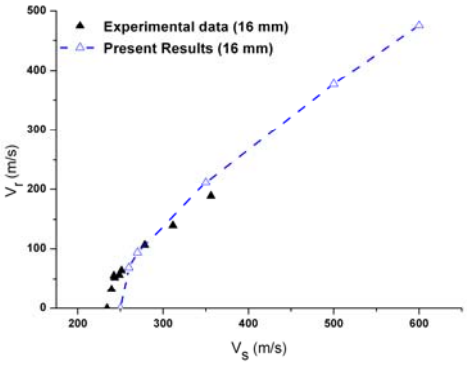

(b) 16mm thick Weldox460E steel plates

Fig.4 Comparisons of the simulation results with the experimental data [12] in terms of residual velocity for 6mm and 16mm thick Weldox460E steel plates struck normally by flat-ended projectiles.

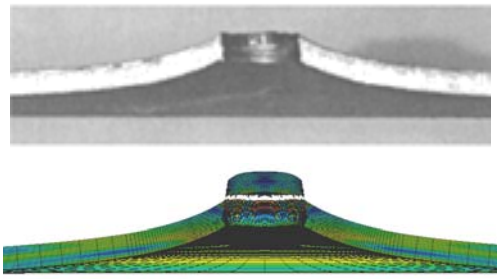

(a) 6mm thick Weldox460E steel plates

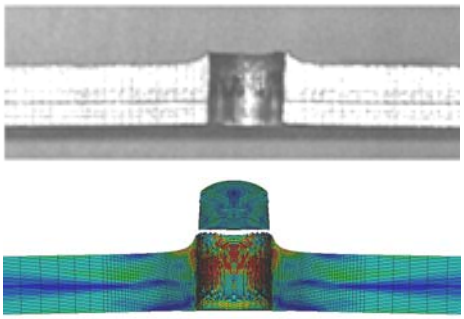

(b) 16mm thick Weldox460E steel plates

Fig.5 Comparisons of the simulation plot and the experimental image of 6mm and 16mm thick Weldox460E steel plate after full perforation.

It is evident from Fig.2 to Fig.5 that the simulation results are in good agreement with the experimental results, and the finite element model is reliable. Based on the present FE model, perforation of 6mm thick Weldox460E steel plates struck normally by rigid conical-nosed projectiles with various cone angles will be analyzed in the following section.

3. Numerical simulations for conical-nosed projectiles with various cone angles

In this section, the perforation behaviors of 6mm thick Weldox460E steel plates under normal impact by conical-nosed projectiles with cone angle θ=20°、60°、100° and 140° are analyzed by numerical simulations. The projectiles with various cone angles have the same effective length L_{eff}, $L_{eff}=4M/\left(\rho_t \pi d^2\right)$, the diameter ($d$) and the mass ($M$) of which are 20mm and 197g, respectively. Thus, the total lengths of projectiles with θ=20°、60°、100° and 140° are 111.2mm, 88.9mm, 83.9mm and 81.2mm, respectively. The strike velocities of the projectiles are 200 m/s.

Fig.6 shows the perforation process of 6mm thick Weldox460E steel plate under normal impact by conical-nosed projectile with θ=20° through numerical simulation. It can be seen clearly from Fig.6 that the materials accumulated aside the perforation hole is formed by radial expansion. Thus, it is deduced that the dominant failure mode here is ductile hole enlargement with global deformation.

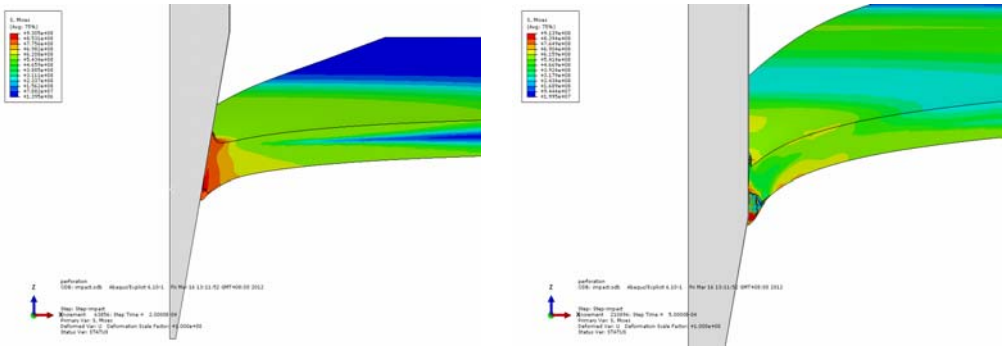

Figure 6. The perforation process of 6mm thick Weldox460E steel plate under normal impact by projectile with θ=20° through numerical simulation.

Fig.7 shows the perforation process of 6mm thick Weldox460E steel plate under normal impact by conical-nosed projectile with θ=60° through numerical simulation. It can be seen clearly from Fig.7 that local bending occurs for the materials beside the projectile, and the dominant failure mode is classified to petalling with global deformation.

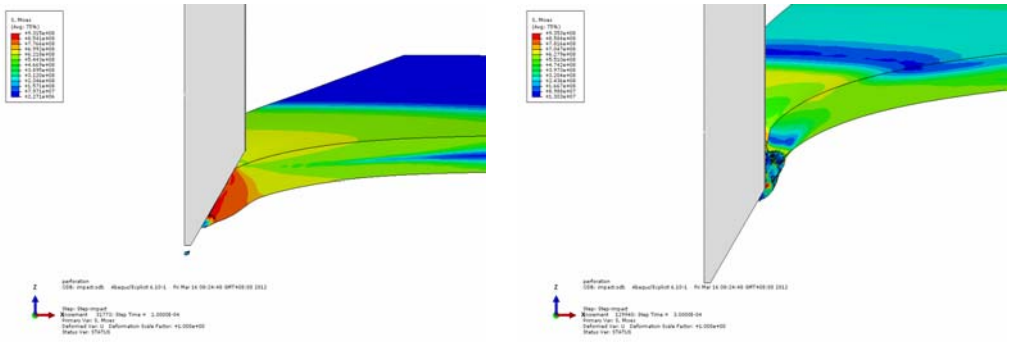

Figure 7. The perforation process of 6mm thick Weldox460E steel plate under normal impact by projectile with θ=60^{o} through numerical simulation.

Fig.8 shows the perforation process of 6mm thick Weldox460E steel plate under normal impact by conical-nosed projectile with θ=100^{o} through numerical simulation. It can be seen from Fig.8 that a plug of diameter larger than the diameter of the projectile is ejected. The crack occurs firstly at the distal surface of the plate, and then propagates to the frontal surface of the plate, finally a full plug is ejected due to stretching and shearing. The plug is formed due to the mixed failure mode of stretching and shearing, and the failure mode here is classified to discing with global deformation.

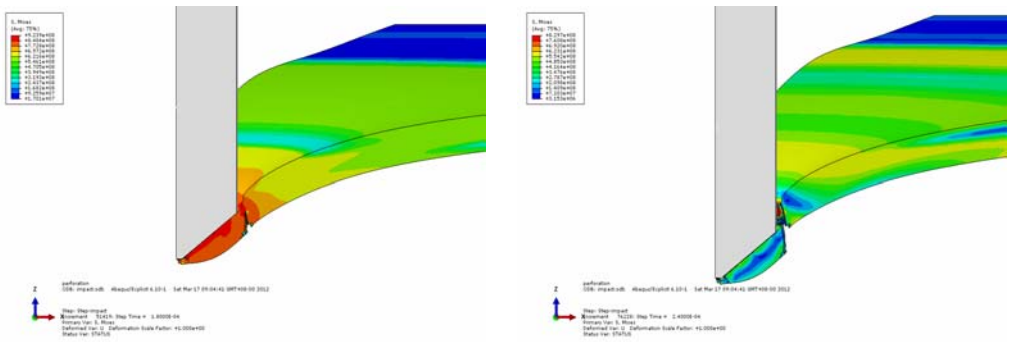

Figure 8. The perforation process of 6mm thick Weldox460E steel plate under normal impact by projectile with θ=100^{o} through numerical simulation.

Fig.9 shows the perforation process of 6mm thick Weldox460E steel plate under normal impact by conical-nosed projectile with θ=140^{o} through numerical simulation. It can be seen from Fig.9 that a plug is ejected which is similar to that in Fig.8, but the difference is that the diameter of the plug here is less than that in Fig.8, which is approximately equal to the diameter of the projectile. The plug is formed mainly due to the failure mode of shearing, and the failure mode here is classified to plugging with global deformation.

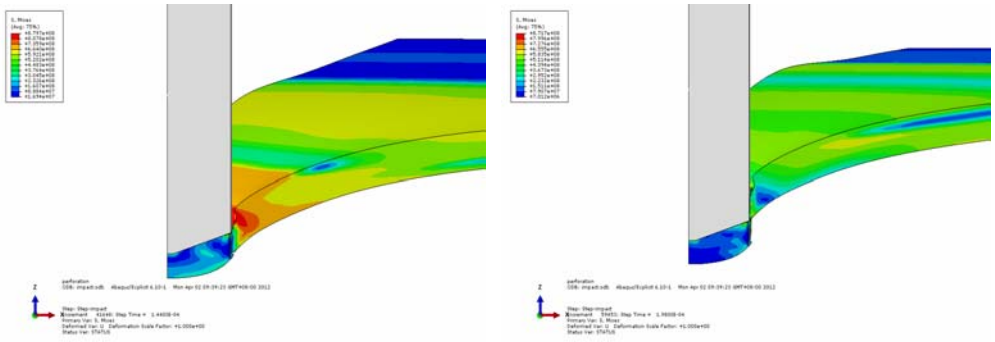

Figure 9. The perforation process of 6mm thick Weldox460E steel plate under normal impact by projectile with θ=140^o through numerical simulation.

As seen from Fig.6 to Fig.9, it is shown that projectile cone angle has significant effect on the perforation modes of 6mm thick Weldox460E steel plates and that for smaller cone angles plates fail by ductile hole enlargement, for medium cone angles plates fail by petalling and for larger cone angles plates fail by discing or plugging.

Fig.10 shows the numerical residual velocity V_r for 6mm thick Weldox460E steel plates struck normally by conical-nosed projectiles with θ=20^o, 60^o, 100^o and 140^o.

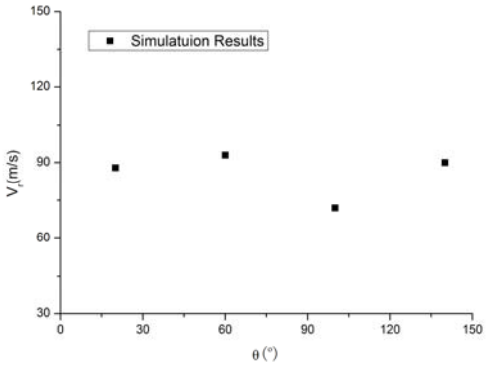

Figure 10. Numerical residual velocity V_r for 6mm thick Weldox460E steel plates struck normally by conical-nosed projectiles with various cone angles

As shown in Fig.10, the residual velocity of projectile is closely related to the failure mode of the target plate, and the residual velocity is not always decreasing sensuously with the increment of the projectile cone angles. The residual velocities for various projectile cone angles θ=20^o, 60^o, 100^o and 140^o in present simulations are 88m/s, 93m/s, 72m/s and 90m/s, respectively. The energy dissipated for the perforation of target plate failed in ductile hole enlargement with global deformation struck normally by conical-nosed projectile with θ=20^o is larger than that for the perforation of target plate failed in petalling with global deformation struck normally by conical-nosed projectile with θ=60^o. The energy dissipated for the perforation of target plate failed in discing with global deformation struck normally by conical-nosed projectile with θ=100^o is larger than those by projectile cone angle θ=20^o and 60^o, and obviously larger than that for the perforation of target plate failed in plugging with global deformation struck normally by conical-nosed projectile with θ=140^o. It is found that the energy dissipated by discing is maximum.

3. Conclusions

In the present paper, a numerical study has been conducted on the perforation of Weldox460E steel plates subjected to impact by rigid conical-nosed projectiles at normal incidence using dynamic finite element code ABAQUS/Explicit. The targets was modelled using the modified Johnson-Cook constitutive relation which was implemented as a user-defined material model by means of a subroutine (VUMAT). The numerical results are in good agreement with the experiments in terms of the patterns of targets after full perforation and the residual velocities, it is shown that the finite element models developed here are reliable. Based on the verified finite element model, numerical simulations are performed on the perforation of 6mm thick Weldox460E steel plates struck normally by conical-nosed projectiles with various cone angles. It is found that the energy dissipated for the perforation is closely related to the failure mode of the target plate, and the energy dissipated is not always increasing sensuously with the increment of the projectile cone angles. It is shown that the energy dissipated by discing is maximum.

References

[1] Backman ME, Goldsmith W. The mechanics of penetration of projectiles into targets. International Journal of Engineering Science, 1978, 16(1): 1-99.

[2] Corbett GG, Reid SR, Johnson W. Impact loading of plates and shells by free-flying projectiles: a review. International Journal of Impact Engineering, 1996, 18(2): 141-230.

[3] Goldsmith W. Non-ideal projectile impact on targets. International Journal of Impact Engineering, 1999, 22(2-3): 95-395.

[4] Borvik T, Langseth M, Hopperstad OS, Malo KA. Perforation of 12 mm thick steel plates by 20 mm diameter projectiles with flat, hemispherical and conical nosed part Ⅰ: experimental study. International Journal of Impact Engineering. 2002, 27(1): 19-35.

[5] Børvik T, Hopperstad OS, Berstad T, Langseth M. Perforation of 12mm thick steel plates by 20mm diameter projectiles with flat, hemispherical and conical noses, Part Ⅱ: numerical simulations. International Journal of Impact Engineering. 2002, 27(1): 37-64.

[6] Dey S, Børvik T, Hopperstad OS, Leinum JR, Langseth M. The effect of target strength on the perforation of steel plates using three different projectile nose shapes. International Journal of Impact Engineering. 2004, 30(8–9): 1005–1038.

[7] Rosenberg Z, Dekel E. Revisiting the perforation of ductile plates by sharp-nosed rigid projectiles. International Journal of Solids and Structures. 2010, 47: 3022-3033.

[8] Iqbal MA, Chakrabarti A, Beniwai S, Gupta NK. 3D numerical simulations of sharp nosed projectile impact on ductile targets. International Journal of Impact Engineering. 2010, 37: 185-195.

[9] Iqbal MA, Gupta G, Gupta NK. 3D numerical simulations of ductile targets subjected to oblique impact by sharp nosed projectiles. International Journal of Solids and Structures. 2010, 47: 224-237.

[10] Gupta NK, Iqbal MA, Sekhon GS. Effect of projectile nose shape, impact velocity and target thickness on deformation behavior of aluminum plates. International Journal of Solids and Structures. 2007, 44: 3411-3439.

[11] Sun WH. Theoretical and numerical study on failure modes of metal plates under normal impact by conical-nosed projectiles. PHD Dissertation, University of Science and Technology of China, 2009.

[12] Børvik T, Hopperstad OS, Langseth M, Malo KA. Effect of target thickness in blunt projectile penetration of Weldox 460 E steel plates. International Journal of Impact Engineering. 2003, 28: 413-464.

[13] He T. A study on the penetration of projectiles into targets made of various materials. PHD Dissertation, University of Science and Technology of China, 2007.

Dynamic fracture of advanced ceramics under impact loading conditions using a miniaturized Kolsky bar

Declan McNamara*, Patricia Alveen[1], Declan Carolan[1], Neal Murphy[1], Alojz Ivanković[1]

[1] School of Mechanical and Materials Engineering, University College Dublin, Ireland
* Corresponding author: Declan.mc-namara@ucdconnect.ie

Abstract
Advanced ceramic materials are frequently used in the machining of hardened steels, aerospace alloys and other abrasive materials. While these materials have many superior properties such as high hardness and abrasive resistance they are still prone to premature failure due to fracture. Accurate fracture properties of such materials are scarce, especially in the dynamic regime. The current work presents a novel combined experimental-numerical approach to determine dynamic fracture behavior. In recent years, much attention has been given to the study of dynamic behavior of materials under stress-wave loading. Experimentation with a modified Kolsky bar and a concurrent numerical investigation using the finite volume method was used in this study. The inherent difficulties in producing large amounts of advanced ceramic means that experiments must be carried out using very small samples. As a result the apparatus has been miniaturised to accommodate such specimen dimensions. The incident and reflected wave histories obtained experimentally in conjunction with the time to fracture of the specimen predicted numerically are used to determine fracture toughness at a number of loading rates.
Presented is a novel and simple test method to determine fracture properties of advanced ceramics using a miniaturised Kolsky bar. Results indicate a change in fracture toughness at increased rates of loading. This may be due to the complicated underlying microstructure of the materials under investigation, which behave differently under varying loading rates.

Keywords Dynamic Fracture, miniaturized Kolsky bar, advanced ceramics

1. Introduction

As opposed to static fracture toughness, no standard methodology yet exists for the determination of the dynamic fracture toughness of materials. Under static conditions the stress intensity factor at the crack tip is proportional to the applied load, under dynamic loading this does not hold true. This is due to the inertial effects, which result from the transient loading conditions. Other factors affecting the determination of dynamic fracture toughness include wave propagation within the test specimen and the accurate determination of crack initiation.

Traditionally dynamic fracture experiments were performed using the instrumented Charpy pendulum [1]. In this test setup strain gauges mounted on the hammerhead measure the response resulting from the impact on a specimen, [2, 3]. While this test method is well established and easily performed there exists a number of drawbacks. During the dynamic impact strong inertial forces affect the load applied at the crack tip. The hammer impact load is recorded by the strain gauge located at its head and this is used to determine the fracture parameters through the resulting load-time history. However due to the inertial forces present the applied load recorded by the

hammer head will be significantly different to that experienced at the crack tip. The impact of the hammer on the specimen will generate longitudinal and traverse stress waves within the specimen and these stress waves will influence the stress intensity factor at the crack tip [4]. Experimental results from the Charpy test are therefore difficult to interpret, as large inertial oscillations are often present in the load-time histories.

To overcome the limitations posed by traditional dynamic test methods much attention has recently been given to the study of dynamic behavior of materials under stress wave loading using a modified Kolsky bar, [5, 6, 7]. The Kolsky bar apparatus allows for fracture testing at rates greater the 10^6 MPa$\sqrt{m}$ s^{-1} therefore simulating more realistic loading conditions experienced by super-hard materials during operation. Both the tensile and compressive loading configurations have been adopted for fracture testing. For the most part compressive stress pulse loading has been most popular and following on from the standard quasi-static setup the high rate-bending configuration has proliferated. Detailed descriptions of all Hopkinson bar fracture tests can be found in a review paper by Fengchun *et al*. [8].

Fracture toughness values presented in this paper should be considered to be measured or apparent fracture toughness's, (K_{1db}) as opposed to the critical dynamic fracture toughness, (K_d). This is due to the effect of notch tip blunting in dynamic fracture tests and the effect of finite notch root radii on the overestimation of the fracture toughness as outlined by Williams and Hodgkinson, [9].

2. Experimental Set-up

2.1. One-Point Bend Fracture apparatus

The one-point bend set-up is a modification of the traditional Kolsky bar apparatus [10], where the transmission bar has been removed. The apparatus consists of a single instrumented cylindrical bar of length 300 mm and diameter 3 mm, Fig. 1. In a typical test a striker impacts the leading edge of the incident bar setting up a longitudinal stress wave. This wave propagates down the incident bar towards the specimen and subsequently reflects at the bar/specimen interface. A portion of the wave is transmitted through the interface into the specimen causing fracture. The degree to which the wave is reflected or transmitted depends on the impedance of the bar and specimen material and will be discussed later. It is of the upmost importance that the striker contact with the incident bar be a planar one. This ensures a trapezoidal wave will be generated and avoids any spurious wave reflection at the impact interface. The compressive wave can be well controlled in terms of duration and amplitude by varying the length and velocity of the striker respectively. The striker must remain less then half the incident bar length so to allow complete unloading of the striker before the arrival of the reflected wave from the impact end. The striker and incident bar both must be made of the same material. In a one-point bend configuration the specimen maintains a single point of contact with the loading apparatus. That is, the specimen remains unsupported throughout the test with no supports to restrain the free-body motion of the specimen. In this way the specimen will fracture due to inertia alone.

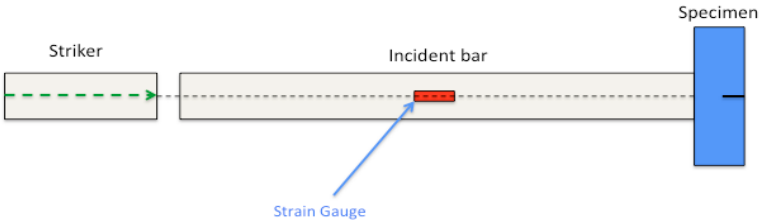

Figure 1. One-Point Bend apparatus

2.2. Material

Tests were carried out using SENB geometries. Due to inherent manufacturing constraints advanced ceramic materials have limitations on available specimen dimensions. Initial testing was carried out on PMMA with specimen span of 18 mm, height of 6 mm and thickness of 3 mm. Testing on the ceramic material was carried out on specimens with a span of 28.5 mm, height 6.25 mm and thickness of 4.76 mm. Future testing will involve specimens whose dimensions are further restricted with a span of 14 mm, height of 5 mm and thickness of 2 mm. The PMMA specimens were notched at 45-degree angle to a depth of 1 mm. Pre-cracks were subsequently introduced using a razor blade. Tests were preformed only on specimens whose pre crack was straight. For brittle materials like ceramics pre cracking is not an option and so samples had a notch root radius of 150 µm for all grades with a notch depth of 1.5 mm. Table 1. shows static fracture toughness values for PMMA and ceramic A and B. The PMMA tests were carried out using the standard three-point bend method, [11]. Static fracture results for the advanced ceramics A and B were taken from a previous study, [12] using a three-blunt notch analytical approach.

Table 1. Static Fracture toughness values

Material	K_{Ic}(MPa$\sqrt{m}$)
PMMA	1.61
Ceramic A	7.70
Ceramic B	2.80

3. Fracture Toughness determination

3.1. Data Reduction

The load applied to the specimen is given below and is based on one-dimensional wave theory, [10]:

$$P(t) = EA_0[\varepsilon_I(t) + \varepsilon_R(t)], \tag{1}$$

where E and A_o are the Young's modulus and cross-sectional area of the bar respectively. The particle velocity at the end of the incident bar is given by:

$$v = C_0[\varepsilon_I(t) - \varepsilon_R(t)], \tag{2}$$

where C_0 is the longitudinal wave velocity of the pressure bar. Integration of the velocity will also yield displacement at the end of the bar.

It is important to note that specimens must be sufficiently brittle so to fully fracture before they loose contact with the incident bar. Once the specimen leaves the end of the bar a free end boundary condition prevails and the above equations are no longer applicable. Up to this time Eq. (1) can be

used to determine the load applied to the specimen up to the point of fracture.

3.2. Fracture time (t_f) Determination

To determine fracture time a small uncalibrated strain gauge was mounted on the specimen close to the crack tip, Fig. 2. The location of the strain gauge is important, as it must be placed within the elastic region but outside the damage zone to yield accurate results [6]. Upon loading, stress within the specimen builds up and the gauge experiences a voltage change. As the crack passes the gauge an unloading wave is generated and a drop of the measured voltage indicates this. The time from the initial voltage rise to the drop off represents the fracture time. Due to the finite size of strain gauges it is difficult to place them exactly at the crack tip. In order to more accurately determine the fracture time a hybrid experimental/numerical approach is undertaken here. Modeling of the fracture specimen using the finite volume method (FVM) was done in OpenFOAM [13,14]. Strain gauge locations on the experimental samples were accurately measured and this data was adopted for the modeling work. Time up to unloading was found to agree well between the two methods. By combining experimental and numerical data increased accuracy of fracture time determination can be ensured.

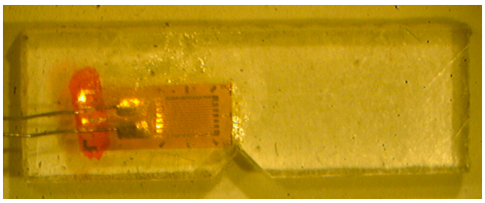

Figure 2. Strain gauge for fracture time detection

3.3. Temporal Stress Intensity Factor Determination

3.3.1. Applied load method

Dynamic fracture toughness (K_{Id}) can be determined as the critical stress intensity factor value at the crack tip at the instant of crack initiation. For Mode I fracture it is approximated as:

$$K_{Id} = K_I(t_f), \tag{3}$$

A closed form solution to predict the SIF from the measured load is applied here [15].

$$K_I(t) = \frac{3SP(t)}{4BW^{3/2}} \frac{\sqrt{\alpha}}{(1-\alpha)^{3/2}(1+3\alpha)} (1.72 + 0.23\alpha + 1.04\alpha^2 - 0.39\alpha^3), \tag{4}$$

where *P(t)* is the applied load to the sample and α is the ratio of crack length to width of the specimen (*a/W*). It has been demonstrated that this equation is valid for different crack to width ratios [8].

3.3.2. Crack tip strain

Another method for determining the SIF evolution experimentally is shown in Eq. (5). This method

relies on the direct measurement of the strain field near the crack tip by means of a strain gauge.

$$K_I(t) = \frac{\varepsilon_y(t) E \sqrt{2\pi r}}{Cos\frac{\theta}{2}\left[1 + Sin\frac{\theta}{2} Sin\frac{3\theta}{2} - \nu(1 - Sin\frac{\theta}{2} Sin\frac{3\theta}{2})\right]}, \quad (5)$$

where r is the radial distance from the crack tip to the strain gauge and θ is the angle from the crack path, [6].

4. Results & Discussion

4.1. PMMA Tests

All tests were performed at ambient temperature. The static fracture toughness has also been determined for comparison. Fig. 3(a) shows a typical incident and reflected strain trace from a fracture test. The striker velocity leaving the muzzle was approximately 8.5 m/s determined using a high-speed camera, which results in a particle velocity of 6 m/s at the load point of the apparatus from Eq. (2). Using Eq. (1) the load applied to the specimen was determined and is illustrated in Fig. 3(b). For this test the value of (a/W) was 0.33 and using Eq. (4) the temporal SIF was found as shown in Fig. 4.

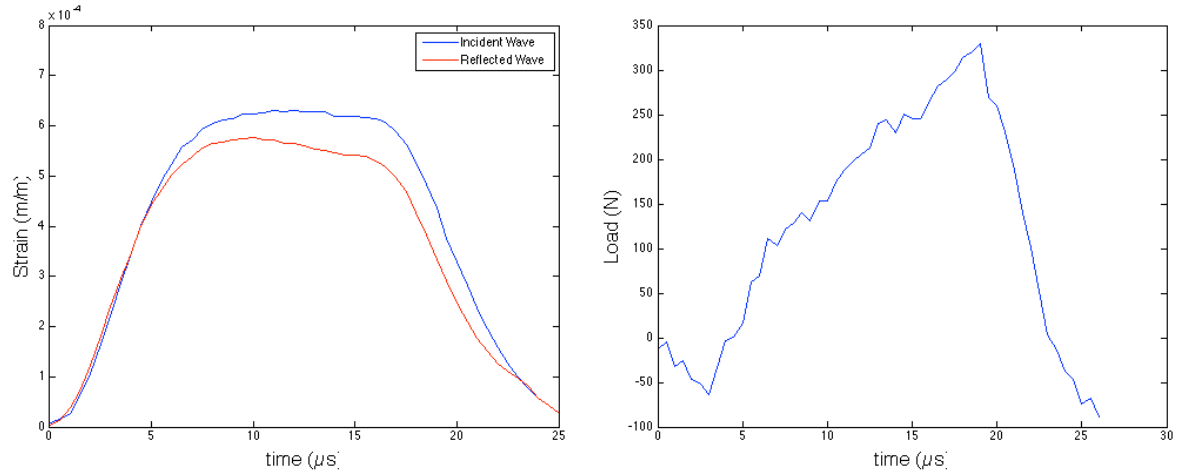

Figure 3(a). Superposition of incident and reflected strain trace, (b) Variation of applied load with time

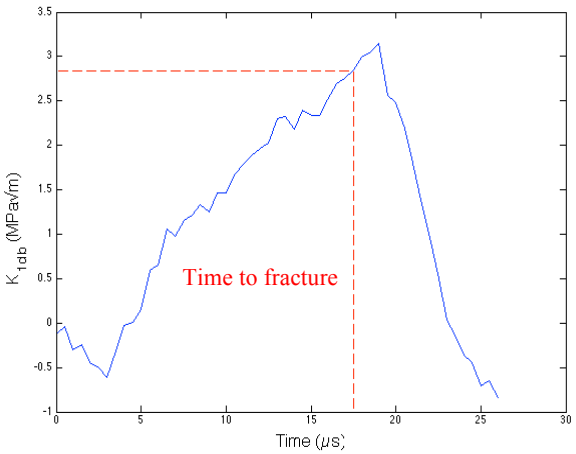

Figure 4. Stress intensity evolution for PMMA at 6m/s

Using both experimental and numerical methods the time to fracture was determined to be 17.5 μs. This yields an apparent dynamic fracture toughness for PMMA of 2.75 MPa√m from the above analysis, Fig. 4.

A number of other tests were carried out at varying loading rates. Fig. 5 shows the stress intensity evolution for a test performed at a velocity of 9.5 m/s. The variation in amplitude of the oscillations between the two tests is as a result of the increased rate of loading.

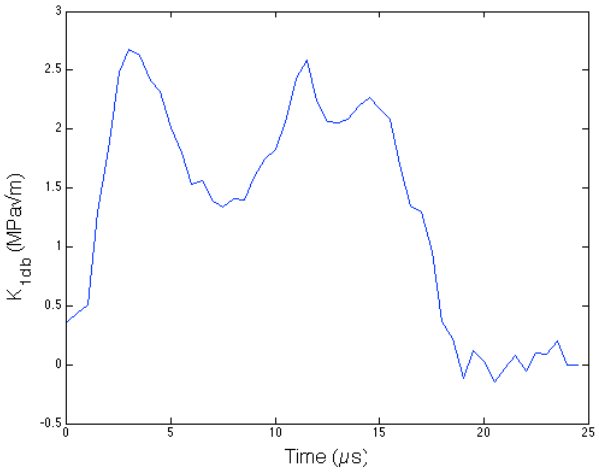

Figure 5. Stress intensity evolution For PMMA at 9.5m/s

Fracture time for the above test was 14.5 μs, which corresponds to an apparent toughness of 2.19 MPa√m. These results agree well with other authors, [5] and show fracture toughness for PMMA increases at dynamic loading rates.

The use of Eq. (5) was shown to greatly underestimate the temporal SIF. For this equation to yield accurate results it is important that the strain measurements be made within the singular zone. The strain gauges used in these tests were 1.5mm in length. Relative to the samples being tested these dimensions are quite large, and while care was taken in their placement, the strain measurements were recorded outside the singular zone therefore leading to inaccurate results. As a result of this the use of strain gauges will be restricted to determining the fracture time for later tests. It should be noted that the use of smaller strain gauges might avoid this problem.

A third method was also tested for comparison. This test procedure uses an impact response curve (IRC) for determination of dynamic fracture toughness, [16,17,18]. This method makes use of the relationship between the dynamic fracture toughness and time to fracture. The IRC is determined once for a specific test condition (impact velocity, specimen material and geometry) using FVM simulation with a contact procedure and subsequently only requires the time to fracture found through experimentation in order to determine the dynamic fracture toughness for successive tests of similar setup.

Fig. 6(a) and (b) show the IRC's determined for an OPB test setup at a particle velocity of 6 m/s using a Young's modulus of 6 GPa and 3 GPa respectively, corresponding to the dynamic and static moduli used by Ivanković and Williams, [19]. In order to determine the IRC for each case the sample was prevented from fracturing. The strain was determined directly at the crack tip in the model within the singular zone, and Eq. (5) was used to calculate the temporal SIF's for these cases. Using the time to fracture determined experimentally from an equivalent test setup the apparent

dynamic fracture toughness is found to be 3.44 MPa√m in the case where the material modulus is taken to be 6 GPa, and 2.84 MPa√m when the modulus is 3 GPa. The model with the higher, dynamic, Young's modulus is shown to overestimate the dynamic fracture toughness when compared to the load-point method presented above. Conversely, when the static Young's modulus of the material (3 GPa) is employed the model predicts an apparent dynamic fracture toughness similar to that of the load-point method, 2.84 MPa√m versus 2.75 MPa√m. This suggests that the static Young's modulus may be a more appropriate measure for this test setup. This point is further reinforced by noting that the quarter period of oscillation (14 µs) of the IRC developed using the dynamic Young's modulus, Fig. 6(a), is less then the experimentally determined fracture time of 17.5 µs, Fig. 4.

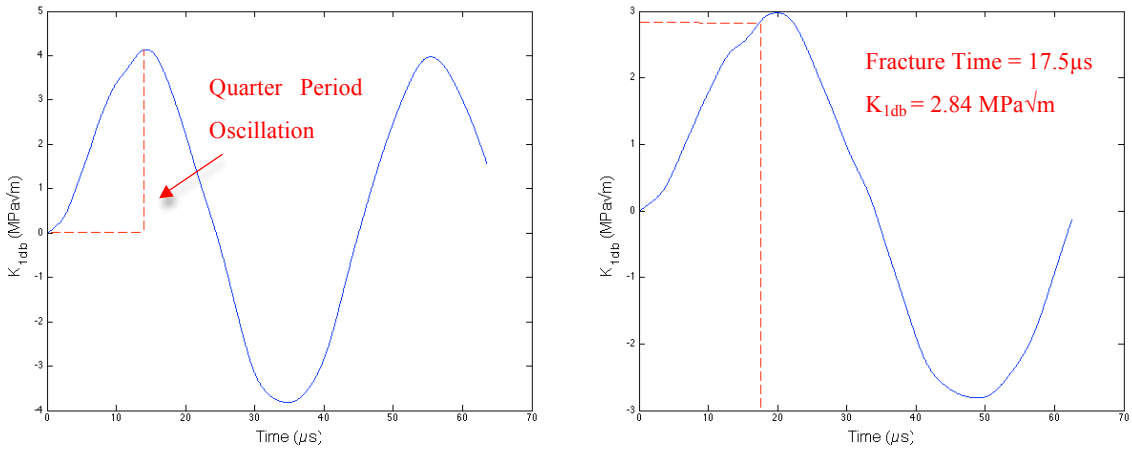

Figure 6(a). Impact Response curve Young's Modulus: 6 GPa, (b) Impact Response curve Young's modulus: 3 GPa

4.2 Advanced Ceramic Tests

A number of tests were carried out on ceramic samples. Due to the inherent difficulty in introducing pre-cracks into hard brittle materials all samples were tested with a blunt notch of 150µm in radius. As a result of this the dynamic fracture toughness values are apparent values. Static fracture toughness values were taken from previous testing [12]. Fig. 7 shows a typical strain trace superimposed on a FVM simulation test with a contact procedure implemented at the incident bar/specimen interface [20]. Very good agreement is observed between experimental and numerical tests. The samples were not instrumented during this round of tests and so only the SIF evolution from the one-dimensional analysis will be calculated. Fig. 8 shows the incident and reflected strain for two tests on samples A and B. The two grades of advanced ceramic vary in both inclusion grain size and second phase material and are denoted A and B. It can be seen from the trace that the degree to which the incident wave is reflected is very similar in both cases. This is to be expected, as at increased rates of loading the values of fracture toughness for both grades of material have been previously shown to be similar [21]. Fig. 9 shows the SIF for both grades of advanced ceramic. The time to fracture for these events was not recorded as mentioned above so a value of fracture toughness at these rates cannot be obtained. It is of interest for future work to instrument the samples using minute strain gauges close to the crack tip as per the PMMA testing. The wave speed velocity in these samples is in the region of 11,000 m/s, resulting in an extremely rapid fracture event. With this in mind future work will also focus on developing the numerical model further to ensure the most accurate determination of fracture time possible.

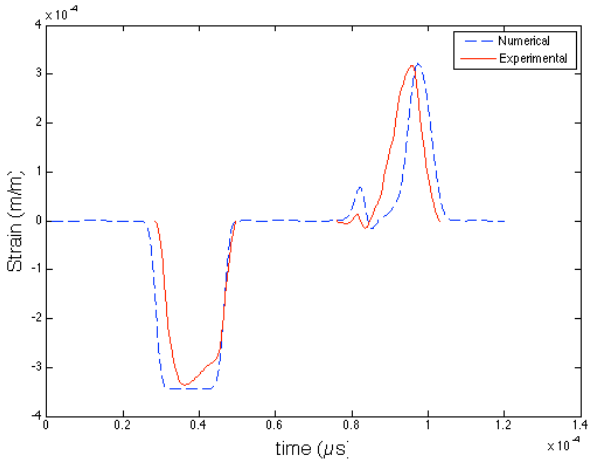

Figure 7. Numerical and experimental incident and reflected wave for ceramic sample

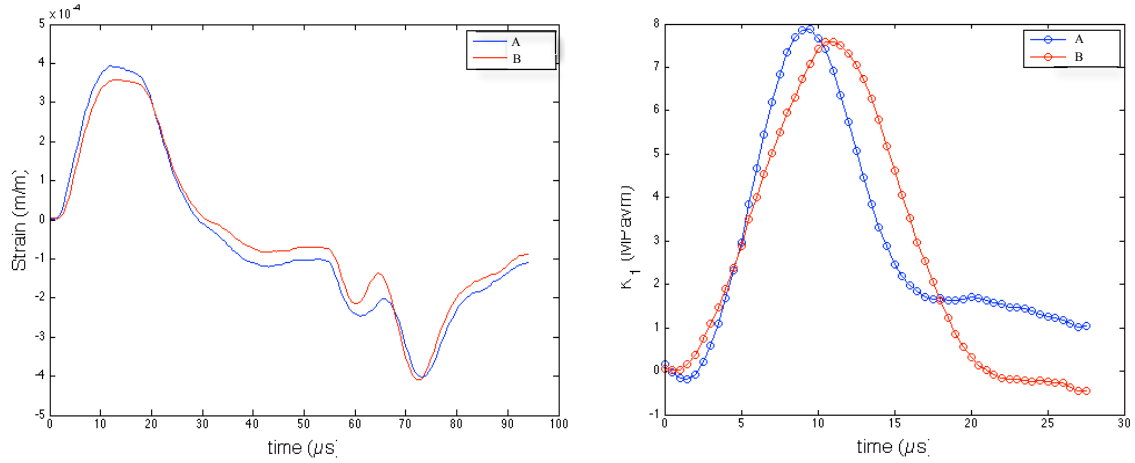

Figure 8(a). Experimental trace from tests on advanced ceramic A & B, (b) SIF evolution for advanced ceramic A & B from Eq. (5)

The difference in the incident and reflected waves in the ceramic tests is much greater than that of the PMMA tests. This is due to the difference in mechanical impedance between the test specimens and the tungsten carbide bar where more of the incident wave was transmitted through the bar/specimen interface. It is desirable to test specimens with similar impedance to that of the bar. In the case of advanced ceramics the impedance difference is low and as a result there is a notable difference between the incident and reflected traces, which allows for the clearer data analysis.

With PMMA its mechanical impedance is much lower then that of the tungsten carbide bars. In view of this fact it is not surprising that the reflected and incident signals are of similar amplitude as very little of the incident wave can be transferred to the specimen for fracture. For relatively low impedance materials it is recommended that a low impedance bar be used as the loading apparatus.

5. Conclusions

A novel experimental method for determining the dynamic fracture toughness of super-hard materials where specimen dimensions are limited was presented. This was achieved using a miniaturized Kolsky bar in one-point fracture. Preliminary tests were undertaken to determine the dynamic fracture toughness of PMMA. It has been shown that at increased loading rates the fracture

toughness of PMMA increases. A comparison of methods to determine SIF evolution was examined. One method using the applied load up to the point of fracture, another method, measuring strain directly on the sample close to the crack tip and a third through the use of an impact response curve. It was shown that strain measurements directly on the sample greatly underestimate the SIF. This is due to the strain measurements being erroneous as they were taken outside the singular zone. The impact response curve yielded apparent dynamic fracture toughness very similar to that of the load-point method. The strain used to calculate the IRC was measured directly on the crack tip in the model, which should lead to a more accurate calculation of SIF even when using static formula. Future testing will focus on detailed experimental work concurrent with numerical analysis to investigate the validity of these methods with emphasis on the use of impact response curves to determine dynamic fracture toughness. No attempt has been made to explain the observed increase in apparent fracture toughness at this stage, although it is in the scope for future testing.

The dynamic SIF evolution of two grades of advanced ceramic was investigated. At high rates of loading the fracture toughness of these grades was shown to decrease from their static values. A numerical model of the one-point bend set up has also been developed and excellent agreement between experimental and numerical results has been achieved. Future work will focus on further development of the model to determine the fracture time, a vital fracture parameter for accurate determination of dynamic fracture toughness.

Acknowledgements

The authors would like to thank Element Six Ltd., Enterprise Ireland and the Irish Research Council for providing financial support for this research.

References

[1] M.G. Charpy, On testing metals by the bending of notched bars. Int. J. Frac. 25 (1984) 287-305.

[2] D.R. Ireland, Critical Review of Instrumental Impact Testing Dynamic Fracture Toughness. The Welding Institute of American Society for Metals, Technical Report (1976) No. 79-55.

[3] W.L. Server, Impact three-point bend testing for notched and precracked specimens. J. Test. Eval., 6.1 (1978) 29-34.

[4] W. Bohme, The influence of stress wave on the dynamic crack tip loading in three- point bend impact. DGM Informationsgesellschaft mbH, Impact Loading and Dynamic Behaviour of Materials, 1 (1988) 305-311.

[5] C. Bacon, J. Farm, J.L. Lataillade, Dynamic fracture toughness determination from load-point displacement. Exp. Mech. 34.3 (1994) 217-223.

[6] G. Weisbrod, D. Rittel, A method for dynamic fracture toughness using short beams. Int. J. Frac., 104.1 (2000) 89-103.

[7] A. Belenky, I. Bar-On, D. Rittel, Static and dynamic fracture of transparent nano-grained alumina. Journal of the Mechanics and Physics of Solids, 58.4 (2010) 484-501.

[8] J. Fengchun, K.S. Vecchio, Hopkinson Bar Loaded Fracture Experimental Technique: A Critical Review of Dynamic Fracture Toughness Tests. Applied Mechanics Review, 62 (2009) 060802.

[9] J.G. Williams and J.M. Hodgkinson, Crack-blunting mechanisms in impact tests on polymers. Proc. R. Soc. Lond. A, 375 (1981) 231-248.

[10] H. Kolsky, An Investigation of the mechanical properties of materials at very high rates of loading. Proc. Phys. Soc Lond, 62.11 (1949) 676.

[11] BSI. Advanced technical ceramics: test methods for determination of fracture toughness of monolithic ceramics. Part 5: single-edge v-notch beam (SEVNB) method. DD CEN 14425-5, British Standards Institution; 2004.

[12] D. Carolan, P. Alveen, A. Ivanković, N. Murphy, Effect of notch root radius on fracture toughness of polycrystalline cubic boron nitride. Eng. Frac. Mech. 78 (2011) 2885-2895.

[13] A. Ivanković and J.G. Williams, The Finite Volume Analysis of Linear Elastic Dynamic Fracture Problems, In *Dynamic Fracture Mechanics*, Chapter **3**, Eds. M. H. Aliabadi, (Computational Mechanics Publications, Southampton), 1995, 101-135.

[14] H. Weller, G. Tabor, H. Jasak, C. Fureby. A tensorial approach to CFD using object oriented techniques. Computers in Physics, 12 (1998) 620– 631 .

[15] I. Villa, J. loya, J. Fernandez-Saez, General expressions for the stress intensity factor of a one-point bend beam, Eng. Frac. Mech., 74.3 (2007) 373-385.

[16] J.F. Kalthoff, S. Winkler, W. Bohme and W. Klemm, Determination of the dynamic fracture toughness K_{1d} in impact by means of response curve. Int. J. Frac. 12 (1980), 277-298.

[17] J.F. Kalthoff, S. Winkler and W. Bohme, A novel procedure for measuring the impact fracture toughness K_{1d} with precracked charpy specimen, Journal de Physique 46 (1985), 363-373.

[18] A. Rager, J.G. Williams and A. Ivanković, Numerical Analysis of the three point bend impact tests for polymers, Int. J. Frac. 135 (2005), 201-217.

[19] A. Ivanković, J.G. Williams, A local modulus analysis of rapid crack propagation in polymers. Int. J. Frac. 64(4) (1993), 251-268.

[20] P. Cardiff, A Karac and A. Ivanković. Development of a finite volume contact solver based on the penalty method. Computational Materials Science (2012).

[21] D. Carolan, A. Ivanković, N. Murphy, A combined experimental-numerical investigation of fracture of Polycrystalline Cubic Boron Nitride. In Press, Accepted Manuscript, Eng. Fract. Mech. http://dx.doi.org/10.1016/j.engfracmech.2012.09.008.

Behavior of interface crack in layered structure under actions of both stress wave and residual stress

ChenWu Wu[1, 2*], XinXin Cheng[1,3], YuChen Yuan[1,3]

[1] Institute of Mechanics, Chinese Academy of Sciences, Beijing 100190, China
[2] Department of Engineering Technology and Industrial Distribution, Texas A&M University, College Station, Texas 77843, USA
[3] School of Physics, University of Chinese Academy of Sciences, Beijing 100049, China
* Corresponding author: chenwuwu@imech.ac.cn & cwwu@tamu.edu

Abstract The propagation characteristic of stress wave impinging at the interface between initially stressed film and substrate is analyzed to reveal the effect of residual stress on the fracture behavior of such layered structure. In particular, the response of the layered structure to both stress wave and residual stress is investigated based on an axis-symmetric model including a centric coin-shape interface crack. The dispersion of the stress wave and the dynamic stress concentration around the interface crack tip are discussed with the crack surface contacting behavior being involved in the model. It is revealed that the strain energy release rate at the crack tip would be dependent on the interface crack length. The results also indicate that the residual stress would influence greatly the in-plane stress of the film and therefore determine the fracture pattern of the film.

Keywords Layered structure, Residual stress, Stress wave, Interface crack

1. Introduction

The impact method with coated bullet was developed by Wu et al [1] to evaluate the interface adhesion of film to substrate. In such measurement, an initial compressive stress pulse is produced by impacting the substrate of the specimen under test with the coated front end, of which the reflection would induce tensile stress around the tested interface. Theoretically, the initial compressive pulse can be calculated as

$$p_0 = -v_0(\rho c)_1(\rho c)_2 / ((\rho c)_1 + (\rho c)_2) . \quad (1)$$

Where v_0 is the relative impinging velocity of the bullet to the specimen, $(rc)_1$ represents the acoustic impedance of the bullet coat and $(rc)_2$ the acoustic impedance of the specimen substrate [2]. The experimental results have revealed that the reflection of the input compressive pulse could separate the film off the substrate clearly [2]. Moreover, it is also indicated that the initial stress state of the specimen may influence the fracture behavior of the film and the interface. Generally speaking, the initial stress, also known as residual stress, varies according to the material treatment processes. Actually, the previous research verified that the film stress and the interface stress around the impact region edge will be greatly changed by the initial stress state in the specimen subjected to coated bullet impact [3].

The fracture may arise first within the film or at the interface depending on the comparison of the stress level to the toughness of the film or the interface. Once the interface crack exists before the specimen is impacted, the interface crack may influence the propagation and evolution of the impinged stress pulse. Therefore, this present work focus on the behavior of the interface crack between the film and substrate under impact test. First, the axis-symmetry cracked model was set up to investigate the impact responses of the structure with treating the initial impact as an input compressive stress pulse as shown in Fig. 1. Then, the propagation and evolution of the stress pulse and thereafter the deformation, stress and strain energy of the specimen are calculated for the cases of different crack length. Finally, the influence of the residual stress on the impact response of the cracked specimen is investigated for the three cases of initially stress free, initially compressed and

initially tensioned film.

2. Theoretical formula and modeling

The axis-symmetry model sketch is shown in Fig. 1, in which the symbol *t_s=5mm* and *t_f* =0.25mm represents the thickness of the substrate and film, respectively; *r_s=50mm* is the radius of the specimen, *r_b=7.5mm* indicates the coverage radius of the impact region. And *l_c* represents the interface crack length and will be set as 10~100 percent of the magnitude of *r_b*. Moreover, the two parameters defining the compressive pulse are $\Delta\tau$ =0.05μs and p_0 =800MPa. The symmetry constraints are applied at the symmetry axis and the displacement at the boundary of the circular specimen are restricted as shown in Fig. 1.

The densities of the substrate and film are 7850kg/m^3 and 8800kg/m^3, respectively. The ideal elasticity is assumed for the specimen and the elastic modulus of the substrate and film are 200e9 Pa and 210e9 Pa, respectively. The Poisson's ratio of the substrate and film are 0.29 and 0.31 respectively.

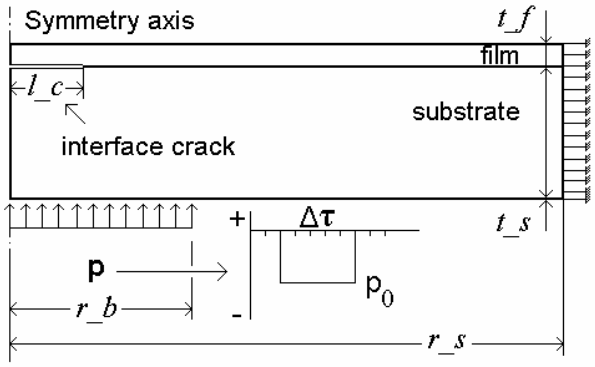

Fig. 1 Model sketch of the system of film and substrate with interface crack

The discretized model is shown in Fig. 2. In detail, the film is divided as five segments through its thickness. Thus, the linear element size is nearly one fifth of the film thickness. The contact elements are adopted at the crack surface for both the film and substrate, for which the coulomb friction law is used to simulate the probable surface friction induced shearing between the crack surfaces.

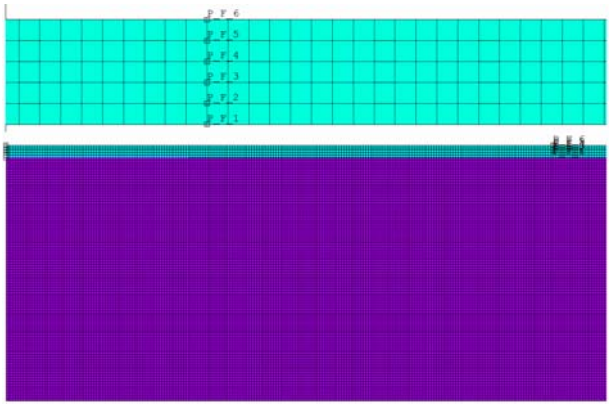

Fig. 2 Discretized model of the film and substrate

As far as the initial stress state is considered, three cases are analyzed. That is, the results denoted by NRS represents the case of the initially stress free film; TRS represents the case of that the film

being initially biaxial tensioned to 300MPa; CRS corresponds to the case that the film being initially biaxial compressed to -300MPa.

3. Results and discussion

The interface normal stress acting at the center point of the impacted region is shown in Fig. 3, which is named as SY_I and the symbol '+' and '-' represent the film side of the interface crack surface and the substrate side, respectively. It is indicated that the interface crack would permit the transmission of compressive stress pulse while deny the transmission of tensile stress. It is also shown that the normal stress is almost continuous across the interface, as one can see that the two curves corresponding to the results of the two nodes across the interface almost identical.

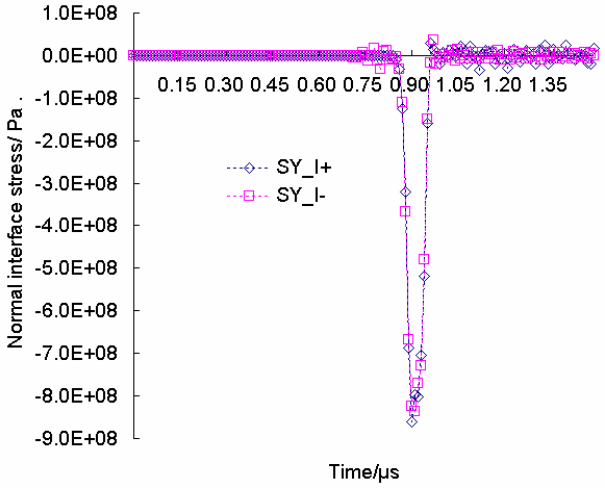

Fig. 3 Normal stress acting at the interface center point

The interface normal stress acting at the third interface node numbered from the interface crack tip is shown in Fig. 4, which is denoted by SY_INTE2 with the symbols '+' and '-' of the same meaning as aforementioned. Great tensile stress pulse appears after the reflection of the transmitted part of the input stress pulse at the free surface of the film. This is thought to be the principle driving force for the interface crack extension.

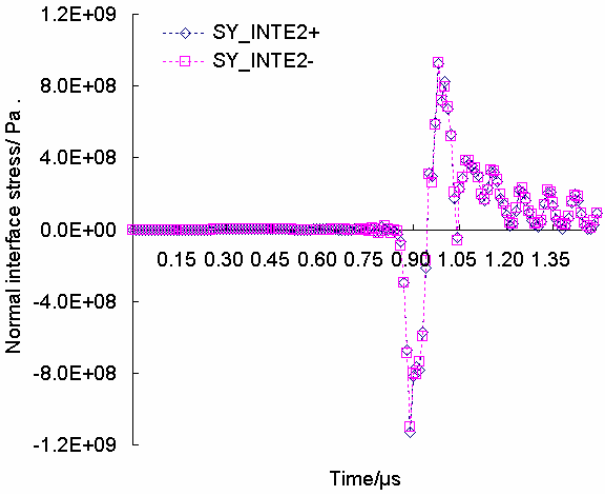

Fig. 4 Normal stress acting at the outer node close to the interface crack tip

The normal stress and shear stress contours for the time point t=1.03μs are shown in Figs.5 and 6,

respectively. It is to be noted that the deformation is magnified by 100 times to reveal the details of the interface crack. Obvious crack open displacement and stress concentration can be found around the crack tip. Moreover, the difference in the normal stress acting where before and after the crack tip the obstructing effects of the interface crack on the propagation of the tensile stress pulse.

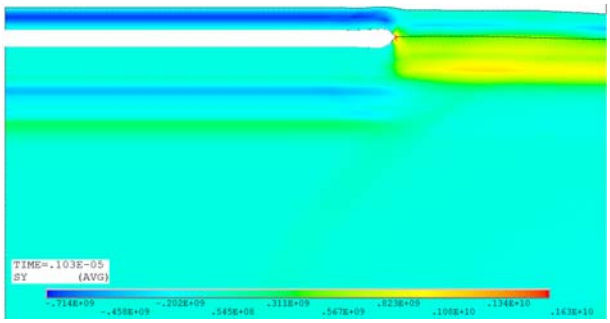

Fig. 5 Magnified contour of stress component SY at the time point t=1.03μs

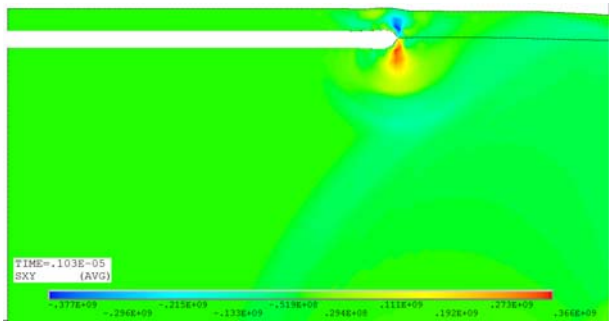

Fig. 6 Magnified contour of stress component SXY at the time point t=1.03μs

The crack open displacement at the node 5μm away from the crack tip is further shown in Fig. 7. It is verified again that the crack is always open after the compressive pulse transmits across the interface crack, although some slight fluctuation arises due to the quick reciprocating of the film under impacting.

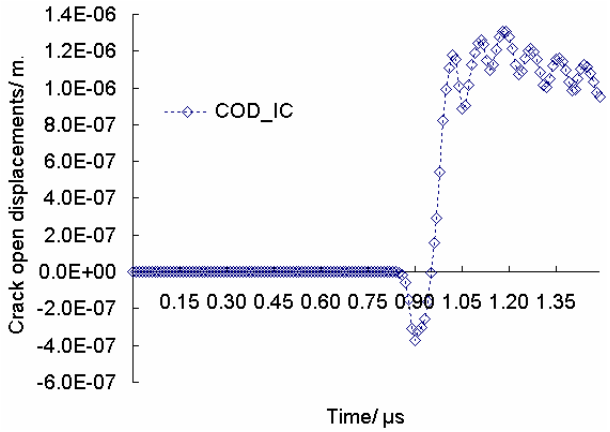

Fig. 7 Crack open displacement at the inner node 5μm away from the crack tip

The peak values of normalized dynamic strain energy release rate [4] (DSERR) versus crack length are shown in Fig. 8 for the model under the three initial stress states, in which the time value in bracket denote the time point when the peak value arises. One can see that the maximum DSERR appears when the crack length if about 65 percent of the impact region radius. One can also see that the peak value of DSERR almost all appears around the time point t=1μs if the crack length is less than 75 percent of the impact region radius, while the time when peak value arises will be

postponed obviously with the increasing of crack length. This may partly due to the dispersion of the stress wave around the impact region edge.

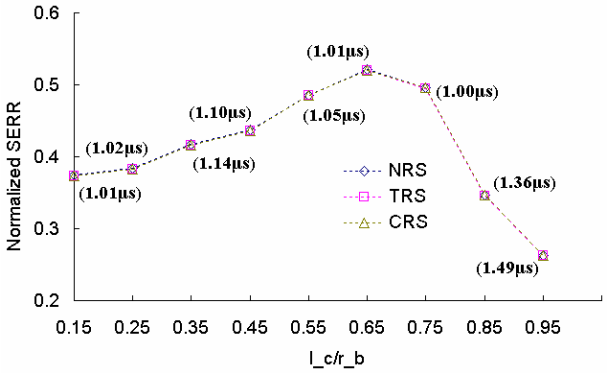

Fig. 8 Peak values of normalized strain energy release rate versus crack length

Anyway, these results in Fig. 8 indicated that the strain release rate is not altered by the in-plane residual stress in the film. Moreover, the interface stresses are neither influenced by the residual stress, as shown in Figs.9 and 10. However, the film stress will be greatly dependent on the residual stress states, which can be found in Fig. 11. A high degree of similarity of the three curves corresponding to the three initial stress states is also in the nature of things considering the ideal elasticity consumption adopted in this model.

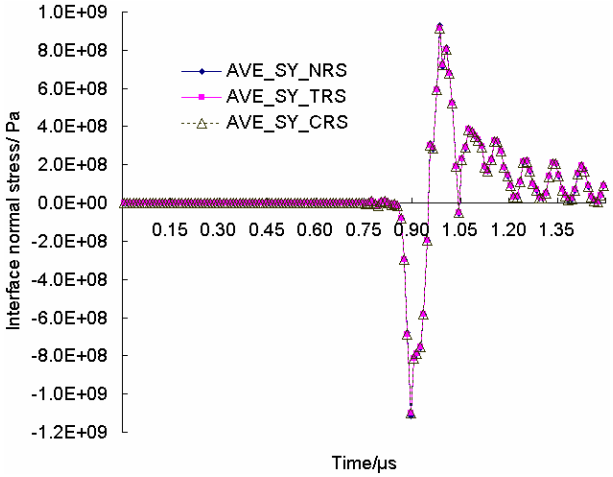

Fig. 9 Normal stress acting at the outer node close to the interface crack tip for the three initial states

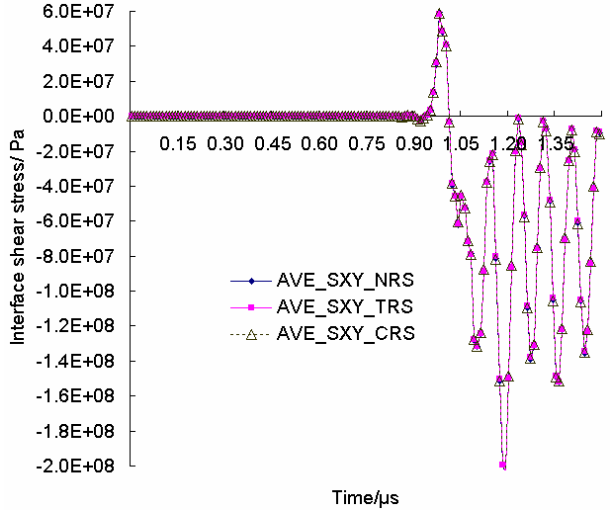

Fig. 10 Shear stress acting at the outer node close to the interface crack tip for the three initial states

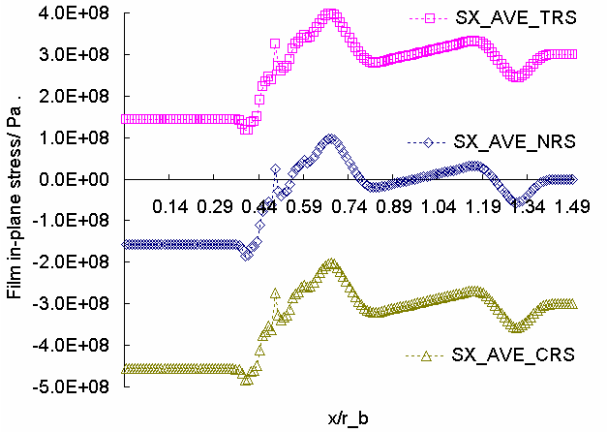

Fig. 11 Film stress at the instant t=1.03μs for the three initial states

For the moment, these results may be theoretically explained by the fact that the action direction of the residual stress is parallel to the interface. Therefore, the load component contributing to the interface separation developed by the in-plane residual stress would be slight when the deflection of the coating is small as considered in the present article. Even so, we hope more physical experimental outcome can be obtained to further support the present cognizance. Actually, a group of relevant tests are undertaken though much difficulty arises in the many sides of it, especially at the quantitative definition of the residual stress and the observation of the interface crack state.

It is also worthwhile to note that these theoretical results are basically drawn from linear dynamic analysis. Such linear modeling could not include the large deformation of the coating, which may lead to more obvious effect of the in-plane residual stress on the interface stress and therefore the interface crack behavior. Moreover, as reveled by Wu [3], the residual stress would influence greatly the total in-plane stress in the coating, which will affect the cracking of the coating under impact. Once the coating fractures around the impact region edge, the interface crack would be arrested around the edge. In comparison, if the coating can endure the impact and maintain intact, the partially released residual stress would affect greatly the interface crack behavior.

4. Conclusions

The model was set up to investigate the behavior of interface crack between the film and substrate subjected to stress wave, in which the crack surface contacting was considered. The dynamic deformation, stress and strain energy versus different crack lengths are calculated for the cases of three initial stress states, that is, initially stress free film, initially compressed film and initially tensioned film.

The history of the normal stress acting at the interface center node indicate that the interface crack permits the transmission of compressive stress while denies the transmission of tensile stress. The dynamic open displacement at the inner node 5μm away from the crack tip further reveals that the crack surfaces seldom contact after separating by the first compressive pulse.

The initial stress state would almost not influence the strain energy release rate of the interface crack or the interface stress around the crack tip if only small strain is taken into account in the modeling. Anyway, the film stress will be greatly changed by the residual stress, which will ultimately determine the fracture of the film.

Acknowledgements

This work was supported by the National Natural Science Foundation of China (Grant No. 11002145).

References

[1] Chen-Wu Wu, Zhi-Lin Wu, Kun Zhang, Guang-Nan Chen, Evaluation of film-substrate adhesion via impact using coated bullets. Journal of Mechanics of Materials and Structures, 10 (2009) 1703–1709.

[2] Zhi-Lin Wu, Chen-Wu Wu, Guang-Nan Chen, Kun Zhang, On a novel method of impact by a front-end-coated bullet to evaluate the interface adhesion between film and substrate. Progress in Organic Coatings, 68 (2010) 19–22.

[3] Chen-Wu Wu, Effect of residual stresses on spallation of the film under impact by coated bullet. Experimental and Applied Mechanics, 6 (2011) 239–252.

[4] De Xie, Sherrill B. Biggers, Jr., Calculation of transient strain energy release rates under impact loading based on the virtual crack closure technique. International Journal of Impact Engineering, 34 (2007) 1047–1060.

Experimental and numerical investigation of fibre-metal laminates during low-velocity impact loading

Yu E Ma[1,*] HaiWei Hu[1] XiaoFeng Xiong[2] QingMao Zhang[2]

[1] School of Aeronautics, Northwestern Polytechnical University, 127, YouYi XiLu, Xi'An, P.R. China,710072

[2] AVIC ChengDu Aircraft Design & Research Institute, ChengDu, P.R. China, 610041

* Corresponding author: ma.yu.e@nwpu.edu.cn

Abstract Fibre-metal laminates(FMLs) that consists of three layers of 2024-T3 aluminium alloy sheets and two layers glass/epoxy composite were studied in this work. The specimens were designed and produced. Low-velocity impact tests were performed successfully on FMLs, using an instrumented falling weight machine. For comparison purposes, similar tests were set up and were carried out on monolithic 2024-T3 sheets. Damage mode and feature of them were compared and studied. ABAQUS software was used to simulate dynamic response and damage evolution of FMLs during impact. It is shown that FMLs have better impact resistance properties than pure aluminum sheets because of the fibre. The damage of FMLs has three clear different steps to damage during impact. The simulation and experiment results agree well with each other.

Keywords Fibre-metal laminates(FMLs), low-velocity impact, damage mode

1. Introduction

Fibre-metal laminates(FMLs) is a type of hybrid material which consists of alternating layers of thin metallic sheets bonded together with fiber reinforced layers[1-8]. During the last decades the application of FMLs in various structures has become increasingly popular, especially in aerospace structures, for its improved fatigue and impact properties [1-5]. There are many articles about experimental [1-3] and modeling [6,7] investigation, regarding to impact resistance of FMLs. While there are a limited number of articles concerning theoretical modeling of impact response of FMLs [8]. Despite of lots of work concerning the impact of FMLs have done, their impact properties still need more understanding and attention.

In this study, low-velocity impact damage resistance of FMLs caused by dropped tools or collisions between service cargo (less than 10 m/s) in aircraft is investigated via both experimental and numerical simulations.

2. Experimental investigation

The FMLs studied in this work were consists of three layers of 2024-T3 aluminium alloy sheets 0.254 mm in thickness and two layers of [0/90/90/0] glass/epoxy composite with each prepreg 0.15 mm in thickness. For comparison purposes, monolithic 2024-T3 sheets of 2 mm in thickness were also studied. According to standard ASTM-D-7136[9]，All specimens were cut into rectangle panels with dimensions of 150×100 mm^2 . There are two types of FMLs specimens, type A with the rolling direction of aluminium sheet or 0 fibre direction parallel to the short side and type B parallel to the long side, and one type of aluminium specimens with rolling direction parallel to the short side. The low-velocity impact tests were conducted using an Instron-Dynatup 9250 instrumented drop-weight impact tester and used an impactor with a 16 mm diameter hemispherical steel head of a total

weight of 6.9025 kg. Tests were performed in the different energies ranging from 5J to 123J. The time history of impact force and impactor displacement was obtained by the test machine. After impact, the residual displacement, indentation depth and the crack length of back surface have been measured.

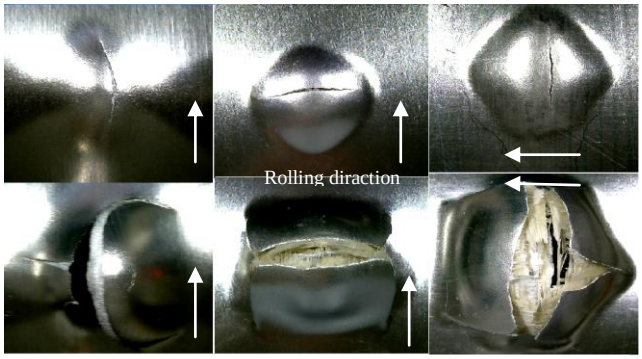

Figure 1. Damage at the non-impacted side of AL and FMLs

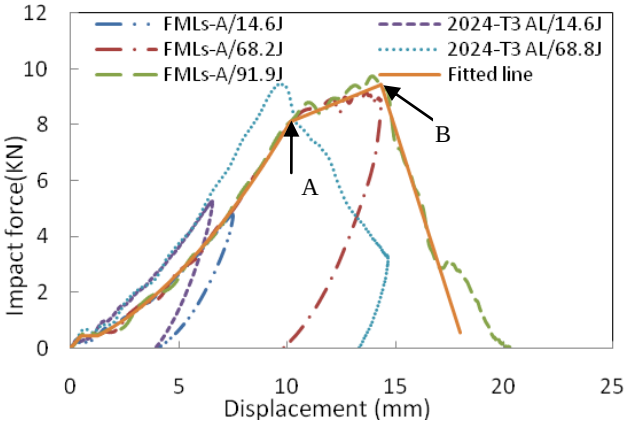

Figure 2.Force-displacement curves

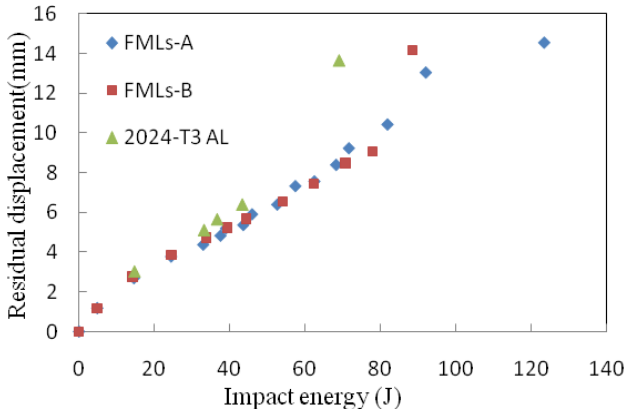

Figure 3.Residual displacement against impact energy

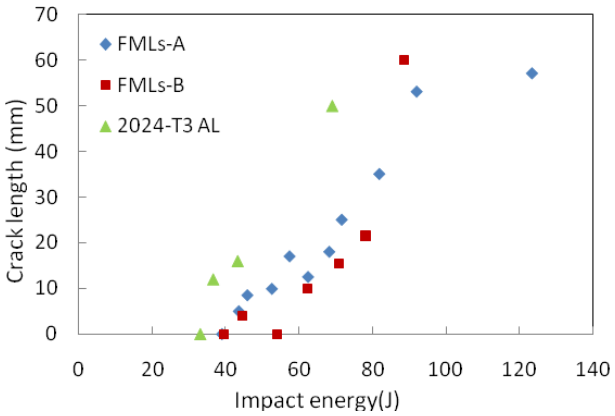

Figure 4. Crack length against impact energy

In Fig.1, damage after the different impact energy was shown and compared between FMLs and 2024T3 sheets. For monolithic 2024-T3 sheets, the first crack was found at non-impact side at impact energy of 36.5J, and almost completely penetrated at energy of 68.8J. The shape of crack was first in rolling direction and growth into "C" shape with high energies. Whereas, for both types of FMLs A and B, the initial crack at non-impact side were found at energy of 43.5J and crack at impact side appeared at 71.5J. It is differently from others work, the first crack found there were perpendicular to rolling direction of aluminium alloy sheets and the adjacent fibre direction. The shape of crack at non-impact side of FMLs was grown into "H" shape at energies of 71.5J. There are little difference between two types of FMLs for the force-displacement curves, indentation depth ,the crack length and others permanent were almost the same at one energy level (see figure 3 and 4). Force-displacement curves were compared in figure 2. It were shown that the route of them kept the same before crack were appeared during loading stage for FMLs and monolithic 2024-T3 sheets respectively, and the quadratic equation can be used to relate the force with displacement. While the path is not coincident in unloading stage, but their slope were basic paralleled that is the

same quadratic equation can be used [5]. There are two inflection points A and B at the force-displacement curves of FMLs. Inflection point A was caused by the crack generation at non-impact side of aluminium alloy sheet, and point B was the ultimate load of FMLs under low-velocity impact which was closed to the ultimate load of monolithic 2024-T3 sheets. The FMLs exhibit aluminium dominated behavior before first crack generated and exhibit fiber dominated failure behavior after the crack generated. The solid line in figure 2 was acquired by fitting the force-displacement curves of FMLs using quadratic and liner segmented function.

3. Numerical simulation

To clarify the relationship between the internal and external damages, dynamic explicit analysis was carried out using the finite element software ABAQUS. The impactor and each layer in three dimensions in the FMLs were modeled as separate parts, see figure 5. Interface layers were inserted into each layer to model interlaminar delamination. The boundary conditions of model FMLs were held four edges fixed. An initial velocity in the vertical direction is prescribed to the impactor, simulating the impact velocity measured during the tests.

The Isotropic elasticity and metal plasticity with ductile damage initial criterion and linear fracture energy damage evolution were used to simulate aluminum alloy failure mechanisms. Orthotropic elasticity in the plane stress field was used for each of the prepreg layers and interfaces layers. The Hashin damage initiation criteria and fracture energy damage evolution implemented in ABAQUS was applied to each ply in the prepreg layers to simulate their failure mechanisms. While the failure of interface layers were modeled as cohesive layers with the max traction-separation damage initial criteria and linear fracture energy damage evolution laws [10].

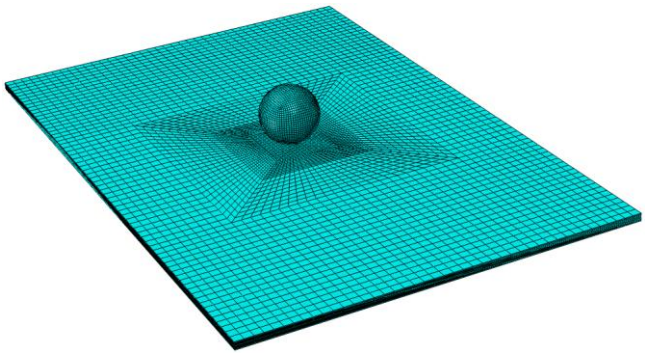

Figure 5. Finite element model

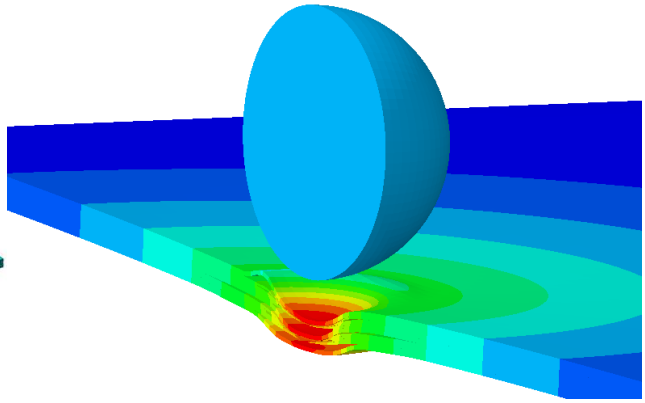

Figure 6. The failure mode of the FMLs subjected to 14.6J impact

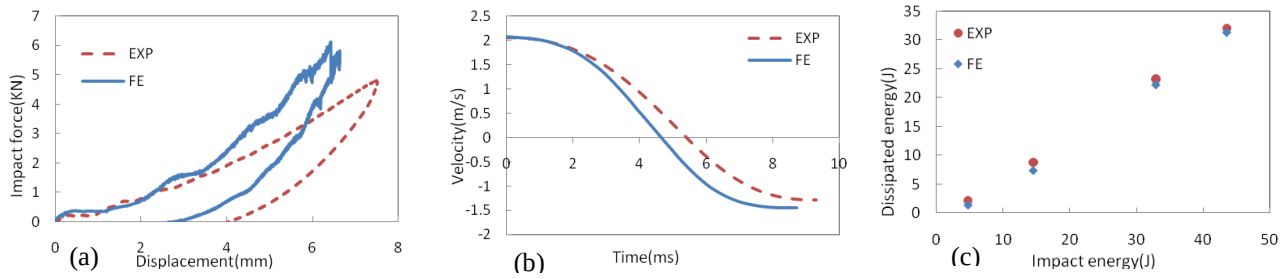

Figure 7. The *F-d* (a), *v-T*(b) and U_d *-U*(c) curves of experiment and finite element results

The finite element model corresponds well with the test results reasonably. Figure 6 shows the

damage of finite element model subjected to the impact energy of 14.6J. This half-specimen plot shows residual depth and interlaminar delamination occurring after impact completed. The experimental and simulated impactor reaction force-displacement and velocity histories curves corresponding to14.6J impacts on the FMLs were plotted in Figure 7(a, b). The experimental tests were not correctly replicated by the simulation results for the maximum impact force was higher, the maximum displacement was lower and impact time was shorter, while the tendency of them was reasonable the same, and the final velocities were much at one, that is the dissipated energies were almost the same. The dissipated energies against several impact energies were plotted in figure 7(c).

4. Conclusion

This study presented an experimental and numerical investigation on low-velocity impact behaviors of the fibre metal laminates (FMLs). Experimental results show that the impact resistance of FMLs was higher than monolithic 2024-T3 sheets for the first crack energy about 15% higher and completely penetration energy about 34% higher. While, the impact resistance of two types of FMLs, which were cut into rectangle panels with the long edge parallel to 90 and 0 fibre separately, were almost the same. Good agreement between finite element results and experimental results such as the internal delamination and dissipated energies were obtained, and hence the model was validated.

Acknowledgement

This paper is sponsored by “National Natural Science Foundation of China (11002111)

References

[1] A.volt, Impact loading on fibre mental laminates[J]. Int. J. Impact Engng Vol. 18, No. 3, pp. 291-307, 1996.

[2] A.volt, M. Krull, Impact damage resistance of various fibre mental laminates[J]. J. PHYS IV FRANCE, 7(1997) C3-1045-1050

[3] G.Caprinoa, G.Spataro, S.D.Luongo, Low-velocity impact behaviour of fibreglass–aluminium laminates[J]. Composites: Part A 35 (2004) 605–616

[4] R.C.Alaerliesten, Fatigue crack propagation and delamination growth in GLARE[D]. PhD Thesis, Delft University of Technology, Delft, 2005.

[5] G. Caprino, V. Lopresto, P. Iaccarino, A simple mechanistic model to predict the macroscopic response of fibreglass–aluminium laminates under low-velocity impact[J]. Composites: Part A 38 (2007) 290–300

[6] H. Nakatani, T. Kosaka, Damage characterization of titanium/GFRP hybrid laminates subjected to low-velocity impact [J], Composites: Part A 42 (2011) 772–781.

[7] J.Y.Fan, Z.W.Guan , W.J.Cantwell, Numerical modeling of perforation failure in fiber metal laminates subjected to low velocity impact loading[J]. Composite structures 93 (2011) 2430-2436

[8] M. Sadighi, R.C.Alderliesten , R.Benedictus, Impact resistance of fiber-metal laminates: A review [J]. International Journal of Impact Engineering 49 (2012) 77-90

[9] ASTM Committee, Designation: D 7136/D 7136M-2005.Standard test method for measuring the damage resistance of a fiber-reinforced polymer matrix composite to a drop-weight impact event[S].United States.

[10] ABAQUS 6.10 documentation.

Analysis of the synergetic effects of blast wave and fragment on concrete bridges

Haiqing Zhu[1,*], Xiedong Zhang[1], Ying Li[1]

1. School of Transportation, Wuhan University of Technology, Wuhan 430070, China

* Corresponding author: zhq7751@163.com

Abstract: The complicated loading caused by explosions is not well understood, so the effect is often simplified when calculated. In order to increase the bridge protective level, a penetrating study of the mechanism of the synergetic effect of blast wave and fragment is necessary. Numerical simulation is used to analyse the dynamic response characteristics and the damage performances of the reinforced concrete bridge. Three conditions were designed to research the synergetic effect of the blast wave and fragment on the bridge. The research indicates that the synergetic effect is larger than the arithmetic sum of the effect of blast wave and fragment separately, which should be taken into account in the protection of bridge.

Keywords: Blast wave, Fragment, Synergetic effect, Dynamic response

1. Introduction

Several decades has witnessed that destroying bridges is the best efficient way to restrict the enemy for cutting off the transportation line and blocking supply in the local conflict. Moreover in many developing areas, infrastructure construction is blooming, blast is the fastest way to demolish the old un-qualified bridges. When bomb or missile exploding, blast wave and fragment are produced and both them impacted on the bridges. In recent years, either blast destroy bridges or fragment penetrate concrete is studied very well. But the complicated combined loading caused by synergetic blast wave and fragment is not well known. However design a blast test to research the synergetic effect is insecure and expensive. Numerical analysis using AUTODYN is the appropriate mean to study the mechanism before material test.

2. Loading characteristics

2.1 Blast wave characteristics

When explosions occur, the energy released at a lighting speed, which produce gas mixture with high temperature (3.5×10^3—4×10^3℃) and high pressure (1×10^4—3×10^4MPa). Since the air initial pressure and density is low, explosive product diffused at a high speed will compress the air nearby, increasing the air pressure, density and temperature drastically, which will develop into blast wave. The blast wave spread rapidly, during the energy spread and deplete, the speed of the blast wave will decay rapidly. When the volume of the explosive product expands big enough, the pressure in it will drop to the original level P_0 of the air nearby. However the product volume will keep expanding to a maximum because of the inertia effect. Then the negative pressure area will occur because the average pressure of the product is lower than the original pressure P_0, and the air nearby will compress the product conversely, which will increase the product pressure. For the air, the first expansion—compression impulse is worthy of study. Classical blast wave spread in air is shown as figure 1.

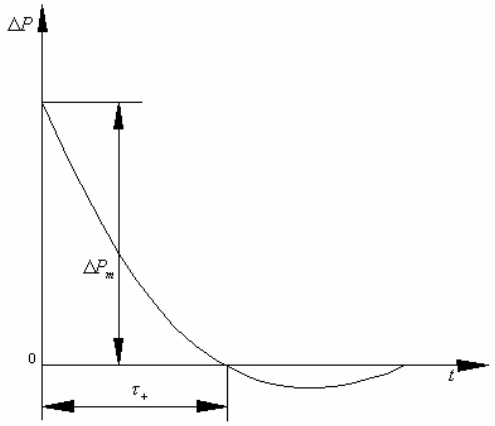

Figure.1 Pressure maximum of the blast wave

The expansion law of the explosive product can be simplified to the polytropic index equation of state [1].

$$PV^{\gamma} = const \tag{1}$$

P is the pressure of the explosive product; V is the volume of the unit quality; γ is the polytropic index, related to the component and density of the explosive product, γ enlarges when the density value increase.

AUTODYN is precise in explosions analysis for its BLAST boundary conditions. In this research, 2kg TNT exploding 2m above the bridge is simulated by AUTODYN [4].

2.2 Fragment characteristics

A large amount fragments are produced when explosion take place, these fragments with high speed will penetrate the bridges.

Mott formula is the most widely used to calculate the fragments' quality [1].

$$\mu^{0.5} = Kt_0(t_0 + d_i)^{1.5}(1 + \frac{M_0}{2m_t})^{0.5} \Big/ d_i \tag{2}$$

$$m_p = 2\mu \tag{3}$$

m_t is the payload quality(kg); m_p is the fragment average quality(kg); t_0 is the thickness of the cartridge case(m); d_i is the internal diameter of the cartridge case(m); K is the explosive material factor($\mathrm{kg}^{1/2}/\mathrm{m}^{3/2}$).

Gurney formula considering cylindrical payload is used to calculate the fragments' initial speed [1].

$$v_0 = \sqrt{2E}\sqrt{\frac{C/m_t}{1 + 0.5C/m_t}} \tag{4}$$

v_0 is the initial speed of the fragments(mgs^{-1}); C is the quality of the explosive materials ($kggm^{-3}$);

$\sqrt{2E}$ is the Gurney factor(or Gurney specific energy), Gurney found the linear relation between the Gurney factor and explosive speed D_e through many tests.

$$\sqrt{2E}=520+0.28D_e \tag{5}$$

In order to simplify the research, this paper chooses spherical fragments with diameter 0.05m and initial speed 1700 ms^{-1}.

3. Models and material parameters

3.1 Bridge model

In order to explain the mechanism clearly, a simple square section with 1m length of each side is used. The superior border has 3 longitudinal steels with diameter 6mm and inferior border has 3 longitudinal steels with diameter 12mm, shown as figure 2.

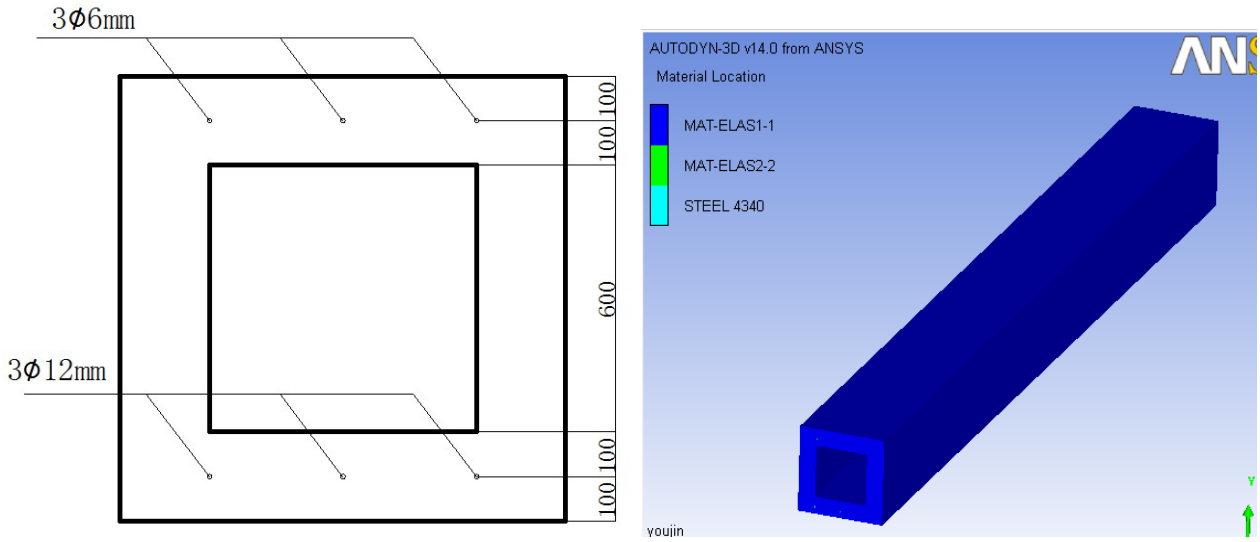

Figure.2 Beam section and 3-D model

3.2 Constitutive relation of the concrete

RHT model [2] was built by Riedel, Hiermaier and Thoma in 1999. The premise of the model formula is that the internal energy of the porous-material and compact-material under the same pressure and temperature are equal. The thermo-motive performances of the concrete under high pressure and the compression behaviors under low pressure will be described clearly by RHT. When the concrete is compacted enough, its state equation is shown as figure 3.

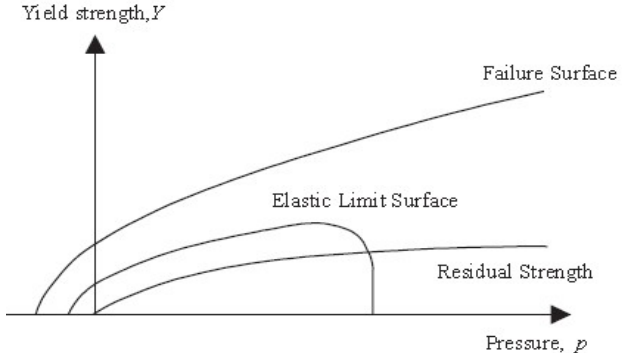

Figure.3 RHT constitutive relation of concrete

3.3 Dynamic constitutive relation of the fragment and steel

In order to describe the structure response to the explosive impact load, several conditions should be taken into account: the strain strengthening phenomenon of the material, the material behaviors under large strain, high strain rate and high temperature, even the material behaviors under the influence of the strain state change and the load history change.

Johnson-cook (JC) strength model [3] is widely used in commercial nonlinear finite-element because of its simple form, distinct concept and precise veracity. JC model is a kind of empirical viscoplasticity constitutive relation, it can describe the hardening effect, strain rate effect and softening temperature effect of metal materials very well.

$$\sigma = (A + B\varepsilon^{n})(1 + C\ln \dot{\varepsilon}^{*})(1 - T^{*m}) \tag{6}$$

$$T^{*} = (T - T_{r})/(T_{m} - T_{r}) \tag{7}$$

σ is equivalent stress(N), ε is equivalent strain, $\dot{\varepsilon}^{*} = \dot{\varepsilon}/\dot{\varepsilon}_{0}$ is dimensionless plastic strain rate, $\dot{\varepsilon}$is static experiment strain,， T is the sample surrounding temperature, T_r is room temperature, T_m is fusion point.

$(A + B\varepsilon^{n})$ describes strain strengthening effect; $(1 + \ln \dot{\varepsilon}^{*})$ describes strain rate strengthening effect; $(1 - (T^{*})^{m})$ describes softening temperature effect. Parameter value shown as follows.

Table1 JC constitutive relation parameters of 4340steel

A(MPa)	B(MPa)	n	C	m	$\dot{\varepsilon}$	T_m (K)
791	510	0.26	0.014	1.03	1	1793

4. Results and analysis

4.1 Damage process of the synergetic effect

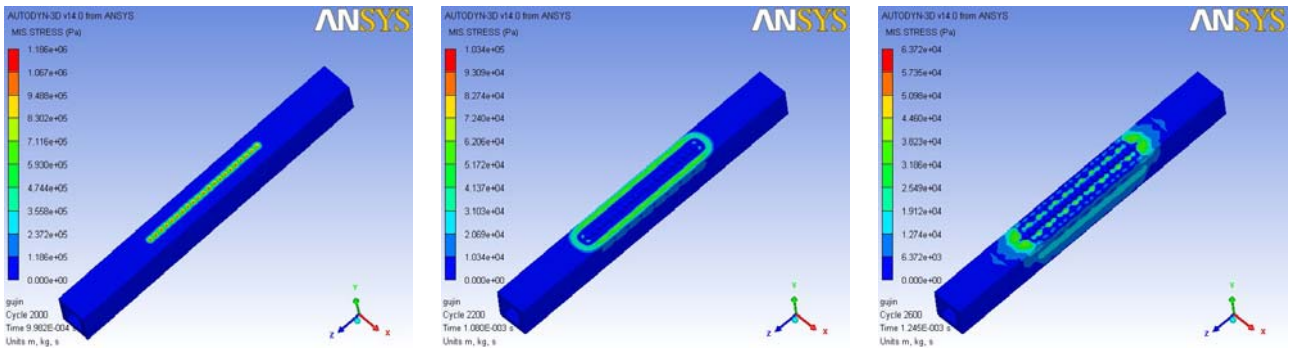

0.998ms 1ms 1.245ms

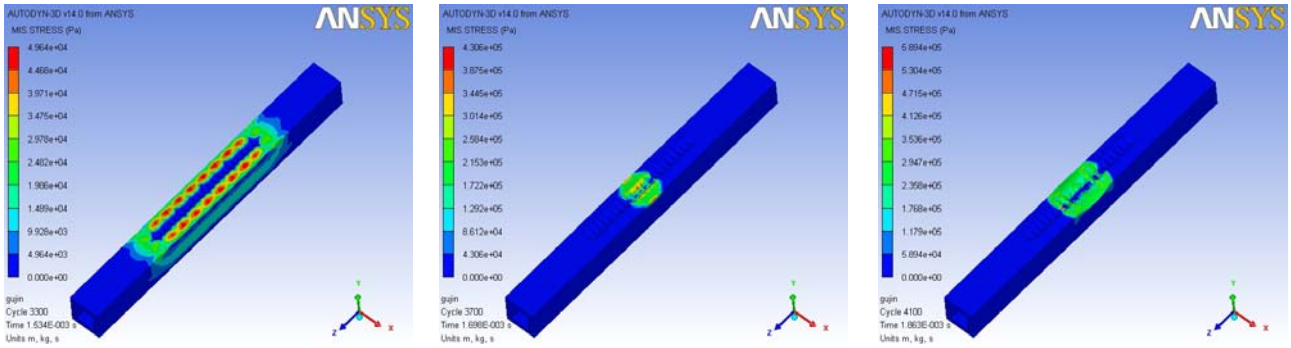

Fig.4 Damage process of the synergetic effect

Because the blast wave and fragments arrive at the bridge at different time, the failure mechanism of the bridge will change at different moment. The failure process of the bridge is divided into 4 stages in AUTODYN.

1st stage(0.998ms-1.245ms): The fragments arrive at the bridge upper surface, the stress wave begin to spread from the upper surface to the lower border in the beam. The fragments with high speed begin to smash the beam to pieces.

2nd stage(1.245ms-1.698ms): The fragments penetrate the beam further, reaching the longitudinal steels, leading a obvious deformation to the longitudinal steels. And the stress wave spread along the longitudinal steels and stirrups, the stress in the corner of the stirrups become larger.

3rd stage(1.698ms-3.33ms): The crest of the blast wave arrive the bridge surface, encountering with the fragments and effect the beam together. Some local deformations begin to occur in the concrete, and expand towards the lower border of the beam. The mid-span of the beam begin damaged.

4th stage(3.33ms- last): Because the fragments are crushed in pieces and its speed decreased, the vibrating beam will became static under the remainder blast wave and its own inertia gradually.

4.2 Failure modes contrast

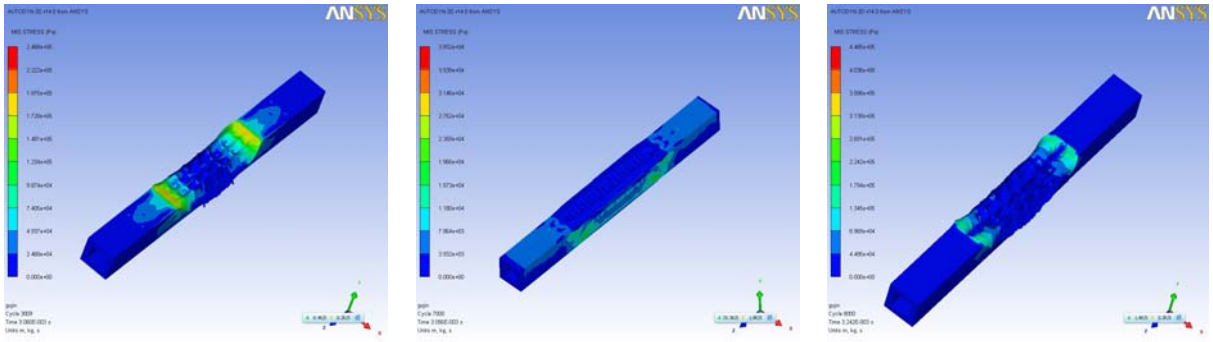

(a)blast loading (b)fragment loading (c)combined loading

Fig.5 failure modes of the concrete beam

Fig.5 (a) when blast loading effect on the bridge separately, the largest deformation occurs in mid-span, steels restrict the beam became more damaged. Some beam border became damaged.

Fig.5 (b) when fragment loading effect on the bridge separately, some pits and holes occur on the beam surface, the longitudinal steels become curved and stressed the main pressure. Fragments pieces splash nearby during the penetrating process.

Fig.5 (b) when combined loading effect on the bridge, the beam damaged seriously. The longitudinal steels yield under the fragments effect and then expand the deformation because of the blast impact wave. The biggest displacement occurs in mid-span, many pits and holes occur on the beam surface, and seriously damage the beam border.

4.3 Dynamic response of the bottom midpoint

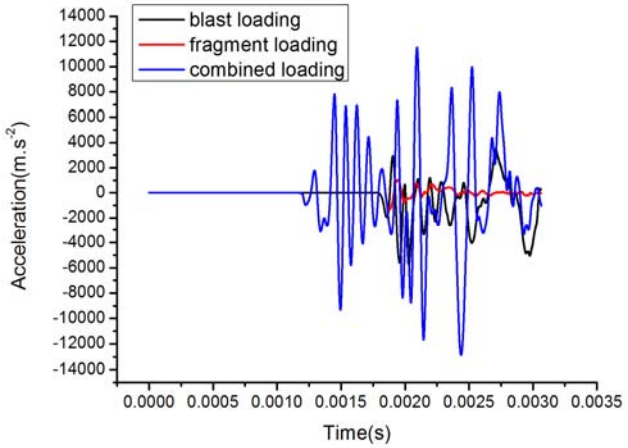

Fig.6 acceleration of the bottom midpoint

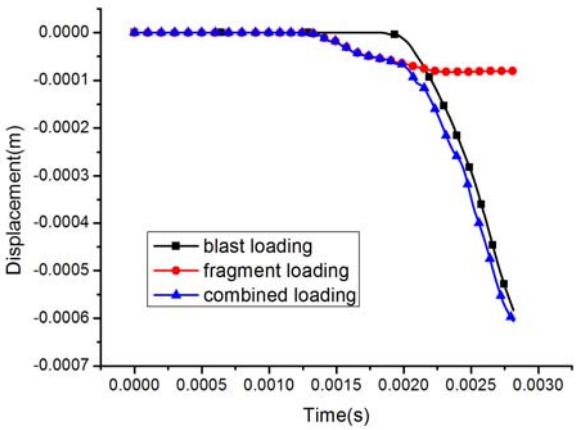

Fig.7 displacement of the bottom midpoint

Figure 6 and 7 indicate that the acceleration response under synergetic effect is larger than the response under fragment or blast wave effect separately, further more larger than the sum of the separate responses. And the displacement response under the synergetic effect is larger than the separate responses.

5. Conclusions

(1)The concrete bridges will be damaged seriously by the synergetic effect of blast wave and fragment.
(2)The synergetic effect to damage the bridge embodied in two ways: impact on the global bridge and destroy the local beam, which will decrease the loading capacity of the bridge.
(3)The acceleration changed seriously under the synergetic effect which should be taken into account in antiknock design.

Reference

[1] Guowei Zhang. Terminal Effect and Application Technology[M].Beijing: National Defence Industry Press, 2006.
[2] Holmquist T.J, Johnson G.R, Cook W.H.A computational constitutive model for concrete subjected to large strains,high strain rates and high pressures[J].14th International Symposium on Ballistics,1995,12(2):591-600.
[3] GR Johnson, W.C., A Constitutive Model and Data for Metals Subjected to Large strains,High Strain Rates and High Temperature, in Proceedings of the seventh international symposium on ballistics. 1983: Netherland.p.541-547.
[4] Century Dynamics AUTODYN Theory Manual, Revision 6.1[M]. California: San Ramon, 2006:25-87.

Effect of Plastic Anisotropy on Shear Localization and Fracture in Automotive Sheets

Jidong Kang[1,*], Raja K. Mishra[2], David S. Wilkinson[3]

[1] CanmetMATERIALS, Natural Resources Canada, Hamilton L8P 0A5, Canada
[2] Chemical and Materials Laboratory, General Motors R&D Center, Warren 48090-9055, U.S.A.
[3] Department of Materials Science and Engineering, McMaster University, Hamilton L88 4L7, Canada
* Corresponding author: jkang@nrcan.gc.ca

Abstract Tensile instability, as characterized by the Considère law, is one of the factors governing formability of metallic sheets. During tensile deformation, material thins in a narrow band due to shear localization, prior to final fracture. Strain rate value within the localized necking band tends to be higher than outside it and final fracture is governed both by the nature of the shear localization as well as the strain rate differential between the neck and the material outside the neck. This paper reports the dependence of shear localization and fracture on plastic anisotropy of the material. Three types of automotive sheet materials, namely IF steel (BCC structure), AA5754 aluminum alloy (FCC) and AZ31 magnesium alloy (HCP) are examined. Digital image correlation is used to follow the development of deformation pattern during tensile tests. The results show that both narrowing and thinning of the tensile sample occur in IF steel, while only thinning occurs in AA5754 and only narrowing occurs in AZ31. These differences arise from the differences in the plastic anisotropy of the three materials, as measured by their r-values. Even though all three materials exhibit ductile fracture, the damage and fracture processes in the three materials differ from each other.

Keywords Shear localization, Plastic anisotropy, automotive sheets, r-value, fracture

1. Introduction

In response to the more stringent regulations on fuel consumption in vehicles, lighweighting via the utilization of aluminum and magnesium alloys are being seen to replace steels for automotive body structural applications. Aluminum can reduce the vehicle weight by 20-30% while magnesium 40-50% compared to a full steel vehicle. A 10% weight reduction will save 6-8% in fuel and related GHG emissions. However, formability of aluminium and magnesium sheets is inferior to that of conventional interstitial free (IF) steel. The formability of alloy sheet can be limited either by instability or fracture depending on the operation [1]. The forming limit is usually defined as the locus in uniform strain space required for the onset of localized necking while the fracture limit is defined as that required for material separation. In uniaxial tension strain path, tensile instability or diffuse necking, as characterized by the Considère law, is one of the factors governing formability of metallic sheets. Further, material thins in a narrow band due to shear localization, prior to final fracture. Strain rate value within the localized necking band tends to be higher than outside it and final fracture is governed both by the nature of the shear localization as well as the strain rate differential between the neck and the material outside the neck. This forms the foundation of the so-called Marciniak-Kuczynski (M-K) approach [2] for forming limit diagram (FLD) analysis. While M-K approach has been successfully applied to prediction of FLD of numerous sheet materials including steels and aluminum alloys, it is commonly recognized that the success of such approach for aluminum alloys depends significantly on the selection of yield functions that represent the effect of plastic anisotropy and texture. On the other hand, whether or not thinning occurs in magnesium alloys is challenged by many experimental observations. For example, for AZ31 sheets, it has been reported that very little thinning occurs during uniaxial tension at room temperature [3] and the deformation process becomes more complicated as a variety of deformation mechanisms become activated at

different elevated temperatures [4-5].

This paper reports the dependence of shear localization and fracture on plastic anisotropy of the material. Three types of automotive sheet materials, namely IF steel (BCC structure), AA5754 aluminum alloy (FCC) and AZ31 magnesium alloy (HCP) are examined. Digital image correlation (DIC) [6-7] is used to follow the development of deformation pattern during tensile deformation. The role of anisotropy in relation to damage and fracture process is also examined through a variety of surface analysis techniques including optical microscopy, scanning electron microscopy (SEM), electron backscatter diffraction (EBSD) and X-ray tomography.

2. Experimental

The three sheet materials used in the present study were 0.7 mm thick IF steel, 2mm thick AA5754 in O-temper and 2mm thick AZ31 in O-temper. IF steel has a BCC structure, AA5754 FCC and AZ31 HCP.
The initial texture is measured by EBSD using TSL OIM software for all three materials. Uniaxial tensile tests are performed at room temperature using ASTM E-8 specimens. Prior to the tests, an ink pattern is applied to each specimen surface. A commercial available optical strain measuring system, Aramis based on digital image correlation is used for DIC measurements.

Plastic anisotropy of metallic materials is usually represented by the plastic strain ratio, r-value, that is defined as [8]

$$r = \frac{\varepsilon_w}{\varepsilon_t} = -\frac{\varepsilon_w}{\varepsilon_l + \varepsilon_w} \tag{1}$$

where ε_l, ε_w, and ε_t are longitudinal, width, and thickness strains, respectively. As thickness strain is difficult to measure, longitudinal and width strains are usually measured to determine the r-value based on the incompressibility criterion along with the assumption of uniform strain distribution over the gage length [8]. In practice, r-value represents material resistance to thinning. In steels, it is generally accepted that higher the r value, higher the FLD.

However, in materials with small amount of plasticity, r-value is not a sensitive parameter. Another parameter, the contraction ratio, q-value, similar to a Poisson's ratio in elasticity, has been proposed and defined as [9]

$$q = -\frac{\varepsilon_w}{\varepsilon_l} \tag{1}$$

It is easily seen that $q=r/(1+r)$.

After tensile tests, necked and fractured specimens are collected for damage and fracture observations using optical microscopy, SEM and X-ray tomography.

3. Results and discussion

Fig. 1 shows the initial texture of IF steel, AA5754 and AZ31 sheets, the later having the basal texture while the former sheets exhibit typical rolling texture.

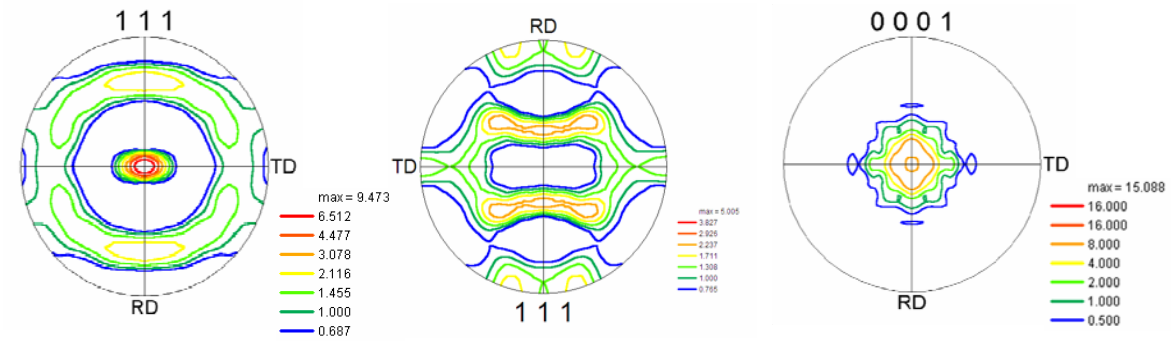

(a) IF steel (b) AA5754 (c)AZ31

Fig. 1 Initial textures of the three alloys

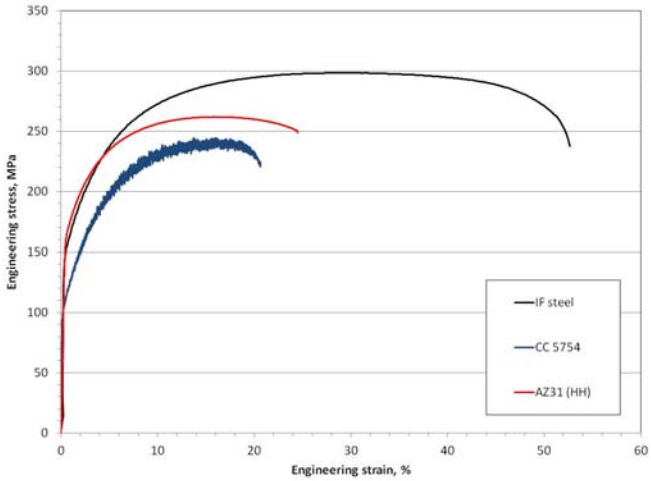

Fig. 2 Engineering stress – engineering strain curves of three alloys

From the engineering stress-engineering strain curves of the three materials (Fig. 2), it is seen that the uniform strain to ultimate tensile stress is 29.6%, 18.0% and 15.8% for IF steel, AA5754 and AZ31, respectively. This is commonly accepted as the strain where diffuse necking is initiated in the materials.

While only diffuse necking can be identified on stress-strain curves, the sequence of deformation occurring during tensile tests, especially the initiation and development of localized necking can be clarified for each material from tensile strain maps obtained from DIC measurements (Fig. 3).

From Fig. 3, it is seen that both thinning and narrowing occurs in IF steel, only thinning in AA5754 and only narrowing in AZ31 following the diffuse neck formation. It is also seen in Fig. 3 (a) and (c) that localized necking occurs in both IF steel and AA5754 before fracture, however, no localized necking occurs in AZ31.

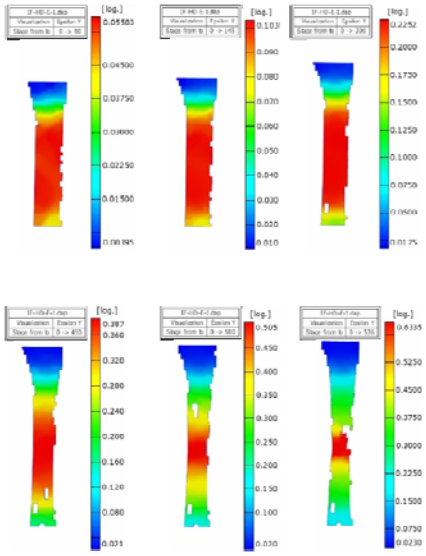

(a) Tensile strain maps in IF steel

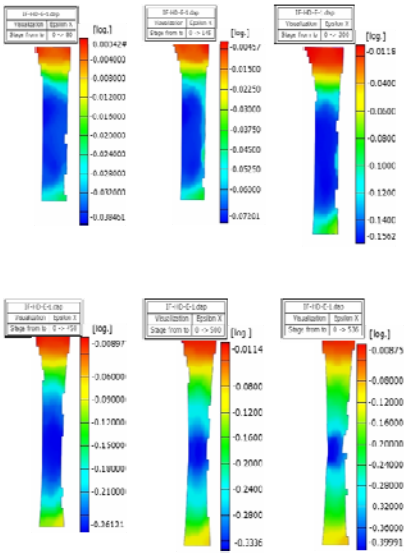

(b) Width strain maps in IF steel

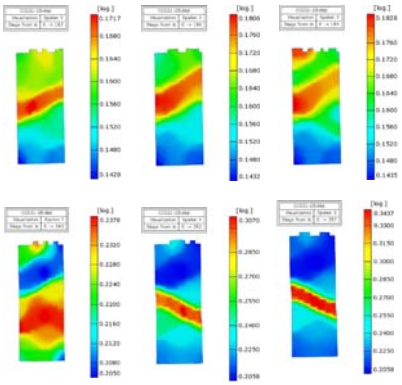

(c) Tensile strain maps in AA5754

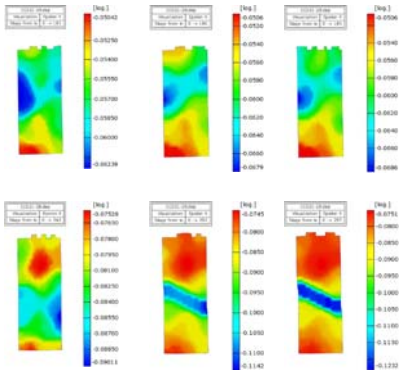

(d) Width strain maps in AA5754

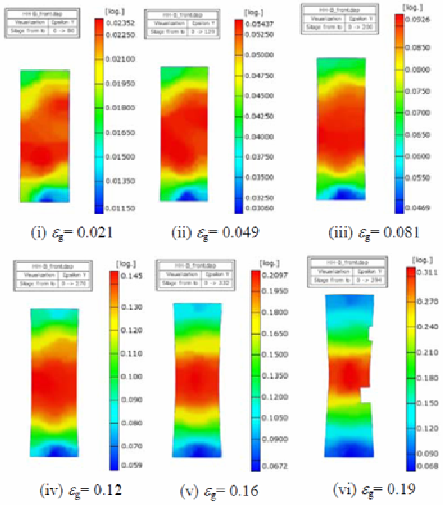

(e) Tensile strain maps in AZ31

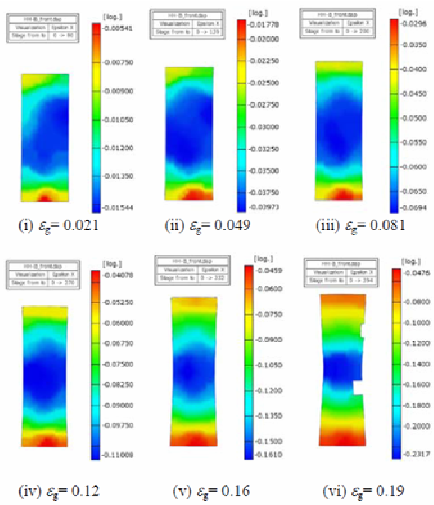

(f) Width strain maps in AZ31

Fig. 3 Deformation development occurring during uniaxial tensile tests

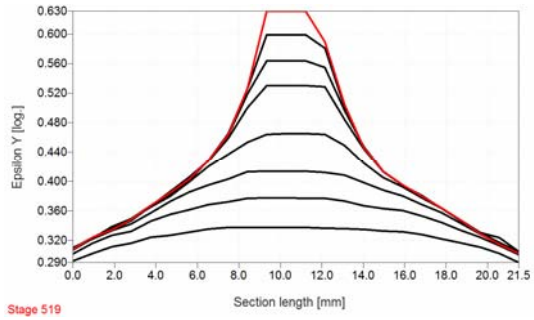

(a) IF steel tensile strains

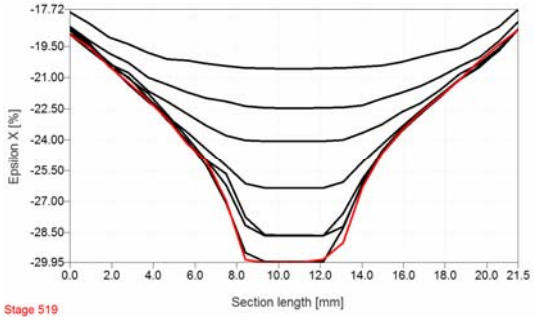

(b) IF steel width strains

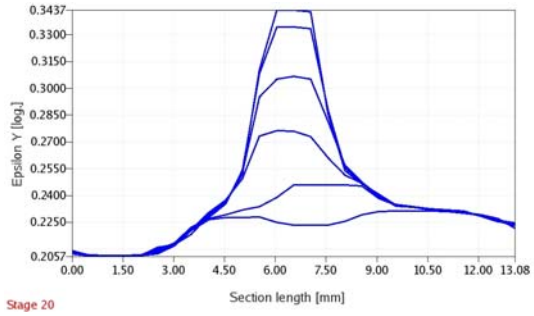

(c) AA5754 tensile strains

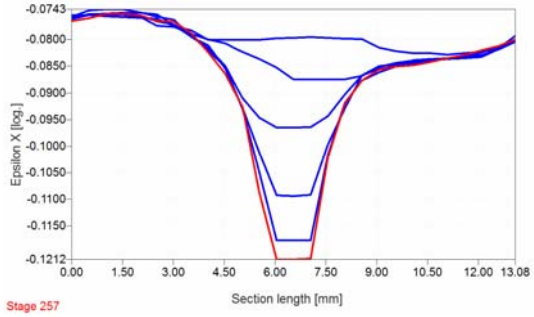

(d) AA5754 width strains

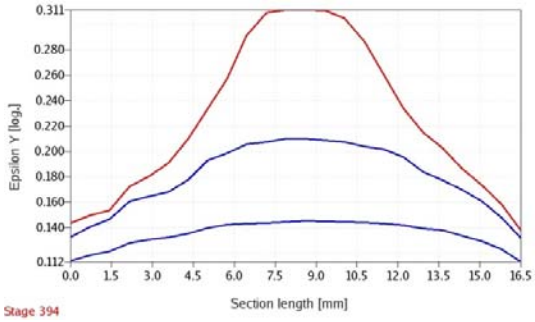

(e) AZ31 tensile strains

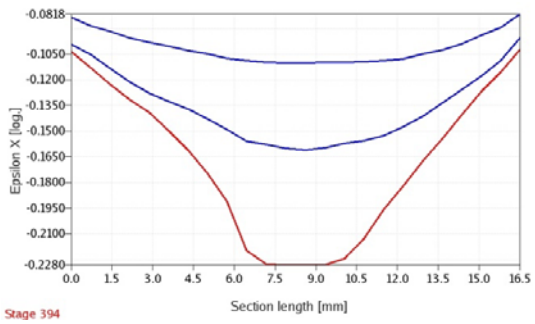

(f) AZ31 width strains

Fig. 4 Line scan of cross section for post-necking strain development in three alloys

Fig. 4 shows the line scans taken through the strain maps at different stages of the deformation. In Fig. 4 (a) and (c), correspondng to IF steel and AA5754, tensile strains become intense in a more and more narrow band while strain outside this area remains unchanged or even is slightly lowered. These are the typical signatures of localized necking in metallic materials. Together with Fig. 3 (a) and (c), it is concluded that localized necking occurs in IF steel and AA5754 sheet materials. However, when looking closely at AZ31 line scan data in Fig. 4 (e) and (f), one observes that both tensile and width strain keep evolving as the global strain increases. This indicates that no localized necking occurs in AZ31. Instead, it transits directly from diffuse necking into final fracture process [3, 14].

From the local strain development (Fig. 5), it is seen that deviation between local and global strains is more significant in IF steel and AA5754 comparing to AZ31.

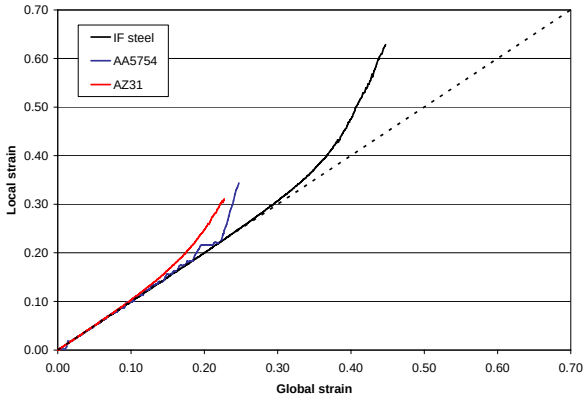

Fig. 5 Local versus global strain in three alloys

It is well known that in AA5754 deformed at room temperature at quasi-static strain rates, premature necking occurs due to the Portevin-Le Chatelier (PLC) effect (e.g. illustrated in the first three maps in Fig. 3 (c)) [1]. A simple model has been established to account for the effect of PLC band strain on reduction of uniform strain to UTS [1]. It is also reported that at a certain combination of temperature and strain rate (e.g. -50 °C and 6×10^{-4}/s), the PLC effect and accompanying premature necking can be removed [1]. It is also reported that the formability of AA5754 can be improved by enhancing specific texture components (e.g. cubic texture) [10]. Traditionally, it is accepted that the higher plastic strain ratio, i.e. r-value, the better formability. In the discussion below, the relationship between plastic anaisotropy and formability is further examined in light of the above observations.

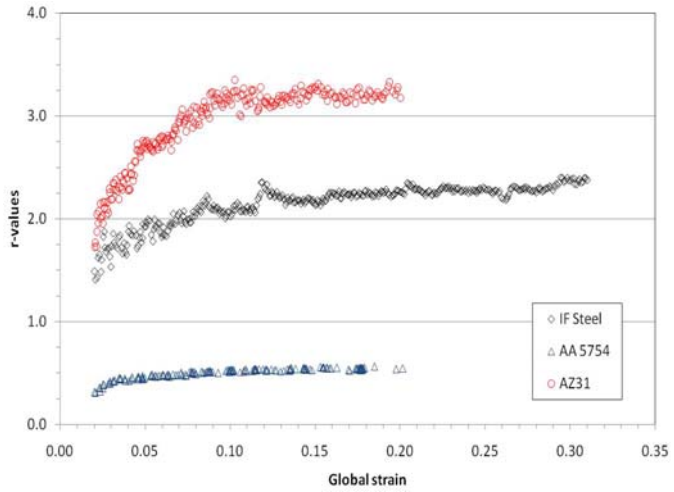

Fig. 6 r-values development in three alloys

When plotting the r-value evolution in the three materials used in the present study (Fig. 6), it is seen that the r-value in AZ31 is the highest (3.2). However AZ31 has the lowest formability in the uniaxial tensile deformation. Eq. (1) is derived with the assumption that material deforms in

length, width and thickness directions and when the material deforms more in width direction than thickness direction to produce a higher r-value, it has improved formability. The contribution of each strain component to r-value and q- value may provide insight into the origin of the anomalous relationship between formability and r-value for AZ31. Fig. 7 shows the relationship between the q-value and strain for the three materials.

It is seen in Fig. 7 that AZ31 has the highest q-value, i.e. most of the deformation is actually concentrated in the width direction while AA5754 has the lowest q-values, with least deformation along the width direction.

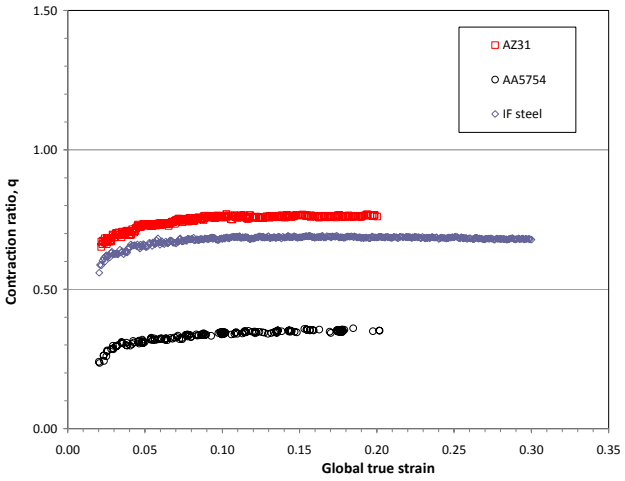

Fig. 7 q-value development in three alloys

Fig. 8 shows the thickness strain in the three materials calculated using the incompressibility criterion. It is clear that there is very little thinning in AZ31, consistent with the q-value results in Fig. 7.

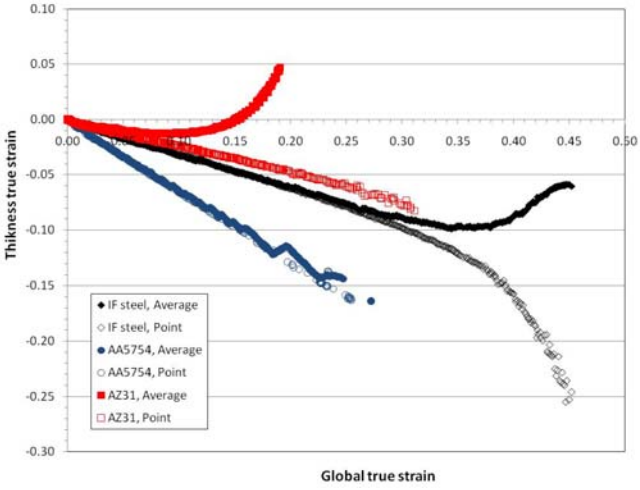

Fig. 8 Thickness strain evolution in three alloys. Note that ‘‘average’’ denotes thickness strain estimated from both tensile strain and width strain from given gage lengths while ‘‘point’’ denotes thickness strain at a point within necked area.

The relationship between damage and shear localization in literature continues to remain ambiguous. Ductile fracture process generally includes three stages, namely void nucleation, void growth and void coalescence. A number of continuum mechanics models have been developed [11-12] to describe this sequence of events. However, the interplay between shear localization and void formation often depends on the materials studied and this effect is not captured in continuum mechanics (macro scale) models. There is very little quantitative data on the development of the complex sequence of damage events in materials such as the ones studied here to ascertain if the existing models can capture any differences in the sequence of events arising from the anisotropic nature of the deformation described above at the microscale.

In IF Steel, limited void growth from aluminum oxide particles has been observed [13] prior to localization in uniaxial tension. It is concluded that damage does not play a role before (or upon) localization, but only beyond localization (Fig. 9 (a) and (b)) [13]. It is in contrast with the observations in other steel alloys [11].

In AA5754, void nucleation is observed only in the very final stage of the tensile deformation and the damage is very localized near the fracture surface [14-16]. This suggests that damage may be a consequence of the fracture process rather than a trigger that determines material ductility (Fig. 9 (c)). Further, it is observed that particle distribution as random particles or in stringers affects the final fracture process. For example, anisotropic distribution of stringers in continuous cast AA5754 sheets significantly reduces the fracture strains [17].

In AZ31, it is revealed by X-ray tomograpghy that microcracks formed at the later stage of diffuse necking (Fig. 9 (d)) contribute to the final fracture without transition into localized necking [18].

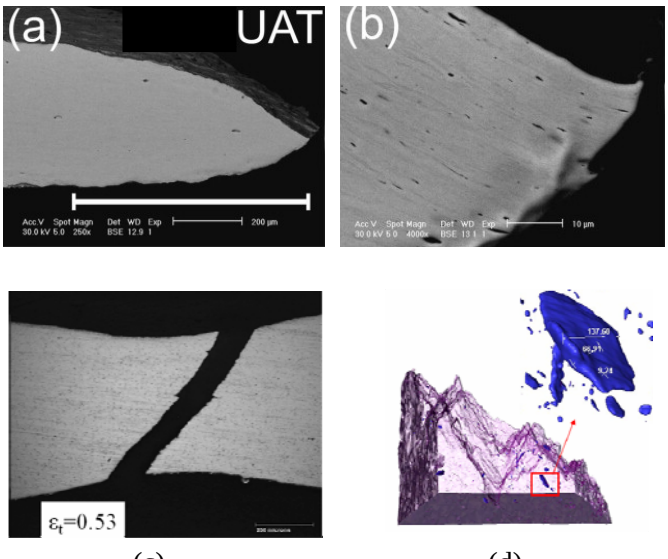

(c) (d)

Fig. 9 Damage and fracture in (a) and (b) cross section of a fractured IF steel specimen [13] showing void growth within localized shear bands, (c) cross section of a fractured AA5754 tensile specimen showing no damage or voids just underneath the fracture surface and (d) fracture surface of an AZ31 alloy tensile specimen revealed by X-ray tomography showing microcracks underneath the fracture surface [18].

Clearly, there is a link between the anisotropy in the deformation process and the development of damage and fracture processes in the three sheet materials. Microcrack formation in AZ31 sheets, for example, is strongly related to the twin formation as a result of the inability of textured AZ31 sheet to deform by dislocation mechanisms alone. IF steel on the other hand deforms by dislocation mechanisms which produce vacancies at high strains, leading to void formation which grow and coalesce to drive the material to failure. AA5754 sheets deform by dislocation mechanisms but voids form not from vacancy condensation at large strains as in IF steel but because of matrix-particle interactions in the sheet which then quickly develops to rupture. The above results suggest the need for developing microscale models that account for these differences in the microstructure and deformation mechanisms between different materials. It is expected that the quantitative data provided above can serve as a starting point for linking the anisotropic deformation with damage processes using a multi-scale (micro and macro scale) simulation strategy.

4. Conclusions

In this paper, we report the dependence of shear localization and fracture on plastic anisotropy of three types of automotive sheet materials, namely IF steel (BCC structure), AA5754 aluminum alloy (FCC) and AZ31 magnesium alloy (HCP). The results show that both narrowing and thinning of the tensile sample occur in IF steel, while only thinning occurs in AA5754 and only narrowing occurs in AZ31. These differences arise from the differences in the plastic anisotropy of the three materials, as measured by their r-values. Even though all three materials exhibit ductile fracture, the damage and fracture processes in the three materials differ from each other – mainly void mechanisms arising due to dislocation interactions in IF steel, premature void formation influenced by particle distribution in AA5754 sheets and premature crack initiation caused by twinning in textured AZ31 sheets. The need for micro-macro model development to link material anisotropy with fracture processes is identified for numerical model development.

Acknowledgements

The authors are grateful for the continuous financial support from Natural Sciences and Engineering Council of Canada (NSERC), General Motors Canada and Initiative for Automotive Manufacturing Innovation (iAMi). JK thanks the support from CanmetMATERIALS, Natural Resources Canada. Valuable technical discussions with scientific staff members in GM R&D Center, Warren, MI, U.S.A. are acknowledged.

References

[1] J. Kang, D. S. Wilkinson, M. Jain, J. D. Embury, A. J. Beaudoin, S. Kim, R. Mishra, A. K. Sachdev, On the sequence of inhomogeneous deformation processes occurring during tensile deformation of strip cast AA5754. *Acta Materialia*, 54(2006), 209-218.

[2] Z. Marciniak, K. Kuczynski, Limit strains in the process of stretch-forming sheet metal, International Journal of Mechanical Sciences, 9(1967), 600-620.

[3] J. Kang, D.S.Wilkinson, R.K.Mishra, W. Yuan, R.S. Mishra, Effect of inhomogeneous deformation on anisotropy of AZ31 magnesium sheet. Materials Science and Engineering A (in press, http://dx.doi.org/10.1016/j.msea.2012.08.117).

[4] Z. Gao, D.S. Wilkinson, J. Kang, Microstructural stability of magnesium alloys during high

temperature deformation, in: K. U. Kainer (ed.), Proceedings of 8th International conference on magnesium alloys and their applications, Wiley-VCH, Weinheim, 2009, pp.745-750.

[5] H. Watanabe, T. Mukai, M. Mabuchi and K. Higashi, Superplastic deformation mechanism in powder metallurgy magnesium alloys and composites. Acta Materialia, 49(2001), 2027-2037.

[6] Aramis v6.02 manual, GOM, Braunschweig, Germany, 2001

[7] J. Kang, D. S. Wilkinson, J. D. Embury, M. Jain, Local strain measurement in a strip cast automotive aluminum alloy sheet. SAE Transactions: Journal of Materials and Manufacturing, 114 (2005), 156-165.

[8] ASTM Standard E517-00, in: ASTM Standard Annual Book vol. 0.3.01, West Conshohocken, PA, USA, 2010.

[9] Hosford and Backofen, Strength and plasticity of textured metals. In: Fundamentals of deformation processing, Proceedings of the 9th Sagamore army materials research conference, Syracuse University Press, Syracuse, 1964, pp.259-292.

[10] K. Yoshida, T. Ishizaka, M. Kuroda, S. Ikawa, The effects of texture on formability of aluminum alloy sheets. Acta Materialia, 55 (2007) 4499-4506.

[11] Viewpoint Set No. 6: Shear bands. Scripta Metall 18(1984), 421.

[12] A.L. Gurson. Continuum theory of ductile rupture by void nucleation and growth. I. Yield criteria and flow rules for porous ductile media. Journal of Engineering Materials and Technology, 99(1977), 2–15.

[13] C.C. Tasana, J.P.M. Hoefnagelsb, C.H.L.J. ten Hornc, M.G.D. Geersb, Experimental analysis of strain path dependent ductile damage mechanics and forming limits. Mechanics of Materials, 41 (2009), 1264–1276.

[14] J. Kang, D. S. Wilkinson, M. Bruhis, M. Jain, P. D. Wu, J. D. Embury, R. K. Mishra, A. K. Sachdev. Shear localization and damage in AA5754 aluminum alloy sheets. Journal of Materials Engineering and Performance. 17(2008), 395-401.

[15] J. Kang, M. Jain, D.S. Wilkinson, J.D. Embury, S. Kim, A.K. Sachdev. Effect of strain path change on forming limits of strip cast automotive aluminum sheets AA5754. In: A.S. Khan (ed.), Dislocations, plasticity and metal forming. Neat Press, Fulton, 2003. pp.181–183.

[16] K. Spencer, S.F. Corbin, D.J. Lloyd. Notch fracture behavior of 5754 automotive aluminum alloys. Materials Science and Engineering A, 332(2002), 81–90.

[17] J. Kang, D. S. Wilkinson, D. V. Malakhov, H. Halim, M. Jain, J. D. Embury, R. K. Mishra, Effect of processing route on the spatial distributions of constituent particles and their role in the fracture process in AA5754 alloy sheet materials, Materials Science and Engineering A, 456 (2007), 85-92.

[18] J. Kang, D. S. Wilkinson, R. K. Mishra, J. D. Embury, E. Essadiqi, A. Javaid. Microstructural Aspects of damage and fracture in AZ31 sheet materials. Journal of Materials Engineering and Performance. Journal of Materials Engineering and Performance. (in press, DOI 10.1007/s11665-012-0399-5).

Crack growth stability analysis with respect to boundary disturbance

Hao Chen[1,*]

[1] Key Laboratory of Earthquake Engineering and Engineering Vibration,
Institute of Engineering Mechanics, CEA, Sanhe, 065201, China
* Corresponding author: chenhao@iem.ac.cn

Abstract Fracture analysis is a high non-linear problem and affected by uncertainties. Because of the limitation of observing technology, accuracy boundary condition can hardly be obtained. Normally, a stochastic model can be used. The difference between reality and numerical model is deemed as disturbance. This paper presents a three-dimension dynamic stability analysis of crack growth under disturbance in boundary condition by using particle discretization scheme finite element method.
The model is a thin epoxy plate with two anti-symmetric notches located in the middle, under uni-axial tensile in longitudinal direction. Two types of disturbance are considered: (i), the disturbance is added to the initial cracks' configuration. The disturbance is modeled by adjusting the position, size and shape of the notches. It shows that changes of the notches' size and position have significant influence on crack growth in the investigated cases; (ii), the disturbance is applied to the displacement boundary condition, which is far from initial cracks. The variability of crack paths of different model sizes under the same disturbance is estimated. The results of the numerical experiment indicate that as the model size increases, the influence of the disturbance becomes weaker. The Saint-Venant principle still holds in the studied crack growth problem.

Keywords Three dimensional dynamic crack growth, particle discretization scheme, finite element method, boundary disturbance, stability analysis

1. Introduction

Fracture analysis is a hot topic in solid mechanics [1]. Both experiments [2] and numerical methods have been developed to investigate the fracture behavior. The physical experiment is a reliable way. However, it costs a lot of resources to conduct. As the accumulation of experimental data increases, the fracture mechanics of more and more materials can be studied by using numerical method, for its convenience and resources saving. In order to increase the reliability of simulation results, a numerical model needs to be built as accurately as possible. However, the current observation equipments and technology have their limitation. Therefore, differences between reality and numerical model exist. Normally, stochastic model can be proposed, and the average value with variances can be used in numerical simulation. The difference between reality and numerical setting is deemed as disturbance in this paper. Since the crack drastically changes the stiffness matrix and strain energy, the dynamic crack propagation becomes a high non-linear problem. Hence, the results may be affected by these uncertainties. In mathematical view point, instability means that when a small perturbation is added to a system, the results will drastically change.

This paper focuses on studying the effect of the boundary condition disturbance on an elastic dynamic fracture problem. The well known Saint-Venant principle tells that, as the distance between the target and disturbance source increases, the effect of the disturbance decreases. Meanwhile, Oguni et al. [3] states that for dynamic fracture stability analysis, the uncertainties can be deemed as disturbance added to the stiffness matrix. As time increases, the effect may be increased or maintained according to system property. Based on these two theories, for boundary disturbance problems, it can be inferred that the effect of disturbance in boundary condition fades as the distance from area of interest increases, and heightens or maintains as time increases. However, since the property of dynamic fracture problem is nonlinear, the effects need to be quantificationally estimated.

Both experiment and numerical simulation can be used to study the effect of boundary disturbance. However, there is an advantage to examine the boundary disturbance effect by using numerical methods. At least two samples are needed to conduct this comparison study. The ideal situation is that all the settings are the same except that a specified disturbance is added in one of the samples' boundary condition. However, in reality, the variability of samples is hard to control, and the designed disturbance in boundary condition cannot be accurately applied. These uncertainties may lead to side effects on this comparison study. While in the numerical analysis, it is much easier to define identical models and add the specified disturbances exactly.

This paper studies the effect of two kinds of boundary disturbances, say, the near and far field disturbances. Here, the adjective, "near" and "far" are used to describe the distance between the boundary with disturbance and the region where crack grows. The target is a thin epoxy resin plate with two anti-symmetric notches located in the middle, subjected to uni-axial tensile in longitudinal direction. The near field disturbance is modelled by adjusting the position, size and shape of the notches. The far field disturbance is modelled by adding disturbance to the displacement boundary condition, which is far from the notches. Several kinds of disturbances are adopted. In order to study the Saint-Venant principle in the fracture problem, the crack paths of different model sizes under the same disturbance are compared.

For numerical simulation of fracture problems, various kinds of numerical methods have been proposed, such as E-FEM, X-FEM [4], discontinuous Galerkin method [5] and meshfree methods [6]. Besides these methods, the newly developed method, called particle discretization scheme finite element method (PDS-FEM) is another candidate [7,8] to calculate three dimensional dynamic crack propagation, for its numerical efficiency and capability of calculating bifurcation, which is important for brittle materials, such as epoxy resin, rock and concrete.

The content of the present paper is as follows: section 2 briefly introduces the characteristics of the adopted numerical method, PDS-FEM. Section 3 and 4 are devoted to study the effect of near and far field disturbances, respectively. Concluding remarks are pointed out in section 5.

2. PDS-FEM

The key idea of PDS-FEM is the discretization scheme. PDS or particle discretization scheme is a scheme which uses two sets of non-overlapping characteristic functions to discretize a function and its derivative. One set is made for Voronoi tessellation, and characteristic functions of this tessellation used to discretize a function. The other set is made for Delaunay tessellation, and characteristic functions of this tessellation are used to discretize function derivatives.

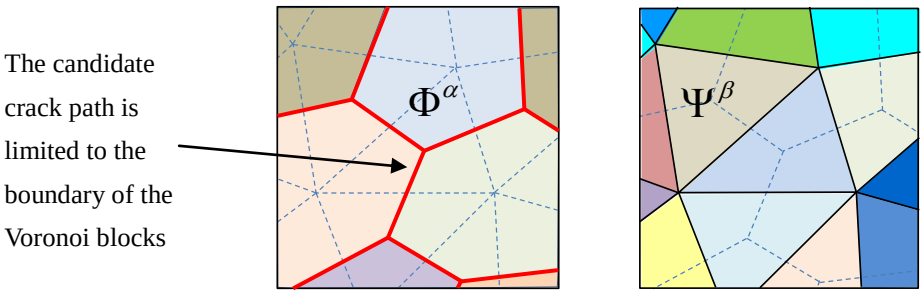

Figure 1. Two dimension decomposition by using particle discretization scheme

Displacement is discretized by the Voronoi, while strain and stress is discretized by Delaunay. As

you can see in Fig. 1, discretized functions are discontinuous everywhere. So, it is easy to model a crack, which is the discontinuity in a function of displacement. The candidate crack paths are limited to the boundary of the Voronoi blocks. For three dimensions decomposition, we can use ordinary tetrahedral mesh instead of triangular mesh as the Delaunay tessellation, and then for each tetrahedral vertex, the Voronoi block containing the vertex is determined by connecting all the centroids of tetrahedrons containing the vertex.

For dynamic analysis, a variation integrator called bilateral symplectic algorithm [9] is adopted as a robust algorithm of the time integration in PDS-FEM [8]. This algorithm is robust for stiffness matrix changes due to crack propagation. Meanwhile it is symplectic, which indicates that the momentum and energy are conserved during the numerical integration.

3. Near field disturbance modeling and simulation

Nowadays, the underground velocity structure and the hypocenter still can hardly be modeled accurately [10-12], let alone the detail fault configuration. According to previous researches, one of the best published results of underground velocity structure modeling with the help of the densest distribution of observation stations in Japan still has more than 10% error [13]. In order to carry out earthquake simulation, the configuration of the fault is always estimated with some variances. The effect of the errors in numerical modeling needs to be estimated. Although far from reality, this section carries out a series of trial simulations to quantificationally study the effect of the cracks' configuration changing on dynamic crack propagation with simple setting.

3.1. Reference model setting

The reference model is a thin epoxy resin plate with two anti-symmetric notches located in the middle, subjected to uniform longitudinal uni-axial tensile; see Fig. 2. The material is set to be linearly elastic; see Table 1. For brittle material, a time dependent material strength failure criterion, call Tuler Butcher criterion is adopted [14]:

$$\int_0^{\tau_f} \left(\sigma_1 - \sigma_0\right)^{\beta} dt \geq K_f \,, \tag{1}$$

where σ_1 and σ_0 are principle stress (tensile stress in this problem) and a threshold stress, τ_f is fracture duration and K_f is the stress impulse for failure. It is assumed that $\beta = 2$ and $K_f = 10^{-8}$. σ_0 is set to be the static tensile strength, and τ_f is assigned to be the time step used in the time integration.

Table 1. Material properties of epoxy resin

Young's modulus (Mpa)	3300
Poisson's ratio	0.38
Tensile strength (Mpa)	35.0
Epoxy density (kg/m^3)	1180

The displacement boundary condition is applied; the bottom end of the model is fixed, and the top end is pulled up in Z direction. The crack tip is modeled as a notch of the height 0.6 mm, the vertical surface of the notch is discretized by 2 elements, averagely. The average mesh size is 1.0 mm at the top and bottom surfaces of the notch. Due to this discretization, the time increment is set as $\Delta t = 7.5 \times 10^{-9}$s.

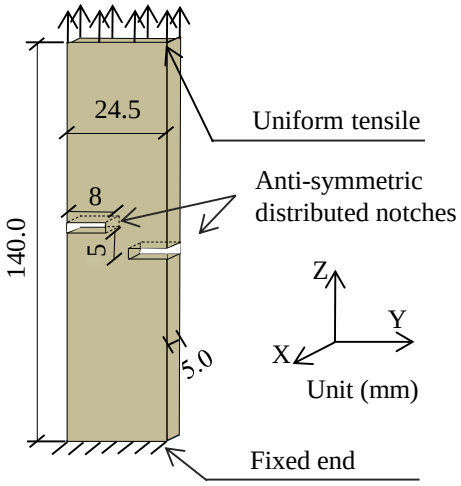

Figure 2. The reference model: epoxy resin thin plate with initial cracks

As aforementioned, the mesh configuration determines the candidate crack paths in PDS-FEM, which introduces local heterogeneity into the target model. In order to reduce the effect of this heterogeneity, finer mesh and lower loading speed can be used. The loading rate is the velocity of the top end, which is set to be V_r = 0.252*m/s*. This velocity is demonstrated to probably generate stable cracks, which means that the crack path solution is not sensitive to the local heterogeneity caused by the mesh setting used in this paper [8]. Also, another mesh with doubled density has been used to make comparison with the current one. The difference is ignorable, which guarantees the availability of current mesh setting for this study.

3.2. Disturbance setting and crack path comparison with reference model

In this sub-section, the near field disturbance is modeled by changing the notches' configuration. The changing is made by adjusting the size, shape and positions of the notches. 3 cases are studied in this part:

(1) Size changing: the left notch size elongates from 8mm to 8.5mm along Y axis, while the right notch size shrinks to 7.5mm.

(2) Position changing: the distance between the anti-symmetric distributed notches changes from 5mm to 4.5 mm.

(3) Out-plane rotation: the notch is designed to rotate along the axis, which is parallel with Y axis, and passes through the centroid of the corresponding notch. Two cases are studied in this paper: (a), left and right notches rotate -5°; and (b), the left rotates -5° and the right rotates 5°. The minus sign indicates that the direction of the rotation points to the Y axis' negative direction according to right hand principle.

(a). Reference model without disturbance

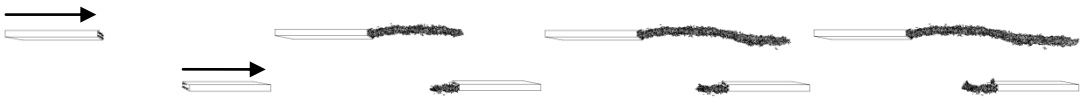

(b). Case 1: left notch elongates 0.5mm, right notches shrinks 0.5mm

(c). Case 2: the two notches get close to each other by 0.5mm

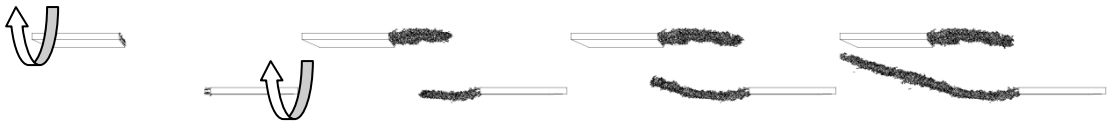

(d). Case 3.a: the two notches rotates 5° in the same direction

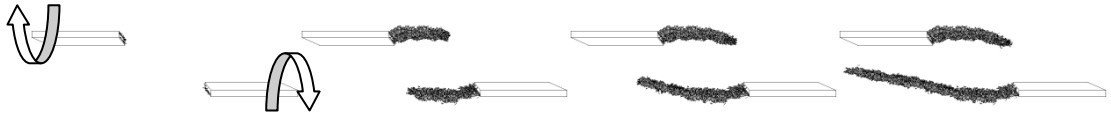

(e). Case 3.b: the two notches rotates 5° in the opposite direction

$t = 30\mu s$ $t = 90\mu s$ $t = 120\mu s$ final state

Figure 3. The near field crack path comparison with reference model

Fig. 3 shows the crack growth process and final states of this dynamic analysis with and without disturbance in notches' configuration. Although the modification is small, the crack path solutions of investigated cases show significant difference except for Case 2. The anti-symmetry property of crack paths solution from the analytical analysis becomes lost [15].

4. Far field disturbance modeling and simulation

4.1. Effect of the degree of heterogeneity

Since the observation technology has its limitation, the boundary condition of analysis model is often proposed in a stochastic way, say, the average with some variances is applied. The variances are used to represent the degree of heterogeneity. The boundary condition with larger variances has stronger effects on crack propagation. The first part of section 4 carries out a series of simulations to numerically examine the effect of the heterogeneity.

The model property is the same as Fig. 2, except that the height is changed to 40mm with the notches still located in the center. In order to avoid element failure near the boundary for the sudden changes caused by the disturbances, the strength of elements within 10mm to the top surface is set to be infinite. The initial tension displacement is 0.075mm for reference model, and the loading rate is set to be uniformly 126mm/s for all the cases. The time step is 5.0×10^{-9} s. Four kinds of disturbance are designed as shown in Table 2. In these formulations, "y" is the Y-axis coordinate of the nodes on top surfaces. The disturbances are added only to the magnitude of nodal displacement boundary condition on top surface along +Z direction. The first one is a half period of sine wave, whose wavelength is 16mm. Case 2 and 3 are two and four periods of sine waves, respectively. The 4th case generates a random number between -0.05mm and 0.05mm for each node on top surface. Except for case 4, the disturbance is set to be uniform along X direction. From Fig. 4, it can be observed that it becomes more and more homogeneous from u_{d1} to u_{d4} (the boundary disturbances are added with 0.075mm in this figure.) For case 4, for a specified area, the average of the disturbance on a certain area tends to be 0. By comparing the stress distribution of models with only

these four kinds of disturbance as boundary condition on top surface, u_{d4} leads to weaker effect for far field stress and larger analysis model; see Fig. 5 (a-d).

Table 2. Four kinds of disturbance added to the displacement boundary condition of the nodes on top surface

Case No.	Formulation of disturbance (mm)
1	$u_{d1} = 0.05 \cdot \sin\left(\frac{y+12.25}{8}\pi\right), -12.25 \le y \le -4.25.$
2	$u_{d2} = 0.05 \cdot \sin\left(\frac{y+12.25}{12.25}2\pi\right), -12.25 \le y \le 12.25.$
3	$u_{d3} = 0.05 \cdot \sin\left(\frac{y+12.25}{12.25}4\pi\right), -12.25 \le y \le 12.25.$
4	$u_{d4} = 0.05 \cdot random(-1,1).$

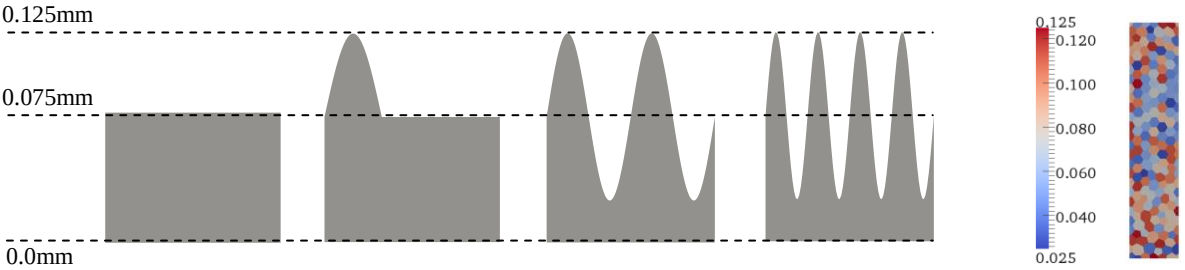

(a) Case 0 (reference) (b) Case 1 (c) Case 2 (d) Case 3 (e) Case 4

Figure 4. Initial displacement boundary condition with disturbances on the top surface (0.075+ u_{d1}~u_{d4}) mm

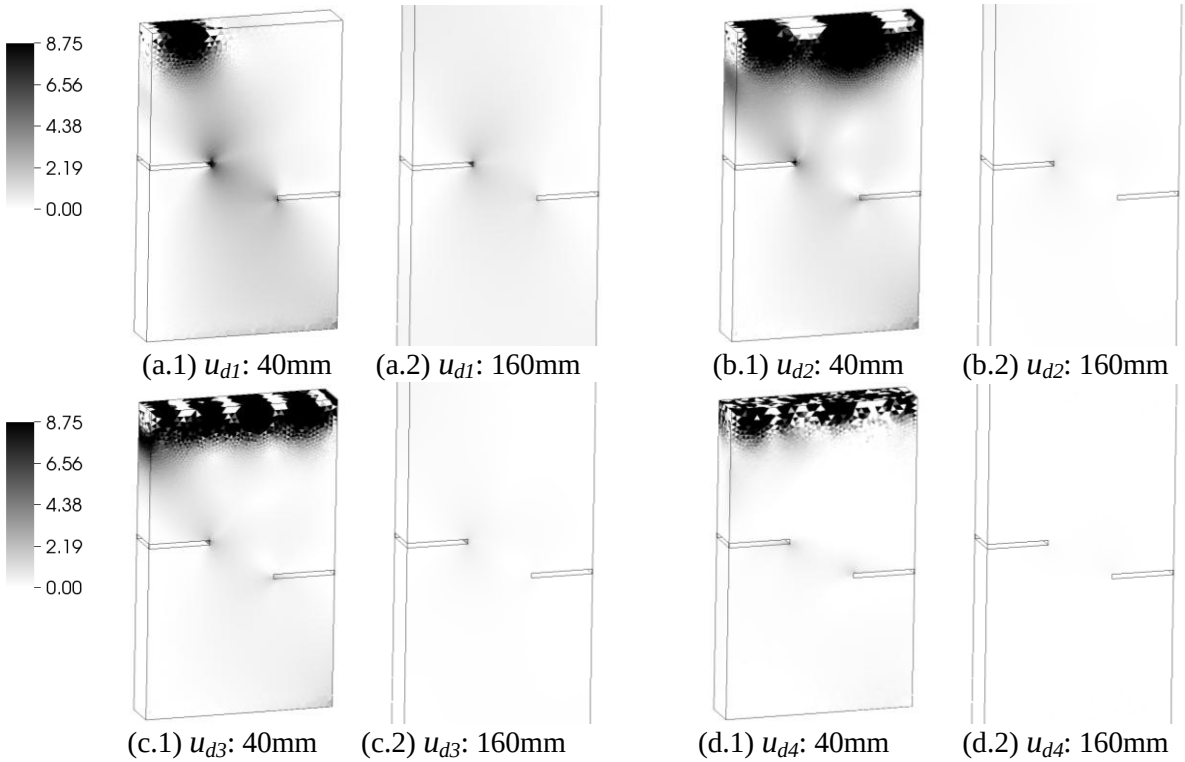

(a.1) u_{d1}: 40mm (a.2) u_{d1}: 160mm (b.1) u_{d2}: 40mm (b.2) u_{d2}: 160mm

(c.1) u_{d3}: 40mm (c.2) u_{d3}: 160mm (d.1) u_{d4}: 40mm (d.2) u_{d4}: 160mm

Figure 5. The tensile principle stress distribution under four kinds of disturbance (u_{d1}~u_{d4}) with different model sizes (left 40mm height, right 160mm height)

(a). Reference model without disturbance

(b). Case 1

(c). Case 2

(d). Case 3

(e). Case 4

$t = 0\mu s$ $t = 10\mu s$ $t = 20\mu s$ $t = 100\mu s$

Figure 6. The crack growth process under different boundary condition

Fig. 6 shows the simulation results. From case 1 to case 4, the crack growth process becomes gradually closer to the one of reference model. The most significant difference happens in the case 1, whose average value of boundary displacement on the top surface is the largest. While the smallest difference is observed in case 4, since the disturbance is added node-wisely, the average value tends to be zero in a relative smaller area compared with case 2 and 3, and it is numerically proved here that the disturbance of this kind has smaller effect on the far field crack growth as expected.

4.2. Effect of distance

The Saint-Venant principle tells that if the distance from the area with disturbance increases, the effect will decrease. The accuracy of observation data is constrained to a certain range. This error could be ignored, since the additional strain becomes smaller as the size of analysis model becomes bigger. However, since the crack growth is a non-linear process, numerical estimation is needed to decide the size of analysis model to ignore the disturbances in boundary condition.

This target is similar with the reference model in section 3. The only differences are made in the length in Z direction and boundary condition. The model height becomes 80mm, 160mm and 320mm. As the model size becomes bigger, the distance between the notches and the top surface, where disturbance exists, becomes longer. In order to keep the same strain rate of these models, the

boundary condition is defined as Table 3. The disturbance of Table 2- Case 2 is used in this section. All the models of different heights are assigned with the same disturbance.

Table 3. Boundary condition of models with different sizes

Height of the model (mm)	Initial tension displacement (mm)	Loading rate (mm/s)
80	0.15	252
160	0.3	504
320	0.6	1008

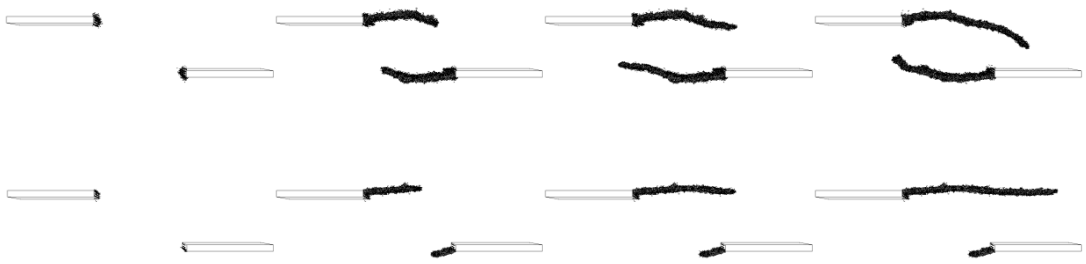

(a). Model of 80mm height without (upper) and with disturbance (lower)

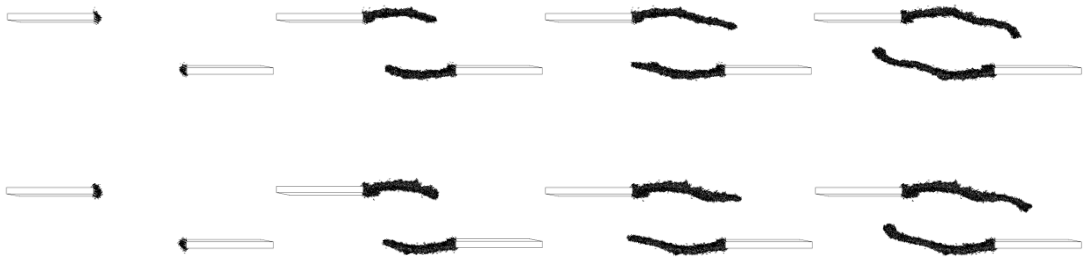

(b). Model of 160mm height without (upper) and with disturbance (lower)

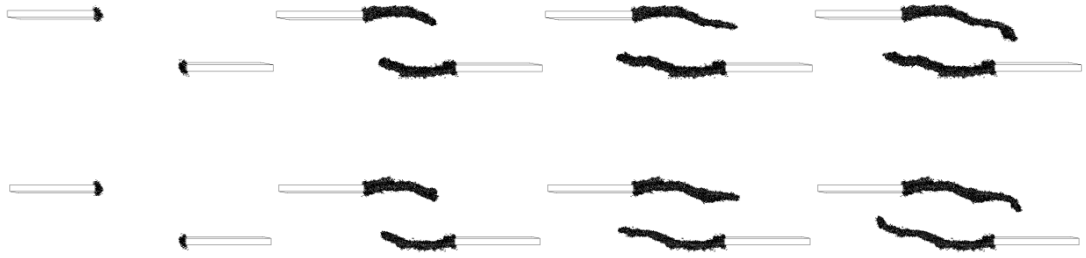

(c). Model of 320mm height without (upper) and with disturbance (lower)

$t = 0\mu s$ $t = 10\mu s$ $t = 20\mu s$ $t = 40\mu s$

Figure 7. The crack path comparison between models with different model height

Fig. 7 shows that the crack path distributions of all the samples without disturbance are anti-symmetric, which are similar to the analytical solution of ideal homogeneous models [14]. Also, these results indicate that the effect of the local heterogeneity generated by these mesh settings can be ignored. As the model size becomes bigger, the difference between models with and without disturbance becomes smaller. For example, the crack path of model of 80mm height with disturbance has one main crack path develop horizontally to the model boundary, the anti-symmetry

of crack paths distribution breaks. While, for the models of 160mm and 320mm height, the crack path solutions are almost the same, which indicates that the designed boundary disturbance has ignorable effect on crack growth for these models sizes. The reasons are: (i), with the same boundary disturbance, the bigger the model is, the smaller the additional stress generated; (ii), as the distance from disturbance becomes bigger, the distribution of additional stress becomes more and more uniform; see the stress distribution comparison between different model sizes in Fig. 5.

5. Conclusion

Nowadays, the observation technology still has some distance to be accuracy enough to generate a numerical model fully describing the real world. With limited data, the differences between numerical modelling and reality exist. For crack propagation problem, which is high non-linear, the effect of the differences is numerically examined by using a simple setting in this paper. For a 3D linear elastic dynamic problem, the near field disturbances lead to significant changes to crack path solution in the invested cases. While, the effect of far field disturbance becomes weaker as the distance from crack tips becomes larger, and becomes stronger as the degree of heterogeneity becomes larger. The Saint-Venant principle still holds in the studied crack growth problem.

Acknowledgements

This research is partially supported by the Central Public-interest Scientific Institution Basal Research Fund of China (Grant No. 2011B-05), China postdoctoral Science Foundation, and Natural Science Foundation of Hei Longjiang Province of China (Grant No. LC2012C32). These supports are greatly appreciated.

References

[1] J. Oliver, Modelling strong discontinuities in solid mechanics via strain softening constitutive equations. Part 1: Fundamentals. Int. J. Num. Meth. Eng., **39**(21), (1996) 3575-3600.
[2] K. Ravi-Chandar, and W. Knauss, An experimental investigation into dynamic fracture: III. On steady-state crack propagation and crack branching. International Journal of Fracture, 26(2), (1984) 141-154.
[3] K. Oguni, L. Wijerathne, T. Okinaka and M. Hori, Crack propagation analysis using PDS-FEM and comparison with fracture experiment. Mech. Mater. Phys. Solid, 41(11), (2009) 1242-1252.
[4] J. Oliver, A. Huespe and P. Sanchez, A comparative study on finite elements for capturing strong discontinuities: E-FEM vs X-FEM. Comput. Method Appl. M., 195(37), (2006) 4732-4752.
[5] F. Stan, Discontinuous Galerkin method for interface crack propagation. Int. J. Mater. Forming 1, (2008) 1127-1130.
[6] W.K. Liu, S. Hao, T. Belytschko, S.F. Li, and C.T. Chang, Multiple scale meshfree methods for damage fracture and localization. Comp. Mater. Sci., 16(1), (1999) 197-205.
[7] M. Hori, K. Oguni, and H. Sakaguchi, Proposal of FEM implemented with particle discretization for analysis of failure phenomena. J. Mech. Phys. Solids: 53(3), (2005) 681-703.
[8] H. Chen, L. Wijrathne, M. Hori, and T. Ichimura, Stability analysis of dynamic crack growth using PDS-FEM. Struct. Eng. Earthq. Eng., 29(1), (2012) 1s-8s.
[9] L. Casett, Efficient symplectic algorithms for numerical simulations of Hamiltonian flows. Phys. Scripta, 51, (1995) 29-34.
[10] H. Hausmann, S. Hoyer, B. Schurr et al., New seismic data improve earthquake location in the Vienna basin area, Austria. Austrian Journal of earth sciences, 103(2), (2010) 2-14
[11] J. Tarasewicz, R. S. White, B. Brandsdóttir and B. Thorbjarnardóttir, Location accuracy of earthquake hypocentres beneath Eyjafjallajkull, Iceland, prior to the 2010 eruptions. JKULL, 61, (2011) 33-50

[12] D.R. Shelly, W.L. Ellsworth, T. Ryberg et al., Precise location of San Andreas Fault tremors near Cholame, California using seismometer clusters: Slip on the deep extension of the fault? Geophysical research letters: 36, (2009) L01303, doi:10.1029/2008GL03637
[13] T. Furumura, T. Hayakawa, M. Nakamura, K. Koketsu, and T. Baba, Development of Long-period Ground Motions from the Nankai Trough, Japan, Earthquakes: Observations and Computer Simulation of the 1944 Tonankai (Mw 8.1) and the 2004 SE Off-Kii Peninsula (Mw 7.4) Earthquakes. Pure and Applied Geophysics, (2008)1-23, DOI 10.1007/s00024-008-0318-8.
[14] B.M. Butcher, L.M. Barker, D.E. Munson and C.D. Lundergan. Influence of Stress History on Time-dependant Spall in Metals. AIAA, Vol. 2:6, (1964) 977-990.
[15] A. Sato, Y. Suzuki, D. Fukahori and K. Sugawara, Application of stress compensation-displacement discontinuity method (SC-DDM) to the crack propagation analysis of multi-crack problem. Shigen-to-Sozai, 120, (2004) 493-499. (In Japanese)

Wrinkling and Delamination of Thin Films on Compliant Substrates

Haixia Mei and Rui Huang*

Department of Aerospace Engineering and Engineering Mechanics, University of Texas, Austin, TX 78712, USA
* Corresponding author: ruihuang@mail.utexas.edu

Abstract When the surface of a soft material is coated with a stiff thin film, compression induced buckling instability of the thin film results in surface wrinkles, and wrinkling of the thin film may lead to fracture and delamination. In this work, cohesive interface elements are employed in finite element analysis to simulate progressive wrinkling and wrinkle-induced delamination of an elastic thin film on a compliant substrate. The critical strain for initiation of wrinkle-induced delamination compares closely with an analytical formula based on a strength criterion. Subsequent growth of the delamination crack depends on the interface toughness. Co-evolution of wrinkling and buckle-delamination is simulated using a sufficiently large model. The interaction between the two buckling modes is elucidated.

Keywords: Thin films, Wrinkling, Delamination

1. Introduction

Stiff thin films on compliant substrates are used in a wide range of technological applications, including flexible electronics [1], thin film metrology [2], and micro/nano-fabrication [3]. Similar material structures are abundant in nature [4]. The mechanical interaction between a stiff film and a compliant substrate leads to a rich variety of phenomena that either limit or inspire practical applications of the hybrid system integrating hard and soft materials. In particular, recent interests in micro/nano-scale thin film materials have exploited mechanical instability (buckling and wrinkling) as an enabling mechanism for novel applications. Mechanics of surface wrinkling has been studied extensively over the last decade [5-17]. While most of these studies have assumed perfect bonding between the film and the substrate, it has been occasionally pointed out that wrinkling may cause interfacial delamination [5, 18, 19]. On the other hand, interfacial delamination is a necessary condition for buckling of thin films attached to relatively stiff substrates [20-22]. Simultaneous buckling and delamination has also been observed in compressed thin films on compliant substrates [23-25]. Some experiments have shown both surface wrinkling and buckle-delamination co-existing in the same film/substrate system [18].

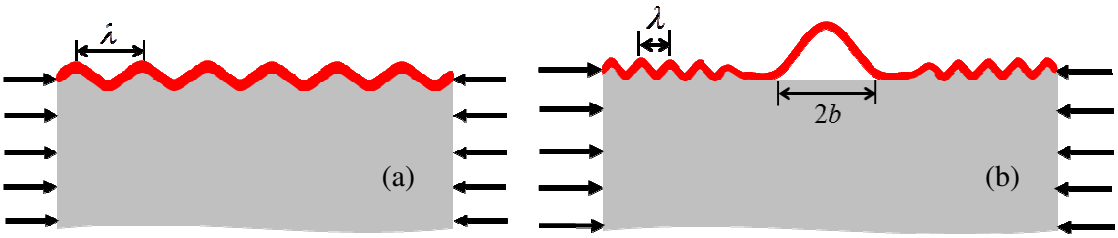

Figure 1. (a) wrinkling with no delamination; (b) Wrinkling and delamination.

In a previous work [18], we proposed a quantitative criterion for selection of the initial buckling mode by comparing the critical conditions for surface wrinkling and buckle delamination. The favored buckling mode at the onset of instability depends on the elastic mismatch between the film and the substrate as well as on the size of pre-existing interfacial delamination. More recently, by analytical and finite element methods, we presented a study on concomitant wrinkling and buckle-delamination for an elastic thin film on a highly compliant substrate [26]. In comparison with a nonlinear finite element analysis, an approximate formula was suggested to estimate the normal traction at the interface and to predict initiation of wrinkle-induced delamination. In this

paper, we present a study on nucleation and subsequent growth of wrinkle-induced delamination using a cohesive zone model.

2. Wrinkling Analysis

Consider an elastic thin film on an elastic compliant substrate, subject to lateral compression. Both the film and the substrate are taken to be linear elastic and isotropic, restricted to small, plane-strain deformation for the present study. Let ε be the nominal compressive strain, relative to the stress-free state. When ε is relatively small, the film/substrate bilayer is uniformly compressed and the surface is flat. When the strain exceeds a critical value, the film buckles and the substrate deforms coherently, forming surface wrinkles (Fig. 1a). The interface between the film and the substrate is assumed to be perfectly bonded in this section. Let h be the thickness of the film, while the substrate is considered infinitely thick. A well-known analytical solution predicts the critical strain for onset of wrinkling [9]:

$$\varepsilon_c = \frac{1}{4}\left(\frac{3\bar{E}_s}{\bar{E}_f}\right)^{2/3}, \tag{1}$$

where $\bar{E} = E/(1-\nu^2)$ is the plane-strain modulus with E for Young's modulus and ν for Poisson's ratio, and the subscripts f and s denote the film and substrate, respectively. The corresponding wrinkle wavelength is

$$\lambda = 2\pi h\left(\frac{\bar{E}_f}{3\bar{E}_s}\right)^{1/3}. \tag{2}$$

In deriving the above analytical solution, the shear traction at the film/substrate interface was assumed to be zero. Alternatively, by assuming zero tangential displacement at the interface, a similar analytical solution can be obtained [8, 13]. The two solutions are identical if the substrate is incompressible ($\nu_s = 0.5$), in which case both the shear traction and tangential displacement are zero. However, when the substrate is compressible ($\nu_s < 0.5$), neither the shear traction nor the tangential displacement is zero at the interface as the film wrinkles. As a result, neither analytical solution accurately accounts for the effect of Poisson's ratio of the substrate [15]. By taking into account both the shear traction and the tangential displacement at the interface, a more accurate analytical solution was developed [26], giving that

$$\varepsilon_c^* = \frac{1}{4}\left(\frac{3\bar{E}_s}{\bar{E}_f}\right)^{2/3}\left[1-\frac{1}{4}\left(\frac{1-2\nu_s}{1-\nu_s}\right)^2\right]^{-2/3}, \tag{3}$$

and

$$\lambda^* = 2\pi h\left(\frac{\bar{E}_f}{3\bar{E}_s}\right)^{1/3}\left[1-\frac{1}{4}\left(\frac{1-2\nu_s}{1-\nu_s}\right)^2\right]^{1/3}. \tag{4}$$

It was shown that, for a compressible substrate ($\nu_s < 0.5$), Eq. (1) underestimates the critical strain and Eq. (2) overestimates the wrinkle wavelength. The difference can be significant, up to about 20% for the critical strain and nearly 10% for the wavelength [26].

Beyond the critical strain, the wrinkle amplitude grows as a function of the nominal strain ε. An approximate solution for the wrinkle amplitude was obtained previously by a nonlinear approach that minimizes the strain energy in the film and the substrate [8, 9], namely

$$A = h\sqrt{\frac{\varepsilon}{\varepsilon_c} - 1}\,. \tag{5}$$

Finite element analysis (FEA) of wrinkling was performed using a two-dimensional (2D) plane-strain model in ABAQUS [26]. By a linear eigenvalue analysis, the finite element model predicted the critical strain for onset of wrinkling and the corresponding eigenmode, in good agreement with the analytical solutions in (3) and (4) when the substrate thickness is sufficiently large. To simulate wrinkle growth beyond the critical strain, a nonlinear post-buckling analysis was performed with the finite element model. Figure 2(a) shows the wrinkle amplitude as a function of the nominal strain for $E_f/E_s = 1000$ and $\nu_f = \nu_s = 1/3$. For comparison, the approximate analytical solution in (5) is plotted as a continuous solid line. The numerical results vary slightly as the amplitude of the initial imperfection (A_0/h) varies. Using a small initial imperfection (A_0/h = 10^{-4}), the numerical results compare closely with the analytical solution, with an abrupt transition at the critical strain. It is thus concluded that the analytical solution (5) is a good approximation for the wrinkle amplitude.

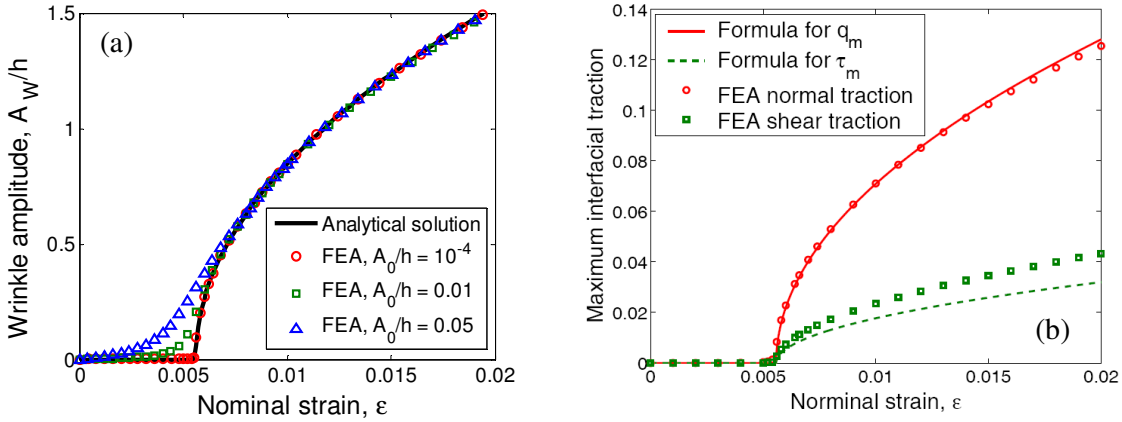

Figure 2. (a) wrinkle amplitude; (b) wrinkling-induced normal and shear tractions.

As the wrinkle amplitude grows, the normal and shear tractions acting on the film/substrate interface increase, which may cause delamination [5, 18, 19]. An approximate formula was derived to estimate the maximum normal traction at the interface [26]:

$$q_m = \frac{4(1-\nu_s)^2}{3-4\nu_s}\bar{E}_s\sqrt{\varepsilon - \varepsilon_c}\,. \tag{6}$$

The maximum shear traction is linearly related to the maximum normal traction, namely

$$\tau_m = \frac{1-2\nu_s}{2(1-\nu_s)}q_m\,. \tag{7}$$

By comparing to the FEA results, as shown in Fig. 2(b), it is found that the maximum normal traction by FEA follows (6) remarkably well, while the formula in (7) underestimates the maximum shear traction. The close agreement for the maximum normal traction suggests that the formula (6) may be used to estimate the critical strain for initiation of wrinkle-induced interfacial delamination. By setting the maximum normal traction equal the interfacial strength ($\hat{\sigma}_{\text{int}}$), the critical strain for initiation of wrinkle-induced delamination is obtained [26]:

$$\varepsilon_{WID} = \varepsilon_c + \left(\frac{3-4\nu_s}{4(1-\nu_s)^2}\frac{\hat{\sigma}_{\text{int}}}{\bar{E}_s}\right)^2. \tag{8}$$

where $\hat{\sigma}_{\text{int}}$ is the peak stress in the normal traction-separation relation for the interface as described by a cohesive zone model [27]. When $\varepsilon > \varepsilon_{WID}$, the interfacial delamination grows concomitantly with buckling (Fig. 1b).

3. Wrinkle-Induced Delamination

To simulate initiation and evolution of wrinkle-induced delamination, a two-dimensional finite element model was constructed in ABAQUS, as illustrated in Fig. 3(a). Both the film and the substrate were modeled by 2D quadrilateral elements (CPE8R). In addition, a layer of cohesive elements (COH2D4) was assigned along the interface to model the interaction between the film and the substrate. The bilinear traction-separation relation, as illustrated in Fig. 3(b), was used to describe the constitutive behavior of the cohesive elements.

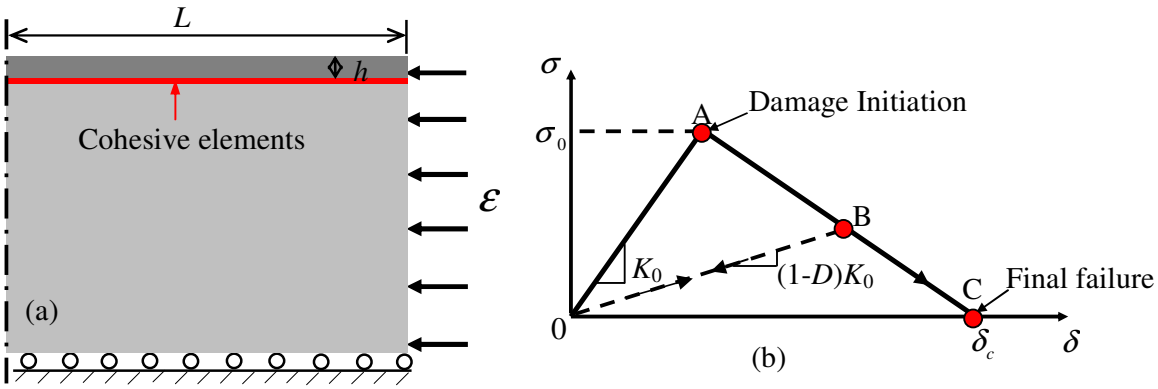

Figure 3. (a) Schematic illustration of the finite element model; (b) Illustration of the bilinear traction-separation law for the cohesive elements in ABAQUS.

A delamination crack along an interface is typically under a mixed-mode condition due to elastic mismatch between the film and the substrate [20]. Consequently, the interfacial properties are required for both modes I and II conditions. For the bilinear traction-separation model, the interfacial properties to be specified include [28]: the initial elastic stiffness K_n and K_s, the cohesive strength σ_n and τ_s, and the interface toughness Γ_I and Γ_{II}. In this section, we ignore the effect of mode mix by taking $K_n = K_s = K_0$, $\sigma_n = \tau_s = \sigma_0$ and $\Gamma_{\text{I}} = \Gamma_{\text{II}} = \Gamma$ for the interface. Previous studies have suggested that the initial elastic stiffness K_0 plays a less important role in cohesive zone modeling. In the present study, the initial stiffness K_0 is taken to be a constant (with $K_0 h / \overline{E}_f = 1$) in all simulations, while the strength (σ_0) and toughness (Γ) are varied. The elastic properties for the film and the substrate are such that $E_f/E_s = 1000$ and $\nu_f = \nu_s = 1/3$.

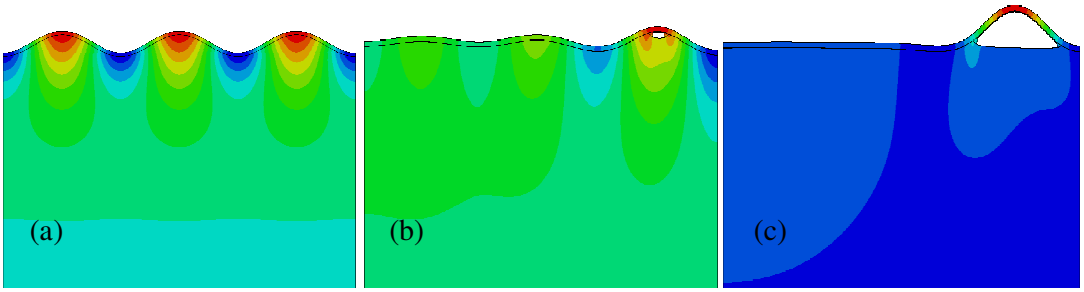

Figure 4. Numerical simulation of progressive wrinkling and interfacial delamination for an elastic thin film on a compliant substrate subject to increasing compression: (a) wrinkling with no delamination; (b) initiation of wrinkle-induced delamination; (c) subsequent growth of interfacial delamination.

Figure 4 shows an example of the numerical simulation. Start from an elastic film perfectly bonded to a compliant substrate (with a small initial perturbation). As the applied compressive strain increases, the film wrinkles first (Fig. 4a), followed by nucleation of an interfacial crack at one of the wrinkle crests (Fig. 4b). Upon subsequent growth of the delamination, buckling of the film becomes localized while the neighboring wrinkles are flattened (Fig. 4c).

In Section 2, initiation of wrinkle-induced delamination is predicted by comparing the maximum normal traction at the interface with the strength of the interface. This strength-based criterion for crack initiation is found to be in good agreement with the numerical results by the cohesive zone modeling approach. With the cohesive interface elements, a nonlinear post-buckling analysis is performed to simulate progressive wrinkling and wrinkle-induce delamination, as shown in Fig. 4. The amplitude of wrinkling or buckling is plotted as a function of the nominal strain in Fig. 5(a) for three different values of the interfacial strength, whereas the interfacial toughness is taken to be a constant, $\Gamma/\overline{E}_f h = 10^{-5}$. For comparison, the wrinkle amplitude without delamination is plotted as a continuous solid line. For each value of the interfacial strength, the wrinkle amplitude follows the solid line before the initiation of delamination. At a critical nominal strain that depends on the interfacial strength, a delamination crack is nucleated and the buckle amplitude at the location of delamination increases abruptly, deviating from the solid line. Thus, the initiation of delamination may be readily observable in experiments by measuring the buckle amplitude.

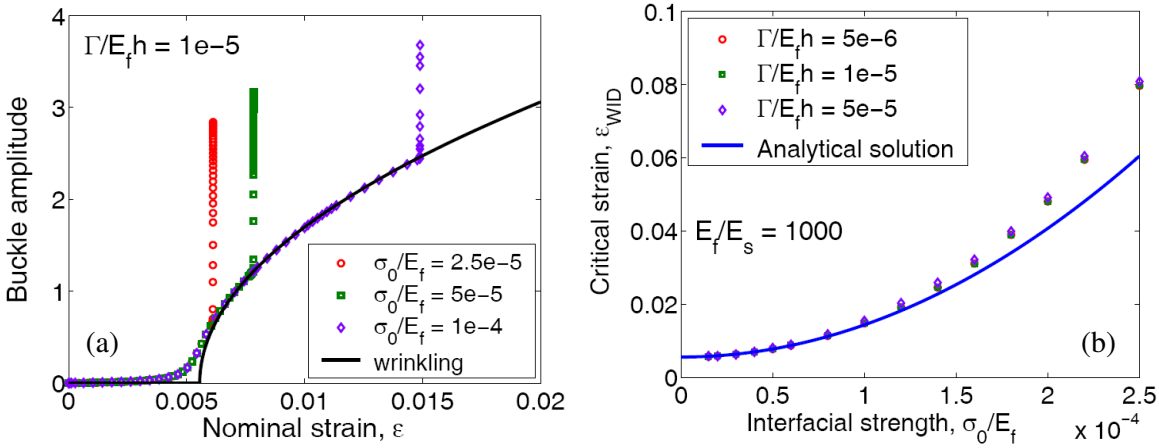

Figure 5. (a) Buckle amplitude as a function of the nominal strain, for three different values of interfacial strength. The solid line represents the wrinkle amplitude by the analytical solution in Eq. (5). (b) The critical strain for initiation of winkle-induced delamination as a function of the interfacial strength.

The critical strain for initiation of wrinkle-induced delamination can be determined from Fig. 5(a). Alternatively, by the cohesive zone model, each cohesive element is characterized by a damage parameter (D), which varies between 0 and 1 during the separation process [28]. Thus, the critical strain for crack nucleation can be determined numerically when the damage parameter reaches 1 for at least one of the cohesive elements. Figure 5(b) plots the critical strain for wrinkle-induced delamination as a function of the interfacial strength, for three different values of interface toughness. For comparison, the critical strain predicted by the analytical formula in Eq. (8) is plotted as the solid line. Clearly, the critical strain is nearly independent of the interface toughness, justifying the strength-based criterion. The numerical results agree closely with the analytical prediction for relatively low interfacial strengths (e.g., $\sigma_0/\overline{E}_f < 10^{-4}$). For higher interfacial strengths, however, Eq. (8) underestimates the critical strain. Apparently, since the critical strain increases with increasing interfacial strength, the linear approximation of the normal traction that leads to Eq. (8) becomes increasingly inaccurate as the strain goes beyond a few per cent.

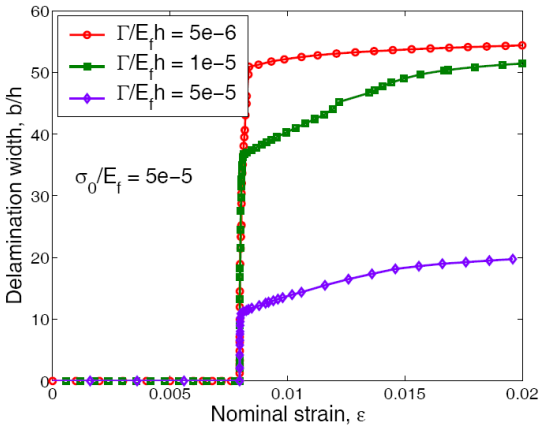

Figure 6. Delamination width as a function of the nominal strain for different values of interface toughness.

While the initiation of wrinkle-induced delamination is independent of the interface toughness, subsequent growth of the delamination crack does depend on the interface toughness. As shown in Figure 6, for an interfacial strength $\sigma_0/\overline{E}_f = 5\times10^{-5}$, the delamination width (b) as a function of the nominal strain is plotted for three different values of interface toughness. The delamination width is determined from the cohesive zone model based on the damage parameters of the cohesive elements. The delamination width remains zero until the critical strain is reached. Upon initiation, the delamination crack grows rapidly, which in turn leads to rapid growth of the buckle amplitude as shown in Fig. 5(a). The growth of the interfacial crack is eventually stabilized with a delamination width depending on the interface toughness. Further increasing the compressive strain, the delamination grows stably. Apparently, under the same nominal strain (greater than the critical strain), the delamination width decreases as the interface toughness increases.

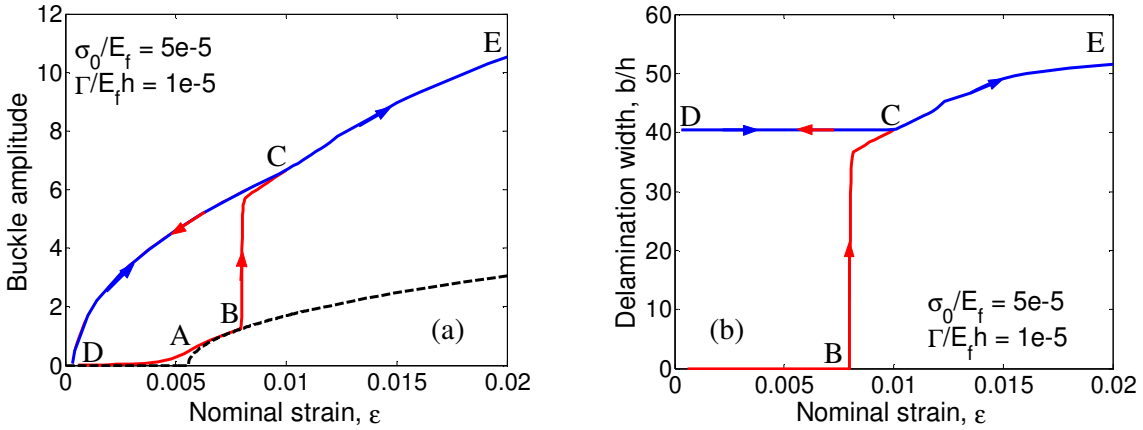

Figure 7. (a) Buckle amplitude and (b) delamination width as a function of the nominal strain during a loading-unloading-reloading cycle.

The cohesive zone elements as implemented in ABAQUS assume an irreversible damage process, which may be used to simulate damage accumulation under cyclic loading. As an example, numerical simulation of a loading-unloading-reloading process is performed, with $\sigma_0/\overline{E}_f = 5\times10^{-5}$ and $\Gamma/\overline{E}_f h = 10^{-5}$. Figure 7(a) shows the buckle amplitude versus the nominal strain. Before the first loading, the interface is perfectly bonded with no damage (D = 0). As the nominal strain increases, wrinkling occurs first at point A (ε ~ 0.00556), and wrinkle-induced delamination initiates at B (ε ~ 0.0076). Subsequently, delamination and buckling co-evolve. The corresponding delamination width is shown in Fig. 7(b). Start unloading at point C (ε = 0.01). The delamination

width remains a constant (b/h ~ 40) during unloading. Meanwhile, the buckle amplitude decreases, following a different path from C to D. The buckle amplitude is nearly zero at D, with the nominal strain (ε ~ 0.000384) corresponding to the critical strain for onset of buckling with b/h ~ 40. Upon reloading, the buckle amplitude follows the same path of unloading from D to C, during which the delamination does not grow. Further increasing the nominal strain beyond C to point E (ε = 0.02), the delamination grows and the buckle amplitude increases. Apparently, the buckle amplitude during reloading follows a drastically different path compared to that for the first loading. Such a behavior qualitatively agrees with an experiment by Vella et al. [25]. However, in their experiment, a discontinuous jump of the buckle amplitude during the first loading was reported, presumably due to the unstable growth of the delamination.

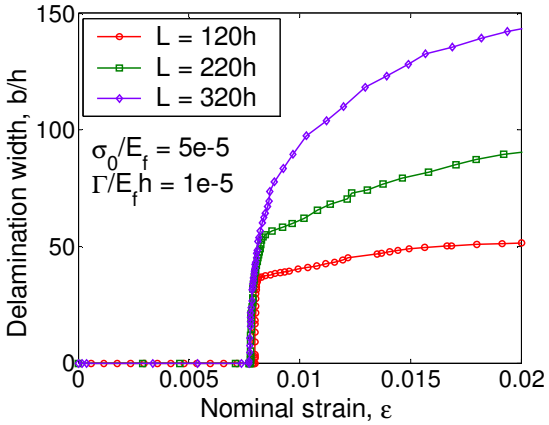

Figure 8. Delamination width as a function of the nominal strain for different lengths used in the finite element model.

It is noted that the growth of buckle-delamination is strongly influenced by the boundary condition. When the crack tip approaches one end of the model, where the symmetric boundary condition is assumed, the energy release rate drops rapidly and the crack is arrested when the energy release rate is less than the interface toughness. Figure 8 shows the delamination width as a function of the nominal strain by finite element models with three different lengths (L). Apparently, as L increases, the delamination width increases upon initiation, while the critical strain for initiation is insensitive to the model size.

With a sufficiently large L/b, the localized buckle-delamination and periodic wrinkles may co-exist [26]. To simulate both initiation and co-evolution of wrinkling and buckle-delamination, the finite element model with cohesive elements is employed with L = 1000h and H = 200h. The bilinear traction-separation relation is assumed for the interface with $\sigma_0/\overline{E}_f = 5\times10^{-5}$ and $\Gamma/\overline{E}_f h = 5\times10^{-5}$. Figure 9 shows the evolution of deformation profiles of the film (solid lines) and the substrate surface (dashed lines) with increasing nominal strain. The film remains flat until the nominal strain reaches the critical strain for wrinkling (ε_W = 0.00556). Beyond the critical strain, periodic wrinkles form as shown in Fig. 9(a) at ε = 0.00758. As the nominal strain increases to the critical value for wrinkle-induced delamination (ε_{WID} = 0.0076), an interfacial crack initiates and grows rapidly, as shown in Figs. 9 (b) and (c) for two strains slightly above the critical strain. The growth of delamination leads to large, localized buckling, which relaxes the compressive stress in the film over a region close to the delamination. As a result, the wrinkles are flattened in the relaxation region. Further away from the delamination, the film remains wrinkled. The size of the relaxation region depends on the relative compliance of the substrate and the delamination width. With continuous growth of the delamination and a finite length (L = 1000h) in the finite element model, all the wrinkles are flatted eventually, as shown in Fig. 9(d).

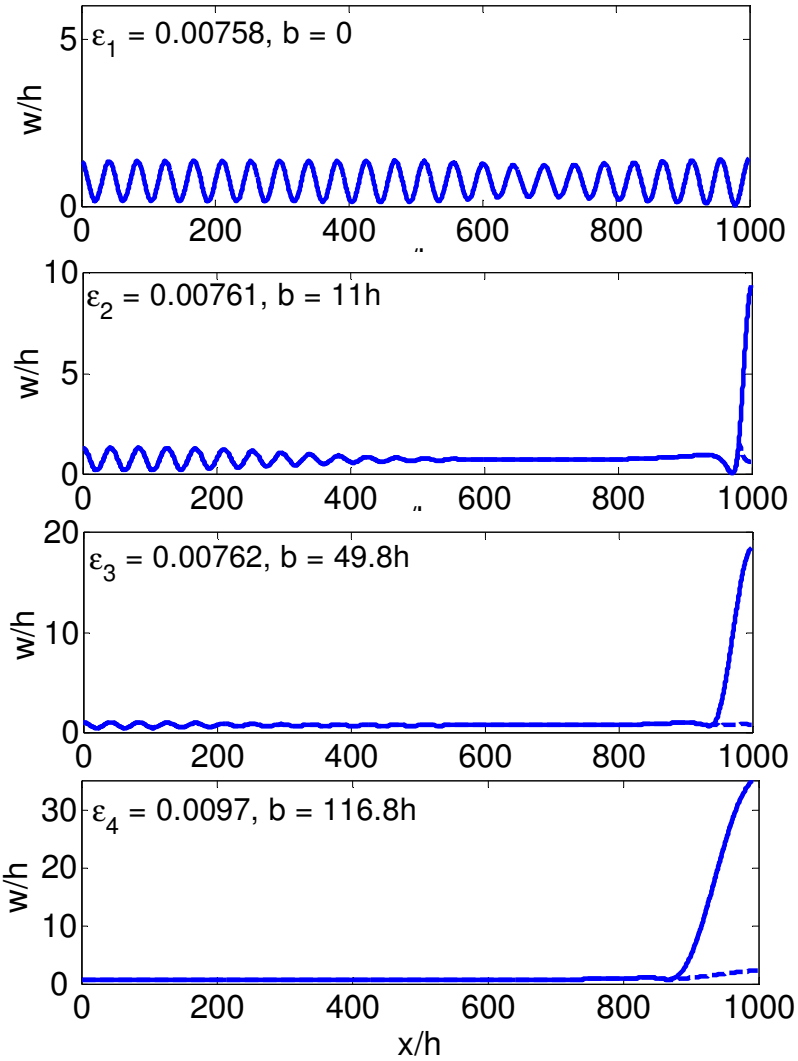

Figure 9. Out-of-plane displacement of the film (solid lines) and the substrate surface (dashed lines) at four different nominal strains: (a) ε = 0.00758; (b) ε = 0.00761 (b = 11h); (c) ε = 0.00762 (b = 49.8h); (d) ε = 0.0097 (b = 116.8h).

4. Summary

Cohesive interface elements are employed in finite element analysis to simulate initiation and growth of wrinkle-induced delamination of an elastic thin film on a compliant substrate. The critical strain for initiation of wrinkle-induced delamination compares closely with an analytical formula based on a strength criterion. Subsequent growth of the delamination crack depends on the interface toughness. Co-evolution of wrinkling and buckle-delamination is simulated using a sufficiently large model. The interaction between the two buckling modes is elucidated.

Acknowledgements

This work was supported by Semiconductor Research Corporation (SRC).

References

1. Rogers, J.A., Someya, T., Huang, Y., 2010. Materials and Mechanics for Stretchable Electronics. Science 327, 1603-1607.
2. Chung, J. Y., Nolte, A.J., Stafford, C.M., 2011. Surface wrinkling: a versatile platform for measuring thin-film properties. Advanced Materials 23, 349-368.

3. Bowden, N., Brittain, S., Evans, A.G., Hutchinson, J.W., and Whitesides, G.M., 1998. Spontaneous formation of ordered structures in thin films of metals supported on an elastomeric polymer. Nature 393, 146-149.
4. Chen, X., and Yin, J., 2010. Buckling patterns of thin films on curved compliant substrates with applications to morphogenesis and three-dimensional micro-fabrication. Soft Matter 6, 5667-5680.
5. Shield, T.W., Kim, K.-S., Shield, R.T., 1994. The buckling of an elastic layer bonded to an elastic substrate in plane strain. J. Appl. Mech. 61, 231-235.
6. Huang, R., and Suo, Z., 2002. Instability of a compressed elastic film on a viscous layer. International Journal of Solids and Structures 39, 1791-1802.
7. Chen, X., and Hutchinson, J.W., 2004. Herringbone buckling patterns of compressed thin films on compliant substrates. J. Appl. Mech. 71,597-603.
8. Huang, R., 2005. Kinetic wrinkling of an elastic film on a viscoelastic substrate. J. Mech. Phys. Solids 53, 63-89.
9. Huang, Z.Y., Hong, W., and Suo, Z., 2005. Nonlinear analysis of wrinkling in a film bonded to a compliant substrate. J. Mech. Phys. Solids 53, 2101-2118.
10. Huang, R., and Im, S.H., 2006. Dynamics of wrinkle growth and coarsening in stressed thin films. Physical Review E 74, 026214.
11. Jiang, H.Q., Khang, D.-Y., Song, J., Sun, Y., Huang, Y., Rogers, J.A., 2007. Finite deformation mechanics in buckled thin films on compliant supports. Proc. Natl. Acad. Sci. 104, 15607–15612.
12. Lee, D., Triantafyllidis, N., Barbar, J.R., Thouless, M.D., 2008. Surface instability of an elastic half space with material properties varying with depth. J. Mech. Phys. Solids 56, 858-868.
13. Audoly, B., and Boudaoud, A., 2008. Buckling of a stiff film bound to a compliant substrate. Part I: formulation, linear stability of cylindrical patterns, secondary bifurcations. J. Mech. Phys. Solids. 56, 2401-2421.
14. Im, S.H., and Huang, R., 2008. Wrinkle Patterns of Anisotropic Crystal Films on Viscoelastic Substrates. J. Mech. Phys. Solids 56, 3315-3330.
15. Cai, S., Breid, D., Crosby, A. J., Suo, Z., Hutchinson, J. W., 2011. Periodic patterns and energy states of buckled films on compliant substrates. J. Mech. Phys. Solids 59, 1094–1114.
16. Sun, J.-Y., Xia, S., Moon, M.-W., Oh, K. H., Kim, K.-S., 2012. Folding wrinkles of a thin stiff layer on a soft substrate. Proc. R. Soc. A 468, 932–953.
17. Cao, Y., Hutchinson, J.W., 2012. Wrinkling phenomena in Neo-Hookean film/substrate bilayers. J. Appl. Mech. 79, 031019.
18. Mei, H., Huang, R., Chung, J.Y., Stafford, C.M., Yu, H.H., 2007. Buckling modes of elastic thin films on elastic substrates. Appl. Phys. Lett. 90, 151902.
19. Goyal, S., Srinivasan, K., Subbarayan, G., Siegmund, T., 2010. On instability-induced debond initiation in thin film systems. Eng. Fracture Mechanics 77, 1298-1313.
20. Hutchinson, J.W., and Suo, Z., 1992. Mixed-mode cracking in layered materials. Adv. Appl. Mech. 29, 63-191.
21. Ortiz, M., and Gioia, G., 1997. Delamination of compressed thin films. Adv. Appl. Mech. 33, 119-192.
22. Moon, M.-W., Chung, J.-W., Lee, K.-R., Oh, K.H., Wang, R., Evans, A.G., 2002. An experimental study of the influence of imperfections on the buckling of compressed thin films. Acta Mater. 50, 1219-1227.
23. Cotterell, B., and Chen, Z., 2000. Buckling and cracking of thin films on compliant substrates under compression. Int. J. Fracture 104, 169-179.
24. Parry, G., Colin, J., Coupeau, C., Foucher, F., Cimetiere, A., Grilhe, J., 2005. Effect of substrate compliance on the global unilateral post-buckling of coatings: AFM observations and finite element calculations. Acta Mater. 53, 441-447.
25. Vella, D., Bico, J., Boudaoud, A., Roman, B., Reis, P.M., 2009. The macroscopic delamination of thin films from elastic substrates. PNAS 106, 10901-10906.
26. Mei, H., Landis, C.M., Huang, R., 2011. Concomitant wrinkling and buckle-delamination of elastic thin films on compliant substrates. Mechanics of Materials 43, 627-642.
27. Hutchinson, J.W., and Evans, A.G., 2000. Mechanics of Materials: Top down approaches to fracture. Acta Mater. 48, 125-135.
28. Mei, H., Gowrishankar, S., Liechti, K. M., Huang, R., 2010. Initiation and propagation of interfacial delamination in integrated thin-film structures. Proc. 12th IEEE Intersociety Conference on Thermal and Thermomechanical Phenomena in Electronic Systems (ITherm), Las Vegas, NV, June 2010.

Estimation of Wheel/Rail Contact Forces Based on an Inverse Technique

Tao Zhu*, Shoune Xiao, Guangwu Yang, Mingmeng Wang

State Key Laboratory of Traction Power, Southwest Jiaotong University, Chengdu 610031, China
* Corresponding author: 232665368@qq.com; hamilyzt@yahoo.cn

Abstract For actual operating conditions, wheel/rail contact forces of high-speed train are very difficult to directly measure. Minimizing the role of driving force between wheel and rail is a key point to ensure railway wheel-rail transport systems in good condition and efficient operation in the long-term. A time-domain inversion method for dynamic loads was proposed. Based on the state space equation, dynamic programming methods and the Bellman principle of optimality, the main theoretical derivation of the inversion mathematical model was given. With a high-speed vehicle system as the research object, accelerations of axle box as input conditions, the vertical and horizontal wheel/rail forces were identified. Inverse results were compared with SIMPACK simulation results which had the same kinetic parameters. The results indicate that the vertical and horizontal wheel/rail forces had the same trend with SIMPACK simulation results. Results from the inverse model were also compared with experiment data. The inverse model has high inverse accuracy, and can be used for real-time monitoring of the running train wheel/rail contact forces.

Keywords inverse technique, wheel/rail contact force, SIMPACK simulation, experiment data

1. Introduction

The estimation of dynamic forces acting on a structure is a problem that has been treated with only partial success. Methods for such estimation include in two categories, direct methods and indirect methods. Direct methods use the placement of force transducers into the load paths at the point of force application. Indirect methods use other sensor types placed at locations on the structure that may not necessarily correspond to the force input locations. Many situations require indirect methods because the forces cannot be measured[1]. For example, the train is subject to a wheel/rail impact load when operating because of rail irregularities and crossing turnouts.

Currently, various methods for inverse identification problem associated with indirect force measurements have been proposed, see for example Ref. [2-4] for an overview. Among them, are two main methods: the frequency domain[5,6]and the time domain method [7,8].

The running stability of a vehicle depends on the wheel/rail interaction. Wheel/rail contact forces play an important role to keep the vehicle stable on straight track and make it able to negotiate through curves smoothly. The possibility of gaining information about wheel–rail contact forces in real time and on-board normal rolling stock vehicles has significant value. But due to the complexity of the inverse identification problem in railway vehicle systems, not much research has been performed in this area. Some papers on this subject focused on impact detection at the contact point[9,10]. Commercially available systems for monitoring wheel-rail health are based on strain measurements at a chosen location on the track, and the track strain will be measured when the train passed [11]. A big disadvantage of the application of such a system is the necessity to locate strain measurement points at many locations on the track, not only time consuming but also expensive[12]. There is a great need to formulate a method that can be based on measurements on the vehicle but not on the track.

This paper presents a new method to identify the time history of input excitation based on the dynamic programming equation. The forces were identified in the time domain by a recursive

formula; the response of the structure was reconstructed by using the identified forces for comparison; and the objective function between the identified and measured values were minimized. The dynamic programming technique possesses inherent limitations that cannot be avoided, however, it still effectively solves these problems during the identification process, and greatly reduces the influence from insufficient known qualities and improper boundary conditions, and obtain decent results comparable with the exact forces. The mathematical model is then applied to estimate the wheel-rail vertical load of a high-speed train, and the inversion results are compared with the rolling and vibrating test-bed and the very detailed SIMPACK model simulation results.

2. Basis of load identification theory

The finite element model of an n-DOFs linear elastic time-invariant structure, the dynamic governing equation is given by:

$$M\ddot{X}(t) + C\dot{X}(t) + KX(t) - F(t) = 0 \tag{1}$$

where M, C, and K are the system mass, damping, and stiffness matrices, respectively; $X(t)$ is the displacement vectors of the structure; and F is the vector of the input excitation forces.

Using the state space formulation, Eq. (1) is converted into a set of first order differential equations as follows:

$$\dot{x} = Ax + Bf \tag{2}$$

For the load identification problem, the known responses of the system M, C, and K are used to solve the unknown input vector $f(s)$ which is in discrete form. In order to facilitate the computer solution, these differential equations are then rewritten as discrete equations using the standard exponential matrix representation.

$$x_{i+1} = Cx_i + Df_i \tag{3}$$

$$y_i = Qx_i \tag{4}$$

where, $C = e^{Ah}$ is the exponential matrix, and together with matrix $D = A^{-1}(C - I)$ is the input influence matrix which represents the dynamics of the system and associates with load. Q is a $m \times 2n$ selection matrix related the measurements to the state variables. x_{i+1} denotes the values at the $(i+1)th$ time step of the computations.

The goal is to find the unknown forcing term f that will cause the system described in Eq.(3) to best match the measurements $\hat{y}_i$. The mathematical representation of a best match is to minimize the least squares error between $\hat{y}_i$ and y_i. This is expressed in matrix-vector notation with the inner product of two vectors (.,.). The least error squares are now expressed as:

$$E = \sum_{i=1}^{N} (y_i - \hat{y}_i)^T \lambda_1 (y_i - \hat{y}_i) + (f_i)^T \lambda_2 (f_i) \tag{5}$$

where T is the transpose of a matrix, y_i and $\hat{y}_i$ are the output variables of the system for the identification formula and measurement, respectively. λ_1 and λ_2 are symmetric positive definite matrices that provide the flexibility of weighting the measurement and the forcing terms. The second term is known as the regularization parameter and the method is called the Tikhonov method. The value of λ_2 is very important for the result, fortunately, there exists a method that can be used to estimate the optimum value of λ_2, see the reference [13].

To minimize the least-squares error E in Eq.(6) over the sequence of the forcing vector, the dynamic programming method and Bellman's Principle of Optimality are applied. This leads to defining the minimize value of E for any initial x and the number of stages, n. Thus:

$$F_n(x) = \min_{f_i} E_n(x, f_i) \tag{7}$$

The recurrence formula can be derived by applying the Principle of Optimality:

$$F_{n-1}(x) = \min_{f_{n-1}}[(Qx_{n-1} - \hat{y}_{n-1})^T \lambda_1 (Qx_{n-1} - \hat{y}_{n-1}) + (f_{n-1})^T \lambda_2 (f_{n-1}) + F_n(Cx_{n-1} + Df_{n-1})] \tag{8}$$

This equation represents the classic dynamic programming structure in that the minimizing at any point is determined by selecting the decision f_{n-1} to minimize the immediate cost (first and second terms) and the remaining cost resulting from the decision (the third term). The solution is obtained by starting at the end of the process, $n = N$, and working backward toward $n = 1$. At the end point $n = N$, the minimum is determined from:

$$F_N(x) = \min_{f_N}[(Qx_N - \hat{y}_N)^T \lambda_1 (Qx_N - \hat{y}_N) + (f_N)^T \lambda_2 (f_N)] \tag{9}$$

At this end point the minimum is obtained by choosing $f_N = 0$ which gives:

$$F_N(x) = \min_{f_N}[(Qx_N - \hat{y}_N)^T \lambda_1 (Qx_N - \hat{y}_N)] \tag{10}$$

Eq.(10) can be expanded to:

$$F_N(x) = (x_N, Q^T \lambda_1 Q x_N) - 2(x_N, Q^T \lambda_1 \hat{y}_N) + (\hat{y}_N, \lambda_1 \hat{y}_N) \tag{11}$$

Eq.(11) can be changed as:

$$F_N(x) = (x_N, R_N x_N) + (x_N, S_N) + q_N \tag{12}$$

where $R_N = Q^T \lambda_1 Q$, $S_N = -2Q^T \lambda_1 \hat{y}_N$, $q_N = (\hat{y}_N, \lambda_1 \hat{y}_N)$.

Eq.(12) shows that F_N is quadratic in x_N. It can be proven inductively that all of the F_n are quadratic in x_n, thus for any n we can write:

$$F_n(x) = (x_n, R_n x_n) + (x_n, S_n) + q_n \tag{13}$$

Substituting Eq.(13) into Eq.(8) and minimizing the equation, the optimal forcing term f^*_{n-1}:

$$(2\lambda_2 + 2D^T R_n D) f^*_{n-1} = -D^T S_n - 2D^T R_n C x_{n-1} \tag{14}$$

For simplification the Eq.(14), let:

$$V_n = (2\lambda_2 + 2D^T R_n D)^{-1} \tag{15}$$

$$H_n = 2D^T R_n \tag{16}$$

Eq.(23) can now be written as:

$$f^*_{n-1} = -V_n D^T S_n - V_n H_n C x_{n-1} \tag{17}$$

These are recurrence formulas required to determine the optimal solution of Eq. (6).

Using Pearson product-moment correlation coefficient to measure the relationship between identification results and actual results, usually expressed by γ. The equation can be expressed by:

$$\gamma = \frac{\sum_{i=1}^{n}(F_{Si} - \bar{F}_S)(F_{Ii} - \bar{F}_I)}{\sqrt{\sum_{i=1}^{n}(F_{Si} - \bar{F}_S)^2}\sqrt{\sum_{i=1}^{n}(F_{Ii} - \bar{F})^2}} \tag{18}$$

where, F_{Si} is the SIMPACK simulation value at each time point, F_{Ii} is the identification value at each time point, $\bar{F}_S$ is the standardization variables of the SIMPACK simulation value, $\bar{F}_I$ is the standardization variables of the identification value.

3. Laboratory verification

First, a laboratory test is performed at TPL at Southwest Jiaotong University using the rolling and vibrating test-bed. The car body vertical acceleration, two bogie frames accelerations and four axle boxes accelerations are measured. Unfortunately, because of the limitation of test conditions, we can not measure the vertical and lateral interface forces directly. So we use a set of measured vertical acceleration response as inputs into the inverse vehicle model to identify other components of the vehicle acceleration responses, and compare with the measured results, by this way to verify the inversion model.

Test scenario is shown in Figure 1, the velocity of the rolling and vibrating test-bed is 250 km/h, the form of rail incentive is actual measured line spectrum of Wu-Guang line.

Figure 1. Test scene of the rolling and vibrating test-bed

Using car body, two bogie frames and the first axle box (numbered from left to right) measured vertical acceleration as input into the inverse vehicle model, the fourth axle box acceleration response and the fourth wheel-set vertical force are identified. See figures 2 and 3.

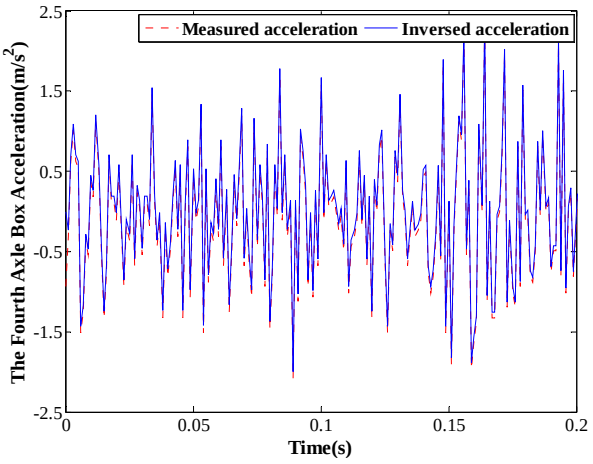

Figure 2. Measured and inversed accelerations for the fourth axle box

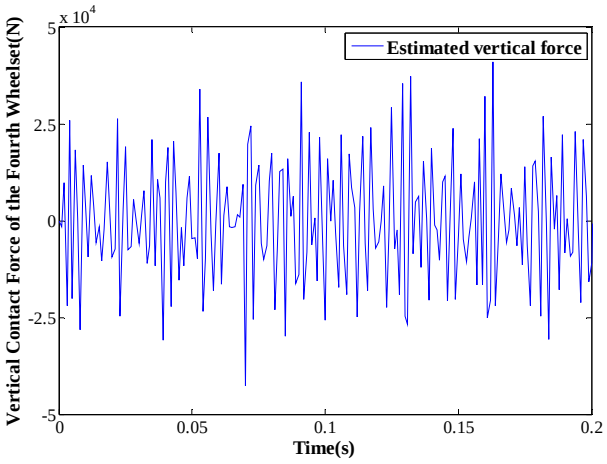

Figure 3. The estimated vertical dynamic contact force for the fourth wheel-set

From figure 2, the acceleration of the fourth axle box which identified by the inverse model is very similar to the measured value, and its correlation coefficient is 0.9756, which can be thought as height correlation. Figure 3 shows the inversed vertical dynamic contact force for the fourth wheel-set, unfortunately, it is unable to be compared with measurement value due to the limitation of test-bed. It is worth noting that, due to the limitation of accelerometers in low frequencies, figure 3 is just the vertical dynamic contact force for the fourth wheel-set, the real vertical force should add the weight reaction force.

4. The application of the inverse model in high-speed train

The commonly used simulation package, SIMPACK, was used to develop a wagon model based on the same parameters as the inverse model. The parameters of the SIMPACK model were the same as the inverse model which was used to generate wheel-rail forces and accelerations at the axle box. These accelerations will be as the input conditions for the inverse mathematical model. In order to make the SIMPACK model replace a practical field test, the vehicle model developed with SIMPACK needs to be a very refined model which includes the nonlinearity of the wheel-rail contact geometry, the nonlinearity of the wheel-rail creep rate and creep forces, the nonlinearity of the vehicle suspension components, and so on.

Taking into account the complexity of the car body systems, as well as many non-linear factors, we need to simplify the body. In this paper, for the vertical and lateral stochastic vibration inverse modeling of the car body, about twenty-seven degrees of freedom are considered.

The measured track irregularity from Beijing to Tianjin was used as the input to the SIMPACK with a simulated velocity of 70 m/s. The resulting axle box accelerations were then used as inputs for the inverse model. The wheel-rail forces were estimated using the MATLAB package. The outputs of the inverse model were the axle box accelerations and wheel-rail reacting forces. The vertical and lateral contact forces of the third wheel-set of the inverse model and the SIMPACK simulation were compared, see Figures 4-5. At the same times, the derailment index which is got from the inverse model and the SIMPACK simulation are also compared. See figure 6.

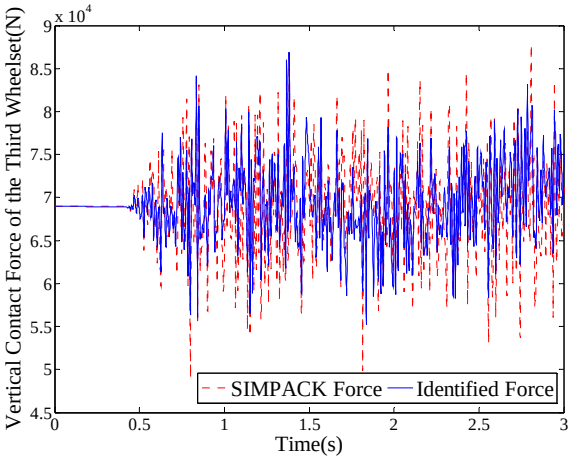

Figure 4. Wheel-rail vertical forces comparison

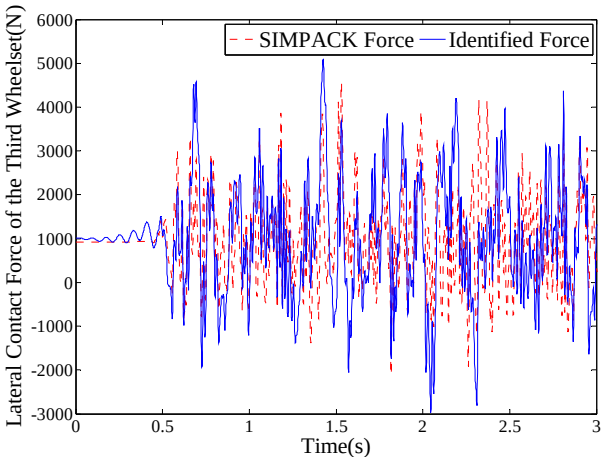

Figure 5. Wheel-rail lateral forces comparison

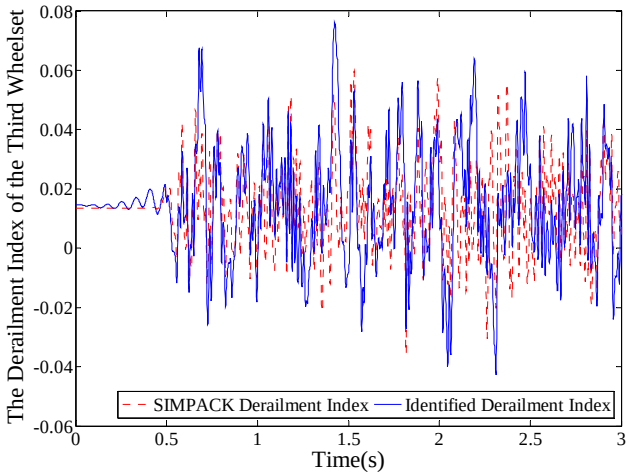

Figure 6. Index coefficient comparison

To compare the results of the SIMPACK simulation and those obtained from the inverse identification method, as shown in Figures 4-5, we can observe that the inverse forces are consistent with the simulation results. Their correlation coefficients are 0.6984 and 0.6235, respectively. By comparing the derailment index, it can be found that the tendencies of the result are also quite accordant.

5. Conclusion

A non-iterative recurrence algorithm for input estimation algorithm mathematical model has been established. Combined with Tikhonovo regularization algorithm, anti-noise ability of the inversion model is enhanced. Based on the response of the accelerations, the method can be applied to the estimation of vertical and lateral contact forces for an operating rail vehicle.

(1)The inversion model is verified by the experiment data of the laboratory test. Using some parts of accelerations which are measured from the rolling and vibrating test-bed to identify the other component of accelerations, and compare with laboratory tests. The results show that the inversion model can be used to identify the unknown output responses for interesting places.

(2) From the time domain, the comparison of the vertical and lateral contact forces results between inverse and SIMPACK models are given. The results show that, the inverse mathematical model has high relatively precision for inversing the wheel/rail contact forces of operation

high-speed vehicle. And their correlation coefficients are greater than 0.5, can be thought as significant correlation.

Since there exist many non-linear factors, such as wheel-rail contact geometry and creep effects, which not only must be taken into account in high-speed train modeling but also make the estimation process of the wheel-rail lateral contact forces are more complex than the vertical contact forces. More research is needed to expand the inverse model which considers the non-linear factors between the wheel and rail. Furthermore, the next step will involve field trial tests to verify the effectiveness of the inverse model.

Acknowledgements

This work was supported in part by the National Natural Science Foundation of China (51275432); National Key Technology R&D Program in the 11th Five year Plan of china （2009BAG12A04-A11）; University Doctor Academics Particularly Science Research Fund (SWJTU09ZT23).

References

[1] T. Zhu, S. N. Xiao, and G. W. Yang, State-of-the-art development of load identification and its application in study on wheel-rail forces. Journal of the China Railway Society, 33 (2011) 29-36. (Chinese).
[2] K. K. Stevens, Force identification problems-an overview. In: Proceedings of SEM Spring Meeting, Houston, (1987) 838–844.
[3] B. J. Dobson, E. Rider, A review of the indirect calculations of excitation forces from measured structural response data. Proc. Inst. Mech. Engrs.: J. Mech. Engrg. Sci., 204 (1990) 69-75.
[4] L. J. L. Nordstrom, T. P. Nordberg, A critical comparison of time domain load identification methods. In: Proceedings of the Sixth International Conference on Motion and Vibration Control, 2 (2002) 1151-1156.
[5] J. Giergiel, T. Uhl, Identification of impact forces in mechanical systems. Arch. Mach. Des., 36 (1989) 321-336.
[6] J. Giergiel, and T. Uhl, Identification of the input excitation forces in mechanical structures. Arch. Transp., 1 (1989)8-24.
[7] B. J. Dobson, E. Rider, A review of the indirect calculation of excitation forces from measured structural response data. J. Mech. Eng. Sci. , 204 (1990) 69-75.
[8] T. Uhl, J. Pieczara, Identification of operational loading forces for mechanical structures. Arch. Transp. ,16 (2003) 109-126.
[9] S. Lechowicz, C. Hunt, Monitoring and managing wheel condition and loading. In: Proceeding of International Symposium for transportation recorders, Arlington, (1999)205-239.
[10] J. Nielsen, A. Johansson, Out of round railway wheels-literature curve. In: Proceedings Of the Institute of Mechanical Engineers – part F, 214 (2002) 79-91.
[11] A. Chudzikiewicz, Selected elements of the contact problems necessary for investigating the rail vehicle system. In: Kisilowski, J., Knothe, K. (eds.) Advanced railway vehicle system dynamics, WNT, Warszawa, 1991.
[12] A. Chudzikiewicz, Elements of vehicle diagnostics. ITE, Radom, 2002.
[13] P. C. Hansen, Analysis of discrete ill-posed problems by means of the L-curve. SIAM Rev. , 34(1992) 561-580.

Seismic Inversion using full wavefied data

XiaoLiang Duan[1*], **Yibo Wang**[2], **Huizhu Yang**[1]

[1]Department of Engineering mechanics, Tsinghua University, 100084, China

[2]Institute of Geology and Geophysics, Chinese Academy of Sciences, 100029, China

*Corresponding author: gfkjdxdxl@yahoo.com.cn

ABSTRACT

Most seismic migration methods stress primary reflection data, it means that multiples is considered as noise and need to be removed prior to migration process. In fact multiples contain important medium property information which can be utilized to improve the quality of image.

By introducing a background model, the difference between the known background properties and unknown real medium properties is inverted. Each gridpoint act as a scatterer in the background media. In our work, Finite-difference contrast source inversion method will be applied in seismic inversion with full wavefield data including surface-related and internal multiples, without including explicit computation of forward problem at each iteration step, this method can employ an inhomogeneous background medium. By solving an optimization problem to reconstruct the contrast function χ, which is a quantity having some connection with the real velocity distribution in the medium. Result of the process is an accurate angle-dependent reflectivity image as well as angle-dependent velocity model in subsurface.

Key words: migration, inversion, anisotropy, multiple, scatter

1. INTRODUCTION

Generally speaking, there are two possible approaches for velocity estimation from surface recorded seismic data, the two methods differ from the domain in which the information is used to update the velocity model. The first approach is formulated in the data space prior to migration, and it involves matching of recorded and simulated data using an approximate velocity model. The second approach is formulated in the image space after migration, in which it involves measuring and correcting image features that indicate model properties inaccuracies.

Nowadays, migration and inversion have been two different approaches to reveal the subsurface information [4,6,9-11], Their fundamental theory is very different. But we can treat migration and inversion as a same form in mathematics. Although they have different physical meaning. So we can incorporate migration and inversion process together to analyze the seismic data[1].

One of the well-known full nonlinear inversion methods based on the integral equation(IE) formulation is the contrast source inversion (CSI) method[7,8]. The main

disadvantage of this approach based on integral equation formulation is that the background medium is usually a simple homogeneous medium.

Finite-difference based contrast source inversion(FDSCI) method is adaptive to the arbitrary inhomogeneous background medium[2,3,5,12], similar to the IE contrast source inversion method, the unknown contrast source and the unknown contrast function are updated alternately to reconstruct the scatters without requiring the solution of forward problem at each iteration step. An attractive feature of FDCSI approach is that the impendence matrix is only dependent on the background medium, which is invariant throughout the inversion process, Hence, the FD operator needs to be inverted only once and the results can be reused for multiple source positions.

2. THEORY

2.1 Joint migration and inversion

In the joint migration and inversion process, first extrapolate the receiver wavefield from depth level z_{m-1} to z_m, then inversion process is applied at depth z_m, and we will use the wavefield from all depth level which represents the internal and surface-related multiples. In full wavefield inversion process, the difference between the known background properties and the unknown real medium properties is inverted. Each gridpoint act as a point scatterer in the background medium, called as contrast source. The total wavefield in the true medium equals the sum of the wavefield of the primary sources in the background and the wavefield of all point scatterers in the background. The contrasts and the total wavefield are alternately updated until the total simulated wavefield matches the recorded wavefield at the detector positions. After that the full wavefield migration is applied to yield the angle-dependent reflectivity, which is solved as a constrained least-squares minimization problem. The two minimization process is in the same mathematic form[1]:

$$Q^{-}(z_m, z_0) - \left[U(z_m, z_m)P^{+}(z_m, z_0) + V(z_m, z_m)P^{-}(z_m, z_0)\right] = \min \tag{1}$$

In which P represents the incident wavefield and Q refers to response of depth z_m

In the migration process, the matrices U and V represent reflectivity:

$$U(z_m, z_m) = (R_1^{\mathrm{U}}, R_2^{\mathrm{U}}, \mathrm{L}\ \ R_k^{\mathrm{U}}, \mathrm{L}\ ) \tag{2}$$

$$V(z_m, z_m) = (R_1^{\mathrm{I}}, R_2^{\mathrm{I}}, \mathrm{L}\ \ R_k^{\mathrm{I}}, \mathrm{L}\ ) \tag{3}$$

In the inversion process, the matrices U and V are same and represent contrast:

$$U(z_m, z_m) = V(z_m, z_m) = (\chi_1, \chi_2, \mathrm{L}\ \ \chi_k, \mathrm{L}\ ) \tag{4}$$

In the JMI process full wavefield extrapolation is applied from z_{m-1} to z_m, using the

wavefield Q_j^+ and p_j^- at depth level z_{m-1}, this extrapolation step yields an estimate of the total wavefield, being denoted by $< p_j >$ at intermediate depth level z_n $(z_{m-1} < z_n < z_m)$:

$$< p_j(z_n, z_0) >= W_0(z_n, z_{m-1}) Q_j^+(z_{m-1}, z_0) + W_0^*(z_n, z_{m-1}) p_j^-(z_{m-1}, z_0) \tag{5}$$

W, W^* represent propagation operator and its conjugate complex respectively.

Next, a full waveform inversion step is applied:

$$p_j(z_n, z_0) =< p_j(z_n, z_0) > + \Delta p_j(z_n, z_0) \tag{6}$$

$$\Delta p_j(z_n, z_0) = \sum_{l=m-1}^{m} G_0(z_n, z_l) \sum_k \chi_k(z_l, z_l) p_{kj}(z_l, z_0) \tag{7}$$

yielding an update of the velocities in each gridpoint of layer (z_{m-1}, z_m) and an update of the wavefield at z_m, G refers to Green's function:

$$p_j^+(z_m, z_0) = W_0(z_m, z_{m-1}) Q_j^+(z_{m-1}, z_0) + \Delta p_j(z_m, z_0) \tag{8}$$

$$Q_j^-(z_m, z_0) = W_0^*(z_m, z_{m-1}) p_j^-(z_{m-1}, z_0) + \Delta p_j(z_{m-1}, z_0) \tag{9}$$

After completion, the updated velocities in layer (z_{m-1}, z_m) as well as the reflectivity and updated wavefield at depth level z_m are known, we can apply the following migration and inversion process at deeper depth recursively.

2.2 Contrast source inversion

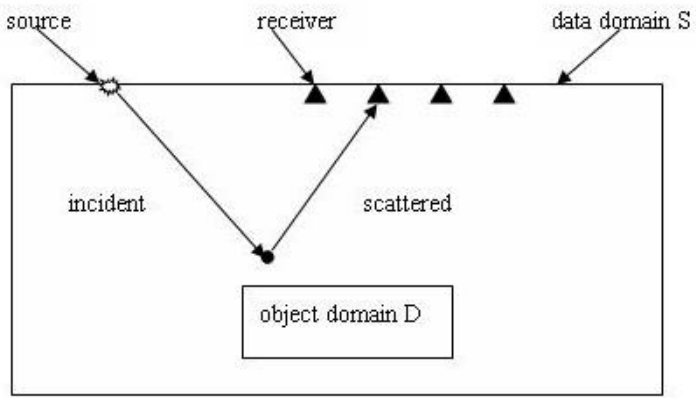

Figure 1. Configuration of the scattering problem

Denote the inversion domain as the object domain D and the data domain S as the domain where the sources and the receivers are located, combination of domain D and domain S are called total domain T (see Figure 1).

Total field $p_j(r)$ satisfies the Helmholtz equation[2,3]:

$$\left[\Delta^2 + k^2(r)\right] p_j(r) = -Q(r, r_j^s), \quad r \in T \tag{10}$$

Where Q is the source term.

We split the total field into its incident and scattered parts:

$$p_j = p_j^{inc} + p_j^{sct} \tag{11}$$

The incident field satisfies the equation:

$$\left[\nabla^2 + k_b^2(r)\right] p^{inc}{}_j(r) = -Q\left(r, r_j^S\right), \quad r \in T \tag{12}$$

Subtracting equation (12) from equation (10), then the scattered field satisfied the equation:

$$\left[\nabla^2 + k_b^2(r)\right] p^{sct}{}_j(r) = -k_b^2(r) w_j(r), \quad r \in T \tag{13}$$

Where $w_j(r)$ are the contrast sources, defined as:

$$w_j(r) = \chi(r)\, p_j(r) \tag{14}$$

In which the contrast function $\chi(r)$ is given by:

$$\chi(r) = \left[\frac{k(r)}{k_b(r)}\right]^2 - 1 = \frac{c^{-2}(r) - c_b^{-2}(r)}{c_b^{-2}(r)} \quad r \in D \tag{15}$$

Here, $c^{-2}(r) = \rho k(r)$ is the velocity of the scattering object, and $c_b^{-2}(r) = \rho k_b(r)$ is the velocity of the background medium.
Equation (13) can be written using operator notation:

$$H_b(p_j^{sct}(r)) = -k_b^2(r) w_j(r), r \in T \tag{16}$$

The solution of equation (16) can be written as:

$$p_j^{sct}(r) = H_b^{-1}\left[-k_b^2(r) w_j(r)\right] = L_b\left[w_j(r)\right], r \in T \tag{17}$$

Introducing an operator M^s that interpolates the field values defined at the finite-difference grids to the appropriate receiver position, the data equation for the contrast function χ can be written as:

$$p^{sct}{}_j(r) = M^s\{L_b[w_j(r')]\} \quad r \in S, r' \in T \tag{18}$$

Introducing an operator M^D that selects fields only on the object domain, we obtain the object equation for the contrast source w_j:

$$\chi p_j^{inc} = w_j - \chi M^D \left\{ L_b \left[w_j \right] \right\} \tag{19}$$

We handle the inverse problem as a minimization of a cost function, being a linear combination of errors in the data equation and the object equation, the method alternatively constructs sequence of contrast sources by a conjugate gradient iterative method such that the cost function is minimized. And the contrast function is then determined to minimize the error in the object equation. The cost function is a superposition of the errors in the data equations and errors in the object equations:

$$F(\chi, w_j) = F^S(w_j) + F^D\left(\chi, w_j\right) = \frac{\sum_j \left\| f_j - M^S \left\{ L_b \left[w_j \right] \right\} \right\|_S^2}{\sum_j \left\| f_j \right\|_S^2} + \frac{\sum_j \left\| \chi p_j^{inc} - w_j + \chi M^D \left\{ L_b \left[w_j \right] \right\} \right\|_D^2}{\sum_j \left\| \chi p_j^{inc} \right\|_D^2} \tag{20}$$

In which f_j is the scattered measured data.

The L_2-norms on domains S and domain D are defined as follow:

$$\left\| v_j \right\|_S^2 = \int_S v_j(r)\overline{v_j(r)}dr \qquad \left\| v_j \right\|_D^2 = \int_D v_j(r)\overline{v_j(r)}dr \tag{21}$$

Where the overbar denote the complex conjugate of a function.

We minimize the cost function (20) by conjugate gradient method, When the updated value of χ is obtained, we can produce the real velocity distribution of the medium. If the value of the cost function is not smaller than the prescribed error criterion, the update step will be repeated until convergence is achieved. The flow of the inversion and migration can be seen in Figure 2.

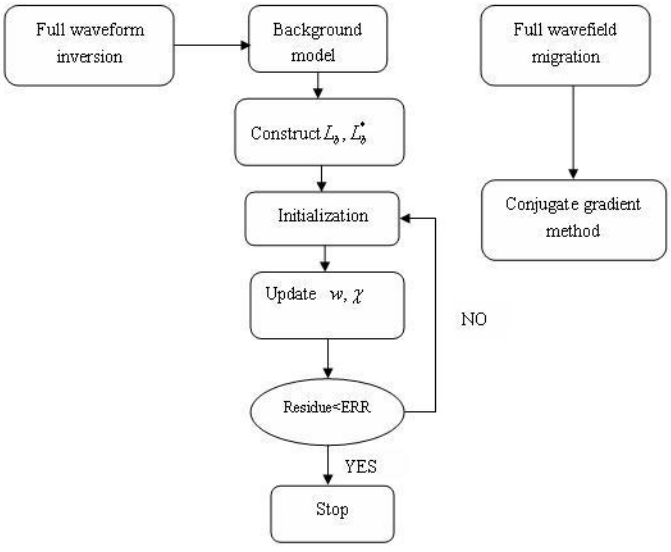

Figure 2. Flowchart of the full wavefield inversion and migration method

SUMMARY

Surface-related and internal multiples can be vital information for revealing the deep subsurface information, because the multiple wavefield can strength the illumination power towards the deeper subsurface. By applying the contrast source inversion method, I wish to produce the accurate velocity distribution and angle-dependent reflectivity of the subsurface model.

ACKNOWLEDGEMENTS

The authors would like to acknowledge Prof. HuiZhu Yang and Prof. YiBo Wang for their suggestions and discussions on this subject.

REFERENCES

[1] A. J. Berkhout. Combining full wavefield migration and full waveform inversion, a glance into the future of seismic imaging. GEOPHYSICS, 77(2012) P.S43-S50.

[2] Aria Abubakar, Wenyi Hu, Tarek M. Habashy, Peter M. van den Berg, Application of the finite-difference contrast-source inversion algorithm to seismic full-waveform data. GEOPHYSICS, 74(2009) WCC47–WCC58.

[3] Aria Abubakar, W Hu, P M van den Berg and T M Habashy. A finite-difference contrast source inversion method.Inverse problems, 24(2008) 065004.

[4] J. Virieux, S. Operto. An overview of full-waveform inversion in exploration geophysics. GEOPHYSICS,74 (2009) P.WCC127-WCC152.

[5] Wenyi Hu, Aria Abubakar, Tarek M.Habashy. Simultaneous multifrequency inversion of full-waveform seismic data. GEOPHYSICS, 74(2009) P.R1-R14.

[6] A. J. Berkhout. Seismic migration, imaging of acoustic energy by wave field extrapolation, a theoretical aspects. Elsevier Press, Netherlands, 1982.

[7] Peter M van Berg, Ralph E Kleinman. A contrast source inversion method. Inverse problem, 13(1997)1607-1620.

[8] P M van den Berg, A L van Broekhoven, A Abubakar. Extended contrast source inversion. Inverse problem. 15(1999)1325-1344.

[9] Laurent Sirgue, R.Gerhard Pratt. Efficient waveform inversion and imaging: A strategy for selecting temporal frequencies.GEOPHYSICS, 69(2004)P.231-248.

[10] John Etgen, Samuel H. Gray, YU Zhang. An overview of depth imaging in exploration geophysics. GEOPHYSICS, (74)(2009)P.WCA5-WCA17.

[11] Dietrich Ristow,Thomas Ruhi. Fourier finite-difference migration.GEOPHYSICS, 59(1994) P.1882-1893.

[12] Aria Abubakar, Tarek M habashy. Peter M van den Berg. Dries Gisolf. The diago nalized contrast source approach: an inversion method beyond the Born approximation. Inverse problems, 21(2005)685-702.

The Attenuation and Dispersion Analyses in Porous and Fractured Medium with Arbitrary Fracture Fill

Liyun Kong[1], Boris Gurevich[2], Tobias M. Müller[3], Yibo Wang[4,*], Huizhu Yang[1]

[1] Department of Engineering Mechanics, Tsinghua University, Beijing 100084, China
[2] Department of Exploration Geophysics, Curtin University of Technology, Western Australia 6845, Australia
[3] CSIRO Petroleum Resources, ARRC, Western Australia 6151, Australia
[4] Institute of Geology and Geophysics, Chinese Academy of Science, Beijing 100029, China
* Corresponding author: wangyibo@mail.igcas.ac.cn

Abstract To study the effect of fractu,re fill on the elastic anisotropy of the rock and frequency-dependent attenuation and dispersion in fractured reservoirs, a model for porous and fractured medium is developed. In this model, the fractured medium is considered as a periodic system of alternating layers of two types: thick porous layers representing the background, and very thin and highly compliant porous layers representing fractures. By taking the simultaneous limits of zero thickness and zero normal stiffness of the thin layers, we obtain expressions for dispersion and attenuation of the P-waves. The results show that in the low-frequency limit the elastic properties of such a medium can be described by Gassmann equation with a composite fluid, while the P-wave speed is relatively high at high frequencies for two layers can be treated as 'hydraulically isolated'. However, there appears to be a critical case where no dispersion is observed, which is caused by the balance of fractures compliance and fluid compressibility filling in them.

Keywords porous media, fracture , attenuation, dispersion

1 Introduction

Flow of the pore fluid by the passing wave is widely believed to be the main cause of attenuation and dispersion of elastic waves in porous rocks. In particular, flow that occurs due to spatial variations of rock or fluid properties on mesoscopic scale (larger than the pore size but smallerthan the wavelength) is considered to be significant at seismic frequencies [1-4]. The magnitude of attenuation and dispersion caused by mesoscopic wave-induced flow is proportional to the squared contrast (variance) of spatial variations of rock or fluid properties. Thus attenuation and dispersion are only significant if the contrast of spatial variations is large.

In recent years, two situations with large contrast in rock/fluid properties have been identified: partial saturation and fractured rock. Partial saturation refers to the situation where a rock is saturated with a mixture of two immiscible fluids with large difference between their properties (say, liquid and gas). When an elastic wave propagates through such a rock, the patches of rock saturated with gas and liquid will deform differently, resulting in pressure gradients and fluid flow [5-8]. Fractured rock refers to a situation where a porous rock is permeated by open fractures. When a wave propagates through such a rock, fractures will deform to a greater extent than the porous background, resulting in fluid flow between pores and fractures [9-13]. These situations (partial saturation and fractures) are usually treated separately: analysis of wave propagation in a partially saturated rock usually ignores variations in elastic properties of the solid frame, while the porous rock permeated by fractures is usually assumed to be saturated with a uniform fluid. However, in some situations, particularly when a fluid such as water or carbon dioxide is injected into a tight hydrocarbon reservoir, fractures may be filled with a different fluid (with capillary forces

preventing fluid mixing). In this paper we consider the simplest situation of this kind: a porous rock saturated with one fluid and permeated by a single set of aligned planar fractures filled with another fluid. For such a medium, we derive a dispersion equation following a method originally proposed by Brajanovski et al. [12] for a porous fractured medium saturated with a single fluid.

The paper is organized as follows. First, we review the theory in case of a medium saturated with a single fluid. Then we extend the method to the situation where the porous background and fractures are saturated with different fluids and derive the corresponding dispersion equation, which yields expressions for dispersion and attenuation due to wave induced flow between pores and fractures. To explore the behavior of attenuation and dispersion, we explore various limiting cases and present several numerical examples. Finally, we discuss the physical nature of the results obtained.

2 Liquid saturated porous and fractured medium

Brajanovski et al. [12] developed a model for a porous medium with aligned fractures. The medium comprises a periodic (with spatial period H) stratified system of alternating layers: relatively thick layers of a background material (with a finite porosity ϕ_b) and relatively thin layers of a high-porosity material representing the fractures. This double porosity model is a limiting case of a periodically layered poroelastic medium studied by White et al. [1] and Norris [14]. Norris showed that for frequencies much smaller than Biot's characteristic frequency $\omega_{\mathrm{B}} = \eta\phi/k\rho_{\mathrm{f}}$, and also much smaller than the resonant frequency of the layering $\omega_{\mathrm{R}} = V_{\mathrm{p}}/H$, the compressional wave modulus of a periodically layered fluid-saturated porous medium composed of two constituents, *b* and *c*, can be written in the form:

$$\frac{1}{C_{33}} = \frac{h_{\mathrm{b}}}{C_{\mathrm{b}}} + \frac{h_{\mathrm{c}}}{C_{\mathrm{c}}} + \frac{\left(\frac{\alpha_{\mathrm{b}}M_{\mathrm{b}}}{C_{\mathrm{b}}} - \frac{\alpha_{\mathrm{c}}M_{\mathrm{c}}}{C_{\mathrm{c}}}\right)^2}{\sqrt{\frac{i\omega\eta_{\mathrm{b}}M_{\mathrm{b}}L_{\mathrm{b}}}{C_{\mathrm{b}}k_{\mathrm{b}}}}\frac{H}{2}\cot\left(\sqrt{\frac{i\omega\eta_{\mathrm{b}}C_{\mathrm{b}}}{k_{\mathrm{b}}M_{\mathrm{b}}L_{\mathrm{b}}}}\frac{h_{\mathrm{b}}H}{2}\right) + \sqrt{\frac{i\omega\eta_{\mathrm{c}}M_{\mathrm{c}}L_{\mathrm{c}}}{k_{\mathrm{c}}C_{\mathrm{c}}}}\frac{H}{2}\cot\left(\sqrt{\frac{i\omega\eta_{\mathrm{c}}C_{\mathrm{c}}}{k_{\mathrm{c}}M_{\mathrm{c}}L_{\mathrm{c}}}}\frac{h_{\mathrm{c}}H}{2}\right)}, \tag{1}$$

In Eq. (1), both constituents are assumed to be made of the same isotropic grain material with bulk modulusK_{g}, shear modulus μ_{g} and density ρ_{g}, but they have different solid frame parameters: porosityϕ, permeability k, dry bulk modulus K, shear modulus μ and thickness fraction h. The layers b and c may be saturated with different fluids with bulk modulus K_{f}, density ρ_{f} and dynamic viscosity η, as indicated by adding 'b' and 'c' in the subscript. Parameter $C_j = L_j + \alpha_j^2 M_j$ denotes the fluid-saturated P-wave modulus of layer j given by Gassmann's equation [15], where $\alpha_j = 1 - \frac{K_j}{K_{\mathrm{g}}}$ is Biot's effective stress coefficient, M_j is pore space modulus defined by $\frac{1}{M_j} = \frac{\alpha_j - \phi_j}{K_{\mathrm{g}}} + \frac{\phi_j}{K_{\mathrm{f}j}}$ and $L_j = K_j + 4\mu_j/3$ is the dry P-wave modulus of the layer j.

To construct a model for a porous medium permeated by parallel fractures, Brajanovski et al. [12] considered parameters with subscript b to represent the porous background, and parameters with subscript c to represent fractures (cracks). They then assumed fractures to be very thin and very

compliant layers and thus considered Eq. (1) in the limit $h_c \to 0$, $K_c \to 0$ and $\mu_c \to 0$ such that both K_c and μ_c (and hence $L_c \to 0$) are O(h_c). By assuming that both pores and fractures are saturated with the same fluid with the viscosity $\eta_b = \eta_c = \eta$, Brajanovski et al [12] obtained the equation

$$\frac{1}{C_{33}} = \frac{1}{C_b} + \frac{\left(\frac{\alpha_b M_b}{C_b} - 1\right)^2}{\sqrt{\frac{i\omega\eta M_b L_b}{C_b k_b}}\frac{H}{2}\cot\left(\sqrt{\frac{i\omega\eta C_b}{k_b M_b L_b}}\frac{h_b H}{2}\right) + \frac{1}{Z_N}}, \tag{2}$$

Where $Z_N = \lim_{h_c \to 0} \frac{h_c}{L_c}$ is the normal excess fracture stiffness of the dry frame given by Schoenberg and Douma [16]. Implicit in the derivation of Eq. (2) was an assumption

$$K_f \gg h_c / Z_N, \tag{3}$$

When both pores and fractures are saturated with a liquid, Eq. (2) exhibits significant attenuation and velocity dispersion. However the model is limited to the case where the fluid is the same in both matrix pores and fractures, and there is an upper limit on the fluid compressibility (Eq. (3)). Below we develop a model that overcomes these limitations.

3 Arbitrary fluid in the fractures

The analysis in the previous section suggests that the effect of fracture fill on the overall modulus of the porous and fractured medium depends on how the fluid bulk modulus scales with h_c as $h_c \to 0$. To analyze this effect, we use the following parameterization

$$K_{fc}/K_g = B h_c, \tag{4}$$

where *B* is a dimensionless nonzero constant that defines the type of fluid in fractures, liquid, gas or intermediate. If *B* is large enough (e.g., if the fluid is a liquid), K_{fc} may satisfy the condition (3). In this case, taking the limit $h_c \to 0$ in Eq. (1), we obtain Eq. (2) with fluid properties K_f and η replaced by the corresponding values for the fluid in the pores K_{fb} and η_b. Conversely, $B = 0$ corresponds to dry fractures.

When $h_c \to 0$, we have $K_c \to 0$, and $\phi_c \to 1$, and thus $\alpha_c \to 1$, $M_c \to K_{fc}$, and $C_c \to L_c + K_{fc}$. Combining these results with the parameterizations (4), and considering $\cot(x) \approx 1/x$ for any complex x with $|x| \ll 1$ and $\cot\left(\sqrt{ix}\right) \to i$ for any real $x \gg 1$, Eq. (1) in the limit $h_c \to 0$ can be simplified as

$$\frac{1}{C_{33}} = \frac{1}{C_b} + \frac{Z_N}{1 + Z_N B K_g} + \frac{\left(\frac{\alpha_b M_b}{C_b} - \frac{Z_N B K_g}{1 + Z_N B K_g}\right)^2}{\sqrt{\frac{i\omega\eta_b M_b L_b}{C_b k_b}}\frac{H}{2}\cot\left(\sqrt{\frac{i\omega\eta_b C_b}{k_b M_b L_b}}\frac{H}{2}\right) + \frac{B K_g}{1 + Z_N B K_g}}, \tag{5}$$

Eq. (5) is the approximation of Eq. (1) for a porous and fractured medium with an arbitrary fracture fill.

Here, we have introduced a dimensionless constant *B* to define the type of fracture fluids, so that we can attain gas and liquid limiting cases. Additionally, we can define low and high frequencies with respect to fluid flow between fractures and background. Therefore, in the following section, we derive and analyze some limiting cases of fluids and frequencies.

4 Limiting cases

4.1 Fluid limits

4.1.1 Liquid in fractures

If the fluid in the fractures is liquid, then $B \gg 1$ and Eq. (5) gives

$$\frac{1}{C_{33}} = \frac{1}{C_{\mathrm{b}}} + \frac{\left(\frac{\alpha_{\mathrm{b}} M_{\mathrm{b}}}{C_{\mathrm{b}}} - 1\right)^2}{\sqrt{\frac{i\omega\eta_{\mathrm{b}} M_{\mathrm{b}} L_{\mathrm{b}}}{C_{\mathrm{b}} k_{\mathrm{b}}}} \frac{H}{2} cot\left(\sqrt{\frac{i\omega\eta_{\mathrm{b}} C_{\mathrm{b}}}{k_{\mathrm{b}} M_{\mathrm{b}} L_{\mathrm{b}}}} \frac{H}{2}\right) + \frac{1}{Z_{\mathrm{N}}}}}, \tag{6}$$

Note that Eq. (6) is exactly the same as Eq. (2). This shows that the result of Brajanovski et al [12] is valid not only if both pores and fractures are saturated with the same liquid, but also when the two liquids are different.

4.1.2 Dry or nearly dry fractures

When fractures are dry or nearly dry, Eq. (5) cannot, strictly speaking, be used because it was derived by assuming that B is nonzero. Instead, we take the limit $B \to 0$, directly in Eq (1). This gives

$$\frac{1}{C_{33}} = \frac{1}{C_{\mathrm{b}}} + Z_{\mathrm{N}} + \frac{\left(\frac{\alpha_{\mathrm{b}} M_{\mathrm{b}}}{C_{\mathrm{b}}}\right)^2}{\sqrt{\frac{i\omega\eta_{\mathrm{b}} M_{\mathrm{b}} L_{\mathrm{b}}}{C_{\mathrm{b}} k_{\mathrm{b}}}} \frac{H}{2} \cot\left(\sqrt{\frac{i\omega\eta_{\mathrm{b}} C_{\mathrm{b}}}{k_{\mathrm{b}} M_{\mathrm{b}} L_{\mathrm{b}}}} \frac{H}{2}\right)}}, \tag{7}$$

Incidentally, exactly the same result is obtained by taking the limit $B \to 0$ in Eq. (5). This means that Eq. (5) is valid even in the limit of small B. Eq. (7) gives the P-wave modulus for a porous medium with dry or gas-filled fractures, and it is quite different from Eq. (5) for liquid case. To further analyze the reason for the difference, we derive the limiting cases of low and high frequencies next.

4.2. Frequency limits

4.2.1 Low frequencies

In the low-frequency limit $\omega \to 0$, the cotangent function in Eq. (5) can be replaced by the inverse of its argument. Thus, Eq. (5) is reduced to

$$\frac{1}{C_{33}} = \frac{1}{C_{\mathrm{b}}} + \frac{1}{\frac{1}{Z_{\mathrm{N}}} + BK_{\mathrm{g}}} + \frac{\left(\frac{\alpha_{\mathrm{b}} M_{\mathrm{b}}}{C_{\mathrm{b}}} - \frac{BK_{\mathrm{g}}}{\frac{1}{Z_{\mathrm{N}}} + BK_{\mathrm{g}}}\right)^2}{\frac{M_{\mathrm{b}} L_{\mathrm{b}}}{C_{\mathrm{b}}} + \frac{BK_{\mathrm{g}}}{1 + Z_{\mathrm{N}} BK_{\mathrm{g}}}}}, \tag{8}$$

In the low frequency limit, the fluid pressure should be fully equilibrated between pores and fractures. Thus in this limit the result must be consistent with the anisotropic Gassmann equations for a fractured medium saturated with a single composite fluid [17] with a bulk modulus defined by

$$\frac{1}{K_{\mathrm{f}}^*} = \frac{S_{\mathrm{fb}}}{K_{\mathrm{fb}}} + \frac{S_{\mathrm{fc}}}{K_{\mathrm{fc}}}, \tag{9}$$

Eq. (9) is known as the Wood equation, and corresponds to so-called uniform saturation of the partial saturation theory [7, 8, 18]. So, if we replace K_{b} with K_{f}^* in Eq. (5), and then take the low

frequency limit, we can also get the same expression as given by Eq. (8).

To clarify the physical meaning of the low-frequency Eq. (8) we again consider liquid and dry (or gas) cases. For liquid-filled fractures (large *B*), we have

$$\frac{1}{C_{33}} = \frac{1}{C_{\mathrm{b}}} + \frac{\left(\frac{\alpha_{\mathrm{b}} M_{\mathrm{b}}}{C_{\mathrm{b}}} - 1\right)^2}{\frac{M_{\mathrm{b}} L_{\mathrm{b}}}{C_{\mathrm{b}}} + \frac{1}{Z_{\mathrm{N}}}}, \tag{10}$$

while for $B \ll 1$

$$\frac{1}{C_{33}} = \frac{1}{L_{\mathrm{b}}} + Z_{\mathrm{N}}, \tag{11}$$

The liquid limit, Eq. (10), corresponds exactly to the low frequency limit of the result of Brajanovski et al [12], with only the bulk modulus of the liquid in the pores affecting the overall modulus. This result may be understood from Eq. (10), which shows that when the bulk moduli of the two fluids are comparable, the effect of the fracture fluid is negligible for its relatively small saturation. In turn, Eq. (11) is exactly the modulus of the dry medium [12, 16]. This is because when K_{fc} is very small (much smaller than $h_{\mathrm{c}} K_{\mathrm{fb}}$), Wood Eq. (10) for the effective fluid modulus reduces to

$$\frac{1}{K_{\mathrm{f}}^*} = \frac{S_{\mathrm{fc}}}{K_{\mathrm{fc}}}, \tag{12}$$

and thus $K_{\mathrm{f}}^* \to 0$, which means that the whole porous and fractured model can be considered as dry or nearly dry medium. Physically, this is the result of the fact that at low frequencies, the pore pressure is equilibrated between pores and fractures, so when the pressure in fractures is zero, thus is also zero in the pores. This is the drained – or dry – limit.

4.2.2 High frequencies

In the high-frequency limit $\omega \to \infty$, the cotangent function in Eq. (5) can be replaced by i. So, we can get the expression of P-wave modulus at high frequencies

$$\frac{1}{C_{33}} = \frac{1}{C_{\mathrm{b}}} + \frac{1}{\frac{1}{Z_{\mathrm{N}}} + B K_{\mathrm{g}}}, \tag{13}$$

In liquid and gas cases we have

$$\frac{1}{C_{33}} = \frac{1}{C_{\mathrm{b}}}, \tag{14}$$

and

$$\frac{1}{C_{33}} = \frac{1}{C_{\mathrm{b}}} + Z_{\mathrm{N}}, \tag{15}$$

respectively.

Note that at high frequencies, the fluid pressure does not have time to equilibrate between pores and fractures, and thus they can be considered 'hydraulically isolated' [12, 17]. Thus the P-wave modulus in this limit corresponds to the modulus of a porous medium with isolated fractures. In the liquid case, the modulus given by Eq. (14) is the same as if there were no fractures. This is because liquid can stiffen the otherwise very compliant fractures so that P-wave velocities for waves propagating parallel and perpendicular to layering are both approximately equal to the modulus of the background medium [12, 16, 19]. Conversely, when fractures are dry, the P-wave modulus (15) is the same as for a medium with dry isolated fractures (cf Eq. (11)).

.

5 Numerical examples

Our main result, Eq. (5), shows that the P-wave modulus is complex-valued and frequency dependent regardless of fluid saturation of fractures. This means that waves will have attenuation and dispersion.

To explore these effects, we compute the complex phase slowness in the direction normal to the fractures $V_p^{-1}=\sqrt{\rho_{\mathrm{b}}/C_{33}}$, where $\rho_{\mathrm{b}}=(1-\phi_{\mathrm{b}})\rho_{\mathrm{g}}+\phi_{\mathrm{b}}\rho_{\mathrm{fb}}$ is mass density of the fluid-saturated background (the effect of fractures on the density can be ignored as their volume fraction is negligibly small). This complex phase slowness can be used to evaluate the frequency dependence of the P-wave phase velocity and attenuation for waves propagating perpendicular to fractures. The P-wave phase speed is the inverse of real part of the complex phase slowness, and the attenuation Q.is given by half the ratio of the real part to the imaginary part of the complex phase slowness.

Now, we rewrite Eq. (5) as a function of normalized frequency Ω [12]

$$\frac{1}{C_{33}}=\frac{h_{\mathrm{b}}}{C_{\mathrm{b}}}+\frac{1}{\frac{L_{\mathrm{b}}(1-\delta_{\mathrm{N}})}{\delta_{\mathrm{N}}}+BK_{\mathrm{g}}}+\frac{\left(\frac{\alpha_{\mathrm{b}}M_{\mathrm{b}}}{C_{\mathrm{b}}}-\frac{BK_{\mathrm{g}}}{\frac{L_{\mathrm{b}}(1-\delta_{\mathrm{N}})}{\delta_{\mathrm{N}}}+BK_{\mathrm{g}}}\right)^2}{L_{\mathrm{b}}\sqrt{i\Omega}*\cot\left(\frac{h_{\mathrm{b}}C_{\mathrm{b}}}{M_{\mathrm{b}}}\sqrt{i\Omega}\right)+\frac{BK_{\mathrm{g}}}{1+\frac{\delta_{\mathrm{N}}}{L_{\mathrm{b}}(1-\delta_{\mathrm{N}})}BK_{\mathrm{g}}}},\tag{16}$$

where $\Omega=\frac{\omega H^2\eta_{\mathrm{b}}M_{\mathrm{b}}}{4C_{\mathrm{b}}k_{\mathrm{b}}L_{\mathrm{b}}}$ is the normalized frequency and $\delta_{\mathrm{N}}=\frac{Z_{\mathrm{N}}L_{\mathrm{b}}}{1+Z_{\mathrm{N}}L_{\mathrm{b}}}$ is a dimensionless (normalized) fracture weakness with values between 0 and 1 [16]. All our calculations are made for a water-saturated sandstone using quartz as the grain material (K_{g}=37GPa, ρ_{g}=2.65×10^{3}kgm^{-3}). The dependency of bulk and shear moduli of the background dry on porosity was assumed to follow the empirical model of Krief et al. [20].

To explore the validity of our approximation, we compare the attenuation and dispersion results with the original Norris [14] model, Eq. (1). For the Norris model, we set fracture parameters to satisfy the assumptions of the approximation (h_{c}=0.001, ϕ_{c}=0.999, δ_{N}=0.2, k_{c}=200mD, η_{fc}=18.1e^{-6}Pa.s). Then, the P-wave speeds and inverse quality factor Q^{-1} are calculated for different values of B, and the results are shown on Fig. 1.Alternatively, we could have given an input value to K_{fc} and then computed B using Eq. (4). However, we prefer to evaluate the results for different values of the dimensionless constant B.

Fig. 1 shows diepersion and attenuation of P-waves propagating along the symmetry axis (normal to fracture plane) for different values of parameter B. Symbols show the values obtained by our approximation, Eq. (5), while the curves correspond to the Norris general solution, Eq. (1). We see that for the whole range of parameter B, the approximation matches the general model very accurately. Curves of dispersion and attenuation have a shape typical for a relaxation phenomenon. It is interesting that dispersion and attenuation is significant for both liquid-filled (B=1000) and dry (B=0.001) fractures, but is much lower for intermediate values of the parameter B. This somewhat

surprising observation can be explained as follows. When both pores and fractures are filled with liquids, the compression caused by the wave will compress the fractures to much greater extent than the background porous material (since fractures are much more compliant than pores), causing the fluid to flow from fractures into pores. Conversely, when the pores are saturated with a liquid and the fractures are dry (or filled with very compressible gas), the compression will cause the flow from pores into fractures (it will be easier to compress gas than deform the fractures). Thus, at some intermediate value of the fluid compressibility (or parameter B), there will be no flow at all, and hence no dispersion or attenuation.

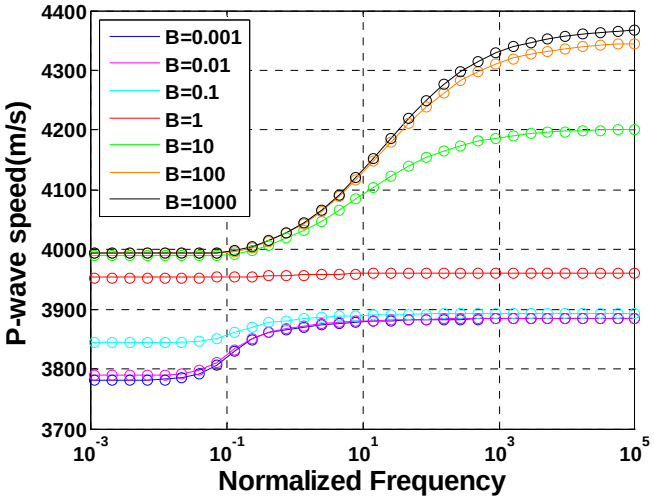

(a)

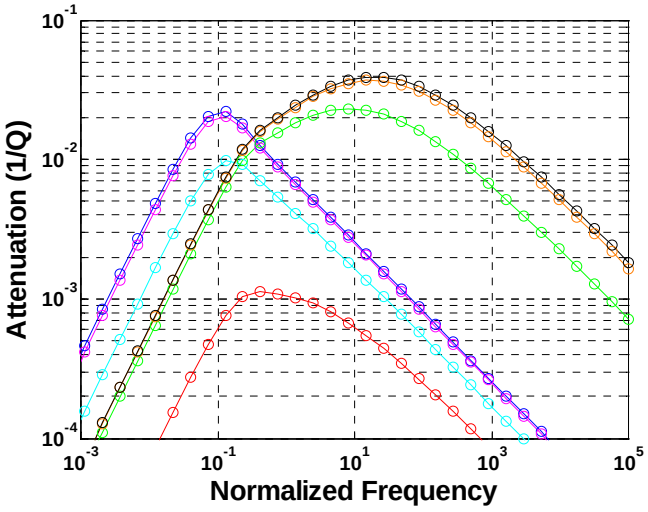

(b)

Figure 1. Frequency dependency of P-wave velocity (a) and inverse quality factor Q^{-1} (b) computed using our approximation (17) and Norris model (1) for different values of the parameter B.

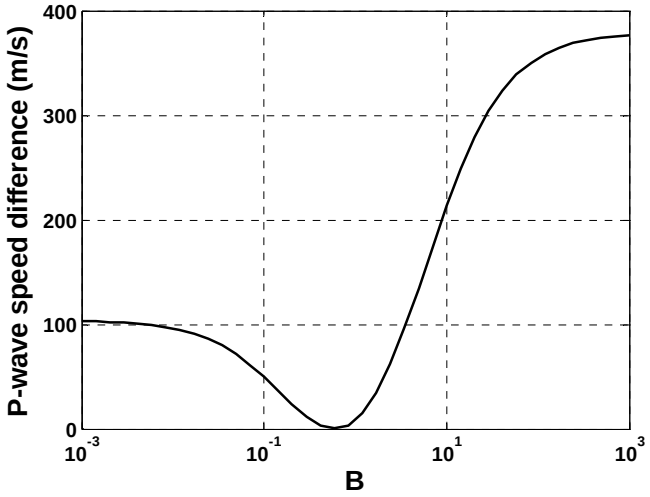

Figure 2. Dispersion magnitude (difference between high- and low-frequency velocities) as a function for parameter B. As B increases, the dispersion first decreases, reaches zero, and then increases again.

Fig. 2 shows the dispersion magnitude (difference between high- and low-frequency velocities) as a function for parameter B. As B increases, the dispersion first decreases, reaches zero, and then increases again. We also see that the dispersion is almost insensitive to B both for very small and very large values of B (corresponding to highly compressible gases and liquids, respectively), but quite sensitive to B for values of B in a range around the critical value where dispersion reaches zero. This critical value can be obtained by equating low- and high-frequency limits, Eqs (8) and (13). This gives

$$B^* = \frac{\alpha_\mathrm{b} M_\mathrm{b}}{C_\mathrm{b} - \alpha_\mathrm{b} M_\mathrm{b}} \frac{1}{K_\mathrm{g}} \frac{1}{Z_\mathrm{N}}, \tag{17}$$

The value B^* given by Eq. (17) corresponds to a critical fracture fluid modulus case, where there will be zero dispersion and attenuation in the general porous and fractured model. For the parameters used in the numerical example of Fig. 1, Eq. (5) gives $B^* \approx 0.59$. This value is quite close to 1.0, and thus we see very small dispersion and attenuation for $B = 1$.

6 Conclusions

We have developed a model for wave propagation in a porous medium with aligned fractures such that pores and fractures can be filled with different fluids. The model considers the fractured medium as a periodic system of alternating layers of two types: thick porous layers representing the background, and very thin and highly compliant porous layers representing fractures. The results show that in the low-frequency limit the elastic properties of such a medium can be described by Gassmann equation with a composite fluid, whose bulk modulus is a harmonic (Wood) average of the moduli of the two fluids. At higher frequencies, the model predicts significant dispersion and attenuation. The dispersion and attenuation are the highest when both pores and fractures are saturated with liquids. The dispersion and attenuation are also significant (but somewhat weaker) when the pores are filled with a liquid but fractures are dry or filled with a highly compressible gas. However, there is an intermediate case where no dispersion is observed. This can be explained by observing that when the medium is uniformly saturated with a liquid, wave-induced compression causes flow from fractures into pores due to high compliance of the fractures. Conversely, when

pores are filled with a liquid but fractures are filled with gas, flow will occur from pores into fractures due to high compressibility of gas. Thus an intermediate case exists where there is no flow and hence no dispersion or attenuation.

Acknowledgments

The authors thank Australia Curtin University, CSIRO and The Twelfth Five-Year National Major Projects of China (2011ZX05004-003) and National Nature Science Foundation of China (41274112) for financial support.

References

[1] J.E. White, N.G. Mikhaylova, F.M. Lyakhovitsky, Low-frequency seismic waves in fluid saturated layered rocks. Izvestija Academy of Sciences USSR, Physics of the Solid Earth, 11 (1975) 654-659.

[2] B. Gurevich, S.L. Lopatnikov, Velocity and attenuation of elastic waves in finely layered porous rocks. Geophys. J. Int., 121 (1995) 933–947.

[3] S.R. Pride, J.H. Harris, D.L. Johnson, A. Mateeva, K.T. Nihei, R.L. Nowack, J.W. Rector, H. Spetzler, R.Wu, T. Yamomoto, J. G. Berryman, M. Fehler, Acquisition/processing —Permeability dependence of seismic amplitudes. The Leading Edge, 22 (2003) 518–525.

[4] T.M. Müller, B. Gurevich, M. Lebede, Seismic wave attenuation and dispersion due to wave-induced flow in porous rocks – a review. Geophysics, 75 (2010) A147–A164.

[5] J.E. White, Computed seismic speeds and attenuation in rocks withpartial gas saturation. Geophysics, 40 (1975) 224–232.

[6] G.A. Gist, Interpreting laboratory velocity measurements in partially gas-saturated rocks. Geophysics, 59 (1994) 1100–1109.

[7] D.L. Johnson, Theory of frequency dependent acoustics in patchy saturated porous media. Journal of the Acoustical Society of America, 110 (2001) 682–694.

[8] J. Toms, T.M. Müller, B. Gurevich, Seismic attenuation in porousrocks with random patchy saturation. Geophysical Prospecting, 55 (2007) 671–678.

[9] J.A. Hudson, T. Pointer, E. Liu, Effective-medium theories for fluid-saturated materials with aligned cracks. Geophysical Prospecting, 49 (2001) 509–522.

[10] M. Chapman, Frequency dependent anisotropy due to mesoscale fractures in the presence of equant porosity. Geophysical Prospecting, 51 (2003) 369–379.

[11] M. Jakobsen, T.A. Johansen, C. McCann, The acoustic signature of fluid flow in complex porous media. Journal of Applied Geophysics, 54 (2003) 219–246.

[12] M. Brajanovski, B. Gurevich, M. Schoenberg, A model for P-wave attenuation and dispersion in a porous medium permeated by aligned fractures. Geophys. J. Int., 163 (2005) 372–384.

[13] B. Gurevich, M. Brajanovski, R.J. Galvin, T.M. Müller, J.T. Stewart, P-wave dispersion and attenuation in fractured and porous reservoirs-poroelasticity approach. Geophysical Prospecting, 57 (2009) 225–237.

[14] A.N. Norris, Low-frequency dispersion and attenuation in partially saturated rocks. J. Acoust. Soc. Am., 94 (1993) 359–370.

[15] F. Gassmann, Über die elastizität poröser medien. Viertel. Naturforsch: Ges. Zürich, 96 (1951) 1–23.

[16] M. Schoenberg, J. Douma, Elastic-wave propagation in media with parallel fractures and aligned cracks. Geophys. Prospect., 36 (1988) 571–590.
[17] B. Gurevich, Elastic properties of saturated porous rocks with aligned fractures. Journal of Applied Geophysics, 54 (2003) 203–218.
[18] G. Mavko, T. Mukerji, J. Dvorkin, The rock physics handbook: Tools for seismic analysis in porous media, Cambridge University Press, 1998.
[19] J.A. Hudson, E. Liu, S. Crampin, The mechanical properties of materials with interconnected cracks and pores. Geophysical Journal International, 124 (1996) 105–112.
[20] M. Krief, J. Garat, J. Stellingwerff, J. Ventre, A petrophysical interpretation using the velocities of P and S waves (Full-Wave Sonic). The Log Analyst, 5 (1990) 355–369.

Analyses of dynamic response and sound radiation of sandwich plate subjected to acoustic excitation under thermal environment

Yuan Liu, Yueming Li*

State Key Laboratory for Strength and Vibration of Mechanical Structures, Xi'an Jiaotong University, China
*Corresponding author: liyueming@mail.xjtu.edu.cn

Abstract In this paper, the dynamic response and sound radiation of sandwich plate subjected to an acoustic excitation under thermal environment are analyzed. The thermal environment is a uniform temperature load. Thermal stress is considered as the membrane force in the plate, while the change of the material property due to the thermal load is ignored. The acoustic excitation applied on the sandwich plate is assumed to be a plane wave. Coupling of the structural vibration and acoustic medium is considered. The equivalent non-classical theory, which takes the effects of rotational inertia and shear deformation into account, is utilized to get the analytical solutions. The effects caused by thermal environment and acoustic excitation are discussed. It is found that the rise of thermal load decreases the natural frequencies and moves response peaks to the low-frequency range. The acoustic excitation doesn't influence the natural characteristics of the sandwich plate, but the incident angle is relative to the number of evident peaks on the response curve. The comparisons of the analytical results and those computed by VA one show the accuracy of the theoretical method.

Keywords Sandwich plate, Thermal environment, Acoustic excitation, Dynamic response

1. Introduction

Sandwich plates are extensively used in the thermal protection system, which is utilized to protect the structure from the damage caused by the high temperature resulting from aerodynamic heating. During the course of the flight, the sandwich plate is exposed to high temperature and harsh mechanical, acoustic excitation. In order to use them efficiently, a good understanding of the dynamic and acoustic characteristics of the sandwich plate under such situation is necessary.

Vibro-acoustic problems of the structures under thermal environment are of great concern. N. Ganesan et al [1, 2] have analyzed vibration and sound radiation characteristics of composite plates under thermal environment numerically. Li et al [3-5] have carried out vibro-acoustic analyses for structures under thermal environment, including the broadband vibro-acoustic response based on hybrid FE-SEA [3], the influence of thermal stress with numerical method [4], and analytical solution for the dynamic and acoustic characteristics of an isotropic plate in thermal environments using classical plate theory [5]. Although a lot of vibro-acoustic problems under thermal environment have been analyzed, few studies can be found for sandwich plates, especially, lack of theoretical investigations.

The aim of this paper is to analyze the vibration and acoustic characteristics of a sandwich plate subjected to an acoustic excitation under thermal environment. Based on the equivalent non-classical theory, this study considers the effects of the shear deformation and the rotational inertia but ignores the compressional deformation. The coupling between the plate and the acoustic medium is taken into account. The influences caused by the thermal environment and the incident angle of the plane wave on the sandwich plates are deeply discussed in the present study.

2. Fundamental formulations

A sandwich plate with dimensions of $a \times b \times (2h_1 + h_2)$ is considered here, as shown in Fig. 1. The plate consists of two isotropic materials for facings and core respectively. The subscripts in the parameter expressions identify the specific materials, 1 for those of facings and 2 for those of core.

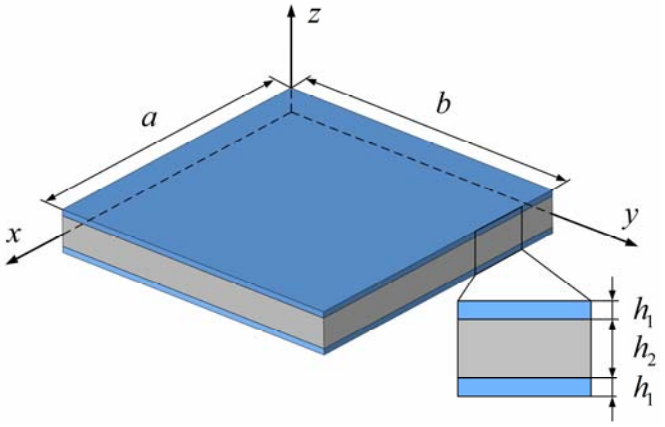

Figure 1. Sandwich plate model

2.1. Governing equations

Based on the non-classical theory, and by adopting the Власов assumption, the governing equations for dynamic analysis considering the membrane forces can be derived as [6]:

$$\begin{cases} \dfrac{G_z h}{k_\tau}\left(\nabla^2 w+\dfrac{\partial \beta_x}{\partial x}+\dfrac{\partial \beta_y}{\partial y}\right)-\rho h\dfrac{\partial^2 w}{\partial t^2}+N_x\dfrac{\partial^2 w}{\partial x^2}+N_y\dfrac{\partial^2 w}{\partial y^2}+2N_{xy}\dfrac{\partial^2 w}{\partial x\partial y}+q=0 \\ D\left(\dfrac{\partial^2 \beta_x}{\partial x^2}+\dfrac{1-\nu}{2}\dfrac{\partial^2 \beta_x}{\partial y^2}+\dfrac{1+\nu}{2}\dfrac{\partial^2 \beta_y}{\partial x\partial y}\right)-\dfrac{G_z h}{k_\tau}\left(\beta_x+\dfrac{\partial w}{\partial x}\right)-\rho J\dfrac{\partial^2 \beta_x}{\partial t^2}=0 \\ D\left(\dfrac{\partial^2 \beta_y}{\partial y^2}+\dfrac{1-\nu}{2}\dfrac{\partial^2 \beta_y}{\partial x^2}+\dfrac{1+\nu}{2}\dfrac{\partial^2 \beta_x}{\partial x\partial y}\right)-\dfrac{G_z h}{k_\tau}\left(\beta_y+\dfrac{\partial w}{\partial y}\right)-\rho J\dfrac{\partial^2 \beta_y}{\partial t^2}=0 \end{cases} \tag{1}$$

where $h=2h_1+h_2$, N_x, N_y and N_{xy} are membrane forces, for this paper, they are generated by thermal stresses. G_z, D, ν, ρh and ρJ are equivalent compositional parameters defined as:

$$G_z=\left[1-3\left(\frac{h_2}{2h}-\frac{h_2^3}{6h^3}\right)\right]\frac{E_1}{2(1+\nu_1)}+3\left(\frac{h_2}{2h}-\frac{h_2^3}{6h^3}\right)\frac{E_2}{2(1+\nu_2)} \tag{2}$$

$$D=\frac{2E_1}{3(1-\nu_1^2)}\left[\left(\frac{h}{2}\right)^3-\left(\frac{h_2}{2}\right)^3\right]+\frac{E_2}{3(1-\nu_2^2)}\left[\left(\frac{h_2}{2}\right)^3-\left(-\frac{h_2}{2}\right)^3\right] \tag{3}$$

$$\nu=\frac{1}{3D}\left\{\frac{2E_1\nu_1}{1-\nu_1^2}\left[\left(\frac{h}{2}\right)^3-\left(\frac{h_2}{2}\right)^3\right]+\frac{E_2\nu_2}{1-\nu_2^2}\left[\left(\frac{h_2}{2}\right)^3-\left(-\frac{h_2}{2}\right)^3\right]\right\} \tag{4}$$

$$\rho h=2\rho_1 h_1+\rho_2 h_2 \tag{5}$$

$$\rho J=\frac{2}{3}\rho_1\left[\left(\frac{h}{2}\right)^3-\left(\frac{h_2}{2}\right)^3\right]+\frac{1}{3}\rho_2\left[\left(\frac{h_2}{2}\right)^3-\left(-\frac{h_2}{2}\right)^3\right] \tag{6}$$

The plate is assumed to be stress-free at the reference temperature T_0. If the plate works under the temperature T, different from T_0, the stress state of the plate will be changed due to the thermal stresses. In this study, all edges are assumed to be simply supported with no in-plane displacement and the temperature is assumed to be uniformly distributed, so the thermal stresses caused by the temperature can be expressed as Eq. (7) [7]:

$$\sigma_x = -\frac{E_i}{1-\nu_i}\alpha_i \Delta T \qquad \sigma_y = -\frac{E_i}{1-\nu_i}\alpha_i \Delta T \qquad \sigma_{xy} = 0 \qquad (i = 1 \text{ or } 2) \tag{7}$$

where $\Delta T = T - T_0$.

The stress resultants caused by thermal stress can be obtained by integrating Eq. (7) along the thickness:

$$N_x = \sum_{k=1}^{3} \frac{-E_k \alpha_k h_k \Delta T}{1-\nu_k} \qquad N_y = \sum_{k=1}^{3} \frac{-E_k \alpha_k h_k \Delta T}{1-\nu_k} \qquad N_{xy} = 0 \tag{8}$$

2.2. Natural frequency and mode

Considering the boundary condition, the modes can be assumed as Eq. (9):

$$\begin{aligned} W_{mn}^{(p)} &= A_{mn}^{(p)} \sin\frac{m\pi}{a}x \sin\frac{n\pi}{b}y \\ \bar{\Psi}_{xmn}^{(p)} &= B_{mn}^{(p)} \cos\frac{m\pi}{a}x \sin\frac{n\pi}{b}y \\ \bar{\Psi}_{ymn}^{(p)} &= C_{mn}^{(p)} \sin\frac{m\pi}{a}x \cos\frac{n\pi}{b}y \end{aligned} \tag{9}$$

Suppose the displacement responses to be expressed as Eq. (10):

$$w = W_{mn}^{(p)} \mathrm{e}^{\mathrm{i}\omega_{mn}^{(p)}t} \qquad \beta_x = \Psi_{xmn}^{(p)} \mathrm{e}^{\mathrm{i}\omega_{mn}^{(p)}t} \qquad \beta_y = \Psi_{ymn}^{(p)} \mathrm{e}^{\mathrm{i}\omega_{mn}^{(p)}t} \tag{10}$$

Substituting Eq. (10) into Eq. (1) and letting q to be zero, Eq. (11) can be obtained:

$$\begin{aligned} &\frac{G_z h}{k_\tau}\left(\nabla^2 \mathrm{W}_{mn}^{(p)} + \frac{\partial \Psi_{xmn}^{(p)}}{\partial x} + \frac{\partial \Psi_{ymn}^{(p)}}{\partial y}\right) + \rho h \omega_{mn}^{(p)2} \mathrm{W}_{mn}^{(p)} + N_x \frac{\partial^2 \mathrm{W}_{mn}^{(p)}}{\partial x^2} + N_y \frac{\partial^2 \mathrm{W}_{mn}^{(p)}}{\partial y^2} + 2N_{xy} \frac{\partial^2 \mathrm{W}_{mn}^{(p)}}{\partial x \partial y} = 0 \\ &D\left(\frac{\partial^2 \Psi_{xmn}^{(p)}}{\partial x^2} + \frac{1-\nu}{2}\frac{\partial^2 \Psi_{xmn}^{(p)}}{\partial y^2} + \frac{1+\nu}{2}\frac{\partial^2 \Psi_{ymn}^{(p)}}{\partial x \partial y}\right) - \frac{G_z h}{k_\tau}\left(\Psi_{xmn}^{(p)} + \frac{\partial \mathrm{W}_{mn}^{(p)}}{\partial x}\right) + \rho J \omega_{mn}^{(p)2} \Psi_{xmn}^{(p)} = 0 \\ &D\left(\frac{\partial^2 \Psi_{ymn}^{(p)}}{\partial y^2} + \frac{1-\nu}{2}\frac{\partial^2 \Psi_{ymn}^{(p)}}{\partial x^2} + \frac{1+\nu}{2}\frac{\partial^2 \Psi_{xmn}^{(p)}}{\partial x \partial y}\right) - \frac{G_z h}{k_\tau}\left(\Psi_{ymn}^{(p)} + \frac{\partial \mathrm{W}_{mn}^{(p)}}{\partial y}\right) + \rho J \omega_{mn}^{(p)2} \Psi_{ymn}^{(p)} = 0 \end{aligned} \tag{11}$$

Substituting Eq. (9) into Eq. (11), one can get a homogeneous linear equations set about $A_{mn}^{(p)}$, $B_{mn}^{(p)}$ and $C_{mn}^{(p)}$. In order to get one set of solution, let 1, $b_{mn}^{(p)}$ and $c_{mn}^{(p)}$ take the place of them

respectively, where $b_{mn}^{(p)} = B_{mn}^{(p)} / A_{mn}^{(p)}$ and $c_{mn}^{(p)} = C_{mn}^{(p)} / A_{mn}^{(p)}$. Thus mode shapes can be rewritten as Eq. (12):

$$\begin{aligned} W_{mn}^{(p)} &= \sin\frac{m\pi}{a}x\sin\frac{n\pi}{b}y \\ \bar{\Psi}_{xmn}^{(p)} &= b_{mn}^{(p)}\cos\frac{m\pi}{a}x\sin\frac{n\pi}{b}y \\ \bar{\Psi}_{ymn}^{(p)} &= c_{mn}^{(p)}\sin\frac{m\pi}{a}x\cos\frac{n\pi}{b}y \end{aligned} \tag{12}$$

If a homogeneous linear equations set exists nonzero solutions, its determinant of the coefficient matrix should be zero. Thus the natural frequency can be obtained by solving Eq. (13):

$$\begin{vmatrix} \frac{G_z h}{k_\tau}(-\frac{m^2\pi^2}{a^2}-\frac{n^2\pi^2}{b^2})+\omega_{mn}^{(p)2}\rho h-\frac{m^2\pi^2}{a^2}N_x-\frac{n^2\pi^2}{b^2}N_y & -\frac{G_z h}{k_\tau}\frac{m\pi}{a} & -\frac{G_z h}{k_\tau}\frac{n\pi}{b} \\ -\frac{G_z h}{k_\tau}\frac{m\pi}{a} & D(-\frac{m^2\pi^2}{a^2}-\frac{1-\nu}{2}\frac{n^2\pi^2}{b^2})-\frac{G_z h}{k_\tau}+\rho J\omega_{mn}^{(p)2} & -\frac{1+\nu}{2}D\frac{mn\pi^2}{ab} \\ -\frac{G_z h}{k_\tau}\frac{n\pi}{b} & -\frac{1+\nu}{2}D\frac{mn\pi^2}{ab} & D(-\frac{n^2\pi^2}{b^2}-\frac{1-\nu}{2}\frac{m^2\pi^2}{a^2})-\frac{G_z h}{k_\tau}+\rho J\omega_{mn}^{(p)2} \end{vmatrix}=0 \tag{13}$$

While $\omega_{mn}^{(p)} = 0$, the critical buckling temperature can be acquired.

By putting the natural frequencies into the equations, the coefficients can be obtained:

$$b_{mn}^{(p)} = \frac{\frac{G_z h}{k_\tau}(-\frac{m^2\pi^2}{a^2}-\frac{n^2\pi^2}{b^2})+\omega_{mn}^{(p)2}\rho h-\frac{m^2\pi^2}{a^2}N_x-\frac{n^2\pi^2}{b^2}N_y}{\frac{G_z h}{k_\tau}(\frac{m\pi}{a}+\frac{n\pi}{b}\frac{D(-\frac{m\pi}{a}-\frac{1-\nu}{2}\frac{an^2\pi}{b^2m})-\frac{G_z ha}{k_\tau m\pi}+\frac{\rho J\omega_{mn}^{(p)2}a}{m\pi}+\frac{1+\nu}{2}D\frac{m\pi}{a}}{D(-\frac{n\pi}{b}-\frac{1-\nu}{2}\frac{bm^2\pi}{a^2n})-\frac{G_z hb}{k_\tau n\pi}+\frac{\rho J\omega_{mn}^{(p)2}b}{n\pi}+\frac{1+\nu}{2}D\frac{n\pi}{b}})} \tag{14}$$

$$c_{mn}^{(p)} = \frac{\frac{G_z h}{k_\tau}(-\frac{m^2\pi^2}{a^2}-\frac{n^2\pi^2}{b^2})+\omega_{mn}^{(p)2}\rho h-\frac{m^2\pi^2}{a^2}N_x-\frac{n^2\pi^2}{b^2}N_y}{\frac{G_z h}{k_\tau}(\frac{m\pi}{a}\frac{D(-\frac{n\pi}{b}-\frac{1-\nu}{2}\frac{bm^2\pi}{a^2n})-\frac{G_z hb}{k_\tau n\pi}+\frac{\rho J\omega_{mn}^{(p)2}b}{n\pi}+\frac{1+\nu}{2}D\frac{n\pi}{b}}{D(-\frac{m\pi}{a}-\frac{1-\nu}{2}\frac{an^2\pi}{b^2m})-\frac{G_z ha}{k_\tau m\pi}+\frac{\rho J\omega_{mn}^{(p)2}a}{m\pi}+\frac{1+\nu}{2}D\frac{m\pi}{a}}+\frac{n\pi}{b})} \tag{15}$$

Considering Eq. (14), Eq. (15) and Eq. (12), one can determine the mode shapes.

2.3. Dynamic analyses

Dynamic responses of the sandwich plate which is subjected to a plane sound wave are discussed in this section.

2.3.1. Acoustic load

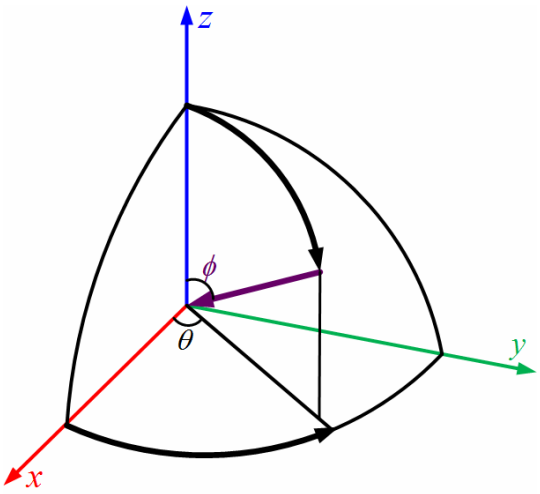

Figure 2. Incident plane wave

The incident angles of plane sound wave are shown in Fig. 2. If neglect the vibration of the plate, the incident and reflected sound pressure can be expressed as Eq. (16-17) [8]:

$$p_i(x,y,z=\frac{2h_1+h_2}{2},t)=P_i\,\mathrm{e}^{\mathrm{i}\omega t-\mathrm{i}k[\sin\phi(x\cos\theta+y\sin\theta)+\frac{2h_1+h_2}{2}\cos\phi]} \tag{16}$$

$$p_r(x,y,z=\frac{2h_1+h_2}{2},t)=P_i\,\mathrm{e}^{\mathrm{i}\omega t-\mathrm{i}k[\sin\phi(x\cos\theta+y\sin\theta)-\frac{2h_1+h_2}{2}\cos\phi]} \tag{17}$$

The dynamic response of an elastic plate excited by the incident wave can modify the resultant sound wave. The plate and acoustic medium have the same normal velocity on the interface. Use Rayleigh's integral (Eq. 18) to calculate the scattered sound pressure produced by the elastic vibration of the plate [9].

$$p_s(x,y,z=\frac{2h_1+h_2}{2},t)=-\frac{\rho_0\omega^2}{2\pi}\int_{S_0}\frac{e^{-\mathrm{i}k\sqrt{(x-x_0)^2+(y-y_0)^2}}}{\sqrt{(x-x_0)^2+(y-y_0)^2}}w(x_0,y_0)dS_0\mathrm{e}^{\mathrm{i}\omega t} \tag{18}$$

An additional pressure components, associated with the wave transmitted into the other side of plate, is added to the loading term in the governing equations. The two plate surfaces partake in identical motions, and the acoustic medium on both sides of the plate are of the same. The phase is, however, different. Thus, on the plate surface this transmitted pressure p_t takes the value $-p_s$ [8].

$$p_t(x,y,z=-\frac{2h_1+h_2}{2},t)=\frac{\rho_0\omega^2}{2\pi}\int_{S_0}\frac{e^{-\mathrm{i}k\sqrt{(x-x_0)^2+(y-y_0)^2}}}{\sqrt{(x-x_0)^2+(y-y_0)^2}}w(x_0,y_0)dS_0\mathrm{e}^{\mathrm{i}\omega t} \tag{19}$$

Resultant acoustic excitation is of the form:

$$q(x,y,t)=p_i+p_r+p_s-p_t \tag{20}$$

Considering Eq. (16-19) and Eq. (20), the loading (Eq. 21) can be obtained:

$$q(x,y,t)=2P_i\cos(\frac{2h_1+h_2}{2}k\cos\phi)\,\mathrm{e}^{\mathrm{i}\omega t-\mathrm{i}k\sin\phi(x\cos\theta+y\sin\theta)}-\frac{\rho_0\omega^2}{\pi}\int_{S_0}\frac{e^{-\mathrm{i}k\sqrt{(x-x_0)^2+(y-y_0)^2}}w(x_0,y_0)}{\sqrt{(x-x_0)^2+(y-y_0)^2}}dS_0\mathrm{e}^{\mathrm{i}\omega t} \tag{21}$$

2.3.2. Vibration responses

Based on mode superposition principle, the dynamic displacement responses can be expanded as Eq. (22):

$$\begin{aligned} w(x,y,t) &= \sum_m \sum_n \sum_p W_{mn}^{(p)}(x,y) T_{mn}^{(p)}(t) \\ \beta_x(x,y,t) &= \sum_m \sum_n \sum_p \Psi_{xmn}^{(p)}(x,y) T_{mn}^{(p)}(t) \\ \beta_y(x,y,t) &= \sum_m \sum_n \sum_p \Psi_{ymn}^{(p)}(x,y) T_{mn}^{(p)}(t) \end{aligned} \tag{22}$$

Assume the time-dependent factor to be $e^{i\omega t}$. Thus,

$$T_{mn}^{(p)}(t) = T_{mn}^{(p)} e^{\mathrm{i}\omega t} \tag{23}$$

Substituting Eq. (22-23) into Eq. (1), in view of the Eq. (11) and the orthogonality for the modes, one can acquire Eq. (24),

$$T_{mn}^{(p)} Z_{mn}^{(p)} + \sum_{k,l,q} Z_{mn}^{kl} T_{kl}^{(q)} = F_{mn} \tag{24}$$

in which:

$$Z_{mn}^{(p)} = \left(\omega_{mn}^{(p)2} - \omega^2\right)\left\{\frac{ab}{4} \times \left[\rho h + \rho J \times (b_{mn}^{(p)^2} + c_{mn}^{(p)^2})\right]\right\}$$

$$F_{mn} = \int_0^a \int_0^b \left\{2P_i \cos\left(\frac{2h_1 + h_2}{2} k \cos\phi\right) \mathrm{e}^{-\mathrm{i}k \sin\phi (x\cos\theta + y\sin\theta)}\right\} \sin\frac{m\pi x}{a} \sin\frac{n\pi y}{b} dxdy$$

$$Z_{mn}^{kl} = \frac{\rho_0 \omega^2}{\pi} \int_0^a \int_0^b \int_0^a \int_0^b \frac{e^{-\mathrm{i}k\sqrt{(x-x_0)^2 + (y-y_0)^2}}}{\sqrt{(x-x_0)^2 + (y-y_0)^2}} \sin\frac{k\pi x_0}{a} \sin\frac{l\pi y_0}{b} \sin\frac{m\pi x}{a} \sin\frac{n\pi y}{b} dx_0 dy_0 dx dy$$

Solving Eq. (24), one can obtain the displacement response. By taking derivative with respect to t, the velocity can be acquired. In accordance with the Rayleigh's integral, the sound pressure at the observation point (x_p, y_p, z_p) above the plate can be got using the velocity (Eq. 25):

$$p(x_p, y_p, z_p, t) = \frac{\mathrm{i}\omega\rho_0}{2\pi} \mathrm{e}^{\mathrm{i}\omega t} \int_\Omega \frac{v(x,y) \cdot \mathrm{e}^{-\mathrm{i}kR}}{R} \mathrm{d}A \tag{25}$$

3. Validation

A simply supported rectangular sandwich plate with dimensions of 400×300×10 mm is considered here for numerical studies, which are carried out to test the validity of the analytical solution.
0.5 mm and 9 mm are the thickness for the facings and the core respectively. The properties for them are listed in Table 1. Structural damping ratio is taken as 0.001.
Use Nastran to test the natural frequencies and modes with FEM (finite element method). The comparisons of the analytical results with those got by numerical approach are shown in Table 2, from which one can see that the two sets of results match with each other very well.

Table 1. Material properties

Material	Young modulus	Poisson'	Density	Coefficient of thermal expansion

	(GPa)	ratio	(kg m^{-3})	(℃$^{-1}$)
Facing	70(1+0.001i)	0.3	2700	2.3E−5
Core	7(1+0.001i)	0.3	1000	1.8E−5

Table 2. Comparisons of the natural frequencies

Modes	With temperature load of 50℃		
	Numerical (Hz)	Analytical (Hz)	Error (%)
(1,1)	245.56	255.44	4.02
(2,1)	645.10	659.75	2.27
(1,2)	955.35	963.44	0.85
(3,1)	1290.6	1304.5	1.07
(2,2)	1318.9	1346.7	2.11
(3,2)	1928.3	1970.6	2.19
(1,3)	2079.4	2079.7	0.02
(4,1)	2166.4	2174.8	0.39

Numerical dynamic responses, used to test the analytical solutions, are obtained using VA one. FEM is utilized to acquire the velocity response, caught at (0.1m, 0.1m), while BEM (boundary element method) is used to get sound pressure level, caught at (0.1m, 0.1m, 3m).

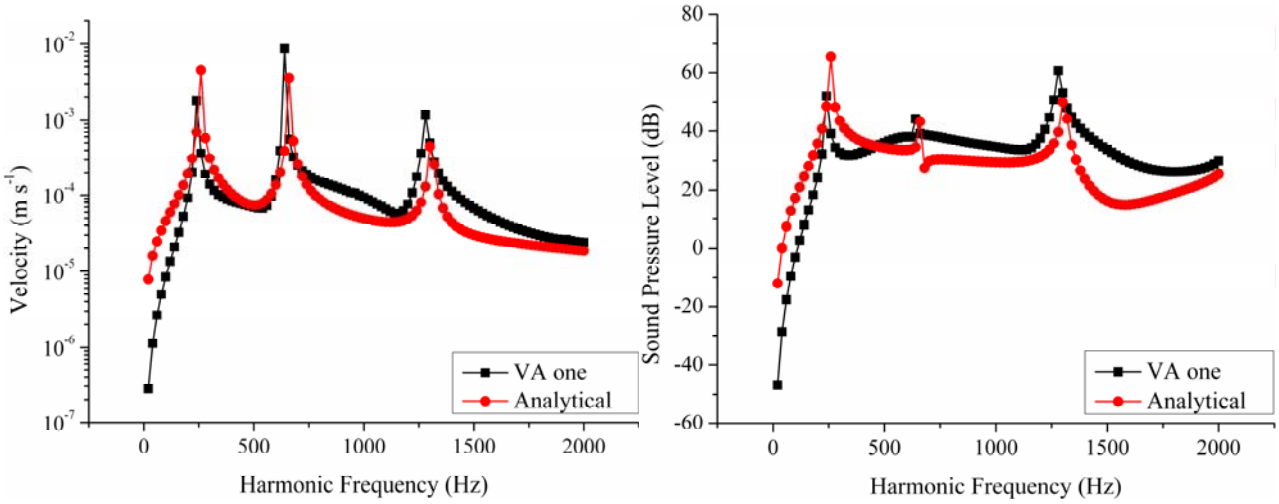

a. Velocity b. Sound Pressure Level

Figure 3. Comparisons of dynamic responses $\Delta T = 50\,°C$ $\phi = 30°$ $\theta = 0°$

From Fig. 3, one can find out that the trends of the response are of the same. There are both three evident peaks on each curve. So far, it could be believable that the present analytical solution is correct based on the above mutual validation.

4. Discussion

4.1. Different thermal loads

Thermal load can change the intrinsic property and influence the dynamic characteristics of the

sandwich plate. To understand the effects caused by the thermal load, several uniform temperature loads, $\Delta T = 0°C, 50°C, 90°C$, are imposed on the plate, whose buckling temperature is verified to be $94°C$.

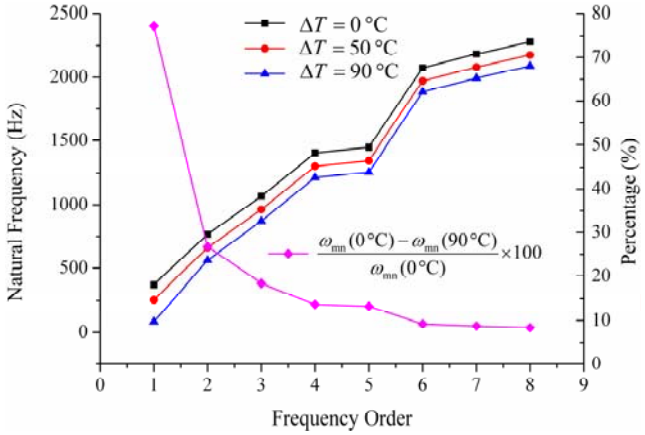

Figure 4. Natural frequency and relative difference

The natural frequencies of the sandwich plate subjected to different thermal load are shown in Fig. 4, from which the trend that the natural frequencies reduce with the temperature rising can be seen obviously. The modes for the plate are the same under different temperature. The relative frequency difference of the first natural frequency is much greater than others, which means the effect induced by thermal load is more obvious in fundamental frequency.

The incident sound wave which is perpendicular to the plane is applied to the plate. The velocity response at (0.1m, 0.1m) and the sound pressure level responses at (0.1m, 0.1m, 3m) are shown in Fig. 5, from which, one can observe that with the thermal load increasing, the peaks of vibration and acoustic responses float to low-frequency range.

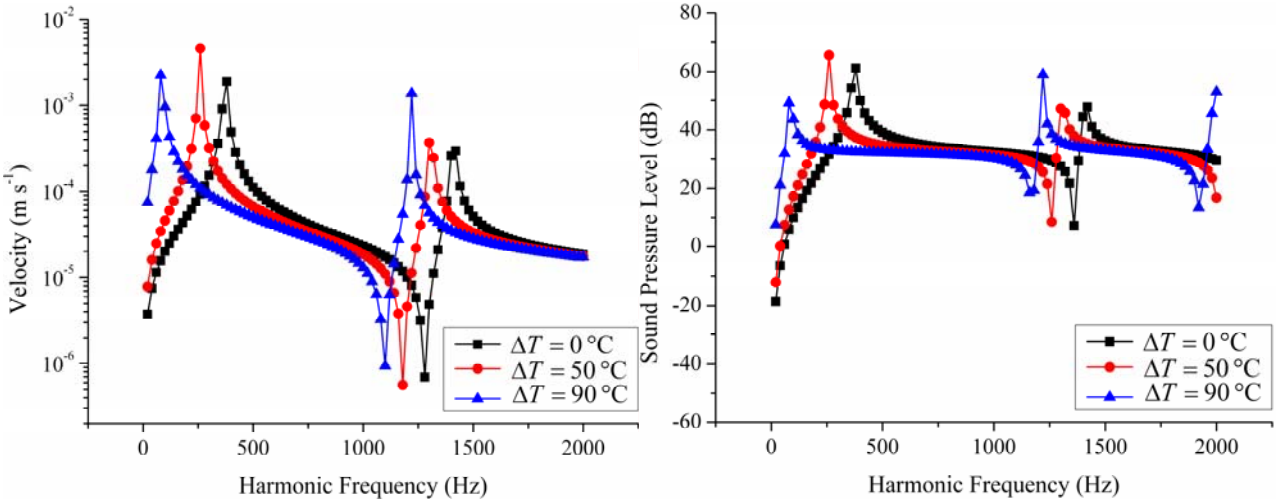

a. Velocity b. Sound Pressure Level

Figure 5. Dynamic responses

4.2. Different incident angles

Plane waves with incident angle of $0°-0°$, $30°-0°, 30°-30°$ are applied on the sandwich plate to discuss the influence caused by the incident angle. Different from the thermal load, the plane sound wave doesn't change the natural characteristics of the plate. Only the dynamic response is affected. The plate is also subjected to a uniform temperature load of $50°C$.

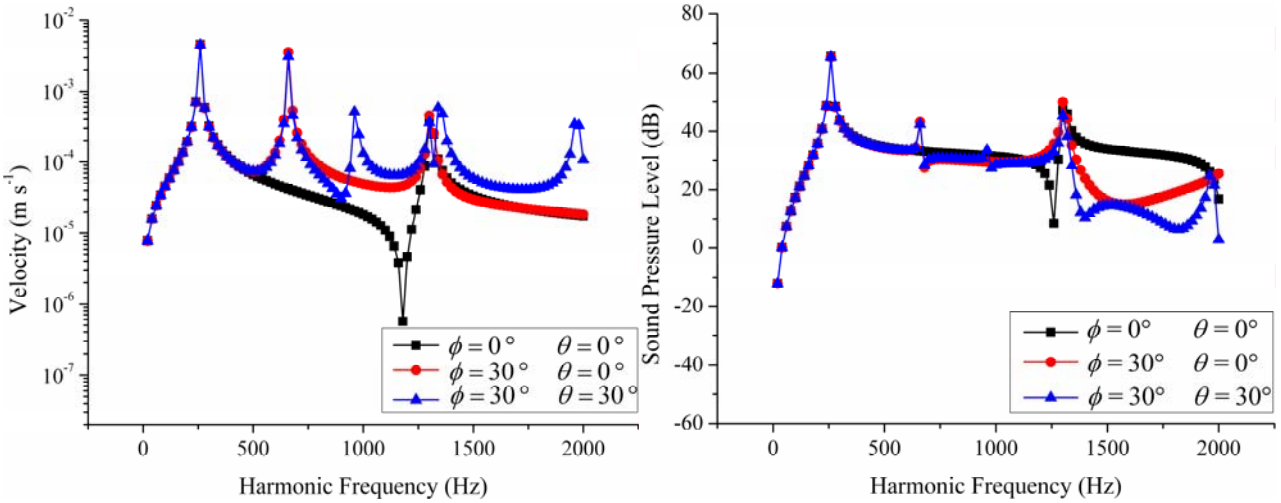

a. Velocity b. Sound Pressure Level

Figure 6. Dynamic responses

From Fig. 6, It is found that the number of the evident peaks is associated with the incident angle of the acoustic excitation. Because the excitation can't influence the natural frequency, the frequencies of peaks on each curve correspond to the natural frequencies of the sandwich plate under the temperature rise of $50°$. The first-order natural mode is markedly excited by all these three sound wave. The three curves are overlapping in the low frequency.

5. Conclusion

In this paper, a method to analyze the dynamic response and sound radiation of the sandwich plate under thermal environment is presented.

The influences caused by thermal environment and acoustic excitation on the sandwich plate are discussed in this paper. Sandwich plates subjected to different thermal loads present different natural property. The natural frequencies decrease and the modes remain the same when the thermal load rises. Thermal environment influences fundamental frequency remarkably, while the effect is less obvious in high natural frequency domain. On the other hand, the dynamic responses are also changed by the thermal load. As the thermal load increases, the peaks of response float to low-frequency range.

The plate imposed on the plane sound wave with different incident angle is analyzed. The acoustic excitation can't affect the natural characteristics of the plate, but the dynamic response is highly associated with the incident angle of the plane wave. Plane waves with different incident angles can excite different number of the evident peaks on the response curve, but the corresponding frequency of each peak can't be affected.

Acknowledgements

The authors are grateful to the National Natural Science Foundation of China (Grant No. 91016008, 11021202).

References

[1] P. Jeyaraj, N. Ganesan, C. Padmanabhan, Vibration and acoustic response of a composite plate with inherent material damping in a thermal environment. Journal of Sound and Vibration, 320 (2009) 322-338.

[2] B. R. Kumar, N. Ganesan, R. Sethuraman, Vibro-acoustic analysis of composite circular disc

with various orthotropic properties under thermal environment. International Journal of Vehicle Noise and Vibration, 4 (2008) 35-69.
[3] X. W. Yang, Y. M. Li, Q. Geng, Broadband Vibro-acoustic Response of Aircraft in High Temperature Environment Based on Hybrid FE-SEA (in Chinese). Acta Aeronautica et Astronautica Sinica, 32 (2011) 1851-1859.
[4] Q. Geng, Y. M. Li, X. W. Yang, Vibro-acoustic numerical analysis of thermally stressed aircraft structure (in Chinese). Chinese Journal of Computational Mechanics, 29 (2012) 99-104.
[5] Q. Geng, Y. M. Li, Analysis of dynamic and acoustic radiation characters for a flat plate under thermal environments. International Journal of Applied Mechanics, accepted.
[6] C. Y. Tsao, The solution of composite plates by equivalent non-classical theory (in Chinese), Acta Mechanica Solida Sinica, 4 (1981), 477-490.
[7] R.B. Hetnarski, M.R. Eslami, Thermal Stresses-Advanced Theory and Applications, Springer, Berlin, 2009.
[8] Miguel C. Junger, David Feit, Sound, Structures, and Their Interaction, 2nd revised edition, The MIT Press, London, 1986.
[9] Z. Y. He, Structural Vibration and Sound Radiation, Harbin Engineering University Press, Harbin, 2001.

Characterization of Mechanical and Physical Properties of Silica Aerogels Using Molecular Dynamics Simulation

Jingjie Yeo[1], Jincheng Lei[2], Zishun Liu[2,*], Teng Yong Ng[1]

[1] School of Mechanical and Aerospace Engineering, Nanyang Technological University, 50 Nanyang Avenue, 639798 (Singapore)
[2] International Centre for Applied Mechanics, State Key Laboratory for Strength and Vibration of Mechanical Structures, Xi'an Jiaotong University, Xi'an, 710049, China
* Corresponding author: zishunliu@mail.xjtu.edu.cn

Abstract Silica aerogels are nanoporous ultralight materials with extreme materials properties: the highest specific surface area of any material; slowest speed of sound through any solid material; excellent thermal insulators. Using molecular dynamics and the Tersoff potential, re-parameterized to simulate silicon dioxide, we have modeled the porous structures of silica aerogels. Our study shows that this potential is more suitable for modeling thermal properties in amorphous silica than the widely-used BKS potential. Increasing densities of aerogel samples are generated using an expanding and quenching process. Analysis of the fractal dimensions indicates a good fit with previous theoretical and experimental results. Each sample's thermal conductivity is determined using reverse non-equilibrium molecular dynamics. Results indicate that the power-law fit of our data reflects the power-law exponent found in experimental studies. The results are also of the same order of magnitude as experimental bulk aerogel, but they are consistently higher. Analysis of the pore size distribution shows, firstly, that such a disparity is due to limited pore sizes represented in a finite nano-sized system, and secondly, that increasing system length scales leads to corresponding increases in the pore sizes that can be represented. Furthermore, we attempt to determine the mechanical properties, such as Young's modulus of aerogel by using the same potential. We can conclude from all these results that our model is very suitable for modeling the mechanical and physical properties of bulk silica aerogel, and that an appropriate system length scale can be chosen to suit the pore size regime of interest.

Keywords molecular dynamics, silica aerogel, nanoporous ultralight materials.

1. Introduction

Silica aerogel is an exceptionally percolated material [1], made from various sol-gel processes and supercritical drying. Some silica aerogel's properties include very low density and extremely high thermal resistance [2, 3]. Previous experimental studies characterized silica aerogel's thermal conductivity and transport mechanisms, and found that the solid thermal conductivity scaled with density via a power law:

$$\lambda_s = C\rho^{\alpha} \tag{1}$$

where α was approximately 1.6 for densities between 0.3 to 1.0g/cm^3 [4]. Previous numerical studies characterizing the properties of silica aerogel [5, 6] include accurate reproductions of the porous and fractal nature of silica aerogels [7-9]. Murillo *et al.* [9] devised an expanding, heating and quenching method to model silica aerogels, obtaining good fits for the elastic moduli in comparison with experimental results. Ng *et al.* [6] employed negative pressure rupturing with the van Beest, Kramer and van Santen (BKS) potential [10, 11], and determined their thermal conductivities. It was found that the power-law fit of the data corresponds to experimental bulk sintered aerogel.

In this study, new methods are used to attain a closer fit of the thermal conductivity, in comparison with experimental data. We have found that the Tersoff potential, re-parameterized to model silicon dioxide, is more suitable than the BKS potential in predicting the thermal conductivity of amorphous silica. The solid thermal conductivity of silica aerogels are determined using reverse non-equilibrium MD (RNEMD) simulations, by generating the porous samples using the method by

Murillo et al. [9] and obtaining aerogel densities in the range of 0.3 to 1.0g/cm^3. The results are plotted and compared against experimental data [4]. The mechanical property, such as Young's modulus is simulated by using same method. The Young's modulus of aerogel with densities in the range of 0.3 to 1.0g/cm^3 is presented also.

2. Simulation Methods

The simulations are performed on the LAMMPS [12] software. The interaction potential used is the Tersoff potential [13], re-parameterized to model interactions between silicon and oxygen [14]. From comparison studies using the BKS potential and Tersoff potential, it is found that the Tersoff potential is more suitable for thermal conductivity studies. , while, the BKS potential augmented with a "24-6" Lennard Jones potential can prevent uncontrollable dynamics at very high temperatures [15]. Using the method by Murillo *et al.* [9], porous aerogel structures can be formed by expanding, heating and quenching, producing aerogels in the density range of 0.3 to 1.0g/cm^3. RNEMD [6, 16-18] can be used to determine the thermal conductivity at each aerogel density, where energies are swapped once every 0.025ps, while the system is kept an average temperature of 300K. This amount of swapping ensures a rapid convergence of the simulated temperature gradient, and produced a linear response within the simulation cell. The system is allowed to equilibrate for a further 1.0ns till a fully linear response has been obtained, and finally, the temperature gradient is averaged over another 50ps. The total solid thermal conductivity can be found by averaging over 5 independent samples at each density. To investigate the Young's modulus with the strain rate 0.0005ps^{-1} for 200ps, the tension tests are carried out on samples of different densities.

3. Results and Discussions

3.1. Thermal conductivity of dense amorphous silica

The thermal conductivity of increasing lengths of amorphous silica is compared with experimental results to validate our MD scheme. These amorphous silica samples are generated by quenching β-cristobalite, from 5000K to 300K. Their thermal conductivities are determined, as shown in Fig. 1 with their error bars.

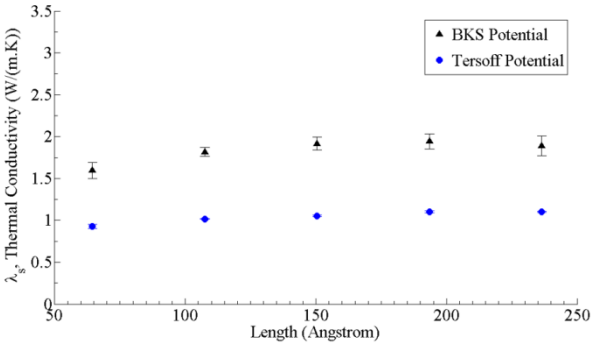

Figure 1. Amorphous silica of various lengths and their thermal conductivities

As the system length increases, so do the thermal conductivity, such that the BKS potential significantly overshoots the thermal conductivity of bulk amorphous silica, which lies between 1.37 – 1.4W/(m.K) [19]. The Tersoff potential plateaus at 1.10 ± 0.01W/(m.K) shows an almost linear dependence with increasing length scales. By extrapolating the results to an infinite length scale, thus representing bulk amorphous silica, the Tersoff potential can give a much better estimation of bulk thermal properties. The inverse of the thermal conductivities versus the inverse of the lengths

($1/\lambda_s$ vs 1/L) are plotted and extrapolated in Fig. 2.

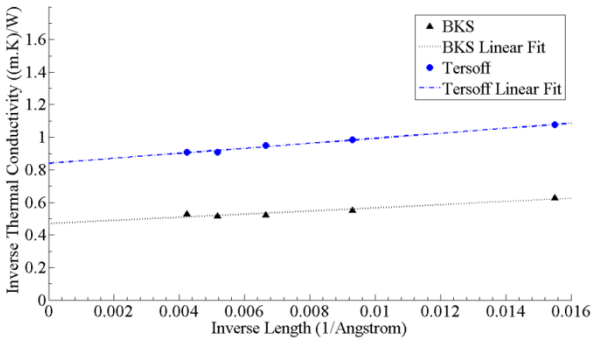

Figure 2. The inverse of the thermal conductivities for amorphous silica systems and their linear extrapolation to infinite lengths

This method gives values of 2.13W/(m.K) for the BKS potential, and 1.19W/(m.K) for the Tersoff potential, at bulk length scales. This gives an error of 55% overestimation for the former, and 13% underestimation for the latter, clearly showing that the re-parameterized Tersoff is much more capable of reproducing bulk thermal properties than the BKS potential can. This is analyzed further by examination of the vibrational density of states (vDOS) of each potential, as shown in Fig. 3, which are obtained through the discrete Fourier transform of the velocity autocorrelation function (VACF) [20].

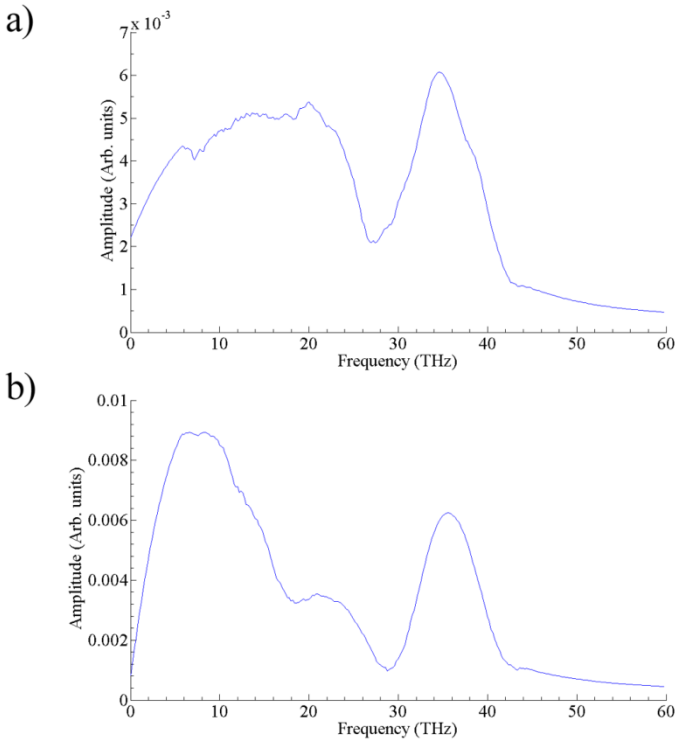

Figure 3. vDos of a) BKS, and b) Tersoff potential

The Tersoff potential clearly shows, as shown in Fig. 6b, the same peaks near the frequencies of 10.5THz, 24.0THz and 36.0THz determined from previous experimental and theoretical results by Laughlin *et al.* [21]. However, the BKS potential, in Fig. 6a, showes no apparent peaks below the 30THz region. Thus, from all these methods presented, we can conclude that the re-parameterized Tersoff potential is a far superior alternative in the thermal characterization of bulk amorphous

silica than the BKS potential.

3.2. Structural correlations of porous silica aerogel

Using the method discussed in Section 2, percolated silica aerogel was simulated on a cubic system of 52,728 atoms, with densities ranging from 0.3 to 1g/cm^3. Fractal dimensions are determined using the method proposed by Kieffer *et al.* [7], where the total radial distributions for each density are calculated, and power-law decays are superimposed on the peak structures to determine the fractal dimensions. These results are plotted in Fig. 4 below along with their error bars, as well as data from previous theoretical studies by Murillo *et al.* [9].

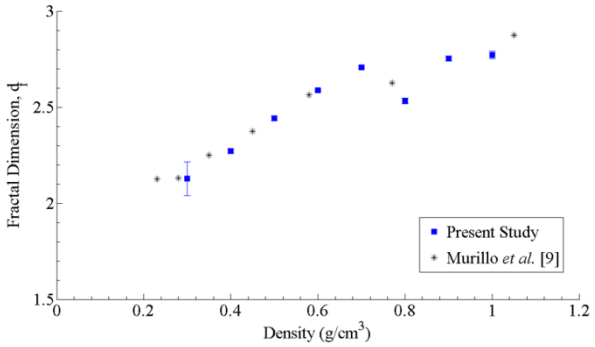

Figure 4. Decreasing fractal dimensions as density decreased

The variation of the fractal dimension, d_f, with density agrees with those found in previous theoretical and experimental studies. Experimental silica aerogel fractal dimensions varies with processing conditions, where it is approximately 1.8 under basic processing conditions, and about 2.2 to 2.4 in both acidic and neutral conditions [22].

3.3. Thermal conductivity of porous silica aerogel

Fig. 5 shows the data obtained, from RNEMD, as a log-scale plot with their corresponding errorbars, and the power-law fit of the data.

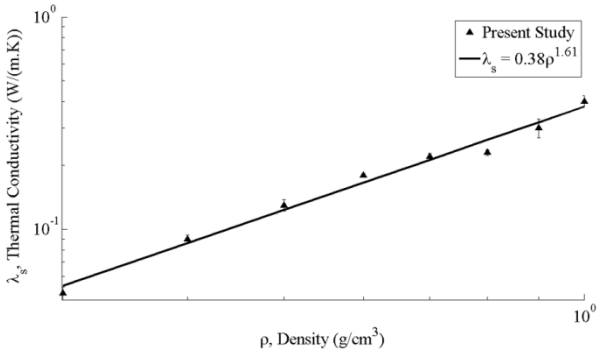

Figure 5. Log-scale plot of the power-law variation of thermal conductivity with density

Thermal conductivity is found to decrease as density decreases, in a non-linear fashion. At the lowest density of 0.3g/cm^3, the thermal conductivity also reaches its lowest value of 0.05 ± 0.003W/(m.K). The power-law exponent, α, of experimental bulk aerogel was found to be 1.6 in the density range of 0.3 to 1.0g/cm^3 [4]. Our results show an α value of 1.61 in this density range, correlating very well with experimental results. Our model is also advantageous in that very low densities are achievable, much lower than 0.1g/cm^3, without any adverse phenomena. A downside

of our current model is that thermal conductivities at each density were 5 times higher than experimental aerogels. The most significant reason is that our model is unable to attain micropores. This can be seen in the pore size distribution of samples of increasing aerogel length scales. Shown in Fig. 6, these plots are calculated using PSDsolv [23], which determines the relative probability of finding pores of different sizes. At a density of 0.3g/cm^3, we generate two different samples with system lengths of 180Å (our current system length at 0.3g/cm^3), and 277Å.

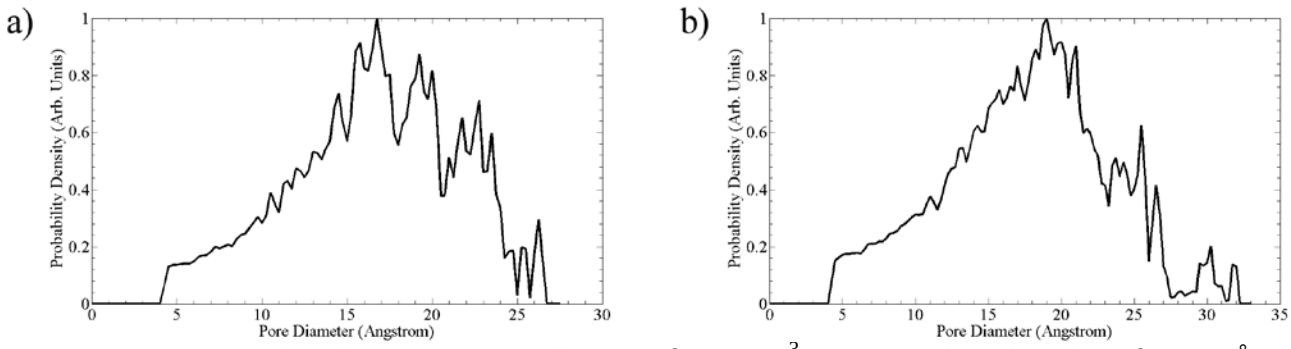

Figure 6. Pore size distribution (PSD) at density of 0.3g/cm^3, at system length scales of a) 180Å, and b) 277Å

The largest pore sizes accessible increase from 27.5Å to 32Å in diameter, as the system length scales increase. The pore sizes attainable are nowhere near the micron-sized diameters in bulk experimental silica aerogels.

3.4. Young's modulus

Using the method discussed in Section 2, the Young's modulus of silica aerogel with different densities ranging from 0.3g/cm^3 to 1.0g/cm^3 are obtained through MD simulation as shown in Fig. 7. A power-law fitt can be used to describe the relationship between Young's modulus and density of samples [9]. From Fig. 7, the exponent of the relationship between Young's modulus and density can obtained and the exponent value is about 2.4313. This value has slightly difference with the result from Murillo *et al*. [9] which was 3.11, while the magnitude of the constant of Young's modulus is almost the same. The discrepancy mainly results from the different interactive potential.

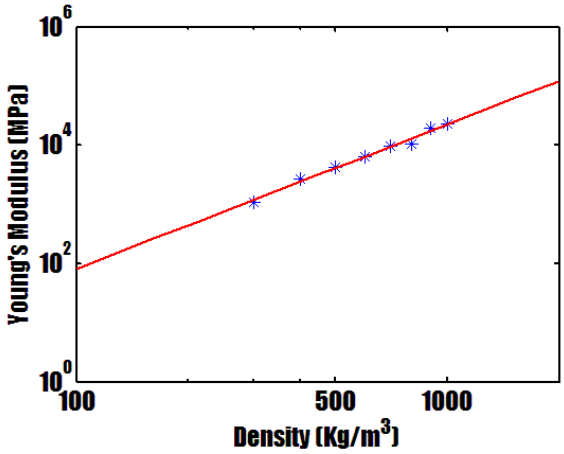

Figure 7. Relation between Young's Modulus and density. (Red line refers to the power-law fitting line, and the blue dots refers to the simulation data.)

4. Conclusions

We have used MD and the re-parameterized Tersoff potential to model the porous structures of silica aerogels. We demonstrate that this potential is suitable for modeling thermal properties in amorphous silica. Using a quenching and expanding process, different densities of aerogel samples are generated. Good fits with previous results are obtained when the fractal dimensions are analyzed. Through RNEMD, their thermal conductivity is determined and the power-law fit of our data corresponds well with experimental studies. Thermal conductivities are also consistently higher than experimental bulk aerogel and analysis of the pore size distribution shows limited pore sizes could be the key issue here.

Acknowledgements

This work is supported by the Agency for Science, Technology and Research (A*STAR), Republic of Singapore. The authors thank the staff in A*STAR Computational Resource Centre for providing valuable technical support. ZS and JC are also grateful for the support from the National Natural Science Foundation of China through grant number 11242011 and number 11021202.

References

[1] S.S. Kistler, Coherent expanded aerogels and jellies. Nature, 127 (1931) 741-741.
[2] J. Fricke, SiO2-Aerogels - Modifications and Applications. J Non-Cryst Solids, 121 (1990) 188-192.
[3] N. Hüsing,U. Schubert, Aerogels - Airy Materials: Chemistry, Structure, and Properties. Angewandte Chemie - International Edition, 37 (1998) 22-45.
[4] J. Fricke, Aerogels - Highly Tenuous Solids with Fascinating Properties. J Non-Cryst Solids, 100 (1988) 169-173.
[5] L.D. Gelb, Simulation and Modeling of Aerogels Using Atomistic and Mesoscale Methods, in: M.A. Aegerter, N. Leventis, and M.M. Koebel (Eds.), Aerogels Handbook, Springer, New York, 2011, pp. 565-581.
[6] T.Y. Ng, J.J. Yeo, Z.S. Liu, A molecular dynamics study of the thermal conductivity of nanoporous silica aerogel, obtained through negative pressure rupturing. J Non-Cryst Solids, 358 (2012) 1350-1355.
[7] J. Kieffer,C.A. Angell, Generation of Fractal Structures by Negative-Pressure Rupturing of SiO2 Glass. J Non-Cryst Solids, 106 (1988) 336-342.
[8] A. Nakano, L.S. Bi, R.K. Kalia, P. Vashishta, Molecular-Dynamics Study of the Structural Correlation of Porous Silica with Use of a Parallel Computer. Phys Rev B, 49 (1994) 9441-9452.
[9] J.S.R. Murillo, M.E. Bachlechner, F.A. Campo, E.J. Barbero, Structure and mechanical properties of silica aerogels and xerogels modeled by molecular dynamics simulation. J Non-Cryst Solids, 356 (2010) 1325-1331.
[10] B.W. van Beest, G.J. Kramer, R.A. van Santen, Force fields for silicas and aluminophosphates based on ab initio calculations. Phys Rev Lett, 64 (1990) 1955-1958.
[11] G.J. Kramer, N.P. Farragher, B.W. van Beest, R.A. van Santen, Interatomic force fields for silicas, aluminophosphates, and zeolites: Derivation based on ab initio calculations. Phys Rev B Condens Matter, 43 (1991) 5068-5080.
[12] S. Plimpton, Fast Parallel Algorithms for Short-Range Molecular-Dynamics. J Comput Phys, 117 (1995) 1-19.
[13] J. Tersoff, Modeling solid-state chemistry: Interatomic potentials for multicomponent systems.

Phys Rev B, 39 (1989) 5566-5568.
[14] S. Munetoh, T. Motooka, K. Moriguchi, A. Shintani, Interatomic potential for Si-O systems using Tersoff parameterization. Computational Materials Science, 39 (2007) 334-339.
[15] A.J.H. McGaughey,M. Kaviany, Thermal conductivity decomposition and analysis using molecular dynamics simulations Part II. Complex silica structures. Int J Heat Mass Tran, 47 (2004) 1799-1816.
[16] F. Muller-Plathe,P. Bordat, Reverse non-equilibrium molecular dynamics. Lect Notes Phys, 640 (2004) 310-326.
[17] T.Y. Ng, J.J. Yeo, Z.S. Liu, A molecular dynamics study of the thermal conductivity of graphene nanoribbons containing dispersed Stone–Thrower–Wales defects. Carbon, 50 (2012) 4887-4893.
[18] J.J. Yeo, Z.S. Liu, T.Y. Ng, Comparing the effects of dispersed Stone–Thrower–Wales defects and double vacancies on the thermal conductivity of graphene nanoribbons. Nanotechnology, 23 (2012) 385702.
[19] M.J. Weber, Glasses, in: Handbook of Optical Materials, CRC Press, Boca Raton, Florida, 2002.
[20] M.T. Dove, Introduction to Lattice Dynamics, Cambridge University Press, Cambridge, 1993.
[21] R.B. Laughlin,J.D. Joannopoulos, Phonons in amorphous silica. Phys Rev B, 16 (1977) 2942-2952.
[22] T. Woignier, J. Phalippou, R. Vacher, J. Pelous, E. Courtens, Different kinds of fractal structures in silica aerogels. J Non-Cryst Solids, 121 (1990) 198-201.
[23] S. Bhattacharya,K.E. Gubbins, Fast Method for Computing Pore Size Distributions of Model Materials. Langmuir, 22 (2006) 7726-7731.

Damage Identification and Influence on Mechanical Properties of Closed Cell Rigid Foams

Liviu Marsavina[1,*], Dan M. Constantinescu[2], Emanoil Linul[1], Tudor Voiconi[1], Dragos A. Apostol[2], Tomasz Sadowski[3]

[1] Department Mechanics and Strength of Materials, Politehnica University of Timisoara, Timisoara 300222, Romania
[2] Department of Strength of Materials, University POLITEHNICA of Bucharest, Bucharest 060042, Romania
[3] Solid Mechanics Department, Lublin University of Technology, Lublin 20-618, Poland
* Corresponding author: msvina@mec.upt.ro

Abstract The effect of damage on mechanical properties of closed-cell foams is numerically investigated. Representative 3D cell structures are considered for the finite element analysis. In the first instance the mechanical properties were obtained on un-damaged structures. The obtained numerical values for Young's modulus and Poisson's are compared with experimental results. Two types of experimental methods were used to determine the mechanical properties of rigid polyurethane foams: Static compression tests providing stress – strain curves and mechanical properties as Young's modulus, yield stress, plateau stress, densification and Digital Image Correlation used for identification of the damage mechanism, observation of bands of deformation, Young's modulus and Poisson's ratio. The influence of density on mechanical properties is also investigated. Two types of damages/defects were defined randomly in finite element analyses by considering missing cell walls and filled cells. The results show that the missing cell walls create a decrease of Young's modulus, while the filled cells produce the increase of Young's modulus.

Keywords Rigid foams, Damage, Mechanical properties, Numerical analysis, Micromechanical models

1. Introduction

Polyurethane foam materials are widely used as cores in sandwich structures. The main characteristics of PUR foams are lightweight, high porosity and good energy absorption capacity, [1,2]. Foam materials crush in compression, while in tension they fail by propagation of a single crack, [3]. Many attempts were performed in order to determine experimentally the compression properties of plastic foams [4-13]. On the other hand, analytical micro-mechanical models based on deformation and fracture of single cell were developed to predict the mechanical properties of foams in compression [14,15]. In recent years the finite element analysis (FEA) micro-mechanical models were used in order to study the effect of damage of cellular structure on the compression properties [16,17]. Usually these models were constructed using 2D beams.

This paper presents the results of mechanical properties for three polyurethane foams under compression loading investigating the effect of density, loading direction and loading rate. The Digital Image Correlation (DIC) technique is employed during compression tests in order to identify the damage mechanisms of foams. Afterwards, using a 3D representative volume of the foam, the effect of damage (missing cells and filled cells) was studied.

2. Experimental program

In order to identify the mechanical properties of the rigid polyurethane (PUR) foams an extensive experimental program was performed. Closed cell rigid PUR foams with three different densities (100, 160 and 301 kg/m^3) were considered for the experimental program, Fig. 1.

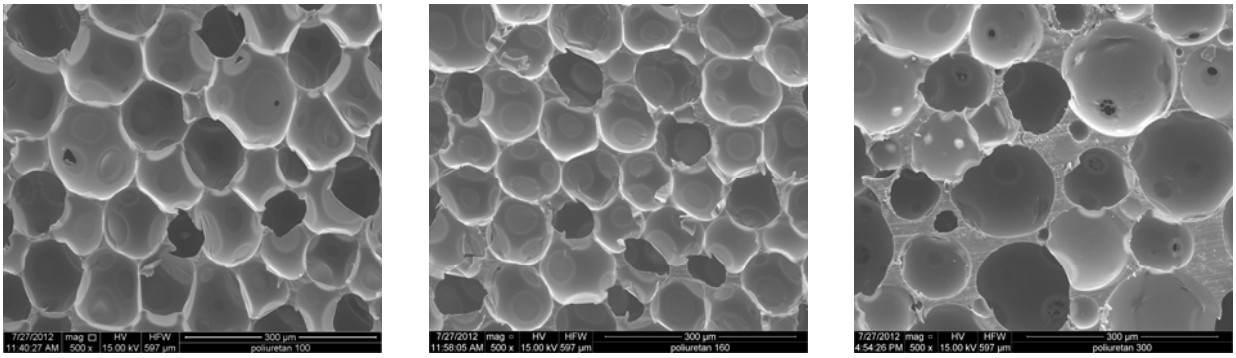

a. density 100 kg/m^3 b. density 160 kg/m^3 c. density 301 kg/m^3

Figure 1. SEM microstructures of closed cell rigid PUR foams (500x).

2.1. Static compression tests

Static compression testes were carried out using a LBG 100kN universal testing machine in the Strength of Materials from POLITEHNICA University of Timişoara, respectively on a Walter+bai 50 kN static and fatigue testing machine from Laboratory of Strength of Materials from University POLITEHNICA of Bucharest. Tests were performed according to ASTM D 1621 at room temperature. Cubic specimens with 50 mm length were used for foam densities 100 and 160 kg/m^3 and with 25 mm length for the 301 kg/m^3 density. The engineering stress-strain diagram shows the non-linear behavior of polyurethane foams in compression, Fig. 2. The following regions could be identified: an initial linear elastic response leading to yield, a small softening in stress after yield, a post-yield plateau and a final sharp rise in compressive stress, corresponding to foam densification. It can be observed that density has a major influence on the behavior of PUR foams.

The influence of the loading direction: in plane (rise direction) and out of plane (transverse direction) is shown in Fig.3. Foam behaviour in transverse direction shows a small hardening after the yield point and no softening.

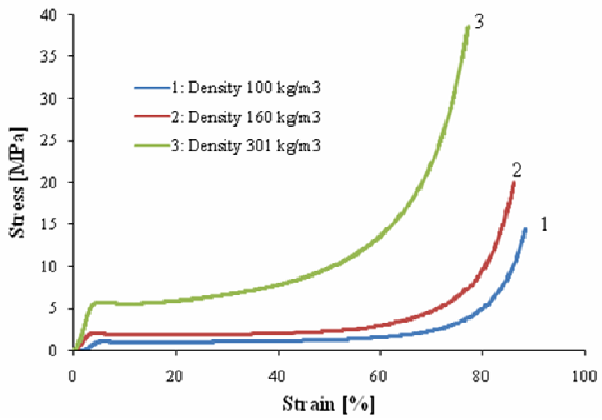

Figure 2. Effect of density.

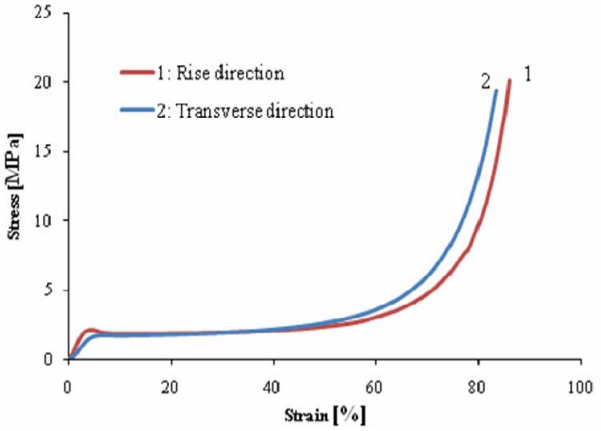

Figure 3. Effect of loading direction.

The compression properties (Young's modulus, yielding stress, plateau stress and densification strain) obtained for the three investigated rigid PUR foams are summarized in Table 1 for a 5 mm/min loading rate.

Table 1. Compression properties of rigid PUR foams

Foam density [kg/m^3]	100		160		301	
Loading direction	rise	transverse	rise	transverse	rise	transverse
E [MPa]	40.38	31.92	81.76	50.83	202.25	201.83
σ_y [MPa]	1.15	1.17	2.09	1.77	5.74	6.69
σ_p [MPa]	1.06	1.14	1.88	1.83	5.98	6.65
ε_d [%]	56.2	55.4	54.4	52.4	54.8	52.5

Young's modulus, yield stress and plateau stress increases with density. For low density foams Young's modulus values are higher in the rise direction, while for the foam with 301 kg/m^3 density Young's modulus are equal in both direction. Also the densification strain is slightly higher in rise direction for all investigated foams. The yield stress and plateau stresses are quite similar in both directions for low density foams, but are higher in transverse direction for foam with 301 kg/m^3 density.

Loading rates between 0.6 and 500 mm/min were used to investigate the influence of loading rate. It could be observed in Fig. 4 that increases in loading rate produces an increase of Young modulus (with approximately 50 % for foam densities 100 and 160 kg/m^3, respectively with 80 % for 301 kg/m^3 foam density) and yield stress (with approximately 67 % for foam densities 100 and 160 kg/m^3, respectively with 73 % for 301 kg/m^3 foam density).

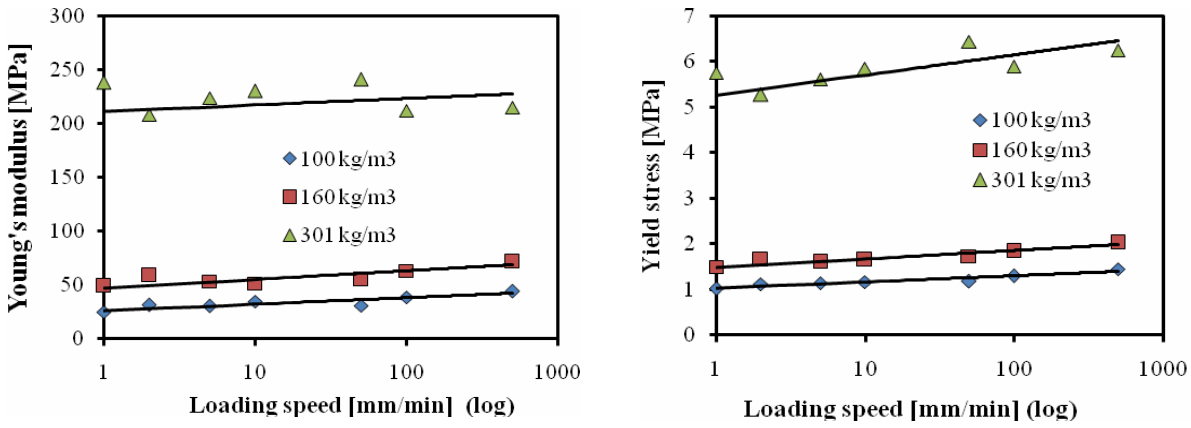

a. Young's modulus b. Yield stress

Figure 4. Effect of loading rate on mechanical properties of PUR foams.

2.2. Digital image correlation investigations

The damage mechanisms of the foams were investigated by the 2D (DIC) technique, using a 5 MPixels camera and by applying a random speckle of paint on the specimen surface. Some analyses were done by using the 3D approach and 2 MPixels cameras. In this case the ARAMIS system was calibrated using a 35 x 28 mm caliber and a facet of 27 x 15 pixels; thus a 44 % facet overlap has been obtained.

Images were recorded at different loads and then processed with the ARAMIS system. A typical engineering stress-strain curve for the foam with 160 kg/m^3 density and major strain plots taken in the relevant parts of the curve is shown in Fig. 5. It can be observed that on the yield point crush bands inclined approximately 45^0 occur, tendency which extends on the plateau and densification

regions.

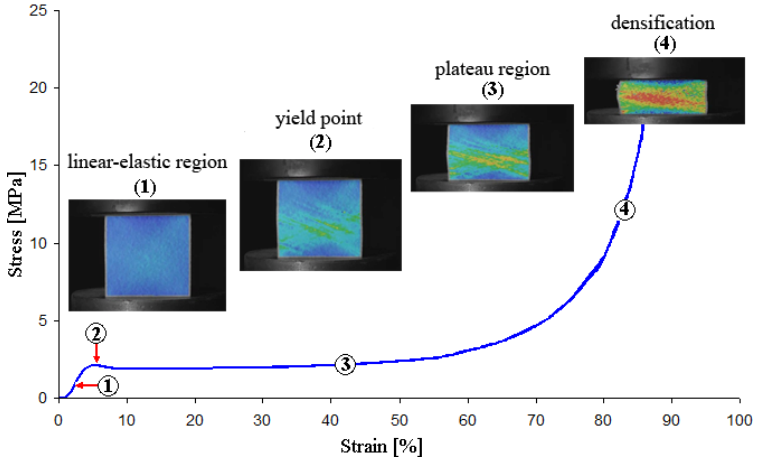

Figure 5. Engineering stress–strain curve with major strain images from ARAMIS system

The DIC measurements in the linear-elastic region allow the determination of Young's modulus E, and Poisson's ratio ν.

For the foam with a density of 301 kg/m^3 (closer to a porous solid) the deformation bands tend to be less inclined. For a loading speed of 1 mm/min in Fig. 6 are shown the following: the current stage in the engineering stress-strain curve (here one in the plateau region is chosen), the vertical displacements and Mises strains in that moment, and the variation of the Mises strains along a vertical line taken in the middle of the specimen (figure upper-left) at different stages of loading – the one represented hereby being depicted by a red curve. In the last registered stage (the last curve) the foam deteriorates significantly – close to 100% – and the curve becomes discontinuous.

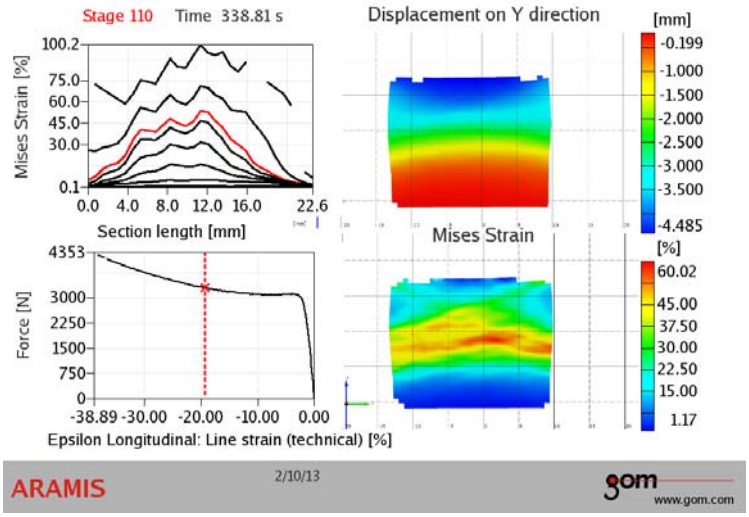

Figure 6. Mises strains and vertical displacements in the plateau region

3. Numerical simulation

Based on the statistical analysis of the closed cells microstructures the geometric parameters were determined and the 3D representative volume (RVE) of the foams was built. Two strategies were considered: a model based on tangent hollow spheres for low density foams (Fig. 7a), respectively a solid cube from which were extracted spheres for higher density foams (Fig. 7b). Polyurethane was considered the material for the cell walls with Young's modulus E_s=1600 MPa and Poisson's ratio

ν= 0.4.

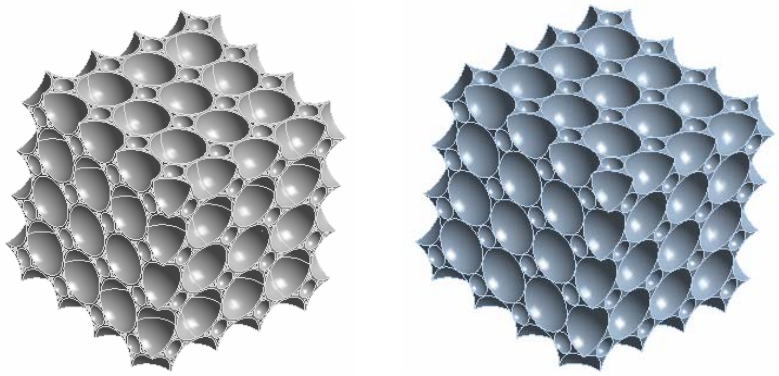

a. Hollow spheres b. Solid with spherical cells

Figure 7. 3D models of the foam RVE

Imposing the periodic boundary conditions and a displacement on the top of the RVE the elastic properties (Young's modulus and Poisson ratio) were determined. Figure 8 presents the results of the equivalent Mises strain.

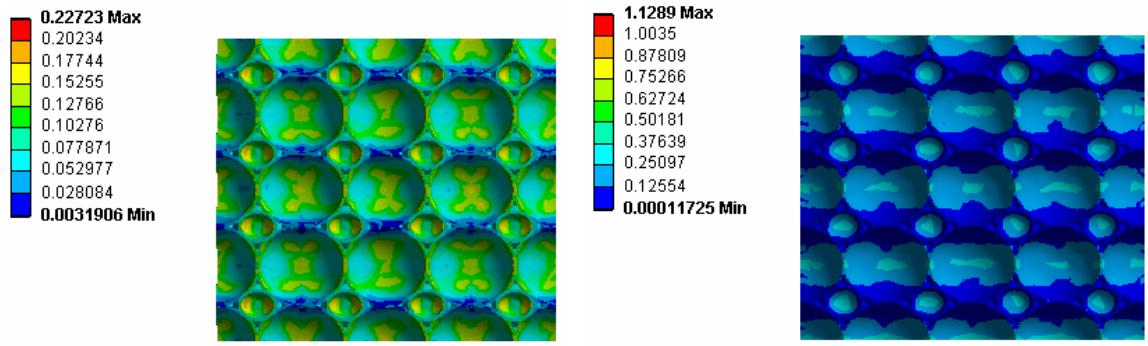

a. Hollow spheres b. Solid with spherical cells

Figure 8. Equivalent Mises strains

Figure 9 presents a comparison between experimental (compression and DIC) and numerical results of Young's modulus (Fig. 9a) and Poisson's ratio (Fig. 9b). A good agreement was obtained between experimental and numerical values for Poisson's ratio and Young's modulus for low density foams. For the higher density foam (301 kg/m^3) a difference of 16% was obtained between compression and DIC values of Young's modulus which could be explained on different methodologies used to record the specimen deformations.

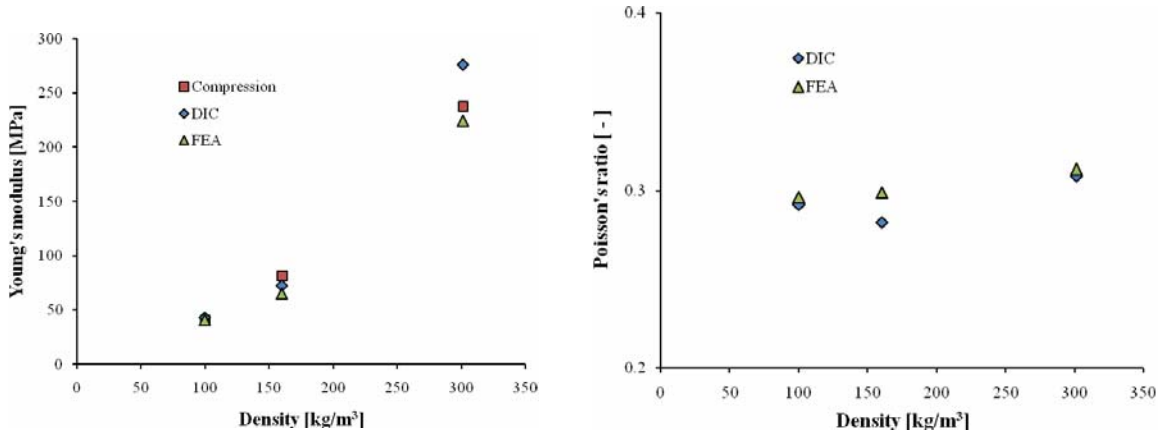

a. Young's modulus b. Poisson's ratio

Figure 9. Comparison between experimental and numerical values of elastic properties of PUR foams

Missing cell walls (for each cell only a single wall was eliminated) and filled cells were considered in the FE analyses in order to investigate the effect of the damage of cellular structures on mechanical properties. Figure 10 presents the influence of damage expressed in terms of normalized Young's modulus (ratio between Young's modulus for damaged structure and for undamaged structure). It can be observed that 7% of missing cell walls decrease the Young modulus with 57%, while 7% of filled cells produce an increase of Young's modulus with 20.5%.

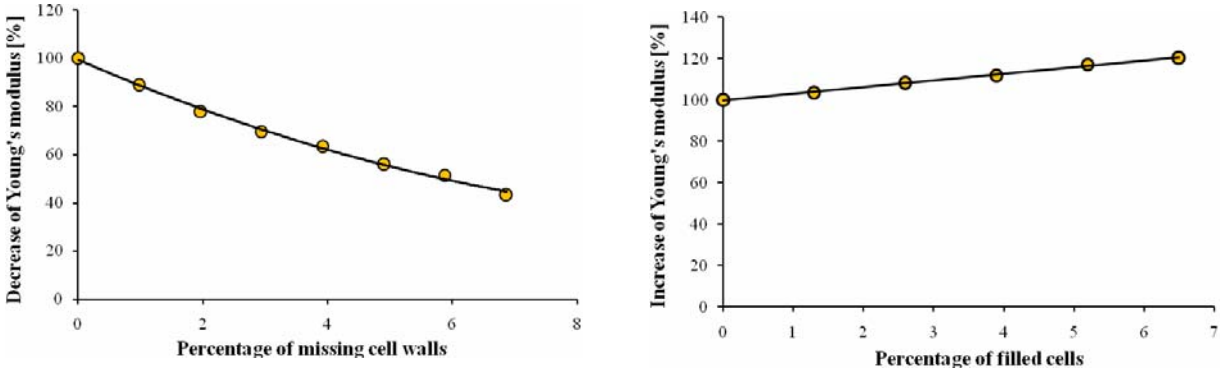

a. Missing cell walls b. Filled cells

Figure 10. Comparison between experimental and numerical values of elastic properties of PUR foams

4. Conclusions

Two experimental methods (compression tests and Digital Image Correlation) were used to determine the mechanical properties of rigid polyurethane foams. The effect of density, loading rate and loading direction were investigated. Ranking the investigated parameters it could be observed that the density has the major influence on mechanical properties, followed by strain rate, and the minor influence is the loading direction.

DIC measurements prove to be a powerful tool in establishing the local damage characteristics and the bands of deformation for the PUR foams. The density of the foam appears to influence the inclination of the deformation bands.

Finite Element Analysis was performed on 3D representative models to predict the elastic constant of polyurethane foams. The predicted values are in good agreement with the experimental ones which validates the numerical methodology. Then the effect of damage, represented by missing cell walls and filled cells, on Young modulus was systematically investigated.

Acknowledgements

This work was supported by a grant of the Romanian National Authority for Scientific Research, CNCS – UEFISCDI, project number PN-II-ID-PCE-2011-3-0456. Parts of experimental results were obtained at Lubin University of Technology, in the facilities of the *Center of Excellence for Modern Composites Applied in Aerospace and Surface Transport Infrastructure* (European Union Seventh Framework Programme (FP7/2007 – 2013), FP7 - REGPOT – 2009 – 1, under grant agreement No: 245479.

References

[1] L.J. Gibson, M.F. Ashby, Cellular solids, Structure and properties, Second edition, Cambridge University Press, Cambridge, 1997.
[2] N.J. Mills, Polymer Foams Handbook: Engineering and Biomechanics Applications and Design Guide, Butterworth-Heinemann, Oxford, 2007.
[3] L. Marsavina, Fracture Mechanics of Cellular Structures, in: Cellular and porous materials in structures and processes, H. Altenbach, A. Ochsner (Eds.), Springer, Wien, 2010.
[4] J.-M. Berthelot, E. Lolive, Non-linear behaviour of foam cores and sandwich materials, Part 1: Materials and modelling, J Sandwich Struct Mater, 4 (2002), 219 – 247.
[6] H.-R. Lin, The structure and property relationships of commercial foamed plastics, Polym Test, 16 (1997), 429 – 443.
[7] F. Saint-Michel, L. Chazeau, J.-Y. Cavaille, E. Chabert, Mechanical properties of high density polyurethane foams: I. Effect of the density, Compos Sci Technol, 66 (2006), 2700–2708.
[8] F. Saint-Michel, L. Chazeau, J.-Y. Cavaille, Mechanical properties of high density polyurethane foams: II. Effect of the filler size, Compos Sci Technol, 66 (2006), 2709–2718.
[9] F. Ramsteiner, N. Fell, S. Forster, Testing the deformation behaviour of polymer foams, Polym Test, 20 (2001), 661 – 670.
[10] F.-P. Chiang, Y. Ding: Size effect on stress–strain relation of neat polyurethane foam, Compos Part B-Eng, 39 (2008), 42–49.
[11] L. Marsavina, T. Sadwski, D.M. Constantinescu, R. Negru, Failure of polyurethane foams under different loading conditions, Key Eng Mat, 385-387 (2009), 205-208.
[12] Z.H. Tu, V.P.W. Smith, C.T. Lim, Plastic deformation models in rigid polyurethane foam under static load, Int J Solids Struct, 38 (2001) 9267-9279.
[13] D.A. Apostol, D.M. Constantinescu, Temperature and speed of testing influence on the densification and recovery of polyurethane foams, Mech Time-Depend Mat, 17 (2013), 111-136.
[14] M. Avalle, G. Belingardi, A. Ibba, Mechanical models of cellular solids: Parameters identification from experimental tests Int J Impact Eng, 34 (2007), 3-27.
[15] L. Marsavina, T. Sadowski, D.M. Constantinescu, R. Negru, Polyurethane foams behaviour. Experiments versus modeling, Key Eng Mat, 399 (2009), 123-130.
[16] A. Ajdari, Mechanical behavior of cellular structures: a finite element study, Northeastern University, Boston, 2008.
[17] X.J. Ren, V.V. Silberschmidt, Numerical modeling of low-density cellular materials, Comp Mater Sci, 43 (2008) 65-74.

Optimal Design of Metallic Corrugated Sandwich Plates to Blast Loading

Jianxun Zhang[1], Qinghua Qin[1,*], Weilong Ai[1], Tao Wang[1, 2], Tiejun Wang[1,*]

[1] State Key Laboratory for Strength and Vibration of Mechanical Structures, Department of Engineering Mechanics, Xi'an Jiaotong University, Xi'an 710049, China
[2] Department of Engineering Physics, Xi'an Research Institute of High-Tech., Xi'an 710025, China
* Corresponding author: qhqin@mail.xjtu.edu.cn; wangtj@mail.xjtu.edu.cn

Abstract Optimal designs of the resistance of metallic corrugated sandwich plates under blast loading are studied numerically and analytically. The dynamic response of metallic sandwich plates under blast loading is numerically analyzed. Comparisons among the corrugated sandwich plates made of the same material and equivalent weight are conducted. The study of weight optimization is carried out, such as the relative core density, core height, the ratio of core height to half-length of the unit, and the thickness ratio of the top face sheet to bottom one. Based on the optimal designs, the sandwich plates possessing better performance are obtained. Three-dimensional finite element (FE) simulations are performed and the FE predictions are in good agreement with the theoretical predictions.

Keywords Sandwich plate, Sinusoidal plate core, Dynamic response, Optimal design

1. Introduction

Lightweight structures have been widely used in engineering, such as vehicles, ships, aircrafts and spacecrafts. Sandwich structures are typical lightweight structures with a number of advantages, e.g. ultralight, high ductility, high crashworthiness, high strength to weight ratio, high stiffness to weight ratio, multifunction. Lightweight metallic sandwich beams, plates and panels with various cores have received great attention. Several kinds of metallic cores are developed, such as metallic foams, lattice materials and corrugated cores [1-3].

In the past decades, some work has been devoted to analyzing the dynamic response of sandwich structures subjected to blast loading. Fleck and Deshpande [4] theoretically investigated the dynamic response of fully clamped metal sandwich beams under uniform transverse blast loading. Subsequently, Qiu et al. [5] developed an analytical model for dynamic response of fully clamped sandwich beams under impulsive loading over a central patch. More recently, Qin and Wang [6] and Qin et al. [7] derived new yield criteria for symmetric and geometrically asymmetric metal sandwich structures, in which the effect of core strength is incorporated. Based on the yield criterion, Qin and Wang [8] and Qin et al. [9] analytically studied the dynamic response of fully clamped metal sandwich beams subjected to impulsive loading using the membrane factor method, in which the interaction of bending and stretching is considered.

Xue and Hutchinson [10] numerically studied the dynamic response of metal sandwich plates subjected to air blast loading. The study of weight optimization was carried out for pyramidal truss, square honeycomb and folded plate with respect to the respective geometric parameters, including core and face sheet thickness, core member aspect ratios and relative density. Zhang et al. [11] numerically studied the resistance of the trapezoidal plate core sandwich plates, and the FE predictions were compared with analytical solutions, showing good agreement. In additions, numerical calculations were carried out to study the dynamic response of metal sandwich panels,

beams and plates with different kinds of cores [12-14] subjected to underwater blast loading and air blast loading.

The objective of this study is to numerically and analytically investigate the optimal design of dynamic response of corrugated metal sandwich plates with sinusoidal plate core. This paper is organized as follows. Firstly, the problem is stated and the topology of sandwich plate with sinusoidal plate core is introduced in Section 2. The analytical solutions to predict the dynamic response of asymmetric sandwich plates are presented in Section 3. In Sections 4 and 5, the analytical solutions of the dynamic response of the sandwich plates under impulsive loading are compared with the finite element results. Furthermore, the study of weight optimization is carried out, such as relative core density, core height, the ratio of core height to half-length of the unit, and the thickness ratio of top and bottom face sheets. Finally, concluding remarks are presented in Section 6.

2. Statement of the problem

Here, we consider a metal sinusoidal plate core sandwich plate with infinite length in x direction under impulsive loading I, as shown in Figs. 1 and 2(a). Clamped conditions are imposed along the two sides in z direction. The top and bottom face sheets with thicknesses h_t and h_b are perfectly bonded to the sinusoidal plate core with the height of the core H_c, as shown in Fig. 2(b). The half-width of the sandwich plate and half-length of the unit cell are L and l, and the thickness of the core web is h_c. The relative core density $\bar{\rho} = \rho_c / \rho_s$ with ρ_c and ρ_s being the density of the core and core web material, respectively, can be calculated as $\bar{\rho} = h_c \cdot l_s \cdot \tan\phi / H_c^2$ [15], where l_s is the arc length of the core web in the half unit cell and $\tan\phi = H_c / l$.

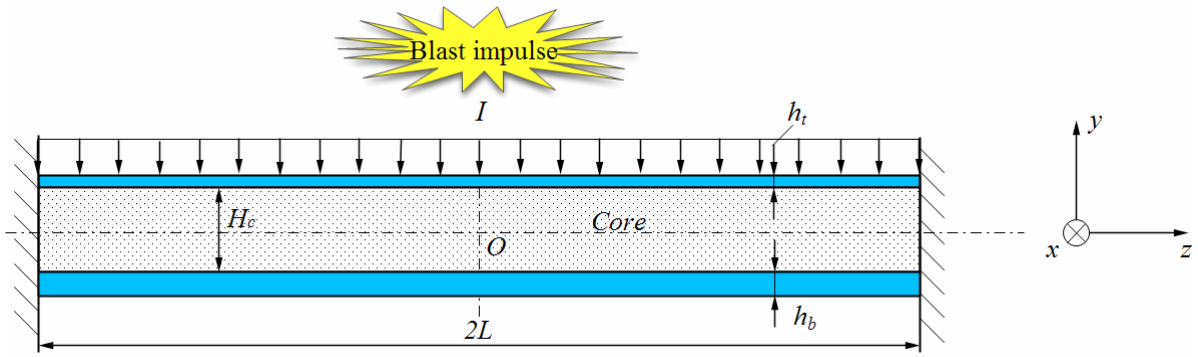

Figure 1. Sketch of a fully clamped sandwich plate subject to impulsive loading

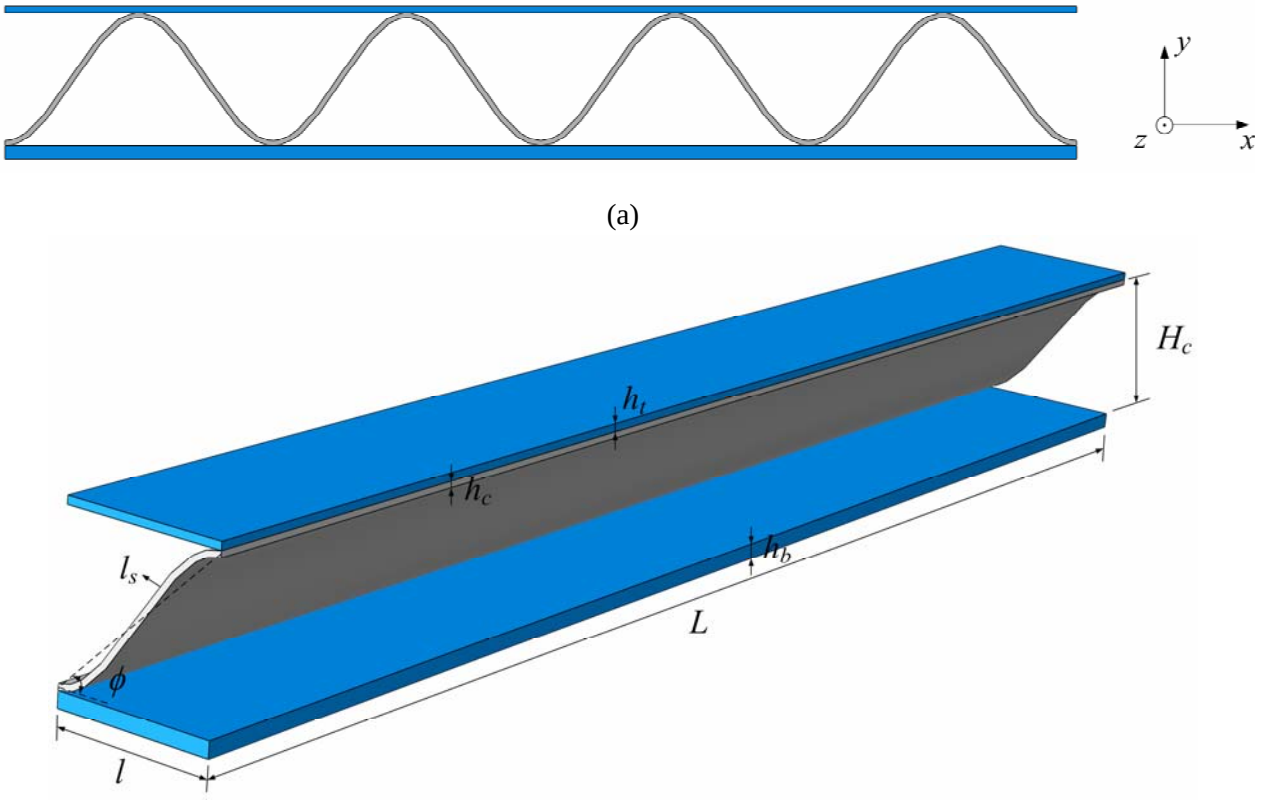

Figure 2. Sketches of the metallic corrugated sandwich plates with sinusoidal plate core. (a) Topology of the sandwich plate, and (b) a quarter of unit cell for the sandwich plate

3. Analytical solutions for the dynamic response of asymmetric sandwich plates

In this section, employing the similar procedure to the plastic-string model [15] for the dynamic response of symmetric sandwich plates, the analytical solutions for dynamic response of the fully clamped asymmetric sandwich plates under the impulsive loading *I* are obtained shown in Fig. 1.

It is assumed that the top and bottom face sheets obey the rigid-perfectly plastic law with the yield strength σ_Y, and the metal sandwich core is modeled as a rigid-perfectly-plastic-locking (*r-p-p-l*) material with a plateau-stress level of σ_{nY} and a critical densification strain ε_D.

The phase of core compression is the same as that for dynamic response of symmetric sandwich beam [4]. It is assumed that the longitudinal plastic membrane force N_p is insensitive to the degree of the core compression [4], and then obtained

$$N_p' = N_p = \sigma_Y b\left(h_t + h_b\right) + \sigma_{lY} b H_c \tag{1}$$

where *b* is the length in *x* direction, σ_Y is the yield strength of face sheet material, and σ_{lY} is the longitudinal compressive strength of core.

The velocity field is assumed as $\dot{w}=\dot{w}_0 z/L$ when $0\le z\le L$, where $\dot{w}_0$ is the velocity at the midspan of the plastic-string, shown in Fig. 3(a) for half of the plastic-string. In the phase of dynamic structural response for the plastic-string model [15], the dynamic response of symmetric sandwich beam is dominated by axial (membrane) force alone. However, the asymmetric sandwich beam has axial (membrane) force N_p' and bending moment *M*, shown in Fig. 3(b). This is because that the plastic neutral surface of asymmetric sandwich structure is usually different from the geometric surface, and the geometric and plastic neutral surfaces of the symmetric sandwich beam are coincident.

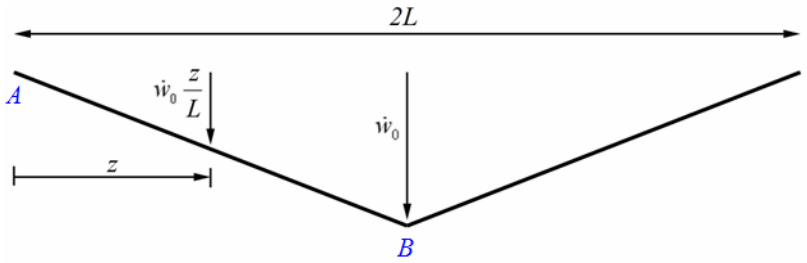

(a)

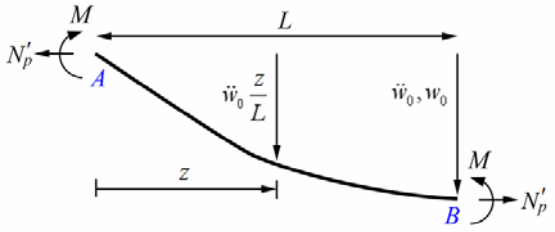

(b)

Figure 3. Sketches of the deformation process of a fully clamped plastic-string. (a) The velocity field and (b) a free body diagram of the half of the plastic-string.

Considering the conservation of the moment of momentum for half of the sandwich plate shown in Fig. 3(b) with respect to the fixed end support Point *A* at time *t*, we have

$$M + N_p' w_0 - M = -\frac{d}{dt}\int_0^L \left(\rho_s b h_t + \rho_s b h_b + \rho_c b H_c\right)\dot{w}z\,dz \tag{2}$$

where w_0 is the deflection at the midspan. The continuity conditions are $w_0(t=0)=0$ and $\dot{w}_0(t=0)=V_f$, where the final common velocity of the core and two face sheets at the end of the core compression stage $V_f = I/\left(\rho_s h_t + \rho_s h_b + \rho_c H_c\right)$ [4]. If $\dot{w}_0\left(t=T_f\right)=0$, the motion of the plastic-string ends. Then, the maximum deflection $w_1 = w_0\left(t=T_f\right)$ and structural response time T_f of the asymmetric sandwich plate can, respectively, be written as

$$w_1 = \frac{IL}{\sqrt{3\left(\sigma_Y h_t + \sigma_Y h_b + \sigma_{lY} H_c\right)\left(\rho_s h_t + \rho_s h_b + \rho_c H_c\right)}} \tag{3}$$

and

$$T_f = \frac{\pi}{2} L \sqrt{\frac{\rho_s h_t + \rho_s h_b + \rho_c H_c}{3\left(\sigma_Y h_t + \sigma_Y h_b + \sigma_{lY} H_c\right)}} \tag{4}$$

To simplify analysis, we introduce the following nondimensional geometric and property variables of the sandwich plate:

$\bar{H}_c = \frac{H_c}{L}$, $\bar{h} = \frac{h_t + h_b}{2H_c}$, $\alpha = \frac{h_t}{h_b}$, $\bar{w}_1 = \frac{w_1}{L}$, $\bar{I} = \frac{I}{\left(\rho_s h_t + \rho_s h_b + \rho_c H_c\right)\sqrt{\sigma_Y / \rho_s}}$, $\bar{\sigma}_l = \frac{\sigma_{lY}}{\sigma_Y}$ and

$\bar{T}_f = \frac{T_f}{L\sqrt{\rho_s / \sigma_Y}}$.

Then, Eqs. (3) and (4) yield the following dimensionless maximum deflection and structural response time of the asymmetric sandwich plate,

$$\bar{w}_1 = \frac{\bar{I}\beta}{\sqrt{3}} \tag{5}$$

and

$$\bar{T}_f = \frac{\pi}{2\sqrt{3}}\beta \tag{6}$$

respectively, where $\beta = \sqrt{\frac{\bar{\rho} + 2\bar{h}}{\bar{\sigma}_l + 2\bar{h}}}$.

Substitution of the equation of normalized longitudinal compressive strength $\bar{\sigma}_l$ for sinusoidal plate core [15] into Eqs. (5) and (6) yields the following dimensionless maximum deflection and structural response time of the asymmetric sandwich plate with sinusoidal plate core,

$$\bar{w}_{1s} = \frac{\bar{I}}{\sqrt{3}} \tag{7}$$

and

$$\bar{T}_{fs} = \frac{\pi}{2\sqrt{3}} \tag{8}$$

Eqs. (5), (6), (7) and (8) can reduce the solutions for the dynamic response of symmetric sandwich plates under the impulsive loading [15].

4. Numerical calculations

Finite element calculations are carried out to predict the dynamic response of the corrugated sandwich plates with sinusoidal plate cores. All simulations have been carried out using ABAQUS/Explicit code. Eight-node linear brick elements with reduced integration (Type C3D8R) are used to model the face sheets and core webs in ABAQUS/CAE software. The uniform distributed impulsive loading *I* per area is applied to the top face sheet of the sandwich plate as a uniform initial velocity $V_0 = I/\rho_s h_t$ [10,12]. Periodic boundary conditions are applied at each end of the repeating unit in *x* direction, and symmetrical boundary conditions about the centerline are adopted. The computational model of the corrugated sandwich plate is shown in Fig. 1(b). All the contact of the plates is modeled by using a general contact algorithm with a frictionless contact option in ABAQUS/Explicit. The vertical, horizontal and rotational displacements of nodes at the ends of the plate are zero. The face sheets and core web are made of stainless steel with yield strength $\sigma_Y = 400\text{MPa}$, Young's modulus $E_s = 200\text{GPa}$, yield strain $\varepsilon_Y = 0.2\%$, elastic Poisson's ratio $v_e = 0.3$, density $\rho_s = 7850\,\text{kg/m}^3$ and linear hardening modulus $E_t/\sigma_Y = 12$, respectively. It is assumed that the face sheets and core web materials have sufficient ductility to be able to sustain deformation without fracture. The face sheets and core webs are modeled as J_2 flow theory of plasticity.

5. Results and discussion

5.1. Effect of the asymmetric factor

Comparisons of the analytical solutions and numerical results for the normalized maximum deflection $\bar{w}_1$ of the bottom face sheets and the nondimensional structural response time $\bar{T}_f$ for the asymmetric sandwich plates subjected to $\bar{I} = 0.25$ are shown in Figs. 4(a) and (b), respectively. The sandwich plates with sinusoidal plate core have $\bar{H}_c = 0.1$, $\bar{h} = 0.08$, $\phi = 45^o$, $\bar{\rho} = 0.055$ and $L = 1\text{m}$. In Fig. 4(a), it is seen the analytical solutions based on Eq. (7) are in good agreement with the numerical results and underestimates the numerical ones a little. Actually, the discrepancies between the analytical and numerical solutions lie in that the analytical procedure does not consider the effects of the wrinkling of face sheets and cores, the strain hardening of the metal material, the effect of shear force and the reduction in momentum provided by the supports in the core compression phase. The discrepancies in high impulsive loading may be due to the assumption that there is full densification of the core in the analytical solution while in the numerical solution there is no distinct densification in the core. In Fig. 4(a), it is seen that the numerical result for the smallest maximum deflection occurs in the case of $\alpha = 0.5$. Moreover, seen the deformed configurations at the impulse value $\bar{I} = 0.25$ in Figs. 5(a) and (b), the deformation of top and bottom face sheets in the case of $\alpha = 2$ both almost keeps horizontal at the midspan, while the top face sheet of the sandwich plate in the case of $\alpha = 0.5$ occurs more evident deformation in the location far away the core web relative to the location bonded to the core. In Fig. 4(b), the analytical

solutions based on Eq. (8) for the structural response time agree well with the numerical results. The numerical results for the structural response time keep almost a constant for the several cases of α.

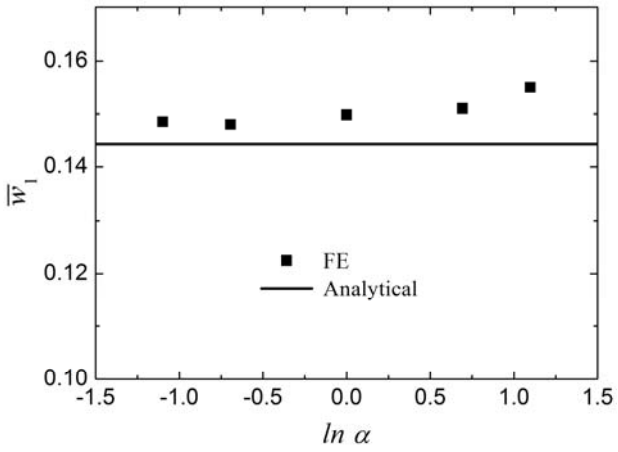

(a)

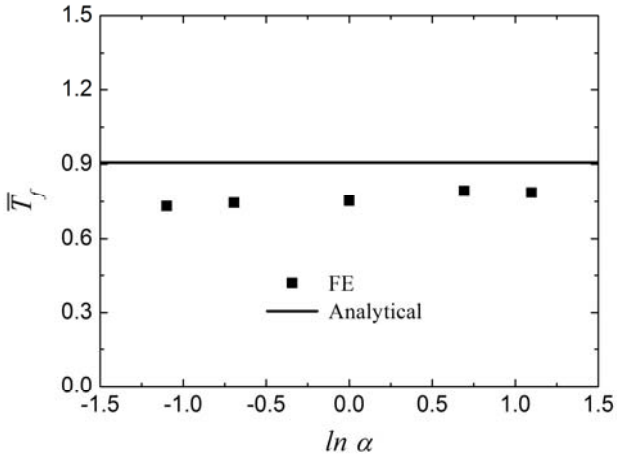

(b)

Figure 4. Analytical solutions and numerical results for (a) the normalized maximum deflection $\overline{w}_1$ of the bottom face sheets and (b) the nondimensional structural response time $\overline{T}_f$ for the asymmetric sandwich plates

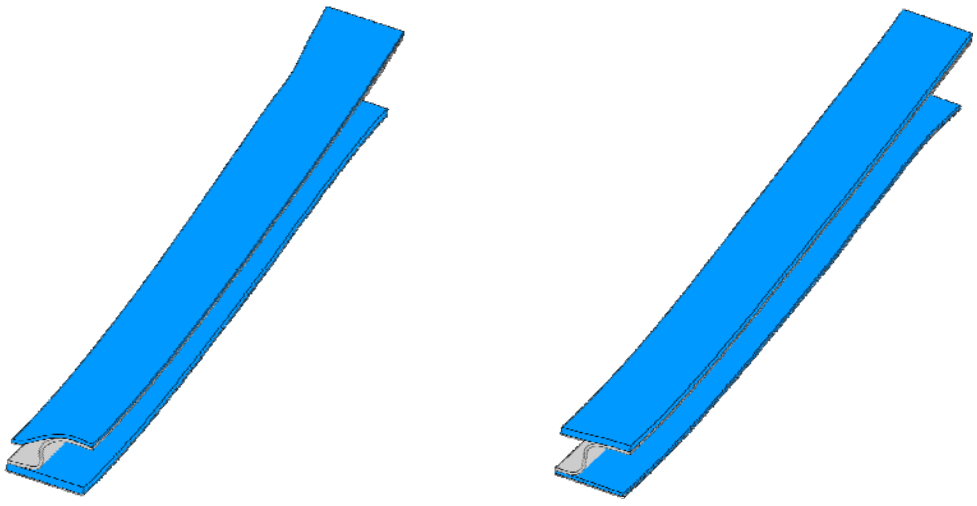

Figure 5. Deformed configurations of sinusoidal plate core sandwich plates subjected to $\overline{I} = 0.25$. (a) The case of $\alpha = 0.5$, (b) the case of $\alpha = 2$

5.2. Effect of the core height

Fig. 6(a) show the effect of the normalized core height $\bar{H}_c$ to the normalized maximum deflection $\bar{w}_1$ of the metal sandwich plates under $\bar{I}=0.25$, in which $\alpha=1$, $2\bar{h}\bar{H}_c+\bar{\rho}\bar{H}_c=0.02$, $\phi=45^o$, $\bar{\rho}=0.04$ and $L=1\text{m}$. Obviously, the analytical solutions [15] agree well with the numerical results for the moderate $\bar{H}_c$, and underestimate and overestimate numerical results for the cases of small and big $\bar{H}_c$. It is readily seen that the angle ϕ significantly affects the numerical results for maximum deflection of bottom face sheets in Fig. 6(a). The normalized maximum deflection of bottom face sheet has smallest value when $\bar{H}_c=0.28$.

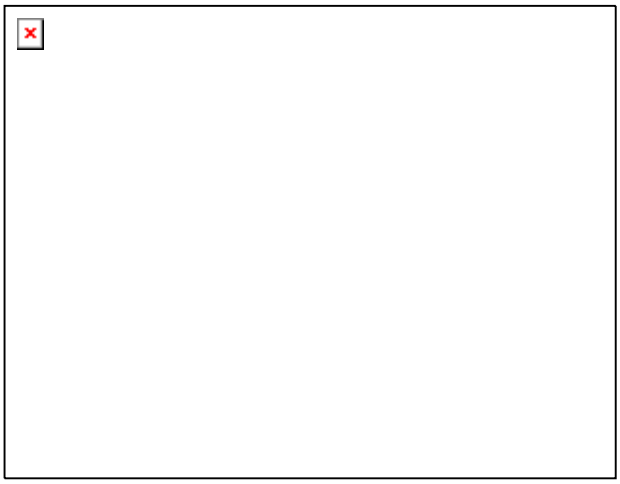

(a)

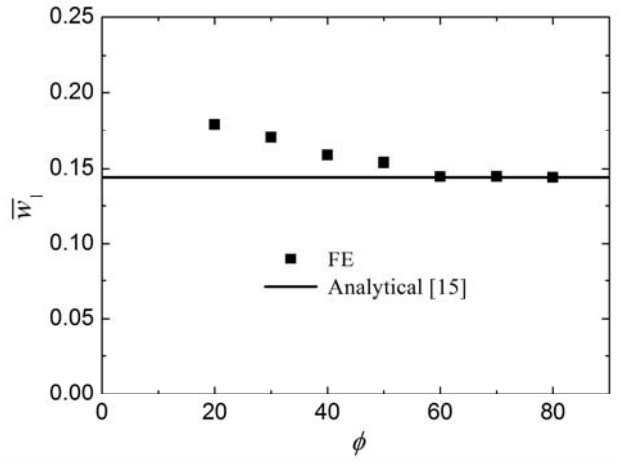

(b)

Figure 6. The effect of the (a) normalized core height $\bar{H}_c$ and (b) angle ϕ to the normalized maximum deflection $\bar{w}_1$ of the bottom face sheets of sandwich plates

5.3. Effect of the ratio of core height to half-length of the unit

Comparisons of the analytical [15] and numerical solutions for the normalised maximum deflection $\bar{w}_1$ of the bottom face sheets of the sandwich plates versus the angle ϕ are shown in Fig. 6(b). The angle ϕ is varied and other values ($\bar{I}=0.25$, $\bar{H}_c=0.1$, $\bar{h}=0.08$, $\bar{\rho}=0.04$, $\alpha=1$ and

$L=1\text{m}$) are fixed. The analytical solutions agree well with the numerical results for the case of big ϕ. The maximum deflection decreases with the increasing of ϕ, and remains more or less constant when ϕ exceeds 60^0. In other words, when ϕ is bigger than 60^0, the blast-resistance performances of the bottom face sheets of the sandwich plates are good.

5.4. Effect of the relative core density

The effect of relative core density $\bar{\rho}$ to the normalized maximum deflection $\bar{w}_1$ of the metal sandwich plates subjected to $\bar{I}=0.25$ is shown in Fig. 7, in which $\bar{H}_c=0.1$, $2\bar{h}\bar{H}_c+\bar{\rho}\bar{H}_c=0.02$, $\phi=45^o$, $\alpha=1$ and $L=1\text{m}$. The analytical solutions [15] are a little smaller than numerical results in a whole, and the bottom face sheet has the smallest maximum deflection at a relative core density 5.5%.

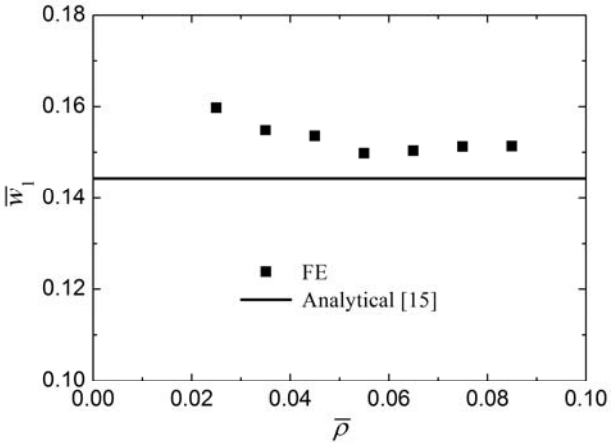

Figure 7. The effect of the relative core density $\bar{\rho}$ to the normalized maximum deflection $\bar{w}_1$ of bottom face sheets of the sandwich plates

6. Concluding remarks

The dynamic response of corrugated sinusoidal plate core sandwich plates under the impulsive loading has been investigated. Good agreement between the analytical predictions and numerical results is achieved. The optimizations of topology with respect to the respective geometric parameters have been obtained. It is shown that the axial force plays an important role in the dynamic large deflection response of corrugated metal sandwich plates and the present analytical procedure is simple and efficient.

Acknowledgements

This work was supported by the National Natural Science Foundation of China (11102146, 11021202 and 11272246), the National Basic Research Program of China (2011CB610301) and the Fundamental Research Funds for the Central Universities.

References

[1] M.F. Ashby, A.G. Evans, N.A. Fleck, J.W. Hutchinson, L.J. Gibson, H.N.G. Wadley, Metal Foams: A Design Guide, Butterworth-Heinemann, London, 2000.

[2] L.J. Gibson, M.F. Ashby, Cellular Solids: Structure and Properties, Cambridge University Press,

Cambridge, UK, 1997.
[3] H.G. Allen, Analysis and Design of Structural Sandwich Panels, Pergamon, Oxford, 1969.
[4] N.A. Fleck, V.S. Deshpande, The resistance of clamped sandwich beams to shock loading. ASME, J Appl Mech, 71 (2004) 386–401.
[5] X. Qiu, V.S. Deshpande, N.A. Fleck, Impulsive loading of clamped monolithic and sandwich beams over a central patch. J Mech Phys Solids, 53 (2005) 1015–1046.
[6] Q.H. Qin, T.J. Wang, An analytical solution for the large deflections of a slender sandwich beam with a metallic foam core under transverse loading by a flat punch. Compos Struct, 88 (2009) 509–518.
[7] Q.H. Qin, J.X. Zhang, Z.J. Wang, T.J. Wang, Large deflection of geometrically asymmetric metal foam core sandwich beam transversely loaded by a flat punch. Int J Aerospace and Lightweight Structures, 1 (2011) 23–46.
[8] Q.H. Qin, T.J. Wang, A theoretical analysis of the dynamic response of metallic sandwich beam under impulsive loading. Eur J Mech A/Solids, 28 (2009) 1014–1025.
[9] Q.H. Qin, T.J. Wang, S.Z. Zhao, Large deflections of metallic sandwich and monolithic beams under locally impulsive loading. Int J Mech Sci, 51 (2009) 752–773.
[10] Z. Xue, J.W. Hutchinson, A comparative study of impulse-resistant metal sandwich plates. Int J Impact Eng, 30 (2004) 1283–1305.
[11] J.X. Zhang, Q.H. Qin, T.J. Wang, The resistance of metallic sandwich plates to blast loading. Key Eng Mater, 462–463 (2011) 349–354.
[12] X. Qiu, V.S. Deshpande, N.A. Fleck, Finite element analysis of the dynamic response of clamped sandwich beams subject to shock loading. Eur J Mech A/Solids, 22 (2003) 801–814.
[13] A. Vaziri, Z. Xue, J.W. Hutchinson, Metal sandwich plates with polymer foam-filled cores. J Mech Mater Struct, 1 (2006) 95–125.
[14] Y. Liang, A.V. Spuskanyuk, S.E. Flores, D.R. Hayhurst, J.W. Hutchinson, R.M. McMeeking, A.G. Evans, The response of metallic sandwich panels to water blast. ASME, J Appl Mech, 74 (2007) 81–99.
[15] J.X. Zhang, Q.H. Qin, T.J. Wang, Compressive strengths and dynamic response of corrugated metal sandwich plates with unfilled and foam-filled sinusoidal plate cores. Acta Mech, (2012) accepted, DOI: 10.1007/s00707-012-0770-5

Evaluation of Microstructure Effect on Anisotropic Mechanical Properties of Hot Rolled AZ31 by AE Analysis

Kousuke Matsumoto[1,*], Takashi Yasutomi[1], Manabu Enoki[1]

[1] Department of Materials Engineering, The University of Tokyo, 7-3-1 Hongo, Bunkyo-ku, Tokyo 113-8656, Japan
* Corresponding author: matsumoto@rme.mm.t.u-tokyo.ac.jp

Abstract Anisotropic properties of twinning and slip deformation of hot rolled and extruded AZ31 Mg alloy have been reported in our previous researches. AE (Acoustic Emission) measurement has been done during the tensile test of specimen with various angles between tensile direction and rolled or extruded direction. AE energy had good correlation with twinning area and 0.2% proof stress. It has been also reported that twinning stress has higher grain size dependence than the stress required for activation of slip because the Hall-Petch slope for twinning is larger than that for slip. In this research, tensile test specimen were prepared from rolled AZ31 with various angles between tensile and rolling directions. In order to change grain size of hot rolled AZ31 Mg alloy, the specimens were annealed at various temperatures. Then in-situ measurement of AE signals was conducted during the tensile test. The mechanical deformations occurring actually were found by EBSD (Electron Backscatter diffraction) and observation of fracture surface. According to the result, the effect that grain size of hot rolled AZ31 Mg alloy gives to anisotropic mechanical properties during the tensile test was quantitatively evaluated by AE analysis.

Keywords Acoustic Emission, AZ31, Annealing, Anisotropy, Twinning

1. Introduction

Mg alloy is a light structural metal with high specific strengths; therefore, its alloys are the most attractive materials to be utilized in the automotive and transportation industries. This is due to their lower density compared to that of other structural materials such as steels and aluminum alloys. However, their poor mechanical properties at the room temperature are considered as an important fault. Grain size refinement is a major way to improve mechanical properties. At this point, Hall-Petch relationship predicts that the material strength increases with decreasing grain size. Its hexagonal close-packed structure also characterizes its mechanical properties. In the former research, anisotropic mechanical properties during tensile test of extruded AZ31 Mg alloy is evaluated by AE analysis [1-6]. In this research, the specimens were produced from hot rolled AZ31 Mg alloy with various angles between tensile and rolling directions. These specimen were annealed at various temperatures in order to change their grain sizes. The effect of various grain sizes on mechanical properties was evaluated by AE energy.

2. Experimental procedure

2.1. Material

The material used in this study was hot rolled AZ31 sheet (Mg – 3.04 % Al – 1.06 % Zn – 0.38 % Mn) with a thickness of 3 mm bought from Osaka Fuji Corporation. The as-received specimen had an average grain size of 9.8μm. In order to change grain size, the as-received specimens were annealed at 285°C for 30 min and 450°C for 30 min. The grain sizes after annealing were 13.5 and 17.9μm for the first and latter conditions, respectively.
To study the anisotropy of mechanical properties, the specimens were prepared with various angles between tensile and rolling directions of 0°, 15°, 30°, 45°, 60°, 75° and 90°, shown in Fig. 1. All tests were carried out at a constant strain rate of 1.67×10^{-4} /s.

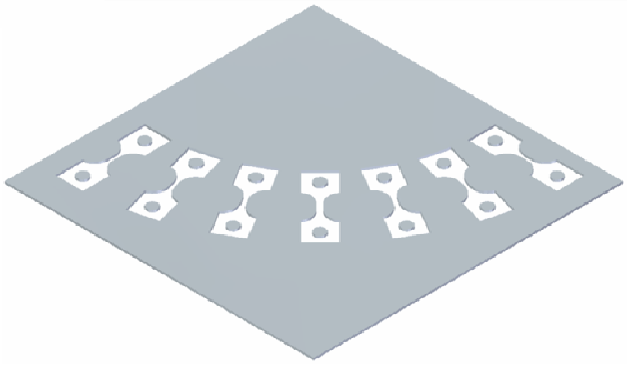

Figure 1. Procedure of cutting specimens

2.2. AE measurement during tensile test

AE measurements were applied with 4 channels in order to remove friction noise from jig of tensile test machine. Positions of AE sensors are shown in Fig. 2. AE sensors used in this study were M304A (Fuji ceramics, Japan). Continuous Waveform Memory (CWM), which was developed by our group, was used to perform AE measurements [7]. The high pass filter was set at 100 kHz. All AE signals are wavelet transformed in order to emphasize dependence of time and frequency. Various threshold levels were set from 60dB to 80dB with an interval of 5dB to detect signals with wide range of amplitude. Then, the data was integrated.

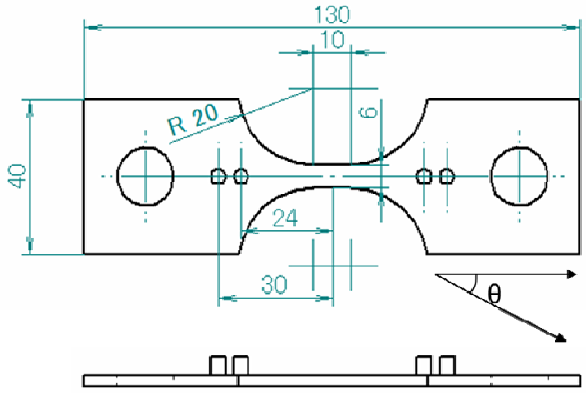

Figure 2. AE sensors positions

2.3. EBSD test

Electron Backscatter Diffraction (EBSD) analysis was performed to evaluate the texture during the tensile testing. The software used in this study was OIM-Analysis 5 of TSL Solutions. Specimens before deformed and after deformed until a strain value of 3% were cut and then polished by a machine called “Cross section Polisher” (CP), which utilizes an argon iron beam to mill the sample. This method prevents any damages from mechanical polishing and therefore the suitable surface for EBSD is easily obtained. Then, automated EBSD scans were performed in the stage control mode with TSL data acquisition software with a step size of 1.5 μm. Average grain size and Schmid factor were calculated from this result. Schmid factor used in this paper is an average value of each grain.

3. Result and discussion

3.1 Microstructure

Initial microstructure of specimens is shown in Fig. 3. As annealing temperature increases, there are less small grains, and the average grain size is larger. Fig 4(a) shows average Schmid factor for twinning of all grains of each angle. In each annealing condition, Schmid factor for twinning is larger at 60° to 90° than another angle. From this tendency, it follows that twinning deformation occurs easily in 60° to 90° specimens. Fig 4(b) shows pole figure for (0002) before tensile test. The (0002) vector shapes ring seen from the RD direction.

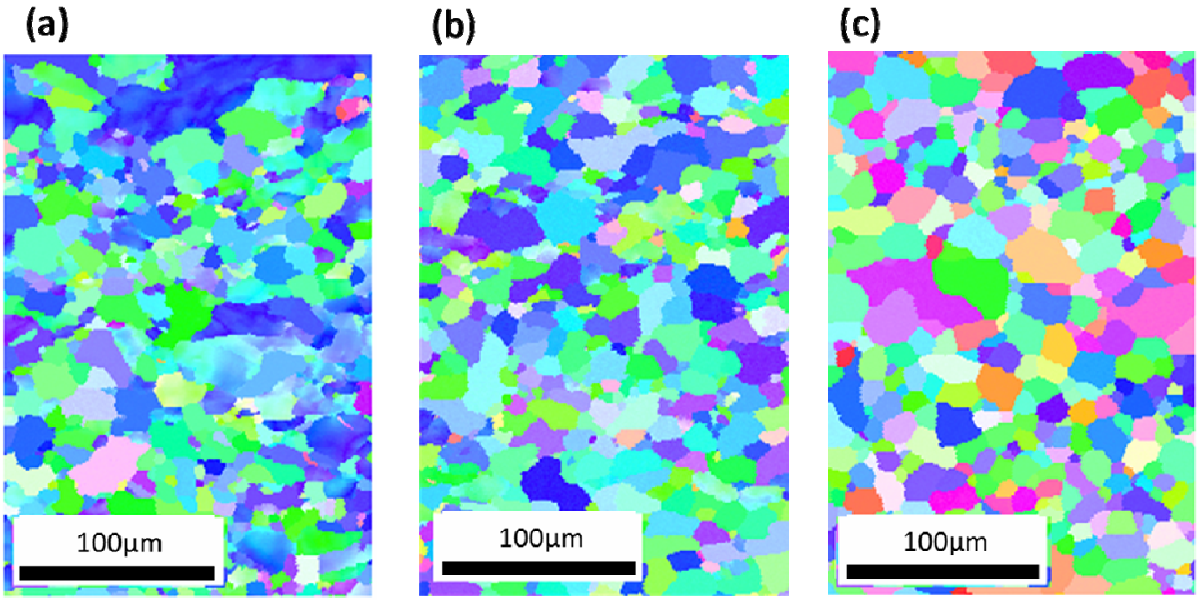

Figure 3. IPF map of (a) as-received, (b) 285°C annealed and (c) 450°C annealed specimens before tensile test

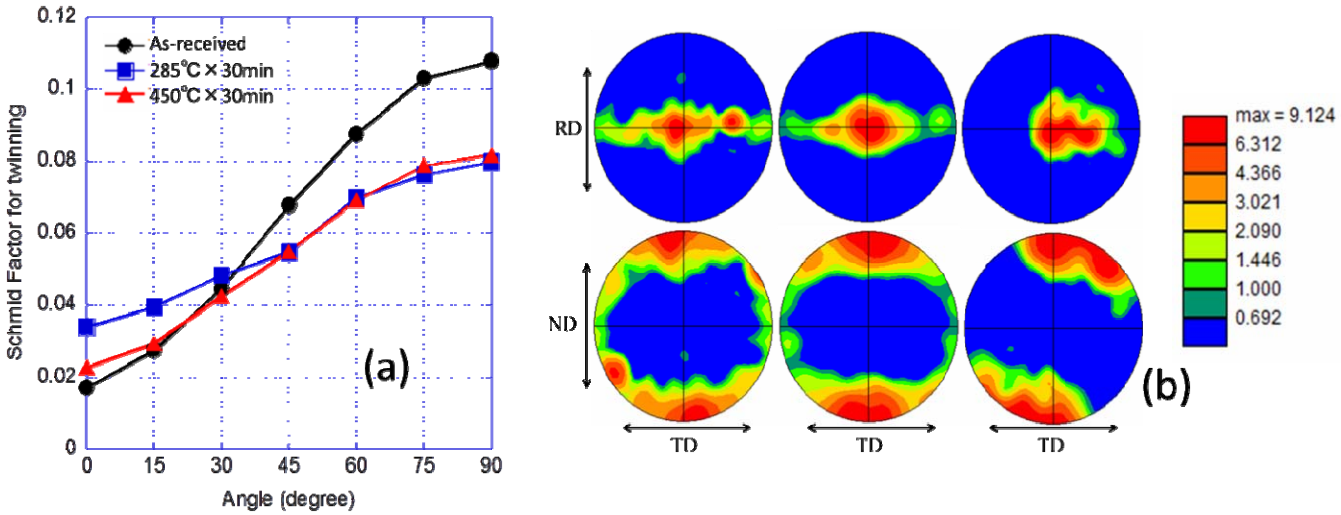

Figure 4. (a) Schmid factor for twinning and (b) pole figure for (0002) before tensile test

3.2. Mechanical properties

Fig. 5 shows strain-stress curve of (a) as-received specimen and (b) 450°C annealed specimen of

each angle. Before and after annealing, nominal stress and strain has different figure in each angle. In other words, strain-stress curve shows anisotropy in each annealing conditions. However, the strength of anisotropy differs by annealing.

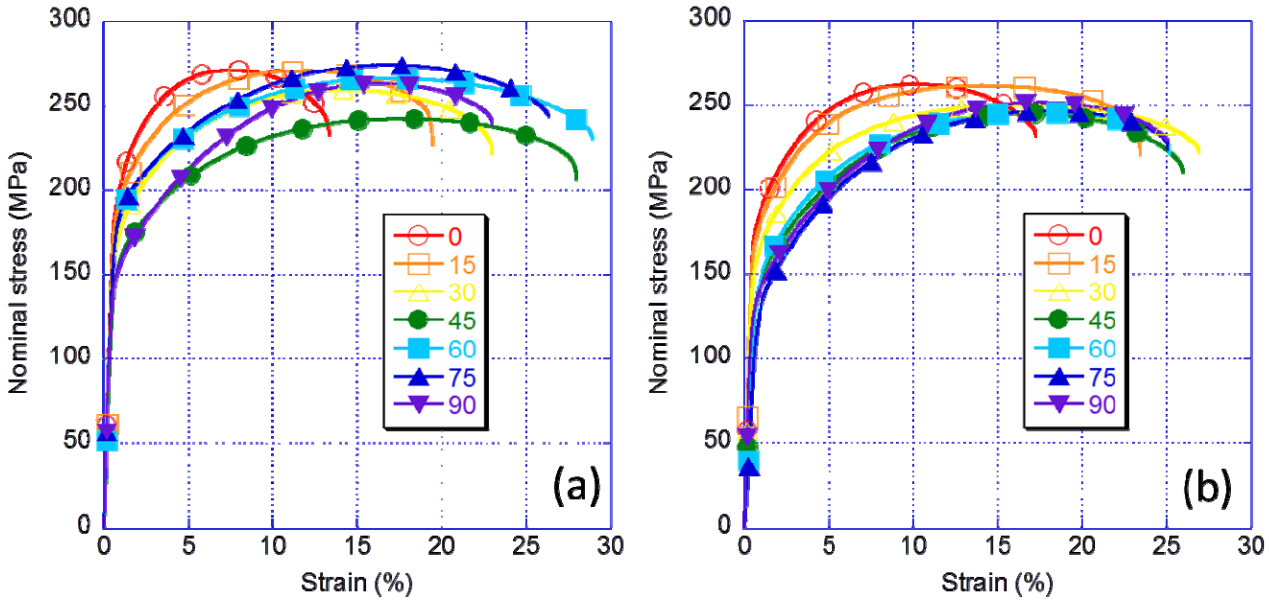

Figure 5. Strain-stress curve of (a) as-received specimen and (b) 450°C annealed specimen

In order to analyze this result, ultimate tensile stress (σ_{max}) and maximum strain (ε_{max}) are plotted in Fig. 6. From Fig. 6(a), ultimate tensile stress is high in 15° and 75°, and is especially low in 45°, so we can see strong anisotropy in as-received specimens. However, in 285° and 450°C annealed specimens, ultimate tensile stress become higher in 45°, and lower in other angles, so it can be said that anisotropy is weakened by annealing. Fig. 6(b) shows that strain also has anisotropy. Strain of as-received specimens is extremely high in 45° to 75°, but by annealing, strain of 0° to 30° becomes higher, on the other hand, strain of 45° to 75° becomes lower. By annealing, strain of 30° to 90° is flat, so it can be said that anisotropy is weaken by annealing.

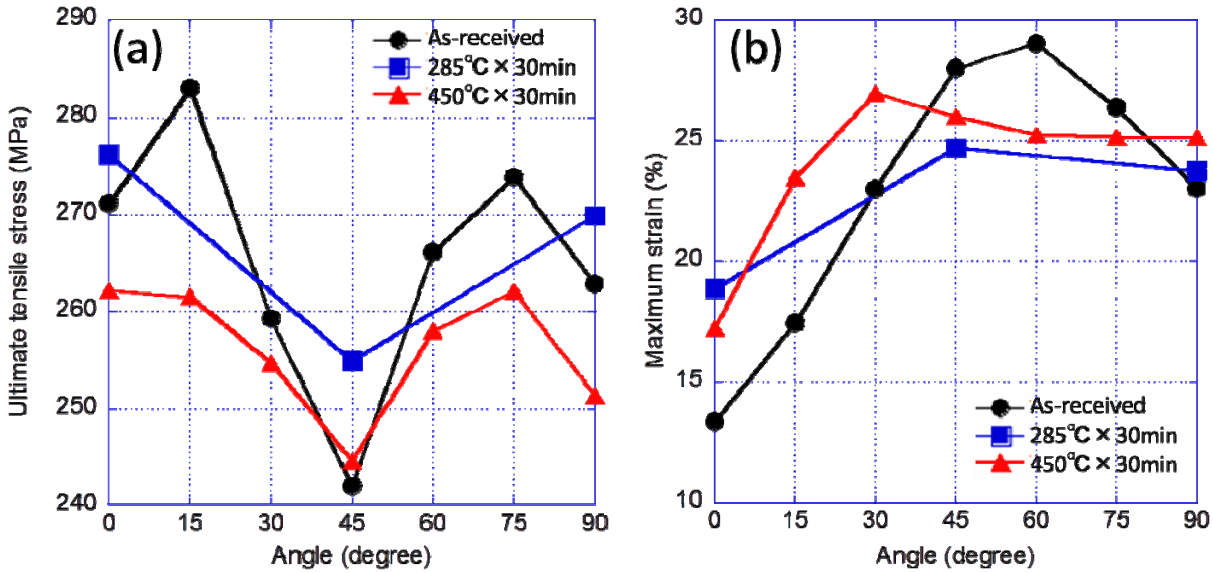

Figure 6. (a) Ultimate tensile stress and (b) Maximum strain of each specimen

However, 0.2% proof stress of each specimens shows different tendency from the former result. Fig. 7 plots 0.2% proof stress of each angle of as-received and 450°C annealed specimens. In both annealing conditions, 0.2% proof stress has anisotropy. Though ultimate tensile stress and maximum strain decreases their anisotropy of all angles by annealing, 0.2% proof stress changes of only 60° to 90° by annealing. In these angle, 0.2% proof stress become high by annealing, and it can be said that anisotropy become even strong in this part. In 0° to 45°, the value of 0.2% proof stress is almost the same in each annealing condition. It is the highest in 0° of all angles and gradually decreases to 45°.

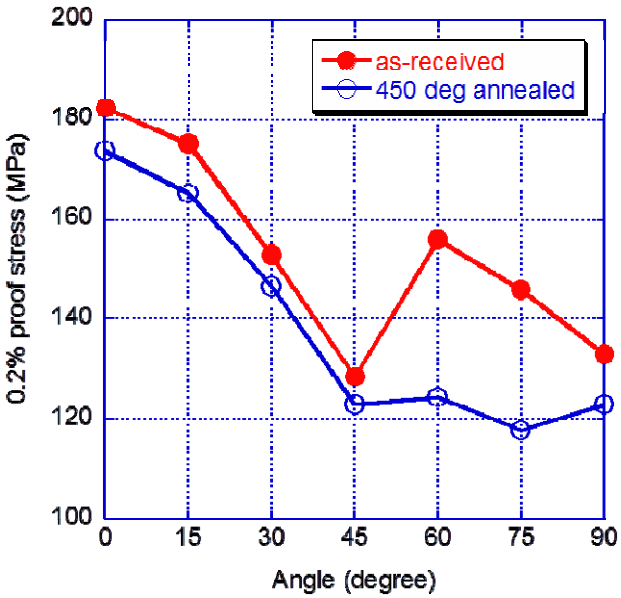

Figure 7. 0.2% proof stress of each angle of as-received and 450°C annealed specimens

3.3. AE measurement

AE result is show in Fig. 8 and Fig. 9. AE measurement was conducted during the tensile test, from start of the test to just before fracture. In each graph, AE result and time stress curve are plotted together in order to connect result of AE measurement and mechanical properties. *x* axis is time, *y* axis is nominal stress and peak frequency of AE signals, and *z* axis is magnitude of AE signals. The value of peak frequency and magnitude is used after wavelet transformed. In all specimens, AE magnitude is high at yield point, so main AE source is related to yielding mechanism. After that, AE magnitude becomes lower gradually as strain increase. In both Fig. 8 and Fig. 9, there are many resemble point. AE magnitude is far higher in 90° than 0° and 45°. Peak frequency is wide range in yield point, but after yielding, AE magnitude is high in high frequency, from about 500 kHz to 600 kHz. The second highest AE magnitude is in frequency of about 300 kHz. In 0°, maximum strain is lowest of all angles, so AE signals is detected in the early time. After annealing, these tendencies are the same. However, AE magnitude of 0° becomes much lower than 45° and 90°.

In order to analyze this AE result, the relationship between AE energy and nominal stress is plotted in Fig. 10. AE energy is calculated as square of AE magnitude and this AE signal is released when nominal stress increases 1 MPa. In Fig 10(a) to (c), AE energy peak (E_{peak}) is extremely high in 90°. AE energy is released from low nominal stress, about 50 MPa, to high nominal stress, about 250 MPa. It is well explained by the fact that AE signals are released at yield point of each specimen.

The nominal stress where AE energy is peak (σ_{AEp}) is low in 90° compared with 0° and 45°. The nominal stress at which AE energy starts to be released ($\sigma_{AEstart}$) is also low, in 90°.

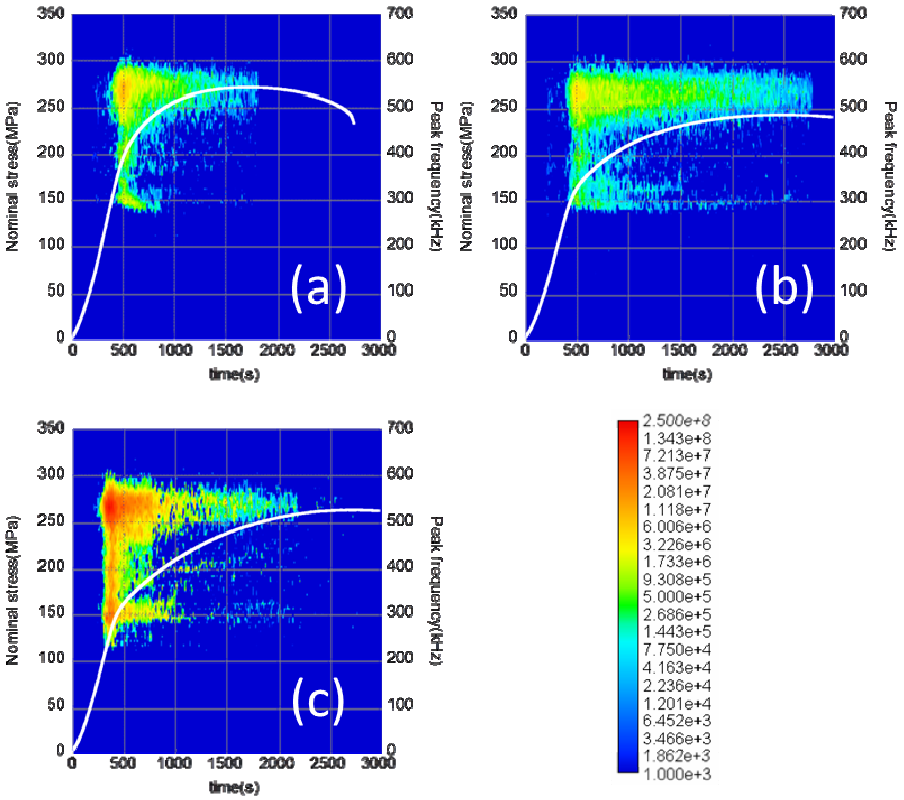

Figure 8. AE magnitude and peak frequency of as-received specimen of (a) 0°, (b) 45° and (c) 90°

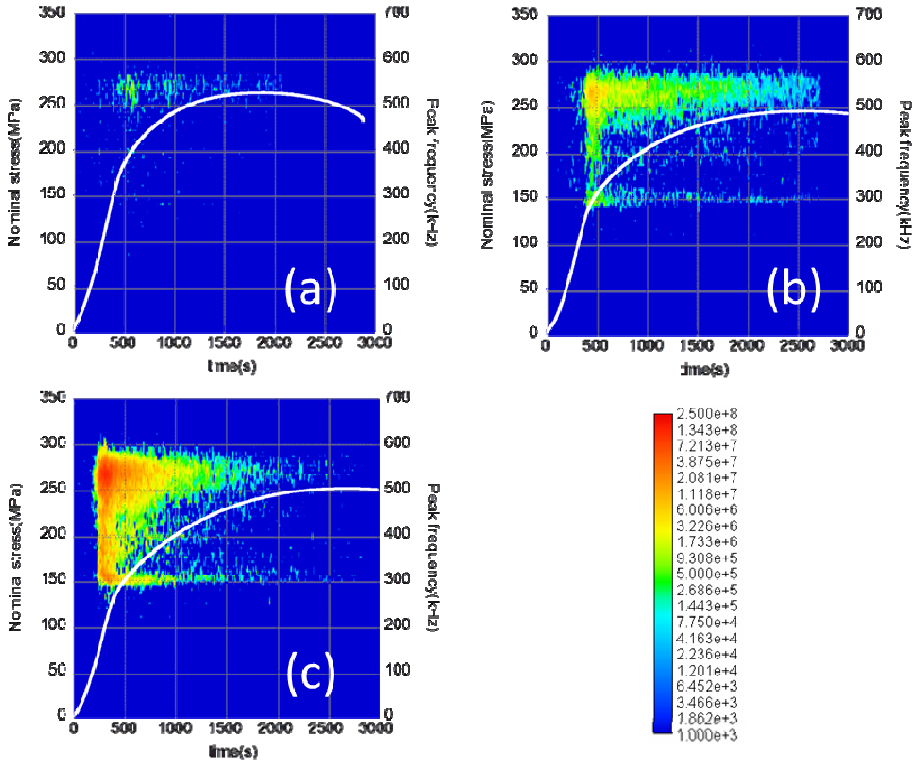

Figure 9. AE magnitude and peak frequency of 450°C annealed specimen of (a) 0°, (b) 45° and (c) 90°

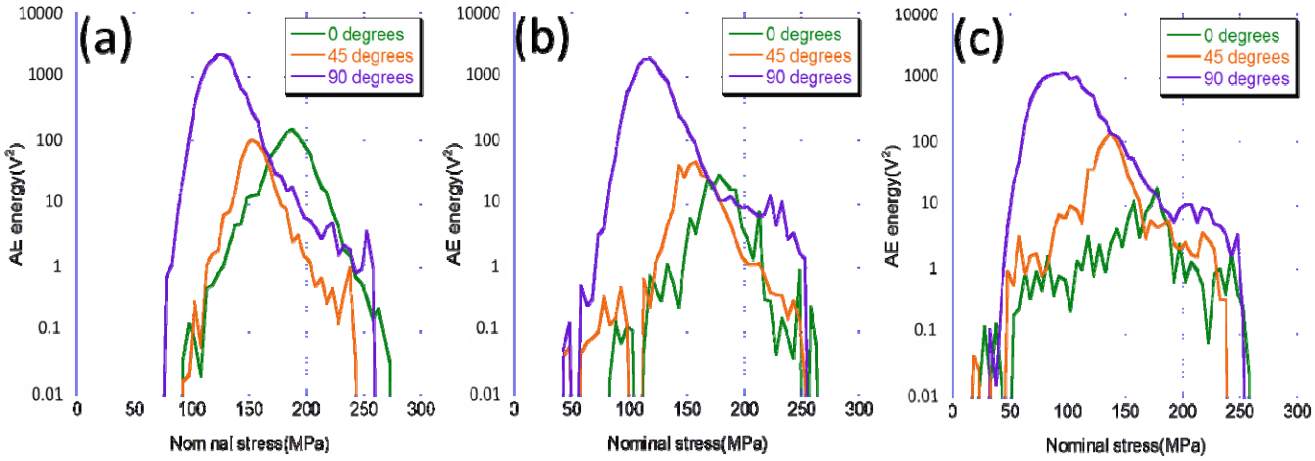

Figure 10. AE energy peak of (a) as-received, (b) 285°C annealed and (c) 450°C annealed specimen

For detail analysis, σ_{AEp} and E_{peak} is plotted in Fig. 11. In each annealing condition, σ_{AEp} become lower and E_{peak} become higher as the angle increases. This tendency is the same in each annealing condition, as-received, 285°C annealed and 450°C annealed. The value is also almost the same. It can be said that σ_{AEp} become lower and E_{peak} become higher when the angle is large for some reason of deformation mechanism.

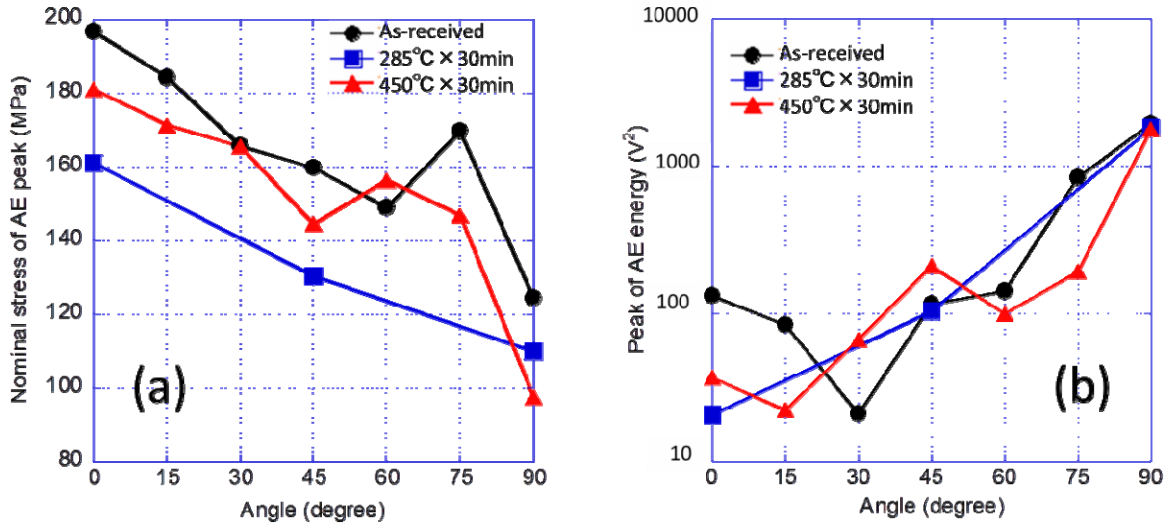

Figure 11. Relationship between tensile angle and (a) nominal stress of AE peak and (b) peak of AE energy of each specimen

In order to see why σ_{AEp} become lower and E_{peak} become higher when the angle is large, x axis is changed to Schmid factor for twinning in Fig. 12. By changing x axis from angle to Schmid factor for twinning, the AE result is connected with mechanical behavior. The abstract of graph is the same as Fig. 10, so it can be said that when Schmid factor for twinning is large, nominal stress of AE peak is low and peak of AE energy is high. The AE result is mainly caused by twinning deformation. When Schmid factor for twinning is large, twinning deformation occurs easily. At low nominal stress twinning deformation occurs, so AE signals released by twinning are detected at lower stress. For the same reason, peak of AE energy is high because the ease of twinning deformation occurring makes more twinning deformation.

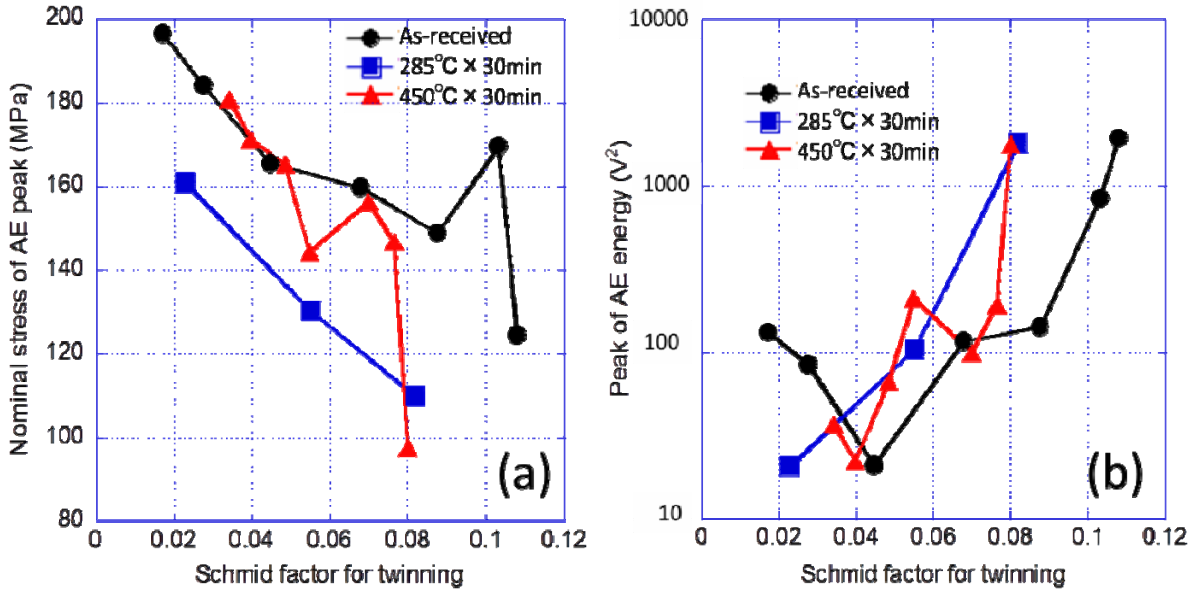

Figure 12. Relationship between Schmid factor for twinning and (a) nominal stress of AE peak and (b) peak of AE energy of each specimen

Fig. 13 shows $\sigma_{AEstart}$ of each angle and each annealing condition. $\sigma_{AEstart}$ is defined as the stress at which AE energy is over 0.01 V^2. At this point, AE energy is especially higher than noise level, and it is easily said that AE energy is released by certain mechanical behavior other than noise. After annealing, in both 285°C and 450°C, $\sigma_{AEstart}$ is almost the same, and the value is less than 20 MPa. However, before annealing, $\sigma_{AEstart}$ is over 30 MPa and has anisotropy. It can be said that when annealed, nominal stress at which AE energy starts to be released is lower and has weaker anisotropy.

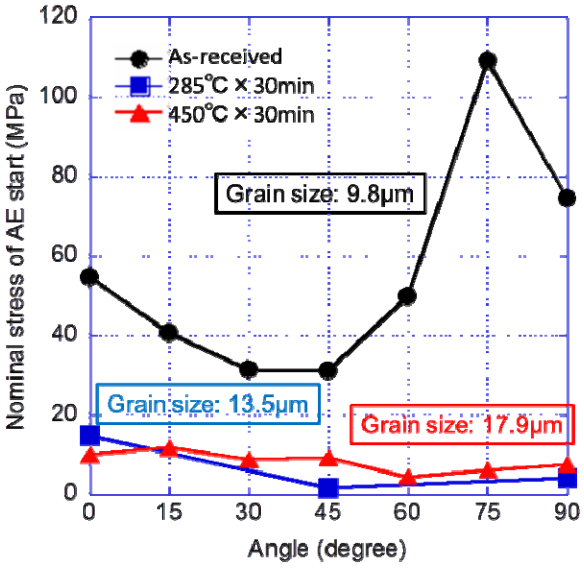

Figure 13. Nominal stress of AE start of each specimen

Fig. 14(a) plotted the relationship between grain size and σ_{AEp}. D is an average grain size, d to the negative one-half power. By annealing, d become larger and D becomes smaller. In each angle, there is linear relationship between D and σ_{AEp}. In other words, Hall-Petch equation, which is shown below, is formed in this result;

.

k, the slope of this equation is larger as the angle increases. Fig. 14(b) shows relationship between *k* and Schmid factor for twinning. In each annealing condition, *k* become larger as Schmid factor for twinning is larger. When Schmid factor for twinning is large, twinning deformation can easily occur, and AE signals are dominated by twinning deformation. Additionally, slope of Hall-Petch equation is larger in twinning than that in slip [8]. For these reason, there is linear relationship between Schmid factor for twinning and k.

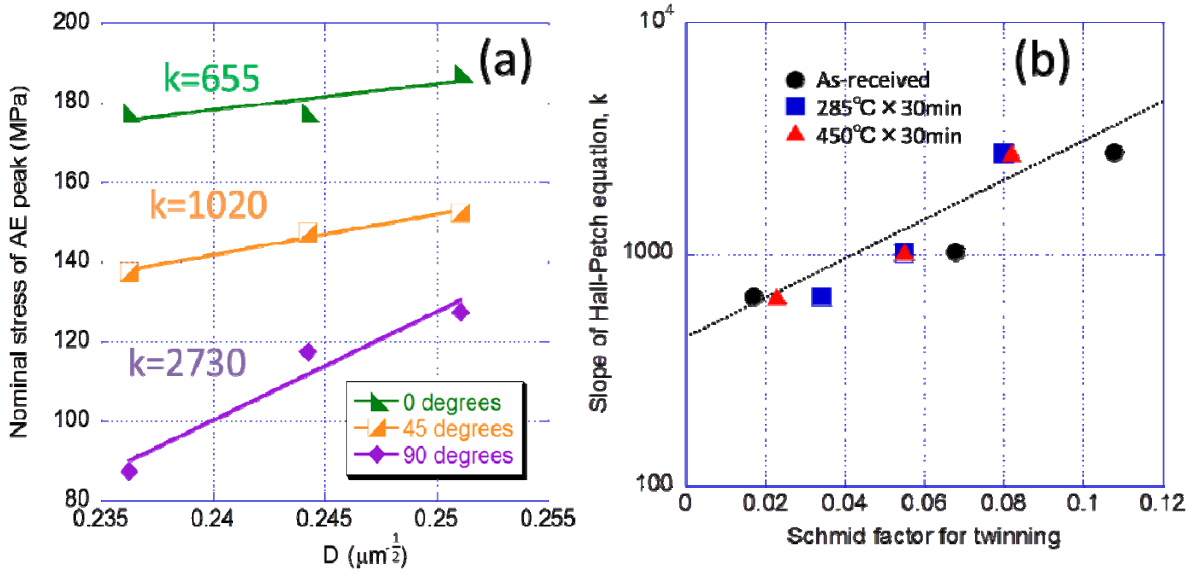

Figure 14. (a) Hall-Petch equation and (b) relationship between slope of the equation and Schmid factor for twinning

4. Conclusion

In the present study, microstructure effect on mechanical properties of AZ31 extruded magnesium alloy is evaluated by AE test and EBSD test, and following conclusions were drawn;

(1) The result of tensile test showed that anisotropy of mechanical properties is weakened by annealing.

(2) Nominal stress of AE energy peak and peak of AE energy were dominated by twinning deformation, so these value changed as Schmid factor for twinning changed.

(3) Nominal stress of AE start showed strong annealing dependence. After annealing, the stress was less than 20 MPa and anisotropy disappeared.

(4) The relationship between nominal stress of AE peak and grain size was well explained by Hall-Petch equation.

(5) Slope of Hall-Petch equation changed as Schmid factor for twinning because twinning deformation is main mechanical behavior in this study.

References

[1] T. Yasutomi and M. Enoki, In-situ evaluation of detwinning behavior in extruded AZ31 mg alloy by AE. Materials Transactions, 53(2012) 1611-1616.

[2] Y. P. Li and M. Enoki, Evaluation of the Twinning Behavior of Polycrystalline Magnesium at Room Temperature by Acoustic Emission. Materials Transactions, 48(2007) 1215-1220.

[3] Y. P. Li and M. Enoki, Deformation and Anelastic Recovery of Pure Magnesium and AZ31B Alloy Investigated by AE. Materials Transactions, 48(2007) 2343-2348.
[4] Y. P. Li and M. Enoki, Recovery Behaviour of Pure Magnesium in Cyclic Compression–Quick Unloading-Recovery Process at Room Temperature Investigated by AE. Materials Transactions, 49(2008) 1800-1805.
[5] Y. P. Li and M. Enoki, Twinning behavior of pure magnesium quantitatively investigated by acoustic emission. Materials Science and Engineering, 536(2012) 8-13.
[6] Y. P. Li and M. Enoki, Anelastic recovery of pure magnesium quantitatively evaluated by acoustic emission. Journal of Materials Research, 26(2011) 3098-3106.
[7] K. Ito and M. Enoki, Acquisition and Analysis of Continuous Acoustic Emission Waveform for Classification of Damage Sources in Ceramic Fiber Mat. Materials Transactions, 48(2007) 1221-1226.
[8] M.R. Barnett, Z. Keshavarz, A.G. Beer and D. Atwell, Influence of grain size on the compressive deformation of wrought Mg-3Al-1Zn. Acta Materialia, 52(2004) 5093-5103.

Mechanical properties of natural fiber polyester composite sandwich panels

Jie Lu[1,*], Bing Yang[2], Nandika D'Souza[2], Sheldon Q Shi[2]

[1] College of Aerospace and Civil Engineering, Harbin Engineering University, Harbin 150001, China
[2] Department of Mechanical and Energy Engineering, University of North Texas, Denton 76207, USA
* Corresponding author: lujie@hrbeu.edu.cn

Abstract In the current work, a novel kenaf fiber reinforced composite sandwich panel was developed and fabricated. The kenaf fiber composites as sandwich face sheets were prepared at 55% (by weight) fiber content. PVC foams were joined using epoxy resin adhesive to fabricate sandwich structures. A series of mechanical tests, such as tensile, three-point bending and double cantilever beam, were carried out to know the mechanical behaviors of sandwich panels. Fracture and failure modes were also reported and discussed. The results show kenaf fiber reinforced composite sandwich panels have potential application in engineering construction of buildings.

Keywords Natural fiber, Sandwich, Mechanical properties, Failure analysis

1. Introduction

In recent years, the use of sandwich structures continues to increase rapidly due to their advantages, such as high strength/weight and stiffness/weight ratios, excellent heat resistance and favorable energy-absorbing capacity. They have been widely used in the satellites, aircraft, ships, automobiles, rail cars, wind energy systems, and bridge and civil constructions [1]. Most sandwich specimens analyzed in the past studies were made of polymer foam cores with composite face sheets or with metal face sheets [2–4]. Additionally, more assembly techniques, such as screw fasteners, adhesively joints, or blazed bonding, can be applied for bonding the core material and the face sheet. These applications and novel manufacturing techniques increase the requirement for the mechanical strengths of the sandwich structures in practical designs.

Another question is that environmental protection becomes increasingly important. Thus, the use of natural fibers as reinforcements of polymer-based composites has been of great interest to many researchers [5–7]. Due to many advantages, such as low density, high specific strength and modulus, relative non-abrasiveness, ease of fiber surface treatment and wide availability. More important, they are renewable and biodegradable. In fact natural fibers are also much cheaper than synthetic fibers and could replace synthetics in many applications.

If according to the design concept of sandwich structures, the natural fibers are used to fabricate the sandwich panel, it is predictable that such a "sandwich structure" with lightweight, high strength, bio-degradable and environmental friendly properties could be obtained. However, few studies have addressed this aspect. The objective of this work was to develop a novel sandwich structure based on natural fiber and PVC foam materials. Fabrication method including sheet molding compound (SMC) and bonding technique was introduced. A series of mechanical tests, such as tensile, bending and fracture properties, were carried out to understand the mechanical behaviors.

2. Materials preparation

Kenaf bast fiber was supplied by Kengro Corp (Charleston, MS, USA). It was short fiber form and

with a length of 5~8mm. The unsaturated polyester resin (UPR) was provided by Ashland Chemicals (AROPOL 6585) with density of 1.12 g/cm^3. The curing agent was obtained from Acros Orgaincs. The sandwich core was Divinycell H-grade H35 PVC foam (DIAB AB Group).

Kenaf fibers reinforced unsaturated polyester resin (UPR) composites were fabricated first as the face sheet of sandwich structure. Then polyesters, fibers, and curing agent were initially weighed to ensure the total fiber loading was 55 wt.%. Each mixture of sandwich face sheet was put into a steel mold and pressed at 5MPa for 2 min to form a mat. Then, the polyester resin with curing agent was poured into the mold and the mat was hot-pressed under a pressure of 5MPa and at a temperature of 150^{o}C for 2 hours. When the fabrication was accomplished, all the panel samples were put into a drier at room temperature for 48 hours for further investigation. The compliant PVC foam core were joined with the upper and lower kenaf fiber reinforced UPR composite panels using epoxy resin.

3. Mechanical properties of sandwich composites

3.1. Tensile test

Tensile specimens were cut from the composite panels. The tensile strength and modulus of the kenaf fiber composite panel were tested on the basis of three replicates with a MTS 810 universal testing system (USA) in accordance with the procedure described in ASTM D 638-10 [8]. The specimen dimensions were 100×20×1.60 mm^3 (Length × Width × Thickness). A tensile fixture was used, with a constant gauge of 60 mm and a crosshead speed of 0.50mm/min. An FEI Quanta Environmental Scanning Electron Microscope (ESEM; FEI Company, Oregon, USA) were used to examine the fracture morphology of the specimens.

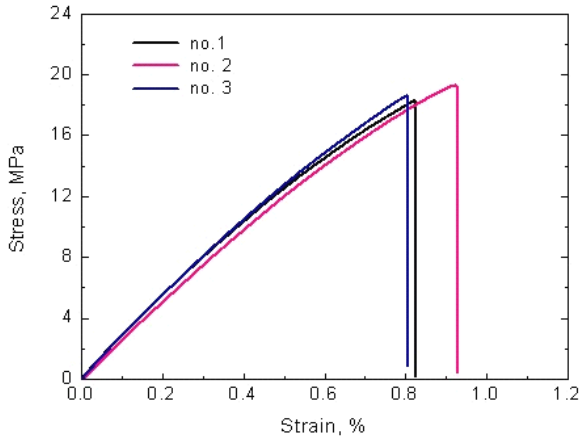

Figure 1. Tensile stress versus strain of kenaf fiber reinforced UPR composite panels

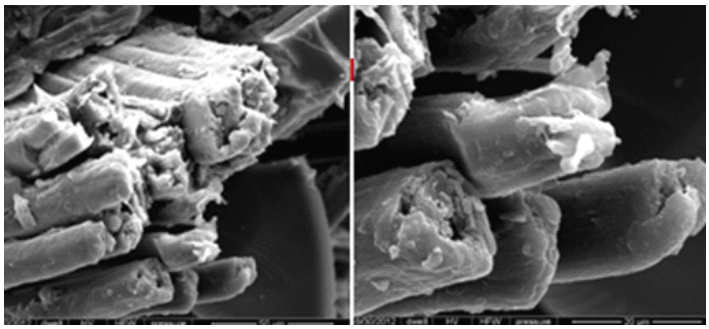

Figure 2. SEM micrographs of composites after tensile failure

In the present study, the tensile properties of the kenaf fiber reinforced UPR composites are displayed in Fig. 1 and summarized in Table 1 showing the peak load, tensile strength, strain at break and young's modulus. Among all tested specimens, kenaf fiber reinforced UPR composites exhibited relative high strength and stiffness characteristics. The tensile stress of sandwich specimens was about 18.21~19.32MPa. On the other hand, the failure strains was 0.81~0.92%. The young's modulus of sandwich panel was 2.05~2.39GPa. Fig. 2 shows the fracture micrograph of kenaf fiber reinforced UPR composites. Good interfacial adhesion of kenaf fiber with polyester resin can be found even though there are some local micro voids. Fiber breakage is the major failure mode.

Table 1. Tensile test results of kenaf fiber reinforced UPR composites

Specimen	Peak load (N)	Max stress (MPa)	Strain at break (%)	Elastic modulus (GPa)
1	582.72	18.21	0.82	2.22
2	621.39	19.32	0.81	2.39
3	594.28	18.86	0.92	2.05

3.2. Bending test

To investigate the characteristics of bending behavior of this novel sandwich panels and also to analyze the shear effects of PVC foam core, three point bending tests were carried out. Sandwich specimens for three-point bending test were cut from the whole sandwich panels. The bending load and deflection of the sandwich composites were tested on the basis of five replicates with a MTS 810 universal testing system (USA) in accordance with the procedure described in ASTM D 7264 [9]. The specimen dimensions were 140×28×28.80 mm^3 (Length × Width × Thickness). Three-point bending fixture was used, with a constant span of 110 mm and a crosshead speed of 2.0mm/min.

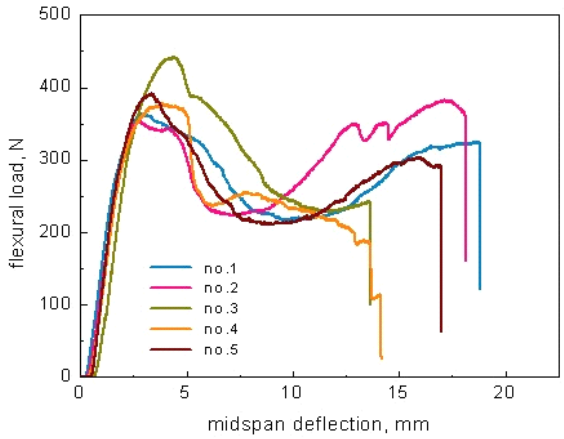

Figure 3. Flexural load versus mid-span deflection of sandwich composite specimens

Fig. 3 shows the flexural load and mid-span deflection of sandwich composite specimens. It could be seen that the whole three-point bending deformation tests included three similar stages for all of specimens. They were linear elastic stage, depressed region and final fracture. The bending properties of sandwich composites were also summarized in Table 2 showing the maximum load, deflection at break, bending stress of face sheet, shear stress in the core, local indentation stress and main failure modes. According to the analysis of [10] , bending stress in face sheet of all tested specimens were 7.79~9.45MPa. The maximum shear stress in the core was 0.29MPa. It was denoted that no shear failure initiated in the sandwich composites. Due to local concentration of loading at mid-span, the major failure mode was local indentation. In the present study, kenaf fiber

was randomly distributed in the unsaturated polyester resin matrix. Bending strength was relative high at rich levels of fiber loading. Otherwise, at a relative low level of fiber loading, due to the limitation of resin strength, during the whole stress transfer process, fracture tended to occur in the voids between fiber and resin. Meanwhile those could be used to explain the low stress fracture in no.1 specimen of experimental results, shown in Fig. 4.

Table 3. Three-point bending test results of sandwich composites

no.	Maximum load (N)	Max Deflection (mm)	σ_f (MPa)	τ (MPa)	σ_{lc} (MPa)	Failure modes
1	365.30	18.82	7.79	0.24	1.37	Upper skin fracture, local indentation
2	381.13	18.17	8.13	0.25	1.43	local indentation
3	443.14	13.65	9.45	0.29	1.67	local indentation
4	378.92	14.19	8.08	0.25	1.42	local indentation, crack in the core
5	391.17	17.01	8.34	0.26	1.47	local indentation

*where,bending stress in the face sheet σ_f , shear stress in the core τ and local indentation stress σ_{lc} were as follows [10]:

$$\sigma_f = \frac{M_{\max}}{t_f hb} \tag{1}$$

$$\tau = \frac{V_{\max}}{hb} \tag{2}$$

$$\sigma_{lc} = \frac{P}{A} \tag{3}$$

$M_{\max}$ is the maximum moment, t_f is the thickness of face sheet, h is the distance between centroids of the face sheets, and b is the specimen width, $V_{\max}$ is the maximum shear, P is the applied load and A is local crushing area.

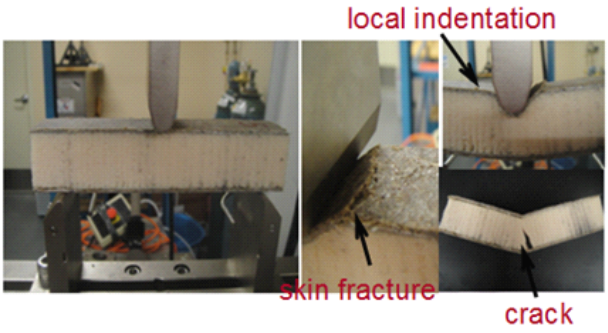

Figure 4. Three-point bending experiment set-up and main failure modes

3.3. Double cantilever beam test

The objective of this part experimental investigation was to understand the fracture behavior and

performance of this novel sandwich composite. The double cantilever beam of the sandwich composites were tested on the basis of three replicates with a Shimadzu universal testing system (model SCG-5KNA, Japan) in accordance with the procedure described in ASTM D 5528 [11]. The specimen dimensions were 160×30×28.8 mm3 (Length × Width × Thickness) with a 25 mm pre-crack. A tensile fixture was used, with a piano hinge amounted on the upper and lower sandwich face sheet and a crosshead speed of 2.0mm/min, shown in Fig. 5. During the process of test, the digital camera was used to real-time record the fracture behavior of the pre-crack and also used to take pictures of the typical fracture behavior.

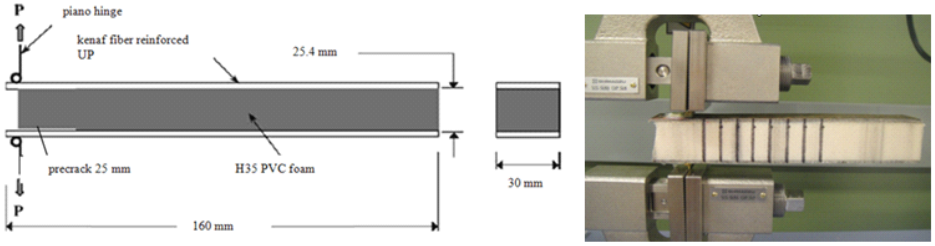

Figure 5. The dimension of double cantilever beam specimens and experiment set-up

A typical load against displacement curve of sandwich specimens during the DCB tests is shown in Fig. 6. The process of fracture can be approximately categorized into four stages based on the observation results and the characteristic load against displacement behavior at each stage, named as I, II, III and IV. In stage I, the load increased approximately linearly to the point A along with the increasing of the open displacement. From the point A to the point B (the stage II), the load against open displacement curve became non-linear. In this stage, the interlaminar delamination initiated between upper sandwich face sheet and PVC foam core and pre-crack developed stably. When stage II fracture completed, the load decreases rapidly from the point B to the point C (the stage III). In stage III, the interlaminar delamination propagated unstably. Beyond the point C, the interlaminar delamination propagation slowly went on. Due to the relative lower randomly distributed fibers in the upper face sheet, skin brittle fracture was found in no.2 specimen.

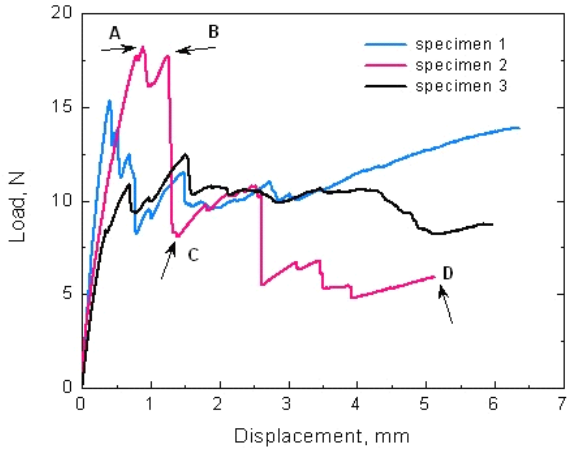

Figure 6. Load against open displacement curves for sandwich composite

According to [12], the strain energy release rate during crack propagation was calculated by,

$$G_c = \frac{\Delta U}{ba} \tag{4}$$

Where, G_c is strain energy release rate, b is the width of the specimen and a is the incremental crack length during the process of test, the energy or work ΔU, is equal to the area under load vs.

displacement curve. In order to calculate the work required to propagate the crack, for all of the specimens, load vs. open displacement of stage II were selected. Meanwhile, the DCB results were summarized in table 4 showing the peak load, open displacement and strain energy release rate Gc. Also compared with some published works, one was for honeycomb sandwich and another was for copper-epoxy interface, it was denoted that this novel sandwich structure exhibited better interlaminar fracture behaviors.

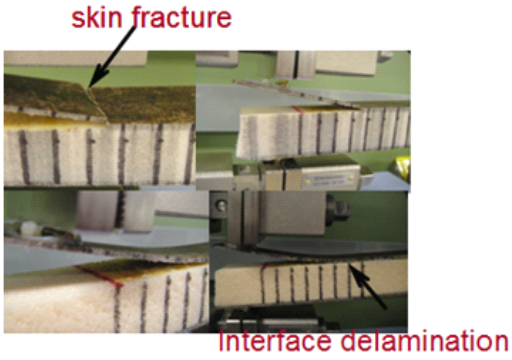

Figure 7. Fracture behavior and propagation of interlaminar delamination of sandwich composite

Table 4. Double cantilever beam test results of sandwich composites

Specimen	Peak load (N)	Open displacement (mm)	Energy release rate (kJ/m^2)	Main failure mode
1	15.37	0.41	0.476	Interface delamination
2	18.27	0.89	0.277	upper skin fracture
3	12.48	1.50	0.423	Interface delamination

4. Conclusions

The following results are obtained,
(1) A novel natural fiber reinforced UPR composite sandwich structure is developed and fabricated.
(2) Mechanical properties results show the elastic modulus of kenaf composite material is about 2.05~2.39GPa. Main failure mode in three-point bending tests is local indentation, while the equivalent flexural stiffness is about 1476~1592N/mm. Meanwhile failure mechanism analysis is accomplished by digital camera and SEM.
(3) Due to lightweight, relative high strength, high elastic modulus and absorb energy, this kind of sandwich structures can be potentially used in civil engineering constructions.

Acknowledgements

This research work was financially supported by the central university scientific research basic project (HEUCFZ1128) of China, National Science Foundation of USA (NSF-PFI 1114389 and NSF-CMMI 1031828). The authors thank Kengro, Inc. and DIAB group, for supplying the raw materials. Also show thanks to Dr. Wen Hu, Mr. Changlei Xia, Mr. Mangesh Nar and Dr. Kaiwen Liang for their help in experiments.

References

[1] D Zenkert. An introduction to sandwich construction. Solihull UK: EMAS, 1995.
[2] SD Clark, RA Shenoi, HG Allen. Modelling the fatigue behaviour of sandwich beams under monotonic, 2-step and block-loading regimes. Compos Sci Technol, 4(1999) 471–486.

[3] E Bozhevolnaya, OT Thomsen. Structurally graded core junctions in sandwich beams: fatigue loading conditions. Compos Struct, 1(2005) 12–23.
[4] IM Daniel, JL Abot. Fabrication, testing and analysis of composite sandwich beams. Compos Sci Technol, 12(2000) 2455–2463.
[5] WL Lai, M Mariatti, JS Mohamad. The properties of woven kenaf and betel palm (Areca catechu) reinforced unsaturated polyester composites. Polym-Plast Technol, 47(2008) 1193–1199.
[6] Cho D, Lee HS, Han SO. Effect of fiber surface modification on the interfacial and mechanical properties of kenaf fiber-reinforced thermoplastic and thermosetting polymer composites. Composi Interfaces, 16(2009) 711–729.
[7] La Mantia FP, M Morreale, Ishak ZAM. Processing and mechanical properties of organic filler-polypropylenecomposites. J Appl Polym Sci, 96(2005) 1906–1913.
[8] ASTM International. Standard test method for tensile properties of plastics. ASTM D638-10. West Conshohocken: ASTM International, 2010.
[9] ASTM International. Standard test method for flexural properties of polymer matrix composite materials. ASTM D7264-07. West Conshohocken: ASTM International, 2007.
[10] GG Gaetano, V Christine, SE Omar. Theoretical design and analysis of a honeycomb panel sandwich structure loaded in pure bending. Eng Fail Anal, 15(2008) 555–562.
[11] ASTM International. Standard test method for mode I interlaminar fracture toughness of unidirectional fiber-reinforced polymer matrix composites. ASTM D5528-07. West Conshohocken: ASTM International, 2007.
[12] SD Pan, LZ Wu, YG Sun, et al. Fracture test for double cantilever beam of honeycomb sandwich panels. Mater Lett, 62(2008) 523–526.

Thermal Stability of Microstructure and Mechanical Properties of Ultrafine-Grained Pure Titanium

Shankun Chen, Qiaoyan Sun*, Lin Xiao, Jun Sun

State Key Laboratory for Mechanical Behavior of Materials, Xi'an Jiaotong University, Xi'an 710049, PR China

* Corresponding author: qysun@mail.xjtu.edu.cn

Abstract Thermal stability of microstructure was investigated of ultrafine-grained (UFG) pure titanium subjected to anneal at 300°C, 400°C, 500°C and 600°C. Hardness variety was used to evaluate the effect of annealing temperature on mechanical properties in UFG titanium. Microstructural observation showed that the average grain size slightly increased in UFG pure titanium annealed below 400°C, while the dislocation density significantly decreased. As the annealing temperature increased to 500°C and 600°C, the average grain size dramatically increased and dislocation density sharply reduced. The hardness almost remained constant, when the annealing temperature was 300°C, while it gradually decreased, as the annealing temperature increased to 400°C. The hardness dramatically decreased in the samples annealed at 500°C and 600°C. The relationship between the microstructural stability and mechanical property variety in UFG Ti during annealing is discussed.

Keywords Ultrafine-grained pure titanium, Thermal stability, Grain size, Hardness

1. Introduction

Research on the ultrafine processing of grains in metals and alloys has attracted a lot of attentions since Prof Valiev and co-workers firstly produced the refined microstructures of less than 1 micron, which has a superior high strength, in copper via equal channel angular pressing (ECAP) technique two decades ago [1-4]. Ultrafine-grained (UFG) metals and alloys have demonstrated the higher combination of strength and ductility than the coarse-grained counterparts. The UFG titanium shows higher corrosion resistance than coarse-grained one due to rapid passivation [5]. Several severe plastic deformation (SPD) techniques have been used to fabricate UFG or nano-grained metals. For example, high pressure torsion (HPT) used for Cu, Cu-Zn, and Cu-Sn alloys [6,7], cumulative roll bonding (ARB) used for some fcc and hcp metals [8-10]. Thermal stability is a big concern for ultrafine-grained materials. Majid Hoseini et.al found that UFG pure titanium had a good thermal stability of microstructure below 450°C [11]. The grain growth activation energy (Q) is close to the self-diffusion activation energy in Ti [12,13]. Although the ultrafine processing of pure titanium has been well studied, little information is available on the thermal stability of mechanical properties and microstructure in UFG pure Ti. The objective of this paper is to study microstructural stability and mechanical property variety in UFG titanium subjected to anneal at different temperatures.

2. Experimental procedure

The UFG pure Ti sheets of 0.2mm in thickness were produced by repeat-rolling with a reduction of 97.5% in thickness at 450°C. Then these sheets were isothermally annealed at 300°C, 400°C, 500°C

and 600°C respectively for 20 minutes in the VTHK-350L vacuum furnace under 10^{-3} Pa. The heating rate was 8-10°C/min. The samples of 30mm×30mm were cut along rolling direction of plates for microstructural examination and micro-hardness measurement. TEM foils were thinned to about 70-80μm by mechanical grinding, and then electronically thinned with a twin jet electropolisher at 25V and -30°C. TEM examinations were carried on with a JEOL JSM-200CX TEM at 160KV. Texture was determined using an X'Pert PRO XRD equipped with a Cu-Kα ray source. Micro-hardness was measured in Tukon 2100B tester with a load of 20g holden for 10 seconds.

3. Results and discussion

3.1 Microstructure evolution of UFG Ti at different annealing temperatures

The optical microstructure in UFG pure Ti samples subjected to anneal at different temperatures is shown in Fig. 1. The as-rolled deformed microstructure remained (Fig.1(a)) and grain boundaries became obscure when the annealing temperature was below 400°C, as shown in Fig. 1(b) and (c). However, as the annealing temperature increased to above 500°C, equiaxed grains were observed, as shown in Fig. 1(d) and (e). Furthermore, the grain size increased with the annealing temperature. The average grain size increased to 3μm and 7μm, respectively, when the annealing temperature increased to 500°C and 600°C.

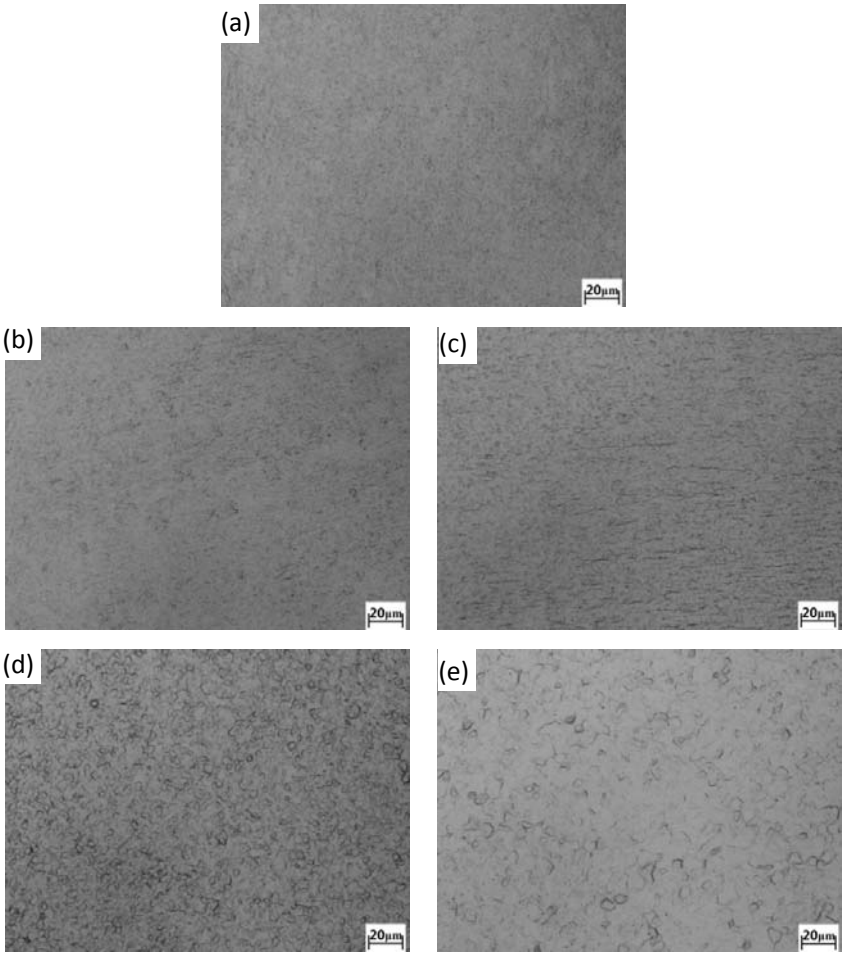

Figure 1. Optical microstructure in UFG Ti samples annealed at different temperatures: (a) as-repeat rolled; (b) 300°C; (c) 400°C; (d) 500°C; (e) 600°C.

TEM examination shows the variety of deformed substructure and grain size with the annealing temperature, as shown in Fig. 2(a) to (e). The ultrafine-grains with a high density of dislocations were produced in the as-rolled samples (Fig.2(a)). The less well-defined grain boundaries and high density of dislocation tangles were the predominant features in the samples subjected to anneal below 400^{o}C, as shown in Fig.2(b) and (c). High density of dislocation cells were formed at 300^{o}C (Fig. 2(b)). Grain boundaries became distinguishable at 400^{o}C (Fig.2(c)). When the annealing temperature was higher than 500^{o}C, well-defined grain boundaries were observed. Most dislocations in the interior of grains disappeared, as shown in Fig.2 (d) and (e). The diameter of grains in the sample annealed at 400^{o}C is larger than that annealed at 300^{o}C. Grain obviously grew and grain size significantly increased as the annealing temperature increased to 500^{o}C and 600^{o}C. The effect of annealing temperature on grain sizes of UFG Ti are summarized in table 1. There is not an obvious increase of grain size under 400^{o}C. It indicates that the deformed microstructure remained stable under 400^{o}C. However, grains apparently grow when the annealing temperature increased to 500^{o}C and 600^{o}C. In other words, microstructural stability was lost over 500^{o}C.

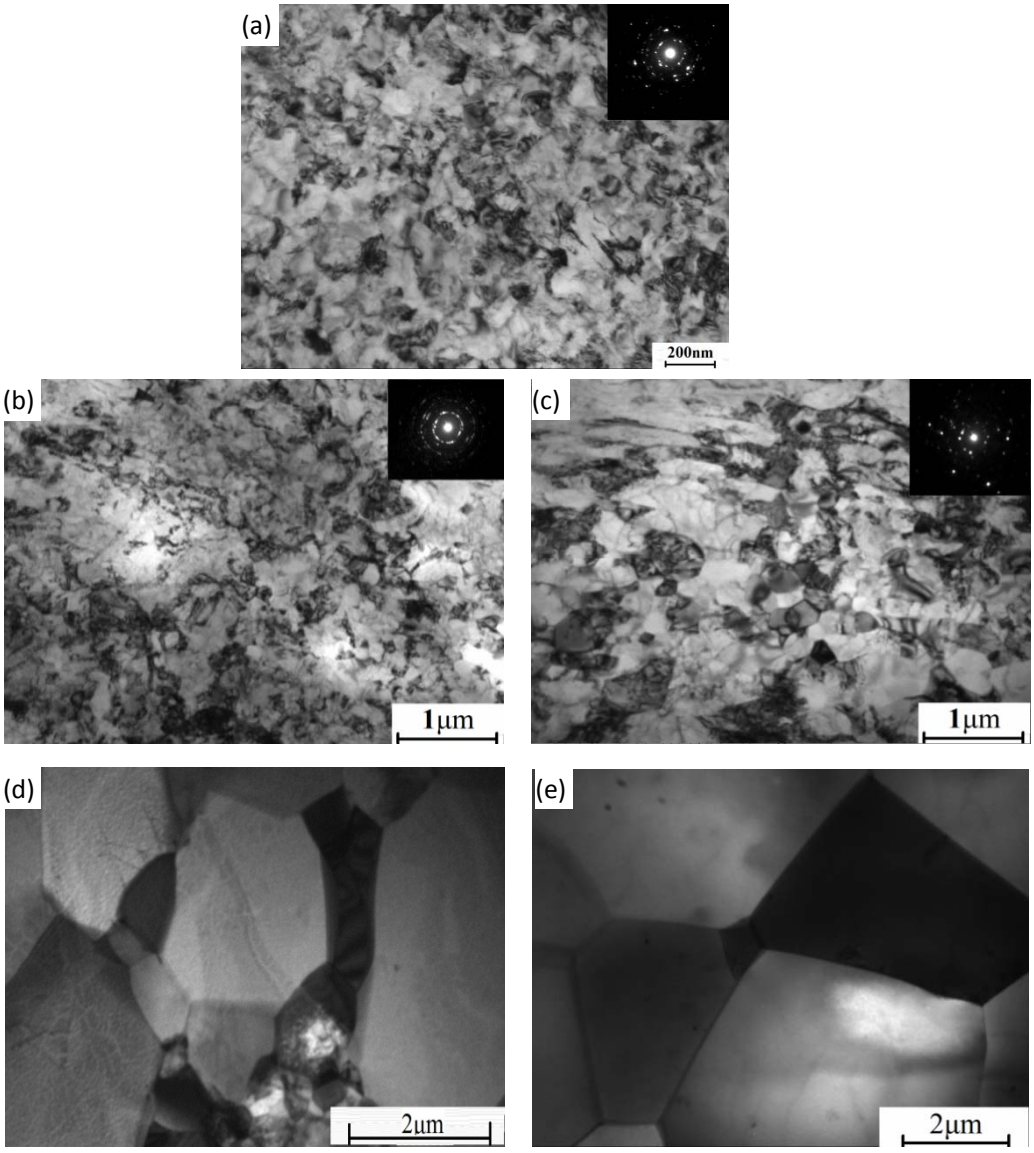

Figure 2 . TEM micrographs in UFG pure titanium annealed at different temperatures:
(a) as-repeat rolled; (b) 300^{o}C; (c) 400^{o}C; (d) 500^{o}C; (e) 600^{o}C.

Table 1. The average grain size in the UFG pure titanium samples annealed at different temperatures

Annealing temperature (^{o}C)	25	300	400	500	600
Average grain size (μm)	0.1	0.2	0.2	3	7

Microstructural observation showed that the average grain size slightly increased when the annealing temperature was less than 400^{o}C. However, the grain size dramatically increased when the annealing temperature was higher than 500^{o}C, as shown in Fig 3. When the annealing temperature is below 400^{o}C, grain size remains constant; however, the distortion and defects in crystal lattice disappear leading to a decrease of the internal stress. When the annealing temperature was higher than 500^{o}C the recrystallization took place in the deformed UFG pure Ti. As a result, the dislocation density remarkably decreased and well-developed grain growth occurred.

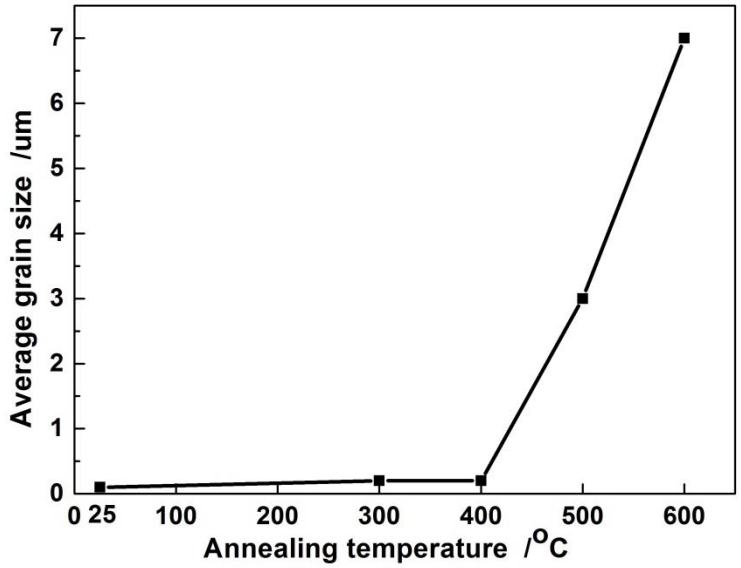

Figure 3. Average grain sizes in UFG pure Ti annealed at different temperatures.

The effect of annealing temperature on texture in UFG titanium is showed in Fig 4. The XRD curve in the initial UFG pure Ti shows that the highest peak is {0002} as shown in Fig 4(a). With increasing annealing temperature to 500°C, the highest peak becomes {10-10}, as shown in Fig 4(b). It means that the lattice rotation took place in UFG titanium during recrystallization.

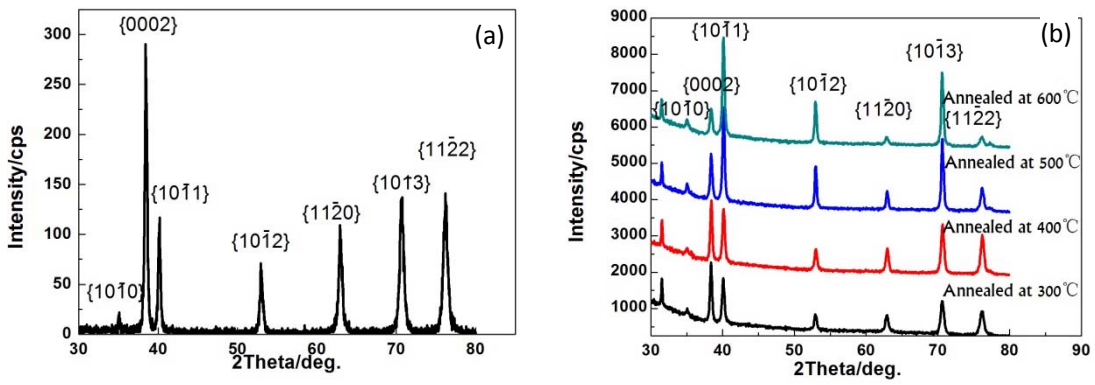

Figure 4. XRD curves of UFG pure titanium annealed at different temperatures

Based on microstructural observation with OM and TEM, it is demonstrated that the microstructure

in UFG pure Ti remains a good thermal stability below 400°C.

3.2 Decrease in hardness during annealing

Hardness was measured in the UFG samples annealed at different temperatures, as shown in Fig 5. The hardness almost remained a constant below 300°C. However, the hardness dramatically decreased when the annealing temperature increased to above 400°C, especially 500°C. The hardness of sample annealed at 600°C is close to that of coarse-grained titanium. This means that the stability of mechanical properties could be kept in the UFG pure Ti below 400°C.

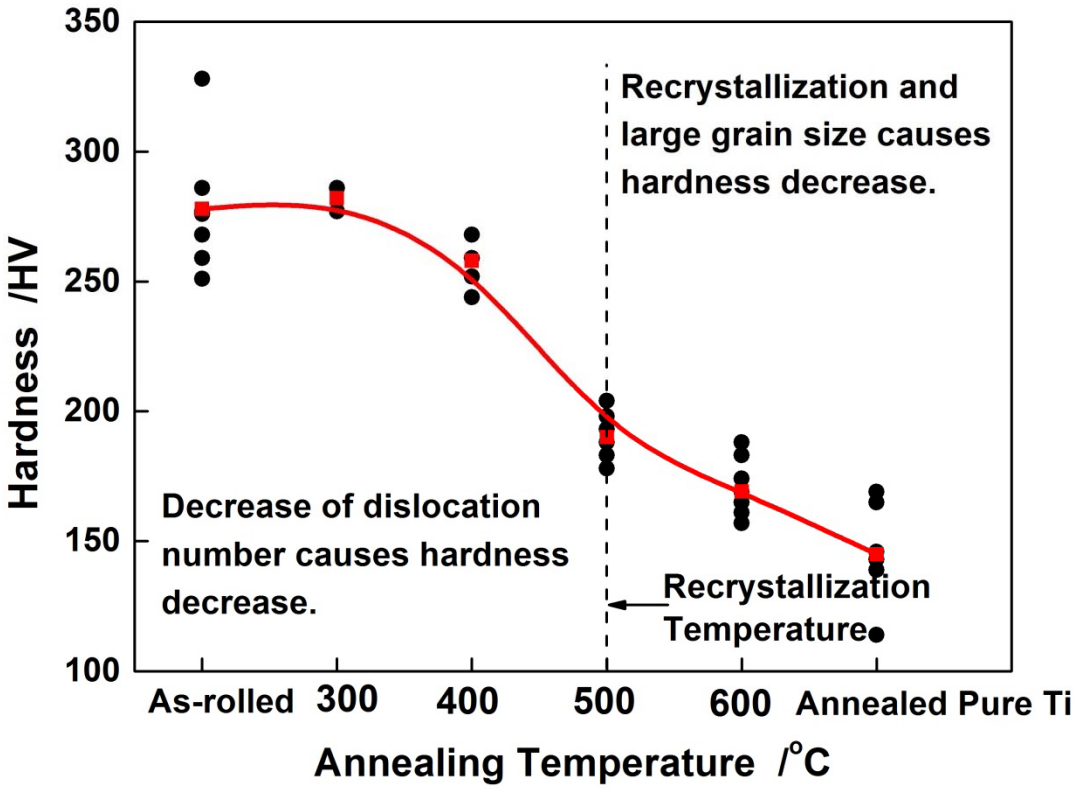

Figure 5. Effect of annealing temperature on micro-hardness in UFG pure titanium

The decrease of hardness in the UFG Ti could be attributed to the following two reasons. When the annealing temperature is below 500°C, the decrease of dislocation density is a predominant factor. While, as the annealing temperature increase to above 500°C, recrystallization and grain growth predominately contributed to the decrease of hardness.

4. Conclusions

1) The average grain size of UFG pure titanium slightly increased when the annealing temperature is lower than 400°C. The microstructure remains stable under 400°C. While the grain size dramatically increased as annealing temperature increased to 500°C or higher. Recrystallization and grain growth took place in ultrafine-grained Ti as annealing temperature is above 500 °C.
2) The rolling texture orientation of UFG pure Ti is {0002} and it disappears when the sample is annealed at 500°C and 600°C.
3) The hardness of UFG Ti slightly decreased when the annealing temperature was lower than

400°C. While, the hardness dramatically decreased as the annealing temperature increased to above 500°C. In former, the decrease of hardness is attributed to the decrease of dislocation density. In the latter, dramatic decrease in hardness results from the recrystallization and grain growth.

Acknowledgements

This project was financially supported by the National Natural Science Foundation of China (51071118, 51271136 and 50831004) the 973 Program of China (2010CB631003), and the 111 Project of China (B06025).

References

[1] Valiev RZ, Krasilnikov NA, Tsenev NK. Plastic deformation of alloys with submicron-grained structure. Mater Sci Eng A, 137 (1991) 35–40.
[2] I. Sabirov, Y. Estrin, M.R. Barnett,et al. Enhanced tensile ductility of an ultra-fine-grained aluminum alloy. Scripta Materialia, 58 (2008) 163–166.
[3] L. Jiang, M.T. Pe′rez-Prado, P.A. Gruber,et al. Texture, microstructure and mechanical properties of equiaxed ultrafine-grained Zr fabricated by accumulative roll bonding. Acta Materialia, 56 (2008) 1228–1242.
[4] H.W. Ho¨ppel ,M. Kautz , C. Xu,et al. An overview: Fatigue behaviour of ultrafine-grained metals and alloys. International Journal of Fatigue, 28 (2006) 1001–1010.
[5] A. Balyanov a, J. Kutnyakova a, N.A. Amirkhanova,et al. Corrosion resistance of ultrafine-grained Ti. Scripta Materialia, 51 (2004) 225–229.
[6] Y.H. Zhao, Z. Horita, T.G. Langdon,et al. Evolution of defect structures during cold rolling of ultrafine-grained Cu and Cu–Zn alloys: Influence of stacking fault energy. Materials Science and Engineering A, 474 (2008) 342–347.
[7] Honggang Jiang, Y. Theodore Zhu, Darryl P. Butt,et al. Microstructural evolution, microhardness and thermal stability of HPT-processed Cu. Materials Science and Engineering A, 290 (2000) 128–138.
[8] Naoki Takata, Seong-Hee Lee, Nobuhiro Tsuji. Ultrafine grained copper alloy sheets having both high strength and high electric conductivity. Materials Letters, 63 (2009) 1757–1760.
[9] Naoya Kamikawa, Nobuhiro Tsuji, Xiaoxu Huang,et al. Quantification of annealed microstructures in ARB processed aluminum. Acta Materialia, 54 (2006) 3055–3066.
[10] Daisuke Terada, Seiya Inoue, Nobuhiro Tsuji. Microstructure and mechanical properties of commercial purity titanium severely deformed by ARB process. J Mater Sci 42 (2007) 1673–1681.
[11] Majid Hoseini, Meysam Hamid Pourian, Florent Bridier, et al. Thermal stability and annealing behavior of ultrafine grained commercially pure titanium. Materials Science and Engineering A, 532 (2012) 58-63.
[12] M.Ravi Shankar, Balkrishna C.Rao, Seongeyl, et al. Severe plastic deformation (SPD) of titanium at near-ambient temperature. Acta Materialia, 54 (2006) 3691-3700.
[13] Xianfeng Jiang, Shunhua Xiang, Nailu Chen. Effect of annealing processes on recrystallization texture of cold rolling pure titanium strip. Material & Heat Treatment, 40 (2011) 18 (in Chinese).

New Trends in the Fracture of Lightweight Structures

Efstathios E. Theotokoglou[1,*], **Gavriil E. Theotokoglou**[1]

[1] School of Applied Mathematical and Physical Sciences
Department of Mechanics Laboratory of Testing and Materials
National Technical University of Athens
Zographou Campus, Theocaris Bld GR-0157 73, Athens, Greece
* Corresponding author: stathis@central.ntua.gr

Abstract Analysis of fractured lightweight structures has been performed in this paper. In particular a sandwich beam under three point bending containing a crack in the core material very close to the upper skin interface and parallel to the longitudinal beam axis is investigated. A numerical study of the fractured sandwich beam is developed calculating the stress intensity factors in order to investigate the fracture very close to upper skin interface under mixed-mode loading conditions. In addition a cohesive damage model is presented to simulate crack propagation and kinking into the core under mixed-mode loading conditions. The crack considered, is analyzed with static non-linear two- dimensional finite element analyses.

Keywords Lightweight structure, Crack Propagation, Stress Intensity Factor, Cohesive Model

1. Introduction

Lightweight composite structures are widely used in aerospace, marine and other modern industrial applications. Sandwich structures used in these applications consist of a lightweight foam core bonded to thin laminas to achieve high values of specific strength and stiffness. One of the main advantages of sandwich structures is their ability to provide increased flexural rigidity without an increase of the structural weight. The core is usually made of PVC, wood, a honeycomb material or lately carbon foam bonded to tough carbon fiber reinforced polyetheretherketone (PEEK) skins. In sandwich structures the foam is typically the weakest part and is the first to fail under static or cyclic loading because it transfers the applied loads as shear stresses. In addition a very critical problem in sandwich structures is the debonding problem between the face and core materials [1-5]. Unstable cracking propagation and kinking in core materials represents one of the weakest failure modes in sandwich composites. The fracture behavior in lightweight composites has been directed toward the understanding of crack propagation, and at the same time toward improving the durability of composites against fracture. A crack flaw may be introduced during processing or subsequent service conditions. It may result from low velocity impact, from eccentricities in the structural load path, or from discontinuities in structures, which induce a significant out-of-plane stress. In our paper a composite beam under three point bending and/or asymmetric three point bending is studied. In the core material of the beam an initially small crack is considered. In this study a computational analysis is developed based on an experimental investigation in composite beams under flexural loading [2]. From the numerical simulations stress intensity factors are calculated using the Finite element method and combined with crack propagation criteria predict the crack kinking into the core under flexural loading. On the other hand cohesive crack models [6, 7] are widely used to simulate crack growth and kinking phenomena. In order to develop numerical methodologies to simulate crack propagation in composite structures, cohesive damage models have attracted much interest [8-13] due to their well established advantages compared to the stress based

and fracture mechanics methods. Taking into consideration that the application of cohesive damage models in sandwich structures for the numerical simulation of the crack propagation is very limited [11-13]; a cohesive model in terms of cohesive parameters will also propose in this study in order to simulate crack propagation and kinking into the core of sandwich structures.
Thus the scope of this study is to numerically investigate the crack propagation and crack kinking into the core of lightweight structures under mixed mode loading conditions and to present a cohesive damage model appropriate to simulate crack propagation into the core. Results from the computational analysis predict the crack growth and kinking under flexural loading.

2. Specimens and Loading Material Testing.

The geometric and the loading conditions for the sandwich are shown in Fig. 1. The sandwich is composed of PVC-core and face sheets from isotropic glass (Table 1). The dimensions of the test specimen were $L = 228.6$ mm (support span) and $b = 63.5$ mm (width). The core thickness was $t_2 = 12.7$ mm and the face sheet thickness was $t_1 = 2.28$ mm. The overall thickness was 17.26 mm.

Static tests were first conducted to generate ultimate strength data [2]. Flexural fatigue tests on sandwich beams were performed at room temperature under load control at a stress ratio of 0.1, using a sinusoidal wave form. Fatigue data was generated for a minimum of three specimens at stress levels of 90%, 85%, 80%, 75%, 70%, 65% and 60% of the ultimate flexural strength. Three distinct damage events take place before the failure of the specimen.

At first crack initiation and propagation was observed on the compression side just below the top face sheet/core interface. This delamination crack was about 1-1.5mm below the interface. The crack runs parallel to the beam axis from the point of initiation towards the end support (Fig. 1). This first damage event occupies about 85% of the fatigue life. The propagated crack kinks at a certain distance and shears through the core thickness. The crack reaches the bottom face sheet/core interface. Finally, delamination takes place at bottom face/core interface using the separation of the core from the face sheet. This is also a rapid event and occupies the remaining 7-8% of fatigue life.

Table 1. Specimen properties

Material	$E\ \left(N/mm^2\right)$	ν
Face sheets (isotropic glass)	16300	0.3
PVC foam core (R75 by DIAB [5])	80	0.4

From the plot of the crack lengths via N (number of cycles) at different stress levels in [2], it is observed that the length of the crack depends on the stress level. Lower is the stress level; the longer is the crack in damage event-1. Thus, at lower stress levels $\left(r = 0.65, 0.70, 0.75\right)$ the first damage event dominates the fatigue life and consequently the crack propagation near the top face core-skin interface, may be used to develop a failure model for sandwich composites.

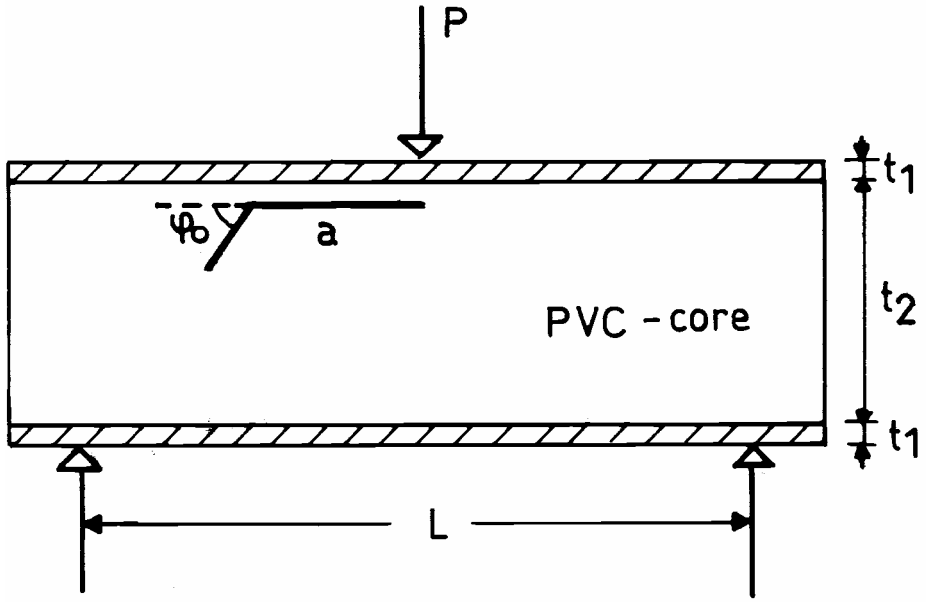

Figure 1. Crack propagation in the core of a sandwich beam under flexural loading

3. Crack Kinking Analysis.

The cracked sandwich beam is analyzed using the finite element method. Because of high stress gradients around the interface, fairly fine mesh consisting of two dimensional plane strain elements was used. The assumption of plane strain is justified throughout.

The finite element analysis is performed with the use of the general purpose finite element programs. The 6 node and 8 node two-dimensional plane strain triangular elements (plane 6) were used in order to model the beam. The frictionless contact area at the crack surfaces is modeled with 2-node linear contact elements, in order to prevent one surface from entering into the other. Singular elements (mid-side nodes at ¼) were used at the two crack tips.

In order to analyze the first damage event, a small crack is considered at about $1.5mm$ below the interface under the central load introduction and parallel to the beam axis. This small crack is considered propagating under the interface. For the different crack lengths the stress intensity factors,

$$\Delta K_1 = K_I^{\max} - K_I^{\min}, \quad \Delta K_{II} = K_{II}^{\max} - K_{II}^{\min}, \tag{1}$$

are calculated automatically from the finite element analysis for the left and right crack tip. The ΔK_I and ΔK_{II} ratios are given in Fig. 2, considering the lower stress level $r = 0.70$ and for the load P to be taken equal to $0.7P_{\text{ultimate}} \left(= 943.46N\right)$, where P_{ultimate} the static failure load of the beam.

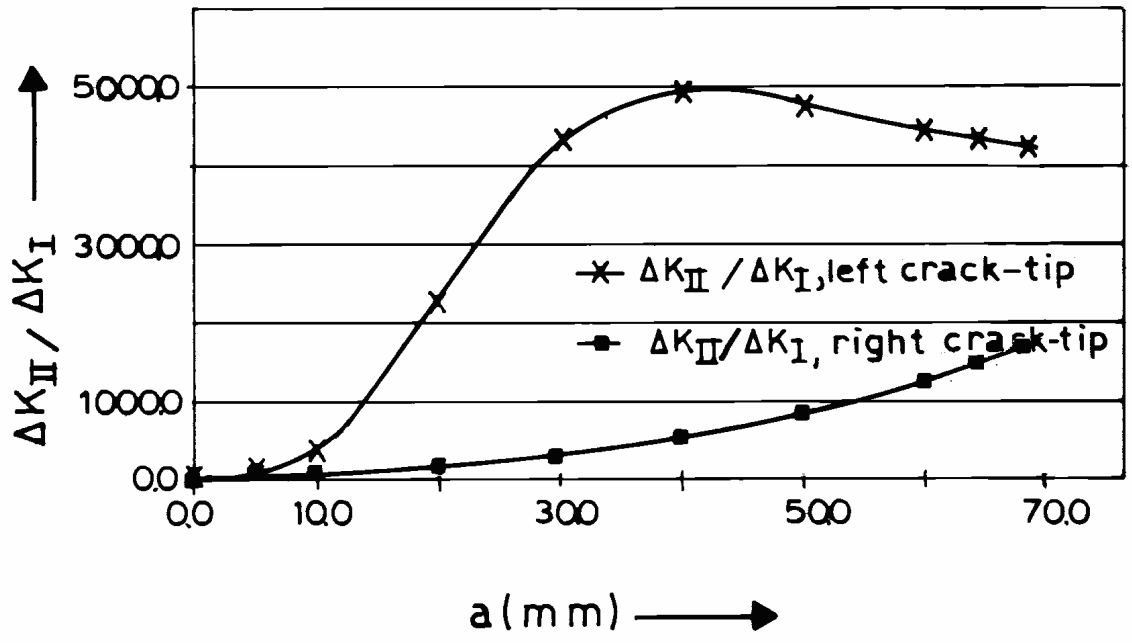

Figure 2. $\Delta K_{II}/\Delta K_I$ ratios for left and right crack-tip for different crack lengths

From the experimental investigation initiation of the crack kinking takes place for a crack length a about $65 \sim 70(mm)$, in an angle φ_0 (Figure 1) of $45° \pm 5°$. Two different crack propagation criteria have been examined to estimate which one should be used in outer to model crack kinking in cross linked PVC sandwich foam cores. At first the Energy density factor criterion [14] is used. According to this criterion, crack initiation occurs in the radial direction in which the local energy density possesses a stationary value. The energy W per unit area A, is expressed by:

$$\frac{dW}{dA} = \frac{S}{r}, \tag{2}$$

where r is the radial distance from the crack tip and S is the strain energy density factor which represents a material element in the distance r from the crack tip. The distance r from the crack tip is assumed to be small compared to the crack length a, and S is given by:

$$S = a_{11}K_I^2 + 2a_{12}K_I K_{II} + a_{22}K_{II}^2 \tag{3}$$

where

$$a_{11} = \frac{1}{16G}\left((1+\cos(\varphi))(\kappa-\cos(\varphi))\right), \quad a_{12} = \frac{1}{16G}\sin(\varphi)(2\cos(\varphi)-(\kappa-1))$$
$$a_{22} = \frac{1}{16G}\left((\kappa+1)(1-\cos(\varphi))+(1+\cos(\varphi))(3\cos(\varphi)-1)\right) \tag{4}$$

and, φ the angle related to the plane of the crack, G the shear modulus of the core material, $\kappa = 3-4\nu$ (plain strain).

The minimum energy density possesses a stationary value which is derived from

$$\frac{\partial S}{\partial \varphi} = 0 \quad \textit{at which} \quad \varphi = \varphi_0 , \tag{5}$$

where φ_0 is the crack propagation angle with respect to the plane of the crack with the minimum energy density.

From the numerical calculations and the core material considered (Table 1), we have:

$$\varphi_0 = \pm 80^\circ ,$$

which is too high comparing with the kinking angle from the experimental investigation.

Secondly the maximum hoop stress is used [15]. The tangential stress component at the vicinity of the crack tip is given by:

$$\sigma_{\theta\theta} = \frac{1}{\sqrt{2\pi r}}\cos\left(\frac{\varphi}{2}\right)\left\{\frac{1}{2}K_I(1+\cos(\varphi))-\frac{3}{2}K_{II}\sin(\varphi)\right\} \tag{6}$$

where r is the distance from the crack tip and $\sigma_{\theta\theta}$ the tangential stress.

According to the maximum hoop stress criterion the crack will propagate in the direction in which $\sigma_{\theta\theta}$ obtains its maximum. The direction of $\max \sigma_{\theta\theta}$ can be found by the relations

$$\frac{\partial \sigma_{\theta\theta}}{\partial \varphi} = 0 , \quad \frac{\partial^2 \sigma_{\theta\theta}}{\partial \varphi} < 0 \tag{7}$$

From the numerical calculations, the following kinking angle is derived

$$\varphi_0 = 42^\circ ,$$

which is in agreement with the test results.

4. Proposed Damage Model

The proposed damage model [8, 11] based on interface finite elements is presented in order to simulate damage onset and growth into the core of a sandwich structure. A linear constitutive relationship between stresses σ and relative displacements δ between homologous points of the interface elements with zero thickness is considered. At first developing the pure-mode model, the constitutive equation before damage starts to grow, is given by:

$$\sigma = D\delta \tag{8}$$

where D is the diagonal matrix containing the penalty parameters (d) in each mode. The values of the penalty parameter must be quite high in order to hold together and prevent interpenetration of the element faces. According to a considerable number of numerical simulations [8, 11], it was determined $d = 10^6 \text{N/mm}^3$. For this value the produced results converge and numerical problems during the nonlinear procedure have been avoided.

After the peak stress $(\sigma_{u,i})$ is reached a gradual softening process between the stress and the relative displacement is observed and is defined as:

$$\sigma = \left(I - E\right) D\delta \tag{9}$$

where I is the identity matrix and E is a diagonal matrix containing the damage parameter:

$$e = \frac{\delta_{u,i}(\delta_i - \delta_{o,i})}{\delta_i(\delta_{u,i} - \delta_{o,i})},\ i = I, II, \tag{10}$$

and, $\delta_{o,i}$, is the displacement corresponding to the onset of damage, and δ_i is the current relative displacement. In pure-mode loading, the strength along other directions is abruptly cancelled. The maximum relative displacement, $\delta_{u,i}$ for which complete failure occurs, is obtained by equating the area under the softening curve to the respective critical fracture energy:

$$G_{c,i} = \frac{1}{2}\sigma_{u,i}\delta_{u,i} \tag{11}$$

In thick composite structures under flexural loading such as in ship hulls, failure is more likely to occur under a mixed-mode situation. Therefore, a formulation for interface elements having zero thickness should include a mixed-mode damage model, which, in this case, is an extension of the pure mode model. Damage initiation may be predicted by using the following criterion [8, 11]:

$$\begin{aligned} &(\frac{\sigma_I}{\sigma_{u,I}})^2+(\frac{\sigma_{II}}{\sigma_{u,II}})^2=1 && \text{if} \quad \sigma_I>0 \\ &\sigma_{II}=\sigma_{u,II} && \text{if} \quad \sigma_I\le 0 \end{aligned} \tag{12}$$

where $\sigma_{u,I}$, $\sigma_{u,II}$ represent the ultimate normal and shear stresses, respectively and it is assumed that normal compressive stress does not induce damage. Providing an equivalent mixed-mode displacement:

$$\delta_e=\sqrt{\delta_I^2+\delta_{II}^2} \tag{13}$$

and a mixed-mode ratio:

$$\beta=\frac{\delta_{II}}{\delta_I} \tag{14}$$

and taking into considering Eq. (8), we have from Eq. (12):

$$(\frac{\delta_{om,I}}{\delta_{o,I}})^2+(\frac{\delta_{om,II}}{\delta_{o,II}})^2=1 \tag{15}$$

where $\delta_{om,i}(i=I,II)$ are the relative displacements at damage initiation, which correspond to the critical interface stresses $\sigma_{um,i}$. Combining Equations (13)-(15), the value of the equivalent mixed-mode displacement leading to damage initiation (δ_{om}) results:

$$\delta_{om} = \frac{\delta_{o,I}\delta_{o,II}\sqrt{1+\beta^2}}{\sqrt{\delta_{o,II}^2 + \beta^2\delta_{o,I}^2}} \tag{16}$$

The mixed-mode damage propagation is simulated considering the linear fracture energetic criterion:

$$\frac{G_I}{G_{Ic}} + \frac{G_{II}}{G_{IIc}} = 1 \tag{17}$$

The released energy in each model at complete failure can be obtained from the area of the triangle:

$$G_i = \frac{1}{2}\sigma_{um,i}\delta_{um,i} \tag{18}$$

being $\delta_{um,i}(i = I, II)$, the relative displacement in each direction for which complete failure occurs. From Equations (8), (11), (13), (14), (17) and (18), the mixed mode relative displacement leading to total failure (δ_{um}) can be obtained:

$$\delta_{um} = \frac{2(1+\beta^2)}{e\delta_{om}}\left[\frac{1}{G_{Ic}} + \frac{\beta^2}{G_{IIc}}\right] \tag{12}$$

The values of δ_e, δ_{om} and δ_{um} are introduced into Eq. (10), instead of δ_i, $\delta_{o,i}$ and $\delta_{u,i}$, thus setting the damage parameter under mixed mode. The mixed mode model proposed is general and it can be applied under any combination of modes.

The same sandwich beam considered in section 3 under three point bending with a crack parallel to the beam axis very close to the upper skin interface (Figure 1), is solved numerically. But in this case we adjust the model according to the demands of the previous analysis. Different models with different cohesive parameters, different crack lengths, different crack positions and orientations, may be confronted. The element type used in this analysis is the four-node two dimensional plane strain elements CPE4 [16]. Different mesh configurations were used in the vicinity of the crack tip and the cohesive layer in order the convergence of the solution to be succeeded. The cohesive layer is placed over the entire plane of crack propagation (Figure 3) by implementing the procedure given in Abaqus [15].

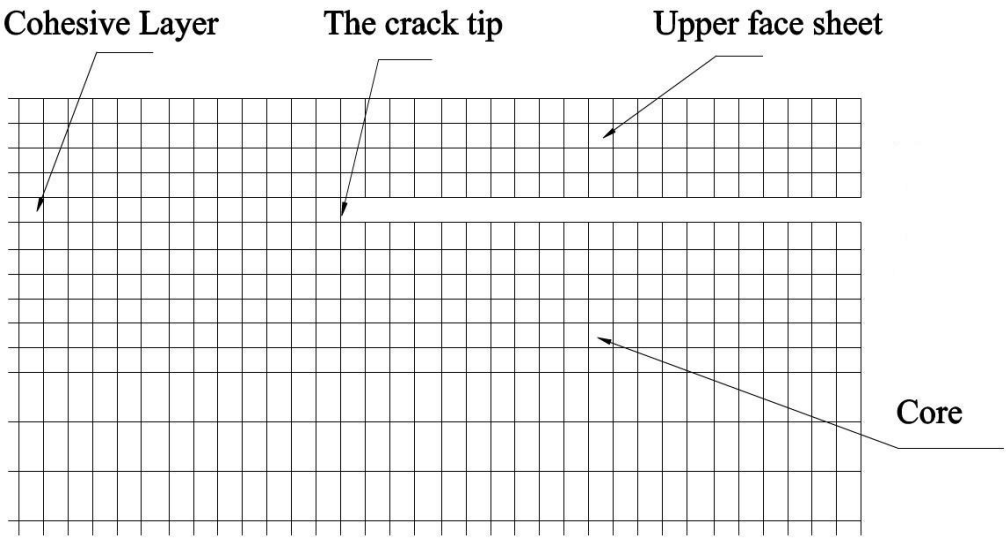

Figure 3. The finite elements mesh at the crack tip.

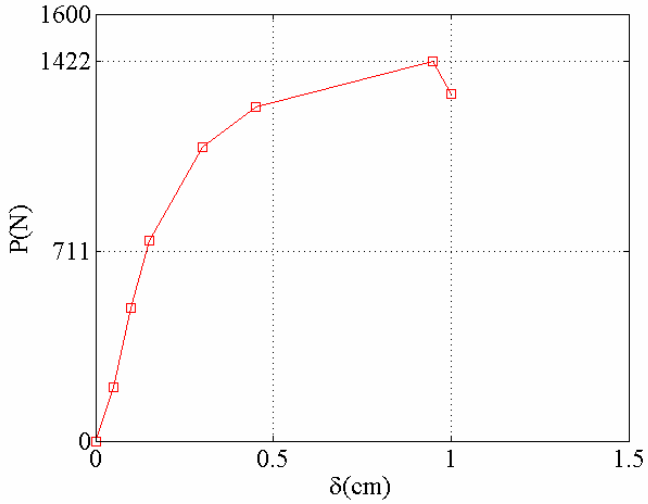

Figure 4. Numerical and experimental results for mixed mode loading

The fractured sandwich beam is modeled according to a mesh generator proposed in [5] which imposes the discretion of the areas of the beam regarding the mesh density and quality in three different regions according to the length of the crack and to crack distance from the upper interface [5]. This discretion is a prerequisite in order to avoid the worthless consumption of computational resources and time. The model shown in Fig. 3 corresponds to the maximum crack length $a \approx 70\text{mm}$ in which about 22500 elements have been used in the finite element analysis. The experimental data and the numerical predictions according to the proposed cohesive law are shown in Figure 4. At the load at failure ($P \simeq 1422\text{N}$) kinking of the crack into the core and catastrophic failure was observed.

5. Conclusions.

In this paper two procedures have been considered for lightweight structures in order to simulate crack propagation and kinking into the core of sandwich structures very close to the upper skin

interface under mixed mode loading conditions. In the first one the crack kinking analysis based on linear fracture mechanics approach and to crack propagation criteria, was considered. Stress intensity factors were calculated and the crack kinking into the core was predicted. In the second one a cohesive damage model was developed to simulate crack propagation and kinking into the core in terms of cohesive parameters. The damage model was implemented in a finite element model. The numerical applications analyzed were in good agreement with the experimental results and in addition predict satisfactory the crack propagation and kinking into the core.

References

[1] L.A. Carlsson, S. Prasad, Interfacial fracture of sandwich beams. Eng Fract Mech, 44 (1993) 581-590.
[2] N. Kulkarni, H. Mahfuz, S. Jeelani, L.A. Carlsson, Fatigue crack growth and life prediction of foam core sandwich composites under flexural loading. Comp Struct, 59 (2003) 499-505.
[3] C. Berggreen, B.C. Simonsen, K.K. Borum, Prediction of debond propagation in sandwich beams under FE-bared Fracture Mechanics and NDI Techniques. Journal Comp Mat, 41 (2007) 493-520.
[4] E.E. Theotokoglou, D. Hortis, L.A. Carlsson, H. Mahfuz, Numerical study of fractured sandwich composites under flexural loading. Journal Sandwich Str Mat, 10 (2008) 75-94.
[5] E.E. Theotokoglou, I.I. Tourlomousis, Crack kinking in sandwich structures under three point bending. Theor Appl Fract Mech, 30 (2010) 158-164.
[6] G.I. Barrenblat, The mathematical theory of equilibrium cracks in brittle fracture. Adv Appl Mech, 7 (1962) 55-129.
[7] X.P. Xu, A. Needleman, Numerical simulations of fast crack growth in brittle solids. J. Mech. Phys. Solids, 42 (1994) 1397-1434.
[8] A.B. de Morais, M.F.S.F. de Moura, J.P.M. Goncalves, P.P. Camanho, Analysis of crack propagation in double cantilever beam tests of multidirectional laminates. Mech Mat, 35 (2003) 641-652.
[9] B.F. Sorensen, P. Kirkegaard, Determination of mixed mode cohesive laws. Engineering Fracture Mechanics, 73, pp. 2642-2661 (2006).
[10] P. Kyoungsoo, G.H. Paulino, J.A. Roesler, A unified potential-based cohesive model of mixed-mode fracture. J. Mech. Phys. Solids, 57 (2009) 891-908.
[11] D.A. Ramantani, M.F.S.F. de Moura, R.D.S.G. Campilho, A.T. Marques, Fracture characterization of sandwich structures interfaces under mode I loading. Comp Sci Techn, 70 (2010) 1386-1394.
[12] D.A. Ramantani, R.D.S.G. Campilho, M.F.S.F. de Moura, A.T. Marques, Stress and failure analysis of repaired sandwich composite beams using a cohesive damage model. Journal Sandwich StrMat, 12 (2010) 369-390.
[13] El- S. Sayed, S. Sridharar, Cohesive layer models for predicting delamination growth and crack kinking in sandwich structures. Int Journal Fr, 117 (2002) 63-84.
[14] G. C. Sih, Strain energy density factor applied to mixed mode crack problems. Int Journal Fr Mech 10 (1974) 305-321.
[15] F. Erdogan, G. C. Sih, On the extension in plates under plane loading and transverse shear. Jour Basic Eng, 85 (1963) 519-527.
[16] Hibbit, Karlsson and Sorensen, Inc., Abaqus/Standard and Abaqus/Explicit version 5.8, Pawtucket, USA (1999).

Effect of Post-Weld Heat Treatment on the Fatigue Properties of Dissimilar Titanium Alloy Joints

S.Q. Wang[1, 2], J.H. Liu[2], D.L. Chen[1,*]

[1]Department of Mechanical and Industrial Engineering, Ryerson University, Toronto, Ontario M5B 2K3, Canada
[2]State Key Laboratory of Solidification Processing, Northwestern Polytechnical University, Xi'an 710072, China
* Corresponding author: dchen@ryerson.ca

Abstract The purpose of this study was to characterize the microstructural change and fatigue resistance of electron beam welded (EBWed) dissimilar joints between Ti-6Al-4V and BT9 (Ti-6.5Al-3.5Mo-1.5Zr) alloys after two types of post-weld heat treatment (PWHT), namely only aging and solution treatment followed by aging (STA). It was observed that no significant microstructural change occurred in the FZ after only aging and the high hardness in the fusion zone (FZ) remained, while coarse acicular α occurred in the FZ in the STA condition, leading to a reduced hardness. Both types of post-welded joints were cyclically stable at lower strain amplitudes of 0.2-0.6%, and exhibited cyclic softening at higher strain amplitudes of 0.8%-1.2%. As the total strain amplitude increased, cyclic stress amplitude increased, while the fatigue life decreased. Fatigue crack initiation occurred from the specimen surface or near-surface defects and propagation was characterized mainly by the formation of characteristic fatigue striations.

Keywords Titanium alloy, Post-weld heat treatment, Microstructure evolution, Strain-controlled fatigue.

1. Introduction

Welding is one of the most widely used and economical joining processes for titanium alloys, which makes it possible to create composite structures in the welded joints for various purposes. However, in the electron beam welding (EBW) and laser beam welding, the fusion zones are known to exhibit poor ductility due to the large prior β grain size and a wholly or partially martensitic microstructure [1]. The low thermal conductivity of titanium alloys causes superheating in the heat-affected zone (HAZ), increases the grain size and gives rise to residual stresses in the HAZ, exerting a negative effect [2]. It is necessary to adjust unstable microstructure of the as-welded joints [3]. The post-weld heat treatment (PWHT) is one of the commonly-used methods which could stabilize microstructure, decrease the inhomogeneity of the structure and increase the mechanical properties of the welded joint. Arenas and Acoff [4] reported that PWHT promotes the formation of γ phase in the fusion zone of a gas tungsten arc (GTA) welded gamma titanium aluminide alloy. Guo *et al.* [5] observed that there was no significant hardness increase in fusion zone (FZ) at Ti-64 side of a dissimilar linear friction weld between Ti-64 and Ti-6246 alloys after PWHT. Tuppen *et al.* [6] performed stress-controlled fatigue tests to determine S-N curves of diffusion-bonded dissimilar Ti-6Al-4V/Ti-4Al-4Mo-2Sn-0.5Si titanium alloy joints. Fu *et al*. [7] studied the effects of electron beam local heat treatment (EBLHT) on strain-controlled fatigue properties of EBWed Ti-6Al-4V alloy joints, and their results showed that Ti-6Al-4V alloy joints with and without EBLHT exhibited cyclic softening and the fatigue life of the joints after EBLHT could increase by 30%. Despite the extensive studies on the weldability of titanium alloys, it is unknown if the PWHT would have a significant effect on the microstructure and cyclic deformation behavior of electron beam welds between Ti-6Al-4V and BT9 (Ti-6.5Al-3.5Mo-1.5Zr) alloy. The aim of this study was, therefore, to identify the effect of two common PWHT processes, namely aging with or without solution heat treatment, on the microstructure and fatigue performance of welded joints.

2. Material and Experimental Procedure

The materials used in the present study were forged 10 mm thick Ti-6Al-4V and BT9 titanium

alloys, with the chemical compositions listed in Tables 1 and 2, respectively. Both alloys were machined into the plates of 140 mm × 80 mm × 10 mm, and then mechanically and chemically cleaned before welding. EBW was performed using HDZ-15B EBW machine with an accelerating voltage (V) of 60 kV, an electron beam current (I_b) of 68 mA, an focus current (I_f) of 2230 mA, and a welding speed (v) of 500 mm/min.

Table 1. Chemical composition of Ti-6Al-4V titanium alloy

Element	Al	V	Fe	C	N	H	O	Ti
Content (wt.%)	6	4	0.3	0.1	0.05	0.015	0.2	balance

Table 2. Chemical composition of BT-9 titanium alloy

Element	Al	Mo	Zr	Si	Fe	C	N	H	O	Ti
Content (wt.%)	6.5	3.5	1.5	0.3	0.25	0.1	0.05	0.012	0.15	balance

PWHT was carried out in a vacuum furnace at a vacuum degree of 10^{-2} Pa. One of the welded joints was subjected to solution treatment at a temperature of 950°C for 1 h followed by furnace cooling and then aging at 550°C for 4 h followed by air cooling, and the other joint was directly subjected to aging at a temperature of 550°C for 4 h followed by air cooling. Microstructures were examined (after etching using Keller's reagent) via optical microscopy. Microhardness was determined across the welded joint of mid-thickness (i.e., at a distance of 5 mm from the bottom surface) using a computerized Buehler hardness tester with a load of 500g and a dwell time of 15s at an interval of 0.1 mm.

Fatigue specimens with a gauge length of 12 mm and a width of 3 mm were machined perpendicularly to the welding direction using electro-discharge machining (EDM). The gauge area was ground up to #600 SiC papers to remove the EDM cutting marks and to achieve a smooth surface. Total strain-controlled, pull-push type fatigue tests were conducted in air at room temperature using a computerized Instron 8801 fatigue testing system at different strain amplitudes up to 1.2%. A triangular waveform with a strain ratio of R_s=-1 was applied at a constant strain rate of 1×10^{-2} s^{-1}, where R_s is the ratio of the minimum strain to the maximum strain. The strain-controlled test at low strain amplitudes was continued until 10,000 cycles, after which it was changed to load control at 50 Hz. At least two specimens were tested at each strain amplitude. Fatigue crack initiation site and crack propagation mechanisms were examined on the fracture surfaces of failed samples using SEM.

3. Results and Discussion

3.1 Microstructure

Fig.1(a) and (b) show the microstructure of the two BMs, respectively. It is seen that both Ti-6Al-4V and BT9 had a typical bimodal microstructure, consisting of a combination of equiaxed α grains and inter-granular $\alpha + \beta$ lamellae. However, Ti-6Al-4V contained more equiaxed α grains than BT9. Fig.1(c), (d) and (e) show a significant microstructural changes in the FZ and HAZ after EBW between Ti-6Al-4V and BT9 alloys. The FZ was mainly composed of acicular and fine martensite α' (Fig.1(d) and (e)) due to the rapid cooling during EBW. The HAZ at Ti-6Al-4V side also consisted of acicular martensite α' (Fig.1(e)) but larger in size. The inner-HAZ at BT9 side consisted of a mixture of acicular martensite α', primary α and metastable β (Fig.1(d)), while the outer-HAZ mainly consisted of primary α and metastable β (Fig.1(c)). Fig.2 shows the microstructure of the joints in the aging condition. From these optical images, no significant

difference of microstructures in both FZ and HAZ was observed between the as-welded and the aging conditions, which was in agreement with the previous observations on the electron beam and laser beam welding of Ti-6Al-4V alloy [7,8]. Fig.3 shows the microstructure of the joints in the PWHT condition of solution heat treatment followed by aging (STA). After STA the microstructure of both FZ and HAZ at Ti-6Al-4V side (Fig.3(a)) became coarse α platelets with interlamellar β, which was due to high solution temperature and slow cooling rate, while α platelets, primary α and interlamellar β appeared in the HAZ at BT9 side (Fig.3(b)).

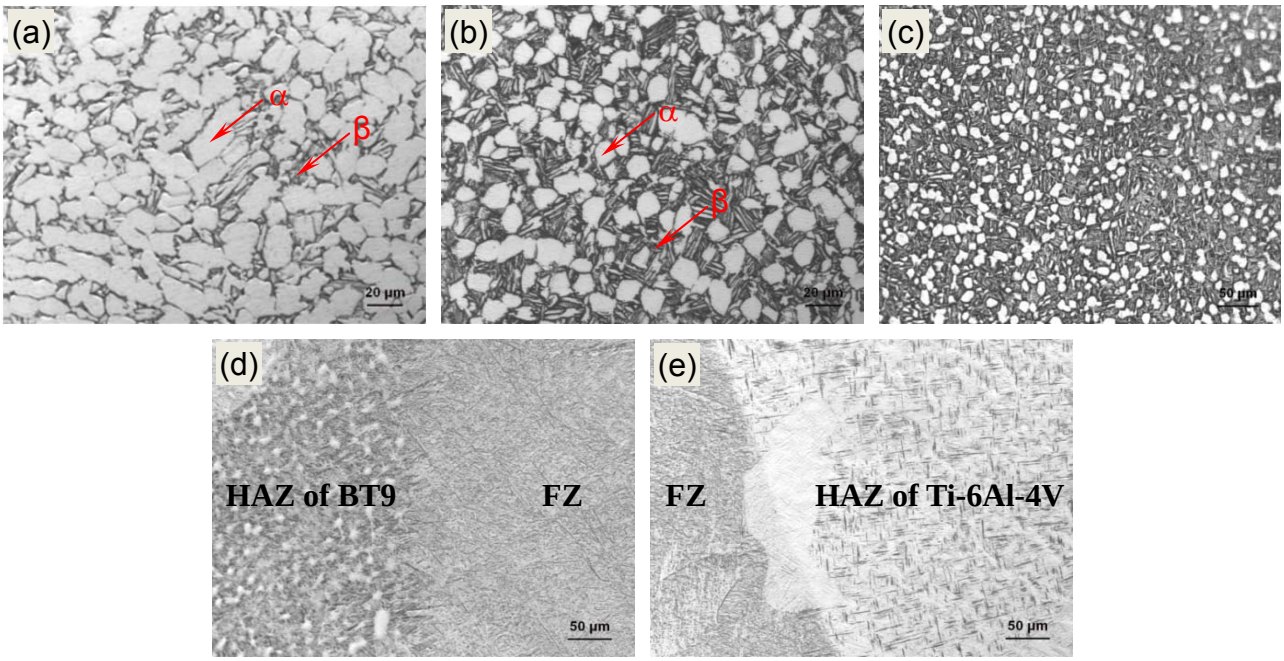

Figure 1. Microstructure of as-welded joint between Ti-6Al-4V and BT9 alloys (a) Ti-6Al-4V BM, (b) BT9 BM, (c) outer-HAZ of BT9, (d) HAZ of BT9 and FZ, and (e) FZ and HAZ of Ti-6Al-4V

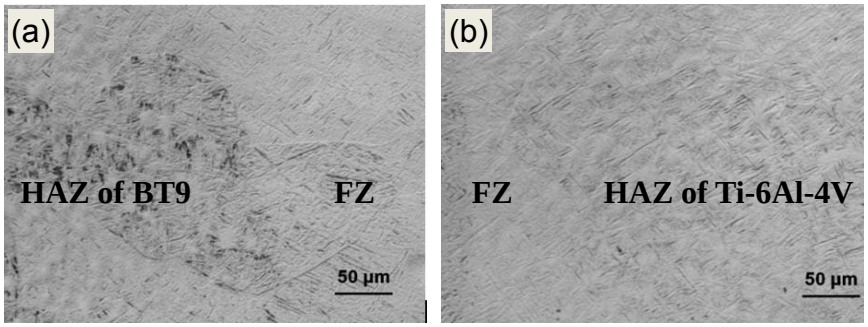

Figure 2. Microstructure of the post-welded joint after aging (a) HAZ of BT9 and FZ, and (b) FZ and HAZ of Ti-6Al-4V

3.2 Microhardness

Vickers microhardness profiles across the dissimilar joint between Ti-6Al-4V and BT9 with and without PWHT are shown in Fig.4. It is seen from Fig.4(a) that an asymmetrical hardness profile across the weld was obtained with an average hardness values of about 300 HV for Ti-6Al-4V BM and approximately 320 HV for BT9 BM, respectively. The higher hardness value in the FZ was due to the formation of martensite in the FZ, as shown in Fig.1(d) and (e). It is observed that the hardness value in the HAZ on the Ti-6Al-4V side was higher than that of the Ti-6Al-4V BM, the hardness value in the inner-HAZ on the BT9 side was also higher than that of the BT9 BM.

However the hardness value in the outer-HAZ was slightly lower than that of the BT9 BM, meaning that a narrow soft zone appeared due to the appearance of β phase as shown in Fig.1(c). The aging treatment at 550°C (Fig.4(a)) led to the elimination of the soft zone at the BT9 side and a slightly higher hardness in the FZ. The increase of hardness was mainly due to the presence of the fine α' and precipitation of some secondary α phase in the β phase both in FZ and HAZ. These results are similar to those reported by Kabir *et al.* [9]. In addition, the microhardness values in the HAZ were also observed to decrease gradually as the distance increased from the FZ border line. This was attributed to the decreasing fine α' and secondary α phase in the HAZ. However, after STA the hardness value in the FZ and HAZ was only slightly higher than or nearly the same as that of the BMs due to the coarse lamellar $\alpha + \beta$ structure (Fig.4(b)). It is of special interest to observe that the narrow soft zone in the outer-HAZ on the BT9 side disappeared as well after STA due to the decomposition of β phase.

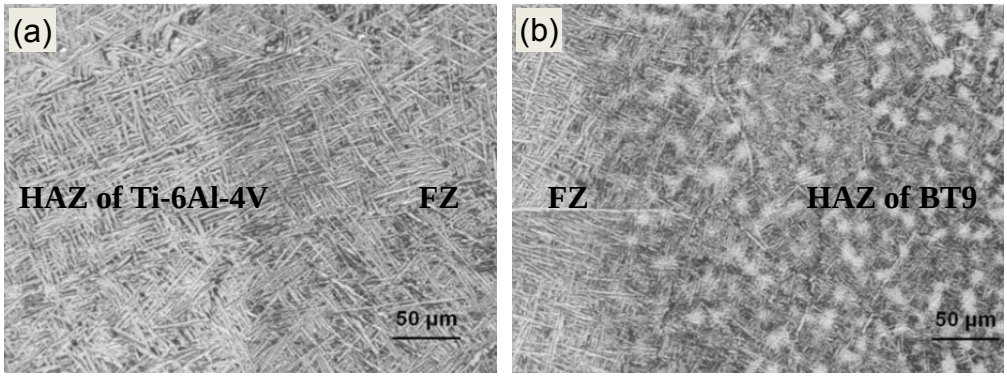

Figure 3. Microstructure of the post-welded joint after STA (a) HAZ of Ti-6Al-4V and FZ, and (b) FZ and HAZ of BT9

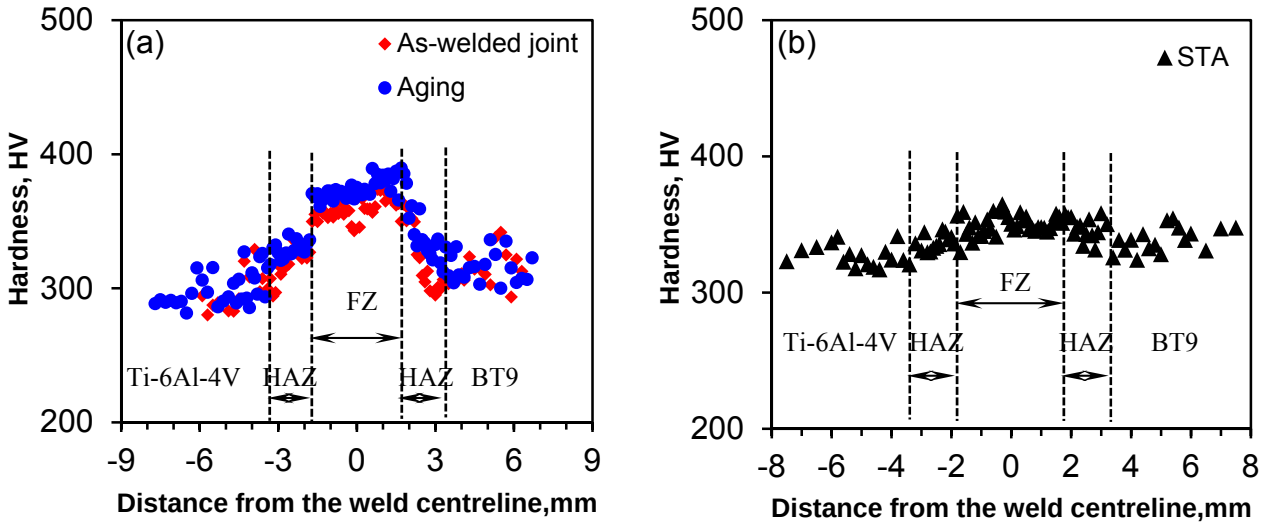

Figure 4. Hardness distribution of the welded joint in (a) as-welded and aging conditions, and (b) STA condition

3.3 Hysteresis loops

The hysteresis loops of the first cycle and mid-life cycle at a total strain amplitude of 1.2% are plotted in Fig 5(a) and (b), respectively. It is seen that the initial tensile (or ascending) phase of the first quarter cycle represented indeed a tensile stress-strain curve tested at a strain rate of 1×10^{-2} s^{-1}. Then the tensile yield strength (YS) of the post-welded joints can be determined from the initial

quarter cycle, and the obtained YS is listed in Table 3. The YS of the post-welded joints in the aging and the STA conditions were almost equal. In addition, the first and mid-life hysteresis loops in both aging and STA conditions were basically symmetrical (Fig.5(a) and (b)). Similar symmetrical hysteresis loops were also observed in titanium alloy [10-13].

3.4 Cyclic deformation response

Figs 6 (a) and (b) show the evolution of cyclic stress amplitude as a function of the number of cycles at different strain amplitudes in the aging and STA conditions, respectively. It is seen that as the applied total strain amplitude increased, cyclic stress amplitude increased and the fatigue life decreased. In both aging and STA conditions, the stress amplitude remained basically constant or stable at the lower strain amplitudes (0.2-0.6%); as the strain amplitude increased (0.8-1.2%) cyclic softening basically occurred, since the post-welded joints lay in a relatively hardened state. Similar cyclic softening characteristics have been documented for titanium alloy under strain-controlled LCF tests [10,14].

Table 3. Fatigue parameters in the aging and STA conditions

Fatigue parameters	σ_y, MPa	n'	K', MPa	σ'_f, MPa	b	ε'_f	c	σ'_y, MPa
Aging	938	0.119	1776	1408	-0.079	0.057	-0.54	865
STA	941	0.116	1759	1412	-0.078	0.109	-0.63	875

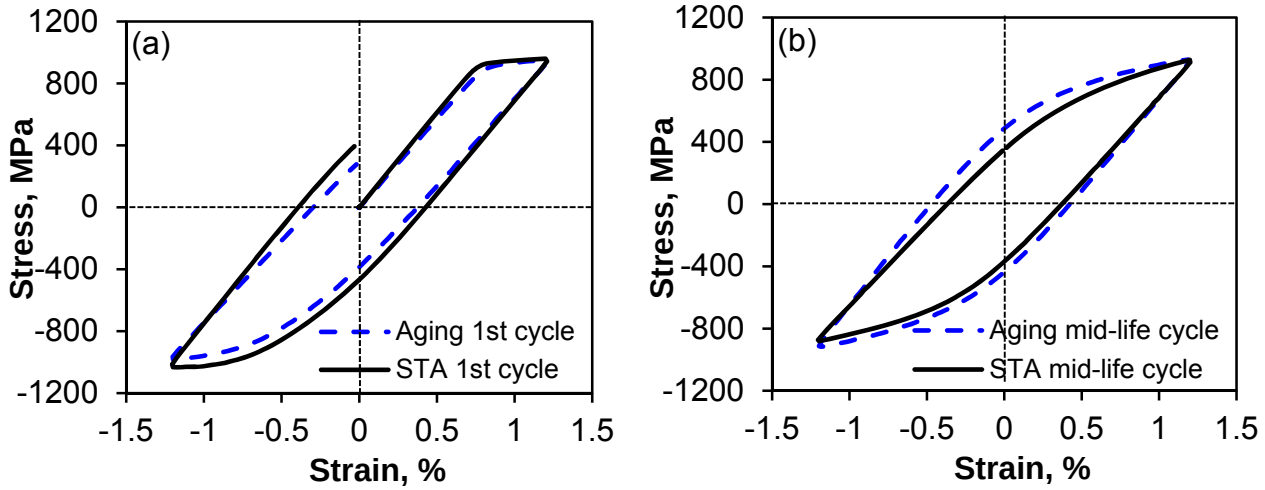

Figure 5. The hysteresis loops at a total strain amplitude of 1.2% and strain ratio of $R_\varepsilon = -1$ for different heat treatment conditions (a) 1st cycle, and (b) the mid-life cycle

Cycling hardening/softening in metals and alloys is known to be dominated by the initial state of the material and the applied strain amplitude. When a material is in its soft/annealed state ($\sigma_{UTS}/\sigma_y \geq 1.4$), cyclic hardening would occur. However, in the hardened state ($\sigma_{UTS}/\sigma_y < 1.2$), cyclic softening would take place [15]. In this study, both types of the post-welded joints exhibited initial cyclic stabilization followed by cyclic softening at the higher strain amplitudes of 0.8-1.2%. The increased degree of cyclic softening with increasing applied strain amplitude might be attributed to the rearrangement and partial annihilation of high density dislocations resulting from EBW [16].

3.5 Fatigue life and fatigue parameters

Fig.7 shows the fatigue lifetime curves of the post-welded joints after aging and STA. Both types of PWHT led to a similar trend of increasing fatigue life with decreasing strain amplitude, and the STA

samples exhibited a slightly lower fatigue life than that of the aging samples at lower strain amplitudes due to the coarser α phase. Based on Basquin equation and Coffin-Manson relation, the total strain amplitude could be expressed as elastic strain amplitude and plastic strain amplitude [15], i.e.,

$$\frac{\Delta\varepsilon_t}{2}=\frac{\Delta\varepsilon_e}{2}+\frac{\Delta\varepsilon_p}{2}=\frac{\sigma'_f\left(2N_f\right)^b}{E}+\varepsilon'_f\left(2N_f\right)^c \quad (1)$$

where E is the Young's modulus, N_f is the fatigue life or number of cycles to failure (the entirety of $2N_f$ is the number of reversals to failure), σ'_f is the fatigue strength coefficient, b is the fatigue strength exponent, ε'_f is the fatigue ductility coefficient, and c is the fatigue ductility exponent. In addition, cyclic deformation behavior is normally considered to be related to the portion of the plastic strain amplitude and is independent of the elastic strain amplitude, which could be expressed by the following equation [15],

$$\frac{\Delta\sigma}{2}=K'\left(\frac{\Delta\varepsilon_p}{2}\right)^{n'}, \quad (2)$$

where $\frac{\Delta\sigma}{2}$ is the mid-life stress amplitude, $\frac{\Delta\varepsilon_p}{2}$ is the mid-life plastic strain amplitude, n' is the cyclic strain-hardening exponent and K' is the cyclic strength coefficient. The obtained fatigue life parameters evaluated on the basis of Equs (1) and (2) were summarized in Table 3. It is also observed that the cyclic strain hardening exponent (n'), the cyclic strength coefficient (K'), fatigue strength coefficient (σ'_f), and cyclic yield strength (σ'_y) of the post-welded joint after aging were nearly the same as that of STA. In general, a smaller absolute value of fatigue strength exponent (b) and fatigue ductility exponent (c) and a larger value of fatigue strength coefficient (σ'_f) and fatigue ductility coefficient (ε'_f) represent a longer fatigue life. This implies that a longer fatigue life of a material in the strain-controlled tests requires a good combination of both high strength and superior ductility. In spite of such a seemingly conflicting effect of the exponent pair (b and c) and the coefficient pair (σ'_f and ε'_f) on the fatigue life, the exponent pair would be expected to play a greater role in the sense of exponential functions. In comparison with STA, the absolute value of c in the aging condition was smaller (while b was nearly the same), and the value of ε'_f was also smaller (while σ'_f remained nearly the same). The combined role of these fatigue life parameters gave no substantial difference between the aging and STA conditions, as also seen in Fig.7. It should be noted that in evaluating the above fatigue life parameters the strain amplitude was limited to a range in-between 0.4% and 1.2%, excluding the strain level with run-out data at which some fatigue samples did not fail at or above 10^7 cycles.

3.6 Fractography

The fracture location of both types of post-welded joints mostly lay in the Ti-6Al-4V BM. Only one sample in the STA condition failed in the HAZ at Ti-6Al-4V side, which might be due to the formation of the coarse α in the HAZ (Fig.3). Fracture surfaces of the fatigued specimens were examined using SEM. Fig.8(a) and Fig.9(a) show an overall view of fracture surfaces of the post-welded joints in the aging and STA conditions at a total strain amplitude of 0.4%, containing regions of fatigue crack initiation, propagation, and final fast fracture. It is seen from these low magnification images that fatigue crack initiated from the specimen surface or near-surface defect, and the river line patterns appeared in both aging and STA conditions which were irregular and

broken and flowed along the crack propagation direction. Fig.8(b)-(c) and Fig.9(b)-(c) show the images near the crack initiation sites and in the crack propagation zone of the fatigued samples at higher magnifications in the aging and STA conditions. In the near-initiation area, a mix of fatigue striations and cleavage-like features could be seen in both aging and STA conditions. Fatigue crack propagation zone was mainly characterized by typical fatigue striations which were perpendicular to the crack propagation direction in both aging and STA conditions.

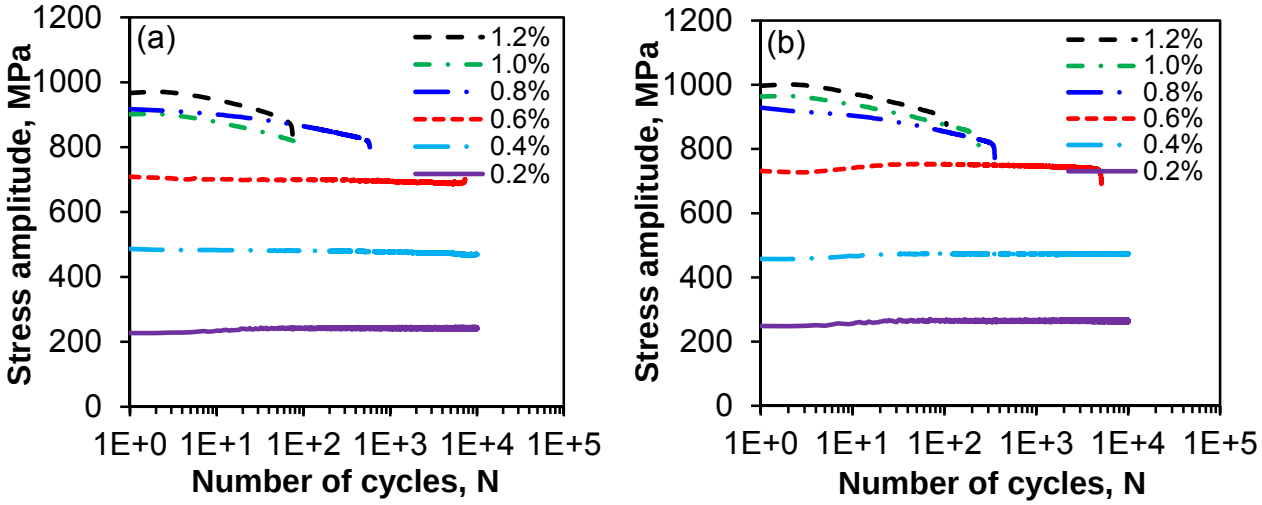

Figure 6. Stress amplitude vs. the number of cycles at different total strain amplitudes in the (a) aging condition, and (b) STA condition

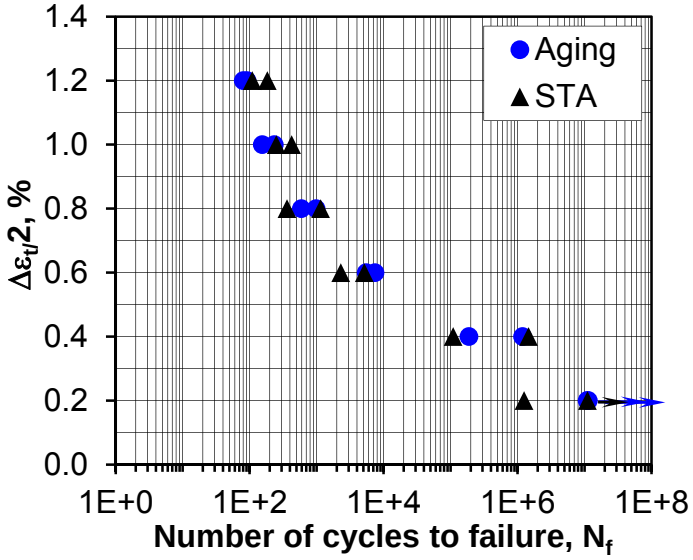

Figure 7. Total strain amplitude as a function of the number of cycles to failure in the aging and STA conditions

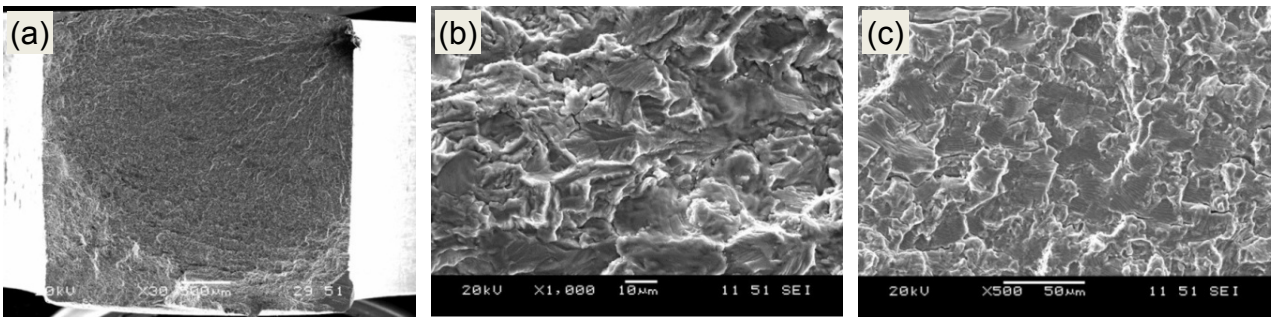

Figure 8. SEM images of fracture surfaces of a post-welded joint in the aging condition, fatigued at a strain

amplitude of 0.4%, (a) an overall view, (b) crack initiation site and (c) crack propagation zone

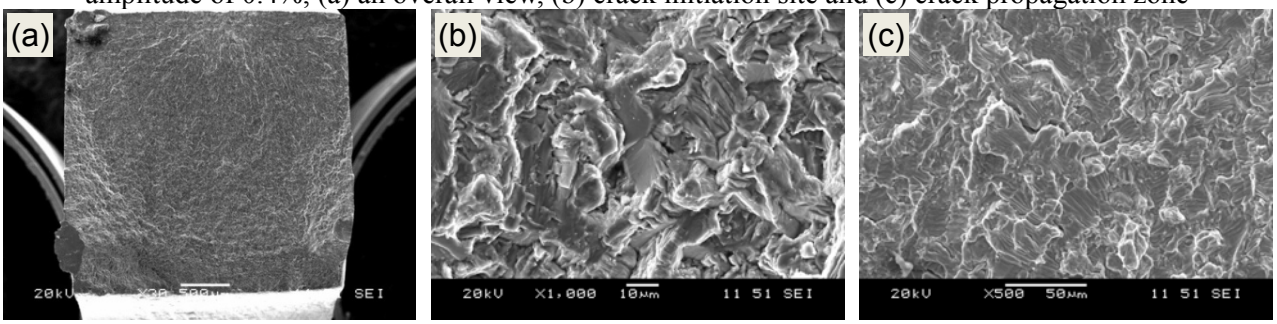

Figure 9. SEM images of fracture surfaces of a post-welded joint in the STA condition, fatigued at a strain amplitude of 0.4%, (a) an overall view, (b) crack initiation site and (c) crack propagation zone

4. Conclusions

1. The microstructure across the dissimilar welded joint exhibited a considerable change, mainly consisting of acicular and fine martensite α' both in the FZ and HAZ of Ti-6Al-4V side, and acicular martensite α', primary α and metastable β in BT9 side, while both BMs of Ti-6Al-4V and BT9 had a microstructure of equiaxed α grains and inter-granular $\alpha + \beta$ lamellae. There was no significant difference in the microstructure of both FZ and HAZ between the as-welded and the aging conditions. However, after STA the microstructure of the FZ and HAZ at Ti-6Al-4V side mainly consisted of coarse α platelets with interlamellar β, while α platelets, primary α and interlamellar β were observed in the HAZ at BT9 side.
2. A characteristic asymmetrical microhardness profile across the dissimilar welded joint was observed with a higher value on the BT9 side than on the Ti-6Al-4V side. The hardness in the FZ was higher than that of both BMs due to the formation of α' martensite arising from the rapid cooling during EBW. A narrow soft zone in the outer-HAZ of BT9 side was observed due to the presence of β phase, while the hardness in the HAZ of Ti-6Al-4V side was higher than that of the Ti-6Al-4V BM. After aging treatment at 550°C the high hardness in FZ remained nearly the same or slightly higher and the narrow soft zone disappeared due to decomposition of β. However, the hardness value of the post-welded joint after STA in both FZ and HAZ was slightly higher than or nearly the same as that of BMs due to the presence of coarsened α.
3. The post-welded joints in both aging and STA conditions displayed cyclic saturation or stabilization in the entire cyclic deformation process at low strain amplitudes up to 0.6%, while cyclic softening occurred after initial cyclic stabilization at higher strain amplitudes. With increasing strain amplitude, the stage of initial cyclic stabilization became gradually shorter.
4. The fatigue life of the aging condition was slightly longer than that of the STA condition at the lower strain amplitudes. In general the strain-controlled fatigue resistance of the post-welded joints in both aging and STA conditions was roughly equivalent.
5. The fatigue fracture of the post-welded joints after aging and STA treatment occurred mostly in Ti-6Al-4V BM. Fatigue crack initiation occurred from the specimen surface or near-surface defect, and crack propagation was mainly characterized by the characteristic fatigue striations coupled with secondary cracks in both aging and STA conditions.

Acknowledgements

The authors would like to thank the Natural Sciences and Engineering Research Council of Canada (NSERC) and AUTO21 Network of Centres of Excellence for the financial support, and

Northwestern Polytechnical University (NWPU), Xi'an, China for providing test materials. One of the authors (D.L. Chen) is also grateful for the financial support by the Premier's Research Excellence Award (PREA), NSERC-Discovery Accelerator Supplement (DAS) Award, Canada Foundation for Innovation (CFI), and Ryerson Research Chair (RRC) program. The authors would also like to thank Messrs. Q. Li, A. Machin, J. Amankrah and R. Churaman for easy access to the laboratory facilities of Ryerson University and their assistance in the experiments.

References

[1] K.K. Murthy, S. Sundaresan, Phase transformations in a welded near α titanium alloy as a function of weld cooling rate and post-weld heat treatment conditions. J Mater Sci, 33 (1998) 817–826.

[2] A.A. Popov, A.G. Illarionov, O.A. Oleneva, Structure and properties of welds of high-alloy titanium alloy after heat treatment. Metal Sci Heat Treat, 52 (2011) 476–480.

[3] G.Q. Wang, Y. Zhao, A.P. Wu, G.S. Zou, J.L. Ren, Microstructure and high-temperature tensile properties of Ti_3Al alloys laser welding joint. Chin J Nonfer Metals, 17 (2007) 1803–1807.

[4] M.F. Arenas, V.L. Acoff, The effect of postweld heat treatment on gas tungsten arc welded gamma titanium aluminide. Scripta Mater, 46 (2002) 241–246.

[5] Y. Guo, Y.L. Chiu, M.M. Attallah, H.Y. Li, S. Bray, P. Bowen, Characterization of dissimilar linear friction welds of α-β titanium alloys. J Mater Eng Perf, 21 (2012) 770–776.

[6] S.J. Tuppen, M.R. Bache, W.E. Voice. A fatigue assessment of dissimilar titanium alloy diffusion bonds. Inter J Fatigue, 27 (2005) 651–658.

[7] P.F. Fu, F.J. Liu, Z.Y. Mao, J.W. Li, Effects of electron beam local heat treatment on fatigue properties for Ti-6Al-4V alloy joints. International Technology and Innovation Conference, Hangzhou, China, November 6-7, 2006, pp. 72–75.

[8] P. Azar, P. Li, P.C. Patnaik, R. Thamburaj, J.-P, Immarigeon, Electron beam weld repair and qualification of titanium fan blades for military gas turbine engine. RTO AVT Specialists' Meeting on "Cost Effective Application of Titanium Alloys in Military Platforms", Loen, Norway, May 7-11, 2001, RTO-MP-069(II), 2001, 18.1–18.16.

[9] A.S.H. Kabir, X.J. Cao, J. Gholipour, P. Wanjara, J. Cuddy, A. Birur, M. Medraj, Effect of postweld heat treatment on microstructure, hardness, and tensile properties of laser-welded Ti-6Al-4V. Metall Mater Trans A, 43 (2012) 4171–4184.

[10] S.J. Li, T.C. Cui, Y.L. Hao, R. Yang, Fatigue properties of a metastable β-type titanium alloy with reversible phase transformation. Acta Biomater, 4 (2008) 305–317.

[11] B. Koch, B. Skrotzki, Strain controlled fatigue testing of the metastable-titanium alloy Ti-6.8Mo-4.5Fe-1.5Al (Timetal LCB). Mater Sci Eng A, 528 (2011) 5999–6005.

[12] Y.H. Lin, K.H. Hu, F.H. Kao, S.H. Wang, J.R. Yang, C.K. Lin, Dynamic strain aging in low cycle fatigue of duplex titanium alloys. Mater Sci Eng A, 528 (2011) 4381–4389.

[13] M. Satoh, S. Horibe, M. Nakamura, H. Uchida, Cyclic deformation and fatigue in TiAl intermetallic compound under plastic strain control. Inter J Fatigue, 32 (2010) 698–702.

[14] J. Plumbridge, M. Stanley, Low cycle fatigue of a titanium 829 alloy. Inter J Fatigue, 4 (1986) 209–216.

[15] E. Dieter, Mechanical Metallurgy, McGraw-Hill, New York, 1986.

[16] A.K. Nag, K.V.U. Praveen, V. Singh, Low cycle fatigue behaviour of Ti-6Al-5Zr-0.5Mo-0.25Si alloy at room temperature. Bull Mater Sci, 29 (2006) 271–275.

Performance of Sandwich Components with Chiral Topology Cores

Marin Sandu[1], Adriana Sandu[1], Dan Mihai Constantinescu[1,*], Ştefan Sorohan[1], Dragoş Alexandru Apostol[1]

[1] Department of Strength of Materials, University POLITEHNICA of Bucharest, Bucharest 060042, Romania
* Corresponding author: dan.constantinescu@upb.ro

Abstract Two thin plates with a stabilizing medium placed between them can be an ideal component for large and lightweight structures with increased strength, stiffness and stability. The application of the novel chiral cellular geometry will lead to the development of structural components with superior elastic and impact resilient properties. This paper proposes the design of lightweight square sandwich panels with aluminum sheets and a core made with a chiral geometry network having parallelogram-shaped nodes. Finite element analyses were undertaken in order to characterize the behavior of the considered panels as having supported edges, and loaded under lateral pressure. Also, the loading in torsion was analyzed in the case when two opposite corners are supported and in the other two corners equal and opposite normal forces are applied. For this loading experimental measurements were also done by using strain gages. The new meta-tetrachiral configurations under investigation can provide significant improvements in the mechanical performance of sandwich components, and may also be considered for advanced designs.

Keywords Sandwich panel, Auxetic core, Meta-chiral topology, Finite element analysis, Strain gage

1. Introduction

The strength and the stiffness properties of a sandwich panel are dependent to a great extent both on the behavior of the faces and of the structure used as core. Classical honeycomb core adopts a saddle shape (anticlastic curvature) upon out-of-plane bending, because its Poisson's ratio is positive. In order to manufacture curved panels, cellular cores that exhibit auxetic properties (negative Poisson's ratio) are used, because of their tendency to form dome-shaped surfaces. Consequently, curved sandwich panels with auxetic cores are basic components of advanced structures, first of all in the aircraft and automotive fabrication. It is evident that the analysis of the behavior of cores and sandwich panels under mechanical and thermal loading is of importance for designers.

In paper [1], the finite element method has been applied to characterize the mechanical properties of re-entrant (auxetic) honeycombs which may be used as cores for sandwich panels with any special properties. In the last two decades, a number of cellular structures have been extensively analyzed [2]-[9]. Especially the periodic core structures with chiral topologies, which contain a number of interconnected basic blocks, have attracted considerable attention. A basic block is "chiral" if it is not super imposable on its mirror image. A basic block is consisting of a node with a number of 3, 4 or 6 ligaments attached to it (Fig. 1). Also, left handed or right handed blocks may be constructed.

In the case of a chiral structure, the nodes are attached on the opposite sides of the same ligament (Fig. 2, a). It is possible to attach the nodes on the same side of each ligament and the corresponding structure will be denominated anti-chiral (Fig. 2, b). A hybrid construction, containing some nodes which are attached to the same side of the ligaments and some others to opposite sides of the ligaments, will be referred as meta-chiral (Fig. 2, c). In two-dimensions (2-D), the nodes may be circular, hexagonal, square, rectangular or with other geometry.

There are many papers which deal with the geometries and the properties of auxetic materials, but there is little information on the behavior of the sandwich panels with chiral configured cores. In this paper, the meta-chiral structure with parallelogram-shaped nodes as in Fig. 3 will be analyzed separately, and as a core of a sandwich panel.

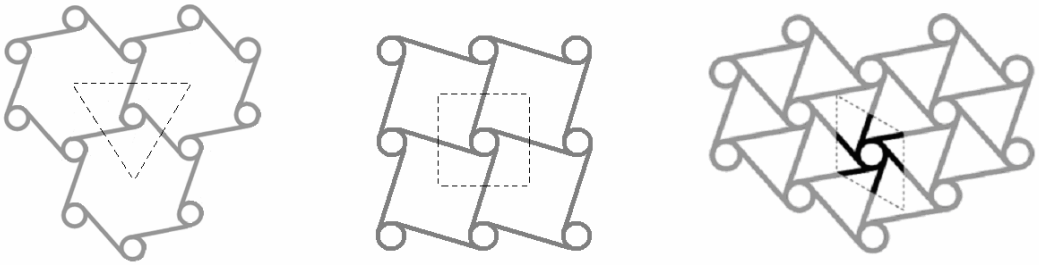

Figure 1. Basic blocks for three chiral structures: a) trichirals, b) tetrachirals, c) hexachirals

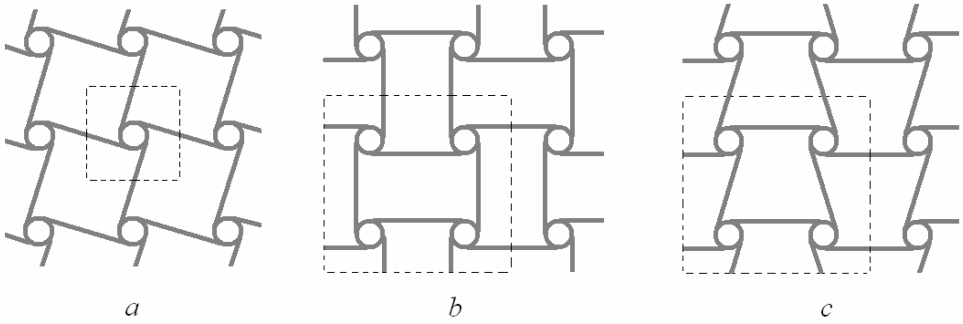

Figure 2. Structures from components of order 4:
a) tetrachirals, b) anti-tetrachirals, c) meta-tetrachirals

It is to note that in the analytical evaluations of auxetic in-plane properties of 2-D chiral, anti-chiral and meta-chiral structures, two different approaches were used: a) rigid ligaments and nodes, connected together through ideal hinges [2]; b) flexible ligaments connected with rigid or deformable nodes [9]. Also, it is possible to evaluate the out-of-plane mechanical properties of a chiral lattice analytically or by means of finite element analysis (FEA) [8,9].

2. Geometry of the analyzed structure and the finite element model

The behavior of the panel presented in Fig. 3 was evaluated by using a FEA model, with ANSYS [10]. The sandwich panel has sheets made from an aluminum alloy (1050 H24) of thickness t_f = 1 mm, glued with araldite AW 106/HV953 U to the core made from rigid polyurethane strips having a section of 5 x 25.4 mm inside the panel and 10 x 25.4 mm on the border of the panel.

The FEA makes possible the characterization of the sandwich panels under several aspects: rigidity, state of stress, fundamental eigenfrequencies and modes of vibration, stability. There were analyzed several cases of loading:

1) simply supported plate, loaded by a lateral pressure of 0.07 MPa;
2) cylindrical bending with the panel supported on two opposite edges and loaded by a lateral pressure of 0.05 MPa;
3) cylindrical bending with the panel supported on the other two opposite edges and loaded by the same lateral pressure of 0.05 MPa;

4) torsion of the panel by applying two equal forces in opposite corners and restricting the movement of the other two corners [11].

In the numerical model the adhesive was considered only in between the upper and lower aluminum sheets and the chiral core which presumably behaves as a monobloc structural component, although the core was built as a "puzzle" from separate parts glued between them.

For the used materials the following material parameters were adopted: aluminum – E = 69000 MPa, v = 0.33, σ_u = 138 MPa (ultimate strength), $\sigma_{y\,0.2}$ = 132 MPa (0.2% offset yield limit), density 2700 kg/m^3; araldite AW 106 – E_a = 1350 MPa, v_a = 0.45, σ_{ua} = 33 MPa, τ_{ua} = 23 MPa, density 1500 kg/m^3; rigid polyurethane foam – E_f = 220 MPa, v_f = 0.3 , density 301 kg/m^3. The allowable stresses will be considered as 100 MPa in aluminum, 5 MPa in the polyurethane foam and 20 MPa in the adhesive.

The dimensions of the panel are: a = 400 mm, b = 48 mm, c = 32 mm, t_f = 1 mm (thickness of the sheets), t_a = 0.3 mm (thickness of the adhesive), t_c = 25.4 mm (thickness of the core), t_s = 5 mm (thickness of the strips used to built the core), t_b = 10 mm (thickness of the border).

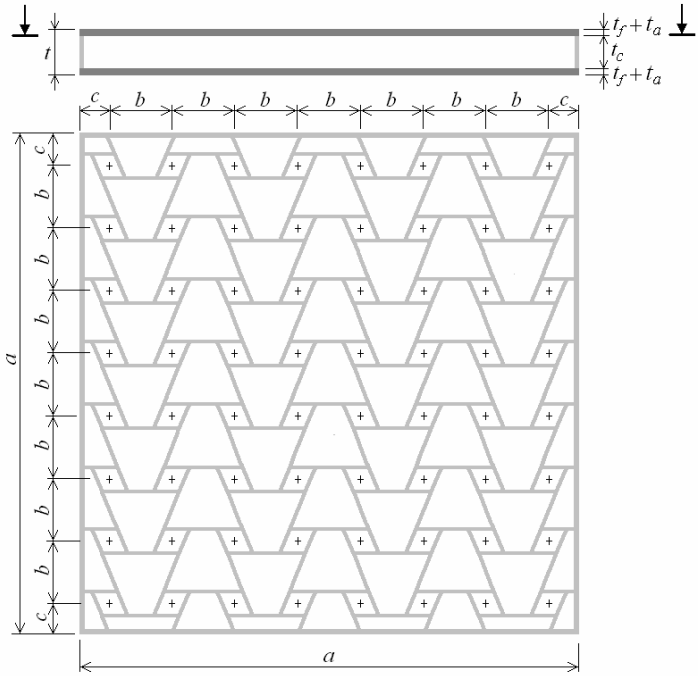

Figure 3. Geometry of the analyzed panel

In generating the chiral network (Fig. 4) was used the basic block obtained by adding to the configuration from Fig. 5 its own image in mirror. The FE mesh is done by using solid 8-noded elements (Brick 8), and resulted as having 134728 elements and 185706 nodes. Two layers of elements were used over the thickness of the strips which form the chiral core and through the thickness of the sheets, and one layer of elements through the thickness of the adhesive.

After a preliminary study it was established that a geometrically nonlinear analysis (large displacements) doesn't lead to results clearly different from the ones obtained in a small

displacement analysis, therefore all the following calculations were done only in the second hypothesis.

By using the densities of the materials mentioned previously the total mass of the sandwich panel resulted as 1.335 kg, from which the mass of the sheets is 65% (0.864 kg), of the core is 31% (0.418 kg), and of the adhesive as 4% (0.053 kg). It is to observe that the mass of proposed chiral foam core represents 35% of the mass corresponding to a compact core made from the same foam and having the same overall sizes, which is of 1.2 kg.

Data were considered in the SI system, therefore in the figures displacements were obtained in meters, and stresses in N/m^2 (10^6 N/m^2 = 1 N/mm^2 = 1 MPa).

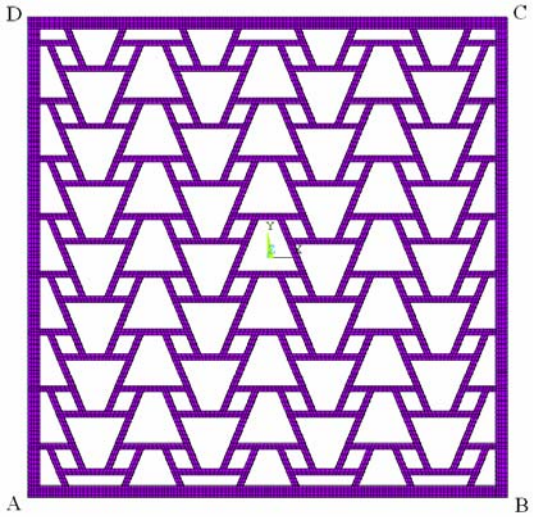

Figure 4. The core discretized with 8-node brick-type finite elements

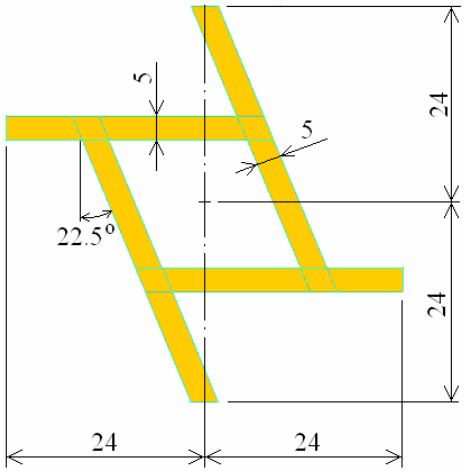

Figure 5. Geometry of the basic semi-block of the meta-tetrachiral core

3. Evaluation of in-plane auxetic properties of the core

The chiral core was initially analyzed separately in order to establish the coefficients of transversal contraction (or of transversal swelling), notated as ν_{xy} and ν_{yx}. The displacements in the plane XY (median plane of the core) were established in two situations (Fig. 4):

I displacements blocked in the direction X on the edge AD and an imposed displacement on the opposite edge (UX = 1 mm);

II displacements blocked in the direction Y on the edge AB and an imposed displacement on the opposite edge (UY = 1 mm).

In general, if L_x and L_y are the overall dimensions of the panel (length and width), the two values of the "Poisson's coefficients", associated to the situations defined in I and II are to be calculated with the relations:

$$\nu_{xy} = -\left(\Delta L_{y,I} / L_y\right) / \left(\Delta L_{x,I} / L_x\right), \qquad \nu_{yx} = -\left(\Delta L_{x,II} / L_x\right) / \left(\Delta L_{y,II} / L_y\right). \tag{1}$$

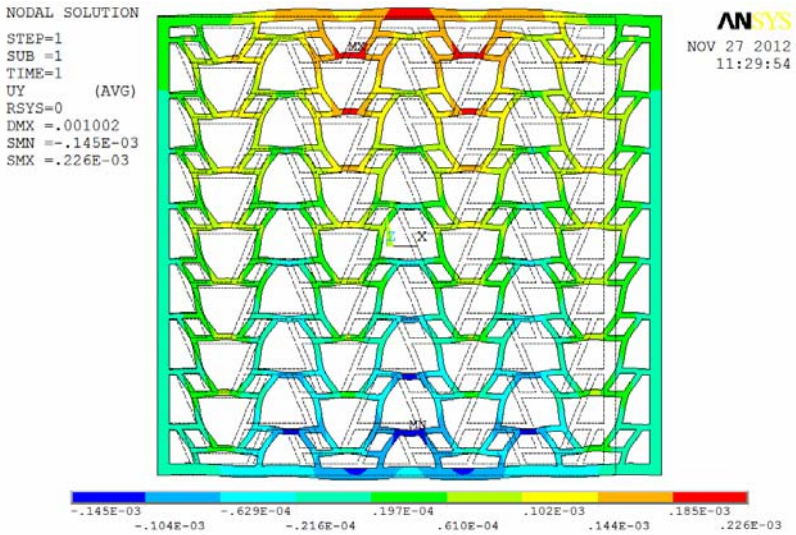

Figure 6. Deformed shape of the core when a relative displacement of 1 mm between the vertical sides is imposed

The results presented in Figs. 6 and 7 show that $\Delta L_{y,I} = 0.226 - (-0.145) = 0.371$ mm, and $\Delta L_{x,II} = 0.159 - (-0.159) = 0.318$ mm. Taking into account that $\Delta L_{x,I} = \Delta L_{y,II} = 1$ mm and that $L_x = L_y = a$, from (1) resulted $\nu_{xy} = -0.371$ and $\nu_{yx} = -0.318$. These negative values show that the core which will be used to build the sandwich panel has auxetic properties.

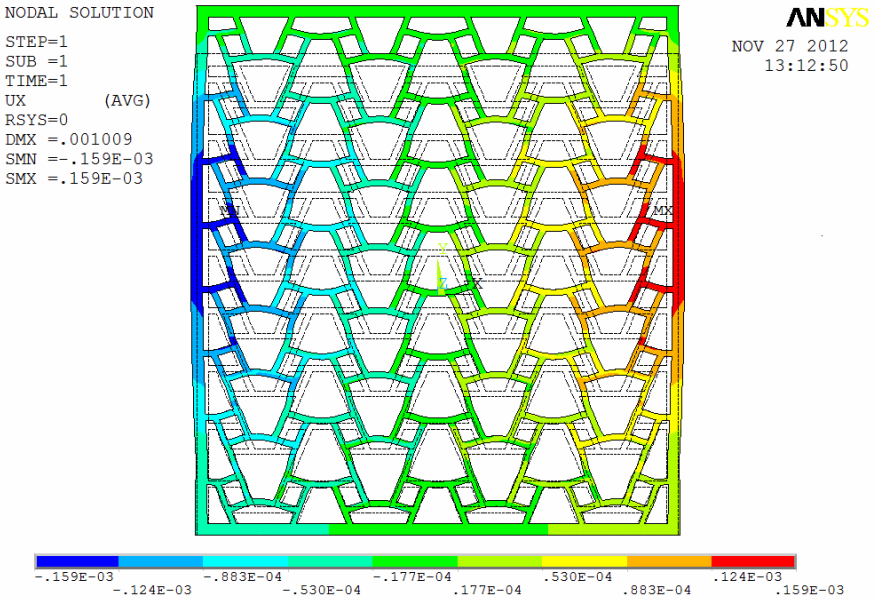

Figure 7. Deformed shape of the core when a relative displacement of 1 mm between the horizontal sides is imposed

4. Results of the FEA in the case of the panel under lateral pressure

4.1. Case of panel simply supported on the contour

The applied loading is a lateral pressure of 0.07 MPa. The obtained results are given in Table 1 and in Figs. 8-13.

It is to be noticed that the maximum von Mises equivalent stresses are lower than the allowable stress values in all the materials. The sandwich plate has a high stiffness as indicated by the maximum deflection (2.589 mm) and a high fundamental eigenfrequency (365 Hz). There is no risk to lose the stability of the plate as the coefficient of safety is 5.97 for the first local buckling mode. Fig. 13 shows a non-uniform distribution of the reactions along the supported contour, thus being explained the increased values of the stresses towards the middle sides of the sheet (Fig. 9).

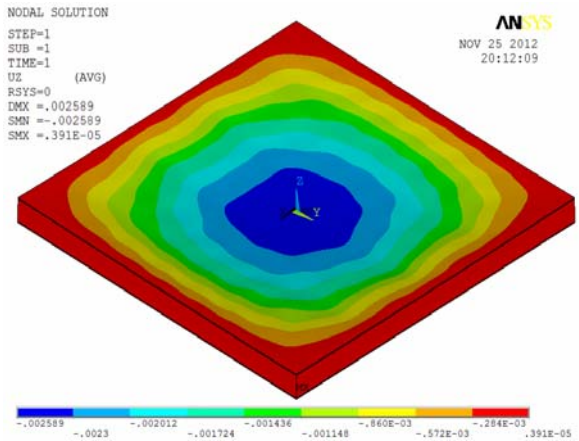

Figure 8. Deformed shape of the panel

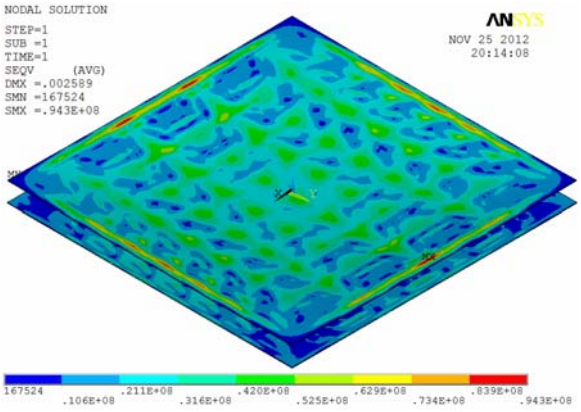

Figure 9. Equivalent stresses in the aluminum sheets

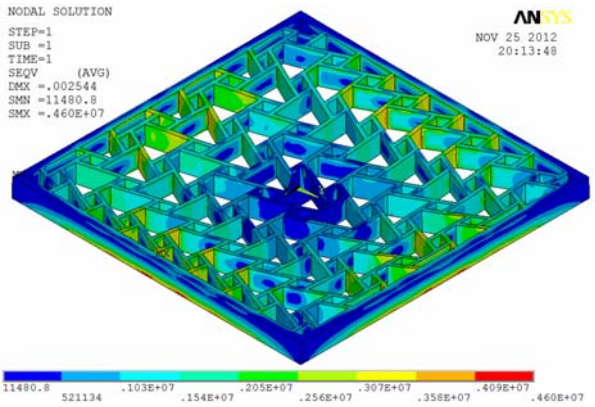

Figure 10. Equivalent stresses into the core

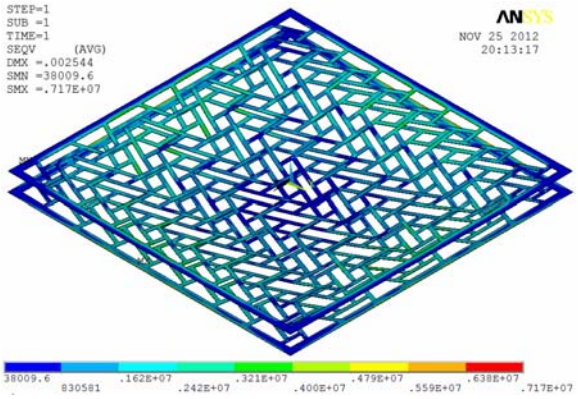

Figure 11. Equivalent stresses into the adhesive

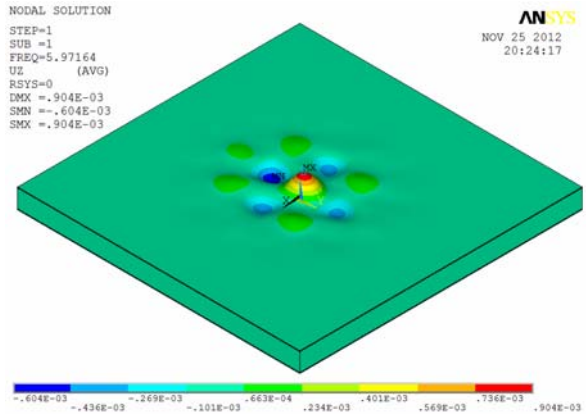

Figure 12. First mode of local buckling

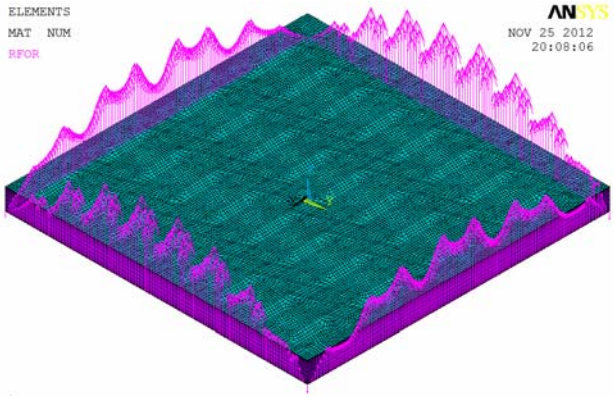

Figure 13. Distribution of the support reactions on the contour of the panel

4.2. Case of panel simply supported on the sides AB and CD (Fig. 4)

The lateral pressure is 0.05 MPa. The obtained results are presented in Table 1 and in Figs. 14-17.

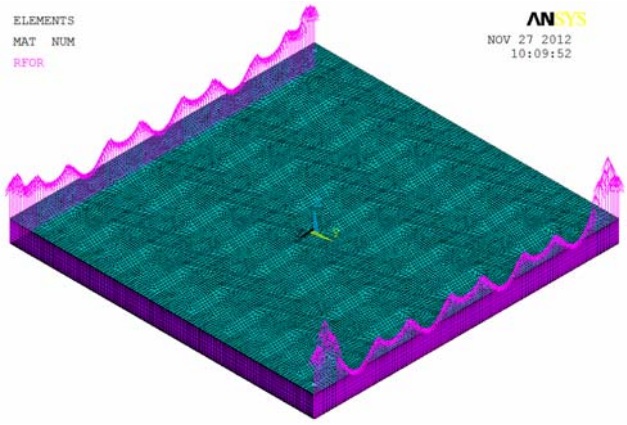

Figure 14. Distribution of the support reactions

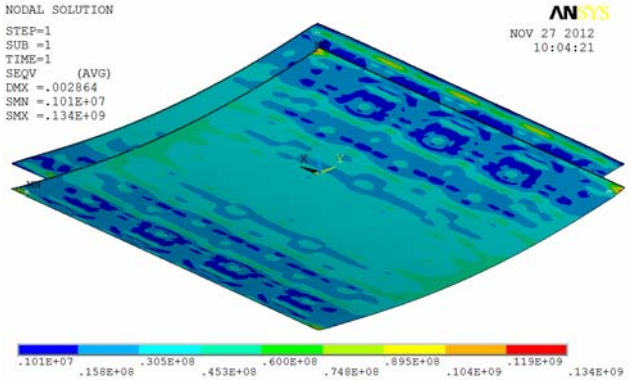

Figure 15. Equivalent stresses in the aluminum sheets

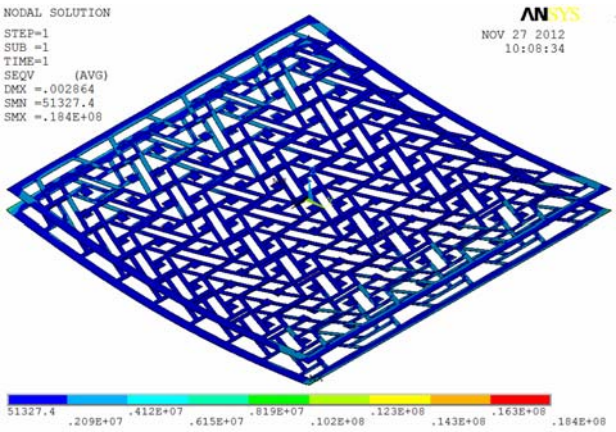

Figure 16. Equivalent stresses in adhesive

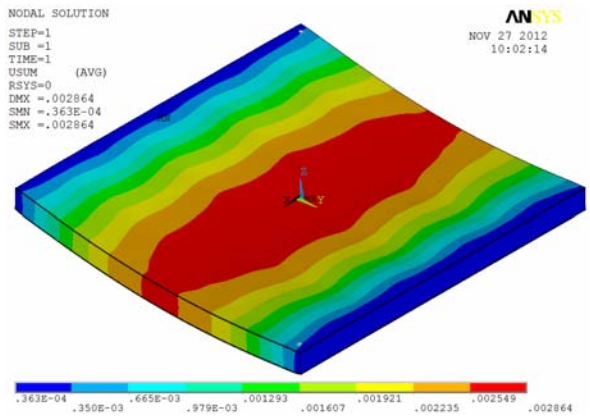

Figure 17. Deformed shape of the panel

4.3. Case of panel simply supported on the sides AD and BC (Fig. 4)

The loading is done by a lateral pressure of 0.05 MPa. The obtained results are presented also in Table 1 and in Figs. 18 and 19.

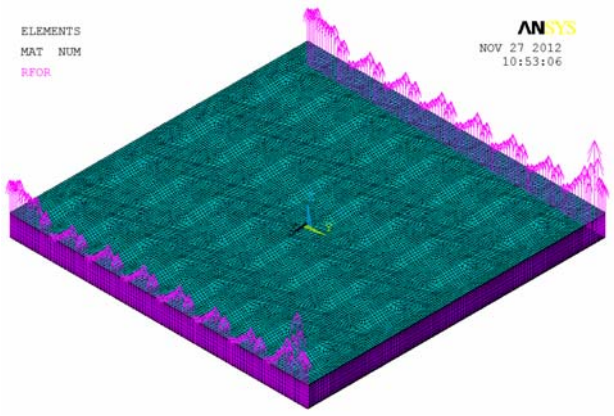

Figure 18. Distribution of the support reactions

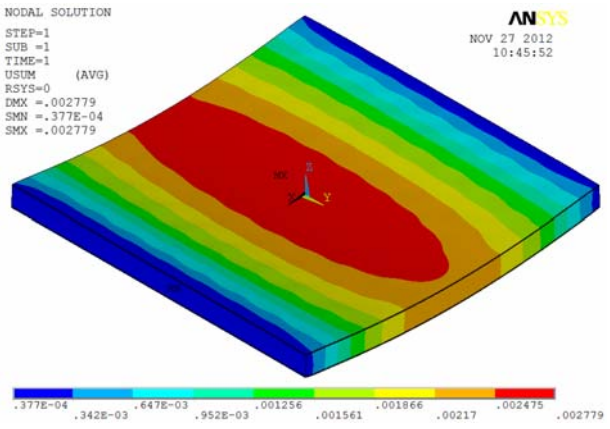

Figure 19. Deformed shape of the panel

Table 1. Results of the finite element analyses

Load case	Type of analysis	Maximum von Mises equivalent stresses [MPa]			Maximum deflection [mm]	Buckling safety coefficient	Fundamental eigenfrequency [Hz]
		Sheets	Core	Adhesive			
1	linear	94.3	4.6	7.17	2.589	5.97	365
1	nonlinear	96.6	4.58	7.12	2.581	5.97	365
2	linear	134	8.95	18.4	2.864	8.09	262
3	linear	133	8.93	18.3	2.779	8.24	265

In the two cases of cylindrical bending the stresses in the sheets, but especially in the core are unacceptably high. As the stresses in the foam have to be reduced to half, the loading has to be decreased from 0.05 MPa to 0.025 MPa. If the pressure has an imposed value (as 0.05 MPa) the thickness of the sheets may be increased and/or a foam with higher density and resistance has to be chosen.

It is interesting to notice that the distribution of the reactions along the edges on which the panel is supported is quite uniform (Figs. 14 and 18), but there are peak values in the vicinity of the corners where extreme values of the stresses in all the components were obtained.

Although it was expected to obtain differences between the two cases of cylindrical bending, the results are very similar; this represents an advantage given by the use of the meta-tetrachiral configuration.

5. Results of the FEA in the case of the panel under torsion

The loading scheme is presented in Fig. 20, in each corner of the plate being applied a force of 500 N, which in the numerical model were distributed on squares of 20x20 mm, as to avoid undesired local effects. The obtained results are presented in Figs. 20-23. In the aluminum sheets the maximum equivalent stress obtained in the corners is 65 MPa (Fig. 22), and in the center is 25 MPa (Fig. 23). In Fig. 23 the middle of the panel is considered the origin of the horizontal axis. The equivalent stress in the adhesive was obtained as about 2 MPa along the border of the core, and a maximum value of 6 MPa resulted again in the corners. In the chiral core the equivalent stress was almost zero in the middle area, about 1 MPa in the border, and a maximum value of 2.9 MPa was again obtained in the corners.

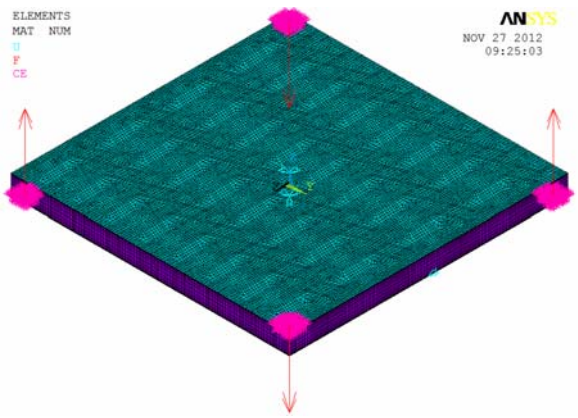

Figure 20. The loading scheme

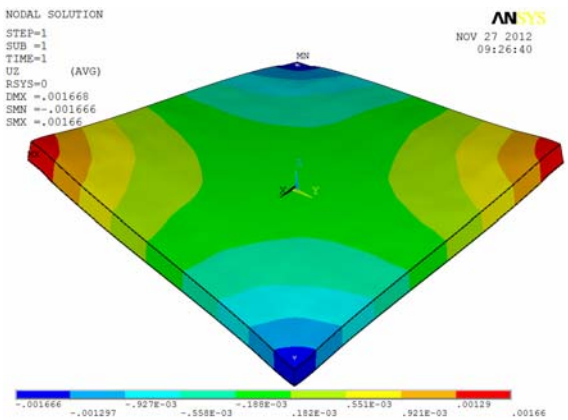

Figure 21. Displacement of the twisted panel

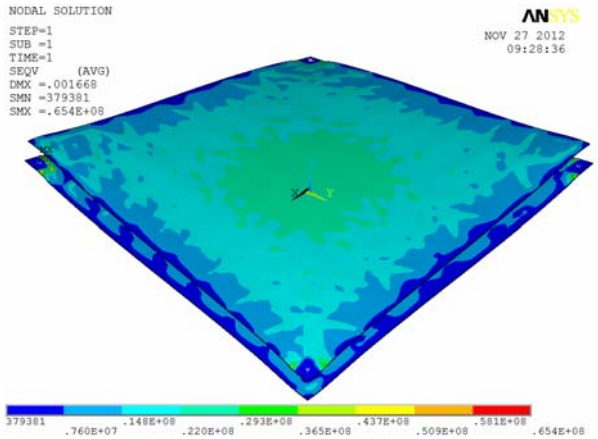

Figure 22. Equivalent stresses in the sheets

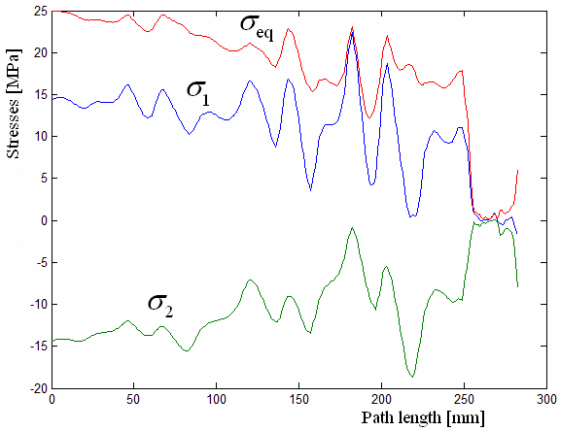

Figure 23. Variation of stresses σ_{eq}, σ_1, σ_2, along a half of the diagonal, on the surface of the panel

6. Experimental evaluation of the sandwich panel under torsion

In Fig. 24 (left) is shown the core of the sandwich panel tested in torsion with the loading scheme from Fig. 24 (right). A strain gage with two measuring grids (SG 1 and SG 2) of type XY93 10/120 (HBM, Germany) was positioned in the middle of the panel along its diagonals in order to measure the principal strains. With these strains were calculated the principal stresses σ_1, σ_2, and then the von Mises equivalent stress, σ_{eq}. For an applied force of 500 N (as in the FEA model) the experimentally established equivalent stress resulted as 23.55 MPa, being a little bit smaller than the 25 MPa value obtained numerically. This result validates the modeling procedure established in the FEA.

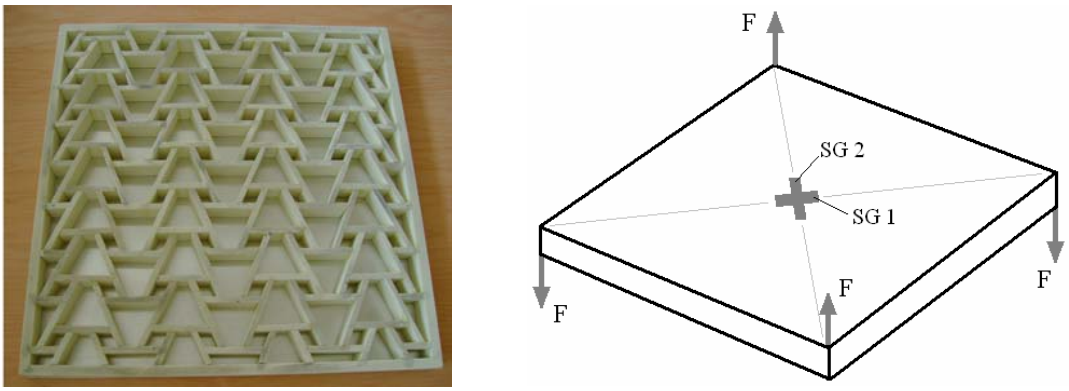

Figure 24. The meta-tetrachiral core manufactured from rigid foam strips and the loading scheme

7. Conclusions

The meta-tetrachiral core analyzed hereby is a new solution which has auxetic properties, and the resulting sandwich panel is stiff and light. Although it has only one plane of symmetry its behavior in bending (Table 1) is almost the same on the two in-plane directions.

This type of geometry, characterized by robust cells having thick walls, confers an important advantage concerning the local stability of the core.

We intend to use this meta-tetrachiral core for curved sandwich panels. By changing the geometry of the basic block (Fig. 5) one can obtain similar chiral core geometries with properties which worth to be investigated. Due to the simple manufacturing technology such panels can be obtained with significant economical advantages.

Acknowledgements

This work was supported by a grant of the Romanian National Authority for Scientific Research, CNDI– UEFISCDI, project number PN-II-PT-PCCA-2011-3.2-0068, contract 206/2012.

References

[1] J.P.M. Whitty, A. Alderson, P. Myler, B. Kandola, Towards the design of sandwich panel composites with enhanced mechanical and thermal properties by variation of the in-plane Poisson's ratios. Composites Part A, 34 (2003) 525-534.

[2] J.N. Grima, R. Gatt, P.S. Farrugia, On the properties of auxetic meta-tetrachiral structures. Phys Solid State, 245 (2008) 511-520.

[3] J.N. Grima, A. Alderson, K. Evans, Negative Poisson's ratios from rotating rectangles. J Comput Methods Sci Technol, 10 (2004) 137-145.

[4] A. Spadoni, M. Ruzzene, Numerical and experimental analysis of the static compliance of chiral truss-core airfoils. Mech Mater Struct, 2 (2007) 965-981.

[5] F. Meraghni, F. Desrumaux, M.L. Benzeggagh, Mechanical behavior of cellular core for structural sandwich panels. Composites Part A, 30 (1999) 767-779.

[6] T. Liu, Z.C. Deng, T.J. Lu, Structural modeling of sandwich structures with lightweight cellular cores. Acta Mech Sin, 23 (2007) 545-559.

[7] Ruzzene M., Applications of chiral cellular structures for the design of innovative structural assemblies, ARO Project no. 45518-EG, Final report, Georgia Institute of Technology, 2008.

[8] J.N. Grima, New auxetic materials, Ph. D. thesis, University of Exeter, 2000.

[9] A. Spadoni, Application of chiral cellular materials for the design of innovative components, Ph.D. thesis, Georgia Institute of Technology, 2008.

[10] ANSYS Inc., "User Manual", Swanson Analysis System, 2009.

[11] F. Aviles, L.A. Carlsson, G. Browning, K. Millay, Investigation of the sandwich plate twist test. Exp Mech, 49 (2009) 813-822.

Tensile Deformation Behavior of a Nickel-base Superalloy under Dynamic Loads

Lei Wang[1,*], Yang Liu[1], Xiu Song[1], Junchao Jin[1], Beijiang Zhang[2]

[1] Key Lab for Anisotropy and Texture of Materials, Northeastern University, Shenyang 110819, Liaoning, P. R. China
[2] Department of High-temperature Materials, Central Iron and Steel Research Institute, Beijing 100083, P. R. China
* Corresponding author: wanglei@mail.neu.edu.cn

Abstract The tensile deformation behavior of a nickel-base superalloy under the dynamic loads was investigated the by the optical microscope, scanning electron microscope and transmission electron microscope. The results shown that the yield strength of the alloy increases with the increasing of strain rate, eapacily at the strain rate higher than 10^1 s^{-1}. While with the increasing of strain rate, the fracture elongation decreases at first, then increases rapidly and shows a minimum value at the strain rate of 10^2 s^{-1}. The manner in which the dislocations go through the strengthening phases may be different during the plastic deformation at different strain rates and it is the main reason of the appearance of inflection point in the change of the strength with the strain rate. The obvious increasing of plasticity of the alloy at high strain rate is depended on the deformation twining during the plastic deformation.

Keywords Superalloy, Dynamic load, Deformation behavior, Dislocation

1. Introduction

Superalloy is a kind of important metallic material for engines in the aerospace industry, which is the key point for determination of the thrust and thrust-weight ratio of advanced engines [1-3]. With the rapid developing aerospace industry, the working condition of the superalloy is becoming more and more severe. In traditional aeroengine manufacturing industry, the mechanical properties and deformation behavior of superalloy used for rotating parts under the actual dynamic load is not given full considerations during its designing of structure, composition and microstructure, which is significantly different compared with that under the static load [4-6]. In fact, the Young's modulus, strength, plasticity and ductility will change with the increasing of strain rate [7-10]. Therefore, the study on the deformation behavior of the alloy under the dynamic load is important for the safety of rotating parts used under the service conditions.
The aim of present study is to investigate the strain rate effects on the tensile deformation behavior of a precipitation strengthened nickel-base superalloy used for aero-engine combustor under dynamic loads. And the mechanism for strain-dependence on strength and ductility of the alloy was also discussed.

2. Experimental Procedures

The chemical compositions (wt%) of the alloy are of 0.038 C, 19.970 Cr, 9.990 W, 5.120 Mo, 2.180 Al, 1.290 Ti, 0.020 Mn, 0.080 Si, and balance Ni. The alloy was double vacuum melted, then forged and hot rolled into plates with the thickness of 1 mm After solution treated at 1150 ℃ for 15 min, the alloy was long-term aged at 800 ℃ for 0 h, 100 h, 200 h, 500 h and 1000 h, respectively. The tensile tests of the alloy were performed at room temperature using MTS 810 testing machine and Zwick HTM 5020 high speed tensile testing machine at a strain rates range of 10^{-3} S^{-1} to 10^3 S^{-1}. The resistance strain gage was setupped on the specimens for synchronous collection of the strains and loads during the dynamic deformation with a sampling frequency of 1 MHz. The microstructure evolution, grain size and the tensile fracture surfaces of the tensile specimen were examined using an optical microscope (OLYMPUS GX71), laser scanning confocal microscope (OLYMPUS OLS 3100) and field emission scanning electron microscope (JEOL 7001). The dislocation configuration near the fracture surface was examined by a transmission electron microscope (TECNAI G^2).

3. Results and Discussion

3.1 Strain rate effect on tensile property

Figure 1 shows tensile properties of the alloy aged with different parameters at various strain rates. It shows a similar strain-rate dependence on yield strength: shallow at the strain rates lower than10^1 s^{-1}, and even steeper with increasing of strain rate, especially when the strain rate is higher than 10^2 s^{-1}. It indicates that the plastic deformation mechanism of the alloy begins to change when the strain rate is higher than 10^1 s^{-1}.

The ductility of an alloy aged for different time also shows variation with the increasing of tensile strain rates, as shown in Fig.1b. When the strain rate is increased from 10^{-3} s^{-1} to 10^2 s^{-1}, the fracture elongation decrease obviously, while, then the fracture elongation increased significantly. From the results, it can be concluded that the plastic deformation mechanism of the alloy changed at the strain rate of 10^2 s^{-1}. When the alloy aged with different aging parameters, the increasing of ductility in the alloy aged for 500 h and 1000 h is less than that for 100 h and 200 h.

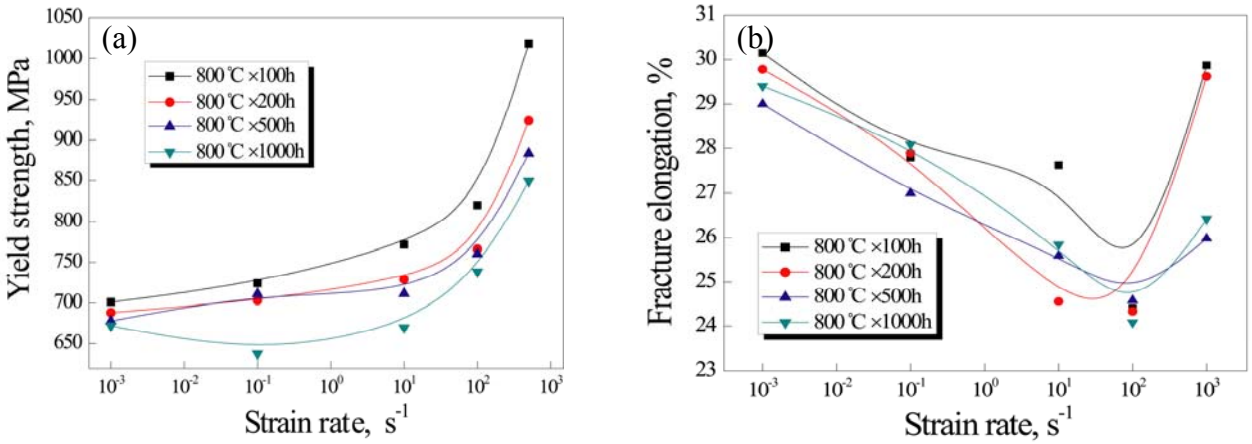

Figure 1. Variation of mechanical properties with the tensile strain rate of the alloy aged by different parameters: (a) yield strength, (b) fracture elongation

3.2 Strain rate effect on tensile fracture morphology

Figure 2 shows the morphologies in fibrous zones of tensile fracture surface of the alloy by aged for 100 h and 100 h with different strain rates. The alloys aged for 100 h and 1000 h exhibit mixed fracture characteristics with ductile and intergranular when the strain rate is lower than 10^{-3} s^{-1}. The small changes can be observed from the fracture morphologies of the alloy with different aging time when the strain rates are increased to 10^3 s^{-1}. It can be found that the percentage of ductile fracture region decreases obviously in the alloy aged for 1000 h as compared with that aged for 100 h at the same strain rate. In addition, the percentage of ductile fracture region in the alloy aged for 1000 h further decreases with the increasing of strain rate and the intergranular fracture characteristics is more apparent.

3.3 Dislocation configurations near fracture surface

Dislocation configurations near the fracture surface in the alloy aged for 200 h at various strain rates are shown in Figure 3. It can be noticed that the dislocation density is not high and it seems no remarkable change with the strain rate of 10^{-3} s^{-1} to 10^1 s^{-1}, while when the strain rate is increased to 10^2 s^{-1}, the dislocation density significantly increases and activation of slip systems can be found with TEM observation. However, when the strain rate is higher than 10^2 s^{-1}, the dislocation density remains stable but dislocation tangles become more severe.

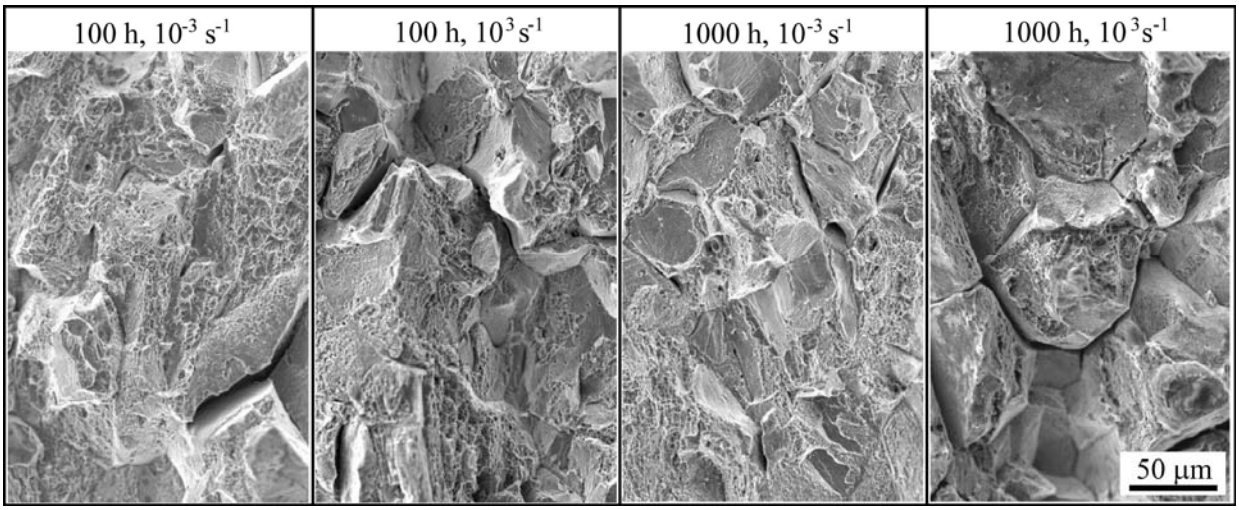

Figure 2. Tensile fracture morphologies in the alloy aged for different time at various strain rates

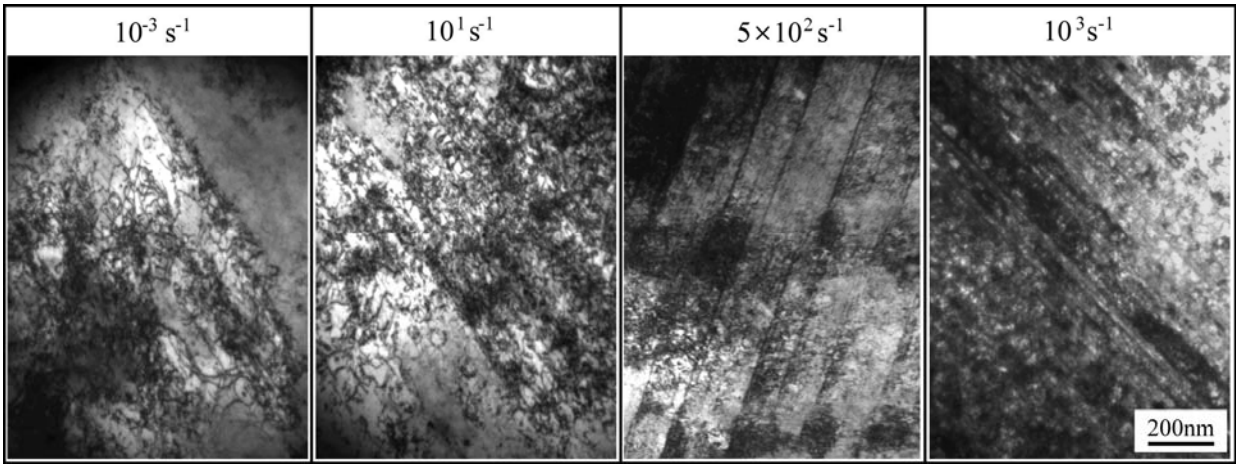

Figure 3. Dislocation configurations near fracture surface in the alloy aged for 200 h at various strain rates

3.4 Mechanism of strain rate effect on dynamic deformation behavior

The stress-strain curves of the alloy aged for 200 h with different strain rates are plotted in Figure 4. It indicates that there is no obvious change of the Young's modulus with the increase of the strain rate. Elastic limit and 0.2% offset yield strength of the alloy increase as the strain rate increase. From Figure 4, it is clear that the stress-strain curves in plastic deformation stage shows strong strain rate-dependence, which is consistent with the results shown in Figure 1. The strength of the alloy exhibits stronger strain rate sensitivity, when the strain rate is upto 10^2 s^{-1}.

It is known that when the force component at a slip system reaches the critical value, the dislocation begins moving. In fact, the dislocation motion is the atom motion in lattice and thus the dislocation motion is time-dependent. As the applied stress increases, the dislocation motion speed increases rapidly. When the specimen undergoes a high loading rate, the acceleration which the dislocation motion needs will be also increased [11]. The dislocation will meet with obstacles continually when it begins moving and this resistance of dislocation motion presents the deformation resistance during plastic deformation from the macroscopic point of view [12]. It is clear that the higher the speed of movable dislocation become, the higher acceleration and resistance of dislocation motion will be.

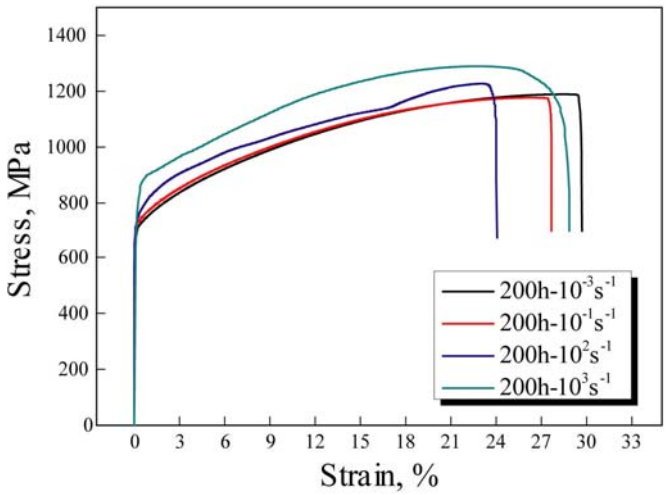

Figure 4. Stress-strain curves of the alloy aged for 200 h at various strain rates

Under the condition of static or quasi-static deformation, the speed of dislocation motion is higher than the deformation speed of materials by the low loading rate. Dislocations have relative enough time for acceleration. At the moment, the acceleration for dislocation moving is very lower, so the time-effect on deformation resistance is not obvious. Therefore, the increasing of yield strength is not high with the increasing of strain rate (lower than10^1 s^{-1}).

When the strain rate is higher than 10^1 s^{-1}, the acceleration of moving dislocation increases, meanwhile, the dislocation moving resistance increases. Consequently, the strength of the alloy increases significantly when the strain rate is higher than 10^2 s^{-1}. It has been found[13] that the dislocation motion is faster at the higher strain rate and the short-range factors inhibiting the dislocation motion such as the Peierls-Nabarro force, thermal vibration of the atoms and electron cloud resistance increases significantly. When the dislocation motion speed exceeds a certain value of about 10^1 $m{\cdot}s^{-1}$, the controlling mechanism of dislocation motion is changed from thermo-activation to short-range damping. And the dislocation motion resistance shows an obvious increase and thus the deformation resistance of the alloy rapidly increases. It indicates that the obvious increasing of the strength as the strain rate higher than 10^2 s^{-1} is related to such factor.

The compatible plastic deformation mechanism of dislocation pile-ups release and crystal rotating exhibits an obvious time-dependence in the alloy when tensile deformation under dynamic loadings [13-15]. And the plastic deformation coordinates by means of activation of dislocation slip systems, as shown in Figure 3. Dislocations are subjected to very high shear stress in a very short time and the shear stress reaches or exceeds the critical resolve shear stress (CRSS) of the dislocation slip systems when the dislocations are not yet ready to move at conventional dislocation slip systems. As a result, the ductility of the alloy shows a marked increase at the same strain rates range as that of the increasing strength.

On the other hard, a large amount of deformation twins have been found near the fracture surface in the alloy, as shown in Figure 5. And the number of deformation twins increases with the increasing of strain rate. Also some dislocation pile-ups around the stacking faults in the crystal can be observed under dynamic loading which is due to the stress concentration. When the dislocation motion is easy, the stress concentration is small. On the contrary, the stress concentration becomes high. It is too late for the dislocations at the dislocation pile-up to move in the alloy during tensile deformation at high strain rate, and thus the stress around the stacking fault increases, which will promote the occurrence of twinning deformation. The existence of a large number of deformation twins in the alloy during tensile deformation at high strain rate makes obvious contribution to increasing of the plastic deformation ability.

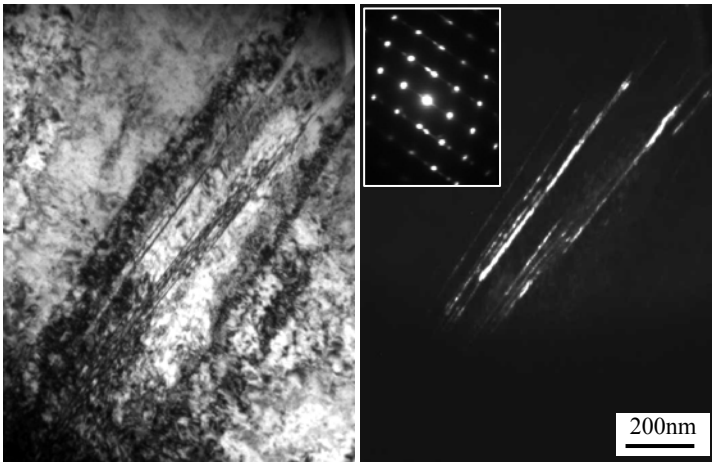

Figure 5. Deformation twins near the fracture surface in the alloy aged for 500 h at strain rate of 5×10^2 s^{-1}

At the same time, the thermal-softening effect often occur caused by heat generation during plastic deformation at higher strain rate [16, 17], which the dislocation moving resistance can be reduced, it also contributes to the increasing of the ductility of the alloy.

4. Conclusions

(1) The yield strength of the alloy exhibits a slight increase when strain rate is lower than 10^1 s^{-1}, while obvious increase when the strain rate is higher than 10^2 s^{-1}.

(2) The fracture elongation of the alloy shows obvious decrease when the strain rate is lower than 10^2 s^{-1}, whereas it shows a rapid increasing when the strain rate is higher than 10^2 s^{-1}.

(3) The deformation resistance of the alloy increases with the increasing of strain rate during deformation at high strain rate due to the increasing of short-range resistance caused by acceleration of dislocation motion. When the strain rate is higher than 10^2 s^{-1}, the significant increasing of the moving dislocation number is the main reason for the increasing of plastic deformation ability. In addition, the twinning deformations as well as thermal-softening caused by the temperature rising at high strain will contribute to the ductility of the alloy too.

Acknowledgements

This research was supported by National Basic Research (973) Program of China (No. 2010CB631203), National High Technology Research and Development (863) Program of China (No. 2012AA03A513) and National Natural Science Foundation of China (No. 51001021, 51171039).

References

[1] S. L. Soo, R. Hood, D. K. Aspinwall, W. E. Voice, C. Sage, Machinability and surface integrity of RR1000 nickel based superalloy. CIRP Ann-Manuf Techn, 60(2011) 89-92.

[2] N. Fang , Q. Wu, A comparative study of the cutting forces in high speed machining of Ti-6Al-4V and Inconel 718 with a round cutting edge tool. J Mater Process Tech, 209(2009) 4385-4389.

[3] R. Sharghi-Moshtagh, S. Asgari, The effect of thermal exposure on the γ′ characteristics in a Ni-base superalloy. J Mater Process Tech, 147(2004) 343-350.

[4] W. S. Lee, C. F. Lin, Plastic deformation and fracture behaviour of Ti-6Al-4V alloy loaded with high strain rate under various temperatures. Mater Sci Eng, A241(1998) 48-59.
[5] X. C. Wei, R. Y. Fu, L. Li, Tensile deformation behavior of cold-rolled TRIP-aided steels over large range of strain rates. Mater Sci Eng, A465(2007) 260-268.
[6] S. Oliver, T. B. Jones, G. Fourlaris, Microstructure and dynamic material performance of high strength and ultra high strength strip steels. Mater Char, 58(2007) 390-396.
[7] R. Smerd, S. Winkler, C. Salisbury, M. Worswick, D. Lloyd, M. Finn, High strain rate tensile testing of automotive aluminum alloy sheet. Int. J. Impact Eng, 32(2005) 541-552.
[8] K. Ishikawa, H. Watanabe, T. Mukai, High strain rate deformation behavior of an AZ91 magnesium alloy at elevated temperatures. Mater Lett, 59(2005) 1511-1515.
[9] A. G. Odeshi, S. Al-ameeri, M. N. Bassim, Effect of high strain rate on plastic deformation of a low alloy steel subjected to ballistic impact. J Mater Process Tech, 162-163(2005) 385-391.
[10] X. Gong, J. L. Fan, B. Y. Huang, J. M. Tian, Microstructure characteristics and a deformation mechanism of fine-grained tungsten heavy alloy under high strain rate compression. Mater Sci Eng, A527(2010) 7565-7570.
[11] M. A. Meyers, Dynamic Behavior of Materials, in: National Defense Industry Press, Beijing, 2006, pp. 225-254.
[12] K. Rajeev, N. N. Sia, Comparison between high and low Strain-Rate deformation of tantalum. Metall Mater Trans, 31A(2000) 815-823.
[13] Y. Liu, L. Wang, S. S. He, F. Feng, X. D. Lu, B. J. Zhang, Effect of long-term aging on dynamic tensile deformation behavior of GH4169 alloy. Acta Metall Sin, 48(2012) 49-55.
[14] J. T. Liu, Z. G. Wang, J. K. Shang, Deformation behaviors of [110] and [112] oriented β-Sn single crystal. Acta Metall Sin, 44(2008) 1409-1414.
[15] Z. L. Liu, X. C. You, Z. Zhuang, A mesoscale investigation of strain rate effect on dynamic deformation of single-crystal copper. Int J Solids Struct, 45(2008) 3674-3687.
[16] K. Rajeev, N. N. Sia, Determination of temperature rise during high strain rate deformation. Mech Mater, 27(1998) 1-12.
[17] A. Rusinek, J. R. Klepaczko, Experiments on heat generated during plastic deformation and stored energy for TRIP steels. Mater Des, 30(2009) 35-48.

Electrical Breakdown of a Metallic Nanowire Mesh

Yuan Li[1,*], Kaoru Tsuchiya[1], Hironori Tohmyoh[1], Masumi Saka[1]

[1] Department of Nanomechanics, Tohoku University, Sendai 980-8579, Japan
* Corresponding author: liyuan@ism.mech.tohoku.ac.jp

Abstract The electrical breakdown of a metallic nanowire mesh induced by Joule heating (i.e., melting) is investigated by solving the corresponding electro-thermal problem, where the effect of electromigration is neglected. A numerical computational program is firstly developed to simulate the temperature profile for a metallic wire mesh and investigate the melting current triggering the melting of mesh segment. The melting process of the mesh structure is investigated by analyzing the variation of melting current with regard to the melting propagation of mesh segment. On this basis, the melting behavior of a system of the mesh equipped with current source is predicted. For both current-controlled and voltage-controlled current source, local instability (i.e., at a constant current/voltage, several mesh segments melt simultaneously) and stable melting (i.e., the increase of current/voltage is necessary for the melting of mesh segment) will happen. Moreover, global instability (i.e., at a constant current, several mesh segments melt until the circuit of mesh opens) will occur only at the mode of current-controlled current source.

Keywords Electrical breakdown, Instability, Joule heating, Metallic nanowire mesh, Stable melting,

1. Introduction

With one-dimensional structure and nanometer-scale diameter, metallic nanowires have shown remarkable electrical, mechanical, optical and chemical properties [1]. Successful assembly of these metallic nanowires into a mesh structure has offered great potential as components for large-scale integrated devices in nanoelectronics and photonics. Recent reports have shown that such mesh can play new roles which are far from the potential of individual nanowires, including transparent conductors, low-cost flexible electronics [2, 3]. It is well known that if an electrically conductive material is subjected to current flow, Joule heating occurs [4]. Joule heating in these metallic nanowires may go beyond degrading the electrical performance of the corresponding metallic nanowire mesh, and therefore deteriorate the reliability of the mesh-based devices. In order to turn around this problem, clarifying the electrical breakdown of a metallic nanowire mesh induced by Joule heating becomes urgent. Up to date, the electrical breakdown of an individual metallic nanowire has been investigated systematically including melting due to Joule heating [5, 6] and due to electromigration [7-10]. The former has been used to cut metallic nanowire in any desirable length [5, 6] for specific purpose, and the latter has been employed to make the nanogap [7, 8] between metal electrodes into which individual molecules can be inserted to measure their electrical properties. However, little is currently known regarding the electrical breakdown of a metallic nanowire mesh, which is expected to show different characteristics because of its unique mesh structure.

In this work, the electrical breakdown of a metallic nanowire mesh induced by Joule heating (i.e., melting) is investigated for the first time. To deal with this type of electro-thermal problem, a numerical simulation method is proposed to determine the associated temperature field for a metallic wire mesh and the variation of the melting current triggering the melting of mesh segment with the melting propagation of mesh segment. By employing the developed computational program, the melting process of a silver (Ag) nanowire mesh structure is clarified by analyzing the variation of melting current during the melting propagation in the mesh. It then indicates the interesting characteristics of the melting behavior for a system of the mesh equipped with current source.

2. Simulation Method for Electrical Breakdown of a Metallic Nanowire Mesh

2.1 Simulation Model and Basic Assumptions

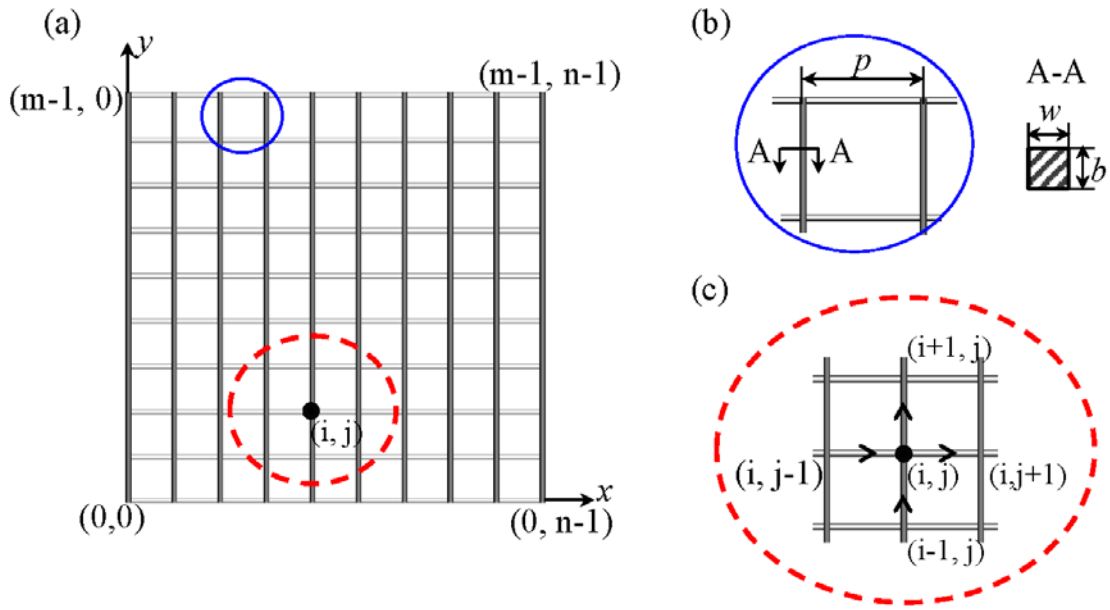

Fig. 1 Schematic illustration of a metallic nanowire mesh (m×n)

A metallic nanowire mesh with size of m×n is schematically illustrated in Fig. 1, which is a uniform rectangular grid of wires with m rows (horizontal wires) and n columns (vertical wires). As shown in Fig.1b, the pitch size is *p*, the wire width and thickness are *w* and *b*, respectively. Due to the complex nature of electro-thermal for a metallic wire mesh, the following assumptions are made: (1) The material of metallic mesh is homogeneous and isotropic; (2) Material properties of metallic mesh are temperature independent; (3) The effect of electromigration is neglected for simplicity.

2.2 Fundamentals of Governing Equations

A mesh node is an intersection of each row and column. Let node (i, j) be the intersection of the $(i+1)^{th}$ row and the $(j+1)^{th}$ column, where i=0, …, m-1; j=0, …, n-1. The wire between two adjacent mesh nodes is called a mesh segment. For the present mesh with size of m×n, the numbers of mesh nodes and mesh segments are m×n and m(n-1)+n(m-1), respectively. The segment between node (i, j-1) and node (i, j) is denoted as $s^{l}_{i,j}$, and the segment between (i, j) and (i, j+1) is denoted as $s^{r}_{i,j}$. Similarly, the segment between node (i-1, j) and (i, j) is denoted as $s^{d}_{i,j}$, and the segment between (i, j) and (i+1, j) is denoted as $s^{u}_{i,j}$. Here, the letters of l, r, d and u stand for the relative positions of the adjacent nodes (i.e., (i, j-1), (i, j+1), (i-1, j), (i+1, j)) to node (i, j), i.e., left, right, down, up, respectively.

For any mesh segment, the current can be calculated using Ohm's law. By considering the node (i, j), the current flowing between four adjacent nodes and it can be obtained as below

$$I_{s^{l}_{i,j}} = j_{s^{l}_{i,j}} A = -\frac{1}{\rho}\frac{U_{(i,j)}-U_{(i,j-1)}}{x_{(i,j)}-x_{(i,j-1)}}A$$

$$I_{s^{r}_{i,j}} = j_{s^{r}_{i,j}} A = -\frac{1}{\rho}\frac{U_{(i,j+1)}-U_{(i,j)}}{x_{(i,j+1)}-x_{(i,j)}}A$$

$$I_{s^{d}_{i,j}} = j_{s^{d}_{i,j}} A = -\frac{1}{\rho}\frac{U_{(i,j)}-U_{(i-1,j)}}{y_{(i,j)}-y_{(i-1,j)}}A$$

$$I_{S^{u}_{i,j}} = j_{S^{u}_{i,j}} A = -\frac{1}{\rho}\frac{U_{(i+1,j)}-U_{(i,j)}}{y_{(i+1,j)}-y_{(i,j)}} A \quad (1)$$

where ρ is the electrical resistivity of material, and A (=wb) is the cross-sectional area of wire. Here, as an example, $I_{S^{l}_{i,j}}, j_{S^{l}_{i,j}}$ are current and current density for mesh segment $s^{l}_{i,j}$; $U_{(i,j)}$ and $x_{(i,j)}, y_{(i,j)}$ are electrical potential and coordinates of node (i, j). It should be noted that as shown in Fig. 1, the origin of the coordinate system is set at the bottom left corner of the mesh, i.e., node (0, 0). The *x*-axis points right and the *y*-axis points up, both of which are taken to be along the wire. Moreover, at any mesh node of (i, j), according to Kirchhoff's current law, we have

$$I_{\text{internal}} + I_{\text{external}} = 0 \quad (2)$$

Here, $I_{\text{internal}}(= I_{S^{l}_{i,j}} - I_{S^{r}_{i,j}} + I_{S^{d}_{i,j}} - I_{S^{u}_{i,j}})$ means the sum of the current flowing into the node (i, j) from different adjacent nodes, and I_{external} represents the external input/output current where the external output current takes the minus value. By considering Eqs. (1) and (2) for all the nodes, the current density at any mesh segment (i.e., $j_{S^{l}_{i,j}}, j_{S^{r}_{i,j}}, j_{S^{d}_{i,j}}, j_{S^{u}_{i,j}}$), and the electrical potential at any mesh node can be obtained.

On the other hand, for any mesh segment, the heat energy, flowing in any mesh segment between two adjacent nodes, can be calculated using Fourier's law of heat conduction as

$$\begin{aligned} Q_{S^{l}_{i,j}} &= q_{S^{l}_{i,j}} A = -\lambda \frac{T_{(i,j)}-T_{(i,j-1)}}{x_{(i,j)}-x_{(i,j-1)}} A \\ Q_{S^{r}_{i,j}} &= q_{S^{r}_{i,j}} A = -\lambda \frac{T_{(i,j+1)}-T_{(i,j)}}{x_{(i,j+1)}-x_{(i,j)}} A \\ Q_{S^{d}_{I,j}} &= q_{S^{d}_{I,j}} A = -\lambda \frac{T_{(i,j)}-T_{(i-1,j)}}{y_{(i,j)}-y_{(i-1,j)}} A \\ Q_{S^{u}_{i,j}} &= q_{S^{u}_{i,j}} A = -\lambda \frac{T_{(i+1,j)}-T_{(i,j)}}{y_{(i+1,j)}-y_{(i,j)}} A \end{aligned} \quad (3)$$

where λ is the thermal conductivity of material. Here, as an instance, $Q_{S^{l}_{i,j}}, q_{S^{l}_{i,j}}$ are heat energy and heat flux for mesh segment $s^{l}_{i,j}$; $T_{(i,j)}$ is the temperature at node (i, j). Moreover, at any mesh node, according to the law of conservation of heat energy, we have

$$Q_{\text{internal}} + Q_{\text{external}} = 0 \quad (4)$$

Here, $Q_{\text{internal}}(= Q_{S^{l}_{i,j}} - Q_{S^{r}_{i,j}} + Q_{S^{d}_{i,j}} - Q_{S^{u}_{i,j}})$ means the sum of the heat energy flowing into the node (i, j) from different adjacent nodes, and Q_{external} represents the external input/output heat energy where the external output heat energy takes the minus value.

It should be noted that when a metallic nanowire is subjected to a steady direct current flow, Joule heating occurs, which, in turn causes increase in temperature of the wire. For simplicity, it is assumed that there is no heat transfer from the surface of the wire to the ambient, and the time-dependence of temperature can be neglected. Then, the heat conduction in the above four mesh segments can be governed by the following one-dimensional Poisson's equations [11]:

$$\begin{aligned} \lambda \frac{d^2 T_{S^{l}_{i,j}}}{dx^2} + \rho j^2_{S^{l}_{i,j}} &= 0 \\ \lambda \frac{d^2 T_{S^{r}_{i,j}}}{dx^2} + \rho j^2_{S^{r}_{i,j}} &= 0 \\ \lambda \frac{d^2 T_{S^{d}_{i,j}}}{dy^2} + \rho j^2_{S^{d}_{i,j}} &= 0 \\ \lambda \frac{d^2 T_{S^{u}_{i,j}}}{dy^2} + \rho j^2_{S^{u}_{i,j}} &= 0 \end{aligned} \quad (5)$$

where $T_{S^{l}_{i,j}}$ as an example is the temperature of mesh segment $s^{l}_{i,j}$.

Using the above Eqs. (3) to (5) for all the nodes, the temperature at any mesh node (i.e., $T_{(i,j-1)}$, $T_{(i,j+1)}$, $T_{(i-1,j)}$, $T_{(i+1,j)}$, $T_{(i,j)}$) can be obtained. For a specific mesh segment, if two ends of it (i.e., two adjacent mesh nodes) have the same temperature, the temperature at its center T^C is also the highest temperature T^{max} in the mesh segment (i.e., $T^C = T^{max}$), which can be calculated [11] as

$$
\begin{aligned}
T^{C}_{S^{l}_{i,j}} &= \frac{\rho}{2\lambda} j^{2}_{S^{l}_{i,j}} \left(\frac{x_{(i,j)}-x_{(i,j-1)}}{2}\right)^{2} + \frac{T_{(i,j)}+T_{(i,j-1)}}{2} \\
T^{C}_{S^{r}_{i,j}} &= \frac{\rho}{2\lambda} j^{2}_{S^{r}_{i,j}} \left(\frac{x_{(i,j)}-x_{(i,j+1)}}{2}\right)^{2} + \frac{T_{(i,j)}+T_{(i,j+1)}}{2} \\
T^{C}_{S^{d}_{i,j}} &= \frac{\rho}{2\lambda} j^{2}_{S^{d}_{i,j}} \left(\frac{y_{(i,j)}-y_{(i-1,j)}}{2}\right)^{2} + \frac{T_{(i,j)}+T_{(i-1,j)}}{2} \\
T^{C}_{S^{u}_{i,j}} &= \frac{\rho}{2\lambda} j^{2}_{S^{u}_{i,j}} \left(\frac{y_{(i,j)}-y_{(i+1,j)}}{2}\right)^{2} + \frac{T_{(i,j)}+T_{(i+1,j)}}{2}
\end{aligned}
\tag{6}
$$

In the present case, most mesh segments have different temperatures at its ends. In view of the very small length of mesh segment of 200μm as shown later in Fig. 3, the temperature at the center of mesh segment is approximately considered as the maximum temperature in mesh segment T^{max} (i.e., $T^C \approx T^{max}$). Once the maximum temperature in a mesh segment T^{max} reaches to the melting point of the material T_m, it is thought that electrical breakdown induced by Joule heating happens at this mesh segment, i.e., this mesh segment melts.

2.3 Computational Procedure

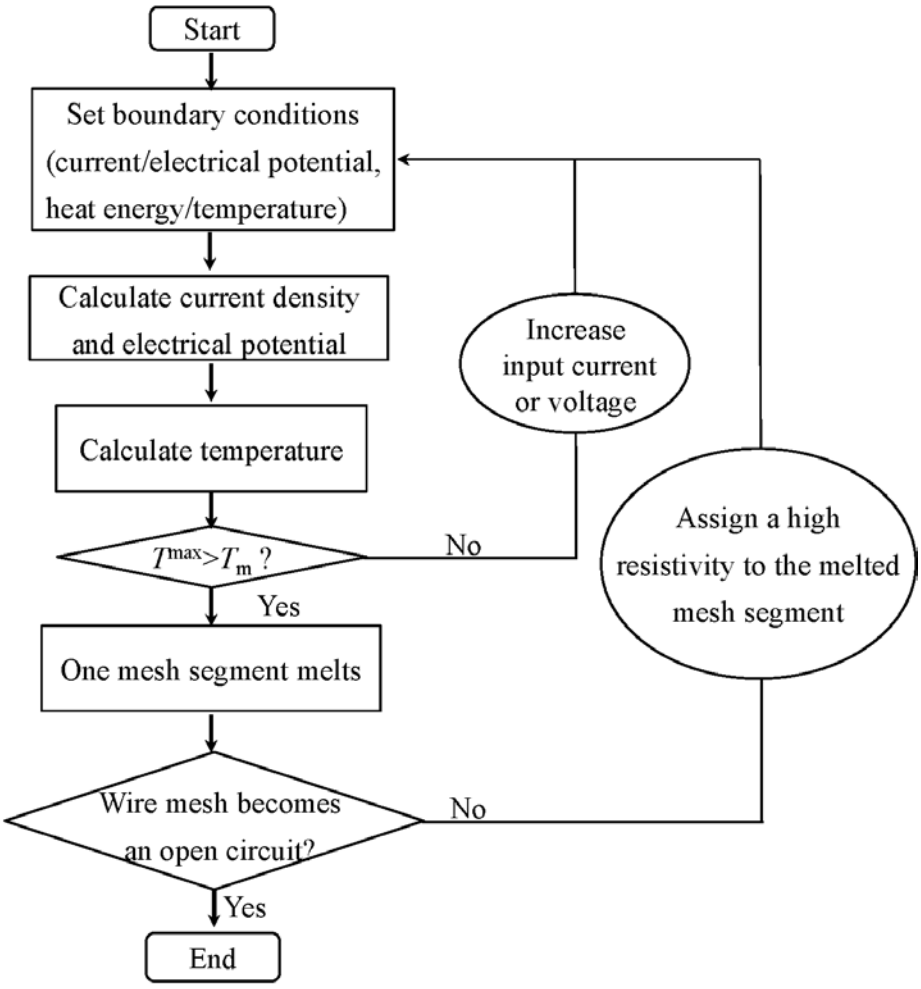

Fig. 2 Flow chart of numerical simulation

A corresponding computational program is developed to solve this electro-thermal problem regarding the electrical breakdown of the metallic nanowire mesh induced by Joule heating. Note that to record precisely the melting current triggering the melting of mesh segment, the increment of current should be tuned to make mesh segment melt one by one. The corresponding simplified flow chart of this program is shown in Fig. 2.

3. Electrical Breakdown of an Ag Nanowire Mesh

3.1 Numerical Model

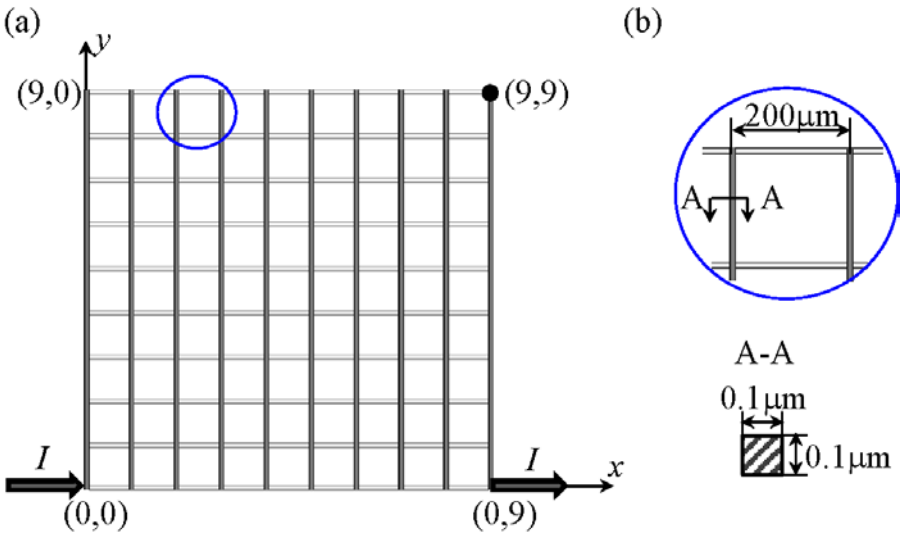

Fig. 3 Schematic illustration of an Ag nanowire mesh (10×10)

Table 1 Physical properties of Ag nanowire

Melting point T_m (K)	873 [12]
Thermal conductivity λ (W/μm·K)	3.346×10^{-4} [13]
Electrical resistivity ρ (Ω·μm)	0.119 [14]

A silver (Ag) nanowire mesh (10×10) as shown in Fig. 3a is considered here. The numbers of mesh nodes and mesh segments are 100 and 180, respectively. The pitch size is p=200μm, both the width and thickness of Ag nanowire are w=b=100nm as shown in Fig.3b. The physical properties of Ag nanowire are listed in Table 1. Note that size effect on the physical properties is taken into consideration for Ag nanowire.

As shown in Fig. 3a, the external current I flows into the mesh from node (0, 0) and flows out of the mesh from node (0, 9), which means that node (0, 0) has an external input current and node (0, 9) has an external output current. For the other nodes, no any external current is given. A constant value is assigned to the electrical potential of node (9, 9). The temperature of boundary nodes (i.e., (i, 0), (0, j), (i, 9), (9, j) where i, j=0,…,9) is room temperature of T_0=300K. There is no any external heat energy for all the other nodes. The developed program is employed to investigate the evolution of the melting current I_m triggering the melting of the mesh segment. Here, in order to make mesh segment melt one by one as much as possible, the increment of the input current is set with a small value of 0.001mA until the melting current is reached. The corresponding melting voltage V_m (i.e., the difference of electrical potential between node (0, 0) and node (0,9)) is also recorded in order to calculate the variation of resistance of the mesh, i.e., R, with regard to the sequential electrical breakdown of mesh segments.

3.2 Results and Discussion

With regard to the melting propagation of mesh segment, the variation of melting current I_m and mesh resistance are shown in Fig. 4a and Fig. 4b. Note that the mesh resistance is the resistance between two mesh nodes where the external current is input and output (i.e., node (0, 0) and node (0, 9)), respectively. Two local parts (c) and (d) in Fig. 4a are enlarged in Fig. 4c and Fig.4d, respectively. In Fig. 4a and Fig. 4c, it is found that when the input current increases up to 0.225mA, the maximum temperature in one mesh segment reaches the melting point of Ag nanowire making the start point of the melting of mesh. For the following melting of the second mesh segment, the melting current decreases to the value of 0.217mA. With the melting propagation of mesh segment, the variation of melting current and voltage shows the repetition of three different trends as marked with arrows in Fig. 4c and Fig. 4d: (I) decrease of both melting current and voltage; (II) increase of both melting current and voltage; (III) decrease of melting current but increase of melting voltage. Finally, the melting of last mesh segment makes the open circuit of the mesh as shown in Fig. 4a. Here, the number of broken mesh segments n_b corresponding to the open circuit of mesh is only 89, which is about one half of the number of the overall mesh segments (i.e., 180) in the intact Ag nanowire mesh. Generally, the nanowire mesh during the whole melting process in this case keeps symmetric, in which the exception is attributed to the minor error during the numerical simulation. On the other hand, the mesh resistance in Fig. 4b increases with the melting propagation of mesh segment, which is independent of the trend of melting current.

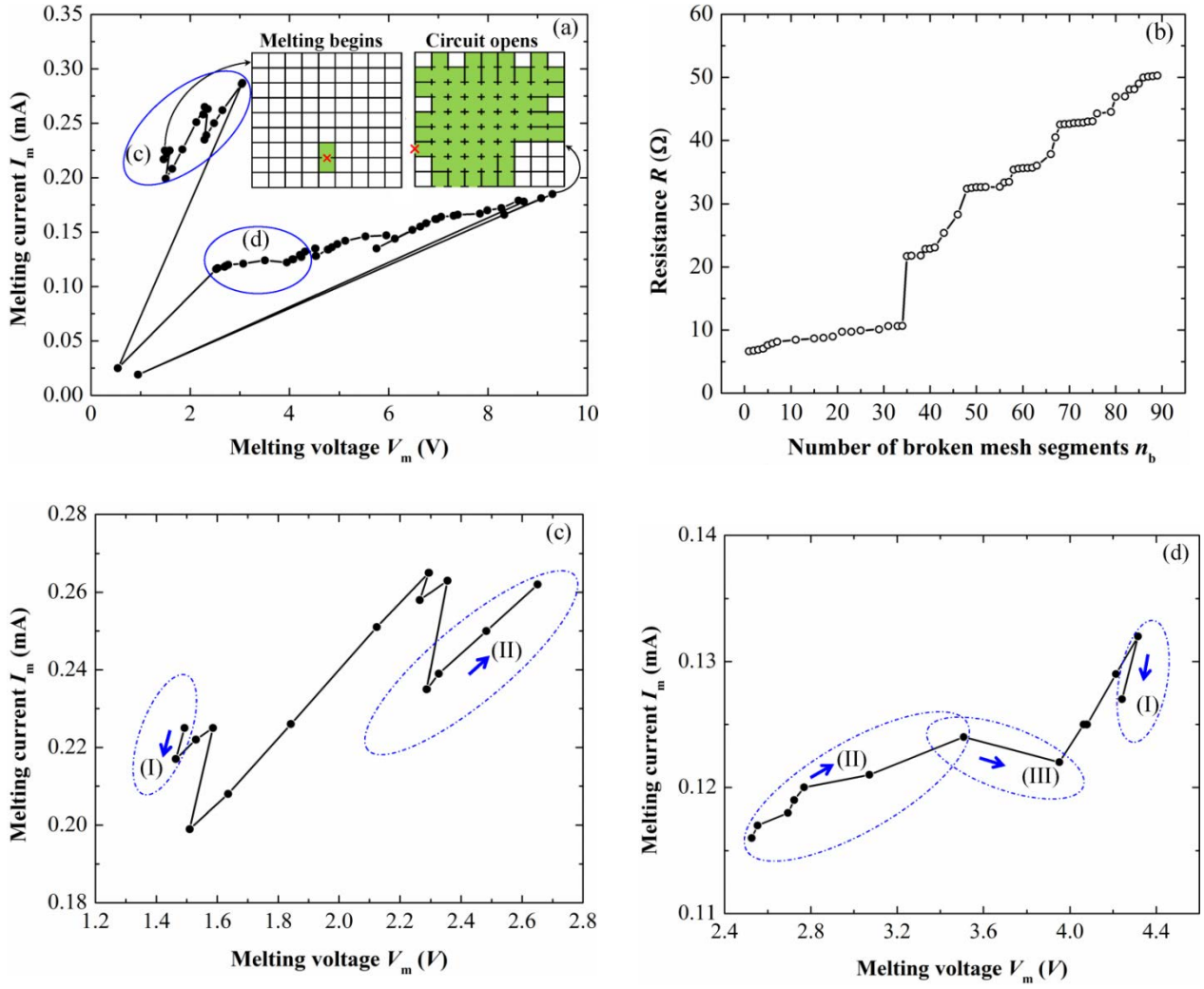

Fig. 4 Numerical melting of an Ag nanowire mesh structure

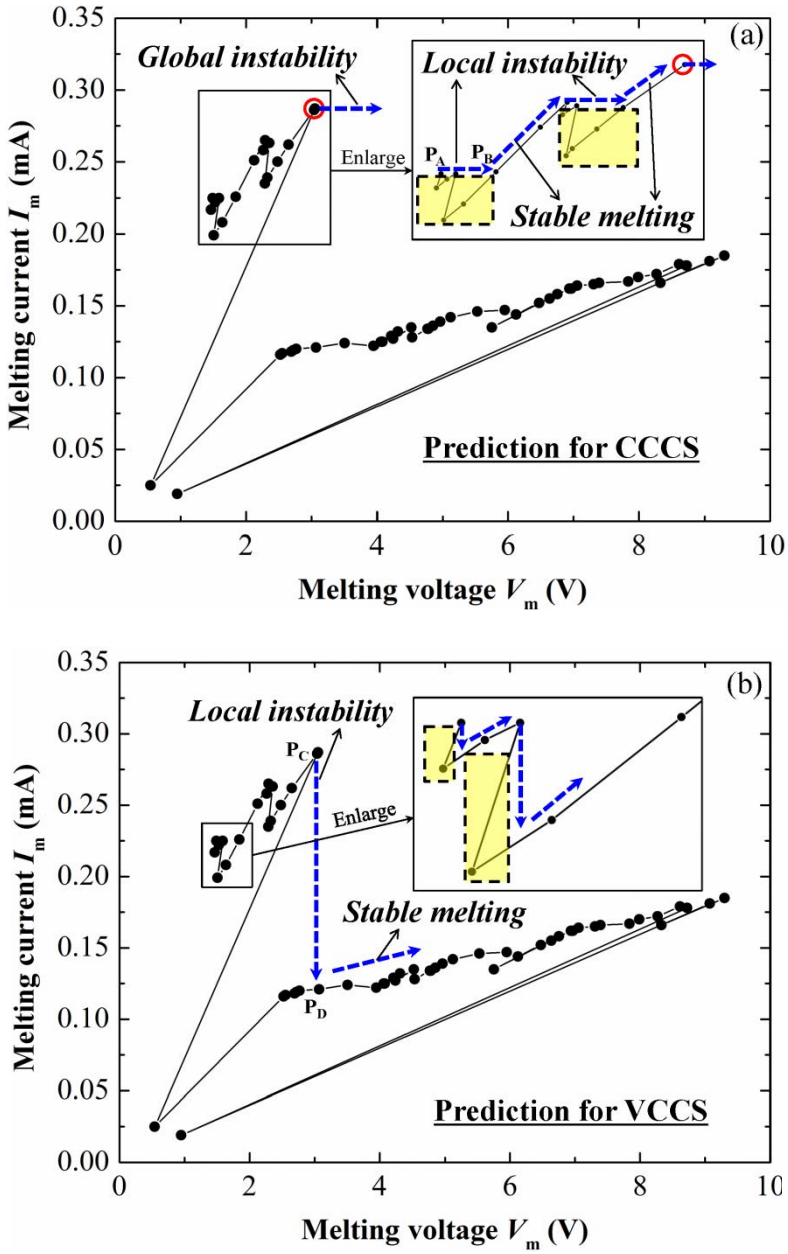

Fig. 5 Predicted experimental melting process of a system of an Ag nanowire mesh equipped with current source
(CCCS: current-controlled current source; VCCS: voltage-controlled current source)

To explain this unique melting behavior of a mesh structure, the melting of an individual nanowire is discussed here to make comparison. The maximum temperature induced by Joule heating in the nanowire increases with increasing current. When the maximum temperature reaches to the melting point of the material, the nanowire will melt, and the melting process of an individual wire is finished. For the mesh structure, on the other hand, the maximum temperature in the mesh, occurring in some place of a mesh segment, initially increases with the increasing current, which is similar with that of the individual nanowire. When the maximum temperature reaches to the melting point of the material, the corresponding mesh segment melts. However, this is just the start point of melting in the mesh structure, and the mesh structure intrinsically takes a consecutive melting

process of large amounts of individual nanowires.

Basically, due to the limit of the properties of current sources, it is difficult to observe the trend of (I) in Fig. 4 (c) and (d) in which both melting current and voltage decrease. Consider a system composed of an Ag nanowire mesh and current source, the corresponding melting behavior can be predicted. As a representative illustration, Fig. 5 is given. For the mode of current-controlled current source (CCCS) in Fig. 5a, such regions with the decrease of current and the subsequent recovery (e.g., the area surrounded by dash rectangular) is difficult to be reproduced in experiment. The dashed arrows indicate the predicted variation of melting current and voltage during experimental melting process of the system. The rightwards dashed arrow means that at a constant current, several mesh segments melt simultaneously leading to the increase of resistance and therefore the increase of the voltage. This phenomenon is defined as ***local instability***, which is a jump (e.g., from point P_A to point P_B in Fig. 5a) when compared to the melting current-voltage curve during numerical melting. The north east dashed arrow indicates that the increase of current is necessary for the further propagation of melting. This behavior is called ***stable melting***. Moreover, the existence of the maximum melting current, marked by a circle in Fig. 5a, tells that if the input current is high enough, the mesh segments will melt simultaneously until the circuit of mesh is open. This phenomenon is denoted as ***global instability***. On the other hand, for the mode of voltage-controlled current source (VCCS) in Fig. 5b, such regions with the decrease of voltage and the subsequent recovery (e.g., the area surrounded by dashed rectangular in the enlarged part) are difficult to realize experimentally. The dashed arrows indicate the predicted variation of melting current and voltage during experimental melting process of the system in a similar strategy with that for the mode of CCCS. There is the repetition of the vertical descent stage and the ascent stage until the circuit of mesh is open. The downwards dashed arrows indicate the vertical descent stages, where the melting of several mesh segments will happen simultaneously at a constant voltage, which shows local instability (e.g., the jump from point P_C to point P_D in Fig. 5b). The north east dashed arrows show the ascent stages, where the increase of voltage is requisite for the melting propagation, which shows stable melting. The only difference from that of CCCS mode is that there is no global instability for VCCS.

4. Conclusions

In the present work, the electrical breakdown of a metallic nanowire mesh induced by Joule heating is investigated by solving the corresponding electro-thermal problem, where the effect of electromigration is neglected for simplicity. A numerical computational program is developed to determine the temperature profile in the mesh, and the melting current triggering the melting of mesh segment. The structural melting of a metallic wire mesh is investigated by clarifying the variation of melting current with regard to the melting propagation of mesh segments. The melting behavior of a system of the mesh equipped with current source in real experiments can then be predicted, in which two modes of current source are discussed in detail. Local instability and stable melting will occur in spite of the mode of current source. Moreover, global instability only happens at the mode of current-controlled current source. This finding deepens the understanding of the electrical breakdown behavior of a metallic nanowire mesh, and may therefore contribute to the development of nanowire-based devices with high reliability.

Acknowledgements

The authors are grateful to be partly supported by Tohoku Leading Women's Jump Up Project for 2013 (J120000428) from the Ministry of Education, Culture, Sports, Science and Technology (MEXT) of Japan.

References

[1] M.S. Dresselhaus, Y.M. Lin, O. Rabin, M.R. Black, G. Dresselhaus, Nanowires, in: B. Bhushan (Eds.), Springer Handbook of Nanotechnology (3rd edition), Springer-Verlag, Heidelberg, 2010, pp.119-168.

[2] M. Kang, H. Park, S. Ahn, L. Guo, Transparent Cu nanowire mesh electrode on flexible substrates fabricated by transfer printing and its application in organic solar cells. Solar Energy Materials & Solar Cells, 94 (2010) 1179-1184.

[3] J. Groep, P. Spinelli, A. Polman, Transparent conducting silver nanowire networks. Nano Lett, 12 (2012) 3138-3144.

[4] H. S. Carslaw, J. C. Jaeger, Conduction of heat in solids, Clarendon, Oxford, 1959, pp. 149-151.

[5] H. Tohmyoh, T. Imaizumi, H. Hayashi, M. Saka, Welding of Pt nanowires by Joule heating. Scripta Mater, 57(2007) 953-956.

[6] H. Tohmyoh, S. Fukui, Manipulation and Joule heat welding of Ag nanowires prepared by atomic migration. J Nanopart Res, 14 (2012) 1116.

[7] H. Park, A. Lilley, A. Alivisatos, J. Park, P. McEuen, Fabrication of metallic electrodes with nanometer separation by electromigration. Appl Phys Lett, 75 (1999) 301-303.

[8] T. Taychatanapat, K. Bolotin, F. Kuemmeth, D. Ralph, Imaging electromigration during the formation of break junctions. Nano Lett, 7 (2007) 652-656.

[9] Q. Huang, C. L., R. Divan, M. Bode, Electrical failure analysis of Au nanowires. IEEE Transaction on Nanotechnology, 7 (2008) 688-692.

[10] J. Zhao, H. Sun, S. Dai, Y. Wang, J. Zhu, Electrical breakdown of nanowires. Nano Lett, 11(2011) 4647-4651.

[11] M. Saka, Y. X. Sun, S. R. Ahmed, Heat conduction in a symmetric body subjected to a current flow of symmetric input and output. Inter J Therm Sci, 48 (2009) 114-121.

[12] A. Mayoral, L. F. Allard, D. Ferrer, R. Esparza, M. Yacaman, On the behavior of Ag nanowires under high temperature: in situ characterization by aberration-corrected STEM. J Mater Chem, 21(2011) 893-898.

[13] J. Xu, A. Munari, E. Dalton, A. Mathewson, K. M. Razeeb, Silver nanowire array-polymer composite as thermal interface material. J Appl Phys, 106 (2009) 124310.

[14] X. Liu, J. Zhu, C. Jin, L. Peng, D. Tang, H. Cheng, In situ electrical measurements of polytypic silver nanowires. Nanotechnology, 19 (2008) 085711.

Growth of Grass Like Architectures on Si Substrate and Its Mechanism Study

Lijiao Hu, Yang Ju*, Hosoi Atsushi

Department of Mechanical Science and Engineering, Nagoya University, Nagoya 464-8603, Japan
* Corresponding author: ju@mech.nagoya-u.ac.jp

Abstract Grass like architectures were synthesized directly on Silicon substrate by thermal oxidation method with nickel catalyst at low temperature. Humidity and catalyst played an important role in the fabrication of the grass like architectures. The morphology of the grass-like architectures was controlled by heating temperature. The grass like architectures were observed by scanning electron microscope (SEM, JSM-7000FK), Energy-dispersive X-ray (EDX) and X-ray diffraction (XRD). The grass like architectures were approximately 8-70μm in size with 1-2.5μm width leaves. The growth of grass like architectures affected by oxidation, vertical stress induced, and horizontal compressive stress was studied in details.

Keywords Grass like architectures, Thermal oxidation, Nickel catalyst, Compressive stress

1. Introduction

Cuprous oxide (Cu_2O) is a p-type semiconductor metal oxide with a direct band gap of about 2.17 eV. Due to its unique optical, electrical, and magnetic properties[1–3], and other properties such as simplicity and low cost of preparation, nontoxic nature, and abundance, it has attracted great attention and been widely applied in solar energy conversion[4], photocatalysis[5], sensors[6], negative electrode materials for lithium-ion batteries[7], electrochromism[8], and antibacterials[9]. The fundamental properties of micro/nanostructure semiconductors are found to be dependent on their architectures, including geometry, morphology, and hierarchical structures[10]. Therefore, great efforts have been devoted to artificially control the morphology of Cu_2O micro/nanocrystals in the past several years[11]. Different Cu_2O nano architectures have been synthesized, such as nanowhiskers[12], nanowires[13], nanocubes[14], nanorods[15], nanospheres[16], nanoflowers[17], nanocages[18]. A variety of methods have been reported to synthesize nanoflowers of different materials. These methods include hydrothermal synthesis[19], sol–gel method[20], chemical vapor deposition[21], ultrasonic pyrolysis[22], electrodeposition method[23], and solution routes[24].

Herein, we have developed novel syntheses of grass like Cu_2O architectures on silicon substrate with nickel-based catalyst at a low temperature. Although many studies proposed the evolution of different structures, the ability to manifest the precise growth mechanism of Cu_2O micro/nanostructures is still quite limited. In this work, the growth mechanism of Cu_2O grass-like architecture on silicon substrate was studied through the phenomenon of several contrast experiments.

2. Experiment

Commercial silicon wafer with a thickness of 0.50 mm was cut into square samples which were 20mm×20mm in size. The substrates were then ultrasonically (BRANSONIC1510) cleaned with acetone, washed with ethanol and de-ionized water sequentially to dissolve the contaminations. Nickel based catalyst used in this experiment was the high temperature electrically conductive coating material (Pyro-DuctTM 598-C, AREMCO, INC.). Catalyst was manually daubed on the silicon substrate as the shape of islands with diameter around 2-3 mm. Cu powder was dispersed around Ni on the substrate. Grass like architectures were then synthesized by heating the sample in wet air atmosphere at 200°C temperature for 3h.

After the heating process, morphologies of the oxidized specimens were characterized by the scanning electron microscopy (SEM, JSM-7000FK), Energy-dispersive X-ray (EDX) and X-ray diffraction (XRD).

3. Results and discussion

3.1. Experiment results

As shown in Fig. 1 grass like architectures, which were 8-70 μm in size with 1-2.5 μm width leaves grew mainly at the edge of the catalyst island. The contrast experiments showed that without the nickel based catalyst there would be no grass like architectures growing on the Si substrate even after the same heating process. Meanwhile, there was no grass like architectures growing on Si substrates which were heated at thermostatic drier and vacuum tank. Therefore, the catalyst, humidity and oxygen atmosphere were considered to be three of the important factors to affect the growth of grass like architectures.

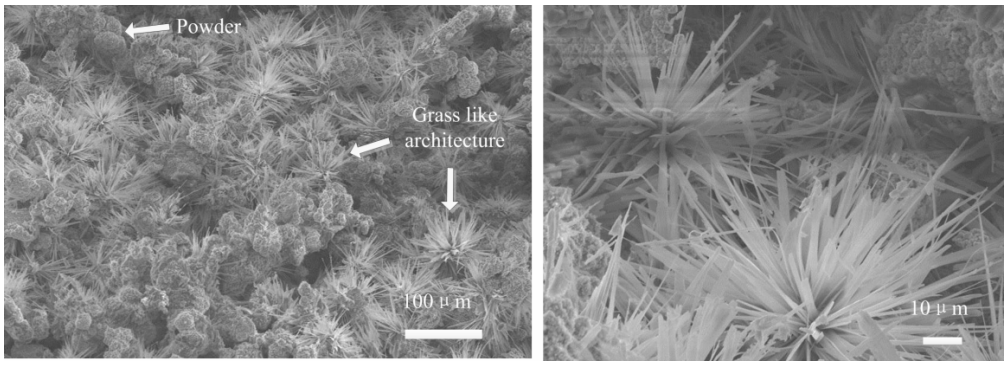

Figure 1. SEM image of grass like architectures

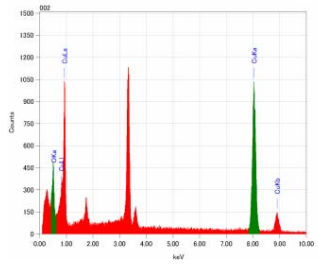

Element	Weight%	Atomic%
O K	12.17	35.50
Cu K	87.83	64.50
Totals	100	

Figure 2. EDX spectra of grass like architectures on Si substrate

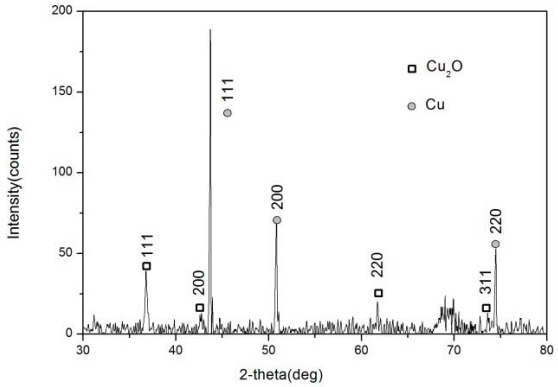

Figure 3. XRD spectra of grass like architectures on Si substrate

Energy-dispersive X-ray (EDX) analysis (Fig.2) indicates that the architectures are composed of Cu elements (35.50%) and oxygen elements (64.50%). The architecture was composed of Cu_2O

grass-like architectures, as confirmed by the X-ray diffraction (XRD) spectrum (Fig.3). The sharp diffraction peaks also indicate the sample is highly crystalline.

3.2. Discussion

The oxide formation appears to proceed via the diffusion of both copper and oxygen. Subsequently, oxidation takes place at the interface between the oxygen in the air and the Cu ions of the copper powders. Cu ions migrate from the inner of powder to the interface, according to stress induce mechanism. Meanwhile, the oxygen diffuses from outside to inside of interface in the opposite direction, according to Flick's first law[25]. As in figure 4, it was suspected that core(Cu)-shell(Cu_2O) composite structure developed in the Cu powder. It was in accord with the aforementioned EDX and XRD results, which were that the composition of grass like architectures was the Cu_2O and the powder was composed of Cu and Cu_2O.

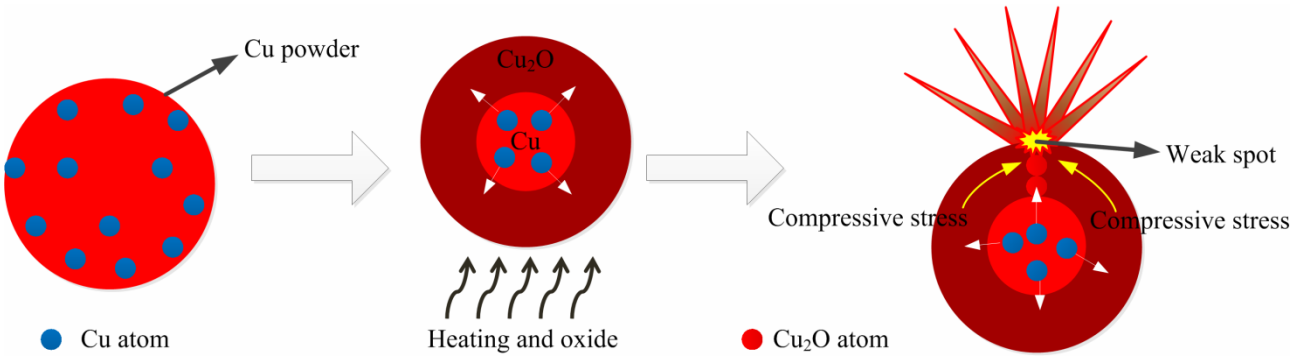

Figure 4. Schematic of atoms migration and its simplified mechanical model

Nickel based high temperature electrical conductive material played an important role in this process. It had the similar character as colloid nickel which has shown to be potential catalysts for selective hydrogenation, such as high surface-to-volume ratio for catalyst. However, colloid nickel can not resist the high temperature environment which is an essential factor for the formation of grass like architectures in our experiments. In our case, environment humidity supplied efficient water vapors from which nickel, as hydrogen absorption catalysts, would absorb hydrogen and left bivalent oxygen ions with two chemical bonds.

Normally, at 200ºC there would have nanowires generated at the surface. However, in our case it was suspected that the tangential direction compressive stress was increased by the composition effect of catalyst, humidity and oxidation during the heating process, as shown in Figure 4. The atom accumulated at the grain boundary under the oxide layer. Finally, with long enough heating time grass like architectures sprouted from the weak spots at the surface of the oxide layer.

It was suspect with longer heating time the core-shell composite structure in the Cu powder would disappear and the powder would be completely oxidized.

4. Conclusion

In summary, grass like architectures which were 8-70μm in size with 1-2.5μm width leaves has been successfully fabricated by thermal oxidation approach. The microstructures and compositions of the samples were characterized by SEM, EDX and XRD. The formation mechanism of grass like architectures were examined and proposed. The results showed that tangential direction compressive stress caused by the oxide layer of the Cu powder surface played a critical role in the

formation of grass like architectures. Compared with other methods for fabricating copper oxide grass like architectures, the method proposed in the paper featured simplicity and cheapness.

References

[1] F.C. Akkari, M. Kanzari, Optical, structural, and electrical properties of Cu2O thin films. Phys. Status Solidi A, 207 (2010) 1647.
[2] L. Liao, B. Yan, F. Hao, G.Z. Xing, J.P. Liu, B.C. Zhao, Z.X. Shen, T. Wu, L. Wang, J.T.L. Thong, C.M. Li, W. Huang, T. Yu, P-type electrical, photoconductive, and anomalous ferromagnetic properties of Cu_2O nanowires. Appl. Phys. Lett., 94 (2009) 113106.
[3] P.H. Shih, J.Y. Ji, Y.R. Ma, S.Y. Wu, Size effect of surface magnetic anisotropy in Cu_2O nanoparticles. J. Appl. Phys. , 103 (2008) 07B735.
[4] R.N. Briskman, A study of electrodeposited cuprous oxide photovoltaic cells. Sol. Energy Mater. Sol. Cells, 27 (1992) 361.
[5] J.Y. Ho, M.H. Huang, Synthesis of Submicrometer-Sized Cu_2O Crystals with Morphological Evolution from Cubic to Hexapod Structures and Their Comparative Photocatalytic Activity. J. Phys. Chem. C, 113 (2009) 14159.
[6] L. Guan, H. Pang, J. Wang, Q. Lu, J. Yin, F. Gao, Fabrication of novel comb-like Cu_2O nanorod-based structures through an interface etching method and their application as ethanol sensors. Chem. Commun., 46 (2010) 7022.
[7] P. Poizot, S. Laruelle, S. Grugeon, L. Dupont, J.M. Tarascon, Nano-sized transition-metal oxides as negative-electrode materials for lithium-ion batteries. Nature, 407 (2000) 496.
[8] O. Akhavan, H. Tohidi, A.Z. Moshfegh, Synthesis and electrochromic study of sol–gel cuprous oxide nanoparticles accumulated on silica thin film. Thin Solid Films, 517 (2009) 6700.
[9] H. Pang, F. Gao, Q.Y. Lu, Morphology effect on antibacterial activity of cuprous oxide. Chem. Commun., 9 (2009) 1076.
[10] A. Ahmed, N. Gajbhiye, S. Namdeo, Low cost, surfactant-less, one pot synthesis of Cu_2O nano-octahedra at room temperature. J. Solid State Chem., 184 (2011) 30.
[11] W.Q. Zhang, L. Shi, K.B. Tang, S.M. Dou, Controllable Synthesis of Cu_2O Microcrystals via a Complexant-Assisted Synthetic Route. Eur. J. Inorg. Chem., 7 (2010) 1103.
[12] Y. Yu, F.P. Du, L.L. Ma, J.L. Li, Y.Y. Zhuang, X.H. Qi, Synthesis of Cu_2O nanowhiskers with CTAB as a template in water-in-oil microemulsion system. RARE METALS. 24 (2005) 283.
[13] Y.W. Tan, X.Y. Xue, Q. Peng, H. Zhao, T.H. Wang, Y.D. Li, Controllable Fabrication and Electrical Performance of Single Crystalline Cu2O Nanowires with High Aspect Ratios. Nano Lett. 7 (2007) 3723.
[14] J.J. Teo, Y. Chang, H.C. Zeng, Fabrications of Hollow Nanocubes of Cu_2O and Cu via Reductive Self-Assembly of CuO Nanocrystals. Langmuir. 22 (2006) 7369.
[15] R.C. Wang, C.H. Li, Dry Synthesis and Photoresponse of Single-Crystalline Cu2O Nanorod Arrays. J. Electrochem.Soc. 159 (2012) K73.
[16] J.T. Zhang, J.F. Liu, Q. Peng, X. Wang, Y.D. Li, Nearly Monodisperse Cu2O and CuO Nanospheres: Preparation and Applications for Sensitive Gas Sensors. Chem. Mater. 18 (2006) 867.
[17] Y.S. Luo, S.Q. Li, Q.F. Ren, J.P. Liu, L.L. Xing, Y. Wang, Y. Yu, Z.J. Jia, J.L. Li, Facile Synthesis of Flowerlike Cu2O Nanoarchitectures by a Solution Phase Route. Cryst. Growth Des. 7 (2007) 87.
[18] C.H. Kuo, M.H. Huang, Fabrication of Truncated Rhombic Dodecahedral Cu2O Nanocages and Nanoframes by Particle Aggregation and Acidic Etching. J. AM. CHEM. SOC. 130 (2008) 12815.
[19] R.H. Wei, H.B. Yang, K. Du, W.Y. Fu, Y.M. Tian, Q.J. Yu, S.K. Liu, M.H. Li, G.T. Zou, A facile method to prepare MoS2 with nanoflower-like morphology. Mater. Chem. Phys. 108 (2008) 188.

[20] K. Haouemi, F. Touati, N. Gharbi, Characterization of a New TiO 2 Nanoflower Prepared by the Sol–Gel Process in a Reverse Microemulsion. J. Inorg. Organomet. Polym. 21 (2011) 929.
[21] T.T. Kang, X.L. Liu, R.Q. Zhang, W.G. Hu, G.W. Cong, F.A. Zhao, Q.S. Zhu, InN nanoflowers grown by metal organic chemical vapor deposition. Appl. Phys. Lett. 89 (2006) 071113.
[22] H.W. Suh, G.Y. Kim, Y.S. Jung, W.K. Choi, D.J. Byun, Growth and properties of ZnO nanoblade and nanoflower prepared by ultrasonic pyrolysis. J. Appl. Phys. 97 (2005) 044305.
[23] J.Y. Xiang, J.P. Tua, Y.F. Yuan, X.L. Wang, X.H. Huang, Z.Y. Zeng, Simple synthesis of surface-modified hierarchical copper oxide spheres with needle-like morphology as anode for lithium ion batteries. Electrochim. Acta. 54 (2009) 1160.
[24] Z.H. Yang, J. Xu, W.X. Zhang, A.P. Liu, S.P. Tang, Controlled synthesis of CuO nanostructures by a simple solution route. J. Solid State Chem. 180 (2007) 1390.
[25] M. Kevin, W. Ong, G. Lee, G. Ho, Formation of hybrid structures copper oxide nanocrystals templated on ultralong copper nanowires for open network sensing at room temperature. Nanotechnology. 22 (2011) 235701.

Monte Carlo Simulation of Fatigue Crack Initiation at Elevated Temperature

Feifei He[1,*], Cher Ming Tan[1,2], Shuai Zhang[1], Shuguang Cheng[3]

[1] School of Electrical and Electronic Engineering, Nanyang Technological University, Singapore 639798
[2] SIMTech-NTU Joint Lab on Reliability, Singapore
[3] School of Materials Science and Engineering, Nanyang Technological University, Singapore 639798
* Corresponding author: ffhe@ntu.edu.sg

Abstract In this paper, a novel way that simulated the micro-crack initiation due to void nucleation under thermal fatigue was proposed using the combination of finite element modeling and Monte Carlo method. A 3D model that simulated the dynamic void nucleation process was constructed using the commercial FEA software ANSYS. The strain and thermal energies of the model due to the applied loads at elevated temperature are calculated. After manually including the grain structures, surface and bonding energies, a number of vacancies were randomly generated and they moved and nucleated according to the energy distributions of the model. To consider the problem at microscopic scale while still maintaining acceptable accuracy, two models are constructed, namely a real-sized full model and a micro-scale sub-model that included the microstructure. The impurities and the residue stresses that may affect the void nucleation process were included in the sub-model as well. The simulation results showed that the vacancies tended to nucleate at the "weak spots".

Keywords Metal fatigue, micro-crack initiation, finite element modeling

1. Introduction

Fatigue is the progressive damage to the material under cyclic loading and unloading. Cracks initiate at the stress concentration centers such as the surfaces, persistent slip bands or grain boundaries. The material eventually fractures even if the load is below its yield strength limit [1].

The initiation of the crack is due to the nucleation of tiny voids during the fatigue process [2]. Many simulation and experimental work had been conducted in the literature to study the crack initiation process using various approaches. For example, Piques *et al.* proposed a crack initiation model in 316L stainless steel based on the intergranular damage accumulation in the crack tip stress-strain field [3]. Nowack *et al.* studied the crack initiation and propagation of a Al 7475 sample under biaxial loading using the modified EVICD approach [4]. Haddar *et al.* developed a 2D model that simulated the crack initiation and shielding effects under thermal fatigue using the linear accumulation damage model [5]. Fine *et al.* predicted the fatigue crack initiation in single crystal iron and copper using the continuum models [6].

However, all the above-mentioned methods are modeled at macroscopic scale (i.e. mm scale). In fact, the voids inside the metal become visible at the size of 1 μm [7], which means the nucleation of the tiny voids start at microscopic scale. Such small crack is outside the regime of the conventional Paris's law and thus the traditional lifetime prediction cannot be applied. Furthermore, at micrometer scale, the change in lattice orientation affects the anisotropic stress distributions near the grain boundaries and this effect should not be ignored.

There is a number of reported works that studied the impact of microstructures on fatigue crack initiation. Vehoff *et al.* predicted the crack initiation at the grain boundary interfaces using the combination of the EBSD methods and the finite element stress analysis [8]. A microstructure sensitive crack nucleation criterion based on the local effective stresses and the non-local plastic strains and strain gradients was proposed by Kirane *et al.* [9]. Manonukul *et al.* developed a polycrystal plasticity finite element model that simulated the fatigue crack initiation based on the

critical resolved shear stress and the critical accumulated slip [10]. However, the dynamic void nucleation process under the applied loads was unable to be observed using the above methods.

Monte Carlo method, based on repeated random sampling algorithm [11], can be used to predict the grain size and structure [5], the crack growth and propagation [12, 13], the fatigue life and S-N curves [14, 15]. Monte Carlo method can also be used to simulate the diffusion and nucleation of the atoms under the applied loads (e.g. current, temperature, stress, etc.) [16-18]. To study the dynamic void nucleation and crack initiation process under fatigue, a novel way was introduced in this paper by incorporating the Monte Carlo method into the finite element models. Using this method, the dynamic motion of the atoms and vacancies before, during and after certain load cycle under the effects of temperature, stress, microstructure and surface condition forces and can be examined. The crack is assumed to initiate at the location of the void nucleation. Pure Al samples are used in this work.

2. Simulation Setup

The simulation is first performed on a dog-bone Al sample with the dimension shown in Figure 1. The chemical composition and the material properties measured from the sample are shown in Table 1 and 2 respectively.

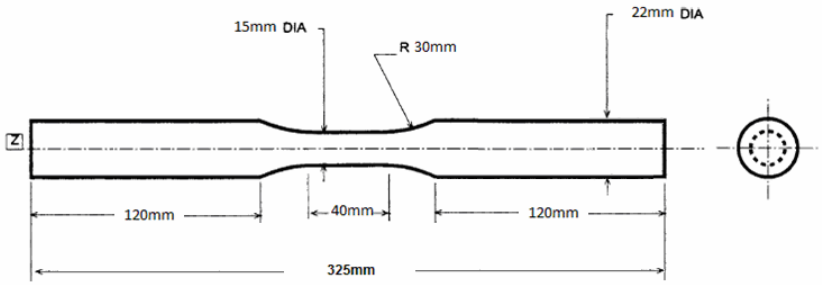

Figure 1. The dimension of the Al sample

Table 1. Chemical composition of the Al sample

ppm (parts per million)														
Al	Si	Fe	Cu	Mn	Mg	Cr	Ni	Zn	Ti	Ga	Pb	B	V	Zr
99.996%	6.20	2.20	0.10	3.90	1.00	1.20	0.30	2.70	1.10	5.50	0.10	0.80	2.40	0.80

Table 2. Physical properties of the Al sample

Young's Modulus (GPa)	Poisson's Ratio	Density (kg/m^3)	Thermal Expansion ($1/^oC$)	Yield Strength (GPa)	Thermal Conductivity ($W/m\cdot^oC$)	Specific Heat ($J/kg\cdot^oC$)
70	0.35	2700	2.24×10^{-5}	280	221.75	899.56

The initial temperature of the sample is assumed to be 27 ^oC and it is placed inside an oven with a constant temperature of 100 ^oC and heated up for 10 minutes. The convection heat transfer coefficient of the sample is 25 $W/m^2\cdot^oC$ [19]. A force of 5 kN is applied at one side of the sample and the other side is fixed and is not free to move. Finite element SOLID 69 and SOLID 45 is used in the thermal and structural-thermal simulation in ANSYS respectively.

To include the microstructure and the surface effects, a 70 μmx60 μmx30 μm sub-model is cut out from the central surface of the dog-bone sample (i.e. the full model), and the grain structures are added to the sub-model according to the EBSD map of this surface. The meshed full model and sub-model are shown in Figure 2. The nodal temperature and stress values extracted from the full model simulation are used as the boundary conditions for performing the sub-model simulation.

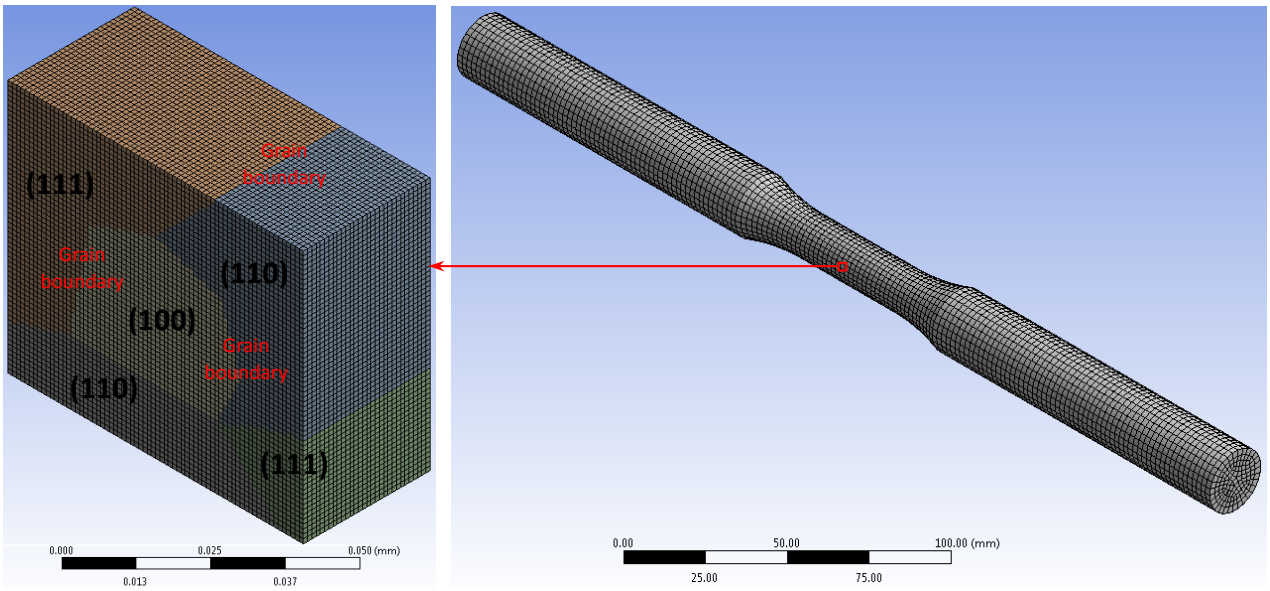

Figure 2. The micro-scale sub-model (left) cut out from the real-sized full model (right)

The nucleation of the voids is due to the movement of the atoms and the vacancies in the material, which is in turn determined by their energy states. With the presence of the external and internal factors, the atoms move and fill in the position of their neighboring vacancies in order to lower the total energy state of the system. The continuous movement causes the nucleation of the voids and the formation of the micro-cracks.

There are three types of energies that determine the total energy state of an atom, namely the thermal energy, the strain energy, and the pairing energy. The thermal and strain energy are external excitations due to the applied temperature and force respectively. The pairing energy is the energy required to excite the atom from its lowest energy state and free it out from its surrounding atoms. The pairing energy is the sum of the total bonding energy of the atom with its nearest neighbors, and is affected by the lattice orientation, the presence of the vacancies and impurities, as well as the surface condition.

The external excitations rise the energy state of the atom and when they are high enough to overcome the energy barrier (i.e. the pairing energy), the atom will become unstable and move to its neighboring vacant lattice site, as shown in Figure 3.

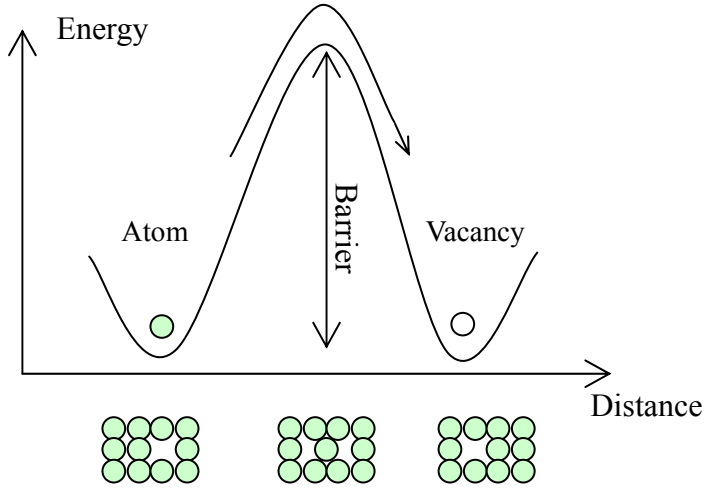

Figure 3. The movement of an atom from its original position into a vacant lattice site

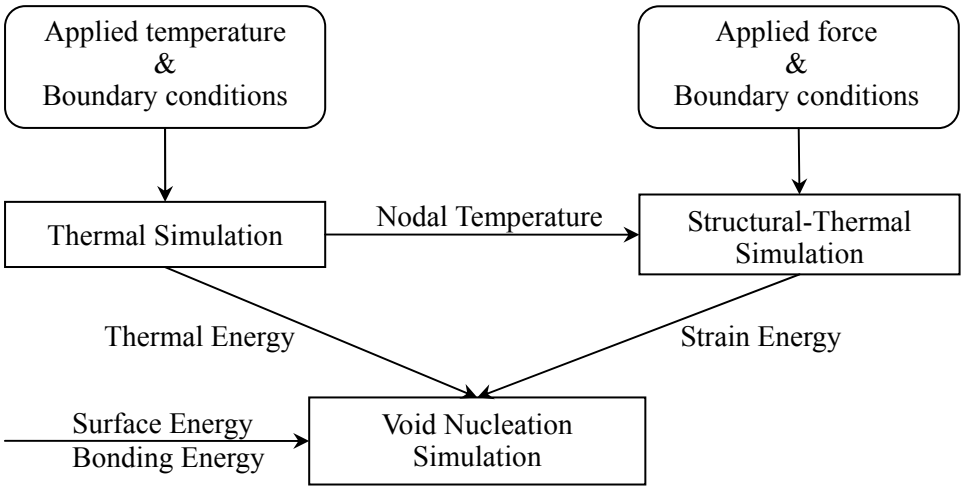

Figure 4. The flow chart of the ANSYS simulation

Figure 4 shows the flow chart of the ANSYS simulation. Based on the values computed in the thermal and structural thermal simulations, the thermal and strain energy are calculated using Equation (1) and (2) respectively [20],

$$E_{th} = N \times \frac{3}{2} k_B T \tag{1}$$

$$E_{str} = E_e^{el} + E_e^{pl} = \frac{1}{2}\{\sigma\}^T \{\varepsilon^{el}\} vol_e + \{\sigma\}^T \{\Delta\varepsilon^{pl}\} vol_e \tag{2}$$

where N is the number of the atoms, T is the location temperature, k_B is the Boltzmann's constant, E_e^{el} and E_e^{pl} are the elastic and plastic strain energy respectively, $\{\sigma\}$ is the stress vector, $\{\varepsilon^{el}\}$ is the elastic strain vector, $\{\Delta\varepsilon^{pl}\}$ is the plastic strain increment, and vol_e is the volume of the atom.

Depending on the position of the atom and the types of its neighboring atoms, the bonding energy are classified as the following categories in our simulation, as shown in Figure 5.

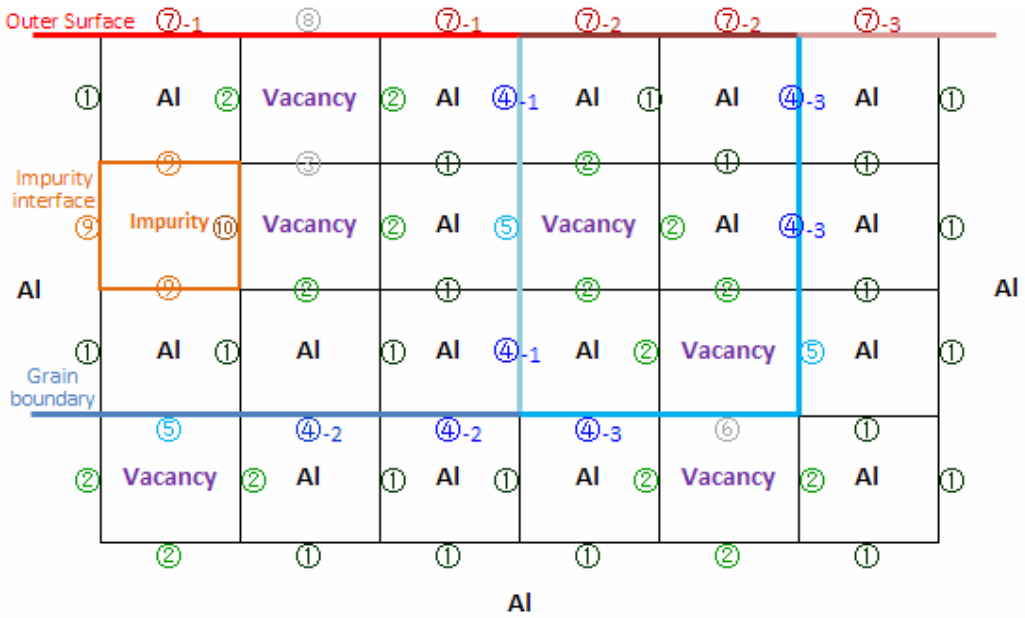

Figure 5. Different types of bonding energies used in the simulation in 2D view

(1) Inside the grain:
- Type 1: bonding energy between the Al atoms

- Type 2: bonding energy between the Al atom and the vacancy
- Type 3: bonding energy between the vacancies

(2) On the grain boundary:
- Type 4: bonding energy between the Al atoms on the grain boundary
- Type 5: bonding energy between the Al atom and the vacancy on the grain boundary
- Type 6: bonding energy between the vacancies on the grain boundary

(3) On the surface:
- Type 7: surface energy of the Al atoms with different lattice orientation
- Type 8: surface energy of the vacancies

(4) In contact with the impurity (if any):
- Type 9: adhesion energy between the Al atom and the impurity
- Type 10: bonding energy between the vacancy and the impurity

The bonding energy between the Al atoms inside the grain is 1.50 eV [21]. The bonding energy between the Al atom and the vacancy is 0.29 eV [22], and that between the vacancies is assumed to be zero. The surface energies of Al for lattice orientation (100), (110), and (111) are calculated as 0.95, 1.02 and 0.79 J/m^2 respectively using the density function theory (DFT) and the VASP software [23]. The surface energy of the vacancy is assumed to be zero. The bonding energy for the atoms on the grain boundary is approximated to be 40% of that inside the grain [24, 25]. The adhesion energy between the Al atom and the impurity (e.g. Si) is 1.09 J/m^2 [26], and 0.20 eV is used as the bonding energy between the vacancy and the Si impurity [27]. The Young's Modulus of Al for lattice orientation (100), (110), and (111) are calculated as 63.05, 71.88 and 76.05 GPa respectively [28].

The probability of atom to fill in its neighboring vacant lattice site is calculated using Equation (3) [16],

$$Probability = \exp\left(-\frac{\Delta E_{th} + \Delta E_{str} + \Delta E_{pair}}{N \times k_B T}\right) \tag{3}$$

where ΔE_{th}, ΔE_{str} and ΔE_{pair} are the change in thermal, strain and pairing energy between the target position and the original position of the atom respectively.

To begin the void nucleation simulation, 0.01% to 0.1% vacancies are randomly generated inside the sub-model depending on whether it is inside the grain or on the grain boundary [29, 30]. A few Si impurities are generated on the grain boundary as well. As the voids are only visible at micrometer scale [7], we assume the initial size of the vacancy to be 1 μm^3, which is also the size of one element in the sub-model. The thermal and strain energy of each element are calculated using Equation (1) and (2), and the pairing energy is calculated based on the position of the element and the number and type of its neighboring elements. In the Monte Carlo subroutine, a vacant site is randomly selected and total change in energy between the selected vacancy and its neighboring elements are computed. The neighboring element exchange position with the vacancy (i.e. fill in the position of the vacant site) if the probability of movement is larger than 0.5 [25]. The continuous position swapping process results in the movement of the vacancies and the nucleation of the voids.

3. Results and discussions

The position of the vacancies at the beginning, during and the end of the simulation after 1500 Monte Carlo cycles are shown in Figure 6(a) (b), and (c) respectively.

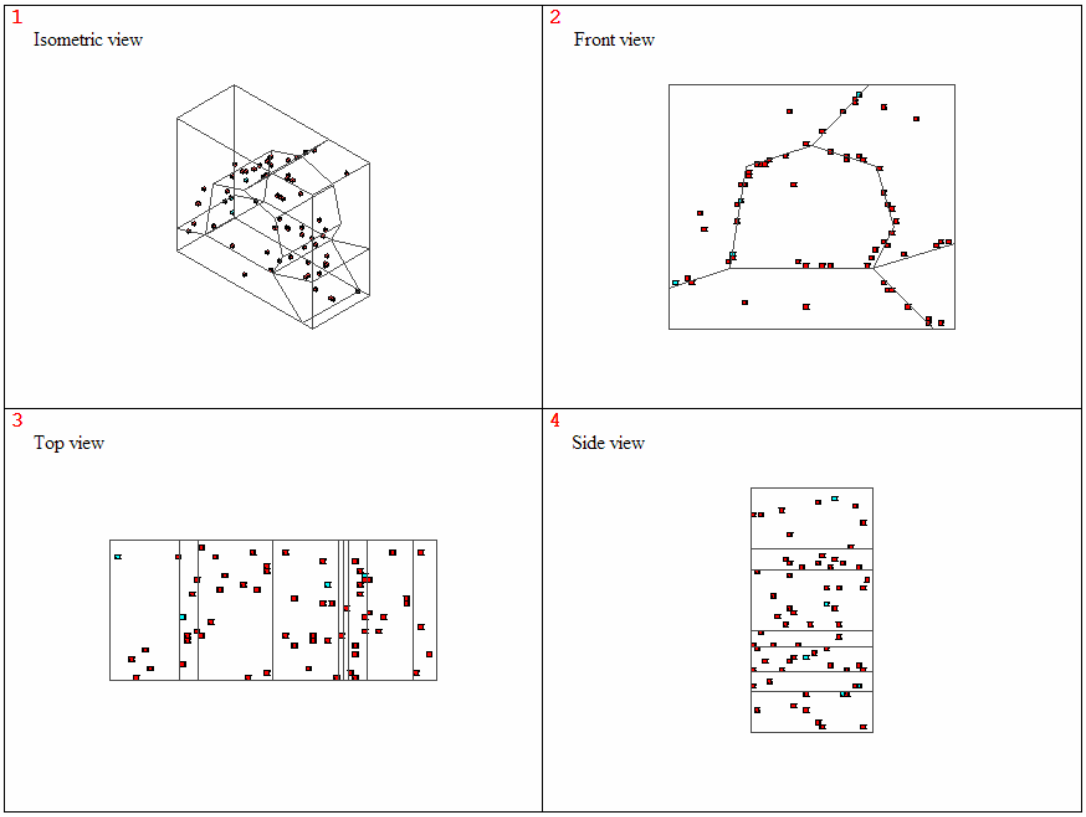
1
Isometric view
2
Front view
3
Top view
4
Side view

(a)

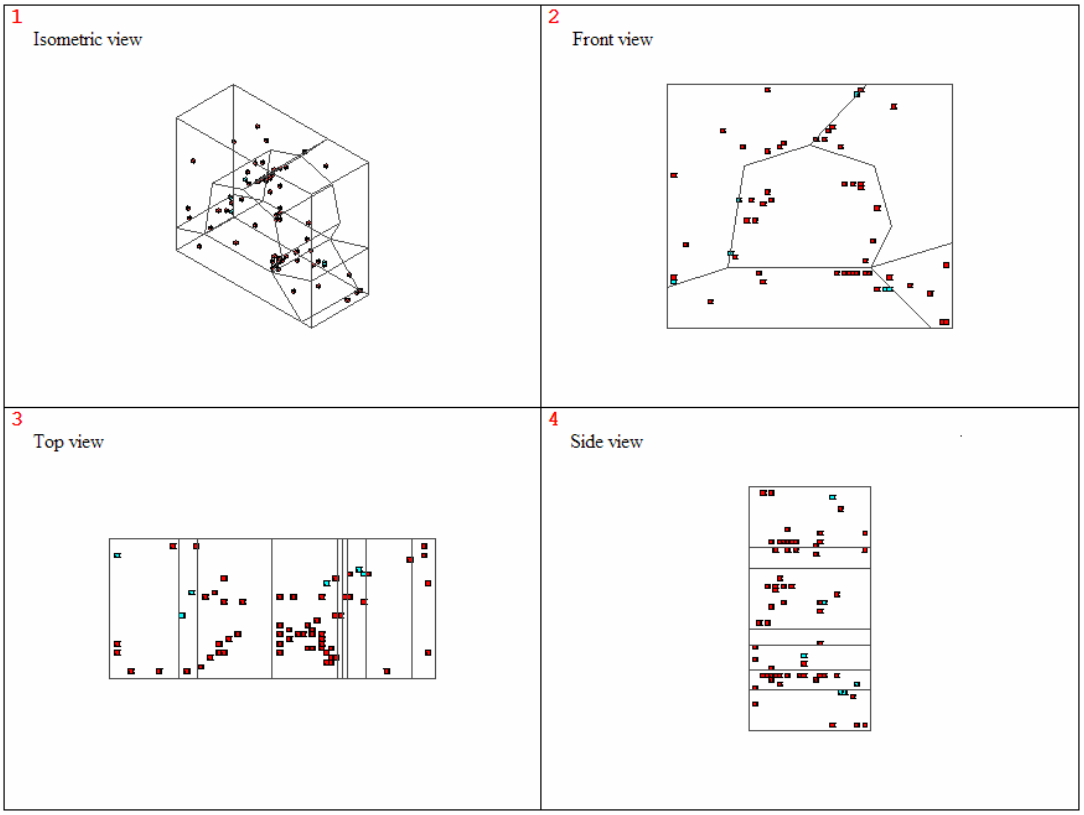
1
Isometric view
2
Front view
3
Top view
4
Side view

(b)

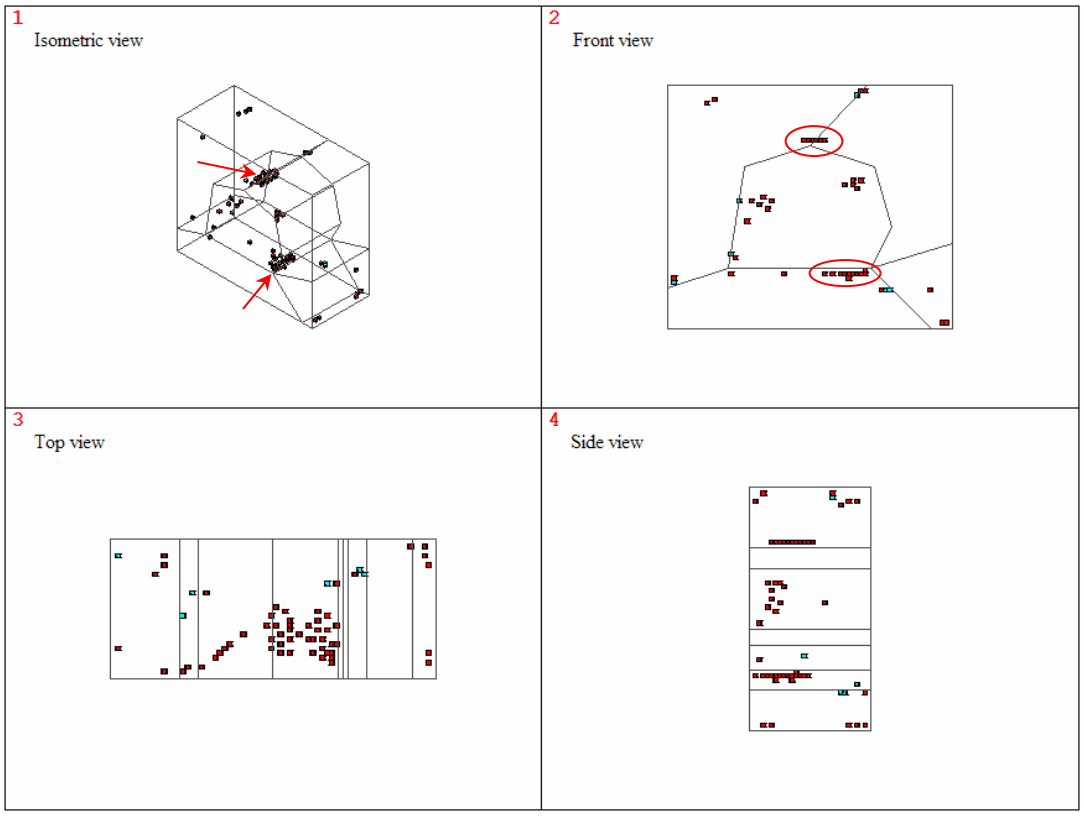

(c)

Figure 6. The vacancy position (a) at the beginning (b) during and (c) at the end of the simulation. The red dots are the vacancies and the blue dots are the impurities.

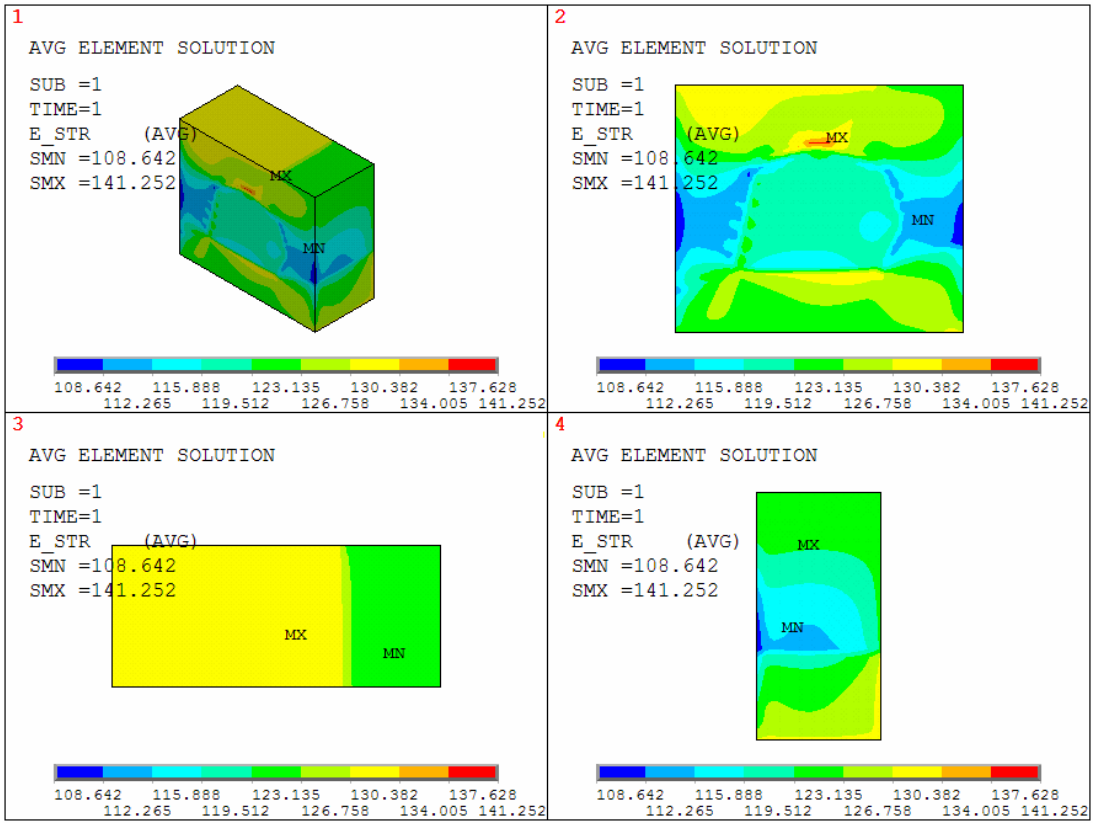

Figure 7. The strain energy distribution of the sub-model. High strain energy concentration is found at grain boundary triple point region.

From Figure 6, it can be seen that most of the vacancies nucleate at the grain boundary triple point region, as shown by the arrows and circles. This is because the stress inhomogeneity between different grains causes the concentration in strain energy along the grain boundary, especially at the triple point, as can be seen in Figure 7. Hence the vacancies tend to move to these regions in order to lower the total energy of the system. On the other hand, the presence of the impurities increases the stress around them slightly. This causes a slight instability in energy in the regions around the impurities. Therefore the impurities are able to attract some of the vacancies as well, and a few red spots are found around the blue spots in Figure 6.

The presence of the residue stress may increase or decrease the stress state on the sub-surface depending on whether it is tensile or compressive. This can affect the void nucleation process as well. The simulation is performed again with 10% increase in sub-surface stress due to tensile residue stress and the final vacancy position is shown in Figure 8. It can be seen that the presence of the residue stress attracts some vacancies to the surface, as shown by the arrows and the rectangle in Figure 8. Additional cracks may form at this region.

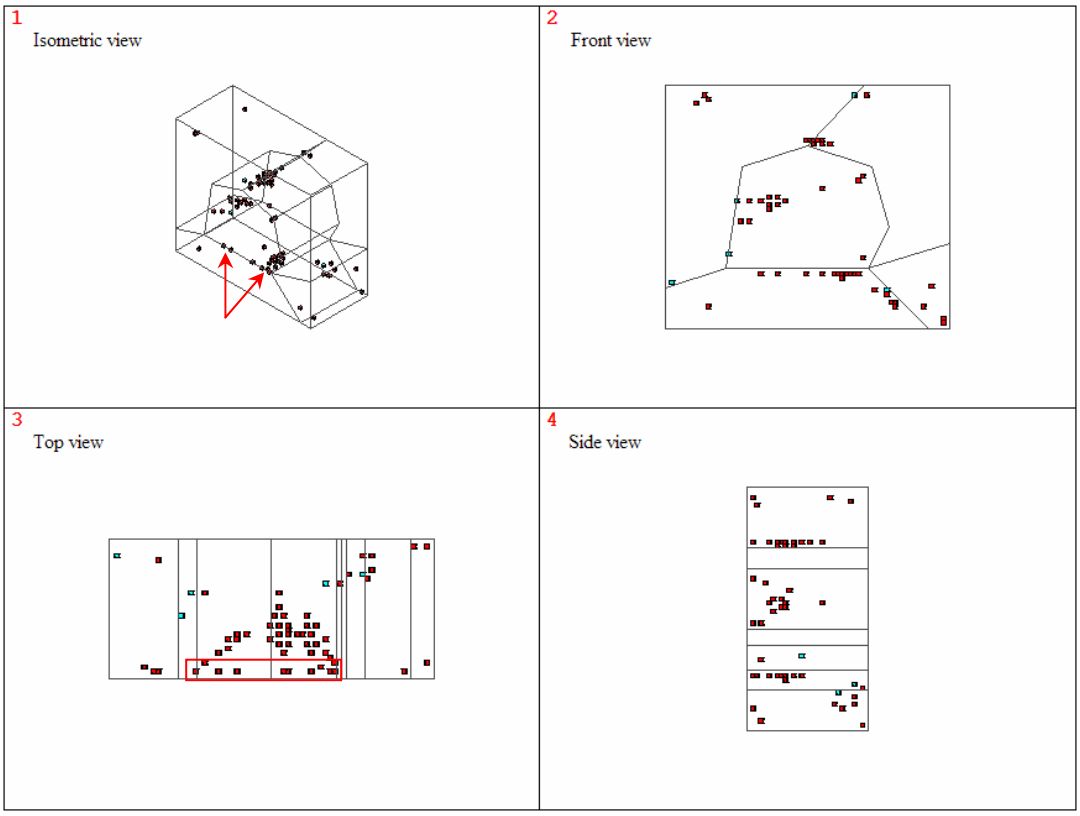

Figure 8. The vacancy position at the end of the simulation with the presence of the residue stress.

4. Conclusions

A finite element model that simulated the void nucleation process under thermal fatigue using the combination of finite element modeling and Monte Carlo method was presented in this paper. The simulation was first performed on a real-sized full model that contained the real time temperature and stress profile of the sample. The simulation was then carried out on a micro-scale sub-model that contained the microstructure and the imperfections, as well as different bonding and surface energies caused by the change in lattice orientation. The movement of the vacancies due to the uneven energy distributions of the model was observed and the void nucleated at the region with higher strain energies (i.e. the “weak spot”). Experimental verification of our method is underway.

References

[1] W.H. Kim, C. Laird, Crack nucleation and state I propagation in high strain fatigue-II mechanism. Acta Metallurgica, (1978) 789-799.
[2] R.L. Lyles, H.G. F. Wilsdorf, Microcrack nucleation and fracture in silver crystals. Acta metall, 23 (1975), 269-277.
[3] R. Piques, P. Bensussan, A. Pineau, Crack initiation and growth under creep and fatigue loading of an austenitic stainless steel. Nuclear Eng and Design, 116 (1989) 293-306.
[4] H. Nowack, D. Hanschmann, W. Ott, K.-H. Trautmann, E. Maldfeld, Crack initiation life behavior under biaxial loading conditions-experimental behavior and prediction. SAE Special Publications, 1280 (1997) 159-183.
[5] N. Haddar, A. Fissolo, 2D simulation of the initiation and propagation of crack array under thermal fatigue. Nuclear Eng and Design, 235 (2005) 945-964.
[6] M.E. Fine, P. Bhat, A model of fatigue crack nucleation in single crystal iron and copper. Mater Sci Eng A, 468-470 (2007) 64-69.
[7] J. Belak, On the nucleation and growth of voids at high strain-rates. J Computer-Aided Materials Design, 5 (1998) 193-206.
[8] H. Vehoff, A. Nykyforchyn, R. Metz, Fatigue crack nucleation at interfaces. Mat Sci Eng A, 387-389 (2004) 546-551.
[9] K. Kirane, S. Ghosh, M. Groeber, A. Bhattacharjee, Grain level dwell fatigue crack nucleation model for Ti alloys using crystal plasticity finite element analysis. J Eng Mat Tech, 131 (2009) 021003.
[10] A. Manonukul, F.P.E. Dunne, High- and low-cycle fatigue crack initiation using polycrystal plasticity. in: Proc Royal Society of London, Series A (Mathematical, Physical and Engineering Sciences), 2004, vol. 460, no. 2047, pp. 1881-903.
[11] K. Binder, D.W. Heermann, Monte Carlo Simulation in Statistical Physics: An Introduction, 4th ed, Springer, Berlin, 2002.
[12] B.N. Cox, W.L. Morris, Monte Carlo simulations of the growth of small fatigue cracks. Eng Fracture Mechanics, 31 (1988) 591-610.
[13] T. Shimokawa, Y. Kakuta, Application of Monte Carlo simulation for fractographic analysis of fatigue crack propagation, Inter J Fatigue, 18 (1996) 321-327.
[14] Y. Zhao, Monte Carlo simulation and modification on the historic probabilistic fatigue S-N curves. in: Proc IEEE 10th Inter Conf on Computer-Aided Industrial Design & Conceptual Design, 2009, pp. 2323-2327.
[15] C.M. Kim, J.K. Kim, C.S. Kim, Fatigue life evaluation of ERW joint in the pipe using Monte-Carlo simulation. Key Eng Mat, 297-300 (2005) 3-9.
[16] T.J. Smy, S.S. Winterton, M.J. Brett, A monte carlo computer simulation of electromigration. J App Phy, 73 (1993) 2821.
[17] P. Bruschi, A. Nannini, M. Piotto, Three-dimensional Monte Carlo simulations of electromigration in polycrystalline thin films. Computational Material science, 17 (2000) 299-304.
[18] W. Li, C.M. Tan, Dynamic simulation of electromigration in polycrystalline interconnect thin film using combined Monte Carlo algorithm and finite element modeling, in: Symp Microelectronics, Singapore, 2006.
[19] http://www.engineeringtoolbox.com/overall-heat-transfer-coefficient-d_434.html
[20] ANSYS, Theory Reference and reference therein
[21] D.R. Askeland, The Science and Engineering of Materials, PWS-Kent Publishing Co., 1987.
[22] J.E Epperson, P Fürnrohr, V. Gerold, Two stages of binding energy between vacancies and in atoms in an Al matrix. Mat Sci and Eng, 19 (1975) 95-103.
[23] X.-G. Wang, A. Chaka, M. Scheffler, Effect of the environment on α-Al_2O_3 (0001) surface structures. Phsical Review Letters, 84 (2000) 3650-3653.

[24] T.V. Zaporozhets, A.M. Gusak, K.N. Tu, S.G. Mhaisalka, Three-dimensional simulation of void migration at the interface between thin metallic film and dielectric under electromigration. Appl Phys Letter, 98 (2005) 103508.

[25] R.R. Atkinson. Ph.D New Brunswick Rutgers, The State University of New Jersey, 2003.

[26] P. Shen, H. Fujii, K. Nogi, Wetting, Adhesion and Adsorption in Al-Si/(0112) α-Alumina System at 1723K. Materials Transactions, 45 (2004) 2857-2863.

[27] J. Burke, A determination of the binding free energy between vacancies and silicon solute atoms in aluminium using an equilibrium method. Philosophical Magazine, 21 (1970) 7-22.

[28] S. Zhang, S. Cheng, H. Su, C.M. Tan, F. He, ab-initio computation of some surface and material properties of Aluminum and Silicon, in preparation for submission to IEEE Trans. On Nanotechnology.

[29] B.V. Guerard, H. Peisl, R. Zitzmann, Equilibrium vacancy concentration measurements on aluminum. Applied Physics B, 3 (1974) 37.

[30] K.M. Carling, G. Wahnstrom, T.R. Mattsson, N. Sandberg, G. Grimvall, Vacancy concentration in Al from combined first-principles and model potential calculations. Phys Review B, 67 (2003) 054101.

Numerical Study of Allowable Current Density for Electromigration Damage of Multilevel Interconnection in Integrated Circuit

Kazuhiko Sasagawa[1,*], Kazuhiro Fujisaki[1], Takahiro Yanagi[1]

[1] Department of Intelligent Machines and System Engineering, Hirosaki University, Hirosaki, 036-8561, Japan
* Corresponding author: sasagawa@cc.hirosaki-u.ac.jp

Abstract The high current density occurring in integrated circuits induces electromigration (EM) of the metal lines used for electric wirings. A void is formed by EM in the line material and the growth of void leads to the line failure. Recently, multilevel interconnection is widely used in electronics devices and MEMS by connecting upper and lower metal lines through vias. The reservoir structure is often constructed in the multilevel interconnection. It is known that there is threshold current density of EM damage in multilevel interconnection with vias. It is important to evaluate the threshold for determination of allowable electric current in the interconnection. In this study, a numerical simulation technique for analyzing the atomic density distribution generated by EM in the line is applied to evaluate the EM risks of metal line in several kinds of the multilevel structures. The thresholds of current density leading to EM change were calculated through the simulations. We confirmed that the atomic density distribution in the line was essential to increase the threshold and to prevent EM damage in the line. And we also showed the simulation technique was useful in the design of safety structure of electric wirings in integrated circuits.

Keywords Integrated Circuit, Reliability, Electromigration, Multilevel Interconnection, Allowable Current Density

1. Introduction

The high current density occurring in integrated circuits induces electromigration (EM) of the metal lines used for electric wirings. EM is a phenomenon that metallic atoms are transported by electron wind and that void, due to depletion of metallic atoms, is formed in the metal line. As the voids are growing the current density in the metal line increases and then the excessive Joule heating leads to metal line failure. Recently, multilevel interconnection is widely used in electronic devices and MEMS by connecting upper and lower metal lines through vias. The structure of interconnect tree and reservoir structure are constructed in the multilevel interconnection. Reservoir structures have an overhang from via connection, and it is usually located at vias on both anode and cathode sides as shown in Fig. 1. Reservoir structure gives delay of EM failure in multilevel interconnection by increasing margin of critical void length. The effect is caused by metallic atoms supplied from the overhanging parts as atom's reservoir to the metal line. The transportation of atoms is induced by tensile stress at the connection part on cathode side via as a result of EM. It is known that there is threshold current density j_{th} of EM damage in multilevel interconnection with vias. It is important to evaluate the threshold for determination of allowable electric current in the interconnection. Some research groups have developed evaluation method of j_{th} [1]. The threshold current density is also evaluated by numerical simulation. The building-up process of atomic density distribution in the line is simulated. And the simulation is based on a governing parameter for EM damage in polycrystalline line AFD^*_{gen} [2]. The parameter is applicable to two-dimensional line shape. Sasagawa et al. have evaluated j_{th} of several kinds of interconnect tree structure [3].
In this study, a numerical simulation technique for analyzing the atomic density distribution generated by EM in the line is applied to evaluate the EM risks of metal line in several kinds of the reservoir structures. The threshold j_{th} of several kinds of straight via-connected line with reservoir are evaluated by the numerical simulation. From the evaluation results, reservoir effects on the threshold current density are discussed.

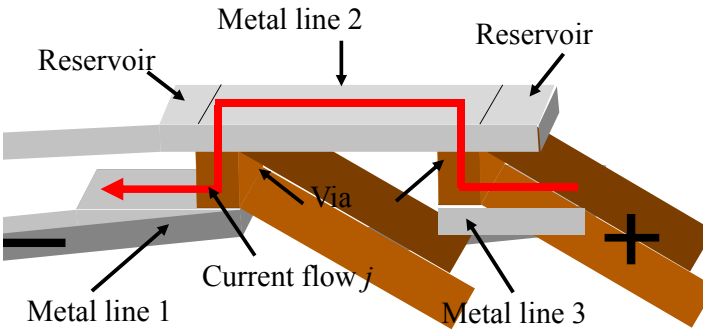

Figure 1. Multilayer interconnection with reservoir structure

2. Simulation method

The governing parameter for EM damage is used for constructing the numerical simulation [2]. The parameter is given by formulation of divergence of atomic flux due to EM. The atomic flux vector **J** is represented by Eq. (1).

$$|\mathbf{J}| = \frac{ND_0}{kT}\exp\left\{-\frac{Q_{gb}+\kappa\Omega(N-N_T)/N_0-\sigma_T\Omega}{kT}\right\}\left(Z^*e\rho j^*-\frac{\kappa\Omega}{N_0}\frac{\partial N}{\partial l}\right) \qquad (1)$$

where N is atomic density, D_0 a prefactor, k Boltzmann's constant, T the absolute temperature, Q_{gb} net activation energy for atomic diffusion, κ the constant relating the change in stress with the change in atomic density under restriction by passivation, N_T the atomic density under tensile thermal stress σ_T, N_0 the atomic density at a reference condition, Ω the atomic volume, Z^* the effective valence and e the electronic charge. ρ is the temperature-dependent resistivity. Symbols j^* and $\partial N/\partial l$ are the components of the current density vector and atomic density gradient in the direction of **J**, respectively. In Eq. (1), the back flow of atoms due to the stress gradient and the effect of the stress generated in the metal line on diffusivity are taken into account.

Grain boundary diffusion is assumed as dominant diffusion mechanism in the simulation, because wide Cu lines covered with passivation layer were supposed. According to literature [4, 5], in wide Cu interconnects, grain boundaries become preferential EM paths rather than lattice and interface diffusions. Sasagawa et al have introduced a grain texture model for calculating atomic flux divergence [6]. So we used the governing parameter for EM damage based on the model even for Cu lines.

Considering atoms going in and out at a unit rectangle, atomic flux divergence in polycrystalline line is formulated as given in Eq. (2).

$$
\begin{aligned}
AFD^{*}_{\mathrm{gb}\theta} = {} & C^{*}_{\mathrm{gb}} N \frac{4}{\sqrt{3}d^{2}} \frac{1}{T} \exp\left\{ - \frac{Q_{\mathrm{gb}} + \kappa\Omega\left(N - N_{\mathrm{T}}\right)/ N_{0} - \sigma_{\mathrm{T}}\Omega}{kT} \right\} \times \\
& \left\langle \sqrt{3}\Delta\varphi \left\{ \left(j_x \cos\theta + j_y \sin\theta \right) Z^{*} e\rho - \frac{\kappa\Omega}{N_0} \left(\frac{\partial N}{\partial x} \cos\theta + \frac{\partial N}{\partial y} \sin\theta \right) \right\} \right. \\
& - \frac{d}{2}\Delta\varphi \left\{ \left(\frac{\partial j_x}{\partial x} - \frac{\partial j_y}{\partial y} \right) Z^{*} e\rho \cos 2\theta - \frac{\kappa\Omega}{N_0} \left(\frac{\partial^2 N}{\partial x^2} \cos\theta + \frac{\partial^2 N}{\partial y^2} \sin\theta \right) \cos 2\theta \right. \\
& \qquad \left. + \left(\frac{\partial j_x}{\partial y} + \frac{\partial j_y}{\partial x} \right) Z^{*} e\rho \sin 2\theta - 2 \frac{\kappa\Omega}{N_0} \frac{\partial^2 N}{\partial x \partial y} \sin 2\theta \right\} \\
& - \frac{\sqrt{3}}{4} d \frac{\kappa\Omega}{N_0} \left(\frac{\partial^2 N}{\partial x^2} + \frac{\partial^2 N}{\partial y^2} \right) - \frac{\kappa\Omega / N_0}{kT} \\
& \quad \times \left[\frac{\sqrt{3}}{4} d \left\{ Z^{*} e\rho \left(j_x \frac{\partial N}{\partial x} + j_y \frac{\partial N}{\partial y} \right) - \frac{\kappa\Omega}{N_0} \left(\frac{\partial N}{\partial x} \frac{\partial N}{\partial x} + \frac{\partial N}{\partial y} \frac{\partial N}{\partial y} \right) \right\} \right. \\
& \quad \left. - \frac{d}{2}\Delta\varphi \left\{ Z^{*} e\rho \left(j_x \frac{\partial N}{\partial y} + j_y \frac{\partial N}{\partial x} \right) - 2 \frac{\kappa\Omega}{N_0} \frac{\partial N}{\partial x} \frac{\partial N}{\partial y} \right\} \sin 2\theta \right] \\
& + \frac{\sqrt{3}d}{4T} \left\{ \frac{Q_{\mathrm{gb}} + \kappa\Omega\left(N - N_{\mathrm{T}}\right)/ N_{0} - \sigma_{\mathrm{T}}\Omega}{kT} - 1 \right\} \\
& \quad \left. \times \left\{ Z^{*} e\rho \left(j_x \frac{\partial N}{\partial y} + j_y \frac{\partial N}{\partial x} \right) - \frac{\kappa\Omega}{N_0} \left(\frac{\partial N}{\partial x} \frac{\partial N}{\partial x} + \frac{\partial N}{\partial y} \frac{\partial N}{\partial y} \right) \right\} \right\rangle, \qquad (2)
\end{aligned}
$$

where C^{*}_{gb} represents the product $D_0\delta$ /k denoting the effective width of the grain boundary by δ, d the average grain size, and $\Delta\varphi$ a constant related to the relative angle between grain boundaries as shown in Fig. 2. The quantities j_x and j_y are components of the current density vector $\boldsymbol{j}$ in Cartesian coordinates, x and y. θ is angle between microstructure unit shown as rectangular in the figure and x axis.

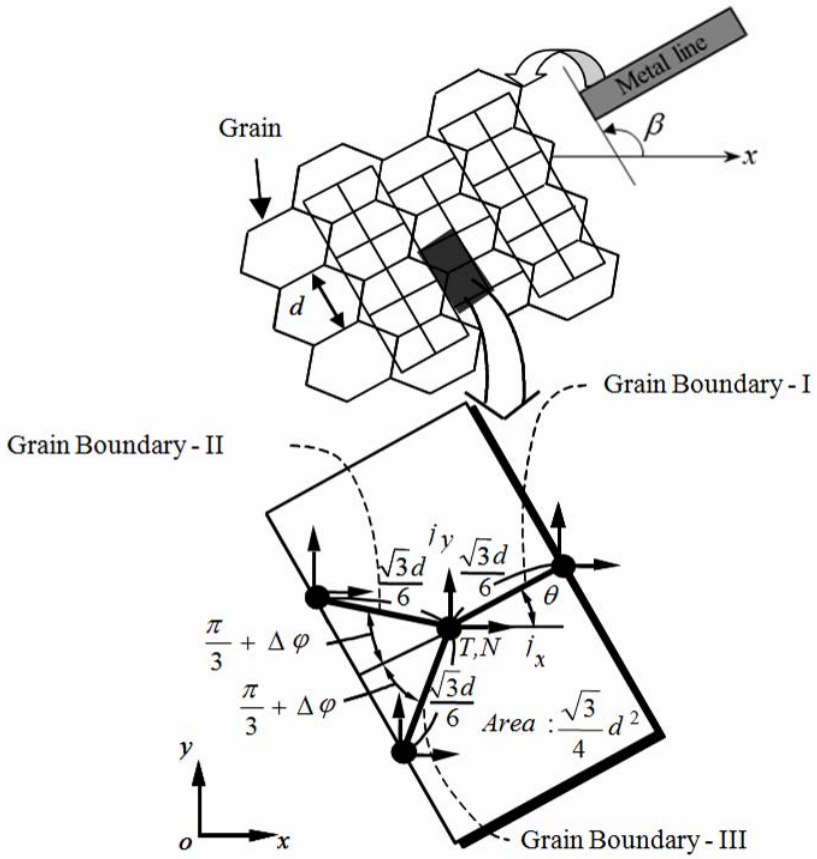

Figure 2. A model of polycrystalline structure

The expectation value of the only positive values of $AFD^*_{gb\theta}$ is obtained, and it represents the parameter governing EM damage, AFD^*_{gen}, concerning void formation in a polycrystalline line as

$$AFD^*_{gen} = \frac{1}{4\pi}\int_0^{2\pi}\left(AFD^*_{gb\theta} + \left|AFD^*_{gb\theta}\right|\right)d\theta \qquad (3)$$

It means the number of atoms decreasing per unit time and unit volume.

At line ends, boundary condition with respect to atomic flow has to be given for the formulation of the parameter at line ends. Namely, there is no coming-in at cathode end of the line and no going-out at anode one. The boundary condition can be expressed by possible zero flux within the microstructure unit being assigned to each θ-range as listed in Table 1 [7].

Table 1. Boundary condition concerning atomic flux

Range-I	Range-II	Range-III
$-2\pi/3+\Delta\varphi+\beta<\theta\leq-\pi/3-\Delta\varphi+\beta$	$-\pi/3-\Delta\varphi+\beta<\theta\leq\beta$	$\beta<\theta\leq\pi/3+\Delta\varphi+\beta$
$J_{II}=J_{III}=0$	$J_{II}=0$	$J_I=J_{II}=0$
Range-IV	Range-V	Range-VI
$\pi/3+\Delta\varphi+\beta<\theta\leq2\pi/3-\Delta\varphi+\beta$	$2\pi/3-\Delta\varphi+\beta<\theta\leq\pi+\beta$	$\pi+\beta<\theta\leq4\pi/3+\Delta\varphi+\beta$
$J_I=0$	$J_I=J_{III}=0$	$J_{III}=0$

Thus, considering coming and going of atoms within the microstructure unit, the atomic flux divergence at the line end, $AFD^*_{\mathrm{gen}|\mathrm{end}}$ is expressed by Eq. (4).

$$AFD^*_{\mathrm{gen}}\big|_{\mathrm{end}} = \frac{2}{\sqrt{3}\pi d^2}\frac{C^*_{gb}N}{T}\exp\left(-\frac{Q_{gb}+\kappa\Omega(N-N_T)/N_0-\sigma_T\Omega}{kT}\right)\Bigg[\ 6D_x\sin\beta-6D_y\cos\beta$$
$$+\frac{\sqrt{3}}{4}\pi d\Bigg\{\ -\frac{\kappa\Omega}{N_0}\left(\frac{\partial^2 N}{\partial x^2}+\frac{\partial^2 N}{\partial y^2}\right)-\frac{\kappa\Omega/N_0}{kT}\left(D_x\frac{\partial N}{\partial x}+D_y\frac{\partial N}{\partial y}\right)$$
$$+\frac{1}{T}\left(\frac{Q_{gb}+\kappa\Omega(N-N_T)/N_0-\sigma_T\Omega}{kT}-1\right)\left(D_x\frac{\partial T}{\partial x}+D_y\frac{\partial T}{\partial y}\right)\Bigg\}\ \Bigg] \qquad (4)$$

where $D_x=Z^*e\rho j_x-\kappa\Omega/N_0(\partial N/\partial x)$, $D_y=Z^*e\rho j_y-\kappa\Omega/N_0(\partial N/\partial y)$. $AFD^*_{\mathrm{gen}|\mathrm{end}}$ expresses the amount of flux divergence at line end and represents the number of atoms decreasing per unit volume and unit time.

Using the governing parameter of EM damage, numerical simulation of atomic density distribution in interconnect is performed under some kinds of input current density, j, at a certain substrate temperature, T_s. The line to be evaluated is two-dimensionally divided into elements and building up process of atomic density distribution is simulated by changing the atomic density of each elements based on the parameter. The boundary condition with respect to temperature is given on both line ends and that with respect to current density is given on via position. Atomic flow is insulated around the metal line. The end-parameter $AFD^*_{\mathrm{gen}|\mathrm{end}}$ is used in elements at cathode and anode ends and on via and AFD^*_{gen} is used for elements except both line ends.

The computational procedure is shown in Fig. 3. At first, the distributions of current density and temperature are calculated by two-dimensional FE analysis. The governing parameters are calculated in each element from the analysis results and the film characteristics. Next, the atomic density related to θ, N^*, is calculated based on the value of the governing parameter. The atomic density in each element N is calculated by averaging N^* among all θ's value. By the repetitive calculation, the atomic density distribution in the line grows with time. The iteration is performed until the atomic density reaches a critical atomic density for damage initiation N^*_{min} or holds a steady state. If atomic density becomes steady state without reaching N^*_{min}, the input current density given in the simulation would be less than j_{th}.

3. Evaluation

We evaluated four line structures as shown in Fig.4. Sample 1 has no reservoir at both ends of line. Sample 2 has two reservoirs located on both vias. Sample 3 has a reservoir located only on the cathode via. And Sample 4 has a reservoir located only on the anode via. In each sample, the reservoir having shorter length was evaluated. After the simulation with current density smaller than the threshold, a steady state distribution of atomic density should be got without reaching critical atomic density N^*_{min}. The smallest value of the atomic density N^* in all elements at steady state is plotted against supposed current density j. From an intersection point of the line of the smallest atomic density N^* and the critical density, the threshold current density is evaluated.

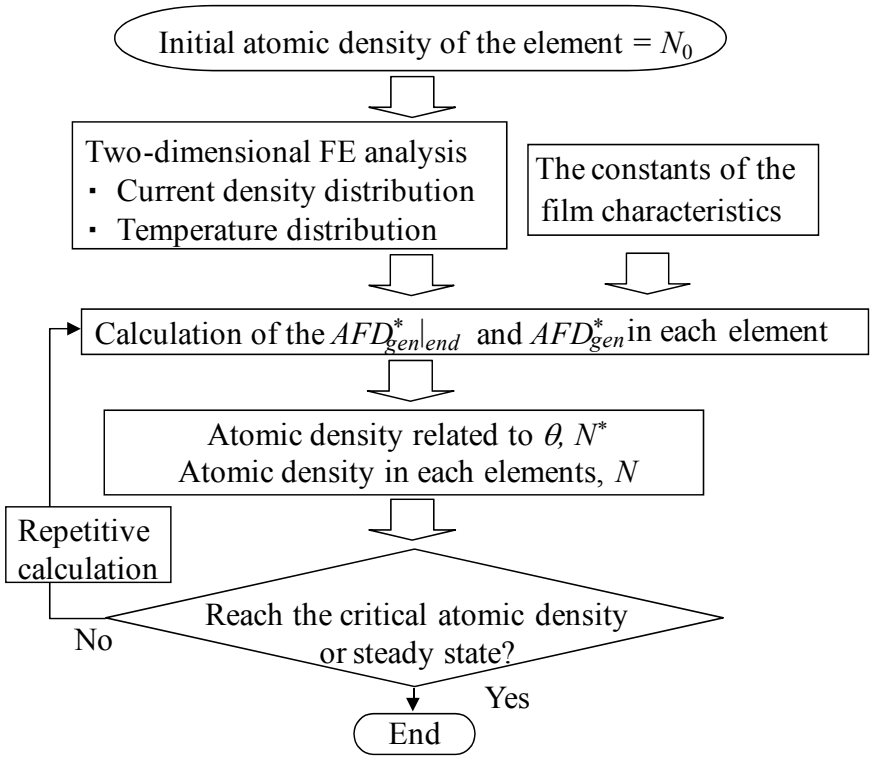

Figure 3. Computational procedure for evaluation of the threshold current density

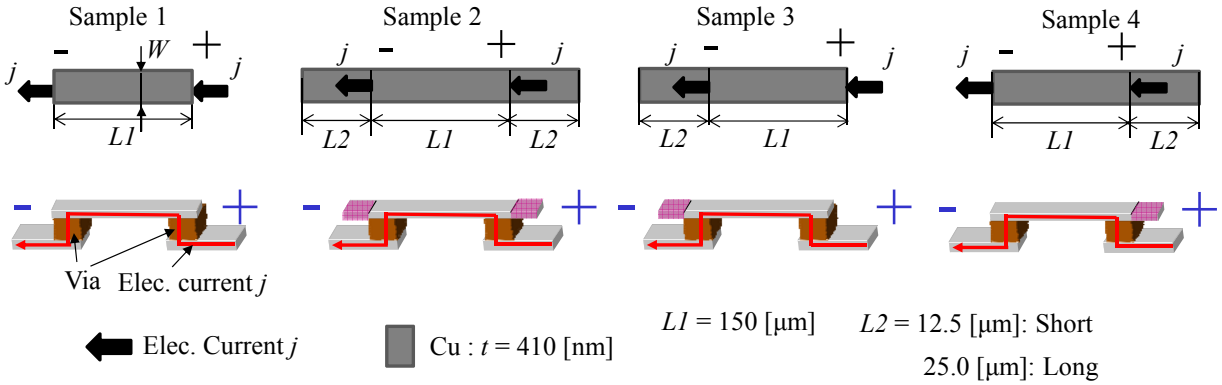

Figure 4. The dimension and structure of the supposed lines

In this simulation, Cu line is assumed having characteristic constants listed in Table 2 [8]-[12]. We supposed three values of input current density, 0.2, 0.4 and 0.6 MA/cm^2. The operating temperature is assumed 573K for all samples.

Table 2. Characteristic constants used in simulation

Characteristic constants	Value	Reference	
D_0 [μm²/s]	3.35	[8]	
Q_{gb} [eV]	1.1	[9]	
Ω [μm³]	3.00×10^{-11}		
Z^*	1	[10]	
ρ_0 [Ωμm]	0.0345 at 573[K]	[11]	
α [K⁻¹]	0.0043 at 573[K]	[11]	
κ [GPa]	42.5	[12]	Cited from results for Al interconnect
N^*_{min} [μm⁻³]	8.40×10^{10}	[12]	
N^*_{max} [μm⁻³]	8.56×10^{10}	[12]	
d [μm]	0.8		

4. Results and discussion

Figure 5 shows the smallest atomic density calculated in the long type reservoir case. The values of threshold current density j_{th} were determined in each sample and listed in Table 3. No reservoir and both reservoirs cases (Sample 1 and 2) were almost the same values. The j_{th} in the cathode reservoir case (Sample 3) showed larger value than those of others. On the other hand, anode reservoir case (Sample 4) showed smaller value than no reservoir case (Sample 1).

According to Eq. (1), if current density is the same, driving force of EM is same. So at steady state, the slope of atomic density corresponds to each other. On the other hand, current density in reservoir is almost zero, and there is not driving force of EM. So at steady state, the slope of atomic density in reservoir becomes almost horizontally. According to conservation law of mass, atomic density distribution in Sample 3 must be shifted upward globally from distribution in Sample 1.

In comparison of length of reservoir, change in j_{th} from Sample 1 or 2 was enhanced by extension of the reservoir.

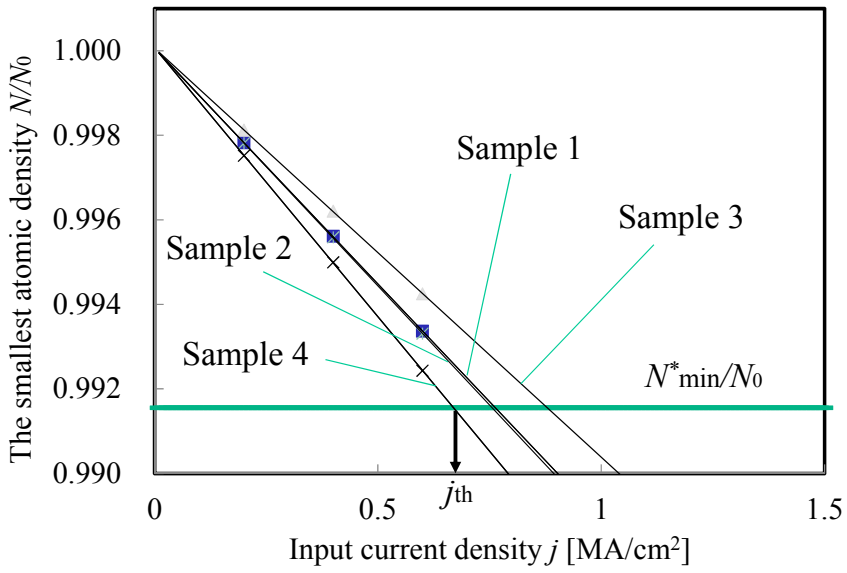

Figure 5. Results of threshold current density in simulation of long type (L_2 =25 μm) reservoir

Table 3. Threshold values of current density j_{th} [MA/cm^2] obtained from simulations

Sample type		1: none	2:+-	3:-	4:+
Reservoir length	Short	0.77	0.76	0.82	0.71
	Long		0.76	0.88	0.67

5. Conclusions

The numerical simulation technique was applied to evaluation of reservoir structure and AFD^*_{gen} -based evaluation of j_{th} was carried out. We found that if a reservoir is located only on the cathode via, the threshold current density of EM damage is increased. And it was concluded that this phenomenon is caused by the change in atomic density distribution among a metal line.

Acknowledgments

This work was partly supported by JSPS under Grant-in-Aid for Scientific Research (B) 21360046.

References

[1] C. S. Hau-Riege, An introduction to Cu electromigration. Microelectronics Reliability, 44 (2004) 195-205.
[2] H. Abé, K. Sasagawa, M. Saka, Electromigration failure of metal lines. International Journal of Fracture, 138 (2006) 219-240.
[3] K. Sasagawa, T. Abo, Evaluation of threshold current density of electromigration damage in interconnect tree with angled Cu lines. Proc. of 12th EMAP (2010) Paper ID:230, 110-116.
[4] M. H. Lin, K. P. Chang, K. C. Su, T. Wang, Effects of width scaling and layout variation on dual damascene copper interconnect electromigration. Microelectronics Reliability, 47 (2007) 2100-2108.
[5] C. -K. Hu, R. Rosenberg, K. Y. Lee, Electromigration path in Cu thin-film lines. Applied Physics Letters, 74 (1999) 2945-2947.
[6] K. Sasagawa, M. Hasegawa, M. Saka, H. Abé, Governing parameter for electromigration damage in the polycrystalline line with a passivation layer. Journal of Applied Physics, 91 (2002) 1882-1890.
[7] M. Hasegawa, K. Sasagawa, M. Saka, H. Abé, Expression of a governing parameter for electromigration damage on metal line ends. Proc. of IPACK'03 (CD-ROM), ASME (2003) IPACK2003-35064.
[8] Z. S. Choi, R. Ronig, C. V. Thompson, Activation energy and prefactor for surface electromigration and void drift in Cu interconnects. Journal of Applied Physics, 102 (2007) 083509.
[9] C. K. Hu, L. Gignac, R. Rosenberg, Electromigration of Cu/low dielectric constant interconnects. Microelectronics Reliability, 46 (2006) 213-231.
[10] C. L. Gan, C. V. Thompson, K. L. Pey, W. K. Choi, Experimental characterization and modeling of the reliability of three-terminal dual-damascene Cu interconnect trees. Journal of Applied Physics, 94 (2003) 1222-1228.
[11] R. S. Figliola, D. E. Beasley, Theory and design for mechanical measurements, Second-ed. John Wiley & Sons, Inc., New York, 1995.
[12] K. Sasagawa, M. Hasegawa, N. Yoshida, M. Saka, H. Abé, Prediction of electromigration failure in passivated polycrystalline line considering passivation thickness. Proc. of InterPACK'03 (CD-ROM), ASME (2003) IPACK2003-35065.

Wear Life Test and Mechanisms of Silicon MEMS Devices under Different Gas Environments

Sihan Shen and Yonggang Meng*

State Key Laboratory of Tribology, Tsinghua University, Beijing 100084, China
* Corresponding author: mengyg@tsinghua.edu.cn

Abstract: Microelectromechanical systems (MEMS) are usually fragile to wear problems. In this research, a bulk-fabricated side-wall Si-MEMS tribotester with the feature of on-chip buckle loading mechanism was designed and used to study the wear life and the mechanisms of early stage wear of resonant MEMS devices in different gas environments. Two distinguishable wear mechanisms are recognized: (1) in dry N_2 or O_2/N_2 mixture environments, wear exhibited an adhesive feature that the instantaneous wear rate is inversely proportional to the wear depth; (2) if corrosive vapors, such as fatty alcohols, are introduced into the environment, chemical reaction can limit the wear rate as a constant. In more complex situation, such as trifluoroethanol vapor, the rubbing process shows a transition from a short adhesive wear phase to a corrosive wear process. The thermal- and tribo-solvolysis could not give a full explanation of the life-time tests for the tested fatty alcohols. Therefore, there must be derivative reactions of grafting groups at silicon surfaces, which cause the instability of such groups. A mechanochemical mechanism is established to understand the stability of grafting groups in friction situation. Compared with fatty alcohols, fluoroalcohol is much more stable and can be used as vapor lubricant for Si-MEMS devices.

Key words: MEMS, wear, solvolysis, mechanochemistry

1. Introduction

Microelectromechanical systems (MEMS) are a class of IC-compatible sophisticated mechanisms to realize highly controllable precision motions at micro/nano scales. Compared with the failure modes of fracture and fatigue, tribological problems, including adhesion, friction and wear, are the main factors which give rise to device failure at such scales owing to the high surface-to-volume ratios of these devices [1]. Until now the adhesion problem can be solved by lowing down the surface energy using self-assembly monolayers (SAM), such as fluoro-substituted tris(dimethylamino)silane [2]. However, SAM could not provide persistent protection of contacting surfaces from wear to achieve enough life-time [2-4]. To overcome the wear problem, lubricant needs to be able to diffuse onto the moving part continuously. Two instances of vapor phase have been successfully used to lubricate tribo-MEMS devices, one is perfluorodecanoic acid vapor using for protecting the aluminum protrusion in Digital Micromirror Device^{TM} [5], and the other is 1-pentanol vapor which is effective to prolong the life-time of silicon micro-tribotester fabricated by Sandia National Laboratory [6]. The possible reasons for the good lubricity of these two lubricants are not exactly the same. For the perfluorodecanoic acid, the competitive adsorption may reduce the corrosion of water on aluminum material, while the 1-pentanol can react with silicon in a soft manner to avoid adhesive wear, which is the most common wear mechanism of silicon materials [7]. In order to expand applications of MEMS, looking for a suitable lubricant and understanding the wear mechanism at micro scales becomes particularly important.

For tribo-MEMS, devices are easy to fail at the early stage of wear, only allowing for blunt rough asperities and a small number of wear debris. To study the early stage of wear, a

bulk-fabricated side-wall micro tribotester is designed to test the wear life of silicon in different vapor environments. In this paper, we first introduce the tribotester and the experimental details. In Section 3, adhesive and corrosive wear are distinguished by the motion mode of the driving shuttle. In Section 4, we analysis the corrosive wear of fatty and fluoro- alcohols, pointing out that the solvolysis can not give a full explanation of tribochemical reactions of fatty alcohols on silicon surfaces. A mechanochemical mechanism is proposed to understand the stability of grafting groups in the presence of friction, helping to explain the stability of fluorocarbon chains on silicon surfaces.

2. Experimental details

Every 50-μm-thick Si-MEMS tribotester consists of a driving shuttle and a pair of loading frames (Fig. 1). The on-chip buckle structure can push the loading frame over a certain displacement to maintain a deflection of the restriction beam to realize 2.7μN or 5.2μN normal loads. For each tribotester, a loading frame and its corresponding restriction beam serves as the reference pair working in the ethanol vapor environment, and the opposite pair is used to study the effects of other environments, such as dry nitrogen or fluoroalcohol vapors. The friction pair to be tested is blown by dry nitrogen or the bubbled vapor stream with saturation lower than 20%. This design can be as far as possible to cancel the interference of device fluctuation in fabrication [8] and give more reasonable judgments of anti-wear effect of candidate lubricants.

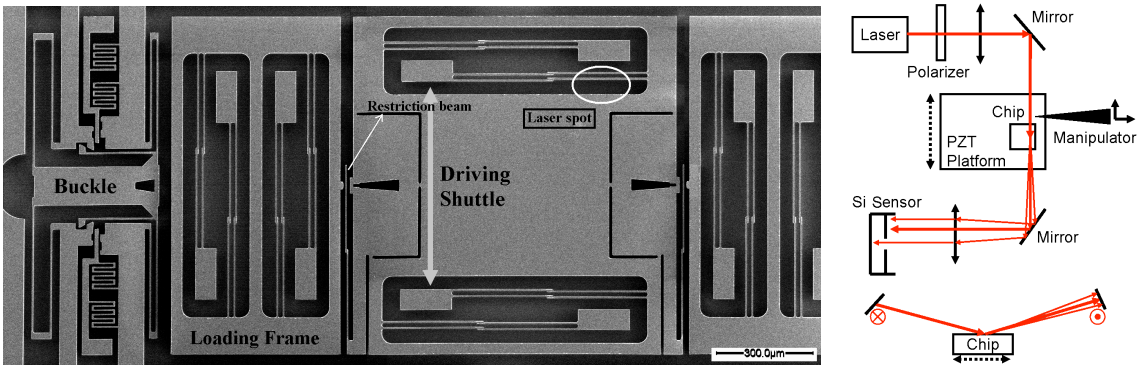

Figure 1. The bulk-fabricated micro- tribotester and the optical path to monitor the vibration of the driving shuttle, top view (up) and side view (down).

To drive the friction pair, the tribotester is stuck to a home-made one dimensional piezoelectric platform to force the shuttle vibrating near its nature frequency. The typical oscillation amplitude of the shuttle is about 4.5μm at 3850Hz. This method can offer a driving force no more than 10μN. And the on-chip buckle loading method avoids the necessity of finding the zero-point in a trial-and-error way. Thus this tribotester can be sensitive enough to observe the early stage of wear from its real starting point in MEMS devices.

The vibration of the shuttle can reflect the friction/wear process. A HeNe 633nm laser focuses onto the edge of the shuttle to reflect a speckle filed. The light intensity of the carefully chose point in this speckle field denotes the position of the shuttle. Since the air resistance is measured only 1/20 of the average friction force, the vibration degradation ΔC ($\Delta C=C_0-C$, C_0 is the vibration amplitude under empty load) reflects the real-time friction force ρ, which has a relationship of $\rho \propto \sqrt{\Delta C}$ deduced from the vibration equation under suitable simplifications [9].

3 Adhesive and corrosive wear mechanisms

After a short while vibration, the tribotester would stop owing to the overlarge friction. Figure 2 shows the worn morphologies of loading heads and restriction beams failed in nitrogen and ethanol vapor environments. On restriction beams only the feature of blunt peaks can be found and the bearing area is no more than 6% of the total nominal contact area. Hence these devices failed at the early stage of wear. The reason of blunt peaks can be inferred from the morphologies of the loading heads, where the worn area concentrated in a small region less than 5μm×5μm with more wear features. For samples in nitrogen atmosphere, scratches and pie-like wear debris distributed on the wear scars, while glass-like materials around bearing spots without scratches were found on samples working in ethanol vapor atmosphere. These glass-like materials can decompose in wet hydrofluoric acid vapor and is considered as the reaction products of silicon and ethanol in rubbing conditions. Therefore wear in nitrogen is attributed to adhesive type while in ethanol vapor it is corrosive type.

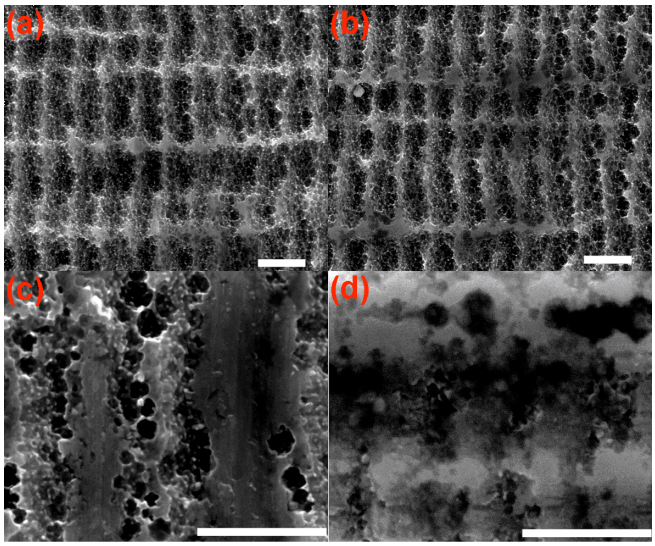

Figure 2. Worn morphologies of driving shuttles (a, b) and loading heads (c, d) after device failure. (a, c) Dry nitrogen atmosphere. (b, d) Ethanol vapor environment. The scale bar is 1μm.

The two wear mechanisms can be further convinced by the shuttle vibration degradation. Assuming each initial rough peak has a parabolic shape $h = r_0 \cdot r^2$ and the average friction force ρ is proportional to the total bearing area $A = N \cdot A_0 = N(\pi \cdot h / r_0)$. For adhesive wear, combining the classical Archard wear equation [10, 11]

$$\frac{A \cdot \Delta h}{v \cdot \Delta t} = \frac{\Delta V}{\Delta s} = \lambda_1 A_r \tag{1}$$

(V is the wear volume, s is the sliding length, v is the sliding speed, and λ_1 is the wear coefficient) and the simplified relationship between atomic contact area A_r and normal load F_n of $A_r=\lambda_2 \cdot F_n$ [12], the transient wear rate is inversely proportional to the wear depth as

$$\frac{dh}{dt} = \lambda_1 \lambda_2 v \frac{F_n}{A} = \left(\frac{\lambda_1 \lambda_2 v \cdot r_0}{\pi \cdot N} \right) \frac{F_n}{h}, \tag{2}$$

which induces $h \propto \sqrt{t}$ or $\rho \propto \sqrt{t}$. And for corrosive wear in strong media, only the reacted materials

will be worn out and the wear rate is limited by the reaction rate, which depends on the activation energy E_a of silicon and adsorbed small molecules:

$$h_0 = \frac{dh}{dt} = d_a K \cdot f_0 \exp[-(E_a - \mathrm{d}E)/k_b T], \tag{3}$$

where d_a is the silicon atom diameter and K is a probability multiplier to express the uniform assignment of multi-contact wear. dE is a modifier for sharp contact between fresh asperities. Since the initial shape can be worn out quickly in bulk-fabricated devices, dE is omitted to prevent redundant discussion [13]. Therefore, the transient wear rate is a time-independent constant, which induces $h = h_0 \cdot t$ or $\rho \propto t$. Therefore, using the relationship of $\rho \propto \sqrt{\Delta C}$, two modes of ΔC should be observed at the beginning of wear.

Figure 3 shows the shuttle vibration degradation in nitrogen and ethanol vapor conditions. The initial degradation can be fitted by the $\Delta C \propto t$ or $\Delta C \propto t^2$ quite well, consistent with the analysis of wear mechanisms from surface morphologies.

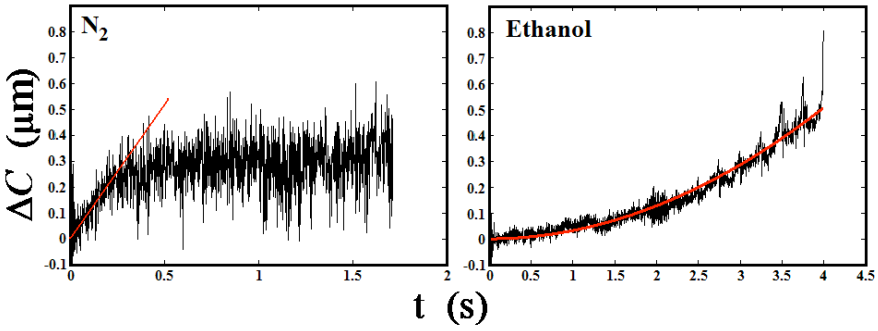

Figure 3. The typical vibration degradation of the driving shuttle in nitrogen and ethanol vapor environments. $\Delta C = d \cdot t^2$ (red line) is used to fit the data for ethanol vapor condition.

More kinds of gas environments have been tested on our tribotesters. In addition to dry nitrogen, O_2/N_2 mixture, n-hexane vapor and HFE 7100 ($CF_3(CF_2)_3OCH_3$) vapor also exhibit adhesive type. According to the density functional theory (DFT) calculation, n-hexane and HFE 7100 have very limited reactivity with silicon materials. Oxygen is easy to react with silicon in tribo-conditions [14]. However, lacking of inert groups, oxygen can not saturate dangling bonds to avoid atom bridges between couple surfaces. Besides ethanol, typical corrosive wear can be found in short chain fatty alcohols, such as methanol and hexanol, as well as propylene oxide. More complex wear processes are observed in water and fluoroalcohol vapor conditions, where a short linear vibration degradation can usually be found before the time-square degradation. Using the DFT calculation, fluoroalcohols show a weaker reactivity than fatty alcohols (Sec. 4). Hence they can not passivate initial sharp asperities as effectively as fatty alcohols to avoid adhesive wear. The reason for the boundary lubrication behavior of water is not very clear. A possible explanation is that silicon surfaces passivated by –OH groups still has possibilities to form atom bridges like Si-O-Si to cause adhesive wear when the local stress is high enough.

Using the time scaling of $\rho \propto \sqrt{t}$ and $\rho \propto t$, the worn area increases in a manner of $t^{3/4}$ and $t^{3/2}$ for adhesive and corrosive wear, respectively. For conventional macro structures, corrosive wear is usually more harmful since it has a superlinear growth. However, for MEMS devices, the permitted

wear volume is light and the wear process fails at its early stage. Near the initial point, the $t^{3/2}$ curve increases slower than that of $t^{3/4}$. That means if suitable chemical reactions are introduced into micro- tribo-devices, corrosive wear can exhibit a longer life-time than adhesive type (Fig. 4).

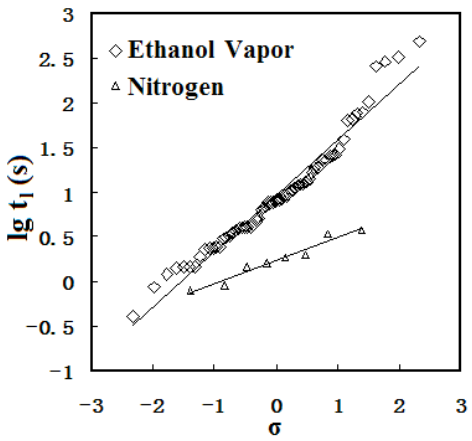

Figure 4. The log-normal distribution of life-time (t_l) in nitrogen and ethanol vapor environments.

4. The life-time test in corrosive vapor environments

Since the initial wear is sensitive to chemical conditions, several vapor environments are tested to study their lubrication effects, including methanol, ethanol, propanol, isopropanol, 2,2,3,3-tetrafluoropropanol, 2,2,2-trifluoroethanol, hexanol, propylene oxide and water. Their life-times compared by the reference pairs in ethanol vapor environments are shown in Fig. 5. According to these results, fluoroalcohols are better lubricant than fatty alcohols.

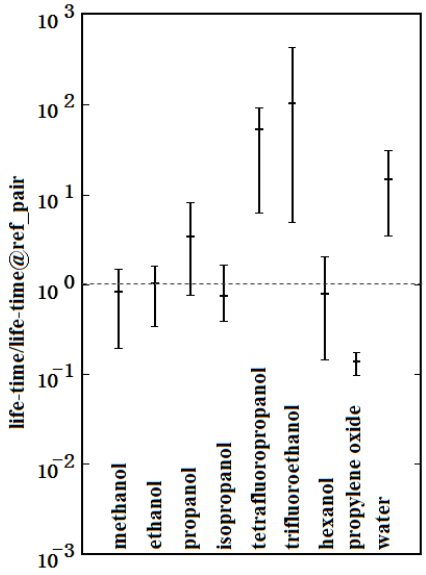

Figure 5. The life-time ratio of different corrosive vapors. The error bars denote the maximum and minimum values for each case.

A basic question is what chemical reactions happen on tribo-surfaces that make fluoroalcohol a better lubricant. For silicon material, especially the silicon dioxide, solvolysis (i.e., hydrolysis for water and alcoholysis for alcohols) is the most important reaction when the environment is filled by

active agents [15-21]. The solvolysis of silicon dioxide with water and fatty alcohols has been studied broadly. In our wear tests, however, the driving frequency is high enough and it is believe that there is not sufficient time to form fully native oxide on tribo-surfaces. Hence the reaction substrate is determined to be silicon instead of silicon dioxide. To compare the solvolysis reactivity of different compounds, the activation energy E_b of reaction

$$\equiv Si_2 - \underset{\|}{Si_1} - OR_1 \quad + \quad R_2OH \quad \rightarrow \quad \equiv Si_2 - H \quad + \quad \underset{\|}{Si_1} \begin{matrix} -OR_1 \\ -OR_2 \end{matrix} \tag{4}$$

is calculated in the framework of the density functional theory where Si(111) cluster model Si_7H1_6 is used (Fig. 6). The calculation is carried out with the Dmol3 software packaged in Material Studio v5.5, employing the BP functional and the DND basis set. Similar model is also used to calculate the hydrolysis barriers for SiO_2(111) and $(HO)_3Si$-O-$Si(OH)_3$, which gives the same transient structures and reaction energies given by Gaussian [22]. The virtual reaction

$$H_{15}Si_6 \equiv Si - OH \quad + \quad HO - Si \equiv H_3 \quad \rightarrow \quad H_{16}Si_6 = \underset{|}{\overset{OH}{Si}} - O - Si \equiv H_3 \tag{5}$$

is used to estimate the upper limit of E_b (149.7kJ/mol) for ROH compounds, where the H-H-H plane in HO-Si≡H_3 is parallel to the Si(111) surface.

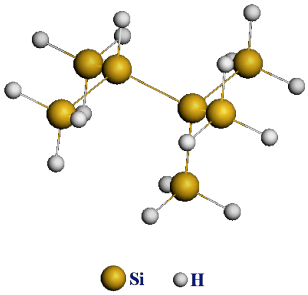

Figure 6. The Si_7H_{16} cluster model used in DFT calculation. H atoms are fully restricted.

Besides the thermal-solvolysis there can be another way to graft carbon chains onto silicon atoms, which depends on the dangling bonds formed in the rubbing process. The friction force in dry nitrogen environment is only several times larger than that in above vapor conditions. Since almost all the driving work in dry nitrogen condition is consumed on the formation of silicon dangling bonds, it is supposed that dangling bonds still forms in vapor conditions. In this paper we ignore the dynamic details in the formation of dangling bonds and use the reaction

$$\equiv Si_1 \bullet \quad + \quad ROH \quad + \quad \bullet Si_2 \equiv \quad \rightarrow \quad \equiv Si_1 - OR + \equiv Si_2 - H \tag{6}$$

to judge the reactivity of dangling bonds with different small molecules and define this reaction in terms of tribo-solvolysis. Two unsaturated Si atoms are used in this reaction to avoid odd number of electrons in DFT calculation. The distance from one Si atom to the other is set to be two times of equilibrium distance to contain the adsorbed small molecules. The energy of Si··Si is 351kJ/mol higher than Si-Si of equilibrium state and the energy change ΔE in Reaction (6) is used as the reactivity of tribo-solvolysis.

Figure 7 shows the DFT calculation results of E_b and ΔE. E_b and ΔE at the reference point are 149.7kJ/mol and -351kJ/mol, respectively. The distance Δ from each compound to the reference

point in kJ/mol can be considered as the activation energy E_a in Eq. (3). Since worn depth of failure devices is about 100-150nm as a constant, the life-time t_l in each vapor environment is theoretically expressed by

$$\lg(t_l / t_{l\_ethanol}) = (\Delta_{ethanol} - \Delta) \times 0.1744. \quad (7)$$

Figure 8 shows the experimental relationship of t_l and Δ of vapors in Fig. 4. Two approximate linear regions are found, one consists of water and fluoroalcohols with the slope of 0.05 and the other includes fatty alcohols with the slope of 0.01. The deviation of the slope from 0.1744 to 0.05 in Region II can be expressed by the non-corrosive stage of the initial wear. And for fatty alcohols, the significant deviation from the theoretical expectation suggests that only the thermal- and tribo-solvolysis is not able to give a full explanation of the tribo-reactions.

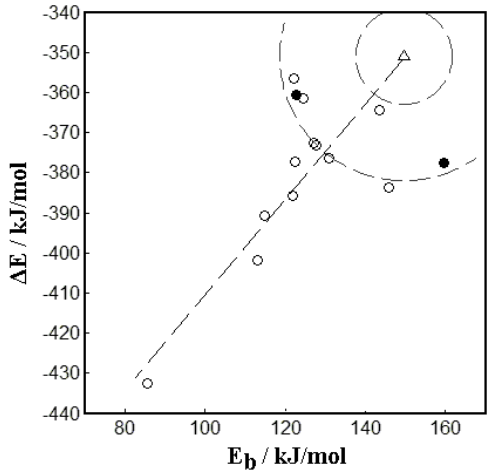

Figure 7. The DFT calculation results of E_b and ΔE. Δ: The reference point, ○: Volatile solvent, ●: Less volatile solvent. Dashed lines are used to guide the sight: along the straight line from top right to bottom left - the reference point, trifluoroethanol, 2-methoxyethanol, propanol, pentanol, hexanol, octanol and propylene oxide, along the arc line from top left to bottom right - tetrafluoropropanol, glycol, isopropanol, ethanol, methanol, 2-methoxyethanol, water and phenol.

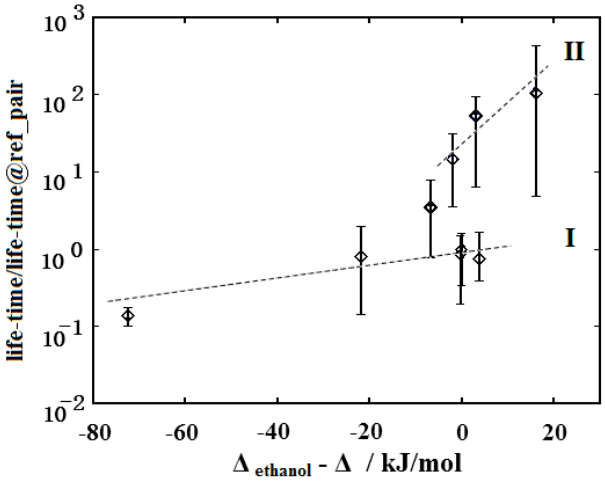

Figure 8. The relationship of life-time test and Δ. From left to right: Region I - propylene oxide, hexanol, propanol, methanol, ethanol and isopropanol, Region II – water, tetrafluoropropanol and trifluoroethanol.

Here we suggest a mechanochemical mechanism to understand the possible degradation routines for grafting groups on silicon surfaces. In tribo-conditions, the dangling bonds may not only form at top silicon atoms but also form by the rupture of grafted carbon groups. Consider the quasi-static vertical stretching of the end carbon atom on hexanol grafted at Si(111) surface in Figure 9. Using the DFT calculation by the Si_7H_{16} model, the chain will break at the end C-C bond, releasing the $CH_3\cdot$ radical. This character gives an explanation of the "tribochemical polymerization" [23] of short C_xH_y compounds found by TOF-SIMS in pentanol lubricating experiments, including surface-MEMS devices [24] and macro- ball(SiO_2)-on-disc(Si) experiments [23]. Figure 10 shows the rupture details of different grafted alcohols. Before a critical strain of approximately the same, the Si-O-R chain is stretched uniformly. And at the critical strain (about 0.2), the chain "breaks" at the end C-C bond, where the energy increase is about 0.86~1.25 times of forming a Si··Si pair. However, different chains have different trends to release carbon radicals. For hexanol, there is a jump at the break point and the CH_3 group is almost fully released to form radical. For ethanol, the jump is not significant and the CH_3 group still has some quantum connection with the main chain when the strain is more than 0.2. The situation of propanol is between ethanol and hexanol. But for fluoroalcohols, the CH_xF_{3-x} group can not get rid of the influence of main chain as fatty alcohols since the Si-O-R chain relaxes in a continuum manner. Therefore, the fluoroalcohols is much more stable than fatty alcohols when they are grafted on silicon surfaces and the latter can degrade by local mechanochemical effect. The longer the alcohol, the easier to break. This degradation may be harmful for lubrication and fluoroalcohols are better lubricant than fatty alcohols.

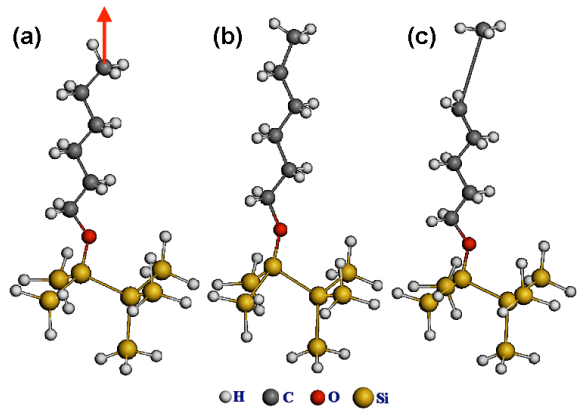

Figure 9. The quasi-static stretching of grafted hexanol on Si_7H_{16} cluster. (a) Initial state, (b) just before C-C break, (c) just after C-C break.

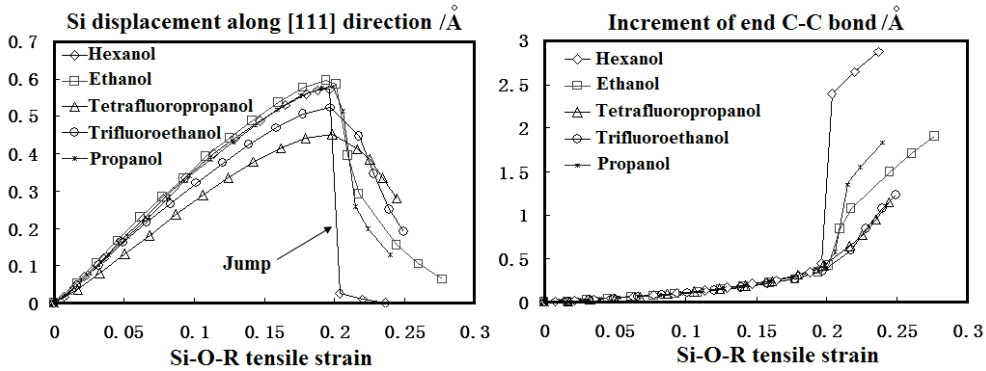

Figure 10. The tensile responses of different grafted alcohols on Si(111) surface.

5. Conclusion

In this research, a bulk-fabricated side-wall Si-MEMS tribotester is fabricated to study the life-time and wear process in different gas environments. By using the on-chip buckle loading method and the resonant driving strategy, the early stage of wear can be studied and classified into adhesive and corrosive types, depending on the gas environment. Since the permitted wear is quite light in MEMS devices, introducing a suitable corrosive vapor, such as alcohol, can relieve the initial wear to prolong the life-time. For fatty alcohols, the thermal- and tribo- solvolysis may not give a full explanation of tribo-reactions. A mechanochemical mechanism is proposed to understand the possible degradation of grafted alcohols on silicon and fluoroalcohols exhibit much more stable than fatty alcohols in the DFT calculation. The average wear life-time ratio in 2,2,2-trifluoroethanol vapor is about 100 times larger than that in ethanol vapor, so trifluoroethanol can give an effective lubrication for silicon devices.

Acknowledgements

This work was supported by the National Natural Science Foundation of China with grant Nos. 91123033 and 51021064.

References

[1] K. Komvopoulos, Surface engineering and microtribology for microelectromechanical systems. Wear, 200 (1996) 305-327

[2] M.G. Hankins, P.J. Resnick, P.J. Clews, et al., Vapor deposition of amino-functionalized self-assembled monolayers on MEMS. Reliability, Testing, and Characterization of MEMS/MOEMS II, 4980 (2003) 238-247

[3] S.T. Patton, W.D. Cowan, K.C. Eapen, J.S. Zabinski, Effect of surface chemistry on the tribological performance of a MEMS electrostatic lateral output motor. Tribol Lett, 9 (2000) 199-209

[4] D.M. Tanner, J.A. Walraven, L.W. Irwin, M.T. Dugger, The effect of humidity on the reliability of a surface micromachined microengine. IEEE International Reliability Physics Symposium Proceedings, (1999) 189-197

[5] S.A. Henck, Lubrication of digital micromirror devices™, Tribol Lett, 3 (1997) 239-24

[6] D.B. Asay, M.T. Dugger, S.H. Kim, In-situ Vapor-Phase Lubrication of MEMS. Tribol Lett, 29 (2008) 67-74

[7] M.N. Gardos, Tribological behavior of polycrystalline and single-crystal silicon. Tribol Lett, 2 (1996) 355-373

[8] S.J. Timpe, D.H. Alsem, D.A. Hook, M.T. Dugger, K. Komvopoulos, Wear of polysilicon surface micromachines operated in high vacuum. J Microelectromech S, 18 (2009) 229-238

[9] S. Shen, Y. Meng, Adhesive and Corrosive Wear at Micro Scales in Different Vapor Environments, submitted to *Friction*.

[10] J.F. Archard, Contact and rubbing of flat surfaces, J Appl Phys, 24 (1953) 981-988

[11] C. Mathew Mate, Tribology on the small scale, Oxford, 2008

[12] Y. Mo, K.T. Turner, I. Szlufarska, Friction laws at the nanoscale. Nature, 457 (2009) 1116-1119

[13] B. Gotsmann, M.A. Lantz, Atomistic wear in a single asperity sliding contact. Phys Rev Lett,

101 (2008) 125501-125504

[14] K. Nakayama, L. Zhang, Work function of scratched silicon surface during O_2 and N_2 adsorption. Jpn J Appl Phys, 39 (2000) 4509-4511

[15] A.C. Lasaga, G.V. Gibbs, Ab-initio quantum mechanical calculations of water-rock interactions: adsorption and hydrolysis reactions. Am J Sci, 290 (1990) 263-295

[16] R. Konecny, D.J. Doren, Adsorption of water on Si(100)-(2x1): A study with density functional theory. J Chem Phys, 106 (1997) 2426-2435

[17] P.L. Silvestrelli, Adsorption of ethanol on Si(100) form first principles calculations. Surf Sci, 552 (2004) 17-26

[18] R. Boukherroub, S. Morin, P. Sharpe, et al., Insights into the formation mechanisms of Si-OR monolayers from the thermal reactions of alcohols and aldehydes with Si(111)-H. Langmuir, 16 (2000) 7429-7434

[19] A.L. Barnette, D.B. Asay, D. Kim, et al., Experimental and Density Functional Theory Study of the Tribochemical Wear Behavior of SiO_2 in Humid and Alcohol Vapor Environments. Langmuir, 25 (2009) 13052-13061

[20] Y. Hibi, Y. Enomoto, Chemical analyses of mechanochemical reaction products of alpha-Si3N4 in ethanol and other lower alcohols. J Mater Sci Lett, 16 (1997) 316-319

[21] H. Seidel, L. Csepregi, A. Heuberger, et al., Anisotropic Etching of Crystalline Silicon in Alkaline-Solutions. 1. Orientation Dependence and Behavior of Passivation Layers. J Electrochem Soc, 137 (1990) 3612-3626

[22] A. Pelmenschikov, H. Strandh, L. Pettersson, et al., Lattice resistance to hydrolysis of Si-O-Si bonds of silicate minerals: Ab initio calculations of a single water attack onto the (001) and (111) beta-cristobalite surfaces. J Phys Chem B, 104 (2000) 5779-5783

[23] A.L. Barnette, D.B. Asay, J.A. Ohlhausen, et al., Tribochemical Polymerization of Adsorbed n-Pentanol on SiO_2 during Rubbing: When Does It Occur and Is It Responsible for Effective Vapor Phase Lubrication? Langmuir, 26 (2010) 16299-16304

[24] M.T. Dugger, Reliable Mechanical Contacts via Vapor Phase Lubrication. Sandia Report, 2009

Study on Radiation induced Mechanical Degradation of Amorphous Silicon Carbide Films

Bo Meng[1], Wei Tang[1], Xuhua Peng[1], Haixia Zhang[1,*]

[1] Institute of Microelectronics, Peking University, 100871, CHINA
* Corresponding author: hxzhang@pku.edu.cn

Abstract In this paper, the radiation effects of 1MeV protons on hydrogenated amorphous SiC films are studied by simulation and experiments. The molecular dynamics simulation by SRIM-2012 software package indicates that compared to crystalline SiC, hydrogenated amorphous SiC may suffer less radiation damage. SiC films with a thickness of 500nm are deposited on silicon substrates by PECVD, and then annealed at about 450℃. The prepared hydrogenated amorphous SiC films are irradiated by 1MeV protons in an electrostatic tandem accelerator at a flux of about 1.4×10^{12} cm^{-2} s^{-1} for 2 hours. The mechanical changes in irradiated silicon carbide films are investigated by nano-indentation and nano-scratch method. The irradiated film suffers a decrease in hardness and Young Modulus, but keeps nearly the same friction coefficient and surface topography as the contrast films.

Keywords Silicon Carbide, Mechanical degradation, Radiation damage

1. Introduction

Silicon carbide was considered as an excellent candidate for Micro-Electro-Mechanical Systems, especially in harsh environments applications [1]. Compared to crystalline SiC, low-stress PECVD SiC thin film is more attractive for CMOS compatible MEMS structures and devices [2]. As with space applications, MEMS devices are working in a complex radiation environment with massive energetic particles and photons. Space radiation induces electrical and mechanical degradation in materials. MEMS structures and devices would suffer mechanical failures and electrical failures after large doses of radiation [3,4]. In recent researches, the radiation effects on crystalline SiC were studied. Microstructural, electrical, mechanical degradation and amorphization of crystalline SiC under ion and neutron irradiation were reported [5–7].

In this work, we focus on the radiation effects of 1MeV protons on amorphous SiC films. SRIM-2012 software package is used to calculate the ions distribution in multiple layers of SiC/Si target. PECVD SiC films are deposited and annealed. The prepared SiC films are irradiated by 1MeV protons at a flux of about 1.4×10^{12} cm^{-2} s^{-1} for 2 hours. The radiation induced mechanical degradations are investigated by nano-indentation and nano-scratch method.

2. Simulation

SRIM-2012 software package, which concerns the stopping and range of ions in matter [8], is used to calculate the ions distribution in SiC and SiC/Si target.

Table 1. The projected range of crystalline SiC and H-SiC.

Samples	Atoms(%)			Projected Range (um)
	Si	C	H	
SiC	50	50		14.95
H-SiC	43	47	10	16.39

Since amorphous SiC films grown by PECVD generally contain a large number of hydrogen atoms, the projected ranges of 1MeV protons in crystalline SiC and hydrogenated amorphous SiC (H-SiC)

were calculated. As the results shown in Table 1, the projected range of crystalline SiC is shorter than hydrogenated amorphous SiC. Due to the existence of hydrogen atoms, hydrogenated SiC with the same width as crystalline SiC may suffers less radiation damage. As the distribution of incident protons in multiple layers of SiC/Si target is showed in Fig. 1, the protons are clustered at the center of projected range.

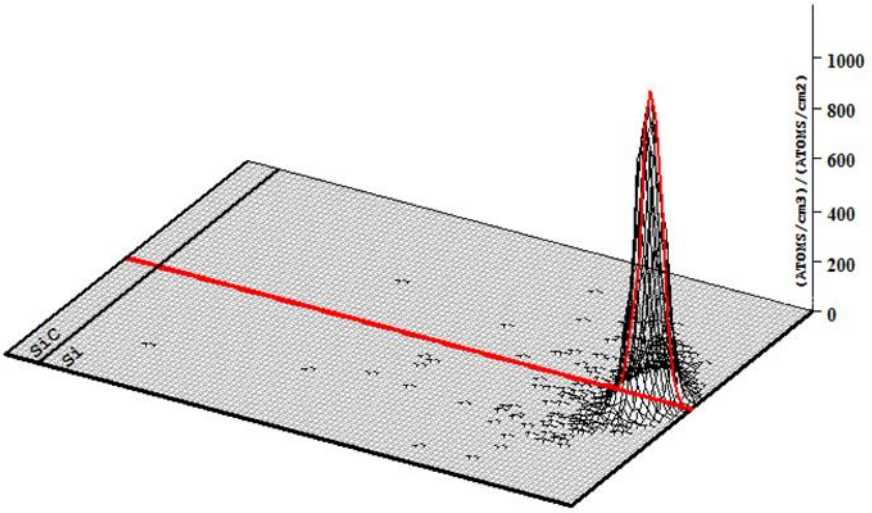

Figure 1. The distribution of incident protons in SiC/Si target.

3. Experiments

3.1 Preparing of amorphous silicon carbide films

500nm amorphous SiC films are deposited on 4 in. (100) silicon substrates by PECVD at 300 ℃. Some of the PECVD parameters are listed in Table 2. In order to get low-stress SiC films which are appropriate for fabricating MEMS structures, a furnace annealing process at about 450 ℃ for about 50 minutes is performed. Thus, the SiC films could be adjusted with a low tensile stress.

Table 2. Parameters of PECVD

Parameters of PECVD	Values
Flow rate of CH4 (sccm)	400
Flow rate of Ar (sccm)	400
Flow rate of NH3 (sccm)	5
Flow rate of SiH4 (sccm)	20
Pressure (mTorr)	1000
Power (W)	300
Temperature (℃)	300

3.2 Radiation on amorphous silicon carbide films

The prepared silicon carbide films were radiated by energetic protons in an electrostatic tandem accelerator at room temperature for 2 hours.

Table 3 illustrates some parameters of radiation experiments. In the accelerator, protons was accelerated to 1MeV. The protons beam was focused on a spot about 2×2 cm^2. The current of the protons beam is 0.9μA, thus the flux reaches 1.4×10^{12} cm^{-2} s^{-1}.

Table 3. Parameters of Radiation experiments

Current	Beam spot size	Flux	Time
0.9μA	4cm^2	1.4×10^{12}/cm^2 s	2h

4. Results and discussion

By nano-indentation, nano-scratch and other methods, the surface roughness, reflectivity, hardness, Young modulus and friction coefficient of irradiated SiC films are measured and analyzed. Deposited amorphous SiC films were employed as contrast samples.

4.1 Surface roughness and reflectivity

Surface topography of the films was observed by nano-indentation scan. As the 3D and plane topography showed in Fig. 2, the irradiated films demonstrates a similar surface topography with the contrast one. The average surface roughness of the irradiated silicon carbide film is 27nm, while the contrast one is 29nm.

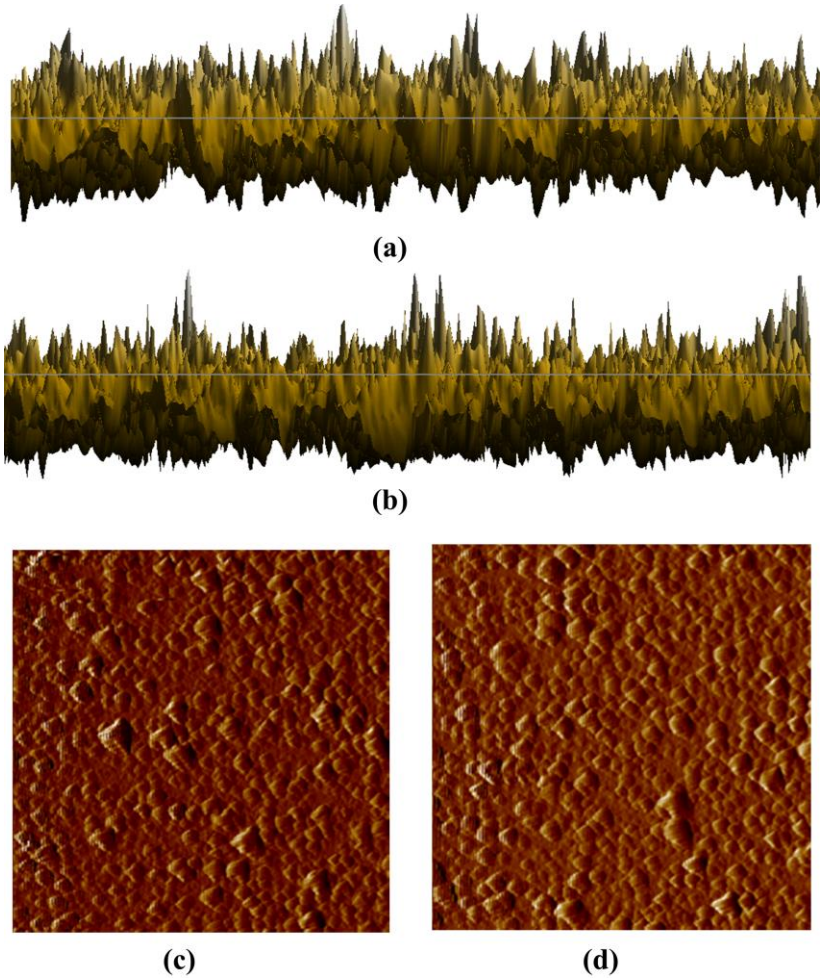

Figure 2. (a) 3D surface topography of irradiated SiC films;
(b) 3D surface topography of contrast SiC films;
(c) Plane surface topography of irradiated SiC films;
(d) Plane surface topography of contrast SiC films.

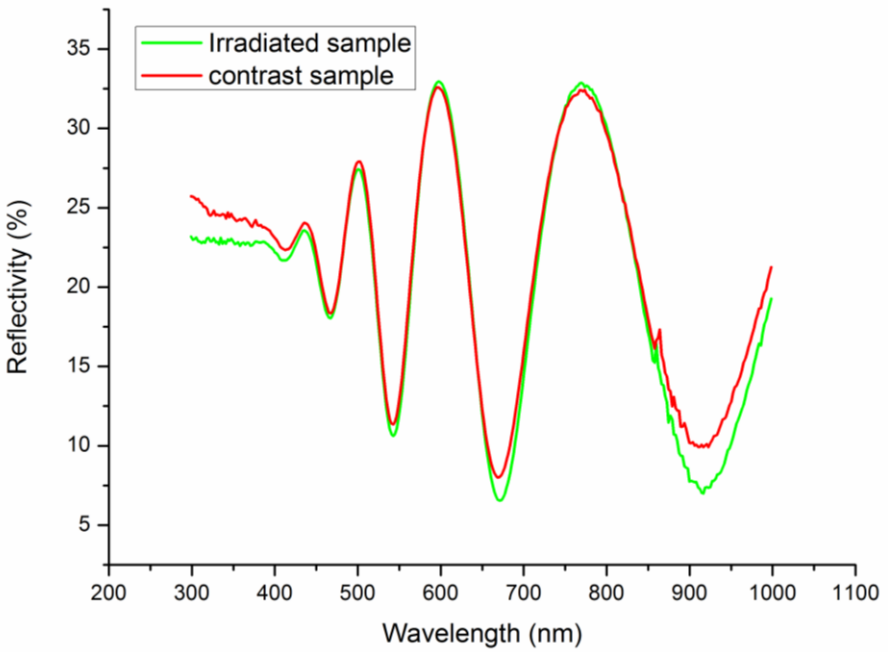

Figure 3. Integrating sphere reflectivity spectrums of SiC films

Integrating sphere reflectivity spectrums of the irradiated films and contrast films are measured at a wavelength range from 300nm to 1000nm. As Fig. 3 shows, the two kind of films demonstrate quite similar spectrums.

4.2. Hardness and Young modulus

Nano-indentation method was employed to measure and calculated the hardness and Young modulus of the films. The displacement in the irradiated films at the maximum load force of 10000μN is 367nm, while the contrast one is 230nm. Fig. 4 shows the load-displacement curves of the films at a load force of 1500μN.

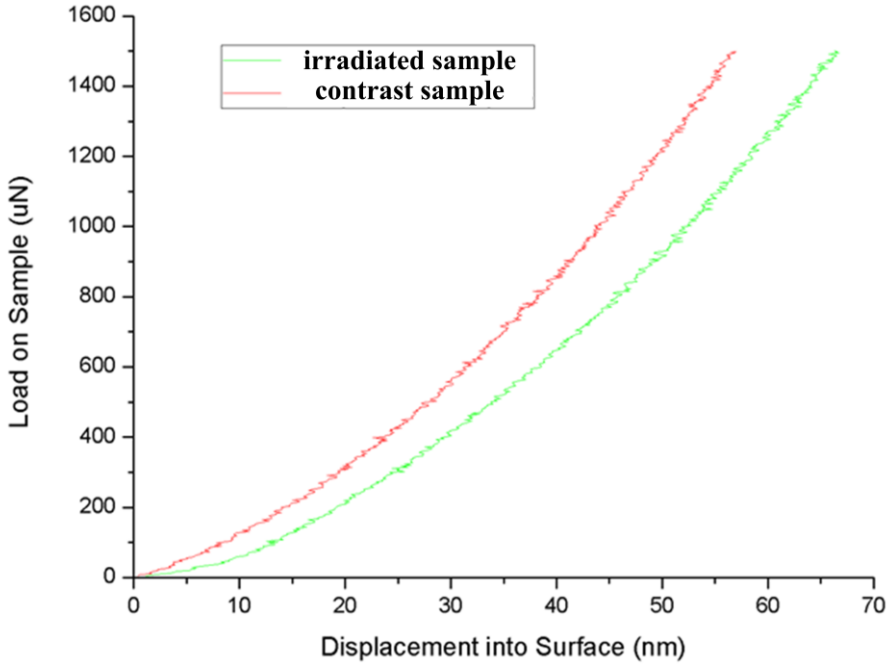

Figure 4. Load-displacement curves of the films in nano-indentation process

The average hardness and Young modulus of the films are calculated and listed in Table 4. The irradiated films demonstrate both lower hardness and young modulus than the contrast one, i.e., the contrast film is more robust than the irradiated film.

Table 4. The average hardness and Young modulus of the films.

Samples	Hardness (GPa)	Young modulus (GPa)
Irradiated samples	9.22	103.54
Contrast samples	10.66	114.46
Difference	15.6%	11%

4.3. Friction coefficient

Nano-scratch method was employed to measure friction coefficients of the films. Load force of 2000μN and 5000μN were used, the results are listed in Table 5. Allowing for the influence of surface roughness of the films, the friction coefficients of the two kinds of films demonstrates no significant difference at each load force. Fig. 5 shows the friction coefficients of the films at a load force of 5000μN during a nano-scratch scan process of 6μm.

Table 5. Friction coefficients at different load force.

Samples	Load Force(μN)	Friction coefficient
Irradiated sample	2000	0.108
	5000	0.154
Contrast sample	2000	0.096
	5000	0.151

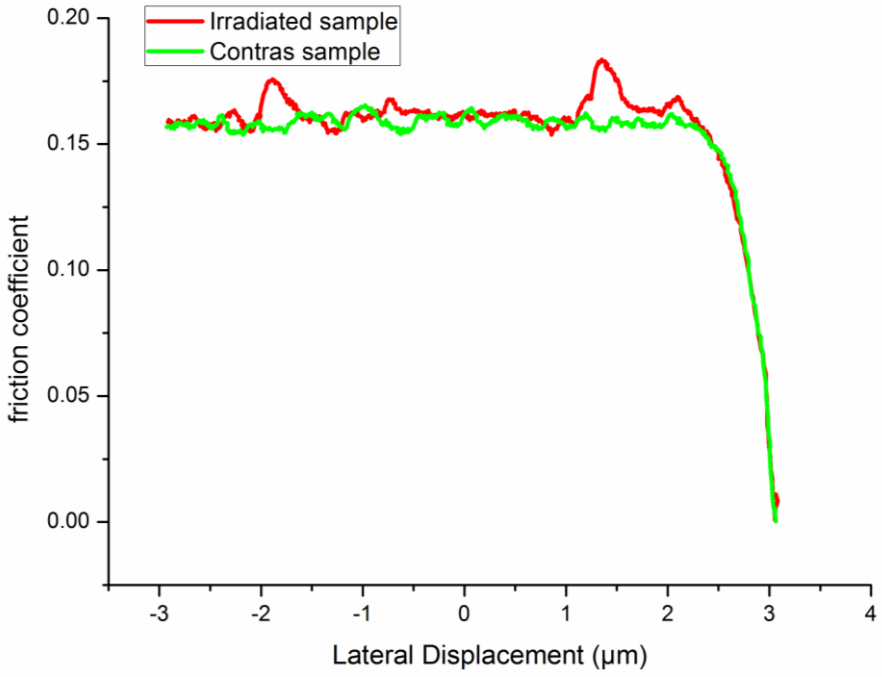

Figure 5. Friction coefficients at a load force of 5000μN during a nano-scratch scan process .

5. Conclusion

The radiation effects of 1MeV protons on amorphous SiC films are studied. According to calculated results of SRIM-2012 software package, the projected range of crystalline SiC is shorter than hydrogenated amorphous SiC. Hydrogenated SiC with the same width as crystalline SiC may

suffers less radiation damage. 500nm SiC films are deposited on 4 in. (100) silicon substrates by PECVD, and then annealed to obtain low stress SiC films. The prepared SiC films are irradiated by 1MeV protons in an accelerator at room temperature for 2 hours. The irradiated film suffers a decrease in hardness and Young modulus, but keeps the same in friction coefficient and surface topography as the contrast films.

Acknowledgements

This work is supported by the National Natural Science Foundation of China (grant nos 91023045 and 61176103), Key Laboratory Fund (no.9140C790103110C7903) and Doctoral Program Fund (no. 20110001110103). The authors appreciate the State Key Laboratory of Nuclear Physics and Technology in Peking University for assist in radiation experiments.

References

[1] P.M. Sarro, Silicon carbide as a new MEMS technology, Sensors and Actuators A: Physical, 82(2000) 210–218.
[2] P.M. Sarro, C.R. deBoer, E. Korkmaz, J.M.W. Laros, Low-stress PECVD SiC thin films for IC-compatible microstructures, Sensors and Actuators A: Physical, 67(1998)175–180.
[3] H. R. Shea, Radiation sensitivity of microelectromechanical system devices, J. Micro/Nanolith. MEMS MOEMS, 8(2009).
[4] E.G. Stassinopoulos, J.P. Raymond, The space radiation environment for electronics, Proceedings of the IEEE, 76(1988)1423–1442.
[5] L.L Snead, S.J Zinkle, J.C Hay, M.C Osborne, Amorphization of SiC under ion and neutron irradiation, Nuclear Instruments and Methods in Physics Research Section B: Beam Interactions with Materials and Atoms, 141(1998)123–132.
[6] M. Ishimaru, I.T Bae, A. Hirata, Y. Hirotsu, J.A. Valdez, K.E. Sickafus, Chemical short-range order in ion-beam-induced amorphous SiC: Irradiation temperature dependence, Nuclear Instruments and Methods in Physics Research Section B: Beam Interactions with Materials and Atoms, 242(2006)473–475.
[7] T. Hernández, E.R. Hodgson, M. Malo, A. Morono, Radiation induced electrical and microstructural degradation at high temperature for HP SiC, Fusion Engineering and Design, 86 (2011) 2442–2445.
[8] J. F. Ziegler, M.D. Ziegler, J.P. Biersack, SRIM-The stopping and range of ions in matter, Nuclear Instruments and Methods in Physics Research Section B: Beam Interactions with Materials and Atoms, 268(2010)1818–1823.

Droplet Ejection and Liquid-solid Separation from Covered Microfluidic Systems

Weiqiang Wang[1,2,*], Thomas B. Jones[2]

[1] School of Mechanical Engineering, Nanjing University of Science and Technology, Nanjing 210094, China
[2] Department of Electrical and Computer Engineering, University of Rochester, Rochester, New York 14627, USA
* Corresponding author: wangweiqiang@njust.edu.cn

Abstract In droplet-based microfluidics, two different types of microsystems are used for droplet manipulation - covered systems based on parallel-plate devices, and open systems based on single-plate devices. Ejecting droplets from covered systems into an open system is an essential operation to build a complete analysis system combining the advantages of both covered and open systems. This paper presents theoretical study and experimental results for ejecting a water and/or oil droplet from a covered into an open system. We use a force analysis method to determine the condition required for a droplet to cross the open/covered edge and demonstrate droplet movements using electric actuation. A bevelled edge structure is developed to facilitate the final liquid-solid separation process, greatly reducing the required actuation voltage.

Keywords electrowetting, electrowetting-on-dielectric (EWOD), microfluidics, dielectrophoresis

1. Introduction

Droplet-based microfluidics (or digital microfluidics) is a fast-developing liquid-handling technology that manipulates liquids in the form of discrete droplets. In integrated devices for droplet-based microfluidics, liquid droplets in contact with dielectric surfaces are moved by applying AC or DC potentials across electrodes patterned beneath the dielectric. There are two types of microsystems for electric actuation of liquid droplets: the covered system, in which voltages are applied across electrodes in both the top and bottom plates, [1-5] and the open system, in which voltages are applied across electrodes on a single plate. [6-10] The mechanism for droplet actuation has been attributed to electrowetting (EW) forces for conductive liquids [1-12], and to dielectrophoretic (DEP) forces for dielectric liquids. [13-16] When voltage is applied across electrodes in a device, a liquid droplet can move towards the activated electrode.

Study on droplet manipulation is usually done in either covered microsystems or open microsystems. The covered system is capable of achieving all the basic fluidic operations- droplet dispensing [3-5,18], moving [1,2], splitting [3,5] and merging [3], and controls droplet volume reliably through dispensing. [4,18] The open system, while lacking the capacity of dispensing or splitting droplets, [5] allows direct access to liquid handling tools on the surface and analytical equipments. Thus, the concept of dual open/covered microsystem combining the advantages of both covered and open systems is developed. [20,21] A covered section dispenses liquid droplets with desired volume and further analytical operation or liquid droplet handling is done on an open section. To achieve this scheme, it is essential to eject a droplet from a covered into an open section of a chip. In this paper, we analyze the possibility of such a motion for both water and oil droplets, and demonstrate experimental results to compare with the results of modeling. A bevelled edge on the top plate makes it possible to minimize the contact area between droplet and the top plate, thus easily separating the liquid-solid interface.

2. Water droplet ejection

An integrated device consisting of a covered section and an open section is illustrated in top and

side views in Figure 1 (a) and (b). The bottom plate consists of a patterned array of addressable electrodes, and the top plate in the covered section is coated with a transparent indium tin oxide (ITO) layer as a continuous ground electrode. The electrodes on bottom plate are coated with a dielectric layer, and both the top and bottom surfaces are covered with Teflon-AF as a hydrophobic film.

To evaluate the prospect of droplet movement from covered to open section by electrical actuation, we conduct force analyses to compare the driving forces with resisting forces. These results provide an estimate for the required voltage for a droplet to achieve such a motion.

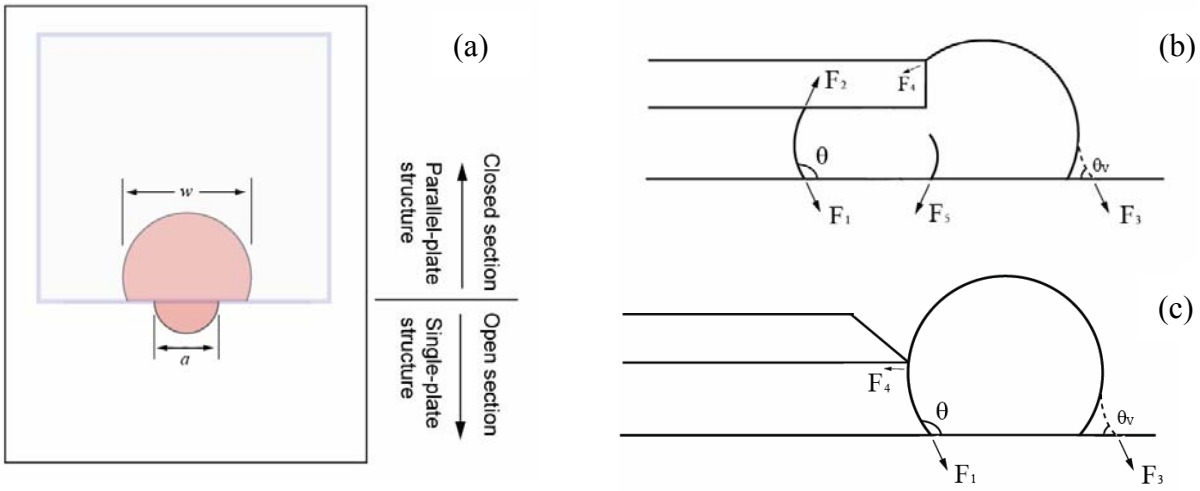

Figure 1. Force balance analysis of a water droplet ejection from covered into an open section. (a) Top view of a water droplet at the covered/open boundary. (b) Forces exerted on a water droplet when it is being moved toward the open section. (c) Liquid-solid separation with beveled edge.

2.1. Force balance analysis

The forces exerted on the droplet at the covered/open interface are illustrated in Figure 1 (b). We can distinguish two distinct contributions in the plane of the structure: the capillary force and the EW force. The capillary force is

$$F_c = F_1\left|\cos\theta\right| + F_2\left|\cos\theta\right| \quad (1)$$

and the EW force is

$$F_{EWOD} = F_3\left|\cos\theta_V\right| + (F_1 - F_5)\left|\cos\theta\right| \quad (2)$$

where $F_1 = F_2 = \gamma w$, $F_3 = \gamma a$, $F_5 = \gamma(w\text{-}a)$. w and a are contact lengths of the droplet in covered and open sections respectively, γ is the surface tension of the liquid droplet. θ_V and θ are the droplet contact angle with and without applied voltage.

When the water droplet is being moved from the covered section to the open substrate, the influence of F_4 can be neglected as there is no motion for the upper portion of droplet that contacts the edge of the ITO plate. Thus, the total force acting on the drop is:

$$F_{total} = F_3\left|\cos\theta_V\right| + (F_1 - F_5)\left|\cos\theta\right| + F_2\left|\cos\theta\right| \quad (3)$$

The three force components in equation (3) tend to move the droplet toward the open section, so we may expect that the droplet gets out the covered section easily. In fact, the water droplet tends to move out even without external applied voltage, in which case the net force becomes $F_2|\cos\theta|$.

When the droplet emerges from the covered section, it still tends to stick to the Teflon-coated ITO plate due to the low interfacial tension between water and Teflon. To facilitate the separation of the liquid droplet and the top plate, we bevel the edge of the top plate as shown in Figure 1 (c). Here the total force acting on the droplet is

$$F_{total} = (F_1|\cos\theta| + F_3|\cos\theta_V|) - F_4 = \gamma a(|\cos\theta| + |\cos\theta_V|) - \gamma a \quad (4)$$

Using $\theta = 115°$, $F_{total} > 0$ gives $\theta_V < 55°$. Because of the contact angle saturation effect, it is not easy to reduce the contact angle of a water droplet to lower than 55° by EW actuation. However, the electromechanical approach of EW theory shows that the EW force experienced by the droplet is independent of the surface profile. [13,14] This result indicates that contact angle saturation does not necessarily limit the maximum EW force that can be applied to a droplet. [17] Converting the contact angle to applied electric voltage by the Lippmann-Young equation, we get V > 105V as the voltage requirement for liquid-solid separation.

2.2. Experimental results of water droplet ejection

We fabricate a number of covered/open integrated devices on glass substrates to test droplet ejection motion. The bottom substrate consists of aluminum electrodes, a 0.5 μm spin-on-glass (SOG) dielectric layer, and a 1μm Teflon-AF layer. The top substrate is coated with an ITO layer and also a 1μm Teflon-AF layer. The spacing between top and bottom substrate is set to be 100 μm.

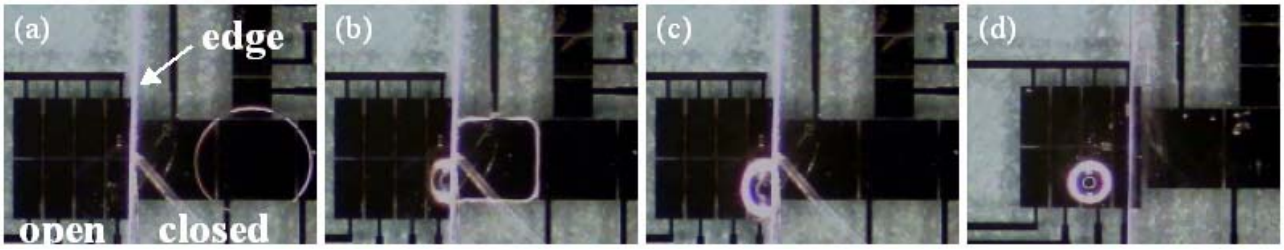

Figure 2. Moving a water drop from covered to open section. (a) The water droplet is initially placed in covered section. (b) The droplet is moved towards covered/open boundary by EW actuation using 100 V_{rms} 100 Hz AC. (c) The droplet enters open section as soon as it arrives at the boundary. (d) The droplet is successfully separated from top plate after applying 300 V_{rms} voltage.

Figure 2 shows video frames of water droplet motion from the covered to the open section. A water droplet is first injected into the covered section, and moved toward the covered/open interface by EW actuation. When the droplet reaches the interface, it is ejected rapidly but still sticks to the top plate. See Figure 2 (c). We then apply voltages ranging from 100 to 300 V_{rms} to separate the droplet and the top ITO plate. Separation is only successful at 300 V_{rms}.

To lower the required voltage for droplet/top plate separation, we bevel the edge of the top ITO plate to minimize the contact area between water droplet and Teflon surface. See Figure 3. Now the droplet can be easily separated by applying a voltage of 90 V_{rms}, which is even lower than the predicted value of 105 V. This is probably because the direction of force F_4 in Figure 1 (c) is not exactly horizontal, making the separation voltage somewhat lower.

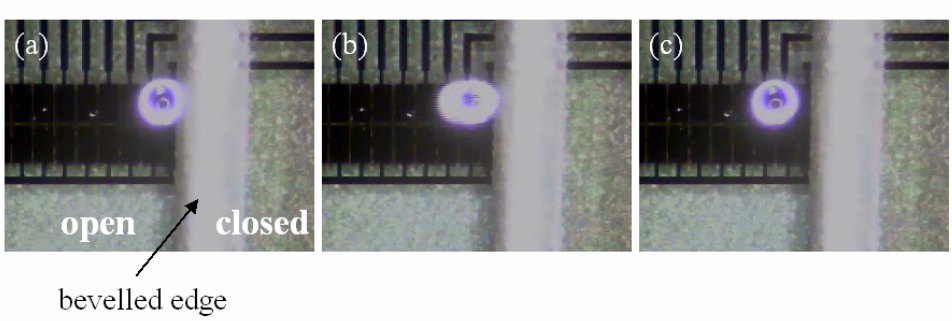

Figure 3. Separating a water drop and ITO plate with bevelled edges. The voltage applied is 90 V_{rms} 100 Hz AC.

3. Oil droplet ejection

Oil droplets have low surface tension and usually small contact angles on solid surfaces. It is likely that an oil droplet will find its way into cracks or small channels due to the capillary effect. As a consequence, it is very difficult to eject an oil droplet from covered into an open section.

3.1. Force balance analysis

The tendency of a liquid to enter narrow channels is commonly recognized as the capillary effect. A classic textbook example is the liquid rising in a vertical glass tube as shown in Figure 4 (a). For our apparatus, the liquid droplet moves horizontally and the goal is to use electrical actuation to overcome the capillary effect. To evaluate the requirements to accomplish this operation, we conduct a force analysis to compare the driving force and resisting forces as shown in Figure 4 (b). The total force acting on the oil drop is:

$$F_{total} = F_{DEP} - F_2\cos\theta - F_4\sin\theta + (F_3\cos\theta + F_5\cos\theta - F_1\cos\theta)$$

$$\approx F_{DEP} - F_2\cos\theta - F_4\sin\theta \qquad (5)$$

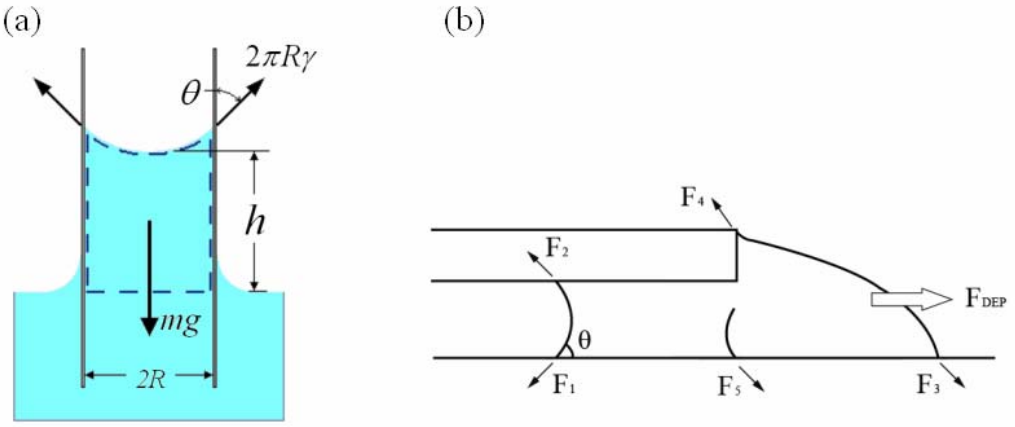

Figure 4. (a) Force analysis for a capillary tube. (b) Force analysis of an oil droplet at the covered/open boundary.

According to our device setup, [18,19] the minimum required voltage to achieve $F_{total} > 0$ is 1292 V and 1555 V for silicone oil and mineral oil, respectively. These high voltages are much greater than the dielectric breakdown voltages of 750 V, so it is impossible to achieve the desired movement by direct actuation. Furthermore, the oil droplet tends to get separated even the DEP force is large enough to overcome the resisting forces. We can understand this issue by considering a quasi-static process where the two plates are slowly separated as shown in Figure 5. The oil droplet sandwiched between parallel plates has a contact angle $\theta < 90°$. The vertical component of the surface tension forces at the upper (or lower) edge and the middle of drop are respectively:

$$F_{edge} = \gamma 2\pi R \sin\theta \tag{6}$$

$$F_m = \gamma 2\pi r \tag{7}$$

As the plates separate, both R and r decrease. Gradually F_{edge} will exceed F_m because r can approach 0. Then, the droplet breaks into two droplets, one each on the top and bottom substrates.

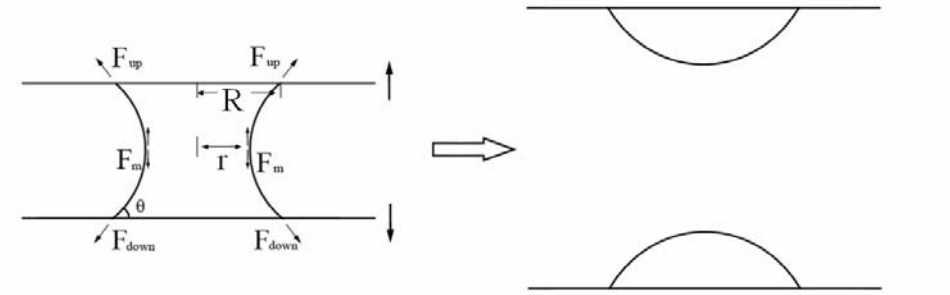

Figure 5. Breaking up of the oil droplet in parallel-plate structure when the two plates are separated far enough from each other.

A solution to this problem is to employ an oleophobic surface for the top plate. When the contact angle is > 90°, R at the upper edge is smaller than r, the oil droplet can be ejected without separation. And the total force acting on the oil droplet become

$$F_{total} = F_{DEP} + F_2 \left|\cos\theta^*\right| - F_4 \sin\theta \tag{8}$$

where θ^* is the oil contact angle against top surface, $\theta^* > 90°$. As F_2 and F_4 counterbalance each other mostly, the oil droplet can be ejected into an open section by DEP actuation.

3.2. Experimental results of oil droplet ejection

We fabricate an oleophobic surface on textured Si wafer and use it as the top plate for oil droplet ejection tests. The fabrication process of oleophobic Si microstructures is similar to that of Tuteja [22] and of Wu [23]. Figure 6 shows a mineral oil droplet sandwiched between a Teflon coated glass substrate (bottom) and a textured Si substrate (top) actuated by DEP. When the oil droplet is delivered to the covered/open boundary, continuous actuation moves the oil droplet to the open section, see Figure 6 (c).

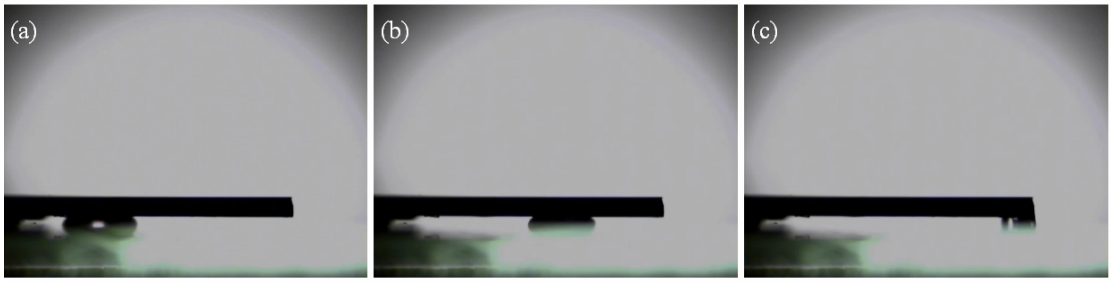

Figure 6. Side view showing the ejection of a mineral oil droplet. The spacing between Teflon coated glass substrate (bottom) and textured Si substrate (top) is 200 μm. The applied voltage is 560 Vrms 100 Hz AC.

The ejected oil droplet on open surface also sticks to the top plate. A beveled edge on the top plate may facilitate the detachment of the oil droplet. Further effort to fabricate an oleophobic beveled structure on the top plate is needed.

4. Conclusion

In this paper, we present theoretical predictions and experimental results on droplet ejection from covered into open microfluidic systems. We use a force balance analysis to predict the condition required to achieve such a motion. This model shows that it is easy to move a water droplet from covered to open section, but oil droplets always tend to stay in a covered section. Ejecting an oil droplet by direct DEP actuation is impossible on Teflon coated surfaces. An oleophobic surface must be used to complete this movement for oil droplet.

Experimental testing of the various predictions is done to demonstrate droplet ejection movements. To detach the water droplet from the top plate, we use a bevelled edge to minimize water-Teflon contact area and thus reduce the applied voltage. For oil droplets, we successfully use an oleophobic Si structure to achieve covered to open movement. Further study to bevel the Si structure is needed.

Acknowledgements

This work was supported by the U.S. Department of Energy, Office of Inertial Confinement Fusion under Cooperative Agreement No. DE-FC52-08NA28302, the University of Rochester, and the New York State Energy Research and Development Authority.

References

[1] M.G. Pollack, R.B. Fair, A.D. Shenderov, Electrowetting-based actuation of liquid droplets for microfluidic applications. Appl Phys Lett, 77 (2000) 1725–1727.
[2] M.G. Pollack, A.D. Shendorov, R.B. Fair, Electro-wetting-based actuation of droplets for integrated microfluidics. Lab Chip, 2 (2002) 96–101.
[3] S.K. Cho, H. Moon, C.J. Kim, Creating, transporting, cutting, and merging liquid droplets by electrowetting-based actuation for digital microfluidic circuits, J Microelectromech Syst, 12 (2003) 70-80.
[4] H. Ren, R.B. Fair, M.G. Pollack, Automated on-chip droplet dispensing with volume control by electro-wetting actuation and capacitance metering. Sens Actuators B, 98 (2004) 319–327.
[5] J. Berthier, Ph. Clementz, O. Raccurt, D. Jary, P. Claustre, C. Peponnet, Y. Fouillet, Computer aided design of an EWOD microdevice. Sens Actuators A, 127 (2006) 283–294.

[6] R.B. Fair, A. Khlystov, V. Srinivasan, V.K. Pamula, K.N. Weaver, Integrated chemical/biochemical sample collection, pre-concentration, and analysis on a digital microfluidic lab-on-a-chip platform. Proc of SPIE, 5591 (2004) 113-124.
[7] C.G. Cooney, C.Y. Chen, M.R. Emerling, A. Nadim, J.D. Sterling, Electrowetting droplet microfluidics on a single planar surface, Microfluid Nanofluid, 2 (2006) 435-446.
[8] M. Abdelgawad, A.R. Wheeler, Rapid prototyping in copper substrates for digital microfluidics, Adv Mater, 19 (2007) 133-137.
[9] P.Y. Paik, V.K. Pamula, K. Chakrabarty, Adaptive cooling of integrated circuits using digital microfluidics, IEEE Tran Very Large Scale Integr (VLSI) Syst, 16 (2008) 432-443.
[10] U.C. Yi, C.J. Kim, Characterization of electrowetting actuation on addressable single-side coplanar electrodes, J Micromech Microeng, 16 (2006) 2053-2059.
[11] F. Mugele, J.C. Baret, Electrowetting: from basics to applications, J Phys: Condens Matter, 17 (2005) R705-R774.
[12] R.B. Fair, Digital microfluidics: is a true lab-on-a-chip possible, Microfluid Nanofluid, 3 (2007) 245-281.
[13] T.B. Jones, On the relationship of dielectrophoresis and electrowetting, Langmuir, 18 (2002) 4437-4443.
[14] T.B. Jones, K.L. Wang, Frequency-dependent electromechanics of aqueous liquids: electrowetting and dielectrophoresis, Langmuir, 20 (2004) 2813-2818.
[15] K.L. Wang, T.B. Jones, Frequency-dependent bifurcation in electromechanical microfluidic structures, J Micromech Microeng, 14 (2004) 761–768.
[16] T.B. Jones, M. Gunji, M. Washizu, M.J. Feldman, Dielectrophoretic liquid actuation and nanodroplet formation, J Appl Phys, 89 (2001) 1441-1448.
[17] F. Mugele, Fundamental challenges in electrowetting: from equilibrium shapes to contact angle saturation and drop dynamics, Soft matter, 5 (2009) 3377-3384.
[18] W.Q. Wang, T.B. Jones, D.R. Harding, On-chip double emulsion droplet assembly using electrowetting-on-dielectric and dielectrophoresis, Fusion Sci and Technol, 59 (2011) 240-249.
[19] W.Q. Wang, T.B. Jones, Microfluidic actuation of insulating liquid droplets in a parallel-plate device, J Phys: Conf Ser, 301 (2011) 012057.
[20] J. Berthier, Ph. Clementz, J.M. Roux, Y. Fouillet, C. Peponnet, Modeling microdrop motion between covered and open regions of EWOD microsystems, Proc 2006 Nanotech Conf, (2006) 685-688.
[21] G. Wang, D. Teng, S.K. Fan, Three-dimensional digital microfluidics and applications, Proc IEEE NEMS, (2012) 415-418.
[22] A. Tuteja, W. Choi, M. Ma, J.M. Mabry, S.A. Mazzella, G.C. Rutledge, G.H. McKinley, R.E. Cohen, Designing superoleophobic surfaces, Science, 318 (2007) 1618-1622.
[23] T. Wu, Y. Suzuki, Engineering superlyophobic surfaces as the microfluidic platform for droplet manipulation, Lab Chip, 11 (2011) 3121-3129.

Core Shell Nanowire Surface Fastener Used for Mechanical and Electrical Room Temperature Bonding

Peng Wang, Yang Ju*, Atsushi Hosoi

Department of Mechanical Science and Engineering, Nagoya University, Nagoya 464-8603, Japan
* Corresponding author: ju@mech.nagoya-u.ac.jp

Abstract This paper presents a method of fabricating surface fastener for the application of mechanical and electrical room temperature bonding based on core shell nanowire array. This surface fastener consists of core shell nanowire array with the copper core and parylene shell. The copper nanowire array on the silicon substrate was prepared through template-assistant electro-deposition, which provided the electrical conductive function. The parylene shell was deposited on Cu nanowire array through CVD method, which provided surface compliance to increase contact areas, thereby realizing larger bonding strength. Through pressing core shell nanowire arrays against each other, the van der Waals forces between the interpenetrating nanowires had a contribution to the room temperature. This room temperature bonding technology may enable the exploration of a wide range applications involving assembly of components in the micro electronics.

Keywords Core shell, Nanowire, Surface fastener

1. Introduction

The continuous trend towards miniaturization and functional density enhancement makes an urgent demand to improve the bonding technology in the surface mount technology. The traditional bonding technology utilizes the solder. However, solder has relatively high electrical properties and copper-tin intermetallics have poor mechanical propertities[1]. An all-copper connection technology has been introduced, but the annealing temperature range of 350-450°C is too high for cost-efficient organic broads or substrates[2]. Moreover, the surface-activated bonding method has been reported, which can be performed at room temperature[3, 4].However, the high electrical resistance (above 1000Ω) may prohibit it application in electrical interconnection. Therefore, to create a bonding technology which not only has good mechanical and electrical property but also does not need high processing temperature is always a destination for the researchers.

With the efficient utilization of von der Waals forces, the gecko can firmly attach to and rapidly detach from varied kinds of surfaces. Many methods have been used to replicate this adhesion mode by some well-arranged micro and nanostructure arrays. Some gecko-inspired adhesive designs with nanowire arrays were cast through porous membranes available from commercial suppliers[5, 6]. Moreover, some special polymer micro and nanostructures, such as mushroom-shaped fibers[7], wedge-shaped fibers[8], bent fibers[9], spatula tips[10], led to bigger strength but also a more complicated manufacturing process. Recently, by using vertically aligned multiwalled carbon nanotube (MWCNT) with curly entangled end segment[11], the extremely high shear adhesion (~100 N/cm^2) was obtained, which was ten times higher than gecko's adhesion strength. Compared with the template method, the chemical vapor deposition method used to fabricate MWCNT is expensive and need high processing temperature.

Recently, a new kind of bonding technique based on core/shell nanowire structure has been demonstrated[12]. Moreover, electrical connector can be obtained through depositing a thin metal film on the nanowires[13]. Although this structure can achieve mechanical interconnection at room room temperature, the high temperature in the fabrication process and the relatively high electrical resistance prohibit their application in the bonding technique in micro electronics. In this paper,

copper/parylene core/shell nanowire surface fastener was investigated and showed much better electrical properties. The copper nanowire array on the silicon substrate was prepared through template-assistant electro-deposition, which provided the electrical conductive function. The parylene shell was deposited on Copper nanowire array through CVD method, which provided surface compliance to increase contact areas, thereby realizing larger bonding strength. In term of pressing the two nanowire array against each other, high adhesion strength was obtained at the same time due to the von der Waals forces between the interleaved nanowires. The according electricity resistance measurement showed that the electrical resistance of core/shell nanowire array was small.

2. Experiment details.

2.1. Electrodeposition of copper nanowires

Polycarbonate (PC) membranes (ISOPORE, Millipore Inc.) containing 0.1 μm diameter pores were used as the templates. The cathode was fabricated through sputtering 50 nm Cr adhesion layer and 100 nm Au seed layer on the substrate. With the help of isolation holders, the PC template was fixed right above the substrate. Copper nanowire arrays were then synthesized by electrodepostion under a constant current of approximately 0.003A. The electro-deposition electrolyte used was a 0.4 M $CuSO_4 \cdot 5H_2O$ solution, adjusted at pH=2 with sulfuric acid. The electro-deposition was performed at room temperature and without stir. After etching in methylene chloride to remove the PC membrane, the freestanding copper nanowire array on the substrate was obtained.

2.2. Parylene coating

As shown in figure 1, parylene-N was deposited on copper nanowire arrays by using a DACS-LAB deposition system. A typical deposition condition used in this work was 160°C for the vaporization of the parylene dimmer precursor, 650°C for the pyrolysis of the dimmer into monomers, and 60mTorr for the vacuum chamber. Through controlling the amount of the loaded precursor, the according thickness of parylene shell could be obtained.

2.3. Testing of parasitic resistance and bonding strength

The samples were connected to each other under the preload of 29.4N，and then the parasitic resistance was measured by the four-point probe method (figure 3a) after the preload was completely removed. During the measurement, electrical current from 0 to 20 mA was applied by the current source to the four-point probe measuring circuits and U-I curves were generated. The shear bonding strengths were tested by measuring the maximum forces that the surface fasteners could afford. The weights of a balance ranging from 1g to 1kg were used to fulfill this testing.

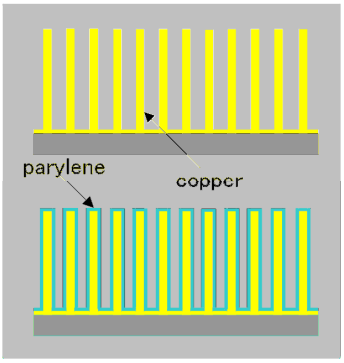

Fig. 1 Schematic of parylene coating

3. Results and discussion

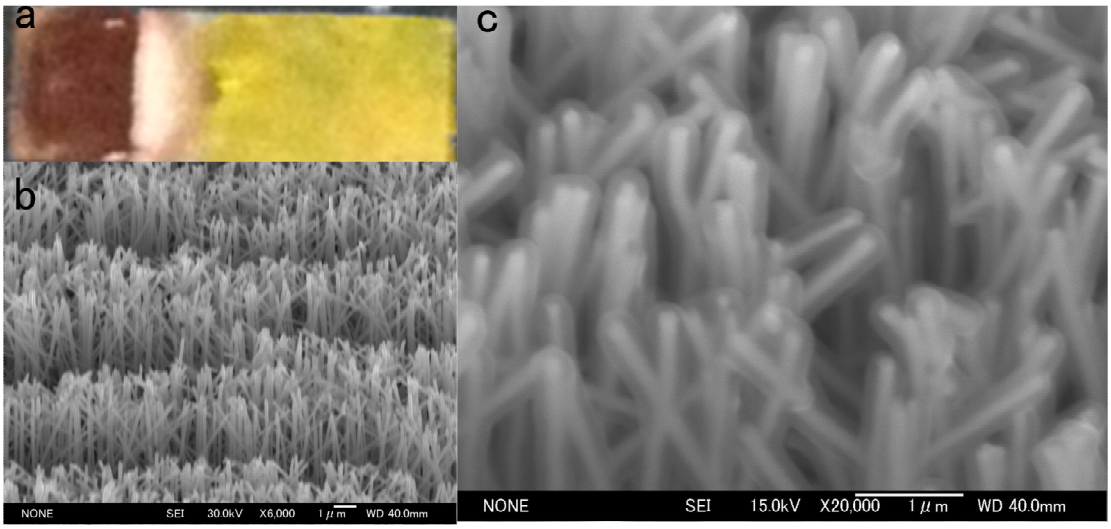

Fig. 2 (a) Photograph of the sample (b) SEM image of the fabricated nanowire array (c) SEM of the nanowire array after the parylene coating

As can be seen in figure 2a, it was easy to distinguish the fastener area from the Au film via their surfaces because the former became red in color. Scanning electron microscopy (SEM) observation (figure 2b) indicated that copper nanowire array grew on all the red area and the length of the nanowire array was uniform in most areas. From figure 2c, many relative dark shells around the bright wires could be observed. Because the parylene is non-conductive, it is darker than the copper in SEM image. The thickness of the shell was measured to be about 50nm.

The voltage-current (*U-I*) curve of interconnected fasteners is shown in figure 3b. The solid line in the figure was obtained through linear fitting of the measured values. Typical Ohmic contact performance was observed and parasitic resistance of 0.82 Ω can be extracted from the slopes of the fitted line. This result is possible to be used as the electrical bonding in surface mount. Figure 4 shows photograph of surface fasteners sustaining a weight of 500g in the shear direction. This bonding strength corresponded to the adhesion strength of 50 KPa. The purpose of our research is to develop a new mechanical and electrical room temperature bonding in surface mount. Regarding to the room temperature bonding or solder in surface mount, there are some design guidelines about the ratio between the component's weight and the bonding area. According to the standard value for second side reflow mounting (R=30g/in^2)[14]. If we consider this weight-area ratio to be R=50g/cm^2, which is more than ten times than the standard value. The bonding strength (S=50kPa) can withstand an acceleration of $a=S/R$=100N/kg>10*g (g=9.8N/kg is the acceleration of gravity). This result means that this room temperature bonding technique can be used in most equipment.

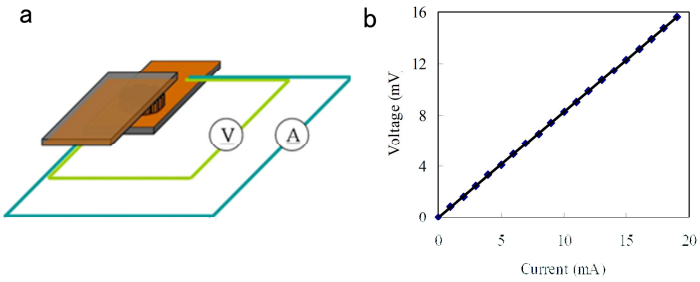

Fig. 3 (a) Schematic of four-point probe measurement (b) Measured *U-I* curves of the bonding

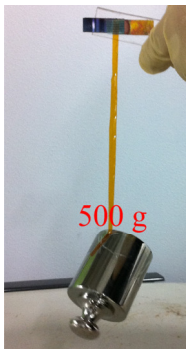

Fig. 4 A photo showing a weight balance of 100g hanging on the interconnected NSFs

4. Conclusions

In conclusion, a new kind of surface fastener composed of copper/parylene core/shell nanowire arrays has been proposed through which electrical and mechanical bonding can be realized at room temperature. Electrical measurement indicated that the electrical resistance of the interconnected nanowire array on the fastener is around 0.82 Ω under the preload of 29.4 N. The bonding strength of approximately 50 kPa was obtained. Therefore, this kind of core/shell nanowire surface fastener is hopeful to be used as electrical and mechanical room temperature bonding in the surface mount.

Acknowledgements

This work was supported in part by the Micro/Nano Mechatronics GCOE for Scientific Research from the Ministry of Education, Culture, Sports, Science and Technology.

References

[1] A. He, T. Osborn, S. A. B. Allen, P. A. Kohl, Low-temperature Bonding of Copper Pillars for All-copper Chip-to-Substrate Interconnections, Electrochem. Solid-State Lett., 9 (2006) 192–195.

[2] K. N. Chen, C. S. Tan, A. Fan, R. Reif, Morphology and bond strength of copper wafer bonding, Electrochem. Solid-State Lett., 7 (2004) 14–16.

[3] R. Takigawa, E. Higurashi, T. Suga, R. Sawada, Room-Temperature Bonding of Vertical-Cavity Surface-Emitting Laser Chips on Si Substrates Using Au Microbumps in Ambient Air, Appl. Phys. Express, 1 (2008) 112201.

[4] E. Higurashi, T. Fukunaga, T. Suga, Low-Temperature Bonding of GaN on Si Using a Nonalloyed Metal Ohmic Contact Layer for GaN-Based Heterogeneous Devices, IEEE Quan. Electron., 48 (2012) 182-186.

[5] J. Lee, B. Bush, R. Maboudian, R. S. Fearing, Directional adhesion of gecko-inspired angled microfiber arrays, Appl. Phys. Lett., 93 (2008) 191910..

[6] J. Lee, C. Majidi, B. Schubert, R. S. Fearing, Sliding-induced adhesion of stiff polymer microfiber arrays. I. Macroscale behavior, J. R. Soc. Interface, 5 (2008) 835-844.

[7] S. Kim, E. Cheung, M. Sitti, Wet Self-Cleaning of Biologically Inspired Elastomer Mushroom Shaped Microfibrillar Adhesives, Langmuir, 25 (2009) 7196-7199.

[8] A. Parness, D. Soto, N. Esparza, N. Gravish, M. Wilkinson, K. Autumn, M. Cutkosky, A microfabricated wedge-shaped adhesive array displaying gecko-like dynamic adhesion, directionality and long lifetime, J. R. Soc. Interface, 6 (2009) 1223-1232.

[9] Kim, T. I., Jeong, H. et al, Stooped Nanohairs: Geometry-Controllable, Unidirectional, Reversible, and Robust Gecko-like Dry Adhesive, Adv. Mater., 21 (2009) 2276-2281.

[10] M. P. Murphy, B. Aksak, M. Sitti, Gecko-Inspired Directional and Controllable Adhesion, Small, 5 (2009) 170-175.

[11] L. T. Qu, L. M. Dai, M. Stone, Z, Xia, Z. L. Wang, Carbon nanotube arrays with strong shear

binding-on and easy normal lifting off, Science, 322 (2008) 238-242.

[12] H. Ko, J. Lee, B. E. Schubert, Y. Chueh, P. W. Leu, R. S. Fearing, and A. Javey, Hybrid Core-Shell Nanowire Forests as Self-Selective Chemical Connectors, Nano lett., 9 (2009) 2054-2058.

[13] R. Kapadia, H. Ko, Y. Chueh, J. Ho, T. Takahashi, Z. Zhang, A. Javey, Hybrid Core-Shell Nanowire Forests for Electrical Connector Applications, Appl. Phys. Lett., 94 (2009) 263110

[14] Y. Liu, D. A. Geiger, D. Shangguan, Determination of Components Candidacy for Second Side Reflow with Lead-Free Solder, IEEE Electronic Component Technology Conference, Orlando, May, 2005, 970-976.

Anchor Design for Microdevice Fabricated by Silicon-on-Glass Process Based on Bonding Strength Consideration

Jun He, Fang Yang, Danqi Zhao, Xian Huang, Wei Wang, Dacheng Zhang*

National Key Laboratory of Science and Technology on Micro/Nano Fabrication, Institute of Microelectronics, Peking University, Beijing 100871, China
* Corresponding author: dchzhang@ime.pku.edu.cn

Abstract In this paper, an array-shaped anchor for microdevice (fabricated by silicon-on-glass (SOG) process) was designed for improving its bonding strength. This design scheme aims to release the coefficient of thermal expansion (CTE) mismatch induced residual stress and decrease the metal electrode layer or particles induced bonding failure risk. To evaluate the bonding performance of the proposed anchor design scheme, numerical simulation and mechanical experiments are carried out on well-established anchor-beam MEMS devices. The scanning electron microscope (SEM) results indicated that the bond yield of the array-shaped anchor was higher than the single anchor. The fracture tests results demonstrated that the torsional bonding strength of the array-shaped anchor was stronger than that of the conventional single anchor in practical application.

Keywords Particles, Bond yield, Torsional bonding strength, Fracture test

1. Introduction

Due to the development of micromachining technology, various micro electro-mechanical system (MEMS) devices (e.g. inertial micro accelerometers, RF/Microwave Devices, microfluidic devices, optical devices) can be fabricated [1–5]. As an important technique in micromachining, the anodic bonding, also known as field-assisted bonding, was firstly developed in the late 1960s by Wallis and Pomerantz [6–8]. Nowadays it has matured into a flexible technology with lots of applications [9]. One of the important applications is constructing micro anchor (bonded structure) for MEMS devices fabricated by the silicon-on-glass (SOG) process, which provides mechanical support or electrical connect to the movable sensing/actuating functional components. Therefore the bond yield and bonding strength of anchors are two of the main aspects for the reliability of MEMS devices [10].With the devices scaling, the bonding strength need to be considered carefully with limited bonding area. Besides, many factors on the bonding surface will lead to a dramatic degradation of the bonding quality and even the bonding failure when the anchor is small; for instance, the metal electrode layer, particles, contaminations and the CTE mismatch induced residual stress [11]. As a result, conventional single anchor is not the optimal choice for small devices. In this paper, a novel array-shaped anchor is proposed to address the above mentioned bonding degradation issues by dividing the single anchor into four identical sub-anchors. For the first time, the correlation between shape/size and bonding strength of the anchor is studied. Theoretical analysis demonstrates the array-shaped anchor improves bond yield and the shock resistance by reducing the bonding failure risk. In addition, the array-shaped anchor is proved to be a perfect way to release the residual stress for the high anchor (Fig 3) as well. Two series of well-established anchor-beam MEMS devices are fabricated by SOG process. The bond yield and torsional bonding strength of the anchors (both conventional and the array-shaped) are measured for

comparison. The experimental results indicated that the proposed array-shaped anchor is performing well and superior to the conventional single anchor ones.

2. Theoretical analysis

The array-shaped anchor design, consisting of four identical square sub-anchors, is illustrated in Fig.1(b). Bonding parameters, the metal electrode layer, particles, other contaminations on the surface within the bonding area, and the residual thermal stress, all these factors affect bonding strength of microdevices. Theoretical comparison between array-shaped anchor and single anchor on bonding quality and residual thermal stress is conducted.

(a) conventional single anchor (b) array-shaped anchor

Figure 1. The different anchor designs

2.1 Bonding quality

When the anchor is small, the metal electrode layer, particles or other contaminations may lead to a dramatic degradation of the bonding quality, even the bonding failure (Fig. 2(a)). But if it happens to array-shaped anchor, the unaffected sub-anchors without particles can be still bonded successfully (Fig. 2(b)), therefore the average bonding quality is better than that of single anchor ones, namely, the array-shaped anchor design improves the bond yield.

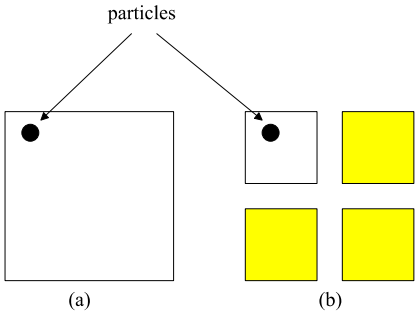

Figure 2. The particles on the surface within the bonding area:
(a) single anchor (b) array-shaped anchor

In addition, the existence of the metal electrode layer or particles will generate defect points on the surface. It is assumed that the ultimate strength of the defect points and normal bonding region is σ_1 and σ_2 respectively ($\sigma_2 > \sigma_1$). When the single anchor's surface stress reaches σ_1, the crack will arise from the defect point, and then propagates until the single anchor fractured because of the brittleness of the monocrystalline silicon (Fig. 2(a)). With regard to array-shaped anchors, when the

surface stress reaches σ_1, the crack will also arise from the defect point, but owing to the sub-anchors without particle contaminations the crack will not propagate. So the ultimate strength of the array-shaped anchor is σ ($\sigma_1 < \sigma < \sigma_2$), which is larger than σ_1, the single anchor's ultimate strength, i.e. improving the shock resistance.

2.2 Residual thermal stress

The array-shaped anchor is conducive to release residual stress caused by CTE mismatch. As a result of the size decrease of the bonding surface, the thermal stress of every sub-anchor surface is much lower than that of the single anchor one [12]. The CTE mismatch between different sub-anchors can be remitted by the bending of sub-anchors. In order to demonstrate advantages of the array-shaped anchor the finite element analysis (FEA) is performed. For silicon and glass, parameters applied in the simulation are shown in table 1. Figure 3 shows the residual thermal stress contour of the bonding surface. The highest stress on the bonding surface of single anchor is 46 MPa, while that of the array-shaped anchor is 34 MPa (table 2). It can be concluded from the FEA results that the array-shaped anchor is beneficial to release the thermal stress.

Table 1. Parameters in FEA

	Young modulus	Poisson ratio	CTE	Bonding temperature	Operating temperature
Glass	62.75 Gpa	0.20	3.25E-6	623 K	300 K
Si	169 Gpa	0.28	2.6E-6	623 K	300 K

Table 2. FEA results of Fig. 3

	Type	Anchor height	Side length of anchor (sub-anchor)	Gap between sub-anchors	Highest stress
Figure 3(a)	Single anchor	40 μm	26 μm		46 MPa
Figure 3(b)	Array-shaped anchor	40 μm	12 μm	2 μm	34 MPa

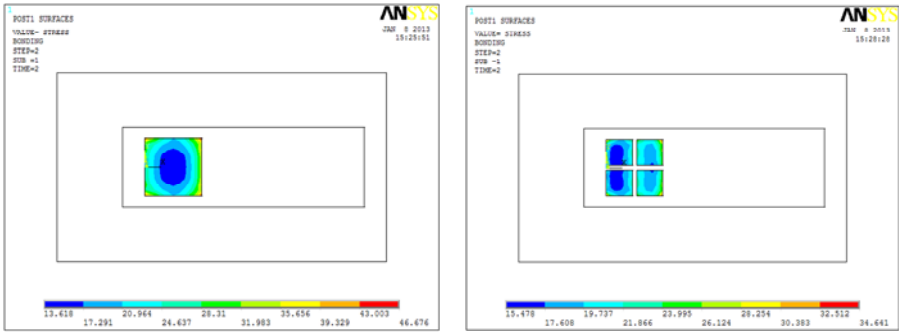

(a)conventional single anchor (b)array-shaped anchor

Figure 3. Contour plot of residual thermal stress of bonding surface (anchor height of 40μm)

Besides, effects of anchor height on thermal stress of the array-shaped anchor are also analyzed.

Figure 4 shows the residual thermal stress contour of bonding surface for the anchor with a height of 4 μm. And detailed results are listed in table 3. It can be concluded that the thermal stress of array-shaped anchor is higher than that of the single anchor. Furthermore, the stress discrepancy reduces as the gap between sub-anchors decreases. The reasons are that sub-anchors could hardly bend when the height of anchors is small, therefore thermal stress cannot be released by bending of the sub-anchors but only by the deformations of the bonding surface. In addition, due to the loss of the bonding surface, the thermal stress of array-shaped anchor is higher. However, this effect can be ignored comparing with ultimate strength in an order of GPa.

Table 3. FEA results of Fig.4

	Type	Anchor height	Side length of anchor (sub-anchor)	Gap between sub-anchors	Highest stress
Figure 4(a)	Single anchor	4 μm	46 μm		85 MPa
Figure 4(b)	Array-shaped anchor	4 μm	16 μm	14 μm	102 MPa
Figure 4(c)	Array-shaped anchor	4 μm	18 μm	10 μm	96 MPa
Figure 4(d)	Array-shaped anchor	4 μm	20 μm	6 μm	91 MPa

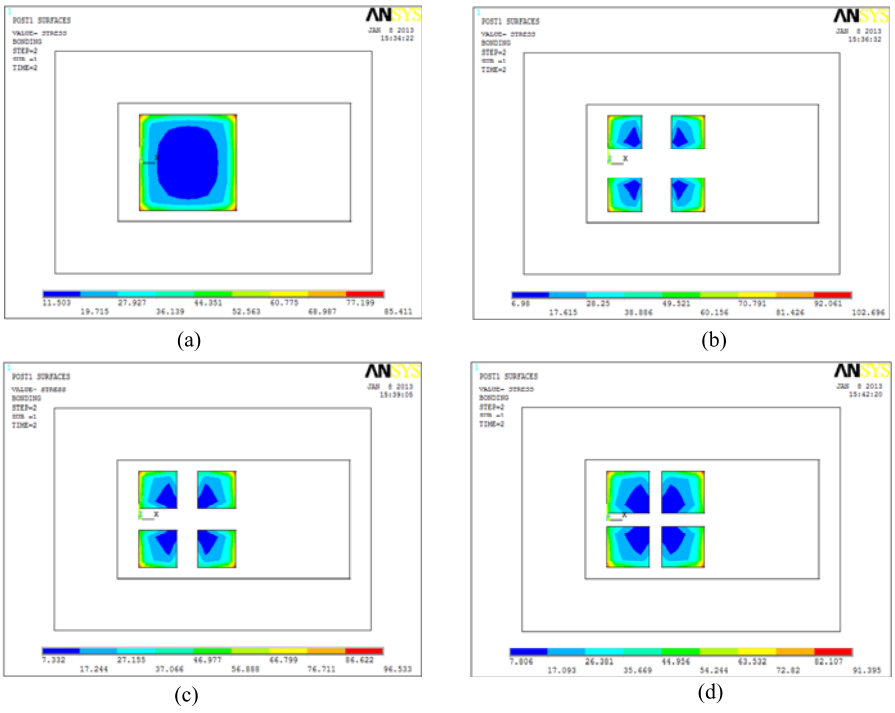

(a) (b) (c) (d)

Figure 4. Contour plot of residual thermal stress of bonding surface (anchor height of 4 μm)

3. Experiments

To evaluate the bonding performance of the proposed anchor design experimentally, two series of

well-established anchor-beam MEMS devices (both conventional and the array-shaped) fabricated by SOG process were carried out to test the bonding quality and the bonding strength in practical application. The basic flow of SOG process (Fig. 5) is described as follows:
(a)Define bonding area, i.e. anchor, by advanced silicon etch (ASE).
(b)Form interconnects on glass wafer by lift-off process.
(c)Anodic bonding and KOH etch.
(d)Release structure by deep reactive ion etching (DRIE).

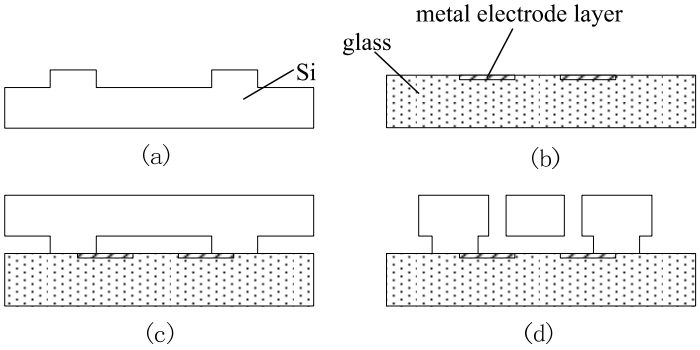

Figure 5. Basic flow of SOG process

3.1 Bonding quality testing device

The bond yield is utilized to evaluate the bonding quality. And various bonding areas are designed to investigate its influence on bond yield for both anchor design schemes. To compare the bond yield conveniently, a similar failure-accelerating method in reliability analysis is introduced. Microdevices are intentionally designed to extreme sizes. On one hand, the anchor is designed to be high enough (anchor height of 30μm). With a higher anchor, the electrostatic force of non-bonding surfaces will reduce and the pressure of bonding surface will decrease accordingly in anodic bonding. As a result, the bonding quality will be poor. On the other hand, the adjacent anchor in a certain direction is designed far enough, because the further adjacent anchor has less assist in anodic bonding of the anchor here.

The structure of the microdevice is shown in Fig. 6. The array-shaped anchor (top) and single anchor (bottom) have the same bonding area. For the array-shaped anchors, in the downward direction, the adjacent anchors are at the same distance with the same bonding area, which excluded the effect of other anchors below. And in the upward direction, the adjacent anchors are the reference anchors, which were at different distances with the same bonding area. From the above analysis it can be concluded that if the distance between the array-shaped anchor and the reference anchor is farther, the bonding quality of the array-shaped anchor would be poorer. For the single anchor, the situation is the same.

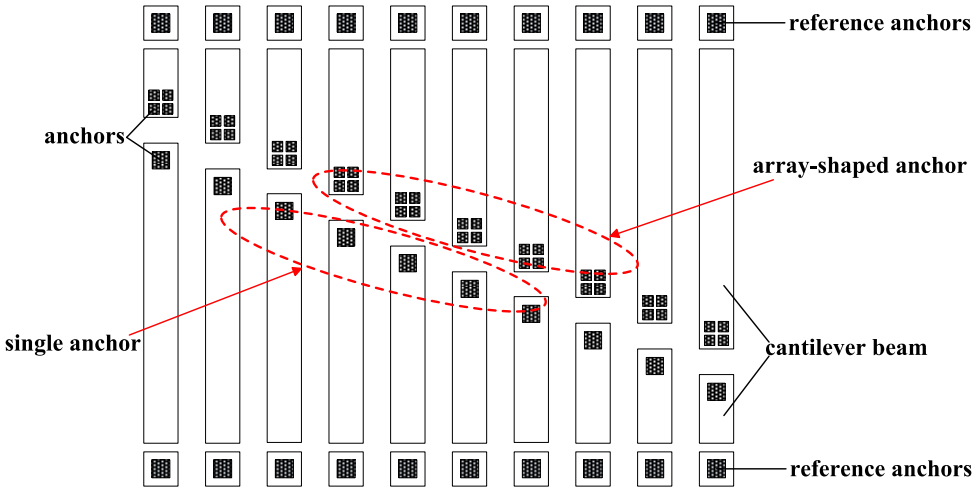

Figure 6. Structure of bonding quality testing device

3.2 Torsional bonding strength testing device

For the horizontal-movable MEMS devices fabricated by SOG process, the conventional measuring methods of bonding strength cannot directly reflect the anchor strength in practical application, because the anchor stands torque when the devices are functioning. Therefore, torsional bonding strength testing device with anchor height of 4 μm and beam thickness of 71 μm is proposed (Fig. 7). The anchor bearing torque when the bonding surface fractures is used to characterize the torsional bonding strength. Specific measuring process goes as follows:

(1) Apply force to the top of the cantilever beam by the probe of the probe station;

(2) Increase the displacement of the probe step by step and record the displacement when the bonding surface fractures;

(3) Use the displacement (from (2)) and calculate the torque by FEA.

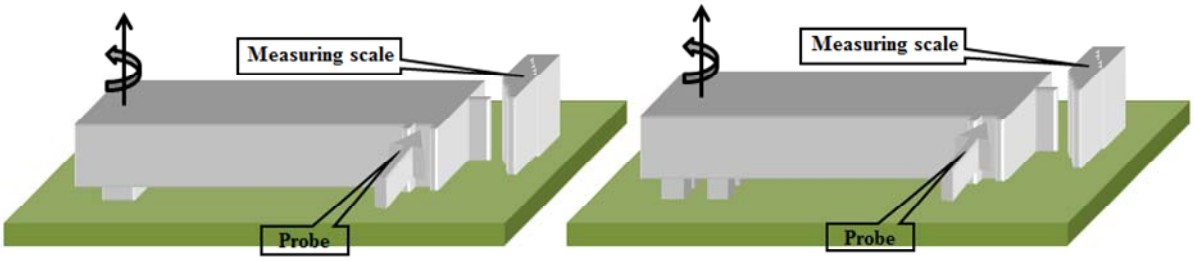

(a) conventional single anchor (b) array-shaped anchor

Figure 7. Structure of torsional bonding strength testing device

4. Results and discussion

4.1 Comparison of bonding quality

Figure 8 shows a scanning electron microscope (SEM) photograph of bonding quality testing devices. The cantilever beams of both array-shaped anchor and single anchor don't drop out when the bonding area was large (Fig. 8(a)). And dropping out happens tempestuously when the bonding

area is small (Fig. 8(b)). The result also shows that the situation of single anchor is severer than that of array-shaped anchor (Fig. 8(b)). It can be concluded that the bonding quality of array-shaped anchor (Fig. 9) is higher than that of the conventional single one and the bonding quality become poorer with a further adjacent reference anchor (Fig. 8(b)).

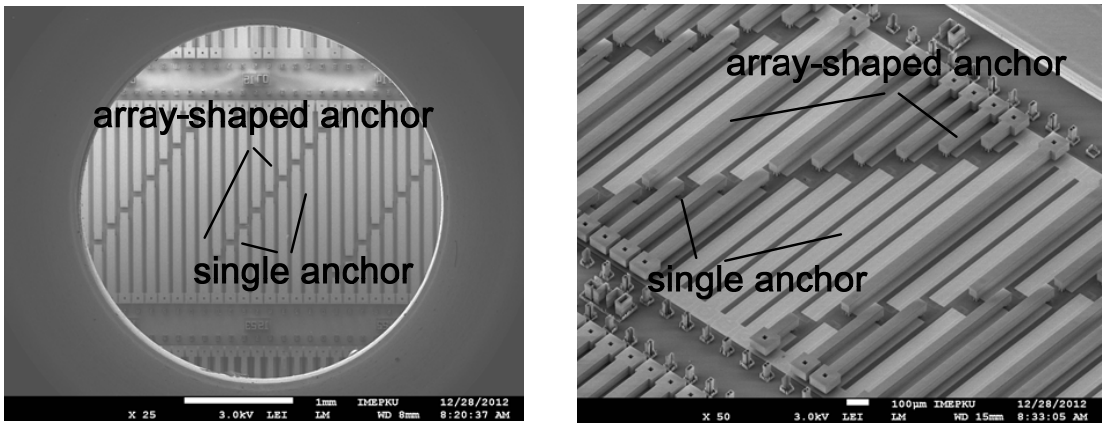

(a) Bonding area of 900 um^2 (b) Bonding area of 196 um^2

Figure 8. SEM photograph of bonding quality testing devices

In order to obtain the bond yield of array-shaped anchor and single anchor, 100 cantilever beams at each bonding area are selected by optical microscope and dropping out situations of them are observed. Figure 10 shows the statistical result, which proves the bonding quality of array-shaped anchor is higher than that of single anchor again. In addition, with the increasing of the bonding area, the bond yield become higher and the bond yield is 100% when the bonding area is bigger than $484\mu m^2$.

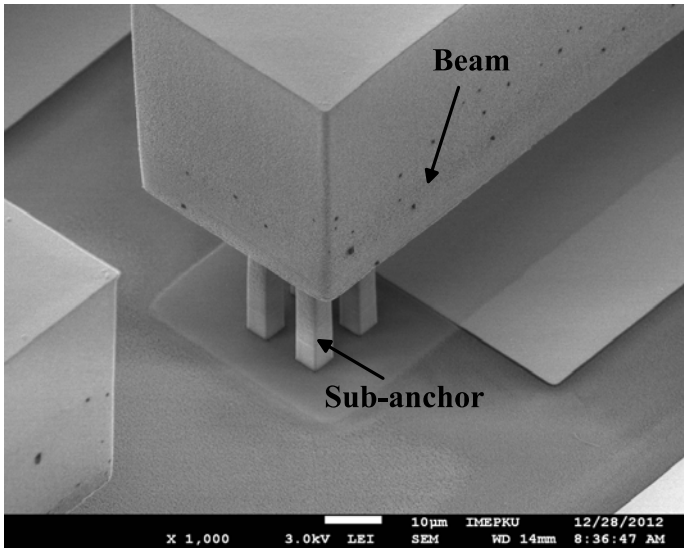

Figure 9. SEM photograph of array-shaped anchor

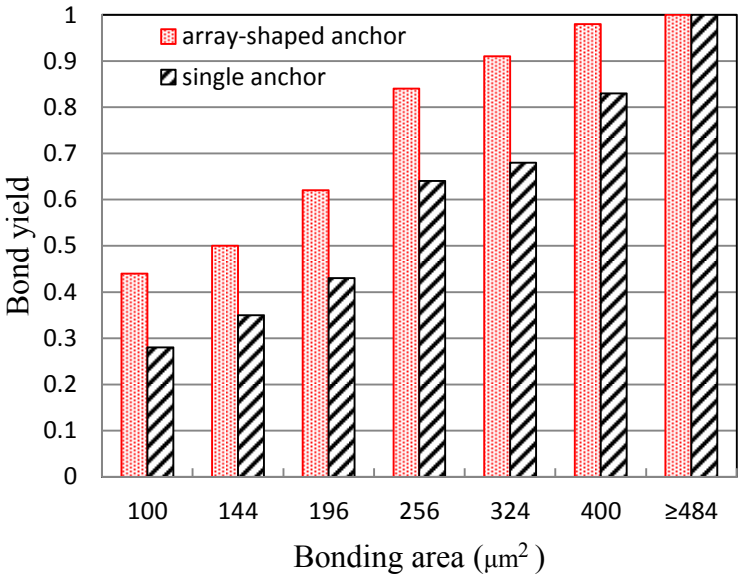

Figure 10. Correlation between bond yield and bonding area

4.2 Comparison of torsional bonding strength

Figure 11 shows a SEM photograph of torsional bonding strength testing devices. To avoid footing effect in DRIE process, protecting metal layer is deposited on glass wafer (Fig. 11(a)). As a result, the actual size of the beam (41.7μm), shown in Fig. 12, is almost the designed size (43μm).

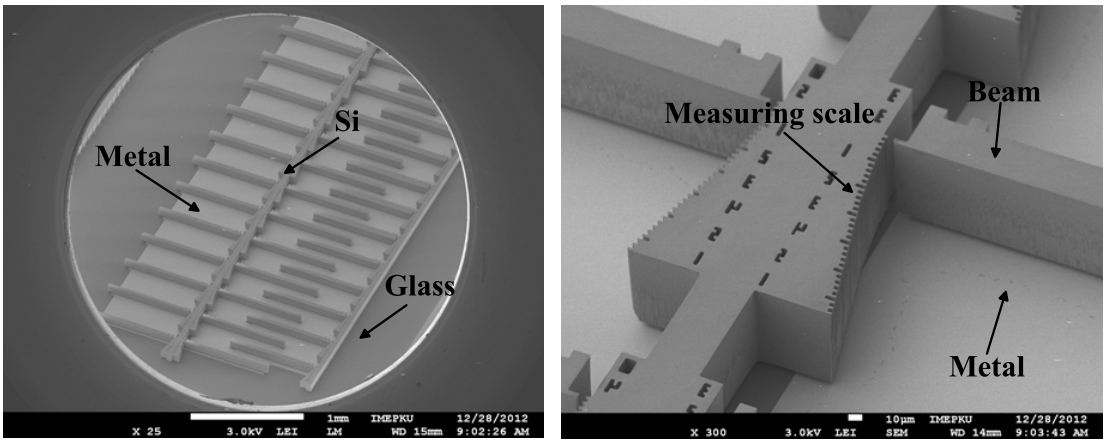

(a) (b)

Figure 11. SEM photograph of torsional bonding strength testing devices

Torsional fracture tests were carried out for both array-shaped anchor and single anchor. Based on the fractured displacements from the fracture tests, the torsional bonding strength is obtained by FEA. Figure 13 shows the correlation between torsional bonding strength and bonding area. The strength of array-shaped anchor is stronger than that of single anchor. And one reason is that the average bonding quality of array-shaped anchor is better than that of single anchor, which can be seen in section 4.1. Another reason is expressed below. There is a low-stress region in the middle of

single anchor bonding surface when the anchor stands torque, and this region contributes little to the bonding strength. However, there is no such low stress region in the array-shaped anchor when it stands torque. Therefore, array-shaped anchor has a stronger torsional bonding strength.

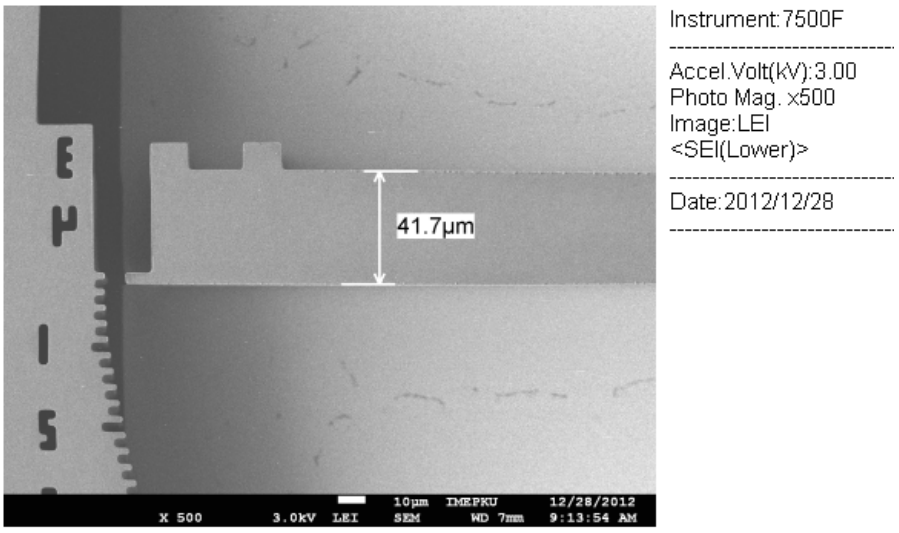

Figure 12. SEM photograph of cantilever beam and measuring scale

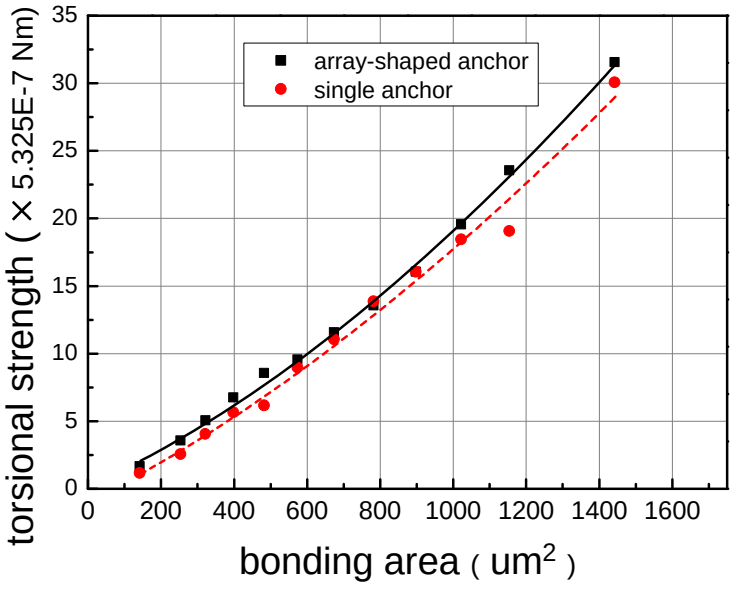

Figure 13. Correlation between torsional bonding strength and bonding area

5. Conclusion

A novel array-shaped anchor design scheme for microdevices fabricated by silicon-on-glass process was proposed. This anchor design was based on bonding strength consideration and consisted of four identical sub-anchors. The bonding quality test has verified that, compared with conventional single anchor, the proposed array-shaped anchor is beneficial to release the CTE mismatch induced

residual stress and decrease the metal electrode layer or particles induced bonding failure risk. Thus the new scheme would achieve a stronger bonding quality and a higher bond yield. From the torsional fracture tests of well-established anchor-beam MEMS devices, we conclude that the torsional bonding strength of array-shaped anchor is stronger than that of single anchor in practical application. This array-shaped anchor has a promising application in microdevice design with scaling-down.

Acknowledgements

This research was supported by National Key Laboratory of Science and Technology on Micro/Nano Fabrication, Institute of Microelectronics, Peking University. It was financed by the National Basic Research Program (also called 973 Program, Project No. 2011CB309502).

References

[1] Nanver, L.K., et al. Special RF/microwave devices in Silicon-on-Glass Technology. in Bipolar/BiCMOS Circuits and Technology Meeting. BCTM . IEEE. 2008.

[2] Larsen, K.P., J.T. Ravnkilde and O. Hansen. SOI silicon on glass for optical MEMS. in TRANSDUCERS, Solid-State Sensors, Actuators and Microsystems, 12th International Conference on. 2003.

[3] Kobayashi, J., et al., A Microfluidic Device for Conducting Gas-Liquid-Solid Hydrogenation Reactions. Science, 2004. 304(5675): p. 1305 -1308.

[4] Boser, B.E. and R.T. Howe, Surface micromachined accelerometers. Solid-State Circuits, IEEE Journal of, 1996. 31(3): p. 366-375.

[5] Najafi, K. Recent progress in micromachining technology and application in implantable biomedical systems. in Micro Machine and Human Science. MHS '95., Proceedings of the Sixth International Symposium on. 1995.

[6] Schmidt, M.A., Wafer-to-wafer bonding for microstructure formation. Proceedings of the IEEE, 1998. 86(8): p. 1575-1585.

[7] Lasky JB., Wafer bonding for silicon-on-insulator technologies. Applied Physics Letters. 1986.48(1): p. 78-80.

[8] Gösele, U., et al., Wafer bonding for microsystems technologies. Sensors and Actuators A: Physical, 1999. 74(1–3): p. 161-168.

[9] Knowles, K.M. and A.T.J. van Helvoort, Anodic bonding. International Materials Reviews, 2006. 51(5): p. 273-311.

[10] Wiemer, M., et al. Waferbond technologies and quality assessment. in Electronic Components and Technology Conference. ECTC . 58th. 2008.

[11] Inzinga, R.A., et al., Characterization and Control of Residual Stress and Curvature in Anodically Bonded Devices and Substrates with Etched Features. 2012. 52(6): p. 637-648.

[12] Chen, W.T. and C.W. Nelson, Thermal Stress in Bonded Joints. IBM Journal of Research and Development, 1979. 23(2): p. 179-188.

Experiments on the mechanical behavior of anodically bonded interlayer of Pyrex Glass/Al/Si

Yu-Qun Hu[1,*], Ya-Pu Zhao[2]

[1] College of Civil Aviation and Flight, Nanjing University of Aeronautics and Astronautics, Nanjing 210016, China
[2] State Key Laboratory of Nonlinear Mechanics (LNM), Institute of Mechanics, Chinese Academy of Sciences, Beijing 100190, China
* Corresponding author: hyq@nuaa.edu.cn

Abstract The MEMS/NEMS devices present an attractive prospect in many areas, especially in aviation and aerospace. Anodic bonding is one of the key technologies for the manufacturing of integrated 3-D structures of these devices. In this paper, based on experiments and detailed analysis, a systematic study will be made in depth for the mechanical behavior of anodically bonded interlayer within micro-scale structures. In accordance with a typical anodically bonded structure from one kind of MEMS micro accelerometer, a series of anodic bonding and mechanical tests were completed, for the behavior of the interlayer under quasi-static loading. The paper also presents the analysis of some important factors which influence the mechanical properties of the anodically bonded structure of Pyrex 7740 Glass/Al/Si. The metal oxidation reaction, dendritic nanostructures, and fractal patterns, which taking place at the bonding interface, were scrutinized. The experimental results demonstrate the thickness effect of the intermediate layer, and that the bonding tensile strength increases with the bonding temperature and voltage, but it decreases with the increase of the thickness of Al intermediate layer. The formation of the nanostructures in the bonding interlayer is also helpful to enhance the anodic bonding strength.

Keywords Anodic bonding, MEMS/NEMS, Intermediate layer,

1. Introduction

Three-dimensional (3-D) integration technologies related to Micro/Nano Electro-Mechanical Systems (MEMS/NEMS) devices is becoming one of focused research areas[1-5]. Anodic bonding is one of the key technologies for the manufacturing of integrated 3-D structures of these devices. In MEMS/NEMS devices, anodic bonding technology, especially for the connection of multilayer materials, offers a great prospect to extend the structural integration of the devices from two-dimensional (2-D) to 3-D, as shown in Figure 1. 3-D integration based on anodic bonding offers the potential for high performance and high-density applications due to lower power consumption, enhanced transmission speeds, better performance, and smaller device size[6].

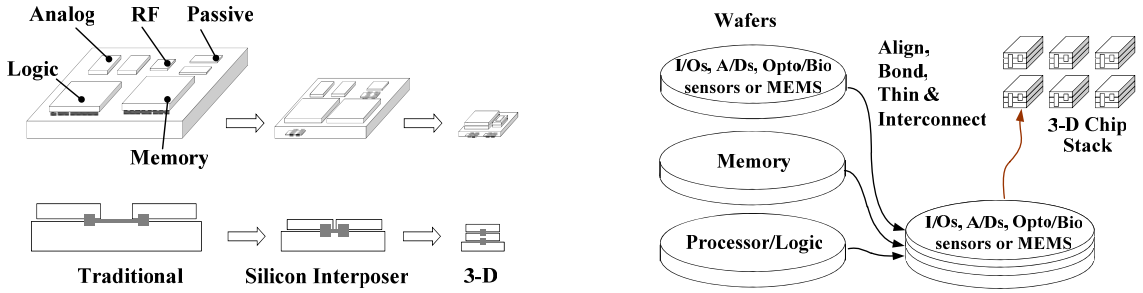

(a) The integration of devices from 2-D to 3-D (b) 3-D integration for MEMS devices

Figure 1. The trend for the integration of MEMS/NEMS devices (revised from reference [1])

Anodic bonding, also known as electrostatic bonding or field-assisted bonding, was developed as a means to connect metals, alloys or semiconductors to conductive glasses. It is also a highly

promising method for joining certain metals or semiconductors to alkali-ion-conductive glasses at decreased temperatures. Compared to other techniques, the main advantage of anodic bonding is that a strong junction interface can be achieved at a reduced bonding temperature by application of an electric field [7-9]. The temperature for anodic bonding is usually lower than the softening point of glass and the melting points of the materials selected for this purpose. Nowadays, there exists a demand for this straightforward and reliable bonding technique in connecting, packaging, or hermetic sealing of more complex micro/nano structures and integrated microcircuits in MEMS/NEMS devices. The promising applications of MEMS devices are still limited by the reliability of MEMS devices, especially in the applications for military and aerospace systems.
Some previous studies [10, 11] show that one of the important structural failure mode is the stripping of micro anchors from its substrate in some type of MEMS devices. On the basis of the structure of these devices, in this paper, we report some mechanical tests on the micro anchors anodically bonded between Pyrex 7740 glass wafer and aluminum thin film coated on crystalline Si wafer.

2. Experimental

2.1. Specimen preparation

The experimental specimens were made by die-level anodic bonding at different temperatures and voltages. The mesa structures are used to avoid the edge micro cracks due to the chip dicing process. Pyrex 7740 glass wafers of 500 μm thickness and 100 mm diameter were cut into 12 mm ×12 mm square chips. The chemical composition of Pyrex 7740 wafer includes 80.8 Mol% SiO_2, 12.0 Mol% B_2O_3, 4.2 Mol% Na_2O, 2.0 Mol% Al_2O_3, 0.6 Mol% K_2O, 0.2 Mol% MgO, and 0.2 Mol% CaO, as shown in Table 1 [12].

Table 1. Chemical composition of Pyrex 7740 glass wafer (Mol%)

SiO_2	B_2O_3	Na_2O	Al_2O_3	K_2O	MgO	CaO
80.8 %	12.0 %	4.2 %	2.0 %	0.6 %	0.2 %	0.2 %

Si wafers were of 100 mm in diameter (double-side polished, p-type, and wafer surface plane (100), and were patterned into mesas with different-sized squares. There are four types of dice with different mesa spacing, as shown in Figure 2. These mesas were of 10 μm in height and were prepared with a deep reactive ion etch (DRIE) process. These patterned Si wafers were coated by an ARC-12M sputtering system with pure aluminum (99.999%). The coated aluminum thin films were of 500 Å, 950 Å, 1500 Å, and 2300 Å in thicknesses respectively. Then these Si wafers were also diced into squares of 12 mm ×12 mm. All square samples were cleaned by deionized water spray rinse in a 100-class clean room and dried by nitrogen gas under pressure.
A pair of glass chip and well-coated crystalline silicon chip was placed between two stainless steel plates, which acted as plate electrodes, and then between two hot plates. The glass side was connected with the cathode, and the silicon side was connected with anode. The schematic of this bonding configuration is shown in Figure 3.

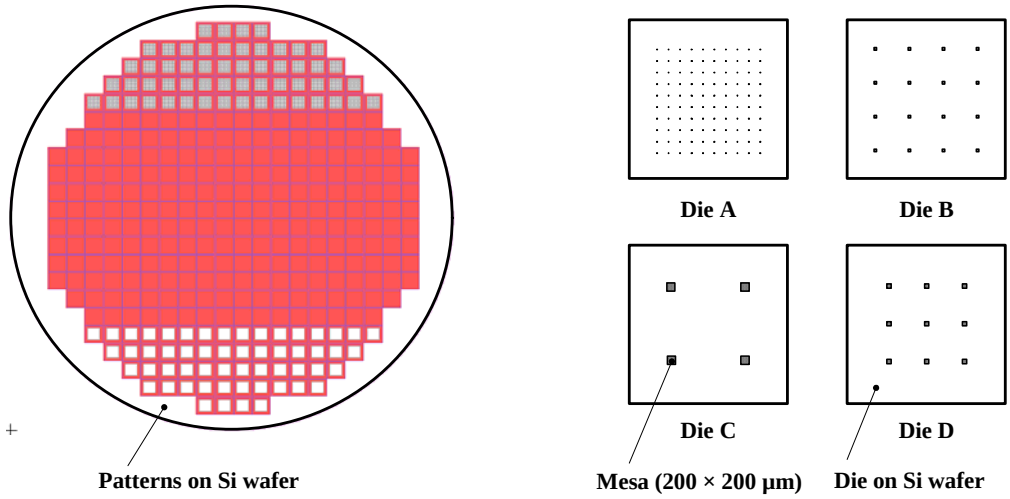

Figure 2. The Silicon wafer patterned with dice

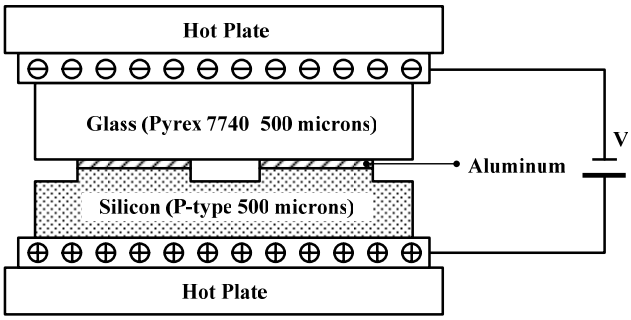

Figure 3. The schematic of specimen bonding configuration

The anodic bonding of these specimens was performed at the temperature range from 300°C to 375°C and at the voltage range from 150V to 500V for less than 30 minutes on an open (non-vacuum) bonding system. The bonding voltage was applied after the selected bonding temperature was reached. When the bonding was completed, the bonded sample was cooled to room temperature in 2 hours.

Before the upcoming tests, all specimens were examined under optical microscope. Some of the glasses were removed to expose the aluminum film for the SEM microanalysis with energy dispersive X-ray (EDX) and EBSD. The specimens were examined in a Sirion 400NC (FEI Field Emission Gun SEM) with the EBSD system (INCA Energy and Crystal System of Oxford).

2.2. Transmission electron microscopy

To prepare TEM test, the bonded samples were cut into small bars with a cross-section of 1.5mm×1.5mm (perpendicular to the interface). These small bars were individually glued into 3mm diameter copper tubes with an inner diameter of 2.2 mm. After the glue was cured on the Nuova II curing stage, these copper tubes were sectioned into slices approximately 750 μm thick, and then ground down to a thickness of about 40 μm and dimpled at the interface. Before argon-ion milling, these foils were attached to molybdenum support rings with an inner diameter of 1 mm. Specimens

were ion milled to electron transparency at room temperature by a Gatan Model 691 precision ion polishing system (PIPS). All TEM specimens were examined in a 300 kV Tecnai F30 (FEI Field Emission Gun TEM with LaB6 filament). STEM and energy dispersive X-ray (EDX) spectroscopy microanalysis were used for chemical analysis.

2.3. Tensile experiment under quasi-static loading

In order to characterize the bonding strength, each bonded chip was diced into 4 mm × 4 mm specimens by an automated dicing saw. Before the tensile test, all samples for tensile tests were examined under an optical microscope with 50× objective lens to exclude defective ones. The specimens were attached to aluminum jigs with glue for the tensile test. The bonding strength was measured by a tensile pulling machine (GATAN Microtest 2000) and the specimen under test was pulled perpendicular to the bonding interface until its rupture. The test pulling speed was 1 mm/min, and the pulling speed and the data acquisition were controlled by a personal computer. In these pulling tests, it was found that the maximum failure loads of these specimens were less than 5 N, and the specimens were easily damaged when they were fixed to rigid fixtures of the test machine. The alignment of the test studs is of critical importance because small deviations will induce bending moments which can cause premature failure of the test sample [13]. To improve the alignment of test samples and to avoid the early failure caused by the force from sample installation, a special fixture was designed with flexible steel wire strand, as shown in Figure 4.

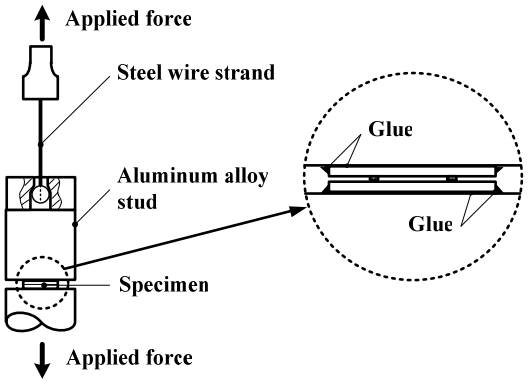

Figure 4. Schematic of fixture for tensile tests

3. Results and discussion

3.1. Fractures in bonded specimens

When all the bonding specimens were examined under optical microscope, fractures were found in some of the specimens, as indicated by white arrows in Figure 5. The fractures occurred in the glass side at the corner of the mesas, and many of them were found in the samples anodically bonded at higher bonding temperature. During the process of anodic bonding, when the bonding temperature was larger than 350°C, the fractures of this type were easily found in some specimens. This kind of fractures seldom occurred in the specimens bonded at the temperature of no more than 350°C. The reason for the occurrence of these fractures is the different thermal expansion coefficient with Pyrex

7740 glass and silicon. The higher the bonding temperature was, the larger the difference of thermal expansion coefficient between the glass and silicon, that is, the larger the residual stress was. The residual stress results in these fractures.

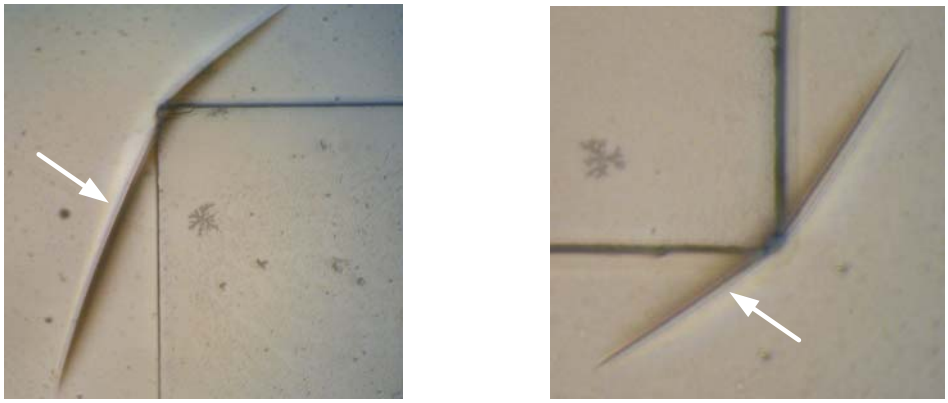

(a) Bonding temperature at 350 °C (b) Bonding temperature at 375 °C

Figure 5. The typical fractures in the samples with Al film of 950 Å

3.2. Fractal patterns and dendritic nanostructures

3.2.1. Fractal patterns

With the optical microscope, many fractal patterns were found in the intermediate aluminum film, as shown in Figure 6. The size of the patterns decreases with the thickness of Al film and increases with the bonding temperature. The fractal patterns in the aluminum film have the characteristics of two-dimensional Diffusion-Limited Aggregation (DLA) model [14, 15]. The fractal dimensions of the typical fractal patterns are calculated by sand-box method [16, 17].

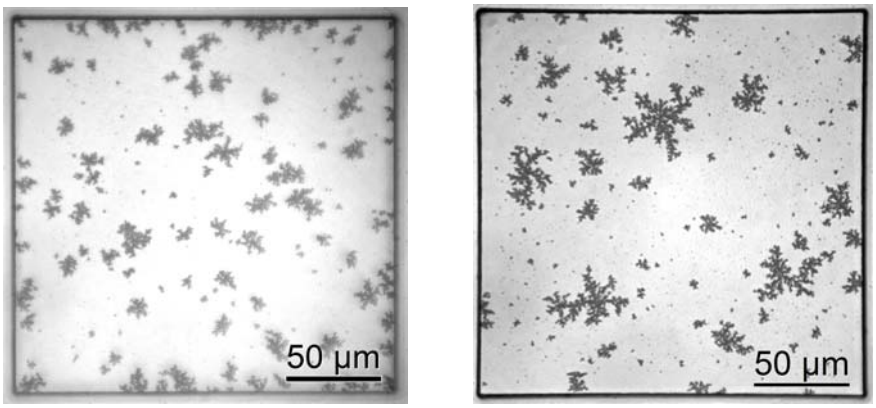

(a) 350 °C (b) 375 °C

Figure 6. Fractal patterns distribution in 500 Å thick Al film at different bonding temperatures

The fractal patterns in the intermediate aluminum film have the typical dimension of 2-D DLA process, and their fractal dimension is around 1.7, as listed in Some fractal patterns were analyzed with the EDX and EBSD systems of INCA. The microanalyses show that the fractal patterns contain the crystalline grains of Aluminum and Silicon. These fractal patterns were formed in the process of anodic bonding due to the limited diffusion and aggregation of Si atoms in the Al film.

These diffused Si atoms mainly originate from the following chemical reaction, $4Al + 3SiO_2 = 2Al_2O_3 + 3Si$. When the temperature is above 300°C, there exists a chemical reaction between the Al and SiO_2 [18]. The silicon dioxides come from the slightly oxidizing of silicon wafer on its exposed surface before the aluminum sputtering process of these silicon wafers.

Table 2.

Some fractal patterns were analyzed with the EDX and EBSD systems of INCA. The microanalyses show that the fractal patterns contain the crystalline grains of Aluminum and Silicon. These fractal patterns were formed in the process of anodic bonding due to the limited diffusion and aggregation of Si atoms in the Al film. These diffused Si atoms mainly originate from the following chemical reaction, $4Al + 3SiO_2 = 2Al_2O_3 + 3Si$. When the temperature is above 300°C, there exists a chemical reaction between the Al and SiO_2 [18]. The silicon dioxides come from the slightly oxidizing of silicon wafer on its exposed surface before the aluminum sputtering process of these silicon wafers.

Table 2. The typical fractal dimensions of the fractal patterns in the Al films[19]

	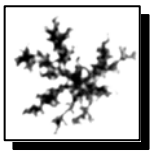				
$D_B = 1.702$	$D_B = 1.695$	$D_B = 1.681$	$D_B = 1.696$	$D_B = 1.700$	$D_B = 1.727$

When the Al film is thin enough, the fractal patterns run through the span of the whole thickness of the film, and bond with the substrate and glass. The strength of chemical bond is 799.6±13.4 kcal/mol for Si-O, 511±3 kcal/mol for Al-O, and 325±7 kcal/mol for Si-Si [20]. Therefore, the fractal pattern improves the bonding strength between the Pyrex glass and the aluminum thin film coated on the silicon substrate.

3.2.2. Dendritic nanostructures

In all anodically-bonded samples, dendritic nanostructures were found in the Pyrex glass near the Al/glass interface, as shown in Figure 7. The dendritic nanostructures, which are seen over the whole thin area, exhibit a similar maximum height of 600-650 nm in the specimens bonded at 350°C, 400 V. These three-dimensional treelike structures have a trunk of tens nanometers in diameter (less than 40 nm). TEM cannot show all the small branches of these 3-D dendritic nanostructures.

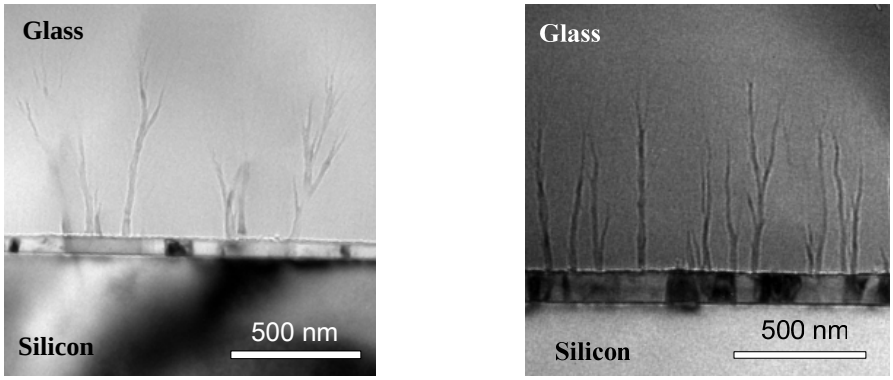

(a) 50 nm aluminum film (b) 95 nm aluminum film

Figure 7. Dendritic nanostructures of specimens at 350°C and 400 V

Figure 8 illustrates the EDX analysis position and element analysis result of the nano dendritic structures under STEM mode. The electron beam scanning path is marked with a black thick line across three trunks of the dendritic structures, as shown in Figure 8(a). Element analysis indicates that the dendritic nanostructures are aluminum enriched, as shown in Figure 8(b). STEM/EDX microanalysis provides enough evidence of diffusion of aluminum into the Pyrex glass during anodic bonding. Examined by EDX, the trunks exhibit lesser counts of silicon and oxygen while the aluminum counts are conspicuously increased.

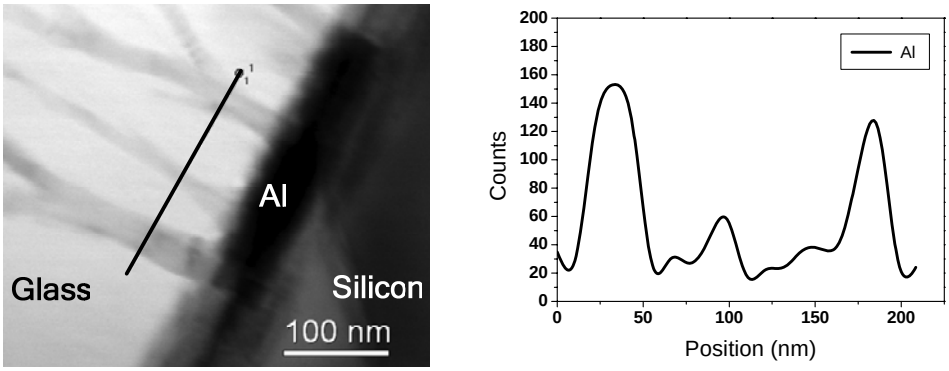

(a) Scanning position (b) Element counting

Figure 8. Scanning position and element counting for EDX analysis

3.2. Bonding strength

The mean bonding tensile strength are shown in Figure 9. Bonding tensile strength, which is averaged from the results of five or more specimens. The measured bonding strength values exhibit a rather large variance around a mean value. This can be attributed to several aspects, such as the misalignment of specimens, the characteristics of bonding behavior [21], the micro defects due to residual stress, and etc. All the specimens pulled apart were also examined with the optical microscope and scanning electron microscope (SEM), and some parts of the aluminum film and the Pyrex glass were residual on the opposite side.

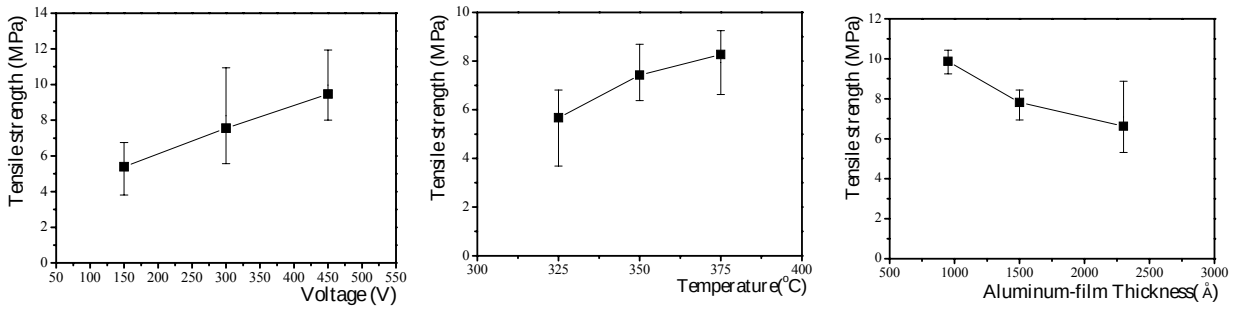

(a) Voltage (b) Temperature (c) Thickness

Figure 9. Bonding tensile strength

Figure 9(a) shows the tensile strength increases with the bonding voltage ranged from 150 to 450 V. The specimens in Figure 9(a) were bonded with 700 μm thick Pyrex 7740 glass wafer at 300°C, and their aluminum film is 1300 Å thick. In the process of anodic bonding, the higher bonding voltage means the larger force produced by the electrostatic field across the bonding interface, and brings about much larger and more intimate contact area between the bonding pairs, that is, more chemical bonds generated at the bonding interface and an enhancement of the bonding strength. On the other hand, the higher the bonding voltage is, the more amounts of movable ions will be produced in the glass and then the more anions, mainly O^{2-}, will accumulate in the bonding glass adjacent to the interface of glass/Al, which provides more opportunities to form the chemical bonds between oxygen and aluminum. Unfortunately, a high bonding voltage will introduce a risk of electric breakdown, and the maximum bonding voltage is limited mainly by the breakdown voltage over the depleted layer.

The tensile test results tell that the maximum failure loads also increases with the bonding temperature from 325 to 375°C, as shown in Figure 9(b). The specimens used in Figure 9(b) were bonded with 500 μm thick Pyrex 7740 glass wafer, and the thickness of aluminum film is 500 Å. Pyrex 7740 glass has a complicated chemical composition and contains some important alkali elements, which are responsible for the ionic current in the glass during the anodic bonding process. The increasing of bonding temperature gives rise to more amounts of the cations, and correspondingly induces a large number of anions to accumulate near the bonding interface, which also provides more opportunities to produce chemical bonds with aluminum in anode and then improves the bonding strength. But a high bonding temperature not only will lead to the degradation of metal leads and integrated circuits in MEMS device, but also will induce large thermal stress. In the high temperature bonding tests, cracks were found in the glass of some specimens due to thermal stress, as shown in Figure 5.

When comparing the tensile failure loads from the specimens which were bonded under the same temperature, voltage, and duration time but with the different thicknesses of aluminum film, we find that their bonding tensile strength increases with the decrease of aluminum film thickness in our tested range, as shown in Figure 9(c). All the tested samples in Figure 9(c) were anodically bonded under 300°C and 400 V. The mean tensile strength increases from 6.6 to 9.9 MPa, while the Al film thickness decreases from 2300 to 950 Å, which indicate a fact that the experimental results show the remarkable size effect. The bonding strength is affected by the thickness of Al film within the tested range of Al thickness.

4. Summary

In summary, the tensile specimens were anodically bonded at the relatively low temperature and voltage, using Pyrex 7740 glass and patterned crystalline silicon chips coated with Al film. To investigate the mechanical behavior of anodically bonded interlayer of Pyrex Glass/Al/Si, the tensile experiments were completed with the newly designed flexible fixtures, and the analysis for the anodically bonded intermediate layer were also made with SEM and TEM.

The formation of the fractal patterns in the process of anodic bonding is due to the limited diffusion, aggregation, and crystallization of Si and Al atoms in the intermediate Al film. These fractal patterns have the fractal dimension of 2-D DLA process, and their fractal dimension is around 1.7.

These fractal patterns in the intermediate Al film consist of Al and Si crystalline grains.The fractal patterns improves the bonding strength between the Pyrex 7740 glass and the Al intermediate layer coated on the crystal silicon substrate.

The formation of the dendritic nanostructures is due to the diffusion and reaction near the glass/Al interface under a non-equilibrium condition during the anodic bonding process. These nanostructures might reveal helpful clues in improving the bonding quality. The dendritic nano-crystalline structures are shown to be one of the key structures for the improvement of strength in anodic bonding.

Test results demonstrated that, the bonding strength increases with the bonding temperature and voltage. This is in agreement with earlier results reported in the literature. But the experiments exhibit that the tensile strength decreases with the increase of the thickness of Al intermediate layer. Although the measured bonding strength values exhibit a rather large variance around a mean value, the experimental results can be referenced qualitatively. With the dimensions of MEMS devices downward, the scale effect in anodically bonded micro anchors should be considerable during the process of device design.

Acknowledgements

We would like to thank Mr. Wan Lap Yeung of Hong Kong University of Science and Technology and Dr. Jijia Xie and Mr. Chuang Feng for their help during specimen preparation and tensile experiments. This work was supported by the National Natural Science Foundation of China (NSFC) (Grant No. 11272144) and the Jiangsu Provincial Natural Science Foundation of China (Grant No. BK2011725).

References

[1] S. Farrens. Wafer and Die Bonding Technologies for 3D Integration. In: Materials and Technologies for 3-D Integration. F. Roozeboom, C. Bower, P. Garrou, et al., Ed. Warrendale: Materials Research Society. 2009. pp. 55-65.

[2] M.M. Koebel, N. El Hawi, J. Lu, et al. Anodic bonding of activated tin solder alloys in the liquid state: A novel large-area hermetic glass sealing method. Solar Energy Materials and Solar Cells. 2011, 95 (11), pp.3001-3008.

[3] Z. Wang, D. Wang, N. Jiao, et al. Nanochannel system fabricated by MEMS microfabrication and atomic force microscopy. Iet Nanobiotechnology. 2011, 5 (4), pp.108-113.

[4] M.M.V. Taklo, N. Lietaer, H.R. Tofteberg, et al. 3D MEMS and IC integration. In: Materials and Technologies for 3-D Integration. F. Roozeboom, C. Bower, P. Garrou, et al., Ed. Warrendale: Materials Research Society. 2009. pp. 211-220.

[5] F. Niklaus, J.-Q. Lu, J.J. McMahon, et al. Wafer-level 3D integration technology platforms for ICs and MEMs. In: Proceedings of the twenty second international vlsi multilevel interconnect conference (VMIC), IMIC. 2005.

[6] J.H. Lau. Recent advances and new trends in nanotechnology and 3D integration for semiconductor industry. 2011 IEEE International 3D Systems Integration Conference (3DIC). 2012, pp.23 pp.-23 pp.

[7] G. Wallis, D.I. Pomerantz. Field Assisted Glass-Metal Sealing. Journal of Applied Physics. 1969, 40 (10), pp.3946-3949.

[8] Q. Xing, G. Sasaki, H. Fukunaga. Interfacial microstructure of anodic-bonded Al/glass. Journal of Materials Science: Materials in Electronics. 2002, 13 (2), pp.83-88.

[9] J. van Elp, P.T.M. Giesen, J.J. van der Velde. Anodic bonding using the low expansion glass ceramic Zerodur. Journal of Vacuum Science and Technology B. 2005, 23 (1), pp.96-98.

[10] L.S. Wang, Y.Q. Hu, Z. Hong, et al. Failure Analysis of Micro-accelerometer under Impact Loading. Journal of Mechanical Strength. 2001, 23 (4), pp.516-522.

[11] Y.Q. Hu, L.S. Wang, Z.J. Zeng, et al. Structural Failure Analysis and Numerical Simulation of Micro-accelerometers under Impulsive Loading. International Journal of Nonlinear Sciences and Numerical Simulation. 2002, 3 (NOS.3-4), pp.311-314.

[12] J.E. Shelby. Effect of radiation on the physical properties of borosilicate glasses. Journal of Applied Physics. 1980, 51 (5), pp.2561-2565.

[13] A. Plößl, G. Kräuter. Wafer direct bonding: tailoring adhesion between brittle materials. Materials Science & Engineering R-Reports. 1999, R25, pp.1-88.

[14] T.A. Witten, L.M. Sander. Diffusion-limited aggregation. Physical Review B. 1983, 27 (9), pp.5686-5697.

[15] T.A. Witten Jr, L.M. Sander. Diffusion-Limited Aggregation, a Kinetic Critical Phenomenon. Physical Review Letters. 1981, 47 (19), pp.1400-1403.

[16] S.R. Forrest, T.A. Witten. Long-range correlations in smoke-particle aggregates. Journal of Physics. A. 1979, 12 (5), pp.L109-L117.

[17] S.W. Russell, J. Li, J.W. Mayer. In situ observation of fractal growth during a-Si crystallization in a Cu3Si matrix. Journal of Applied Physics. 1991, 70 (9), pp.5153-5155.

[18] N.J. Chou, J.M. Eldridge. Effects of material and processing parameters on the dielectric strength of thermally grown SiO_2 films. Journal of the Electrochemical Society. 1970, 117 (10), pp.1287-1293.

[19] Y.Q. Hu, Y.P. Zhao, T.X. Yu. Fractal Pattern Formation in Anodic Bonding of Pyrex Glass/Al/Si. International Journal of Nonlinear Sciences and Numerical Simulation. 2008, 9 (4), pp.315-322.

[20] D.R. Lide. Handbook of Chemistry and Physics. Boca Raton, FL: CRC Press. 2005.

[21] B. Müller, A. Stoffel. Tensile strength characterization of low-temperature fusion-bonded silicon wafers. Journal of Micromechanics and Microengineering. 1991, 1 (3), pp.161-166.

Micromechanical modeling and numerical simulation of ablation of 3D C/C composites

Na Liu , Qingsheng Yang*

Department of Engineering Mechanics, Beijing University of Technology, Beijing, 100124, China
* Corresponding author: Email: qsyang@bjut.edu.cn; Tel: 86-10-67396333

Abstract Carbon-carbon (C/C) composites, in which a carbon matrix is reinforced by carbon fibers, are mainly used as thermo-structural protections in the aerospace engineering. The ablation of C/C composites at high-temperature causes mass loss, which is dominated by coupling effect of physical, chemical and mechanical factors. This paper classified the C/C ablation into three types according to the ablation mechanism: linear-rate reaction, parabolic-rate reaction and logarithmic-rate reaction. In this work, a micromechanical model of C/C composite with high-temperature heat conduction was established. A linear heat-transfer finite element analysis was carried out for revealing the damage morphology of C/C composites at an ultra high temperature.

Keywords C/C composites, ablation, surface recession, thermal damage

1. Introduction

Thermal protection materials, which are highly required in advanced thermal protection systems and envisioned for use on future hypersonic and space craft, will inevitably be subjected to utmost high temperature and strong oxidizing environment, such as the intercontinental ballistic missile nose cap often suffer an ultra high temperature of 7000~8000K atmosphere, dozens of megawatt heat flow density, unexpected high erosion of particle cloud and nuclear radiation in reentry [1]. Ablation phenomenon is frequent occurrence on the re-entry progress of space shuttle or rocket caused by aerodynamic heating, which can heat the surface of spacecraft up to a extremely high temperature in seconds. The thermal energy may lead to solid surface melting, evaporation, sublimation or decomposition of solid surface in the ultra temperature environment. Therefore, it is important for protecting the inner structure and astronauts from high temperature thermal damage.

Carbon-carbon(C/C) composites consist of carbon matrix and reinforced carbon fibers[2] and possess a series of excellent mechanical properties, such as high temperature resistance, low density, high specific modulus, high specific strength, small coefficient of thermal expansion, high ablation resistance and high temperature resistant. Therefore, C/C composites are widely used in technological applications as excellent ablation resistance and thermal protection materials, e.g. solid rocket motor (SRM) nozzle throats, reentry rocket nose cone, missile nose-tips and leading edges [3,4]. In the ablation process, the sublimation or decomposition of C/C composites will take away lots of heat and the surface temperature of aerospace craft will be effectually lowered down. Consequently, the ablation resistance of C/C composites is directly related to the strengths of astrovehicle, determining the achievement of task scheduled. Hence, the research on the ablation of C/C composites has a great significance.

In generally, researchers investigate the ablation mechanism of C/C composites in high temperature environment from two aspects: experiment research and numerical simulation research. The experiment is an effective method to understand the ablation mechanism of C/C composites. Unfortunately, the experimental simulation is extremely expensive because of the complexity of the extreme environmental conditions. Therefore, computer-based numerical simulation, which can predict the thermo-mechanical response of these composite heat shields, have become an effective method for analyzing the ablation behavior of C/C composites. Ultimately, it will achieve the design

purpose of C/C thermal protective materials based on the ablation research and simulation

In recent study, Aspa et al.[5] carried out a one-dimensional diffusion model to describe the effective surface ablation recession. Their analysis focused on the ablation of diffuse-controlled reaction. Vignoles et al.[6,7] investigated surface roughness of C/C composites by SEM. They discovered that fibers, matrices and interphase have different ablation resistance, which usually leads to typical surface roughness feature. In their work, a three-dimensional reaction-diffusion local model was set up to simulate the formation of the typical needle shape of the carbon fibers during ablation. Laborde et al.[8] established a damage model for carbon-carbon orthotropic composite materials with a special attention to the thermo-mechanical effects. They performed a numerical solution using an implicit incremental scheme implemented in ABAQUS.

The origanization of the paper is as follows. In the section 2, a brief introduction is given of ablation mechanism of C/C composites. Section 3 is devoted to classify the C/C ablation recession into three types according to the ablation mechanism. In section 4, a mesoscopic analytical model of C/C composite with high temperature heat conduction was established. The analysis used a heat-transfer finite element in ABAQUS to simulate the ablation morphology of C/C composites at ultra high temperature. The last section is the summary of the main conclusion resulted from the present work.

2. Ablation mechanism of C/C composites

There are mainly two types of carbon-oxygen (C/O) reaction for C/C composites in oxidation atmosphere: $C+O_2=CO_2$ and$2C+O_2=2CO$.
In the ablation process, the surrounding oxygen is transferred to the surface of the C/C composites. Ablation reaction primarily occurred on the surface of those materials, which resulted in mass loss with melting, sublimation and particle erosion. Then with the inward diffusion of oxygen in the surface microcracks and pores of C/C structure, further oxidation occurred. During the reaction process, fiber and matrix are oxidized simultaneously. Whereas the reaction rate of fibers is lower than the matrix. That means, along with the aggravation of ablation, the first melted interface layers separate the fibers and matrix. Ultimately, the fibers are burned into needle shape, while the around matrix are eroded into cylindrical shell. Fig.1 shows the ablation process of a C/C composite.

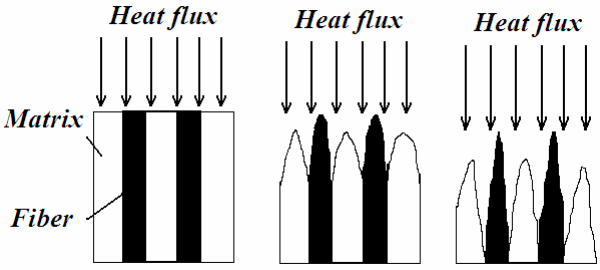

Figure 1. The ablation of the C/C composites

3. Ablation reaction rate of C/C composites

The oxidation reaction of C/C composites without high-temperature oxidation resistant coating is time-independent, and is mainly controlled by gas/solid interface reaction rate. In this case, the mass loss rate of C/C composites is linear with response time, as shown in Equation 1.

$$\frac{\Delta m}{A} = k_l t \tag{1}$$

where $\frac{\Delta m}{A}$ is the mass loss of C/C composites per unit area; k_l denotes coefficient of linearity

relation, which is determined by experiment; and *t* is the reaction time. Fig.2 shows the recession location of the ablation surface during the ablation process.

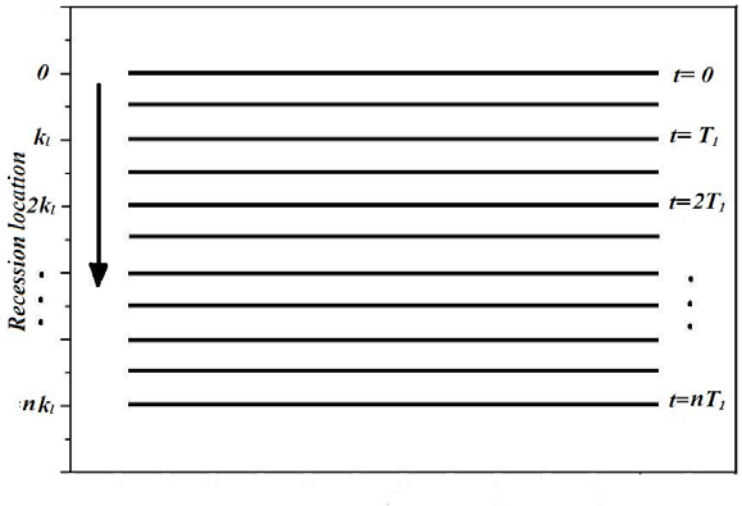

Figure 2. Recession location of the ablation surface

The ablation reaction of C/C composites with high-temperature oxidation resistant coating follows the parabolic-rate law, and the reaction rate is inversely proportional to the square root of time, which is determined by the diffusion rate of oxygen in the inner material, as shown in Equation 2.

$$\left(\frac{\Delta m}{A}\right)^2 = k_p t \tag{2}$$

where k_p is the parabolic rate constant or diffusion constant, which is derived from Arrhenius law as shown in Equation 3.

$$k_p = k_0 \, exp\left(-\frac{Q}{RT}\right) \tag{3}$$

where k_0 is the constant obtained by experiment; Q is the activation energy of oxidation; and R presents gas constant; T is the reaction temperature.

Logarithmic rate reaction is suitable for C/C composites with silicon elements. Early in the reaction process of ablation, the oxidation of silicon elements is rapidly, and silicon oxide produced from the oxidation between silicon and oxygen can generate a compact oxide layer covering the surface of C/C composites. The generated SiO_2 layer will prevent further diffusion of the oxygen and then increase the ablation resistance of the C/C. With the exacerbated of oxidation, the ablation of C/C composites will become severe and accompany with mass loss. Hence, the logarithmic-rate reaction mechanism is only appropriate for representing the early reaction of the C/C composites with silicon in lower high temperature.

3. Analytical model

C/C composite is a homogeneous multi-scale material. In microstructure, the “skeleton” of the composite consists of unidirectional bundles made of several thousands of fibers which are linked together by a pitch-based matrix. The formation of the typical roughness patterns of C/C composites in ablation process depends on the unidirectional fibers perpendicular to material surface. Due to the different ablation rates between carbon matrix and carbon fibers, the unidirectional fibers perpendicular to material surface will separate from the carbon base, expose to the external

oxidation environment, and take the shape of “needle clusters”. This paper focuses on the unit cell model of C/C composites in micromechanical structure, analyzing the change laws of C/C composites in high temperature thermal radiation and predicting the ablation morphology change.

There are two basic kinds of unit cell model of C/C composites. The first model, as shown in figure 3, is a hexahedron representative volume element (RVE), in which matrix and fibers are assumed homogeneous and isotropic, and the internal pores are negligible. The second model is a cylinder RVE, in which the fiber bundles are fit together into a 3D C/C structure. This meso-structure forms a network of meso-scale pores, as shown in figure 4.

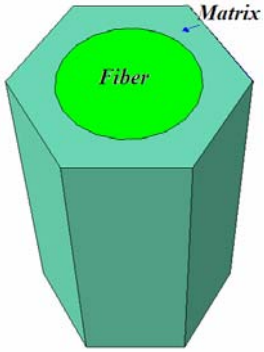

Figure 3. Hexahedron RVE of C/C

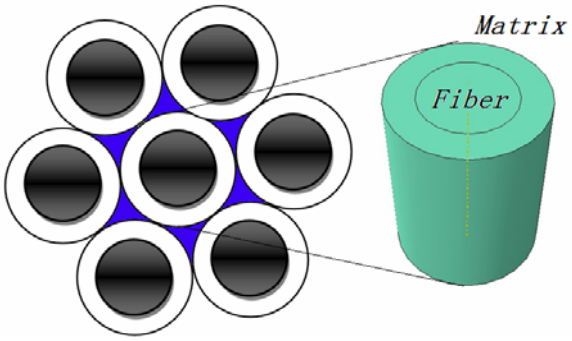

Figure 4. Cylinder RVE of C/C

In the finite element software of Abaqus, the thermal radiation analysis can be conducted according to the following steps: (ⅰ)modeling, (ⅱ) defining the materials property, (ⅲ) assembly model, (ⅳ) creating heat conduction steps and interaction, (ⅴ) applying boundary condition and load, (ⅵ) meshing and selecting element type, (ⅶ) creating analysis job, (ⅷ) results visualization.

The physical properties of C/C composite in the two models are listed in table 1. In the thermal radiation analysis, the physical constants of absolute zero temperature and Stefan-Boltzmann constants are -273.15 ℃ and 5.67E-8 W/(m^2 • k^4).

Table 1. Physical properties of C/C composites in the simulation models

Characteristic	Density	Elastic modulus	Poission’s ratio	Thermal conductivity	Specific heat
Unit	kg/m^3	GPa	--	W/(m • ℃)	J/(Kg • ℃)
Fiber	2000	230	0.22	1.15	5000
Matrix	1600	4.07	0.25	10.38	1000

Both of the two models use standard linear heat transfer element type DCC3D8 to analyze the thermal radiation. We assume the heat transfer is a transient state. It is subjected to surface radiation with ambient temperature of 2000℃ on top of the RVE and predefined temperature field of 300℃. We ignore the mass diffusion during the ablation process. The governing equation is

$$[C]\{\dot{T}\}+[K]\{T\}=\{F_q\}+\{F_r\},$$

where [C] is the element capacitance matrix, [K] is the sum conductivity matrix of heat conduction and thermal radiation. {F_q } and { F_r} are the load vectors due to applied heat flux and radiation respectively. We can obtain the temperature distribution in the C/C composite, and then calculate the heat flux by the following rule:

$$q = A((T-T^Z)^4-(T^0-T^Z)^4)$$

where A is the radiation constant , which was set to be one emissivity times the Stefan-Boltzmann constant; T^Z is the value of absolute zero on the temperature scale being used.

4. Numerical results

Damage analysis of hexahedron RVE in the ablation process was carried out first. The numerical example was presented to bring out for analyzing the potential ablation damage location. The finite element model was implemented in ABAQUS using a heat transfer element to analyze the ablation property of C/C composites during high temperature radiation of 2000℃. Figure 5 shows the heat flux distribution in a time of 0.13 seconds. The thermal flux magnitude of the 14 nodes along the circumscribed circle radius of the hexahedron is shown in figure 6.

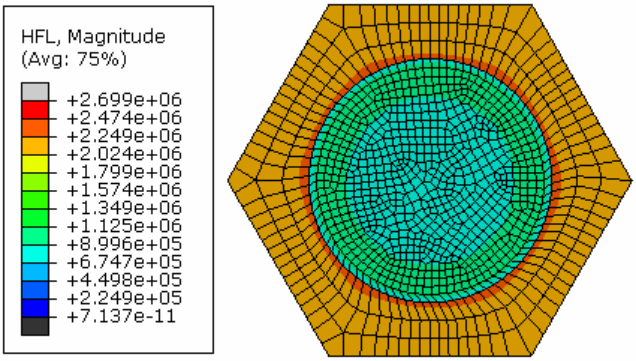

Figure 5. Heat flux distribution in micromechanical structure at 0.13seconds

The simulation result indicated that the heat flux at the interface between fiber and matrix is maximum, which make the interface damage easily, as shown in red colored area in figure 5. The result in figure 6 demonstrated that because of the mismatch between fibers and matrix, the thermal flux at the interface jumps to a higher value than the values inside the fiber, implying the debonding between fibers and matrix may happen during the ablation process.

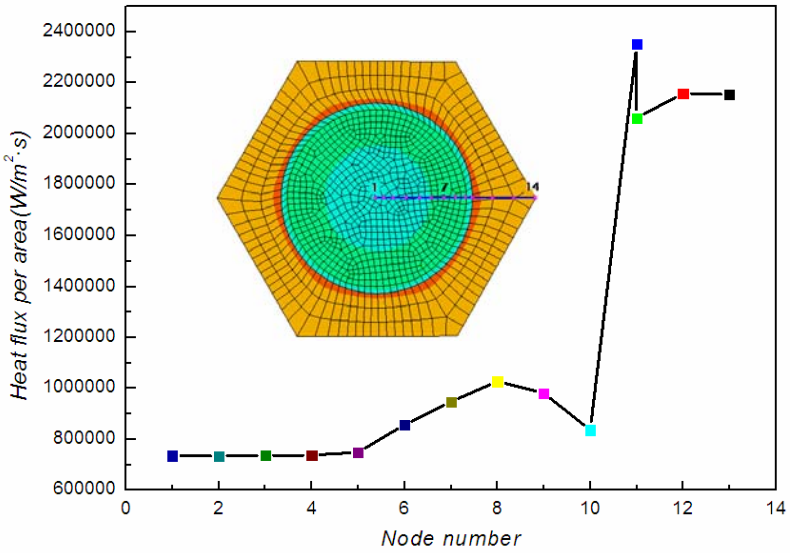

Figure 6. Variation of heat flux of selected nodes

Next, the damage analysis of Cylinder RVE in the ablation process was conducted. The numerical simulation focused on the temperature rise period of cylinder RVE in ultra thermal radiation environment. According to the symmetry of the cylinder RVE of C/C composites, a 3D axisymmetric model was established in software ABAQUS. The heat-transfer element was used to simulation the progress of temperature rising up during the ultra thermal radiation. It was subjected to specified surface radiation interaction with a temperature of 2000℃on the surfaces except the

bottom one. Both matrix and fibers are assumed homogeneous and isotropic. Figure 7 (a) illustrates the axisymmetric model of cylinder RVE, and the mark numbers of selected nodes are shown in meshed model in Figure 7(b).

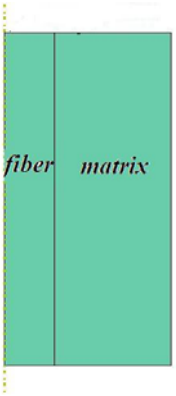

(a)

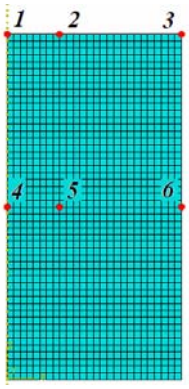

(b)

Figure 7 (a) Axisymmetrical model (b) Selected node numbers

The ablation morphology of C/C composites is determined by the temperature when the oxidation is adequate. As shown in Figure 8, it was indicated that the carbon fiber presented a cone head, and the carbon fibers took the shape of needles after ablation processes. The total ablation time was about 50 seconds. In the ablation process, the temperature of the material came to balance in 40s. The results indicate that the ablation morphology of C/C takes the shape of typically “needle clusters” due to the mismatch of the thermal property of the carbon fibers and matrixes.

The analysis result is consistent with experimental results in Ref.9. Figure 9 illustrates that the temperature gradient of material surface exposed to the external environment changes greatly, which will increase the incidence of material surface damage.

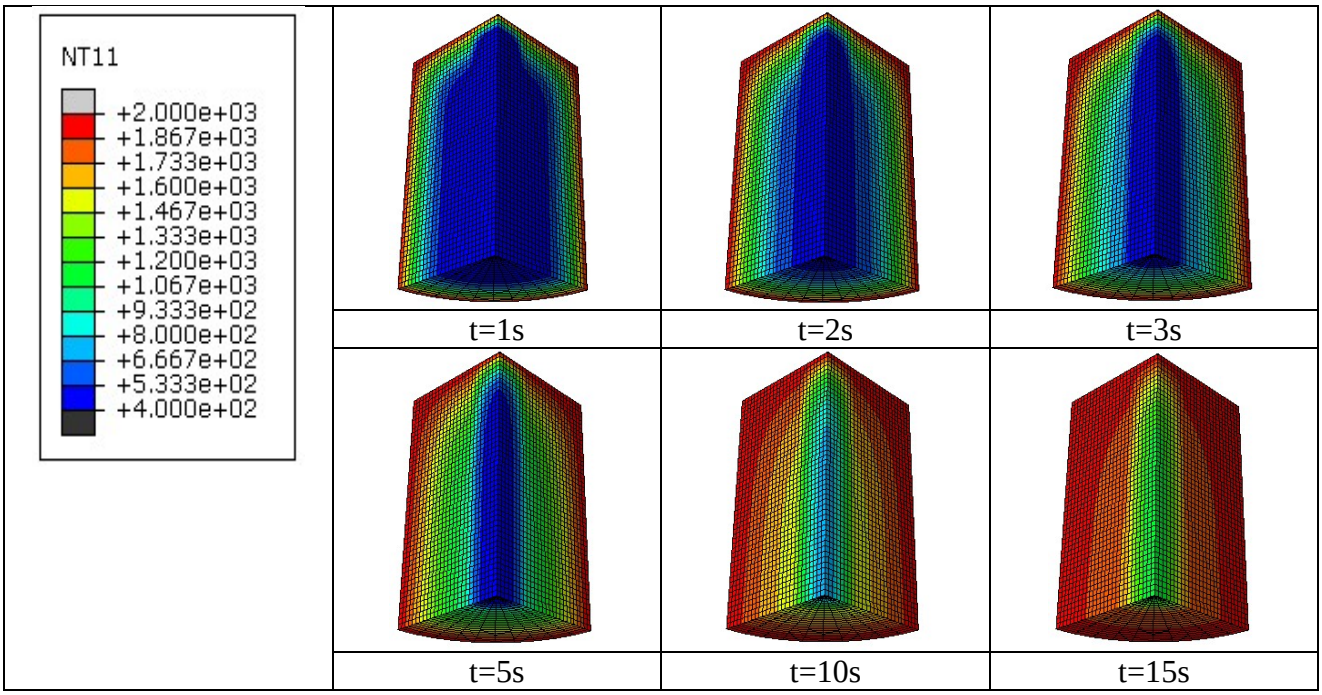

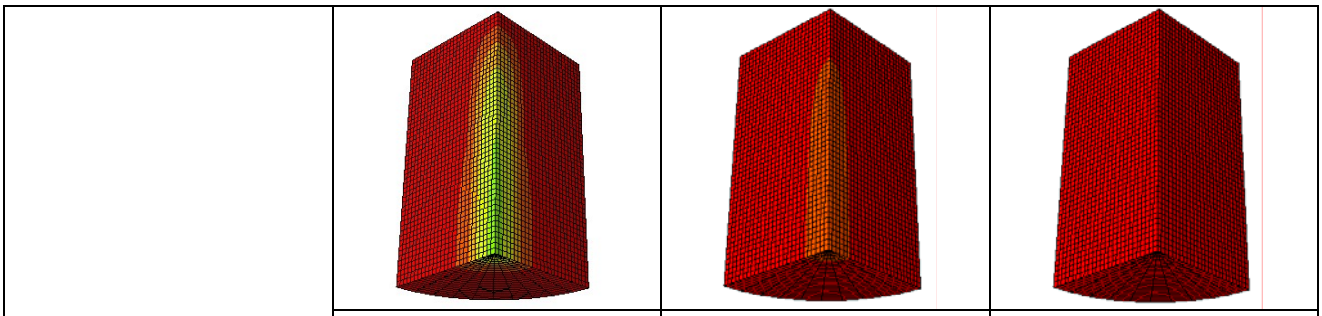

Figure 8. Temperature distribution of cylinder C/C RVE during thermal radiation

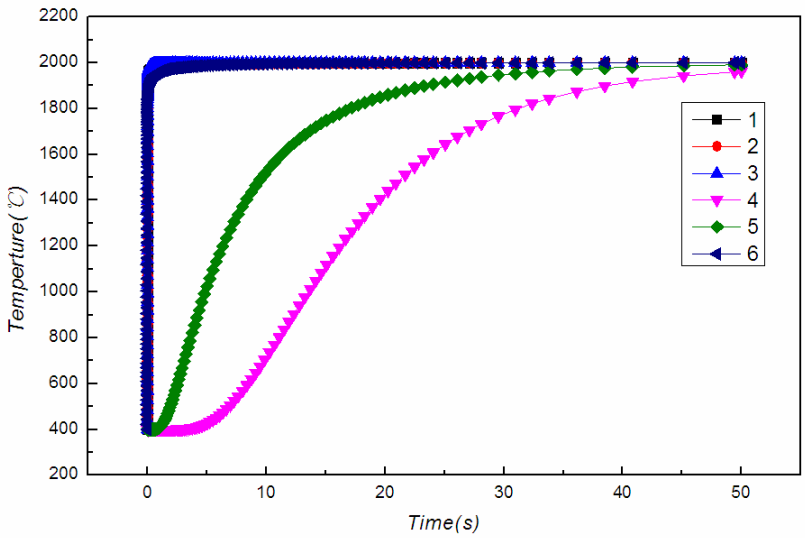

Figure 9. Temperature change process of selected nodes

5. Conclusion

In this paper, the ablation damage of C/C composites in high temperature radiation environment was investigated. The conclusions can be remarked as follows.

(1) The mismatch of ablation rate between fiber and matrix leads to a high heat flux and damage at the interface during thermal radiation.

(2) The ablation morphology of C/C composites takes the shape of typical “needle clusters” due to the mismatch of the thermal property of the carbon fibers and matrixes.

Acknowledgements

The authors gratefully acknowledge the support from Foundation of China under grant #11172012 and the Municipal Natural Science Foundation of Beijing under grant #3092006.

References

[1] F.J. Yi, J. Liang, S.H. Meng, S.Y. Du. Study on ablation mechanism and models of heatshield composites. Journal of Solid Rocket Technology. 23(2000) 48-56.

[2] J.D. Buckley. Carbon-carbon materials and composites. USA: Noyes Pulications. 1993.

[3] R.P. Nathan. Modeling of Ablation of Carbon-Carbon Composite Thermal Protection System. Collection of Technical Papers - 39th AIAA Thermophysics Conference. 2(2007) 1307-1314.

[4] Z.P. Li. Major advancement and development trends of TPS composites. Fuhe Cailiao Xuebao/Acta Materiae Compositae Sinica. 28(2011) 1-9.

[5] Y. Aspa, M. Quintard, F. Plazanet, C. Descamps and G. L. Vignoles. Ablation of Carbon/Carbon Composites: Direct Numerical Simulation and Effective Behavior. Ceramic Engineering and Science Proceeding. 26(2005) 99-106.

[6] J. Lachaud, G. L. Vignoles, J. M. Goyheneche and J. F. Epherre. Ablation in Carbon/Carbon Composites: Microscopic Observations and 3D Numerical Simulation of Surface Roughness Evolution. Ceramic Transactions. 191(2006) 149-160.

[7] G. L. Vignoles, J. Lachaud, Y. Aspa and M. Quintard. Effective Surface Recession Laws for the Physico-Chemical Ablation of C/C Composite Materials. Ceramic Engineering and Science Proceedings. 32(2010) 351-360.

[8] P. Laborde, B. Toson and M. Odunlami. High Temperature Damage Model for Carbon–Carbon Composites. European Journal of Mechanics - A/Solids. 30(2011) 256-268.

[9] S. Farhan, K. Li, L. Guo, Q. Gao and F. Lan. Effect of Density and Fibre Orientation On the Ablation Behaviour of Carbon-Carbon Composites. New Carbon Materials. 25(2010) 161-167.